The Flade Potential of Iron Passivated by Various Inorganic Corrosion Inhibitors

Herbert H. Uhlig and Peter F. King[1]

Department of Metallurgy, Massachusetts Institute of Technology, Cambridge, Massachusetts

ABSTRACT

The characteristic potential obtained just before decay of passivity (Flade potential) was measured for iron passivated by ferrates, nitrites, chromates, molybdates, tungstates, conc. HNO_3, and by anodic polarization in H_2SO_4. The Flade potential is linear with *p*H, of slope 0.059 up to approximately *p*H 4.5. Above this value up to *p*H 11.5, the potentials tend to follow an extension of the data in acids in the case of iron passivated by chromates and nitrites, but reach a constant value for iron passivated anodically or by conc. HNO_3. The standard Flade potential (*p*H = 0) for various passivators is increasingly noble in the order: nitrite (—0.50 v); chromate, ferrate, molybdate (—0.54 v); tungstate (—0.61 v); and anodic polarization or conc. HNO_3 (—0.64 v). The average of these values is in reasonable accord with previously reported values and only small observed deviations from the average indicate that the structure and composition of the passive film on iron is largely independent of the passivation process.

This is explained by a primary passive film consisting essentially of a monolayer of chemisorbed oxygen atoms through gaps of which a layer of O_2 molecules is chemisorbed. The calculated free energy of formation of such a film (—30,000 cal/mole ads. O), the chemical equivalents of passive film substance (0.01 coulomb/cm^2), and the oxidizing capacity (12×10^{-8} equivalents/cm^2) are all consistent with independent data obtained by others for oxygen adsorption on iron, coulometry, and reaction of the passive film with CrO_3^- to form CrO_4^{--}.

The mechanism of passivity, accordingly, is proposed to consist of: (*a*) adsorption of the passivator on the metal or metal oxide surface; (*b*) depolarization of cathodic areas by the passivator accompanied by anodic passivation of residual small areas of exposed metal; the adsorbed oxygen film is formed at anodes by discharge and combination of OH^- at current densities above approximately 17 amp/cm^2 in accord with data of Franck; and (c) very slow formation of iron oxides with continual repair of the adsorbed oxygen film by electrochemical action, as described, at pores in the oxide. Oxide formation is accelerated by elevated temperatures and presence of certain anions, e.g., Cl^-.

It is proposed that the greater stability of the passive film formed by some passivators is accounted for by supplementary adsorption of the passivator on the passive film, accompanied by shift of the Flade potential to a less noble value.

In 1911, Flade (1) showed that if iron is passivated in concentrated HNO_3 or by anodic polarization in dilute H_2SO_4, the decay of passivity with time is represented: first, by a steep fall of potential in the active direction; second, by a less steep change lasting for a fraction of a minute to several minutes; and third, by a steep descent to the active value. The value of potential immediately preceding the steep descent was called by Flade the "umschlagspunkt" and by later workers the Flade potential. This critical potential was shown by Flade to be more noble the higher the concentration of acid in which the decay took place, and also that the value at constant *p*H became more active by about 50 mv as the temperature was decreased from 15° to 0°C. Franck (2) showed that the Flade potential E_F for iron in acid media accurately followed the relation (A.C.S. Sign Convention):

$$E_F(\text{volt}) = -0.58 + 0.058\,p\text{H}$$

suggesting, therefore, a reversible thermodynamic relationship to *p*H of the activating acid. Rocha and Lennartz (3) measured the Flade potentials for Fe-Cr alloys and Cr in H_2SO_4, their values for which showed a slope of potential plotted with *p*H of 0.058 for alloys below about 12% Cr and 2 x 0.058 for alloys of higher Cr content. Earlier, Müller and Cupr (4) provided data for potential behavior of Cr which show on plotting vs. *p*H a slope of 0.058 characteristic for spontaneous activation of Cr in various acids, and 2 x 0.058 for Cr activated by cathodic polarization. Recently Cartledge and Sympson (5) demonstrated that iron passivated by sodium molybdate, tungstate, and chromate or by potassium pertechnetate also exhibits Flade potentials that are linear with *p*H, of slope 0.058, the average absolute values for which parallel those by Franck for iron passivated in con-

[1] Present address: Dow Chemical Company, Midland, Michigan.

centrated HNO_3 or anodically in H_2SO_4. The present measurements explore Flade potentials for iron passivated by ferrates and nitrites in addition to chromates, molybdates, tungstates, concentrated HNO_3, and by anodic polarization in H_2SO_4. The experimental procedure differs somewhat from that used by Cartledge and Sympson, and the *p*H range is increased to include the alkaline region.

Experimental Procedure

Electrodes of about 2 cm^2 area were prepared from mild steel. This composition has an advantage over higher purity iron in that passivity is found to be more stable during transfer from the passivating solution to the activating solution. Carbon steels are more readily passivated by concentrated HNO_3 than is pure iron (6), probably because of cementite present as a second phase in the carbon steels which acts as the noble component of a galvanic couple, hastening anodic passivation of the metallic phase (ferrite). For example, coupling of platinum to iron also hastens passivity. Cementite, accordingly, stabilizes passivity probably by allowing galvanic action to continue during transfer of the specimen. Flade showed earlier (1) that carbon steel or electrolytic iron exhibits essentially the same "umschlagspunkt."

The electrode was assembled with a nickel wire silver soldered to a stem machined on the steel specimen, the wire being enclosed by an 8 mm diameter glass tube. A Teflon gasket maintained a water-tight seal between steel and glass tube at one end, with constant contact being effected by means of a screw, nut, and rubber grommet attached to the wire at the other end. The gasket was machined so as to insure against crevices or leakage which if not avoided made it difficult to obtain optimum passivity.

Passivator solutions were made up from reagent grade salts and distilled water in the following concentrations: (*a*) 0.0025*M* and 0.1*M* $NaNO_2$, (*b*) 0.0025*M* K_2CrO_4, (c) 0.0025*M* Na_2WO_4, (*d*) 0.0025*M* Na_2MoO_4. In addition, concentrated CP HNO_3 was used, and 0.1% K_2FeO_4 solution prepared according to the method described by Thompson, Ockerman, and Schreyer (7).

Electrodes were passivated by immersion in one of the above solutions for a period of usually several minutes up to 1 hr, or whatever time was required to achieve a stable noble potential. Electrodes were then washed successively in 3 beakers of distilled water, and finally immersed in water adjusted to a known *p*H by means of HNO_3, H_2SO_4, or NaOH. It made no apparent difference whether HNO_3 or H_2SO_4 was used for adjustment in the lower *p*H range. The decay of potential vs. time was measured with reference to Ag-AgCl, 0.1*N* KCl electrode using a Na_2SO_4 salt bridge and employing an electronic galvanometer and portable potentiometer. Corrections were not made for liquid junction potentials. Typical decay curves are shown in Fig. 1. The potential obtained just before the abrupt drop was recorded as the Flade potential. Cartledge and Sympson used instead the average value of the potential at the plateau preceding breakdown, but this procedure differs from that first described by Flade. It seems to us more likely that the potential corresponding to

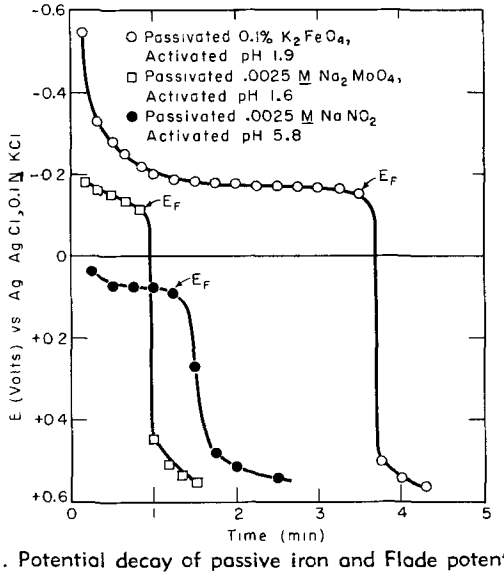

Fig. 1. Potential decay of passive iron and Flade potential E_F

the thinnest passive film, i.e., just before the steep decline, represents the equilibrium state between film and solution, and that it is this potential in which we have most interest. In any case, however, the relatively large experimental error in determining the Flade potential makes the particular procedure in this regard of small consequence. This is evident from the relatively good correspondence of our data with those of Cartledge and Sympson.

The procedure used by the latter authors for activating their electrodes consisted of adding sodium sulfate to the passivator solution until passivity decayed, without removal of the electrode. Our method was to remove the electrode from the passivator solution, wash it, and then place it in an aqueous solution of known *p*H. The latter procedure produced a sharper change from the passive to active state, with apparently less experimental scatter.

Results

Flade potentials determined as described above, where each point represents one or more runs, are plotted vs. *p*H in the acid range up to *p*H 4.5 in Fig. 2 and 3. Although a single line of slope 0.059 and intercept at −0.57 v for *p*H = 0 might have been drawn through all the points with maximum deviation of about ±150 mv, the pattern of data favors individual straight lines through points relating to a

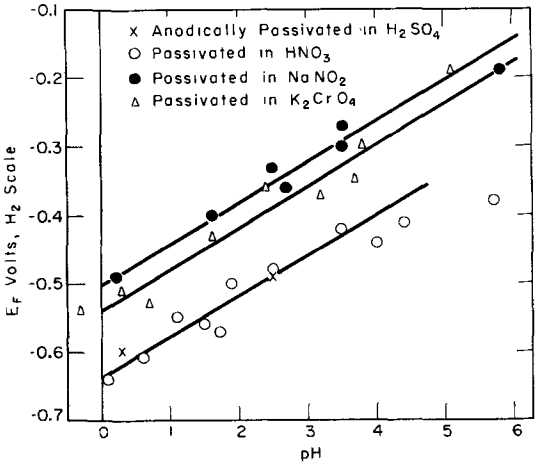

Fig. 2. Flade potentials for iron in acid range

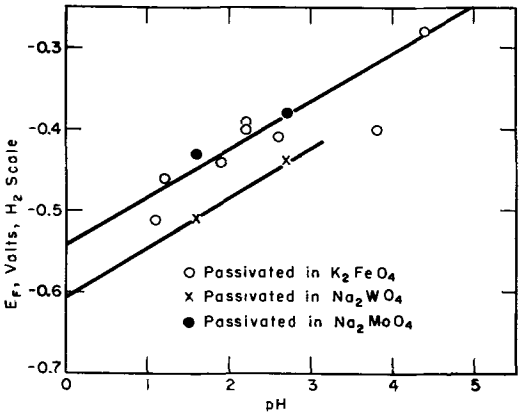

Fig. 3. Flade potentials for iron in acid range

given passivator. All lines so drawn have a slope of approximately 0.059, but the intercepts are increasingly noble in the following order:

	Passivator	Approx. intercept, $pH = 0$ (H_2 scale) v
1.	$NaNO_2$	—0.50
2.	K_2CrO_4, K_2FeO_4, Na_2MoO_4	—0.54
3.	Na_2WO_4	—0.61
4.	Anodic polarization in H_2SO_4; conc. HNO_3	—0.64

Measurements in the near-neutral and alkaline range were not as reproducible, and passivator solutions behaved with greater individual differences in comparison to their behavior in acid environments. Data are plotted in Fig. 4.

Potentials of Fig. 2 and 3 agree in slope with those reported by Franck, and by Cartledge and Sympson. The average intercept at $pH = 0$ of —0.57 v is also close to the average value of their data. However, drawing the best line through individual points for passivation by HNO_3, or anodically in H_2SO_4, produces an intercept of —0.64 v, which is more noble than the average by 0.07 v. This value can be compared with the still more noble standard Flade potential reported by Rocha and Lennartz for iron anodically passivated in H_2SO_4 equal to —0.68 v.

There is a tendency for Flade potentials of iron previously passivated in K_2CrO_4 and then activated in alkaline solutions to follow an extrapolation of data obtained in acid media as indicated by the dotted line of Fig. 4. Two points for $NaNO_2$ fall

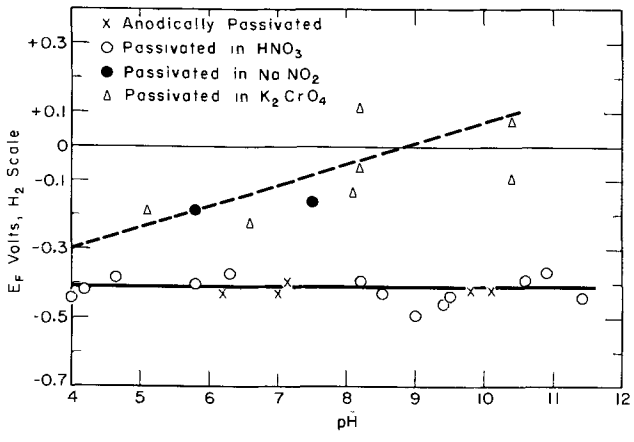

Fig. 4. Flade potentials for iron in near-neutral and alkaline ranges.

within the same region. These data as mentioned earlier are inherently more difficult to reproduce, particularly since breakdown of passivity is sluggish in the alkaline region and sometimes does not occur at all within a reasonable time. More definite conclusions are reached in this region for iron passivated in concentrated HNO_3 or by anodic polarization. Flade potentials lie on a line of zero slope from pH 4 to 11.4, the mean value for which, —0.41 v, is considerably more noble than comparable values for nitrite or chromate.

Discussion

It is significant that all Flade potentials whether in the alkaline or acid region are more noble by several tenths volt than corresponds to potentials for any of the several oxides of iron in equilibrium with metallic iron (8, 9). Hence, the passive film does not appear to be any single known iron oxide. Vetter (9, 10), in order to account for the facts, hypothesized a high potential gradient within a film of Fe_2O_3 overlying a film of Fe_3O_4. Göhr and Lange (11) and Schottky (12) discussed various possible ionic equilibria within the oxide or at the oxide surface.

Göhr and Lange by assuming equilibrium between a layer of γFe_2O_3 overlying a layer of Fe_3O_4, and making certain assumptions regarding the free energy of formation of γFe_2O_3, show that the following reaction may account for the Flade potential:

$$Fe_3O_4 + 1/2\ H_2O \rightarrow 3/2\ \gamma Fe_2O_3 + 2H^+ + 2e$$

Heusler, Weil, and Bonhoeffer (13) concur in a model based on γFe_2O_3 overlying Fe_3O_4. Cartledge (14) suggested an inner oxide, e.g., an abnormal "FeO," in contact with an outer iron oxide in a higher oxidation state to account for the Flade potential.

Some of the assumptions upon which these proposals are made immediately run into difficulty in explaining the Flade potential of Cr (0.2 v) which is also more noble than corresponds to Cr_2O_3 in equilibrium with Cr and for which only one known oxide forms on the metal surface. Furthermore, the total observed thickness of passive film substance, assuming it to be an oxide, is hardly sufficient to accommodate two layers of oxides. For example, the approximate number of chemical equivalents of passive film substance on iron as measured by coulometry (15) or by the oxidizing capacity of the film (16) corresponds to only 0.01 coulomb/cm^2 apparent surface. Assuming that the roughness factor for pickled iron is similar to the measured value of 4 for 18-8 stainless steel pickled in hydrochloric-sulfuric acids (17), the value becomes 0.0025 coulomb/cm^2 absolute surface. This figure becomes larger as iron is polarized to more noble potentials, but becomes smaller as the Flade potential is approached where the passive film reaches minimum thickness consistent with retention of passivity. Hence assuming 0.0025 coulomb/cm^2, the average thickness is 14Å if the passive film is composed of Fe_3O_4, and it can be thinner;[2] if it is γFe_2O_3, the corresponding

[2] Employing for Fe_3O_4 and γFe_2O_3 equivalent weights and densities of 28.9, 26.6, and 5.2, 5.1, respectively. The above thickness of the passive film should not be confused with thicker layers of oxide (25-100Å) residual on iron surfaces after passivity has decayed. This matter is discussed later.

thicknes is 13Å. But the unit cell dimensions of Fe_3O_4 and γFe_2O_3 are 8.3 to 8.4Å (18, 19), the sum of which is 16.7Å. Hence, it does not seem likely that thermodynamic properties of bulk oxides, as employed by Göhr and Lange, for example, can have much significance with respect to properties of the passive film near the Flade potential where the total thickness is less than the sum of the unit cell dimensions. Along the same lines, it is difficult to conceive of a high potential gradient ($>10^6$ v/cm) in a Fe_2O_3 film overlying Fe_3O_4 as hypothesized by Vetter, where the Fe_2O_3 layer has a thickness less than the dimensions of the unit cell. A third difficulty with this duplex oxide film model is that, so far, it has not been able to explain the ability of the passive film to oxidize CrO_2^- to CrO_4^{--} as measured by Uhlig and O'Connor (16).

These difficulties are overcome by the suggestion (20) that the passive film is not an abnormal oxide or double oxide, but is essentially chemisorbed oxygen instead, and that the Flade potential corresponds to the following equilibrium:

$$3H_2O + \text{Fe surface} \leftrightarrows O\cdot O_2 \text{ (adsorbed on Fe)} + 6H^+ + 6e \qquad [1]$$

The standard potential for this reaction (pH = 0) is —0.58 v according to Franck's data or —0.64 v according to Fig. 2. The structure $O\cdot O_2$ (ads. on Fe) signifies a complete monolayer of chemisorbed oxygen atoms through gaps of which a further layer of O_2 molecules is chemisorbed in accord with the suggested structure of chemisorbed oxygen on tungsten (21). This structure is consistent with the observed approximate 0.01 coulomb/cm² apparent surface of passive film substance. At the Flade potential, as mentioned earlier, the film is somewhat thinner than corresponds to $O\cdot O_2$, and may more nearly correspond to a film of atomic oxygen. For passive potentials more noble than the Flade potential, the film probably contains not only chemisorbed oxygen additional to an atomic monolayer, but also adsorbed OH, the amount depending on the extent to which iron is polarized anodically by the passivation process.

On breakdown of passivity in accord with:

$$O\cdot O_2 \text{ (ads. on Fe)} + 2Fe + 3H_2O \rightarrow Fe(OH)_3$$

a residual film of Fe_2O_3, 60Å thick is accounted for, in reasonable agreement with measurements of Schwarz (22) and Gulbransen (23). It is the decomposed passive film which was observed by electron diffraction measurements of Mayne and Pryor (24) which they reported as γFe_2O_3.

A major support for chemisorbed oxygen as the composition of the passive film comes from thermodynamic data. From Tompkin's measurements (25) on the direct chemisorption of gaseous oxygen on iron, ΔH° = —75,000 cal/mole O_2. The standard entropy of adsorption ΔS° is approximately equal to —46.2 e.u. (26) with a standard state of half surface coverage. Hence, since ΔH° is not sensitive to the extent of surface coverage (27) we can use the relation ΔG°, the free energy of adsorption, = $\Delta H^\circ - T\Delta S^\circ$ = —61,300 cal/mole oxygen adsorbed. Accordingly:

$$3/2\ O_2 + \text{Fe surface} \rightarrow O\cdot O_2 \text{ (ads. on Fe)}$$
$$\Delta G^\circ = -3/2 \times 61{,}300 \text{ cal} \qquad [2]$$
$$3H_2O \rightarrow 6H^+ + 3/2\ O_2 + 6e^-$$
$$\Delta G^\circ = 170{,}000 \text{ cal (28)} \qquad [3]$$

Adding [2] and [3]:

$$3H_2O + \text{Fe surface} \rightarrow O\cdot O_2 \text{ (ads. on Fe)} + 6H^+ + 6e^-$$
$$\Delta G^\circ = +78{,}000 \text{ cal} \qquad [4]$$

The corresponding standard potential E° equal to $-\Delta G^\circ/6F$ is —0.56 v. This value agrees within reasonable limits with the measured values of —0.58, —0.64, and —0.68 v quoted previously.

Bonhoeffer (29) and his co-workers showed that passivation of iron in concentrated HNO_3 proceeds by an electrochemical reaction in which nitrous acid, HNO_2, acts as a strong cathodic depolarizer. The major part of the iron surface serves as cathode resulting in very high current densities reaching approximately 17 amp/cm² (2) at small residual anodic surfaces. These high anodic current densities produce the passive film, which in turn becomes the seat of the continuing cathodic reaction, thereby favoring spread of passivity over all the surface.

The nitrous acid resulting from reduction of HNO_3 plays a very important part as depolarizer, therefore, in passivation by nitric acid. It is proposed herewith that the passivators reported in this paper act also by depolarization to produce the passive state, and that the resulting composition and structure of the passive film are basically the same in all cases. The similarity of Flade potentials makes this conclusion plausible. Chromates, for example, first adsorb on the iron surface, and on iron oxides if present, and as such act as cathodic depolarizers. Since adsorption and depolarization occur over the entire surface, current densities at gaps in the adsorbed film easily reach the order of 17 amp/cm². The ultimate passive film, which is essentially chemisorbed oxygen resulting from discharge and combination of OH^-, is formed by anodic polarizaton. It is formed at a rate measurably slower than for nitric acid presumably because of the slower rate of cathodic reduction of chromates as compared with HNO_2.[3] This slower re-

[3] Uhlig and O'Connor (16) proposed that ferrates or similar higher valence iron compounds form when iron reacts with concentrated HNO_3 and that such compounds adsorbed on iron probably constitute the passive film. They calculated the amount of adsorbed ferrate on the iron surface from the ability of the passive film to oxidize CrO_2^- to CrO_4^{--} in NaOH solution.

It now appears from the foregoing data that it is not necessary to assume formation of ferrates as such as source of the observed oxidizing property of the film. Instead, adsorbed oxygen expressed as $O\cdot O_2$ (ads. on Fe) can also account for the facts. This adsorbed oxygen is related to the ferrate structure in that strongly alkaline media convert the adsorbed film continuously to ferrates in accord with the reaction:

$O\cdot O_2$ (ads. on Fe) + Fe + 2NaOH → $Na_2FeO_4 + H_2O$ + Fe surface

as is observed when iron is polarized anodically in concentrated NaOH.

In dilute NaOH, ferrates act as passivators in accord with:

$$2Na_2FeO_4 + 5H_2O + \text{Fe surface} \rightarrow O\cdot O_2 \text{ (ads. on Fe)} + 2Fe(OH)_3 + 4NaOH$$

Iron immersed in K_2FeO_4, therefore, preforms the passive film and no initial reaction occurs on subsequent immersion of iron into conc. HNO_3, a reaction that is necessary otherwise to form a minimum concentration of HNO_2 to serve as depolarizer (16).

The herein-described mechanism of passivation by chromates (and similar passivators) modifies the earlier proposal by one of us that the primary passive film consists of chromate adsorbed directly on the metal. From present data, formation of such a film more likely is the first stage of passivation. This is followed by formation of the anodically produced oxygen film, which is actually the primary passive film. Iron oxides form more slowly as a third stage process, but they contribute relatively less to corrosion resistance compared to the adsorbed oxygen film which continues at the base of pores in such oxide layers so long as chromates are present in solution. Elevated temperatures and certain anions (e.g., Cl^-) accelerate formation of iron oxide and accompanying reduction of chromate.

duction can account for the fact that it requires only seconds for passivation of iron in conc. HNO_3 but about ½ to 1 hr for the passive film to form completely in chromates as indicated by potential measurements (30), and from experiments on the effect of pre-immersion of iron in chromates on the rate of reaction with concentrated HNO_3 (31).[4]

The above described reaction of iron with dichromate can proceed as follows:

$$Cr_2O_7^{--} + 14H^+ + 6e^- \rightarrow 2Cr^{+++} + 7H_2O \qquad E^\circ = 1.33 \text{ v} \qquad [5]$$

$$3H_2O + \text{Fe surface} \rightarrow 6e^- + 6H^+ + O\cdot O_2 \text{ (ads. on Fe)} \qquad E^\circ = -0.54 \text{ v} \qquad [6]$$

Adding [5] and [6]:

$$Cr_2O_7^{--} + 8H^+ + \text{Fe surface} \rightarrow 2Cr^{+++} + 4H_2O + O\cdot O_2 \text{ (ads. on Fe)} \qquad E^\circ = 0.79 \text{ v} \qquad [7]$$

The positive value of emf for reaction [7] indicates that the reaction can go spontaneously; in other words, dichromate can produce the chemisorbed passive film by anodic polarization in the same way as can conc. HNO_3 or direct anodic polarization in H_2SO_4. It is reasonable that a similar reaction should occur in alkaline media forming perhaps basic chromic chromate (32) as end product, but free energy data for this reaction are not available.

According to reaction [7], each mole $Cr_2O_7^{--}$ which is reduced to form the passive film forms two moles Cr^{+++}. If Cr^{+++} so produced is retained on the metal surface, perhaps as hydrated Cr_2O_3 or adsorbed as the ion, the amount so formed is an indication of the number of equivalents of passive film substance per unit surface. Geary (33) found 3×10^{16} Cr atoms/cm² or 5×10^{-8} g-atom/cm² retained on an iron surface after passivation by dichromate using radioactive Cr as tracer. In this experiment, the iron surface was hydrogen-reduced at 1000°C, then exposed to deaerated 0.0005*M* $Cr_2O_7^{--}$ solution of *p*H 1.9 for 2 to 17.5 hr avoiding contact with air. The iron surface was washed in distilled water before counting. The same approximate amount of residual Cr was reported by Brasher and Stove (34), by Powers and Hackerman (35), and by Cohen and Beck (36) for air-exposed iron. This quantity of chromium, calculated in accord with conditions of reaction [7], corresponds to 2.5×10^{-8} mole $O\cdot O_2$ (ads. on Fe)/cm²[5] or 15×10^{-8} equivalents of passive film substance per cm². This value is in good agreement with the maximum amount of passive film substance on iron (2×10^{-8} mole $O\cdot O_2$ ads. on Fe/cm² or 12×10^{-8} equivalents of passive film substance/cm²) found by O'Connor (16) from the oxidizing capacity of the passive film.[6] It is also in accord with Weil's value of about 0.01 coulomb/cm² passive film substance as determined by coulometry ($15 \times 10^{-8} \times 96{,}500 = 0.014$ coulomb).

It is probable that most other passivators operate by a mechanism similar to that outlined above for chromates. This mechanism explains why sulfates or perchlorates are not passivators even though they have the XO_4^{n-} structure. Ions of this kind either do not reduce, or do so too slowly to fulfill the requirements of a cathodic depolarizer. On the other hand, oxidizing substances such as chlorides for which the minimum current density for anodic passivation is very high or infinite, also do not meet the requirements of a passivator. Hypochlorous acid and ferric chloride are in this category. Alkaline inhibitors such as Na_3PO_4, Na_2CO_3, and NaOH act as passivators only in the presence of dissolved oxygen (37, 38) and hence the cathodic reduction of these substances is not required for passivation. Instead, most alkaline substances probably displace adsorbed H, the latter tending to form whenever iron is exposed to an aqueous environment, and favor adsorption of OH^- together with oxygen on the metal surface. Hence for these substances an adsorbed oxygen-hydroxyl ion film can form directly without the necessity of anodic polarization. This same situation applies to Cr and the stainless steels which become spontaneously passive on exposure to air.

Dissolved oxygen is also required for passivation of iron by molybdates and tungstates (38). A possible explanation is that oxygen as well as the passivator adsorbs on the metal thereby increasing cathodic and decreasing anodic areas. This extension of cathodic sites and limitation of anodic sites favors attainment of the critical current density necessary for anodic passivation. Oxygen may be necessary, in other words, because molydates and tungstates are not sufficiently good cathodic depolarizers on a clean iron surface, but they become effective if the galvanic current accompanying their cathodic reduction is restricted to smaller anodic areas as when oxygen is present on the surface.

With chromates, dissolved oxygen is not necessary for passivation, but oxygen does increase the rate of passivation (31) in accord with the mechanism just described.

The passive film formed by pertechnetates may also consist essentially of chemisorbed oxygen. From data by Cartledge and Smith (39) for the reaction:

$$TcO_2(c) + 2H_2O \rightarrow TcO_4^-(aq) + 4H^+ + 3e \qquad E^\circ = -0.738 \text{ v} \qquad [8]$$

it is concluded that the following reaction is spontaneous:

$$2TcO_4^- + 2H^+ + \text{Fe surface} \rightarrow O\cdot O_2 \text{ (ads. on Fe)} + H_2O + 2TcO_2 \qquad E^\circ = +0.20 \text{ v} \qquad [9]$$

Radioactive counts by Cartledge (40) on an iron surface passivated by TcO_4^- corresponding to amounts of Tc much less than 4×10^{-8} g-atom/cm² suggests that reduced TcO_4^-, whatever its composition, enters solution rather than precipitating or adsorbing on the metal surface, in contrast to the situation for

[4] When the passive film is previously formed by immersion of iron in O_2-saturated 0.1% $K_2Cr_2O_7$ for more than but not less than ½ hr, no measurable iron reacts on subsequent immersion in concentrated HNO_3, whereas for air-exposed iron, omitting chromate immersion, about 0.04 mg/cm² (16) reacts before the iron-HNO_3 reaction subsides. In deaerated 0.1% $K_2Cr_2O_7$, the time to reach optimum passivity is longer (approx. 2 hr).

[5] This calculated amount should be reduced by the amount of chromate irreversibly adsorbed on the passive film itself. Since a close-packed monolayer of CrO_4^{--} (diam. = 5.4Å) on a surface of roughness factor = 3 amounts to only 0.2×10^{-8} mole/cm², the correction is small.

[6] The reaction studied by O'Connor is assumed (20) to be the following:

$$O\cdot O_2 \text{ (ads. on Fe)} + Fe + OH^- + CrO_2^- + H_2O \rightarrow Fe(OH)_3 + CrO_4^{--} \qquad \Delta G^\circ = -33{,}000 \text{ cal}$$

He found that a maximum of 2×10^{-8} mole CrO_4^{--} was formed per cm² of passive iron, which was reported as equivalent to 2×10^{-8} mole ferrate/cm² instead of 2×10^{-8} mole $O\cdot O_2$ (ads. on Fe)/cm².

chromates. There is also the possibility that a monolayer or partial monolayer of adsorbed TcO_4^- can in itself satisfy surface affinities, as does CO adsorbed on 18-8 in HCl, without reduction. This seems less likely in view of the fact that Cl^- or SO_4^{--} can and do stimulate reduction of TcO_4^- by metallic iron (41), similar to accelerated reduction of other passivators in presence of these ions.

The slightly more active standard Flade potentials for iron passivated by nitrites and chromates as compared with concentrated HNO_3 or anodic passivation in H_2SO_4 (Fig. 2) is evidence of a slightly greater stability of the passive film formed by the first two substances. This stability is also evident from the usually longer time it requires for passivity to break down using chromates as compared with the less stable passive film formed by HNO_3 or by anodic polarization. The greater stability can be accounted for by adsorption of the passivator substance itself, subsequent to the passivation process, directly on the chemisorbed oxygen film, thereby reducing the over-all free energy of the system. Adsorption of passivator on an underlying oxide layer was proposed by Powers and Hackerman (35, 42) based on contact potential measurements, where, however, an adsorbed oxygen layer would also fit the facts. For example, the following adsorption can occur:

$$O \cdot O_2 \text{ (ads. on Fe)} + H_2CrO_4 \rightarrow$$
$$O \cdot O_2 \cdot H \cdot H \cdot CrO_4 \text{ (ads. on Fe)}$$

the free energy change for which is calculated to be −13,700 cal based on −0.54 v for the standard Flade potential for iron passivated by chromates compared to −0.64 v in concentrated HNO_3. If there is supplementary adsorption of Fe^{+++} or $Fe(NO_3)_3$ on the passive film in HNO_3, as seems likely, the calculated ΔG° is for displacement of such an adsorbate by H_2CrO_4. In other words, the interaction between passivator and passive film on which passivator is adsorbed can account for slight variations in Flade potential and for the observed differences in stability of the passive film. On this basis, nitrites adsorb on the passive film more strongly than do chromates, ferrates, and molybdates (Fig. 2, 3), and the latter in turn more strongly than tungstates.

Reasons for the constant Flade potential in the region of *p*H 4 to 11.5 when iron is passivated anodically or by HNO_3 probably depend on change in mechanism of passive film breakdown for less acid environments. It is known that corrosion of iron in HNO_3 or H_2SO_4 continues even when it is passive, hence, it is not unlikely that the surface *p*H rises and that an insoluble basic ferric salt or ferric hydroxide forms as end product of passive decay in solutions of *p*H as low as 4 to 5.

Since considerable ferric nitrate or ferric sulfate forms at the iron surface just prior to passivity, we can assume with justification that Fe^{+++} or $Fe(NO_3)_3$ adsorbs on the passive film. Accordingly a plausible reaction accounting for breakdown of passivity, which is independent of *p*H, is the following:

$$2Fe^{+++} \cdot O \cdot O_2 \text{ (ads. on Fe)} + 3H_2O \rightarrow 2Fe(OH)_3 - 6e$$
$$\Delta G^\circ = -75{,}440 \text{ cal}$$

The standard free energy change for this reaction is based on standard free energies of formation of $Fe(OH)_3$(s), Fe^{+++}(aq), $O \cdot O_2$ (ads. on Fe) and H_2O(l), equal to −166,000, −2,530, −81,500,[7] and −56,690 cal per mole, respectively, discounting the small free energy of adsorption of Fe^{+++} on the passive film. The standard potential is accordingly 0.54 v, or −0.54 v for the same reaction written as an oxidation step. This is to be compared with the observed potential of −0.41 v (Fig. 4). The difference of 0.13 v is probably due, other than to experimental error, to free energy of adsorption of Fe^{+++} not included in the calculation, and possibly to reaction products differing in composition from $Fe(OH)_3$. The above reaction does not go when iron is passivated by chromates and similar passivators because soluble ferric salts are not formed in high concentration, and hence are not adsorbed on the passive film. Accordingly, for such passivators breakdown of passivity in alkalies follows a course not much different from that in acids, as is observed.

Acknowledgment

The authors are grateful for support of this research by the Office of Naval Research.

Manuscript received March 7, 1958. This paper was prepared for delivery before the Ottawa Meeting, Sept. 28-Oct. 2, 1958.

Any discussion of this paper will appear in a Discussion Section to be published in the December 1959 JOURNAL.

REFERENCES

1. F. Flade, *Z. physik. Chem.*, **76**, 513 (1911).
2. U. F. Franck, *Z. Naturforsch.*, **4a**, 378 (1949).
3. H. J. Rocha and G. Lennartz, *Arch. Eisenhüttenw.*, **26**, 117 (1955).
4. E. Müller and V. Cupr., *Z. Elektrochem.*, **43**, 42 (1937).
5. G. Cartledge and R. Sympson, *J. Phys. Chem.*, **61**, 973 (1957).
6. "Corrosion Handbook," p. 140, edited by H. H. Uhlig, John Wiley & Sons, Inc., New York (1948).
7. G. Thompson, L. Ockerman, and J. Schreyer, *J. Am. Chem. Soc.*, **73**, 1379 (1951).
8. H. Beinert and K. Bonhoeffer, *Z. Elektrochem.*, **47**, 536 (1941).
9. K. Vetter, "International Symposium on Passivity," Heiligenberg, West Germany, September 1957.
10. K. Vetter, *Z. Elektrochem.*, **58**, 230 (1954).
11. H. Göhr and E. Lange, *Naturwiss.*, **43**, 12 (1956); *Z. Elektrochem.*, **61**, 1291 (1957).
12. W. Schottky, "Halbleiterprobleme," II, p. 233, F. Vieweg u. Sohn., Braunschweig (1955).
13. K. Heusler, K. Weil, and K. Bonhoeffer, *Z. physik. Chem., N. F.*, **15**, 149 (1958).
14. G. Cartledge, *J. Phys. Chem.*, **60**, 1571 (1956).
15. K. Weil, *Z. Elektrochem.*, **59**, 11 (1955).
16. H. Uhlig and T. O'Connor, *This Journal*, **102**, 562 (1955).
17. T. O'Connor and H. Uhlig, *J. Phys. Chem.*, **61**, 402 (1957).
18. L. Welo and O. Baudisch, *Phil. Mag.*, **50**, 399 (1925).
19. A. Claassen, *Proc. Phys. Soc.*, **38**, 482 (1926).
20. H. H. Uhlig, "International Symposium on Passivity," Heiligenberg, West Germany, September 1957.
21. J. Becker, *Ann. N. Y. Acad. Sci.*, **58**, 723 (1954).
22. W. Schwarz, *Z. Elektrochem.*, **59**, 11 (1955).
23. E. Gulbransen, *Trans. Electrochem. Soc.*, **82**, 375 (1942).
24. J. Mayne and M. Pryor, *J. Chem. Soc., (London)*, **1949**, 1831.

[7] Per 3/2 mole O_2.

25. Quoted by B. Trapnell, "Chemisorption," p. 215, Academic Press, New York (1955).
26. Ref. (25), p. 212. Approximated from the value for N_2 chemisorbed on Fe. The value for oxygen has not been reported.
27. Ref. (25), p. 213.
28. "Oxidation Potentials," W. M. Latimer, Prentice-Hall, Inc., New York (1952).
29. K. F. Bonhoeffer, *Z. Metallkunde*, **44**, 77 (1953).
30. R. M. Burns, *J. Appl. Phys.*, **8**, 400 (1937).
31. H. Uhlig and H. Gatos, *This Journal*, **99**, 250 (1952).
32. Ref. (28), p. 249.
33. H. Uhlig and A. Geary, *This Journal*, **101**, 221 (1954).
34. D. Brasher and E. Stove, *Chem. & Ind.*, **1952**, No. 8, 171.
35. R. Powers and N. Hackerman, *This Journal*, **100**, 314 (1953).
36. M. Cohen and A. Beck, "International Symposium on Passivity," Heiligenberg, West Germany, September 1957.
37. H. H. Uhlig, *Metaux & Corrosion*, **23**, 204 (1947).
38. M. Pryor and M. Cohen, *This Journal*, **100**, 203 (1953).
39. G. Cartledge and W. Smith, Jr., *J. Phys. Chem.*, **59**, 1111 (1955).
40. G. Cartledge, *ibid.*, **59**, 979 (1955).
41. G. Cartledge, *Corrosion*, **11**, 355t (1955); *J. Phys. Chem.*, **60**, 28 (1956).
42. N. Hackerman and R. Powers, *J. Phys. Chem.*, **57**, 139 (1953).

Some Observations on the Mechanism of Inhibition

A. C. Makrides

Metals Research Laboratories, Electro Metallurgical Company, Division of Union Carbide Corporation, Niagara Falls, New York

ABSTRACT

Thiocyanic and citric acids are efficient inhibitors of dissolution of iron in dilute HNO_3 solutions. It is concluded that inhibition does not generally involve "poisoning" the combination step in the hydrogen evolution reaction. Some observations on the kinetics of dissolution of iron in dilute HNO_3 solutions are also presented.

There is little doubt that organic compounds which inhibit dissolution of metals in acids adsorb at the metal-solution interface. There are a number of ways in which the resultant adsorbed film could modify the kinetics of the dissolution process. It has been suggested (1) that adsorbed inhibitor on iron deactivates "active centers" at which the reaction

$$H_{ads} + H_{ads} \rightarrow H_2(g) \qquad [1]$$

between adsorbed hydrogen atoms takes place. According to this view, inhibition of iron dissolution is closely associated with occurrence of reaction [1].

Polarization studies with some organic compounds led Elze and Fischer (2) to the conclusion that inhibition of hydrogen discharge governs the process of dissolution in the presence of inhibitors. The particular inhibitors used by these authors had a negligible effect in the presence of an oxidizing agent (Fe^{+++}). From this result, it was maintained that inhibitors function only if reaction [1] above, which according to Elze and Fischer (2) is sensitive to inhibitors, is included in the over-all dissolution process.

It was pointed out (3, 4) that work of King and Hillner (5) indicates that some organic compounds function as inhibitors in strongly oxidizing solutions where reaction [1] is unimportant. However, the relevance of the work of King and Hillner (5) to the elucidation of the mechanism of inhibitor action was questioned on the ground that the observed decrease in dissolution rate may have been due to pH changes of the bulk solution (6).

Makrides and Hackerman (4, 7) found that butyl thiourea inhibits dissolution of iron in $FeCl_3$-HCl solutions. Any bulk effect of butyl thiourea at the concentrations employed was negligible. It was of interest, therefore, to establish whether other compounds function as inhibitors in oxidizing solutions where reaction [1] may be neglected.

Experimental

The rotating cylinder technique was used (8). Armco iron cylinders (99.92-99.96% iron content), 0.94 cm in diameter and about 8 cm long, were rotated at 250 cm/sec linear speed in 400 ml of solution. The cylinders were polished with 2/0 emery paper and were degreased with CCl_4. Only the lateral surface was exposed to solution, the top and bottom parts as well as the edges being covered with paraffin. The exposed area was measured for each cylinder.

Nitric acid solutions of desired concentration were made from stock by dilution. The HNO_3 concentration was determined by titration. Water was doubly distilled, one distillation being from dilute, alkaline $KMnO_4$.

Stock solutions containing HSCN and citric acid were prepared by dissolving a weighed quantity of the corresponding potassium salt in an equivalent quantity of HNO_3 solution. Desired inhibitor concentrations were obtained by diluting stock with HNO_3 solutions of selected concentration. With this procedure, the hydrogen ion concentration in solutions containing inhibitors was at least equal, and generally greater, than in corresponding solutions without inhibitors.

All solutions were thermostated to within $\pm 0.1°C$.

Results and Discussion

Solutions similar to the ones employed by King and Hillner (6) were used originally. First order rate constants were calculated from

$$k = \frac{2.30\,V_s}{At} \log \frac{X_\infty}{X_\infty - X} \qquad [2]$$

Here, V_s is the volume of solution, A the projected surface area, X the weight loss in time t (300 sec), and X_∞ the calculated weight loss for $t \to \infty$. Table I shows that k varied, with no apparent trend, over the concentration range examined. If the (Cl^-) concentration is varied, while that of (H^+) is constant, k at first is independent of C_{Cl^-}, but shows a maximum at larger (Cl^-) concentrations (Table II). Tables I and II indicate that the rate in solutions containing (Cl^-) depends both on total concentration and on the ratio of KNO_3 to HCl concentration.

These results are in general agreement with the work of Abramson and King (9) who have shown that dissolution of iron in KNO_3-HCl solutions is complex. Since there is no apparent reason for using such mixtures, rather than HNO_3 alone, the procedure of King and Hillner (6) was modified to exclude chloride ion.

Dissolution rates in HNO_3 are given Tables III through VI. The results may be summarized as follows: (*a*) approximately two moles of hydrogen ion are consumed per mole of iron dissolved; (*b*) the rate constant decreases regularly with increasing HNO_3 concentration; (*c*) addition of KNO_3 increases the dissolution rate; with $C_{NO_3^-} \sim 2C_{H^+}$, the rate constant increased by about 15% (Table V); (*d*) addition of (H^+) increases the dissolution rate considerably more than addition of (NO_3^-); with $C_{H^+} \sim 2C_{NO_3^-}$, the rate increased by a factor of about 2 (Table VI).

Observations (*a*), (*c*), and (*d*) suggest that in HNO_3 solutions diffusion of (H^+) largely determines the rate at which dissolution takes place. The (H^+) concentration at the interface, therefore, may be considered negligible. The (NO_3^-) concentration at the interface is also less than in the bulk, but the decrease probably does not exceed 20-25%. While it is not possible to state whether (H^+) is consumed by reaction with reduction products of (NO_3^-) or by reaction with (NO_3^-) after discharge, it may be concluded, in view of the excess of (NO_3^-) over (H^+) at the interface,[1] that the concentration of adsorbed atomic hydrogen is negligible. Under these conditions, the contribution of reaction [1] to the overall rate may be neglected.

The decrease of the specific rate constant with increasing HNO_3 concentration is probably caused, at least in part, by changes of the diffusion coefficient. Since the reaction is under diffusion control,

$$k = D/\delta$$

where δ, the equivalent thickness of the boundary layer, may be assumed independent of concentration (10, 11); D, however, is a function of concentration. Any simple correction for this dependence is not possible here, particularly in view of the unknown

[1] Electrical neutrality is, of course, preserved by an equivalent amount of ferrous ion.

Table I

$T = 30° \pm 0.1°C$; $V = 250$ cm/sec

Concentration, M	k, cm/sec*
0.030 KNO_3 + 0.0124 HCl	0.0387
0.060 KNO_3 + 0.0248 HCl	0.0344
0.090 KNO_3 + 0.0372 HCl	0.0321
0.120 KNO_3 + 0.0496 HCl	0.0404

* King and Hillner (5) find $k = 0.0351$ for 0.06 KNO_3 + 0.02 HCl at the same (250 cm/sec) linear speed.

Table II

$T = 30° \pm 0.1°C$; $V = 250$ cm/sec

Concentration, M	k, cm/sec
0.0231 HNO_3	0.0400
0.0231 HNO_3 + 0.000125 KCl	0.0406
0.0231 HNO_3 + 0.00250 KCl	0.0412
0.0231 HNO_3 + 0.00375 KCl	0.0409
0.0231 HNO_3 + 0.00500 KCl	0.0413
0.0231 HNO_3 + 0.0113 KCl	0.0430
0.0231 HNO_3 + 0.0226 KCl	0.0426
0.0231 HNO_3 + 0.0452 KCl	0.0410

Table III

$T = 30° \pm 0.1°C$; $t = 300$ sec

HNO_3 concentration, M	Wt. loss, mg	Wt. loss from (H^+) consumption, mg*
0.0357	122	120
0.0462	171	162
0.0925	288	260

* Calculated from decrease in (H^+), as determined by titration, assuming $2H^+$ are consumed per mole iron dissolved.

Table IV

$T = 30° \pm 0.1°C$; $V = 250$ cm/sec

HNO_3 concentration, M	k, cm/sec
0.0126	0.0422
0.0231	0.0400
0.0357	0.0384
0.0462	0.0356
0.0925	0.0318

Table V

$T = 30° \pm 0.1°C$; $t = 300$ sec

Concentration, M	Wt. loss, mg/10 cm²	k, cm/sec
0.0231 HNO_3	62.0	0.0400
0.0231 HNO_3 + 0.0020 KNO_3	66.0	0.0430
0.0231 HNO_3 + 0.0040 KNO_3	67.0	0.0436
0.0231 HNO_3 + 0.0075 KNO_3	65.5	0.0426
0.0231 HNO_3 + 0.0125 KNO_3	68.5	0.0452
0.0231 HNO_3 + 0.0250 KNO_3	69.5	0.0465

Table VI

$T = 30° \pm 0.1°C$; $t = 300$ sec

Concentration, M	Wt. loss, mg/10 cm²*
0.0231 HNO_3	62.0
0.0231 HNO_3 + 0.0077 $HClO_4$	81.0
0.0231 HNO_3 + 0.0128 $HClO_4$	88.5
0.0231 HNO_3 + 0.0256 $HClO_4$	105.5

* Weight loss in $HClO_4$ solutions only was 3-3.5 mg.

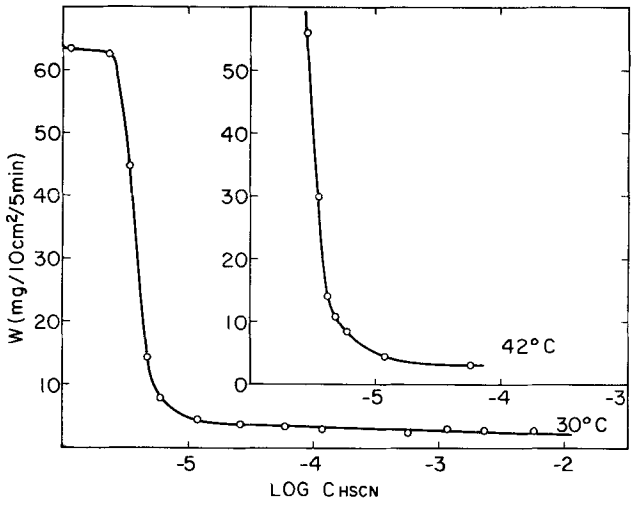

Fig. 1. Rate of dissolution in 0.0231M HNO_3 solutions containing HSCN.

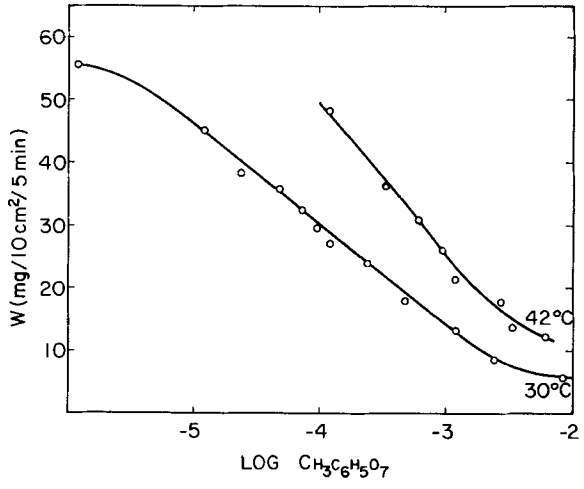

Fig. 2. Rate of dissolution in 0.0231M HNO_3 solutions containing citric acid.

effect of ferrous (or ferric) ions on the activity coefficient of (H^+). There is also the possibility that lack of constancy of k denotes that first order kinetics do not adequately describe the dissolution process in HNO_3 solutions.

Inhibition

Thiocyanic and citric acids were used as inhibitors. HSCN is known to be a good inhibitor in nonoxidizing H_2SO_4 solutions (12), while $H_3C_6H_5O_7$ appeared to be a promising inhibitor according to King and Hillner (6). Runs were made at 30° and 42°C. Results are given in Fig. 1 and 2. In both cases, the solution was 0.0231M HNO_3.

Both compounds proved to be efficient inhibitors. HSCN in particular shows essentially complete inhibition at concentrations above 5×10^{-6} to 1×10^{-5}M. Runs for periods up to 30 min showed that at least half the weight loss observed in this concentration range occurred while the system achieved a steady state. If, as commonly assumed, inhibitors function by adsorption, at small concentrations an appreciable amount of HSCN is removed from solution. At small times, therefore, the solution next to the surface may be depleted and the rate at which adsorption takes place is then limited by the rate of HSCN transport to the interface. From the weight loss-time curve in 5×10^{-6}M HSCN solutions, it was estimated that the time required for adsorption to come to completion was of the order of 1 min.

Of the two compounds used, HSCN is the better inhibitor. It may be inferred that it is adsorbed more firmly. This is borne out by the essentially negligible change in rate observed on raising the temperature to 42°C. The same temperature increase, however, shifts the curve for citric acid toward higher dissolution rates.

It is perhaps worth while to point out again that in neither case can the observed decrease in rate be attributed to a decrease in hydrogen ion concentration of the bulk solution.

Conclusions

Inhibition of iron dissolution under conditions where reaction [1] is negligible by compounds which also inhibit dissolution of iron in nonoxidizing acids suggests that the mechanism of inhibition does not involve, generally, poisoning of the combination reaction between adsorbed hydrogen atoms.

Manuscript received July 17, 1958.

Any discussion of this paper will appear in a Discussion Section to be published in the December 1959 JOURNAL.

REFERENCES

1. J. O'M. Bockris and B. E. Conway, *J. Phys. Coll. Chem.*, **53**, 527 (1949).
2. J. Elze and F. Fischer, *This Journal*, **99**, 259 (1952).
3. A. C. Makrides, *ibid.*, **101**, 635 (1954).
4. A. C. Makrides and N. Hackerman, *J. Phys. Chem.*, **59**, 707 (1955).
5. C. V. King and E. Hillner, *This Journal*, **101**, 79 (1954).
6. C. V. King and E. Hillner, *ibid.*, **101**, 635 (1954).
7. A. C. Makrides and N. Hackerman, *Ind. Eng. Chem.*, **47**, 1773 (1955).
8. A. C. Makrides, N. M. Komodromos, and N. Hackerman, *This Journal*, **102**, 363 (1955); A. C. Makrides and N. Hackerman, *ibid.*, **105**, 156 (1958).
9. M. B. Abramson and C. V. King, *J. Am. Chem. Soc.*, **61**, 2290 (1939).
10. J. N. Agar, *Disc. Faraday Soc.*, **1**, 26 (1947).
11. C. V. King, *J. Am. Chem. Soc.*, **57**, 828 (1935).
12. L. Cavallaro and G. Bolognesi, *Atti Accad. Sci. Ferrara*, **24**, No. 1 (1946-47).

Oxidation of Titanium, Zirconium, and Hafnium

G. R. Wallwork and A. E. Jenkins

School of Metallurgy, New South Wales University of Technology, Sydney, Australia

ABSTRACT

A metallographic study of the high-temperature oxidation of titanium, zirconium, and hafnium has shown that alterations in the rate equations relating to such processes may be associated with the establishment of oxygen diffusion gradients in the surface layers of the metal. It has been shown that these diffusion gradients in the metal extend in depth during an initial period in which the total rate of oxidation is given by the familiar parabolic equation. Subsequent changes in oxidation behavior have been related to observed alterations in the form of these gradients.

The high-temperature oxidation of the metals titanium, zirconium, and hafnium has been investigated on many occasions over the last decade. However, there is still much uncertainty concerning the oxidation characteristics of these metals, and the aim of this investigation has been to extend the available experimental results, most of which have been obtained from gravimetric or volumetric oxidation rate measurements.

Earlier work on the oxidation of Ti and Zr (1-3) has shown that, following an initial period, the parabolic rate equations become linear with further passage of time. Smeltzer and Simnad (4) investigated the oxidation of Hf and reported that logarithmic, parabolic, and linear equations describe the oxidation of this metal over the temperature range 350°-1200°C.

The structure of scales formed on Ti in air has been described by Morton and Baldwin (5) and in air and oxygen by Kinna and Knorr (6), and the scales formed on pure Zr in oxygen in the temperature range 500°-700°C have been described by Belle and Mallett (7).

Previous work by one of the authors (1, 2) has indicated the need for a more detailed metallographic examination of the oxidized specimens, and this has now been carried out subsequent to the development of a suitable metallographic technique.

Experimental Procedure

Metal specimens (1.0 x 0.5 x 0.1 cm) prepared as described by Jenkins (1) were oxidized in pure oxygen produced by the thermal decomposition of potassium permanganate. The system was initially evacuated to 15μ Hg, flushed with oxygen, re-evacuated, and then filled to atmospheric pressure. A furnace operating at the required temperature was drawn over a silica tube which contained a specimen hanging from a Pt wire in the oxygen atmosphere. The iodide-refined Ti metal was supplied by the Phillips Laboratories, Eindhoven, and the analysis was reported by Corbett (8). The Hf-free Zr was obtained from the U.S.A.E.C. and the Hf, containing 3-4% Zr, was supplied by the Westinghouse Electric Corporation. The oxidized specimens were mounted on edge in a cold setting polyester resin and abraded on 120, 320, and 400 mesh SiC papers followed by wax laps made from 400, 600, and 850 mesh SiC. Polishing was carried out by first rubbing lightly on a napless cloth impregnated with 1μ diamond paste and then on selvyt cloth carrying an aqueous paste of MgO. The thickness of scale was measured with a filar eyepiece on cross sections of metallographically polished, oxidized specimens. The presence of oxygen in the Ti lattice could be detected by an increase in hardness of the metal, and measurements were therefore made on specimen cross sections utilizing a Leitz microhardness instrument with a standard 124° diamond indenter.

Results

Titanium

Experiments performed in the range 800°-1000°C for long periods indicated that scaling of Ti was influenced greatly by the extent of an oxygen diffusion gradient in the metal phase of the oxidizing specimen. It was noted that the form of this gradient altered during the oxidation at corners and sides of strip specimens, and that ultimately the gradient beneath the main faces of such specimens was affected by the penetration of oxygen to the center of the strip. Further discussion relating to the form of scaling under such conditions is left to a later stage, and the following comments concern the scaling observed on flat surfaces of thick specimens.

The scales.—Two different types of scale were observed. Below 800°C only thin, gray adherent films were obtained, e.g., 0.2 mm thick after 75 hr at 750°C, which on metallographic examination in polarized light proved to be translucent. The gray appearance of the oxidized specimens is considered to be due to reflections from the metal surface beneath the translucent rutile. Above 800°C the scales were pale yellow, and microscopically they exhibited a characteristic form of lamination or banding. On closer examination these layers appeared to alternate in color from translucent yellow to gray, Fig. 1. Platinum marker experiments using wires wrapped around the original specimens showed that the oxide was formed at the metal/oxide interface, and this conclusion was later verified by the use of

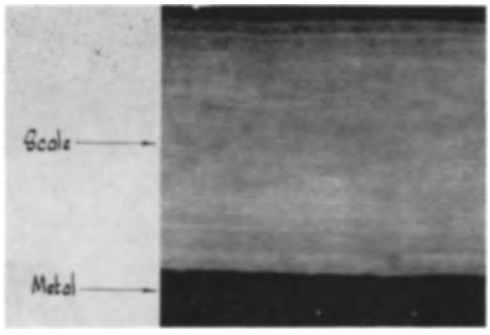

Fig. 1. Scale formed on Ti metal oxidized for 72 hr at 850°C, showing the characteristic form of lamination or banding. (Polarized light, x 250).

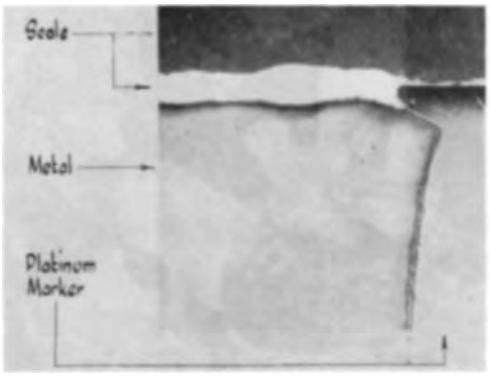

Fig. 2. Scale formed on Ti oxidized for 24 hr at 800°C, showing the inward movement of scale past the Pt marker. (Polarized light, x 125).

Pt plugs inserted through the specimens (Fig. 2). X-ray diffraction studies of the scales and metal cores confirmed that rutile was the only oxide present. The scales, although separated from the metal core on cooling from the oxidation temperature, must have remained in close contact with the oxidizing metal during the tests as they were readily absorbed by the metal when the gaseous supply of oxygen was withdrawn and the tests contained in vacuum for some hours at the same temperature.

The metal core.—Metallographic examination of a cross section of metal cores from oxidized specimens showed that the surface layers contained oxygen in solid solution. In the etched condition these cores taken from specimens oxidized below 800°C showed an oxygen saturated zone outlined by a fine black line just beneath the surface. Above this temperature a much wider band appeared Fig. 3. Previous work (1) had shown that microhardness traverses could be used to follow the form of an oxygen diffusion gradient in Ti. This technique was used to establish the form of the gradients below the saturated surface zone in each section. For each temperature a particular oxygen gradient was established in the core, the extent of penetration being initially time dependent. However, with increasing time the gradient reached a steady state, an example being given in Fig. 4. The time necessary to produce this condition decreased with increasing temperature and coincided with the change from a parabolic to a linear rate equation.

Zirconium and Hafnium

Scales, formed on both metals between 700° and 950°C, were dark gray and adhered to the metal core on cooling. However, the scales were white where they had lifted away from the metal during oxidation. Metallographic examination revealed some cavities penetrating to the metal surface in an otherwise dense, featureless scale structure devoid of layering. Belle and Mallett (7) published a photomicrograph of scale formed on Zr heated in oxygen between 500° and 700°C, and the similarity with the results obtained in the present study indicates that the form of the scale remains unchanged in the range 500°-950°C. Measurements of scale thickness after 24 hr showed a linear increase with respect to both time and temperature. Microhardness traverses revealed that steady oxygen gradients were also established in the cores of these two metals; the periods necessary to accomplish this increased in the order Ti, Zr, and Hf.

"Edge Effect"

Above 800°C, the scales formed on Ti were sufficiently thick to examine in detail, particularly along the edges and corners. At such sites, the yellow translucent scale was invariably thinner than on the main faces and had a crystalline structure distinct from the banded structure obtained elsewhere, Fig. 5. The form of the oxygen gradient in the metal core beneath these edges was traced and its total depth of penetration is shown in Fig. 6 for a specimen oxidized at 850°C for 72 hr.

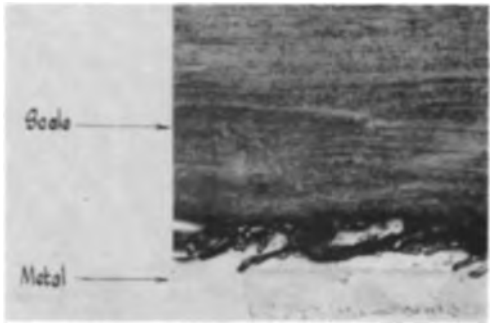

Fig. 3. Same as Fig. 2. The oxygen-saturated zone in the metal core shows as a dark etching band in bright-field illumination. (x 250).

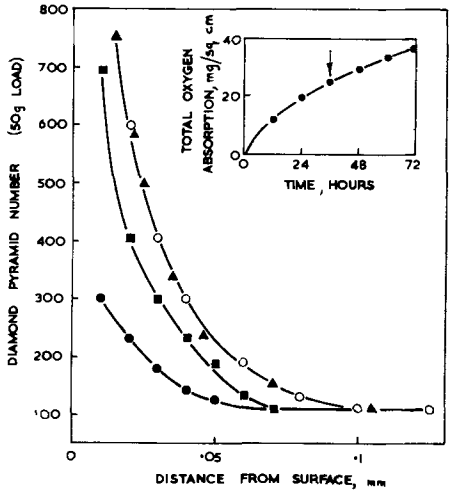

Fig. 4. Penetration hardness curves, showing the development of the gradient and the change from a parabolic to linear rate equation on specimens oxidized at 850°C. ●, 12 hr; ■, 24 hr: ▲, 36 hr; ○, 48 hr.

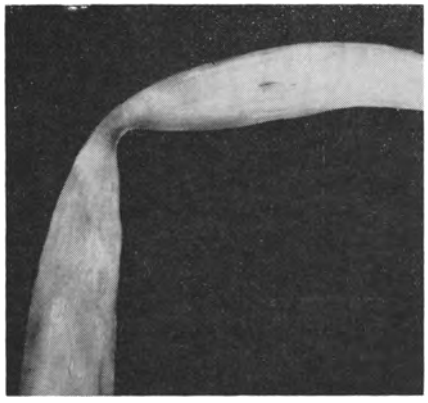

Fig. 5. Section through the center of a specimen of Ti showing the scale formed on a corner ("edge effect"), oxidized at 850°C, for 72 hr. (Polarized light, x 50).

Quite clearly the extent of oxygen penetration into the metal core at the edges was greater than on the flat faces and this affected the form and thickness of the scale at these sites.

Oxidation of Thin Specimens

In the early stages of the investigation, the importance of maintaining oxygen-free metal at the center of reacting specimens was not fully appreciated. Although specimens 1 cm thick were used in later experiments, oxidation at 1000°C for periods in excess of approximately 5 hr produced scaling changes which were attributed to an interruption in the movement of the diffusing oxygen gradient in the metal. This was apparently caused by oxygen penetrating to the center zone of the specimens because the onset of a change in scaling behavior at these high temperatures was noted to vary with the thickness of the specimen. Results of tests carried out under conditions where the diffusion gradient was affected are given in Fig. 7-9. Figure 7 is a cross section of a thin Ti specimen oxidized at 850°C for 72 hr. Initially a normal layered pale yellow scale of considerable thickness was produced (the layers were not reproduced in Fig. 7 so that other features could be high-lighted). However, due to the thinness of the metal specimen, the diffusion

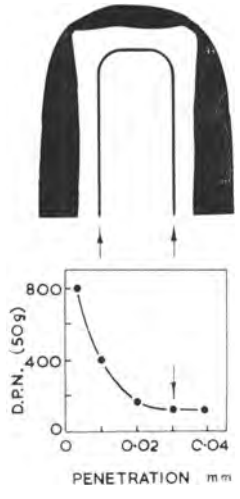

Fig. 6. Shadowgraph of the scale formed on the end of a Ti specimen oxidized for 72 hr at 850°C, showing the position of the extremity of the oxygen gradient and its position in relation to the scale.

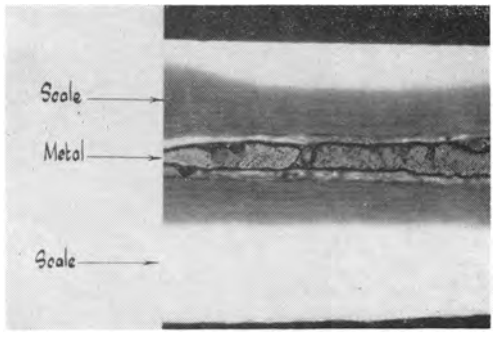

Fig. 7. Scale formed on a thin Ti specimen oxidized for 72 hr at 850°C, showing the effect of through oxidation.

gradients have met in the center, preventing further unhindered progress of the gradients. It is suggested that as a result of a reduced rate of oxygen diffusion into the metal core discoloration of the laminated scale commenced with the onset of cation diffusion outward through the scale toward the gas/scale interface. The metal core eventually received sufficient oxygen to become completely saturated and even produced a film of lower oxide (mainly purple Ti_2O_3) on the large solid particles remaining. As a general rule, the conversion of oxygen-saturated Ti to rutile will by-pass the lower oxides because, as suggested in the following discussion, very thin layers or fragments of oxygen-saturated Ti which have split off from the core are intermittently converted to rutile.

Two additional observations were made on specimens oxidized above 950°C (Fig. 8 and 9). Whenever oxidation conditions permitted the penetration of oxygen to the center zone of each metal specimen, a line of demarcation could be observed in the scale on metallographic examination (Fig. 8). This photomicrograph was prepared from a specimen oxidized at 1000°C for 6 hr, the specimen thickness being such that oxygen penetrated to the center regions. Marker experiments proved that this demarcation line represented the original metal surface. Scale appearing between this line and the metal surface apparently formed during the initial period of oxidation prior to the oxygen penetrating to the center of the metal and possessed the characteristic layered structure (Fig. 1). However, the

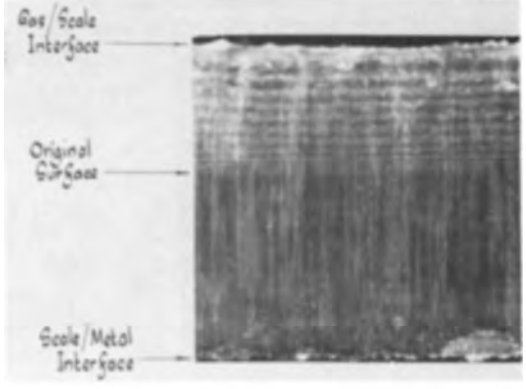

Fig. 8. Scale formed on a Ti specimen oxidized for 6 hr at 1000°C, in which the gradient in the core has been reduced by through oxidation. The columnar structure and the layering in the outer and inner sections of the scale are shown.

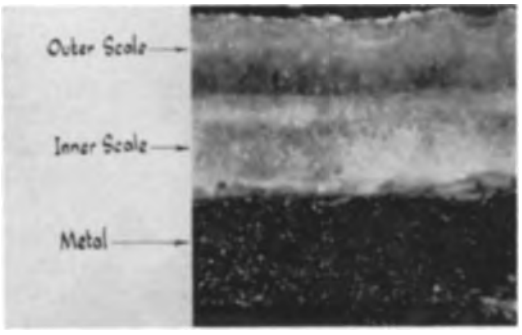

Fig. 9. Scale formed on Ti oxidized for 24 hr at 1000°C, showing the saturated metal core and the two recrystallized layers in the scale.

scale formed between the demarcation line and the gas interface must have been produced as a result of the diffusion of metal cations to the gas interface, and it is evident that the periodicity of the banding has lengthened noticeably toward the end of the oxidation. This portion of the scale forms when the demand for oxygen by the metal phase is reduced for some reason, such as oxygen penetrating to the center of the metal. Microhardness traverses on the remnant metal core beneath the scale shown in Fig. 8 revealed a decrease in oxygen concentration at the surface and a rise at the center, which supports the suggestion concerning reduced oxygen demand by the core. The scale exhibited a gray metallic luster, except at the corners and edges which consisted of large equiaxed crystals. The unusual columnar structure superimposed on the scale structure in Fig. 8 appears to be the result of some cooling phenomenon. The authors believe that a similar observation has been made on rapidly cooled UO_2 crystal aggregates.

Figure 9, taken from a thin specimen oxidized for 24 hr at 1000°C, shows a photomicrograph of the scale produced when the metal core has become completely saturated with oxygen. The two-layer scale is composed of equiaxed translucent yellow crystals of rutile, probably formed at the temperature of test. The core contains a second phase, TiO, which apparently has been rejected during cooling of the saturated solution comprising the core.

Discussion

Earlier work (1, 3) has established that after a brief interval Ti and Zr oxidize according to parabolic rate equations transforming to linear for prolonged periods of time. It is now suggested that the rate equation obeyed by Hf also undergoes a transformation from parabolic to linear upon the establishment of a steady oxygen gradient in the core of the oxidizing specimens. Apart from Loriers' explanation (9) based on a change in scale porosity this transformation has been interpreted in the past as indicating a transition from a diffusion-controlled process (parabolic equation) to a process in which resistance to further diffusion is offered by a barrier of fixed dimensions (linear equation). This barrier was believed to exist in the oxide scale, and the diffusion process was thought to be one in which oxygen penetrated by an anion vacancy mechanism. Metallographic examination has not yet revealed any obvious barrier in any of the scales examined, and density measurements (1) show a 7% porosity at room temperature for rutile scales formed on Ti between 700° and 950°C. However, x-ray diffraction, metallographic, and microhardness techniques have shown that a saturated surface zone together with a steady oxygen gradient is established eventually in the metal core after a period which coincides with the change from parabolic to linear oxidation.

It is now proposed that the scale is not operating as a diffusion barrier in the temperature range considered and that the oxidaiton of Ti, Zr, and Hf is controlled by interstitial diffusion of oxygen in the metal phase. It is considered that the exposure of clean surfaces of these metals to oxygen at high temperatures results first in a rapid gas absorption together with a transient increase in temperature, the gas concentration also rising in the surface layer. Scale formation probably follows the establishment of a saturated surface layer. The conversion of oxygen-saturated metal to rutile is considered to involve an exfoliation of very thin surface layers from the core, conversion to rutile following immediately as the detached metal is exposed to an atmosphere of relatively high oxygen potential. At the high temperature involved, the semiplastic oxide, under stress, would tend to sinter to the previously formed scale, although the junction line may well prove not to be perfect and so lead to the layered scale structure. No layering has been observed in the scales formed on Zr or Hf and this could indicate a difference in the conversion process at the metal/oxide interface.

Scale thickness measurements suggest that the actual scaling rate remains constant during the initial period of parabolic oxidation, whereas the rate of total oxygen absorption decreases with time, the decrease probably reflecting the establishment of the oxygen gradient in the metal core. This would explain the observed parabolic to linear transition in the rate of total oxygen absorption, because a stage must be reached at which the oxygen absorption by the metal core balances the conversion reaction at the metal/oxide interface. Oxygen entering the core then would be used periodically to establish saturated conditions in the core surface and to convert the detached layers to rutile. The following modified parabolic equation should apply during the establishment of the oxygen gradient in the metal,

$$\frac{dn}{dt} = \frac{K_1}{K_2 + n}$$

where n is the number of oxygen molecules absorbed at time t, and K_1 and K_2 are the rate constants for the diffusion and interface reactions. Integrating between the limits (n_0, n), $(0, t)$ we obtain the equation

$$n - n_0 = \Delta n = 2K_1 \left(\frac{t}{\Delta n}\right) - 2(n_0 + K_2)$$

Mathematical substitution in this equation will result in evaluation of the constants K_1 and K_2.

Finally, the influence of the diffusion gradient on the oxidation of Ti is revealed if, for some reason, the gradient of the core is upset. This can occur at corners and edges of specimens where the gradient is extended in depth and also over the main faces of thin specimens in which oxygen has penetrated to the center of the core. When this occurs, the gradient is apparently reduced, the absorption of oxygen by the core is therefore reduced and, if the specimen is scaling in the linear region, the scaling rate must then decrease. The experimental results suggest that the subsequent alteration in scaling behavior then depends on the temperature. Below about 900°C, it appears that a thinner scale remains over such sites, with the possibility of recrystallization at the corners and edges. However, at higher temperatures, it appears that the decrease in the absorption of oxygen at the core surface results in a longer period elapsing between the continuous process of saturation and separation of the core surface layers. Cation diffusion out through the attached scale structure is then observed. Once the usual exfoliation process occurs at the core surface, cation diffusion is halted temporarily until actual contact between scale and core again develops, and this is registered in the widening layered structure (Fig. 8) observed in the outer scale zone of those specimens which have produced a double scale. If this explanation is correct, it would be expected that, as a result of further oxidation of the core and therefore a slower rate of oxygen absorption, an increase in the period elapsing between the detachment of core surface layers would be observed. The result would be that the outermost scale layers formed by cation diffusion, having been the most recent formed, should show the widest banding. It is concluded from the absence of such effects below 850°C (cation diffusion is seen to have commenced in Fig. 4) that the ratio of the diffusivity of Ti cations in rutile to that of interstitial oxygen in the metal may perhaps be increasing with increasing temperature and at a rate such that oxidation at temperatures in the vicinity of 1200°C involves only outward diffusion of the metal cation to the gas-scale interface. Finally, when complete oxygen saturation of the core is approached at high temperatures, it is considered that the scale must eventually recrystallize to form the characteristic pale yellow rutile shown in Fig. 9. Oxygen demand by the core must then be very low, and cation diffusion would operate only as long as contact existed between the scale and the core.

Conclusion

The results of this investigation suggest that the scaling behavior of Ti, Zr, and Hf is controlled by the diffusion of oxygen in the metal phase. The presence of oxygen in the metal core has been used to explain the change in the rate equations during the oxidation of these metals. In the past this has been attributed to a scale barrier of constant thickness, but no such barrier has been detected. However, a diffusion barrier of constant depth is eventually established in the metal core and this is associated with the parabolic to linear transformation. It is considered that the actual isothermal scaling rate for these metals may well prove to be approximately constant, and that the initial parabolic rate of oxygen absorption is associated with the establishment of an oxygen diffusion gradient in the metal core as well as the scaling reaction. Further discussions based on these proposals has produced an explanation for certain effects commonly observed during the high-temperature oxidation of Ti.

Finally, a number of metals other than Ti, Zr, and Hf exhibit a significant oxygen solubility at high temperatures, and therefore their scaling behavior is being examined now along similar lines.

Acknowledgments

The work described in this paper was carried out in the School of Metallurgy at the New South Wales University of Technology, Australia. During the period involved, one of the authors (G.R.W.) held an Australian Atomic Energy Commission Postgraduate Studentship. The authors wish to express their thanks to Professor Rupert Myers for the provision of laboratory facilities and to the Australian Atomic Energy Commission for continued financial support.

Manuscript received March 10, 1958.

Any discussion of this paper will appear in a Discussion Section to be published in the December 1959 JOURNAL.

REFERENCES

1. A. E. Jenkins, *J. Inst. Metals*, **82**, 213 (1953-4).
2. A. E. Jenkins, *ibid.*, **84**, 1 (1955-6).
3. L. F. Kendall, A.E.C. Research & development report H.W. 39190 Sept. (1955).
4. W. W. Smeltzer and M. T. Simnad, *Acta Met.*, **5**, 328 (1957).
5. P. H. Morton and W. M. Baldwin, Jr., *J. Metals*, **4**, 854 (1952).
6. W. Kinna and W. Knorr, *Z. Metallk.*, **47**, 594 (1956).
7. J. Belle and M. W. Mallett, *This Journal*, **101**, 339 (1954).
8. J. A. Corbett, *Analyst*, **76**, 652 (1951).
9. J. Loriers, *Compt. rend.*, **231**, 522 (1950).

The Electrical Resistance of Oxide Films on Zirconium in Relation to Corrosion

R. D. Misch and F. H. Gunzel, Jr.

Argonne National Laboratory, Lemont, Illinois

ABSTRACT

The conductivity of anodic and corrosion films on zirconium was found to increase during heating in vacuum. The conductivity changes at 450°C were studied on anodic films which were 0.6, 0.75, 0.9, and 1.5 μ in thickness. The change in conductivity was attributed to the diffusion of anion vacancies into the oxide with an estimated diffusion coefficient of 4×10^{-13} cm^2 sec^{-1}. Corrosion films produced in water at 350°C appeared to have higher diffusion coefficients. Among the materials zirconium, Zircaloy-1, and Zircaloy-2, specimens of zirconium had the highest corrosion rates and diffusivities (as judged by the conductivity changes). Consequently, an effect of vacuum heating on corrosion was expected and subsequently confirmed. Enhanced oxide growth was observed after corroded specimens were heated at 600°C for 1 min. The increase in weight gain was greater than would be expected from a simple restoration of dissolved oxide.

The corrosion of zirconium in water at high temperature is a sensitive function of metal composition (1). Consideration of this problem has focused attention on changes in the oxide film as a result of additives. An analysis of such effects has been given by Thomas (2). The present study was designed to determine whether the resistance of the oxide plays a role in the corrosion process.

In the case of highly conductive oxides like FeO the effect of small concentrations of impurities is negligible. Zirconium oxide, however, is an insulator at room temperature, and impurities might be expected to decrease its electrical resistivity. Consequently, the resistivity of the corrosion film should reflect the presence of various impurities. The incorporation of such impurities in the oxide has been observed in a 2.5% Sn-Zr alloy where the Sn was found in solid solution in the ZrO_2 layer (3).

Other elements such as Ti, U, Fe, Cr, and Ni have ionic sizes favorable for substitutional replacement of Zr^{4+} in the oxide lattice. Titanium and uranium increase the corrosion rate of Zr in water, while the other elements in small amounts cause a decrease. One may conclude that crystallographic changes are not of primary importance so that emphasis can be directed to changes in the oxide defect structure as determining corrosion behavior. Resistance measurements should be of value in resolving this problem.

A study of the resistance of corrosion films at room temperature was made by Akimov and Clark (4). The film was touched with a mercury droplet. The present technique is similar to that of Savage (5) who examined the resistance of electrical contacts. Contact with the oxide was made with a wire probe, and the underlying Zr formed the other contact.

The oxide on a metal is not a homogeneous, isotropic solid, and the role of inclusions and defects cannot be overlooked. Freshly prepared anodic or corrosion oxide on Zr is an insulator at room temperature, and a low resistance area is an indication of a conducting inclusion. Other factors which influence the data are discussed below.

Experimental

Procedure.—All measurements were made by resting the polished tip of a 10-g Pt probe on the oxidized surface of Zr specimens. The probe made electrical contact through the oxide to another Pt wire spot welded to the Zr. In all measurements the voltage across the oxide was 10 mv, and the current was read on a galvanometer with a sensitivity of 0.005μa/mm of deflection. The circuit and probe are shown in Fig. 1. The magnitude of the current was independent of polarity; usually the probe was maintained positive to the Zr. The Zr specimen rested in the center of a 1-in. diameter Pt tube fur-

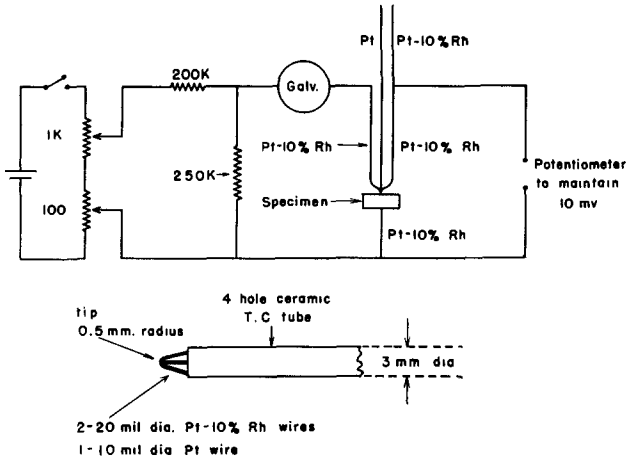

Fig. 1. Schematic drawing of circuit and construction of probe for measuring film conductivity and temperature.

nace, 8 in. long. The furnace was mounted in an 18-in. bell jar which was evacuated to 10^{-6} mm Hg pressure before heating. At 450°C the vacuum was 10^{-5} mm Hg or better.

Materials.—The study was made on reactor grade Zr, Zircaloy-1, and Zircaloy-2. Hafnium was present to approximately 0.02% in all these materials. Specimens were cut from rolled plates having the analyses given below:

Zirconium: (all ppm) 200 O, 70-350 C, 60-150 N, 30-100 Al, 2-10 Cr, 5-20 Cu, 200-700 Fe, 1-20 Mg, 2-7 Mn, 40-80 Ni; each less than 50 ppm: Si, Ti. This material is classified Grade 1 on the basis of corrosion testing in water.

Zircaloy-1: 2.5% Sn, other individual elements below 0.01%.

Zircaloy-2: 1.43% Sn, 0.108% Fe, 0.105% Cr, 0.048% Ni, 0.0032% N, with 30 ppm Al, 50 ppm Ca, 170 ppm Hf, 60 ppm Pb, 50 ppm Si, 15 ppm Ti.

All specimens were prepared by wet grinding to 400 grit paper and etching in a solution of 50 ml 70% HNO_3, 50 ml distilled water, 8 ml 47% HF. Etching time was 1 min at room temperature.

Anodic films.—Anodic films were produced by applying constant voltage to a cell with Zr as the anode and Pt as the cathode. In the present work the electrolyte was purified saturated H_3BO_3 at room temperature. This electrolyte had a high resistance but permitted anodizing up to 500 v. In anodizing of this type the film thickness is proportional to the applied voltage (1). The gain in weight of Zr anodized according to the procedure used in this study was found to be in good agreement with the data of Polling and Charlesby (6), i.e., 0.46 μg cm^{-2} v^{-1}. Charlesby assumed a density of 5.67 g cm^{-3} which gave a thickness-voltage relation of 30Å v^{-1}.

The dependence of film thickness on voltage was also shown by measuring the capacitance of the Zr anode in the electrolyte. The second electrode was Pt gauze. Effectively, the Zr and electrolyte were the plates of the condenser. A General Radio Company Type 650-A bridge was used. It was expedient to substitute acetic acid for boric acid when measuring capacitance in view of the high resistance of the latter soluton. The data are shown in Fig. 2. Zircaloy-2 could not be anodized above 300 v which limited the range in which the film thickness could be varied. This fact was attributed to oxygen evolution at inclusions.

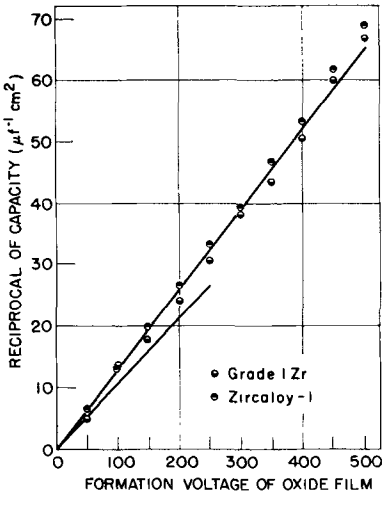

Fig. 2. Reciprocal of capacity of anodic films as a function of the voltage of anodizing of Zr and Zircaloy-1, anodized in boric acid, measured in 1N acetic acid. The short line is from data of Charlesby (14).

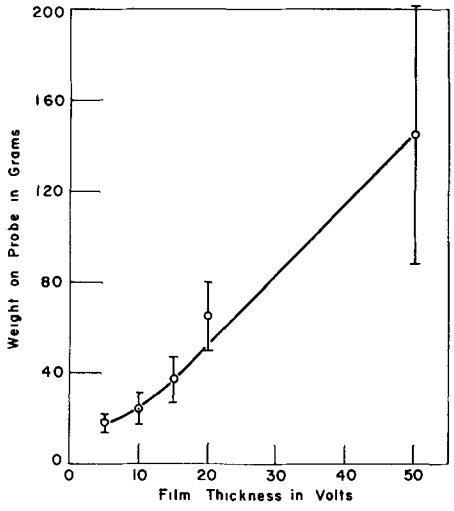

Fig. 3. Region of electrical breakdown of the anodic film on Zr as a function of probe weight and film thickness. The solid line bracketing each point indicates standard deviation.

Autoclave films.—Autoclave films were produced by exposing specimens to degassed, distilled water at 350° ±5°C for periods from 16 hr to 2 weeks. The resultant films were adherent, and weight gains were a measure of film thickness.

Weight on the probe.—The probe rested on the surface with a weight of 10 g. To be certain that the film was not damaged by this weight the maximum tolerable weight at room temperature was determined for different film thicknesses. The data are given in Fig. 3. The film broke down electrically above the line, producing a short circuit. The applied voltage was 10 mv prior to breakdown. An average of 30 points was examined for each anodic film thickness.

Contact area.—The contact area of the probe was very small. To determine this area the 10-g probe was placed on smooth Pt, the resistance was measured, and the area was calculated from the formula of Holm (7). An average of numerous measurements gave a contact area of $1.5 \pm 0.5 \times 10^{-6}$ cm^2. This is the largest error in estimating resistivity.

Results

Effect of Heating in Vacuum

No current was detected when the probe was placed on anodic or autoclave films at room temperature. However, when a specimen was heated in vacuum, current became measurable at 350°C and higher. The conductivity increased with time as well as temperature, and a reversible temperature coefficient could not be obtained. Film history, thickness, and temperature were all found to influence the conductivity changes.

Preliminary work in which specimens were heated and cooled showed that the ZrO_2 films became better conductors and remained so as long as the vacuum

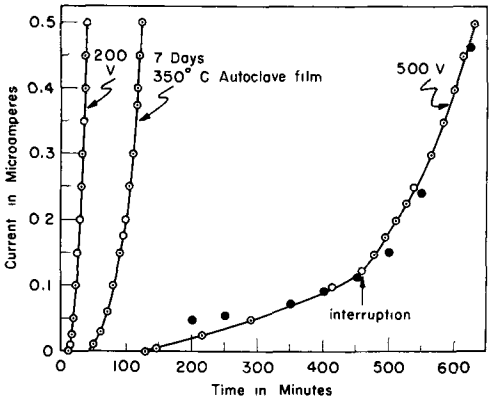

Fig. 4. Typical examples of the change in conduction of the oxide in Zr held at 450°C in vacuum.

was maintained. The conductivity often dropped when air was admitted.

At constant temperature the conductivity increased at a rate dependent on temperature. At 350°C there was no perceptible conductivity up to 16 hr. At 450°C the change in the film was apparent in a matter of minutes. Typical results for heating different specimens are shown in Fig. 4.

Weight gains of these specimens were as follows: 200 v anodized film, 9.1 mg/dm^2; autoclave film, 31.0 mg/dm^2 (somewhat higher than average); 500 v anodized film 22.8 mg/dm^2. These data were for single trials, but the reproducibility may be judged from Fig. 5-7. The "interruption" on the 500 v curve indicates an overnight interval during which the specimen was in vacuum at room temperature. When heating was resumed, the current returned within several minutes to the magnitude recorded just before cooling.

Anodic films of increasing thickness.—To measure the effect of film thickness, a series of anodic films formed at different voltages was studied. The voltages were 200, 250, 300, and 500 and the corresponding weight gains were 9.1, 11.4, 13.7, and 22.8 mg/dm^2. Assuming 5.67 g cm^{-3} as the density (6) the thicknesses of these films were 0.6, 0.75, 0.9, and 1.5μ. The conductivity was measured at 450°C in vacuum,

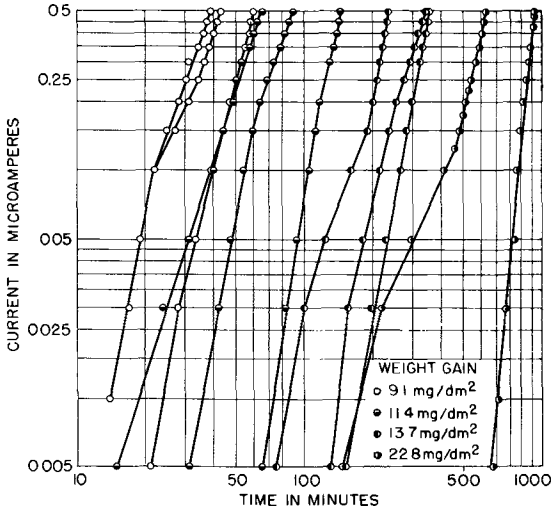

Fig. 5. Current vs. time curves for anodic oxide films on Grade I Zr held at 450°C in vacuum.

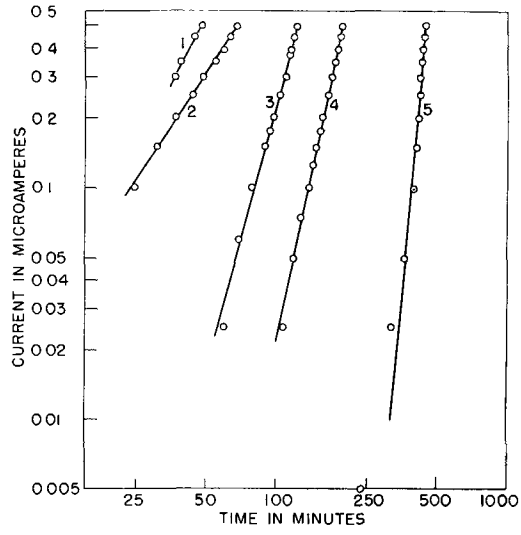

Fig. 6. Current vs. time curves for autoclave films on specimens of arc-melted Zr crystal bar having an average weight gain of 19 mg/dm^2 after 1 week in water at 350°C. Each specimen was held at 450°C in vacuum. Specimens 1, 2, and 3 exhibited patches of gray or white oxide; specimens 4 and 5 were black and uniform.

and the data are plotted as log current (with 10 mv across film) vs. log time in Fig. 5.

Autoclave films.—Here all the specimens had weight gains very close to 21 mg/dm^2. The alloys had uniform black films, while the Zr specimens showed occasional white patches. Measurements were made only on the coherent black film.

The curves for Zr are given in Fig. 6 and the curves for the two alloys in Fig. 7. In the latter case the experimental points are shown only for Zircaloy-2. The experimental data for Zircaloy-1 were in good agreement with the lines as shown, and the points were omitted to avoid overlapping. The slopes of the curves on the autoclave films were similar to those for the anodic films. The experimental spread for Zr was large as compared to the alloys.

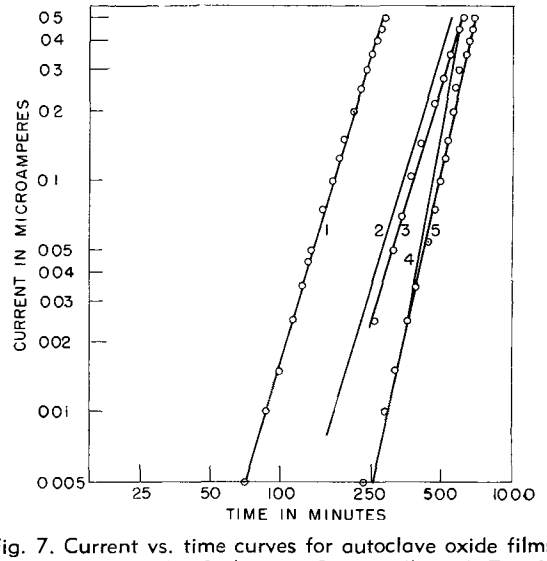

Fig. 7. Current vs. time curves for autoclave oxide films on specimens of Zircaloy-1 (curves 2 and 4) and Zircaloy-2 (curves 1, 3, and 5) having an average weight gain of 24 mg/dm^2 after 1 week in water at 350°C. Specimens were held at 450°C in vacuum.

Vacuum heating and corrosion rate.—The existence of a conductivity effect suggested that the corrosion rates might be increased by vacuum heating. With rapid heating to sufficiently high temperatures the corrosion oxide film became a good conductor at room temperature over its entire surface. The subsequent corrosion behavior should indicate whether film growth is affected. For this purpose the corrosion of Zr specimens was compared before and after a rapid heating to 600°C followed by rapid cooling. The corrosion film was conducting after this treatment. Zirconium specimens were exposed to water at 350°C, periodically removed, and vacuum heated. Comparison with controls revealed no effect of the heating. Consequently, the heating time in vacuum was extended as follows: The specimen was brought to 600°C in 30 sec, kept at 600° for 1 min, and cooled below 400° in 30 sec. The vacuum was 10^{-5} mm Hg or better. This procedure was employed on both Zr and Zircaloy-2 specimens after 16-hr intervals of exposure to degassed water at 350°C. Upon removal from the autoclave the heated films were again insulating.

One set of specimens was used as a control; the other set was vacuum heated before and during the corrosion test. An additional set of specimens was vacuum heated at the same time, but corrosion testing was not carried out until the vacuum heating was discontinued after 320 hr of corrosion exposure.

The corrosion weight gains are shown in Fig. 8 and 9. Initially, the heated specimens had lower weight gains, but they continued to gain weight when the control specimens were leveling off. It was found in a preliminary experiment that these low weight gains did not appear when the vacuum heating preceding the corrosion exposure was omitted. Consequently, the initial low weight gains may be due to a different surface after the vacuum treatment.

The effect of vacuum heating did not last, as shown by the leveling of the curve after 320 hr when this treatment was ended. The four specimens of each material which were vacuum heated and then corrosion tested (data not shown) had essentially the same weight gains as the standards which were

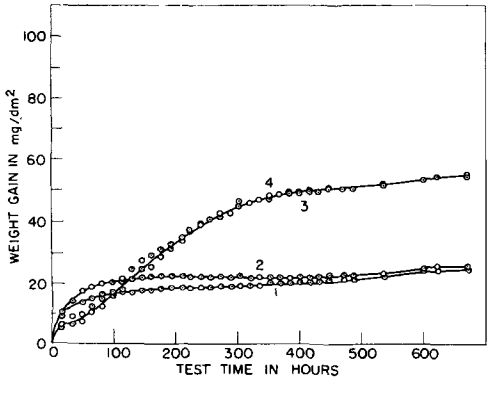

Fig. 8. Weight gains of four specimens of arc-melted Zr, corrosion tested simultaneously in water at 350°C. No. 3 and No. 4 were heated at 600°C for 1 min at the time of each weighing up to and including 320 hr (also prior to testing). Heating was discontinued after this point. Specimen No. 1 and No. 2 were not heated.

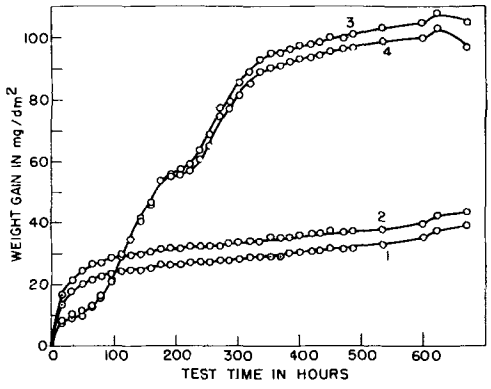

Fig. 9. Weight gains of four Zircaloy-2 specimens, corrosion tested simultaneously in water at 350°C. No. 3 and No. 4 were heated at 600°C for 1 min at the time of each weighing up to and including 320 hr (also prior to testing). Heating was discontinued after this point. Specimen No. 1 and No. 2 were not heated.

not heated. This ruled out any metallurgical effect. Specimen weights were always checked before and after the vacuum heating and did not vary by more than 0.5 mg/dm². This was negligible in comparison to the corrosion weight gains.

At the end of the test the specimens numbered 1 and 2 had a uniform dark lustrous appearance indicative of a protective oxide, for both Zr and Zircaloy-2. Specimens 3 and 4 were light gray. Under a microscope the light gray oxide was seen to vary from gray to white with white predominating. The film on the Zircaloy-2 was breaking away along the lines of inclusions. The Zr surfaces had tiny brown and black spots which were probably deposits from the autoclave.

Discussion

Vacuum heating has been shown to influence both the electrical conductivity of the oxide on Zr and its corrosion rate in water at 350°C. The reasons for electrical changes in the oxide will be considered before discussing the effect of vacuum heating on corrosion.

The nature of the Zr-ZrO_2 system suggests that diffusion is responsible for the conductivity changes. The most likely mechanism to account for the observed changes is the loss of oxygen to the metal which would be accompanied by the formation of anion vacancies in the oxide. The very low dissociation pressure of ZrO_2 (10^{-40} atm at 450°C) is evidence that oxygen will not escape to the vacuum.

The current-time curves can be explained on the basis that the resistance of the oxide drops rapidly with the penetration of anion vacancies. The mean displacement of a diffusing species is $\sqrt{2Dt}$, where D is the diffusion coefficient and t is time (12). If the major part of the observed electrical resistance is provided by the unpenetrated oxide (of unchanged resistivity), one may write

$$i = \frac{k\,V}{\delta - \sqrt{2Dt}} \qquad [1]$$

where i is the current through the film, V is the applied voltage, k is a constant proportional to the area of the contact, and δ is the film thickness. At 450°C

Table I. Diffusion coefficients, D, calculated from the data of Fig. 5 (Anodic oxide on Grade 1 Zr at 450°C)

Anodizing voltage	Film thickness μ	D x 10^{13} (cm^2 sec^{-1}) As calculated	Average for each film thickness
200	0.60	7.6 6.7 4.9	6.4
250	0.75	6.9 5.2 3.2	5.1
300	0.90	2.8 1.9 1.9	2.2
500	1.5	2.9 1.8	2.4

the change in film thickness due to dissolution can be neglected.

This equation provides a reasonable representation of the observed data as indicated in Fig. 4 where the solid points were calculated from Eq. [1] using the values $D = 2.72 \times 10^{-13}$ cm^2 sec^{-1} and $k = 3.1 \times 10^{-5}$ μa^{-1} cm^{-1}. These empirical values were calculated from two points on the experimental curve (0.05 μa, 290 min and 0.4 μa, 600 min); k was an average for these points.

Two points from a curve are sufficient to solve for D from the equation

$$\frac{i_2}{i_1} = \frac{\delta - \sqrt{2Dt_1}}{\delta - \sqrt{2Dt_2}} \qquad [2]$$

Using i_2 as 0.5 μamp and i_1 as 0.025 μamp, the diffusion coefficient was calculated for the curves of Fig. 5. The resulting values are shown in Table I. The average from all the curves was 4.0×10^{-13} cm^2 sec^{-1}.

This result may be compared with 2×10^{-15} cm^2 sec^{-1} which Pemsler (8) obtained for the diffusion of oxygen into Zr metal at 450°C. The difference between 4.0×10^{-13} and 2×10^{-15} is consistent with the observation that conductivity changes can be observed in films where dissolution is almost insignificant. However, in the absence of corroborative information it should not be concluded that the "vacancy diffusivities" presented here are valid diffusion coefficients.

The conductivity changes of the corrosion oxide films on Zr showed a wide variation although the films were of equivalent thickness. The following diffusivities for the corrosion films heated at 450°C were calculated in the same manner as for the anodic films (the designations refer to Fig. 6): Curve 1, 2.5×10^{-12} cm^2 sec^{-1}; curve 2, 2.1×10^{-12} cm^2 sec^{-1}; curve 3, 1.4×10^{-12} cm^2 sec^{-1}; curve 4, 0.86×10^{-12} cm^2 sec^{-1}; curve 5, 0.38×10^{-12} cm^2 sec^{-1}.

As would be expected, curve 5 represents a lower diffusion coefficient than curve 1.

The better reproducibility of the curves for Zircaloy-1 and 2 suggests that the oxide is more homogeneous on these alloys than on Zr. The curves for these alloys are similar to curve 5 for Zr so that a comparable diffusivity can be expected. It is possible that a low diffusivity as estimated from conductivity changes may be related to a low corrosion rate.

The effect of vacuum heating on corrosion cannot be explained readily. The increase of electrical conductivity during heating indicates that changes are taking place within the oxide. In addition, some of the oxide is dissolving as a result of oxygen diffusion into the Zr. The rate of dissolution has been used to determine the diffusivity of oxygen in Zr (8).

Considering the latter process, the effect is to make the oxide film slightly thinner. In previous work (11), using the same equipment as this study, it was shown that about 100Å of oxide was dissolved while heating 1 min at 600°C. This is somewhat smaller than the results of Pemsler (8) where approximately 250Å would be expected to dissolve in the first minute. Using the smaller number the decrease in thickness would be 0.2μ after twenty heatings. This corresponds to 3 mg/dm^2 of oxygen. The final differences in weight gains between heated and unheated specimens were much larger than this, indicating that the weight increases are not simply due to the restoration of dissolved oxide.

As already mentioned the heated film did not remain conducting after exposure in the autoclave but was apparently restored to its original insulating character. This suggests that the defect structure produced by heating is eliminated by re-exposure to water. In such a case a weight gain would be expected, corresponding to a filling of vacancies.

As shown by the data on corrosion weight gains a specimen gained weight each time it was vacuum heated and returned to the autoclave. In the case of Zr which had a weight gain of 40 mg/dm^2 without heating, the additional weight gain after each vacuum heating and re-exposure was approximately 2.5 mg/dm^2. The latter figure represents 6% of the oxygen in the film before re-exposure in the autoclave. Consequently, one may postulate that 6% of the oxygen sites were emptied by diffusion during vacuum heating and refilled upon subsequent exposure in the autoclave.

Under the same circumstances, the 40 mg/dm^2 film on Zircaloy-2 gained about 5 mg/dm^2, representing a 12.5% vacancy concentration. These percentages seem unreasonably high because the oxygen consumed in the dissolution of oxide at 600° (100Å) is only 0.15 mg/dm^2 or 0.4% of 40 mg/dm^2. This suggests that other factors are increasing the corrosion rate.

Perhaps the structure of the oxide is changed by heating, or the diffusion of oxygen into the Zr promotes the subsequent conversion of some of this diffused layer into oxide during corrosion. More evidence concerning these factors is desirable.

This phenomenon may be related to the "memory" effect noted by Thomas (13) where Zr specimens maintained a high corrosion rate after the corrosion temperature was lowered.

Acknowledgment

The authors are indebted to J. E. Draley for discussion relating to this work.

Manuscript received May 3, 1957. This paper was prepared for delivery before the Pittsburgh Meeting, Oct. 9-13, 1955. The work was performed under the auspices of the U. S. A. E. C.

Any discussion of this paper will appear in a Discussion Section to be published in the December 1959 JOURNAL.

REFERENCES

1. B. Lustman and F. Kerze, Jr., Editors, "The Metallurgy of Zirconium," Chapter 11, Corrosion of Zirconium and Its Alloys, McGraw-Hill Book Co., New York (1955).
2. J. Chirigos and D. E. Thomas, Proc. AEC Metallurgy Conf. March 1952, p. 337, Report TID-5084.
3. R. D. Misch, Unpublished research.
4. G. V. Akimov and G. B. Clark, *Trudy Inst. Fiz. Khim., Akad. Nauk SSSR*, **4**, Issledovaniya Korrozii Metallov. No. 3, 3 (1952).
5. R. H. Savage and D. G. Flom, *Ann. N. Y. Acad. Sci.*, **58**, 946 (1954).
6. J. J. Polling and A. Charlesby, *Proc. Phys. Soc. (London)*, **67B**, 201 (1954).
7. Ragnar Holm, "Electric Contacts," Hugo Gebers Forlag, Stockholm (1946).
8. J. P. Pemsler, U.S.A.E.C. Report NMI-1177 May 31, 1957; also *This Journal*, **105**, 315 (1958).
9. T. J. Gray, "The Defect Solid State" Interscience Publishers, Inc., New York (1957).
10. L. Young, *Trans. Faraday Soc.*, **51**, 1250 (1955).
11. R. D. Misch, *Acta Met.*, **5**, 179 (1957).
12. W. Jost, "Diffusion in Solids, Liquids, Gases," Academic Press, New York (1952).
13. D. E. Thomas and S. Kass, *This Journal*, **103**, 478 (1956).
14. A. Charlesby, *Acta Met.*, **1**, 340 (1953).

The Structure of Electro-Deposited Nickel

B. C. Banerjee and A. Goswami

National Chemical Laboratory, Poona, India

ABSTRACT

An electron diffraction study was made on the crystal structure, orientation, and mode of growth of nickel deposits from sulfate-chloride-boric acid and chloride-boric acid baths under various bath conditions. The effect of *p*H, temperature, concentration, current density, mechanical stirring, etc., and of additions such as hydrogen peroxide, nickel nitrate, and sodium chloride was investigated on polycrystalline substrates. Depending on bath conditions various preferred orientations (one-degree), mixed or otherwise, were developed and their causes have been discussed in detail. These have been correlated also with the mode of cathodic crystal growth process.

It has been shown previously that the crystal structure and orientations of electrodeposited nickel are profoundly affected by the bath conditions (1-5). In what follows an account is given of a comparative survey of the crystal orientations in deposits from nickel chloride and sulfate-chloride baths as commonly used in industrial plating.

Experimental

In order to restrict the substrate influence on crystal size and orientation of electrodeposits, mechanically polished brass disks (70:30) of about 3.0 cm^2 significant area were used as cathodes, the nonsignificant portions being covered with collodion. Compositions of the baths were: (*a*) $NiSO_4 \cdot 7H_2O$ 280 g/l + $NiCl_2 \cdot 6H_2O$ 48 g/l + H_3BO_3 31 g/l; (*b*) $NiCl_2 \cdot 6H_2O$ 150 g/l + H_3BO_3 31 g/l; (c) $NiCl_2 \cdot 6H_2O$ 280 g/l + H_3BO_3 31 g/l; and (*d*) $NiSO_4 \cdot 7H_2O$ 280 g/l + H_3BO_3 31 g/l. The chemicals used were of AR or CP quality. The above solutions were purified and adjusted to desired *p*H values in the manner described previously (3). Unless otherwise stated, the current density employed was 10 ma/cm^2, and the solutions were unstirred. When stirring was resorted to, the sweep of the glass propeller was close to the cathode surface.

After electrodeposition, the specimens were washed thoroughly with distilled water, with alcohol, and then immediately examined in a Finch-type electron diffraction camera (6) working with 45-65 kv electrons, the camera length being about 50 cm. The lattice parameter of the deposit was determined by dusting graphite powder over the specimens and using $11\bar{2}0$ ring of graphite ($d_{11\bar{2}0} = 1.230$Å) as the internal standard. Since the reflection technique was used, the diffraction of electrons was due to the top surface layers only. In order to study the change of surface structure with time of deposition, specimens were examined by electron diffraction at various deposit thicknesses.

The deposition was carried out to well beyond the stage where the polycrystalline deposits had developed preferred orientations (one-degree). By preferred orientation, it is meant that the polycrystalline deposits had a common lattice row normal to the deposit surface, or in other words had a common lattice plane parallel to the deposit or substrate surface. The orientation plane is generally indicated by {hkl}.

Results

The appearance of nickel deposits varied from semibright and dull matte to dark gray or even black, depending on the deposition conditions. Pitting and pinholes were observed in deposits formed under the conditions giving rise to profuse hydrogen evolution. Electron diffraction studies of the cathode surface revealed that the deposits were initially polycrystalline but randomly disposed; with increasing thickness, the deposits developed one degree orientations determined by bath conditions. The lattice constant of the coatings ($a_o = 3.543$Å) was found to be similar to that of f.c.c. nickel (7). Occasionally, however, hexagonal form of nickel

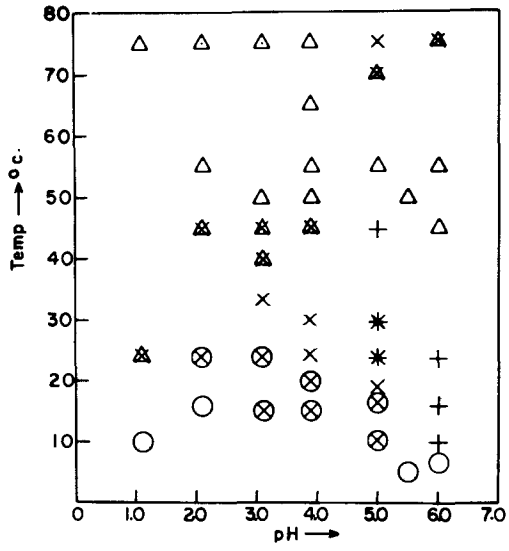

Fig. 1. Change in orientations of nickel deposits with pH and temperature; bath (a). × means {100} orn; △ means {110} orn; + means {211} + {10$\bar{1}$0} orn; O means {210} orn.

(7) also appeared along with the f.c.c. structure. The results are shown in Fig. 1-7.

Influence of Various Factors

pH and temperature.—It will be seen from Fig. 1-3 that, with increasing bath temperature, the orientations changed eventually from {210} (○) to {110} (△) irrespective of *p*H values. At an intermediate range, however, depending on *p*H and bath composition, {100} (×) and a mixed {211} + {10$\bar{1}$0}$_{hex}$ (+) orientations were generally observed.

Metal ion concentration.—The orientations of the deposit crystals were also influenced by metal ion concentrations. Baths (*a*) and (*b*) under different *p*H conditions were diluted in the ratio of 1:1, 1:3, and 1:9 maintaining the *p*H in each case the same as that of the undiluted bath. Thus with gradual dilution, the initial {211} + {10$\bar{1}$0}$_{hex}$ (+) orientations changed to {100} (×) and finally to {110} (△)

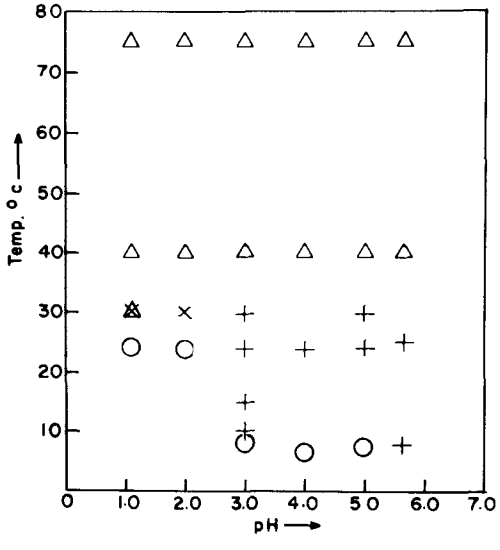

Fig. 2. Change in orientations of nickel deposits with pH and temperature; bath (b). Symbols have same meaning as in Fig. 1.

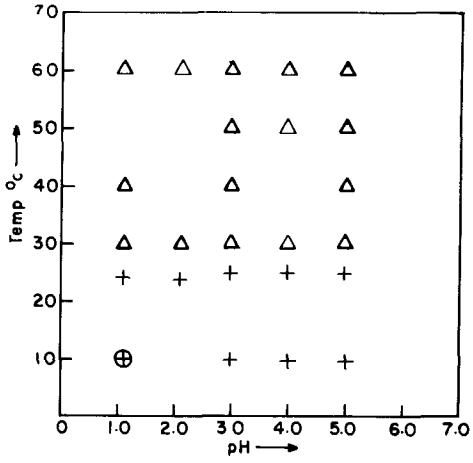

Fig. 3. Change in orientations of nickel deposits with pH and temperature; bath (c). Symbols have same meaning as in Fig. 1.

as can be seen from Fig. 4. Similar results were also obtained even when the concentration of boric acid was maintained to 31 g/l in the diluted baths. This suggests that boric acid content has no significant effect on the orientations of nickel deposits.

Oxidizing agents.—The addition of hydrogen peroxide or nickel nitrate to the baths suppressed pitting of deposits and also affected the crystal orientations (Fig. 5a and 5b). Addition of hydrogen peroxide (≅1 g/l) resulted in the {210} orientation (○) gradually changing to {100} (×) or {211} + {10$\bar{1}$0}$_{hex}$ (+) at all *p*H ranges and at temperatures up to 35°C. At higher temperatures, however, hydrogen peroxide decomposed without oxidizing hydrogen evolved at the cathode, and no further change in orientation was observed. With further increase in hydrogen peroxide concentration, the crystal orientations changed to {110} (△) (Fig. 5a). If the concentration of hydrogen peroxide was still further increased, the deposits became rough and were often covered with basic nickel salts.

Nickel nitrate (about 0.8 g/l), on the other hand, favored {110} (△) orientation of the deposit crystals under conditions which would otherwise have developed {210} (○), {100} (×), or {211} + {10$\bar{1}$0}$_{hex}$ (+) orientations (Fig. 5b).

Mechanical stirring.—Stirring of the solutions affected the crystal orientation by reducing the con-

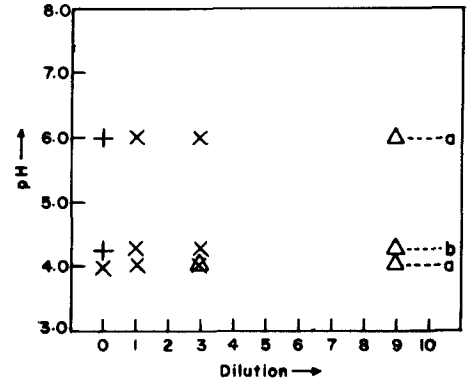

Fig. 4. Change in orientations of nickel deposits with dilution and pH; baths (a) and (b). Symbols have same meaning as in Fig. 1.

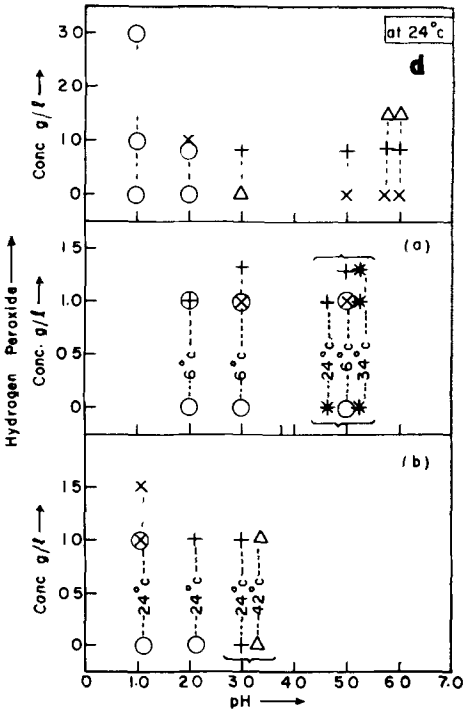

Fig. 5. (a) Change in orientations of nickel deposits with hydrogen peroxide and pH; bath (a), (b), and (d); Fig. 5 (b). With nickel nitrate. Symbols have same meaning as in Fig. 1.

centration gradient in the catholyte layer and possibly also by facilitating the removal of hydrogen from the cathode surface. Thus, instead of the {210} (○) orientation of the deposit-crystals favored at a low temperature in a still bath, a mixture of {210} (○) and {100} (×) orientations occurred at 250 rpm and, finally, {211} + $\{10\bar{1}0\}_{hex}$ (+) orientations at about 1000 rpm (Fig. 6). Similarly, instead of the {110} (△) orientation normally developed at 55°C in an unstirred bath, a {100} (×) orientation appeared at 300 rpm. Mechanical stirring, however, did not affect the continued development of {100} (×) or {211} + $\{10\bar{1}0\}_{hex}$ (+) orientations when the unstirred were favorable to the formation of these orientations.

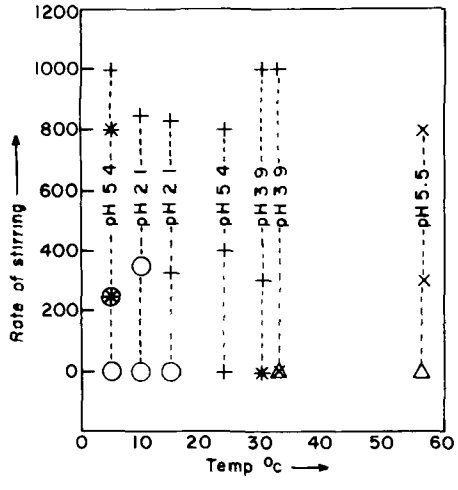

Fig. 6. Change in orientations of nickel deposits with rate of stirring and temperature; bath (a). Symbols have same meaning as in Fig. 1.

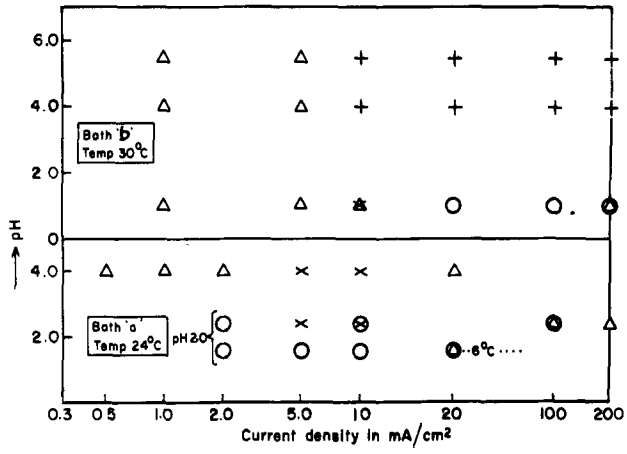

Fig. 7. Change in orientations of nickel deposits with current density and pH; baths (a) and (b)

Current density.—The effect of current density on the deposition of nickel is very interesting. It may be seen (Fig. 7) that except at low temperature, the deposits developed {110} (△) orientation in the lower current density range. At an intermediate range of current density, however, either {100} (×) or {211} + $\{10\bar{1}0\}_{hex}$ (+) orientations were favored. At a still higher current density {110} (△) orientation was developed sometimes accompanied by {210} (○) orientation, especially at low pH ranges. In bath (c), however, lateral {100} (×), {211} + $\{10\bar{1}0\}_{hex}$ (+) types of deposits were always obtained, even at a current density as high as 200 ma/cm^2.

Chloride ion concentration.—An increase in the chloride ion concentration in the bath generally favored {211} + $\{10\bar{1}0\}_{hex}$ (+) orientations in place of {100} (×) and the bath could tolerate a higher current density range than the usual. Figure 8 shows typical {211} + $\{10\bar{1}0\}_{hex}$ orientations of the deposit crystals.

Discussion

The mode of cathodic crystal growth and its influence on the orientation of the resulting deposits have recently been discussed by Finch and coworkers (1, 2) and ourselves (3-5, 8). The orientations developed in electrodeposits are determined primarily by the growth process of the deposits. The chief factors controlling the process are: (*a*) rate of supply of cations through the diffusion layer to

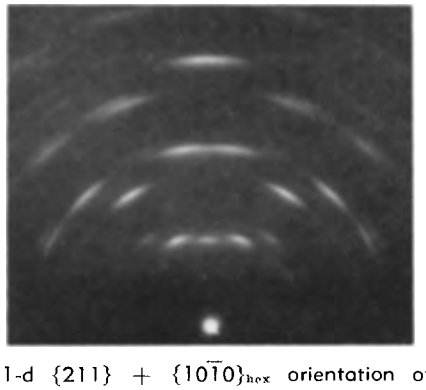

Fig. 8. 1-d {211} + $\{10\bar{1}0\}_{hex}$ orientation of nickel deposits.

the cathode; (*b*) rate of discharge of cations; (*c*) thickness of the diffusion layer; and (*d*) formation of films near the cathode surface region. Any change in the deposition conditions may materially affect one or more of the above factors determining the over-all deposition process and thus modify the orientation of the deposited crystals. When the rate of supply of metal ions to the catholyte is plentiful compared with the rate of their discharge, the deposits grow laterally with a densely packed plane lying parallel to the substrate surface. On the other hand, when the rate of supply of cations at the cathode is inadequate, resulting in an impoverishment of metal ions at the catholyte, the deposit-crystals grow outward in such a way that a densely packed atom row is normal to the cathode surface. In the case of nickel {111}, {100} (×), and also {211} + $\{10\bar{1}0\}_{hex}$ (+) orientations, as recently shown by Goswami (8), are characteristics of lateral growth-deposits whereas {110} (△) indicates an outgrowth mechanism.

Other orientations also may develop due to factors which come into play during deposition. The appearance of {210} (○) orientation, for instance, seems to be associated with the adsorption or otherwise of hydrogen, presumably atomic, by the deposits which are known to be in a highly active condition when freshly deposited (9). This is evident from the change of orientation from {210} (○) to {100} (×) or $\{10\bar{1}0\}_{hex}$ and {211} (+) effected by the addition of hydrogen peroxide to the bath (Fig. 5a). The rate of discharge of hydrogen ions at the cathode will be increased due to the oxidation of atomic hydrogen to water molecules in the presence of hydrogen peroxide. This will, no doubt, facilitate the formation, precipitation, and occlusion on the cathode surface of colloidal nickel hydroxides or basic salts, thus reducing the effective metal ion concentration in the catholyte and favoring an outgrowth mechanism.

Nickel nitrate influences the orientation of the deposits in a different manner. Hydrogen, atomic or molecular, formed at the cathode reduces the nitrate in its immediate vicinity finally to ammonia which in turn forms nickel ammonium complexes. The effective metal ion concentration thus reduced should favor outgrowth.

Mechanical stirring, as has been mentioned before, reduces the thickness of the catholyte layer and maintains metal ion concentration at the cathode surface region; hence orientations of the deposits tend to be characteristic of the lateral growth. By disturbing the adsorption of hydrogen at the cathode, mechanical agitation also reduces and ultimately eliminates pitting pinholes in the deposit surface.

When a bath is much diluted, the effective metal ion concentration is low and hence the deposits are of outgrowth type as has been experimentally observed by us.

The effect of temperature on the crystal is peculiar. A higher temperature should increase the mobility of the ions and at the same time reduce the thickness of the diffusion layer. Normally this should favor lateral growth-deposits. On the other hand, our experimental results show that higher temperatures favor outgrowth-deposits at all *p*H conditions excepting in bath (*a*) at 75°C at *p*H 5.0. This may be due to the increased rate of hydrolysis of the nickel salts with the rise of bath temperature. It is well known that nickel salts hydrolyze to hydroxides or basic salts when the *p*H of the solution is appropriate at room temperature and this is increased still more at higher temperatures. This leads to outgrowth-deposit.

The effect of high current density is generally to increase the rate of discharge of metal ions at the cathode without a corresponding increase in their rate of supply to cathode surface region, thereby causing an impoverishment of cations at the cathode surface and thus favoring outgrowth. The formation of lateral-growth deposits at an intermediate current density range may also be similarly understood. A very peculiar observation, as mentioned before, was the development of {110} (△) orientation at very low current densities. This cannot be explained easily. The effect of current density and temperature will be discussed in a separate paper.

An increase in chloride ion concentration generally induces crystal twinning and ultimately results in a new orientation. This has recently been studied in detail on single-crystal substrates. The development of {211} + $\{10\bar{1}0\}$ (+) orientation in the concentrated chloride bath can thus be easily understood, but it is not yet clear why chloride ions should favor twinned structures. However, it is known that these ions are adsorbed more easily by the cathode surface than the bivalent sulfate ions (12), and hence it may be possible that they influence the potential energy configuration of the substrate surface, thereby inducing a twinned structure on the deposits.

Acknowledgment

The authors' thanks are due to Professor G. I. Finch and Dr. A. B. Biswas for their keen interest in the work.

Manuscript received April 11, 1957.

Any discussion of this paper will appear in a Discussion Section to be published in the December 1959 JOURNAL.

REFERENCES

1. G. I. Finch, H. Wilman, and L. Yang, *Disc. Faraday Soc.*, **1**, 144 (1947).
2. G. I. Finch and D. N. Layton, *J. Electrodepositors Tech. Soc.*, **27**, 215 (1951).
3. B. C. Banerjee and A. Goswami, *J. Sci. Industr. Res.*, **14B**, 322 (1955).
4. B. C. Banerjee and A. Goswami, *ibid.*, **16B**, 144 (1957).
5. A. Goswami, *ibid.*, **16B**, 315 (1957).
6. G. I. Finch and H. Wilman, *Ergeb. exakt. Naturwiss.*, **16**, 353 (1937).
7. W. R. A. Wycoff, "Crystal Structure," Interscience Publications, New York (1957).
8. A. Goswami, *J. Sci. Industr. Res.*, **15B**, 322 (1956).
9. C. C. Roth and H. Leidheiser, *This Journal*, **100**, 553 (1953).
10. A. W. Hothersall and R. A. F. Hammond, *Trans. Faraday Soc.*, **30**, 1079 (1934).
11. D. J. Macnaughton, G. E. Gardam, and R. A. F. Hamond, *ibid.*, **29**, 729 (1933).
12. J. Heyrovsky, *Disc. Faraday Soc.*, **1**, 212 (1947).

The System ZnO-CdO-B_2O_3, Phase Relationships, and Fluorescence

D. E. Harrison

Luminescent Materials Laboratory, Lamp Wire and Phosphors Department, General Electric Company, Cleveland, Ohio

and

F. A. Hummel

Department of Ceramic Technology, The Pennsylvania State University, University Park, Pennsylvania

ABSTRACT

The subsolidus phase relationships were investigated using x-ray and petrographic methods. Two compounds were isolated: $2ZnO \cdot CdO \cdot B_2O_3$ which fuses at about 860°C and $ZnO \cdot 2CdO \cdot 2B_2O_3$ which melts congruently at 797° ± 3°C. Excitation by either 2537Å or cathode rays produces a maximum orange (6200Å) fluorescence in $2ZnO \cdot CdO \cdot B_2O_3$ with 0.004 wt % Mn and a maximum red (6400Å) fluorescence in $ZnO \cdot 2CdO \cdot 2B_2O_3$ with 0.080 wt % Mn. The fluorescence of $ZnO \cdot 2CdO \cdot 2B_2O_3$ was examined using Ag, Sn, Tl, Pb, and Sb as single activators as well as sensitizers with Mn.

Ohno (1) claimed a region of manganese activated zinc-cadmium borate compositions which when blended with $MgWO_4$ yielded a white fluorescent substance. Interest in the zinc-cadmium borate component and the lack of any phase data in this ternary system stimulated the present investigation.

The study was limited to the determination of compatibility triangles, isolation of compounds, and examination of the fluorescence of certain compositions with various activators.

Experimental Procedure

Mallinckrodt reagent-grade boric acid and cadmium carbonate, and New Jersey Zinc Company U.S.P. zinc oxide were used as starting materials. Reagent-grade $MnSO_4$, $Mn(NO_3)_2$, $AgNO_3$, Tl_2CO_3, $Pb(NO_3)_2$, SnO_2, or Sb_2O_3 were used as activators.

The ingredients were ground in an agate mortar with acetone until dry. Calcines were prepared in platinum crucibles at temperatures ranging from 700° to 900°C for periods from 8 to 48 hr.

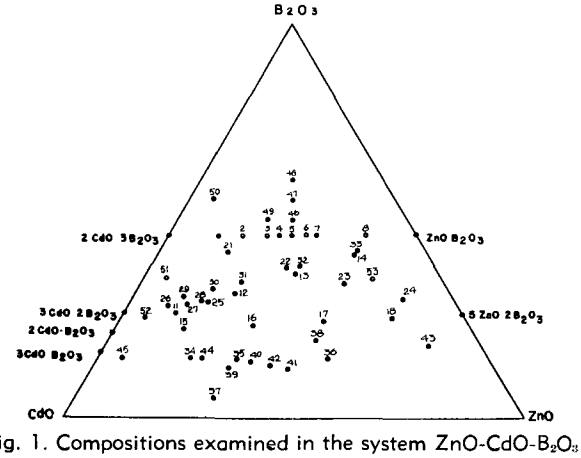

Fig. 1. Compositions examined in the system ZnO-CdO-B_2O_3

X-ray data were obtained from Norelco and General Electric recording spectrometers using $Cu_{K\alpha}$ radiation (λ = 1.537Å) filtered with nickel.

The immersion technique was used to determine the refractive indexes of crystals to an accuracy of ±0.002, using white light and index oils which were calibrated with an Abbe refractometer.

Differential thermal analysis (DTA) data were obtained with automatically recording apparatus described by Gruver (2).

Emission curves were obtained with an automatically recording General Electric spectroradiometer. Visual examinations were made under 2537Å, 3650Å, and cathode-ray excitation.

Compositions.—The compositions examined are listed in Table I and are shown graphically in Fig. 1.

Experimental Results and Discussion

Phase relationships.—The compatibility triangles were determined by comparing the x-ray data of ternary compositions with the data for binary compounds in the systems CdO-B_2O_3 and ZnO-B_2O_3 as reported by Subbarao and Hummel (3) and Harrison and Hummel (4), respectively.

Two new ternary compounds were discovered and individually prepared, and the compatibility triangles were determined as shown in Fig. 2. An unidentified phase is situated in the subtriangle $3CdO \cdot B_2O_3$-$2ZnO \cdot CdO \cdot B_2O_3$-$ZnO$, but its exact composition is not readily discernible because of the extensive solubility of $3CdO \cdot B_2O_3$ and ZnO in $2ZnO \cdot CdO \cdot B_2O_3$.

Table I. Composition of ZnO-CdO-B_2O_3 mixtures

No.	Molar composition ZnO	CdO	B_2O_3
1	1.00	2.61	4.91
2	1.00	1.51	3.26
3	1.00	0.97	2.46
4	1.00	1.24	2.16
5	1.00	0.65	1.97
6	1.00	0.53	1.80
7	1.00	0.43	0.89
8	1.00	0.16	1.24
9	1.00	—	1.00
10	—	1.00	0.50
11	1.00	3.71	2.86
12	1.00	1.39	0.92
13	1.00	0.62	0.71
14	1.00	0.23	1.12
15	1.00	2.68	1.74
16	1.00	0.99	0.90
17	1.00	0.45	0.62
18	1.00	0.17	0.62
19	1.00	—	0.40
20	—	1.00	1.50
21	1.00	1.88	3.22
22	1.00	0.70	1.47
23	1.00	0.31	0.87
24	1.00	0.12	0.58
25	1.00	2.00	2.00
26	1.00	4.71	3.81
27	1.00	2.91	2.61
28	1.00	2.23	2.21
29	1.00	3.17	3.31
30	1.00	2.01	2.34
31	1.00	1.29	1.86
32	1.00	0.58	1.39
33	1.00	0.22	1.14
34	1.00	2.06	0.87
35	1.00	1.16	5.83
36	1.00	0.44	0.35
37	1.00	1.37	0.20
38	1.00	0.50	0.50
39	1.00	1.25	0.50
40	1.00	0.94	0.47
41	1.00	0.67	0.33
42	1.00	0.80	0.40
43	1.00	0.10	0.30
44	1.00	1.75	0.75
45	1.00	10.21	3.52
46	1.00	0.64	2.34
47	1.00	0.63	2.86
48	1.00	0.63	3.50
49	1.00	1.00	3.00
50	1.00	5.11	12.95
51	1.00	7.66	8.25
52	1.00	8.93	5.89
53	1.00	0.19	0.82
54	—	1.00	0.67
55	—	1.00	0.33

The compound 2ZnO:CdO:B_2O_3 (2:1:1) is biaxial negative with a very small 2 v angle and R.I. of $n_\alpha = 1.709$, $n_\beta > 1.79$, $n_\gamma > 1.79$. Because of the difficulty in obtaining this composition as a glass, neither the nature of the fusion nor the exact melting temperatures could be determined by the conventional quench technique. However, DTA revealed an endothermic peak at 860°C at which temperature the sample fused. X-ray examination of 2:1:1 after firing at various temperatures supported the DTA data that no polymorphs existed between 100°C and the fusion temperature. A characteristic x-ray pattern is given in Table II.

Crystals of the compound ZnO:2CdO:$2B_2O_3$ (1:2:2) remained too small, even after prolonged heat treatment, to determine their optical properties accurately. However, 1:2:2 exhibited high birefringence with maximum and minimum R.I. of about 1.78 and 1.75, respectively. The 1:2:2 compound melts congruently at 797° ±3°C and it has no polymorphs between 100°C and its fusion temperature. A characteristic x-ray pattern is given in Table II.

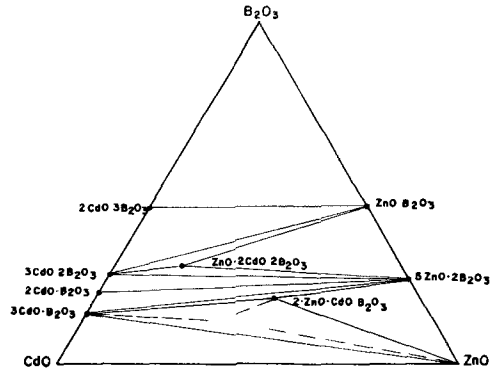

Fig. 2. Compatibility triangles in the system ZnO-CdO-B_2O_3

With the exception of the subtriangle $3CdO\cdot B_2O_3$-$2ZnO\cdot CdO\cdot B_2O_3$-ZnO, petrographic and x-ray data revealed no extensive solid solution in the ternary system. The compound 1:2:2 gave no evidence of solid solubility between it and compatible phases.

Fluorescent studies.—The compounds 2:1:1 and 1:2:2 were prepared with various Mn concentrations. Excitation by either 2537Å or cathode rays, but not 3650Å, gave an orange (6200Å) fluorescence in 2:1:1 and a red (6400Å) fluorescence in 1:2:2. Variation in Mn concentration in either 2:1:1 or 1:2:2 affected the fluorescent intensity, but it did not produce any noticeable shift in the emission

Table II. Characteristic x-ray patterns

$2ZnO\cdot CdO\cdot B_2O_3$ d	I/I_o	$ZnO\cdot 2CdO\cdot 2B_2O_3$ d	I/I_o
4.21	40	9.12	20
3.39	5	5.31	25
3.23	5	4.48	50
3.11	5	4.42	10
2.93	100	3.36	30
2.32	20	3.25	30
2.67	20	3.21	25
2.61	10	3.07	55
2.51	10	3.02	60
2.48	15	2.98	85
2.40	55	2.87	55
2.34	10	2.71	100
2.08	15	2.64	30
2.04	15	2.51	15
1.855	40	2.41	5
1.834	20	2.38	20
1.734	5	2.24	5
1.678	5	2.20	15
1.629	10	2.12	15
1.575	10	2.08	20
1.556	15	2.04	15
1.469	25	1.953	35
1.459	10	1.845	10
1.389	10	1.824	15
1.318	5	1.790	10
1.293	5	1.771	5
1.247	5	1.749	10
1.203	5	1.722	25
1.148	5	1.689	25
1.112	5	1.680	10
		1.626	10
		1.600	10
		1.556	15
		1.506	10
		1.465	10
		1.423	5
		1.388	5

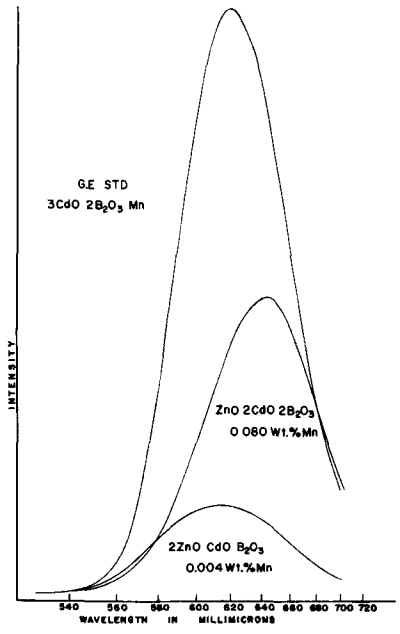

Fig. 3. Spectral distribution and relative intensities excited by 2537Å radiation.

spectrum. Optimum brightness occurred at 0.004 wt % Mn in 2:1:1 and at 0.080 wt % Mn in 1:2:2. Manganese concentrations in the range 1 to 5 ppm were sufficient to activate either 2:1:1 or 1:2:2. However, decreasing fluorescent brightness with decreasing Mn concentration indicates that the pure compounds are not luminescent. The small amounts of Mn necessary to activate the ternary compounds did not appear to introduce new phases.

Spectral distributions of 2:1:1:Mn and 1:2:2:Mn compared to Std. G.E. $3CdO \cdot 2B_2O_3$:Mn using 2537Å excitation are shown in Fig. 3. The intensities are relative to Std. G.E. cadmium borate phosphor and thus give a comparison of absolute intensities obtained. Visual examination of the phosphors under cathode rays gave results comparable to those obtained by 2537Å excitation.

The rarity of red (6400Å) emitting borate phosphors directed attention to 1:2:2 as a possible matrix for other activators. These included Ag, Tl, Pb, Sn, and Sb as single activators, as well as sensitizers with Mn. Only one level of activator concentration at 0.1 wt % was investigated. Since the phosphors were prepared under oxidizing conditions, Sn^{4+} was probably the oxidation state involved.

After firing the singly activated 1:2:2 compositions at 700°-750°C for from 8 to 12 hr, visual examination with excitation by 2537Å, but not 3650Å, gave a weak red fluorescence. The sample prepared without the addition of an activator remained dead after this heat treatment.

When viewed through a Corning No. 2418 red filter, the Tl addition showed the greatest brightness followed in order of decreasing brightness by Sb, Ag, Pb, and Sn additions. Only the Pb-activated phosphor showed a blue band in addition to the weak red band when viewed through a Corning No. 5850 blue filter.

Increasing the firing temperature to values close to the melting temperature of 1:2:2 (797° ±3°C) produced weak red fluorescence in the activated as well as the "nonactivated" phosphors.

Evidently the addition of Tl, Sb, Ag, Pb, or Sn sensitized the residual Mn present in the nonactivated material when the phosphor was prepared at the lower temperature. Also, the additive may have had a mineralizing effect on the phosphor matrix. With the exception of Pb none of these additions introduced emission bands of their own.

When either Tl, Ag, Sn, Pb, or Sb was used as a sensitizer with Mn, all at concentrations of 0.1 wt %, and when the compositions were fired at 700°-750°C for from 8 to 12 hr, excitation by 2537Å or cathode rays, but not 3650Å, produced a bright red fluorescence. Mn + Tl and Mn + Ag additions were brighter and exhibited much shorter afterglows than did Mn additions alone. Thus an Mn + Tl activated 1:2:2 composition fired at 700°-750°C was as bright as a phosphor activated with Mn alone and fired close to the melting point. When viewed through a Corning No. 2418 red filter, Mn + Tl addition showed the greatest brightness followed in order of decreasing brightness by Mn + Ag, Mn alone, Mn + Sn, Mn + Pb, and Mn + Sb additions. None of these phosphors showed a blue component when examined through a Corning No. 5850 blue filter.

The differences in fluorescent brightness between the various additions became smaller as the firing temperature approached the melting point. However, the brightness did not exceed that produced by Mn + Tl at the lower temperature. Both the Mn + Tl and Mn + Ag additions exhibited shorter afterglows at the higher firing temperature than did Mn additions alone.

Manuscript received April 18, 1958. This paper was prepared for delivery before the New York Meeting, April 27-May 1, 1958. It is a part of a thesis submitted by D. E. Harrison in partial fulfillment of the requirements for the Ph.D. degree to The Pennsylvania State University; contribution No. 57-83 from the College of Mineral Industries, The Pennsylvania State University.

Any discussion of this paper will appear in a Discussion Section to be published in the December 1959 JOURNAL.

REFERENCES

1. Y. Ohno, Japanese Pat. No. 3354, Oct. 9, 1950; *C. A.*, 46: 9998d.
2. R. M. Gruver, *J. Am. Ceram. Soc.*, **31**, 323 (1948).
3. E. C. Subbarao and F. A. Hummel, *This Journal*, **103**, 29 (1956).
4. D. E. Harrison and F. A. Hummel, *ibid.*, **103**, 493 (1956).

Activation of ZnS and (Zn,Cd)S Phosphors by Gold and Other Elements

S. T. Henderson, P. W. Ranby, and Margaret B. Halstead

Thorn Electrical Industries, Ltd., Enfield, Middlesex, England

ABSTRACT

A study has been made of the spectral emission characteristics of zinc and zinc-cadmium sulfide phosphors, activated by gold and excited by long wave ultraviolet at 25° and —120°C. The positions and heights of the Gaussian sub-bands constituting the emission were examined and compared with those derived from the series activated by copper, silver, and chloride ("self-activated"). Copper and gold produce the most similar phosphors, with 3 sub-bands each; silver and chloride give 2 sub-bands, and resemble each other particularly in the effects associated with crystallographic change. Linear relations in the peak locations and an energy diagram are discussed. Other observations concern cathode-excitation, the effects of substituting selenium for sulfur, and a recently reported emission band of higher frequency.

The zinc and zinc cadmium sulfide phosphors have been investigated very extensively, especially with activation by Cu, Au, and Mn. There has been comparatively little interest in Au as the impurity metal, and it is remarkable that these sulfides are the only phosphors, so far as is known, which can be activated by Au. In the following a survey is given of work published hitherto on the subject.

Indications of ZnS:Au as a distinct phosphor began when a blue emission band was observed in a slightly different position from that of "unactivated" ZnS under excitation by ultraviolet (1, 2) or cathode rays (3). Since then a number of observations have been made on the emission peaks of ZnS with trivalent cations and variable Au content (4), and the cathodoluminescent efficiency of this material (5); on the emission shift due to incorporation of ZnO (6); and on the glow curve of ZnS:Au,Cl (7). More recently Arpiarian has used ZnS:Au to study intensification and killing effects produced by Fe, Co, and Ni (8), and Destriau has found that field-enhanced luminescence of (Zn,Cd)S:Mn under x-rays is improved by traces of Au in the phosphor (9).

The well-known (Zn,Cd)S series has received little attention in regard to activation by Au. This activator was mentioned by Leverenz as applicable to the (Zn,Cd)(S,Se) series but no emission data were quoted (10). Byler attempted to explain the effects of changing CdS content by assuming a set of emission bands in fixed positions and independent of the activator (Cu,Ag,Au, Mn, or none) (11). The most extensive investigation on record is concerned with developing a single phosphor of white cathodoluminescence, namely, (Zn,Cd)S:Ag,Au,Al; in this case the emission data for (Zn,Cd)S:Au were presented only as chromaticity plots (12).

There is no doubt that Au is a specific activator, although in the past the blue band it produces in ZnS has sometimes been mistaken for that in ZnS without added metal activator.

The present work is concerned primarily with the effects of activation by Au, but for comparison other better known activators also have been used. The properties of ZnS phosphors with the various activators and different preparative details are first considered, particularly with regard to the effects on emission band positions and intensities of changes of temperature or of crystal form. Next, phosphors in the (Zn,Cd)S series with the same activators are discussed, with special reference to the shift of the bands as the CdS content is changed. A search for regular progressions between different series with Cu, Ag, and Au activators has been unrewarding, although interesting comparisons between Cu and Au have emerged. The individual behavior of activators is in fact much more striking than their similarities.

It has been reported previously that the frequencies of emission band peaks in the (Zn,Cd)S series, under cathode-ray excitation, give closely linear plots against weight proportions of the matrix (3). This inexplicable relation applies reasonably well to most of the data in the present work, but the apparently more rational scale of molecular proportions has been used in the graphical presentation. Other variables have been plotted against peak band wave number; of these only the c_o dimension of the hexagonal lattice gave any approach to linearity.

Measurement and Presentation of Emission Spectra

In the present work long wave-length ultraviolet excitation has been used in the main, with a few observations made under cathode-ray excitation. Samples were generally contained in a brass cell with a quartz window for exposure to 125-w mercury arc lamps in Wood's glass bulbs. This excitation by the group of lines near 3650Å produced a phosphor brightness of the order of 0.25 to 0.5 stilb. For the experiments on cooled samples the powder was used in the apparatus shown in Fig. 1. This

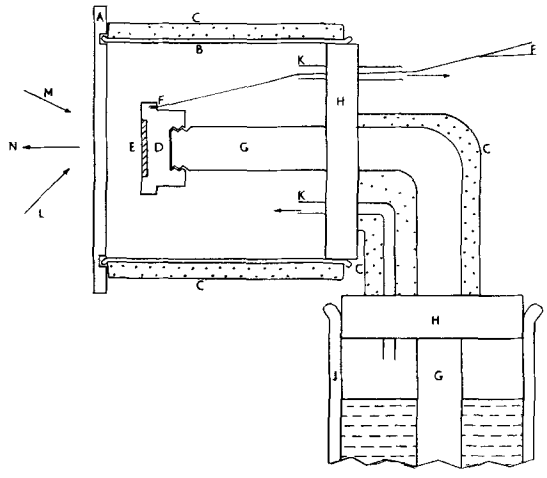

Fig. 1. Apparatus for excitation under ultraviolet at low temperature. A, Lucite plate; B, glass; C, asbestos and silica wool insulation; D, phosphor container detachable by screwing; E, phosphor compressed into cavity; F, thermocouple; G, copper rod; H, corks; J, Dewar flask of liquid oxygen; K, glass tubes for oxygen circulation; L, air stream to prevent condensation; M, ultraviolet beam; N, to spectrograph slit.

produced reasonably low phosphor temperatures without a vacuum enclosure, and condensation on the phosphor was prevented by a stream of evaporated oxygen.

Spectral emission curves were measured on a spectrophotometer previously described (13), with an exit slit width of 5Å at 4000Å and 42Å at 7000Å. Beyond the latter wave length the low sensitivity of the 1P22 photomultiplier and the background radiation from the mercury lamps made the measurements unreliable. Although wave lengths in the visible spectrum are more familiar than wave numbers and are largely used in the literature of phosphor emission bands, in the present work wave numbers have been used to permit analysis of the emission bands into Gaussian sub-bands. Therefore, emission curves are drawn with ordinates representing relative energy emitted per unit wave number interval instead of the usual energy per unit wave length interval. The Gaussian bands isolated from these curves were taken to be the ultimate components of the emission and were considered as the basic experimental data. This agreement of emission curves with a sum of Gaussians is of somewhat uncertain significance, but it provides a convenient method of analysis and presentation. Peak intensities of the bands have been examined in detail; band widths were found to be not very consistent, and therefore band areas (equivalent to energy) were not used.

ZnS with Au and Other Activators

Preparation.—Samples were prepared by mixing pure precipitated ZnS with aqueous solutions to give 5% by weight of chloride ion (added as an equimolecular mixture of sodium and magnesium chlorides) and 0.01% by weight of Au, Ag, or Cu, as chloride, nitrate, or sulfate, respectively. After drying, the finely powdered mixtures were heated in 100-g quantities for 1 hr at 1100°-1150°C in air in plugged silica tubes, then removed from the furnace to cool. The products were washed free from fluxes, dried, and sieved. Other phosphors were prepared in a precisely similar manner but omitting the heavy metal addition. Also, a few samples of cubic structure were made by firing at 800°C, and of partially cubic structure by firing at 1100°C in the presence of excess of S contained in the raw ZnS. Other workers have referred to ZnS with no other foreign ion than chloride as "self-activated," "zinc activated," or "unactivated." In the following the term "chloride activated" is used. The residual chloride in these materials is in fact of the usual order of activator proportions. The metal-activated phosphors also contain small amounts of chloride and are described as ZnS:Au,Cl, etc.

Emission characteristics.—When activated by Au instead of by Cu, Ag, or Cl, ZnS emits two closely overlapping bands with peaks about 600Å apart; these are of the same order of intensity when the excitation is by long wave-length ultraviolet. There is in addition a weaker band in the yellow region. The over-all effect is that the fluorescence is much paler than for the other phosphors examined and is of a light bluish green color, similar in hue to that of 80 mole % ZnS·20% CdS:Ag,Cl, or 85%ZnS·15%CdS:Cl, but less saturated (see Fig 2. and 3 for examples of emission curves).

Table I summarizes the average values for emission peak positions. Wave lengths are given to correspond to the wave numbers: it must be emphasized that such values are not really equivalent owing to the different shapes of the wave number and wave-length curves. Peak values read off directly from the latter curves are included for comparison.

Table II shows changes observed on cooling the samples during excitation. Details are included for preparations of similar composition but different crystal structure.

Table III summarizes changes at 25°C caused by these different structures.

For Table I accuracy is estimated at ±100 cm^{-1} except for the more uncertain bracketed values. The

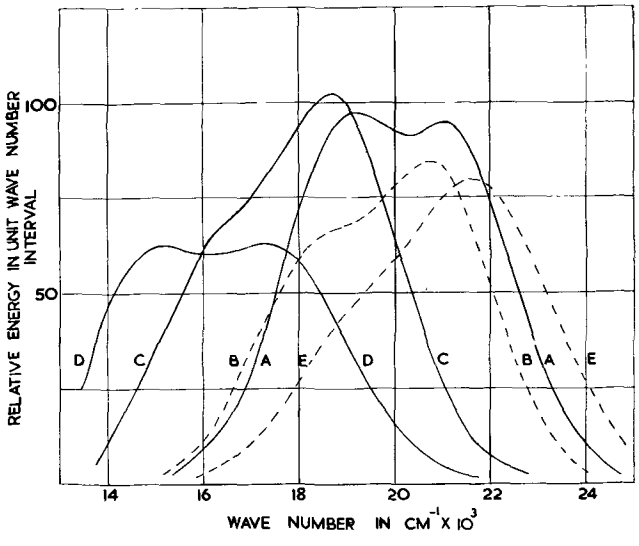

Fig. 2. Spectral emission of Au activated phosphors at 25°C. A, B, C, D: 0, 2.7, 16.5, 30 mole % CdS, respectively. E: 0% CdS, cathode-ray excitation.

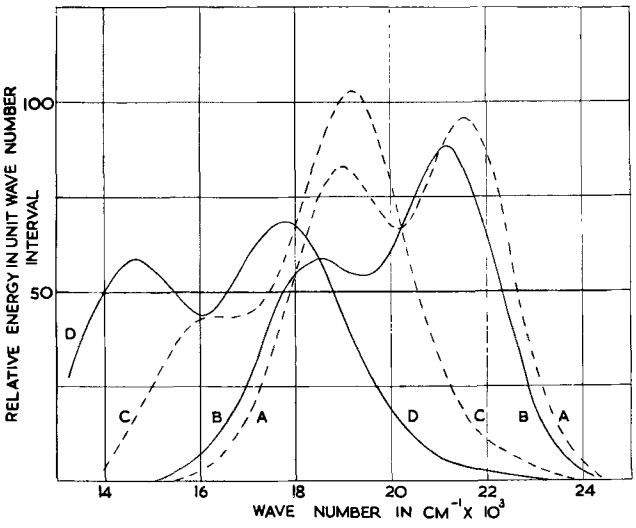

Fig. 3. Spectral emission of Au activated phosphors at —120°C. A, B, C, D: 02.7, 16.5, 30 mole % CdS, respectively.

convention adopted is to number the bands in order from the blue end of the spectrum, as Au I, II, etc. A band appearing only at low temperature is not included in this scheme (see Discussion).

Band peak positions.—The most interesting feature is the similarity between Au and Cu as activators. The well marked shifts to increased wave number on cooling and the contrary effect observed for ZnS:Cl agree with the findings of Tomlinson for his "self-blue" and "Cu-blue" bands (14) and of Shrader and Larach for their blue bands in ZnS:I, ZnS:Cu,I, and ZnS:Ag,halide (15).

For ZnS:Ag,Cl there is a small increase of wave number in Ag I on cooling. This places Ag with Cu and Au, as chemical considerations would suggest. Silver activation however is known to show anomalous behavior compared with Cu and Cl when ultraviolet excitation of cubic samples is changed to cathode-ray excitation (3). Other unusual effects have been described also for Ag in (Zn,Cd)S (16). To summarize present information on this topic:

(*A*) Cu, Ag, and Au at about 0.01% concentration and with Cl also, in cubic or hexagonal ZnS under ultraviolet, produce an increase of wave number on cooling, and Cl alone shows the reverse effect.

(*B*) A change to cathode-ray excitation increases wave number for Cl and Cu,Cl (cubic), and Au,Cl (hexagonal), but the reverse is true for Ag,Cl (cubic).

(*C*) Under cathode-ray excitation, cooling increases wave number for Cu,Cl (cubic), and decreases it for Ag,Cl and for Cl (cubic). It appears that it would be worth-while to pursue such measurements in the hope of correlating some of the variables.

Of the small bands isolated, Ag II and Cl II have not been reported before, while Cu III is probably the yellow band at 5800Å described by Froelich, but not the red band at 6700Å which moves to a lower wave number on cooling (17, 18).

Most of the samples considered in this paper were entirely hexagonal in structure. Table III shows considerable shifts of bands to lower wave numbers for cubic forms of ZnS with metal activators, and for a ZnS:Cl with about 50% cubic structure. Shifts of —400 to —600 cm^{-1} have been reported for this crystallographic change in ZnS:Cl, ZnS:Cu,Cl, and ZnS:Ag,Cl (19). The changes mentioned in this paragraph are all for excitation at room temperature; cooling introduces more complications.

Relations between band peak intensities.—The relative heights of the peaks vary with method of preparation of the phosphor, and with temperature of excitation. In almost every case the ratio of blue Au I to green Au II is increased by cooling to —120°C, that is, the green band is suppressed, as with Cu II. Another similarity to Cu is provided by an increase of the green band with more Au.

Modifications of the phosphor preparation, using several rates of cooling graded from instantaneous quenching in water to 16 hours' cooling in the furnace, made a progressive increase of Au II at the expense of Au I as the cooling became faster, and the more so for higher initial firing temperature.

Table I. Positions and ratios of peak intensities of component bands of ZnS: ultraviolet excitation at 25°C. Alternative values are for different samples. Cl is present in all samples

	Au (hex)	Au (cub)	Cu (hex)	Cu (cub)	Ag (hex)	Ag (cub)	Cl (hex)	Cl*
Band I	21150	20700	22400	21700	22900	22100	22250	21650 cm
II	18550	18000	19250	18750	21000	20000	(19500)	(19100)
III	(16950)	(16500)	(17000)	(17200)				
Band I†	4730	4830	4460	4610	4370	4520	4490	4620Å
II	5390	5560	5190	5330	4760	5000	5130	5240Å
III	5900	6060	5880	5810Å				
Main peak‡ (wave length)	4710	4800	5150	5300	4350	4500	4460	4580Å
Ratio of peak energy								
I : II	1.2,1.4	1.7	0.13,0.11	0.16,0.15	6.1,9.9	7.4	8.8,9.9	9.4,9.0
I : III	9.3,6.7	16.8	4.5,2.9					

* 50:50 cubic:hexagonal.
† By direct conversion from the wave number data above.
‡ From wave-length emission curves.

Table II. Shifts of component bands of ZnS and peak intensity changes by cooling from 25° to −120°C (±10°). Separate results shown for 0.01% hexagonal are from different samples

Activator	% Metal activator	Crystal structure	Shift of peak in cm^{-1}			Change in peak intensity ratio	
			Band I	Band II	Band III	I:II	I:III
	0.01	Hex	+350	+200	+400	1.20–1.22	9.3–8.7
			+340	+170	+250	1.41–1.55	6.7–10.0
		Cub	+125	+200	+150	1.7–1.7	16.8–17.6
Au,Cl	0.002	Hex	+160	+170	+250	2.55–2.23	11.1–15.6
	0.1	Hex	~ 0	~ 0		0.48–0.81	
	0.01	Hex	+225	+100	+800	0.13–0.20	4.5–3.0
			+230	+ 85	+600	0.11–0.19	2.9–2.9
Cu,Cl		Cub	+375	+ 80	+175	0.16–0.22	1.25–2.4
	0.01	Hex	− 10				
			+140				
			+100				
Ag,Cl		Cub	+150				
	(~0.01 Cl)	Hex	−250				
			− 80				
Cl		50:50 Cub-hex	−175				

Quenching also produced unusual results on the positions of Au I and II when the phosphor was excited at −120°C. The hexagonal form showed small or no shifts compared with excitation at room temperature, while the cubic suffered wave number decreases of 200-300 cm^{-1} instead of the "normal" increases given in Table II.

Cathodoluminescence.—A few phosphors were examined when scanned by a defocused spot at 14 kv and 3 μa/cm^2. This produced an approximate doubling of the blue band at the expense of the others. Of the ZnS:Au,Cl samples, those with 0.01% Au showed shifts of all three bands, to wave numbers higher by 100-450 cm^{-1}, compared with ultraviolet excitation (see Fig. 2 for an example).

Selenium replacement in ZnS.—When Se replaces increasing proportions of S in ZnS:Au,Cl, phosphors result which resemble the (Zn,Cd)S:Au,Cl series under ultraviolet. The color changes are produced in part by the suppression of Au I and in part by shifts in the positions of Au I and II which are smaller than those found with equivalent substitution of CdS. For instance, a sample containing 27.6% of ZnSe has an emission curve which is nearly a pure Gaussian of Au II, peak 17875 cm^{-1}, and with a visual color close to that of (Zn,Cd)S:Au,Cl containing 20% CdS. At −120°C the Au I band is largely restored in relation to Au II for those phosphors with smaller ZnSe contents.

Table III. Shifts of component bands of ZnS at 25°C by change from hexagonal to cubic structure

	Band I	Band II	Band III
0.01% Au,Cl	−450	−550	−450 cm^{-1}
0.1% Au,Cl	−400	−350	
0.01% Ag,Cl	−800	−1000	
0.01% Cu,Cl	−700	−500	+200
Cl (50% cubic)	−600	−400	

(Zn,Cd)S Series with Au and Other Activators

Au *activator: preparation, composition, and spectral characteristics.*—Samples were prepared by the general method described above, replacing proportions of ZnS in the initial mixture by an equal weight of precipitated CdS, usually in multiples of a nominal 10% by weight of ZnS up to 80% CdS. The percentages of ZnS and CdS in the phosphors were determined by analysis involving the initial removal of Cd by precipitation with phenyl trimethyl ammonium iodide; the Zn was then precipitated by 8-hydroxyquinoline, followed by the standard volumetric estimation. The precipitated Cd was determined volumetrically by iodate. In the text and figures percentages of CdS given are molecular values unless stated otherwise. The analyzed CdS weight percentages were up to 4% less than the nominal values (increasing with CdS content), this difference arising largely from a small amount of ZnS present in the CdS raw material.

In appearance under ultraviolet the Au,Cl series varies from pale bluish green to very pale yellow to colors resembling those of higher members of the other series. The unsaturated color of phosphors low in CdS is very marked, but at 25% CdS the yellow fluorescence is similar to that of 10% CdS:Cu, Cl, 50% CdS:Ag,Cl, and 35% CdS:Cl. Examples of emission curves at 25° and −120°C appear in Fig. 2 and 3, and of resolution into sub-bands in Fig. 4. The peak wave numbers are plotted against molecular percentage of CdS in Fig. 6, which also includes a weight percentage plot for Au I.

Cathode-ray excitation gave results similar to those for ZnS, namely, a relatively doubled emis-

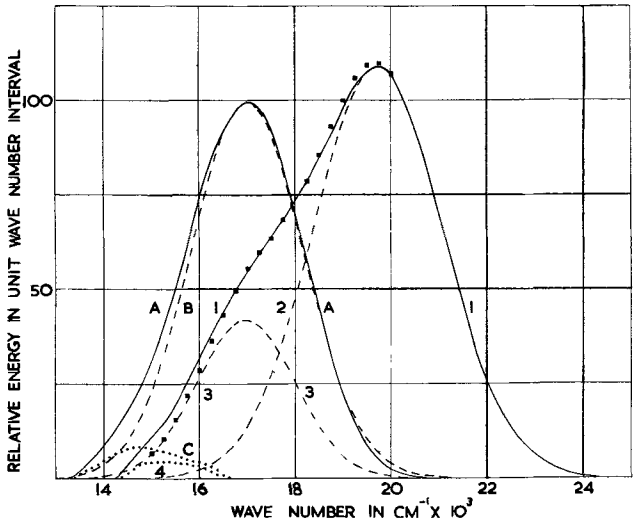

Fig. 4. Resolution of emission curves at 25°C into Gaussian sub-bands. Solid line, measured emission; broken line, Gaussian; dotted line, remainder not resolved into Gaussians; square points, sums of constituent Gaussians. 1-4: 8.5 mole % CdS: Au, Cl; A-C: 48 mole % CdS: Ag, Cl.

sion of band Au I compared with ultraviolet excitation, and band shifts between 100 and 300 cm^{-1} to higher wave numbers.

Other activators.—Samples were made with 0.01% Cu or Ag, or without metal addition, all with chloride. In the last mentioned type, analysis of well-washed samples established the residual chloride content to be 0.007% by weight in a 3.5% CdS phosphor and 0.01% in a 7% CdS phosphor, compared with 0.008% in a ZnS:Cl.

Examples of band resolution are given in Fig. 4 and 5, while peak wave number data from the complete series are presented in Fig. 7-9, where linear relations are evident as in Fig. 6. The Cu II band is also plotted on a weight percentage scale.

It will be observed that qualitatively Cu resembles Au in its band structure: to visual inspection the Cu and Au phosphors are similar in their long phosphorescence which contrasts with the short afterglow in the Ag series. There is a resemblance between the slopes of the Ag and Cl plots, but all the

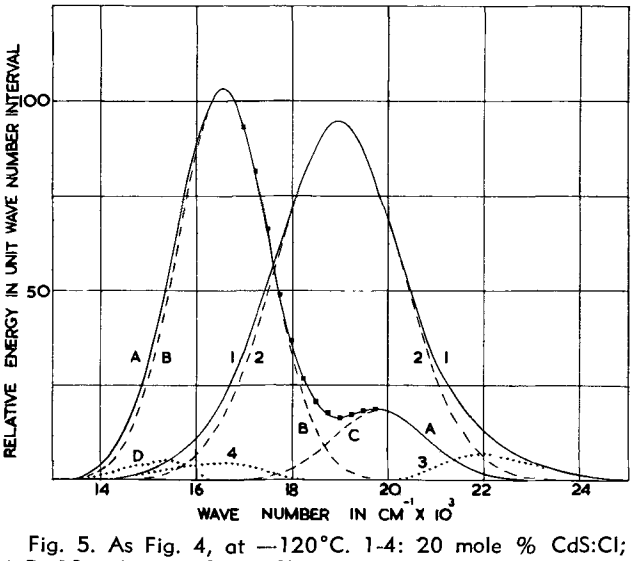

Fig. 5. As Fig. 4, at —120°C. 1-4: 20 mole % CdS:Cl; A-D: 18 mole % CdS: Cu, Cl.

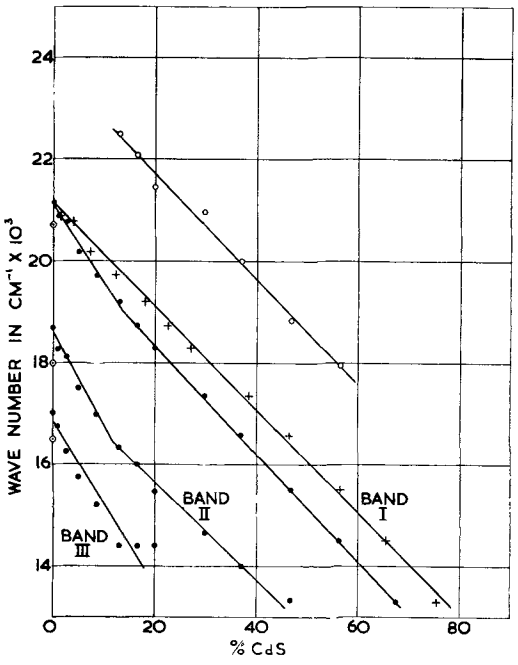

Fig. 6. Location of emission band peaks of (Zn, Cd)S: Au, Cl at 25°C. Circled points, cubic samples; open circles, low temperature peak; crosses, plot with weight percentage obscissae.

series show a break at about 15 mole % CdS. If weight proportions are used for plotting, the data for Cu and Au may be expressed by straight lines from 0 to 80% CdS, while Ag and Cl require broken lines like those in Fig. 8 and 9. These breaks occur near the point at which cubic forms can no longer be made as CdS content increases, owing to the preponderance of the hexagonal CdS structure.

Another series of samples was fired at 1100°C without metallic activator but with ZnS containing much free S, which assists the formation of the cubic structure below about 15 mole % CdS. The emission

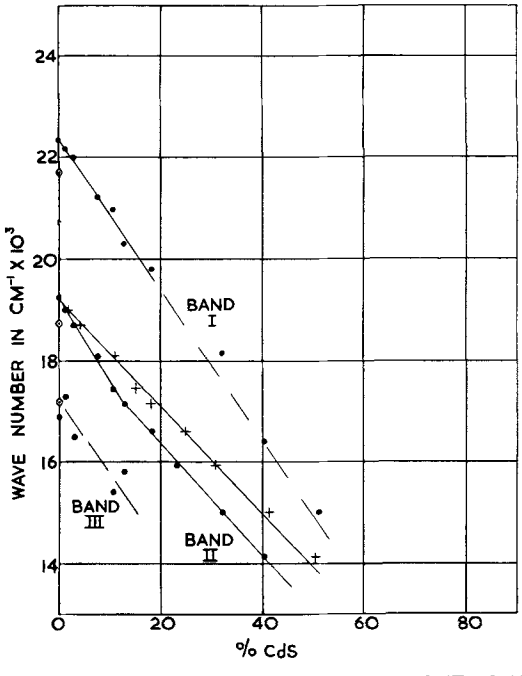

Fig. 7. Location of emission band peaks of (Zn,Cd)S:Cu, Cl at 25°C. Circled points, cubic samples; crosses, plot with weight percentage abscissae.

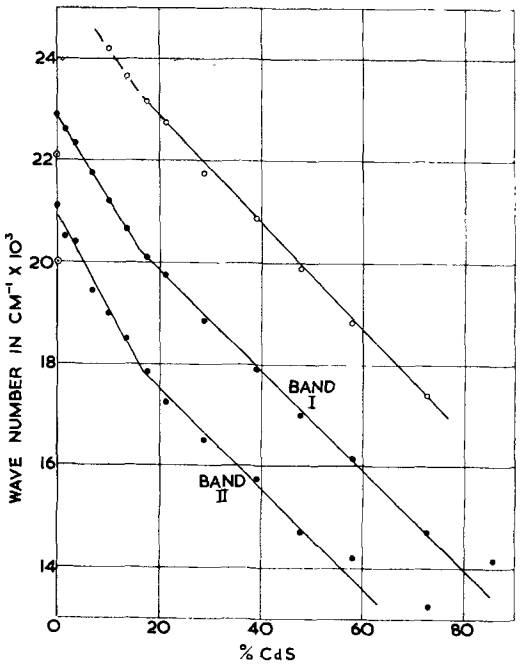

Fig. 8. Location of emission band peaks of (Zn,Cd)S:Ag, Cl at 25°C. Circled points, cubic samples; open circles, low temperature peak.

band peaks of these materials lie on the general plots above 15% CdS, but below this point the wave numbers are lower, as shown in Fig. 9 for band Cl I.

The peak intensities of the bands in the (Zn,Cd)S series with any of the four types of activator decrease as the CdS content rises to 10-15%, the fall of intensity being between 10 and 30%; a rise follows by which the values for 0% CdS may be reached or exceeded (at a CdS content of 15-30%); finally with more CdS a general fall occurs. In Fig. 2 and 3 the ordinates (except for the cathode-ray excitation example) are nearly proportional to the true intensities.

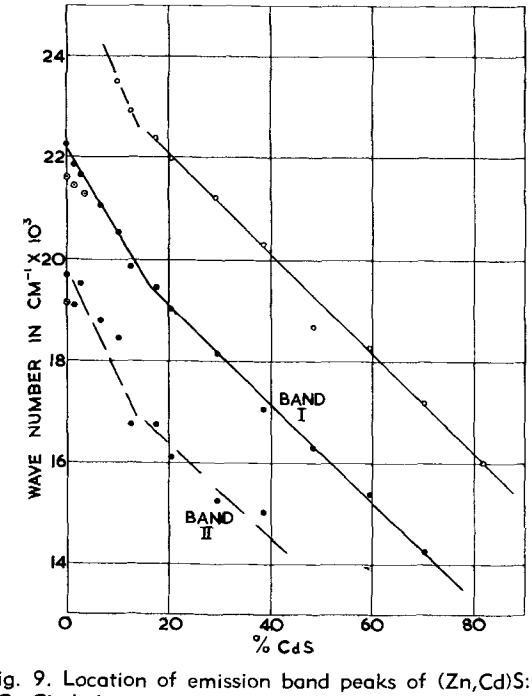

Fig. 9. Location of emission band peaks of (Zn,Cd)S:Cl at 25°C. Circled points, partially cubic samples; open circles, low temperature peak.

Table IV. Slopes of band peak plots in $-cm^{-1}$/1 mole% CdS, for main hexagonal series

Activator	Band I <15% CdS	Band I >15% CdS	Band II <15% CdS	Band II >15% CdS	Band III <15% CdS	Band III >15% CdS
Au,Cl, 25°C	152	107	180	97	174 ?	
Au,Cl, −120°	176	101	192	104	176	
Cu,Cl, 25°	150	?	158	110	150 ?	
Cu,Cl, −120°	165	125	171	113	164	
Ag,Cl, 25°	161	99	184	97		
Ag,Cl, −120°	155	97	178	101		
Cl, 25°	167	97	200 ?	95 ?		
Cl, −120°	154	95	170	98		

Low temperature effects in the (Zn,Cd)S *series.*— The emission spectra of the series with four different activators have been investigated at −120°C. When plotted in the manner of Fig. 6-9 the component band peaks lie on lines of similar slopes, and with the same breaks, as those of the corresponding bands at 25°C. These plots are not reproduced here. They show closer fit of points to lines owing to the sharper band structure at −120°C. In the case of Cu I at 25°C it is difficult to isolate this small component from the emission, and the plot in Fig. 7 is irregular. At −120°C a more normal pattern reappears; see Table IV, which summarizes all the measurements and indicates some similarity of Cu and Au on the one hand, and of Ag and Cl on the other.

The uppermost lines on Fig. 6, 8, and 9 refer to another band, not hitherto mentioned, found only at the low temperature; this is discussed in the next section.

Discussion

Reference has been made to the representation of emission band peak positions in terms of straight line plots. These varied linear relations are difficult to interpret, although their occurrence is quite striking. The data are probably not sufficiently precise to determine the exact relations which exist, but one interesting possibility is suggested below.

The emission band structure and its behavior on temperature change are important in relation to the theory of activator center structure and of energy levels. For Cu a third long wave-length band has been confirmed, and for Au three bands have been demonstrated. With both activators band II appears to be the typical one due to the metal, possibly as Cu^{+} or Au^{+} substituted for Zn^{++}. If the blue bands Cu I and Au I are assumed due to Cl producing cation vacancies, in the way that Bowers and Melamed have proposed for Cl "blue I," the anomaly arises that these bands differ from Cl I in their response to cooling (20). It is therefore suggested that, contrary to the views of Bowers and Melamed, blue Cu I and Au I are not due to the presence of cation vacancies even though all the phosphors did contain chloride. When, besides the chloride, an activating metal is also present, its effect seems to predominate.

With regard to the emission changes by cooling the main series of hexagonal phosphors, it is reasonable to attribute all the bands in ZnS and (Zn,Cd)S with Au or Cu to associated groups of acceptor levels near the valence band, whereas Cl as sole activator produces donor levels nearer the con-

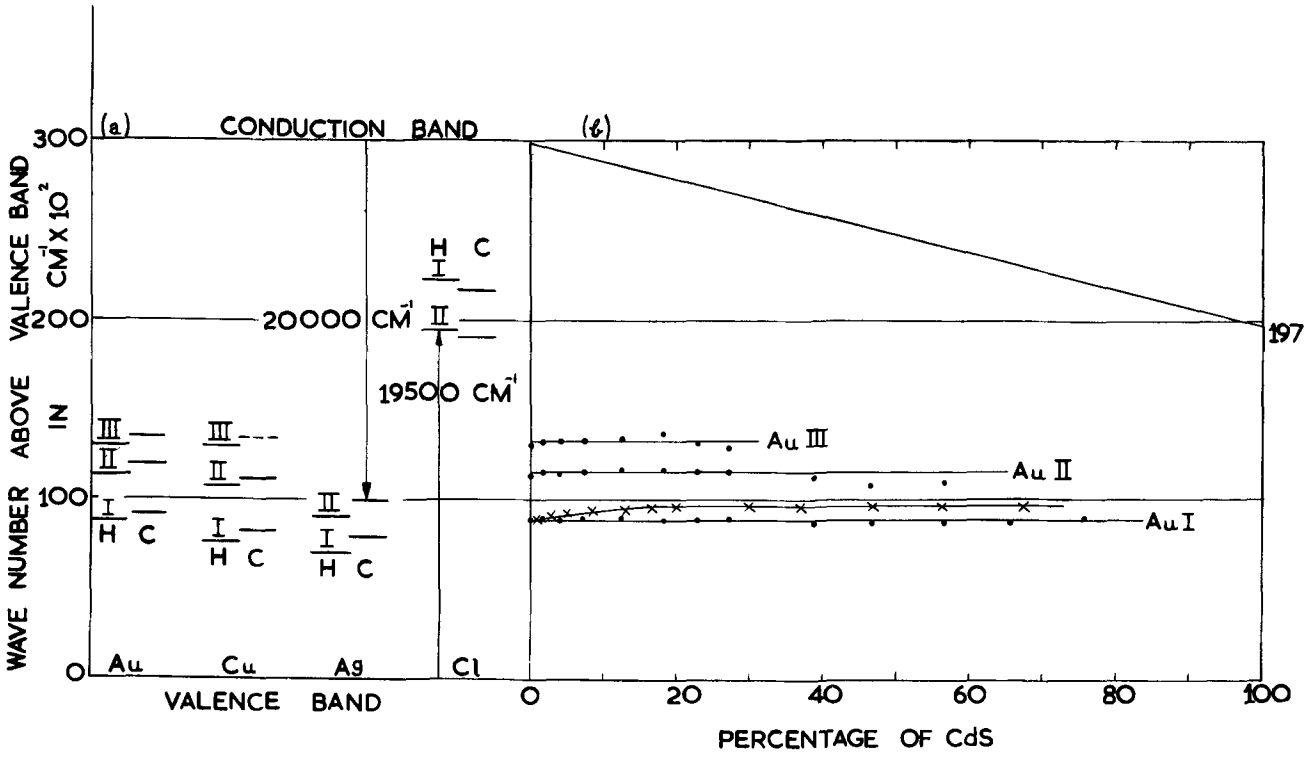

Fig. 10. (a) Energy level diagram for Cu, Ag, Au, Cl bands in ZnS at 25°C. Arrows indicate luminescent transitions; H, levels for hexagonal crystals; C, for cubic. (b) Energy level diagram for Au bands in (Zn, Cd)S. Points, plotted on weight percentage of CdS; crosses, plotted on colecular percentage.

duction band in the sense of the model of Lambe and Klick (21). These different types of radiative transition may account for the differences in temperature effects. Figure 10a gives the simplest energy diagram on these assumptions. Over the temperature range used in the work, the energy gap in the ZnS crystal increases by about 300-500 cm^{-1} according to determinations by Coogan and others (22). The observed emission band shifts on cooling suggest that the Au, Cu, and Ag levels remain nearly in the same position with respect to the valence band as the energy gap increases. In contrast, for Cl alone the levels must approach the valence band appreciably on cooling. All the shifts discussed are very small compared with the energy gap or the radiated quanta, and they are so easily altered by change of phosphor preparation method that the above details cannot be generally applicable. The approximate constancy of the separation between activator and valence band is shown better by assuming a linear variation of the energy gap between ZnS and CdS, the observed emission wave numbers being then plotted from the conduction band downward, as in Fig. 10b for the gold-activated series, where abscissae give weight percentages of CdS. A recent extensive study of (Zn,Cd)S phosphors by Hoogenstraaten develops similar ideas on activator levels (23). He refers to molecular proportions of CdS, but in Fig. 10b this scale is seen to give worse agreement with a linear relation than does the weight proportion scale; in fact the line for Au I could be drawn in two sections, as in Fig. 6, and the part above 15% CdS would be parallel to the x-axis.

A band of shorter wave length than those already discussed, and not included in the band numbering, was found only under excitation at −120°C, and for phosphors with over 10 mole % CdS. Peak locations are shown in Figs. 6, 7, and 9 on the lines which are all of the same slope (-102 ± 2 cm^{-1}/1 mole % CdS), with possibly a steeper part below 15% CdS making extrapolation difficult; however it is likely that the 0% CdS value is that attributed by Melamed (24) to the emission due to anion vacancies in cooled ZnS, namely 3950Å or approximately 25000 cm^{-1}. Similarly van Gool (24, 25) has reported a band in CdS:Ag at 6200Å or approximately 16000 cm^{-1}. The present results extrapolated would give a much higher wave length. This band did not appear with Cu activator except doubtfully in a few samples of low CdS content, and at 25°C.

There is clearly a great deal more to be discovered about the emission spectra of these phosphors and their mutual relations. Correlation with other physical parameters may be difficult or impossible but this is merely a consequence of the most striking characteristic of phosphors as a whole, namely the extreme sensitivity of their emission, both qualitative and quantitative, compared with any other measurable properties.

Manuscript received May 19, 1958.

Any discussion of this paper will appear in a Discussion Section to be published in the December 1959 JOURNAL.

REFERENCES

1. C. J. Milner, "Luminescence," Faraday Society, London, 1938, Discussion, p. 101.
2. H. W. Leverenz and F. Seitz, *J. Appl. Phys.*, **10**, 479 (1939).
3. S. T. Henderson, *Proc. Roy. Soc.* **A173**, 323 (1939).
4. F. A. Kröger and J. Dikhoff, *Physica*, **16**, 297 (1950).
5. A. Bril and H. A. Klasens, *Philips Research Repts.*, **7**, 401 (1952).

6. F. A. Kröger and J. A. M. Dikhoff, *This Journal*, **99**, 144 (1952).
7. W. Hoogenstraaten, *ibid.*, **100**, 356 (1953).
8. N. Arpiarian, *C. R. Acad. Sci. (Paris)*, **240**, 1202, 1333 (1955).
9. G. Destriau, Paper presented at Electrochem. Soc. Meeting, Washington, May 14, 1957, Abstract 24.
10. H. W. Leverenz, *et al.*, "Solid Luminescent Materials," Cornell 1946 Symposium, p. 205.
11. W. H. Byler, *J. Opt. Soc. Amer.*, **37**, 920 (1947).
12 F. A. Kröger, A. Bril, and J. A. M. Dikhoff, *Philips Research Repts.*, **7**, 241 (1952).
13. S. T. Henderson and M. B. Halstead, *Brit. J. Appl. Phys.*, **3**, 255 (1952).
14. T. B. Tomlinson, *J. Electronics*, **2**, 166 (1956).
15. R. E. Shrader and S. Larach, *Phys. Rev.*, **103**, 1899 (1956).
16. E. B. Fehr, A. I. Friedman, F. J. Studer, and G. R. Fonda, *J. Opt. Soc. Amer.*, **42**, 917 (1952).
17. H. C. Froelich, *This Journal*, **100**, 280 (1953).
18. M. H. Aven and R. M. Potter, *ibid.*, **105**, 134 (1958).
19. F. A. Kröger and J. E. Hellingman, *ibid.*, **93**, 156 (1948).
20. F. Bowers and N. T. Melamed, *Phys. Rev.*, **99**, 1781 (1956).
21. J. Lambe and C. C. Klick, *ibid.*, **98**, 909 (1955).
22. C. K. Coogan, *Proc. Phys. Soc.*, **B70**, 845 (1957).
23. W. Hoogenstraaten, Thesis, Amsterdam, Feb. 1958.
24. N. T. Melamed, *Phys. Rev.*, **107**, 1727 (1957).
25. W. van Gool, *Philips Research Repts.*, **13**, 157 (1958).

Particle Size Effects and the Distribution of Barriers in Electroluminescent Zinc Sulfide Phosphors

Paul Goldberg

Central Research Laboratories, Sylvania Electric Products Inc., Bayside, New York

ABSTRACT

The particle size of electroluminescent phosphors is found to be a significant factor in empirical equations describing brightness-voltage relationships. These observations can be understood by considering the following factors: (*a*) number and distribution of barriers in a single particle, (*b*) division among the barriers of the voltage drop per particle, and (*c*) dependence on the particle size of the voltage drop per particle. Equations are derived which permit a comparison of the brightness of different phosphors.

In the recent literature on the electroluminescence of zinc sulfide, the barrier concept finds wide support. According to this mechanism electrons are accelerated in the barrier region and cause excitation through impact ionization of luminescent centers (1-6). Radiation occurs when the ionized centers and free electrons recombine. The barrier picture is appealing for at least two reasons. First, it provides an explanation of how an electric field can raise electrons to several electron volts above their ground states without electrical breakdown of the crystals. Second, the concept of localized barriers correlates well with the observed inhomogeneous distribution of emitted light (2, 7, 8).

Information on the number and distribution of barriers is not obtained easily. This is particularly true of powder layers. Electroluminescent phosphors are reported to possess both "surface" (2) and "volume" (9) electroluminescence, reflecting possible differences in barrier distribution. The present work is one approach for obtaining information on the number and distribution of barriers in polycrystalline phosphors.

If it is assumed that the barriers are located near the surface of the particles, one may ask what happens to the electroluminescent properties as the specific surface, (i.e., particle size) is varied. To study this problem effectively, a series of electroluminescent phosphors is needed in which the members have equal chemical and physical properties but have varying particle sizes. While it is hardly feasible to synthesize separately the individual members of such a series, one promising approach is through fractionation by particle size. Most of the work presented here employed this technique.

Experimental Technique and Results

The starting materials were two phosphors representative of the blue- and green-emitting materials of Homer, *et al.* (10). These were fractionated according to particle size by settling from water or aqueous glycerine solutions. Turbulent stirring of the suspensions with a surface active agent prior to settling reduced flocculation. Also, the green-emitting phosphor was subjected to ultrasonic vibration as an added measure to break up agglomerates. Nevertheless, some aggregation undoubtedly occurred prior to settling as some of the fractions showed a plurality of log-normal distributions. Unfractionated phosphors showed only a single log-normal distribution. Individual particles were mainly globoid. A few particles showed triangular faces with rounded corners.

The measurement of the luminous emittance of the powders was made using a cell similar to that described by Lehmann with castor oil as the suspending dielectric (11). The cell dimensions were 1 x 1 x 0.005 in. A 1P22 photomultiplier was used as the detector. The phosphor concentration was held at a fixed volume fraction of 0.25 for all measurements. The experimental spread in duplicating a given emittance measurement, including factors for making the castor oil slurries, loading the cell, and aging it under an applied field, is about 10%.

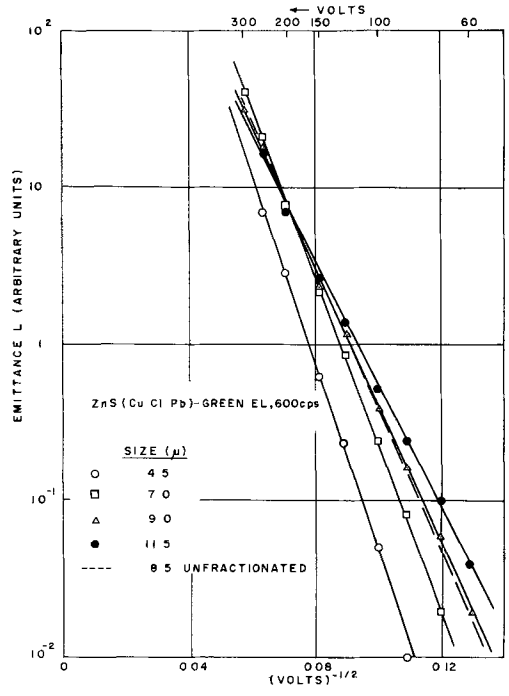

Fig. 1. Brightness-voltage characteristics of a green-emitting electroluminescent powder and some representative fractions.

It has been demonstrated by Zalm (2) and Alfrey and Taylor (3) that brightness data are well represented by straight lines when the log of the luminous emittance L is plotted vs. $V^{-1/2}$, where V is the rms applied voltage. Figure 1 shows the emittance-voltage data of four fractions and of the unfractionated green-emitting electroluminescent powder plotted in this way for a frequency of 600 cps. There is a distinct regularity in the variation of the slopes and the apparent intercepts with particle size. Variations in the emittances of up to an order of magnitude at 60-70 v are evident. Figure 2 shows the data taken at 6000 cps for the blue-emitting phosphor, with a similar result. For both phosphors the effect has been observed at other frequencies in the range 60-6000 cps.

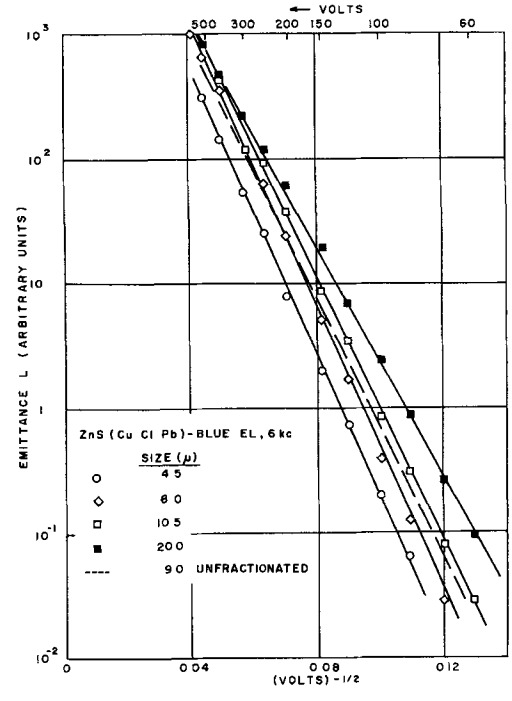

Fig. 2. Brightness-voltage characteristics of a blue-emitting electroluminescent powder and some representative fractions.

Analysis of Results

An attempt will be made to analyze the emittance data in terms of the luminous flux from each particle. This flux itself originates at point sources of emission. We shall assume that a potential barrier exists at each point source and the flux from it is determined by the voltage drop, V_B, across the barrier. V_B will be determined largely by the voltage applied to the cell. However, it may have different values depending on the particle size and the number and distribution of barriers in each particle. The procedure will be to evaluate V_B for a given applied voltage and for different types of distributions. We then may express the dependence of the flux from each point source on the applied voltage and the parameters describing the particular distribution of barriers. The emittance of the cell is obtained by summing the flux from each point source in a particle and then summing the contributions to the total emittance from each particle in the cell. Lehmann discussed this approach but did not attempt a quantitative development (12) .

For the a-c case, V_B will vary with time during a cycle and, therefore, we must visualize it as corresponding to an average value. Zalm (2) and Alfrey and Taylor (3) have discussed this point and also the factors which determine how much of the voltage applied to the crystal appears across the barrier.

The voltage dependence of the luminous flux from the individual point sources will be assumed to be of the same form as the dependence of the emittance of the whole cell.[1] Thus the flux F_B from one point source of those making up a given particle is

$$F_B = F_o \exp\left(-b'/V_B^{1/2}\right) \qquad [1]$$

where F_o and b' are parameters which are independent of voltage.

To evaluate V_B in terms of the voltage applied to the crystal we shall assume that the electroluminescent layer is represented by a mixture of two homogeneous dielectrics. The phosphor phase is considered to be a rectangular array of cubic phosphor grains of uniform size dispersed in the insulating medium between plane parallel electrodes in the manner shown in Fig. 3. Following Roberts (12), the electric field in a particle E_p is proportional to the mean applied field E_m through a factor dependent upon the ratio, r, of matrix and phosphor dielectric constants, and the volume fraction v of the phosphor, i.e., $E_p = E_m \cdot f(r, v)$. The voltage drop V_p across one of the cubes in Fig. 3 is thus

$$V_p = (Va/l) \cdot f(r, v) \qquad [2]$$

where V is the applied voltage, l the distance between electrodes, and a the cube edge.

At this point some choice must be made as to the

[1] Zalm (2) measured the flux from single grains of electroluminescent ZnS and showed that the dependence of the emission from single grains follows closely that of the composite cell.

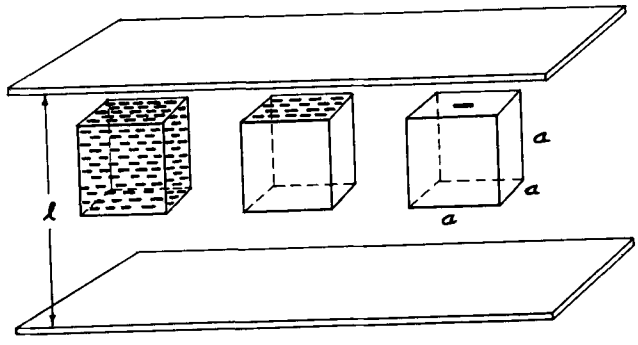

$F_B \sim \exp(-bV_B^{-1/2})$

Fig. 3. Schematic diagram of electroluminescent particles with (a) volume distribution of barriers, (b) surface distribution of barriers, and (c) a constant number of barriers per grain, unity in the case pictured.

distribution of potential barriers in the particle. The choice of the distribution will determine how much of the voltage applied to the crystal as a whole will appear across each barrier and, therefore, governs the magnitude of the luminous flux from the region near each barrier. Three cases will be considered: (*a*) uniform distribution of barriers throughout the volume of the grain; (*b*) uniform distribution of barriers over the surface of the grain; and (c) constant number of barriers per grain regardless of dimensions.

These cases are represented schematically in Fig. 3 and considered in detail below.

(*a*) *Uniform distribution of barriers throughout the crystal volume.*—Let the volume density of a system of identical barriers be n_v/cm^3. Then along a line of force through a crystal with rectangular orientation relative to the electrodes there will be $n_v^{1/3}$ barriers per cm.[2] In a crystal of edge a cm there are $n_v^{1/3}a$ barriers through the crystal in the direction of the applied field. Dividing the V_p by this number of barriers gives for the voltage drop per barrier

$$V_B = V_p/n_v^{1/3}a = (V/ln_v^{1/3}) \cdot f(r, v) \qquad [3]$$

and substitution in Eq. [1] gives for the luminous flux from the region near each barrier

$$F_B = F_o \exp[-b/(V/ln_v^{1/3})^{1/2}];\ b \equiv b'/f^{1/2}(r, v) \qquad [4]$$

There are n_va^3 barriers in the grain and the total flux F_p from the particle is $F_p = n_va^3\ F_B$. For a volume fraction of phosphor v in the suspending dielectric the number of grains N per cm^3 of suspension is v/a^3. The flux per cm^3 of suspension is $F = F_pv/a^3 = vn_vF_B$ or from Eq. [4]:

$$F = vn_vF_o \exp[-b/(V/ln_v^{1/3})^{1/2}] \qquad [5]$$

The luminous emittance L from a layer of the suspension l cm thick is proportional to $F \cdot l$ and therefore

$$L \sim vn_vlF_o \exp[-b/(V/ln_v^{1/3})^{1/2}] \qquad [6]$$

Thus, as the particle size a does not occur in Eq. [6], neither the intercepts nor the slopes of data plotted as in Fig. 1 should depend on particle size for grains with a volume distribution of barriers.

(*b*) *Uniform distribution of barriers on the surface of the grains.*—Let us next consider the barriers to be distributed over the surface of the grains at a concentration of n_s barriers per cm^2. The number of barriers on one cube face is n_sa^2. Also, as there is only one barrier along any line of force perpendicular to the surface, the full voltage applied to the grain will appear across each barrier.[3] Thus, $V_B = V_P = (Va/l)\ f(r, v)$. Therefore from Eq. [1]:

$$F_B = F_o \exp[-b/(Va/l)^{1/2}] \qquad [7]$$

The flux from each particle is $F_P = n_sa^2F_B$. The total flux per cm^3 is $F = vn_sF_B/a$ and the emittance is given by

$$L \sim (vn_slF_o/a) \exp[-b/(Va/l)^{1/2}] \qquad [8]$$

Here both the slope and intercept of log L vs. $V^{-1/2}$ will vary with particle size. It is seen from Eq. [8] that for all particle sizes, plots of log (La) vs. $(Va/l)^{-1/2}$ should be coincident.

(*c*) *Constant number of barriers per grain.*—Next let us visualize a specific number of barriers, n, to exist on the surface of each particle and let n be constant for all particle sizes. The entire voltage drop per crystal is across the barrier as in case (*b*), and again $V_B = V_P = (Va/l)\ f(r, v)$. The total flux per particle is

$$F_P = nF_o \exp[-b/(Va/l)^{1/2}] \qquad [9]$$

and

$$L \sim (vnlF_o/a^3) \exp[-b/(Va/l)^{1/2}] \qquad [10]$$

where again

$$b \equiv b'/f^{1/2}(r, v)$$

Here too, both the intercept and the slope of log L vs. $V^{-1/2}$ vary with particle size. In contrast to the previous section, plots of log (La^3) vs. $(Va/l)^{-1/2}$ for various particle sizes should be coincident. The data in Fig. 1 and 2 eliminate the possibility of a volume concentration of barriers, as prominent particle size effects are evident. The model of a surface density of barriers is also not satisfied by the data, as Fig. 4 shows a test of Eq. [8] for the fractions in Fig. 1. While the slopes of separate fractions show some degree of uniformity in Fig. 4, there is still a wide discrepancy among the intercepts. Good agreement with case (c) is found for the data of Fig. 1. The application of Eq. [10] to these data is shown in Fig. 5. The simple model of a constant number of barriers per grain fits well for this phosphor.

While the blue-emitting phosphor of Fig. 2 shows pronounced particle size effects, the data are not satisfied by Eq. [10]. This is seen in Fig. 6; a dependence of slope on particle size still persists. For this phosphor it can be shown that the slopes in Fig. 2 vary roughly as $a^{-1/4}$.

The development presented above can also be tested with unfractionated phosphors of differing mean particle size. Figure 7 shows a plot of the slope of (log L vs. $V^{-1/2}$) vs. $a^{-1/2}$ for a group of blue-emit-

[2] The number of barriers in the direction of the lines of electrical force will actually be proportional to $n_v^{1/3}$. Setting the number of barriers/cm equal to $n_v^{1/3}$ simply introduces a different arbitrary constant at a later point.

[3] We visualize the barriers on only one side of the crystal to be operative during one half cycle of a.c. and those on the opposite side during the following half cycle.

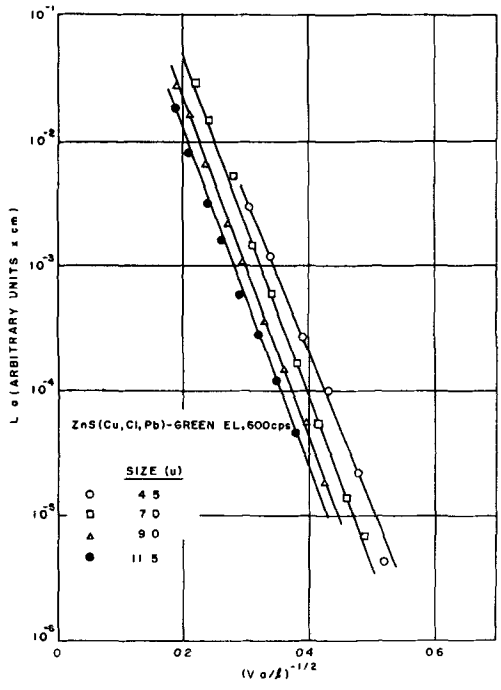

Fig. 4. Test of Eq. [8] corresponding to a surface density of barriers (case b). Data are taken from Fig. 1.

ting phosphors of the ZnS:Cu, Cl, Pb or ZnS:Cu, Cl type. The data fall close to a straight line with a slope greater than zero. This eliminates the possibility that the group is characterized by a volume distribution of barriers. It is not possible, however, to distinguish between cases (b) and (c) for these phosphors.

It should be mentioned that, for a given field strength, Eq. [10] predicts a particle size a_m which gives maximum emittance: $a_m = b^2/36(V/l)$. This condition arises from the fact that as a decreases, the number of emitting particles per cm^3 increases.

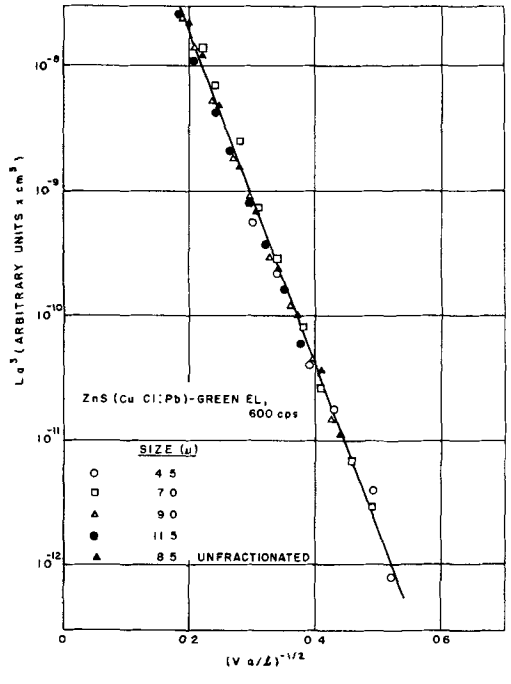

Fig. 5. Test of Eq. [10] corresponding to a constant number of barriers per grain (case c) for the data of Fig. 1.

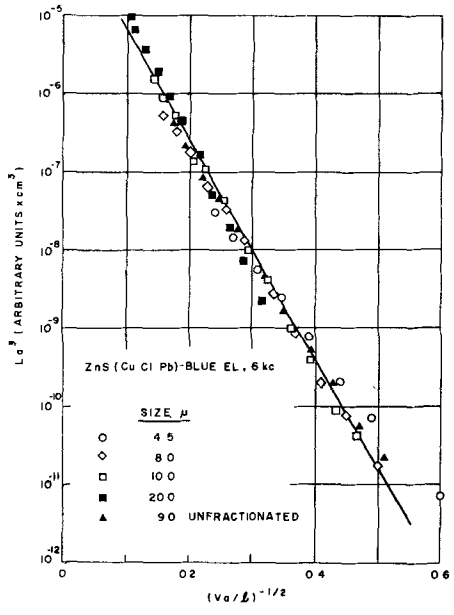

Fig. 6. Test of Eq. [10] corresponding to a constant number of barriers per grain (case c) for the data of Fig. 2.

At the same time however, the luminous flux per particle decreases with decreasing particle size.

Discussion

The data presented above show that the particle size is a significant factor in the brightness-voltage characteristics of electroluminescent phosphors. Limited agreement is obtained between the data and a simple theory based on a specific distribution of barriers in the phosphor particles. For both the fractionated green-emitting phosphor and the unfractionated group of Fig. 7 the slopes of the exp $(V^{-1/2})$ lines vary as $a^{-1/2}$. In particular, the data for this fractionated phosphor support case (c) corresponding to a constant number of barriers per grain. It should be emphasized that this concept, being derived as it is from the emittance data, applies only to the barriers which are active in the excitation processes. Other barriers or similar physicochemical constructs may be present in the particles but are not revealed by the emittance data.

The reasons for the failure of the blue-emitting phosphor of Fig. 2 to show the same detailed behavior as the green-emitting one are not clear. The assumptions regarding the identity of chemical com-

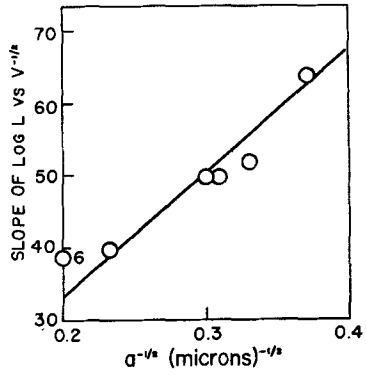

Fig. 7. Slopes (of log L vs $V^{-1/2}$ plots) vs. $a^{-1/2}$ for some unfractionated blue-emitting electroluminescent phosphors with various thermal histories and particle sizes.

position of the fractions and the existence of a simple distribution of barriers possibly need closer examination. Poor separation during fractionation may also be a factor as the blue-emitting phosphor did not have the benefit of ultrasonic dispersion prior to settling.

The development assumes that for barriers distributed as in cases (*b*) and (c), the voltage drop per barrier V_B will be determined largely by the grain size. This concept finds support in the work of Waymouth and Bitter (8), who studied the effects of geometric crystal orientation, relative to the field vector, on the emission from individual particles. They examined particles of elongated shape in which single spots of emission could be observed. These spots were brightest when the field was parallel to the long axis of the particle. One possible interpretation of this from the present work is that the elongated particle exhibits the greatest "effective particle size" when oriented parallel to the field, causing V_B and therefore F_B to be larger than for any other orientation.

We can only speculate at present on the number of barriers per grain for case (c). The choice of one barrier per grain is attractive. Waymouth and Bitter examined a large number of single grains of phosphors also synthesized by the method of Homer, *et al.* (10) and observed brightness waves with only one major emission peak per cycle. If more than one barrier were operative in a crystal, then emission during each of the two half cycles would be expected.

In practical electroluminescent cells the grains are not cubic and perfectly oriented. However, the aim of the development is to produce the correct functionality in equations relating light output to particle size. Absolute values are not of concern. The shape might have been taken to be something other than cubic with the same result; the cube of a characteristic linear dimension would enter into the pre-exponential factor in Eq. [10] and as the negative ½ power in the exponential term, regardless of particle geometry. Neither does the fact that only polydisperse materials can be obtained by fractionation limit the validity of the arguments. It is seen that the unfractionated powder behaves as if it were a fraction with the effective particle size equal to the average.

It is possible to employ the present analysis in several ways. First, it provides a possible approach to distinguishing between classes of phosphors possessing dissimilar distributions of barriers. However, the equations do not provide means for distinguishing between surface and volume barriers. For instance, Eq. [10] can be obtained by choosing a small value for the number of barriers in each grain and distributing them throughout the volume. If the density of such barriers is low, so that a single line of force through the crystal sees only one barrier, then the equation so derived is exactly of the same form as Eq. [10]. For other phosphors, distributions not considered here may be of importance.

Second, if the distribution of barriers can be established, the characteristics of phosphors with different particle sizes can be compared, with allowance for size. Thus if the data for a pair of phosphors are plotted as in Fig. 4, comparison of the ordinates for a specified value of the abscissa gives a measure of the relative light output corrected to the same particle size and applied field.

Third, it may be possible to employ the analysis for a better understanding of the factors which influence the efficiency of the excitation process. Figure 7 shows that a constant slope exists for several electroluminescent phosphors of the ZnS:Cu, Cl type. Theoretical arguments have been advanced which state that the slopes are related to the probability that an electron accelerated in the region of a potential barrier will result in impact ionization (2, 3). Changes in the composition of the phosphor which change the slopes may yield information on the chemical and physical factors which govern the properties of the barriers.

Acknowledgments

It is a pleasure to thank B. E. Bartels, D. R. Frankl, A. K. Levine, A. L. Solomon, and R. N. Summergrad for stimulating and helpful discussions. Thanks are also due D. H. Baird for reading the manuscript and suggesting improvements. The aid of J. T. Ragusin and G. Klecak in the fractionations and the particle size determinations is gratefully acknowledged.

Manuscript received May 23, 1958. This paper was prepared for delivery before the New York Meeting, April 27-May 1, 1958.

Any discussion of this paper will appear in a Discussion Section to be published in the December 1959 JOURNAL.

REFERENCES

1. G. Destriau and H. F. Ivey, *Proc. I. R. E.*, **43**, 1911 (1955).
2. P. Zalm, *Philips Research Repts.*, **11**, 353 (1956); **11**, 417 (1956).
3. G. F. Alfrey and J. B. Taylor, *Proc. Phys. Soc.*, **B78**, 775 (1955).
4. W. W. Piper and F. E. Williams, *Brit. J. Appl. Phys.*, Supplement No. 4, S39 (1955); *Phys. Rev.* **87**, 151 (1952).
5. D. R. Frankl, *Phys. Rev.*, **100**, 1105 (1955); *Sylvania Technologist*, **9**, 6 (1956).
6. G. F. Neumark, *Sylvania Technologist*, **10**, 29 (1957).
7. S. Roberts, *J. Opt. Soc. Amer.*, **43**, 590 (1953).
8. J. F. Waymouth and F. Bitter, *Phys. Rev.*, **95**, 941 (1954).
9. A. H. McKeag and E. G. Steward, *This Journal*, **104**, 41 (1957).
10. H. H. Homer, R. M. Rulon, and K. H. Butler, *ibid.*, **100**, 566 (1953).
11. W. Lehmann, *ibid.*, **103**, 24 (1956).
12. W. Lehmann, *ibid.*, **103**, 667 (1956).

A Method for the Purification of Selenium

S. Nielsen and R. J. Heritage

Royal Radar Establishment, Great Malvern, England

ABSTRACT

A method has been worked out for purifying selenium based on the formation and decomposition of hydrogen selenide. Details of an apparatus capable of producing about 10 g/hr of extremely high purity selenium are given. Several analytical methods used in examining the product are outlined.

Selenium is recovered industrially from two main sources (*a*) flue dust obtained in burning pyrites in the manufacture of H_2SO_4, and (*b*) anode slimes from electrolytic refining, particularly of Cu. Usually the crushed ore is roasted in air and the SeO_2 formed, sublimes, and is collected in water. Selenium is recovered from this solution by reaction with SO_2 according to the equation

$$H_2SeO_3 + 2SO_2 + H_2O = Se + 2H_2SO_4$$

Material prepared in this way is approximately 99.5% pure, the main impurities being S and Te (1).

Further purification has been achieved in several ways. Henkels (2) recommended a 4-stage procedure: (*a*) distillation of the Se at atmospheric pressure, (*b*) conversion to SeO_2, (*c*) purification of the SeO_2 by sublimation, (*d*) recovery of the Se by reaction of the dioxide with gaseous ammonia according to the equation

$$3SeO_2 + 3NH_3 = 3Se + 2N_2 + H_2O$$

High purity Se has also been produced commercially by the ammonia reduction of SeO_2, which has been prepared by the catalytic vapor phase oxidation of Se (3). A recent patent (4) pointed out that selenium could be obtained spectrographically pure by a direct solution method. In this process Se was dissolved in a hot aqueous solution of sodium sulfite and a small quantity of aluminum sulfate solution added. Aluminum hydroxide precipitated, carrying with it impurities present in the solution. After filtration, purified Se was precipitated on cooling. Nijland (5) recommended a sublimation procedure at a pressure of 10^{-3} mm Hg and claimed that sublimation was much better than distillation. Also methods based on the purification of SeO_2 in solution using ion exchange resins have been used (6).

Distillation and sublimation techniques are to be preferred since they are simple and the purification of other chemicals is not required. However our experiments with radiotracers suggested that to achieve a significant reduction in impurities repeated sublimation would be necessary. Our attempts to purify Se by zone melting were also without success.

Selenium doped with 10 ppm of radioactive Cu and Sb was sublimed in a simple tube-type apparatus. The results indicated that the Cu content of the sublimate was reduced to about 0.5 ppm and the Sb content to about 0.2 ppm.

An ingot of Se which had been previously doped with 100 ppm of each of the impurities shown in Table II was zone-melted in a sealed evacuated silica tube. After 30 passes, samples taken from along the ingot were examined spectrographically, but no movement of impurities could be detected. The ingot length was ~30 cm, the zone length ~2 cm, although there was a pronounced tendency for supercooling, and the rate of zone travel was 5 cm/hr.

These experiments suggested that neither sublimation nor zone melting processes were particularly effective, and we report here a new method which we believe to provide very pure Se. The method involves the formation and decomposition of H_2Se. Hydrogen selenide is formed by bubbling purified hydrogen through molten Se at 650°C. The H_2Se is decomposed by passing the gas through a silica tube maintained at 1000°C. With a suitably constructed tube about 70% of the selenide is decomposed. Undecomposed H_2Se is condensed in a liquid air trap and later allowed to recirculate through the decomposition tube. In this way practically all the H_2Se is decomposed. The Se liberated is collected by melting into a silica crucible.

The only other elements likely to form hydrides under these conditions and consequently those likely to be impurities in the final material are F, Cl, Br, I, O, S, Te, P, As, and Sb. The first 6 of these elements form hydrides more readily than Se and the others less readily. Further, the hydrides of the first 6 are less easily decomposed at 1000°C than H_2Se, while the others are more easily decomposed (cf. Table I). The difference in stability is utilized in this process. Further purification of the H_2Se could be obtained by fractional distillation (cf. Table I) or gas chromatographic procedures, but we have not found these necessary.

The advantage of the process lies in the purity which can be obtained in one operation. For instance, it has been shown using radiotracers that, if 1 ppm of the Cu or Sb is added to the starting material, there is an improvement of the order of 10^4. It is clear also that very low grade Se can be purified in this way. A serious disadvantage, however, is that H_2Se is very toxic and consequently care must be

Table I. Physical properties of hydrides

	HF	HCl	HBr	HI	H_2O	H_2S	H_2Se	H_2Te	H_3N	H_3P	H_3As	H_3Sb
MP	−92.3	−112	−88.5	−50	0	−82	−64	−51	−77	−133	−113	−88
BP	+19.4	−84	−67	−35	100	−61	−42	−4	−33	−87	−55	−17
Approx. % decomp. at 1000°C	—	10^{-2}	10^{-1}	35	0	15	75	10^2			10^2	10^2

taken to avoid leakages when assembling and handling the apparatus.

Apparatus

The general arrangement of the apparatus, as illustrated in Fig. 1, is described below, followed by details of the individual units. Hydrogen is purified (H_2 purifier) and bubbled through molten Se where a portion is converted into H_2Se (H_2Se generator). The gas stream then passes though trap I at 300°C and through trap II at −20°C. During the first ½ hour's operation the gas is led direct to waste with taps B and D being open and taps C and E closed. After this time, tap D is closed and C and E opened and the gas stream is led into condenser I. This is maintained at −196°C by surrounding it with liquid nitrogen when H_2Se is condensed. When a suitable quantity of H_2Se has been collected, the hydrogen flow is stopped, taps A and B are closed, and the H_2Se is allowed to evaporate into a silica tube maintained at 1000°C (decomposition tower). In this

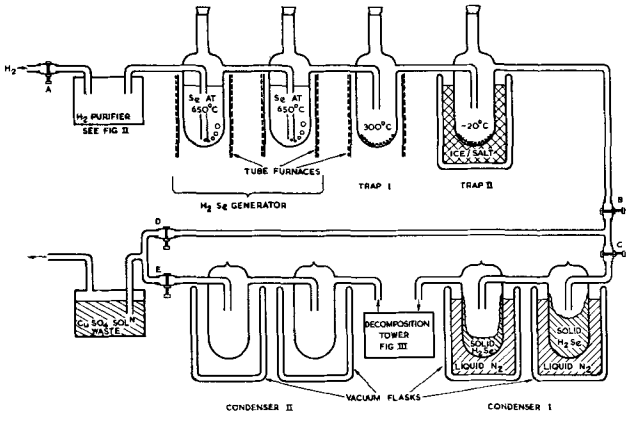

Fig. 1. General arrangement of apparatus

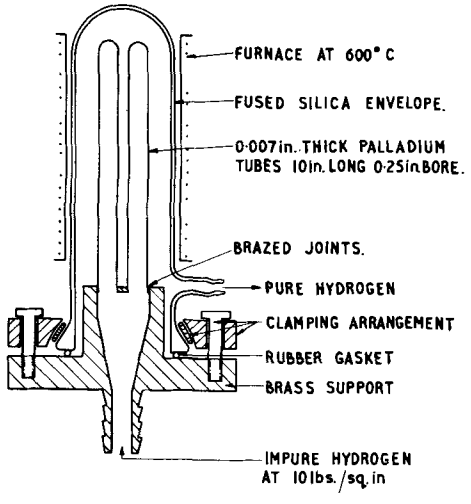

Fig. 2. Hydrogen purifier

tower H_2Se is cracked into its elements and the Se is collected by melting into a silica tube. Most of the undecomposed H_2Se is trapped in condenser II which is surrounded by liquid nitrogen and any which passes through this is converted into copper selenide by bubbling through a solution of copper sulfate (waste). After the H_2Se in condenser I has been passed through the tower, tap E is closed and D opened and the selenide in condenser II is allowed to evaporate through the decomposition tower in the reverse direction. Any undecomposed H_2Se then passes into waste where it is converted into copper selenide.

Periodically, crude Se is added to the generator and the purified Se collected from the tower. Hydrogen selenide can be recovered from waste by reaction of the copper selenide with acid.

Hydrogen Purifier

We have used oxygen-free hydrogen which has been further purified by passing through a palladium diffusion unit (Fig. 2) followed by a liquid air trap. In most of our experiments, a flow rate of 2 l/hr was maintained. When flow rates of 10 l/hr were used the hydrogen was purified by passing through a "Deoxo" catalytic purifier[1] again followed by a liquid air trap.

Generator

The purified hydrogen is passed through molten Se in a simple trap-type apparatus illustrated in Fig. 1. The apparatus is made of fused quartz and contains 150 g of crude Se. The Se is introduced in pellet form via a long arm closed with a rubber bung. For the first ½ hour's operation the Se is maintained at 550°C and after this time at 650°C.

A temperature of 550°C is used initially when volatile materials and elements which react readily with hydrogen are expelled from the Se, these being sent direct to waste. During the remainder of the operation a temperature of 650°C is maintained. At this temperature the reaction $H_2 + Se = H_2Se$ precedes more rapidly than at 575°C, the temperature at which the concentration of H_2Se in the equilibrium mixture is greatest (7). Actually we have used two generators coupled in series to insure that a near equilibrium concentration of H_2Se is attained. The fact that the second generator does not lose weight suggests that this may be so. Under these conditions, we expect those materials such as the halides, oxygen, and sulfur, which form hydrides more readily than selenium, to be removed during the preliminary ½ hr at 550°C. We have found from doping experiments that Te, As, and Sb are not carried over under the normal experimental conditions. The only

[1] Made by Baker Platinum Ltd.

impurities likely to be present in the gas stream leaving the generator are volatile materials such as hydrocarbons, etc., not removed by the preliminary stage and particles which are carried along in the gas stream.

Impurity Traps

Trap I is maintained at 300°C such that any hydrides of As, Sb, and Te which may be present would be decomposed. Trap II is cooled in an ice/salt mixture at −20°C to collect any particles carried over in the gas stream and any vapors which may be condensed at this temperature, e.g., mercury or water. Both the traps are of the same design as the generator and made of fused quartz (cf. Fig. 1).

Condensers

The gas stream is then passed into condenser I which is maintained at −183°C. The condensers are made of quartz, and a very simple design such as illustrated in Fig. 1 is satisfactory. Two condensers of 300-ml capacity, coupled in series could be used with the generator for about 4 hr. After this time, the H_2Se is allowed to evaporate over into the decomposition tower. The condensation and subsequent distillation result in further purification of the H_2Se and also enable the gas to be recirculated through the tower.

Decomposition Tower

From preliminary experiments we found that a decomposition tower of the type illustrated in Fig. 3 was very satisfactory. It appeared that the H_2Se needed to be raised to 1000°C and then the products cooled rapidly, so that they did not reform H_2Se. Selenium condenses at points shown in Fig. 3 and is melted with a bunsen burner into a silica collecting crucible.

Under equilibrium conditions, at 1000°C, about 75% of the H_2Se is decomposed. Table I indicates the extent to which the other hydrides decompose at 1000°C. From this, it is suggested that only sulfur and iodine may appear in the final product, and the concentrations of these will be appreciably reduced.

Any H_2Se which escapes the condensers, passes into waste. This consists of two bubblers. The first bubbler contains 50% H_2SO_4 to prevent water and oxygen diffusing back into the tower. The second contains copper sulfate solution in which the H_2Se decomposes according to the reaction $H_2Se+CuSO_4=CuSe+H_2SO_4$. Periodically the copper sulfate is renewed.

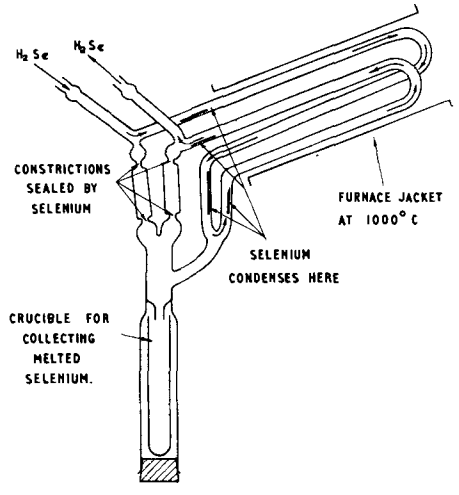

Fig. 3. Decomposition tower

Taps and Assembly

The units of the apparatus have been sealed to each other, but the final assembly is fragile. We have found it more convenient to use polythene, silicone rubber, or rubber tubing to connect the units. The tubing quickly becomes coated with a layer of Se which would tend to reduce any possible exchange reaction. The separate units are cleaned by soaking in a mixture of HNO_3 and HF, washing with metal-free water and finally with distilled acetone. The units are heated to a high temperature in air to remove adhering liquid and then heated by a flame when assembled in the apparatus with a stream of hydrogen passing through.

Results

The efficiency of the process was estimated by weighing the generator before and after an experiment and weighing the amount of purified Se obtained. In a typical experiment the following results were obtained: 28 g of Se was used in the generator and the H_2Se produced was trapped in condenser I. When this was allowed to evaporate through the tower, 20 g (70%) of Se was formed. Undecomposed H_2Se which was trapped in condenser II was recycled through the tower and yielded a further 4 g (14%) Se. The total yield of the process was, therefore, 84%. In an experiment not using condenser I, the gas mixture leaving the generator being passed directly into the decomposition tower, the following typical figures were obtained: 33 g of Se was used in the generator and 21 g (64%) of Se was obtained after passing through the tower. The undecomposed H_2Se trapped in condenser II was recirculated through the tower and a further 8 g (24%) produced, giving a total yield of 88%. The efficiency of the process is seen to be high and yields near 100% are possible if the undecomposed H_2Se is recirculated through the tower after condensing.

Analytical Tests

1. Selenium doped with 100 ppm of each of the elements Cu, Hg, Pb, Sn, Ag, Bi, Fe, Si, and 500 ppm

Table II. Results of analytical test No. 1

Impurity	Initial ppm	Final	Detection limit ppm
Cu	100	Not detected	0.2
Hg	100	Not detected	1
Pb	100	Not detected	1
Sn	100	Not detected	10
Ag	100	Not detected	0.1
Bi	100	Not detected	20
Fe	100	?*	10
Si	100	?*	20
As	500	Not detected	300
Sb	500	Not detected	50
Te	500	Not detected	200

* Traces of these were also visible with blank electrodes.

of As, Cb, and Te was used in the generator and the purified Se examined spectrographically. Ten-mg samples of Se were arced at 6 amp D.C. between graphite electrodes on Hilger Medium Quartz Spectrograph. Results are given in Table II. The limit of detection of the process was obtained by successive dilution of the doped Se.

2. Selenium doped with 1 ppm of radioactive Sb and Cu (separately) was used in the generator. After operation, traps I and II, condensers I and II, and the purified Se were examined for radioactivity. Quantitative estimation of the impurity content was obtained by dissolving the Se in HNO_3 and using a solution counting method.

3. The Li, Na, and K content of the purified Se was examined, using an Evans flame photometer. Samples of Se (10 g) were dissolved in concentrated HNO_3 (30 ml) and the solution evaporated to dryness. Selenium dioxide was then sublimed at 300°C. The residue was taken up in warm metal-free water (10 ml) and examined in the photometer. Calibration, using a series of standards, indicated that the galvanometer reading on the photometer varied linearly with concentration in the ranges 0-1 ppm for Na, 0-3 ppm for Li, and 0-5 ppm for K, with a standard deviation of ±0.05, ±0.1, and ±0.1 ppm, respectively. These tests also indicated that Na, Li, and K, were not lost during the evaporation of SeO_2. Results with purified Se are given in Table III.

4. Copper, silver, mercury, tin, zinc, lead, indium, and bismuth in the purified Se were estimated using the following procedure. Selenium (5 g) was dissolved in warm concentrated HNO_3 (20 ml) and the solution adjusted to pH 9.5 with ammonia. The solution was then extracted with 5 ml of a 0.005% solution of dithizone (diphenylthiocarbazone) in chloroform. The chloroform extract was then allowed to drip on to a sample of ammonium sulfate (5 mg) maintained at 85°C. The chloroform evaporated leaving the solute adsorbed on the ammonium sulfate; this was then arced on the spectrograph as described previously. Checks on the limit of detection were made by introducing impurities as nitrates into the solution of Se in HNO_3. Results are given in Table III. We found that it was necessary to redistill all the reagents in quartz apparatus and to carry out all operations in quartz vessels to avoid pickup of traces of impurity from glass. It was also advantageous to work in clean laboratory with still air.

5. We are also greatly indebted to the Boliden Mining Co., Skelleftehamn, Sweden, for the analytical results presented in Table IV, which, we understand, were obtained by a modified spectrographic technique.

Analytical Results

The results of the analytical experiments are shown in Tables II and III.

Our analytical techniques could detect no difference in the impurity content of the final Se whether the H_2Se was condensed before entering the decomposition tower or allowed directly through.

In the experiments with radioactive Cu no trace of radioactivity could be detected in the final Se or in any part of the apparatus except the generator.

Table III. Results of analytical tests Nos. III and IV

Method	Impurity	ppm in purified selenium	Detection limit ppm
Flame photometer	Li	Not detected	0.07
	Na	0.25	0.02
	K	0.3	0.10
Dithizone Extraction and spectrograph	Zn	Not detected	1
	Cu	0.04	0.04
	Ag	0.04	0.04
	Pb	Not detected	0.4
	Hg	Not detected	0.5
	Bi	Not detected	1
	In	Not detected	2
	Sn	Not detected	1

As 1 ppm of Cu was used, this means less than 2×10^{-3} ppm was present in the purified Se. Using radioactive Sb, however, a trace of activity was found in trap II and the final material appeared to contain about 10^{-5} ppm. Selenium obtained when H_2Se from condenser II was recycled through the decomposition tower showed no trace of activity.

Combined results of the analysis suggest that traces of Na, As, Pb, and Cu may be present in the purified material. Although the total amount of impurity appears to be small, the difficulty of analysis at these concentrations precludes an accurate estimate.

Discussion

If Cu is regarded as typical of cations which do not form hydrides, then the experiment using radioactive Cu indicates that such cations are not carried over during the purification procedure. The presence of Cu shown by direct analysis suggests that it has either been picked up from the silica apparatus or has been introduced during the transfer operation. We have also found it extremely difficult to remove traces of Cu from the reagents. It is probable that the other cations indicated by the analysis are also introduced in these ways. The experiment with radioactive Sb suggests that traces of the hydride of Sb may be formed during the experiment but an improvement of 10^5 may be expected.

It is not certain, at present, whether the As present in the final material has been transferred as the hydride or is due to pickup from the silica apparatus, in which it is known to be present. The absence of detectable S and Te in the product is encouraging

Table IV. Results of the Boliden analysis

Impurity	Impurity content in sample	Detection limit ppm	Impurity	Impurity content in sample	Detection limit ppm
Ag	Not detected	0.03	Ca	Not detected	1
Cu	0.20 ppm	0.1	Cr	Not detected	0.3
Hg	Not detected	0.5	Mg	Not detected	0.3
Fe	0.60 ppm	0.3	Mn	Not detected	0.1
K	Not detected	0.3	Ni	Not detected	0.3
Na	0.40 ppm	0.1	Pb	0.6 ppm	0.3
Te	Not detected	1	Sb	Not detected	1
Al	Not detected	0.3	Si	Not detected	1
As	1.0 ppm	1	Sn	Not detected	0.3
Bi	Not detected	0.1	S	Not detected	5
Zn	Not detected	1	Ce	Not detected	2

and suggests that these are at least substantially reduced by the process.

The amount of Se which could be purified appears to be limited only by the rate of flow of hydrogen through the Se. Flow rates of 10 l/hr result in production of about 10 g of Se/hr. It is important that the flow rate is such that H_2Se attains 1000°C in the decomposition stage. Analytical results (cf. Table II) suggest that quite impure Se may be refined in this way.

It may be mentioned that the purified H_2Se may be decomposed chemically if suitably pure reagents are available and may also be converted directly into a metal selenide should this be required.

Acknowledgment

The authors wish to acknowledge the help and interest shown by the Boliden Mining Company, Skelleftehamn, Sweden. They are also indebted to Miss I. Betteridge and Messrs. A. Fray, D. Maines, and J. Conaboy for help with the apparatus and to Miss P. Butcher for some of the analytical work. Acknowledgment is made to the Controller, Her Majesty's Stationery Office for permission to publish this paper.

Manuscript received July 16, 1957.

Any discussion of this paper will appear in a Discussion Section to be published in the December 1959 JOURNAL.

REFERENCES

1. B. S. Hopkins, "Chemistry of the Less Familiar Elements," Stipes Publishing Co., Chicago, Ill. (1939).
2. H. W. Henkels, *J. Appl. Phys.*, **21**, 725 (1950).
3. (a) C. W. Clark and E. M. Elkin (to Canadian Copper Refiners Ltd.) U.S. Pat. 2,406,666, Aug. 27, 1946; (b) C. W. Clark, E. M. Elkin, and G. R. Waitkins (to Canadian Copper Refiners Ltd.) U.S. Pat. 2,409,835 Oct. 22, 1946.
4. A. Voigt and H. Krebs (to Deutsche Gold-und-Silber-Scheideanstalt vorm. Roessler), British Pat. 698,228, Oct. 7, 1953.
5. L. M. Nijland, *Philips Research Repts.*, **9**, 259 (1954).
6. British Drug Houses, Poole, England, Private communication.
7. J. W. Mellor, "A Comprehensive Treatise on Inorganic and Theoretical Chemistry," Vol. X, p. 759, Longmans, Green and Co., London (1930).

Electrodeposition of High-Purity Chromium

F. E. Block, P. C. Good, and G. Asai

Bureau of Mines, Region I, Albany, Oregon

ABSTRACT

Thick chromium deposits were prepared by the electrolysis of aqueous chromic acid baths. Metal containing 0.005% oxygen, less than 0.002% nitrogen, and only traces of metallic impurities was obtained upon electrolysis of purified solutions at elevated temperatures. After consumable electrode arc-melting, this type of chromium could be hot-worked to rod and drawn to wire that was ductile at room temperature.

The electrolysis of chromic acid solutions was selected for study as a method of preparing high-purity chromium because metallic impurities may be excluded easily and gaseous impurities remain at very low levels. Although a low current efficiency is obtained in electrowinning chromium from hexavalent solutions and chromic anhydride is an expensive reagent, this method was adopted because it was found that metal could be prepared sufficiently pure to permit a study of its properties without additional purification steps which, in turn, are costly.

Electrodeposition from chromic acid solutions has been practiced from the time Fink (1) patented his process in 1926; however, its use has been confined mainly to decorative plating. Adcock (2) prepared massive deposits in 1927 as a means of making chromium for physical studies, but it was not until more recently that Greenaway (3) and the Bureau of Mines, United States Department of the Interior (4) employed high-temperature baths operated at high current density to yield thick deposits of low-oxygen chromium.

Brenner, Burkhead, and Jennings (5) investigated the properties of thin chromium electrodeposits plated under widely differing conditions of solution concentration, temperature, and current density. Their work indicated that the level of oxygen contamination in the electrodeposits was governed primarily by the temperature of deposition, with high temperatures favoring lower oxygen contents. Consequently, high-temperature baths were employed exclusively in this work. It has been demonstrated (6-8) that oxygen has little effect on the ductility of chromium metal; however, the object of this investigation was the preparation of the pure metal for direct study and for alloy studies, and since oxygen is generally the major contaminant in chromium, efforts were made to maintain a low oxygen level.

Experimental Work

Description of Apparatus

A number of different cells and procedures were studied during the course of the investigation, but only the more recent apparatus used in preparing metal for fabrication studies is described here.

The bath was maintained in a circular steel tank 18 in. in diameter and 16 in. in height lined on the inside with unplasticized polyvinyl chloride. This

was found to be one of the few corrosion-resistant nonmetallic materials that would withstand the operating temperatures of 90°C. A 6-in. diameter aluminum tube in the center of the cell served as cathode. In earlier runs the anode consisted of a 16-in. diameter coil of ¾-in. lead tubing which served also as a cooling coil. In later runs the cell comprised a lead vessel in a steel container, and the cell was used as an anode, the electrolyte being cooled by circulating water in the annular space between the cell and the steel container. In either type of cell the flow of water was regulated with a Powers regulator[1] activated by a temperature-sensitive, lead-sheathed bulb in the electrolyte. The tubular lead anode was more effective in removing heat and controlling temperature at high current densities, but the lead-pot type suffered less anodic corrosion.

Because the bath was operated at its boiling point and was in a constant state of violent agitation, due to the large amount of hydrogen being produced, a Micarta cover was fitted over the cell to direct the escaping mist and vapors to a glass reflux condenser which returned them to the cell. Losses of uncondensed liquid were made up from a reservoir placed above the cell and connected to a constant-level device to maintain a uniform electrolyte level in the cell.

Cell Operation

The electrolyte was made up by dissolving chromium trioxide in distilled water and adding sulfate ion as H_2SO_4.

Since the electrolyte was used repeatedly, impurities were prevented from building up by contacting the solution with a cation-exchange resin before each run. A 4-in. diameter resin bed 30 in. deep was employed. By analyzing the H_2SO_4 solution used to regenerate the resin, it was determined that Al, Cu, Fe, Ni, Si, and Sn were being removed by this treatment.

Cation-exchange resins of the sulfonated polystyrene type have been recommended (8) for treating strongly oxidizing solutions, such as chromic acid. Although this general type was employed, there was considerable variation with respect to stability among the different resins tested. Amberlite IR-120 was found to be highly resistant to oxidation at room temperature when used with solutions containing up to 250 g/l of chromic acid.

During electrolysis the chromium concentration in the electrolyte was determined twice daily by specific gravity measurements and adjusted by the addition of chromium trioxide to the feed reservoir or directly into the cell. The sulfate ion concentration was adjusted at the beginning of each run.

Direct current was supplied to the electrodes from a 4000-amp selenium rectifier.

To take advantage of the relationship between operating temperature and the oxygen content of the deposit, the electrolyte temperature was maintained near the boiling point. Since early deposition tests at lower operating temperatures had confirmed the temperature-oxygen content relationship as reported by Brenner and co-workers (5), all runs in this investigation were made in the 85°-90°C range.

During electrolysis, the deposit appeared first as a smooth surface having a matte finish, but as deposition continued it changed to a more nodular form. Because the electrolyte had poor throwing power, the nodules grew quickly into long dendrites, which eventually broke from the cathode and dropped to the bottom of the cell. Although the dendrites could be recovered as metal, it was necessary to treat them with nitric acid to remove lead chromate, which sloughed off the anode and mixed with the dendrites. Also, the dendrites consistently contained more oxygen than the adherent deposits.

For these reasons attempts were made to minimize the growth of dendrites. This could be accomplished to some degree by changing cathodes at shorter intervals before the dendrites formed; however, the thinner deposits were very difficult to remove from the cathode by mechanical methods. It was found that a deposition interval of 72 hr generally yielded a deposit between 1/16 and 3/32 in. thick, which was plated in a highly stressed condition. A deposit of this nature could be removed by striking the cathode a sharp blow with a hammer. Scoring the surface of the aluminum cathode into 1-in. squares before electrolysis caused a thinner deposit to be formed at the score marks and facilitated removal of the deposit.

Experimental Results

Table I shows the results of 72- and 96-hr deposition tests at cathode current densities ranging from 340 to 1100 amp/ft^2 and with various electrolyte compositions. Analyses were performed on specimens taken from ingots arc-melted from representative portions of the deposit. Oxygen and hydrogen were determined by vacuum fusion analysis, and nitrogen was determined either by vacuum fusion or Kjeldahl analysis.

Figure 1 is a plot of the data appearing in Table I and shows the relationship between the cathode current density and the proportion of the cathode deposit that appeared as loose dendrites. This plot indicates the advantage of operating at lower cur-

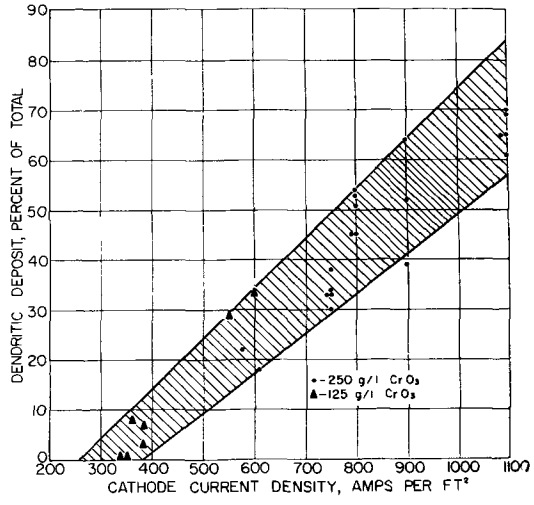

Fig. 1. Effect of current density on cathode deposit

[1] The Powers Regulator Company, Skokie, Ill.

Table I. Results of electrolytic tests

Run No.	Hr	Bath composition			Cathode current density, amp/ft²	Cathode current efficiency, %	Dendrite deposit %	*	Analysis, ppm			
		SO_4, g/l	CrO_3, g/l	Ratio, CrO_3/SO_4					O_2	H_2	N_2	C
1	72	2.5	125	50	340	12.3	0	P	410	2	10	110
2	96	1.0	125	125	350	7.7	0	P	50	1	20	80
3	96	2.2	85	39	350	10.2	20					
4	96	2.1	125	60	365	11.6	8					
5	96	2.6	125	48	385	13.1	7					
6	72	2.5	125	50	385	13.6	3					
7	72	3.9	125	32	550	10.5	29	P	55	1	<30	250
8	72	5.2	250	48	580	8.8	22	P	140	2	<50	
9	72	3.9	125	32	600	8.4	33	P	1150	7	20	55
10	72	7.8	250	32	610	8.4	18	P	50	<1	<30	
11	72	2.5	250	100	750	9.7	33	P	100	3	<20	
								D	920	3	<20	
12	72	2.5	250	100	750	8.6	38	P	120	5	<20	
								D	590	5	<20	
13	72	2.5	250	100	750	8.6	34	P	40	1	<20	
								D	600	5	<20	
14	72	2.5	250	100	750	11.2	33	P	250	4	<20	
								D	355	6	<20	
15	72	2.5	250	100	750	10.7	30	P	134	2	85	
								D	836	4	<20	
16	76	2.5	250	100	800	8.7	53	P	150	934	<20	740
								D	970	<20	<20	160
17	72	2.5	250	100	800	7.8	45	P	215	14	<20	370
								D	1170	<20	<20	<50
18	72	2.5	250	100	800	8.5	51	P	120	<20	<20	<50
								D	260	<20	<20	<50
19	72	2.5	250	100	800	7.5	45	P	130	<20	<20	<50
								D	740	5	<20	160
20	72	2.5	250	100	800	7.3	54	P	200		<20	<50
								D	920		<20	<50
21	72	2.5	250	100	900	9.4	52	P	210		<20	490
								D	1170		<20	80
22	72	2.5	250	100	900	12.8	64					
23	72	2.5	250	100	900	8.5	39					
24	72	2.5	250	100	1100	8.8	65					
25	72	2.5	250	100	1100	7.3	65					
26	72	2.5	250	100	1100	8.5	69	P	220	5	<20	
27	72	2.5	250	100	1100	8.4	70	D	1140	10	<20	
28	72	2.5	250	100	1100	8.9	61					

* P = deposit adhering to cathode; D = dendrite deposit fallen from cathode.

rent densities if a greater proportion of low-oxygen, solid deposits are desired. These data are not strictly comparable, because larger amounts of chromium usually were deposited in the tests at higher current densities, and a greater proportion of dendrites might be expected under these circumstances. However, the relationship appears to be independent of either the current efficiency or time of deposition, which might also be expected to influence the results if the relative amount of deposit was a major factor.

Table I indicates that the current efficiency was independent of the current density at constant bath composition. These data also suggest that optimum current efficiencies were obtained when baths were used having CrO_3 to SO_4 ratios of approximately 50, with somewhat lower efficiencies resulting from either higher or lower ratios. In this respect, the present investigation is in general agreement with the work of Greenaway (3).

At constant temperatures the oxygen content of the deposit appeared to be independent of both current density and bath composition. In all instances the dendritic deposits were found to contain a significantly higher amount of oxygen than the corresponding deposits which adhered to the cathode; however, the dendrites also exhibited a significantly greater amount of surface, which might account for the higher oxygen level. Usually the deposit which was removed from the cathode was found to contain between 50 and 250 ppm oxygen and less than 20 ppm nitrogen.

Metallic impurities were not determined quantitatively, but qualitative spectrographic analysis indicated that the deposits usually contained trace amounts of aluminum, iron, or silicon. There was no detectable difference between the dendritic or adherent deposits with respect to metallic impurities.

Figure 2 shows photomicrographs of arc-melted chromium representing both types of deposits. The increased amount of second-phase material in the dendritic deposit illustrates the higher oxygen level in this material.

Physical Testing

For evaluation, the deposits were consolidated by the inert atmosphere, cold mold, arc-melting technique. Homogeneous samples were prepared for analysis by melting a 50-g representative portion of

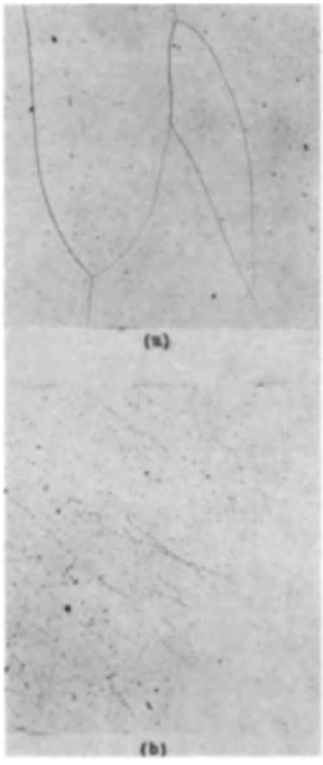

Fig. 2. Photomicrographs of arc-melted, as-cast chromium electrodeposits, chromic acid-electrolytic etch. (a) Adherent deposit 40 ppm oxygen, (b) dendritic deposit 600 ppm oxygen. Magnification 100X before reduction for publication.

each deposit, employing a nonconsumable tungsten electrode for arc melting. Larger ingots were prepared for physical studies by melting the chromium as a consumable electrode into a 2-in. diameter, water-cooled copper crucible. In this case the deposit was crushed to pass minus-8-mesh and compressed into 1-in. by 1-in. electrodes 10 in. long. The electrodes were sintered 8 hr in purified hydrogen at 1200°C to increase their mechanical strength.

Tensile tests were made on wire specimens prepared from the arc-cast ingots. Ingots were scalped, sheathed in stainless steel, and swaged at 1100°C to approximately 1-in. diameter. The 1-in. diameter swaged rods were recrystallized by heating to 1200°C sheathed in mild steel and swaged to approximately 0.25-in. diameter. After recrystallization the rods were reduced to 0.125-in. diameter test wire by drawing through tungsten carbide dies at 350°C. All of the specimens were tested in the 50% worked condition. Tensile specimens were prepared by stopping off the ends and electrolytically

Table II. Tensile strength of wire at 25°C

Specimen No.	Ingot analysis, ppm			Wire analysis, ppm N	U.T.S., 1000 psi.	Elongation, % in 1 in.
	O	H	N			
W-65	245	6.7	<50	40	69	10
				40	69	16
W-82	245	6.7	<50	50	68	15
				50	68	16
W-88	245	6.7	<50	30	57	26
SA, 17, 286	—	—	—	210	72	0
				—	70	0
SA 16, 284	40	2	<30	220	77	0
				—	74	0

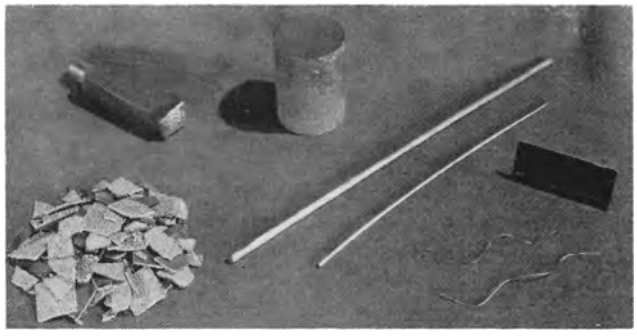

Fig. 3. Stages employed in preparing chromium wires from electrodeposit.

etching the wire surface in the center portion to yield a reduced section along the gauge length. In this work, as in previous investigations (9, 10), the full ductility of the material was not realized until a thin surface layer had been removed from the specimens by etching. Although the wires could not be bent before etching, after removal of the surface layer the wires could be reverse-bent by hand repeatedly without fracture.

Table II shows the results of tensile tests at 25°C representing specimens prepared from two ingot melts. Because of the opportunity for gaseous contamination during the sintering, arc-melting, and annealing steps, the broken tensile specimens were analyzed for nitrogen content as shown. The results indicate that material containing 50 ppm or less nitrogen is ductile, while chromium containing on the order of 200 ppm nitrogen has no ductility. This shows the importance of preparing and maintaining a low nitrogen content in the metal if ductility is desired.

Figure 3 represents the stages employed in preparing chromium wires, showing the electrodeposit, a section of partly melted consumable electrode, an ingot section, swaged rod, and drawn and etched ductile wire.

Conclusions

High-purity chromium can be prepared conveniently by high-temperature electrodeposition from purified chromic acid solutions, yielding deposits containing only trace amounts of metallic impurities, with oxygen the chief impurity. After having been melted and worked into shapes, electrolytic chromium exhibits tensile properties comparable to chromium prepared by refining commercial grade material by hydrogen treatment. The low nitrogen content of electrodeposited metal favors this method as a means of preparing chromium for physical studies.

Manuscript received Dec. 3, 1957. This paper was prepared for delivery before the Buffalo Meeting, Oct. 6-10, 1957.

Any discussion of this paper will appear in a Discussion Section to be published in the December 1959 JOURNAL.

REFERENCES

1. C. G. Fink, U. S. Pat. 1,581,188 (1926).
2. F. Adcock, *J. Iron and Steel Inst.*, **115**, 369 (1927).
3. H. T. Greenaway, *J. Inst. Metals*, **83**, 1576 (1954-55).
4. P. M. Gruzensky and F. E. Block, *U. S. Bur. Mines Rep. Invest. 5035*, January 1957.
5. G. Asai and H. Johansen, "Final Report on Massive

Chromium" to Army Ordnance Corps, Watertown Arsenal Laboratory, Watertown, Mass., Sept. 15, 1953.
6. A. Brenner, P. Burkhead, and C. Jennings, *J. Res. Nat. Bur. Standards*, **40**, 31 (1948).
7. G. Asai and E. T. Hayes, "Mechanical Properties of Bureau of Mines' Chromium," Ductile Chromium ASM, p. 138 (1957).
8. W. H. Smith and A. U. Seybolt, "Effects of Impurities on the Ductility of Chromium," Ductile Chromium, ASM, p. 169 (1957).
9. R. L. Costa, *Ind. and Eng. Chem.*, **42**, 308 (1950).
10. H. L. Wain, F. Henderson, and S. T. M. Johnstone, *J. Inst. Metals*, **83**, 133 (1954-1955).
11. H. A. Johansen and G. Asai, *This Journal*, **101**, 604 (1954).

Some Effects of Pressure on Consumable Electrode Arc Melting

J. W. Suiter[1]

Mines Branch, Department of Mines and Technical Surveys, Ottawa, Ontario, Canada

ABSTRACT

The effect of pressure in a consumable electrode arc furnace on the weight of metal melted per unit of energy dissipated was investigated while melting titanium electrodes of negative and positive polarity and steel electrodes of negative polarity. Provided that the arc length was sufficiently short, the weight of metal melted per unit of energy dissipated increased continuously as the pressure of argon was decreased from 650 to 1×10^{-2} mm Hg.

Many workers (1, 2) have reported the weight of metal melted per unit of energy dissipated in consumable electrode arc melting, but in most cases the experiments were done only at a few widely separated pressures. Beall, *et al.* (3) have reported the effects of varying the pressure in the range 10-760 mm Hg when melting titanium electrodes in an argon atmosphere. However, the present emphasis on vacuum arc melting has made it desirable to extend their investigations to lower pressures.

The paper reports the effects of varying the argon pressure in the range of 1×10^{-2} to 650 mm Hg on the weight of metal melted per unit of energy dissipated when melting titanium and steel in a consumable electrode arc furnace.

Materials and Experimental Procedure

The titanium electrodes were produced by welding, end to end, compacts of sponge titanium (20.4 x 5.1 x 5.1 cm) each weighing 1600 g. The mild steel (0.1% C) electrodes consisted of rolled bar 3.8 x 3.8 cm in cross section. These electrodes were attached to a water-cooled copper electrode stub which passed through a sliding seal in the top of the furnace. The electrodes were melted into a mold 34 cm long and 12 cm in diameter, producing ingots of 4-5 kg weight.

Power for melting was supplied by three motor-generator welding machines connected in parallel. The same generator settings were used in all experiments, and the arc current and voltage were allowed to vary with the pressure.

During melting the feed rate of the electrode was adjusted by the operator while observing the arc voltage pattern on a direct current oscilloscope and also the arc voltage and current as indicated by conventional meters. The desirable arc length was such that the pattern on the oscilloscope indicated the presence of occasional, momentary dead shorts. It was thought that these momentary dead shorts were due to droplets of molten metal shorting between the electrode and the molten pool. It was not possible to measure such an arc length but it appeared to be less than 1 cm. For some melts at pressures of 25 and 10 mm Hg, an arc length of approximately 8 cm was deliberately maintained; these were duplicates of melts made at the same pressures with a normal short arc length. The long arc length was used to determine what effect the presence of positionally unstable arcs would have on the weight of metal melted per unit of energy dissipated. It was possible to observe, through a sight glass, the presence or absence of positionally unstable arcs within the mold.

In the pressure range 10-650 mm Hg a static atmosphere of argon was used, but in the pressure range 10^{-1}-10 mm Hg it was necessary to remove gas from the system while melting to maintain a constant pressure. No argon was used for pressures less than 10^{-1} mm Hg which were obtained by continuously evacuating the furnace so that the steady pressure during melting depended on the speed of the pumps being used and the amount of gas evolved from the electrode. The gas pressure was measured in the body of the furnace, for it has been shown (4) that this pressure is very close to that in the melting region of this type of furnace if there are no volatile materials in the electrode. There were only very small quantities of volatile materials in the steel electrodes used in these experiments, but the titanium electrodes contained such volatiles as magnesium and magnesium chloride. Thus, the pressure measured in the body of the furnace did not indicate accurately the pressure in the melting region when melting titanium electrodes at very low pressures.

The energy dissipated during melting was calculated from the arc voltage, the arc current, and the time of the melting operation.

[1] Present address: Baillieu Laboratory, The University of Melbourne, Victoria, Australia.

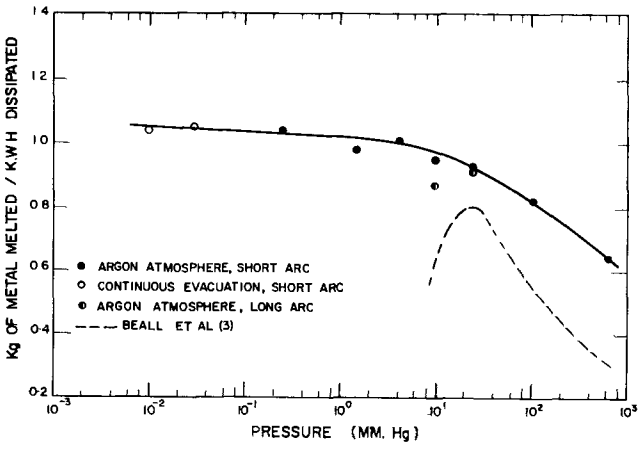

Fig. 1. Effect of pressure on the weight of titanium melted per unit of energy dissipated when melting electrodes of negative polarity.

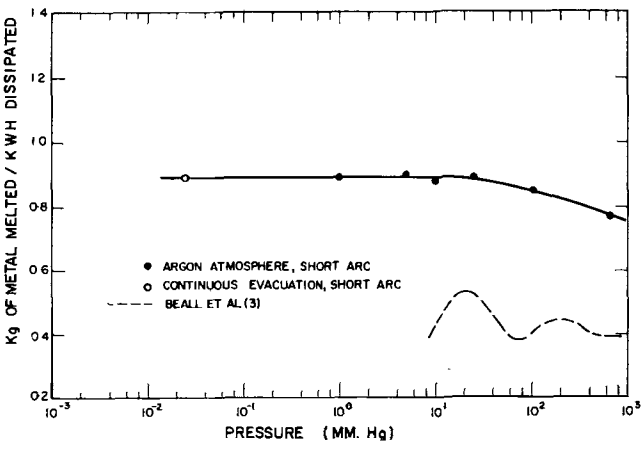

Fig. 2. Effect of pressure on the weight of titanium melted per unit of energy dissipated when melting electrodes of positive polarity.

Results

The effect of pressure on the weight of metal melted per unit of energy dissipated when melting titanium electrodes of negative polarity is shown in Fig. 1. As the pressure was decreased from 650 mm Hg to approximately 10 mm Hg the weight of metal melted per unit of energy dissipated increased, but at lower pressures the increase was less marked. As the pressure was decreased the arc voltage decreased from 36 v at 650 mm Hg pressure to 28 v at pressures less than 5 mm Hg, and in the same pressure range the arc current increased from 1800 to 2200 amp.

In the pressure range 2 x 10^{-1} to 20 mm Hg, positionally unstable arcs were seen occasionally within the mold, but these were eliminated by decreasing the arc length. Two electrodes were melted at 25 and 10 mm Hg pressure while maintaining an arc length of approximately 8 cm. At a pressure of 25 mm Hg, melting with a long arc had little effect on the weight of metal melted per unit of energy dissipated. At 10 mm Hg pressure, the weight of metal melted per unit of energy dissipated was less when melting with a long arc, and there was also a large increase in the amount of positionally unstable arcs within the mold.

Figure 2 shows that the weight of metal melted per unit of energy dissipated increases with decreasing pressure when melting titanium electrodes of positive polarity, but the increase is less than when melting titanium electrodes of negative polarity (compare Fig. 1 and 2). Thus, at low pressures the weight of metal melted per unit of energy dissipated was higher when melting electrodes of negative polarity, but near atmospheric pressure the position was reversed.

The effect of pressure on the weight of metal melted per unit of energy dissipated when melting steel electrodes of negative polarity is shown in Fig. 3. The results are similar to those obtained when melting titanium electrodes of negative polarity. At all pressures the weight of steel melted per unit of energy dissipated was greater than that of titanium, but this result was not unexpected in view of the different heat contents of the two materials at temperatures just above their melting points. As in the case of titanium electrodes of negative polarity, a

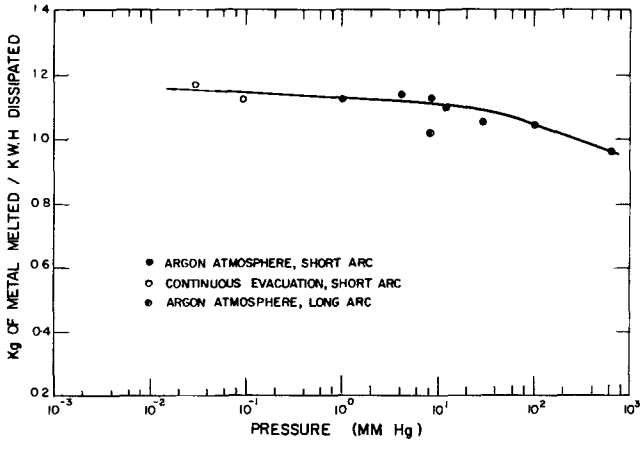

Fig. 3. Effect of pressure on the weight of steel melted per unit of energy dissipated when melting electrodes of negative polarity.

long arc at a pressure of 8 mm Hg led to positionally unstable arcs and a decreased weight of steel melted per unit of energy dissipated.

Discussion

When melting titanium electrodes of negative and positive polarity and steel electrodes of negative polarity in a consumable electrode arc furnace, the weight of metal melted per unit of energy dissipated increased continuously as the pressure was decreased. Beall, *et al.*, (3) have reported the results of melting titanium electrodes in argon atmospheres in the pressure range of 10-760 mm Hg, and they found a sharp decrease in the weight of titanium melted per unit of energy dissipated as the pressure was reduced below 20 mm Hg (see Fig. 1 and 2). Beall, *et al.* suggested that this decrease was due to the formation of positionally unstable arcs. The present work confirmed that the formation of these arcs led to a decreased weight of metal melted per unit of energy dissipated but that by maintaining a sufficiently short arc length these positionally unstable arcs could be avoided. If they were avoided, then the weight of metal melted per unit of energy dissipated increased continuously as the pressure decreased. Beall, *et al.* used two horizontally opposed electrodes in a relatively large furnace in their experiments,

and the different size and arrangement of electrodes used in the two sets of experiments may account for the different values of the weight of titanium melted per unit of energy dissipated that were obtained in the two sets of experiments near atmospheric pressure.

Although most of the melting experiments were done in an argon atmosphere, no argon was used for the melts when the furnace was evacuated continuously, and the pressure during melting was less than 1×10^{-1} mm Hg. Since the results obtained under these conditions followed the same trend as those obtained when melting in an argon atmosphere, it appeared that at very low pressures the atmosphere in which melting occurred had little effect on the weight of metal melted per unit of energy dissipated. The steel electrodes contained very little volatile material, and the composition of the gas in the melting region when melting these electrodes under continuous evacuation differed greatly from the gas composition when melting titanium electrodes. These changes in the composition of the gas in the melting region appeared to affect neither the behavior of the arc nor the weight of metal melted per unit of energy dissipated.

Acknowledgments

The work was done under the general direction of H. V. Kinsey, of the Department of Mines and Technical Surveys, Ottawa, and was made possible by the award of a Fellowship by the National Research Council of Canada. Thanks are due to R. H. Landry, technician, for assistance with the experimental work.

Manuscript received May 19, 1958. This paper was prepared for delivery before the Ottawa Meeting, Sept. 28-Oct. 2, 1958.

Any discussion of this paper will appear in a Discussion Section to be published in the December 1959 JOURNAL.

REFERENCES

1. W. H. Smith, "Arcs in Inert Atmospheres and Vacuum," W. E. Kuhn, Editor, p. 41, John Wiley & Sons, Inc., New York (1956).
2. J. L. Ham and C. B. Sibley, *J. Metals*, **9**, 976 (1957).
3. R. A. Beall, F. W. Wood, J. O. Borg, and H. L. Gilbert, "Production of Titanium Castings," Rept. of Investigation 5265, Bureau of Mines, U. S. Department of the Interior, Washington (1956).
4. J. W. Suiter, *This Journal*, **105**, 44 (1958).

Tungsten Zone Melting by Electron Bombardment

R. G. Carlson

Lamp Wire and Phosphors Department, General Electric Company, Cleveland, Ohio

ABSTRACT

An apparatus for refining tungsten in vacuum by the floating zone method is described. It consists of four components: vacuum system, power supply, anode support, and traversing cathode. Included is a brief résumé on the theory of refining by this technique. Spectrographic analyses along the length of a purified tungsten rod indicate that molybdenum may not be removed by zone refining, but rather by volatilization. Further, x-ray diffraction studies show that tungsten rods purified in this manner are single crystals and these crystals as grown from the melt do not exhibit preferential growth. It is demonstrated, by bending one of the single crystals, that the purified tungsten rods have relatively high ductility.

Zone melting, developed by Pfann (1), has attracted great interest as a process for the purification of metals. In this process a small molten zone traverses the length of a solid rod. Impurities that are more soluble in the liquid phase than in the solid phase migrate with the molten zone, leaving behind a purer metal. In the case of zone melting tungsten purification also occurs because of the outgassing and volatilization of impurities.

It is exceedingly difficult, if not impossible, to retain W in a molten state by conventional techniques without impairing its purity because of the refractory nature of this metal. Tungsten can be zone melted by utilizing the floating zone technique and heating by electron bombardment. The principle of this heating, simply the blasting of a material anode with electrons through a high potential gradient, is not new nor unique since it has long been used in the outgassing of electronic vacuum tubes and occurs in the operation of x-ray tubes. However, because of the characteristics inherent in electron bombardment heating, i.e., ability to operate at low pressures, ability to direct and concentrate the heat, ease of temperature control over a wide range, and relative simplicity of the power supply, this type of heating is employed advantageously in laboratory (2-4) as well as commercial furnaces (5).

This paper covers the design and construction of an Electron Bombardment Zone Melting Apparatus (EBZMA), includes a brief discussion on the theory of purification, and presents data on the removal of Mo and on crystal orientation.

Electron Bombardment Zone Melting Apparatus

The equipment consists of four components: vacuum system, power supply, anode support, and traversing cathode.

Vacuum system.—The anode and cathode are enclosed by a Pyrex bell jar 10½ in. in diameter and 14 in. high mounted on a brass plate (Fig. 1). There

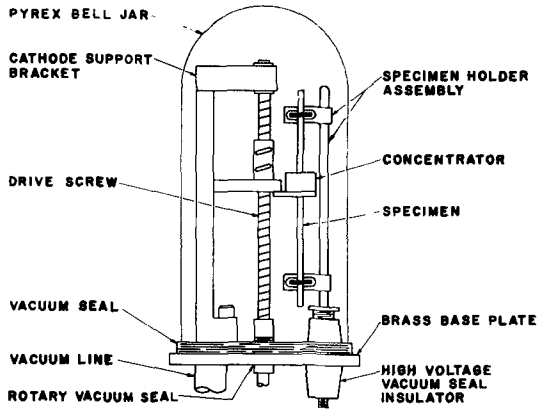

Fig. 1. Schematic drawing of the vacuum system

are five holes in this plate: three ⅝-in. diameter holes for electrical binding posts; one 2-in. diameter hole for the vacuum line; and one rotating "O" ring seal for the cathode traversing helix.

The 2-in. vacuum line is constructed with a vertical pipe extending down to a "T" section. One leg of this section forms a liquid nitrogen trap; the other leg is connected to a MCF-60 CEC oil diffusion pump, which in turn is backed up by a Kinney KC-2 mechanical pump.

Power supply.—A small power unit supplies d.c. at a maximum of 5000 v and 300 ma. It consists of a variac that limits the 110 a-c volt power to the high voltage transformer. This high voltage is then rectified by a pair of 866 A half-wave mercury rectifier tubes. The positive side of this high voltage is fed through the high-voltage-high-vacuum-throughput to the anode support. The cathode is the ground terminal. Figure 2 is a schematic of the power supply.

Anode support.—The support shown in Fig. 1 can accommodate rods up to ¼ in. in diameter. The upper and lower holding blocks are critical parts. They should possess four properties: (*a*) high melting point; (*b*) stable material in order that W is not contaminated, i.e., low vapor pressure; (*c*) high electrical conductivity; (*d*) low thermal conductivity. No one material has all these properties, but because of its superiority in the first three properties and its ability to be easily fabricated, Mo is used. A small groove in each block at the point of specimen contact reduces the heat transfer.

The specimen is held in position in each of the

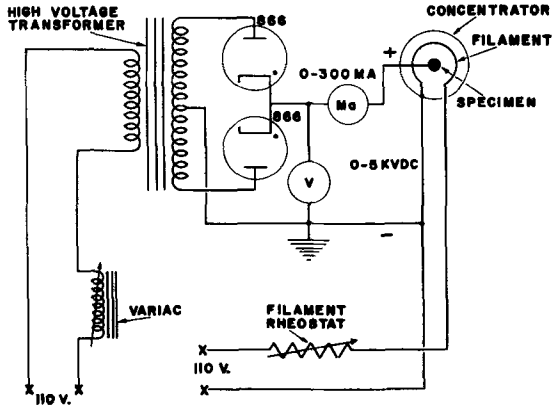

Fig. 2. Schematic drawing of the power supply

holders by flat tungsten strip that acts as a spring contact. This spring serves a dual purpose. One is to support the rod during the movement of the floating zone and the other is to allow the specimen to expand and contract in the heating and cooling operation.

Traversing cathode.—The cathode is the moving terminal; it is composed of a filament that emits the electrons, a concentrator that directs the flow of the electrons, and a mechanism that moves the cathode with respect to the stationary tungsten rod.

Traversal of the specimen occurs by the movement of a screw drive with the torque being transmitted through a rotating "O" ring seal in the brass plate. The torque is supplied through a gear train by a 3 rpm a-c reversible motor. The output of the gear train varies from 0.1 to 12 rpm producing a cathode movement of 0.3-4 cm/min.

The concentration of the electrons to the anode is an important factor. This is achieved by enclosing a W filament with a Mo concentrator of the same potential. To obtain more efficient concentration the sides of the concentrator are parabolic. The top and bottom are changeable disks with different diameter center holes, approximately ⅛ in. diameter larger than the specimen diameter.

The W filament, 15 mils in diameter, is heated by a 110 a-c power supply as shown in Fig. 2. The filament rheostat regulates the current flow to obtain sufficient emission of electrons to melt the sample, i.e., in the order of 200-250 ma.

Theory

In the zone refining process the molten zone is moved repeatedly in the same direction. Solute elements that depress the melting point of the solvent metal concentrate in the terminal end of the rod and have a distribution coefficient, k, less than one. Solute elements that increase the melting point have a k value greater than one and tend to concentrate at the starting end. The distribution coefficient is defined by the equation

$$k = \frac{N^s}{N^l} \qquad [1]$$

where N^s is mole fraction of the solute in the solid phase and N^l is the mole fraction in the liquid phase.

The distribution coefficient can be determined simply by referring to a phase diagram. From the Mo-W equilibrium phase diagram (6), the equilibrium distribution coefficient (k_o) for Mo in W is found to be 0.91.

Another approach in the determination of the distribution coefficient would be to utilize thermodynamics and, if the alloy forms ideal liquid and solid solutions, apply the well-known van't Hoff equation

$$\ln \frac{N_{Mo}{}^{l}}{N_{Mo}{}^{s}} = -\frac{\Delta H_f{}^{Mo}}{R}\left(\frac{1}{T} - \frac{1}{T_M{}^{Mo}}\right) = K_{Mo} \qquad [2]$$

or

$$\frac{N_A{}^{l}}{N_A{}^{s}} = e^{K_{Mo}} \qquad [3]$$

then

$$k_o = \frac{1}{e^{K_{Mo}}} \qquad [4]$$

where T equals the temperature considered, in this case the melting point of W, 3680°K; T_M^{Mo} equals the melting point of Mo, 2900°K; ΔH_f^{Mo} equals the heat of fusion for Mo, 6700 cal/mole; R equals gas constant. From Eq. [4] we determine that k_o equals 0.78.

As originally stated, purification of W also occurs by outgassing and the volatilization of metallic impurities on fusion in vacuum. In this particular case we will consider only the volatilizaton of Mo. The vapor pressure ($p°$Mo) for Mo at a temperature slightly above the melting point of W, 3800°K, equals 3.83 mm Hg, while the vapor pressure for W, at the same temperature, equals 0.046 mm Hg. If the mole fraction of Mo (N_{Mo}) is assumed to be 0.00002, by assuming ideality ($a_{Mo} = N_{Mo}$) and using Raoult's law ($p = a \cdot p°$Mo), the vapor pressure of Mo in the melt is 7.7×10^{-5} mm Hg. This would indicate that, if the pressure of Mo in the environment was less than 7.7×10^{-5} mm Hg, Mo would volatilize from the melt. The rate of evaporation can be calculated from the formula (9)

$$\frac{m}{t \cdot A} = P\sqrt{\frac{M}{2\pi RT}} = G \qquad [7]$$

where P is pressure (microbars); M, molecular weight; A, area (cm²); t, time (sec); R, gas constant (8.31×10^7 erg/°K/mole); T, temperature (°K); m evaporation (gr), or the ratio of the evaporation rates can be determined from the equation

$$\frac{G_{Mo}}{G_W} = \frac{P_{Mo}}{P_W}\sqrt{\frac{M_{Mo}}{M_W}} \qquad [8]$$

From this equation the ratio of evaporation rate of Mo to W is found to be 1.21×10^{-3}, i.e., of the metal evaporated during melting, 0.121% by weight is Mo.

Results

Many rods have been zone melted with this apparatus; two of the zone melted rods after five passes are shown in Fig. 3. It was found on evaluation of the purified rods that they were high in purity, single crystals, and exhibited a comparatively large amount of ductility.

It is difficult to obtain quantitative data on samples containing less than 10 ppm of an impurity. The initial concentration of all elements other than Mo were less than 10 ppm and could not be detected by spectrographic analysis. The initial concentration of Mo was estimated to be of the order of 10 ppm. To determine the amount of Mo present after the bar was traversed five times at a speed of 0.33 cm/min the rod was severed at intervals along its length. Each end of the severed section was arced against its adjacent section. The initial concentration in the rod was arbitrarily assigned the value of 10. In Fig. 4, the relative amounts of Mo, as determined by quantitative optical spectrography, are plotted against the distance along the zone purified rod.

An apparent discrepancy existed at the beginning and the end of the zone melted portion. According to the theory of zone purification, if $k < 1$, a zone of higher purity should be present at the start and a concentration of the impurities at the end. Because this did not occur, it was reasoned that either a distribution coefficient greater than one existed, or possibly the Mo evaporated from the zone melted region.

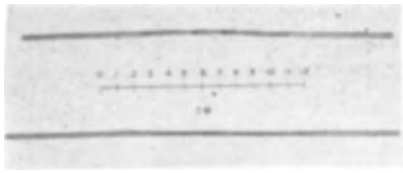

Fig. 3. Zone melted W rods, after five zone passes

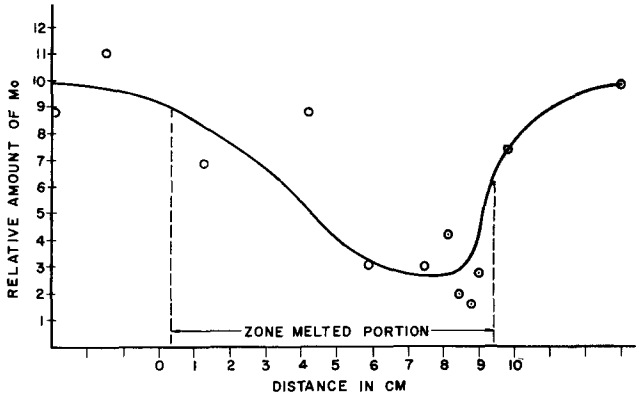

Fig. 4. Relative concentration of Mo vs. distance in zone melted portion.

To substantiate the absence of an increase in Mo concentration at the end of the rod, five separate analyses were obtained in this region. If a zone of higher Mo concentration was present, it must have existed in a length less than 4 mm long, and this is not very probable. On the basis that $k_o = 0.91$, the lowest possible concentration of Mo that could exist after 5 passes was calculated to be 6.24, assuming equilibrium existed and that the original concentration of Mo = 10. Using the same assumption and now $k_o = 0.78$, the lowest concentration was calculated to be 2.89. This latter value, as can be noted in Fig. 4, falls in the range of the lowest concentration. Of course, this lowest concentration of the solute should have occurred at the start. More work is currently being performed to support the validity of these initial results.

To determine the orientations of the rods and to ascertain if the rods after zone melting were single crystals, six were examined by x-ray diffraction utilizing the transmission Laue technique, and two were examined metallographically. Results of x-ray

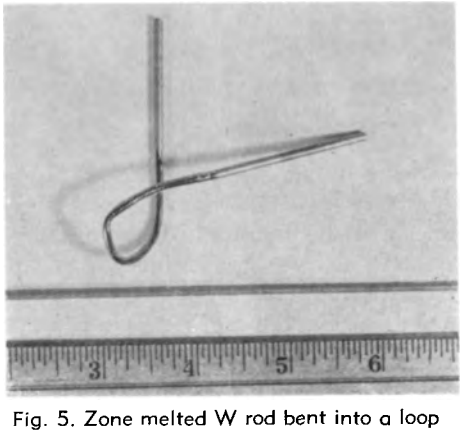

Fig. 5. Zone melted W rod bent into a loop

Table I. Crystal orientation

Plane	Angle between major plane normal and rod axis 1	1A	ZMW-1	ZMW-2	ZMW-3	ZMW-4
(100)	37	33	38	25	6	18
(110)	20	14	7	21	42	32
(111)	22	29	33	32	49	37

orientation determination are recorded in Table I. These suggest that no one preferential direction of growth existed, Rod 1A and ZMW-1 were examined at several points along the length of the crystal, and it was determined that the orientation remained the same, indicating only one crystal of the same orientation existed. Metallographic observation confirmed these results, that the rod was a single crystal along its length.

A qualitative measure of the high ductility at room temperature was obtained; this is shown in Fig. 5. Here the ⅛-in. zone melted tungsten rod was bent approximately 270° into a loop.

Conclusions

Single crystals of tungsten can be grown in the Electron Bombardment Zone Melting Apparatus. These crystals are greatly purified and exhibit a larger amount of ductility than can be obtained in an equivalent sized polycrystalline material.

Acknowledgments

The author gratefully acknowledges the assistance of J. H. Moorhead with the design and operation of this apparatus. Further, the assistance of R. Madden and J. Fagel in obtaining the spectrographic analysis, and of S. Leber for the x-ray orientation determinations is acknowledged.

Manuscript received June 9, 1958. This paper was prepared for delivery before the New York Meeting, April 27-May 1, 1958.

Any discussion of this paper will appear in a Discussion Section to be published in the December 1959 JOURNAL.

REFERENCES

1. W. G. Pfann, "Zone Melting," John Wiley & Sons, New York (1958).
2. W. A. Rocco and G. W. Sears, *Rev. Sci. Instrum.*, **27**, 1 (1956).
3. A. Calverly, M. Davis, and R. F. Lever, *J. Sci. Instr.*, **34**, 142 (1957).
4. P. G. England and H. N. Jones, *ibid.*, **35**, 66 (1958).
5. Temescal Metallurgical, *Chem. Eng. News*, Feb. 10, 1958.
6. W. P. Sykes, "A.S.M. Metals Handbook," p. 1230 (1948).
7. J. Chipman and A. Hayes, *Trans. A.I.M.E.*, **135**, 85 (1939).
8. L. S. Darken and R. W. Gurry, "Physical Chemistry of Metals," McGraw-Hill Book Co., New York (1953).
9. H. Jones, I. Langmuir, and G. MacKay, *Phys. Rev.*, (2) **30**, 201 (1927).

Vapor Pressure of Niobium

Rudolph Speiser

Department of Metallurgy, The Ohio State University, Columbus, Ohio

P. Blackburn

Research Laboratory, Westinghouse Electric Corporation, Pittsburgh, Pennsylvania

H. L. Johnston

H. L. Johnston Associates, Columbus, Ohio

ABSTRACT

The Langmuir method has been used to determine the vapor pressure of niobium. An accommodation coefficient of unity was assumed. Least square treatment of the vapor pressure data yields the equation

$$\log P_{atm} = -\frac{(40{,}169)}{T} + 8.872$$

The heat of sublimation at absolute zero, ΔH°_0, is 171.80 ± 0.49 and $\Delta H^\circ_{298.15}$ is 172.53 kcal/g atom.

Prior to this investigation, the only data (1) available for the computation of vapor pressures of Nb was the rate of sublimation from a Nb wire heated by the passage of an electric current. Since these measurements were made at only three temperatures, and since the temperature measurement depended on an accurate determination of the emissivity of the wire, it was decided to repeat these measurements using the method and apparatus described in previous publications (2). The Langmuir method was employed, and an accommodation coefficient of unity was assumed.

Experimental

The measurements consisted of determining the rate at which a Nb surface sublimed into a high vacuum. The sample was supplied by the Fansteel Corporation and was assayed at a purity of 99.9%. The sample was in a form of an annular ring 0.985 in. OD, 0.374 in. ID, and 0.357 in. thick. The effective internal area (3) of the annular ring was computed from the expression

$$\text{Eff. area} = \pi b(\sqrt{a^2 + b^2} - b) \qquad [1]$$

where a is the inside diameter and b, the thickness.

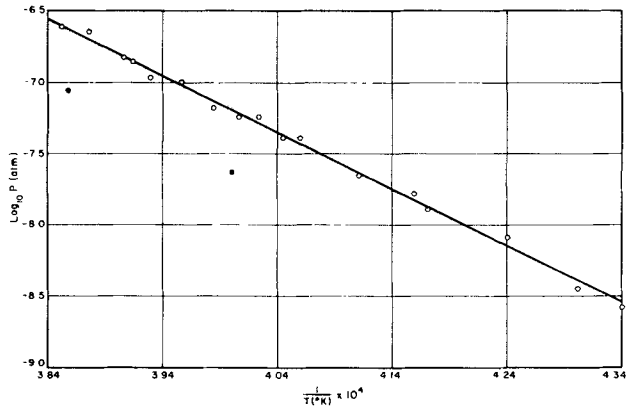

Fig. 1. Plot of the logarithm of the pressure of Nb in atmospheres vs. the reciprocal of the absolute temperature. Solid circles represent the data of Reimann and Grant (1).

Table I. Vapor pressure of Nb

Temp, °K	Weight loss, g	Eff. time, min.	Evap. rate, g/cm²/sec	Pressure, atm
2304	0.00791	326.7	2.3423×10^{-8}	2.6311×10^{-9}
2325	0.00881	274.4	3.1208×10^{-8}	3.5216×10^{-9}
2358	0.01733	236.0	7.1368×10^{-8}	8.0977×10^{-9}
2397	0.01206	105.4	1.1091×10^{-7}	1.2708×10^{-8}
2404	0.02600	174.2	1.4402×10^{-7}	1.6526×10^{-8}
2432	0.01941	97.1	1.9343×10^{-7}	2.2323×10^{-8}
2463	0.01495	41.5	3.4881×10^{-7}	4.0512×10^{-8}
2472	0.01134	30.8	3.5520×10^{-7}	4.1329×10^{-8}
2485	0.01568	30.4	4.9777×10^{-7}	5.8069×10^{-8}
2496	0.01735	33.6	4.9787×10^{-7}	5.7032×10^{-8}
2510	0.02501	42.4	5.6649×10^{-7}	6.6418×10^{-8}
2528	0.02694	30.1	8.6111×10^{-7}	1.0132×10^{-7}
2545	0.02172	23.2	9.0269×10^{-7}	1.0657×10^{-7}
2555	0.02684	21.8	1.1803×10^{-6}	1.3963×10^{-7}
2566	0.04075	31.7	1.2338×10^{-6}	1.4626×10^{-7}
2580	0.04827	25.0	1.8615×10^{-6}	2.2127×10^{-7}
2596	0.04340	20.4	2.0495×10^{-6}	2.4438×10^{-7}

Table II. Thermodynamic functions of Nb

Temp, °K	$\frac{(F°-H°_0)_g}{T}$	$\frac{(F°-H°_0)_s}{T}$	$-R \ln P$	$\Delta H°_0$ kcal	
2304	51.41	15.66	39.28	172.87	
2325	51.46	15.71	38.70	173.10	
2358	51.55	15.82	37.05	171.62	
2397	51.65	15.92	36.15	172.30	
2404	51.67	15.94	35.63	171.55	
2432	51.74	16.02	35.03	172.06	
2463	51.82	16.11	33.85	171.33	
2472	51.85	16.13	33.81	171.88	
2485	51.88	16.17	33.13	171.07	
2496	51.91	16.20	33.17	171.92	
2510	51.94	16.23	32.86	172.11	
2528	51.98	16.27	32.02	171.22	
2545	52.02	16.31	31.92	172.11	
2555	52.05	16.34	31.38	171.41	
2566	52.07	16.36	31.29	171.92	
2580	52.12	16.40	30.47	170.77	
2596	52.16	16.46	30.27	171.26	
			Mean	171.80	±0.49

The area of the sample was also corrected for the thermal expansions from room temperature to the temperature of the measurement. The sample was placed in a metal cell (2) and after thorough outgassing was then heated by induction under a vacuum of the order of 10^{-6} mm.

The effective time at the temperature of measurement was determined as described previously (2).

Temperatures were measured under black body conditions by sighting into a hole drilled into the sample. A L&N disappearing filament optical pyrometer which had been calibrated by the National Bureau of Standards and frequently checked against a standard lamp furnished by the Bureau was used to measure the temperature. Pyrometer readings were reproduced to ±2°.

Results and Discussion

Experimental results are plotted as log P_{atm} vs. $1/T$ in Fig. 1 and summarized in Table I. Thermodynamic functions are tabulated in Table II; the thermal data for solid and gaseous Nb were taken from the compilation of Stull and Sinke (4). The computed value of $\Delta H°_0$, the heat of sublimation at 0°K, is 171.80 ±0.49 kcal/g atom. This value is to be compared with a $\Delta H°_0$ value of 176.82 kcal/g atom computed from the vapor pressure data of Reimann and Grant at 2600°K. Vapor pressures in this research are higher by a factor of 2.8 than those measured by Reimann and Grant. An error of 70° in the temperature scale could account for this discrepancy, and an error of this magnitude is quite possible when temperature measurements dependent on the emissivity of a surface are made.

Least square treatment of the vapor pressure data for Nb yields the equation

$$\log P_{atm} = -\frac{(40{,}169)}{T} + 8.872 \qquad [2]$$

These data also yield a value of $\Delta H°_{298.15}$ of 172.53 kcal/g atom.

Manuscript received July 14, 1958. This paper was prepared for delivery before the New York Meeting, April 27-May 1, 1958.

Any discussion of this paper will appear in a Discussion Section to be published in the December 1959 JOURNAL.

REFERENCES

1. A. L. Reimann and C. K. Grant, *Phil. Mag.*, **22**, 34 (1936).
2. R. Speiser and J. W. Spretnak in "Vacuum Metallurgy," p. 155, Electrochem. Soc., Inc. (1955); R. Speiser and H. L. Johnston, *Trans. ASM*, **42**, 283 (1950).
3. R. B. Holden, R. Speiser, and H. L. Johnston, *J. Am. Chem. Soc.*, **70**, 3897 (1948).
4. D. R. Stull and G. C. Sinke, "Thermodynamic Properties of the Elements," Am. Chem. Soc. (1956).

The Occurrence of Impurities in Rock Salt, Solar Salt, and Purified Sodium Chloride

Arthur Bloomberg and Kurt Ladenburg

Research Laboratory, International Salt Company, Inc., New York, New York

ABSTRACT

Because of the known interference of certain impurities and the suspected effect of others in the electrolytic cell processes for the production of sodium and chlorine-caustic soda, the presence or absence of thirty-five elements in sodium chloride samples was investigated spectrographically, allowing detection of extremely low concentrations. Results are reported for rock salt from four different locations, for three different solar salts, and for purified salt from two separate plants.

The chlorine caustic industry has reliable information (1-4) regarding the influence of trace impurities on the electrolysis of sodium chloride by the mercury cell process. The presence of certain metals (V, Mo, Cr, and Ti) in concentrations as low as 0.25 mg/liter of brine (equivalent to 0.8 ppm in dry sodium chloride) decreases cathodic current efficiency considerably.

The sodium chloride brines used are derived from different sources and from various locations, viz., rock salt, brought to the surface dry; rock salt, dissolved underground and pumped to the surface through brine wells; natural underground brines; solar salt; vacuum pan salt.

Although rock salt and raw brines are usually purified before use, it is of considerable interest to know to what extent the harmful metals occur in the salt. Since the literature provides practically no information on this subject, a spectrographic investigation of different types of sodium chloride from different locations was undertaken. Rock salt samples were obtained from Louisiana, Michigan, New York, and the Dominican Republic; solar salt from California, The Great Salt Lake, and the Bahamas; purified vacuum pan salt from Louisiana and New York.

Considerable variation exists in quantity, and some variation in kind, of impurities found in natural salt deposits.Unrefined rock salt contains some water-insoluble matter, mostly anhydrite, plus traces of other minerals: dolomite, hematite, quartz, celestite, clay (aluminum silicate), etc. Since trace quantities were to be determined, an effort was made to determine the variance in results between duplicate analyses and between samples taken from the production line at least one week apart. The analyses on rock salt from New York, Michigan, and Louisiana were run in duplicate on two samples taken at different times. A single analysis of the purified salt was made on two samples taken several weeks apart. Kilogram samples were used in all analyses to increase precision and to compensate for the non-uniform distribution of impurities in the rock salt deposits. In no instance, where more than one analysis was made on salt from a given source, was there any wide discrepancy in results between the several samples.

Solar salt may contain traces of many of the constituents of sea water, depending on the control exercised during the evaporation and crystallization process. Most of the natural impurities are water-soluble except for mechanical contaminants such as clay or calcium sulfate from pan bottoms, or windblown dust.

Purified vacuum pan salt was included to indicate, by difference, the extent to which trace elements are removed by chemical purification.

Experimental

A kilogram of salt was dissolved in 3500 ml of distilled water, allowed to stand over night, and then filtered through Whatman No. 41 paper. The residue was washed with several portions of distilled water, the washes being added to the brine. The filter paper and insolubles were dried over night at 110°C. The paper was separated and ashed separately. The residue was added to the ash and the total weighed as "insolubles." This was ground in an agate mortar and analyzed spectrographically. In the case of the purified salt samples there was no insoluble portion.

The trace elements in the soluble fraction were precipitated with H_2S from slightly alkaline brine, using high-purity lead as a carrier.

The filtered brine was made alkaline with 5 ml of C.P. NH_4OH. Fifty mg of 99.99+% lead, as a lead nitrate solution, was added to act as "carrier." The precipitation of the sulfides was carried out under a slight pressure of water-washed H_2S and with stirring. A blank containing 5 ml NH_4OH and 50.0 mg Pb was run along with the brine samples. To avoid colloid formation, the solution was evaporated to 400-500 ml before the H_2S was added.

In the analysis of the sulfides, the following metals were determined quantitatively with the aid of specially prepared standards: Ni, Co, Cr, Cu, Mn, Zn, Fe, and V. All other analyses were made semiquantitatively.

Table I

Element	Limit of detection (ppm) Insol.	Sulfide	Mother liq.	Wave length Å
				3082.1
Al	0.1	0.00025	5	3092.7
				2528.5
Sb	0.1	0.00025	5	2598.0
As	0.2	0.0005	10	2780.2
Ba	0.02	0.00005	1	4554.0
Bi	0.02	0.00005	1	3067.7
Cd	0.1	0.00025	5	3261.0
Ca	0.02	0.00005	1	4226.7
Ce	0.02	0.00005	1	8521.1
Cr	0.1	0.00025	5	4254.3
Co	0.1	0.00025	5	3453.5
Cu	0.01	0.000025	0.5	3273.9
Ga	0.02	0.00005	1	2943.6
Ge	0.02	0.00005	1	3039.0
In	0.02	0.00005	1	3256.1
Fe	0.02	0.00005	1	3020.6
Pb	0.02	0.00005	1	2833.1
Li	0.02	0.00005	1	6707.8
Mg	0.1	0.00025	5	2852.1
Mn	0.02	0.00005	1	2798.2
Mo	0.1	0.00025	5	3193.9
Ni	0.1	0.00025	5	3414.7
P	1	0.0025	50	2535.6
K	0.02	0.00005	1	7664.8
Rb	0.02	0.00005	1	7800.2
Si	0.1	0.00025	5	2881.5
Ag	0.01	0.000025	0.5	3280.6
Na	0.02	0.00005	1	5889.9
Sr	0.02	0.00005	1	4607.3
Tl	0.1	0.00025	5	3519.2
Sn	0.02	0.00005	1	2839.9
Ti	0.1	0.00025	5	3078.6
W	1	0.0025	50	2944.4
V	0.02	0.00005	1	3185.4
Zn	0.1	0.00025	5	3345.0
Zr	0.1	0.00025	5	3601.2

The precipitate was allowed to settle over night and was then separated from the alkaline brine by centrifuging. It was washed several times with slightly alkaline H_2S-saturated distilled water. The washed precipitate was then transferred to a crucible, dried at 110°C, and analyzed spectrographically as was the alkaline "mother liquor." Since no information was available on the efficiency of this method of separation of trace elements, a separate spectrographic analyses was also made on the filtered mother liquor.[1]

To evaluate the contribution of the water impurities to the mother liquor analysis, the alkaline solution, after the removal of the sulfides in the blank analysis, was evaporated to dryness and the residue analyzed spectrographically.

All spectrographs were made using a Bausch and Lomb Littrow instrument. Samples were burned to completion using a d-c arc. Fifty mg of the "insolubles" or 100 mg of the salt obtained by evaporating the mother liquor was used for each analysis. The standards were prepared by adding 0.01 mg of each of the metals to 50.0 mg of high-purity lead and converting to sulfate. In each analysis of the "Sulfide Precipitate," the entire precipitate was converted to sulfates and burned to completion. The standard sulfate sample contained the equivalent of 0.01 ppm of each of the metals based on the original sample weight of 1000 g.

Discussion of Results

Table I gives the minimum concentration of each element detectable by the techniques used and the wave lengths used for detection. The data give the maximum amount of each element found.

Tables II and III give the analyses of the different salt samples. To conserve space the analyses of the sulfides and the mother liquors are combined under the heading of "Brines." The alkali metals and alkaline earth metals were not found in the sulfide precipitate. The only metallic impurities found in the filtered mother liquor were Cu, Fe, and Mn. These were close to the limit of detection and may be due largely to trace impurities in the graphite electrodes. The values listed for these metals in the brine column are based on analysis of the sulfides. Silicon

[1] Vanadium content of Pacific Coast solar salt found spectrographically, 5 ppb; independent analysis by colorimetric method, 7 ppb.

Table II

Element	Rock salt samples: Michigan Insoluble	Michigan Brine	New York Insoluble	New York Brine	ppm Element in sample: Louisiana Insoluble	Louisiana Brine	Caribbean Insoluble	Caribbean Brine
Al	750	0.09	900	0.9	150	0.09	>1000	0.9
Ba	25	N	10	N	N	N	100	N
Ca	—	—	—	—	—	—	—	—
Cr	N	0.01	N	0.01	N	<0.005	1.8	0.06
Co	N	<0.005	N	<0.005	N	<0.005	N	<0.005
Cu	5	0.3	1	0.09	1	0.03	18	0.2
Fe	250	0.9	1000	0.5	90	0.2	<1000	0.08
Pb	2	—	0.2	—	2	—	18	—
Mg	1000	500	1000	90	1000	90	>1000	900
Mn	10	0.04	100	0.03	100	1.2	180	0.1
Ni	N	0.08	N	0.01	N	0.012	1.0	0.03
K	200	9000	1000	5000	100	9000	180	9000
Si	1000	—	>1000	—	200	—	>1000	—
Ag	N	<0.005	N	<0.005	0.2	0.09	N	0.09
Na	100	—	200	—	1000	—	180	—
Sr	1000	9000	200	900	100	900	100	900
Sn	N	N	N	N	N	N	0.2	0.09
Ti	10	<0.005	200	<0.005	2	<0.005	180	0.09
V	N	<0.005	10	<0.005	N	<0.005	N	0.09
Zn	N	0.20	2	0.34	N	0.05	N	0.2
Zr	N	N	2	N	N	N	1.8	N

Table III

ppm Element in sample

Element	Purified salt		Solar salt					
			Caribbean		Great Salt Lake		Pacific Coast	
	New York	Louisiana	Insoluble	Brine	Insoluble	Brine	Insoluble	Brine
Al	0.09	0.05	18	0.9	15	0.009	>15	0.09
Ba	N	N	1	N	0.9	N	0.9	N
Ca	90	90	—	—	15	—	<15	—
Cr	<0.005	<0.005	N	0.02	0.05	<0.005	0.09	<0.005
Co	<0.005	<0.005	N	<0.005	N	<0.005	N	<0.005
Cu	0.57	0.04	0.2	0.2	0.9	0.008	0.5	0.1
Fe	0.25	0.20	18	0.3	<15	0.01	>15	0.08
Pb	—	—	0.1	—	0.5	—	0.05	—
Mg	9	9	—	900	>15	900	>15	900
Mn	0.002	0.009	0.2	0.003	0.9	<0.005	0.9	0.01
Ni	0.04	0.005	N	0.01	0.05	<0.005	0.09	0.009
K	90	90	1.8	9000	0.9	5000	0.9	5000
Si	—	—	—	—	>15	—	<15	—
Ag	0.009	0.009	N	0.09	N	0.009	N	0.009
Na	—	—	18	—	>15	—	<15	—
Sr	9	N	18	900	0.05	50	0.09	500
Sn	N	N	1.8	0.09	0.005	N	0.009	0.009
Ti	0.09	0.009	0.2	0.09	<15	N	<15	N
V	<0.005	0.008	N	0.06	N	<0.005	N	0.005
Zn	<0.01	<0.01	N	0.07	N	<0.005	N	0.01
Zr	N	N	N	N	0.09	N	0.09	N

was estimated only in the insoluble portion. Sufficient silicon can be extracted from laboratory glassware to show up in the spectra of the sulfides and mother liquors.

Where semi-quantitative analyses were made, the higher value of the range is listed. The symbol "N" in the tables indicates that the element was not detected, and (-) indicates that the concentration was not estimated. All values are corrected for the concentrations found in the blanks. An element listed in Table I, but not in the other tables, indicates that the element was not detected in either the insoluble or soluble portion.

Manuscript received April 2, 1958. This paper was prepared for delivery before the New York Meeting, April 27-May 1, 1958.

Any discussion of this paper will appear in a Discussion Section to be published in the December 1959 JOURNAL.

REFERENCES

1. G. Angel and T. Lunden, *This Journal*, **99**, 435 (1952).
2. G. Angel and R. Brämmland, *ibid.*, **99**, 442 (1952).
3. G. Angel, T. Lunden, and R. Brämmland, *ibid.*, **100**, 39 (1953).
4. G. Angel, T. Lunden, S. Dahlerus, and R. Brämmland, *ibid.*, **102**, 124 (1955).
5. G. Angel, T. Lunden, S. Dahlerus, and R. Brämmland, *ibid.*, **102**, 246 (1955).

The Oxygen Electrode

I. Isotopic Investigation of Electrode Mechanisms

Myron O. Davies,[1] Milton Clark,[2] Ernest Yeager, and Frank Hovorka

Department of Chemistry, Western Reserve University, Cleveland, Ohio

ABSTRACT

Isotopic techniques involving O^{18} have been used to study the cathodic and anodic properties of the oxygen-peroxide couple on partially hydrophobic, active carbon electrodes in alkaline solution. The isotopic analyses have been carried out with an analytical mass spectrometer. For the cathodic reaction, tracer and equilibration experiments prove that all of the peroxide oxygen originates from gaseous oxygen and that the O-O bond is not actually broken in the formation of the peroxide. Tracer experiments also indicate that the oxygen gas liberated during the anodic oxidation of the HO_2^- ion contains only peroxide oxygen. These results are interpreted in terms of various possible reaction mechanisms.

Various investigators (1-5) have demonstrated the reversibility of the oxygen-peroxide couple on active carbon electrodes in alkaline solution in the absence of a polarizing current. The over-all electrode reaction in alkaline solution may be represented as follows:

$$O_2 + H_2O + 2e \rightleftharpoons OH^- + HO_2^-$$

[1] Present address: N.A.S.A. Laboratory, Cleveland, Ohio.
[2] Present address: National Carbon Co., Cleveland, Ohio.

Cathodic (5,6) as well as anodic (7) polarization measurements[3] at Western Reserve University have indicated that the activation polarization associated with the oxygen-peroxide couple on active carbon in alkaline solution is generally small even at apparent current densities as high as 500 ma/cm^2. Concentration polarization involving the perhydroxide ion and molecular oxygen transport are the predominant sources of polarization under these conditions. As a result, polarization measurements have yielded only limited information concerning the electrode mechanisms associated with the oxygen-peroxide couple.

The following questions have been raised concerning the cathodic reaction:

(*A*) Does all of the peroxide oxygen originate from molecular oxygen? (*B*) Is the oxygen-oxygen bond actually broken in the formation of the peroxide? Similar questions have been proposed for the reverse anodic reaction. On a theoretical basis, the answer to the first question should be positive and to the second question negative, but no one had ever proved it conclusively.

The present experiments involving isotopic techniques represent an attempt to provide a definite proof. While tracer experiments involving O^{18} can be used to answer the first question, equilibration experiments are necessary to answer the second question. All of the isotopic experiments described in this paper have been carried out under substantially reversible electrochemical conditions.

Experimental Procedures

Isotopic concentrations in non-equilibrated oxygen gas.—In terms of the isotopes 16 and 18, oxygen gas contains the three molecular species O^{16}-O^{16}, O^{18}-O^{16}, and O^{18}-O^{18}. The O^{18}-enriched gas available for these experiments is approximately 1.4% O^{18} on an atomic basis. The concentration of O^{18}-O^{16} is twice the O^{18} concentration because there are two chances for the inclusion of an O^{18} atom in a given molecule (see Table I). The concentration of O^{18}-O^{18}, however, is approximately the square of the O^{18} concentration since the probability of two simultaneous, substantially independent events is involved. The latter is true only if the gas is completely equilibrated. Consider the results of diluting this O^{18}-enriched gas sample with oxygen gas containing no O^{18} in a 1:1 ratio. Table I indicates the concentrations for the case of nonequilibration and equilibration. For the former, the concentration of the species O^{19}-O^{18} is reduced by a factor of two, whereas in the latter case the concentration is reduced fourfold.

In the present research, various experiments have been performed in which nonequilibrated oxygen gas is converted to hydrogen peroxide. The peroxide is then oxidized to yield oxygen gas which is subsequently examined with a mass spectrometer to see if it has been equilibrated. From this information it is possible to establish whether the oxygen bond has been broken during any step.

[3] These polarization studies will be the subject of later papers in this series.

Table I. Effects of dilution on isotopic concentrations

	O^{18} %	O^{18}-O^{16} %	O^{18}-O^{18} %
1. Original sample	1.4	2.8	0.02
2. Diluted sample (1:1)			
a. Equilibrated	0.7	1.4	0.005
b. Nonequilibrated	0.7	1.4	0.01

Preparation of O^{18}-enriched gas.—The oxygen gas used in the isotope experiments was prepared by the electrolysis of O^{18}-enriched water (1.4% H_2O^{18}).[4] Sufficient H_2SO_4 was added to provide an approximately 1M solution. The electrolysis was carried out in an H-cell between smooth platinum electrodes. The oxygen gas was collected by means of an automatic system and stored as a liquid at liquid nitrogen temperatures for subsequent use.

Electrolytic cells.—Two cells of different design were required for the cathodic and anodic experiments. Figure 1 shows the cell used for the cathodic experiments. The cathode consisted of a porous graphite plug with a layer of active carbon approximately 1 mm thick on the surface exposed to the electrolyte. The apparent area of the cathode was approximately 3 cm^2. The oxygen gas was introduced through the rear side through inlet F. The side arm E, which was submerged in the water within a test tube, served as a pressure control by venting excess gas. The anode consisted of a 1-cm^2 piece of smooth platinum, which was enclosed in a separate compartment with a small hole connecting to the main cathode compartment. This arrangement reduced greatly the rate at which the peroxide generated at the cathode diffused to the anode where it would be oxidized. Oxygen liberated at the anode did not diffuse to the cathode in any appreciable amounts.

The active carbon layer on the cathode must serve the dual purpose of providing sites for the electrochemical reduction as well as a means by which molecular oxygen is readily transported to these sites. The effective transport of oxygen in the electrode structure has been shown (5, 6) to require a

[4] Obtained from the Stuart Oxygen Co. of California.

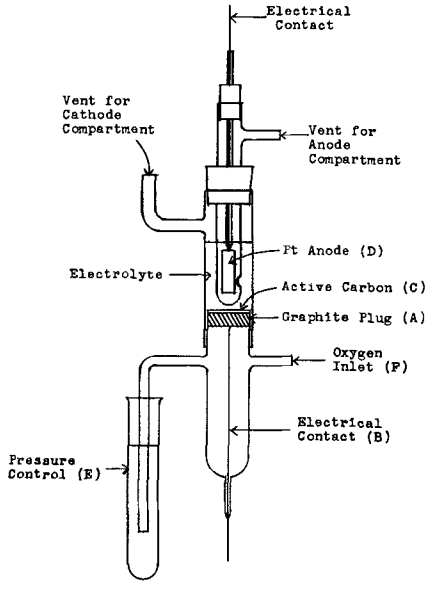

Fig. 1. Cathodic cell for O^{18} experiments

microporous structure containing no solution. For these reasons, the active carbon electrode must be partially hydrophobic to prevent the penetration of the solution into the porous structure. While active carbon itself is somewhat hydrophobic to alkaline solutions, additional waterproofing is obtained through the use of a material such as polyethylene, paraffin, or gum rubber, which also functions as a binder. In the present work, the active carbon layer was applied to the graphite plug by a technique similar to that used by Berl (1). A benzene suspension of active carbon containing gum rubber (5% by weight of carbon) was sprayed with a small atomizer onto the porous graphite plug. The graphite plug was warmed with an infrared lamp both before and after spraying and suction applied on the rear surface of the plug to expedite the rapid and complete removal of the benzene from the active carbon layer. Nuchar C 115[5] was chosen as the active carbon because cathodes prepared from this carbon have low polarization and do not decompose hydrogen peroxide very readily.

The cell used for the anodic experiments is shown in Fig. 2. The anode, A, consisted of a smooth platinum electrode with an area of approximately 3 cm^2. This platinum electrode was corrugated so that it would fit under the hood, B, and then was sprayed on both sides with active carbon by a procedure similar to that used for the preparation of the cathodes in Fig. 1. A small piece of platinum foil, C, located outside of the hood served as the cathode. The oxygen gas resulting from the anodic oxidation of the hydrogen peroxide in the solution was collected in the tube, E.

Cathode measurements.—Two types of cathodic experiments were carried out with the cell in Fig. 1. In one, ordinary oxygen (Linde) was used in conjunction with an enriched 1M KOH solution, prepared by dissolving analytical grade KOH in O^{18}-enriched water. In the second, the electrolytic solution was unenriched, but a 1:1 mixture of enriched oxygen and ordinary oxygen gas was fed to the cathode. No hydrogen peroxide was added to the electrolyte in the cathodic experiments.

[5] Product of West Virginia Pulp and Paper Co.

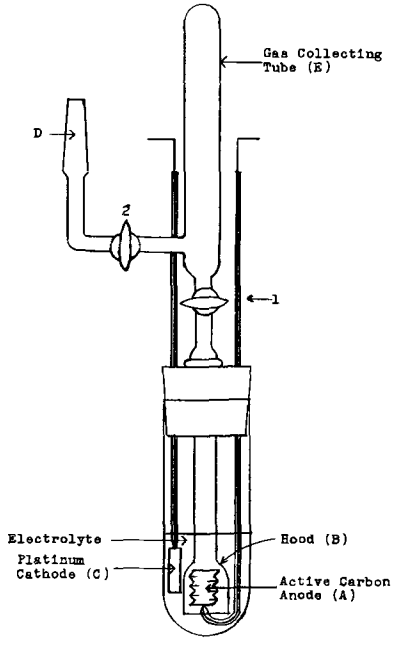

Fig. 2. Anodic cell for O^{18} experiments

In the experiment using the enriched oxygen mixture, the 1:1 mixture of enriched and unenriched oxygen was prepared by condensing an equal volume of Linde tank oxygen (U.S.P.) into the same tube in which the electrolytically produced, O^{18}-enriched oxygen had been collected. The two gases were mixed by distilling them over into another tube which was kept in a Dewar of liquid nitrogen until used in the electrochemical experiment. The outlet of this tube was connected to inlet F of the cathodic cell, the stopcock opened, and the Dewar lowered just enough to allow the oxygen to boil at such a rate that a steady stream of bubbles came from the outlet tube immersed in test tube E. For the majority of the experiments using only unenriched oxygen, the oxygen tank was connected directly to inlet F and the appropriate rate of flow obtained by means of the needle valve of the tank regulator.

After the oxygen flow had been adjusted, approximately 10 ml of electrolyte was added to the cell and the current turned on. Reduction was continued for 15 min after which the sample was quickly transferred to the peroxide decomposing system to be described shortly. Although it is possible for O^{18} to exchange between HO_2^- and H_2O, it has been shown (as will be described later) that no significant exchange occurs within 30 min. In all experiments this was the maximum time allowed to elapse from the beginning of the experiment until the solution was frozen in the peroxide decomposing system.

Anodic measurements.—The electrolyte consisted of 5M KOH prepared with O^{18}-enriched water to which sufficient 90% unstabilized H_2O_2 was added to yield a solution of approximately 0.9M with respect to peroxide. A volume of 25 ml of solution was required to fill the cell in Fig. 2. The solution was sucked up within the cell as far as stopcock 1. This stopcock was then closed and tube E was evacuated through outlet D, after which stopcock 2 was closed. The current was then turned on.

All of the oxygen liberated from the anode, as well as some oxygen resulting from the decomposition of hydrogen peroxide, was collected in the upper part of the tube above the hood below stopcock 1. Hydrogen from the cathode escaped into the atmosphere. From time to time oxygen which had collected in the upper part of the hood tube was admitted to the evacuated collecting tube E by opening stopcock 1. Care was taken to allow as little electrolyte as possible to be sucked into the upper tube. When sufficient oxygen gas had been obtained for the pressure in tube E to be 1 atm, the current was turned off. The total length of time from the introduction of the peroxide to the electrolyte until the end of the electrolysis was not more than 30 min.

After the completion of the electrolysis, the oxygen gas in tube E was passed through a dry ice-methanol trap to remove moisture and transferred to a storage bulb for subsequent mass spectrometer analysis.

Table II. Results of isotopic experiments

Conditions	O^{18}-O^{16} %	O^{18}-O^{18} %
A. Adsorption of enriched, nonequilibrated oxygen on active carbon at liquid nitrogen temperature, followed by desorption.		
1. Experimental	1.54	0.012
Expected if equilibration occurred	1.58	0.0062
Expected if no equilibration occurred	1.58	0.012
2. Experimental	1.50	0.0096
Expected if equilibration occurred	1.48	0.0055
Expected if no equilibration occurred	1.48	0.0086
B. Unenriched hydrogen peroxide in alkaline solution with enriched water for 30 min.		
Experimental	0.41	0.0008
Expected if no exchange	0.40	0.0004
Expected if complete exchange	2.8	0.020
C. Peroxide formed cathodically at an active carbon electrode in basic solution, using enriched, nonequilibrated oxygen and unenriched water.		
1. Experimental	1.27	0.0078
Expected if the oxygen in the peroxide came from the water only	0.40	0.0004
Expected if the oxygen in the peroxide came from the oxygen gas only		
With equilibration	1.24	0.0038
With no equilibration	1.24	0.0067
2. Experimental	1.37	0.0086
Expected if the oxygen in the peroxide came from the water only	0.40	0.0004
Expected if the oxgen in the peroxide came from the oxygen gas only		
With equilibration	1.41	0.0050
With no equilibration	1.41	0.0083
D. Peroxide formed cathodically at an active carbon electrode in basic solution, using tank oxygen and enriched water.		
1. Experimental	0.45	0.0023
Expected if the oxygen in the peroxide came from the water only	2.80	0.020
Expected if the oxygen in the peroxide came from the oxygen gas only	0.43	0.0026
2. Experimental	0.45	0.0021
Expected if the oxygen in the peroxide came from the water only	2.80	0.020
Expected if the oxygen in the peroxide came from the oxygen gas only	0.41	0.0022
3. Experimental	0.42	0.0029
Expected if the oxygen in the peroxide came from the water only	2.80	0.020
Expected if the oxygen in the peroxide came from the oxygen gas only	0.41	0.0021
E. Peroxide formed cathodically at an active carbon electrode in basic solution using enriched water and unenriched oxygen gas prepared by partial evaporation of liquefied tank gas.		
1. Experimental	0.42	0.00088
Expected if the oxygen in the peroxide came from the water only	2.80	0.020
Expected if the oxygen in the peroxide came from the oxygen gas only	0.40	0.00089
2. Experimental	0.43	0.00094
Expected if the oxygen in the peroxide came from the water only	2.80	0.020
Expected if the oxygen in the peroxide came from the oxygen gas only	0.40	0.00089
F. Oxygen gas formed anodically at an active carbon electrode in basic solution containing unenriched hydrogen peroxide.		
1. Experimental (with unenriched water)	0.39	0.00076
2. Experimental (with enriched water)	0.38	0.0014
Expected if the oxygen came from the water	2.80	0.020
Expected if the oxygen came from the peroxide	0.39	0.00076

Analytical procedures.—The hydrogen peroxide samples were decomposed with ceric sulfate as an oxidant in order to recover the peroxide oxygen for mass spectrometer analysis. Cahill and Taube (8) have shown that oxidation with this reagent liberates oxygen exclusively from the peroxide without exchange with oxygen of the water. These workers also believed that the rupture of the oxygen-oxygen bond does not occur in the oxidation of hydrogen peroxide with this reagent. The present experimental work verifies this conclusion.

Prior to the oxidation with ceric sulfate, the hydrogen peroxide solutions as well as the ceric sulfate-sulfuric acid solutions were degassed[6] to remove any dissolved molecular oxygen. The oxygen gas from the oxidation of the hydrogen peroxide was dried by means of a dry ice-methanol trap and then stored in a glass bulb for subsequent isotopic analysis.

A Consolidated Engineering analytical mass spectrometer (modified type 21-101) was used for all the isotopic analyses. This instrument was equipped with a nonmagnetic stainless steel analyzer tube in which the ionization zone was thermostated to 250° ±0.3°C. The surface of the tungsten filament within the analyzer tube was kept well carbided to minimize the attack of the filament by the oxygen gas. The mass spectrum for each sample was scanned from mass number 26 to 42 in order to include the peaks for nitrogen and argon, if present, as well as the various isotopic O_2 peaks. It was necessary to scan this range twice for each sample, once at high amplifier sensitivity and once at low amplifier sensitivity, because the high sensitivities required to give measurable 36 peaks (O^{18}-O^{18}) gave 32 peaks (O^{16}-O^{16}) which were too large to record. Mass 34 peaks (O^{18}-O^{16}) were measurable at both sensitivities.

The calculations of the relative isotopic concentrations are based on the assumption that the isotopic concentrations are directly proportional to the peak heights minus the background peak heights on the records from the mass spectrometer with the same proportionality constant for all three mass numbers: 32, 34, and 36. This assumption is justified only if the accelerating voltages used in the mass spectrometer are approximately the same for the various mass numbers. Such was the case in the present work. Corrections were made for nonlinearity in the recording system. An additional correction was necessary for the 36 peaks corresponding to O^{18}-O^{18}. Argon occurs as an impurity in oxygen gas prepared by liquefaction of air to the extent of about 0.5%. Evidence of this situation is readily apparent from the relatively prominent mass number 40 peaks in the mass spectra. Since argon has an isotope of mass 36, it has been necessary to apply a correction for this isotope. The ratio of the 36 to 40 peaks for argon is 0.31 to 99.68 in argon in the air (10). This ratio was assumed to apply to the argon in the oxygen gas as an approximation, although the actual ratio is probably higher because of the fractional distillation involved in the preparation of oxygen gas from air. The height of the 40 peak multiplied by 0.003 was subtracted from the 36 peak.

[6] For details concerning the procedure used for the recovery of the peroxide oxygen, see Ref. (9).

Experimental Results

Preliminary Experiments

Several preliminary experiments were carried out to become familiar with the techniques as well as to check certain aspects of the electrochemical experiments which might prove troublesome. The first experiment involved the adsorption of nonequilibrated oxygen gas on an active carbon sample (Nuchar C115) from which physically adsorbed gas had been removed previously. After 45 min at liquid nitrogen temperatures, the gas was desorbed by warming the sample of carbon to room temperature. The amount of gas adsorbed at the liquid nitrogen temperatures was just slightly less than that corresponding to a monolayer coverage as determined by earlier surface area measurements. The data in part A of Table II indicate that no equilibration occurred within the limits of reproducibility of the experiment. Since this experiment was for the most part at liquid nitrogen temperatures, the results do not imply that equilibration does not take place at room temperatures to some extent. Reproducibility generally was limited by contaminants in the oxygen gas, and to a lesser extent, background associated with the mass spectrometer.

The second preliminary experiment involved a check to see if appreciable exchange between oxygen in the water and oxygen in the peroxide occurs in alkaline solution during the time periods required for the electrochemical experiments. If such an exchange had occurred to any significant extent, the electrochemical experiments would have been invalidated. Sufficient 90% unenriched, nonstabilized hydrogen peroxide was added to a 1.4M KOH solution containing enriched water (approximately 1.4% O^{18}) to yield approximately 0.4M H_2O_2 solution. After 30 min the H_2O_2 was decomposed by the procedure described previously. The results are given in part B of Table II and indicate no exchange of peroxide oxygen and water oxygen within the limits of reproducibility during a period of 30 min. This was the maximum length of time during which H_2O_2 and H_2O were in contact in alkaline solution in the subsequent electrochemical experiments.

Electrochemical Experiments

In parts C to E of Table II are summarized the results of the cathodic experiments with O^{18}-enriched gas and water. In part F the results for the anodic experiments with O^{18}-enriched water are given.

All of the expected values for the O^{18}-O^{16} percentages in Table II are based on the original concentration of this species in the oxygen gas or the water involved in the experiment, as the case may be. In parts A and C the expected non-equilibration values for O^{18}-O^{18} are the same as for the original nonequilibrated enriched gas, while the expected equilibration values for O^{18}-O^{18} are calculated from the concentration of O^{18}-O^{16} in the original oxygen gas. The expected values for the concentration of O^{18}-O^{18} in parts D, E, and F of the table are based on the original oxygen gas used in the experiment or calculated on the basis of the atomic per cent O^{18} in the water, depending on which prediction is involved. In the predictions based on the O^{18} content of the original water used in preparing the solution, no correction was made for the small dilution effect of the base on the O^{18} content of the resulting solution.

Examination of the data revealed one fact which required further investigation. Unenriched oxgyen should contain only 0.0004% of O^{18}-O^{18}. Experimental values were consistently higher than this, as is evident in part D of Table II. If the unenriched oxygen gas was first liquefied and a fraction distilled off, the results were found to be closer to the expected values. An unenriched oxygen sample thus treated gave results of 0.40% for O^{18}-O^{16} and 0.0009% for O^{18}-O^{18}.

The remaining discrepancy of approximately twofold between the calculated value of 0.0004% for O^{18}-O^{18} and the measured value of 0.0009% for O^{18}-O^{18} is not surprising because these values are near the limit of sensitivity of the mass spectrometer and because relatively large background corrections are involved. The analyses of oxygen obtained from H_2O_2 produced cathodically from unenriched oxygen gas which had been fractionally distilled in the above manner also gave lower results for O^{18}-O^{18}. The data for two such experiments in 1M KOH with enriched water are given in part E of Table II. The agreement is considerably better than in part D. The nature of the impurity in the unenriched Linde U.S.P. oxygen which caused the discrepancies is not known, but apparently it is carried through the entire experimental procedure when the oxygen is not first distilled.

Conclusions

The data in parts C to F of Table II support the following conclusions concerning the oxygen-peroxide couple on active carbon in alkaline solution:

1. In the reduction of oxygen gas to hydrogen peroxide, all of the peroxide oxygen originates from the molecular oxygen. The reverse is also true for the anodic oxidation of peroxide to oxygen gas.

2. In the cathodic formation of hydrogen peroxide, the O-O bond is modified in type but not actually broken. In addition it is evident that the O-O bond is not broken in the oxidation of hydrogen peroxide with ceric sulfate in acid solution.

The following are three possible mechanisms for the oxygen cathode on carbon in alkaline solution:

Mechanism 1

$$H_2O + e \rightarrow H\ (ads) + OH^- \quad [1a]$$
$$O_2\ (gas) \rightarrow O_2\ (ads) \quad [1b]$$
$$O_2\ (ads) + H\ (ads) \rightarrow HO_2\ (ads) \quad [1c]$$
$$HO_2\ (ads) + e \rightarrow HO_2^- \quad [1d]$$

Mechanism 2

$$H_2O + e \rightarrow H\ (ads) + OH^- \quad [2a]$$
$$O_2\ (gas) \rightarrow O_2\ (ads) \quad [2b]$$
$$O_2\ (ads) + H\ (ads) \rightarrow HO_2\ (ads) \quad [2c]$$
$$HO_2\ (ads) + H\ (ads) \rightarrow H_2O_2 \quad [2d]$$
$$OH^- + H_2O_2 \rightarrow H_2O + O_2H^- \quad [2e]$$

Mechanism 3

$$O_2\ (gas) \rightarrow O_2\ (ads) \quad [3a]$$
$$O_2\ (ads) + H_2O + 2e \rightarrow HO_2^- + OH^- \quad [3b]$$

where step [3b] is intended to represent the direct electrochemical reduction of O_2 (ads) to HO_2^- without intermediate reactions involving adsorbed hydrogen. Step [3b] may proceed by several steps: for example,

$$O_2 \text{ (ads)} + H_2O + e^- \rightarrow HO_2 \text{ (ads)} + OH^-$$
$$HO_2 \text{ (ads)} + e^- \rightarrow HO_2^-$$

The authors favor mechanism 3, but the first two mechanisms involving chemi-adsorbed hydrogen cannot be discarded on the basis of information available at present.

It is not possible to distinguish between these mechanisms on the basis of the present isotope experiments. Mechanisms 1 and 2 may be considered as corresponding to hydrogen electrodes with the surface concentration of adsorbed hydrogen depressed by the reactions with adsorbed oxygen.

In later papers in this series, an attempt will be made to elucidate further the electrode mechanism in terms of cathodic and anodic polarization measurements for the oxygen-peroxide couple. In addition, fractionation experiments involving the oxygen-peroxide couple are planned.[7]

Acknowledgments

The authors are pleased to acknowledge the support of this research by the Office of Naval Research under Contract Nonr 58100 and by E. I. du Pont de Nemours and Company through a graduate fellowship to one of the authors (M.O.D.)

Manuscript received April 3, 1958. This paper was prepared for delivery before the Cincinnati Meeting, May 1-5, 1955.

Any discussion of this paper will appear in a Discussion Section to be published in the December 1959 JOURNAL.

[7] It is interesting to note that fractionation experiments involving the anodic formation of oxygen on various surfaces have been reported by Anbar and Taube (11).

REFERENCES

1. W. G. Berl, *Trans. Electrochem. Soc.*, **83**, 253 (1943).
2. R. Weisz and S. Jaffe, *ibid.*, **93**, 128 (1948).
3. K. Kordesch and A. Marko, *Oster. Chem. Ztg.*, **53**, 125 (1951).
4. K. Kordesch and F. Martinola, *Monatsch.*, **84**, 39 (1953).
5. R. Witherspoon, H. Urbach, E. Yeager, and F. Hovorka, Technical Report 4, Office of Naval Research Contract Nonr 58100, Western Reserve University, 1954.
6. M. Davies, M. Clark, E. Yeager, and F. Hovorka, Paper 163, Cincinnati Meeting, Electrochemical Society, May 1-5, 1955. (Theoretical Division Enlarged Abstract Booklet, pp. 52-4.)
7. M. Clark, M. Davies, E. Yeager, and F. Hovorka, Paper 28, Cleveland Meeting, Electrochemical Society, October 3, 1956.
8. A. Cahill and H. Taube, *J. Am. Chem. Soc.*, **74**, 2312 (1952).
9. M. Davies, M. Clark, E. Yeager, and F. Hovorka, Technical Report 6, Office of Naval Research, Contract Nonr 58100, Western Reserve University, 1956.
10. F. Aston, "Mass Spectra and Isotopes," p. 262, Edward Arnold and Co., London (1948).
11. M. Anbar and H. Taube, *J. Am. Chem. Soc.*, **78**, 3252 (1956).

Technical Notes

Magnesium-Bismuth Oxide Dry Cells

C. K. Morehouse and R. Glicksman

RCA Laboratories, Radio Corporation of America, Princeton, New Jersey

The oxides of mercury, thallium, and lead have been studied extensively as cathode materials for electrochemical cells. Mercuric oxide and lead dioxide are of practical significance, finding use as cathode materials in the zinc-mercuric oxide dry cell (1, 2) and the lead-acid storage cell (3, 4). Thallium(III) oxide (5), despite its desirable electrochemical properties, has not proved of practical value probably because of its high cost and two step voltage-time discharge curve during current flow (6). Bismuth oxide, the next oxide in this series, also has some attractive physical and chemical properties for use as a cathode material in electrochemical cells. For example, it has a low solubility in neutral solutions, is stable over a wide temperature range, and has a flat voltage-time discharge curve during current flow (6). Although bismuth oxide has a considerably lower reversible electrode potential than manganese dioxide and mercuric oxide cathode materials used at present in commercial dry cells, it does have greater theoretical ampere-minute capacity per unit of weight (20.7 amp-min/g) and volume (176 amp-min/cc) than these materials. Using the half-cell technique for evaluating cathode materials (7), it has been found that a bismuth oxide electrode operates at a potential (vs. hydrogen) of −0.30 to −0.40 v over a wide range of current densities and at an electrode efficiency in excess of 90% when discharged at a constant current drain of 0.005 amp/g in an aqueous solution of magnesium bromide (250 g/l $MgBr_2 \cdot 6H_2O$).

Heil (13) describes a cell containing a mixture of bismuth oxide and manganese dioxide coupled with a zinc anode, while Edison (14-17) refers to the use of bismuth oxide in a nickel-iron storage cell, claiming that the addition of bismuth oxide to the electrodes results in improved performance. However, no practical dry cells containing this material have

been reported, probably because of the low resultant voltage obtained when coupling this cathode with a zinc anode.

In this paper the construction and performance characteristics of magnesium-bismuth oxide dry cells are described.

Experimental

Magnesium-bismuth oxide dry cells were assembled, using an impact extruded magnesium AA-size (height 1.82 in., OD 0.521 in., ID 0.441 in.) can, composed of AZ10A Dow Chemical Company alloy. The magnesium cans were lined with a piece of Nibroc salt-free paper (2¼ x 2¼ x 0.002 in. thick), and an extruded slug of cathode mix inserted in the lined can and consolidated. A carbon rod (height 1.787 in., diameter 0.159 in.) containing a brass cap was then inserted in the center of the cathode mix and the cells sealed with a rosin base wax seal in the conventional manner. Each cell contained approximately 10 g of cathode mix of the following formulation:

	% by weight
Bismuth oxide	54.7
Shawinigan acetylene black	6.8
Barium chromate	1.9
Electrolyte (an aqueous solution of 500 g/l $MgBr_2 \cdot 6H_2O$ and 1.0 g/l $Li_2CrO_4 \cdot 2H_2O$)	36.6

The open-circuit voltage of the bismuth oxide dry cells ranges between 1.60 and 1.65 v, the high voltage being due either to adsorbed air in the cathode mix or to the small amount of chromate which is added to inhibit the corrosion of the magnesium anode. When current is withdrawn from the cells, the voltage drops to a low value followed by a gradual increase to its operating voltage level. After the initial voltage drop, the cells have a flat voltage discharge curve operating slightly above 1.00 v for most of their useful discharge life as illustrated in Fig. 1. The initial voltage drop, which is believed to be due to changes which occur at the bismuth oxide electrode, is more noticeable at the high current drains and is different from that experienced with other magnesium dry cells.

Performance data in terms of hours of continuous service to a 0.90 v end voltage vs. load resistance are presented in Fig. 2. Also included are watt-minute capacity per unit of weight and volume data plotted against average continuous power output in milliwatts.

A favorable shelf life for the magnesium-bismuth dry cell is indicated by the fact that AA-size dry cells have given 75-80% of initial capacity as measured on 50- and 150-ohm continuous discharge tests to a 0.90 v end voltage after storage for 18 and 24 months at 70°F, 50% R. H.

The magnesium-bismuth oxide dry cells described in this paper have a flatter voltage-discharge curve and give more hours of service on continuous tests to end voltages of 1.00 v and lower than both the zinc-manganese dioxide Leclanché and magnesium-manganese dioxide (18) dry cells. At the present state of the development the technical difficulties

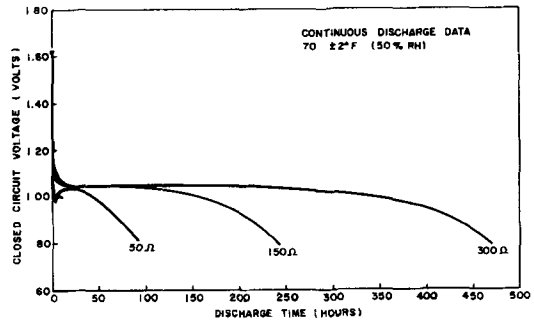

Fig. 1. AA-size magnesium-bismuth oxide dry cells discharged continuously through 50-, 150-, and 300-ohm resistances at 70° ± 2°F (50% R. H.).

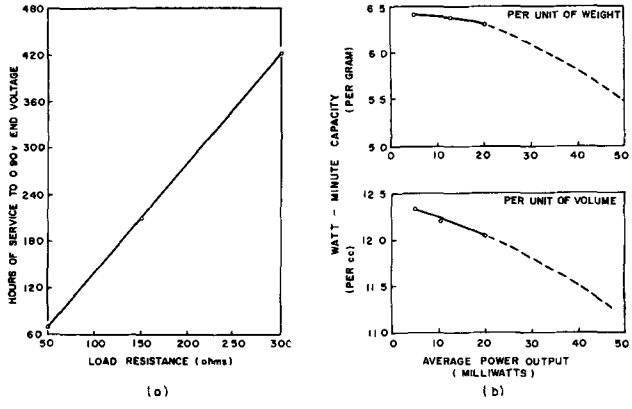

Fig. 2. Capacity data for AA-size magnesium-bismuth oxide cells in (a) hours of service to a 0.90 v end voltage vs. load resistance (b) watt-minutes per unit of volume and weight vs. average power output (capacity and average power computed to 0.90 v end voltages from continuous discharge data).

associated with these new cells are: (*a*) "delayed action," (*b*) high internal impedance, and (*c*) loss in capacity on light intermittent tests. These difficulties are believed to be associated with the magnesium electrode and can be solved with further research and development. It should be recognized, however, that bismuth oxide is inherently more expensive than manganese dioxide and, even if the technical problems can be overcome, these magnesium-bismuth oxide dry cells probably would find only limited application.

Acknowledgment

The authors wish to express their appreciation to Mr. G. R. Ganges for assisting in gathering some of the cell data.

Manuscript received March 7, 1958. This paper was prepared for delivery before the Ottawa Meeting, Sept. 28-Oct. 2, 1958.

Any discussion of this paper will appear in a Discussion Section to be published in the December 1959 JOURNAL.

REFERENCES

1. S. Ruben, *Trans. Electrochem. Soc.*, **92**, 219 (1947).
2. M. Friedman and C. E. McCauley, *ibid.*, **92**, 81 (1947).
3. G. W. Vinal, "Storage Batteries," 4th ed., John Wiley & Sons, Inc., New York (1954).
4. C. Drucker and A. Finkelstein, "Galvanische Elemente und Akkumulatoren," Akad. Verlag, Leipsig (1932).
5. S. Glasstone and A. Hickling, "Electrolytic Oxidation and Reduction," p. 105, D. Van Nostrand Co., Inc., New York (1936).

6. R. Glicksman and C. K. Morehouse, *This Journal*, **104**, 589 (1957).
7. C. K. Morehouse and R. Glicksman, *ibid.*, **103**, 94 (1956).
8. G. W. Vinal, *Elec. Eng.*, **67**, 456 (1948).
9. W. S. Herbert, *This Journal*, **99**, 190C (1952).
10. G. Leclanchés, *Mondes*, **16**, 532 (1868).
11. W. M. Latimer, "Oxidation Potentials," Prentice-Hall, Inc., New York (1952).
12. A. Walkley, *This Journal*, **99**, 209C (1952).
13. A. Heil, U.S. Pat. 1,195,677, Aug. 22, 1916.
14. T. A. Edison, U.S. Pat. 946,540, Jan. 18, 1910.
15. T. A. Edison, U.S. Pat. 999,762, Aug. 8, 1911.
16. T. A. Edison, U.S. Pat. 1,034,002, July 30, 1912.
17. T. A. Edison, U.S. Pat. 1,036,471, Aug. 20, 1912.
18. R. C. Kirk, P. F. George, and A. B. Fry, *This Journal*, **99**, 323 (1952).

Corrosion Product and Inhibitor Films on Aluminum

H. W. McCune

Miami Valley Laboratories, The Procter & Gamble Company, Cincinnati, Ohio

Effect of Inhibitors on Triphosphate Sorption

When aluminum corrodes in an alkaline sodium triphosphate solution, phosphate is incorporated into the surface oxide film on the metal (1). Corrosion in such sequestering solutions is more rapid than in most other alkaline solutions at the same pH, perhaps because a complex of Al(III) and sequestrant forms in the oxide surface at the solution-solid interface and plays an important role. Sodium silicate, potassium permanganate, and sodium chromate have been suggested as inhibitors for Al exposed to alkaline solutions (2). Sodium silicate has been suggested specifically for sodium pyrophosphate and sodium triphosphate solutions and has found wide application as an inhibitor in household detergent mixtures containing polyphosphates (3, 4). A comparison of the character of the corrosion product film with the inhibitor films was thought to bear on the mechanism of corrosion by sequestering agents and on the inhibition of such corrosion. The effect inhibitors have on the amount of triphosphate appearing on the surface of Al exposed to inhibited solutions of sodium triphosphate was first determined.

In Table I, the entries under "$Na_5P_3O_{10}$ deposited" were calculated from the phosphorus-32 activity sorbed on the Al specimens which were exposed to uninhibited and inhibited radioactive sodium triphosphate solutions. Triphosphate ion is probably the chief phosphate species sorbed. Hydrolysis in the bulk test solution is negligible, so only if a surface-catalyzed hydrolysis takes place would much lower phosphate be sorbed. The sorbed phosphate will be spoken of as "triphosphate," recognizing that its identity has not been proven. The specimens were weighed before and after exposure under stagnant conditions and after a standard dip in concentrated HNO_3 (5). Determination of the weight loss in HNO_3 is usually a rough measure of corrosion products. The "Total weight loss" of Table I is the sum of weight lost during exposure and during the HNO_3 dip. The metal was prepared as was described previously (1). The reported weight loss data were determined using 7.62 x 1.90 cm specimens. In the tracer determination of phosphate deposition, 1.90 x 1.90 cm specimens were used for convenience in counting. The sensitivity of the radiochemical determination was 0.001 mg/cm^2 and the precision was ±0.001 mg/cm^2 (95% confidence level).

Table I. Effect of inhibitors on triphosphate sorption

(0.02% inhibitor, 0.18% $Na_5P_3{}^{32}O_{10}$, 3.0 hr, 60°C, pH 9.5, 6.9 ml solution/cm^2 3003 Al)

Inhibitor	$Na_5P_3O_{10}$ deposited, mg/cm^2	Weight loss in HNO_3, mg/cm^2	Total weight loss, mg/cm^2
None	0.017	0.05	0.59
SiO_2 (sod. silicate)	0.000	0.00	0.01
$KMnO_4$	0.003	0.03	0.06*
K_2CrO_4	0.024	0.07	0.39

* Weight gain.

When sodium silicate was present at inhibitory concentrations, triphosphate was prevented from depositing in the film. Potassium permanganate almost eliminated phosphate deposition and formed a highly effective inhibitory coating. The film was highly colored, indicating that permanganate had been included in it. Potassium chromate increased the amount of phosphate deposited and had a slight inhibitory effect. The concentrated HNO_3 removed all of the radioactive phosphorus in these experiments except in the permanganate experiment, where it removed none. In the permanganate experiment determination of weight loss in HNO_3 obviously does not represent all of the corrosion products. The adsorbed triphosphate was roughly one-third of the total corrosion product in the uninhibited test and in the potassium chromate test. Not enough silica or corrosion product to be weighed was deposited with the silicate inhibitor in these experiments.

The attack of uninhibited alkaline triphosphate solutions on Al might be by way of the complexing of aluminum ions in solution, or by the formation of surface complexes with the oxide film, which is suggested by the incorporation of triphosphate into the film. The fact that the effective corrosion inhibitors, silicate and permanganate, largely prevent the incorporation of phosphate in the film and a poor inhibitor, chromate, does not prevent incorporation of triphosphate adds some support to the suggested role of the surface complex in increasing corrosion.

Sorption of Silicate

It has been reported that the hydrous metal oxide corrosion product plays an essential part by inter-

acting with silicate ions or silica to attach the protective film to the metal; chemical analysis, microscopic examination, and x-ray diffraction indicate that the film is mostly amorphous silica (6). The report that the siliceous film cannot continue to grow on itself (7) is a further indication of the importance of the metal oxide. Examination of the sorption of silicate on Al might indicate whether an inhibitory concentration is sufficient to cover the metal surface.

A sorption isotherm was determined using granular Al, reported to contain 1% or less impurity, which was given a wash with very dilute alkali followed by three washes with distilled water, a rinse in ethanol, and air drying. The 200-270 mesh fraction was taken, and the average particle size with respect to surface was determined microscopically. The specific surface was calculated to be 7.9 x 10^3 cm^2/g. Sodium silicate solutions were made from filtered stock solution and analyzed for silica colorimetrically before and after shaking with the metal for 0.5 and 1.5 hr; there was no difference in the results obtained at these two times. The weight of the sorbate was calculated as SiO_2 from the decrease in solution concentration. The error introduced by loss of solvent to sorbent is estimated to be negligible compared to the variability of the data. If the weight of water sorbed is equal to the weight of the siliceous aluminum oxide film (see below), the volume of the solution would be changed less than 1%. Sodium triphosphate was absent in these experiments, but this appears to be justified by the absence of triphosphate from the inhibitory film formed when both silicate and triphosphate were in the solution.

The results in Fig. 1 show that at 60°C sorption on Al from a sodium silicate solution is essentially complete at about 0.45 mg SiO_2 per g of Al. From the specific surface of the Al granules used, this is 5.7 x 10^{-5} mg/cm^2. If it is assumed that the true area was determined microscopically and that SiO_2 molecules with an area of 12.3 sq Å are sorbed (8), calculation indicates a coverage of 0.7. However, these are not very good assumptions, and whether less than a monolayer, a monolayer, or a few monolayers saturate the surface is unimportant for understanding corrosion inhibition in this case. The equilibrium concentration of SiO_2 corresponding to saturation of the surface is 150-250 mg/100 ml, which is an order of magnitude greater than the concentration of about 10-20 mg/100 ml which inhibits corrosion at the same temperature (4) (Table I). Apparently silicate by itself does not cover the metal but cooperates with the hydrous aluminum oxide to form the protective film.

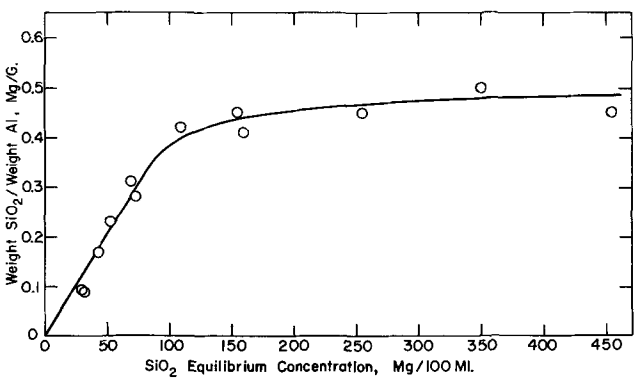

Fig. 1. Sorption isotherm of silica on Al at 60°C

Hypotheses advanced to explain how Si is built into the surface film on protected metals involve interaction of some combination of ions of the metal or the hydrous metal oxide with silicate ions or "silica micelles" (6). It is not possible to progress much further by examining the existence of possible reactants under pertinent conditions. The possibility of reaction of free aluminum ions can be dismissed in favor of aluminum ions bonded with water, hydroxide ions, and oxide ions and forming a continuous hydrous oxide film covering the metal surface. A reasonable picture of the reaction might be hydrous aluminum oxide reacting with monomeric or low molecular weight silicic acid, perhaps slightly ionized, depending on the pH (9), to produce an aluminum silicate. The aluminum ion is small enough to replace Si to some extent, adopting a coordination number of four toward oxygen, as half of the aluminum ions do in sillimanite, Al_2SiO_5, and as is common in other aluminosilicates (10). Aluminum is corroded much more rapidly by uninhibited triphosphate solutions and is protected much more effectively from sodium triphosphate solutions at low concentrations of silicates than is Zn, Ni, Ag, brass (4), Cu, or Pb. The decreased effectiveness of the inhibitor may be because the ions of these metals and alloys are larger than the aluminum ions and are not incorporated easily into metallosilicate structures.

Characterization of Isolated Films

Surface films were collected by exposing 50 to 150 dm^2 of Al foil (1100 purity, 0.0002 in. thick), then dissolving the metal in 5% bromine in methanol. The remaining solid film was filtered off on sintered glass, washed with methanol, and dried at 80°C before weighing. An exposure of 3 hr in 0.18% sodium triphosphate solution at 60°C gave 0.04 mg of corrosion products film per cm^2. This weight agreed fairly well with the weight loss in HNO_3 (Table I). It was found by chemical analysis that a similar film contained phosphorus equivalent to 0.016 mg $Na_5P_3O_{10}$ per cm^2 (1) which agrees well with the value in Table I determined by the use of P-32. Evidently the Al_2O_3 film contains a substantial fraction of phosphate. The triphosphate solution with sodium silicate equivalent to 0.02% silica added and also adjusted to pH 9.5, gave a film weighing 0.0013 mg/cm^2 under the same conditions. A correction of 0.0008 mg/cm^2 for the insoluble material in the clean, untreated foil must be subtracted from the weights collected. Clearly the inhibitory film is very thin, a few tens of angstroms thick. X-ray diffraction indicated that the insoluble material from the foil itself contained crystalline Si and a little Cu; after ignition, a pattern for a crystalline aluminum silicate was obtained, indicating the presence of Al from the air-formed film initially present on the foil.

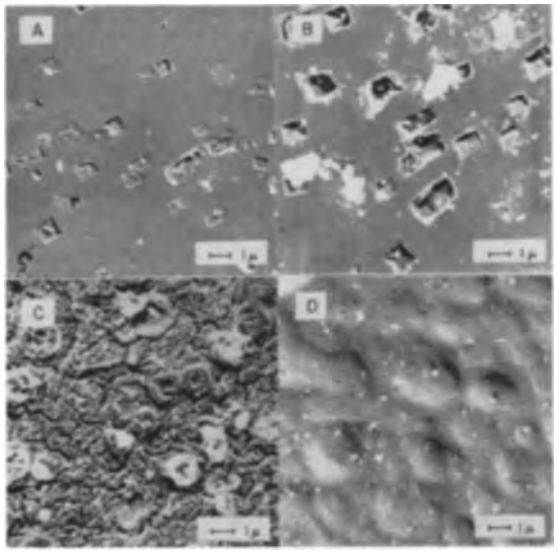

Fig. 2. Electron micrographs of Al surfaces: A, polished and etched; B, after exposure to 0.18% $Na_5P_3O_{10}$, 0.02% SiO_2, 3 hr, 60°C, pH 9.5; C, same as B without the SiO_2; D, same as C after corrosion products were removed in concentrated HNO_3.

Neither sample of film from treated foils gave crystalline x-ray diffraction lines other than those of Si and Cu, with CuK_α radiation.

Electron Microscopy of the Surface

Portions of the 3003 sheet Al were electropolished in an aqueous solution of methanol and perchloric acid. The samples were then lightly etched in a methanol solution of bromine for 15-30 sec, washed, and exposed to the corrosive conditions of interest. After removal of the metal from the test solutions, liquid was blown off with an air jet. Chromium replicas about 150Å thick were prepared by oblique evaporation and freed by dissolving the aluminum in bromine-methanol. To demonstrate that the results were not affected by the method of sample preparation, additional samples were prepared by polishing with an abrasive and etching with a dilute HNO_3-HF-HCl solution. Similar electron micrographs were obtained, but electropolishing followed by bromine-methanol etch gave more nearly reproducible surfaces and more sharply defined etch pits.

Sheet Al is polycrystalline, but the electron micrographs shown include portions of only one or a few crystallites. Electropolishing gave a smooth, abrasive-free surface like the background of Fig. 2A. The samples were all etched in bromine-methanol to remove, by dissolving the metal, any film left by polishing and to give a texture to the surface which might permit observation of surface films. Rectangular etch pits developed and, from their orientation, show that Fig. 2A includes parts of two crystallites. In electron micrographs of samples exposed to triphosphate solutions inhibited with sodium silicate there was no evidence of a continuous film covering the surface and obscuring the edges of the pits (Fig. 2B). Evidently the siliceous film is textureless, and probably it is very thin. The white, irregular unshadowed particles prominent in Fig. 2B and 2D are absent in many other micrographs of similar subjects; hence it is concluded that they are accidental contamination. The set of micrographs shown in Fig. 2 was chosen from the sets available as the most informative over-all despite the contamination. In a majority of micrographs, the rectangular pits appear larger in samples exposed to inhibited triphosphate solution than in the etched blanks, but this does not necessarily represent a real difference. When the inhibitor was omitted, corrosion product was built up, and the metal was attacked within the crystallites (Fig. 2C). A dip in concentrated HNO_3 removed the corrosion products and revealed that corrosion gave rise to shallow circular pits (Fig. 2D).

Acknowledgment

The author wishes to express his thanks to A. P. Murphy, who is responsible for the light and electron microscopy, and to W. E. Cooley for aid in preparing the manuscript.

Manuscript received April 10, 1958.

Any discussion of this paper will appear in a Discussion Section to be published in the December 1959 JOURNAL.

REFERENCES

1. H. W. McCune, *Ind. Eng. Chem.*, **50**, 67 (1958).
2. J. M. Bryan, "Aluminium and Aluminium Alloys in the Food Industry," H. M. Stationery Office, London (1948).
3. J. C. Harris, "Metal Cleaning Bibliographical Abstracts," Am. Soc. Testing Materials, Spec. Tech. Publ., 90B (1953) and 90C (1954).
4. R. Getty, N. W. McCready, and W. Stericker, ASTM Bull. No. 205, April (1955).
5. "ASTM Standard, 1952, Part 2, Non-ferrous Metals," p. 1045. ASTM Designation: B185-43T.
6. L. Lehrman and H. L. Shuldener, *J. Am. Water Works Assoc.*, **43**, 175 (1951).
7. J. G. Vail, "Soluble Silicates," Monograph No. 116, Am. Chem. Soc., Vol. II, p. 248ff, Reinhold Publishing Corp., New York (1952).
8. P. F. Holt and D. T. King, *J. Chem. Soc.*, **1955**, 773.
9. R. K. Iler, "The Colloid Chemistry of Silica and Silicates," Cornell University Press, Ithaca, N. Y (1955).
10. A. F. Wells, "Structural Inorganic Chemistry," 2nd ed., p. 569, Oxford University Press, London (1950).

Additives and Grain Refinement

D. A. Vermilyea

Research Laboratory, General Electric Company, Schenectady, New York

Most commercial plating baths contain some addition agent which is added to produce a desirable structure in the deposits. These addition agents are usually high molecular weight organic compounds or colloids, small ions or molecules being generally not very effective (1). The purpose of this note is to suggest a mechanism by which such addition agents may modify the crystal structure of electrodeposits. Silver will be used as an example.

It has often been observed (2-4) that the deposition of Ag from a $AgNO_3$ solution containing high molecular weight organic compounds may result in the formation of filaments or "whiskers" of Ag. Whiskers of Cu have also been reported (5, 6). A theory to account for such growth has been given by Price, Vermilyea, and Webb (7). According to the theory, organic molecules adsorb on the crystal and interfere with the motion of lattice steps over the surface. When the concentration of molecules adsorbed on the surface is above a critical value depending on the overvoltage, step motion is completely blocked and no further growth of the crystal occurs. On the other hand, molecules adsorbed on a rapidly growing surface are thought to be incorporated into the crystal as lattice steps move around and past them. According to this picture, therefore, molecules adsorbed on the surface interfere with growth; they may be removed from the surface by incorporation into the crystal. If the crystal grows rapidly enough, the surface will be kept clean because adsorbed molecules are buried as fast as they reach the surface by diffusion. At slower growth rates adsorbate reaches the surface faster than it can be buried; the surface becomes severely contaminated, and growth stops.

A major prediction of the theory of Price, Vermilyea, and Webb (7) is that there is a critical current density for the continued growth of a metal crystal in a solution containing large, strongly adsorbed molecules. At the critical current density there is a balance between the rate of diffusion of molecules to the surface and the rate of incorporation into the crystal. The equation for the critical current density for a spherical crystal of a given metal for a given metal ion concentration and temperature is

$$I_c = \text{const}\left(\frac{C_i}{r}\right)^{1/3} \qquad [1]$$

where C_i is the concentration of adsorbate in the solution, and r is the radius of the crystal. Equation [1] is valid for crystals with radii less than about 10 μ. Typical critical current densities observed from whisker growth experiments range from 0.1-10 amp/cm^2; somewhat larger values may be expected with the larger additive concentrations used commercially.

Now consider the electrodeposition of a metal from a solution containing some substance, either organic compound or colloidal material, which is strongly adsorbed on the electrode surface. Before the application of current, the electrode will be completely contaminated. When a current is passed through the cell the electrode potential will rise until deposition begins to occur on the most active sites of the electrode. Crystals would probably start growing at many points on the surface. The overvoltage required to start the deposition would be large because of the initial contamination of the electrode, and the crystals once nucleated would grow very rapidly. Consequently, there would be a rapid and considerable concentration polarization in the vicinity of each growing crystal.

Now consider just one of the many small growing crystals. Around the crystal there will be a hemispherical diffusion field, and if the crystal is small ($< 10\mu$ diam) the gradient at the crystal surface will be proportional to the concentration difference between the bulk of the solution and the surface of the crystal and to the reciprocal of the crystal radius. As the crystal grows a larger concentration difference is required to maintain the same concentration gradient at the surface. When the concentration of metal ions at the surface has become essentially zero it will no longer be possible to maintain the same gradient at the crystal surface, and further growth of the crystal will result in a rapid decrease in the current density.

It is clear, therefore, that eventually it will not be possible to maintain the critical current density of Eq. [1], and that the crystal surfaces will become contaminated and stop growing.

On the electrode as a whole, crystals will continually nucleate, grow, reach a limiting size, become contaminated, and stop growing. It is unlikely that a new crystal will nucleate near or on one which has just stopped growing because the solution in that area is depleted of metal ions. The tendency of new crystals to start as far as possible from ones which just stopped will insure a uniform coverage of the electrode.

It is possible to estimate the size of the crystals which result from such a process. The current density at a growing crystal is given by

$$I = zFD\frac{dC}{dr} \qquad [2]$$

where I is the current density, z the ionic charge, F the Faraday constant, D the diffusion coefficient, and dC/dr the concentration gradient at the crystal surface. For a small hemispherical crystal $dC/dr \sim \Delta C/r$, and hence with $D \sim 10^{-5}$cm^2/sec, $\Delta C_{max} = 10^{-3}$ mole/cc, $I_{max} = 10^{-3}/r$. Hence, if the critical current density is

10 amp/cm^2 the maximum particle size is about 1μ, a reasonable size for a fine-grained deposit.

This simple picture accounts for the very fine grain size produced by additives and for the uniformity of the deposit. It also accounts for the fact that the addition agents which are effective in altering the structure of the deposit are invariably incorporated into the deposit in rather large quantities (of the order of a percent) (8). It also accounts for the absence of specificity reported by Fischer (9); since almost the only requirements for effectiveness are that the units of the additive be large and strongly adsorbed, it is apparent that many substances can accomplish about the same result.

Manuscript received June 18, 1958.

Any discussion of this paper will appear in a Discussion Section to be published in the December 1959 JOURNAL.

REFERENCES

1. H. Fischer, "Elektrolytische Abscheidung und Elektrokristallisation Von Metallen," p. 270, Springer, Berlin (1956).
2. K. M. Gorbunova and A. I. Zhukova, *J. Phys. Chem. U.S.S.R.*, **23**, 605 (1949).
3. K. M. Gorbunova and P. D. Dankov, *ibid.*, **23**, 616 (1949).
4. L. Graf and W. Morgenstern, *Z. Naturforsch.*, **10a**, 345 (1955).
5. P. A. Van der Meulen and H. V. Lindstrom, *This Journal*, **103**, 390 (1956).
6. T. C. J. Ovenston, C. A. Parker, and A. E. Robinson, *ibid.*, **104**, 607 (1957).
7. P. B. Price, D. A. Vermilyea, and M. B. Webb, to be *Acta Met.*, **6**, 524 (1958).
8. Ref. (1), p. 519.
9. Ref. (1), p. 236.

Measurement of Carbon-Metal Contact Resistances

H. L. Foltz and M. R. Hertz

Technical Division, Goodyear Atomic Corporation, Portsmouth, Ohio

The use of large quantities of elemental fluorine in AEC gaseous diffusion plants has led to numerous research projects concerning materials suitable for use in fluorine generators. The cell being used at present to generate fluorine consists basically of a Monel shell and head assembly from which wire mesh diaphrams, steel cathode, and carbon anode subassemblies are suspended.

One of the major causes of low power efficiency and early cell failure has been the electrical deterioration of the carbon anode-metal connection in the anode subassemblies. Since an initially high contact resistance would be conducive to heating of the carbon anode-bus-bar joint with further corrosion of the contact areas, still higher resistance, and so on, work has been completed to determine the relation between contact pressure and contact resistance for various carbon-metal joints. From this work it has been determined that of five metals tested, copper and beryllium copper give the lowest contact resistance, followed by phosphor bronze, magnesium, and steel.

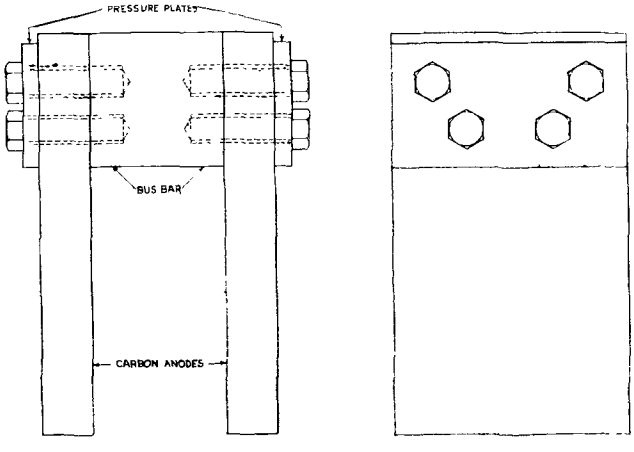

Fig. 1. Anode clamping assembly

Measurements of anode-bar contact resistance as a function of torque did not give consistent results, possibly because of pressure plate warping or a nonlinear increase in thread friction as torque was increased.

As shown in Fig. 1, the carbon anodes are clamped between the bus bar and pressure plates by four ¾-in. steel cap screws per anode. The contact areas of the anodes are specified to be ground smooth and parallel. Original cell assembly specifications called for the cap screws to be torqued to 85 ft lb, which is approximately equivalent to 1400 psi pressure on the anode contact area, the exact pressure being a function of the condition of the threads and their lubrication.

In Fig. 2 the test set-up used is shown. A carbon sample block was compressed between the two metal contact plates by means of a hand operated hydraulic press; the force was applied through a Baldwin SR-4, Type U-1 load cell, which was coupled to a type M strain indicator. Precautions were taken to make sure that the load was applied to the specimen on the vertical axis. The load cell-indicator combination was checked against an Olson testing machine and was found to have an accuracy of ± ¼% of full range (5000 lb). One metal contact plate was insulated from the press so that resistance measurements could be made between the two plates.

For resistance measurement current and potential leads, attached to the contact plates, were connected to a Biddle Model 713 "Ductor" Low Resistance Ohmmeter. This instrument operates on a somewhat similar principle to that of a Kelvin bridge, except that it incorporates a special highly sensitive D'Arsonval-type meter with both a current and a voltage coil to replace the bridge circuit. Thus, increased current tends to decrease the reading, while increased voltage increases the reading. The meter has a basic 0 to 100 micro-ohm range with five

10 amp/cm^2 the maximum particle size is about 1μ, a reasonable size for a fine-grained deposit.

This simple picture accounts for the very fine grain size produced by additives and for the uniformity of the deposit. It also accounts for the fact that the addition agents which are effective in altering the structure of the deposit are invariably incorporated into the deposit in rather large quantities (of the order of a percent) (8). It also accounts for the absence of specificity reported by Fischer (9); since almost the only requirements for effectiveness are that the units of the additive be large and strongly adsorbed, it is apparent that many substances can accomplish about the same result.

Manuscript received June 18, 1958.

Any discussion of this paper will appear in a Discussion Section to be published in the December 1959 JOURNAL.

REFERENCES

1. H. Fischer, "Elektrolytische Abscheidung und Elektrokristallisation Von Metallen," p. 270, Springer, Berlin (1956).
2. K. M. Gorbunova and A. I. Zhukova, *J. Phys. Chem. U.S.S.R.*, **23**, 605 (1949).
3. K. M. Gorbunova and P. D. Dankov, *ibid.*, **23**, 616 (1949).
4. L. Graf and W. Morgenstern, *Z. Naturforsch.*, **10a**, 345 (1955).
5. P. A. Van der Meulen and H. V. Lindstrom, *This Journal*, **103**, 390 (1956).
6. T. C. J. Ovenston, C. A. Parker, and A. E. Robinson, *ibid.*, **104**, 607 (1957).
7. P. B. Price, D. A. Vermilyea, and M. B. Webb, to be *Acta Met.*, **6**, 524 (1958).
8. Ref. (1), p. 519.
9. Ref. (1), p. 236.

Measurement of Carbon-Metal Contact Resistances

H. L. Foltz and M. R. Hertz

Technical Division, Goodyear Atomic Corporation, Portsmouth, Ohio

The use of large quantities of elemental fluorine in AEC gaseous diffusion plants has led to numerous research projects concerning materials suitable for use in fluorine generators. The cell being used at present to generate fluorine consists basically of a Monel shell and head assembly from which wire mesh diaphrams, steel cathode, and carbon anode subassemblies are suspended.

One of the major causes of low power efficiency and early cell failure has been the electrical deterioration of the carbon anode-metal connection in the anode subassemblies. Since an initially high contact resistance would be conducive to heating of the carbon anode-bus-bar joint with further corrosion of the contact areas, still higher resistance, and so on, work has been completed to determine the relation between contact pressure and contact resistance for various carbon-metal joints. From this work it has been determined that of five metals tested, copper and beryllium copper give the lowest contact resistance, followed by phosphor bronze, magnesium, and steel.

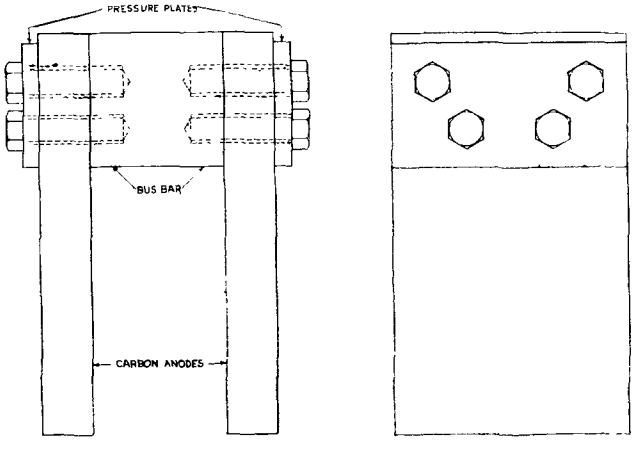

Fig. 1. Anode clamping assembly

Measurements of anode-bar contact resistance as a function of torque did not give consistent results, possibly because of pressure plate warping or a nonlinear increase in thread friction as torque was increased.

As shown in Fig. 1, the carbon anodes are clamped between the bus bar and pressure plates by four ¾-in. steel cap screws per anode. The contact areas of the anodes are specified to be ground smooth and parallel. Original cell assembly specifications called for the cap screws to be torqued to 85 ft lb, which is approximately equivalent to 1400 psi pressure on the anode contact area, the exact pressure being a function of the condition of the threads and their lubrication.

In Fig. 2 the test set-up used is shown. A carbon sample block was compressed between the two metal contact plates by means of a hand operated hydraulic press; the force was applied through a Baldwin SR-4, Type U-1 load cell, which was coupled to a type M strain indicator. Precautions were taken to make sure that the load was applied to the specimen on the vertical axis. The load cell-indicator combination was checked against an Olson testing machine and was found to have an accuracy of ± ¼% of full range (5000 lb). One metal contact plate was insulated from the press so that resistance measurements could be made between the two plates.

For resistance measurement current and potential leads, attached to the contact plates, were connected to a Biddle Model 713 "Ductor" Low Resistance Ohmmeter. This instrument operates on a somewhat similar principle to that of a Kelvin bridge, except that it incorporates a special highly sensitive D'Arsonval-type meter with both a current and a voltage coil to replace the bridge circuit. Thus, increased current tends to decrease the reading, while increased voltage increases the reading. The meter has a basic 0 to 100 micro-ohm range with five

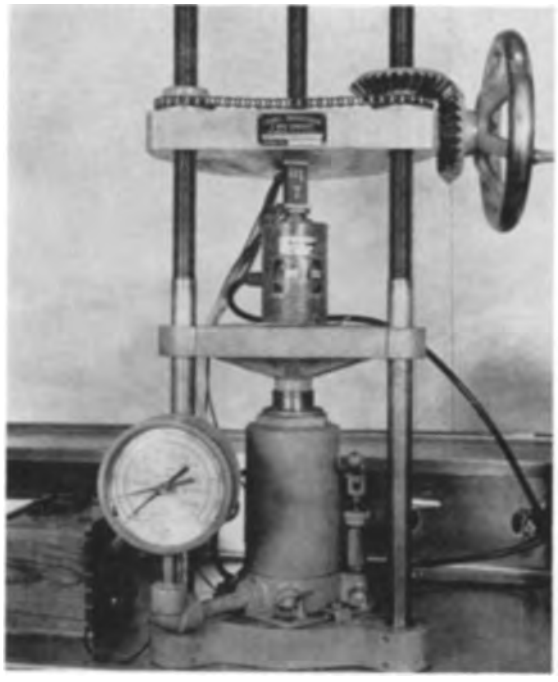

Fig. 2. Compressing carbon block samples between metal contact plates.

decade multiplying ranges giving an over-all range of 0-1 ohm with an accuracy of 1% of full scale for any range. This permits an error approaching 10% at certain readings.

Carbon sample blocks, 1 in.^{2} in cross section and approximately 2 in. high, were cut from the contact area of anodes so that the original surface was retained for the contact pressure vs. resistance measurements. For steel contacts, sections were cut from actual steel pressure plates, while for other metal contacts various metal stock was used, finished with a series of grades of emery paper of increasing fineness.

The actual resistance reading was that for two 1-in.^{2} carbon-metal contact areas and of a 2-in. length of carbon 1 in.^{2} in cross section, all in series. Contact resistance per square inch of area is then:

$$R = (R_t - R_c)/2$$

where R_t is the resistance measured on the meter and R_c is the specific resistance of the carbon in ohms per cubic inch. Since the potential leads were attached directly to the contact plates, the resistance of the metal plates themselves could be disregarded. This was checked by pressing the two plates together while resistance was measured. The resistance was found to be negligible even though an added metal-metal contact was involved.

The specific resistance of National Carbon Company Type YBD carbon, which is not graphite, as given by the manufacturer, is 1550 μ ohms/in.^{3}. This value was obtained by measuring the resistance of a large number of full size anodes lengthwise, using a Kelvin bridge. When this figure was used for the specific resistance of carbon in preliminary tests, the results were somewhat variable from sample to sample. However, when resistance vs. pressure curves were run several times on the same carbon sample block, there was little variation.

Variation could be attributed either to differences in the condition of the carbon contact surfaces from sample to sample, or to differences between the specific resistance of the carbon in the various samples. Since the anodes are formed by extrusion in a lengthwise direction, there should be some difference in carbon density in various locations in the anode, and some pore orientation should occur in the lengthwise direction. This in turn could be expected to result in a lower specific resistance of carbon lengthwise than across the anodes, the latter applying to this experiment. In addition, the National Carbon Company has measured air permeabilities twice as great in the lengthwise as in the transverse direction. Twenty-eight blocks, nominally 1 x 1 x 2 in., were cut from each of two anode blades, half lengthwise, as National Carbon measured resistance, and half transversely, the ends being the normal contact area. They were each placed in the press between pressure plates in the normal manner and resistance measured between two scribe marks, 1 in. apart. Exact dimensions were measured with a micrometer calipers. Values for transverse specific resistance varied from 1600 to 2100 μ ohms/in.^{3} with an average of 1810 μ ohms/in.^{3}. Standard deviation was approximately 100 μ ohms/in.^{3}. With samples cut in the lengthwise direction, variation was similar but the average value of specific resistance was 1190 μ ohms/in.^{3}. This was somewhat lower than that obtained by National Carbon Company. In view of the large variation between samples, the specific resistance was measured for each block and this value used in calculating contact resistance.

Several samples were loaded over a range of pressures from 600 to 5000 psi. Pressure was increased by 400-lb increments up to 5000 lb and then decreased by the same increments back to 600 lb, 5000 psi approaches the compressive strength of carbon and should be avoided for design purposes. The plots of contact resistance vs. pressure were found to approximate straight lines on a log-log graph, although the slopes were slightly smaller for the unloading curves. These plots are shown in Fig. 3.

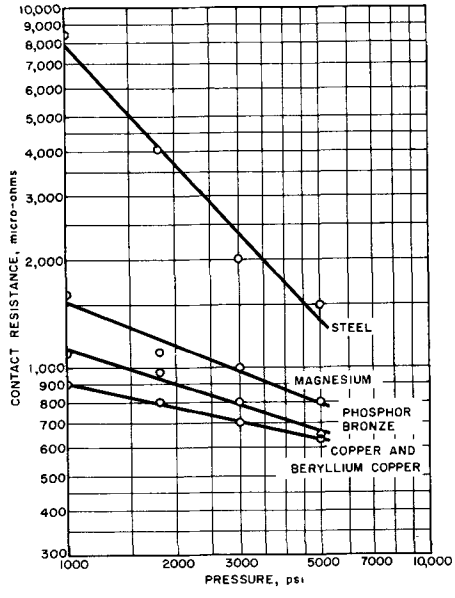

Fig. 3. Contact resistance as a function of pressure

It can be seen that, while the steel-carbon contact resistance decreases rapidly when pressure increases, it never approaches the copper-carbon contact resistance and is greater than the contact resistance of any of the other metals tested.

It has been proposed that the measured contact resistance in newly assembled cells might give some indication of the expected performance of the cell. Since humidity of the anode storage and assembly environment is one factor that is not controlled, a test was made to determine the contact resistance-pressure function of anode material which had been oven dried as compared to that which had been stored for some time in an atmosphere at 100% humidity. Some samples were dried for 165 hr at 210°C, while others were stored for 96 hr in a desiccator containing a wet sponge. When tested with both copper and steel no significant difference in contact resistance was found between dried samples, those which were in equilibrium with the laboratory atmosphere, and those stored at 100% humidity.

In the cell, the carbon metal contact is exposed to a mixture of fluorine and hydrogen fluoride gases, as well as to the liquid electrolyte which may enter the joint through capillary action in the somewhat porous carbon anode.

With the experimental set-up used it was impossible to expose the contact to a fluorine atmosphere while under pressure. The metal plates, however, were fluorinated for 48 hr with 100% fluorine at 100°C. The metal plates were then removed and contact resistance against carbon determined as before. Care was exercised that the fluorinated layer was undisturbed. Results are shown in Table I.

The increase in contact resistance was negligible for beryllium-copper, a factor of approximately three for copper and magnesium, and a factor of five for phosphor-bronze. Contact resistance for steel could not be measured with the normal equipment and was found to be greater than 20 megohms when measured with a conventional ohmmeter. It must be noted that the fluorination was done with dry fluorine which contained no hydrogen fluoride. Fluorination in a cell might not affect the micro-areas of the metal actually in contact with carbon. However, the extreme insulating value of the fluoride layer on steel indicates that this metal is of doubtful value as a contact material in a fluorine cell.

Table I. Contact resistance-pressure values for carbon-fluorinated metal

Pressure psi	Steel megohms	Contact resistance in micro-ohms/in.^{2} Mg	Phosphor-Bronze	Cu	Be-Cu
1000	>20	3560	4830	2330	900
1800	>20	2440	3170	1610	683
3000	>20	1760	2260	1140	575
5000	>20	1230	1600	858	517

The resistance-pressure relationship for any metal has the general equation:

$$R = a P^m$$

where R is contact resistance, a, a constant, P, pressure, and m, slope of log-log plot. Both a and m are different for each metal.

From the results it is apparent that the largest unit pressure possible, applied uniformly over the contact surfaces, results in the lowest contact resistance. The use of copper alloys and magnesium result in lower contact resistance than does the use of steel. Copper contact plates have been used for at least fifteen years and the tests confirm the suitability. Steel appears to be of doubtful value in this application.

Manuscript received May 16, 1958. The work on this paper was performed under Contract AT-(33-2)-1 with the U. S. Atomic Energy Commission.

Any discussion of this paper will appear in a Discussion Section to be published in the December 1959 JOURNAL.

REFERENCE

1. R. L. Murray, S. G. Osborne, and M. S. Kircher, *Ind. Eng. Chem.*, **39**, 249 (1947).

Technical Review

Electrodeposition of Powders for Powder Metallurgy

C. L. Mantell

Department of Chemical Engineering, Newark College of Engineering, Newark, New Jersey

ABSTRACT

A very large number of articles are made by powder metallurgical methods from electrolytically reduced powders. In powder production, cathode current densities are much higher than those of refining; loosely adherent deposits are produced. These are dried, surface oxides removed, and classified by screening. Important electrolytic powders are those of copper, iron, nickel, zinc, some alloys, as well as duplexes. Operating details are reviewed.

Metal deposited at the cathode varies widely in its characteristics, depending on the electrolyte itself, the ions present, and operating conditions. Silver deposited from a solution of $AgNO_3$ forms large, readily visible crystals. Tin from a solution of $SnCl_2$ will form long needles which may rapidly "bridge" from the anode to the cathode. Lead from a chloride or acetate solution gives crystals different from those from a chlorate or perchlorate electrolyte. Nickel deposits from a sulfate bath are hard and may be polished but not with ease, while nickel from a naphthalene sulfonate gives bright deposits needing little if any polishing.

In plating, efficiency of utilization of electrical energy is secondary to quality. High current and energy efficiencies may be sacrificed without upsetting the economics of the operation. Particularly where thermal or chemical processes compete, power cost in refining is a major item; maximum current and energy efficiencies are vital. In electroforming, of which metal powder production is a form, conditions approach refining to a far greater degree than plating, as the procedures compete with thermal and mechanical disintegration procedures.

The nature of the electrolyte, its pH, metallic ion concentration, anodic and cathodic current density, temperature, the simplicity or complexity of the metallic ion including its primary and secondary ionization, as well as the presence of modifying or "addition" agents, have effects on the character of the deposit.

The crystalline structures of cathode deposits may be classified as follows:

Group I. The initial nuclei or crystals continue to grow throughout the deposit forming (*A*) isolated crystals: which are (*a*) symmetrical or (*b*) acicular; or giving rise to (*B*) contiguous crystals: which may be (*a*) columnar or (*b*) fibrous.

Group II. Part of the initial nuclei or crystals continue to grow. These are (*A*) conical ("normal") or (*B*) twinned.

Group III. The nuclei or crystals do not grow for any extended period. Their shapes are (*A*) broken (compact), or (*B*) arboreal, sometimes called "fernlike" ("treed"), or (*C*) powdery (spongy), and (*D*) slimelike.

If any addition which would increase the cathode polarization be made to the solution, the number of crystal nuclei increases. The current densities may be increased, and the effective metal ion might be decreased in the film or thin layer of solution adjacent to the cathode by (*a*) diluting the solution; (*b*) decreasing the temperature, which in turn reduces diffusion and convection; (c) adding a salt having an ion common with those already present; (*d*) introducing a colloid; (*e*) increasing the viscosity of the solution; and (*f*) causing the formation of complex ions. These factors increase the difference in cathode potential, the number of crystal nuclei, and the production of fine-grained deposits.

Dissociation, ionic migration, diffusion, and convection, particularly at the surface of the cathode, replenish the metal ion concentration. Growth of existing crystals may be favored by acceleration of these factors. The tendency of metals such as silver and lead, when deposited from nitrate solutions, to form isolated crystals is partly the result of the relatively large change in density of the solution produced by the removal of the metal. The effects of various factors upon the structure of deposits are summarized in Table I.

Decreasing the metal ion concentration decreases the size of the crystals. Fine-grained, bright, or hard deposits are produced at low temperatures, while increase of temperature causes coarse or soft deposits. The effects of increases of current density and

Table I. Direction of effects on structure of deposits

Change in operating condition	Change in structure group*
Increase metal salt concentration	III → II → I
Increase metal ion concentration	III → II → I
Agitate solution	III → II → I
Elevate temperature	III → II → I
Increase conductivity of solution	III → II → I
Add colloids to solution	I → II → III
Increase viscosity of solution	I → II → III
Increase current density	I → II → III

* Groups as described above in the text.

temperature are in opposite directions. Therefore, it is possible to obtain fine-grained deposits in warm solutions at a high current density. Addition of colloids in more than small amounts, increase of viscosity, and increase in current density tend in the direction of broken crystals, arboreal, or powdery electrolytic precipitates.

Deposited metal powders are represented by the Group III type of crystals. They are "poor" electroplates. Powder production is favored by low metal concentration, low metal ion concentration, unagitated solutions, low temperatures, solutions of low conductivity, addition of colloids, increases in viscosity, and marked increases in current density. The effect of each variable is not of the same order of magnitude; the effects are cumulative and interdependent; changes in concentration may be of greater importance than variation of temperature; vigorous agitation may offset the effect of increase of current density.

Electrolytic powders of commercial importance are of two varieties. Loose crystals may be formed in the cells as nonadherent powders, or the powder may result from grinding relatively hard, brittle, partially coherent deposits. Examples of the first class are Cu, Zn, Ni, Ag, and Pb; of the second Fe and Mn. These will be briefly described from the viewpoint of their production. While electrolytic Zn, Ni, and Pb powders are interesting, they are commercially unimportant in that powders of these metals are the result of other methods; industrially only electrolytic Cu, Fe, and Mn command markets. Silver crystals are the conventional result of electrolytic refining. Disintegration converts them to a powder.

The powders all command "shape" premiums in price over ingot metal or cathode chip of the same purity.

In practice, cathode current densities are higher than those of refining, so that loosely adherent spongy deposits which are periodically removed by scraping or tapping devices or by electrolyte circulation may be produced. In the case of Cu powder, acid electrolytes of lower metal and higher acid concentration than those used for refining or plating are preferred. When operated at high cathode density and with hydrogen evolution, the finely divided metal crystals often have a fernlike appearance under the microscope. It is necessary to remove the cathode frequently; otherwise the effective area of the deposit is increased to such an extent that the current density is lowered and coarse deposits formed.

The fineness of the powder may be varied over a considerable range by changes in the composition, temperature of the electrolyte, and variation of the cathode current density, as well as by the introduction of addition agents, reducing compounds, or substances which are cathodically reduced and anodically oxidized but are not plated out. Cathode current densities are different from those at the anode, usually higher. The deposited powders are washed, dried in inert or reducing atmospheres, and cooled to room temperature.

Copper

French electrolytic copper powders were produced through the addition of colloidal materials, such as H_2SO_4-treated glucose, for example, to the electrolyte (1). The colloid was thought to make possible the production of extremely fine powders with the elimination of hydrogen evolution at the cathode and higher current efficiencies. American production of copper powder made the material in modified refining tanks from selected regular anodes and smooth copper cathodes.

Large quantities of industrial Cu powders are electrolytic. They are made by electrodeposition using a soluble anode and a nonattackable cathode. The electrolytic step transforms solid Cu into discrete, finely divided particles of controlled and reproducible characteristics. Since high purity is essential, the anodes are electrolytically refined Cu. Large-scale attempts to use anodes of lower purity so that refining and powder formation could be combined have been commercial failures because of the wide variations in the characteristics of the end product. Insoluble anodes have been investigated, but have not proved commercially feasible for the production of high-grade Cu powders.

The cathodes are lead alloy sheet. Silicon-iron, briquetted iron oxide, various stainless steels, magnetite, and graphite, have not been satisfactory.

The electrodes are arranged in parallel in lead-lined or rubber-lined tanks, and are frequently inspected as in refinery practice for irregularities to insure uniform current density and elimination of short circuits in the cells.

In contrast to the copper refining practice, electrolysis is carried out at current densities from 5 to 10 times higher, at lower temperatures and low concentrations, and low circulation. By control at various levels, marketable copper powder is produced varying from 1.5 to 3.5 g/cm^3 in apparent density and from 30 to 98% minus 325-mesh in particle size. The widely differing demands of powder metallurgy make this necessary.

Copper deposits as discrete particles at the cathode and is collected at the bottom of the cell, or as a loosely adherent deposit which may be lifted from the cell and washed off the cathodes. Periodically the sludge is removed, filtered, and washed free of electrolyte. The large surface area and activity of wet Cu powder make thorough washing and immediate drying essential to avoid oxidation of the Cu particles.

The powder is dried in controlled-atmosphere, continuous furnaces. Reducing conditions are main-

tained to remove surface oxides. The furnaces are operated at 315°-760°C (600°-1400°F) in atmospheres of 10-30% hydrogen and 5-20% carbon monoxide. Furnace conditions are closely controlled. Excessive fritting or sintering of the powder into a ductile mass must be avoided.

The discharge from the furnaces is fed to high-velocity impact mills to break up clusters without excessive cold working and hardening. Powder which is milled too lightly will contain a high percentage of agglomerated fines. Powder milled too heavily will contain flakes, roughly spherical, or cold-worked particles which will destroy its compacting qualities.

Size fractionation is by screening and air separation. The various fractions are stored in airtight, dessicated containers. Blending of the various fractions produces desired types of powder.

Lead

Mantell described the preparation of Cu-coated Pb powder using an acetate electrolyte with Cu and Pb anodes and Ni cathodes at cathode current densities of 18 amp/ft^2 at a power consumption of 1.5 kwhr/lb of 200-mesh powder containing 60% Cu and 40% Pb (2). These have been used for bearings whose operating temperatures may exceed the melting point of Pb. No lead "bleeding" results.

Zinc

Electrolytic zinc powder is made from flue dust with a caustic leach liquor and an electrolyte of sodium hydroxide and sodium zincate. The product shows a typical fern-leaf appearance of sizes 45-60 μ long. Zinc dust is employed as a reducing agent in the manufacture of hydrosulfites and in the preparation of organic compounds. Commercial operating data of a plant employing hollow magnesium alloy cathodes are given in Table II.

Nickel

Electrolytic Ni has been made by Mantell (3) employing an NH_4Cl electrolyte whose pH was adjusted by means of NaOH, using Ni anodes and cathodes. Operating details are given in Table II.

Lead

The inter-relation of operating conditions in producing lead powder was shown by Crownover (4) who found: "Spongy deposits were formed at lead concentrations between 7.23 and 16.2 oz per gal and free HBF_4 concentrations between 51.5 and 27.6 oz per gal at current densities ranging from 1,325 to 177 amp per sq ft for 2 minute deposition periods. Particle size increased with increasing time of deposit and decreasing current density. Dendritic growths formed on the edge of the cathodes at current densities between 257 and 835 amp per sq ft and electrolyte concentrations of 16.6 to 28.1 oz per gal lead and 27.6 to 12.4 oz per gal free HBF_4 for deposition periods of 4 to 30 minutes. Easily removable powdered lead could not be produced at current densities between 299 and 835 amp per sq ft when the electrolyte contained 28.1 oz per gal lead and 12.4 oz per gal free HBF_4. A firm adhering deposit formed on the cathode at a current density of 1,100 amp per sq ft. No difference was noted in the use of copper, carbon steel or stainless steel for cathodes."

Table II. Operating details—electrolytic Zn and Ni powders

	Electrolytic zinc powder	Electrolytic nickel
Raw material	High-grade Zn flue dust	Ni
Cell:		
Material of construction	Steel, rubber-lined	Steel, rubber-lined
Capacity, lb/day	110	
Electrolyte:		
Feed	200 g/l NaOH, 10 g/l Zn	300 g/l NH_4Cl, 2 g/l NaOH
Effluent	200 g/l NaOH, 9 g/l Zn	
Temperature, °C	30	23-26
Method of feed	Gravity	
Circulation method	Rubber-lined pump	
Current:		
Current per cell, amp	2,500	
C.d. anode, amp/ft^2		10-20
C.d. cathode, amp/ft^2	120-150	20-30
Current efficiency, %	80-90	55
Volts per cell	3.4	1.4-1.5
Power consumption:		
Kwhr per lb metal	1.37	1.13
Lb metal per kwhr	0.73	0.88
Anode	Ni sheet	Ni
Cathode	Hollow iron or Mg alloy (Elektron)	Sheet Ni
Electrode spacing	1.18 in. (30 mm)	1.5 in.
Final product, % metal	Paste 35-45 Zn, dry dust 85-95	98-99

Iron

Electrodeposition of iron dates back to 1846 when Bottger used a bath of $FeSO_4 \cdot 7H_2O$ and NH_4Cl. Bietz in 1869 produced electrolytic Fe and employed it for making magnetic tests. Siemens (5) in 1889 proposed a general process in which sulfide-iron minerals were leached with ferric chloride or sulfate, the Fe deposited from the leach liquors on a cathode in a diaphragm cell, and the leach regenerated. The first serious attempt to produce electrolytic Fe in quantities was in 1904 (6), when the metal was deposited from a mixture of ferrous and ammonium sulfates at a current density of 6-10 amp/ft^2 (0.65-1 amp/dm^2) at 30°C and an average emf of 1 v. In the plant of the Western Electric Company (7) the anodes were cast steel and the bath carried slightly on the alkaline side so that a considerable amount of oxides would be deposited in the cathode to make the latter brittle and easily ground up in connection with the manufacture of electrical "loading coils." It was not necessary to make a pure grade of Fe. A further modification of the Burgess process was used by the Westinghouse Electric & Manufacturing Company (8) in which a pure grade of Fe was produced for use in the manufacture of alloys for electromagnetic machinery and instruments. Commercially pure Fe anodes were used, but the refining range of the process was very small. Cathodic products would often be produced which were too high in either C or S or both.

In 1914 an electrolytic iron plant was installed at

Table III. Data on production of electrolytic Fe powder and electrolytic Mn

	Iron	Manganese
Electrolyte:		
Sp gr	1.1	
Percentage Fe	4.6 (50 g/l)	
*p*H	4.5	
Temperature, °C	50	35-40
Circulation, gal/min	3.0	
Circulation apparatus	Centrifugal pumps	Centrifugal pumps
Anolyte:		
Mn, g/l, as $MnSO_4$		10-18
H_2SO_4, g/l		25-35
$(NH_4)_2SO_4$, g/l		120-140
*p*H		1-1.4
Catholyte feed:		
Mn, g/l, as $MnSO_4$		25-35
$(NH_4)_2SO_4$, g/l		125-135
*p*H		7.2-7.6
Current:		
Amp/ft²	25	40
Voltage per tank	2.5	5+
Current, voltage, and kw of d-c apparatus	2940 amp 85 v 250 kw	6000 amp 600 v
Current efficiency, %	90	65-70
Kwhr/lb metal, d.c.	1.20	4-4.5
Kwhr/lb metal, a.c.		5-5.25
Lb metal per kw-day	20.0	4.07
Anodes:		
Composition	Steel plate, 99%	Lead alloy
Length, width, thickness	24 x 18 x 1 in.	
Weight, lb	120	
Mode of suspension	Welded to hanger bars	Welded to hanger bars
Anode spacing, in.	5	
Life	12 days	3 years
Scrap, %	20	None
Number per cell	21	21
Cathodes:		
Length, width, thickness	18 x 22½ x 20 in. gauge	36 x 18 x 1/16 in.
Weight, lb	5½	
Mode of suspension	Welded to hanger bars	Welded to hanger bars
Replaced after ? days	2-3	1.5-2
Weight, lb	15-22	
Material		Stainless steel
Number per cell	20	20
Deposition tanks		
Material of construction	Haveg	Concrete, lead or plastic lined
Length, width, depth	10 ft x 30 in. x 30 in.	
Number of anodes, cathodes	21, 20	21, 20
Electric connection	Series	Series
Amp/in.² cross section of busbar	1000	1000
Anode mud:		
Percentage of anode	17	
Composition	Metallic iron and other metal oxides and sulfates	MnO_2
Removed after ? days	8	

Grenoble, France (9), in which a hot neutral solution of ferrous chloride was employed as an electrolyte to which iron oxide was added as a depolarizer, with cast-iron anodes and rapidly rotating mandrels for cathodes. Both tubing and plates were produced of electrolytic Fe of good purity, showing Fe 99.967%, C 0.008%, Mn 0.009%, P 0.002%, Si 0.014%, S trace (10). In commercial operation the electrolyte was circulated over Fe turnings, and iron oxide was added; or else air was blown in to keep the H^+ ion concentration of the solution low. Current density was 93-105 amp/ft² (10-11 amp/dm²) at a temperature of 80°C. The small hydrogen content of the metal was removed by annealing at 900°C. Power requirements were of the order of 1.8 kwhr/lb.

A bath used in Germany, originated by Fischer (11), contained 450 g $FeCl_2$, 500 g anhydrous $CaCl_2$, 750 g water, operated at 90°-110°C at 93-185 amp/ft² (10-20 amp/dm²). Owing to the high working temperature, the Fe deposited is relatively free from hydrogen and is therefore not brittle. It has a purity of at least 99.95% and can be deposited in thick, dense layers.

With the development of powder metallurgy, a demand for Fe powder arose. Part of this is met by electrolytic iron made by Plastic Metals of Johnstown, Pa. The operating conditions are tabulated in Table III (12).

Manganese

Manganese powder is the product of grinding electrolytic "cathode chip" metal in ball mills in nitrogen, helium, or argon atmospheres with particular care to keep temperatures low because of the pyrophoric nature of the powder. More recently Mn powder has been made successfully on crushing rolls. Manganese powder finds tonnage applications in welding rods and coatings therefore, as well as magnetic materials.

Manganese is electrowon from reduced ores or equivalent Mn containing materials which are

leached with return electrolyte, which when purified becomes cell feed (13). Operating conditions are given in Table III.

In the preparation of electrolyte from which the metal is deposited, the solution is purified completely of Fe, As, Sb, Sn, Pb, Ni, Co, Mo, SiO_2, Al; Ca and Mg are also removed. Diaphragms are around the cathodes, and the anolyte fills the cell around the diaphragms.

The electrowinning of Mn depends on very pure solutions. In addition, there is dependence on the combination of factors such as concentration, pH, temperature, current density, cathode and anode material, rate of flow to the cells, as well as other variables. Problems of dealing with an alkaline catholyte and an acid anolyte in a two-compartment cell, as well as the impossibility of considering any of the variables separately because of their influence on each other, cause Mn electrowinning to be almost in a class by itself. It demands much more delicate control than does the electrowinning of Zn and Cu, for it carries all their problems and many more.

Manuscript received July 15, 1957. This paper was prepared for delivery before the Buffalo Meeting, Oct. 6-10, 1957.

Any discussion of this paper will appear in a Discussion Section to be published in the December 1959 JOURNAL.

REFERENCES

1. E. Drouilly, U. S. Pat. 1,799,157 (1931); S. A. Tréfileries et Laminoirs du Havre, British Pat. 303,984 (1929); B. Leach and Henry and Leigh Slater Ltd., French Pat. 511,428 (1920); S. A. Tréfileries et Laminoirs du Havre, French Pat. 656,777 (1929).
2. C. L. Mantell, U. S. Pat. 2,182,567 (1939).
3. C. L. Mantell, U.S. Pat. 2,233,103 (1941).
4. J. B. Crownover, M.S. in ChE Thesis, Newark College of Engineering, Newark, N. J. (1952).
5. H. Siemens, U. S. Pat. 415,576 (1889).
6. C. F. Burgess and C. Hambuechen, *Trans. Am. Electrochem. Soc.*, **5**, 201 (1904).
7. B. Speed and G. W. Elman, *J. Am. Inst. Elec. Eng.*, **40**, 596 (1921).
8. P. H. Brace, *ibid.*, **44**, 922 (1925).
9. L. Guillet, *Electrician*, **74**, 79 (1914); *Engineering*, **98**, 413 (1914).
10. J. Escard, *Génie civil*, **75**, 165, 199, 225 (1919); *Elec. Rev.*, **76**, 610 (1920).
11. F. Fischer, *Z. Elektrochem.*, **15**, 595 (1909); O. W. Storey, *Trans. Am. Electrochem. Soc.*, **29**, 357 (1916).
12. B. T. du Pont, Private communication.
13. C. L. Mantell, *J. (and Trans.) Electrochem. Soc.*, **94**, 323 (1948).

Brief Communication

On the Hydrogen Evolution Reaction

Ralph J. Brodd

National Bureau of Standards, Washington, D. C.

Theoretical calculations of the rates of electrochemical reactions have been the subject of many publications. Most treatments in recent years involve the assumption of an activated complex and suffer in that the energy terms for the activated complex cannot be evaluated accurately. In the case of electrode reactions it would appear that a promising line of approach to take would involve the assumption that the charge transfer at the electrode occurs by a tunneling process and that this tunneling process is the controlling factor in the rate of the reaction (1).

Kinetic theories of the hydrogen evolution reaction usually assume that the initial reaction step at an elecrode is

$$H^+ \text{ (sol'n)} + e \underset{M}{\rightarrow} H \qquad [1]$$

It can be shown that the rate of this reaction may be approximated from (1) by

$$\text{rate} = \Gamma \exp(-\Delta U/kT) \qquad [2]$$

where

$$\Gamma = \exp\left[-\frac{(2m)^{1/2}}{h}(\phi)^{1/2} R\right] \qquad [3]$$

and

$$\Delta U = \phi - E_a - \frac{e^2}{4R} + (E_{zpc} + \chi) \qquad [4]$$

In these equations e, h, k, m, and T have their usual significance. ϕ is the work function of the metal electrode, E_a is the electron affinity of H^+ in Eq. [1], E_{zpc} is the potential of the hydrogen electrode vs. the zero point of charge, χ is the surface potential for hydrogen adsorption on the metal, and R is the distance of approach of hydrogen ions to the surface of the metal when the charge transfer occurs. R is assumed to be 0.49Å, the average of the Goldschmidt and Bohr radius of the hydrogen atom.

In Table I are found the results of calculations

Table I. Calculated and experimental rates of hydrogen evolution reaction

Metal	Cal'd. rate, amp/cm²	Expt'l. rate (2), amp/cm²
Hg	5.8×10^{-13}	2×10^{-12}
Ni	2.5×10^{-4}	1×10^{-6}
Cu	2.5×10^{-7}	2×10^{-7}
Ta	7.2×10^{-6}	1×10^{-5}

of the rates of the hydrogen evolution reaction at the reversible potential, and H^+ (sol'n) concentration of unity. Experimental rates of the hydrogen evolution reaction at approximately the same conditions are given for comparative purposes.

The table shows that the calculated and experimental values are in fairly good agreement. Since the calculated values are very sensitive functions of R, E_{zpc}, and χ, as seen in Eqs. [3] and [4], the agreement is fortuitous in some cases.

The following model may be associated with the process given in Eq. [1]. The metal electrode is assumed to be a perfect conductor. The electron from the metal electrode moves through an energy barrier at the surface of the electrode described by the Γ function in which the barrier height is ϕ and the barrier width is R. Then, at distance R from the electrode the electron combines with a proton from the hydrogen ion solvation complex in the electrical double layer to form a hydrogen atom. A somewhat similar model in principle has been proposed by Gurney (3).

Manuscript received Aug. 22, 1958.

Any discussion of this paper will appear in a Discussion Section to be published in the December 1959 JOURNAL.

REFERENCES

1. J. Weiss, *Proc. Roy. Soc. (London)*, **A222**, 128 (1954).
2. J. O'M. Bockris, National Bureau of Standards "Electrochemical Constants," Circular 524 (1953), P243.
3. R. W. Gurney, *Proc. Roy. Soc. (London)*, **A134**, 137 (1931).

Zinc-Mercuric Dioxysulfate Dry Cell

Samuel Ruben

Ruben Laboratories, New Rochelle, New York

ABSTRACT

A dry cell is described which provides some of the desirable characteristics of the mercuric oxide alkaline cell while allowing the use of inexpensive conventional dry cell construction. The system is $Zn/ZnSO_4/HgSO_4 \cdot 2HgO + C$ and has an over-all reaction of $3Zn + HgSO_4 \cdot 2HgO \rightarrow ZnSO_4 + 2ZnO + 3Hg$. A relatively flat discharge characteristic is obtained within the proper limits of current density. The cell capacity is directly referable to the $HgSO_4 \cdot 2HgO$ or $3HgO \cdot SO_3$ content.

The alkaline mercuric oxide cell (1-3) possesses a number of characteristics, particularly for specialized use such as military applications where compactness, long shelf life, and storage at high ambient temperatures are necessary. It is used in commercial applications requiring cells of high capacity in small dimensions such as in hearing aids and other miniaturized electronic devices. One specific characteristic of this system, the maintenance of a flat discharge voltage and low impedance during discharge, has been of particular advantage in transistor applications.

An electrochemical system has been developed which is suitable for many applications and which combines some of the desirable discharge characteristics of the mercuric oxide cell with the low cost structure of the Leclanché zinc-carbon cell.

In the past, attempts have apparently been made (4) to use mercury compounds in the cathode of a nonalkaline dry cell, but these have failed because of inherent limitations of the materials used.

Zinc-Mercuric Dioxysulfate Cell

In the new cell, which might be termed the Mercury-Zinc Carbon Cell, the cathode reactant is a basic mercurial compound, such as mercuric dioxysulfate, and the electrolyte is a zinc sulfate solution in which the cathode is stable. The anode is zinc. The combination permits conventional zinc carbon cylindrical and flat cell constructions.

The electrochemical system in the presence of an aqueous solution of zinc sulfate can be expressed as

$$Zn/ZnSO_4/HgSO_4 \cdot 2HgO + C$$

with an over-all reaction on the discharge as

$$3Zn + HgSO_4 \cdot 2HgO \rightarrow ZnSO_4 + 2ZnO + 3Hg$$

In addition to the reactive components it is desirable to add a buffer agent to raise and maintain the *p*H of the electrolyte in the desired range to reduce the solubility of the mercuric dioxysulfate to a minimum. Various buffers have been used, such as the addition of calcium carbonate to the cathode mix or the addition of acetate to the electrolyte, to maintain the *p*H in the range of 5 to 6.

An inhibitor such as potassium dichromate is added to the electrolyte to inhibit continued amalgamation of anode by the slight amount of active cathode material in solution. The cathode is spaced from the anode by a paper cellophane laminate processed to provide barrier action and control of electrolyte transfer.

Construction of the Cell

The dry mix is composed of 8 parts mercuric dioxysulfate and 1 part acetylene black.

The electrolyte consists of a 20% solution of $ZnSO_4 \cdot 7H_2O$ to which 1% of $K_2Cr_2O_7$ is added. The electrolyte is added to the dry mix in the proportions of 1 part electrolyte to 2 parts dry mix.

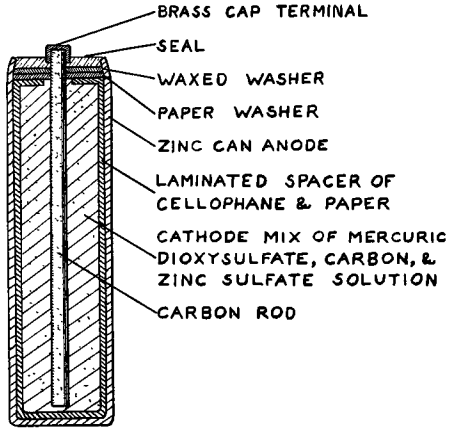

Fig. 1. Construction and components of the zinc-mercuric dioxysulfate cell.

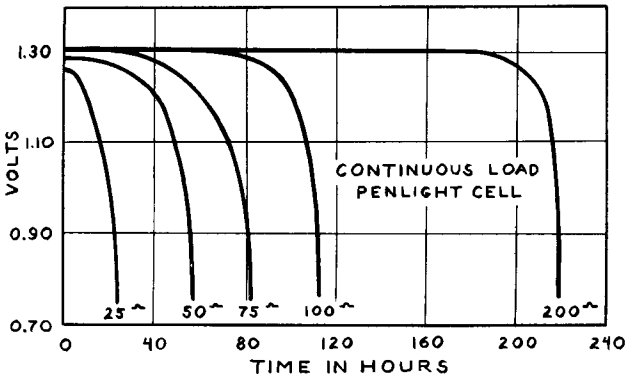

Fig. 2. Discharge characteristics of an AA-size cell discharged continuously at loads of 25, 50, 75, 100, and 200 ohm.

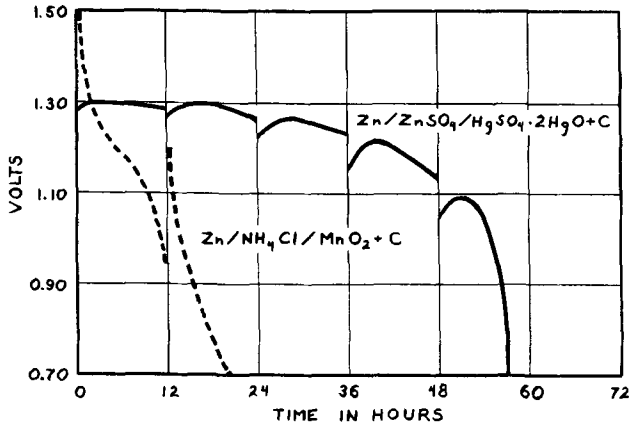

Fig. 3. Discharge characteristics of an AA-size cell discharged at 50 ohms 12 hr/day.

The zinc can is lined with a spacer which consists of a laminate of 0.004 in. paper and 0.0009 in. cellophane cemented together and coated with an aqueous glycerine gum arabic solution. The paper side of the laminate contacts the zinc can.

No free space is incorporated in the cell since there is negligible expansion of the bobbin during use. The top edge of the zinc can is rolled over and the space between the rolled edge and waxed washer on top of the bobbin filled with sealing compound. This gives a secure top seal and holds the bobbin in intimate contact with the lined can. The can thickness is about 0.004 in. greater than used in standard zinc-carbon cells to allow higher capacity without puncture at end of life.

Freshly made cells have an open-circuit voltage of 1.45 v. This stabilizes with initial use or on shelf to 1.36 v. The closed circuit potential has 1.3 v for loads within the rated current density.

Due to the high efficiency of the cathode mix, the capacity per unit volume exceeds that of the conventional zinc-carbon cell and is directly referable to the $HgSO_4 \cdot 2HgO$ content. The theoretical capacity of the $HgSO_4 \cdot 2HgO$ is approximately 0.22 amp-hr/g and the practical capacity, 0.21 amp-hr/g. Cells connected to a gas collecting apparatus and maintained at 45°C (113°F) have shown negligible gas evolution over several months tests.

Electrical Characteristics

Figure 1 illustrates the construction and components of the cell.

Figure 2 illustrates the discharge characteristic of AA (penlight) size cells discharged continuously through resistances of 25, 50, 75, 100, and 200 ohms.

Figure 3 illustrates the discharge characteristics of AA (penlight) size cells discharged intermittently 12 hr per day through a resistance of 50 ohms. Similar discharge of a commercial Leclanché cell of the same size is included for comparison.

Figure 4 illustrates the discharge characteristics of AA cells after 8 months' casual storage.

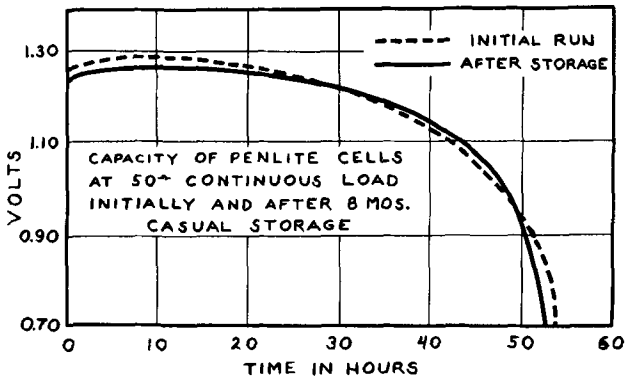

Fig. 4. Discharge characteristics of AA cells after 8 months' casual storage.

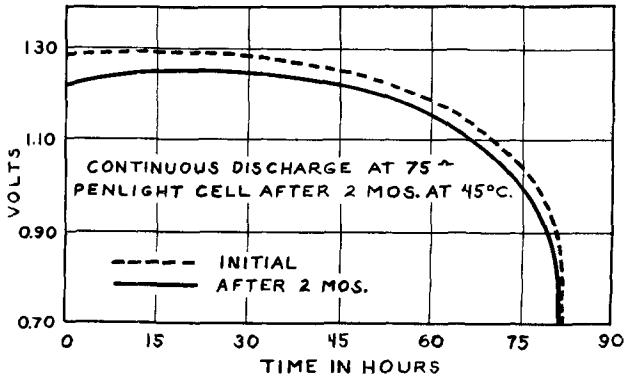

Fig. 5. Discharge characteristics of AA-size cells after 2 months' storage at 45°C (113°F).

Figure 5 illustrates the discharge characteristics of AA-size cells after two months' storage at 45°C (113°F).

The initial impedance of an AA-size cell at 1000 cycles is eight-tenths ohms and the impedance after continuous discharge is one ohm. On intermittent loads the impedance is higher at the start of each cycle and decreases to the normal value.

The weight of an AA-size cell constructed with a capacity of 1360 ma-hr is 20 g.

In summary, the new cell described has some desirable characteristics where a low current discharge is required over long periods of time with a flat voltage output. One such application has been for electronic clocks where D-size cells have been operating for a year with a total capacity of 8.0 amp-hr.

Manuscript received June 9, 1958. This paper was prepared for delivery before the Ottawa Meeting, Sept. 28-Oct. 2, 1958.

Any discussion of this paper will appear in a Discussion Section to be published in the December 1959 JOURNAL.

REFERENCES

1. S. Ruben, U. S. Pat. 2,814,664 (1957).
2. M. Friedman and C. E. McCawley, *Trans. Electrochem. Soc.*, **92**, 195 (1947).
3. S. Ruben, *ibid.*, **92**, 183 (1947).
4. A. Heil, German Pat. 212,468 (1908).

The Potential of the Manganese Dioxide Electrode and the Surface Composition of the Oxide

Akiya Kozawa[1]

Department of Applied Chemistry, Faculty of Engineering, Nagoya University, Nagoya, Japan

ABSTRACT

When manganese dioxide is heated, the electrode potential decreases with the heating temperature. This potential decrease cannot be explained as a phase transformation nor as an ordinary decomposition of MnO_2 to Mn_2O_3. A lower oxide film is formed on the surface of MnO_2 when it is heated at temperatures up to 450°C. The potential decrease on heating can be explained as the result of the lower oxide film formation, the potential of manganese dioxide depending on the surface oxidation state. The reaction of Mn^{++} in slightly alkaline electrolyte with MnO_2 gives a similar decrease in potential explainable as a surface effect.

When a MnO_2 electrode is discharged the potential decreases gradually as reduction takes place to a lower oxide such as Mn_2O_3 (or MnOOH) or to Mn^{++} ion. To understand the potential decrease, we must know what factors determine the electrode potential.

The potential of the MnO_2 electrode in neutral or alkaline solution free from manganese(II) ion may be expressed by

$$E = E^\circ - 0.059\ pH - \frac{RT}{2F} \ln \frac{a_{Mn_2O_3}}{(a_{MnO_2})^2} \qquad [1]$$

$$E^\circ_{red} = 1.014$$

corresponding to the reaction

$$2MnO_2 + 2H^+ + 2e = Mn_2O_3 + H_2O \qquad [2]$$

However, the potential seems to be dependent on the composition of the oxide surface rather than on the activities of two separate phases in neutral electrolyte (2). In this paper the effect on the potential of alteration of the surface composition of MnO_2 by heating at moderate temperatures and by the adsorption of Mn(II) ion is considered. Heating at 100°-450°C affects the potential, the discharge capacity, and the water content (2-5) although the decomposition temperature is higher than this, 480°-580°C for different kinds of manganese dioxide. The decrease in potential on heating has been ascribed to a change in crystal form (5).[2] The experiments to be described lead to a different explanation, namely, that the change in potential is the result of loss of oxygen at the surface.

[1] Present address: Department of Chemistry, Western Reserve University, Cleveland, Ohio.

[2] The idea that different phases of manganese dioxide may have different potentials can be tested by calculating the approximate free energy difference between γ-MnO_2 and β-MnO_2 using the decomposition temperature of MnO_2 to Mn_2O_3 at 1 atm pressure. The decomposition temperature is measured as 480°C for γ-MnO_2 and 580°C for β-MnO_2 from the author's thermal balance experiments, which can be seen to be the starting point of the decomposition in Fig. 1. From the Nernst approximation formula $\log P_{O_2} = \Delta H/4.579T + 1.75 \log T + 2.8$, ΔH is calculated for each MnO_2, then the potential difference $\Delta E = (\Delta H_{480} - \Delta H_{580})/4F + T(\Delta S_{480} - \Delta S_{580})/4F$ is obtained, where the second term is neglected. The results shows γ-MnO_2 should be 44 mv higher than β-MnO_2 in potential. The 44 mv is too small to explain the potential decrease (about 250 mv) on heating.

Experimental

Preparation of oxides.—An electrolytic oxide, presumably γ-MnO_2, was prepared by electrodeposition from an acid bath at 97°-98°C with a current density of 1.74 amp/dm². Initially the bath was 0.85 mole/l $MnSO_4$ and 0.03 mole/l H_2SO_4 and at the end 0.48 mole/l $MnSO_4$ and 0.51 mole/l H_2SO_4.

Figure 1 gives the result of a differential thermal analysis of this MnO_2 along with one of natural pyrolusite. The electrolytic oxide was ground to pass through a 100-mesh sieve. The powdered sample was washed with hot 2*N* H_2SO_4 several times, then several times with water, and finally with very dilute ammonia solution. It was dried at 80°C for 10 hr. Samples of this oxide, of the oxide before washing, and of a natural pyrolusite were heated at various temperatures from 160° to 438°C for 1 hr in an electric furnace in air.

Some of the γ-MnO_2 was heated to constant weight at 800°C. The resulting oxide was shown by analysis to be Mn_2O_3.

Potential of heated MnO_2.—The potentials of the heated oxides were measured as follows. A 1.00-g sample of each oxide was placed in 50 ml of 2M NH_4Cl and NH_3, pH 8.35, in an Erlenmeyer flask, shaken occasionally for 3 hr, and then digested overnight at room temperature. The mixture was cen-

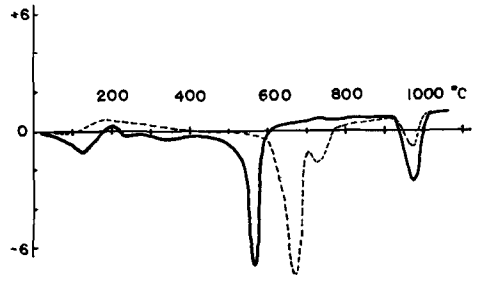

Fig. 1. Differential thermal analysis of manganese dioxides. The temperature was raised at a rate of 2°C/min. —— electrolytic MnO_2 (γ-MnO_2), - - - - - pyrolusite (β-MnO_2).

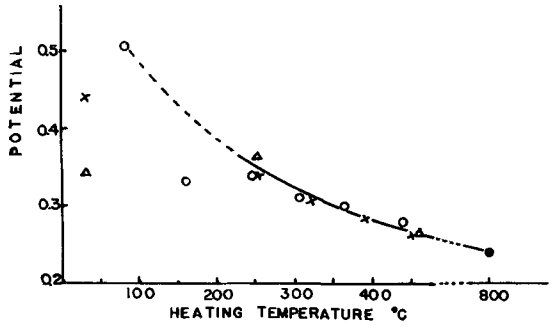

Fig. 2. Potentials, corrected to pH8, vs. saturated calomel electrode of heated manganese dioxides. O, electrolytic MnO_2 washed with H_2SO_4, X, electrolytic MnO_2 not washed; △, natural pyrolusite (β-MnO_2); •, Mn_2O_3 made from the electrolytic MnO_2 by heating at 800°C.

trifuged in a 15-ml centrifuge tube with a narrow bottom. A platinum foil electrode was inserted in the manganese dioxide layer at the bottom of the centrifuge tube. The potential then was measured against a saturated calomel electrode and the *p*H of the solution was measured by a glass electrode *p*H meter.

Results are shown in Fig. 2 for all potentials which were corrected to *p*H 8.0 assuming a change of −60 mv per *p*H unit. It is clear that the potential decreases with heating temperature between 250° and 450°C regardless of the kind of manganese dioxide and of acid washing. Although three different unheated samples gave very different potentials, they came to agreement on heating above 250°C. The potential after heating to 450°C was fairly close to that of Mn_2O_3, although the composition was not much different from that of the original unheated sample, as shown in Fig. 3.

Analysis of the heated MnO_2 was carried out by the $FeSO_4$ method for available oxygen and by the $NaBiO_3$ method for total Mn. The calculated x values in MnO_x, as shown in Fig. 3, decrease with heating temperature from 1.977 to 1.946.

According to Fig. 1 no extensive decomposition takes place below 450°C, and the small change in x-value (in MnO_x) confirms this. Heating at 250°C did not give a continuous change; after 1 hr the x-value (in MnO_x) was 1.965, after 4 hr, 1.963, and after 6 hr, 1.964. Previously (2) heating at 450°C gave a similar result. Maxwell and Thirsk observed

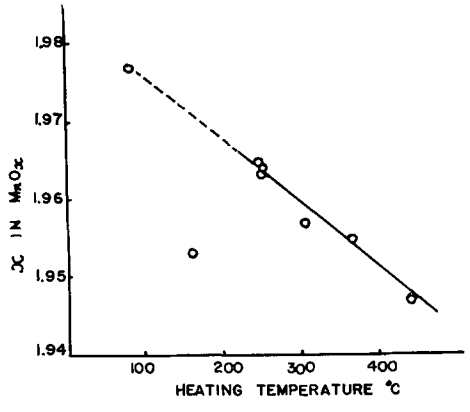

Fig. 3. Results of analysis of electrolytic MnO_2 heated at various temperatures; values of x in MnO_x. Three points around 250°C are for different heating times, 1, 4, and 6 hr.

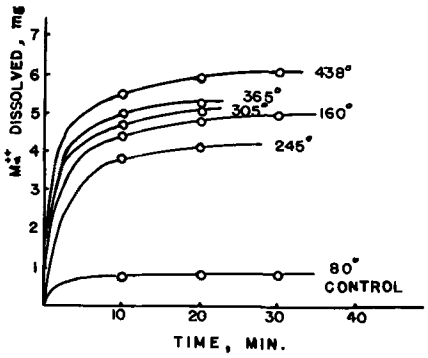

Fig. 4. Manganese (II) ion dissolution from heated manganese dioxide (0.5 g) by 1N H_2SO_4 stirring at room temperature. After 10 min stirring, it was allowed to stand for 5 min which was not counted in the abscissa of this figure. Heating temperatures of MnO_2 are indicated in the figure.

a similar decrease in x value of MnO_2 heated under O_2 atmosphere (6).

The sample of γ-MnO_2 heated at 160° differed in x value, potential, and also in dissolution of Mn^{++} (as shown in Fig. 4) from what would be expected on the basis of the data for the other heated oxides. A similar deviation was observed previously (2). That the deviation is real and not the result of an error is suggested.

Changes on heating can be shown to be the result of the MnO_2 surface. Samples of the heated oxides (of electrolytic origin) of 0.50 g each were mixed with 50 ml of 1*N* H_2SO_4, the mixtures being stirred at room temperature for exactly 10 min. After 5 min, a 5-ml sample of the supernatant solution was taken for Mn^{++} ion determination. The sample was added to 5 ml of 0.01M E.D.T.A. solution and buffer ($NH_4Cl + NH_3$) added to adjust the *p*H at 9 to 9.5. Then the excess E.D.T.A. was titrated with a standard $ZnSO_4$ solution (0.0100M) using Eriochrom Black T as indicator. In this method, small particles of manganese dioxide, if any are present, do not interfere. Then the mixture of MnO_2 and H_2SO_4 solution was stirred again for 10 min and, after 5 minutes' standing, another sample was analyzed, and the whole procedure repeated a third time.

Results are shown in Fig. 4. The unheated original MnO_2 (control in Fig. 4) was washed with 2*N* H_2SO_4 previous to the experiment and gave only a little Mn(II) ion dissolved. Most of the Mn(II) ion dissolves in 10 min.

The larger amount of Mn(II) dissolved from heated MnO_2 may be considered as the result of lower oxide formation on the surface of manganese dioxide by heating. Increase of heating temperature gives an increase in Mn(II) ion dissolved, except that the 160°C curve is out of place, as mentioned above.

The decrease in x-value of the various samples can be compared with the Mn(II) ion dissolved by acid. A decrease in x from 1.977 for the original sample to 1.947 for the sample heated at 438°C corresponds to the reduction of about 3% of the total Mn from Mn(IV) to Mn(II). In the 0.5-g sample treated with acid, 3% of the total Mn, or 8.6 mg, should have been Mn(II) according to the analysis and calculation. The acid treatment extracted 5.9

mg of Mn(II) according to Fig. 4, but this should be corrected by 0.8 mg extracted from the unheated sample, leaving 5.1 mg additional extractable Mn(II) as the result of heating. This is 59% of the total estimated from the analysis.

Another experiment was carried out to confirm the lower oxide formation on the surface of MnO_2 using three kinds of MnO_2: γ-MnO_2 or electrolytic MnO_2, α-MnO_2 or cryptomelane made from the electrolytic MnO_2 by autoclaving with NH_4Cl solution at 170°C (7), and β-MnO_2 or natural pyrolusite. Two grams of each sample heated at various temperatures for 3 hr were shaken with a $MnSO_4$ solution buffered with acetic acid-sodium acetate (*p*H, 5.4), then the supernatant solution was analyzed to determine the adsorption of the divalent manganese ion on the manganese dioxide. Results are shown in Fig. 5. The absolute value of the Mn(II) ion adsorption should be affected by the surface area and the original surface oxidation state of the manganese dioxides. However, the results show that the higher the heating temperature the smaller is the adsorption. This means the more of the lower oxide on the surface the less of a reaction between MnO_2 and Mn(II) ion to form the lower oxide, $MnO_2 + Mn^{++} \rightarrow Mn_2O_3$.

From the above results it seems possible to conclude that the potential decrease of heated manganese dioxide is the result of lower oxide formation on the surface, and also that the potential of manganese dioxide depends mainly on the surface oxidation state.

In an electron diffraction study of manganese dioxide, Butler and Thirsk (8) found a lower oxide on the surface of manganese dioxide, but they pointed out that it may have been formed there by the bombardment with electrons.

Potential change on heating various MnO_2 *samples.*—Samples of four oxides: B, electrolytic MnO_2 or γ-MnO_2; A, sample B treated by Na_2CO_3 solution for dry-cell use; C, natural ore, probably α-MnO_2; D, natural pyrolusite or β-MnO, were heated at various temperatures for 3-4 hr. Then 5.00 g of each sample was digested with 25 ml of 0.5M NH_4Cl solution for 5 days at 25°C with occasional shaking. The potentials and *p*H values of the solutions were measured as described before. Results are shown in Fig. 6. On heating below 250°C no regularity was found between the *p*H and the potential, and those points are omitted from Fig. 6. However, above 250°C a straight line relationship for each temperature was obtained between *p*H and potential irrespective of the kind of manganese dioxide, and the slope was near the theoretical 0.059 v per *p*H unit.

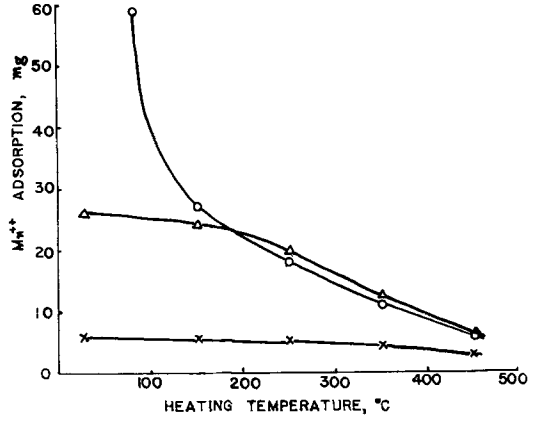

Fig. 5. Adsorption of Mn^{++} on MnO_2 heated. o, γ-MnO_2; △, α-MnO_2; x, β-MnO_2. 2-g sample was shaken with 50 ml of NaAc-HAc buffered solution containing $MnSO_4$ (100 mg as Mn^{++}), pH 5.4.

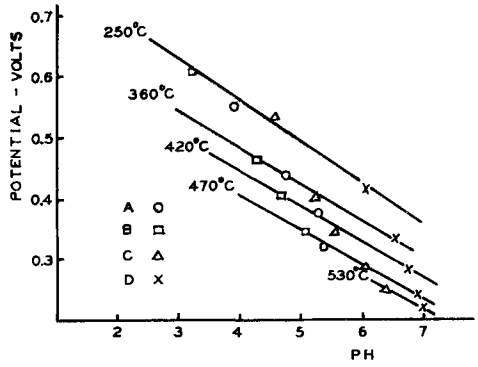

Fig. 6. Potentials of various MnO_2 samples after heating. Potentials were measured against a 0.1N calomel electrode. A, B, γ-MnO_2; C, probably α-MnO_2; D, β-MnO_2.

This result can be interpreted in terms of a surface layer of lower oxide. Originally each of the four samples had its individual surface oxidation state, so there was no consistent relation between the potentials of different samples and the *p*H. However, on heating at 250°C or higher the surface attains the same oxidation state for all, determined only by the temperature and irrespective of the original surface oxidation state, crystal structure, and chemical composition of the interior of the crystals.

Potential of MnO_2 *with a known amount of lower oxide on the surface.*—MnO_2 reacts with Mn(II) ion in a solution of suitable *p*H as follows:

$$MnO_2 + Mn^{++} + H_2O \rightarrow Mn_2O_3 + 2H^+ \qquad [3]$$

and the lower oxide (Mn_2O_3 or MnOOH) will remain on the surface of the MnO_2. When MnO_2 having a known surface area reacts with a known amount of Mn(II) ion, we can calculate the percentage of surface covered by the lower oxide. Therefore, a quantitative relation between the electrode potential and the surface oxidation state can be established. Some experiments were carried out to examine this point of view.

Powdered MnO_2 made by electrodeposition was washed with 2*N* H_2SO_4 several times to remove lower oxide and then washed with water and dried at 80°C. The sample had a surface area of 60 m^2/g as measured by the B.E.T. method by N_2 adsorption at liquid nitrogen temperature. Samples of 1.50 g were treated with 50 ml of 0.5M NH_4Cl containing varying amounts of manganese sulfate (0-180 mg of Mn^{++}). The *p*H of the solution was adjusted to around 8 by addition of NH_3. The mixtures were heated at about 70°C for 1 hr with occasional shaking and allowed to stand overnight at room temperature. Then the potential and *p*H of the solution were measured. Colorimetric tests showed that the

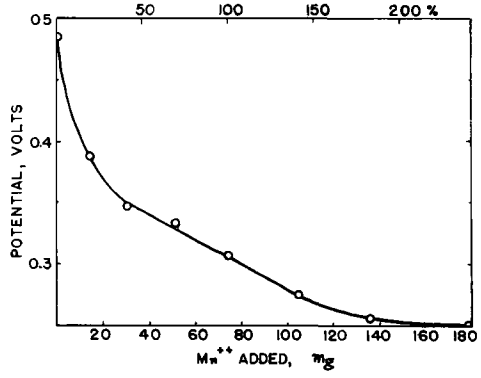

Fig. 7. Potential (vs. saturated calomel electrode) of manganese dioxide with known amount of lower oxide on the surface. The upper obscissa scale represents the percentage of the surface covered by lower oxide.

supernatant solution contained no detectable Mn(II) ion; that is, all Mn^{++} added had reacted with the manganese dioxide. Figure 7 shows the potentials corrected to *p*H 8 using a theoretical coefficient, −60 mv/*p*H. The lower scale of abscissas represents divalent manganese added to 1.50 g of the manganese dioxide. The upper scale represents the percentage of the surface covered by lower oxide assuming that all Mn(II) ion added remains on the surface of MnO_2.

The number of manganese atoms on the MnO_2 surface can be calculated from $n = \left(\frac{d \times N}{MnO_2} \right)^{2/3} \times 100^2 \times S$, in which d is the density of MnO_2 taken as 4.020 found from pycnometer measurements for this sample, N is Avogadro's number, MnO_2 represents the formular weight, and S is the surface area (m^2/g). Let it be assumed that for each atom of Mn(IV) on the surface one Mn^{++} ion from the solution is added to form Mn_2O_3 as indicated in Eq. [3]. Then 75.4 mg of Mn^{++} is necessary to cover the total surface of 1.5 g of this MnO_2 by Mn_2O_3.

The results in Fig. 7 show that one and half layer or two layer coverage of the MnO_2 surface by Mn_2O_3 gives nearly the same potential as that of Mn_2O_3, which is shown in Fig. 2.

From the data in Fig. 7, E° in Eq. [1] can be calculated, if the ratio $a_{Mn_2O_3}/a_{MnO_2}$ is taken to be the ratio in the surface. When 50% of the surface is covered in Mn_2O_3, E is 0.342 v (from Fig. 7). If activity coefficients can be neglected, Eq. [1] becomes:

$$0.342 = E^\circ - (0.059 \times 8) - 0$$

Then, E° is 0.814 v referred to the calomel electrode or 1.056 v referred to the hydrogen electrode. This is near enough to the calculated value 1.014 v from thermal data to support the assumption that the potential is determined by the composition of the surface.

Discussion

When a MnO_2 electrode is discharged the potential decreases and on interruption of the discharge the potential is recovered. As one of the factors to explain the potential recovering process, the following mechanism has been considered (9). On the discharge of MnO_2, lower oxides (Mn_2O_3 or MnOOH) may be formed on the surface of MnO_2, and on interruption the lower oxides may start to diffuse into the interior of the MnO_2, namely, a rearrangement between the surface and the inside may take place in such a way that only electrons and protons are moving (10).

The results given in the present paper have shown that the lower oxide on the surface of MnO_2 is fairly stable (from experiments shown in Fig. 5-7) even for electrolytic MnO_2 containing water (about 8%) which may help to move proton. The potential of the MnO_2 electrode, therefore, is dependent mainly on the surface oxidation state of the dioxide instead of the activity of the whole oxide.

Therefore it seems that the rate of the rearrangement process would be very slow if there is any contribution of it to the potential recovery process.

Acknowledgment

The author wishes to express his appreciation to Professor W. C. Vosburgh, Duke University, who has given much helpful advice in preparation of this paper and particularly under whom the experiments of Fig. 7 have been carried out. The author is indebted to Dr. K. Nagasawa, Nagoya University of Japan, for the differential thermal analysis. This portion of the work was supported in part by the Office of Naval Research.

Thanks are also due Professor E. Yeager and Professor F. Hovorka, Western Reserve University, and Professor K. Sasaki, Nagoya University, Japan, for their encouragement and valuable comments.

Manuscript received July 28, 1958. This paper was presented at the Cleveland Local Section meeting of The Electrochemical Society on April 8, 1958.

Any discussion of this paper will appear in a Discussion Section to be published in the December 1959 JOURNAL.

REFERENCES

1. A. M. Moussard, J. Brenet, F. Jolas, M. Pourbaix, and J. Van Muylder, Proceeding of the Sixth Meeting of the International Committee for Electrochemical Thermodynamics and Kinetics, p. 190 (1954).
2. A. Kozawa and K. Sasaki, *J. Electrochem. Soc. Japan*, **22**, 569 (1954).
3. K. Sasaki and A. Kozawa, *ibid.*, **25**, 273 (1957).
4. K. Sasaki and A. Kozawa, *ibid.*, **25**, 115 (1957).
5. J. Brenet and A. M. Briot, *Compt. rend.*, **232**, 1300, 2021 (1951).
6. K. H. Maxwell and H. R. Thirsk, *J. Chem. Soc.*, **1955**, 4057.
7. H. F. McMurdie, *Trans. Electrochem. Soc.*, **86**, 313 (1944).
8. G. Butler and H. R. Thirsk, *This Journal*, **100**, 297 (1953).
9. J. J. Coleman, *Trans. Electrochem. Soc.*, **90**, 545 (1946).
10. D. T. Ferrell and W. C. Vosburgh, *This Journal*, **98**, 334 (1951).

Anodic Dissolution of Magnesium Alloys in Aqueous Salt Solutions

R. Glicksman

RCA Laboratories, Radio Corporation of America, Princeton, New Jersey

ABSTRACT

The anodic dissolution of a magnesium AZ10A alloy has been studied by measuring corrosion rates and electrode potentials as functions of current density, pH, and electrolyte concentration. Results are interpreted in terms of a rate-controlling proton transfer step through a surface film of magnesium oxide and/or hydroxide.

The effect of different alloy compositions and soluble metal additives to the electrolyte on the anodic corrosion rate and electrode potential also has been measured.

Although the theoretical advantages of magnesium as an anode for primary batteries have been recognized for well over fifty years (1), nothing significant had been reported on a Mg dry cell until the recent work of Kirk, George, and Fry (2, 3). Their cell, which is patterned after the conventional Leclanché cell, contains a magnesium alloy anode, a manganese dioxide cathode, and a magnesium bromide electrolyte. More recently, magnesium dry cells containing a magnesium bromide electrolyte and organic cathode materials have been reported (4, 5).

These developments indicate that magnesium may find extensive use in primary cells. However, some basic problems present themselves. One of these is the poor electrode efficiency of the magnesium alloys. Information on the mechanism of anodic dissolution should help to explain these low electrode efficiencies and could indicate new approaches that might be taken to improve anode performance. In the present investigation the anodic dissolution of an AZ10A magnesium alloy has been studied by measuring corrosion rates and electrode potentials as functions of current density, pH, and electrolyte concentration. The effect of different alloy compositions and soluble metal additives to the electrolyte on the anodic corrosion rate and electrode potential also has been measured.

Experimental

Corrosion rates were obtained by measuring the amount of hydrogen liberated at a magnesium anode while it was undergoing anodic dissolution. The apparatus used in making these measurements is shown in Fig. 1. A carbon rod was used as the cathode, while the anode consisted of cylinders of magnesium approximately 2.5 cm in diameter and 2.5 cm long. These were mounted on a steel shaft with ends protected by plastic washers. The remainder of the shaft was protected by a close fitting Bakelite sleeve, which is set tightly on a ground glass male joint.

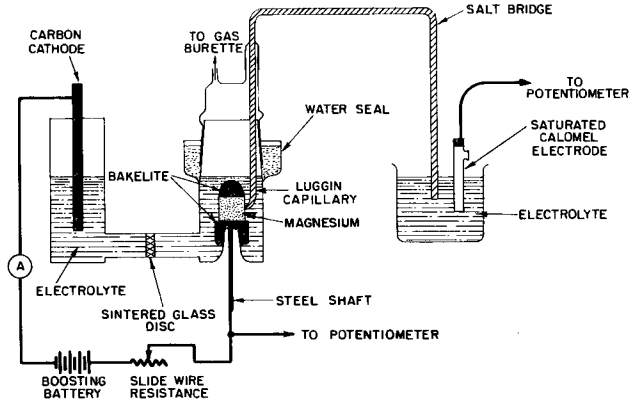

Fig. 1. Apparatus used to investigate magnesium corrosion rates and anode potentials.

The current flow in the circuit was maintained constant by means of a variable resistance and booster battery, and the hydrogen was collected in a gas buret in the usual manner. The procedure and apparatus were checked by measuring the volume of hydrogen liberated at a platinum electrode in 2*N* HCl solution, which corresponded to within 1% of the theoretical amount of hydrogen expected, based on calculations using Faraday's law.

The magnesium specimens, compositions of which are shown in Table I, were prepared by etching them in dilute acetic acid for 1-2 min and washing them in distilled water. Solutions were prepared with Fisher purified magnesium bromide and certified sodium bromide reagents using doubly distilled water. All solutions were saturated with Fisher N. F. magnesium hydroxide reagent.

The duration of each run was 3 hr except in the more corrosive solutions where quantities of hydrogen in excess of 100 cc were evolved in shorter time intervals. With but few exceptions all reported measurements represent the average of two or three runs, and each result was obtained with fresh electrolyte and a newly prepared magnesium cylinder. Duplicate runs varied from 1 to 3% for most of the

Table I. Local corrosion rates, electrode potentials, and anode efficiencies of various commercial magnesium alloys dissolving anodically in 2N $MgBr_2$ electrolyte [st'd with $Mg(OH)_2$] at a current density of 2.0 ma/cm²

Alloy*	Composition, %†					Maximum† impurities, %		Anode efficiency, %	Anode potential, v	Corrosion rate × 10^{-2} mdd
	Al	Zn	Mn	Ca	Zr	Ni	Fe			
Commercially pure magnesium	—	—	0.15 Max.	—	—	0.001	—	63.5	1.327	12.5
AZ10A	0.8-1.2	0.3-0.5	0.15 Max.	0.1-0.25	—	0.001	0.002	68.3	1.287	10.2
AZ31B	2.5-3.5	0.7-1.3	0.20 Min.	0.04 Max.	—	0.005	0.005	67.0	1.232	10.7
AZ80A	7.9-9.2	0.2-0.8	0.15 Min.	—	—	0.005	0.005	68.9	1.227	9.8
ZK60A†	—	4.8-6.5	—	—	0.45 Min.	—	—	58.3	1.233	15.6
M1A	—	—	1.20 Min.	0.08-0.14	—	0.01	—	52.6	1.328	19.6

* Alloys obtained from Dow Chemical Co. and White Metal Rolling and Stamping Corp.
† Data supplied by the Dow Chemical Co.

measurements, while a variation of 5-6% was obtained with the more corrosive solutions. Average values in terms of mg/dm²/day (mdd) are reported for the dissolution rates.

All runs were made at room temperature which varied from 24°-30°C during the course of this investigation. The effect of temperature on the corrosion rate over this temperature range has been shown to be negligible (6), and duplicate runs made at varying temperatures indicate no correction for this factor was necessary. Measurements of the effect of dissolved oxygen on the corrosion of magnesium in magnesium bromide solution (7) showed it has little or no effect on the corrosion rate, a result in agreement with previously reported data (8). Therefore, this factor was not controlled either.

The magnesium potentials were measured with a L&N type K potentiometer at the completion of each run using a Luggin capillary and a saturated calomel reference electrode as shown in Fig. 1. The reported potentials are all steady-state values and represent the average of two or three measurements. The individual measurements had a reproducibility of ±0.001 v for the majority of the runs.

Effect of Current Density

The effect of a polarizing current on the dissolution rate of a magnesium AZ10A alloy[1] in 2*N* $MgBr_2$ solution is shown in Fig. 2. When the specimen is made anodic, the observed dissolution rate is the sum of the rate due to the external current as defined by

$$Mg \rightarrow Mg^{++} + 2e^- \qquad [1]$$

and the rate due to local action as defined by

$$Mg + 2H_2O \rightarrow Mg(OH)_2 + H_2 \qquad [2]$$

It is seen that the local corrosion rate increases with increasing anodic current density. This is known in the theory of corrosion as the negative difference effect. For magnesium, the magnitude of this effect has been found by Robinson (9) to be dependent on

[1] This alloy, which was furnished by the Dow Chemical Co., consists principally of magnesium, but contains in addition 1% aluminum and 0.5% zinc.

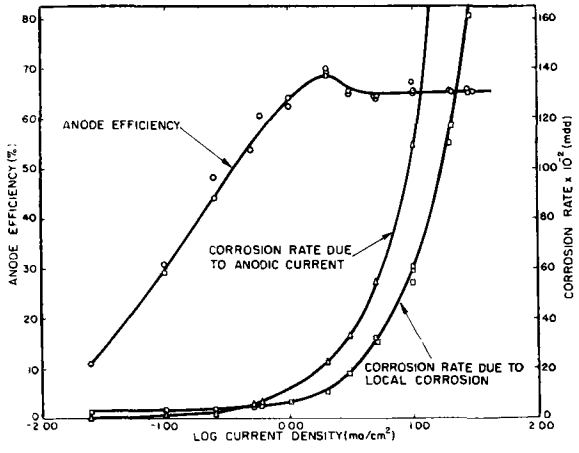

Fig. 2. Effect of current density on the local corrosion rate and anode efficiency of a magnesium AZ10A alloy dissolving in 2N $MgBr_2$ electrolyte [st'd with $Mg(OH)_2$].

both the electrolyte and anode composition including alloy ingredients and level of impurities.

For such an anode, the electrode efficiency is given by the following relationship:

Electrode efficiency =

$$\frac{\text{number of Faradays passed through the circuit}}{\text{number of equivalents of magnesium dissolved}} \times 100 \qquad [3]$$

i.e., by the rate of useful corrosion over the total dissolution rate. For many anodes the electrode efficiencies would approach 100% as a limit. However, if the rate of local corrosion were to increase with the rate of useful corrosion, efficiencies would tend to approach a limiting value of less than 100%. This is indicated by the anode efficiency curve for the magnesium AZ10A alloy which reaches a limiting efficiency of 65% at current densities above 1 ma/cm² in the 2*N* $MgBr_2$ electrolyte, although efficiency values as high as 68-69% are attained at a current density of 2 ma/cm².

Figure 3 is a plot of the negative difference effect obtained on a magnesium AZ10A alloy in 2*N* $MgBr_2$ vs. the anodic current density. It is seen that the

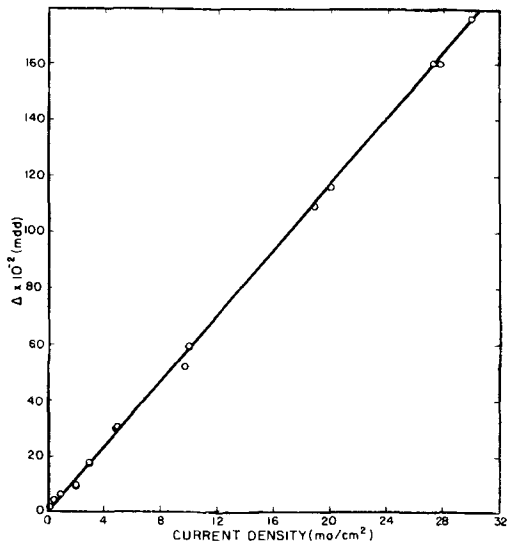

Fig. 3. Effect of current density on the negative difference effect obtained from a magnesium AZ10A alloy in 2N $MgBr_2$ electrolyte [st'd with $Mg(OH)_2$].

difference effect is directly proportional to the galvanic current up to 30 ma/cm². This type of effect has also been observed on magnesium corroding in a 3% NaCl solution (10) and is usually found with very active anodic metals covered by a protective layer. The positive effect is found in the absence of a protective layer as in the case of magnesium dissolving in HCl (11). Similarly, aluminum anodes show positive difference effects in certain corrosive electrolytes such as NaOH (12) and HF (13) which can dissolve the protective film, while the negative effect shows up in HCl (13) because of the presence of a film on the metal. The work of Kroenig and Uspenskaja (10) indicates that the magnitude of the negative difference effect increases with the thickness of the oxide layer.

There are two hypotheses which explain the negative difference effect. The first of these attributes the increased corrosion of magnesium to the destruction of the anodic films with increased current density, resulting in continuous exposure of impurity particles which serve as sites for cathode reactions (13, 14). The second hypothesis explains the experimental results by assuming that unipositive magnesium is formed as an unstable intermediate. Oxidation of this species to the common dispositive state by water

$$2Mg^{+} + H_2O \rightarrow MgO + Mg^{++} + H_2 \qquad [4]$$

was held responsible for hydrogen evolution (15, 16). All efforts to isolate and identify a compound containing unipositive magnesium thus far have been unsuccessful. Although the various experimental observations on the magnesium anode can be explained by either of these hypotheses, the experimental evidence available at the present time cannot serve as a convincing demonstration of the correctness of one or the other of these hypotheses.

It is proposed that a more appropriate model with which to consider the anodic corrosion of magnesium is one in which the over-all rate is controlled by the rate of either proton or magnesium ion transport through a surface film of magnesium oxide and/or hydroxide. (Control by proton transfer appears more likely because of the apparent ease with which magnesium ions penetrate the film during anodic dissolution.) This model, suggested by Casey and Bergeron (17) to explain the dissolution rates of magnesium in acidic salt solutions, is used to explain the experimental data in the present study. Thus, the negative difference effect could be attributed to the action of the polarizing current in breaking down the protective film. This would manifest itself as an increased rate of local corrosion, since changes in the structure of the film due to the anodic current would be reflected by changes in the rate of passage of any particle through the film.

Effect of Soluble Metal Additives to the Electrolyte

In the corrosion of metals, where the cathode process is hydrogen evolution, the nature of the cathode material, specifically its hydrogen overvoltage, plays an important role in the corrosion reaction (18). Thus the galvanic currents observed when magnesium anodes were coupled with various other metals in a 3% NaCl solution bore no relationship to the reversible electrode potentials of these metals, but were governed by their hydrogen overvoltages, the metals of lowest overvoltage permitting the greatest galvanic currents. In regard to promoting corrosion, the elements arranged in an increasing order of effect, were found by Kroenig and Kostylev (19) to be Hg, Zn, Mn, Pb, Cu, Ni, Fe, Al, and Pt.

In order to study the effect of impurities on the anodic dissolution rate of the magnesium AZ10A alloy, corrosion rates and electrode potentials were measured in a 2*N* $MgBr_2$ electrolyte containing various soluble metal additives in the form of their bromide salts. Solutions were made up by adding 1 g of the metallic bromide to a liter of 2*N* $MgBr_2$ electrolyte and saturating the resultant solution with magnesium hydroxide to maintain the *p*H constant. Experimental measurements were made with solutions containing the following salts: $ZnBr_2$, $PbBr_2$, TlBr, $AlBr_3$, $MnBr_2$, Hg_2Br_2, $CdBr_2$, $CuBr_2$, AgBr, and $PtBr_4$.

In Fig. 4, the local corrosion rates are plotted against the logarithm of the exchange current for the hydrogen evolution reaction on the corresponding metal. The exchange currents, which provide a standard state at which the velocities of the reaction $2H^{+} + 2e^{-} \rightarrow H_2$ on various metals can be com-

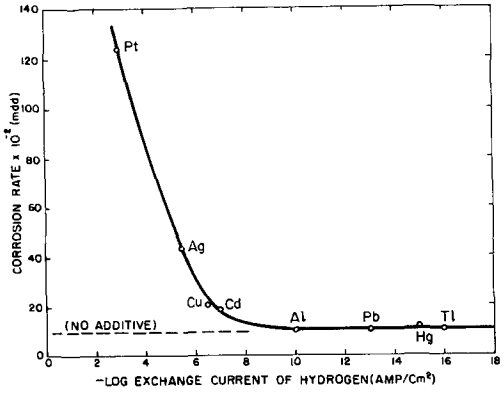

Fig. 4. Effect of various soluble metal bromide additives on the corrosion rate of a magnesium AZ10A alloy dissolving anodically in a 2N $MgBr_2$ electrolyte [st'd with $Mg(OH)_2$] at a current density of 2.0 ma/cm².

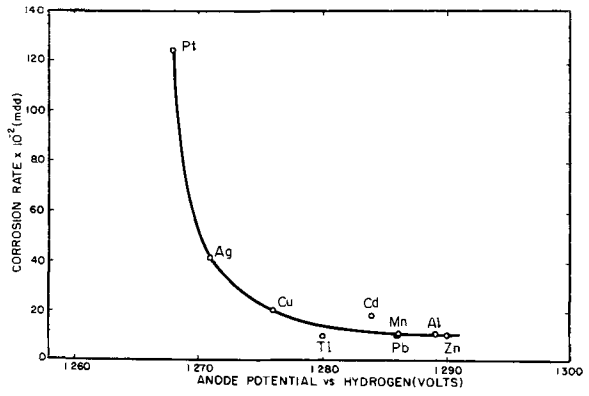

Fig. 5. Relationship between the corrosion rate and anode potential of a magnesium AZ10A alloy dissolving anodically in a 2N $MgBr_2$ electrolyte [st'd with $Mg(OH)_2$] containing various soluble metal bromide additives at a current density of 2.0 ma/cm².

pared, were estimated from the data available in the literature (20-22). For the corrosion of magnesium in a neutral or slightly alkaline aqueous salt solution, it is seen that a small quantity of low overpotential metal in the solution greatly accelerates the corrosion reaction. Apparently these metals are deposited on or in the oxide film and form centers on which hydrogen can come off more easily. Metals having hydrogen exchange currents of 10^{-9} or less appear to have little effect on the local corrosion rate as measured under these experimental conditions.[2]

The effect of the various additives on the anode potential is illustrated in Fig. 5, where the corrosion rate is plotted vs. magnesium potential. It is seen that, with the metal additives which cause little or no change in the corrosion rate, the anode potentials range from 1.280 to 1.290 v as compared to a potential of 1.287 v in solutions containing no additives. The low overpotential metal additives, such as Cu, Ag, and Pt, which cause a marked increase in the corrosion rates, lower the magnesium potential by 0.01-0.02 v, the greatest effect occurring with the Pt additive.

Assuming the anodic polarization curve of magnesium is the same for all these solutions, any differences in the corrosion currents and potentials would be dependent on the cathodic polarization curve. If the cathodic areas possess a low overpotential, the cathodic polarization curve slopes down less than if the overpotential is high. Thus the current is greater, and the potential more noble, in agreement with the experimental data.

The effect of the Hg additive on the potential was quite marked, resulting in an anode potential of 1.376 v, a value too high to be shown in Fig. 5. The high potential encountered with this additive is believed due to the partial removal of the magnesium oxide film by amalgamation. This type of behavior is similar to that found for amalgamated aluminum anodes. The effectiveness of the Hg additive in maintaining a low corrosion rate, despite the absence of a controlling oxide film, is attributed to the difficulty of proton discharge on this high overvoltage metal.

[2] The corrosion rates of the magnesium AZ10A alloy in solutions containing $ZnBr_2$ and $MnBr_2$ were 10.0 and 10.8 x 10^2 mdd, respectively. These results were not included in Fig. 4 because their hydrogen exchange currents were not known.

Effect of Electrolyte

The effect of electrolyte concentration and pH on the local corrosion rate and electrode potential of a magnesium AZ10A alloy dissolving anodically in various magnesium and sodium bromide solutions is shown in Fig. 6.

It is seen that the corrosion rate of magnesium in the magnesium bromide solutions increases approximately linearly with decreasing electrolyte pH over the range of 6.3-8.1 pH units. At pH values greater than 8.1, the corrosion rate approaches a constant value of 12.7 x 10^2 mdd, which corresponds to an anode efficiency of 63%. The minimum in the corrosion rate occurs at a pH of 8.1, corresponding to an anode efficiency of 68%.

In contrast to the marked change in electrolyte pH with magnesium bromide concentration, which is a consequence of the common ion effect, the sodium bromide electrolyte shows only a 0.7 variation in pH over a concentration range of 1.0-6.0 *N*. Over this small range of pH 9-10 the corrosion rate is essentially constant at a value of 11.5-12.1 x 10^2 mdd. This result is comparable to those obtained in magnesium bromide electrolytes having pH values of 8 or higher.

The effect of electrolyte pH on the anode potential of the magnesium AZ10A alloy also is illustrated in Fig. 6. For the magnesium bromide electrolyte it is seen that the anode potential falls rapidly with increasing pH in the basic pH range. For the weakly acidic solutions the potential varies only slightly with pH, approaching a constant value of 1.36 v. In contrast to the marked drop in potential observed in the weakly basic magnesium bromide solutions, the anode potential in the sodium bromide electrolytes decreases only 0.04 v in the pH range 9.3-10.0.

The data in Fig. 6 can be explained in terms of the effect of these electrolytes on the structure of a surface film which must be magnesium oxide and/or magnesium hydroxide. This film is more easily penetrable at low pH values because the OH^- ion concentration is too low to maintain an effective magnesium hydroxide film. Thus at low pH values,

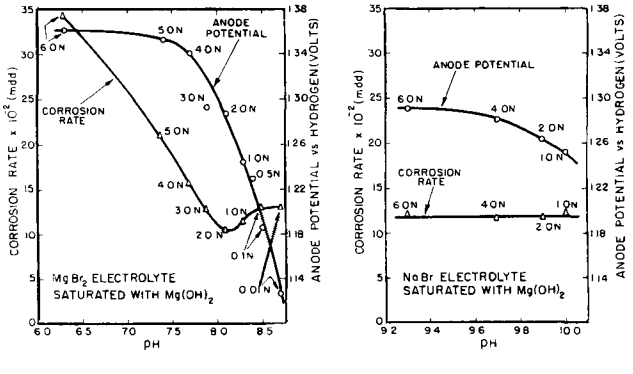

Fig. 6. Effect of pH on the corrosion rate and anode potential of a magnesium AZ10A alloy dissolving anodically in various $MgBr_2$ and NaBr electrolytes [st'd with $Mg(OH)_2$] at a current density of 2.0 ma/cm².

high corrosion rates and high anode potentials are observed.

At high *p*H values the OH^- ion concentration of the electrolyte controls the precipitation of the Mg^{++} ions produced at the anode, which, according to Robinson (9), are precipitated so close to the anode as to stifle the anodic reaction. This results in more cathodic potentials, a decrease in local corrosion, and excessive polarization of the anode.

In an intermediate *p*H range, precipitation of magnesium hydroxide occurs at a sufficient distance from the active anodic areas to permit the anodes to function normally. It is in this *p*H range that other properties of the electrolyte exert a greater influence over such factors as local corrosion and anode potential. Since the magnesium bromide and sodium bromide electrolytes appear to operate in this intermediate *p*H range, the similar corrosion rates in the 1.0-6.0*N* NaBr and 0.01-3.0*N* $MgBr_2$ electrolytes are to be expected, despite the differences in electrolyte *p*H. At the higher magnesium bromide electrolyte concentrations, *p*H becomes the dominant factor, and the corrosion rates in the magnesium bromide solutions are much greater than in the sodium bromide electrolyte.

The slightly lower corrosion rates found in the 1.0-3.0*N* $MgBr_2$ electrolytes as compared to the more basic sodium bromide electrolytes are similar to the type of results obtained by Casey and Bergeron (17), who found that the dissolution rates of magnesium in acidified potassium chloride solutions are greater than those in comparable magnesium chloride solutions of the same *p*H. Their results were explained on the basis of a thicker or less porous oxide film on magnesium in the magnesium chloride electrolyte, formed as a result of the lower solubility of magnesium hydroxide in the magnesium chloride solutions. The lower solubility in this electrolyte is a consequence of the common ion effect. Thus, if the rate of dissolution of magnesium in aqueous salt solution depends on the solubility of the magnesium hydroxide film, as was first suggested by Whitby (23, 24), it follows that corrosion rates would be greatest in those electrolytes where a thinner or more porous oxide film on magnesium is obtained.

The electrode potential data in Fig. 6 can be explained in the following way. Because of the higher *p*H of the sodium bromide solutions, the potential of magnesium, when measured at a current density of 2.0 ma/cm^2, is more anodic for the concentrated (3.0-6.0*N*) $MgBr_2$ solutions. However, for the more dilute magnesium bromide solutions the anode potential decreases rapidly with increasing *p*H, becoming more cathodic than the potentials measured in the sodium bromide electrolytes. These lower potentials are attributed in part to the effect of the Mg^{++} ions in stifling the anode reaction with increasing *p*H. In addition a significant portion of the potential ennoblement at the low magnesium bromide concentrations is due to the decreased bromide ion concentration of the electrolyte.

Effect of Anode Composition

It has been shown by Hannawalt, Nelson, and Peloubet (25) that the presence of certain impurities and alloying metals has a marked effect on the corrosion characteristics of magnesium alloys in an aqueous salt solution. They determined tolerance limits of impurities such as Fe and Ni, for magnesium and some of its alloys. When the amount of the element present exceeds this tolerance limit, there results a large increase in corrosion rate. These findings point to the importance of knowing the concentration of deleterious impurities and their tolerance limits when investigating alloy effects. In addition, it must be realized that the corrosion behavior of magnesium alloys in other electrolytes will be different from that in the 3% NaCl solution of Hanawalt, *et al.* and care should be exercised in extending their results to other electrolyte systems.

In Table I are presented corrosion rates and anode efficiencies of six different commercial magnesium alloys along with their compositions and significant metal impurities. It is seen that magnesium alloys containing aluminum and manganese operate at higher anode efficiencies than commercially pure magnesium, as well as the ZK60A and M1A magnesium alloys. Alloying the magnesium with aluminum permits removing most of the major cathodic impurity, iron, by precipitation with manganese. The corrosion resistance of such high-purity alloys is very good and, as anodes, they perform more efficiently than any of the magnesium compositions tested to date (9).

Also presented in Table I are anode potentials of these alloys, when measured in a 2*N* $MgBr_2$ electrolyte at a current density of 2.0 ma/cm^2. It is seen that the alloys containing Al or Zn are 0.04-0.10 v more cathodic than commercially pure magnesium. The pure magnesium has a potential of 1.33 v on the normal hydrogen scale, as compared to values of 1.23-1.29 v for the Mg-Al alloys, whose potential is more anodic with decreasing amounts of Al. This type of behavior has been found by other investigators with other electrolytes (9, 26).

Conclusions

It is proposed that the most appropriate model with which to consider the anodic corrosion of magnesium in aqueous salt solutions is one in which the over-all rate is controlled by the rate of proton transport through a surface film of magnesium oxide and/or hydroxide. The anodic corrosion rates and potentials of a magnesium AZ10A alloy in various magnesium bromide and sodium bromide electrolytes can be explained in terms of the effect of these electrolytes on the structure of this film.

It has also been shown that the presence of certain low overvoltage metal impurities, such as Cu, Ag, and Pt, with hydrogen exchange currents greater than 10^{-9} amp/cm^2, have a deleterious effect on the corrosion characteristics of magnesium alloys in an aqueous salt solution.

Acknowledgments

The author wishes to express his appreciation to G. S. Lozier and C. K. Morehouse for their many helpful suggestions during the course of this investigation.

Manuscript received May 5, 1958. This paper was prepared for delivery before the New York Meeting, April 27-May 1, 1958.

Any discussion of this paper will appear in a Discussion Section to be published in the December 1959 JOURNAL.

REFERENCES

1. C. K. Morehouse, *This Journal*, **99**, 187C (1952).
2. R. C. Kirk and A. B. Fry, *J. (and Trans.) Electrochem. Soc.*, **94**, 277 (1948).
3. R. C. Kirk, P. F. George, and A. B. Fry, *This Journal*, **99**, 323 (1952).
4. C. K. Morehouse and R. Glicksman, *ibid.*, **105**, 306 (1958).
5. C. K. Morehouse and R. Glicksman, *ibid.*, **105**, 619 (1958).
6. H. H. Uhlig, Editor, "Corrosion Handbook," pp. 218-222, John Wiley & Sons, Inc., New York (1948).
7. R. Laity, Unpublished work.
8. Ref. (6), p. 218.
9. H. A. Robinson, *Trans. Electrochem. Soc.*, **90**, 485 (1946).
10. W. O. Kroenig and V. N. Uspenskaja, *Korrosion u. Metallschutz*, **11**, 10 (1935).
11. B. Roald and W. Beck, *This Journal*, **98**, 277 (1951).
12. M. A. Streicher, *J. (and Trans.) Electrochem. Soc.*, **93**, 285 (1948).
13. M. E. Straumanis and Y. N. Wang, *This Journal*, **102**, 304 (1955).
14. R. E. McNulty and J. D. Hanawalt, *Trans. Electrochem. Soc.*, **81**, 423 (1942).
15. R. L. Petty, A. W. Davidson, and J. Kleinberg, *J. Am. Chem. Soc.*, **76**, 363 (1954).
16. J. H. Greenblatt, *This Journal*, **103**, 539 (1956).
17. E. J. Casey and R. E. Bergeron, *Can. J. Chem.*, **31**, 849 (1953).
18. Ref. (6), p. 490.
19. W. Kroenig and G. Kostylev, *Z. Metallk.*, **25**, 144 (1933).
20. J. O. 'M. Bockris, "Modern Aspects of Electrochemistry," p. 199, Academic Press Inc., New York (1954).
21. J. O. 'M. Bockris, "Electrochemical Constants," pp. 252-257, National Bureau of Standards Circular 524 (1953).
22. J. A. V. Butler, "Electrical Phenomena at Interfaces," pp. 164-165, Macmillan Co., New York (1951).
23. L. Whitby, *Trans. Faraday Soc.*, **31**, 638 (1935).
24. L. Whitby, *ibid.*, **29**, 1318 (1933).
25. J. D. Hanawalt, C. E. Nelson, and J. A. Peloubet, *Trans. Am. Inst. Min. Met. Eng.*, **147**, 273 (1943).
26. J. A. Boyer, Aeronautics, 12th Ann. Rep. Nat. Adv. Comm. 445 (1926).

Electrolytic Transition of Ag_2O to AgO in Alkaline Solutions

Thedford P. Dirkse and George J. Werkema

Department of Chemistry, Calvin College, Grand Rapids, Michigan

ABSTRACT

An interrupted current technique was used to study the electrolytic oxidation of silver in alkaline solutions. The short voltage peak just preceding the stage corresponding to the production of AgO in the voltage-time curves is interpreted as being due to the high electrical resistance to the Ag_2O layer.

During the anodic treatment of silver in alkaline solutions a two level curve is obtained when voltage is plotted against time. Such a curve, obtained by a constant current oxidation, is shown on Fig. 1. Part a corresponds to the formation of Ag_2O, part c to the formation of AgO, and d to the evolution of oxygen. The work reported here deals with the peak represented by b. Such a peak may or may not be present also at the beginning of stage a, but is usually present during the transition from stage a to stage c. It is found whether a constant current or a constant potential process is used. It is also found in the charging curves for commercial silver-zinc batteries.

Although very little has been written about this peak, two different explanations for it appear in the literature. The first was given by Hickling and Taylor (1) who suggested that the peak corresponds to the change

$$Ag_2O + 4OH^- \rightarrow Ag_2O_3 + 2H_2O + 4e \qquad [1]$$

and the Ag_2O_3, being unstable, quickly decomposes as follows:

$$Ag_2O + Ag_2O_3 \rightarrow 4AgO \qquad [2]$$

As soon as this latter reaction begins the voltage begins to decline from the peak. This mechanism, whereby the oxidation of Ag^+ to Ag^{++} proceeds through the formation of Ag^{+++}, has been proposed also for acid solutions by others.

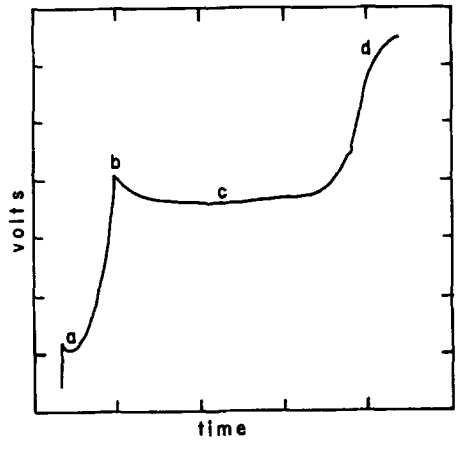

Fig. 1. Typical voltage-time curve for constant current oxidation of silver in KOH solution.

Yost (2) studied the catalytic effect of Ag^+ on the oxidation of Cr^{+++} by persulfuric acid. He suggested a mechanism for this action in which the persulfate first oxidized the Ag^+ to Ag^{+++} and the latter, in turn, oxidized the Cr^{+++} to dichromate. This mechanism is consistent with the kinetic data obtained for this process. Later Noyes, *et al.* (3) studied the rate of oxidation of $AgNO_3$ by ozone in acid solution and interpreted their kinetic data in a way similar to that of Yost. A study of the rate of reduction of Ag^{++} by water in acid solution showed this process to be fairly complex, but it was suggested that Ag^{+++} was an intermediate in this reaction also (4). Gordon and Wahl (5) used a similar mechanism to explain their data on the rate of the exchange reaction between Ag^+ and Ag^{++}.

This interpretation has, however, not gone unchallenged. Bawn and Margerison (6) studied the oxidation of a hydrazyl using Ag^+ and persulfuric acid. They suggest that their results can be interpreted in a manner similar to that proposed by Yost (2). However, they contend also that such results can be interpreted just as well without assuming the formation of Ag^{+++} as an intermediate. They prefer a mechanism involving the formation of free radicals and Ag^{++}.

Aside from the fact of the existence or nonexistence of tripositive silver, it is doubtful whether peak b in Fig. 1 is due to its formation. This peak is obtained even when the potential of the silver electrode is kept 100-150 mv above the reversible potential of the Ag_2O-AgO couple in alkaline solution, and such a potential is not of sufficient magnitude to result in the formation of Ag^{+++} from Ag^+ or Ag^{++}. This value is lower than that generally accepted as the potential of Ag^{+++}-Ag^{++} in alkaline solutions (7).

Another explanation of this peak has been given by Jones, *et al.* (8). They suggest that the transition from Ag_2O to AgO proceeds with difficulty and the peak represents the difficulty of forming centers of AgO in the lattice of Ag_2O. They also suggest that some Ag_2O_3 may be formed, but at the end rather than at the beginning of stage c.

Because of this divergence of opinions, and because of the possibility that a proper understanding of the meaning of this peak may afford a clue to the unravelling of the kinetics of these particular electrode reactions, a special effort was made to study this phenomenon further.

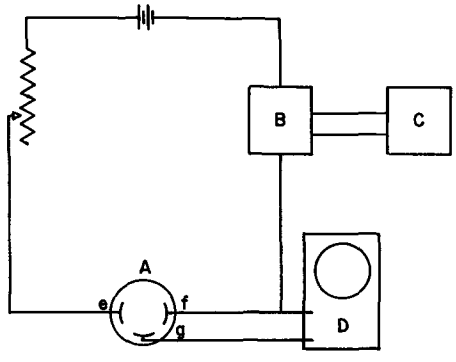

Fig. 2. Schematic diagram of interrupter apparatus. A, cell; B, Western Electric 275 Relay; C, sine wave generator; D, oscilloscope; e, auxiliory silver electrode; f, working electrode; g, reference electrode.

Experimental

The method used in this study involved the passage of interrupted current through the electrode. The voltage changes were observed on an oscilloscope both during passage of the current and during decay (open-circuit condition). A schematic diagram of the apparatus is shown on Fig. 2. The Western Electric 275 relay served as a current interrupter, and frequency of interruption was governed by the frequency delivered by the sine wave generator. The working electrode was a silver wire with about 0.5 cm^2 surface area. Constant current processes were used in all this work. The auxiliary and reference electrodes were relatively large pieces of silver screen. The traces on the oscilloscope were recorded photographically. All runs were made at room temperature. The variables studied were: concentration of KOH, current density, and effect of oxygen. The last of these was studied by bubbling air through the solution and then making an identical run except for the fact that purified nitrogen was bubbled through the solution during the run.

Results

The nature and shape of the traces obtained were the same whether air or nitrogen was bubbled through the electrolyte during the run. Consequently, the phenomena observed were not due to the presence or absence of oxygen in the electrolyte.

In all cases the electrolyte was a solution of KOH. A change in the concentration of the electrolyte did not give rise to any changes in the traces that were obtained. When the more concentrated KOH solutions were used the electrolyte gradually became discolored due to the presence of finely divided particles of silver oxides. Furthermore, since the silver oxides are slightly soluble in KOH solutions, it was possible that the nature of the decay curve could be affected by the solubility of the oxides produced during passage of current. For these reasons, the results used here are those obtained when 1*N* KOH was the electrolyte.

Types of the traces that were obtained are shown on Fig. 3. These were all traced from photographs taken during the runs. Similar traces were obtained

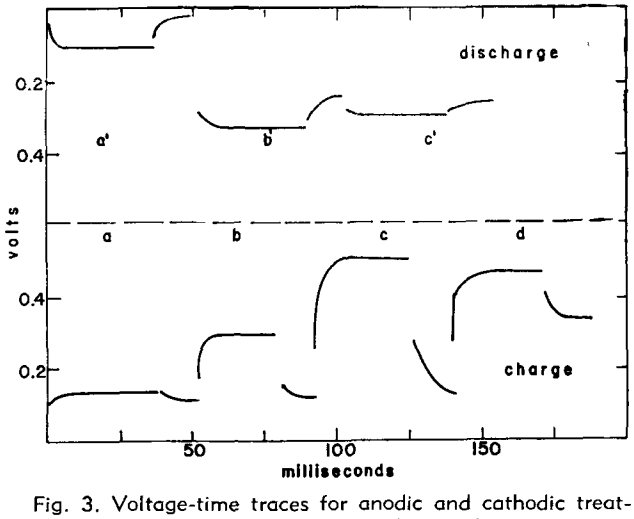

Fig. 3. Voltage-time traces for anodic and cathodic treatment of silver electrode in N KOH solution. Current density, 7 ma/cm^2.

over an apparent current density range of 1-10 ma/cm^2. The voltages are expressed as the difference between that of the working electrode and of the reference electrode. A base line was recorded before beginning each charge or discharge. The charge curves on Fig. 3 are given in the order in which they appear. At the beginning of the charge the traces are of the type shown in panel a. As the treatment continues the amplitude of this curve increases slightly. This is followed by a rapid transition from type a to type c. Panel b represents an intermediate in this transition. In each case the decay curve shows that Ag_2O is the oxide still on the surface. The curve in panel c represents the peak referred to in Fig. 1. Curve d is of the type that follows the transition from a to c. It should be noted that the decay curve now shows the presence of AgO on the electrode, and at the same time the charging voltage is lower than that in panel c. Traces of the type shown in panel d continue for a while, and then the voltage levels become higher as gassing begins.

During discharge a similar sequence takes place, see the upper set of curves in Fig. 3. Here the top border of the graph represents the base line obtained before the discharge was begun. Panel a' represents the kind of trace obtained at the beginning of discharge. The decay curve shows the presence of AgO. Then there follows a rapid transition to traces such as shown in panel c'. Panel b' shows an intermediate trace. Here again the voltage during passage of current (discharge) is lower in panel b' than in panel c'. This is similar to the peak obtained on charge.

Discussion

It is suggested here that these phenomena can be interpreted in terms of the resistance of the Ag_2O layer that is formed on the electrode. It has been pointed out (9) that the electrical resistance of Ag_2O is considerably greater than that of AgO. According to this interpretation, then, as the oxidation of silver proceeds, a film of Ag_2O is formed on the surface of the electrode. As this film builds up, the electrical resistance at the electrode-electrolyte interface increases. When this film completely covers the surface, the resistance, and consequently the *IR* drop also, increases giving rise to the peak represented by b in Fig. 1. The traces on Fig. 3 also show a relatively large *IR* drop at this point (panel c). As soon as some of this Ag_2O is changed to AgO, the resistance of the surface film decreases, the *IR* drop decreases, and the open-circuit voltage (on decay) rises to that of AgO. As more AgO is formed the resistance of the surface film and the voltage decrease slightly.

This explanation also accounts for the phenomena observed on discharge. As the discharge progresses, AgO is changed to Ag_2O and the resistance of the surface layer increases. When all the surface AgO has been changed to Ag_2O this resistance is at its maximum and there is the greatest voltage loss on discharge. The open-circuit voltage is that of Ag_2O, Fig. 3 b'. This trace also shows a large *IR* drop. On further discharge the Ag_2O changes to Ag and the resistance of the surface layer decreases. Consequently, the discharge voltage is a little higher, Fig. 3 c'.

It is believed that this interpretation is more consistent with the data obtained than are the other interpretations that have been offered. The existence of Ag_2O_3 is doubtful, particularly in alkaline solutions. Moreover, if Ag_2O_3 were an intermediate in the formation of AgO from Ag_2O, this might account for peak b in Fig. 1 but would not account for a corresponding dip in the discharge curve when the AgO is gone.

Similar reasoning tends to eliminate the idea that the peak on charge is due to the difficulty of forming AgO nuclei in an Ag_2O lattice. Again, this suggestion can be used to account for the charge phenomenon, but it does not account for a similar event on discharge.

Acknowledgment

The authors wish to express their appreciation and thanks to the Office of Naval Research for sponsoring the work reported here under Contract No. Nonr-1682(01), and to Mr. S. Schuldiner for his suggestions with respect to the experimental procedures.

Manuscript received July 16, 1958.

Any discussion of this paper will appear in a Discussion Section to be published in the December 1959 JOURNAL.

REFERENCES

1. A. Hickling and D. Taylor, *Disc. Faraday Soc.*, **1**, 277 (1947).
2. D. M. Yost, *J. Am. Chem. Soc.*, **48**, 152 (1926).
3. A. A. Noyes, J. L. Hoard, and K. S. Pitzer, *ibid.*, **57**, 1221 (1935).
4. A.A. Noyes, C. D. Coryell, F. Stitt, and A. Kossiakoff, *ibid.*, **59**, 1316 (1937).
5. B. M. Gordon and A. C. Wahl, *ibid.*, **80**, 273 (1958).
6. C. E. H. Bawn and D. Margerison, *Trans. Faraday Soc.*, **51**, 925 (1955).
7. R. Luther and F. Pokorny, *Z. anorg. u. allgem. Chem.*, **57**, 290 (1908).
8. P. Jones, H. Thirsk, and W. F. K. Wynne-Jones, *Trans. Faraday Soc.*, **52**, 1003 (1956).
9. M. Le Blanc and H. Sachse, *Physik. Z.*, **32**, 887 (1931).

Strain Electrometry and Corrosion, IV

Film Properties and Strain Potential

J. Calvin Giddings, Albert G. Funk, Carl J. Christensen, and Henry Eyring

University of Utah, Salt Lake City, Utah

ABSTRACT

Measurements of the strain transients have been recorded here for several metal electrodes including copper, aluminum, zinc, nickel, silver, and iron. The magnitude of the transients as a function of the percentage strain are treated by an extension of previous theoretical results. It is found that the transients depend on the position of an electrode in the emf series and on the protective nature of the film as predicted by the theoretical considerations. In addition, several experiments have been reported concerning the effect of corrosion inhibitors and organic coatings on strain transients. Some possible theoretical interpretations are made on these preliminary results.

It has been shown that the magnitude of the strain transient for a metallic wire is related to the chemical and physical nature of the protective film along with the chemical nature of the surrounding solution (1-3). In order to extend this study of rapid interface reactions we have measured and compared strain transients for a group of metals possessing films of greatly differing nature. It has been found possible to correlate approximately the relative values of these transients with the position of the metal in the electromotive series, for the same per cent strain, of the metals used (Cu, Al, Zn, Ni, Ag, and Fe). This is done using the concept that a stationary electrode potential is fixed when the rates of competing anodic and cathodic reactions are equal. A sudden strain causes film rupture, and temporary changes of the interface rates occur. The change is in such a direction as to account for the clean metal surface exposed when the film is broken. Metals such as aluminum show transients as high as a volt since, when the highly protective film is removed, the surface of the aluminum, which is very electropositive, reacts to yield aluminum ion. Metals such as iron, however, show much smaller transients, in the range of 100-200 mv. This results since the protective film on iron is sufficiently porous that the straining of the metal causes a relatively small increase in anodic area compared to that obtained by straining aluminum.

According to the same picture metals only slightly electropositive would be expected also to show small transients. The transient of silver is about 50 mv in confirmation of this general picture. The above picture can be written in a quantitative form that approximately describes these voltage transients under various conditions. In particular, an equation has been derived that relates the maximum voltage change, $-\Delta V_m$, to the fractional elongation of the wire electrode. Strain electrometry is another tool that can be used for the elucidation of the complex reactions of corrosion inhibitors. Preliminary results have been obtained in this important field.

The experimental methods used in strain electrometry have been described elsewhere (2, 3). The potentials recorded here are measured and recorded against the saturated calomel electrode.

Strain Transients of Metals

It is convenient to study the potential transients of strain electrometry in relation to Fig. 1. This schematic diagram is similar to one presented in an earlier publication (1), but here it is extended to include an approximate description of several metals.

Each electrode reaction has a reverse reaction acting to charge the electrode in the opposite direction. If only one reaction and its reverse were operative, an equilibrium electrode potential would be realized. These are denoted by the solid lines in Fig. 1. If more than one reaction is operative, the final, steady-state potential will differ from all of the equilibrium potentials. It will, however, lie nearest the equilibrium potential established by the fastest reactions. The steady-state potentials are shown as dotted lines. Potentials shown in Fig. 1 conform to the European sign convention.

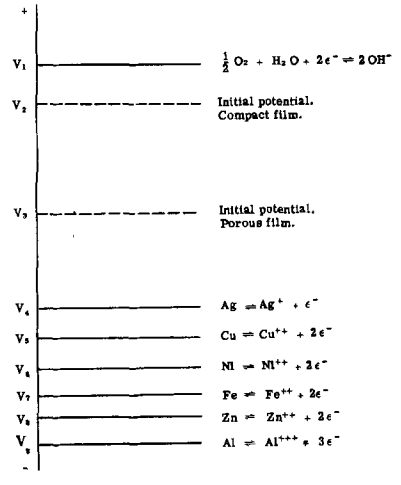

Fig. 1. Schematic diagram of equilibrium potentials and steady-state potentials for electrode reactions.

In most aerated solutions there are two reactions of paramount importance in establishing the steady-state potential. These are the oxygen reaction, tending to establish the potential at V_1, and the metal, metal-ion reaction tending to establish the potential, in the typical case of Ni, at V_6. If the metal possesses a highly protective film, the metal, metal-ion reaction is slowed considerably, since it has the equivalent of a small anodic area and the initial (before strain) steady-state potential is near the oxygen equilibrium potential, V_1. Such metals are Ag, Cu, Ni, and Al with a steady-state potential shown at V_2. These potentials are not all equal, but schematically they may be considered to be the same.

In the case of metals with a porous film, metal ions can escape easily into solution, and the initial steady-state potential is established nearer the metal, metal-ion pair. Probable examples are Fe and Zn with an initial, steady-state potential, V_3.

When the metal electrode is suddenly strained, the brittle oxide film is ruptured, thus increasing the anodic area. This greatly facilitates the metal, metal-ion reaction and establishes a new potential nearer the metal, metal-ion pair. This potential is of short duration since various factors, such as regrowth of the oxide film and concentration polarization (caused by corrosion of the metal), tend to reestablish it at the original value.

It is clear from this discussion that the transient potential is dependent on the amount of strain. A larger strain causes the new potential to establish itself nearer the metal, metal-ion pair. Thus the potential difference that is recorded at the point of maximum change, ΔV_m, becomes more negative as strain increases. We return to this point later.

The strain transient recorded for a given metal, ΔV_m, is the difference between the initial steady-state potential and a potential that is close to that particular metal, metal-ion pair. This increases in magnitude (the values of ΔV_m are negative) as (*a*) the metal becomes more electropositive (higher in the emf series), thus establishing a larger negative potential with strain, and (*b*) the metal has a more compact film, for which the initial potential is more positive. Silver has the smallest transient, since it is not electropositive. It is likely in this case that hydrogen and metallic impurities in the silver cause the strain transient since, unless Ag^+ is extremely dilute, the Ag, Ag^+ equilibrium is higher than that for oxygen. (The reason, of course, that Fig. 1 is schematic is that every equilibrium potential depends on the concentration of some ionic species. Since these are greatly changed from one metal to another, due to polarization, etc., a completely accurate diagram cannot be made.) The value of $(-\Delta V_m)$ for silver at 7% strain is 39 mv, as shown in Table I.

Beyond silver, the value of $-\Delta V_m$ at 7% strain increases in the order of Cu, Fe, Ni, Zn, and Al; whereas, in order of increasing emf, they are Ag, Cu, Ni, Fe, Zn, and Al. The order of Fe and Ni has been reversed since the emf, by itself, does not account for the magnitude of the transient. This is better illustrated in Fig. 2 where $(-\Delta V_m)$ is plotted against emf. A smooth curve is obtained with the exceptions of Fe and Zn. These lie below the curve in accord with the picture that a porous film will reduce the observed magnitude of the transient.

Table I. Transient potentials in distilled water at 7% strain; temperature, 25°C

Metal	Strain transient (approximate), mv
Aluminum	—800
Zinc	—224
Nickel	—194
Iron	—148
Copper	—95
Silver	—39

Dependence of Voltage on Relative Strain

It is useful to derive an approximate equation showing the dependence of $(-\Delta V_m)$ on the applied strain on the electrode. An equation derived in an earlier paper (1) reads

$$-\Delta V_m = \frac{kT}{ze} \ln \left(\frac{\epsilon u_{i0}\, \epsilon v^1_{i0}}{\epsilon u^1_{i0}\, \epsilon v_{i0}} \right)$$

where the terms, u_{i0}, u^1_{i0}, v_{i0}, v^1_{i0} are various reaction velocities (cm^{-2} sec^{-1}) of processes that transfer charge across the metal-solution interface: v_{i0}, *i*th anodic velocity, before strain; v^1_{i0}, *i*th cathodic velocity, before strain; u_{i0}, *i*th anodic velocity, after strain; u^1_{i0}, *i*th cathodic velocity, after strain. The reaction velocity "after strain" is the reaction velocity where the transient acquires a maximum value. The zero subscript simply means that these reaction velocities are all measured at some standard voltage. This voltage can be arbitrarily picked without changing the ratio of terms in Eq. [1]. The other terms are Boltzmann's constant, *k*; the electron charge unit, *e*; the temperature, *T*; and the average charge, in electron charge units, transferred across the interface in a single process, *z*.

Approximations made in the derivations of Eq. [1] include, (*a*) the charge transferred in the *i*th

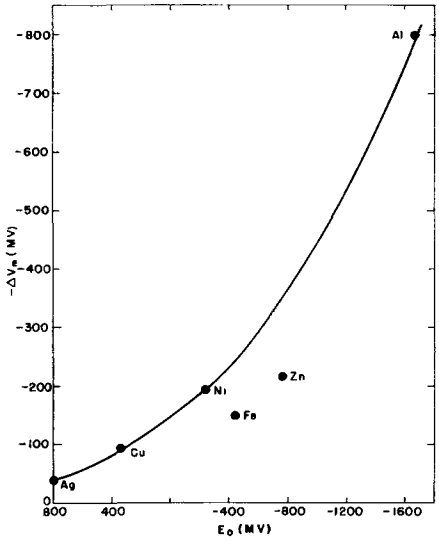

Fig. 2. Strain transients vs. the emf of metal electrodes. Distilled water at 25°C.

process, z_i, can be replaced by some average charge for all processes, z, and, (b) the potential energy barriers for these charge-transfer processes are symmetrical. In view of these approximations, and those to be introduced, only a rough agreement with experiment is expected.

The simplest assumption that can be made with respect to Eq. [1] is that the cathodic reaction velocity (at the fixed reference potential) is not changed as the electrode is strained.

$$\epsilon v^1_{io} = \epsilon u^1_{io} \qquad [2]$$

The anodic reaction velocities at this potential, however, are increased since deformation of the metal increases the anodic area. We can assume that this increase in the anodic rate is proportional to the relative elongation of the electrode, s.

$$\epsilon u_{io} = \epsilon v_{io} + gs \qquad [3]$$

where g is the relative anodic rate of a clean metal surface.

As s approaches zero, the anodic velocity after strain, u_{io}, must approach the anodic velocity before strain, v_{io}, as in Eq. [3].

When Eqs. [2] and [3] are substituted into Eq. [1], we obtain

$$-\Delta V_m = \frac{kT}{ze} \ln (1 + \alpha s) \qquad [4]$$

where $\alpha = g/\epsilon v_{io}$. This equation follows the approximate form of the experimental data, as shown in Fig. 3 for Cu. Best fit is obtained when $z = 0.92$ and $\alpha = 407$. For most of the metals used, αs is considerably larger than unity in the higher range of s. When this assumption can be made, Eq. [4] has only the term (αs) remaining in the logarithm. Although this assumption results in a considerable error, particularly for Ag, Zn, and Fe, it is justified considering the approximate nature of the other assumptions introduced. With this assumption, then, we can write Eq. [4] as

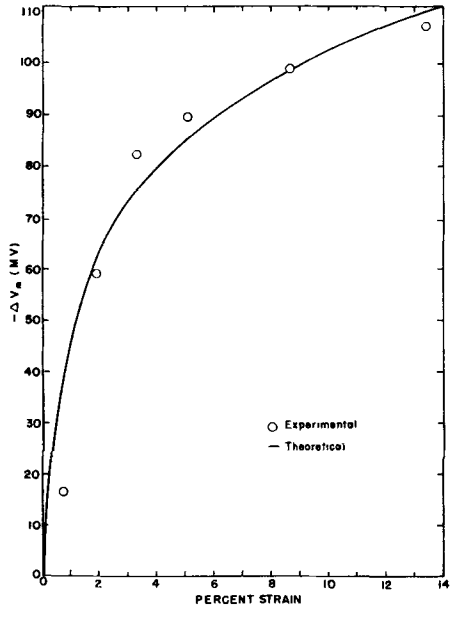

Fig. 3. Strain transient vs. per cent strain of copper

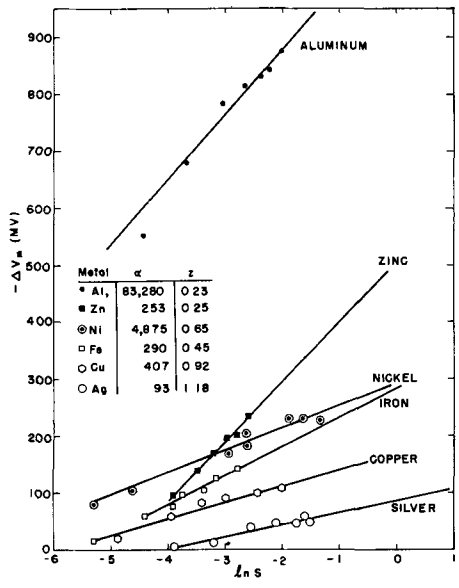

Fig. 4. Strain transients vs. ln (strain). Distilled water at 25°C.

$$-\Delta V_m = \frac{kT}{ze} \ln \alpha + \frac{kT}{ze} \ln s \qquad [5]$$

A plot of $-\Delta V_m$ vs. ln s is shown in Fig. 4. The slope of the line, kT/ze, determines z. The intercept at ln $s = 0$ is kT ln α/ze. The values of z are of the right order except for Zn and Al. Whether this discrepancy is due to the back reaction of metal ions (thus violating Eq. [2]), or to some other effect, has not been ascertained.

The quantity α, as determined from experimental data, is interesting in its dependence on the nature of the metal and the oxide film. Since $\alpha = g/\epsilon v_{io}$, it is determined by g, the relative anodic rate of a clean metal surface, and ϵv_{io} which is the anodic reaction rate of a metal surrounded by an oxide film. The latter quantity is proportional to the rate of dissolution of the metal ion through the oxide film, or the corrosion rate. The former quantity, g, should be an increasing function of the emf of the metal since the emf is a measure of the anodic rate of the clean metal surface. The values of α increase in the order, Ag, Zn, Fe, Cu, Ni, Al, which is the order in the emf series if Zn and Fe are excluded. Zinc and iron have unusually small values of α since the corrosion rate of these metals, appearing in the term ϵv_{io}, is large.

Corrosion Inhibitors

The reactions due to corrosion inhibitors and promoters are expected to reflect themselves in the measured strain transients. The nature of the change in these transients depends on the type of reactions occurring. Thus, with most metals, a pH decrease leads to film dissolution, and a resultant decrease in the transient voltage. At the same time corrosion rates have been increased due to decreased film protection. In practice, many other reactions occur simultaneously and complicate the over-all picture, thus a sufficient pH decrease inhibits some corrosion processes (4). It is still valuable, however, to suggest the effects of single contributing reactions. These reactions may be important in the following ways.

Corrosion inhibitors and promoters are responsible for changing the rates of various electrode reactions. The changed reaction rates are reflected both in corrosion measurements and in strain-electrometry measurements. The latter shows promise of providing a rapid and sensitive measurement of reactions involved in corrosion. A good deal of additional knowledge is needed before this method can be employed generally. Preliminary results are reported here.

An acid is a common example of a corrosion promoter. The corrosion rate is greater and the strain-transient is smaller upon the addition of an acid. Both effects are due to the dissolution of the protective film. As indicated earlier, the strain-transient is a measure of the protective nature of the film, and if this is changed by added substances it is indicated immediately in an altered strain transient.

Inhibitors and promoters are involved in a large number of reactions in addition to those that dissolve the protective film. Although these cannot be enumerated fully at present, a number of reasonable postulates can be made. We may assume, for instance, that some added substances alter the structure of the film—something short of dissolution. Depending on the structure change, corrosion may be promoted or inhibited. Another reaction that has been discussed extensively is ion and molecular adsorption; such adsorption is effective in inhibiting the anodic dissolution of the metal (5-8).

It is well known that the corrosion rate of any given metal depends on the potential of the metal with respect to its environment (9). This potential can be altered by electrical means or by chemical reactions. Thus the addition of oxygen to a metal surface leads to a more positive potential in an aqueous environment; this in turn speeds the reaction of metal ions, $M \rightarrow M^{n+} + ne^-$, and thus the corrosion rate is increased. In some cases however, the adsorption of oxygen inhibits corrosion due to its effect on the oxide film. Thus oxygen can work simultaneously in opposite ways in its effect on corrosion rates. Similar effects might be expected for many additives.

One class of corrosion inhibitors are strong oxidizing agents such as $KMnO_4$ and $K_2Cr_2O_7$. These substances usually act in such a way as to make the potential more positive. This effect by itself would promote corrosion, so apparently there are additional effects (6-8, 10). Another effect such as the surface adsorption (7, 8) of MnO^-_4 or $Cr_2O^=$ must be responsible for the inhibiting effect.

Table II shows the effect of these inhibitors on aluminum, brass, zinc, iron, and copper in different solutions. The value of the potential is given before strain, V_o, and at the maximum of the transient. V_m, the difference, is the maximum value of the strain transient (the potential amplitude) $V_m - V_o = \Delta V_m$.

Several interesting features are shown in Table II. First, it may be seen that the V_o of Al is not shifted in the positive direction by $KMnO_4$. It is expected that in this strongly basic solution other reactions are rapid enough to overshadow the oxidation of the metal by $KMnO_4$. This reaction, of course, would shift the potential in the positive direction. When the electrode is strained, V_m is more positive in the presence than in the absence of inhibitor. It is possible that the reduction of $KMnO_4$ has been catalyzed by some newly exposed surface sites.

Table II. Effect of oxidizing inhibitors on strain transients and electrode potentials. Saturated calomel reference is used, 4% strain.

Electrode and solution	Inhibitors		Without inhibitors, mv	With inhibitors, mv
Copper in HOH	0.2% $K_2Cr_2O_7$	V_o	4	35
		V_m	−81	59
		ΔV_m	−85	24
Copper in $CaCl_2$ (one half saturated)	0.07% Na_2CrO_4	V_o	−350	−250
		V_m	−373	−270
		ΔV_m	−23	−20
Aluminum in 10% NaCl	0.1% K_2CrO_7	V_o	−680	−680
		V_m	−1430	−1430
		ΔV_m	−750	−750
Aluminum in 0.3 *N* NaOH	0.1% $KMnO_4$	V_o	−1300	−1300
		V_m	−1317	−1274
		ΔV_m	−17	26
Brass in HOH	0.2% $K_2Cr_2O_7$	V_o	−32	142
		V_m	−157	22
		ΔV_m	−125	−120
Brass in $CaCl_2$ (one half saturated)	0.07% Na_2CrO_4	V_o	−400	−215
		V_m	−449	−246
		ΔV_m	−49	−31
Zinc in HOH	0.2% $K_2Cr_2O_7$	V_o	−690	−440
		V_m	−863	−580
		ΔV_m	−173	−140
Iron in HOH	0.2% $K_2Cr_2O_7$	V_o	−250	72
		V_m	−382	−179
		ΔV_m	−132	−107

Several of the strain transients involve two peaks instead of one. Only the larger peak is shown in Table II. Copper in distilled water with inhibitor shows a negative transient with $\Delta V_m = -15$ mv and a positive transient with $\Delta V_m = +24$ mv. In calcium chloride solution with inhibitor the two amplitudes are −20 mv and +16 mv. The time elapse between the two peaks is approximately 0.25 sec in the first case and 1.5 sec in the second. Only a single peak is observed in the absence of inhibitor. Aluminum shows a similar behavior, but the first peak, a negative one, occurs with an amplitude of only about 1 mv.

In the cases mentioned above, it appears that the reactions occurring in the first 0.01 sec or so after strain are the same as when the inhibitor is not present. After this very rapid negative surge, supposedly due to anodic dissolution of the metal, a cathodic process becomes predominant. Either the effect of cathodic reactions has increased, or anodic reaction rates have decreased. It is possible that new surface sites are exposed with strain, and the anodic reaction proceeds briefly before the inhibitor becomes effective in this newly exposed region. Or it is possible that the inhibitor must diffuse to the new surface, after which it becomes reduced in a cathode reaction. In either case, this effect is an interesting reflection of inhibitor reactions.

A great number of substances are used to decrease corrosion other than those already discussed. A few examples are shown in Table III. Especially prominent in protecting metals against corrosion are those substances that form a distinct physical coating in addition to any that might exist by virtue of

Table III. Effects of inhibitors and organic coatings on strain transients and electrode potentials. Saturated calomel reference is used; strain, 4%

Electrode and solution	Inhibitors		Without inhibitors, mv	With inhibitors, mv
Nickel in HOH	Black paint	V_o	—170	—250
		V_m	—285	—262
		ΔV_m	—115	—12
Nickel in HOH	Red enamel	V_o	—170	—240
		V_m	—345	—260
		ΔV_m	—175	—20
Iron in HOH	Black paint	V_o	—250	—300
		V_m	—282	—328
		ΔV_m	—132	—28
Iron in HOH	Red enamel	V_o	—250	—334
		V_m	—282	—374
		ΔV_m	—132	—40
Iron in gylcerol	0.6% oleic acid	V_o	—125	—180
		V_m	—185	—192
		ΔV_m	—60	—12
Iron in 3% NaCl	20% $NaNO_2$	V_o	—520	—200
		V_m	—538	—322
		ΔV_m	—18	—122

the metal oxide on the surface. Films formed by organic substances fall into the general classes (11): paints, varnishes, enamels, lacquers, plastic films, and bitumens. The results of strain-electrometry measurements with a paint and a varnish are reported here as examples of organic coatings. Results were obtained with both Ni and Fe, and are reported in Table III. The initial potentials become negative when the coating is applied (with excessively thick coatings the electrode is insulated to such an extent that the potential cannot be measured). The strain transients are smaller than without the coating. The potential at the maximum of the transient, V_m, is not strongly altered when the coating is used. Apparently the new film is partially ruptured just as oxide films are. Since V_m is about the same in either case, similar regions of anodic (metallic) surface must be exposed.

These results give an indication of the brittleness and the protective nature of the artificial coatings as well as showing their role in altering the potential in comparison to inhibitors.

Acknowledgment

The authors would like to acknowledge grants from the Atomic Energy Commission, Contract No. At (11-1)-82, Project No. 1, and Army Ordnance Research Contract No. DA-94-495-ORD-959, in support of this work.

Manuscript received May 5, 1958.

Any discussion of this paper will appear in a Discussion Section to be published in the December 1959 JOURNAL.

REFERENCES

1. A. G. Funk, J. C. Giddings, C. J. Christensen, and H. Eyring, *Proc. Nat'l. Acad. Sci.*, **43**, 421 (1957).
2. A. G. Funk, J. C. Giddings, C. J. Christensen, and H. Eyring, *J. Phys. Chem.*, **61**, 1179 (1957).
3. A. G. Funk, D. N. Chakravarty, H. Eyring, and C. J. Christensen, *Z. Physik. Chem.*, **15**, 64 (1958).
4. H. H. Uhlig, "Corrosion Handbook," p. 20, John Wiley & Sons, Inc., New York (1948).
5. G. H. Cartledge. *J. Phys. Chem.*, **60**, 28 (1956).
6. N. Hackerman, and S. J. Stephens, *J. Phys. Chem.*, **58**, 904 (1954); N. Hackerman, and R. A. Powers, *ibid.*, **57**, 139 (1953).
7. H. H. Uhlig and A. Geary, *This Journal*, **101**, 215 (1954); H. H. Uhlig, *Chem. Eng. News*, **29**, 3154 (1946).
8. H. C. Gatos, *Corrosion*, **12**, 39 (1956); H. C. Gatos, *This Journal*, **101**, 433 (1954).
9. O. Gatty and E. C. R. Spooner, "The Electrode-Potential Behavior of Corroding Metals in Aqueous Solutions," Clarendon Press, p. 22, Oxford (1938).
10. U. R. Evans, "Metallic Corrosion Passivity and Protection," Edward Arnold and Co., London (1948).
11. K. G. Compton, *Corrosion*, **4**, 112 (1948).

Oriented Dioxide Films on Uranium

J. T. Waber, J. A. O'Rourke, and R. Kleinberg

University of California, Los Alamos Scientific Laboratory, Los Alamos, New Mexico

ABSTRACT

The growth habit of UO_2 on uranium during the oxidation by water vapor has been analyzed with the aid of detailed x-ray diffraction work and pole figures. The dioxide grows with a (110) planar texture which bears no epitaxial relation to the underlying metal crystallites. Although the polycrystalline alpha uranium has a strong and anisotropic preferred orientation as a result of fabrication, the oxide forms without azimuthal directionality in the plane of contact. The lack of alignment in the plane of contact also was confirmed in an experiment with a single crystal of uranium.

The texture of UO_2 formed during annealing in vacuum also was found to be planar without significant directionality. In such cases, the (100) planes were parallel to the surface of the metal substrate, and large amounts of uranium monoxide always were present in such films. Subsequent oxidation of specimens covered with the (100) texture yielded the characteristic (110) dioxide texture.

In incidental experimental work on the vapor deposition of UO_2 the octahedral or (111) texture was observed on glass and tantalum substrates, and the cubic or (100) texture was developed on several ionic substrates.

In a preliminary investigation, the rate law for the formation of uranium dioxide under conditions which produce such oriented films was found to be logarithmic.

Oriented layers of uranium dioxide form without any evident relationship to the orientation of parent metal during high-temperature exposure to moderate vacuum and water vapor. This occurrence appears to be unusual since it is commonly thought that the first layers of oxide are oriented epitaxially with the parent metal. For example, Gulbransen and Ruka (1), employing electron diffraction, showed that strongly oriented films are obtained on iron in $H_2 + H_2O$ mixtures and that these bear a rational epitaxial relationship to underlying metal. Mehl and McCandless (2) oxidized single crystals of iron in wet hydrogen and obtained the same epitaxial relations by x-ray diffraction on films thick enough to show interference colors.

Mehl, McCandless, and Rhines (3) were probably the first investigators to discuss the orientation of Cu_2O on copper. The results of eleven subsequent studies were reviewed by Lawless and Gwathmey (4). These authors made a very careful investigation of the degree of orientation of Cu_2O as a function of temperature, oxide thickness, and crystal face of the copper crystal. The degree of orientation increased with reaction temperature but decreased with oxide thickness. These studies were all conducted on relatively thick films.

Recently Harris, Ball, and Gwathmey (5) published the results of a very thorough electron microscope and electron diffraction study of the first few Angstroms of Cu_2O formed on copper single crystals. They found that the degree as well as the symmetry of orientation increased with oxide thickness. This confirmed the earlier observation of Pinsker and Tatrinova (6). More specifically, Harris, Ball, and Gwathmey observed that the thin films were composed of small oxide crystals having ". . . particular planes parallel to particular planes of the copper and random orientation about the plane normal. This orientation is designated type II. The oriented oxide of the thicker films was made up of oxide crystals with particular planes parallel to particular planes of the copper but with a common zone axis in the plane. This orientation is designated as type III. The common planes were: $(110)Cu_2O//(311)Cu$, $(111)Cu_2O//(111)Cu$, and $(111)Cu_2O//(100)Cu$. The common zone axis was [110]." That is, in thicker films, the degree of orientation increased so that the [110] direction in the oxide became parallel to [110] direction on the underlying copper. This parallelism was discussed also by Lawless and Gwathmey (4).

Oxide films with only one degree of orientation (type II cited by Harris, *et al.*) generally have not been recognized as they are evidenced only by unusual differences in line intensities on the diffraction pattern. Kerr and Wilman (7), in a recent electron diffraction study, reported that BeO forms on randomly oriented beryllium (either abraded or electropolished) with a (001) planar orientation at temperatures from 400° to 500°C and with a mean (100) orientation above 700°C.

Although unusual differences in line intensities on a diffraction pattern imply preferred orientation of the material under study it is difficult to identify the texture with certainty from these alone. Usually a pole figure technique is the only satisfactory method of studying texture. Very thin films are not readily studied by x-ray diffraction techniques, however, and the more complicated methods entailed in the study of texture by electron diffraction methods must be utilized. As far as the authors are

aware, only Harris, Ball, and Gwathmey have been able to verify in this way the suspected orientation of initially formed films.

Fortunately, for studies of UO_2 films, x-ray diffraction methods are adequate. Films of UO_2, thin enough to exhibit interference colors (200-300Å), can be studied satisfactorily by x-ray techniques.

It was possible in the present research to form, in a moderate vacuum, one planar orientation of UO_2 without azimuthal alignment in the surface plane and subsequently to convert it to a second planar orientation when the specimens were heated and oxidized in water vapor. To a large extent, the experiments described here deal with oxide films formed on polycrystalline uranium sheet. Both abraded and electropolished samples were studied. An experiment with a single crystal of uranium metal confirmed the conclusion that the growth habit of UO_2 films does not bear a unique relationship to the orientation of the underlying metal.

Pertinent Crystal Structures

An excellent summary of the physical and chemical properties of uranium metal has been published (8). With increasing temperature, at 668°C the orthorhombic alpha phase changes to a complex tetragonal beta phase. Above 774°C, the latter changes to the body-centered cubic phase which is then stable to the melting point at 1132°C.

Uranium dioxide is the principal compound formed during oxidation of uranium. It has the CaF_2 structure, and the stoichiometric compound has a lattice parameter of $a_o = 5.470$Å. Belle and Lustman (9) have reviewed the extensive information on the physical properties and chemical reactivity of UO_2. An oxide, referred to in this paper as the monoxide, having an x-ray structure compatible with the composition UO (an NaCl type structure with $a_o = 4.93$Å) has been observed by many investigators to form during the vacuum annealing of uranium. There is doubt that it is an equilibrium phase in the U-O system.

Experiment

The texture of the cold-rolled metal was first studied prior to oxidation. The reader is referred to a standard text (11) for details of constructing pole figures and interpreting orientation textures from them. Using a modified Schulz camera mounted on a Norelco wide range goniometer (10), pole figures were prepared from samples of sheet which had received varying amounts of cold reduction, both with and without subsequent annealing. Since only the center 60° of each pole figure could be obtained from the flat sheet as such, longitudinal and transverse sections through the sheet were necessary to complete each pole figure. These were prepared by sectioning the sheet in the appropriate directions, as indicated in Fig. 1, and then rotating the segments 90° about their long axis and bolting them together again. In the following discussions the bolted compacts which had been prepared from longitudinally sectioned segments, i.e., those which had been rotated 90° about the rolling direction RD as axis, are designated by the letter L following the sample number, while those prepared from transverse sections are designated by the letter T.

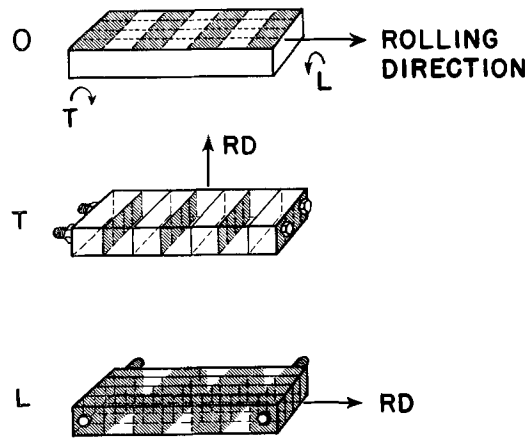

Fig. 1. Surfaces of uranium presented for oxidation by the rolled metol as well as the bolted compacts.

Since the oxide did not deposit epitaxially, details of the various metal textures developed during rolling are omitted here. It is sufficient to show that highly oriented textures were developed. This fact is demonstrated in Fig. 2, which shows the pole figure of an 86% cold-rolled uranium sheet. The same major texture developed here with a spread between (102)[010] to (203)[010] was evidenced by all the unrecrystallized samples used in this work. Different crystallographic planes, then, are predominantly parallel to the surface in the normal, transverse, and longitudinal samples. For example, if the (102) planes are parallel to the surface of the rolled sheet, (010) and (203) planes are parallel to the surface in the transverse and longitudinal sections, respectively.

The pole figure study of the dioxide presented a somewhat different problem. Here the (110) or (100) textures were developed on all of the sections, and were developed independently of the orientation of the underlying metal. Only the inner 60° of the pole figure could be plotted from an examination of the oxidized surfaces as such, and any study of the outer periphery would involve oxidizing the flat segments nearly to completion and then rotating

Fig. 2. The (111) pole figure of cold rolled alpha uranium

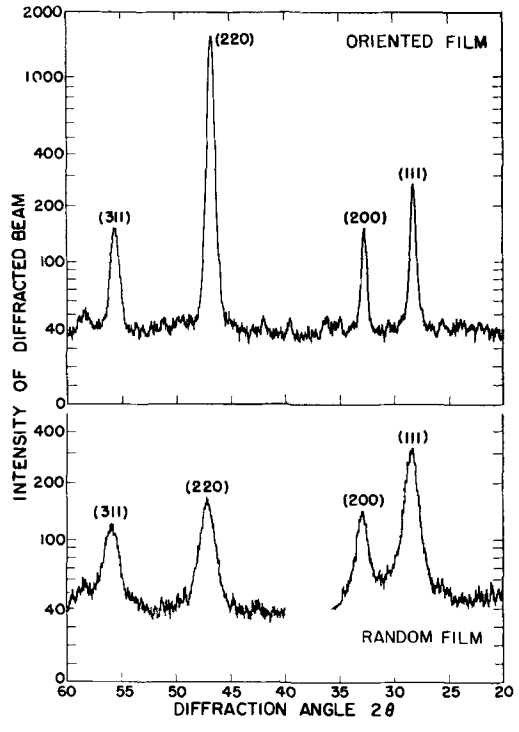

Fig. 3. Powder patterns token of UO_2 films on uranium. Intensities ore plotted on a logarithmic scale. The randomly oriented film occurred on a uranium sample after 10-hr immersion in boiling water. Ratio of the intensity of (220) to (111) is equal to the ideal value of 0.46. The oriented film occurred on the uranium after 40-min exposure to 22 mm water vapor at 400°C. The intensity ratio $I_{(220)}/I_{(111)}$ was 6.6. The triplet of alpha uranium lines which lie near the Debye 2θ angle of 36° has been omitted in the random pattern to simplify the pattern and reduce confusion.

them 90° about the long axis and bolting them together, as illustrated in Fig. 1. The necessity for resorting to this lengthy procedure was overcome by preparing pole traces of several different planes and using known crystallographic relationships for completing the analysis.

Once the nature of the orientation texture has been established, a semiquantitative estimate of the degree of orientation could be obtained from the relative intensities of lines on a diffractometer tracing. The ratios $I_{(220)}/I_{(111)}$ and $I_{(200)}/I_{(111)}$ were utilized in much of the oxidation study to evaluate the development of the (110) and (100) textures. An example of such a tracing is given in Fig. 3, together with a tracing illustrating a nearly random texture. The oriented film pattern is from a sheet sample oxidized in water vapor and exhibiting a fairly strong (110) texture. Here, the ratio of $I_{(220)}/I_{(111)}$ is 6.6, and values as high as 35 were observed in the course of the experiments. The intensity ratios for a random sample using various planes are given in Table I.

Table I. Calculated relative intensities of x-ray diffraction lines for uranium dioxide

Plane (hkl)	$I_{(hkl)}/I_{(111)}$
111	1.00
200	0.38
220	0.46
331	0.51
222	0.11

Table II. Relative intensity of oxide x-ray reflections following oxidation in vacuo

Specimen No.	Test conditions			Relative intensity		UO_2 intensity ratios	
	°C	hr	mm Hg	UO (111)	UO_2 (111)	$I_{(200)}/I_{(111)}$	$I_{(220)}/I_{(111)}$
2130	400	1½	10^{-5}	20	25	6.4	1.0
1952	600	½	10^{-6}	170	50	3.0	0.4
1954	600	¼	10^{-6}	70	20	3.75	0.3
1802	1000	19	10^{-5}	210	32	1.56	0.6

Results

Several pole figures were constructed for mechanically polished specimens heated in a vacuum of 10^{-5} mm Hg or better. This metal was oxidized by the residual gas in the vacuum system. Both uranium dioxide and uranium monoxide were present in the film. Analysis of the pole figures for these vacuum treated specimens established that the (100) planes of the dioxide were formed parallel to the metal substrate during vacuum oxidation.

Oxidation experiments were conducted at 400°, 600°, and 1000°C. Results are summarized in Table II. At each of these temperatures, the dioxide is oriented principally with its (100) planes parallel to the specimen surface. Uranium monoxide was formed simultaneously in all such films, and the restraint it imposed on the texture of the dioxide is not known.

The relative amounts of monoxide in the films are indicated somewhat semiquantitatively by the relative intensities of the (111) lines of the UO and UO_2, since the scattering factor for this plane of the monoxide is approximately 91% of that for the dioxide. More quantitative estimates would require that both oxides have a similar or random orientation.

Oxidation in water vapor appears to favor the formation of the (110) or dodecahedral orientation. Several (110) and (100) pole figures were prepared from samples oxidized in water vapor. One such pole figure is presented in Fig. 4 to illustrate the relatively small spread in the angle of inclination between the pole of plane investigated and the [110] pole of the oxide. The weak directionality indicated by the broken "ring" in Fig. 4 is believed to result from the physical dimensions of the sample (the x-ray beam covered an area slightly larger than the sample in one of its orientations) rather than from any real directionality. A strong (100) texture having little or no directionality was always developed during vacuum annealing.

Starting with the oxidized sheet having the (100) or cubic texture it was possible to oxidize the metal further in water vapor and develop the (110) orientation. Admittedly, the texture was less highly oriented when preformed layers were present. One metal sample was oxidized in vacuum at 600°C and examined by x-ray diffraction to establish the nature of the film. This sample and another mechanically polished piece of the same rolled stock were placed in the furnace and oxidized at 600°C and at a water vapor pressure of 0.3 mm Hg. After x-ray determination, the two samples were replaced in the furnace and oxidized for 1 hr at 6.2 mm pressure. As indicated in Table III a significant increase in the

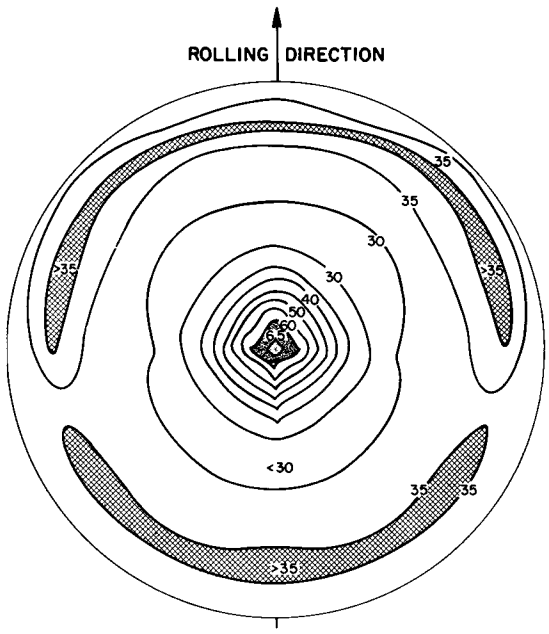

Fig. 4. Typical (110) pole figure of uranium dioxide which was formed on rolled alpha uranium sheet by oxidation in water vapor. Only the inner 60° of the stereographic projection is drawn here. The central peak and the incomplete ring illustrate the lack of significant azimuthol directionality. The intensity ratio $I_{(220)}/I_{(111)}$ was 5.6.

(110) component was observed. Specimen 1954 (Table II) was subsequently oxidized in water vapor at 600°C. Pole figures constructed using the (200) and (220) planes of UO_2 confirmed that the UO_2 was forming with the (110) planes predominantly parallel to the specimen surface.

Bolted metal compacts were oxidized for 40 min at 400°C and at 17-28.4 mm Hg water pressures. Pertinent test data are presented in Table IV. The electropolished specimen, 2130L, was heated in vacuum (10^{-5} mm Hg) at 400°C for 90 min. The predominant orientation appeared to be that of the (100) UO_2 planes parallel to the surface. This sample was oxidized to form sample 2131 which then exhibited a pronounced (110) or dodecahedral texture. The preformed (100) orientation, then, did not deter the (110) formation on subsequent oxidation.

Pole figure studies of samples, oxidized as indicated in Table III and IV, established that the uranium dioxide formed with a planar orientation on

Table III. Comparison of the degree of orientation resulting from the oxidation of preformed films at 600°C

Specimen No.	Treatment given	Orientation ratio* $I_{(220)}/I_{(200)}$†	$I_{(200)}/I_{(111)}$
1952	Vacuum, ½ hr	0.25, 0.09	1.6, 3.8
1952	Vacuum, 1 hr	0.25, 0.20	1.7, 3.3
1952a	Vacuum + 0.3 mm Hg	0.23, 0.30	2.0, 1.5
1952b	Vacuum + 0.3 mm + 6.2 mm	0.45, 0.48	0.79, 0.83
1966	0.3 mm	0.74, 0.89	5.4, 4.0
1966a	0.3 mm + 6.2 mm	1.29, 1.86	4.0, 4.0

* Duplicate values are for observations made, respectively, parallel and transverse to the rolling direction.
† Intensity ratio for random samples is 1.21.

Table IV. Orientation ratios and test conditions

Specimen No.	Preliminary treatment	Water pressure	Ratio of intensities $I_{(220)}/I_{(111)}$	$I_{(200)}/I_{(111)}$
2130L	Electropolished	Vacuum	1.0	6.4
2131L	Vac. anneal	28.4 mm Hg	1.0	0.30
2132L	Electropolished	28.4	1.80	0.59
2133T	Electropolished	17.0	18.2	1.47
2134T	Electropolished	17.0	35.0	2.70
2135L	Front, electropolished	22.1	2.4	0.26
2135L	Back, after mech. polish	22.1	2.7	0.27
2136L	Electropolished	22.1	6.4	0.5

the sheet surface, and that there was definitely no epitaxial relationship between this oxide and the underlying metal. Longitudinal, transverse, and normal samples of the same rolled sheet all exhibited identical textures when oxidized under like conditions.

A second texture develops, during this recrystallization of uranium, with the [140] pole parallel to the original rolling direction and with the poles of the planes parallel to the sheet surface having a small spread about [112]. By using bolted compacts, two other metal planes were examined to ascertain whether they influenced the oxide orientation markedly. Six such compacts were oxidized simultaneously in 20 mm Hg water pressure for 3 hr at 450°C. Data are summarized in Table V.

It is reasonable to conclude that the same dodecahedral texture devoid of azimuthal directionality developed on the recrystallized metal as well.

Single-Crystal Experiment

It was possible to confirm these conclusions with a "single crystal" of uranium obtained from Argonne National Laboratory. It was a cylinder approximately ⅛ in. in diameter and ⅜ in. long, and contained five grains. The largest of these grains filled the central cross section of the cylinder and extended along the axis in both directions.

Following oxidation in water vapor at 450°C and a pressure of 15 mm Hg for 17 min, it was examined by Olsen,[1] using a cylindrical x-ray camera. Six photographs were taken at different angles normal to the cylindrical axis; three of these photographs were overlapping oscillation patterns covering an angular range of 44°. Fairly uniform diffraction

[1] C. E. Olsen, Los Alamos Scientific Laboratory, Los Alamos, N. Mex.

Table V. Orientation ratios for the oxidation of rolled and recrystallized uranium sheet

Specimen No.	Ratio of intensities $I_{(220)}/I_{(111)}$	$I_{(200)}/I_{(111)}$
	Rolled Sheet	
2918 as rolled	4.82	1.38
2919 longitudinal	2.46	0.34
2920 transverse	3.20	0.38
	Recrystallized Sheet	
4123 as rolled	5.21	1.37
4124 longitudinal	1.89	0.43
4125 transverse	1.44	0.57

"rings" were obtained and there was no evidence of preferred alignment between the metal and oxide. The (110) planar orientation was concluded to have formed on the cylindrical metal surface.

Other Observations of Oxide Orientation

Numerous additional examples of the preferred growth habits of UO_2 can be gained from a study of the literature. Uranite and other minerals involving partial replacement of the uranium atoms, such as thorianite, occur mainly as cubes and octahedrons (12). Occasionally, dodecahedrons are found.

The octahedral or (111) growth habit was observed during an electron diffraction (13) study of a vapor deposit of UO_2 formed on a smooth glass substrate. When it was deposited under similar conditions on tantalum, the [111] pole was not perpendicular to the substrate as on glass but was inclined to it, which suggests that the higher thermal conductivity of tantalum reduced the substrate surface temperature and thus reduced the surface mobility.

Wilman and co-workers (7, 14-16) have discussed numerous examples of oriented overgrowths. In particular, they evaporated various metals and ionic salts onto substrates in such a way that the line of flight taken by the evaporating substance was oblique to the surface of the substrate. Low melting materials were observed to be arranged with some rational and densely packed plane parallel to the substrate surface. However, with refractory materials, the orientation axis of the deposit was inclined to the surface presented by the substrate, and the direction of preferred growth was approximately parallel to the line of flight. When the substrate has good thermal conductivity the kinetic energy of the depositing material is reduced and the molecules lose a portion of their surface mobility. If the substrate does not conduct heat well, high surface temperatures, high surface mobilities, and thus more perfectly oriented deposits are to be expected.

The cubic or (100) growth habit was observed for heated substrates (17). Uranium dioxide was distilled from a tungsten boat at approximately 2800°C in an evacuated system containing a few millimeters of hydrogen and was deposited onto a polished single crystal of either CaF_2 or KBr which was held at approximately 600°C. The deposit showed preferred orientation with the (200) line being very prominent.

Thus vapor deposition favors the same two growth habits that are found in naturally occurring crystals. The dodecahedral habit, however, is associated with the oxidation of uranium. Mogard (18) reported that, during the corrosion of uranium in molten sodium, uranium dioxide forms by combining with the small amounts of oxygen dissolved and entrained as Na_2O in the molten sodium. The films formed at 475°C exhibited the (110) planar orientation. At higher temperatures, a porous and relatively nonoriented layer occurred on top of the coherent hard oxide layer adjacent to the base metal. During the cathodic vacuum etching of uranium in tank argon, thin UO_2 films form. These films are formed with the (110) planes parallel to the metal substrate.

These observations suggest that the formation of this dodecahedral orientation results from growth of the oxide film in a preferred direction. The interfacial temperature of the uranium is probably high enough during oxidation to permit surface migration and preferred growth of those oxide crystallites which are favorably oriented.

Rate Law Involved

Rate data were obtained in connection with the orientation of the oxide. It is surprising that a logarithmic law is followed. Doubtless this can only occur at such a high temperature because of the low pressure of the oxidant, water.

The change in weight of the specimen was determined from the extension of a fused silica spiral spring. By using three springs, which were each able to support 3-g loads safely, and by arranging them in tandem, a spring constant of 10.84 cm/g was obtained at room temperature. A 1-mg change in weight corresponded to a 0.108-mm extension, which could be read easily with a cathetometer. The spring constant was determined with the furnace in place and with the specimen, bucket, and a portion of the spring at 400°C. For example, it was found that the helix, with the bucket containing a piece of gold, changed in length from 40.950 cm at room temperature to 41.150 cm at 400°C mainly as a result of the change in the spring constant.

The system was evacuated and the specimen brought to temperature and equilibrated for approximately 1 hr. The water was admitted to the system by breaking a sealed ampoule in that portion of the system at room temperature. The initial cathetometer reading was taken approximately ½ min after the reaction commenced.

The high-purity uranium metal used for this test was rolled to approximately 0.002 in. thick sheet and annealed. This annealed sheet was cut and polished through 4/0 metallographic paper. An extension of 0.1 mm corresponded to a weight increase of 30.67 $\mu g/cm^2$ of the specimen.

Typical weight changes with time are illustrated in Fig. 5 for two separate runs conducted at 400°C

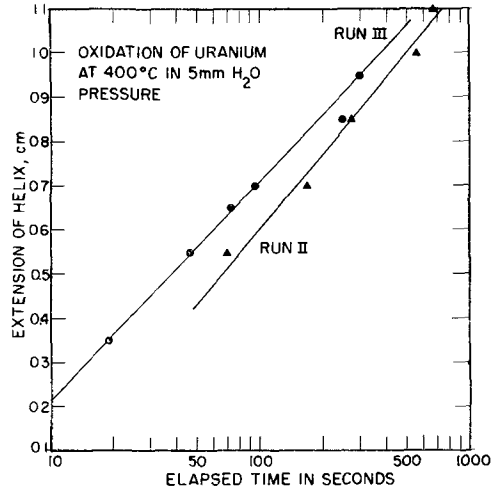

Fig. 5. Semi-logarithmic plot of the length of the silica helical spring vs. the duration of oxidation. Data are for two separate runs at 400°C.

and 5 mm water pressure. A logarithmic growth law was obtained with a fair degree of reproducibility.

The orientation of the oxide was examined after removal of the samples from the furnace. The ratios $I_{(220)}/I_{(111)}$ were found to be 1.1 for Run II and 2.15 for Run III.

Discussion

Several hypotheses could be advanced which would afford an explanation for the formation of the planar texture of the overgrowth. One of the most logical explanations would involve the use of dislocation theory. A thin layer of oxide next to the metal is disorganized and is not aligned epitaxially with the metal. A few oxide grains will contain, or form, one dislocation emerging essentially perpendicular to the specimen surface. Diffusion of ions along this dislocation will be relatively rapid, as has been indicated by the experiments of Turnbull and Hoffman (19, 20) on the self-diffusion of silver along grain boundaries. Inward diffusion of oxygen along such dislocation "pipes" will increase the rate of oxidation. Thus oxide grains with favorably oriented dislocations will penetrate faster. The favored grains need have no azimuthal relation to the substrate. At a later stage, when such a grain has penetrated more deeply than most, the diffusion resistance along this dislocation pipe will increase until it is equal to that along most paths. The tip of the favorably oriented grain will then advance inwardly at almost the same rate as does the bulk of the oxide. However, an alternative path lying partly along the dislocation and partly perpendicular to it has lower resistance. Thus the penetrating grain will spread laterally near the interface and will become roughly pyramidal. The high temperature in the oxide film from the heat of reaction will facilitate the recrystallization of the disorganized oxide thus enlarging the large favorable grains. Experiments to establish the essential features of this explanation are in progress.

Two important studies have been reported recently. Miller and Lawless (22) have obtained electron-photomicrographs of spiral growth terraces such as are associated with screw dislocations on Cu_2O polyhedra formed on copper single crystals. An experiment by Harris, Ball, and Gwathmey (5) strongly indicated that the nucleation and formation of Cu_2O polyhedra was related to dislocations in the copper itself. These polyhedra are oriented with a common [110] zone axis in the interface as cited above for the thick oxide films (4, 5). Webb and Foreng (23) have observed the formation of α-Al_2O_3 whiskers and platelets during the oxidation of aluminum or of Al_3Ti in wet hydrogen at 1300°-1500°K. Invariably the whiskers were single crystals with the [001] direction parallel to the principal growth direction. Dragsdorf and Webb (24) have shown that these whiskers contain screw dislocations. Terraced growth steps have been observed optically on α-Al_2O_3 platelets.

The formation of a smooth oxide film of uniform thickness can no longer be envisaged as the proper description. The growth and nucleation of discrete oxide grains are the dominant processes initially. Similar phenomena have been observed for the formation of AgBr on silver by Newman and Pashley (25). More work is needed to elucidate the role of dislocations in the metal substrate and in the compound formed.

Belle and Lustman (9) have reviewed the evidence which leads to the conclusion that ionic migration in UO_2 occurs by the diffusion of anions. The formation of anti-Frenkel defects (interchange between an anion in its sublattice with a vacant interstitial site) contributes to the higher mobility of anions in the fluorite lattice as Ure (21) has shown for doped CaF_2. Because of this anion diffusion, the dioxide grows inward during the oxidation of uranium leaving superficial markers unaffected on the original surface. Thus external growth patterns are not anticipated in the UO_2.

Conclusion

It has been shown that uranium dioxide formed by the reaction of uranium with water vapor at moderate temperatures occurs with a distinctive growth habit. The (110) planes of the dioxide lie parallel to the surface of the polycrystalline uranium substrate. No evidence was found for an epitaxial relation between the metal and the oxide. Although preformed dioxide films having a (100) planar texture were developed, subsequent oxidation yielded the (110) texture.

The formation of the dodecahedral texture is uncommon in naturally occurring crystals or in vapor deposition. The planar texture is explained on the basis of recrystallization of the oxide and preferential growth of oxide grains containing favorably oriented dislocations.

Acknowledgment

The authors are deeply indebted to Professor Robert Brick for his interest in the problem and for his valuable suggestions during the course of the work. The single crystal of uranium was generously given by Dr. Frank G. Foote of Argonne National Laboratory. The assistance of many members of the laboratory in connection with the experimental work and the preparation of this report is gratefully acknowledged. Particularly we should like to mention Donald Prys and Marguerite Coleman. Dr. R. B. Roof, Jr., calculated the intensity of the lines in the UO_2 x-ray diffraction pattern. Edward S. Wright, Dawn D. Whyte, and William R. Hickey contributed to the experimental work.

Manuscript received Nov. 26, 1956. A portion of this paper was prepared for delivery before the Cleveland Meeting, Sept. 30-Oct. 4, 1956 and a portion was reported at the Gordon Research Conference on Oxidation Processes, New London, N. H., July 1954. The work was done under the auspices of the Atomic Energy Commission.

Any discussion of this paper will appear in a Discussion Section to be published in the December 1959 JOURNAL.

REFERENCES

1. E. A. Gulbransen and R. Ruka, *This Journal*, **99**, 360 (1952); *Ind. Eng. Chem.*, **43**, 697 (1951).
2. R. F. Mehl and E. L. McCandless, *Trans. Am. Inst. Mining Met. Eng.*, **125**, 531 (1937); *Nature*, **137**, 702 (1934).
3. R. F. Mehl, E. L. McCandless, and F. N. Rhines, *Nature*, **134**, 1009 (1934).

4. K. R. Lawless and A. T. Gwathmey, *Acta Met.*, **4**, 153 (1956).
5. W. W. Harris, F. L. Ball, and A. T. Gwathmey, *ibid.*, **5**, 574 (1957).
6. Z. G. Pinsker and L. I. Tatrinova, "Electron Diffraction," p. 262, Butterworth Scientific Publ., London (1953).
7. J. S. Kerr and H. Wilman, *J. Inst. Met.*, **84**, 383 (1956).
8. J. J. Katz and G. T. Seaborg, "The Chemistry of the Actinide Elements," p. 124 ff, Methuen and Co., London (1957).
9. J. Belle and B. Lustman, "The Properties of UO_2," Atomic Energy Commission Document WAPD-184 (Sept. 1957).
10. Anon. "Schulz Integrating Reflection Goniometer," Am. Soc. Test. Mat. Tentative Stand. E49-86T Revised 1954.
11. C. S. Barrett, "Structure of Metals," p. 154 ff, McGraw-Hill Book Co., New York (1943).
12. J. J. Katz and E. Rabinowitch, "The Chemistry of Uranium," p. 77, Nat. Nucl. Ener. Ser. VIII-5, McGraw-Hill Book Co., New York (1952).
13. J. T. Waber, D. D. Whyte, and C. E. Olsen, submitted to *This Journal*.
14. D. M. Evans and H. Wilman, *Proc. Phys. Soc.*, **63A**, 298 (1950).
15. D. M. Evans and H. Wilman, *Acta Cryst.*, **5**, 731 (1952).
16. H. Wilman, *Proc. Phys. Soc.*, **64A**, 329 (1951).
17. E. T. Teatum, Unpublished work.
18. H. Mogard, Int. Conf. Peaceful Uses Atomic Ener., A/CONF./P/787, vol. 9, p. 318.
19. D. Turnbull and R. E. Hoffman, *Acta Met.*, **2**, 419 (1954).
20. R. E. Hoffman, *ibid.*, **4**, 97 (1956).
21. R. W. Ure, Jr., *J. Chem. Phys.*, **26**, 1363 (1957).
22. G. T. Miller and K. R. Lawless, *J. Appl. Phys.*, **29**, 863 (1958).
23. W. W. Webb and W. G. Foreng, *ibid.*, **28**, 1449 (1957).
24. R. D. Dragsdorf and W. W. Webb, *ibid.*, **29**, 817 (1958).
25. R. C. Newman and D. W. Pashley, *Phil. Mag.*, **46**, 927 (1955).

Kinetics of the Uranium-Steam Reaction

B. E. Hopkinson[1]

Atomic Energy Research Establishment, Harwell, England

ABSTRACT

Reaction rates of unalloyed uranium with super heated steam at 160°-1400°C and 1 atm pressure have been determined by a thermogravimetric method. Up to 880°C the reaction follows a linear rate law with maximum rates at approximately 300° and 750°C. Above 880°C a parabolic rate law applies for the first 60-120 min, after which corrosion is linear; the oxide formed in the initial period gives protection to the underlying metal, and the subsequent linear rate is as low as that at about 200°C. X-ray diffraction of the reaction product indicated that uranium dioxide was formed over almost the whole temperature range.

Previous quantitative work on this reaction has been confined to temperatures below 600°C. The earliest investigations (1) reported uranium to be attacked rapidly by steam from 150° to 400°C, with a reaction product of uranium dioxide at the lower temperatures; this changed to U_3O_8 on rise of temperature until at 400°C U_3O_8 constituted about 92% of the total oxide produced. Other workers (2) found that steam reacted rapidly with uranium turnings at 250°C to give a mixture of uranium dioxide and uranium hydride, but at 600° and 1000°C only uranium dioxide and hydrogen were formed; no U_3O_8 was reported at any temperature.

Huddle (3) gave some experimental data up to 600°C and also assessed the kinetic possibilities at higher temperatures, concluding that the uranium dioxide formed would be sufficiently protective to give a low reaction rate. The reaction rates obtained here indicate that the uranium oxide does in fact tend to be protective at high temperatures.

Experimental

Materials

Uranium.—Two different sizes of uranium specimens were used. The first, of rectangular shape, was satisfactory at low temperatures but oxidized completely in a few minutes at 750°C. It was therefore replaced by a larger cylindrical sample for experiments above 600°C.

The rectangular specimens weighed about 6.5 g and were approximately 1.3 x 1.9 x 0.15 cm (surface area 5.7 cm^2). They were fabricated by rolling as-cast Springfields uranium into a sheet at 450°C and punching out to size. The cylinders weighed 30 g and were approximately 1.26 cm in diameter and 1.27 cm in height. They were cut from a bar of cast uranium and machined to the approximate dimensions. Before the experiment each specimen was polished to 00 emery paper under oil, degreased in acetone, and stood for 12 hr in a desiccator over calcium chloride.

Steam.—Steam was obtained from a main supply, the line pressure being reduced by a valve which maintained the pressure inside the reaction chamber slightly above one atmosphere.

Argon.—Argon was used to provide an inert atmosphere when preheating the specimen to reaction temperature. It was purified from oxygen and nitrogen by passing over calcium turnings at 600°C followed by bubbling through Na/K alloy at room temperature.

[1] Present address: Research Laboratory, The International Nickel Company, Inc., Bayonne, N. J.

Procedure

The reaction rate was followed by continuous weighing of the specimen on a modified thermobalance. The apparatus was as described by Kubaschewski and Hopkins (4) except for the provision of a heater to prevent condensation of steam on the platinum suspension wire where it emerged from the reaction chamber.

A platinum or nichrome wound furnace maintained the specimen temperature, which was measured by a chromel/alumel or platinum/platinum rhodium thermocouple placed adjacent to the specimen in a silica "pocket." The thermocouple measured the temperature of the gas stream, which may be lower than that of the specimen by an amount depending on the degree of self-heating. This self-heating, due to the exothermic nature of the reaction, is unavoidable. At 350°C it can be as large as 150°C (3) but above 880°C, when the protective oxide scale has formed, the heat of reaction is not likely to contribute materially to the specimen temperature when compared with the external heat input. The actual temperature fluctuations recorded were between 10° and 40°C for each experimental run.

When carrying out the experiment, the furnace, argon purifier, and heating tapes were brought up to the appropriate temperature, the specimen placed in the fused silica reaction chamber, and argon flushed through. After elevating the furnace to a position around the specimen and preheating in a flow of argon to the required temperature for about 30 min, steam was admitted at roughly 2 l/min. Weight increases were recorded at appropriate time intervals. After the required period, the steam flow was stopped and the specimen cooled in argon before removal. In nearly all experiments the specimen showed a small weight increase when being preheated, and this was attributed to impurities still remaining in the argon after purification.

The specimens were always enclosed in a basket of platinum gauze (52 mesh) to retain oxide that fell away from the metal; the basket in turn was suspended from the balance.

Table I. Rates of reaction over the temperature range 160°-1400°C

Average temp, °C	Linear reaction rate as weight gain in mg/cm²/min	Value of index n in the equation $y = kt^n$ applied to first 60-120 min of reaction
160	0.02	
200	0.1, 0.1, 0.08	
230	0.3, 0.3, 1.6	
250	0.9, 1,6, 1.6	
270	1.7, 1.9, 1.9	
300	2.0, 2.4, 2.7	
330	2.1	
350	1.6	
370	1.9	
380	1.6	
400	1.8	
420	1.2, 1.8, 1.4	
450	1.1, 1.7	
500	0.9, 1.0, 1.3	
520	1.0, 0.6	
550	0.7, 1.0, 0.8, 1.1	
600	1.5, 1.7, 1.3	
650	1.4, 1.5	
700	1.3, 6	
730	6	
780	4	
820	3	
840	3	
880	0.2	0.52
890	0.3	0.46
930	0.3	0.46
970	0.3, 0.2	0.50
1000	0.2, 0.3	0.42
1020	0.2, 0.3	0.50
1060	0.3	0.49
1200	3.8	
1400	4.8	

Results

The rates of corrosion, i.e., the slope of the curves, are detailed in Table I. Usually several values of the reaction rate were determined at each temperature by independent experiments.

The scatter of rates shown in this table may be due partly to lack of control of temperature because of self-heating and partly to other variations in the experimental conditions, e. g., traces of oxygen in the steam supply.

The behavior of solid uranium in steam from 160° to 880°C is represented by a linear relationship between weight increase and time; an exception is at 230°C. Figures 1(a) and 1(b) show typical curves for this part of the temperature range

From 880° to 1060°C the curves [Fig. 1(c)] are initially parabolic changing to linear after times ranging from 60 to 120 min. The linear rates are detailed in Table I. The parabolic or near-parabolic nature of the initial part of the curve was shown by the slope of a log-log plot of weight increase per unit area (y) against time (t). This slope should ideally be 0.50. Actual values are reported in Table I, column 3.

Two experiments were carried out with molten uranium. Figure 2 shows that at about 1200° and 1400°C the rate fell initially with time to a steady value of 4-5 mg/cm²/min. Some difference in the form of the two oxidation curves was evident.

Figure 3 shows the linear reaction rate of each specimen plotted against the temperature of the experiment.

Other observations.—The physical nature of the reaction product varied with the temperature of oxidation. Below 500°C the oxide was a voluminous fine powder, but above this temperature larger particles began to appear. Above 880°C the oxide formed a complete shell, which adhered to the uranium and remained intact on cooling the specimen to room temperature. When cold, this shell could be stripped off easily. Figure 4 shows typical changes in the reaction product with temperature. The bulk densities of the oxide produced at higher temperatures were measured by weighing in air and water and are given in Table II.

The reaction products over the temperature range 200°-1400°C were examined by x-ray diffraction. All the samples gave a uranium dioxide type pattern except one at 300°C which appeared to be U_3O_8; this does not imply a stoichiometric composition of $UO_{2.0}$

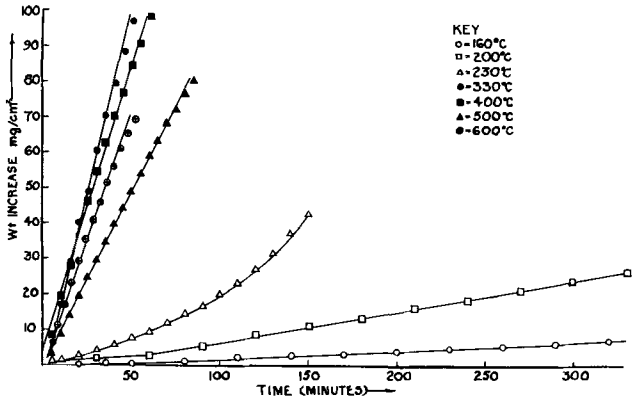

Fig. 1 (a). Uranium in steam 160°-600°C. Plot of weight increase (mg/cm²) V time (min).

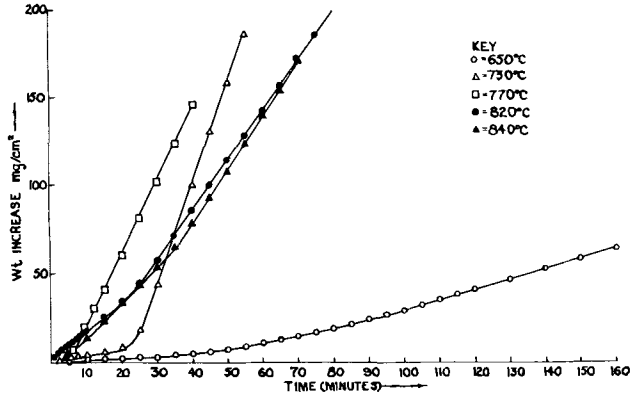

Fig. 1 (b). Uranium in steam 650°-840°C. Plot of weight increase (mg/cm²) V time (min).

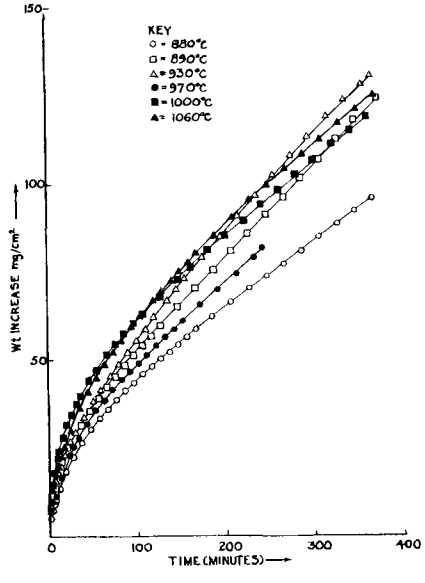

Fig. 1 (c). Uranium in steam 880°-1060°C. Plot of weight increase (mg/cm²) V time (min).

but is typical of compositions between $UO_{2.0}$ (α-UO_2) and $UO_{2.24}$ (β-UO_2).

Three specimens which had been exposed to steam at 200°, 930°, and 1060°C were examined metallographically. The 930° and 1060°C specimens showed similar characteristics and are considered together. The outer layer of oxide, about 1 mm thick, had flaked off, but an adherent coating approximately 5μ thick remained. No evidence of preferential grain boundary attack was observed, and inclusions originally in the uranium appeared unchanged in the oxide. These inclusions were thought to be uranium monocarbide since they etched black in a mixture of equal parts of nitric acid and water. After corrosion, inclusions of a new type were present in addition to the carbide. These consisted of light brown areas (Fig. 5) generally serpent-like in shape at grain boundaries and almost invariably containing a spine of small, dark, fairly equiaxed inclusions. The brown inclusions occupied about 0.25 vol % of the material and were more numerous in the center than the periphery. Mogard and Cabane (5) indicate that this type of inclusion is uranium hydride. The solubility of hydrogen in γ-uranium is 15-17 ppm but is less than 2 ppm in α-uranium (6). Since 0.25 vol % of uranium hydride corresponds to 18 ppm of hydrogen, it appears that during corrosion with steam the uranium becomes saturated with hydrogen which precipitates on cooling.

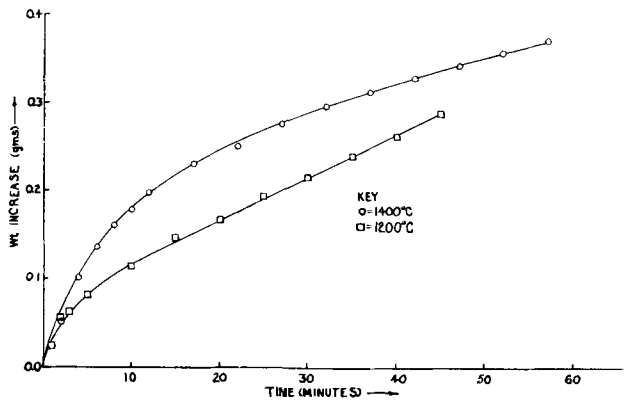

Fig. 2. Molten uranium in steam. Approximate surface area of molten uranium exposed to steam = 0.9 cm².

Examination of the specimen corroded at 200°C showed no such hydride. Except for a few large fissures, attack was fairly uniform, and no trace of preferential attack along the grain boundaries was found. The fissures ran parallel to strings of uranium carbide inclusions, but the carbide content in the region of the fissures did not appear above average. Uranium hydride was found near the tips of the fissures, either along the stringers of carbide inclusions or as needles at an angle to the fissure (Fig. 6).

Discussion

From the results obtained on solid specimens two oxidation maxima are observed at approximately 300° and 750°C, with two minimum at about 550° and from 800°-1050°C.

It is possible to explain the first maximum at 300°C by considering the rate of variation of uranium hydride formation with temperature. Uranium hydride is unstable above 433°C under 1 atm partial pressure of hydrogen, and the rate of reaction be-

Table II. Bulk densities of the oxide scales formed above 880°C

Temperature of formation, °C	Scale thickness, cm	Density g/cc
970	0.07	10.95
1000	0.11	11.00
1020	0.14	10.97

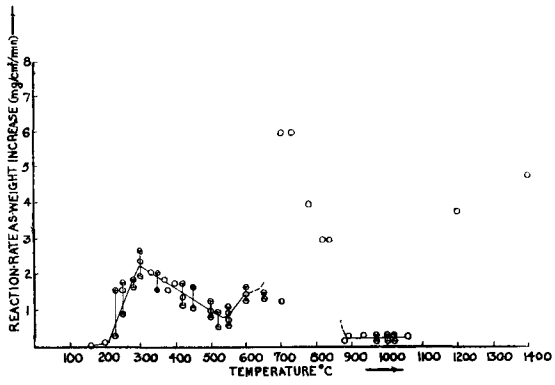

Fig. 3. Plot of reaction rate (mg/cm²/min) V temperature (°C).

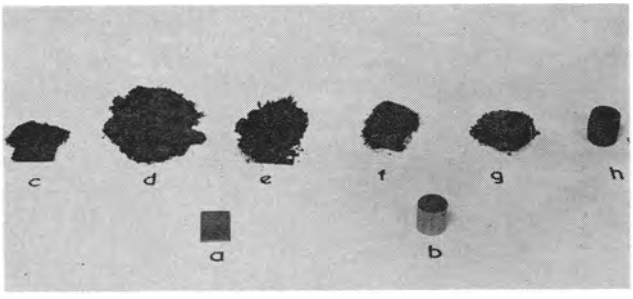

Fig. 4. Photograph of uranium specimens before and after corrosion in steam: (a) rectangular specimen before corrosion; (b) cylindrical specimen before corrosion; (c) specimen after exposure to steam at 200°C for 6¾ hr; (d) specimen after exposure to steam at 300°C for ¾ hr; (e) specimen after exposure to steam at 500°C for 1 hr, 40 min; (f) specimen after exposure to steam at 700°C for 20 min; (g) specimen after exposure to steam at 840°C for 1 hr, 20 min; (h) specimen after exposure to steam at 1000°C for 6 hr.

tween uranium and gaseous hydrogen reaches a maximum at 225°-250°C. It has been reported (7) that below 450°C uranium reacts with steam to give a mixture of hydride and oxide according to the equation

$$U + H_2O \rightarrow UH_3 + UO_2$$

and that the uranium hydride reacts slowly (8) with more steam to give uranium dioxide. Therefore, reaction below 450°C should yield a mixture of uranium hydride and uranium dioxide,[2] the latter predominating, as confirmed by metallographic examination of a specimen corroded at 200°C. It is probably justified to infer therefore that the maximum oxidation rate of uranium by steam at 300°C is determined by the variation of the rate of uranium hydride formation with temperature.

Above 500°C, hydride formation is improbable and the reaction may be written

$$U + H_2O \rightarrow UO_2 + H_2$$

the hydrogen being evolved as a gas or dissolving in the metallic uranium. In the temperature region above 500°C the cohesive properties of the oxide become important as a rate-determining factor. Up to 500°C the reaction product is in the form of a fine

[2] It is not clear whether the U_3O_8 found at 300°C is a definite reaction product (1) or results from air oxidation of uranium dioxide or uranium hydride after removal from the apparatus.

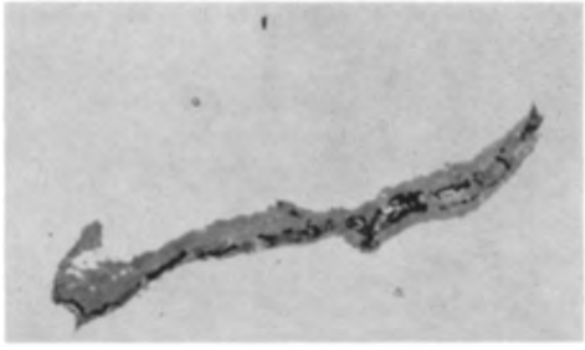

Fig. 5. Hydride precipitate in specimen after exposure to steam at 1060°C and cooled to room temperature. Magnification 1200X.

Fig. 6. Tip of fissure in uranium corroded at 200°C. Magnification 312X.

powder, but above 500°C granular particles are formed. Normal sintering of uranium dioxide occurs at about 1300°C (0.6 Tm), but it has been suggested that the presence of steam enhances the sintering characteristics of uranium dioxide (9). Also, an oxide film growing on the metal may behave differently from discrete oxide particles. The high reaction rates observed in part of this temperature range, i.e., 700°-880°C, may result from the increased surface area caused by the specimen splaying out at the top and bottom during oxidation. Why this occurs only between 700° to 880°C is not clear, but it may be that at these temperatures the oxide does not sinter sufficiently to protect the uranium completely, and that the stresses developed as the scale grows prove too much for continued cohesion, resulting in breakdown and high oxidation rate. It was noted that an induction period of up to 20 min occurred in experiments betwen 650° and 840°C before the reaction rate increased to a high value. This may indicate a change in mechanism but, since the size of the specimen had to be increased to work in this region, this also may have influenced the appearance of an induction period.

It is above 880°C that the most significant change in the rate of the reaction occurs. Above this temperature a hard compact scale forms, the density lying between 10.95 and 11.00 g/cc which compares well with theoretical values from lattice parameters given by Grönvold (10) viz., 10.954 g/cc for $UO_{2.00}$ and 11.297 g/cc for $UO_{2.25}$.

The results from 880° to 1060°C show large initial weight gains increasing roughly according to a parabolic law. After 60-120 min however, a change occurs and the weight increase becomes linear with time and continues linear for the rest of the experiment.

The rate in the linear range is between 0.2 and 0.3 mg/cm²/min over the temperature range 880°-1060°C. Therefore once an oxide film has been formed, the reaction rate between uranium and

steam is smaller above 880°C than at any lower temperature down to about 200°C.

To explain this, the two rate laws which characterize the reaction may be discussed briefly.

(*A*) The parabolic rate law can be expressed as $y = kt^{1/2}$ and traditionally is derived from the diffusion of reactants through the oxide as the rate-determining step.

(*B*) The linear law $y = kt$ can be ascribed to oxidation of metal by the following two mechansims: (i) when the rate-controlling step is a surface reaction at one of the interfaces; (ii) if the rate is controlled by diffusion through an oxide layer of constant thickness.

The change from parabolic to linear oxidation with time at constant temperature has been reported for a number of reactions (11-16).

To explain the change from a parabolic to linear oxidation rate three mechansims may be considered. First, the heat of oxidation could result in self-heating of the specimen, thereby increasing the temperature and rate of oxidation. Second, if the surface area changes as oxidation proceeds (i.e., a decrease in roughness) this may cause a change in the oxidation rate. Davies and Birchenall (13) explained the initial parabolic oxidation of titanium in oxygen as being due to a change of surface area as oxidation proceeded, the over-all rate-controlling stage being the interface reaction of oxygen and titanium oxide. Third, there is the idea of a "barrier film" of constant thickness controlling the rate of oxidation. This mechanism has been used to explain the majority of transitions from parabolic to linear-type rate laws.

A mechanism involving control by an oxide layer of constant thickness appears to serve the facts of the uranium-steam reaction above 880°C and is put forward to explain these results.

The actual diffusing species through the oxide layer is probably anionic. The presence of uranium hydride in the metal after corrosion at high temperatures in steam indicates that hydrogen either as molecular hydrogen, protons, or hydroxyl ions is able to penetrate to the uranium in some way. One suggestion (3) is that water vapor is first chemisorbed on the uranium dioxide at the oxide/steam interface. The chemisorbed complex then produces hydroxyl ions, which are further reduced at the metal/oxide interface, the hydrogen dissolving in the metal. The hydrogen is precipitated as hydride in the grain boundaries when the specimen is cooled within the hydride formation range.

Conclusions

The rate of attack of uranium by steam varies with temperature over the range 160°-1060°C, and two maxima are obtained at about 300° and 750°C. Above 880°C however, a protective scale is formed, due to coalescence of the oxide. Once this scale has been produced the rates of oxidation above 880°C are smaller than those found between 200° and 880°C.

From the results given the trend of the reaction has been indicated, but further work will be needed to confirm the true rate-controlling mechanisms over the whole temperature range.

Acknowledgments

Thanks are due to K. A. Peakall for some of the early experimental work, to Dr. D. K. Thomas for the x-ray diffraction studies, and to P. E. Madsen for the metallographic examination. For helpful discussion and constructive criticism the author is indebted to Mr. R. A. U. Huddle, Dr. H. M. Finniston, Mr. J. N. Wanklyn, and Dr. P. Murray.

Manuscript received Dec. 23, 1957. This paper was prepared for delivery before the Ottawa Meeting, Sept. 28-Oct. 2, 1958.

Any discussion of this paper will appear in a Discussion Section to be published in the December 1959 JOURNAL.

REFERENCES

1. T. Wathen, BR-233. "Corrosion of Uranium Metal in Air and Steam at Various Temperatures," Imperial Chemical Industries, May 1943.
2. J. J. Katz and E. Rabinowitch, "Chemistry of Uranium," N.N.E.S. Vol. VIII, p. 167, McGraw Hill Book Co., New York (1951).
3. R. A. U. Huddle, A.E.R.E., M/R 1281, "The Uranium Steam Reaction," (1953).
4. O. Kubaschewski and B. E. Hopkins, "Oxidation of Metals and Alloys," p. 90 Butterworth's Scientific Publications, London (1953).
5. H. Mogard and B. Cabane, *Rev. Met.*, **51**, 617 (1954).
6. J. J. Katz and E. Rabinowitch, *op. cit.*, p. 183.
7. J. C. Warf, U.S.A.E.C. Report No. MDDC. 1391 (1943).
8. J. J. Katz and E. Rabinowitch, *op. cit.*, p. 202.
9. P. Murray, Private communication.
10. F. J. Gronvold, *Inorganic and Nuclear Chemistry*, **1**, 357 (1955).
11. D. Cubicciotti, *J. Am. Chem. Soc.*, **74**, 1200 (1952).
12. P. Levesque and D. Cubicciotti, *ibid.*, **73**, 2028 (1951).
13. M. H. Davies and C. E. Birchenall, *J. Metals*, **3**, 877 (1951).
14. A. F. Gerds and M. W. Mallet, *This Journal*, **101**, 175 (1954).
15. E. A. Gulbransen and K. F. Andrew, *ibid.*, **97**, 383 (1950).
16. D. Cubicciotti, *J. Am. Chem. Soc.*, **74**, 1079 (1952).

Tarnishing Reactions of Silver in Iodine Atmospheres

Donald M. Smyth and Marjorie Cutler

Sprague Electric Company, North Adams, Massachusetts

ABSTRACT

The tarnishing of silver in halogen vapors, particularly iodine vapor, has been studied as a function of reaction temperature, halogen pressure, silver purity, and concentration of foreign vapors in the halogen atmosphere for reaction times up to several hours. The reaction temperature range studied was 25°-150°C for reactions in iodine and up to 200° in bromine and chlorine. In pure halogen vapor the reactions follow the familiar parabolic rate expression and are proportional to the square root of the halogen pressure. In the presence of small partial pressures of water or carbon tetrachloride vapor, however, the tarnishing rate is suppressed and is independent of the tarnish film thickness.

The tarnishing of silver in halogen atmospheres has been described by several investigators using various techniques (1-4). Since the publishing of Wagner's theory of the mechanism of these reactions (1, 5), however, very little work has been done on the tarnishing of undoped silver in halogen vapor, and, in particular, there has been no evaluation of the role played by foreign gases in the halogen atmosphere. Neither has there been any extensive study of these tarnishing reactions in the temperature range 25°-150°C. This range of reaction temperature has been examined in this laboratory for the silver-iodine system for silver samples of differing purity and for pure iodine atmospheres and iodine atmospheres containing water vapor or carbon tetrachloride vapor. Exploratory experiments have also been made on the effect of water vapor and carbon tetrachloride vapor on the tarnishing rate of silver in bromine and chlorine atmospheres.

Previous publications in this field are in agreement that the high-temperature tarnishing of silver in halogen vapor follows a parabolic rate expression

$$x^2 = kt \qquad [1]$$

where x is the tarnish film thickness, t the reaction time, and k the rate constant. The reaction rate has been found to be proportional to the square root of the halogen pressure, $P_{X_2}^{1/2}$, and inversely proportional to the concentration of cation vacancies, $[Ag^+]$, in the silver halide. The cation vacancy content can be controlled by the addition of polyvalent metallic impurities to the silver (2, 3). Our experiments in the reaction temperature range 25°-200°C indicate that the factors determining the tarnishing rate are essentially the same in the case of tarnishing reactions in pure halogen vapors. In the presence of even small partial pressures of water or carbon tetrachloride vapors, however, the nature of the reaction is altered completely. Reaction rates become independent of tarnish film thickness and follow a linear expression,

$$x = at \qquad [2]$$

where a is a new rate constant. Reaction rates are relatively insensitive to reaction temperature and halogen pressure under these conditions.

Experimental

The reactions were followed by measuring the weight increase of silver foil in a halogen atmosphere by the extension of a quartz fiber spring balance (McBain balance). The silver samples were cut from 0.001-in. foil and had a geometrical surface area of 19.4 cm^2. The samples were cleaned just prior to use by a dip in concentrated cyanide solution to remove atmospheric tarnish and by a light etch in dilute nitric acid. After being rinsed and air dried, the specimens were weighed and hung in the reaction chamber on the end of the quartz fiber spring. The iodine pressure was determined by thermostatting iodine crystals. In order to avoid condensation of iodine, the atmosphere surrounding the experimental system was heated slightly above the temperature of the iodine crystals.

When all parts of the apparatus had reached temperature equilibrium and the system had been evacuated to less than 30 μ pressure, the iodine container was opened to the reaction chamber. As the spring oscillations caused by the flow of iodine vapor into the reaction chamber ceased, an initial spring level reading was taken and the timer started. The spring depression then was measured every 1-5 min for a total time of ½-6 hr depending on the reaction rate. To terminate the reaction, the system was evacuated and flushed with air; then the sample was removed and weighed. The difference between the actual total weight increase and the weight increase which occurred during the measured reaction time as calculated from the total spring depression gave the amount of reaction which occurred before the first reading was taken. This initial amount of reaction was transformed into an equivalent spring depression which was added to each measured spring depression. These corrected values thus correspond to the total weight increase of the sample normalized to the clean, unreacted silver foil. This procedure was necessary because of the possible shift of the equilibrium spring position during the large, initial oscillations. The

square of the corrected spring depression was plotted against the reaction time, and the slope of this line when transformed into appropriate units gives the reaction rate constant k. (Microscopic examination of cross-sectioned samples showed that the bulk density of the silver halides can be used to calculate the film thickness.)

The technique was slightly more involved when the reaction rate was measured in the presence of a foreign vapor. In this case, a second isolated and thermostatted container was added to the apparatus to hold the thoroughly outgassed water or carbon tetrachloride. The two vapor sources generally were held at different temperatures and thus could not be opened to the system at the same time. An initial film of tarnish product was formed on the silver by exposure to halogen and foreign vapor. Then the reaction was halted and this initial film was exposed to the foreign vapor for 15 min after which the reaction rate with iodine was measured. No subsequent readmission of foreign vapor was necessary since additional exposures at the same pressure did not change the reaction rate.

Materials.—The silver[1] was of the following types:

1. Commercial silver, nominally 99.9+% pure. Spectrographic analysis showed copper to be the major impurity with a concentration of the order of 0.05% with lead, iron, and calcium being present in slightly lesser concentration.[2]

2. Laboratory refined silver, initially prepared as a powder 99.995+% pure. Some surface contamination may occur during rolling but this is probably removed by the etch treatment.

3. Cadmium doped silver prepared from laboratory refined silver. This alloy contained 0.046% cadmium according to the suppliers assay. The copper content was 0.003% and no other impurity was present in concentration greater than 0.001%.

Matheson, Coleman, and Bell Reagent iodine crystals (resublimed) were used without further purification. Baker Reagent Grade bromine was dried by several passes through a tube of anhydrous calcium sulfate. Baker and Adamson Reagent carbon tetrachloride was used without further purification. The source of water vapor was demineralized water of greater than 1 megohm cm resistivity.

Several quartz springs were used during this investigation, all having spring constants of about 0.05 g/cm. The spring constants were determined by measuring the extension caused by known loads over the pertinent load range and were found to be constant within ±5% over the entire experimental temperature range. The spring depression could be read to ±5μ through a 10X telescope mounted on a micrometer head.

Results

The experimental results may be summarized as follows: the reaction of silver with pure halogen atmospheres followed parabolic rate expressions, Eq. [1], except for some deviations observed during the first few minutes of reaction; in halogen atmospheres containing water or carbon tetrachloride vapor above some minimum pressure the reaction rates were linear with time and followed Eq. [2]. The reaction rates behaved reversibly to changes in halogen pressure and foreign gas pressure but not to changes in reaction temperature since a decrease in reaction temperature does not change the reaction rate to the rate obtained when the reaction is started at the lower temperature. All of these factors will be discussed in detail.

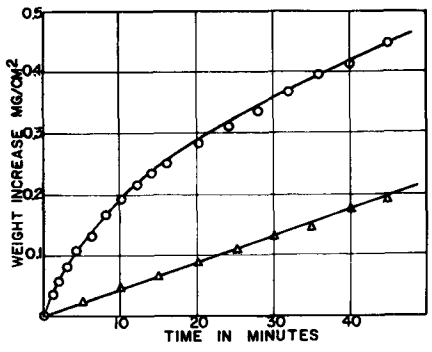

Fig. 1. Tarnishing of silver in 0.2 mm iodine vapor at 39°C. ○ Pure iodine vapor; △ iodine vapor plus 0.37 mm H_2O vapor.

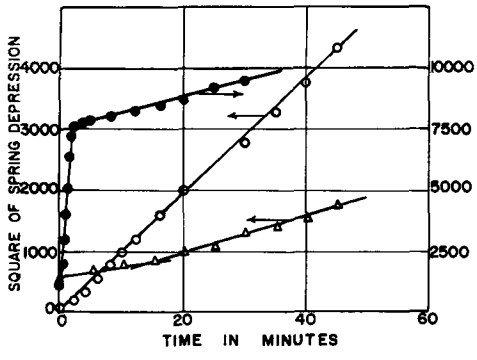

Fig. 2. Tarnishing of laboratory refined silver (99.99+%) in 0.2 mm pure iodine vapor. Typical experimental data. ○ Parabolic throughout, reaction at 69°C; △ slow initial reaction at 68°C; • fast initial reaction at 137°C; the arrows indicate the ordinate scale to be used with each set of data.

Typical tarnishing data are shown in Fig. 1 for the silver-iodine system. Similar results were obtained for the silver-bromine and silver-chlorine systems. The figure shows data obtained from two reactions performed under identical conditions except for the presence of a small partial pressure of water vapor in one case (laboratory refined silver was used in each experiment). Figure 2 shows the types of initial deviation from parabolic reaction rates observed for the reaction of silver with pure iodine vapor. Almost all of the reactions of fine silver and some of those of laboratory refined silver followed a simple parabolic expression throughout the measured time. A large number of the reactions with laboratory refined silver had an initial, slow reaction rate which changed into a final rate after 2-15 min. For each batch of laboratory refined silver, there was a temperature between 100° and 130°C above which the reaction initially proceeded very rapidly for several minutes before abruptly slowing down to a rate comparable to that observed at lower temperatures. Above 145°

[1] Obtained from Handy and Harman, 82 Fulton St., New York, N. Y.

[2] Analysis carried out by Lucius Pitkin, Inc., 47 Fulton St., New York, N. Y.

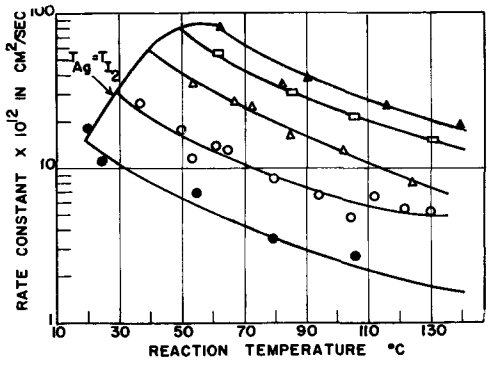

Fig. 3. Tarnishing of "fine" silver (99.9+%) in pure iodine vapor. Iodine pressures: • 0.20 mm; ○ 0.47 mm; △ 1.0 mm; □ 2.2 mm; ▲ 4.3 mm.

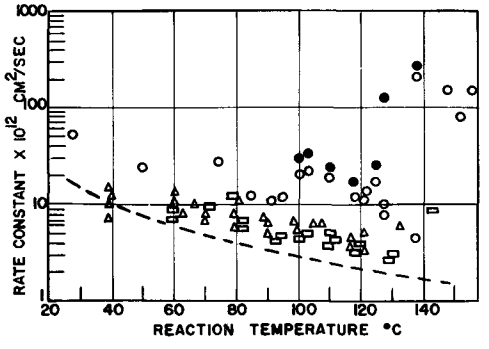

Fig. 4. Tarnishing of laboratory refined silver (99.99+%) in 0.2 mm pure iodine vapor. △, ○ Two different batches of pure silver; • initial fast reaction for batch designated as ○; □ pure silver plus 0.046% cadmium; — — — averaged data for 99.9+% silver.

(the transition temperature for the phase change $\alpha AgI \rightarrow \beta AgI$) the fast reaction rate continued without change. This initial fast reaction also was observed for some lots of fine silver at temperatures just below the transition temperature.

In Fig. 3 and 4 are shown the results of a large number of tarnishing experiments carried out under a variety of conditions. The reaction rates of commercial purity silver (99.9+%) with pure iodine vapor as a function of reaction temperature with iodine pressure as a parameter are shown in Fig. 3. Each point represents an individual tarnishing experiment at constant temperature and iodine pressure, and smooth curves have been drawn through points obtained at the same iodine pressure. The tarnishing rates are expressed in terms of the parabolic tarnishing constant k in Eq. [1] in units of (cm of film thickness)^2/sec. The line in Fig. 3 which is labeled $T_{Ag} = T_{I_2}$ connects points at which the iodine pressure is in equilibrium with the reaction temperature.

In Fig. 4 are shown the results of a large number of tarnishing experiments on high-purity and cadmium doped high-purity silver. The rate of the brief, initial reaction is not shown in this figure except for the very fast initial reaction observed in the higher temperature range, and this is designated by the symbol •. The variation in reaction rate for separate lots of silver (represented by different symbols) is apparent in this figure as is the scatter of reaction rates within the same batch. The effect of divalent metallic impurities is shown by the cadmium doped samples. All of the experiments in Fig. 4 were carried out in 0.2-mm iodine pressure and the dashed line represents the averaged tarnishing data for the commercial grade silver in iodine vapor of this pressure.

The tarnishing rates of the commercial grade silver and of silver heavily doped with cadmium are not reversible with temperature as shown by the following experiment. If a piece of commercial grade silver foil is tarnished at 30° and the reaction temperature is then raised to 100°, the reaction rates correspond to the values for these temperatures shown in Fig. 3. If, however, the reaction temperature is reduced to 30° again, the reaction rate increases only a fraction of the amount required to restore the original rate found at this temperature. The same effect is obtained when a tarnish film is heated a few minutes at the higher temperature without exposure to iodine vapor. A similar but more striking behavior is noted when fine silver containing 0.09% cadmium is tarnished. The initial tarnishing rate is similar to that of undoped silver but, after "annealing" an initial tarnish film, the subsequent reaction rate may be lowered by as much as a factor of 50. Thus, the exposure of a tarnish film to a higher temperature tends to lower the rates of subsequent reactions carried out at lower temperatures, and the effect is more pronounced in less pure silver. These phenomena will be discussed further with respect to the mechanism of these reactions.

Laboratory refined silver was employed for the tarnishing experiments carried out in iodine in the presence of water or carbon tetrachloride vapor. The reaction rates in 0.20 mm of iodine vapor as a function of water vapor pressure at three different reaction temperatures and as a function of carbon tetrachloride vapor pressure at one reaction temperature are shown in Fig. 5. In this case, the reaction rate constant represents the constant, a, in the rate expression of Eq. [2], indicating that the reaction rate is independent of film thickness. For water vapor pressures below 0.1 mm, the reaction follows the same parabolic rate equation found for the anhydrous reaction. There is a narrow, intermediate range of water vapor pressure in which the reaction rate is erratic and is sometimes linear and sometimes parabolic. For higher water vapor pressures, the reaction rate is always linear and gradually decreases with

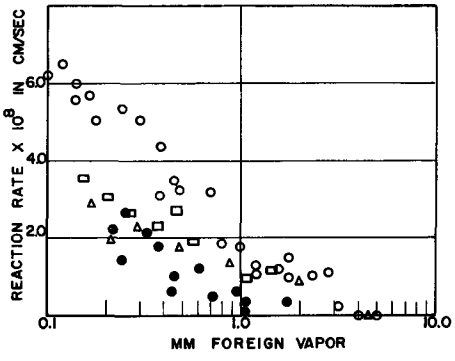

Fig. 5. Tarnishing of laboratory refined silver in 0.2 mm iodine vapor plus H_2O or CCl_4 vapor. □ H_2O vapor, reaction at 40°; ○ H_2O vapor, reaction at 69°; △ H_2O vapor, reaction at 101°; • CCl_4 vapor, reaction at 33°.

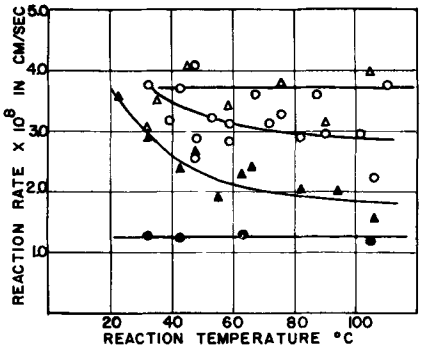

Fig. 6. Tarnishing of laboratory refined silver in iodine vapor plus 0.26 mm water vapor. Iodine pressures: △ 0.47 mm; ○ 0.20 mm; ▲ 0.11 mm; • 0.04 mm.

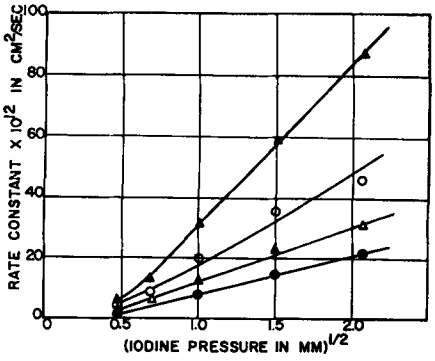

Fig. 7. Tarnishing rate of "fine" silver as a function of $\sqrt{P_{I_2}}$. Reaction temperatures: • 60°C; △ 80°C; ○ 100°C; ▲ 130°C.

increasing water vapor pressure until at a water vapor pressure of 4 mm the reaction becomes too slow to observe. It is not clear whether the reaction actually stops in the presence of larger concentrations of water vapor or whether it decreases steadily but remains finite. The situation is similar for carbon tetrachloride except that this vapor is apparently somewhat more effective in suppressing the tarnishing rate than is water vapor.

Figure 6 shows the reaction rate of silver with moist iodine vapor as a function of reaction temperature with iodine vapor pressure as the parameter. Although the results are scattered, it is clear that the reaction temperature has very little effect on the reaction rate and that the reaction rate increases with iodine vapor pressure.

A few tarnishing experiments were also carried out in bromine atmospheres and the results were similar to those found for iodine. The reaction of silver with anhydrous bromine follows parabolic rate expressions, while the wet bromine atmospheres give linear reaction rates. One major difference from the iodine reactions was that the linear reaction rate did not change with the water vapor pressure. Thus at a reaction temperature of 105° and a bromine pressure of 43 mm, the linear reaction rate constant, a, was $6 \pm 2 \times 10^{-8}$ cm/sec in nine experiments over the water vapor pressure range 0.06-1.5 mm. The reaction temperature was also found to have little effect on the reaction rate since at a water vapor pressure of 1.0 mm and a bromine pressure of 43 mm, the reaction rate less than doubled between 105° and 190°C. Over the same temperature range the anhydrous parabolic rate constant increased by a factor of about 700.

In 600 mm of chlorine vapor and 0.045 mm of water vapor the laboratory refined silver tarnished at a linear rate of 0.5×10^{-8} cm/sec at 172° and 2.0×10^{-8} cm/sec at 194°.

Discussion

Tarnishing in Pure Halogen Vapor

It is assumed that the anhydrous tarnishing reactions proceed according to the theory of Wagner (1, 5). This states that the parabolic reaction rate is determined by the diffusion of an ionic or electronic species across the bulk of the tarnish film and proposes the following equilibrium reaction at the halide-halogen interface

$$\tfrac{1}{2}\,X_2\,(\text{gas}) = AgX + \boxed{Ag^+} + \textcircled{e^-} \qquad [3]$$

where X is a halogen, $\boxed{Ag^+}$ is a silver ion vacancy, and $\textcircled{e^-}$ is an electron hole in the electronic structure of the silver halide. If we consider the silver halides as predominantly ionic conductors, the migration of electron holes across the silver halide must be the rate-determining step. Assuming that the ionic disorder of the lattice is large compared with the cation vacancies injected according to Eq. [3], the theory predicts the following dependence of the parabolic rate constant, k, on the halogen pressure, P_{X_2}, the cation vacancy concentration, $\boxed{Ag^+}$, and the mass action constant, K, for Eq. [3]

$$k \propto \frac{K\,P_{X_2}^{1/2}}{\boxed{Ag^+}} \qquad [4]$$

The proportionality of the tarnishing rate with $\sqrt{P_{I_2}}$ is shown in Fig. 7 in which reaction rate constants taken from the smooth curves in Fig. 3 are plotted against $\sqrt{P_{I_2}}$ for several different reaction temperatures. This proportionality apparently does not hold for very low iodine pressures. The inverse proportionality to the cation vacancy concentration has been demonstrated by other workers for other silver halides at higher reaction temperatures by adding a sufficient amount of impurity to determine the cation vacancy concentration (2, 3).

All of the rate-determining factors in Eq. [4] should behave reversibly to changes in temperature except perhaps the cation vacancy concentration. The irreversible "annealing" effect observed for reactions of the low-purity silver and the more striking effect observed with cadmium doped silver points to the vacancy content as an important factor in determining the rate. The cation vacancy concentration depends on the purity of the halide since the substitution of a polyvalent cation M^{a+}, for a monovalent silver ion in the lattice requires the formation of n-1 cation vacancies to maintain electrical neutrality. Teltow (6) determined the solubility limits of $CdBr_2$, $PbBr_2$, and $ZnBr_2$ in AgBr over a considerable temperature range, and by extrapolation of his results it is clear that the solubilities will be only a small fraction of a per cent at tempera-

tures below 150°. The behavior of the iodides may be assumed to be quite similar. It is not unreasonable to expect that for a silver sample of low purity there will be sufficient polyvalent metal ions to saturate the halide lattice up to an appreciable temperature. Thus as the reaction temperature increases, the concentration of dissolved impurities in the AgI also increases due to the increase in solubility. As a result, the quantity $[Ag^+]$ increases and from Eq. [4], the reaction rate decreases with increasing temperature. At these low concentrations the concentration of dissolved impurities would probably not decrease reversibly with decreasing temperature but would remain in a state of supersaturation. This would account for the irreversibility of the reaction rate with temperature as observed for the lower purity silver. In addition to this factor, there may be a temperature dependence arising from K, but this should behave reversibly to temperature changes.

If the ionic conductivity of the silver halide is playing any part in controlling the reaction rate, the polycrystalline nature of the tarnish film may be important since there is evidence that ionic conduction takes place very readily along grain boundaries (7). In this case, the annealing effect could be enhanced by a decreased concentration of grain boundaries due to a growth in crystal size in heated tarnish films.

The nature of the temperature coefficient of reaction rate found here supports some of the earlier work on the Ag-I_2 system. Tammann (4) found no change in reaction rate in the temperature range 15°-100°C. Dubrisay (8) observed a slight decrease in tarnishing rate as the reaction temperature was raised from 24° to 60°. Balarew (9) found a very slight increase in reaction rate between 50° and 70°, followed by a slight decrease again at 100° and a sharp dip in reaction rate at 120°. This pronounced minimum in tarnishing rate has not been reported elsewhere. All of these works employed the interference color technique to measure the tarnish film thickness and thus deal with thinner films than discussed in this paper. It is of interest to note that the behavior is similar over such a wide range of film thickness. Evans and Bannister (10) made an extensive study of the rate of reaction of silver with organic solutions of iodine and found that the reaction rate at 35° is about twice that at 0° for carbon tetrachloride solutions of iodine. The use of organic solvents may invalidate a direct comparison to reactions in pure iodine vapor however.

The brief, rapid reaction rates noted for pure silver reacting with iodine vapor at reaction temperatures just below the α-β phase transition temperature of AgI (145°C) are of the same magnitude as the continuous reaction rates observed above the transition temperature. Thus it appears that the initial film may have the α phase structure for 1-3 min after which it abruptly changes back to the phase in equilibrium at the reaction temperature. It was considered that the samples might be heating themselves above the transition temperature by their own heat of reaction. This possibility was investigated numerically by Miss Alma Marcus of these laboratories, who computed the temperature rise of a sample considering the heat evolved by the reaction and the heat loss through radiation and conduction. It was found that for typical reaction conditions the rise in sample temperature would reach a maximum of 1.4°C after 1.7 sec and this is insufficient to explain the experimental results. It is possible that the crystalline structure of the silver substrate may influence that of the initial silver iodide film and that close to the transition temperature the high temperature structure is favored. This would conflict with the observation of Tammann and Köster (11) that the phase transition takes place at 145°C even for layers of silver iodide on silver which show optical interference colors.

The initial, slow reaction rate observed in some reactions of high-purity silver at temperatures below 100° does not fit in with the general behavior outlined above and is not understood at present.

Tarnishing in the Presence of Foreign Vapors

The linear rate expression, Eq. [2], followed by the tarnishing reactions carried out in the presence of foreign vapors implies that the rate-determining factor is an interface phenomenon and hence independent of the tarnish film thickness. This factor has not been identified experimentally but it is suspected that adsorption of the impurity gas on the halide surface results in modification in the space charge layer at the AgI surface adjacent to the iodine atmosphere. Speculations along this line will be the subject of a future publication from this laboratory. The diffusion rate of the halogen through the adsorbed film of foreign vapor may also be of importance.

The experimental results from the Ag-I_2 system (see Fig. 4 and 5) indicate that the amount of foreign vapor is the main rate-determining factor since the reaction temperature has no significant effect and the influence of iodine pressure is small. The two gaseous atmospheres extensively investigated in this work, iodine with water vapor and iodine with carbon tetrachloride vapor, show that the effect is not dependent on the polarity of the foreign molecule since the nonpolar carbon tetrachloride is even slightly more effective in suppressing the reaction rate than is water. This fact implies that a wide variety of vapors would act similarly to the two investigated here. The results also show that a foreign vapor is not consumed by the tarnishing reaction. Once the tarnish film has been exposed thoroughly to the foreign vapor, the reaction rate continues unchanged for hours without further addition of water or CCl_4 vapor, and neither do subsequent additions at the same vapor pressure alter the reaction rate. The effect is perfectly reversible and the tarnishing rate can be changed immediately in either direction by suitable adjustment of the pressure of the foreign vapor.

Since the character of the tarnish film does not seem to be altered by the presence of the foreign vapor, the reaction rate for any particular experiment will be parabolic or linear depending on whether the bulk diffusion process or the interface process is the slower. Thus for very low foreign vapor pressures,

the interface process will not be slower than hole diffusion and the reaction will be parabolic. The rate of diffusion will decrease as the tarnish film thickens and it will eventually become the rate-determining step regardless of the experimental conditions unless the foreign vapor completely stops the reaction. The ideal situation can be described by the following simplified considerations. The reaction rate will follow the linear rate equation (Eq. [2]) unless the diffusion process is rate determining, in which case the reaction follows the parabolic rate expression (Eq. [1]). A change from the linear to the parabolic reaction will occur at the film thickness, x_1, at which the reaction rate dx/dt is the same for both equations

$$x_1 = \frac{k}{2a} \qquad [5]$$

This thickness will be reached after a reaction time t_1,

$$t_1 = \frac{k}{2a^2} \qquad [6]$$

Subsequent to the time t_1 the reaction will follow the expression

$$x^2 = k\left(t - \frac{k}{4a^2}\right) \text{ for } x > x_1 \qquad [7]$$

where $k/4a^2$ is the difference in times that the parabolic and linear reactions would require to build up a tarnish film x_1 cm thick starting from bare silver. This behavior is illustrated in Fig. 8 which compares the tarnishing rate in dry iodine with two reactions carried out in the presence of water vapor. In the presence of 0.94 mm of water vapor the reaction follows a linear rate throughout (Eq. [6] indicates that the transition to a parabola should occur after 295 min of reaction). The data shown for reaction in the presence of 0.26 mm of water vapor have been found to follow Eq. [2] and [7] with $a = 3.3 \times 10^{-8}$ cm/sec, $k = 8.7 \times 10^{-12}$ cm^2/sec, and a transition time of 52 min. (The fact that the initial linear reaction does not extrapolate to the origin of coordinates has been taken into account.) These rate values are in satisfactory agreement with the average anhydrous tarnishing rate, $k = 9.5 \times 10^{-12}$ cm^2/sec, and moist tarnishing rate, $a = 3 \times 10^{-8}$ cm/sec, observed under similar conditions for the same batch of silver foil.

The effect of moisture on the tarnishing rate explains some of the previously published results of

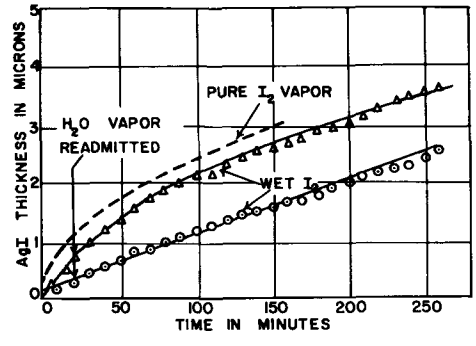

Fig. 8. Influence of moisture content of atmosphere on tarnishing rate of laboratory refined silver at 35°C in 0.2 mm iodine vapor. — — — Averaged data from reactions in pure iodine vapor; △ 0.26 mm H_2O vapor; ○ 0.94 mm H_2O vapor.

tarnishing reactions of silver with halogens. In many instances the reactions did not follow a parabolic rate expression and this can almost invariably be explained by the presence of moisture in the halogen vapor. For example, Hartung measured the tarnishing rate of silver with iodine and bromine at 25° (12, 13). The iodine atmosphere was obtained from an aqueous KI-I_2 solution and thus was saturated with water vapor. The tarnishing rates followed linear rate equations for the range of iodine concentrations studied. Hartung does not describe any purification or drying of his bromine and it was undoubtedly moist since the reaction rates were found to be linear after an initial fast reaction lasting about 100 sec.

Kohlschütter and Krähenbühl investigated the reaction of silver with iodine and found some variation in reaction rate depending on the dryness of the halogen atmosphere (14). Their results do not follow either parabolic or linear rate expressions but some intermediate rate equation. It is possible that their data follow the linear expression for the initial reaction period and then transform into a parabolic reaction rate as described above, but since the authors give no quantitative data, it is not possible to investigate this possibility thoroughly. Using Cl_2 and Br_2, Kohlschütter and Krähenbühl found faster reactions with silver in the presence of moisture than in the dry halogen. The use of streams of N_2 or CO_2 to carry the halogen over the silver may have had some influence on the reaction rate.

Several publications report observations which conflict with those described here (15-19). In general, these papers contain very little quantitative data and are therefore difficult to evaluate.

Other tarnishing reaction systems have been observed to be affected by the presence of water vapor. Solovjev (20) has found that there is apparently an optimum water vapor pressure for maximum reaction rate of copper with iodine. He also noted a decrease in reaction rate of iron with iodine with decreasing water vapor pressure. Bircumshaw and Everdell found a linear reaction rate for copper reacting with aqueous solutions of KI and I_2 (21) whereas the reaction rate depended on the tarnish film thickness in organic iodine solutions (22). The authors attribute this behavior to a wetting and penetration of the tarnish film by the aqueous solutions while the organic solutions do not wet the film and the reaction can proceed only by bulk diffusion through the iodide. Campbell and Thomas (23) investigated the oxidation of copper in dry and moist oxygen. In dry oxygen the reaction was parabolic while in moist oxygen the results had a smaller dependence on the film thickness. In general, these experiments show the care necessary in controlling all of the experimental conditions in order to obtain meaningful results. Even the presence of what might be usually considered "inert" gases may drastically alter the nature of the reaction.

Acknowledgments

The work reported herein was carried out under United States Army Signal Laboratories Contracts DA-26-039-sc-63151 and DA-36-039-sc-72349. The

authors wish to express their appreciation to Dr. Kurt Lehovec of these laboratories for much stimulating discussion and advice.

Manuscript received March 12, 1958.

Any discussion of this paper will appear in a Discussion Section to be published in the December 1959 JOURNAL.

REFERENCES

1. C. Wagner, *Z. physik. Chem.*, **32B**, 447 (1936).
2. C. Gensch and K. Hauffe, *ibid.*, **195**, 386 (1950).
3. K. Hauffe and C. Gensch, *ibid.*, **195**, 116 (1950).
4. G. Tammann, *Z. anorg. Chem.*, **3**, 78 (1920).
5. C. Wagner, *Z. physik., Chem.*, **21B**, 25 (1933).
6. J. Teltow, *Ann. Phys.*, **6**, 63 (1949).
7. I. Pfeiffer, K. Hauffe, and W. Jaenicke, *Z. Elektrochem.*, **56**, 728 (1952).
8. R. Dubrisay, *Compt. rend.*, **229**, 829 (1949).
9. D. Balarew, *Koll. Z.*, **101**, 47 (1942).
10. U. R. Evans and L. C. Bannister, *Proc. Roy. Soc., London*, **125A**, 370 (1929).
11. G. Tammann and W. Köster, *Z. anorg. u. allgem. Chem.*, **123**, 196 (1922).
12. E. J. Hartung, *J. Chem. Soc.*, **1926**, 1349.
13. E. J. Hartung, *ibid.*, **1924**, 2198.
14. V. Kohlschütter and E. Krähenbühl, *Z. Elektrochem.*, **29**, 570 (1923).
15. H. B. Linford and M. J. Ford, *J. (and Trans.) Electrochem. Soc.*, **93**, 16 (1948).
16. M. H. Brown, W. B. DeLong, and J. R. Auld, *Ind. Eng. Chem.*, **39**, 839 (1947).
17. R. Weiner, *Arch. Metallk.*, **1**, 281 (1947).
18. S. Shimadzu, *Mem. Coll. Sci. Kyoto Imp. Univ. Ser.*, **A19**, 229 (1936); *Chem. Zentr.*, (1937) II, 3575.
19. E. Raub, *Degussa-Metallberichte*, **1**, 39 (1941).
20. A. V. Solovjev, *Compt. rend USSR*, **4**, 185 (1935).
21. L. L. Bircumshaw and M. H. Everdell, *J. Chem. Soc.*, **1942**, 598.
22. L. L. Bircumshaw and M. H. Everdell, *ibid.*, **1947**, 1119.
23. W. E. Campbell and U. B. Thomas, *Trans. Electrochem. Soc.*, **91**, 623 (1947).

Potential Studies on Passivity to Corrosion Induced by Pretreatment Processes for Metals

I. Aluminum

K. S. Rajagopalan

Central Electrochemical Research Institute, Karaikudi, India

ABSTRACT

Potential and polarization characteristics of aluminum which has been subjected to various chemical oxidation processes are reported. It is shown that a more negative initial electrode potential is recorded by the treated metal as compared to the untreated metal. The cathodic polarization curve of the treated metal is also much steeper. These results are satisfactorily explained by the application of the Glasstone, Laidler, and Eyring theory of electrode processes to the potential of a corroding metal.

Electrode potential measurements have been widely used in studying corrosion and corrosion inhibition (1-6). Such measurements have thrown valuable light on the intrinsic corrodibility of metals and alloys, the manner in which corrosion-inhibitive constituents added to the corrosive medium affect the corrosion process, and have also helped in understanding the role played by various types of pigments. Similarly, anodic and cathodic polarization curves of corroding metals have given valuable information on the mechanism of inhibition by corrosion inhibitors (7, 8). Numerous chemical processes have been developed in recent years which improve the resistance of metals to corrosion in different corrosive environments by the formation of thin, protective oxide, chromate, or phosphate films (9-14). The resistance to corrosion conferred by these treatments have been studied mainly by means of accelerated corrosion and field tests. Potential and polarization studies with the object of obtaining an insight into the mechanism by which chemical surface treatments confer passivity to the metal surface have, however, not yet been carried out. This paper is the first of a series describing such studies and concerns aluminum for which a number of simple processes involving only a dip treatment are known.

Experimental

Metal.—Indal 2 S to B.S. 1470 (commercially pure aluminum of 99% purity) from Indian Aluminum Co., Belur, Calcutta, cut into 1 x 1 in. specimens was used.

Scratch-free material was cut into the size required and given a high degree of polish with cloth buff soaked with wet pumice (15). This was followed by solvent cleaning in hot benzene and acetone, cleaning with alkaline cleaner (16), rinsing with cold water, and treatment in one of the following processes:

1. *MBV process* (17): 5-min treatment at 90°-100°C in solution containing 5% sodium carbonate and 1.5% sodium chromate.

2. *E.W. process* (18): 10-min treatment at 90°-100°C in MBV solution to which 0.1% sodium silicate has also been added.

3. *Pylumin process* (19): 5-min treatment at 95°-100°C in solution containing 6% sodium carbonate, 2% sodium chromate, and 0.2% disodium phosphate.

4. *Alrok process* (20): 20-min treatment at boiling point in solution containing 2% sodium chromate and 0.5% potassium dichromate.

5. *Chrome pickle* (21): Dipping for 2 min at 60°-70°C in solution containing 17.5% (w/v) chromic acid and 3.5% (w/v) H_2SO_4.

6. *Phosphoric acid pre-treatment* (22): 5-min treatment in cold solution containing 10% (v/v) of orthophosphoric acid (85%), 70% (v/v) butyl alcohol, and 20% water.

7. *Acid cleaning* (23): 5-min immersion in cold solution of 5.6% of phosphoric acid (v/v) and 1.7% chromic acid.

8. *Chemical polishing* (24): 5-min treatment at 90°C in solution 80% (v/v) of phosphoric acid (85%), 3.5% (v/v) nitric acid, and 16% water. After treatment, the specimens were given a thorough rinse in cold water and dried with a hot air blower.

Procedure

The procedure followed was similar to that described by Brasher (25) with the difference that the sealing of the junction between metal and the external lead and glass tube was done in three stages using different mixtures of beeswax-rosin, beeswax-ceresin, and ceresin. This seal remained unaffected up to 60 days. The corroding medium, 3% NaCl in water, was contained in a 600 ml beaker and the specimen was fitted by means of rubber cork to the perspex cover of the beaker and lowered into the solution to a depth of 1 in. below the solution level. The test solution was aerated for 15 min before test to saturate it with oxygen.

Potentials were measured against a saturated calomel electrode using a Beckman *p*H meter as the null instrument. Only 10^{-11} amp passed on off balance. Polarization studies were carried out by external application of current with a duplicate specimen as the auxiliary electrode and the potentials measured as before. All measurements were made at 35° ± 0.1°C.

Results

Potentials given by a replicate number of untreated specimens and specimens treated by the MBV process immediately after immersion in sodium chromate solution are given in Table I. The instantaneous potentials of untreated aluminum are found to be reproducible with ±10 mv while more variation is observed in the case of the treated specimens.

Potentials of treated and untreated metal were recorded frequently up to a period of 4 hr and then at the end of 1 and 2 days. Results are given in Table II.

The potential of untreated aluminum is found to be fairly steady for several hours at −0.745 v and then falls to more negative values, indicating failure of the protective oxide film in the corroding medium containing chloride ion in solution. The potential of the treated metal, which is highly negative to start with, rises quickly to the potential of untreated aluminum and falls again.

Reproducibility of potential-time curves with untreated and treated metal.—Potential-time curves given by replicate specimens of treated and untreated metal up to a period of 60 days are plotted in Fig. 1. It is seen from the figure that the potential-time curves of the untreated metal are generally characterized by a gradual drift in the course of 4 days to a constant potential which is 200 mv more negative; that of treated metal is, on the other hand, characterized by a rapid rise in the course of a day to the initial potential of untreated aluminum followed by a much slower fall. The extent of drift with

Table I. Reproducibility of initial electrode potential vs. saturated calomel electrode at 35°C

No.	Untreated metal	Metal treated by MBV process
1	−0.761	−1.028
2	−0.745	−1.128
3	−0.753	−1.081
4	−0.740	−1.052

Table II. Change in potential in the first few hours

No.	Time	Potential of untreated metal	Potential of treated metal
1	0 min	−0.745	−1.081
2	5 min	−0.745	−1.021
3	10 min	−0.748	−0.991
4	15 min	−0.748	−0.954
5	30 min	−0.748	−0.825
6	1 hr	−0.748	−0.740
7	2 hr	−0.748	−0.745
8	3 hr	−0.748	−0.753
9	4 hr	−0.753	−0.787
10	1 day	−0.835	−0.857
11	2 days	−0.837	−0.868

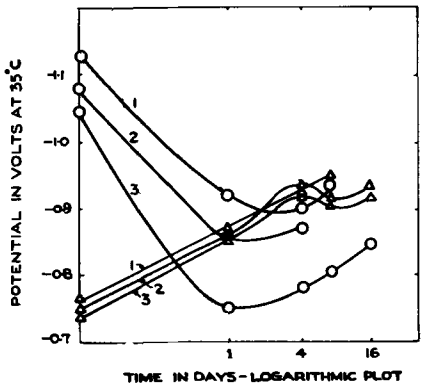

Fig. 1. Reproducibility of potential-time curves of untreated aluminum and aluminum treated by MBV process. △, untreated Al, O, Al treated by MBV process. Potentials were measured against saturated calomel electrode.

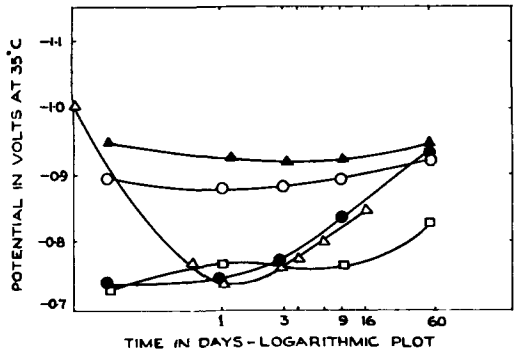

Fig. 2. Potential-time curves of aluminum treated by different pretreatment processes. •, untreated Al, □, EW process, ▲, Alrok process, O, Pylumin process, △, MBV process. Potentials were measured against saturated calomel electrode.

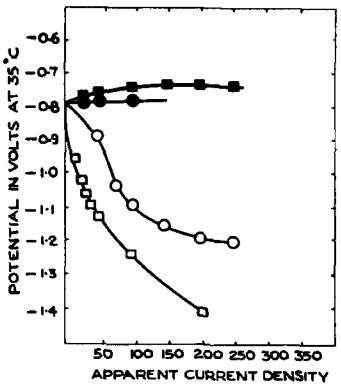

Fig. 3. Polarization curves of treated and untreated aluminum. Untreated Al, O cathodic, • anodic; MVB treated Al, □ cathodic, ■ anodic. Potentials were measured against saturated calomel electrode. Current density is in $\mu a/in.^2$.

time of immersion is, however, not so reproducible in the case of treated metal.

Potential-time curves of aluminum treated by different pretreatment processes. — Potential-time curves of aluminum treated by three more processes are given in Fig. 2 along with those of untreated metal and metal treated by MBV process.

It is seen from Fig. 1 and 2 that the rise in potential of untreated metal is not significant beyond 7 days. The initial potential of metal treated by the EW process is the same as that of untreated metal, and this potential falls at a much slower rate than that of untreated metal. The metal treated by the Alrok process gives a highly negative initial potential to start with, and there is not much change in this potential with time. Metal treated by the Pylumin process behaves similarly.

Initial potentials and changes in potential of aluminum treated by etching and polishing solutions.— An understanding of the data obtained with various passivating solutions may be facilitated if the effects of chemical treatments which involve etching, cleaning, or polishing of the surface on the potential are known. Therefore, the metal was treated by four solutions, one of which just etched the surface, the other cleaned it free of oxide film, the third one primed the surface for painting, and the last one gave a chemical polish. Results obtained are given in Table III.

It is seen from Table III that the behavior of the metal treated by any of the above methods is generally similar to that of untreated metal. The initial potential is the same as that of untreated metal, and this potential increases fairly rapidly to a more negative potential similar to untreated metal.

Polarization curves of untreated aluminum and aluminum treated by MBV process.—It is known that increased cathodic polarization of aluminum takes place when dc currents of the order of 100 μa are passed from an external source through the metal as cathode, and hardly any polarization is observed with the metal as the anode (26-28). The effect of MBV treatment on the anodic and cathodic polarization curves of aluminum is, therefore, of interest. Anodic and cathodic polarization curves of treated and untreated aluminum are compared in Fig. 3.

It is seen that the cathodic polarization curve is made much steeper by treatment, and comparatively little change is observed at the anode.

Table III. Effects of chemical treatments not involving passivation

No.	Time	Chrome pickle	Phosphoric acid wash	Acid cleaning	Chemical polishing
1	0 hr	—0.737	—0.727	—0.760	—0.767
2	1 day	—0.813	—0.769	—0.796	—0.752
3	45 days	—0.922	—0.933	—0.939	—0.887

Discussion

The fall in potential of untreated aluminum with time in the chloride medium is readily understood in terms of classical ideas on the meaning of electrode potential. It is associated with the breakdown of the protective oxide film and the final potential of —0.9 v signifies the equilibrium state between the breakdown of the oxide film by the corrosive action of chloride ions and repair of this film by oxygen present in the liquid. It is more difficult to understand the highly negative initial potential observed with metal treated by MBV, Pylumin, and Alrok processes. Passivation of a metal surface is usually accompanied by the potential becoming ennobled. Here, however, there are a number of systems where this is not the case. Mears (29) has shown, however, that, if the over-all electrode potential of a corroding metal is given by the convergence point of the polarization curve of the local anodes and cathodes (30), then instances can occur where passivity of the metal surface is accompanied by shifting of the electrode potential in the negative direction.

The greater corrosion resistance of more electronegative aluminum as compared to steel in salt solutions is believed to arise from such a mechanism. This shift of potential in the negative direction, according to Mears, arises from increased polarization of the local cathodes. When the MBV treated metal is polarized cathodically by the application of external emf (see Fig. 3), the treated metal is polarized to a much greater extent than the untreated metal at equal current densities. The extent to which the two metals are polarized anodically does not differ to a significant extent. The more negative initial potential of MBV-treated aluminum and the polarization data are, therefore, explained satisfactorily in terms of this mechanism. But, as Mears pointed out, this approach has substantial limitations. First, it may not be correct to assume that anodic and cathodic polarization curves obtained by the application of an external current reproduce the polarization behavior of the local anodes and cathodes in the absence of an applied emf. Second, the indirect methods (7, 31) that have been suggested for measuring the polarization curves of the local anodes and cathodes stipulate a number of conditions which cannot be met in the case of the present systems. Further, the changes in potential with time, e.g., rapid rise in potential of MBV treated metal to that of untreated aluminum, do not lend themselves easily to explanation on the basis of the above mechanism.

It was considered worth while, therefore, to see if the Glasstone, Laidler, and Eyring theory of rate processes (32) threw more light on the significance of such potential changes. According to this theory, the rate of the forward and reverse processes taking place at an electrode and the magnitudes of the currents flowing in the two directions as a result can be expressed in the form of an equation involving the concentration terms controlling each reaction, the specific velocity of the reaction, energy transfer coefficient, number of electrons involved in the electrode reaction, and the potential of the electrode, each of which can be measured under well-defined circumstances. The reactions taking place at each of the two electrodes constituting any one of the innumerable local cells present on a corroding metal also can be expressed in terms of such an equation. At each electrode, there is a forward and reverse reaction and there is a net flow of current. The local cells of a corroding metal are, however, short circuited through the metal and the total net current at all the local anodes equals the total net current at all the local cathodes. The two currents can, therefore, be balanced as follows:[1]

Net cathodic current from all the local cells:

$$i_1 = Z \cdot f \cdot A_c \left\{ \prod_1^{\nu i} (a_i^{\nu_i}) \cdot K_1 \cdot e^{-\alpha' Z f v/RT} - \underbrace{\prod_1^{\nu i} (a_i \nu_i) \cdot K'_1 \cdot e^{(1-\alpha')Z f v/RT}}_{\text{negligible}} \right. \quad [1]$$

where A_c = total cathodic area in cm^2, $\prod_1^{\nu i} (a_i \nu_i)$ = product of concentration terms controlling the cathodic reaction, K_1 = specific velocity of the reduction reaction in cathodic areas, α' = symmetry factor or energy transfer coefficient, Z = No. of electrons involved in the electrode reaction f = 96,500 (coulombs/mole, v = potential, R = gas constant, and T = temp °K

Net anodic current from all the local cells:

$$i_2 = A_a \cdot Zf\{(\underset{\text{negligible}}{\quad}) - \prod_1^{\nu_2^1} (a_i \cdot \nu_i) \cdot K_2^1 \cdot e^{(1-\alpha'')Z f v/RT} \quad [2]$$

where A_a = total anode area in cm^2, K_2 is the specific velocity of the oxidation reaction in anodic areas and α'' is the symmetry factor.

In the present case, potentials of the treated and untreated metal in 3% NaCl solution are all in the range of −0.7 to −1.2 v in which the anodic reaction terms of Eq. [1] and the cathodic reaction term of Eq. [2] would be negligible. Therefore, $i_1 = i_2$, where positive value denotes a cathodic current and negative value denotes anodic current, and

$$e^{-Z.v.f(\alpha'+1-\alpha'')/RT} = \frac{A_a \prod_1^{\nu_2^1} (a_i \cdot \nu_i) \cdot K_2^1}{A_c \cdot \prod_1^{\nu_1} (a_i \cdot \nu_i) K_1} \quad [3]$$

and

$$-v = \frac{RT}{Z \cdot f \cdot (\alpha' + 1 - \alpha'')} \cdot \ln \frac{A_a \prod_1^{\nu_2^1} (a_i \cdot \nu_i) \cdot K_2^1}{A_c \prod_1^{\nu_1} (a_i \cdot \nu_i) K_1} \quad [4]$$

$$-v = \frac{RT}{Z \cdot f \cdot (\alpha' + 1 - \alpha'')} \cdot \ln \frac{A_a \cdot X_2}{A_c \cdot X_1} \quad [5]$$

where

$$X_2^1 = \prod_1^{\nu_2^1} (a_i \cdot \nu_i) K_2^1 \text{ and } X_1 = \prod_1^{\nu_1} (a_i \cdot \nu_i) K_1$$

Application of Eq. [5] to the behavior of untreated and treated aluminum in chloride solutions is of interest. From the tendency of aluminum to suffer localized corrosion or pitting, it may be concluded that A_a must be small compared to A_c. From the fact that the corroding metal registers a high negative potential, it also may be concluded with the help of the above equation that $A_a \cdot X_2$ must be greater than $A_c \cdot X_1$ and X_2 must be much greater than X_1. The observed steep polarization of the metal when it is made cathodic by an external emf is in agreement with the idea of $A_c \cdot X_1$ being small. Similarly, the sluggishness with which the metal polarizes, when it is made the anode, is in agreement with the idea of $A_c \cdot X_2$ being large. The steeper cathodic polarization curve for the treated metal means that $A_c \cdot X_1$ is smaller than it was before treatment. This change is more likely to have taken place in respect to the effective area of the cathode A_c rather than in respect to the velocity factor. The effective cathodic area must, therefore, be considered to have diminished as a result of treatment. It also is seen from the above equation that when $A_c \cdot X_1$ becomes smaller the potential of the metal also falls. This is exactly what is observed in the case of the passivation treatments under study.

According to this interpretation the shift of potential of treated aluminum in the negative direction after immersion in the corroding solution arises from an increase in the anodic area, which is in conformity with the idea of breakdown of the film. The rise in potential of treated metal immediately after immersion should, according to this view, indicate an increase in the effective cathodic area, and this apparently comes to a stop when the solution has permeated all the pores of the treated metal. This approach also explains why treatments such as the EW process, which form extremely thin films similar to the naturally formed oxide films and which are practically free from pores, do not show such a tendency. In this case, the fall in potential with time is slower than that of untreated aluminum, thereby indicating that the production of anodic points is much less favored by the film formed under the conditions of this process than in the case of the natural oxide film. Observations made with specimens treated in solutions which have essentially a cleaning or smoothing effect on the metal surface are also explained. The initial potentials as well as the main trend of the potential time-curves of these specimens are parallel to the untreated metal. This shows that no film formation or conversion of the surface has taken place which is different from that which

[1] After this paper was completed, the author came across an interesting paper by M. Takahashi [*J. Electrochem. Soc. Japan*, 25, (4) E 36 1957] giving the derivation of the equations for the potential of the corroding metal on the basis of the Glasstone, Laidler, and Eyring theory of rate processes as well as the experimental verification of the same.

happened to the untreated metal during exposure to air. The final potentials of untreated aluminum and aluminum treated by the different passivation processes do not differ considerably. This nearness of these electrode potentials despite the fact that the corrosion rate of treated aluminum is much lower than that of untreated aluminum can only be understood if the factor dominating the observed potential is the ratio between the anodic and cathodic areas. As long as this ratio remains the same, the potential will not differ considerably, but the corrosion rate may be markedly minimized if both anodic and cathodic areas are diminished. This leads to the important conclusion that the factor responsible for passivation by these treatments is the diminution in the cathodic area. The tendency of aluminum to be subjected to localized corrosion or pitting may, therefore, be expected to be minimized by the chemical oxidation processes investigated, unlike anodic inhibitors, e.g., chromates and phosphates.

Acknowledgment

Thanks of the author are due to Dr. K. S. G. Doss, Director of the Central Electrochemical Research Institute, for his valuable suggestions in regard to the discussions in this paper.

Manuscript received Nov. 12, 1957.

Any discussion of this paper will appear in a Discussion Section to be published in the December 1959 JOURNAL.

REFERENCES

1. O. Gatty and E. C. R. Spooner, "The Electrode Potential Behaviour of Corroding Metals in Aqueous Solutions," Clarendon Press, Oxford (1938).
2. U. R. Evans, "Metallic Corrosion, Passivity and Protection," Edward Arnold and Co., London (1946).
3. H. H. Uhlig, Editor, "Corrosion Handbook," John Wiley & Sons, Inc., New York (1948).
4. Internationales Kolloquim Uber Die Passivitat Der Metalle, Heiligenberg, 1957.
5. M. Cohen, *Corrosion*, **9**, 372 (1953).
6. M. J. Pryor, *This Journal*, **101**, 141 (1954).
7. T. P. May and F. L. LaQue, *Corrosion*, **10**, 91 (1954).
8. H. C. Gatos, *ibid.*, **12**, 23 (1956).
9. S. Wernick and R. Pinner, "Surface Treatment and Finishing of Aluminium and Its Alloys," Robert Draper Ltd., England (1956).
10. W. E. Pocock, *Metal Finishing*, **52**, 49 (Dec. 1954).
11. H. A. Holden, *Sheet Metal Ind.*, **23**, 1539 (1946).
12. R. P. Drysdale, Trans. Inst. *Metal Finishing*, **31**, 23 (1954).
13. R. Kerr, *J. Soc. Chem. Ind.*, **65**, 101 (1946).
14. S. C. Britton and R. M. Angles, *J. Appl. Chem.*, **4**, 351 (1954).
15. A.S.T.M. Standards, 1944, B 117-44T, (1), 1843.
16. Aluminium Development Association Information Bulletin No. 13 "Surface Finishing of Aluminium."
17. G. Eckert, Hauszeit *V.A.W. Erftwerk A.G. Aluminium*, **3**, 349 (1931).
18. W. Helling and H. Neunzig, *Aluminium*, **20**, 536 (1938).
19. Pyrene Co., Ltd., British Pat. 441,088 (1936).
20. S. Wernick and R. Pinner, *op. cit.*, p. 189.
21. H. Bengston, *Trans. Electrochem. Soc.*, **88**, 307 (1945).
22. U.S. Army Specn. 98-20007.
23. Reynolds Metal Co., "Finishes for Aluminium" Sec. 1 (1946).
24. Aluminium Co., of America, British Pat. 659,747 (1951).
25. D. M. Brasher, *Electroplating and Metal Finishing*, **9**, 280 (1956).
26. R. H. Brown and R. B. Mears, *J. (and Trans.) Electrochem. Soc.*, **94**, 495 (1948).
27. R. Ergang, H. Masing, and M. S. Mohling, *Z. Elektrochem.*, 56 (1952).
28. M. J. Pryor and D. S. Keir, *This Journal*, **102**, 605 (1955).
29. R. B. Mears and R. H. Brown, *ibid.*, **97**, 75 (1950).
30. U. R. Evans, *J. Franklin Inst.*, **208**, 52 (1929).
31. W. J. Schwerdtfeger and O. N. Mcdorman, *This Journal*, **99**, 407 (1952).
32. S. Glasstone, K. J. Laidler, and H. Eyring, "Theory of Rate Processes," McGraw Hill Book Co., New York (1941).

Mechanism of Electrodeposition of Nickel from Liquid Ammonia Solutions of Spin-Free Nickel(II) Complexes

George W. Watt and David A. Hazlehurst

Department of Chemistry, The University of Texas, Austin, Texas

ABSTRACT

Data on cathode current efficiencies for the electrolysis of solutions of $[Ni(NH_3)_6]^{2+}$, $[Ni(en)_3]^{2+}$, and $[Ni(dn)_2]^{2+}$ in the presence of Br^-, I^-, and SCN^- are interpreted on the basis of an S_N2 mechanism in which the rate-controlling step is most probably dependent on the translabilizing effect of the entering ligand that is involved in the formation of an initial transition state complex.

Continued interest in the electrodeposition of metals from nonaqueous media (1-5) from both theoretical and practical viewpoints has prompted us to re-examine certain data that were obtained several years ago. It was observed that deposition from ammonia solutions of hexamminenickel(II) bromide, trisethylenediaminenickel(II) bromide, and bisdiethylenetriaminenickel(II) bromide occurred at negligibly low rates; upon addition of the potassium salts of Br^-, I^-, and SCN^-, however, deposition occurred at markedly increased rates that were dependent on the identity of the added anionic ligands. It is of interest to consider these data in the light of generalizations and mechanisms proposed by Lyons

(6-8) with reference to deposition from aqueous solutions, and to propose an alternative mechanism for the genesis of a transition state complex.

Experimental

Materials.—Hexamminenickel(II) bromide (calculated: Br^-, 49.9; found: Br^-, 50.0) was prepared as described elsewhere (9). Trisethylenediaminenickel(II) bromide 1-hydrate was prepared as described by Werner and Megerle (10); the anhydrous salt (calculated: Br^-, 39.9; found: Br^-, 40.1) resulted upon heating the 1-hydrate for several hours at 100°-105°. Similarly, bisdiethylenetriaminenickel (II) bromide (calculated: Br^-, 37.6; found: Br^-, 37.6) was formed from the corresponding 1-hydrate (11).

Equipment and procedures.—The equipment employed was essentially the same as that described by Booth and Merlub-Sobel (12) except that the design of the electrode holders was such that the electrodes could be removed readily for direct weighing before and after electrolysis. Nickel anodes (Ni, 99.5) and bright platinum cathodes were used in all of the experiments reported here. The electrical circuit included a silver coulometer and otherwise was conventional in all respects.

The electrolysis cell was predried, thoroughly, and strictly anhydrous conditions were maintained in all experiments. The solvent ammonia was dried over sodium amide and, just prior to use, was bubbled through a solution of potassium in ammonia. The ammonia was condensed at −45°, after which the temperature was raised to and maintained at a temperature just slightly below the normal boiling point of the solvent (−33.5°). Following electrolysis, the ammonia solution was siphoned from the cell and the electrodes were washed, dried, and weighed. After evaporation of the solvent from the combined electrolytic solution and washings, Ni^{2+} could be determined gravimetrically by the dimethylglyoxime method.

Experimental data.—In a series of experiments involving the cationic nickel(II) complexes indicated above, the total solution volume was 75 ml, the concentration of the nickel(II) salt was 0.02*M*, the concentration of the added potassium salts was 0.1*M*, and the current density was 0.54 ± 0.05 ma/cm^2. Other pertinent data are included in Table I.

Table I. Electrolysis of liquid ammonia solutions of nickel(II) salts

	Added salt	Potential, v	Time, hr	Cathode current efficiency, %
$[Ni(NH_3)_6]Br_2$	KBr	2.85	3.0	3
	KI	1.57	3.0	80
	KSCN	1.50	3.0	108
$[Ni(en)_3]Br_2$	KBr	3.00	2.0	9
	KI	1.72	2.1	75
	KSCN	1.48	3.0	105
$[Ni(dn)_2]Br_2$	KBr	2.80	1.0	12
	KI	1.88	1.5	67
	KSCN	1.55	3.0	109

Although bright adherent deposits of nickel were obtained in the electrolysis of ammonia solutions of tetramminenickel(II) thiocyanate (13), the deposits in the experiments reported here were less satisfactory but nevertheless sufficiently adherent not to introduce appreciable errors in determining the total nickel deposited by direct weighing of the cathodes. Neither microscopic examination nor electron photomicrographs served to reveal any consistent characteristics of the deposits as a function of the ligands employed.

Discussion

With reference to the electrodeposition of metals from cationic complexes, Vlcek (14) has proposed that the essential step involves the formation of a zerovalent species, after which metal-ligand bond breaking leaves the free metal as a deposit on the cathode. If such a mechanism were operative, it is not immediately apparent in the present case why cathode current efficiencies should be influenced so profoundly by specific anionic ligands.

Lyons (7) suggested a primary heterolytic dissociation, or S_N1 mechanism[1] in which metal-ligand bond breaking provides an available bonding orbital for the establishment of a partially metallic bond with the cathode lattice.

We wish to propose, largely on the basis of the results reported above, that there is an alternative and more probable mechanism. The nickel(II) complexes used in the present studies are all of the octahedral sp^3d^2 or spin-free type. If the observed trends in cathode current efficiencies may be assumed to have even qualitative kinetic significance, it seems reasonable to assume that the primary reaction involves an initial nucleophilic attack by the added anions, e.g., Br^-, I^-, and SCN^-. Thus, it is assumed that an S_N2 mechanism is operative, that the coordination number of nickel in the transition state complex is seven, and that rupture of one of the original metal-ligand bonds occurs trans to the incoming anionic ligand. Accordingly, a bonding orbital is made available and the subsequent events may well occur as pictured by Lyons (7). Irrespective of the stereochemical configuration of the transition state complex and regardless of whether cis or trans attack is involved, the proposed S_N2 mechanism suggests two possible rate-limiting steps both of which must take into account the fact that the neutral solvent molecules as incoming ligands are potentially competitive with the added anionic ligands. In view of the data in Table I, however, it seems apparent that the solvent molecule is not thus competitive.

First, the formation of a transition state complex may be rate limiting and dependent on the relative nucleophilic character of the incoming ligands. From Table I it may be seen that the increasing order of cathode current efficiencies for the three added anionic ligands is $Br^- < I^- < SCN^-$. Although still of questionable status (15) and in any event probably not quantitatively applicable to ammonia solutions, the order of nucleophilic constants (16, 17) for these

[1] The nomenclature employed herein is that recommended by Basolo and Pearson (15).

ions is $Br^- < SCN^- < I^-$. A second and more attractive alternative would assume that bond breaking is the rate-limiting step; in this case the observed rates should correspond to the relative translabilizing effects of the entering ligands. If we may assume the same order for octahedral as for square planar complexes (18), i.e., $NH_3 < Br^- < I^- < SCN^-$ (where only the relative position of the latter is in doubt, but nevertheless reasonable) then the correlation with the data of Table I is self-evident.

It is our intention to provide further experimental data bearing on this question.

Acknowledgments

This work was supported in part by the U. S. Atomic Energy Commission, Contract AT-(40-1)-1639. The nickel anodes used in these studies were supplied by the International Nickel Co.

Manuscript received Sept. 3, 1958.

Any discussion of this paper will appear in a Discussion Section to be published in the December 1959 JOURNAL.

REFERENCES

1. A. Brenner, *This Journal*, **103**, 652 (1956).
2. J. H. Connor and A. Brenner, *ibid.*, **103**, 657 (1956).
3. W. E. Reid, Jr., J. M. Bish, and A. Brenner, *ibid.*, **104**, 21 (1957).
4. G. B. Wood and A. Brenner, *ibid.*, **104**, 29 (1957).
5. J. H. Connor, W. E. Reid, Jr., and G. B. Wood, *ibid.*, **104**, 38 (1957).
6. E. H. Lyons, Jr., *ibid.*, **101**, 363 (1954).
7. E. H. Lyons, Jr., *ibid.*, **101**, 376 (1954).
8. E. H. Lyons, Jr., J. C. Bailar, Jr., and H. A. Laitinen, *ibid.*, **101**, 410 (1954).
9. G. W. Watt, "Inorganic Syntheses," Vol. 3, p. 194, McGraw-Hill Book Company, Inc., New York (1950).
10. A. Werner and W. Megerle, *Z. anorg. Chem.*, **21**, 213 (1899).
11. J. G. Breckenridge, *Can. J. Research*, **26B**, 11 (1948).
12. H. S. Booth and M. Merlub-Sobel, *J. Phys. Chem.*, **35**, 3303 (1931).
13. G. W. Watt and D. A. Hazlehurst, Unpublished work.
14. A. A. Vlcek, *Nature*, **177**, 1043 (1956); *Z. Elektrochem.*, **61**, 1014 (1957).
15. F. Basolo and R. G. Pearson, "Mechanisms of Inorganic Reactions," John Wiley & Sons, Inc., New York (1958).
16. C. G. Swain and C. B. Scott, *J. Am. Chem. Soc.*, **75**, 141 (1953).
17. J. O. Edwards, *ibid.*, **76**, 1540 (1954).
18. J. Chatt, L. A. Duncanson, and L. M. Venanzi, *J. Chem. Soc.*, **1955**, 4456.

Electrodeposition of Molybdenum

T. T. Campbell

U. S. Bureau of Mines, Albany, Oregon

ABSTRACT

Electrodeposition studies performed at the Northwest Electrodevelopment Laboratory of the U. S. Bureau of Mines, Albany, Oregon, are described. Research was directed toward the electrodeposition of molybdenum from nonaqueous media such as liquid ammonia, formamide, acetamide, hydrazine, and other organic solvents and the preparation of pure anhydrous molybdenum halides. While thin plates of molybdenum were obtained, the growth of massive deposits was not realized.

The requirements of modern technology for materials possessing high temperature strength and corrosion resistance properties has, in recent years, stimulated an intensified ilnterest in molybdenum.

Molybdenum is produced commercially by hydrogen reduction of molybdenum oxides. The metal powder resulting from this treatment is not of uniform quality and purity although it can be converted into usable forms by powder metallurgy techniques.

While the literature reports many claims for the successful electrodeposition of Mo (1), thorough analyses of and attempts by later investigators to duplicate these claims lead to the conclusion that the only practicable method of electrodepositing molybdenum is from the fused salt bath recently developed by Brenner and Senderoff of the U. S. Bureau of Standards (2). The prevailing opinion is that electrodeposition of pure Mo from aqueous solutions is unlikely. On the other hand, the use of organic solvents, fused salt baths, and other nonaqueous solvents such as hydrazine or liquid ammonia as media for the electrodeposition of Mo has had only limited attention. Efforts to electrodeposit Mo at the Albany station of the U. S. Bureau of Mines were restricted mainly to studies in nonaqueous solvents since a preliminary period spent in duplicating other published methods proved fruitless.

Discussion

It is doubtful whether simple ions as such are present in solutions containing Mo compounds, either because of reactions occurring between the solutes and solvents or because of the tendency of Mo ions to form polyions by polymerisation and condensation reactions. In addition, Mo compounds may disproportionate to give complex compounds in which the metal ion may exist in any of its oxidation states. It is probable that only complex systems result during efforts to electrodeposit Mo, regardless of the media used.

Studies of electrode potentials in fused salt baths carried out by Brenner and Senderoff (2) indicate that the reduction of Mo to trivalent oxides proceeds at a more noble potential than does reduction to

metal. The same situation apparently holds true either in aqueous or organic solutions, and on this basis it would seem that oxygen or oxygen containing compounds must be absent from the electrolytic system in order to obtain the metal. Reduction of Mo ions *in situ* by hydrogen, postulated as a mechanism in chromium deposition, does not occur; this fact, and the low hydrogen overvoltage of Mo (3) are major factors preventing deposition of Mo from aqueous systems.

While the metal can be deposited from the fused salt baths developed by Brenner and Senderoff, the utility of their techniques from an economic standpoint does not appear promising. The procedures outlined offer formidable difficulties such as operation of corrosive fused salt baths at temperatures ranging from 600° to 900°C with the necessity of complete exclusion of air or moisture from the cell. While these baths presumably could be useful for specialized electroplating or electroforming operations, it is doubtful if they could be adapted to widespread general usage.

On the basis of the foregoing discussion, it appears obvious that a practicable solution to the problem of Mo deposition is needed. The application of nonaqueous solvents other than fused salt baths to the problem of Mo deposition offers many interesting possibilities: (*a*) studies can be made on systems from which oxygen or oxygen containing compounds can be completely excluded; (*b*) exploration in a comparatively new and untried field of research is possible; and (c) if successful, research of this type may provide a new approach for the electrodeposition of other rare and refractory metals.

Experimental Procedures and Apparatus

For reasons previously expressed, it was considered desirable to conduct tests in systems which completely excluded oxygen either in the solutes or the solvents. This program necessitated careful examination of methods for preparing Mo compounds. Much of the work was restricted to molybdenum chlorides and bromides since these compounds proved reasonably soluble in many of the solvents studied. Most of the solvents had relatively high dielectric constants although solvents were not excluded from study even when the dielectric constant was of a rather low order.

Since the majority of the work carried out in this study was exploratory in nature, the equipment and procedures utilized were varied in nature. In general, Pyrex beakers of 250-500 ml capacity were used as cells, although small rectangular glass cells (800 ml capacity), U tube cells, and 3-necked Pyrex flasks were utilized during various phases of the investigation. Those tests carried out under an inert atmosphere usually were carried out in 3-necked flasks or in Pyrex tubes sealed with rubber stoppers. Argon or helium atmospheres were maintained above those systems which were sensitive to carbon dioxide, oxygen, or moisture. The liquid ammonia study was carried out in equipment similar to that described by Merlub-Sobel (4). Liquid ammonia cells were operated at either low temperatures (below −33°C) and atmospheric pressure, or at room temperature when a high pressure (above 145 psig) cell was used. After initial study in the field of aqueous electrolysis proved unsuccessful, the solubility of various Mo compounds in organic and other nonaqueous solvents was determined. Quantitative solubility tests were carried out in a temperature controlled (±1°C) water bath in the 25°-100°C range and in an ondina oil bath (a USP grade mineral oil) for temperatures up to 200°C. The Mo compounds were added in 100-mg quantities to 50 ml of the solvent until insoluble material remained for at least 1 hr. The temperature was increased by 20°C increments with periodic additions of solute until the highest practicable operating temperature for the particular solvent was reached. The maximum solubility of the solutes over a wide temperature range was obtained by this procedure. Qualitative data on solubilities were also obtained on many of the systems studied. Since solubility data of Mo compounds in nonaqueous solvents are not generally available in the literature, the results of this work are presented in Table I.

Conductivity tests were made on all of the solvents in which Mo compounds were reasonably soluble. Column 5 of Table I indicates those solvents which were conducting or nonconducting, along with other pertinent remarks. Anodes and cathodes of graphite, copper, iron, platinum, molybdenum, stainless steel, lead, etc., were used, the particular electrode material used depending on the type of solvent employed. A Beckman (Model H-2) *p*H meter was used to determine *p*H values during the course of the study. A 50 amp-24 v capacity selenium rectifier was used as a source of d-c current.

Electrolytic tests generally covered a wide range of current densities and temperatures over varying periods of time. The course of electrolyses was followed by observation of current, voltage, and *p*H readings. The effectiveness of any particular system for Mo deposition was determined by visual inspection of the cathode. Whenever metallic deposits were obtained they were subjected to x-ray diffraction study and to spectrographic analyses. While no massive deposits of Mo were obtained from any of the systems studied, thin deposits of Mo and alloys of Mo with Fe, Pb, or Pt were readily obtained. The usual cathode products were lower oxides, hydroxides, or other reduced compounds of Mo.

Because of the great number of systems covered during this study and the negative character of some of the results, it is impracticable to show all the data obtained. For this reason, Table II shows only the data for those experiments which either gave thin deposits of pure Mo or alloys of Mo with other metals.

Preparation and Handling of Mo Halides

Since much of the work described utilized either the chlorides or bromides of Mo as solutes, the preparation of these compounds required detailed attention. The preparation of the dichloride and dibromide of Mo posed no particular problem as disproportionation of molybdenum tribromide in a 2-in. Vycor tube was found to proceed smoothly at 600°C to give molybdenum dibromide and disproportiona-

Table I. Solubility of Mo Compounds in water and non aqueous solvents

Compound	Solvent	Temp, °C	Solubility g/l	Remarks
MoS_2	Alkaline polysulfide	—	51.5	Low solubility
MoS_2	Formamide	180	Insol.	
MoS_2	Acetamide	200	Insol.	
MoS_2	Triethanolamine	215	50	
MoS_2	Pyridine hydrochloride	70	v.sl.s.	
MoS_3	Alkaline polysulfide	—	>50	Low solubility
$MoBr_2$	Water	To 100	Insol.	
$MoBr_2$	Carbon tetrachloride	Room	Insol.	
$MoBr_2$	Hydrazine hydrochloride (65%) Water (35%)	Room	>1.0	
$MoBr_2$	Water (75%) Hydrazine (25%)	Room		Violent reaction
$MoBr_2$	Ethylene diamine	Room	Sol.	Visible reaction
$MoBr_2$	Cyclohexanol	Room	Insol.	Suspension formed
$MoBr_2$	Aniline	Room		
$MoBr_3$	Hydrazine (95%)	25-30	—	Violent reaction
$MoBr_3$	Cyclohexanol	Room	51.5	Suspension formed
$MoBr_3$	Water (50%) Tartaric acid (50%)	Room	51.5	Conducting
$MoBr_3$	Dextrose (50%) Water (50%)	Room	51.5	Conducting
$MoBr_3$	Tartaric acid	170	51.5	Conducting
$MoBr_3$	Liquid ammonia	—35	—	Reaction to give solid ppt.
$MoBr_3$	Liquid ammonia Ammonium nitrate eutectic	20	10	Nonconducting
$MoCl_3$	Pyridine hydrochloride	70	~570	Soluble with reaction to give clear amber solution that solidifies at 35°-40°C conducting
$MoCl_3$	Liquid ammonia Diethyl amine	—35	Insol.	
$MoCl_3$	Liquid ammonia	—35	15-20	Some reaction to give solid ppt.
$MoCl_3$	Ethyl chloride (10 ml) Benzene (20 ml)	Room	10	
$MoCl_3$	Liquid ammonia Ammonium nitrate eutectic	20	10	Nonconducting
$MoCl_3$	Aniline (10 ml) Ethyl bromide (5 ml)	Room	10	Conducting
$MoCl_5$	Carbon tetrachloride	Room	51.5	Conducting
$MoCl_5$	Pyridine hydrochloride	70	~400	Soluble with reaction to give clear brown solution
$MoCl_5$	Methyl alcohol	Room	v.s.	Soluble with reaction to give conducting solution
$MoCl_5$	Ethyl alcohol	Room	v.s.	Soluble with reaction to give conducting solution
$MoCl_5$	Liquid ammonia	—35	—	Reaction to give solid ppt.
$MoCl_5$	Aniline	Room	<5	Nonconducting
$MoCl_5$	Ethyl bromide	Room	16	Nonconducting
$MoCl_5$	Benzene	Room	<5	Nonconducting
$MoCl_5$	Ethylene diamine	Room	—	Reaction
$MoCl_5$	Hydrazine (95%)	Room	—	Violent reaction
$MoCl_5$	Acetone	Room	Sol.	Reaction to give green solution, conducting
$MoCl_5$	Acetic anhydride (10 ml) Formamide (15 ml)	Room	300	Conducting
$MoCl_5$	Aniline (10 ml) Ethyl bromide (5 ml)	Room	50	Low conductivity
$MoCl_5$	Liquid ammonia Ammonium nitrate Eutectic	20	40	Nonconducting
$MoCl_5$	Phenyl ethyl bromide	150-200	180-200	Conducting
$MoCl_5$	Pyridine hydrobromide	40	~60	Soluble with reaction to give red solution
$MoCl_5$	Pyridine (10 ml) Phenol (10 ml)	50	~100	Soluble with reaction to give green solution
$MoCl_5$	Ethyl chloride (10 ml) Benzene (20 ml)	Room	10	Low conductivity
$MoCl_5$	Ethyl bromide (10 ml) Benzene (20 ml)	Room	~60	Low conductivity
Na_2MoO_4	Formamide	150	200	Solidification-conducting
Na_2MoO_4	Acetamide	203	Insol.	Conducting
Na_2MoO_4	Triethanolamine	215	>50	Low conductivity
Na_2MoO_4	Pyridine hydrochloride	70	~38	
$(NH_4)_2MoO_4$	Formamide	180	~200	Solidification-conducting
$(NH_4)_2MoO_4$	Acetamide	170	~100	Conducting
$(NH_4)_2MoO_4$	Triethanolamine	170	~250	Conducting
$(NH_4)_2MoO_4$	Pyridine hydrochloride	70-100	~95	Soluble with reaction, pyridine decomp. at 100°C, conducting

Key: v.s., very soluble, in excess of 50 g/l; s., soluble, 10-50 g/l; sl.s., slightly soluble, 1-10 g/l; insol., <1 g/l.

Table II. Electrolytic test data on the electrodeposition of Mo

Solvent	Vol, ml	Solute	Weight, g	E, v	I, amp	Cathode current density, amp/ft²	Temp, °C	Anode	Cathode	Remarks
Acetic acid	108	MoO_3	1	Max 15	2 9-29	47-470	18-80	Graphite	Copper	Slight deposit at low CD. At higher CD's thin deposits of metal, then oxides. pH = 5.8-6.4
Ammonium hydroxide (concentrate)	100									
Acetamide	100	$MoCl_5$	1	—	—	465	120-130	Platinum	Copper	Metallic appearing deposit
Acetamide	100	$MoCl_5$	2	—	—	93	105-150 90-130	Platinum	Copper	Dark metal deposit. Heating indicates Mo present
Acetamide	200	$MoCl_5$	7	—	—	74.3-557	80-155	Platinum	Copper	Metallic deposit covered with oxide
Acetamide	100	$MoCl_5$	7	—	—	56	80-115	Molybdenum	Copper	Black oxides with faint blush of metal. Slight attack on anode
Acetamide	500	$MoCl_5$	25	7.5	0.75	0.35	80	Graphite	Copper	Metallic blush
Acetamide	200	$MoCl_5$	1-7	—	—	74.5-557	80-155	Iron	Copper	Thin metallic deposits
Acetamide	116	$MoCl_5$	7	—	—	46.5-111.5	100	Platinum	Copper	Pt-Mo deposit
Acetamide	258	$MoCl_5$	23.6	4.0	1.11	20	80-90	Graphite	Copper	Metal blush at 4 hr, nonadherent deposit on cathode
Hydrazine	10									
Ethylene diamine	200									
Acetamide	195.6	$MoCl_5$	20	3.8	0.5	1.03	90	Graphite	Copper	Metal blush on back of cathode
Hydrazine	10									
Ethylene diamine	100									
Acetamide	300	$MoCl_5$	23.6	4.0	1.1	2.0	80-90	Graphite	Copper	Metal blush after 4 hr
Hydrazine	10									
Ethylene diamine	200									
Acetamide	86.3	$MoCl_5$	5	5.0-7.0	0.5	102	75-80	Graphite	Copper	Metallic blush formed. Was displaced by dense black film
Pyridine	10									
Acetamide	432	$MoCl_5$	25	0.75	7.5	9.39	80	Graphite	Copper	Metallic blush on one side
Pyridine	300									Metallic growth on edges
Acetamide	100	$MoCl_5$	5	5-7	0.5	173	75-80	Graphite	Copper	Metal blush replaced by black film
Pyridine	10									
Formamide	100	$MoCl_5$	2.4	—	—	140-460	80-120	Graphite	Copper	Blushes on metal and oxides. Higher CD produces dull deposit
Formamide	100	Na_2MoO_4	10	—	—	74-148	40-140	Platinum	Copper	Metallic blush. Pt-Mo alloy
Formamide	100	MoO_3	10	—	—	18.5-371	25-110	Platinum	Copper	Metal blush on edges of cathode
Formamide	100	$(NH_4)_2MoO_4$	10	—	—	186-372	23-90	Platinum	Copper	Thin deposit covering cathode
Formamide	50	$MoCl_5$	1	—	—	37-613	30-89	Graphite	Copper	Few oxides. Faint blush of metal
Water	5									
Formamide	400	$MoCl_5$	15	0.1	1.5	1.6	35	Graphite	Stainless steel	Metallic blush covered by spongy black deposit
Pyradine	100									
Hydrazine	5									
Formamide	100	Na_2MoO_4	5	10	1	46.5	—	Graphite	Copper	Thin bright metallic-like deposit
Versene	10									
Formamide	100	Na_2MoO_4	5	7.5-8.5	0.5	23.2	25-35	Graphite	Copper	Light metallic deposit on edges of cathode
Versene	10									
Formamide	100	Na_2MoO_4	5	9-18	1.5	69.6	25-65	Graphite	Copper	Thin metallic plate on face of cathode
Formamide	100	Na_2MoO_4	5	11	1	46.4	25-55	Graphite	Copper	Same as above run
Versene	10									
Formamide	100	Na_2MoO_4	5	9-18	2	92.9	35-95	Graphite	Copper	Metal blush
Versene	10									
Formamide	100	MoO_3	5	5	1	46.5	25-60	Graphite	Copper	Bluish cast. Metallic deposit covered with oxides
Versene reg.	10	85%								
Formamide	100	MoO_3	5	5	2	92.9	25-85	Graphite	Copper	Deposit similar as previous run
Versene reg.	10	85%								
Formamide	100	MoO_3	5	7-15	3	139.5	25-105	Graphite	Copper	No metal deposit. Temp. probably too high
Versene reg.	10	85%								
Glycol	500	$Na_2MoO_4 \cdot 2H_2O$	17.5	20	—	3.6	20	Iron	Copper	Thin gray metallic deposit
Glycol	500	$Na_2MoO_4 \cdot 2H_2O$	17.5	3.5	—	19	80-112	Iron	Copper	Gray deposit mostly iron. Some Mo
Hydrazine	25	$MoCl_5$	5	2.4	0.7	100	22	Stainless steel	Copper	Metal blush on Cu cathode
Ammonium hydroxide (concentrate)	25									
Hydrazine	25	$MoCl_5$	5	2.4	0.7	101	22	Graphite	Copper	Metal blush
Ammonium hydroxide (concentrate	25									
Water	170	H_2MoO_4	320	—	—	185-465	22-55	Lead	Copper	Thin Pb-Mo alloy deposit
Sulfuric acid (concentrate)	1665	85%								
Water	200	$N_2H_4 \cdot 2HCl$	20	2.1-3.0	0.5-3.3	18-108	20-50	Copper	Stainless steel	Thin metallic deposit on cathode
		MoO_3	8							
		NH_4Cl	20							
Water	100	$N_2H_4 \cdot 2HCl$	10	2.0	2.4	—	22	Copper	Stainless steel	Metal blush on cathode
		MoO_3	8							
		NH_4Cl	20							
Water	100	MoO_3	8	2.4	2.0	—	22	Copper	Stainless steel	Metal blush
		NH_4Cl	20							
		$N_2H_4 \cdot 2HCl$	10							
Water	500	KOH	50	3.5	—	20	45-50	Graphite	Copper	Metal blush on cathode
		$Na_2MoO_4 \cdot 2H_2O$	100							
Water	500	$Na_3C_6H_5O_7 \cdot 2H_2O$	44	4	—	93	26-44	Iron	Copper	Fe-Mo alloy
		$Na_2MoO_4 \cdot 2H_2O$	36.5							
		Na_2SO_4	14							
Water	500	$Na_3C_6H_5O_7 \cdot 2H_2O$	44	7	—	1.85	30-66	Iron	Copper	Fe-Mo alloy
		$Na_2MoO_4 \cdot 2H_2O$	36.5							
		Na_2SO_4	14							
Water	500	$Na_3C_6H_5O_7 \cdot 2H_2O$	44	4	—	93	26-40	Graphite	Copper	Bluish black metallic deposit
		$Na_2MoO_4 \cdot 2H_2O$	36.5							
		Na_2SO_4	14							
Water	500	$Na_3C_6H_5O_7 \cdot 2H_2O$	44	20	—	93	28-52	Graphite	Copper	Bluish black metallic deposit
		$Na_2MoO_4 \cdot 2H_2O$	36.5							
		Na_2SO_4	14							
Water	500	NaOH	120	2.0	—	90	50-55	Iron	Copper	Thin gray metallic deposit
		$Na_2MoO_4 \cdot 2H_2O$	50							
Water	500	NaOH	120	3.25	—	180	20-40	Iron	Copper	Thin gray metallic deposit
		$Na_2MoO_4 \cdot 2H_2O$	50							
Water	500	NaOH	120	5.0	—	360	20-65	Iron	Copper	Thin gray metallic deposit
		$Na_2MoO_4 \cdot 2H_2O$	50							
Water	50	MoO_3	5	6.2-14	8.2-16.3	70-300	28-85	Graphite	Copper	No massive deposits. Only thin plates. pH = 5.5-7.0
Acetic acid	10	$KC_2H_3O_2$	50							
		$NH_4C_2H_3O_2$	50							
Water	130	$KC_2H_3O_2$	100	—	—	90-180	22-72	Graphite	Copper	Metal blushes obtained at low CD's. Oxides only at higher CD. pH = 5.5-6.75
Acetic acid	50	MoO_3	5							
Water	50	$NaC_2H_3O_2$	20	—	—	18-300	20-75	Lead	Copper	No deposit at low CD
Acetic acid	36	MoO_3	5							Lead deposits at higher CD along with Mo.pH = 4-5
Water	200	NH_4Cl	20	2.1-3.0	0.5-3.3	18-108	22-50	Graphite	Stainless steel	Metal blush on cathode
Hydrazine hydrochloride	20	MoO_3	8							
Water	100	MoO_3	8	1.7-2.4	2.0-2.4	—	22-70	Stainless steel	Copper	Metal blush
Hydrazine hydrochloride	10	NH_4Cl	20							
Water	100	MoO_3	1	2.4	0.5	—	22	Stainless steel	Graphite	Very thin metal blush
Hydrazine hydrochloride	20									

tion of molybdenum trichloride at 600°-650°C gave good yields of molybdenum dichloride.

Direct chlorination of Mo powder at 350°-400°C was found to give a product whose major constituent was the pentachloride. The product almost always contained some unreacted metal powder and small amounts of lower valent chlorides. Direct chlorination of molybdenum disulfide in a Ni-lined vertical shaft type chlorinator at 500°C was attempted. Pure molybdenum pentachloride could not be isolated by this method. The product was contaminated with molybdenum compounds that contained sulfur (Mo_2S_3) which tended either to sublime along with the molybdenum pentachloride or were carried over by entrainment. Efforts to free the molybdenum pentachloride of sulfur compounds by sublimation at 280°C were unsuccessful.

Molybdenum trichloride was prepared by the reaction of molybdenum pentachloride with powdered molybdenum at 350°C as shown in the equation below:

$$3MoCl_5 + 2Mo \xrightarrow{350°C} 5MoCl_3$$

Direct bromination of Mo powder at 300°-350°C produced a mixture of molybdenum tribromide and molybdenum tetrabromide; however, analyses indicated the product to be primarily tribromide.

With the exception of the dibromides, tribromides, and the dichlorides, the halides of molybdenum are all hygroscopic, sensitive to oxygen and moisture in the air, and form oxycompounds readily.

The preparation of definite compounds was not successful except in the case of the divalent halides; in all other cases the products were contaminated to some extent with unreacted metal powder or were a mixture of tri, tetra, and pentavalent halides.

In order to prevent the formation of oxy compounds, it was necessary to exercise extreme precautions while transferring the halides from the reaction tubes to storage vessels and finally to the electrolytic cells. Large rubber transfer tubes, filled with argon gas, were used at all times to prevent air contamination of the halides. The prepared halides were stored in bottles under an argon atmosphere and sealed with polyethylene tape which was in turn paraffin covered. Avoidance of these procedures inevitably led to rapid contamination of the halides and the formation of oxy compounds.

Conclusions

The inability to obtain pure massive Mo deposits from either aqueous or nonaqueous systems containing oxygen compounds probably is caused in part by the low overvoltage of hydrogen on Mo and by the fact that deposition of oxides occurs at a more noble potential than does reduction to metal. While many thin plates of Mo were obtained during this study, once the cathode was covered with a thin film of Mo, the following situations developed: (*a*) passivation set in, (*b*) hydrogen, nitrogen, or ammonia evolved at the cathode, (c) lower oxides, hydroxides, or other reduced compounds continued to deposit at the cathode.

In several instances, alloys of Mo with Fe, Pt, or Pb were obtained; the source of the alloying agent in most instances originated from the anode.

Reduction of molybdenum ions to metal *in situ* by hydrogen, postulated as a possible mechanism for Cr deposition, does not seem to occur. Recovery and examination of the Mo salts, after evaporation of the solvents, indicated that Mo halides readily form a wide variety of complex compounds with nonaqueous solvents. It is doubtful if simple molybdenum ions were present in any of the systems studied.

Both qualitative and quantitative solubility data for a number of Mo compounds in a variety of organic solvents are shown.

While massive deposits of Mo were not obtained, the results obtained in this study are encouraging. The application of much higher current densities than those reported in this study, coupled with more stringent atmosphere control, may well provide a means toward the electrodeposition of massive Mo.

The use of nonaqueous solvents in conjunction with anhydrous Mo compounds, while faced with serious difficulties, offers an interesting and challenging approach to a very difficult problem.

Manuscript received April 13, 1956. This paper was prepared for delivery before the San Francisco Meeting, April 29-May 3, 1956.

Any discussion of this paper will appear in a Discussion Section to be published in the December 1959 JOURNAL.

REFERENCES

1. T. T. Campbell and A. Jones, Information Circular 7723, U. S. Dept. of Interior, July 1955.
2. A. Brenner and S. Sanderoff, *This Journal*, **101**, 16, 33 (1954).
3. J. O. Bockris, *Trans. Faraday Soc.*, **43**, 417 (1947).
4. H. S. Booth and M. Merlub-Sobel, *J. Phys. Chem.*, **35**, 3303 (1931).

Microfurnace for Thermal Microscopy and Studies at High Temperatures

W. A. Lambertson and G. Lewis

Research and Development Division, The Carborundum Company, Niagara Falls, New York

ABSTRACT

A small laboratory furnace is described for use in high-temperature microscopy and for determining chemical compatibility, wetting, sintering, and temperatures of apparent melting up to 3000°C (5433°F). The furnace shell is a water-cooled, 5-in. copper tee and is of such construction as to afford a controlled atmosphere. Water-cooled electrodes are designed to hold refractory metal strip heaters (either plain or with a wedge for better black body conditions) or special-machined graphite heaters. Stepless power input is provided by variac-controlled, saturable core reactor.

Furnace Description

Figure 1 shows the furnace diagram. The furnace shell was fabricated from 12.7 cm (5 in.) ID copper tubing which was cut and welded to form a "T". Cooling was provided by 6.25 mm (¼ in.) copper tubing tracing welded to the outside of the shell. The ends of the furnace through which pass the terminal connections were isolated electrically from the furnace shell by Teflon rings, and an atmospheric seal is provided by "O" ring seals. Water-cooled terminal connections, fabricated from 1.9 cm (¾ in.) diameter copper rod, were led into the furnace through rubber gasketed CGB cable connector seals in the end plates. The seals provide both an electrical and atmospheric seal, and, when loosened, permit the terminals to be rotated easily or moved in and out. Each terminal had interchangeable threaded end pieces which served as adapters so that several types of heater configurations may be used.

The furnace is loaded through an "O" ring sealed cover, about 5 in. in diameter, on the center leg of the "T." This cover has a 1-in. diameter sight port for visual observation and temperature determination of the sample. There are two additional sight ports, one directly opposite the sight port in the cover and one displaced 30° from the center line passing through the two former ones. Three ports are needed for high-temperature microscopy work, one for the microscope, one for an arc light which provides additional illumination when necessary, and one for an optical pyrometer.

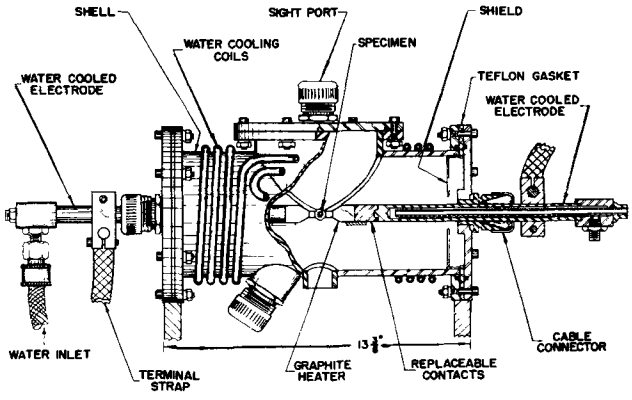

Fig. 1. High-temperature microscopy furnace

Heaters.—Three types of resistors have been used. The furnace was originally designed to use two refractory metal strip heaters 7.6 x 1.27 x 0.00127 cm (3 x 0.5 x 0.005 in.) (top Fig. 2) for wetting angle studies. The metal strips are clamped in copper holders; the sample rests on the lower heater while the upper strip functions as a radiation guard heater. For oxidizing atmospheres, a platinum-40% rhodium metal strip (mp 1900°C) is used. With inert atmospheres, a tantalum, tungsten, or molybdenum strip is used for still higher temperatures.

Reaction of some samples with metal heaters is sometimes a problem, and crucibles of boron nitride or thoria are placed on the lower heater to hold the sample. Boron nitride is satisfactory as a crucible up to 2000°C, but at higher temperatures it reacts with the heater. A guard ring of tungsten is placed around the crucible to reduce radiation loss from the side and to make the temperature more uniform.

In melting point studies it was found that reactions between the materials under study and the heater strip were sometimes severe, so a heater was constructed from a graphite block 7.6 cm (3 in.) long by 1.9 cm (¾ in.) square at the terminals. The central section was made considerably smaller in area and contains a thin-walled cylindrical furnace chamber (Fig. 2). This cylinder provides a hot zone with a 6.25 mm (¼ in.) inner diameter by 1.59 cm (⅝ in.) high. The sample is generally formed into 3.2 mm (⅛ in.) diameter rod about 2.54 cm (1 in.) long and is supported on a graphite pedestal. Several refractory metal shields are placed around the heater to reduce radiation losses.

At temperatures above 2500°C, even with a flowing argon atmosphere, there is sufficient vaporization of graphite to cause problems of contamination of the sample. A small amount of work has been done on the possibility of using heaters made from the high melting tantalum carbide-zirconium carbide solid solution. These heaters are difficult to fabricate and very susceptible to thermal shock. A few have

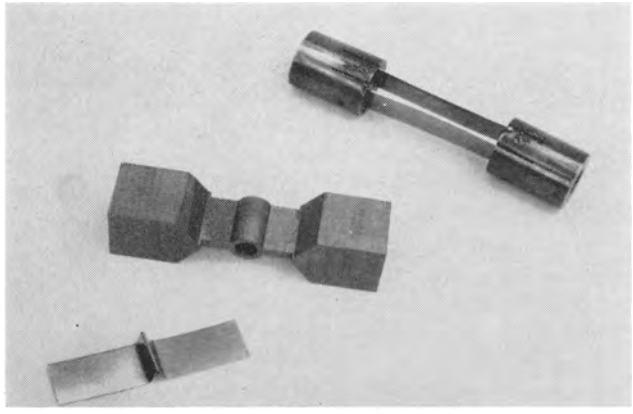

Fig. 2. Furnace heaters, double wedge, graphite block, and "V" types.

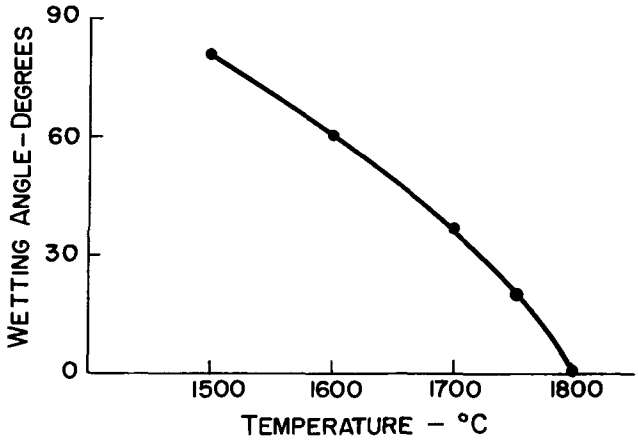

Fig. 4. Wetting of SiC by $FeSi_2$

been used satisfactorily, but further development work is needed to reduce thermal shock problems. A second technique which has proved helpful is to line the inside of the graphite heater with tantalum or tungsten foil.

Power supply.—The saturable core reactor d-c bias is controlled by a manually operated powerstat on a 110-v line, through a small transformer which reduces the voltage, and then through a rectifier to provide d-c control. This manual control is entirely satisfactory for most applications of the furnace, because the firing times are usually short. Four 5 kva step-down transformers are used with the primaries in parallel and the secondaries in series. Figure 3 shows the power consumption for various types of heaters. Maximum secondary current drawn is slightly in excess of 500 amp.

Temperature measurement.—In addition there are two other sources of uncertainty in knowing the temperature of the sample.

The optical pyrometer is accurate to ±13.9°C and this was checked regularly by comparison with a standard. Temperature is read through a Vycor sight glass which adsorbs a certain, though small, amount of energy at the wave length used for measurement, 0.65μ. The sight glass was calibrated using an optical standardization apparatus, and the correction factor corresponded with the simplified Wein equation, $1/T_t - 1/T_a = C$, where T_t is equal to the true absolute temperature, T_a is the apparent absolute temperature, and C is the calibration constant. The value of this constant was found to be -6.7×10^{-6} and resulted in the addition of 35°C at 2040°C, the melting point of aluminum oxide.

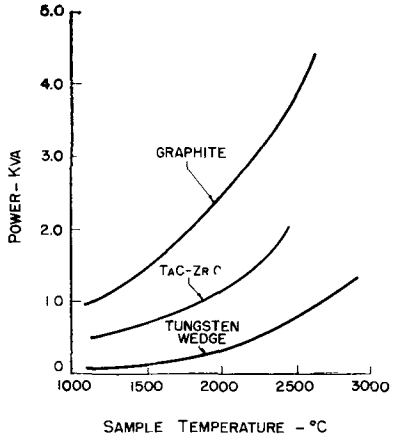

Fig. 3. Micro furnace-power-temperature relationship.

The variation from black body conditions in the furnace constitutes a source of error. Because the sample can be seen when it is melted in this furnace, true black body conditions are not obtained. The effective emissivity falls between one and the true emissivity of the material under test. Using a material of high purity for which the melting point is well established, it is possible to calculate the apparent emissivity if the correction constants are known for the optical pyrometer and the sight glass. The apparent melting temperature of aluminum oxide and the literature value for aluminum oxide, 2040°C was used to calculate the emissivity as 0.9594. Assuming that the apparent emissivity does not change at higher temperatures, and for other oxides the emissivity correction for the zirconia melting point, 2656°C, is 16°C, and for the urania melting point 2740°C, 17°C.

Experimental Results with Furnace

Melting Points

Table I shows some of the melting points which have been obtained compared with values from the literature. Aluminum oxide is readily available in high-purity form and its melting point is well established. This material was used as a standard for checking the sight glass calibration and for calculating the effect of emissivity on the experimental conditions. High-purity zirconia is available in quantity, and represents an excellent high-temperature standard material. Zirconia with 2% hafnia was chosen as a standard because of some previous work (3). High-purity urania is available, but may not be a good standard because of the possible variations in the uranium to oxygen ratios.

The reason the melting point of alumina checked satisfactorily and those for zirconia and urania by two different methods did not is not understood. Lambertson and Mueller (3) used a tungsten crucible ¼ in. in diameter by 2 in. long heated in a tungsten heater ¾ in. in diameter by 6 in. long. They obtained black body conditions. Melting was determined by observing the sample before and after

Table I. Oxide melting points

Material	Number of tests	Melting point, °C±20°C	Value from literature
Al_2O_3	5	2030(A)*	2040± 5°C(2)
		2040(B)†	2040±20°C(3)
ZrO_2(2% HfO_2)	3	2656(A)	2710±20°C(3)
		2672(B)	2677 (4)
ZrO_2(HfO_2 free)	4	2690(A)	
HfO_2(5% ZrO_2)	4	2770(A)	2777 (4)
UO_2	3	2740(A)	2750±40°C(2)
		2757(B)	2878±22°C(3)
			2860±45°C(5)

* (A) Corrected for sight glass absorption.
† (B) Corrected for sight glass absorption and a calculated emissivity of 0.9594.

Table II. Sources and compositions of melting point materials

1. Al_2O_3 —99.99+ Linde Air Products, Type A —5175, Lot #P—196
2. ZrO_2 —99.87% (ZrO_2 + 2% HfO_2)—Titanium Alloy Manufacturing Division, National Lead Co.—Specially purified
3. ZrO_2—Hf free—99.5% ZrO_2—The Carborundum Metals Co., Akron, Ohio
4. HfO_2 —95+%—The Carborundum Metals Co., Akron, Ohio.
5. UO_2 —99.9+%—The Mallinckrodt Chemical Co., Source Grade

heating. The crucible bottom may have been at a lower temperature than that indicated through radiant heat loss. In the present work only the part that melts is seen but deviation from black body conditions presents a source of error.

Wetting Angles

Wetting angles of $FeSi_2$ on SiC vs. temperature are plotted in Fig. 4. In this work the sample is placed on a pin or in a crucible on strips and heated to the test temperature. It is then held for a few seconds, the furnace turned off, and the sample quenched by the rapid cooling of the furnace. The sample is removed from the furnace and ground so that the angle between the melt and the crystal can be seen easily. This is then projected on a screen and the angle measured.

Acknowledgments

The authors would like to express their appreciation to Mr. Henry N. Baumann for his suggestions, to Dr. F. K. Davey for his work on the power supply and the development of the graphite heater, and to many others of the Carborundum Company who contributed their ideas, suggestions, and help in obtaining the data presented in this report.

REFERENCES

1. H. N. Baumann, Jr., *Bull. Am. Ceram. Soc.*, **27** (7), 267 (1948).
2. L. G. Wisnyi and S. W. Pijanowski, Ceramic Information Meeting held at Oak Ridge National Laboratory, Oct. 1-3, 1956, *TID*-7530 (Pt. 1) p. 46, April 1957.
3. W. A. Lambertson and M. H. Mueller, *J. Am. Ceramic Soc.*, **36**, (10) 329, (11) 365, (12) 397 (1953).
4. F. von Henning, *Naturwissenschaften*, **13**, 661 (1925).
5. T. C. Ehlert and J. L. Margrave, *J. Am. Ceram. Soc.*, **41**, [8], 330 (1958).

Zirconium Coating of Uranium by the Iodide Process

W. L. Robb[1]

Knolls Atomic Power Laboratory
(Operated for Atomic Energy Commission by General Electric Company), Schenectady, N. Y.

ABSTRACT

A method for coating uranium metal with a bonded layer of crystalline zirconium metal has been developed. It consists of thermally decomposing zirconium iodide vapors on the surface of uranium metal heated to about 1100°C in vacuum. Prior to coating, the uranium metal surface is cleaned by iodizing it and then vaporizing the uranium iodide. Greatly increased diffusion between the uranium and deposited zirconium can be obtained if the uranium is alloyed previously with as little as 0.5% zirconium. This increased diffusion improves the corrosion resistance of the coatings.

The desirability of coating uranium or uranium alloy fuel elements with zirconium arises from the excellent corrosion resistance of zirconium, plus its low thermal neutron cross section. Of particular interest are 1-10 mil thick zirconium "sweater" coatings, for use as secondary corrosion resistant barriers. This paper describes one of the more successful methods for achieving such a coating.

The coating process examined in this study was based on the van-Arkel-de-Boer (1) process for producing pure zirconium metal. It consisted of first forming volatile zirconium iodides, and second, decomposing or disproportionating these iodides on the hot surface of a uranium specimen (2). The process is carried out most successfully in an evacuated system, although coatings of less desirable nature can be obtained in the presence of an inert gas or a reducing gas such as H_2.

[1] Present address: Research Laboratory, General Electric Company, Schenectady, N. Y.

Experimental

The apparatus used to coat 1 x ¾ in. uranium disks is shown in Fig. 1. The uranium disk was heated inductively by a 5 kw Ajax converter, the disk's temperature being measured by an optical

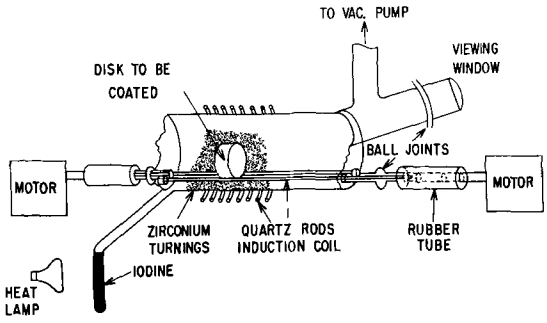

Fig. 1. Cut-away viewing of vapor coating apparatus with disk rotator.

pyrometer through a glass window. Uranium temperatures of 1050°-1100°C could be maintained to ±5°C. The zirconium was in the form of 10-mil turnings twisted into cigar shaped bundles which were then placed in the tube around the uranium. It was necessary that the ends of the bundles did not complete a circle within the induction field. Thus the zirconium was heated mainly by radiation from the uranium disk. This was sufficient to heat the zirconium to 200°-400°C. The iodine pressure was controlled by regulating the temperature of the iodine supply tube generally between 20°-50°C.

The coating cell was evacuated continuously, using a fore pump and diffusion pump, although once a thin coating of zirconium had been deposited and the uranium and zirconium had been completely degassed, the coating cell could be operated without continuous evacuation.

A somewhat thicker coating was obtained near the edge of the sample as compared to the middle due to (*a*) the nearness to the zirconium supply, and (*b*) the higher temperature of the edge of the disk as compared to the middle.

In order to coat a disk completely in one operation, the uranium disk was supported on rods which could be rotated continuously. Quartz rods were found suitable for the rollers as long as the rate of rotation was sufficiently rapid and the weight of the disk not too high. Otherwise the uranium was oxidized by the quartz, and nonbonded coatings resulted. Required rates of rotation for the rods were 1-3 rpm. The rod diameters for 1-in. diameter uranium disks were about 3/16 in. Thin metal foils of tantalum and molybdenum were tried as covers for the quartz rods but were not useful since the foil stuck to the hot uranium.

Prior to coating a specimen, the uranium was cleaned by an acid dip or by electrocleaning. The simplest method of cleaning consisted of dipping the uranium sample in concentrated nitric acid, followed by a water rinse and an acetone rinse. The sample was placed in the coating cell, which then was evacuated as quickly as possible. After the cell had been evacuated to better than 0.01μ Hg (with leak rates of less than 8μ ft^3/hr) the liquid nitrogen was removed from the iodine supply and the induction furnace turned on. As the uranium disk became hot it was iodized, forming UI_4 which vaporized from the surface as the disk reached red heat. This served to clean the surface just prior to coating and was a most important step in obtaining bonded coatings. As the temperature of the uranium approached 1080°C the equilibrium of the reaction:

$$U + \frac{X}{2} I_2 \rightleftharpoons UI_x$$

shifted more and more to the left. Thus, at coating temperature, the iodization rate of U could be reduced greatly by maintaining the iodine pressure below 60μ Hg (3).

By the time the uranium had reached 1050°C (2-4 min), ZrI_4 was already being formed and could be seen condensed on the cold outlet of the deposition cell. Coating of the uranium had to begin immediately in order to prevent the formation of a diffusion blocking layer of uranium oxide. Coating times of ½-6 hr were tried, with rates as high as 2-3 mils/hr being obtained. Runs usually were 2-3 hr long, at 1 to 2 mils/hr coating rate.

Coated samples were removed from the apparatus under a purge of N_2, A, or He gas to prevent oxidation of the condensed ZrI_4. This eliminated the need to clean the apparatus after every coating test.

Results and Discussion

By means of the equipment and procedures described above, zirconium coatings have been applied on uranium disks and cylinders of various shapes and sizes. A photograph of a typical coating, shown in Fig. 2, illustrates the very crystalline nature of the deposited zirconium. The nature of the diffusion bond of the zirconium to the uranium can be seen in Fig. 3. The diffusion was considerably less than expected from measured diffusion rates of uranium and zirconium (4). Furthermore, the annealing of coated uranium disks did not increase the diffusion layer thickness noticeably.

Fig. 2. Zirconium coated uranium disk, actual size

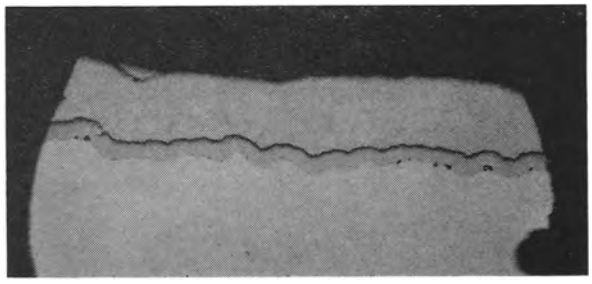

Fig. 3. Zirconium coating on uranium. Magnification 250X B.F.

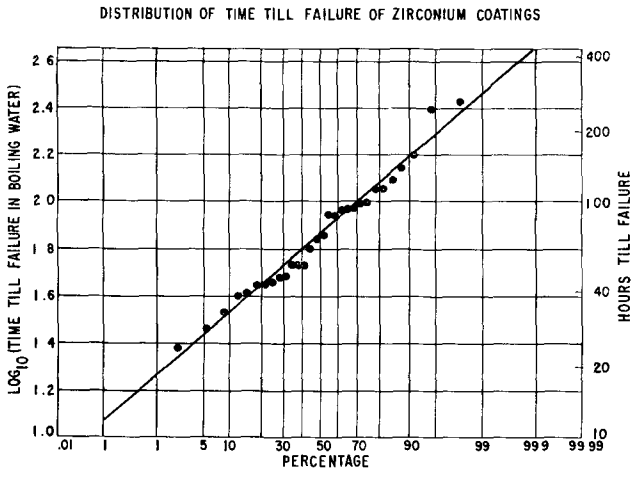

Fig. 4. Distribution of time until failure of zirconium coatings.

The corrosion resistance of these coatings was determined by noting the time required for their rupture or penetration in boiling water. More specifically, failure was indicated by UO_2 powder in the water, by a blister on the surface of the coated specimen, or by the enlarging of a pore hole on the surface. The times required until failure of coatings on pure uranium are shown on a probability graph, Fig. 4, and it is seen that the log mean time till failure for 30 samples was 73 hr.

Except for the cases where failure of the coatings was due to a poor diffusion bond (caused by poor cleaning or by uranium oxidation on heating), the most common cause of failure was porosity of the crystalline coatings. As a result, several methods for reducing this porosity were tried. These methods and their results are listed in Table I.

As is seen from the table, no major improvement in corrosion resistance was observed for any of the additional treatments. It was observed, however, that coatings on the sides of disks which were rolled on the quartz rods while the zirconium was being deposited were not nearly as porous, nor as brightly crystalline, as were the unpressed faces of the disks. If a practical way could be found to deform or to press the zirconium deposit continually over the entire disk while the deposit was being laid down, less porous coatings could be obtained.

Table I. Corrosion times in boiling water of zirconium coatings on pure uranium disks

	Hours until failure in boiling water
Coatings deposited in 1-2 hr	115, 115, 161, 87, 44, 49, 29
Coatings deposited in 2-3 hr	94, 73, 126, 54, 88, 72, 54, 54, 94, 91, 64, 41, 98, 45, 48
Coatings deposited in 3-5 hr	250, 24, 100, 34, 46, 40
Coatings deposited in 5-6 hr	142, 271
Coatings vacuum annealed after coating	69, 47, 112, 164, 48, 78
Coatings ball milled	51, 121, 21
Coatings shot blasted	74, 74
Coatings hot pressed	116, 114, 73, 71
Coatings with Ni and Zr co-deposited	49, 88, 21, 38, 24, 117, 134, 157, 67, 67, 116, 70, 41, 17, 72, 73, 22, 77
Coatings deposited in reverse plating runs	190, 60

The codeposition of Ni from $Ni(CO)_4$ and Zr from ZrI_4 results in a lower melting Ni-Zr and Ni-U alloy being formed. This causes increased diffusion between the U and Zr, and when carefully controlled could result in improved coatings. Figure 5 shows this increased diffusion. The presence of Ni in the coating was verified by x-ray fluorescence measurements, but the occlusions in the Zr coating were not identified and could be either nickel, zirconium oxide, or zirconium carbide. The scattered appearance of these occlusions is due to the intermittent introduction of nickel-carbonyl into the coating chamber.

Depositing the zirconium coating on a uranium alloy disk previously alloyed with a small amount of zirconium resulted in markedly improved corrosion resistance of the zirconium coatings. This had been noticed by Campbell and Powell (5) on a cementation process for depositing zirconium on uranium. Figures 6 and 7 show zirconium deposited on a 99% U —1% Zr alloy and illustrate the type of diffusion obtained when zirconium is deposited on the uranium alloy. As would be expected from previously measured diffusion rates of U in Zr (4), the uranium is completely diffused through the zirconium coating and 1 mil layers machined off the outer surface of coatings have analyzed as high as 43% uranium. X-ray diffraction measurements on successive 1 mil layers indicate a concentration profile going from alpha zirconium through epsilon phase uranium-zirconium alloy to alpha uranium. Uranium metal alloys containing from 0.5 to 4% zirconium were coated and over this range the results were very similar. Figure 8 shows several coated alloy disks. The

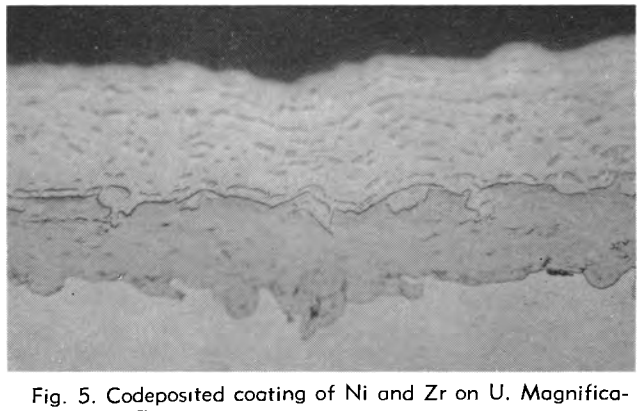

Fig. 5. Codeposited coating of Ni and Zr on U. Magnification 500X B.F.

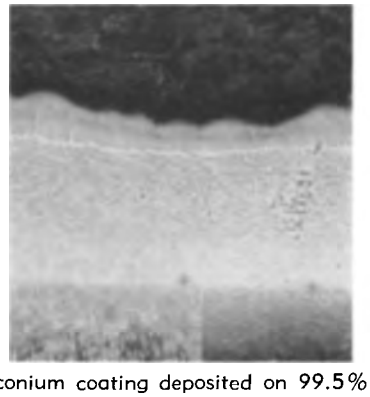

Fig. 6. Zirconium coating deposited on 99.5% U—0.5% Zr alloy. Magnification 250X B.F.

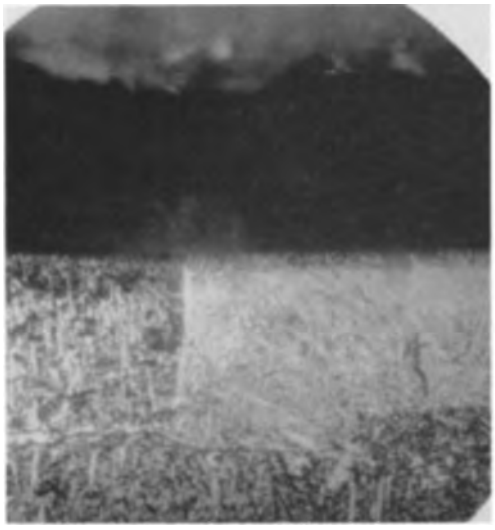

Fig. 7. Zirconium coating deposited on 99.5% U—0.5% Zr alloy. Magnification 250X Pol.

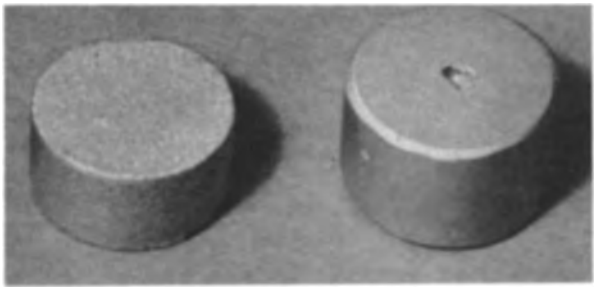

Fig. 8. Photographs of Zr deposited on U-Zr alloy. Magnification 1X.

coatings on these alloy disks are very smooth compared to the macro crystalline coating deposited on uranium and shown in Fig. 2. Corrosion tests on the coated alloy samples showed greatly increased protection (Table II). For example, a coating deposited in 1 hr and annealed for 1 hr lasted 447 hr and was still intact at the end of the test. Some failures occurred in less than 100 hr but they could be accounted for largely by pits or holes in the uranium alloy metal used. Although the inside of the holes were coated to some extent, the holes still presented weak spots in the coatings.

The zirconium apparently fixes the carbon usually found in uranium, thus preventing its migration to the uranium-zirconium coating interface. Since ZrC is more stable than UC, it would be expected that the carbon in the uranium would diffuse to the zirconium, and in this way cause a ZrC diffusion blocking layer to be formed at the U-Zr interface. This explains why the expected amount of codiffusion between U and Zr was not observed in the initial coating experiments.

Conclusions

It is possible, but difficult, to obtain pore-free zirconium coatings on present grade uranium metal. Under carefully controlled conditions the coatings probably can be made to resist boiling water consistently for over 100 hr. On low zirconium alloy specimens (or possibly on uranium containing very little carbon) pore free coatings can be obtained easily, and coatings to resist 100°C boiling water for over 200 hr or 170°C water for 80 hr should be produced easily.

Table II. Corrosion times of zirconium coatings on uranium-zirconium alloy disks

Run No.	% Zr alloyed with U	Time of run	Annealing Time	Annealing Temp	Time to failure in water at °C	
248	0.5	3			232+	100
274	0.5	2			47	100
277	0.5	2			37	100
259	1.0	2			168	100
278	1.0	2			177	
260	1.0	1	1	1100	447+	100
261	1.0	0.5	0.5	1100	141	100
263	1.0	1.5	1.5	1100	214	100
265	1.0	2	1	1100*	242	100
253	2.5	3			85	100
255	2.5	2.5			309+	100
280	2.5	2				
254	4.0	2.5			264	100
279	0.5	2	65	800	80	170
266	1.0	1.5			12	170
267	1.0	1			18	170
268	1.0	1	48	800	72	170
255	2.5	2.5			24	170
262	4.0	3	0.5	1100	24	170

* Quenched from the beta phase for grain refinement.

So far only coatings on uranium or uranium-zirconium alloys have been described. However, the method also has been used at KAPL to coat thorium and graphite. Other reactor materials including beryllium metal, beryllium carbide, beryllium oxide, boron, and boron carbide, may also be coated in the same manner.

Although this method of coating is limited in use by the high temperature required for the decomposition of zirconium tetraiodide, it does represent a possible method for producing coatings of zirconium metal. The cost for this type of coating probably will be higher than that for electroplated coatings. But, for specialized cases where diffusion bonded and corrosion resistant coatings of low neutron cross section are required, it alone affords a method of producing thin bonded zirconium coatings.

Acknowledgment

The author wishes to thank F. J. Shipko, F. J. Clark, R. L. Myers, and A. C. Schafer for their technical assistance during this project.

Manuscript received June 27, 1958. This paper was prepared for delivery before the New York Meeting, April 27-May 1, 1958.

Any discussion of this paper will appear in a Discussion Section to be published in the December 1959 JOURNAL.

REFERENCES

1. A. E. van Arkel and J. H. de Boer, *Z. anorg. u. allgem. Chem.*, **148**, 345 (1925).
2. I. E. Campbell, C. F. Powell, D. H. Nowicki, and B. W. Gonser, *J. (and Trans.) Electrochem. Soc.*, **96**, 318 (1949).
3. C. H. Prescott, Jr., F. L. Reynolds, and H. A. Holmes, "The Preparation of Uranium Metal by Thermal Dissociation of the Iodide," MDDC-437, April 18, 1946.
4. Y. Adda, J. Philibert, and C. Mairy, *Compt. rend.*, **243**, 1115 (1956).
5. I. E. Campbell and C. F. Powell, Private communication.

Transport Numbers and Ionic Mobilities in the System Potassium Chloride-Lead Chloride

Frederick R. Duke and Richard A. Fleming

Institute for Atomic Research and Department of Chemistry, Iowa State College, Ames, Iowa

ABSTRACT

Values of ionic transport numbers and ionic mobilities were determined for the fused system potassium chloride-lead chloride. Cation transport numbers were found: 0.24 for $PbCl_2$ at 525°C, 0.62 for KCl at 850°C. In each mixture, t_- deviated positively and t_+ and t_{++} deviated negatively from linearity when plotted against equivalent fraction. The initial, very rapid depression of total equivalent conductance from that of pure KCl, caused by addition of small amounts of $PbCl_2$, was found to be due to the depression of the ionic conductance of K^+ rather than complexing between Pb^{++} and Cl^- as had been supposed previously. The relative mobilities of K^+ and Pb^{++} were compared with those of Li^+ and Pb^{++} in the system LiCl-$PbCl_2$, calculated from available literature data.

The transport numbers and mobilities of the ions in a mixture of $AgNO_3$ and $NaNO_3$ have been determined (1). This system proved to be ideal in the sense that the ionic mobilities were independent of composition. The system $PbCl_2$-KCl is of interest because of the possibility of complex ion formation involving Pb^{++} and Cl^-; furthermore, it might be expected that a mixture of a biunivalent salt with a uniunivalent one would show a different behavior from the $AgNO_3$-$NaNO_3$ system.

Complex ions of Pb^{++} and Cl^- in the molten system $PbCl_2$-KCl have been reported on the basis of phase diagram (2), electrical conductance (3), surface tension (4), and molar volume measurements (5). In addition, previous studies on transport numbers in this system have indicated that complex ions might play a large role in the mobility of the ions. Lorenz and Ruckstuhl (6) observed that the lead ions are apparently anionic ($PbCl_3^-$ or $PbCl_4^=$) in mixtures containing more than about 25 mole % KCl. Wirths (7), using radioactive Pb^{++} as tracer, obtained some evidence that lead ion migrated toward the anode in mixtures of $PbCl_2$ and KCl. These transport studies were lacking in precision, however. With more precise experimental techniques available, the present work on the $PbCl_2$-KCl system was done.

Experimental

Two experimental quantities must be determined in order to calculate the transport numbers of the three ions. One of these, designated ϕ by Aziz and Wetmore (8) (where $\phi = 1 - t_{++} - E_1 t_-$), is related to experimental values by $\phi = (E_2 N_1 - E_1 N_2)/Z$, where t_{++}, t_+, and t_- are the transport numbers of Pb^{++}, K^+, and Cl^- ions, respectively, E_1 and E_2 are the original equivalent fractions of $PbCl_2$ and KCl, respectively, N_1 and N_2 are the total number of equivalents of $PbCl_2$ and KCl in the anode compartment after electrolysis between Pb electrodes, and Z is the charge transferred in faradays. The other experimental quantity is t_- measured directly by radio tracer methods.

Apparatus.—The cell used in the determination of ϕ and t_- is shown in Fig. 1. The low temperature runs were done in Pyrex with the membrane consisting of an ultrafine Pyrex disk. For high temperature, the cell was made of quartz; the membrane was specially prepared for each cell from commercial fine porosity quartz disks. To reduce the porosity of the fine quartz disks, ethyl silicate and concentrated HCl were allowed to react in the disk, with a heating period (850°C) after each treatment, until sufficiently fine porosity was obtained. The porosity was calibrated by measuring the time required for 1 ml of water to pass through the disk under 1 atm pressure. Disks having "water times" above 600 sec were found to be satisfactory. Contact to the electrodes was made through loosely fitting caps, with tungsten wires passing through the center tube in the cap.

The furnace used was a Marshall tube furnace with external compensating taps on the heating coil. The temperature was controlled by a chromel-alumel thermocouple which operated a Brown indicating controller. In addition, the furnace contained an indicating chromel-alumel thermocouple connected to a L&N No. 8662 potentiometer with reference junction compensator. The center zone of the furnace

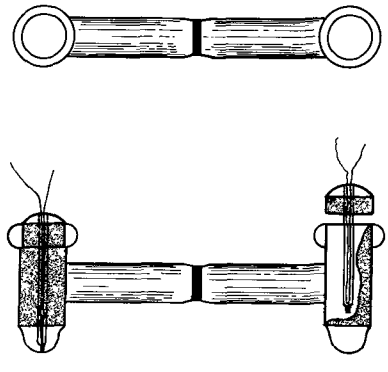

Fig. 1. Transport cell

had a temperature gradient of less than 5° and could be controlled to ±1°C of any desired temperature at a given point. Direct current up to 300 ma was available through a bank of selenium rectifiers in a smoothing capacitance-inductance circuit. A Model 100 Berkeley Decimal Scalar was used in making all radioactivity counts.

Determination of ϕ.—The cell shown in Fig. 1 was loaded with an intimate mixture of reagent grade solid KCl and $PbCl_2$. Pure lead metal was used for the electrodes. In general, the amount of molten salt filled the horizontal tube of the cell only partially, allowing a large surface area and minimizing differences in head across the membrane as the experiment proceeded. After a suitable quantity of electricity had been passed, the cell was broken at the membrane and the catholyte and anolyte collected separately and analyzed as follows. The weighed samples were pulverized, heated in boiling water, cooled, and filtered. This procedure was repeated three times, thus removing all of the KCl and part of the $PbCl_2$. The remaining $PbCl_2$ was dried and weighed. The filtrate was titrated with the sodium salt of cyclohexanediaminetetraacetic acid (9) to determine the dissolved lead, and K^+ was precipitated and weighed as the tetraphenylborate (10).

Determination of t_-.—Radioactive Cl^{36} with a half-life of 3.08×10^5 years, was used as tracer. If all the radioactive chloride is placed initially in the cathode compartment of the cell shown in Fig. 1, it can be shown that

$$t_- = K_a C_a E_c / K_c C_c Z \qquad [1]$$

where C_a is the counting rate of the anolyte, corrected for diffusion, after passage of Z faradays, C_c is the counting rate of the catholyte before the run, and E_c is the total number of equivalents of Cl^- in the catholyte initially. K_a and K_c take into account the aliquation and the geometry of the counted sample so that, for example, $K_a C_a$ gives the amount of Cl^* in the anode compartment. For K_a to equal K_c, the counting efficiencies and the aliquation and other similar variables must be the same when counting catholyte and anolyte.

After the current was run, the cell was broken at the membrane and the anolyte and catholyte samples were collected carefully and weighed. For analysis, a $NaCl^*$-$PbCl_2^*$ sample was homogenized by completely dissolving it in boiling water. This was followed by concentrating portions of the solution by evaporation and then cooling to precipitate $PbCl_2^*$, the form in which Cl^{36} was counted. The original portion size and the extent of concentration by evaporation were adjusted so that a final $PbCl_2^*$ weight of about 0.1 g was obtained, after water and acetone rinses to remove KCl^*. From the observed counting rates of five or six samples, the counting rate of a 0.1000-g sample of $PbCl_2$ was determined. This weight represents 0.000719 equivalents of Cl^-. By knowing the total number of equivalents of Cl^- in the sample, the radioactive Cl^- aliquot of 0.1000 g $PbCl_2$ was determined, and the total counting rate of the sample was found by multiplication.

The final weight of the anolyte sample was known. The final concentration of the anolyte was calculated from the results of ϕ runs made on samples of the same composition. Thus, total Cl^- and then the anolyte's uncorrected counting rate were calculated. To determine C_a, one need only correct the observed counting rate for leakage and diffusion of Cl^* into the anolyte.

Values of C_c were obtained in two ways. Proceeding exactly as in the case of the anolyte sample, one can determine an observed final counting rate for the catholyte. Then one need only add the uncorrected anolyte counting rate to this term to determine the initial counting rate of the catholyte. Alternately, one may proceed so that in every run exactly the same number of equivalents of Cl^- are present initially in the catholyte. Also, one may introduce Cl^* from an active KCl^* (or $PbCl_2^*$) stock and use the same weight of stock for each run. Then C_c will be the same for each run and, if the same number of faradays are passed in each run, Eq. [1] simplifies to

$$t_- = AC_a \qquad [2]$$

This method demands care in weighing out a homogeneous radiochlorine source, but it is time saving. The value of A is known once $K_c C_c$ has been determined, and each catholyte need not be collected individually and counted.

Diffusion leakage corrections were made by reference to a calibration plot of "water times" vs. diffusion leakage determined on a number of membranes. The calibration plot is a straight line, and corrections amounted to 5% or less of the total radioactivity transferred across the membrane in all experiments.

Results

Experimental results are summarized in Table I. The equivalent and mole fractions of KCl in the KCl-$PbCl_2$ mixtures are listed in the first two columns, for seven compositions studied (a to g) at the temperatures listed in the third column. The experimentally determined values of ϕ and t_- are listed in the fourth and fifth columns, respectively. The definition $\phi = 1 - t_{++} - E_1 t_-$ involves the equivalent

Table I. Values of the parameter ϕ, of the ionic transport numbers, and of the equivalent conductance λ in the KCl-$PbCl_2$ system

E (KCl)	X (KCl)	Temp, °C	ϕ	t_-	t_+	t_{++}	λ
0.000	0.000 (g)	525	0	0.76±0.01	0.00±0.016	0.24±0.01	45.28
0.087	0.160 (f)	525	0.115±0.011	0.74±0.02	0.05±0.023	0.17±0.023	42.64
0.185	0.312 (e)	525	0.257±0.015	0.71±0.02	0.12±0.023	0.17±0.024	39.65
0.297	0.458 (d)	525	0.389±0.012	0.68±0.03	0.19±0.024	0.13±0.025	36.23
0.461	0.631 (c)	525	0.599±0.012	0.60±0.03	0.32±0.032	0.08±0.023	35.14
0.461	0.631 (c)	850	0.604±0.012	0.58±0.03	0.32±0.035	0.10±0.023	72.99
0.681	0.810 (b)	850	0.789±0.012	0.50±0.04	0.46±0.037	0.04±0.023	79.97
1.000	1.000 (a)	850	1.000	0.38±0.04	0.62±0.04	0.00	118.75

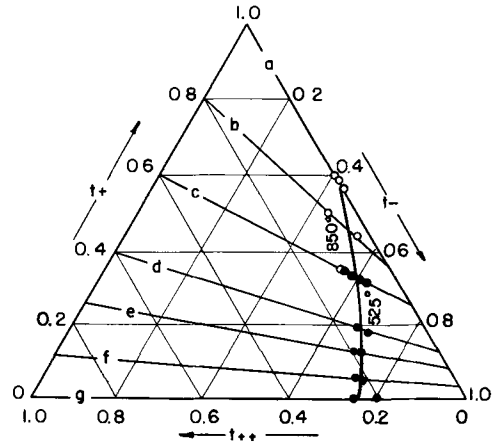

Fig. 2. Triangular diagram of the three transport numbers t_-, t_+, and t_{++} in fused KCl-$PbCl_2$ systems at several compositions: (a) pure KCl; (b) 19.0 mole % $PbCl_2$; (c) 36.9 mole % $PbCl_2$; (d) 54.2 mole % $PbCl_2$; (e) 68.8 mole % $PbCl_2$; (f) 84.0 mole % $PbCl_2$; (g) pure $PbCl_2$; and at 525° (•) and 850°C (O). The straight lines (a to g) correspond to the experimental values of the parameter ϕ (Table I). Experimental points correspond to the measured values to t_- (Table I), plotted for each composition (a to g) on the appropriate ϕ line. The smooth curve drawn through the points defines the transport numbers t_-, t_+, and t_{++} as a function of composition (a to g).

fraction E_1 of $PbCl_2$ which is simply equal to $1 - E_2 = 1 - E(\text{KCl})$. The corresponding mole fractions are $X_1 = E_1/(2 - E_1)$ and $X_2 = 2E_2/(1 + E_2)$ for $PbCl_2$ and KCl, respectively.

Since t_- was determined independently by the use of a radiochlorine tracer, as described, the definition of ϕ above and the relation $1 = t_- + t_+ + t_{++}$ provide a system of two equations which can be solved for the two unknowns t_+ and t_{++}, once the value of ϕ has been determined experimentally, as described.

Since the three transport numbers add up to unity, the equilateral triangular diagram (Fig. 2) lends itself particularly well to this solution for two unknowns. The defining equation for the parameter ϕ corresponds to a straight line in this diagram, whose intercept on the $t_- = 0$ axis (left side of Fig. 2) is $t_{++} = 1 - \phi$, and whose intercept on the $t_{++} = 0$ axis (right side of Fig. 2) is $t_- = (1 - \phi)/E_1$.

Seven straight lines (marked a to g) have been drawn in Fig. 2, corresponding to the seven compositions studied and to their experimentally determined values of ϕ (Table I). For line c, the values of ϕ at 525° and 850°C coincided within experimental error. Once the ϕ lines were drawn in Fig. 2, the experimentally determined t_- points (Table I) could be plotted, each set of points being plotted on the ϕ line corresponding to the same composition. The locus of these t_- points defines the three transport numbers for each one of the seven compositions studied. The smooth curve drawn through the points shows how the transport numbers t_-, t_+, and t_{++} vary as the composition goes from line a (KCl) to g ($PbCl_2$). The lack of a break in the curve in line c suggests that the transport numbers are insensitive to temperature changes between 525° and 850°C. The values of t_+ and t_{++} given in the sixth and seventh columns of Table I were read off the intersections of the smooth curve with the ϕ lines in Fig. 2.

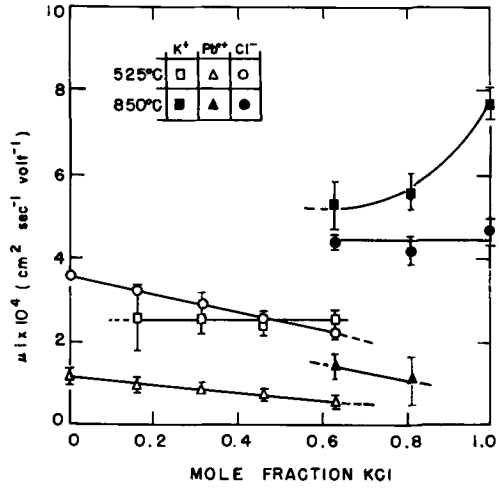

Fig. 3. Mobility of the ions vs. mole fraction in the fused KCl-$PbCl_2$ system.

Equivalent conductance data for the $PbCl_2$-KCl system are available from density data of Boardman, Dorman, and Heymann (11) and specific conductance data of Bloom and Heymann (3). The conductance data of Yaffe and Van Artsdalen (12) were used for pure KCl. The total equivalent conductances λ of the mixtures are given in the last column of Table I. The ionic equivalent conductances λ_i may be calculated from the equation $\lambda_i = t_i\lambda/E_i$, where t_i is the transport number and E_i the equivalent fraction of the i^{th} ion. The ionic mobilities, $u_i = \lambda_i/F$, are shown in Fig. 3, as a function of composition. It is noteworthy that the transport numbers for pure $PbCl_2$ determined here with radiotracers agree very well with those determined using the bubble cell (13, 14).

Discussion

The most striking observation provided by the data is the rapid decrease in mobility of K^+ ion upon addition of $PbCl_2$ to KCl. This observation is understandable if Pb^{++} ion is present in $PbCl_2$ and if Pb^{++} ion combines with negative holes, the holes into which K^+ ion would normally move. The lowering of the K^+ ion mobility cannot be due to the formation of complex ions; the chemical nature of K^+ ion is not that of complex former. On the other hand, the fairly high mobility of Pb^{++} ion is greater than one would expect on the assumption that Pb^{++} ion moves into doubly charged negative holes; such doubly charged holes should be difficult to create energetically and, in the presence of the singly charged Cl^- anion, should split readily into two singly charged holes. To accommodate both facts, the mobility of Pb^{++} ions and the combining of Pb^{++} ion with negative holes, it is necessary to postulate an equilibrium between Pb^{++} and $PbCl^+$, the latter accounting for the mobility of the Pb^{++} ions. The general change in mobility of Cl^- and Pb^{++} ions with composition change is gradual enough to be accommodated by general changes in the properties of the medium in which the ions move.

The disagreement between the present data and those of Lorenz and Ruckstuhl (6) is explained easily on the basis of leakage of salt through the membrane of the cell. Values of ϕ are very insensitive to such leakage. As mentioned previously, there is no effect on ϕ if the composition of the melt flow-

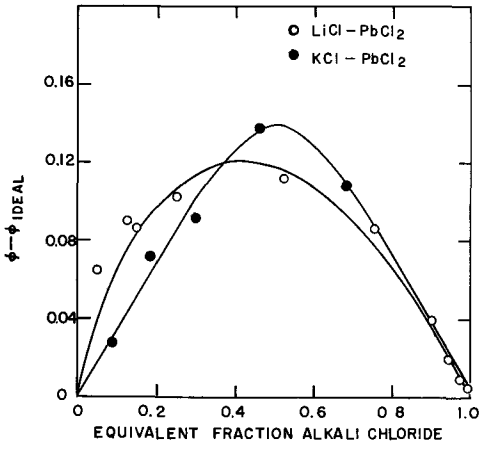

Fig. 4. Comparison of the ϕ parameter for fused $LiCl-PbCl_2$ systems at 650°C [O, cf. Ref. (15)] and for fused $KCl-PbCl_2$ systems at 525° and 850°C (•, cf. Table I); ϕ_{ideal} is here taken equal to the equivalent fraction of alkali chloride in both mixtures (see text).

ing through the disk is that of the original sample. Values of t_+ determined by a change of weight method, such as that used by Lorenz and Ruckstuhl, are extremely sensitive to leakage, while values of t_+ determined radiochemically in an experiment such as is outlined here are much less sensitive. This is because of the immediate dilution of Cl^{36} by the anolyte. The effect of temperature on the transport number is small. In changing from 525° to 850°C, the transport numbers for all of the ions remain constant within experimental error. The temperature change here is sufficiently large that if there were significant differences in the activation energies for mobility of the ions, there would be a sensible change in the transport numbers. Note that the mobilities of the ions change very appreciably in this temperature interval.

An interesting experiment was performed recently by Klemm and Monse (15). With an ingeniously devised moving boundary, they determined relative mobilities of cations in the system $LiCl-PbCl_2$. In essence, they determined ϕ for this system. It can be shown that $\phi = b_{13}E_1/(b_{13}E_1 + b_{23}E_2)$, where b_{13} and b_{23} are Klemm and Monse's notation for the mobility of $1(Li^+)$ and $2(Pb^{++})$ with respect to $3(Cl^-)$, and E_1 and E_2 are (here only) the equivalent fractions of uni- and divalent salts. The similarities and dissimilarities of the two alkali chloride-lead chloride systems are such as to make their data of obvious interest. Values of ϕ in this system were computed together with values of $\phi - \phi_{ideal}$; ϕ_{ideal} becomes numerically equal to the equivalent fraction of the alkali chloride, if the simplifying assumption can be made that uni- and divalent cations have the same mobility.

With this simplifying assumption, ϕ_{ideal} is the same for corresponding equivalent concentrations in the two systems; values of ϕ are compared most easily by looking at the sensitive function, $\phi - \phi_{ideal}$. These values are presented in Fig. 4. It is interesting to note the close similarity in the behavior of the two systems. Nothing can be said regarding absolute values of t_+ and λ_+ in the $LiCl-PbCl_2$ system, however, until an independent set of determinations relating them to measurable quantities is available.

Manuscript received Dec. 27, 1957. Contribution No. 581. Work was performed in the Ames Laboratory of the U.S.A.E.C.

Any discussion of this paper will appear in a Discussion Section to be published in the December 1959 JOURNAL.

REFERENCES

1. F. R. Duke, R. Laity, and B. Owens, *This Journal*, **104**, 299 (1957).
2. R. Lorenz and W. Ruckstuhl, *Z. anorg. Chem.*, **51**, 70 (1906).
3. H. Bloom and E. Heymann, *Proc. Roy. Soc. (London)*, **A188**, 392 (1946).
4. J. L. Dahl, "Surface Tensions of Some Binary Fused Salt Systems," unpublished Ph. D. Thesis, Iowa State College Library, Ames, Iowa (1957).
5. N. K. Boardman, F. H. Dorman, and E. Heymann, *J. Phys. and Colloid Chem.*, **53**, 375 (1949).
6. R. Lorenz and W. Ruckstuhl, *Z. anorg. Chem.*, **52**, 41 (1907).
7. G. Wirths, *Z. Elektrochem.*, **43**, 486 (1937).
8. P. M. Aziz and F. E. W. Wetmore, *Can. J. Chem.*, **30**, 779 (1952).
9. T. C. Loomis, "Metal Chelates of Cyclohexanediaminetetraacetic Acid," Thesis, Iowa State College Library, Ames, Iowa.
10. H. J. Cluley, *Analyst*, **80**, 354 (1955).
11. N. K. Boardman, F. H. Dorman, and E. Heymann, *J. Phys. and Colloid Chem.*, **53**, 375 (1949).
12. I. S. Yaffe and E. R. Van Artsdalen, *J. Phys. Chem.*, **60**, 1125 (1956).
13. F. R. Duke and R. W. Laity, *J. Phys. Chem.*, **59**, 549 (1955).
14. M. R. Lorenz and George J. Janz, "Transference Numbers in Molten Salts," Armed Services Technical Information Agency Technical Note 57-240. ASTIA Document Service Center, Dayton 2, Ohio. 1957. (Mimeographed).
15. V. A. Klemm and E. H. Monse, *Z. Naturforsch.*, **12a**, 319 (1957).

Galvanic Behavior in Fused Electrolytes

I. The Nominal System Mg/LiCl-KCl/Ni

Sidney M. Selis,[1] Guy R. B. Elliott,[2] and Laurence P. McGinnis

Diamond Ordnance Fuze Laboratories, Washington, D. C.

ABSTRACT

The galvanic function of cells containing hygroscopic molten electrolytes involves hydroxide ion as an active material if no stronger oxidizing agent is present. For the system without additional components two sets of reactions are postulated; the operative set would depend on the temperature range. At lower temperatures (390°-440°C), hydroxide ion is cathodically reduced to hydrogen gas plus oxide ion; at higher temperatures (445°-535°C), nickel(II) oxide, formed by the action of hydroxide ion on nickel metal, is the cathodically reduced species. In both temperature ranges magnesium oxide is formed at the anode. At higher temperatures, the magnesium and nickel electrodes obey Nernst's law with respect to the additions of magnesium, nickel, and oxide ions in the concentration range of interest. The electrodes are reversible and of the second kind.

The galvanic system of interest here nominally includes a magnesium anode, an electrolyte which is a molten mixture of potassium chloride and lithium chloride, and a nickel cathode. In the course of the work, the effects of additional components were noted but only to assist in the postulation of electrode reactions. The system is related to some which have been discussed before (1), but it contains no strong oxidant and therefore is not capable of supplying appreciable currents.

On the basis of the present work, half-cell reactions are postulated and, at least under certain conditions, electrode reversibility is demonstrated.

Experimental

Materials.—The nickel(II) oxide, potassium chloride, lithium chloride, lithium carbonate, nickel(II) chloride hexahydrate, and silver chloride were of the usual reagent grade and were not purified further. The nickel content in the nickel(II) chloride hexahydrate was determined gravimetrically by the dimethylglyoxime method. Reagent grade magnesium chloride hexahydrate was dehydrated by a method similar to that of Kelley and Moore (2). All solid chemicals were handled, as far as possible, in a "dry room" (relative humidity 6% under usual room temperature and pressure).

The hydrogen and helium gases were dried by bubbling through concentrated sulfuric acid followed by passage over potassium hydroxide pellets.

The sheet magnesium, generally 0.13 mm thick, was of the commercial electrolytic grade (over 99.5% pure). The impurities included small amounts of silver, aluminum, copper, and calcium as determined by spectrographic analysis. Just prior to use, the dark film on the metal was removed by immersion in 1% hydrochloric acid solution followed by thorough rinsing in distilled water. The metal was wiped dry with a soft lint-free paper.

The sheet nickel was also 0.13 mm thick and was of a good commercial grade (over 99.5% pure). A spectrographic analysis revealed small amounts of zinc, iron, and cobalt. It was found that, other than a thorough washing with a mild soap and water, no treatment of the metal surface was needed.

Another type of electrode material was sintered nickel plate. The preparation and properties of this material have been described by Fleischer (3). This porous material was thoroughly rubbed with nickel (II) oxide to provide a nickel, nickel oxide electrode. (The original sintered plate was not impregnated with nickel hydroxide as described by Fleischer.)

Procedure.—The electrodes were prepared from 3.8-mm strips of the magnesium and nickel. One end of each strip was joined to tungsten wire leads by spot welding. These strips were inserted into lengths of 7-mm Pyrex tubing which were sealed at one end to the tungsten so that copper wire could be joined to the latter. At the other end of the glass tubes, 10 mm of electrode strip protruded. The total length of the electrode assemblies was about 25 cm, of which 3-4 cm was to be submerged in the electrolyte.

Except for minor differences, the cell arrangement was similar to that pictured by Jennings (4). A magnesium and a nickel electrode assembly, a Pyrex thermocouple protection tube, and a Pyrex gas inlet tube were inserted through a cap and sealed in place. The faces of the electrodes were oriented directly opposite to each other and the thermocouple occupied a central position. The electrode tubes were placed approximately 3 cm apart.

For individual electrode polarization measurements, a large cylindrical working electrode of sheet nickel was used. The reference electrodes were contained in 7-mm Pyrex tubing closed at one end. The

[1] Present address: Catalyst Research Corporation, Baltimore, Md.
[2] Present address: University of California, Los Alamos Scientific Laboratory, Los Alamos, N. Mex.

reference system was either Ag(c), AgCl (1, unit mole fraction), or Ni(c), KCl-LiCl-NiCl (1, mole fraction 1.00×10^{-3}) in glass. The silver or nickel electrode leads were 2-3 mm in diameter.

To start a run, a 38 x 200 mm Pyrex test tube was charged with the initial electrolyte salts. This was then placed in a noninductively wound electric furnace, and the cell temperature was adjusted to approximately 320°C by the use of a variable autotransformer. This temperature was maintained until most of the adsorbed water was removed. The temperature then was increased and when the electrolyte was molten, the electrodes, thermocouple tube, and gas inlet tube were positioned.

When a hydrogen or helium atmosphere was used, the gas was slowly bubbled through the melt for 30-60 min. (The loose fit between cap and test tube permitted the escape of gas.) The gas flow was stopped some minutes before emf readings were made.

Electromotive forces of cells and of chromel-p-alumel thermocouples were measured with a null-balancing potentiometer (cell emf's to the nearest centivolt). Temperature values are correct to about ±1°C. The current through the polarized electrodes was measured with a d-c milliameter. The current source was a storage battery with a voltage divider.

The x-ray analysis of the matter insoluble in the molten electrolyte, which was observed on the electrodes and at the bottom of the cell, was accomplished with powder samples mounted in a Debye-Scherer camera. A copper target was used in providing the 30 kv x-radiation. Sixteen-hour exposures were made, and d/n values as determined were checked against known tabulated values.

Results

Electrolyte composition.—Nominally the electrolyte composition was the eutectic mixture of potassium and lithium chlorides and the stated amounts of added components. This eutectic composition is 58 mole % of lithium chloride and 42 mole % of potassium chloride. The eutectic temperature as 354°C [cf. Solomons, *et al.* (5)]. Actually, water and hydroxide ion were also included as demonstrated by Laitinen, *et al.* in terms of polarographic residual current measurements and cold trap collection of water (6). The presence of these species also was shown clearly by the present authors. Quantities of water were collected in a cold trap on evacuation of tubes containing electrolyte; pieces of calcium reacted with the electrolyte to release hydrogen gas. Of course, the presence of hydroxide ion at elevated temperatures implies the additional presence of oxide ion.

Measurements of hydrogen-ion concentration were made on water solutions of frozen electrolyte containing only the eutectic chloride mixture. The pH values were such as to indicate concentrations of hydroxide and oxide ions in the electrolyte ($[OH^-] + 2[O^=]$) to be of the order of 10^{-3} moles/liter.

Behavior at lower temperatures (390°-440°C).—To assist in the postulation of reactions, the effects of internal atmosphere were determined for cells Mg/KCl-LiCl/Ni at 420°C. Unit pressures of air, hydrogen, and helium were used; cells under reduced pressure were measured also. Steady cell potentials were reproducible to within ±0.01 v.

The results of measurements with different atmospheres at 420°C can be summarized as follows: (*a*) with ordinary air atmosphere, the emf was 1.67 v; (*b*) with dry hydrogen atmosphere, 1.58 v; (c) with dry helium atmosphere, 1.67 v; and (*d*) under reduced pressure (10μ Hg), 1.61 v.

It is apparent that, while the use of dry hydrogen gave a lower potential than that of an air-atmosphere cell, the use of dry helium had no such measurable effect. Moreover, evacuation of a cell also depressed the potential, but not as much as the hydrogen atmosphere did.

When an external resistive load was placed across the electrodes, such that electrode current densities were about 10 ma/cm^2, gas was evolved from the nickel cathode. This evolution ceased when the load was removed.

In order to obtain some qualitative information as to the reversibility of the magnesium and nickel electrodes at 420°C, anodic and cathodic polarization measurements were made on both electrodes. For current densities of 3 ma/cm^2, there were no overpotentials within experimental error (±0.01 v). Apparently because of the low ohmic resistance of the electrolyte and the small amounts of current used, measured polarizations were independent of the placement of the reference electrodes.

Starting with a temperature of about 390°C, cells of the type Mg/KCl-LiCl/Ni were heated slowly to 440°C, and the emf was studied as a function of temperature. The portion of the curve in Fig. 1, which has a steep slope, is fairly well established. The points were derived from three separate cells. For a given temperature in this region, the potential remains stable for at least 1 hr. On reversing the direction of temperature change, the emf eventually stabilizes at the value associated with a given temperature.

From the observed dE/dT in the 390°-440°C region, a cell reaction entropy of 55 cal/°C/mole was calculated for a two-electron transfer.

X-ray examinations of the scrapings from electrodes used in the lower temperature range revealed magnesium oxide. No oxide of nickel was detected.

Behavior at higher temperatures (445°-535°C).—

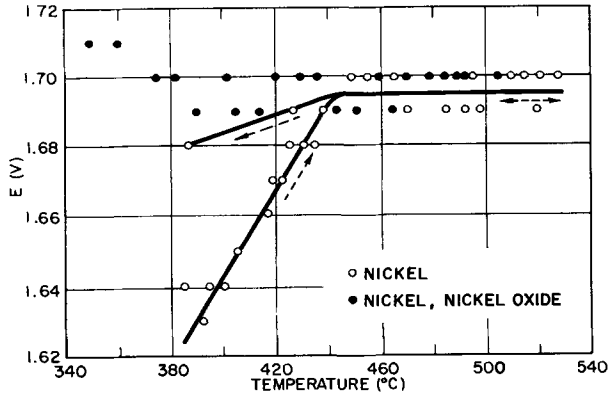

Fig. 1. Electromotive force vs. temperature for the nominal system Mg/KCl-LiCl/Ni.

Upon increasing the temperature of the system Mg/KCl-LiCl/Ni to 445°C, a leveling-off occurs, and on lowering the temperature, a higher potential persists as shown in Fig. 1. The higher potential of 1.70 v also was observed at all temperatures, on heating and cooling, by using a sintered nickel positive electrode into which had been rubbed nickel(II) oxide (NiO).

Examination of cells in the higher temperature region with magnesium and bright nickel electrodes (NiO not deliberately added) revealed the presence of insoluble matter on the electrodes and at the bottom of the cell. X-ray analysis of this material indicated MgO and NiO.

The potentials of magnesium and nickel electrodes at 480°C were studied as a function of concentrations of magnesium (Fig. 2), nickel (Fig. 3), and oxide (Fig. 4) ions in the electrolyte. The ions were introduced by adding to the electrolyte magnesium chloride, nickel chloride hexahydrate, and lithium carbonate, respectively. Often as much as 2 hr was required for stabilization of the potential. However, a stable potential would usually remain so for several hours, and emf values could be confirmed by repetitive measurements with duplicate cells.

Values given in Fig. 2-4 are electrode potentials with respect to the Ag, AgCl (1), glass electrode. At the beginning of a run, the composition of the electrolyte would nominally include both magnesium and nickel chlorides at mole fractions of 3.16×10^{-4} (log N = −3.50). In any one run, only one type of ion was added.

It will be noted that the addition of magnesium or nickel ions causes the electrode potentials of both magnesium and nickel electrodes to rise (become more noble) linearly with the logarithm of the mole fraction of the added ion (Fig. 2 and 3); on the other hand, the addition of oxide ion causes the potentials of both electrodes to fall (become less noble, Fig. 4).

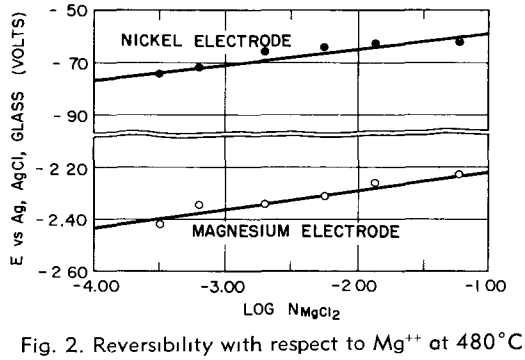

Fig. 2. Reversibility with respect to Mg^{++} at 480°C

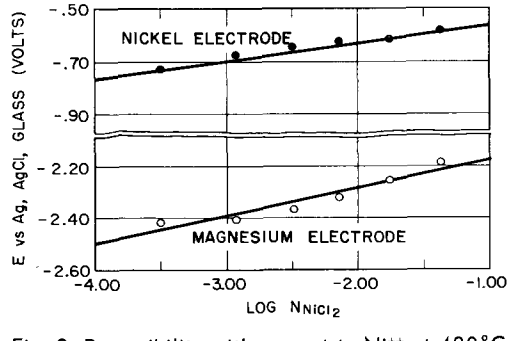

Fig. 3. Reversibility with respect to Ni^{++} at 480°C

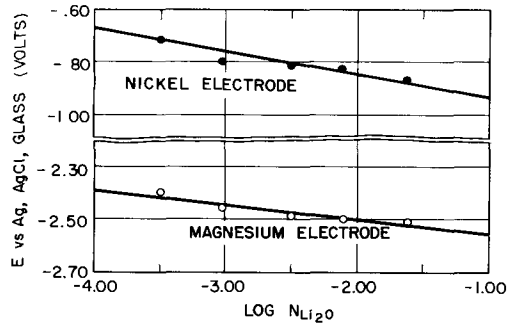

Fig. 4. Reversibility with respect to $O^{=}$ at 480°C

The slopes of the potential-log N curves are given in Table I. The theoretical slopes of ±0.075 are equal to 2.303 *RT*/2F.

Discussion

Cells at Lower Temperatures

On the basis of experimental observations reviewed above, the authors suggest reactions [1a, b, and c] below for the system at 390°-440°C. At the anode,

$$Mg(c) + O^{=}(l) \rightarrow MgO(c) + 2e^{-} \qquad [1a]$$

At the cathode,

$$2OH^{-}(l) + 2e^{-} \rightarrow H_2(g) + 2O^{=}(l) \qquad [1b]$$

Net reaction,

$$Mg(c) + 2OH^{-}(l) \rightarrow MgO(c) + H_2(g) + O^{=}(l) \qquad [1c]$$

Supporting evidence may be summarized as follows: (*a*) The emf was responsive to changes in the internal atmosphere. As compared with an air atmosphere, the use of hydrogen resulted in a depressed emf; vacuum partially restored the cell potential; a helium atmosphere had no particular effect. (*b*) There is definite evidence for the presence of hydroxide ion and/or water. (c) With fairly low current densities, gassing at the cathode was observed upon application of load. Attendant cell polarization was not excessive. (*d*) The cell reaction has a high apparent entropy, which is consistent with the formation of gas. (*e*) X-ray analysis of the anode surface revealed magnesium oxide. A study of the cathode showed no oxide of nickel for cells used in the lower temperature range.

Cells at Higher Temperatures

On heating above 445°C, the emf was relatively unresponsive to temperature change. The observed (and reproducible) discontinuity in the emf-temperature curve suggests a change in mechanism, and indeed, nickel(II) oxide is to be found on the cathode surface if the latter is heated above 450°C in the electrolyte. The negligible entropy of reaction at the

Table I. Slopes of electrode potential vs. log N curves at 480°C

Added ion	Electrodes: Observed Mg v	Observed Ni v	Theoretical Mg v	Theoretical Ni v
Mg^{++}	+0.070	+0.060	+0.075	+0.075
Ni^{++}	+0.110	+0.070	+0.075	+0.075
$O^{=}$	−0.057	−0.090	−0.075	−0.075

higher temperatures indicates disappearance of the gas phase reaction.

Reactions postulated for the system at higher temperatures are as follows. At the anode, [1a] as above, and at the cathode,

$$NiO(c) + 2e^- \rightarrow Ni(c) + O^= (l) \qquad [2a]$$

Net reaction,

$$Mg(c) + NiO(c) \rightarrow MgO(c) + Ni(c) \qquad [2b]$$

It is suggested that the nickel oxide is formed by reaction [3]

$$Ni(c) + 2OH^-(l) \rightarrow NiO(c) + H_2(g) + O^= \qquad [3]$$

This reaction becomes thermodynamically possible in the temperature region of interest. The presence of water and hydroxide ion, which react with both magnesium and nickel to form metal, metal oxide electrodes, has been discussed above.

Lack of information on the free energy of oxide ion in solution does not permit calculation of emf's in the lower temperature region. However, reaction [2b] is amenable to an approximate calculation of potential. Coughlin (7) gives the following standard free energies at 450°C

$$Mg(c) + \tfrac{1}{2}O_2(g) \rightarrow MgO(c),$$

$$\Delta F^\circ_{450^\circ C} = -125.1 \pm 0.2 \text{ kcal} \qquad [4]$$

$$NiO(c) \rightarrow Ni(c) + \tfrac{1}{2}O_2(g),$$

$$\Delta F^\circ_{450^\circ C} = +41.2 \pm 0.1 \text{ kcal} \qquad [5]$$

The sum of reactions [4] and [5] gives, for reaction [2b] $\Delta F^\circ_{450^\circ C}$ -83.9 ± 0.3 kcal. This is equivalent to a standard emf of 1.82 ± 0.01 v. The observed value is 1.70 ± 0.01 v.

The difference between the calculated E° and the observed emf is about a tenth of a volt. However, it should not be inferred that the nickel oxide in the actual cell is at unit activity. Verwey (8) and Tichenor (9) discuss the presence of lithium ion in the nickel oxide lattice. The former induces the presence of nickel(III) oxide which can combine with Li_2O (10). Nickel(II) oxide itself forms a solid solution with lithium oxide, at least on the surface (11).

In any case, the half-reactions [1a] and [2a] are electrodes of the second kind as evidenced by the data in Fig. 2, 3, and 4. That is to say, the magnesium and nickel electrodes are constituted by a metal, a partially soluble metal oxide, and oxide ion in solution. As metal ion is added, it reacts with oxide ion in the electrolyte, and since the oxides are only partially soluble, relationships [A] and [B] will hold:[3]

[3] E′ and K′ imply the use of concentrations instead of activities. Activity coefficients are not known but it is assumed that they are constant throughout the concentration ranges of interest.

$$[Mg^{++}][O^=] = K'_1 \qquad [A]$$

$$[Ni^{++}][O^=] = K'_2 \qquad [B]$$

The Nernst equations for the electrode potentials of the magnesium and nickel electrodes are given by the relationships,

$$E(Mg,Mg^{++}) = E^{\circ\prime}(Mg,Mg^{++}) + (RT/2F) \ln [Mg^{++}]$$
$$= E^{\circ\prime}(Mg,Mg^{++}) + (RT/2F) \ln K'_1/[O^=], \qquad [C]$$

$$E(Ni,Ni^{++}) = E^{\circ\prime}(Ni,Ni^{++}) + (RT/2F) \ln [Ni^{++}]$$
$$= E^{\circ\prime}(Ni,Ni^{++}) + (RT/2F) \ln K'_2/[O^=] \qquad [D]$$

The slopes of E vs. log N_{MgCl_2} or log N_{NiCl_2} curves are calculated to be $+0.075$ v; the slope of the E vs. log N_{Li_2O} curve is calculated to be -0.075 v. These are to be compared with the experimental values in Table I. The authors consider the agreement to be good considering the various experimental difficulties.

Relationships [C] and [D] may be combined to give relationship [E] which expresses the emf of the nominal system:

$$E \text{ (system)} = E^{\circ\prime}(Ni,Ni^{++}) - E^{\circ\prime}(Mg,Mg^{++}) + (RT/2F) \ln K'_2/K'_1 \qquad [E]$$

It can be seen that this latter emf should be independent of the concentrations of magnesium, nickel, or oxide ions for a given temperature.

Manuscript received June 14, 1954. This paper was prepared for delivery at the Cincinnati Meeting, May 1-5, 1955.

Any discussion of this paper will appear in a Discussion Section to be published in the December 1959 JOURNAL.

REFERENCES

1. R. B. Goodrich and R. C. Evans, *This Journal*, **99**, 207C (1952).
2. K. K. Kelley and G. E. Moore, *J. Am. Chem. Soc.*, **65**, 1264 (1943).
3. A. Fleischer, *Trans. Electrochem. Soc.*, **94**, 289 (1948).
4. C. W. Jennings, *This Journal*, **103**, 531 (1956).
5. C. Solomons, J. Goodkin, H. J. Gardner, and G. J. Janz, *J. Phys. Chem.*, **62**, 248 (1958).
6. H. A. Laitinen, W. S. Ferguson, and R. A. Osteryoung, *This Journal*, **104**, 516 (1957).
7. J. P. Coughlin, Bur. of Mines Bull. 542, Washington (1954).
8. E. J. W. Verwey, *Bull. soc. chim. France*, Mises au point D122 (1949).
9. R. L. Tichenor, *Ind. Eng. Chem.*, **44**, 973 (1952).
10. L. D. Dyer, D. S. Borie, and G. P. Smith, *J. Am. Chem. Soc.*, **76**, 1499 (1954).
11. P. J. Fensham, *J. Am. Chem. Soc.*, **76**, 969 (1954).

Enhanced Surface Reactions

III. Adsorption of Gases on Prepared Ruthenium Surfaces

Manfred J. D. Low and H. Austin Taylor

Nichols Laboratory, New York University, New York, New York

ABSTRACT

Rates of adsorption of H_2, CO, and O_2 on $Ru \cdot Al_2O_3$ catalyst surfaces prepared by pre-adsorption of gases were studied. Pre-adsorption of CO increases the rate and extent of H_2 adsorption. Adsorption of CO and of O_2 irreversibly poisons the surface. The Elovich equation is applicable to the data. The results are discussed in terms of a site-creation mechanism. It is found that the pre-adsorption of a gas may influence both the initial and the ambient rates of adsorption to various and at times opposite extents, resulting in several types of "poisoning."

In the study of chemisorption, catalysis, and similar surface processes it is of interest to examine the effects of one gas on the reaction of another with a solid surface. Whereas numerous examples of the "poisoning" of chemisorption and heterogeneous, catalytic processes exist, relatively few data on the opposite effect are to be found in the literature. A study of the effects of one pre-adsorbed gas on the adsorption kinetics of another has been undertaken, and is presented here.

Experimental

A commercial catalyst of 0.5% Ru on alumina was used as adsorbent. A 28-g sample of the solid was placed in a Vycor tube which was subsequently sealed to a conventional constant volume adsorption system. The adsorbent was heated to 500°C and evacuated for about 10 hr to a pressure of 10^{-6} mm Hg or less. Appreciable amounts of gas and water were evolved during the first hour of pumping. The catalyst retained its original black color.

Palladium-filtered H_2 was admitted to the catalyst at 500°C and 1 atm pressure. After a few minutes the catalyst turned gray and retained that color until exposure to oxygen occurred. Subsequent reduction with hydrogen restored the gray color. After being in contact with H_2 for 10 min the system was pumped on for 2 hr at 500° to 10^{-6} mm Hg or less. Experiments on H_2 adsorption were then made. All experiments were done with the adsorbent at 100°C and were numbered consecutively in the order of execution. Volumes are reported in ml. N.T.P. At the completion of each experiment the system was evacuated, the adsorbent heated to 500°C and pumped on at that temperature for 10 hr, with the exception of several "pretreatments" described later. All H_2 was purified by passage through Pd. Carbon monoxide was prepared by dehydration of formic acid with H_2SO_4. Oxygen was purified by passage through a train of ascarite and drierite traps.

Surface preparation.—To prepare the catalyst by pre-adsorption, the following general procedure was adopted. After the 10-hr pumping period, the catalyst was isolated from the system, cooled, and then thermostatted to 100° ± 0.1°C in a steam bath. A predetermined amount of pre-adsorbate was placed in the system of known volume, and the pressure was measured. The stopcock isolating the adsorbent was then opened, admitting the gas to the catalyst chamber. Within 1 min or less the pressure in the system, measured on a manometer containing dibutyl phthalate (DBP), fell to less than 0.1 mm. After about 30 min the adsorbent was isolated and the system evacuated. Gas to be adsorbed "on top of" the first gas was placed in the system at a predetermined pressure. This gas was then admitted to the prepared adsorbent, and the rate of gas-uptake was measured.

Results

Adsorption of hydrogen.—The rate of adsorption of H_2 was measured on the catalyst immediately after the initial H_2 treatment described above. The kinetics of H_2 adsorption on this adsorbent have been studied previously (1). It was found then, as now (Table I), that the kinetics obeyed the Elovich equation (2)

$$\frac{dq}{dt} = a\, e^{-\alpha q}$$

q being the amount of gas adsorbed at time t, a and α constants depending on temperature and initial gas pressure (1-3, 7). The data were internally con-

Table I. Adsorption of H_2 on Ru surfaces pretreated with CO

Run No.	Pi, cm DBP	q_{CO}, ml NTP	α_1, ml^{-1}	α_2, ml^{-1}	ln $a_1\alpha_1$	ln $a_2\alpha_2$
1	69.9	—	3.5	4.6	6.44	8.80
2	69.5	—	3.65	4.8	6.68	10.98
3	70.6	0.30	2.7	3.8	4.88	7.41
4	70.2	—	3.4	4.7	6.15	8.99
6	70.2	1.01	1.33	2.6	1.95	4.98
7	70.0	3.18	0.98	1.4	1.34	2.53
8	69.9	6.50	0.65	0.74	0.73	1.01
9	70.0	1.01	1.76	3.3	2.72	6.39
10	69.9	1.33	1.58	3.1	2.42	6.28
11	70.2	0.27	2.4	4.3	3.87	7.92
12	69.8	1.64	1.46	2.4	2.16	4.58
13	69.9	—	3.3	4.8	5.22	8.10
30	70.8	—	2.5	4.3	4.03	7.75

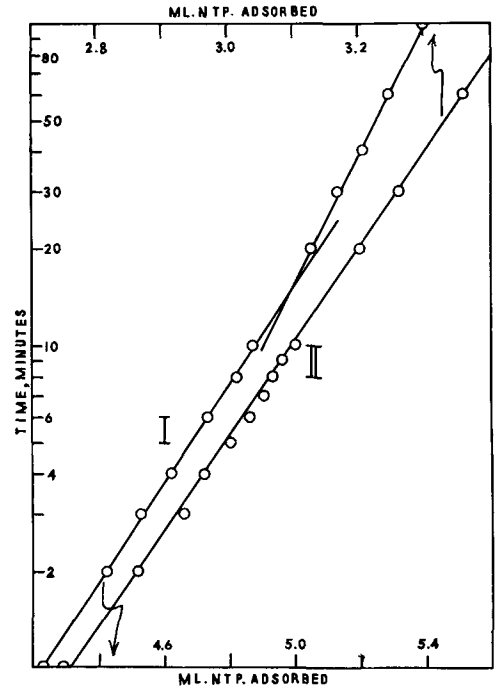

Fig. 1. Adsorption of H_2 on untreated Ru surfaces: I, Run No. 1, 100°C; Pi: 73.8 cm DBP; II, 100°C; Pi: 65 cm DBP.

sistent and well represented by the integrated Elovich equation,

$$q = \frac{2.3}{\alpha} \log_{10} (1 + a\alpha t)$$

Because $a\alpha t > 1$, this is tantamount to representation of data by $q - \log_{10} t$ plots. Whereas in the previous study linear $q - \log_{10} t$, or Elovich, plots were obtained, isothermal anomalies (2) were found in plots of the data of present experiments. Figure 1 shows a plot of the data of Run No. 1 and also that of a comparable run of the previous investigation.

At the end of the previous investigation (1) the catalyst was removed. Fresh adsorbent from the same batch of catalyst used previously was added to the sample to bring its weight to 28 g. It seems plausible, in view of the results to be discussed later, that the break in plot I of Fig. 1 and in other Elovich plots was caused by contamination, possibly

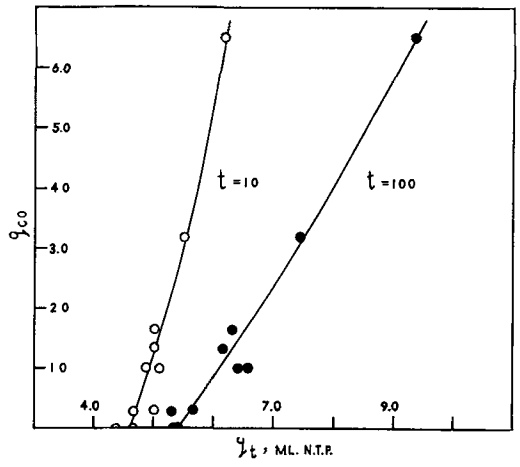

Fig. 3. Adsorption of H_2 on top of CO. The variations of the amount of H_2 adsorbed at time t, qt, with variation in q_{CO}.

by atmospheric oxygen not removed by the initial H_2 treatment of the present investigation.

Adsorption of hydrogen on surfaces containing CO.—Data for eight such experiments are given in Table I. The rate of H_2 adsorption on surfaces containing varying amounts of CO was measured. In each case, the $q - \log_{10} t$ plot of the data resulted in a straight line which, after a certain time, abruptly changed in slope in a fashion similar to that of plot I, Fig. 1. The constants a and α for the initial and final part of each plot were designated by subscripts 1 and 2, respectively. All runs were made at approximately the same initial hydrogen pressure. Inspection of the data reveals some scatter of parameter values, but nevertheless interesting results.

Figure 2 to 4 show the type of relation obtained on plotting several parameters against the amount of pre-adsorbed CO, q_{CO}. In general, it appears that the ambient rates and extents of H_2 adsorption are enhanced, but that the initial rates are decreased, by the pre-adsorption of CO.

Adsorption of CO.—At the end of run 13 the system was evacuated and the temperature of the adsorbent raised to 500° in 20 min. The hot adsorbent was exposed to CO at 80 cm DBP for 2 min, and then pumped on at 500° for 5 min. This CO pretreat-

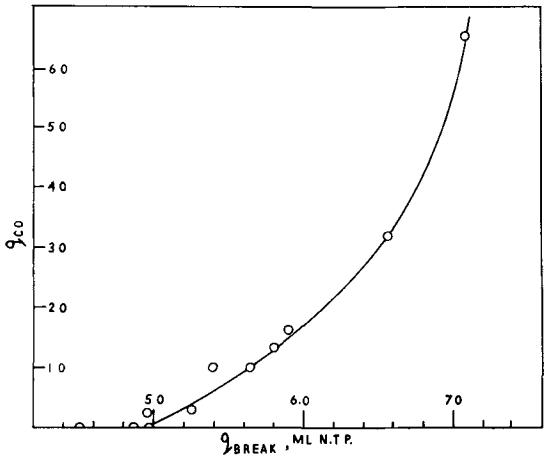

Fig. 2. Adsorption of H_2 on top of CO. The variation of the q-coordinate of the isothermol anomaly, q_{break}, with variation in q_{CO}.

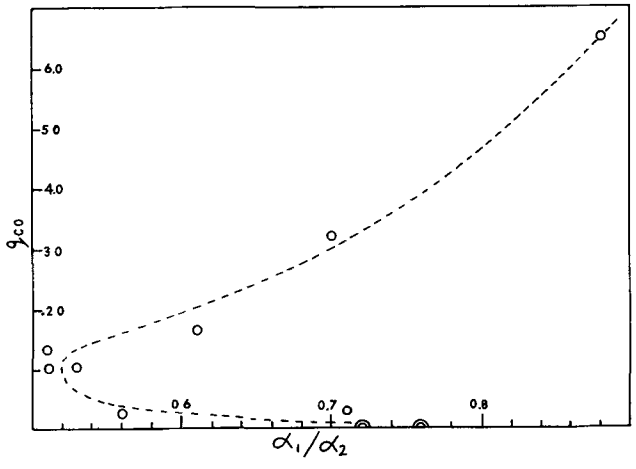

Fig. 4. Adsorption of H_2 on top of CO. The variation of the ratio α_1/α_2, the ratio of ambient rates, with q_{CO}.

ment was repeated twice. The adsorbent was then pumped down to 10^{-6} mm Hg or less for about 12 hr at 500°. Various runs using CO were then made, the parameters of four being given in Table II.

It was found that the experiments were not reproducible and that extreme scatter of parameter values was obtained: there was no gradual change in parameter values with change in the amount of pre-adsorbed H_2. Also, the total amounts of CO adsorbed at 100 min show a steady decrease, dropping from 16.28 ml (run 16) to 13.70 ml (run 29), suggesting that progressive poisoning of the surface occurred.

It is interesting to note that in the first runs using CO on the unprepared surface, Elovich plots wihout breaks were obtained, whereas the data of experiments on surfaces prepared with H_2 (with the exception of the terminal run 29 with 0.08 ml pre-adsorbed H_2) gave discontinuous Elovich plots.

Repetition of hydrogen adsorption.—In order to determine whether the adsorbent had been damaged by the CO pre-adsorption experiments, the H_2 adsorption on an unprepared surface was repeated. After the usual pump-off at the end of run 29, H_2 was admitted to the catalyst at 500° for 5 min at 42 cm DBP. The catalyst was then pumped on for 5 min at that temperature. This treatment was repeated three times, after which the catalyst was pumped on overnight at 500°. Run 30 was then made. The magnitude of the parameters of that run, in comparison to those of runs, 1, 2, and 4, suggests that the surface had been permanently damaged. In view of this it seems possible and perhaps probable that CO poisoning was responsible for the failure of H_2 on O_2 and of O_2 on H_2 experiments, since all may be on top of CO.

Adsorption of oxygen.—An attempt was made to determine the influence of pre-adsorbed H_2 on the adsorption of O_2, and the influence of pre-adsorbed O_2 on the adsorption of H_2. The experiments were not reproducible. It seems probable that, as in the case of CO, an accumulation of irremovable gas occurred on the surface.

Some qualitative information was obtained from ten experiments. (*A*) Each experiment showed internal consistency in obeyance of the Elovich equation. (*B*) Pre-adsorption of O_2 enhances the rate and extent of adsorption of H_2 (Fig. 5).

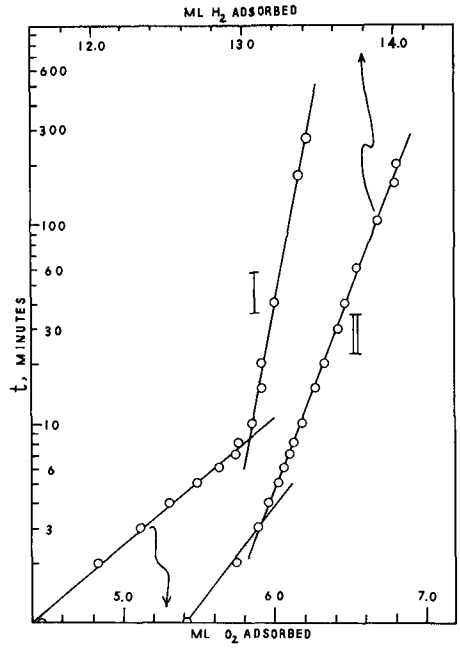

Fig. 5. Adsorption of O_2 and of H_2: I. Adsorption of O_2 on unprepared Ru, Run 33; II, H_2 on top of 0.78 ml O_2, Run 35.

Discussion

The adsorption of H_2 on top of CO is faster and more extensive than that on untreated surfaces. An explanation, in classical terms, comes readily to mind. After 100 min, 5.40 ml of H_2 (run 1) but 16.28 ml CO (run 16) are adsorbed on untreated surfaces. Pretreatment of a surface with CO might therefore cause a part of the surface, originally inert, to take up H_2, or H_2 may form surface H-CO complexes, or H_2 may literally be adsorbing on top of adsorbed CO molecules.

Such effects and mechanisms have been found previously, mainly in equilibrium studies such as the following. The work of Griffin (4) on the effect of pre-adsorbed CO on the adsorption of H_2, and that of White and Benton (5) on the effect of H_2 on Ni "poisoned" with CO are examples. A more recent work is that of Sastri and Wiswanathan (6). The adsorption of CO and H_2 was studied on a Fischer-Tropsch Co-ThO_2-kieselguhr catalyst on which H_2 and CO, respectively, had been pre-adsorbed. It was found that at any temperature the H_2 adsorption was enhanced the higher the amount of pre-adsorbed CO, that for a particular amount of CO the enhancement was larger the higher the temperature, and that the enhancement caused was relatively larger the smaller the volume of gas pre-adsorbed. These effects were explained in terms of surface complexes, since the amounts of pre-adsorbed gas were too small to account for the enhancement by a mechanism whereby one gas became adsorbed on top of the other. A similar postulate was made by White and Benton who, finding that CO enhanced H_2 adsorption, argued that ". . . either the CO can increase the activity of the already active areas, or it can stimulate those areas which do not function until higher pressures, or it can create entirely new areas . . ." (5). Because only small amounts of CO gave the effect, it was suggested that increased adsorption was due to an enlargement of active areas, which are produced by having very small amounts of CO adsorbed on them.

Examination of the present data and reference to "poisoning" effects discussed previously (2, 7, 8) suggest that a more generally applicable approach is desirable. A more general mechanism may be deduced from the theories of Taylor and Thon. It has been shown (2, 7-10) that surface site creation can occur by a branching chain mechanism initiated by the reaction of an active particle, G, with a surface atom, S, causing a "dissociation" of the atom into two adsorption sites, V. The over-all reaction for the branched chain may be written,

$$G + nS \rightarrow GV + (2n-1)\ V$$

Table II. Adsorption of CO, O_2, H_2

Run No.	Pi, cm DBP	α_1 ml^{-1}	α_2 ml^{-1}	ln $a_1\alpha_1$	ln $a_2\alpha_2$	
16	73.8	1.90	—	11.45	—	(a)
17	74.2	2.00	—	11.88	—	(a)
24	73.7	0.98	2.4	5.00	13.08	(b)
28	74.2	0.65	2.4	3.2	12.01	(c)
33	60.2	1.48	15.3	2.83	2.89	(d)
35	75.6	2.3	4.5	12.61	25.17	(e)

(a) CO on untreated surface.
(b) CO on top of 2.58 ml pre-adsorbed H_2.
(c) CO on top of 0.65 ml pre-adsorbed H_2.
(d) O_2 on untreated surface.
(e) H_2 on top of 0.78 ml pre-adsorbed O_2.

The excess (2n-1) sites can be active for adsorption or, alternatively, may suffer bimolecular decay. Enhancement or retardation of chemisorption rates or of the extent of chemisorption by pre-adsorbed gases may be explained in terms of that general mechanism. The effect of an impurity may be expected to be either one, or a combination of, two general effects: (*A*) the initial site creation process may be affected, i.e., the parameter n (chain length) may be greater or smaller than usual; (*B*) the bimolecular decay process may be affected, poisons permitting easier recombination of sites, promoters hindering the decay and thus permitting a longer "site-life." Several combinations of *A* and *B* are thus possible.

In the present case of H_2 adsorbed on top of CO, the initial rate, a_1, is seen to decrease with increasing q_{CO} (Table I), a_1 falling from about 10^6 on the pure surface to about 10^1 on a surface having 6.5 ml of pre-adsorbed CO. Simultaneously, the total amounts adsorbed at $t = 100$ min increase (Fig. 3) and the parameters α, reflecting the reciprocal ambient rates, decrease. It appears that the initial site creation process was hindered, and that fewer sites were available initially for the adsorption of H_2. Thus the increase in the adsorption process seems to be wholly due to a reduced site decay rate.

Conversely, the parameters of run 35 (Table II) suggest that the site creation process was affected mainly. In this case, on adsorbing H_2 on top of 0.78 ml O_2, a_1 was changed from 10^6 to 10^{12}, while α_1 declined slightly: it appears that many more sites were created initially than in the case of H_2 adsorption on the untreated surface. The over-all effect is thus one of "promotion."

Further over-all effects may be predicted. An outright "poisoning" may occur, where both the initial and ambient rates of adsorption are decreased. The lack of reproducibility of CO adsorption rates and the diminution in the extent of adsorption of that gas, noted above, may be ascribed to such an effect: the rate of site recombination is greatly increased and the initial site creation process hindered, resulting in outright, true poisoning. Such true poisoning is also shown by Iijima's data (11, 12): the pre-adsorption of mercury or of CN by a Ni catalyst decreases both the initial and ambient rates of adsorption of H_2.

Also, a "pseudo-poisoning" may occur, in which case the ambient rate is decreased, but the initial rate is increased. The pre-adsorption of a gas thus may cause increased total adsorption, but at greatly reduced rates, the bulk of the gas adsorbing in a very short time.

It appears that the reverse of the last example may exist: there may be decreased total adsorption, but at a higher rate. Agliardi and Morelli (13) thus found that when cobalt catalyst is poisoned with CO, less H_2 is adsorbed, but also that the rate of adsorption is greater, than by cobalt not poisoned by CO. This case may be ascribed to the dual action of a decreased initial site creation and a hindered rate of site decay. A further example of pseudo-poisoning is given by Iijima's data (12) on the adsorption of H_2 on top of CO on a Ni catalyst. The total adsorption after 19 hr decreases, the parameters α_1 increase, and the initial rates a_1 increase, with increasing amount of pre-adsorbed CO.

These considerations suggest that the determination of rates of adsorption may be more fruitful in pre-adsorption studies than the usual static isotherm or isobar measurements.

It has been postulated previously (2) that the isothermal anomalies sometimes found are due to a change-over of the adsorption process from one type of adsorption site to another. Recently this postulate has been supported by Meller (14), who derived the Elovich equation by assuming the chemisorption process to consist of two independent but simultaneous processes.

Such a mechanism also is implied to be operative at the present time. Thus the appearance of a break in the Elovich plots of data of CO adsorption on H_2-treated surfaces, while no such breaks were found to occur with CO adsorptions on untreated surfaces, may be said to be due to the influence of H_2 on the site creation of decay mechanism. Similarly, the displacement of amount adsorbed, q_{BREAK}, at the discontinuity in Elovich plots with increasing amounts of pre-adsorbed gas—a behavior also apparent in the data of Iijima—may be bound up with such a mechanism (Fig. 2).

Not enough data exist at present for a quantitative treatment of these effects, but qualitatively the above mechanism may be applied to the various relations shown by Fig. 2-4. However, because the presence or absence of isothermal anomalies seems to depend on the past history of the surface, there may be no real significance, from a general quantitative point of view, between the relations of parameters vs. q_{poison} for several different poisons. Further work is in progress.

Acknowledgment

The authors wish to thank Dr. T. Freund for performing several experiments.

Manuscript received Jan. 24, 1958.

Any discussion of this paper will appear in a Discussion Section to be published in the December 1959 JOURNAL.

REFERENCES

1. M. J. D. Low and H. A. Taylor, to be published.
2. H. A. Taylor and N. Thon, *J. Am. Chem Soc.*, **74**, 4169 (1952).
3. L. Leibowitz, M. J. D. Low, and H. A. Taylor, *J. Phys. Chem.*, **62**, 471 (1958).

4. C. W. Griffin, *J. Am. Chem. Soc.*, **49**, 2136 (1927); **56**, 845 (1934); **57**, 1206 (1935).
5. T. A. White and F. Benton, *J. Phys. Chem.*, **35**, 1784 (1931).
6. M. V. C. Sastri and T. S. Viswanathan, *J. Am. Chem. Soc.*, **77**, 3967 (1955).
7. H. A. Taylor, *Ann. N. Y. Acad. Sci.*, **58**, 798 (1954).
8. H. A. Taylor, Peter C. Reilly Lectures in Chemistry, Vol. XII, Univ. of Notre Dame Press (1956).
9. M. J. D. Low and H. A. Taylor, *This Journal*, **104**, 439 (1957).
10. M. J. D. Low, *ibid.*, **105**, 104 (1958).
11. S. Iijima, *Rev. Phys. Chem. Japan*, **12**, 148 (1938).
12. S. Iijima, *ibid.*, **13**, 1 (1938).
13. N. Agliardi and S. Morelli, *Gazz. chim. ital.*, **78**, 707 (1948).
14. A. Meller, *Monatsh.*, **87**, 491 (1956).

Technical Notes

Electrolytic Preparation of Titanium from Fused Salts

II. Design of Laboratory Cells

Marshall B. Alpert, James A. Hamilton, Frank J. Schultz, and William F. Sullivan

Titanium Division, Research Department, National Lead Company, Sayreville, New Jersey

Previously a process was described for the preparation of Ti metal by the electrolysis of an alkali or an alkaline earth metal chloride melt containing the reduced chlorides of Ti (1). The reduced chlorides were prepared *in situ* by electrolytically reducing $TiCl_4$ introduced through a hollow cathode. Variables important in obtaining a good yield of coarsely crystallized, ductile Ti metal adhering to the cathode included careful sealing of the cell, maintenance of the soluble Ti largely in the divalent state, and avoidance of melt agitation during metal deposition. Provision of an adequate diaphragm and gas barrier arrangement to avoid oxidation of soluble reduced Ti at the anode was also considered.

The relation between design and function of externally heated laboratory cells is an important factor. Modifications were made in the single diaphragm cell leading, on the one hand, to diaphragm cells operating continuously rather than on a charge-strip basis and, on the other hand, to alternative deposition procedures. These include both one-step diaphragmless and electrorefining procedures.

Single Diaphragmed Cell

The usual laboratory single diaphragm cell used, of approximately 10-liter capacity and externally heated by a Globar furnace, is similar to the cell illustrated in Fig. 1, except that no diaphragm surrounded the introduction cathode. The porous, fused alumina diaphragm rests on a pedestal, since it has been found that, as long as the diaphragm is not under tension by support from above, no difficulty is experienced with breakage in the fused salt system. The gas barrier is fitted inside the diaphragm so that the Cl_2 atmosphere does not contact the catholyte containing reduced Ti; spacing is sufficiently close to insure that practically no rising Cl_2 bubbles slip between the diaphragm and the gas barrier. Current efficiencies for Cl_2 gas were about 90% with this arrangement. The cell may be pressure tested for air leakage even while hot by use of an attached manometer. It is essential that the cell be sealed carefully from atmospheric contamination. Laboratory equipment of this type has been operated for periods of over three months without breakdown.

Certain limitations are inherent in this cell. The current for extended periods of operation is limited to about 60-100 amp to avoid obstructing the relatively small cross section (7.5 cm diameter) of the diaphragm and gas barrier with salt spray. The relatively small size of the anode and cathodes resulted in a rather high cell resistance, for example, 0.06 ohm with $SrCl_2$-NaCl supporting electrolyte at 700°C. This situation was improved by a concentric design with the graphite anode as a ring external to the diaphragm. Such a cell with a resistance of only 0.01 ohm was studied. The small amount of catholyte (2.8 l) resulted in an inconveniently short charging

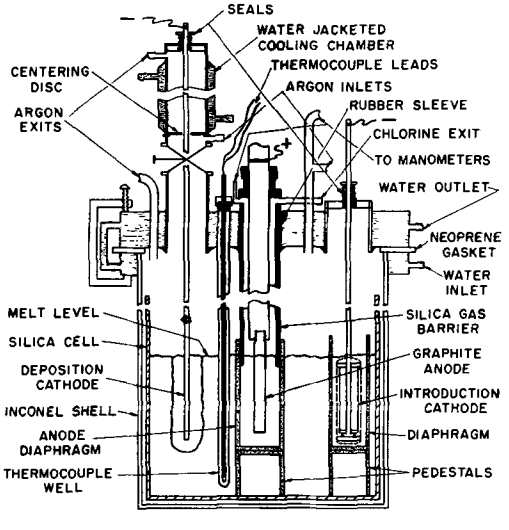

Fig. 1. Schematic drawing of double diaphragm cell

and stripping cycle, and the placing of the necessary accessory parts was difficult because of the small space available.

A major disadvantage of the single diaphragm cell is that the $TiCl_4$ must first be charged to the cell and then the reduced titanium chlorides electrolyzed to yield Ti metal in cyclic rather than continuous operation. Two factors imposed this requirement. Operation of the hollow cathode caused agitation of the melt in the vicinity of the deposition cathode and thereby reduced the crystal size and quality of the metal produced. In the second place, polarization of the hollow cathode at current densities above about 0.1 amp cm^{-2} resulted in the deposition of significant amounts of Ti metal at this electrode. Therefore, introduction of $TiCl_4$ at a rate of one mole per two faradays gave less than optimum degree of reduction for the melt, unless low hollow cathode current densities were employed or the melt was further reduced at low current densities prior to the metal deposition stage.

Some of the difficulties with cyclic operation may be eliminated by avoiding the use of a diaphragm entirely. If the current through the introduction cathode is increased to a value of approximately $4/f$ faradays per mole of $TiCl_4$, where f is the current efficiency of the cell, the reduced titanium chlorides formed exist only transiently and do not escape in significant amounts from the vicinity of the introduction cathode. The melt therefore is substantially free of reduced Ti salts and no diaphragm is required (6,7).

Double Diaphragm Cell

Figure 1 shows a cell in which the introduction cathode is also surrounded with a porous fused alumina diaphragm similar to the anode diaphragm (2). This cell permitted continuous reduction of $TiCl_4$ to Ti metal. When a high soluble Ti concentration was built up within the introduction diaphragm, the amount of Ti introduced as $TiCl_4$ and the amount leaving the introduction catholyte for the deposition catholyte were balanced by hydrostatic flow. The hydrostatic head resulting in this flow stems from the weight of $TiCl_4$ being added and from ionic migration effects (1). The deposition of coarsely crystallized, ductile metal was obtained while $TiCl_4$ was continuously introduced, since agitation of the melt about the hollow cathode no longer disturbed the electrolyte about the deposition cathode. In addition, polarization of the hollow cathode did not prevent maintenance of the degree of reduction of the melt desired, a level of at least 70% Ti^{++}. In this case polarization of the hollow cathode occurred at a higher current density because of the higher concentration of total Ti and hence of Ti^{+++} in the introduction catholyte melt. Also, metal produced by polarization was ultimately dissolved in the introduction catholyte by reaction with either $TiCl_4$ or $TiCl_3$.

During continuous operation of the cell illustrated in Fig. 1 approximately 50 amp was passed through the introduction cathode while 45 amp was the deposition current. Typically, using the $SrCl_2$-NaCl eutectic melt as supporting electrolyte, the concentration of reduced titanium chloride was about 6M in the introduction catholyte and about 0.6M in the deposition catholyte; approximately 80% was Ti^{++}. Current efficiencies averaged 90% and recoveries were about 80% ductile Ti metal. The anode gas was 98.6% Cl_2 and 1.4% $TiCl_4$

Titanium Bed Introduction Cell

An alternative cell design which also allows continuity of operation and, in addition, can be used to produce secondary as well as primary metal, is shown in Fig. 2. In this design, $TiCl_4$ was reacted with a bed of Ti metal to produce the reduced titanium chlorides required for the deposition of Ti metal. The bed of Ti metal may be replenished either by adding a portion of the deposited metal or by adding Ti metal scrap. In the cell illustrated in Fig. 2 alternate deposits were dropped to the bed. The net reactions are given by the equations

$$\left(\frac{4}{N} - 1\right) \text{Ti (scrap or dropped deposit)} + TiCl_4 \rightarrow \frac{4}{N} TiCl_N \text{ (chemical)}$$

$$\frac{4}{N} TiCl_N \xrightarrow{4/f \text{ faradays}} \frac{4}{N} Ti + 2Cl_2 \text{ (electrochemical)}$$

$$\left(\frac{4}{N} - 1\right) \text{Ti (scrap or dropped deposit)} + TiCl_4 \xrightarrow{4/f \text{ faradays}} \frac{4}{N} Ti + 2Cl_2 \text{ (over-all)}$$

where N is the apparent valence of the Ti dissolved in the melt and f is the current efficiency of the cell. Note that when scrap Ti is employed instead of dropped deposits and the Ti dissolved in the melt is maintained largely in the divalent state, each $4/f$ faradays produced 1 mole of primary metal and also almost 1 mole of secondary metal. In a simple primary cell the same amount of current would produce only 1 mole of Ti metal. In the cell illustrated the electrolyte selected was a mixture of 8% $SrCl_2$ and 92% NaCl, requiring an operating temperature of about 830°C. The current was 65 amp with the $TiCl_4$ feed rate at 1.6 g/min. The concentration of reduced titanium chloride, approximately 80% divalent Ti, was maintained about 0.25M in the catholyte.

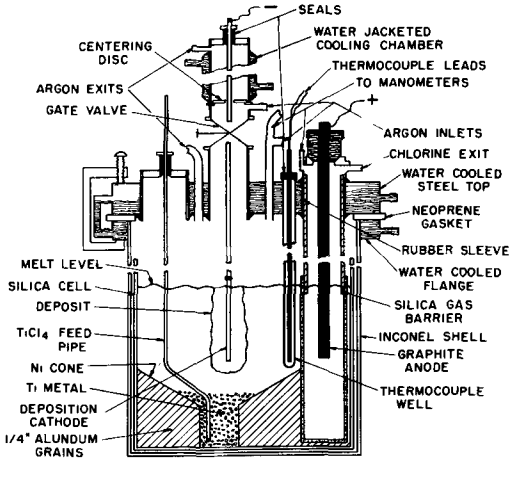

Fig. 2. Schematic drawing of titanium bed cell

Recovery averaged about 83% of ductile Ti metal. A further improvement in design which completely avoids any disturbance of the catholyte during $TiCl_4$ introduction may be realized in the case of scrap metal by using a design similar to the double diaphragm cell. The scrap metal is added to the introduction catholyte.

Refining of scrap Ti metal may also be accomplished separately by using a cell with a scrap Ti anode. Such cells are particularly simple to construct, since neither a gas barrier nor a diaphragm is used, and no protection against corrosive Cl_2 is required. At low current densities the anode dissolves to yield reduced titanium chlorides substantially at concentrations set by the equilibrium

$$Ti + 2TiCl_3 \rightleftharpoons 3TiCl_2$$

and, since Ti is deposited from the same melt at close to reversible conditions, the cell emf is small, less than 0.1 v at 700°C, $SrCl_2$-NaCl melt, anode current density 0.25 amp cm^{-2}. At higher anode current densities increasing amounts of Ti^{3+} are produced because of anodic polarization and the cell emf is increased. Most contaminating metals are left effectively at the anode and oxygen remains as a reduced titanium oxide anode sludge (3-5).

Acknowledgments

The technical assistance of Thomas M. Buck, Daniel Kaufman, Bryce H. McMullen, and Lawrence S. White is gratefully acknowledged.

Manuscript received July 2, 1958. This paper was prepared for delivery before the Ottawa Meeting, Sept. 28-Oct. 2, 1958.

Any discussion of this paper will appear in a Discussion Section to be published in the December 1959 JOURNAL.

REFERENCES

1. M. B. Alpert, F. J. Schultz, and W. F. Sullivan, *This Journal*, **104**, 555 (1957).
2. M. B. Alpert and J. A. Hamilton (To National Lead Co.), U. S. Pat. 2,760,930, Aug. 28, 1956.
3. J. R. Nettle, D. H. Baker, Jr., and F. S. Wartman, "Electrorefining Titanium Metal," U. S. Bur. Mines, Rept. Invest. 5315 (1957).
4. R. S. Dean, W. W. Gullett, F. X. McCawley, and I. Hornstein, Industrial Laboratories, **8** (4), 4 (April 1957).
5. F. J. Schultz and T. M. Buck, (To National Lead Co.), U. S. Pat. 2,734,856, Feb. 14, 1956.
6. M. B. Alpert, W. R. Opie, F. J. Schultz, and K. Svanstrom (To Titan Company, Inc.), Argentine Pat. 88,505, March 17, 1953.
7. W. R. Opie and K. A. Svanstrom, "Electrodeposition of Titanium from Fused Chloride Baths Using $TiCl_4$ as a Feed Material," to be published in *Trans. A.I.M.E.*

Process for Electrolytic Extraction of Titanium Metal from Titanium Carbide Anodes

Guy Ervin, Jr., Herbert F. G. Ueltz, and Malcolm E. Washburn

Research and Development Department, Norton Company, Worcester, Massachusetts

Extractive metallurgy of titanium has been discussed in several review articles (1-8). Increasing interest has been shown in molten salt electrolysis using soluble anodes, but confined chiefly to electrorefining, in which high-purity metal is recovered from scrap or other sources of impure metal. However, one article (9) and several patents (10-14) deal with production of Ti by electrolysis of soluble anodes containing TiC.

The key to the process is the fact that, although TiC is a metal carbide with a limiting composition of 1:1, it behaves during electrolysis as though it were metal with high carbon content. Since the other refractory carbides probably have the same property, the method is potentially applicable to production of Zr and other refractory metals.

The work reported here was started in this laboratory several years ago. It shows that better than 90% of the Ti in TiC can be extracted electrolytically in fused halide baths and deposited as dendritic Ti metal. The dendritic deposit contains entrapped electrolyte which must be removed by leaching with dilute acid. Current efficiency and product quality are variable and depend on several factors including electrode configuration, physical and chemical characteristics of the TiC anode, chemical composition of the electrolyte, and to a lesser extent on current densities and temperature of the bath.

Experimental

The cell used for most of the experiments consisted of a graphite crucible lined with carbon-bonded TiC and containing the molten electrolyte, with a metal cathode mounted centrally in the bath, and with an external container of nickel or steel, closures being made with rubber O-rings clamped between water-cooled flanges. Operation was in a purified argon atmosphere, and precautions were taken to remove traces of air and moisture from all raw materials and cell parts. Several sizes of cell were used, varying in metal product capacity from 20 g to 12 lb.

Carbon-bonding of TiC in the anode was achieved either by sintering at about 2300°C or more commonly by forming a mixture of the carbide with pitch, molding to shape, and baking at 1000°-1200°C in inert atmosphere to drive off pitch volatiles. Anodes formed in this way from pitch were strong and porous, with good electrical conductivity, and their use permitted rather complete electrolytic extraction of the Ti in the TiC.

Some typical results are shown in the following Tables I and II.

Table I. Electrolytic titanium from titanium carbide

Anode composition,‡ %			Electrolyte composition*	Cathode C.D., amp/cm²	Voltage	Current efficiency Ti^{+4} basis	Metal Composition, %			Hardness† BHN
Ti	C	Fe					Fe	C	O**	
69	24	0.15	LiCl-KCl	2	3.8	45%	0.2	0.4	0.3	310
66	31	0.15	NaCl-$TiCl_3$	2	3.6	65	0.5	0.5	0.5	380
70	27	0.6	NaCl-K_2TiF_6	2	4.5	49	0.6	0.02	0.14	174
67	31	0.1	NaCl-K_2TiF_6	2	4.5	47	0.1	0.3	0.3	250
79	20	0.03	NaCl-K_2TiF_6	2.5	4.1	51	0.1	0.05	0.12	157

Table II. Electrolytic refining of titanium

99.4	0.15	0.1	NaCl-$TiCl_2$	1.5	0.7	130	0.03	0.02	0.12	120
99.1	0.02	0.7	NaCl-K_2TiF_6	1	0.5	105	0.01	0.00	0.11	104

* When $TiCl_3$ or $TiCl_2$ was present the concentration was 5% Ti, K_2TiF_6 in the bath corresponded to 3% Ti. Temperature approximated 850°C in all cases.
** Oxygen was calculated from hardness plus Fe and C analyses.
† Measured as Rockwell C or B and converted to BHN.
‡ Exclusive of the carbon bond. Note that in all cases but one, substantial quantities of free carbon were present, above the stoichiometric value of 20%.

Metal could be produced with electrolytes containing no Ti initially, or with $TiCl_3$ present, but coarser crystals were produced with electrolytes containing K_2TiF_6. Figure 1 shows metal dendrites typical of the cathode deposits described in the last row of Table I, made from relatively pure TiC.

Table II shows data on electrorefining of primary metal made electrolytically from TiC. This produced much coarser crystals, of the type shown in Fig. 2, and purity was improved.

Discussion

Dissolved Ti in the bath is trivalent, when the anode is TiC. If a bath containing $TiCl_2$ is used, it rapidly converts to $TiCl_3$, contrary to the behavior with Ti metal anodes. The theoretical basis for this is that the electrode potential at the anode due to decomposition of TiC is lower for formation of Ti^{+3} (0.59 v) than for Ti^{+2} (0.89 v). Furthermore this potential probably exceeds that for oxidation of Ti^{+2} to Ti^{+3} so that, before any Ti ion is produced anodically from the TiC, all of the $TiCl_2$ in the vicinity of the anode is oxidized to $TiCl_3$. This makes it impossible to use iron cells and iron anodes as has been done elsewhere (15) because $TiCl_3$ attacks iron. For the same reason little refining with respect to iron can be expected when the anode is TiC.

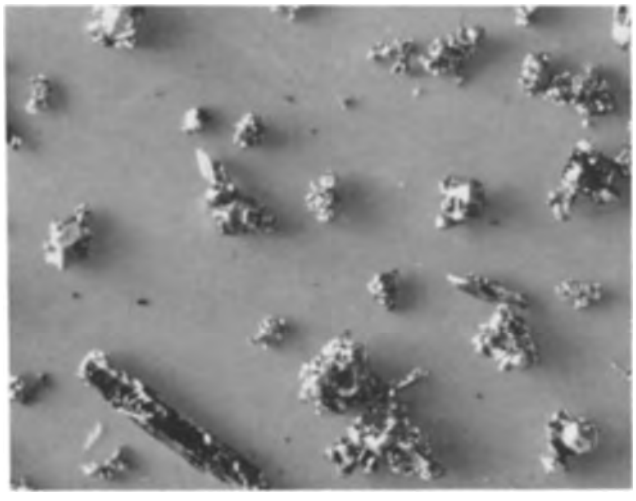

Fig. 1. Titanium metal dendrites 99.6% Ti, BHN 157, made from TiC anode. Magnification, X25.

Fig. 2. Titanium crystals 99.8% Ti, BHN 110, made by two-stage electrolysis from TiC. Magnification X8.

Important impurities other than iron to be considered are carbon and oxygen. Carbon contamination was caused by loosening of particles from the anode, but could be kept below about 0.05% C by proper bonding of the anode. Oxygen contamination kept decreasing during the course of the project as techniques were improved. There was no evidence of any transfer of oxygen from the carbide anode to the product, and it seems probable that metal of suitably low oxygen content could be produced in larger equipment. However, direct oxygen analyses of TiC and the metal produced from it were not made so that direct evidence for refinement with respect to oxygen is lacking. Estimating oxygen by difference indicated that metal with 0.1 to 0.2% oxygen was produced from arc-furnace TiC containing 0.5% or more oxygen.

Conclusion

Titanium metal powder can be produced in fused salt electrolyte from titanium carbide anodes. Purity of the metal is adequate for many uses including

powder metallurgy and for feed material to an electrorefining process making maximum purity metal. There is a reasonable expectation that commercial development would lead to higher product purity direct from TiC.

One of the cheapest ways to get metal from its oxide is to reduce the oxide with carbon, if possible. Reduction of titanium oxide with carbon does not yield metal but does yield metal-like carbide from which metal can be produced electrolytically. Viewed in these simple terms the method has strong commercial potential for titanium metal production.

Manuscript received May 8, 1958.

Any discussion of this paper will appear in a Discussion Section to be published in the December 1959 JOURNAL.

REFERENCES

1. N. S. Spence, *Can. Mining Met. Bull.*, **1951**, 21.
2. M. Cook, *J. Inst. Metals*, **82**, 93 (1953).
3. W. J. Kroll, *Metall.*, **9**, 1, 366 (1955).
4. *Chemical Week*, **76**, No. 8, pp. 35-54, Feb. 19, 1955.
5. P. Herasymenko, New York Univ.-Amer. Soc. for Metals Titanium Course, Sept. 12-16, 1955.
6. M. E. Sibert and M. A. Steinberg, *J. Metals*, **8**, 1160 (1956).
7. L. M. Pidgeon, *Metal Prog.*, Vol. 70, Aug. '56 p. 81; Oct. '56 p. 79; Nov. '56 p. 75.
8. *Chemical Week*, **79**, No. 23, pp. 55-64, December 8, 1956.
9. B. S. Hickman and G. M. Willis, *Proc. Australasian Inst. Mining & Met.*, **178**, 29 (1956).
10. S. C. Pyk, Swedish Pat. 137,626, July 24, 1952.
11. E. Wainer (to Horizons Titanium Corp.) U. S. Pat. 2,722,509, Nov. 1, 1955.
12. G. Ervin, Jr. and H. F. G. Ueltz (to Norton Co.) Brit. Pat. 744,396, Oct. 5, 1956; U. S. Pat. 2,837,478, June 3, 1958.
13. B. C. Raynes, M. E. Sibert, and J. T. Burwell, Jr. (to Horizons Titanium Corp.) U. S. Pat. 2,813,069, Nov. 12, 1957.
14. M. E. Washburn (to Norton Co.) U. S. Pat. 2,838,454, June 10, 1958.
15. D. H. Baker, Jr. and J. R. Nettle, Paper presented at New York Meeting AIME, February 1956.

Comparison of the Life of Linings in Rotating and Stationary Phosphorus Furnaces

M. M. Striplin, Jr., J. M. Potts, and E. C. Marks

Tennessee Valley Authority, Wilson Dam, Alabama

The first commercial-size rotating phosphorus furnace, a TVA development (2), was placed in operation in October 1950. The furnace is similar to the rotating alloy and carbide furnaces described by Ellefsen (1). It is of about 10,000-kw capacity and has been operated with conventional stationary furnaces as an integral part of the TVA plant. Except for information on the life of the furnace lining, which is a factor of major importance, fairly complete operating results on the rotating furnace have been published (3). Now, further information is presented which compares the life of the lining in this furnace with those of the TVA stationary furnaces.

TVA operates five rectangular stationary furnaces of conventional design and one round rotating furnace. Unless hot spots show up to indicate the need for repairs, the furnaces are normally operated at least 2 years between lining inspections. At the time of inspection, superficial damage to the lining is repaired by ramming in hot carbon paste, although such repairs to the surface of the hearth are of doubtful value. Major repairs involve replacement of a substantial number of carbon blocks used in the lining, or the entire lining.

Data on the performance of the linings in the TVA furnaces during the 8 years since the rotating furnace was started show a big advantage in favor of the rotating furnace (see Table I). For the stationary furnaces, the record shows that during the 8-year period, there were 12 times when holes developed in the furnaces unexpectedly spilling the molten contents (tapouts). Only minor repairs that could be made from the outside of the furnaces were sufficient in some cases, while others involved major repairs. Hot spots developed frequently, causing a need for decreased power input and special precautions to avoid further damage. Operation on low power usually was continued until such time as the hot spots disappeared or it was decided to shut down for major repairs to the lining. Twelve major repairs were made to the stationary furnaces during this period; this averaged a major repair to each furnace once every 3 years.

In comparison, during the same period, the rotating furnace had no hot spots, no tapouts, and no major repairs. The only patching has been after each of the four inspections, when carbon paste was used to cover eroded surfaces caused by normal wear and by the tools used to dig out the charge. The last inspection showed the original floor of this furnace to be in excellent condition. Erosion of the carbon amounted to about 2.54 cm/year (the thickness of the carbon floor is 104 cm).

Even at the slag line, there has been little or no wear of the carbon blocks in the rotating furnace. In the stationary furnaces, this is an area of high normal wear. This contrast was experienced even though the outer surfaces of the electrodes in the rotating furnace are 27% closer to the side walls than in any of the other furnaces. Maintenance costs have been considerably less on the rotating furnace than on the stationary furnaces.

For the same hearth area, the rotating furnace has a higher kilowatt capacity than the stationary furnaces. As an example, this factor expressed as kilowatts per square meter of hearth area (power density) shows the rotating furnace to have been oper-

Table I. Comparison of TVA rotating and stationary phosphorus furnaces

	Stationary furnace No.						Rotating furnace No.
	2	3	4	5	6	Avg	1
Nominal rating, kw	9500	8700	7500	16,000	16,000	—	10,000
Area of hearth, sq m	26.8	28.1	23.6	37.6	40.1	—	19.9
Hearth power density, kw/sq m	354	310	318	426	399	361	503
Distance from outer surface of electrode to side wall, m	1.52	1.55	1.37	1.77	1.77	—	1.12
Maximum voltage (transformer taps), v	375	300	260	500	500	—	375
Age of lining as of October 1950, yr and mo	6-2	2-2	1-10	2-0	1-10	2-10	0
Calendar time in operation,* %	78.4	75.3	66.0†	79.3	86.9	77.1	79.9
Number of major repairs to lining* ‡	2	2	2	4	2	2.4	0

* Since October 1950.
† Retired from service in 1957.
‡ Substantial replacement of carbon blocks required, as distinguished from minor repairs with carbon paste.

ated at a value of 503 as compared with 310 to 426 for the other furnaces. Localized overheating or overexposure of the lining to corrosive conditions occurs in stationary furnaces because the furnace lining remains in the same relative position with respect to the tips of the electrodes, which are the focal points of energy input to the furnaces. In the rotating furnace no area of the lining remains near the tips of the electrodes very long. Localized overexposure is thereby avoided and more energy can be concentrated into the same space. Also, whatever normal wear is encountered is more uniformly distributed.

One of the few features of the original design of the rotating furnace that failed to give completely satisfactory service was the molten lead seal, which was provided at the juncture between the stationary roof and rotating crucible to prevent the escape of gas. This seal required considerable attention and maintenance. After 5½ years of operation, the seal was replaced with a 51-cm water seal. Fresh water is fed continuously to the seal and is allowed to overflow down the furnace shell as supplemental cooling water. The new seal has required no maintenance and has given good service.

The TVA rotating furnace, although relatively small in comparison with the furnaces constructed recently by industry, has demonstrated adequately that rotating furnaces have important advantages over stationary furnaces. The feasibility of rotating larger phosphorus and other types of furnaces has been demonstrated by industry.

The trend in the phosphorus industry seems to be away from furnaces with the electrodes arranged in line and toward furnaces with a triangular arrangement of the electrodes. The electrical load is more equally distributed to each electrode in these furnaces than in furnaces with the electrodes arranged in line. Even distribution of the electrical load may contribute to longer life of the furnace lining and is beneficial in other respects. Inasmuch as it is possible to operate a round furnace at a slightly higher power input when the furnace is rotated, the cost of a rotating furnace per unit of capacity is essentially the same as that of a stationary round furnace. Additional rotating phosphorus furnaces may be expected as soon as the benefits to be derived from this type furnace are fully appreciated.

Manuscript received June 16, 1958.

Any discussion of this paper will appear in a Discussion Section to be published in the December 1959 JOURNAL.

REFERENCES

1. J. Ellefsen, *Trans. Electrochem. Soc.*, **89**, 307 (1946).
2. M. M. Striplin, Jr., S. A. Hardin, and W. H. Bundy, U. S. Pat. 2,744,944, May 8, 1956.
3. M. M. Striplin, Jr., G. H. Megar, and J. M. Potts, *Chem. Eng.*, **60**, 201 (September 1953).

June 1959 Discussion Section

A Discussion Section, covering papers published in the July–December 1958 JOURNALS, is scheduled for publication in the June 1959 issue. Any discussion which did not reach the Editor in time for inclusion in the December 1958 Discussion Section will be included in the June 1959 issue.

Those who plan to contribute remarks for this Discussion Section should submit their comments or questions in triplicate to the Managing Editor of the JOURNAL, 1860 Broadway, New York 23, N. Y., *not later than March 2, 1959*. All discussion will be forwarded to the author, or authors, for reply before being printed in the JOURNAL.

Technical Feature

Electrolysis of Organic Solvents with Reference to the Electrodeposition of Metals[1]

Abner Brenner

National Bureau of Standards, Washington, D. C.

This lecture was instituted to honor the memory of one of the founders of our society, J. W. Richards. Since it is now many years since he died, and since few of us had a personal acquaintance with him, it is fitting that I say a few words about him. He was not only one of the organizers of the Society, but also its first president, holding office in 1903. He served as Secretary-Treasurer for 17 years until his death in 1921. He was very active in both the administrative and scientific affairs of the Society and commented on most of the papers that were presented at the annual meetings. He was known the world over as an eminent metallurgist and served on numerous technical committees. He made one of his greatest contributions to science in his capacity as Professor of Metallurgy at Lehigh University where he taught until the time of his death. He was the author of two textbooks on metallurgical subjects.

In appraising the list of previous Richards Lectures, I note that 12 lectures have been given previously at an average interval of 2.5 years. Since there is an interval of five years between this lecture and the previous one, I assume that the Society intentionally passed the thirteenth, and that this one should be considered as the fourteenth. Can it be that the directors of the Society are superstitious?

I have also noted with interest that the previous lectures have covered such subjects as history, metallurgy, and electronics. Only one lecture, the last one, dealt with an electrochemical subject—overvoltage. I believe that the lecture that I am giving this afternoon is also an innovation, because it is the first one concerned with electrodeposition. No doubt some members of the audience are glad to see that electrochemistry is finally winning public recognition.

The subject of this lecture is the "Electrolysis of Organic Solvents with Reference to the Electrodeposition of Metals." Since this is a rather specialized subject and since electrodeposition is not usually presented at the Spring Meeting, I was pleased to see so many members assembling for the lecture. I mentioned this to Dr. Steinberg just before starting, and he replied that, inasmuch as it was raining outside, the members had no where else to go.

Research on the electrolysis of organic solutions has been sadly neglected in favor of a slavish devotion to aqueous systems. I did not understand this attitude until I happened to see a cartoon pinned on a laboratory bulletin board that made clear the reason for this. It depicted a students' laboratory. A voluptuous young woman was working at the bench blissfully unaware that she was the cynosure of two pairs of male eyes, focused from across the room. One male student was saying to the other, "and just think, she is over 90% water!" The great practical importance of water in our daily living has induced scientists to study aqueous systems far beyond their scientific importance. There are many more new phenomena to be discovered in the study of nonaqueous[2] systems.

The subject matter of this lecture is divided into two parts. Beginning with the more complex subject, attempts to electrodeposit metals from nonaqueous media are discussed and next, the more fundamental subject, the electrolysis of nonaqueous solvents themselves.

Deposition from Nonaqueous Media

The first interest in electrodeposition of metals from nonaqueous media developed in connection with the measurement of the conductivity of solutions. It was natural that the investigator should seek to determine whether conducting solutions would yield electrodeposits as do aqueous solutions. The first record is the work of Laszczynski (1) in 1895, who was measuring the conductivity of solutions of salts in acetone. He electrolyzed several of the solutions and observed that the deposits on the cathode gassed or sparked if placed in water. He concluded that lithium and potassium had been deposited. He also deposited silver. Within the next five years both he (2) and Kahlenberg (3) electrodeposited several metals from pyridine solutions. Kahlenberg showed that, under the best conditions, the theoretical quantity of metal deposited.

During the next 25 years the deposition of metals from a small number of solvents was studied in a qualitative fashion. This early work has been re-

[1] This paper was presented as the J. W. Richards Memorial Lecture, April 28, 1958, at the New York Meeting.

[2] In this paper nonaqueous systems do not include fused salts.

viewed by Audrieth (4). Among the solvents used were acetone, pyridine, ethylenediamine, ammonia, formamide, and acetamide. Apparently nitrogen-containing solvents commanded the most attention. Grignard reagents were electrolyzed and yielded mossy deposits of magnesium (5).

The amount of early work was rather small and attracted little interest. Within the last decade there has been a revived interest in the study of nonaqueous media because of the possibility of depositing some of the less common metals which cannot be deposited from aqueous solution.

About 30 metals can be deposited from aqueous solution. These metals will be referred to as the aqueous group and the other metals as the nonaqueous group. The early studies of nonaqueous solvents dealt mainly with the aqueous group of metals. Since these metals can be deposited more readily and in a purer condition from water solution, these studies were of little practical interest. Few of the nonaqueous group of metals were deposited. Lithium and some other alkali metals were purported to have been deposited. However, the purity was not substantiated by analysis and certainly many of the deposits were far from pure, as Pospekhov (6) has shown. Furthermore, since the metals could be obtained more readily by deposition from fused electrolytes, there was no incentive to further study.

The nonaqueous group of metals which has been of more recent interest contains the light metals, beryllium, aluminum, and magnesium; the semiconductor, germanium; and the refractory metals, titanium, zirconium, tungsten, and molybdenum. Of these by far the most attention has been given to the deposition of aluminum. Furthermore, aluminum is the only nonaqueous metal that can be considered to have been successfully deposited. By this is meant that the metal can be obtained at high cathode current efficiency in high purity and with good physical properties.

Studies at the National Bureau of Standards

This lecture is largely, although not exclusively, concerned with the work done by the Electrodeposition Section of the National Bureau of Standards. Our work in this field started rather suddenly. About 1950 we became interested in the electrodeposition of aluminum and were repeating some of the recently published work. About this time lithium aluminum hydride became commercially available and we studied the electrolysis of ether solutions of this compound. These experiments led to the development of a new type of nonaqueous plating bath (7). The Navy Bureau of Aeronautics sponsored further investigations of the process because of the possibility of electroforming aluminum wave guides. This interest seemed to have kindled a spark. Other Government agencies became interested in depositing some one of the less common metals for various purposes. The AEC sponsored a project on the deposition of beryllium (8); the Wright Air Development Center, on the deposition of titanium and zirconium (9); and Springfield Armory, on the deposition of molybdenum. An investigation of the deposition of magnesium (10) was also carried out. Although some interesting developments resulted, they were not the practical objectives desired by the sponsors, and after a period of three or four years the program ceased about as suddenly as it had started.

I wish to mention briefly some of the equipment used in our work with nonaqueous solvents. Since many of the experiments involved the preparation and use of compounds, such as metal alkyls and borohydrides, which were sensitive to air or moisture or even spontaneously inflammable, the techniques and equipment used were somewhat different from those used in ordinary plating experiments. Indispensable to our work were inert atmosphere chambers (11) of which two were constructed. A dry atmosphere of helium was circulated continuously through the chambers and deoxygenated. For running electrolytic experiments in the laboratory some special cells were designed (12) which excluded the air and yet allowed the cathodes to be removed and examined, and fresh ones put in if necessary.

Since aluminum is the nonaqueous metal which has received most study and also is the one most successfully deposited, it is discussed in some detail as a typical example. Space does not permit the mention of all of the early attempts to deposit this metal from organic solvents. A partially successful deposition was done by Blue and Mathers (13) from organic solutions similar to the Friedel-Craft reagents and from aluminum alkyl halide solutions. The deposits were not of good quality. The first successful deposition of aluminum from a nonaqueous solution at room temperature was accomplished by Hurley and Wier (14) using a solution of aluminum chloride in ethyl pyridinium bromide. This bath had more the characteristics of a molten salt bath than a typical bath made from an organic solvent. Menzel (15) deposited aluminum from solutions of aluminum ethyl or aluminum phenyl and aluminum chloride in toluene.

At the National Bureau of Standards a hydride plating bath was developed which yielded a pure, ductile deposit of aluminum (7). The bath consisted of aluminum chloride dissolved in ether with the addition of lithium aluminum hydride. Evans and Kennedy (16) by conductometric studies have shown that the ionizing complex in this type of solution is probably $Al_2Cl_5^+ \cdot AlH_4^-$. Deposits several hundredths of an inch thick were readily obtained from the bath. To prevent formation of nodules, methyl borate was used as an addition agent.

The bath had some interesting characteristics. It had a limited life and could tolerate the presence of oxygen but not moisture. Baths were used up to periods of a year or more by occasionally rejuvenating them with lithium aluminum hydride. Decomposition of the bath occurred mainly during electrolysis, not as a result of atmospheric attack. During operation hydrogen was given off at both the cathode and anode, but the quantity was greater at the anode than at the cathode. Apparently the decomposition of the bath occurred anodically, although aluminum went into solution with 100% anode current efficiency. Another peculiarity of the

bath was that the amount of aluminum deposited from it was about equivalent to the amount of aluminum that had been added to the bath as aluminum chloride. The aluminum that went into solution anodically did not appear to enter into the same kind of chemical combination as the aluminum initially introduced, and apparently metal did not deposit readily from this anodically dissolved aluminum. Thus, additional aluminum chloride had to be added to the bath at intervals. Eventually, the bath became so viscous that it could not be used any longer. Up to this point about 250 g Al had been deposited from about 1 l of bath.

Some experiments were made to determine whether the hydrogen that was liberated at the anode in the electrolysis of the aluminum plating bath would cause embrittlement of steel. We used steel rings to test this and found that the rings were embrittled more severely than in a water solution. The decrease in breaking load was 30-50%. Cathodic discharge of hydrogen from several other organic solvents did not cause appreciable hydrogen embrittlement.

More recently another bath for depositing aluminum has been developed by Ziegler (17) in Germany, the man of polyethylene fame. This bath is unique because it involves the formation of a complex between triethyl or methyl aluminum and sodium fluoride. The aluminum alkyl by itself does not conduct the current, but the complex does and yields very pure aluminum on electrolysis. We have prepared the bath and confirmed that it does operate satisfactorily. Also the complex can be prepared in ether solution and then is much less inflammable.

Most recently, Murphy and Doumas (18) reported the deposition of aluminum from aluminum chloride dissolved in an ethereal solution of butyl amine. We have not had much success with this bath. A private communication to me indicates that the deposit may be an aluminum compound.

I shall briefly touch on our work with some of the other elements (8-10) of the nonaqueous group and then attempt to summarize the state of our knowledge. I believe that the work will be easier to follow if it is organized with respect to the type of compound involved rather than to take each metal separately.

The success of the hydride bath for depositing aluminum led us to attempt the deposition of other metals from similar types of baths, but the hydride bath appears to be specific for aluminum. Soluble hydrides of titanium and zirconium could not be prepared as lithium aluminum hydride precipitated the elements or a compound from ether solution. Ethereal solutions containing beryllium aluminum hydride and magnesium aluminum hydride were prepared and yielded alloys containing aluminum and the other metal, but the quality of the deposits was rather poor.

The metal alkyls were investigated as electrolytes because Grignard reagents had yielded magnesium on electrolysis. Our experience with the magnesium deposits was unsatisfactory as they were not dense and coherent. Beryllium was deposited from an ethereal solution of beryllium dimethyl, the best results being obtained from a solution that contained both beryllium dimethyl and beryllium chloride. The beryllium was about 95% pure under the best conditions. We made a number of attempts to prepare alkyl derivatives of titanium and zirconium but all of these ended in failure, although a number of interesting compounds were encountered which we did not have time to investigate. Solutions of the cyclopentadienyl derivatives of titanium and zirconium conducted poorly and did not yield metal on electrolysis.

The most interesting phase of the work was the preparation and electrolysis of metallic borohydrides. The metallic borohydrides had only recently been prepared when we started our work. The pure borohydrides of aluminum and zirconium are liquids but they do not conduct. In ether solution, the borohydrides of aluminum, magnesium, and beryllium conduct, and alloys are obtained containing the metal and boron. The most interesting deposit was one containing about 30% boron, the remainder beryllium. The ether solutions of titanium and zirconium borohydrides did not yield the metals on electrolysis. However, by mixing the aluminum hydride plating bath with borohydride solutions of titanium or zirconium, deposits were obtained which contained aluminum, boron, and titanium or zirconium. The refractory metals were not present in large percentages. The titanium content was about 7% and zirconium between 15 and 40%.

We also attempted to prepare a molybdenum borohydride, by the dry reaction of molybdenum pentachloride, or molybdenum hexafluoride, with $LiBH_4$, but after the apparatus blew up twice we gave up. However, a molybdenum compound containing borohydride radical and chloride was obtained by a reaction in solution. In the course of our program on nonaqueous plating we made a considerable number of attempts to deposit molybdenum, but all these were negative and it is not likely that we shall publish the results of that investigation.

To complete the picture of the deposition of the less common metals from organic solutions, germanium was deposited from a solution of germanium tetrachloride in propylene glycol by Szekely (19). Because the cathode current efficiency was less than 1%, the process is not practicable. The claim of Müller and associates (20) to having deposited some of the alkaline earth metals from pyridine solution is open to question since they did not actually isolate the metals but only examined the current density potential relations during the electrolysis. Several investigators have made unsuccessful attempts to deposit the rare earths from basic solvents (21). Jonassen (22) has been unsuccessful in depositing tungsten or molybdenum from a wide variety of compounds and complexes dissolved in various organic and inorganic solvents.

Discussion of Nonaqueous Plating

Now I wish to evaluate the work that has been done in the field of nonaqueous deposition with respect to its practicability, its achievements, and its theoretical interest. Certainly there is no practical

interest in the deposition from nonaqueous media of those metals which can be deposited from water solution. The success which has attended the efforts to obtain the nonaqueous group of metals has not been very great. As already mentioned, aluminum is the only nonaqueous metal that can be deposited conveniently in a satisfactory physical condition and with a good cathode current efficiency. Some commercial interest has been manifested in the deposition of aluminum, but no actual uses have developed. At one time there was some interest in depositing aluminum on copper wire. The aluminum was to be anodized and thus form a high temperature insulation for the wire, but it is not known whether this process was actually tried. The deposition of other nonaqueous metals has not been sufficiently successful even to consider practical applications.

In general the metals which separate from nonaqueous media are less pure than those obtained from water solution. This may be caused partly by incomplete reduction and partly by adsorption of the organic material on the nascent surface of the metal. Adsorption also occurs to some extent in deposition of metals from aqueous solutions, but since the solvent molecules are much smaller the adsorption is much less. As examples of the contamination of metals deposited from nonaqueous solution, Pospekhov (6) showed that the alkali metals deposited from nitrobenzene solution in some instances contained only 25% of the metal. In our own work we were unsuccessful in obtaining satisfactory nickel or cobalt deposits from organic solvents. They were stressed and exfoliated. The nickel deposits were only 85% metallic. Some of the beryllium deposits obtained from the alkyl baths contained so many inclusions that if scratched they spontaneously ignited.

The last topic to be considered concerns the generalizations that are helpful in investigating nonaqueous deposition. Before taking these up, it is necessary to dispose of some ideas that have been suggested but which are not applicable. The magnitude of the dielectric constant of a solvent has been considered an index of its ability to form conducting solutions and, by inference, good plating baths. However, this criterion is not valid because ether is a good nonaqueous solvent for depositing several metals and yet its dielectric constant is only about 4.5. On the other hand, anhydrous HCN, which has a high dielectric constant, is not a particularly good electrolytic solvent. Incidentally, even if one could predict solutions that would be conductive, it would be of little help to nonaqueous plating, because the difficulty is not in finding conductive solutions but in finding conductive solutions that yield metals on electrolysis.

Water and a number of other polar solvents such as acetone, alcohol, and dimethylformamide, which readily form conducting solutions, have themselves in the pure state an appreciable electrical conductivity of about 10^{-7} ohm^{-1} cm^{-1}. This conductivity might seem to be an index of a good electrolytic solvent. However, this generalization is vitiated by the fact that ether has a conductivity of about 4×10^{-13} ohm^{-1} cm^{-1}. Toluene has a conductivity of 10^{-14} ohm^{-1} cm^{-1}, and yet aluminum can be deposited from certain toluene solutions.

The crystal structure of a compound is regarded as an index of its ability to ionize and form a conducting solution when dissolved. This idea is expressed tacitly when a salt is said to have an ionic structure. However, the solute is not the only factor, inasmuch as the solvent plays an equally important role. An "ionic" compound which forms a conducting solution in water does not necessarily form a conducting solution in nonaqueous solvents.

In considering those few generalizations which are helpful in nonaqueous plating, it is necessary to discuss the aqueous and nonaqueous groups of metals separately. The aqueous group can be deposited readily from polar solvents using common salts in many instances. This subject is not of interest in the present discussion and need not be considered further.

The nonaqueous group of metals may be divided into two subgroups: (*A*) active metals like the alkali and alkaline earth metals, which are too active to be deposited from aqueous solution, and (*B*) less active metals such as tungsten, germanium, etc., which are thermodynamically capable of depositing from aqueous solution (12, 23) but do not because of the nonreactivity of their ions. The alkali metals, as already mentioned, have been deposited from a few organic solvents. Presumably this is possible because in these solvents the hydrogen is more strongly bound than in water and the deposition potential of these metals can be attained.

However, little success has attended the deposition of the (*B*) subgroup of nonaqueous metals. The nonreactivity of their ions seems to be as much of a stumbling block in nonaqueous as in aqueous media. In fact, alloys of tungsten and molybdenum are more readily deposited from aqueous than from nonaqueous solutions. The fact that lithium and sodium can be deposited from the very solution containing one of the subgroup (*B*) metals further confirms the fact that the difficulty is not one of thermodynamics.

The metals magnesium, aluminum, titanium, zirconium, and beryllium, because of the difficulty of depositing them, seem to belong more to subgroup (*B*) than (*A*). The following generalizations apply to them. The best plating solutions appear to be made from solvents and solutes that can coordinate mutually. The solvents and solutes are probably similar to the classes of compounds that have been designated as Lewis bases and acids. The only useful solvents are those containing a weak coordinating center, for example, the oxygen atom of an ether or the double bond of an aromatic hydrocarbon. Other solvents with a more unsaturated coordinating center, for example, nitrogen or carbonyl groups, form too stable a complex. On the other hand, solvents which have virtually no coordinating ability, such as aliphatic hydrocarbons, do not even form conducting solutions.

The solutes found useful for depositing metals are very specific: certain halides, metal alkyls, hydrides, and borohydrides. The conventional solutes—ordinary salts—which are useful for aqueous solutions are of no value in nonaqueous plating. In no case

has the salt of an oxyacid been useful for depositing the metals considered here.

To summarize, the electrodeposition of the nonaqueous group of metals is intensely interesting from an academic and theoretical point of view, but it does not have a bright future for practical purposes. It is unlikely that baths for depositing the subgroup (*B*) metals can be developed by systematically and empirically trying all available compounds of the elements in all available solvents. The further developments will probably depend on the general development of the chemistry of complexes; that is, new types of complexes will have to be produced. It is likely that the type of complex that will solve the problem of depositing some of the nonaqueous metals has not yet been prepared.

Electrolysis of Organic Solvents

Background and Literature

Our attempts to electrodeposit some of the metals of the nonaqueous group, although lacking in practical success, have made us cognizant of the vast, unexplored field of nonaqueous electrochemistry. In our researches many nonaqueous conducting solutions were prepared and electrolyzed without obtaining a metal at the cathode, indeed, in many instances without any visible signs of reaction. Thus we became interested in the nature of the electrode reactions, not only as a matter of curiosity, but also because basic information might eventually lead to a better approach to the electrodeposition of metals.

After some deliberation and exploratory work we decided on a research dealing with the electrolysis of pure nonaqueous solvents, mainly organic solvents, as being the most basic study in electrolysis that could be undertaken. We were interested in the mechanism of the electrode reactions, the products formed, and the dynamic potentials involved. The electrolyses to be studied were analogous to the electrolytic decomposition of water. Electrolyses in which a compound was added to the solvent to impart conductivity were not excluded from the investigation, but it would be necessary to show, eventually, that the electrolytic decomposition of the solvent, as in the case of water, was independent of the nature of the conducting additive.

In the introduction to the previous section, the statement was made that the electrochemistry of nonaqueous systems has been largely neglected. To this can be added the observation that, in the study of the electrochemistry of the nonaqueous systems, dynamic electrode processes have been slighted in favor of the measurement of static potentials and conductivities. Measurements of potentials without an identification of the electrode reactions do not possess much meaning. The lack of interest in electrolyses of nonaqueous systems becomes evident from a perusal of several monographs. The books by Jander (24) and Audrieth (25) which deal with nonaqueous solvents contain little information on electrolyses. Brockman's book (26) deals almost exclusively with the electrolysis of organic compounds in aqueous solutions. The "Electrochemie Nichtwässeriger Lösungen" of Walden (27) is mainly concerned with the conductivity of solutions. Measurements of conductivity have little direct relation to electrolysis. This is evident, since conductivities can be measured by methods that do not involve electrolysis, for example, by the use of induced currents.

Studies of the electrolysis of inorganic solvents other than water are few. In most instances the interest centered on the electrolysis of a dissolved substance rather than of the solvent. Cady and Taft (28, 29) attempted to study electrolytic oxidation and reduction in liquid sulfur dioxide and in phosphorus oxychloride but were not very successful. The electrolysis of sulfur dioxide and of solutions of salts in sulfur dioxide was studied by several investigators (30), but the results were inconclusive. Stefan and Nagel (31) noted that electrolysis of solutions of various organic compounds in ammonia yielded only nitrogen and hydrogen on electrolysis, and the organic compound was frequently recovered unchanged.

Although a number of investigations have involved the electrolysis of organic solutions, in most of these the interest also was centered on the electrolytic decomposition of a substance dissolved in the solvent, the latter playing a minor role. The attempts to deposit metals from organic solutions form the largest group of investigations and these already have been discussed adequately. The remainder of the literature deals with organic solutions that undergo complicated reactions on electrolysis. The electrolysis of ether solutions of Grignard reagents (5) has been studied thoroughly. The electrolysis of organic solvents containing dissolved hydrogen fluoride (32) has become of commercial importance. Another 15 or 20 references (33) cover most of the subject of electrolysis of organic solutions, but as already noted these dealt with the dissolved substances rather than with the solvent.

Work at the National Bureau of Standards

The study of the electrolysis of nonaqueous solvents at the NBS is at an early stage. Preliminary investigation showed that various difficulties attended the electrolysis of some organic solvents, for example, the formation of tarry materials. One class of compounds that seemed amenable to study was the amides. Thus far we have electrolytically decomposed several simple amides. Most of the work has been done with formamide and dimethylformamide in a simple cell having both electrodes in the same compartment. The main products of the electrolysis of formamide are hydrogen and cyanuric acid. This had previously been shown by Schaum and Schneider (33c). The products formed in the electrolysis of dimethylformamide have not yet been identified.

Since eventually the anode and cathode reactions must be studied separately, a divided cell must be used. Conventional equipment, such as U-tubes or H-tubes of the types used for transference experiments, is not suitable, because a considerable electrical migration of material occurs when an appreciable fraction of a faraday is passed during electrolysis to provide sufficient reaction products for examination. The use of a porous diaphragm between the cathode and anode compartment, which is a common practice, is not successful in dealing with

nonaqueous solvents because electro-osmosis is considerable. To prevent it the diaphragm must be very porous.

Several different types of divided cells have been constructed. The most promising type consists of three compartments, one each for the anode and cathode and a chamber between these two. By allowing fresh solvent continually to flow through the middle compartment to a discard, products from either the anolyte or catholyte that migrate into the center chamber are removed before they can migrate into the opposite electrode chamber. Some further modifications of the flowing junction type of cell are contemplated.

The performance of a given electrolytic cell in keeping the anolyte and catholyte from mixing was determined qualitatively by electrolyzing boron trifluoride etherate with copper electrodes. Copper which dissolved at the anode was precipitated as metal by reaction products that formed in the catholyte. Thus the presence of copper on the walls of the vessel was evidence that mixing or electrical transport of the contents of the compartments had occurred. The apparatus with the flowing junction had only a slight deposit of copper.

Future Program

The study of the variables involved in electrolysis will be directed toward answering the following questions:

1. Are the products of electrolysis of the pure solvent the same as those obtained in the presence of a conducting additive or obtained in the electrolysis of an aqueous solution of the solvent?

2. Do the solvents have a definite decomposition potential?

3. Can the solvents be arranged in a series, either on the basis of the decomposition potential or of the enthalpy change of the electrolysis, such that in a mixture the solvent lower in the series is preferentially decomposed electrolytically?

More specifically, by electrolyzing various substituted amides we hope to arrive at an understanding of the mechanism of the electrolysis.

In conclusion, a systematic study of the electrolysis of nonaqueous media will greatly advance the science of electrochemistry and contribute to the chemistry of nonaqueous solvents. The electrolysis of nonaqueous media is probably the most neglected field of inquiry in both electrochemistry and the chemistry of nonaqueous solutions. At the present time most of the knowledge of electrolysis has been obtained from aqueous solutions, and many of the phenomena observed for water may be specific for that solvent. The study of the electrolysis of a large number of other solvents will lead to generalizations that cannot be obtained from a study of a single solvent.

Manuscript received Sept. 8, 1958. This paper is the Richards Memorial Lecture presented at the New York Meeting, April 27-May 1, 1958.

Any discussion of this paper will appear in a Discussion Section to be published in the December 1959 JOURNAL.

REFERENCES

1. St. v. Lacszczynski, *Z. Elektrochem.*, **2**, 55 (1895).
2. St. v. Lacszczynski and St. v. Gorski, *ibid.*, **4**, 290 (1897).
3. L. Kahlenberg. *J. Phys. Chem.*, **3**, 602 (1899); *ibid.*, **4**, 349 (1900).
4. L. F. Audrieth and H. W. Nelson, *Chem. Rev.*, **8**, 335 (1931).
5. Jolibois, *Compt. rend.*, **155**, 353 (1912); *ibid.*, **156**, 712 (1913).
   Rodebush and Peterson, *J. Am. Chem. Soc.*, **51**, 638 (1929).
   Kondyrew and Manojew, *Ber.*, **58**, 469 (1925).
   J. Kondyrew, *J. Russ. Phys. Chem. Soc.*, **60**, 545 (1928).
   J. M. Nelson and W. V. Evans, *J. Am. Chem. Soc.*, **39**, 82 (1917).
   L. W. Gaddum and H. E. French, *ibid.*, **49**, 1295 (1927).
   H. E. French and M. Drane, *ibid.*, **52**, 4904 (1930).
   W. V. Evans and F. H. Lee, *ibid.*, **55**, 1474 (1933).
   W. V. Evans and F. H. Lee, *ibid.*, **56**, 654 (1934); *ibid.*, **57**, 489 (1935).
   W. V. Evans and E. Field, *ibid.*, **58**, 720 (1936).
   W. V. Evans and E. Field, *ibid.*, **58**, 2284 (1936).
   W. V. Evans and D. Braithwaite, *ibid.*, **61**, 898 (1939).
   W. V. Evans, D. Braithwaite, and E. Field, *ibid.*, **62**, 534 (1940).
   W. V. Evans and Fang-Hsun Lee, *Nanking J.*, **6**, 29 (1936).
6. D. A. Pospekhov, *J. Appl. Chem. USSR*, **27**, 552 (1954).
7. D. E. Couch and A. Brenner, *This Journal*, **99**, 234 (1952).
   J. H. Connor and A. Brenner, *ibid.*, **103**, 657 (1956).
8. G. B. Wood and A. Brenner, *ibid.*, **104**, 29 (1957).
9. W. E. Reid, Jr., J. M. Bish, and A. Brenner, *ibid.*, **104**, 21 (1957).
10. J. H. Connor, W. E. Reid, Jr., and G. B. Wood, *ibid.*, **104**, 38 (1957).
11. J. M. Sherfey, *Ind. Eng. Chem.*, **46**, 435 (1954).
12. A. Brenner, *This Journal*, **103**, 652 (1956).
13. R. D. Blue and F. C. Mathers, *Trans. Electrochem. Soc.* **63**, 231 (1933); **65**, 339 (1934); **69** 519 (1936).
14. F. H. Hurley and T. P. Wier, Jr., *This Journal*, **98**, 203 (1951); *ibid.*, 207.
15. W. Menzel, *Z. anorg. u. allgem. Chem.*, **269**, 52 (1952).
16. G. G. Evans, J. K. Kennedy, Jr., and F. P. Del Greco, *J. Inorg. & Nuclear Chem.*, **4**, 40 (1957).
17. K. Ziegler and H. Lehmkuhl, *Z. anorg. u. allgem. Chem.*, **283**, 414 (1956).
18. A. C. Doumas, Virginia Polytechnic Inst. (1955).
    N. F. Murphy and A. C. Doumas, *Proc. Am. Electroplaters' Soc.*, 162 (1956).
19. G. Szekely, *This Journal*, **98**, 318 (1951).
20. R. Muller, F. Holzl, W. Knaus, F. Planisberg, and K. Prett, *Monatsh.*, **44**, 219 (1923).
21. P. A. Zimmerman, Doctoral dissertation, Univ. of Illinois (1951).
    V. D. Aftandilian, *ibid.*, (1954).
    G. W. Cullen, *ibid.*, (1956).
    T. Moeller and P. A. Zimmerman, *Science*, **120**, 539 (1954).
    G. W. Cullen, *Dissertation Abst.*, **17**, 234 (1957).
    T. Moeller and T. M. Yappan, *J. Inorg. & Nuclear Chem.*, **4**, 216 (1957).
22. H. B. Jonassen, Tulane Univ. (Last report, March 12, 1957).
23. A. Brenner, *Rec. Chem. Progress*, **16**, 241 (1955).
24. G. Jander, "Die Chemie In Wasserähnlichen Lösungsmitteln," Springer-Verlag, Berlin (1949).
25. L. F. Audrieth and J. Kleinberg, "Non-aqueous Solvents as Media for Chemical Reactions, John Wiley & Sons, Inc., New York (1953).
26. C. J. Brockman, "Electro-organic Chemistry," John Wiley & Sons, Inc., New York (1926).

27. P. Walden, "Electrochemie Nichtwässriger Lösungen," Johann Ambrosius, Leipzig (1924).
28. H. P. Cady and R. Taft, *J. Phys. Chem.*, **29**, 1075 (1925).
29. H. P. Cady and R. Taft, *ibid.*, 1057 (1925).
30. B. D. Steele, *Chem. News*, **96**, 224 (1908).
L. S. Bagster and B. D. Steele, *Chem. News* **105**, 157 (1912); *Trans. Faraday Soc.*, **8**, 51 (1913).
M. Centnerszewer and J. Drucker, *Z. Elektrochem.*, **29**, 210 (1923).
31. S. Goldschmidt and F. Nagel, *Ber.*, **64B**, 1744 (1931).
32. J. H. Simons and Co-workers, *J. (and Trans.) Electrochem. Soc.*, **95**, 47 (1949).
33a. K. Hopfgartner, Electrolysis of Salts of Aliphatic Acids in Solutions of their Respective Anhydrous Parent Acids, *Monatsh.*, **32**, 523 (1911).
b. C. Schall, Electrolysis in Nonaqueous Solvents, *Z. Elektrochem.*, **19**, 830 (1914).
c. K. Schaum and H. Schneider, Uber die Darstellung von Cyanursäure und Allophansäure-Estern aus Formamide auf Elektrochemischem Wege, *Ber.*, **56**, 2460 (1923).
d. F. Fichter and R. E. Meyer, Electrolysis of Acetates in Absolute Methanol, *Helv. Chem. Acta*, **16**, 1408 (1933).
e. F. Fichter and R. E. Meyer, Electrolysis of Benzoic and 2.6 Dimethyl -4 -tert-butyl-benzoic Acids mixed with their Salts in Absolute Methanol, *Helv. Chim. Acta*, **17**, 535 (1934).
f. G. Giacomello and A. Mayer, The Electrolysis of Some Organic Substances in Nonaqueous Media I, *Gazz. chim. ital.*, **65**, 546 (1935).
g. G. Giacomello and M. Lentine, The Electrolysis of Some Organic Substances in Nonaqueous Medium II, *Gazz. chim. ital.*, **66**, 350 (1936).
h. M. Centnerszwer and J. Szper, Electrolysis of Salts in Anhydrous Glycerol, *Bull. intern. acad. polon. sci., (Classe sci. math. nat.)*, **A**, 378 (1936).
i. A. Hickling and J. V. Westwood, Electrolytic Oxidation, XI. The Electrolysis of Acid Ester Salts in Nonaqueous Solutions and the Mechanism of the Crum Brown-Walker Synthesis, *J. Chem. Soc.*, **1939**, 1109.
j. J. J. Lingane, C. G. Swain, and M. Fields, Polarographically Controlled Synthesis, with Particular Reference to Organic Chemistry, *J. Am. Chem. Soc.* **65**, 1348 (1943).
k. E. D. Fultz and J. H. Wood, Electrolysis Studies in Organic Solvents. Rensselaer Polytechnic Inst. ASTIA 103081 Aug. 1956.
l. H. C. Mandell, Jr. (Univ. of Pa., Philadelphia) Univ. Microfilms (Ann Arbor, Mich.) Publ. No. 7801, 196 pp.; *Dissertation Abstr.*, **14**, 769 (1954); Chemical and Electrochemical Studies of Nonaqueous Solutions of Boron Tribromide.
m. S. Wawzonek, E. W. Blaha, R. Berkey, and M. E. Runner, Polarographic Studies in Acetonitrile and Dimethylformamide II. Behavior of Aromatic Olefins and Hydrocarbons, *This Journal*, **102**, 235 (1955).
n. G. Jander and H. Knauer, Ionic Reactions in Absolute Diethyl Ether as a Solvent. III. The application of high-voltage electrolysis to the investigation of the dissociation of several metal halides in ether solution and their transposition with alkali alcoholates, *Z. anorg. Chem.*, **287**, 138 (1956).
o. H. Breederveld and E. C. Kooyman, The electrolysis of some 3-arylpropionic acids; isomerization of free radicals, *Rec. trav. chim.*, **76**, 297 (1957).
p. A. P. Stuart, Hydrazine Manufacture U. S. Pat. 2,813,067, Nov. 12, 1957.

Brief Communication

Composition and Properties of Saturated Solutions of ZnO in KOH

Thedford P. Dirkse

Calvin College, Grand Rapids, Michigan

In many alkaline batteries a soluble zinc anode is used. This produces, on discharge, a solution of ZnO or zincate in the electrolyte. To deal with such solutions theoretically, it is often necessary to know the values for certain physical properties of such solutions. For that reason saturated solutions of ZnO in KOH were prepared and studied at different temperatures.

All KOH solutions were made by addition of water to a saturated stock solution. C.P. ZnO was added to these KOH solutions. Because of the possibility of phase changes, the solutions were allowed to stand at least several months before analysis. Pyrex glass and polyethylene containers were used. Several different series of solutions were prepared at 25°C and run independently of each other. Some of the solutions were saturated at a higher temperature before being cooled and allowed to equilibrate at the desired temperature; some solutions were saturated at the temperature indicated; some were saturated by allowing water to evaporate at a consider-

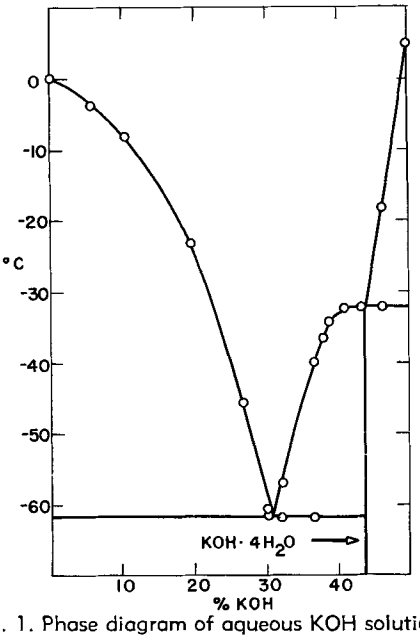

Fig. 1. Phase diagram of aqueous KOH solutions

ably reduced pressure; and some were prepared by dilution of more concentrated solutions.

Each solution was analyzed for potassium and zinc. All the potassium analyses were made spectrophotometrically (1, 2). Zinc was determined most often by titration with standardized potassium ferrocyanide solution, but also spectrophotometrically using dithizone (3). All solutions were filtered through glass filtering crucibles before analysis. Precautions were taken to avoid contact with CO_2. The melting points of aqueous KOH solutions were determined from cooling and warming curves. Duplicates and checks were run constantly and the results agreed to within 0.1°C.

Results are given in the accompanying Tables I and II and Fig. 1. The solid phases were ZnO and various hydrates of KOH. In operating batteries the zinc content, and hence density and viscosity, may rise temporarily considerably above the values given here (4).

Table I. Composition and properties of saturated solutions of ZnO in aqueous KOH at 25°C

% K	% Zn	Density, g/cm³	Relative viscosity	Sp. cond. ohm⁻¹ cm⁻¹
3.66	0.28			
4.93	0.48			
8.18	0.55	1.1076	1.302	0.370
15.0	1.83	1.2258	1.865	0.521
21.3	3.61	1.3616	3.120	0.500
21.9	3.71	1.3637	3.123	0.492
28.9	6.34	1.5356	7.624	0.317
30.9	8.41			
35.3	10.20			
36.0	11.05			
36.1	10.53			
36.3	7.91			
36.4	6.02			
37.7	2.28			

Table II. Composition of saturated solutions of ZnO in aqueous KOH

44.6°C		3°C	
% K	% Zn	% K	% Zn
10.05	0.80	7.90	0.55
17.62	2.30	14.01	1.74
22.1	4.33	20.01	3.82
31.8	7.48	21.29	3.97
34.4	9.29	26.9	5.36
34.7	11.05	32.2	7.89
38.6	0.81	32.6	4.31
38.8	2.03		
38.3	3.49		
39.1	2.78		
40.1	2.29		
−20°C		**−30°C**	
17.4	2.38	17.1	2.43
18.8	2.96	19.4	3.04
15.4	2.38	17.4	2.46
17.3	2.28	21.9	3.85
21.4	3.80	24	4.89
24.3	5.28	29.9	0.52
28.0	0.95	30.8	0.32
28.6	0.25		

REFERENCES

1. E. Amdur, *Ind. Eng. Chem.*, Anal. Ed., **12**, 731 (1940).
2. R. Faber, T. P. Dirkse, *Anal. Chem.*, **25**, 808 (1953).
3. H. Cowling, E. J. Miller, *Ind. Eng. Chem.*, Anal. Ed., **13**, 145 (1941).
4. T. P. Dirkse, *This Journal*, **102**, 497 (1955).

Manuscript received Oct. 13, 1958. Work on this paper was performed under Contract N7 onr-496, T.O. 1 with the Office of Naval Research. Reproduction in whole or in part is permitted for any purpose of the United States Government.

Any discussion of this paper will appear in a Discussion Section to be published in the December 1959 JOURNAL.

Ammonia Vapor Activated Batteries

H. S. Gleason and J. M. Freund
Apparatus & Optical Division, Eastman Kodak Company, Rochester, New York

and L. J. Minnick and W. F. Meyers
G. and W. H. Corson, Inc., Plymouth Meeting, Pennsylvania

ABSTRACT

A new type of reserve battery is described. In storage, the solvent for the electrolyte, liquid ammonia, is kept separate from the dry, deliquescent solute. On activation, ammonia vapor is released to condense rapidly in the cells and energize the battery. A large number of practical cells can be built using this principle. Characteristics of several are presented. Some properties of electrolytes in liquid ammonia are also discussed.

For more than a century the solvent properties of liquid ammonia have intrigued chemists. A large body of literature has derived from the research of Franklin and of Kraus and their students. Franklin (1), Audrieth and Kleinberg (2), and Sneed, *et al.* (3) have surveyed liquid ammonia chemistry.

Many substances dissolve in liquid ammonia to form conducting solutions. Most investigators have been concerned with dilute solutions, particularly their behavior with respect to relationships such as those of Debye and Hückel, Onsager, and Walden. The solutions used in the batteries under discussion are highly concentrated, and, as in the case of concentrated aqueous solutions, adequate theoretical relationships between various properties and concentration have not been derived. The literature on concentrated solutions deals largely with the solubility of salts at various temperatures. This information is well summarized by both Audrieth and Kleinberg (2) and Sneed, *et al.* (3). Data are also given by Seidell (4).

Vapor pressure studies on the systems NH_4SCN-NH_4NO_3-NH_3 and NH_4SCN-NH_3-H_2O were made by Foote, Brinkley, and Hunter (5-7) and on solutions of NH_4Cl, NH_4Br, NH_4I, and NH_4NO_3 in NH_3 by Hunt and Larsen (8).

The conductance at −40°C of solutions of eighteen salts was measured by Pleskov (9), whose data extend only to regions of moderate concentration. Specific conductances at 0°C for the system NH_4SCN-NH_3 are given by Foote and Hunter (7).

Standard oxidation potentials in liquid ammonia are discussed by Jolly (10) whose table includes most of the previously published data. A series of papers on potentiometric titrations in liquid ammonia has been published by Watt and his students (11).

The development of ammonia vapor activated batteries derives from research into the recovery of calcium from lime deposits carried out by Minnick and Presgrave (12), who developed a process for electrowinning this metal from solutions of its salts in liquid ammonia at −50°C. The process was later enlarged to include other materials such as alkali metals. In the course of investigating these cells, a rechargeable current-producing cell system capable of delivering about 4.5 v was discovered. It was possible to operate lamps and other devices for a considerable period with the cell at −50°C. The physical chemistry of electrolyte solutions potentially desirable for use in batteries was extensively studied by Minnick, Presgrave, and Meyers, and the behavior of elementary cells incorporating various electrodes was investigated with the particular objective of high-rate, short-duration discharge. Many cells suitable for such applications were found to self-discharge rapidly and were deemed unsatisfactory for batteries in general.

An interesting discovery during these studies was that a cell could be built in which one constituent of the electrolyte was placed in a dry condition between the electrodes. Activation of the cell was accomplished merely by exposure to a vapor, in this case ammonia. Among the advantages of gas or vapor activation is the fact that there is no liquid to be moved as in the conventional types of reserve batteries. The geometry of the stack is therefore less critical and internal short circuits arising from electrolytic paths across edges are virtually eliminated.

Electrolytes

The ammonium salts, which are the acids in liquid ammonia chemistry, and salts with nitrogen-containing anions are useful as solutes for AVA (ammonia vapor activated) batteries. NH_4SCN solutions, for example, have been found particularly effective. On exposure of the dry salt to ammonia vapor, condensation occurs rapidly, forming a colorless solution. The vapor pressure of saturated solutions is less than 4% of that of pure ammonia at temperatures between −55° and +75°C and never exceeds 1 atm in this range. For some solutions formed in AVA batteries, pressures may be well above atmospheric under extreme environmental conditions.

The conductance of NH_4SCN solutions is high over a wide temperature range and has a smaller temperature coefficient than is characteristic of

aqueous solutions. Foote and Hunter (5) list specific conductances at 0°C ranging from 0.20 to 0.11 ohm^{-1} cm^{-1} for solutions ranging from 25 to 43 mole % NH_4SCN. This high conductivity is related in part to the low viscosity of the solvent.

Other solutes and mixtures of solutes have been used successfully in AVA cells, although in most instances the rate of condensation is appreciably slower than when NH_4SCN is used.

Electrodes

The principal metals used for anodes have been magnesium, zinc, and lead. The magnesium has usually been an alloy of the AZ31 series, but pure vapor-deposited magnesium has also been tried. Both rolled zinc, either pure or containing a small percentage of lead and cadmium, and electroplated zinc have been used. The lead anodes have generally been electrodeposits, but some tests were made using lead foil. In no case has there been any appreciable difference in performance between the "pure" coatings and the alloys. Experiments have also been performed using cadmium, lithium, lithium-aluminum alloys, calcium, and other anodes.

Much of the work has included the use of manganese dioxide and lead dioxide cathodes. The former has been electro ore mixed with carbon black for the most part, but some tests have also been run with MnO_2 electrodeposited on carbon rods. The lead dioxide has usually been electrodeposited on a stainless steel base. An extensive test program using silver chloride and silver oxide cathodes was fairly successful. However, the high solubility of silver compounds in ammonia limits their usefulness for many applications. Numerous other materials can be used as cathodes.

Structures

Most of the development studies on AVA cells have been carried out using cells of laminar construction. Thin electrodes were blanked from strip stock, between which one or more dry electrolyte pads were placed. The basic experimental cells have been annular in shape, with NH_3 admitted from the center. Electrolyte pads have comprised a porous vehicle, of which filter paper is a typical example, impregnated from an aqueous solution of the desired salt and dried. It has been found that for a given vehicle, the weight of salt impregnated per unit area from a solution of given concentration is reproducible within 10%, even with rudimentary controls, and that the uniformity of impregnation of the vehicle in sheet form is acceptable. Inclusion of more than one electrolyte pad in a cell permits the use of differing amounts of salt in the catholyte and the anolyte pads. Some 20 cellulose papers ranging in free volume from 35 to 82% and two glass fiber papers of 29 and 95% free volume have been used.

In the cells using MnO_2-C as the depolarizer mix, a somewhat similar construction has generally been employed. The basic cells have been sandwiches of circular disks, with NH_3 admitted from the outer perimeter. The anode has been the same type of material used in the annular cells. The pads, however, have been blanked and then impregnated by addition of a definite volume of solution from a buret. The MnO_2-C has been pelletized by compression, and a carbon cathode has been used. Corson has also done some work with cylindrical cells using variations of the typical Leclanché cell structure.

Cells are connected as required by the application and are placed in a suitable container, which to date has been either steel or aluminum, although magnesium is also practical. The ammonia source may be either external, in which case a suitable fitting is provided, or internal, using a releaser within the battery actuated by a mechanical or electrical impulse. Depending on the rapidity of activation required, a source of heat may be included in the releaser to achieve rapid evaporation of NH_3.

The container is hermetically sealed after evacuation to a "soft" vacuum of 1 mm Hg or slightly less, primarily to remove all but the last traces of water or NH_3 and to avoid back pressure in the cells. The battery is provided with an exhaust hole over which a cap is soldered under vacuum. The cap may be unsoldered in an ammonia atmosphere and the battery checked electrically. The NH_3 is then exhausted, the battery re-evacuated, and the cap resoldered returning the battery to an inert condition. This feature is unique among reserve batteries insofar as the authors are aware, and should enhance the reliability of the product.

Cell Characteristics

The program to evaluate design parameters has comprised thousands of cell discharges. Each particular construction of cell has been tested at room temperature by discharge at constant current immediately after activation from a source of NH_3 at about 10 atm to depletion of the cell by exhaustion of depolarizer or electrolyte. The evaluation has included tests at several current densities. Variations in construction have involved (*a*) the anode metal, (*b*) the amount of depolarizer on the cathode, and (*c*) the type of electrolyte vehicle and the effect of varying the salt content thereof. The more promising constructions are then evaluated at several temperatures and also by testing after various periods of activated stand.

The nature of the electrolyte solutions has dictated that even the most elementary tests be conducted in special test vessels; working in open vessels or in glass is impractical. For repeated use in test equipment, parts coming in contact with cell components are best made of Teflon or polyethylene, although nylon is adequate unless the stand time or discharge is prolonged. Insulation of wires requires also that Teflon, nylon, polyethylene, or similar materials be used.

As expected, there is no one combination of components that gives the best performance under all conditions. Figures 1, 2, and 3 present discharge voltages as a function of delivered capacity for the $Mg/NH_4SCN/PbO_2$, $Zn/NH_4SCN/PbO_2$, and $Pb/NH_4SCN/PbO_2$ systems, using for each the construction

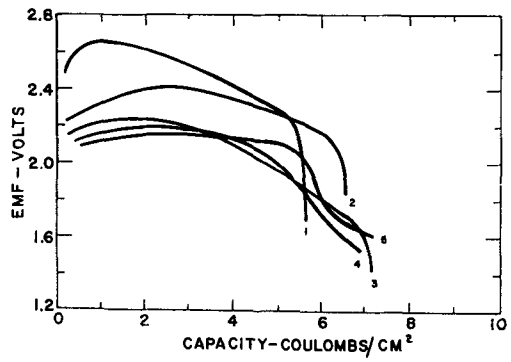

Fig. 1. Discharge characteristics of $Mg/NH_4SCN/PbO_2$ AVA cells at 25°C (77°F).
(Theoretical capacity, based on NH_4SCN, 10 coulombs/cm²)

Curve	Current density	
	ma/cm²	ma/in.²
1	7.7	50
2	15.5	100
3	23.7	153
4	35.3	228
5	47.3	305

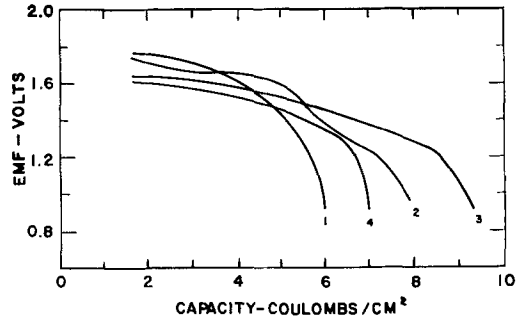

Fig. 2. Discharge characteristics of $Zn/NH_4SCN/PbO_2$ AVA cells at 25°C (77°F).
(Theoretical capacity, based on NH_4SCN, 12 coulombs/cm²)

Curve	Current density	
	ma/cm²	ma/in.²
1	23.7	153
2	35.3	228
3	59.2	382
4	70.8	457

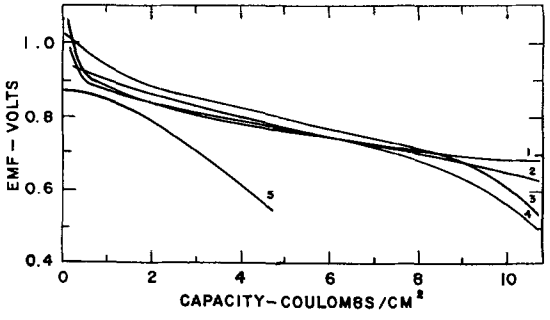

Fig. 3. Discharge characteristics of $Pb/NH_4SCN/PbO_2$ AVA cells at 25°C (77°F).
(Theoretical capacity, based on PbO_2, 11 coulombs/cm²)

Curve	Current Density	
	ma/cm²	ma/in.²
1	0.15	0.95
2	1.5	9.5
3	7.4	47.5
4	29.4	190
5	88	570

that has thus far given the most energy per unit volume of cell. The most efficient Mg and Zn cells, on this basis, are electrolyte limited. Their capacity depends on the amount of NH_4SCN initially in the cell and not on the total amount of PbO_2 present. On the other hand, Pb cells with the same amounts of NH_4SCN and PbO_2 are limited in capacity by the depletion of PbO_2. This results from the relatively rapid reaction of Mg and Zn with the acid solution, which removes NH_4^+ ion that would have been available for the cathode reaction. Lead, however, is cathodic to hydrogen in acid solutions in ammonia. This makes it possible to operate lead cells for long periods at very light loads or after extended activated stand, whereas Mg or Zn cells are subject to rapid self-discharge. Figures 4, 5, and 6 show capacity to depletion of Mg, Zn, and Pb cells, respectively, as a function of current density. Current densities are cited in terms of the equal apparent areas of the electrodes. The effect of self-discharge in the Mg and Zn cells may be perceived by comparing the ordinates with the theoretical capacities of 10 and 12 coulombs/cm², respectively. At current densities below 31 ma/cm² (200 ma/in.²), the Pb cells operate essentially at 100% cathode efficiency. If the proportion of NH_4SCN in Mg or Zn cells is made large with respect to the amount of PbO_2 on the cathode, the PbO_2 can be made limiting so that efficiency of Mg or Zn cells approaches 100% based on PbO_2. The energy density suffers considerably in doing this.

Figure 7 shows the effect of temperature on cell capacity for the $Zn/NH_4SCN/PbO_2$ system. The results are attributed to more rapid corrosion of the Zn as the temperature is increased.

Tests of the $Mg/NH_4SCN/MnO_2$-C cell have been concerned with modifications of the electrolyte to reduce or eliminate the self-discharge at the anode. Self-discharge in this system can be reduced significantly by using additives that buffer the electrolyte, neutral salts such as $Mg(SCN)_2$, or substances that limit the diffusion of NH_4^+ ion toward the anode to a rate less than that of transport toward the cathode.

The ability to evacuate AVA cells rapidly has been used to obtain information on chemical changes as a function of stand time and discharge. Such tests show qualitatively that on activation there is a reaction between MnO_2 and SCN^- ion, resulting in an appreciable decrease in the available oxygen of the depolarizer mix. However, a product of this reaction is presumably thiocyanogen, which is available as a depolarizer in the cell, but which is leached from the MnO_2 prior to analysis for available oxygen. The increase in Mg^{++} ion in the cell was found to be the sum of the amounts formed by self-discharge, as determined from stand tests without discharge and the amount electrochemically equivalent to the capacity delivered.

A unique apparatus for analyzing the characteristics of the components of operating cells has been developed by Meyers. It involves a Haring cell operated with breaker techniques. It is intended to describe this test method in a future paper. Tests

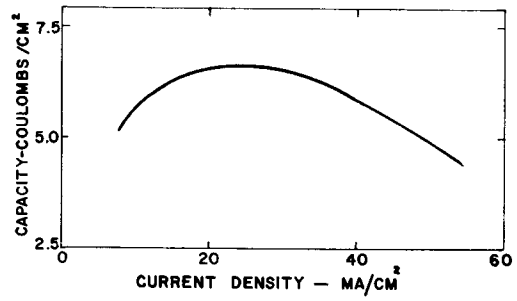

Fig. 4. Capacity to NH_4SCN depletion for Mg/NH_4SCN/PbO_2 AVA cells at 25°C (77°F). Theoretical capacity = 10 coulombs/cm².

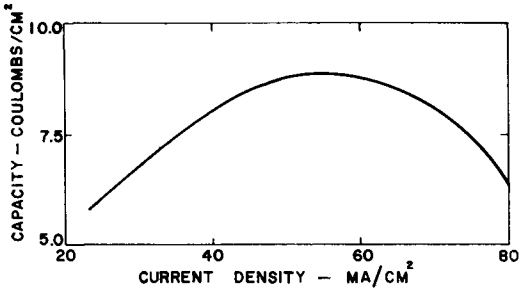

Fig. 5. Capacity to NH_4SCN depletion for Zn/NH_4SCN/PbO_2 AVA cells at 25°C (77°F). Theoretical capacity — 12 coulombs/cm².

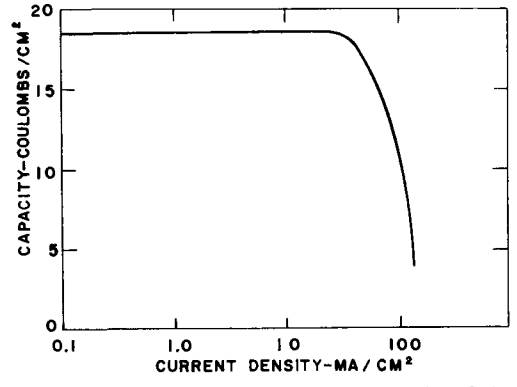

Fig. 6. Capacity to PbO_2 depletion for Pb/NH_4SCN/PbO_2 AVA cells at 25°C (77°F). Theoretical capacity — 18.6 coulombs/cm².

of the Mg/NH_4SCN/MnO_2-C cell showed that anode polarization increases at a small constant rate during discharge. The anode, electrolyte, and over-all cell resistances also increase linearly during discharge. The resistivity of the cells was initially 55 ohm-cm and increased to 100 ohm-cm during complete discharge (to 0 v), the major part of the increase being in the anode film. Similar evaluation of cells with PbO_2 cathodes is now in process. Surge discharges of Pb/PbO_2 cells of 0.3 amp/cm² (2.0 amp/in.²) for 10 msec result in over 80% instantaneous recovery of voltage on removal of the load, and complete recovery within 2 msec. Surges of 0.15 amp/cm² (1.0 amp/in.²) for 100 msec result in better than 90% recovery in 10 msec.

Although few tests have been conducted at temperatures below —25°C, liquid system reserve batteries have operated as well at —55°C as at room temperature. Small vapor activated batteries have also been successfully activated and operated at —55°C. On the basis of work to date, the capabilities of AVA batteries appear to lie in the range

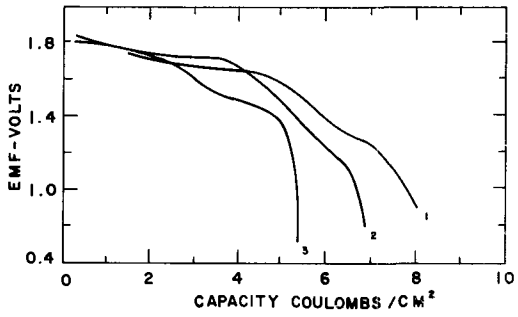

Fig. 7. Effect of temperature on discharge of Zn/NH_4SCN/PbO_2 AVA cells at 35.3 ma/cm² (228 ma/in.²). Curve 1 at 25°C, curve 2 at 50°C, curve 3 at 70°C.

of 1.0 wmin/cm³ (0.3 whr/in.³) for high rate discharges (over 25 ma/cm²) to more than 3.6 wmin/cm³ (1 whr/in.³) for low rate applications (under 3 ma/cm²). These are equivalent to a range of 0.6 to 2.5 wmin/g (5 to 20 whr/lb).

Acknowledgments

The development program has received support for the Department of Defense under several research and development contracts. The data reported in this paper were obtained in the course of work sponsored by the United States Army Signal Engineering Laboratories under Contracts DA-36-039 SC-71232 and DA-36-039 SC-72306.

The authors wish also to acknowledge the important roles in this program of C. Presgrave of G. and W. H. Corson, Inc., and of T. A. Hale, K. R. Scribner, J. R. Flynn, and V. M. Bryant, Jr., of the Eastman Kodak Company.

Manuscript received Nov. 25, 1957. This paper was prepared for delivery before the Buffalo Meeting, Oct. 6-10, 1957.

Any discussion of this paper will appear in a Discussion Section to be published in the December 1959 JOURNAL.

REFERENCES

1. E. C. Franklin, "The Nitrogen System of Compounds," Reinhold Publishing Co., New York (1935).
2. L. F. Audrieth and J. Kleinberg, "Non-Aqueous Solvents," John Wiley & Sons, Inc., New York (1953).
3. "Comprehensive Inorganic Chemistry," M. C. Sneed and R. C. Brasted, Editors, Vol. 5; "Nitrogen, Phosphorus, Arsenic, Antimony, and Bismuth" by H. H. Sisler; and "Nonaqueous Chemistry" by A. R. Pray, D. Van Nostrand Co., Inc., Princeton, N. J. (1956).
4. A. Seidell, "Solubilities of Inorganic and Metal-Organic Compounds," 3rd ed., Vol. I, D. Van Nostrand and Co., New York (1940) and "Supplement to the Third Edition" (1952).
5. H. W. Foote and M. A. Hunter, *J. Am. Chem. Soc.*, **42**, 69 (1920).
6. H. W. Foote and S. R. Brinkley, *ibid.*, **43**, 1018 (1921).
7. H. W. Foote, *J. Am. Chem. Soc.*, **43**, 1031 (1921).
8. H. Hunt and W. E. Larsen, *J. Phys. Chem.*, **38**, 801 (1934).
9. V. Pleskov, *Acta Physicochim. U. R. S. S.*, **5**, 509 (1936).
10. W. L. Jolly, *J. Chem. Ed.*, **33**, 512 (1956).
11. For example, G. W. Watt and D. M. Sewards, *This Journal*, **102**, 46 (1954) which also gives references to earlier papers.
12. L. J. Minnick and C. Presgrave (to G. and W. H. Corson, Inc.) U. S. Pat. 2,615,838, Oct. 28, 1952.

General and Intergranular Corrosion of Austenitic Stainless Steels in Acids

Effect of Cations in the Acids and the Influence of Heat Treatment and Grain Size of the Steel

Michael A. Streicher

Engineering Research Laboratory, Engineering Department, E. I. du Pont de Nemours & Co., Inc., Wilmington, Delaware

ABSTRACT

Corrosion of stainless steels by nitric acid is determined largely by the crystallography of grain boundaries. There is preferential attack even on annealed steels. Increasing the rate of dissolution, either by an anodic current or by oxidizing cations, intensifies intergranular penetration. The same crystallographic factors which determine preferential corrosion also determine the precipitation of chromium carbides. Their presence leads to a very great intensification of intergranular attack, as does sigma phase, even as an invisible, pre-precipitation constituent.

Oxidizing cations, such as Cr^{+6}, Ce^{+4}, and Fe^{+3}, increase the corrosion of stainless steels in nitric acid by cathodic depolarization, by shifting the open-circuit potential of cathodic areas toward more noble values and, probably, by depolarization of anodic areas.

The effect of surface finish on corrosion rate is largely a function of the true (absolute) area produced by various finishes.

Ferric ions in ferric sulfate-sulfuric acid solution greatly inhibit general, or grain-face, corrosion by anodic polarization. In place of the reduction of hydrogen ions and the evolution of hydrogen gas at cathodic areas, ferric ions are reduced. The consumption of ferric ions is electrochemically equivalent to the weight of steel dissolved. On steels containing intergranularly precipitated chromium carbides, intergranular attack leads to dislodgment of grains and a readily detectable weight loss.

Data obtained in sulfuric acid solutions containing ferric nitrate in place of ferric sulfate suggest that it may be possible to develop a 24-hr evaluation test with this solution.

The action of cupric sulfate in copper sulfate-sulfuric acid solution is similar to that of ferric ions. However, intergranular attack on susceptible steels does not dislodge grains readily, and, therefore, weight loss cannot be used for routine evaluation of the results.

Intergranular attack in this solution is greatly accelerated by metallic copper immersed simultaneously with the stainless steel specimen or in contact with it. This acceleration is a result of the formation of cuprous ions and of galvanic action by copper, which is the anode of this couple. The resulting galvanic current and the cuprous ions reduce anodic polarization most readily at grain boundaries containing chromium carbide precipitate and thereby greatly increase the rate of intergranular penetration. Sigma phase does not lead to accelerated intergranular attack in this solution.

The influence of grain size on intergranular corrosion depends on the method used for measurement, change in electrical resistance or weight-loss, and composition of the corroding acid solution.

Dissolution of stainless steels in all three acid solutions is predominantly under anodic control. The difference in grain surface corrosion and in intergranular penetration at susceptible boundaries is attributed primarily to a lower anodic polarizability of the metal in such grain boundary zones rather than to any difference which may exist in the open-circuit potentials of grain surfaces and grain boundaries.

The intensity of intergranular attack on stainless steels exposed to certain acid solutions may range from light etching of grain boundaries, which merely outlines the granular structure, to intense penetration, which may lead to complete loss of mechanical strength or even disintegration of the metal. Whether corrosion is predominantly by intergranular or by general attack depends on the difference in the rate of corrosion of the grain-boundary zones and of the grain faces. This difference in rates is determined by

the structure and composition of the grain boundaries and by the composition of the corroding solution.

In the present investigation a detailed study has been made of the type of intergranular attack produced by three acid solutions which are used, or have been proposed for use, in evaluation tests. These are nitric acid, ferric sulfate-sulfuric acid, and copper sulfate-sulfuric acid solutions. Special attention has been given to the electrochemical action of the cations encountered in these solutions, either as inhibitors of general corrosion or as corrosion products, which may accelerate or retard intergranular attack. Among the pertinent factors in the stainless steels, chromium carbides, sigma phase, and grain size have been investigated in their effect on intergranular attack.

It was essential to know whether or not a given specimen had been made susceptible previously to intergranular attack by heat treatments which formed intergranular precipitates of chromium carbides and/or sigma phase. The presence or absence of chromium carbide precipitate was determined by electrolytic etching in oxalic acid. This etch, originally described by Ellinger (1), has been developed into a standard testing method (2, 3). A 10% solution of oxalic acid is used for anodic etching at a current density of 1 amp/cm^2 for 1.5 min. In the absence of chromium carbides a "step structure" is formed, Figure 1A. Evidence of chromium carbide precipitate is shown by ditches at the grain boundaries. If the ditches do not envelope any one grain completely, the etch is classified as "dual structure," and if one or more grains are completely surrounded, as "ditch structure," Figure 1B. To detect susceptibility to intergranular attack associated with sigma phase, the steels were tested in nitric acid, since it was found that this is the only method which will detect the presence of certain kinds of sigma phase.

Corrosion in Nitric Acid

The investigations in nitric acid were made in boiling, 65% acid solution. This is the temperature and concentration of acid used in the standard nitric acid test (2) first proposed by Huey (4). In the standard test the weight loss of a specimen of known surface area (20-40 cm^2) is determined after each of five 48-hr exposure periods. New acid is used for each of these periods. Tests are made in 1-liter wide-mouth Erlenmeyer flasks, containing 600 ml of acid. Evaporation is prevented by a "cold-finger" type of condenser and the specimens are held in glass cradles. (This apparatus was also used for tests with the other acids.) On a steel (Table I) which is resistant to accelerated intergranular attack, the corrosion rate (slope of annealed line, Fig. 2) is low and constant throughout the entire exposure period. The surface structure produced on this type of

Table I. Analyses of steels used

Steel AISI type	Code	Weight per cent					
		Cr	Ni	Mo	C	Si	Mn
304	FK-2	19.2	10.7	—	0.031	0.35	0.94
304	DT-2	18.3	10.7	—	0.06	0.45	0.098
304	HM-3	18.5	9.24	—	0.06	0.51	1.14
304	M304	18.3	9.3	—	0.063	0.37	0.80
316L	FI-4	16.2	13.2	2.2	0.020	0.47	1.6
316L	FH-5	17.7	13.2	2.40	0.026	—	—
316	M316	17.7	12.6	2.45	0.046	0.61	1.68
316L	FI-6	18.9	12.8	2.37	0.022	0.44	1.85
316L	EM-9	17.9	13.3	2.55	0.025	—	—
316L	FI-2	17.3	12.9	2.28	0.022	—	—
316L	FI-9	18.5	12.8	3.00	0.018	—	—
316	EW-6	17.4	12.7	1.89	0.053	0.44	1.60
316	GT-8	16.7	11.3	2.18	0.074	0.35	1.62

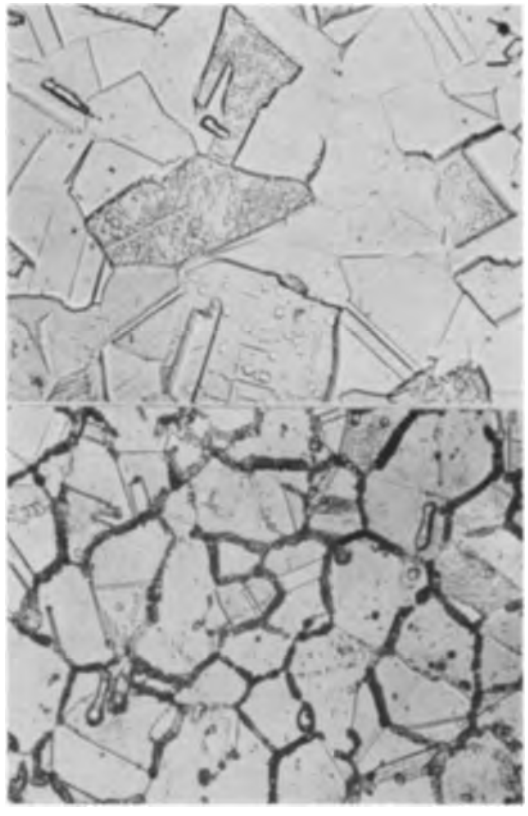

Fig. 1. Oxalic acid etch structure: A (top), annealed, step structure; B (bottom), heated 3 hr at 1250°F, ditch structure. Etched 1.5 min at 1 amp/cm^2. Steel AISI-304, FK-2 (analysis Table I). Magnification 500X before reduction for publication.

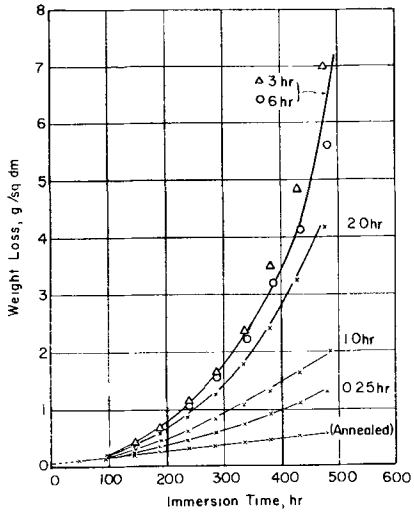

Fig. 2. Corrosion of AISI-304 stainless steel in boiling 65% nitric acid. Various degrees of susceptibility to intergranular attack produced by heating at 1250°F for periods indicated. Steel: FK-2, 0.031% C. (A weight loss of 1.0 g/dm^2 in 240 hr is equivalent to a corrosion rate of 0.0015 in./mo).

specimen during exposure to nitric acid is shown in Fig. 3A. It is apparent that even on a steel which is resistant to accelerated intergranular attack there is some etching at the grain boundaries which is so slow that it does not lead to undermining of these grains. In contrast, on susceptible specimens the attack at the grain boundaries leads to undermining and dislodgment of grains (Fig. 3B) and, consequently, to progressively increasing corrosion rates (slopes of tangents of curves in Fig. 2). The factors determining the rate of increase in slopes of these curves, such as composition of the steel, its heat treatment, and grain size, are dealt with throughout this discussion.

Influence of Surface Finish

The curves of Fig. 2 do not pass through the origin when extrapolated to zero exposure time, i.e., the corrosion rate at the beginning is high compared to the subsequent rate of attack. Specimens used for the tests of Fig. 2 were ground to an 80-grit finish. To determine whether this finish is responsible for the high initial corrosion rate, a number of specimens having other finishes, sand blasted, polished, and pickled, were exposed to nitric acid. Results have been plotted in Fig. 4 and show that both the high initial corrosion rate and the constant rate reached after 48-96 hr are a function of the type of surface finish.

On specimens having a smooth finish, produced by polishing or bright pickling, the corrosion rate is constant throughout the exposure period. Only when

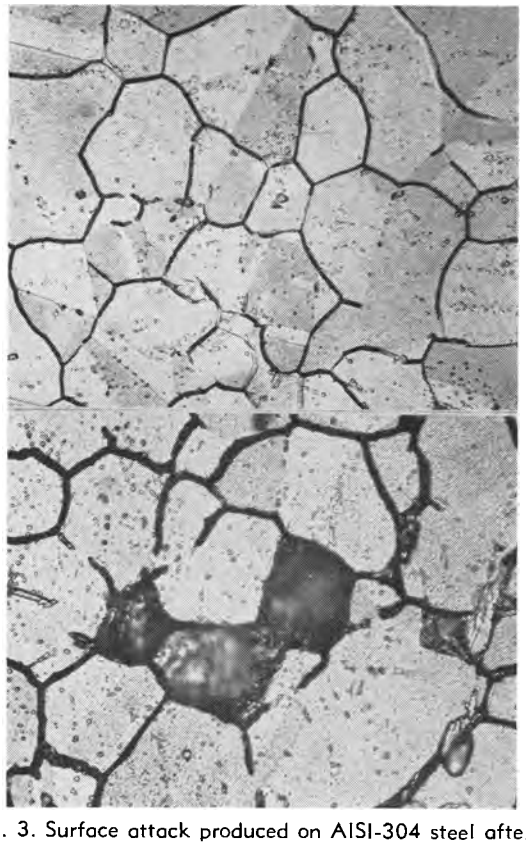

Fig. 3. Surface attack produced on AISI-304 steel after 80 hr of exposure to boiling 65% nitric acid. A (top), annealed; B (bottom), heated 3 hr at 1250°F. Steel: FK-2, 0.031% C. Magnification 500X before reduction for publication.

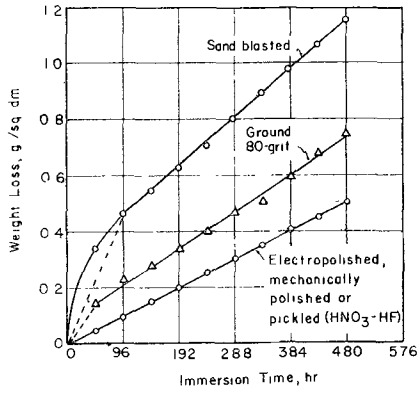

Fig. 4. Influence of surface finish on corrosion of AISI-304 steel in boiling 65% nitric acid. Annealed steel, heated 1 hr at 1950°F, W.Q.

the finishing operation produces sharp edges, as in grinding (abrading) or sand blasting, is there a high initial corrosion rate, which gradually decreases until it reaches a constant value.

Examination of the surface of the ground specimen at 750X shows that many edges and scratches on the ridges and valleys of the main grinding contours are eliminated during the first 50 hr of exposure. The main ridges remain, even after 500 hr of immersion, and suggest that the differences in corrosion rates during the period of changing rates and of constant slope (Fig. 4) are related to absolute areas. Thus, the slopes increase with the roughness of the surface finish. These observations are supported by some surface-area measurements made by O'Connor and Uhlig (5) on austenitic stainless steels. They found roughness factors (ratios of absolute to geometric areas) of 1.1 for electropolished, 1.4 for HNO_3-HF pickled, and 3.1 for (2/0) abraded finishes.

Unless otherwise noted, all specimens used in this investigation were given an 80-grit finish.

Stresses and metal deformation produced by surface treatments do not appear to have an appreciable effect on corrosion rates. The rate of the mechanically polished specimen is the same as that of the electropolished specimen. Also, it is of interest that the various surface finishes do not change the electrode potential of the steel when exposed to boiling 65% nitric acid. Measurements were made with the apparatus shown in Fig. 5.

Method of Measuring Electrode Potentials

The arrangement shown in Fig. 5 was used throughout this investigation to measure electrode potentials on stainless steels in boiling, concentrated acids. A 1-liter wide-mouth Erlenmeyer flask with a cold finger condenser was modified for this purpose. To make contact with the calomel cell a glass tube with a fritted glass filter at its end was sealed into the flask. This filter retarded movement of the acid electrolyte in and out of the flask. A glass tube was sealed into the condenser for the stainless steel wire used to make electrical contact with the specimen. This wire was welded to the specimen, covered with a plastic coating, and bent, as shown, to prevent condensate from running onto the specimen. At the top of the condenser, rubber tubing and a clamp were

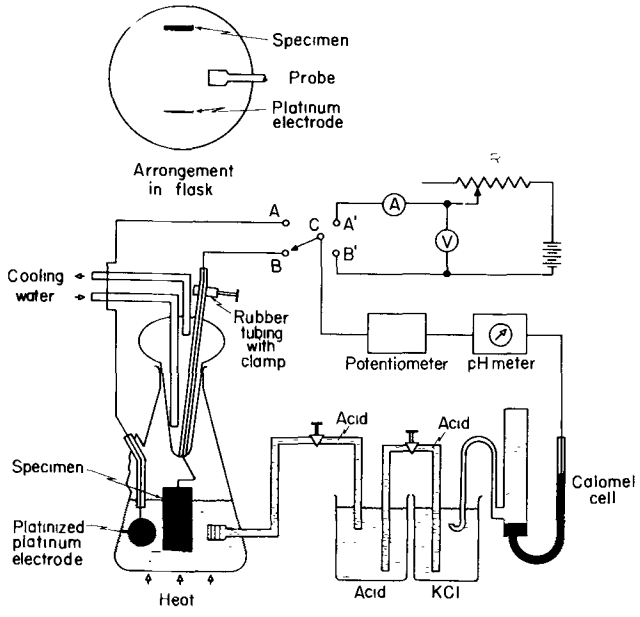

Fig. 5. Apparatus used for electrode potential measurements in boiling acids. As the reference cell, a saturated potassium chloride calomel cell was used.

used to prevent the loss of vapor from this glass tube. For anodic and cathodic polarization by an external current and for potential measurements, a platinized platinum electrode was inserted in the flask via a ground glass joint.

To prevent mutual contamination of acid electrolyte and the calomel cell, bridges were used. Only the flask was heated. The temperature of the calomel cell was 40°C. No temperature or junction potential corrections have been applied to the measurements reported.

Potential measurements on the stainless steel specimen or the platinum electrode were made by using a *p*H meter, with an impedance of 10^{10} to 10^{12} ohms, as a nil current indicator connected in series with a potentiometer (6). For polarization measurements, the circuit shown in Fig. 5 was used.

Effect of Corrosion Products

As the stainless steels dissolve, iron, chromium, and nickel corrosion products accumulate in the nitric acid solution. DeLong (7) has shown that, of

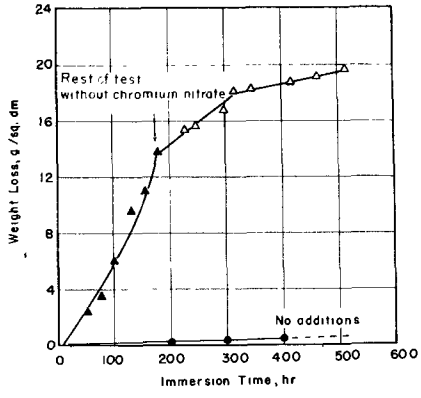

Fig. 6. Effect of chromium nitrate additions on the corrosion of AISI-304 in 65% boiling nitric acid. Steel: annealed condition, heated 1 hr at 1950°F, W.Q., HM-3. Addition: 1.26 g $Cr(NO_3)_3 \cdot 9H_2O$ in 600 ml acid for a solution containing 0.02% Cr (0.005 mole/liter). Solution changed every 24 hr.

these, only dissolved chromium affects corrosion in the concentrations likely to be encountered during evaluation tests. He found that concentrations greater than about 0.004% chromium (0.033 g Cr in 600 ml 65% nitric acid) greatly increase the rate of corrosion. Tests were made to determine the form and the mechanism of corrosion responsible for this great increase caused by dissolved chromium.

Previous investigators (8-11) have shown that acceleration is due to the action of chromium in the hexavalent state. When chromium dissolves in acids, it enters the solution as divalent ions, blue, which are rapidly converted to the trivalent state, green. These ions are then oxidized more gradually in nitric acid to the hexavalent state, orange. A green solution of 0.005 mole/l trivalent chromium in 65%, boiling nitric acid turns orange in 24 hr. For some of the tests described below, trivalent chromium was added to simulate as closely as possible the action of chromium dissolving from stainless steel.

A 1-cm^2 area was electropolished on the AISI-304 specimens for metallographic observation of the form of corrosion. New solutions were used every 24 hr. The weight-loss measurements have been plotted in Fig. 6, and microstructures are given in Fig. 7. Results on AISI-321 steel (not shown) were similar.

From these figures it is apparent that dissolved

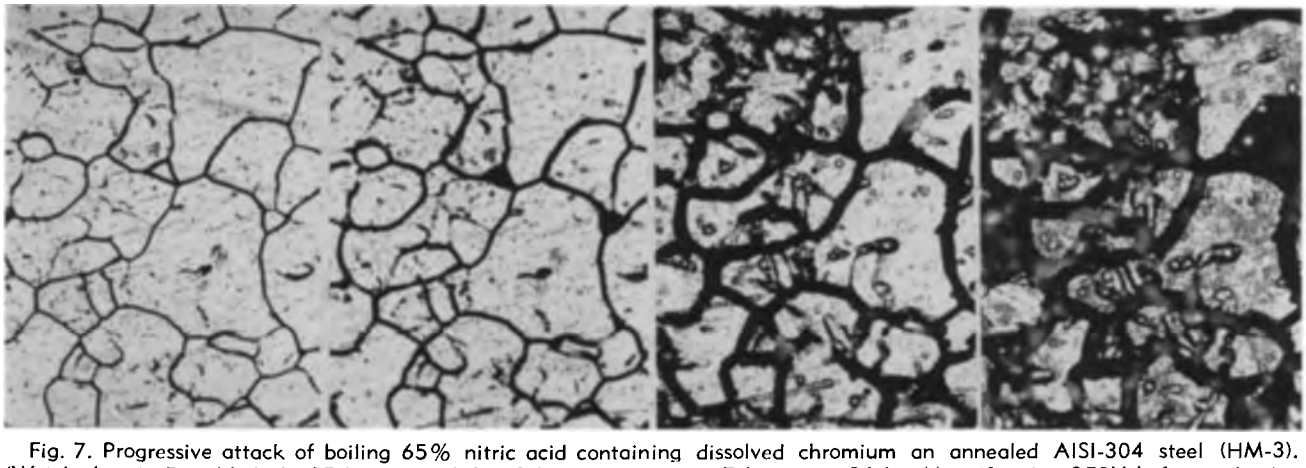

Fig. 7. Progressive attack of boiling 65% nitric acid containing dissolved chromium an annealed AISI-304 steel (HM-3). (Weight loss in Fig. 6.) Left, 15 hr; center left, 21 hr; center right, 47 hr; right, 96 hr. Magnification 250X before reduction for publication.

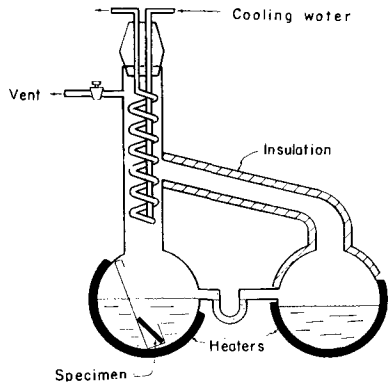

Fig. 8. Apparatus for continuous removal of soluble corrosion products from boiling solutions. Both 1-liter flasks are heated electrically. Corrosion products accumulate in specimen-free flask.

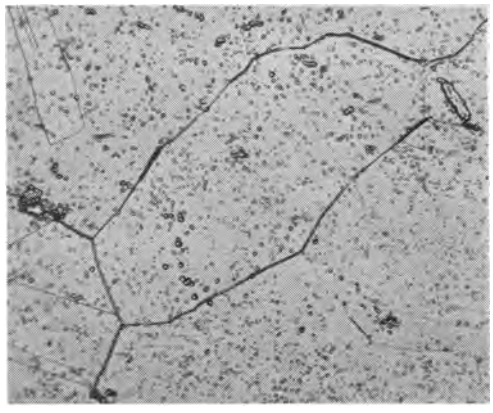

Fig. 9. Corrosion of annealed AISI-304 steel in pure nitric acid. Specimen exposed 254 hr to boiling 65% nitric acid in apparatus of Fig. 8. Magnification 500X before reduction for publication.

chromium greatly increases the weight loss of annealed stainless steels, largely as a result of accelerated intergranular attack. Grains are dislodged, even though both steels tested are in the annealed condition and do not contain any intergranularly precipitated chromium carbides or sigma phase. There is also some increase in general, or grain-face, corrosion, but most of the weight loss is due to grain dropping.

When a specimen which has been exposed to nitric acid containing chromium is immersed in pure nitric acid, the higher weight losses persist until these loosened layers have been removed completely. There is a gradual decrease in rate until the rate of the annealed steel is approached (Fig. 6).[1] Another factor which prolongs higher weight losses is the dissolution of the dislodged grains in the fresh nitric acid. Accumulation of hexavalent chromium is accelerated in this way.

Further tests on the effect of dissolved chromium were made to establish whether accelerated corrosion is by intergranular attack on other grades of stainless steels. Annealed specimens of AISI-304, 347, and 430 (17% Cr, no Ni) were immersed in boiling, 65% nitric acid containing direct additions of hexavalent chromium, 0.10 mole/l CrO_3. Within 2 hr very rapid intergranular attack produced dislodgment of appreciable numbers of grains on all three steels.

Continuous removal of corrosion products.—This intense intergranular attack on annealed steels produced by small amounts of added hexavalent chromium suggests that the chromium corrosion product which inevitably accumulates even during the 48-hr standard exposure periods used between renewal of acid may be the cause of grooving on annealed steel (Fig. 3A). The apparatus of Fig. 8 was used to determine whether there is intergranular grooving even when corrosion products are removed continuously. Its design is based on the principle of the multisample tester of DeLong (7). Each 1-liter flask contains about 500 ml of 65% nitric acid at the beginning of the test. The vapors from the solution containing the specimen (tester) are condensed and returned to this flask. Pure vapors from the other flask (boiler) are carried over to the cooling coil and condensed into the tester, causing a continuous overflow of solution containing corrosion products into the boiler, where they accumulate. This solution turns yellow during the test, while the solution with the specimen remains clear, even during a 500-hr test.

A metallographically polished specimen of annealed AISI-304 steel was exposed to 65% nitric acid for 516 hr in this apparatus without change of acid. The weight loss was 0.18 g. Analysis of the acid in the tester gave 1.1 ppm Fe, 0.12 ppm Ni, and less than 0.1 ppm Cr. Figure 9 shows the grooving at grain boundaries which took place even with continual removal of corrosion products.

In standard 48-hr flask tests the grain boundary grooves formed in this way accumulate chromium ion corrosion products, which then intensify the grooving action. The high corrosion rates observed on very small grained, annealed stainless steels are due to this type of action. Such steels have more grain boundaries per unit area of surface than large-grained steel. The grooving of very small grains may even lead to undermining and dislodgment of grains on annealed steels exposed to nitric acid solutions which are renewed every 48 hr.

Grain boundary grooves on annealed stainless steels may also be formed by making the steel anodic with an external current and an auxiliary electrode in 65% nitric acid (Fig. 10).[2] Longer etching or higher current densities make these grooves deeper and wider and lead to some grain dropping (Fig. 10B). Note the absence of grooves at the sides of twin boundaries (Fig. 10A). Preferential attack at grain boundaries of single-phase metals has also been found in other systems to be a function of the orientation of the two grains making up the boundary and its direction (12). Grooving in Fig. 3A and 9 shows evidence of this effect.

Mechanism of acceleration by oxidizing cations.—Hexavalent chromium is readily reduced at cathodic areas on steels exposed to acid solutions.

[1] Accelerated intergranular corrosion caused by precipitation of chromium carbides also is increased greatly by dissolved chromium in nitric acid. A concentration of 0.02% dissolved chromium increased the rate of a sensitized specimen by a factor of 10.

[2] These grooves are in contrast to the step structure produced on this same specimen by anodic etching in oxalic, sulfuric, and other acids.

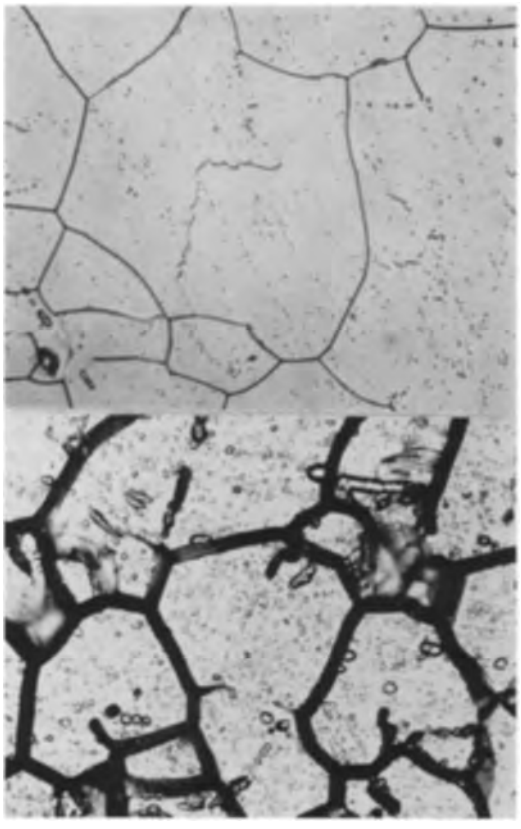

Fig. 10. Microstructure produced by anodic dissolution of annealed AISI-304 steel in 65% nitric acid. Etched at 0.02 amp/cm², temperature 25°C. A (top), 15 min; B (bottom) 60 min. Magnification 500X before reduction for publication.

$$Cr_2O_7^{-2} + 14H^+ + 6e = 2Cr^{+3} + 7H_2O$$

This reaction takes place more readily at cathodic points on the metal surface than does the reduction of hydrogen ions or of nitric acid. As a result, there is acceleration (depolarization) of the cathodic reaction. This makes possible a corresponding increase in the anodic, metal dissolution reaction. In this sense, the effect of oxidizing cations and of an anodic, external current is the same, i.e., the removal of electrons from the metal is accelerated. The result of this acceleration of dissolution, preferential grain boundary attack, is also the same in both cases (Fig. 7 and 10). The process is self-accelerating because hexavalent chromium ions accumulate more rapidly in the grooves, which tend to retard their diffusion into the solution.[3]

The effect of two other oxidizing cations, Fe^{+3} and Ce^{+4}, was also investigated. Weight-loss data obtained with ferric nitrate additions are plotted in Fig. 11A. Relatively large amounts are required before there is an appreciable increase in corrosion rate. As in the case of hexavalent chromium, the increase is largely a result of intergranular attack. Because of the high concentration of ferric ions required and the much greater effectiveness of dissolved chromium, their influence is not observed in nitric acid testing solutions containing only those ferric ions formed from dissolving stainless steels.

[3] Concentration of chromium-ion corrosion products in cavities is also responsible for accelerated attack at cross-sectional surfaces of bar stock, end-face corrosion. Hexavalent chromium collects in the small pits frequently formed when inclusions are removed by acid corrosion. These pits are then greatly enlarged by the rapid intergranular attack produced by the chromium ions.

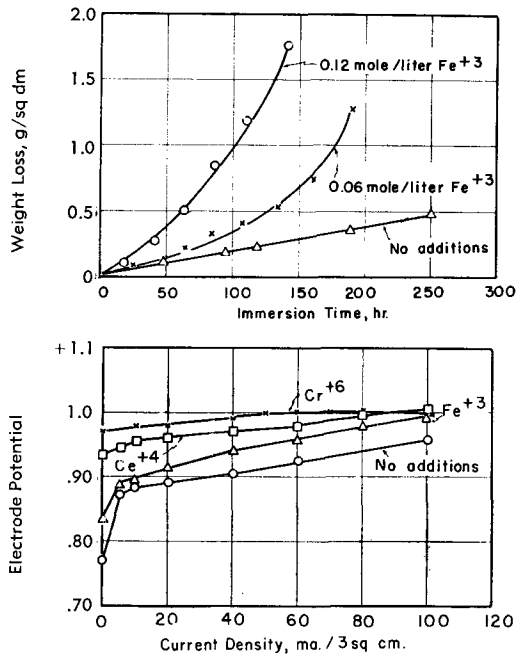

Fig. 11. Effect of cations in nitric acid on corrosion of stainless steel. A (top), acceleration of intergranular attack by ferric nitrate; Addition: $Fe(NO_3)_3 \cdot 9H_2O$, solution changed every 48 hr. B (bottom), anodic polarization of stainless steel. Concentration of cations: 0.10M. Additions: $Fe(NO_3)_3 \cdot 9H_2O$, CrO_3, and $Ce(HSO_4)_4$. Potential: against saturated KCl, calomel electrode, apparatus, Fig. 5.

What property of these ions determines the amount of acceleration, the oxidation potential, the valence change, or their influence on anodic and cathodic polarization? In another system in which oxidizing cations accelerate corrosion, iron dissolving in sulfuric acid, Gatos (6) found that the increase in corrosion was proportional to the concentration of the cation and its valence change in the reduction reaction. The rate of corrosion in this system depended on the rate of diffusion of the cations to the cathodic points on the surface of the metal rather than on a partially protective film on anodic areas. Since the diffusion rate was nearly the same for most cations investigated, it followed that the amount of acceleration was a function of the valence change of each ion. For the case of stainless steels in nitric acid, McIntosh (9) has suggested that the oxidation potential of the cations is the determining factor.

Polarization and corrosion rate tests were made to obtain data on this problem. The corrosion of annealed AISI-304 steel was determined in boiling, 65% nitric acid solutions, each of which contained 0.10 mole/l of a different oxidizing cation, hexavalent chromium, trivalent iron, and tetravalent cerium. Weight-loss measurements, together with other pertinent data, are given in Table II. These data show that the valence change involved in the cathodic reaction does not determine the corrosion rate, i.e., cathodic depolarization, while accelerating the rate of dissolution, is not the rate-controlling process. This indicates that the rate-controlling process is a combination of changes in the open-circuit potential of cathodic areas and, probably, in anodic polarization. The potentials of cathodic areas are changed in the cathodic direction to various de-

Table II. Effect of oxidizing cations on corrosion of AISI-304 steel in boiling 65% nitric acid

Cation*	(Concentration 0.10 mole/l) Electrode potential, Measured, Pt‡	Electrode potential, Measured, Stainless steel	Valence change	Weight loss, g/dm² 2 hr	Weight loss, g/dm² 8 hr**
HNO_3	+1.07 (1.20) +	+0.75 (0.95) +			
Fe^{+3}	+1.05	+0.79	1	0.0†	0.1
Cr^{+6}	+1.13	+0.97	3	1.4	10.3
Ce^{+4}	+1.22	+0.94	1	1.7	6.0

* Added as $Fe(NO_3)_3 \cdot 9H_2O$, CrO_3, and $Ce(HSO_4)_4$.
** After 8 hr the effect of Cr^{+6} is greater than that of Ce^{+4} because there is profuse grain dropping in the Cr^{+6} solution, while in Ce^{+4} solution there is less intergranular penetration, more widening of grain boundaries, and, therefore, almost no grain dropping.
† As is shown in Fig. 11A, there is acceleration of corrosion by ferric ions, but this is not sufficient to be detectable in a 2-hr exposure.
‡ Potential of platinized platinum electrode vs. saturated KCl calomel electrode.
+ Potential increases gradually with time at boiling temperature, 122°C.

grees by different cations; these changes increase the difference in the open-circuit potentials and, therefore, the corrosion rate (Table II).

A possible effect of the cations on the anodic polarization (formation, dissolution, and permeability of the protective film) is indicated by the data of Fig. 11B. As stainless steel is made anodic in nitric acid by an external current, its potential increases in the cathodic direction. However, the change in potential per milliampere of current depends greatly on the cations in the solution. The change in potential produced by a 100 ma current is 0.20 v for nitric acid without additions, 0.05 v for Cr^{+6}, 0.07 v for Ce^{+4}, and 0.16 v for Fe^{+3}. Thus, the ions which have the greatest effect on the corrosion rate also are most effective in reducing anodic polarization. These anodic polarization measurements suggest, but do not prove, the effect of cations on the anodic process, because the local cell current to which the external anodic currents of Fig. 11B are added also vary with the type of cation in the solution.[4]

These factors have been summarized in the schematic diagram of Fig. 12. Oxidizing cations increase the corrosion of stainless steel in nitric acid by cathodic depolarization (increase in rate of cathodic reaction), by shifting the open-circuit potential of cathodic areas toward more noble values and thereby increasing the open-circuit potential of the local cell,

[4] In ferric sulfate-sulfuric acid solution (see below) Cartledge (24) has found by radiotracer techniques that dissolved cations became part of the anodic film.

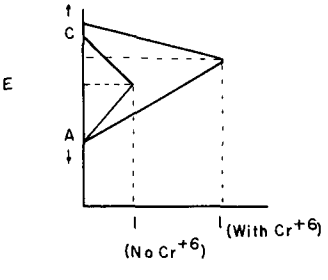

Fig. 12. Schematic potential-current diagram of local-cell action on stainless steel in nitric acid. Effect of dissolved chromium. "C" and "A" are open-circuit potentials of the local cathodic and anodic areas, and "I" is the corrosion current.

and, probably, by anodic depolarization (decreasing the protective properties of the anodic films).

Effect of Heat Treatment

Exposure of austenitic stainless steels to temperatures in the range of 1000°-1600°F may produce either or both of two types (chromium carbide and sigma phase) of susceptibility to intergranular attack, depending on the composition of the steel. The degree of susceptibility to intergranular attack increases with increasing temperature of heat treatment to a maximum at about 1250°F and then decreases with further increases in temperature. Heat treatments above 1700°F, with water quenching, do not result in appreciable susceptibility to intergranular attack in these steels (13).

The sigma phase responsible for susceptibility to intergranular attack may or may not be detectable in the microstructure. It can be revealed with certainty only by exposure of the steel to the nitric acid test. An example of this phenomenon is given by the steel whose microstructure is shown in Fig. 13. Because of the low carbon content there is no precipitation of chromium carbides after heating 1 hr at 1250°F, nor is there any visible formation of sigma phase. Yet the nitric acid corrosion rate is 35 times as great as that of an annealed specimen of the same heat of steel. While such examples are not common, similar behavior has been described by other investigators (14, 15).

In steels containing more than about 0.007-0.009% carbon, chromium carbides may be formed by heat treatments in the range of 1050°-1300°F. This lower limit of solubility was determined (14, 16) by heat treatments lasting from one day to three weeks.

The formation and growth of chromium carbides at grain boundaries can be shown by very gradual cooling of a large-grained specimen. Electrolytic etching reveals the dendritic impression in the steel left when the carbide is removed (Fig. 14A). An actual dendritic carbide, isolated from this steel, is shown in Fig. 14B. The carbide was isolated by the method of Mahla and Nielsen (17) who have made an extensive investigation of isolated carbides. A solution of bromine in anhydrous methanol was used to dissolve the stainless steel. The carbides were left

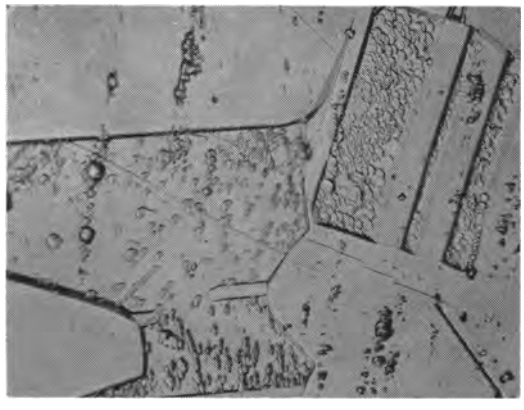

Fig. 13. Electrolytic etch of AISI-316L steel in 10% oxalic acid. Steel: FI-4 (0.020% C, 16.2% Cr) heated 1 hr at 1250°F. Etch: 1 amp/cm² for 1.5 min. Step structure: nitric acid corrosion rate 0.04 in./mo. Magnification 500X before reduction for publication.

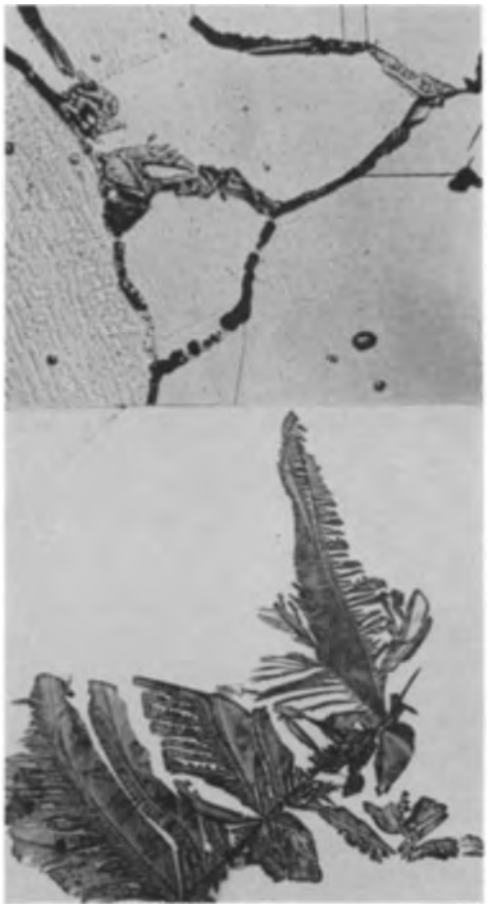

Fig. 14. Carbide precipitation in AISI-304 steel. A (top), etched electrolytically in oxalic acid. Traces of dendritic carbides (magnification 1000X before reduction for publication); B (bottom) electron photomicrograph of dendritic carbide isolated in bromine-methanol solution (magnification 5000X before reduction for publication). Steel: 0.05% C heated to 2000°F (1080°C) in evacuated, sealed quartz tube and furnace cooled.

behind in a residue layer, from which they were collected, washed, dried, and caught on a screen for examination in an electron microscope. As in the case of grain-boundary grooving of annealed steel, intergranular precipitation of chromium carbides depends on the structure of the grain boundaries. Thus, brief exposure at 1250°F produces carbides at certain preferred sites, and longer heating results in precipitation in most grain boundaries except twin boundaries. Prolonged heating (100 hr) precipitates carbides even at twin boundaries (18). This dependence of intergranular precipitation on the orientation of the grains has been observed in other alloys (19, 20).[5]

As the length of time of heat treatment at 1250°F is increased, more and more grains are completely enveloped by carbide precipitate. Upon subsequent exposure to boiling nitric acid, these grains are readily dislodged and the corrosion rate of the steel is increased (Fig. 2). It is apparent that a 1- or 2-hr sensitizing treatment of this steel at 1250°F does not produce the maximum possible amount of susceptibility to intergranular corrosion.

[5] During the formation and growth of chromium carbides the metal adjacent to the carbide is depleted in chromium. Since the carbides grow away from the boundary in very thin plates, the zone of metal depleted in chromium is parallel to the carbide and not to the grain boundary.

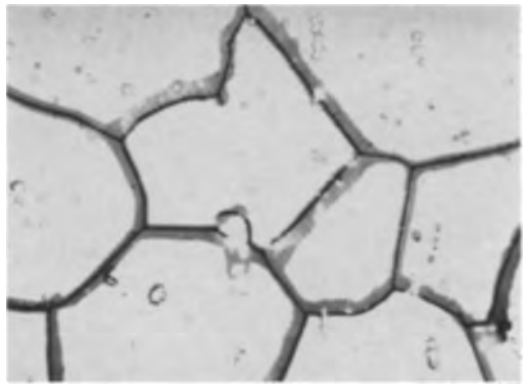

Fig. 15. Intergranular attack on AISI-316L steel in boiling 65% nitric acid. Print made from two superimposed negatives taken of the same surface area after 30 and 124 hr of exposure to acid. Narrow, dark lines show original location of grain boundaries. Steel: FH-5 (0.026% C) heated 1 hr at 1300°F. Magnification 500X before reduction for publication.

A further indication of the influence of grain orientation on intergranular precipitation and attack is given in metallographic studies of progressive corrosion. By photographing the same area of a corroding specimen after various periods of exposure to nitric acid, a series of negatives is obtained which shows the widening of grain boundary grooves. A print, made by superimposing a negative taken near the beginning of the test on one taken after considerable intergranular attack has taken place, shows the relative contributions to the grooves made by each grain (Fig. 15). In agreement with observations on intergranular precipitation, the amount of metal dissolved from various grains to make the grooves varies greatly. The grain in the center is oriented in such a way in relation to those adjacent that it contributes practically no metal to the grooves made in the exposed surface. Thus, the same crystallographic factors which determine preferential attack on annealed steel also determine the location of precipitates whose presence leads to a very great intensification of intergranular attack.

Susceptibility to intergranular attack on sensitized steel could not be detected by electrode potential measurements. Annealed and sensitized AISI-304 specimens had the same electrode potentials in boiling 65% nitric acid. This suggests that dissolution is under anodic control, i.e., the greater rate of intergranular attack on sensitized steel is a result of a lower polarizability as compared with that of the grain boundaries of annealed specimens.

Corrosion in Ferric Sulfate-Sulfuric Acid Solutions

Recent work (21) on the inhibition of corrosion of stainless steels in various acids by ferric salts has led to the development of a new test for evaluating the susceptibility of austenitic stainless steels to intergranular attack. This ferric sulfate-50% sulfuric acid test (22) is specific for revealing only the chromium carbide type of susceptibility to intergranular attack in unstabilized steels and requires only 120-hr testing time.

Mechanism of Ferric-Ion Inhibition

The minimum amount of ferric ions required for inhibition was determined for 50 and 60% solutions

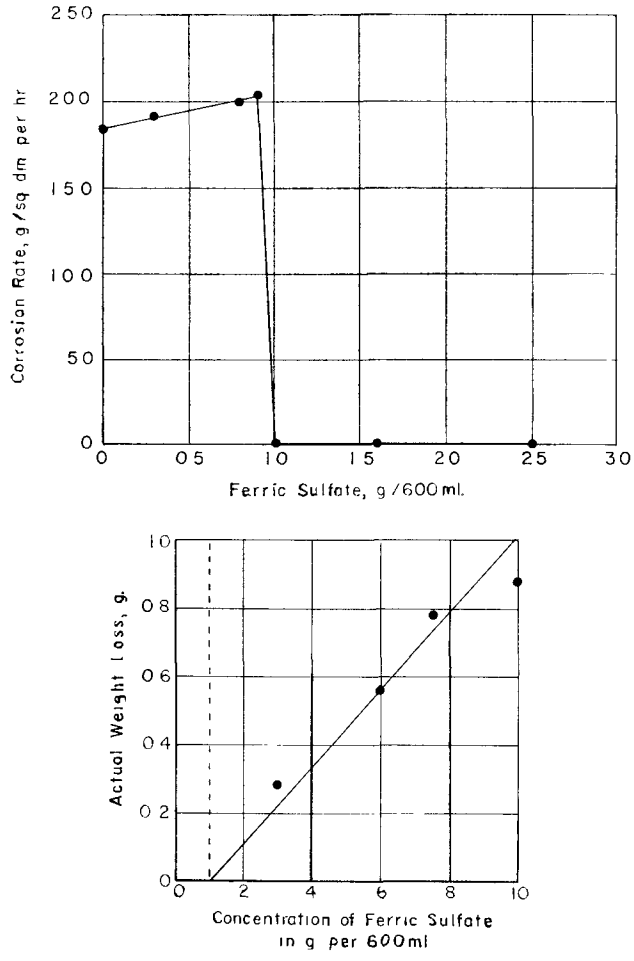

Fig. 16. Effect of ferric sulfate on corrosion of annealed AISI-304 steel in boiling 60% sulfuric acid. Ferric sulfate: 75% $Fe_2(SO_4)_3$. A (top), minimum amount of ferric sulfate required for inhibition; B (bottom), consumption of ferric sulfate. Weight loss of stainless steel at time of exhaustion of ferric sulfate as a function of amount of ferric sulfate added initially.

of boiling sulfuric acid by exposing specimens of AISI-304 stainless steel to a series of flasks to which various amounts of ferric sulfate had been added. At low concentrations of ferric ions there was no appreciable change in the very high, uninhibited corrosion rate (Fig. 16A). At a certain concentration (1 g ferric sulfate per 600 ml of 60% and 0.8 g in 50% acid) there was a sudden decrease in rate to a very low value. Corrosion was reduced from 200 to 0.037 g/dm²/hr in 60% acid.[6]

Clues to the mechanism of this process of inhibition are the absence of any hydrogen gas bubbles on the stainless steel, even though there is readily detectable corrosion, and the gradual dissolution of excess ferric sulfate in boiling acid solutions containing rapidly corroding (sensitized) stainless steel specimens. These observations suggest that ferric ions are consumed during inhibition.

When 18 Cr-8 Ni steel dissolves, divalent iron, chromium, and nickel are formed (reaction [1]). In acid solutions this anodic process is electrochemically equivalent to the discharge of hydrogen ions at cathodic areas (reaction [2]). However, in the presence of ferric ions, reaction [2] may be completely replaced by the reduction of ferric ions (reaction [3]) which results in consumption of inhibitor.

$$\left.\begin{matrix}Fe\\Cr\\Ni\end{matrix}\right\} \xrightarrow{-e} Fe^{+2} + Cr^{+2} + Ni^{+2} \qquad [1]$$

$$2H^{+} + 2e \rightarrow 2H \rightarrow H_2 \qquad [2]$$

$$Fe^{+3} + e \rightarrow Fe^{+2} \qquad [3]$$

The consumption of ferric ions to an amount just below the minimum required for inhibition is clearly indicated by the sudden onset of profuse evolution of hydrogen (change from reaction [3] to [2]).

To obtain data on the relationship of dissolution of stainless steel and the consumption of ferric ions, tests were made on coils of annealed stainless steel foil in a series of flasks containing 60% boiling sulfuric acid with various amounts of ferric sulfate in excess of the minimum amount (1 g/600 ml) needed for inhibition. This system was selected to obtain accurate weight loss-time data, which could be extrapolated 1 or 2 hr. Total testing time had to be restricted to about 7 hr because it was observed that there is gradual conversion of ferrous to ferric ions in boiling sulfuric acid solution.[7]

To expose large surface areas of steel which would provide readily detectable weight losses in periods of 0.5-7 hr the foil was made into cylindrical coils of about 600 cm² total surface area. From one to three coils were immersed in the flasks containing various amounts of ferric sulfate. The weight-loss-time data resulted in a straight line for all coils. At the instant of sudden activation (profuse hydrogen evolution) the total length of time of immersion was noted and used to determine the weight of metal dissolved by a small extrapolation of the weight loss-time line. In Fig. 16B these weight losses have been plotted against the total amount of ferric sulfate added at the beginning of the test.

The origin of the line in Fig. 16B is at 1 g ferric sulfate because the amount consumed is only that in excess of the minimum amount required for inhibition. Dissolution of 1 g of stainless steel is accompanied by the consumption of 9 g of ferric sulfate. This is in good agreement with the theoretical value of 9.7 g, derived[8] on the assumption that reactions [1] and [3] describe the process. This agreement between observed and theoretical amounts of ferric ion consumption, together with the fact that no hydrogen gas bubbles were observed in any of the solutions, some of which contained as much as 1500 cm²

[6] Sixty per cent acid was used for these tests to provide measurable corrosion rates in 7 hr or less. In the ferric sulfate-sulfuric acid test for detecting susceptibility to intergranular attack 50% acid is used (22). The minimum concentration of ferric ions required for inhibition depends on the alloy content of the steel and, therefore, may vary somewhat for different heats of 18-8 stainless steel (21). Larger concentrations of ferric ions are required to suppress corrosion of an active specimen than to prevent the onset of corrosion of an uncorroded specimen.

[7] Conversion of ferrous to ferric ions was detected by periodically exposing a stainless steel specimen to a boiling 50% solution of sulfuric acid containing 15 g per 600 ml of ferrous sulfate (colorless). This solution gradually turned yellow. When the specimen was immersed after 31 hr of boiling, it remained passive; i.e., at least 0.17 g per 600 ml of ferric ions (the minimum amount required for inhibition) had been formed.

[8] The stainless steel used was 18.9% Cr, 9.27% Ni, and, by difference, 71.8% Fe. One gram of this steel contains 0.018 moles of metal. Each mole of metal dissolving to divalent ions consumes two moles of ferric ions. The ferric sulfate used contained 20.8% iron by analysis, or one mole of ferric ions in 269 g of ferric sulfate. Therefore, the amount of ferric sulfate consumed during the dissolution of 1 g of steel is $2 \times 0.018 \times 269 = 9.7$ g.

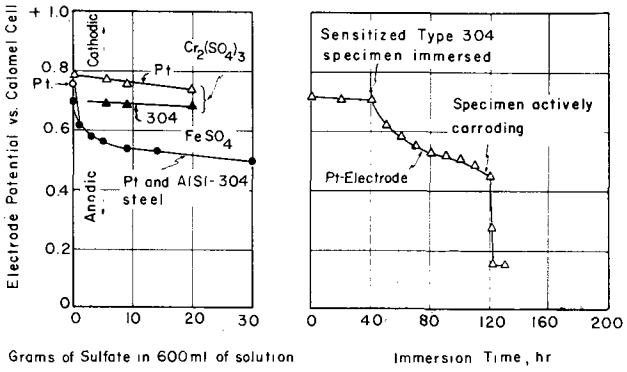

Fig. 17. Electrode potentials in boiling solutions of 50% sulfuric acid containing 15 g/600 ml of ferric sulfate. (For apparatus used see Fig. 5; all potentials measured against saturated potassium chloride calomel electrode.) A (left), effect of synthetic corrosion products on electrode potential; B (right), effect of corroding stainless steel specimen on potential of platinum electrode.

of corroding surface, shows that the reduction of ferric ions is electrochemically equivalent to the amount of metal dissolved. The corrosion current involved in reactions [1] and [3] in boiling 60% acid was derived from the weight loss, exposure time, and area of the specimen, and found to be 0.026 ma/cm^2.

Electrode potential measurements.—In 50% boiling sulfuric acid, 18 Cr-8 Ni steel has a potential of −0.34 v. With ferric ions the potential changes about 1 v in the noble direction to +0.70 v. When additions of small amounts of ferrous ions are made to the ferric sulfate-sulfuric acid solution, either as corrosion product from dissolving stainless steel or as an addition in the form of ferrous sulfate, the potential of stainless steel is the same as that of the platinum electrode, Fig. 17. Thus, the anodic areas on the steel are polarized to the potential of the cathodic areas on which the reduction of ferric ions takes place. The potential is the same for annealed and for sensitized steel and is independent of acid concentration (Table IV).

Neither ferrous ions nor other corrosion products affect corrosion in ferric sulfate-sulfuric acid solution (22). The effect of nickel and chromium sulfate additions on electrode potentials is shown in Fig. 17A. Divalent chromium (light blue) is rapidly changed to the trivalent (dark green) state in these solutions. Hexavalent chromium (orange-red), which accelerates corrosion of stainless steel, does not form in sulfuric acid during the dissolution process. This is in contrast to the behavior in nitric acid in which trivalent chromium is oxidized to the hexavalent state.

When ferrous ions accumulate from dissolving steel and reduction of ferric ions, the potential gradually changes in the anodic direction. As soon as the ferric ion concentration has been reduced to a value below that required for inhibition, the stainless steel becomes active and there is a further, rapid change to more negative potentials (Fig. 17B).

Rapid cathodic reduction of ferric ions in turn accelerates the anodic reaction, i.e., the dissolution of metal in pores of the protective film. The surge of metal (Fe, Cr, Ni) ions produced then makes possible the rapid formation of more film which heals the pores. [In the case of *iron* dissolving in sulfuric acid

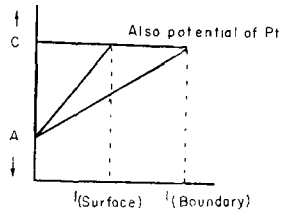

Fig. 18. Schematic potential-current diagram of local-cell action on stainless steel in ferric sulfate-sulfuric acid solution containing some ferrous ions. "C" and "A" are the open-circuit potentials of the local cathodic and anodic areas, and "I" is the corrosion current.

containing ferric ions the anodic corrosion product, ferrous ions, cannot form a protective film, and the result is an increase in the corrosion rate (6).] The passive state is dynamic. There is continual breakdown and repair of the surface. Ferric ions in solution and the ferrous ions formed by their reduction probably aid in the formation of this film (24).[9] There is also a possibility that film formation is promoted by oxygen evolved in the thermal reaction of water with ferric ions (25). The rate of dissolution of this film in the acid and/or the rate of diffusion of ions through the film determine the corrosion rate of the steel.[10]

The fact that the potential of annealed and of sensitized (chromium carbide type) steel is the same indicates that dissolution is under anodic control. The difference in grain face corrosion and intergranular penetration is primarily a result of the lower polarizability of the metal in grain boundary zones containing chromium carbide precipitate, rather than of any difference which may exist in open circuit potentials of grain centers and grain boundaries. This is also the case in nitric and in copper sulfate-sulfuric acid solution.[11]

A schematic diagram of local cell polarization is given in Fig. 18. The intersection of the polarization lines is the measured potential. Since the potential of stainless steel is the same as that of the platinized platinum electrode, the corrosion current "I" depends on the slope of the line representing anodic polarization. At grain boundaries containing chromium carbides and, therefore, a zone depleted in chromium, polarizability is less than at grain surfaces.

Intergranular Corrosion

Ferric ions greatly retard general, or grain face, corrosion (23). However, intergranular attack cannot be suppressed. As the concentration of sulfuric

[9] As a result, anodic polarization may be affected by cations in the solution. This may be different from polarization produced on stainless steel in pure sulfuric acid solutions by an anodic external current. Local cell polarization has, therefore, been described in terms of the simplified, schematic diagrams of the type of Fig. 18, rather than in reference to a specific polarization curve determined in pure acid solutions by means of an external current.

[10] In sulfuric acid solutions, without ferric ions, anodic polarization and consequent suppression of corrosion of stainless steel may be produced by means of an external electrical current or by aeration (26-29, 50, 55). Alloying additions of about 0.1% platinum and palladium to stainless steel have also been used to provide areas in the surface on which the rates of cathodic reactions are increased to permit more rapid formation of protective films on anodic areas (51).

Metal dissolution in aqueous media by diffusion of cations through protective films has been proposed by Petrocelli (48), Hoar and Evans (49), and Vetter (57).

[11] Support for this mechanism is given by electrode potential measurements made on grain surfaces and grain boundaries of large grained sensitized specimens using the technique described by Dix (53). There was no difference in these potentials in a solution of nitric-hydrofluoric acid. Similar measurements have been made by Standifer (54), who also found that the potentials of susceptible boundaries are the same as those of grain surfaces in several acids.

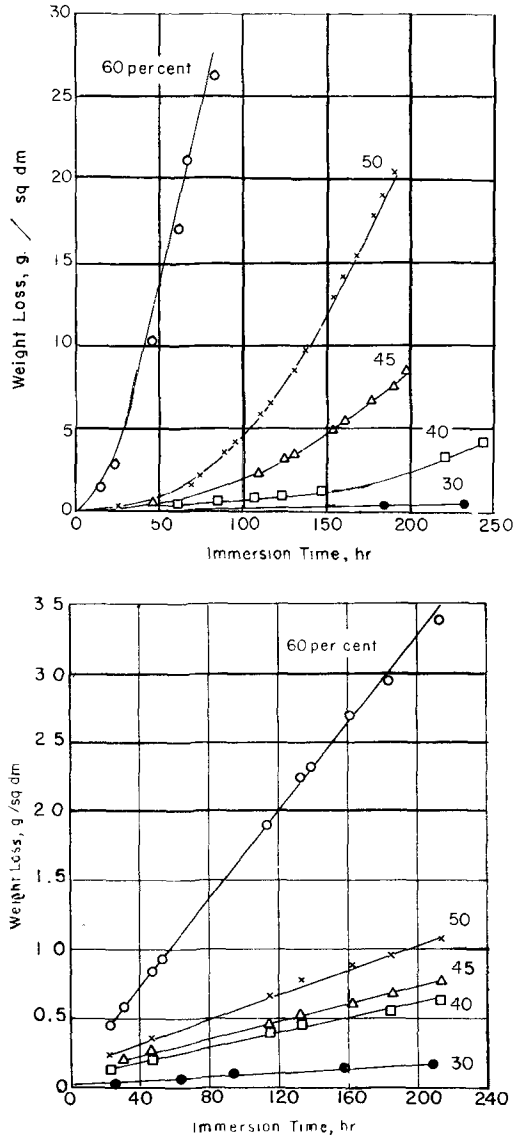

Fig. 19. Effect of concentration of sulfuric acid on corrosion of AISI-304 steel in boiling ferric sulfate-sulfuric acid solution (22). Solution: 600 ml with 15 g ferric sulfate (acid concentrations in weight per cent). Specimens: A (top), AISI-304 (M304, Table I) heated 1 hr at 1250°F; B (bottom), (M304, Table I) annealed.

acid is increased from 30 to 60% there is a large increase in intergranular corrosion of a steel containing chromium carbides (Fig. 19A). The morphology of intergranular penetration remains unchanged in this range of acid concentration (data in section on "Comparison of Types of Intergranular Attack"). General corrosion also increases as the acid concentration is increased (Fig. 19B). At a given length of exposure time, the ratio of intergranular to general corrosion is a measure of the resolving power or sensitivity of the solution to detect susceptibility to intergranular attack. Increases in acid concentration and testing time increase the ratio (22).

Intergranular corrosion in this solution leads to undermining and dislodgment of grains (Fig. 20) at a rate about twice that in the nitric acid test. This is shown by a comparison of ratios as given in Table III. On the AISI-304 steels the ratios obtained in 120 hr of exposure in the ferric sulfate-sulfuric acid solution are the same as those found after 240 hr of

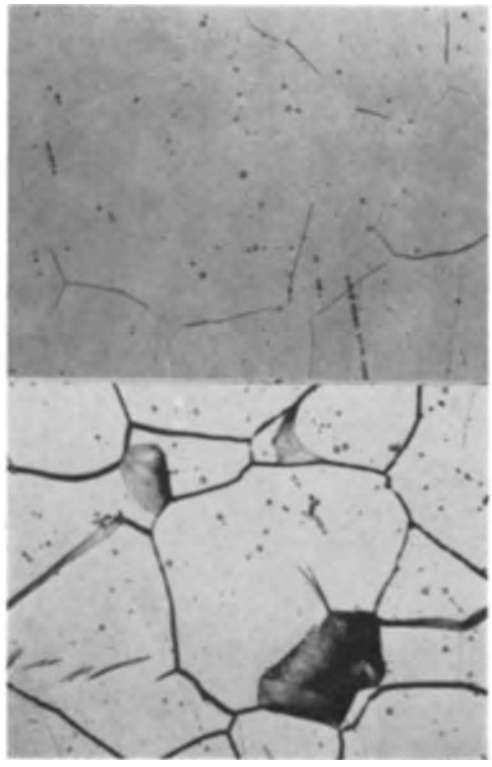

Fig. 20. Corrosion of AISI-316 steel in boiling ferric sulfate-sulfuric acid solution. Solution: 50% sulfuric acid containing 15 g/600 ml ferric sulfate. Steel: M316, analysis Table I. A (top), annealed, M316, after 20-hr exposure; B (bottom), sensitized, 1 hr 1250°F, after 20 hr exposure. Magnification 500X before reduction for publication.

testing in the nitric acid test. The conditions of acid concentration and testing time of the new evaluation test were selected on the basis of this type of data.

Table III also shows that on AISI-316 and 316L steels the ferric sulfate-sulfuric acid test does not reveal the type of susceptibility associated with sigma phase. Most of these steels have very high ratios in nitric acid but have a ratio of unity in the 120-hr ferric sulfate-sulfuric acid test. For example, steel FI-4, which does not contain any carbides after

Table III. Comparison of evaluation tests

(Types of susceptibility to intergranular attack and use of ferric sulfate and ferric nitrate)

Steel AISI	Code†	Ratio of weight losses* 65% nitric acid 240 hr	50% sulfuric acid Ferric sulfate 120 hr	50% sulfuric acid Ferric sulfate 240 hr	50% sulfuric acid Ferric nitrate(d) 24 hr
304	M304(a)	12.8	11.8	23.8	28.0
304	FK-2(a)	2.1	2.1	3.7	2.1
316L	FI-4(a)	35.6	1.4	1.7	1.0
316	M316(a)	19.0	7.8	18.5	—
316L	FI-6(b)	133.0‡	1.0	1.5	—
316L	EM-9(c)	3.3‡	1.0	1.2	—
316L	FI-2(b)	20.4‡	1.4	2.4	—
316L	FI-9(b)	210.0‡	1.3	2.2	—

* Weight loss of heat-treated specimen, (g/dm²)
Weight loss of annealed specimen, (g/dm²)

† (a) Heated 1 hr at 1250°F, W.Q.
(b) Heated 1 hr at 1300°F, W.Q.
(c) Heated 4 hr at 1600°F, W.Q.
(d) 35.5 g/liter $Fe(NO_3)_3 \cdot 9H_2O$

‡ Calculated from data given in Ref. (42).

heating 1 hr at 1250°F (Fig. 13), has a ratio of 35.6 in the nitric acid test as a result of severe intergranular corrosion of the sensitized specimen. In the ferric sulfate-sulfuric acid test there is essentially no intergranular attack on this steel even though there is some grain boundary grooving. This is a more severe form of the grooving shown on annealed AISI-316 steel in Fig. 20A.

Use of other ferric salts and other acids.—Corrosion and inhibition may be influenced greatly by the anion of the ferric compounds used for inhibition. Thus, ferric chloride and bromide readily break down passive films and lead to severe pitting (21, 30). The oxalate is decomposed in sulfuric acid solution, and the products of decomposition reduce ferric to ferrous ions.

Also, the anion of the ferric salt may affect the rate of intergranular attack. For example, ferric nitrate increases the rate of intergranular attack as compared with the rate obtained with ferric sulfate. The comparison of ratios in Table III suggests that a 24-hr test with the ferric nitrate inhibitor is equivalent in resolving power to a 120-hr ferric sulfate-sulfuric acid or a 240-hr nitric acid test. Thus, it may be possible to develop a 24-hr ferric nitrate-sulfuric acid test.

A further development of accelerated evaluation tests for susceptibility to intergranular attack may be possible by the combined use in these tests of ferric compounds and the very acid to which the steel is to be exposed in plant service. Ferric ions inhibit general corrosion in a number of acids, e.g., acetic, formic, oxalic, sulfamic, and sodium bisulfate (21). The use of ferric compounds in these acids makes it possible to use boiling solutions at acid concentrations selected to give the most rapid intergranular attack on susceptible steels. Thus, if a certain steel is to be used in acetic acid service, its susceptibility to intergranular attack might be determined by exposing it in boiling, ferric-ion inhibited, 20% acetic acid.

Corrosion in Copper Sulfate-Sulfuric Acid Solution

This combination of reagents, originally developed by Hatfield (31), has been widely used to determine the susceptibility of austenitic stainless steels to intergranular corrosion. Exposure to this solution at boiling temperatures produces intergranular attack only on steels containing intergranularly precipitated chromium carbides (13, 32, 33). The attacked zone at grain boundaries is such that the large majority of grains remain in place. Also, general corrosion on grain faces is very low. As a result, the change in weight, even on steels susceptible to intergranular attack, is very small and has not been used as a routine means of measuring the extent of intergranular corrosion.[12]

The most commonly used method for routine evaluation of this test consists of bending a 2-cm wide by 5- or 8-cm long specimen through 180° and examining the surface for cracks, which indicate intergranular attack. This qualitative evaluation method has actually been found to be a more sensitive indication of intergranular corrosion than measurement of changes in electrical resistance (33) or of weight loss. For resistance measurements, first used by Rutherford and Aborn (35), a modified Kelvin bridge, thin specimens, 4- to 10-cm long, and exposure periods of hundreds of hours are required.

A method of greatly accelerating intergranular attack in the copper sulfate-sulfuric acid solutions has recently been developed by Rocha (36). This consists of placing the stainless steel specimen in contact with copper metal chips during exposure in the test solution. As a result, the exposure time is reduced from 200 to 24 or 48 hr before evaluation by the bend test.

Intergranular Corrosion

A boiling solution of 15.7% sulfuric acid and 5.7% $CuSO_4$ (by weight) was used for all tests. This was prepared by adding 100 g $CuSO_4 \cdot 5H_2O$ and 100 ml H_2SO_4 (sp gr 1.84) to 840 ml of water (37). Apparatus was the same as that used for the nitric acid and the ferric sulfate-sulfuric acid solutions, i.e., a 1-liter Erlenmeyer flask, containing 600 ml of solution, with a cold finger condenser. To avoid accumulation of corrosion products frequent changes of solutions were made. For electrical resistance measurements the stainless steel specimens were machined and ground to a cross section of 0.6 x 0.15 cm and a length of 3 to 6 cm. Any heat treatments required were made on the specimens before machining.

Changes in electrical resistance of these specimens were measured with a precision Kelvin bridge. These resistances varied from 0.001 ohm on specimens before testing to about 0.06 ohm on specimens whose grain boundaries were extensively corroded. All resistance measurements were converted to per cent change in resistance. By determining this change for segments of various lengths of one specimen, it was found that the per cent change in resistance was independent of the length of specimens used in this investigation.

Before resistance measurements are made the specimens must be immersed in acetone to remove residual liquids and soluble solids from corroded grain boundaries

Dislodgment of grains in the cupric sulfate-sulfuric acid solution is very slow, especially from AISI-316 steels. Even though the grain boundaries may be penetrated enough to make a 6-cm long specimen bend under its own weight the surface may be almost unchanged in appearance. In the case of AISI-304 steels, grains are dislodged more readily and the specimens sometimes break in handling.

Effect of metallic copper.—Quantitative data were obtained on the acceleration of intergranular attack produced by immersion of metallic copper in the testing solution. Three types of tests were made: (*a*) simple immersion of stainless steel in cupric sulfate-sulfuric acid solution, (*b*) simultaneous immersion with metallic copper, but not in contact, and (c) immersion of steel in contact with copper. Contact with metallic copper was provided by partially filling the glass cradles, used to hold the steel specimen, with copper turnings. A weighed and measured cop-

[12] An intergranularly corroded specimen gives off a dull sound when dropped on a hard surface. This effect has been investigated by oscillographic analysis (34).

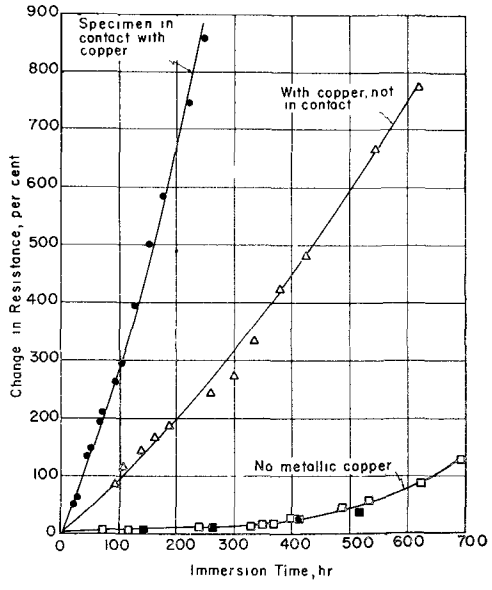

Fig. 21. Change in electrical resistance of sensitized AISI-316 steel in boiling copper sulfate-sulfuric acid solution. Effect of metallic copper. Solution: 15.7% H_2SO_4 and 5.7% $CuSO_4$. Steel: AISI-316 (EW-6) heated 1 hr at 1250°F.

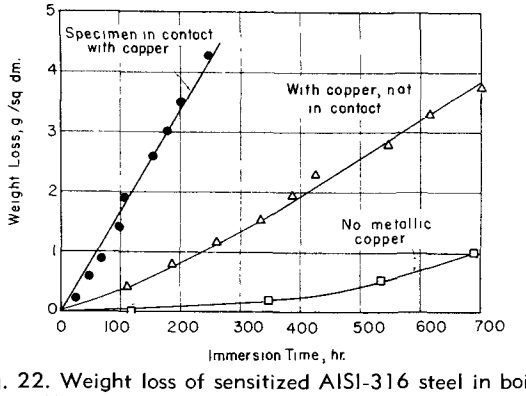

Fig. 22. Weight loss of sensitized AISI-316 steel in boiling copper sulfate-sulfuric acid solution. Same tests as Fig. 21.

per specimen was used for the simultaneous immersion tests.

The results of electrical resistance and weight-loss measurements are given in Fig. 21-23. It is apparent that without the use of metallic copper the rate of intergranular attack is very slow. After 240 hr the change in resistance is only 10% and the weight loss only 0.1 g/dm² (in a 120-hr exposure in 65% nitric acid the weight loss of this steel was 31.5 g/dm²). Simultaneous immersion of the copper, about 20 cm² in area, increases the rate of intergranular attack by a factor of 24 (at 240 hr of immersion) as determined by change in resistance (Fig. 21). Contact with the copper specimen produces a further increase in the rate of attack—by a factor of 85 over the copper-free test. These differences in rates of intergranular attack also are reflected in the weight losses (Fig. 22).

To determine whether this increase of corrosion by copper is a result of simple acceleration of the type of intergranular attack observed without immersion of copper, or the result of a change in the geometry of grain-boundary attack the per cent changes in resistance have been plotted against the weight losses (Fig. 23). In this graph the time factor has been eliminated. The resulting relationship of resistance change to weight loss is the same for all three tests. Thus, metallic copper increases corrosion by accelerating the type of intergranular attack produced in the absence of copper, rather than by changing the character of grain boundary attack.

A photomicrograph of intergranular attack produced in copper sulfate-sulfuric acid solution with the stainless steel in contact with copper is shown in Fig. 24. Even though the attacked grain-boundary zone is very narrow in comparison with that produced in nitric acid and ferric sulfate-sulfuric acid solutions (Fig. 3 and 20), there has been enough penetration to undermine and dislodge grains.

Effect of sensitizing time.—Increasing the heat treatment at 1250°F from 1 hr to 2 hr increases the amount of intergranularly precipitated chromium carbides and probably also the size of the carbides. Figure 25 indicates that the character of intergranular attack on specimens of the same heat of steel is changed by varying the length of time of sensitizing. Each specimen has its own resistance change vs. weight relationship. Greater amounts of carbide precipitate produce a more rapid increase in resistance than in weight loss in the cupric sulfate-sulfuric acid solution (without metallic copper). The rate of intergranular penetration increases more rapidly than does grain dropping.

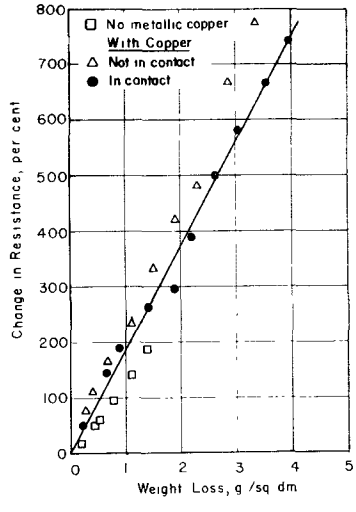

Fig. 23. Relationship of change in electrical resistance and weight loss of sensitized AISI-316 steel in boiling copper sulfate-sulfuric acid solution. Same tests as Fig. 21.

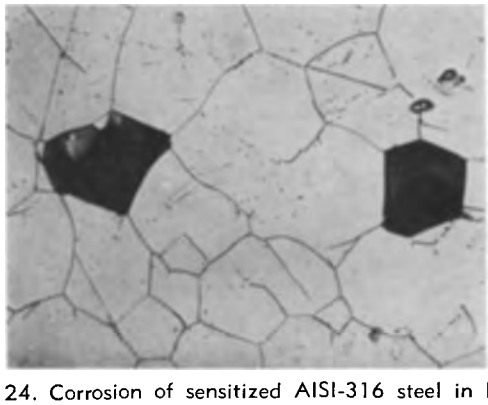

Fig. 24. Corrosion of sensitized AISI-316 steel in boiling copper sulfate-sulfuric acid solution. Specimen in contact with copper. Steel: AISI-316 (EW-6) heated 1 hr at 1250°F. Exposure: 23 hr. Magnification 500X before reduction for publication.

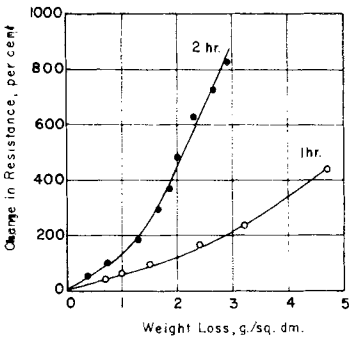

Fig. 25. Effect of length of time of heat treatment on intergranular penetration in boiling copper sulfate-sulfuric acid solution. AISI-316 (M 316) heated at 1250°F. As shown. Tests made without metallic copper.

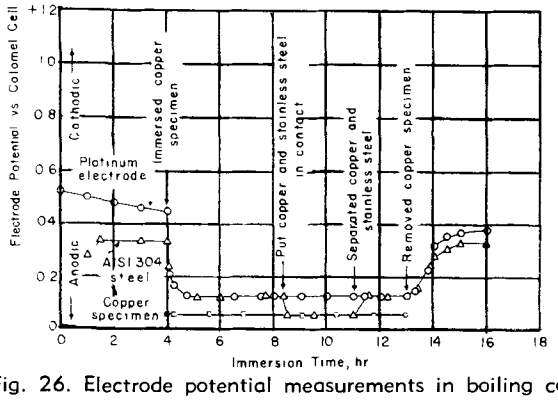

Fig. 26. Electrode potential measurements in boiling copper sulfate-sulfuric acid solutions. Effect of metallic copper. Solution: 15.7% sulfuric acid and 5.7% $CuSO_4$. (For apparatus used see Fig. 5; all potentials measured against saturated potassium chloride calomel electrode).

Tests have also been made in cupric sulfate-sulfuric acid solution on steels containing the sigma type of intergranular susceptibility. The results, discussed below, are in agreement with those of previous investigators (13, 32, 33) and show that the sigma type of susceptibility does not lead to accelerated intergranular attack in this solution.

Effect of dissolved iron.—Ferrous sulfate was added to copper sulfate solutions to give a concentration of 1.3 to 2.6 g/l of ferrous ions. Dissolved iron in this range of concentration was without effect on the weight loss of annealed or of sensitized steel, with or without metallic copper in the solution. However, in some tests dissolved iron reduced the change in resistance of sensitized specimens, which is in agreement with results of Brauns and Pier (39), who reported a decrease in intergranular attack (no metallic copper) as determined by the bend test, which indicates total penetration, as does the change in resistance.

Electrode Potential Measurements

Potential measurements in boiling solutions of copper sulfate-sulfuric acid of the same concentration as described above were made to provide data for an interpretation of the action of metallic copper and the mechanism of dissolution in this solution. Some results have been plotted in Fig. 26.

Initially, the potential of the platinized platinum electrode is about +0.53 v and that of a stainless steel specimen, +0.34 v. Immersion of a piece of copper (40 cm^2 surface area) in this solution, but not in contact with either the stainless or platinum electrode, very rapidly changes the potential of both electrodes in the anodic (active) direction to +0.13 v. Both electrodes now have the same potential, which is constant. The potential of the copper is constant at 0.06 v. When the copper is put in contact with the stainless electrode there is a further change in potential of the steel in the active direction to that of copper, which remains unchanged (large surface area). The potential of the solution (Pt electrode) remains unchanged. Breaking contact between the stainless steel electrode and the copper specimen reestablishes the potential of the stainless steel at the same value as that of the platinum electrode. Upon removal of the copper specimen the potentials of both platinum and stainless steel electrodes increase in the cathodic direction. As in the beginning, the platinum electrode assumes the more cathodic potential. These measurements are readily reproducible and are the same on annealed and on sensitized steel.

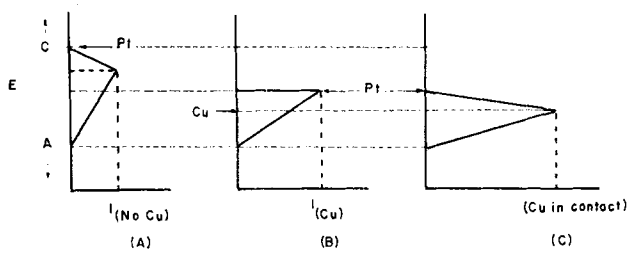

Fig. 27. Schematic potential-current diagrams of local-cell action on stainless steel in copper sulfate-sulfuric acid solution. Effect of metallic copper. "C" and "A" are the open-circuit potentials of the local cathodic and anodic areas, and "I" is the corrosion current. The electrode potentials of a platinized platinum electrode and the metallic copper, immersed together with the stainless steel, are indicated by arrows.

The action of metallic copper in this solution is shown by a comparison of weight-loss measurements obtained on copper in boiling sulfuric acid, with and without cupric sulfate. Without cupric sulfate the weight loss was about 0.3 g/dm^2 in 20 hr. Addition of cupric sulfate to make a 5.7% $CuSO_4$ solution increased this weight loss 40-fold by cupric-ion corrosion.

$$Cu + Cu^{+2} \rightarrow 2Cu^{+1}$$

Accumulation of cuprous ions in the cupric sulfate-sulfuric acid solution changes the potential in the anodic direction to the same value on both the platinum and stainless steel electrodes, which indicates that the local anodes are polarized to the potential of the cathodic areas. Thus, in copper sulfate-sulfuric acid solution, as well as in the other two acid solutions investigated, corrosion of stainless steel is controlled by the polarizability of anodic areas. These changes in potential are shown schematically in terms of local cell action in Fig. 27A and B.

When the copper specimen is put in contact with the stainless steel there is a further change in the potential of the steel, in the anodic direction, to that of the copper. (The potential of the platinum electrode remains constant.) This change indicates cathodic polarization of the steel.[13] Therefore, stainless

[13] Making an electrode a cathode by means of an external current either has no effect on its potential or changes it in the anodic direction. In turn, anodic polarization changes the potential in the cathodic direction.

steel is the cathode of the steel-copper galvanic couple.[14] There is a simultaneous reduction in anodic polarization, primarily at susceptible grain boundaries, and, consequently, an increase in corrosion rate, or corrosion current, in terms of the diagram in Fig. 27C. In this system cathodic polarization increases corrosion.[15] As suggested by Rocha (36) the copper contact produces dissolution of the stainless steel at a constant potential, i.e., the copper provides a very simple equivalent of a constant-potential instrument, a potentiostat.

Since copper is the anode of the galvanic couple with stainless steel, it might be expected that its rate of corrosion is increased. However, no increase was observed because of the very great difference in the corrosion rates of the stainless steel and the copper. The galvanic current produced by the couple doubles the corrosion rate of the stainless steel (Fig. 22). Only a small fraction of this is actually due to metal dissolution; most is a result of grain-dropping. The galvanic current passing to the stainless steel from the rapidly corroding copper (0.65 g/dm²/hr) produced such a small increment in this rate that it could not be detected.

Dissolution of stainless steel in cupric sulfate-sulfuric acid solution without metallic copper gradually changes the oxidation reduction potential of the solution in the anodic direction as cuprous ions are formed by reduction of cupric ions on the surface of the steel. However, in the presence of relatively large concentrations of dissolved ferrous ions this shift is suppressed. In agreement with Brauns and Pier (39) it was found that 1-3 g/l of ferrous ions retards or prevents the change of potential in the anodic direction. Ferrous ions were oxidized to the ferric state. A blue solution containing 1.3 g/l ferrous ions becomes blue-green in 12 hr at boiling temperature. When metallic copper was added, dissolved iron remained in the ferrous state and the potentials of copper and of stainless steel in contact with it were the same as in solutions without iron.

Comparison of Types of Intergranular Attack

In this concluding section the techniques described in the previous parts are used for a comparison and interpretation of the types of intergranular attack produced by various solutions. The data have been summarized in terms of criteria which can be used to compare the applicability of these corroding acids for routine evaluation tests. A description of experimental work undertaken to reveal the effect of grain size on intergranular corrosion concludes the discussion.

Effect of Acids

Some results obtained on AISI-304 and 316 steels in the three acid solutions discussed above are shown in Fig. 28. In these two graphs the effect of length of testing time has again been eliminated by plotting change in resistance against the weight loss of a given (sensitized) steel. Elimination of the testing time facilitates the comparison of types of intergranular attack, because the factors in the acids which determine the rate of intergranular penetration do not affect its character. Thus, it was shown (Fig. 23) that the very great acceleration of intergranular attack caused by the use of metallic copper in the copper sulfate-sulfuric acid test does not alter the characteristics of this attack. This is also the case for increasing acid concentration which greatly affects the rate of corrosion in the ferric sulfate-sulfuric acid solution (Fig. 19). The data on AISI-304 and 316 steels in Fig. 28, obtained in 15.7 and 50% acid, provide the evidence for this observation. Even though corrosion on the AISI-316 steel is increased 300-fold in 77 hr by this increase, the points for both concentrations fall on one line. A discussion of "characteristics of intergranular penetration" is given below.

The relationship of change in resistance and weight loss on intergranularly corroding specimens may be described with reference to an imaginary specimen suffering uniform general corrosion. Cal-

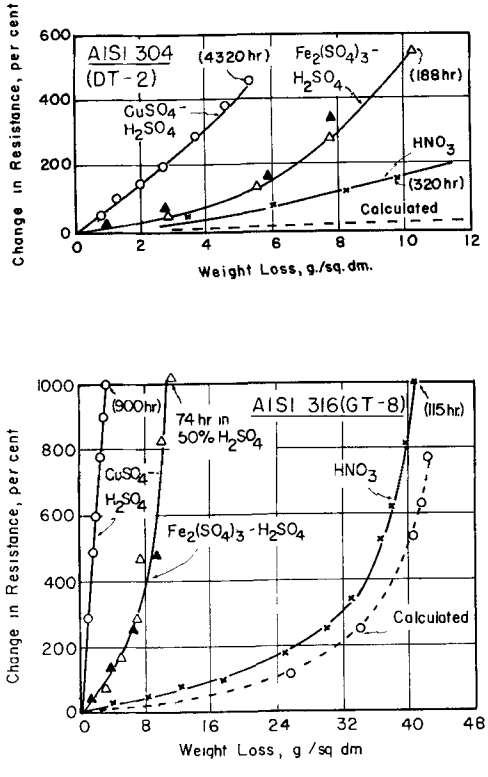

Fig. 28. Comparison of intergranular penetration and weight loss in three boiling acid solutions. Steels: A (top), AISI-304 (DT-2) heated 1 hr at 1250°F; B (bottom), AISI-316 (GT-8) heated 1 hr at 1950°F, then 1 hr at 1250°F. Solutions: O, 15.7% H_2SO_4 — 5.7% $CuSO_4$ (no metallic copper); △, 50% H_2SO_4 — $Fe_2(SO_4)_3$; ▲, 15.7% H_2SO_4 — $Fe_2(SO_4)_3$; x, 65% HNO_3.

[14] Confirmation of this relationship in the copper-stainless steel couple was obtained in a test in which the current and its direction in this couple were measured. Specimens of copper and stainless steel, connected through a microammeter, were partially immersed in boiling sulfuric acid without cupric sulfate. The stainless steel dissolved with vigorous evolution of hydrogen and was the anode of the couple. When the couple was immersed in a second solution of sulfuric acid of the same concentration containing cupric sulfate, evolution of hydrogen on the stainless steel was suppressed. There was a reversal and a large decrease of the current between the specimens. The stainless steel became the cathode and the copper became the anode of the galvanic couple.

[15] This is in contrast to the behavior of some metals in nearly neutral solutions. Cathodic polarization frequently reduces corrosion in such systems (cathodic protection). On metals exposed to solutions in which they evolve hydrogen [steels in acids, aluminum in sodium hydroxide (38)] cathodic polarization usually does not affect the corrosion rate.

culations[16] were made of the per cent change in resistance as a function of the weight loss of such a stainless steel specimen (of similar cross-sectional area as those used in the laboratory tests) and have been plotted in Fig. 28. At a given weight loss the difference in per cent change in resistance between the calculated curve and one of the experimental curves is an indication of the extent of intergranular penetration beyond the metal surface produced by grain dropping. This difference in per cent resistance change is a measure of the grain boundary attack which has taken place, but which did not contribute to the weight loss. (The assumption is that the weight loss is very largely due to dislodged grains rather than to dissolved grain boundary material.)

Examination of the curves in Fig. 28 shows that intergranular penetration in addition to that indicated by weight loss measurements is greatest in copper sulfate-sulfuric acid solution and least in nitric acid. Also, this type of penetration is less for AISI-304 than for 316 steel in the two sulfuric acid solutions. These conclusions are in agreement with the qualitative observations made on corroded specimens. In the copper sulfate solution there is relatively little dislodgment of grains as compared with that produced in the other tests. Also, in copper sulfate-sulfuric acid solution grain dropping on AISI-304 steel is greater than on the 316 steel. On both steels there is more intergranular penetration beyond the surface in the ferric sulfate-sulfuric acid than in the nitric acid solution.

The slopes of the curves in Fig. 28 are determined by the ratio of intergranular penetration along susceptible grain boundaries to the rate of grain surface corrosion. If the rate of grain surface corrosion is low, there is little widening of grain boundary grooves following dissolution of the zone which contains chromium carbide or sigma phase constituent, and, therefore, the grains tend to remain in place (large slope). High rates of grain surface corrosion lead to widening of the attacked zone and to profuse grain dropping (low slope). In the narrow space formed by dissolution of the grain boundary zone the ratio of surface area to volume of solution is much greater than in the bulk solution. As a result, corrosion products may have a great effect on subsequent dissolution in these confined spaces.

Data on specimens corroding in ferric sulfate-sulfuric acid solution of various concentrations of acid support this view of the importance of the ratio of intergranular to grain surface corrosion. The resistance change-weight loss relationship in this solution is the same for 15.7 and 50% acid (Fig. 28). Thus, the ratio of intergranular penetration to grain surface corrosion should be independent of acid concentration. Evidence for this can be derived from the data plotted in Fig. 19, which shows the effect of acid concentration on the corrosion of annealed and of sensitized steel in ferric sulfate-sulfuric acid solutions. For this comparison the weight loss on sensitized specimens (Fig. 19A) may be used as a measure of intergranular penetration. From Fig. 28, it is apparent that the penetration measured by weight loss does not represent the total depth of penetration. Also, there is a relatively small amount of general corrosion reflected in this weight loss. However, these factors are eliminated by determining the ratio of intergranular to grain surface corrosion in solutions of various acid concentrations at the same stage of intergranular disintegration, i.e., at the same weight loss of the sensitized specimens, rather than at a certain time of immersion.

At a weight loss of 8.0 g/dm^2 the specimen (Fig. 19A) in 45% acid has corroded 192 hr. The weight loss of an annealed specimen in 45% acid after 192 hr is 0.70 g/dm^2, and the ratio of intergranular to grain surface corrosion is 8.0/0.70 = 11.4. Identical ratios are obtained in 50 and 60% acid. At a weight loss of 4.0 g/dm^2 the ratios are 5.7(40%), 7.25(45%), 7.25(50%), 7.25(60%). Thus, the ratio of intergranular to grain surface corrosion is independent of acid concentration.

The data of Fig. 23 show that the ratio of intergranular to grain-face corrosion in the copper sulfate-sulfuric acid solution is unaffected by the action of metallic copper.

In nitric acid, corrosion products, especially hexavalent chromium, greatly accelerate corrosion and cause widening of the spaces between the grains. Consequently, the depth of the layer of grains removed is almost equal to the depth of intergranular penetration (Fig. 28).

To compare corrosion currents and the corresponding electrode potentials in the three acid solutions, corrosion rates of annealed specimens have been converted to milliamperes per square centimeter, Table IV. Even though the corrosion current in ferric sulfate-sulfuric acid solutions varies by a factor of 88 in the range of 10-60% acid, the potential is essentially the same at all concentrations.

Effect of Chromium Carbide and Sigma Phase

The effect of length of time of sensitization on intergranular penetration and grain dropping de-

Table IV. Corrosion currents and electrode potentials of annealed AISI 304 (M304) steel in boiling acid solutions

Solution	Corrosion current,* ma/cm^2	Electrode potential, (Sat. KCl electrode), v
Copper sulfate-15.7% sulfuric acid (in contact with copper)	0.00074	+0.06
Nitric acid (65%)	0.0040	+0.75-0.95
Ferric sulfate-sulfuric acid 5.5 g/l Fe^{+3} + 1.15 g/l Fe^{+2}		
10% H_2SO_4	0.00043	+0.60†
30% H_2SO_4	0.0018	+0.60†
50% H_2SO_4	0.012	+0.59†
60% H_2SO_4	0.038	+0.61†

* Calculated from corrosion rates, which are constant with immersion time on annealed chromium carbide- and sigma phase-free) steel.

† Also the potential of platenized platinum electrode in these solutions.

[16] The per cent change in resistance was derived from

$$\% \Delta R = \frac{R_t - R_o}{R_o}(100) = \frac{A_o - A_t}{A_t}(100)$$

where R_t, R_o, A_t, and A_o are the resistances and areas of cross sections of the specimens, at the beginning of the test and after exposure, t. To relate change in resistance to weight loss a specimen of 100 cm^2 surface area (neglecting the ends) 0.15 × 0.60 cm in cross section (66.6 cm long) was assumed. Using 8.04 g/cm^3 as the density for 18 Cr-8 Ni stainless steel, the changes in weight for various changes in cross-sectional areas of the specimen was calculated. These same cross-sectional areas were used in the formula above to determine the accompanying change in resistance.

pends on the solution to which the steel is exposed. Results obtained in copper sulfate-sulfuric acid solution have been plotted in Fig. 25. Intergranular penetration (per cent change in resistance) per gram of weight loss is greater on the specimen heated for 2 hr at 1250°F than for that heated 1 hr. Comparable tests have been made in ferric sulfate-sulfuric acid and in nitric acid solutions.

In ferric sulfate-sulfuric acid the difference in change in resistance between specimens heated 1 and 2 hr at 1250°F was only 35% at a weight loss of 8 g. This is much less than in the copper sulfate-sulfuric acid solution. Also, penetration per gram of weight loss was greater for the specimen heated 1 hr than for the 2-hr specimen. In nitric acid intergranular penetration and grain dropping were identical on both specimens. The data for the 1- and the 2-hr specimens, when plotted as in Fig. 25, fell on one curve. As expected, the rate of change in resistance and the rate of weight loss for a given length of exposure time was greatest in all three solutions for the specimen sensitized 2 hr.

These observations may also be interpreted in terms of the ratio of intergranular to grain face corrosion and the role of corrosion products. Increasing the length of sensitizing time from 1 to 2 hr increases the amount of chromium carbides formed and, to some extent, their size, i.e., the distance which they grow into the grains. There is some increase in widening of grooves and, therefore, an increase in grain dropping, and a consequent decrease of the slope of the resistance change-weight loss curve. In the ferric sulfate-sulfuric acid solution, in which corrosion products do not affect corrosion, there is such a decrease. In the copper sulfate-sulfuric acid solution increasing the length of sensitizing time increases intergranular penetration without a corresponding increase in grain dropping. In nitric acid, the accelerating effect of corrosion products obscures the influence of length of time of sensitizing. Again, grain boundaries are widened and lead to such rapid dislodgment that there is little penetration ahead of the surface produced by grain dropping.

For a comparison of the action of the acid solutions on various types of steels, the ratio of the corrosion rate (at a given exposure time) of a sensitized specimen to that of an annealed specimen of the same heat of steel has been applied. This ratio, which has already been used in connection with Table III, is a sensitive measure of the power of a solution to detect susceptibility to intergranular attack. In addition, it eliminates any changes in corrosion rates caused by small variations in alloy composition of the steels.

When these solutions are used for routine evaluation by means of weight-loss determinations, it usually is not necessary to test an annealed specimen along with the one being evaluated. The corrosion rate of the latter is compared with the maximum permissible rate established for the given solution and type of stainless steel. Selection of this maximum permissible rate is based, in part, on the known general or grain face corrosion.

There is one exception to this practice. In nitric-hydrofluoric acid solutions general corrosion is very sensitive to variations in alloy content (chromium) of the stainless steels. In the range of 16-19% Cr the corrosion rate of a group of AISI-316 steels varied from 2.7 to 0.8 in./mo; i.e., by a factor of 3. This solution has been employed occasionally as a qualitative method for detecting weld decay (32, 40, 41) and has been used in this investigation for comparison with the other three solutions. Because of the relatively large influence of small variations in chromium content on grain-face corrosion the ratio must be determined even for routine evaluation purposes.

A summary of results obtained on five different heats of steel is given in Table V. The susceptibility to intergranular attack in these steels varies from the pure chromium carbide type (AISI-304) to the pure sigma phase type (AISI-316L, FI-4). A combination of both types is illustrated by the two AISI-316 heats (M316, GT-8).

First, all specimens, except FI-4, show some completely encircled grains in the oxalic acid etch structure after heating 1 hr at 1250° (and 2 hr in the case of M316) and are, therefore, classed as "ditch" struc-

Table V. Comparison of tests

Test	Steel: AISI 304 (I-9)*	AISI 304 (FK-2)*	AISI 316 (GT-8)*	AISI 316 (M316)*	AISI 316† (M316)*	AISI 316L (FI-4)*
	Ratio**					
Oxalic acid						
Etch structure (*a*)	Ditch	Ditch	Ditch	Ditch	Ditch	Step
Nitric-hydrofluoric acid test (*b*)	4	1.5	9	6	40	1.0
Ferric sulfate-sulfuric acid test (*c*)	11	2	26 (*f*)	8	34	1
Copper sulfate-sulfuric acid test (*d*)						
Exposure: 1000 hr						
Change in resistance, %	20	3	1475	40	568	1
Ratio of weight losses	4	2	34	7	20	1
Nitric acid test (*e*)	15	2	185 (*g*)	19	141	36

* Refers to Laboratory Code, Analysis, Table I.
** Ratio of weight loss on sensitized to weight loss on annealed specimen.
† Sensitized 2 hr at 1250°F.
‡ (*a*) Standard oxalic acid etch of sensitized specimen.
(*b*) 10% HNO_3-3% HF at 65°C, 1-hr test.
(*c*) Ferric sulfate—50% sulfuric acid test, 120 hr.
(*d*) 5.7% $CuSO_4$-15.7% H_2SO_4 (no metallic copper).
(*e*) Standard 240-hr nitric acid test.
(*f*) 77-hr exposure.
(*g*) Only 120-hr exposure.

tures. The number of grains completely encircled varies from only a few grains on FK-2 to complete encirclement of almost all grains on I-9, GT-8, and M316. Only the FI-4 (0.020% C) steel is entirely free of chromium carbides after the sensitizing treatment (Fig. 13).

A comparison of the ratios obtained in nitric-hydrofluoric acid, ferric sulfate-sulfuric acid, and the 1000-hr cupric sulfate-sulfuric acid test shows that all these solutions give similar results. They reflect the chromium carbide type of intergranular susceptibility. The ratios of the FK-2 steel are smaller than those of the higher carbon, I-9 steel. Among the 316 steels the GT-8 heat is consistently higher than the M316 steel, which has been sensitized 1 hr. Extending the sensitizing treatment of M316 to 2 hr increases the ratio in all of these solutions. Also, the FI-4 steel, which is free of carbides, has a ratio of unity. In the copper sulfate test resistance measurement is a more sensitive indicator of intergranular attack than the ratio based on weight loss. The discrepancy between the ratio and the per cent change in resistance increases rapidly at the higher ratios.

In the *nitric acid* test the ratios on I-9 and FK-2 follow the trend of the other tests. However, on FI-4 there is a large increase in intergranular corrosion due to sigma phase, which is not detectable in the microstructure.[17] The relatively large ratios in nitric acid of the AISI-316 heats, especially GT-8,[18] are also caused by sigma phase in combination with chromium carbides.

All five tests reveal the presence of the chromium carbide type of susceptibility to intergranular attack. The sigma type is detected only in nitric acid.[19] Since the sigma type in 316 steel is known to cause intergranular attack only in nitric acid (42), one of the other quantitative evaluation tests could be used for routine evaluation of all stainless steels, except those AISI-316 and 316L steels which are intended for use in nitric acid. In determining which of these is the most promising, the following factors are of importance.

The most sensitive quantitative measure of intergranular attack in the copper sulfate-sulfuric acid test is the change in electrical resistance. Specialized apparatus is required for such measurements, and the test specimen must be relatively long and thin. Weight losses in this solution are relatively small and not nearly so sensitive as in the other solutions.[20] The nitric-hydrofluoric acid test is rapid (4 hr or less) (56), but requires testing of two specimens because evaluation is by ratio. Special equipment and care are required for handling hydrofluoric acid and holding the solution at a temperature considerably below the boiling point. For these, and other reasons, the 120-hr ferric sulfate-sulfuric acid test has been proposed to meet the need for a quantitative method of evaluating austenitic stainless steels for the chromium carbide type of susceptibility to intergranular attack in unstabilized stainless steels (22).

[17] An attempt was made to detect this phase by electrolytic etching in 15 other reagents, which included sulfuric, chromic, phosphoric, citric, and formic acid. In every case, a step structure similar to that obtained in the oxalic acid etch was the result. Intergranular attack in this steel in nitric acid is, therefore, associated with a preprecipitation form of the sigma constituent.

[18] Note that the ratio given in Table V is only for a 120-hr exposure in nitric acid. After the regular 240-hr test this ratio would be much greater.

[19] In terms of the polarization concepts developed above, this indicates that the presence of chromium carbides leads to a decrease in polarizability at grain boundaries in all five solutions. However, sigma phase, which is also a chromium-rich phase, occurring in 18 Cr-8 Ni-Mo steel, decreases polarizability of grain boundary zones only in nitric acid.

[20] For example, it was not possible to detect by weight loss or resistance change the relatively small variations in intergranular attack produced by various lengths of sensitizing heat treatments on FK-2 steel. In nitric acid these changes were readily found, as shown in Fig. 2.

Effect of Grain Size

Discussions of grain dropping and intergranular penetration, as given above, lead to the problem of the influence of grain geometry on these processes. Does the grain size of the steel affect the rate of intergranular corrosion? On the basis of corrosion tests in sulfuric acid, with and without copper sulfate, Newell (43) has concluded that susceptibility to intergranular attack increases with grain size. Rutherford and Aborn (35) and Ferri (44) have made resistance measurements on specimens exposed to copper sulfate-sulfuric acid solution, which also showed more rapid intergranular penetration on large than on small grained steel. On the basis of these observations some investigators (35, 43, 45, 46) have concluded that intergranular carbide precipitation per unit surface of grain boundary is a function of grain size. However, on steels corroding in nitric and other acids it has frequently been observed in the present investigation that small-grained steels drop grains after shorter exposure periods than large-grained specimens. Also, on specimens having grains of various sizes the smallest are the first ones to be dislodged. Furthermore, they are the most likely to be surrounded completely by ditching in the oxalic acid etch structures.

In order to obtain quantitative data on this problem, specimens having appreciably different grain sizes were required. Various combinations of mechanical deformation and heat treatments were tried to induce grain growth. These were unsuccessful. The only method found to produce exaggerated growth was a cyclic heat treatment. A group of AISI-304 specimens was welded into a stainless steel vessel and heated to 2200°F for 7 hr and then furnace cooled. This procedure was repeated three times. The over-all diameter of the grains was thus increased from 0.04 mm to 3 mm.

It was evident that there had been some decarburization of the specimens during these heat treatments. They were bright as a result of oxide removal by reaction with carbon in the steel. Examination of carbides isolated from these specimens, after sensitizing heat treatments, showed that these were entirely different in size and shape from those found in this steel before the high-temperature heat treatments. Thus, besides grain growth, there had been other changes which were known to affect intergranular penetration. (Figure 25 shows that a 2-hr sensitizing treatment results in a different type of intergranular attack than 1-hr treatment.) For these reasons, the data obtained on these specimens are not presented in detail but are used for qualitative comparison with those of another heat of steel in which a

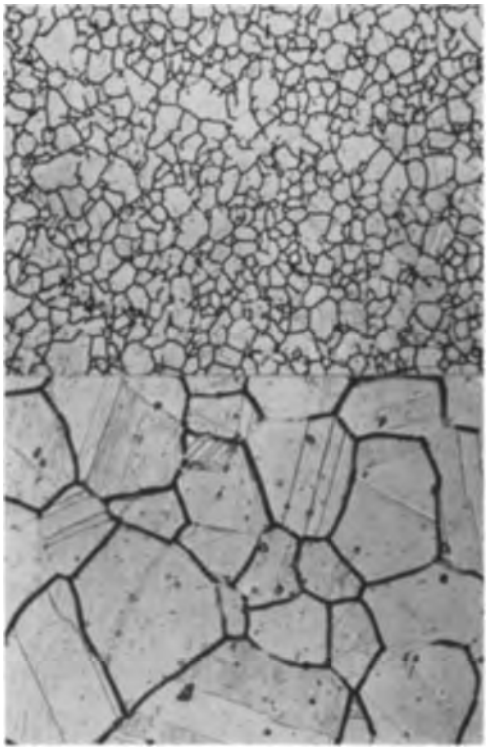

Fig. 29. Microstructure of AISI-316 steel used for grain size study. Steel: AISI-316 (GT-8, Table I). Etched electrolytically in oxalic acid. A (top), steel as received and heated 1 hr at 1250°F (unusually small grain size); B (bottom), heated first for 1 hr at 1950°F, W.Q., and then 1 hr at 1250°F. Magnification 500X before reduction for publication.

Fig. 30. Electron photomicrographs of carbides isolated from sensitized AISI-316 steel. Steel: GT-8, specimens same as Fig. 29. A (top), from small-grained specimen; B (bottom), from large-grained specimen. Magnification 20,000X before reduction for publication.

variation in grain size was induced without extensive heat treatments.

A heat of AISI-316 (GT-8) steel was found which had an unusually small, uniform grain size (Fig. 29A). This was readily changed to a normal grain size by a 1-hr heat treatment at 1950°F. The ratio of internal boundary area of the small-grained to the large-grained steel as determined by the method of random sectioning (47) was 5.7. Carbides were isolated from both types of specimens and examined in the electron microscope. The shapes and sizes of the carbides appear unchanged by this grain growth (Fig. 30A and B). As might be expected, the quantity of carbides remaining after some metal had been dissolved was much greater on the small-grained than on the large-grained specimen. Results obtained on sensitized large and small-grained specimens of this steel in three acid solutions have been plotted in Fig. 31.

The relatively high carbon content (0.074% C) of this steel leads to very high corrosion rates in all tests. An appreciable amount of the sigma type of susceptibility has also been formed during sensitization (Table V). The rates in nitric acid were so high that it was not possible to complete the standard 240-hr test because the ⅛-in. thick specimens became too thin.

In all three tests, Fig. 31, the small-grained specimens had a greater weight loss (corrosion rate) than the large-grained specimens, especially in the copper sulfate-sulfuric acid solution.[21] (This was also the case on the normal and large-grained AISI-304 steel.) However, changes in resistance are greater on the large-grained specimen in nitric acid and in ferric sulfate-sulfuric acid solution. In copper sulfate-sulfuric acid the small-grained specimen shows the greatest increase. This reversal may be due to an unusual amount of grain dropping, which is implied in the high weight loss in this solution. The grains are so small that there is profuse dropping even on an

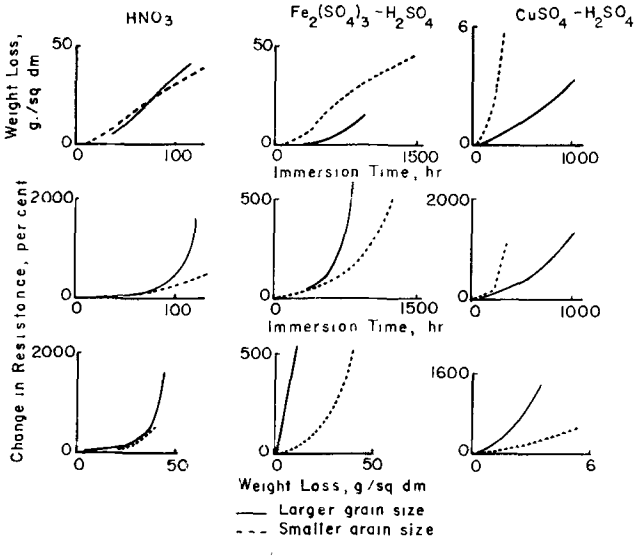

Fig. 31. Effect of grain size on intergranular corrosion of sensitized AISI-316 steel in three boiling acids. Steel: AISI-316 (GT-8) in two grain sizes as shown in Fig. 29. Specimens heated 1 hr at 1250°F. Solutions: 65% nitric acid; ferric sulfate, 15.7% sulfuric acid; 5.7% cupric sulfate, 15.7% sulfuric acid (no metallic copper).

[21] There is less difference between the two specimens in nitric acid than in the other solutions, and after about 80 hr the curves cross. Rapid accumulation of corrosion products and consequent acceleration by hexavalent chromium may have obscured the effect of grain size.

AISI-316 steel. Normal or large grains are not readily dislodged by this solution.

Despite these differences in behavior, the resistance change accompanying a given weight loss is greater on the large-grained specimen in all three solutions (bottom row, Fig. 31). Because small grains drop more readily, the results on the smaller steel are closer to the calculated curve.

In conclusion, the effect of grain size on corrosion depends on the method of measurement (weight loss or resistance change) and on the testing solution. While the total amount of intergranularly precipitated chromium carbides is greater in the small-grained than in the large-grained steel, the amount of carbide per unit area of internal grain surface is probably the same in both. Only when the diameter of the small grains approaches the width of the grain boundary zone containing chromium carbides will the grain size affect the amount of precipitate per unit area. The width of this zone depends, among other factors, on the length of time of the sensitizing treatment, i.e., the size of the carbides (cf. Fig. 14B and 30).

Acknowledgment

The writer wishes to thank S. J. Kucharsey for his assistance with this investigation.

Manuscript received April 16, 1958. This paper was prepared for delivery before the Ottawa Meeting, Sept. 28-Oct. 2, 1958.

Any discussion of this paper will appear in a Discussion Section to be published in the December 1959 JOURNAL.

REFERENCES

1. G. A. Ellinger, *Trans. Am. Soc. Metals*, **24**, 26 (1936).
2. ASTM Book of Standards, 1955, Part I, p. 1108, "Tentative Recommended Practice of Boiling Nitric Acid Test for Corrosion Resisting Steels," (A262-55T).
3. M. A. Streicher, *ASTM Bull.*, **188**, 35 (February 1953), *Werkstoffe u. Korrosion*, **5**, 363 (1954).
4. W. R. Huey, *Trans. Am. Soc. Steel Treating*, **18**, 1126 (1930).
5. T. L. O'Connor and H. H. Uhlig, *J. Phys. & Colloid Chem.*, **61**, 402 (1957).
6. H. C. Gatos, *Corrosion*, **12**, 322 (1956).
7. W. B. DeLong, "Symposium on Evaluation Tests for Stainless Steels," ASTM Special Tech. Publ. 93, 211 (1949).
8. M. M. Kurtepov, G. V. Akimov, and N. N. Bardizh, *Doklady Akad. Nauk SSSR*, **87**, 625 (1952).
9. A. B. McIntosh, *Chemistry & Industry*, **1957**, 687.
10. J. E. Truman, *J. Appl. Chem.*, **4**, 273 (1954).
11. M. M. Kurtepov and G. V. Akimov, *Doklady Akad. Nauk SSSR*, **87**, 93 (1952).
12. P. Lacombe, Physical Soc. Bristol Conference Report, 91 (1948).
13. M. H. Brown, W. B. DeLong, and W. R. Myers, "Symposium on Evaluation Tests for Stainless Steels," ASTM Special Tech. Publ. 93, 103 (1949).
14. J. J. Heger and J. L. Hamilton, *Corrosion*, **11**, 6 (1955).
15. A. J. Lena, Discussions in *Trans. ASM*, **45**, 446 (1953).
16. S. J. Rosenberg and C. R. Irish, *J. Research Nat. Bur. Standards*, **48**, 40 (1952).
17. E. M. Mahla and N. A. Nielsen, *Trans.* A.S.M., **43**, 290 (1951).
18. A. J. Lena, Private communication.
19. P. J. E. Forsyth, G. J. Metcalfe, R. King, and B. Chalmers, *Nature*, **158**, 875 (1946).
20. W. G. Gruhl and D. Ammann, *Acta Met.*, **3**, 347 (1955).
21. M. A. Streicher, *Corrosion*, **14**, 59 (1958); (to du Pont Co.) U. S. Pat. 2,793,190 and 2,793,191, May 21, 1957.
22. M. A. Streicher, ASTM Bulletin No. 229, p. 77, April 1958.
23. W. H. Hatfield, *Trans. Electrochem. Soc.*, **46**, 297 (1924).
24. G. H. Cartledge, *Nature*, **177**, 181 (1956), and *This Journal*, **104**, 420 (1957).
25. W. Good and W. A. B. Purdon, *Chemistry & Industry* (London), **1955**, 1594.
26. H. J. Rocha and G. Lennartz, *Arch. Eisenhüttenw.*, **26**, 117 (1955).
27. C. Carius, *ibid.*, **26**, 769 (1955).
28. C. Edeleanu, *Nature*, **173**, 739 (1954).
29. E. H. Phelps and D. C. Vreeland, *Corrosion*, **13**, 619 (1957).
30. M. A. Streicher, *This Journal*, **103**, 375 (1956).
31. J. H. G. Monypenny, "Stainless Iron and Steel," Vol. I, 99, Chapman and Hall, Ltd., London (1951).
32. W. O. Binder and C. M. Brown, "Symposium on Evaluation Tests for Stainless Steels," ASTM Special Tech. Publ. 93, 146-171 (1959).
33. H. Ebling and M. A. Scheil, "Symposium on Evaluation Tests for Stainless Steels," ASTM Special Tech. Publ. 93, 121-138 (1949).
34. O. Masi and A. Ferri, *Met. ital.*, **44**, 207 (1952).
35. J. B. Rutherford and R. H. Aborn, *Trans. Amer. Inst. Mining Met. Engrs.*, **100**, 293 (1932).
36. H. J. Rocha, Discussion in Reference (39).
37. ASTM Book of Standards, 1955, Part I, 1135, "Tentative Recommended Practice for Conducting the Acidified Copper Sulfate Test for Intergranular Attack in Austenitic Stainless Steels," (A393-55T).
38. M. A. Streicher, *J. (and Trans.) Electrochem. Soc.*, **93**, 285 (1948).
39. E. Brauns and G. Pier, *Stahl u. Eisen*, **75**, 579 (1955).
40. F. K. Bloom and M. E. Carruthers, "Symposium on Evaluation Tests for Stainless Steels," ASTM Special Tech. Publ. 93, 87-100 (1949).
41. H. Zitter, *Arch. Eisenhüttenw.*, **28**, 401 (1957).
42. D. Warren, Submitted to *Corrosion* (1959).
43. H. D. Newell, *Trans. Am. Soc. Steel Treating*, **19**, 673 (1932).
44. A. Ferri, *Met. ital.*, **43**, 432 (1951).
45. F. J. Phillips, *Trans. A.S.M.*, **39**, 891 (1947).
46. E. C. Bain, R. H. Aborn, and J. J. B. Rutherford, *Trans. Am. Soc. Steel Treating*, **21**, 481 (1933).
47. C. S. Smith and L. Guttman, *J. Metals*, **5**, 81 (1953).
48. J. V. Petrocelli, *This Journal*, **97**, 10 (1950).
49. T. P. Hoar and U. R. Evans, *ibid.*, **99**, 212 (1952).
50. I. D. G. Berwick and U. R. Evans, *J. Appl. Chem.*, **2**, 576 (1952).
51. N. D. Tomashov, G. P. Sinelshchikova, and M. A. Vedeneeva, *Zhur. Fiz. Khim.*, **23**, 3 (1949), discussed in Platinum Metals Review, **2**, 117 (1958).
52. G. Masing, T. Heumann, and H. Jesper, *Arch. Eisenhüttenw.*, **25**, 169 (1954).
53. E. H. Dix, *Trans. Am. Inst. Mining Met. Engrs.*, **137**, 11 (1940).
54. L. R. Standifer, Thesis, The Ohio State University, Columbus, Ohio (1952).
55. C. Carius, *Arch. Eisenhüttenw.*, **29**, 449 (1958).
56. D. Warren, *ASTM Bull.*, **230**, 45 (May 1958).
57. K. J. Vetter, *Z. Elektrochem.*, **62**, 642 (1958).

The Diffusion of Oxygen in Alpha and Beta Zircaloy 2 and Zircaloy 3 at High Temperatures

M. W. Mallett, W. M. Albrecht, and P. R. Wilson[1]

Battelle Memorial Institute, Columbus, Ohio

ABSTRACT

The diffusion rates of oxygen in alpha and beta Zircaloy 2 and Zircaloy 3 were determined in the range 1000°-1500°C. For alpha Zircaloy 2, the variation of the diffusion coefficient, D, in cm²/sec, with temperature is given by the equation

$$D_\alpha = 0.196 \exp(-41{,}000 \pm 1500/RT)$$

For beta Zircaloy 2,

$$D_\beta = 0.0453 \exp(-28{,}200 \pm 2400/RT)$$

Spot checks of the diffusion of oxygen in alpha and beta Zircaloy 3 to 1100° and 1400°C show that the rates are in close agreement with those for oxygen in Zircaloy 2.

The diffusion coefficients for oxygen in beta Zircaloy 2 and Zircaloy 3 are about 10 times greater than those for nitrogen in high-purity beta zirconium.

The water and steam corrosion of Zircaloy 2 has been investigated up to 400°C (1, 2). The corrosion reaction proceeds principally by formation of a surface film of ZrO_2. One of the processes that occurs during the reaction is the diffusion of oxygen in the metal. At the temperatures that have been investigated, the diffusion rates are very slow and do not contribute to the over-all corrosion process. However, at high temperatures above 1000°C or so, the rate of diffusion becomes appreciable and may play a large part in the over-all reaction. Therefore, as part of a study of the high-temperature corrosion of Zircaloy 2 and Zircaloy 3, the diffusion coefficients of oxygen in the alpha and beta phases of the materials were determined at 1000°-1500°C. Rather complete data were obtained for Zircaloy 2. The diffusion in Zircaloy 3 was spot checked to obtain a few rates for comparison with those for oxygen in Zircaloy 2.

Experimental

Materials

The Zircaloy 2 and Zircaloy 3 for this work were fabricated into 5/8-in.-diameter rods. Specimens for the experiments were machined from these rods. Analyses of both alloys were obtained by spectrographic, chemical, and vacuum-fusion techniques. Results are given in Table I.

Oxygen was prepared by the thermal decomposition of degassed potassium permanganate as described by Hoge (3). It was dried with a dry ice-acetone cold trap.

Zirconium-Oxygen Phase Diagram

Knowledge of the phase diagrams of the Zircaloy 2 and Zircaloy 3 oxygen systems should be known in preparing suitable diffusion specimens to determine diffusion coefficients, but no information is available on either system. However, it is believed that the zirconium-oxygen system (4) is very similar to the Zircaloy-oxygen systems since the basic structure of the alloys is not changed from that of zirconium, that is, alpha and beta Zircaloy alloys have the same structures as alpha and beta zirconium. Therefore, the zirconium-oxygen system was used as a source of oxygen-concentration data needed for diffusion studies of the Zircaloy materials. A partial phase diagram of the zirconium-oxygen system is reproduced in Fig. 1. The portion of the diagram of interest for this study is that from 1000° to 1500°C. In this range, the beta-alpha plus beta boundary represents the maximum solubility of oxygen in beta (solid solution) zirconium. The alpha plus beta-alpha boundary represents the lowest oxygen concentration required to maintain a single phase of alpha (solid solution) zirconium. The alpha-alpha plus ZrO_2 boundary represents the maximum solubility of oxygen in alpha zirconium.

Table I. Analyses of Zircaloy 2 and Zircaloy 3

Element	Amount present, wt %	
	Zircaloy 2	Zircaloy 3
Sn	1.5	0.22
Fe	0.20	0.34
Cr	0.05	0.03
Ni	0.03	0.005
Si	0.007	0.05
Al	0.006	0.005
Mn	0.002	0.01
Mg	0.002	0.001
Pb	0.002	—
O_2	0.089	0.14
N_2	0.003	0.01
H_2	0.002	0.003

[1] Present address: Department of Chemistry, University of Massachusetts, Amherst, Mass.

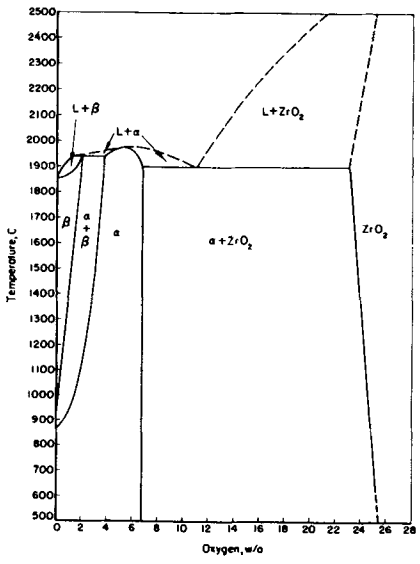

Fig. 1. Partial phase diagram of the zirconium-oxygen system.

Concentration-Gradient Technique

The concentration-gradient technique (5) was used to determine the diffusion coefficients for oxygen in beta-phase Zircaloy 2 and Zircaloy 3. Essentially, the method consists of analyzing the concentration gradient in a cylindrical specimen resulting from reaction with oxygen at a given temperature for a predetermined length of time. The diffusion coefficient was determined from the concentration gradient by a graphical method.

Specimens having gradients were prepared as follows. A Zircaloy 2 (or Zircaloy 3) cylinder about 1 cm in diameter and 4 cm long was dry abraded with 240-grit silicon carbide paper. After the dimensions of the cylinder were measured, the specimen was placed in the Vycor furnace tube of a modified Sieverts apparatus (2). The sample then was induction heated in a vacuum for 1 hr at the temperature of the run. Temperatures were measured under black-body conditions with an optical pyrometer. With the sample at the desired temperature, an amount of oxygen (based on the maximum solubility in beta phase at desired temperature) calculated to maintain a thin oxide film on the sample was added to the reaction chamber. The sample was heated for a length of time sufficient to prepare a suitable gradient; that is, enough oxygen was diffused to just begin to affect the core. At the end of this time, the sample was quenched as rapidly as possible. Temperatures below 500°C were attained in less than 30 sec. At 500°C and below, diffusion is extremely slow so that very little movement of oxygen occurred below this temperature. The film on the sample contained the phases shown in the phase diagram, Fig. 1. Proceeding from right to left on the diagram at the temperature of the run, the outer layer is ZrO_2; beneath this is a very thin layer of alpha solid solution. Beneath this is the beta core which contains the oxygen gradient being measured. It should be noted that two-phase regions are not produced by diffusion in a heterogeneous binary system (6).

Since diffusion occurs from the ends of the cylinder as well as the sides, lengths equal to the radius were cut from each end of the specimen and discarded. This insured that the remaining sample would have a concentration gradient as uniform as possible from end to end. The remainder of the sample was machined radially into layers of equal weight and each layer analyzed for oxygen by the vacuum-fusion method. Diffusion coefficients then were determined by the graphical method, using the average oxygen concentrations of the layers, the average radii, and the time. The thin surface layer, which contains alpha and oxide phases, was not used in the calculations.

Moving-Boundary Technique

The diffusion coefficients of oxygen in the alpha phase of Zircaloy 2 (and Zircaloy 3) were determined by the moving-boundary technique described by Jost (5).[2] This method was developed by Wagner for the case of diffusion into a heterogeneous system of given over-all concentration. The mathematical treatment of this case is based on the fact that a displacement, ξ, of the phase boundary produced by the diffusion of a single species is proportional to the square root of the time of diffusion, i.e.,

$$\xi = 2\gamma\sqrt{Dt} \qquad [1]$$

where ξ is the displacement of the phase boundary, cm; γ, a dimensionless parameter characteristic of the system; D, diffusion coefficient, cm²/sec; and t, time, sec. The parameter, γ, is defined as follows:

$$\frac{C_s - C_{II,I}}{C_{II,I} - C_0} = \sqrt{\pi}\,\gamma \exp\gamma^2 \operatorname{erf}\gamma \qquad [2]$$

where C_s, $C_{II,I}$, and C_0 are concentrations of the diffusing species at various phase boundaries. In the present case, for a given temperature, C_s is the maximum solubility of oxygen in the alpha phase, $C_{II,I}$ is the oxygen concentration at the alpha plus beta-alpha boundary, and C_0 is the oxygen concentration at the beta-alpha plus beta boundary. The term erf γ is the "gaussian error function." Values of erf γ may be found in Jost (7) and Carslaw and Jaeger (8). The value for γ was determined from Eq. [2] by a graphical method.

To determine the value of the diffusion coefficient, it is necessary to have values of ξ, t, and γ at a given temperature. The slope of the plot of ξ vs. $t^{1/2}$ is equal to $2\gamma\sqrt{D}$ from which D may be evaluated.

Experimental techniques used to obtain the moving-boundary measurements are as follows. A cylindrical specimen about 1 cm in diameter by 4 cm long was prepared as described above for the gradient method. A calculated quantity of oxygen, C_0, was then added in slight excess to saturate completely the beta phase at the experimental temperature. This sample was heated at temperature for 6 to 8 hr. The specimen then was quenched to room temperature. To check the homogeneity of the

[2] Jost presents the solution of Fick's law for movement of a boundary in a plate. Brief calculations showed that for small displacements of the boundary in a cylinder, the equations for plates could be used in calculating diffusion coefficients without introducing significant errors.

specimen, metallographic examination was made of a cross section. A uniform distribution of a few alpha grains in a beta zirconium matrix was observed. This would be expected since even slight lowering of the temperature would supersaturate the beta phase in respect to oxygen. The alpha grains must have formed during the 30-sec cooling required to reach a temperature below which diffusion was negligible. This cooling time introduces an error of not more than 10% in measuring the minimum diffusion time of 5 min. At maximum diffusion times (120 min) the error was less than 0.4%.

The surface oxide (excess oxygen) was abraded from the surface of the sample which was then cut into three cylinders. The cylinders were heated in an oxygen atmosphere at temperature for various periods of time. A calculated quantity of oxygen was reacted to maintain an oxide film at all times but to keep its thickness at a minimum. The thickness of the oxide was always less than 5% of the alpha layer and was ignored in all calculations. At the end of the heating period, the sample was quenched as rapidly as possible and cut in half diametrically. The cross section was examined metallographically to determine the movement of the alpha-beta boundary. The diameter of the beta core was measured and subtracted from the original diameter of the cylinder. From this, the displacement of the boundary was determined. Then, the diffusion coefficient was determined from the slope of a plot of the displacement, ξ, against $t^{1/2}$.

Results and Discussion

The diffusion coefficients for oxygen in alpha and beta Zircaloy 2 were determined in the range 1000°-1500°C at 100°C intervals. Experimental diffusion times ranged from 5 to 120 min. Attempts were made to obtain coefficients at 1600°C; however, no suitable gradients or moving boundaries could be prepared. The experimental times (less than 5 min) at 1600°C necessary to prepare optimum diffusion samples were so short that errors in the measurement of the time required to quench to room temperature would introduce large errors in the estimation of actual diffusion times. The data obtained on a gradient prepared in beta Zircaloy 2 at 1100°C for 35 min are shown in Fig. 2 The thicknesses of the machined layers and the average oxygen concentration of each layer are shown. The solid line is the theoretical curve derived from diffusion theory (5) for this gradient. It is seen that there is good agreement between the experimentally determined concentrations and the theoretical curve. Also, it was found that the terminal solubilities of oxygen in beta Zircaloy 2 (obtained from concentration gradients) agreed with those for oxygen in pure zirconium. It is seen from Table II that with the exception of the 1400°C value these solubilities show an average difference of only 0.03 wt %. This supports the earlier assumption that the Zircaloy(s)- and zirconium-oxygen phase relationships are closely similar. The 1100°C terminal oxygen solubility for beta Zircaloy 3 also agrees with zirconium data, but again the

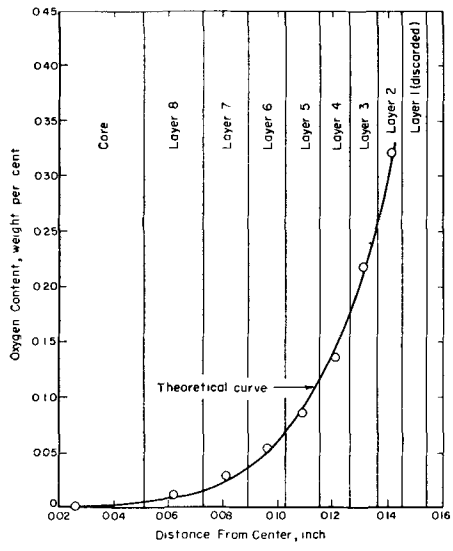

Fig. 2. Oxygen concentration gradient prepared in beta Zircaloy 2 at 1100°C for 35 min.

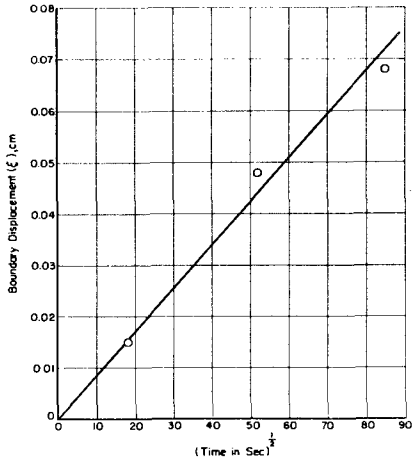

Fig. 3. Variation of displacement of alpha-beta boundary with time for oxygen in alpha Zircaloy 2 at 1200°C.

1400°C value shows a large discrepancy. The fact that the greatest differences were noted at 1400°C is believed to be coincidental rather than systemic. In Fig. 3 is shown a typical plot of the alpha-beta boundary displacement, ξ, against $t^{1/2}$ for alpha Zircaloy 2 at 1200°C. The slope of the line is equal to $2\gamma\sqrt{D}$. At 1200°C, the value of γ is 0.895. From

Table II. Terminal solubility of oxygen in beta Zircaloy 2 and beta Zircaloy 3

	Oxygen, wt %				
	Pure Zr*	Zircaloy 2		Zircaloy 3	
Temperature, °C	Solubility	Solubility	Difference†	Solubility	Difference†
1000	0.20	0.25	0.05	—	—
1100	0.38	0.44	0.06	0.42	0.04
1200	0.62	0.61	0.01	—	—
1300	0.83	0.80	0.03	—	—
1400	1.05	0.80	(0.25)	1.3	(0.25)
1500	1.29	1.3	0.01	—	—
		Average difference 0.03			

* From Ref. (4).
† Difference from pure zirconium.

Table III. Diffusion coefficients for oxygen in alpha and beta Zircaloy 2 and Zircaloy 3

Material	Diffusion coefficient, cm²/sec, at temperature indicated, °C					
	1000	1100	1200	1300	1400	1500
Zircaloy 2, alpha	1.8×10^{-8}	4.8×10^{-8}	2.3×10^{-7}	3.6×10^{-7}	7.9×10^{-7}	1.7×10^{-6}
Zircaloy 2, beta	8.2×10^{-7}	1.4×10^{-6}	2.4×10^{-6}	3.8×10^{-6}	8.1×10^{-6}	2.4×10^{-5}
Zircaloy 3, alpha	—	5.8×10^{-8}	—	—	1.4×10^{-6}	—
Zircaloy 3, beta	—	1.4×10^{-6}	—	—	6.5×10^{-6}	—

these values the diffusion coefficient was calculated. All the data are given in Table III. The diffusion coefficients for oxygen in alpha Zircaloy 2 range from 1.8×10^{-8} cm²/sec at 1000°C to 1.7×10^{-6} cm²/sec at 1500°C. Those for oxygen in beta Zircaloy 2 range from 8.2×10^{-7} cm²/sec at 1000°C to 2.4×10^{-5} cm²/sec at 1500°C.

In Fig. 4 and 5 are shown the variations of the diffusion coefficients with temperature for alpha Zircaloy 2 and beta Zircaloy 2, respectively. The logarithms of the diffusion coefficients are plotted against the reciprocal of temperature (Arrhenius-type plot). Equations for the best straight lines through the points were determined by the method of least squares. The equation for the diffusion coefficient, D, in cm²/sec, for oxygen in alpha Zircaloy 2 is

$$D = 0.196 \exp [(-41{,}000 \pm 1500)/RT] \quad [3]$$

For oxygen in beta Zircaloy 2,

$$D = 0.0453 \exp [(-28{,}200 \pm 2400)/RT] \quad [4]$$

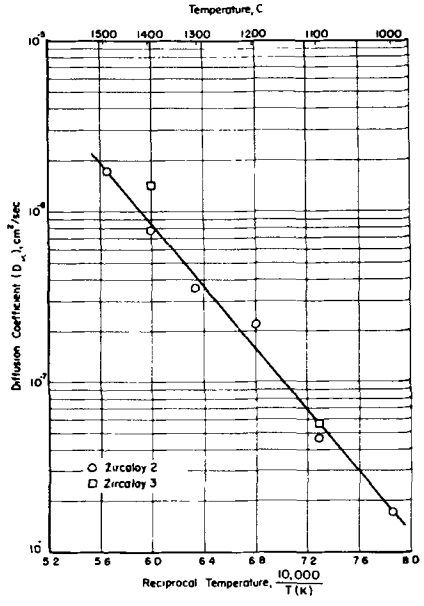

Fig. 4. Temperature variation of the diffusion coefficient for oxygen in alpha Zircaloy 2 and Zircaloy 3.

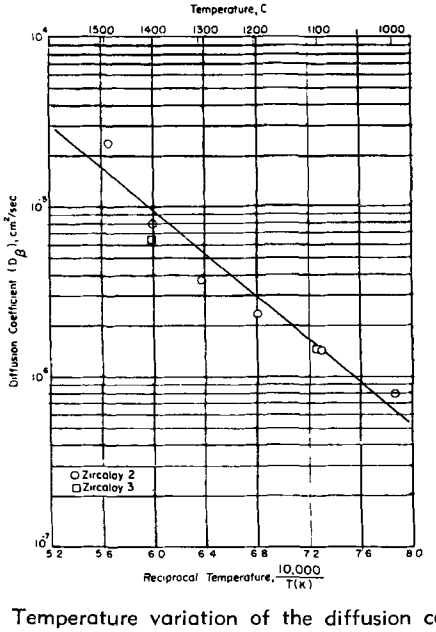

Fig. 5. Temperature variation of the diffusion coefficient for oxygen in beta Zircaloy 2 and Zircaloy 3.

The diffusion coefficients for oxygen in alpha and beta Zircaloy 3 were determined at 1100° and 1400°C. The values also are given in Table III and plotted in Fig. 4 and 5. It is seen that they are in good agreement with those for Zircaloy 2. Apparently, the alloying constituents in the range studied have very little effect on the diffusion of oxygen.

The diffusion coefficients for oxygen in beta Zircaloy 2 and Zircaloy 3 are greater (about 10 times) than those for nitrogen in high-purity beta zirconium (9). This difference probably arises from the differences in the size of the diffusing species, oxygen and nitrogen, and not from differences in the alloying constituents. The atomic radius of oxygen is 0.60Å and that of nitrogen is 0.71Å. Since oxygen is the smaller atom, it would be expected to diffuse faster.

Manuscript received Sept. 3, 1957. Work performed under subcontract to the Bettis Laboratory of the Atomic Energy Commission, operated by Westinghouse Electric Corporation. This paper was prepared for delivery before the Ottawa Meeting, Sept. 28-Oct. 2, 1958.

Any discussion of this paper will appear in a Discussion Section to be published in the December 1959 JOURNAL.

REFERENCES

1. D. E. Thomas, "Metallurgy of Zirconium," **VII-4** 608, McGraw Hill Book Co., New York (1955).
2. D. E. Thomas and S. Kass, Jr., *This Journal*, **104**, 261 (1957).
3. H. J. Hoge, *J. Research Nat. Bur. Standards*, **44**, 321 (1950).
4. R. F. Domagala and D. J. McPherson, *Trans. Am. Inst. Mining Met. Engrs.*, **200**, 238 (1954).
5. M. W. Mallett, E. M. Baroody, H. R. Nelson, and C. A. Papp, *This Journal*, **100**, 103 (1953).
6. F. N. Rhines, "Surface Treatment of Metals," p. 122, American Society for Metals, Cleveland, Ohio, (1941).
7. W. Jost, "Diffusion," p. 71, Academic Press, Inc., New York (1952).
8. H. Carslaw and J. C. Jaeger, "Conduction of Heat in Solids," Oxford University Press, London (1948).
9. M. W. Mallett, J. Belle, and B. B. Cleland, *This Journal*, **101**, 1 (1954).

Reaction of Aluminum and Carbon Tetrachloride, I

J. D. Minford, M. H. Brown, and R. H. Brown

Alcoa Research Laboratories, Aluminum Company of America, New Kensington, Pennsylvania

ABSTRACT

Many aluminum alloys are corroded severely by boiling CCl_4. Two of the products of the reaction are aluminum chloride and hexachloroethane. The presence of anhydrous aluminum chloride accelerates the reaction. A number of chemical agents can retard this reaction apparently by combining with aluminum chloride as it is produced. The reaction of aluminum alloys drops off rapidly as the magnesium content increases.

Aluminum reacts rapidly with boiling carbon tetrachloride to form aluminum chloride and hexachloroethane (1) as follows:

$$2Al + 6CCl_4 \rightarrow 2AlCl_3 + 3C_2Cl_6 \qquad [1]$$

Previous investigations have been concerned with the effect of impurities in the carbon tetrachloride and the relative rate of attack on different alloys. However, there has been little evidence to establish a suitable reaction mechanism. Since the use of aluminum with halogenated hydrocarbons has important commercial applications, a need exists for better understanding of the mechanism of the reaction.

Stern and Uhlig (2) investigated certain phases of the reaction between aluminum and boiling carbon tetrachloride and concluded that an induction period of about 70 min exists during which no reaction takes place. It was found that the length of the induction time could be increased in the presence of either water or carbon disulfide and decreased in the presence of the corrosion products (Eq. [1]). They also found no consistent difference in corrosion rates between cathode and anode from either galvanic coupling or an applied potential of 1.5 v. When they applied a potential of 1000 v, the anode corroded about 1 hr before the cathode, but this was described as being the result of a premature breakdown of the protective coating on the aluminum surface. These authors interpreted these results as excluding an electrochemical mechanism and concluded that the reaction proceeds by a "typical direct chemical reaction."

In a subsequent paper Stern and Uhlig (3) proposed that the reaction proceeded by a free radical mechanism. This conclusion was based on the fact that the reacting solution is colored and that water and oxygen, which increase the induction period, also are known to combine with free radicals. Also, substances such as quinone, 1, 4-napthoquinone, and nitrobenzene, which have been listed as free radical suppressors, act as inhibitors for this reaction. Additional experiments to supplement this data and determine the feasibility of this free radical mechanism will be presented in a subsequent paper (3a).

The importance of the practical application of aluminum with halogenated hydrocarbons has led to considerable investigation during the last seven years. As a result, significant data pertinent to the mechanism, not available in the literature, have been obtained.

Characteristics of the Reaction (99.99% Al)

Visible effects.—Most of the experiments were carried out in a 500-ml round-bottomed glass flask connected to a reflux condenser by a ground glass joint. Two hundred and fifty milliliters of carbon tetrachloride were placed in the flask and heated on an electric hot plate. The aluminum specimens (0.064 x ½ x 3 in.) were placed in the carbon tetrachloride after the boiling point was reached.

As previously reported (2) it was observed that the first sign of corrosion usually appeared as a small black spot of corrosion product on the surface of the specimen after about 30 min. These spots increased in number until the entire surface was covered. The solution turned a faint pink after several hours and gradually darkened, finally becoming black with the formation of a large amount of insoluble black corrosion product. When the solution was filtered to remove the black insoluble product and then evaporated, a yellow residue was left indicating that a soluble reaction product had been formed.

Weight loss vs. time relationships.—The weight loss data given in Table I show that very little corrosion occurred in the first hour, but following that it proceeded rapidly. This apparent induction period had been observed previously (2). As will be shown in the second paper (3a) the reaction proceeds from time zero.

Effect of temperature on reaction.—Zappi (4) has

Table I. Corrosion weight losses of 99.99% aluminum in boiling carbon tetrachloride

Specimen No.	Exposure time, hr	Weight loss, g
1	1.00	0.0024
2	1.75	0.1652
3	2.25	0.2146
4	3.00	0.4252
5	4.00	0.7257
6	4.50	1.0822
7	5.50	1.3862
8	6.50	1.6843
9	7.00	2.0022

Table II. Corrosion resistance of aluminum alloys to carbon tetrachloride at room temperature*

Alloy	CCl_4 purity	Time, mo	Weight loss, g	Observation
99.99% Al	Tech.	18	0.015†	No visual corrosion
99.99% Al	C. P.	18	0.012	No visual corrosion
3003	Tech.	18	0.002	No visual corrosion
3003	C. P.	18	0.007	No visual corrosion
5052	Tech.	18	0.006	No visual corrosion
5052	C. P.	18	0.009	No visual corrosion
5154	Tech.	18	0.008	No visual corrosion
5154	C. P.	18	0.005	No visual corrosion

* Aluminum alloys formed into storage containers with a weld midway up the side wall were half filled with carbon tetrachloride. The containers were stored in a tilted position so that only half of the weld bead was immersed.
† The weight losses represent averages from duplicate storage tests. The initial weights of the containers were about 270 g.
Note: The exposed area was 45 in.^{2}.

reported that no reaction occurred between aluminum and carbon tetrachloride at room temperature in a four-month test period. When aluminum was sealed in a tube with carbon tetrachloride and heated to 110°C, however, rapid reaction ensued.

Observations of the present authors indicate a rather critical temperature dependence for this reaction. The reaction proceeded rapidly at the boiling point of carbon tetrachloride (77°C), but very little reaction occurred at 50°C over a 60-day test period and none occurred in 18 months at room temperature (see Table II).

Yields of reaction products—Although Rhodes and Carty (1) stated that aluminum and carbon tetrachloride react to form aluminum chloride and hexachloroethane, two additional experiments were carried out to determine the yields based on the above reaction and to see if any additional reactions were involved.

The yield of the soluble fraction (assumed to be entirely hexachloroethane) in duplicate runs was 41.2 and 48.7% of the theoretical and the yield of insoluble fraction (assumed to be entirely aluminum chloride) was 83.8 and 100.6% of the theoretical. The theoretical yields were calculated from the weight loss of aluminum assuming that hexachloroethane and aluminum chloride were the only products formed according to the following reaction:

$$2Al + 6CCl_4 \rightarrow 3C_2Cl_6 + 2AlCl_3$$

Examination of fraction originally insoluble in carbon tetrachloride.—An x-ray diffraction analysis of the carbon tetrachloride insoluble fraction showed that aluminum chloride was the only identifiable component. Chemical analyses for aluminum and inorganic chlorides are shown in Table III.

The insoluble fraction does not appear to be pure aluminum chloride because the ratio of chlorine atoms to aluminum atoms was 2.74 instead of 3 as in pure aluminum chloride. In this case Stern (5) reported the Cl/Al ratio to be 2.8. These results indicate that some of the aluminum valence bonds were linked to some element other than chlorine. Since carbon and chlorine were the only elements present in addition to aluminum, it seems apparent that about 8.7% of the aluminum valence bonds were linked directly with carbon.

Table III. Chemical analysis of fraction originally insoluble

Sample No.	Al, %	Inorganic Cl, %	Ratio Cl atoms / Al atoms
1	18.6	67.3	2.74
2	18.9	68.1	2.74

The black carbon tetrachloride insoluble fraction almost completely dissolved in water with evolution of heat. A small quantity of the black material is insoluble in water. If this water insoluble material is dried and placed in carbon tetrachloride, it dissolves readily forming a dark brown colored solution. Upon evaporation of the carbon tetrachloride, a black resinous material is left behind. The carbon tetrachloride insoluble fraction contained 3.18% of this resinous material. Chemical analysis of the black resinous material revealed that its carbon content was 42.2%. These data are in accord with previously reported information (2).

The fact that this black resinous material is insoluble in carbon tetrachloride until it is treated with water suggests that an aluminum-carbon-chlorine complex is formed which is broken up by reaction with water. The formation of a resinous solid indicates that the complex must have a high molecular weight.

Examination of the fraction originally soluble in carbon tetrachloride—The carbon tetrachloride soluble fraction was a yellow solid. Chemical analysis showed that the aluminum content was less than 0.005%. An x-ray diffraction analysis of the soluble fraction revealed that it was mainly hexachloroethane. The soluble fraction also was analyzed by index of refraction measurements. In this method of structural determination, an equation developed by one of the authors was used (6).

$$n-1 = \frac{5.07}{\frac{m-1}{dA}}$$

Where n is the refractive index; m, the molecular weight; d, the density; and A, the sum of constants based on actual atomic volumes (A) of the atoms in the molecule ($A = 0.821$ for carbon, 1.800 for chlorine, and 0.436 for a double bond). For hexachloroethane, $A = (2)\ (0.821) + (6)\ (1.800) = 12.442$.

In using this method, the index of refraction for the structural formula in question is calculated using the measured density for the unknown. If the structural formula is correct, the calculated value of refractive index should agree with the observed value.

Since hexachloroethane is a solid it was necessary to dissolve the soluble fraction in a solvent to make the refractive index measurements. The solvent used was 1, 2, 4 trichlorobenzene. The value of m/A for the trichlorobenzene was determined experimentally as 14.19 by determining d and n in the equation $m/A = \frac{5.07d + (d-1)\ d}{n-1}$. When using a mix-

ture of two compounds the values of m and A should be average values based on the molecular percentages of the two components. The composition of the solution used was 22.3 mole % soluble fraction and 77.7 mole % trichlorobenzene.

If the soluble fraction was 100% hexachloroethane, the m/A value for the solution would be 15.25, whereas, the measured value was 15.17 ± 0.01. These results indicate that the soluble fraction was not pure hexachloroethane. It seems logical to assume that some of the hexachloroethane could have reacted with aluminum to form high molecular weight carbon-chlorine compounds. Several possible formulations of this type are given below along with the calculated m/A values if they replaced hexachloroethane completely in the trichlorobenzene solution.

Type of compound	Structure	m/A (calc.)
Straight chain polymer	$\begin{bmatrix} Cl\ Cl\ Cl\ Cl \\ -C\ -C\ -C\ -C- \\ Cl\ Cl\ Cl\ Cl \end{bmatrix}_n$	15.20
Branched chain polymer	$\begin{bmatrix} Cl \\ -C- \\ \prime \end{bmatrix}_n$	15.10
Unsaturated straight chain polymer	$\begin{bmatrix} Cl & Cl \\ -C = & C- \end{bmatrix}_n$	15.08
Unsaturated branched chain polymer	$\begin{bmatrix} & Cl \\ -C = & C- \\ \prime & \end{bmatrix}_n$	14.37

The evidence indicates that the small amount of impurity in the soluble fraction is not a straight chain polymer. The presence of branched chain, unsaturated straight chain, or unsaturated branched chain polymers could lower the m/A value from 15.25 for pure hexochloroethane to the 15.17 value actually measured.

Indications are that the impurities in the soluble fraction are intermediate compounds in the formation of the black resinous material since their carbon contents are between those of hexachloroethane and the black resinous material.

Table IV. Effect of reaction products on the corrosion of 99.99% aluminum in boiling carbon tetrachloride

Specimen No.	Conditions	Time, hr	Weight loss, g
1	Corrosion products from 1.6701 g spec.	1.00	0.3251
2	Corrosion products from 1.7359 g spec.	1.00	0.3774
3	Saturated with $AlCl_3$	0.25	0.0105
4	Saturated with $AlCl_3$	0.50	0.2738
5	Saturated with $AlCl_3$	1.00	0.6157
6	Saturated with $AlCl_3$	2.00	1.3378
7	Saturated with $AlCl_3$	3.25	1.6999
8	Saturated with $AlCl_3$	4.00	2.4072
9	Saturated with $AlCl_3$	4.50	2.7282
10	0.5% (by wt) hexachloroethane	4.00	0.9222
11	0.5% (by wt) hexachloroethane	4.50	1.1880
12	0.5% (by wt) hexachloroethane	5.50	1.5364
13	0.5% (by wt) hexachloroethane	6.50	1.8670

Effects of Reaction Product on Reaction

Tests were run exposing 99.99% aluminum specimens in solutions containing reaction products from previous exposures. The results given in Table IV show that the presence of reaction products increased the initial corrosion rate. Since aluminum chloride and hexachloroethane are the main reaction products, tests were run with additions of these two compounds to fresh carbon tetrachloride to determine their influence on the reaction. Since aluminum chloride is only slightly soluble in carbon tetrachloride, a saturated solution was used. An excess of anhydrous aluminum chloride was added to carbon tetrachloride and refluxed for 1 hr. The carbon tetrachloride then was decanted into another flask for the corrosion tests. It was observed that a faint pink color, which gradually darkened, developed in the boiling carbon tetrachloride saturated with aluminum chloride. No color developed when hexachloroethane was dissolved in boiling carbon tetrachloride.

The results of these tests are given in Table IV. This information in graphical form along with data from Table I is shown in Fig. 1. The presence of hexachloroethane had no detectable effect on the reaction, but the addition of aluminum chloride had a marked accelerating effect. This indicates that aluminum chloride acts as a reaction accelerator, probably through the formation of complexes with carbon tetrachloride.

Effective Retarding Agents

On the basis of the preceding discussion of factors that markedly affect the reaction of aluminum with carbon tetrachloride, it is obvious that aluminum chloride is one of the most potent promoters accelerating the reaction. The possibility was considered that chemical agents could retard this reaction by combining with the aluminum chloride to retard its effect on the reaction. In this manner, the stimulating effect normally produced on the carbon tetrachloride-aluminum reaction would be retarded.

Since benzoyl chloride has been reported in the literature to form a molecular complex with aluminum chloride (7), it should have a retarding effect

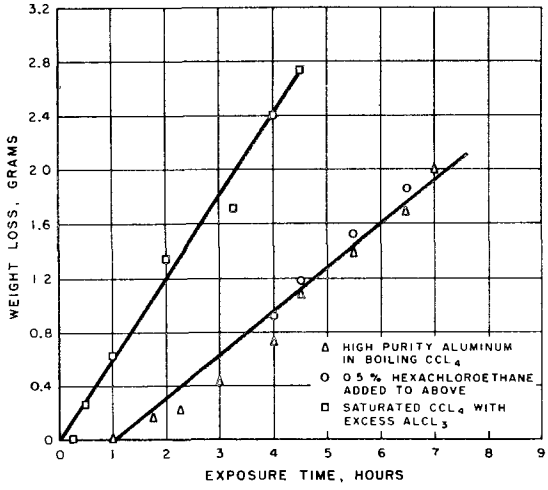

Fig. 1. Effect of anhydrous aluminum chloride and hexachloroethane additions.

on the reaction between aluminum and carbon tetrachloride by complexing the aluminum chloride and rendering the aluminum chloride unavailable for accelerating the reaction. Since significant retardation was obtained when 1% of freshly distilled benzoyl chloride was added to the carbon tetrachloride, the theory of an inhibitor operating by complexing the aluminum chloride was demonstrated.

It was also shown that the corrosiveness of carbon tetrachloride for aluminum was decidedly greater in the presence of a given added quantity of aluminum chloride than in the presence of the same quantity of aluminum chloride combined with benzoyl chloride in a molecular complex. The fact that aluminum reacted with somewhat greater rapidity in the presence of this complex than in the absence of any added aluminum chloride was attributed to the effect of some small amount of aluminum chloride that did not complex with the benzoyl chloride. This was further confirmed by the fact that the solution of carbon tetrachloride containing the complex became colored in a short time as if a relatively small amount of the total aluminum chloride had been separately added to the carbon tetrachloride (i.e., was not combined in the complex).

Additional support for the theory that retarding agents operate by complexing aluminum chloride was obtained by converting a corrosive carbon tetrachloride solution containing added aluminum chloride into a noncorrosive solution by removing the colored aluminum chloride-carbon tetrachloride complex that forms when aluminum chloride is heated with carbon tetrachloride. This was accomplished by the addition of any one of three different retarders (2, 5 hexanedione, ethyl acetoacetate, aluminum nitrate $.9H_2O$) in the following manner. Sufficient anhydrous aluminum chloride was added to refluxing carbon tetrachloride to produce the deep color associated with the beginning stages of the corrosion of aluminum in the halogenated hydrocarbon. If 1% by weight of either of three different retarding agents (i.e., an excess with respect to the amount of added aluminum chloride) was added, the characteristic color was rapidly removed and the carbon tetrachloride became noncorrosive to aluminum. Subsequent analysis disclosed that all the detectable aluminum chloride was now in the precipitate which formed simultaneously as the color of the solution disappeared. All compounds that were known to be effective retarding agents precipitated aluminum chloride in this manner. The explanation of the results of this type of experiment can be explained most satisfactorily in terms of the previously projected theory of complexing the aluminum chloride. It now appeared to be a logical step to search for new retarding agents among chemical compounds that offered the possibility of known or projected reactivity with aluminum chloride.

The possibility that acid anhydrides might have retardation properties was predicted on the basis of the use of anhydrides in organic syntheses with aluminum chloride acting as a catalyst through a complex intermediate. Both acetic anhydride and phthalic anhydride acted as effective retarding agents, although the possibility of conversion to the corresponding acid made their practical use questionable. Phthalic anhydride, however, proved to be equally effective as a retarder in the presence or absence of water in refluxing carbon tetrachloride. Phthalic acid, on the other hand, was ineffective as a retarding agent unless water was present in the carbon tetrachloride. The equilibrium established between the anhydride or the acid and water in carbon tetrachloride that affords such excellent retardation is not known at this time. Phthalic anhydride, itself, has proved to be the best retarder at the lowest levels (0.1-0.2% by weight) of all the retarding agents investigated.

One successful class of retarders for this reaction is the carbonyl compounds. Acetone is the simplest member of this series and its complexing with $AlCl_3$ has been reported (8). Acetone serves as an effective retarder at a concentration of 0.2% by weight. The difficulty of maintaining an adequate concentration of acetone is increased, however, because of its relatively low boiling point. A more effective carbonyl agent is 2,5-hexanedione. Although the ratio of C=O/C is the same as in acetone, some advantage is obtained through the lower volatility as well as in the possibility of chelation. Other effective carbonyl-type retarding agents that react with aluminum chloride are acetophenone (9, 10) and benzophenone (10). They offer the advantage of a lower volatility than acetone but require a larger addition of retarder because of the increased molecular weight. On the other hand, they are not so effective on a weight basis as 2,5-hexanedione but are considerably cheaper.

Other retarding agents related to the carbonyl compounds are the esters that contain the group

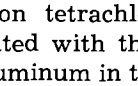

—C—O—R. A number of different esters have been reported to form complexes with aluminum chloride (11, 12). Ethyl acetate and ethyl acetoacetate both proved to be good retarders for this reaction. Ethyl acetate has the advantage of having about the same boiling point as carbon tetrachloride which might be desirable in certain industrial applications. Ethyl acetoacetate is the better retarder of the two as might be expected because of the combination of a carbonyl and an ester group as well as offering the possibility of chelation.

Some heterocyclic ring system compounds such as thiophene, pyrrole, and quinoline act as effective retarding agents. These compounds were selected for several reasons. For example, all of them enter into condensation reactions in the presence of aluminum chloride in which it is often necessary for the aluminum chloride to be present in a mole-for-mole ratio or greater. They might also work since onium-type compounds could be produced in such situations where a Lewis type acid, such as aluminum chloride, comes in contact with a Lewis type base such as the heterocyclic atom in these ring systems.

Several olefin-type compounds (cyclohexene and isoprene) in which no heterocyclic atom is present also were effective although to a lesser extent than the other retarders previously mentioned. There is a basis for selecting olefins since olefins formed by pyrolysis of paraffins in the presence of aluminum chloride polymerize and remain bound fast with the aluminum chloride according to Nenitzescu (13-15). The specificity of the olefinic linkage was demonstrated by showing that cyclohexane has no retardation effect. On the other hand, benzene does have some retardation effect although, as might be expected, it is not so good as cyclohexene; this is because the compound is aromatic and hence none of the bonds have 100% double bond character.

It has been shown that another halogenated hydrocarbon that could complex $AlCl_3$ was capable of retarding the reaction with carbon tetrachloride. Benzyl chloride, for example, will complex with aluminum chloride and will retard the reaction when present at a concentration of 1%. Benzyl chloride, itself, is reactive toward aluminum at its boiling point.

Two amines which retard the reaction (triethylamine, 2-methyl-2-amino-1 propanol) have the ability to remove almost quantitatively aluminum chloride from a carbon tetrachloride solution saturated with aluminum chloride. The response to the addition of the amine is immediate and can be followed by noting the loss of pink color in the solution as well as by analysis for the aluminum in filtered carbon tetrachloride solution. Other amine retarding agents are methylamine, diethylamine, trimethylamine, n-butylamine, 3-methoxypropylamine, and cyclohexylamine. One of the disadvantages of the amines as practical retarders is their separate reactivity with carbon tetrachloride to form voluminous precipitates; however, under some conditions amines may be practical.

The ability of 21 hydrated inorganic salts to retard this reaction has been noted. The salts tested were generally in four classifications: nitrates, sulfates, chlorides, and sulfides. Only the hydrated nitrate and sulfide salts were retarding agents. Unlike the anhydrous salt, the hydrated aluminum chloride did not accelerate the reaction rate. The attempt to relate this phenomena to the coordination number of the metal ion of the salt was unsuccessful. Likewise, when the equivalent of the total water of crystallization was added as water to the carbon tetrachloride, its retarding influence was not nearly as effective as the hydrated inorganic salt.

On the assumption that an agent that might chelate $AlCl_3$ would be an effective retarder, 8-hydroxyquinoline was added at levels of 1% or less. Comparison on a weight basis shows that 8-hydroxyquinoline is one of the two best retarders (the other is phthalic anhydride).

Table V. Effect of retarding agents on reactivity in carbon tetrachloride in contact with aluminum

Additive (1% by wt of each)	Reactivity (first visible attack) In CCl_4	In CCl_4 saturated with $AlCl_3$
None	1 hr	<5 min
Amines		
1, 6-hexanediamine	None (88 hr)	None (72 hr)
3-methoxypropylamine*	After 40 hr	After 72 hr
2-methyl-2-amino-1-propanol	None (88 hr)	None (264 hr)
Triethylamine	None (88 hr)	None (72 hr)
Carbonyls		
Acetone*	None (40 hr)	<20 hr
2, 5-hexanedione	None (576 hr)	After 72 hr
Esters		
Ethyl acetate*	None (336 hr)	After 21 hr
Ethyl acetoacetate	None (678 hr)	After 21 hr
Acid anhydrides		
Acetic anhydride	None (96 hr)	None (120 hr)
Phthalic anhydride	None (336 hr, 0.2%)	None (192 hr)
Organic acid + water		
Acetic acid + water	None (40 hr)	After 20 hr
Phthalic acid + water	None (144 hr)	None (144 hr)
Heterocyclic compounds		
Pyrrole	None (96 hr)	After 72 hr
Quinoline	None (96 hr)	After 66 hr
Thiophene	None (144 hr)	None (72 hr)
Olefins		
Cyclohexene	After 192 hr	After 35 min
Aromatic compounds		
1, 4 naphthaquinone*	None (40 hr)	None (68 hr)
Nitrobenzene*	None (216 hr)	Slight (120 hr)
Quinone*	Slight (40 hr)	None (68 hr)
1, 3, 5 trinitrobenzene	None (40 hr)	<16 hr
Inorganic salt		
Aluminum nitrate .9 H_2O	None (96 hr)	<6 hr
Water (equivalent to above)	Extensive (40 hr)	<6 hr
Chelating agent		
8-hydroxyquinoline	None (216 hr)	None (192 hr)

* These additives had been investigated previously (3).

Table VI. Effect of magnesium content in aluminum alloys on corrosion rate in boiling CCl_4

Alloy	Exposure time, hr	Specimen size, in.	Weight loss, g	Calc. vol. metal loss, in.³/in.²/yr.	Nominal magnesium content, %
Solution used—CCl_4					
99.99% Al	7.83	1/16 × 1/2 × 3	1.6950	12.1	0
99.99% Al	7.5	1/16 × 1/2 × 3	1.6111	12.0	0
99.99% Al	7.0	1/16 × 1/2 × 3	2.0022	16.1	0
3003-H14	16	1/16 × 1/2 × 3	2.2480	7.76	0
3004-H14	6.75 days	1/16 × 1/2 × 3	0.5377	0.183	1.0
5052-H34	6.75 days	1/16 × 1/2 × 3	0.3868	0.132	2.5
5356-H34	6 days	1/16 × 1/2 × 3	0.1891	0.0740	5.2
112	48	1/2 × 2	1.4946	1.263	0
195	48	1/4 × 1/2 × 3	1.0173	0.857	0
214	12.67 days	1/4 × 1/2 × 3	1.9174	0.256	3.8
220	7 days	1/4 × 1/2 × 3	0.0027	0.0009	10.0
220	7 days	1/4 × 1/2 × 3	0.0019	0.0006	10.0
356-T6	48	1/4 × 1/2 × 3	0.5668	0.482	0.3
Mg	6 days	1/16 × 1/2 × 3	0.0006	0.0007	100
Mg	3 days	1/16 × 1/2 × 3	0.0003	0.0002	100
Solution used—CCl_4 saturated with $AlCl_3$					
5356	17	1/16 × 1/2 × 3	0.1711	0.564	5.2
5356	24	1/16 × 1/2 × 3	0.2578	0.602	5.2
220	24	1/4 × 1/2 × 3	0.0122	0.0285	10.0
220	7 days	1/4 × 1/2 × 3	0.0586	0.0196	10.0
Mg	96	1/16 × 1/2 × 3	0.0024	0.0022	100
Mg	24	1/16 × 1/2 × 3	0.0096	0.0352	100
Solution used—CCl_4 plus 0.5% $AlCl_3$					
Mg	20.5	1/16 × 1/2 × 3	0.0289	0.124	100
Mg	96	1/16 × 1/2 × 3	0.0282	0.0260	100

Tests for Evaluating Effectiveness of Retarding Agents

Since some retarders seemed capable of protecting aluminum for almost indefinite periods of time, some means of accelerating the test was needed to determine the relative effectiveness of the retarders. Exposure of aluminum specimens to refluxing carbon tetrachloride saturated with aluminum chloride is a much more stringent test than exposing them to refluxing pure carbon tetrachloride. To establish the relative effectiveness of the best known retarders, the same concentration by weight of each retarder was added to carbon tetrachloride saturated with aluminum chloride at room temperature. In order to insure that uniform conditions were maintained, the carbon tetrachloride was degassed in a dry box with nitrogen flushing through both the solution and the box. The total volume of carbon tetrachloride to be employed was saturated with $AlCl_3$ inside the box. The carbon tetrachloride was transferred to reflux flasks inside the box and the retarder and specimens added before the flask was stoppered. The time necessary for corrosion to appear on the aluminum specimen exposed in the boiling solution was a measure of the relative efficiency of the retarder. For example, some of the retarders classified in order of decreasing effectiveness were as follows: phthalic anhydride, 8-hydroxyquinoline, 2,5-hexanedione, ethyl acetoacetate, ethyl acetate, aluminum nitrate·$9H_2O$, and cyclohexene. The first two retarders completely prevented reaction under this condition for the five day test period. The actual periods of retardation are given in Table V.

Reaction of Carbon Tetrachloride with Magnesium and Aluminum Alloys

Tests were run with magnesium and ten aluminum alloys. The results given in Table VI and Fig. 2 show that magnesium in aluminum alloys has a pronounced effect on the corrosion rate. The corrosion

Table VII. Effect of $AlCl_3$ and $MgCl_2$ on the corrosion of magnesium and aluminum alloys in CCl_4

Alloy	Exposure time, hr	Specimen size, in.	Additive	Weight loss, g	Calc. vol. metal loss, in.³/in.²/yr.
5356	17	1/16 × 1/2 × 3	Saturated with $AlCl_3$	0.1711	0.564
	24	1/16 × 1/2 × 3	Saturated with $AlCl_3$	0.2578	0.602
220	24	1/4 × 1/2 × 3	Saturated with $AlCl_3$	0.0122	0.0285
	7	1/4 × 1/2 × 3	Saturated with $AlCl_3$	0.0586	0.0196
Mg	96	1/16 × 1/2 × 3	Saturated with $AlCl_3$	0.0024	0.0022
	24	1/16 × 1/2 × 3	Saturated with $AlCl_3$	0.0096	0.0352
Mg	20.5	1/16 × 1/2 × 3	0.5% $AlCl_3$	0.0289	0.124
	96	1/16 × 1/2 × 3	0.5% $AlCl_3$	0.0282	0.0260
99.99% Al	3	1/16 × 1/2 × 3	0.5% $MgCl_2$	0.8544	16.0
	3	1/16 × 1/2 × 3	0.5% $MgCl_2$	1.3874	26.0
99.99% Al	3	1/16 × 1/2 × 3	0.25% Mg turnings	0.7757	14.5
	3	1/16 × 1/2 × 3	0.25% Mg turnings	0.4438	8.32

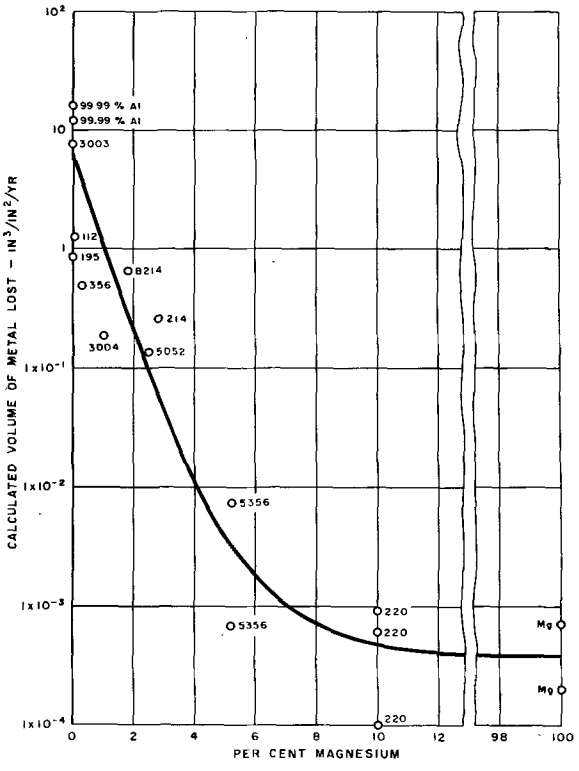

Fig. 2. Effect of magnesium content of aluminum alloys on corrosion rate in boiling CCl_4.

rate drops off rapidly as the magnesium content increases, becoming negligible for 220 cast aluminum alloy and magnesium. It should be pointed out that in Table VI and Fig. 2 varying exposure times were used to calculate the values of $in.^3/in.^2/yr$ and, hence, these values may not represent the true rates.

Tests also were run exposing magnesium and aluminum alloys 5356 and 220 to carbon tetrachloride saturated with aluminum chloride. The results given in Table VII show that the presence of aluminum chloride increased the corrosion rates of magnesium as well as the aluminum alloys. It was shown also that the presence of magnesium chloride or magnesium turnings had no significant effect on the corrosion of 99.99% aluminum in refluxing carbon tetrachloride. These results indicate that magnesium must be present as an alloying constituent in order to retard the reaction.

Conclusions

1. As reported by several others (1,2,5), many aluminum alloys are corroded severely by boiling carbon tetrachloride.

2. The reaction decreases rapidly when the temperature is dropped from the boiling point (77°C) to 50°C and is insignificant at room temperature. Some alloys show great resistance to carbon tetrachloride, even at the boiling point.

3. The addition of reaction products to carbon tetrachloride increases the initial reaction rate. Hexachloroethane had no effect on the reaction. Aluminum chloride, however, promotes the reaction and, when initially present, the reaction attains within a few minutes the same rate that is reached after several hours when starting with fresh carbon tetrachloride. This indicates that aluminum chloride acts as a reaction accelerator, probably through the formation of complexes with the carbon tetrachloride.

4. Chemical agents which can retard this reaction probably operate by combining with the aluminum chloride as it is produced. In this manner, the accelerating effect normally produced by the aluminum chloride is absent. Only anhydrous aluminum chloride accelerates corrosion.

5. Certain chemical agents that act as retarders for this reaction have shown the ability to decolorize a boiling solution of carbon tetrachloride containing aluminum chloride and to precipitate simultaneously and quantitatively in complexed form the aluminum chloride from the solution. Such a solution is noncorrosive if the retarder has been added in excess of that amount necessary to precipitate all the aluminum chloride.

6. Classes of retarding agent have been selected on the basis of known or projected reactivity with aluminum chloride. Some of the successful classes of retarders are acid anhydrides, amines, esters, heterocyclic compounds, halogenated hydrocarbons (which can complex aluminum chloride), ketones, olefins, and chelating agents in general. Certain hydrated nitrate and sulfide inorganic salts also were effective although the mechanism of their retardative ability is not clearly understood.

7. Reaction of aluminum alloys in boiling carbon tetrachloride drops off rapidly as the magnesium content increases. Addition of magnesium chloride or the presence of magnesium metal in carbon tetrachloride has no significant effect on the corrosion of high purity aluminum.

Manuscript received Nov. 13, 1957. This paper was prepared for delivery before the Buffalo Meeting, Oct. 6-10, 1957.

Any discussion of this paper will appear in a Discussion Section to be published in the December 1959 JOURNAL.

REFERENCES

1. F. H. Rhodes and J. T. Carty, *Ind. Eng. Chem.*, **17**, 909 (1925).
2. M. Stern and H. H. Uhlig, *This Journal*, **99**, 381, 389 (1952).
3. M. Stern and H. H. Uhlig, *ibid*, **100**, 543 (1953).
3a. R. H. Brown, E. H. Cook, M. H. Brown, and J. D. Minford, *ibid.*, **106**, 192 (1959).
4. E. V. Zappi, *Anales. soc. quim. argentina*, **2**, 217 (1914).
5. M. Stern, Thesis M.I.T. (1952).
6. M. H. Brown, Thesis Iowa State College (1949).
7. G. Perrier, *Compt. rend.*, **116**, 1298 (1893).
8. H. Funk, J. Schormuller, and W. Hensinger, *Z. anorg. u. allgem. chem.*, **204**, 361 (1932).
9. E. P. Kohler, *Am. Chem. J.* **27**, 241 (1902).
10. B. Menshutkin, *J. Russ, Phys. Chem. Soc.*, **42**, 1298 (1910).
11. J. W. Walker and A. Spencer, *J. Chem. Soc.*, **85**, 1106 (1904).
12. G. Gustavson, *Bull. Soc. Chem.* (2), **34**, 322 (1880).
13. C. D. Nenitzescu and I. P. Cantuniari, *Ber.*, **65**, 1449 (1932).
14. C. D. Nenitzescu and I. G. Gavat, *Ann.*, **519**, 260 (1935).
15. C. D. Nenitzescu and D. Curcaneanu, *Ber.*, **70**, 346 (1937).

Reaction of Aluminum and Carbon Tetrachloride, II

R. H. Brown, E. H. Cook, M. H. Brown, and J. D. Minford

Alcoa Research Laboratories, Aluminum Company of America, New Kensington, Pennsylvania

ABSTRACT

The mechanism of the reaction between aluminum and boiling carbon tetrachloride appears to be electrochemical. Conductivity measurements indicate that the reaction starts as soon as the aluminum is exposed to the boiling solution. The increase in the conductivity with time is caused by the presence of $AlCl_3$ and parallels the increase in weight of aluminum reacted as the reaction proceeds. The application of a cathodic current prevents attack of an aluminum specimen, indicating that the initial attack is caused by the presence of an ionic species. Trace amounts of the reaction product hexachloroethane were produced electrochemically in the absence of any aluminum.

Substances that retard the reaction apparently function by forming inactive complexes with the $AlCl_3$. The rate-determining step in the reaction does not appear to involve free radicals since the majority of the effective inhibitors failed to react with known free radicals.

It has been shown (1) that two of the products of the reaction between aluminum and carbon tetrachloride, are aluminum chloride and hexachloroethane. Evidence was also obtained for the presence of high molecular weight carbon-chlorine compounds soluble in carbon tetrachloride and high molecular weight carbon, chlorine, and aluminum compounds which were insoluble in carbon tetrachloride.

A rather critical temperature dependence can be shown for this reaction, ranging from rapid reaction at the boiling point to negligible reaction in eighteen months at room temperature.

The presence of the reaction products accelerates the reaction because of the presence of aluminum chloride. Hexachloroethane has no effect on the reaction. The aluminum chloride acts as a reaction accelerator probably through the formation of complexes with the carbon tetrachloride.

Chemical agents that act as retarders do so by reaction with the aluminum chloride as it is produced. This was demonstrated by quantitatively removing the aluminum chloride from a corrosive boiling carbon tetrachloride solution and rendering it noncorrosive in the process.

A number of classes of retarding agents were discovered on the basis of known or projected reactivity with aluminum chloride. Some of these were acid anhydrides, amines, esters, heterocyclic compounds, halogenated hydrocarbons (which can complex aluminum chloride), ketones, olefins, and chelating agents in general. Retardation was also secured with a number of hydrated inorganic nitrates and sulfides for less definitive reasons.

Reaction of aluminum alloys in boiling carbon tetrachloride drops off rapidly with increasing magnesium content. Magnesium metal or magnesium chloride has no significant effect on this reaction.

Studies of Conductivity

High-purity (99.99%) aluminum is attacked severely in boiling carbon tetrachloride but is resistant to carbon tetrachloride at room temperature. Since the conductivity of carbon tetrachloride is much higher at the boiling point than at room temperature, it was thought that a relationship might exist beween conductivity and corrosion.

The apparatus shown in Fig. 1 was used to measure conductivity. As shown in Fig. 2, the conductivity increased steadily for about 5 hr after aluminum specimens were immersed in boiling carbon tetrachloride, indicating that the conductivity increased as the corrosion products increased. On the basis of weight loss measurements, there would appear to be an induction period of about 1 hr; however, the more sensitive conductivity measurements show that the reaction starts soon after the aluminum is placed in the boiling carbon tetrachloride (see also Fig. 11). Since aluminum chloride and hexachloroethane were identified as two of

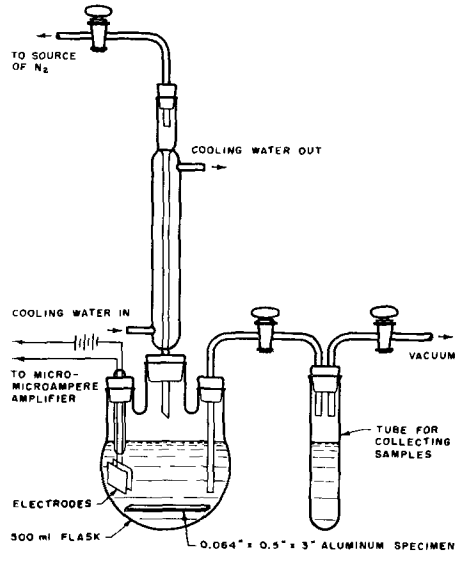

Fig. 1. Apparatus used for measuring conductivity and removing samples simultaneously.

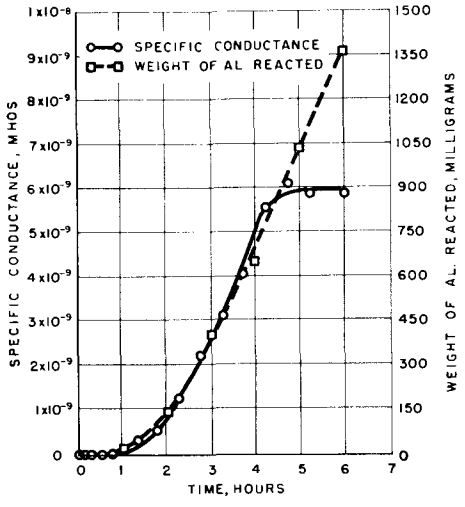

Fig. 2. Plot of specific conductance and weight of aluminum reacted vs. time.

the corrosion products, these compounds were added singly to determine the effect of each compound on conductivity. As shown in Fig. 3, aluminum chloride had a marked effect. The conductivity increased rapidly during the first 20 min and then leveled off. The reaction resulting when an aluminum specimen was added after the conductivity leveled off, caused the conductivity to rise to a value about ten times that of carbon tetrachloride saturated with aluminum chloride, indicating that additional ionized complexes are formed. No significant change in conductivity occurred when hexachloroethane was added to boiling carbon tetrachloride.

In another experiment, samples of solutions were withdrawn periodically and analyzed for aluminum at the same time as conductivity measurements were being made on the solution remaining in the flask. The results are shown in Table I and Fig. 2. The data show that the increase of conductivity and weight of aluminum reacted in the carbon tetrachloride roughly parallel each other in the first 4.5 hr. In Fig. 4,[1] a comparison of the curves of conductivity and total aluminum reacted shows that the aluminum reacted increases linearly with specific conductivity up to 5×10^{-9} mhos. The specific conductivity reaches a limiting value of about 6×10^{-9} mhos while the total aluminum reacted continues to increase. It can be seen in Fig. 5[2] that the reaction rate increases with increasing specific conductivity and levels off as the specific conductivity approaches 6×10^{-9} mhos. As shown in Fig. 6, the reaction rate increases with time up to 4 hr, where it reaches a constant value. As can be seen in Fig. 2, the specific conductance also reaches a limiting value after about 4 hr. These results which indicate a relationship between the reaction rate and specific conductivity suggest that ions may be involved in the reaction.

The conductance of a solution is proportional to the mobility and number of ions in the solution. The

[1] Figure 4 was plotted by taking points from the two curves on Fig. 2 for the same time, and plotting the points against each other.

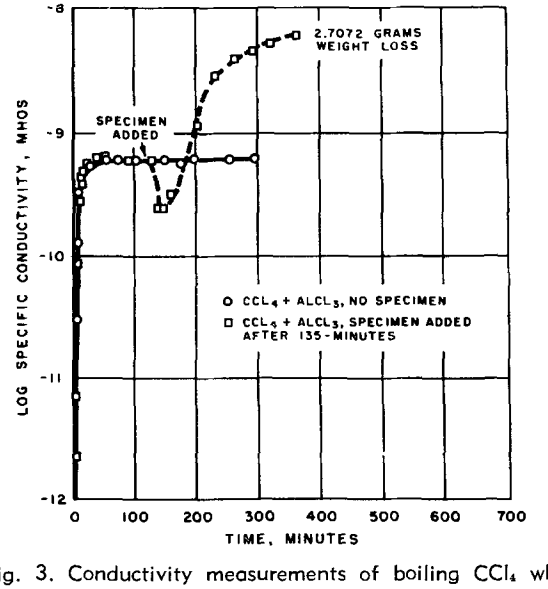

Fig. 3. Conductivity measurements of boiling CCl_4 while $AlCl_3$ was going into solution.

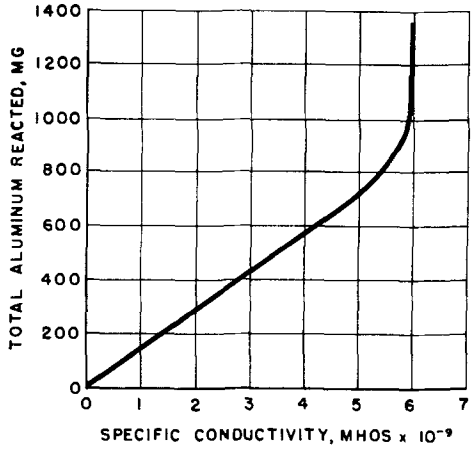

Fig. 4. Plot of total aluminum reacted vs. specific conductivity.

[2] The reaction rate was calculated from the slope of the weight of aluminum reacted vs. time curve shown in Fig. 2. The slope at a given time was plotted against the specific conductance value at the same time.

Table I. Data on per cent dissolved aluminum and conductivity

Time, min	Volume of* sample, ml	Weight of Al in samples, mg	Weight % Al dissolved in CCl_4	Total Al dissolved in CCl_4, mg	Specific conductivity, mhos
0	25	0	0	0	6.80×10^{-12}
10	—	—	—	—	1.78×10^{-11}
20	—	—	—	—	1.78×10^{-11}
30	—	—	—	—	4.40×10^{-11}
40	—	—	—	—	5.90×10^{-11}
50	—	—	—	—	9.15×10^{-11}
60	27.5	1.2	0.00274	21.8	—
80	—	—	—	—	3.15×10^{-10}
100	—	—	—	—	5.40×10^{-10}
120	27	8.1	0.0188	143	—
140	—	—	—	—	1.25×10^{-9}
160	—	—	—	—	2.24×10^{-9}
180	29	25.6	0.0553	403	—
200	—	—	—	—	3.12×10^{-9}
220	—	—	—	—	4.08×10^{-9}
240	28	41.2	0.0891	650	—
260	—	—	—	—	5.56×10^{-9}
280	—	—	—	—	6.10×10^{-9}
300	29	71.0	0.154	1033	—
330	—	—	—	—	5.87×10^{-9}
360	29	97.6	0.211	1367	5.87×10^{-9}

* Initial volume of CCl_4 = 500 cc.

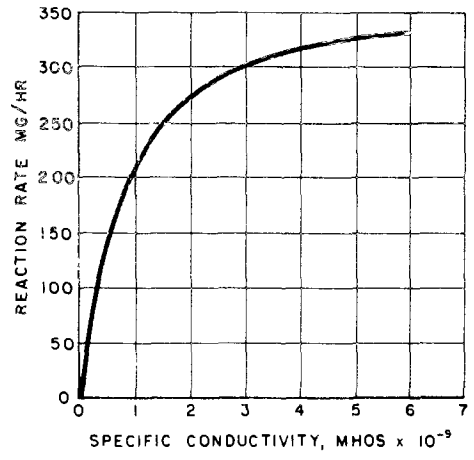

Fig. 5. Plot of reaction rate vs. specific conductivity

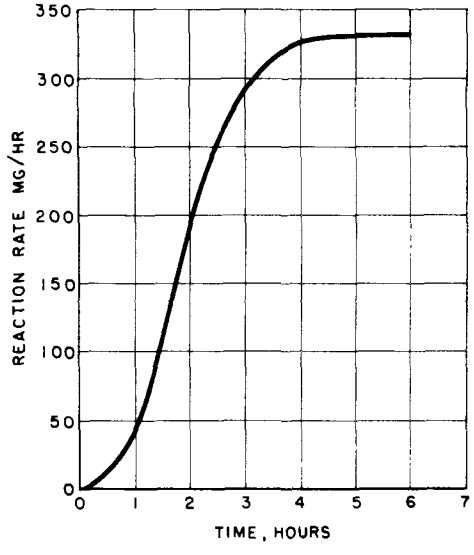

Fig. 6. Plot of reaction rate vs. time

slope of the line from a plot of log specific conductance vs. $1/T$ is the temperature coefficient. The smaller the temperature coefficient the greater the number of ions in a given solution. The relationship can be demonstrated by comparing the temperature coefficients for distilled water and the more highly ionized 0.01M KCl solution. The temperature coefficients are —0.208 for distilled water and —0.084 for 0.01M aqueous potassium chloride solution (2).

Figure 7 shows the effect on the temperature coefficient of carbon tetrachloride due to addition of aluminum chloride or corrosion products from the aluminum-carbon tetrachloride reaction. These results show that the addition of aluminum chloride to carbon tetrachloride decreases the temperature coefficient, indicating that the addition of aluminum chloride increases the number of ions. The presence of aluminum corrosion products further decreases the temperature coefficient indicating an additional increase in the number of ions. These results also suggest that an ionic mechanism may be involved.

The increase in conductivity with time that accompanies the reaction between aluminum and carbon tetrachloride is observed in other corrosion reactions occurring in aqueous solutions. Since conductance in solution depends on the presence of ions, this indicates that this reaction may proceed by

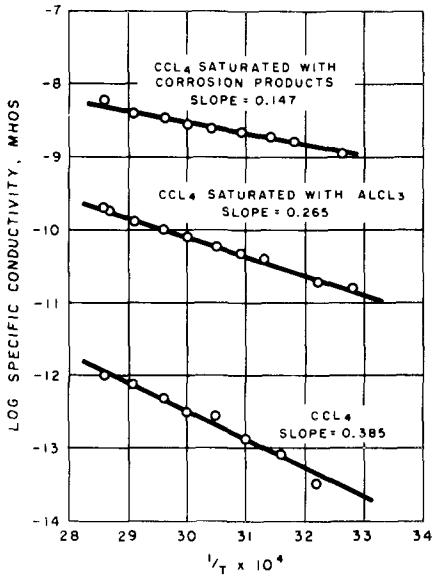

Fig. 7. Temperature coefficients for CCl_4 and CCl_4 saturated with $AlCl_3$ and corrosion products.

an electrochemical mechanism involving oxidation and reduction (3). For these reasons, electrochemical relationships that might be involved were further investigated. For example, if it could be shown that the reaction with carbon tetrachloride could be prevented by cathodically protecting the aluminum, this would support an electrochemical mechanism. However, it should be pointed out that the inability to protect the aluminum cathodically would not be sufficient to disprove such a mechanism. A reduction or an increase in the corrosion rate caused by the coupling to dissimilar metals or by an applied current would lend support to an ionic mechanism.

Effect of Galvanic Corrosion

A sample of high-purity sheet aluminum (99.99% Al) was coupled to a mild steel sheet specimen in boiling carbon tetrachloride. The electrodes were 1 in. apart. The exposed area of each specimen was approximately 3 in.^{2} and the initial galvanic current between the specimens was 2×10^{-11} amp. When the boiling carbon tetrachloride was saturated with aluminum chloride, in order to increase the conductance, the galvanic current increased over a 15-min period and leveled off at a value of 10×10^{-9} amp. During this time, the solution darkened, and the aluminum specimen became coated with corrosion product, while the steel specimen remained clean. The evidence of a current flow as a result of bimetallic coupling further indicated the analogy with similar reactions occurring in aqueous solutions. The fact that Stern and Uhlig (4) were unable to notice an increased weight loss effect from bimetallic coupling based on a 6-hr test in carbon tetrachloride is understandable in view of the very high solution resistance encountered between electrodes. The corrosion of aluminum in carbon tetrachloride could proceed by an electrochemical mechanism to give high corrosion rates if the local anodes and cathodes on the surface of the aluminum are only a few angstroms apart. This proximity of anode and cathode would enable the reaction to proceed at relatively

rapid rates even though the resistance of the solution were high.

Observations with an Applied Potential

Based on results with galvanic couples one would expect an externally applied current to protect an aluminum specimen cathodically in boiling carbon tetrachloride. To study the effects of an applied cathodic and anodic current on an aluminum specimen in carbon tetrachloride, a rather high emf source is required to overcome the resistance of the carbon tetrachloride. For the following experiment a potential source of 200 v d.c. was used.

To prevent attack on the portions of the electrodes in the vapor phase, the possibility of a coating resistant to boiling carbon tetrachloride and its vapors was investigated. It was found that an anodic coating (Alumilite[3] 204) prevented attack except at the edges of an aluminum sheet. By using round rods with rounded ends it was found that these anodic coatings almost completely retarded the attack. Round rods 99.99% Al, ¼ in. in diameter with rounded ends, were given Alumilite 204 treatment except for a band ½ in. long located ¼ in. from the end of the rod.

When an external potential was applied across two round aluminum rods (⅜ in. apart) of 99.99% Al in 400 cc of boiling carbon tetrachloride saturated with aluminum chloride, the corrosion of the cathode was slightly retarded, whereas the corrosion of the anode began almost immediately. A blank placed in the same solution clearly shows that the corrosion of the anode was accelerated and that of the cathode was slightly retarded (Fig. 8). Initially the current passing between the two electrodes was 10 x 10^{-8} amp. After about 200 min the rate of attack of the cathode increased and approached that of the anode. The current at this point increased to 110 x 10^{-8} amp. This increase in current was caused by an increase in solution conductivity because of the presence of aluminum corrosion products. At this point the solution was rather dark and the attack of both specimens was caused largely by local action rather than by the applied current. At the time the experiment was discontinued the current through the solution was 200 x 10^{-8} amp. This increase in current with a constant applied potential parallels the increase in conductivity which accompanies the corrosion of aluminum in boiling carbon tetrachloride.

[3] Trade name of Aluminum Company of America.

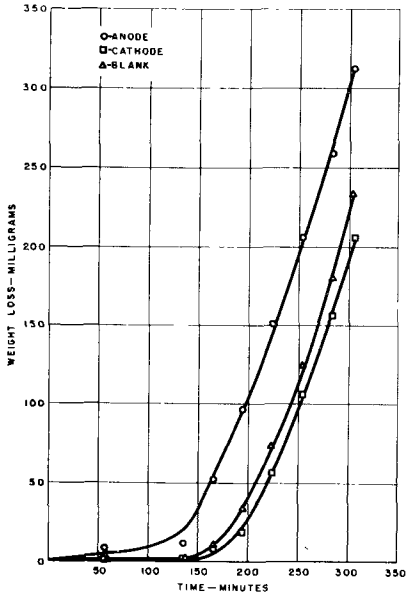

Fig. 8. Effect of an applied potential on aluminum rods in boiling carbon tetrachloride saturated with aluminum chloride.

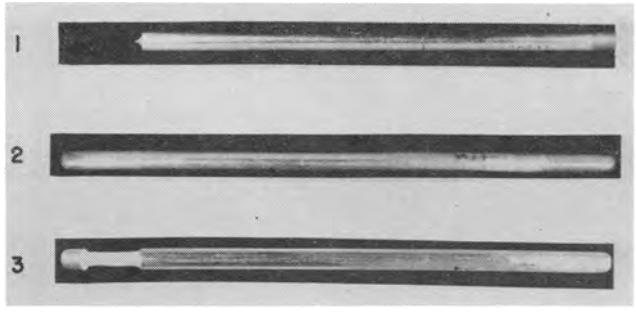

Fig. 9. Cathodic protection of aluminum in carbon tetrachloride: 1, An aluminum rod suspended in boiling carbon tetrachloride for four days (no cathodic current applied); 2, an aluminum rod suspended in boiling carbon tetrachloride for 28 days, with an applied cathodic current of 5 x 10^{-9} amperes. This specimen was completely protected; 3, The cathodically protected specimen 48 hr after the applied cathodic current had been removed.

In view of the above results, an experiment was devised to determine whether a specimen could be protected cathodically in boiling carbon tetrachloride. When an aluminum rod was suspended in boiling carbon tetrachloride, the unanodized portion completely reacted within four days, although the attack did not begin until about the third day (Fig. 9). This increase in induction time indicated the significance of eliminating corners and rough edges from the specimens.

When a potential of 220 v was applied across the aluminum rod and a cylindrical platinum gauze (the aluminum being the cathode), no attack of the aluminum specimens by boiling carbon tetrachloride was observed after 28 days (Fig. 9). The average current between the electrodes was 5 x 10^{-9} amp. This current was relatively constant over the 28-day time interval.

When the applied potential was removed, the corrosion of the aluminum began within 30 hr; in 48 hr the attack was severe (Fig. 9). This experiment was then repeated with lower currents and shorter periods of observation. The results indicate that cathodic protection was complete for the period of observation (Table II).

Table II. Cathodic protection of aluminum in boiling CCl_4

	Current, amp			Number of days the experiment was continued	Aluminum detected
	Initial	Maximum	Average		
(a)	"No Current"			3	Severe attack
(b)	8×10^{-11}	2.4×10^{-10}	2.2×10^{-10}	12	0.075 mg/l
(c)	2×10^{-10}	20×10^{-10}	10×10^{-10}	10	0.018 mg/l
(d)	6×10^{-10}	7×10^{-10}	6×10^{-10}	11	0.155 mg/l
(e)	5×10^{-9}	6×10^{-9}	5×10^{-9}	28	None detected

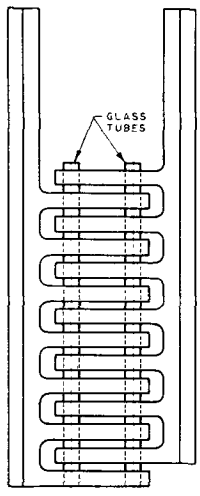

Fig. 10. Schematic diagram of corbon electrodes used for electrochemical production of hexachloroethane from carbon tetrachloride.

In the case of (*b*) and (*e*) (Table II), when the current was removed after the time of observation, corrosion began within 24 and 30 hr, respectively. All these results are indicative of an electrochemical mechanism for the attack of aluminum by carbon tetrachloride.

It was not possible to protect cathodically an aluminum rod in carbon tetrachloride saturated with aluminum chloride at the reflux temperature. It was estimated from the rate of attack of an aluminum specimen in this solution that a current density of at least 50 ma/cm^2 would be required to prevent attack of the aluminum. With the high resistance of the solution, such a current could be obtained only with excessively high applied potentials.

Thus, the reaction in carbon tetrachloride can be prevented for an indefinite period by cathodically protecting the aluminum with an applied potential. Therefore, it is concluded that the initial attack of the aluminum is caused by the presence of an ionic species.

During the corrosion of an aluminum specimen in boiling carbon tetrachloride, the energy supplied by the oxidation of the aluminum produces hexachloroethane as a reduction product. If reduction of the carbon tetrachloride to hexachloroethane can be produced in the absence of metallic aluminum by means of an applied potential, this fact would lend support to an electrochemical mechanism.

Graphite electrodes were constructed (Fig. 10) to give a large surface area and a small distance between anode and cathode. Each electrode consisted of seven plates (3 x 1¾ x ¼ in.) placed ½ in. apart. The electrodes were then placed so that the distance between each plate was about ⅛ in. Platinum was used to connect the electrode to the potential source.

Approximately 1 liter of carbon tetrachloride was added to the cell using aluminum chloride as the electrolyte. At a potential of 850 v the average current in the cell was 200 μa for a period of twelve days. At the end of the twelve-day period, the solution was filtered and the carbon tetrachloride evaporated on a water bath to a volume of about 50 cc. Because of the ease of sublimation of hexachloroethane, the remainder of the solution was evaporated at room temperature. The concentrated solution was yellow. When the solution was evaporated to dryness, an odor resembling hexachloroethane was detected in the residue (which also contained some aluminum chloride).

By means of infrared spectroscopy, hexachloroethane was detected, but special techniques were necessary. The hexachloroethane has two detectable absorption bands; one is rather weak while the stronger band is masked by carbon tetrachloride absorption. Because of the volatility of the product and its low yield, it was impossible to obtain a large enough sample to identify the weaker band of hexachloroethane. Consequently, the residue from the carbon tetrachloride evaporation was dissolved in spectral pure cyclohexane and submitted for analyses. Hexachloroethane was detected in this solution at the stronger wave length (12.77 μ). In an identical experiment in which there was no applied current, no hexachloroethane could be detected by the above procedure.

Relationship of Conductivity to Retarding Agents

Since the conductivity is markedly affected by the concentration of aluminum chloride in carbon tetrachloride solution, any factors that affect the aluminum chloride would also result in conductivity changes. Hence, the addition of retarding agents to colored carbon tetrachloride solutions containing anhydrous aluminum chloride should result in a subsequent drop of the conductivity to essentially the level of pure carbon tetrachloride (Fig. 11).

The results shown in Table III indicate that a good retarding agent can be generally predicted based on its ability to lower the conductivity of the corrosive carbon tetrachloride solution. Of all the retarding agents tested, only the addition of cyclohexene to the carbon tetrachloride-aluminum chloride solution failed to lower the conductivity by ap-

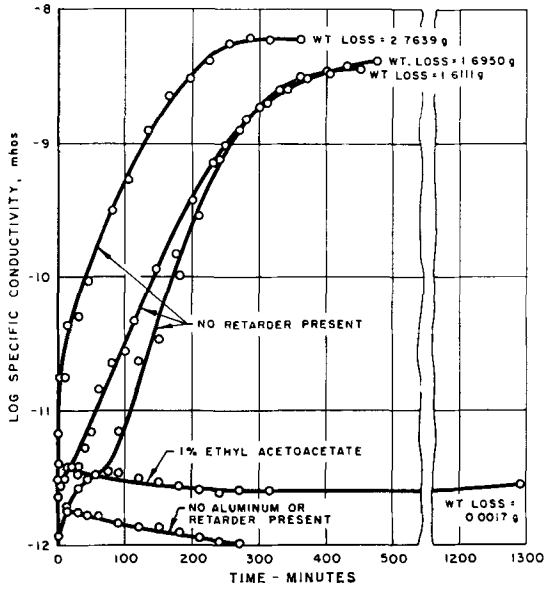

Fig. 11. Conductivity measurements on boiling carbon tetrachloride with and without aluminum specimens and retarders present.

Table III. Effect of retarding agents or reactivity and conductivity in carbon tetrachloride in contact with aluminum

Additive	Reactivity (first visible attack) in CCl_4	Initial specific conductivity, mhos	
		in CCl_4 + additive	in CCl_4 + additive + $AlCl_3$
None	1 hr	4×10^{-12}	2×10^{-10}
Amines			
1, 6 Hexanediamine	None (88 hr)	9×10^{-12}	Prevented by ppt
3-methoxypropylamine	After 40 hr	3×10^{-12}	2×10^{-11}
2-methyl-2-amino-1-propanol	None (88 hr)	7×10^{-12}	8×10^{-13}
Triethylamine	None (88 hr)	8×10^{-12}	2×10^{-11}
Carbonyls			
Acetone	None (40 hr)	2×10^{-12}	1×10^{-12}
2, 5 Hexanedione	None (576 hr)	4×10^{-12}	2×10^{-12}
Esters			
Ethyl acetate	None (336 hr)	2×10^{-13}	4×10^{-11}
Ethyl Acetoacetate	None (678 hr)	4×10^{-12}	3×10^{-11}
Acid Anhydrides			
Acetic anhydride	None (96 hr)	2×10^{-12}	4×10^{-11}
Phthalic anhydride	None (336 hr, 0.2%)	2×10^{-12}	8×10^{-13}
Organic Acid + Water			
Acetic acid + water	None (40 hr)	3×10^{-12}	8×10^{-13}
Phthalic acid + water	None (144 hr)	1×10^{-12}	8×10^{-12}
Heterocyclic Compounds			
Pyrrole	None (96 hr)	2×10^{-12}	3×10^{-12}
Quinoline	None (96 hr)	8×10^{-13}	3×10^{-12}
Thiophene	None (144 hr)	8×10^{-12}	2×10^{-11}
Olefins			
Cyclohexene	After 192 hr	3×10^{-12}	1×10^{-10}
Aromatic Compounds			
1, 4 Naphthaquinone	None (40 hr)	2×10^{-12}	2×10^{-12}
Nitrobenzene	None (216 hr)	9×10^{-12}	1×10^{-12}
Quinone	Slight (40 hr)	2×10^{-12}	4×10^{-12}
1, 3, 5 Trinitrobenzene	None (40 hr)	6×10^{-13}	2×10^{-11}
Inorganic Salt			
Aluminum nitrate·$9H_2O$	None (96 hr)	2×10^{-12}	5×10^{-13}
Water (equivalent to above)	Extensive (40 hr)	5×10^{-13}	2×10^{-12}
Chelating Agent			
8-Hydroxyquinoline	None (216 hr)	2×10^{-12}	1×10^{-11}

proximately a factor of ten or more. It should be pointed out that this particular agent was also considered least effective as a retarding agent when evaluated with a test specimen in a carbon tetrachloride solution initially saturated with anhydrous aluminum chloride. It can also be seen in Table III that the various retarding agents at 1% concentration have negligible effect on the conductivity of pure carbon tetrachloride. Accordingly, it is presumed that the conductivity changes are the result primarily of interaction of the colored ionized complex (between carbon tetrachloride and anhydrous aluminum chloride) and the retarding agent. It does not appear, however, that a direct proportional relationship exists between the ability of an agent to lower the conductivity a specific amount and its effectiveness as a retarding agent. For example, 8-hydroxyquinoline, 2,5 hexanedione, and phthalic anhydride are all highly effective retarding agents by actual test and do lower the conductivity of carbon tetrachloride-aluminum chloride solution but not to the same degree. For example these compounds lower the conductivity by factors of 20, 100, and 250, respectively.

One practical application of this relationship might be to follow the conductivity of a closed aluminum system containing inhibited carbon tetrachloride. A warning that the concentration of the retarding agent was inadequate would be indicated by a rise in conductivity. Addition of more retarding agent followed by a drop in the conductivity would mean the carbon tetrachloride was again adequately inhibited. Conceivably, this type of control could be exercised with other halogenated hydrocarbons where similar relationships between conductivity, aluminum chloride, and retarding agents might be established.

Discussion of Possible Alternate Free Radical Theory

As pointed out by Stern and Uhlig (5) several theoretical reasons indicate that the reaction may proceed by means of a free radical mechanism. It was concluded, therefore, that the reaction was initiated by free radicals whose formation accelerated with time until the rate of generation equaled the rate of destruction. This could be one of several possible explanations for the constant corrosion rate found for high-purity aluminum in carbon tetrachloride. However, an ionic mechanism would also be consistent with the observed data. In the following equilibrium,

$$AlCl_3 + CCl_4 \rightleftharpoons (CCl_3)^+ + (AlCl_4)^-$$

the concentration of the ionic species is so small that a steady-state condition would soon be obtained. In view of the complexity of the reaction, it would not be unreasonable to assume that some of the steps may involve free radicals. However, our data indicates that the rate-determining step is one involving an electrochemical mechanism.

Stern and Uhlig (5) have shown that certain free radical supressors are capable of retarding the aluminum-carbon tetrachloride reaction. If effective retarders do combine with free radicals, this would be another indication that the rate-controlling step is free radical in nature.

Tests for Free Radicals

The following experiments were carried out to determine whether or not free radicals are present in measurable quantities in boiling carbon tetrachloride. A solution of triphenylmethyl free radicals was prepared by dissolving 0.25 g triphenylchloromethane in 50 ml of benzene and adding 3 g of zinc filings and allowing the mixture to stand at room temperature for 6 hr in a sealed bottle. The presence of free triphenylmethyl radicals was indicated by the appearance of a yellowish-orange color. The free radicals form according to the reaction shown below:

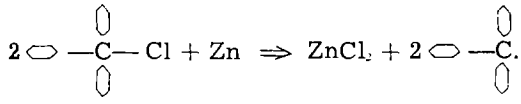

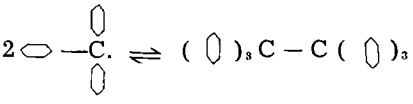

The solution of free radicals in benzene was decanted and added to 50 ml of carbon tetrachloride and the mixture refluxed under nitrogen for 10 min. The color did not fade during this period. The solution was then divided into two portions. One portion was placed in a bottle and sealed to exclude air. The color of this solution did not fade. The other portion was poured into an open beaker. The color of this solution faded completely within a few minutes indicating that the color was caused by the presence of free radicals and that the free radicals were destroyed by reaction with oxygen when the solution was exposed to air. One of the properties of triarylmethyl free radicals is the rapid absorption of atmospheric oxygen to form colorless triarylmethyl peroxides (6). If appreciable amounts of free radicals were present in the boiling carbon tetrachloride, it would be expected that the free radicals would be removed by the following reactions causing the color of the solution to fade in a short time:

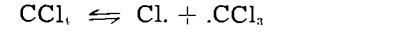

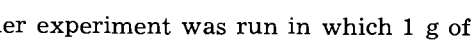

Another experiment was run in which 1 g of zinc filings, 50 ml of benzene and 50 ml of carbon tetrachloride were placed in a reflux flask and brought to the boiling point, 0.25 g of triphenylchloromethane was then added and the flask flushed with nitrogen. A dark yellow-orange color appeared in a short time. After refluxing for 10 min the solution was decanted and divided in two portions. One portion was sealed in a glass bottle and remained colored; the other portion was poured into an open beaker and became colorless within a few minutes. A blank was run in which 1 g of zinc filings, 50 ml of benzene, and 50 ml of carbon tetrachloride were refluxed for 30 min. This solution did not develop any color. The above results indicate that the rate of formation of free radicals from carbon tetrachloride was too low to prevent the formation of triphenylmethyl free radicals.

A number of the retarder materials investigated in this laboratory (1) as well as some mentioned by Stern and Uhlig (5) were tested for their ability to react with triphenylmethyl free radicals.

Some amines have already been mentioned as being reactive with aluminum chloride as well as carbon tetrachloride. The amine, 3-methoxypropylamine, does, in addition, react with triphenylmethyl free radicals almost as rapidly as the free radical reacts with air with the resultant solution becoming water clear. On the other hand, retarders containing carbonyl groups such as ethyl acetate, ethyl acetoacetate, 2,5-hexanedione, and phthalic anhydride which range from good to excellent as retarding agents do not react with solutions of this free radical species, and it is necessary to expose these solutions to air in order to decolorize them. Acetone was an exception to this rule.

Heterocyclic ring-type compound retarders such as thiophene did not react with the triphenylmethyl free radical. The olefin, cyclohexene, which is only a fair retarder for the carbon tetrachloride reaction, readily reacts with the colored free radical. The inorganic salt Al $(NO_3)_3 \cdot 9H_2O$, an effective retarder, can also decolorize the colored free radical solution.

Two of the free radical supressors mentioned by Stern and Uhlig (5), quinone and napthaquinone, could not be evaluated by this method since both materials give yellow colored solutions in benzene. However, nitrobenzene, another retarder mentioned by Stern and Uhlig, did react to the extent that small amounts of nitrobenzene lightened the deep yellow color of the free radical solution and air did not further lighten the color.

On the basis of the above results, it was concluded that the ability of a substance to react or not react with triphenylmethyl free radicals bears no relationship to its ability to retard the carbon tetrachloride-aluminum reaction. Therefore, the evidence indicates that the rate-determining step for this latter reaction is controlled largely by an electrochemical mechanism (7).

Results with Other Halogenated Hydrocarbons

This proposed electrochemical mechanism applies only to carbon tetrachloride and was not established for other halogenated hydrocarbons. High-purity aluminum specimens could not be cathodically protected in the case of the eight other halogenated hydrocarbons tested. From the initial high rates of attack, relatively high current densities would be required to achieve cathodic protection if the mechanism were electrochemical. These high current densities were not possible with the available equipment. The halogenated hydrocarbons were 2- chloro -2- methylbutane, 2-chloro -2- methylpropene, (1, 4-dichlorobutane), (1, 1, 2, 2- tetrachloroethane), α-chlorotoluene, methlychloroform, (1, 1, 2- trichloroethane), and 3- chloro -2- methylpropene. The inability to achieve cathodic protection in these cases

could be explained by (*a*) inability to achieve the minimum cathodic current required because of high solution resistance and limited emf source, or (*b*) the rate-controlling step being other than electrochemical.

Summary

1. Conductivity of a boiling carbon tetrachloride solution with high-purity aluminum present increases steadily as the reaction proceeds and after about 4-5 hr reaches a constant value.

2. Addition of hexachloroethane to boiling carbon tetrachloride has no effect on conductivity, but addition of aluminum chloride produces an immediate elevation of the conductivity. An additional elevation of the conductivity can be secured by reacting an aluminum specimen in this solution, suggesting that additional ionized complexes are formed.

3. Increase of conductivity in a corroding solution parallels the increase in weight per cent aluminum in solution which occurs as the reaction proceeds. However, the more sensitive conductivity measurements show that the reaction starts soon after the aluminum is placed in the boiling carbon tetrachloride; hence the induction period referred to in previous literature reports is only an "apparent induction time."

4. The fact that the reaction rate increases with increasing conductivity suggests an electrochemical mechanism. Changes in the temperature coefficient of the conductivity in the presence and absence of corrosion products also suggests this type of mechanism.

5. Cathodic protection successfully prevented the corrosion of high-purity aluminum in boiling carbon tetrachloride. This also supports an electrochemical mechanism since it must be concluded that the initial attack of the aluminum is caused by the presence of an ionic species.

6. Additional evidence for an electrochemical mechanism was obtained by producing an identifiable amount of hexachloroethane (a primary reaction product) by electrolysis of a carbon tetrachloride solution saturated with aluminum chloride.

7. The addition of retarding agents resulted in an alteration of the ionized aluminum chloride-carbon tetrachloride complex so that the conductivity dropped essentially to that of pure boiling carbon tetrachloride. There is no direct proportional relationship between the ability of an agent to lower the conductivity a specific amount and its effectiveness as a retarding agent. Following the pattern of conductivity in the carbon tetrachloride solution should, however, be indicative of the level of protection of a retarder agent added to the solution.

8. There was no apparent reaction between triphenylmethyl free radicals in benzene and boiling carbon tetrachloride, although a portion of the same solution reacted with the oxygen of the air. Similarly, triphenylmethyl free radicals could be made in the presence of boiling carbon tetrachloride, indicating that the rate of formation of free radicals in carbon tetrachloride, if present, was too low to prevent the formation of the triphenylmethyl free radicals by reaction.

9. Several of the retarder materials listed in previous publications were tested for their ability to react with triphenylmethyl free radicals. There was no relationship between the ability of a substance to retard this carbon tetrachloride-aluminum reaction and to react with triphenylmethyl free radicals.

Manuscript received Nov. 13, 1957. This paper was prepared for delivery before the Buffalo Meeting, Oct. 6-10, 1957.

Any discussion of this paper will appear in a Discussion Section to be published in the December 1959 JOURNAL.

REFERENCES

1. J. D. Minford, M. H. Brown, and R. H. Brown, *This Journal*, **106**, 185 (1959).
2. International Critical Tables VI, 152, 230.
3. L. P. Hammett, "Physical Organic Chemistry," p. 142, 310 f. McGraw-Hill Book Co., New York (1940).
4. M. Stern and H. H. Uhlig, *This Journal*, **99**, 381 (1952).
5. M. Stern and H. H. Uhlig, *ibid.*, **100**, 543 (1953).
6. M. Gomberg and L. H. Cone, *Ber.*, **37**, 3538 (1904).
7. E. R. Alexander, "Principles of Ionic Organic Reactions," p. 2, John Wiley & Sons, Inc. New York, (1950).

Copper-Activated Calcium Orthophosphate and Related Phosphors

Yasuo Uehara, Yoshimasa Kobuke, and Isoo Masuda

Matsuda Research Laboratory, Tokyo Shibaura Electric Co., Ltd., Kawasaki, Japan

ABSTRACT

The preparation and properties of copper-activated calcium orthophosphate and related phosphors are described. Copper-activated β-calcium orthophosphate phosphor fired in a reducing atmosphere produces a strong blue fluorescence peaked at 4800Å under excitation by 2537Å and cathode rays. With partial substitution of Ca by bivalent metals such as Be, Cd, and Sr the emission remains unchanged, while introduction of Mg and Zn gives a strong violet fluorescence peaked at about 4400Å and 4500Å, respectively. Phosphors containing boron produce a blue to greenish yellow fluorescence depending on the content of boron. All of these phosphors give a strong thermoluminescence. Only the blue fluorescent phosphor gives also a weak red emission stimulated by 3650Å radiation. Introduction of Mn or Sn as secondary activators into Cu-activated β-calcium orthophosphate or into the Cu-activated substituted phosphors gives rise to a red band due to Mn or Sn in addition to the original blue or violet band. The luminescent properties of zinc or cadmium orthophosphate are similar in some respects to those of zinc or cadmium sulfide phosphors.

Calcium metaphosphate and halophosphate activated with Cu have been reported to produce a weak blue fluorescence (1). According to the present investigation, calcium orthophosphate with added Cu and fired in air shows practically no fluorescence at room temperature under excitation by 2537Å, 3650Å, and cathode rays. However, calcium orthophosphate containing Cu which was fired in a reducing atmosphere was found to give a strong blue fluorescence under excitation by 2537Å and cathode rays. This phosphor also shows a strong blue thermoluminescence and a weak red emission stimulated by 3650Å. The present paper describes the preparation and properties of Cu-activated calcium orthophosphate fired in a reducing atmosphere and related phosphors.

Preparation and Structure of Phosphors

Calcium orthophosphate phosphors were prepared from dibasic calcium phosphate ($CaHPO_4$) and calcium carbonate. These materials were prepared from purified solutions of dibasic ammonium phosphate, calcium chloride, and ammonium carbonate. A solution of purified copper sulfate was added to a mixture of 2 mole dibasic calcium phosphate and 0.9 mole calcium carbonate. The blend was dried at about 200°C, then milled to assure intimate mixture. It was fired in a silica tube in an electrically heated furnace for about 30 min at 1100°C in air. The air-cooled powder was reground and fired in a reducing atmosphere for about 30 min at 1100°C, then cooled in the same atmosphere. As the reducing gas, a mixture of 75% nitrogen and 25% hydrogen was used for the most part. If pure hydrogen was used as a reducing gas, the resulting powder showed a grayish color and low fluorescent efficiency due to excessive reduction.

Optimal concentration of the activator was about 5×10^{-3} g-atom Cu for 1 mole calcium orthophosphate. Any departure of the activator concentration from its optimal value leads to a rapid decrease of the fluorescent intensity under excitation by 2537Å at room temperature, as shown in Fig. 1.

In order to obtain the brightest phosphor, it is preferable to use an amount of calcium carbonate about 10 mole % less than that required for the stoichiometric composition, as shown above. Even in this case, it was verified by x-ray analysis that the resulting phosphor has the calcium orthophosphate structure. Copper-activated calcium orthophosphate fired above about 1200°C in the same atmosphere shows only a weak blue fluorescence under excitation by 2537Å and cathode rays at room temperature, in contrast with the phosphor fired below about 1200°C. It was also verified by x-ray analysis that the former had α-form structure and the latter had β-form structure.

With partial substitution of bivalent metals such as Be, Mg, Zn, Cd, and Sr for Ca in the Cu-activated β-calcium orthophosphate, similarly efficient phosphors can be obtained. However, substitution of about 7 mole % Ca by Ba results in a weakly purple fluorescent phosphor. Phosphors containing Mn or Sn as secondary activators were prepared by

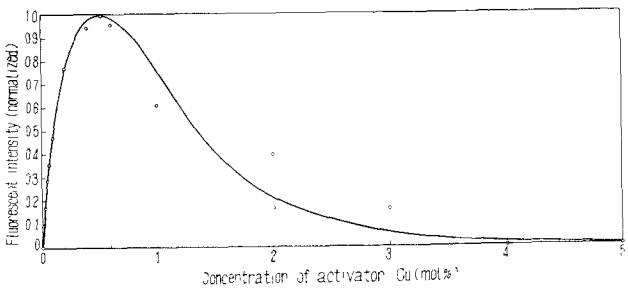

Fig. 1. Relative fluorescent intensity vs. activator concentration of Cu-activated β-calcium orthophosphate phosphors fired in a reducing atmosphere. Excitation with 2537Å at room temperature.

the same method as Cu-activated β-calcium orthophosphate.

Measurement Techniques

The spectral energy distribution of the phosphor excited by 2537Å was measured with a Zeiss three glass prism spectrograph which was equipped with an exit slit and a photomultiplier. This allowed its use as a constant deviation type monochrometer whose resolving power corresponded to a single 60° prism having 21-cm base length. The spectral sensitivity of this optical system was calibrated by use of a standard lamp.

In order to investigate the absorption characteristics of the phosphor, the spectral reflectance of a phosphor layer of about 2-mm thickness was measured relative to that of a plaque of smoked magnesium oxide whose spectral reflectance was measured previously. The spectral range from about 2300Å to the visible part of the spectrum was covered. This measurement was carried out with a Beckmann-type monochrometer combined with a photomultiplier. As a light source a low pressure hydrogen lamp was used. The arrangement of the optical system was similar to that reported by Botden and Kröger (2). In the measurement of the spectral reflectance, various cut-off filters were used to eliminate the fluorescent radiation from the reflected light. Using this apparatus, the quantum efficiency of fluorescence also was measured. The detailed method of the measurement and measured results for various phosphors, except some typical phosphors which are described below, will be published elsewhere.

Decay characteristics of Cu-activated β-calcium orthophosphate excited by cathode rays at room temperature were measured with a demountable cathode ray tube. The phosphor was placed as a uniform layer of powder in a shallow, nickel plated brass cup. A square wave of voltage from a Hewlett Packard 212A pulse generator was fed to the grid of the electron gun of the cathode-ray tube. The pulse width and frequency of excitation were variable. The emitted light was received by a RCA 1P21 photomultiplier through a glass window of the cathode-ray tube. Its output was fed to the vertical amplifier of a Tektronix 545 oscilloscope.

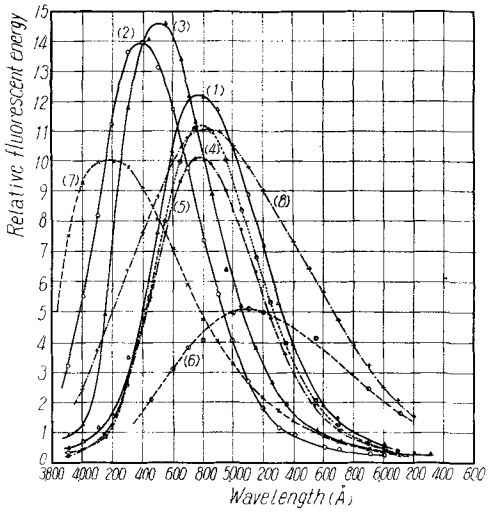

Fig. 2. Spectral energy distribution of Cu-activated calcium orthophosphate and substituted orthophosphates fired in reducing atmospheres, in comparison with tungstate phosphors. All phosphors excited with the same intensity of 2537Å at room temperature. Curve 1, 2.9 CaO · P_2O_5: 5 x 10^{-3} Cu; curve 2, 2.5 CaO · 0.4 MgO · P_2O_5 x 10^{-3} Cu; curve 3, 2.7 CaO · 0.2 ZnO · P_2O_5:5 x 10^{-3} Cu; curve 4, 2.7 CaO · 0.2 CdO · P_2O_5 x 10^{-3} Cu; curve 5, 2.7 CaO · 0.2 SrO · P_2O_5 x 10^{-3} Cu; curve 6, 2.9 CaO · 0.15 B_2O_3 · P_2O_5 x 10^{-3} Cu; curve 7, $CaWO_4$; curve 8, $MgWO_4$.

The decay characteristics of the persistent phosphorescence with 2537Å excitation at 297°-298°K were measured with a Brown Electronik Recording Electrometer in combination with a photomultiplier. Periods of constant excitation by 2537Å varied from 10 sec to 6 hr. Curves of the decay characteristics were recorded with the recording electrometer for periods of time from 1 to 100 min after the end of excitation.

The buildup and decay characteristics of thermoluminescence with a thin layer of the phosphor which was excited by 2537Å at about 280°K and then heated at about 465°K were measured by using the recording electrometer combined with a photomultiplier. However, the rate of buildup of thermoluminescence was too fast to be measured accurately by this method, and only the rate of decay could be determined.

Phosphor Characteristics

Emission under excitation by 2537Å, 3650Å, and cathode rays.—Cu-activated β-calcium orthophosphate fired in a reducing atmosphere shows a strong blue fluorescence peaked at 4800Å under excitation by 2537Å and cathode rays, while with 3650Å excitation it produces only an extremely weak blue fluorescence at room temperature. The spectral energy distribution of this phosphor excited by 2537Å at room temperature is shown by curve 1 in Fig. 2, compared with that of calcium tungstate (curve 7) and magnesium tungstate (curve 8). All the curves shown in Fig. 2 were obtained under conditions of constant 2537Å intensity and identical geometry of the optical system.

Cu-activated β-calcium orthophosphate fired in air shows practically no fluorescence at room or low temperature under excitation by 2537Å, 3650Å, and cathode rays, as mentioned before, but it produces a very weak blue fluorescence at temperatures higher than about 500°K with 2537Å excitation. Cu-activated α-calcium orthophosphate fired in a reducing atmosphere shows only a weak blue fluorescence under excitation by 2537Å and cathode rays at room temperature, as mentioned before. Therefore, only Cu-activated β-calcium orthophosphate fired in a reducing atmosphere can give an efficient fluorescence.

Partial substitution of Be, Cd, and Sr for Ca in Cu-activated β-calcium orthophosphate fired in a reducing atmosphere has very little effect on the intensity and color of fluorescence. The substituted orthophosphate phosphors containing 0.2 g-atoms of the bivalent metals mentioned above still produce a fairly strong fluorescence, but as the amount of bivalent metals is further increased, the intensity of the fluorescence gradually decreases. The spectral energy distribution curves of the substituted

phosphors containing 0.2 g-atoms of Cd and Sr are shown by curves 4 and 5 in Fig. 2.

Partial substitution of Mg and Zn for Ca in Cu-activated β-calcium orthophosphate shifts the peak of emission toward shorter wave lengths and increases the efficiency of fluorescence. The peak position of the substituted phosphors containing 0.4 g-atoms of Mg and 0.2 g-atoms of Zn are 4400Å and 4500Å, respectively, as shown by curves 2 and 3 in Fig. 2. The band widths of the phosphors mentioned above are very narrow compared with that of calcium or magnesium tungstate. Fluorescent lamps made with these phosphors show a very saturated blue or violet color and the average output in 20-w fluorescent lamps made with Cu-activated β-calcium orthophosphate was 370 lumens at 100 hr.

If boron compounds such as ammonium borate or boric oxide are introduced into Cu-activated β-calcium orthophosphate in amounts of 0.1 mole, the color of fluorescence is practically identical with that of the original phosphor, but as the amount of boric oxide is further increased, the color of the fluorescence shifts gradually from blue to green and finally to greenish yellow with about 0.4 mole of boric oxide. Besides, the intensity of the fluorescence is lowered as the amount of boric oxide is increased. The phosphor containing about 0.15 mole of boric oxide gives a very broad band peaked at 5100Å, as shown by curve 6 in Fig. 2.

Copper-activated orthophosphates of Be, Mg, Sr, and Ba which were prepared by firing at 850°-950°C in air for 30 min and then in a reducing gas for 30 min show essentially no fluorescence under excitation by 2537Å, 3650Å, and cathode rays at any temperature ranging from room to liquid air temperature. However, Cu-activated zinc orthophosphate fired in a reducing atmosphere at 850°C gives a green fluorescence of moderate intensity at room temperature with 3650Å excitation and a very weak green fluorescence with 2537Å excitation, but not with cathode ray excitation. At liquid air temperature, the fluorescence increases in intensity without change of color. Pure zinc orthophosphate without added activator and fired in a reducing atmosphere at 800°C, also produces a weak green emission peaked at 5000Å at room temperature but only with 3650Å excitation. At liquid air temperature, it shows a green fluorescence of moderate intensity under excitation by both 3650Å and 2537Å.

Copper-activated cadmium orthophosphate fired in a reducing atmosphere at 850°-900°C gives a weak orange fluorescence at liquid air temperature only with 2537Å excitation, but it does not fluoresce at room temperature under excitation by either 2537Å, 3650Å, or cathode rays. However, pure cadmium orthophosphate without added impurities and fired at 900°C in a reducing atmosphere or in nitrogen gives a weak whitish yellow fluorescence at room temperature with 2537Å excitation. At liquid air temperature, the fluorescence increases in intensity. Pure cadmium orthophosphate fired in air at 850°C for 30 min shows a weak whitish yellow fluorescence at liquid air temperature under excitation by 2537Å and 3650Å. At room temperature, it shows no fluorescence under excitation by 2537Å, 3650Å, and cathode rays.

Introduction of Mn, in addition to Cu, into β-calcium orthophosphate fired in a reducing atmosphere produces a whitish purple fluorescence which consists of a blue band and a sensitized red band. Calcium orthophosphate doubly activated with Cu and Sn and fired in a reducing atmosphere produces a blue to whitish red fluorescence depending on the Sn concentration. With partial substitution of Mg and Zn for Ca in β-calcium orthophosphate containing Mn or Sn, in addition to Cu, the peaks of the red band due to Mn or Sn, as well as that of the blue or violet band due to Cu, are shifted toward shorter wave lengths. As a typical example, the spectral energy distribution of β-calcium orthophosphate doubly activated with Cu and Sn, calcium magnesium orthophosphate containing 0.2 g-atoms of Mg and 2.7 g-atoms of Ca and doubly activated with Cu and Sn, and calcium orthophosphate doubly activated with Cu and Mn are shown by curves 1, 2, and 3 in Fig. 3. These curves were obtained under the same conditions as those for Fig. 2 and the ordinate scale is the same as that of Fig. 2.

The peak positions of the red bands of β-calcium orthophosphate doubly activated with Cu and Sn, and with Cu and Mn are about 6300Å and 6600Å, respectively, as seen in Fig. 3, and they are in good agreement with those of the corresponding bands of β-calcium orthophosphate activated with Sn alone and with Sn and Mn which have already been reported by Butler (3).

As clearly seen in Fig. 2, the peak intensity of calcium orthophosphate, calcium·magnesium orthophosphate, and calcium·zinc orthophosphate activated with Cu is larger than that of calcium or magnesium tungstate. The measured quantum efficiency of fluorescence of Cu-activated calcium·magnesium orthophosphate and calcium orthophosphate was about 0.9 and 0.8, respectively, with 2537Å excitation at room temperature. Considering a rather large absorption of the phosphors in the visible part of the spectrum, a correction for absorption loss must be made in order to evaluate the intrinsic quantum efficiency of fluorescence. Ac-

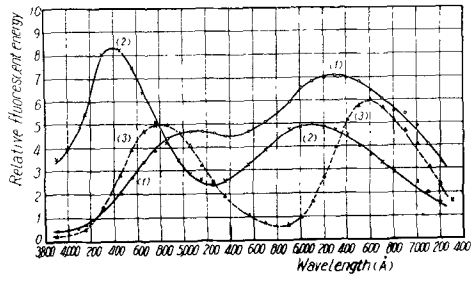

Fig. 3. Spectral energy distribution of orthophosphates doubly activated with Cu and Sn or Mn and fired in reducing atmospheres. All phosphors excited with the same intensity of 2537Å at room temperature. Curve 1, 2.9 CaO · P_2O_5:5 × 10^{-3} Cu + 5 × 10^{-3} Sn; curve 2, 2.7 CaO · 0.2 MgO · P_2O_5 × 10^{-3} Cu + 5 × 10^{-3} Sn; curve 3, 2.9 CaO · P_2O_5:5 × 10^{-3} Cu + 3 × 10^{-2} Mn.

cording to Bril and Klasens (4), the intrinsic quantum efficiency of fluorescence, νi, is given by

$$\nu i = \frac{2}{1 + R\infty}\,\nu m,$$

where νm is the measured quantum efficiency of fluorescence and $R\infty$ is the reflectance of the phosphor layer having practically infinite thickness. Since the value of $R\infty$ for both Cu-activated calcium·magnesium orthophosphate and calcium·orthophosphate was about 0.8 over the wide range of the visible part of the spectrum, a value close to unity was obtained for the intrinsic quantum efficiency of Cu-activated calcium·magnesium orthophosphate with 2537Å excitation at room temperature. The intrinsic quantum efficiency of Cu-activated β-calcium orthophosphate evaluated by the same method was about 0.9 with 2537Å excitation at room temperature, and a value of about 0.1 with 3650Å excitation at about 600°K was estimated.

Temperature dependence of fluorescent intensity.—The temperature dependence of fluorescent intensity of a typical β-calcium orthophosphate activated with 0.5 mole % Cu and fired in a reducing atmosphere is shown in Fig. 4. Curves 1 and 2 were obtained under excitation by 2537Å and 3650Å, respectively, and show a remarkable difference in behavior.

Although the emission peak of Cu-activated calcium orthophosphate shifts slightly toward shorter wave lengths at temperatures higher than room temperature, the effect of variation of the peak position on the measured intensity of fluorescence at higher temperatures will be small. Since the intensity of exciting radiation used in this measurement is rather weak, the intensity of fluorescence at various temperatures will be proportional to the quantum efficiency of fluorescence at the corresponding temperatures. The units of the ordinate in Fig. 4 are given so that the curves shown in this diagram express the temperature dependence of the intrinsic quantum efficiency of fluorescence.

The temperature dependence curves of fluorescent intensity of the Cu-activated phosphors substituted with Be, Mg, Zn, Cd, and Sr were similar to that of Cu-activated β-calcium orthophosphate.

Absorption.—The reflection spectra of typical phosphors measured at room temperature are

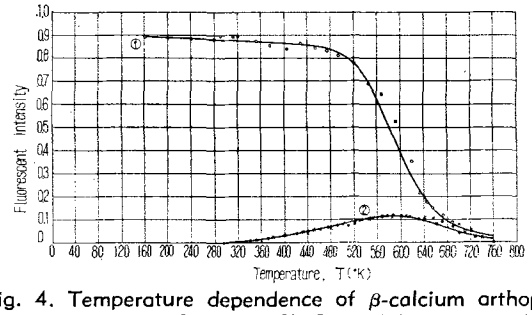

Fig. 4. Temperature dependence of β-calcium orthophosphate activated with 0.5 mole % Cu and fired in a reducing atmosphere. (Ordinate is equivalent to the intrinsic quantum efficiency of fluorescence). Curve 1, 2537Å excitation; curve 2, 3650Å excitation.

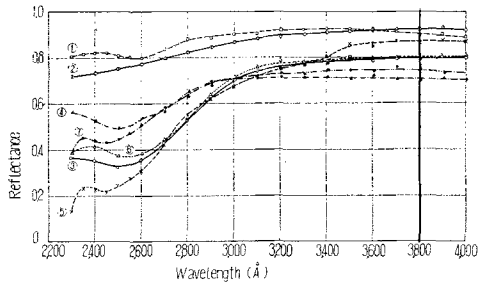

Fig. 5. Reflection spectra of pure and Cu-activated calcium orthophosphates and related phosphors at room temperature. Curve 1, β—2.9 CaO · P_2O_5 fired in a reducing atmosphere; curve 2, β—2.9 CaO · P_2O_5 fired in air; curve 3, β—2.9 CaO · P_2O_5:5 x 10^{-3} Cu fired in a reducing atmosphere; curve 4, α—2.9 CaO · P_2O_5:5 x 10^{-3} Cu fired in a reducing atmosphere; curve 5, β—2.9 CaO · P_2O_5:5 x 10^{-3} Cu fired in air; curve 6, β—2.5 CaO · 0.4 MgO · P_2O_5:5 x 10^{-3} Cu fired in a reducing atmosphere; curve 7, β—2.9 CaO · 0.15 B_2O_3 · P_2O_5:5 x 10^{-3} Cu fired in a reducing atmosphere.

illustrated in Fig. 5. Pure calcium orthophosphates fired in air or in a reducing atmosphere give rather flat reflection curves throughout the measured range of the spectrum, as shown by curves 1 and 2 in Fig. 5.

Copper-activated β-calcium orthophosphate fired in a reducing atmosphere gives a pronounced absorption band ranging from about 3100Å down to the short wave-length region of the spectrum and peaking at about 2550Å, as shown by curve 3 in Fig. 5. The reflection spectra of this phosphor measured at higher temperatures were practically identical with curve 3 in Fig. 5. Therefore, the temperature dependence of fluorescent intensity shown in Fig. 4 will be essentially independent of the absorption transition probability in the activator center.

The absorption of Cu-activated α-calcium orthophosphate shown by curve 4 in Fig. 5 is shallower than that of Cu-activated β-calcium orthophosphate in the shorter wave-length region below about 3000Å, but in the long wave-length region the situation is reverse. The shallowness of the absorption in the α-form, as well as the difference in structure, may be responsible for the low efficiency of its fluorescence. It is interesting that the absorption of Cu-activated β-calcium orthophosphate fired in air is stronger than that of the phosphor fired in a reducing atmosphere, at least in the shorter wave-length region below about 2700Å, as shown by curve 5 in Fig. 5. This fact, together with the temperature dependence of fluorescent intensity mentioned before, suggests that the trapping or quenching effect of this phosphor is much stronger than that of the phosphor fired in a reducing atmosphere.

The effect of the introduction of Mg or boron in Cu-activated calcium orthophosphate is shown by curves 6 and 7 in Fig. 5.

The measured reflection spectra of pure zinc orthophosphate and cadmium orthophosphate, which were prepared by firing in air or nitrogen, showed a flat and strong absorption with absorption edges at about 3900Å and 3200Å, respectively. The interesting fact was found that the characteristic ab-

sorption of these phosphors was decreased by the introduction of Cu or by firing in a reducing atmosphere. Detailed quantitative results will be published elsewhere.

The properties of zinc and cadmium orthophosphate phosphors, for example, absorption and emission characteristics, thus resemble those of zinc sulfide phosphors.

Although the detailed results of the reflection spectra of bivalent metal phosphates (except for a series of calcium orthophosphates) will be published elsewhere, it will be noted here that all curves of the reflection spectra of magnesium, strontium, and barium orthophosphate with added copper and fired in a reducing atmosphere were similar in shape to those of pure calcium orthophosphate (curves 1 and 2 in Fig. 5), but they were deeper in absorption. The average reflectance of these phosphors in the spectral region from 2300Å to 4000Å was about 0.7, 0.65, and 0.55, respectively. The detailed hue of color of these powders depends on the nature of the matrix. The natural color of the magnesium, strontium, and barium orthophosphates is reddish, grayish, and reddish, respectively.

Decay characteristics of phosphorescence.—The measured decay characteristics of the phosphorescence of Cu-activated β-calcium orthophosphate were of a monomolecular type under excitation by both 2537Å and cathode rays. The measured decay constants of this phosphor were 0.13 μsec for a fast component of afterglow and 1.6 μsec for a slow component under excitation by cathode rays of about 5 kv and 0.07 μsec pulse width at room temperature.

The measured decay constants for the components of the persistent phosphorescence with 2537Å excitation were 3.87 hr, 24.6 min, 4.13 min, and 0.931 min at 297°-298°K and their relative light sums were 100, 19.7, 6.9, and 3.9, respectively. The intensity of the persistent phosphorescence is extremely weak and the initial intensity of the most persistent component of the phosphorescence was of the order of 10^{-4} compared with the fluorescent intensity at about 300°K. The color of the phosphorescent light was identical with that of the fluorescent light.

Thermoluminescence.—Copper-activated β-calcium orthophosphate fired in a reducing atmosphere shows a strong blue thermoluminescence when it is heated after a previous exposure to 2537Å radiation for more than 10 min, and even after storage in the dark for times longer than about 10 hr at about 280°K. The intensity of thermoluminescence is dependent on the intensity of 2537Å, time of exposure to 2537Å, and temperature during excitation as well as the heating temperature. When the excitation by 2537Å is made at low temperature such as liquid air temperature or at higher temperatures than about 500°K, the phosphor shows no thermoluminescence. The brightest thermoluminescence was obtained after excitation by 2537Å at about 280°K. The phosphor excited with 3650Å showed no thermoluminescence.

The decay characteristics of thermoluminescence at a constant heating temperature were exponential. The decay constant of thermoluminescence measured at 465°K was about 10 sec. The rise time was very fast compared with the decay time. The characteristics of thermoluminescence of Cu-activated orthophosphate phosphors containing Be, Mg, Zn, Cd, Sr, and boron are similar to those of Cu-activated β-calcium orthophosphate, and only detailed behaviors are dependent on the amount of the added elements.

Stimulation by 3650Å radiation.—When Cu-activated β-calcium orthophosphate fired in a reducing atmosphere was first excited to saturation with 2537Å and then irradiated with 3650Å, it produced a weak red emission. The peak of the red emission was judged to be in the spectral range from 6000Å to 6500Å, according to visual inspection. The intensity of the red emission depended on the duration and intensity of the 2537Å excitation and on the intensity of the 3650Å radiation, but it was insensitive to the time of storage after exposure to 2537Å radiation as well as thermoluminescence. Indeed, we could observe the red emission after more than 10 hr following the excitation at about 280°K. This duration time for the stimulated red emission together with the thermoluminescence is of the same order as that of the most persistent component of the phosphorescence, whose decay constant is 3.87 hr at about 298°K. The red emission showed a very fast rise time, but its decay time was as long as minutes under stimulation by 3650Å of moderate intensity at room temperature. The brightest red emission was observed under excitation by 2537Å at about 280°K.

The blue fluorescent orthophosphate phosphors containing Be, Cd, Sr, or boron also gave the stimulated red emission, but the violet fluorescent orthophosphate phosphors containing Mg or Zn did not produce the red emission at all over a wide range of temperatures at which excitation was made with 2537Å.

In order to investigate the effect of impurities on the stimulation, a number of compounds of elements were added in the preparation of Cu-activated β-calcium orthophosphate. Introduction of about 0.01 mole of compounds of Ce, Zr, Mo, Ni, Se, V, Cr, Au, U, Co, Sn, and Mn per mole of Cu-activated β-calcium orthophosphate suppressed the red emission. On the other hand, introduction of K, Na, As, and boron compounds enhanced the red emission. However, if the amount of these added impurities except boron exceeded about 0.1 mole per mole of the matrix, the red emission was also suppressed completely.

Discussion

Although the properties of the phosphors here described are more complicated than those of the usual oxide-type phosphors, it does not seem to be difficult to give a straightforward theoretical interpretation, at least qualitatively. Quantitative explantations have already been formulated by one (6) of the present authors, and detailed results will be published in the near future. Therefore, only a qualitative discussion for the observed results is given here.

It is reasonable to suppose that the activator of Cu-activated β-calcium orthophosphate fired in a reducing atmosphere is different from that of the phosphor fired in air, because their respective characteristics of emission and absorption are quite different. Considering the firing process, it is natural to assume that the activator center of the phosphor fired in air may be formed by a Cu^{++}ion, while that of the phosphor fired in a reducing atmosphere may be ascribed to a Cu^{+}ion. Indeed no paramagnetic resonance absorption was detected in Cu-activated β-calcium orthophosphate fired in a reducing atmosphere.[1] The grayish color of the phosphor prepared by firing in pure hydrogen may be attributed to colloidal copper formed through a process of reduction from Cu^{+} ion to Cu atom as may be understood from the following consideration. Referring to the color of the magnesium, strontium, and barium orthophosphates mentioned before, we assume that the copper added to these phosphates is dispersed uniformly in the matrix in the form of neutral atoms, and we can then expect a pronounced characteristic absorption due to the Cu atoms in the near u.v. or visible region of the spectrum which, however, is contrary to the observed results. Therefore, the natural color of these phosphates may be attributed to the colloidal copper dispersed in the matrix. For the same reason, the grayish color of Cu-activated calcium orthophosphate fired in pure hydrogen may be ascribed to the same origin, as mentioned before.

Referring to the position of the activator in Cu-activated calcium orthophosphate, and assuming that the activators occupy interstitial sites in the lattice, we cannot find any convincing reason why copper cannot be introduced into the matrix of magnesium, strontium, or barium phosphate as an effective activator. However, the experimental results mentioned above will be explained by assuming that the activator in Cu-activated calcium orthophosphate can replace Ca^{++}ions at lattice sites in the form of Cu^{++} or Cu^{+}ions, as suggested above. If we consider the Cu^{+}ion to be the activator in Cu-activated β-calcium orthophosphate fired in a reducing atmosphere, we must assume that a vacancy of a single O^{--}ion may be generated by the replacement of two Ca^{++}ions by Cu^{+}ions in order to satisfy the condition of charge neutrality in the phosphor.

According to the above consideration concerning the activator center in Cu-activated β-calcium orthophosphate fired in a reducing atmosphere, the allowed transition of $^1S_0 \rightarrow {}^3P_1^0$ may be responsible for the absorption band peaking at about 2550Å, and also the transition $^1S_0 \rightarrow {}^3D_{1,2,3}$ or $^1D_2$ for the weak absorption in the spectral range above about 3100Å. Although the latter transition is originally forbidden in a free Cu^{+}ion, we can expect that it will be allowed by the interactions between the activator center and lattice ions. If the trapping state for the most persistent component of phosphorescence, thermoluminescence, and stimulation is attributed to the $^3P_2^0$ or $^3P_0^0$ states because of their similar decay constants, the stimulation by 3650Å may be caused by the absorption transition $^3P_2^0$ or $^3P_0^0 \rightarrow {}^1P_1^0$ and the red emission by the transition $^1P_1^0 \rightarrow {}^1S_0$ which is allowed. This absorption transition in a free Cu^{+}ion is originally forbidden because of the same odd parity of the spectrum terms. However, if we assume that it will be allowed by the interactions between the activator center and Ca^{++}ions in the lattice, we can explain the experimental result that no stimulated red emission could be observed in the phosphors containing Mg or Zn in the following way. The transition $^3P_2^0,0 \rightarrow {}^1P_0^0$ may become completely forbidden in the phosphor containing Mg or Zn because of the small interactions between the activator center and Mg^{++} or Zn^{++} ions which have smaller ionic radii than Ca^{++} ions; thus it results in complete suppression of the red emission. Incidentally, the effect of the introduction of boron on the stimulated red emission will be explained satisfactorily in a similar way. The observed peak position of the emission band peaking at a longer wave length and the large width of the emission band of the phosphor containing boron in contrast with those of the phosphor containing Mg or Zn suggests large interactions in the activator center. Thus we can expect an enhanced red emission of the phosphor containing boron in accordance with the observed result.

The experimental result that neither thermoluminescence nor stimulation could be observed under excitation by 2537Å at lower or higher temperatures, as mentioned before, suggests that some activation energy will be necessary for the transition $^3P_1^0 \rightarrow {}^3P_2^0,0$ in the activator center.

The effect of boron introduced in the phosphor on the fluorescence and stimulated red emission is quite different compared with that of the other elements, as mentioned before. We are inclined to believe that boron may replace phosphorus in the matrix.

Acknowledgment

The authors wish to express their sincere thanks to Dr. Tsuneo Harada for his continuous support and encouragement. Part of this paper was presented at the Annual Meeting of the Japan Chemical Society in Tokyo, April 1-5, 1955.

Manuscript received April 28, 1958.

Any discussion of this paper will appear in a Discussion Section to be published in the December 1959 JOURNAL.

[1] The authors are obliged to Professor Hidetaro Abe of Ochanomizu University, Tokyo, for this measurement.

REFERENCES

1. F. A. Kröger, "Some Aspects of the Luminescence of Solids," p. 268, Elsevier Publishing Co., Inc., New York (1948); A. H. McKeag and P. W. Ranby, U. S. Patent 2,664,401.
2. T. H. J. Botden and F. A. Kröger, *Physica*, **15**, 747 (1949).
3. K. H. Butler, *This Journal*, **100**, 250 (1953).
4. A. Bril and H. A. Klasens, *Philips Tech. Rev.*, **15**, 63 (1953).
5. Y. Uehara, Y. Kobuke, I. Masuda, K. Maed, and M. Yamanaka, presented at the Second Symposium of the Atomic Power Commission, Tokyo, Feb. 7-9, 1958.
6. Y. Uehara, paper presented at the Annual Meeting of the Chemical Society of Japan, Tokyo, April 1-5, 1955; Kyoto, April 2-6, 1956; Tokyo, April 4-8, 1957.

Crystal Growth of Electrodeposited Zinc

An Electron Diffraction and Electron Microscopic Study

Ryoitiro Sato

Mitsubishi Metal Mining and Metallurgical Laboratory, Omiya City, Saitama Prefecture, Japan

ABSTRACT

Crystallographic aspects of zinc electrodeposited on to polycrystalline cathode from $ZnSO_4 + H_2SO_4 + H_2O$ baths with or without organic colloids have been investigated by electron diffraction (reflection method) and electron microscopy (replica method). At the initial stage of deposition, the zinc layer always consists of fine-grained crystallites oriented at random. As the zinc layer becomes thicker, some of these crystallites grow larger to yield a fiber orientation depending on the depositing condition. For such relatively thick zinc layers deposited under various degrees of influence of hydrogen and/or organic colloids, the orientation and texture are interpreted from standpoint of crystal growth.

Electron diffraction investigations of crystal growth of a variety of metals at the cathode during electrodeposition have so far been carried out by many authors (1-10). Although a comprehensive interpretation of their results is given by Finch, *et al.* (7), crystal growth of metals of lower symmetry has not yet been sufficiently explained, contrary to that of cubic metals. For this reason, zinc, a hexagonal metal, was chosen for this investigation, and it has been approached first in a study of crystal growth on a polycrystalline cathode.

Although addition of organic colloids to the electrolytic bath is of great technical importance, the crystallographic aspects of their effects have been studied little by means of electron diffraction. Again, zinc, which has moderate inhibitor sensitivity (11, 12), is suitable for such a study.

Thus, this paper reports electron diffraction (reflection method) and electron microscopic (replica method) investigations of zinc films electrodeposited under the following conditions: insoluble anode, polycrystalline cathode, and $ZnSO_4 + H_2SO_4 + H_2O$ baths (with or without addition of various organic colloids).

Experimental

The aqueous solution of $ZnSO_4 \cdot 7H_2O$ was purified by zinc dust. The organic colloids used were proteins (glue, gelatin, and albumin), a gum (gum arabic), and carbohydrates (dextrin, soluble starch, and saponin).

Electrodeposition was carried out in a 300-ml beaker, using a platinum plate as anode (1 cm x 1 cm x 0.2 mm) and a mechanically polished plate of α-brass as cathode (1 cm x 1 cm x 1 mm). These were separated by 4 cm. Depositing time varied from several seconds to 20 min. Immediately after taking out the cathode, it was washed successively with running water, distilled water, and acetone. To avoid chemical change of the cathode after the deposition, the procedure was carried out rapidly.

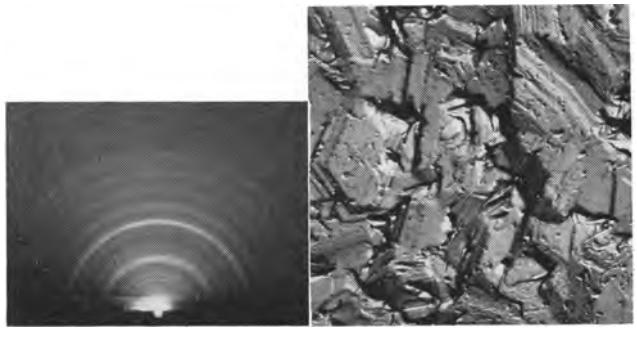

Fig. 1a (left). Electron diffraction pattern; Fig. 1b (right). Electron micrograph, magnification 5,000X. Bath: Zn 50 g/l; room temperature; $D_k = 3.5$ amp/dm^2; $C_{eff} = \sim 100\%$; θ (mean thickness) $= 38 \times 10^3$ Å. Hydrated basic zinc sulfate covering zinc layer.

The accelerating voltage of the electron beams for diffraction work was 35-50 kv. The sample to plate distance was 30 cm. To obtain the electron micrographs of the surface of the deposited layer, a two-stage replica method (acetylcellulose-carbon, followed by shadowing with Ge) was adopted. Usually the cathode which had served as the sample for the electron diffraction was itself subsequently observed by the electron microscope.

Results and Discussion

Experiments Using Baths Containing No Organic Colloids

(I) In some cases a diffraction pattern due to a substance other than zinc was obtained (Fig. 1a). In the corresponding electron micrograph (Fig. 1b) the substance covering the zinc layer is observed. Since the pattern is more marked with the baths containing comparatively low concentrations of the free acid, the substance is probably soluble in sulfuric acid. The analysis of the pattern is given in Table I. The data of hydrated basic zinc sulfate ($4ZnO \cdot SO_3 \cdot 7H_2O$) (13) agree fairly well with the analysis of Table I. The pattern appears invariably

Table I. Analysis of the Debye-Scherrer rings of Fig. 1a

Spacing, Å	Intensity
4.3	m
3.7	m
2.8	st
2.6	st
2.47	w
2.15	w
1.79	w
1.57	st
1.35	m
1.18	m
1.02	m
0.90	m

as Debye-Scherrer rings, showing no particular orientation relationship of the substance to the underlying zinc layer.

(II) In the zinc patterns obtained, almost always two blurred halos are observed, the one at the inside of the innermost ring of zinc and the other between the (10.2)-ring and the (11.0)-ring (e.g., Fig. 2a, 4a, and 5a). The same pair of halos appeared also in the pattern from the zinc layer deposited from a cyanide bath. The halos can be ascribed neither to minute crystallites of hydrated basic zinc sulfate nor to those of zinc oxide, which might be formed by oxidation of the deposited zinc.

(III) In the zinc patterns the (00.2)-ring is usually imperceptible. This anomaly in intensity of the diffraction patterns shows that the crystallites of the deposit are flat plates parallel to the basal plane (14). This is supported by the corresponding electron micrographs (e.g., Fig. 3b, 4b, and 5b).

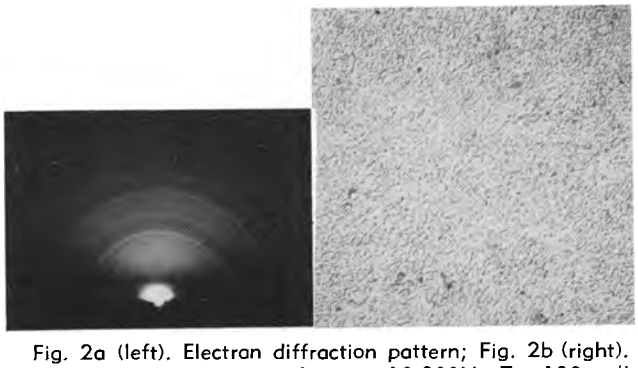

Fig. 2a (left). Electron diffraction pattern; Fig. 2b (right). Electron micrograph, magnification 10,000X. Zn 100 g/l + H_2SO_4 100 g/l; room temperature; D_k = 4 amp/dm²; θ = 700 Å. Random orientation.

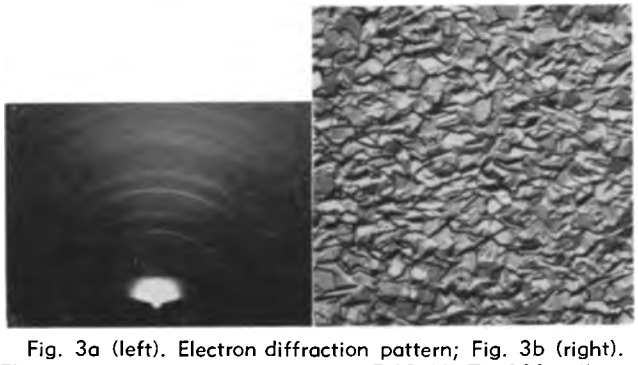

Fig. 3a (left). Electron diffraction pattern; Fig. 3b (right). Electron micrograph, magnification 5,000X. Zn 100 g/l + H_2SO_4 100 g/l; room temperature; D_k = 4 amp/dm²; θ = 6.3 x 10^3 Å. Random orientation.

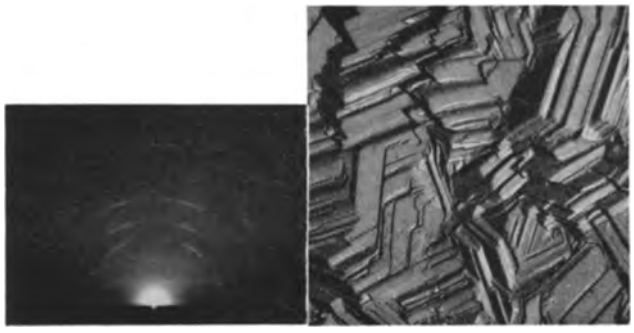

Fig. 4a (left). Electron diffraction pattern; Fig. 4b (right) electron micrograph, magnification 5,000X. Zn 100 g/l + H_2SO_4 100 g/l; room temperature; D_k = 4 amp/dm²; C_{eff} = 92%; θ = 54 x 10^3 Å. Plane of orientation : (11.l), l ≈ 4.

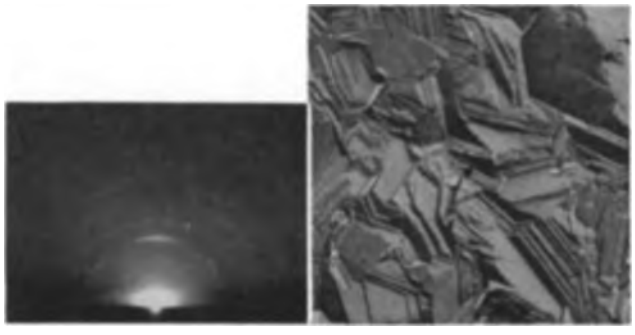

Fig. 5a (left). Electron diffraction pattern; Fig. 5b (right) electron micrograph, magnification 5,000X. Zn 10 g/l + H_2SO_4 100 g/l; room temperature; D_k = 3 amp/dm²; C_{eff} = 58%; θ = 50 x 10^3 Å. Plane of orientation : (10.l), l ≈ 1.

(IV) All of the zinc patterns show that the zinc crystallites take a fiber orientation (including random orientation), whose axis stands upright to the cathode surface. To denote such a fiber orientation, its "plane of orientation," i.e., the crystallographic plane of zinc which tends to lie parallel to the surface, is used in the following descriptions.

(V) With various bath compositions and depositing conditions, the zinc layer deposited in initial stages (up to several thousand angstroms in thickness) consists invariably of fine-grained crystallites (approximate dimension : 300Å in Fig. 2b, and 5000Å in Fig. 3b), and the tendency for a fiber orientation is very weak (Fig. 2a and 3a). This is in harmony with the results of Finch, *et al.* (7).

(VI) With continued deposition, the crystallites grow larger and a fiber orientation characteristic of the bath composition appears (Fig 4a, 4b, 5a, and 5b). According to Bauer (15), this kind of orientation should be called orientation due to crystal growth (vide infra). Table II gives a summary of the orientations. Variations in the temperature and in the current density within the ranges of the experimental conditions of plating had no noticeable effects on the plane of orientation.

(VII) According to Table II, except for deposits from baths having relatively high ratios of H_2SO_4/Zn, (11.*l*)-orientation (Fig. 4a and 4b) is invariably obtained. The occurrence of this orientation may be explained as follows. Since the surface of the growing layer is not atomically flat parallel to the cathode surface (as evidenced by the electron

micrographs, as well as by the spotty nature of the diffraction patterns), the zinc ions are carried to the surface from any direction in the bath. Under such a condition, among the many crystallites which were oriented randomly in the initial stage of the deposition, only those having by chance an orientation favorable to growth do grow and become predominant over those having unfavorable orientations. This favorable orientation is most likely determined by the relation of the growth velocities (or the surface energies) of various crystallographic planes. Thus, it is supposed that every crystallite near the surface of the relatively thick zinc layer has a tendency to be bounded by three crystallographic planes, i.e., the plane of the lowest outward velocity (basal plane) and a pair of planes of the second lowest outward velocity. If for the latter planes two prismatic planes of the first order, (10.0), [or two pyramidal planes of the first order, (10.1)] are assumed, the occurrence of the (11.l)-orientation is readily understood (Fig. 6). Although the value of l (not necessarily an integer) should be determined by the competition in the growth of the basal plane and the above prismatic (or pyramidal) plane, the quantitative data on their outward velocities of growth are not available. In this connection, the reversed order of the outward velocities of growth due to Stranski, *et al.* (16-19), together with the order of the reticular densities, are listed in Table III for various crystallographic planes of close-packed hexagonal metal. The morphology observed in the electron micrographs of Fig. 4b seems to support the point of view of this paragraph. Finch, *et al.* (7) postponed the explanation for their observation of (11.2)-orientation of electrodeposited cadmium. This may also be accounted for along the above line (15).

(VIII) As seen from Table II, when the ratio H_2SO_4/Zn of the bath is relatively high, the (11.l)-orientation is replaced by the (10.l)-orientation (Fig. 5a and 5b). This change may be related to the increased hydrogen evolution which occurs with these baths. Straumanis made observations on

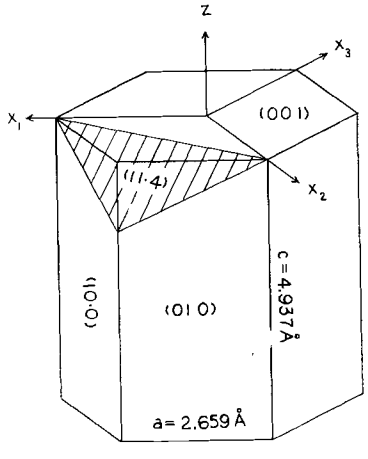

Fig. 6. Explanation of the occurrence of the (11.l)-orientation. Only (00.1) and (10.0) are depicted as the permanent faces determining the plane of orientation. l is assumed to be 4.

Table II. Plane of orientation characteristic of the bath composition

Bath composition, g/l	Plane of orientation
Zn 50 Zn 50, H_2SO_4 50 Zn 100, H_2SO_4 100 Zn 100, H_2SO_4 200	(11.l), $l \approx 4$, with angular tolerance of about ±15°
Zn 10, H_2SO_4 50 Zn 10, H_2SO_4 100	(10.l), $l \approx 1$, with angular tolerance of about ±15°

Mean thickness (θ), 10-100 × 10^3Å; temperature, room temperature—80°C; current density (D_k), 1-15 amp/dm².

the crystal growth of zinc, which was formed by evaporation in hydrogen atmospheres (21). According to him, under hydrogen pressures lower than ~4 mm Hg the permanent crystallographic faces of zinc are: (00.1) (basal planes), (10.0) (prismatic planes of the first order), (10.1) (pyramidal planes of the first order), and (11.0) (prismatic planes of the second order). When his results are compared with the theory of Stranski, *et al.* (16-19), it seems that differences in growth velocities of the planes of lower indices of zinc (except for the basal plane) are slight, and that even a reversal of the velocities can be effected by the presence of hydrogen. Such a reversal of growth velocities of planes resulting from adsorption of impurity is discussed by Smekal (19). In (VII) the occurrence of the (11.l)-orientation was explained by assuming that the permanent faces of zinc are the basal plane and a pair of prismatic (or pyramidal) planes of the first order. Now, taking into account the consideration regarding the reversal of the growth velocities of the planes, if a pair of prismatic planes of the second order is substituted for the pair of the first order, the (10.l)-orientation is reasonably reached in the same manner as in (VII).

Results and Discussion

Experiments Using Baths Containing Organic Colloids

The effects on the zinc plating by minor quantities of addition agents, which eventually lead to structural modifications of the deposited layer, are caused by complex factors such as a change in viscosity of the bath, cathode polarization, hydrogen overvoltage, current efficiency, etc. However, the

Table III. Relative velocities of growth and relative reticular densities of planes of close-packed hexagonal metal

(*hk.l*)	Reversed order of the outward velocities of growth	Order of reticular densities
(00.1)	1	1
(10.0)	2	3*
(10.1)	4	5
(10.2)	3	
(10.3)	6	
(11.0)	5	2
(11.2)		4*

* For zinc the third and the fourth are reversed, owing to its deviation of c/a ratio (1.857) (20) from the ideal value (1.633).

most essential function of an addition agent on the deposited layer seems to lie in its adsorption on the surface of the layer. A simple measure of adsorbability of an organic colloid is the well-known "gold number," which refers to the protective action of the colloid on red gold sol. Note that a lower value of gold number means a higher adsorbability (or protective action) of the colloid. The gold numbers of the organic colloids used in the present experiments are listed in Table IV (22). Their values were estimated roughly by using the red gold sol prepared by utilizing the reducing flame of coal gas (23). The obtained values fell in the ranges shown in Table IV.

As mentioned earlier, the (11.*l*)-orientation is characteristic of the zinc layer electrodeposited from the baths of $ZnSO_4 + H_2SO_4 + H_2O$ system, except for the baths of relatively higher values of the ratio H_2SO_4/Zn. Consequently, in most of the following experiments to clarify the effects of organic colloids on the structure of deposited zinc, the concentrations of zinc and sulfuric acid were chosen both as 100 g/l, since, with no addition agents, this is a bath which leads invariably to the (11.*l*)-orientation (Table II). The temperature of the bath, the current density for the deposition, and the mean thickness of the deposited layer were room temperature, ~4 amp/dm², and $20 - 60 \times 10^3$ Å, respectively. The results of the electron diffraction investigations are summarized in Fig. 7, and some of the electron micrographs are reproduced in Fig. 8b and 9-12.

(I) It is generally accepted that the flatness of the surface of the electrodeposited layer becomes improved by adding an organic colloid to the bath, as the result of its ability to increase cathode polarization and, therefore, throwing power of the bath. Although such a tendency is actually observed with the naked eye with baths of relatively low concentrations of an organic colloid which is a protein or carbohydrate (roughly up to 50 mg/l), the surface is liable to become inhomogeneous with higher concentrations of the colloid. This seems due to the adherence of hydrogen bubbles to the surface, resulting from the increased viscosity of the bath. Gum arabic shows a somewhat different behavior; it makes the surface inhomogeneous at a concentration as low as 10 mg/l and yields a fine-grained surface of blackish appearance at 500 mg/l (Fig. 8b). Unfortunately, it is impossible to obtain

Table IV. Gold numbers of biocolloids used (22)

Colloid		Gold number, mg sol/100 cm³
Protein	Glue	0.05-0.1
	Gelatin	0.05-0.1
	Albumin	0.3-2
Gum	Gum arabic	1.5-2.5
Carbohydrate	Dextrin	20-70
	Starch	50-250
	Saponin	230

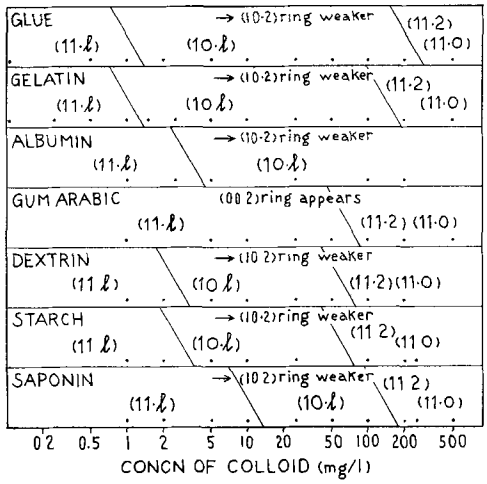

Fig. 7. Effects of organic colloids on plane of orientation. Each fiber orientation involves angular tolerance of about ±15°. Bath : Zn 100 g/l + H_2SO_4 100 g/l + organic colloid; room temperature; D_k : ~ 4 amp/dm²; θ : 20-60 x 10^3 Å. The zinc layers deposited from the baths containing the addition agent concentrations marked by the dots were investigated by electron diffraction and microscopy.

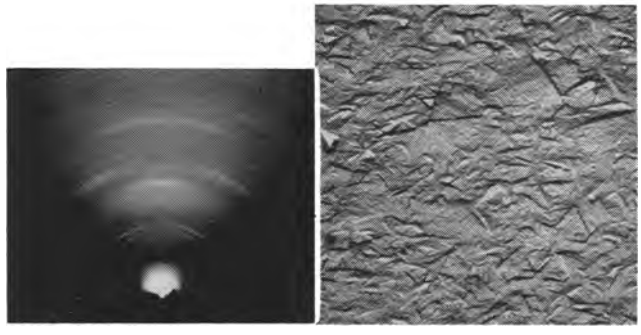

Fig. 8a (left). Electron diffraction pattern; Fig. 8b (right). Electron micrograph, magnification 5,000X. Zn 100 g/l + H_2SO_4 100 g/l + gum arabic 500 mg/l; room temperature; D_k = 4 amp/dm²; C_{eff} = 45%; θ = 24 x 10^3 Å. Plane of orientation : (11.0).

precise values of current efficiency, since the weight increase of the cathode on deposition is usually only several milligrams. It is roughly 92% in the case of no colloids and decreases with the concentration of a colloid down to 65-80% with 200 mg/l addition.

(II) As before, the (00.2)-ring is generally barely perceptible, showing the flatness of the crystallites parallel to the basal plane (layer structure). With the addition of a protein or carbohydrate, besides the low intensity of the (00.2)-ring, the (10.2)-ring shows a tendency to decrease in intensity with increasing concentration. Since among the planes of lower indices, which yield strong reflections, the (10.2)-plane makes a relatively low angle with the basal plane, this is accounted for by the further predominance of the layer structure and agrees with the discussion by Smekal (19) on crystal growth under the presence of impurity. This change of the degree of layer structure with the concentration of addition agent is also morphologically observed in a series of electron micrographs in the case of dextrin (Fig. 4b and 9-12). With gum arabic such a change of the layer structure is not observed. Moreover, it is

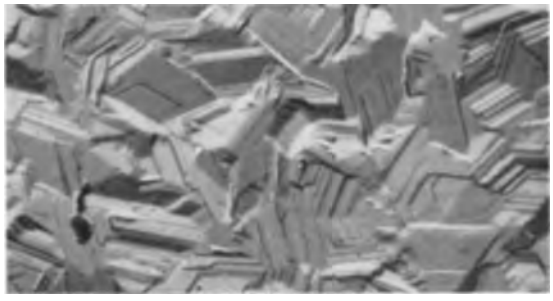

Fig. 9

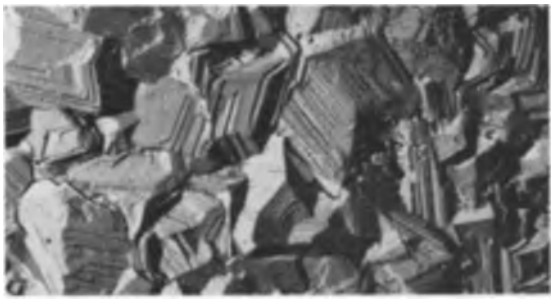

Fig. 10

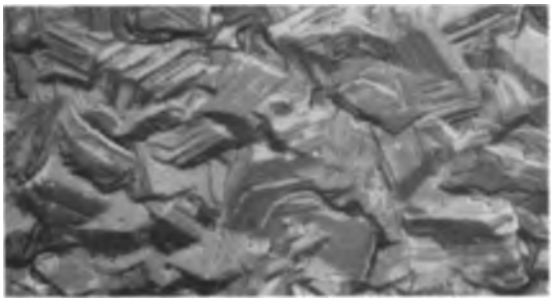

Fig. 11

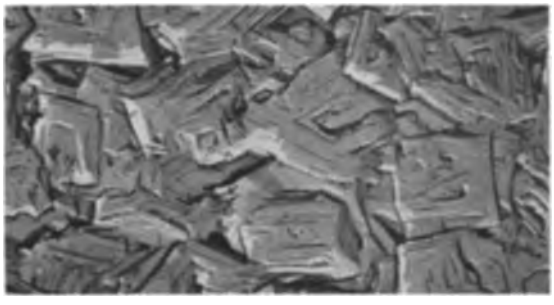

Fig. 12

Fig. 9-12. Electron micrographs, each magnification 5,000X. Zn 100 g/l + H_2SO_4 100 g/l + dextrin (2 mg/l, 10 mg/l, 25 mg/l, and 200 mg/l, respectively); room temperature; $D_k = \sim 4$ amp/dm^2; $C_{eff} = 88$, 86, 82, and 70%, respectively; $\theta = \sim 40 \times 10^3$ Å. Plane of orientation : (11.l), (10.l), (10.l), and (11.0), respectively.

remarkable that the (00.2)-ring appears with 10-50 mg/l of gum arabic (Fig. 7). This seems to have some relation to the inhomogeneity of the zinc layer, which has been touched on just above.

(III) Figure 7 shows changes of plane of orientation with concentration of the seven addition agents. Apart from the case of gum arabic, the following sequence of changes is general:

$$(11.l), l \approx 4 \rightarrow (10.l), l \approx 1 \rightarrow (11.2) \rightarrow (11.0)$$

each fiber orientation involving a considerable angular tolerance of about ± 15°. To the first, (11.l) → (10.l), the discussion made in (VIII) above applies, if it is assumed that the role of hydrogen is now played by organic colloid. This line of consideration is also preferable for elucidation of the predominance of the layer structure with increasing addition agent, which was touched on in (II). The final (11.0)-orientation (Fig. 8a) is an orientation, where the most densely packed atom rows in the most densely packed lattice plane (basal plane) stand upright to the cathode surface. When the concentration of addition agent is sufficiently high, resulting in high viscosity of the bath and low current efficiency for the deposition, the supply of zinc ions to the hollows of the surface and the mobility of zinc ions at the surface are both supposed to be insufficient. It should be understood that the (11.0)-orientation derives from such a situation. The (11.2)-orientation is most likely a transient stage before reaching the final (11.0)-orientation. With gum arabic it is remarkable that the plane of orientation changes from (11.l) directly to (11.2) → (11.0).

(IV) In Fig. 12 a square structure is noticeable. This structure is also observed with high concentrations of others carbohydrates, starch, and saponin. In these cases the plane of orientation is (11.0), and flat plates thin in the direction of c-axis, which lies parallel to the cathode surface, are supposed to be piled up to form a block. If such a block is oriented to an adjacent block of the same nature so as to form twinning on (10.2)-plane, the square structure should appear. It is well known that the twinning plane of close-packed hexagonal metals, such as zinc, is (10.2) (24). For zinc, (10.2) makes 47° 0′ with (00.1), the doubled value of which is near 90°. With proteins this square structure is less noticeable and with gum arabic is never encountered.

(V) In comparing Fig. 7 with Table IV, a reasonable correlation between the gold number of a colloid and its ability to change the orientation of deposited zinc is found in three proteins and in three carbohydrates. However, in spite of the much higher values of the gold number of carbohydrates as compared with those of proteins, they are not so ineffective in changing the orientation. This might be accounted for by the difference of their states of hydration and electric charge in the bath. Elucidation in detail must be postponed. An exceptionally weak ability of gum arabic to change the orientation is remarkable, together with its peculiarity in many aspects mentioned in the foregoing paragraphs.

Conclusion

It has been shown that many experimental results concerning the orientation and texture of electrodeposited zinc layer can be reasonably interpreted from the standpoint of development of crystallographic planes under various degrees of influence of hydrogen and/or organic colloids. However, the interpretation is considerably simplified. The fiber orientations observed in the present study invariably involve some tolerance. This implies that the crystallographic planes other

than those which determine the orientation are not necessarily excluded, presumably owing to slight differences among the surface energies of many crystallographic planes. This situation is reflected in the fine structure of the diffraction spots, which is to reveal the external crystallographic planes. Close examination of the fine structure of the spots shows that it is too complex to permit a simple interpretation, although generally the nature of the fine structure does not contradict the line of consideration described so far.

Acknowledgments

The author wishes to acknowledge with grateful thanks the support and permission to publish this article of Mr. S. Yamagata and Mr. M. Kamada, Director and Assistant Director of our Laboratory, respectively, and Mr. H. Kurama, Manager of our Research Section. The author thanks sincerely Dr. H. Hagihara, Kobayasi Institute of Physical Research, for his interest and discussions. His heartful thanks are due to Messrs. B. Ishii and Y. Kikuchi for their assistance.

Manuscript received June 23, 1958.

Any discussion of this paper will appear in a Discussion Section to be published in the December 1959 JOURNAL.

REFERENCES

1. G. P. Thompson, *Proc. Roy. Soc.*, **133**, 1 (1931).
2. G. I. Finch and C. H. Sun, *Trans. Faraday Soc.*, **32**, 852 (1936).
3. W. Cochrane, *Proc. Phys. Soc.*, **48**, 723 (1936).
4. A. G. Quarrell, *ibid.*, **49**, 3 (1937).
5. G. I. Finch and A. I. Williams, *Trans. Faraday Soc.*, **33**, 564 (1937).
6. G. I. Finch, A. G. Quarrell, and H. Wilman, *Discussions Faraday Soc.*, "The Structure of Metallic Coatings, Films and Surfaces," 1058 **1935**.
7. G. I. Finch, H. Wilman, and L. Yang, *ibid.*, "Electrode Processes," 144 **1947**.
8. G. I. Finch, *Z. Elektrochem.*, **54**, 457 (1950).
9. L. Yang, *This Journal*, **101**, 456 (1954).
10. S. Yoshioka and H. Yamamoto, *J. Metal Finishing Soc. Japan*, **6**, 110 (1955) (in Japanese).
11. H. Fischer, *Z. Elektrochem.*, **49**, 342 (1943); **49**, 376 (1943).
12. H. Fischer, "Elektrolytische Abscheidung und Elektrokristallisation von Metallen," Springer-Verlag, Berlin (1954).
13. A. S. T. M., "X-Ray Powder Data File," 3-0797.
14. J. M. Bijvoet, N. H. Kolkmeijer, and C. H. MacGillavry, "Röntgenanalyse von Krystallen," p. 94, Julius Springer, Berlin (1940).
15. E. Bauer, *Z. Krist.*, **107**, 265 (1956); **107**, 290 (1956).
16. I. N. Stranski and R. Kaishew, *ibid.*, **78**, 373 (1931).
17. I. N. Stranski and L. Krastanow, *ibid.*, **83**, 155 (1932).
18. I. N. Stranski, *Discussions Faraday Soc.*, "Crystal Growth," 13 **1949**.
19. A. Smekal, "Strukturempfindliche Eigenschaften der Kristalle" in "Handbuch der Physik," Vol. 24/2 (Aufbau der zusammenhängenden Materie), Julius Springer, Berlin (1933).
20. R. W. G. Wyckoff, "Crystal Structures," Vol. 1, Interscience Publishers, Inc., New York (1948).
21. M. Straumanis, *Z. phys. Chem.*, **B13**, 316 (1931); **B19**, 63 (1932).
22. A. Kuhn, "Kolloidchemisches Taschenbuch," Leipzig (1944).
23. Z. Samesima, *J. Chem. Soc. Japan*, **54**, 695 (1933) (in Japanese).
24. C. S. Barrett, "Structure of Metals," McGraw-Hill Book Co., Inc., New York (1952).

Changes in Trapping Levels of Zinc Sulfide Phosphors Resulting from Positive Ion Bombardment

William T. Allen[1] and C. H. Bachman

Department of Physics, Syracuse University, Syracuse, New York

ABSTRACT

Utilizing a decay method which consisted of measuring the amount of visible light emitted by the ZnS:Ag phosphor 5.0 msec after excitation by weak ultraviolet, studies were made of the changes in trap distribution on the surface of phosphor crystals which previously had been bombarded by Ar^+, H_2^+, and O_2^+ ions. Interpretation of results was limited to first order kinetics.

The results showed that bombardment by ions caused an increase in the number of traps at the lowest trapping level, 0.28 ev deep, as well as the creation of new traps at depths slightly greater and slightly less than 0.28 ev. This effect was independent of the ion used for bombardment.

In addition, ion bombardment caused new traps to appear at deeper trapping levels: 0.37 ev for Ar^+ ion bombardment, 0.38 ev for H_2^+ ion bombardment, and 0.39 ev for O_2^+ ion bombardment. For the latter, the peak in the difference curve is quite sharp and clearly located at 345°K, locating its depth at 0.39 ev. This corresponds to the next trapping level with increasing depth reported in the literature and thus may indicate that this trapping level is caused by the presence of oxygen in ZnS phosphors.

Ion bombardment, as a cause of deterioration in zinc sulfide phosphors, has been studied by many authors (1-8). In recent years, all research has been done with the working hypothesis that the reduced luminescence is caused by the creation of electronic levels between the valence band and the conduction band, such states making possible direct transition from the conduction band to the valence band.

It was considered desirable to investigate the dis-

[1] Present address: Franklin and Marshall College, Lancaster, Pa.

tribution of states between the valence band and the conduction band and the distribution of the states as a result of ion bombardment on the surface of the crystals.

The Lambe-Klick model (9) for luminescence in zinc sulfide was assumed valid. The depth of a state was designated as the energy difference between the state and the top of the valence band. States with depths less than 1 electron volt (ev) can influence the decay of a phosphor and customarily are called traps.

The usual method for investigating trap distributions is by the use of glow curves, a technique developed by Randall and Wilkins (10). In measuring a glow curve, the phosphor is first cooled to a very low temperature, so that electrons in the traps are stabilized, that is to say, their half-life is much longer than the time required to perform the experiment. Then the phosphor is excited at this low temperature by irradiation with ultraviolet (u.v.) light in order to fill the traps. If, now, the phosphor is warmed at a slow rate, traps filled with holes will be emptied. These holes, thermally excited to the valence band, will be attracted to the luminescent centers. The electron and hole are now in a position to recombine, giving up one photon of visible light, and the phosphor will glow as a result of a great number of these recombinations.

The temperature at which a particular trapping level becomes unstable depends on its depth, the deeper traps becoming unstable as the temperature gets higher. A curve of light output vs. temperature is called a glow curve and can be assumed to represent a trap depth distribution. For example, if a phosphor contains traps at two different depths, then the glow curve will have two different peaks, each representing one of the trapping levels.

Using glow curve techniques, Bube (11) has found that traps are present in ZnS at five distinct trapping levels. These are revealed by five distinct glow peaks at −120°C, −60°C, −25°C, −15°C, and 90°C. Any change in the methods of preparation or in the activator used will not alter the temperature at which these peaks exist but will change the relative heights of the peaks, and hence, the relative numbers of traps represented by each peak.

In the past few years, studies have been made to improve the interpretation of glow curves by considering the second order kinetics or retrapping. Such analyses not only involve consideration of holes thermally excited to the valence band finding their way to luminescent centers, but also holes thermally excited to the valence band and then retrapped and excited again to the valence band one or more times before finding their way to luminescent centers. Satisfactory interpretation of glow curves where more than one level of trap is present and where second order kinetics are considered is very difficult to achieve. It is customary in the literature to present glow curves showing light ouput as a function of temperature at a particular heating rate and leave it for the reader to interpret.

Very roughly, it can be said that if T is the temperature of a glow peak (10), then $E = 20\ kT$, where E is the trap depth and k is Boltzmann's constant. This could mean that a peak occurring at room temperature will represent a trap depth of approximately 0.5 ev.

A decay measurement consists of exciting the phosphor with u.v., cutting off this excitation, and measuring the phosphorescent light output of the phosphor as a function of time, the temperature remaining constant.

In the present investigation a problem arose in that impinging ions with energies of the order of 10 kev do not penetrate the crystal sufficiently so that changes can be observed by the use of glow curves. This is because in the excitation which precedes the warming in a glow curve measurement, the phosphor is maintained for at least several minutes under u.v. radiation, and traps are filled as deeply into the crystal as the u.v. can penetrate. Glow curve measurements are then essentially the determination of trap distributions throughout the volume of the crystal. Any change, therefore, in the distribution of traps in the surface will be largely masked by the response of the remainder of the crystal which has not been damaged.

Young (4) has shown that the deterioration of the phosphor lies in a very thin surface layer, its thickness being of the order of 0.1μ for bombardment by ions of energies in the order of 10 kev. Since the phosphor crystals ordinarily used in television screens have diameters of about 10μ, the volume of the layer is the order of 1% of the volume of the crystals, and for this reason ion bombardment by ions, the energies of which are in the order of 10 kev, does not affect glow curves of the phosphors appreciably.

However, it was observed that a phosphor damaged by ion bombardment exhibits increased phosphorescence when irradiated by low intensity u.v. for times in the order of hundredths of a second. This is because the excitation is only sufficient to fill traps on the surface of the phosphor crystal, and such surface traps are filled preferentially. This observation led to a technique in which observations of the decay characteristics yield information concerning the trap distribution.

Theory for Decay Measurements

Let P be the probability that a hole in a single trapping level of depth E will escape, then,

$$P = \frac{1}{t_d} = G\left[\exp\left(-\frac{E}{kT}\right)\right] \qquad [1]$$

where t_d is the decay time, i.e., the time for the number of holes in a trapping level to reduce to $1/e$ of its value at cutoff, E is the trap depth, k is Boltzmann's constant, T is the temperature in degrees Kelvin, and G is a constant of the order of 10^8 given by Randall and Wilkins (10) and represents the vibration frequency of an atom in the lattice (10^{12} vib./sec) multiplied by the probability that a hole in a trapping state having received enough energy from the lattice to undergo a transition to the valence band will do so.

Figure 1 shows a plot of p_T/p_{T_0} vs. time, where p_T is the density of holes in traps at any time, and p_{T_0} is the density of holes in this trapping level at cutoff. The observed visible light, I, is proportional to the

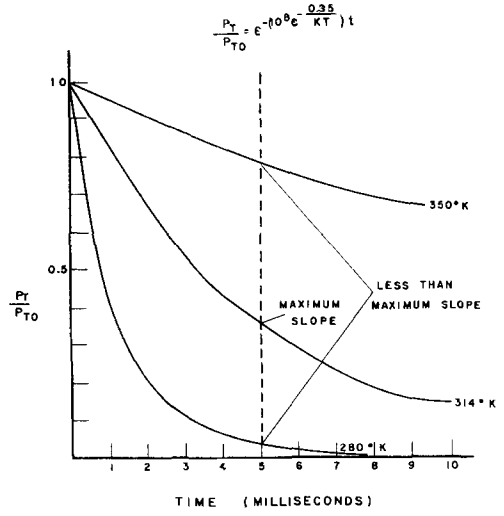

Fig. 1. P_T/P_{To} vs. time for various temperatures

rate of change of p_T with respect to time, or is proportional to the slope of the p_T/p_{To} vs. time curve. If measurements are made at a particular time, say 5 msec after cutoff, it can be seen that the maximum slope occurs at neither a high nor a low temperature, but somewhere between. Location of the temperature at which a peak occurs can be done in the following way:

If we consider a single trapping level of depth E, then from Eq. [1]

$$p_T = p_{To} \exp\left\{-G\left[exp\left(-\frac{E}{kT}\right)\right]t\right\} \qquad [2]$$

The light output I due to this single trapping level as a function of time after cutoff is equal to

$$I = V\frac{\partial p_T}{\partial t} = S\,p_{To} \exp\left\{-\left[\frac{E}{kT} + Gt\exp\left(-\frac{E}{kT}\right)\right]\right\} \qquad [3]$$

where V and S are proportionality constants.

I will be a maximum value when

$$\frac{\partial I}{\partial T} = 0 = Up_{To} \exp\left\{-\left[\frac{E}{kT} + Gt\exp\left(-\frac{E}{kT}\right)\right]\right\} \left\{\frac{E}{kT^2} - Gt\left[\exp\left(-\frac{E}{kT}\right)\right]\frac{E}{kT^2}\right\} \qquad [4]$$

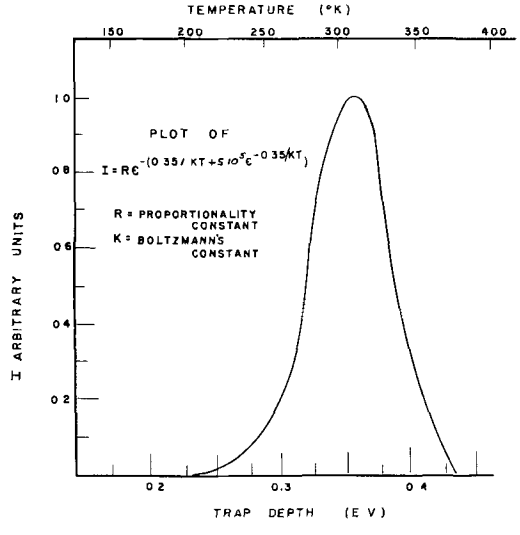

Fig. 2. I vs. temperature at 5.0 msec

where U is a proportionality constant.

$$\exp\left(-\frac{E}{kT}\right) = \frac{1}{Gt}$$

Hence a peak occurs at

$$E = (\log Gt)\,kT = 2.3\,(\log_{10} Gt)\,kT \qquad [5]$$

Thus if measurements are made 5 msec after cutoff, I will be a maximum, or a peak should occur at

$$E = 13.1\,kT \qquad [6]$$

Figure 2 is a plot of I vs. T as a result of holes trapped at a single trapping level of depth arbitrarily chosen to be 0.35 ev. It should be noted that the curve peaks rather sharply at its maximum point and also that it is not completely symmetrical in that it approaches zero much faster at high temperatures than at low temperatures.

It is interesting to compare Eq. [5] with the results obtained by Randall and Wilkins (10). If, in performing a glow curve experiment, the rising in temperature is suddenly stopped at a glow curve peak, then the visible light, according to Randall and Wilkins, will be emitted, but will decay to $1/e$ of its value in a certain amount of time in the order of 10 sec. Substituting $t = 10$ sec in Eq. [5], we have

$$E = (2.3\,\log_{10} 10^8)\,(10\,kT)$$

$$E = (2.3)\,(9\,kT) = 20.7\,kT \qquad [7]$$

or almost exactly the formula given by Randall and Wilkins.

If, during excitation, u.v. light irradiates the phosphor for an amount of time sufficient to allow the emitted light to reach a constant value, an equilibrium exists between the holes in the traps and the holes in the valence band, that is to say, the number of holes entering the traps must equal the number of holes which are thermally ejected from the traps. This can be expressed by the following equation, which should be valid if we consider only one trapping level at cutoff.

$$pb\,(\tau - p_{To}) = p_{To}\,G\left[\exp\left(-\frac{E}{kT}\right)\right] \qquad [8]$$

where p is the density of holes in the valence band, τ is the density of traps, p_{To} is the density of holes in the traps at cutoff, $(\tau - p_{To})$ is the density of empty traps, and b is a constant representing the product of the capture cross section of a trap and the velocity of a hole in the valence band.

Solving for p_{To}

$$p_{To} = \frac{\tau}{1 - \frac{G}{pb}\left[\exp\left(-\frac{E}{kT}\right)\right]} \qquad [9]$$

showing that at cutoff p_{To} is proportional to the number of traps. Since according to Eq. [3], I is proportional to p_{To} then it also, by Eq. [9] is proportional to τ, the density of traps.

It is obvious that by plotting I vs. temperature, where measurements are made 5 msec after cutoff, a curve possessing peaks should be obtained from Eq. [6]. The height of a peak should give a qualitative indication of the density of traps at a particular trapping level, according to Eq. [9]. Since the

heights of the peaks can at best only be compared qualitatively and since the efficiency of the phosphor decreases markedly at higher temperatures, it was decided to measure I/I_0 instead of I, where I_0 is the visible light output of the phosphor at cutoff. The I/I_0 vs. temperature curves therefore should be similar to glow curves except that there should be a shift in the position of the peaks. The amount of such shift can be obtained by dividing Eq. [6] by Eq. [8]

$$\frac{T_{I/I_0}}{T_0} = 1.58 \qquad [10]$$

Thus peaks determined by the decay method should be at temperatures about 60% higher than those from glow curves.

Since ion damage occurs very near the surface of phosphor crystals, it is of importance that a method be utilized which measures only surface effects. In the method of glow curves, every effort must be made to saturate all of the traps as deeply into the crystals as possible in order that the glow will consist of a measurable amount of light. If, however, I/I_0 measurements are made, weak u.v. can be used, and allowed to fall onto the phosphor for a small amount of time, so that only surface traps are preferentially filled during irradiation and can be detected during decay.

The above derivation assumed only first order kinetics, i.e., retrapping is not considered. The reason for this is that there is no way of determining the ratio of the number of filled traps to the total number of traps for any trap depth at cutoff (p_0/τ), since the phosphor is flashed with ultraviolet for a brief period of time and the traps are not saturated. Also (p_0/τ) is not constant at all distances from the surface of the crystal, and an average value of (p_0/τ) would require information not available at the present writing.

Procedure

Description of Phosphor Used

The ZnS phosphor was provided by the General Electric Company and was the blue component of phosphor used for the luminescent screens in earlier television tubes. This phosphor contained 0.015% chlorine by weight, 0.015% sodium by weight, and 0.04% ZnO by weight. The average particle size was 9μ. The phosphor contained 0.05% silver by weight as activator, which was introduced into the crystal with a sodium chloride flux (amounts of retained sodium and chlorine listed above) by heating to about 1000°C for about a half hour. The phosphor was examined by standard x-ray diffraction methods and found to be completely hexagonal.

The phosphor was water settled to a thickness of 0.01 g/cm^2 on aluminum slides 20 mils thick, measuring 15 x 30 mm. Previous to settling, the slides and the beakers used were carefully boiled in detergent and rinsed several times in doubly distilled water. The water used for settling was also doubly distilled.

Description of Equipment Used for Ion Bombardment

The ion bombardment equipment is shown in Fig. 3. The main part of the bell jar can be maintained at a relatively high vacuum (10^{-4} mm or better), and the small discharge chamber can be maintained at about 20μ.

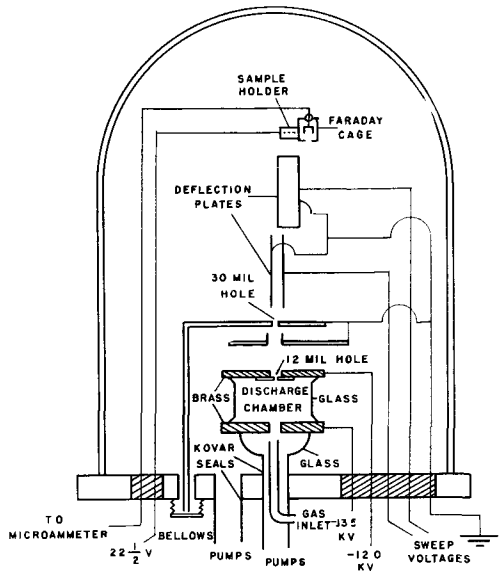

Fig. 3. Apparatus for bombarding phosphors with ions

The center support of the system is a length of heavy cane glass, and all electrical connections are fastened to the cane by means of ring stand clamps.

The output of a 30-kv power supply is applied across a string of 30, 1-megohm resistors. The positive end of the string is grounded and the negative end of the string is connected to the bottom plate of the discharge chamber. A center tap is connected through a 10 megohm resistor to the top plate of the discharge chamber.

With the pressure at 20μ and a voltage applied to the top and bottom plates of the discharge chamber, a discharge results causing positive ions to be produced. The electric field between the plates causes the ions to be accelerated upwards. A ½-in. hole, drilled in the top plate of the chamber is covered by a piece of 5-mil thick tantalum in which a 12-mil hole is drilled. Ions, produced in the chamber, pass through the hole and are accelerated by the electric field in the space between the top plate of the chamber and the next plate, which is at ground potential. Immediately above this plate is a thin sheet of aluminum, 10-mils thick, in the middle of which is drilled an aperture 1½ mm in diameter for the purpose of controlling the diameter of the beam. As an aid to lining up the apparatus, the position of this aperture can be controlled from outside of the bell jar by means of a metal bellows.

The ions proceed upward through two sets of parallel plates, arranged so that one set of plates is perpendicular to the other, but with one pair displaced laterally to allow removal of neutral particles. The electric field between these plates controls the lateral position of the beam at all times, as voltages of from 0 to 10,000 v can be applied to one plate of each set, the other remaining at ground potential. Sweep voltages of 3 and 1/10 cps are used. The sample is mounted with the phosphor facing downward or toward the beam. The sample holder and sample are operated at −22.5 v when the beam, aimed into the hole of the Faraday cage, is being measured in

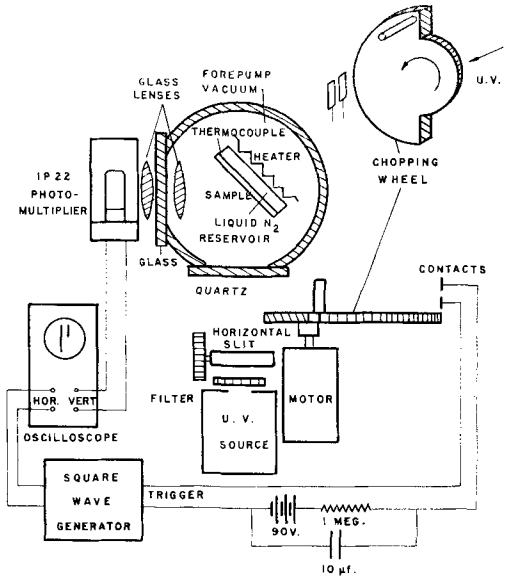

Fig. 4. Apparatus for measuring I/I_0 vs. temperature

order to retard the emission of secondary electrons from the inside of the Faraday cage, but are operated at ground potential when the beam is bombarding the sample.

Apparatus for measuring amount of fluorescent light emitted by the phosphor after a given amount of time.—This apparatus is shown in Fig. 4. The u.v. radiation is produced by the standard Beckman u.v. accessory kit which is intended for use with the Beckman DU spectrophotometer. This source is a hydrogen arc which is rich in u.v. at all wave lengths from 2000 to 4000Å.

First the light is passed through a Corning 9863 filter which passes most of the u.v. emitted by the hydrogen arc, but cuts out the visible light. The light then is passed through a narrow slit, which can be varied in width. Next, the beam is chopped by a wheel rotating at about 25 rps, so that u.v. light passes for 20 msec and is cut off for an equal amount of time. The time required for the intensity of the u.v. to reduce to a negligible value is measured by using a photomultiplier tube and an oscilloscope. This time is less than 50 μsec, which is 1% of the time during which the measurements were made. The chopped beam passes through a quartz window into a chamber maintained at forepump vacuum and onto the phosphor sample which is placed at a 45° angle to the beam.

The sample is so arranged that its temperature can be varied from −150° to +200°C and is in a vacuum in order to avoid the formation of frost on the sample when at low temperatures. All temperatures are measured using a copper-constantan thermocouple and a L&N thermocouple potentiometer. Melting ice is used as a temperature reference junction. The emitted visible light from the phosphor is collected by a lens within the vacuum chamber, transmitted through the glass window, and converged by a second lens onto an RCA 1P22 photomultiplier tube. The electrical signal from the photomultiplier tube is applied with amplification to the vertical plates of an oscilloscope.

The chopping wheel carried a small metal protrusion so arranged that at the time of u.v. light cutoff an electrical contact is made with two wires, thus triggering a Tektronix #162 wave form generator. The wave form generator gives a square pulse 5 msec in duration every time it is triggered. This pulse is then applied to the horizontal plates of the oscilloscope.

The pattern on the screen of the oscilloscope consists of two vertical lines. The vertical deflection is dependent on the light output of the phosphor. The first vertical line indicates the light output under u.v. irradiation. The second, displaced to the right, gives the light output during the 5 msec pulse. By setting the vertical amplifier of the oscilloscope so that top termination of the first vertical line is at 100 on the screen scale and so that the beam is a zero when no u.v. light shines on the phosphor, the termination of the second line immediately gives the percentage of light emitted from the phosphor 5 msec after cutoff.

It was necessary to insure that the u.v. light falling on the phosphor was constant and equal for all samples measured. Before and after each run, a phototube was placed in the vacuum chamber at the exact point where the phosphor was placed during a run, and it was found that, if a half-hour warmup was allowed, the light output never varied more than 1%.

Ion-burning of samples.—With the sample in place and the system evacuated, potentials are applied to create the ion beam. This is deflected into the Faraday cage for current measurement, after which the sweep voltages are applied to the deflection plates, so that the beam now traces a square raster on the phosphor sample. Bombardment is allowed to continue for a length of time dependent on the number of particles per square centimeter desired.

The beam is redirected into the Faraday cage for a check on intensity. The beam current is assumed to be constant throughout the bombardment if the measurements made before and after bombardment are equal.

The sample is then examined under u.v. light and the unaffected portion, which fluoresces brighter than the affected part, is scraped off. The bare aluminum is painted with aquadag to reduce reflected u.v. light. The area of the affected portion is measured so that with measurements of beam current and time of bombardment, the density of particles per square centimeter can be computed.

Measurements.—With the samples in place the chamber is evacuated and the sample is cooled to −150°C by pouring liquid nitrogen into the reservoir The chopping wheel is then rotated at about 25 rps, and the triggered pulse generator is activated.

The heater coils are activated then so that the temperature of the sample increases at no more than 4°C/min. This is sufficiently slow so that glow curve effects can be neglected. The temperature is measured at all times with the thermocouple potentiometer and measurements of I/I_0 are made every 0.25 mv. This amounts to taking a measurement every 10°C at low temperatures and every 4°C at high temperatures.

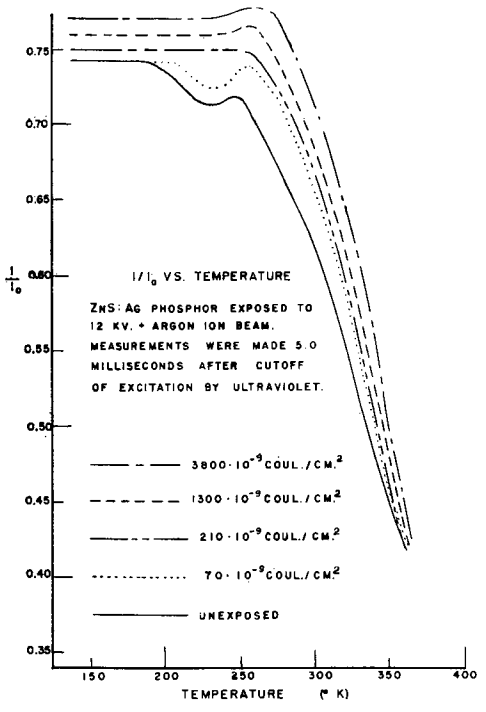

Fig. 5. I/I_0 vs. temperature for argon bombardment

Experimental Results

The curves shown in Fig. 5 represent I/I_0 measurements made on ZnS:Ag phosphor which had been previously bombarded by 12 kv ions of Ar^+.

There are significant differences in the I/I_0 vs. temperature curves for varying degrees of ion bombardment. Whereas the difference in I/I_0 is as much as 12% for some temperatures, it does not always appear to be significant, due to the large negative slope of these curves. For this reason the I/I_0 vs. temperature curve for the unbombarded phosphor was subtracted from the I/I_0 curve for the bombarded phosphor. In this way, it was possible to emphasize the difference in the decay as a result of bombardment. The difference curves are shown in Fig. 6 for argon bombardment; Fig. 7 and 8 show similar difference curves for samples which had been bombarded with H_2^+ and O_2^+ ions.

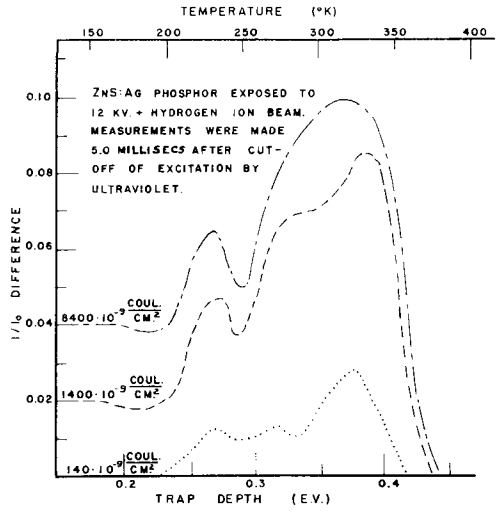

Fig. 7. I/I_0 vs. temperature (difference curve) for hydrogen

In the I/I_0 vs. temperature curve for the standard unbombarded phosphor, it is observed that a peak exists at 250°K. Since this is the lowest observable peak, it is assumed to be due to the trapping level represented by the glow curve peak at −120°C or 153°K. This means that experimentally the ratio

$$\frac{T_{I/I_0}}{T_G} = \frac{250^\circ}{153^\circ} = 1.63 \qquad [11]$$

which agrees very closely with Eq. [10], where the ratio is 1.58. This discrepancy of about 3% is perhaps explained by retrapping or second order kinetics. Since the saturation of traps in this decay method is not attempted, one would expect the percentage of unfilled traps to be higher than that encountered in glow curve measurements. Therefore, the probability of trapping would be somewhat larger since holes excited to the valence band would encounter a greater number of empty traps in which to be trapped. In general the retrapping effect shifts the peak to higher temperatures, as holes which are retrapped on the low temperature side of the peak predicted by first order theory do not recombine with electrons at centers to emit visible light. Also on the high temperature side of the peak predicted

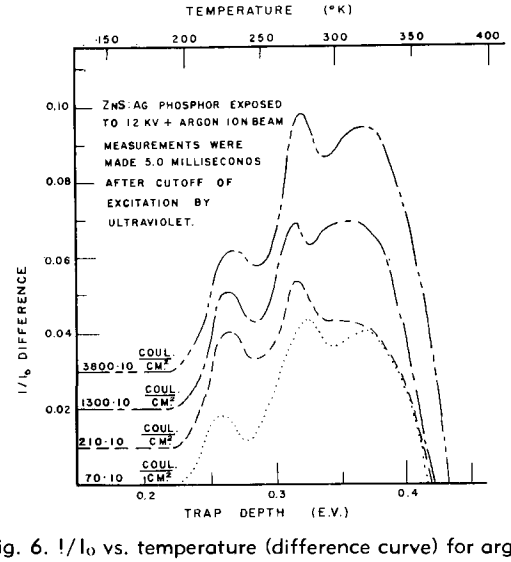

Fig. 6. I/I_0 vs. temperature (difference curve) for argon

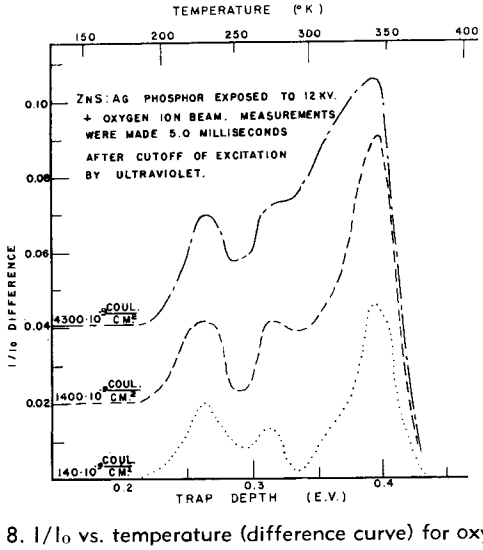

Fig. 8. I/I_0 vs. temperature (difference curve) for oxygen

by first order theory, the probability of holes being thermally ejected from traps becomes very large since it is an exponential function of temperature, whereas the probability of recombination with empty traps is only proportional to the number of empty traps. Accordingly the value of I/I_0 at temperatures below the peak predicted by first order theory should be reduced and at temperatures above the peak predicted by first order theory, I/I_0 should remain about the same. In this way retrapping will tend to cause a peak to shift slightly to the higher temperature.

From the I/I_0 difference vs. temperature curves, Fig. 6-8, one can conclude the following:

1. In general, the heights of the I/I_0 difference vs. temperature curves are dependent on the degrees of bombardment. It appears that small ion exposures are very efficient in creating traps, whereas increased ion exposures yield diminishing changes in the I/I_0 difference vs. temperature curves. There is an apparent saturation of traps at this depth.

2. All I/I_0 difference vs. temperature curves show two peaks, located at 230° and 290°K, that are equally distant from the 250°K peak in the I/I_0 vs. temperature curve. The closeness of these two peaks to the 250°K peak indicates that possibly the new traps at these two levels are related to the 250°K peak. If bombardment by ions had only increased the population in the trapping level represented by the 250°K peak, then the I/I_0 difference vs. temperature curve would have shown a single peak at 250°K. However, if the bombardment had produced new trapping levels not only at the discrete trap depth represented by the 250°K peak but also at levels slightly greater and smaller in depth, then the difference curve would show two peaks on either side of 250°K. This was observed.

It is evident that traps at a depth of 0.28 ev which are represented in the I/I_0 vs. temperature curve by a peak at 250°K are not only increased in number, since the height of the I/I_0 vs. temperature curve was shown in Eq. [9] to be proportional to the number of traps at a particular level, but also, following bombardment, traps exist at depths slightly greater and slightly less than 0.28 ev.

This is not in agreement with work by Martin (8) who found that this trapping level in ZnS:Ag was decreased rather than increased by ion bombardment. He used 45 kev hydrogen ions and measured trap distribution by use of glow curves.

3. In all of the I/I_0 difference vs. temperature curves, another large peak appeared at a somewhat higher temperature. As can be seen in Fig. 6-8, this was dependent on the ion used for bombardment, as the peak in the argon curves was at 315°K, in the hydrogen curves at 330°K, and in the oxygen curves at 345°K, corresponding to trap depths of 0.37, 0.38, and 0.39 ev, respectively.

It is interesting to note that the distinct oxygen peak a 345°K corresponded almost exactly to the predicted second peak at 344°K. Although this certainly is not conclusive evidence, it is clearly indicative that this trap depth of 0.39 ev might be caused by oxygen in the ZnS:Ag crystal replacing sulfur in the lattice either substitutionally or interstitially.

4. Values of I/I_0 were increased at low temperatures as a result of ion bombardment. This might indicate trapping levels of depths below 0.28 ev, but such have not been reported previously in the literature. Such values of I/I_0, which at low temperatures are constant with respect to temperature, but which increase as a result of ion bombardment, may be explained in two different ways.

First, it is possible to assume that, since surfaces are being studied, other trapping levels can exist and these can have a depth distribution which is constant. This assumption appears unlikely as traps are associated with particular kinds of imperfections in the lattice and would be preferentially located at particular levels.

Second, it should be noted that the theoretical curve of I vs. T in Fig. 2 is not symmetrical, but has a tail which is significantly large at low temperatures. It is possible that the tails of many of these curves added together give what appears to be a higher value of I/I_0 constant with respect to temperature.

If the destruction of luminescence is simply a matter of producing levels between the valence band and the conduction band so that radiationless or infrared emitting transitions can take place, then the number of paths for the recombination of electrons and holes will be increased, and the time t_a for the density of holes in the valence band to drop to $1/e$ of its initial value will be decreased. In all of the measurements made, t_a was always observed to increase as a result of ion bombardment. The data gathered at low temperatures indicate that: (*a*) these levels were not produced; (*b*) these levels may be produced, but their effect is overcompensated by the destruction of centers; and (c) these levels may be produced but their effect is overcompensated by the low temperature tail of the curve I vs. T, shown in Eq. [2].

Manuscript received June 11, 1958. This paper has been scheduled for presentation at the Philadelphia Meeting, May 3-7, 1959. The work on this paper was sponsored by the office of Ordnance Research, Department of the Army.

Any discussion of this paper will appear in a Discussion Section to be published in the December 1959 JOURNAL.

REFERENCES

1. B. Stech, *Z. Naturforsch.*, **7a**, 175 (1952).
2. W. Hanle and K. H. Rau, *Z. Phys.*, **133**, 297 (1952).
3. A. W. Smith and J. Turkevich, *Phys. Rev.*, **94**, 857 (1954).
4. J. R. Young, *J. Appl. Phys.*, **26**, 1302 (1955).
5. W. Berthold, *Naturwissenschaften*, **42**, 436 (1955).
6. H. P. Gilfrich, *Z. Phys.*, **145**, 241 (1956).
7. A. W. Smith, *Phys. Rev.*, **101**, 1263 (1956).
8. W. Martin, *Z. Phys.*, **147**, 582 (1957).
9. J. Lambe and C. C. Klick, *Phys. Rev.*, **98**, 909 (1955).
10. J. T. Randall and M. H. F. Wilkins, *Proc. Roy. Soc.*, **A184**, 366 (1945).
11. R. H. Bube, *Phys. Rec.*, **90**, 70 (1953).

Influence of Firing Conditions, Composition, and Screening Media on the Zeta Potentials of ZnS Phosphors as Related to Adherence to Glass Surfaces

Boris Levy[1]

Electron Tube Division, Radio Corporation of America, Lancaster, Pennsylvania

ABSTRACT

Zeta potentials were determined by the streaming potential method as a function of firing conditions, flux, activator, phosphor coating, and type and concentration of screening media. The effect of these factors on adherence was determined by the jet impingement method. Positive zeta potentials were obtained in $Ba(Ac)_2$ solutions and in H_2O during all stages of phosphor preparation prior to the coating operation. Either positive or negative potentials are obtained with the finished phosphor depending on the type of coating used. Firing conditions also have been found to be important in determining the sign of the zeta potential. A general trend toward enhanced wet adherence with decreasing negative zeta potential and increasing positive zeta potential has been noted.

The influence of electrolyte concentration on the zeta potentials of ZnS powders was measured with solutions of the following materials: $Ba(Ac)_2$, K_2SiO_3, $Ba(Ac)_2$-K_2SiO_3 mixtures, $(NH_4)_2Cr_2O_7$, polyvinyl alcohol, and mixtures of $(NH_4)_2Cr_2O_7$ and polyvinyl alcohol.

Adherence of a phosphor to a glass faceplate is one of the important factors involved in the manufacture of television tubes. The phosphor is commonly applied to the glass by either a settling (1) or slurry technique (2). Both methods involve the preparation of a phosphor suspension containing water, an electrolyte, and a bonding agent, but the nature of the electrolyte and bonding agent differs for the two methods. Different phosphors, or even the same phosphor handled in slightly different manners often have wide variations in screening properties. The concentrations of electrolyte and bonding agent also have marked effects on screen characteristics.

Hazel and co-workers have demonstrated a correlation between zeta or electrokinetic potential and adherence in settled screens (3-5). They found a decrease in the magnitude of the zeta potential with increasing concentration of either $Ba(Ac)_2$ or K_2SiO_3-$Ba(Ac)_2$ mixtures. Similar results were obtained with powdered glass. In the systems in which the potential of the phosphor and glass were negative, measurements of the adherence of the phosphor to glass surfaces indicated enhanced adherence with a decrease in the magnitude of the zeta potential. The explanation offered by Hazel was that the repulsive forces between the two similarly charged surfaces were reduced, thereby giving the silicate a chance to bind the phosphor to the glass in a more compact network.

The present study is an outgrowth of Hazel's work in that it attempts to discover the factors of importance in a phosphor preparation and handling that influence the electrical properties of its surface. To this end streaming potential experiments were performed at various stages of phosphor preparation and under a variety of conditions that might occur in screen application. Attempts were made to correlate the results with adherence measurements.

Experimental

Materials.—Measurements are made on either commercial RCA phosphor powders or on specially prepared samples as described in Table I. Demineralized water is used in the preparation of all solutions used in the measurements. Reagent-grade $Ba(Ac)_2$, KCl, and $(NH_4)_2Cr_2O_7$ are used. The potassium silicate solutions are prepared from Sylvania PS5 (0.96M K_2O-3.05M SiO_2), and the polyvinyl alcohol (PVA) solutions are prepared from du Pont Elvanol #52-22.

Apparatus.—The streaming-potential apparatus used in these experiments combines several of the features used by Gaudin and Fuerstenau (10) and by Hazel and his co-workers (3-5). Calomel electrodes, as used by Hazel, are employed for most of the potential measurements when a L&N Type K potentiometer and galvanometer are used in the measuring circuit. Perforated platinum electrodes, sealed to the ends of specially ground 24/40 standard taper joints, are used for the conductivity measurements. The joints are ground in such a way that a piece of filter paper can be placed over the ends of the electrodes without interfering with the fit of the joints. The filter paper helps to confine the powdered sample in the streaming potential cell between the platinum electrodes. When preparing the streaming potential cell one of the 24/40 joints is sealed with Apiezon W wax and a suspension of powder

[1] Present address: Radiation and Nucleonics Laboratory, Materials Engineering Departments, Westinghouse Electric Corporation, Engineering Center, East Pittsburgh, Pa.

Table I. Streaming potential measurements in 5.8 x 10^{-4}M $Ba(Ac)_2$ and relative wet adherence measurements
Experiments with firing conditions

Test No.	Description of sample	Zeta potential, mv	Relative wet adherence
1	RCA 33-Z-10; ZnS prepared by ppt. from $ZnSO_4$ solution with H_2S. Lot #1877	+13.1	1.3
2	RCA 33-Z-19 Lot #1869	+13.6	1.6
3	RCA 33-Z-19 Lot #1784	+14.3	1.5
4	RCA 33-Z-19 Lot #1869 fired in H_2S for 1 hr at 1000°C, flushed with N_2	−6.50	
5	Sample and firing as Test 4	−6.73	
6	RCA 33-Z-19 Lot #1869 fired in H_2S for 1 hr at 1000°C, flushed with N_2	+9.41	2.1
7	Same sample and firing as Test 6	+10.7	
8	RCA 33-Z-19 Lot #1869 fired in H_2S for 1 hr at 1000°C, flushed with N_2 (more extended N_2 flushing than with previous samples)	−3.64	1.3
9	Same sample and firing as Test 8	−2.62	1.6
10	RCA 33-Z-19 Lot #1869 fired in H_2S for 1 hr at 1000°C, flushed with N_2. Samples 10-12 were fired in the same furnace simultaneously, with Test 10 in the hottest region, Test 11 in the next hottest, and Test 12 in the coolest region	−8.49	0.96
11		−3.24	1.5
12		−2.89	1.6
13	RCA 33-Z-19 Lot #1869 fired in H_2S for 1 hr at 975°C, N_2 for ½ hr at 975°C, cooled in N_2	−3.53	
14	RCA 33-Z-19 Lot #1869 fired in H_2S for 1½ hr at 975°C, cooled in H_2S	+18.5	2.6
15	Fired same as Test 13	−4.62	1.8
16	Fired same as Test 13, but at 1100°C	+4.43	3.3
16a	Fired same as Test 13, but at 1100°C	+13.1	1.3
17	Repeat of Test 16 (new H_2S cylinder)	−6.17	1.8
18	Fired same as Test 14, but at 1100°C	+6.09	2.5
19	Starting material Test 14, heated in vacuum furnace for 2 hr at 160°C	+12.7	1.8
20	Starting material Test 15, rinsed with dilute NH_4OH, dried	+2.28	1.8
21	RCA 33-Z-19 Lot #1869 plus 2% NaCl, no Ag, fired at 975°C for 1¼ hr in air, covered, washed with H_2O	+16.9	1.8
22	RCA 33-Z-19 Lot #1869 plus 2% NaCl plus 0.015% Ag fired at 975°C for 1¼ hr in air, covered, washed with H_2O	+16.8	1.6
23	RCA 33-Z-19 Lot #1869 plus 4% NH_4Cl plus 0.015% Ag fired at 975°C for 1¼ hr in air, covered, washed with H_2O	+18.9	1.8
24	RCA 33-Z-19 Lot #1869 plus 2% $CaCl_2$ plus 0.015% Ag fired at 975°C for 1¼ hr in air, covered, not washed	+20.3	3.3
25	RCA 33-Z-19 Lot #1869 plus 4% NH_4 plus 0.015% Ag fired at 975°C for 1¼ hr in air, covered, washed with H_2O	+18.7	2.2
26	RCA 33-Z-19 Lot #1869 fired at 975°C for 1¼ hr in air, open tube	+24.9	1.9
27	RCA 33-Z-19 Lot #1869 fired at 975°C for 1¼ hr in N_2, cooled in N_2	+16.3	1.6
28	RCA 33-Z-19 Lot #1869 fired at 975°C for 1¼ hr in air, flushed with N_2	+25.1	2.2
	Experiments at various stages of phosphor preparation		
29	RCA Phosphor 33-Z-265, uncoated, ZnS:0.015% Ag (100 g) coated with 3 cc of 5% silicate* + 0.1 g $ZnSO_4$ specially prepared	+10.2	1.9
30	RCA Phosphor 33-Z-265, uncoated, (100 g) coated with 5 cc of 5% silicate* + 0.1 g $ZnSO_4$	−19.8	2.3
31	RCA Phosphor 33-Z-265, uncoated, (100 g) coated with 15 cc of 5% silicate* + 0.1 g $ZnSO_4$	−31.4	2.7
32	RCA Phosphor 33-Z-265, standard product, (100 g) coated with 3 cc of 5% silicate* + 0.1 g $ZnSO_4$	−19.4	1.5
33	RCA Phosphor 33-Z-265, uncoated, with 0.5% ZnS	Positive in H_2O	2.2
34	RCA Phosphor 33-Z-265, uncoated, coated with CaCdZn hydroxy apatite	Negative in H_2O	2.3
35	RCA Phosphor 33-Z-265, uncoated, factory product	+27.4	1.9
36	RCA Phosphor 33-Z-285, ZnS:0.01% Ag coated with CaCdZn hydroxy apatite	−8.28	2.3
37	RCA Phosphor 33-Z-285, ZnS:0.01% Ag coated 0.1% $Mg(BO_2)_2$, 0.2% BaO, 0.2% SiO_2	−23.0	1.2
38	RCA 33-Z-285, ZnS:0.01% Ag coated with 0.75% $Mg(BO_2)_2$, 0.2% BaO, 0.2% SiO_2	−13.7	2.6
39	RCA 33-Z-386A, (ZnCd)S: 0.003% Ag coated with CaCdZn hydroxy apatite	−3.38	4.1

* 5% by volume silicate solution prepared from a stock solution containing 0.96M K_2O and 3.05M SiO_2.

poured into the open end of the cell. Suction is applied in order to achieve a tight packing. The other electrode then is sealed into place. Occasionally, when a *p*H meter or an electrometer is used, the platinum electrodes are employed for the potential measurements.

Experimental procedure.—In the streaming-potential experiments, care is taken to rinse out all sections of the apparatus with the liquid being used in the experiments. Measurements are made at several pressures (10-50 cm Hg) and with the liquid flowing in both directions. Potential and conductance measurements are made at each pressure, and sufficient time is allowed for the system to come to equilibrium before each measurement is made. The system is then disassembled, rinsed with 0.010M KCl, and reassembled in order to determine the cell constant of the streaming potential cell under flow conditions analogous to those used in streaming potential determinations.

The formula used to calculate zeta potentials from the experimental data is:

$$\zeta = \frac{4\pi\eta K}{D} \cdot \frac{E}{P}$$

where ζ is zeta potential (mv); η, viscosity of the solution, (poise); D, dielectric constant of the solution; K, specific conductance of the solution within the plug ($ohms^{-1}$); E, streaming potential (mv); and P, driving pressure (dynes/cm).[2]

Assuming that the viscosity (η) and the dielectric (D) of the solution do not differ appreciably from pure water, the following formula is used for the calculation at 25°C:

$$\zeta = 9.69 \times 10^4 \frac{KE}{P}$$

Experimental Results

Effect of firing conditions.—The first experiments performed in this investigation were made with precipitated ZnS (Table I). Because the surface condition of the powder is of paramount importance in streaming potential measurements, some way of removing adsorbed ions on the ZnS was thought desirable. The ZnS used in these experiments was prepared by bubbling H_2S into a solution of $ZnSO_4$. Under these conditions one may reasonably expect that adsorbed Zn^{++} and $SO_4^{=}$ ions will be present on the ZnS surface. If an excess of Zn^{++} ions are on the surface, there will also be a possibility of ZnO formation. The method of obtaining ZnS free of $SO_4^{=}$, Zn^{++}, and ZnO recommended by Larach and Thomsen (11) was used in this study. It consists of firing precipitated ZnS in H_2S at ~1000°C.

Streaming potential measurements on the ZnS powder prepared in this manner initially gave negative zeta potentials in 5.8×10^{-4}M $Ba(Ac)_2$ (Table I, Test No. 4 and 5). Changes in sign, of this nature, indicate rather radical changes in the condition of the surface. Further investigation of firing conditions showed that it is possible to obtain either positive or negative zeta potentials with a given sample of ZnS. For negative zeta potentials, the method used should be:

Method A

1. Fire ZnS in H_2S at 975°C for 1 hr.
2. With the sample at 975°C, flow N_2 through the furnace for ½ hr.
3. Allow the sample to cool in a N_2 atmosphere.

For positive zeta potential the ZnS sample is:

Method B

1. Fired in H_2S at 975°C for 1½ hr, and
2. Allowed to come to room temperature in an H_2S atmosphere.

These results were found to be reproducible as may be seen in Table I. When the H_2S used in the firing was taken from an almost empty cylinder, Method A yielded phosphors having a positive zeta potential (Test 16). Negative phosphors were always obtained when fresh cylinders of H_2S were used on the samples fired according to Method A. Impurities in the H_2S cylinder (definite infrared spectrum evidence for CH_2Cl_2 was found) which become more pronounced as the cylinder is almost empty may be the cause of the positive zeta potentials obtained when samples were fired by Method A (Test 16). Since O_2 is a usual contaminent in nitrogen cylinders, it is possible that ZnO or chemisorbed O_2 may be formed on the surface of the powder when Method A is used. Method B will probably result in adsorbed H_2S.

The ZnS transition temperature for the transformation from cubic to hexagonal form occurs at 1020°C. Tests 16, 17, and 18 were fired at 1100°C. The other firings were below this temperature. There is some indication that crystal habit affects the zeta potential, but it is felt that not enough experiments were performed above the transition temperature to come to any definite conclusions concerning this point.

Several attempts were made to treat a sample that had been fired by Method A with H_2S in order to cause the streaming potential to become positive. Hydrogen sulfide was allowed to come in contact with dry phosphor and with phosphor-water suspensions. The sign of the potential remained unaltered in all cases. Samples fired by Method B were vacuum heated to 160°C in an unsuccessful attempt to remove adsorbed H_2S and cause the samples to revert to negative potentials (Test 19).

Samples of ZnS that were prepared by Method A and had negative zeta potentials were rinsed with a dilute NH_4OH solution (Test 20). This treatment caused the streaming potential to become positive. X-ray analysis of the ZnS samples before and after treatment with the NH_4OH solution revealed several unidentified lines in the sample treated with the NH_4OH that were not present in the untreated sample. NH_4OH treatment commonly is used commercially to neutralize any excess H_2SO_4, formed during the precipitation of the ZnS, that has not been removed by water rinsing.

Streaming potential measurements at various stages of phosphor preparation.—Streaming potential experiments were performed next on a ZnS phosphor during various stages of preparation. Experiments on several lots of precipitated ZnS all resulted in positive zeta potentials in $Ba(Ac)_2$ (5.84×10^{-4}M) (Tests 1, 2, and 3). When various fluxes such as NH_4Cl, NaCl, and $CaCl_2$ were used to incorporate the Ag activator into the ZnS, the zeta potential still remained positive (Tests 21 through 25). It was not until the phosphor was coated with silicate that the zeta potential became negative in the $Ba(Ac)_2$ solution (Test 32). A phosphor that had been fluxed with the NaCl and activated with 0.015% Ag was coated with ZnS. The coating was applied by bubbling H_2S into a suspension of the uncoated phosphor resulting in the formation of an amorphous layer of ZnS on the surface. This phosphor was found to have a positive zeta potential in H_2O (Test 33). CaCdZn hydroxyapatite coatings give negative potentials (Tests 34, 36, and 39). Several experiments were performed using various amounts of silicate coating, and the results indicate that the magnitude of the negative potential increases with increased amounts of silicate (Tests 30, 31, and 32). Tests 37 and 38 show that $Mg(Bo_2)_2$ coatings give negative zeta potentials with the RCA 33-Z-285 phosphor.

Streaming potential experiments on a ZnS:0.015% Ag, *uncoated phosphor* (33-Z-265 *uncoated*).—(*a*)

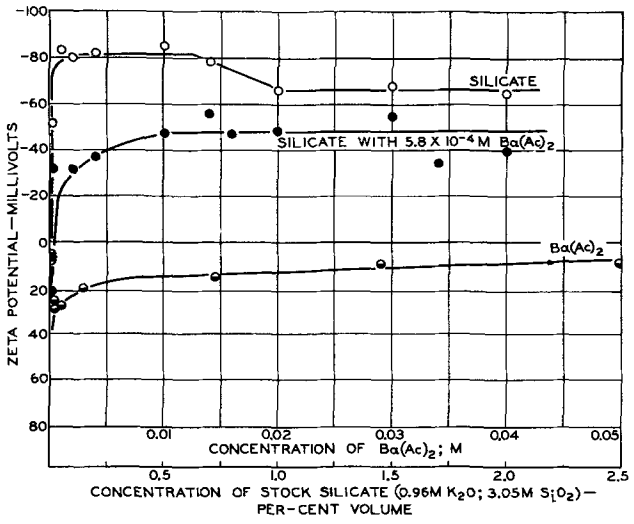

Fig. 1. Zeta potential of RCA phosphor 33-Z-265, uncoated (ZnS:0.015% Ag) as a function of (a) $Ba(Ac)_2$ concentration, (b) silicate concentration, (c) silicate concentration with 5.8×10^{-4}M $Ba(Ac)_2$.

$Ba(Ac)_2$ solution: The results of these experiments are shown in Fig. 1 where the calculated zeta potentials are plotted as a function of the molar concentration of $Ba(Ac)_2$. It is seen that the zeta potential starts at a value of +30 mv at the lowest concentration and falls to a plateau value of about +10 mv at higher concentrations.

(*b*) Silicate: In Fig. 1 the zeta potential is plotted as a function of silicate concentration. The zeta potential starts out with positive values at low silicate concentrations, goes through zero, and continues to increase in magnitude until it reaches a value of about −80 mv. It remains fairly steady at this value and then proceeds to decrease in magnitude in the conventional manner to a plateau value of about −65 mv.

(c) $Ba(Ac)_2$-silicate system, $Ba(Ac)_2$ conc. held constant at 5.8×10^{-4}M: These results are also given in Fig. 1. A comparison of the curves in Fig. 1 shows that the added $Ba(Ac)_2$ has the effect of lowering the magnitude of the zeta potential over those obtained with silicate dose.

Several experiments were performed using 9.93×10^{-4}M $Ba(Ac)_2$ plus 0.05% silicate and 0.2% silicate. The zeta potentials were −6.32 and −23.6 mv, respectively, indicating that additional $Ba(Ac)_2$ further suppresses the magnitude of the potentials as compared to that obtained with silicate.

(*d*) Polyvinyl alcohol-ammonium dichromate system: Streaming potential experiments with PVA have been performed on the regular product 33-Z-265 phosphor (ZnS:0.015% Ag, silicate coated) and on uncoated 33-Z-265 phosphor. The results, given in Table II, show that the PVA does not change the sign of the zeta potential of these phosphors from that in pure water. As will be remembered, potassium silicate solutions caused a reversal from positive to negative in the sign of the zeta potential of the uncoated phosphor.

With $(NH_4)_2Cr_2O_7$ as the streaming electrolyte, the same phosphors gave unusual results. Particular difficulty was encountered with the uncoated phosphor. The streaming potential was found to start out positive and to drop rapidly in magnitude. In some cases when the direction of liquid flow was reversed, the measured potential did not reverse sign in the normal manner. The coated 33-Z-265 also showed some tendency toward a decrease in magnitude of the zeta potential with time, but to a much smaller degree than the uncoated material. The zeta potential of the coated phosphor was negative in all cases and ranged from about −25 to −13 mv with time. The concentrations of $(NH_4)_2Cr_2O_7$ used were 0.001 and 0.0005 wt %.

Table II

RCA Phosphor No.	Per cent of PVA	Zeta potential, mv
33-Z-265 uncoated	0.149	+9.77
33-Z-265	0.149	−12.21
33-Z-265 uncoated	0.0149	+13.89

Experiments using PVA (0.0149 wt %) plus $(NH_4)_2Cr_2O_7$ (0.0005 wt %) were performed on the coated and uncoated phosphor. The coated 33-Z-265 had zeta potentials that ranged with time from −8 to −3.5 mv. The potential of uncoated 33-Z-265 ranged from +31 to +6.5 mv. These changes in zeta potential with time are probably due to chemical interaction of the $(NH_4)_2Cr_2O_7$ with the phosphor and could possibly be used as a means of estimating how well a phosphor has been coated.

Adherence measurements.—Table I and Fig. 2 give zeta potential and adherence data on a number of samples prepared by various firing conditions and with different fluxes and coatings. A water jet impingement method (12) for evaluating wet adherence was used. It consists of first dispersing the sample to be tested in a solution containing 9.25×10^{-5}M $Ba(Ac)_2$ and 0.22% stock potassium silicate and then allowing the sample to settle to the bottom of the vessel. After the prescribed time (20 min) has elapsed, a glass capillary tube with an inner diameter of 1.2 mm is immersed into the vessel and a jet of water allowed to impinge through a given height of liquid (1 in.) onto the settled powder. The geometry and hydrostatic pressure applied to the capillary

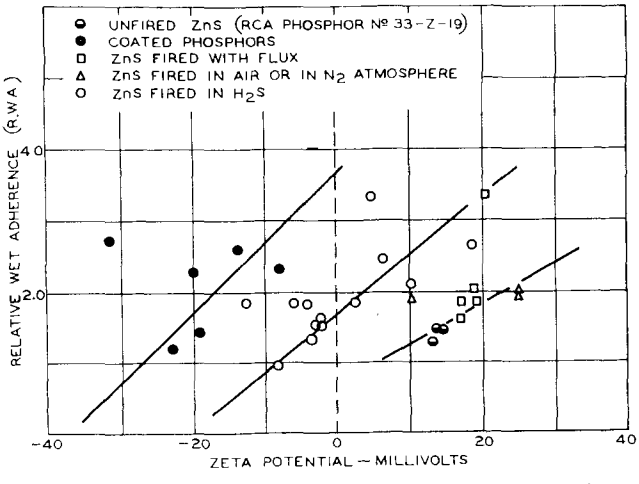

Fig. 2. Correlation between zeta potential and relative wet adherence.

Table III

Conc. $Ba(Ac)_2$, M	Hole diameter*, mm Standard phosphor	Uncoated phosphor
1.06×10^{-3}	8.2	17.2
8.57×10^{-4}	9.3	22.3
8.57×10^{-5}	28.7	38.5
8.57×10^{-6}		39.3

* Large hole diameter indicates poor adherence.

are kept constant (jet-flow rate equals 153 cc/min). The data in Table I for relative wet adherence (RWA) are the reciprocal of the eroded area produced by the water jet on the sample being studied, divided by the reciprocal of the area obtained with a standard sample, and multiplied by 4.05 (the RWA of the standard phosphor).

Wet-adherence measurements using the jet-impingement technique, but with the data reported in terms of eroded hole diameter, were performed on the uncoated 33-Z-265 phosphor as a function of $Ba(Ac)_2$ concentration. The concentration of the silicate was 0.81% of the stock solution. Results are given in Table III.

It is apparent that the uncoated 33-Z-265 phosphor has comparatively poor wet adherence. The fact that the jet impingement test with the uncoated phosphor results in hole diameters that increase with decreasing concentration indicates that it has a negative zeta potential when suspended in the silicate for the wet adherence test. The streaming potential experiments confirm this assumption.

Discussion

The results of the experiments on the effect of firing conditions on the sign of the zeta potential indicate the importance of surface conditions. The difference in sign between ZnS samples that have been fired in H_2S and flushed with N_2 (negative zeta potential) and those fired in H_2S and allowed to cool in H_2S (positive zeta potential) may possibly be due to adsorbed H_2S, in the latter case, and O_2 adsorption or ZnO formation, due to impurities in the N_2, in the former case.

Samples allowed to cool in H_2S may be expected to behave quite differently from those cooled in N_2. Undoubtedly, H_2S will be adsorbed which, when placed in H_2O, will have the opportunity of dissociating into H^+ and HS^- ions. If the H^+ ions remain adsorbed, the diffuse part of the double layer must have an excess of negative charge. This negative charge will result in the observed positive values for the streaming potential and zeta potential. It was not possible to detect any differences in *p*H of water suspensions of ZnS samples prepared by the methods mentioned above, probably because the concentration of HS^- ions discharged from the surface of the powder cooled in H_2S was too small to be effective.

It is difficult to establish from the experiments that have been performed thus far whether the impurities in the N_2 contribute measurably to the resulting zeta potentials. The negative zeta potentials obtained by firing in H_2S and flushing with N_2 may be due to ZnO or O_2 on a ZnS substrate, or simply to ZnS.

The NH_4OH treatment of the sample that had been treated by Method A caused the potential to become positive. Because zinc complexes with NH_3, an adsorbed zinc-ammonia complex may be the cause of the sign reversal. The x-ray data indicate the possible formation of a new species in the NH_4OH treated sample, but the intensity is too low to allow for positive identification.

The streaming potential experiments performed at various stages of phosphor preparation also indicate the importance of surface conditions as compared to bulk modification of a ZnS powder. Thus, the streaming potential was found to remain positive during all stages of phosphor preparation until the coating operation. Additions of various fluxes, as well as Ag activator, resulted in powders with positive potentials. All of the streaming-potential experiments performed by various workers on phosphors have been with finished products (3-5). In all cases but one, negative potentials were obtained. Hazel and Schnabel (4) found that du Pont #1630 (ZnS; ZnCdS) had a positive potential in the absence of K_2SiO_3. They suggest that the positive potential was due to the flux or other impurities. The present findings indicate that the positive potentials are not due to the flux, because the original ZnS starting material has a positive potential. A ZnS coated ZnS:0.015% Ag phosphor was found to have a positive potential. Silicate coatings result in negative potentials with the magnitude of the potential increasing with heavier coatings. The ZnS coated phosphors have all of the free-flowing characteristics that have been found desirable in phosphor coatings that have negative potentials. This information permits the selection of a coating with either a positive or negative potential should a particular screen-application technique indicate one or the other to be most desirable.

Streaming-potential experiments on the ZnS: 0.015% Ag uncoated phosphor (33-Z-265) as a function of $Ba(Ac)_2$ concentration, silicate concentration, and $Ba(Ac)_2$-silicate mixtures are shown in Fig. 1. The curve for zeta potential vs. $Ba(Ac)_2$ concentration shows the usual reduction of the zeta potential with increased concentration of electrolyte as a result of condensation of the diffuse part of the electrical double layer. As may be seen from the curve for zeta potential vs. silicate concentration there is a reversal in the sign of the zeta potential from positive to negative with increasing silicate concentration. The region of rapid increase in negative values of the zeta potential with increasing silicate concentration may indicate only partial coating of the phosphor with silicate. From 0.05 to 0.7% silicate, the phosphor may be completely coated with silicate. It is only at concentrations higher than 0.7% stock silicate that compression of the electrical double layer, caused by additional adsorption of ions into the inner Helmholtz plane and, consequently, reduction in magnitude of the zeta potential, becomes predominant. With an ordinary electrolyte, the zeta potential falls to values considcrably lower than the −64.5 mv at 2.0% stock silicate found in the present system. This reduction may be due to the tendency

of the silicate ions to associate into micells which will result in only a relatively small increase in the concentration of free ions with an increase in silicate concentration.

Comparison of the curve for zeta potential vs. silicate concentration with the curve for zeta potential vs. silicate concentration plus 5.8×10^{-4}M $Ba(Ac)_2$ shows that the added $Ba(Ac)_2$ (5.8×10^{-4}M) has the effect of lowering the magnitude of the zeta potential and of shifting the curve toward the higher concentration range. A possible explanation is that the silicate is forced to compete with the Ba^{++} ions for adsorption sites, despite the fact that different charge types are involved. For example, an adsorbed silicate ion at a positively charged site may prevent adsorption of a Ba^{++} ion at an adjacent negatively charged site by steric hindrance. The silicate ions overbalance the Ba^{++} ions because they cause a phosphor that has positive zeta potentials in H_2O or in $Ba(Ac)_2$ solutions to become negative. The lowered magnitude of the negative zeta potential in $Ba(Ac)_2$ as compared to that found with silicate alone indicates partial adsorption of the Ba^{++} ions in the inner Helmholtz plane in the region of low silicate concentration. Another mechanism that would contribute to the lowered potentials would be strongly adsorbed Ba^{++} ions on top of the adsorbed silicate ions. The drop in the zeta potential, after the maximum value of the negative potential has been obtained, is less pronounced than for the silicate system. This difference is to be expected because the $Ba(Ac)_2$ will tend to gel the silicate system at these higher concentrations, in effect reducing the number of ions available to cause compression of the electrical double layer and, therefore, reduction of the zeta potential.

The experiments with PVA and ammonium dichromate indicate that the PVA does not change the sign of the potential of the uncoated phosphor as compared to that found with water, and also that some reaction occurs between the phosphor and the ammonium dichromate. Perhaps the ZnS is oxidized to the sulfate. The silicate coated phosphor is more resistant to attack by the dichromate, as is evident from the smaller zeta potential change with time as compared to that observed for the uncoated material. Streaming potential measurements on systems of this type may be useful in studying chemical reactions which would otherwise remain undetectable.

Attempts to correlate wet-adherence measurements, performed in 9.25×10^{-5}M $Ba(Ac)_2$ and 0.22% stock silicate, with zeta potential data have not been completely successful. This variance may be due largely to the tendency of the silicate, used in making the RWA measurements, to coat the sample and at least partially mask the electrical properties of the original material. Thus, while there is a trend toward increasing RWA with decreasing zeta potential, the results are not conclusive as there is considerable scatter in the experimental data (Table I and Fig. 2). The best correlation is found with the coated phosphors that have negative zeta potentials in 5.8×10^{-4}M $Ba(Ac)_2$. Thus far, no attempt has been made to study the effect of shape and size distribution on the relative wet adherence and the zeta potential. Because the samples studied were prepared under different conditions of firing, fluxing, activation, and coating, the lack of correlation is not surprising. If the samples are grouped according to treatment when the data are plotted, as has been done in Fig. 2, fair correlation is obtained. It should be re-emphasized, however, that the best correlation between zeta potential and wet adherence is found if the same sample is used and its zeta potential is altered by changing the concentration of the electrolyte.

Conclusions

1. The zeta potential of ZnS may be altered in sign depending on firing technique. Apparently, adsorbed H_2S plays an important role.
2. NH_4OH washing can change the zeta potential of a ZnS sample that has been fired in H_2S and flushed with N_2 from negative to positive. The change is due possibly to an adsorbed zinc ammonia complex.
3. ZnS phosphors have positive zeta potentials during all stages of preparation prior to the coating operation. Silicate coatings yield negative potentials, while ZnS coatings yield positive potentials. These experiments illustrate the importance of surface conditions as compared to bulk properties in determining the zeta potential.
4. The influence of electrolyte concentration on the zeta potential of a ZnS:0.015% Ag, uncoated phosphor has been determined with $Ba(Ac)_2$, potassium silicate, and $Ba(Ac)_2$-potassium silicate mixtures. Similar experiments were performed in the PVA-ammonium dichromate system for the coated as well as the uncoated phosphor. The dichromate interacts chemically with the phosphor, causing rapid changes in the zeta potential.
5. Zeta potential data have been correlated with adhesion measurements.

Acknowledgment

The author is happy to acknowledge the assistance of L. E. Whitmer and Dr. S. A. Harper, who prepared many of the samples used in these experiments. Mrs. K. Maisane performed a major share of the streaming potential experiments concerned with the effect of electrolyte concentration, and her help is gratefully appreciated. Dr. D. J. Donahue and Dr. R. N. Summergrad assisted in many instances with helpful discussion and suggestions.

Manuscript received May 19, 1958. This paper was prepared for delivery before the New York Meeting, April 27-May 1, 1958.

Any discussion of this paper will appear in a Discussion Section to be published in the December 1959 JOURNAL.

REFERENCES

1. M. Sadowsky, *J. (and Trans.) Electrochem. Soc.*, **95**, 112 (1949).
2. D. J. Donahue, *RCA Engineer*, **1**, No. 3, 10 (1955).
3. R. Edelberg and J. F. Hazel, *J. (and Trans.) Electrochem. Soc.*, **96**, 13 (1949).
4. J. F. Hazel and G. L. Schnable, *This Journal*, **100**, 65 (1953).
5. J. F. Hazel and G. L. Schnable, *J. Phys. Chem.*, **58**, 812 (1954).
6. See *Electrical Phenomena at Interfaces*, The Macmillan Company, New York, 1951, J. A. V. Butler, Chap. II and III.

7. J. J. Bikerman, *Trans. Faraday Soc.*, **36**, 154 (1940).
8. D. R. Briggs, *J. Phys. Chem.*, **33**, 641 (1928).
9. J. Th. G. Overbeek and P. W. O. Wijga, *Rec. Trav. chim.*, **65**, 556 (1946).
10. A. M. Gaudin and D. W. Fuerstenau, *Mining Engineering*, January 1955, pp. 1-7.
11. S. Larach and S. M. Thomsen, *Anal. Chem.*, **26**, 1600 (1954).
12. A. S. T. M., F-1 subcommittee No. 7 on Luminescent Materials is currently considering a number of methods of measuring wet adherence one of which is the method being used by RCA, briefly described in this paper.

Associated Donor-Acceptor Luminescent Centers in Zinc Sulfide Phosphors

E. F. Apple and F. E. Williams

Research Laboratory, General Electric Company, Schenectady, New York

ABSTRACT

Zinc sulfide activated with copper or silver and coactivated with gallium or indium shows two emission bands. The shorter wave-length band does not involve the ground state of the coactivator or donor, whereas the longer wave-length band does. Both bands involve the ground state of the activator or acceptor. The factors contributing to the emission intensities from the various associated donor-acceptor pairs are discussed theoretically. The dependences on temperature and on concentrations of activator and coactivator are in accord with the longer wave-length band involving a highly associated donor-acceptor pair. In addition, the energy levels of the donors, as obtained from thermoluminescent data, are correlated on the basis of the model with the differences in the transition energies of the two emission bands of these phosphors.

Zinc sulfide phosphors coactivated with Group III elements of the Periodic Table have been reported to have a long wave-length emission band in addition to the short wave-length emission band associated with activation by Group I elements and with self-activation. Kröger and Dikhoff (1), for example, reported long wave-length emission in phosphors coactivated with Sc, Ga, or In. The emission bands peaked at 5250Å with Sc, 5700Å with Ga, and 6800Å with In and were relatively independent of the identity of the activator. They also observed that the substitution of ZnS in part by CdS had less effect on the long wave-length emission spectra than on the short wave-length emission spectra. Klasens (2) attributed these long wave-length bands to the radiative recombination of a free hole with an electron trapped at the coactivator. Froelich (3) reported long wave-length emission for Cu and self-activated ZnS phosphors which were coactivated with quite high concentrations of Al. Emission peaks are at 5880 and 5000Å, respectively. Apple (4) has reported that the crystalline structure influences the relative intensities of the two emission bands observed with ZnS: x(Cu, Ag, Au), y(Ga, In) phosphors in which $x < y$. The long wave-length emission was found to be enhanced in hexagonal ZnS. He has suggested that this effect may be related to a change in association of activator and coactivator.

In this investigation a comprehensive study of ZnS:x(Cu or Ag), y(Ga or In) was made. The spectra of the long wave-length emission are found to depend on the identities of both activator and coactivator. The relative intensities of the long and short wave-length emission depend on concentrations of activator and coactivator and on temperature of excitation. These experimental results are explained by means of a model for the long wave-length emission center consisting of a highly associated activator-coactivator center. This center is similar to the associated donor-acceptor system proposed by Prener and Williams (5) to explain the short wave-length emission by radiative transitions from excited states of the donor to the ground state of the acceptor but is different in that the donor and acceptor responsible for the long wave-length emission are more closely associated so that radiative transitions occur from the ground state of the donor to the ground state of the acceptor.

Experimental Results

The phosphor mixes usually were made by adding aqueous solutions of activator and coactivator to a water slurry of ZnS (G.E. luminescent grade); in a few cases the activator and coactivator were added as the solid ternary sulfides, i.e., $CuGaS_2$, $CuInS_2$, or $AgGaS_2$ in the absence of water. The mixes were fired in an H_2S stream either at 950°C to give a cubic material or at 1150°C to give a hexagonal phosphor. The H_2S used was bubbled through $Ba(OH)_2$ solution, then through drying columns containing silica gel and P_2O_5 and a cold trap held at −50°C before coming in contact with the sample.

Emission spectra of the phosphors under 3650Å excitation[1] are shown in Fig. 1-4. Concentrations are given in gram-atoms added per mole ZnS, but the amounts of activator and Ga present after firing were equivalent to the amounts added, whereas the

[1] Essentially 3650Å radiation was obtained from a G.E. mercury lamp, #H100-FL4, in conjunction with Corning #5840 and Kopp #41 uv filters. The spectra were recorded on an automatic spectroradiometer which plots radiant energy flux vs. wave length.

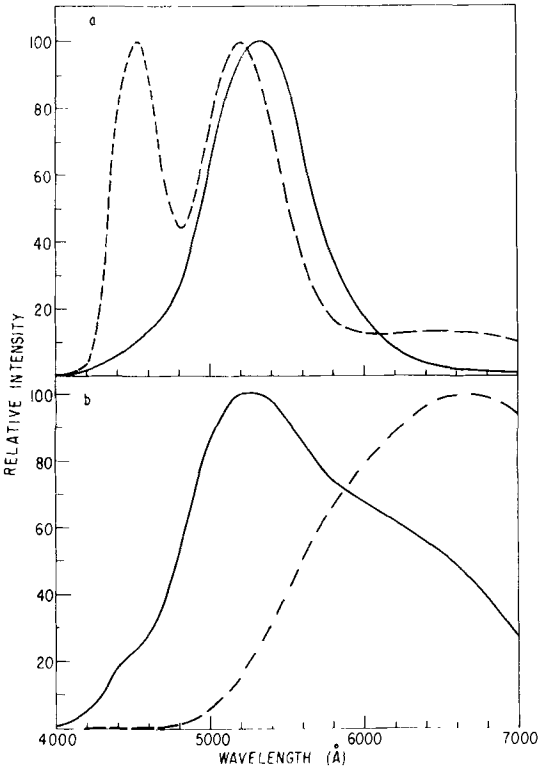

Fig. 1. Emission spectra of ZnS:10^{-4} Cu, 10^{-4} Ga; a, cubic structure; b, hexagonal structure; 3650Å excitation; ——— room temperature - - - - - —196°C.

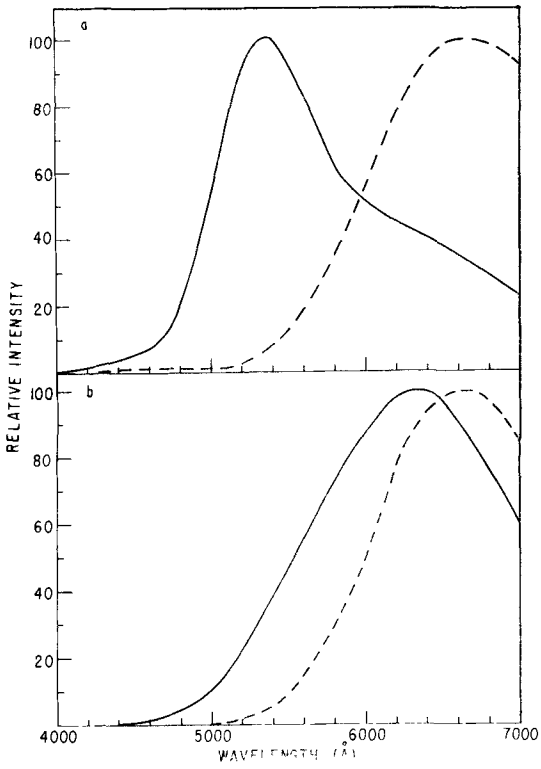

Fig. 2. Emission spectra of ZnS:10^{-4} Cu, 2×10^{-4} In; captions as in Fig. 1.

final In concentration, because of volatization, was approximately equal to the concentration of activator present. Although most of the phosphors were prepared in purified H_2S, they could be made equally well in sealed, evacuated quartz tubes, S_2(p = 30 atm), N_2, or H_2, provided that water and oxygen were excluded in the phosphor preparation.

This class of phosphors clearly shows two emission bands.[2] The shorter wave-length emission, which is in the blue with Ag and in the green with Cu, is dependent on the identity of the activator only, while the longer wave-length emission, which is in the yellow with Ag and orange with Cu, depends on the identity of both activator and coactivator. For example, the longer wave-length emission peaks at 5900Å in ZnS:Ag,Ga and at 6150Å in ZnS:Ag,In.

The relative intensities of the two bands are determined by such parameters as concentration of activator and coactivator, temperature during excitation, identity of coactivator, crystal structure, and firing temperature.

An increase in concentration of activator and coactivator causes an increase in the long to short wave-length emission ratio. For example, consider the emission in cubic ZnS:Cu,In. Below 10^{-5} Cu and In, virtually no contribution from the orange band is observed under excitation at room temperature. Increase in concentration of Cu and In from 10^{-5} causes an increase in the orange emission until at 3 x 10^{-4} Cu and In the intensity of the orange band is about equal to that of the green band and above this concentration, the orange band predominates. In Ga-coactivated phosphors, the shorter wave-length band predominates in samples containing up to about 10^{-2} Cu and Ga. Related to the concentration effect is the dependence of the longer to shorter wave-length emission ratio on firing temperature. In cubic ZnS: 10^{-4} Cu, 2 x 10^{-4} In, this ratio at room temperature is 0.31, 0.27, 0.26 for samples fired at and air-cooled from 600°, 700°, and 900°C, respectively.

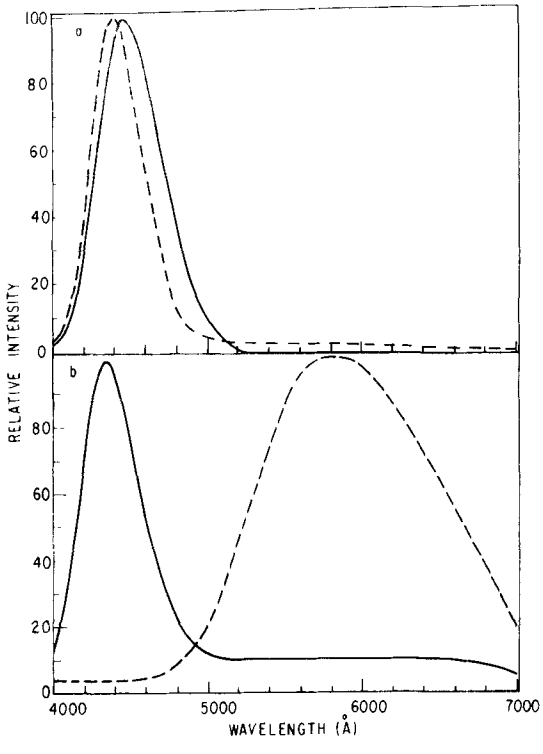

Fig. 3. Emission spectra of ZnS:10^{-4} Ag, 10^{-4} Ga; captions as in Fig. 1.

[2] The additional band at 4500Å observed only in cubic ZnS:Cu, Ga is not discussed in this paper.

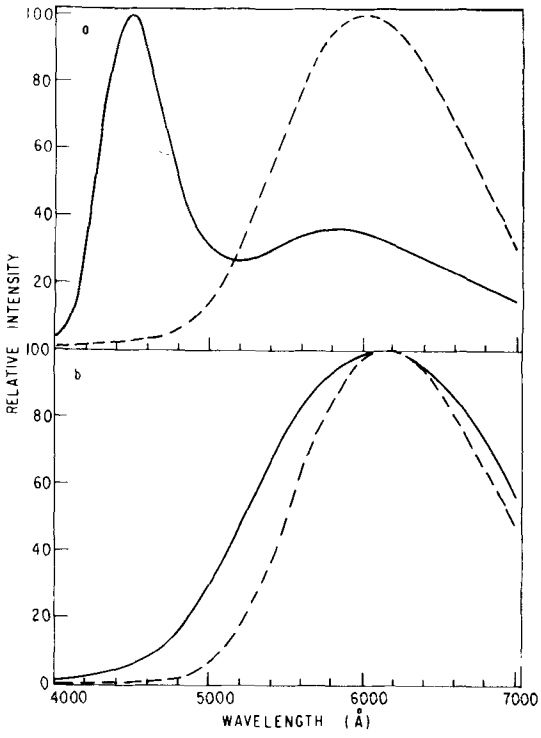

Fig. 4. Emission spectra of ZnS:10^{-4} Ag, 2 × 10^{-4} In; captions as in Fig. 1.

As is evident from Fig. 1-4 the longer wave-length emission is favored under excitation at lower temperatures. The temperature dependence of emission of the phosphors was determined by recording the spectra as the sample contained on a large Cu block in vacuum was cooled slowly from about 275°C to room temperature. Below room temperature, the block was cooled by the addition of small quantities of liquid nitrogen. The temperature change during measurement of the spectrum was in no case greater than 5°C. Figure 5 shows some of the spectra obtained on hexagonal ZnS:10^{-4} Cu, 2 x 10^{-4} In at the temperatures indicated. Even at 255°C, where temperature quenching has begun, the contribution of the orange band is considerable. The slight shift in the spectra at lower temperatures is due in part to the disappearance of the green band below —140°C. Cubic ZnS:10^{-4} Cu, 2 x 10^{-4} In shows the same general temperature dependence, but above 100°C the orange contribution to the spectra is small and the change from predominantly orange to green emission occurs at —35° to 0°C. The green-orange change in emission occurs at lower temperatures as the concentration of Cu and In is decreased. This is observed for both cubic and hexagonal phosphors. Figure 6 shows the temperature dependence of emission for hexagonal ZnS:10^{-4} Cu, 10^{-4} Ga. Above 100°C, the contribution from the orange band is again very small. These data indicate that the temperature dependence of emission at a given concentration of activator and coactivator is determined by the identity of the coactivator. In ZnS:Ag,Ga or In, the data were limited to below about 80°C where temperature quenching of luminescence begins. Consequently, the yellow to blue emission shift was not observed in hexagonal ZnS:Ag,In.

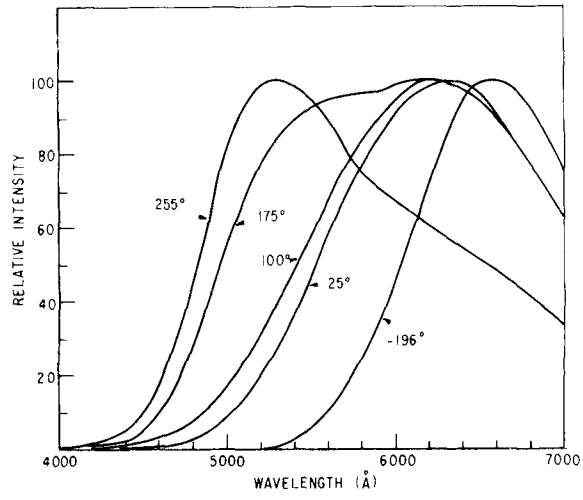

Fig. 5. Emission spectra of hexagonal ZnS:10^{-4} Cu, 2 × 10^{-4} In at indicated temperature using 3650Å excitation.

The effect of structure of the ZnS in luminescence has been mentioned heretofore in connection with the concentration- and temperature-dependent properties of the phosphors. At a given concentration of activator and coactivator, the longer wave-length emission is enhanced in the hexagonal phase of ZnS as, again, is shown in Fig. 1-4. On annealing a hexagonal phosphor for an extended time at 800°-900°C, the shorter wave-length emission typical of cubic phosphors increases concurrently with increase in the amount of cubic phase present. The effect is reversible with change in structure. Also, phosphors with emission spectra characteristic of those prepared at 1150°C can be made at temperatures as low as 600°C provided hexagonal ZnS is used in preparation of the phosphor mixes. The structure of these phosphors remains hexagonal during the 1-hr firing period at 600°C.

Glow curves were obtained on samples previously excited by a BH-4 lamp at —195°C for a 5-min period, and then heated at a rate of 10°C/min. The glow intensity was measured with an RCA 5819 PM tube with S-4 response. Glow peaks apparently resulting from In occur at —140° and —60°C. The thermoluminescence changes from the longer to the shorter wave-length emission during these glow experiments. The high-temperature glow peak at 100°-

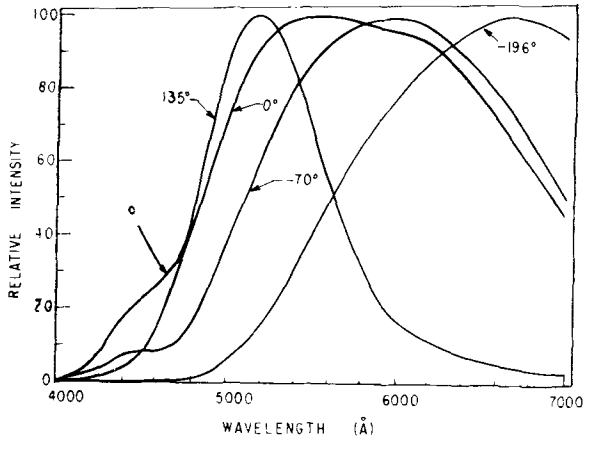

Fig. 6. Emission spectra of hexagonal ZnS:10^{-4} Cu, 10^{-4} Ga at indicated temperature using 3650Å excitation.

140°C observed with Cu-activated materials changes position with change in concentration.

Theoretical Analysis

As a consequence of the association of activator and coactivator impurities into donor-acceptor pairs, a unique impurity system is not expected in these phosphors, but rather a distribution of diatomic centers each characterized by a different interimpurity distance is expected. These pairs will each have a different energy level structure and transition probabilities for excitation and emission.

Prener and Williams (5) have proposed a model for the luminescent center defined in this paper as the short wave-length luminescent center. In this model, the transitions responsible for the short wave-length emission occur between excited states of the donor and the ground state of the acceptor in an associated, but not nearest neighbor, coactivator-activator pair. Because excited states of the donor are involved, the emission is independent of the chemical identity of the coactivator. Recently, Williams (6) extended the original concept of associated pairs at second, third, and fourth nearest-neighbor sites to more widely separated pairs of nonrandomly distributed donors and acceptors contributing to short wave-length emission. The present analysis is consistent with the short wave-length emission involving pairs with sufficiently great interimpurity spacing such that only radiative transitions from excited donor states to the ground state of the acceptor can occur with appreciable probability. The ground state of the donor for these pairs will function as an electron trap. These pairs will be designated s-type and are shown on the left of the band model in Fig. 7. The emission process also is indicated with the transition probability A_s.

We propose that the long wave-length emission arises from coactivator-activator pairs sufficiently closely associated so that radiative transitions may occur directly from the ground state of the donor to the ground state of the acceptor. The probability of this transition depends, of course, on overlap of the ground state donor and acceptor wave functions. Because the energies of the ground states are dependent on the identities of donor and acceptor, respectively, the transition energy for the long wave-length emission will be dependent on the chemical identities of both the coactivator and the activator. These pairs will be designated as l-type and are shown on the right in Fig. 7 along with the emission process indicated by the transition probability A_l.

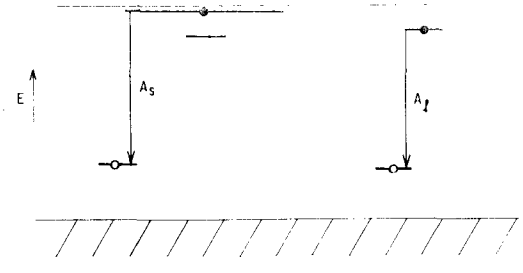

Fig. 7. Band theory model for the short and long wave-length luminescent centers.

The relative intensities of the short and long wave-length emission bands can be analyzed theoretically most readily for temperatures sufficiently great so that thermal equilibrium applies among the electron states and separately among the hole states. The ratio of intensities from s- and from l-type centers will then be of the following form:

$$\frac{I_s}{I_l} = \frac{\rho_s}{\rho_l} \cdot \frac{P(\epsilon_s)}{P(\epsilon_l)} \cdot \frac{A_s}{A_l} \cdot \frac{\alpha_s}{\alpha_l} \qquad [1]$$

where the ρ's, P's, A's, and α's are, respectively, the densities of states, occupational probabilities for each state, transition probabilities for emission, and fractions of pairs responsible for the s- and l-type emission.

Because the s-centers are believed to comprise all the coactivator-activator pairs in which any excited donor state has a finite matrix element for a radiative transition with the ground state of the acceptor and since there are many excited donor states characterized by different spatial extensions of their wave functions, a distribution of pairs with different interimpurity spacings is expected to contribute to α_s. On the other hand, the l-centers probably comprise a unique pair, or at most a narrow distribution of pairs, because the interimpurity spacing must be such that a finite matrix element for a radiation transition exists between the ground states of the donor and acceptor. Only a small fraction α_l of the pairs are consistent with this requirement. In the following analysis the ratio α_s/α_l will be determined theoretically in an approximation consistent with being large compared to unity. From the formula of Prener (7), we obtain:

$$\frac{\alpha_s}{\alpha_l} = \frac{\sum_{l+1}^{\infty}\alpha_m}{\alpha_l} = \frac{\sum_{l+1}^{\infty} Ac\, Z_m e^{e^2/KrmkT_D}\, e^{-c\sum_1^m Z_j}}{Ac\, Z_l\, e^{e^2/KrlkT_D}\, e^{-c\sum_1^l Z_j}} \qquad [2]$$

where Z_j is the number of sites of the jth type and T_D is the temperature during preparation below which diffusion over interimpurity distances cannot occur. We then make a continuum approximation (8) for the pairs of the s-type and replace the sums by integrals. In this approximation $(Z_{l+1} - Z_l) \rightarrow dZ = 4\pi r^2 dr$, and

$$\frac{\alpha_s}{\alpha_l} = 4\pi Z_l^{-1} e^{c\sum_1^l Z_j} \int_{r_l}^{\infty} r^2 e^{\frac{e^2}{KkT_D}\left(\frac{1}{r}-\frac{1}{r_l}\right)} e^{-\frac{4}{3}\pi r^3 c}\, dr \qquad [3]$$

For $T_D \approx 10^8$ °K and $l \geqq 3 (r_l \geqq 7\text{Å})$, the factor $e^{\frac{e^2}{KkT_D}\left(\frac{1}{r}-\frac{1}{r_l}\right)}$ is a sufficiently slowly varying function of r from r_l to ∞ so that a weighted average value can be removed from the integrand. The result is integrated and the relation $\frac{4}{3}\pi r_l^3 = \sum_1^l Z$, between the continuum approximation and the lattice is utilized to yield the following approximate relation:

$$\frac{\alpha_s}{\alpha_l} \approx c^{-1} Z_l^{-1} \left[e^{\frac{e^2}{KkT_D}\left(\frac{1}{r_s}-\frac{1}{r_l}\right)} \right] \qquad [4]$$

in which r_s can be interpreted as a weighted average interimpurity distance for the s-type centers. The factor α_s/α_l will favor s-type emission and is clearly

dependent on the concentration c of activators and coactivators.

On the other hand, the factor in Eq. [1] which takes account of the occupational probabilities of emitting states of the s- and l-type centers favors l-type emission and is strongly temperature-dependent. This is evident from Fig. 7 and also from the equilibrium approximation. For ordinary excitation intensities the fraction of centers excited simultaneously will be sufficiently small so that Boltzmann statistics may be used. The difference in emission spectra of the two bands is a measure of the difference in energies of the states of the two types of centers. We may write, therefore

$$\frac{P(\epsilon_s)}{P(\epsilon_l)} \approx e^{-\frac{hc}{kT}\left(\frac{1}{\lambda_s}-\frac{1}{\lambda_l}\right)} \qquad [5]$$

This formula will be in error by the difference in polarization energy of the two types of centers following emission. This error may be as great as the difference between the thermal depth and the optical depth of the donor. At low temperatures the occupational probabilities will not be determined by equilibrium considerations but rather by detailed balance between excitation and emission within each coactivator-activator pair. Under these conditions Eq. [5] will not apply, and an appreciable fraction of s-type pairs will no longer contribute to emission at low temperatures in the steady state because of electron trapping in the ground state of the donor of these pairs.

The ratio of densities of states ρ_s/ρ_l and transition probabilities for emission A_s/A_l are both expected to be of the order of unity and not appreciably dependent on temperature or concentration of luminescent centers. In the l-type center, emission is exclusively from the ground state of the donor so that ρ_l is obviously unity. The excited states in the highly associated l-type pair have been perturbed back to the conduction band edge (5). In an s-type center the lower excited states which give a finite matrix element for radiative recombination with the positive hole in the associated acceptor contribute to ρ_s, the higher excited states having been perturbed back into the conduction band (5). Since the s-type centers comprise a distribution of pairs with different interimpurity spacings $r_m > r_l$, the identities of the excited states contributing to ρ_s will vary with r_m; however, their number is expected to be a constant small integer. The magnitudes of the matrix elements A for radiative recombination with the positive hole in the associated acceptor should be comparable for s- and l-type emission.

In addition, the ratio I_s/I_l has been investigated with the assumption that the transitions between the unperturbed conduction band states and the ground state of the acceptor are responsible for s-type emission. With this assumption, the same dependence on temperature and impurity concentration is obtained as in the foregoing analysis. However, a pronounced dependence of I_s/I_l on excitation intensity is obtained because I_s is proportional to both the concentration of the electrons in the conduction band and the concentration of empty acceptors, whereas I_l is proportional only to the concentration of empty acceptors. This is not the case with the analysis based on s-type emission involving excited donor or perturbed conduction band states since, for this analysis, both I_s and I_l are proportional only to the concentration of empty acceptors.

The model illustrated in Fig. 7, in addition to providing the basis for the preceding analysis of the relative intensities of the short and long wave-length emission bands, provides a basis for relating the transition energies for emission to other luminescent properties. For example, the ground state of the donor in the s-type center is an electron trap, and therefore, the depth of the trap should be approximately equal to the difference in transition energies for the two emission bands.

$$E_T \approx hc\left(\frac{1}{\lambda_s}-\frac{1}{\lambda_l}\right) \qquad [6]$$

This relation is more nearly correct for the optical, rather than the thermal, trap depth. In addition, this relation is based on the assumption that the energies of the ground states of the donor and acceptor are independent of whether the association is into s-type or l-type pairs.

Since the energies of the states of the donor and acceptor do depend on association, the accuracy with which Eq. [6] is in accord with experiment permits placing an approximate limit on the degree of association of the l-type pairs. Williams (9) recently has examined theoretically the donor-acceptor pair system, which is a two-particle system consisting of an electron and a positive hole bound in the field of a finite dipole. The analysis is similar to the Heitler-London treatment of the hydrogen molecule and takes account of the overlap of the donor and acceptor wave functions. This overlap was neglected in the analysis of Hoogenstraaten (10). The transition energy for emission E_e for pairs characterized by the interimpurity spacing r_i and by radial wave functions for the separated donor and acceptor of the form $a^{-3/2}e^{-r/a}$ is:

$$E_e = -\frac{e^2}{Ka}e^{-2r_i/a}\left[\frac{a}{r_i}+\frac{5}{8}-\frac{3}{4}\frac{r_i}{a}-\frac{1}{6}\frac{r_i^2}{a^2}\right] - \frac{e^2}{12a}\left(\frac{1}{K_o}-\frac{1}{K}\right)e^{-2r_i/a}\left[4\frac{r_i^2}{a^2}+18\frac{r_i}{a}+9\right] + \frac{e^2}{K_o r_i} - E_D - E_A + E_G \qquad [7]$$

where E_D and E_A are the ionization energies for the separated donor and acceptor, K and K_o are the static and optical dielectric constants, and E_G is the band gap. For pairs consisting of donors and acceptors both located at sites of the same sign and with $E_D \geqq 0.5$ ev and $E_A \geqq 0.5$ ev, the perturbation of the ground states and consequent increase in E_e will be quite accurately e^2/Kr_i. The error involved in using Eq. [6] to calculate thermal trap depths tends to cancel the error involved in assuming the energies of the donor and acceptor states to be independent of degree of association.

Interpretation of Experimental Results

The longer wave-length emission is attributed to radiative transitions involving the ground states of highly associated donor-acceptor pairs and consequently should depend on the chemical identity of

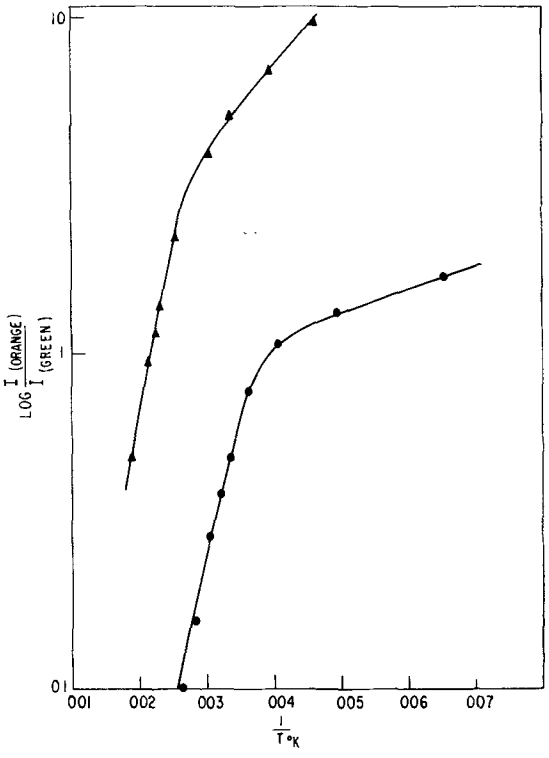

Fig. 8. log I orange/I green vs. 1/T ——— 3650Å excitation; ▲, hexagonal ZnS:10^{-4} Cu, 2 × 10^{-4} In; ●, hexagonal ZnS:10^{-4} Cu, 10^{-4} Ga.

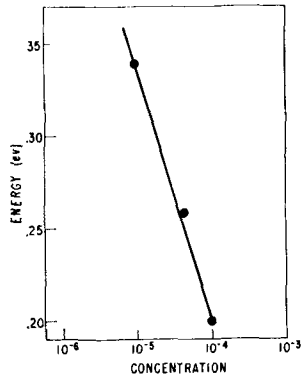

Fig. 9. E (slope from Fig. 8) vs. log concentration Cu in ZnS:Cu, In.

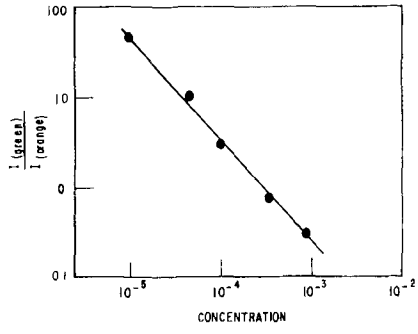

Fig. 10. log I orange/I green vs. log concentration Cu in cubic ZnS:Cu, In.

both donor and acceptor. This has been observed experimentally as has already been pointed out with ZnS:Ag,Ga and ZnS:Ag,In. In ZnS:Cu,Ga and ZnS:Cu,In, the difference in spectral distributions of the long wave-length emissions is less marked but present.

In addition, the model for the long wave-length center is in agreement with the fact that the temperature dependent properties are determined primarily by the identity of the coactivator, since the energy level of the activator for both the short and long wave emission is nearly identical, whereas different energies are associated with the Ga and In levels. The latter was pointed out by Hoogenstraaten (10) for the trap depths for Ga and In. This was confirmed in the glow curve measurements of the present study. In Fig. 8 the log of the ratio of orange to green intensities is plotted against the reciprocal of the absolute temperature for hexagonal ZnS:10^{-4} Cu, Ga and hexagonal ZnS:10^{-4} Cu, 2 x 10^{-4} In. The slopes of these plots are the differences in energies of the *s*- and *l*-type centers in their emitting states and are approximately the difference in energies of the donor levels responsible for the short and long wave-length emissions. The total quantum efficiency does not decrease in this temperature interval, and the effects of competing nonradiative processes can therefore be neglected. The nonlinear portions of the plots observed at lower temperatures indicate the absence of thermal equilibrium. The slope is 0.12 ev for ZnS:Cu,Ga and 0.20 ev for ZnS:Cu,In. Although these energies are lower than the values of the trap depths, i.e., 0.50 ev for In and 0.42 ev for Ga, the energy differences are in the right direction and the 0.08 ev difference between Ga and In is the same as the difference in energies reported for the trap depths (10). With decrease in concentration of activator and coactivator, the energies become larger as is shown in Fig. 9. This effect of concentration is qualitatively in accord with the changes in energy level structures of the two types of centers predicted by Eq. [7] since the contribution from each pair changes with concentration.

Using Eq. [6], the trap depths for In and Ga as calculated from emission spectra of Cu-activated materials are 0.47 ev for In and 0.44 for Ga which compare favorably with the thermal trap depths described above. In the case of Ag-activated phosphors, however, the values obtained are 0.80 for In and 0.72 for Ga. The difference in calculated trap depths is 0.08 ev, however.

Equation [4] predicts a slope of minus one between log I_s/I_l and log C, and Fig. 10 shows such a dependence in the cubic ZnS:Cu,In system.

The ratio I_s/I_l was found to be approximately independent of excitation intensity. This experimental result is consistent with the prediction of the theoretical analysis in the Theoretical Analysis Section based on *s*-emission involving excited donor states of donor-acceptor pairs, and is contrary to the results of the analysis based on *s*-emission involving conduction electrons.

In the section on Experimental Results it was pointed out that a higher concentration of Ga than of In is necessary to make the long wave-length emission predominate. Superficially, this might seem in conflict with the model since Ga has the shallower trap depth and consequent greater spatial extension of its wave functions so that sufficient overlap for radiative transitions to a less closely associated ac-

Table I

	I, ev	II, ev	III, ev	IV, ev
Hex. ZnS: Cu, Ga	2.39	0.42	1.97	1.89
Hex. ZnS: Cu, In	2.39	0.50	1.89	1.88
Hex. ZnS: Ag, Ga	2.78	0.42	2.36	2.10
Hex. ZnS: Ag, In	2.78	0.50	2.28	2.02

I. Energy of short wave-length emission peak.
II. Trap depth of coactivator (10).
III. I-II calculated energy for long wave-length emission.
IV. Observed energy at long wave-length emission peak.

ceptor at a lower concentration would be expected. However, as is evident from Eq. [5] the ratio of occupational probabilities $P(\epsilon_s)/P(\epsilon_l)$ not only strongly favors the long wave-length emission but also is strongly dependent on the energy of the ground state of the donor. The Ga, compared to In, is less favored by this factor to emit in the long wave-length band so that an increased concentration of Ga over In is necessary to attain comparable values of I_s/I_l in these two materials.

In Table I, the energy at the long wave-length emission peak is compared to that calculated from thermal and optical data involving the trap depth of the coactivator and the emission peak of the short wave-length process, respectively. The difference in these two values should give approximately the energy of the long wave-length emission in accordance with Eq. [6]. In the Cu-activated materials, this relation is satisfied but with Ag-activated phosphors the calculated and observed values differ by 0.26 ev in both cases.[3] Because of this approximate agreement of Eq. [6] with experiment a lower limit on the value of l is suggested. From Eq. [7] an increase in the transition energy E_e for nearest-neighbor pairs ($l = 1$) of 3/4 ev is predicted for these phosphors; an increase of 1/2 ev for second-nearest neighbors pairs ($l = 2$); and an increase of 2/5 ev for third-nearest neighbors pairs ($l = 3$). Only $l \geqq 4$ is consistent with the success of Eq. [6]. In addition, the interimpurity distance r_l is different for the cubic and hexagonal structures if $l \geqq 3$, and this may account in part for the dependence on crystal structure of the relative intensities of the short and long wave-length bands.

An interesting sequel to the work reported here is a preliminary study of the effect of Cd substitution on ZnS phosphors showing the long wave-length emission. In hexagonal ZnS: 10^{-4}Cu,In, substitution of up to 15 mole % CdS causes an increase in the ratio of intensities of the short wave-length to long wave-length emission at room temperature. These data are consistent with the analysis of the occupational probabilities of electrons in the emitting states of the s- and l-type centers as discussed in this paper. Up to 15% CdS substitution essentially decreases the depth of the ground state of the donor and thus increases the competition of the short wave-length process with the long wave-length process. A more detailed account of this work will appear in a future communication.

In summary, the long wave-length emission bands observed in ZnS: (Cu or Ag), (Ga or In) phosphors are attributed to transitions between the ground state of the donor and the ground state of the acceptor in highly associated coactivator-activator pairs. The short wave-length emission apparently involves transitions between excited donor states and the ground state of the acceptor in less highly associated pairs characterized by a distribution of interimpurity distances. The spectra and the dependence on temperature and on pair concentration of the intensities of the short and long wave-length bands are in accord with this model.

It is predicted that at low temperatures the centers responsible for the long wave-length emission should be capable of excitation at longer wave lengths than the short wave-length centers, and excitation of single crystals under these conditions with polarized light should yield polarized long wave-length emission since the highly associated pairs have a strong anisotropy.

[3] It should be pointed out that observed and calculated values of the long wave-length emission in ZnS: Au, In agree very well.

Acknowledgment

We wish to acknowledge the contributions from the following people: Mrs. D. J. Weil for sample preparation; Dr. J. S. Prener for suggestions and critical review; Dr. P. D. Johnson for glow-curve measurements; Dr. F. J. Studer for measurement of emission spectra.

Manuscript received Aug. 4, 1958. This paper was prepared for delivery before the New York Meeting, April 27-May 1, 1958.

Any discussion of this paper will appear in a Discussion Section to be published in the December 1959 JOURNAL.

REFERENCES

1. F. A. Kröger and J. Dikhoff, *Physica*, **16**, 297 (1950).
2. H. A. Klasens, *This Journal*, **100**, 72 (1953).
3. H. C. Froelich, *ibid.*, **100**, 496 (1953).
4. E. F. Apple, *ibid.*, **105**, 251 (1958).
5. J. S. Prener and F. E. Williams, *Phys. Rev.*, **101**, 1427 (1956); *This Journal*, **103**, 342 (1956); *J. phys. radium*, **17**, 667 (1956).
6. F. E. Williams, *J. Opt. Soc. Amer.*, **47**, 869 (1957).
7. J. S. Prener, *J. Chem. Phys.*, **25**, 1294 (1956).
8. H. Reiss, *ibid.*, **25**, 400 (1956).
9. F. E. Williams, To be published.
10. W. Hoogenstraaten, Thesis, University of Amsterdam, February 1958.

Effect of Various Etches on Recombination Centers at Germanium Surfaces

George Wallis[1] and Shyh Wang[2]

Sylvania Electric Products, Inc., Woburn, Massachusetts

ABSTRACT

Germanium samples were etched with CP-4, hydrogen peroxide, iodine A, electrolytic, and silver etch. The density, energy levels, and capture probabilities of the recombination centers were measured before and after the etched samples were baked. It was found that iodine A and electrolytic etches produce recombination centers of one type, and the remaining etches, centers of another type. Baking converted the centers found on iodine A etched surfaces into the type of centers that are characteristic of surfaces etched with CP-4, hydrogen peroxide, and silver etches. When surfaces were prepared with an etch other than iodine A, baking increased the density but did not affect the types of the centers. The different etches did not produce significant differences in maximum surface recombination velocity either before or after baking.

During recent years, it has become evident that the recombination process on germanium surfaces is described fully by the Shockley-Read theory (1). Good theoretical fits to experimental results can be obtained if it is assumed that the recombination centers are at discrete energy levels, and it has been our experience that within experimental error the same type of recombination centers is found on CP-4 etched surfaces irrespective of conductivity type. The present work was undertaken in order to find out what effect different etches have on the recombination centers. The etches under investigation were CP-4, hydrogen peroxide etch, iodine A etch, electrolytic etch, and silver etch (see appendix). Our results indicate that under favorable conditions all of the above etches produce comparable densities of recombination centers. However, iodine A and the electrolytic etch produce recombination centers of one type while the remaining etches produce centers of a different type. As far as maximum surface recombination velocity is concerned, a range of values between 100 and 200 cm/sec was found for all etches. Baking of the etched samples under atmospheric conditions at 100°C for periods in excess of 16 hr increased the density of recombination centers by varying amounts. In addition, baking converted the type of recombination center found on iodine A etched surfaces into the type characteristic of CP-4, hydrogen peroxide, and silver etch. Baking did not change the type of recombination center when the surfaces were treated previously with any etch other than iodine A.

Theory and Procedure

Previous investigation of the fast states at a CP-4 etched germanium surface has indicated that the following simple model is adequate (2). The fast states are located at four discrete energy levels within the forbidden gap, as shown in Fig. 1. Each of the levels is associated with four parameters, i.e., energy, density, capture probability for holes, and capture probability for electrons. The levels near the two band edges have a larger density than the levels near the center of the gap; however, the levels near the band edges have much smaller capture probabilities for electrons and/or holes. When the surface potential (energy difference between Fermi-level and intrinsic Fermi-level at surface) is in a range $-6\ kT$ to $+2\ kT$, the field effect is controlled by all four levels, but the surface recombination process is controlled primarily by the two levels near the center of the gap. The latter therefore will be referred to as surface recombination centers. It turns out that within experimental error the parameters in the theoretical expression for surface recombination velocity are the same for either recombination level. Hence, the two levels are regarded as constituting one type of recombination centers, having the same capture probabilities for holes and electrons. In view of these simplifications, we are concerned with ten rather than sixteen parameters, i.e., the densities and energies of the four levels, and the capture probabilities for holes and electrons of the pair of recombination centers.

When a freshly etched sample is exposed to various ambient atmospheres, some of these parameters

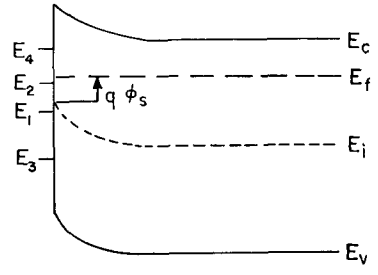

Fig. 1. Band structure of Ge near surface. E_1, E_2, E_3, and E_4 are the energy levels of the four groups of fast states at the germanium-oxide interface.

[1] Present address: Clevite Transistor Products, Waltham, Mass.

[2] Present address: Department of Electrical Engineering, University of California, Berkeley, Calif.

evidently change. A consistent interpretation is possible if it is assumed that only the densities of the pair of recombination centers change, and that they change in such a way that the ratio of the densities remains constant.

In the presence of a single type of recombination center with energy level E_t and capture probabilities for electrons c_n and for holes c_p, the photoconductance G_L of a thin sample[3] is given by

$$G_L = k\tau_{eff} = k\{1/\tau + N_t\,(c_p c_n)^{1/2}\,(n_o + p_o)/an_i[C + \cosh q\,(\phi_s - \phi_o)/kT]\}^{-1} \quad [1]$$

where k is a proportionality constant; τ_{eff} and τ are the effective and the bulk lifetime, respectively; N_t is the density of the centers; n_o and p_o are the equilibrium electron and hole concentrations; n_i is the intrinsic carrier concentration; a is the thickness of a sample; ϕ_s is the surface potential; $2q\phi_o/kT = \ln (c_p/c_n)$; $C = \cosh (E_t - E_i - q\phi_o)/kT$; and E_i is the intrinsic Fermi level. The effective lifetime is related to the surface recombination velocity v_s by the equation $\tau_{eff} = [1/\tau + 2v_s/a]^{-1}$.

A range of ϕ_s values can be obtained by exposing a sample to a Brattain-Bardeen cycle (3) of dry oxygen, sparked oxygen, and wet nitrogen. During the cycle, a series of simultaneous measurements of G_L and ϕ_s can be made. The determination of C and ϕ_o from the experimental curves of G_L vs. ϕ_s is straightforward provided N_t, C, and ϕ_o remain constant during a cycle. We believe that C and ϕ_o satisfy this condition. However, N_t did not remain constant on the freshly etched surfaces under discussion. Hence, C and ϕ_o had to be determined by a less direct method (4) which is independent of N_t.

When a small a-c field is applied normal to the surface of a sample, the change in photoconductance ΔG_L may be expressed as

$$\frac{\Delta G_L}{G_L} = (\tau_{eff}/\tau - 1)\,\frac{\sinh q\,(\phi_s - \phi_o)/kT}{C + \cosh q\,(\phi_s - \phi_o)/kT}\,\frac{q\Delta\phi_s}{2kT} \quad [2]$$

This equation contains the same parameters C and ϕ_o as Eq. [1], but it does not contain N_t explicitly. The change in surface potential with field, $\Delta\phi_s$, can be calculated from the field effect conductance, ΔG_s, for a given value of ϕ_s by use of the expression

$$\Delta G_s = \frac{\partial G_s}{\partial \phi_s}\,\Delta\phi_s \quad [3]$$

where $\partial G_s/\partial\phi_s$ is a known function of ϕ_s.

Experimentally, a series of simultaneous measurements of the following four quantities is made during a Brattain-Bardeen cycle: (*a*) surface potential ϕ_s, calculated from the d-c surface conductance; (*b*) field effect conductance, ΔG_s, for a small a-c field applied normal to the surface; (*c*) the a-c photoconductance G_L which results when a region of the sample is illuminated with chopped light from a water filtered light source;[4] (*d*) the change in conductance ΔG with an a-c field of the same strength as in (*b*), measured in the presence of d-c light of the same intensity as the chopped light in (c). ΔG (4) is found to be the sum of the change in photoconductance ΔG_L and the dark field-effect conductance ΔG_s.

From these four quantities, a plot of $\Delta G_L/G_L$ vs. ϕ_s may be constructed which can be fitted by Eq. [2] by means of the adjustable parameters C and ϕ_o. Relative changes in the density of the recombination centers can be deduced by comparing the experimental plot of G_L vs. ϕ_s with Eq. [1] into which the previously derived values of C and ϕ_o have been substituted.

Finally, the densities of the recombination centers and the other two surface states are deduced as follows. In the field-effect experiment, the total charge, induced by the a-c field, is the sum of the charge in the space charge region, ΔQ_{sc}, and the charge in the surface states, ΔQ_{ss}. The total induced charge is known, and ΔQ_{sc} can be computed for each experimental point from the equation

$$\Delta Q_{sc} = \frac{\partial Q_{sc}}{\partial \phi_s}\,\Delta\phi_s \quad [4]$$

where $\partial Q_{sc}/\partial\phi_s$ is a known function of ϕ_s, and $\Delta\phi_s$ is obtained from the field effect by use of Eq. [3]. Hence, one can construct a curve of ΔQ_{ss} vs. ϕ_s. From the latter, the density of each of the surface states can be deduced by curve fitting to the equation

$$\Delta Q_{ss} = q\sum_{n=1}^{4} N_{tn}\,\frac{\exp y_n}{(1 + \exp y_n)^2}\,\frac{q\Delta\phi_s}{kT} \quad [5]$$

where $y_n = (E_{tn} - E_i - q\phi_s)/kT$, and the summation is over the four states.

All samples used in this work were cut from a single crystal of n-type Ge. The resistivity of the samples was 18 ohm-cm and the bulk lifetime about 1000 μsec. All samples were oriented along the same plane (321) in order to exclude possible structural effects. The thickness of the samples was between 7 and 25 mil. Samples were hand polished, and their ends plated with Rh. Ohmic contacts were soldered to the plated ends, and two further contacts which served as voltage probes were soldered to one side of the samples. During an etch, the plated and soldered areas were masked by Apiezon W wax. After etching, the samples were rinsed in distilled water, the wax was dissolved in Triad,[5] and the Triad in turn was rinsed off with acetone, alcohol, and distilled water, in this order. After the last rinse was dried off, the sample was mounted in a glass holder and placed in a double-walled glass tube. Water from a thermostatically controlled tank was pumped through the region between the two walls. Thus, the temperature of the sample during a cycle was kept at 29° ± 0.05°C. Furthermore, the water served to filter out penetrating light.

The d-c conductance was measured to five significant figures. From the conductance, the surface potential was calculated without taking Schrieffer's correction (5) into consideration. The field-effect measurements were made with a 32 cps sinusoidal voltage, using essentially Low's circuit (6). The peak field strength was 4000 v/cm. The photoconductance

[3] The thickness a of the sample must be less than a diffusion length.

[4] The theoretical expressions hold only if injection is limited to the surface. Hence, nonpenetrating light must be used.

[5] Detrex Chemical Industries, Inc., Detroit, Mich.

Table I

Etch		$(v_s)_{max.}$ cm/sec.	$q\phi_o/kT = \frac{1}{2}\ln(c_p/c_n)$	C	$(N_{to})_1 \times 10^{-10}$, cm^{-2}	$(E_{t1}-E_i)/kT$	$(E_{t2}-E_t)/kT$	$\sigma_p \times 10^{16}$, cm^2	$\sigma_n \times 10^{16}$, cm^2	$(N_t)_3 \times 10^{-12}$, cm^{-2}
CP-4	Pre-bake	150	1.1	8	4.6	—1.7	3.9	27.6	3.1	0.7
	Post bake	306	1.1	6	8.2	—1.4	3.6	25.5	2.8	2.2
H_2O_2	Pre-bake	235	1.1	7	6.3	—1.5	3.7	30.0	3.3	0.8
	Post bake	535	1.4	7	12.9	—1.2	4.0	44.2	2.7	2.1
Iodine A	Pre-bake	162	1.9	8	4.6	—0.9	4.7	67.1	1.5	1.1
	Post bake	403	0.9	7	18.1	—1.7	3.5	14.7	2.5	2.2
Electrolytic	Pre-bake	131	1.9	8	2.5	—0.9	4.7	106.0	2.4	0.9
	Post bake	1100	1.9	6	16.7	—0.6	4.4	101.0	2.3	2.1
Silver	Pre-bake	170	1.1	10	7.3	—1.7	3.9	27.6	3.1	0.8
	Post bake	600	1.4	8	19.7	—1.4	3.6	25.5	2.8	—

Summary of results: $(N_{to})_1$ refers to the density of recombination centers below the intrinsic Fermi level and was measured at $\phi_s = \phi_o$. The density of the recombination centers above the intrinsic Fermi level was found to be $(N_{to})_2 = \frac{1}{2}(N_{to})_1$. $(N_t)_3$ refers to the density of the levels near the valence band which are seen in the field effect but are found to have a negligible effect on surface recombination. The values of $(N_t)_3$ were computed on the assumption that the level is located at $E_t - E_i = -6.8$ kT. The contribution of $(N_t)_3$ to the field effect was negligible on the silver-etched baked surface. The capture cross sections σ_p and σ_n for holes and electrons, respectively, refer to the recombination centers. They are related to the corresponding capture probabilities c_p and c_n by the equations $c_p = v_t\sigma_p$, $c_n = v_t\sigma_n$, where v_t is the thermal velocity 10^7cm/sec at room temperature.

was measured with light from a tungsten lamp chopped at 60 cps. The injection never exceeded 10% of the equilibrium bulk majority carrier concentration. Usually the photoconductance measurement was checked by a direct measurement of effective lifetime by means of the photoconductive decay method. The surface potential was changed by exposing the sample to Brattain-Bardeen cycles of sparked oxygen, dry oxygen or nitrogen, and nitrogen bubbled slowly through distilled water. The oxygen was sparked with a Tesla coil for short periods of time (usually less than a second). The gases were preheated to the temperature of the sample. Measurements were made before and after the samples were baked in a dry room atmosphere at 100°C for a period of 16 hr or more.

Results and Discussion

A summary of the results is presented in Table I. In Fig. 2, we show experimental points of $\Delta G_L/G_L$ and theoretical fits (solid lines) plotted as a function of ϕ_s for surfaces freshly etched with silver etch, electrolytic etch, iodine A etch, and H_2O_2 etch. Corresponding plots for CP-4 have been shown in a previous paper (2). It will be noticed that the theoretical plots (based on Eq. [2]) fit the experimental points quite closely throughout the experimental range of ϕ_s. Notice, also, that there appear to exist two distinct values of ϕ_o, i.e., 1.1 kT and 1.9 kT. The significance of these two values is discussed below. With ϕ_o given by the value of ϕ_s at which $\Delta G_L/G_L$ vanishes, C was the only parameter in each fit. From ϕ_o and C, the energy levels of the recombination centers were deduced for each curve.

Figure 3 presents curves of surface recombination velocity v_s vs. ϕ_s for the same surfaces as the curves in Fig. 2. For comparison's sake, we have added a theoretical curve (dashed line) based on Eq. [1], with the parameters C and ϕ_o, appropriate for the H_2O_2-etched surface and with $(N_t)_1$ and $(N_t)_2$ assumed constant. The experimental curve (triangles) is much flatter and rises beyond the maximum of the theoretical curve. The discrepancies between the experimental and theoretical curves are due entirely to changes in $(N_t)_1$ and $(N_t)_2$ during the cycle. If we had failed to take these changes into consideration,

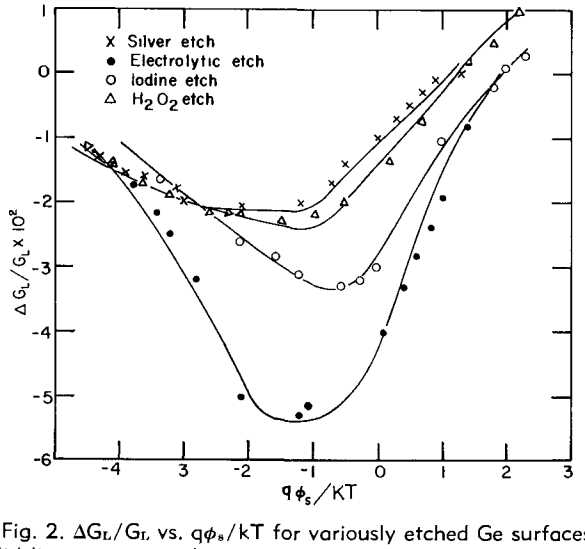

Fig. 2. $\Delta G_L/G_L$ vs. $q\phi_s/kT$ for variously etched Ge surfaces. Solid lines represent theoretical fits to the experimental data.

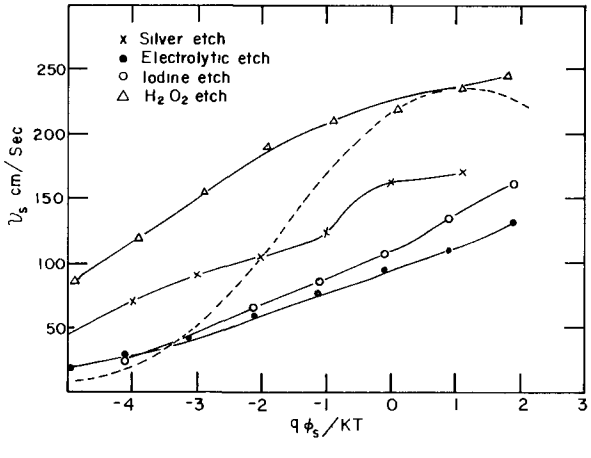

Fig. 3. Surface recombination velocity, v_s, vs. surface potential $q\phi_s/kT$ for the same surfaces as in Fig. 2. Solid lines represent the experimental data. Dashed curve was computed from Eq. [1] for the hydrogen peroxide-etched surface, with the parameters C and ϕ_o as deduced from the corresponding plot in Fig. 2, and with $(N_t)_1$ and $(N_t)_2$ assumed constant.

and if we had attempted to analyze the v_s vs. ϕ_s curves on the basis of Eq. [1], we would have obtained much larger values of C and ϕ_o. These values would have been inconsistent with the experimental $\Delta G_L/G_L$ curves.

By comparison of experimental and theoretical curves of v_s vs. ϕ_s, one can deduce whether relative changes in the density of the two recombination centers have taken place during a Brattain-Bardeen cycle. Typical relative changes for an H_2O_2 etched surface several days after etching (solid line) and after baking (dashed curve) are shown in Fig. 4. N_{to} is the density at the time ϕ_o was measured. N_t is not a function of ϕ_s but has been plotted against ϕ_s merely for convenience. For each curve, the extreme point at the left represents the density of centers immediately after oxygen was sparked. The extreme points at the right were in both cases taken in an ambient of wet nitrogen. Evidently, the baked surface was far more stable than the unbaked surface. Comparable amounts of sparking increased the density of centers on the unbaked surface by a factor of ten, as compared to an increase of less than two for the baked surface. Upon sparking, the unbaked surface became more p-type than the baked surface. On the other hand, in wet nitrogen, the unbaked surface became somewhat less n-type than the baked surface. Therefore, baking appears to make the surface more n-type. Moreover, the same Brattain-Bardeen cycle swung the surface potential of the unbaked surface through a larger range than that of the baked surface. Although these results were not strictly reproducible, these tendencies usually have been observed.

Figure 5 shows plots of $kT\Delta Q_{ss}/q\Delta\phi_s$ vs. ϕ_s for the same surfaces as in Fig. 2. The points were computed from the experimental plots of ΔG_s vs. ϕ_s, as described above. The theoretical fits are based on Eq. [7] which contains eight parameters, i.e., the densities and energies of the four levels. The energy levels near the band edges were far enough removed

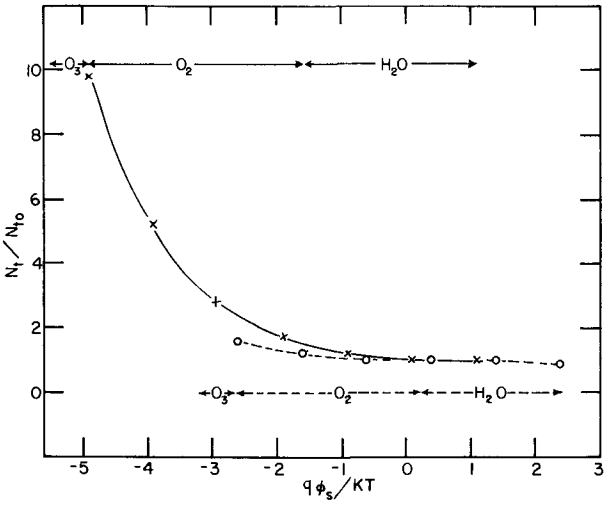

Fig. 4. Normalized density of the recombination centers, N_t/N_{to} vs. surface potential, $q\phi_s/kT$, for the hydrogen peroxide-etched surface during a Brattain-Bardeen cycle. Normalization was arbitrarily carried out at the point $\phi_s = \phi_o$. The solid curve refers to the freshly etched sample, and the dashed curve refers to the same sample after baking.

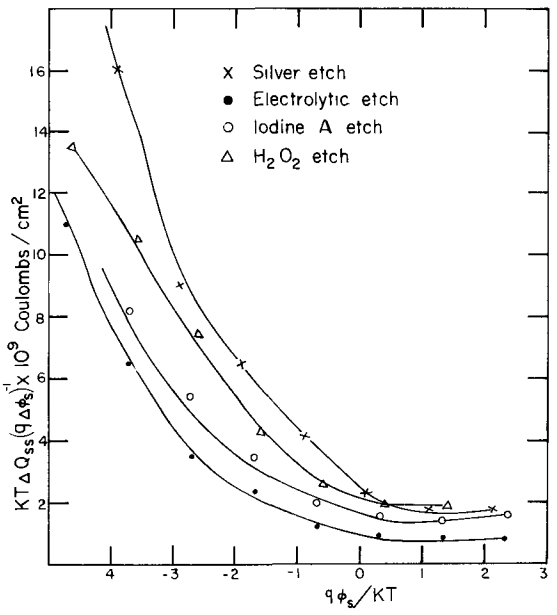

Fig. 5. Change of charge in the fast states per unit change in surface potential, $kT\Delta Q_{ss}/q\Delta\phi_s$, vs. surface potential, $q\phi_s/kT$, for the surfaces shown in Fig. 2 and 3. Solid curves represent theoretical fits to the experimental data.

from our range of ϕ_s values so that the two respective terms $N_{tn} \exp y_n (1 + \exp y_n)^{-2}$, $n = 3,4$, could be replaced by $(N_t)_3 \exp y_3 = A_3 \exp(-q\phi_s/kT)$, where $A_3 = (N_t)_3 \exp(E_{t3} - E_i)/kT$ for the level near the valence band $(E_{t3} - E_i < 0)$, and by $(N_t)_4 \exp(-y_4) = A_4 \exp q\phi_s/kT$, where $A_4 = (N_t)_4 \exp -(E_{t4} - E_i)/kT$ for the level near the conduction band $(E_{t4} - E_i > 0)$. For the energy levels of the states near the center of the forbidden gap (recombination centers), we used the values deduced from Fig. 2. As previously stated, it was assumed that the ratio of the densities of the two recombination centers remained constant during a Brattain-Bardeen cycle. The relative changes in the density of either recombination center were read off from plots such as Fig. 4. Thus, the solid lines in Fig. 5 represent four parameter fits, the parameters being the densities $(N_{to})_1$ and $(N_{to})_2$ of the recombination centers and A_3 and A_4 of the centers near the band edges. The density $(N_{to})_1$ of the recombination center below the center of the gap, $E_{t1} - E_i < 0$, has been found generally to be larger than the density $(N_{to})_2$ of the other recombination center. Almost invariably, the best fits were obtained by setting $(N_{to})_1 = 2\ (N_{to})_2$. The values for the density N_{t3} of the fast states near the valence band were calculated from A_3 on the assumption (2) that the states were located at the level $E_t - E_i = -6.8\ kT$. This level could not be determined with great accuracy. The level near the conduction band contributed relatively little to the field effect. Hence, there is considerable uncertainty about the values of A_4, and since, in addition, there is some doubt about the location of the level, we did not calculate the corresponding densities.

Before the data can be discussed, one must make an estimate of the errors involved in the measurements. No over-all estimates can be given because the accuracy of the different measurements is not the same throughout the experimental range of ϕ_s.

For instance, near the minimum in surface conductance, a large change in ϕ_s corresponds to a small change in surface conductance so that accurate determination of ϕ_s is very difficult. However, when $\phi_s - \phi_{min}$[6] becomes larger than kT, the situation is reversed: a small change in ϕ_s corresponds to a larger change in surface conductance so that fairly accurate determination of ϕ_s becomes possible. On the other hand, the determination of ΔG_L is less accurate near $\phi_s = \phi_o$ than it is for other regions of ϕ_s since it represents the difference between two large quantities, i.e., ΔG and ΔG_s.

We estimate that our values of ϕ_o are reliable to $\pm 0.3\ kT$, the uncertainty being due to inaccuracy in the measurement of ϕ_s and ΔG_L. Values of C were obtained from fits to the $\Delta G_L/G_L$ vs. ϕ_s curves and are estimated to be accurate to 20%. The energy levels were calculated from the values of C and ϕ_o and are reliable to about $\pm 0.5\ kT$. The densities of the recombination centers were obtained from a comparison of three curves, i.e., $\Delta G_L/G_L$ vs. ϕ_s, ΔG_s vs. ϕ_s, and G_L vs. ϕ_s. Moreover, the values are quite sensitive to the exact values for the energy levels. Therefore, they are probably only reliable to about 50%. Finally, the error in the values of $\sqrt{c_p c_n}$ involving C and N_t is also of the order of 50%.

We can summarize the results as follows:

(i) The values of ϕ_o in Table I fall into two groups: one around 1.1 kT and the other around 1.9 kT. With an estimated error of $\pm 0.3\ kT$, one might at first sight hesitate as to whether this difference in ϕ_o should be interpreted as a single level or several levels. However, repeated experiments with electrolytically etched surfaces consistently gave larger values of ϕ_o than were obtained on CP-4 etched surfaces. Hence, we conclude that recombination centers exist at two types of discrete levels, a pair of "CP-4 levels" with a ϕ_o of about 1.1 kT and a pair of "electrolytic levels" with a ϕ_o of about 1.9 kT. It is seen from the table that the pair of "electrolytic levels" are separated by about the same energy interval as the pair of "CP-4 levels" but are displaced from the latter by about 0.8 kT. The capture probabilities for electrons, c_n, have approximately the same value for the two types of levels. However, the capture probabilities for holes, c_p, of the "electrolytic levels" are larger than those of the "CP-4 levels" by a factor of about three.

(ii) After samples etched with iodine A were baked, the initial "electrolytic levels" were found to have been replaced by CP-4 levels. On surfaces prepared with any of the other etches, the same type of centers were observed before and after baking. In all cases, the density of the recombination centers was larger after baking than before baking. The increase in the density of recombination centers during baking appears to take place in a few hours. Further baking at the same temperature has little effect on the density of the centers. This seems to argue for the existence of an equilibrium concentration of recombination centers.

If the baked samples are allowed to stand in a dry atmosphere at room temperature for several days, the density of the centers usually decreases somewhat from the high value immediately after baking. However, the density of centers never recovers to the initial value before baking.

(iii) When a sample is exposed to sparked oxygen, the changes in the density of recombination centers depend on three factors, (a) intensity of the spark, (b) duration of the sparking, (c) history of the sample. The changes are largest for freshly etched samples, and they are small for aged and baked samples. On freshly etched samples, the density of recombination centers often is increased by an order of magnitude when the ambient oxygen is sparked for a fraction of a second. No comparable increases in density have ever been observed after baking. Whereas recovery after baking is very slow and the decrease in density is small, after sparking the recovery is almost complete after about half an hour.

(iv) Exposure of a freshly etched sample to water vapor increases the density of recombination centers by amounts depending on (a) humidity, (b) length of exposure, and (c) history of the sample. The changes are quite gradual, but they can get as large as a factor of twenty if the sample is kept in a humid atmosphere for several hours.

When the humid atmosphere is replaced by a dry ambient, a slow recovery in the density of recombination centers usually is observed. Frequently, the density recovers to a value somewhat smaller than the value before exposure to water vapor. Sometimes, however, no change in density is apparent for an hour or more. A detailed study of these effects has not been made yet.

(v) Irrespective of which of the etches was used, the surface potential of a newly etched sample in a dry oxygen atmosphere was usually near the intrinsic Fermi level, but its exact value depended on the washing procedure after etching. After baking, the surface potential was invariably such as to make the surface more n-type. This is in agreement with the observation of other workers (7) according to which oxidation of a sample tends to make the surface n-type. We have also observed in agreement with other authors (7) that comparable Brattain-Bardeen cycles produce large changes in surface potential on some surfaces and small changes on others. There is an indication that baking and aging of the surface tends to cut down the range over which the surface potential can be changed. When a baked surface is rinsed in distilled water, the range over which the surface potential can be changed is increased and the density in recombination centers is decreased.

Baking, exposure to sparked oxygen, and exposure to water vapor all tend to increase the density of recombination centers and to decrease the range of surface potential. Baking and exposure to sparked oxygen clearly promote oxidation of the Ge surface. The effect of water vapor is more complicated. In part, water vapor may be expected to dissolve small amounts of soluble oxide. In part, water vapor appears to promote the oxidation of insoluble GeO to soluble GeO_2. Thus, our results strongly suggest that

[6] ϕ_{min} is the value of ϕ_s for minimum conductance and is given by $kT/q \ln(bn_o/p_o)$ where b is the ratio of electron to hole mobility.

the density of the recombination centers depends on the condition of the oxide films.

The recombination levels probably arise wherever there is a mismatch between the bulk Ge and the oxide film, at the edges and corners and at imperfections of any kind. Since the oxide films appear to be largely amorphous (8), epitaxical growth probably is confined to small regions where the films nucleate, and regions of mismatch abound. A further important source for imperfections may be the lack of stoichiometry in the film. For instance, surplus oxygen atoms at the interface could provide recombination levels. Another source of recombination centers may be fluorine which is believed to be present in the films (8). In general, it can be said that the density of the recombination centers is probably a measure of the amount of disorder at the germanium-oxide interface. We conclude, therefore, that such oxidation processes as baking, exposure to water vapor, and exposure to sparked oxygen all increase the degree of disorder at the interface. During subsequent exposure to a dry ambient, some degree of order is gradually restored. This throws an interesting light on the details of the oxidation process.

The results in (ii) suggest that not only the density but also the type of recombination centers depend on the oxide film. Any correlation between the type of recombination center and some property of the oxide film is extremely difficult as the following remarks show. Since the centers are probably at the germanium-oxide interface, one would expect that they would be affected only by a few monolayers of film nearest the interface. It is possible that these first monolayers are not representative of the rest of the film. In addition, the oxide films are probably inhomogeneous; both monoxide and dioxide as well as impurity atoms from the etching solution may be present in varying amounts (8). It should also be emphasized that the condition of the first few monolayers at the time of an experimental run may be different from their condition immediately after the etch. A time interval of at least several hours between etch and first run was required to mount the sample and allow it to get into thermal equilibrium with the tube. During most of this time, the sample was kept in a dry atmosphere, but it is nevertheless possible that changes occurred in the oxide film. Further changes undoubtedly occurred during the Brattain-Bardeen cycle. Whether, and to what extent, the few monolayers nearest the germanium-oxide interface were affected presumably depended on the thickness and porosity of the remainder of the film.

It is possible that both types of centers are present simultaneously on an etched surface. Usually, one type of center will be dominant, but in some cases, both may contribute to the recombination process in appreciable amounts. In such cases, our interpretation in terms of a single type of recombination center would be an oversimplification, and the parameters derived on the basis of such an interpretation would, in fact, represent averages over both types of centers. If this is the correct interpretation, it must, however, be assumed that the relative contributions of the two types of centers remained approximately constant during a Brattain-Bardeen cycle. Otherwise, the $\Delta G_L/G_L$ curves could not have been fitted with single values of C and ϕ_o throughout a cycle.

So far, the discussion has been limited to the centers near the intrinsic Fermi level which largely control the recombination process. The existence of another pair of levels near the band edges is indicated clearly by the field effect. The density of these levels is usually an order of magnitude larger than the density of levels near the center of the gap. However, their capture probabilities for electrons and/or holes are so small that their net effect on the recombination process is negligible in the range of surface potential which was used in this work. Likewise, the range of surface potential was too small to ascertain the energy of the levels with any accuracy. On relatively freshly etched surfaces the density of the levels near the band edges was increased by baking. It is possible that some changes in density also occurred during exposure to a Brattain-Bardeen cycle. However, in the analysis, we assumed that the density of the states near the band edges remained constant during a cycle so as not to introduce further parameters. From the quality of the fits in Fig. 4, it appears that, if changes in density did occur, they were relatively small.

Extensive work on the recombination centers on CP-4 etched surfaces has been reported by Brattain and Garrett (9) and by Many and Gerlich (10). The same levels were seen also in field effect measurements by Montgomery and Brown (11) and by Bardeen, *et al.* (12). All of these authors agree that there exists a discrete level near the conduction band and a discrete level near the valence band. There is, however, some disagreement as to whether the levels near the center of the gap are continuously distributed or discrete. Continuous distributions are assumed by Brattain and Garrett, Montgomery and Brown, and by Bardeen, *et al.* Two discrete levels are assumed by Many and Gerlich and by the authors. It is agreed generally that the field effect data at room temperature can be interpreted equally well on either assumption. The low temperature field-effect data of Montgomery and Brown also could be interpreted in terms of discrete levels provided the assumption is made that the density of the levels was smaller at low temperatures than it was at high temperatures. This assumption would explain the small slope of their low-temperature curve of change of charge in surface states vs. surface potential. Surface recombination velocity data have been fitted most closely when discrete levels were assumed.

A comparison of our results and those of Many and Gerlich will be made after a brief description of their procedures and underlying assumptions. Whereas we obtained variations in ϕ_s by exposing the sample to the Brattain-Bardeen cycle, Many and Gerlich varied ϕ_s by the application of high a-c fields normal to the two surfaces of a sample. Measurements of surface conductivity and effective lifetime were made at peak field, peaks of different ampli-

tudes corresponding to different values of ϕ_s. During a run, a sample was kept in a constant atmosphere. In analyzing their data, Many and Gerlich used essentially Eq. [1] and assumed that N_t as well as C and ϕ_o remained constant during a run. By contrast, our analysis was based on Eqs. [2] and [3] and the assumption that C and ϕ_o, but not N_t, remained constant during a run.

Both procedures are open to criticism. Many and Gerlich's assumption that N_t remains constant during a run may not be entirely correct in view of the observations by Statz, *et al.* (13) according to which large applied fields appear to produce changes in the density of surface states. It is frequently difficult to tell from an analysis of the v_s vs. ϕ_s curves whether changes in the density of recombination centers have, in fact, occurred during a run. On the other hand, our assumption that C and ϕ_o remain constant during a Brattain-Bardeen cycle also may be questioned. Indeed, Many and Gerlich conclude that the C and ϕ_o values on a CP-4 etched surface vary through a range larger than the experimental error, and that the values depend both on the history of the sample and on the ambient atmosphere. This would mean that several types of recombination centers can exist on CP-4 etched surfaces, with one type being dominant under one set of ambient conditions, and another type dominant under different ambient conditions. Such a view would present two difficulties:

1. According to Many and Gerlich, $C = 6$ in nitrogen and $C = 12$ in oxygen and sparked oxygen. In the part of the ambient cycle in which we changed from oxygen to nitrogen, the fit to the $\Delta G_L/G_L$ curve is quite sensitive to C, and a change in the value of C by 50% should have been easily detectable. No such changes have been found.

2. During repeated cycles, ϕ_o was found sometimes immediately after the oxygen was sparked, and sometimes, at a considerable time after sparking, during which time the sample stood in a dry oxygen or nitrogen atmosphere. Occasionally, ϕ_o was found in a cycle from which the sparking of oxygen was omitted. Since, according to Many and Gerlich, $\phi_o = 0.35\ kT$ in oxygen and nitrogen and $\phi_o = 0.97\ kT$ in sparked oxygen, one would expect to measure different ϕ_o values depending on the details of the cycle. Within experimental error, we have found no such dependence. Thus, we conclude that we observed during a Brattain-Bardeen cycle either a single type of recombination center or, conceivably, two types of centers whose relative contributions to the recombination process remained approximately constant during the cycle.

Possible explanations for the discrepancies between our results and those of Many and Gerlich are the following. The dependence of C and ϕ_o on an ambient gas may show up only after extended exposure of a sample to the gas. Alternatively, it is possible that once a surface has acquired the recombination centers characteristic of sparked oxygen, it becomes immune to the growth of other types of centers upon subsequent exposure to different ambients.

Another difference between the work of Many and Gerlich and ours is concerned with the interpretation of the parameter $C = \cosh\ (E_t - E_i - q\phi_o)/kT$. The v_s vs. ϕ_s curve has the same shape irrespective of whether recombination centers are located at the level $E_t - E_i = q\phi_o + kT$ arcosh C or at the level $E_t - E_i = q\phi_o - kT$ arcosh C or at both levels. Since ϕ_o/kT is assumed to be temperature independent, the correct level could be deduced in principle from the measurement of C at two different temperatures. Temperature measurements were made by Many and Gerlich, and the results suggest that the recombination center lies at the level $E_t - E_i = q\phi_o + kT$ arcosh C. However, the results are not sufficiently accurate to make this conclusion altogether convincing. We rather incline to the view that recombination centers are located at both levels because the field effect measurements indicate that there exist fast states at both these levels. As far as the principal conclusions of this work are concerned, it does not matter whether one or both of the levels act as recombination centers.

A numerical comparison of results for CP-4 etched surfaces follows. Many and Gerlich find ϕ_o to have a range of values between 0.35 and 1.70 kT under the ambient conditions: vacuum, oxygen, nitrogen, hydrogen, and sparked oxygen. This is to be compared to our value of $1.1 \pm 0.3\ kT$. Many and Gerlich's values for C under the above ambient conditions range from 6.1 to 29.0, while the values found by us for all etches before and after baking are in the range 8 ± 2. From their values of C and ϕ_o, Many and Gerlich calculate that the recombination centers are located at a range of $E_t - E_i$ between 2.9 and 6 kT compared to our corresponding range $3.9 \pm 0.5\ kT$. From their field-effect measurements, Many and Gerlich find another state at about $-1\ kT$. Our corresponding value is $-1.7 \pm 0.5\ kT$. If Montgomery and Brown (11) interpret their field-effect data on the basis of discrete levels, they also find these levels at 3.9 kT and $-1\ kT$. In the calculation of ϕ_s, Many and Gerlich used the Schrieffer correction whereas Montgomery and Brown and the authors did not. Within the range of ϕ_s under discussion, the Schrieffer correction is not important.

The effect of various etches on surface recombination velocity has also been investigated by McKelvey and Longini (14). Their results indicate that progressively larger surface recombination velocities are obtained on n-type germanium with silver, hydrogen peroxide, CP-4, and electrolytic etches. However, large spreads in surface recombination velocity were produced in repeated treatments with a particular etch, and the spreads for different etches were found to overlap. These results cannot be strictly compared with ours because simultaneous measurements of surface potential were not made. However, if McKelvey and Longini made their measurements on thoroughly dried samples and in a dry atmosphere, it is probable that their results represent only 50% or less of the respective maximum surface recombination velocities, corresponding to $\phi_o - \phi_s > 3\ kT$. If this assumption is made, our values of surface recombination velocity (see Table I) are consistent with their range of values. Unlike McKelvey and Longini, we did not observe that some etches produce consistently smaller surface recombination velocities than others.

Acknowledgments

The authors are grateful to P. Wang and J. Flynn for assistance with the chemical aspects of this work and for valuable discussions.

Manuscript received May 15, 1958. This paper was prepared for delivery before the New York Meeting, April 27-May 1, 1958.

Any discussion of this paper will appear in a Discussion Section to be published in the December 1959 JOURNAL.

REFERENCES

1. W. Shockley and W. T. Read, *Phys. Rev.*, **87**, 835 (1952); See also D. T. Stevenson and R. J. Keyes, *Physica*, **20**, 1041 (1954).
2. S. Wang and G. Wallis, *Phys. Rev.*, **107**, 947 (1957).
3. W. H. Brattain and J. Bardeen, *Bell System Tech. J.*, **32**, 1 (1953).
4. S. Wang and G. Wallis, *Phys. Rev.*, **105**, 1459 (1957).
5. J. R. Schrieffer, *ibid.*, **97**, 641 (1955).
6. C. G. E. Low, *Proc. Phys., Soc. (London)*, **B68**, 10 (1955).
7. M. Lasser, C. Wysocki, and B. Bernstein, *Phys. Rev.*, **105**, 491 (1957).
8. S. G. Ellis, *J. Appl. Phys.*, **28**, 1262 (1957).
9. W. H. Brattain and C. G. B. Garrett, *Bell System Tech. J.*, **35**, 1019 (1956); C. G. B. Garrett and W. H. Brattain, *ibid.*, **35**, 1041 (1956).
10. A. Many and D. Gerlich, *Phys. Rev.*, **107**, 404 (1957).
11. H. C. Montgomery and W. L. Brown, *ibid.*, **103**, 865 (1956).
12. J. Bardeen, R. E. Coovert, S. R. Morrison, J. R. Schrieffer, and R. Sun, *Phys. Rev.*, **104**, 47 (1956).
13. H. Statz, G. A. de Mars, L. Davis, Jr., and A. Adams, Jr., "Semiconductor Surface Physics," p. 139, University of Pennsylvania Press, Philadelphia (1957).
14. J. P. McKelvey and R. L. Longini, *J. Appl Phys.*, **25**, 634 (1954).

APPENDIX

The composition of the five etches used in this work are given below. The reagents are: 70% HNO_3, 48% HF, 30% H_2O_2, 100% HAc.

CP-4: 50 cc HNO_3, 30 cc HAc, 30 cc HF, 0.6 cc bromine.

Hydrogen peroxide: 10 cc HF, 20 cc H_2O_2, 20 cc H_2O.

Iodine A: 30 cc HNO_3, 33 cc HAc, 15 cc HF, 90 mg iodine.

Electrolytic: 2M KOH, 3 v.

Silver: 20 cc HNO_3, 40 cc H_2O, 40 cc. HF, 2 g $AgNO_3$.

Principles and Applications of the Iodide Process

A. C. Loonam

Consulting Engineer, 70 East 45th Street, New York, New York

ABSTRACT

The thermodynamic factors favoring deposition of elements from vapors of their iodides are the low heats of formation of those iodides and the ease with which diatomic iodine dissociates at moderately high temperatures. The vapor pressure of the element and the stability of its lower iodides determine the temperature and pressure range in which deposition can occur. The lower pressure limit for deposition at a given temperature is set by the vapor pressure of the deposited element and the upper limit by the stabilities of the lower iodides. At very low pressures, deposition is a first order heterogeneous reaction, every iodide molecule which strikes the surface adding to the deposit. As the pressure is increased, the deposition rate falls off and eventually becomes zero order, the rate being governed by that at which I atoms evaporate from the saturated surface. At higher pressures the deposition reaction is diffusion-controlled. Factors influencing the character of the deposits, the removal of impurities, and the deposition of alloys are discussed.

The iodide process was introduced by van Arkel and de Boer in 1925 (1). Shapiro (2) gave an excellent account of the development of the process through about 1954. Much of the information in the Government reports to which he referred has since appeared in the technical literature or in patents.

The elements which have been deposited by the iodide process and convenient temperatures for their deposition are listed in Table I.

Some Fundamentals of the Process

To be capable of being refined by the van Arkel-de Boer process, an element must fulfill two requirements:

1. It must be capable of existing in a solid or liquid state at some condition of temperature and pressure in equilibrium with gas containing a high atomic ratio of iodine to element. Thus, both Ti and Zr are in equilibrium with gases containing ratios of I to metal of 80 and higher at temperatures of 1100°C and above at low pressures. It is desirable that the element have a high melting point and a low vapor pressure to permit deposition as the more convenient solid at pressures where high efficiency can be obtained; but neither is essential as shown by the deposition of molten U and the fact that the relatively volatile Si can be deposited from the vapor of its tetraiodide just as well as the much less volatile Zr.

Table I. Elements prepared by thermal dissociation of their iodides

Element	Deposition temperature, °C	Element	Deposition temperature, °C
Be	700-900	Si	1000
Cr	1100	Th	1700
Cu	900	Ti	1400
Fe	1100	U	1100
Hf	1600	V	1200
Ni	1030	Zr	1400
Pa	—		

2. The element must be capable of reacting readily with the gaseous products of the deposition reaction at the same pressure and another temperature to yield a gaseous product with a low atomic ratio of I to element. For example, crude Ti and Zr react readily with I at temperatures in the neighborhood of 200°C to produce gaseous TiI_4 and ZrI_4.

These two statements are perfectly general. It is not essential that the deposition temperature be higher than that of the crude. In an excellent recent paper, Schäfer and Morcher (3) showed that Si can be made to travel either up or down a temperature gradient via the vapors of its iodides by varying the pressure, high pressures favoring transport down the gradient owing to the reversible reaction

$$SiI_4 + Si = 2SiI_2 \qquad [1]$$

and low pressures favoring transport up the gradient via dissociation of SiI_2 and SiI_4

$$SiI_2 = Si + 2I \qquad [2]$$

$$SiI_4 = Si + 4I \qquad [3]$$

In both cases the Si is transported from the region where a gas with a low atomic ratio of I to Si is in equilibrium with the element to the region in which this ratio is higher.

Theoretically, at least, a pressure gradient should have the same general effect as a temperature gradient. Thus, at a suitable temperature, a relatively low pressure should cause reaction [1] to proceed as written, while increasing the pressure should cause it to reverse, thus making Si travel up the pressure gradient. Conversely, reactions [2] and [3] take place at low pressures, but are reversed at higher pressures with the result that Si travels down the pressure gradient.

However, all applications of the iodide process to date have been based on formation or supply of iodide vapors at low temperatures and pressures and their dissociation at high temperatures at essentially the same pressure, i.e., transport up a temperature gradient. Accordingly, this discussion is confined to that phase of the subject.

Thermodynamics of the Process

The most important thermodynamic factors in the iodide process are the low heats of formation of the iodides and the ease with which diatomic iodine dissociates. The latter, data for which are given in Table II, is perhaps the more important of the two factors because, especially with the higher valence elements, it produces a large increase in the number of moles of gas when the iodides dissociate. Accordingly, the dissociation reactions have large positive entropies and, even though the heats of formation of the iodides are moderately high, the free energies of dissociation decrease rapidly with increasing temperature. Thus, $\Delta S°$ at 25°C for the reaction

$$ZrI_{4(g)} = Zr_{(c)} + 4I_{(g)}$$

is about +75 e.u. Furthermore, the expression for the equilibrium constant for this reaction contains the pressure of atomic I to the 4th power, so that even if the value of this constant is rather small, it can still mean that a respectable pressure of I vapor exists in equilibrium with the metal.

Table II. Dissociation of diatomic iodine

Temp, °C	K*	Percent dissociated at 1 atm	100 mm	10 mm	1 mm	0.1 mm
600	2.10×10^{-4}	0.72	2.00	6.31	19.6	53.4
800	1.09×10^{-2}	5.2	14.2	41.4	82.1	97.7
1000	0.166	19.9	48.9	87.1	98.4	
1100	0.482	32.8	69.1	95.0		
1200	1.22	48.3	83.5	97.9		
1300	2.73	63.7	91.6			

* Equilibrium constant, $(pI)^2/pI_2$; p in atmospheres.

It follows from the foregoing that the process should become less well adapted in going from tetraiodides to tri-, di-, and monoiodides. Although, as will be seen later, other factors are also important, this is generally true. It is the author's opinion that monomeric monoiodides which have respectable stabilities in the vapor state cannot be decomposed by dissociation to give solid or liquid metal. Since there is only one mole of gas on each side of the reaction equation, there is no pronounced increase in entropy and therefore no marked reduction in free energy upon heating. The fact that deposition of Ag from AgI vapor has not been reported is to be expected on this basis. It also follows that an element forming a stable gaseous monomeric monoiodide cannot be deposited by dissociation. Indeed, it can readily be shown that deposition of a metal by dissociation of a gaseous iodide, MI_n, requires that the equilibrium constant at the deposition temperature for the reaction,

$$MI_{(g)} = M_{(c,\,l)} + I_{(g)}$$

be greater than $(n\text{-}1)$, i.e., MI must be definitely unstable and to a greater extent the greater the value of n.

The author believes that the monoiodides of Al and perhaps those of the rare earth metals are sufficiently stable to prevent deposition by dissociation. Like Al, such metals probably could be transported down a temperature gradient by disproportionation. In this connection it is to be expected that a high heat of vaporization of the element to be deposited would favor instability of a monoiodide, causing it to break down to the condensed element and gaseous atomic I.

However, if the monoiodide is polymeric in the vapor state, conditions would be quite different. Thus, Brewer and Lofgren's (4) results indicate that the cuprous halides exist as trimers in the vapor state. The condition is now

$$Cu_3I_{3(g)} = 3Cu_{(c)} + 3I_{(g)}$$

indicating a considerable entropy increase. The fact that deposition of Cu from its iodide has been reported therefore is excellent independent evidence of the soundness of these workers' views.

The fact that many of the transition metals are deposited readily from the vapors of their diiodides

may be attributed to the low heats of formation of these vapors resulting from their relatively high heats of vaporization. A comparatively small entropy increase therefore is sufficient to promote instability on heating. There is also good evidence that they are dimeric so that the entropy situation becomes similar to that of the tetraiodides with the advantage that two atoms of metal are deposited for every iodide molecule decomposing.

It is readily apparent that there must be, at any given temperature, a lower pressure limit below which deposition cannot take place. This is at the point where the rate of deposition just equals the rate of evaporation of the deposited element due to its own vapor pressure. At lower pressures the rate of evaporation will exceed that of deposition and there will be a net loss or "chewing" of the deposit.

It is not so readily apparent that an upper pressure limit can also exist. This happens with tri- and higher iodides if subiodides above the mono compound have appreciable stabilities in the gaseous state. Under such conditions there must be a pressure at which the atomic ratio of I to element in the gases in equilibrium with the deposit just equals that in the iodide used for transport. There is therefore no deposition at this point. Reduction of the pressure below this value results in deposition, while an increase produces attack or chewing. The author discovered this situation in the deposition of Ti from TiI_4 many years ago (5), a fact later confirmed by Runnalls and Pidgeon (6) who located this point at a TiI_4 pressure of 38 mm Hg at 1500°C. Schäfer and Morcher (3) located it at several temperatures in the Si-SiI_4 system, e.g., 15 mm of SiI_4 at 1160°, calling it "the critical decomposition pressure"; while Emelyanov, Bystrov, and Evstyukhin (7) found it in the Zr-ZrI_4 system.

Plotting of the percentage iodide decomposition at equilibrium against the pressure in such a system yields a curve which starts at zero at the pressure corresponding to the lower deposition limit, rises to a maximum, falls off to zero again at the upper deposition limit, and then passes into the region of negative decomposition or attack. Such a curve for deposition of Sn from SnI_4 at 1300°C is shown in Fig. 1.

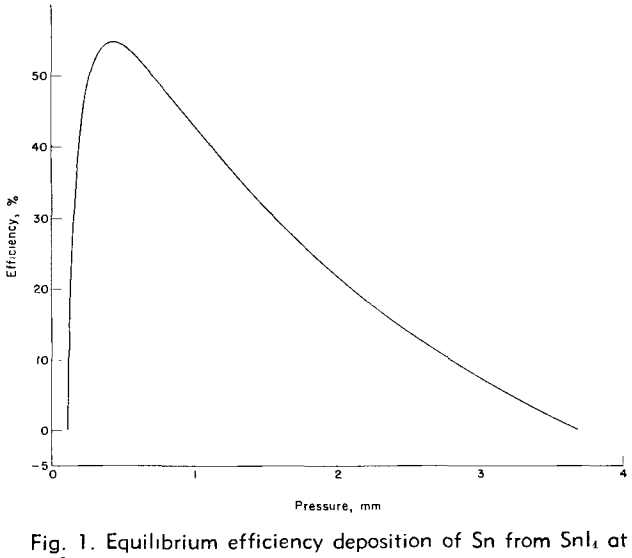

Fig. 1. Equilibrium efficiency deposition of Sn from SnI_4 at 1300°C.

In general, the value of the upper critical pressure increases with temperature. It can also be raised by reducing the ratio of I to element in the gas contacting the deposition surface and indeed may disappear altogether, but the fact remains that there will be no net decomposition of the highest iodide at pressures above its upper deposition limit. In this connection, it is important to note that, given a fixed temperature and pressure in the presence of deposit and I gases alone, the equilibrium composition of the gases will be the same regardless of the starting material.

In systems where lower iodides do not exist, the decomposition efficiency-pressure curve starts at zero and rises to a maximum as before, but then falls more slowly, approaching the zero axis asymptotically.

Given sufficient reliable thermodynamic data, it is relatively easy to calculate whether a given element can be deposited from the vapors of its iodides and, if so, the pressures and temperatures at which it can occur and the equilibrium efficiencies obtainable. At present, however, although the situation is slowly improving, no such fund of data is available for any element. It is therefore necessary to resort to estimates and even educated guesses. On the basis of these and also by analogy with other cases the author believes that B, C, Co, Ge, Mo, Nb, Ta, Sn, and perhaps Re, can be deposited from the vapors of their iodides. This statement does not mean that all of these elements can be refined by the van Arkel-de Boer process. In some cases, e.g., carbon, it would be necessary to prepare the iodide by an external process.

Kinetics of the Deposition Reaction

The writer believes that in the region represented by the lefthand leg of the curve in Fig. 1 and at low pressure, i.e., in the free molecule region where the Knudsen number (the ratio of the mean free path to the diameter of the deposition surface) is greater than about 10, the deposition reaction is a heterogeneous one, the rate being given by the Knudsen equation with an accommodation efficiency of unity, i.e., every iodide molecule which strikes the surface adds to the deposit. The reaction is therefore first order modified perhaps by the rate of evaporation of the metal itself, the activation energy is zero, and the deposition rate is proportional to the exposed surface area. This high efficiency is in accord with the findings of Holden and Kopelman (8) and Döring and Molière (9) with Zr. The author calculated the vapor pressure of TiI_4 from Fast's deposition rate at a bulb temperature of 50°C on this basis, and obtained a value which, when combined with that at the melting point derived from the data of Blocher and Campbell, yielded a figure for the heat of fusion of TiI_4 only 1.3% lower than that determined calorimetrically. Furthermore, calculation of the vapor pressure of ZrI_4 from Fast's rate of deposition of Zr at 150°C gave a value equal to 72% of that given by Rahlfs and Fischer's simple log $P - 1/T$ equation (10) and

120% of that obtained from the free energy equation using what is believed to be an accurate expression for the specific heat difference. Finally, rates of deposition of chromium from CrI_2 vapor were very close to 1.4 times those to be expected on the basis of measurements of the vapor pressure of the iodide if it were a monomer in the gaseous state and almost exactly that to be expected if it were a dimer, thus providing evidence that the latter is the case. Indeed, measurement of the rate of deposition of a metal is recommended as a method for determining the vapor pressure of its iodides at low pressures (11).

Since the primary deposition reaction is so highly efficient, it follows that it must be at least nonendothermic and more probably strongly exothermic. In the author's opinion the only one which can fulfill this requirement is the direct reaction of the incident molecule with the deposition surface to produce an atom of deposit and a chemisorbed monolayer of I atoms, i.e.

$$MI_n(g) = M_{(c)} + nI_{(ads)}$$

Such a mechanism would require heats of adsorption of I atoms on Ti and Zr of at least 42 and 50 kcal, respectively. They could be considerably higher than these values and still be consistent with that of 53.7 kcal found by Van Praagh and Rideal (12) for I atoms on Pt. The author believes that the chemisorbed I is mobile at deposition temperatures and that it evaporates at a rate consistent with its heat of adsorption.

On the basis of this mechanism, the deposition reaction should be first order with 100% efficiency so long as a large part of the deposition surface is free of adsorbed I, the rate of evaporation of I atoms just equalling that of deposition. On continued increase in pressure, however, the chemisorbed I layer covers a larger and larger fraction of the surface until ultimately it forms a complete monolayer. At this point the deposition reaction should become zero order, the deposition rate being governed solely by the rate of evaporation of the I. There is meager evidence that the point of complete surface coverage is identical with the maximum in the equilibrium efficiency curve of Fig. 1.

It is to be expected that any free I striking the deposition surface will also deposit with 100% efficiency. If its pressure and therefore its deposition rate is high enough to cause formation of the monolayer, it should reduce the rate of metal deposition, but it should have little or no effect at lower pressures.

It is believed that the foregoing mechanism applies to cases, such as the deposition of Cr from Cr_2I_4, in which lower iodides do not play any part. If, on the other hand, lower iodides can be formed, the reaction also approaches zero order, but attack of the metal begins via the I monolayer. This is in accord with the results of Langmuir on the reaction of oxygen with tungsten. He found (13) that at low pressure, oxygen formed a chemisorbed monolayer of atoms on the tungsten surface which evaporated as atoms at high temperature and was not readily reduced by hydrogen or other reducing agents. Furthermore, it showed no tendency to form WO_3. On raising the pressure of oxygen above that required to form the monolayer, however, formation of WO_3 set in.

The foregoing picture applies only to the free molecule region. As the pressure is increased with suitable adjustment of the temperature to maintain deposition, a point is ultimately reached where diffusion becomes an important, and ultimately, the controlling factor, the deposition rate being governed by that at which the iodide molecules diffuse to the deposition surface through the adjacent stationary gas film and the I atoms diffuse away.

Schäfer, Jacob, and Etzel have recently published two important papers on this phase of the subject (14, 15), in the first of which they discuss the theory of the transport of condensed phases through a temperature gradient via reversible gaseous reactions, and in the second of which they give experimental data for the transport of Fe and Ni via the vapors of their iodides and present calculations showing that the results can be accounted for by assuming equilibrium at both ends of the gradient with transport by diffusion. They secured good agreement between experimental and calculated results on the basis of diffusion coefficients derived from kinetic theory. They bring out that their treatment holds only within a definite pressure range. Presumably at lower pressures the foregoing free molecule form of transport applies, while at higher pressures transport is promoted by convection. Schäfer and Morcher (3) also discuss this subject.

One consequence of diffusion control is that the rate of deposition on a cylindrical surface, such as a filament coaxial with a cylinder of crude, becomes constant per unit length and independent of filament diameter. Shapiro and others (2) analyzed this situation and showed that the rate should be not quite independent of filament diameter, but inversely proportional to the log of the ratio of the inside diameter of the cylinder of crude to the diameter of the filament, similar to the conduction of heat radially through a cylindrical wall. In the corresponding heat transfer case, Kyte, Madden, and Piret found (16) that the ratio of the effective diameter of the stationary gas film to that of the filament was an inverse function of the Grashof and Prandtl numbers and the ratio of diameter to the length of the filament. They also took the mean free paths of the gas molecules into account at low pressures and small filament diameters.

Some of the foregoing statements regarding conditions in the range where diffusion is controlling must be accepted with qualifications. The one that the deposition rate on a filament is nearly independent of diameter is true only for relatively large diameters. That this must be so follows from the simple fact that, given any reasonable rate of deposition per unit length of, say a ½-in. filament and indefinitely reducing the diameter, a point must be reached where the original deposition rate cannot possibly be maintained because an insufficient number of iodide molecules strike the surface.

The surface reaction then becomes controlling and the rate proportional to the square of the diameter. A relation beween the deposition rate as a function of diameter and the Knudsen number probably exists for any given temperature, although the change in the diffusion gradient would also have to be taken into account.

The assumption of equilibrium at both ends of a temperature gradient is probably valid for systems in which both temperatures are high and also at the high temperature ends of other systems, but it certainly is not valid in the refining of Ti, Zr, and probably Hf with crude temperatures of 100°-200°C. These processes depend on the dynamic formation of the volatile tetraiodides instead of the much less volatile di- and triiodides which are in thermodynamic equilibrium with the metals. Under equilibrium conditions it is necessary to go to temperatures above 400°C to secure adequate vapor and dissociation pressures of the lower iodides.

These metals therefore have two distinct ranges of crude temperatures in which the process can be operated and which, as will be seen later, can yield deposits of quite different properties. As Fast has shown with Ti (17) and Döring and Molière with Zr (9), a temperature range of zero or low deposition rate can be found between them under suitable conditions, the lower limit of this gap being determined by the upper pressure deposition limit of the tetraiodides and the rate at which they are reduced, and the upper limit by the vapor and dissociation pressures of the lower iodides. Incidentally, the author believes that the tetraiodides are the primary products of the reaction of I with these metals at low temperatures and that formation of lower iodides is a secondary reaction.

Finally, the assumption of a simple diffusion gradient in the cases of Ti and Zr may be an oversimplification. In the range between 200° and 1400°C, two potentially important processes can take place in the gas phase, namely combination of I atoms at temperatures below about 900° and tetraiodide dissociation above 1000°C. There is reason to believe that both processes should be active even at the low pressure ordinarily prevailing. It is known that such reversible reactions markedly increase the thermal conductivity of a gas and they could have similar effects on other transport properties. It is possible that relatively few tetraiodide molecules reach the deposition surface at high surface temperatures and pressures where diffusion is controlling.

As Shapiro showed when he compared the rate of deposition of Zr from cut up crystal bar with that from Kroll process sponge (2), the reactivity of the crude can also be rate-controlling.

Removal of Impurities

In general, the purpose of an iodide process is to secure a high purity product. The elimination of impurities is therefore of the utmost importance. Both equilibrium and dynamic considerations are important in this connection.

If the iodide to be dissociated is prepared in a separate operation, it can be purified by any of the usual methods, filtration, fractional condensation, crystallization from a solvent, sublimation, fractional distillation, and even zone refining (18-20). Furthermore, these unit operations can be modified to meet special requirements. Thus KI has been added to a mixture of TiI_4 and AlI_3, which have very similar boiling points, to form $KAlI_4$ which is not volatile at a low red heat and from which the TiI_4 can be readily boiled away (21). Again, Zr and Hf have been separated by taking advantage of the difference in reducibility of their tetraiodides to less volatile lower iodides (22). Finally, U and Zr have been separated in a mixture of iodides produced by iodination of reactor fuel by fractionally condensing the less volatile U iodide and allowing the ZrI_4 to pass on (23).

One is somewhat more restricted when the operation is confined to a single unit as in the de Boer-van Arkel process, but even here advantage can be taken of a number of equilibrium and dynamic effects. In this connection, it is worth noting that I does not react with C or the oxides of any of the heavy polyvalent metals except perhaps those of Cd and Hg at any reasonable temperature. Indeed, the reverse is the case. The iodides of these metals can readily be roasted to oxide and iodine vapor in air or oxygen.

Probably the elements most readily refined by the de Boer-van Arkel process are Ti, Zr, and Hf. At the low crude temperatures possible when transfer takes place via the volatile tetraiodides, nitrides, carbonitrides, silicides, and perhaps other intermetallic compounds, as well as oxides and carbides, are unattacked, while the iodides of divalent metals have negligible vapor pressures if they are formed.

To secure the maximum benefit of these advantages, it is necessary to maintain a low temperature of the crude metal. This material can have considerable resistance to heat flow and, if reasonably thick, the surface facing that on which deposition is taking place can have a temperature at which the divalent iodides have large vapor pressures, carbonitrides and silicon are attacked by iodine, and even carbon monoxide can be formed by reaction of liberated carbon with oxides with consequent transfer of both components. Carbon monoxide can exist in equilibrium with iodine and iodide vapors at high temperatures.

Close control of the temperature of the crude may permit some interesting separations. Thus, Fast (24) secured no appreciable deposit from ZrI_4 at a bulb temperature of 100°C because of the low vapor pressure of the iodide, but he secured a considerable deposit of Ti from TiI_4 at a bulb temperature of 50° (17). Possibly Zr and Hf might be separated similarly.

One apparently neglected field has been the introduction of foreign substances into the units to aid in separations. This would seem to have definite possibilities. Thus, following Blumenthal and Smith (21), KI might be introduced into a Ti unit to prevent transfer of Al and other metals. Similar separations might be made among the fourth group

metals. Thus, KI does not form a complex with TiI_4 but it may with ZrI_4 or HfI_4. It is worth noting in this connection that there is less tendency to complex formation in the tetraiodide-alkali iodide systems than in the corresponding chloride systems, but that the tendency increases with the atomic weight of the alkali metal. Thus, K_2SnCl_6 is well known, but only Rb_2SnI_6 and Cs_2SnI_6 are known in the anhydrous state.

Another possibility is the introduction of an oxide. Chaigneau recently published two papers on the preparation of a large number of iodides by reaction of the corresponding oxides with AlI_3 at moderate temperatures (25, 26). Of the 29 oxides tried, 26, including TiO_2 and ZrO_2, yielded pure iodides; only one, Cb_2O_5, yielded an appreciable quantity of oxyiodide; and two, Cr_2O_3 and B_2O_3, did not react. There was no report on SiO_2.

Presumably, then, the presence of TiO_2 in a Ti bulb could prevent transfer of Al if the reaction rate were fast enough. Indeed, it should be possible to make up a list of elements in order of ease of conversion of their oxides to iodides with the alkali metals at the top and B and Al near the bottom.

Formation of stable "intermetallic" compounds does not appear promising from a thermodynamic standpoint because of the presence of free I in the system. However, empirical research could disclose compounds of value because of the slowness with which they react. Thus, addition of C might reduce the rate of transfer of strong carbide formers, while Ti might prevent transfer of N.

Application of the de Boer-van Arkel process to the divalent transition metals as well as U, and, to some extent, Th, presents greater difficulties because the high crude temperatures necessary to secure useful iodide pressures promote attack on nitrides and other relatively inert compounds as well as formation of CO by reaction of C with the generally less stable oxides. Furthermore, all iodides have appreciable vapor pressures at these temperatures, making separations more difficult.

Another factor of importance in the case of Cr, V, Fe, Co, and Ni is that their diiodides have appreciable dissociation pressures in the temperature range where their vapor pressures are appreciable (15, 27-29). Accordingly, the I pressure gradient is from that at the deposition surface to a finite value and not to zero at the crude. This could mean that, if there were any considerable temperature gradient in the crude metal, the vapor pressure of the iodide would tend to be fixed by the cold end of that gradient and the minimum I pressure by the hot end. This would reduce diffusion of both components with a consequent reduction in deposition rate.

However, the situation is by no means entirely unfavorable, as shown by the appearance of iodide chromium on the market. Because of the instability of the iodide vapors, deposition surface temperatures can be considerably lower than for the Ti group metals (cf Table I).

When operated under optimum conditions, the process can yield products of extraordinarily high purity. On the basis of his experiments with spent uranium reactor fuel, Robb (23) concluded that the process is capable of producing better decontamination than any of the known pyrometallurgical processes under study and that theoretical considerations and study of the vapor pressures of the pertinent iodides indicate that separation from every fission product should be possible. Additional evidence to this effect is the recent production of ultra pure Si (19, 20, 30).

Finally, one curious fact is that a sample of iodide Cr, analyzed by the radioactivation method at Oak Ridge, was found to contain less I than one of chromate electrolytic metal analyzed at the same time (31).

Character of the Deposits

One generalization which has appeared in the study of the iodide process is that diiodides, such as FeI_2 and CrI_2, tend to yield spiny, noncompact, noncoherent deposits. Compact deposits can be secured by proper choice of conditions, but even then the coherence is low because of low adhesion between the individual grains. On the other hand, the tetraiodides of Ti, Zr, and Hf, readily give compact, coherent deposits which can be mechanically worked directly.

Factors responsible for this situation are:

1. The high-temperature gradient in the deposition of Ti, Zr, and Hf from their tetraiodides and the fact that, for Ti and Zr at least, there is a temperature at which deposition changes to attack. Accordingly, a "sprout" or protuberance cannot grow very far, and the growing deposit maintains a reasonably smooth surface. With the divalent metals on the other hand, there are no lower iodides to produce a deposition limit, and the low volatility of their diiodides requires a high crude temperature, thereby reducing the temperature gradient. Furthermore, because of the high temperature of the crude, the gases leaving are nearly in thermodynamic equilibrium with it, thereby reducing the concentration gradient. Hence, a sprout can grow quite a distance without being attacked.

In support of this viewpoint are the facts that Ti deposited at high crude temperatures, where the temperature gradient is less and lower iodides participate in the transport, is much less compact than that deposited at low crude temperatures, and that Th, which requires relatively high crude temperatures because of the low volatility of its tetraiodide (bp 839°C) also gives noncoherent deposits according to Veigel, Sherwood, and Campbell (32).

2. The greater volatility of the divalent transition metals. At 1300°C, the vapor pressure of Cr is 417 times and that of Fe 90 times that of Ti, the most volatile of the fourth group transition metals. Accordingly, these metals have a much greater tendency to sublime from the high temperatures of crevices in the deposits to the ends of sprouts. The monoiodides of the divalent metals could enhance the rate of this transport down the temperature gradient. As pointed out they can be more stable than those of the tetravalent metals without preventing deposition.

Deposition of Alloys

Alloys can be deposited by the iodide process. De Boer and Fast (33-35) prepared alloys of Zr with Sn and Al, as well as Ti-Zr and Zr-Hf alloys over their entire composition ranges, while Shapiro (2) prepared alloys of Zr with Cr, Fe, Ni, and Sn. Very recently, Robb (23) reported deposition of U-Zr alloys ranging in Zr content from 16 to 97% from a 40% Zr-60% U alloy by changing conditions.

Factors of importance in the preparation of alloys are: (*a*) relative stability of the iodides; (*b*) relative volatility of the iodides; (*c*) relative volatility of the metals. By employing a high filament temperature, de Boer and Fast (33) prepared Fe-free Zr from a contaminated feed, the volatilized Fe collecting on the cooler electrode. High transfer efficiencies of Fe have, however, been obtained under other conditions (2); (*d*) thermodynamic activity of the second metal in the alloy. If extensive solid solutions or stable compounds are formed, even metals which cannot be deposited in the pure state from their iodides can be codeposited as alloys as shown by the foregoing preparation of Zr-Al alloys.

This whole subject may be summed up in the statement that, if alloys are desired, conditions for obtaining high purity should be avoided. Of course, the converse is also true.

Acknowledgment

The author wishes to thank the Chilean Iodine Educational Bureau, Inc., for permission to present this paper and for its sponsorship of studies of the iodide process at Battelle Memorial Institute, as well as Drs. Ivor E. Campbell and John M. Blocher, Jr., and others of the Battelle staff for many pleasant and illuminating discussions of the process.

Manuscript received July 2, 1958. This paper was prepared for delivery before the New York Meeting, April 27-May 1, 1958.

Any discussion of this paper will appear in a Discussion Section to be published in the December 1959 JOURNAL.

REFERENCES

1. A. E. van Arkel and J. H. de Boer, *Z. anorg. u. allgem. Chem.*, **148**, 345 (1925).
2. Z. M. Shapiro, Chapter 5 in "The Metallurgy of Zirconium," B. Lustman and F. Kerze, Jr., McGraw-Hill Book Co., New York (1955).
3. Harald Schäfer and Bernhard Morcher, *Z. anorg. u. allgem. Chem.*, **290**, 279 (1957).
4. Leo Brewer and Norman L. Lofgren, *J. Am. Chem. Soc.*, **72**, 3038 (1950).
5. A. C. Loonam, U. S. Pat. 2,694,654, Nov. 16, 1954.
6. O. J. C. Runnalls and L. M. Pidgeon, *Trans. Am. Inst. Mining Met. Eng.*, **194**, 843 (1952).
7. V. S. Emelyanov, P. D. Bystrov, and A. I. Evstyukhin, *J. Nuclear Energy*, **4**, 253 (1957).
8. Robert B. Holden and Bernard Kopelman, *This Journal*, **100**, 120 (1953).
9. H. Döring and K. Molière, *Z. Elektrochem.*, **56**, 403 (1952).
10. O. Rahlfs and W. Fischer, *Z. anorg. u. allgem. Chem.*, **211**, 349 (1933).
11. J. M. Blocher, Jr., Personal communication.
12. Gordon Van Praagh and Eric K. Rideal, *Proc. Roy. Soc. (London)*, **A134**, 385 (1931).
13. Irving Langmuir, *J. Chem. Soc.*, **1940**, 511.
14. Harald Schäfer, Herbert Jacob, and Karl Etzel, *Z. anorg. u. allgem. Chem.*, **286**, 27 (1956).
15. *Ibid.*, pp. 42-55.
16. J. R. Kyte, A. J. Madden, and Edgar L. Piret, *Chem. Eng. Progr.*, **49**, 653 (1953).
17. J. D. Fast, *Z. anorg. u. allgem. Chem.*, **241**, 42 (1939).
18. A. C. Loonam, U. S. Patents 2,694,652-3-4, Nov. 16, 1954.
19. B. Rubin, G. H. Moates, and J. R. Weiner, *This Journal*, **104**, 656 (1957).
20. G. Szekely, *ibid.*, 663.
21. W. B. Blumenthal and H. Smith, *Ind. Eng. Chem.*, **42**, 249 (1950).
22. Commonwealth Scientific and Industrial Research Organization, Australian Pat. 4831/54, Nov. 22, 1954.
23. W. L. Robb, Knolls Atomic Power Laboratory Report KAPL-1788, May 1, 1957.
24. J. D. Fast, *Z. anorg. u. allgem. Chem.*, **239**, 145 (1938).
25. Marcel Chaigneau, *Compt. rend.*, **242**, 263 (1956).
26. Marcel Chaigneau, *Bull. soc. chim. France*, **1957**, 886.
27. J. W. Nash, H. R. Ogden, R. E. Durtschi, and I. E. Campbell, *This Journal*, **100**, 272 (1953).
28. H. Schäfer and W. J. Hones, *Z. anorg. u. allgem. Chem.*, **288**, 62 (1956).
29. T. L. Allen, *J. Am. Chem. Soc.*, **78**, 5476 (1956).
30. C. S. Herrick and J. G. Krieble, Report No. 57-RL-1825, General Electric Research Laboratory, Schenectady, October 1957.
31. J. M. Blocher, Jr., Discussion, Symposium on Ductile Chromium, American Society for Metals, Philadelphia, Pa., October 18, 1955.
32. N. D. Veigel, E. M. Sherwood, and I. E. Campbell, *This Journal*, **102**, 687 (1955).
33. J. H. de Boer and J. D. Fast, *Z. anorg. u. allgem. Chem.*, **187**, 177 (1930).
34. *Ibid.* 193.
35. J. D. Fast, *Rec. trav. chim.*, **58**, 973 (1939).

Techniques and Results of Zone Refining Some Metals

J. H. Wernick, D. Dorsi, and J. J. Byrnes

Bell Telephone Laboratories, Inc., Murray Hill, New Jersey

ABSTRACT

Techniques and results are given for the floating zone refining of Ni, Ti, V, and for boat zone refining of Al and Au. These elements have been purified by zone melting. A considerable amount of purification was obtained by volatilization during floating zone melting.

The need for purer metals for basic research and development purposes is great. Because of these needs, we have zone refined a number of metals by floating zone and boat techniques. Some of the results are discussed here.

Floating Zone Refining Equipment

The floating zone refining was done in vacuum in a vapor plating unit[1] adapted for this work. It is similar to the unit used by Buehler (1). Figure 1 shows a schematic drawing of the equipment. The liquid nitrogen trap, diffusion, and mechanical pumps are not shown. The ends of the rod to be zone refined are placed in quartz holders which in turn are held in the yoke by chucks made of stainless steel. The upper chuck (Fig. 2) is so designed that, as the chuck body moves upward, the steel balls prevent the chuck body from returning to its original position.[2] This prevents squeezing out of the molten zone after melting. The yoke is attached to a water-cooled push-rod which passes through an O-ring vacuum seal (Fig. 3) on the base plate. The high-frequency power leads pass through a coaxial vacuum seal, the details of which are shown in Fig. 4. The pressure attained prior to heating is 10^{-6} mm Hg and rises to 10^{-5} mm Hg during refining.

Radio frequency power is obtained from an Ecco 10-kw output generator at a frequency of either 5 mc or 450 kc. The tank circuit for the 450-kc frequency is located within the unit, whereas the tank circuit for 5 mc is located under the base plate of the vacuum system to minimize power loss (Fig. 1). A frequency of about 5 mc was used exclusively for

[1] Consolidated Electrodynamics Corporation LCI-18 Vacuum Coater.

[2] This chuck, as well as the mechanical feed mechanism, was designed by J. J. Gillich.

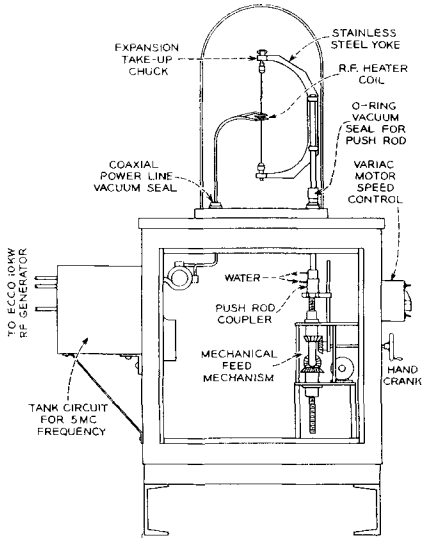

Fig. 1. Vacuum floating zone refiner

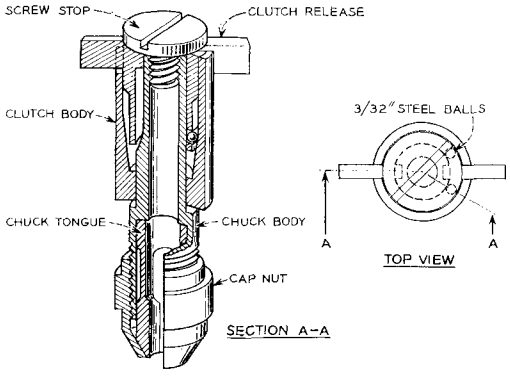

Fig. 2. Expansion take-up chuck

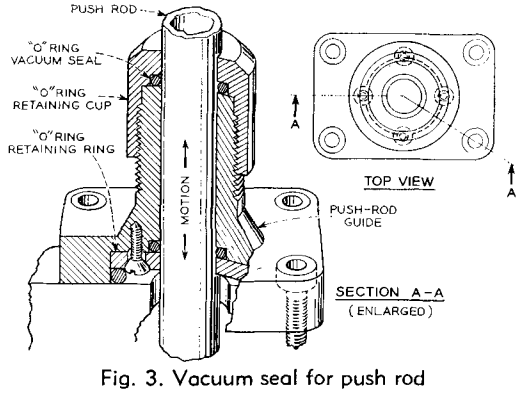

Fig. 3. Vacuum seal for push rod

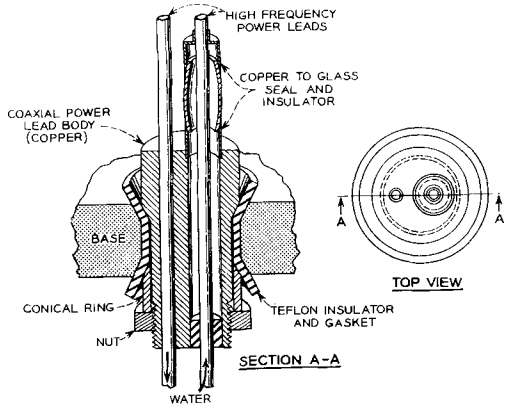

Fig. 4. Vacuum seal for coaxial high frequency leads

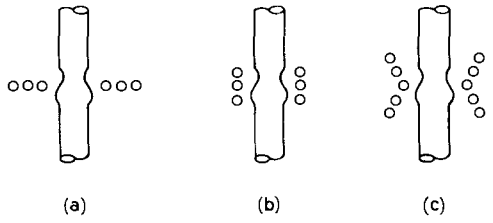

Fig. 5. Induction work coils for (a) Ni, (b) Ti, and (c) V

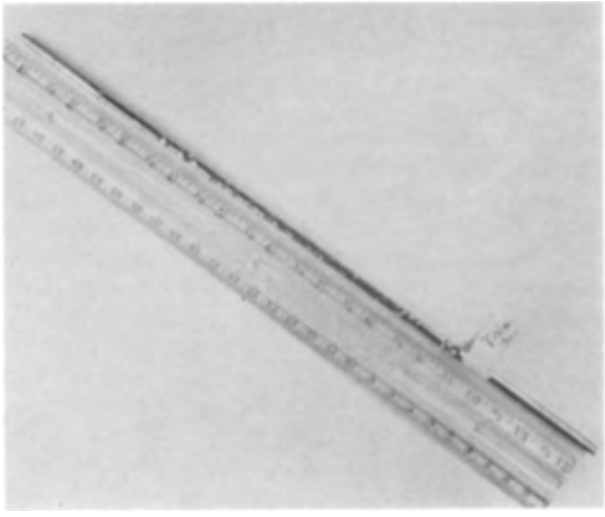

Fig. 6. Zone melted 3/16 in. D Ni rod

the floating zone refining of metals, although a frequency of 450 kc could also be used.

The work coils are made of 3/16 in. D copper tubing, and those used for Ni, Ti, and V (a, b, and c, respectively) are illustrated in Fig. 5. Some trial and error effort is involved in determining the proper coil, because one needs a sufficient concentration of power and yet obtain a stable zone. The zone travel rate was 0.07 in./min for these elements, and the zone lengths varied from ¼ to ⅜ in. For the case of Ni, the zone melted bar was more uniform in cross section when the zone traveled from top to bottom.

Floating Zone Melting Results

Figures 6, 7, and 8 are photographs of zone melted Ni, Ti, and V rods. The starting high purity Ni was obtained from K. M. Olsen and was made by a crucible melting technique(2). The analytical data for this Ni are shown in Table I (2). Examination of the phase diagrams of Ni with the metal impurities indicates that the equilibrium distribution coefficients for these impurities in Ni are not too different from unity.

The zone refined Ni (2¼ in./hr travel rate) was evaluated by measuring the residual resistances, at liquid He temperature, of sections of the zone refined ingot, as described by Kunzler and Wernick (3). A decrease in the residual resistance indicates purification. Figure 9 shows the resistance ratio $R_{4.2°K}/R_{273°K}$ (residual resistance) as a function of position along the bar. The control data are for the unmelted sections at the ends. Note that crucibleless zone melting, after four passes, resulted in purification, mainly by volatilization of volatile impurities, as indicated by the absence of appreciable pile up of impurities at either end.

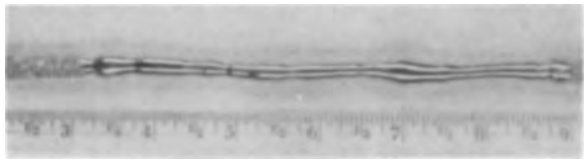

Fig. 7. Zone melted ¼ in. D Ti rod

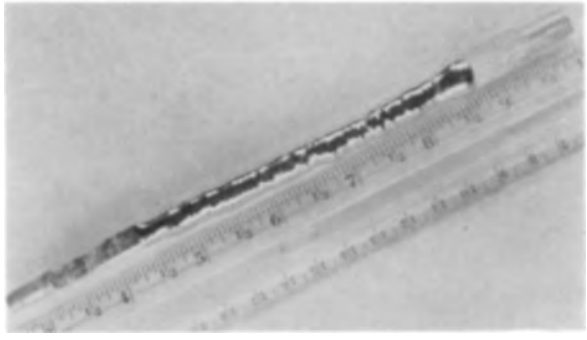

Fig. 8. Zone melted ⅜ in. D V rod

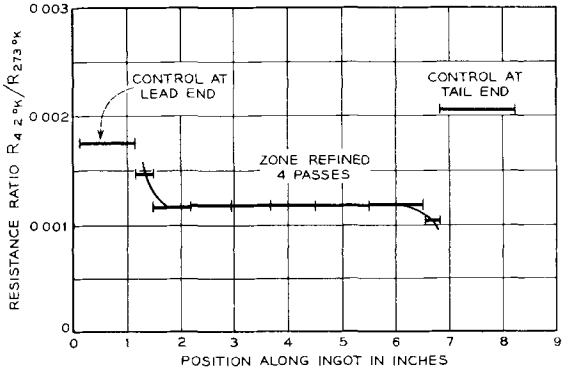

Fig. 9. Low-temperature resistivity of floating zone refined Ni

The zone melted Ti bar (6 passes, 1¼ in./hr travel rate) was analyzed spectroscopically. Titanium is not cubic, and residual resistance measurements for determining purity would be difficult to interpret unless one has a single crystal. Quantitative analytical data are shown in Table II. It appears that purification was mainly due to volatilization, as indicated by the absence of appreciable pile up of impurities at either end. No carbon and oxygen analyses were obtained.

The qualitative spectroscopic data for zone melted V (6 passes, 2¼ in./hr travel rate) are shown in Table III. Purification was obtained both by movement of impurities and by volatilization.

Boat Zone Melting Results for Al and Au

The zone refining of aluminum in Al_2O_3 boats has been discussed by Albert, *et al.* (4), Caron (5),

Table I. Analysis of BTL nickel used for zone refining

Element	% by weight
Fe	<0.005
Si	<0.005
Cu	<0.001
Mg	<0.005
C	0.001
S	0.001
O	0.0015
H	0.0001
N	0.0001

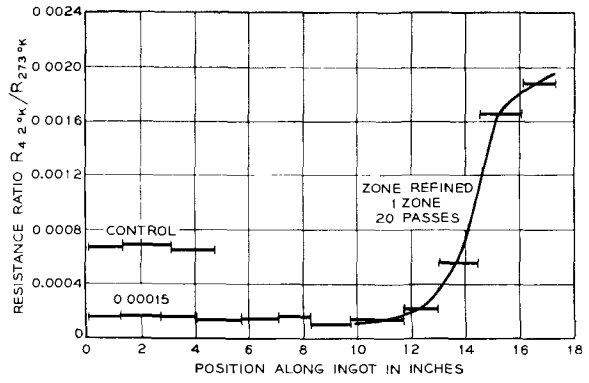

Fig. 10. Low-temperature resistivity of zone refined Al 99.999+%.

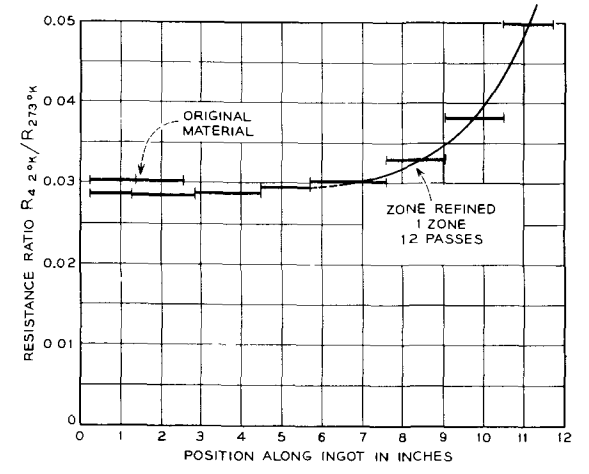

Fig. 11. Low-temperature resistivity of zone refined Au

Montariol (6), and in graphite boats by Demmler (7). We have zone refined Al in graphite boats[3] in a flowing purified argon atmosphere (4.9 in./hr travel rate). The graphite boat is first degassed *in vacuo* at a temperature estimated to be 1200°C. The argon is cleaned by passing it through a bed of drying agent, Linde Molecular sieve, and then through a bed of steel wool held at 600°C. Induction heating (450 kc) was used for zone refining. Mass transfer during zone refining is excessive, and it is prevented by tilting the refiner. This also aids in maintaining a zone of given size during refining. Figure 10 shows a plot of resistance ratio vs. distance along the length of a zone refined bar.[4] Also shown are the resistance ratio data for an annealed section of the original ½ in. D rod (marked control). It is apparent that zone refining was effective in increasing the purity of the 99.999+% Al. Table IV compares the reciprocal resistance ratios of zone refined Alcoa 99.99+% and AIAG 99.999+% Al ingots. The impure ends were not removed at any time during refining.

Gold was also zone refined by induction heating in a degassed graphite boat in a flowing argon atmosphere (3.6 in./hr travel rate). The residual resistance data for an ingot are shown in Fig. 11. Note that some zone refining was accomplished, but that there was also some impurity pickup from the surroundings, as indicated by the rather large pile-up of impurities at the impure end. The nature and source of the external impurities are not known at present.

[3] A limited discussion of this work appears in Ref. 3.

[4] The starting 99.999% Al used for this zone refining work was kindly furnished by Aluminium-Industrie-Aktien-Gesselschaft, Neuhausen am Rheinfall, Switzerland. The American supplier for this material is United Mineral and Chemical Corp., New York, N. Y.

Table II. Spectrochemical quantitative analysis of floating zone refined titanium

	Original	Lead section	End section
Ni	0.062	0.018	0.0051
Mn	0.015	N.D.	N.D.
Mg	0.010	0.0043	0.0043
Fe	0.042	0.0087	0.017
Si	0.24	0.062	0.11
Cu	0.006	0.0008	0.0007
Ca	0.033	0.014	0.014
Al	0.0088	N.D.	N.D.
Mg	(<0.005) *	N.D.	N.D.

N.D., not detected.
* Qualitative estimate.

Table III. Qualitative spectroscopic analytical data for zone melted vanadium (in weight per cent)

Element	Control (unmelted) portion	Lead section	Center section	End section
Al	<0.001	<0.03	N.D.*	N.D.
Ca	<0.001	<0.03	N.D.	N.D.
Co	<0.03	<0.001	<0.001	<0.005
Cr	<0.03	<0.001	<0.001	<0.001
Cu	<0.005	<0.001	<0.001	<0.001
Fe	<0.03	<0.005	<0.001	<0.001
Mg	<0.001	<0.005	<0.001	N.D.
Mn	<0.03	<0.001	N.D.	N.D.
Si	<0.03	0.01-0.3	0.01-0.3	<0.03
Ti	N.D.	<0.005	N.D.	N.D.
W	0.03	0.03	0.03	0.03

* N.D., not detected.
Alkaline earth elements not detected.

Acknowledgments

The authors wish to thank J. E. Kunzler for advice concerning the residual resistance measurements; K. E. Benson for experimental assistance; E. K. Jaycox and D. Babusci for the spectroscopic analysis; and E. Buehler for suggesting the yoke design for the floating zone apparatus.

Manuscript received Aug. 13, 1958. This paper was prepared for delivery before the New York Meeting, April 27-May 1, 1958.

Table IV. Resistance ratios for zone refined Al

Starting material	Original $R_{273°K}/R_{4.2°K}$	Zone refined $R_{273°K}/R_{4.2°K}$	Atmosphere	Passes	Boat
Alcoa 99.99+ (Ref. 3)	800	5000	Argon (purified)	20	Graphite
AIAG 99.999+%	1500	6600	Argon (purified)	20	Graphite

Any discussion of this paper will appear in a Discussion Section to be published in the December 1959 JOURNAL.

REFERENCES

1. E. Buehler, to be published in Transactions of the Metallurgical Society, AIME.
2. K. M. Olsen, *Metal Prog.*, **72**, 105 (1957).
3. J. E. Kunzler and J. H. Wernick, Transactions of the Metallurgical Society, AIME, **212**, 856 (1958).
4. P. Albert, F. Montariol, R. Reich, and G. Chaudron, in "Radioisotope Conference," p. 75, Vol. 2, J. E. Johnson, Editor, Academic Press, New York (1954).
5. M. Caron, Proceedings of a Meeting Held by Commissions 1 and 2 of International Institute of Refrigeration in Louvain, Belgium, Sept. 4-7, 51 (1956).
6. F. Montariol, *ibid.*, p. 63.
7. A. W. Demmler, Jr., *Trans. Am. Inst. Mining Met. Engrs.*, **206**, 958 (1956).

Effects of Electrolytes and of Gelatin on the Half-Wave Potentials of Carbon Tetrachloride, Dibromoacetate, and p-Dinitrobenzene

Leif E. I. Hummelstedt and L. B. Rogers

Department of Chemistry and Laboratory for Nuclear Science, Massachusetts Institute of Technology, Cambridge, Massachusetts

ABSTRACT

Polarograms were obtained in media in which reductions of each compound occurred on both sides of the electrocapillary maximum. Capillary-active anions retarded the less cathodic reduction steps and capillary-active tetramethylammonium ion facilitated the second reduction steps of carbon tetrachloride and the dibromoacetate ion. Capillary-inactive calcium ion had little effect on the halogenated compounds, but it greatly facilitated the second reduction of p-dinitrobenzene thereby suggesting ion-pair formation with the known divalent intermediate

Gelatin, for the first time, was found to shift a reduction to less cathodic values. This occurred only in acidic media when the reduction took place on the negative branch of the electrocapillary curve. The shift was attributed to the presence of protonated gelatin in the double layer.

In an earlier study of the effect of added electrolyte on the half-wave potentials of carbon tetrachloride (1), the possibility existed that the observed changes, which had been attributed to changes in the double layer at the electrode surface, might have been due to changes in junction potential. In the present study, the effects of electrolytes were re-examined using a large concentration of a relatively inert electrolyte in order to minimize changes in junction potential. By examining two different waves of the same compound, each on a different side of the electrocapillary maximum, it was possible to isolate selective influences. By using a single medium for studying carbon tetrachloride, dibromoacetic acid, and p-dinitrobenzene, it was possible to distinguish further between different types of electrolyte effects.

Experimental Details

Apparatus.—Polarograms were obtained using a Sargent Model XXI recording polarograph. The initial and final potentials of each polarogram were measured with a Rubicon or a Sargent potentiometer. All measurements were made against an external saturated calomel electrode (S.C.E) which was connected to the polarographic cell by means of a salt bridge which contained 1*M* potassium chloride. The end of the salt bridge which dipped into the sample was closed by a Vycor plug, the other, by an agar plug. The capillary used throughout the experiments had a value for $m^{2/3}t^{1/6}$ of 1.32 $mg^{2/3}$ $sec^{-1/2}$ at -0.800 v vs. S.C.E. in 0.9*M* potassium chloride. The resistance of the polarographic cell circuit was measured using an Industrial Instruments Company conductivity bridge, Model RC-1B. The *p*H measurements were made using a glass electrode in conjunction with a Beckman H or G *p*H meter.

Reagents and solutions.—Most of the chemicals were analytical reagent grade. However, the dibromoacetic acid was a research sample kindly furnished by Dr. Vernon Stenger of the Dow Chemical Company. The tetramethylammonium chloride was the polarographic grade of Southwestern Analytical Chemicals. The p-dinitrobenzene, after recrystallization from ethanol, had a melting point of 173.2°-173.7°C.

Carbon tetrachloride and dibromoacetic acid were added in the form of methanol solutions to solutions of background electrolyte. The p-dinitrobenzene was added as either a methanol or ethanol solution. Most of the experiments were performed using a high concentration of lithium chloride (2.0*M*) as supporting electrolyte in 41% methanol. Other electrolytes were added to such a solution as solids. To make the background alkaline, the *p*H was adjusted by adding sodium hydroxide; to make it acidic, a phthalate buffer was prepared in the manner described by Pearson (2). In adjusting the apparent *p*H of some of these buffers in different concentrations of alcohol, hydrochloric acid was added. Gelatin was added as an aqueous 0.50% solution.

Procedures.—The polarographic solutions, which were generally 50 ml, were deaerated with prepurified nitrogen that had been passed through a portion of the supporting electrolyte before entering the polarographic cell. Usually 15 min of deaeration was sufficient to remove the oxygen. In working with carbon tetrachloride, the supporting electrolyte was first deaerated for 15 min, whereupon 1.00 ml of the stock solution containing carbon tetrachloride was added and the solution deaerated for an additional period of 1.5 min.

All data were corrected for residual current and *IR* drop. All experiments were performed using a mercury height of 102 cm and a thermostatic bath held at 24.0°C. Electrocapillary curves were determined from recordings for at least 100 drops at each potential.

Results

Effect of Monovalent Ions

Figure 1a shows the effect of potassium thiocyanate and tetramethylammonium chloride, respectively, on the half-wave potentials of carbon tetrachloride solutions in alkaline 2.0*M* lithium chloride containing 41% by volume of methanol. It is apparent that the addition of relatively small amounts of potassium thiocyanate shifted the first wave of carbon tetrachloride in a more cathodic direction, while the second was shifted slightly in the opposite direction. Addition of tetramethylammonium chloride, on the other hand, had no effect on the first wave, while the second was shifted to markedly less cathodic potentials. Addition of an equimolar mixture of potassium thiocyanate and tetramethylammonium chloride simultaneously shifted the first wave toward more cathodic potentials and the second wave toward less cathodic. The shifts observed for the mixture were about half those for the separate components (−0.066 v vs. −0.116 v and +0.181 v vs +0.274 v).

The results of a similar experiment using dibromoacetic acid, a compound extensively studied by Elving, *et al.* (3) are shown in Fig. 1b. The shift in half-wave potential for the second wave was smaller than that for the corresponding wave for carbon tetrachloride, probably because the former is closer to the electrocapillary maximum. The importance of such a factor is qualitatively illustrated by the data of Elving, *et al.* (4) on α-bromo-n-butyric acid. Comparison of Fig. 2 with Fig. 1a and 1b shows that the electrocapillary maximum lay as expected between the two polarographic waves of both carbon tetrachloride and the dibromoacetate ion. Electrocapillary curves for separate additions of either potassium thiocyanate or tetramethylammonium chloride had maxima which fell in the same region of potential as those in Fig. 2.

In an earlier study of carbon tetrachloride by Lothe and Rogers (1) similar shifts in polarographic waves were demonstrated, but contributions from changes in junction potential were present because a high concentration of background electrolyte had not been used. In order to check the constancy of the liquid junction potential in the present study polarograms of 2 x 10^{-3}*M* thallium (I) were run in the same background medium. On addition of a mixture giving 0.05*M* potassium thiocyanate and 0.05*M* tetramethylammonium chloride, the half-wave potential remained constant at −0.447 v; an increase in concentration to 0.20*M* caused only a slight shift to −0.454 v (further complexing of thallium?). The largest effect of the "active" salts on the half-wave potentials of carbon tetrachloride occurred for additions of 0.05*M* or less for which the 2*M* lithium chloride did indeed hold the liquid junction potential constant.

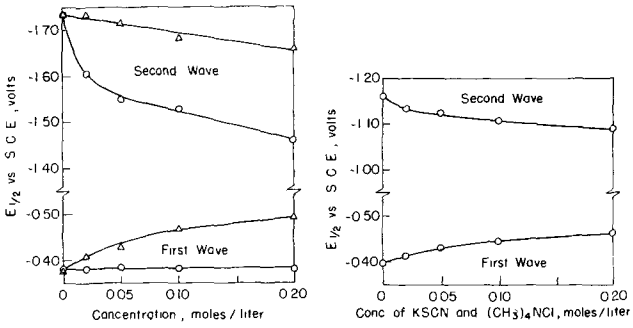

Fig. 1. Effect of electrolytes on the half-wave potentials of carbon tetrachloride and dibromoacetate in solutions of 2.0M lithium chloride and 41% methanol having an apparent pH of 10.9: (a) (left), addition of KSCN (Δ) and $(CH_3)_4NCl$ (O) to 10^{-3}M carbon tetrachloride; (b) (right), addition of an equimolar mixture of KSCN and $(CH_3)_4NCl$ to 1.7 × 10^{-3}M dibromoacetate.

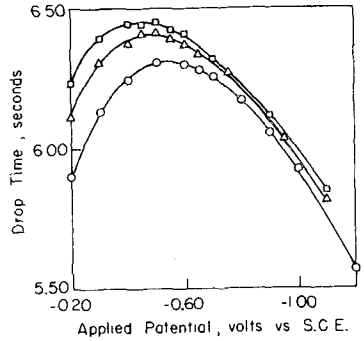

Fig. 2. Drop time as function of applied potential in 2.0M lithium chloride and 41% methanol with different additions of an equimolar mixture of KSCN and $(CH_3)_4NCl$ (□—no addition; Δ—0.05M; O—0.20M). Apparent pH, 10.9.

To evaluate the effect of competition of lithium and chloride ions for positions at the interface, additions of an equimolar mixture of potassium thiocyanate and tetramethylammonium chloride were made to solutions of carbon tetrachloride containing lower initial concentrations of background electrolytes. A change from 2.0*M* to 1.0*M* lithium chloride resulted in a slightly greater shift in each half-wave potential in the range up to 0.05*M* of each electrolyte but, for larger additions, virtually the same shifts were found as those shown for the more concentrated lithium chloride. When 0.60*M* potassium nitrate was substituted for lithium chloride as a supporting electrolyte, the second wave could not be measured because of decomposition of the background. However, the shift of the first wave was practically identical with that observed for 1.0*M* lithium chloride.

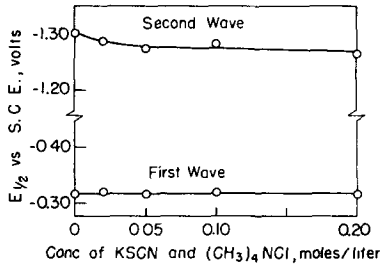

Fig. 3. Effect of an equimolar mixture of KSCN and $(CH_3)_4NCl$ on the half-wave potentials of $10^{-4}M$ p-dinitrobenzene in solutions of 2.0M lithium chloride and 41% methanols having an apparent pH of 10.9.

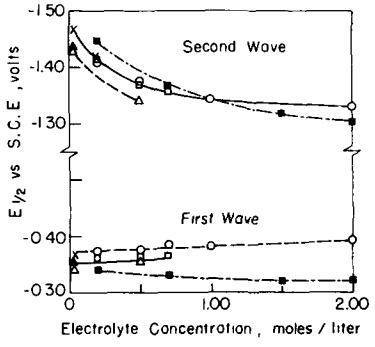

Fig. 4. Effect of electrolytes on the half-wave potentials of $10^{-4}M$ p-dinitrobenzene in 41% methanol. □—KCl, ○—KSCN, △—$(CH_3)_4NCl$, ×—KI, ▲—$(CH_3)_4NI$, ■—LiCl. The apparent pH is approximately 11.9 except for solutions containing LiCl which caused a decrease to 10.9. ——— "Inactive" ions; - - - "Active" ions; - . - . - LiCl curves.

After the similarities of carbon tetrachloride and dibromoacetic acid had been established, p-dinitrobenzene was studied because it represented a different type of reducible group. In the case of an organic halide the transfer of one electron (possibly two) is followed by rapid elimination of a halide ion. The first wave of p-dinitrobenzene in alkaline solution corresponds to a two-electron change with formation of a relatively stable divalent ion; the second wave to formation of p-hydroxylaminoaniline (5). Hence, the organic halides involve electron-transfer to neutral (or monovalent) species whereas the second alkaline reduction step of p-dinitrobenzene goes through a stable divalent intermediate.

Figure 3 indicates that the first wave of p-dinitrobenzene in 2*M* lithium chloride was unaffected by an equimolar mixture of potassium thiocyanate and tetramethylammonium chloride whereas the second wave was shifted, but only slightly, toward less cathodic potentials.

In the absence of 2*M* lithium chloride (Fig. 4) the second wave was shifted considerably by an increase in ionic strength. Potassium chloride, potassium thiocyanate, and potassium iodide behaved the same. Points for tetramethylammonium chloride and tetramethylammonium iodide fell at less cathodic potentials, indicating that the tetramethylammonium ion had a greater effect than potassium. In going from 0.2 to 2.0*M* lithium chloride, the apparent *p*H decreased from 11.55 to 10.90, a change that was confirmed using a hydrogen electrode (6). Correction for the change in *p*H would make the lithium curve essentially parallel to, but more cathodic than, the potassium curve, indicating that lithium by itself was less effective than potassium.

Lithium chloride also caused a small amount of shift in the first wave which, according to Holleck and Exner (5), should be practically independent of the *p*H in the alkaline range. It is possible that a shift of this magnitude (0.02 v) could be caused by a change in liquid junction potential. Although all the electrolytes had only a small effect, values for the first half-wave potential in the presence of thiocyanate or iodide are consistently more negative than the corresponding values for chloride, in accord with known differences in capillary activity of those anions (7).

Agreement between the present study and the earlier one by Holleck and Exner (5) was good for the first wave. However, their values for the second wave were more cathodic (nearly −1.6 v vs. −1.3 v) in spite of the fact that their lower concentration of methanol (20%) would normally be expected to result in a less cathodic wave. Figure 4 shows that a difference in ionic strength is the chief source of the discrepancy since they did not use as highly concentrated background electrolyte.

Though the above discussion refers only to two waves of p-dinitrobenzene, Holleck and Exner (5) showed that this compound has three polarographic waves at intermediate values of *p*H. At high values of *p*H the middle wave is not present but, under the conditions of the present experiment, a small wave was still visible at about −0.88 v. Unfortunately this wave was too small to permit accurate half-wave measurements, so changes in its position were not included in the study. As a further complication, a new wave was observed to grow in at slightly more positive potentials when the solution was allowed to stand a few hours before a polarogram was run. It was established that p-nitroanisole was the compound produced in alkaline methanol.

Effects of Divalent Ions

Prior studies on the reduction of ketones (8) and nitrate ion (9) have indicated that di- and trivalent cations resulted in a less cathodic half-wave potential than monovalent ions of comparable concentration. It was surprising, therefore, to find that the addition of calcium chloride in an amount sufficient to produce a 0.05*M* solution had little effect on the first and second waves of carbon tetrachloride and dibromoacetic acid. In contrast, the second wave for p-dinitrobenzene shifted +56 mv although the first wave remained constant. Barium chloride was also tried and gave a shift of +23 mv for the second wave, but unfortunately a precipitate formed which decreased the concentration of barium by an unknown amount. The fact that calcium exerted little effect on the second waves of the halides (compared to tetra alkylammonium ion) is probably due to its lack of electrocapillary activity (10).

The greater effect of calcium ion on the second wave of p-dinitrobenzene appears to be due to ion-

pair formation with the stable divalent intermediate. Ion-pair formation would decrease the effective negative field around the nitro body and would facilitate further reduction. The acidic reduction of p-dinitrobenzene as well as the acidic and alkaline reductions of o-dinitrobenzene, none of which involve a stable charged intermediate (5), show little effect of calcium (6). The fact that changes in the concentrations of lithium and potassium ions had nearly the same effect as changes in tetramethylammonium ion, plus the fact that doubly charged calcium had a much greater effect than any monovalent cation, suggests that the shift is associated with charge rather than electrocapillary activity.

Effect of Gelatin

In early exploratory runs with p-dinitrobenzene in acidic solutions, gelatin exhibited unusual effects which made further investigation seem worthwhile. In acidic media, p-dinitrobenzene is reduced in two steps, the first corresponding to formation of p-hydroxylaminonitrobenzene and the second to p-hydroxylaminoaniline (5).

Two series of runs were made in different concentrations of ethanol. In one the apparent pH of the buffer was adjusted to 4.1 by the addition of hydrochloric acid, while in the second the electrolyte concentration was held constant and the apparent pH allowed to increase with alcohol concentration. At the lowest ethanol concentration (8%) a maximum was formed on the second wave of p-dinitrobenzene unless 0.002% gelating was present. Hence, the half-wave potential of the second wave in the absence of gelatin was somewhat uncertain in 8% ethanol. At higher ethanol concentrations no maxima were observed even in the absence of gelatin.

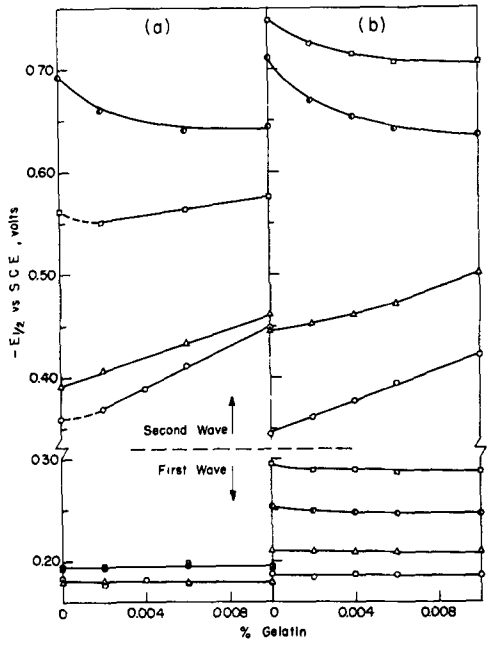

Fig. 5. Effect of gelatin on the half-wave potentials of 10^{-4}M p-dinitrobenzene in 0.07M phthalate buffers of varying ethanol concentration (O—8%; △—29%; ∅—49%; □—73%). (a) Apparent pH maintained constant at 4.1 by adding HCl when increasing the ethanol concentration. (b) Apparent pH allowed to increase with ethanol concentration.

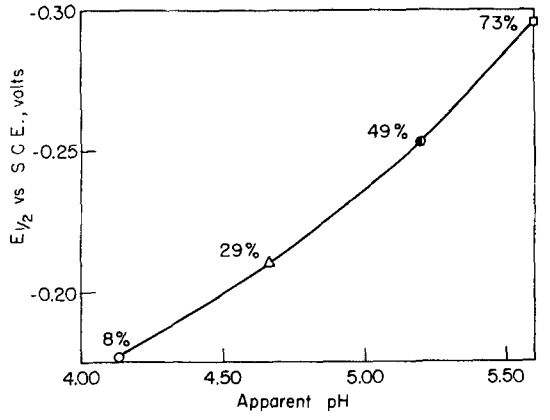

Fig. 6. Changes in the half-wave potential of the first wave of 10^{-4}M p-dinitrobenzene as function of the apparent pH of solutions of different ethanol content with 0.07M potassium acid phthalate as supporting electrolyte.

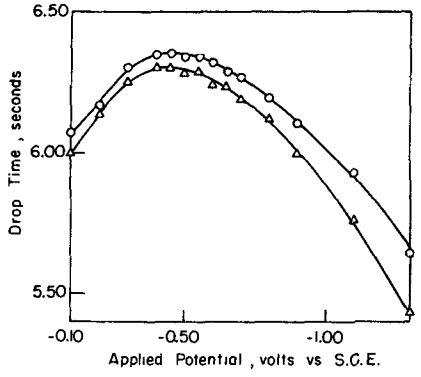

Fig. 7. Effect of gelatin on the electrocapillary curve in 0.07M potassium acid phthalate and 29% ethanol (O—no gelatin added; △—0.01% gelatin present).

As shown in Fig. 5a and 5b gelatin had no effect on the first wave. This probably indicates that this wave is more nearly reversible in character than the second. The shift observed for the half-wave potential as a function of alcohol in Fig. 5b is largely due to a change in pH, though Fig. 6 shows the change to be somewhat greater than expected, i.e., 85 mv per unit of apparent pH. This undoubtedly reflects a change in the composition of the solvent and in the resulting junction potential. This solvent effect is also indicated by the slight cathodic shift of the first wave with increasing ethanol concentration, at constant apparent pH, shown in Fig. 5a.

The behavior of the second wave with a change in concentration of gelatin was complex. At the 8 and 29% levels of alcohol, the difficulty of reduction increased almost linearly with concentration. At the 49% level, reduction was facilitated, an effect not previously reported for gelatin. This must have been due to superposition of a second factor which counteracted the generally observed retardation. Electrocapillary data of the type shown in Fig. 7 showed that these reductions were taking place on the negative branch of the electrocapillary curve. Hence, the acceleration is probably due to protonated gelatin in the double layer.

At the 73% level, the effect of gelatin differed in the two series. In Fig. 5a where the reduction fell

only slightly on the negative side of the electrocapillary maximum (due to a large increase in ionic strength when a large amount of hydrochloric acid had to be added to attain an apparent pH of 4.1), the retarding effect was predominant. In Fig. 5b, the positive-ion effect was still predominant, but smaller, even though the reduction took place at a more cathodic potential than in 49% alcohol. This probably reflects less extensive protonation of the gelatin in the lower dielectric medium, as well as a possible denaturization.

Confirmation of the protonation hypothesis may be found by noting in Table I that, at pH 10.9 where protonation was very slight, the retarding effect was always observed regardless of position of the reduction relative to the electrocapillary maximum. This indicates that the positive-ion effect was indeed the cause of the reversal observed in acidic medium. The only reservations that must be made are: (*a*) the fact that the reduction mechanism for p-dinitrobenzene differs in acidic and alkaline media, and (*b*) a small positive shift was observed for the second wave of carbon tetrachloride. However, the latter data are very uncertain due to superposition of the carbon tetrachloride reduction on that of the background electrolyte.

Discussion

The present study confirms the importance of the position of a polarographic wave relative to the electrocapillary maximum in determining whether one can expect anion or cation effects on the half-wave potential of an electron-transfer controlled reaction (1). Although Ashworth (8) was one of the first to report the influence of cations on irreversible organic reductions (benzophenone and fluorenone) and the fact that similar compounds may react differently to the same ion, the conditions under which the two ketones were examined were not strictly comparable. Thus, his results are difficult to analyze. The present study indicates that one may be able to differentiate between different roles played by the electrolytes. In one case the effect may be a general one and probably depends only on the presence of excess anions or cations sufficiently close to the electrode surface to change the potential at the point where reduction takes place. [There is evidence that tetraalkylammonium ions are not appreciably solvated and are electrocapillary active (11).] Therefore, calcium ion, in spite of its greater charge, may have had less effect on the halide reductions because its solvated ion is not appreciably concentrated by adsorption at the interface. The comparatively small effects in 2*M* lithium chloride of capillary-active monovalent ions on p-dinitrobenzene may be the result of the more nearly reversible character of the waves (especially the first).

The large effect of calcium on the alkaline reduction of p-dinitrobenzene was discussed earlier. Although this may be a specific effect of calcium ion, it appears more probable that the specificity is associated with the divalent intermediate formed in this particular mechanism. However, electrocapillary-inactive ions may exert an additional characteristic influence. Unfortunately, the alkaline reduction of p-dinitrobenzene did not lend itself to such a study because most difficultly reducible multivalent cations form hydroxide complexes or precipitates. However, good examples of specific cation effects have been reported for the electrochemical reduction of nitrate which is affected by a number of multivalent cations in addition to calcium. Collat and Lingane (12) found the products to be quite different if obtained in the presence of uranyl ion instead of lanthanum (III). In fact, somewhat different yields of products resulted in shifting from lanthanum (III) to cerium (III).

The half-wave potentials for irreversible reactions are usually affected by changes in concentration of the reducible substance so the concentration was held constant. However, the volatility of carbon tetrachloride made difficult the maintenance of a constant concentration throughout a series of experiments, so the effect of a change in concentration on the half-wave potential was briefly investigated. A change from 4.1×10^{-4} to 4.1×10^{-3} *M* caused a shift in half-wave potential of about +10 mv, an insignificant amount compared to most of the shifts that were observed.

It was recognized that the results obtained with solutions at apparent pH 10.9 would be open to some question because of the absence of a buffer. Unfortunately, higher concentrations of sodium hydroxide, which would have been better buffers, would also have prevented the study of the calcium effect by precipitating the hydroxide. As a compromise, the concentration of sodium hydroxide used was 0.007*M* which would serve rather well as a buffer for the pH-sensitive reduction of 1×10^{-4} *M* p-dinitrobenzene. The calculated pH of 11.85 was actually observed in the absence of a large concentration of background electrolyte, but the presence of 2.0*M* lithium chloride caused a decrease in apparent pH to 10.9. This decrease was checked and substantially confirmed using a hydrogen electrode although there was a small sodium and lithium error (6).

Table I. Effect of gelatin on the half-wave potentials of carbon tetrachloride, dibromoacetate, and p-dinitrobenzene in 2.0M lithium chloride and 41% methanol of apparent pH 10.9

	Carbon tetrachloride		Dibromoacetate		p-Dinitrobenzene	
Gelatin, %	First wave	Second wave	First wave	Second wave	First wave	Second wave
0	−0.39	−1.71*	−0.414	−1.179	−0.315	−1.284
0.01	−0.42	−1.68*	−0.443	−1.194	−0.318	−1.316

* Values for the second wave of carbon tetrachloride are uncertain due to superposition of the reduction on that of the background electrolyte.

Acknowledgment

The authors are grateful to Dr. Vernon Stenger for providing the dibromoacetic acid, to Dr. William H. Reinmuth for many stimulating discussions and the opportunity to read one of his manuscripts during its preparation. This work was supported in part by the Atomic Energy Commission.

Manuscript received March 28, 1958.

Any discussion of this paper will appear in a Discussion Section to be published in the December 1959 JOURNAL.

REFERENCES

1. J. L. Lothe and L. B. Rogers, *This Journal*, **101**, 258 (1954).
2. J. Pearson, *Trans. Faraday Soc.*, **44**, 683 (1948).
3. P. J. Elving, I. Rosenthal, and M. K. Kramer, *J. Am. Chem. Soc.*, **73**, 1717 (1951).
4. P. J. Elving, J. C. Komyathy, R. E. Van Atta, C.-S. Tang, and I. Rosenthal, *Anal. Chem.*, **23**, 1218 (1951).
5. L. Holleck and H. J. Exner, *Z. Elektrochem.*, **56**, 677 (1952).
6. R. F. Breese, Private communication.
7. D. C. Grahame, *Chem. Revs.*, **41**, p. 451, Table I, (1947).
8. M. Ashworth, *Collection Czech. Chem. Commun.*, **13**, 229 (1948).
9. M. Tokuoka and J. Ruzicka, *ibid.*, **6**, 339 (1934).
10. W. H. Reinmuth, Private communication.
11. G. Sutra, *J. Chim. Phys.*, **43**, 189, 279 (1946); *see also*: G. Darmois and E. Darmois, *Compt. rend.*, **238**, 971 (1954).
12. J. W. Collat and J. J. Lingane, *J. Am. Chem. Soc.*, **76**, 4214 (1954).

Kinetics of the Cathodic Reduction of Anions: Germanium Oxides

Mino Green[1] and P. H. Robinson

Lincoln Laboratory, Massachusetts Institute of Technology, Lexington, Massachusetts

ABSTRACT

The electrochemical cell Hg(Na)|GeO_2, NaOH(aq)|Pt, gives GeH_4, Ge, and H_2 as end products at the cathode. GeH_4 yields have been obtained with a current efficiency of >40% and a mass conversion efficiency of >80%. The partial currents of GeH_4, Ge, and H_2 have been measured as a function of electrolyte composition, cathode potential, and cathode diffusion boundary layer thickness. A highly reducing reactive intermediate has been detected in solution with a mean life of ~4 min. The value of the Tafel slope for GeH_4 evolution was found to be -56 ± 2 mv per decade. The mechanism for the over-all reaction $GeO_3^= + 7\ H_2O + 8\ e^- \rightarrow GeH_4 + 10\ OH^-$ is discussed and the most likely mechanisms up to the rate-determining step are narrowed down to three possible cases. Further experiments for the final determination of the rate-determining step are suggested.

The work reported here had two main objects: (*a*) the determination of the optimum conditions for the electrochemical preparation of germane, GeH_4; and (*b*) an investigation of the kinetics and mechanism of the cathodic reduction of anions in the light of recent advances in the theory of electrode processes, e.g., Ref. (1). It has been found that the system Na(Hg)|NaOH, GeO_2(aq)|Pt, anode, gives high yields of GeH_4 and therefore it is this system which is discussed here.

Experimental

Materials.—Unless otherwise specified reagent grade chemicals were used. The GeO_2 used contained less than 1 ppm w/w total metallic impurities. The Hg used was triply distilled and all other metallic electrodes used were designated "spectroscopically pure."

Estimation of GeH_4-H_2 ratios.—The gaseous product from the cathode was a mixture of GeH_4 and H_2; no other gaseous species were detected, nor were there any other volatile hydrides of Ge. The GeH_4-H_2 ratio was determined using a Rayleigh-Zeiss interferometer. The essentials of the analytical method, which depended on measuring the differences between the refractive indexes of hydrogen and a GeH_4-H_2 mixture, have been reported elsewhere (2). The procedure has been modified somewhat to extend the range to 100% GeH_4: the accuracy of the method was ± 0.004 mole fraction GeH_4.

[1] Present address: Zenith Radio Corporation, Chicago, Ill.

Cell assembly.—The assembly of Fig. 1 was used where quantitative gas collection was required. The system was cooled by flowing water. Current was obtained from a 110 ± 1 v d-c generator and the other circuitry was conventional. The anode con-

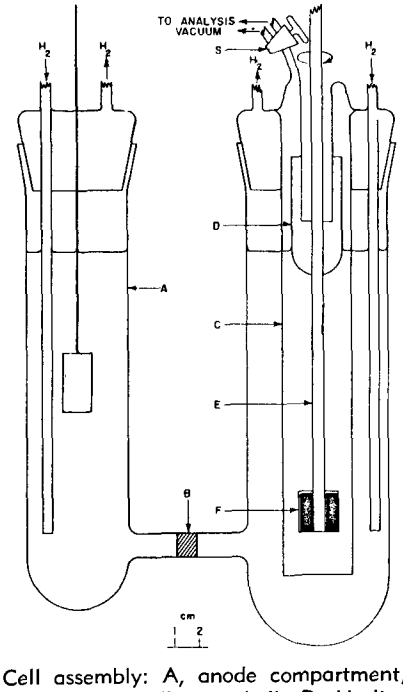

Fig. 1. Cell assembly: A, anode compartment; B, porous disk (medium); C, gas collecting bell; D, Hg-liquid seal; E, "Teflon" shaft; F, Hg cathode.

Manuscript received March 28, 1958.

Any discussion of this paper will appear in a Discussion Section to be published in the December 1959 JOURNAL.

REFERENCES

1. J. L. Lothe and L. B. Rogers, *This Journal*, **101**, 258 (1954).
2. J. Pearson, *Trans. Faraday Soc.*, **44**, 683 (1948).
3. P. J. Elving, I. Rosenthal, and M. K. Kramer, *J. Am. Chem. Soc.*, **73**, 1717 (1951).
4. P. J. Elving, J. C. Komyathy, R. E. Van Atta, C.-S. Tang, and I. Rosenthal, *Anal. Chem.*, **23**, 1218 (1951).
5. L. Holleck and H. J. Exner, *Z. Elektrochem.*, **56**, 677 (1952).
6. R. F. Breese, Private communication.
7. D. C. Grahame, *Chem. Revs.*, **41**, p. 451, Table I, (1947).
8. M. Ashworth, *Collection Czech. Chem. Commun.*, **13**, 229 (1948).
9. M. Tokuoka and J. Ruzicka, *ibid.*, **6**, 339 (1934).
10. W. H. Reinmuth, Private communication.
11. G. Sutra, *J. Chim. Phys.*, **43**, 189, 279 (1946); *see also*: G. Darmois and E. Darmois, *Compt. rend.*, **238**, 971 (1954).
12. J. W. Collat and J. J. Lingane, *J. Am. Chem. Soc.*, **76**, 4214 (1954).

Kinetics of the Cathodic Reduction of Anions: Germanium Oxides

Mino Green[1] and P. H. Robinson

Lincoln Laboratory, Massachusetts Institute of Technology, Lexington, Massachusetts

ABSTRACT

The electrochemical cell Hg(Na)|GeO_2, NaOH(aq)|Pt, gives GeH_4, Ge, and H_2 as end products at the cathode. GeH_4 yields have been obtained with a current efficiency of >40% and a mass conversion efficiency of >80%. The partial currents of GeH_4, Ge, and H_2 have been measured as a function of electrolyte composition, cathode potential, and cathode diffusion boundary layer thickness. A highly reducing reactive intermediate has been detected in solution with a mean life of ~4 min. The value of the Tafel slope for GeH_4 evolution was found to be -56 ± 2 mv per decade. The mechanism for the over-all reaction $GeO_3^= + 7\ H_2O + 8\ e^- \rightarrow GeH_4 + 10\ OH^-$ is discussed and the most likely mechanisms up to the rate-determining step are narrowed down to three possible cases. Further experiments for the final determination of the rate-determining step are suggested.

The work reported here had two main objects: (*a*) the determination of the optimum conditions for the electrochemical preparation of germane, GeH_4; and (*b*) an investigation of the kinetics and mechanism of the cathodic reduction of anions in the light of recent advances in the theory of electrode processes, e.g., Ref. (1). It has been found that the system Na(Hg)|NaOH, GeO_2(aq)|Pt, anode, gives high yields of GeH_4 and therefore it is this system which is discussed here.

Experimental

Materials.—Unless otherwise specified reagent grade chemicals were used. The GeO_2 used contained less than 1 ppm w/w total metallic impurities. The Hg used was triply distilled and all other metallic electrodes used were designated "spectroscopically pure."

Estimation of GeH_4-H_2 ratios.—The gaseous product from the cathode was a mixture of GeH_4 and H_2; no other gaseous species were detected, nor were there any other volatile hydrides of Ge. The GeH_4-H_2 ratio was determined using a Rayleigh-Zeiss interferometer. The essentials of the analytical method, which depended on measuring the differences between the refractive indexes of hydrogen and a GeH_4-H_2 mixture, have been reported elsewhere (2). The procedure has been modified somewhat to extend the range to 100% GeH_4: the accuracy of the method was ± 0.004 mole fraction GeH_4.

[1] Present address: Zenith Radio Corporation, Chicago, Ill.

Cell assembly.—The assembly of Fig. 1 was used where quantitative gas collection was required. The system was cooled by flowing water. Current was obtained from a 110 ± 1 v d-c generator and the other circuitry was conventional. The anode con-

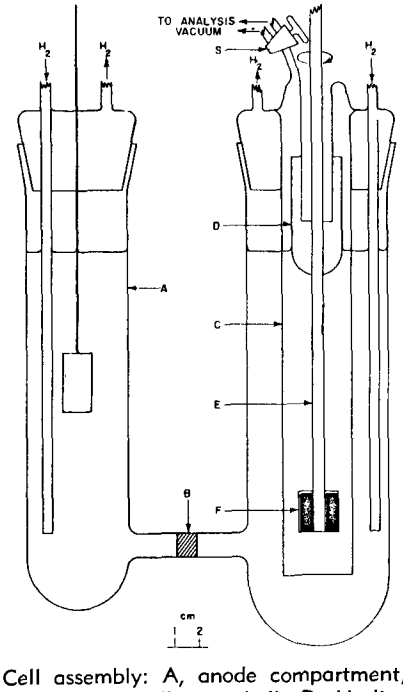

Fig. 1. Cell assembly: A, anode compartment; B, porous disk (medium); C, gas collecting bell; D, Hg-liquid seal; E, "Teflon" shaft; F, Hg cathode.

sisted of Pt(A = 4 cm^2) and the cathode was contained in a cup attached to a Teflon rod. Electrical contact was made to the mercury in the cup by means of a platinum wire which passed down the center of the stirring rod. The exposed area of mercury was about 0.8 cm^2, and the volume of mercury was about 0.5 cc. The cathode could be spun to speeds up to 800 rpm. Gas produced at the cathode was collected in the bell. No corrosion of the glass cup containing the cathode was observed.

A typical run was performed as follows: Current corresponding to the desired current density at the cathode was passed through the cell. The cathode was "run-in" for a suitable time after which liquid was drawn up in the bell to the stopcock, S. At this point the current was recorded continuously on a strip-chart recorder. One determination was completed when the liquid in the bell was displaced by gas down to the level of the cathode surface. Then the gas was transferred to the evacuated collecting bulb via a mixed calcium chloride-barium oxide drying column. The run-in of the cathode was necessary since the sodium first formed at the cathode dissolved in the mercury (fresh Hg used for each run), and only after the cathode reached a certain Na-Hg composition did gas evolution occur. After a further period of electrolysis a determination of composition, etc., was made and this was repeated. The second determination usually gave the same results as the first, indicating that the cathode had reached a limiting Na concentration for both cases. If the second determination did not give the same values as the first, a further determination was carried out and this invariably gave, within experimental error, the same values as the preceding run. Since reproducible yield results were obtained in the manner just outlined, it is reasonable to assume that no error arises out of the possible solubility of GeH_4 in the electrolyte. The temperature near the cathode was 25° ± 3°C for all current densities up to ~ 2 amp-cm^{-2}; for higher current densities (not used in kinetic analysis) the cathode rose to somewhat higher temperatures.

The information available from each run was: the amount and composition of the evolved gas, the rpm of the cathode, and the total coulombs passed. The volume of the bell (about 80 cc) was determined by weighing the amount of Hg required to fill it to the point where cathode/electrolyte contact was broken. The number of moles of GeH_4 produced was calculated taking into account the temperature, atmospheric pressure, and water vapor pressure above the particular electrolyte being used. The coulombs passed were measured by graphical integration of the current-time recording. The rotary speed of the cathode was measured by a stroboscopic illumination method.

Determination of cathode potential.—The potential of the cathode with current passing was determined in an H-shaped cell, using the cathode and Luggin arrangement of Fig. 2. The object of this Luggin capillary arrangement, used by Piontelli and Polli (3), was to avoid measuring any resistive potential drop in the solution. The geometrical surface

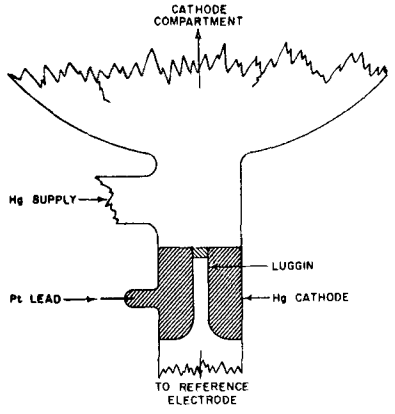

Fig. 2. Backside Luggin capillary arrangement

area of the cathode was 0.31 cm^2 and the outside diameter of the Luggin was 0.02 cm with a wall thickness of about 0.004 cm. In a measurement of cathode potential the Hg was always kept filled to the tip of the Luggin; any excess Hg passed out through the Luggin. Measurements of potential were made at the lowest current density first. The cathode potential measured was in each case the steady-state value, i.e., a run-in period was necessary to allow the Na concentration of the cathode to reach its limiting value (cf. above).

Cathode potential measurements were made in NaOH and also in solutions of GeO_2 and NaOH. Yield values also were determined in the case of GeO_2/NaOH solutions in a cell similar to that shown in Fig. 1 but with the cathode at the bottom of the cathode compartment and identical in construction with that shown in Fig. 2 but without a Luggin. The aim of making the two arrangements identical was to obtain the same hydrodynamical conditions at the cathode. Note that there was no rotation of the cathode in either case; in fact, nearly all the electrolysis data reported here refer to a stationary cathode. It was shown that the cathode potential depended only on the partial current of hydrogen; this enabled an evaluation of the cathode potential if the hydrogen current was known.

Measurement of the lifetime of an intermediate product.—Some of the results reported below pointed to the possible production of an intermediate product which was sufficiently long lived so that there could be substantial diffusion of this material from the cathode into solution. If such an intermediate product were present in solution, it would be a stronger reducing agent than Ge. ($GeO_2 + 4H^+ + 4e_o^- = Ge + 2H_2O$: $e = -[0.15 + 0.059\,pH + 0.015\,pG]$, where pG is the negative of the logarithm of the GeO_2 concentration.) Thus, if Ge/GeO_2 is added to an acid solution containing vanadium (III) and vanadium (II) ions ($V^{3+} + e^- = V^{2+}$: $e^o = -0.255$) no reduction of vanadium (III) will take place, if the conditions of the experiment are such that $e_{GeO_2/Ge}$ and $e_{V^{3+}/V^{2+}}$ are more positive than −0.15 v and more negative than about −0.2 v, respectively. But if this supposedly highly reducing intermediate product were added, a reduction of vanadium(III) might well occur.

A solution of known concentration of vanadyl sulphate in 8*N* HCl was reduced to the V^{2+} state with

Table I. Dependence of mean values* of ϕ, i_{GeH_4} and i_{Ge}, on current density and electrolyte composition

Composition†	ϕ‡	i_{GeH_4}	i_{Ge}
	c.d. = 3.10^{-2} amp-cm^{-2}		
2.0(2.5)	4.83×10^{-3}	1.2×10^{-4}	2.32×10^{-2}
	c.d. = 1.10^{-1} amp-cm^{-2}		
2.0(2.5)	0.0488	5.04×10^{-3}	7.06×10^{-2}
	c.d. = 8×10^{-1} amp-cm^{-2}		
2.0(2.5)	0.172	0.314	0.120
	c.d. = 1.2 amp-cm^{-2}		
5.5(1.6)	0.0900	0.294	0.170
3.0(1.6)	0.1200	0.378	0.188
2.0(1.6)	0.1199	0.361	0.169
2.0(2.0)	0.1498	0.436	0.144
3.0(2.0)	0.1384	0.402	0.151
5.5(2.0)	0.1261	0.378	0.118
8.0(2.0)	0.0820	0.251	0.215
3.0(2.8)	0.1839	0.521	0.106
5.5(2.8)	0.1479	0.412	0.206
8.0(2.8)	0.1175	0.346	0.188
	c.d. = 2.4 amp-cm^{-2}		
2.0(1.0)	0.0605	0.398	—
2.1(1.0)	0.0584	0.427	0.237
2.1(1.0)	(S)0.0422	0.384	0.264
3.0(1.0)	0.0568	0.360	—
4.0(1.0)	0.0421	0.322	—
5.0(1.0)	0.0398	0.302	—
6.0(1.0)	0.0340	0.281	—
7.0(1.0)	0.0278	0.235	—
8.0(1.0)	0.0192	0.166	—
9.0(1.0)	0.0113	0.086	—
10.0(1.0)	0.0099	0.084	—
5.5(1.3)	0.0611	0.427	0.245
2.25(1.4)	0.1026	0.650	0.293
2.0(1.5)	0.1100	0.778	0.0564
4.0(1.5)	0.0885	0.576	0.344
7.0(1.5)	0.0490	0.403	0.0451
9.0(1.5)	0.0300	0.218	—
4.6(1.8)	0.1010	0.641	0.301
2.0(2.0)	0.1367	0.713	—
3.0(2.0)	0.1310	0.749	—
5.0(2.0)	0.1160	0.806	—
7.0(2.0)	0.0755	0.552	0.158
8.0(2.0)	0.0625	0.458	0.212
2.4(2.1)	0.1444	0.811	0.383
2.0(2.25)	0.1623	0.902	0.301
2.0(2.4)	0.1610	0.960	0.185
3.0(2.4)	0.1563	0.917	—
5.0(2.4)	0.1344	0.794	—
7.0(2.4)	0.1010	0.593	0.484
9.0(2.4)	0.0750	0.497	0.362
2.0(2.5)	0.1734	0.907	0.414
2.5(2.5)	0.1630	0.924	0.266
8.0(2.5)	0.0820	0.578	0.204
9.5(2.5)	0.0615	0.442	0.262
3.0(2.6)	0.1605	0.924	0.269
7.0(2.6)	0.1020	0.655	0.299
8.5(2.6)	0.0860	0.590	0.240
2.0(2.7)	0.1832	1.018	—
3.0(2.7)	0.1730	0.974	0.258
4.0(2.7)	0.1495	0.847	—
5.5(2.7)	0.1309	0.890	0.0234
5.5(2.7)	(S)0.1315	0.706	0.152
7.0(2.7)	0.1164	0.742	0.241
10.0(2.7)	0.0667	0.439	0.152
2.75(2.75)	0.1724	0.931	0.392
3.4(2.8)	0.1630	0.924	0.293
3.8(2.8)	0.1600	0.922	0.399
2.0(3.0)	0.1914	1.034	—
3.0(3.0)	0.1728	1.010	—
3.5(3.0)	0.1730	0.936	0.343
4.0(3.0)	0.1612	0.972	—
5.0(3.0)	0.1507	0.991	—
7.0(3.0)	0.1200	1.013	—
8.0(3.0)	0.1030	0.898	—
10.0(3.0)	0.0738	0.631	—
4.5(3.1)	0.1640	0.888	0.369
	c.d. = 4.8 amp-cm^{-2}		
2.0(1.6)	0.0986	1.440	0.0890
3.0(1.6)	0.0970	1.272	0.566
5.5(1.6)	0.0592	0.965	0.0638
2.0(2.0)	0.1184	1.704	0.276
3.0(2.0)	0.1090	1.709	0.725
5.5(2.0)	0.0929	1.248	0.624
8.0(2.0)	0.0346	0.504	—
3.0(2.8)	0.1445	1.632	0.576
5.5(2.8)	0.1289	1.656	0.320
8.0(2.8)	0.0782	1.277	0.450

* Maximum errors in ϕ, i_{GeH_4}, and i_{Ge} are about ±0.5%, ±1.5%, and ±3%, respectively.
† Composition is given as normality NaOH and GeO_2 g/100 ml in brackets.
‡ Mole fraction GeH_4 in $GeH_4 - H_2$ mixture.
(S) Electrode rotated at ~250 rpm. Electrode stationary in all other cases.

Sn. This solution then was placed in a small beaker, and with nitrogen bubbling through the solution the oxidation-reduction potential of the V^{2+}/V^{3+} couple at a platinum electrode was measured against a calomel reference electrode. Then oxygen was bubbled through the solution until most, but not all, of the V^{2+} had been oxidized, as shown by the potential of the platinum electrode (from which the V^{2+}/V^{3+} ratio could be determined). All of the solution (about 10 ml) from the cathode compartment of a small electrolysis cell which had been in operation for about 20 min was drained off, filtered, and equal aliquots of the filtrate added to the $V^{2+} - V^{3+}$ containing solution at regular time intervals. The change in potential of the $V^{2+} - V^{3+}$ solution was measured each time; these changes occurred in a few seconds, and each time the potential remained constant at the new value. From these measurements it was possible to calculate (see later) the reducing power of the solution at each addition and thus to obtain a measure of the lifetime of the strongly reducing substance in the GeO_2/NaOH solution. The same experiments were repeated but without GeO_2 in the NaOH solution; this time material from the cathode compartment did not affect the V^{2+}/V^{3+} couple. Finally powdered Ge was added to the $V^{2+} - V^{3+}$ solution to determine its effect on the redox potential; it was undetectable.

Diffusion layer thickness.—A small quantity (~10^{-5} M) of tagged $Hg(CN)_2$ was added to the electrolyte in the cathode compartment of a cell similar to that shown in Fig. 1 but containing no bell and no stirring arrangement. $Hg(CN)_2$ is reduced readily at a Hg cathode and, since the concentration of the tracer is small, its partial current density can confidently be expected to be its limiting current. Hence a determination of the rate of removal of $Hg(CN)_2$ from

solution can be used to calculate the effective thickness of the diffusion layer, δ. Thus,

$$\frac{1}{\delta} = \frac{S}{DtA} \ln (n_o/n)$$

where S is the volume of solution in the cathode compartment; D is the diffusion coefficient for Hg $(CN)_2$; t is time of electrolysis; A is the surface area of the electrode; and n_o and n are the initial and final radioactivity of the solution, respectively.

Results

Partial currents.—The partial currents for the products of electrolysis, GeH_4, Ge, and H_2 are given in Table I and Fig. 3 and 4. The variation of ϕ, mole fraction of GeH_4 in the gas, with the nature of the cathode material was examined; results are shown in Table II. There is no simple relation apparent between yield and the hydrogen overpotential.

Cathode potential.—Hydrogen overpotential measurements on the cathode as a function of current density, 10^{-2} to 1 amp-cm^{-2}, in solutions of 2 and 10N NaOH are shown in Fig. 5. The Tafel b-function obtained is in agreement with the over-all results of Bockris and Watson (4) obtained at lower current densities and for more dilute NaOH solutions. Cathode potential measurements also were made with a solution of 2N NaOH containing 2 g GeO_2/100 ml; a plot of the cathode potential against the current density for hydrogen evolution gave a curve identical with curve 1 in Fig. 5. Thus the cathode potential in the presence of GeO_2 can be defined as long as the hydrogen current is known.

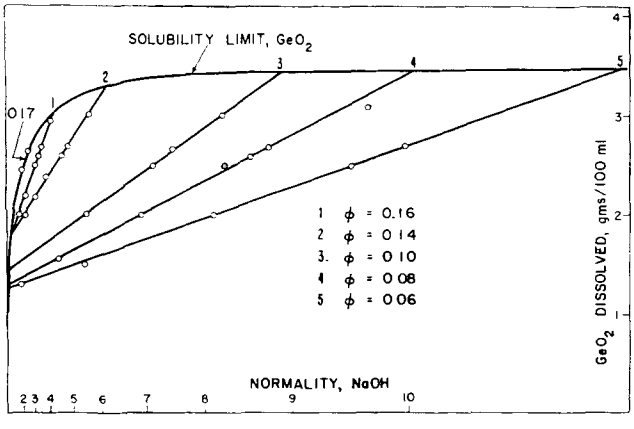

Fig. 3. Lines of constant yield, ϕ, current density 2.4 amp-cm^{-2}

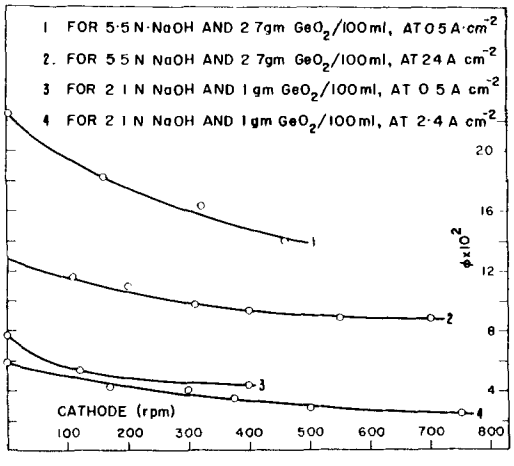

Fig. 4. Variation of ϕ with cathode rotation

Table II. Yield, ϕ, at different cathodes
Electrolyte composition: 10N NaOH, 2 g GeO_2/100 ml

Cathode material	Current density, amp-cm^{-2}	ϕ
Hg (Na)	0.90	0.19
Pb	0.88	0.0460
Th	0.90	0.019
Ge (p-type)	8.0	0.0102
Ge (n-type)	8.0	0.0058
Ta	1.45	0.0006
Pt	0.25	<0.0005

ϕ = mole fraction GeH_4 in GeH_4 – H_2 mixtures.

A plot of i_{GeH_4} vs. cathode potential (Fig. 8) yields a Tafel slope of -56 ± 2 mv per decade. It is quite possible, however, that the appropriate current to use is not i_{GeH_4}, since, as has been noted above, an intermediate product (abb. I.P.) diffuses away from the cathode. If the I.P. occurs before the rate-determining step, then η vs. i_{GeH_4} is the correct way to obtain the overpotential for the GeH_4 production process. If, on the other hand, the I.P. occurs after the rate-determining step, then the current of material going through the rate-determining transition state will be

$$I = i_{GeH_4} + (8/m) i_{Ge}$$

where m is the number of stages of reduction (from $GeO_3^=$) that the I.P. has gone through. This presupposes that i_{Ge} is due to the I. P., and this interpretation of the facts is suggested by the result that, as stirring at the cathode is increased, i_{GeH_4} decreases and i_{Ge} increases. Furthermore, if Ge were produced at the cathode, the comparative yield of GeH_4 would be very much lower since Ge electrodes give very low GeH_4 yields (whence the reaction Ge → GeH_4 would appear to go with difficulty). Since no plot of η vs. ln I for values of m from 1 to 4 yields a single Tafel slope, it is suggested that the I.P. occurs before the rate-determining transition state.

Intermediate product.—The reducing power of solution drawn from the cathode compartment is shown as a function of time in Fig. 6. The initial concentration of V^{2+}, $(a_{V^{2+}})_{t=0}$, was known and $(a_{V^{2+}})_{t=0} << (a_{V^{3+}})_{t=0}$, i.e., 10^{-4} N: 1N; since the over-all change in $a_{V^{2+}}$ was from 10^{-4} N to 1.8×10^{-4} N the concentration of the V^{3+} can be taken as constant. Thus the change in potential, ΔE, due to reduction of

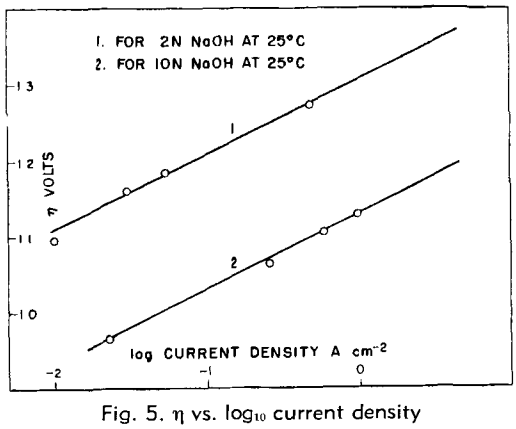

Fig. 5. η vs. $\log_{10}$ current density

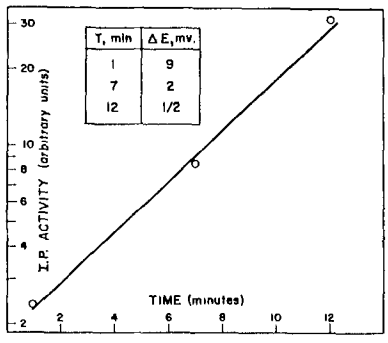

Fig. 6. Decay of intermediate product

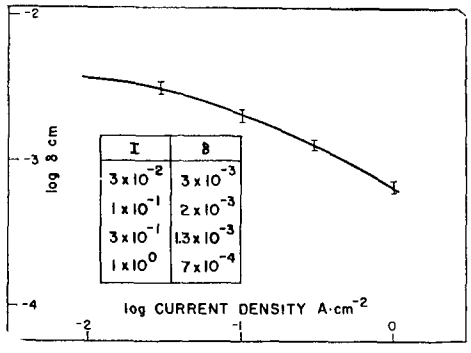

Fig. 7. Change of diffusion layer thickness with current density.

V^{3+}, by reactive intermediate at a time t' after removal from the cathode compartment is,

$$\Delta E = RT/F \ln [(a_{V^{2+}})_{t=t'}/(a_{V^{2+}})_{t=0}]$$

The concentration of the intermediate product is proportional to the amount of V^{3+} reduced, i.e., $\propto [(a_{V^{2+}})_{t=t'} - (a_{V^{2+}})_{t=0}]$. Upon a further addition of reactive intermediate, the new V^{2+} concentration can be determined from the potential change and so the concentration of reactive intermediate at time t'' was

$$\propto [(a_{V^{2+}})_{t=t''} - (a_{V^{2+}})_{t=t'}], \text{ etc.}$$

The slope of the line of $\log_{10} [(\Delta a_{V^{2+}})_{\Delta t}]$ vs. t (Fig. 6) gave a mean life for the intermediate product of 4.3 min: this presupposes a monomolecular decay process.

The nature of the intermediate product has not been established by direct chemical means. However, it has been shown that the intermediate product does not give rise to H_2 in solution. An electrolysis cell with a U-shaped cathode compartment was used; the cathode was in one limb and the other limb was filled completely with electrolyte. Convective mixing was relatively unhampered as shown by the Ge particles first formed near the cathode appearing in the opposite limb in ~ 1 min. There was no accumulation of H_2 gas in the sealed limb after prolonged electrolysis.

Diffusion layer.—The measurement of diffusion layer thickness for various current densities in 2*N* NaOH solution, using tagged $Hg(CN)_2$, is shown in Fig. 7. The presence of GeO_2 in solution could not be tolerated since the Ge metal produced might well adsorb some of the $Hg(CN)_2$. That $Hg(CN)_2$ is the only diffusing mercury species has been established by Tomes (5). Its diffusion coefficient in 10^{-2} *N* NaOH is (6) 1.56×10^{-5} cm^2 sec^{-1} at 28°C. The diffusion coefficient for $Hg(CN)_2$ in more concentrated solutions of NaOH has been calculated from this value assuming Stokes law applies, values for the viscosity of aqueous solutions of NaOH being available (7). The applicability of Stokes law for the diffusion of zinc sulfate and zinc acetate in various concentrations of NaOH solution has been tested by Brasher and Jones (8) and has been found to be valid: it is therefore reasonable to assume that $Hg(CN)_2$ in NaOH solutions also obeys Stokes law.

Discussion

The experiments of Pugh (9) and Carpéni (10) have shown that, when GeO_2 is dissolved in NaOH solutions of $pH \geqq 13$, the Ge will be present as $GeO_3^=$; all the solutions used in this study were of $pH > 14$.

Transport to the cathode.—The variation of ϕ with current density and cathode stirring rate suggests that the over-all electrochemical process is not entirely activation controlled; thus it is necessary to consider the diffusion of various ions toward and away from the cathode. The primary species moving to the cathode are Na^+ and $GeO_3^=$. Na^+ ions move to the cathode under a favorable potential gradient and $GeO_3^=$ ions approach the cathode by diffusion and convection in an adverse potential gradient. Wagner (11) has treated these cases in a theoretical study of the electroreduction of anions in solutions of high electrolyte concentration. The solution of the diffusion equation for the discharge of Na^+ shows that the Na^+ concentration at the cathode does not rise above 1.1 times the bulk Na^+ concentration for the highest current densities employed in this study. The Na^+ concentration is enhanced at the cathode since discharged Na^+ ions react with water; the change in water concentration at the cathode is insignificant. The transport rate per unit time per unit area along the x-coordinate (which is normal to the surface of the electrode and is measured from the cathode) of ions of type i to the cathode under steady-state conditions, is given by (11)

$$\frac{1}{A}\frac{dn_i}{dt} = -c_i D_i \left(\frac{\partial \ln c_i}{\partial x} + \frac{z_i F}{RT}\frac{\partial \Psi}{\partial x} \right) \quad [1]$$

where the symbols are: dn_i/dt, number of moles of i passing cross section, A, per unit time; D_i, diffusion coefficient of ions of type i; c_i, their concentration; z_i, their valence; F, the Faraday; Ψ, electrical potential; R, gas constant; and T, absolute temperature. It is reasonable to make the simplifying assumption that the cathode is covered by a static diffusion layer, thickness δ, beyond which concentration differences are negligible owing to convective mixing: concentration changes will occur only between $x = 0$ and $x = \delta$. In Eq. [1] the first term on the right hand side accounts for transport due to a concentration gradient, and the second term accounts for electrolyte migration. As Wagner points out, if the potential difference across the diffusion layer is $< RT/F$ (0.025 v at room temperature) then the potential gradient will have little effect on anion migration. The value of $(\partial\Psi/\partial x)\delta$ was always <0.025 v in the systems studied. This argument assumes an

essentially linear potential gradient across δ. The validity of this assumption is not in question except at short distances from the electrode, $<10^{-6}$ cm (δ is typically 10^{-3} cm) when deviations from local charge neutrality can occur, i.e., the region of the Stern double layer. Since all the solutions used were concentrated electrolytes it is known that (12) a diffuse layer (i.e., Gouy layer) was not present, so Eq. [1] will be applicable up to the outer Helmholtz plane of the cathode.

The transport of ions from the bulk of the electrolyte to the outer Helmholtz plane has been considered thus far. An outline of the derivation of the equation for electron transfer to an anion follows. Consider the electrochemical reaction

$$A^{z-} + e^- \rightarrow A^{(z+1)-} \qquad [2]$$

For zero applied p.d. the initial state for this reaction is A^{z-} ions in the outer Helmholtz plane and electrons in the cathode. The final state is $A^{(z+1)-}$ anions partially adsorbed on the cathode. When a p.d. η is applied across the Helmholtz double layer the change in Galvani p.d. is η and if the dipole distribution in the Helmholtz double layer is taken to be unchanged, and the fractional surface coverage due to $A^{(z+1)-}$ is far from unity or close to unity (i.e, 0.9) then η may be equated to the Volta p.d. across the Helmholtz double layer. That is, η is due to the building up of excess, equal and opposite charge, on either side of the Helmholtz double layer. This is the usual assumption made in current theories of hydrogen overpotential and seems to be in accord with the facts. If the potential in the outer Helmholtz plane is arbitrarily taken as zero, then an applied (negative) potential η will increase the potential energy of the electrons in the cathode by an amount $F\eta$ per mole. That is, the potential energy of the initial state is increased by amount $F\eta$ per mole. The potential energy of the final state is raised by $(d_o - d/d)F\eta$ per mole, where d_o is the thickness of the Helmholtz double layer and d is the distance from the metal side of the Helmholtz double layer to the species $A^{(z+1)-}$. Thus the applied p.d. will have reduced the activation energy for the forward path of reaction [2] by

$$\beta F\eta(d/d_o) \qquad [3]$$

where β is the Tafel symmetry factor [discussed fully by Bockris (1)]. Since d_o is taken to be 5 to 10 times greater than $(d_o - d)$, the term (d/d_o) in Eq. [3] can be neglected. Whence, in the form usual for electron transfer reactions from the cathode, the forward velocity of reaction [2] is given by

$$i = i_o \exp(-\beta F\eta/RT) \qquad [4]$$

The limiting current, i_l, for $GeO_3^=$ calculated from Eq. [1], using a typical set of values, shows for all but the highest current densities that $i << i_l$: this gives rise to two limiting cases for GeH_4 evolution,

$$i_{GeH_4} = i_o[\exp(-\alpha\eta F/RT)] \qquad [5]$$

and

$$i_{GeH_4} = i_l[1 - \exp(\eta 8F/RT)] \qquad [6]$$

where, for the GeH_4 formation reaction, i_o is the exchange current and α is the Tafel transfer coefficient. Eqs. [5] and [6] are for activation and diffusion controlled processes, respectively. A plot of log i_{GeH_4} vs. cathode potential (Fig. 8) obeys the form of Eq. [5] over a range of >0.2 v and four decades of current density. Thus it is concluded that the GeH_4 formation reaction is largely activation controlled.

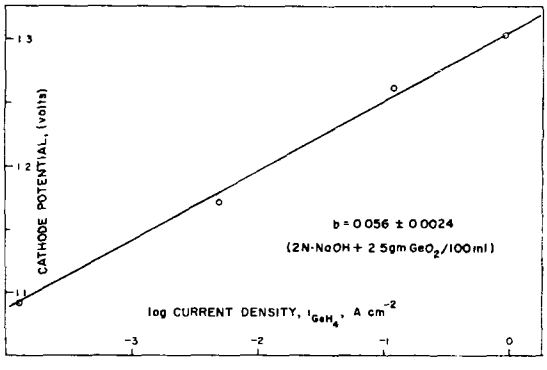

Fig. 8. Tafel curve for GeH_4 evolution reaction

Consecutive electrode processes.—The $GeO_3^=$ reduction process is taken to be a sequence of consecutive reactions. The method of handling such reactions is outlined below. Christiansen (13) has shown how the steady-state reaction rate for an open sequence of reactions can be represented in terms of the rate constants of the elementary reactions and the concentration of the stable components. In a sequence of reactions such as

$$A_1 \underset{s_{-1}}{\overset{s_1}{\rightleftharpoons}} X_1 + B_1\,,\; X_1 + A_2 \underset{s_{-2}}{\overset{s_2}{\rightleftharpoons}} X_2 + B_2 \ldots \text{ etc.} \qquad [7]$$

where the A's and B's are stable components and the X's are reactive intermediates and s and s_- are the forward and reverse reaction rates, respectively. A set of quantities ω are defined such that:

$$\omega_1 = s_1 = k_1 c_{A_1}$$

$$\omega_{-1} = \frac{s_{-1}}{c_{X_1}} = k_{-1} c_{B_1}$$

$$\omega_{-n} = s_{-n} = k_{-n} c_{B_n}$$

The principle of detailed balance is assumed, whence the over-all reaction rate, S, is given by:

$$S = s_1 - s_{-1} = s_2 - s_{-2} \ldots = \omega_1 - \omega_{-1} c_{X_1} = \omega_2 c_{X_1} - \omega_{-2} c_{X_2} \ldots$$

This gives rise to an expression for S which can be written generally as:

$$S = \frac{\prod_{k=1}^{k=n} \omega_k}{\sum_{m=2}^{m=n+1} \prod_{k=m}^{n} \omega_k \prod_{l=1}^{l=m-2} \omega_{-l}} \qquad [8]$$

where m goes from 2 to $n+1$ and $\prod_a^b = 1$ if $b < a$.

Bockris (14) first applied this method to the calculation of the over-all rate of electrochemical reac-

tions for oxygen evolution. The essential change to be made from the application to chemical kinetics is that the rate constants in reactions involving charge transfers are potential dependent. Thus, for a cathodic reaction, the rate constant for a partial cathodic reaction becomes

$$\vec{k} = k \exp [-\beta \Delta \xi nF/RT] \qquad [9]$$

where $\vec{k}$ and $\vec{k}$ are the electrochemical and chemical rate constants, respectively; $\Delta\xi$ is the Galvani p.d. between the electrode and the solution; and n is the number of electrons transferred. Correspondingly for the partial anodic reaction

$$\overleftarrow{k} = k \exp [(1-\beta) \Delta \xi nF/RT] \qquad [10]$$

These rate constants, utilized in partial reactions which involve charge transfer, give rise to potential terms in the final expression for the over-all reaction, and hence allow the evaluation of $\partial\Delta\xi/\partial \ln n_i$, i.e., the Tafel slope, b, characteristic of a given reaction mechanism. Thus a typical reaction sequence is examined for each partial reaction, in turn, being the rate-determining step (r.d.s.). In each case it can be taken that the reactions preceding the r.d.s. are fast, so that $k_+/k_- = K$, an "equilibrium" constant. Further, if $k_{+\text{r.d.s.}} \to k_{-\text{r.d.s.}} \to 0$, and $k_{+\text{r.d.s.}} \geqq 10\, k_{-\text{r.d.s.}}$, then all terms involving $k_{-\text{r.d.s.}}$ in the denominator of Eq. [8] can be neglected. This gives rise to a simple expression for the over-all rate which involves only one rate constant, i.e., $k_{+\text{r.d.s.}}$, and Eq. [8] can be written for the ith rate-determining step:

$$S = \prod_{k=1}^{k=i} \omega_k \Big/ \prod_{k=1}^{k=(i-1)} \omega_{-k} \qquad [11]$$

This expression is used here in the evolution of various reaction paths.

Mechanism of $GeO_3^= \to GeH_4$ *reaction.*—The final chemical products occurring at the cathode are H_2, Ge, and GeH_4. The reduction of $GeO_3^=$ to give GeH_4 can be represented by the over-all stoichiometric equation,

$$GeO_3^= + 7H_2O + 8\, e_0^- \to GeH_4 + 10\, OH^-$$

The over-all reduction reaction is taken to occur in a set of simple consecutive reactions, i.e., it is taken to be an open sequence of reactions. Since it is unlikely that the first step in the reduction of the $GeO_3^=$ ion can occur in two different, and approximately equally probable ways, the production of Ge must be taken to be due to a branch reaction in the $GeO_3^= \to GeH_4$ reaction sequence. If absorbed hydrogen atoms are used at any stage in the reduction of $GeO_3^=$ ions, then the $GeO_3^= \to GeH_4$ reaction sequence is complex, and H_2 evolution can be considered to be a branch reaction. But, if $GeO_3^= \to GeH_4$ does not involve the use of absorbed hydrogen atoms, then H_2 evolution is a process which occurs in parallel with the $GeO_3^=$ reduction process.

If atomic hydrogen is used in the reduction process it must be treated as one of the "stable" products, A, in the reaction sequence, Eq. [7]. Since the reaction which produces atomic hydrogen cannot be treated as in equilibrium as compared with the r.d.s. of the $GeO_3^= \to GeH_4$ reaction an expression for the steady-state concentration of atomic hydrogen is required. Bockris and Watson (4) have shown that the reaction of sodium atoms with water is the rate-determining step in the hydrogen evolution reaction on mercury cathodes in aqueous NaOH solutions. Whence, assuming the reaction

$$Na + H_2O \to Na^+ + OH^- + H$$

The surface concentration of atomic hydrogen will be directly proportional to the surface sodium atom concentration (the activity of water is taken to be large and invariant). Furthermore, these workers found that the surface activity of sodium atoms is proportional to $\exp(-F\eta/2RT)$; thus,

$$c_H = C \exp(-F\eta/2RT) \qquad [12]$$

where C is a constant at constant electrolyte composition.

Unfortunately the work of Bockris and Watson (4) is not completely convincing, e.g., these workers accept the experimental fact that the reaction rate of sodium atoms with water depends on the square root of the sodium concentration but do not show in their proposed reaction mechanism how this comes about. Also, they assume that barium amalgams behave in a similar way, but Kaplsan and Jofa (15) have shown that for Ba the reaction rate with water is proportional to $[Ba]^{1/4}$. Bockris and Watson, however, present cogent reasons for rejecting all other simple reaction paths for the hydrogen evolution reaction of sodium amalgam electrodes in NaOH solution other than the mechanism mentioned above. Thus in the absence of evidence to the contrary the mechanism of Bockris and Watson must be accepted, bearing in mind that the analysis given below would have to be re-examined in the light of any new and contrary development arising out of this point.

Table III. Potential dependent factors introduced into Eq. [11] by an elementary reaction. $x \equiv \eta F/RT$ (when $\beta = \frac{1}{2}$)

Reaction	Factor r.d.s.	Factor Equil.
1. $A^{z-} + e^- \to A^{(z+1)-}$	$e^{-x/2}$	e^{-x}
2. $A^{z-} + H \to HA^{z-}$	$e^{-x/2}$	$e^{-x/2}$
3. $A^{z-} + H + e^- \to HA^{(z+1)-}$	e^{-x}	$e^{-3x/2}$

By means of Eqs. [11] and [12] Table III lists the factor that an elementary reaction will introduce into the final expression for S, depending on whether the reaction is rate determining or precedes the r.d.s. whence it is treated as being in equilibrium. The Tafel slope for the $GeO_3^= \to GeH_4$ reaction is $-RT/F$, from experiment. Use of Eq. [11] shows that each successive stage of reduction leads to a smaller Tafel slope. Thus the possible reaction paths up to the rate-determining step which give a Tafel slope of $-RT/F$ can be written, viz:

(i) $$GeO_3^= + e^- \xrightarrow{\text{fast}} GeO_3^{\equiv}$$
$$GeO_3^{\equiv} + H_2O \xrightarrow{\text{slow}} H\,GeO_3^= + OH^-$$

(ii) $$GeO_3^{=} + H \xrightarrow{fast} H\,GeO_3^{=}$$

$$H\,GeO_3^{=} + H_2O \xrightarrow{slow} H_2GeO_2^{-} + OH^{-}$$

or,

$$(H\,GeO_3^{=} \xrightarrow{slow} GeO_2^{-} + OH^{-})$$

(iii) $$GeO_3^{=} + H \xrightarrow{fast} GeO_2^{-} + OH^{-}$$

$$GeO_2^{-} + H_2O \xrightarrow{slow} H\,GeO_2 + OH^{-}$$

(iv) $$GeO_3^{=} + H + e \xrightarrow{slow} H\,GeO_3^{=}$$

(v) $$GeO_3^{=} + H + e \xrightarrow{slow} GeO_2^{=} + OH^{-}$$

Since an intermediate product of high reducing power appears to diffuse away from the electrode before the r.d.s., from (i) to (v), this must be GeO_3^{3-}, $HGeO_3^{2-}$, or GeO_2^{-}. Thus the reactions (iv) and (v) are excluded as possible reaction paths since $GeO_3^{=}$ is the only Ge species before the rate-determining transition state. It is not possible to say on the basis of the work done here which of the remaining possibilities, (i), (ii), or (iii) is the actual mechanism. However, it should be possible to distinguish between reduction by electron transfer and reduction by atomic hydrogen on the basis of two further experiments, viz., (*a*) reduction in divalent alkali metal solutions, rather than NaOH, where $c_H \propto \exp(-\eta F/RT)$ should give different Tafel slopes if atomic hydrogen is involved in the reduction; (*b*) reduction at high current densities where the surface concentration of atomic hydrogen reaches a limiting value (4) should give $\partial\eta/\partial \ln i \rightarrow 0$ if atomic hydrogen is used in the r.d.s.; otherwise there should be no variation in the Tafel slope with current density.

Acknowledgment

The authors are pleased to acknowledge their thanks to Professor Carl Wagner and Professor J. O'M. Bockris for their interest and helpful suggestions. The method for determining the diffusion layer thickness was based on a suggestion of Professor Wagner's.

Manuscript received March 14, 1958. The research reported in this document was supported jointly by the Army, Navy, and Air Force under contract with M.I.T.

Any discussion of this paper will appear in a Discussion Section to be published in the December 1959 JOURNAL.

REFERENCES

1. J. O'M. Bockris, "Modern Aspects of Electrochemistry," p. 180, Butterworths Scientific Publications, London (1954).
1a. *Ibid.*, p. 190.
2. M. Green and P. H. Robinson, *Anal. Chem.*, **25**, 1913 (1953).
3. R. Piontelli and G. Polli, *Gazz. Chim. Ital.*, **78**, 717 (1948); R. Piontelli, *Z. Elektrochem.*, **55**, 128 (1951).
4. J. O'M. Bockris and R. G. H. Watson, *J. Chim. Phys.*, **49**, 070 (1952).
5. J. Tomes, *Collection Szechoslav. Chem. Communs.*, **9**, 12, 81, 150 (1937); see also I. M. Kolthoff and J. J. Lingane, "Polarography," p. 232, Interscience Publishers, New York (1952).
6. J. Newman, Private communication.
7. "International Critical Tables," New York, **5**, 15 (1926).
8. D. M. Brasher and F. R. Jones, *Trans. Faraday Soc.*, **42**, 775 (1946).
9. W. Pugh, *J. Chem. Soc.*, **1929**, 1537.
10. G. Carpéni, *Bull. Soc. Chem., France*, **15**, 629 (1948).
11. C. Wagner, *This Journal*, **101**, 181 (1954).
12. D. C. Grahame, *Chem. Revs.*, **41**, 441 (1947).
13. J. A. Christiansen, *Z. Physik. Chem.* (*B*), **28**, 303 (1935); *ibid.*, **33**, 145 (1936).
14. J. O'M. Bockris, *J. Chem. Phys.*, **24**, 817 (1956).
15. O. L. Kaplsan and Z. A. Jofa, *Zhur. Fiz Khim.*, **26**, 193 (1952); *ibid.*, **26**, 201 (1952).

The Electrical Conductivity of Sweat

II. The Interionic Attraction Factor and the Conductivity of Undiluted Sweat in the Study of Cystic Fibrosis

Andre J. deBethune and Truman S. Licht

Department of Chemistry, Boston College, Chestnut Hill, Massachusetts

and Milton Stern and Harry Shwachman

Division of Laboratories and Research, Children's Medical Center, and Department of Pediatrics, Harvard Medical School, Boston, Massachusetts

ABSTRACT

The electrical conductivity of sweat is a useful criterion for the study and diagnosis of *cystic fibrosis*. The sweat conductivity usually is determined from measurements on diluted sweat solutions. A method of calculation is presented to account for the interionic attraction effects due to the greater ionic strength in the undiluted parent sweat sample. This introduces a correction of the order of 10% in the conductivity based on the dependence of equivalent conductance on ionic strength. Experimental verification of the correction is given for synthetic mixtures of sodium and potassium chlorides and for a natural sweat sample. Sweat conductivity data obtained from a study of 77 control subjects and 47 cystic fibrosis patients are summarized, after application of this correction.

In a study of the electrolyte content of thermally induced eccrine sweat, Licht, Stern, and Shwachman (1) described a technique for the measurement of the electrical conductivity of sweat. They reported values of sweat conductivity for subjects with and without the disease *cystic fibrosis* and showed that for cystic fibrosis patients a threefold elevation of sweat conductivity was obtained which was significant enough to be used as a diagnostic criterion.

The method of obtaining sweat samples by collection on a weighed gauze pad and elution of electrolytes with distilled water necessitates that chemical and physical tests be performed on diluted solutions. As pointed out in (1) calculation of sweat conductivity from data obtained in diluted sweat solutions, without taking into account the interionic attraction effects due to greater ionic strength in the parent sample, results in conductivities approximately 10% too high. While this error is of no significance when sweat conductivity is used as a diagnostic criterion for cystic fibrosis, it does become important when sweat conductivities are correlated with ionic composition, a study which is currently in progress and will be reported elsewhere. The present paper attempts to develop a method of calculation which introduces a correction for the dependence of equivalent conductance on ionic strength. Conductivity data are presented for sodium and potassium chloride mixtures and for pure sweat and diluted sweat solutions which show that sweat conductivities calculated by this corrected method are reliable within 2 to 3%. Sweat conductivities presented in (1) from a study of 77 control subjects and 47 cystic fibrosis patients are recalculated. Availability of these more accurate values will permit correlation with analytical information and aid in the further elucidation of the electrolyte constitution of sweat.

Experimental

The thermal induction of sweat by placing the subject in a plastic bag, the collection of sweat on a weighed gauze pad, and the subsequent measurement of the diluted sweat sample in a special 3-ml conductivity cell with the Serfass conductance bridge has been described in (1). To establish the validity of the interionic attraction factor (described below), it was necessary to collect pure sweat not exposed to air long enough for evaporation to occur. Using a 1-ml pipette as a capillary tube, drops of pure sweat were collected. The volumes of such samples ranged from 0.2 to 1 ml and their conductivity could be measured directly in a Sunderman conductivity pipette[1] with a cell constant of 12.7 cm^{-1}. This pipette, which has a nominal capacity of 0.5 ml, could be used for measuring as little as 0.2 ml by floating the sample on top of mercury (mercury in the stem only). Five to fiftyfold dilutions were prepared with conductivity water and the conductivity again measured. The specific conductance of mixtures of sodium and potassium chloride in the range of pure and diluted sweat samples were measured also.

Theoretical

In (1), the sweat conductivity (i.e., the specific conductance of sweat in micromhos per centimeter),

[1] Available from Arthur H. Thomas Co., Philadelphia, Pa.

to be here denoted by L_s', was calculated from experimental observables by the relation

$$L_s' = (J_o - J_b)KF \qquad [1]$$

where J_o and J_b are the observed conductances in micromhos at 25°C of the diluted sweat solutions and blank solutions, respectively; K is the cell constant in cm^{-1}; F, the dilution factor, is the volume ratio of diluted to undiluted sweat. The grouping $(J_o - J_b)K = L_d$ is the observed conductivity of the diluted sweat solution. Multiplication by the dilution factor F is based on the tacit assumption that conductivity is a linear function of concentration.

This assumption is approximately valid for strong electrolytes over narrow concentration ranges and corresponds to the hypothesis that ionic mobilities and equivalent ionic conductances are constants independent of ionic strength. In point of fact, interionic attraction effects lead to a decrease of ionic mobilities and ionic conductances with increasing ionic strength (2-4).

Over the range of dilution factors F (5-fold to 58-fold) utilized in (1), the equivalent conductances of sodium, potassium, and chloride ions drop by about 5 to 15% in going from the diluted to the parent sweat sample, and the sweat conductivities calculated by Eq. [1] are too high by the same amount.

It is therefore desirable to correct the sweat conductivities L_s'. This can be done by the equation

$$L_s = L_dFS = L_s'S \qquad [2]$$

where L_s is the "corrected" sweat conductivity, and the interionic attraction factor S accounts for the drop-off of the equivalent conductances with increasing ionic strength.

The conductivity L of any electrolyte (in micromhos per centimeter) is equal to the summation of terms of the form $c_j\Lambda_j$ where c_j is the number of milliequivalents per liter and Λ_j is the equivalent conductance of the j^{th} electrolyte. By taking the ratio of L_s to L_dF, it can be shown that the factor S is given by

$$S = \Sigma(x_j\Lambda_j)_s/\Sigma(x_j\Lambda_j)_d \qquad [3]$$

where x_j is the equivalent fraction of the j^{th} electrolyte in the total electrolyte content (normality of j/ total normality of all electrolytes). In both cases, the Λ_j's are determined by the total ionic environment (5, 6), i.e., by the total ionic strength, of the liquid: either the parent sweat sample s or the diluted sweat sample d.

Table I. Conductivity of NaCl—KCl mixtures (25°C)

c (KCl), mEq/l	c (NaCl), mEq/l	L (observed), μmho/cm	L (calculated, Eq. [4]), μmho/cm
100	0	(12,896)	12,896
0	100	10,590	10,674
50	50	11,790	11,785
25	75	11,200	11,230
10	0	1414	1413
0	10	1178	1185
5	5	1288	1299
2.5	7.5	1266	1242
1	1	268	268.5

The composition of sweat (1, 7-10) is such that 60-90% of the conductivity may be attributed to sodium and potassium chlorides, the remainder being due chiefly to calcium, sulfate, and lactate. The pH ranges from 4 to 7. Sodium chloride constitutes 50-90% of the sum of the sodium and potassium chloride normality. It was therefore decided, as an approximation, to restrict the summations in [3] to the two salts j = NaCl, and KCl. Since Λ values for the mixtures of these salts were not readily available, the Λ's of the pure salts were used (4a, 11). It was postulated that *the Λ of a salt in a mixture is equal to the Λ of the same pure salt at the same total ionic strength.* This postulate was verified experimentally by us for synthetic mixtures of sodium and potassium chlorides in the total chloride concentration range of 2 to 100 mEq/l, and shown to be valid within the experimental error of the measured conductivity (1%) (Table I). The calculated values in Table I were computed from

$$L(\mu\text{mho/cm}) = (c\Lambda)_{KCl} + (c\Lambda)_{NaCl} \qquad [4]$$

where the c's are in milliequivalents per liter, and the Λ's are chosen in accordance with the *ionic strength postulate* stated above.

In 1911, Bray and Hunt (12) determined the conductivities of mixtures of sodium chloride and hydrochloric acid. Their observed conductivities agreed with values calculated from the ionic strength postulate within about 1% up to ionic strengths of about 0.1M. Deviations due to the "mixture effect" (5,6) of cations of widely different mobilities with a common anion are to be expected and tend to make the conductivity calculated from the ionic strength postulate slightly high. Bray and Hunt consistently observed a small but systematic deviation in this direction. In their work, this deviation reached a maximum in equimolar mixtures of the two electrolytes, dropping off as the mixtures approached either one or the other pure electrolyte. These maximum mixture effect deviations attained the values: 2.0% in a mixture of 100 mEq/l of HCl and NaCl; 1.1%, in 20 mEq/l of each; 0.68%, in 5 mEq/l of each. Since the mobilities of potassium and sodium ions are much closer than those of hydrogen and sodium ions, the mixture effect should be smaller in sweat and in the synthetic mixtures akin to sweat investigated in the present study than it was in Bray and Hunt's studies. It was felt by us that the mixture effect could be neglected safely, and that the ionic strength postulate should be reliable within 1% or better in the present instance.

The calculation of the interionic attraction factor S is best illustrated by an example. Consider a "parent sweat sample" initially 0.100N in chloride ion. By a 50-fold dilution, this is reduced to 0.002N in the "diluted sweat solution." The Λ's of pure KCl and NaCl at 25°C are, respectively, 128.96 and 106.74 mho cm^2 Eq^{-1} at 0.1N, and 145.80 and 122.70

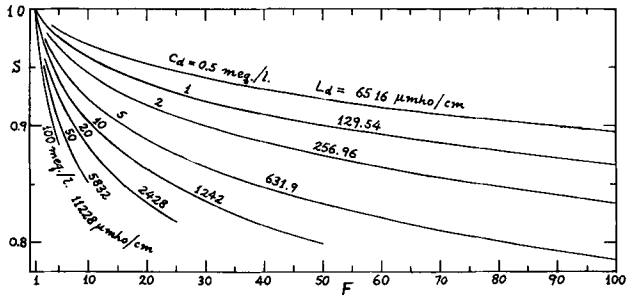

Fig. 1. Interionic attraction factor S for a 25 eq. % KCl : 75 eq. % NaCl mixture as a function of dilution factor F, diluted sweat sample electrolyte concentration c_d (in milliequivalents per liter), and diluted sample conductivity L_d (in micromhos per centimeter at 25°C).

at 0.002*N* (4, 11). The *S* factor calculated from Eq. [3] then takes on the value 0.884, 0.881, 0.878, 0.874, and 0.870, as the equivalent ratio of KCl:NaCl goes from 100:0 to 75:25, 50:50, 25:75, and 0:100, respectively. At less than 50-fold dilution, the spread in *S* values is even less. Thus the *S* factor is an insensitive function of the actual KCl to NaCl ratio. The 25KCl : 75NaCl equivalent ratio was arbitrarily selected as representative of the bulk of sweat samples, and was used in the construction of the family of *S* curves plotted in Fig. 1. Here, the *S* factor is given as a function of two variables, the total chloride concentration c_d of the diluted sample (in mEq/l), and the dilution factor *F*. In addition, each curve (of constant c_d) is identified by the appropriate value of L_d, the diluted sample conductivity (in micromhos per centimeter at 25°C) calculated from Eq. [4].

In practice, the interionic attraction factor *S* is determined as follows. The available empirical data on any actual sweat sample are, as already noted, the diluted sweat conductivity $L_d = (J_o - J_b)K$ and the dilution factor *F*. The value of *S* is then read off the curves of Fig. 1, at the proper value of *F*, by visual interpolation between the several L_d values. The final "corrected" sweat conductivity L_s is then calculated as $(J_o - J_b)KFS$.

Sweat Conductivity

To establish the validity of the interionic attraction factor *S*, pure sweat samples were collected from three subjects as described above and the conductivity of undiluted and diluted portions measured. Table II shows the data obtained for one of these samples from a cystic fibrosis patient whose undiluted sweat conductivity was measured directly

Table II. Comparison of observed and calculated sweat conductivities for a pure and diluted sweat sample (25.0°C, cell constant K = 12.7 cm^{-1}) (CF Subject No. 1693)

L_d (observed), μmho/cm	*F*	*S*	L_s' (uncorrected), μmho/cm	L_s (corrected), μmho/cm
15,500*	1*	1*	15,500*	15,500*
3430	5	0.918	17,150	15,740
1780	10	0.893	17,780	15,880
916	20	0.875	18,320	16,030
352	50	0.87	17,590	15,300

* Pure undiluted sweat.

Table III. Typical sweat conductivity data for subjects with and without cystic fibrosis (25°C)

Subject No.	L_d (observed), μmho/cm	Dilution factor, *F*	Interionic attraction factor, *S*	Sweat conductivity: L_s' (uncorrected), μmho/cm	Sweat conductivity: L_s (corrected), μmho/cm
A. For Children with Cystic Fibrosis					
474	229	47.43	0.879	10,860	9540
505	1274	10.60	0.897	13,510	12,110
532	550	21.31	0.896	11,720	10,500
646	2655	5.36	0.920	14,240	13,090
654	481	35.49	0.871	17,060	14,860
B. Healthy Children and those with Miscellaneous Diseases (Control Group)					
513	215	20.55	0.927	4420	4100
520	477	11.48	0.941	5480	5150
526	286	12.95	0.933	3710	3460
650	103	57.69	0.912	5940	5420
651	733	4.68	0.955	3430	3270

C. Summary of Sweat Conductivity Data

Group	No. in group	Sweat conductivity: Mean, μmho/cm	Group standard deviation, μmho/cm	Range, μmho/cm
Cystic fibrosis	47	(uncorrected) L_s' = 16,150	3500	9000-24,640
		(corrected) L_s = 14,380	3130	8030-21,260
Control group	77	(uncorrected) L_s' = 5560	2360	2080-14,380
		(corrected) L_s = 5080	2160	1970-13,340

as 15,500 μmho/cm. The sample was diluted five to fifty-fold, and the conductivity measured again. The uncorrected "sweat conductivities" L_s' calculated by Eq. [1] ranged from 17,150 to 18,320, about 11 to 18% high. Application of the *S* factor (Fig. 1) yielded "corrected sweat conductivities" L_s ranging from 15,300 to 16,030, i.e., from 1.3% low to 3.4% high, the average error being 2.2% for the dilutions of this one sample. On all three subjects, uncorrected conductivities L_s' ranged from 7 to 23% high; values corrected by use of the *S* factor ranged from 2.7% low to 5.7% high, the average error being 3.3%.

In Table III, typical sweat conductivity data, originally presented in (1), are recalculated from Eq. [2] employing the interionic attraction factor. The mean, group standard deviation, and range of sweat conductivities for 77 subjects in a control group and 47 patients with cystic fibrosis are presented in summary. It is noted that a significant change in conductivity values occurs as a result of the application of the *S* factor. The corrected values can be used as a basis for a further correlation between conductivity and electrolyte content currently in progress.

Acknowledgment

The authors wish to express their thanks to the International Nickel Company, Inc., of New York, and to the National Cystic Fibrosis Research Foundation for Grants-in-Aid in support of this work.

Manuscript received April 29, 1958.

Any discussion of this paper will appear in a Discussion Section to be published in the December 1959 JOURNAL.

REFERENCES

1. T. S. Licht, M. Stern, and H. Shwachman, *Clinical Chem.*, **3**, 37 (1957).
2. P. Debye and E. Hückel, *Physik Z.*, **24**, 185, 305 (1923).
3. L. Onsager, *ibid.*, **27**, 388 (1926); **28** 277 (1928).
4. D. A. MacInnes, "The Principles of Electrochemistry," p. 339, Reinhold Publishing Co., New York (1939).
5. L. Onsager and R. M. Fuoss, *J. Phys. Chem.*, **36**, 2689 (1932).
6. H. S. Harned and B. B. Owen, "The Physical Chemistry of Electrolytic Solutions," 3rd. ed., Reinhold Publishing Co., New York (1958).
7. S. Robinson and A. H. Robinson, *Physiol. Rev.*, **34**, 202 (1954).
8. S. Rothman, "Physiology and Biochemistry of the Skin," University of Chicago Press, Chicago (1954).
9. Y. Kuno, "Human Perspiration," p. 224, Charles C. Thomas, Springfield, Ill. (1956).
10. H. Shwachman, M. Stern, R. R. Dooley, and E. A. Higgins, *Clinical Chem.*, **2**, 393 (1956).
11. F. H. MacDougall, "Physical Chemistry," 3rd ed., p. 504, MacMillan Co., New York (1952).
12. W. C. Bray and F. L. Hunt, *J. Am. Chem. Soc.*, **33**, 788 (1911).

The System LiF-LiCl, LiF-NaCl, LiF-KCl

H. M. Haendler, P. S. Sennett, and C. M. Wheeler, Jr.

Department of Chemistry, University of New Hampshire, Durham, New Hampshire

ABSTRACT

Liquid-solid equilibrium data for the systems LiF-LiCl, LiF-NaCl, LiF-KCl were obtained through the concentration range 0-100 mole % LiF. These data were used to test the formula

$$T_{calc} = T_m \left(\frac{1 + x^2 \Delta F^\circ / L}{1 - \frac{2RT_m \ln (1 - X)}{L}} \right)$$

for the prediction of liquidus temperatures. Activities were calculated from experimental data by

$$a_{M_1A_1} = (1 - X)_{M_1} \cdot (1 - X)_{A_1} e^{X_{M_2} \cdot X_{A_2} \cdot \Delta F^\circ / RT}$$

It was shown that the activities of salt components can be calculated by this formula, if the difference in the sum of lattice energies of the reactants and products of mixing is not too large.

Although phase relationships in fused salt systems have been studied for many years, it is only recently that the practical applications of these relationships have become apparent. One promising new application is in the purification and separation of metals by extraction with fused salt media (1). Of particular interest are systems containing fused LiF as one of the components. Botschwar (2) and Bergman (3) have published data for the system LiF-LiCl. However these phase diagrams are not in agreement, exhibiting a difference in liquidus temperatures over a wide concentration range and a substantial difference in the eutectic temperature and composition. Flood (4) has reported data for the system LiF-KCl over a limited concentration range. The work reported in this paper defines more accurately the system LiF-LiCl and extends the reported data for the system LiF-KCl through the entire concentration range, 0-100 mole % LiF. This paper also presents new data for the system LiF-NaCl.

In addition to determining phase diagrams for binary systems of fused salt systems, it is also of interest to use these data where possible to determine the activities of the salt components in the binary systems. An important contribution to this problem has been made by Flood (4, 5). His equations have been tested with the data reported in this work. For systems with components of similar lattice energies, Flood's equations for the determination of activities and prediction of liquidus temperatures are much better than the Clausius-Clapeyron equation for ideal solutions, when the Temkin model for ideal solutions is used.

Experimental

All chemicals were reagent grade and were used after drying without further purification. Mixtures were prepared by accurate weighing of components and melting in a nickel sample holder. A gas stirring device, described by Campbell and Prodan (6), was used for the LiF-LiCl system and the NaCl-rich portion of the LiF-NaCl system. A nickel stirring paddle connected to a variable speed motor was used for the LiF-rich portion of the LiF-NaCl system and the entire LiF-KCl system.

Temperatures were measured using chromel-alumel thermocouples, calibrated at the melting point of Bureau of Standards samples of aluminum and zinc. The emf of the thermocouple was measured by a L&N Type G two point recording potentiometer and a Rubicon Type B potentiometer.

The samples were heated for ½ to 1 hr at 100° above the expected freezing point. When supercooling was not a problem, the current through the furnace was completely turned off and the sample was

allowed to cool at the rate of about 20°C/min. When supercooling was encountered, the cooling rate was adjusted to 5°C/min.

There was no evidence that the nickel sample holder reacted appreciably with the melt. The pure salts apparently attacked the cell to a lesser extent than did mixtures of intermediate composition. As an example of the extent of corrosion, electrolytic determination of nickel present in the LiF-LiCl system at 10 mole % LiF, gave 0.08, 0.07, and 0.08% nickel in three determinations. X-ray powder pattern data also substantiated these results.

Results

The system LiF-LiCl.—Temperature-composition data were obtained for the LiF-LiCl system over the concentration range 0 to 100 mole % LiF. An eutectic composition of 30.5 mole % LiF was observed, melting at 501°C. Botschwar (2) reported 20 mole % LiF at a eutectic temperature 485°C, Bergman (3) reported 30.5 mole % LiF, 484°C. There was no evidence of compound formation or of solid solutions. The experimental data are recorded in Table I. Figure 1 is a plot of these data. Also plotted are the theoretical liquidus curves for solutions of this system, as calculated from the Clausius-Clapeyron equation.

The System LiF-NaCl.—Temperature-composition data were obtained for the LiF-NaCl system over the concentration range 0 to 100 mole % LiF. The eutectic for this system occurs at 41.5 mole % LiF and 680°C. The phase diagram for this system is similar to that for the LiF-LiCl system, exhibiting a single eutectic, with no evidence of compound formation or solid solutions.

The 50-90 mole % LiF region of this system presented considerable experimental difficulties because of supercooling. Supercooling apparently did not occur in any other composition range. Thermal analysis of mixtures in this range were performed initially using a cell with an air stirring device. Data using this equipment were not reproducible and varied consistently by 10°C from the data reported here. When a more vigorous mechanical stirring device was used, supercooling became small enough so that reproducible results were obtained. The results obtained while using the mechanical stirrer are included in Table II since their reproducibility is considerably better. The values included in Table II and plotted in Fig. 2 for 50-90 mole % LiF are averages of three determinations with a maximum difference of ±2°C.

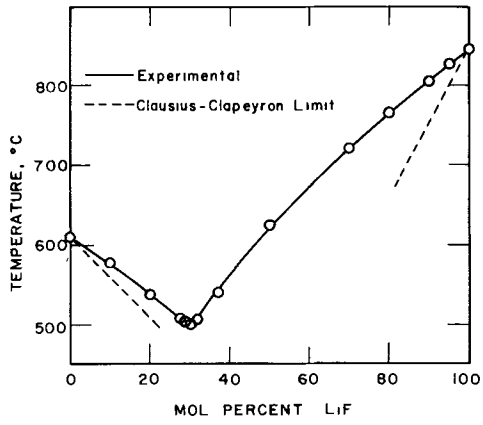

Fig. 1. The system LiF-LiCl

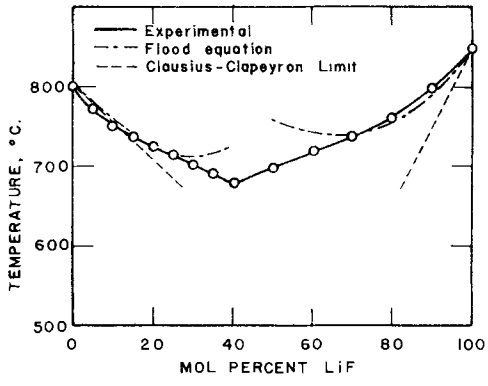

Fig. 2. The system LiF-NaCl

Table II records the experimental data for the system LiF-NaCl. Figure 2 includes a plot of these experimental data and the theoretical liquidus curves for ideal solutions of this system as calculated from the Clausius-Clapeyron equation and Flood's equation.

The System LiF-KCl.—The temperature-composition data obtained for this system in the concentration range 0-100 mole % LiF are listed in Table III.

A plot of these data is shown in Fig. 3, with the theoretical liquidus curves for this system as pre-

Table I. System LiF-LiCl

Composition, mole % LiF	Temperature, °C Liquidus	Eutectic
0.0 (100% LiCl)	—	610
10.0	577	500
20.0	538	499
27.4	509	501
29.0	504	501
30.0	—	501
32.0	509	501
36.9	543	502
50.0	626	502
70.0	723	502
80.0	769	502
90.0	805	502
95.0	830	—
100.0	—	848

Table II. System LiF-NaCl

Composition, mole % LiF	Temperature, °C Liquidus	Eutectic
0.0 (100% NaCl)	—	802
5.0	775	676
10.0	752	679
15.0	742	679
20.0	729	681
25.0	717	681
30.0	704	681
35.0	694	680
40.0	—	681
50.0	700	—
60.0	720	—
70.0	740	—
80.0	764	680
90.0	800	680
100.0	—	848

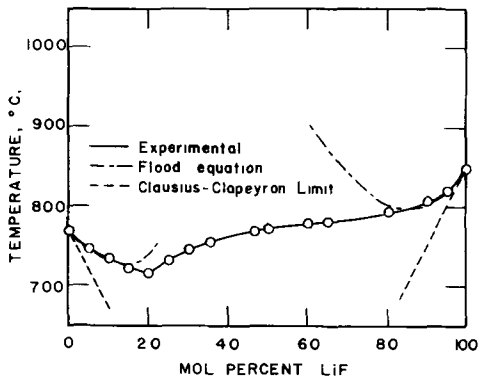

Fig. 3. The system LiF-KCl

dicted by the equations of Clausius-Clapeyron and Flood. This system forms a eutectic at 20 mole % LiF and 715°C. Flood (4) does not list specific eutectic data for this system, but his phase diagram shows eutectic behavior consistent with that which was observed in this work. As will be noted in Fig. 3, the liquidus curve for the potassium chloride side of the eutectic is fairly regular with a slight curvature. On the lithium fluoride side of the eutectic, however, the liquidus curve exhibits a point of inflection. The shape of this curve and its deviation from the general shape of the corresponding curve in the previous two systems can be accounted for in two ways.

The first possible explanation of this curve is that the two components tend toward the formation of an equimolar binary compound. This would account for the abrupt change in the freezing point near the eutectic and the slow change of freezing point with composition in the 40-80 mole % LiF region.

A second explanation for the shape of this type of phase diagram is given by Sidgwick and Ewbank (7). Curves of this shape are due to a submerged miscibility gap. This miscibility gap is unstable with respect to the liquidus curve, that is, it occurs at a lower temperature than the liquidus curve. Presumably if the melt could be supercooled below the liquidus temperature, two liquid phases in metastable equilibrium would appear. This can actually be accomplished in systems where the miscibility gap is not far below the liquidus temperature. It is assumed that solid solubility in these systems is negligible since none of the experimental data indicated any solid solution formation.

Table III. System LiF-KCl

Composition, mole % LiF	Temperature, °C Liquidus	Eutectic
0.0 (100% KCl)	—	772
5.0	747	—
10.0	736	716
15.0	722	714
20.0	—	716
25.0	732	—
30.0	747	—
35.0	755	—
46.4	767	714
50.0	772	—
60.0	780	—
65.0	783	—
80.0	795	713
90.0	805	712
95.0	819	—
100.0	—	848

Discussion

From a comparison of Fig. 1, 2, and 3 it can be seen that the deviations from ideality on the lithium fluoride side of the eutectic increases in the order LiCl-NaCl-KCl. The most pronounced deviation occurs in the LiF-KCl system on the lithium fluoride side of the eutectic. Of the three systems studied, it is to be expected, based on the influence of ionic sizes and radius ratios, that the maximum deviation from ideality would appear in this system. The apparent tendency toward the formation of two immiscible liquid solutions is consistent with the higher lattice energy of lithium fluoride and the consequent higher attractive forces operative in the fused salt media.

An improvement over the Clausius-Clapeyron equation for calculating the liquidus temperature is given by Flood's equation (4).

$$T_{calc} = T_m \left[\frac{1 + X^2 \Delta F^\circ / L}{1 - \frac{2RT_m \ln (1 - X)}{L}} \right] \qquad [1]$$

Using the solution reaction of KCl in LiF as an example, the terms of this equation have the following meaning: where ΔF° is standard free energy change of the reaction

$$KCl + LiF \rightarrow LiCl + KF$$

L is molar heat of fusion of major component (LiF); T_{calc}, liquidus temperature of melt of mole fraction X; T_m, melting temperature (degrees Absolute) of major component; X, mole fraction of minor component (KCl), M_2A_2; 1 — X, mole fraction of major component, M_1A_1.

It is of interest to determine the activities of the salt components of the two binary systems LiF-NaCl and LiF-KCl. The major component of the binary salt mixtures may be considered the solvent. The activity of the solvent is related to the depression in freezing point of the solvent by the equation (negligible solid solubility assumed)

$$\ln a_{M_1A_1} = \frac{L}{R}\left(\frac{1}{T_m} - \frac{1}{T}\right) \qquad [2]$$

where $a_{M_1A_1}$ is the activity of the major component M_1A_1; L is the heat of fusion of the major component, considered to be constant; T_m is the melting point of the major component in the pure state; and T°K is the experimentally observed temperature for a solution of mole fraction 1 — X.

The activity coefficient $\gamma_{M_1A_1} = \dfrac{a_{M_1A_1}}{(1 - X)_{M_1}(1 - X)_{A_1}}$.

The value of $a_{M_1A_1}$ is calculated from Eq. [2]. The activity coefficients calculated in this fashion will be called γ exp in this paper.

These equations permit the calculation of activities and activity coefficients from liquidus curve temperatures. The equations developed by Flood are intended to provide a means of theoretically calculating the activities and liquidus temperatures for a

binary system, using free energy, heat of fusion, and concentration data.

For the mixing $M_1A_1 + M_2A_2 = M_2A_1 + M_1A_2$, the activity of M_1A_1 may be calculated using Flood's simplified formula

$$a_{M_1A_1} = (1 - X)_{M_1} \cdot (1 - X)_{A_1} \cdot e^{X_{M_2} \cdot X_{A_2} \cdot \Delta F^\circ / RT}$$

where ΔF° is the standard free energy change for the reaction as written.

The activity coefficient may be calculated using

$$\ln \gamma M_1A_1 = X_{M_2} \cdot X_{A_2} \cdot \Delta F^\circ / RT$$

The quantitative comparison between calculated and experimentally determined activity, activity coefficient, and liquidus temperature values is given in Table IV-VII.

Table IV. System LiF-KCl (LiF as solvent)

	T°K		a		γ	
$(1-X)_{LiF}$	exp.	calc.	exp.	calc.	exp.	calc.
1	1121					
0.95	1092	1089	0.93	0.92	1.03	1.02
0.90	1078	1073	0.89	0.87	1.10	1.08
0.80	1068	1074	0.86	0.87	1.34	1.38
0.65	1056	1143	0.84	1.15	1.99	2.71
0.60	1053	1178	0.83	1.32	2.30	3.69
0.50	1045	1258	0.81	1.96	3.24	7.85
0.46	1040	1288	0.80	2.33	3.78	11.00
0.35	1028	1370	0.77	4.22	6.28	34.90
0.30	1020	1435	0.75	5.61	8.33	62.70
0.25	1005	1423	0.71	4.10	11.36	65.90

Table V. System LiF-KCl (KCl as solvent)

	T°K		a		γ	
$(1-X)_{KCl}$	exp.	calc.	exp.	calc.	exp.	calc.
1	1045					
0.95	1020	1016	0.93	0.92	1.03	1.02
0.90	1009	1002	0.90	0.88	1.11	1.09
0.85	995	998	0.86	0.87	1.19	1.21

Table VI. LiF-NaCl (LiF as solvent)

	T°		a		γ	
$(1-X)_{LiF}$	exp.	calc.	exp.	calc.	exp.	calc.
1	1121					
0.90	1073	1060	0.88	0.89	1.08	1.04
0.80	1037	1027	0.79	0.76	1.23	1.19
0.70	1013	1015	0.74	0.74	1.51	1.51
0.60	993	1018	0.69	0.76	1.91	2.15
0.50	973	1029	0.64	0.82	2.56	3.29

Table VII. LiF-NaCl (NaCl as solvent)

	T°		a		γ	
$(1-X)_{NaCl}$	exp.	calc.	exp.	calc.	exp.	calc.
1	1075					
0.95	1048	1046	0.92	0.91	1.02	1.01
0.90	1025	1024	0.85	0.85	1.05	1.05
0.85	1015	1006	0.82	0.80	1.13	1.11
0.80	1002	996	0.79	0.77	1.23	1.24
0.75	990	990	0.75	0.75	1.33	1.34
0.70	977	987	0.72	0.75	1.47	1.53
0.65	967	988	0.69	0.76	1.63	1.80

Free energies of formation and heats of fusion were taken from National Bureau of Standards Circular 500.

The development of Flood's equation assumes that the entropy condition of the fused salt melt is that of an ideal ion mixture; each cation is surrounded by anions and vice versa; the cations as well as the anions are statistically distributed at random. In addition it is assumed that the heat of mixing is equal to zero. Thus the calculated liquidus temperature and activities of the components are related through the free energy change of mixing to the entropy condition of the mixture.

In a system such as LiF + NaCl = LiCl + Na F the difference in lattice energies of the reactants and products of mixing is much less than for the system Li F + K Cl = LiCl + KF. One may suppose, then, that the entropy condition required by Flood's treatment would more nearly be approximated by the LiF-NaCl system. Consequently liquidus temperature calculated by his equation should more closely correspond to the experimental temperatures for this system than for the LiF-KCl system, in which a greater difference in lattice energies is observed. This is the case and is evident from the plots in Fig. 2 and 3. The theoretically calculated liquidus curve for the LiF-NaCl system is in fair agreement with the experimental curve over a wide concentration range. However, in the LiF-KCl system large positive deviations are observed at concentrations greater than 25 mole % LiF. Apparently due to the strong interionic forces between the Li^+ and F^- ions, the random distribution of cations and anions of the Li^+, F^-, K^+, Cl^- mixture is not realized in these more concentrated solutions. In the LiF-NaCl system the bond energies of the products of mixing more nearly equal those of the reactants. This should provide for a more random distribution of the Li^+, F^-, Na^+, Cl^- ions and consequently for better agreement between theoretical and experimental activities and liquidus temperatures.

Flood (4) has shown that the activities of salt components with lower lattice energies can be calculated accurately with his simplified theoretical formula. The data and calculations reported here for the LiF-NaCl system indicate that the formula can also be used with fair results for a system in which the lattice energies of the components are large, providing the difference in the sum of lattice energies of reactants and products of mixing is not too great. For systems in which the difference in lattice energies of the components is large, the formula fails for solutions of even moderate concentrations.

Acknowledgment

This research was supported in part by the Atomic Energy Commission.

Manuscript received March 7, 1958.

Any discussion of this paper will appear in a Discussion Section to be published in the December 1959 JOURNAL.

REFERENCES

1. D. W. Bareis, R. H. Wiswall, Jr., and W. E. Winsche, *Nucleonics*, **12**, 16 (1954).

2. A. A. Botschwar, *Z. anorg. Chem.*, **210**, 163 (1933).
3. A. G. Bergman and E. I. Banashek, *Izvest. Saktora Fiz-Khim. Anal., Akad. Nauk. S.S.S.R.*, **23**, 201 (1953); *C. A.*, **48**, 9170a (1954).
4. H. Flood, O. Fykse, and S. Urnes, *Z. Elektrochem.*, **59**, 364 (1955).
5. H. Flood, T. Forland, and K. Grjotheim, *Z. anorg. Chem.*, **276**, 289 (1954).
6. A. N. Campbell and L. A. Prodan, *J. Am. Chem. Soc.*, **70**, 553 (1948).
7. N. W. Sidgwick and E. K. Ewbank. *J. Chem. Soc.*, **119**, 979 (1921).

Technical Notes

Study of Magnetic Oxides by Cathode Rays

S. Yamaguchi

Scientific Research Institute, Tokyo, Japan

The path of cathode rays is deflected by a magnetic field (Lorentz effect). This effect is observable in the electron diffraction pattern obtained from a ferromagnetic substance. In the present study, the magnetic states of two ferromagnetic oxides were investigated by means of electron diffraction.

The two specimens employed were ferromagnetic pure nickel oxide (NiO) and an oxide permanent magnet of practical use (Fe_2O_3:NiO:ZnO = 50:15:35 by weight). The weight of the specimen used for the experiment was about 1 mg.

In Fig. 1, the diffraction rings from a powder of the nickel oxide and those from a nonferromagnetic gold foil are photographed on the same dry plate by means of double exposure. In this procedure, the wave length of the electron beam applied and the position of the photographic plate were kept fixed. It is noticeable in Fig. 1 that the diffraction rings from these two substances are not co-centric. This implies that the paths of the electrons are magnetically perturbed by the ferromagnetic specimen.

In Fig. 2, the diffraction rings from a nonferromagnetic aluminum oxide (böhmite) (1) and those from the gold foil are photographed by the same process as for Fig. 1. In this photograph all the diffraction rings are co-centric, i.e., there is no magnetic effect on the electrons. Figure 2 corresponds to the result of a blank test for magnetic analysis.

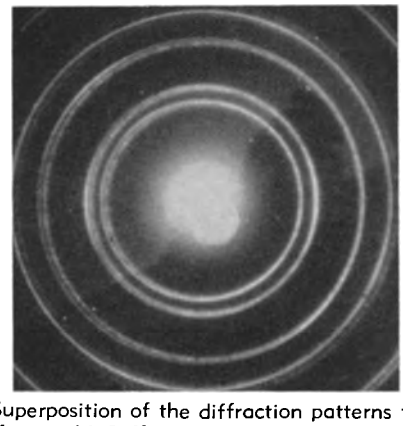

Fig. 1. Superposition of the diffraction patterns from nickel oxide and from gold. Diffraction rings of the former and those of the latter are excentric as the result of Lorentz effect. Wave length, 0.0292Å. Camera length, 495 mm. Positive enlarged 2.1 times.

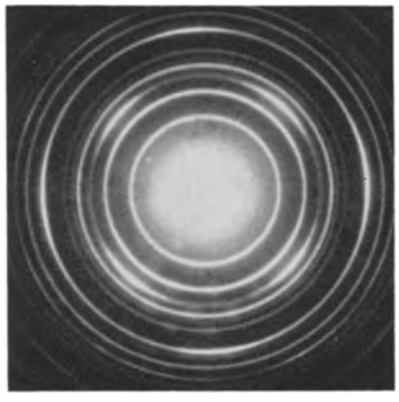

Fig. 2. Superposition of the diffraction patterns from bohmite and from gold. All the rings are co-centric. No Lorentz effect.

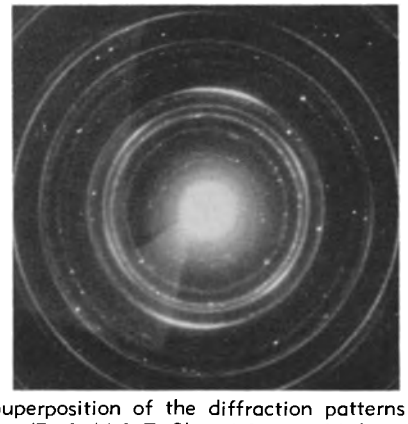

Fig. 3. Superposition of the diffraction patterns from the oxide magnet (Fe_2O_3-NiO-ZnO) and from gold. Lorentz effect. Wave length, 0.0302Å.

The diffraction pattern of Fig. 3 was observed from a powder of the oxide permanent magnet and from the gold foil in the same way as for Fig. 1 and 2. In Fig. 3, the diffraction rings of the oxide and those of gold are not co-centric.

From the diffraction figures thus prepared, it is possible to estimate the strength H of the magnetic field given by the ferromagnetic oxide.

$$H = \frac{m}{e}\frac{v}{lL} \cdot \Delta x$$

or

$$H = \frac{h}{e\lambda lL} \cdot \Delta x \qquad [1]$$

where e is electron charge (1.6×10^{-20} CGSEMU); m, electron mass; v, velocity of electrons; L, camera length (495 mm); h, Planck's constant (6.6×10^{-27} erg sec); l, width of the magnetic field (about 0.5 mm); λ, wave length of the electron wave; and Δx, observed deflection of the electron beam.

In Fig. 1 and Fig. 3,

$$\Delta x = 0.2 \text{ mm } (\lambda = 0.0292\text{Å})$$

and

$$\Delta x = 0.1 \text{ mm } (\lambda = 0.0302\text{Å}),$$

respectively.

According to Eq. [1], therefore,

$$H = 11.4 \text{ and } 5.53 \text{ gauss, respectively.}$$

It is thus possible to investigate ferromagnetic oxides magnetochemically as well as crystallographically by means of electron diffraction.

Manuscript received Sept. 30, 1957.

Any discussion of this paper will appear in a Discussion Section to be published in the December 1959 JOURNAL.

REFERENCE

1. S. Yamaguchi, *Z. anal. Chem.*, **155**, 21 (1957).

The Mechanism of Blackening of Nickel Anodes

Thomas C. Franklin and Jack Goodwyn

Chemistry Department, Baylor University, Waco, Texas

In the process of depositing black nickel using a nickel wire anode and cathode and a modification of the bath used by Moline (1) it was noted that the anode as well as the cathode became black. Meyer (2) gave the composition of solutions in which nickel may be blackened without passing current, but no mention was made of the composition of the black coating nor of the mechanism of its formation. Since the solutions used by Meyer and Moline were similar, the coatings were assumed to be the same. This paper describes an investigation on the composition of the black deposit and the mechanism by which it was formed.

Experimental Methods and Results

Composition of the anode coating.—The bath used contained $NiSO_4 \cdot 6H_2O$, 70 g/l; $(NH_4)_2SO_4$, 37 g/l; $ZnSO_4 \cdot 7H_2O$, 34.3 g/l; and KSCN, 17.9 g/l, and was operated at a pH of 5.0, a temperature of 30°C, and a current density of 11 amp/m^2. All chemicals were reagent grade. To determine which component of this bath caused the blackening of the anode, an aqueous solution of each component was prepared, adjusted to a pH of 5.0 with HCl, and a small piece of nickel wire was placed in each solution. The nickel wire in the solution containing potassium thiocyanate darkened in two days. When the pH was lowered to 2.0, the solution darkened the wire in 7 hr. With current passing, both solutions darkened the anode within 6 min. None of the solutions containing the other components blackened the nickel wire. The odor of H_2S was noticed above those test tubes containing potassium thiocyanate.

To identify the reaction which liberated the H_2S, a series of test tubes was prepared with moistened lead acetate paper fastened over the mouth of each test tube. Each tube contained 20 ml of water, 1 g of potassium thiocyanate, and 2 ml of concentrated HCl. To these test tubes 1 g portions of different substances were added and the results were noted. These results are summarized in Table I.

The yellow solid which settled out of the blank solution (No. 1) was a polymerization product of thiocyanic acid (3). Metal ions evidently retard this polymerization as evidenced by the fact that 12 days were required for the formation of crystals in the solutions containing the cobalt and nickel ions and that 15 days were required with zinc ions present. The blackening of the lead acetate paper above test tubes 1, 4, 6, and 7 was due to H_2S from the hydrolysis of thiocyanic acid. The fact that H_2S was generated more rapidly in the solutions con-

Table I. Effect of various materials on acidified potassium thiocyanate solutions

	Material added	Results observed
1.	None	Lead acetate paper blackened in 5 days. Yellow crystals precipitated in 12 hr
2.	Nickel wire	Lead acetate paper blackened in 3 hr
3.	Tin (II) chloride	Lead acetate paper blackened in 3 hr. Brown precipitate formed in solution
4.	Zinc chloride	Only slight darkening of lead acetate paper in 3 days. Crystals formed in solution in 15 days
5.	Copper (II) chloride	Black precipitate [copper(II) thiocyanate] formed in the solution immediately
6.	Cobalt (II) chloride	Slight darkening of lead acetate paper in 3 days. Crystals formed in solution in 12 days
7.	Nickel (II) chloride	Slight darkening of lead acetate paper in 3 days. Crystals formed in solution in 12 days

taining the metal ions than in the blank was due to the inhibition of the polymerization by the metal ions thus making the hydrolysis the major reaction. In the presence of the reducing agents, tin (II) chloride and nickel wire, the evolution of H_2S was much more rapid and proceeded by a reduction similar to the following:

$$2CNS^- + 2Sn^{++} \rightarrow SnS_2 + 2CN^- + Sn^{++++}$$

Both chemical tests and x-ray diffraction showed the presence of nickel sulfide in the anode coating.

Mechanism of formation of the anode coatings.— An examination of the data shows that the reduction of the thiocyanic acid by nickel wire produced a coating in 7 hr while the anodic reaction produced a coating in 6 min. It seems unreasonable that the nickel anode was the reducing agent. Therefore it was postulated that the nickel anode was oxidized to nickel (I) and these ions then acted as the reducing agent on the thiocyanate ion. Kleinberg (4) has postulated a similar mechanism for the anodic dissolution of magnesium in the presence of oxidizing agents.

Because of the formation of nickel (II) sulfide on the anode, it was impossible to check coulometrically the valence of nickel as it went into solution in the presence of the thiocyanate ion. To avoid this difficulty, the nickel was anodically oxidized in solutions containing potassium bromate in place of the thiocyanate. Thus the valence could be checked and any bromine produced by the reduction of the bromate could be detected by odor and by its ability to bleach methyl red indicator. The electrolysis was carried out in a 400 ml beaker containing a 100 ml porous porcelain cup as the anode compartment. Sulfuric acid was used rather than HCl in order to prevent reaction between the chloride and bromate ions. An oxy-hydrogen coulometer, modeled after that of Lingane (5), was used. The potassium bromate was added in the form of a 0.1177M solution. A nickel wire of the same diameter and length as the anode was placed in a solution identical in composition to the anode solution and was left there for the duration of each electrolysis. The small change in weight of this blank was subtracted from the change in weight of the anode to give the exact loss of weight due to electrolytic oxidation. Results are given in Table II.

As can be seen, the valence of nickel anodically dissolved in H_2SO_4 averaged 2.02 ± 0.03. However, in the presence of potassium bromate, the valence of the nickel going into solution dropped below two (runs 3-7 and 15-23). It will be noticed that on repeated use of the bromate solution the valence rose toward two as the bromate concentration was lowered. The introduction of a fresh solution or the addition of more bromate always caused the valence to drop. At the completion of each electrolysis, it was found that the anolyte had a distinct odor of bromine and that it would bleach methyl-red readily. It was not possible to make an extended study since slight changes in current density or in pH caused oxygen to be evolved at the anode.

In order to establish further the existence of nickel (I) as an intermediate in the anodic dissolution of nickel, the nickel was oxidized anodically at low current densities (0.13 amp/m^2) in acetonitrile containing tetramethylammonium chloride as a supporting electrolyte. In this solvent corrosion was not possible. The apparatus was an H-tube with the compartments separated by means of a fine porosity sintered glass disk. The temperature was maintained at 7°C in order to minimize electro-osmosis. Results are summarized in Table III. In all cases it can be seen that part of the nickel dissolves as nickel (I).

Table II. Effect of potassium bromate on the anodic dissolution of nickel in sulfuric acid solution

Run No.	Electrolyte	Current density, amp/m^2	Change in wt of anode, g	Loss in wt of blank, g	Dissolution time, min	N-number of Faradays per mole	Remarks
1	0.171*N* H_2SO_4	8.40	0.0121	0.0012	30	2.00	
2	0.171*N* H_2SO_4	8.40	0.0084	0.0010	20	1.98	
3	0.171*N* H_2SO_4 + 5 ml $KBrO_3$	8.40	0.0153	0.0005	30	1.48	
4	0.171*N* H_2SO_4 + 5 ml $KBrO_3$	8.40	0.0105	0.0010	20	1.54	
5	0.171*N* H_2SO_4 + 5 ml $KBrO_3$	4.54	0.0093	0.0012	30	1.41	
6	0.171*N* H_2SO_4 + 5 ml $KBrO_3$	8.40	0.0218	0.0044	70	1.17	
7	0.171*N* H_2SO_4 + 5 ml $KBrO_3$	8.40	0.0187	0.0027	60	1.17	
8	0.1676*N* H_2SO_4	4.72	0.0080	0.0005	40	2.02	
9	0.1676*N* H_2SO_4	4.44	0.0078	0.0006	40	1.97	
10	0.1*N* H_2SO_4	2.83	0.0045	0.0003	40	2.05	
11	0.0378*N* H_2SO_4	2.88	0.0050	0.0004	40	1.98	
12	0.0378*N* H_2SO_4	2.88	0.0051	0.0007	40	2.06	
13	0.0378*N* H_2SO_4	4.60	0.0077	0.0004	40	2.05	
14	0.0378*N* H_2SO_4	4.60	0.0059	—	30	2.06	
15	0.1046*N* H_2SO_4 + 5 ml $KBrO_3$	2.77	0.0082	0.0015	50	1.64	
16	0.1046*N* H_2SO_4 + 5 ml $KBrO_3$	2.62	0.0072	0.0014	50	1.78	Soln. 15 reused
17	0.1046*N* H_2SO_4 + 5 ml $KBrO_3$	2.43	0.0060	0.0020	40	1.93	Soln. 16 reused
18	0.1046*N* H_2SO_4 + 5 ml $KBrO_3$	2.52	0.0070	0.0012	40	1.40	Soln. 17 + 5 ml of $KBrO_3$
19	0.1046*N* H_2SO_4 + 5 ml $KBrO_3$	2.52	0.0069	0.0012	40	1.42	Soln. 18 reused
20	0.1676*N* H_2SO_4 + 5 ml $KBrO_3$	4.05	0.0100	0.0017	40	1.56	
21	0.1676*N* H_2SO_4 + 5 ml $KBrO_3$	4.20	0.0095	0.0025	40	1.90	Soln. 20 reused
22	0.1676*N* H_2SO_4 + 5 ml $KBrO_3$	4.56	0.0110	0.0017	40	1.59	Fresh soln.
23	0.1676*N* H_2SO_4 + 5 ml $KBrO_3$	4.47	0.0112	0.0011	40	1.44	Fresh soln.

Table III. Anodic dissolution of nickel in acetonitrile containing tetramethyl ammonium chloride

Total weight loss, g	N-number of Faradays per mole
0.0213	1.85
0.0230	1.67
0.0285	1.35

From these experiments it was concluded that the black coating formed on nickel anodes in baths containing thiocyanate was nickel sulfide formed by the following series of reactions:

$$Ni \rightarrow Ni^{+} + e$$

$$2Ni^{+} + CNS^{-} \rightarrow NiS + CN^{-} + Ni^{++}$$

These reactions might also be expected to occur to some extent at the cathode in black nickel plating baths. It is known that these black cathodic plates contain nickel sulfide. Sanborn and Orlemann (6) have shown the formation of an intermediate Ni (I) ion during the electrolytic reduction of Ni (II) in concentrated salt solutions. Therefore it is reasonable to expect that part of the nickel sulfide arises from the above reactions.

Acknowledgment

This work was sponsored by the Office of Ordnance Research, U. S. Army.

Manuscript received Oct. 28, 1957.

Any discussion of this paper will appear in a Discussion Section to be published in the December 1959 JOURNAL.

REFERENCES

1. W. E. Moline, *Proc. Am. Electroplater's Soc.*, **1943**, 21.
2. W. R. Meyer, *ibid.*, **1943**, 90.
3. N. V Sidgwick, "The Organic Chemistry of Nitrogen," p. 333, Oxford University Press, London (1937).
4. Jacob Kleinberg, *J. Am. Chem. Soc.*, **76**, 363 (1954).
5. J. J. Lingane, *ibid.*, **67**, 1916 (1945).
6. R. H. Sanborn and E. F. Orlemann, *ibid.*, **78**, 4852 (1956).

ZnS Phosphors with P, As, Sb Coactivators

E. F. Apple

Research Laboratory, General Electric Company, Schenectady, New York

In ZnS:P,Cl and ZnS:As,Cl phosphors (1, 2) it is thought that both the Group V element and chlorine occupy S sites in the ZnS lattice. This configuration gives rise to an acceptor-donor luminescent system in which P and As are acceptors or activators and chlorine is a donor or coactivator (3). Emission spectra under 3650Å excitation show a broad band in the yellow with P and a broad band in the yellow-orange with As.

If P or As or Sb is incorporated in ZnS along with Cu, only the blue and green emissions typical of Cu-activated ZnS are observed. These phosphors, which contain (before firing) from 5×10^{-6} to 5×10^{-4} g-atoms Cu/mole ZnS with equal to five times as much Group V element, are prepared in an H_2S stream or in a sealed, evacuated quartz tube at 950°C. Figure 1 shows the emission spectra of ZnS: 10^{-4} Cu, 5×10^{-4} As both under 3650Å and cathode-ray excitation. The spectra of corresponding ZnS: Cu,P and ZnS:Cu,Sb phosphors are almost identical with those shown. Note that under cathode-ray excitation the blue band disappears almost completely. This blue emission, which peaks at about 4450Å, is probably the "Cu-blue" emission previously described in the literature (4, 5). The self-activated blue emission in cubic ZnS peaks at 4600°-4700Å and has a much broader half-width than the blue emission band in ZnS:Cu,As. Increasing the temperature of preparation of ZnS:Cu,As causes an increase in the blue emission and decrease in the green emission intensity. It should be mentioned that ZnS:Cu, ZnS:P, ZnS:As, or ZnS:Sb are all practically nonluminescent when prepared in H_2S at 950°C.

The absence of the P-yellow and As-orange emissions in ZnS:Cu, P and ZnS:Cu, As, respectively, indicates that in the presence of Cu the Group V element assumes a different role than when in the presence of halogens. Because of the similarity in emission to ZnS:Cu,Al, in which Al is a donor, it is concluded that the Group V elements are donors (coactivators) when incorporated in ZnS along with Cu, the acceptor or activator. It is probable that the Group V element occupies a Zn

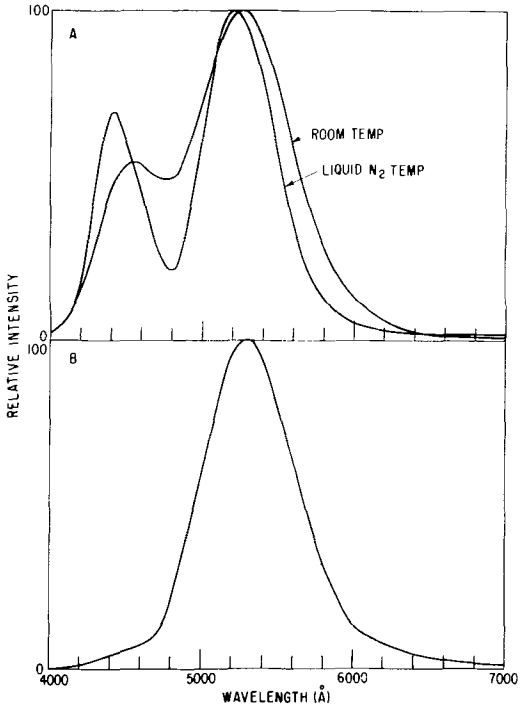

Fig. 1. ZnS: 10^{-4} Cu, 5×10^{-4} g-atoms As/mole ZnS; fired in H_2S at 950°C. A, 3650Å excitation; B, CR excitation (15 kv, 3μa/cm^2).

site when incorporated as a donor, a situation not unexpected; As and Sb occupy metal lattice sites in several ternary sulfides whose structures are related to the zinc blende or wurtzite modifications of ZnS. Phosphors with Group V coactivators have slightly weaker emissions and shorter afterglows than those with Group III coactivators such as Al. Also, Group V elements do not give rise to the self-activated blue center in ZnS.

In covalent compounds, Sb (or As) usually forms only three strong bonds and usually has only three nearest neighbors. For instance, Cu_3SbS_3 has the zinc blende structure in which the Cu and Sb atoms occupy metal sites and one quarter of the S sites are vacant. $CuSbS_2$ has a more complicated structure, related to the wurtzite structure, in which each Sb atom forms three strong pyramidal bonds and Cu four tetrahedral bonds to S atoms. Sb_2S_3 itself has a chain structure in which each Sb atom has three nearest-neighbor S atoms. Arsenic forms similar compounds with correspondingly complex structures (6). In contrast, $CuAlS_2$ and Al_2S_3 both have structures in which the metal atoms are tetrahedrally bonded to four equidistant S atoms (7). In addition to effects on luminescent processes, the differences in bonding between ternary sulfides of Al and As or Sb may be responsible for the more limited solubilities of added impurities in the phosphors containing Cu along with the Group V element. ZnS phosphors containing more than 10^{-3} g-atoms Cu/mole ZnS and equal to five times as much P, As, or Sb, have a very gray body color, and are only weakly luminescent. Presumably, a multiphase system exists. However, ZnS:Cu,Al or $ZnS:CuGaS_2$ phosphors containing 10^{-3} Cu have a light body color, exhibit a fairly bright green luminescence, and are single phase systems (8, 9).

In summary, it has been shown that P, As, and Sb may, under special conditions, function as coactivators in ZnS phosphors. Whether the Group V element acts as an activator and substitutes on S sites or a coactivator and substitutes on Zn sites depends on which type of compensating impurity is incorporated simultaneously. In the presence of halogen, the substitution occurs at S sites, whereas with Cu it occurs at Zn sites.

Preliminary experiments indicate that P, As, and Sb are also coactivators in ZnS phosphors containing Ag or Au activators.

Manuscript received Sept. 25, 1958.

Any discussion of this paper will appear in a Discussion Section to be published in the December 1959 JOURNAL.

REFERENCES

1. A. H. McKeag and P. W. Ranby, *This Journal*, **96**, 85 (1949).
2. J. S. Prener, *ibid.*, **98**, 406 (1951).
3. J. S. Prener and F. E. Williams, *ibid.*, **103**, 342 (1956).
4. F. A. Kröger and N. W. Smit, *Physica*, **16**, 317 (1950).
5. F. A. Kröger and J. Dikhoff, *ibid.*, **16**, 297 (1950).
6. A. F. Wells, "Structural Inorganic Chemistry," pp. 402-405, Oxford Press (1950).
7. H. Hahn, G. Frank, W. Klinger, A. Meyer, and G. Störger, *Z. anorg. u. allgem. Chem.*, **271**, 153 (1953).
8. H. C. Froelich, *This Journal*, **100**, 496 (1953).
9. E. F. Apple, *ibid.*, **105**, 251 (1958).

Brief Communication

Titanium Coatings on Molybdenum Wire

Robert L. Bronnes

Philips Laboratories, Irvington-on-Hudson, New York

In an electron tube, the level of primary grid emission is dependent on many factors, including grid and cathode temperatures, rate of supply of evaporation products from emitter material in the cathode, and evolution of gases. Espersen and Rogers of these Laboratories have shown that the emission level may be lowered by controlling grid temperatures and by choosing grid materials which are not readily activated by contamination with evaporation products from the cathode (1). Titanium, in comparison to molybdenum and other commonly used grid materials, is remarkably insensitive to such activation, but does not have sufficient high-temperature rigidity to maintain the anode-grid-cathode spacings. In order to combine the low-level emission characteristics of titanium with the rigidity of molybdenum, a method was developed for depositing a layer of titanium on molybdenum by the evaporation of metallic titanium.

Apparatus and Method

The materials required are 0.010-in. molybdenum wire, 0.010-in. titanium wire, and a 0.020-in. helical tungsten wire heater coil having a diameter of 0.5-in. and 8 complete turns, 1-in. long. The steps required are:

1. Degrease the molybdenum, tungsten, and titanium wires in acetone.

2. Hydrogen-fire the molybdenum and tungsten wires at 1100°C for 30 min to remove surface contamination and reduce surface oxides.

3. Mount the molybdenum wire vertically on a bulb stem inside the tungsten coil. Approximately 50 mg of titanium wire are wrapped uniformly around the tungsten coil.

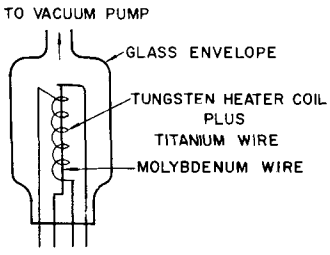

Fig. 1. Evaporation assembly

Fig. 2. Titanium coated molybdenum wire. Original magnification 900X.

4. Thoroughly degrease the assembly in trichlorethylene vapor.

5. Seal the assembly in a glass envelope (Fig. 1), mount on a vacuum pump, evacuate, and bake-out at 450°C for 1 hr. A vacuum of ca 2 x 10^{-7} mm Hg should be obtained.

6. Raise the temperature of the molybdenum wire to 1600°C[1] for degassing, while maintaining a vacuum of at least 6 x 10^{-5} mm Hg. Degas until a vacuum of ca 2 x 10^{-6} mm Hg is obtained. Note power requirements.

7. Lower the temperature of the molybdenum wire to 900°C. A vacuum of ca 6 x 10^{-7} mm Hg should be obtained. Note power requirements.

8. While the temperature of the molybdenum wire is held at 900°C, slowly raise the temperature of the tungsten heater coil to a few degrees above the melting point of titanium. Maintain a vacuum of ca 6 x 10^{-5} mm Hg, and hold at this temperature for 5 min. After the heater coil has cooled down, a vacuum of ca 6 x 10^{-7} mm Hg should be obtained. Since the glass envelope will become opaque during the evaporation of titanium, the temperature of the molybdenum wire can be maintained only by reference to the power requirements noted in Step No. 7.

9. Raise the temperature of the molybdenum wire to 1600°C by using the power requirements noted in Step No. 6. Hold for 1 min.

10. Allow the assembly to cool down and remove from the vacuum pump.

[1] All temperatures are uncorrected, as measured with a L&N optical pyrometer.

Results and Discussion

Smooth, uniform coatings have been obtained by this method with good reproducibility of results. Bonding occurs during deposition and during final heating by the formation of a molybdenum-titanium alloy. The titanium coating and alloyed region are clearly visible in Fig. 2.

If the parts have been carefully processed and a good vacuum maintained, the coatings will be of good physical integrity, firmly bonded and adherent to the molybdenum, and sufficiently ductile so that rupturing will not occur on moderate flexing.

While this process has been described as a laboratory procedure, it is possible to modify the apparatus to permit continuous processing of wire in any desired lengths.

Manuscript received Oct. 20, 1958.

Any discussion of this paper will appear in a Discussion Section to be published in the December 1959 JOURNAL.

REFERENCE

1. G. A. Espersen and J. W. Rogers, IRE Transactions of the Professional Group on Electron Devices, Vol. ED-3, No. 2, pp. 100-107, April, 1956.

Batteries with Solid Ion Exchange Electrolytes

I. Secondary Cells Employing Metal Electrodes

W. T. Grubb

Research Laboratory, General Electric Company, Schenectady, New York

ABSTRACT

Highly conducting ion exchange polymers can be employed as solid electrolytes in batteries. Their resistivities are intermediate between aqueous electrolytes and the usual inorganic solid electrolytes. Cells containing pairs of metal electrodes behave reversibly. Their emf's form an additive series for the examples tested and are only slightly less than those of their aqueous analogs.

In this paper the phrase ion-exchange battery is used to denote a galvanic cell in which the electrolyte is a solid (although somewhat hydrated) ionically conducting ionizing polymer of the type commonly called ion exchange resins. In these materials the self-diffusion rates and ionic conductances are simply interrelated as has been demonstrated by Coryell and Spregler (1).

Ion exchangers have been used as separating membranes in cells containing two or more electrolyte compartments such as the Daniell cell disclosed by Juda, *et al.* (2) and the concentration battery proposed by Meyer (3). They have been employed to depolarize cells by removing a reaction product (4, 5). They have been employed to supply a reacting ion to the cell reaction. For example, Robinson (6) has disclosed the use of a permanganate anion exchange resin as a cathode depolarizer in an analog of the Leclanché cell.

The present investigation has been concerned with the ion exchange polymers acting as electrolytes wherein the current is entirely conducted by the ionizing polymer itself. At the same time it maintains the physical structure of the cell. The role of the ion exchanger is analogous to that of a silver halide in the more conventional type of solid-electrolyte cells (7) except that the conductance is several orders of magnitude higher. Also, there are more possibilities for the ion-exchange battery since the mobile ion may be selected at will simply by exchanging the electrolyte into a suitable ionic state.

Materials and Methods

Ion exchange membranes.—Synthetic polymers containing strongly ionized sulfonate groups were used. A review (8) of the typical ion-exchange properties and structures may be found helpful. Particular use was made of ion-exchange membranes which consist of sheets of ion-exchange polymer very resistant to direct flow of liquids but highly permeable to ions. Two commercial membranes were employed: Amberplex C-1,[1] a sulfonated polystyrene resin finely comminuted and held in a matrix of an inert polymer; and Nepton CR-51,[2] a homogeneous sheet of sulfonated phenol formaldehyde polymer. These two membranes possess somewhat different electrical and mechanical properties. Hereafter they are referred to as Amberplex and Nepton membranes, respectively.

Conditioning of membranes.—The ion-exchange membranes were converted into a desired ionic form by successive equilibration in several portions of a solution of the cation in question as described by Juda, *et al.* (9). In all cases, the "free" electrolyte was removed by extensive washing with distilled water. In several cases the membrane was equilibrated with water in ethylene glycol, using a large excess of solution and equilibrating for 24 hr or more. The solution contained 12.0% by weight of water or a mole fraction of 0.32. The water-ethylene glycol system obeys Raoult's law (10) approximately.

Solvating liquids.—Laboratory distilled (ρ = 500,000 ohm-cm) water was employed as the aqueous solvate to saturate the membranes. Ethylene glycol, U.S.P. grade, was redistilled at reduced pressure under dry N_2 atmosphere.

Cell construction.—Two cell construction methods have been employed in this work. For high-area cells (A = 10 cm^2) the metal foils have been backed up by ½-in. plexiglas blocks, and the electrolyte has been sealed from evaporation by surrounding it with a silicone rubber gasket. In these cells, the electrolyte overlaps the electrodes to prevent any possibility of edge shorting. Low-area cells (A = 0.3 cm^2) were constructed in trubore tubing (½ in. ID). In this case the electrode and the electrolyte do not overlap but are of the same size, being cut with the same punch and die. Data obtained on the two sizes of cells were mutually consistent.

The metals were of commercial purity, except for copper which was oxygen-free.

Electrical measurements.—Potential measurements were usually made with a Rubicon potentiometer to the nearest millivolt. Currents were obtained to about ½% using a Sensitive Instrument Co. polyranger. These measurements are adequate to the purpose at hand.

[1] Rohm & Haas Co., Resinous Products Div., Philadelphia, Pa.
[2] Ionics, Inc., Cambridge, Mass.

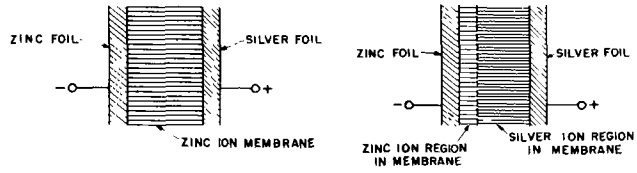

Fig. 1. Schematic diagram of silver-zinc cell. Left, uncharged cell, emf 0.8-1.2 v, right, charged cell, emf 1.4-1.5 v.

Results

Among the possible combinations of electrode and ion-exchanger electrolyte, those in which a metal is in contact with an electrolyte containing ions of the same metal coordinated with the fixed sites on the polymer are probably the simplest. While these might be constructed as primary cells by the use of two metals and two ion-exchange membranes in appropriate ionic state, a simpler method is to form such a cell by charging a single-electrolyte cell. The process is shown diagrammatically in Fig. 1. The cell initially contains an electrolyte in the zinc state between zinc and silver foils. The charging current produces a silver ion region next to the silver electrode.

In order to prove the nature of the charging process, the cell was set up as in Fig. 1 and charged with a known current for a measured time interval. It was then disassembled, the electrolyte washed, and analyzed. The total charge input was 2.00 ma for 4.08 hr, corresponding to 32.8 mg Ag. The analysis for total silver in the membrane was 32.0 mg Ag, indicating quantitative agreement within the error of measuring the total charge.

Both phenolic (Nepton type) and polystyrene (Amberplex type) electrolytes were employed in silver-zinc cells. Measurements of cell voltage as a function of both charging and of discharging current reveal that the emf is a linear function of the current, with the line passing smoothly through the zero current axis, as seen from representative plots in Fig. 2 and 3. Table I identifies the compositions and dimensions of the various cells, and the first column refers to the appropriate curve of Fig. 2 and 3. Data were obtained at 25° ± 0.05°C.

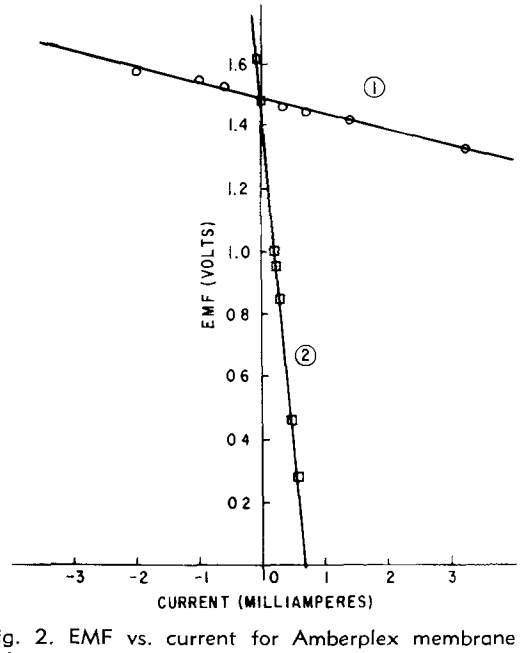

Fig. 2. EMF vs. current for Amberplex membrane cells. Numbers on curves refer to experiment numbers in Table I.

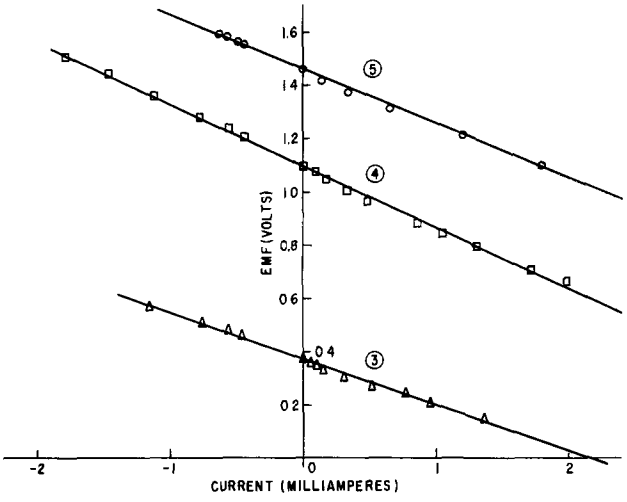

Fig. 3. EMF vs. current for Nepton membrane cells. Numbers on curves refer to experiment numbers in Table I.

In every case the cell was charged at 2.0 ma for 30 min. From the measured capacity data for the H^+ form of the ion exchange membranes, this amount of charge supplies the more noble metal ion to about 4% of the sites in the electrolyte (the membrane capacities per unit volume are similar for Amberplex and Nepton membranes). The data of Fig. 2 and 3 are the emf values after about 10 sec on the given load (or charge).

It might be supposed that concentration polarization is prevented by the nature of the ion exchanger electrolyte since the distribution of ions and their concentrations are held nearly constant by the immobile polymer network. However, concentration polarization actually does occur in the present cells when they are placed on heavier loads for short time intervals. This may be caused by solvate moving with the ions as hydration shells (11).

The present cells are analogous to cells with liquid junctions in conventional electrochemistry. It is likely that liquid junctions are absent in the present cells; first, because of the nature of the electrolyte which requires that the transference number is unity for cations, and second, because of the fixed sites in the network polymer, cross diffusion at the bound-

Table I

Expt. No.	Metal pair	Type of electrolyte	Solvate	Area of cell, cm²	Thickness of cell, cm
1.	Ag-Zn	Amberplex	H_2O	10.0	0.088
2.	Ag-Zn	Amberplex	H_2O + ethylene glycol[a]	10.0	0.088
4.	Cu-Zn	Nepton	H_2O + ethylene glycol[a]	10.0	0.081
5.	Ag-Zn	Nepton	H_2O + ethylene glycol[a]	10.0	0.081
3.	Ag-Cu	Nepton	H_2O + ethylene glycol[a]	10.0	0.081

[a] Concentration = 12.0% by weight of water.

ary of the regions of different ionic form occurs in the manner of an ion exchange reaction and is therefore equal in each direction.

The lines in Fig. 2 and 3 were determined by the method of least squares. In Table II are tabulated the constants for the equations of these lines, which all are of the form, $E = A - bi$ with E in practical volts and i in milliamperes.

The correlation coefficient (12), r, is a measure of the degree to which the least squares line represents the experimental points. It may be concluded that the experimental points are quite well represented by straight lines of constant slope, and therefore within errors of measurement the half-cells of the type metal/ion-exchange polymer, metal salt are reversible when metals such as silver, copper, or zinc are employed. Further evidence of the reversibility of the metal-ion exchanger half-cells is the additivity of potentials using the same electrolyte. From the data of experiments 3, 4, and 5 it is observed that A (3) + A (4) = 1.46_4 and A (5) = 1.46_0.

The internal resistances of the cells are equal to $b \times 10^3$ and represent a composite of two ionic forms of the ion exchanger.

Experiments 1 and 2 illustrate the fact that solvation of the electrolyte has little effect on the emf of a typical cell but has a large effect on the internal resistance. The very slight variation of emf observed when the water activity in the ion exchanger is reduced by a factor of about 3 indicates that the activity ratio of the two ions in the electrolyte is virtually unaffected by the partial removal of the water of solvation and its replacement by ethylene glycol. This effect could be interpreted as being due to the change of dielectric constant which influences the activity of ions in ion exchangers in a manner unspecific as to the nature of the ion. The very marked effect on conductivity is probably caused by a variation in the amount of association between the fixed sites and the mobile ions. This would also be expected from variation of the dielectric constant of the solvating liquid.

A number of cells were put through charge and discharge cycles. In a typical case, a cell of the type of experiment 1, Table I, was charged for 5 hr at 1.0 ma and then placed on a fixed load resistance. The discharge current as a function of time is plotted in Fig. 4. After 5 hr, there had been recovered approximately 80% of the charge input. When cells of the type of experiment 5, Table I, were tested in a similar manner, the charge recovery was only about 40%. Little charge could be recovered from cells

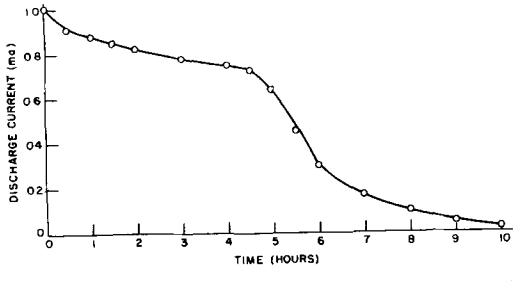

Fig. 4. Discharge current vs. time for Amberplex electrolyte cell. Dimensions: d= 0.088 cm, A = 35 cm²; local resistance = 420 ohms; charge = 1 ma for 5 hr.

Table II.

Expt. No.	A	b	r
1	1.48_5	0.0492	0.993
2	1.48_1	2.20	0.999
3	0.368	0.171	0.996
4	1.09_6	0.232_2	0.999
5	1.46_0	0.205	0.996

which were charged and then allowed to stand for 24 hr before discharging.

Figure 1 represents an idealized situation. The boundary between ionic forms is not sharp as shown but becomes "smeared out" by cross diffusion, and this happens rather quickly in highly conducting systems. Moderate stability is produced by use of partial aqueous solvation, using solutions of water in another polar liquid (e.g., ethylene glycol). Even in this case, silver ions eventually reach the zinc electrode and deposit because of cross diffusion. Such processes destroy the cell for practical purposes.

To prevent silver ion from reaching the zinc foil a barrier layer is needed. One way of achieving this is by use of a highly selective ion exchange resin, and some progress toward this has already been made (13). A more versatile solution perhaps lies in the use of complex ions. If one ion of the cell pair forms a stable complex anion, then an anion exchange resin membrane would effectively protect the less noble metal foil. This modification of the basic cell has not been tried yet experimentally.

The present paper discussed the application of ion exchange resins as solid electrolytes in a secondary cell system employing two metal electrodes and demonstrated that these cells are electrochemically reversible. A study of several types of primary cells employing ion exchange resin solid-state electrolytes has been made and will be reported in a subsequent publication.

Acknowledgment

The author wishes to thank his associates in this laboratory, Dr. J. L. Weininger and Dr. D. L. Douglas for helpful discussions and Mr. Paul R. Schmidt for experimental assistance in a portion of the work reported here.

Manuscript received Jan. 8, 1958.

Any discussion of this paper will appear in a Discussion Section to be published in the December 1959 JOURNAL.

REFERENCES

1. K. S. Spiegler and C. D. Coryell, *J. Phys. Chem.*, **57**, 687 (1953).
2. W. Juda and W. A. McRae, U. S. Pat. 2,636,851, April 28, 1953.
3. K. H. Meyer, *Helv. Chim. Acta.*, **23**, 795 (1940); cf. G. Manecke, U. S. Pat. 2,700,063.
4. E. C. Pitzer, U. S. Pat. 2,607,809, Aug. 19,1952.
5. C. K. Morehouse, U. S. Pat. 2,771,381, Nov. 20, 1956.
6. P. Robinson, U. S. Pat. 2,786,088, March 19, 1957.
7. K. Lehovec and J. Broder, *This Journal*, **101**, 208 (1952).
8. F. C. Nachod and J. Schubert, "Ion Exchange Technology," pp. 144-5, Academic Press, New York (1956).
9. W. Juda, N. W. Rosenberg, J. A. Marinsky, and A. A. Kasper, *J. Am. Chem. Soc.*, **74**, 3736 (1952).

10. H. M. Trimble and W. Potts, *Ind. Eng. Chem.*, **27**, 66 (1935).
11. A. G. Winger, R. Ferguson, and R. Kunin, *J. Phys. Chem.*, **60**, 556 (1956).
12. W. L. Gore, "Statistical Methods for Chemical Experimentation," p. 132, Interscience Publishers, Inc., New York (1952).
13. D. K. Hale, *Research*, **9**, 104 (1956).

Controlled Potential Reactions of Cadmium and Silver in Alkaline Solution

George T. Croft

Edison Laboratory, Thomas A. Edison Industries, McGraw-Edison Company, West Orange, New Jersey

ABSTRACT

Data are reported on the electrochemical oxidation and reduction of both cadmium and silver in potassium hydroxide electrolyte obtained using techniques in which the overpotential was the independent and the current the dependent variable. The rate of oxidation of cadmium is maximum at overpotentials of 18.0 and approximately 40.0 mv. The rate of reduction of cadmium and the rate of oxidation of silver are both monotonically increasing functions of the overpotential.

Very few electrochemical reactions are investigated by methods which use the overpotential as the independent and the current as the dependent variable. However, the application of such methods to investigations of electrochemical reactions which produce insoluble oxide films on the electrode yields information on the kinetics of the reaction not realizable by the conventional procedures which utilize the current as the independent variable (1). Methods utilizing control of the overpotential have here been applied to the study of reactions of cadmium and silver in potassium hydroxide electrolyte with new and important results.

It is well known that the rate of most electrochemical reactions depends exponentially on the overpotential, therefore a measurement of rate as a function of overpotential is inherently a more sensitive indicator of the kinetics of the reaction than a measurement of the overvoltage as a function of the current. Furthermore, given the overpotential as an independent variable we can choose from a number of possibilities a particular reaction for investigation. If the current is the independent variable, the electrode system may seek the kinetically most favorable reaction, especially if the electrode tends toward passivity, rather than the reaction under investigation. By controlling the overpotential we can determine the influence on the reaction rate of thickening of the oxide layer with time. For example, if the rate-limiting step in the oxide growth is transport of ions through the oxide already formed on the electrode and if the driving force is a gradient in the electrostatic potential, the current density is given by

$$I = \left(\frac{\sigma\phi}{2\Omega}\right)^{1/2} t^{-1/2} \qquad [1]$$

If the driving force is a gradient in ion concentration, the current is given by

$$I = \left(\frac{kT}{e}\frac{\sigma}{2\Omega}\right)^{1/2} \left(1 - \exp - \frac{e\phi}{eT}\right)^{1/2} t^{-1/2} \qquad [2]$$

The quantity ϕ is the overpotential, σ the ionic conductivity, T the temperature, t the time, Ω the volume of oxide formed per coulomb of electricity, and k and e are the Boltzmann constant and the charge on the electron, respectively.

Equations [1] and [2] indicate that, if experimental conditions are such that a simple growth law is observed (in this case a parabolic growth law), we might tentatively assume that the reaction rate is given by an equation of the form

$$I = F(\phi)t^{-1/2} \qquad [3]$$

where $F(\phi)$ is some function of the overpotential.

Two methods based on this approach were used to investigate the oxidation and reduction of cadmium and silver in potassium hydroxide electrolyte. Using the first method, the fixed potential method, we measure as a function of time the current required to maintain oxidation at a constant overpotential. We find that after sufficient time has elapsed the current and time are related by an equation of the form of Eq. [3]. Thus once it is established that the oxide grows according to a parabolic growth law, we interpret $F(\phi)$ as a function relating the rate of the reaction to the overpotential.

In employing the second method, an electrode is first oxidized at a fixed rate (constant current) until it becomes passive. This state of the electrode corresponds to the onset of the $t^{-1/2}$ current dependence observed using the fixed potential technique. The electrode is then oxidized or reduced at a rate such that ϕ follows the form of a triangular wave. Simultaneously the current necessary to make the electrode potential follow this wave shape is recorded. Thus if the change in thickness of the oxide layer is negligible during the anodic or cathodic swing of ϕ, measurements of I as a function of ϕ yield $F(\phi)$ vs. ϕ directly. Both methods of measurement yield the result that for anodic values of ϕ, $F(\phi)$ for cadmium electrodes has at least one maximum and often two. Furthermore, the overpotential

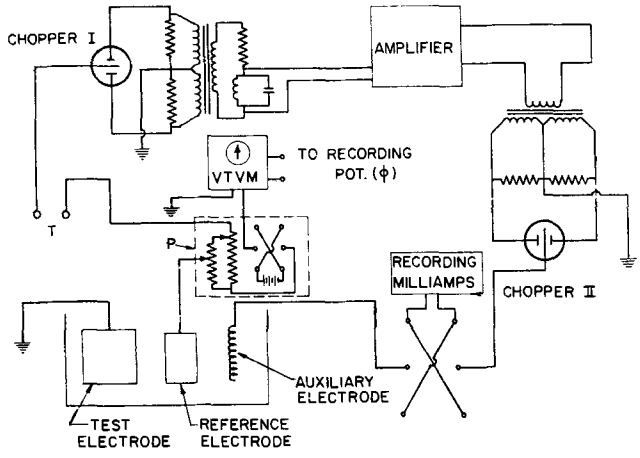

Fig. 1. Block diagram of control circuit used to maintain a given electrode overpotential.

observed during constant current oxidation (before passivity occurs) is equal to the potential corresponding to one of the maxima in the $F(\phi)$ vs. ϕ curve. Similar results were obtained for silver electrodes except that $F(\phi)$ has only one maximum and this for cathodic potentials. The overpotential observed during constant current reduction of the silver electrode is equal to the potential corresponding to the maximum in $F(\phi)$.

Apparatus and Sample Preparation

A block diagram of the instrumentation developed to oxidize or reduce a test electrode at any desired overpotential is shown in Fig. 1. The circuit is designed so that any difference between the desired potential fed in at terminals T and the test electrode potential produces a flow of current through the test electrode via the auxiliary electrode. This current, either cathodic or anodic, causes a change in the test electrode potential which reduces to zero the difference in potential between the test and input potential.

Control of the electrode potential is achieved by converting the difference potential by means of a chopper (Chopper I) to a 400 cps signal which is amplified and used to drive a power amplifier. The output of the power amplifier is fed into the output chopper (Chopper II) which is synchronized with the input chopper. Such synchronization leads to a direct current output which is fed back through the test electrode via the auxiliary electrode in such a direction that the difference potential is reduced to zero.

The potentiometer P is used to buck out the test electrode-reference potential. The reference used was a partially discharged nickel electrode from an Edison nickel-iron-alkaline storage battery. The current and potential were measured on a recording milliammeter and a self-balancing recording potentiometer. Using this circuit one can force the electrode to oxidize at a fixed potential and record the current as a function of time, or make the potential follow some predetermined function of time and record the current necessary to produce this potential variation. If the current through the test electrode does not exceed 25 ma, the circuit maintains the desired potential (either anodic or cathodic) to within ± 0.2 mv.

The cells used in both the fixed and sweeping potential measurements were of conventional design. Nitrogen was bubbled through the electrolyte in the fixed potential cell to reduce the dissolved oxygen concentration and to provide stirring of the electrolyte.

The cadmium electrodes used in the fixed potential experiments were prepared by electroplating cadmium onto nickel plates whose dimensions were 3.7 x 5.2 cm. The cadmium overlay was 0.005-0.01 cm thick and completely covered the underlying metal. The electrodes were cleaned by washing and scouring, followed by an overnight reduction at a cathodic potential of 37.5 mv.

The electrodes used in the sweeping potential experiments on cadmium were made from spectrographically pure Johnson-Matthey cadmium rods which were rolled into sheets, from which were cut electrodes of dimensions 2.86 x 3.00 cm. The electrodes were mounted in an epoxy resin with only one side exposed to the electrolyte.

The following procedure was used prior to recording the sweeping potential data. First the electrode was electrolytically polished in phosphoric acid and washed in distilled water. It was then placed in the cell and reduced at a high current density (approximately 1 amp/cm^2). Hydrogen was evolved over the surface until the electrolyte in the cell was thoroughly flushed with hydrogen. The cathodic current was turned off and the electrode was then oxidized at a fixed anodic current (1 ma/cm^2). When ϕ rose to 30 mv anodic, the current was turned off and the electrode was left to return to thermodynamic equilibrium. The electrode was then alternately oxidized and reduced so that ϕ followed the form of a triangular wave. Simultaneously the current necessary to produce this potential variation was recorded.

Fixed Potential Data—Cadmium

The electrochemical reaction studied was

$$Cd + 2OH^- \rightarrow Cd(OH)_2 + 2e$$

This was established by analysis of the x-ray diffraction lines of the reaction product. No evidence of CdO was observed.

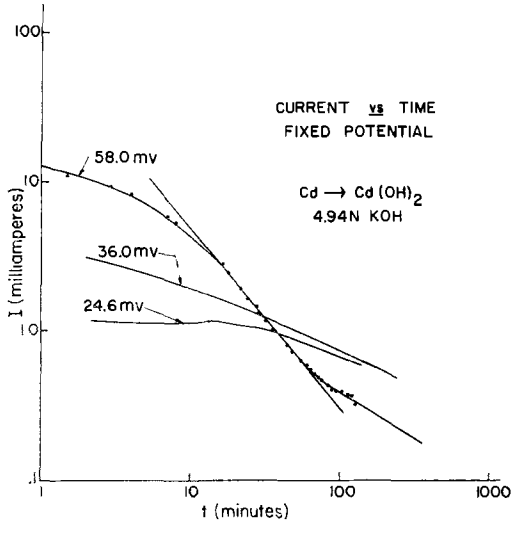

Fig. 2. Log I vs. log t curves for cadmium electrodes oxidized at fixed potential.

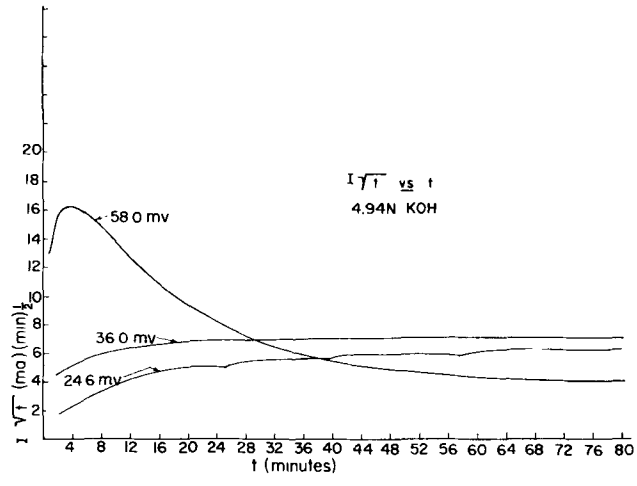

Fig. 3. The quantity $It^{1/2}$ vs. t for cadmium electrodes oxidized at fixed potential. No oxide present initially.

A typical series of log current vs. log time curves are shown in Fig. 2. Each of these curves was obtained by starting with an oxide-free surface previously maintained overnight at a cathodic potential (37.5 mv) and then instantaneously switched to a predetermined anodic potential.

After an initial slow decay, the current for the $\phi = 24.6$ and 36.0 mv runs begins to follow an equation of the form of Eq. [3]. At higher potentials (58 mv) the I vs. t curve has three portions. In the first portion the current decays slowly with time, in the second the current is proportional to t^{-1}, and in the third portion the current is proportional to $t^{-1/2}$.

The quantity $It^{1/2}$ obtained from the data shown in Fig. 2 is plotted vs. t in Fig. 3. For each potential the product $It^{1/2}$ tends toward a constant final value independent of time. This behavior follows directly from the $t^{-1/2}$ decay of current which starts after sufficient time has elapsed. The quantity $It^{1/2}$ for the $\phi = 24.6$ mv run exhibits a number of steps. This is probably caused by cracking or shearing off of the oxide film which exposes unoxidized cadmium to the electrolyte, which then oxidizes anew, etc.

Data similar to those in Fig. 3 are shown in Fig. 4. These results were obtained by suddenly advancing the electrode potential to 36.0 mv after the electrode had oxidized at 24.6 mv until the current was proportional to $t^{-1/2}$. More oxide was grown at this potential until the current decay was again proportional to $t^{-1/2}$. The potential was then suddenly made more anodic and more oxide was grown, etc. These data show that when sufficient time has elapsed after the sudden rise in anodic potential the product $It^{1/2}$ approaches a constant even if an initial oxide is present on the cadmium electrode. In this particular example $It^{1/2}$ tends toward the same value obtained if no oxide was present initially.

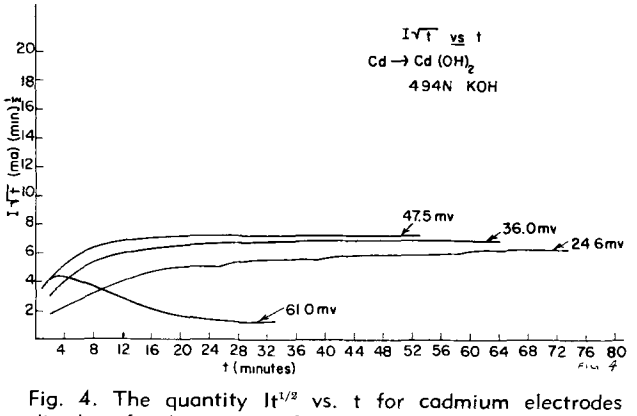

Fig. 4. The quantity $It^{1/2}$ vs. t for cadmium electrodes oxidized at fixed potential. Oxide present initially.

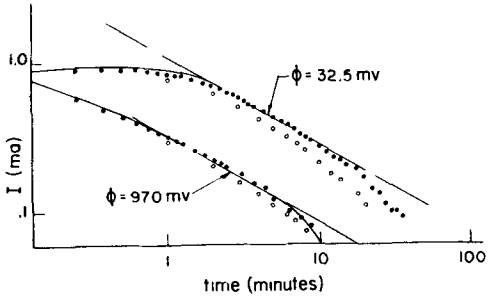

Fig. 5. Log I vs. log t for a cadmium electrode initially in the passive state. The electrode was 2.8 x 3.0 cm with one side exposed to electrolyte.

The characteristic shape of the curves shown in Fig. 2 to 4 is a reproducible function of ϕ, but the currents at equivalent times after application of anodic potentials were not generally reproducible. The curves shown represent some of the more reproducible runs.

Figure 5 is a plot of log I vs. log t obtained by the fixed potential method using electrodes which were first oxidized at constant current until the overpotential rose to 30 mv. (As the constant current overpotential rises to a value greater than 30 mv, the electrode rapidly approaches the passive state. Thus these electrodes for all practical purposes were in the passive state.) The current necessary to force the electrode to oxidize at a fixed potential is greater at 30 mv than at 97 mv. This is consistent with the fixed potential observations on electrodes not previously oxidized.

By fitting the I vs. t data in the $t^{-1/2}$ portion of the curve to Eq. [3] a number of determinations of $F(\phi)$ were made. Values of $F(\phi)$ determined by this procedure are shown plotted vs. ϕ in Fig. 6. Points obtained from additional I vs. t data not shown in this report are also plotted in this figure. The scatter of the points indicates the difficulty of achieving reproducibility from sample to sample, but qualita-

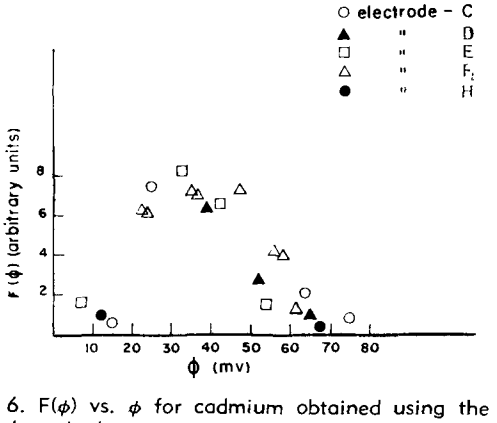

Fig. 6. F(ϕ) vs. ϕ for cadmium obtained using the fixed potential method.

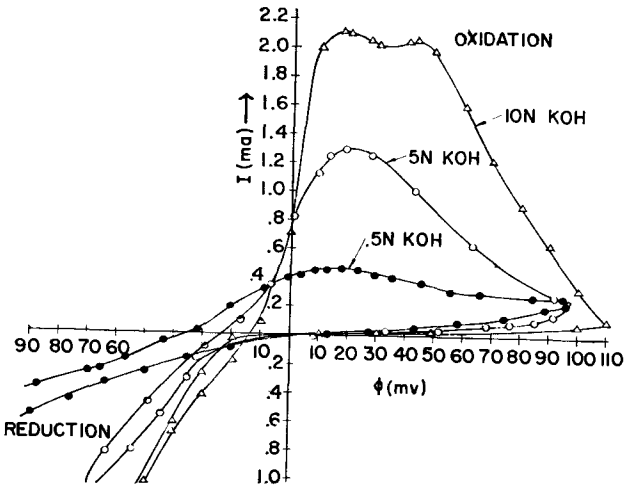

Fig. 7. Rate of oxidation and reduction of a cadmium electrode vs. overpotential obtained by the sweeping potential method.

tively the points show that $F(\phi)$ increases with ϕ to a maximum which lies between 18 and 40 mv. As ϕ is increased to potentials beyond the maximum, $F(\phi)$ decreases rapidly.

Thus fixed potential measurements on electrodes oxidized in a number of ways all indicate that in the final portion of the I vs. t curve the current is proportional to $t^{-1/2}$. This dependence of current on time corresponds to a *parabolic growth law*. Furthermore, besides being a function of time, the rate of growth is a peculiar function of potential which has a maximum for values of ϕ between 18 and 40 mv. Because of the difficulty of forming reproducible electrode surfaces, the potential at which the rate is maximum cannot be determined with great precision by the fixed potential method. However, the data indicate that there is a potential at which the parabolic growth rate is maximum. This result is confirmed by data presented below.

Sweeping Potential Data—Cadmium and Silver

The problem of forming reproducible electrode areas is partially eliminated if one uses the sweeping potential method. This method yields $F(\phi)$ vs. ϕ directly, and all the data are recorded using only one area, i.e., that associated with a single electrode.

Figure 7 is a plot of I vs. ϕ obtained using the sweeping potential method and is typical of the behavior of pure cadmium electrodes. There is at least one potential at which the rate of oxidation is maximum ($\phi = 18$ mv), and often the rate has a peak at $\phi \cong 40$ mv. The rate of reduction is a monotonically increasing function of the overpotential. The data also show a trend toward an increased current density at equivalent potentials as the (OH^-) concentration in the electrolyte increases. It is difficult to make a quantitative statement about effects of (OH^-) concentration changes because of the problem of maintaining reproducible surfaces from electrode to electrode.

Additional data were obtained on cadmium electrodes by simply increasing ϕ linearly with time with no subsequent reversal of potential. The data shown in Fig. 8 with $F(\phi)$ normalized also show peaks at $\phi = 18$ and $\phi = 40$ mv. These curves, when compared with the data plotted in Fig. 6, indicate that both methods, i.e., either fixed or sweeping potential, lead to the result that the rate of oxidation of cadmium in alkaline electrolyte is a function of potential and this function has at least one maximum in the range of potential between $\phi = 18$ and 40 mv. Comparison of Fig. 7 and 8 shows that when the electrode is forced to follow a cyclic variation of ϕ the details of the I vs. ϕ curves near the origin are altered, but the position of the maxima in $F(\phi)$ are unaltered.

These are very important new results. They show clearly that the rate of oxidation of the cadmium electrode is a function of the overpotential, that there is a potential at which the rate is maximum, and that the rate is a multivalued function of the overpotential.

Figure 9 shows I vs. ϕ data obtained using the sweeping potential method and electrodes containing 1 atomic % of indium alloyed with cadmium. These electrodes were 1 x 1 cm in dimension and were also mounted in resin with one side exposed to the electrolyte.

The addition of indium to cadmium electrodes causes supression of the 20 mv peak and the appearance of an additional peak between 60 and 70 mv. The 40 mv peak in the anodic quadrant remains, but a peak in the rate of reduction, i.e., in the cathodic quadrant, is introduced. Thus an indium impurity can introduce new peaks in both the rate of oxidation and reduction and can eliminate peaks associated with the pure electrode.

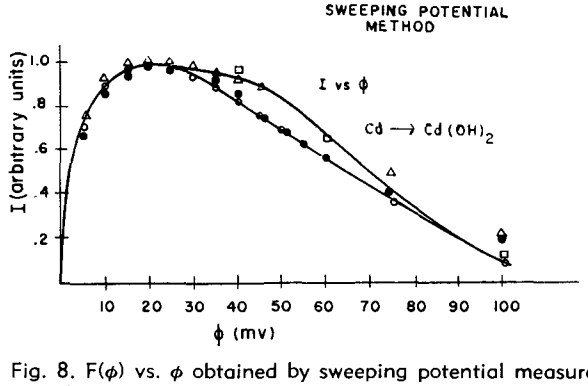

Fig. 8. $F(\phi)$ vs. ϕ obtained by sweeping potential measurements. $F(\phi)$ is normalized to its maximum value. The points represent values obtained in a number of different runs using sweep rates ranging from 4.7 to 22.8 mv/sec.

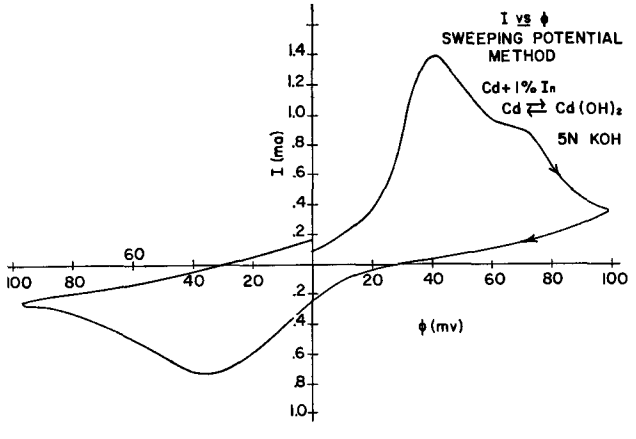

Fig. 9. Rate of oxidation and reduction vs. overpotential for a cadmium electrode containing 1 atomic % indium.

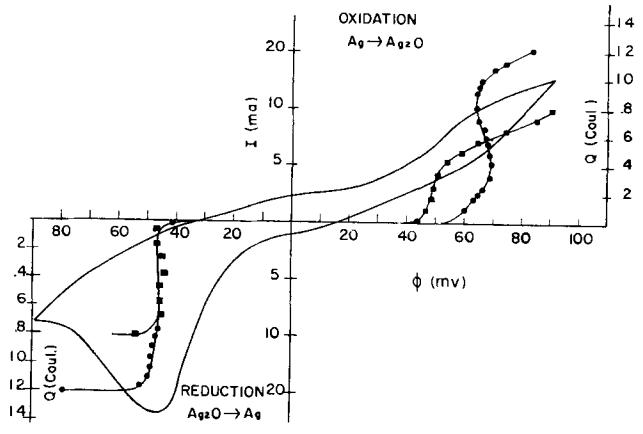

Fig. 10. Comparison of data for silver electrodes using either the overpotentiol, ϕ, or the capacity, Q, os the independent variable. Q in coulombs vs. ϕ is superimposed on the rate vs. ϕ data by plotting both the rate of oxidation and capacity data on the ordinate. —●—● reduced at 2 ma/cm²; —■—■ reduced at 10 ma/cm².

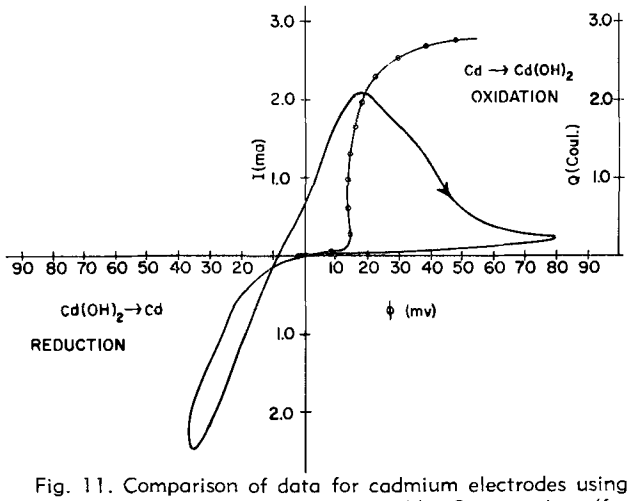

Fig. 11. Comparison of data for cadmium electrodes using either ϕ or Q as the independent variable. Q vs. ϕ data (for oxidation only) is superimposed on the normal I vs. ϕ plot by plotting both I and Q on the ordinate. Constant current oxidation was at 5 ma/cm².

The rate of oxidation and reduction of silver electrodes in KOH electrolyte vs. overpotential was also measured using the sweeping potential technique. The electrodes were plates 1 x 1 cm cast from 99.98% pure silver and mounted in epoxy resin with one polished side exposed to the electrolyte. The studies were made on the reaction,

$$2\,Ag + 2\,OH^- \rightleftarrows Ag_2O + H_2O + 2\,e$$

Figure 10 is a plot of I vs. ϕ data obtained using a silver electrode. (Constant current oxidation data discussed later are superimposed on this plot.) The rate of oxidation is a monotonically increasing function of overpotential, but a strong peak in the rate appears at 46 mv in the reduction quadrant.

Comparison of Overpotential vs. Charge and Current vs. Overpotential Data

The results of constant current oxidation and reduction of a silver electrode are shown in Fig. 10. The overpotential is plotted as a function of the charge Q where $Q = It$. Q is now the independent variable. Superimposed on this plot is the I vs. ϕ curve, where ϕ is the independent variable, which shows that when reduced at constant current the silver electrode overpotential drops to the value corresponding to the maximum in the I vs. ϕ reduction curve. The overpotential remains constant until all of the Ag_2O is reduced to Ag.

A similar plot using cadmium as the electrode is shown in Fig. 11. The constant current anodic overpotential rises to a value which corresponds closely to the potential at the first peak in the I vs. ϕ plots for pure cadmium. The constant current overpotential remains approximately constant at this value over a wide range of Q, but as ϕ exceeds 20 mv, $d\phi/dQ$ increases rapidly with ϕ until the oxidation reaction ceases, and the electrode becomes passive. Thus it appears that there is some fundamental connection between the rate of oxidation as a function of overpotential and the constant current oxidation and reduction characteristics of the electrodes.

The results of the measurements are best summarized in Fig. 10 and 11. It is evident that the rate of oxidation or reduction of Cd and Ag electrodes is a function of ϕ and that it is maximum at particular values of ϕ. There is a connection between the values of ϕ at which the rate of oxidation or reduction is maximum and the overpotential that the electrode seeks under constant current oxidation or reduction conditions. For example, the maximum rate of reduction of Ag_2O to Ag occurs at $\phi = 46.0$ mv and, if this electrode is reduced at constant current, the overpotential drops to 46.0 mv and remains constant until all of the Ag_2O is reduced. Similarly one of the peaks in the rate of oxidation of cadmium occurs around 18 mv which corresponds approximately to the constant current overpotential. As the potential rises above this value the electrode goes rapidly over into the passive state.

The constant current cathodic overpotential of the silver electrode agrees favorably with the value (0.04 v) obtained by Glicksman and Morehouse (2). Comparison of these data is probably legitimate because measurements of overpotential vs. current density on the Ag_2O to Ag system (see Fig. 10) indicate that the overpotential is relatively insensitive to the current density. The value of the constant current overpotential observed by Rozentsveig, *et al.* (3) agrees favorably with our value as does the general shape of the ϕ vs. Q curves.

Discussion of Results and Conclusions

The dependence of rate of oxidation on potential has been measured by two methods and both agree qualitatively. The fixed potential studies of cadmium indicate that if the current is proportional to $t^{-1/2}$ the rate of oxidation is maximum for potentials between $\phi = 18$ and 40 mv. The sweeping potential results show that the rate of oxidation of cadmium is maximum at two values of ϕ, one at approximately 18 mv and the other at 40 mv, and that an impurity in the metal such as indium can influence the potential at which the rate is maximum. Thus the results from each method are in good agreement.

The fixed potential experiments show that after sufficient time has elapsed the rate of oxidation follows a parabolic growth law. A parabolic growth

law is consistent with at least two hypotheses. One is that the necessary electron transfer process in the growth of $Cd(OH)_2$ occurs at the metal-electrolyte interface and that metal ion goes into solution and later precipitates on the metal as $Cd(OH)_2$. The parabolic growth characteristic sets in when the precipitated oxide completely covers the metal except for small pores. The rate is then limited by transport of the Cd^{+2} ion or an equivalent through the pores. As the oxide grows, the Cd^{+2} ion path increases, thus causing a current proportional to $t^{-1/2}$. Muller (4) has advanced a theory of passivity based on this mechanism.

The other hypothesis is that the cadmium ion, or OH^- ion, moves through the oxide and that the electron transfer process occurs at the oxide-electrolyte interface. Using this hypothesis, the parabolic growth law sets in when the exchange currents associated with the metal-oxide and oxide electrolyte boundaries are large compared with the rate of growth so that the rate is limited only by transport through the oxide. As the oxide thickens, the resistance increases and the current required to maintain the imposed potential decreases, thus yielding a parabolic growth law.

The following experimental facts support the latter hypothesis, namely, that the oxide grows by transport of mass and electricity through the oxide and that the solution process is not relevant.

The observations of steps in the $It^{1/2}$ vs. t curve (Fig. 5) are difficult to explain by any other mechanism than local cracking of an adherent solid oxide film which exposes a clean metal surface to the electrolyte for further oxidation. If the solution-precipitation process were relevant, there would be no way of developing strains necessary to cause cracking. Furthermore, if the solution-precipitation process were relevant, the overpotential would be a result of either a gradient in electrostatic potential or gradient in concentration of dissolving species in the pores connecting the metal to the electrolyte. Thus $F(\phi)$ vs. ϕ as determined by the fixed potential method would fit either the expression in Eq. [1] or Eq. [2]. Clearly it fits neither expression, indicating that the solution-precipitation process is not the relevant process in oxidation of cadmium.

We have also noticed that $Cd(OH)_2$ formed by a precipitation process differs in color from that formed by electrochemical oxidation of cadmium. Electrochemically prepared $Cd(OH)_2$ is yellow and we have observed that it is bleached white when exposed to x-rays. Precipitated $Cd(OH)_2$ is white. Again it is difficult to explain (*a*) the difference in color of the two compounds formed (according to the solution precipitation process) the same way, and (*b*) presence of traps in a presumably precipitated compound which are bleached out by x-rays.

One additional fact supporting the solid-state hypothesis is related to the $F(\phi)$ vs. ϕ data. The effects observed using the sweeping potential technique are similar to those observed in oscillographic polarography (6). One then might conclude that the sweeping potential effects are purely polarographic in character. However, it is difficult to reconcile this view with the fact of agreement in the rate of oxidation vs. overpotential data as determined by both the sweeping and fixed potential techniques. If one were observing only a polarographic effect, one would not observe a peak in $F(\phi)$ vs. ϕ using the fixed potential technique. The quantity $F(\phi)$ would be a monotonically increasing function of ϕ with no peaks. Thus the solution hypothesis is not consistent with the facts, and one is forced to the alternate, that of growth controlled by some solid-state mechanism.

Accepting the solid-state hypothesis the data so far not discussed are given the following tentative interpretation.

The 58-mv curve in Fig. 2 shows a continuous transition of the rate of oxidation from a t^{-1} to a $t^{-1/2}$ dependence on the time. The t^{-1} dependence of the rate of electrochemical oxidation corresponds to the logarithmic growth law often observed in air oxidation processes. A logarithmic growth rate is a result of transport of ions through a compound or across an interface, either metal-metal oxide or metal oxide-electrolyte, caused by a large local electric field intensity such that there is no local thermodynamic equilibrium. Thus the 58-mv curve suggests that, for values of ϕ in excess of the overpotential for maximum parabolic growth rate, ions are initially transported either through the hydroxide film or across an interface under nonequilibrium conditions and that, as the film thickens, the internal field is reduced until the ions come to local thermodynamic equilibrium at the interfaces and in the interior of the hydroxide thus yielding a parabolic growth law.

It is of interest to note that the rate-limiting step in the t^{-1} part of the curve could be transferred across either interface. If this is true, additional measurements of rate vs. time in the high overpotential region could lead to a determination of the exchange current at the relevant interface.

Again taking the solid-state view, the new $F(\phi)$ vs. ϕ curve (see Fig. 9) obtained by addition of indium to the cadmium electrode is also given the following tentative interpretation.

It is very probable that some indium becomes incorporated in the cadmium hydroxide lattice causing changes in the type and number of imperfections in the hydroxide. If this is true, the effects caused by indium suggest that the peaks are related to the type of imperfections in the cadmium hydroxide crystal.

If the growth of the hydroxide is via transport of mass and electricity through the hydroxide (as the evidence indicates), the dependence of rate on overpotential must then be related to the transport properties of the hydroxide subject to the boundary conditions imposed by the metal-hydroxide and hydroxide-electrolyte interfaces. Our results indicate that the boundary conditions are related to the electrode overpotential. A more detailed discussion of the implications of this result and an interpretation of the $F(\phi)$ vs. ϕ curves is in preparation and will be published later.

Acknowledgments

The author is indebted to his colleagues at the Edison Laboratory and in particular to Dr. J. B.

Johnson and Dr. Donald Tuomi for many stimulating discussions and helpful criticism of the manuscript. The author thanks the members of the supporting staff for the assistance in preparing the manuscript and Dr. Donald W. Collier, Director of the Edison Laboratory, for permission to publish.

Manuscript received June 3, 1958. This paper was presented before the Ottawa Meeting, Sept. 28-Oct. 2, 1958.

Any discussion of this paper will appear in a Discussion Section to be published in the December 1959 JOURNAL.

REFERENCES

1. M. Fleischmann and H. R. Thirsk, *Trans. Faraday Soc.*, **51**, 71 (1955).
2. R. Glicksman and C. K. Morehouse, *This Journal*, **104**, 599 (1957).
3. S. A. Rozentsveig, B. V. Ershler, E. L. Shtrum, and M. M. Ostanina, *Trudy Soveshchaniya Elektrokhim. Akad. Nauk. S. S. S. R. Otdel. Khim. Nauk 1950*, 571 (1953).
4. W. J. Muller, *Trans. Faraday Soc.*, **27**, 737 (1931).
5. Phyllis E. Lake and E. J. Casey, *This Journal*, **105**, 52 (1958).
6. Paul Delahay, "New Instrumental Methods In Electrochemistry," p. 122, Interscience Publishers Inc., New York (1954).

The Stability and Solubility of AgO in Alkaline Solutions

Thedford P. Dirkse and Brandon Wiers

Department of Chemistry, Calvin College, Grand Rapids, Michigan

ABSTRACT

Silver oxide is stable in boiling water and decomposes but very little at room temperature in strongly alkaline solutions. The presence of Ag_2O does not affect this stability, but the presence of unoxidized silver does increase the rate of decomposition. When AgO dissolves in strongly alkaline solutions the dissolved form is primarily AgO and $Ag(OH)_3^-$. The standard free energy of formation of the latter is —85,380 cal/mole.

Silver(II) oxide, AgO, has been known for some time and is now available commercially. Various methods for its preparation have been reported as well as several studies of its properties. Yet, in spite of all this, there is still confusion as to the nature and characteristics of this substance. There is conflicting information on its crystal structure as well as its stability.

The work reported here is the result of a study that has been made of AgO to eliminate some of this confusion and to determine some physical chemical constants.

In general there are two methods for preparing AgO. One of these is the electrolytic oxidation of silver in alkaline solution, or of silver ion in acid solution. However, it is difficult to get a pure product by this method. Our studies of the electrolytic oxidation of silver in alkaline solutions have shown that it is very difficult to oxidize silver completely to AgO. Denison (1) indicates that unoxidized silver is always present. In the preparation of the oxide by oxidation in acid solutions it is difficult to remove the last traces of anion.

The other method of preparation uses chemical oxidizing agents on silver ions. Various oxidizing agents have been suggested, e.g., MnO_4^-, $S_2O_8^{--}$, and ozone, but potassium persulfate in strongly alkaline solutions apparently gives the purest product (2, 3). In our work we used either a product prepared by this method or a commercially available material.

Experimental

Three types of analyses were performed on each batch of material to determine its purity. Samples of AgO were analyzed for oxygen content by heating to drive off oxygen; for silver by the Volhard method; and for oxidizing power by treating with KI and titrating the liberated I_2 with thiosulfate (4). These analyses indicated that the material was always better than 97%, and usually closer to 99% AgO.

In the solubility measurements, the mixtures were quickly filtered through sintered glass filtering crucibles and acidified with HNO_3 to reduce Ag^{++} to Ag^+ (4, 5). The sample was then titrated potentiometrically using a KI reagent and a silver electrode. The reference electrode was a saturated calomel electrode. The same precautions and techniques were used as are described in reference (6).

The KOH solutions were prepared by dilution of a stock solution to which some $Ba(OH)_2$ had been added to remove carbonate.

X-ray diffraction patterns were obtained from a plane surface of the material made by pasting the sample on a platinum screen. A Norelco x-ray unit was used. The radiation was produced by a copper cathode, and a nickel foil served as a filter.

Results

X-ray diffraction patterns.—Schwab and Hartmann (7) prepared AgO by several different methods and, in general, obtained the same x-ray diffraction pattern for each preparation. However, a somewhat different pattern was obtained from a sample prepared by extensive oxidation of silver with ozone, and from an oxide prepared by anodizing silver nitrate between platinum electrodes and then boiling the product in water. These latter patterns were also obtained by others (8) from similarly prepared oxides. This difference in x-ray patterns indicates a

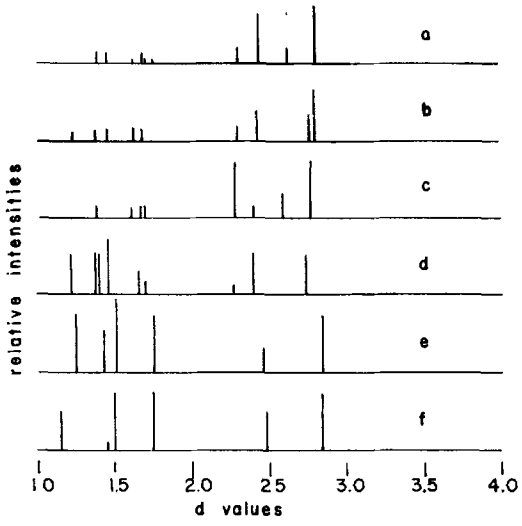

Fig. 1. X-ray diffraction patterns for AgO: (a) commercially available AgO; (b) AgO formed by anodizing Ag in KOH solutions; (c) AgO formed as in (b) but containing excess oxygen, $AgO_{1.17}$; (d) most AgO specimens prepared by Schwab and Hartmann (7); (e) AgO prepared by extensive ozonization of Ag (7); (f) AgO prepared from product obtained by anodizing $AgNO_3$ (7, 8).

difference in structure. Samples prepared by these latter two methods have often been suspected of containing Ag_2O_3 (9). It is possible that some such substance is formed and, being unstable, readily loses oxygen giving, in effect, AgO with somewhat larger lattice parameters.

Much of the work that has been reported on AgO has been based on a study of samples prepared by anodizing silver nitrate. Since such a sample has a different x-ray pattern than the AgO prepared by other methods, it is possible that its properties are also different. The oxides used in our work gave x-ray patterns similar to those of most of the preparations studied by Schwab and Hartmann. This pattern is also obtained from the AgO prepared by the electrolytic oxidation of silver in KOH solutions, Fig. 1. The relative intensities of these lines are not necessarily comparable since some of these patterns were obtained from powders and others from a plane surface.

Stability in aqueous solutions.—Since AgO is a strong oxidizing agent, it is possible that it may be unstable in water. However, reaction [1] is not

$$4AgO + 2H_2O \rightarrow 4Ag^+ + 4OH^- + O_2 \qquad [1]$$

thermodynamically spontaneous. Jirsa, *et al.* (4) studied this by placing AgO in boiling water and observed that the extent of decomposition of AgO increased with the amount of water used. Their explanation was that the decomposition continued until the water was saturated with AgOH. However, it is possible that the AgOH could precipitate as Ag_2O, and thus the decomposition of AgO by water would continue. The extent of decomposition would then depend on the time of boiling rather than the amount of water used.

In our attempt to test this, samples of AgO were placed for 1.5 hr in varying amounts of boiling water. The purity of the samples was determined iodometrically (4). There was no decomposition of AgO with such treatment (see Table I). In fact, the boiling water appears to purify the samples somewhat. It should be noted here that the oxide used by Jirsa and co-workers was prepared from the material produced by the anodization of a $AgNO_3$ solution.

In another test, samples of AgO were placed for 1.5 hr in boiling solutions of $AgNO_3$. Here there was a marked effect on the AgO, Table II. This likely was due to the hydronium ion. The *p*H of the 2.0*N* $AgNO_3$ was 3.5. AgO does decompose in acid solutions (4, 5). The ΔF°_{298} for reaction [2] is

$$4AgO + 4H^+ \rightarrow 4Ag^+ + O_2 + 2H_2O \qquad [2]$$

about −54 kcal.

It is of interest to note whether this stability of AgO changes at still higher *p*H values. Portions of AgO were allowed to stand in KOH solutions at room temperature. Samples were taken at various time intervals to determine the extent of decomposition. Results are given in Table III. It is obvious that a very slight, but definite, deterioration takes place.

To test this stability further, samples of AgO were prepared by treating silver anodically in KOH solutions. After treatment these specimens were soaked in distilled water to remove KOH, dried in a stream of purified nitrogen, and then placed in a desiccator for at least a day. The weight gained in this process was assumed to be due to oxygen. One of these specimens was anodized for several weeks in order to get complete conversion to AgO. This was verified by x-ray diffraction pattern and by analysis. The other sample was anodized for a few days and, while the surface was converted to AgO, not all the Ag was

Table I. Effect of boiling water on AgO

Ml water	% AgO after boiling
—	97.7
25	97.8
50	98.1
300	98.3
500	98.2

Table II. Effect of boiling $AgNO_3$ on AgO

Solution	% AgO after boiling
H_2O	97.6
0.1*N* $AgNO_3$	95.6
0.5*N* $AgNO_3$	94.2
1.0*N* $AgNO_3$	92.3
2.0*N* $AgNO_3$	88.3

Table III. Stability of AgO in KOH solutions

Days	% AgO after treatment	
	13% KOH	7% KOH saturated with Ag_2O
0	97.6	97.6
1	97.2	97.2
3	96.9	97.5
7	95.6	97.2
14	96.5	97.3
60	94.7	96.3

oxidized to AgO. The total composition could be represented by $AgO_{0.38}$. Both samples were kept in the dark in 30% KOH solutions for 4 months at room temperature. At the end of this time the pure sample had lost 2% of its weight. The amount that could have dissolved would have been only about 0.06% of the original weight. The x-ray diffraction pattern of the surface showed only lines of AgO. Hence any appreciable amount of Ag_2O that formed did not remain on the surface of the electrode. Some may have been shed by the electrode. There was a small amount of dark colored material at the bottom of the test tube when the sample was finally examined.

At the end of the 4 months the $AgO_{0.38}$ had lost only about 0.3% by weight, but this represented all the AgO there was on that electrode since the x-ray diffraction patterns showed that the surface had been completely converted to Ag_2O. Measurement of the potential of this electrode vs. a zinc electrode showed the presence of AgO at the end of 2 months.

These results indicate that pure AgO does decompose slightly even in the more concentrated KOH solutions. This decomposition may be due to the presence of local cell action, with a potential of about 200 mv.

$$2\,OH^- \rightarrow H_2O + \tfrac{1}{2}\,O_2 + 2e \qquad E^\circ = -0.4 \text{ v}$$

$$2AgO + H_2O + 2e \rightarrow Ag_2O + 2\,OH^- \qquad E^\circ = +0.6 \text{ v}$$

This decomposition of AgO would be hastened by the presence of impurities such as Ag. However, at room temperature even this process takes place slowly, as indicated by the very slight decomposition of the $AgO_{0.38}$ preparation over a period of time.

It is possible that Ag_2O may decompose AgO catalytically, but there was no evidence for this even in boiling solutions of KOH, Fig. 2.

Solubility in KOH solutions.—The solubility of AgO in KOH solutions was measured at 25°C. The samples were allowed to equilibrate for at least 2 days although later work showed that equilibrium was reached in a few hours. Some of the results are given on Fig. 3. The solubility is a function of the OH^- ion concentration. This indicates that the AgO dissolves by reacting with the OH^- ions. So far as

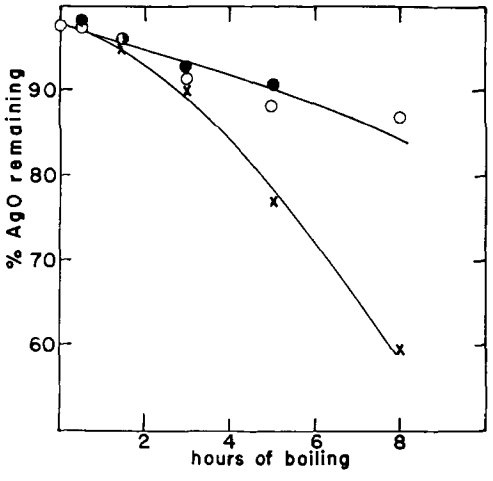

Fig. 2. Effect of boiling solutions of KOH on AgO: O, 7.5% KOH; •, 7.3% KOH saturated with Ag_2O; x, 14.1% KOH.

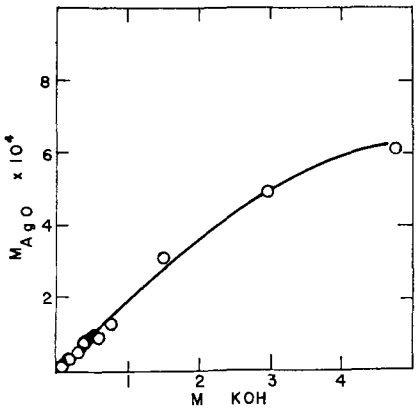

Fig. 3. Solubility of AgO in KOH solutions at 25°C

comparison can be made, these values are the same as those for Ag_2O (6). This is striking because ordinarily the higher valence oxide is more acidic.

Results obtained in more dilute solutions were treated to determine equilibrium constants for the formation of certain ions (10). Assume the following equilibria in solution.

$$AgO + H_2O \rightleftharpoons Ag(OH)_2 \qquad [3]$$

$$AgO + OH^- + H_2O \rightleftharpoons Ag(OH)_3^- \qquad [4]$$

$$AgO + 2\,OH^- + H_2O \rightleftharpoons Ag(OH)_4^{--} \qquad [5]$$

The total solubility, S, then can be expressed as

$$S = M_{AgO} + M_{Ag(OH)_3^-} + M_{Ag(OH)_4^{--}} \qquad [6]$$

or

$$S = M_{AgO} + K_2 M_{OH^-} + K_3 (M_{OH^-})^2/[y \pm (1-1)]^2 \qquad [7]$$

where K_2 is the equilibrium constant for reaction [4] and K_3 for reaction [5], the activities of AgO and H_2O being taken as unity. If now a plot of S vs. M_{OH^-} is made, it is evident from equation [7] that the extrapolated value is M_{AgO} or $M_{Ag(OH)_2}$. Such a plot is shown on Fig. 4. The extrapolated value is 0.27 x 10^{-5}M.

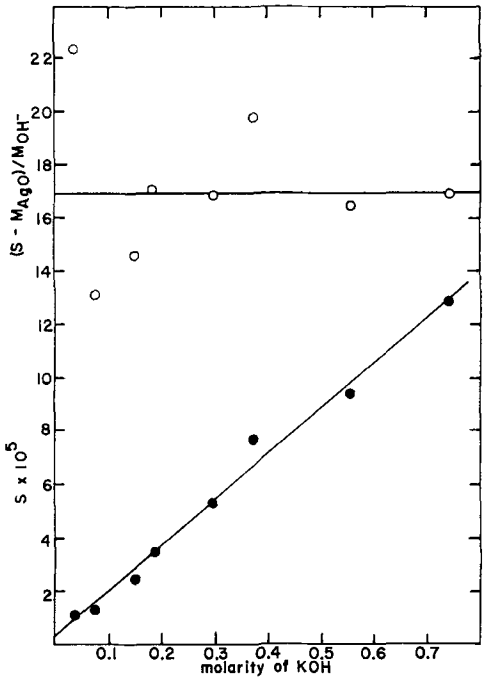

Fig. 4. Plot to determine value of M_{AgO} and K_2

Rearranging equation [7]

$$(S - M_{AgO})/M_{OH^-} = K_2 + K_3 M_{OH^-}/[y \pm (1-1)]^2 \quad [8]$$

Plotting the left hand member vs. M_{OH^-} and extrapolating now gives the value of K_2. This is shown on the upper portion of Fig. 4. The value for K_2 is 17 x 10^{-5}. Since this plot is parallel to the base line, the value of K_3 is zero. Consequently, the dissolved form consists of AgO or $Ag(OH)_2$ and $Ag(OH)_3^-$. Using the same technique the concentration of $AgOH^+$ is shown to be negligible.

$$AgO + H_2O \rightleftarrows AgOH^+ + OH^- \quad [9]$$

A similar treatment of the data of Johnston, *et al.* (6) shows the dissolved form of Ag_2O in alkaline solutions to be Ag_2O or AgOH and $Ag(OH)_2^-$. The value of the equilibrium constant for the formation of the latter is 3.6 x 10^{-3}. Thus, although the total solubility of Ag_2O and AgO in alkaline solutions is practically the same, the concentration of $Ag(OH)_3^-$ is greater than that of $Ag(OH)_2^-$.

Since K_{298} for reaction [4] is 1.7 x 10^{-4} the value of ΔF°_{298} for this reaction is +5150 cal. Using accepted values for the free energy of formation of H_2O and OH^-, and +3615 cal/mole for AgO (11), ΔF°_{298} for $Ag(OH)_3^-$ is −85,380 cal/mole. Likewise, ΔF°_{298} for $Ag(OH)_2^-$ is −57,065 cal/mole.

The rate of solution of AgO in KOH solutions was also studied. This was done by stirring the KOH solutions with solid AgO and analyzing samples of the solution for dissolved AgO. This solubility passes through a rather sharp peak, Fig. 5. This has been observed by others also (12). A similar phenomenon has been noted in perchloric acid (13). It was suggested that this could be due to a solid phase transition. This is a possibility, although x-ray diffraction measurements gave no difference in patterns. Nor is this phenomenon due to a decomposition of AgO. The residue left after allowing AgO to stand in contact with the KOH solutions for several days was analyzed iodometrically, and there was no evidence of decomposition. The residue showed as much oxidizing ability after standing as before. If this peak were due to a reaction such as [10] then the

$$4Ag(OH)_3^- \rightarrow 2Ag_2O + O_2 + 4OH^- + 4H_2O \quad [10]$$

residue would gradually change from AgO to Ag_2O. This reaction is thermodynamically possible, but neither weight measurements, analysis, nor x-ray diffraction patterns indicate that this or similar reactions take place unless, e.g., metallic silver is present. If this peak is due to a phase transition, e.g.,

$$AgO\ (A) + H_2O + OH^- \rightarrow Ag(OH)_3^- \quad [11]$$

$$Ag(OH)_3^- \rightarrow AgO(B) + H_2O + OH^- \quad [12]$$

it is a rapid transition and one not detected by our x-ray diffraction measurements. Furthermore, this peak was observed with samples of AgO obtained by treating $AgNO_3$ with $K_2S_2O_8$ in a strongly alkaline solution, so it is unlikely that further contact with alkaline solutions would cause such a phase change.

It is possible that this peak in the solubility curve is due merely to a time lag necessary for a reaction such as [12] to take place and thus some time is necessary before solubility equilibrium is truly established.

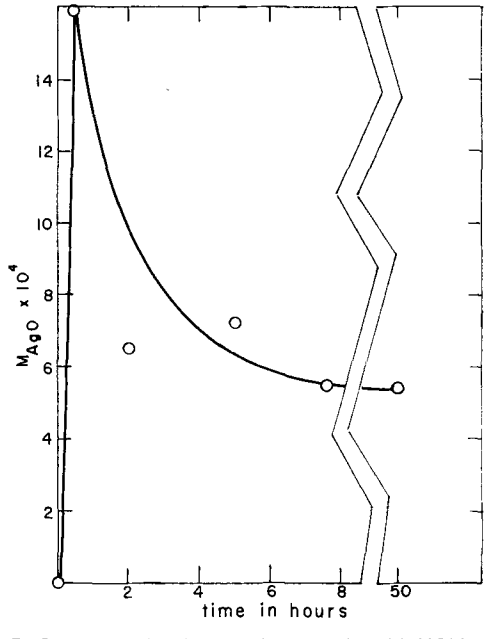

Fig. 5. Rate of solubility of AgO in 4.75M KOH at room temperature.

Acknowledgment

The authors wish to express thanks to the Office of Naval Research for a grant under which this work was undertaken, and to Merck and Company for supplying samples of AgO.

Manuscript received Oct. 8, 1958.

Any discussion of this paper will appear in a Discussion Section to be published in the December 1959 JOURNAL.

REFERENCES

1. I. A. Denison, *Trans. Electrochem. Soc.*, **90**, 387 (1946).
2. F. Jirsa, *Collection Czechoslav. Chem. Commun.*, **14**, 445 (1949).
3. J. C. Bailar, "Inorganic Syntheses," Vol. IV, p. 12, McGraw-Hill Book Co., New York (1953).
4. F. Jirsa, J. Jelinek, and J. Srbek, *Z. anorg. u. allgem. Chem.*, **158**, 33 (1926).
5. F. Jirsa and J. Jelinek, *ibid.*, **148**, 130 (1925).
6. H. L. Johnston, F. Cuta, and A. B. Garrett, *J. Am. Chem. Soc.*, **55**, 2311 (1933).
7. G. M. Schwab and G. Hartmann, *Z. anorg. u. allgem. Chem.*, **281**, 183 (1955).
8. P. Jones and H. R. Thirsk, *Trans. Faraday Soc.*, **50**, 732 (1954).
9. R. Luther and F. Pokorny, *Z. anorg. u. allgem. Chem.*, **57**, 290 (1908); G. Baborovsky and G. Kuzma, *Z. physik. Chem.*, **67**, 48 (1909); H. C. P. Weber, *Trans. Am. Electrochem. Soc.*, **32**, 391 (1917).
10. T. P. Dirkse, C. Postmus, and R. Vandenbosch, *J. Am. Chem. Soc.*, **76**, 6022 (1954).
11. T. P. Dirkse, Unpublished work.
12. H. P. Gregor, N. Nakajima, D. H. Gold, E. M. Loebl, G. K. Hoeschele, and R. Dogan, "A Study of the Application of Ion Exchange to Electric Batteries," Report of 31 August 1954 on Contract No. NObs-62383, Polytechnic Institute of Brooklyn, Brooklyn, N. Y.
13. A. A. Noyes, D. De Vault, C. D. Coryell, and T. J. Deahl, *J. Am. Chem. Soc.*, **59**, 1326 (1937).

Investigation of the Electrochemical Characteristics of Organic Compounds

III. Nitroalkanes

R. Glicksman and C. K. Morehouse

RCA Laboratories, Radio Corporation of America, Princeton, New Jersey

ABSTRACT

A theory based on the electron density in the vicinity of a reducible nitro group which had been used to explain the effect of substituent groups and their position on the operating potential of aromatic nitro compounds has been extended to the nitroalkane compounds. The high theoretical ampere-minute capacity of the nitroalkane compounds, along with their high operating potentials, show these compounds to have considerable promise for use as cathode materials in primary cells.

Previous studies (1-3) of the electrochemical characteristics of organic N-halogen, aromatic C-nitroso, and aromatic nitro compounds have suggested the use of these materials as cathodes in primary cells because of their high theoretical ampere-minute capacities and practical operating potentials.

The performance characteristics of dry cells containing aromatic nitro and C-nitroso compounds as cathodes coupled with a magnesium anode and a magnesium bromide electrolyte have been described in previous papers (4, 5). These cells have many performance characteristics superior to those of existing commercial dry cells.

On the basis of these studies, the most promising class of organic cathode materials appears to be the aromatic nitro compounds because of their high theoretical ampere-minute capacity, both on a weight and volume basis. Since the aromatic nitro compounds represent only one class of a large number of organic compounds, extensive studies were made of the electrochemical characteristics of other organic nitro compounds. This paper deals with the work on the nitroalkanes.

Apparatus and Technique

Because of the irreversible nature of the electrode reaction and polarization effects encountered during current flow, the electrochemical characteristics of many inorganic and organic compounds often cannot be predicted by thermodynamic calculations and a knowledge of their physical and chemical properties. A technique, previously described by the authors (6), has been used to measure the operating potential during current flow and the coulombic capacity of various nitroalkane compounds. This technique consists in discharging at a constant current, in a large volume of electrolyte, a 0.5-g [1] sample of the nitroalkane cathode material mixed with 0.05 g of Shawinigan acetylene black. The change in cathode potential with time was measured with a L&N Type K potentiometer using a saturated calomel reference electrode. The measured potentials were corrected for the *IR* drop associated with the apparatus and electrolyte by means of an oscillographic technique (7).

All half-cell potential data reported in this paper are referred to the normal hydrogen scale and include a liquid junction potential, which in most cases is small and can be neglected.

For most of the measurements an aqueous magnesium bromide electrolyte and a magnesium anode were used, while, in studying the effect of pH on potential, a zinc anode was employed with the acidic NH_4Cl-$ZnCl_2$-H_2O and basic NaOH-H_2O electrolytes.

Effect of Substituted Groups on the Electrode Potential of Nitroalkanes

Experimental Results

Presented in Fig. 1 are half-cell discharge curves for nitrobenzene and some low-molecular-weight nitroalkane compounds, discharged at a rate of 0.030 amp/ml of cathode material in a 250 g/l $MgBr_2 \cdot 6H_2O$ electrolyte. It is seen that these simple primary nitroalkane compounds operate at lower potentials than nitrobenzene under these conditions of discharge. The latter finding is in general agreement

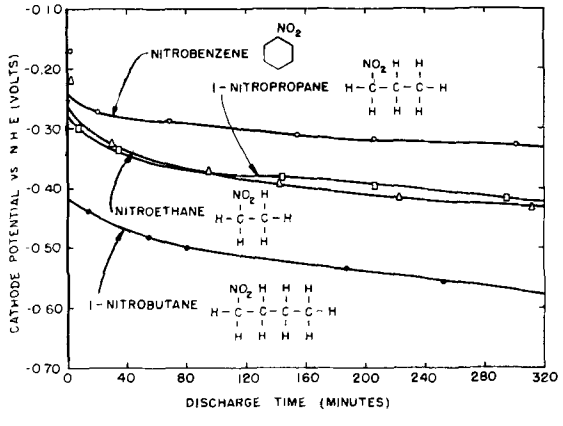

Fig. 1. Cathode potential of various nitroalkane compounds discharged in 250 g/l $MgBr_2 \cdot 6H_2O$ electrolyte at a rate of 0.030 amp/ml.

[1] Liquid compounds were tested by mixing 0.5 ml of the compound with Shawinigan acetylene black, discharging the resultant mix at the required rate, and making half-cell potential measurements in the usual manner.

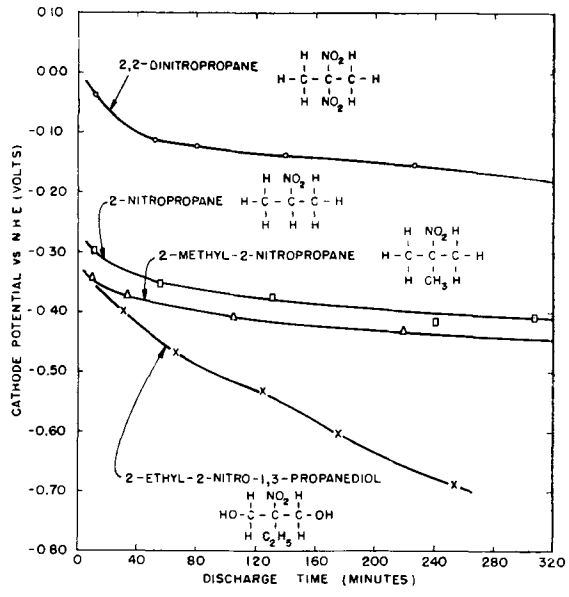

Fig. 2. Effect of substituted groups on the cathode potential of 2-nitropropane discharged in 250 g/l $MgBr_2 \cdot 6H_2O$ electrolyte at a rate of 0.030 amp/ml and 0.030 amp/g.

with polarographic data (8) obtained from these compounds over a wide range of *p*H values.

To test the effect of substituted groups on the electrode potential of the nitroalkane compounds, some 2-substituted 2-nitropropane derivatives were discharged in the $MgBr_2$ electrolyte. From the data presented in Fig. 2, it is seen that those compounds having electron-repelling groups such as $-CH_3$, and $-C_2H_5$, substituted in the 2-position of 2-nitropropane operate at lower potentials than the parent compound, while a compound such as 2, 2-dinitropropane, with a strongly electron attracting $-NO_2$ group in the 2-position, operates at a potential 0.25 v higher than 2-nitropropane.

In Fig. 3 are presented discharge data for a series of chloronitropropane isomers discharged at a rate of 0.030 amp/ml in the 250 g/l $MgBr_2 \cdot 6H_2O$ electrolyte. As with the nitroaromatic compounds (2), the position as well as the type of substituted group

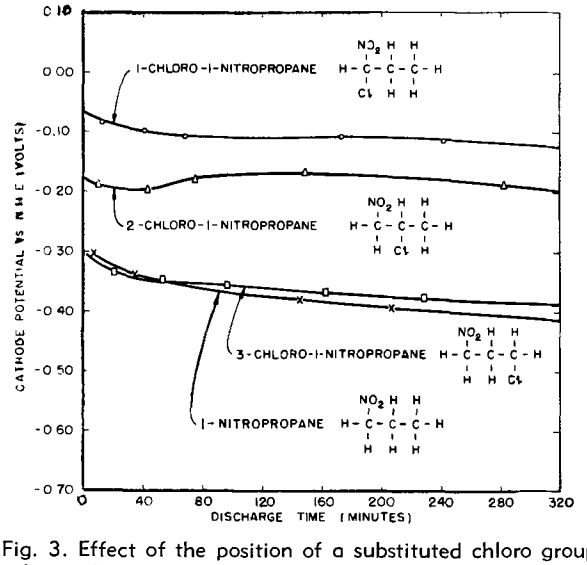

Fig. 3. Effect of the position of a substituted chloro group on the cathode potential of 1-nitropropane discharged in 250 g/l $MgBr_2 \cdot 6H_2O$ electrolyte at a rate of 0.030 amp/ml.

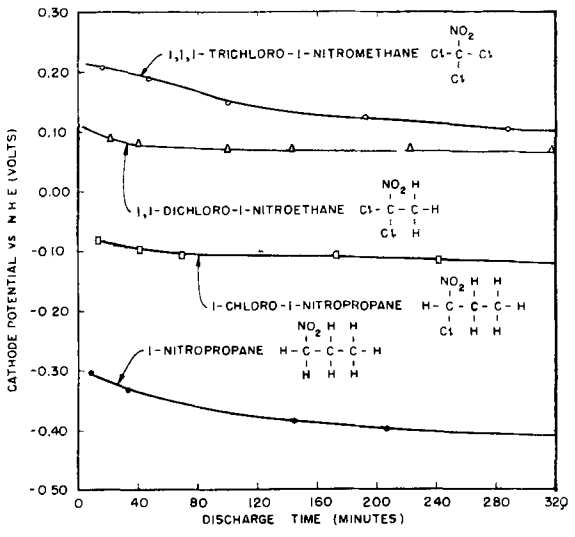

Fig. 4. Effect of the oddition of successive chloro groups to a nitro-carbon atom of a nitroalkane compound discharged in 250 g/l $MgBr_2 \cdot 6H_2O$ electrolyte at a rate of 0.030 amp/ml.

appears to have a pronounced effect on the operating potential of nitroalkane compounds as evidenced by the progressively higher potentials obtained when the electron attracting —Cl group is successively substituted in the 3-, 2-, and 1-position of 1-nitropropane. The effect of the —Cl group in raising the potential of 1-nitropropane is seen to be appreciable only for the 1- and 2-positions, having very little effect when substituted in the 3-position.

The addition of a second and third —Cl group to a primary nitro carbon atom raises the operating potential of a nitroalkane compound still higher, as evidenced by the discharge curves in Fig. 4 for the various mono-, di-, and tri-chloronitroalkane compounds. It is interesting to note that, although the potential increases with each succeeding chloro addition, the potential increases at a decreasing rate, the increase being approximately 0.25-0.30 v for the

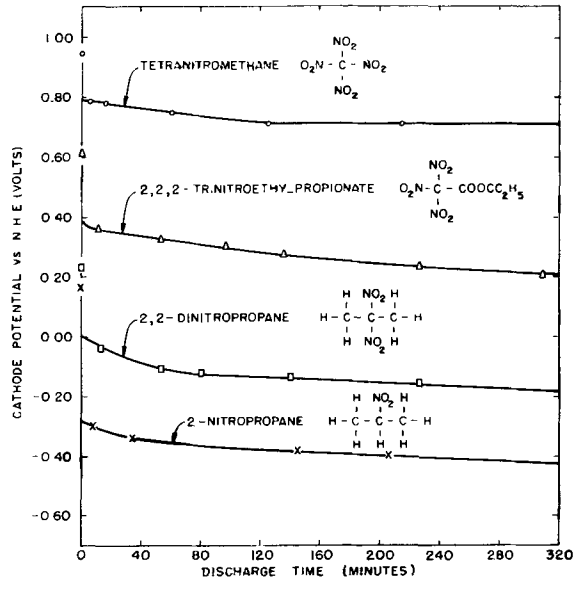

Fig. 5. Effect of the addition of successive nitro groups to a nitro-carbon atom of a nitroalkane compound discharged in 250 g/l $MgBr_2 \cdot 6H_2O$ electrolyte at a rate of 0.030 amp/ml.

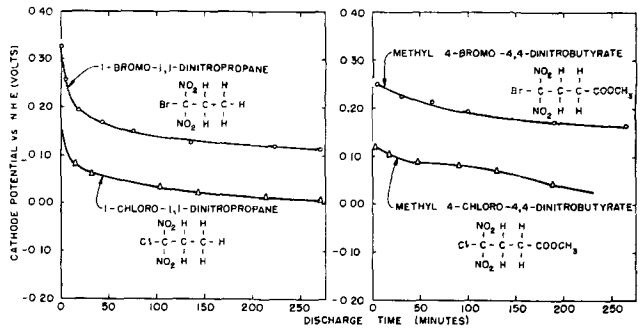

Fig. 6. Cathode potential of various bromo and chlorodinitroalkane compounds dischorged in 250 g/l $MgBr_2 \cdot 6H_2O$ electrolyte at a rate of 0.030 amp/ml.

addition of the first —Cl group, 0.18-0.20 v for the second, and 0.03-0.12 v for the addition of a third chloro group to a dichloronitro compound.[2]

The effect on potential of adding successive $-NO_2$ groups to a nitro carbon atom is shown in Fig. 5 where it is seen that the potential of the various nitroalkane compounds increases with each succeeding addition of a $-NO_2$ group. The increase in potential due to this strongly electron attracting group is greater than that found for the —Cl group, as evidenced by the considerably higher cathode potential of tetranitromethane compared to that of trichloronitromethane.

In Fig. 6 are presented discharge data for two pairs of bromo- and chlorodinitroalkane compounds, discharged at a rate of 0.030 amp/ml in 250 g/l $MgBr_2 \cdot 6H_2O$ electrolyte. Under these conditions of discharge the bromodinitroalkane compounds operate at potentials 0.1 v higher than those of the corresponding chlorodinitroalkane compounds.

Discussion

The cathode potential of aromatic nitro compounds has been shown to be dependent on the type and position of the substituent group or groups on the ring (2). This has been explained on the basis of the electron distribution in the molecule. For example, in substituted nitrobenzenes, the introduction on the ring of electron-attracting groups, such as —CHO, —CN, and —Cl, decreases the electron density in the vicinity of the nitro group, thus increasing its affinity for electrons and facilitating its reduction. Conversely, electron-repelling groups such as $-CH_3$, —OH, and $-NH_2$ increase the electron density around the nitro group, thus decreasing its affinity for electrons, resulting in compounds which are more difficultly reduced, i.e., with compounds having a lower cathodic discharge potential than the parent nitrobenzene.

The data presented in Figs. 2-5 also can be explained on the basis of the same theory. For example, it is seen from Fig. 2 that the effect of substituted electron attracting and electron-repelling groups on the potential of a nitroalkane compound during current flow is similar to that found for the nitrobenzene compounds. Further, the increase in potential due to the addition of a $-NO_2$ group to the nitro-carbon atom of a nitroalkane is greater than that found for the addition of a $-NO_2$ group to the para, meta, or ortho position of nitrobenzene. This is attributed to the fact that, for the nitroalkane compound, the substituted $-NO_2$ group is directly on the carbon atom containing the reducible nitro group, while for nitrobenzene such a grouping is impossible, and the effect of a nitro group must be transmitted through the ring carbon atoms.

By the same reasoning, one would expect the effect of an electron-attracting chloro group on the potential of a nitroalkane compound to diminish rapidly as saturated hydrocarbon groups are interposed between it and the $-NO_2$ group. The discharge curves in Fig. 3 for a series of chloro-nitropropane isomers bear out this reasoning. This same effect is operative for a wide variety of other organic reactions (9, 10).

Similarly, the cathode potential of a nitroalkane compound can be increased by the addition of successive electron-attracting groups to the nitro-carbon atom. The effect of each substituted group is to lower the electron density in the vicinity of the reducible nitro group, thus increasing its affinity for electrons and facilitating its reduction. This type of behavior is illustrated by the discharge curves presented in Fig. 4 and 5 for the various mono-, di-, and tri-chloronitro, and the mono-, di-, tri-, and tetranitroalkane compounds.

It has been shown previously that substituted chloro groups raise the cathode potential of nitroalkane compounds. This is in accord with theory. However, contrary to theory, the data in Fig. 6 show that bromo substituted compounds operate at higher potentials under current drain than their corresponding chloro compounds. The reason for this is not known.

As with the aromatic nitro compounds, it is recognized that the reduction of nitroalkane compounds involves the acceptance of hydrogen ions as well as electrons, and either or both might be involved in the rate-determining step. However, the data presented in Fig. 2-5, can be explained readily on the basis of a rate-determining electron transfer step.

Coulombic Capacities and Operating Potentials of Solid Nitroalkane Compounds

Tabulated in Table I are theoretical capacity and electrode efficiency data for some nitroalkane compounds compared with a few aromatic nitro compounds and two of the cathode materials now used in commercial dry cells. The theoretical capacities of the nitro compounds were computed by means of Faraday's Law, with the assumption that each nitro group is reduced to the amino stage, with a corresponding 6-electron change.

It is seen that the listed nitroalkane compounds have theoretical ampere-minute capacities per unit of weight approximately 2 to 10 times those of manganese dioxide and mercuric oxide. The capacities of some of these nitroalkane compounds are comparable to those of the aromatic nitro compounds. As with the aromatic nitro compounds, the low densities of the nitroalkane compounds result in a greatly reduced theoretical capacity advantage over the in-

[2] In making this comparison, it is assumed that the operating potentials of comparable chloronitroalkane derivatives, such as 1, 1-dichloro-1-nitroethane and 1, 1-dichloro-1-nitropropane, are approximately the same.

Table I. Theoretical capacities and electrode efficiencies of various cathode materials

Cathode	Physical state	Theoretical capacity, amp-min/g	Electrode efficiencies,* %
Conventional dry cell cathode materials			
Manganese Dioxide	Solid	18.5	66†
Mercuric Oxide	Solid	14.9	70
Aromatic nitro compounds			
Nitrobenzene	Liquid	78.4	—
m-Dinitrobenzene	Solid	115	77
1, 3, 5-Trinitrobenzene	Solid	136	—
Nitroalkane compounds			
2-Nitropropane	Liquid	109	—
2, 2-Dinitropropane	Waxy solid	144	—
Tetranitromethane	Liquid	196	—
2, 4, 6-Trichloro-2, 4, 6-trinitroheptane	Solid	89.3	32
4-Bromo-4, 4-dinitrobutyric acid	Solid	75.1	36
1, 1, 3, 3-Tetrabromo-2, 2-dimethyl-1, 3-dinitropropane	Solid	40.4	50
1, 1, 3, 3-Tetrachloro-2, 2-dimethyl-1, 3-dinitropropane	Solid	64.3	48
1, 1, 4, 4-Tetrabromo-1, 4-dinitrobutane	Solid	41.7	52

* Efficiency calculation based on a −0.40 v cut off.
† Efficiency calculation based on an 85% MnO_2 content.

organic compounds, when these cathode materials are rated on a volume basis (2).

The most attractive of these cathode materials is tetranitromethane, which has a theoretical ampere-minute per gram capacity comparable to that of oxygen, and which, when coupled with a magnesium anode in a magnesium bromide electrolyte, results in a galvanic cell which operates at 2.0-2.1 v for the first reduction step.

Despite the attractive electrochemical properties of tetranitromethane and other nitroalkane compounds, many of these compounds are liquids or are unstable, and for that reason their use in primary cells would be limited. However, these liquid oxidizing agents have potential use as cathodes in continuous-feed cell systems and deserve serious consideration for this application.

There are, however, a number of solid nitroalkane compounds available which, because of their high theoretical ampere-minute capacities and operating potentials, show considerable promise for use as cathodes in primary cells. Coulometric studies of some of these compounds in a magnesium bromide electrolyte are presented in Fig. 7-10, while the electrode efficiencies[3] of a few of these are given in Table I. The results were obtained by discharging a 0.5-g sample of the compounds at a constant current drain of 0.005 amp/g, and measuring the change in half-cell potential with time by the same technique as previously described.

[3] Electrode efficiencies calculated on the basis of a −0.40 v end voltage.

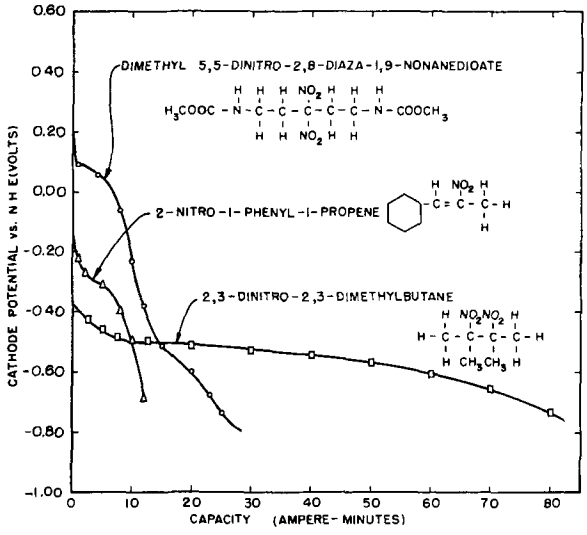

Fig. 7. Half-cell potential studies of various nitro and dinitroalkane compounds discharged in 250 g/l $MgBr_2 \cdot 6H_2O$ electrolyte at a rate of 0.005 amp/g.

Nitro and Dinitroalkane Compounds

The data presented in Fig. 7 illustrate the fact that an electron-attracting group must be attached to the carbon atom containing the reducible nitro group in order to get useful potentials from nitroalkane compounds. For the compound dimethyl 5,5-dinitro -2,8-diaza -1,9-nonanedioate such a grouping is available, and the reduction of the nitro group takes place at a half-cell potential of 0.00 to +0.10 v.

The low operating potential of the "vic"-2,3-dinitro-2,3-dimethylbutane compound as compared to that of the "gem"[4]-dinitro compound is attributed to the diminished effect of the $-NO_2$ groups on each other as saturated carbon groups are interposed between them, while the higher operating potential of 2-nitro-1-phenyl-1-propene as compared to other mononitroalkane compounds is believed to be due to the effect of the unsaturated double bond in lowering the electron density in the vicinity of the reducible $-NO_2$ group.

Despite their practical operating potentials, the gem-dinitro and 2-nitro-1-phenyl-1-propene compounds have poor electrode efficiencies, as measured under these conditions of evaluation.

[4] The prefix "gem" denotes attachment of both nitro groups to the same carbon atom, while "vic" denotes attachment to adjoining carbon atoms.

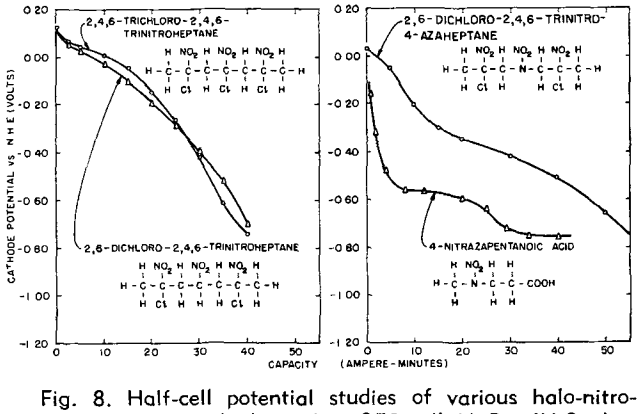

Fig. 8. Half-cell potential studies of various halo-nitroalkane compounds discharged in 250 g/l $MgBr_2 \cdot 6H_2O$ electrolyte at a rate of 0.005 amp/g.

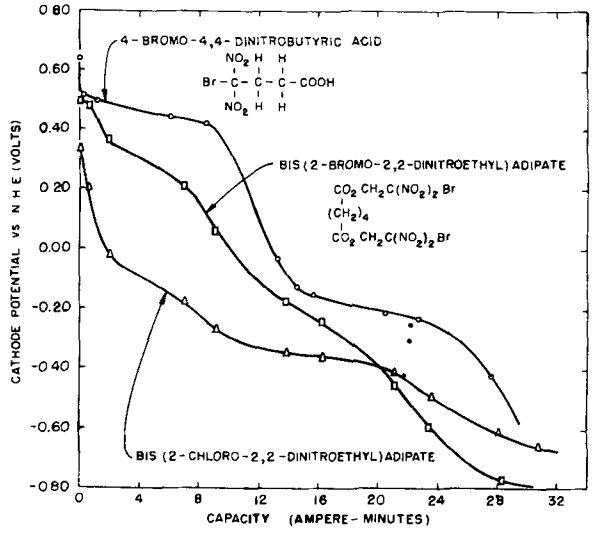

Fig. 9. Half-cell potential studies of various halo-dinitroalkane compounds discharged in 250 g/l $MgBr_2 \cdot 6H_2O$ electrolyte at a rate of 0.005 amp/g.

Halo-Nitroalkane Compounds

The high operating potential of 1-chloro-1-nitropropane (Fig. 3) prompted a search for structurally similar solid chloronitroalkane compounds, which in addition contain a high percentage by weight of the $-NO_2$ group. Presented in Fig. 8, are data obtained on a number of such compounds, which were discharged at a rate of 0.005 amp/g in a $MgBr_2$ electrolyte. It is seen that both 2,6-dichloro-, and 2,4,6-trichloro-2,4,6-trinitroheptane operate at potentials close to that of 1-chloro-1-nitropropane and give capacities of 30 amp-min/g to a −0.40 v cut off, these capacities being approximately twice the theoretical limit of the inorganic cathode materials. Although these compounds operate at slightly higher potentials than aromatic dinitro compounds such as m-dinitrobenzene, the high electrode efficiency of the latter compound (77%) makes it a more attractive cathode material than a compound such as 2,4,6-trichloro-2,4,6-trinitroheptane which operates at an efficiency of 32% and gives one-third the capacity of the aromatic dinitro compound in a $MgBr_2$ electrolyte.

Also included in Fig. 8 are discharge data for two compounds containing a N-NO_2 grouping. From a comparison of the discharge curves of 2,6-dichloro-2,4,6-trinitroheptane with 2,6-dichloro-2,4,6-trinitro-4-azaheptane, and 4-nitrazapentanoic acid with those of the primary nitroalkane compounds (Fig. 1), it would appear that those compounds containing a N-NO_2 grouping operate at lower potentials than comparable compounds containing a C-NO_2 grouping. A similar type of relationship has been found for the operating potential of C-nitroso and N-nitroso compounds (3).

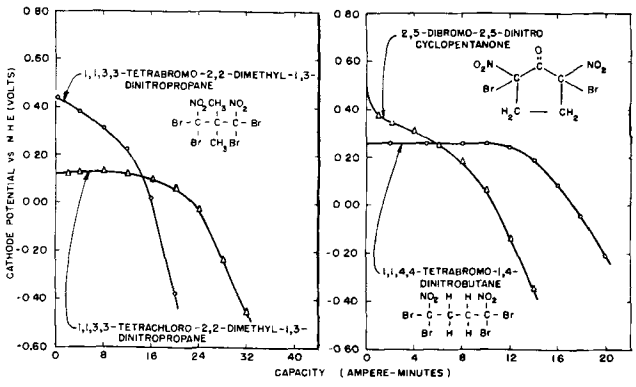

Fig. 10. Half-cell potential studies of various dihalonitroalkane compounds discharged in 250 g/l $MgBr_2 \cdot 6H_2O$ electrolyte at a rate of 0.005 amp/g.

Halo-Dinitro and Dihalo-Nitroalkane Compounds

It has been shown previously that liquid nitroalkane compounds containing halo-dinitro and dihalonitro groups would operate at higher potentials than the halo-nitroalkane compounds which have just been considered. A number of solid nitroalkane compounds containing these groupings were evaluated as cathodes in a $MgBr_2$ electrolyte, and the results are presented in Fig. 9 and 10.

The halo-dinitroalkane compounds exhibit a two-step discharge curve, probably due to the reduction of one nitro group at a time. The most attractive of these compounds, 4-bromo-4,4-dinitrobutyric acid, operates at a half-cell potential of +0.4 to +0.5 v for the first reduction step and between −0.1 and −0.2 v for the second step. The large difference in potential between the two stages of discharge is undesirable for many primary cell applications, and this together with their poor electrode efficiencies (36% for 4-bromo-4,4-dinitrobutyric acid) would limit the use of these halo-dinitroalkane materials as cathodes in primary cells at the present state of development.

The dihalo-nitroalkane derivatives, whose discharge curves are shown in Fig. 10, comprise another promising class of solid nitroalkane compounds. These compounds, which exhibit relatively flat voltage discharge curves, also operate at higher potentials than their corresponding halo-nitroalkane compounds.

The discharge curves of 1,1,3,3-tetrabromo- and 1,1,3,3-tetrachloro-2,2-dimethyl-1,3-dinitropropane further emphasize the fact that bromo-nitro compounds operate at higher potentials than their corresponding chloro-nitro compounds. Another interesting discharge curve is that of 2,5-dibromo-2,5-dinitrocylopentanone, because of the relatively high operating potential of this monobromo-nitro compound as compared to the dibromo-nitro compounds. The high potential of this compound is believed due to the effect of the electron attracting keto group in raising the potential of the adjacent Br-C-NO_2 groups.

Although the electrode efficiencies of the dihalonitro compounds are low (48-52%) compared to those of the aromatic nitro compounds (70-90%), they represent the best efficiencies which have been attained from any of the solid nitroalkane compounds. The poor electrode efficiencies of the nitroalkanes can be attributed either to the relative difficulty in completely reducing a nitroalkane to its corresponding amine, or to the fact that, under present conditions of discharge, the electrolytic reduction of the nitroalkane compound does not take place to the amine but to some intermediate stage. On the

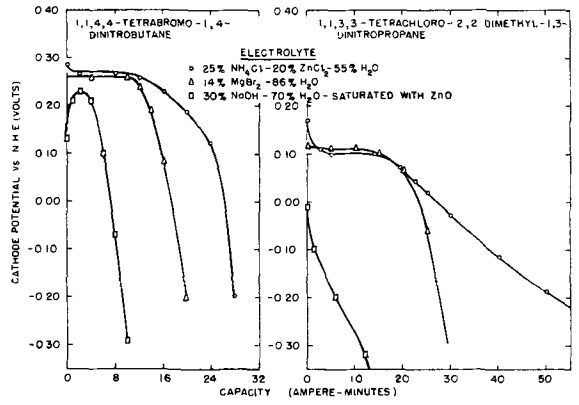

Fig. 11. Half-cell potential studies of 1,1,4,4-tetrabromo-1,4-dinitrobutane and 1,1,3,3-tetrachloro-2,2-dimethyl-1,3-dinitropropane discharged in various electrolytes at a rate of 0.005 amp/g.

basis of the above study, no satisfactory statement can be made about either possibility, and additional study of the reaction mechanism is needed in order to resolve this problem.

A review of the literature revealed that the reduction of mononitroalkanes to primary amines may be effected with a wide variety of reducing agents under various conditions (11-13). Strong reducing conditions yield amines. Hydrogen and a catalyst (Pt, Pd) are most frequently used, but good yields of amine have been reported from reductions by metals and acids, as well as by electrolytic methods. Mild reduction of primary and secondary nitroalkanes with zinc and acetic acid yields aldoximes and ketoximes, respectively, while still milder reducing conditions such as zinc in water or aqueous NH_4Cl yields the N-alkylhydroxylamine.

Additional coulometric studies of 1,1,4,4-tetrabromo-1,4-dinitrobutane and 1,1,3,3-tetrachloro-2,2-dimethyl-1,3-dinitropropane in electrolytes of different *p*H are presented in Fig. 11. It is seen that the cathode capacities of these compounds increase with decreasing *p*H of the electrolyte, especially when taken to a low end potential. However, the capacities obtained in the acidic NH_4Cl-$ZnCl_2$ electrolyte are still considerably less than the theoretical capacities of these compounds when calculated on the basis of a 6-electron change per $-NO_2$ group.

The poor capacities obtained from the nitroalkane compounds in the strongly basic NaOH electrolyte is

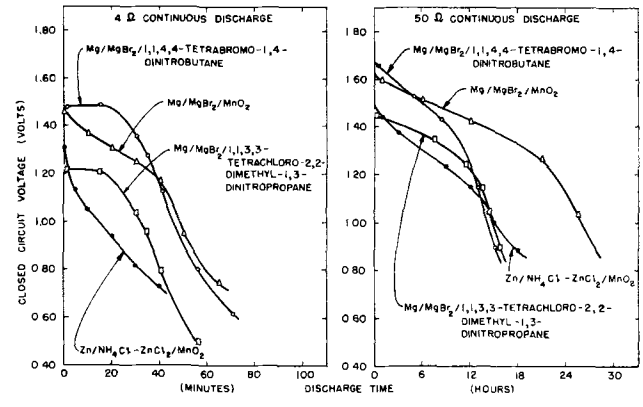

Fig. 12. AA-size dry cells discharged continuously through 4 and 50-ohm resistances at 70° ± 2°F (50% RH).

similar to that encountered for the aromatic dinitro compounds and could be attributed to the presence of side products which are formed by the condensation of the primary reduction products. In addition, nitroalkanes in the presence of alkaline reagents may undergo oxidation-reduction and extensive decomposition reactions, with a concommitant loss in cathode capacity.

It is interesting to note that the effect of *p*H on the operating potential of these nitroalkane compounds is very small, a relationship quite different than that found for the aromatic dinitro compounds (2). This type of behavior agrees with that found from polarographic studies, which show that the half-wave potentials of the nitroalkanes change only slightly with *p*H, while those of the nitroaromatics show a considerable variation with *p*H (8).

Experimental Dry Cell Data

Experimental dry cells containing 1,1,3,3-tetrachloro-2,2-dimethyl-1,3-dinitropropane and 1,1,4,4-tetrabromo-1,4-dinitrobutane cathodes were assembled in the usual manner (4) using an impact extruded Mg AA-size can be composed of an AZIOA Dow Chemical Co. alloy, and a 500 g/l $MgBr_2 \cdot 6H_2O$ electrolyte. The cathode mix (weighing approximately 5 g) consisted of two parts by weight of the nitroalkane compound to one part by weight of Cabot experimental battery black.

The performance characteristics of these magnesium-nitroalkane AA-size dry cells on a 4- and 50-ohm continuous discharge test are shown in Fig. 12. Included for comparison are performance data for comparable size commercial Leclanché, and Mg/$MgBr_2$/MnO_2 dry cells (14) of the type being developed by the Dow Chemical Company.

On the 4-ohm continuous discharge test, it is seen that the magnesium-nitroalkane cells are superior to the Leclanché cell both on the basis of minutes of service to specified end voltages, and operating voltage. Compared to the Mg-MnO_2 cell, the magnesium-1,1,4,4-tetrabromo-1,4-dinitrobutane cell operates at a higher voltage and gives comparable minutes of service to the inorganic cell.

On the lighter drain 50-ohm continuous discharge test, both organic cells give comparable hours of service to the Leclanché cell to a 0.90 v end point but are inferior to the Mg-MnO_2 cell in this respect. The organic cells, however, operate at higher voltages than the Leclanché cell on this test, while the magnesium-1,1,4,4-tetrabromo-1,4-dinitrobutane cell has a voltage comparable to that of the Mg-MnO_2 cell.

These results, while only representing the data obtained on two nitroalkane cathode materials, demonstrate the possible practical application of these materials in primary cells.

Summary

1. A theory based on the electron density in the vicinity of a reducible nitro group is presented which explains the effect of substituent groups and their position on the operating potential of nitroalkanes. For example, the effect of an electron-attracting chloro group on the potential of a nitroalkane diminishes rapidly as saturated hydrocarbon groups

are interposed between it and the nitro group. It is also seen that the addition of successive chloro or nitro groups to a primary nitro carbon atom increases the potential of the parent nitroalkane compound with each succeeding addition of the electron attracting group.

2. Coulometric studies in a $MgBr_2$ electrolyte indicate electrode efficiencies of 36-52% can be obtained from a number of solid nitroalkane compounds, assuming a 6-electron change per nitro group. The latter assumption is in doubt, however, since the reduction mechanism is not known.

3. Magnesium-nitroalkane dry cells have been assembled, and the performance characteristics of these cells indicate that nitroalkane compounds show promise for use as cathodes in primary cells.

Acknowledgment

The authors wish to express their appreciation to Mr. A. M. Cooke and Dr. R. S. Egly of Commercial Solvents Corporation and Dr. M. H. Gold of Aerojet-General Corporation for supplying many of the chemicals used in this investigation. Thanks are due also to Mr. G. R. Ganges of this laboratory for assembling and testing the dry cells.

Manuscript received July 7, 1958. This paper was presented before the Ottawa Meeting, Sept. 28-Oct. 2, 1958.

Any discussion of this paper will appear in a Discussion Section to be published in the December 1959 JOURNAL.

REFERENCES

1. C. K. Morehouse and R. Glicksman, *This Journal*, **104**, 467 (1957).
2. R. Glicksman and C. K. Morehouse, *ibid.*, **105**, 299 (1958).
3. R. Glicksman and C. K. Morehouse, *ibid.*, **105**, 613 (1958).
4. C. K. Morehouse and R. Glicksman, *ibid.*, **105**, 306 (1958).
5. C. K. Morehouse and R. Glicksman, *ibid.*, **105**, 619 (1958).
6. C. K. Morehouse and R. Glicksman, *ibid.*, **103**, 94 (1956).
7. R. Glicksman and C. K. Morehouse, *ibid.*, **102**, 273 (1955).
8. I. M. Kolthoff and J. J. Lingane, "Polarography," Vol. II, Chapter XLII, Interscience Publishers, New York (1952).
9. L. F. Fieser and M. Fieser, "Organic Chemistry," 3rd ed., pp. 162-164, Reinhold Publishing Corp., New York (1956).
10. C. R. Noller, "Chemistry of Organic Compounds," p. 430, W. B. Saunders Co., Philadelphia (1951).
11. H. B. Hass and E. F. Riley, *Chem. Revs.*, **32**, 373 (1943).
12. H. B. Hass, E. F. Riley, and H. Schechter, "The Science of Petroleum," Oxford Univ. Press, Vol. V. pt II.
13. N. Levy, and J. D. Rose, *Quart. Rev.*, **2**, 358 (1948).
14. R. C. Kirk, P. F. George, and A. B. Fry, *This Journal*, **99**, 323 (1952).

Oxidation Studies on the Iron-Chromium-Aluminum Heater Alloys

Earl A. Gulbransen and Kenneth F. Andrew

Research Laboratories, Westinghouse Electric Corporation, Pittsburgh, Pennsylvania

ABSTRACT

The oxidation behavior of three iron-chromium-aluminum alloys was studied using sensitive weight gain techniques. In addition, x-ray diffraction methods were used to determine the crystal structure and composition of the oxide films. The adhesion characteristics of the oxide film to the metal were tested by introducing strains into the metal oxide system during oxidation.

Rate studies show a change in rate for the three alloys near 900°C. Between 900° to 1050°C the rate of oxidation remained nearly constant; above 1050°C it increased again. X-ray diffraction studies suggest that a crystal structure transformation was occurring in the oxide. At 1050°C, α-Al_2O_3 was the main oxide in the scale.

The parabolic rate law was used to interpret the rate data. Deviations occurred during the initial reaction period as a result of crystal structure transformations in the film. Heats of activation of 76 to 77 kcal/mole were calculated for the range 700°-900°C.

Strain oxidation studies showed the oxide scale on the high aluminum alloy to be less susceptible to damage than the lower aluminum content alloys. These studies were correlated directly with practical performance tests.

Thermodynamic analyses of the several types of solid-solid and solid-gas reactions were used to interpret the rate and structure studies. Preliminary design principles were proposed for heat resistant alloys.

Heater alloys have been characterized by three important properties: (*a*) high melting point, (*b*) high resistance to oxidation, and (c) good mechanical properties. For extreme service conditions, two types of alloys have been used: (*a*) Ni-Cr alloys of nominal composition 80% Ni and 20% Cr, and (*b*) Fe-Cr-Al alloys of nominal composition 20-25% Cr, 4-6% Al, balance Fe. Both alloy systems consist of a single phase with the Ni-Cr alloys having the austenitic structure and the Fe-Cr-Al alloys the ferritic structure.

The maximum operating temperature in the final analysis is limited by the alloy's solidus point. This is about 1440°C for the Fe-Cr-Al alloys and 1380°C

for the Ni-Cr alloys. Neither series of alloys can be used at temperatures near their solidus point as the rate of oxidation and scaling becomes excessively high and the mechanical properties become poor. At extreme temperatures the oxidation resistance of the alloy determines, in part, the usefulness of the alloy as a high-temperature material.

The oxidation resistance of metals has been related to the formation of lattice defects and the diffusion of cations, anions, and electrons through these defects (1,2). This picture, based on a uniform oxide film, is probably too simple as has been shown by the formation of oxide needles, whiskers, and platelets (3, 4) on the scale. These suggest that certain areas of the metal are much more reactive than the rest of the surface.

If the metal is oxidized under periodic temperature cycles or when subjected to stresses or to a strain, the oxide-metal interface may be damaged (5). As a result, the rate of oxidation increases. The oxidation resistance of the alloy for these conditions is governed not only by diffusion processes but also by the chemical and physical properties of the oxide, alloy, and oxide-alloy interface.

The objectives of this study are: (*a*) to determine the kinetics of the oxidation of three Fe-Cr-Al alloys as a function of time, temperature, and alloy composition, (*b*) to determine the effect of strain on the oxidation process, (*c*) to determine the crystal structure of the oxide scales, and (*d*) to interpret from the experimental observations and thermodynamic analysis the high heat resistance of the Fe-Cr-Al alloys.

Literature.—von Kantzow (6) first observed that the heat resistance of steels was improved by alloying with aluminum. A series of alloys of Fe-Cr and Al were developed and patented. Since 1932 these alloys have been manufactured under the name of Kanthal[1] alloys.

The heat resistance of Fe-Al and Fe-Cr alloys has been studied by several groups (7-12). Hauttman (7) showed the strong effect of increasing the Al content between 4 and 9% at 1000°C. Al_2O_3 was found in the oxide layer on a 9.44% Al alloy. Scheil and Schulz (8) in a study of Cr-Al steels at 1200°C showed that the most oxidation resistant alloys were covered with a white aluminum oxide scale. At temperatures above 1000°C an Al content of greater than 4% was necessary to get a high degree of oxidation resistance. The high oxidation resistance properties and high electrical resistance suggested the use of Al-Cr steels for heater alloys. Ziegler (9) and Portevin, Pretet, and Jolivet (10) also noted the beneficial affect of adding Al to improve the oxidation resistance of steels.

The nature of the scaling process in the oxidation of steels containing Ni, Cr, and Al has been discussed by Krainer, Wetternik, and Carius (11). The loss by scaling was lowest for steel containing 24% Cr and 5% Al and having a scale of Al_2O_3. However, the resistance of the layer to scaling with temperature fluctuations was best for a Cr_2O_3 scale and poorest for an Al_2O_3 scale.

[1] Kanthal is a proprietory name for a series of heater alloys manufactured by Kanthal Corp., Stamford, Conn.

The segregation of aluminum atoms in Al-Cr-Fe alloys toward the periphery is discussed by Sektova (12). Sektova also noted the strong effect of Al to improve the oxidation resistance of these alloys.

Experimental

The vacuum microbalance method has been described (13-15). In this study a microbalance of low sensitivity, 4.39μg/0.001 cm deflection, was used. A total weight change of about 7 mg could be measured with a sensitivity of 1.10×10^{-6} g. This low sensitivity microbalance together with the use of smaller specimens increased the range of the measuring system by a factor of 25.

A vacuum grade mullite furnace tube contained the sample. It was sealed directly to the Pyrex glass system. With the specimen in the furnace tube at 1100°C, a McLeod gauge pressure of 3×10^{-6} mm Hg was readily obtained in the system. The vacuum system and gas preparation system have been described (15).

The furnace temperature was controlled to about ±1.5°C. There was no evidence of a temperature gradient along the 2.25-cm specimen during oxidation.

Weight changes occurring during the reaction were followed in a semicontinuous manner by observing a pointer on a balance beam using a micrometer microscope. Readings of the balance were taken *in vacuo* before reaction at temperature, during the reaction in oxygen, and after reaction *in vacuo*. Weight changes due to reaction of carbon in the metal with the surface oxide and to vaporization of metallic elements from the alloy were small.

Specimens used in this study were three types of commercial heater alloys obtained from the Kanthal Corporation. Table I shows the approximate and spectroscopic analysis of the alloys and their ratings as heater alloys. The 0.025-cm thick specimens were prepared from 0.63 cm wide strips and had surface areas of about 2.25 cm^2. Sample weight was about 0.1886 g. Sections of the strip were abraded starting with No. 1 polishing paper and finishing through 4/0 paper. To avoid oxidation, the last stage was carried out under purified kerosene. After abrading, the samples were cleaned with soap and water, distilled water, petroleum ether, and absolute alcohol, and stored in a desiccator.

Strain oxidation.—Earlier studies of the Ni-Cr series of alloys (5) and the studies of Krainer. Wetternik, and Carius (11) have shown that constant temperature studies cannot be used alone to evaluate the protective characteristics of a particular alloy if the alloy is subjected to stress or to a strain in its use. To give a more complete picture of the physical and chemical factors involved in high-temperature oxidation, a new test method called strain oxidation was developed. In this method the metal is oxidized to a given weight gain, removed from the balance system and strained 1-4% in a tensile machine. After cutting a smaller section of the sample free from grip marks, the specimen was placed in the balance system and re-oxidized. Rate calculations before and after strain were made on a 1 cm^2 basis. To achieve

Table I. a. Approximate composition* Fe-Cr-Al alloys (Kanthal Corporation)

Weight per cent

Alloy	C	Si	Mn	Cr	Al	Co	Fe	Relative useful life at 1200°C
1	0.07	0.65	0.26	23.0	5.7	0.57	Balance	175
2	0.06	0.74	0.27	22.4	5.1	0.59	Balance	150
3	0.07	0.65	0.22	21.7	4.5	0.58	Balance	100

b. Spectroscopic analyses† (Westinghouse)

Weight per cent

Alloy	Mo	Ni	Cu	Zr	Pb‡	Sn	Mg	V	Ca
1	<0.01	<0.1	~0.01	0.01-0.05	<0.01	<0.05	<0.001	<0.01	<0.01
2	0.5-0.9	0.1-0.5	~0.01	Not detected	<0.03	<0.05	<0.001	<0.01	<0.01
3	<0.01	<0.1	~0.01	Not detected	<0.01	<0.05	<0.001	<0.01	<0.01

* Traces of other elements to improve oxidation resistance.
† Tested for but not detected: Nb, Ta, Ti, and Ce.
‡ Erratic segregation.

a strain of 1% a stress corresponding to the yield point or greater was imposed on the sample.

X-ray diffraction method.—Filtered Cr K_α radiation was used with a fine focus x-ray diffraction tube. The diffraction patterns were made at room temperature using a 9 cm Unicam camera.

Oxide samples were removed from the alloy by electrochemical stripping (16). After washing several times in distilled water, the oxide films were rolled on to small glass capillary tubes for mounting in the x-ray camera.

Results

The three alloys were oxidized at 600°-1100°C using an oxygen pressure of 7.6 cm Hg for a reaction time of 2 hr. Weight gain during reaction was calculated in units of micrograms per square centimeter.

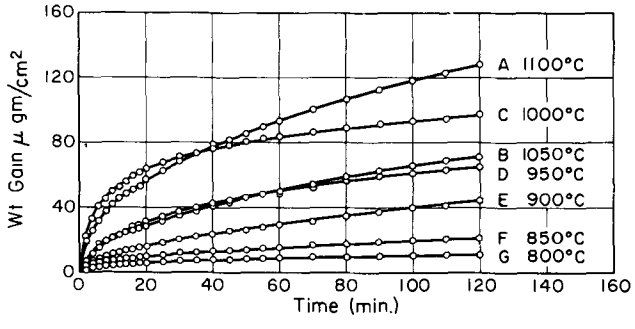

Fig. 1. Effect of temperature on oxidation Fe-Cr-Al alloy 1, 7.6 cm Hg of O_2, abraded through 4/0.

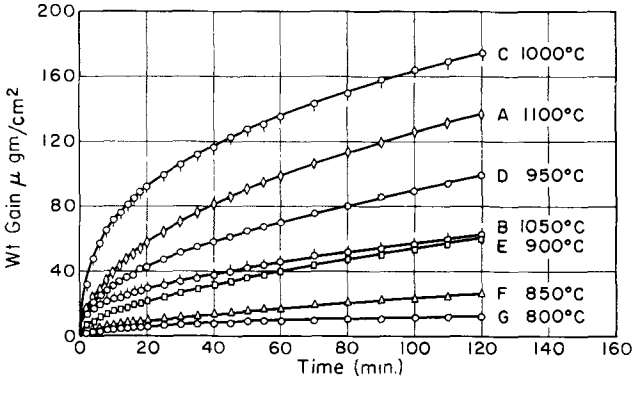

Fig. 2. Effect of temperature on oxidation of Fe-Cr-Al alloy 2, 7.6 cm Hg of O_2, abraded through 4/0.

X-ray diffraction analysis suggested that the oxides were largely α-Al_2O_3 and Cr_2O_3. Assuming α-Al_2O_3 and a surface roughness ratio of unity, a value of 54 was calculated for the relation between the oxide thickness in angstroms and the weight gain in micrograms per square centimeter.

Time and temperature.—Figures 1-3 show oxidation curves for the three alloys in the range 800°-1100°C. There was a rapid initial reaction rate in all curves, with the rate decreasing as the oxide film grows. No evidence was found for a linear rate law for the times studied. All of the oxides were grayish-black and were adherent to the alloy when cooled to room temperature.

Below 900°C the oxidation curves show a strong dependence on the temperature. However, between 900° and 1050°C, the rate was nearly constant for each of the alloys. Above 1050°C it increased again with temperature.

This nearly constant rate of reaction between 950° and 1050°C is of great interest and suggests that major structural changes were occurring in the alloy or in the oxide scale.

A comparison of the rate of oxidation of the three alloys at 1100°C shows only minor differences in the amount of oxidation or in the final rate of oxidation. Practical performance tests of alloys in Table I show alloy 1 to be superior to 2 and 3.

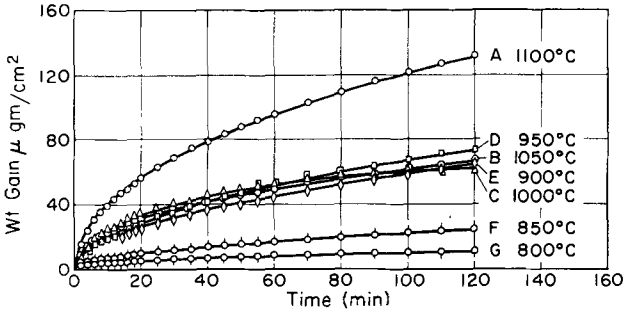

Fig. 3. Effect of temperature on oxidation of Fe-Cr-Al alloy 3, 7.6 cm Hg of O_2, abraded through 4/0.

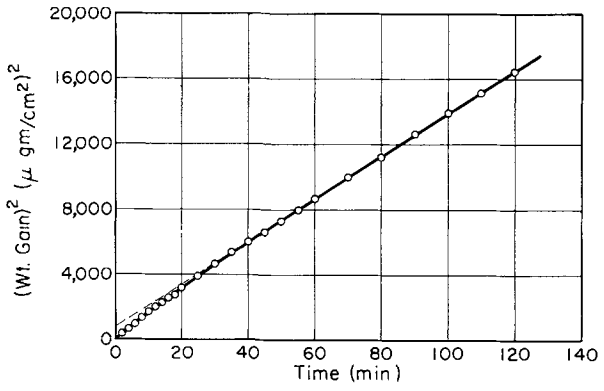

Fig. 4. Oxidation Fe-Cr-Al alloy 2, 1100°C, 7.6 cm Hg of O_2, abraded through 4/0, parabolic plot, A = 2.16 x 10^{-12} $(g/cm^2)^2$ sec^{-1}.

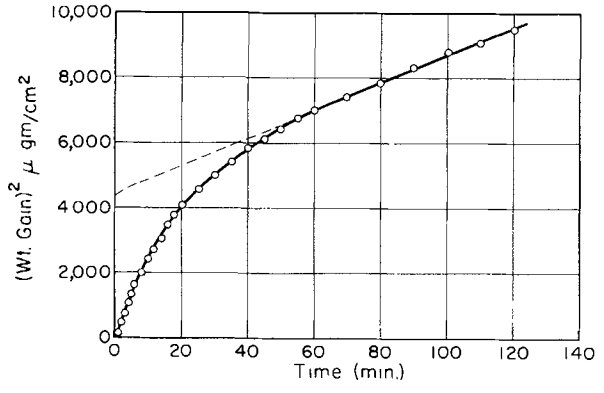

Fig. 5. Oxidation Fe-Cr-Al alloy 2, 1000°C, 7.6 cm Hg of O_2, abraded through 4/0, parabolic plot, A = 0.695 x 10^{-12} $(g/cm^2)^2$ sec^{-1}.

Parabolic rate law.—The parabolic rate law is useful in evaluating the nature of oxidation reactions even though deviations may occur, since the law is based on fundamental physical principles (1, 2). Physical and chemical changes occurring in the oxide film are noted as deviations from the rate law.

The equation states that $W^2 = At + C$. Here W is the weight gain, t is the time, and A and C are constants. Figure 4 shows a parabolic rate law plot at 1100°C for alloy 2. Agreement with the theoretical law was good except for the initial part of the reaction.

From 750° to 900°C the parabolic rate law constant increases during the first several hours of reaction over the initial value, while above and below this temperature range the parabolic rate law constant decreases with time. These effects also may be related to minor changes in the composition or physical structure of the oxide film. In the temperature range 900°-1050°C a major change occurred in the alloy or oxide film, since the temperature coefficient of the reaction was near zero. A change also occurs in the oxide film or alloy as a function of time for this temperature range. This was seen in the 1000°C parabolic rate law plot shown in Fig. 5. The parabolic rate law constant decreased rapidly during the first 60 min of reaction after which a nearly constant value was found.

Temperature dependence.—Figures 6 to 8 show plots of the logarithm of the parabolic rate law constant A vs. $1/T$ for the three alloys. Below 900°C a

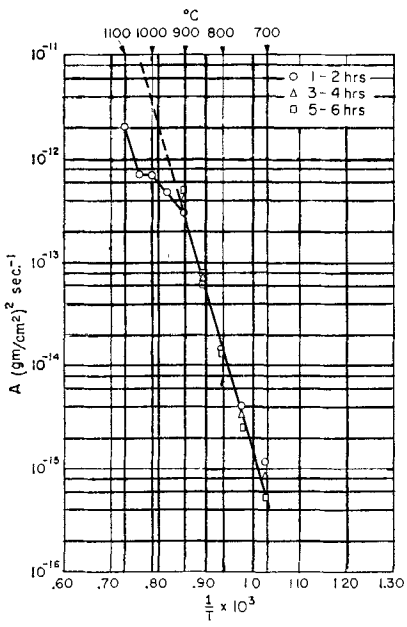

Fig. 6. Oxidation Fe-Cr-Al alloy 1, log A vs. 1/TΔH = 76,900 cal/mole.

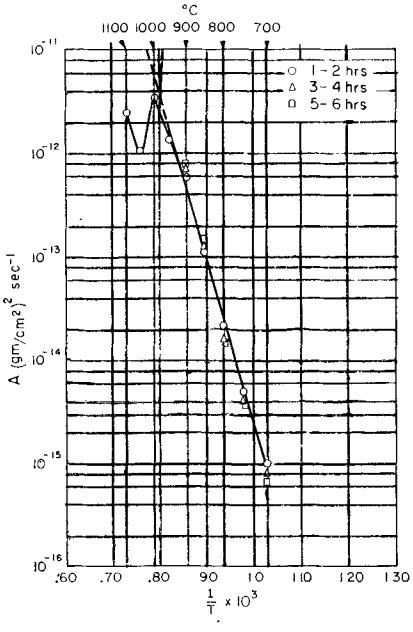

Fig. 7. Oxidation Fe-Cr-Al alloy 2, log A vs. 1/TΔH = 76,900 cal/mole.

straight line relationship was observed. Between 900° and 1050°C the plots show the transition phenomenon already noted. The slopes of the log A vs. $1/T$ plot and the absolute values of A for the three alloys were similar. Analysis of the slopes of Fig. 6-8 for alloys 1 and 2 shows heats of activation of 76,900 cal/mole and for alloy 3, 76,500 cal/mole. These are very high for oxidation processes.

Strain Oxidation

The several alloy specimens were oxidized at 900°C to form an oxide film of about 44.7μg/cm^2 or an estimated oxide thickness of 2410Å. After straining 2-4%, the specimens were re-oxidized at 900°C.

Figure 9 shows the results for a 2% strain for alloy 1. The oxidation curve after 2% strain was nearly continuous with the curve for the initial oxidation.

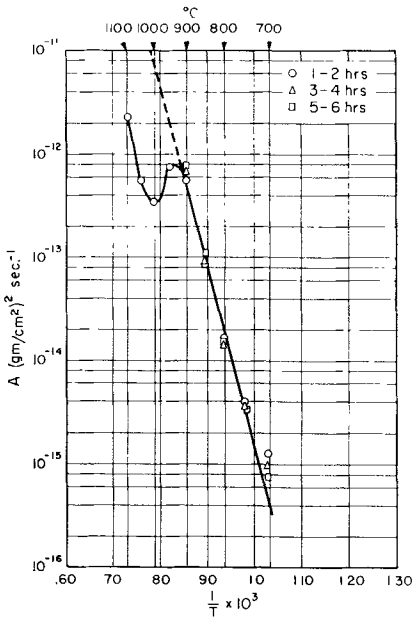

Fig. 8. Oxidation Fe-Cr-Al alloy 3, log A vs. 1/T $-\Delta H = 76{,}500$ cal/mole.

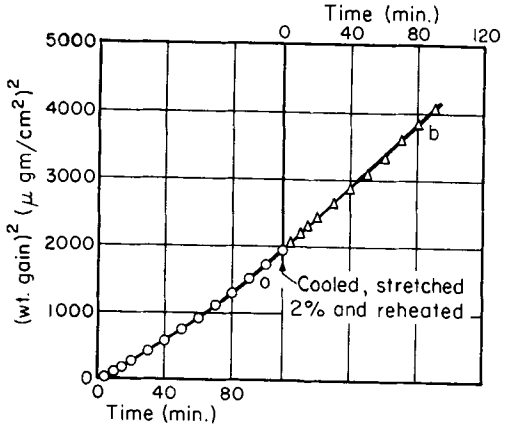

Fig. 9. Strain oxidation of Fe-Cr-Al alloy 1, 2% strain: a, 900°C, 7.6 cm Hg of O_2, A= 3.55×10^{-13} $(g/cm^2)^2/sec$; b, 900°C, 7.6 cm Hg of O_2, after cooling, stretching 2% and reheating, A = 4.0×10^{-13} $(g/cm^2)^2/sec$.

Figure 10 shows the strain-oxidation curve for alloy 1 for a 4% strain. A marked change in the course of oxidation was noted as a result of the 4% strain.

The usual effect of strain between the several oxide layers and the metal is flaking of the oxide with loss of protection of the metal (5). For heat resistant alloys 1-4% strain may not visually destroy the bonding between the oxide and metal but localized damage on a microscopic or submicroscopic level may occur which affects the rate of oxidation.

Some damage in the oxide or at the interface between metal and oxide has occurred as a result of 4% strain of alloy 1 as shown in Fig. 10. This damage was smaller than that observed on other alloys for the same amount of strain (5). Two types of damage are postulated to occur as a result of straining of the alloy. The first is a short-term damage which is rapidly repaired by further oxidation. The second is long-term damage. This damage involves an increase in the rate of reaction which continues over long periods of time. A comparison of the parabolic rate law constants before and after strain shows some

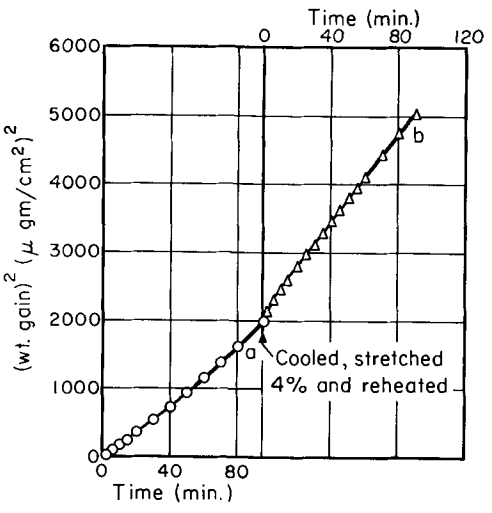

Fig. 10. Strain oxidation of Fe-Cr-Al alloy 1, 4% strain: a, 900°C, 7.6 cm Hg of O_2, A = 4.09×10^{-13} $(g/cm^2)^2/sec$; b, 900°C, 7.6 cm Hg of O_2, after cooling, stretching 4% and reheating, A = 5.12×10^{-13} $(g/cm^2)^2/sec$.

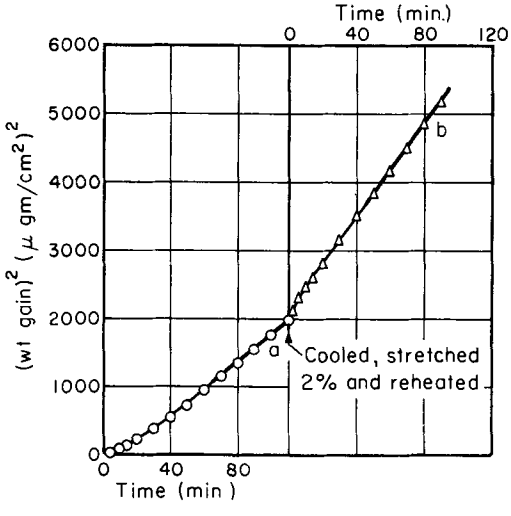

Fig. 11. Strain oxidation of Fe-Cr-Al alloy 2, 2% strain: a, 900°C, 7.6 cm Hg of O_2, A = 3.40×10^{-13} $(g/cm^2)^2/sec$; b, 900°C, 7.6 cm Hg of O_2, after cooling, stretching 2% and reheating, A = 6.41×10^{-13} $(g/cm^2)^2/sec$.

long-period damage for both 2 and 4% strains for alloy 1.

Figures 11 and 12 show the results of strain oxidation studies of alloys 2 and 3. Both alloys show short- and long-period damage resulting from a 2% strain. A comparison of the strain oxidation tests for alloys 1, 2, and 3 show alloy 1 to be superior. These results are in agreement with the useful life tests given in Table I. The useful life tests are temperature cycling tests and are used to evaluate heater alloys.

Crystal Structure Studies

Table II shows the results of crystal structure studies on 2-hr oxidation experiments for the three alloys and for the several temperatures. Crystal structure studies were made above and below the transition temperature region of 1000°C. The x-ray diffraction patterns showed sharp lines for all of the oxide scales studied.

Complete identification of all of the diffraction lines was not possible since the stripping process re-

Table II. Summary crystal structure studies Fe-Cr-Al alloys

Temp, °C	Alloy 1 Crystal structures	Temp, °C	Alloy 2 Crystal structures	Temp, °C	Alloy 3 Crystal structures
		850	α-Al_2O_3 s.a. Cr_2O_3 s.a. MnO	800	α-Al_2O_3 Cr_2O_3 MnO
950	α-Al_2O_3 s.a.* Cr_2O_3 tr.† MnO	950	α-Al_2O_3 tr. Cr_2O_3	900	α-Al_2O_3 Cr_2O_3 MnO
1050	α-Al_2O_3 s.a. α-Fe_2O_3	1050	α-Al_2O_3	1050	α-Al_2O_3 MnO tr. Cr_2O_3
	tr. spinel $a_o = 8.12$Å		tr. spinel $a_o = 8.12$Å		tr. spinel $a_o = 8.12$Å

* s.a. = small amount.
† tr. = trace.

moves carbides, nitrides, etc. from the surface layer of the alloy. As a result a number of extra reflections occur. Identification of the major oxide components was readily made. Oxides present in trace amounts were identified with less reliability by two or three characteristic reflections.

Alpha-Al_2O_3 was the principle oxide found in all of the oxide scales shown in Table II. Cr_2O_3 and MnO appear in the oxide scale at temperatures of 900°C and lower. The identification of MnO is open to some question since its diffraction pattern is nearly identical to those for NbC, NbN, and TaC (17). These compounds could conceivably be present in trace amounts in high-temperature alloys. Spectroscopic analyses of the alloys in Table I showed no evidence for Nb or Ta in the metal.

In the transition temperature zone the Cr_2O_3 content of the oxide scale decreases. In addition, a spinel, probably $FeO \cdot Al_2O_3$, appears in the oxide having a parameter of 8.12Å (17). These changes in oxide composition occur for all of the alloys.

Alloy 3 containing the lowest amounts of Al, Cr, and Mn shows the largest amount of MnO structure in the oxide scale. Alloy 3 also shows the largest amount of damage in the oxide in strain oxidation tests.

We conclude that crystal structure differences exist in the oxide scales of the three alloys as a result of minor differences in alloy composition. These crystal structural differences affect the adhesion properties of the oxide as shown by the strain oxidation studies or by practical performance tests. These differences do not appreciably affect the rate of oxidation at constant temperatures above and below the transition temperature zone.

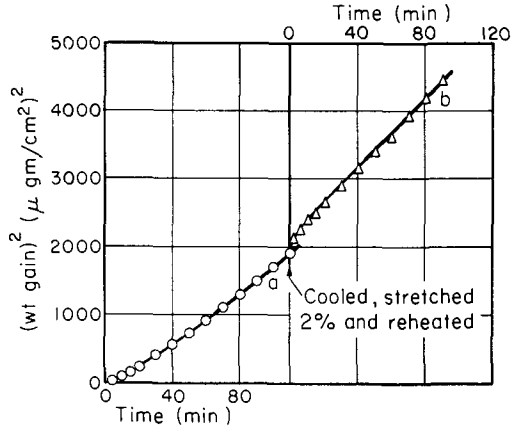

Fig. 12. Strain oxidation of Fe-Cr-Al alloy 3, 2% strain: a, 900°C, 7.6 cm Hg of O_2, $A = 3.29 \times 10^{-13}$ $(g/cm^2)^2/sec$; b, 900°C, 7.6 cm Hg of O_2, after cooling, stretching 2% and reheating, $A = 4.34 \times 10^{-13}$ $(g/cm^2)^2/sec$.

Thermodynamic Interpretation

Table III shows the principal types of reactions which may occur in the oxidation of Fe-Cr-Al alloys. These determine in part the constitution of the oxide scale formed at high temperatures. Precise calculations of the thermodynamic properties of the oxidation products necessitate consideration of the relative rates of attack of the several metals and interdiffusion processes in the alloy, as pointed out by Wagner (18) for a number of binary systems.

The thermodynamic evidence given below for most of these reactions assumes a standard state of unit activity for the component metals. For many of the calculations, the activity correction is small compared to the free energy change in the reaction itself.

Table IV shows logarithms of the dissociation

Table III. Types of surface reactions occurring on Fe-Cr-Al alloys

A. Direct oxidation
$2Cr(s) + 3/2O_2(g) \rightleftarrows Cr_2O_3(s)$, etc.
B. Solid phase reactions
$2Al(s) + Cr_2O_3(s) \rightleftarrows Al_2O_3(s) + 2Cr(s)$, etc.
C. Formation of spinels
$FeO(s) + Al_2O_3(s) \rightleftarrows FeO \cdot Al_2O_3(s)$, etc.
D. Formation of silicates
$Al_2O_3(s) + SiO_2(s) \rightleftarrows Al_2O_3 \cdot SiO_2(s)$, etc.
E. Decarburization reactions
$Cr_2O_3(s) + 3C(\text{solid solution}) \rightleftarrows 2Cr(s) + 3CO(g)$, etc.
F. Vaporization reactions
$Cr(s) \rightleftarrows Cr(g)$, etc.

Table IV. Dissociation pressures of the oxides

Temp, °C	$-\log p_{O_2}$ atmospheres					
	Fe_2O_3	Al_2O_3	Cr_2O_3	SiO_2	MnO	CoO
25	85.5	184.6	121.8	144.6	127.2	75.4
200	50.8	112.4	73.4	87.6	77.4	44.5
400	33.0	75.7	48.9	58.8	52.1	28.9
600	23.4	55.8	35.6	43.2	38.4	20.4
800	17.4	43.3	27.3	33.5	29.8	15.1
1000	13.3	34.7	21.6	26.8	24.0	11.4
1200	10.3	28.4	17.4	21.9	19.6	8.8

Table V. Solid phase reactions of ferric and chromic oxides with Cr, Al, Si, and Mn

1. $2Cr\ (s) + Fe_2O_3\ (s) \rightleftarrows Cr_2O_3\ (s) + 2Fe\ (s)$
2. $2Al\ (s, l) + Fe_2O_3\ (s) \rightleftarrows Al_2O_3\ (s) + 2Fe\ (s)$
3. $2Al\ (s, l) + Cr_2O_3\ (s) \rightleftarrows Al_2O_3\ (s) + 2Cr\ (s)$
4. $3Mn\ (s) + Fe_2O_3\ (s) \rightleftarrows 3MnO\ (s) + 2Fe\ (s)$
5. $3Si\ (s) + 2Fe_2O_3\ (s) \rightleftarrows 3SiO_2\ (s) + 4Fe\ (s)$
6. $3Si\ (s) + 2Cr_2O_3\ (s) \rightleftarrows 3SiO_2\ (s) + 4Cr\ (s)$

Temp, °C	$\log_{10}K$ Reaction 1	Reaction 2	Reaction 3	Reaction 4	Reaction 5	Reaction 6
25	+54.1	+148.2	+94.1	+62.1	+176.4	+68.3
200	33.9	92.4	58.5	39.9	110.5	42.6
400	23.8	63.9	40.1	28.6	77.3	29.8
600	18.4	48.6	30.2	22.5	59.5	22.8
800	14.9	38.9	24.0	18.6	48.2	18.5
1000	12.5	32.2	19.7	16.1	40.5	15.5
1200	10.8	27.2	16.4	14.0	34.9	13.4

pressures of the oxides from 25° to 1200°C as calculated from equations given by Kubaschewski and Evans (19). All of the oxides are stable in the atmospheres and temperatures used in the oxidation experiments.

The equilibrium constants for the several solid phase reactions are given in Table V. All are thermodynamically possible over the temperature range. Although ferric oxide may form initially, both Cr and Al can react to form chromium and aluminum oxide as shown by the positive values of $\log_{10}K$. Eventually aluminum oxide should constitute the bulk of the oxide film.

X-ray crystal structure studies (Table II) confirm the thermodynamic predictions that Al_2O_3 should be the chief oxide in the scale. Solid phase reactions may account for the decreases in chromium oxide content of the scale at temperatures above 900°C. The presence of MnO may be due to the high mobility of manganese and to its high thermodynamic stability.

The formation of spinels or other mixed oxide systems may be expected but thermodynamic data for spinels other than Fe_3O_4 are not available. However, the stability of the several spinels of interest can be deduced from structural information. Table VI shows the lattice parameters of some of the known aluminates (17) having the spinel structure as a function of the ionic radii of the bivalent ions. Table VI shows that Co, Fe, and Mn can form spinels with aluminum

Table VI. Parameters of aluminate spinels of a number of metals

Divalent metal	Atomic number	Radius of ion, Å	Parameter of oxide MO,* Å	Parameter of aluminate (17), Å
Ni	28	0.74	4.168	8.06
Mg	12	0.75	4.203	8.10
Co	27	0.78	4.24	8.085
Fe	26	0.80	4.332†	8.119
Zn	30	0.83		8.087
Cu	29			8.09
Mn	25	0.83	4.4345	8.28
Cd	48	0.99	4.689	
Ca	20	1.05	4.797	

* Coordination number of six.
† Stoichiometric composition.

Table VII. Vapor pressure of metals

Temp, °C	$\log_{10}K_p$ Fe	Cr	Al	Si	Mn	Co
400		—23.1	—18.2	—26.3	—14.5	—25.3
600		—16.1	—12.5	—18.55	—9.6	—17.8
800		—11.65	—8.95	—13.7	—6.5	—13.05
900		—9.95	—7.6	—11.8	—5.3	—11.25
1000	—9.83	—8.55	—6.5	—10.3	—4.35	—9.75
1100	—8.63	—7.4	—5.5	—8.9	—3.5	—8.5
1200		—6.4	—4.7	—7.85	—2.8	—7.35

oxide. Even though Mn and Co are present in minor amounts in the alloy, they can substitute in the spinel structure and thus appear in the oxide film.

The formation of silicates may be expected from phase diagram studies of the oxides (20). These compounds can exert a major influence on the oxidation process since they may concentrate at the oxide-alloy interface.

The role of the decarburization reaction is not understood. Calculations using data from Kubaschewski and Evans (19) show that, if a carbon content of 0.05% is assumed for the reaction of carbon with ferric oxide, the equilibrium carbon monoxide pressure is 1 atm at 1000°C. Similar calculations for chromic oxide, aluminum oxide, and silicon dioxide show the reaction to occur under vacuum conditions at 1000°C. As the carbon content is depleted, the importance of this reaction diminishes.

Table VII shows the vapor pressures of the metals of interest in this study from 25° to 1200°C. Except for iron the data are calculated from a recent survey by Stull and Sinke (21). The data for iron are taken from a recent study by the authors (22) using the vacuum microbalance method. The measured values for the vapor pressure of iron were lower than the extrapolated values given by Stull and Sinke (21).

Weight loss calculations based on Table VII for oxide free Fe-Cr-Al alloys show rapid evaporation of Al, Cr, and Mn above 1000°C in high vacuum. However, rapid evaporation of these metals has not been observed in our studies or in other studies (6) on these alloys.

In another study (22) the weight loss curves for oxide free surfaces of pure iron, a 5 Al-Fe alloy and a 5 Al-23 Cr-Fe alloy, were determined. The alloys were prepared from pure metals. The 5 Al-Fe alloy gave a weight loss curve somewhat lower than that for pure iron while the 5 Al-23 Cr-Fe alloy gave a weight loss curve a little higher than that for iron. Chemical analyses of the vaporized deposits showed the vapor from the 5 Al-Fe alloy consisted essentially of iron, while the vapor from the 5 Al-23 Cr-Fe alloy consisted largely of Cr and Fe. We conclude that Al does not vaporize effectively from a 5 Al-Fe alloy. However, Cr and Fe do vaporize from an oxide free surface of a 5 Al-23 Cr-Fe alloy. Other studies (6, 22) show that oxidation of an Fe-Cr-Al alloy reduces the evaporation losses at 1050°C. Since Cr_2O_3 is not an important component in the oxide scale at 1050°C, one must conclude that α-Al_2O_3 acts as a barrier to the diffusion of chromium.

Table VII shows manganese to have a high vapor pressure. In these alloys manganese is probably com-

bined with sulfur or with oxygen thus lowering its activity, and little manganese would vaporize.

Effect of Vapor Pressure in Oxidation

With the exception of oxidation resistant metals and alloy at high temperatures, the vapor pressure of the metal has no direct effect on the mechanism of oxidation. This is because breakdown of normal oxidation processes occurs by other mechanisms, such as loss of adhesion at the oxide-metal interface. The first evidence for a vapor pressure effect was found in the oxidation of chromium (23). The rapid increase in the rate of oxidation of chromium was explained as short circuiting by vaporization of normal ion transfer and diffusion processes. This occurs when the transfer of metal ions into the oxide by evaporation approaches the rate of reaction. Vapor transfer of metal can occur at surfaces other than the metal-oxide interface. In this sense the normal diffusion processes are short circuited. The present study shows a rapid increase in the rate of oxidation at 1050°C for the Fe-Cr-Al alloys. The vapor pressure of the metallic components may be important in the high-temperature oxidation of these alloys, as in the case of chromium.

The vapor pressure effect can be studied in two ways. Compare the rate of evaporation of metal atoms from a free surface with the reaction rate expressed in terms of metal atoms leaving the oxide-metal interface. Since the rate of evaporation has a higher temperature coefficient than the rate of oxidation, a sharp break in the rate of oxidation should occur at the temperature where the two rates intersect. Crystal structure studies also can be used to show the vapor pressure effect. If the volatility of a certain metal becomes important, the oxide of this metal could appear in the oxide film even though other metals form more stable oxides.

Alloy 1 having the lowest rate of oxidation in the 1-2 hr period is the best alloy for checking the vapor pressure effect. Figure 13 shows a plot of the rate of oxidation in terms of both iron and aluminum reacting and the experimental weight loss data for the 5 Al-23 Cr-Fe alloy. The rate of oxidation shows a sharp break at the temperature where the metal transfer by evaporation equals the rate of reaction.

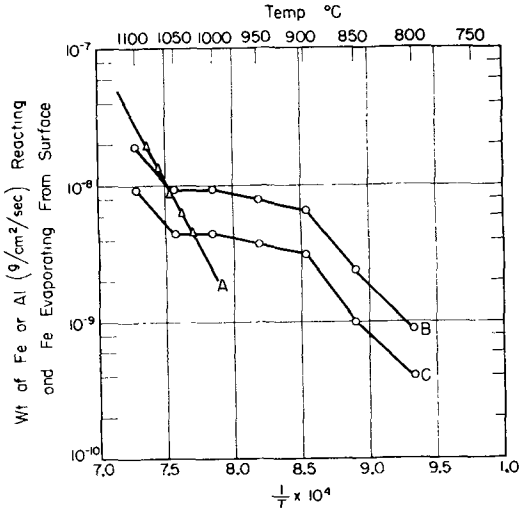

Fig. 13. Comparison weight loss 5Al-23Cr-Fe alloy (curve A) with rate of oxidation in terms of Fe (curve B) or Al (curve C), log rate vs. 1/T, alloy 1.

Table II shows the oxide scale at 1050°C to be α-Fe_2O_3, α-Al_2O_3, and a low parameter spinel (probably $FeO \cdot Al_2O_3$). Below 1050°C iron oxides were not observed. Both the rate studies and crystal structure studies show that the high-temperature rate of oxidation and crystal structure of the scale are related closely to the vapor pressure of the metals in the alloy. The α-Al_2O_3 scale limits in some manner the vapor pressure effect of chromium.

Table II shows for alloy 3, which has the lowest useful life value, the formation of MnO and a trace of Cr_2O_3. This suggests that the lower aluminum content of the alloy 3 is not limiting the formation of MnO and Cr_2O_3 in the oxide scale.

General Principles

The selection of metals for high heat resistant alloys based on iron should be made on the following principles: (*a*) alloying elements should lower the rate of oxidation; (*b*) solid phase reaction should be considered so as to give an oxide having a good crystal structure match with the metal; this property should maximize adherence of the oxide to the metal and minimize the effects of stress or strain; and (c) alloying elements should be chosen to lower the alloy vapor pressure and to limit the vapor pressure of the more volatile but still desirable elements.

Those studies show that increasing the chromium and aluminum contents in alloys 1 to 3 improves the physical properties of the oxide-metal interface as determined by the strain oxidation experiments. A smaller improvement is noted on the constant temperature oxidation rate.

Summary

Three Fe-Cr-Al alloys were studied systematically in regard to their oxidation behavior from 700° to 1100°C. Kinetic studies were made using the vacuum microbalance method. Crystal structure studies were made on the oxide film electrochemically removed from the oxidized alloy. Strain-oxidation studies were made to determine the adherence characteristics of the oxide film. The experimental results were interpreted by thermodynamic and rate analyses of the oxide-metal systems.

Kinetic studies show a unique change in rate of oxidation at 900°C. Over the range of 900°-1050°C the rate of oxidation was nearly constant. Above 1050°C the rate of oxidation again increased. The parabolic rate law could be applied with initial deviations over the complete temperature range. For the temperature range 700°-900°C a logarithmic plot of the parabolic rate law constants vs. $1/T$ gave a straight line and calculated heats of activation of 76-77 kcal/mole for the three alloys.

Crystal structure studies showed α-Al_2O_3 to be the main oxide over the temperature range. Below 950°C some Cr_2O_3 and MnO were observed. These oxides decreased in the oxide scale on passing through the transition temperature region. At 1050°C the oxide was largely α-Al_2O_3.

The crystal studies confirmed thermodynamic predictions as to the composition of the scale. Solid phase reactions of aluminum with chromium oxide were proposed to explain the shift in oxide composition at 950°C.

Strain oxidation studies showed the oxide scale on alloy 1 to be less susceptible to damage than the scale on alloys 2 and 3. These studies can be correlated with practical performance tests.

Comparison of the rate of oxidation with available vapor pressure data showed that metal transfer by vaporization was the rate-controlling factor in the oxidation of Fe-Cr-Al alloys at 1050°C and above. Design principles were proposed for high heat resistant alloys.

The Fe-Cr-Al alloys are good examples of well designed high heat resistant alloys.

Manuscript received April 23, 1958. This paper was presented before the Ottawa Meeting, Sept. 28-Oct. 2, 1958.

Any discussion of this paper will appear in a Discussion Section to be published in the December 1959 JOURNAL.

REFERENCES

1. C. Wagner, *Z. physik. Chem.*, **21B**, 25 (1933).
2. C. Wagner, "Atom Movements," p. 153, American Society for Metals (1951).
3. G. Pfefforkorn, *Naturwissenshaften*, **40**, 551 (1953); *Z. Metallk.*, **46**, 204 (1955).
4. E. A. Gulbransen, T. P. Copan, and D. van Rooyen, Westinghouse Research Report 6-94602-1-R5, Sept. 1957; Presented to AIME Chicago Meeting, November 1957.
5. E. A. Gulbransen and K. F. Andrew, ASTM Technical Publication No. 171, p. 35, February 2, 1955.
6. Private communication, Kanthal Corp., Stamford, Conn.
7. A. Hauttman, *Stahl u. Eisen*, **51**, 65 (1931).
8. E. Scheil and E. H. Schulz, *Arch. Eisenhüttenw.*, **6**, 155 (1932).
9. N. A. Ziegler, *Trans. Am. Inst. Mining Met. Engrs.*, **100**, 267 (1932).
10. A. Portevin, E. Pretet, and H. Jolivet, *Rev. met.*, **31**, 101, 186, 219 (1934).
11. H. Krainer, L. Wetternik, and E. Carius, *Arch. Eisenhüttenw.*, **22**, 103 (1951).
12. I. Sektova, *Fiz.-Khim., Anal.*, **16**, 122 (1948).
13. E. A. Gulbransen, *Trans. Electrochem. Soc.*, **81**, 187 (1942).
14. E. A. Gulbransen, *Rev. Sci. Instruments*, **15**, 201 (1944).
15. E. A. Gulbransen, "Advances in Catalysis," Vol. V, p. 119, Academic Press, Inc., New York (1953).
16. E. A. Gulbransen, R. T. Phelps, and J. W. Hickman, *Ind. Eng. Chem.*, **18**, 391 (1946).
17. J. D. H. Donnay and W. Nowacki, "Crystal Data," Memoir No. 60, The Geological Society of America, April 1, 1954, New York.
18. C. Wagner, *This Journal*, **103**, 571 (1956).
19. O. Kubaschewski and E. Evans, "Metallurgical Thermochemistry," John Wiley & Sons, Inc., New York (1956).
20. F. P. Hall and H. Insley, "Phase Diagrams for Ceramists," Am. Ceram. Soc., Columbus, Ohio, (1947).
21. D. R. Stull and G. C. Sinke, "Thermodynamic Properties of the Elements," American Chemical Society, Washington, D. C. (November 1956).
22. E. A. Gulbransen and K. F. Andrew, To be published.
23. E. A. Gulbransen and K. F. Andrew, *This Journal*, **104**, 334 (1957).

Deposition of New Chromium-Iron Alloy Plate of Banded Structure

L. D. McGraw, J. A. Gurklis, and C. L. Faust

Electrochemical Engineering Division, Battelle Memorial Institute, Columbus, Ohio

and J. E. Bride

Diamond Alkali Company, Cleveland, Ohio

ABSTRACT

A new bath composition and its operating conditions are described for electrodeposition of hard, bright, chromium-iron alloy plate having banded microstructure. A precipitation mechanism is proposed to account for the microstructure of the plate. The process produces plate having almost the same physical properties as conventional hard chromium from a bath composition not based on chromic acid. The plating rate and cathode current efficiency for the alloy are higher than for plating chromium from a conventional bath.

A high-speed chromium-iron-alloy plating process was developed in these laboratories (1). The bath is essentially a chromic- and ferric-alum solution with additions of ammonium sulfate and other salts. In the course of the development program, it was observed that bright chromium-iron-alloy plate having banded microstructure was obtained when hypophosphite was used as a bath additive.

The opportunity to study this particular alloy plate arose when a program for the Navy Department (2) had as its objective the development of hard, wear-resistant plate from a high-efficiency bath. Since plates of laminar (banded) structure resemble conventional hard chromium, they were developed with the ultimate objective of improved abrasion resistance.

Preliminary experiments.—Preliminary efforts were successful in depositing bright chromium-iron alloy having banded microstructure onto 2.5-cm (1-in.)-diameter circular areas of steel cathodes

shielded by a 0.8-cm (5/16-in)-deep plastic frame under the following conditions:

Bath composition (3)

700 g/l chrome alum [$Cr(NH_4)(SO_4)_2 \cdot 12H_2O$] (76 g/l chromium)
13.6 g/l ferrous ammonium sulfate [$Fe(NH_4)_2(SO_4)_2 \cdot 6H_2O$]
25 g/l magnesium sulfate ($MgSO_4 \cdot 7H_2O$)
100 g/l ammonium sulfate [$(NH_4)_2SO_4$]
0.2 g/l sodium dihydrogen phosphate ($NaH_2PO_4 \cdot H_2O$)

Operating conditions

Temperature	60°C (140°F)
*p*H	1.5
Cathode current density	54 amp/dm² (500 amp/ft²)

Lead or chromium-iron alloy anodes were satisfactory for oxidizing and maintaining iron in the ferric state, a condition necessary for the best plating results. The initial oxidation of the iron to the ferric state could also be carried out by the addition of chromic acid to the bath. Apparently phosphate, an oxidation product of hypophosphite, could have been responsible for similar bright, banded plate obtained in earlier work.

Mechanism for the Deposition of Chromium-Iron Alloy Having Banded Structure

The apparent mechanism responsible for laminar structure of deposits taken from a chromic-ferric sulfate bath containing small amounts of phosphate is that grain refinement and banding result from precipitation of ferric phosphate in the cathode film during electrodeposition. Since confirmation of this mechanism would make development of the bath an easier problem, experiments were designed for this purpose. If the mechanism were correct, silicate, arsenate, and vanadate additions to the bath should have an effect similar to phosphate additions. All these anions form insoluble compounds with ferric iron. Using the conditions for plating with the phosphate additive, the new anions were substituted for phosphate in amounts varying from 0.1 to 1.2 g/l. The results showed the new anions to have the same effect as phosphate with the exception that larger amounts were required (1.2 g/l as opposed to 0.2 g/l).

Actually, the new anions were an improvement over the phosphate additive, because the concentrations required for producing deposits with banded microstructure were not so critical. Slight excess amounts of phosphate caused burning, but this was not true with the other anions. High current density [43-65 amp/dm² (400-600 amp/ft²)] was required to obtain the desired effects with phosphate and the other anion additives mentioned. The mechanism was supported further by the knowledge that ferric salts of phosphoric, silicic, arsenic, and vanadic acids are insoluble in solutions having *p*H near 2.7, and that cathode film *p*H values are higher than bath *p*H which varied from 0.8 to 2.0 in the tests.

Development of Bath for Deposition of Plate Having Banded Structure

The precipitation mechanism developed in the preceding section suggested the changes necessary to develop a practical bath composition. A buffer was required to equalize the *p*H over the entire face of the cathode so that masking of the cathodes with thick frames would not be necessary.

Many amino acids, such as aminoacetic acid (glycine), have isoelectric points in the *p*H range 2.0 to 2.2 and good buffering capacity in the *p*H range 1 to 3. They should permit deposition of laminar plate uniformly over broad flat cathodes by maintaining uniformly high *p*H in the cathode film. Glycine additions, ranging in concentration from 0.5 to 3.0 g/l, were made to the following bath:

450 g/l basic chromic sulfate (76 g/l chromium)[1]
13.5 g/l ferrous ammonium sulfate [$Fe(NH_4)_2(SO_4)_2 \cdot 6H_2O$] (or 16.6 g/l ferric ammonium sulfate [$NH_4Fe(SO_4)_2 \cdot 12H_2O$])
20 g/l magnesium sulfate ($MgSO_4 \cdot 7H_2O$)
100 g/l ammonium sulfate [$(NH_4)_2SO_4$]
1 g/l silicon dioxide (added as water glass, 29.5% SiO_2)

with the result that uniform deposition of laminar chromium-iron-alloy plate could be achieved on flat rectangular steel panels without any form of shielding under the following conditions:

Temperature	54°C (130°F)
*p*H	0.8-1.3
Cathode current density	21-28 amp/dm² (200-260 amp/ft²)
Agitation (work bar)	None to 50 cpm with 3.8-cm (1.5-in.) stroke
Cathodes	Steel-5 x 15 cm (2 x 6 in.) or 3.8 x 10 cm (1.5 x 4 in.)
Glycine concentration (g/l)	0.5 to 3.0
Oxidation state	Iron all ferric with little or no Cr^{+6}.

[1] Technical grade purchased from Mutual Chemical Company of America.

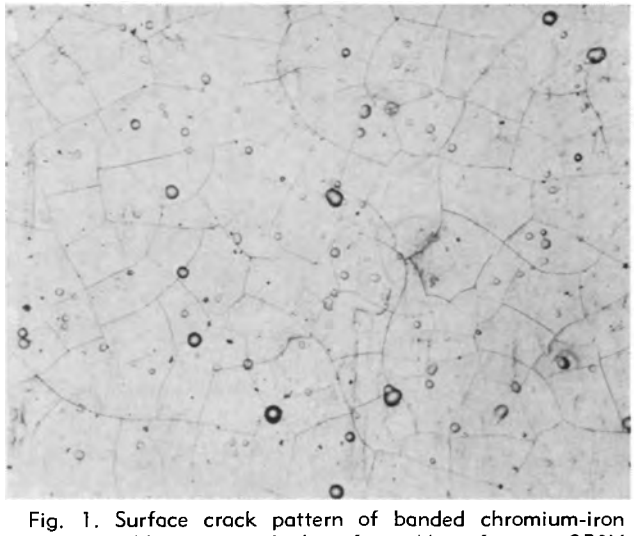

Fig. 1. Surface crack pattern of banded chromium-iron alloy plate. Note: untouched surface. Magnification 250X before reduction for publication.

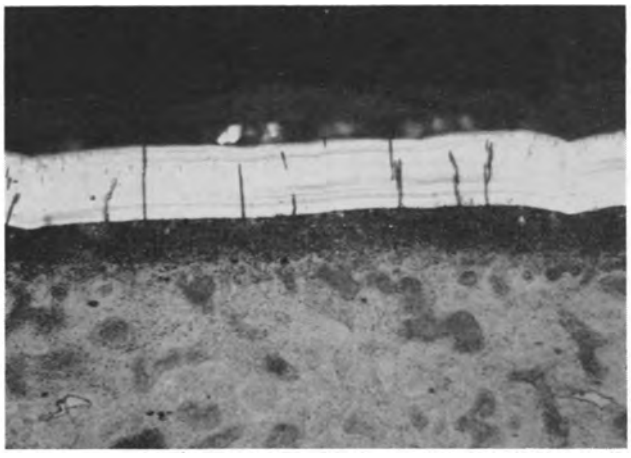

Fig. 2 Polished and etched cross section of banded chromium-iron alloy plate. Note: electrolytically etched in dilute oxalic acid. Magnification 500X before reduction for publication.

Data derived from the operation of this bath include the metallographical examination of fourteen deposits to verify the relation between brightness of the deposits and banded microstructure. Uniformly bright plate and complete lack of columnar structure were observed for operating conditions and bath composition cited above. The function of bath constituents was indicated by the following observations:

1. Only mat columnar plate could be obtained if the *p*H was so low as to solubilize ferric silicate or if the concentration of ferric iron was too low to cause precipitation of ferric silicate at *p*H 3.
2. Without a buffer (glycine) to equalize pH over the cathode surface, plastic shielding frames and current densities on the order of 53 to 63 amp/dm^2 (500 to 600 amp/ft^2) were required for production of uniformly bright and banded plate.

Bath composition was fixed to obtain plate of desired physical characteristics described below. Hence there could be little variation in plate composition from the neighborhood of 85Cr-15Fe. Bath composition was followed by chemical analysis. Iron was maintained by addition of ferrous sulfate or by occasional shifting between soluble Cr-Fe alloy anodes and platinum anodes. The oxidation state of iron was maintained with chromic acid. A few grams per liter of excess chromic acid had no observable effect on the characteristics of the plate. It is noteworthy that no hexavalent chromium had to be present to obtain the alloy plate which resembles hard chromium so long as most of the iron was in the ferric condition.

Bath life and glycine stability were not studied. However, baths were operated 3-4 hr daily for several weeks without any apparent deterioration or need for addition of more glycine.

The procedure according to which the bath was prepared was critical. Solutions of all chromic salts hydrolyze slowly when the temperature is raised. An equilibrium is attained more rapidly when they are cooled from an elevated temperature (over 80°C) to the desired temperature. For this reason a detailed description for bath formulation is given.

Bath formulation.—Basic chromic sulfate is added gradually (with constant stirring) to water at 82°C (180°F). The initial volume of water is about 60% of the final volume of the bath. When all but a small residue of insoluble matter is dissolved, the ammonium sulfate, ferrous ammonium sulfate, and magnesium sulfate are added with continued stirring. Next, the water glass solution diluted with twice its weight of water is added with vigorous stirring to avoid precipitation of silicic acid.[2]

The solution, still at 82°C, is treated with 0.3 g/l activated carbon,[3] usually added as a 4% suspension in water to facilitate wetting. The bath is then aged 4 hr at 82°C and 16 hr or longer at near plating temperature. Next, it is filtered at plating temperature, and the *p*H is adjusted to 1.3 (measured at 55°C)[4] with sulfuric acid. The glycine is then added (preferably 1 g/l), and enough chromic acid is added to give a positive external test for hexavalent chromium using S-diphenyl-carbazide indicator.

Typical plate containing 85Cr-15Fe is obtained immediately at 55°C, 21 amp/dm^2 (200 amp/ft^2) cathode and anode current density, using soluble chromium-iron alloy anodes (85Cr-15Fe). The cathode current efficiency is about 35% based on trivalent chromium. Compared with a conventional hexavalent bath with a cathode current efficiency of about 15% (basis Cr^{+6}) the trivalent bath with a cathode current efficiency of 35% (basis Cr^{+3}) yields about 4.6 times more deposit per unit of electrical current. Such an improvement in electrical efficiency has long been sought in chromium plating. The plating rate is 0.0076 cm/hr (0.003 in./hr) at 230 amp/ft^2 cathode current density.

Properties of the Plate

The plate, containing about 85% chromium and 15% iron, has a banded microstructure with a crack pattern (Fig. 1 and 2) similar to that of conventional chromium plate. The as-plated hardness of the plate is 1000 to 1025 Knoop (0.5 kg load) which is about the same as for conventional hard chromium plate. Thin plates up to at least 0.0025 cm (0.001 in.) have the appearance of decorative chromium plate. Thick deposits are still bright, but hazy, because of micronodules (see photomicrograph of untouched surface, Fig. 1.) Plates as thick as 0.025 cm (0.010 in.) were mat.

The rate of wear on the Taber Abraser,[5] after a short period of initial wear at 0.65 mg per thousand cycles, is 0.00 to 0.03 mg per thousand cycles. The wear for conventional hard chromium by the same method was 0.00 to 0.01 mg per thousand cycles. The as-plated stress[6] in the deposit is tensile and amounts to 5,000 kg/cm^2 (28,000 psi). This might be termed

[2] The solubility of silica as $Si(OH)_4$ is *p*H independent and is about 0.01% at 25°C and 0.02% at 57°C (4).

[3] Activated carbon, Grade S-51, Darco Department, Atlas Powder Company, New York, New York, was used throughout this work.

[4] The *p*H was always measured with a glass electrode standardized at room temperature.

[5] Research Model E-4010, Taber Instrument Corporation, North Tonawanda, New York.

[6] The stress measurements were made with a Brenner-Senderoff Contractometer, Champion Manufacturing Co., New York, N. Y.

residual stress, since stress had been relieved somewhat by cracking.

The frequency of the cracks in the channel-type crack pattern does not appear to vary significantly with bath pH between 1.0 and 1.3, nor with glycine content between 0.5 and 1.5 g/l. Crack counts indicate 250-340 cracks per linear cm (640 to 870 cracks per linear inch) or an average plateau diameter of about 0.0038 cm (0.0015 in.).

Conclusions

The results of this research show that a new chromium alloy electroplate containing a minor amount of iron and otherwise having physical properties close to those of conventional hard chromium (*a*) can be obtained from a bath composition involving little or no chromic acid; (*b*) derives its characteristic banded microstructure from a precipitation mechanism; (*c*) can be deposited at a rate of 0.0076 cm/hr (0.003 in./hr) at a cathode current efficiency of near 35% based on trivalent chromium; and (*d*) can be used as a hard, bright decorative plate. Further study of this interesting bath is required to obtain practical information relative to bath life and to establish a system of soluble and insoluble anodes to maintain bath composition.

Acknowledgment

The authors wish to acknowledge the sponsorship of the Navy Department, Bureau of Aeronautics, which made the investigation possible and to express their appreciation to the Navy Department for permission to publish portions of the work conducted under the contract cited in the introduction.

Manuscript received Aug. 29, 1958.

Any discussion of this paper will appear in a Discussion Section to be published in the December 1959 JOURNAL.

REFERENCES

1. C. A. Snavely, C. L. Faust, and J. E. Bride, U. S. Pat. 2,693,444 Nov. 2, 1954.
2. Navy Department, Bureau of Aeronautics, U. S. Government Contract NOa(s)-51-713-C (Aer-Ct-43), dated March 28, 1951. See also, L. D. McGraw, "Electrodeposition of New Chromium and Chromium-Alloy Plate," PB 111911, Office of Technical Services, Washington, D. C.
3. See ref. (1).
4. G. B. Alexander, W. M. Heston, and R. K. Iler, *J. Phys. Chem.*, **58**, 453 (1954).

Electroplating on Certain Transition Metals

(Groups IV, V, VI)

E. B. Saubestre[1]

Central Research Laboratories, Sylvania Electric Products Inc., Bayside, N. Y.

ABSTRACT

It has been found that transition metals of groups IV, V, and VI can be plated adherently in the as-plated condition by being subjected first to a cathodic treatment which probably covers the surface with a hydride. By this technique, it is possible to eliminate etching prior to plating, permitting better control of dimensional tolerances. If the part is to be heated after plating, the procedure is to deposit a thin film of nickel or iron after the cathodic treatment, vacuum fire, then plate as desired. The method was used to produce adherent coatings of Ni and Cu on Ti, Zr, Nb, Ta, Mo, and W.

A further study was made of Nb and Nb-Ti alloys, in which an anodizing procedure was developed which permits subsequent electroplating of Fe or Ni without requiring etching (thereby permitting close control of dimensions) or annealing treatments (useful where delicate assemblies are involved).

In the past decade, the transition metals of groups IV to VI have become of increasing commercial importance. Accordingly, there has arisen a demand for electrodeposition on these metals. The main reasons for such electrodeposition are: (*a*) to improve corrosion or high-temperature resistance, and (*b*) to permit ready joining by soldering, brazing, or welding.

Conventional methods.—The usual method of plating other metals on these elements has involved the following steps: "activation" by etching in a suitable acid, deposition of a thin film of nickel or iron; removal of adsorbed gases; and finally heat treating to improve adhesion of the electrodeposited coating to the substrate. Table I gives recent literature references on the subject; in all cases, a heat treatment is applied after subsequent electrodeposition.

The effect of the etch commonly employed in the methods in Table I is to remove scale, oxide films, and the like, remove skins formed by fabricating techniques, and present a fresh, clean surface for plating. In the case of immersion treatments, the oxidizing agent is hydrogen ion, so that the surfaces also tend to become coated with metal hydride or occluded hydrogen during etching. This is especially true of the group V metals, which are especially prone to hydride formation. For this reason, it is worthy of note that such preplating treatments as cathodic cleaning, commonly employed in preparing many conventional metals for electroplating, have

[1] Present address: Enthone, Inc., New Haven, Conn.

Table I.

Group	Metal	Etch	Method of application	Plating	Ref.
IV	Ti	$HF-CH_3COOH$	a.c.	Cr	1
		$HF-CH_3COOH$	Cathodic or anodic	Cu	1
		$SnCl_2$	Immersion	Displacement Cu	2
		HF-HOAc	Immersion; then, a.c.	Cr	37
		$HF-HNO_3-H_2SO_4-FeSO_4-Al_2(SO_4)_3$	Cathodic; anodic; cathodic	*	38
		$HF-HBF_4$	Immersion	Ag strike in BF_4^- soln.	39
		$HF-HCl$; $HF-HNO_3$	Immersion	Zn (fluoride-ethylene glycol)	3
		$H_3PO_4-H_2SO_4$	Anodic	Zn (fluoride-ethylene glycol)	3
		$AlCl_3$ in ether	Anodic	Al (ether-lithium aluminum hydride)	4
		HF-ethylene glycol	Anodic	Cu	5
		$HF-CuSO_4$	Immersion	Cr	6
		$HF-Na_2Cr_2O_7$	Immersion	Cr	6
	Zr	$HF-NH_4F$	Immersion	Immersion Zn or Ni plating	7, 8
		$HF-NH_4F$	Immersion	Displacement In	9
	Hf	Little published data. Zr methods should work.			
V	V	$Na_2CO_3-NaHCO_3$	Anodic	*	10
	Nb	HF	a.c.	Ni; Fe	11, 7
	Ta	HF-HCl	Anodic	*	12
		HF-HCl	Anodic	*	13
		$HF-H_2SO_4$	Anodic	*	14
		NH_4F-formamide	Anodic	*	15
VI	Mo	$KOH-K_3Fe(CN)_6$	Immersion	Cr (after anodic etch in Cr plating solution)	16, 7
		HCl	Immersion	Cr (after anodic etch in Cr plating solution)	17
		Cu-Zn plating solution	Cathodic	Ni; Fe (after heating to 1000°C to volatilize Zn)	18
		Au strike	Cathodic	Au (after heating to 1400°C)	19
		HF	Immersion	Cr (after anodic etch in Cr plating solution)	20
		H_2SO_4	Anodic	Cr strike, then Ni strike and plate	21
	W	$KOH-K_3Fe(CN)_6$	Immersion	Cr (after anodic etch in Cr plating solution)	7
		Cu-Zn plating solution	Cathodic	Ni; Fe (after heating to 1000°C to volatilize Zn)	18
		Au strike	Cathodic	Au (after heating to 1400°C)	19
		$HF-HNO_3$	Immersion	*	22
		H_2O_2-oxalic	Immersion	*	23
		$H_3PO_4-HClO_4$	Immersion	*	24
		$K_3Fe(CN)_6$	Immersion	*	25

* These references are not directly concerned with plating, but the etches used should be satisfactory prior to plating.

not been mentioned in connection with the substrates of interest in this paper. An exception noted in the tabulation above is the use of strike solutions, which are in effect combined cathodic cleaning and plating solutions.

The principal emphasis found in the literature when electrolytic preplating treatments are employed, is upon anodic treatments, which presumably minimize hydrogen occlusion, or hydride formation. Such treatments, however, are not desirable where accurate dimensional tolerances are involved.

In the course of commercially plating on some of these substrates, a very brief laboratory review was made of typical procedures contained in the table above. In general, it was found that both immersion etch and anodic etch procedures gave reasonably satisfactory results. However, during the course of this limited investigation, intermittent troubles were encountered, usually due to peeling of the as-deposited coating, and also blistering of the coating during the baking step. It was at first thought that these occasional difficulties were due to excessive occlusion of gases, such as hydrogen, on the surface of the substrate prior to plating. Therefore, a preliminary vacuum bake was employed prior to plating. Plating adhesion was found to deteriorate markedly as a result of this operation. This then suggested the possibility that good adhesion was favored by occluded gases, and that perhaps an important function of the preplating etch was to provide such a surface. If true, then it should be possible to substitute for the conventional etch a cathodic treatment in an electrolyte which does not chemically attack the substrate.

It is recognized that impurities often greatly affect the type of results obtained in studies of this type. The substrate used (except for Nb and Nb-Ti alloys) were obtained from A. D. Mackay, and analyzed better than 99.9%; however, no further analyses were made of the impurity contents. The nickel plating solution employed contained the following impurities: Mn, 0.48 g/l; Co, 0.46 g/l; Mg, 0.19 g/l; Fe, 0.028 g/l; Al, 0.018 g/l; Zn, 0.014 g/l; Cu, 0.007 g/l; others, 0.005 g/l. No analysis was made of the nickel

electrodeposits on the substrates discussed in this paper. However, nickel deposits on steel made from the same bath as above indicated an impurity analysis consistent with the above figures.

The reagents used for cathodic treatment were A.C.S. reagent grade.

"Hydride" Plating Procedure

It was indeed found that deliberate evolution of hydrogen on the substrate surface prior to plating markedly improved adhesion of the electrodeposit in the as-plated condition. The essential step in the preplating treatment is cathodic treatment of the metal so as to cause adsorption of hydrogen (with probable formation of surface "hydrides"). This cathodic treatment may be carried out in any electrolyte which does not contain ions of platable metals. Conveniently, dilute mineral acid or alkali metal hydroxide solutions may be used. In this method, the acid etching step may be eliminated, so that no dimensional changes in the substrate occur. However, if the original surface of the substrate is unsound (scale, metallurgically unsound surface skins, etc.) an etch is needed for cleaning purposes.

An example of the procedure is:

1. Soak in alkaline cleaning solution at 180°-200°F.
2. Rinse.
3. Etch in 10% (wt) HF (see Note 1). Immersion—Ti, Zr, Hf. Anodic at 50 asf—V, Nb, Ta, Mo, W.
4. Rinse.
5. Cathodic for 5-15 sec at 10-100 asf at room temperature in a suitable electrolyte (see Note 2).
6. Rinse.
7. Nickel plate for 30 sec to 2 min: $NiSO_4 \cdot 6H_2O$, 300 g/l; $NiCl_2 \cdot 6H_2O$, 37.5 g/l; H_3BO_3, 37.5 g/l; 65°C; 5-100 asf; pH = 4.
8. Rinse.
9. Plate as desired.

Note 1. This step is optional, and is needed only if it is desired to remove the surface and prepare a new, clean one.

Note 2. Suitable electrolytes are 2% (wt) HCl, H_2SO_4, HNO_3, HF, KOH, NaOH. The anode should be inert; platinum was used in the laboratory study.

If the part which has been plated is to be subjected to high temperatures during use the hydrogen present under the deposit (in any form) will cause blistering, and lifting of the deposit may result. For such applications, the following procedure is used:

1-8. As above.
9. Dry.
10. Vacuum fire at 450°-750°C until gas ceases to be evolved.
11. Nickel strike (Wood's nickel), then plate as desired.

In either of the above procedures, iron plating may be substituted for nickel plating in step 7.

The above procedures were used to obtain adherent deposits (0.2-0.3 mils thick) of Ni and Cu on Ti, Zr, Nb, Ta, Mo, and W. It is concluded that the procedure would be satisfactory for plating any group IV, V, or transition metal. Adhesion was determined qualitatively only. In the case of wire substrates, conventional bend tests were employed. For rigid substrates, knife or chisel tests were employed. Details of such tests have been given by Ferguson (33). Adhesion was determined on 0.2-0.3 mil deposits only. Undoubtedly, lower adhesion values would be obtained with thicker coatings. However, within the range of coating thicknesses which was explored, the above method gave results equal to or better than those obtained using conventional etching treatments.

Hydrides on the Surface

The above procedure has been referred to as a "hydride" plating process. The reason for this was to distinguish this procedure from use of conventional cathodic cleaning, as for example, in the preparation of zinc base die castings for electrodeposition, or in the activation of stainless steels prior to plating. In these cases, the saturation of the surface with hydrogen, *per se*, is not the object of the treatment. For the transition metals under discussion, such cathodic treatments have apparently been largely avoided in the past, because of the known ease with which these metals form hydrides. By contrast, this method employed here deliberately saturates the surface with hydrogen.

The word hydride was put in quotation marks in the preceding section because, unfortunately, the very limited scope of the work did not permit proper examination of the cathodically treated surfaces to verify the manner in which the hydrogen was present. However, general reviews on metal hydrides (34, 35) suggest that the hydrides of interest in this paper are so-called "metallic" hydrides. Such materials possess a metallic structure and have metal alloy-like characteristics, lacking stoichiometric formulas characteristic of true electron bonding [for example, Moeller (35) cites $ZrH_{1.92}$, $TaH_{0.76}$, $VH_{0.56}$]. X-ray determinations show the lattice of the substrate metals to be distorted, suggesting that the diffusion of hydrogen is interstitial in nature, resembling formation of a metallic solid solution. The hydrogen probably is present in the atomic state, in view of the strong reducing properties of such hydrides. There is evidence that transition metals of group IV, and to a lesser extent, those of group V, form semimetallic hydrides, i.e., hydrides in which evidence of chemical bonding is stronger, and stoichiometric formulas can be obtained. A hypothesis concerning the role of such semimetallic hydrides in plating is presented below.

In any event, all the transition metals are characterized by a tendency to absorb, occlude, or chemically bond with enormous amounts of hydrogen (palladium, for example, taking up 1000 of its volume of hydrogen when treated cathodically). With reference to the procedures discussed in this paper, Hüttig (36) found that Ta takes up about 0.8 H/Ta at room temperature, this figure falling to a very low value above 700°C, indicating that a true chemical bonding is not present, at least at elevated temperatures. Transition metals of group VIII (Fe,

Co, Ni) have high permeabilities at elevated temperatures, but absorb little hydrogen reversibly at elevated temperatures. Thus, Hüttig (36) cites an absorption of 0.0004 H/Ni, Fe, or less at 700°C. Thus, in the procedures outlined in this paper, the heat treatment after plating would serve to remove hydrogen from the substrate without adversely effecting the plated deposit. When hydrides of the metals discussed above are removed by heating in a vacuum, decomposition is virtually complete at 800°C (27, 32).

No investigation was made of why it is desirable to have a surface covered with hydride prior to plating (if, indeed, such is the case). Possibly, lattice structure is of importance in this connection. Transition metals of groups V and VI are body-centered cubic. Metals of group IV may be hexagonal close packed, but hydrogen tends to stabilize the body-centered cubic form (the β-form) (26). Niobium and tantalum hydrides, at lower hydrogen levels, show a definite body-centered cubic lattice (27, 28). With higher hydrogen contents, transition metal hydrides of groups IV and V tend to form face-centered cubic or face-centered tetragonal structures (29-31). Since nickel is usually deposited in a face-centered cubic lattice, it can be seen why the presence of a hydride of similar structure would augment adhesion since electrodeposits adhere best when deposited in the same lattice form as that of the substrate.

Electroplating on Niobium and Niobium-Titanium Alloys

In the course of the laboratory investigation cited above, particular attention was paid to the problem of plating on niobium and a 75% Nb-25% Ti alloy. The procedure given above was found satisfactory. Equally satisfactory is an etch method suggested by Faust and Beach (7):

1. Etch in HF (49% wt) with a.c. at 200 asf.
2. Rinse.
3. Dip in 50% (vol) HNO_3 (s.g. 1.43) and 2% (vol) HF (49% wt) to desmut.
4. Rinse.
5. Plate with Ni or Fe.
6. Bake at 400°F for 22 hr.
7. Heat treat at 1300°F for 1 hr to insure good diffusion bonding.

However, this method is not ideal when close dimensional tolerances are to be maintained. The "hydride" plating procedure would get around this problem, but involves heat treatments just as does the method of Faust and Beach. Accordingly, further work was done to determine whether a method could be developed which would avoid both etching and annealing treatments, for cases where close dimensional tolerances must be maintained and where the nature of the assembly does not permit annealing. Following the type of procedure used successfully with metals such as aluminum, a brief investigation was made of the feasibility of anodizing the substrate as a basis for electrodeposits. Such a procedure would remove no readily detectable amount of metal, require no activation step, eliminate smutting, and obviate the need for subsequent annealing operations to remove occluded hydrogen and/or hydride.

The procedure when using the anodizing method is:

1. Soak in alkaline cleaning solution at 90°C for 2 min. Any strong ferrous electrocleaner may be employed satisfactorily.
2. Rinse.
3. Anodic in 10% (wt) NaOH solution at about 5 v at room temperature to produce yellow (straw) colored film on the substrate. (Any metal not attacked by NaOH may be used as cathode.)
4. Rinse.
5. Coat with nickel or iron: $NiCl_2 \cdot 6H_2O$, 220 g/l; HCl (sp. gr. 1.18), 125 ml/l; 25°C; 30 asf.

When visibly covered with nickel, rinse and plate: $NiSO_4 \cdot 6H_2O$, 300 g/l; $NiCl_2 \cdot 6H_2O$, 37.5 g/l; H_3BO_3, 37.5 g/l; 65°C; 5-10 asf; pH = 4.

Or, if iron is desired: $FeSO_4 \cdot 7H_2O$, 300 g/l; $FeCl_2 \cdot 4H_2O$, 40 g/l; $(NH_4)_2SO_4$, 15 g/l; 60°C; 10-20 asf; pH = 4.

6. Rinse.
7. Dry.
8. Heat to red heat in air, or in vacuum for about 2 min.

In the anodizing treatment, the color of the anodized film is critical, the other conditions are not. For example, the NaOH may be as dilute as desired, consistent with rendering the solution conductive. It may be as concentrated as desired, up to the limit of solubility. Temperature of the solution may lie anywhere between freezing and boiling. Formation of an improper film may be detected readily by visual means, by observing the color, as follows: (a) colorless—too thin, (b) yellowish-brown—slightly too thick, and (c) blue or purple—much too thick.

In general, increased film thickness is favored by lower temperatures, higher solute concentration, and higher voltage. Therefore, based on the color of film obtained, suitable adjustment of temperature, concentration, and voltage may be made. The NaOH may be replaced by other alkali metal hydroxides, alkaline salts such as alkali metal phosphates, carbonates, and silicates, and by proprietary alkaline cleaning solutions, particularly those designed for cleaning ferrous parts.

It is possible to combine the cleaning and anodizing steps by utilizing PR in the cleaning step:

1. PR treatment in a strong alkaline electrocleaning solution at 90°C at about 5 v, with a cycle of 8 sec anodic and 4 sec cathodic, with treatment time of 2 min.
2. As in steps 4-8 above.

No metallographic cross sections were prepared, but careful stripping indicated that the anodized coating remains on the Nb or Nb-Ti after electroplating. This anodizing procedure has been used to electrodeposit Ni and Fe on Nb and on an alloy of 75% Nb and 25% Ti. Heating the deposit to red heat did not cause blistering or peeling of the deposit, and adhesion remained good, (as determined qualitatively) in spite of the absence of a baking step. Thus, the anodizing method has the advantage over the acid etching and cathodic treatment methods of not requiring an annealing step, and has the advantage over the acid etching method of not attacking the substrate appreciably.

Manuscript received June 16, 1958. This paper was prepared for delivery before the Ottawa Meeting, Sept. 28-Oct. 2, 1958.

Any discussion of this paper will appear in a Discussion Section to be published in the December 1959 JOURNAL.

REFERENCES

1. C. L. Stanley and A. Brenner, *Proc. Am. Electroplaters' Soc.*, **43**, 123 (1956).
2. F. Beuckman and W. Tucker, U. S. Pat. 2,801,213 (1957).
3. M. Richaud, *Corrosion*, **4**, 400 (1956); *Electroplating and Metal Finishing*, **9**, 303 (1956).
4. D. E. Couch and A. Brenner, *This Journal*, **99**, 234 (1952).
5. W. H. Colner, M. Feinleib, and J. N. Reding, *Ibid.*, **100**, 485 (1953).
6. L. Missel, *Proc. Am. Electroplaters' Soc.*, **43**, 17 (1956); *Metal Finishing*, **55**, No. 9, 46 (1957); U. S. Pat., 2,829,091 (1958).
7. C. L. Faust and J. G. Beach, *Plating*, **43**, 1134 (1956).
8. W. C. Schickner, J. G. Beach, and C. L. Faust, *This Journal*, **100**, 289 (1953).
9. BMI 809, 15 pp. (1953).*
10. C. M. Brown, U. S. Pat. 2,803,596 (1957).
11. J. G. Beach and C. L. Faust, BMI 1004 (1954).*
12. G. J. Kahan, U. S. Pat. 2,775,553 (1956).
13. J. F. Gall and H. C. Miller, U. S. Pat. 2,481,306 (1949).
14. J. F. Gall and H. C. Miller, U. S. Pat. 2.466,095, (1949).
15. A. L. Jenny, U. S. Pat., 2,742,416 (1956).
16. L. E. Vaaler, C. A. Snavely, and C. L. Faust, BMI 813 (1953).*
17. C. Levy, *Proc. Am. Electroplaters' Soc.*, **43**, 219 (1956).
18. S. S. Brenner, U. S. Pat. 2,805,192 (1957).
19. A. G. Russell, U. S. Pat., 2,816,066 (1957).
20. R. J. Runck, *This Journal*, **104**, 74 (1957).
21. A. Korbelak, *Plating*, **40**, 1126 (1953).
22. D. Robbins, *Metallurgia*, **55**, 257 (1957).
23. S. I. Gusev and U. I. Kumov, *Zhur. Anal. Khim.*, **3**, 373 (1948).
24. W. R. Schoeller and A. R. Powell, "Analysis of Minerals and Ores of the Rarer Elements," p. 207, Chas. Griffin and Co., London (1940).
25. G. W. Keilholtz and M. J. Bergin, U. S. Pat. 2,566,615 (1951).
26. D. P. Smith, "Hydrogen in Metals," Chicago Univ. Press, Chicago (1948).
27. Ya. S. Umanskii, *Zhur. Fiz. Khim.*, **14**, 332 (1940).
28. F. H. Horn and W. T. Zeigler, *J. Am. Chem. Soc.*, **69**, 2762 (1947).
29. J. Fitzwilliam, A. R. Kaufman, and C. F. Squire, *J. Chem. Phys.*, **9**, 678 (1941).
30. G. Hagg, *Z. physik. Chem.*, **11B**, 433 (1930).
31. E. A. Gulbransen and K. F. Andrew, *This Journal*, **96**, 364 (1949).
32. W. G. Guldner and L. A. Wooten, *Trans. Electrochem. Soc.*, **93**, 223 (1948).
33. A. L. Furguson, AES Research Reprints, Serial 1 and 2 (1946).
34. D. T. Hurd, "An Introduction to the Chemistry of the Hydrides," John Wiley & Sons, New York (1952).
35. T. Moeller, "Inorganic Chemistry," 403-416, John Wiley & Sons, New York (1952).
36. G. Hüttig, *Z. angew. Chem.*, **39**, 67 (1926).
37. C. L. Stanley and A. Brenner, *Proc. Am. Electroplaters' Soc.*, **43**, 123 (1956).
38. J. J. Dailey, *Aviation Week*, **66**, 79 (May 13, 1957).
39. G. W. Slomin and M. P. Christensen, U. S. Pat., 2,798,843 (1957).

* These reports are available through OTS, Dept. of Commerce, Washington 25, D. C.

A Radioisotopic Study of Leveling in Bright Nickel Electroplating Baths

Seward E. Beacom and Bernard J. Riley

Research Laboratories, General Motors Corporation, Detroit, Michigan

ABSTRACT

A radioisotope-containing addition agent has been synthesized and used as a component in a bright and leveling nickel bath. Investigation by autoradiography and counting techniques shows that this agent is deposited preferentially at the high points of an irregular surface, thereby substantiating a part of leveling theory. The radioactive addition agent also is used in an attempt to understand better the mechanism of formation of laminations in this type of nickel deposit.

In the sequence of events which leads to the production of brilliant, chromium plated parts, the chromium must be deposited on a bright and smooth nickel surface. Such a surface may be produced by buffing a matte or a semi-bright nickel deposit. As an alternative, it is possible to deposit directly, from baths containing organic addition agents, a nickel plate which is bright and which also tends to fill in the micro-irregularities of a surface to make it smooth. Any process which eliminates buffing operations is desirable.

The recognition that certain plating solutions can deposit more than the expected amount of metal in the small recesses or scratches in the basis metal to produce a smoother surface was reported by Meyer (1) in 1940 and also recognized in the patent literature, prior to the noteworthy contribution of Gardam (1a) in 1947. Although this phenomenon subsequently has been known by a variety of terms, such as "smoothing action" and "hiding power," here it is called "leveling." Leveling has been defined by Thomas (2) as the ability of an electroplating solution to produce deposits relatively thicker in small recesses and relatively thinner on small protrusions with an ultimate decrease in the depth or height of the small surface irregularities. If an irregular surface is considered to be a series of peaks and recesses, then any such action which deposits

more metal in a recess than on a peak contradicts normal plating expectancy. In normal plating, more metal would be deposited on the high current density areas which are the high points, or peaks, of an irregular surface. Thus, in addition to its practical significance, the phenomenon of leveling poses a problem which has enlisted the attention of many investigators, and which has led directly to the study reported here. For a comprehensive review of the whole problem of leveling, the report of Leffler and Leidheiser (3) is most informative.

There has been much speculation concerning the mechanism by which the phenomenon of leveling may occur in the electrodeposition of bright nickel. The situation is complicated by lack of agreement among investigators as to the effect on leveling of various plating conditions, including current density, temperature, agitation, and addition agent concentration (2, 4-7). There is, however, general agreement that an increase in polarization accompanies leveling action (4, 6-12). Some theories of the phenomenon assume that an organic addition agent which promotes leveling is adsorbed or codeposited onto the high points, or peaks, of an irregular surface (2, 4, 7-15). This adsorbed material presumably leads to localized polarization which partially inhibits the deposition of metal at the peaks and diverts current flow to recessed areas. Recent work of Watson and Edwards (7) supports this view. They show conclusively that there is increased polarization in solutions possessing leveling ability. Further, they apparently have identified the presence of addition agents in nickel deposits by a staining technique which, for example, caused a darkening on the peak areas of a deposit obtained from a bath containing thiourea. In his study of laminations, Vanderkooi (15) considered that the dark bands present in deposits contain either included addition agents or their reduction products. These observations point up the need for a technique which will show unambiguously the location of addition agents in leveling nickel deposits.

With the particular solutions used in this study, the deposits formed are laminated in structure. While it is known that leveling can be achieved in unlaminated deposits, a theory which can account at least in part for leveling must be compatible with lamination formation.

The purpose of this study is twofold: to determine if an organic agent known to promote leveling is adsorbed preferentially or codeposited on the high points of an irregular surface, and to develop radiotracer techniques suitable for determining the location, within electrodeposits, of a radioactive organic addition agent.

The work of Vanderkooi (15) has shown that the brightener system sodium allyl sulfonate (16) and N-allyl quinaldinium bromide (17) produces bright, leveling, and laminated nickel deposits. These organic addition agents were used in a Watts type nickel bath to produce the electrodeposits examined in this study. The sodium allyl sulfonate was radioactive due to the use of S-35 in its synthesis.

Experimental

Synthesis of radioactive sodium allyl sulfonate.—The microsynthesis of sodium allyl sulfonate containing the radioactive isotope S-35 is one reported by Hoekstra (18). The metathesis reaction is carried out between allyl bromide and sodium sulfite containing S-35 as the labeled atom. One-millimole amounts of each of the reactants are heated together in a closed system at 60°C for 35 hr. Excess allyl bromide is extracted by ether using a Soxhlet extractor. The product was dissolved in water to yield a solution concentration such that 1 ml contained approximately 0.003 g of radioactive sodium allyl sulfonate. A radiochemical analysis of the final product showed a recovery of about 95% of the original activity present in the sodium sulfite.

Plating procedure.—The stock nickel solution was a Watts type bath containing nickel sulfate, 300 g/l; nickel chloride, 30 g/l; boric acid, 30 g/l; and a proprietary wetting agent, 5 ml/l. The *p*H was adjusted to 3.0. Plating was carried out in a small Lucite cell, 2 in. long by 1 in. wide by 3 in. deep. A temperature of 56°-58°C was maintained by immersing the plating cell in a constant temperature water bath. The anode was electrolytic nickel, and agitation was provided by a Hull Cell agitator operating a Lucite paddle which made 110 oscillations per minute. The current density range was from 10 to 55.5 amp/ft^2, and the plating times varied from 20 to 100 min depending upon the thickness of deposit desired. Due to rapid changes in *p*H of the small volume of solution used, frequent additions of dilute sulfuric acid were made to maintain a *p*H range from 2.6 to 3.5.

Inasmuch as a surface consisting of peaks and recesses was desired, grooved cathodes were prepared from brass blocks 1.75 in. by 1 in. by 0.125 in. Grooves 0.030 in. deep, with an included angle of 90°, were cut into one face of the blocks parallel to the long edge. The cathodes had 13 peaks and 12 recesses. To obtain foils of the plated metal, it was necessary to provide a passivated surface. Therefore, the brass cathodes were plated first with a thin deposit of nickel from a sulfamate bath and then passivated by immersion for 1 min in a 0.05% potassium dichromate solution.

The organic addition agent was added to the nickel stock solution in the form of radioactive sodium allyl sulfonate (1 ml equals approximately 0.003 g). Additional nonradioactive sodium allyl sulfonate was added to bring the total concentration up to a range of from 1.5 to 2 g/l. In some of the experiments, a second organic addition agent, N-allyl quinaldinium bromide,[1] was added in sufficient amounts to produce concentrations from 2 to 6 mg/l. All of the additions and plating procedures were carried out under radiochemically safe conditions.

At the conclusion of plating, the cathode was withdrawn from the cell, rinsed with distilled water, and then a scalpel was used to remove the foil from the cathode block. The foil was scrubbed on both top and bottom to remove any adhering material, rinsed with water and with alcohol, and then dried under an infrared lamp preparatory to counting and

[1] Prepared by N. Vanderkooi, Jr., Wayne State University.

Table I. Plating conditions and results

Foil number	Plating time, min	Amp	Current density, asf	Brighter concentration, mg/ml: No. 1 active	No. 1 inactive	No. 2 inactive	Result
21	100	0.3	27.3	3	0	0.6	Foil intact, dull
25	100	0.3	27.3	6	0	0.6	Foil intact, dull
26	100	0.2	18.2	6	0	0.6	Foil intact, dull
31	100	0.2	18.2	3	198	0	Foil intact, bright, brittle
34	100	0.2	18.2	3	302	0	Foil intact, dull, brittle
36	100	0.2	18.2	3	198	0.4	Foil intact, dull, very brittle
38	100	0.2	18.2	3	198	0.5	Foil intact, bright, brittle
41	100	0.2	18.2	3	198	0.3	Foil intact, dull, brittle
51	40	0.45	41	3	150	0.2	Foil intact, semi-bright, tough
54	25	0.45	41	3	150	0.2	Foil intact, bright, tough

autoradiography. The data pertinent to the plating conditions and foils produced are presented in Table I. These results are representative of the 65 plating experiments carried out and the 55 nickel foils produced. The foils varied in thickness from 0.0005 to 0.0025 in.

To check whether or not these solutions and conditions produced leveling, portions of cathodes with two different degrees of surface irregularities were plated under conditions identical with those reported above. Duplicate specimens were plated, one in a solution containing only sodium allyl sulfonate, the other in a solution containing both sodium allyl sulfonate and N-allyl quinaldinium bromide. The plated specimens were cross-sectioned, mounted, polished, and etched in 1-1 nitric acid-acetic acid. Fig. 1 shows photomicrographs of a precision reference specimen of surface roughness (2), with a

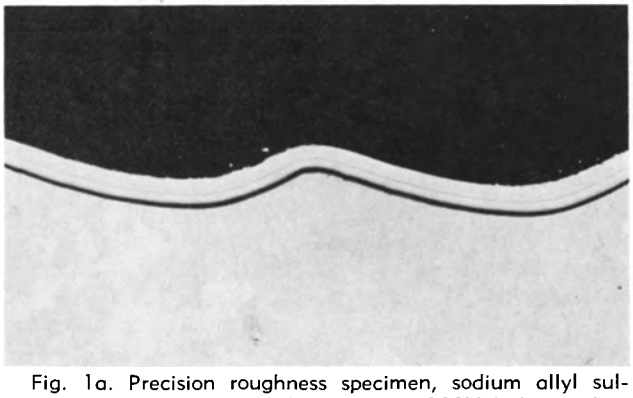

Fig. 1a. Precision roughness specimen, sodium allyl sulfonate, nitric-acetic etch. Magnification 100X before reduction for publication.

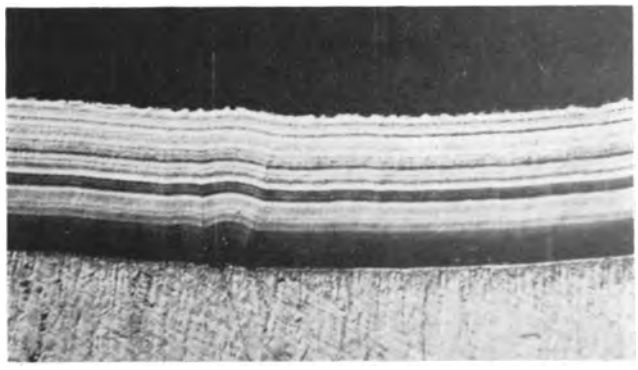

Fig. 1b. Precision roughness specimen, sodium allyl sulfonate nitric-acetic etch. Magnification 500X before reduction for publication.

peak-to-valley height of 0.002 in., plated from a solution containing sodium allyl sulfonate. The original and final roughness measurements made with a topographic microscope showed that leveling did occur. The solution containing both addition agents produced similar leveling.

Counting procedures and autoradiography.—The counting of the plated cathodes and the foils removed from these cathodes was carried out in a proportional flow counter. This procedure provided a gross count of the activity on the top and bottom of the foils but gave no information relative to the distribution of the radioactivity across the surface of the sample. It did, however, give data which were useful in computing autoradiographic exposure times. Several innovations were tried to give more quantitatively useful data which might augment the results of autoradiography. A 0.005-in. thick piece of lead foil was corrugated to duplicate the surface of the nickel foils by pressing the lead into the grooves of one of the cathodes. A single slit, 0.002 in. wide by 1 in. long, was cut in the center of one peak. This piece was then overlayed on a radioactive foil so as to expose only one peak at a time. In this manner, all of the peaks on a foil were counted individually. By turning the lead foil over, it was possible to fit the slit into a valley and count each valley individually. Continuing in this way, a profile of the peak and valley counts was made for both sides of a foil. The results of this method are shown in Table II.

The primary source of information on the distribution of the radioactivity over the surface of a foil has been autoradiography. Since the S-35 gives off a very weak beta ray, it was considered necessary to have the foil in direct contact with the film. Therefore, most of the foils were flattened mechanically, placed between two pieces of film, and then weighted to insure good contact. Past experience has shown that both chemical and pressure effects on the film can result from this method of exposure. In order to insure that everything which appeared on the final autoradiogram was due to radioactivity and not to side effects, foils containing no radioactivity were exposed under identical conditions to check possible chemical interaction and the effects of pressure. These tests showed no influence of side effects. Although several types of film were used,

Table II. Lead slit counting data

Top of Foil*			
Foil A		Foil B	
Peak	Recess	Peak	Recess
125	94	42	27
115	72	33	33
115	53	76	53
143	63	47	81
213	80	177	91
226	163	163	160
224	212	94	97
125	65	147	34
106	64	43	28
55	55	59	45
79	57	58	

Bottom of Foil*			
Foil A		Foil B	
Obverse of the peak	Obverse of the recess	Obverse of the peak	Obverse of the recess
248	143	145	58
198	103	133	77
152	133	134	84
120	112	154	65
207	102	135	100
254	113	190	128
227	163	212	126
150	146	176	101
146	129	163	82
181	158	144	80
242	129	102	

* Counting was done left to right on the top of the foil and right to left on the bottom so that the values in the columns are matched. All values are counts per minute.

the autoradiograms shown in this report were made on Eastman Kodak Type AA film.

Composite data on the counting and autoradiographic exposures are given in Table III, and representative autoradiograms of the top and bottom surfaces are shown in Fig. 2.

The reproductions of the autoradiograms shown in Fig. 2 are positives which are identical with the original autoradiograms. The dark areas indicate the regions of the foils which contain radioactivity. Since it was necessary to make an intermediate negative to achieve this reproduction, some detail has been sacrificed. All of the notches or holes cut into the foils and visible in the autoradiograms were cut so as to identify a peak area. This system of notching not only allowed identification of the individual foils by the number and position of such notches, but also precisely located the peaks and recesses on a given foil.

In addition to visual inspection, densitometric readings on a recording densitometer have been made and are recorded below each autoradiogram in Fig. 2. The apparatus employed was a L&N Linear Recording Densitometer with a General Motors Research Laboratories light source and scanning device. A slit width of 0.005 in. (0.127 mm) was used since narrower ones did not contribute to detail and led to larger instrument fluctuations.

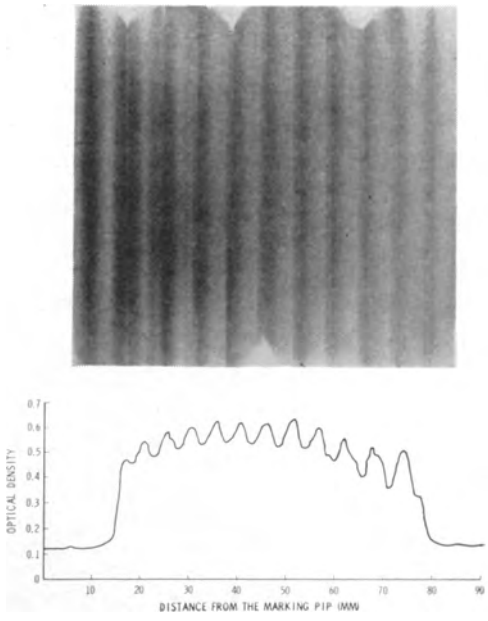

Fig. 2a. Autoradiogram and densitometer trace for the "top" of a foil containing only sodium allyl sulfonate.

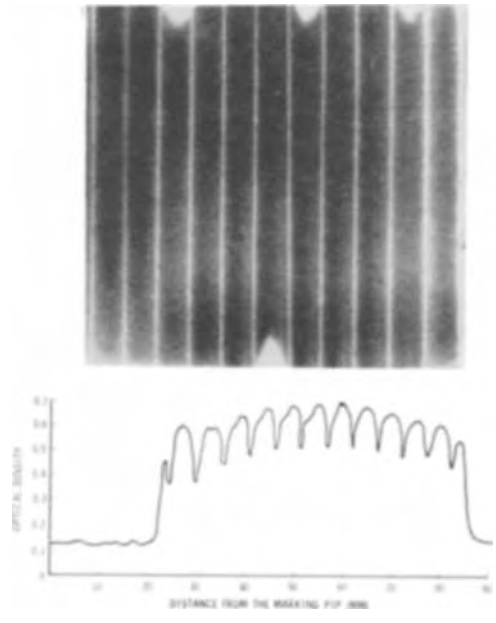

Fig. 2b. Autoradiogram and densitometer trace for the "bottom" of a foil containing only sodium allyl sulfonate.

Because this system recorded a marking pip each 0.5 mm, it was possible, by placing a mark near the edge of the autoradiogram, to measure distances from the edge accurately. The instrument was calibrated with a standard step wedge prior to use. Thus, the densities recorded are the actual densities from the exposure to radioactivity when all possible variables in the film processing are kept constant.

As was indicated previously, most of the foils were flattened mechanically to obviate the differences in distance between the peaks and recesses, and the film, during autoradiography. Some of the foils were quite brittle, thereby making this flattening process very difficult. A check was made, therefore, with a representative foil, to determine if the mechanical flattening gave any advantage,

Table III. Counting data and autoradiography

Foil No.	Counts, cpm/cm²	Type of film	Exposure time, hr	Results		
				Image	Detail	ground
21	T-12*	KK	833	Fair	Poor	Heavy
	B-10*	KK	833	Fair	Poor	Heavy
25	T-22	KK	833	Good	Fair	Heavy
	B-30	KK	833	Good	Fair	Heavy
26	T-15	KK	1268	Poor	Poor	Heavy
	B-13	KK	1268	Poor	Poor	Heavy
31	T-1830	K	22	Good	Fair	Heavy
		AA	67	Good	Good	Light
	B-2320	K	22	Good	Good	Heavy
		AA	67	Excellent	Excellent	Light
34	T-850	AA	141	Good	Fair	Light
	B-895	AA	141	Excellent	Good	Light
36	—	AA	66	Good	Good	Light
	B-2231	AA	66	Good	Good	Light
38	T-901	KK	18	Fair	Fair	Heavy
		AA	48	Good	Good	Light
		AA	146	Excellent	Excellent	Light
	B-2116	KK	18	Good	Good	Heavy
		AA	48	Good	Good	Light
		AA	67	Excellent	Excellent	Light
41	T-736	AA	67	Poor	Poor	Light
	B-1656	AA	67	Good	Fair	Light
51	T-585	AA	67	Excellent	Excellent	Light
	B-1434	AA	67	Excellent	Excellent	Light
54	T-804	AA	67	Good	Good	Light
	B-1221	AA	67	Excellent	Excellent	Light

* T—top of foil; B—bottom of foil.
Film processing conditions: temperature, 19°-20°C (67°-69°F); development time, 4-6 min; developed emulsions on both sides of film.

either for the autoradiogram or for the subsequent densitometer trace. The foil was formed and then exposed for a given length of time to produce its characteristic autoradiogram. The foil was flattened then and another autoradiogram obtained on the same type of film which was exposed for the same length of time and processed under the same conditions. Visually there were no significant differences noted on the autoradiogram, and the densitometer traces, shown in Fig. 3, indicated that there was no advantage in mechanically flattening these foils.

Results and Discussion

An examination of the autoradiograms shown in Fig. 2 reveals a greater darkening on those portions of the film which were irradiated by the peaks of the foils. In those autoradiograms labeled "top," the difference in density of the lines produced by peaks and recesses is evident, but there is also greater smearing of radioactivity than is apparent on the corresponding "bottom" autoradiograms. The concentration of activity in both instances, however, is much higher on the peaks than in the recesses. This is especially true with the "bottom" autoradiograms which show that the activity is concentrated on the obverse of the "top" peaks. This differential darkening of the films means that there is greater radioactivity emanating from the peaks than from the recesses.

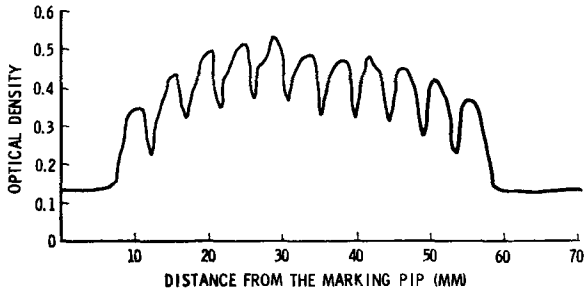

Fig. 3a. Densitometer trace of an autoradiogram made from a foil as it was removed from the brass cathode.

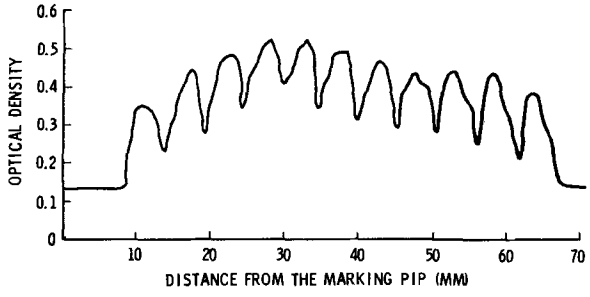

Fig. 3b. Densitometer trace of an autoradiogram made from the same foil after it was mechanically flattened.

The slit-counting data for radioactivity on the peaks and in the recesses, recorded in Table II, serve as quantitative confirmation of the results shown visually by the autoradiograms. Likewise, the densitometer traces made from the autoradiograms show quantitatively the results of distribution of radioactivity over the entire surface. The concentration of activity is highest on the peaks of the "top" autoradiograms and on the obverse of the peaks on the "bottom" autoradiograms. These traces also indicate the manner in which radioactivity increases from a minimum at the bottom of a recess to the maximum at a peak.

In explanation of these results, it is apparent that the ratio of radioactive material (sodium allyl sulfonate or a reduction product containing the S-35) to deposited metal is greater on the peaks than in the recesses. Consequently, there is less self-absorption of the radioactivity by the thinner nickel metal on the peaks and, therefore, a greater darkening of the film occurs. This explanation is consistent with the fact that in leveling less metal is deposited on the peaks and more metal is deposited in the recesses of an irregular surface. In order to initiate the leveling process, the addition agent first must be concentrated preferentially on the peaks. The autoradiograms and the slit-counting data appear to confirm the assumption of a preferential adsorption or codeposition of the addition agent on the peaks. Actually these results, as well as those recorded in the literature, show only that the agent is concentrated at the peak area. The mechanism of this concentrating action has not yet been demonstrated satisfactorily. While some investigators (7, 14) have shown that certain addition agents apparently are deposited with the metal in an unchanged or unreduced state, the work of Hoekstra (18) and Vanderkooi (15) strongly indicates, in the case of sodium allyl sulfonate, that its reduction

product, sulfide ion, is present in the electrodeposited nickel metal. The present work, with this same addition agent, shows only that the labeled S-35 atom is located in the deposit as no attempt was made to distinguish between the possible presence of the sulfonate or the sulfide.

With the type of bath employed in this study, the leveling process is accompanied by the formation of laminations (2, 4, 6, 9, 11, 15, 18, 19). Several investigators (6, 15, 18) have speculated that the "dark" bands contain sulfur, probably in the form of sulfide. It has been proposed by Vanderkooi (15) that the "dark" bands are formed by the reaction between nickel and the reduction product of the sodium allyl sulfonate, while the "light" bands are nickel metal. In order to account for the formation of these laminations, as they accompany the leveling process, it is convenient to assume that both phenomena start with a preferential adsorption of the addition agent on the peaks. It would appear, from an inspection of Fig. 1, that the formation of the laminations is some type of cyclic process wherein alternate layers of metal, and the addition agent or its reduction product, are deposited. The start of this cyclic process and the inhibition of metal deposition on the peaks can be explained by an assumption of preferential adsorption of addition agent.

Summary

A radioactive organic addition agent, sodium allyl sulfonate, containing the beta-emitting S-35 atom, has been synthesized. This addition agent has been used as a component in a bright nickel plating bath to produce leveling nickel deposits. A radiochemical technique has been developed to locate radioactivity in the deposited metal. Autoradiograms and counting data from the nickel foils produced show that the radioactive addition agent, or its reduction products, is preferentially adsorbed or codeposited on the high points of an irregular surface. On the basis of this evidence, confirmation is obtained for a theory which accounts partially for leveling action in the type of bright and leveling nickel solutions considered in this study.

Acknowledgment

The authors are grateful for the assistance provided by several members of the Research Laboratories staff who carried out analytical, photographic, and metallographic procedures.

Manuscript received Oct. 8, 1958. This paper was prepared for delivery before the Ottawa Meeting, Sept. 28-Oct. 2, 1958.

Any discussion of this paper will appear in a Discussion Section to be published in the December 1959 JOURNAL.

REFERENCES

1. W. R. Meyer, *Metal Ind.*, **38**, 212 (1940).
1a. G. E. Gardam, *J. Electrodepositors' Tech. Soc.*, **22**, 155 (1947).
2. J. D. Thomas, *Proc. Am. Electroplaters' Soc.*, **43**, 60 (1956).
3. E. B. Leffler and H. Leidheiser, Jr., AES Research Report, No. 37, Am. Electroplaters' Soc., 1957; also in *Plating*, **44**, 388 (1957).
4. D. G. Foulke, *Metal Finishing*, **54**, No. 10, 52 (1956).
5. H. Leidheiser, Jr., *Trans. Inst. Metal Finishing*, **31**, 207 (1954).
6. E. Raub and M. Wittum, *Metal Industry and Metal Finishing*, **38**, 206, 315, 429 (1940).
7. S. A. Watson and J. Edwards, *Trans. Inst. Met. Finishing*, **34**, Advance Copy No. 1 (1957).
8. H. Schmellenmeier, *Korrosion u. Metallschutz*, **21**, 9 (1945).
9. D. G. Foulke and O. Kardos, *Proc. Am. Electroplaters' Soc.*, **43**, 172 (1956).
10. G. E. Gardam, *Proc. Third Intern. Electrodeposition Conf.*, **1947**, 203.
11. E. Raub, *Plating*, **45**, 486 (1958).
12. E. Bertorelli, I. R. Bellabono, and C. R. Bordonali, *Trans. Inst. Metal Finishing*, **35**, Advance Copy No. 4 (1958).
13. A. H. DuRose, W. P. Karash, and K. S. Willson, *Proc. Am. Electroplaters' Soc.*, **37**, 193 (1950).
14. J. L. Dye and O. J. Klingenmeier, *This Journal*, **104**, 275 (1957).
15. N. Vanderkooi, Jr., Doctoral Dissertation, Wayne State University, 1958.
16. H. Brown, U. S. Pat. 2,191,813, Feb. 12, 1940; 2,523,-190, Sept. 19, 1950; 2,550,449, April 24, 1951; 2,648,628, Aug. 11, 1953.
17. H. Brown, U. S. Pat. 2,647,866, Aug. 4, 1953.
18. J. J. Hoekstra, Doctoral Dissertation, Wayne State University, 1957.
19. K. M. Gorbunova, I. V. Ivanovskaya, and N. A. Shishakov, *Zhur. Fiz. Khim.*, **25**, 981 (1951), Insdoc Translation, No. 1172.

Determination of Crystal Orientation by High Intensity Reflectograms

G. H. Schwuttke

Research Laboratories, Sylvania Electric Products, Inc., Bayside, New York

ABSTRACT

An instrument based on the light figure technique for optical orientation of Ge and Si is described which fulfills all requirements for a fast precision orientation of single crystals. The dependence of high intensity reflectograms on etching conditions is shown and standard etching specifications are given.

Reflectograms are light figures obtained by the reflection of light from an etched crystal surface. This method has been developed by mineralogists to obtain information on the location of crystallographic planes and zones in crystals. Many investigators (1) contributed to the light figure method. The method was first applied to germanium and silicon by Wynne and Goldberg (2) and Faust (3). More recently Wolff, Clark, and Wilbur (4) showed that reflectograms of Ge and Si turned out to be very clear and distinct in accordance with the low coordination number and the strong directional bonding forces of these materials.

If reflectograms are used for the orientation of monocrystals, they give excellent accuracy, competing with that achieved by the use of Laue's back reflection technique. Crystals can be oriented accurately by means of reflectograms as already shown for Ge and Si by Wolff and co-workers (4) who oriented Ge and Si single crystals using the (111) reflection within 1.5 min of arc.

The purpose of this paper is to report on a practical instrument for routine orientation work. By use of this instrument it is possible to orient a crystal in any direction and then cut along this predetermined direction without removing the crystal from its original mount. The reflectograms produced are very bright, so the instrument can be operated in a well-illuminated room. The accuracy of orientation is limited by the goniometer error to 12 min of arc for the (111), (110), and (100) reflections in Ge and Si.

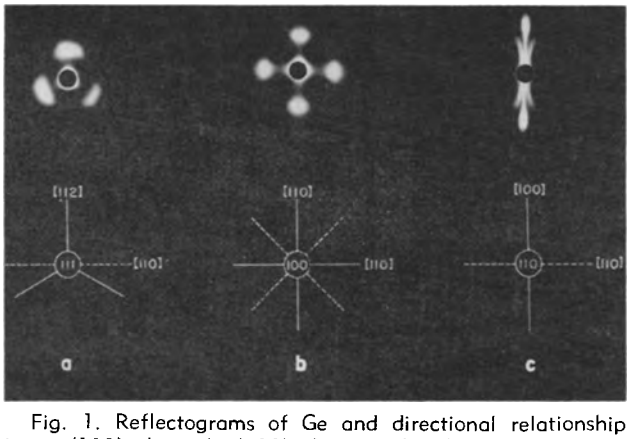

Fig. 1. Reflectograms of Ge and directional relationship in: a, (111) plane; b, (100) plane; c, (110) plane.

Instrument and Method

For optical orientation the crystal surface first is ground and then etched in a specified way. A large number of pits of microscopic size thus are created at the surface of the crystal. These pits are bounded by minute facets which are more or less perfect planes. If a beam of light is directed to such a surface, it splits into a number of components after reflection. If the reflected beam is intercepted by a screen, a light pattern or reflectogram is seen. These patterns show the symmetry of the crystal in the direction of the incident light beam. The pattern for the [111] direction thus shows threefold symmetry (Fig. 1a), the pattern for the [100] direction fourfold symmetry (Fig. 1b), and the pattern for the [110] direction twofold symmetry (Fig. 1c).

The instrument (Fig. 2) consists of an optical system A and a goniometer B for mounting the specimen. The sample can be rotated in both the vertical and horizontal plane without changing the crystal surface to screen distance. A third circle attachment C allows a complete rotation about the horizontal axis of the mounted crystal. The optical system A consists of a 30 watt concentrated arc lamp and a f/1.9 Cintar lens of 50 mm focal length. The screen is a steel plate covered with white paper. A convergent beam of light is focused on the screen, thus achieving very bright reflectograms (5). To orient an ingot, it is cemented onto attachment D as shown in Fig. 2 and D is placed in grooves on goniometer B after removing slice attachment C. The goniometer is built strongly enough to be placed on a cutting machine.

Crystal orientation with a precision of $\pm$ 0.5° of arc is easy to achieve without too much concern for the etching technique. For greater accuracy, however, the etching process is critical. The perfection and shape of the pits developed is strongly dependent on composition of etchant, temperature of etchant, and etching time. For instance, the action of the etching medium might be such that only cubic planes are exposed, thus producing in the (111) plane the well known triangular pit, formed by a three sided pyramid; in the (110) plane an indentation which is saddle shaped; and in the (100) plane a square hole with an uneven bottom. Since the surface in the lower part of these pits is uneven, the resulting reflection is diffused. If these diffused

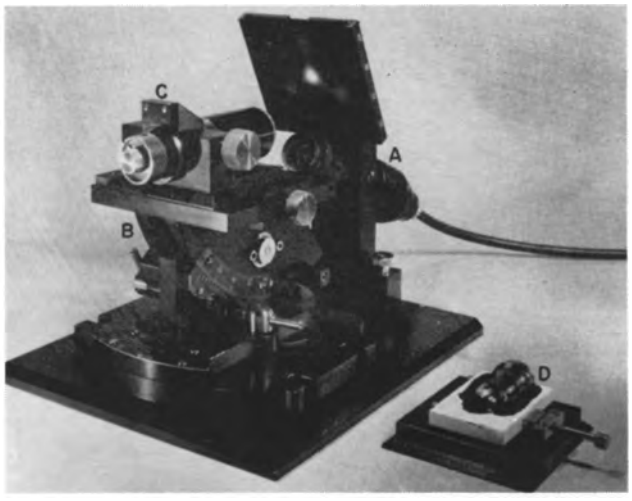

Fig. 2. Instrument for optical orientation: A, optical system; B, goniometer, transferable to cutting mochine; C, third circle attachment; D, ingot mounted for orientation and cutting.

reflections are used for orienting crystals, the accuracy will be less than that obtainable with distinct light figures which correspond to etch pits with flat bottom sections parallel to the plane to be oriented.

The following experimental procedure was adopted: the crystal surface to be checked was hand polished on a glass plate using a water slurry of 500 mesh silica and then etched. The etching solutions, the etching time, and etching temperature as used for Ge and Si are given in Table I. It should be noted that these data apply only to fresh etching solutions. Different etching solutions can be used, but of the ones tried, those listed in Table I gave the most intense reflectograms.

The side walls of the pits in all three planes show a terraced arrangement, corresponding to high index or vicinal planes. These side walls are responsible for the reflections adjacent to the distinct (111), (110), and (100) reflections and aid in identifying different reflections, but their degree of perfection is strongly dependent on etching variables (see Fig. 4 in Ref. 4).

Reflectograms can be used for orientation of single crystals and bicrystals, for tilt angle determination in bicrystals, and many other applications. Once the crystal is etched, measurements can be made in approximately 2 min, a great improvement over the Laue back reflection method.

Table I

	Reflection	Composition of etchant	Time, min	Temp, °C
Ge	(100)	1½ P. HF 2 P. H_2O_2	12	24
	(110)	4 P. H_2O	12	30
	(111)	1 P. HF 2 P. H_2O_2 4 P. H_2O	6	24
Si	(100)	50% NaOH solution	12	65
	(110)	or	12	65
	(111)	50% KOH solution	6	65

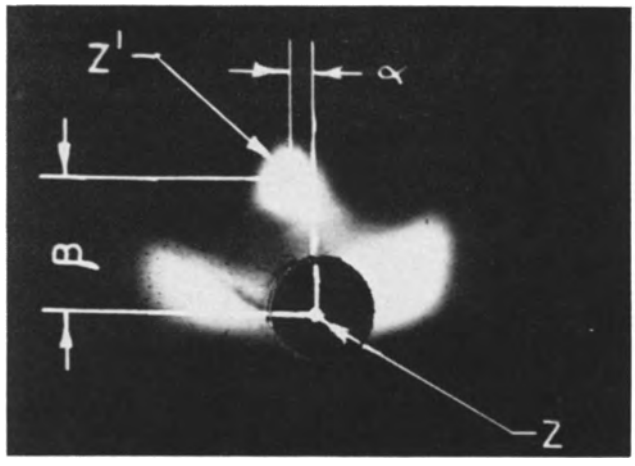

Fig. 3. Ge-(111) reflectogram of 10° misorientation

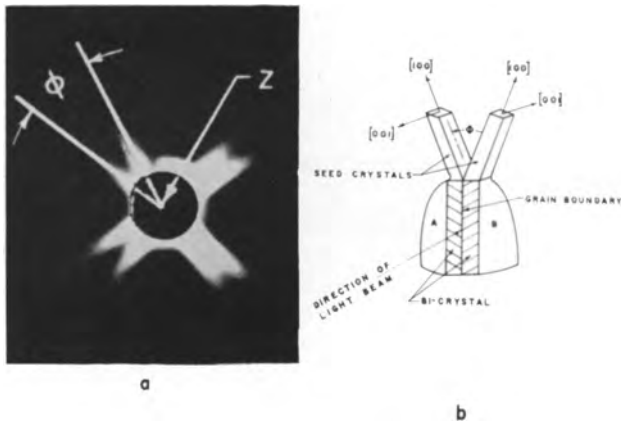

Fig. 4. (a) Tilt angle ϕ determination in a bicrystal by means of reflectograms. (b) Sketch of a bicrystal showing tilt angle ϕ between the two crystals.

Figure 3 shows a (111) reflectogram of a Ge crystal which is approximately 10° off orientation. The angle of deviation is given by α and β and is measured by turning the goniometer circles until the center reflection coincides with a predetermined point on the screen obtained for zero settings of the goniometer from a mounted mirror. The horizontal and vertical scale readings of the goniometer then give the amount of misorientation.

An example of tilt angle determination in a bicrystal is represented in Fig. 4a. This picture shows a reflectogram of a bicrystal taken in such a way that the light beam was straddling the grain boundary. The bicrystal is tilted around the [001] direction as shown schematically in Fig. 4b, therefore the reflectogram is taken in the (001) plane which is common to both crystals. Two superimposed (001) patterns show up. The tilt angle is the rotation angle ϕ which can be measured easily.

Acknowledgment

This work was initiated by Dr. H. F. Mataré. The author is also indebted to Messers E. Haffner and M. Adler who designed the instrument and to P. Riggio and A. Piorkow who built the instrument. Thanks are also due to R. Modena who prepared all the numerous samples.

Manuscript received June 2, 1958. This paper was presented before the New York Meeting, April 27-May 1, 1958.

Any discussion of this paper will appear in a Discussion Section to be published in the December 1959 JOURNAL.

REFERENCES

1. V. Goldschmidt and F. E. Wright (with exhaustive reference to the literature), N. Jb. Min. Beil-Bd., **17**, 355-390 (1903).
2. Wynne and Goldberg, *Trans. AIME*, **197**, 436 (1953).
3. J. W. Faust, IRE conference June 1953, ECS meeting in Cincinnati, May 1955, and ECS meeting in San Francisco, May 1956.
4. G. A. Wolff, J. M. Wilbur, J. C. Clark, *Z. Electrochem.*, **61**, 101 (1957).
5. G. H. Schwuttke, *Sylvania Technologist*, **XI**, 2 (1958).

Water-Stabilized Arc Tests on Nonmetallic Materials

M. Dank, R. A. Nelson, W. R. Sheridan,[1] and W. H. Sutton

Missiles and Space Vehicles Department, General Electric Company, Philadelphia, Pennsylvania

ABSTRACT

Evaluation of erosion rates on possible high-temperature resistant materials have been carried out in a water-stabilized arc. General classes of materials tested include: graphites and impregnated graphites; ceramics, principally oxides; plastic-ceramic composites; and reinforced ceramics. Results on erosion rates as a function of power dissipated in the arc and time are given, and a general ranking of these materials for high-temperature use is discussed.

Components to function at ultra-high temperatures for short periods range from liners for uncooled rocket engines, where the heat is generated internally, to leading surfaces of high-speed airplanes and missiles which are subject to large heat fluxes as the result of aerodynamic heating, to the experimental machines used in thermo-nuclear research. Temperatures may range up to thousands of degrees; the time of exposure ranges from fractions of a second to minutes.

In order to select or develop materials from which such components can be made, samples of the materials must be tested in an environment comparable to that to which they will be exposed in service. It is desirable that the test duplicate not only the high temperature, but also structural loading, thermal shock, and attack by the gaseous environment to be imposed on the component. One device which has been found useful for the rapid and economical evaluation of materials for resistance to high-temperature gas flow is the fluid-stabilized electric arc.

An arc operating in the vortex formed by a rapidly swirling body of water has developed extremely high temperatures (1). This is due to the increased current density arising from the restricted cross-sectional area of the vortex and the cooling of the outer arc regions, which forces most of the current to flow in the center. Peters (2) described an arc in which the cathode consisted of a plate with a hole from which a stream of "plasma" is issued.

The arc used in the present work is struck in a vortex of water between a ½-in. diameter graphite rod as anode, and a graphite cathode which is in the form of a disk with a 3/16-in. hole in the center. The cathode is mounted in a water-cooled horizontal metal plate, which is at ground potential, while the anode is held by a collet in a vertical position directly below the hole in the cathode. Figure 1 is a schematic diagram of the water-stabilized arc. A Lucite "swirl chamber" surrounds the anode. During operation, water is introduced tangentially into this chamber at 36 psi and forms the vortex in which the arc burns.

The power supply consists of four welding generators connected in series. It has been found desirable for stable operation to dissipate about one half the power in a ballast resistor connected in series with the arc, since when the arc is first struck the voltage and current tend to fluctuate. The sample is

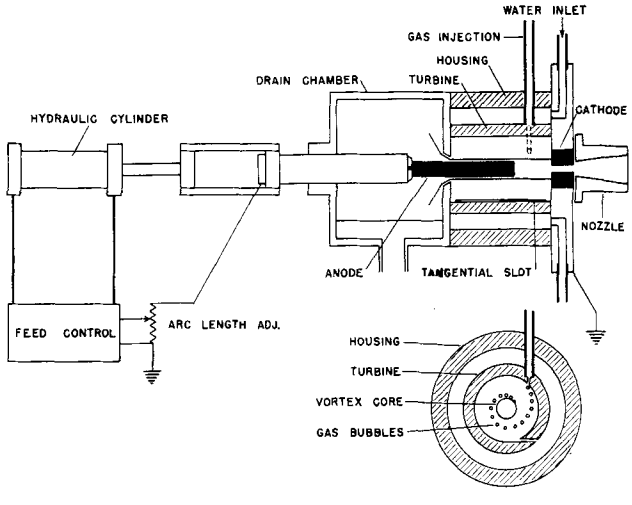

Fig. 1. Schematic diagram of water-stabilized arc

[1] Present address: Sylvania Electric Products, Inc., Buffalo, N. Y.

not introduced into the testing position until stable operation has been obtained. Arc voltage is maintained at 180 v by means of a voltage-sensing device connected across the arc and controlling a hydraulic mechanism which feeds the lower electrode at the proper rate to maintain this voltage. The current under these conditions is 350 amp, giving a power dissipation at the arc of 63 kw.

The samples are ½-in. diameter rods 3 or 4 in. long. Usually flat ended samples are used, but in some cases hemispherical ends have been provided: the hemispherical shape is generally lost rapidly. The sample is introduced so that its axis is aligned with the axis of the arc and its end is one inch above the hole in the cathode. An exposure time of ten seconds is usual and an automatic timer records the exact duration of exposure.

With such a facility it is possible to compare various materials for resistance to high temperature. Samples are weighed and their length measured before and after test. Results may be expressed as rate of loss in milligrams per kilowatt second and as loss of length. Such comparisons appear to be valid as long as exposure conditions are held constant.

It would of course be very desirable to define exactly the conditions to which the samples are exposed, but to date such exact definition has not been possible. Temperature, velocity, and composition of the plasma jet should be different at different locations within the jet.

Work has begun to measure conditions within the jet and some preliminary estimates are available. Temperatures have been estimated from 7,000° to 12,000°K, and velocities from 100 to 1000 m/sec. The composition at the center of the jet has been estimated to be as follows: 10% vaporized carbon; 5% carbon particles from the electrodes; 25% water vapor; 50% dissociated water vapor; 10% ionized atoms and molecules.

In spite of this uncertainty, the arc, used with constant operating conditions, is an excellent tool for preliminary screening and comparison of various materials. However, one useful parameter which may be measured with some accuracy is the rate of heat transfer to a body placed in the jet some distance from the cathode opening. By the use of both solid metal and water-cooled metal calorimeters, it has been possible to establish heat transfer rates averaged radially at various distances from the cathode. Typical results, using a graphite nozzle as a cathode to expand the jet, are shown in Fig. 2.

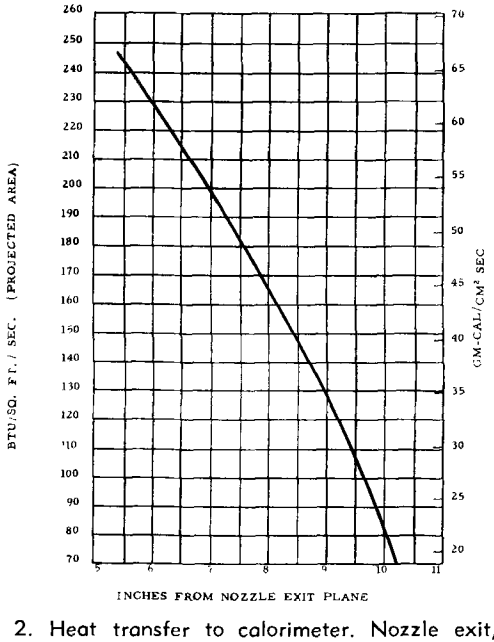

Fig. 2. Heat transfer to calorimeter. Nozzle exit, 1-in. diameter.

Not only is it important to determine which materials are most suitable for component fabrication, but also why. A high decomposition temperature and high specific heat are undoubtedly an advantage. An endothermic decomposition would also be favorable. Samples with low thermal conductivity appear to have an advantage; this is doubly useful since the interior of a component made of such material would remain at a relatively low temperature and better retain its mechanical properties during the service life of the component. An additional advantage of materials with low thermal conductivity is that the surface reaches an extremely high temperature, and heat flux due to radiation from the adjacent hot gases is minimized.

Various classes of nonmetallic inorganic materials have been fabricated and tested in the water-stabilized arc. These include: (*a*) graphites and impregnated graphites, (*b*) ceramics and reinforced ceramics, (c) ceramic-and-plastic composites.

It should be borne in mind that the ranking given these materials is based simply on erosion rates exhibited in the arc and with a high heat influx-short time application in mind. The ranking for a different environment (lower temperatures, longer times) may be very different.

Graphite and Impregnated Graphites

Graphite has many desirable high-temperature properties which makes it a likely structural material: its refractoriness, low density, low thermal expansion, high-temperature strength, availability of the raw material, machinability, etc. Unfortunately, the oxidation resistance, erosion resistance, and mechanical strength at intermediate temperatures may be too low to permit immediate utilization of any present graphite as a high-temperature structural material particularly in large pieces.

According to current theories, the permeable macrostructure which permits oxygen to penetrate the interior of the material and its microstructure, which is highly reactive to oxygen-containing gases at high temperatures, explains the low oxidation resistance of graphite. The use of pitch binders which partially volatilize during baking and graphitization results in a highly permeable macrostructure, while crystallization into a lamellar structure with weak binding between planes explains the ability of oxygen to break the interplanar bonds which results in low erosion resistance.

Attempts to overcome the undesirable effects of oxidation and erosion include experiments on densification, metal oxide and carbide coatings, and impregnation, chiefly liquid metal and liquid glass im-

Table I. Typical results of water-stabilized arc test on graphites

Material	Grain size*	Impregnant	Length erosion in 10 sec, cm	Weight erosion, mg/kw sec	Final structural state of graphite compared to start
Graphite Z2 (1) extruded	F	None	0.15	0.84	Same
			0.13	0.97	Same
Graphite Z2 (1) extruded	F	None	0.21	0.69	Same
			0.22	0.79	Same
Graphite Z3 (1) molded	F	None	0.25	0.72	Same
			0.23	0.70	
Graphite Z21 (2)	C	None	0.28	0.83	Same
			0.23	0.90	
Graphite Z22 (2)	M	None	0.23	0.65	
			0.20		Same
Carbon Z23 (2)	C	None		End spalled	
Graphite (5)	F	None	0.13	1.10	Same
			0.23	0.61	
Graphite 1 (7)			0.20	0.67	Same
			0.20	0.62	
Graphite 4 (8)		Yes	0.25	0.81	Same
			0.20	0.87	

* F, fine; M, medium; C, coarse.

pregnation of porous graphite. This last approach seems to be the most promising and the most likely to improve the high temperature oxidation and erosion resistance of graphite.

Above 1500°C, graphite becomes stronger mechanically in contrast to most nongraphitic materials; below this temperature, its mechanical strength is about 1/10 that of metals. Its thermal shock resistance is excellent compared to most ceramics but poor compared to metals. It shows practically no ductility below 2200°C, which means there is no relief of localized or unequal stress internally. However, recent work at the Jet Propulsion Laboratory has shown some ductility above 2200°C.

Graphite Materials System

Graphite materials systems can be divided into at least three types: (*a*) graphite structures filled with impregnant: the pores in the massive graphite being filled with an impregnant; (*b*) inorganic or organic structures filled with graphite powder; for example, a cast block of concrete having some of the same replaced by graphite powder; (c) an all-refractory system: a system in which all the ingredients are as equally refractory as graphite. An example would be titanium carbide; here the ingredients could all be added before the mass is graphitized.

Results of water-stabilized arc testing of graphites from many commercial sources showed a very small spread in erosion rates, the average value of which was 1.1 mg/kw sec. The average length loss was 0.25 cm, somewhat higher for more porous graphites.

The best impregnated graphites were found to be a series of composition consisting of silicon carbide and graphite, or silicon metal and graphite which converts to SiC on firing. These show a weight erosion of about 0.6 mg/kw sec and a length loss equivalent to the pure graphite. Since no other impregnant gave better results than pure graphite, the superiority of the carbide-bonded graphite systems seems established, although nitride and boride bonded systems are still to be tested. Other impregnants tested include: oxalic acid, epoxy resin, aluminum sulfate, sulfur, iodine, boric acid, and many others.

Typical test results for graphites and impregnated graphites are given in Tables I and II.

Ceramics and Reinforced Ceramics

Ceramic materials, in general, have poor thermal shock resistance because of their relatively high coefficients of thermal expansion and brittle characteristics. For this reason, most ceramic bodies are not suitable for applications where severe temperature gradients exist. However, successful attempts have been made to increase thermal shock resistance greatly by reducing considerably the thermal expansion coefficients. Unfortunately, the low-expansion ceramic materials are not very refractory. Another approach for improving thermal shock resistance has been to use refractory bodies which are relatively soft and similar to plaster of paris in texture. These materials, when exposed to sudden temperature changes, fail locally at the exposed surfaces while still retaining their strength.

The results of the arc tests on simple ceramics, mostly oxides, are given in Table III.

All samples were obtained from commercial suppliers and were given no further treatment. The fused MgO samples were in the form of 2 x 2-in. plates varying from ¼ to 1 in. in thickness. Since the plasma jet covered only a ½ in. circle in the center of the MgO plates, this undoubtedly contributed to the severe thermal shock observed.

A series of ceramic aggregates (listed in Table IV) reinforced by a cementing agent were tested; these unfired cemented bodies had previously exhibited excellent thermal shock resistance when subjected to the exhaust of a rocket motor. Several samples were made from castable mixes containing water, calcium-aluminate cement, or phosphoric acid, and aggregates of bubble alumina and zirconia, magnesia, several grades of commercial alumina grain, and silicon carbide. These samples were tested in the water arc, and the results are shown along with those of other materials in Table IV.

Table II. Typical results of water-stabilized arc tests on impregnated graphites

Material	Grain size†	Impregnant	Length erosion in 10 sec, cm	Weight erosion, mg/kw sec	Final structural state of graphite compared to start
Silicon carbide and graphite			0.51	0.51	
			0.51	0.54	Same
	F	None	0.25	0.73	
Graphite (5)			0.23	0.98	Same
Graphite (5)	F	Repitch treated and regraphitized		1.64	Same
			0.18	2.30	
		Copper	0.03	0.49	
Graphite (5)			0.03	0.47	Same
		Sodium	0.08	0.96	
Graphite (5)		Borate	0.15	0.81	Same
	F	Some initial oxidation	0.30	1.94	
Graphite (5)			0.28	1.56	Same
Graphite Al	C	None	0.25	0.86	Same
			Average	1.55	
Graphite Al	C	Sod. sulfate	0.13	1.88	Same or
		Na_2SO_4 3%	0.18	1.85	better
Graphite Bl	F	None	0.23	0.90	
			0.20	Average	Same
			0.20		
Graphite Bl	F	Sod. ammonium hydrogen phosphate hydrated	0.15	4.02	
			0.13	3.91	Same
		7%			
Porous graphite	M	None	1.02, 0.88, 1.02*	1.96, 1.73	Same as porous graphite
Porous graphite	M	Boric acid	2.28	1.56	Slightly weaker than
		5%	2.28	2.66	porous graphite
Porous graphite	M	Epoxy resin	0.51	13.7	Much weaker
		34%	1.10	15.7	
Porous graphite	M	Oxalic acid	0.76	12.3	Same as porous graph-
		36%	1.10	11.5	ite; piece in very good condition
Porous graphite	M	Polyester	0.38		"Waterburn" and
		35%	0.51		warped
Porous graphite	M	Sod. phosphate tribasic crystal	0.76	11.5	Same as porous graphite
		39%			
Porous graphite	M	Aluminum sulfate hydrated	1.27	10.9	Much weaker
				7.2	
		30%			
Porous graphite	M	Sulfur	0.51	14.2	Same as porous graph-
		47%	0.76	20.8	ite
Porous graphite	M	Iodine	0.76	30.4	Same as porous graph-
		59%		34.7	ite

† F, fine; M, medium; C, coarse.
* Surface temperature by optical pyrometer 2450°C.

The various samples made of Al_2O_3 and MgO eroded quite rapidly compared to the SiC aggregates. Therefore, it appears that the aggregate-type rather than bond-type is more important with regard to erosion resistance. The results indicate that there are no significant differences between samples having different aggregate-size distributions, water content, density, and methods of preparation (casting, troweling, or tamping).

Ceramic-and-Plastic Composites

Although compositions containing organic plastics are not ordinarily considered as refractory materials, certain ceramic-plastic compositions show a surprisingly low erosion rate in the water-stabilized arc tests.

At 3000°C, the organic plastic decomposes into gas and residual carbon as coke on the surface. When glass is present, it fuses and forms a thin viscous layer on the surface which reduces the heat transfer to the model and protects it from the chemical action of the hot gases.

In the 8000°C plasma, even the glass is volatilized, so no liquid protective layer is formed. Here the erosion rate depends on the heat absorbed in converting plastic and glass to vapor at some high temperature and, in the case of supersonic flow, the reduction in heat transfer associated with the addition of the gas to the boundary layer. Since the atoms of the organic part are lighter than those of the glass, the volume of gas generated from a gram of the all-organic material is substantially higher than that from the glass-reinforced material.

Results of arc testing are given in Table V and relative erosion rates for ceramic plastic composites at different temperatures are given in Table VI.

Table III. Water-stabilized arc tests on simple ceramics

Material	Wt. loss, g/sec	Wt. loss, mg kw^{-1} sec^{-1}	Average wt. loss, mg kw^{-1} sec^{-1}	Length loss, cm	Comments
Silica-bonded SiC	0.103	1.64	1.61	0.38	
	0.098	1.55		0.33	
	0.103	1.64		0.13	
Fused MgO	0.054	0.86	1.65	0.23	Severe thermal shock
	0.119	1.89		0.28	
	0.139	2.21		0.36	
Fused quartz (SiO_2)	0.139	2.11	2.07	0.71	White opaque SiO_2 at cold end
	0.128	2.03			
SiC (self-bonded)	0.402	6.40	6.40	—	White coating of SiO_2
Al_2O_3	0.508	8.06	6.86	1.04	
	0.365	5.65		0.86	
Fused mullite	0.524	8.32	8.22	1.68	
	0.531	8.43		1.65	
	0.449	7.92		1.62	
Glass-bonded mica	0.918	14.6	11.4	3.82	Glassy surface after test
	0.511	8.12		2.06	
ZrO_2	0.778	12.35	12.98	1.40	
	0.735	11.65		1.58	
	0.943	14.95		1.86	

Table IV. Water-stabilized arc tests on reinforced ceramics

Principal aggregate	Bond type	Wt. loss, g/sec	Average wt. loss, mg kw^{-1} sec^{-1}	Length loss, cm
Al_2O_3	Phosphoric acid	—	7.00	—
Al_2O_3	Phosphoric acid	—	8.40	1.42
Al_2O_3	Phosphoric acid	0.540	7.80	0.98
Bubble Al_2O_3	Phosphoric acid	—	7.30	—
Al_2O_3	Phosphoric acid	0.576	7.56	0.88
Al_2O_3	Phosphoric acid	0.608	9.65	1.68
Al_2O_3	Phosphoric acid	—	7.20	0.86
Fused Al_2O_3	Phosphoric acid	—	7.50	—
Fused Al_2O_3	Phosphoric acid	0.538	8.58	1.47
Fused Al_2O_3	Phosphoric acid	0.515	8.15	1.42
Bubble Al_2O_3	Calcium aluminate	—	6.80	—
Al_2O_3	Calcium aluminate	0.559	8.86	1.40
Fused Al_2O_3	Calcium aluminate	0.635	10.07	1.65
Fused MgO	Calcium aluminate	—	7.00	—
Fused MgO	Calcium aluminate	0.435	6.90	1.24
SiC	Calcium aluminate	0.161	2.57	0.56
Fused mullite	Calcium aluminate	0.484	7.65	0.96
Bubble ZrO_2	Calcium aluminate	0.646	10.25	1.85

Table V. Behavior of various materials exposed to the water-stabilized arc (½-in. diameter rods)

	Weight loss mg/kw-sec
Chopped glass cloth-high temp. phenolic B	6.0
Chopped glass cloth-high temp. phenolic D, 27% resin	2.7
Chopped glass cloth-high temp. phenolic D, 37% resin	2.2
Chopped glass cloth-high temp. phenolic D, 44% resin	2.2
Chopped glass cloth-high temp. phenolic D, 65% resin	1.5
Chopped refrasil cloth-high temp. phenolic D, 41% resin	2.3
Chopped nylon cloth-high temp. phenolic D, 57% resin	1.1

Table VI. Relative erosion rates of various materials vs. temperature of exposure

Material	Temperature, °C 1800	2500	7000
Phenolic-glass cloth, 27% resin	1.0	2.7	2.5
Phenolic-glass cloth, 37%	1.2	2.5	2.0
Phenolic-glass cloth, 44% resin	1.6	2.2	2.0
Phenolic-glass cloth, 65% resin	1.7	1.5	1.4
Phenolic-glass cloth, 41% resin	1.4	1.0	2.1
Phenolic-nylon cloth, 57% resin	4.7	2.5	1.0

Conclusions

1. A small water-stabilized arc, as described herein, is a suitable device for screening materials considered for short time service at extremely high temperatures. A large number of samples may be tested rapidly and at relatively low cost.

2. The results listed below have been obtained under the conditions described. Only the better plastics and ceramics are included; for example, some ceramics spalled badly and are omitted from consideration.

Materials	Loss of length (When exposed for 10 sec in the plasma 1 in. from the cathode)
Graphite	0.04 to 0.16
Graphite (impregnated)	0.04 to 0.13
Reinforced plastics	0.12 to 0.47
Ceramics	0.13 to 0.40
Copper*	1.0

* Copper is shown here for comparison only.

3. Extrapolation of these results to other thermal and chemical environments or longer periods of time should not be attempted.

Manuscript received July 25, 1958. This paper was presented at the New York Meeting, April 27-May 1, 1958.

Any discussion of this paper will appear in a Discussion Section to be published in the December 1959 JOURNAL.

REFERENCES

1. H. Maecker, *Z. Physik*, **129**, 108 (1951).
2. T. Peters, *ibid.*, **135**, 573 (1953).

An Investigation of the Compound Silicon Boride (SiB_6)

Carl F. Cline

Research and Development Division, The Carborundum Company, Niagara Falls, New York

ABSTRACT

Single crystals of the compound silicon hexaboride have been prepared. Laue, rotation, and Weissenberg photographs indicate an orthorhombic cell with lattice parameters a = 14.39 ± 0.01, b = 18.27 ± 0.01, and c = 9.88 ± 0.01Å. The pycnometer density is 2.43 g/cm³. The average electrical resistivity of single crystals, based on a probe technique, is 0.2 ohm-cm. The melting point is 1950°C. SiB_6 has a Knoop hardness, with a 100-g load, of 1910 kg/mm².

The interest in hard and refractory materials has been prevalent from times dating back to Moissan at the turn of the century. Among the most elusive of these refractory compounds have been the borides of silicon.

Moissan and Stock (1) reported in their original work that they had prepared, by fusion of the elements, two borides, SiB_3 and SiB_6. The SiB_3 was obtained as black rhombic plates with a density of 2.52 g/cm³, and the SiB_6 as black irregular crystals with a density of 2.47 g/cm³. The borides were reported to be hard, to have high melting points, and to conduct electricity.

These properties interested other researchers (2-5) who were unsuccessful in their attempts to duplicate the original work. Recently, Samsonov and Latysheva (6) have reported the properties of a tetragonal SiB_3 phase prepared by hot-pressing the elements. Their results and interpretations were questioned by Ormont (7) who found discrepancies in their x-ray data. Samsonov and Latysheva also prepared a compound, SiB_6, which was studied by Zhuravlev (8) who reported a structure isomorphous with CaB_6.

Concurrent with the Russian research, a study of the silicon-boron system was underway in our laboratories. A preliminary report (9) has been issued on the formation of the compound SiB_6.

Experimental

Preparation.—A review of the methods of preparation of refractory borides and silicides indicated that the synthesis by a combination of the elements was the most logical place to start. The initial experiments were carried out by hot-pressing boron and silicon in a 1 to 3 weight ratio to a temperature of 1700°C. The hot-pressing was performed by induction heating of a graphite mold, which had a boron nitride liner and plungers, using a pressure of 2000 psi and an argon atmosphere. This technique permitted a minimum amount of carbon contamination. Spectrographic analyses of the boron and silicon are given in Table I. The x-ray identification of material obtained by the hot-pressing was difficult due to the presence in the system of unreacted boron which has a complex powder pattern.

To overcome this problem, synthesis experiments were carried out by fusion of the elements at a temperature of approximately 2250°C in an atmosphere of argon. The hold time at 2250°C was usually 1 hr. Fusion was carried out in a boron nitride crucible with a boron nitride lid. The crucible was placed in a graphite susceptor and heated by induction. Fusion experiments were carried out using weight ratios of silicon to boron ranging from 2:1 to 3:1. This was done so that sufficient silicon would be available to react with all of the boron, since a chemical separation of the boron from silicon boride would be extremely difficult. The fused mass was removed from the boron nitride crucible and acid-treated with a mixture of HF and HNO_3 to remove the last traces of free silicon. The crystals were then fused with KOH to remove boron nitride which had formed on the surface. A photomicrograph of a typical melt is shown in Fig. 1. A picture of the crystals after treatment is shown in Fig. 2. After treatment of the melt, the SiB_6 crystals are black and opaque, even when crushed to a fine particle size.

Table I. Spectroscopic analysis of silicon metal from Electro Metallurgical Co. (−30 +80 mesh, high purity, acid treated with HCl)

	%
Fe	0.01
Al	0.01
B	0.003
Ca	0.005
Mn	0.0005
Mg	0.0002

Spectroscopic analysis of Pacific Coast Borax*, (95-97%) amorphous boron

	%
Fe	0.7
Al	0.01
Mn	0.1
Si	1.0 (approx.)
Cu	0.01
Cr	0.008
Ca	0.02
Mg	0.7

Major impurity: 0 not determined

* Pacific Coast Borax Co., 100 Park Ave., New York 17, N. Y.

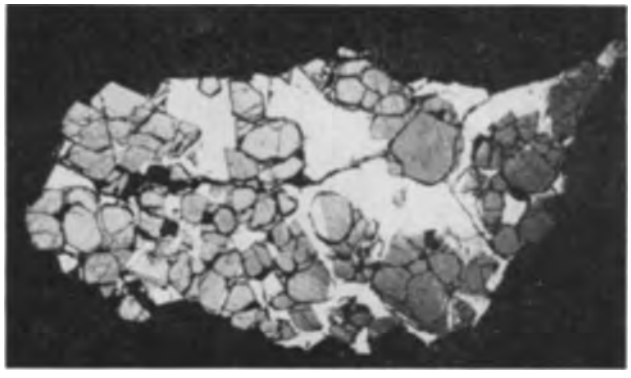

Fig. 1. Typical silicon-boron melt. Magnification 6X

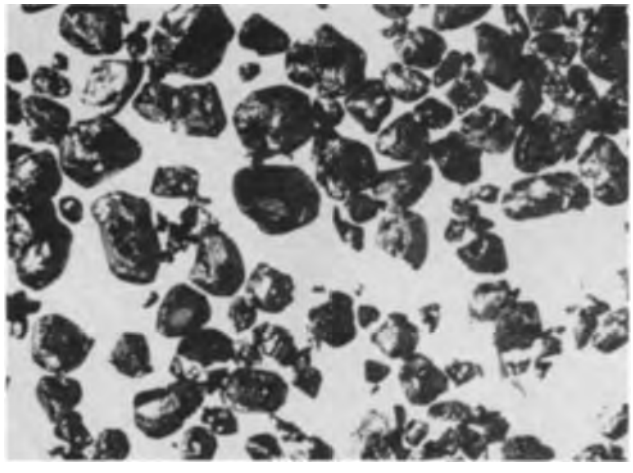

Fig. 2. SiB_6 crystals after acid treatment. Magnification 6X

Structure.—A single crystal obtained by the fusion technique shown in Fig. 3 was examined using Laue, rotation, and Weissenberg techniques. The results indicated that the system was orthorhombic with unit cell dimensions of $a = 14.39$, $b = 18.27$, and $c = 9.88$Å. The sample was crushed and a powder pattern was run using a Geiger counter diffractometer. The measured interplanar spacings, as well as the relative intensities, are listed in Table II. CuK α radiation was used in all cases.

The number of molecules per unit cell, Z, was calculated from the pycnometer density of the compound. Using the observed density of 2.43 g/cc, a value of $Z = 40.9$ was obtained.

Chemical analysis.—The wet chemical analysis of silicon boride was carried out by first crushing the treated crystals down to −97 mesh particle size in a hardened steel mortar. A 0.2-g sample was analyzed for boron by the method of Blumenthal (10). The silicon analysis required a 0.5-g sample and was carried out using the conventional sodium carbonate fusion. The boron was removed by dissolving out the oxide, after the fusion, by acidifying and treating with methyl alcohol. The alcohol-treated mass was then evaporated to remove methyl borate. Percentages of boron and silicon in crystals prepared by the fusion technique average 69.7 and 29.3, respectively. Values are shown in Table III.

The chemical analysis of SiB_6 is quite close to theoretical values of 69.8% boron and 30.2% silicon. In all cases the boron analyses were run in duplicate. Nitrogen analyses indicated less than 0.2% N_2 present in the crystals. The SiB_6 is not appreciably affected by solutions of the common acids.

Physical properties.—The apparent melting point of SiB_6 was measured in a small graphite resistance furnace and a value of 1950°C obtained. The melting point of Pacific Coast Borax "fused" boron was 2130°C, as observed in the same furnace.

A schematic drawing of the internal construction of the melting point furnace is shown in Fig. 4. The behavior of the sample is followed visually through a special close-range optical pyrometer equipped with additional filters designed to extend its operating range to 4200°C. Samples were placed inside a hole drilled in a boron nitride rod. The rod was mounted vertically in a graphite pedestal and the graphite heater placed around the sample. Radiation shields were used around the heater to reduce power loss by radiation. Stepless control of power input to the heater was afforded by a Variac-controlled saturable core reactor. Before a run the furnace was evacuated and then filled with argon. The argon was allowed to flow during the run.

The furnace was calibrated by measuring the melting points of Al_2O_3, ZrO_2, and HfO_2. The melting

Table II. X-ray diffraction data for SiB_6

"d" (A)	I*	"d"	I*
11.47	20	2.74	50
9.12	10	2.71	60
7.62	20	2.67	60
5.57	10	2.63	40
4.92	100	2.60	40
4.62	40	2.56	30
4.35	70	2.53	30
4.23 (Doublet)	80	2.48	20
4.15	50	2.47	20
3.99	20	2.40	30
3.86	40	2.36	30
3.70	30	2.34	20
3.53	10	2.26	20
3.45	30	2.21	20
3.39	30	2.15	10
3.25	40	2.11	10
3.18	30	2.08	10
3.10	20	2.04	20
3.05	20	2.01	10
2.98	30	1.98	10
2.93	30	1.93	10
2.85	80		
1.89	20		
1.85	20		
1.83	20		
1.82	20		
1.77	20		
1.71	40		
1.67	30		
1.62	40		
1.57	20		
1.552	20		
1.546	10		
1.482	30		
1.444	30		
1.434	30		
1.424	30		
1.369	10		
1.356	20		
1.350	20		

Fig. 3. Single crystal of SiB_6. Magnification 22X

points agreed with published values within experimental error which was assumed to be ± 20°. Correction for the glass window in the furnace was made using Wien's law. A more complete description of the apparatus is given by Lambertson and Lewis (11).

The electrical resistivity of crystals of SiB_6 was determined by a "probe" method (12, 13). The resistivity was of the order of 0.2 ohm-cm as compared with 6×10^3 ohm-cm for the resistivity of the boron used. It is not possible from these measurements to conclude a reason for this low resistivity for SiB_6; however it is consistent with the low resistivity reported for B_4C (14).

The hardness of SiB_6 was measured on single crystals which were mounted in black bakelite. Samples of silicon carbide, boron, and boron carbide were mounted in the same mount so that a direct comparison could be made. The mount was first rough-polished on a 100-grit diamond wheel. The final polishing was done with a 400-grit diamond wheel followed by 500-grit SiC waterproof paper with a final finish using diamond dust on a polishing cloth.

The samples were indented using a Leitz Mini-load Durimet Tester. The indenter was the Knoop diamond point and the load 100 g in all cases. The hardness values are listed in Table IV.

Table III. Chemical analysis of SiB_6

Sample	Percentage boron	Percentage silicon
1*	76.53	23.02
2†	69.05	29.43
3†	70.30	28.92
4†	70.16	29.48
5†	69.4	29.3
Theoretical Composition		
Boron	69.8	
Silicon	30.2	

* Hot pressed slug (had free boron).
† Single crystals by fusion of elements.
Note: Percentages were obtained after treatment of the melt with HF + HNO_3 to remove free silicon followed by fusion with KOH to removed boron nitride. Nitrogen was analyzed to be less than 0.2%.

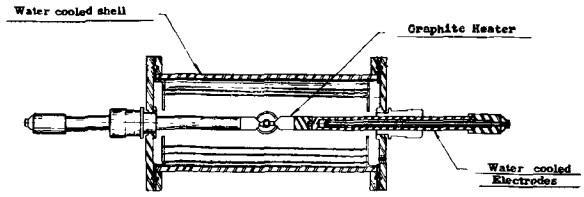

Fig. 4. Schematic drawing of melting point furnace

Discussion of Results

The difficulties experienced by previous investigators in preparing single crystals of SiB_6, as evidenced by the literature survey, appear to have been the result of several factors, of which the most pertinent are:

1. In most instances the reaction was carried out at too low a temperature. It appears that it is necessary to be above the melting point of boron, which is approximately 2130°C.
2. Reactions generally were carried out in the presence of carbon, which appears detrimental to the reaction since silicon and boron tend to form their respective carbides. The fact that a crucible material such as boron nitride was available was indeed fortunate, since silicon carbide and graphite had proven unsatisfactory.
3. A slow cooling rate is essential particularly since indirect evidence indicates that a peritectic reaction is involved.
4. A sufficient amount of silicon is necessary to react with all of the boron, as the final separation of SiB_6 from boron or other compounds is extremely difficult. With this in mind it appears that a two to one weight ratio of silicon to boron is satisfactory.

Structure—Cell dimensions were determined from rotation and Weissenberg photographs.

The orthorhombic structure reported here for SiB_6 is not in agreement with the CaB_6 structure reported by Zhuravlev. X-ray data reported by Zhuravlev matches that for CaB_6, but since no chemical analysis is reported it is not possible to conclude that the pattern applies to SiB_6. The solution to the complete structure should prove interesting since a similarity to B_4C (15, 16) is indicated.

Table IV. Knoop hardness measurements

	L*	Range HK_{100}	Avg. HK_{100}
Boron	24.3	1940-2630	2410
B_4C	21.6	2910-3160	3050
SiC	23.6	2510-2580	2560
SiB_6	27.3	1740-2050	1910

$$HK_{100} = \text{Knoop hardness} = \frac{14230.\,P}{L^2}$$

where P = load grams, L = length of indentation in microns.

* Values for L are an average of 10 indentations.

The chemistry of the borides indicates that one might well expect various other borides of silicon, but as yet no evidence for the SiB_3 phase reported by Moissan has been found.

Physical properties.—The density as determined by the pycnometer method is quite reproducible. The value of 2.43 g/cm³ is slightly less than the 2.47 g/cm³ quoted by Moissan. The density for SiB_3 (2.43 — 2.49 g/cm³) as determined by Samsonov indicates a compound similar to SiB_6 The density of the SiB_6 prepared by Samsonov was reported by Zhuravlev to be 2.16 g/cm³.

The observed melting point for SiB_6 is approximately 1950°C, which is about 200°C below that of elemental boron.

The breakdown of SiB_6 upon melting as observed by x-ray studies suggests a peritectic reaction, but further work will be necessary before the various phases of the binary diagram are established.

The measured hardness of SiB_6 is lower than anticipated from the reported hardness of silicon borides. In view of the hardness values reported by Samsonov it is felt that there may be other silicon borides that will give the expected hardness. SiB_6 is not as prone to cracking under loading as boron or boron carbide.

Summary

1. Single crystals of silicon boride (SiB_6) have been prepared and identified by wet chemical and x-ray analyses.

2. SiB_6 has an orthorhombic structure with unit cell dimensions of a = 14.39, b = 18.27, and c = 9.88Å.

3. SiB_6 has a density of 2.43 g/cm³ based on pycnometer measurements.

4. The number of molecules per unit cell based on a density of 2.43 g/cm³ is 40.9.

5. The melting point of SiB_6 is approximately 1950°C.

6. The electrical resistivity is approximately 0.2 ohm-cm based on probe measurements of single crystals.

7. The Knoop hardness of SiB_6 is approximately 1910 kg/mm² using a 100-g load.

Manuscript received Aug. 7, 1958. This research was carried out in partial fulfillment for the M.Sc. degree at Niagara University.

Any discussion of this paper will appear in a Discussion Section to be published in the December 1959 JOURNAL.

REFERENCES

1. H. Moissan and A. Stock, *Compt. rend.*, **131** (1900).
2. O. P. Watts, Thesis, University of Wisconsin, (1906).
3. F. Tone, *Ind. & Eng. Chem., Ind. Ed.*, **30**, No. 2, 232 (1938).
4. L. Brewer, D. L. Sawyer, D. H. Templeton, and C. H. Dauben, *J. Am. Cer. Soc.*, **173** (1952).
5. J. A. Stavrolakis, *ibid.*, **35**, No. 2 (1956).
6. G. V. Samsonov and V. P. Latysheva, *Doklady Academia Nauk., S.S.S.R.*, **105**, No. 3, 499 (1955).
7. M. A. Gurevich, V. A. Epel'baum, and B. F. Ormont, *Zhur. Neorg. Khim.*, **2**, 206 (1957).
8. N. N. Zhuravlev, *Kristallografia*, **1**, 666 (1956).
9. C. F. Cline, *Nature*, **181**, 476 (1958).
10. H. Blumenthal, *Anal. Chem.*, **23**, 992 (1951).
11. W. Lambertson and G. Lewis, Paper presented at the New York Meeting, April 1958, of The Electrochemical Society.
12. Torrey and Whitmer, "Crystal Rectifiers," p. 24, McGraw Hill Book Co., New York (1948).
13. W. C. Shaw, D. E. Hudson, and G. C. Danielson, Iowa State College-380, August (1953).
14. "High Temperature Technology," p. 120, John Wiley & Sons, Inc., New York (1956).
15. H. K. Clark and J. L. Hoard, *J. Am. Chem. Soc.*, **65**, 2115 (1943).
16. R. Adamsky, *Acta Cryst.*, **11**, 744 (1958).

The Electrolytic Preparation of *p*-Methoxyphenylacetonitrile

S. Wawzonek and J. D. Fredrickson

Department of Chemistry, State University of Iowa, Iowa City, Iowa

ABSTRACT

Conditions necessary for the electrolytic preparation of *p*-methoxyphenylacetonitrile from α-hydroxy-*p*-methoxyphenylacetonitrile and its esters were determined polarographically. Polarographic reduction waves were obtained in dioxane and water only in the presence of tetrabutylammonium iodide and tetramethylammonium iodide. Alpha-benzoxy-*p*-methoxyphenylacetonitrile which was reduced at the most positive potential gave no reduction wave in the presence of either ammonium chloride or lithium chloride.

On the basis of the ease of reduction and ease of preparation α-benzoxy-*p*-methoxyphenylacetonitrile was used as the starting material in the large scale reduction at a mercury cathode and gave *p*-methoxyphenylacetonitrile in yields averaging 65%.

The preparation of *p*-methoxyphenylacetonitrile is of interest since this compound is an intermediate in the synthesis of numerous alkaloids and synthetic drugs (1, 2). The chemical methods reported are numerous and have involved the metathetical reaction of anisyl chloride with alkali cyanides, the nitration of phenylacetonitrile followed by reduction, diazotization, hydrolysis, and methylation, the catalytic reduction of α-benzoxy-*p*-methoxyphenylacetonitrile, and the reaction of acetic anhydride with the oxime of *p*-methoxyphenylpyruvic acid (3).

The present study describes the electrolytic preparation of *p*-methoxyphenylacetonitrile from α-benzoxy-*p*-methoxyphenylacetonitrile. Polarographic

data were used to determine the conditions necessary for the electrolysis and the derivative of α-hydroxy-p-methoxyphenylacetonitrile most suitable for this preparation.

Experimental

The esters of α-hydroxy-p-methoxyphenylacetonitrile and α-hydroxyphenylacetonitrile (mandelonitrile) were studied polarographically in solutions having the following compositions: (*A*) 0.175*M* tetrabutylammonium iodide and 0.0048% methyl red in 75% dioxane; (*B*) 0.175*M* tetrabutylammonium iodide in 75% dioxane; (*C*) 0.0972*M* tetramethylammonium iodide in 47% dioxane; and (*D*) 0.1312*M* tetramethylammonium iodide in 50% dioxane.

The current voltage curves were obtained with a Fisher Elecdropode having a current scale calibration of 0.0196μa/unit on the galvanometer scale at a sensitivity of one and a Sargent Model XII polarograph having a current scale calibration of 0.00497 μa/mm at a sensitivity of one.

All measurements were made in a water thermostat at 25° ± 0.1° using both a cell with a mercury pool as an anode and a H-type cell fitted with a saturated calomel electrode. The potential of the mercury pool was measured in the various solutions against a saturated calomel electrode (S.C.E.) using a sintered glass salt bridge of the type described by Laitinen (4).

The dropping mercury electrode had the following characteristics. At a pressure of 70 cm of mercury the drop time in 0.1N KCl was 4.3 sec. (open circuit). The value of m was 1.58 mg sec^{-1} with a calculated value of $m^{2/3}t^{1/6}$ of 1.73 $mg^{2/3}$ $sec^{-1/2}$.

Materials.—The dioxane was purified by refluxing with metallic sodium until the molten sodium remained shiny. This process usually required about a week. The ammonium chloride, lithium chloride, and tetramethylammonium iodide used were of a reagent grade. Tetrabutylammonium iodide (5), α-benzoxyphenylacetonitrile (6), α-ethoxycarbonyloxyphenylacetonitrile (6), α-hydroxy-p-methoxyphenylacetonitrile (6), α-ethoxycarbonyloxy-p-methoxyphenylacetonitrile (7), α-benzoxy-p-methoxyphenylacetonitrile (6), and α-acetoxy-p-methoxyphenylacetonitrile (8) were made according to the directions given in the literature.

Electrolysis.—The reduction was carried out in a circular battery jar, 15.7 cm in diameter and surrounded by an ice bath. A 5 x 13 cm porous cup, which was 4-mm thick, was used as the anode compartment and was supported by a small Lucite stand 3 cm above the surface of the mercury pool used as the cathode. The cathode had an area of 193.8 cm^2 and was connected to the external circuit by a glass tube filled with mercury and with a small platinum wire sealed in one end. The anode was a large platinum gauze electrode. An efficient mechanical stirrer was mounted in the cathode compartment close to the surface of the mercury pool.

The anode and cathode compartments were filled with 1700 ml of 0.1*M* tetramethylammonium iodide in 50% dioxane. To the cathode solution α-benzoxy-p-methoxyphenylacetonitrile (20.0 g) was added. The line potential was 80 v. The initial current of 1.7 amp increased to 3.9 amp in the first 20 min as the temperature increased from 21.5° to 50.0°. This current, which corresponded to a current density of 0.020 amp/cm^2, and the temperature were maintained at this point for an additional hour. Gas evolution occurred after 1 hr of electrolysis. To insure complete reduction the electrolysis was continued for a total of 6 hr during which time the current density dropped to 0.010 amp and the temperature to 30°. During the entire period the cathode solution was kept neutral by the dropwise addition of glacial acetic acid (10.65 ml). The resulting catholyte was treated with 800 ml of water, and the dioxane was removed under reduced pressure as an azeotrope. The resulting solution which contained an oil was then extracted with ether. The ether extract after washing with 5% hydrochloric acid and 5% sodium hydroxide gave 13.75 g of an oil which gave two fractions when distilled under reduced pressure. The first (2.5 g) of these, bp 100°-120° (20 mm) corresponded in boiling point to benzyl alcohol; it was not, however, investigated any further. The second fraction (6.3 g, 57% yield), bp 163.5°-164° (22 mm) consisted of p-methoxyphenylacetonitrile, $n_D^{17.0} = 1.5392$. Further proof for the structure was obtained by condensing the product with anisaldehyde in the presence of alkali (9). The product α-(p-methoxyphenyl)-p-methoxycinnamonitrile melted at 107°-109° and did not depress the melting point of an authentic sample (10).

In a smaller run using 10 g of α-benzoxy-p-methoxyphenylacetonitrile 4 g of p-methoxyphenylacetonitrile was obtained (72.5% yield).

Results

The polarographic data obtained for the various substituted phenylacetonitriles are given in Table I.

All the the compounds except α-hydroxy-p-methoxyphenylacetonitrile gave well-defined waves. The latter gave a drawn out wave.

Alpha - benzoxy - p - methoxyphenylacetonitrile failed to give a polarographic wave in either 0.1*M* ammonium chloride or 0.1*M* lithium chloride in 75% dioxane.

The large-scale electrolytic reduction of α-benzoxy-p-methoxyphenylacetonitrile in 50% dioxane containing 0.1*M* tetramethylammonium iodide gave

Table I. Half-wave potentials and diffusion currrent constants for various substituted phenylacetonitriles

Compound -phenylacetonitrile	Concn. millimoles liter	Solution*	$E_{1/2}$ (v) S.C.E.	I_d†
α-Benzoxy	1.00	A	—1.65	2.86
α-Ethoxycarbonyloxy	1.00	D	—2.12	3.62
α-Hydroxy-p-methoxy	1.00	B	—1.72	1.73
α-Acetoxy-p-methoxy	1.05	B	—2.02	1.92
α-Benzoxy-p-methoxy	1.00	A	—1.65	2.06
α-Benzoxy-p-methoxy	0.055	C	—1.73	1.60
α-Ethoxycarbonyloxy-p-methoxy	1.01	B	—2.07	5.17

* For the composition see the Experimental section.
† $I_d = i_d/Cm^{2/3}t^{1/6}$.

in two runs p-methoxyphenylacetonitrile in yields amounting to 57 and 72.5%, respectively.

Discussion of Results

An examination of the results in Table I indicates that the α-benzoxy derivatives of the two phenylacetonitriles are reduced more easily than the other esters. This behavior points to a greater tendency for the phenyl group in comparison with the ethoxy and methyl groups to withdraw electrons from the ester linkage and thus make this bond more susceptible to reduction. A similar effect is found in the corresponding analogous acids; benzoic acid is more acidic than acetic acid. No value is reported for the dissociation of ethyl bicarbonate, but this acid would be expected to have approximately the same acidity as carbonic acid since the inductive effect of the ethoxy group approximates that of the hydroxyl grouping.

The diffusion current constant obtained for these benzoates pointed to the following electrode reaction.

$$p\text{-}CH_3OC_6H_4\underset{\displaystyle OCOC_6H_5}{\underset{|}{C}}HCN + 2e + H_2O \rightarrow$$
$$p\text{-}CH_3OC_6H_4CH_2CN + C_6H_5COO^- + OH^-$$

This process was confirmed by the formation of p-methoxyphenylacetonitrile in a large-scale reduction. No benzoic acid was isolated in this reduction since the potential was not controlled. A fraction boiling at approximately the same point as benzyl alcohol was obtained, however, and may be formed from the benzoate ion since this is reducible at more negative potentials.

Alpha-hydroxy-p-methoxyphenylacetonitrile and α-acetoxy-p-methoxyphenylacetonitrile from their diffusion current constants undergo a similar reduction to p-methoxyphenylacetonitrile and hydroxide and acetate ions, respectively. The lower values obtained for the currents may be caused by decomposition of these compounds in solution.

The higher diffusion coefficient constants obtained for the α-ethoxycarbonyloxy derivatives suggests that possibly four electrons are involved in the reduction of these compounds. The reduction of these esters to the phenylacetonitrile would involve two electrons and produce the ethyl carbonate ion. This ion can hydrolyze at the dropping mercury electrode to carbon dioxide and ethanol. Carbon dioxide has been shown to undergo reduction at the dropping mercury electrode to formic acid (11) and would be the basis for the higher current observed. The overall electrode reaction for the reduction of the α-ethoxycarbonyloxy derivatives would be the following:

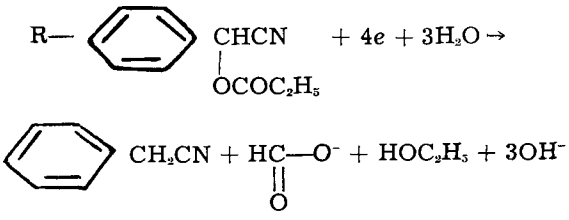

On the basis of the ease of reduction and the ease of preparation α-benzoxy-p-methoxyphenylacetonitrile was used as the starting material for the large-scale electrolytic preparation of p-methoxyphenylacetonitrile. Tetramethylammonium iodide was used as the supporting electrolyte because it was less expensive than the tetrabutylammonium iodide. The average yield of 65% obtained indicated that the electrolytic method offered a suitable way for the preparation of p-methoxyphenylacetonitrile.

Manuscript received Sept. 19, 1958. This paper was abstracted in part from the M.S. Thesis of one of the authors (J.D.F.).

Any discussion of this paper will appear in a Discussion Section to be published in the December 1959 JOURNAL.

REFERENCES

1. O. Kromalka, *Ber.*, **75**, 123 (1942).
2. C. Mentzer, D. Molho, and D. Billet, *Bull. soc. chim.*, **1946**, 271.
3. For the references involved see *Org. Syntheses*, **36**, 50 (1956).
4. H. A. Laitinen, *Ind. Eng. Chem., Anal. Ed.*, **13**, 393 (1941).
5. H. A. Laitinen and S. Wawzonek, *J. Am. Chem. Soc.*, **64**, 1765 (1942).
6. F. Francis and O. C. M. Davis, *J. Chem. Soc.*, **95**, 1404 (1909).
7. J. S. Buck, *J. Am. Chem. Soc.*, **55**, 2593 (1933).
8. K. Kindler, *Arch. Pharm.*, **269**, 70 (1931).
9. *Org. Syntheses*, **29**, 83 (1949).
10. J. B. Niederl and A. J. Ziering, *J. Am. Chem. Soc.*, **64**, 885 (1942).
11. T. E. Teeter and P. van Rysselberghe, *Proc. 6th Meeting Intern. Comm. Electrochem. Thermodynam. and Kinet.*, **1955**, 538.

The Electrochemistry of Nickel

I. Codeposition of Nickel and Hydrogen from Simple Aqueous Solutions

John Yeager,[1] J. P. Cels,[2] Ernest Yeager, and Frank Hovorka

Department of Chemistry, Western Reserve University, Cleveland, Ohio

ABSTRACT

The simultaneous electrodeposition of nickel and hydrogen has been studied in chloride and sulfate solutions and the individual polarization curves determined from efficiency measurements. Nickel polarization has a Tafel slope of 0.10 and is independent of *p*H and type of anion at constant nickel ion activity. The nickel polarization data can be explained readily in terms of the transfer of a nickel ion from the solution across an unsymmetrical potential energy barrier to the metal phase. The hydrogen overvoltage evaluated during codeposition at constant *p*H is substantially the same for both chloride and sulfate solutions with a Tafel slope of 0.12. Hydrogen and nickel deposition appear to occur without any appreciable interdependence over the range of conditions involved in the present work.

The electrodeposition of nickel has been studied by various workers in the terms of polarization measurements (1-8), structural studies (9-13), and efficiency measurements (7, 14). With only a few exceptions, these measurements have been made in nickel solutions containing two or more anions in appreciable concentrations and often various addition agents. Experimental results obtained with such relatively complicated systems are not conducive to fundamental interpretation.

The present investigation has been directed to the determination of the various parameters associated with the electrodeposition of nickel from relatively simple aqueous solutions containing only one type of anion at a time in any appreciable concentration, i.e., sulfate or chloride. The cathodic polarization and current efficiency with respect to nickel deposition have been measured in sulfate and in chloride solutions as a function of nickel ion concentration, *p*H, and temperature. From these data, the activation polarization for both nickel deposition and hydrogen deposition has been calculated (15) as a function of current density for each process.

Reiser and Fischer (7) have reported on the simultaneous deposition of hydrogen and nickel from a nickel chloride-hydrochloric acid solution and have calculated the individual polarization curves according to the procedure mentioned above. These authors then compared the nickel polarization curve from the simultaneous discharge with the corresponding curve for the deposition of nickel from a boric acid buffered, nickel chloride solution for which the efficiency was close to 100%. Hydrogen polarization for the simultaneous discharge was compared with that for a nickel surface in a pure hydrochloric acid solution. The polarization curves for nickel electrodeposited from the two different solutions were found to be reasonably close in view of the differences in the nickel ion activities and the possibility of nickel hydroxide formation near the cathode at a *p*H as high as 4.4. Major differences were found for the hydrogen overvoltage curves. On the basis of the latter comparison, Reiser and Fischer concluded that the hydrogen and nickel deposition processes are dependent on each other during codeposition on a nickel surface.

Such comparisons are not without question. For example, in the hydrogen overvoltage comparison, no consideration appears to have been given to the differences in the hydrogen ion activities or salt effects. A specific objective of the present research has been to examine further the interdependence of the polarization curves for nickel and hydrogen during simultaneous discharge in terms of the dependence of these processes on nickel and hydrogen ion activities in both chloride and sulfate solutions.

Apparatus

Such factors as mass transport, current distribution, electrochemical purity, and temperature must be controlled carefully in polarization measurements. The polarization cell shown in Fig. 1 has been designed with these factors in mind. The Pyrex cell consists of two U-tubes at right angles to each other with the two U-tubes joined by a T-connection at the cathode compartment. Several small sidearms (not shown) have been incorporated to facilitate the introduction of auxiliary electrodes and a solution bridge to an external reference electrode for *p*H measurements as well as for the filling and subsequent withdrawal of the solution from the cell. The cathode assembly was introduced through a ground joint at the top of the cell while the anode was introduced through a second ground joint (not shown) in the other end of the U-section containing the cathode. The centrifugal glass stirrer and associated drive system, represented diagrammatically

[1] Present address: National Carbon Research Laboratories, Parma, Ohio.
[2] Present address: The Kemet Company, Cleveland, Ohio.

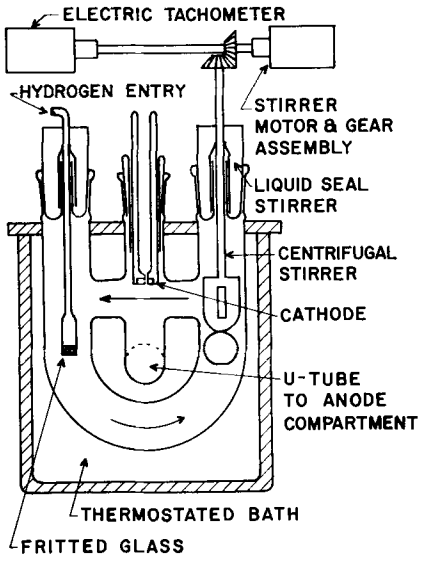

Fig. 1. Polarization cell

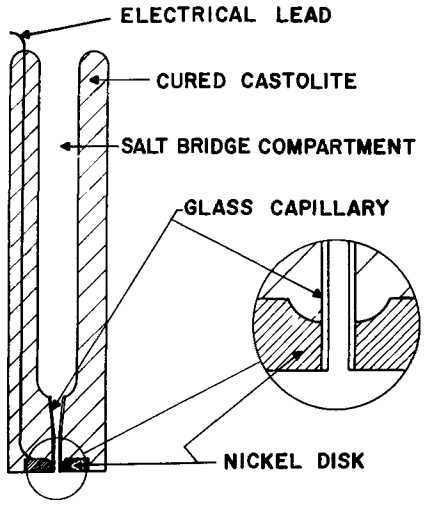

Fig. 2. Plastic cathode assembly with rear-type Luggin capillary.

in Fig. 1, were used to circulate the electrolyte past the cathode surface at a controlled rate with the direction of flow as shown by the arrows. The solution within the cell was saturated with purified hydrogen gas, usually by means of a fritted glass disk. Temperature was controlled to ±0.05°C by means of a thermostatic control mounted within the outer bath in Fig. 1.

The majority of the polarization measurements have been made by the direct method. The Luggin capillary was introduced through the rear of the cathode since this arrangement did not interfere with the flow of the solution past the cathode surface. This advantage more than offsets the possible disadvantage associated with slightly nonuniform current density distribution at the electrode surface. Any *IR* drop effects associated with the use of the rear Luggin capillary arrangement were shown to be negligible on the basis of a check made by the interrupter method.

The cathode design is shown in Fig. 2. A metal disk with an area of approximately 1 cm^2 and a thickness of 1/8 in. was mounted in the cured plastic Castolite.[3] A glass capillary tube with an internal diameter of 1/16 in. extended from the inside of the cathode assembly to the outside. The outside end of the glass capillary tube was ground so as to be flush with the surface of the nickel disk. Electrolytic leakage between the inside of the cathode assembly and the nickel through a path around the outside of the glass capillary tube was not a problem since the capillary tube was cast in the plastic.

The reference electrode for the cathodic polarization measurements was a mercury-mercurous chloride, saturated potassium chloride, reference electrode (S.C.E.). Reagent grade chemicals and triply distilled mercury were used in the preparation of the reference electrode. For all measurements, the reference electrode was maintained at the same temperature as the polarization cell. In order to minimize contamination of the solution within the cathode compartment, an intermediate solution bridge filled with the same solution as in the cell was used between the solution in the rear of the cathode assembly and the reference electrode. Two asbestos-filled capillaries were placed in this solution bridge to prevent any appreciable convection.

The anode for the polarization measurements in nickel sulfate solutions consisted of a platinum foil in the form of a cylinder. This cylinder was welded to a platinum wire which, in turn, was sealed into a soft glass tube. For the chloride solutions, the platinum anode was not used because of possible difficulties associated with liberation of chlorine within the cell. For the chloride solutions, the anode consisted of a cylinder of nickel with a thick plate of nickel electrodeposited from a Watts bath which had been prepared from reagent grade chemicals. The anode was inserted into the cell through a ring-sealed joint. A separate gas vent was incorporated in the anode compartment in order that any gaseous products liberated at the anode would be swept out with the hydrogen, and hence, would not reach the cathode compartment. The anodic efficiency in the chloride solutions with the electroplated nickel anode was close to 100%.

Polarization was measured with a L&N K-1 potentiometer in conjunction with an Eppley unsaturated Weston standard cell. A conventional regulated, filtered powder supply capable of delivering 350 v at 200 ma with a large series resistance was used as a source of polarizing current. The current through the cell was determined by measuring the *IR* drop developed across a standard 10.00-ohm resistance in series with the cell.

The velocity of the electrolytic solution was determined as a function of the voltage output of the electrical tachometer by means of a Pitot tube with an entrance of 1 mm ID. By varying the position of the tip of the Pitot tube in the cathode compartment, it was established that the velocity of the solution was at a maximum at a level corresponding to approximately the top of the intersection in Fig. 1. For this reason, the cathode assembly was placed in the cell in such a way that the cathode surface was

[3] Castolite Company, Woodstock, Ill. This plastic is an unsaturated polyester resin and is insoluble in all common solvents when properly cured.

just a slight distance below the top of this intersection. The final velocity vs. tachometer measurements were made with the cathode assembly in the cell.

Experimental Procedure

The solutions were prepared from recrystallized reagent grade nickel sulfate and chloride. The effect of pre-electrolysis of the electrolytic solutions with platinum electrodes was examined during the preliminary polarization measurements and found to be negligible at potentials for which appreciable nickel electrodeposition occurred. This finding concerning pre-electrolysis is somewhat surprising in view of the general need for pre-electrolysis in polarization studies. The effects of impurities on the polarization, however, are probably considerably less in the case of the deposition of a metal wherein a new surface is constantly being created. At higher *p*H, the pre-electrolysis caused considerable changes in the *p*H. As a result, pre-electrolysis was not used for the majority of the measurements reported in this paper.

The exact concentration of nickel in the various solutions was determined by the cyanide method (16). The *p*H of each solution was determined by measuring the potential of a hydrogen electrode in the particular electrolyte vs. an S.C.E. While the precision of these measurements was of the order of 0.01 *p*H unit, the accuracy was less because of liquid junction potentials. The *p*H of each solution was adjusted to specific values through the addition of either hydrochloric or sulfuric acid to the electrolyte.

The preparation of the cathode surface was as follows. The nickel cathode was first abraded to yield a fresh surface with medium grade (320 A) silicon carbide, waterproof emery paper, wetted with water, and then polished further with fine waterproof emery paper (400 A) until the surface of the nickel disk appeared uniformly smooth. The electrode surface was subsequently etched for 45 sec in a 5*N* nitric acid solution. After the surface was thoroughly rinsed with distilled water, the cathode was quickly inserted into the polarization cell and the solution velocity adjusted to approximately 45 cm/sec in the bulk of the solution adjacent to the cathode. The polarizing current was then adjusted to 15 ma/cm^2, and the electrodeposition of nickel continued at this current density for 10 min. This period of time has been found sufficient for the cathode to attain an essentially steady-state condition with respect to potential.

After 10 min of preplating, the polarization was carefully measured at a current density of exactly 15 ma/cm^2. The current density was then increased to 55 ma/cm^2 and the potential recorded again as soon as a stable value was attained. This usually required less than 30 sec. Polarization measurements were made subsequently at current densities of 45, 35, 25, 10, 6, 4, 2, 1, 4, and 15 ma/cm^2. In each case, a second repeat run was made under similar circumstances with a 10-min preplate period. In the second run, polarization measurements were made at the current densities of 15, 50, 40, 30, 20, 15, 12, 8, 5, 3, 1.5, 3, 5, and 15 ma/cm^2. Area increments under these conditions were negligible. After the completion of the run, the *p*H of the electrolyte was again checked with the hydrogen electrode. The *p*H change during any one run usually was less than 0.02 *p*H unit.

The cathode efficiencies for the electrodeposition of nickel were determined at the potentials associated with current densities of 55, 40, 25, 15, 8, and 5 ma/cm^2 for each solution composition and temperature involved in the polarization studies. In some cases, the amount of nickel that could be deposited in any reasonable time was so small that conventional weighing operations were not suited to the determination of the amount of nickel electrodeposited. Consequently, the procedure adopted for this purpose involved the anodic dissolution of the deposited nickel in hydrochloric acid solution followed by the analysis of the solution for nickel by the cyanide method (16). The electrolytic cell used for the anodic dissolution is described elsewhere in detail (17). The cathode assemblies used in the efficiency studies were similar in design to those shown in Fig. 2 with the exception that the disk of nickel was replaced with a similar disk of silver. The silver surface was preplated with nickel at a current density of 15 ma/cm^2 for 10 min in much the same fashion as in the case of the polarization measurements. The amount of nickel electrodeposited during the preplate time was carefully determined and subtracted from the total amount of nickel deposited on the cathode in the subsequent measurements.

The structural properties of the electrodeposited nickel were examined by means of x-ray diffraction techniques. A modified Wyllie (18) camera, specifically constructed for the examination of electrodeposits, was used for this work. A North American Phillips x-ray diffraction tube with a cobalt target provided an incident x-ray beam at an angle of approximately 15° relative to the surface of the electrodeposit. A cylindrical projection of the diffracted x-rays was obtained. The depth in the deposit to which the x-ray pattern was sensitive was checked by depositing a known amount of nickel on a silver surface and then examining the diffraction pattern for lines corresponding to silver. In the final x-ray examination, the deposit thickness was adjusted so as to prevent the preplated nickel from registering directly in the x-ray diffraction patterns. Because of the relatively small angle of incidence of the x-ray beam, deposits of only a few ten-thousandths of an inch thickness were generally sufficient.

Experimental Results

Flow rate.—At 45°C for all of the solutions involved in the present work, the cathodic polarization was found to approach a limiting value with increasing flow rate even at current densities as high as 55 ma/cm^2. This was not the case at 25°C in the more dilute solutions. Even at the highest available solution velocities (50 cm/sec) in the 0.12M nickel sulfate, the polarization attained a limiting value only at current densities less than 25 ma/cm^2. For this reason, the majority of the polarization measurements have been made at 45°C. Although the

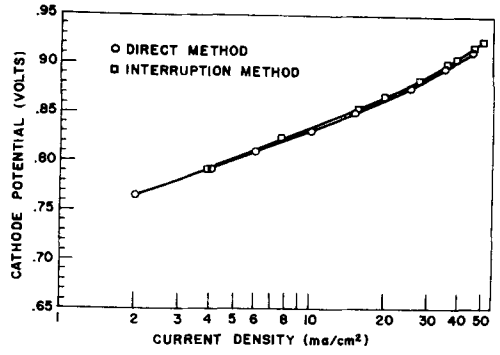

Fig. 3. Comparison of polarization measurements by the direct and interrupter methods. Potentials are negative to the saturated KCl calomel electrode (S.C.E.) at the same temperature. Solution: 0.5M $NiCl_2$ with a pH of 2.0 at 25°C, adjusted by addition of HCl.

polarization attained a limiting value as the solution velocity was increased, it cannot be assumed that the concentration polarization was negligible. The increase of the velocity of flow in the bulk of the solution beyond a certain value probably has relatively little effect on the effective thickness of the diffusion layer at the cathode solution interface. The attainment of a limiting value for the polarization at high flow rates, however, is important because reproducible concentration gradients are then established at the electrode surface. In no case was a limiting current density found with respect to the discharge of either nickel or hydrogen. Unless otherwise indicated, all of the polarization measurements reported in this paper were made with a maximum flow rate in the bulk of the electrolyte adjacent to the cathode surface of 45 cm/sec.

Reproducibility.—In Fig. 3, cathode potentials (negative to an S.C.E. reference) are plotted against total current density for a 0.5M nickel chloride solution with a pH of 2.0 at 25°C. The data noted by the circles were obtained by the procedures described above, whereas the data indicated by the squares were obtained in subsequent measurements by Griffis (19) in a glass polarization cell of somewhat different design. The interrupter method was used for the latter measurements with cathodes of 0.25 cm^2 area with purified hydrogen gas bubbled through the solution. The electronic equipment has been described previously (20). In both cases, the

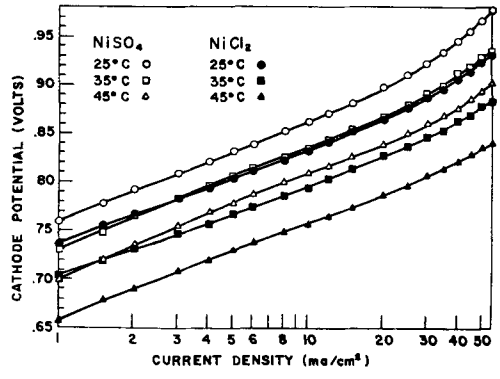

Fig. 4. Dependence of cathode potentials on current density at various temperatures in 0.5M salt solutions of pH 2.0. Potentials negative to S.C.E. at the same temperature; pH adjusted by addition of HCl or H_2SO_4.

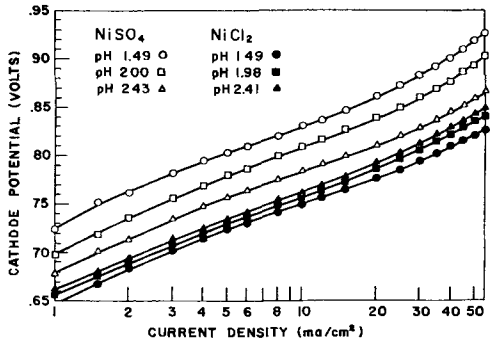

Fig. 5. Dependence of cathode potentials on current density at various pH in 0.5M salt solutions at 45°C.

flow rates in the solution adjacent to the cathode were in excess of 40 cm/sec. The agreement between the two independent sets of measurements is within ±2 mv.

Further evidence of the reproducibility in the present work can be found in Fig. 4-6 in terms of the smooth curves which can be drawn through the experimental points despite the fact that two separate runs were involved in obtaining the points for each curve. The agreement between the polarization measured at 15 ma/cm^2 at the start of each run and that measured at the same current density at the end of each run was usually within ±1 mv and at the worse ±3 mv.

Polarization data.—In Fig. 4-6 are presented typical cathodic polarization data for the simultaneous deposition of nickel and hydrogen from chloride and sulfate solutions for various temperatures, pH, and nickel salt concentrations. The ordinates represent cathode potentials (negative to S.C.E.) and include a small liquid junction potential. Variations in the junction potential with solution composition are believed to be small compared to the changes in the cathode potentials arising directly because of changes in the activities of the hydrogen and nickel ions. Current densities represented in these figures are based on the apparent areas of the cathodes.

Polarization measurements have been limited to apparent current densities of 10^{-3} to 10^{-1} a/cm^2 for the following reasons. At current densities below 10^{-3} a/cm^2, the predominant process is the discharge of hydrogen and the polarization values become somewhat nonreproducible, probably because of insufficient control of impurities. Under such circumstances, impurity effects are accumulative. At cur-

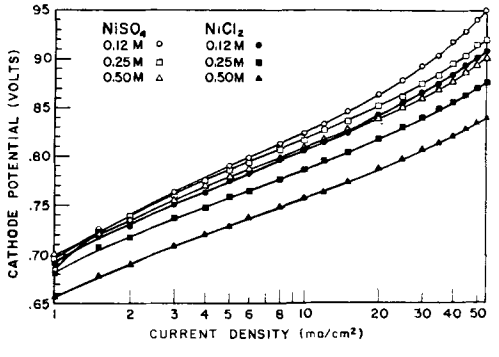

Fig. 6. Dependence of cathode potentials on current density at various salt concentrations at pH 2.0 and 45°C.

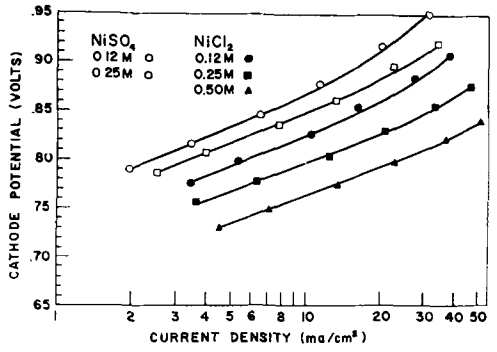

Fig. 7. Dependence of cathode potential on current density for nickel electrodeposition at various salt concentrations at pH 2.0 and 45°C.

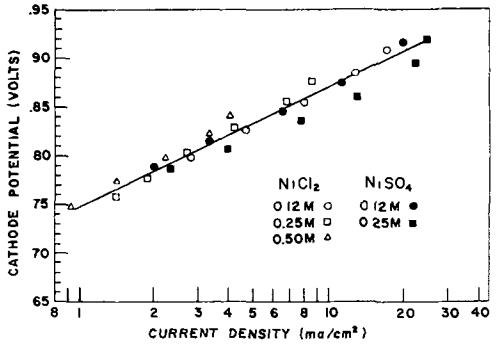

Fig. 10. Dependence of cathode potential on current density for hydrogen discharge at various salt concentrations at pH 2.0 and 45°C.

rent densities above 10^{-1} a/cm^2, concentration polarization becomes significant in solutions of relatively low nickel ion concentration and high pH.

Polarization curves for the discharge of nickel at 45°C are presented in Fig. 7-9 for various nickel ion concentrations, pH, and temperatures. These curves have been derived from the over-all polarization data and the efficiency data. At least part of the deviation from linearity at higher current densities is associated with concentration polarization, and perhaps all of it.

In Fig. 10-12 are the polarization curves for the discharge of hydrogen at various nickel salt concentrations, pH, and temperatures. As in the case of the nickel polarization curves, deviations from linearity can be explained in terms of concentration polarization. Mass transport problems should be particularly severe at the higher pH as is evident from the curve for pH 2.43 in the 0.5M $NiSO_4$ solution in Fig. 11.

The differential capacity of the nickel cathode was measured by the interrupter method in the 0.50M nickel sulfate solution at a pH of 2.0 and temperature of 45°C. The value was found to be 75 ± 3 μf/cm^2 of apparent surface area over the complete range of potentials represented in Fig. 4-6. If the value of 28.8 μf/cm^2 of true surface area as determined by Brodd and Hackerman (21) for nickel in 1M Na_2SO_4 at 30°C is assumed applicable at potentials negative with respect to the zero point of charge, the roughness factor is approximately 2.5. In Fig. 10, the hydrogen polarization exhibits little variation with the type or concentration of nickel salt. Likewise in Fig. 8, the nickel polarization exhibits only minor dependence on pH particularly in chloride solution. This implies that the roughness factor does not change to any appreciable extent with pH, salt type, or salt concentration. Little question exists as to the constancy of the roughness factor during a

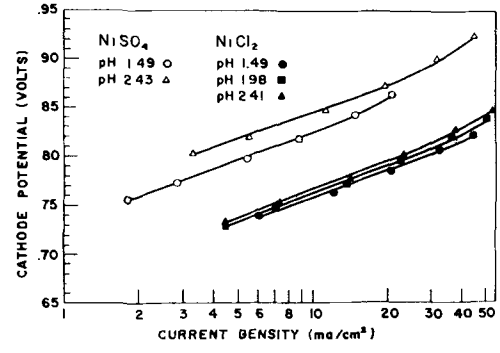

Fig. 8. Dependence of cathode potential on current density for nickel electrodeposition at various pH in 0.5M salt solutions at 45°C.

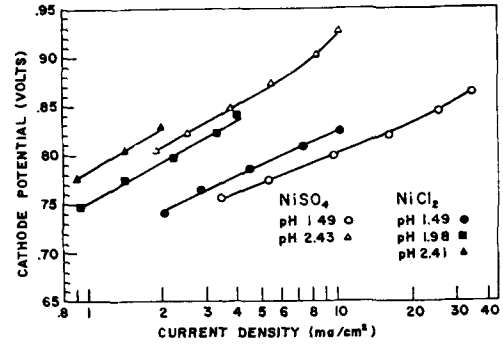

Fig. 11. Dependence of cathode potential on current density for hydrogen discharge at various pH in 0.5M salt solutions at 45°C.

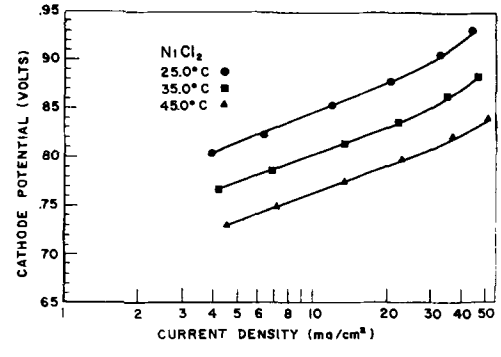

Fig. 9. Dependence of cathode potential on current density for nickel electrodeposition at various temperatures in 0.5M nickel chloride at pH 2.0.

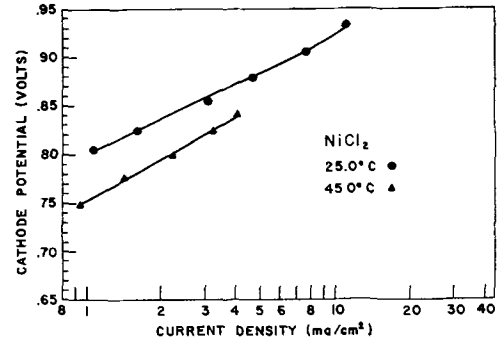

Fig. 12. Dependence of cathode potential on current density for hydrogen discharge at various temperatures in 0.5M nickel chloride at pH 2.0.

Table I. Polarization data for hydrogen discharge and nickel deposition

Salt	Molarity	Temp, °C	pH	Hydrogen discharge*			Nickel deposition		
				B	α	$-\log i_o$	B	αz	$-\log i_o$
$NiCl_2$	0.50	25	2.00	0.123	0.48	6.6	0.103	0.57	5.4
	0.12	45	2.00	0.130	0.49	5.9	0.103	0.61	5.0
	0.25	45	2.00	0.139	0.45	5.8	0.098	0.64	4.7
	0.50	45	2.00	0.134	0.47	5.9	0.098	0.64	4.5
	0.50	45	1.49	0.120	0.53	6.1	0.093	0.68	4.6
	0.50	45	2.41	(0.143)	(0.44)	(5.6)	0.100	0.63	4.5
$NiSO_4$	0.12	45	2.00	0.117	0.54	6.4	0.105	0.60	5.0
	0.25	45	2.00	0.111	0.57	6.4	0.104	0.61	5.0
	0.50	45	1.49	0.120	0.53	6.1	0.093	0.68	5.0
	0.50	45	2.43	(0.144)	(0.44)	(6.6)	0.091	0.69	5.5

* Bracketted values are dubious because of concentration polarization with respect to hydrogen ions or because of limited accuracy for the hydrogen discharge current. When the efficiency for nickel deposition is close to 100%, the errors in the hydrogen discharge current become quite significant.

given polarization run in view of the reproducibility of the initial and final polarization values at a total current density of 15 ma/cm^2.

In Table I are summarized the polarization data for the discharge of hydrogen and nickel ions in terms of the Tafel slopes (B), the logarithms of the exchange current i_o in a/cm^2 of apparent area, and αz, where α is the fraction of the potential effective in changing the energy of activation for the cathodic rate-determining step, and z is the charge of the species passing over the energy barrier. For hydrogen, $z = 1$, while for nickel, z can be assumed to be equal to 2 if the rate-determining step involves the transfer of a nickel ion from the solution to the metal phase. The coefficient α is approximately 0.50 for hydrogen discharge with no significant difference in this coefficient between the sulfate and chloride solutions within the limits of experimental error. Likewise, the average value for the coefficient αz for nickel discharge is 0.65 and does not appear to differ significantly between sulfate and chloride solutions.

The calculation of the values for log i_o requires a knowledge of the reversible potentials of the hydrogen and nickel electrodes in the particular electrolytic solutions involved in the present work. For hydrogen, this is not a problem since the potentials of the reversible hydrogen electrode in these electrolytic solutions vs. S.C.E. were determined directly as part of the adjustment of the solutions to particular pH values. In the case of nickel, however, the reversible potential vs. the S.C.E. is much more difficult to establish because the reversible potentials could not be measured directly under the present experimental conditions. Furthermore, the best literature values for the standard electrode potential for nickel are probably accurate only to 10 mv. Even with data for the standard electrode potential for nickel, the uncertainties concerning liquid junction potentials and single ion activities interfere with the accurate calculation of the potential difference between the reversible nickel electrode and the S.C.E. In the present work, this potential has been evaluated for both sulfate and chloride solutions on the basis of the following equation:

$$E = -0.470-(1.0\cdot 10^{-3})(t-25) + (0.9915)(10^{-4})\ T \log a_+ \qquad [1]$$

where a_+ is the activity of the nickelous ion and t and T are the temperature on the Centigrade and absolute scales, respectively. This equation is based on the data of Carr and Bonilla (22) for the thermogalvanic potentials of nickel in 0.1 and 1.0M nickel sulfate solutions. In using the above equation for chloride as well as sulfate solutions, the assumption has been made that the liquid junction potentials and the temperature coefficients are the same for the chloride solutions as for the sulfate solutions. This assumption is probably valid to within a few millivolts.

The activities of the nickelous ion have been calculated for the sulfate solutions from the mean activity coefficients evaluated by Harned and Owen (23) from the isopiestic vapor pressure data of Robinson and Jones (24), and for the chloride solutions (25) from the isopiestic vapor pressure measurements of Robinson and Stokes (26). For the nickel sulfate solutions, the activity coefficient of nickelous ion has been assumed equal to the mean activity coefficient. For the chloride solutions, the activity coefficient of the nickelous ion was set equal to the square of the mean activity coefficient on the basis of the Debye limiting law. Furthermore, the values for the activity coefficients at 45°C have been assumed to be the same as at 25°C, an approximation which appears justified in view of the limited accuracy of Eq. [1]. In the case of the nickel sulfate solutions of pH 1.49, the amount of sulfuric acid added in the course of adjusting the pH was appreciable compared to the nickel sulfate concentration (0.5M). This partially was taken into account in the activity coefficient calculations by using the mean activity coefficient of nickel sulfate solutions of the same ionic strength as that of the sulfuric acid-nickel sulfate solutions.

The accuracy of the values for the apparent exchange current i_o is limited more by the accuracy of the value for the Tafel slope than the reversible potential. The uncertainty in the Tafel slope is particularly great for solutions in which either the concentration polarization is appreciable or the current densities for hydrogen discharge are uncertain because only a small fraction of the total current is involved in hydrogen discharge, e.g., hydrogen polarization curve in Fig. 11 for 0.5M nickel chloride at pH 2.41. On the basis of the roughness factor of

Table II. Orientation and grain size of nickel electrodeposited at 45°C

Salt	pH	Current density, ma/cm²	Orientation*	Grain size†
0.5M $NiSO_4$	1.5	5	R	1
		15	[100]	2
		40	[100]W	2
	2.5	5	R	1
		15	[100]	2
		40	[110]	1
0.5M $NiCl_2$	1.5	5	R	2
		15	[100]	3
		40	[100]W	3
	2.5	5	R	2
		15	R	4
		40	[100]W	2

* Random = R; Weak = W.
† Grain size scale: 1 to 4 (increasing size).

2.5, discussed earlier, the quantity −0.4 should be added to log i_o values in Table I to obtain the logarithm of the exchange current per unit true area.

X-ray diffraction.—The x-ray diffraction studies indicated that all of the deposits at 45°C from chloride and sulfate solutions have a face-centered cubic lattice. The diffraction patterns show a tendency for two types of preferred orientations as well as small changes in grain size. These results are summarized in Table II on a relative basis. In no case was the tendency for preferred orientation strong. The lack of any preferred orientation at the low current densities is surprising, particularly since the preplate had a small tendency for the [100] plane to be parallel to the surface. At the higher current densities, the [110] plane tends to be parallel to the surface for the sulfate solutions.

The grain size is compared qualitatively on a scale of 1 to 4, where 1 represents the finest grain and 4 the coarsest for the samples which were examined. This scale is believed to have covered a small range of grain size with the variation in size between the limits of the scale estimated to have been less than 1 to 3. No consistent trend is evident with increasing current density, although the grain size was generally smaller with the nickel sulfate solutions than the nickel chloride solutions.

Table III. Hydrogen overvoltage data for nickel in hydrochloric and sulfuric acid solutions according to other workers

Electrolyte	Temp, °C	Tafel slope	−log i_o	Worker
0.0003M HCl	—*	0.090	6.7	L., L., & F.(30)
0.0012M HCl	—	0.090	6.7	L., L., & F.
0.013M HCl	—	0.10	6.5	L., L., & F.
0.15M HCl	—	0.10	6.0	L., L., & F.
0.001M HCl	20	0.093	6.6	B. & P.(29)
0.001M HCl	40	0.104	6.0	B. & P.
0.01M HCl	20	0.091	6.7	B. & P.
0.01M HCl	40	0.094	6.1	B. & P.
0.1M HCl	20	0.104	6.0	B. & P.
0.1M HCl	40	0.106	5.7	B. & P.
1.0M HCl	20	0.109	5.4	B. & P.
1.0M HCl	40	0.120	4.2	B. & P.
1M $NiCl_2$ + 1M HCl	20	0.06	9.5	R. & F.(7)
1M $NiCl_2$ + 1M HCl	30	0.07	8.3	R. & F.
1M $NiCl_2$ + 1M HCl	40	0.07	8.1	R. & F.
1M $NiCl_2$ + 1M HCl	50	0.07	8.1	R. & F.
0.1M H_2SO_4	25	0.110	6.6	B. & R.(31)
0.01M H_2SO_4	25	0.110	6.4	J., Y., & H.(27)
0.05M H_2SO_4	25	0.095	6.3	J., Y., & H.
0.5M H_2SO_4	25	0.097	4.5	J., Y., & H.
0.05M H_2SO_4 + 0.45M K_2SO_4	25	0.135	6.6	J., Y., & H.

* No temperatures appear to have been given by Lukovzev, Levina, and Frumkin (30).

Interpretation of Experimental Results

In systems involving simultaneous electrode processes, the assumption is often made that the current densities associated with the individual processes can be calculated on the basis of a constant effective area for each process. In Fig. 7-12 for nickel and hydrogen discharge, the Tafel slopes are substantially constant over a tenfold change in current density in the instances where concentration polarization is not large. This constancy of the Tafel slopes supports the above stated assumption. Likewise, the hydrogen discharge appears to be independent of nickel deposition on the basis of the linearity in the Tafel plots for hydrogen as well as the minor and probably negligible effect which variations in nickel salt concentration appear to have on the hydrogen polarization curves (see Fig. 10).

The values for the derivative of the cathode potential with respect to pH at constant hydrogen discharge current, evaluated near the middle of the linear ranges in Fig. 11, are 0.11 and 0.10 for hydrogen discharge[4] from sulfate solutions and from chloride solutions, respectively, provided the curve for pH 2.41 in 0.5M nickel chloride is not considered. These values compare favorably with the value of $2.3RT/\alpha F$ predicted (28) for the dependence of the electrode potential on pH when hydrogen is deposited in acid solution in the presence of a neutral salt for the case where either the hydrogen ion discharge step or the electrochemical desorption step is rate-determining. This relatively close agreement however, is to be expected only in the absence of specific ionic adsorption.

Unfortunately, hydrogen overvoltage data are not generally available in the literature for purposes of comparison with the present data since it is necessary to duplicate both pH and ionic strength. Table III summarizes hydrogen overvoltage data of Bockris and Potter (29) and of Lukovzev, Levina, and Frumkin (30) for room temperatures. Values for the 0.01 and 0.013*N* hydrochloric acid solutions in Table III differ by small, although significant amounts from the Tafel slope of 0.123 and the log i_o value of −6.6 listed in Table I for the 0.5M nickel chloride solution of pH 2.0 at 25°C. Such differences might be anticipated in view of the large concentration of salt present during the codeposition of hydrogen with nickel as well as the dependence of the Tafel slope on the pretreatment of the nickel surface (27).

The Tafel slopes and log i_o, calculated from the graphs published by Reiser and Fischer (7), also have been listed in Table III. These values are based

[4] Values for −log i_o in Table I are far too limited in accuracy to permit the effects of varying pH on the kinetics to be examined in terms of the apparent exchange current density.

on polarization measurements obtained during the simultaneous deposition of hydrogen and nickel. They differ from those obtained by other workers in Table III as well as in the present investigation. Hydrogen overvoltage measurements in sulfuric acid by Bowden and Rideal (31), and Jefferys, Yeager, and Hovorka (27) also have been presented in Table III. It is interesting to note that the Tafel slope is higher in sulfuric acid containing an excess of potassium sulfate. If the Tafel slope for hydrogen on nickel in sulfuric acid tends, in general, to be higher in the presence of a salt, then this may explain the slightly higher slopes obtained for hydrogen overvoltage in the present work.

The heat of activation for the discharge process at the reversible potential of the hydrogen electrode may be calculated on the basis of the following equation:

$$\Delta H^* = \alpha z F[T(\partial\eta/\partial T)_i - \eta] \qquad [2]$$

provided α is independent of temperature. If this equation is applied to the data in Table I for the 0.5M nickel chloride solution at *p*H 2 and at temperatures of 25° and 45°, ΔH^* is approximately +12 kcal, averaged over this temperature range. Considerable question exists, however, as to the accuracy of this value. A change in the roughness factor between 25° and 45° would cause a relatively large error. It is to be compared with values of 6.9 kcal and 16.3 kcal obtained by Bockris and Potter for 0.1*N* and 1.0*N* hydrochloric acid solutions, respectively. A knowledge of the Tafel slope, the exchange current density, and the approximate energy of activation for hydrogen overvoltage on nickel has not proved sufficient to resolve the question (32, 33) as to whether the rate-determining step is proton discharge ($H^+_{aq} + e^- \rightarrow H_{ads}$) or electrochemical desorption ($H^+_{aq} + H_{ads.} + e^- \rightarrow H_2$).

From Fig. 7 to 9, it is evident that the polarization associated with nickel electrodeposition is substantially independent of *p*H and follows the Tafel type dependence on current density. Deviations from linearity at higher current densities are probably associated with concentration polarization. These results support the conclusion that the rate-determining step associated with the nickel deposition is independent of hydrogen discharge over the range of conditions represented in the present work.

The apparent lack of interdependence between nickel deposition and hydrogen discharge can be explained on the basis that the number of sites available for nickel deposition does not vary appreciably with *p*H or potential and that the total number of sites available for each process is very large compared to the actual number of sites involved at any instant.

On the basis of the Tafel slopes listed in Table I, the value for αz is approximately 0.65. Such a value appears reasonable in terms of the transfer of a nickel ion from the solution across an unsymmetrical potential energy barrier to the solid phase as the rate-determining step for the nickel polarization. If this is the case, $z = 2$ and $\alpha = 1/3$. The data in Fig. 7-9 do not appear compatible with rate-determining steps involving transfer of nickel from metastable surface sites to stable lattice sites. It is interesting to note that Yuza and Kopyl (1) in 1940 reported a Tafel slope corresponding to $\alpha \cong 1/2$ on the basis of oscillographic studies of nickel electrodeposition from a 1M nickel chloride solution buffered with boric acid. In 1935, Essin and Alfimova (14), primarily from current efficiency measurements, deduced a value of $\alpha = 0.39$ for nickel sulfate over a range of concentrations and temperatures. The Tafel slope calculated from the graphs of Reiser and Fischer (7) is approximately 0.09 at 40°C for the electrodeposition of nickel from a 1.0M $NiCl_2$ — 1.0M HCl solution as well as a 0.26M $NiCl_2$ solution buffered with boric acid to *p*H 4.4. This Tafel slope corresponds to $\alpha = 0.3$ for $z = 2$.

The variation of the cathodic potential with the nickel ion activity expressed as the derivative $(\partial E/\partial \log a_+)_i$ has been found to be 0.12 for both the chloride and the sulfate solutions on the basis of the data represented in Fig. 7. Nickel ion activities have been calculated on the same basis as described earlier in conjunction with the determination of the reversible nickel potentials. Unfortunately, present day treatments of the double layer structure are not adequate to permit a quantitative prediction of $(\partial E/\partial \log a_+)_i$ with relatively concentrated solutions of polyvalent electrolytes such as $NiCl_2$ wherein complexing occurs. Furthermore, considerable question exists as to the significance of single ion activities evaluated in such solutions by the procedure indicated earlier.

In general, the deposition of nickel from a chloride solution occurs at lower potentials with corresponding higher current efficiencies than from sulfate solutions of the same concentration. This difference between chloride and sulfate solutions is as would be predicted on the basis of the nickel ion activities for the solutions represented in Fig. 7. In the sulfate solutions, the nickel activity coefficients are considerably lower than in chloride solutions. Thus, differences between chloride and sulfate solutions are not evidence of any specific anion effects.

As in the case of the hydrogen polarization data, the energy of activation for nickel deposition may be calculated from Eq. [2], provided the surface roughness factor and α are substantially independent of temperature and the method of ascertaining the reversible potential for nickel relative to the saturated calomel reference electrode is reliable. On the basis of the apparent exchange currents listed in Table I for 0.5M $NiCl_2$ at *p*H 2.0 for 25° and 45°C, the activation energy for nickel is +21 kcal or approximately twice that for hydrogen discharge.

A detailed discussion of the kinetics of the rate-determining steps involved in the nickel deposition will not be given at this time but will be postponed until after the publication of later papers in this series involving the electrodeposition of nickel from mixed solvent systems and the anodic properties of nickel in simple chloride and sulfate solutions.

Acknowledgments

The authors are pleased to acknowledge the support of this research by the Harshaw Chemical

Company through fellowships to two of the authors (John Yeager and J. P. Cels). This research has also been supported by the Office of Naval Research under Contract Nonr 58100. The authors express their appreciation to Robert Griffis and Richard Jefferys who carried out some of the supplementary work cited in this paper.

Manuscript received July 9, 1958. This paper was presented at the New York Meeting April 27-May 1, 1958.

Any discussion of this paper will appear in a Discussion Section to be published in the December 1959 JOURNAL.

REFERENCES

1. V. Yuza and L. Kopyl, *J. Phys. Chem. (U.S.S.R.)*, **14**, 1074 (1940).
2. O. Essin and M. Laskarev, *ibid*, **13**, 186 (1939).
3. A. Vagramyan and Z. Solovéva, *Doklady Akad. Nauk. (U.S.S.R.)*, **77**, 629 (1950).
4. A. Gorbachev and Y. Yurkevich, *J. Chem. Phys. (U.S.S.R.)*, **28**, 1120 (1954).
5. F. Salt, *Discussion Faraday Soc.*, **1**, 169 (1947).
6. G. Gardam, *ibid.*, **1**, 182 (1947).
7. H. Reiser and H. Fischer, *Z. Elektrochem.*, **58**, 668 (1954).
8. H. Fischer, M. Seipt, and G. Morlock, *ibid.*, **59**, 440 (1955).
9. E. Yang, *This Journal*, **97**, 241 (1950).
10. G. Clark and S. Simonson, *ibid.*, **98**, 110 (1951).
11. H. Leidheiser and A. Gwathmey, *ibid.*, **98**, 225 (1951).
12. A. Brenner, V. Zentner, and C. Jennings, *Plating*, **39**, 857 (1952).
13. H. Fischer, "Elektrolytische Abscheidung und Elektrokristallisation von Metallen," pp. 623-638, Springer-Verlag, Berlin (1954).
14. O. Essin and E. Alfimova, *Trans. Electrochem. Soc.*, **68**, 417 (1935).
15. See, e.g., G. Kortum and J. Bockris, "Textbook of Electrochemistry," Vol. II, p. 443, Elsevier Publishing Co., New York (1951).
16. I. Kolthoff and V. Stenger, "Volumetric Analysis," Vol. II, 2nd ed., p. 283, Interscience Publishers, New York (1947).
17. J. P. Cels, Ph. D. Dissertation, Western Reserve University, (1954).
18. M. Wyllie, *Rev. Sci. Instruments*, **18**, 426 (1947).
19. R. Griffis, Ph.D. Dissertation, Western Reserve University (1956).
20. E. Yeager, T. Oey, D. Staicopoulos, and F. Hovorka, Technical Report 6, Office of Naval Research Contract N7onr 47002, Western Reserve University (1951).
21. R. Brodd and N. Hackerman, *This Journal*, **104**, 704 (1957).
22. C. Carr and C. Bonilla, *ibid.*, **99**. 475 (1952).
23. H. Harned and B. Owen, "The Physical Chemistry of Electrolytic Solutions," 2nd ed., p. 427, Reinhold Publishing Co., New York (1950).
24. R. Robinson and R. Jones, *J. Am. Chem. Soc.*, **58**, 959 (1936).
25. Reference (23), p. 567.
26. R. Robinson and R. Stokes, *Trans. Faraday Soc.*, **36**, 1137 (1940)
27. R. Jefferys, E. Yeager, and F. Hovorka, Paper 129, San Francisco Meeting, Electrochemical Society, April 30 to May 3, 1956.
28. A. N. Frumkin, *Z. phys. Chem.*, **164**, 121 (1933); *Acta Physicochim., URSS*, **6**, 502 (1937); *ibid.*, **7**, 475 (1935). See summary in J. Bockris, "Modern Aspects of Electrochemistry," p. 209, Butherworth Scientific Publications, London (1954).
29. J. Bockris and E. Potter, *J. Chem. Phys.*, **20**, 614 (1952).
30. P. Lukovsev, S. Levina, and A. Frumkin, *J. Phys. Chem. (U.S.S.R.)*, **13**, 916 (1939).
31. F. Bowden and E. Rideal, *Proc. Roy. Soc., London*, **A120**, 86 (1928).
32. B. Conway and J. Bockris, *J. Chem. Phys.*, **26**, 532 (1957).
33. B. Conway and J. Bockris, *Can J. Chem.*, **35**, 1124 (1957).

Streaming Potentials of Corundum in Aqueous Organic Electrolyte Solutions

D. W. Fuerstenau[1] and H. J. Modi[2]

Department of Metallurgy, Massachusetts Institute of Technology, Cambridge, Massachusetts

ABSTRACT

The effect of certain 12-carbon anionic and cationic surface-active compounds on the zeta potential of corundum at different pH values has been evaluated from streaming potential measurements. These measurements, made under conditions of both positive and negative surface charge, indicate that long-chained ions are adsorbed appreciably only when the solid and organic ions are oppositely charged. An adsorption mechanism involving electrostatic attraction and hydrocarbon chain association is discussed using the Stern model of the double layer.

The structure of the double layer has been the subject of considerable interest during the past few years. Although most of the work published deals with theoretical considerations, a number of experimental studies utilizing electrokinetic or electrochemical techniques have also been reported. The effects of organic electrolytes on the properties of the electrical double layer are important in flotation and other processes dependent on surface properties, but still the technical literature on the subject is exceedingly scant. Streaming potential experiments on quartz have shown that aminium ions are strongly adsorbed and are able to change the sign of the electrokinetic or zeta potential, ζ, because ions adsorbed

[1] Present address: Kaiser Aluminum & Chemical Corp., Permanente, Calif.
[2] Present address: National Cash Register Co., Dayton, Ohio.

in the Stern layer associate through Van der Waals attraction between their hydrocarbon chains (1, 2) Aminium ions begin to associate at the quartz-solution interface at pH 7 when their bulk concentration is about one-hundredfold less than their bulk critical micelle concentration (2). The experiments with quartz were carried out with a negatively charged surface, but corundum offers the possibility of working with an oxide mineral that can be readily charged positively or negatively since the zero point of charge occurs at pH 9.4 (3). The object of this paper, therefore, is to present the results of an electrokinetic investigation of corundum in solutions containing long-chained organic ions under conditions of both positive and negative surface charge, and to discuss an adsorption mechanism in terms of experimental results.

Experimental Materials and Method

The preparation and treatment of crushed corundum and the equipment and general techniques used in this investigation have been described previously in detail (3, 4). Great care was exercised in using reagents of the highest purity. Dodecylammonium chloride was obtained from Armour and Company, Chicago, Illinois, and sodium dodecyl sulfate and sodium dodecyl sulfonate were both supplied by Colgate-Palmolive Company, Jersey City, New Jersey. A sample of pure sodium laurate was prepared by neutralizing a warm solution of recrystallized lauric acid (mp 43.3°C) in absolute alcohol with an equivalent amount of a warm solution of metallic sodium in absolute alcohol. The white, waxy precipitate which formed was filtered, washed with alcohol, and dried at 90°C.

Experimental Results

Since H^+ and OH^- are potential-determining ions for alumina (3-5), the pH was maintained constant for each series of experiments. At pH values below 9.4, the alumina surface is positively charged, and at higher pH values it is negatively charged. Thus, by controlling the solution pH it is possible to study the effect of an anion or a cation on the electrokinetic potential of a positively or negatively charged surface.

Anionic organic electrolytes.—Zeta potentials of corundum were determined in aqueous solutions of sodium dodecyl sulfate, sodium dodecyl sulfonate, and sodium laurate at pH 6.5. Sodium dodecyl sulfate and sodium dodecyl sulfonate are both completely dissociated in aqueous solutions in the concentration range investigated. Since the pK of lauric acid (6) is about 5.3 and its solubility is 1.2×10^{-5} moles per liter (7), at pH 6.5 the undissociated acid should precipitate from 2×10^{-4}M additions of sodium laurate. The critical micelle concentrations of these anionic organic electrolytes are the following: sodium dodecyl sulfate, 0.8×10^{-2}M; sodium dodecyl sulfonate, 1.0×10^{-2}M; sodium laurate, 2.4×10^{-2}M.

Experimental results are presented in Fig. 1 along with measurements for sodium nitrate added for comparative purposes. The zeta potential curves are characterized by certain common features. First, the

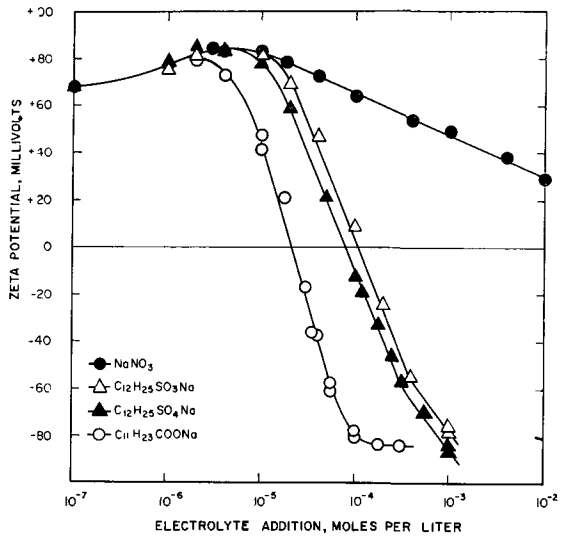

Fig. 1. Zeta potential of corundum in aqueous solutions of sodium laurate, sodium dodecyl sulfate, sodium dodecyl sulfonate, and sodium nitrate at pH 6.5.

experimental values of ζ indicate that all three organic electrolytes function like a simple 1:1 valent inorganic electrolyte (like $NaNO_3$) in dilute solutions. Second, sharp breaks occur in the curves for organic electrolytes with the zeta potential becoming negative, and third, the curves contain a portion where the slope decreases again. In the case of sodium laurate solutions, however, the slope is abruptly reduced to zero by the precipitation of undissociated lauric acid. The slope of the straight line portion of the ζ-log c curve for sodium nitrate is 17 mv, whereas for sodium dodecyl sulfate and sulfonate, it is 102 mv. For sodium laurate, it is 135 mv.

To illustrate the effect of the magnitude and sign of surface charge on the sharp break in the zeta potential curve, measurements were also made at pH 4 and 11 in sodium dodecyl sulfate solutions. In Fig. 2, ζ is plotted as a function of the concentration of both

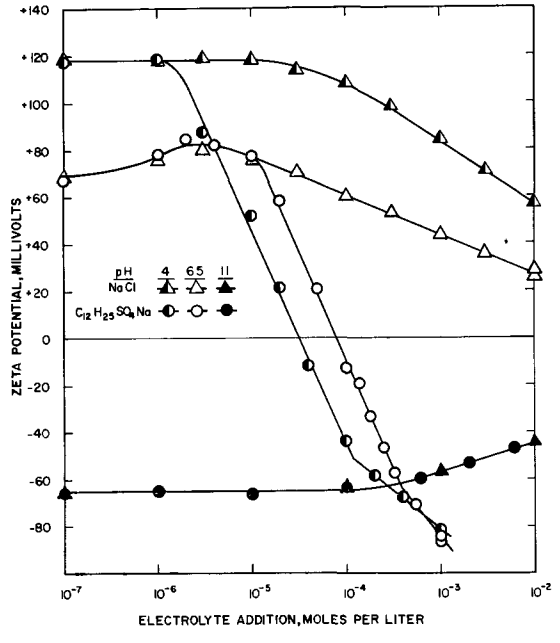

Fig. 2. Zeta potential of corundum in aqueous solutions of sodium dodecyl sulfate and sodium chloride at pH 4, 6.5, and 11.

sodium dodecyl sulfate and sodium chloride at pH 4, 6.5, and 11. It is seen that the sharp break in the ζ-log c curve occurs at nearly a tenfold greater dilution at pH 4 than at pH 6.5, but the slope $d\zeta/d$ log c is still 102 mv. In contrast, $d\zeta/d$ log c for the NaCl curves is only 17 mv and 27 mv at pH 6.5 and 4, respectively. Under conditions where corundum is negatively charged (pH 11), however, the two curves are nearly identical, the slope being —12.5 mv.

Cationic organic electrolytes.—Since anionic paraffin-chain electrolytes bring about an abrupt reversal in the sign of ζ when the surface is positively charged, it seemed reasonable that positively charged organic ions should produce similar changes under converse conditions. To study this experimentally, the zeta potential was determined in aqueous solutions of dodecylammonium chloride at pH 6.5, 10, and 11. The pK for the hydrolysis of dodecylamine is 3.4 and the solubility of dodecylamine is 2×10^{-5} moles per liter (8). At pH 10 and 11, the ratio RNH_3^+/RNH_2 is 4.3 and 0.43, respectively. The critical micelle concentration for dodecylammonium chloride is 1.3×10^{-2}M.

Experimental data are presented in Fig. 3 along with data for sodium chloride added for comparative purposes. At pH 6.5, when corundum is positively charged, dodecylammonium chloride behaves as an ordinary indifferent electrolyte, such as NaCl, because identical values are obtained in solutions of equal concentration. However, when corundum is negatively charged, dodecylammonium ions abruptly change the sign of ζ once a critical concentration is reached. For instance, in the ascending portion of the curve at pH 11, $d\zeta/d$ log c is nearly —350 mv. However, with further additions of dodecylammonium chloride the slope drops back to zero because of the precipitation of free amine. At pH 10, a similarly shaped curve is also obtained, although ζ becomes somewhat less positive as more dodecylammonium chloride is added. This results from the fact that, once the solubility of the free amine is exceeded, addition of dodecylammonium chloride at constant pH is equivalent to adding more NaCl, which increases the ionic strength and compresses the double layer, thereby reducing the zeta potential.

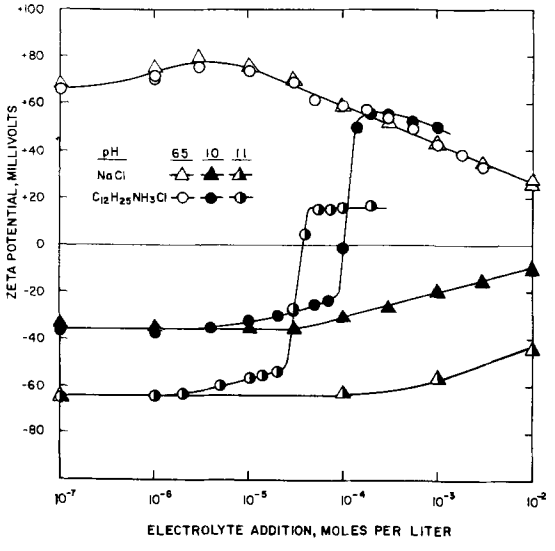

Fig. 3. Zeta potential of corundum in aqueous solutions of dodecylammonium chloride and sodium chloride at pH 6.5, 10, and 11.

Discussion of Results

Since H^+ and OH^- are potential-determining ions for corundum (3, 5), the surface potential, ψ_o, of corundum depends on the pH of the solution, and its value in volts can be calculated from

$$\psi_o = \frac{kT}{ve} \ln \frac{a_{H^+}}{a_{H_o^+}} = 0.059 \ [9.4 - pH] \qquad [1]$$

where a_{H^+} is the activity of H^+ in solution and $a_{H_o^+}$ is their activity at the zero point of charge, namely, pH 9.4 (3). In Eq. [1], k is Boltzmann's constant, T is absolute temperature in degrees Kelvin, v is the valency of H^+ (sign of charge included), and e is the electronic charge. The surface potential is +300 mv, +170 mv, —30 mv, and —90 mv at pH 4, pH 6.5, pH 10, and pH 11, respectively. In conductivity water, the values of ζ should approach ψ_o, but surface conductance has lowered the calculated value of ζ to +70 mv because the measurements were made with particles (10, 11). Experimental measurements of ζ with particles and capillaries made of the same glass have shown that data obtained with capillaries are 80, 50, and 17% higher in 10^{-6}, 10^{-5}, and 10^{-4}M KNO_3 solutions, respectively, than the values determined with particles (10). However, in the present investigation, we are essentially concerned with the conditions where ζ changes sign, and these conditions do not depend on particle size.

Monovalent inorganic electrolytes, such as NaCl or $NaNO_3$, reduce ζ to practically zero in highly concentrated solutions through compression of the electrical double layer (3), but under no condition do they change its sign. Monovalent organic ions, on the other hand, can change the sign of ζ provided they are charged oppositely to the surface. Under conditions wherein the organic ion and the solid surface are charged oppositely, ζ-log c curves indicate that organic ions are adsorbed as individual counter ions through coulombic attraction for the surface until a certain critical concentration is reached within the double layer when the hydrocarbon chains of the ions adsorbed in the Stern layer begin to associate and change the sign of ζ. Because of the analogy of this phenomenon to micelle formation in the bulk solution, the associated organic ions in the Stern layer have been called hemi-micelles (1, 2). The reduction of the slope of the ζ-log c curves at higher concentrations results either from monolayer coverage (in the case of dodecyl sulfate and sulfonate ions) or from precipitation of a neutral molecule (lauric acid or dodecylamine).

Stern first pointed out that the work W_i required to bring an ion from the bulk of the solution to a point in the double layer at potential ψ_i might involve not only electrostatic work

$$W_i = ve\,\psi_i \qquad [2]$$

but also chemical work, ϕ:

$$W_i = ve\,\psi_i - \phi \qquad [3]$$

If the adsorbed ion possesses a long hydrocarbon chain, Van der Waals association between hydrocarbon chains of similarly adsorbed ions will give rise to an additional work term, ϕ':

$$W_i = ve\,\psi_i - \phi - \phi' \qquad [4]$$

From the data presented in Fig. 2 and 3, it can be seen that reversal of ζ occurs only when the solid and organic ion are oppositely charged, meaning that the organic ions are adsorbed appreciably only when they can function as counter ions at the interface. Since these long-chained electrolytes affect ζ in a manner identical to any indifferent electrolyte under conditions of like charge, they have no chemical affinity for alumina and, consequently for this system, ϕ is zero. Thus, the inner Helmholtz plane will be empty and the heads of the adsorbed organic ions will lie in the outer Helmholtz or Stern plane. Under conditions represented by the initial portion of the ζ-log c curves, the force of adsorption is simply electrostatic and ϕ' is zero, whereas under conditions corresponding to the second and third parts of the curves, Van der Waals force of association between hydrocarbon chains becomes operative and ϕ' has a finite value. However, ϕ' is not constant and will depend on the orientation of the adsorbed organic ions in the Stern layer. Thus, the attractive force between the adsorbed organic ions will increase from zero to a value that is approximately the energy gained by taking the hydrocarbon chain out of water; namely, 1.1 kT per CH_2 group in the chain (9). The rate at which ϕ' becomes effective is illustrated qualitatively by any of the graphs.

Qualitatively, dodecyl sulfate ions change the sign of ζ at a lower bulk concentration than is required for dodecyl sulfonate ions, which is in accord with their relative critical micelle concentrations. However, even though the critical micelle concentration of sodium laurate is somewhat higher than that for sodium dodecyl sulfate, laurate ions begin to associate at the corundum-solution interface at a lower bulk concentration than is required for sodium dodecyl sulfate. At pH 6.5, the ratio of laurate ions to lauric acid molecules in solution is 16, that is, nearly 6% of the sodium laurate added is present as undissociated lauric acid. In the bulk solution this concentration of 12-carbon neutral molecules is not sufficient to lower the cmc (12), but it must be a major factor in adsorption at the solid-solution interface. If a laurate ion is anchored in the Stern plane, a lauric acid molecule can then be adsorbed through association of hydrocarbon chains. Another laurate ion can then be adsorbed through Van der Waals attraction between its hydrocarbon chain and that of an anchored lauric acid molecule. In this case repulsion between the charged laurate ion heads will be lower because of the intervening uncharged molecule. This is rpresented by F_{rep} in Fig. 4. If association of organic molecules with organic ions takes place before the Stern layer is sufficiently populated with enough organic ions for the ions to associate by themselves, ϕ' should already have a finite value when the curves begin to break sharply. Observation of Fig. 3 shows that the ζ-log c curves

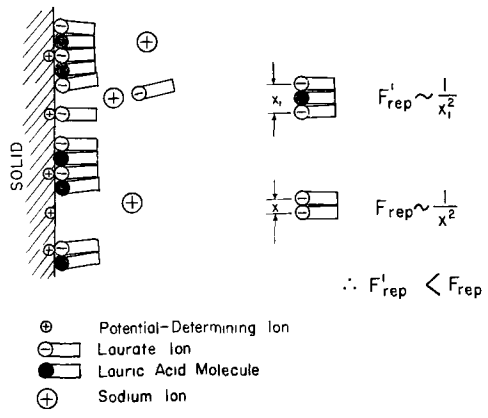

Fig. 4. Schematic representation of double layer when neutral molecules are present.

for dodecylammonium chloride (pH 10 and 11) begin to deviate from the curves for NaCl at concentrations above 2×10^{-6}M. This deviation increases gradually until it is 12 mv at the point where the ζ-log c curve breaks sharply. Thus, ϕ' for the system involving dodecylammonium chloride in alkaline solutions is zero only until 2×10^{-6} mole of the organic salt has been added. Because of the presence of the dodecylamine molecules, ϕ' begins to increase gradually for 2×10^{-6}M additions, but it increases sharply at the abrupt break in the ζ-log c curves. If the organic salt is a strong electrolyte, organic molecules are absent and the ζ-log c curves do not deviate from those of NaCl before the sharp break (Fig. 2).

Increasing the surface potential, that is, lowering the pH from 6.5 to 4.0, was found to reduce the bulk concentration of dodecyl sulfate ions which is required for the adsorbed ions to associate (Fig. 2). This results from the increased adsorption of counter ions. It should be pointed out that competition exists for sites in the double layer because the concentration of Cl^- is 10^{-4}M. At pH 11, sodium dodecyl sulfate affects ζ in a manner identical to sodium chloride. This indicates that the counter ions in each case are sodium ions and that dodecyl sulfate ions have no chemical affinity for corundum. In this case no association can take place because the concentration of dodecyl sulfate ions next to the surface is only about one-tenth of the bulk concentration.

A quantitative estimate of the value of ϕ' can be made by looking at the double layer under conditions where ζ is zero. For this quantitative treatment, the Stern plane must be assumed to coincide with the shear plane in streaming experiments in order that ζ equals ψ_s, the potential at the Stern plane. Under conditions where ζ is zero, all the counter ions occur in the Stern plane and consequently the double layer consists only of a molecular condenser.

The capacity C_s of the molecular condenser will be assumed to be constant and the relation with the surface charge σ where ζ is zero can be expressed by

$$\sigma = \psi_o\, C_s \qquad [5]$$

The charge of the Stern plane, σ_s, which is equal to but opposite in sign to the surface charge for this

Table I. Data for the calculation of ϕ' with Eq. [8a] when ζ is zero

Electrolyte	pH	ψ_o, mv	y	K'	c_o	ϕ', kT
Sodium dodecyl sulfate	6.5	+170	6.8	10.9	8.2×10^{-5}M	8.9
Sodium dodecyl sulfate	4.0	+300	12	10.9	3.3×10^{-5}	10.9
Sodium dodecyl sulfate	11.0	—90	—3.6	—	—	0
Sodium dodecyl sulfonate	6.5	+170	6.8	10.9	1.2×10^{-4}	8.6
Sodium laurate	6.5	+170	6.8	22.2	2.5×10^{-5}	9.4
Dodecylammonium chloride	6.5	+170	6.8	—	—	0
Dodecylammonium chloride	10.0	—30	—1.3	21.2	8.9×10^{-5}	6.9
Dodecylammonium chloride	11.0	—90	—3.6	21.2	1.2×10^{-5}	9.5

model, is given by

$$\sigma_s = 2\ rnve \exp\left(\frac{\phi'}{kT}\right) \qquad [6]$$

when ζ is zero (13). In Eq. [6] r is the radius of the ion under consideration, that is, the head of the organic ion charged oppositely to the surface, and n is the number of such ions per cc of bulk solution.

For the molecular condenser:

$$\psi_o C_s = \sigma = -\sigma_s = -2\ rnve \exp\left(\frac{\phi'}{kT}\right) \qquad [7]$$

Multiplying both sides of the equation by ve/kT and rearranging terms gives

$$\frac{ve\,\psi_o}{kT} = -\left(\frac{ve}{kTC_s}\right) 2\ rnve \exp\left(\frac{\phi'}{kT}\right) \qquad [8]$$

$$vy = -K' c_o \exp\left(\frac{\phi'}{kT}\right) \qquad [8a]$$

where y is $e\psi_o/kT$ (ψ_o being evaluated from Eq. [1]), K' is $\frac{2\,v^2e^2r}{kTC_s}$ $(N/1000)$. Here N is 6.02×10^{23} molecules per mole, and c_o is the concentration in moles per liter of the organic electrolyte to bring the value of ζ to zero. Evaluation of ϕ' depends on the value and constancy of C_s, the mathematical identity of the Stern plane and the shear plane (obviously the shear plane exists outside the hydrocarbon chains of the adsorbed organic ions, but for use of Eq. [8] ψ_s must be zero when ζ is zero), and the presence or lack of a layer of water molecules between the adsorbed ions and the surface. For the present calculation, the large sulfate and sulfonate ion (2.9Å radius) will be considered to be dehydrated, and consequently the capacity of the Stern layer will be about 25 $\mu F/cm^2$. Because of the similarity in behavior between ammonium ions and the aminium ions (2), the aminium ions are probably separated from the surface by a layer of water molecules and C_s will thereby be about $15\mu F/cm^2$ (14). The value of r in Eq. [8] then must be the radius of the aminium head plus one water molecule, or a total of 4.2Å. Similarly, the relatively small soap ion (which would be 1.7Å when the tail is perpendicular to the surface) will be considered to be separated by a layer of water molecules from the surface. Consequently, the value of r in Eq. [8] will be 4.4Å and C_s will be $15\mu F/cm^2$.

The results of calculating ϕ' with Eq. [8] when ζ is zero are presented in Table I. The concentration of dodeclyammonium ions must be corrected to account for hydrolysis at pH 10 and 11.

In our picture of the adsorption mechanism, the adsorption potential ϕ' is zero until the organic ions in the Stern layer begin to associate, this being depicted by the deviation of the ζ-log c curve of an organic electrolyte from a surface-inactive inorganic electrolyte. For example, in the system involving corundum in aqueous solutions of sodium dodecyl sulfate at pH 6.5, ϕ' will be zero until the bulk concentration of sodium dodecyl sulfate reaches 10^{-5}M. Thereupon, ϕ' begins to increase as the adsorbed ions associate, reaching a value of about 8.9 kT when the bulk concentration is 8×10^{-5}M. Under these conditions ζ is zero. The value of ϕ' will continue to increase until the Stern layer is filled. Under these conditions ϕ' will approach 12 kT if all but the end CH_3 group is out of water. Beyond this point, adsorption probably will occur in multilayers. A plot of ϕ' vs. the logarithm of the concentration of sodium dodecyl sulfate yields a fairly straight line if ϕ' is zero at the first break in the ζ-log c curve (10^{-5}M), 8.9 kT when ζ is zero (8×10^{-5}M), and 12 kT at the second break in the ζ-log c curve (3×10^{-4}M). The slope of this curve $d\phi'/d$ log c is about 9 kT. A similar plot of the data at pH 4 shows that $d\phi'/d$ log c is reduced to about 7 kT. This reduction probably reflects the competition between dodecyl sulfate ions and chloride ions at the surface. For sodium laurate, $d\phi'/d$ log c is about 8 kT. Since the solubility limit of dodecylamine is rapidly reached, $d\phi'/d$ log c is over 300 kT (note the steep slopes in Fig. 3) for the systems involving dodecylammonium chloride at pH 10 and 11.

In this paper, the adsorption potential ϕ' which arises through association of hydrocarbon chains has been evaluated by considering the double layer as a molecular condenser when ζ is zero. Since ϕ' appears as an exponent in Eq. [8], its value does not change appreciably with the change in capacity of the Stern layer. However, adsorption measurements should be carried out to determine the actual value of the capacity of the molecular condenser in order to ascertain whether the organic ions are hydrated or not in the Stern layer.

Summary

The effect of 12-carbon organic ions on the zeta potential of corundum has been measured by stream-

ing potential techniques. Experimental data indicate that organic ions are adsorbed appreciably only under conditions where the solid and the organic ions are charged oppositely. Adsorption takes place as individual ions until a sufficiently high concentration is attained in the Stern layer to permit association of their hydrocarbon chains. This association results in increased adsorption which can be represented by an adsorption potential in the Boltzmann equation. By considering the double layer to be a molecular condenser when ζ is zero, the adsorption potential resulting from association of hydrocarbon chains was evaluated. The presence of uncharged long-chained molecules reduces the bulk concentration required for association next to the surface.

Acknowledgments

This research was made possible through the financial support provided by the Aluminum Company of America. The interest of Professors A. M. Gaudin and P. L. de Bruyn in this work is appreciated. The authors also wish to thank Dr. H. J. Harwood, Armour and Company, for a sample of purified dodecylammonium chloride and Dr. A. I. Gebhart, Colgate Palmolive Company, for samples of purified sodium dodecyl sulfate and sodium dodecyl sulfonate.

Manuscript received June 30, 1958. This paper was presented before the New York Meeting, April 27-May 1, 1958.

Any discussion of this paper will appear in a Discussion Section to be published in the December 1959 JOURNAL.

REFERENCES

1. A. M. Gaudin and D. W. Fuerstenau, *Trans. Am. Inst. Mining Met. Engrs.*, **202**, 958 (1955).
2. D. W. Fuerstenau, *J. Phys. Chem.*, **60**, 981 (1956).
3. H. J. Modi and D. W. Fuerstenau, *ibid.*, **61**, 649 (1957).
4. H. J. Modi, "Electrokinetic Properties and Flotation Behavior of Corundum," Sc.D. Thesis, Massachusetts Institute of Technology (1956).
5. W. D. Harkins, "The Physical Chemistry of Surface Films," Ch. 4 and 6, Reinhold Publishing Corp., New York (1952).
6. K. L. Sutherland and I. W. Wark, "Principles of Flotation," Aust. Inst. of Min. and Met., Melbourne (1955).
7. L. M. John and J. W. McBain, *J. Am. Oil Chemists' Soc.*, **25**, 40 (1948).
8. P. L. de Bruyn, *Trans. Am. Inst. Mining Met. Engrs.*, **202**, 291 (1955).
9. K. Shinoda, *J. Phys. Chem.*, **58** 1136 (1954).
10. B. N. Ghosh, B. K. Chadhury, and P. K. De, *Trans. Far. Soc.*, **50**, 955 (1954).
11. J. Th. G. Overbeek and P. W. O. Wijga, *Rec. trav. chim.*, **65**, 556 (1946).
12. Y. Ooshika, *J. Colloid Sci.*, **9**, 254 (1954).
13. D. C. Grahame, *Chem. Rev.*, **40**, 441 (1947).
14. E. L. Mackor, *Rec. trav. chim.*, **70**, 763 (1951).

Capacities of Solid Metal-Solution Interfaces

J. J. McMullen[1] and Norman Hackerman

Department of Chemistry, University of Texas, Austin, Texas

ABSTRACT

An electric analog of the metal-solution interface was assumed and E vs. t changes were deduced mathematically for application of a square wave voltage. The analysis was verified using actual electric components, and it was demonstrated that the component of capacity could be measured readily. The method was applied with some success to each of the following systems: mercury in 0.1N Na_2SO_4, platinum, silver, copper, aluminum, and tantalum in 1N Na_2SO_4.

At various times investigators have attempted to determine roughness factors (ratios of true to apparent surface areas) of metal electrodes by means of capacity measurements. Assumptions usually made in these attempts included (*a*) that all metals have the same capacities at potentials slightly anodic (positive) to their hydrogen evolution potentials, and (*b*) that for mercury the apparent surface area is the true surface area. Thus if the capacity per square centimeter of apparent area for the metal M was C_M (at a potential just short of hydrogen evolution) and that for mercury C_{Hg} (at a similar potential) then the roughness factor of the metal M was C_M/C_{Hg}.

Assumption (*b*) is reasonable. However, assumption (*a*) is not entirely tenable. The small amount of information in the literature concerning capacities of solid metal electrodes shows wide discrepancies. Grahame (1) has published very useful papers concerning the differential capacity of mercury. Solid metal electrodes, however, have not been investigated systematically. Of course, differential capacities of solid electrodes cannot be checked by electrocapillary methods and as a result electrical double layer (edl) theory concerning solid metal electrodes has not been as extensively treated as has that of the mercury-solution system.

Several experimental techniques have been utilized to measure differential capacities of mercury-solution interfaces. The most sensitive method is the impedance bridge method. Grahame (1) has used this method extensively and reports an accuracy of better than 1%. The major drawback of this method is its inapplicability to large capacities. Bowden and Rideal (2) devised a method of measuring capacities by direct charging. They observed the potential change resulting from the passage of a known direct current for a known length of time. The potential changes involved, however, were of the order of 0.5 v, and the capacities calculated were, therefore, an

[1] Present address: Aluminum Research Center, Olin Mathieson Chemical Corp., New Haven, Connecticut.

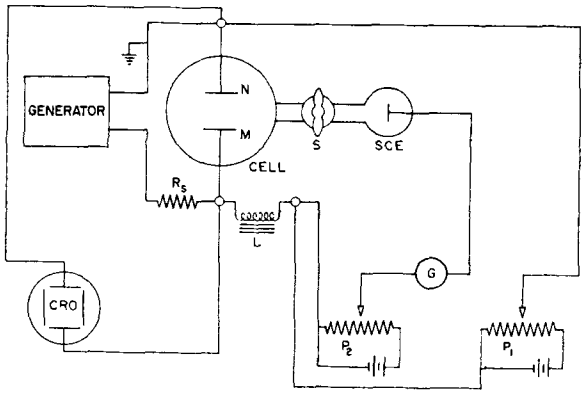

Fig. 1. Circuit diagram

average over a large potential change. Wagner (3) used a ballistic galvanometer to measure the charge required to polarize a silver specimen 0.1 v.

Methods involving direct charging all assumed that any current supplied to the electrode was involved in charging the edl. In effect, the assumption was made that the interface behaved as an ideally polarizable one.

Brodd and Hackerman (4) reported results obtained with solid metal electrodes showing a correlation between areas calculated from capacity data and areas measured by krypton adsorption. Their capacity data were obtained from time-potential traces observed when a square-wave signal was applied to the electrodes. This method has been modified and utilized here in an attempt to determine the differential capacity curves for several solid metal-solution interfaces.

Experimental

The circuit diagram is shown in Fig. 1. The source of the square wave voltage was a Model 202-A function generator manufactured by Hewlett-Packard. The generator applied a square wave voltage, across the series resistance, R_s, to the electrodes N and M. The potential change across the cell was observed on the cathode-ray oscilloscope, CRO. Potentiometer P_1 was used to polarize electrode M using N as an auxiliary electrode. Potentiometer P_2 measured the potential of M with respect to the saturated calomel electrode, SCE. L was an inductance placed in the circuit to keep the alternating current from the direct current parts of the circuit. For each measurement the CRO was connected to the generator to obtain a trace of the input square wave. Permanent records of the traces were obtained photographically.

The Pyrex cells used for measurements and for reservoir are, respectively, A and B in Fig. 2. The mercury electrode M was formed in a Pyrex cup with an inside diameter of 2.5 cm. The mercury level was controlled so that the top of the mercury meniscus was tangent to the plane at the top of the cup. A fresh surface was obtained by overflowing the mercury from the cup. A platinized platinum screen cylinder, N, suspended through the top of the cell and surrounding the mercury electrode, was in series with the mercury electrode in the a-c circuit. The area of the platinum screen cylinder was very large compared to that of the mercury; hence its capacity was large and its effect on the cell impedance should have been negligible. The saturated calomel electrode, SCE, was immersed in the solution in a small side cell connected to the main cell A through the closed stopcock S_2.

A ball joint and closed stopcock S_1 connected the main cell A with cell B. Cell B served as a pre-electrolysis cell and reservoir for solution. Pre-electrolysis with a current of 3 ma was carried out for at least 12 hr.

Bureau of Mines grade A helium, reported as 99.99% pure, was bubbled through a saturator and passed into cells A and B. The helium stirred the solution and provided an inert atmosphere. After pre-electrolysis and at least 4 hr of helium flushing, the helium pressure was used to force solution from B into A.

Distilled water was redistilled from alkaline permanganate to remove any organic matter. The mercury was triple-distilled instrument mercury. Other metals were used as wires put into the solution through the tip of the cell. Pretreatment of wires consisted of degreasing, washing with dilute sulfuric acid, and rinsing with distilled water.

The importance of avoiding grease contamination has been demonstrated (5). No grease was used in any part of the apparatus employed in these experiments.

Analysis of time-potential curve.—In the study of time-potential curves obtained with a square wave, it is helpful to consider the time-potential changes at the electrode surface in terms of an analogous electric circuit. Various simple and complex arrangements of resistors and capacitors have been utilized to represent the behavior of such an interface. One of the simplest, Fig. 3, consists of a condenser (C) in parallel with a resistance (R_p), both being in series with another resistance (R_e). In the present case the square wave passed through resistance R_s before entering the cell. The potential difference between points A and B was observed on the

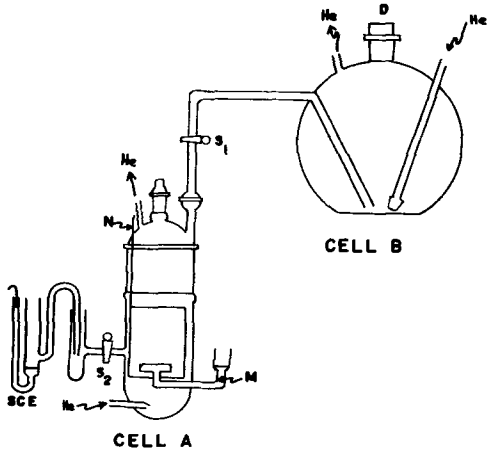

Fig. 2. Polarization cell and reservoir

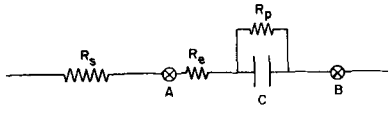

Fig. 3. Electric analog circuit

CRO. Three cases were examined to determine the time-potential behavior to be expected under different conditions.

Case I: $R_p = \alpha$; $R_e = 0$

If the simplifying assumptions are made that the interface is an ideally polarizable one and that the resistance of the solution is zero, then R_p is infinite and R_e is zero. The equation for the change of voltage (E_c) between points A and B, in this case, is

$$E_c = E_i\,[1 - \exp\,(-t/R_sC)] \qquad [1]$$

where t is time and E_i is the input voltage. The value of E_c approaches the value of the input voltage, exponentially, with increasing time. At short time intervals, $t << R_sC$, the exponential in Eq. [1] was expanded to give

$$E_c = E_it/R_sC \qquad [2]$$

In this time interval E_c is a linear function of time. With reversal of the current, i.e., on the second half of the square wave cycle, another linear function, with slope of opposite sign, is obtained. The composite result for small time intervals is a triangular trace on the CRO.

Case II: $R_p \neq \alpha$; $R_e = 0$

If the interface is not an ideally polarizable one, R_p has a finite value. The equation for the change in voltage is now:

$$E_c = \frac{E_iR_p}{(R_s + R_p)}\left[1 - \exp\frac{\{-t(R_p + R_s)\}}{CR_pR_s}\right] \qquad [3]$$

At short time intervals, $t << CR_pR_s/(R_p + R_s)$, the exponential in Eq. [3] was expanded to give Eq. [2]. The form of the trace is thus the same as in Case I.

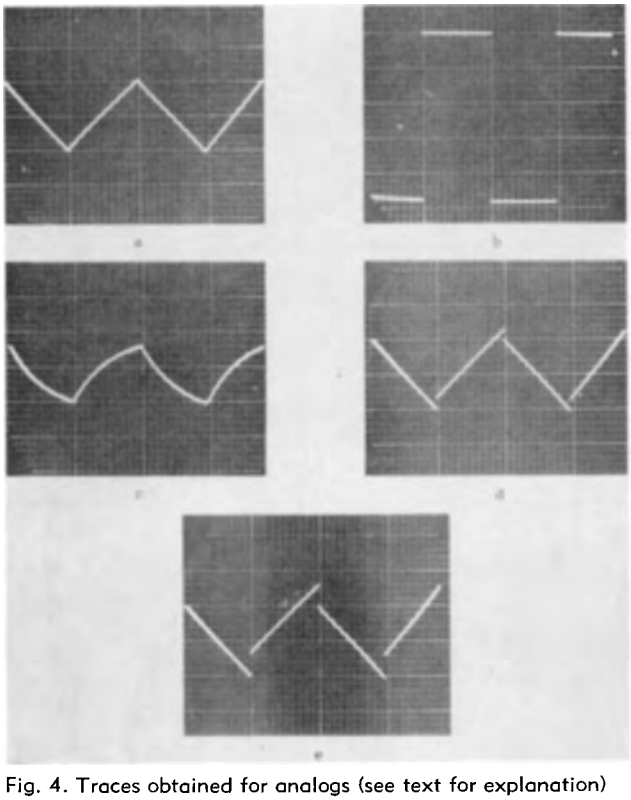

Fig. 4. Traces obtained for analogs (see text for explanation)

Case III: $R_p \neq \alpha$; $R_e \neq 0$

Introduction of R_e into the system results in discontinuities in the time-potential curve. These potential drops are representative of IR_e, where I is the current. The equation of each half-cycle obtained on the oscilloscope is thus:

$$E_c = IR_e + E_it/R_sC \qquad [4]$$

In all three cases, therefore, Eq. [2] gives the dependence of E_c on t for small values of time. Differentiating Eq. [2] with respect to time gives

$$dE_c/dt = E_i/R_sC \qquad [5]$$

If the frequency of the input square wave is selected to give a triangular trace on the oscilloscope, then the absolute values of the slope for each half-cycle is given by Eq. [5].

The three cases given above were studied experimentally by obtaining oscilloscope traces for the respective electrical circuits.

Figure 4a is a photograph of the CRO trace for the time-potential curve with the circuit described in Case I (Fig. 3). Here C was a 37μF commercial electrolytic condenser, R_s was a 15,000-ohm resistor, and the input voltage, E_i, was 100 cps square wave. A trace of the input voltage E_i, attenuated 100:1, is shown in Fig. 4b.

From the slope of the trace in Fig. 4a, and the known values of the input voltage (E_i) and of R_s, the capacity of condenser C can be calculated with Eq. [5]. The time for one half-cycle was 0.005 sec; the voltage rose 10 divisions in this time, giving the slope 2 x 10^3 div./sec. Therefore,

$$C = (dt/dE_c)\,(E_i/R_s) = \left(\frac{1}{2 \times 10^3}\right)\frac{12(100)}{15{,}000} = 40\mu F$$

This is in good agreement with 37μF measured by the conventional bridge method.

Figure 4c shows a trace obtained with a circuit described under Case II. Here, C was a 54μF condenser, R_p a 100-ohm resistor, R_s a 15,000-ohm resistor, and the frequency 50 cps. The time-potential curve is not a triangular wave. However, when the frequency of the input square wave was increased to 500 cps the output trace was triangular and the calculated capacity was 58μF. An increase in the amplitude of the input square wave, at this same frequency, resulted in a triangular trace with increased slope, and looked just like the trace in Fig. 4a. The product of the reciprocal of the slope and the input voltage remained constant, however, and the calculated capacity was again 58μF.

Figure 4d shows a trace obtained with a circuit described by Case III. Here C was a 54μF condenser, R_p 100 ohms, R_s 15,000 ohms, R_e 13 ohms, and the frequency 500 cps. The time-potential curve showed discontinuities between the linear portions. The calculated capacity was 58μF. The IR_e drop, (Fig. 4d), was 1.5 divisions. When R_e was doubled to 26 ohms, the discontinuity doubled in size (Fig. 4e) to 3 divisions. The calculated capacity remained the same, since the slope of the linear portions did not change.

Results and Discussion

Mercury.—The mercury-solution interface was investigated as another check, since the results could be compared with those of other workers. The Pyrex cup containing the mercury had an inside diameter of 2.5 cm. Assuming the surface of the mercury to be planar, the surface area was 5 cm^2. If the curvature of the surface were taken into consideration, the area could be as high as 6 cm^2. The former value was used here.

The solution used was 0.1*N* Na_2SO_4, and all experiments were conducted at 30° ± 1°C. The potential values given refer to the saturated calomel electrode. A 15,000-ohm resistor was used as the series resistance R_s throughout the rest of the experiments. Application of the square wave voltage, employed to carry out the capacity measurements, changed the potential of the electrodes somewhat. The change of potential was less than 10 divisions on the CRO. Since the sensitivity of the CRO was approximately 1.5 mv/division, the uncertainty in the measured potentials of the electrodes were less than 0.02 v.

Figure 5a is a photograph of a typical time-potential trace obtained with mercury electrodes. The potential of the mercury was −0.2 v in this case. The time-potential trace is a triangular wave with discontinuities between the linear portions. This type of trace corresponds to Case III. The calculated capacity was 154μF or 31$\mu F/cm^2$.

Capacity measurements were made at potentials varying from 0.0 to −1.0 v. These potentials were obtained by polarizing the mercury electrode with an auxiliary potentiometer. The differential capacity curve is shown in Fig. 6.

Grahame (1) found the potential at the zero point of charge (zpc) of mercury in 0.1*N* Na_2SO_4 to be −0.44 v. Therefore, for the purposes of discussion, the curve in Fig. 6 may be divided into three regions: (*a*) a region of potentials more negative than the zpc (cathodic branch of the curve), (*b*) a region of potentials more positive than the zpc (anodic branch of the curve), and (c) a region of potentials in the immediate vicinity of the zpc.

The capacity on the cathodic branch is independent of the potential and has a constant value of 19 $\mu F/cm^2$. This value would be 16$\mu F/cm^2$ if the higher surface area value were used. The constancy of the capacity along this branch of the curve has been verified experimentally many times. The value obtained here agrees with Proskurnin and Frumkin (6), Barclay and Butler (7), and Philpot (8). Grahame's experimental value was 16$\mu F/cm^2$.

The anodic branch of the curve does not show the broad flat portion found on the cathodic branch. However, for a narrow region of potentials, the curve has a slope close to zero. The average capacity in this region was about 33$\mu F/cm^2$. Grahame's curve shows such a "hump" at about 35$\mu F/cm^2$.

In the region of the zpc, a transitional portion of the curve occurs with capacities intermediate between those for the cathodic and anodic branches of the curve. In very dilute solutions (N/100 and less), this region exhibits a more or less sharp minimum. Even with 0.1*N* Na_2SO_4 Grahame found a minimum of the order of 1 or 2$\mu F/cm^2$. The sensitivity of the present measurements is insufficient to permit observation of such a shallow minimum in the curve.

Platinum.—In order to avoid the large solution resistance encountered in dilute solutions, the remaining experiments were conducted in 1*N* Na_2SO_4. The platinum electrodes were 20 cm in length and were cut from smooth wire having a diameter of 0.04 cm. The apparent electrode area was 2.5 cm^2.

A photograph of a typical time-potential trace obtained with platinum electrodes is shown in Fig. 5b. The time-potential trace is again of the type discussed under Case III above. However, the IR_e drop is considerably less than with mercury in 0.1*N* Na_2SO_4 (compare Fig. 5a and 5b).

Results of the capacity measurements, at potentials varying from 0.0 to 1.4 v, are shown in Fig. 7. The shape of the curve obtained is similar to that for mercury. Three regions are evident: a portion where the capacity is fairly constant at approximately 80μF, a narrow region having a capacity of

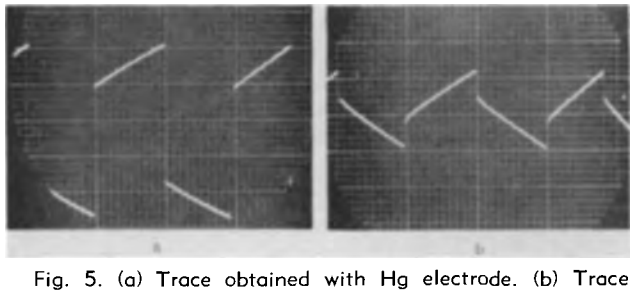

Fig. 5. (a) Trace obtained with Hg electrode. (b) Trace obtained with Pt electrode.

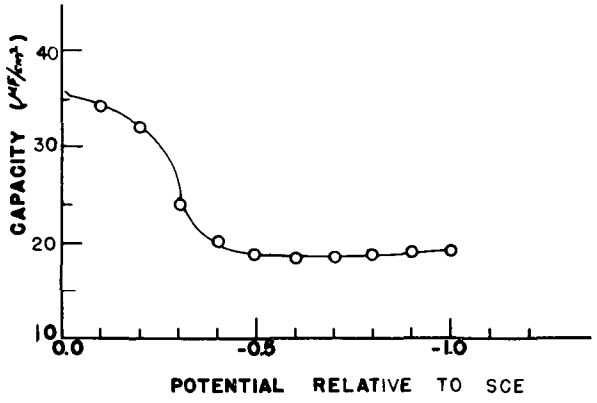

Fig. 6. Differential capacity curve for Hg-0.1N Na_2SO_4

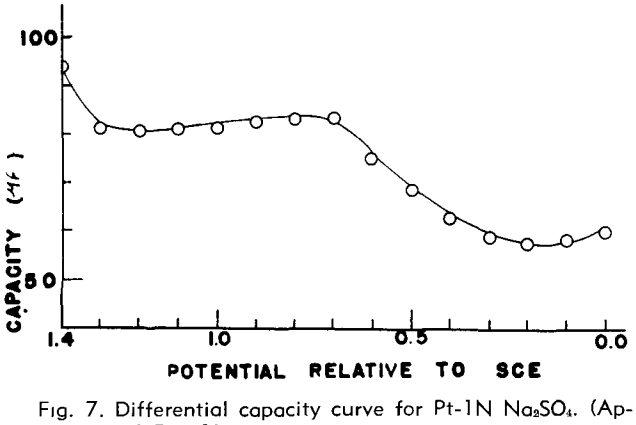

Fig. 7. Differential capacity curve for Pt-1N Na_2SO_4. (Apparent area 2.5 cm^2.)

approximately 58 μF, and a connecting portion with intermediate capacities.

These regions can be interpreted in the same fashion as for the curve obtained for mercury in 0.1*N* Na_2SO_4. The transitional portion of the curve is expected to be in the neighborhood of the zpc. Therefore, the zpc for platinum in this solution should be 0.5 ± 0.2 v. Robertson (9) has obtained a capacity minimum, for platinum in 1*N* HCl, at 0.79 v. A value of −0.04 v in acidified 1*N* Na_2SO_4 by contact angle measurements has also been reported (10).

The cathodic portion of the curve, with total capacities of the order of 54 μF, is the region of cation predomination in the double layer. Using the apparent area of the electrodes, the capacity was approximately 22 μF/cm^2. On the anodic portion the capacity was 32 μF/cm^2.

Silver.—The apparent area of the silver electrodes was 1.3 cm^2. The polarization caused by the square wave voltage was less than 15 mv.

The results of capacity measurements, at potentials of 0.0 to −1.2 v, are shown in Fig. 8. The shape of the curve is similar to that obtained for the mercury-solution interface. The zero point of charge has been reported for silver, in 0.1*N* KNO_3, as −0.233 v (11). A hump appears, in the vicinity of this potential, on the capacity-potential curve. Similar humps have been observed in the region of the zero point of charge for capacity-potential curves obtained for mercury in concentrated solutions. Grahame (1) has suggested that the humps arise from the mutual electrostatic repulsion of ions in the double layer. Watanabe, Tsuji, and Ueda (12) have suggested that this phenomenon is related more to mercury-ion interaction than to ion-ion interaction. The appearance of this phenomenon with silver and not with platinum seems to favor the latter suggestion.

The cathodic portion of the curve shows a capacity of approximately 58 μF. This would be the region of cation predomination in the solution side of the double layer. The capacity was approximately 45 μF/cm^2. This apparently high value of the capacity is not unreasonable. Wagner (3) has reported values of the order of 100 μF/cm^2 for "smooth" silver wires.

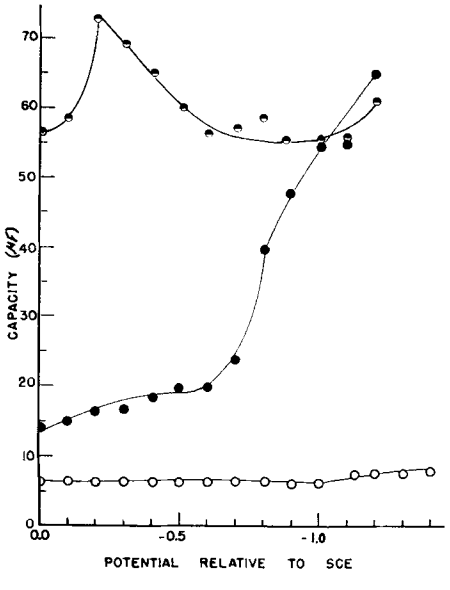

Fig. 8. Half-filled circle: Differential capacity curve for Ag-1N Na_2SO_4. (Apparent area 1.3 cm^2.) Open circle: Differential capacity curve for Al-1N Na_2SO_4. (Apparent area 2.5 cm^2.) Solid circle: Differential capacity curve for Al-1N Na_2SO_4 after cathodic treatment.

Aluminum.—The apparent surface area of the aluminum electrodes was 2.5 cm^2. The results of capacity measurements are shown in Fig. 8. The shape of this curve has no similarity to the curve obtained for mercury. The capacity is fairly constant over the range of potentials at which it was measured. The low values of the capacities, about 3 μF/cm^2 of apparent surface, are not surprising, since aluminum is normally covered with an oxide film. Rakov and Ershler (13) obtained 7 μF/cm^2 for an oxide covered electrode. The capacity of the oxide film is small compared to the capacity of the double layer. Therefore, the measured capacity would be primarily that of the oxide film. The capacity of the film is not dependent upon the potential. This explains the apparent nondependence of the measured capacity upon the potential.

Estimates of the thickness of oxide films on metals have been made by capacity measurements (14). Wanklyn (15) has used capacity measurements to study the protective character of oxide films on zirconium alloys. In these measurements the double layer capacity was neglected. Assuming the film substance to be γAl_2O_3, and using a value of 8 for the dielectric constant (16), the film thickness was calculated to be approximately 20Å.

A potential large enough to evolve hydrogen at the aluminum electrode was applied, momentarily, between it and an auxiliary electrode placed in the small side cell. The capacity was measured at potentials progressively more anodic. The results of these measurements are shown in the upper curve in Fig. 8. The capacity was found to be much higher after this treatment but decreased with time and the potential of the aluminum became progressively more anodic. The values of the capacity after cathodic treatment were in all cases substantially higher but fairly irreproducible. It is likely that the rise in capacity after cathodic pretreatment may be caused by the oxide film thinning due to the local increase in *p*H at the electrode.

Tantalum.—The apparent area of the tantalum electrodes was 1.6 cm^2. The results of the capacity measurements are shown in Fig. 9. The shape of this curve is very similar to that of aluminum. Tantalum, like aluminum, is normally covered by an oxide film. Therefore, the low values obtained for the capacities are in no way unusual. The average value of the capacity was approximately 9 μF/cm^2. Capacities were measured at progressively more anodic potentials to observe possible evidence of increased oxide formation. From Fig. 9 it can be seen that there is a continuous slow trend toward lower capacities. This lowering of capacity at more anodic potentials suggests the formation of more oxide on the surface of the tantalum.

Copper.—The apparent surface area of the copper

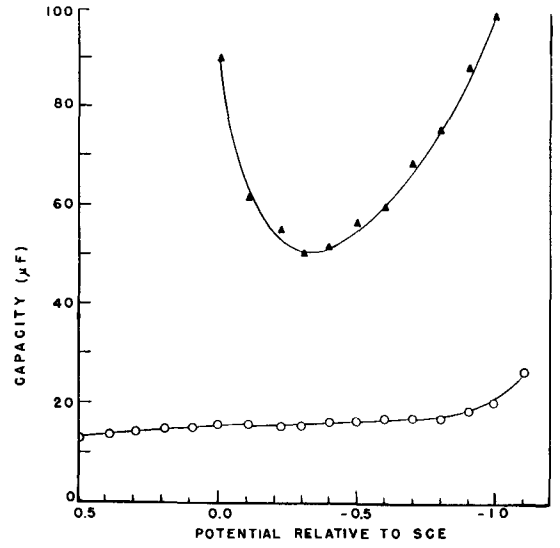

Fig. 9. Open circle: Differential capacity curve for Ta-IN Na_2SO_4. (Apparent area 1.6 cm^2.) Solid triangle: Differential capacity curve for Cu-IN Na_2SO_4. (Apparent area 2.4 cm^2.)

electrodes was 2.4 cm^2. The capacity-potential curve is shown in Fig. 9.

Since no value of the zpc could be found in the literature, an approximation method, as used earlier by Brodd and Hackerman (4), was tried. The work function for copper is 4.6 ev (17) and for mercury 4.5 ev (18). The difference between these two is 0.1 v. The zpc for mercury is −0.44 v; therefore, the zpc for copper is approximately −0.3 v. It is further noted that this approximation is made more approximate because of the variations in the values of the work functions found in the literature.

The capacity-potential curve (Fig. 9) shows a minimum of capacity at a potential of about −0.3 v. The shape of the curve is similar to that of mercury in that the capacity goes through a minimum. The anodic branch is similar to the anodic branch of the curves obtained for mercury in solutions containing anions which specifically adsorb (1). The results indicate that sulfate ion has specifically adsorbed on the copper.

The cathodic portion of the curve does not display a broad flat minimum as with mercury. The rise in capacity occurs with mercury but at much more cathodic potentials. This difference could be accounted for by the high hydrogen overvoltage on mercury and the smaller overvoltage on copper.

The minimum of capacity corresponds to 21 $\mu F/cm^2$. Winkler (19) reported a capacity of 23 $\mu F/cm^2$ for cathodic charging of copper.

Conclusions

The results obtained for electric analogs and the agreement of the results obtained for the mercury-solution interface with those of other workers attest to the reliability of the method.

The shapes of the differential capacity curves reported indicate that for most metals only a limited potential range is available for capacity measurements from which to estimate surface areas.

The capacity-potential curves obtained for film covered metals, aluminum and tantalum, suggests the applicability of the method to film formation and film removal studies. Further work along these lines is underway.

Acknowledgment

The authors are pleased to express their appreciation to the Office of Naval Research for the financial support of this work, and also to Dr. P. V. Popat for a number of very fruitful discussions.

Manuscript received June 6, 1958. This paper was prepared for delivery before the Washington, D. C. Meeting, May 12-16, 1957.

Any discussion of this paper will appear in a Discussion Section to be published in the December 1959 JOURNAL.

REFERENCES

1. D. C. Grahame, *Chem. Rev.*, **41**, 441 (1947); *Ann. Rev. Phys. Chem.*, **6**, 337 (1955).
2. F. P. Bowden and E. K. Rideal, *Proc. Roy. Soc., London*, **120A**, 59, 80 (1928).
3. C. Wagner, *This Journal*, **97**, 72 (1950).
4. R. J. Brodd and N. Hackerman, *ibid.*, **104**, 704 (1957).
5. M. Proskurnin and M. A. Vorsina, *Compt. rend. Acad. Sci. U.R.S.S.*, **24**, 915 (1939).
6. M. Proskurnin and A. Frumkin, *Trans. Faraday Soc.*, **31**, 110 (1935).
7. I. M. Barclay and J. A. V. Butler, *ibid.*, **36**, 128 (1940).
8. L. St. J. Philpot, *Phil. Mag.*, **13**, 775 (1932).
9. W. D. Robertson, *This Journal*, **100**, 194 (1953).
10. A. Frumkin and B. Kabanov, *Physik. Z. Sowjetunion*, **5**, 418 (1934).
11. V. I. Veselovsky, *Acta physicochim. U.R.S.S.*, **11**, 815 (1939).
12. A. Watanabe, F. Tsuji, and S. Veda, *Bull. Inst. Chem. Research, Kyoto Univ.*, **34**, 1 (1956).
13. A. A. Rakov, T. I. Borisova, and B. Ershler, *Zhur. Fiz. Khim.*, **22**, 1390 (1948).
14. L. Young, *Trans. Faraday Soc.*, **51**, 1250 (1955).
15. J. N. Wanklyn, *Nature*, **177**, 849 (1956).
16. Von W. G. Burgers, A. Claassen, and J. Zernike, *Z. Physik*, **74**, 593 (1932).
17. E. W. J. Mitchell and J. W. Mitchell, *Proc. Roy. Soc., (London)*, **210A**, 70 (1954).
18. N. K. Adam, "The Physics and Chemistry of Surfaces," p. 310, 3rd Edition, Oxford University Press, London (1941).
19. C. A. Winkler, *Can. J. Chem.*, **31**, 306 (1953).

Preparation and Properties of Improved Protamine Collodion Matrix Membranes of Extreme Ionic Selectivity

Marc Lewis[1] and Karl Sollner

National Institute of Arthritis and Metabolic Diseases, National Institutes of Health, Public Health Service, U. S. Department of Health, Education, and Welfare, Bethesda, Maryland

ABSTRACT

Improved protamine collodion matrix membranes of extreme electrochemical activity were prepared by the adsorption of purified protamine from aqueous solutions on preformed highly porous collodion membranes whose porosity was subsequently reduced by drying. The most useful permselective membranes give rise to concentration potentials which agree with the calculated thermodynamic maximum potential in potassium chloride cells up to 0.1*N*/0.05*N* within the meaningfulness of the method. At higher concentrations the measured potentials become gradually less than the theoretical value. The more highly selective membranes have anion permeabilities which in 0.1*N* KCl are 250 to 450 times greater than the cation permeabilities and 2,000 to 12,000 times greater in 0.01*N* solutions. With solutions of $CaCl_2$ these ratios were at least two orders of magnitude greater. The ohmic resistances of the permselective membranes of highest selectivity (as measured in 0.1*N* KCl) may be adjusted from about 10 ohm-cm^2 upward.

The first membranes which combined a high degree of anionic selectivity with great stability and low resistance were the permselective protamine collodion matrix membranes described by Carr, Gregor, and Sollner (1-5).[2] They were prepared by the adsorption of protamine from buffered ($\cong$ pH 10.5) aqueous protamine sulfate solutions on collodion membranes of high porosity which were subsequently dried under carefully controlled conditions. The most important shortcoming of these membranes was their limited ionic selectivity; their permeabilities for anions even at concentrations as low as 0.01 and 0.001*N* were only 30-50 times greater than those for cations. This low ratio severely restricts the usefulness of these membranes in many studies.

Anion selective membranes of high resistance have been prepared by Albrink and Fuoss (6). Membranes of the permselective type were described in recent years by Bonhoeffer and Manecke (7), Winger, Bodamer, and Kunin (8), Wetstone and Gregor (9), and others (10-12). For our purpose these membranes have somewhat too low ionic selectivities, especially at higher concentrations, and too high unit area exchange capacities. Also the porosities and resistances of these membranes cannot be as readily adjusted at will as those of collodion matrix membranes.

Collodion matrix membranes of extreme anion selectivity which are free from these limitations and shortcomings were prepared some years ago in this laboratory by the adsorption from aqueous solution of poly-2-vinyl-N-methylpyridinium bromide (and several other basic synthetic polyelectrolytes) on preformed highly porous collodion membranes whose porosity was subsequently reduced by drying (13). The most useful of these membranes give rise to concentration potentials which agree closely with the calculated thermodynamic maximum potentials in potassium chloride cells up to 0.1*N*/0.05*N*. The more highly selective membranes have anion permeabilities which in 0.1*N* KCl are 500-1300 times greater than the cation permeabilities, and in 0.01*N* solutions 5,000-32,000 times greater. With solutions of $CaCl_2$ these ratios are two to three orders of magnitude greater. The ohmic resistances of these membranes as measured in 0.1*N* KCl may be adjusted from about 10 ohm-cm^2 upward (13). While otherwise fully satisfactory for many physicochemical investigations and model studies of biological interest, these membranes quite unexpectedly show a peculiarity which restricts their usefulness for certain purposes. The rates of self-exchange of critical ions between solutions across these membranes do not agree with those calculated from the Nernst-Einstein equation, whereas this equation describes satisfactorily the results of self-exchange studies with protamine collodion matrix membranes, or with (cation selective) oxidized collodion and sulfonated polystyrene collodion matrix membranes (14).

In order to prepare anion selective membranes of extreme ionic selectivity which behave in the manner postulated by the Nernst-Einstein equation with respect to the rate of exchange of ions across them, it seemed best to try to improve the ionic selectivity of the otherwise satisfactory protamine collodion

[1] Public Health Service Research Fellow; Present address: National Institute of Dental Research, Bethesda, Md.

[2] Protamines are simple strongly basic proteins, ordinarily derived from salmon sperm, with molecular weights of about 4000 in the hydroxyl form. They are of somewhat varying composition, most probably consisting of nineteen molecules of arginine, a dibasic amino acid with a pK of 10.5 to 11, and six or seven monobasic amino acids. The ionizable groups in the protamine molecule, which are not blocked by the formation of peptide linkages, are: one carboxyl group, one imino group, and nineteen guanidino groups.

matrix membrane. This seemed desirable also in view of the planned use of these membranes in studies of biological interest because the chemical nature of protamine is more similar to that of biological membranes than that of synthetic polyelectrolytes, such as poly-2-vinyl-N-methylpyridinium salts.

The looked for improvement, as previously indicated (1), must be presumed to consist either of the removal (or the chemical blocking) of the carboxyl group which is an inherent, terminal part of the protamine molecule, of the removal of acidic impurities contained in the commercial preparations, or of a combination of the two. If the presence of some acidic impurities in the protaminic preparations used is the cause of the deficient ionic selectivity of the membranes, the solution of the problem could be expected from a thorough purification of the protamine preparations.

Preliminary experiments with the commercial protamine preparations available at present regularly yielded membranes of higher ionic selectivity than those described previously, with considerable differences according to the particular batch of protamine used. Different samples of protamine were found to be of different purity as evidenced also by differences in color, from pure white to distinctly yellow, the least yellowish preparations generally yielding the best membranes. This observation also agrees with the results of earlier attempts to purify protamine in which the repeated dissolution and reprecipitation of commercial protamine preparations had led in some instances, but not in a satisfactorily reproducible manner, to membranes of greatly increased anionic selectivity (15).

Thus, the thorough purification of protamine was the obvious initial step in our attempt to improve the ionic selectivity of protamine collodion matrix membranes.

Preparation of Improved Permselective Protamine Collodion Matrix Membranes

A consistently successful method of purifying protamine to a degree adequate for our purpose is the following: Fifty grams of commercial protamine sulfate is extracted repeatedly with ethyl ether until a sample of the ether on evaporation does not leave any trace of residue. (With preparations already free of lipid-like ether soluble contaminants this step may be omitted.) The ether-wet protamine sulfate is dried, and a nearly saturated, approximately 6.5% aqueous solution is prepared (which in all instances proved to be very close to neutral). To remove all impurities of an acidic (anionic) character from this solution, it was passed through a column consisting of 1 kg of strong base anion exchange resin (Amberlite IRA —400) in the chloride form. While the protamine solution is run slowly through the column, the eluate is continuously tested with trichloroacetic acid and discarded until a positive test, a white precipitate, is obtained. After the last of the protamine solution has been run on the column, the column is slowly washed with distilled water and the eluate collected until it no longer gives a positive reaction with trichloroacetic acid. The solution containing the protamine (now in the chloride form) may either be diluted appropriately and used directly in the preparation of membranes, or dry protamine chloride may be obtained as a fine white powder by the conventional method of freezing and drying *in vacuo*. It might be added that this purified protamine chloride when reconverted to protamine sulfate on an ion exchange column yielded membranes which are significantly inferior in ionic selectivity to those prepared with the purified protamine in the chloride state.

The preparation of permselective membranes consists of casting collodion membranes of high porosity, followed by adsorption on the membranes of protamine from aqueous solutions, and controlled drying (1, 2). Three-layer membranes were prepared routinely at room temperature and at relative humidities between 20% and 50% from a 4.0% solution of Parlodion (Mallinckrodt) in 50:50 ether-alcohol containing 2% water. This solution was poured over 25 x 100 mm test tubes rotating in the horizontal position. Ordinarily, the first layer was dried 3.0 min, and the second 3.5 min; 4.0 min after the third layer was poured the membranes were immersed in water. When membranes of higher resistance were desired, these drying periods were each extended by 30 sec. After being washed for an hour in several changes of water, the membranes were slipped off their casting tubes and washed for 3 to 4 hr. They were then immersed in a solution containing 10 g of protamine chloride per liter, buffered to a pH of about 10.5 with a sodium hydroxide-sodium borate-sodium chloride buffer (0.05*N* NaOH, 0.05*N* $Na_2B_4O_7 \cdot 10H_2O$, 0.375*N* NaCl).[3] The membranes were kept in this solution for periods ranging from 12 to 48 hr depending on the resistance desired, shorter immersion times yielding membranes of higher resistance. Thereafter the membranes were washed for 5 min in distilled water, replaced on their casting tubes, and dried for 24 hr in a humidistat over saturated $CaCl_2$ solution, at a relative humidity of 31%. Next, the membranes were placed in water for 2 hr, removed from their casting tubes, and tied with linen thread to glass rings fitted into their open ends. They were again dried for 24 hr at 31% relative humidity and then placed in 0.1*N* KCl solution. After an aging period of several days in this solution, their properties are virtually constant. These test tube shaped membranes were about 30-40 μ thick, transparent, glass clear, and smooth.

The permselective membranes prepared with the purified protamine preparations, like the earlier types of protamine collodion matrix membranes, are very stable. They do not show any significant deterioration either in ionic selectivity or in mechanical strength over periods of a few years when stored in 0.1*N* KCl solution to which a preservative such as thymol was added for protection against mold growth. With respect to stability the protamine collodion matrix membranes are superior to the poly-2-vinyl-N-methylpyridinium collodion matrix

[3] These solutions of protamine could be used repeatedly with adjustment of pH as necessary. They were stored routinely in a refrigerator to prevent bacterial growth and other forms of deterioration.

Table I. Properties and functional behavior of various permselective protamine collodion matrix membranes

1 Time of immersion in 1% protamine chloride, hr	2 Anion-exchange capacity, meq/g	3 Anion-exchange capacity, μeq/cm^2	4 Water content, %	5 Rate of osmotic water movement (0.2M sucrose), mm^3/hr 100 cm	6 Av. unit area resistance[c] in 0.1N KCl, ρ^* (t = 25.00°), ohm-cm^2	7 Av. concn. potential[c] 0.4N KCl | 0.2N KCl (t = 25.00°), mv
12[a]	0.141	0.76	7.6	15.0	4500 (1620)	—15.32 (0.08)
24[a]	0.163	0.99	8.5	16.0	2130 (780)	—15.66 (0.05)
8[b]	0.229	1.36	9.6	22.0	660 (310)	—15.62 (0.06)
52[a]	0.304	1.91	12.7	36.0	189 (66)	—15.43 (0.06)
16[b]	0.359	2.43	22.1	88.0	45.0 (9.0)	—15.22 (0.13)
32[b]	0.410	2.59	22.2	255.0	17.7 (8.5)	—15.18 (0.18)

[a] Drying times of 3.5, 4.0, and 4.5 min.
[b] Drying times of 3.0, 3.5, and 4.0 min.
[c] Figures in parentheses indicate maximum deviation from mean value.

membranes, some of which become very brittle in a period of two months.

Properties of Improved Protamine Collodion Matrix Membranes

For a series of survey experiments, six different sets of twelve membranes each were prepared under carefully controlled conditions and characterized by (*a*) anion-exchange capacity, (*b*) water content, (*c*) rate of osmotic water movement, (*d*) ohmic resistance in contact with 0.1N KCl solution, and (*e*) concentration potential in the cell 0.4N KCl | membrane | 0.2N KCl (see Table I).

Following the survey, membranes of the types most useful for physicochemical investigations were studied for their electromotive properties in KCl concentration cells over a wide range of concentrations, the concentration ratio being 2:1 (see Table II). One of these membranes was tested similarly in analogous cells with HCl, KNO_3, KIO_3, and K-Acetate (see Table III). The rates of exchange of critical ions (anions) and of noncritical ions (cations) across representative membranes at three concentrations, 1.0N, 0.1N, and 0.01N, were determined as a measure of their absolute permeabilities and ionic selectivities, and the corresponding ratios, the ionic selectivities of the membranes, calculated (see Table IV). In addition the bi-ionic potentials across several representative membranes were measured with various pairs of critical ions.

The anion-exchange capacity was determined with three or four membranes selected at random from each of the six sets. The membranes were slit open lengthwise, and 5.0 x 7.0 cm rectangles cut from the flat portions were placed in 0.1N KCl solutions which were changed several times during a week to assure that all accessible fixed charged groups were in the chloride form. The membranes were then washed with distilled water for several days until chloride could not be detected in the wash water. The chloride ions in the membranes were then displaced by immersing each group of three or four membranes in 20 ml of 0.5N $NaNO_3$ solution. After standing three days with occasional stirring, the $NaNO_3$ solutions were analyzed for chloride ion and the anion-exchange capacities of the membranes in μeq/cm^2 calculated. The dry weights of the membranes (see below) were used to calculate the anion-exchange capacities per gram of dry membrane.

The water content was measured with the flat membranes used in the anion-exchange measurements. They were reconverted to the chloride form, washed, blotted dry with filter paper, placed immediately in tared weighing bottles, and weighed in the wet state. They were then dried over phosphorus pentoxide *in vacuo*. The loss in weight was taken as the water content. The reproducibility of the measurements was about ±0.5 g, when the results are expressed as g water/100 g wet membrane.

The rate of osmotic water movement across a membrane was measured by filling the test tube shaped membrane with a 0.2M solution of sucrose (for which they are virtually impermeable), fitting it with a rubber stopper carrying a graduated capillary manometer tube, and placing it in a beaker of water at 25° ± 0.05°. After thermal equilibrium was reached, the rise of the liquid in the capillary gave

Table II. Concentration dependence of the concentration potentials (c_1:c_2 = 2:1) with solutions of KCl across representative permselective protamine collodion matrix membranes of different resistance (t = 25.00° ± 0.05°)

Concn. of electrolyte soln. c_1:c_2, equiv/l	Theor. max., mv	ρ^* = 10.0 ohm-cm^2, mv	ρ^* = 49.5 ohm-cm^2, mv	ρ^* = 188 ohm-cm^2, mv	ρ^* = 660 ohm-cm^2, mv	ρ^* = 2300 ohm-cm^2, mv
0.002/0.001	—17.45	—17.17	—17.28	—17.30	—17.31	—17.31
0.004/0.002	—17.31	—	—17.19	—17.20	—17.20	—17.18
0.01/0.005	—17.10	—17.06	—17.10	—17.10	—17.10	—17.10
0.02/0.01	—16.86	—16.76	—16.83	—16.84	—16.84	—16.83
0.04/0.02	—16.63	—16.45	—16.54	—16.55	—16.56	—16.55
0.1/0.05	—16.30	—16.06	—16.16	—16.18	—16.19	—16.18
0.2/0.1	—16.11	—15.75	—15.85	—15.88	—15.91	—15.91
0.4/0.2	—15.95	—15.03	—15.33	—15.40	—15.64	—15.67
1/0.5	—16.32	—14.43	—14.54	—14.92	—14.93	—14.86
2/1.0	—17.3	—12.33	—13.33	—13.63	—14.08	—14.25

Table III. Concentration potentials (c_1:c_2 = 2:1) of several electrolytes across a permselective protamine collodion matrix membrane (ρ^* = 660 ohm-cm²) (t = 25.00° ± 0.05°C)

Concentration of electrolyte solutions c_1/c_2	Concentration potential Theoretical maximum $E_{max.}$	Concentration potential Experimental (corrected) $E_{exp.}$	Diffusion potential, E_1, in free solution $E_{1(calc.)}$	Diffusion potential, E_1, in free solution $E_{1(exp.)}$
	A. Potassium iodate			
equiv/liter	mv	mv	mv	mv
0.002/0.001	—17.5	—17.0	5.5	5.0
0.004/0.002	—17.3	—16.8	5.5	5.0
0.010/0.005	—16.9	—16.8	5.4	5.0
0.020/0.010	—16.7	—16.6	5.3	5.1
0.040/0.020	—16.1	—16.0	5.2	5.0
0.100/0.050	—15.1	—14.9	5.0	4.9
0.200/0.100	—14.1	—13.8	4.8	4.7
0.400/0.200	—	—	—	—
	B. Potassium nitrate			
equiv/liter	mv	mv	mv	mv
0.002/0.001	—17.52	—16.98	0.27	0.27
0.004/0.002	—17.40	—16.92	0.27	0.32
0.010/0.005	—17.12	—16.76	0.28	0.38
0.020/0.010	—16.72	—16.50	0.29	0.46
0.040/0.020	—16.27	—16.12	0.29	0.54
0.100/0.050	—15.58	—15.26	0.31	0.64
0.200/0.100	—15.02	—14.92	0.34	0.85
0.400/0.200	—14.19	—13.95	0.39	1.00
	C. Potassium acetate			
equiv/liter	mv	mv	mv	mv
0.002/0.001	—17.43	—17.02	5.07	5.15
0.004/0.002	—17.34	—17.13	5.09	5.06
0.010/0.005	—17.16	—16.94	5.11	4.84
0.020/0.010	—16.97	—16.85	5.11	4.56
0.040/0.020	—16.82	—16.77	5.18	4.23
0.100/0.050	—16.79	—16.63	5.35	4.08
0.200/0.100	—16.85	—16.55	5.50	3.95
0.400/0.200	—17.27	—16.20	5.82	3.86
	D. Hydrochloric acid			
equiv/liter	mv	mv		
0.002/0.001	—17.45	—17.30	Concentration	
0.004/0.002	—17.34	—17.09	potentials were	
0.010/0.005	—17.15	—17.12	measured with	
0.020/0.010	—16.97	—16.93	Ag/AgCl elec-	
0.040/0.020	—16.84	—16.70	trodes; see text.	
0.100/0.050	—16.76	—16.43		
0.200/0.100	—16.87	—15.60		
0.400/0.200	—17.49	—14.23		

the rate of water transport, the reproducibility of these measurements being about ±10%.

The ohmic resistance of the membranes in 0.1N KCl solution, ρ^*, was measured at 25° ± 0.05° using the Kohlrausch method as previously described (16). From the measured resistance and the known free area of the membrane (about 50 cm²) the unit area resistance was computed.[4] The reproducibility of the membrane resistance from day to day was about ± 3%.

The concentration potentials of the membranes were measured at 25° ±0.05° using saturated calomel half-cells with saturated potassium chloride-agar bridges, except in the case of the HCl-cells in which Ag|AgCl electrodes, prepared by the method of Rule and La Mer, were used (17). Stirring had no effect at any concentration with membranes of ρ^* of several hundred ohm-cm² and more. With membranes having a ρ^* of about 100 ohm-cm², stirring was necessary at concentrations below about 0.2N/0.1N; otherwise, particularly at the lowest concentrations, the potentials were up to 0.5 mv too low. The majority of the potential measurements were reproducible within ± 0.05 mv except with the highest and lowest concentrations used, where the error may be twice as large.

From these raw data the true concentration potentials were obtained by the following two procedures. Where Ag/AgCl electrodes were used the difference of the two electrode potentials was computed from the Nernst equation using the known mean activities of the pairs of KCl solutions under consideration, and subtracting this computed value from the experimentally determined potential. In the case of the cells with which calomel half-cells and saturated KCl-agar bridges were used for the potential measurements, the corrections for the asymmetry of the two liquid-junction potentials, potassium chloride-agar bridge | electrolyte c_1 | electrolyte c_2 | potassium chloride-agar bridge, were determined by the following method which had also been used on prior occasions (4, 18). It is based on the assumption that it is possible to calculate with considerable accuracy (from the Nernst equation and known ionic mobility data) the liquid-junction potentials, $E_{1(calc.)}$, arising between solutions of the same electrolyte at different concentrations. These calculated liquid-junction potentials, $E_{1(calc.)}$ are compared with the experimental liquid-junction potentials, $E_{1(exp.)}$, in the membrane-free cells: saturated calomel electrode | saturated potassium chloride | saturated potassium chloride-agar bridge | electrolyte c_2 | electrolyte c_1 | saturated potassium chloride-agar bridge | saturated potassium chloride | saturated calomel electrode. The difference between these two values, $E_{1(calc.)} - E_{1(exp.)}$, is taken as the value of the asymmetry of two liquid-junction potentials at the tips of the agar bridges; it is applied as a correction to the concentration potentials measured across the membrane.

The values of $E_{1(exp.)}$ were measured with a simple W-shaped tube with a glass stopcock in the middle; otherwise the instruments used and the technique employed were the same as were used for the determination of the concentration potentials across membranes. The reproducibility of the $E_{1(exp.)}$ data, except at the lowest concentrations used, is better than ±0.05 mv. The various values for $E_{1(exp.)}$ and $E_{1(calc.)}$ are given in Table III for the neutral salts except KCl. With KCl cells with a concentration ratio of 2:1 (Tables I and II) the correction is —0.33 mv independent of the concentration. All data

[4] Dimensionally this resistance in ohm-cm², the reciprocal of the unit area conductance which is expressed in moh/cm². The designation of the unit resistance as ohm/cm² which is common in the literature (including some older publications from this laboratory) is dimensionally in error.

Table IV. Rates of movement of critical and noncritical ions across several permselective protamine collodion matrix membranes at various concentration levels in the system KCl (c_1) || NH_4Cl (c_1)

1	2	3	4	5	6	7	8	9	10
	Concentration 0.1N			Concentration 0.1N			Concentration 0.01N		
Membrane ρ*, ohm-cm²	Initial rate of movement of Cl⁻ μeq/hr cm²	Initial rate of movement of NH_4^+ μeq/hr cm²	Ratio of initial rates of movement of Cl⁻ to NH_4^+	Initial rate of movement of Cl⁻ μeq/hr cm²	Initial rate of movement of NH_4^+ μeq/hr cm²	Ratio of initial rates of movement of Cl⁻ to NH_4^+	Initial rate of movement of Cl⁻ μeq/hr cm²	Initial rate of movement of NH_4^+ μeq/hr cm²	Ratio of initial rates of movement of Cl⁻ to NH_4^+
5040	0.366	0.025	14.6	0.192	7.8×10^{-4}	250	0.180	5.8×10^{-5}	3100
2780	0.638	0.034	18.7	0.376	1.1×10^{-3}	340	0.304	4.6×10^{-5}	6600
450	4.64	0.380	12.2	2.46	5.6×10^{-3}	450	1.71	2.00×10^{-4}	8550
113	17.9	1.09	16.4	8.34	2.10×10^{-2}	400	5.56	4.6×10^{-4}	12000
24.5	121	16.7	7.2	42.8	2.69×10^{-1}	160	15.0	6.5×10^{-3}	2300
9.5	267	33.6	7.9	110	1.18	93	17.2	1.36×10^{-2}	1250

on membrane concentration potentials given in this paper are appropriately corrected.

The thermodynamically possible maximum values of the concentration potential were calculated in the conventional manner assuming that the only process occurring across an ideal membrane is the reversible transfer of the critical ions from the one solution to the other, and that the activity of the critical ions, the anions, at any given concentration is equal to the mean activity of the electrolyte ($a_- = a_\pm$). The activity coefficients were taken from Harned and Owen and from Robinson and Stokes, and converted from the molality to a normality basis (19, 20).

For the measurement of the rate of exchange of the anions a membrane filled with a KCl solution containing radioactive Cl^{36} was placed in a large volume of solution of nonradioactive KCl of the same concentration. Both solutions were stirred. Aliquots of the outer solution were withdrawn periodically and their radioactivity determined. The initial rate of anion exchange was calculated from the fraction of the radioactive chloride exchanging for stable chloride per unit time.[5]

The strictly comparable initial rate of exchange of the cations can be obtained from analogous experiments only with membranes of very low resistance and a significant leak because of the short half life ($t_{1/2}$ = 12.4 hr) of the available potassium isotope K^{42}. Instead, with the membranes of the extremely low cation leak of particular interest here, the rate of exchange of cations between an NH_4Cl and a KCl solution of equal concentration was determined by conventional microanalysis. The use of the data for these rates instead of those for the self-exchange of K^+ seems unobjectionable for the present purpose for the following reasons: (*a*) the behavior of NH_4^+ and K^+ ions in solution is very similar, and likewise, with cation selective membranes, as is evident from the fact that the bi-ionic potential, NH_4^+ | cation selective permselective membrane | K^+ is very low, at best of the order of a few millivolts; (*b*) the rates of exchange $K^{39+} \leftrightarrows K^{42+}$ and $NH_4^+ \rightleftarrows K^+$ across permselective poly-2-vinyl-N-methylpyridinium collodion matrix membranes have been found to agree satisfactorily in the case of those membranes with which both rates could be determined (14).

In addition, a few analogous experiments on the rates of exchange of critical and noncritical ions were carried out with $CaCl_2$ solutions in which the rates of exchange of the bivalent noncritical Ca^{++} ions were obtained by the use of Ca^{45} ($t_{1/2}$ = 152 days).

The bi-ionic potential in cells of the type 0.1*N* KCl | membrane | 0.1*N* KX where X may be any anion other than chloride, was measured (with all the precautions described recently elsewhere), using saturated calomel half-cells with saturated potassium chloride-agar bridges (21). The measurements were reproducible in general within ±0.5 mv. No corrections were made for the asymmetry of the liquid junction potentials at the tips of the two agar bridges.

Discussion

The exchange capacity per gram of membrane (Table I, column 2) is of interest primarily in correlation to certain aspects of the Teorell, Meyer-Sievers theory of the electrochemical behavior of membranes. This point will be touched upon later.

The exchange capacity per square centimeter of the membranes (Table I, column 3) is low, of the order of 1 to 2.5 μeq/cm² with the most useful of these membranes. Thus, in many types of experiments, it is possible to use membranes whose exchange capacities are low relative to the number of equivalents of ionic constituents in the surrounding solutions. This is of importance in many physicochemical investigations such as, for example, in the electrometric determination of ionic activities and in the study of Donnan equilibria.

The water content of the membranes (Table I, column 4) is the higher the longer the time of immersion of the membranes in the protamine solution and the less dried, that is, the more porous the membranes were during this immersion.

The rate of osmotic water movement across the membranes (Table I, column 5) is greater the higher the water content (cf. col. 4). The water movement across the membranes which is measured under a driving force corresponding to 50 m of water pressure is low except in the case of those with the highest protamine content. The low water permeabilities are helpful in studies where it is necessary to keep solutions of different water activity separate for long periods.

The resistances (Table I, column 6) of the membranes of a given type prepared under nominally identical conditions show substantial variations. Small increments in anion-exchange capacity are accompanied by great differences in resistance.

[5] A detailed account of the experimental technique is planned for a forthcoming paper on the exchange of ions across permselective membranes by Gottlieb and Sollner, in preparation (14).

The degree to which the concentration potentials (Table I, column 7) of the membranes deviate from the theoretical maximum at the 0.4/0.2*N* KCl concentration level can be estimated by comparing them with the calculated theoretical maximum potential, —15.95 mv.

The concentration potentials across the membranes with medium protamine contents approach the maximum theoretical potential more closely than do those with very low or very high protamine contents. The lower concentration potential obtained with the membrane with the lowest protamine contents is very probably due to the absence of charged groups at critical points in some of the pores of these membranes. With membranes of high protamine content the lower concentration potentials are undoubtedly due to the larger average pore size of these membranes which is correlated with their higher water content (cf. col. 4).

In connection with the Teorell, Meyer-Sievers theory (22, 23) it is of interest to look for a correlation of the selectivities of the various membranes as manifested by their concentration potentials and the equivalent concentrations of fixed basic wall groups (or exchangeable counter ions) in the pore water of the membranes. The latter values as derived from col. 3 and 4 of Table I, assuming all of the water to be available, are in order of increasing anion exchange capacity per gram of wet membrane, 1.7, 1.8, 2.2, 2.1, 1.3, and 1.4 equiv/l. These values are identical with the selectivity constants of the Teorell, Meyer-Sievers theory. The theory postulates the concentration potentials to be the higher the greater the equivalent concentration of active groups in the pore water of the membrane. The empirically found correlation is more of a general qualitative than of a quantitative nature.

Table II on the concentration dependence of the concentration potential in KCl cells shows that the potentials at the lowest concentrations are 0.15 — 0.28 mv below the calculated maximum; at 0.01/0.005*N* and 0.02/0.01*N* the agreement is perfect within the accuracy of the measurements, except possibly with the membrane of lowest resistance. With more concentrated solutions the deviations become greater. The electromotive behavior of the permselective protamine membranes in this series of concentration cells is virtually the same as that of the analogous strong-base type poly-2-vinyl-N-methylpyridinium bromide collodion matrix membranes (13).

Table III gives the calculated and the (corrected) experimental concentration potentials in cells with four different electrolytes, KIO_3, KNO_3, K-Acetate, and HCl, together with the calculated and experimental liquid junction potentials obtained with the three neutral electrolytes (on which the corrections of the measured potential values are based). In all instances, as above with the KCl cells, the agreement between the theoretical and experimental concentration potentials is best in a medium range of concentrations.

In order to facilitate visualization of the data on concentration potentials a part of the data of Table II and the data of Table III are represented graphically in Fig. 1. The deviations of the experimental values from the calculated ones at the higher concentrations do not require any comment; it is in full agreement with the fixed charge theory (22, 23). Deviations between the two sets of data at the lower and particularly the lowest concentrations, which are quite systematic and, with the neutral salts, far in excess of any probable error, are not explained by the fixed charge theory as commonly understood. They duplicate earlier observations with the older type of permselective protamine collodion matrix membrane (4) and with poly-2-vinyl-N-methylpyridinium collodion matrix membranes (13). Analogous deviations at the lowest concentrations were also observed with strong acid sulfonated polystyrene collodion membranes (24). We are inclined to attribute this effect to the ions of the water, specifically to the drift of the experimental cells toward the state of membrane hydrolysis predicted by the theory of membrane equilibria. Preliminary experiments support this view, without as yet definitely proving its correctness. We hope to report on this matter in the near future.

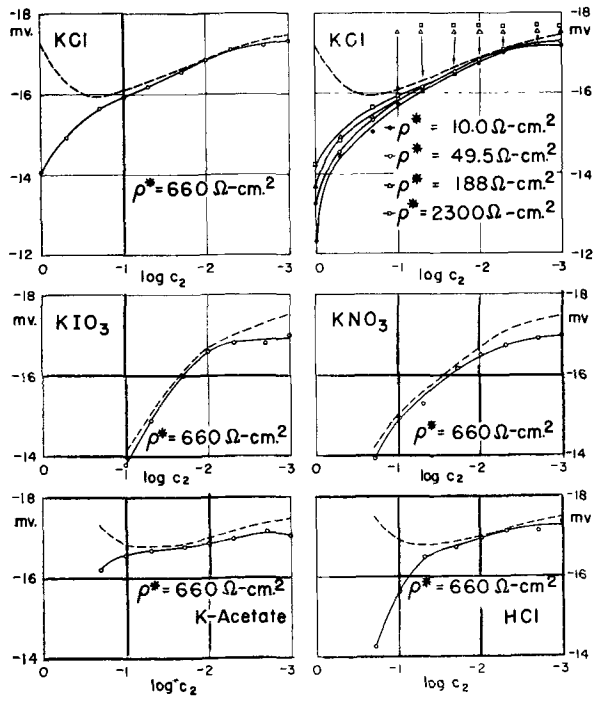

Fig. 1. Concentration potentials (c_1:c_2 = 2:1) of several electrolytes across typical permselective protamine collodion matrix membranes.

It was recognized some time ago that the deviations of the measured concentration potentials from the theoretically possible maximum values, particularly in the case of membranes of high ionic selectivity, do not furnish an adequate basis for a calculation of the numerical value of the ionic selectivities of such membranes (25). A variety of complicating factors is now generally recognized (26).

First, nonthermodynamic assumptions are made in the calculation of the theoretical maximum potential; and, likewise, in assigning a part of the measured potential of a concentration cell to the membrane concentration potential a nonthermody-

namic, at least semi-empirical correction procedure must be used, such as that outlined above. Second, there are definite limitations of the accuracy with which the potential measurements may be made. In particular, if a membrane is not of virtually ideal ionic selectivity and if the solutions are very dilute, the concentrations of electrolyte in the nonstirred, adhering water layers of the membrane may be significantly different from those in the bulk solutions. The measured potential would thus be lower than that which would arise if the concentrations in the adhering water layers and bulk solutions were the same. Expressed in another way, the true ionic selectivity of the membrane would be higher than that calculated in a straightforward manner from the measured concentration potential. Further, membrane hydrolysis may also lower the measured potential in dilute solutions of neutral electrolytes. In addition, the ions move across the membranes in a hydrated state, thereby transporting water of hydration from a compartment of lower to the compartment of higher water activity (and possibly some additional water by an electrophoretic effect). There may also be an opposing osmotic streaming of water which the diffusing critical ions must overcome. All these effects would tend to reduce the electromotive efficiency of the critical ions, thus reducing the concentration potential below the value which is calculated for the condition of no solvent transport between the two solutions. These latter possibilities, in recent years, have been the subject of intensive theoretical and experimental work (21, 26-29). Thus it is apparent that the degree of the ionic selectivity of highly ion selective membranes is better established by a more direct method, namely, on the basis of the relative permeabilities of the critical and noncritical ions as determined from the rates of self-exchange of these ions across a membrane (13, 14, 24, 25).

The initial rates of movement of critical ions, the anions, across the various membranes in the systems at 0.1*N* (Table IV, column 5) are inversely proportional to their standard resistances, ρ^*, (which is also measured with 0.1*N* solution) as postulated by the Nernst-Einstein equation for the rate of self-diffusion. With 1*N* and 0.01*N* solutions (columns 2 and 8 of Table IV) the rates of self-exchange of the critical ions show only a semi-quantitative inverse proportionality to the standard resistance of the membranes, ρ^*.

The initial rate of movement of the noncritical ions, the cations, (columns 3, 6, and 9 of Table IV) shows a considerably steeper inverse relationship with the standard membrane resistance than that observed with the critical ions.

The rates of exchange of the critical ions across a given membrane in 0.01 and 1*N* solutions differ by a factor of about 2 with the membrane of the highest standard resistance to a factor of about 15 with the membrane of lowest resistance. The rate of exchange of the noncritical ions varies over the same concentration interval by a factor of about 430 for the membrane with the highest resistance, to a factor of about 2500 for the lowest resistance membrane.

The ionic selectivities of the various permselective membranes, that is, the ratio of the initial rates of exchange of the critical to those of the noncritical ions (columns 4, 7, and 10 of Table IV) are very much greater at the lower than at the higher concentrations, in agreement with all previous experience.

The correlation between membrane resistance and selectivity is not straightforward; the best membrane with a selectivity of 12,000:1 in 0.01*N* KCl solution is of medium resistance. The degree of ionic selectivity of the permselective protamine collodion matrix membranes closely approaches, but does not quite reach, that of the analogous permselective poly-2-vinyl-N-methylpyridinium collodion matrix membranes (13).

The small "leaks" of noncritical ions which correspond to these high ionic selectivities (numerically their reciprocals) circumscribe the conditions under which these membranes can be used without significant disturbances due to this imperfection.

The selectivities of the improved permselective protamine collodion matrix membranes, in the presence of univalent anions and bivalent cations (not shown in the tables) as determined with 0.1*N* $CaCl_2$ solutions containing radioactive Ca^{45}, and membranes of 10, 23, 108, and 402 ohm-cm^2 in 0.1*N* KCl were found to be 10.400, 15.000, 48.000, and 151.000 ohm-cm^2, respectively. With more dilute solutions these selectivities can be safely assumed to be considerably higher.

The bi-ionic potentials across the permselective collodion matrix membranes prepared with purified protamine preparations, as may be expected *a priori*, are very similar in magnitude to those obtained earlier with membranes made with less pure preparations (30). Some of the bi-ionic potentials, E_{bip}, obtained (with 0.1*N* solutions) across a membrane with a standard resistance, ρ^*, of 660 ohm-cm^2 were: NaCl || NaSCN, + 31.4 mv; NaCl || $NaNO_3$, + 21.1 mv; NaCl || NaI, + 16.3; NaCl || NIO_3, − 38.3 mv; NaCl || Na-acetate, − 46.0 mv; and NaCl || Na-propionate, − 52.5 mv, the signs referring to the charge of the solutions on the right side.

The improvement in the ionic selectivity of the membranes prepared with purified protamine over those prepared with the commercial preparations obviously must be ascribed to the removal of some strongly adsorbable impurities of acidic character which are removed by the treatment with the ion exchange resin since it can hardly be assumed that the treatment with an ion-exchange column alters the chemical structure of protamine itself. As is evident from the data, the carboxylic end groups of the protamine molecules do not affect adversely the ionic selectivity of the membranes to any significant extent, in spite of the fact that they represent about 5% of the potentially dissociable groups of the protamine molecule.

Several factors should be considered to account for the functional ineffectiveness in the membrane of the carboxylic end groups of the protamine molecule. First, many of these groups may be blocked functionally by combination with a basic group

either of the same or of some other protamine molecule. Second, the cationic counterions of the sparsely distributed acidic groups, even if dissociated completely off the latter,[6] would have to migrate past numerous interposed positive wall groups. Being strongly repelled by these groups of the same charge, the cations are unable to move from the vicinity of one of the acidic groups to the next and thus are more or less permanently confined to the location which they had occupied when the membrane was prepared.

The high ionic selectivities of the improved protamine collodion matrix membrane which are evident from Tables I-IV demonstrate that the purpose of this investigation has been achieved, namely, to produce membranes which are free of the main shortcoming of the previous protamine membranes, their inadequate degree of ionic selectivity, and which fulfill the predictions of the Nernst-Einstein equation with respect to the correlation of their resistance and the rate of self-exchange of ions across them.

[6] Due to the mode of preparation of the membranes, the carboxyl groups may be present in the hydrogen state with the hydrogen ion dissociated off to a very limited degree only.

Manuscript received June 16, 1958. This paper was presented at the New York Meeting, April 27-May 1, 1958.

Any discussion of this paper will appear in a Discussion Section to be published in the December 1959 JOURNAL.

REFERENCES

1. C. W. Carr, H. P. Gregor, and K. Sollner, *J. Gen. Physiol.*, **28**, 179 (1945).
2. H. P. Gregor and K. Sollner, *J. Phys. Chem.*, **50**, 88 (1946).
3. H. P. Gregor and K. Sollner, *ibid.*, **54**, 325 (1950).
4. K. Sollner and H. P. Gregor, *ibid.*, **54**, 330 (1950).
5. H. P. Gregor and K. Sollner, *J. Colloid Sci.* **7**, 37 (1952).
6. W. S. Albrink and R. M. Fuoss, *J. Gen. Physiol.*, **32**, 453 (1949).
7. G. Manecke and K. F. Bonhoeffer, *Z. Elektrochem.*, **55**, 475 (1951).
8. A. G. Winger, G. W. Bodamer, and R. Kunin, *This Journal*, **100**, 178 (1953).
9. D. M. Wetstone and H. P. Gregor, *J. Phys. Chem.*, **61**, 151 (1957).
10. A. Nishihara, Y. Mineki, and M. Sekino, *Reports of Research Laboratory, Asahi Glass Co.*, **6**, 20 (1956).
11. W. Juda and A. A. Kasper, U. S. Pat. 2,731,425, Jan. 17, 1956.
12. J. T. Clarke, U. S. Pat. 2,730,768, 2,731,408, 2,731,411, Jan. 17, 1956; 2,732,351, Jan. 24, 1956; 2,756,202, July 24, 1956.
13. M. H. Gottlieb, R. Neihof, and K. Sollner, *J. Phys. Chem.*, **61**, 154 (1957).
14. M. H. Gottlieb and K. Sollner, in preparation; J. Wagner and K. Sollner, in preparation.
15. R. Neihof, Ph.D. Thesis, University of Minnesota, Minneapolis 1950.
16. H. P. Gregor and K. Sollner, *J. Phys. Chem.*, **50**, 53 (1946).
17. C. K. Rule and V. K. La Mer, *J. Am. Chem. Soc.*, **58**, 2339 (1936).
18. K. Sollner and H. P. Gregor, *J. Phys. Chem.*, **51**, 299 (1947).
19. H. S. Harned and B. Owen, "The Physical Chemistry of Electrolytic Solutions," 2nd ed., Reinhold Publishing Corp., New York (1950).
20. R. A. Robinson and R. H. Stokes, "Electrolyte Solutions," Academic Press Inc., New York, and Butterworth Scientific Publications, London (1955).
21. S. Dray and K. Sollner, *Biochim. et Biophys. Acta*, **18**, 341 (1955).
22. T. Teorell, *Proc. Soc. Exptl. Biol. Med.*, **33**, 282 (1935); *Proc. Natl. Acad. Sci. U. S.*, **21**, 152 (1935); *Z. Elektrochem.*, **55**, 460 (1951); *Progr. Biophys. and Biophys. Chem.*, **3**, 305 (1953); *Discussions Faraday Soc.*, **21**, 9 (1956).
23. K. H. Meyer and J. F. Sievers, *Helv. Chem. Acta*, **19**, 649, 665, 987 (1936).
24. R. Neihof, *J. Phys. Chem.*, **58**, 916 (1954).
25. K. Sollner and H. P. Gregor, *ibid.*, **51**, 299 (1947).
26. K. Sollner, *This Journal*, **97**, 139C (1950).
27. A. J. Staverman, *Trans. Faraday Soc.*, **48**, 176 (1952).
28. G. Scatchard, *J. Am. Chem. Soc.*, **75**, 2883 (1953).
29. *Membrane Phenomena*, Discussions of the Faraday Society No. 21, The Faraday Society, and Aberdeen University Press Ltd., Aberdeen, 1956.

December 1959 Discussion Section

A Discussion Section, covering papers published in the January-June 1959 JOURNALS, is scheduled for publication in the December 1959 issue. Any discussion which did not reach the Editor in time for inclusion in the June 1959 Discussion Section will be included in the December 1959 issue.

Those who plan to contribute remarks for this Discussion Section should submit their comments or questions in triplicate to the Managing Editor of the JOURNAL, 1860 Broadway, New York 23, N. Y. *not later than September 1, 1959.* All discussions will be forwarded to the author(s) for reply before being printed in the JOURNAL.

Electrochemical Kinetics of the Anodic Formation of Oxide Films

Pierre Van Rysselberghe

Department of Chemistry and Chemical Engineering, Stanford University, Stanford, California

and Herman A. Johansen

Research Laboratories, Westinghouse Electric Corporation, Pittsburgh, Pennsylvania

ABSTRACT

The total electric potential difference between a metal and a solution across an oxide film being built up by a constant anodic current is decomposed into three contributions: differences at the interphases metal-oxide and oxide-solution, both subject to activation overvoltage, and the difference across the oxide layer. For one or the other of the interphases the case of linearity of overvoltage with the logarithm of the current (in the range of large currents) and that of proportionality of overvoltage with current (in the range of small currents) are examined in some detail, and previously obtained experimental data for three types of titanium, for hafnium, and for tantalum are analyzed in terms of the proposed theoretical treatment. Numerical values are obtained for the various parameters appearing in the equations: thickness of the interphase, exchange current, electric potential difference, and electric field at zero current. Possibilities for refinement and extension of the treatment are mentioned.

The theory advanced by Cabrera and Mott (1) on the basis of earlier work by Mott (2) to explain the rate of growth of oxide films on metals usually has been regarded as directly applicable to the case of anodic oxidation. The present authors and their collaborators (3-5) have applied it to the interpretation of data obtained in the anodic oxidation of several metals. From the evolution with time of the potential of the metal (measured against an unpolarized electrode) during oxidation at constant current they were able to verify that the unitary rate of change of potential, $(1/I) \cdot (\partial E/\partial t)_I$, in which I is the apparent current density, E the relative potential of the metal, t the time, corresponding to the flats in the curves $\log(\partial E/\partial t)_I$ vs. $\log t$ at constant I was, over the range of currents utilized (1 to 100 μa/cm^2), a linear function of $\log I$. This situation is implied in the Cabrera-Mott theory which thus was regarded as essentially verified.

In a more detailed analysis of our recently published data (5) on the anodic oxidation of Al, Cr, Hf, Nb, Ta, Ti, and V in saturated ammonium borate at 25°C, it was found interesting to interpret these data on the basis of an electrochemical approach involving the use of the current-overvoltage relationships of electrochemical kinetics at the metal-oxide and at the oxide-solution interphase. Regardless of the detailed circumstances of the passage of the current through the oxide film itself, it appears probable that, at the metal-oxide interphase, the net process is the transfer of metallic ions from the metal to the oxide and that, at the oxide-solution interphase, the net process is the transfer of oxide or hydroxyl ions from the solution to the oxide. The treatment presented here does not depend on an *a priori* decision as to which process (that across the metal-oxide interphase, that across the oxide itself, or that across the oxide-solution interphase) is rate-determining. In a steady state, with the same current passing through the three portions of the over-all metal-solution system, the evaluation of the velocity of one of the three processes serves for the two other processes as well. This has been the guiding idea of one of us in previous treatments of overvoltage phenomena (6).

Following Cabrera and Mott (1) and Vermilyea (7) we shall neglect the possibility of the presence of a space charge anywhere in the over-all interphase, the electric field being then constant from the bulk of the metal to the bulk of the solution.

Electrochemical Theory of Anodic Oxidation

Consider a metallic phase α separated from an electrolyte solution β by a film γ of oxide (Fig. 1). Between the terminal plane a' of the metal and the oxide in bulk there is a transition layer a'a and between the oxide in bulk and the solution in bulk there is a transition layer bb'. The oxide has the thickness X from a to b. The thicknesses a'a and bb' are called x_a and x_b, respectively, and will be regarded as independent of time. We shall restrict ourselves to values of X large enough to prevent any overlapping or mutual influence of the transition

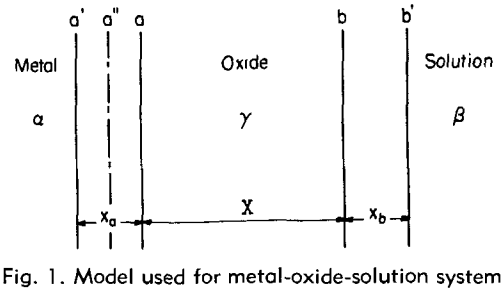

Fig. 1. Model used for metal-oxide-solution system

regions a'a and bb' but small enough to remain in the range of thin films.

The electric potential difference from metal to solution is given by

$$\phi_a - \phi_\beta = (x_a + x_b + X) \cdot F \qquad [1]$$

in which F represents the electric field. Calling w the mass of oxide formed per coulomb and d the density of the oxide we have

$$X = X_o + wIt/d \qquad [2]$$

In electrochemical terms the situation at the a'a interphase can be described as follows. It should be clear that this analysis is equally applicable to the interphase bb'. We shall consider the two extreme cases of: (a) a Tafel relation between current and overvoltage, and (b) proportionality between current and overvoltage. In this latter case, as well as in the intermediate one corresponding to proportionality of current with the hyperbolic sine of $zF\eta/2RT$ (z being the number of Faradays F carried by one gram-ion, η the overvoltage, R the molar gas constant, and T the absolute temperature; the transfer coefficient is taken as equal to ½ for both the anodic and the cathodic direction) the net current is the resultant of a forward anodic current and of a reverse cathodic current. Such a situation may conceivably occur at very low net currents both in a'a and in bb', even though the anodic current through the oxide itself might still be unopposed.

Case 1.—We have the following Tafel relation:

$$(\phi_{a'} - \phi_a)_I = (\phi_{a'} - \phi_a)_{I=0} + \frac{RT}{\tau_a zF} \cdot \ln \frac{I}{I_{0a}} = x_a \cdot F \qquad [3]$$

in which τ_a is the transfer coefficient (equal to the ratio of distance a'a" to distance a'a in which a" is the activated position of the metallic ion moving across the barrier from a' to a), ln represents the natural logarithm, and I_{0a} is the extrapolated exchange current at the a'a barrier. Since

$$\phi_a - \phi_\beta = (x_a + x_b + X_0 + wIt/d) \cdot F \qquad [4]$$

we have, combining with Eq. [3] and differentiating with respect to t at constant I, E differing from $\phi_a - \phi_\beta$ by a constant:

$$\frac{1}{I} \cdot \left(\frac{\partial E}{\partial t}\right)_I = \frac{RTw}{\tau_a dx_a zF} \cdot \ln \frac{I}{I_{0a}} +$$

$$(\phi_{a'} - \phi_a)_{I=0} \cdot \frac{w}{dx_a} = \frac{w}{d} \cdot F \qquad [5]$$

an expression independent of t which thus is expected to be valid only along the horizontal portions of the experimental plots of $\log(\partial E/\partial t)_I$ vs. $\log t$ for constant I. This situation is that which we actually verified with several of the metals previously reported on (3-5). Equation [5] was found to apply satisfactorily from current densities of 100 μa/cm^2 down to 1. However, plots of unitary rates vs. I rather than vs. $\log I$ (8) indicated a definite possibility that the lower current densities, from 5 to 1, might be in or very near the range of applicability of Case 2.

Table I. Data on anodic oxidation of Ti, Hf, and Ta in saturated ammonium borate at 25°C

Metal	Oxide	Density of oxide	x_a, Å	I_{0a}, μa/cm^2	$(\phi_{a'} - \phi_a)_0$, mv	F_0, 10^6 v/cm	F_{100}, 10^6 v/cm
Ti (iodide)	TiO_2	4.22	8.7	1.7	205	2.3	3.0
Ti (Kroll)	TiO_2	4.22	7.1	2.5	176	2.6	3.2
Ti (cold worked)	TiO_2	4.22	7.9	1.1	214	2.5	3.4
Hf	HfO_2	9.68	8.0	1.5	225	2.8	3.6
Ta	Ta_2O_5	8.5	6.0	1.7	94	1.6	2.3

Case 2.—When the cathodic counter-current in a'a cannot be neglected the net current is given by a difference between two Tafel expressions which, upon expansion and limitation to first power terms in the overvoltage (a procedure justified when $\tau_a F\eta/RT$ becomes sufficiently smaller than 1) gives:

$$(\phi_{a'} - \phi_a)_I = (\phi_{a'} - \phi_a)_{I=0} + \frac{RTI}{(\tau_a + \tau'_a) zFI_{0a}} = x_a \cdot F \qquad [6]$$

Instead of Eq. [5] we now have:

$$\frac{1}{I} \cdot \left(\frac{\partial E}{\partial t}\right)_I = \frac{RTwI}{(\tau_a + \tau'_a) dx_a zFI_{0a}} +$$

$$(\phi_{a'} - \phi_a)_{I=0} \cdot \frac{w}{dx_a} = \frac{w}{d} \cdot F \qquad [7]$$

an expression which, like Eq. [5], is time-independent and which we may expect to find verified along the horizontal portions of the plots of $\log(\partial E/\partial t)_I$ vs. $\log t$ for sufficiently small values of I. Let us note that Eq. [7] leads to the possibility of determining the field at zero current from the intercepts of the linear plots of $(1/I) \cdot (\partial E/\partial t)_I$ vs. I. This is of course not possible with the linear plots of $(1/I) \cdot (\partial E/\partial t)_I$ vs. $\log I$ corresponding to Eq. [5]. However, by combining information obtainable from Eq. [5] and [7] and on the basis of plausible assumptions concerning d, τ_a, and τ'_a we can arrive at numerical values for all the quantities appearing in these two equations. We have done this for a number of metals by applying Eq. [7] to the range of 5 to 1 μa/cm^2, taking the slope provided by these two points to be the coefficient of I in Eq. [7]. In two cases out of five [the first two of Table I, see (8)] the plots were linear in the range 1-5-10 μa/cm^2, while in the other three cases a hyperbolic sine type of behavior appears to hold in the 5-10-20 range.

Application to Titanium, Hafnium, and Tantalum

In Eq. [5] and [7] the experimental quantities are the unitary rate $(1/I) \cdot (\partial E/\partial t)_I$, the temperature T and the current density I. In addition these equations contain the constants R, w, z, and F. We assume that the density d of each oxide is equal to that of the oxide in bulk, that τ_a and τ'_a are both equal to 0.5. On this basis it is readily seen that the coefficient of ln I in Eq. [5] immediately will give us the value of x_a. Introducing this value of x_a in the coefficient of I in Eq. [7] we obtain the value of I_{0a}. It is interesting to note, as is shown in Table I, that, in the

five cases for which these calculations were carried out, I_{0a} turns out to fall within the 1 to 5 μa/cm^2 range, an indication that this range either corresponds to the exact applicability of the proportionality between current and overvoltage or is one of transition from hyperbolic sine behavior to proportionality. Even if this second alternative were to be the more correct one, it appears to be of extreme interest to pursue the calculations on the basis of proportionality for the 1 to 5 range and thus to obtain from our measured unitary rates at least approximate values for quantities which otherwise would not be accessible: exchange currents, electric potential differences across a'a or bb' interphases and electric fields at I equal to or different from zero.

Another indication in support of our procedure is the following: the term $(\phi_{a'} - \phi_a)_{I=0} \cdot (w/dx_a)$ should have, for internal consistency between Eq. [5] and [7] and their respective ranges of validity, the same value in these two formulas. We verified that this was practically the case by transporting into Eq. [5] the value of $(\phi_{a'} - \phi_a)_{I=0} \cdot (w/dx_a)$ derived from Eq. [7] and calculating the value of I_{0a} required for verification of Eq. [5]. In the case of hafnium, for instance, I_{0a} obtained from Eq. [7] is 1.5 μa/cm^2, while the value obtained from Eq. [5] by the procedure just outlined is 0.9, a very satisfactory agreement in view of the fact that a verification of the order of magnitude was all that had been expected.

The results of the calculations described above are given in Table I for three kinds of titanium (iodide process, Kroll process-annealed, Kroll process-34% cold worked), hafnium, and tantalum. The experimental details concerning these and other metals have been given earlier (5). The formula of the oxide, its density, the thickness x_a, the exchange current I_{0a}, the electric potential difference $(\phi_{a'} - \phi_a)_{I=0}$, the field F_0 at zero current and the field F_{100} at $I = 100$ μa/cm^2 are given for each metal.

Our calculations have been carried out without introducing any roughness factor because of the lack of any reliable information concerning its value and also because its theoretical role in the considerations developed here is by no means clear. It may be that the values of x_a empirically obtained in the calculations include an effective roughness factor. Using an arbitrary value of 2, for instance, the actual values of x_a would be those of Table I divided by 2.

Recall that the exchange current I_{0a} is proportional to exp $(-\Delta G^*/RT)$ in which ΔG^* is the chemical free enthalpy of activation, the electrical portion of the total free enthalpy of activation at zero net current having been separated in the first term on the right hand side of Eq. [3]. The values of I_{0a} and ΔG^* thus vary in opposite directions. It is interesting to note that, of the three kinds of titanium considered here, the Kroll process-annealed has the lowest ΔG^* and the Kroll process-cold worked has the highest, with the iodide process type having an intermediate ΔG^*, the total range of variation being about 500 cal/gram-ion.

In concluding we wish to stress that the calculations presented here should be regarded as having only qualitative significance. They should serve as illustrations for a theoretical approach which appears to be in the right direction and which could be refined without any major difficulty. In particular it would be a simple matter to introduce discontinuities in the electric field at the planes a and b and thereby to take into account the possible presence of space charges. The overvoltage-current relationships at the interphases a'a and bb' may each be, for a given current, of one of three possible types (Tafel, hyperbolic sine, proportionality) giving rise to a total of nine possibilities. In accordance with a recent study by one of us (9) on the dependence of reaction rates on affinities, which we are in the process of extending to electrochemical reactions, elementary reactions with rates varying exponentially with their affinities (here currents varying exponentially with the electrochemical affinities or overvoltages) are rate-determining, while elementary reactions with rates proportional to their affinities (here currents proportional to the electrochemical affinities or overvoltages) are regarded as practically reversible steps. If, in the cases discussed above, the current-overvoltage relationship applying to the thickness X of the oxide itself remains of the Tafel (or Cabrera-Mott) type throughout the whole range of currents, i.e., from 100 to 1 μa/cm^2, the corresponding step (passage of metallic ions from a to b, but, as a conceivable alternative, passage of oxide ions from b to a) is definitely rate-determining in the range of small currents, i.e., here 5 to 1 μa/cm^2. On the other hand, at the higher currents, the actual rate-determining step may be either the passage of metallic ions from a' to a or the passage of oxide ions from b' to b. In this latter case a variation with the composition of the solution of the parameters calculated in the present paper would be expected. In this manner it would become possible to examine the influence of the composition of the solution on the characteristics of the film-building process. Such an influence has already been detected experimentally in the case of zirconium and its alloys (10, 11).

Acknowledgment

The work reported in the present paper was part of a project carried out under a Research Fellowship granted to one of the authors (H. A. J.) by the Research Foundation of the Aluminum Company of America to which appreciation is hereby expressed. The experimental work (5, 8) on which the foregoing theoretical developments are based was performed in the Department of Chemistry of the University of Oregon at Eugene, Oregon.

Manuscript received Jan. 2, 1957.

Any discussion of this paper will appear in a Discussion Section to be published in the December 1959 JOURNAL.

REFERENCES

1. N. Cabrera and N. F. Mott, Reports on Prog. in Physics, **12**, 163 (1948).
2. N. F. Mott, *Trans. Faraday Soc.*, **35**, 1175 (1939); **36**, 1 (1940); **43**, 429 (1947).
3. M. Maraghini, G. B. Adams, Jr., and P. Van Rysselberghe, *This Journal*, **101**, 400 (1954).
4. G. B. Adams, Jr., P. Van Rysselberghe, and M. Maraghini, *ibid.*, **102**, 502 (1955).

5. H. A. Johansen, G. B. Adams, Jr., and P. Van Rysselberghe, *ibid.*, **104**, 339 (1957).
6. P. Van Rysselberghe, *J. Chem. Phys.*, **17**, 1226 (1949); **20**, 1522 (1952); *J. chim. phys.*, **49**, C 47 (1952); "Electrochemical Affinity," Hermann & Co., Paris (1955).
7. D. A. Vermilyea, *Acta Met.*, **1**, 282 (1953); **2**, 476, 482 (1954).
8. H. A. Johansen, Ph.D. Thesis, University of Oregon, Eugene, Ore., 1956.
9. P. Van Rysselberghe, *J. Chem. Phys.*, **29**, 640 (1958).
10. C. E. Borchers, Ph.D. Thesis, University of Oregon, Eugene, Oregon, 1956.
11. G. B. Adams, Jr., C. E. Borchers, and P. Van Rysselberghe, Technical Report to the Atomic Energy Commission, AECU 3388, 1957.

Technical Notes

Electrochemical Aspects of Stress Corrosion

D. K. Priest

Research Division, The Pfaudler Company, Rochester, New York

In recent years there has been some discussion of a "mechanical" mechanism for stress-corrosion cracking (1-5). In much of this work discussions of mechanism are based on the combination of a mechanical step and an electrochemical step, these being regarded as alternate and discrete actions which contribute to the total phenomenon. Those holding this viewpoint with respect to the mechanism of stress-corrosion believe that purely mechanical cracking is the major contribution toward stress-corrosion cracking and that electrochemical reaction or corrosion acts only as a means of triggering the mechanical cracking.

It is believed that some experimental evidence available indicates another, more logical mechanism for stress-corrosion, and this paper is devoted to discussion of a mechanism for stress-corrosion believed to be in best agreement with observable data.

Harwood, in a review of the phenomenon, discussed several theories of stress-corrosion (6). These theories can be divided into two main areas of belief, a mechanical mechanism, triggered at intervals by very local corrosive attack and an electrochemical mechanism in which corrosive attack occurs continuously as a primary contributing factor with the role of stress being that of causing local electrode potential changes. Such potential changes might be caused by stress-induced changes in filming mechanisms or by cold work of local metal volumes.

Brown and Dix (7) supported an electrochemical mechanism. Their work dealt primarily with intergranular stress corrosion, however, and strong evidence was presented for the existence of preferential paths for corrosion along grain boundaries. Extensions of the electrochemical theory into the area of transgranular stress-corrosion have been made by Logan (8), Priest, Beck, and Fontana (9, 10), among others.

Although the mechanical theory was early expressed by Keating (1), in recent years Edeleanu (4), Harwood (5) and others have held similar although more sophisticated views wherein the electrochemical contribution to stress-corrosion was viewed as a triggering mechanism for a purely mechanical fracture. This expanded viewpoint was made necessary in view of the demonstration of the effectiveness of cathodic protection in preventing stress-corrosion cracking and in slowing or stopping stress-corrosion already in progress.

Loading Previously Cracked Specimens

Unpublished data and observations recorded by the writer some years ago are of interest in support of the electrochemical theory of stress-corrosion. In an investigation of stress corrosion in a magnesium-base alloy (9), several interesting experiments were performed. In one case stress-corrosion cracking of the J1 alloy (6% Al, 1% Zn, balance Mg) in an inhibited sodium chloride solution was allowed to proceed until the test specimen was cracked halfway through, at which time it was removed from the test solution, washed and dried, and subjected to additional stress. The imposition of additional stress resulted in no further cracking and caused only ductile bending of the remainder of the cross section. Such cracked specimens could only be cracked further in air by impact loading, in which case the surface appearance of the impact fracture was far different than the surface appearance of the fracture caused by stress-corrosion cracking.

Corrosion Current Measurements

A consideration of the mechanical triggering idea is that measured corrosion currents should assume different values according to whether or not mechanical failure or electrochemical corrosion is taking place within a given time interval. Thus, if purely mechanical cracking is occurring, the corrosion current should be zero or appreciably decreased and, if mechanical cracking is not taking place at the instant of time considered, then corrosion current should assume some maximum value.

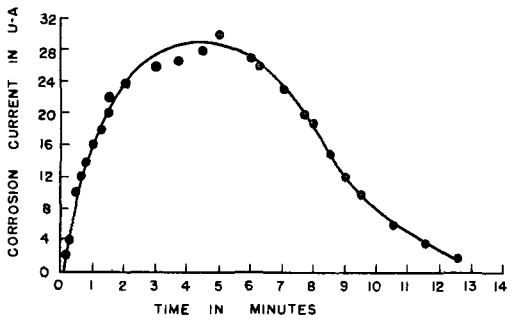

The data presented in Fig. 1 were recorded for a transgranular stress corrosion failure of J1 alloy under testing and measuring conditions described in detail previously (9). The J1 alloy was made to crack in an inhibited sodium chloride solution and, using an electrode physically separated from the anodic crack as cathode, corrosion currents were measured. The data of Fig. 1, recorded at intervals of a minute or less, indicate that the measured currents did not fluctuate and did not increase or decrease in a step-wise manner. Further, continuous visual observation of the microammeter revealed no needle "flicker" or other evidence of changing current. This behavior of the corrosion current suggests that the electrochemical nature of stress-corrosion process is continuous and that purely mechanical cracking plays no role in the mechanism.

Cathodic Protection

Harwood (5) suggests that at some point in the cracking process, the influence of mechanical cracking might be too great to counteract with cathodic protection. In contrast, the writer's experiments indicate that application of cathodic protection to a specimen undergoing stress-corrosion controlled the *rate* of stress-corrosion at all stages of cracking.

Figure 1 presents typical corrosion current-cracking time data obtained for transgranular stress corrosion cracking with the magnesium-base alloy, J1. The data cover the total cracking of a specimen from crack initiation to essentially complete failure. Current values were measured as described previously. The shape of the curve in Fig. 1 is due to the fact that the specimens were stressed by the constant deflection method so that stress values at the crack base varied from zero (before initiation) to a maximum (when crack was halfway through the specimen cross section) to zero (as relief occurred because of the ductile behavior of the reduced cross section of the nearly completely cracked specimen). At any stage in the cracking process, the amount of cathodic protection current needed to stop the attack was proportional to the corrosion current being generated at the time of application of protection. Further, at all stages of the process the addition of lesser amounts of cathodic protection current slowed the stress corrosion cracking so that "failure time" was increased.

Corrosion Rates

Complete cracking of a specimen 3/16 in. thick took place in about 20 min, but the major portion of the cracking occurred in approximately 10 min and, during this time, two-thirds or about ⅛ in. of the specimen was cut through. During the fastest cracking period, therefore, a rate of 0.0125 in./min was attained. This is approximately 6500 in./year, a very high corrosion rate.

It should not be assumed that the explanation for this very large corrosion rate lies in proposing extensive mechanical cracking. On the contrary, corrosion can account for all of the metal loss necessary to produce such rapid cracking. If a crack width of 100 unit cells is assumed, a transgranular stress corrosion crack along the basal plane of the magnesium-base J1 alloy would be approximately 520Å or 5.2×10^{-6} cm in width. Since, experimentally, the average rate of crack propagation during its actively cracking period was of the order of ⅛ in. in 10 min (0.03 cm/min), then in 1 min the volume of metal lost in a crack the width of the 3/16-in. specimen (0.4763 cm) would be 7.43×10^{-6} cc. Using 1.8 g/cc for the density of the J1 alloy, the weight loss would be 1.34×10^{-7} g.

Another approximation of weight loss can be made by using measured corrosion current values (Fig. 1). During the active portion of cracking, corrosion current flow was at least 20 μa or 1.2×10^{-3} coulombs/min. By Faraday's law, the weight of metal lost should be 1.51×10^{-7} g.

These two weight loss approximations reduce to corrosion rates of 6,210 ipy (7.79×10^{6} mdd) and 7,000 ipy (8.77×10^{6} mdd), respectively, for cracks 100 unit cells in width.

Corrosion rate values thus derived strongly support the idea that electrochemical action is the primary cause and reason for the stress-corrosion cracking. These calculations, while admittedly approximate, could be considerably in error and still demonstrate the existence of extremely large corrosion rate values.

Visual Perception of Stress Corrosion

Still another area of discussion may clarify the essentially electrochemical nature of stress corrosion cracking. Reference has been made by Harwood (5) to the motion picture produced by Priest, Fontana, and Beck (9) with respect to visual evidence of the noncontinuous nature of stress-corrosion cracking. While the motion picture does show that the crack progresses nonlinearly with time, this does not necessarily indicate a series of sharp mechanical failures triggered by corrosion. It is the writer's belief that cracking is going on continuously, but is perhaps not always continuously visible. It must be remembered that this motion picture provides only a two-dimensional view of something occurring in three dimensions. With this in mind, it is evident that noncontinuous crack propagation observed on a surface could be caused by continuous cracking taking place beneath the viewed surface. As soon as this unseen cracking progressed far enough, the surface in view would tear quickly and do so in a semiductile fashion, that is, in the manner typical of ductile metal failure at the base of a notch. This analysis is compatible with the observations recorded in the film, and it is concluded that the plastic deformation revealed in the motion picture is the result of crack

propagation and not the cause of crack propagation. The role of stress, then, is that of maintaining film-free areas or, by very local deformation, causing an anodic change in electrode potential at the tip of an advancing stress corrosion crack.

Summary and Conclusions

Much of what has been discussed refers specifically to the author's work with the Jl alloy, but the fact remains that the electrochemical nature of stress corrosion has been demonstrated for other systems as well as the work discussed in this paper. In view of experimental evidence with regard to crack corrosion rates, cathodic protection and the nature of measured corrosion currents, it seems unlikely that purely mechanical cracking plays any discrete part in the stress corrosion process unless a distinctly brittle phase exists.

It is concluded that in ductile materials transgranular stress corrosion takes place only under the driving force of a continuous electrochemical action which causes very localized removal of metal by corrosion. The site of metal removal (the crack tip) and the direction of cracking are determined by stress acting to cause localized potential differences through the interruption of film forming mechanisms or by intense, localized plastic deformation.

Manuscript received Sept. 10, 1958.

Any discussion of this paper will appear in a Discussion Section to be published in the December 1959 JOURNAL.

REFERENCES

1. F. H. Keating, Symposium on Internal Stresses in Metals and Alloys, p. 311, Institute of Metals, London (1948).
2. P. T. Gilbert and S. E. Hadden, *J. Inst. Metals*, **77**, 237 (1950).
3. C. Edeleanu, *ibid.*, 80, 187 (1952).
4. "Stress Corrosion Cracking and Embrittlement," W. D. Robertson, Editor, chapter by C. Edeleanu, p. 126, John Wiley & Sons, Inc., New York (1956).
5. "Stress Corrosion Cracking and Embrittlement," W. D. Robertson, Editor, chapter by J. J. Harwood, p. 1, John Wiley & Sons, Inc., New York (1956).
6. J. J. Harwood, *Corrosion*, **6**, 249, 290 (1950).
7. R. B. Mears, R. H. Brown, and E. H. Dix, Jr., "Symposium on Stress-Corrosion Cracking of Metals," p. 323, ASTM-AIME, York, Pa., 1944.
8. H. L. Logan, *J. Research Natl. Bur. Standards*, **48**, 99 (1952).
9. D. K. Priest, F. H. Beck, and M. G. Fontana, *Trans. ASM*, **47**, 473 (1955).
10. "Stress-Corrosion Cracking and Embrittlement," W. D. Robertson, Editor, chapter by D. K. Priest, p. 81, John Wiley & Sons, Inc., New York (1956).
11. "Stress-Corrosion Cracking and Embrittlement," W. D. Robertson, Editor, chapter by T. P. Hoar, and J. G. Hines, p. 107, John Wiley & Sons, Inc., New York (1956).

Evaluation of the Homogeneity of Germanium Single Crystals by Photovoltaic Scanning

J. Oroshnik and A. Many[1]

Research Laboratories, Sylvania Electric Products Inc., Bayside, New York

It is well known (1, 2) that photovoltages due to resistivity gradients in the bulk can exist in semiconducting crystals. This phenomenon is generally referred to as the "bulk photovoltaic effect." Resistivity inhomogeneities constitute small junctions throughout the material which allow charge separation to take place. These junctions give rise to easily observed photovoltages generally of the order of hundreds of microvolts. Photovoltages due to p-n junctions are usually in the range of tenths of a volt.

Consider, for example, an n-type germanium sample having rectangular shape with contacts at the ends. If this crystal is illuminated at some point along its length where $(d\rho/dx) > 0$, a voltage will be observed across the sample with the right-hand contact (at $x = k$) positive (left-hand contact at $x = 0$ grounded). Similar reasoning holds for p-type material, in which case the voltages are reversed.

Since the photovoltage depends on the existence of a resistivity gradient, it is a derivative quantity. Therefore, the integrated signal corresponds qualitatively to the changes in resistivity.

This phenomenon can be used as a sensitive and rapid tool for exploring the homogeneity of single-crystal germanium samples that may otherwise appear to be very uniform. The experimental arrangement is shown schematically in Fig. 1. A low-speed

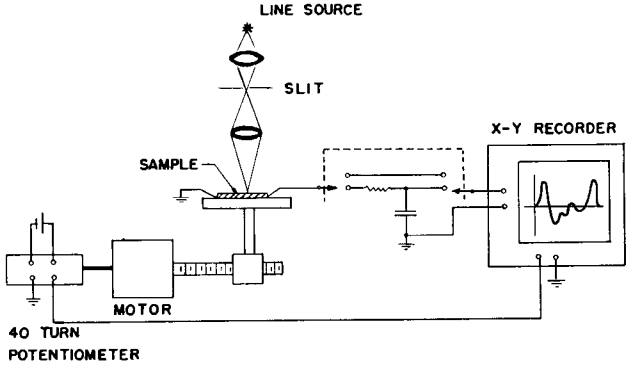

Fig. 1. Schematic of photovoltage scanning system

motor drives the crystal sample under a narrow band of white light focussed on the surface. A 40-turn potentiometer is driven simultaneously, and the voltage from it drives the x-axis of the recorder. Either the direct photovoltage signal, or the integrated photovoltage as desired, is, after suitable amplification, fed into the y-axis of the recorder. A direct plot of signal versus position is thus obtained for any sample.

Figure 2 shows the experimental results for an n-type germanium sample that would ordinarily be considered as being fairly uniform over a significant part of its length. The upper curve is the photo-

[1] Present address: The Hebrew University, Jerusalem, Israel.

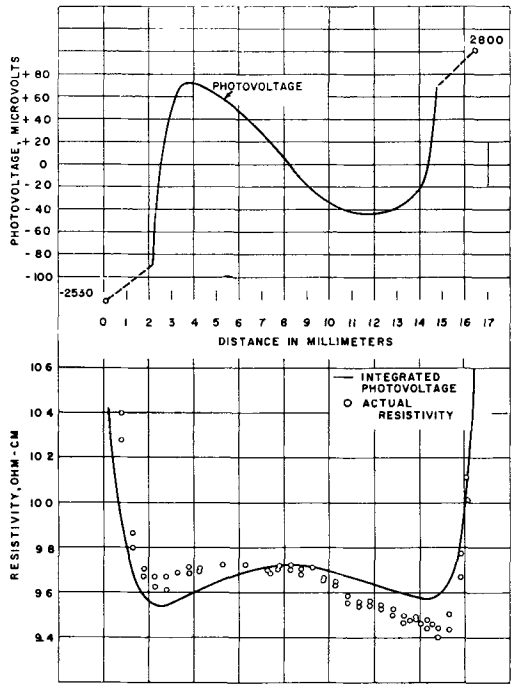

Fig. 2. Photovoltage and resistivity scan of on n-type germanium sample.

voltage scan—microvolts vs. distance along the sample in millimeters. This curve shows three points where the signal is zero, indicating that a combination of three maxima and minima will occur in the resistivity curve. The lower diagram represents the resistivity scan for this sample. The solid curve is the result of integrating the photovoltage, while the circles represent the actual resistivity measurements. The resistivity measurements were taken with a two-point probe. An electrometer was used to measure voltages, and a constant-current generator supplied the sweep current to the sample. Reasonably good agreement is apparent. In the central portion of the crystal, that is, around 8 mm, the resistivity changes are of the order of 0.1%, while the photovoltages in the same region are large and distinct. It is also clear that the zero photovoltage signals coincide exactly with the maxima and minima of the resistivity curve.

To explore a crystal wafer, deep trenches are cut into the crystal on one of the large faces, in the vicinity of the contacts. This procedure greatly reduces the effective lifetime of the minority carriers in the vicinity of the contact and alleviates troublesome photosignals that may arise.

Figure 3 is a diagram of such a (p-type) germanium wafer. A contact is soldered continuously along the left- and right-hand edges of the wafer. The pair of vertical lines at each end represent the trenches. A set of direct and integrated photovoltage scans (as in Fig. 2), were taken on this wafer from $x = 0$ to $x = 22.5$ mm, and $y = 0$ to $y = 19.8$ mm.

The integrated values of the photovoltage signals are plotted directly, and a resistivity map of the wafer is then prepared. The heavy lines in this map are lines connecting points of equal resistivity *change,* plotted in terms of microvolts. For convenience, let us call these lines *isorhos.* This mapping is still a very qualitative picture of the wafer. However, sufficient information can be gleaned from such a diagram so as to determine the region from which a sample having the highest uniformity can be obtained. For example, the section of the wafer in Fig. 3 between $x = 0$ and $x = 3$ mm indicates small resistivity changes as compared to other possible sections.

The section between $x = 0$ and $x = 3$ mm was cut out of this wafer and the measurements on it are shown in Fig. 4. The upper curve is the photovoltage scan, and the lower solid curve is the direct integration of it. As before, the circles represent the actual resistivity measurements. The fit between the two is clearly good.

This evaluation method has some distinct advantages over probe methods. First, it is fast; the photoscan and integration can be made in less than 1 min. Second, it is the only way known of making a detailed estimate of the homogeneity of a wafer before cutting it. Third, the photo method of estimating resistivity changes is applicable under conditions where probe methods are very difficult, as, for example, when the sample is held at liquid nitrogen temperatures.

Thus far there has been reasonable success in obtaining relative values of resistivity changes by photoscanning. By taking into account such important factors as the lifetime of the material, the photo-

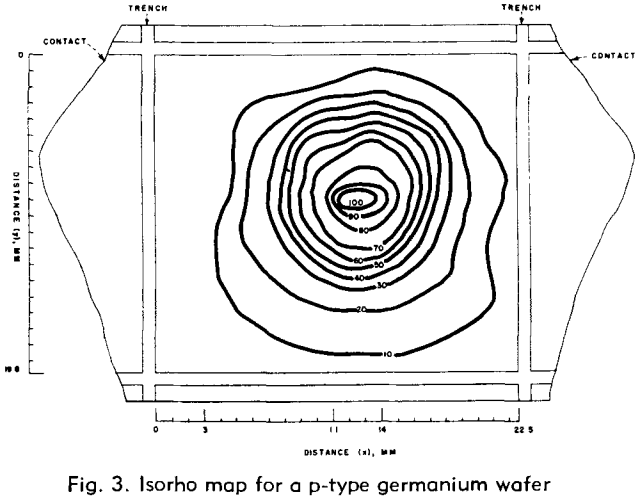

Fig. 3. Isorho map for a p-type germanium wafer

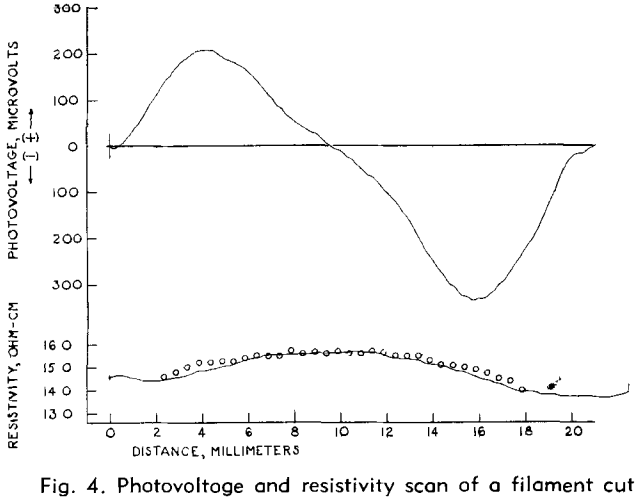

Fig. 4. Photovoltage and resistivity scan of a filament cut from the wafer of Fig. 3.

voltaic scanning method should be suitable for approximating the actual values of the resistivity changes in ohm-centimeters.

Acknowledgment

The authors are particularly indebted to Mr. Alfred Willis, of this laboratory, for the preparation of samples and his assistance in performing this work; to Mr. M. Adler, of the Design Group for the design of the mechanical components; and to Mr. M. Thomsen and Mr. A. Piorkow of the machine shop for the fabrication.

Manuscript received June 2, 1958. This paper was presented at the New York Meeting, April 27-May 1, 1958.

Any discussion of this paper will appear in a Discussion Section to be published in the December 1959 JOURNAL.

REFERENCES

1. J. Tauc, *Czech. J. Phys.*, **5**, 178 (1955).
2. Z. Trousil, *ibid.*, **6**, 96 (1956).

Technical Feature

Production of Electrolytic Copper Powder

Frank Wills

Technical Department, American Metal Climax, Inc., New York, New York

E. J. Clugston[1]

Amco Research Inc., Subsidiary, American Metal Climax, Inc., New York, New York

ABSTRACT

A detailed description of the operation, equipment, and quality control used in the commercial production of electrolytic copper powder[2] is presented. The effect of electrochemical and mechanical variables on the physical characteristics of electrolytic copper powder is also reviewed.

Roll has discussed (1) the advantages and improved properties obtainable by the use of electrolytic metal powders. The present paper describes the production of electrolytic copper powder. The plant[3] is an integrated copper smelter and refinery which processes concentrates, blister and scrap to fire refined, electrolytic and OFHC[4] brand copper. In addition to electrolytic copper powder, the plant also produces atomized copper-lead based powders as well as solder and tin powders.

Electrolytic copper powder, based on the work of Drouilly (2), has been produced by the refinery for twenty-five years. During this period the production capacity of copper powder was increased from 20,000 to over 1,000,000 lb/month. Simultaneously, with increased production capacity, many improvements have been made in production and control techniques, resulting in a better and more uniform product.

The physical characteristics such as particle size, apparent density, flow rate, and dimensional change on sintering of electrolytically deposited copper powder are affected by a number of factors. The most important of these are the current density, copper and acid content and the temperature and circulation rate of the copper sulfate electrolyte. Although electrochemical variables can be controlled to produce a powder within a relatively narrow range of physical properties, they cannot be controlled sufficiently to yield a product which meets the rigid specifications required by the consumer. Consequently, further processing operations on the washed powder are required such as furnacing in a controlled atmosphere, grinding, screening, and blending.

The basic electrochemical theory of electrorefining and electroplating is identical to that of electrolytic powder deposition. The electrochemical conditions affecting the type of deposit, however, are controlled in powder production so as to yield a deposit which is the opposite of that desired in refining and electroplating where a hard, dense and smooth, adherent cathode is the object. An excellent paper on the theories covering metal powder deposition has been presented by Mehl (3). Wranglen (4) also defines the three basic factors responsible for the formation of powdery and spongy deposits as low metal overvoltage, depletion of the metal content of the cathode film, and the formation of basic material in the cathode film. Only the first two factors are of importance in this case.

While the generalities noted above do produce spongy deposits, it is necessary to control the following variables to produce a powder within a specified range of physical properties. These are: (*a*) electrolyte composition (acid and copper content); (*b*) electrolyte temperature; (*c*) electrolyte circulation rate; (*d*) current density; (*e*) size and type of anode and cathode; (*f*) electrode spacing; and (*g*) brush-down interval.

The last variable is very important since it not only controls the type of deposit which builds up on the cathode, but also prevents excessive variations

Table I. Effect of brush-down interval

Brush-down interval, hr	Apparent density, g/cc	Dimensional change, %
1	2.15	0.55
4	2.18	0.58
8	2.35	1.62

[1] Present address: Reading Metals Refining Corp., Reading, Pa.
[2] By the U. S. Metals Refining Co.
[3] United States Metal Refining Co., Carteret, N. J.
[4] Registered trademark of American Metal Climax, Inc.

Table II. Effect of temperature Cu in bath, 8.5 g/l

Temperature, °C	Apparent density, g/cc	Dimensional change, %
50	2.15	0.55
55	2.40	1.75
60	2.70	2.12
65	2.85	2.50

Table III. Effect of copper content in bath; temp, 55°C

Copper content, g/l	Apparent density, g/cc	Dimensional change, %
5	1.90	1.13
6	2.05	1.30
7	2.18	1.44
8	2.32	1.60

in the cathode area, with consequent lowering of the current density. Tables I, II, and III indicate the effect of three of the above variables on the apparent density and the per cent dimensional change on sintering.

Electrolytic Operations

A section of the regular electrolytic copper refining plant, or tank house, is used for the production of electrolytic copper powder. The powder section uses the same type of cell as is found in the regular tank house and is also supplied with direct current from the main power plant. Electrolyte and electrical conditions for the two units are different, but by suitable alteration of piping and bus bars, sections can be switched from electrolytic copper refining to powder production and vice versa. This flexibility allows for considerable leeway in operating capacity of the two units.

At the present time, six sections or groups of cells, containing 16 cells each, are available for powder production. In addition, copper powder is also produced by four-cell liberator sections which control the electrolyte copper content by plating from the electrolyte solution instead of from copper anodes. The cells of four of the regular sections are constructed of wood, with adjacent cells having common side walls. The dimensions are 11 ft long by 3½ ft wide by 4 ft high (I.D.). These tanks are completely lined with 8-lb, 6% antimonial lead. The remaining two regular sections and the liberators are made of individual self-supporting, glass-fiber reinforced, polyester cells. The plastic cells are superior to the lead-lined cells from an electrical viewpoint, since stray currents and current leakage are minimized. To evaluate plastic tanks for use in the powder plant several different design and fabrication methods were used. While several units have demonstrated excellent serviceability, other tanks have developed leaks due to separation of the fiber-glass laminations. Repairs to these tanks is an arduous task since it is difficult to determine where the leak originates in the laminated structure.

All cells are supported by concrete piers standing in the basement floor. For electrical insulation from the ground, the columns are capped with glass and are protected from electrolyte leaks by plastic shields. Each cell is equipped with a solution outlet 15 in. from the bottom for partial draining. This outlet, in conjunction with a stand pipe which controls the solution level in the tank, is also used as an outlet for the circulating electrolyte. Another outlet in the cell bottom is used for complete draining.

Originally the sections were built on two levels so that the electrolyte flowed from the tank in the upper tier to the lower lying parallel tank before returning to storage for recirculation. Due to the change in both copper content and temperature of the electrolyte in flowing through the two tanks, powder deposited in the lower section was much coarser and heavier. To overcome this nonuniformity in powder production, all sections are now built on the same level and each tank has individual circulation. Electrolyte is pumped from basement storage tanks to an elevated head tank. From there it flows to manifolds on each section by gravity, and then into the back and the top of the cell. Thus circulation of electrolyte in the tanks is top to bottom. This yields a finer, more homogeneous powder than bottom to top circulation. Electrolyte returns to the basement storage by gravity.

The cathodes, which have been the subject of considerable experimentation, are now 6% antimonial lead, 24 x 34 x ⅜ in. and weigh about 150 lb each. Polished copper, aluminum, stainless steel, rolled and cast lead, as well as carbon, have been tried but none proved as satisfactory as the presently used material. For better contact, these cathodes are cast directly on the ½ x 1½ x 46 in. copper bars by which they are suspended. The lead cathodes have an average life of several years.

Each cell is loaded with eighteen lead cathodes at a spacing of 7 in. centers, and nineteen copper anodes which are hung between the cathodes. The electrodes in each cell are in parallel with each other, and the cells and sections are in series with each other. The bus bars from which the electrodes hang are notched, which prevents the electrodes from shifting and also gives better contact, permitting 20% higher amperage operation.

Power is supplied to the cells by a 1500 kw motor generator set at 10,000-13,000 amp, the power being conducted to the cells by a 21 square inch bus bar. At 12,000 amp, the current density on the anodes is 50 amp/ft^2.

During electrolysis, some of the deposited powder sloughs off and falls to the bottom of the cell. To prevent short circuiting between anodes and cathodes, causing a decrease in cathode current density and deposition of large particles, the cathodes are brushed down periodically with a long handled rubber squeegee. Several other methods such as continuous vibrating, shaking, and hammering have been tried, but none has been practicable.

At the end of the three-day operating cycle the power is turned off in that particular section. The electrolyte is drained to a level just above the top of the powder. The anodes and cathodes are washed down and removed from the cells by an overhead crane which services the entire powder section. The bottom outlet is opened and the remaining electro-

lyte drained from the tank along with a small amount of powder which is later cleaned from the solution launders.

The powder is scooped from the bottom of the cell by a motorized clam-shell bucket attached to the overhead crane. Damage to the cell bottom is prevented by wooden or plastic boards placed in the cell.

The subsequent powder washing operation is one of the most important steps in the whole production cycle. All traces of electrolyte must be removed from the powder, otherwise an impure and easily oxidizable material will be produced. In addition, any sulfate remaining in the powder will cause repeated breakdowns in the electrically heated furnaces used in the finishing operation. Until several years ago, a 40-in. batch type Tolhurst centrifuge was used to remove the electrolyte from the wet powder, followed by a clean water wash. Due to the high speed of the centrifuge, the powder was compacted causing particles to densify, making production of low density powder impossible. Production of low density powder was possible only by percolation washing in wooden boxes. Due to channeling, washing was frequently poor, and consequently time-consuming to achieve complete removal of electrolyte.

A system of washing and dewatering has been developed which improves the copper powder operation immensely. The present system, which is operating very efficiently, involves dumping of the powder from the clam-shell bucket into a 400 cubic foot tank. Water is added to slurry the powder which is then pumped by a Wilfley centrifugal pump to one of two 400 cubic foot surge tanks. Here, the slurry is adjusted to the proper consistency and then pumped to a 60 in. diameter horizontal Oliver continuous filter. The filter dewaters the slurry, washes it twice with clean water, and then dewaters it to about 20% moisture. A rotating screw removes the moist powder from the filter.

Since the density ratio of powder to solution is approximately 8:1, special precautions must be taken to prevent settling of powder in pipes, tanks, pumps, valves, etc. Although considerable preliminary test work was done to determine critical velocities and powder characteristics after pumping, a lengthy start-up period was needed in the plant before trouble-free operation was obtained. The irregular structure of the powder complicated matters even more, since once powder starts to settle out in the system, the powder particles interlock resulting in a very solid and hard-to-remove plug.

All equipment external to the cells is constructed of stainless steel type 316 and has given satisfactory service.

Because of the low acid content and relatively low temperature of the electrolyte, as well as the high resistance of the lead cathodes and high current density used, the power consumption is considerably higher than for copper refining. The average voltage per tank is 0.9-1.1 v compared to normally less than 0.25 v for copper refining. The ampere efficiency at the anode is in excess of 95%, but at the cathode it is somewhat less than 90% because of the deposition of hydrogen and relatively rapid redissolution of fine copper powder.

Preparation

The wet powder, which oxidizes readily because of its finely divided state and active surface, is now ready for the finishing operations. Certain of its properties, especially the apparent density and the dimensional change on sintering, have been produced in the powder during electrodeposition. To produce an acceptable grade of powder, however, a furnacing operation followed by grinding and screening with subsequent blending of the finished powder is needed.

As in the electrolytic operations, considerable improvements have been made in the processing division. When operations were begun in 1932, 6-in. tube furnaces were used to treat the powder. Small boats held the wet powder and were pushed through the furnace by hand. As demand increased and better equipment became available, the first of a series of four chain-driven pan furnaces was installed in 1937. These furnaces are 60 ft over-all in length having a three-section, 30-ft electrically heated zone and a 30-ft water jacketed cooling zone. Manually filled and compacted paper-lined copper pans were used to hold the powder. In order to meet increasing demand and to achieve improved production methods, a mesh belt furnace was installed in 1951 to supercede the pan-type furnaces. Various other improvements were also made in the grinding and classifying system.

Due to the location of the electrolytic production unit and the processing plant, the filtered product must presently be transported to the finishing division. A ten-ton fork lift truck which carries three boxes per trip is used for this job. Pumping has been considered, but, because of the difficulties encountered in even the short distance pumping in the tank house, improved systems must be developed before this will be feasible. Added factors are the possible and very probable detrimental changes that long distance pumping will have on powder characteristics.

Powder is dumped from the transfer boxes into the charge hopper of the mesh belt furnace. Dimensions for this furnace are identical to the above described pan furnaces. The continuous mesh belt, made of Cambriloy 25-20 alloy wire, is driven by a variable speed drive and operates at 1-7 in./min. To prevent wet powder from falling through the belt, a continuous high wet strength paper sheet is interposed between the belt and the powder. A roller after the charge hopper compresses the powder to improve heat transfer and to prevent loose powder from falling off the belt. After the belt enters the furnace and all water has been driven off, the paper burns, but by this time the powder has sintered sufficiently to prevent any of it from falling through the meshes of the belt.

Furnace atmosphere is produced in exothermic gas producing units.[5] Natural gas and air are burned in a ratio of approximately 1:6 to give a gas con-

[5] General Electric Co.

taining 17% H_2, 12% CO, 4% CO_2, balance N_2. Refrigeration lowers the dewpoint to 30°-40°F. Gas is fed to the furnace counter-currently, which improves reduction and improves cooling of the cake.

The furnace operation accomplishes the following: (*a*) drying the powder; (*b*) reducing oxide; (*c*) sintering the fines; (*d*) altering physical properties including apparent density and sintering characteristics.

By varying furnacing temperature between 900°-1450°F and concurrently varying furnacing time by changing the belt speed, large changes in the amount of fines, the apparent density, and to some extent the dimensional change characteristics can be effected. This furnacing operation is consequently the second point where powder properties can be changed to meet final specifications.

Depending on furnace conditions, the sintered powder discharges as a soft to a hard cake which cannot be broken by hand. Discharge temperature is maintained low enough to prevent re-oxidation of the powder. As the cake discharges, it is broken by grappling hooks and given a preliminary crushing in a 40 hp hammer mill to ¼ in. The crushed cake is next lifted to the main grinding system by a bucket elevator.

Fine grinding is done by Mikro-Pulverizers. These are high-speed water-cooled hammer mills equipped with Stellite faced hammers. Feed rate to the mills, the mill speed, and the screen opening under the mill can all be varied to obtain the desired powder characteristics. Normal operating conditions are: (*a*) 3000 - 4500 rpm; (*b*) 500 - 1000 lb/hr mill; (*c*) 1/16 - 3/32-in. screen opening; (*d*) screen hole shape: round, elliptical, slots.

The grinding operation becomes the third operation where powder characteristics can be changed. Each grinding system consists of two Mikro-Pulverizers in series. One or both units can be used to grind the powder, depending on the type desired. The ground powder is then moved to screen hoppers. These discharge into Sprout Waldron bolting reel screens equipped with a beater arm. Oversize powder from the screen is returned to a secondary grinding system which again consists of two Mikro-Pulverizers and screen. The minus 100 mesh powder is next classified in a Gayco air classifier. Fines from this unit are collected in 24-gal drums and moved to the blending floor. Oversize from the air classifier can either be removed from the system or, if desired, be again returned to the grinding system.

The grinding and classifying system consists of seven banks of Mikro-Pulverizers, screens, air classifiers, and the necessary bucket elevators and screw conveyors. Ground material starts in the first unit, and oversize, or material for regrinding to change its characteristics, is then ground and classified progressively through the whole system. The product from the final unit has been worked considerably and represents the highest density material produced. Its apparent density is above 3.5 g/cc and its application is for specialized uses. Oversize from this system is rejected and sent to the casting building for remelting.

Powder that discharges from the system is stored in closed drums to which silica gel containers are added to control humidity and prevent oxidation. Each drum of powder is sampled and its weight, apparent density, flow, and screen characteristics recorded.

To produce a lot of finished powder to meet customer specifications, the correct type of powder is selected from the storage drums and mixed in one of three Gemco double cone blenders. The lot size is generally 20,000 lb/blender charge and, before a lot is withdrawn from the blender into shipping drums, all specifications have been checked by the Control Department and approved for shipment.

In order to control all phases of the operation, a well-equipped production control laboratory is maintained. The control laboratory checks both electrolytic and finishing operations and the following samples are taken and tested.

1. Daily composite of cell powder: Tested for particle size distribution, flow, and apparent density.
2. Electrolyte sample: Tested for copper content and acidity.
3. Daily composite of filtered powder: Tested for washing, particle size, flow, apparent density, dimensional change on sintering, and sintered strength.
4. Hourly furnace discharge cake: Tested for temperature.
5. Shift composite of discharge: Analyzed for oxygen content.
6. Daily composite of furnace production: Tested for particle size distribution, apparent density, oxygen content, dimensional change on sintering, and sintered strength.
7. Daily composite of finished production lots: Tested for chemical assay: Cu, Pb, O_2, C, S, HNO_3 insol., grease.
8. Daily composite of main finished powder production: Tested for screen analysis, flow, apparent density, and dimensional change on sintering.

Table IV. Powder specifications

Type	Apparent density, g/cc	Flow, sec/50g	Screen analysis		Dimensional change, %	Chemical analysis %		
			+100 mesh	−325 mesh		Cu	H_2 loss	HNO_3 insol.
LC	1.5-1.75	(Scott)	0.1 Max.	90 Min.	—	99.0 Min.	0.75 Max.	0.03 Max.
C	2.1-2.5	(Scott)	0.1 Max.	90-95 Min.	—	99.0 Min.	0.75 Max.	0.03 Max.
A	2.4-2.6	32 Max.	0.5 Max.	22-32	—	99.5 Min.	0.30 Max.	0.03 Max.
B	2.5-2.6	32 Max.	0.2 Max.	43-53	—	99.5 Min.	0.30 Max.	0.03 Max.
U	2.5-2.6	35 Max.	0.2 Max.	55-65	0.3-1.8	98.4	0.40 Max.	0.03 Max.
HM	2.6-2.7	35 Max.	0.2 Max.	60-70	—	99.25	0.50 Max.	0.03 Max.
AJL	3.5-4.0	24 Max.	0.8 Max.	35-45	—	99.25	0.30	0.03 Max.

9. Monthly composite of finished production lots: Tested for tensile strength and green strength.

10. Production lots: Tested for screen analysis, apparent density, flow, dimensional change on sintering, green strength, and chemical assay.

This amount of testing has been found necessary to give a satisfactory degree of control over all operations and to assure consistent uniform powder production.

Table IV shows some of the types of powder produced. These range from the very light and fine LC type to the heavy and coarse material which is designated AJL. All other grades produced lie between these types.

To supplement the control section, a fully equipped powder research laboratory is also maintained. This unit has the responsibility of developing and improving production methods and to assist the operations generally. Since the United States Metals Refining Company also produces other powders, the laboratory has units for producing atomized powders, and an electrolytic section which consists of electroplating tanks which range in size from battery jars to full size units. The laboratory is also fully equipped with presses and sintering furnaces to study the effect of all processing variables on finished product characteristics. Process variables can consequently be fully evaluated in the laboratory before large scale tests are made in the production unit.

Manuscript received Oct. 13, 1958. This paper was prepared for delivery before the Buffalo Meeting, Oct. 6-10, 1957.

Any discussion of this paper will appear in a Discussion Section to be published in the December 1959 JOURNAL.

REFERENCES

1. K. H. Roll, Paper presented at The Electrochemical Society Meeting, Buffalo, N. Y., Oct. 9, 1957.
2. Drouilly, U. S. Pat. 1,799,157, April 7, 1931.
3. E. Mehl, Developments in the Production and Quality of Metal Powders, Meeting, Church House, London, Dec. 4, 1957.
4. G. Wranglen, *This Journal*, **97**, 353 (1950).

Brief Communication

The Structure of AgO

Alvin J. Salkind and William C. Zeek

The Electric Storage Battery Company, Research Center, Yardley, Pennsylvania

The structure of silver oxide (AgO) has been of interest to members of the Society as evidenced by recent articles (1) in the *Journal*, and by discussions at the Ottawa Meeting.

We would like to draw the attention of readers of this *Journal* to a group of researchers whose earlier contributions to this field are often overlooked. We refer to the work of Vladimiro Scatturin and his associates at the University of Padua. Their most recent paper was entitled "The Crystalline Structure of AgO" (2).

They investigated the crystal structure of AgO using both copper and iron radiation and listed in their paper 36 reflections obtained with Fe Kα radiation. They were able to index all these reflections by the Ito method and concluded that the compound was monoclinic, Space Group C_2^6 h = C 2/C with the following parameters.

$a = 5.85_2$Å	$b = 3.47_8$	$c = 5.49_5$
$\beta = 107°30'$	$V = 106.7$Å^3	$Z = 4$

The authors also discussed the position of the atoms and concluded that with the atoms as follows:

4 Ag in ¼, ¼, 0; ¾, ¼, ½; + (000; ½, ½, 0)

4 O in 0, Y, ¼; 0, Y, ¾; + (000; ½, ½, 0)

the most probable value for the parameter Y was 0.084.

Comparisons are also drawn with the spacings commonly found in other silver compounds.

REFERENCES

1. W. Graff and H. H. Stadelmaier, *This Journal*, **105**, 446 (1958).
2. V. Scatturin, P. Bellon, and R. Zannetti, "La Ricerca Scientifica 7" 2163 (1957).

Oxidation of Aqueous Ferrous Sulfate by Glow Discharge

H. A. Dewhurst, J. F. Flagg, and P. K. Watson

Research Laboratory, General Electric Company, Schenectady, New York

A variety of chemical reactions may be produced in aqueous solution by "glow discharge electrolysis." The observed chemical effects have been attributed to ions which are produced in the vapor phase by the discharge (1-3). It is well known that in glow discharges several chemically active species are formed in addition to the ions. These include atoms, radicals, metastables, as well as photons, all of

which can, under favorable conditions, produce chemical reactions in aqueous solution. We have recently carried out experiments which were designed to differentiate between the effectiveness of the positive ions and of the electrically neutral species in the glow discharge oxidation of ferrous sulfate. The portion of the total oxidation attributable to charged species was determined by interposing a platinum grid between the discharge point and the solution. The grid was used as the negative electrode in the cell so that it collected the positive ions from the discharge. However, because of its open construction, it had very little effect on the electrically neutral species.

The discharge cell was similar to that used by Hickling and Linacre (2) with the exception of the grid and the fact that the platinum cathode was placed directly in the aqueous solution. The anode was a stainless steel hypodermic needle situated approximately 1.0 cm above the surface of the solution. Deaerated 0.01M ferrous ammonium sulfate solutions (5-10 ml) 1.0*N* in H_2SO_4 were used. The amount of oxidation was determined by spectrophotometric measurement of ferric ion at 305 mμ (4). The total current was measured with a Keithley electrometer. Oxidation yields are reported in terms of the number of equivalents of ferric ion produced per Faraday of charge. Experiments were carried out at about 25 mm pressure under which conditions the discharge operated in water vapor. Other experiments were conducted at 760 mm pressure with either a static or flowing (3 liters/min) atmosphere of pure nitrogen. The results of these experiments are shown in Table I.

Table I. Glow discharge oxidation of aqueous ferrous sulfate
Fe^{2+} = 0.01M in 1.0N H_2SO_4

Pressure, mm Hg	Voltage, kv	Current, μamp	Fe^{3+} Ions/Faraday Grid*	No Grid
25 (Static)	1.1	100	0.6	25
	1.2	1000	0.3	11
	0.65	4200	0.2	11
760 (Static)	10.5	50	5.5	13.5
760 (Flow)	4.2	8.5	0.8	8.7†
	4.8	50	1.4	9
	7.0	100	0.9	10

* 3 mil wire, 80 wires/in.
† Current was 4.0 μamp.

Results at low pressure show that species removed by the grid account for at least 95% of the observed oxidation. The inverse dependence of the oxidation yield on current will be discussed in a later publication. We note that yields under our conditions are greater than yields observed by Hickling and Linacre (2).

Results at 760 mm pressure under static conditions show that about 60% of the oxidation could be accounted for by species removed by the grid. Under flow conditions, however, the grid prevented about 90% of the oxidations. We attribute the decreased effectiveness of the grid under static conditions to the presence of water vapor in the discharge region. In other experiments it was observed that under flow conditions presaturation of the nitrogen with water increased the yield to that obtained under static conditions.

In connection with these studies we have also examined the effect of various gases, ferrous sulfate concentration, and polarity on the yields. An oscillographic study has been made of the electrical characteristics of the discharge, under conditions used in these experiments. Details of these and related studies will appear in a subsequent publication.

Acknowledgment

The authors wish to acknowledge helpful discussions with Dr. K. H. Kingdon.

Manuscript received Nov. 17, 1958.

Any discussion of this paper will appear in a Discussion Section to be published in the December 1959 JOURNAL.

REFERENCES

1. R. A. Davies and A. Hickling, *J. Chem. Soc.*, **1952**, 3595.
2. A. Hickling and J. K. Linacre, *ibid.*, **1954**, 711.
3. A. R. Denaro and A. Hickling, *This Journal*, **105**, 265 (1958).
4. H. A. Dewhurst, *Trans. Faraday Soc.*, **49**, 1174 (1953).

Correction

In the December 1958 issue of the JOURNAL, page 728, paper entitled "Electron Mobility in InP," the authors' names should be M. Glicksman and K. Weiser. Dr. Glicksman's name was misspelled.

The Anodic Oxides of Lead

Jeanne Burbank

U. S. Naval Research Laboratory, Washington, D. C.

ABSTRACT

The anodic oxides formed on lead under varying potential and *p*H were identified by x-ray and electron diffraction. Pure lead specimens were anodized at selected constant potentials to develop anodic coatings of sufficient thickness to give strong x-ray patterns. The domains of occurrence of: α and β PbO_2, yellow and red PbO, and the intermediate oxides, Pb_3O_4, and PbO_x were determined for acid and alkaline electrolytes. The intermediate oxides are not believed to be direct anodic oxides, but to represent chemical reaction products. The occurrence of certain of the oxides may be attributable to an initial electrochemical oxidation of water. The identifications have been presented in potential-*p*H phase diagrams.

Coincident with a study of the positive grid corrosion of the lead-acid storage cell, the anodic oxides formed on lead at various potentials in H_2SO_4 were identified by x-ray and electron diffraction (1, 2). Considered in the light of the potential-*p*H phase diagrams for the system (3), it became evident that certain aspects of the diagrams could be verified by application of diffraction techniques to anodic products formed on lead under controlled conditions of potential and *p*H. Furthermore, it was of interest to know which of the many oxides of lead occur as direct anodic products.

The potential-*p*H diagram is an isothermal phase diagram showing the various valence states of a metal, solubilities of oxides and salts, areas of thermodynamic stability of solid phases, ionic species, and their homogeneous and heterogeneous equilibria. The original presentation of the diagrams for the lead system (3) was based on available thermodynamic information. This present study was undertaken to identify the solid oxide phases appearing on lead as anodic products and to expand the usefulness of the diagrams by verification of the stable and metastable equilibria. In addition, it was desired to clarify the apparent thermodynamic anomaly of the simultaneous occurrence of the two crystallographic modifications of PbO_2 and of tetragonal PbO as anodic products on lead in acid solutions, and relate the known corrosion domains to those predicted on the basis of the diagrams.

Lead forms a number of oxides and Table I presents selected references (4-24) and the designations used in this report. An exhaustive listing has not been attempted. The hydrated lead monoxides have not been included because these materials are not well-established crystallographic identities. Bystrom (25) has presented a survey of the sterochemistry of the lead oxides.

Previous studies have indicated that the corrosion processes on the lead anode in H_2SO_4 at selected positive potentials included a group of reactions quite distinct from the reversible PbO_2, $PbSO_4$ and Pb, $PbSO_4$ electrode reactions (1, 2, 26-28). In order to clarify further the anodic corrosion reactions on lead, this detailed identification of the anodic products was undertaken.

Experimental

The anodic deposits formed on lead at controlled potential and *p*H were determined by polarizing pure lead sheet under fixed conditions and identifying the anodic products by x-ray and electron diffraction patterns taken by reflection from the anodized surfaces. The standard diffraction patterns used for identification are found in the X-ray Powder Data File (29) or in one or more of the references cited for each oxide in Table I.

The electrolytes used in this study were made from C. P. chemicals and distilled water. In the solutions near neutral limited amounts of CO_2 did not interfere with the observations. In order to check this a few experiments were carried out with freshly boiled distilled water and KOH very low in CO_2, in a closed cell. The results of these anodic tests were identical with those obtained in fresh solutions with nominal concentrations of CO_2. Fresh KOH solution was prepared for each run in which it was used. Values of reference electrode potentials were taken from the literature (30-33).

A Beckmann *p*H meter using a glass electrode, saturated calomel reference electrode, and standard buffer solutions were used to monitor the *p*H of the electrolytes. Solutions were made with C. P. reagents to approximate values and their actual *p*H's determined. Whenever feasible, the reference electrodes were used in the same solutions during anodization to eliminate liquid junctions. In sulfuric acid solutions, the electrode was Hg_2SO_4, Hg and in KOH solutions, HgO, Hg. Potentials were converted to the standard hydrogen electrode for this report.

Anodizations were carried out in glass cells, and usually only a few hours were required to develop coatings sufficiently heavy to give excellent x-ray diffraction patterns. Some specimens were anodized for longer periods of time, and as much as one week. The constant potential regulator described by Work and Wales (34) was used as the source of polarizing potential. A negative electrode of Pb or Pt gauze

Table I. Some known oxides of lead

	Formula*	Lattice	Other designations	Reaction with Acids	References
	PbO_y*	Orthorhombic	Litharge, yellow		(4, 5)
	PbO_t*	Orthorhombic-pseudotetragonal	Distorted PbO, yellow, brown, red	$PbO + 2H^+ = Pb^{++} + H_2O$	(6)
	Red PbO	Tetragonal	Massicot, red		(7, 8)
	PbO	Hexagonal	Yellow Litharge		(9)
$PbO \cdot xPbO_2$* or PbO_x*	Pb_3O_4*	Tetragonal	Minimum-orange Red lead	$Pb_3O_4 + 4H^+ = 2Pb^{++} + \beta PbO_2 + 2H_2O$	(6, 9-11)
	Pb_7O_{11}	Orthorhombic-pseudotetragonal	Black minium		(6, 12-17)
	Pb_5O_8		$PbO_{1.38-1.51}$ maroon to	$PbO_x + 2H^+ = Pb^{++} + \alpha PbO_2 + H_2O$	
	Pb_2O_3	Orthorhombic-pseudocubic	$PbO_{1.47-1.57}$ black	$1.33 \leqq x \leqq 1.57$	
		Monoclinic			(16, 18, 19)
	βPbO_2*	Tetragonal	Beta; $PbO_{1.87-2.02}$	Insoluble or dissolves as divalent Pb	(6, 13, 20, 21)
	αPbO_2*	Orthorhombic	Alpha; $PbO_{1.94-2.02}$		(22-24)

* Symbols used in this report.

was of such area that a constant positive polarization potential was obtained.

C. P. lead sheet to be anodized was annealed at 100°C for six weeks, cleaned of its air-formed oxide film by washing in saturated ammonium acetate solution, rinsing in water and inserting into the electrolyte while wet. Anodic polarization was begun simultaneously with insertion into the electrolyte, and the first few minutes of polarization was monitored carefully with a bench potentiometer and reference electrode to determine that the desired anodic potential was applied to the positive electrode.

At the termination of polarization, the electrode was removed from the solution, and rinsed in water, blotted dry on tissue, and placed immediately in the diffraction apparatus. The patterns were recorded as soon as possible after mounting.

GE-XRD-5 x-ray diffraction equipment was used with copper and iron targets, and electron diffraction examination was carried out with the diffraction attachment of an RCA-EMU-2 electron microscope.

In order to determine whether the two polymorphic forms of PbO_2 were readily interconvertible by crystallization from alkaline or acid media several tests were made on C. P. βPbO_2. Beta PbO_2 was dissolved in KOH solution, in concentrated HNO_3 solutions, and filtered with water aspiration. Water was added dropwise to the filtrates and, when sufficient material had hydrolyzed, it was collected on a filter and identified by x-ray diffraction examination.

C.P. βPbO_2 was treated with solid KOH and sufficient water to form a slurry. After several days' digestion at room temperature, large water-clear crystals formed up to 2 cm in diameter. These were washed free of excess PbO_2 with distilled water, and then placed in contact with a few drops of *N* KOH solution. They were slowly converted to dark brown powder which was examined by x-ray diffraction. The residual unconverted PbO_2 was also examined by diffraction.

Large clear crystals up to 6 mm in diameter formed from C.P. PbO_2 when treated with concentrated HNO_3. These were washed free of excess PbO_2, and placed in contact with dilute HNO_3 at room temperature. They were converted gradually to a brown powder that was examined by x-ray diffraction.

Essentially identical potential arrests are reported in many polarization studies of lead anodes in alkalies and only a few are cited here (35-38). Consider-

Table II. Electrolytes and anodic potentials used in this study

pH	Electrolyte Composition	Potential in volts with respect to standard hydrogen electrode — Anodic lead specimens			
−0.63	3.5*N* H_2SO_4	2.08	1.87	1.62	1.30
		2.07	1.86	1.59	1.10
		1.90	1.70	1.56	1.06
2.5	*N* $NaSO_4$	1.85	1.19	0.32	
	H_2SO_4*	1.57	1.17	0.02	
7	M K_2SO_4	1.33	1.05	1.00	
	N Na_2SO_4	1.4	1.00	0.51	
		1.20	0.80	−0.30	
12	*N*/1000 KOH	0.85	0.45	−0.41	
14.5	3*N* KOH	1.03	0.67	0.38	0.27
		0.98	0.45	0.36	−0.57
		0.85	0.43	0.33	−0.66
		Platinum anode potentials			
2.5	0.1M $Pb(NO_3)_2$	2.3	1.47	1.32	
8	0.1M $Pb(NO_3)_2$ KOH*	1.8	1.30	1.1	
14.5	3*N* KOH PbO**	1.06	0.34		

* Sufficient quantities of these reagents were added to adjust the pH to the indicated values.
** Excess solid PbO was present in the cell during electrolysis.

ation of such reports enabled judicious choice of the potentials used for the anodic treatments of this study.

Table II is a list of the electrolytes, and the potentials, employed in these anodization studies. Certain experiments were rerun many times in order that the identification should be conclusive. Certain other areas, where there seemed no possibility of question, were identified with only a few runs. The anodic products formed on lead in H_2SO_4 solutions have been reported earlier (1,2).

Some anodic coatings were laminated, and the material at the solution interface was removed by wiping the electrode with dry tissue, or by scoring around the edge of the electrode and lifting off the outer layer.

By using spot tests (39) it was possible to detect the appearance of a highly oxidizing material on the electrode surface considerably below the potentials where PbO_2 or the intermediate oxides became apparent in the x-ray diffraction patterns from specimens anodized in the strong acid range. Sheet lead specimens were anodized in H_2SO_4 solutions at carefully monitored potentials within a range ± 0.1 v to the theoretical reversible O_2,H_2O potential. After anodizations as long as 24 hr, the electrodes were removed from the electrolyte and dropped into the selected reagent: acetic acid when the benzidine test was used and starch-KI solution when this was used.

In order to verify the reported deposition of α and β PbO_2 as residues from the intermediate oxides, Pb_3O_4 and PbO_x were extracted with H_2SO_4, $NH_4C_2H_8O_2$ (saturated solution), HNO_3, and $HC_2H_3O_2$. The residues were rinsed in water, sucked dry on a filter, and the diffraction patterns recorded.

Neutral, acid and alkaline solutions of lead were electrolized between platinum electrodes. The potentials at which lead dioxide first deposited on the anode were observed, and the initial and final deposits were examined by x-ray diffraction.

αPbO_2 was heated in air at temperatures between 150° and 400° and the decomposition followed by x-ray diffraction examination of the products. The temperature range between 290°-305° was examined in steps of 2° with heating times of 48 hr. The decomposition was compared with that reported and verified for C.P. βPbO_2 (6, 13, 17).

Results and Discussion

The solid anodic products formed on lead at fixed pH and potential are divided into two categories: (*a*) the product of the anodic reaction at the solution interface; and (*b*) the product of the anodic reaction at the metal interface. These may be the same or different reactions, and there may or may not be other reactions between cell components. Thorough familiarity with the potential-pH diagram originally published (3) for the system is assumed, and this report deals mainly with the solid oxide phases associated with certain conditions of potential and pH at room temperature, but does not include solubility data.

Free energy values have been used to calculate the equilibrium potentials of this report in conformity with the original presentation of the potential-pH diagram; however, the free energy of formation of PbO_2 used by Delahay, Pourbaix, and Van Ryssel-berghe was only −50.86 kcal. Latimer gives a value of −52.34 kcal (40).

The domain of thermodynamic stability of metallic lead may approach that of PbO_2, and the equilibrium expected between the metal and this oxide has been calculated (28)

$$\beta PbO_2 + 4H^+ + 4e^- = Pb + 2H_2O \qquad [1]$$
$$E = 0.6775 - 0.0591\ pH$$

However, it is known that metallic lead usually tends to dissolve in the presence of PbO_2 and will be oxidized in a mixture containing excess higher oxide; or if metallic lead is in excess, the higher oxide will be discharged (41, 42). The electrochemical instability of PbO_2 in strong H_2SO_4 solutions at potentials below the reversible $PbSO_4$, PbO_2 electrode has been discussed by Lander (28). But at the potential of reaction [1], metallic lead is thermodynamically stable in the presence of PbO_2. However at this potential PbO_2 is not thermodynamically stable with respect to PbO_t or Pb^{++}. Therefore when the potential of a lead anode is raised above that of reaction [1], any formation of PbO_2 from metallic lead would tend to undergo the reaction

$$PbO_2 + 2H^+ + 2e^- = PbO_t + H_2O \qquad [2]$$
$$E = 1.107 - 0.0591\ pH$$

until the reversible potential for this reaction is exceeded. At potentials above those of reaction [1], metallic lead is unstable with respect to both PbO_t and PbO_2.

Anodic oxides at the solution interface.—It has been reported and was verified in this study that electrolysis of Pb^{++} solutions between platinum electrodes develops deposits largely of βPbO_2 from acid and αPbO_2 from alkaline solutions. Either or both polymorphs may be deposited from certain solutions depending on current density (potential) (23, 24).

Figure 1 shows the anodic oxides identified in this study at the electrode-solution interface on lead polarized in solutions of varying pH at several potentials. The lines for the oxidation of water to ozone and H_2O_2 have been added for reference. The effect of anions other than sulfate has not been indicated on the diagram; however, the corresponding salts will precipitate at the solution interface. The accumulations of solid products on the anode surfaces appear as oxides or hydrated oxides intermixed with the salts owing to depletion of the anolyte in anions.

The areas designated as PbO_y, βPbO_2, and the hydrous oxides (43) indicated on the diagram, Fig. 1, are not at thermodynamic equilibrium. Lead dissolves in solutions of pH less than 9.4 as the divalent Pb^{++} to form a saturated solution adjacent to the electrode, and when the rate of solution exceeds the rate of diffusion of anions from the bulk of the electrolyte the oxide crystallizes as a chemical deposit from this solution. The deposits designated in Fig. 1 of the hydrous oxides and the yellow glistening crystals of orthorhombic PbO_y are in this category and form normal and basic salts with anions present.

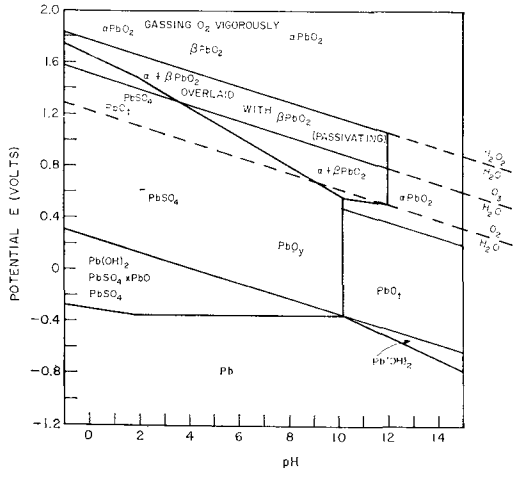

Fig. 1. Anodic oxides on lead at the solution interface. This diagram indicates the areas of occurrence of the solid oxide phases identified by x-ray and electron diffraction, and obtained on anodization of lead metal at fixed pH and potential. The lines for the following equilibria have been added

$$O_3 + 6H^+ + 6e^- = 3H_2O$$
$$E = 1.51 - 0.0591\ pH \quad P_{O_3} = 1\ atm$$
$$H_2O_2 + 2H^+ + 2e^- = 2H_2O$$
$$E = 1.77 - 0.0591\ pH \quad a_{H_2O_2} = 1M$$

Anions present in the electrolytes will form normal and basic salts with the lower oxides as indicated in the original potential -pH diagram of the system (3).

The open-circuit potential of the lead electrode is controlled by the amount of Pb^{++} in solution and is independent of pH. Above pH of 9.4 lead passes into solution as biplumbite ion, and the reaction has a slope 0.089 vs. pH. By impressing anodic potential on the system, more and more salt and oxide will be deposited unless a uniform coherent coating forms on the surface (passivation). These phenomena have been described in detail by Wolf and Bonilla for a large number of anions (44).

The crystals of PbO_y deposit in platelets shown by x-ray diffraction to be parallel to the c_o face typical of solution-grown crystals of this material. It does not form dense passivating films but grossly crystalline deposits. It is an anodic oxide in the sense that it is the solid deposited from saturated lead ion solutions.

At more elevated potentials such an electrode becomes covered with a layer of PbO_t in which the crystals of PbO_y are embedded. The domains of solubility of the two polymorphs of PbO_2 intrude into this area at higher pH, and a mixture of the four oxides is obtained. It is in this area that the intermediate oxides Pb_3O_4 and PbO_x as chemical reaction products will form after a time, but the electrode does not passivate. Only above the line indicated in Fig. 1 corresponding to the theoretical reversible O_3/H_2O reaction does passivation appear. The corrosion reaction of the metal surface is primarily a divalent one up to a potential corresponding to the reversible ozone reaction, while the deposition of tetravalent oxide takes place at the solution interface, resulting in a mixture of di- and tetravalent products.

In solutions of pH 12 and higher, a lead anode becomes covered with a deposit of hydrated lead oxide designated as $Pb(OH)_2$ in Fig. 1, and subsequently with a tetragonal oxide designated as PbO_t. If the potential is increased, plumbate ion is formed in the solution, and the surface of the electrode becomes covered with a layer of αPbO_2. There is an underlying layer of PbO_t which may react with the αPbO_2 formed at the solution interface to produce the intermediate oxides.

It may be possible to limit the deposition of αPbO_2 from alkaline solutions to a rate comparable to its chemical reaction rate with PbO_t and thereby obtain a deposit at the solution interface of the intermediate oxides, but such a condition was not observed in this work during anodization. Self-discharge may also produce such a surface. These intermediate oxides do not appear to be deposited directly from oxidation-reduction reactions, but from chemical combinations, i.e.

$$\left.\begin{aligned} PbO + PbO_2 &= Pb_2O_3 \\ 2PbO + PbO_2 &= Pb_3O_4 \end{aligned}\right\} \text{designated } PbO_t \cdot xPbO_2$$

An infinitude of stoichiometries is possible in such anodic products.

X-ray diffraction examination shows that βPbO_2 is obtained by hydrolysis of both acid and alkaline solutions of tetravalent lead ion, and is the main product deposited electrolytically from acidic Pb^{++} solutions at elevated potentials. Anodization of metallic lead, however, produces a mixture of α and βPbO_2 at elevated potentials. The anodic deposition of βPbO_2 in alkaline solutions occurs simultaneously with the evolution of O_2 gas. It therefore probably deposits by hydrolysis at the local areas on the anode where alkalinity is reduced by the gassing reaction.

Anodic oxides at the metal interface.—The x-ray and electron diffraction examination of the anodic products developed on Pb at various pH and potential conditions showed that the metal-coating interface exhibited the same oxides throughout the pH range, at the same potentials relative to the reversible hydrogen electrode in the same solutions (not the standard electrode). This means that the anodic reactions have slopes of 0.059 vs. pH. The solid phases identified in this study are indicated in Fig. 2.

When the potential of a lead surface exceeds the line bounding the lower extent of the area designated as $Pb(OH)_2$, a film of the solid hydrous oxide forms on the metal surface.

When the potential of a lead anode is raised above the line representing the reaction:

$$PbO_t + 2H^+ + 2e = Pb + H_2O \qquad E_o = 0.248$$

in Fig. 2, the lead becomes covered by a layer of PbO_t. This oxide has a tetragonal lattice showing a characteristic combination of sharp and diffuse lines in its diffraction patterns (6,13, 14). It is considered more reactive than either of the normal monoxides, and it appears on a lead anode in both acid and alkaline media. Katz described this as orthorhombic pseudotetragonal PbO (6). In alkaline solutions heavy coatings of this material appear yellow when wet with electrolyte, but are pale peach in color when dry and may form beautiful glossy coatings on a lead electrode. It has been described as a yellow

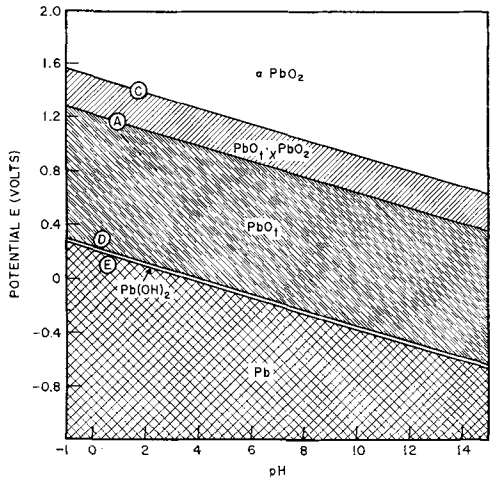

Fig. 2. Anodic oxides of lead at the metal interface. This diagram indicates the areas of occurrence of the solid oxide phases obtained at the metal-coating interface on anodization of lead at fixed potential and pH. The reactions represented by the lines D and E bounding Pb and the phases $Pb(OH)_2$ and PbO_t will be recognized from the original diagram (3), and were found to occur at essentially their reversible potentials throughout the pH range. The exception is the boundary between PbO_t and PbO_2. The intermediate region labeled $PbO \cdot xPbO_2$, representing oxides and mixtures of oxides of di- and tetravalent lead, was found to appear between the reversible oxygen and ozone potentials, lines A and C. Above line C, αPbO_2 is the principal anodic oxide at the metal interface. The reactions are represented as follows

(A) $O_2 + 4H^+ + 4e^- = 2H_2O$
$E = 1.228 - 0.0591\ pH \qquad P_{O_2} = 1\ atm$

(C) $O_3 + 6H^+ + 6e^- = 3H_2O$
$E = 1.51 - 0.0591\ pH \qquad P_{O_3} = 1\ atm$

(D) $PbO_t + 2H^+ + 2e^- = Pb + H_2O$
$E = 0.258 - 0.0591\ pH$

(E) $Pb(OH)_2 + 2H^+ + 2e^- = Pb + 2H_2O$
$E = 0.242 - 0.0591\ pH$

scum (37). Thermodynamically this oxide is stable up to a potential described by the reaction:

$$PbO_2 + 2H^+ + 2e = PbO_t + H_2O \qquad E_o = 1.107$$

The area associated with PbO_t is one of rapid corrosion of the anode unless there is a passivating layer of salt at the solution interface that permits establishment of metastable equilibrium. In sulfuric acid $PbSO_4$ serves this purpose, but in alkaline solutions no passivation occurs and the anode continues to corrode at high rates.

The area designated in Fig. 2 as $PbO \cdot xPbO_2$ is determined by both diffraction examination and spot tests. In this area PbO_2 as such is not detected by diffraction examination at the metal interface. In acid solutions the product is PbO_t giving a spot test for a highly oxidizing material after polarization above a potential corresponding to the theoretical reversible oxygen potential. The highly oxidizing material is considered in this report to be tetravalent lead. It appears immediately above the O_2/H_2O electrode potential and is not observed in the area where H_2O_2 could form from O_2 reduction. In neutral and alkaline solutions a mixture of the oxides Pb_3O_4, PbO_x, and PbO_t is observed. The reason for the difference in anodic materials developed in highly acid and in neutral or alkaline solutions is that PbO_2 varies in solubility with the pH at the solution interface. It is discharged in strong acid solutions, preventing accumulation of significant amounts of tetravalent lead. Both forms of PbO_2 are formed at the solution interface at higher pH so that larger amounts of tetravalent material do accumulate. In the alkaline solutions of $pH > 9.4$, the electrode is covered with a gray or black film of PbO_2 which is loose and may be lifted off the electrode revealing a layer colored bright orange, yellow, and peach giving the diffraction patterns for PbO_t, Pb_3O_4, and PbO_x. Lead is corroding under these conditions by a divalent mechanism (26, 28, 35, 36) forming PbO_t, part of which is being oxidized to PbO_2, and acted on at the solution interface by plumbate ion. The anodic products designated $PbO_t \cdot xPbO_2$ at the metal interface represent the mixture obtained by chemical reaction of these materials.

The existence of this area is belived to be caused by the relative rates of these several reactions

$$Pb + H_2O = PbO_t + 2H^+ + 2e^-$$

$$2H_2O = 2(O)_{aq} + 4H^+ + 4e^-$$

$$PbO_t + (O)_{aq} = PbO_2$$

$$\left.\begin{aligned} PbO_t + PbO_2 &= Pb_2O_3 \\ 2PbO_t + PbO_2 &= Pb_3O_4 \end{aligned}\right\} \text{Designated } PbO_t \cdot xPbO_2$$

The following mechanism is suggested: The anodic current may take two paths: (*a*) it corrodes Pb to form PbO_t or divalent products; (*b*) it oxidizes H_2O to $O_{2(aq)}$ which reacts with PbO_t to form the intermediate oxides (6, 13). Lander (26, 28) showed that within experimental limits all the current went to a divalent corrosion mechanism up to a potential of 1.58 v in acid solutions, and only above that potential did a tetravalent corrosion mechanism become significant. Grube and Glasstone (35, 36) showed a similar divalent corrosion mechanism in NaOH solutions up to a corresponding potential. It is suggested that the kinetics of the electrochemical reactions determine the anodic corrosion rate, and above potentials expressed by line C, Fig. 2, PbO_2 is present directly on the metallic surface. Line C corresponds to the reversible oxidation potential of water to ozone.

$$O_3 + 6H^+ + 6e^- = 3H_2O \qquad E_o = 1.51$$

The fact that the passivation of Pb in both acids and alkalies occurs just above this potential, that the reaction has a slope of 0.059 vs. pH, that it exceeds the potentials for formation of PbO_2 from Pb and PbO_t indicates that the corrosion reactions occurring at this potential may be related to water oxidation reactions.

The kinetic analyses of Lander (26) show that when lead is polarized above the potential for oxidation of water to O_2, the reaction mechanism changes. It was further determined that the anodic corrosion rates were related to the square of the water activity up to a potential corresponding to the maximum in the rate. Above this potential the relationship of the corrosion rate to water activity has values "ranging between two and four" (27). The water oxidation reactions to give O_2 and O_3 depend on the square and cube of the water activity, respectively.

The steps in the over-all water oxidation mechanisms are not known at the present time. The relation of the oxidation processes of the lead anodes to the water activity does not prove that $O_2(aq)$ or $O_3(aq)$ is liberated in these reactions; however, it does suggest that the anodic processes depend on the simultaneous reaction of two and more water molecules. It is possible that Pb or PbO_t catalyzes the water oxidation reaction, and that the subsequent step is reaction of Pb and PbO_t with the water oxidation product to form the intermediate oxides rather than molecular gas evolution.

If the lead anode in alkaline solutions is disturbed while in the laminated condition, before polarization above line C, Fig. 2, so that PbO_2 is mechanically brought into physical contact with the base lead metal, oxygen gas begins to be evolved at a potential lower than it will be from an undisturbed electrode. This effect, described by earlier workers (35), was verified in this study. With this positive identification of the anodic materials, it is concluded that PbO_2 must be in direct contact with the metal surface for the oxygen gas liberation reaction to take place and that the reaction may be associated with oxidation of H_2O or $(OH)^-$ to H_2O_2.[1]

It should be emphasized that this is a study of the dynamic anodization of lead under the potential and pH conditions indicated. Polarization of lead within the area designated $PbO \cdot xPbO_2$ does not establish a passivating coating on the surface, and anodic corrosion rates are high. Deposition of PbO_2 at the solution interface does not comprise a protective coating.

The area indicated at αPbO_2 in Fig. 2 is characterized by a heavy deposit of this material directly on the electrode, providing other reactions do not interfere. This material has not been well characterized chemically, and is probably the low-temperature polymorph (45).

X-ray diffraction examination of the residues obtained on air ignition of αPbO_2 at temperatures corresponding to those reported for thermal degradation of βPbO_2 (6, 17) showed evidence that prior to decomposition α converted to βPbO_2. The conversion temperature lies between 296° and 301°C. Subsequent thermal decomposition, determined by x-ray diffraction examination, follows the same path as βPbO_2.

It may be concluded from this examination of the oxides occurring at the metal-coating interface on anodic lead specimens that the oxides formed are: $Pb(OH)_2$; PbO_t and αPbO_2. The potentials for these reactions have a slope of 0.0591 vs. pH and are believed to represent the electrochemical reactions of lead with water and its oxidation products.

The reaction of metallic lead with water to form PbO_t takes place near the calculated reversible potential. Arrests appear near the theoretical potential in both acid and alkaline solutions on both anodic and cathodic treatment, and PbO_t is observed by diffraction examination of the surface. This indicates that the oxidation proceeds by direct reaction with water molecules or hydroxyl ions at the electrode interface and that no preliminary oxidation of water occurs in this reaction. But the reaction forming PbO_2 at the metal interface should probably be written to indicate that water is first oxidized to an oxygen species and the solid anodic products result from secondary reactions. This suggests that the anodic studies of lead may offer a method for kinetic analysis of the water, oxygen electrodes.

Anions and passivation.—As pointed out previously and discussed extensively by Wolf and Bonilla (44) anions present in the solutions will react with the lead ion and/or the lower oxides, and the corresponding salt will be deposited at the solution interface. If the anion is suitable, a tight passivating film is deposited on the anode surface [i.e., $Pb_3(PO_4)_2$, PbI_2, $PbSO_4$] (44, 46), and continued polarization of the electrode will result in the characteristic anodic oxide at the metal-coating interface. If the lead salt of the anion is not passivating, the electrode process may be changed by only very high current densities or cell potentials (47).

A picturization of a cross section of an anodic lead surface is shown in Fig. 3. This indicates the reaction products identified on the anode surface at pH = 0, and the reference potentials are presented in the left margin. The cross section is schematic;

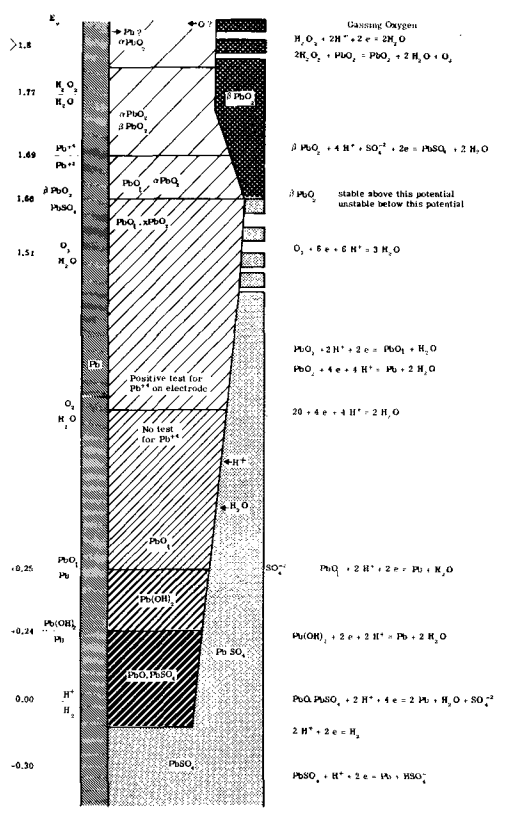

Fig. 3. Schematic cross-section of an anodic lead surface in H_2SO_4 at pH = 0. Anodic products identified by diffraction techniques on a lead surface held at constant potential in sulfuric acid are indicated. Electrochemical reactions are shown at the right within the areas where they were observed to occur. Some E_0 values are indicated at the left for orientation purposes. At the potential 1.8 v oxygen gas is evolved, and a hydrogen peroxide reaction mechanism is indicated as suggested by the potential. At this potential lead is represented as corroding by either migration of Pb or O in the film. The mechanism of this corrosion process is not known at the present time.

[1] The reactions in alkaline solution may be written with $(OH)^-$ rather than H^+, and the HO_2^- reactions have different slopes, but for simplicity these are not included in this discussion.

however, it indicates that as the potential is increased the $PbSO_4$ coating appears to become thinner while the PbO_t layer becomes increasingly thicker. Some suggested reactions are indicated at the right of the drawing. The solid phases identified by diffraction examination are indicated within the potential ranges where they were observed. Areas corresponding to high corrosion rates are indicated as porosity in the outer coating. These rates were determined by Lander under constant potential anodization (26, 28). Several reactions appear near their reversible potentials, exhibiting little polarization, and it is thought that the superficial $PbSO_4$ coating is permeable to H^+ ion and water, but not to SO_4^- ion (26, 44). The action of this passivating film is to permit establishment of pseudo equilibrium in an electrochemical reaction in an environment where the reaction would normally be driven in a destructive direction. This, of course, describes the condition called metastable equilibrium.

As the potential is increased, the lead sulfate present on the surface may be converted to βPbO_2. Electron diffraction examination of the anodic products indicates that the βPbO_2 is a polycrystalline coating at the solution interface. Beneath this is a thin layer of a mixture of the two polymorphs of PbO_2 (1, 2). These materials are believed to arise from two reactions forming PbO_2, one from the base lead and PbO_t and the other from $PbSO_4$.

The oxygen gassing reaction at elevated potentials has been indicated as going by way of the formation of H_2O_2 (possible at these potentials) and being decomposed catalytically by the PbO_2. This is merely a representation and suggestion of a possible oxygen liberation mechanism which potential appears to be related to the peroxide reaction in both acid and alkaline solutions (48, 49). The lead metal is represented as corroding by migration of an oxygen species in and lead outward through an αPbO_2 coating at very elevated potentials. Lead exhibits an increased corrosion rate (26, 28), and αPbO_2 comprises the major portion of the anodic product at these potentials, but it is not known whether the mechanism involves attack of the lead through fissures in the coating or migration through a continuous film.

Conclusions

The areas of occurrence of the anodic lead oxide phases are indicated on the potential-pH phase diagrams of Fig. 1 and 2. There appear to be two sets of anodic reactions, producing different anodic products. Some of the observed oxides are believed to be electrode species, and some deposits from saturated solutions and chemical reactions.

The occurrence of αPbO_2 as an anodic product on lead in acid solutions has been attributed to oxidation of PbO_t and lead metal by the preliminary oxidation of water.

It is suggested that the corrosion rate of lead depends on the kinetics of these water reactions, and that inhibition of corrosion depends on the imposition of a "corrosion" current and potential that results in a steady-state condition in which PbO_2 is maintained in direct contact with the base metal. Upon anodic polarization of a clean lead surface, it is necessary to "overshoot" the steady-state potential and current in order to generate the required materials, but once the materials are formed in the solution and on the electrode surface then only a minimal current is required to maintain passivation. The low corrosion rate of telephone battery service (50) is believed to be a reflection of this requirement.

The passivation domains originally outlined to correspond to the domains of thermodynamic stability of PbO_2 and $PbSO_4$ (3) should be modified to indicate two areas of passivation: one where the composite coating of $PbSO_4$ and PbO_t is protective below line A in Fig. 2; and the other above line C. These passivation domains are separated by an area of intense corrosion believed to be caused by the electrochemical oxidation of water at the metal interface at a rate insufficient to maintain a passivating coating of PbO_2 on the metal surface.

X-ray diffraction examination of calcined αPbO_2 suggests that it is the low-temperature polymorph and is converted to βPbO_2 at approximately 300°C in air.

The potentials associated with gassing oxygen from a PbO_2 electrode indicate that the reaction may go by way of peroxide in both acid and alkaline media.

Manuscript received Mar. 24, 1958. This paper was prepared for delivery before the Buffalo Meeting, Oct. 6-10, 1959.

Any discussion of this paper will appear in a Discussion Section to be published in the December 1959 JOURNAL.

REFERENCES

1. J. Burbank, *This Journal*, **103**, 87 (1956).
2. J. Burbank, *ibid*, **104**, 693 (1957).
3. P. Delahay, M. Pourbaix, and P. Van Rysselberghe, *ibid.*, **98**, 57 (1951).
4. A. Bystrom, *Arkiv. Kemi. Min. Geol.*, **17B**, No. 8 (1943).
5. F. Halla and F. Pawlek, *Z. Phys. Chem.*, **128**, 49 (1927).
6. T. Katz, *Ann. Chim.*, **5**, 5 (1950).
7. R. G. Dickinson and J. G. Friauf, *J. Am. Chem. Soc.*, **46**, 2457 (1924).
8. W. J. Moore and L. Pauling, *ibid.*, **63**, 1392 (1941).
9. P. E. Jensen and E. J. Ritchie, Paper presented at the Buffalo Meeting, Electrochemical Society, Oct. 7-10, 1957.
10. S. T. Gross, *J. Am. Chem. Soc.*, **65**, 1107 (1943).
11. A. Bystrom and A. Westgren, *Arkiv. Kemi. Min. Geol.*, **16B**, No. 14 (1943).
12. M. LeBlanc and E. Eberius, *Z. Phys. Chem.*, **160A**, 69 (1932).
13. A. Bystrom, *Arkiv. Kemi. Min. Geol.*, **20A**, No. 11 (1945).
14. G. L. Clark and J. Rowan, *J. Am. Chem. Soc.*, **63**, 1302 (1941).
15. C. Holtermann, *Ann. Chim.*, **14**, 121 (1940).
16. G. L. Clark, N. C. Schieltz, and T. T. Quirke, *J. Am. Chem. Soc.*, **59**, 2305 (1937).
17. G. Butler and J. L. Copp, *J. Chem. Soc.*, **1956**, 725.
18. S. T. Gross. *J. Am. Chem. Soc.*, **63**, 1168 (1941).
19. A. Bystrom, *Arkiv. Kemi. Min. Geol.*, **18A**, No. 23 (1944).
20. A. E. Van Arkel, *Physica*, **5**, 162 (1925).
21. A. Ferrari, *Rend. d. Acc. Nag. d. Lincei*, **2**, 186 (1925).
22. J. A. Darbyshire, *J. Chem. Soc.*, **1932**, 211.
23. A. I. Zaslavskii, J. D. Kondrashov, and S. S. Toklachev, *Doklady Akad. Nauk. S.S.S.R.*, **75**, 559 (1950).

24. A. I. Zaslavskii and S. S. Toklachev, *J. Phys. Chem. S.S.S.R.*, **26**, 743 (1952).
25. A. Bystrom, *Arkiv. Kemi. Min. Geol.*, **25A**, No. 13 (1947).
26. J. J. Lander, *This Journal*, **98**, 213 (1951).
27. J. J. Lander, *ibid.*, **98**, 220 (1951).
28. J. J. Lander, *ibid.*, **103**, 1 (1956).
29. X-Ray Powder Data File, Amer. Soc. Testing Mat., Philadelphia, 1950-1957.
30. Ming Chow, *J. Am. Chem. Soc.*, **42**, 488 (1920).
31. W. C. Vosburgh and D. N. Craig, *ibid.*, **51**, 2009 (1929).
32. H. S. Harned and W. J. Hamer, *ibid.*, **57**, 27 (1935).
33. H. S. Harned and W. J. Hamer, *ibid.*, **57**, 9 (1935).
34. G. W. Work and C. P. Wales, *This Journal*, **104**, 67 (1957).
35. S. Glasstone, *J. Chem. Soc. Trans. II*, **121**, 2091 (1922).
36. G. Grube, *Z. Elektrochem.*, **28**, 273 (1922).
37. N. P. Fedotieff, B. P. Artamonoff, and N. J. Rasmerova, J. Electrodepositors' Tech. Soc., **12**, 26 (1937).
38. P. Jones, H. R. Thirsk, and W. F. K. Wynne-Jones, *Trans. Faraday Soc.*, **52**, 1003 (1956).
39. F. Feigl, "Qualitative Analysis by Spot Tests," Nordeman Publishing Co., New York (1939).
40. W. M. Latimer, "Oxidation States of the Elements and Their Potentials in Aqueous Solutions," 2nd ed., Prentice-Hall, New York (1952).
41. S. Glasstone, *J. Chem. Soc. Trans. II*, **121**, 1469 (1922).
42. L. V. Andrews and D. J. Brown, *J. Am. Chem. Soc.*, **56**, 388 (1934).
43. G. L. Clark and W. P. Tyler, *ibid.*, **61**, 58 (1939).
44. E. F. Wolf and C. F Bonilla, *Trans. Electrochem. Soc.*, **79**, 307 (1941).
45. H. Bode and E. Voss, *Z. Elektrochem.*, **60**, 1053 (1956).
46. J. Kamecki, Z. Zembura, and J. Trau, *Roczniki Chem.*, **30**, 261 (1956).
47. R. Piontelli and G. Poli, *Z. Elektrochem.*, **62**, 320 (1958).
48. M. Pourbaix, "Thermodynamics of Dilute Aqueous Solutions," Trans. by J. N. Agar, Edward Arnold and Co., London (1949).
49. P. Delahay, M. Pourbaix, and P. Van Rysselberghe, *Ind. Chim. Belge.*, **16**, 396 (1951).
50. U. B. Thomas, F. T. Forster, and H. E. Haring, *Trans. Electrochem. Soc.*, **92**, 322 (1947).

Evidence for a Logarithmic Oxidation Process for Stainless Steel in Aqueous Systems

Milton Stern

Metals Research Laboratories, Union Carbide Metals Company, Division of Union Carbide Corporation, Niagara Falls, New York

ABSTRACT

Upon immersion of a passive stainless steel electrode into an oxidizing ferrous-ferric aqueous solution, the mixed potential of the electrode gradually approaches the reversible redox potential of the solution. During this period, an oxidation process occurs, the rate of which decreases with time. The process is most likely oxidation of metal since the potential range over which it occurs is more active than the estimated reversible oxygen potential for the system, and no other oxidation reaction is likely. The kinetics of oxidation of stainless steel are similar to kinetics reported for anodic oxidation of metals which form thin amorphous oxides. Therefore, it is believed that evidence has been obtained for growth of a similar type of oxide on stainless steel. At constant potential, the oxidation process can be described closely by a logarithmic oxidation equation. Also, the kinetics are consistent with equations which describe ion current through thin oxides as a function of the field across the oxide.

A study of ferrous-ferric electrode kinetics on stainless steel surfaces has been reported (1). The data supported theoretical equations which describe potential-current relationships for such a system. All rate measurements were conducted on electrodes whose potential, with no applied current, was very close to the reversible ferrous-ferric potential. However, it was also shown that stainless steel does not exhibit this potential immediately after immersion in the oxidizing solution. The electrode is initially more active than a platinum electrode in the same solution and slowly approaches the platinum potential over a period of several thousand minutes in a manner already illustrated (1). No effort was made to explain the processes occurring during this time interval; however, pertinent data were obtained which, at that time, were not particularly clear. A better understanding of the nature of the system now provides a reasonable explanation of this initial potential-time dependence, and the purpose of this discussion is to describe the kinetics of the processes which occur.

Experimental

The experimental procedure was described earlier (1, 2) and only pertinent details are repeated. The environment was either a mixture of ferrous and ferric sulfate in water or a mixture of ferrous and ferric chloride containing sodium nitrate as a pitting inhibitor. Solutions were oxygen-free. Platinized platinum was used as reference and as auxiliary electrodes during polarization. The material was commercial Type 304 stainless steel. Sample preparation involved thorough degreasing, activation in concentrated HCl until hydrogen evolution was ob-

served, a rinse in distilled water, brief (approximately 5 sec) immersion in concentrated HNO_3, a second rinse, and immediate introduction into the cell. This treatment produces a passive surface prior to immersion in the electrolyte. The initial potential-time behavior was recorded using a L&N pH meter which drove an appropriate potential recorder. Since platinized platinum was used as a reference, the approach of the stainless steel electrode to the reversible potential could be observed readily by watching the approach of the recorder indication to zero. During this time interval, a measurement not reported earlier was conducted. It involved periodic anodic polarization of the sample to the platinum potential and determination of the current required to do this. The procedure required a maximum of about 10 sec and did not affect the normal potential-time behavior significantly. To minimize the time during which the sample was polarized, an anodic current was applied to produce a zero recorder reading, after which the polarizing circuit was opened. The value of current required to polarize to the platinum potential was determined by substituting a shunt for the cell in the series polarizing circuit and measuring current through the series circuit without the presence of the cell. Values of resistance in the circuit were high so that the current was not significantly affected by introduction or removal of the effective resistance represented by the cell. This procedure was repeated periodically from the first few minutes after the electrode was introduced into the solution to the time when the potential was essentially stationary.

These measurements were not conducted with a view toward interpretation in the manner presented below. Rather, they were done to determine whether it was possible to measure the instantaneous corrosion rate of the material by a method described by Vetter (3). He reported that the corrosion rate of passive iron in concentrated nitric acid can be determined electrochemically by polarizing the surface anodically to the potential of platinum in the same solution. The current required to polarize is equivalent to the corrosion current. Measurements of this type were discontinued when it was realized that very special electrochemical conditions, described elsewhere (4), are required for the method to work. A sufficient number of experiments of this type were conducted to provide convincing evidence that the observations described below are correct for stainless steel. Since, qualitatively, similar potential-time behavior was observed for other materials, it is possible that the analysis presented below could well apply to the various other surfaces which were used to study ferrous-ferric oxidation-reduction kinetics. However, data for these other metals are not available.

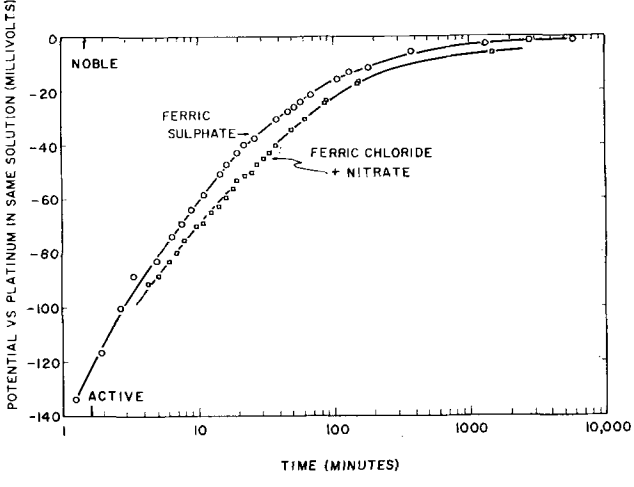

Fig. 1. Potential as a function of time for stainless steel

Time-Potential Measurements

Figure 1 illustrates the potential-time behavior described above. The circles represent data in ferric-ferrous sulfate and are the data reported earlier (1) without explanation. The squares apply to a ferrous-ferric chloride system containing nitrate. Kinetic data for oxidation and reduction of ferrous and ferric ions have already been reported for these systems. In the sulfate solution with a ferrous-ferric reversible potential of +0.770 v, the exchange current, i_o, is 0.045 μamp/cm^2; the Tafel slope for reduction of ferric ions, β_c, is 0.123 v; the Tafel slope for oxidation of ferrous ions, β_a, 0.102 v. For the chloride system (2) with a reversible potential of +0.824 v, i_o, is 0.063 μamp/cm^2; β_c is 0.146; β_a is 0.165. These measurements were made after the electrodes had come to a steady-state potential very close to the reversible ferrous-ferric potential.

Anodic Polarization Measurements

It is assumed that the above kinetic parameters apply to the system very soon after the electrode is immersed and that they do not change during the time the potential approaches that of platinum. Justification for this important assumption is presented later. If this assumption is correct, another oxidation reaction, in addition to oxidation of ferrous ions, must be occurring during this time. According to the theory of the mixed potential, the system must satisfy the following relation:

$$\overleftarrow{i_{Fe^{++}}} + \overleftarrow{i_m} = \overrightarrow{i_{Fe^{+++}}} \qquad [1]$$

where $\overleftarrow{i_{Fe^{++}}}$ (μamp/cm^2) is the rate of oxidation of ferrous ions; $\overleftarrow{i_m}$ is the rate of oxidation of a second oxidation process, and $\overrightarrow{i_{Fe^{+++}}}$ is the rate of reduction of ferric ions. Equation [1] simply states that there can be no net oxidation or reduction in the system and holds at any time where no external current is applied. The most likely process represented by $\overleftarrow{i_m}$ is oxidation of metal, particularly since potentials involved are more active than the reversible oxygen potential and oxygen evolution is not likely.

Upon anodic polarization to the potential of platinum ($\eta = o$), with an applied current, $\overleftarrow{i_p}$, the equation satisfied is:

$$\overleftarrow{i_p} = (\overleftarrow{i_{Fe^{++}}} + \overleftarrow{i_m}) - \overrightarrow{i_{Fe^{+++}}} \qquad [2]$$

but at $\eta = o$, $\overleftarrow{i_{Fe^{++}}} = \overrightarrow{i_{Fe^{+++}}} = i_o$, so that

$$\overleftarrow{i_m} = \overleftarrow{i_p} \qquad [3]$$

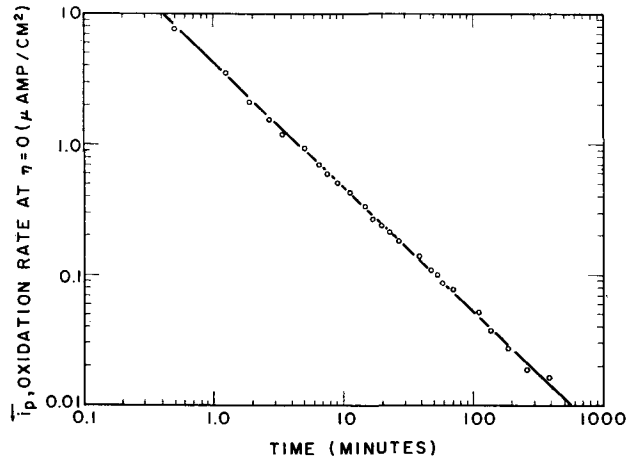

Fig. 2. Oxidation rate at zero overvoltage as a function of time for stainless steel in a ferric-ferrous sulfate solution with reversible potential of +0.770 v.

As described above, $\overleftarrow{i_p}$ was measured as a function of time. Consequently, the kinetics of metal oxidation *at constant potential* can be described in considerable detail solely from this type of measurement. Since the data range over three orders of magnitude, it is convenient to plot them on logarithmic scales. Data for sulfate solution are given in Fig. 2. The points fall on a good straight line, the slope of which is close to minus one. This means that $\overleftarrow{i_m}$ is inversely proportional to time.

$$\overleftarrow{i_m} = \frac{k'}{t} \qquad [4]$$

Consider that $\overleftarrow{i_m}$ represents the rate of oxidation of metal to form an oxide of some type in accordance with a process similar to $M + H_2O \rightarrow MO + 2H^+ + 2e$. Then $\overleftarrow{i_m}$ is proportional to the rate of growth of oxide thickness

$$\overleftarrow{i_m} = \frac{k''dx}{dt} \qquad [5]$$

where x is the oxide film thickness. Therefore,

$$\frac{dx}{dt} = \frac{k}{t} \qquad [6]$$

and upon integration a logarithmic oxidation equation is obtained

$$x = A + B \log t \qquad [7]$$

Whether one considers x an oxide film thickness or simply the weight of metal oxidized, it is quite clear that the kinetics of the process at constant potential closely approximate the general logarithmic oxidation equation.

Generally, Eq. [7] applies to oxidation at low temperatures when thin films are formed.

Relation to Other Work on Oxidation of Metals

Considerable work has been reported on oxidation kinetics of metals such as aluminum, tantalum, columbium, and zirconium, where amorphous oxide films are formed. Much of the experimental work has been directed toward determination of the applicability of the Mott and Cabrera (5) type of equation which relates ionic current through an oxide film with the field, F, across the film.

$$i = \alpha e^{\beta F} \qquad [8]$$

For example, Charlesby has worked with aluminum (6) and zirconium (7) and reports general agreement with Eq. [8]. Van Rysselberghe and co-workers (8) extended work with zirconium to much thinner films than those investigated by Charlesby and also found Eq. [8] valid. Young (9) reports that results for columbium may be expressed by this equation. Vermilyea (10) has conducted extensive studies on the formation of anodic oxide films on tantalum and finds that at constant temperature results are described by an equation similar in form to [8]. However, detailed work has shown that the Mott and Cabrera theory is not adequate for describing all observed phenomena, and efforts to provide modifications or new theories have appeared (11-14).

It is not the purpose of this work to evaluate any of these detailed descriptions. Rather, an effort will be made to show that observed kinetics of stainless steel anodic oxidation are very similar in form to observed kinetics for anodic oxidation of aluminum, columbium, tantalum, and zirconium where amorphous oxide films are produced.

At constant potential, Eq. [8] [where i is proportional to dx/dt and $F = E/x$] may be put in the form of the so-called inverse logarithmic equation by making suitable approximations (5).

$$\frac{1}{x} = a - b \log t \qquad [9]$$

It is particularly difficult to distinguish experimentally between Eqs. [7] and [9]. Measurements over better than two orders of magnitude in time are required. This is described clearly by Vermilyea and illustrated by his data for anodic oxidation (10) and dry oxidation (15) of tantalum. Thus, it is possible that the thickness-time relation observed here for stainless steel could also fit the inverse logarithmic equation and be consistent with Eq. [8].

Charlesby (6) in work with anodized aluminum tried to determine whether his data best fit Eq. [8] or whether they are best described by the strong field emission formula of Fowler and Nordheim (16).

$$i = \alpha F^2 e^{(-B/F)} \qquad [10]$$

He also illustrates the difficulty involved and further reports that the Guntherschulze and Betz' (17) data for tantalum fit Eqs. [8] and [10] equally well. Charlesby's data of particular interest here involve decay of current with time at constant potential, exactly the experimental conditions used for stainless steel in Fig. 2. He shows mathematically that for systems described by Eq. [8], $(d \log i)/(d \log t)$ varies with βF. Over a range of βF values from 10 to 50, which should cover many real systems, $(d \log i)/(d \log t)$ varies from −0.87 to −0.96. For Eq. [10], with B/F values from 10 to 30, $(d \log i)/(d \log t)$ varies from −0.984 to −0.998. These values are closer to −1 than the corresponding values for Eq. [8] and may serve to distinguish between the

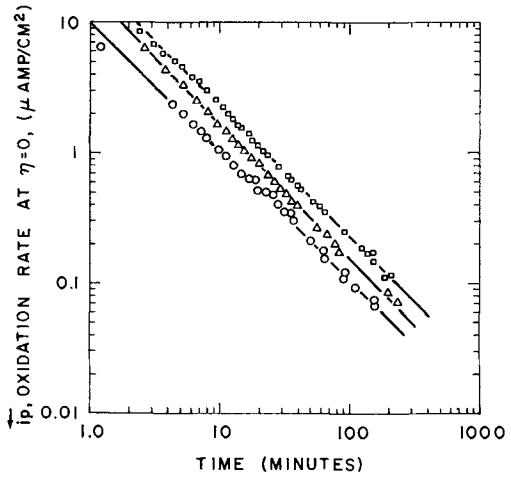

Fig. 3. Oxidation rate at zero overvoltage as a function of time for stainless steel in ferric-ferrous chloride solutions containing nitrate with reversible potentials of +0.824 v (circles), +0.823 v (triangles), and +0.809 v (squares).

two. Charlesby favored Eq. [8] for his data, but reported the results as inconclusive.

The line drawn through the points on Fig. 2 has a slope, $(d \log i)/(d \log t)$, of −0.96. Although values of B and F are not known for the stainless steel system, these data alone indicate that Eq. [8] may apply. However, similar data for three chloride systems are shown in Fig. 3. The circles are for the ferrous-ferric chloride system illustrated in Fig. 1. The squares and triangular points are for stainless steel in a similar solution with reversible ferrous-ferric potentials of +0.809 and +0.823 v, respectively. The straight lines drawn through the three sets of data have slopes of −1.0 (circles), −1.0 (squares), and −0.97 (triangles).

It is evident from the above discussion that the oxidation kinetics observed for stainless steel at constant potential in the oxidizing aqueous environments investigated can be considered to comply reasonably well with either the logarithmic or inverse logarithmic oxidation equations. Also, the data can be considered reasonably consistent with either Eqs. [8] or [10] describing ion current as a function of field across an oxide.

Dependence of Metal Oxidation Rate on Potential

For Eq. [8], which is favored by most work on anodic oxidation, $dF/(d \log i)$, is a constant[1] which is often referred to as the Tafel slope by Dewald (11) and Young (9). Thus, at constant film thickness, $dE/(d \log i)$ is a constant. The rapid (~10-sec) anodic polarization measurements described above for determination of $\overleftarrow{i_p}$ may be considered polarization at constant film thickness. Thus, one would expect a straight line relation between potential and log $\overleftarrow{i_m}$ at any time t. While extensive data showing the variation of $\overleftarrow{i_m}$ with potential at constant time cannot be obtained by the methods used, two points at any time have been measured. This is best described with the aid of a schematic

[1] There is now evidence that β in Eq. [8] is not strictly independent of field (14, 18). However, for the situation described, the change in field is quite small, and this relation may be considered to apply.

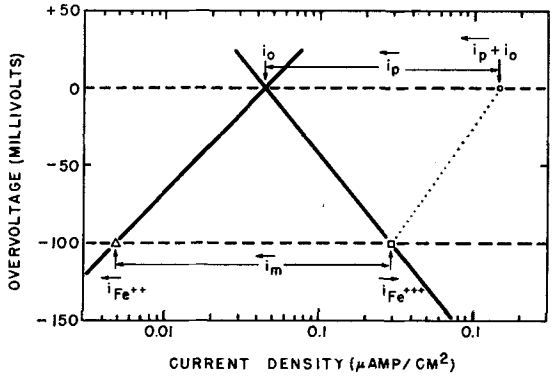

Fig. 4. Schematic polarization diagram showing the position of partial currents during the approach to a steady-state potential.

polarization diagram using the assumption (described above) that the ferrous-ferric oxidation-reduction kinetics are constant with time. With the measured kinetic parameters in sulfate solution used as an example, Fig. 4 illustrates the relation between the various partial currents during the approach to a steady state. Potentials are referred to platinized platinum in the same solution. The two solid Tafel lines represent the rate of oxidation and reduction of ferrous and ferric ions as a function of potential. Since these do not vary at any time (t) during the approach to the platinum potential, the magnitudes of $\overleftarrow{i_{Fe^{++}}}$ and $\overrightarrow{i_{Fe^{+++}}}$ are known from a knowledge of the mixed potential. For example, when the potential is −100 mv, $\overleftarrow{i_{Fe^{++}}}$ is about 0.005 μamp/cm² and $\overrightarrow{i_{Fe^{+++}}}$ is about 0.30 μamp/cm². These values are shown as the triangles and squares on Fig. 4. From Eq. [1], $\overleftarrow{i_m}$ is the difference between these values or approximately 0.30 μamp/cm². Therefore, the point representing $\overrightarrow{i_{Fe^{+++}}}$ also represents $\overleftarrow{i_m}$ when $\overleftarrow{i_{Fe^{++}}}$ is negligible and, in any case, represents the total anodic current.

Upon rapid anodic polarization to the potential of platinum, another value of $\overleftarrow{i_m}$ is determined as shown by Eqs. [2] and [3]. At this potential, $\overleftarrow{i_m} + \overleftarrow{i_{Fe^{++}}}$ represents the total anodic current. Since $\overleftarrow{i_m} = \overleftarrow{i_p}$ and $\overleftarrow{i_{Fe^{++}}} = \overleftarrow{i_o}$, $\overleftarrow{i_p} + i_o$ also represent the total anodic current. Therefore, the dotted line on Fig. 4 connecting $\overleftarrow{i_p} + i_o$ with $\overrightarrow{i_{Fe^{+++}}}$ represents the total anodic polarization curve of the system when the mixed potential is −100 mv. As described above, when the potential is far from the reversible potential, $\overleftarrow{i_{Fe^{++}}}$ is negligible and the dotted line represents the change of $\overleftarrow{i_m}$ with potential. At longer times, when η is small, $\overleftarrow{i_{Fe^{++}}}$ can no longer be neglected, and an analogous dotted line would represent the sum of two logarithmic curves which, over the small potential increment considered, may also be represented by a single Tafel line (19).

As described above, $\overleftarrow{i_p}$ was measured periodically during the approach of the sample potential to that

of platinum in the same solution. The exchange current and Tafel lines were measured after the electrode had reached a steady potential value. Constructing a similar plot to Fig. 4, the data for the sulfate system are shown in Fig. 5. The square points which lie along the Tafel line for ferric reduction are measured potentials at various times during the approach to zero overvoltage. They are the same points illustrated in Fig. 1 and are placed on this figure using the assumption that ferrous-ferric kinetics are independent of time. The circles are values of $\overleftarrow{i_p} + i_o$, where $\overleftarrow{i_p}$ is also measured during the approach to zero overvoltage. The solid lines connecting circles and squares represent data obtained at the same time (within about 10 sec), the time after immersion in the cell being indicated along the appropriate line. The lines are not exactly parallel, those at the shorter times exhibiting a higher slope. The lines at short times should more nearly represent $\overleftarrow{i_m}$ as a function of potential since $\overleftarrow{i_{Fe^{++}}}$ is insignificant, while the lines at long times are influenced by $\overleftarrow{i_{Fe^{+++}}}$. Unfortunately, for short times, the interval during which the sample is anodically polarized is significant in respect to the total time, so that these data cannot be considered as accurate as those for which the sample has been immersed for long times.

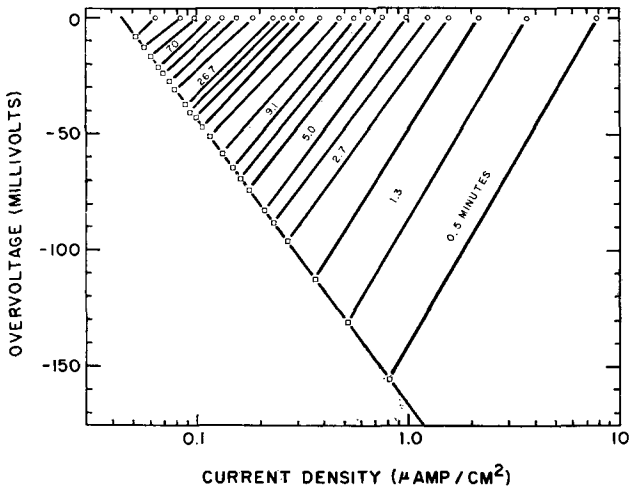

Fig. 5. Total anodic polarization curve for stainless steel as a function of time during the approach to a steady-state potential in ferric-ferrous sulfate with a reversible potential of +0.770 v.

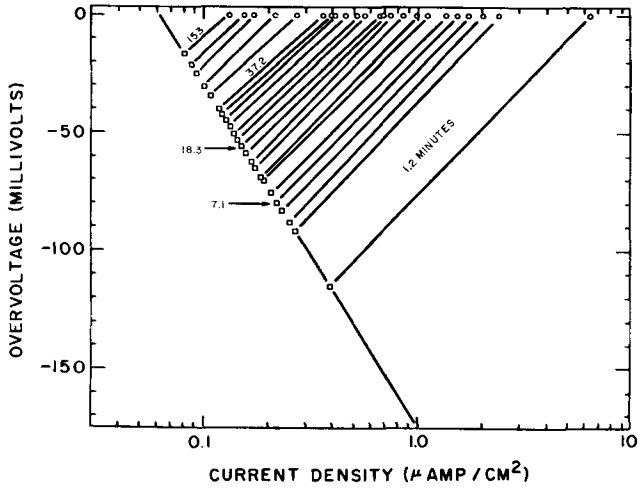

Fig. 6. Total anodic polarization curve for stainless steel as a function of time during the approach to a steady-state potential in ferric-ferrous chloride containing nitrate with a reversible potential of +0.824 v.

Figure 6 shows a similar plot for the chloride system. Here the total polarization lines are all more nearly parallel.

Regardless of whether one considers the family of total polarization curves parallel or not (and one would not expect them necessarily to be parallel since two different processes, $\overleftarrow{i_m}$ and $\overleftarrow{i_{Fe^{++}}}$, with possibly different β values are involved), it is evident that $\overleftarrow{i_m}$ appears to be a logarithmic function of potential as required by Eq. [8].

Potential-Time Behavior

The initial potential-time behavior is explained readily in terms of the processes described above. The potential decreases in the manner shown in Fig. 1 because an anodic Tafel line (representing $\overleftarrow{i_m}$ as a function of E) sweeps from right to left across the polarization curves of $\overleftarrow{i_{Fe^{++}}}$ and $\overrightarrow{i_{Fe^{+++}}}$. The mixed potential at any time is that value at which the sum of all the rates of oxidation ($\overleftarrow{i_{Fe^{++}}} + \overleftarrow{i_m}$) equals the rate of reduction ($\overrightarrow{i_{Fe^{+++}}}$). At short times, $\overleftarrow{i_{Fe^{++}}}$ is negligible and the potential is determined primarily by $\overleftarrow{i_m}$ which is changing rapidly. When $\overleftarrow{i_m}$ approaches $\overleftarrow{i_{Fe^{++}}}$, the potential is determined by the sum of these two currents. In this interval, $\overleftarrow{i_m}$ is changing less rapidly. Finally, when $\overleftarrow{i_m}$ becomes negligible in comparison to $\overleftarrow{i_{Fe^{++}}}$, the total anodic current is essentially $\overleftarrow{i_{Fe^{++}}}$. In this condition, $\overleftarrow{i_{Fe^{++}}} = \overrightarrow{i_{Fe^{+++}}}$ (or the exchange current), and the metal exhibits the reversible ferrous-ferric potential of the solution where $\eta = o$. The potential no longer changes with time.

Oxide Film Thickness

The oxidation kinetics observed for stainless steel during the approach of its mixed potential to that of platinum in ferric-ferrous solutions are similar to kinetics observed for anodic oxidation of metals which are known to form thin amorphous films. This is evidence that similar films are formed on the iron-chromium-nickel alloy.

An estimate of the thickness of the film formed at constant potential may be made by determining the number of coulombs involved in the observations reported in Fig. 2. Integrating the current-time relationship between 1 min and 400 min produces a value of 1.3 (10^{-3}) coulombs/cm^2. Considering the relationship applies from 1 sec to 1000 min increases this value to 2.5 (10^{-3}) coulombs/cm^2. Using 2 (10^{-4}) g/coulomb for the electrochemical equivalent for oxidation of the alloy, gives a value of approximately 5 (10^{-7}) g/cm^2 for the weight of metal oxidized after 1000 min. Assuming the oxide has the formula M_2O_3 with average molecular weight of 150 and metal atomic weight of 55, the weight of oxide

produced is approximately 7 (10^{-7}) g/cm^2 or 0.7 μg/cm^2. With a surface roughness factor of 2.5, this value is reduced to 0.3 μg/cm^2. This may be compared with Rhodin's (20) values of 0.5 to 1.0 μg/cm^2 obtained by weighing oxides stripped from stainless steels. Assuming an oxide density of 5 g/cm^3, the oxide thickness grown in the oxidizing solution after passivation in nitric acid is 6Å, a value which could easily be in error by a factor of two, considering the assumptions which are involved.

The calculation is made primarily to show that experimental values of current are consistent with a process involving logarithmic growth of thin oxide films.

General Discussion

The important assumption made in this entire analysis is that the ferrous-ferric kinetics remain constant with time during the approach of the potential to the reversible redox value of the solution. No absolute proof for the validity of this assumption can be presented. However, it appears quite reasonable, and the entire kinetic description based on this assumption is quite self-consistent.

It should perhaps be mentioned that construction of Fig. 5 and 6 to produce a family of curves which are so nearly parallel provides a very severe test of both the assumption involved and the experimental data. Note, for example, the points along the platinum potential are values of $\overleftarrow{i_p} + i_o$, where i_o is quite significant in respect to $\overleftarrow{i_p}$ for an appreciable fraction of the total anodic curves shown. If i_o or β_c for the ferric-ferrous system were to change appreciably with time, it would be highly unlikely that construction of Fig. 5 and 6 would have produced such a parallel array of anodic curves. This perhaps provides some justification for the assumption. Further, the assumption is consistent with a redox process occurring on an oxide surface, since one would not necessarily expect redox kinetics to change as the oxide becomes thicker provided the rate is not limited by the rate of electron transfer through the oxide.

Perhaps anodic oxidation kinetics for stainless steel, similar to that described here, have not been heretofore reported because stainless steel exhibits a transpassive potential region. That is, at relatively noble potentials, stainless steel dissolves rapidly, whereas oxides on other metals can support much higher fields. Also, overvoltages for oxygen evolution on metals like tantalum, zirconium, columbium, and aluminum are relatively high in comparison to the overvoltage for the process on stainless steel. Thus, the potential range where such kinetics can be observed for stainless steel is much more limited than that which exists for metals which can be anodized readily. Since the oxide on stainless steel apparently cannot support high fields, the thickness cannot readily be built up to the interference color range.

In most work on anodic oxide films, the field required to produce growth is applied externally, whereas here the redox system is considered to provide the field. This is consistent with considerations of Young (9), Dewald (11), Vermilyea (10), and Van Rysselberghe (8), who all have taken into account the field produced by electrochemical processes in solution as well as the field created by an applied potential.

Acknowledgments

The author would like to acknowledge critical discussions with Drs. N. D. Greene, A. C. Makrides, and H. Wissenberg. Dr. Makrides pointed out that the kinetics observed at constant potential can be described by a logarithmic oxidation equation. This led to the interpretation presented here.

Manuscript received Nov. 18, 1958.

Any discussion of this paper will appear in a Discussion Section to be published in the December 1959 JOURNAL.

REFERENCES

1. M. Stern, *This Journal*, **104**, 559 (1957).
2. M. Stern, *ibid.*, **104**, 600 (1957).
3. K. J. Vetter, *Z. Elektrochem.*, **56**, 814 (1952).
4. M. Stern, *This Journal*, **105**, 638 (1958).
5. N. Mott and N. Cabrera, *Repts. Prog. in Phys.*, **12**, 163 (1949).
6. A. Charlesby, *Proc. Phys. Soc. London*, **B66**, 317 (1953).
7. A. Charlesby, *Acta Met.*, **1**, 340 (1953).
8. G. B. Adams, N. Maraghini, and P. Van Rysselberghe, "Proc. 6th Meeting, International Committee for Electrochemical Thermodynamics and Kinetics," p. 249, Butterworths Scientific Publications, London (1955).
9. L. Young, *Trans. Faraday Soc.*, **50**, 159 (1954); **52**, 502 and 515 (1956).
10. D. A. Vermilyea, *Acta Met.*, **1**, 282 (1953).
11. J. F. Dewald, *This Journal*, **102**, 1 (1955); *J. Phys. Chem. Solids*, **2**, 55 (1957).
12. C. P. Bean, J. C. Fisher, and D. A. Vermilyea, *Phys. Rev.*, **101**, 551 (1956).
13. H. H. Uhlig, *Acta Met.*, **4**, 541 (1956).
14. P. Winkel, C. A. Pistovius, and W. Ch. van Geel, *Philips Res. Repts.*, **13**, 277 (1958).
15. D. A. Vermilyea, *Acta Met.*, **6**, 166 (1958).
16. R. H. Fowler and L. Nordheim, *Proc. Royal Soc. A*, **119**, 173 (1928).
17. A. Güntherschulze and H. Betz, *Z. Physik*, **92**, 367 (1934).
18. D. A. Vermilyea, *This Journal*, **102**, 655 (1955).
19. M. Stern, *ibid.*, **104**, 645 (1957).
20. T. N. Rhodin, *Ann. N. Y. Acad. Sci.*, **58**, 855 (1954).

Role of Thiourea in the Electrodeposition of Copper

Bacon Ke, John J. Hoekstra,[1] Bienvenido C. Sison, Jr.,[2] and Dan Trivich

Department of Chemistry, Wayne State University, Detroit, Michigan

ABSTRACT

Single crystal spheres of copper were used to study the effect of thiourea on the plating of copper from an acid bath and the adsorption of thiourea on copper. By x-ray diffraction methods, it was found that instead of the normal tendency of copper to receive single-crystal deposits on the (111) regions from the acid bath, the presence of thiourea caused a uniform bright polycrystalline deposit to be received over the entire sphere. By the use of thiourea labelled with S-35, it was found that thiourea was strongly but fairly uniformly adsorbed on the spheres. It is concluded that the adsorption of thiourea is general with no preference for any crystal face of copper and that the adsorbed thiourea interferes with the crystal growth of the copper electrodeposit.

During the development of modern electroplating practice, it was found that the inclusion of small amounts of the proper addition or brightening agent in the plating bath results in marked changes in the nature of the deposit obtained from the bath. In most cases addition agents are used to obtain smooth bright deposits although they also may be used in some cases to improve other properties. In some cases addition agents permit the use of higher current densities and, as is the case particularly with some bright nickel baths, produce a leveling action, whereby the plated surface is smoother than the original surface. The amount of addition agent required to produce these effects is surprisingly small, and the action of the addition agent is often specific for a particular bath.

The advent of bright plating represents a considerable commercial advance in the field of electrodeposition. In particular, substantial savings in cost and effort have been made since a good deal of the hand finishing previously used can be eliminated.

The early history of bright plating has been reviewed by Rubinstein (1) and by Henricks (2). The discovery of the brighteners used in the various plating baths was accidental in some cases, and in others was the result of painstaking experimentation, almost invariably by means of repeated test platings on a small scale. However comparatively little research effort has been devoted to incisive inquiry into the mechanism of bright plating. Henricks (2) reviewed several theories proposed for the mechanism of bright plating. The most prominent of these theories are the reducing menstruum theory of Kern (3), the adsorption theory of Bancroft (4) [cf. Blum (5)], the complex theory of Mathers (6), and the cathode interference theory of Hunt (7). Each of these proposed theories explains some of the phenomena associated with brightener action, but none of these completely explains all of the facts observed. While the explanations of the mechanism of bright plating are still obscure, the prevalent opinion among more recent workers (8) is that some form of adsorption is involved. The development of a satisfactory theory of bright plating will be of importance in bringing about the development of further bright baths of commercial utility.

A successful theory of bright plating must explain most or all of the following aspects of bright plating: the refinement of the deposit in regard to crystal size and the production of bright, smooth surfaces; the frequent accompaniment by leveling action; the extension of the current density range; the specific nature of the structure of the brightener; inclusion of the brightener or its reaction products in the deposit; the accompaniment of polarization; and the possible change of orientation in deposits.

The specific action of particular agents in certain baths is one of the characteristics that is hardest to explain. It is puzzling that some small variations in the structure of a brightener can ruin its brightening ability and that often there is little carry-over of the brightening power of a particular compound from one bath to another. This suggests that a proper theory of brightening should take into account this specificity in the nature of the brightener and its relation to the metal being plated.

In the face of these facts, we agree with the prevalent hypothesis that brightening is primarily the result of some form of adsorption. Our assumption of this point of view is based particularly on the fact that the molar concentration of the brightener is always much less than the molar concentration of the metal ion. Clearly then it is not possible for a small amount of brightener to form a complex with any substantial fraction of a large amount of metal ion. The most plausible mechanism in which such small amount of brightener can control the disposition of a large amount of metal must require that its action be localized principally at a surface. While it is possible that a brightener is carried into the cathode film in the form of a complex, or that it may exist at or near the electrode surface as a complex, this appears to us to be incidental to the real mechanism.

One could postulate several variations of adsorption mechanisms. One we shall call "structure-sen-

[1] General Motors Fellow at Wayne University, 1954-5.

[2] General Motors Fellow at Wayne University, 1954.

sitive," i.e., the adsorption of the brightener is selective, so that only molecules of a certain size, shape, and chemical structure can be adsorbed on the metal surface. This corresponds to something like chemisorption and may require a suitable spacing between metal atoms on the surface of the electrodeposit to hold the organic molecules. To test this, single crystals of copper were used in this investigation to carry out the adsorption studies. Plating tests were also made with the single crystals, and x-ray studies were made of the deposits on the various faces of the crystal obtained in the absence as well as in the presence of the brightening agent.

Another type of adsorption that could be postulated might be called "current density sensitive," or better "shape sensitive," i.e., the adsorption of the brightener molecules on the cathode surface occurs under electrolysis conditions regardless of the nature of the crystalline structure of the cathode but dependent on the surface contour of the electrode. Here primary consideration is given to the leveling action in certain bright baths, in which the expected low current density areas grow faster than the high current density areas, suggesting the possibility that the high current density areas are blocked preferentially by these compounds. It should be mentioned here that leveling is a microscale phenomenon and that the high and low current density areas being referred to here are micro protrusions and recesses. Relatively less attention was given to the leveling aspect of the subject in the present work. Some investigations of this aspect are in progress and will be reported later. The subject of leveling has recently been reviewed by Leffler and Leidheiser (19).

These types of adsorption may be viewed as physically independent but not necessarily always separate. There could be situations where one type of mechanism operates to the entire exclusion of the others and *vice versa,* but it would be more likely that any real situation would show some contribution from each. The degree to which each mechanism would be represented will probably vary from case to case. It should be mentioned that these postulated variations of an adsorption mechanism are not original with the present authors and that suggestions reminiscent of them can be found in the work of a number of other authors [e.g. (8, 19-24)].

The bath chosen for initial investigation was the acid copper bath using thiourea as a brightener, since this bath appeared to be simpler than others which might have been chosen. Typical compositions for bright acid copper baths are given by Blum (8a), Clifton and Phillips (9), and Beaver (10).

Electrodeposition Studies on Copper Single Crystal Spheres from the Acid Copper Bath

In the structure-sensitive hypothesis, it was suggested that adsorption processes might be operative in which a particular match would occur between the interatomic distances in the brightener molecule and those in the metal crystals of the surface of the electrodeposit. It appeared that such processes could be studied to good advantage by the use of large single crystals of metals.

The desirability of using metal single crystals in any studies in which the metal surface is concerned has been well demonstrated by Gwathmey, Leidheiser, and co-workers (11). Since an ordinary metal specimen is composed of many small crystallites which may have random orientations, the value of a measured surface property of such a specimen is a composite and variable average value of contributions due to exposed crystallite surfaces of many orientations. Such a surface is not readily reproducible and is not suitable for incisive studies of adsorption and other surface phenomena on metals. For such investigations metal single crystals can provide a more readily reproducible surface of better known character and can allow one to choose surfaces parallel to particular crystal planes for study. Single crystal spheres are useful in metal surface studies because a sphere permits all possible crystal faces to be exposed for study in any given experiment and under competitive conditions.

In the present research, two types of studies employing copper single crystals were made. The first type was the electrodeposition of copper on single crystal spheres from plain acid copper plating baths and from acid copper baths containing thiourea as a brightener. The second type was the study of the adsorption of the brightener, thiourea, on copper crystal spheres by means of radiotracer techniques. Plating studies are presented in this section and the radiotracer adsorption studies are presented later. The object of both types of experiments was to determine the relation between crystal structure of the copper metal and brightener action.

Experimental

Copper single crystal rods were grown by the Bridgman method in a resistance furnace which is a modification of one described by Gwathmey and Benton (11a) and also by a method using an induction heated stationary graphite crucible, developed here (12). The copper used was Baker's C.P. shot and also "high-purity" rods.[3] The single crystal rods obtained were machined into spheres by means of a lathe attachment and method developed here (13). Following the machining operation the spheres were first polished mechanically with abrasive papers and then electropolished until etching showed that all worked material had been removed. In general, the procedure followed was that outlined by Gwathmey and Benton (11a). The crystal spheres were further annealed at 1000°C in a nitrogen atmosphere for approximately 12 hr using a Lindberg CF-1 tube furnace. The area of the spheres was determined from micrometer measurements for current density calculations.

Plating experiments were conducted in 1-liter beakers which were immersed in a 25°C thermostat. The experimental electrolyte used was a standard acid copper bath: 205g/l $CuSO_4 \cdot 5H_2O$ and 50 g/l conc. H_2SO_4 (sp gr 1.84).[4] Trace organic impurities which had been found to cause poor results were removed by stirring some activated charcoal[5] into the

[3] Obtained from the American Smelting and Refining Co.

[4] Both chemicals were Baker and Adamson Reagent Grade.

[5] Darco Red Label grade.

solution at 60°C, allowing the solution to stand a short time, and filtering to remove the carbon. The anodes were thin, high-purity copper rods.[3] The single crystal sphere as cathode was immersed in the center of the cell.

Two series of plating experiments were performed; one series in a plain acid copper bath and the other in a bright acid copper bath, run at a fixed current density of 5 amp/dm^2 at 25°C for plating times of 1, 5, 10, and 20 min, corresponding to approximate deposit thicknesses of 1, 5, 10, 20 μ. The bright plating bath was the same as the plain bath, but contained 0.01 g/l of thiourea (Matheson, further purified by recrystallization from alcohol) in addition. At the beginning of a plating experiment the sphere was again electropolished for 5 min to remove oxide films; then the sphere was rinsed with water and immediately placed in the plating bath. Plating was begun at the current calculated to give the desired current density. The plating bath was agitated by bubbling filtered air through it. Immediately after plating, the spheres were rinsed with water, dried carefully with tissue paper, and then lacquered by dipping in a 4% solution of Saran F-120 in methyl ethyl ketone. The lacquer coating was advisable to preserve the deposit from oxidation to allow subsequent examination by x-ray diffraction. The appearance of the deposit was observed and in some cases photographed.

X-ray diffraction photographs were taken of the deposits on various crystal faces using the back reflection technique. Some early experiments were done with a General Electric XRD-3 x-ray diffraction unit but most of the work reported here was done with a North American Phillips model 5001 unit, using a copper target tube and one of the pin-hole ports. The camera was a Sachs type back reflection camera consisting of a cassette and pin-hole system.

The crystal sphere was mounted in a two-circle goniometer which enabled positioning the desired crystal face normal to the beam and 3 cm from the film. The white radiation necessary for the examination of single crystal structures was obtained by running the copper tube at 48 kv, 16 ma. In the case of polycrystalline deposits, usually two x-ray diffraction patterns were taken, one with white radiation and one with monochromatic radiation which accentuate the single crystal and the polycrystalline structures, respectively. The monochromatic radiation was the copper K-α line, which was obtained by running the tube at 30 kv, and 24 ma and using a 0.00075-in. nickel filter at the window of the x-ray tube. The film used was Eastman Kodak "No Screen" medical x-ray film and the exposure time was 1-1½ hr.

Results

It should be mentioned that the single crystal spheres before plating were bright and uniform in appearance following the polishing and electropolishing procedures. Plating these spheres with copper from the plain acid bath resulted in the development of characteristic patterns of striking symmetry [as first observed by Gwathmey and co-workers (11c)]. The deposit in the (100) region consisted of a matte area in the form of a square, while the deposit in the (111) region consisted of a bright triangle. There were six such square areas parallel to the faces of a cube and eight such triangles perpendicular to the body diagonals of a cube. Further we have found that this same pattern was obtained over a substantial range of temperatures and current densities (14). As a matter of fact, the patterns are so characteristic of copper electroplates on good single crystals from a pure bath that they may be used as a test of good procedures. The adequacy of the preparation, handling, cleaning, and plating conditions could be judged by the distinctness of the electroplated patterns obtained. For example, electropolishing insufficient to remove worked surface would result in an irregularly patterned deposit. The annealing treatment of the single crystals and the activated carbon treatment of the plating baths were instituted because such plating tests indicated their advisability. Many plating tests were made and the ones quoted are representative.

The structure of the electrodeposits on the single crystal bases plated in the plain acid copper bath is shown by the x-ray diffraction patterns in Fig. 1. In the bright (111) region, the patterns characteristic of a single crystal structure were obtained for plating times up to 10 min. Even a 20-min plate showed strong preferred orientation. In the matte (100) region, the structure is shown to be polycrystalline at a much earlier stage in the course of plating.

In contrast to the patterned deposits from the plain bath, the bright deposit obtained from a bath containing thiourea was bright and uniform over the entire sphere with no indication of the structure of the underlying single crystal base. Also, x-ray

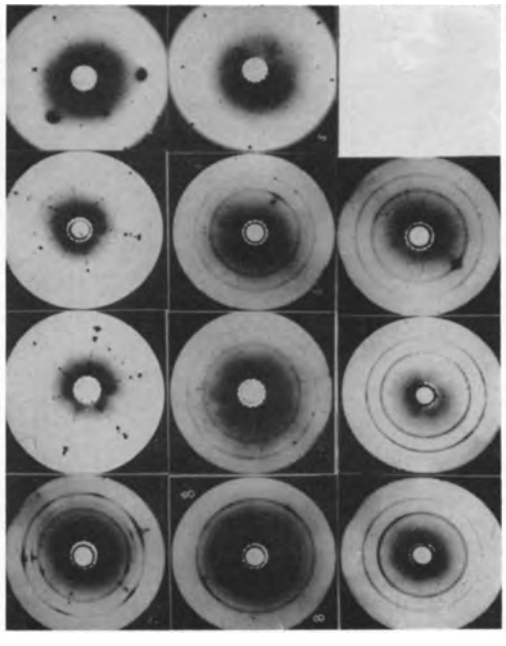

Fig. 1. X-ray diffraction patterns for copper electrodeposits of various thicknesses on copper single crystal spheres plated in an acid copper bath. First column is for white radiation on (111) face; second, white radiation on (100) face; and third, monochromatic radiation on (100) face. Plating times at 25°C at 5 amp/dm^2 from top to bottom: 1, 5, 10, and 20 min.

diffraction studies showed the deposit to have the same structure over the entire sphere. In this case the bright deposit was found to have a polycrystalline structure even in very thin deposits, in contrast to the single crystal bright deposit obtained on the (111) region from a plain acid bath.

Discussion of Plating Results

These results show that under normal plating conditions electrodeposition from the acid copper bath has the greatest tendency to continue the structure of the base crystal on the (111) faces. On the (100) faces, the process is sufficiently less favorable that a polycrystalline deposit is obtained. In a related study by Leidheiser and Gwathmey (11e), it was found in the electrodeposition of nickel from a Watts bath on copper single crystals that the favored direction for continuation of the single crystal structure was on the (100) face. The preferential direction of growth of metal crystals in electrodeposition is probably a composite effect of the influence of a number of variables, including the base crystal, bath composition, and plating conditions. It is well known that this same tendency for the electrodeposit from some baths to continue the structure of the base metal exists even in the case of polycrystalline metal bases when properly prepared [cf. (8a) p. 89].

Under the usual plating conditions on a polycrystalline base metal of doubtful cleanliness, the orienting influence of the base becomes less important, and the observed orientation in electrodeposits is more likely to be determined by bath composition and plating conditions. Electrodeposits from comparatively simple salt solutions frequently have a preferred crystal orientation and commonly exhibit a fiber structure perpendicular to the base metal and extending in the direction of the current flow (15). Fischer (8c) has evolved an extended classification system of crystal structures in electrodeposits and has also dealt extensively with the effect of inhibitors on electrodeposition, Microscopic examination of coarser deposits such as from the acid copper bath reveals a predominance of long columnar grains, One might expect that the long direction of such crystals would be the same as the preferred direction for the continuation of single crystal structure and thus establish a correlation to the preferred orientation in the polycrystalline deposits. Some support for this point of view can be found in the results of Leidheiser and co-workers who found that the Watts nickel bath gives a preferred (100) orientation in polycrystalline deposits (16) and that it continues the single crystal structure on (100) faces of a single crystal (11e), although this conclusion is clouded by the fact that the single crystal base was of copper.

The more striking results of the experiments of this section are the profound effects of the thiourea on the electrodeposition of copper. The most important effect is the ability of the thiourea to interfere with the normal tendency of the acid copper bath to continue the propagation of a metal single crystal on the (111) faces. Similarly the interference operates on the growing crystals on the (100) faces of the single crystal sphere limiting their growth also, as evidenced by the fact that the matte coarsely crystalline deposits normally obtained in these regions from the plain bath becomes refined into a finely crystalline bright deposit from a bath containing thiourea. Thus the copper electrodeposits from a bright bath on single crystals show a uniform polycrystalline structure with no trace of influence from the base single crystal.

It would be expected that copper electrodeposits made on a polycrystalline base would also show the inhibition effect of brighteners. Microscopic examination was made of copper electrodeposits from a standard acid copper bath and from bright acid copper using thiourea as a brightener. The nonbright deposit exhibited the typical coarse, grainy structure with some tendency toward a columnar structure. In the bright deposit there was no evidence of graininess and columnar growth. While no grain structure can be resolved, bright deposits are crystalline as shown by our x-ray results and as shown for nickel by Denise and Leidheiser (16), and others. It is interesting to note that the bright copper deposit obtained from an acid bath containing thiourea exhibits the laminar structure which is frequently, if not invariably, found in bright electrodeposits.

It is not possible from these plating results to decide whether thiourea exercises its inhibiting action on only certain crystal faces. While grain refinement could occur in the case of the electrodeposition of a metal of such highly symmetrical crystal structure as copper if adsorption were to occur on only certain crystal faces, one cannot exclude the possibility that inhibition could occur on several types of faces and perhaps even on all faces indiscriminately. One possible method of deciding between these various possibilities is a direct meaurement of adsorption using tracer methods.

Radiotracer Studies of the Adsorption of Thiourea on Copper Single Crystals

In the preceding section it was shown that the presence of thiourea in the acid copper bath profoundly influenced the crystalline structure of the copper electrodeposit and that this influence, or at least the effect of this influence, appeared to be greater on (111) faces than on the (100) faces. It was suggested that the adsorption of thiourea on copper might be selective on the various crystal faces. In order to make a direct experimental test of this possibility, radiotracer studies were undertaken.

Metal single crystals in the form of spheres are well suited to studies of this type because the surface of a single crystal sphere presents all possible crystal planes and all possible interatomic distances to the reaction medium being studied. If the reaction of the medium with the metal is a function of crystal face and spacing, a definite macroscopic pattern will develop on the surface of the crystal sphere. Gwathmey, *et al.* (11) have shown numerous examples of this pattern development such as those resulting from the etching action of a solution of cupric chloride in hydrochloric acid on copper single crystal spheres, the deposition of carbon on nickel crystal spheres during the thermal decomposition of car-

bon monoxide, oxidation films, wetting by lubricants, electrodeposition, etc.

Accordingly, if thiourea is adsorbed selectively on particular crystal faces of copper because of a preference for a particular interatomic spacing, then it is reasonable to expect that the adsorbed material would be arranged in such a regular macroscopic pattern on the crystal sphere. If thiourea-S^{35} is employed in the adsorption study, by means of the appropriate radioactivity detection technique, it should be possible to determine whether or not a radioactivity pattern corresponding to an adsorption pattern occurs. Since the films of interest would be expected to be monomolecular, sensitive detection methods are required.

Experimental

Electrolytically polished single crystal spheres such as described in the preceding section were used to carry out the adsorption studies. Immediately after they were taken out of the polishing bath and washed in running water, the spheres were dipped in solutions containing carrier-free thiourea-S^{35} which had been synthesized according to the procedure of Bills and Ronzio (17). Two types of solutions were used; one being an aqueous solution containing 0.01 g/l thiourea-S^{35} and the other being a typical acid copper plating bath of the composition used in the preceding section to which 0.01 g/l thiourea-S^{35} had been added. The time of immersion in the solution was usually 30 min to insure the attainment of equilibrium. Exposures were also made of short flash electrodeposits as well as simple immersion without current.

Gas phase adsorption experiments were conducted in a glass tube similar to the outside jacket of a vacuum sublimator. The crystal was suspended from a glass hook at the bottom of the solid ground glass stopper used to close the tube. A small amount of radioactive thiourea was dropped into the tube which was then evacuated at room temperature. After evacuation, the temperature of the whole tube was raised by means of an infra-red lamp operated through a transformer. At 50°C, the adsorption was allowed to continue for about 12 hr, while for a temperature of 100°C it was heated for 30 min and 1 hr in two experiments.

Two methods were employed for the detection of radiation on the spheres which had been exposed to the thiourea-S^{35} in various media. One was an autoradiographic method and the other a method employing a two-circle goniometer and a Geiger counter with scaler. These two methods with their results will be treated separately below.

The autoradiographic detection method of the present work is based on the fact that a photographic emulsion is darkened by the β-particles from the S^{35} in the thiourea-S^{35}. The location of the blackening on development serves as a means of determining the location of the adsorbed thiourea. The procedure used, patterned after that described by Gomberg (18), is as follows. After the adsorption procedure, each sphere was coated with a thin, chemically inert coating of Saran by dipping the sphere into a 4% solution of Saran F-120[6] in methyl ethyl ketone. This coating prevents the subsequent photographic emulsion from reacting with the copper base, and at the same time it is transparent to all radiations coming out. The 4% solution leaves about 2.5 μ of protective plastic coating. After this coating was dried, the photographic emulsion was applied over it.

The emulsion used was du Pont's DH dehydrated emulsion which was prepared, applied, and developed according to the instructions of the manufacturer. All handling, dissolving, coating, and processing steps were carried out in a photographic darkroom equipped with a du Pont S-55x safelight. The emulsion was applied by simply dipping the crystal sphere into the emulsion and rotating the sphere to spread the emulsion evenly over the entire surface. After the application of the emulsion the spheres were placed in a rack in a well closed dark box for exposure. Exposure times were determined from the β-count per unit area per unit time of the individual sphere and the emulsion requirement of 5×10^6 emissions per cm^2 for suitable contrast. The emulsion dried during the first part of the exposure period, and after exposure the film was developed and fixed without peeling it from the sphere.

The experimental results using the autoradiographic technique all turned out to be quite similar. All of the emulsion coatings developed to be uniformly dark over the surface of each sphere. In no case could any gradation be detected in the darkening, and certainly no regular pattern of localization of any kind was evident. The only conclusion that could be drawn was that the adsorption was uniform and that no preferential adsorption of thiourea on the copper single crystal spheres occurred. Several factors existed which gave a basis for doubting the validity of the autoradiographic results, among them possible migration of sensitive material in the emulsion during drying and subsequent exposure time, saturation and reversal effects in the exposure, and imperfect insulation of the emulsion from the base copper by the Saran coating allowing catalytic non-exposure reduction of the silver. These were proved to be unnecessary worries by further tests on blanks and graded exposures, but it was felt desirable in any case to proceed with an independent method of radiation detection employing the two-circle goniometer and Geiger counter.

The apparatus shown in Fig. 2 was used to count directly the emissions from various locations on the sphere. It consisted of a two-circle goniometer for fixing the position of the sphere and a TGC-2 mica window (2.3 g/cm^2) Geiger counter tube (Tracerlab, Inc.) which was used with a Raychronix Model A-4 64-scaler.

The crystal sphere was held in the goniometer clamp in such a position that the axes of both vertical and horizontal rotation passed through the center of the sphere. The crystal holder could be rotated 360° about its own axis and simultaneously through 180° about the vertical axis. Thus, any point on a hemisphere of the crystal sphere could be located

[6] Dow Chemical Co. vinyldene chloride.

Fig. 2. Apparatus used for scanning the radioactivity on copper single crystal spheres having adsorbed thiourea-S^{35}.

with respect to a chosen reference point which, in this case, was the pole of the horizontal axis opposite the handle of the crystal.

The Geiger tube was held horizontally on a ring stand. In front of and parallel to the Geiger tube window, 8 mm away, was a ⅛-in. lead sheet, in the middle of which was a small hole of known size, so positioned that the hole was in the horizontal plane through the horizontal axis and along a radius through the vertical axis. When the Geiger tube and lead shield were fixed in position, the crystal sphere could be so rotated that all positions on the hemisphere could be located and its emissions counted. The surface of the sphere was about 1 mm from the load shield so that emissions from the surface would give a fairly true representation of the number of counts from an area of the order of that of the hole in the lead sheet.

A typical set of counting results is shown in the polar projection of Fig. 3. The size of the black dots is proportional to the number of counts. The number of counts is referred to a pin-hole area of 0.0914 cm². The background count is subtracted. The locations of the various crystallographic regions on the crystal are also projected on the chart.

The direct counting method in the main substantiated the results of the autoradiographic method. While a finer discrimination in the detection of the degree of adsorption was possible, in that the counts varied from 50 to 90 over different points, again no definite pattern of adsorption could be detected. As shown in Fig. 3, no correlation can be found between strong and weak adsorption and crystallographic position.

The important result of the experiments of this section is that thiourea is strongly adsorbed on the various faces of a copper single crystal sphere. Contrary to the predictions of the structure sensitive hypothesis, no localization of adsorption was found which might have resulted if a specific fit were required between the brightener structure and interatomic distances on the metal crystal surface.

The differences in the amount of adsorption on the various parts of the single crystal spheres were not large in that they covered only a twofold range of variation. Such small variations might have been due to differences in metal surface areas or to migration of the brightener during the drainage and drying periods. In any case the differences were too small to differentiate between the various crystal faces in terms of adsorption power so that the present results lead to the conclusion that the adsorption of the thiourea is uniform on the various crystal faces.

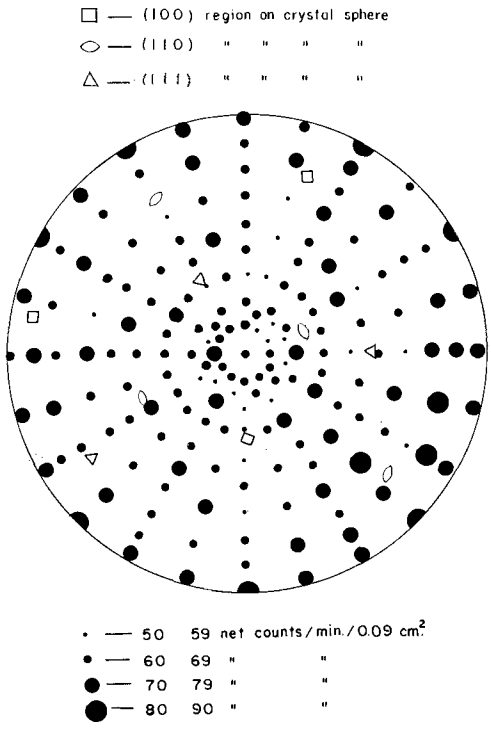

Fig. 3. Polar projection plot of radioactivity from adsorbed thiourea-S^{35} on a copper single crystal sphere. Smallest circles represent 50-59 counts/min/area of 0.09 cm²; next, 60-69; then, 70-79; and largest, 80-90. Crystallographic regions are represented: (100) by squares, (110) by ellipses, and (111) by triangles.

However, while these results are valid for the conditions used, there remains a lingering suspicion that other methods of carrying out the experiments might reveal a preferential adsorption. Perhaps in the present experiments, the adsorption is sufficient to saturate all faces, indicating that the media studied here have plenty of thiourea available for even the presumably weakest adsorbing faces of the copper to take on substantially the saturation amount of thiourea. This possibility suggests further experiments such as a mapping of the entire concentration vs. adsorption curve for thiourea on copper, or adsorption studies similar to the ones done here but in a medium with insufficient material to give saturation, or selective desorption studies by washing with various solvents, by heating, etc., performed on a saturated single crystal.

Summary and Conclusions

It has been shown by direct tracer measurements that thiourea is strongly adsorbed on the surface of a copper metal crystal or electrode. This adsorption takes place even in the absence of applied potential or electrolysis conditions, but this does not exclude the possibility of modification and perhaps enhancement of the adsorption under conditions of electrolysis.

The effect of the thiourea on the metal electrode during electrodeposition of copper from the acid bath is to modify the crystal structure of the deposit severely. The action of the brightener is one of inhibition of the crystal growth process so that there is a relative enhancement of the nucleation process. This results in a finer grained deposit. The adsorption process appears to have no selectivity for the various crystal faces of the metal so that the inhibition must be a general one governed by conditions other than crystal character of the metal.

Manuscript received Sept. 3, 1957. Most of the work was performed under Contract DA-20-018-ORD-12079 between Wayne University and the Office of Ordnance Research, U. S. Army, during the period of February 1952 to January 1954. Some later confirmatory work is included. Further details are given in Ref. (25).

Any discussion of this paper will appear in a Discussion Section to be published in the December 1959 JOURNAL.

REFERENCES

1. M. Rubinstein, *Metal Finishing*, **48**, No. 5, 54; **78**, No. 8, 51, 58 (1950).
2. J. A. Henricks, *Trans. Electrochem. Soc.*, **82**, 113 (1942).
3. E. F. Kern, *ibid.*, **15**, 441 (1909).
4. W. D. Bancroft, *ibid.*, **23**, 266 (1913).
5. Wm. Blum, Trans. *ibid.*, **36**, 213 (1919).
6. F. C. Mathers, *ibid.*, **29**, 417 (1916); **38**, 133 (1920).
7. L. B. Hunt, *J. Phys. Chem.*, **36**, 1006 (1932); *Trans. Am. Electrochem. Soc.*, **65**, 413 (1934).
8. (a) Wm. Blum and G. B. Hogaboom, "Principles of Electroplating and Electroforming," McGraw-Hill Book Co., New York 1949).
   (b) Wm. Blum and W. R. Meyer, "Modern Electroplating," A. G. Gray, Editor, p. 43, John Wiley & Sons, New York (1953).
   (c) H. Fischer, "Elektrolytische Abscheidung und Elektrokristallisation von Metallen," Springer-Verlag, Berlin, (1954).
9. F. L. Clifton and W. M. Phillips, *Proc. Am. Electroplaters Soc.*, **1942**, 92.
10. J. F. Beaver, Jr. U. S. Pat. 2,391,289, Dec. 18, 1945.
11. (a) A. T. Gwathmey and A. F. Benton, *J. Phys. Chem.*, **44**, 35 (1940).
    (b) A. T. Gwathmey and A. F. Benton, *ibid.*, **46**, 969 (1942).
    (c) H. Leidheiser, Jr., and A. T. Gwathmey, *Trans Electrochem. Soc.*, **91**, 95 (1947).
    (d) A. T. Gwathmey, Proc. Pittsburgh International Conference on Surface Reactions, Corrosion Publishing Co., Pittsburgh (1948).
    (e) H. Leidheiser, Jr., and A. T. Gwathmey, *This Journal*, **98**, 225 (1951).
12. B. Ke, Ph.D. Thesis, Wayne University (1952).
13. B. Ke, J. J. Hoekstra, and D. Trivich, *Rev. Sci. Instr.*, **25**, 1033 (1954).
14. B. C. Sison, Jr., M. S. Thesis, Wayne University (1955).
15. C. S. Barrett, "Structure of Metals," p. 439, McGraw-Hill Book Co., New York (1943).
16. F. Denise and H. Leidheiser, Jr., *This Journal*, **100**, 490 (1953).
17. C. W. Bills and A. R. Ronzio, AECU-619 (1949).
18. H. J. Gomberg, *Nucleonics*, **9**, 28 (1951).
19. E. B. Leffler and H. Leidheiser, Jr., *Plating*, **44**, 388 (1957).
20. J. D. Thomas, *Proc. Am. Electroplaters' Soc.*, **43**, 60 (1956).
21. O. Kardos, *ibid.*, **43**, 181 (1956).
22. D. G. Foulke and O. Kardos, *ibid.*, **43**, 172 (1956).
23. A. W. Hothersall and G. E. Gardam, *J. Electrodepositors' Tech. Soc.*, **15**, 127 (1939).
24. H. Leidheiser, Jr., *Z. Elektrochem.*, **59**, 756 (1955).
25. D. Trivich, Technical Report No. 1 (Aug. 1953) and Final Report (Oct. 1954) on Contract DA-20-018-ORD-12079, Office of Ordnance Research.

The Source of the Nitrogen Impurity in Electrodeposited Chromium

N. Ryan and E. J. Lumley

Aeronautical Research Laboratories, Department of Supply, Commonwealth of Australia, Melbourne, Victoria, Australia

ABSTRACT

High-purity chromium deposited from chromic acid electrolytes containing either sulfate or fluoride catalysts invariably contains small amounts of nitrogen as an undesirable impurity. The amount of this nitrogen impurity is shown to be increased by increased nitrate ion concentration in the electrolyte but not affected by dissolved atmospheric nitrogen or ammonium compounds. It is demonstrated that the nitrate impurity is decomposed at the cathode by reduction with hydrogen to form ammonia as the major product. Some of the atomic nitrogen which is possibly formed at a stage during this reduction is probably adsorbed continuously into the electrodeposited metal.

The nitrogen content of high-purity chromium produced by the electrolysis of chromic acid electrolytes varies according to the bath conditions (1-3). In the chromium prepared at these laboratories it is usually present in the range 0.001-0.004%. Investigations into the ductile-brittle behavior of chromium and its alloys have revealed that small increases in the nitrogen impurity can influence the mechanical properties detrimentally to a remarkable degree (4,3). Hence there is a strong need to eliminate, as far as possible, this nitrogen impurity and for this reason to trace its source.

Possible sources of primary nitrogen contamination immediately apparent are: (*a*) atmospheric nitrogen dissolved in the electrolyte, and (*b*) nitrogen-containing compounds dissolved in the electrolyte.

If atmospheric nitrogen were the main source of

the nitrogen contamination it would be expected that chromium deposited by electrolysis in an atmosphere free from nitrogen would have a low nitrogen content, while that produced under high nitrogen concentrations would have a higher value.

Regarding the second source, the most commonly occurring nitrogen impurity in chromic acid is the nitrate ion, probably arising from the nitric acid wash during manufacture. The nitrate impurity is present in amounts usually of the order 0.004%. This appears a relatively small value, but represents 0.003 g of available nirogen in 1 liter of a 300 g/l chromic acid solution. If 5 g[1] of chromium containing 0.003 wt % nitrogen is deposited from this solution, only 0.00015 g of the 0.003 g of available nitrogen is used. Therefore, it is possible that the nitrogen contamination of electrodeposited chromium could originate from the nitrate impurity in the electrolyte. If this is the case, an increase in the electrolyte nitrate impurity should result in increased nitrogen contamination of the electrodeposited metal.

The experiments here described were carried out to test the above hypotheses.

In general, electrolysis in the sulfate- and fluoride-containing electrolytes was carried out for 5-hr and 1-hr periods, respectively. Because of the higher current efficiencies when using the fluoride electrolytes (2),[2] hourly runs produced sufficient chromium for analysis.

Apparatus

The apparatus, basically a completely enclosed glass vessel, was designed primarily to investigate the effect of dissolved atmospheric nitrogen and was subsequently employed for all experiments. It consisted of two sections: (i) the cell section for 300 ml of electrolyte, cathode, and anode, and (ii) the upper section connected to the cell via a ground glass socket joint. This section contained inlet and outlet arms for (*a*) introduction of the electrolyte, (*b*) anode and cathode connections, and (*c*) a reflux condenser (through which passed gases generated during electrolysis) to reduce evaporation losses.

The chromium was deposited on ½ in. diameter, 2 in. long copper tubes which were subsequently removed by digestion in nitric acid. Pure lead anodes were used in sulfate electrolytes, and 0.5% tin-lead anodes in the fluoride electrolytes. The nitric acid extraction does not influence the nitrogen content of the chromium as it has been found that chromium chipped from the electrode has the same value as that extracted in the nitric acid. Power to the cell was supplied by a 60-amp capacity selenium rectifier.

It has been found (2) that only slight contamination of the electrolyte with SiF_6^{--} occurs when using the fluoride electrolytes in glass vessels.

Chemical analysis.—The chromic acid used contained between 0.002-0.004% nitrate impurity together with the following nominal impurities 0.02% SO_4, 0.01% Fe, and 0.1% Na.

The oxygen content of the chromium deposits was determined using the "Adcock" method and the nitrogen content was determined by a semi-micro Kjeldahl procedure using a colorimetric finish for the low nitrogen values and an acid-alkali titration finish for the high nitrogen values.

Results

Effect of electrolyte atmosphere.—The conditions of electrolysis and the composition of the electrolytes used in these tests are recorded in Table I.

In the first test series, no precautions were taken to exclude air contamination, and these runs are recorded in Table I as having been deposited in an air atmosphere. This however is not entirely correct as the oxygen and hydrogen produced during electrolysis rapidly replaces the air above the electrolyte in the enclosed vessel. Results had been obtained previously for chromium deposited from open vats under otherwise similar conditions, and these showed the same gas content as the chromium produced "in air" in the experimental cell. In the second series of tests a rapid stream of nitrogen was bubbled through the electrolyte during plating.

To investigate deposition under nitrogen-free conditions the apparatus was completely evacuated and flushed with pure hydrogen. The electrolyte was introduced from an attached reservoir, into the evacuated vessel while the current was applied through the electrodes. The oxygen and hydrogen generated were free to escape through the reflux condenser via a water seal, once the internal pressure exceeded that of the external atmosphere.

Analyses of the chromium deposit obtained under the above conditions are recorded in Table I. It is apparent that dissolved nitrogen has an insignificant

[1] The approximate weight of chromium deposited from 1 l of electrolyte during a normal production run in the chromic acid-sulfate electrolyte.

[2] For brevity, the terms "fluoride electrolyte" and "sulfate electrolyte" are used to denote chromic acid solution containing fluoride and sulfate additions, respectively. "Fluoride chromium" and "sulfate chromium" similarly refer to the products of these electrolytes.

Table I. Effect of electrolyte atmosphere

Electrolyte composition CrO_3, g/l	SO_4, g/l	F, g/l	Atmosphere	Current density, amp/ft²	Temp, °C	Current efficiency, %	Oxygen, wt %	Nitrogen, wt %
300	4	—	Air	954	80	11	0.02	0.002
300	4	—	Nitrogen bubbled through	910	82	12	0.02	0.002
300	4	—	Evacuated prior to run	1000	80	10.5	0.015	0.002
295	—	5.4	Air	960	100	39	0.03	0.003
295	—	5.4	Nitrogen bubbled through	980	100	37.5	0.02	0.003

Probable analytical error of nitrogen figures is ±0.0004%. Results given to first significant figure.

Table II. Effect of nitrate impurity in electrolyte

Electrolyte composition								
CrO_3, g/l	SO_4, g/l	F, g/l	NO_3, g/l	Current density, amp/ft²	Temp, °C	Current efficiency, %	Oxygen, wt %	Nitrogen, wt %
300	4	—	0.012	1000	82	12	0.02	0.002
300	4	—	0.1	980	80	12.5	0.02	0.4*
300	4	—	0.5	980	84	10.6	0.02	0.8*
300	—	5.2	0.006	880	100	35	0.02	0.001
290	—	5.4	0.2	910	100	39	0.03	0.28
290	—	5.4	0.15	900	100	37	0.03	0.19

* These results are given only to the first decimal place, as the method used for the analysis was not fully suited to such high nitrogen contents.

influence on the amount of nitrogen codeposited with the chromium.

Effect of nitrate impurity in the electrolyte.—Chromium was deposited under the conditions detailed in Table II from 300 g/l as-received chromic acid solutions containing either 4 g/l sulfate or 5.4 g/l fluoride as the active catalyst, the nitrate impurity being 0.012 g/l and 0.006 g/l, respectively. The chromium obtained from these tests was found to contain 0.002 wt % and 0.001 wt % nitrogen, respectively. These deposits were used as comparison standards.

In order to vary the nitrate impurity, nitric acid was added to electrolytes of similar composition to the above, and electrolysis was carried out under the conditions described in Table II. These deposits were analyzed for both oxygen and nitrogen, and results showed that the nitrogen content of the chromium was increased markedly.

Effect of electrolyte temperature.—Investigations into the production of high purity chromium from various electrolytes have given some indication that reduction in nitrogen content of the chromium occurs with increasing electrolyte temperature (2). In these experiments chromic acid with only trace amounts of nitrate impurity was used. Chromium deposited from an electrolyte containing sulfate at 100°C was found to contain less than the chemically detectable amount of nitrogen, but, as shown in Table III, the current efficiency was only 2.5%.

For a further series of tests, an electrolyte containing 300 g/l CrO_3, 5.3 g/l F, and 1 g/l NO_3 was prepared. This was electrolyzed at 1000 amp/ft² for 1-hr periods at 70°, 85°, 92°, and 100°C. Analyses of the chromium deposits obtained from these experiments are recorded in Table III. They indicate that the nitrogen content was unaffected by electrolyte temperature.

Effect of ammonium compounds in the electrolyte.—It is well known that ammonia is produced during the electrolytic reduction of nitrates. In order to find the effect of this ammonia on the nitrogen content of the electrodeposited chromium, the following tests were performed. Normal chromic acid electrolytes in which the active catalyst radicals were introduced as the corresponding ammonium salts were electrolyzed under the conditions listed in Table IV. The results indicate that the ammonium ion does not influence the nitrogen content of the chromium to any significant extent since the nitrogen values obtained lie within the usual scatter found in successive chromium deposits during normal production.

Electrolytic reduction of nitrate impurity.—In the preceding sections of this paper it has been demonstrated that there is a definite relationship between nitrate additions to the chromic acid electrolyte and the increased nitrogen content of the electrodeposited metal, while molecular nitrogen and ammonium compounds are without effect. The manner in which this contamination takes place is a matter for speculation and has been discussed briefly in a previous report (5). Nitrogen is obviously introduced into the chromium at some stage during the electrolytic reduction of the nitrate electrolyte impurity.

In order to study this relationship more closely a solution containing 300 g/l CrO_3, 5.84 g/l F, and 2.7 g/l NO_3 was prepared. This solution was electrolyzed at 100°C and 1015 amp/ft² current density. Chromium deposits were plated from this electrolyte for consecutive time intervals of 1 hr, ½ hr, ¾ hr, and ½ hr. Fresh cathodes were used for each successive electrodeposition. These deposits were analyzed to determine the nitrogen content, and samples of the electrolyte, after each succeeding deposit,

Table III. Effect of electrolyte temperature

Electrolyte composition								
CrO_3, g/l	SO_4, g/l	F, g/l	NO_3, g/l	Current density, amp/ft²	Temp, °C	Current efficiency, %	Oxygen, wt %	Nitrogen, wt %
300	4	—	0.012	960	82	10	0.02	0.002
300	4	—	0.012	984	100	2.5	Not detected	
310	—	5.25	0.006	1100	100	40	0.03	0.003
300	—	5.3	1	1000	70	26	0.18	0.098
300	—	5.3	1	1000	84	32	0.12	0.10
300	—	5.3	1	1000	92	36	0.09	0.096
300	—	5.3	1	1000	100	39	0.03	0.098

Table IV. Influence of ammonium compounds

Electrolyte composition									
CrO_3, g/l	SO_4, g/l	SO_4 as $(NH_4)_2SO_4$, g/l	F, g/l	F as NH_4F, g/l	Current density, amp/ft²	Temp, °C	Current efficiency, %	Oxygen, wt %	Nitrogen, wt %
300	4	—	—	—	960	82	10	0.02	0.002
300	—	4.2	—	—	980	84	11	0.01	0.003
300	—	—	5.2	—	880	100	35	0.02	0.001
300	—	—	—	5	910	100	39.5	0.03	0.002

Table V. Electrolyte composition, 300 g/l CrO_3, 5.84 g/l F. Electrolyte temp. 100°C; current density 1015 amp/ft²; current efficiency 32%

	NO_3,* g/l	NH_3, g/l	NO_3 equivalent of NH_3 produced, g/l	Nitrogen in electrodeposit, wt %
Fresh solution	2.7	0.0023	—	—
1-hr deposition	0.052	0.55	2.0	0.24
1½-hr deposition	0.024	0.64	2.3	0.084
2¼-hr deposition	0.012	0.70	2.4	0.040
2¾-hr deposition	0.008	0.74	2.7	0.025

* The nitrate ion was added as potassium nitrate.

were analyzed to determine ammonia and residual nitrate, i.e., during the 1-hr deposition the nitrate was reduced from 2.7 to 0.052 g/l and so on. Results are recorded in Table V and Fig. 1.

It can be seen that the nitrate content decreased rapidly during the first hour of electrolysis and then more steadily with time, the ammonia content showing a corresponding increase. The nitrogen content of the chromium samples decreased with the nitrate content of the electrolyte.

Discussion

The main conclusions to be drawn from this investigation are that dissolved nitrogen and ammonium salts in the electrolyte do not influence the nitrogen contamination of electrodeposited chromium, but that nitrate impurities markedly raise the nitrogen pickup. Increasing the electrolyte temperature does not in any way effect a reduction in the nitrogen impurity, at least in electrolytes containing fluoride and considerable amounts of nitrate. However, the limited evidence from the sulfate electrolyte could suggest a decrease in nitrogen content with increasing electrolyte temperature. It has been shown in Table V and Fig. 1 that the progressive electrolytic reduction of nitrate results mainly in production of an equivalent amount of ammonium ion, and that the reaction follows a typical reaction rate time curve, asymptotic to the time axis. This implies long times for substantially complete conversion of nitrate to ammonia.

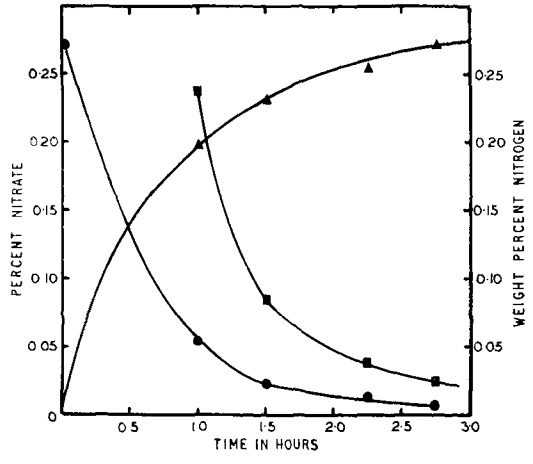

Fig. 1. ●—Reduction in nitrate during electrolysis; ▲—increase in ammonia in electrolyte expressed as equivalent nitrate; ■—nitrogen content in successive chromium deposits.

The manner by which nitrogen enters the chromium is not definitely known. The nitrogen impurity in the chromium is obviously introduced at some stage during electrolytic reduction of the electrolyte nitrate impurity. It is possible that atomic nitrogen is formed at some stage during this reduction, and that a portion of this nitrogen enters the electrodeposited chromium (5). The electrochemical reduction of nitrate is known to be complex (6), and many nitrogen-containing compounds can be formed depending on the various cathode conditions.

It is obvious that if some means could be found of eliminating the nitrate impurity in chromic acid electrolytes the nitrogen content of electrodeposited chromium could be reduced to a much lower level than is normally obtained at present. It is suggested that the impurity could at least be substantially reduced by electrolyzing solutions of chromic acid for long periods under conditions favoring the generation of large volumes of hydrogen at the cathode without any recoverable chromium deposition. Low concentrations of nitrate may however be very difficult to remove. Low-nitrate chromic acid could also be produced by replacing the nitric acid wash during manufacture by hydrofluoric acid, or by repeated recrystallization.

Acknowledgments

The authors wish to express their thanks to Mr. A. R. Edwards for his helpful criticism in the preparation of this paper which is published by permission of the Chief Scientist, Department of Supply, Australia.

Manuscript received Aug. 25, 1958.

Any discussion of this paper will appear in a Discussion Section to be published in the December 1959 JOURNAL.

REFERENCES

1. H. T. Greenaway, *J. Inst. Metals*, **83**, 121 (1954-5).
2. N. E. Ryan, Report A.R.L./Met 26, Oct. 1957.
3. "Ductile Chromium," American Society for Metals, Cleveland, Ohio (1957).
4. H. L. Wain, E. Henderson, S. T. M. Johnstone, and N. Louat, *J. Inst. Metals*, **86**, 281 (1957-58).
5. E. J. Lumley, A.R.L./Met. Note 7 Feb. 1957.
6. M. J. N. Pourbaix, "Thermodynamics of Dilute Aqueous Solutions," Edward Arnold and Co., London.

Electroplating on Thorium

John G. Beach and Glenn R. Schaer

Battelle Memorial Institute, Columbus, Ohio

ABSTRACT

A method was developed for treating thorium whereby adherent electroplates of most metals can be applied. The method involves anodic pickling in hydrochloric acid and chemical pickling in sulfuric acid prior to plating. Factors affecting the adherence and protective qualities of the coatings are discussed.

The use of thorium in nuclear reactors prompted an interest in coatings that could provide desirable surface properties. Thorium, like magnesium, uranium, and zinc, oxidizes easily and corrodes readily in boiling water.

Coatings on thorium that could prevent oxidation and corrosion, or that would aid joining to other metals, for example by soldering, were deemed desirable. A process for plating on thorium has been worked out (1), and electroplated and conversion coatings that protect thorium in boiling water were studied briefly (2).

A review of the known properties of thorium and its compounds plus its electrochemical activity suggested that the problems involved should be similar to those encountered in plating on aluminum, magnesium, and uranium. The principal problem was the preparation and activation of the thorium surface. When the thorium was properly prepared, most metals could be electrodeposited satisfactorily by established procedures. Known methods for preparing aluminum, magnesium, and uranium for electroplating did not provide satisfactory adherence of electrodeposits on thorium. However, the method developed in these studies for plating on thorium is also applicable to aluminum.

Method of Electroplating on Thorium

Pretreatment of thorium.—Anodic and chemical pickling were used to activate thorium for electroplating. The procedure is as follows: descale mechanically (abrasive blast, machine, etc.); degrease (trichlorethylene); cathodic alkaline clean, conventional multipurpose alkaline cleaner, 180°F, 25 amp/ft^2, 2 min; cold-water rinse; anodic pickle, hydrochloric acid, 1.2*N* HCl, HCl (1.19 g/cc)—10% by volume, 80 = 10°F, 50 amp/ft^2, 5 min; chemical pickle (without rinsing), sulfuric acid, 3.6*N* H_2SO_4, H_2SO_4 (1.84 g/cc)—10% by volume, 80 = 10°F, immersion 5 min; cold-water rinse; electroplate (immerse with the current on).

Electroplating on pretreated thorium.—The above pretreatment permitted adherent electroplating of aluminum, chromium, copper, gold, indium, iron, lead, nickel, silver, tin, and zinc directly on thorium. The listing below describes the types of solutions that were used.

Metal Plated	Type of Solution
Aluminum	Aluminum chloride—lithium chloride—ether (3)
Chromium	Chromium acid—sulfuric acid (4)
Copper	Copper sulfate—sulfuric acid (4)
Iron	Iron sulfate—chloride—formate (5)
Nickel	High *p*H bath (6) (used for direct plating on aluminum)
Gold	Cyanide (4)
Indium	Cyanide (4)
Silver	Cyanide (4)
Zinc	Acid sulfate (4)
Lead	Complex alkaline tartrate (7)
Tin	Alkaline stannate (4)

Although most types of plating baths are suitable for plating on thorium not all plating baths were satisfactory. For example, chloride-containing baths that had a *p*H lower than 4 were unsatisfactory. Also, the high-temperature chromic acid solution for depositing low-contraction chromium was unsuitable for direct deposition on thorium.

Stripping of electrodeposits.—Most electrodeposits could be stripped, with little or no attack on the thorium, by immersion of the plated thorium in 50% nitric acid or by anodic treatment in a caustic solution.

Electropolishing (Anodizing) of Thorium

Electropolishing was tried as a means of improving the thorium surface for plating. Thorium treated anodically under the following conditions was smoothened uniformly but retained a film that prevented uniform activation for plating. However, the film presumed to be thorium phosphate also provided protection against oxidation and corrosion.

Sulfuric acid	9*N* H_2SO_4
Phosphoric acid	11*N* H_3PO_4
130°F	150 amp/ft^2

1500 amp-min/ft^2/mil of surface metal removed

Heating the electropolished thorium in vacuum at 600°F for about 30 min increased the protective quality of the anodized film.

Evaluation of Coatings on Thorium

Qualitative adherence, solderability, thermal-cycling, and corrosion tests were made to provide data for engineering design of protective coatings on thorium.

For the research reported here, "adherence" is narrowly defined as the attachment at the basis metal-electroplate interface. The term "bond strength" (8) is used to indicate the force required to separate the electroplated metal from the basis metal regardless of the location of fracture. Bond strength is of ultimate importance and whether or not a given bond strength is satisfactory is, of course, governed by the end use.

Adherence.—The adherence of the above electroplates to pretreated thorium was excellent. In no case could the electroplated metal be peeled from the thorium at the electroplate-thorium interface by the tests described below.

Adherence tests for copper, nickel, and silver-plated thorium were made by: filing and/or grinding across the interface (in a direction to drag the plate away from the thorium); chiseling along the interface; and bending a flat 40-mil-thick specimen around a ¼-in. mandrel, reflattening, and bending back around the mandrel. A minimum thickness of 1 mil of electroplate was deposited for the above tests.

Solderability.—Soldering copper- or nickel-plated thorium pieces together with a lap joint and separating by flexing the joint fractured the sample in the soft solder. Thus the adherence of the plate exceeded the strength of the soft solder, about 6000 psi.

Cyclic heating and cooling.—Copper-, nickel-, and silver-plated thorium specimens were cyclicly heated (in argon) for 15 min at 100° intervals up to 700°C successively and quenched through air into cold water. Zinc-plated thorium was heated only to 400°C.

Bend tests were made to find the temperature at which diffusion alloying would degrade the bond strength. The bond of zinc-plated thorium was satisfactory after heating to 400°C (19°C below the melting point of zinc). The bond of copper-, nickel-, and silver-plated thorium was satisfactory up to 500° or 600°C. Since thorium metal or alloy remained firmly attached to the electroplates when the samples were bent after heating to 600° or 700°C, the bond failure was attributed to the interfacial alloy layers that were weaker than the electrodeposited metal or the thorium.

Thorium is known to alloy with most metals. Interdiffusion of the electroclad metal and the thorium, along with the melting point of the clad or eutectic alloys formed, appears to establish limiting conditions for the use of plated thorium at elevated temperatures.

Corrosion.—Thorium corrodes readily in hot water, oxidizing and/or hydrating to form a layer of loose powdery corrosion products that can be brushed off easily. Corrosion weight changes of +72 mdd to −14 mdd have been reported. No doubt the variance in data is due to retention or removal of loose corrosion products for obtaining the weight-change data.

Table I. Corrosion rate in distilled water at 203°F (95°C)
Duration of test: 6 weeks

Surface coating on thorium	Corrosion rate in mdd
None*	−7.4
Anodized*	−1.7
Anodized and heated*	−0.7
Copper electroclad†	+0.9

* Loose corrosion products removed before weighing.
† Copper was plated in several steps with intermediate burnishing (to close porosity) and periodic heat treating in vacuum at 400°C (to decompose hydrides and remove entrained hydrogen). Copper tarnished during corrosion.

Anodizing (electropolishing) and heat treating or copper electrocladding appreciably reduced the corrosion of thorium. The corrosion data are presented in Table I. The corrosion of thorium was reduced about 90% by anodizing and heating to form a protective thorium phosphate film. The slight weight gain for copper-electroclad thorium was attributed to tarnishing of the copper and possibly to entrapment of water in the copper cladding.

Conclusions

Thorium surfaces pretreated by anodic pickling in hydrochloric acid and chemical pickling in sulfuric acid can be electroplated with coatings of most metals. The adherence of the plated coatings is excellent and passes all the conventional adherence tests. Electroplated metals on thorium can protect thorium in boiling water and can aid soldering and/or joining to other metals. The use of electroclad metals on thorium for high-temperaure applications will depend on the proper selection of metals that form suitable alloys with thorium by interdiffusion.

Copper, iron, nickel, and silver directly on thorium offer promise for protecting thorium. However, further data on the diffusion of the electroplated metals and thorium along with the properties of the alloys formed are needed.

Electropolishing (anodizing) of thorium and heat treating imparts a protective coating that resists hot-water corrosion.

Manuscript received Sept. 25, 1958. This paper was prepared for delivery before the Ottawa Meeting, Sept. 28-Oct. 2, 1958. Work was performed under AEC Contract W-7405-Eng-92.

Any discussion of this paper will appear in a Discussion Section to be published in the December 1959 JOURNAL.

REFERENCES

1. J. G. Beach, G. R. Schaer, and C. L. Faust "Electroplating of Metals on Thorium," Report BMI T-7 (Feb. 1 1949).
2. J. G. Beach, W. C. Schickner, L. E. Vaaler, and C. L. Faust, "Electroplating on Thorium," Report BMI 802 (Jan. 9, 1953).
3. D. E. Couch and A. Brenner, *This Journal*, **99**, 234 (1952).
4. "Metal Finishing Guidebook," 27th Ed., published by Metals and Plastics Publications, Inc. (1959).
5. J. G. Beach, *Plating*, **43**, 616 (1956).
6. J. G. Beach and C. L. Faust, *This Journal*, **100**, 276 (1953).
7. A. W. Liger (Battelle Memorial Institute), U. S. Pat. 2,474.092, June 21, 1949.
8. C. L. Faust, *Monthly Rev. Am. Electroplaters' Soc.*, 223 March 1946, (see errata, May 1946, issue); *Plating*, 1221, December 1948.

The Effect of Magnesium Salts on Nickel Plating Baths

Ahmad Geneidy[1] **and W. A. Koehler**

Department of Chemical Engineering, West Virginia University, Morgantown, West Virginia

and Willi Machu

Department of Chemical Engineering, Cairo University, Cairo, Egypt

ABSTRACT

The effect of magnesium salts was measured in Watts-type and Wesley all-chloride type nickel plating baths. The deposition potential of nickel was lowered (metal became more noble), polarization was reduced, and results on decomposition potentials were inconclusive. Nickel deposited from all baths under test had a face-centered cubic lattice, and magnesium was present only in spectroscopic traces. It was found that addition of magnesium salts increased cathode current efficiency, improved throwing power, and reduced porosity of the nickel, as revealed by the ferroxyl test. At low concentrations of magnesium salts the mechanical properties of nickel deposits were not changed materially, but at high concentrations deposits were harder, more brittle, and had a higher tensile strength. The effect on residual stress in nickel deposits was not measured.

It has been shown that properties of electrodeposited nickel are dependent on a number of factors. One of these is the nature and concentration of the so-called "conducting salts"; the most common of these salts are those of sodium, ammonium, and magnesium.

Addition of magnesium salts to nickel baths has aroused a controversial issue in the plating industry, since many beneficial and some harmful effects have been observed and reported. Opinions expressed by scientific workers as well as by practical platers were, in many cases, conflicting. Data to support both sides of the argument have appeared in the literature. However, no systematic study confirmed with quantitative data has yet been conducted. Needless to say, the presence of such data will, undoubtedly, help the plater to control behavior of the bath as well as properties of the deposit. To this end the present investigation was directed. Carefully controlled tests were made to determine the net effect of magnesium salts on the operation of nickel baths and on the properties of nickel deposit, and whether or not these effects are due to codeposition of magnesium.

The chief advantage of adding conducting salts to nickel plating baths is to increase the conductivity of the baths. Apart from the economic advantage of increasing the conductivity, better conductivity usually leads to better deposits, prevents formation of trees and rough deposits (1), and improves the throwing power (2-4). The effect of magnesium salts on the conductivity of nickel plating baths was reported by Hammond (5) and by Nicol (6). Reactions, functions, and mechanisms of magnesium and other conducting salts were discussed at length (8-11).

As a conducting salt, magnesium sulfate was added to nickel baths since the very beginning of the nickel plating industry. Adams, who commercialized nickel plating in Boston in 1869 (12), introduced in the following year his well-known patent (13) of a nickel bath containing magnesium salts and in 1899 Kugel established another patent (14).

The first study on the effect of magnesium was conducted in 1902 by Coehn (15) followed by Siemens in 1904 (16). Since then, magnesium sulfate additions have been recommended for nickel baths used in various fields of applications; for commercial rapid (17-20) and barrel plating (21) and also for plating on iron and stainless steel (22), as well as on nonferrous metals and alloys, particularly zinc and zinc base die castings (23-32) aluminum and is alloys (33-41), and lead (42).

Magnesium sulfate additions have also been reported in nickel baths recommended for producing a rust-resisting nickel plate (43, 44), a detachable and elastic nickel film on a nickel base (45), and for plating phonograph records (46). Magnesium sulfate has also been added to improve throwing power (47), to produce mat silver-white deposits (48) that are free from pitting (49).

Nickel deposited from baths containing magnesium sulfate is soft, easy to buff (50), and can be bent, twisted, or rolled without stripping or peeling off the plate (51). However, Makar'eva (52) found that the addition increases hardness and produces a deposit that is more lustrous and more uniform in texture, and that changed very little with change in current density or temperature. The effect of magnesium on stress is not yet agreed upon (53, 54).

Robinson (55) considered magnesium sulfate as the most suitable conducting salt in nickel baths. Baths containing this salt kept up their metallic concentration, produced even anode corrosion, and showed no pitting. Nickel deposited from such baths were whiter, resisted action of acids and did not rust as quickly, retained their luster longer, and were

[1] Present address: Cairo University, Cairo, Egypt.

more readily cleaned and polished than deposits obtained in the absence of magnesium sulfate. Thirteen years later, Barrows (56) confirmed Robinson's findings relative to that "indifferently recognized aid to better plating."

In spite of reported beneficial effects of adding magnesium sulfate to nickel plating baths, some objections against its use had been raised (57-59).

Magnesium chloride additions are also common, although to a lesser extent. The function is either to increase conductivity (60) or to increase anode corrosion in sulfate baths (61-65) or as a halogen carrier in a bright bath (66).

In addition to being introduced intentionally as magnesium slats, magnesium can be also introduced in small amounts from nickel salts (67), nickel anodes (68-71), water (72-74), and from chemicals added to introduce ions or radicals other than magnesium (75-77).

Experimental

Purification and preparation of the test baths.— This was effected in a Pyrex glass cylindrical container. Heating was accomplished by immersing the container in a constant temperature water bath while agitating by bubbling purified compressed air through a perforated Pyrex glass coil which rested on the bottom of the container. Air was purified by passing it through columns packed with glass wool and charcoal to capture any entrained oil.

Concentrated solutions of plater's grade nickel sulfate and of nickel chloride were prepared and to each solution 2 ml of 30% hydrogen peroxide was added per liter of solution. The temperature was raised to 70°-75°C (158°-167°F), and the *p*H was then raised to 5.8 by slow addition of a freshly prepared slurry of nickel carbonate. Solutions were stirred vigorously at that temperature and *p*H for 2 hr, after which the precipitates were allowed to settle. After filtration, the solutions were electrolyzed at low current density. Due to the limited available quantity of electrolytic nickel, platinum anodes were used; cathodes consisted of thin nickel sheets to avoid the possibility of introduction of impurities at very low current density areas, as might be the case if steel or nickel plated steel were used. Electrolysis was continued at 0.2 amp/dm^2 (2 a.s.f.) until 120 amp-hr/gal were passed, and then at 0.5 amp/dm^2 (4.6 a.s.f.) until at least 30 amp-hr/gal had passed. Finally, the solutions were electrolyzed at 5 amp/dm^2 (46 a.s.f.) for 6 hr. The hot and well-agitated solutions were then treated with 7.5 g/l (1 oz/gal) of activated carbon. After allowing the solutions to stand for a few hours, they were filtered.

The effectiveness of this purification cycle was tested by spectroscopic analysis of a nickel sheet deposited nonadherently on a stainless steel cathode at the specified operating conditions. After thus purifying the separate concentrated solutions of nickel sulfate and nickel chloride, test baths shown in Table I were prepared by mixing and/or dilution of purified concentrated solutions.

Baths chosen for this investigation are the Watts sulfate and Wesley all-chloride types of nickel baths since they are the two most commonly used baths apart from the bright ones. Of the different types of Watts baths, the one selected was chosen because it is very widely used in actual practice; it has nearly the same nickel content as the Wesley bath, and it has been subjected to some investigations.

Since anions have a decided influence on the character of the deposit, it was decided to add magnesium sulfate to Watts bath and magnesium chloride to Wesley bath. Furthermore, in order to permit a fair comparison of the effects of magnesium ions in the two baths, magnesium salts were added in equinormal amounts rather than in equal percentages. Concentrations of the magnesium salts were selected to cover the range of usual additions. In order to facilitate reference to the different test baths, a bath symbol was assigned to each type; the letter S (sulfate) is a symbol of the Watts sulfate bath while C (chloride) indicates the Wesley chloride bath. The bath symbol is followed by a numeral which indicates the normality of the magnesium salt added.

Operating conditions. — Operating conditions chosen for this investigation were as follows: current density, 4.3 amp/dm^2 (40 a.s.f.); temperature, 60°C (140°F); *p*H (electrometric) 2.

Measurement of cathode and decomposition potentials.—Measurements of the deposition potentials were effected in a small rectangular glass trough measuring 15 x 6 x 6 cm. The two anodes and the cathode measuring 6 x 1.0 x 0.1 cm each were cut from electrolytic nickel sheet and placed 5 cm apart. Although dimensions of the electrodes did not allow ideal conditions of uniform density, results thus obtained were in agreement with those obtained by Wesley and Roehl (78) with measurements made in a box similar to Haring cell which provides better means for measuring electrode potentials. The close

Table I. Composition of the test nickel baths

Bath No.	Bath symbol	Bath type	Constituents in g/l					
			$NiSO_4 \cdot 7H_2O$	$NiCl_2 \cdot 6H_2O$	H_3BO_3	$MgSO_4 \cdot 7H_2O$	$MgCl_2 \cdot 6H_2O$	NaCl
1	S-0.0	Watts	325	45	30	—	—	—
2	S-0.1	Watts	325	45	30	12.3 (0.1*N*)	—	—
3	S-1.0	Watts	325	45	30	123 (1.0*N*)	—	—
4	S-2.0	Watts	325	45	30	246 (2.0*N*)	—	—
5	C-0.0	Wesley	—	300	30	—	—	—
6	C-0.1	Wesley	—	300	30	—	10.2 (0.1*N*)	—
7	C-1.0	Wesley	—	300	30	—	102 (1.0*N*)	—
8	C-2.0	Wesley	—	300	30	—	204 (2.0*N*)	—
9	C-2.0Na	Wesley	—	300	30	—	—	117 (2.0*N*)

agreement between the two data indicate the reliability of the measurements carried out in the previously mentioned manner. Moreover, we were chiefly concerned with reproducible relative values rather than exact absolute ones. The potential of the cathode was measured against a saturated calomel electrode. Connection with the cathode was effected through a glass U-tube, one stem of which was drawn to a capillary, which was bent through 90° and pressed against the cathode.

The electrolysis cell, containing 400-500 ml of solution under test, was immersed in a constant-temperature water bath at 50° ± 0.1°C, while the calomel electrode was at room temperature. The solution was not stirred. No difference was observed when the solutions were tested as prepared or after being boiled to expel dissolved oxygen. After recording the static potential, a very small current was applied for a sufficient length of time to attain equilibrium. Equilibrium was assumed to exist if two consecutive readings of the potential made 4 or 5 min apart differed only by a fraction of a millivolt. Usually equilibrium was attained within 20 min.

Decomposition potentials were made in the same cell and in the same manner except that the electrodes were all made of platinum sheet. No effort was made to measure decomposition potentials with great precision.

Cathode current efficiency and throwing power.—Cathode current efficiencies were determined by the increase in weight of a nickel cathode. Measurements were made in a rectangular glass trough 12 x 7 x 6.5 cm (4¾ x 2¾ x 2½ in.). The two anodes and the cathode were all cut from thin nickel sheet 1 mm (0.04 in.) thick. With the cathode placed midway between the two anodes and the area of all electrodes exactly filling the cross section of the trough, a uniform current density was secured on the cathode.

Measurements were made in triplicate with the efficiency cell at 60°C while a copper coulometer connected in series was at room temperature. For each bath, the current efficiency was determined at three current densities: 2.1, 4.3, and 6.4 amp/dm^2 (20, 40, and 60 a.s.f.). Results were reproducible to ±1%.

Throwing power determinations were made in the same troughs. The anodes were perforated with 3/32 in. holes. Determinations were made at two primary current distribution ratios: 5:1 and 2:1. In calculating the current density, only the areas of the two sides of the cathode facing the anode were considered. A run lasted usually 45 min.

Mechanical properties.—For testing mechanical properties, a sheet of nickel 0.25 mm (0.01 in.) thick was prepared from each bath by plating nonadherently on a stainless steel sheet, type 302, about 0.079 mm (0.031 in.) thick. The cathode measured 20 x 18.7 cm (8 x 7.5 in.)

The plating jar consisted of a rectangular glass trough measuring 20.6 cm long x 36.5 cm high x 16.2 cm wide (8¼ in. x 3 in. x 6.5 in.). The anode consisted of electrolytic nickel which was analyzed by spectroscopic methods and was enclosed in a high-quality cotton bag. One anode and one cathode were used, both filling the cross section of the plating jar. The pH of the solution, which always tended to rise, was kept constant at the required value by allowing acid to drip from a buret. Agitation of the solution was effected by two electrically driven propeller-type glass rods. Pitting was prevented by adding 0.4-0.5 ml of 30% hydrogen peroxide to every liter of the bath. Decomposition of the hydrogen peroxide was ascertained by testing with a dilute solution of potassium permanganate.

The electroformed nickel sheet obtained from each bath was cut into 2.5 cm (1 in.) strips with the long dimension corresponding to the horizontal dimension of the original sheet. Strips were then machined to the form recommended by A.S.T.M. specifications E8-46 for thin sheet material, except that the length of the strip was 18.7 cm (7.5 in.) instead of 20.3 cm (8 in.). Specimens were tested in a Baldwin hydraulic testing machine. After the tensile strength test was completed, the zone where fracture occurred was noted and the dimensions of that zone, previously measured, were used in the calculation of the cross-sectional area. The per cent elongation was calculated by the increase of a 5 cm (2 in.) gauge length. Usually two sets of gauge marks were made in the reduced section of the specimen so that the fracture would very likely take place with one, if not both pairs. However, in some specimens the fracture occurred just near or even outside the gauge marks; in such cases no elongation measurements were obtained. At least five specimens of each type of deposit were tested. Reproducibility of the tensile strength measurements was within 10% while that of the elongation measurements was very much poorer, although all specimens were free of pits and microscopic defects.

Hardness measurements were made by an Eberbach microhardness tester using a load of 323.2 g. Indentations were made on the cross section of the deposit (cross-sectional hardness) as well as on the inner surface of the deposit which was adjacent to the basis metal (surface hardness). Usually, at least seven hardness measurements were taken for each type of deposit. Reproducibility of the results was within 10%.

Structure.—To obtain samples for metallographic examination, two small pieces were cut from the electroformed nickel sheet; one of these pieces was mounted in Bakelite in such a way that the cross section perpendicular to its plated surface was exposed. The other piece was mounted so that the surface originally adjacent to the stainless steel cathode was exposed. Electrolytic etching using different electrolytes under varying conditions did not give satisfactory results. Good results were obtained through using the "flat solution," consisting of a mixture of equal volumes of concentrated nitric and glacial acetic acids. The structure was photographed in a Bausch and Lomb metallograph.

X-ray patterns were obtained by the powder method in a North American Philips Diffraction unit using a cobalt tube and an iron filter.

Porosity.—Samples for porosity were obtained by coating a thin layer of nickel 0.025 ± 0.0025 mm (0.001 ± 0.0001 in.) thick on low carbon (0.15% C)

steel pieces measuring 18.7 x 20 cm (7.5 in. x 8 in.). Steel cathodes were prepared according to the A.S.T.M Designation B 183-49 (79).

The corrosive solution used was that recommended by Thon, *et al.* (80) which consists of 50 g/l of potassium ferricyanide and 0.2 g/l sodium chloride. The test was carried out in the manner mentioned in the British Standard 1224-1945. At least five determinations were made from each bath.

Determination of magnesium. — Spectrograms were obtained by shaping two pieces of the electroformed nickel sheets from each bath to form the two electrodes for the spectrograph. These were then excited by a d-c arc at 5 amp for 60 sec. The nickel standard was excited for 5 sec only. Analysis was then conducted in the usual manner using the internal standard method.

Results

Cathode potentials and cathode polarization curves are shown in Fig. 1, 2, and 3. Figures 4 and 5 show the effect of magnesium on the cell voltages and on the decomposition potentials of the different baths.

Results of cathode current efficiencies are shown in Fig. 6 and 7.

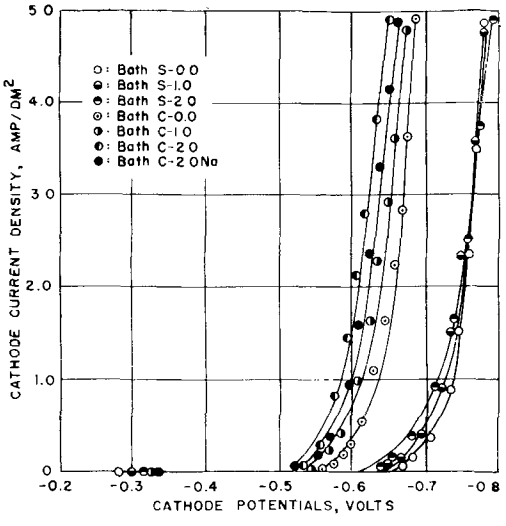

Fig. 1. Cathode potentials for nickel baths at 50°C against a saturated calomel electrode.

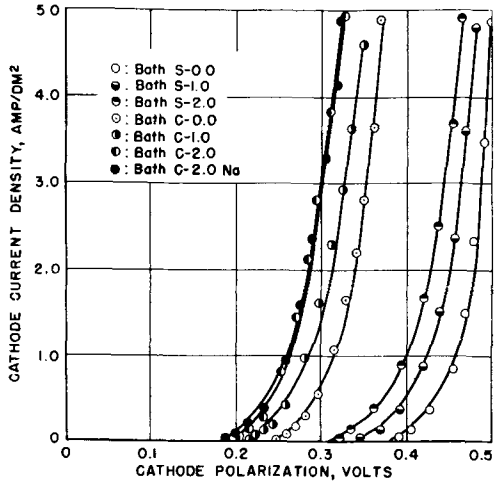

Fig. 2. Cathode polarization in nickel baths at 50°C

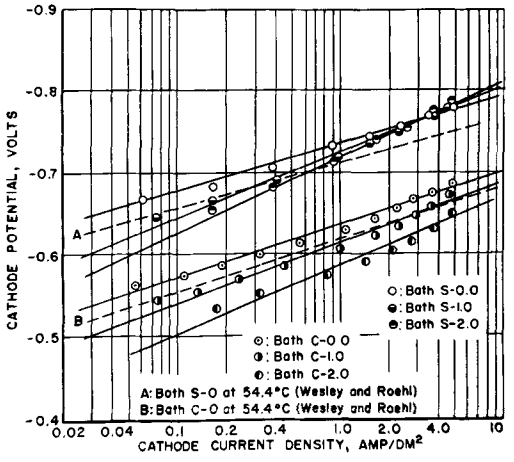

Fig. 3. Cathode potential vs. current density curves for nickel baths.

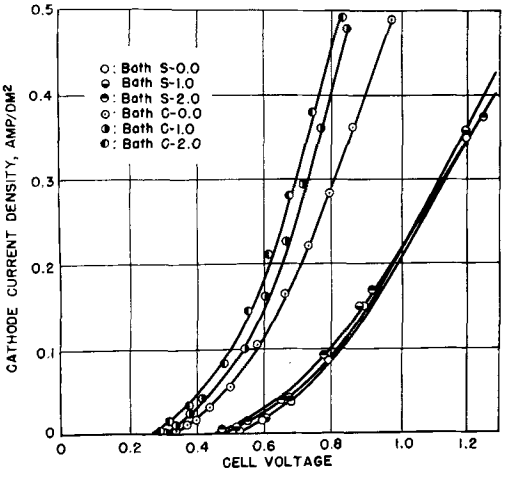

Fig. 4. Cell voltages in nickel baths

Throwing power data are plotted in Fig. 8. Data are submitted on the three scales: Haring and Blum scale (3), Heatley's modification (81), and the British Standard Institution (B.S.I.) scale. Each point on each curve is the average of three determinations.

Mechanical properties data are plotted in Fig. 9, 10, and 11. In Fig. 10, the elongation value corresponding to bath S-0.1 was not included since the fracture of the specimens occurred either outside the gauge marks or just adjacent to them.

Photomicrographs of the various deposits are shown in Fig. 12, 13, 14, and 15. X-ray patterns for the Wesley baths are shown in Fig. 16.

Corrosion resistance data are plotted in Fig. 17. Corrosion resistance is expressed as the reciprocal of the number of spots revealed by the ferroxyl test per square decimeter of the tested deposit.

Figure 18 shows spectrograms obtained from the standard nickel specimen and deposits from Wesley-type baths.

Table II summarizes some of the important data obtained in this investigation.

Discussion

Deposition potential, polarization, and decomposition potential.—Deposition potential and polarization data were investigated since they influence the

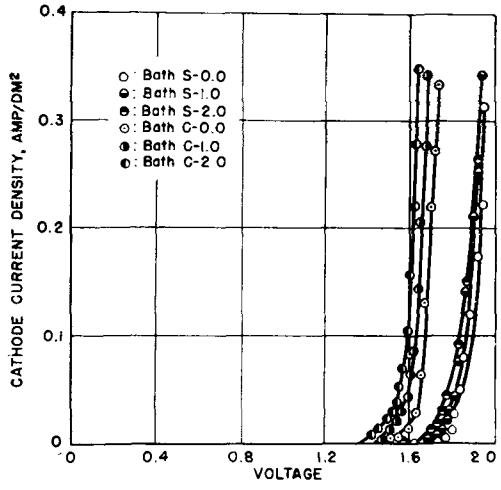

Fig. 5. Decomposition potentials for nickel baths at 50°C

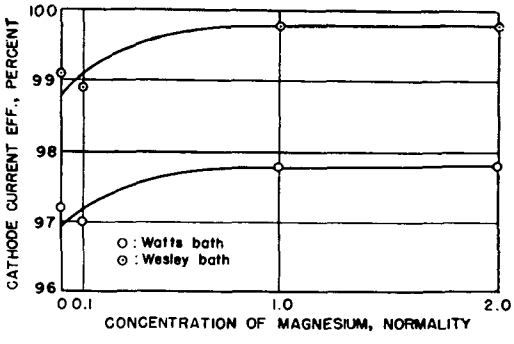

Fig. 6. Effect of magnesium content of nickel baths on the cathode current efficiency at 50°C and 40 a.s.f.

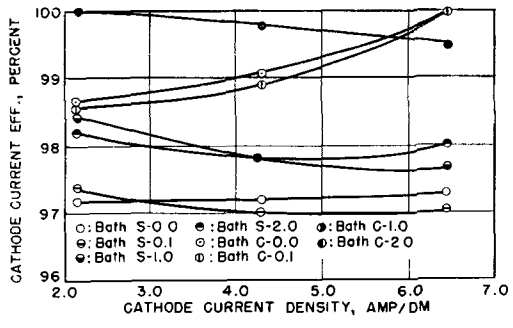

Fig. 7. Effect of the magnesium content of nickel baths on the rate of change of cathode efficiency with current density.

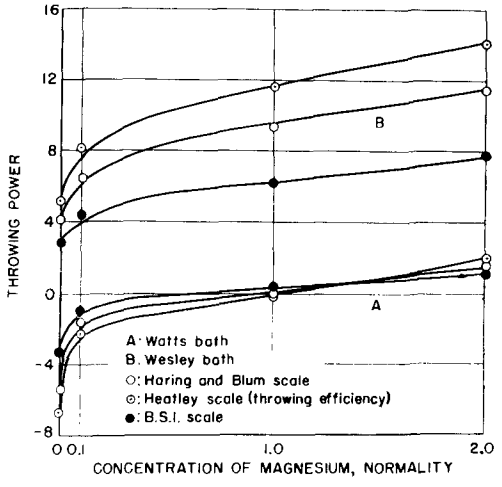

Fig. 8. Effect of the magnesium content of nickel baths on the throwing power. (Linear ratio, L = 5).

following four characteristics (82): (*a*) structure of the deposit; (*b*) cathode current efficiency; (*c*) throwing power; and (*d*) alloy deposition.

It has been shown by others that there exists a relation between cathodic polarization and the structure of the deposit (1, 83-85). In some cases, the relation was not verified (86-90). This led to the introduction of the "interference" concept (91). However it is believed by some investigators that there must be some connection between cathode potentials and formation of electrodeposited metal (92).

Concerning throwing power, high cathodic polarization improves that important property (93, 2, 94). In this respect, the significant criterion is the slope of the cathode potential vs. current density curve.

Cathodic polarization affects alloy deposition in the same manner as it affects hydrogen evolution.

In the present study it is evident from Fig. 1 and 2 that addition of magnesium slightly makes the potential of nickel more noble and lowers cathodic polarization. That this effect is not due to formation of insoluble magnesium hydroxide is shown by the fact that bath C-2.0Na showed the same trend as the other baths.

The previous result is not in agreement with that of Thompson (27) who reported that magnesium increased cathodic polarization and cathodic current

Table II. Effect of adding magnesium salts on the operation of Watts and Wesley baths and on the physical properties of the electrodeposited nickel

Bath	Cathode efficiency at 40 a.s.f., %	Throwing* power	Tensile strength, psi	Elongation,† %	Hardness‡ Vickers	Corrosion resistance	Magnesium content in deposit, %
S-0.0	97.2	—5.4	6700	17.6	143	12.0	—
S-0.1	97.0	—1.7	6400	—	142	20.8	0.011
S-1.0	97.8	—0.3	6300	19.3	144	37.0	0.014
S-2.0	97.8	1.6	7700	13.7	163	100.0	0.014
C-0.0	99.1	4.2	9200	16.1	204	12.3	—
C-0.1	98.9	6.5	9000	14.9	204	14.5	0.014
C-1.0	99.8	9.3	9400	16.7	202	58.8	0.018
C-2.0	99.8	11.5	9700	10.9	224	76.9	0.021

* As measured in a throwing power box with a linear ratio of 5:1 applying the Haring and Blum formula.
† In 2-in. gauge marks.
‡ Determined by an Eberbach microhardness tester applying a load of 323.2 grams.

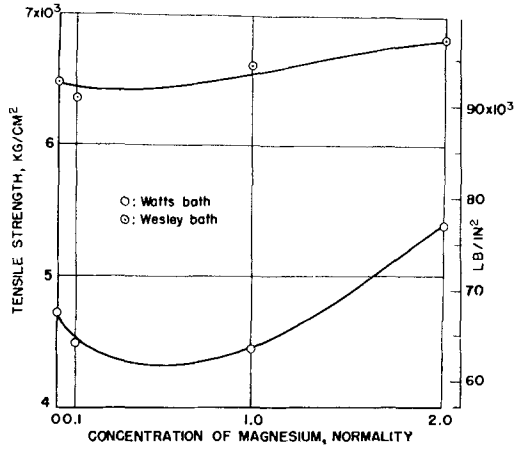

Fig. 9. Effect of the magnesium content of nickel baths on the tensile strength of the deposits.

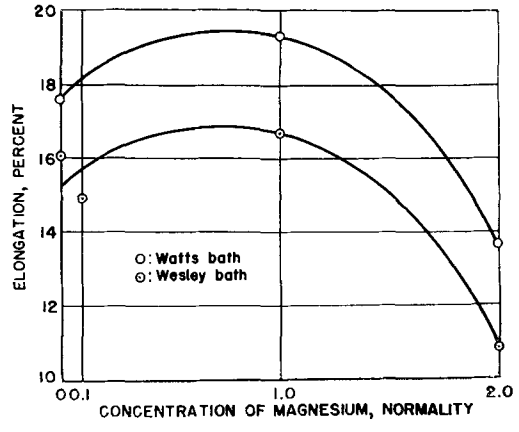

Fig. 10. Effect of the magnesium content of nickel baths on the elongation of the deposits.

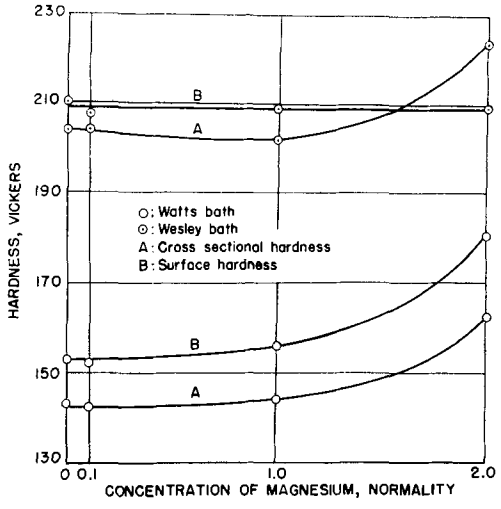

Fig. 11. Effect of the magnesium content of nickel baths on the hardness of the deposits.

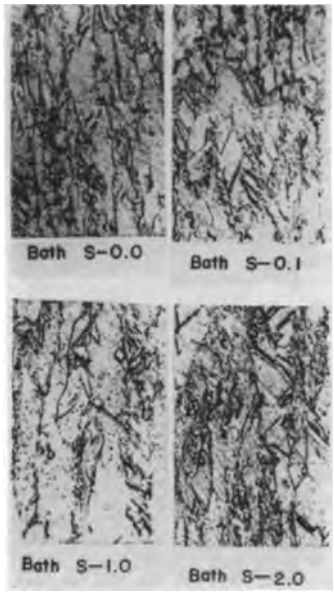

Fig. 12. Effect of the magnesium content of Watts-type bath on the structure of electrodeposited nickel. Section parallel to the direction of growth of deposit. Magnification 250X.

efficiency as well. Thompson attributed these two contradictory phenomena to the common ion effect and to increased density and viscosity of the solution due to addition of magnesium salt. If this is the case, addition of magnesium chloride to a nickel chloride bath should also increase cathodic polarization. However, this was not verified by Verdick, *et al.* (95) who found that, at high concentrations of magnesium chloride, nickel was deposited more easily. These workers tried to explain this and similar phenomena by a theory involving complex ion formation.

It seems that the problem is open to more fundamental study to establish the possibility of complex ion formation and to reveal the part played by the degree of dissociation and solvation of molecules and similar factors which govern the very nature of the delicate process of deposition.

Figure 3 shows that the addition of magnesium increases the slope of the cathode potential vs. current density curve. This should tend to improve the throwing power of the baths.

Curves of Fig. 5 indicate that addition of magnesium causes a slight decrease in the over-all potential. This decrease may be entirely due to decrease in resistance of the bath.

Cathode current efficiency.—Cathode current efficiency is significant as it determines the useful portion of electric power consumed, liberation of hydrogen, maintenance of a constant pH during plating, and throwing power of plating baths.

Figure 6 shows that the baths under test have high cathodic current efficiencies. There is, however, a slight increase in these efficiencies after addition of magnesium. This is in agreement with results obtained earlier (27).

Concerning the rate of change of cathodic current efficiency with current density which affects throwing power, Fig. 7 indicates that there is no consistent change in one direction or the other, and differences observed are within the reproducibility of results and experimental errors. It is concluded, therefore, that this factor will have very little, if any, effect at all on the throwing power of the nickel baths under test under the conditions of this investigation.

Throwing power.—Good throwing power is a desirable property in plating solutions since it is generally found that a bath with a good throwing power

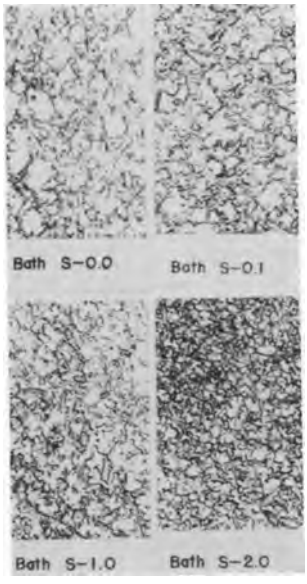

Fig. 13. Effect of the magnesium content of Watts-type bath on the structure of electrodeposited nickel. Section perpendicular to direction of growth of deposit. Magnification 250X.

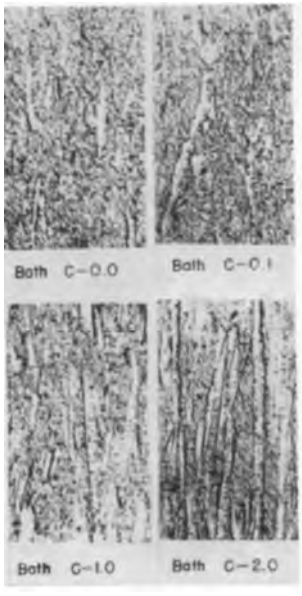

Fig. 14. Effect of magnesium content of Wesley-type bath on the structure of electrodeposited nickel. Section parallel to direction of growth of deposit. Magnification 250X.

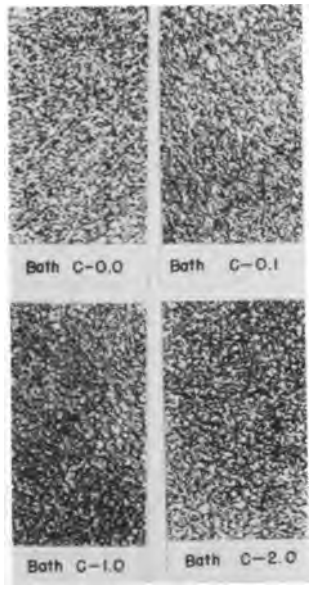

Fig. 15. Effect of magnesium content of Wesley bath on the structure of electrodeposited nickel. Section perpendicular to direction of growth of deposit. Magnification 250X.

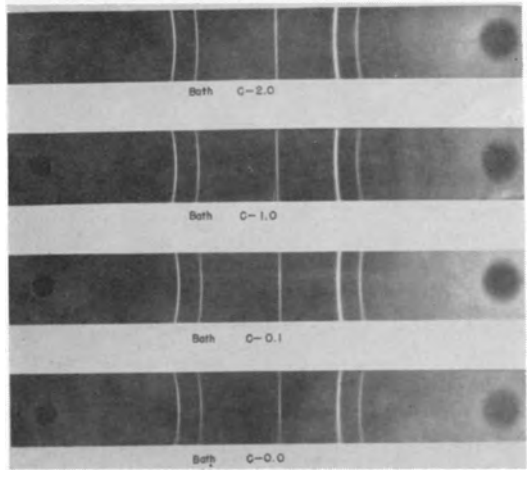

Fig. 16. Powder method diffraction patterns of nickel deposited from Wesley baths.

usually yields a good smooth deposit. It helps to give uniform thickness of plate with subsequent economic advantage. It is also important in plating more electronegative metals and alloys.

Figure 8 shows that there is a small but consistent increase in throwing power with increasing concentrations of magnesium. There was contradiction in the results of earlier investigations (27, 59). However, magnesium sulfate was usually added to improve the throwing power in nickel baths (47, 50).

The effect of magnesium can be predicted by analyzing its effect on the three factors which determine throwing power, namely, conductivity, rate of change of cathode potential and of cathode current efficiency with current density. By referring to Fig. 4 and to the work of Hammond (5) and Thompson (27) it will be clear that addition of magnesium sulfate increases the conductivity of nickel baths. Also, it was previously shown that addition of magnesium increases the slope of the cathode potential vs. current density curves. The third factor is not affected as has already been stated. It may be concluded therefore that addition of magnesium improves the throwing power partly due to an increase in conductivity of the bath and partly due to an increase in the rate of change of cathode potential with current density.

Mechanical properties.—Mechanical properties are of prime importance in determining the engineering qualities of electrodeposited metals. The tensile strength indicates the amount of distending force per unit area that the deposit can withstand before its fracture. Ductility is important if the plate is subjected to deformation or to machining operations. Elongation is associated with ductility and is usually taken as a measure of the latter. Hardness is also important in determining the ease of polishing and buffing. It is related to the resistance of abrasion.

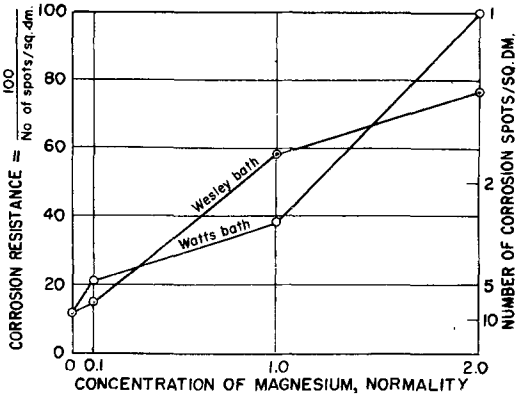

Fig. 17. Effect of magnesium content of nickel baths on the corrosion resistance of the deposits.

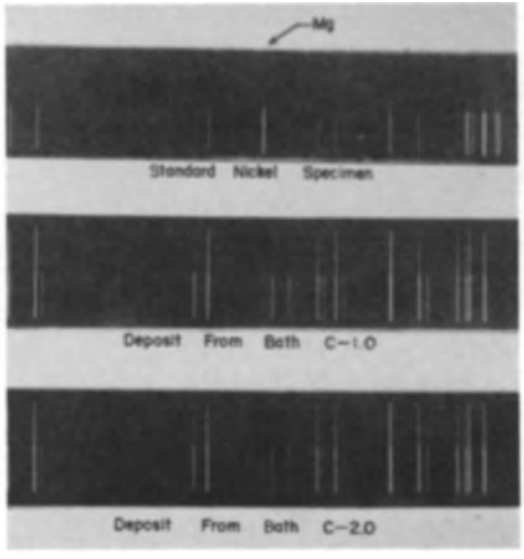

Fig. 18. Magnesium lines in the spectrum of nickel deposited from Wesley bath containing different concentrations of magnesium chloride.

Mechanical properties are affected by a large number of factors and many theories have been propounded to account for the net influence of these factors, the latest being that of Brenner and his associates (96).

Figures 9, 10, and 11 show that up to a concentration of one normal of magnesium salts, there is no appreciable change in the mechanical properties. When the concentration of the salts is twice normal, the resultant deposit has a higher tensile strength, is less ductile, and is harder. Opinions concerning the effect of magnesium are quite contradictory (97, 52, 73, 50). The recent investigation of Brenner and his associates (96) has proved that addition of 0.5*N* sodium sulfate or potassium sulfate to Watts-type bath did not result in any appreciable effect on mechanical properties. This has been shown, in the present investigation, to be true also in the case of magnesium salts up to a concentration of 1*N*. It is also found that the effect of magnesium is almost independent of the anion associated with it. The effect of high concentration of magnesium could not be attributed to codeposition of magnesium since this metal was found only in spectroscopic amounts as will be demonstrated later. The effect may be attributed to different factors such as increased density and viscosity of the solution, changing the rate of arrival of hydrogen and nickel ions to the cathode surface, or changing the nature and thickness of the cathode film. Unfortunately, our present knowledge based on available data is not quite sufficient to clear out this point.

Figure 11 shows that there is some difference between the cross-sectional and surface hardness with a general trend toward greater hardness on the surface. A similar phenomenon was observed by Cuthbertson (98) who attributed it to the anisotropic nature of electrodeposits, but it may also be due to the finer grain size of the deposit first laid down.

Structure.—The structure of electrodeposits is quite significant because of the relation which exists between it and mechanical properties. The structure was studied in the two directions parallel to the two different directions of linear crystallization, i.e., parallel to and normal to the cathode.

The effect of magnesium on structure has not been reported except in very few general statements (7, 99). In the present investigation, some modification in the structure was noticed usually at higher concentration of magnesium. In Fig. 13, for example, it is seen that the surface structure of the deposit obtained from bath S-2.0 is somewhat finer than that obtained from bath S-0.0. Also, in Fig. 14, the deposit from bath C-2.0 has a more pronounced needle-like structure. It has already been demonstrated that this modification in structure is accompanied by a change in hardness.

Structure by x-ray diffraction.—X-ray diffraction methods were conducted to examine the influence of magnesium on the crystal structure of electrodeposited nickel, and to detect the presence of magnesium or nickel-magnesium alloys if they were present in a fairly large percentage, as was reported earlier.

X-ray diffraction patterns, Fig. 16, show that the addition of magnesium has not changed the crystalline structure of nickel which is deposited from all baths under test with a face-centered cubic structure. It has been reported previously that, according to conditions, nickel can be deposited with a face-centered cubic structure or a hexagonal close-packed structure or a combination of both (100-102).

The patterns show also that magnesium lines do not appear. It is concluded, therefore, that nickel deposits do not contain magnesium or nickel-magnesium alloys, at least not in appreciable amounts. This necessitated further analysis of the deposits for trace amounts by spectroscopic methods.

Porosity.—Porosity determines to a large extent the protective value of nickel in ordinary atmospheres. Many methods have been used for determination of porosity. While atmospheric exposure tests are the most reliable, the ferroxyl tests are extensively applied and, in many cases, they give the best reproducible results which are parallel to those obtained by atmospheric exposure tests. In the present investigation, porosity was determined by hot water and ferroxyl tests. The former did not give consistent results.

Figure 17 shows that there is no essential difference in the porosity of deposits, expressed as corrosion resistance, between the Watts- and Wesley-type baths. However, the addition of magnesium to both baths has resulted in a marked increase in corrosion resistance of the resultant deposit. Increased corrosion resistance may be the result of the lower deposition potential mentioned before. This may have reduced the tendency for the nickel deposits to be pitted.

Magnesium in nickel deposits.—Early investigators had reported that magnesium was codeposited with nickel at fairly high percentages (15, 16, 103, 97), which may amount to as high as 10%. These results had led to the belief that magnesium is codeposited with nickel from aqueous solutions and that changes in the nature (104) and whiteness (29) of these deposits are attributed to such deposition. Later investigations could not verify these earlier claims (27, 59, 105) and neither does the present investigation. Table II shows that magnesium is found in deposits from baths containing magnesium but only in spectroscopic amounts. There is, however, a gradual increase in the magnesium content following concentration of magnesium in the bath. The source of the magnesium present may be either from occluded solution or from magnesium hydroxide inclusions which may have been precipitated at the high *p*H prevailing in the cathode film.

Conclusions

As a result of the present investigation, it is concluded that addition of high concentration of magnesium to nickel baths makes the deposition potential of nickel more noble, reduces cathode polarization, does not change the face-centered cubic lattice of nickel, codeposits only spectroscopic traces of magnesium, increases cathode current efficiency slightly, improves the throwing power, reduces porosity, and makes nickel deposits harder, stronger, and less ductile.

In the plating industry, use can be made of the effect of magnesium additions to nickel baths. It is shown that by addition of 2*N* magnesium sulfate to the Watts bath, properties of the new bath, bath S-2.0, lie nearly midway between those of Watts and Wesley baths. This can be realized easily by inspection of Table II. It is true that the same effect can be brought about by increasing the chloride content of the Watts bath, but addition of magnesium sulfate has certain advantages:

1. Magnesium sulfate is less expensive than nickel chloride.
2. The corrosive nature of the Watts bath will not be increased, whereas it will be much increased if the nickel chloride content is increased. In the latter case, additional precautions against corrosion of the equipment will be necessary.
3. In the presence of magnesium salts, nickel baths hold their metallic concentration better than they do without magnesium salts; addition of acid to correct the *p*H is less often needed.
4. Addition of magnesium sulfate will improve the corrosion resistance of the deposit, whereas increasing the nickel chloride content will not improve that property. An evidence of this is the fact that the Wesley bath, which is made solely of nickel chloride, gives deposits having corrosion resistance identical to that of deposits obtained from the Watts bath. This result was found by Wesley and Carey (106) and was confirmed in the present work.

It is worthy to note that the above point stimulates the necessity of further research to determine whether or not addition of still higher concentration of magnesium sulfate to Watts bath will result in deposits having mechanical properties closer to those of deposits obtained from Wesley bath without the disadvantage of higher tensile stresses characteristic of these deposits.

Acknowledgment

Acknowledgment is made to the International Nickel Company, Inc., for furnishing materials used in this investigation.

Manuscript received Feb. 21, 1957.

Any discussion of this paper will appear in a Discussion Section to be published in the December 1959 JOURNAL.

REFERENCES

1. W. D. Bancroft, *Trans. Am. Electrochem. Soc.*, **23**, 261 (1913).
2. W. G. Horsch and Tyler Fuwa, *ibid.*, **41**, 363 (1922).
3. H. E. Haring and William Blum, *ibid.*, **44**, 313 (1923).
4. E. Mantzell, *Z. Elektrochem.*, **43**, 174 (1937).
5. L. D. Hammond, *Trans. Am. Electrochem. Soc.*, **45**, 219 (1924).
6. A. E. Nicol, *Metal Ind.* (London), **30**, 90 (1927).
7. E. F. Kern, *Trans. Am. Electrochem. Soc.*, **15**, 441 (1909).
8. F. J. Liscomb, *Quart. Rev. Am. Electroplaters' Soc.*, **1**, No. 2, 10 (1913).
9. E. W. Heil, *Monthly Rev. Am. Electroplaters' Soc.*, **3**, No. 8, 4 (1916).
10. William Blum, *Trans. Am. Electrochem. Soc.* **36**, 213 (1919).
11. C. H. Proctor, *Metal Ind.* (N. Y.) **19**, March 1921.
12. Isaac Adams, *Trans. Am. Electrochem. Soc.*, **9**, 211 (1906).
13. Isaac Adams, U. S. Pat. 100,961, March 22, 1870.
14. M. Kugel, German Pat. 117,054 Nov. 5, 1899.
15. Alfred Coehn, *Z. Elektrochem.*, **8**, 593 (1902).
16. Siemens, *Z. Anorg. Chem.*, **41**, 249 (1904).
17. K. Altmannsberger, *Oberflachentech.*, **8**, 185 (1931); *Metals and Alloys, Cur. Met. Lit. Abs.*, **2**, 306 (1931).
18. Eugen Werner, *Oberflachentech.*, **12**, 219 (1935).
19. N. I. Larin, *Korroziya i Bor'ba s Nei*, **5**, No. 3-4, 112 (1939).
20. C. W. J. Morley, *Electroplating*, **3**, 400 (1950).
21. Henry Strow, *Proc. Am. Electroplaters' Soc.*, **1947**, 201.
22. H. Krause, *Korrosion u. Metallschutz*, **16**, 304 (1940).
23. C. H. Proctor, *Metal Ind.* (N. Y.), **11**, 11 (1913).
24. R. J. Hazucha, *Monthly Rev. Am. Electroplaters' Soc.*, **4**, No. 10, 11 (1917).
25. S. Herrich, *Metal Ind.*, (N. Y.), **20**, 354 (1922).
26. A. K. Graham, *Trans. Am. Electrochem. Soc.*, **44**, 347 (1923).
27. M. R. Thompson, *ibid.*, **47**, 163 (1925).
28. C. H. Proctor, *Metal Ind.*, (N. Y.), **23**, 415 (1925).
29. C. H. Proctor and O. J. Sizelove, *Monthly Rev. Am. Electroplaters' Soc.*, **12**, No. 7, 15 (1925).
30. Samuel Gordon, *Metal Cleaning Finishing*, **2**, 765 (1930).
31. Marcel Ballay, *Trans. Electrochem. Soc.*, **62**, 91 (1932).

32. J. L. Roberts, Jr., *Monthly Rev. Am. Electroplaters' Soc.*, **23**, No. 3, 24 (1936).
33. C. H. Proctor, *Metal Ind.*, (N.Y.), **17**, 25 (1919).
34. Benjamin Fess, *Monthly Rev. Am. Electroplaters' Soc.*, **16**, No. 11, 7 (1929).
35. Eugen Werner, *Metallborse*, **20**, 1434 (1930).
36. A. V. Re, *Trans. Electrochem. Soc.*, **61**, 337 (1932).
37. H. Krause, *Mitt. Forschungsinst. Probieramt Edelmetalle*, **7**, 87 (1933).
38. M. Ballay, *Rev. Aluminum*, **11**, 2365 (1934).
39. G. Blonda, *Chimica*, **2**, 237 (1935); *Chemie et Industrie*, **35**, 328 (1935).
40. Jean Frasch, French Pat. 810,010, March 13, 1937.
41. Eugen Werner, *Werkstatt u. Betrieb*, **72**, 103 (1939).
42. Joseph Underwood, *Monthly Rev. Am. Electroplaters' Soc.*, **5**, 16, 44 (1929).
43. T. C. Eichstadt, *Metal Ind.* (London), **26**, 603 (1925).
44. Anon, *Metallwaren-Ind. u. Galvano-Tech.*, **23**, 605 (1925).
45. S. M. Kochergin, *J. Appl. Chem.* (U.S.S.R.), **12**, 44 (in French, 45) (1939).
46. S. Herrich, *Metal Ind.* (N. Y.), **16** (1918).
47. J. Underwood, *Monthly Rev. Am. Electroplaters' Soc.*, **13**, No. 9, 14 (1926).
48. L. M. Evlannikov and D. S. Neiman, *Trans. Leningrad Ind. Inst.*, 1939 No. 1, Sec. Met. No. 1, 3.
49. H. J. Richards and F. P. Menninges, *Monthly Rev. Am. Electroplaters' Soc.*, **12**, No. 7, 23 (1925).
50. Myron B. Diggin, *ibid.*, **33**, 513, 524 (1946).
51. J. Walters, *ibid.*, **4**, No. 5, 10 (1917).
52. S. Makar'eva, *Bull. acad. sci. U.S.S.R., Classe sci. math. nat., Ser. chim.*, (1938), 1211 (in English), 1223.
53. V. Kohlschuetter and E. Vuilleumier, *Z. Elektrochem.*, **24**, 300 (1918).
54. Bernard Martin, *Proc. Am. Electroplaters' Soc.*, June 1944, 206.
55. D. W. Robinson, *Metal Ind.* (N. Y.), **14**, 133 (1916).
56. W. S. Barrows, *Can. Machinery*, **40**, No. 19, **71** (1929).
57. Joseph Haas, Jr., *Metal Ind.* (N. Y.), **19**, 364 (1921).
58. C. P. Madsen, *Trans. Am. Electrochem. Soc.*, **39**, 483 (1921).
59. R. E. Harr, *Trans. Electrochem. Soc.*, **68**, 425 (1935).
60. W. A. Wesley, *et al.*, *Proc. Am. Electroplaters' Soc.*, **36**, 79 (1949).
61. F. C. Mathers, *et al.*, *Trans. Am. Electrochem. Soc.*, **29**, 383 (1916).
62. E. P. Later, *Foundry*, **45**, 333 (1917).
63. R. L. Dorrance and W. C. Gardiner, *Trans. Am. Electrochem. Soc.*, **54**, 303 (1928).
64. V. M. Guskov and A. Z. Rivkind, *Metallurg*, **9**, No. 1, 69 (1934).
65. Myron Diggin, *Monthly Rev. Am. Electroplaters' Soc.*, **28**, 793 (1941).
66. Max Schlotter, Brit. Pat. 459,887, Jan. 18, 1937.
67. M. R. Thompson and C. T. Thomas, *Trans. Am. Electrochem. Soc.*, **42**, 79 (1922).
68. C. T. Thomas and William Blum, *ibid.*, **45**, 193 (1924).
69. E. Raub, *Mitt. Forschungsinst Probieramt Edelmetalle*, **10**, 37 (1936).
70. C. G. Beiber and M. P. Buck, (to the International Nickel Co., Inc.) U. S. Pat. 2,117,284, May 17, 1938.
71. H. Silman, "Chemical and Electroplated Finishes," p. 286, Chapman and Hall Ltd., London (1952).
72. G. B. Hogaboom, *Metal Ind.* (N. Y.), **37**, 165 (1939).
73. M. B. Diggin, *Metal Finishing*, **39**, 13 (1941).
74. J. B. Kushner, *Monthly Rev. Am. Electroplaters' Soc.*, **29**, 751 (1942).
75. Henry Brown, (to The Udylite Corp.) U. S. Pat. 2,523,190-1, Sept. 19, 1950.
76. Henry Brown, (to The Udylite Corp.) U. S. Pat. 2,523,190-1, Sept. 19, 1950.
77. H. Komusaari, *Metalloberflache*, **6**, No. 11, 162 (1952).
78. W. A. Wesley and E. J. Roehl, *Trans. Electrochem. Soc.*, **86**, 419 (1944).
79. "Specifications and Tests for Electrodeposited Metallic Coatings," American Society for Testing Materials, Philadelphia, Pa. (1949).
80. N. Thon and Denis Kelemen, *Proc. Am. Electroplaters' Soc.*, **1947**, 128.
81. A. Harold Heatley, *Trans. Am. Electrochem. Soc.*, **44**, 283 (1923).
82. H. Bandes, *Metal Finishing*, **44**, 516 (1946).
83. A. H. W. Aten and L. M. Boerlage, *Rec. Trav. Chim. Pay-Bas*, **39**, 720 (1920).
84. William Blum and H. S. Rawdon, *Trans. Am. Electrochem. Soc.*, **44**, 397 (1923).
85. V. Kohlschutter, *ibid.*, **45**, 229 (1924).
86. H. E. Haring, *ibid.*, **49**, 417 (1926).
87. A. K. Graham, *ibid.*, **52**, 157 (1929).
88. D. J. Macnaughtan and A. W. Hothersall, *Trans. Faraday Soc.*, **24**, 387 (1928).
89. S. Glasstone and E. B. Sanigar, *Trans. Faraday Soc.*, **25**, 590 (1929).
90. B. Clark and E. O. Jones, *ibid.*, **25**, 583 (1929); **26**, 96 (1930).
91. L. B. Hunt, *J. Phys. Chem.*, **36**, 1006 (1932).
92. S. Glasstone, *Trans. Faraday Soc.*, **31**, 1232 (1935).
93. Kurt Arndt and Oskar Clemens, *Chem. Ztg.*, **46**, 925 (1922).
94. H. E. Haring, *Trans. Am. Electrochem. Soc.*, **46**, 109 (1924).
95. Ralph Verdieck, *et al.*, *Trans. Electrochem. Soc.*, **80**, 41 (1941).
96. A. Brenner, *et al.*, *Plating*, **39**, 865 (1952).
97. K. Engermann, *Review d'Electrochemie et d'Electrometallurgie*, p. 199, July 1912.
98. J. W. Cuthbertson, *Trans. Electrochem. Soc.*, **77**, 157 (1940).
99. R. S. Dean and M. Y. Chang, *Chem. Met. Eng.*, **19**, 83 (1918).
100. A. Colombani and J. Wyart, *Compt. rend.*, **215**, 129 (1942).
101. Ling Yang, Ph.D. Thesis University of London (1948).
102. Ling Yang, *J. Electrochem. Soc.*, **97**, 241 (1950).
103. K. Engermann, *Z. Elektrochem.*, **17**, 910 (1911).
104. A. J. Allmand and H. J. T. Ellingham, "The Principles of Applied Electrochemistry," 2nd ed., p. 361, Edward Arnold and Company, London, (1924).
105. A. A. Bulakh, *Korroziya i Bor'ba s Nei*, **4**, No. 2, 164 (1938).
106. W. A. Wesley and J. W. Carey, *Trans. Electrochem. Soc.*, **75**, 209 (1939).

Color Centers in Cadmium Fluoride

Martin Rubenstein[1] and Ephraim Banks

Department of Chemistry, Polytechnic Institute of Brooklyn, Brooklyn, New York

ABSTRACT

Single crystals of CdF_2, purified and containing additions of NaF, CeF_3, and equimolar quantities of NaF and CeF_3, were grown from the melt in graphite crucibles in a helium atmosphere.

Physical constants of CdF_2 were measured. Optical transmission spectra were obtained before and after x-irradiation on slices of single crystals (about 1.5 mm thick), at 28°, —78°, —190°C. Crystals containing 0.05-4 mole % NaF, when irradiated at 28° or at —78°C, showed a radiation-induced absorption near the fundamental absorption edge; this induced absorption is stable at 28°C. These same crystals, when irradiated at —190°C, showed another absorption which is unstable at —78°C. CdF_2, pure, and containing low concentrations of CeF_3, NaF, or equimolar CeF_3 and NaF, all showed one x-ray induced absorption band, unstable above —10°C. CdF_2 x-irradiated at room temperature showed a very stable absorption band.

Color centers in alkali halides (1, 2), and to a lesser extent in alkaline earth halides (3-5), have been and are being investigated extensively. Only limited data have been published on the compound CdF_2 (6, 7), and there have been no investigations on color centers in this compound.

The density, melting point, optical transmission spectrum, and lattice constant of CdF_2 have been reported (6, 7). These characteristics were reinvestigated and are reported here. Since no color centers had been reported in CdF_2, we obtained transmission spectra (200-1200 mμ and 2000-15,000 mμ) of single crystals of CdF_2, pure, and with various additions before and after x-irradiation at 28°C (room temperature), —78°C (acetone and solid CO_2), and —190°C (liquid nitrogen).

Experimental Procedures

Chemical compounds and materials.—"Standard luminescent" grade $CdCO_3$ powder[2] was purified by dissolving the carbonate in concentrated aqueous ammonia solution, filtering repeatedly, precipitating with concentrated aqueous hydrofluoric acid, and leaching this precipitate repeatedly with boiling concentrated aqueous hydrofluoric acid. The purified CdF_2 was dried and used in the preparation of single crystals with and without additives.

Cerium (III) fluoride (CeF_3) was prepared by dissolving ammonium hexanitratocerate (IV)[3] in water and reducing with 3% aqueous H_2O_2 solution; a gelatinous precipitate was obtained on acidification with aqueous hydrofluoric acid, washed repeatedly with doubly distilled water, centrifuged, and heated to dryness.

Growth of single crystals.—Single crystals of about 8 g in weight were prepared by placing CdF_2 powder, with or without additions, in covered graphite[4] crucibles; the crucibles were placed in vitreous silica tubes (one end closed); a flow of helium (purified) was maintained in the silica tube; the silica tube was placed in a furnace. The furnace temperature was raised to 1120°C and the setting of the furnace controller was lowered in a step-wise manner (cut down 10° in 2 min, held for 8 min, and then this cycle was repeated) until room temperature was reached. The additions of CeF_3 were prepared by mixing CeF_3, prepared by using the method mentioned in the previous section; the additions of NaF were prepared by mixing reagent grade NaF with CdF_2. The smaller concentration additions were made by using portions of solid solutions of larger concentrations.

Density measurements.—The density of CdF_2 was obtained by using a 10 ml solid pycnometer, fragments of melted CdF_2 (each fragment about 5 mm in diameter), and doubly distilled water as the immersion liquid. The water level in the pycnometer was reached by using a water bath maintained at 36.5°C.

Melting point.—The melting point of pure CdF_2 was determined by recording heating curves. The CdF_2 powder was placed in a graphite crucible with the same apparatus as used for crystal growth. The temperature was measured by a Pt-Pt 10% Rh thermocouple whose junction was positioned in the wall of the graphite crucible—the distance between the thermocouple junction and the melt being less than 1/32 in. The thermocouple was calibrated using gold (mp 1063°C). The furnace temperature was raised and the arrest in the plot of thermocouple temperature vs. time was noted as the melting point.

Lattice constants.—The lattice constants of pure CdF_2 and CdF_2 with additions were obtained by means of the Debye-Scherrer technique, using a 57.32 mm radius Straumanis-type camera with nickel-filtered copper radiation. Eight back-reflection lines of the x-ray diffraction diagram were measured and the precision lattice constants were

[1] Present address: Materials Engineering Depts., Solid State Electronics Engineering Dept., Westinghouse Electric Corporation, Pittsburgh, Pa.

[2] Mallinckrodt.

[3] G. F. Smith Chemical Co., certified grade. NaF was reagent grade.

[4] AUC grade from National Carbon Corp.

calculated by the Straumanis calibration (8) and the Bradley-Jay (9) extrapolations.

Crystal slices.—The single crystals grown were cylinders about 12.5 mm in diameter and 12.5 mm in height. These crystals were sliced with a diamond-impregnated saw on a milling machine. These slices were mounted in polystyrene, polished with emery papers, and the final polishing was accomplished on a metallurgist's wheel using a silk cloth, Linde "B" Alumina, and water as a lubricant.

Optical measurements.—The transmission measurements were obtained at 28°C by a Process and Instruments Co. recording spectrophotometer, and at other temperatures by a Beckman DU Spectrophotometer, using a modified cell described by Casler, Pringsheim, and Yuster (10). The primary modifications were: standard tapered joints were replaced by ball and socket joints to provide maneuverability, and the beryllium window was replaced by an aluminum foil (0.2 mm) window. Transmissions were measured against an air path.

Irradiation.—The crystal slices were x-irradiated by a Machlett OEG-50-6 x-ray tube. The tungsten target permitted the generation of a white radiation x-ray spectrum. The tube was run as a self-rectified tube at 26 ma and 42 peak kv.

Ultraviolet irradiation was accomplished by a Conte-Glo lamp (3650Å). Infrared irradiation was obtained by a commercial infrared lamp.

Results

Physical constants.—The density of CdF_2 as previously reported (6) was 6.33 ± 0.06 g/cm³. Our pycnometric value for purified CdF_2 was 6.40 ± 0.02 g/cm³. The density calculated from the lattice constant (5.3883Å) was 6.386 g/cm³. The pycnometric density of CdF_2 with 16 mole % CeF_3 in solid solution was 6.32 ± 0.02 g/cm³.

The melting point of CdF_2 as previously reported was $1049° \pm 2°C$ (6). Our value from melting point curves of purified CdF_2 was $1072° \pm 2°C$.

The lattice constant of CdF_2 (fluorite structure) previously was reported as 5.3880 ± 0.0005Å (6). Our value for the lattice constant of purified CdF_2 was 5.3883 ± 0.0005Å. The difference between these two values probably is not significant.

The lattice constants of CdF_2 with additions of NaF indicate that the limit of solid solution is at 3 mole % NaF; the lattice constants form a straight line function from pure CdF_2 to the limit of solubility of NaF in CdF_2, with lattice constants increasing with NaF concentration. Concentrations greater than 3 mole % NaF produced no further increase in lattice constant, but did produce a two phase system. The lattice constant of a sample with 3 mole % NaF in CdF_2 is 5.3897 ± 0.0005Å, which is an expansion

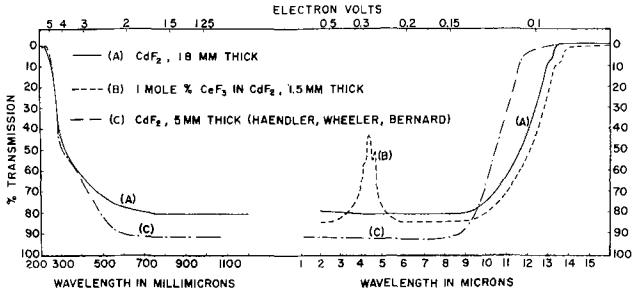

Fig. 1. Optical transmission spectra of single crystals

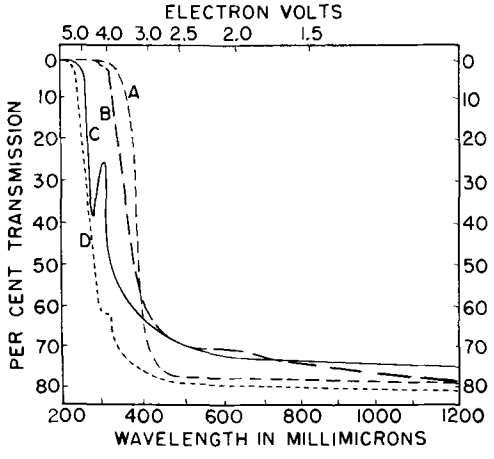

Fig. 2. Optical transmission spectra of CdF_2 with additions of CeF_3 measured at 28°C. A, CdF_2 with 10 mole % CeF_3; B, CdF_2 with 1 mole % CeF_3; C, CdF_2 with 0.01 mole % CeF_3; D, CdF_2 with 0.0005 mole % CeF_3.

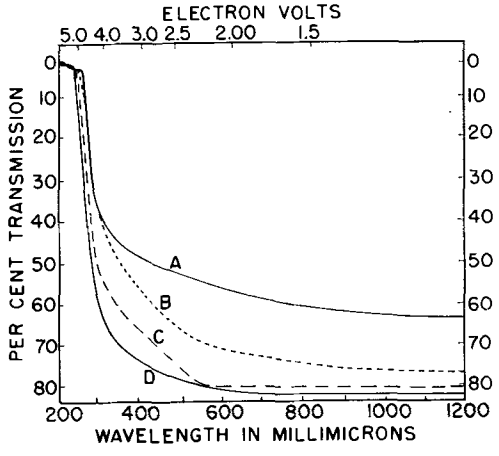

Fig. 3. Optical transmission spectra of CdF_2 with additions of NaF, measured at 28°C. A, CdF_2 with 5 mole % NaF; B, CdF_2 with 1 mole % NaF; C, CdF_2 with 0.05 mole % NaF; D, CdF_2 with 0.005 mole % NaF.

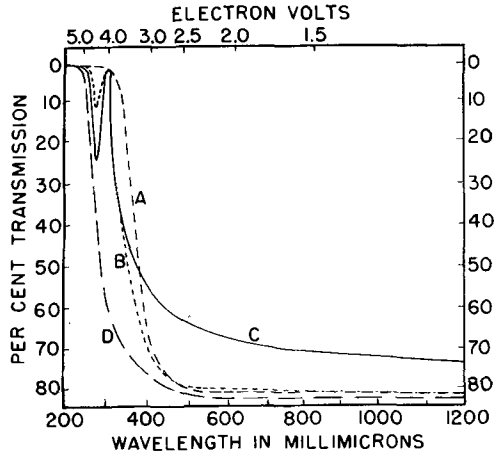

Fig. 4. Optical transmission spectra of CdF_2 with equimolar additions of NaF and CeF_3, measured at 28°C. A, CdF_2 with 5 mole % NaF and 5 mole % CeF_3; B, CdF_2 with 0.5 mole % NaF and 0.5 mole % CeF_3; C, CdF_2 with 0.05 mole % NaF and 0.05 mole % CeF_3; D, CdF_2 with 0.0005 mole % NaF and 0.0005 mole % CeF_3.

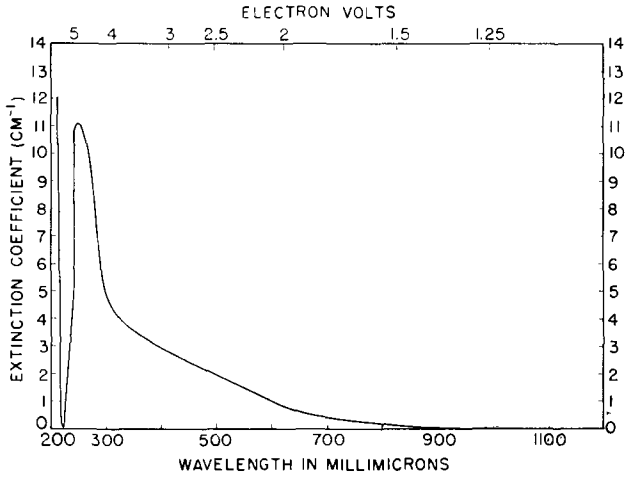

Fig. 5. Absorption spectrum of CdF_2 x-irradiated for 13 hr, x-irradiated and measured at 28°C.

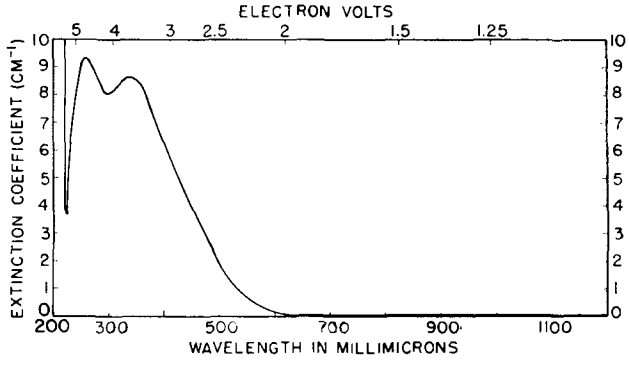

Fig. 6. Absorption spectrum of CdF_2 x-irradiated for 5 hr, x-irradiated and measured at —190°C.

of 0.0014 ± 0.0005Å. Similarly the lattice constants of CdF_2 with additions of CeF_3 indicate that the limit of solid solution is at 18 mole % CeF_3; this series also demonstrates a linear lattice expansion to 5.5032 ± 0.0005Å for the 18 mole % sample, which is an expansion of 0.0064 ± 0.0005Å per mole % CeF_3 in CdF_2. The lattice constant of a sample with 16 mole % CeF_3 in CdF_2 is 5.4890 ± 0.0005Å.

The maximum solubility of equimolar additions of NaF and CeF_3 in CdF_2 is 4.75 mole % NaF and CeF_3; this sample has a lattice constant of 5.4091 ± 0.0005Å. It should be noted that this lattice constant value would be attained in the solid solution containing no NaF at a composition of only 3.5 mole % CeF_3.

The optical transmission spectra from our data and from Haendler's (7) data are shown in Fig. 1. The fundamental absorption edge (the center of the portion of the transmission spectrum having the greatest slope before zero transmission) is at 265 mμ. Transmission spectra of polished crystal slices of CdF_2 with additions of CeF_3, NaF, and equimolar additions of CeF_3 and NaF are shown in Fig. 2, 3, and 4.

The transmission from 700 mμ to 10μ is almost constant with transmission of about 80%. At 10μ the transmission begins to fall and by 13.1μ there is no transmission; this edge is due to reststrahlen. In the range 2-15μ, crystals of CdF_2, purified, and with additions of NaF gave the same spectrum. However, CdF_2 crystals with CeF_3 and with equimolar additions of NaF and CeF_3, in addition to the reststrahlen edge, demonstrated another set of peaks around 4.40μ (2880 cm^{-1}). Two shoulders on both sides of the main peak at 4.17μ (2400 cm^{-1}), and at 4.64μ (2150 cm^{-1}) are observed in crystals of CdF_2 with CeF_3. In crystals with equimolar additions of CeF_3 and NaF, the main peak shifts to 4.45μ (2250 cm^{-1}) and the two shoulders appear at 4.18μ (2390 cm^{-1}) and 4.63μ (2160 cm^{-1}). The shoulder at the largest wave length is much more poorly defined with NaF plus CeF_3 in CdF_2 than with CeF_3 alone in CdF_2.

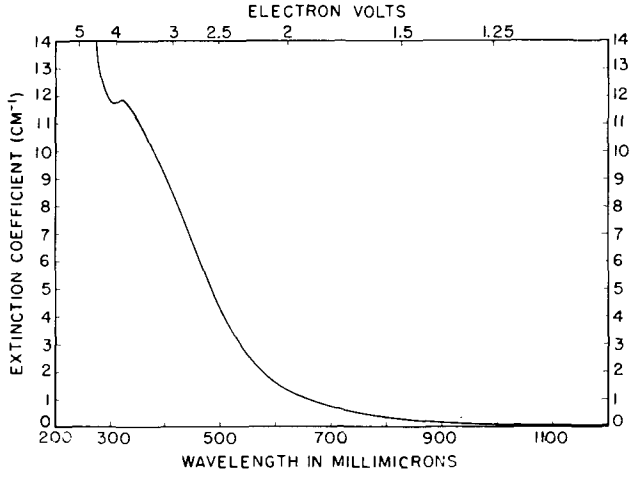

Fig. 7. Absorption spectrum of CdF_2 with 1 mole % NaF, x-irradiated 3.5 hr at 28°C, measured at —190°C.

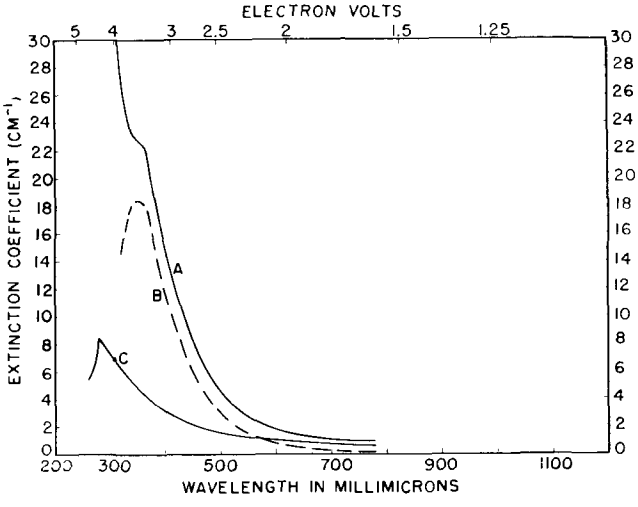

Fig. 8. Absorption spectra of CdF_2 with 1 mole % NaF. A, X-irradiated 2.6 hr at 28°C, measured at 28°C; B, Portion of Curve A bleached by heating 8 hr in 150°C oven; C, Portion of Curve A unbleached by heating 8 hr in 150°C oven.

X-radiation-induced absorption bands.—Four apparently independent x-ray-induced absorption bands were observed.

I. CdF_2 irradiated for several hours at room temperature causes an absorption band peaking at 255 mμ (see Fig. 5). This band does not bleach with heat (up to 150°C), ultraviolet radiation, or infrared radiation.

II. CdF_2, pure, and containing low concentrations of CeF_3 (less than 0.0005 mole % CeF_3), low equimolar concentrations of CeF_3 and NaF (less than 0.0005 mole % CeF_3 and NaF), and low concentra-

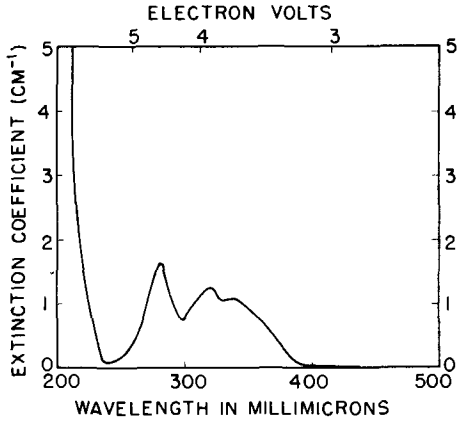

Fig. 9. Absorption spectrum of CdF_2 with 4 mole % NaF, x-irradiated 2.5 hr at —190°C, and measured at —190°C.

tions of NaF (less than 0.0005 mole % NaF) showed a double band (see Fig. 6). This band was produced by x-irradiation at —190°, or —78°C and was completely bleached by raising the temperature above —10°C. Irradiation with 3650Å at —190°, or —78°C, produced no bleaching.

III. CdF_2 with additions of NaF (in concentrations greater than 0.05 mole % NaF) when x-irradiated at —78° or 28°C produced an absorption band which could not be bleached completely. The band was relatively stable at 28°C. Partial bleaching could be accomplished by heating the crystal to 100° or 150°C in an oven, or by irradiating with 3650Å, or by irradiating with a commercial infrared lamp. The absorption band in Fig. 7 has a smaller extinction coefficient than that in Fig. 8A because the crystal in Fig. 7 was positioned further from the focal point and received a smaller dose of x-rays. Figure 8B shows that portion of A bleached by heating in an oven. Figure 8C shows the portion of A unbleached by this heating.

IV. CdF_2 with additions of NaF (also in concentrations greater than 0.05 mole % NaF) when x-irradiated and measured at —190°C produced the absorption bands in Fig. 9. This absorption was bleached by raising the temperature to —78°C or by irradiation with 3650Å at —190°C. This is a triple band.

To calculate the number of color centers per cubic centimeter, we assume that the expression derived by Smakula (11) applies. Smakula applied the theory of dispersion to F-center bands of alkali halide crystals to determine the density of F-centers. Among his assumptions were the following: the absorption transition is analogous to the 1s-2p transition in atomic hydrogen; the extinction coefficient of the bulk material is zero in the vicinity of the F-center bands. Since the bands are close to the absorption edge, this equation cannot apply exactly.

Table I summarizes some data on the above mentioned four primary x-ray induced absorptions.

Discussion and Conclusions

If one compares the transmission spectrum of 0.005 mole % NaF in CdF_2 (Fig. 3, curve D) and the spectrum of the CdF_2 without any additions (Fig. 1), one notices that the transmission of the CdF_2 with NaF is greater than that of the CdF_2 without any additions in the visible and in part of the ultraviolet. This difference of transmission is real and not instrumental. This apparent anomaly is probably caused by $S^=$ ions. If CdS is added to CdF_2 in a concentration of 1 ppm, the resulting crystal is quite yellow. The optical absorption at wave lengths less than 5000Å is total. The CdF_2 crystals prepared in this investigation undoubtedly had some $S^=$ ions but much less than 1 ppm. The addition of NaF to CdF_2, even at low concentrations of NaF, seemed to reduce the $S^=$ ion concentration.

CdF_2 with 16 mole % CeF_3 has a pycnometric density of 6.32 ± 0.02 g/cm³ and a lattice constant of 5.4921 ± 0.0005Å. A density of 6.335 g/cm³ may be calculated using this lattice constant, by assuming that a Ce (III) ion substitutes for a Cd (II) ion and an interstitial fluoride ion is present for charge compensation. If one uses a molecular weight assuming that two Ce (III) ions substitute for three Cd (II) ions, the calculated density would be 5.851 g/cm³. Therefore, it is concluded that a Ce (III) ion substitutes for a Cd (II) ion and the charge compensatory ion is an interstitial fluoride ion. This conclusion is consistent with the findings of Zintl and Udgard (12) on the CaF_2-YF_3 system and the findings of Ketelaar and Williams (13) on the SrF_2-LaF_3 system. Although the substitutional Ce (III) ion would tend to cause a small electrostatic contraction

Table I. Description of absorption bands

Crystal	Band	Position of peak, mμ	Position of peak, e.v.	Absorption coefficient in cm⁻¹ at peak	Half bandwidth, e.v.	No. of color centers (Smakula equation*)
Pure CdF_2, x-irradiated 15 hr at 28°C, and measured at —190°C	I, Fig. 5	255	4.85	0.97	11.1	1.125×10^{17}
Pure CdF_2, x-irradiated and measured at —190°C	II, Fig. 6	340	3.64	8.6	1.62	1.45×10^{17}
CdF_2 with 1 mole % NaF, irradiated at 28°C and measured at —190°C	III, Fig. 7	315	3.92	11.9	2.38	2.95×10^{17}
CdF_2 with 1 mole % NaF, irradiated and measured at 28°C	III, Fig. 8A	350	3.53	21.6	1.56	3.50×10^{17}
Bleachable portion of Fig. 8A	III, Fig. 8B	350	3.53	18.2	1.18	2.24×10^{17}
Unbleachable portion of Fig. 8A	III, Fig. 8C	280	4.42	8.0	1.32	1.10×10^{17}
CdF_2 with 4 mole % NaF, irradiated and measured at —190°C	IV, Fig. 9	340	3.64	1.1	0.60	6.87×10^{16}
		320	3.86	1.25	0.55	7.16×10^{16}

* The oscillator strength is assumed to be unity in these calculated values.

of the lattice, the larger size of the Ce (III) ion (ionic radius of Cd (II) = 0.97Å; ionic radius of Ce (III) = 1.07Å) would tend to cause an appreciable expansion of the lattice, and the interstitial fluoride ion (ionic radius = 1.33Å) would also cause an appreciable expansion of the lattice.

CdF_2 crystals with additions of NaF show a small lattice expansion: 0.0005Å/mole % of NaF. The expansion of CeF_3 in CdF_2 shows a much larger expansion of 0.0064Å/mole % of CeF_3. If the Na (I) ion were to enter the CdF_2 lattice interstitially in any way (either a fluoride ion could also enter interstitially or a Cd (II) ion vacancy could allow two interstitial Na (I) ions to enter the lattice) one would expect a larger lattice expansion than observed. Therefore, it has been assumed that on this basis and on the x-ray induced absorption band data (discussed in the next paragraphs), each Na (I) ion entering the CdF_2 lattice does so substitutionally for a Cd (II), and an anionic vacancy is present to achieve electrical neutrality.

In the case of solid solutions of NaF in CdF_2, both the substitution of Na (I) ion for Cd (II) ion and the formation of anionic vacancies would lead to an expansion of the lattice by virtue of the local decrease in charge density. The expansion is probably diminished by the decrease in overlap repulsion when a Cd (II) ion is replaced by a Na (I) ion and when fluoride ions are removed. This may account for the relatively small expansion actually observed. Since the ionic radius of Cd (II) ion is 0.97Å and the ionic radius of Na (I) ion is also 0.97Å, no expansion or contraction of the lattice would be expected because of a difference in ionic radii.

It seems quite apparent that the number of anionic vacancies has been reduced by a similar reduction of the number of interstitial fluoride ions in crystals of CdF_2 with equimolar additions of CeF_3 and NaF (the number of anionic vacancies here is compared to solid solutions of CdF_2 and NaF and the number of interstitial fluoride ions here is compared to solid solutions of CdF_2 and CeF_3), for the following reasons:

1. The crystals of CdF_2 with equimolar additions of CeF_3 and NaF (in concentrations greater than 0.05 mole % CeF_3 and NaF) did not show x-ray induced absorption stable at room temperature, while crystals of CdF_2 with NaF additions greater than 0.05 mole % demonstrate this absorption band (Fig. 7).

2. We have proved that CdF_2 with additions of CeF_3 has an interstitial fluoride ion for each substitutional Ce (III) ion. The lattice constant of such crystals of CdF_2 with equimolar additions of CeF_3 and NaF is less than if the same percentage of CeF_3 alone were incorporated (the expansion of CdF_2/mole % NaF is 0.0005Å, the expansion of CdF_2/mole % CeF_3 is 0.0064Å, and the expansion of CdF_2 with equimolar additions of CeF_3 and NaF is 0.0044Å/mole % of CeF_3 or NaF). Since we have indicated that CdF_2 with additions of NaF has an anionic vacancy for each substituted Na (I) ion, and since CdF_2 with additions of CeF_3 produces interstitial fluoride ions, the combination of NaF and CeF_3 incorporated together allows most of the interstitial fluoride ions to enter the anionic vacancies.

It has been proved (14) that the shoulder at about 4.18 μ (2400 cm^{-1}) is an artifact caused by CO_2 absorption in the beam path of the spectrophotometer. In using a double-beam spectrophotometer in this region of the spectrum, the response of the recording pen falls to zero since the CO_2 in the air is high enough to cause almost total absorption in both beams. In this region the electrical circuit becomes insensitive so that if the transmission is the same below and above this region, there is usually a small pip, which has been subtracted in Fig. 1A (the spectrophotometer is insensitive immediately about 4.18 μ, but is quite sensitive at wave lengths above and below this immediate region). In the case of solutions of CeF_3 in CdF_2, the absorption spectra of the crystal are rising to a peak in the region of 4.18 μ (Fig. 1B), and it could not be decided whether this was a separate peak or an artifact caused by the CO_2 absorption. Using a single-beam spectrophotometer and a nitrogen gas path for the beam instead of air, it was proved that this was not a separate peak but merely an artifact due to the CO_2 absorption (14). Mandel also obtained a value of 2×10^{-6} oscillators per atom from the calculated intensity of the absorption of the Ce (III) ion involving only a 4f shell transition. He has suggested, by analogy with other work on rare earth spectra, that this infrared absorption may be the $2_{F_{5/2}}$-$2_{F_{7/2}}$ transition.

The x-ray induced absorption band which is stable at 28°C could involve electrons trapped at anionic vacancies, since the crystals demonstrating this absorption do have a high concentration of anionic vacancies before x-irradiation. This band was resolvable into a bleachable and a difficultly bleachable(unbleached portion) band (see Fig. 8). Since bleaching by means of 3650Å irradiation was observed at temperatures as low as −78°C (but no bleaching was observed at −190°C), we must assume a thermal step is involved in the bleaching [Gurney and Mott indicate that a thermal step is necessary for the bleaching of F-centers in alkali halides (15)].The more difficultly bleached band may involve the absence of levels sufficiently shallow for the thermal step to be accomplished at the temperature at which the measurements were made.

Since the x-ray induced absorption band (Fig. 7) which is stable at room temperature is not observed when crystals of NaF in CdF_2 are x-irradiated at −190°C, one must conclude that a thermal step is involved in the production of the centers causing this band. The triple absorption band (Fig. 9) produced when NaF in CdF_2 is x-irradiated at −190°C is bleached by 3650Å irradiation or by warming to −78°C.

The absorption band (Fig. 6) common to pure CdF_2 and CdF_2 with low concentrations of cerium (III) fluoride, NaF, and equimolar additions of NaF and CeF_3 is not bleached by 3650Å at −78°C, or −190°C, but is bleached by warming to temperatures greater than −10°C. This band is independent of the impurities added to CdF_2. Apparently bleaching requires only a thermal step.

The increase in extinction coefficients at the high energy end of the spectra in Fig. 5, 6, and 9 is due to the logarithmic differences between the reciprocals

of small transmissions of questionable accuracy. Since the Beckman spectrophotometer is not as accurate at very low transmissions as it is at higher transmissions, the values of the transmissions at small transmissions are not very accurate, the differences between such small transmissions are less accurate, and the logarithms of such differences exaggerate the inaccuracy. Therefore, it is doubtful whether the increase in extinction coefficients at the high energy end of the spectra involved is real.

Acknowledgment

The authors wish to thank Henry F. Ivey for reading this manuscript.

Manuscript received Nov. 10, 1958. This paper is part of a thesis submitted by one of the authors (M.R.) in partial fulfillment of requirements for the Ph.D. degree to the Polytechnic Institute of Brooklyn. This paper was prepared for delivery before the Washington, D. C., Meeting, May 13-16, 1957.

Any discussion of this paper will appear in a Discussion Section to be published in the December 1959 JOURNAL.

REFERENCES

1. F. Seitz, *Revs. Modern Phys.*, **18**, 384 (1946).
2. F. Seitz, *ibid.*, **26**, 6 (1954).
3. A. Smakula, *Phys. Rev.*, **77**, 408 (1950).
4. S. Barile, *J. Chem. Phys.*, **20**, 297 (1952).
5. J. H. Schulman, R. J. Ginther, and R. D. Kirk, *ibid.*, **20**, 1966 (1952).
6. H. M. Haendler and W. J. Bernard, *J. Am. Chem. Soc.*, **73**, 5218 (1951).
7. H. M. Haendler, G. M. Wheeler, Jr., and W. J. Bernard, *J. Optical Soc. Am.*, **43**, 215 (1953).
8. M. E. Straumanis, *J. Appl. Phys.*, **20**, 726 (1949).
9. A. J. Bradley and A. H. Jay, *Proc. Phys. Soc.*, **44**, 563 (1932).
10. R. Casler, P. Pringsheim, and P. Yuster, *J. Chem. Phys.*, **18**, 887 (1950).
11. A. Smakula, *Z. Physik*, **59**, 603 (1930).
12. E. Zintl and A. Udgard, *Z. anorg. u. allgem. Chem.*, **240**, 150 (1939).
13. J. A. A. Ketelaar and P. J. H. Williams, *Rec. trav. chim.*, **56**, 29 (1937).
14. G. Mandel, Bachelor's Dissertation, Polytechnic Institute of Brooklyn, 1957.
15. (a) R. W. Gurney and N. F. Mott, *Trans. Faraday Soc.*, **34**, 506 (1938).
    (b) N. F. Mott, *Proc. Phys. Soc.*, **50**, 196 (1938).

The Luminescent Center in Self-Activated ZnS Phosphors

J. S. Prener and D. J. Weil

Research Laboratory, General Electric Company, Schenectady, New York

ABSTRACT

A model for the ground state of the self-activated luminescent center in ZnS phosphors proposed by Prener and Williams in 1956 has been confirmed experimentally. It is shown that a Zn vacancy is involved in the blue luminescence and that the spectrum depends on whether the required coactivator can occupy a Zn or S site near the vacancy. The calculated energy levels of the center using a simple model are in qualitative agreement with the observed spectra.

If pure ZnS is heated to a high temperature in the presence of a halogen (e.g., NaCl or H_2S, HCl gas mixture) or with small amounts of Al or Ga (1), a blue emitting phosphor is obtained. The atomic nature of the defect responsible for this "self-activated" emission has been the subject of much discussion in the literature (2, 3). Recognizing that a neutral Zn vacancy may act as a double acceptor, Kröger and Vink (2) proposed that this defect was such a vacancy with one of the bound holes ionized. However, a concentration of such centers of about 2×10^{19} cm^{-3} or greater should have led to a measurable paramagnetic contribution to the magnetic susceptibility of this phosphor in the experiments of Bowers and Melamed (3); yet they failed to find such a contribution. More recently, Prener and Williams suggested that the defect in question consists of a Zn vacancy in which both the holes are ionized, leaving the vacancy doubly negatively charged, and an ionized donor impurity (Cl, Br, I, Al, or Ga) associated at nearest possible sites in the ZnS lattice (4). Such a center, in its ground electronic state, is not paramagnetic.

It is the purpose of this paper to present experimental evidence for such an associated center. The role of Zn vacancies in the formation of the center is shown by the expected variation in the intensity of the blue fluorescence with changes in the pressure of S vapor over the phosphor during preparation. That the coactivator is also part of the center is shown by the differences in spectral distribution of the fluorescence when halogens or group IIIB elements are used as coactivator impurities. Deductions based on a model for such a center are shown to be consistent with these observed differences.

In a series of papers Bube (5) and Addamiano (6) discussed the preparation of self-activated ZnS with blue fluorescence, by high-temperature firing in air or nitrogen without the use of any added coactivators. Their interpretation was that the center responsible for the fluorescence was a Zn vacancy which was formed thermally at high temperatures. Careful and numerous experiments performed in our laboratories have convinced us that previous observations were the result of faulty experimental techniques. If a "luminescent grade" of ZnS is carefully protected from dust and is fired in a stream of purified, dry H_2S in clean apparatus, first at low temperatures (400°C for several hours) and then slowly at increasingly higher temperatures until 1150°-1200°C is reached, no visible luminescence is found even at liquid nitrogen temperature! If, on the

other hand, the firing temperature is raised rapidly to 1150°C, very frequently bright blue luminescence is indeed observed. We presume that even the best ZnS available probably has some coprecipitated halide which can be volatilized or converted to sulfide by low temperature H_2S firing. At higher temperatures the halogen may diffuse into the ZnS lattice producing the characteristic blue luminescence. Our general conclusion is therefore that under conditions most likely to produce Zn vacancies (H_2S firing rather than nitrogen) no self-activated luminescence can be induced in ZnS without the use of coactivators.

Experimental and Results

Emission Spectra of ZnS:xCu:yAl as a Function of Atmosphere during Preparation

Many phosphors containing various amounts of Cu and Al were prepared by adding appropriate quantities of copper sulfate and aluminum sulfate solutions to pure ZnS and firing at 950°-975°C for 2 hr in a stream of purified and dry H_2S. Parts of these phosphors, all of which showed bright blue and green fluorescence under 3650Å excitation, were refired in oxygen-free, dry H_2 for an additional 2 hr at the same temperature. Emission spectra were taken at liquid nitrogen temperatures with 3650Å excitation (General Electric BH-4 high-pressure mercury lamp with a Corning 5840 filter) using a recording spectroradiometer. The powdered samples were contained in a holder which permitted us to position each sample accurately with respect to the exciting light and the entrance slit of the spectroradiometer and also to obtain spectra at low temperatures.

In Fig. 1 are shown emission spectra, typical of many obtained, for phosphors in which $x = 0$, $x < y$, $x = y$, and $x > y$. The results show the sensitivity of the "self-activated blue" emission to H_2 refiring and the absence of any such marked effect on the "copper green" emission and the "copper blue" emission always obtained when $x > y$. The different spectral distribution of the copper blue band at liquid nitrogen temperatures compared to the self-activated blue emission has been cited as evidence that two different types of centers are responsible for these two blue bands (7). The different behavior of the fluorescent intensity after H_2 refiring is further evidence for this.

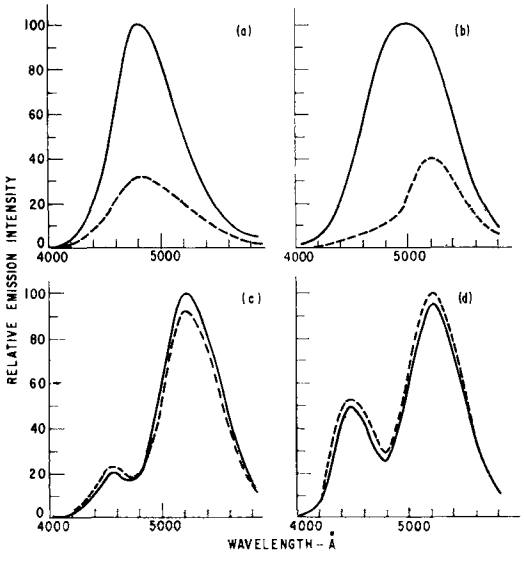

Fig. 1. Typical emission spectra at —196°C with 3650Å excitation of ZnS:xCu:yAl phosphors fired at 950°C in H_2S ——————; and refired at 950°C in H_2 - - - - - -. (a) $x = 0$; $y = 10^{-4}$; (b) $x = 2 \times 10^{-6}$; $y = 10^{-4}$; (c) $x = 10^{-4}$; $y = 10^{-4}$; (d) $x = 10^{-4}$; $y = 10^{-5}$.

To test the reversibility of this effect on the intensity of the blue self-activated emission after H_2 refiring, as well as its reproducibility, four phosphor samples were prepared, all of the composition ZnS:5 x 10^{-6} Cu:10^{-4} Al. These were then subjected to the following firing schedules at 975°C: (*a*) 2 hr in H_2S; (*b*) 2 hr in H_2S followed by 2 hr in H_2; (c) 2 hr in H_2S, 2 hr in H_2, 2 hr in H_2S; (*d*) 2 hr in H_2S, 2 hr in H_2, 2 hr in H_2S, and finally 2 hr in H_2. The emission spectra shown in Fig. 2 show again that there is a marked decrease in the intensity of the blue self-activated band on H_2 refiring. Furthermore, the effect is clearly reversible and reproducible. There appears also to be a small decrease in the green copper band intensity after H_2 refiring of those phosphors in which $y > x$. For $y = x$ and $y < x$, no such effect is observed within the limits of experimental reproducibility. The effect of H_2 refiring on the green band is very much smaller than on the self-activated blue band. The reason for this effect is not known at present but may very well be due to the increased association at nearest neighbor sites of the negatively charged copper acceptors with the larger concentration of available positively charged Al donors available at the high temperature when the phosphor is fired in H_2 and ionized Zn vacancies are destroyed. The effect of H_2 refining on the intensity of the self-activated blue emission described above for ZnS:Al has also been observed in ZnS:Ga phosphors. (See the third section of Discussion).

Spectral Distribution of the Self-Activated Emission in Cubic ZnS

ZnS:Al and ZnS:Ga phosphors were prepared as described in the previous section, except that the firing was carried out at 850°C. ZnS:Cl and ZnS:Br phosphors were prepared by firing ZnS in a stream of H_2S containing several per cent of anhydrous HCl or HBr at 850°C for 2 hr. Bright blue fluorescing materials were obtained in all cases. The low firing

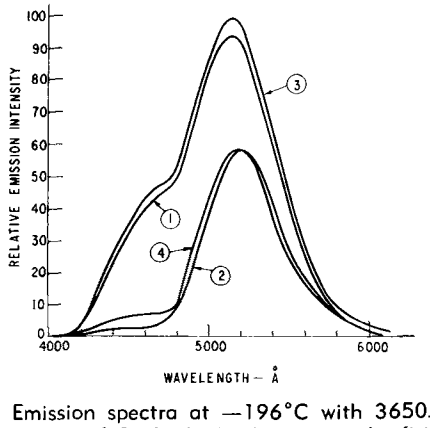

Fig. 2. Emission spectra at —196°C with 3650Å excitation of ZnS:5 x 10^{-6} Cu:10^{-4} Al subjected to the firing schedules described in the text.

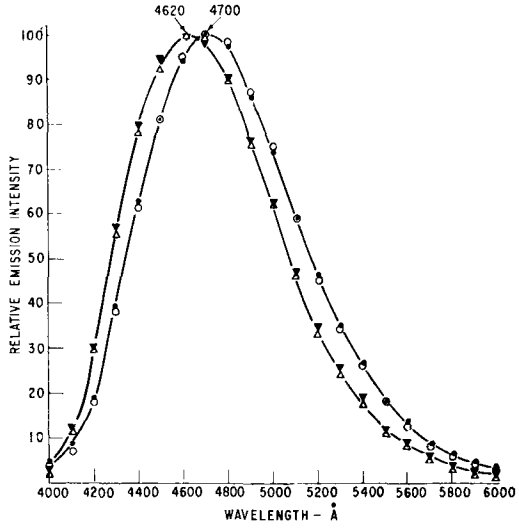

Fig. 3. Emission spectra at room temperature with 3650Å excitation of ZnS:10^{-3} Al, solid circle; ZnS:10^{-3} Ga, open circle; ZnS:Cl, open triangle; ZnS:B, solid inverted triangle; all fired at 850°C.

temperatures were used to assure the absence of any hexagonal phase in the ZnS phosphors, since it is known that the emission spectra are different for the cubic and hexagonal phases. The absence of any hexagonal phase was confirmed by obtaining long exposure x-ray diffraction patterns of the fired phosphors.

The emission spectra of four phosphors taken at room temperature are shown in Fig. 3. It is seen that the spectra of ZnS:Al and ZnS:Ga are identical as are the spectra of ZnS:Cl and ZnS:Br. However, the peak of the emission band of the latter two phosphors occurs at about 80Å toward shorter wave lengths than the peak of the first two phosphors. This effect of the coactivator impurity on the spectral distribution of the self-activated blue emission was also observed by Kröger and Dikhoff (1), although they placed no significance on this difference and indicated that the blue emission was independent of the coactivator. We believe this 80Å difference to be significant and this is discussed later in this paper.

The emission spectra of those phosphors containing halogen were also found to be independent of how the halogen was introduced. In Fig. 4, the emission spectra of halogen-containing phosphors prepared from HCl and H_2S, HBr and H_2S, NaCl, and NaI are compared to the phosphor ZnS:Al (10^{-3}) by plotting the ratios of the emission intensities (normalized to unity at 4700Å) at various wave lengths. The emission spectrum of the self-activated emission was found not to depend on the concentration of the coactivator. In Fig. 5, emission spectra of ZnS:Al (10^{-4}, 5 x 10^{-5}) and ZnS:Ga (10^{-3}, 10^{-4}) are compared to ZnS:Al (10^{-3}) by again plotting the ratios of emission intensities. Similar measurements of the emission intensity of various phosphors as a function of wave length compared to ZnS:Al (10^{-3}) also showed that the emission spectra were dependent neither on firing temperature so long as no hexagonal ZnS were formed, nor on the intensity of the exciting ultraviolet. The general conclusion is that

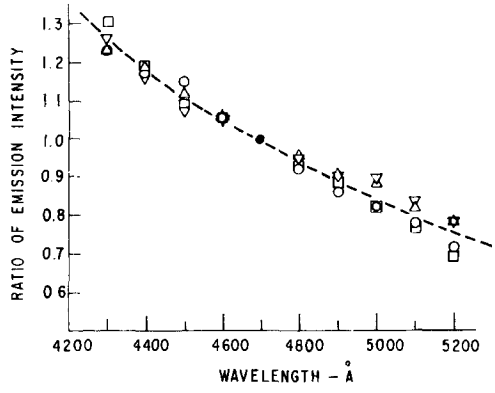

Fig. 4. Ratio of the emission intensity at room temperature and 3650Å excitation of the various phosphors given below to the emission intensity of ZnS:10^{-3} Al, as a function of wave length. (Intensities normalized to unity at 4700Å). Open circle, ZnS fired in H_2S containing HCl at 850°C; open square, ZnS fired in H_2S containing HBr at 850°C; open triangle, ZnS:5%NaCl fired in N_2 at 850°C; open inverted triangle, ZnS:2%NaI fired in N_2 at 925°C.

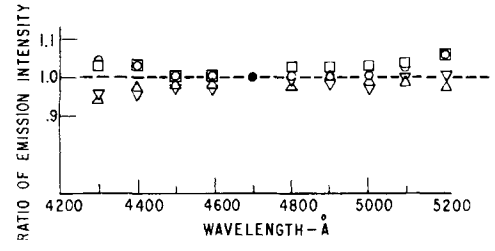

Fig. 5. Ratio of the emission intensity at room temperature and 3650Å excitation of the various phosphors given below to the emission intensity of ZnS:10^{-3} Al as a function of wave length. (Intensities normalized to unity at 4700Å). All phosphors were fired in H_2S at 850°C. Open circle, ZnS:10^{-4} Al; open square, ZnS:5 x 10^{-5} Al; open triangle, ZnS:10^{-3} Ga; open inverted triangle, ZnS:10^{-4} Ga.

the spectral distribution of the blue emission depended only on whether the coactivator used was one of the Group III or Group VII elements.

Discussion

Formation and Ionization of Zn Vacancies

ZnS phosphors prepared by firing at high temperatures will contain neutral Zn vacancies and S vacancies (V_{Zn}^0 and V_S^0) whose equilibrium concentration will depend on the temperature and pressure of S in the gas phase with which the solid is in equilibrium. The assumption will be made that lattice defects in ZnS are primarily vacancies, not interstitials. Work on CdS (8), CdSe (9), and other binary compounds has indicated that metal atom vacancies can behave as acceptors. Since the removal of a neutral Zn atom from ZnS removes two of the eight electrons in the four bonds to the neighboring sulfurs, a neutral Zn vacancy has two holes bound in its vicinity. These may be thermally ionized into the valence band as shown in Eqs. [1] and [2].

$$V_{Zn}^0 \rightleftharpoons V_{Zn}^{-1} + p - \epsilon_1 \quad [1]$$

$$V_{Zn}^{-1} \rightleftharpoons V_{Zn}^{-2} + p - \epsilon_2 \quad [2]$$

In these equations, p represents a hole in the valence band, and ϵ_1 and ϵ_2 are the thermal ionization energies. The energy released by the optical capture of a hole into V_{Zn}^{-1} can be computed approximately us-

ing a Bethe model (10). This energy would be equal to the ionization energy of a hydrogen atom in a polarizable medium whose static dielectric constant is that of ZnS. Similarly the energy released on capturing a hole optically into V_{Zn}^{-2} should be approximately the ionization energy of He^{+1} in a polarizable medium (11). For ZnS, with a static dielectric constant of 8, these energies are 0.21 e.v. and 0.84 e.v. These values can only be approximate for ZnS due to the fact that the holes move in small orbits around the charged Zn vacancies so that the details of the potential in the vicinity of the vacancy are important. Once the hole is captured in the center, the atoms surrounding the vacancy will move to new equilibrium positions, and the energy required for the optical ionization of the hole will be greater than 0.21 or 0.84 e.v. depending on the lattice polarization energy. The thermal ionization energies ϵ_1 and ϵ_2 will lie somewhere between these two limits (12).

Association of Charged Zinc Vacancies and Ionized Donor Impurities

Coactivator impurities such as Al or Cl in ZnS are donors and therefore constitute a single positively charged species when ionized (13). For the thermal ionization of Al we have

$$Al^0 \rightleftharpoons Al^{+1} + n - \epsilon_3 \qquad [3]$$

Here n is a conduction electron. These ionized centers interact coulombically with negatively charged Zn vacancies, and the equilibrium distribution of these two defects will therefore be a nonrandom one. Of particular interest is the strong interaction between V_{Zn}^{-2} and Al^{+1} or Cl^{+1}. For a concentration of each of 10^{-4}M at 1000°K, the fraction of V_{Zn}^{-2} and Al^{+1} associated into $V_{Zn}^{-2} - Al^{+1}$ pairs at neighboring Zn sites is about 0.9 (14). For $V_{Zn}^{-2} - Cl^{+1}$ the fraction will be even higher. At a large distance the associated pair appears as a single negative charge in ZnS and should therefore be capable of binding a hole in a localized orbital. This hole can be thermally ionized as follows

$$(V_{Zn} - Al)^0 \rightleftharpoons (V_{Zn} - Al)^{-1} + p - \epsilon_4 \qquad [4]$$

The energy released by the optical capture of a hole into the ionized acceptor can be estimated using a Bethe-type model in which the hole moves in the potential of a $-2e$ and a $+1e$ charge separated by a distance R in a polarizable medium. For cubic ZnS the distance R is 2.35Å when Cl, Br, or I are the donors and 3.84Å when Al or Ga are the donors. The particular group IIIB or VIIB impurity used would be expected to affect the position of the localized level only to a slight extent because the trapped hole moves in an orbit close to the doubly negatively charged Zn vacancy and therefore does not feel the inner potential peculiar to the donor impurity. Our primary interest is the difference in the binding energy of a hole to the two types of associated pairs characterized by the different distances R and particularly the sign of this difference. Therefore, the binding energy of a hole to such an associated pair embedded in a medium of dielectric constant 8 was calculated as a function of R. At very small or very large values of R the binding energy

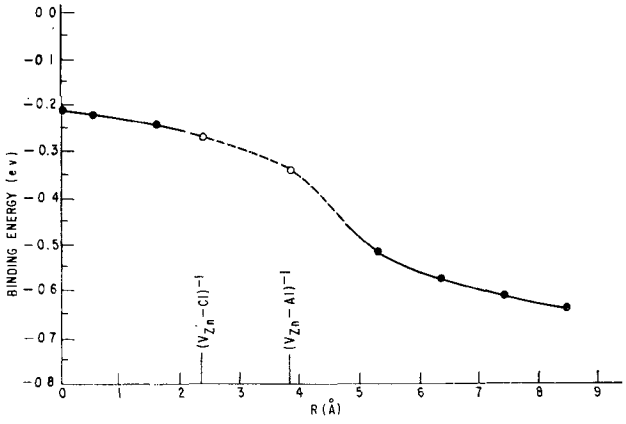

Fig. 6. Binding energy of a positive hole to fixed charges of —2e and +1e separated by a distance R (Å) in a polarizable medium of dielectric constant 8.

of a hole can be obtained by a perturbation treatment using hydrogen 1s wave functions. The binding energy in electron volts is:

$$E(\text{small } R) = -\frac{27.2}{2k^2} + \frac{27.2}{k^2R}\left[(0.529\,k - R) - (0.529\,k + R)\,e^{-2R/0.529\,k}\right] \qquad [5]$$

$$E(\text{large } R) = -\frac{54.4}{k^2} + \frac{27.2}{k^2R}\left[0.529\,k - (0.529\,k + 2R)\,e^{-4R/0.529\,k}\right] \qquad [6]$$

E is shown as a function of R in Fig. 6 for the dielectric constant $k = 8$. The two values of R of particular interest do not lie within the range where the simple perturbation treatment would be expected to be valid. Accordingly, for these two distances the energies were calculated using the continued fraction solutions given by Baber and Hassé for the ground state of the unsymmetrical hydrogen molecule ion (15). These two values are also given in Fig. 6 and are seen to differ by 0.07 e.v., the level due to $(V_{Zn} - Al; Ga)^{-1}$ lying higher above the valence band than the level due to $(V_{Zn} - Cl; Br; I)^{-1}$. This energy difference amounts to a 100Å difference at 4700Å and is therefore in accord with the observed difference of the emission spectra as shown in Fig. 3, both as to the direction and magnitude of the difference, provided that we assume that the lattice polarization energy following excitation of the phosphor is largely independent of the donor impurity making up the center. As was pointed out, the hole moves in an orbit close to the Zn vacancy so that it is not unreasonable to imagine that it is the vacancy which primarily governs the lattice polarization.

Concentration of Luminescent Centers $(V_{Zn} - Al)^{-1}$ as a Function of Sulfur Pressure

ZnS, heated for a sufficiently long time in a very slow stream of a gas, will attain a stoichiometry dependent on the composition of the gas (16). When H_2 is used as the gas atmosphere during firing we can show that the final effective sulfur pressure with which the solid phase is in equilibrium and which therefore determines the stoichiometry of the solid

is obtained by a solution of the equation (taking sulfur to be S_2 molecules in gas phase):

$$2p_{S_2}^{3/2} + K_d P_{H_2} p_{S_2} - K_p = 0 \quad [7]$$

P_{H_2} is the pressure of H_2, usually 1 atm, and K_d is the equilibrium constant for the dissociation of H_2S.

$$H_2 + \frac{1}{2} S_2 \rightleftharpoons H_2S \quad [8]$$

$$K_d = (p_{H_2S}/p_{S_2}^{1/2} \cdot p_{H_2}) \quad [9]$$

K_p is the equilibrium constant for the dissociation of ZnS molecules in the gas phase multiplied by the equilibrium pressure of ZnS molecules at the firing temperature:

$$ZnS \text{ (solid)} \rightleftharpoons ZnS \text{ (gas)}; \; p_{ZnS} = \text{constant} \quad [10]$$

$$ZnS \text{ (g)} \rightleftharpoons Zn \text{ (g)} + \frac{1}{2} S_2 \text{ (g)} \quad [11]$$

$$K_p = K_{ZnS} \cdot p_{ZnS} = p_{Zn} \cdot p_{S_2}^{1/2} \quad [12]$$

At 1000°K, Kelley (17) gives K_d as 144 $atm^{-1/2}$ and, according to Pogorelyi (18), $K_p = 1.63 \times 10^{-10}$ $atm^{3/2}$. With $P_{H_2} = 1$ atm, we get from Eq. [7] that $p_{S_2}^{1/2} = 1.06 \times 10^{-6}$ $atm^{1/2}$. On the other hand, if H_2S is used as the firing gas, we can show that p_{S_2} is obtained from:

$$2K_d p_{S_2}^2 + 2p_{S_2}^{3/2} - p_{S_2}^{1/2} (P_{H_2S} + K_p K_d) - K_p = 0 \quad [13]$$

With P_{H_2S}, the initial pressure of H_2S, equal to 1 atm, we get from Eq. [13] that $p_{S_2}^{1/2} = 0.15$ $atm^{1/2}$. These results show that firing ZnS phosphors for a sufficiently long time in a slow stream of H_2S at 1000°K followed by H_2 is equivalent to lowering the square root of the sulfur pressure by about five orders of magnitude.

We did not determine whether or not the gas flow rates we used were sufficiently slow to maintain equilibrium between the solid and gas phases. Thus in our experiments the ratio of effective values of $p_{S_2}^{1/2}$ might very well not have been as low as 10^{-5}. For this and, more important, for other reasons to be pointed out in the following paragraphs, only a qualitative comparison of experiment with calculations can be made at this time.

The method developed by Kröger and Vink (19) for calculating the concentrations of various defects as a function of sulfur pressure, can be applied to the system ZnS:Al (2.54×10^{18} cm^{-3}) by using the values of the equilibrium constants given in Table I.

If the concentrations of defects, impurities and charge carriers are expressed as number per cubic centimeter, then K_1 to K_4, which are the equilibrium constants for the reactions given in Eqs. [1] to [4], are taken to have the form $K = 2(2\pi mkT/h^2)^{3/2} \exp(-\epsilon/kT)$, the free electron mass being used. K_g is the equilibrium constant for the thermal production of electron-hole pairs.

$$ZnS \text{ (ground state)} \rightarrow n + p - \epsilon_g \quad [14]$$

$$K_g = [n]\,[p] \quad [15]$$

K_g is taken to be of the form $4\,(2\pi mkT/h^2)^3 \exp(-\epsilon_g/kT)$. Finally, the reciprocal of K_a is the equilibrium constant for the dissociation of the associated pair

$$(V_{Zn} - Al)^{-1} \rightleftharpoons V_{Zn}^{-2} + Al^{+1} \quad [16]$$

$$K_a = [(V_{Zn} - Al)^{-1}]/[V_{Zn}^{-2}]\,[Al^{+1}] \quad [17]$$

Neutral Zn vacancies are formed by the reaction

$$(1 - \delta)\; ZnS + \delta/2\; S_2 \rightleftharpoons Zn_{1-\delta}\; (V_{Zn}^{0})_\delta S \quad [18]$$

The application of the law of mass action for $\delta << 1$ gives

$$K_v = [V_{Zn}^{0}]\; p_{S_2}^{-1/2}\; cm^{-3}\; atm^{-1/2} \quad [19]$$

Since K_v is unknown for ZnS, the concentrations of all other defects and charge carriers were calculated as functions of $K_v\, p_{S_2}^{1/2}$ for ZnS:Al (2.54×10^{18} cm^{-3}) at 1000°K using the method of reference (19). The Schottky constant for ZnS, giving the equilibrium product of the concentrations of neutral Zn and S vacancies, is also unknown, so that we assumed that, in the range of sulfur pressures used, the concentration of ionized sulfur vacancies which can act as donors was much less than the concentration of Al^{+1}. After the high-temperature concentrations were determined, the concentrations at liquid nitrogen temperature were found by assuming that the total concentration of lattice defects and associated pairs is frozen in at 1000°K as the phosphor is cooled, whereas electrons and holes distribute themselves among the various available states in accordance with the equilibrium Eqs. [1] to [4] and [14] using the values of the equilibrium constants at 77°K also given in Table I. The results, shown graphically in Fig. 7, are to be taken only as an indication of the behavior of ZnS:Al because of the approximations used, some of which have been cited. Somewhat different approximations would still lead to the same general qualitative behavior with varying sulfur pressure. Nevertheless, it is of interest to note that the model used leads to the concentration of

$$(V_{Zn} - Al)^{-1}$$

Table I. Equilibrium constants for the system ZnS:Al

	Temp, 77°K		Temp, 1000°K		
	K_i	ϵ_i (e.v.)*	K_i	ϵ_i (e.v)*	Remarks
K_a	—	—	2.3×10^{-17}	—	From calc. deg. of assoc. (14)
K_1	2.1×10^{-20}	0.58	4.1×10^{17}	0.51	Assumed same as K_4
K_2	3.3×10^{-136}	2.32	7.6×10^{9}	2.0	ϵ_2 taken as four times ϵ_1
K_3	1.2×10^{2}	0.25	1.2×10^{19}	0.22	From thermal glow curve data (20)
K_4	2.1×10^{-20}	0.58	4.1×10^{17}	0.51	From temperature quenching data (21)
K_g	1.6×10^{-204}	3.66	1.6×10^{24}	3.20	From optical band gap data applying a correction of -5×10^{-4} ev/deg (22).

* All levels assumed to decrease with temperature at the same rate as the optical band gap.

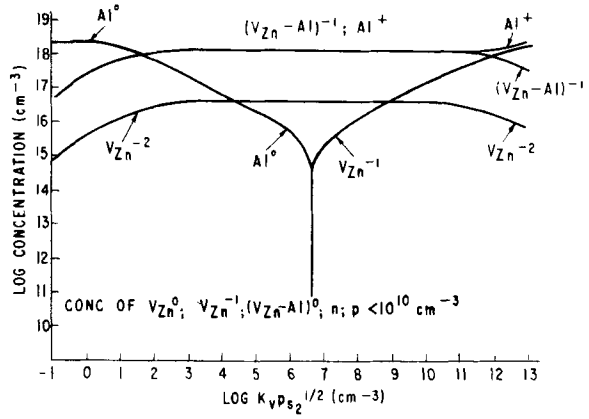

Fig. 7. Concentration of defects in ZnS:Al (2.54×10^{18} cm^{-3}) at —196°C after equilibration at 1000°K and various pressures of sulfur in the gas phase.

being practically constant at one-half the total Al concentration over a range of values of $p_{S_2}^{1/2}$ of about eight orders of magnitude. The indicated decrease in the concentration of this associated pair at low sulfur pressures is in accord with the experimental results given in this paper and the interpretation that a Zn vacancy is part of the luminescent center. The indicated decrease in the concentration of self-activated luminescent centers at high sulfur pressures was observed in CdS:Ga by Kröger, *et al.* (8), although the authors interpreted their results differently. Also, over a wide range of sulfur pressures the concentrations of Al°, V_{Zn}^0, V_{Zn}^{-1}, and $(V_{Zn} - Al)^0$ are less than 2×10^{16} cm^{-3}. Since these would be paramagnetic defects, it can be seen that only under special conditions of preparation would this phosphor be expected to have a measurable paramagnetic susceptibility.

Summary

Associated $(V_{Zn} - Al; Ga)^{-1}$ or $(V_{Zn} - Cl; Br; I)^{-1}$ pairs can form in ZnS containing Al, Ga, or a halogen as an impurity due to the strong coulombic interaction between ionized donor impurities and Zn vacancies. Calculations show their concentration can remain fairly constant at one-half the concentration of the donor impurity over a considerable range of sulfur pressures. At decreasing sulfur pressures the concentration of these pairs decreases. This is in accord with the observed decrease in the intensity of the blue luminescence after H_2 refiring of the self-activated phosphor.

The peak of emission spectrum of the blue luminescence depends on whether a group IIIB or group VIIB element is used as a coactivator indicating that the coactivator is a part of the luminescent center. Simple considerations suggest that the observed shift in peak position is in the right direction and of the correct order of magnitude.

On the basis of these results we conclude that the luminescent center in self-activated ZnS is a V_{Zn}^{-2} associated with the coactivator at a nearest possible site in ZnS. The associated pair gives rise to a localized acceptor level above the valence band just as do the usual activators such as Cu or Ag.

Acknowledgments

The authors acknowledge the help given them by Dr. F. J. Studer and Miss G. Lloyd in obtaining the emission spectra of the many phosphors prepared in the course of this study. Dr. B. Segall aided greatly in obtaining the solutions to the two-center problem used in this paper. Dr. D. T. F. Marple carried out the careful measurements of intensity ratio as a function of wave length of many phosphors containing Al, Ga, Cl, and Br. Finally the many discussions with Dr. F. E. Williams were instrumental in clarifying our ideas on the interpretation of the data and the model presented here for the self-activated luminescent center.

Manuscript received Oct. 27, 1958. This paper was prepared for delivery before the New York Meeting, April 27-May 1, 1958.

Any discussion of this paper will appear in a Discussion Section to be published in the December 1959 JOURNAL.

REFERENCES

1. F. A. Kröger and J. Dikhoff, *Physica*, **26**, 297 (1950).
2. F. A. Kröger and H. J. Vink, *J. Chem. Phys.*, **22**, 250 (1954).
3. R. Bowers and N. T. Melamed, *Phys. Rev.*, **99**, 1781 (1955).
4. J. S. Prener and F. E. Wiliams, *J. Chem. Phys.*, **25**, 361 (1956).
5. R. H. Bube, *Phys. Rev.*, **80**, 655 (1950); *J. Chem. Phys.*, **20**, 708 (1952); *J. Phys. Chem.*, **57**, 785 (1953).
6. A. Addamiano, *J. Chem. Phys.*, **23**, 1541 (1955).
7. R. E. Schrader and S. Larach, *Phys. Rev.*, **103**, 1899 (1956).
8. F. A. Kröger, H. J. Vink, and J. Van den Boomgaard, *Z. physik. Chem.*, **203**, 1 (1954).
9. D. de Nobel, Thesis, University of Leiden, May, 1958.
10. H. Bethe, M.I.T. Radiation Laboratory Report No. 43-12 (1942).
11. H. M. James and K. Lark-Horowitz, *Z. physik. Chem.*, **198**, 107 (1951).
12. M. Schön, *Z. Naturforschg.*, **6a**, 287 (1951).
13. J. S. Prener and F. E. Williams, *This Journal*, **103**, 342 (1956).
14. J. S. Prener, *J. Chem. Phys.*, **25**, 1294 (1956).
15. W. G. Baber and H. R. Hassé, *Proc. Cambridge Phil. Soc.*, **31**, 564 (1935).
16. J. Bloem and F. A. Kröger, *Z. physik. Chem. (Frankfurt)*, **7**, 15 (1956).
17. K. K. Kelley, *U. S. Bur. Mines Bull. 406* p. 20 (1937).
18. A. D. Pogorelyi, *J. Phys. Chem. U.S.S.R.*, **22**, 731 (1948).
19. F A. Kröger and H. J. Vink, Relations between the Concentrations of Imperfections in Crystalline Solids, in "Solid State Physics," Vol. 3, pp. 307-435, Academic Press, Inc. (1956).
20. W. Hoogenstraaten, *This Journal*, **100**, 356 (1953); F. A. Kröger, *Physica*, **21**, 637 (1956).
21. M. Schön, *Z. Naturforschg.*, **6a**, 287 (1951).
22. W. W. Piper, *Phys. Rev.*, **92**, 23 (1953).

A Double Diffused Silicon High-Frequency Switching Transistor Produced by Oxide Masking Techniques

J. F. Aschner, C. A. Bittmann, W. F. J. Hare, and J. J. Kleimack

Bell Telephone Laboratories, Incorporated, Murray Hill, New Jersey

ABSTRACT

The relative merits of two double diffused transistor structures are discussed, one of which employs a localized emitter. A process for producing the localized emitter structure is described employing the masking property of SiO_2 against the subsequent phosphorus diffusion. The dimensions of each emitter are controlled closely by etching away this oxide mask from only those regions not protected by a specially prepared photo resist coating. Transistors have been produced which switch 30 ma with a gain of 12, in times in which the sum of the turn-on, storage, and turn-off time is less than 0.1 μsec. Small signal alphas of 0.97, and alpha cut-off frequencies in the common base connection in excess of 300 mc have been achieved.

The need for high-frequency transistors, requiring extremely narrow base layers, has led to the development of new fabrication techniques. The adaptation of solid-state diffusion (1) has been found to permit a high degree of control of both the depth and concentration of an impurity necessary to produce such layers. In this paper an n-p-n silicon switching transistor is discussed, in which both the emitter and base layers are formed by diffusion. By making use of the masking properties of a specially prepared oxide layer, precise regulation of the geometry of the emitter region is attained. The electrical characteristics of transistors prepared by these techniques are presented.

Double Diffused Structure

In Fig. 1(a) the essential features of a transistor produced by a double diffusion process (2) are illustrated. A p-type impurity is diffused first into the n-type wafer to form a collector junction about 0.2 mils from the surface. An n-type emitter dopant having a much higher impurity concentration is then diffused into this layer. This overcompensates the original diffused impurity until such a depth is reached that their concentrations are equal. The emitter junction, so formed, is located at this depth. The separation of the two junctions, defining the base layer, can be reproduced to within 0.005 mils.

In this type of transistor, since the emitter layer entirely covers the base layer, a metallic base contact is alloyed through the emitter. Furthermore, the regrowth region around this contact must form a rectifying junction with the emitter layer, in order for the device to operate as a transistor; otherwise, the base would be shorted to the emitter. With a suitable choice of materials, this technique is quite feasible, and transistors have been built this way. However, certain limitations are imposed. In order to have a rectifying junction between the base contact and the emitter layer through which it passes, an upper limit is placed on the surface concentration of the emitter diffusant, thus limiting emitter efficiency. Alternatively, the highly doped portion of the emitter immediately surrounding the base contact may be removed by an etching process. The latter, in fact, is the preferred choice but suffers from control difficulties as the electrical characteristics of the transistor are quite sensitive to the depth reached by this etch.

The present paper is concerned with a process in which the masking properties of a silicon dioxide layer against certain diffusants have been exploited to circumvent these difficulties (3, 4). By removing the oxide from selected regions on the surface, the emitter diffusant can penetrate into the base layer only at each of these designated areas, leaving the base layer exposed to the surface everywhere else [Fig. 1(b)]. Contact to the base region thus may be made without difficulty after the remaining oxide has been removed. The elimination of any emitter etch and the freedom to make use of high emitter

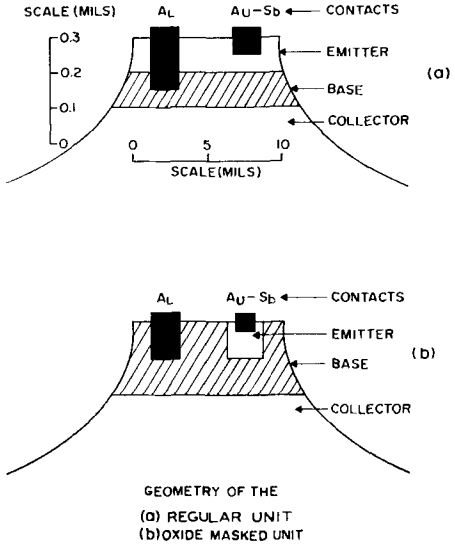

Fig. 1. Cross section of two double diffused transistor structures. Geometry of (a) regular unit, (b) oxide masked unit.

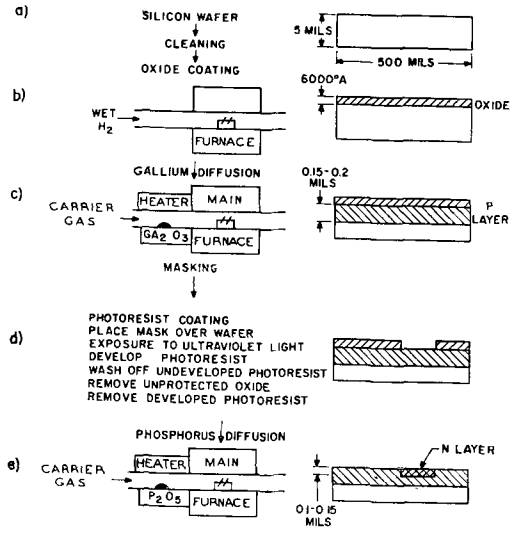

Fig. 2. Detailed diffusion and masking process.

concentrations are considerable advantages. In addition, limiting the emitter area results in a lower emitter capacity.

Oxide-Masking Technique

The masking process is illustrated in detail in Fig. 2. N-type silicon wafers of about 0.3 ohm-cm resistivity are cut into squares and lapped to obtain the highly polished surface essential to the production of uniform diffused junctions. A silicon dioxide layer is now grown over the surface; a simple method is illustrated, in which wet hydrogen is passed over the heated wafers to produce the 8000Å oxide layer required. Using the technique developed by Frosch (3, 4), the base layer dopant, gallium, is diffused into the wafer to a depth of about 0.2 mils. The oxide coating only slightly inhibits the rate of gallium diffusion.

The oxide now must be removed, selectively, from the 100 3 mil x 6 mil designated areas on the surface into which emitters are to be diffused. For clarity, only one emitter area, much enlarged, is shown in Fig. 2. To achieve this, the wafer is dipped into a photo resist solution,[1] dried in air, and exposed to ultraviolet light through a film mask which covers only those areas which are to be the emitters. The photo resist over these areas is not exposed to the light and, after the exposed portion is developed, is easily washed off in water. The oxide unprotected by the photo resist is removed in a slow etch. Finally, all of the photo resist is dissolved to give the structure in Fig. 2(d).

The second diffusion, with phosphorus as the impurity, is now carried out. In the time necessary to diffuse through the exposed regions to the required depth of about 0.1 mil, there is no diffusion through the oxide. To produce much deeper emitter junctions, thicker oxide layers would have to be prepared to insure complete masking. The final diffused structure of a single transistor is shown in Fig. 2(e).

To illustrate the control attained over the geometry of the emitters, an actual photomicrograph of

[1] Such as one made by the Eastman Kodak Co. A description of the general properties of this material is given in the pamphlet "Industrial Uses of Kodak Photo Resist," a manual prepared by Eastman Kodak Co., Rochester 4, N. Y.

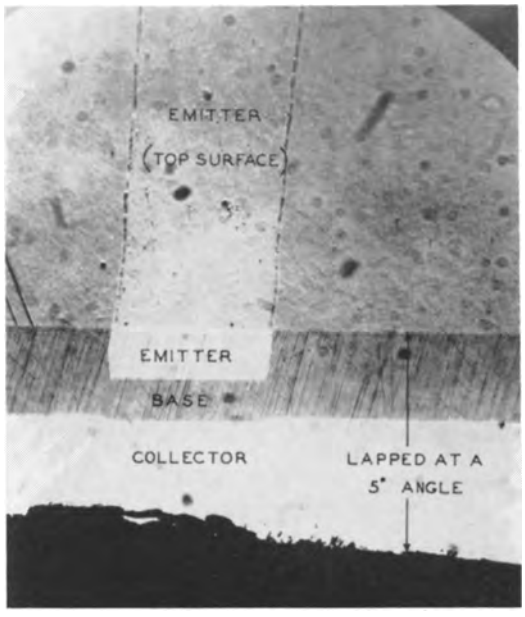

Fig. 3. Photomicrograph of an oxide masked double diffused unit. The junction has been exposed by beveling at a slight angle and staining the p-layer.

a unit is presented in Fig. 3. The transistor has been lapped at an angle of five degrees to the surface and the base layer stained with a hydrofluoric-nitric acid etch (5) to delineate the junctions clearly. Both collector and emitter junctions are seen to be quite straight, any imperfections being much less than the layer thicknesses.

In the next step, Au-Sb emitter contacts and Al base contacts are evaporated through masks. To insure that the former fall entirely within the emitter areas and that the latter are positioned accurately close to the emitter edges but within the base layer, the masks are indexed carefully with respect to the original film mask used to prepare the emitters. Again, considerable control is needed in the definition of the emitter areas on the surface to prevent emitter-to-base shorts. The unlapped part of the wafer in the photomicrograph of Fig. 3, showing one such emitter area prior to the evaporation of contacts, clearly illustrates the close control of the emitter geometry that can be achieved by this masking technique.

The subsequent fabrication process follows standard procedures of collector bonding, lead attachment, and encapsulation.

Results and Discussion

The electrical characteristics of n-p-n, silicon, switching transistors prepared using the above techniques are presented in Table I. The base layers are normally from 0.05 to 0.10 mils in width. As some of the electrical parameters are quite sensitive to this width, results from some experimental units with a much thinner base layer (0.029 mils) are also shown.

The static characteristics of the normal units show a high collector to emitter breakdown voltage, a low emitter junction breakdown due to the high impurity gradient at this junction, and the low reverse saturation currents expected with silicon devices.

Table I.

	Normal median values	Thin base median values	Units
Number of units	9	20	
Emitter thickness	0.09	0.04	mils
Base thickness	0.08	0.029	mils
BV_{CBO} at $I_{co} = 1\ \mu a$	65	27	volts
BV_{EBO} at $I_{eo} = 1\ \mu a$	3	8	volts
I_{co} at $V_{CB} = 4.5$ V	2×10^{-10}	9×10^{-9}	amps
C_c at $V_{CB} = 4.5$ V	5	6	$\mu\mu f$
hie at $V_{CE} = 5V$, $I_c = 10$ ma	400	450	ohms
Switching times			
at $I_c = 30$ ma, $I_{B_1} = 2.5$ ma			
$V_{B_2} = O$ V			
t_0	0.03	0.03	μsec
t_1	0.03	0.03	μsec
t_2	0.04	0.03	μsec
V_{CE} at $I_C = 30$ ma, $I_B = 2.5$ ma	0.5	0.9	volts
V_{BE} at $I_C = 30$ ma, $I_B = 2.5$ ma	0.9	1.1	volts
Small signal alpha			
at $V_{CB} = 4.5$ V			
$I_E = 0.1$ ma	0.927	0.939	
1 ma	0.960	0.976	
10 ma	0.973	0.987	
30 ma	0.972	0.985	
hfe at f = 30 mc, $V_{CE} = 5V$	14	21	db
$I_E = 5$ ma			

The small size of the unit is reflected in the low collector capacitance of 5 $\mu\mu f$. Base resistances of 200-300 ohms are encountered normally.

The electrical parameters of interest for switching applications also are summarized in Table I. In the circuit used for measuring the switching time, the units are usually in the ON or saturation condition, with 2.5 ma base drive and 30 ma collector current. They are turned off by a negative pulse to the base which thus is driven to ground potential. The total switching time is the sum of storage time t_1, turn-off time t_2, and turn-on time t_0. For switching 30 ma with a gain of 12, total switching times of the order of 0.1 μsec have been measured.

Finally, the gain characteristics are given. The low-frequency short-circuit current gain, alpha, is fairly high for this transistor and varies only slightly over the operating range. The variation both with emitter current and collector voltage is presented in Fig. 4. The fact that alpha is independent of the reverse collector voltage is of considerable advantage in the design of circuits using the unit. The advantage gained from the use of such a narrow base device is apparent from the current gain at high frequency (hfe). For the normal units, the measured gain of 14 db at 30 mc corresponds to an alpha cut-off frequency of approximately 150 mc.

An analysis of the data for the extremely thin base experimental units emphasizes the favorable high-frequency behavior. The gain has been measured as a function of frequency both for the common emitter and common base connection (Fig. 5) for a thin base unit. The alpha cut-off frequency of 350 mc is comparable to the best germanium transistors if the difference in mobility is taken into account. These units also show a small but significant

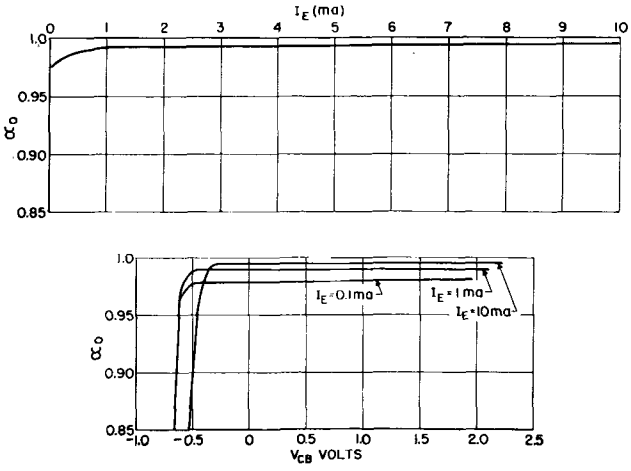

Fig. 4. The variation of alpha with emitter current and collector voltage for an oxide masked unit.

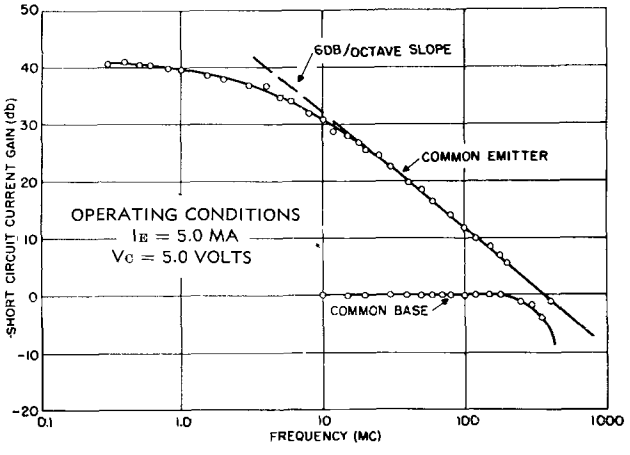

Fig. 5. The current gain vs. frequency for a thin base unit, both in the common emitter and common base connection.

improvement in the low frequency alpha. The collector to base reverse breakdown voltage is substantially lower than in the regular units due to reach-through effects; however, it is still high enough for many switching circuit applications.

Acknowledgments

The authors wish to acknowledge the contributions of W. C. Hittinger, who suggested this approach to the problem, M. Mandel (now at Stanford University), and D. L. Kushler. Thanks are also due to D. E. Thomas for making the frequency measurements.

Manuscript received July 18, 1958. This paper was prepared for delivery before the New York Meeting, April 27-May 1, 1958.

Any discussion of this paper will appear in a Discussion Section to be published in the December 1959 JOURNAL.

REFERENCES

1. C. A. Lee, *Bell System Tech. J.*, **35**, 23 (1956).
2. M. Tanenbaum and D. E. Thomas, *ibid.*, **35**, 1 (1956).
3. C. J. Frosch and L. Derick, U. S. Pat. 2,802,760.
4. C. J. Frosch and L. Derick, *This Journal*, **104**, 547 (1957).
5. C. S. Fuller and J. A. Ditzenberger, *J. Applied Phys.*, **27**, 544 (1956).

Equilibrium Reduction of Tungsten Oxides by Hydrogen

Robert C. Griffis

Refractory Metals Laboratory, General Electric Company, Cleveland, Ohio

ABSTRACT

A complete study has been made of the heterogeneous equilibrium involving the four tungsten oxides, water, and hydrogen, using a modified static equilibrium apparatus. These data show that the initial results, previously reported, are in error due to thermal diffusion. The new data were used to compute the standard heats of formation and entropies of the solid oxide species as follows:

WO_2, $\Delta H_f^\circ = -134.0 \pm 0.7$ kcal/g-atom W, $S^\circ_{298} = 19.7 \pm 1.0$ e.u./g-atom W
$WO_{2.72}(W_{18}O_{49})$, $\Delta H_f^\circ = -180.3 \pm 1.4$ kcal/g-atom W, $S^\circ_{298} = 25.0 \pm 1.4$ e.u./g-atom W
$WO_{2.90}(W_{20}O_{58})$, $\Delta H_f^\circ = -193.1 \pm 1.4$ kcal/g-atom W, $S^\circ_{298} = 23.6 \pm 1.4$ e.u./g-atom W
WO_3, $\Delta H_f^\circ = -202.8 \pm 1.4$ kcal/g-atom W, $S^\circ_{298} = 19.1 \pm 1.4$ e.u./g-atom W

Since the previous paper (1) there have been several significant developments in the literature which warrant notice. The high-temperature form (above 740°C) of WO_3 has been the subject of two more investigations (2, 3). Vasil'eva, *et al.* (3) have made a thermodynamic study of the series of suboxides formed from the high-temperature species of WO_3. They reported that the structure of the oxide formed by the reduction of WO_3 is determined by the structure of the WO_3. This gives rise to a series of heretofore unreported tungsten suboxides. In addition to this, some very interesting evidence as to metallic nature of beta tungsten has been presented (4, 5).

The purpose of this paper is to discuss the etiology of the thermal diffusion error in the initial results for the heterogeneous equilibrium involving H_2-W-WO_2-H_2, and to present new data for the heterogeneous equilibrium involving the complete reduction of WO_3 to W.

Experimental Procedure

All reagents were prepared as previously described (1). X-ray analyses of the products of the equilibrium reactions are discussed in the next section.

The extension of the reported experimental techniques to the higher oxide systems was found to be impracticable (1). The limiting H_2O vapor pressure resulted in large relative errors when the value of K_p was greater than one. It was experimentally difficult to thermostat the condensing bulb at higher than room temperature since provision had to be made for cooling the cold finger. There was also an indication of increased mass transfer of the oxides in the vapor phases, especially at high H_2O vapor pressures and temperatures. This increase in volatility in the presence of H_2O has been reported in the literature (6, 7). Effects encountered here were cumulative in nature only, and the amount of oxide lost in any one run was negligible, but the effects of 10-20 runs resulted in a visible oxide film at the exit of the reaction chamber. The original reaction chamber, due to its circular nature, could not be cleaned out in a reasonable time. The situation was aggravated also by accidental spillage inside the chamber.

Apparatus.—The design and construction of the new experimental apparatus closely followed the original work of Emmett and Schultz (8). The entire apparatus is present in Fig. 1. It should be noted that the hot reaction gases over the sample are pumped into the restricted section of the reaction chamber and thence to the H_2O vapor saturator. This design also facilitates removal of the chamber for periodic cleaning. The temperature of the water bath is regulated to within ±0.02°C by means of a mercury thermoregulator and zero current relay. The container is a Pyrex glass jar 12 in. in diameter and 18 in. high, holding approximately 7 gal of double distilled water. It is fitted with a plastic cover to minimize evaporation losses and to keep out dust. The supports for the water saturator and man-

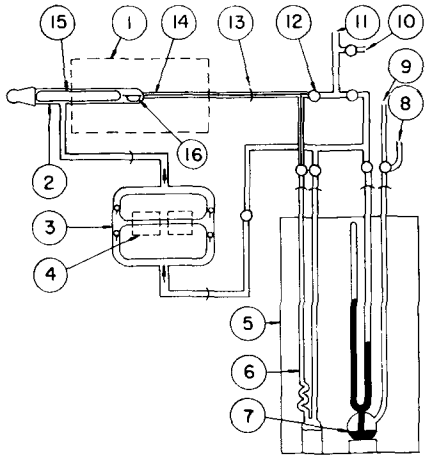

Fig. 1. Equilibrium apparatus: 1, furnace; 2, quartz reaction chamber; 3, gas pump; 4, solenoids; 5, thermostated, constant temperature water bath; 6, water vapor saturator; 7, mercury manometer; 8, to atmosphere; 9, to high vacuum; 10, to hydrogen or argon; 11, to high vacuum manifold; 12, 4 mm high vacuum stopcocks; 13, 18/7 spherical high vacuum glass joints; 14, restricted section and exit capillary; 15, sealed quartz tube used as plug; 16, sample boat.

ometer are fashioned from brass, copper, and Teflon.

The basic design for the gas solenoid pump was furnished by Seybolt (9) and is similar to that recently described by Bennett (10). A Teflon encased drill rod is used as a piston. This piston was machined to give a tight fit in ½ in. OD Pyrex glass tubing. This size of glass tubing was chosen so as to fit the readily available commercial solenoids. The piston was then hand lapped to give a smooth sliding action. A port is also provided for easy removal of the piston, if necessary. Small blocks of iron transformer core were placed on the upper part of the glass tube on the outside of the solenoids next to the vertical sections of the pump. When the solenoid is energized the iron blocks attract the iron core of the piston and tend to lengthen the stroke. This action results in a floating effect which enables the pump to run continuously for 8-10 hr at a temperature of 60°C without variation in pumping speed. The pumping frequency is 60 cycles/min and is obtained by a cam, synchronous motor, and breaker point assembly. The pumping capacity was measured as 250 cc/min by a water displacement method at atmospheric pressure. There was no evidence of decomposition of the Teflon piston at 60°C when it was operated in a vacuum.

All the glass tubing, including stopcocks, is heated with asbestos-covered resistance wire and wrapped with Al foil strips. The high vacuum stopcocks operate efficiently at 60°C if the proper greasing technique is used. Enough heat is conducted from the quartz reaction chamber to prevent condensation of H_2O in this section. The H_2O vapor pressure therefore is determined only by the temperature of the water bath which is carefully regulated. The same reaction furnace was used. The constant temperature zone (± 1°C) was increased to 4 cm due to increased end insulation and radiation shielding. The control thermocouple and recorder were rechecked against a Bureau of Standards Certificate Pt-Pt-10%Rh to ± 1°C for the entire temperature range. The mercury manometer readings were made with a precision cathetometer to ±0.03 mm.

This new experimental apparatus was used to determine once again the Fe-H_2O-H_2-Fe_3O_4 equilibrium over the temperature range 400°-550°C. Data were some 20% higher than those obtained with the initial apparatus, while data for the system H_2-W-WO_2-H_2O were slightly lower than the previous data. Vasil'eva and Gerasimov (11) suggested some changes in the experimental apparatus. They were of the opinion that the flow of the hot reaction gases was not great enough to eliminate thermal diffusion. At their suggestion the exit capillary of the reaction chamber was made 1 mm ID and most of the space in the reaction chamber was occupied by inserting a sealed quartz tube after the sample boat was inserted. This resulted in a much higher flow of gases through the hot reaction zone.

These improvements enabled data to be obtained for the system Fe-H_2O-H_2-Fe_3O_4 which agreed essentially with that obtained using the original apparatus (1); however, the K_p's now obtained for the system H_2-W-WO_2-H_2O were considerably lower than those obtained previously. The apparent paradox can be explained by examining the conditions under which the original apparatus was used. In the original apparatus the entire reaction chamber was insulated by Al foil guards. The auxiliary furnace was operated at about 300°C while the reaction furnace varied from 400° to 550°C for the reference Fe-H_2O-H_2-Fe_3O_4 system. Under these conditions the temperature gradient was not large enough over the closed tube chamber to bring thermal diffusion effects into play and/or convection circulation was sufficient to overcome this effect. In working with the tungsten oxide system, however, the temperature ranged from 500° to 1000°C. Under these conditions the effects of thermal diffusion evidently had a considerable influence on the data obtained.

Therefore, it is believed that thermal diffusion effects were eliminated in the system described above because; (*A*) the positive pressure action of the pump maintained a forced circulation of the reaction gases; (*B*) the velocity of the gases in the reaction chamber was increased by eliminating as much as possible of the dead space by means of the sealed quartz tube; and (*C*) the exit gases were conducted by means of a 1 mm capillary directly to the water vapor saturator.

X-ray studies.—The x-ray investigation was concerned with two areas of interest. The first area involved routine x-ray examinations of the solid phases in the equilibrium samples, using powder camera techniques. This study showed only the tungsten oxide phases as reported by Magneli, *et al.* (12).

The second area of interest concerned the new structures of the suboxides described by Vasil'eva, *et al.* (3). Samples in this study consisted of the pure tungsten oxides in contrast to the solid two-phase samples encountered in the equilibrium samples. A General Electric XRD-5 x-ray diffractometer was used to examine the quenched samples so as to obtain the data as soon as possible. Copper K radiation was used since the resolution achieved was sufficient for this study. It has been pointed out that reliable determination of angular position and intensities of the diffraction peaks requires considerable attention to the preparation and mounting of the sample powders (13). The samples were mounted according to the procedure as outlined by McCreery (14). Several samples were examined for each oxide in order to detect gross variations. The pure oxide samples were sealed in quartz tubes after careful evacuation at less than 0.1 μ pressure for a period of 8 hr. These capsules were held at 1000°C for approximately 18 hr. The samples were quenched to room temperature by dropping the hot capsule into a reservoir of water. The quenched powder which was still under vacuum was removed by breaking the capsule. Total time required for quenching and preparing the sample was 3 min. In one instance a sample of WO_3 was heated in air, quenched directly into water, filtered, washed with acetone for drying purposes, and then prepared for x-ray.

Table I. Equilibrium data for the system WO_3-H_2-$WO_{2.90}$-H_2O

Temp, °C	$K_p = \frac{P_{H_2O}}{P_{H_2}}$	Temp, °C	$K_p = \frac{P_{H_2O}}{P_{H_2}}$	Temp, °C	$K_p = \frac{P_{H_2O}}{P_{H_2}}$
600	2.30	700	5.10	800	8.40
600	2.21	700	4.91	800	9.20
600	2.39	700	5.30	800	9.61
600	2.28	700	5.24	800	9.12
600	2.25	700	5.05	800	9.71
600	2.32	700	5.12	800	9.54

Table II. Equilibrium data for the system $WO_{2.90}$-H_2-$WO_{2.72}$-H_2O

Temp, °C	$K_p = \frac{P_{H_2O}}{P_{H_2}}$	Temp, °C	$K_p = \frac{P_{H_2O}}{P_{H_2}}$	Temp, °C	$K_p = \frac{P_{H_2O}}{P_{H_2}}$
600	1.20	700	3.20	800	7.20
600	1.25	700	3.10	800	7.37
600	1.17	700	3.27	800	7.02
600	1.19	700	3.30	800	7.15
600	1.21	700	3.17	800	7.23
600	1.23	700	3.22	800	7.10

Table III. Equilibrium data for the system $WO_{2.72}$-H_2-WO_2-H_2O

Temp, °C	$K_p = \frac{P_{H_2O}}{P_{H_2}}$	Temp, °C	$K_p = \frac{P_{H_2O}}{P_{H_2}}$	Temp, °C	$K_p = \frac{P_{H_2O}}{P_{H_2}}$
600	0.880	700	1.10	800	1.31
600	0.892	700	1.05	800	1.29
600	0.894	700	1.13	800	1.35
600	0.873	700	1.08	800	1.33
600	0.850	700	1.10	800	1.27
600	0.861	700	1.05	800	1.33
900	1.50				
900	1.45				
900	1.54				
900	1.48				
900	1.51				
900	1.47				

Table IV. Equilibrium data for the system WO_2-H_2-W-H_2O

Temp, °C	$K_p = \frac{P_{H_2O}}{P_{H_2}}$	Temp, °C	$K_p = \frac{P_{H_2O}}{P_{H_2}}$	Temp, °C	$K_p = \frac{P_{H_2O}}{P_{H_2}}$
600	0.175	700	0.269	800	0.390
600	0.168	700	0.272	800	0.385
600	0.178	700	0.260	800	0.394
600	0.164	700	0.267	800	0.401
600	0.173	700	0.265	800	0.388
600	0.171	700	0.263	800	0.386
900	0.535	1000	0.687		
900	0.521	1000	0.667		
900	0.540	1000	0.690		
900	0.550	1000	0.665		
900	0.525	1000	0.670		
900	0.531	1000	0.683		

Results and Discussion

All of the data was obtained by alternate reduction and oxidation of the samples. The sample consisted of a mixture of the two solid phases concerned for the particular heterogeneous equilibrium being investigated. This is in contradistinction to the method of Vasil'eva, *et al.* (3) who prepared the phases *in situ* by the reduction of WO_3. The two phases were introduced in order to achieve equilibrium conditions as soon as was practicable and to avoid excessive sintering effects which sometimes invalidate the data obtained for experimental runs involving long times and/or high equilibrium gas ratios. The 2-g sample was evacuated to less than 0.1 μ and held there for at least 3 hr. Each sample was subjected to conditioning runs under oxidizing and reducing conditions before the final run was made. The system was evacuated after the final equilibrium measurements were made and the sample cooled to room temperature. All equilibrium samples then were examined by x-ray, using powder camera techniques, to identify the solid phases present. The temperature regions investigated were limited by the significant volatility of the higher tungsten oxides in the presence of water vapor, as was pointed out in the first paragraph.

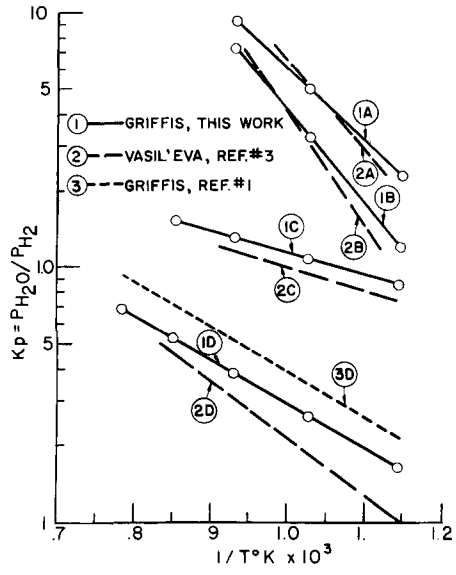

Fig. 2. Plot of log $K_p = \frac{P_{H_2O}}{P_{H_2}}$ vs. $\frac{1}{T°K}$ for the systems:

(1A)(2A)—WO_3-H_2-$WO_{2.90}$-H_2O
(1B)(2B)—$WO_{2.90}$-H_2-$WO_{2.72}$-H_2O
(1C)(2C)—$WO_{2.72}$-H_2-WO_2-H_2O
(1D)(2D)(3D)—WO_2-H_2-W-H_2O

The data are summarized in Tables I-IV, and Fig. 2.

C_p's for the equilibrium reactions were calculated on the basis of literature values for H_2, H_2O, WO_3 (15), W (16), and Kopp's rule for the tungsten oxides since no literature values are available. The equilibrium values in Tables I-IV were treated by means of sigma functions and the method of least squares. Literature values (17) of $\Delta F°_{298}$ (−109, 200 cal) and $\Delta H°_{298}$ (−115, 600 cal) for the reaction $2H_2 + O_2 \rightarrow 2H_2O$ were used to calculate $\Delta H°_f$ for each oxide. The standard entropy values of W and O_2 (18) were used to calculate the standard entropies of the oxides. The results of these calculations are tabulated in Table V.

The lack of reliable heat capacity data accounts for the large estimated error assigned to these values. The heats of formation reported here (Table VI) are compared with those obtained by direct combustion techniques (1).

Table V. Results of thermodynamic calculations

(A) $10\ WO_3 + H_2 \rightarrow 10\ WO_{2.90} + H_2O$

$\Delta H^\circ = 42{,}300 + 1.90T - 33.1 \times 10^{-3} T^2 + 0.04 \times 10^5 T^{-1}$

$\Delta F^\circ = 42{,}300 - 1.90T\ln T + 33.1 \times 10^{-3} T^2 + 0.02 \times 10^{-5} T^{-1} - 66.0T$

$\Delta H^\circ_{298} = +39.9 \pm 1.0$ kcal

$\Delta F^\circ_{298} = +22.4 \pm 1.0$ kcal

$W + 3/2\ O_2 \rightarrow WO_3$

$\Delta H^\circ_{298} = -202.8 \pm 1.4$ kcal/g-atom W

$S^\circ_{298}\ WO_3 = 19.1 \pm 1.4$ e.u./g-atom W

(B) $100/18\ WO_{2.90} + H_2 \rightarrow 100/18\ WO_{2.72} + H_2O$

$\Delta H^\circ = 19{,}100 - 3.35T + 0.89 \times 10^{-3} T^2 + 0.04 \times 10^5 T^{-1}$

$\Delta F^\circ = 19{,}100 + 3.35T\ln T - 0.89 \times 10^{-3} T^2 + 0.02 \times 10^5 T^{-1} - 44.1T$

$\Delta H^\circ_{298} = +18.2 \pm 1.0$ kcal

$\Delta F^\circ_{298} = +11.6 \pm 1.0$ kcal

$W + \frac{2.90}{2} O_2 \rightarrow WO_{2.90}$

$\Delta H^\circ_{298} = -193.1 \pm 1.4$ kcal/g-atom W

$S^\circ_{298}\ WO_{2.90} = 23.6 \pm 1.4$ e.u./g-atom W

(C) $100/72\ WO_{2.72} + H_2 \rightarrow 100/72\ WO_2 + H_2O$

$\Delta H^\circ = 6110 - 3.35T + 0.89 \times 10^{-3} T^2 + 0.04 \times 10^5 T^{-1}$

$\Delta F^\circ = 6110 + 3.35T\ln T - 0.89 \times 10^{-3} T^2 + 0.02 \times 10^5 T^{-1} - 28.6T$

$\Delta H^\circ_{298} = 5.2 \pm 1.0$ kcal

$\Delta F^\circ_{298} = 3.2 \pm 1.0$ kcal

$W + \frac{2.72}{2} O_2 \rightarrow WO_{2.72}$

$\Delta H^\circ_{298} = -180.3 \pm 1.4$ kcal/g-atom W

$S^\circ_{298}\ WO_{2.72} = 25.0 \pm 1.4$ e.u./g-atom W

(D) $\frac{1}{2}\ WO_2 + H_2 \rightarrow \frac{1}{2}\ W + H_2O$

$\Delta H^\circ = 10{,}125 - 3.48T + 1.08 \times 10^{-3} T^2 + 0.04 \times 10^5 T^{-1}$

$\Delta F^\circ = 10{,}125 + 3.48T\ln T - 1.08 \times 10^{-3} T^2 + 0.02 \times 10^5 T^{-1} - 30.7T$

$\Delta H^\circ_{298} = +9.2 \pm 0.5$ kcal

$\Delta F^\circ_{298} = +6.8 \pm 0.5$ kcal

$W + O_2 \rightarrow WO_2$

$\Delta H^\circ_{298} = 134.0 \pm 0.7$ kcal/g-atom W

$S^\circ_{298}\ WO_2 = 19.7 \pm 1.0$ e.u./g-atom W

Table VI. Heats of formation of tungsten oxides

Oxide	ΔH_f° kcal/g-atom W Combustion	Equilibrium
WO_3	-199 ± 1	-202.8 ± 1.4
$WO_{2.90}$	-193 ± 1	-193.1 ± 1.4
$WO_{2.72}$	-183 ± 1	-180.3 ± 1.4
WO_2	-137 ± 1	-134.0 ± 0.7

The x-ray examination of the equilibrium samples, as was previously pointed out, showed no evidence of the structure reported by Vasil'eva, *et al.* (3). The structure of the equilibrium oxide phases corresponded only to those reported by Magneli, *et al.* (12).

The x-ray examination of the pure oxides phases, as outlined under the second area of interest, was also unsuccessful in revealing any new structures for the tungsten oxides. All of the samples heated at 1000°C and quenched gave only the tungsten oxide patterns as previously reported (12). The tetragonal structure of WO_3 above 740°C had been confirmed by dilatometric (19), x-ray, and differential thermal analysis data (20-22). Perri, *et al.* (2) showed that there is a smooth transition from the monoclinic form of WO_3 to the orthorhombic form at about 300°C, and a sharp transition to the tetragonal form at 720°C. The high-temperature form (above 740°C) of WO_3 was described as orthorhombic by Vasil'eva on the basis of examination of rapidly cooled samples of WO_3. As stated above, this study failed to detect any "quenched-in" high-temperature form. The one sample of WO_3, which was cooled by pouring the hot powder into H_2O, did show some evidence of increase in the *d* values obtained from 001, 020, 200 reflections. This comportment indicates a shift to the orthorhombic structure. The peaks were recorded in their normal positions, however, after 15 min. The data obtained from the diffractometer, especially at slow scanning speeds, were sufficiently precise so as to show the possible shift in structure for all the tungsten oxides. The question as to whether the tungsten oxides prepared *in situ* by Vasil'eva and subsequently cooled rapidly have a different structure from those prepared by direct synthesis, using WO_3 and W, is difficult since the high-temperature structure for WO_3 was not reported by Vasil'eva. The equilibrium data certainly suggest that there is a distinct and measurable difference. Further work is planned in examining the phase transitions of each of the oxides by means of a high-temperature x-ray camera. The characteristics of those oxides prepared by reduction of WO_3 *in situ* and those prepared by direct synthesis of WO_3 and W (12) will be compared.

Acknowledgments

The author wishes to thank many members of the Refractory Metals Laboratory, and other divisions of the General Electric Company for their helpful assistance. He wishes to thank Dr. A. U. Seybolt for the gas pump design. He is especially grateful for the helpful discussion with Professor Gerasinov and Candidate Chem. Science Vasil'eva.

Manuscript received Nov. 5, 1958. This paper was prepared for delivery before the Buffalo Meeting, Oct. 6-10, 1957.

Any discussion of this paper will appear in a Discussion Section to be published in the December 1959 JOURNAL.

REFERENCES

1. R. C. Griffis, *This Journal*, **105**, 398 (1958).
2. J. A. Perri, E. Banks, and B. Post, *J. Appl. Phys.*, **28**, 1272 (1957).
3. I. A. Vasil'eva, Ya. I. Gerasimov, and Yu. P. Simanov, *J. Phys. Chem.* (U.S.S.R.), **331**, 682 (1957).
4. T. Millner, A. J. Hegedus, K. Sasvari, and J. Neugebauer, *Z. anorg. u. allgem. Chem.*, **289**, 288 (1957).
5. J. Neugebauer, A. Hegedus, and T. Millner, *ibid.*, **293**, 241 (1957).
6. T. Millner and J. Neugebauer, *Nature*, **163**, 601 (1949).
7. O. Glemser and H. Volz, *Naturwissenschaften*, **43**, 33 (1956).
8. P. Emmett and J. Schultz, *J. Am. Chem. Soc.*, **55**, 1376 (1933).
9. A. U. Seybolt, Private communications.
10. W. Bennett, *Rev. Sci. Inst.*, **28**, 1092 (1957).
11. I. A. Vasil'eva and Ya. I. Gerasimov, Private communications.
12. A. Magneli, G. Anderson, B. Bloomberg, and L. Kihlborg, *Anal. Chem.*, **24**, 1998 (1952).

13. H. Klug and L. Alexander, "X-ray Diffraction Procedures," pp. 290-305, John Wiley & Sons, Inc., New York (1954).
14. G. L. McCreery, *J. Am. Ceram. Soc.*, **32**, 141 (1949).
15. O. Kubaschewski and E. Evans, "Metallurgical Thermochemistry," pp. 312, 320, John Wiley & Sons, Inc., New York (1956).
16. K. K. Kelley, *U. S. Bur. Mines Bull. 476* (1949).
17. O. Kubaschewski and E. Evans, *op. cit.*, p. 248, 334.
18. K. K. Kelley, *U. S. Bur. Mines Bull. 434* (1948).
19. M. Foex, *Compt. rend.*, **200**, 917 (1945).
20. R. Ueda and T. Ichinokawa, *Phys. Rev.*, **82**, 563 (1951).
21. S. Sawada, *ibid.*, **91**, 1010 (1953).
22. W. Kehl, R. Hay, and D. Wahl, *J. Appl. Phys.*, **23**, 212 (1952).

Polarographic Behavior of Nitro and Nitrosoguanidine

Gerald C. Whitnack and E. St. Clair Gantz[1]

General Research Branch, U. S. Naval Ordnance Test Station, China Lake, California

ABSTRACT

The general behavior of nitro and nitrosoguanidine at the dropping mercury electrode has been studied under various alkaline, neutral, and acidic conditions. Different mechanisms of reduction are postulated and discussed. Optimum conditions are specified, with other details, both for the determination of the nitroso compound in the presence of the nitro compound, and for the reduction of the nitro compound to either the amino or nitroso compound. Half-wave potentials, diffusion current constants, and n-values are reported for each compound in several media. The multiple waves obtained with these compounds at some *p*H values are discussed in terms of different ionic and molecular forms in solution.

The reduction of nitroguanidine has been a subject of considerable study for many years (1-5). Nitrosoguanidine has been established as the first product in the chemical reduction of nitroguanidine (1, 3). Thiele described the preparation of nitrosoguanidine by the careful reduction of nitroguanidine with tin and dilute hydrochloric acid. Steinbach (5) studied the chemical reduction of nitroguanidine in neutral, acidic, and alkaline solutions and the electrochemical reduction in acidic and alkaline solutions. He showed that the product of the chemical reduction depended mainly on the type of reducing agent and the amount of reductant present. Aminoguanidine and nitrosoguanidine were the end products. Smith and Sabetta, and Davis and Rosenquist (4, 23) proposed a method for the preparation of nitrosoguanidine by the reduction of nitroguanidine with zinc dust in an ammonium chloride solution. The oxidation potential for the half-cell, nitro-nitrosoguanidine, has been measured (4,6); however, very little fundamental information has been reported on the polarographic behavior of this very involved system.

Nitro and nitrosoguanidine exhibit amphoteric characteristics (7) and their different possible molecular and ionic forms have been the subject of considerable controversy (8-13). The dissociation constants of several derivatives of nitroguanidine (14) and the effect of substituents on the absorption spectrum of nitroguanidine have been determined spectrophotometrically (15). A hydroxylaminoguanidine intermediate has been proposed in the reduction of nitroguanidine by titanium (III) chloride (16).

In the fall of 1955, a paper on the polarographic behavior of nitro and nitrosoguanidine was published by Lanza, *et al.* (17). In addition, Namba and Suzuki (18) in 1955 published some work on nitrourea and nitroguanidine. In general, where their work overlapped with the work presented in this report, good agreement was obtained.

The present study was initiated so that additional fundamental knowledge about the mechanism and products of reduction and the general polarographic behavior of nitro and nitrosoguanidine might be obtained. It is the purpose of this report to present and discuss such data.

Experimental

Apparatus and materials.—A Sargent Model XXI recording polarograph and a Fisher "Elecdropode" were used in these studies. Mercury pool potentials and half-wave potentials ($E_{1/2}$) vs. the saturated calomel electrode (SCE) were determined with the "Elecdropode" (19). The $E_{1/2}$ values (vs. Hg pool) were calculated by the method of intersecting lines from polarograms obtained with the Sargent Model XXI polarograph. It is recognized that $E_{1/2}$ (vs. Hg pool) values do not have exact significance and are reported for relative comparison only. The potential of the mercury pool was fairly constant in a Britton and Robinson buffer system through the *p*H 3-7 range.

Solutions used in these studies had cell resistances of less than 500 ohms (as determined with a Wheatstone bridge) and the *iR* correction was negligible in computing the $E_{1/2}$ values (20). All *p*H measurements were made with a Beckman Model G *p*H meter.

Several dropping mercury electrodes were used in this work. The $m^{2/3}t^{1/6}$ values are reported in the tables.

Small borosilicate glass beakers (30 ml) were used as polarographic cells. A rubber stopper to which were attached the dropping mercury elec-

[1] Present address: Aircraft Gas Turbine Division, General Electric Co., Cincinnati, Ohio.

trode, contact electrode, and a glass tube with a fritted disk, was placed over the top of the small beakers. The current-voltage curves were obtained in a constant temperature bath at 30° ± 0.1°C.

Dissolved oxygen was removed from all solutions with pure nitrogen just prior to the polarographic examination. The nitrogen was passed through a portion of the solution being examined polarographically and finally through the solution in the polarographic cell.

Clark and Lubs' and Britton and Robinson buffer solutions (21, 22) were prepared double strength (2x), and then the buffer was added to varying amounts of aqueous stock solutions of nitro and nitrosoguanidine so that the final polarographic solutions were about 0.1M in buffer. Methyl red (0.001%) was used as a maxima suppressor in these studies, and redistilled mercury, C.P. grade, was used as the anode. The ionic strength of the polarographic solutions was controlled carefully by the addition of ionic strength agents whenever needed.

Nitrosoguanidine was prepared by the method of Davis and Rosenquist (23). The material was recrystallized once from water and analyzed 98.6% by a permanganate titration.

The nitroguanidine used in this work was a commercial grade known as "picrite." This material was recrystallized three time from distilled water and had a melting point of 234°-236°C.

Diffusion Coefficient and n-*Value Measurements*

The diffusion coefficient (D) for nitroguanidine was determined by a procedure adapted from that employed by Stokes (24). In this method, porous diaphragm cells were used, which embodied a magnetic stirring mechanism. The cells were calibrated by the usual method of allowing 0.1M potassium chloride to diffuse into water at 25°C until 25% had passed through the diaphragm. The diffusion constant of potassium chloride for these conditions is known to be 1.867×10^{-5} cm²/sec.

Since nitrosoguanidine decomposes in aqueous solutions (25), a more rapid method of determining its diffusion coefficient and n-value was needed. A millicoulometric method reported by Reynolds (26), and recently modified in this laboratory (27), was employed. In this method the polarograph served as a coulometer and a source of constant applied potential. The integration method was used in calculation. An n-value for nitroguanidine was also determined by this technique.

Results and Discussion

Effect of pH, mercury height, and concentration.— Nitro and nitrosoguanidine were investigated in ammonium chloride and ammonium sulfate solutions (pH 4.5). Only one wave was observed for nitroguanidine in these salt solutions, and the $E_{1/2}$ was more negative in the ammonium sulfate solution than in the ammonium chloride solution. However, in 1N HCl and H_2SO_4 solutions, two waves were observed. The $E_{1/2}$ values were more negative in the H_2SO_4 solution than in the HCl solution. Nitrosoguanidine gave two waves in the salt solutions but only one in the 1N acid solutions. Thus it appeared

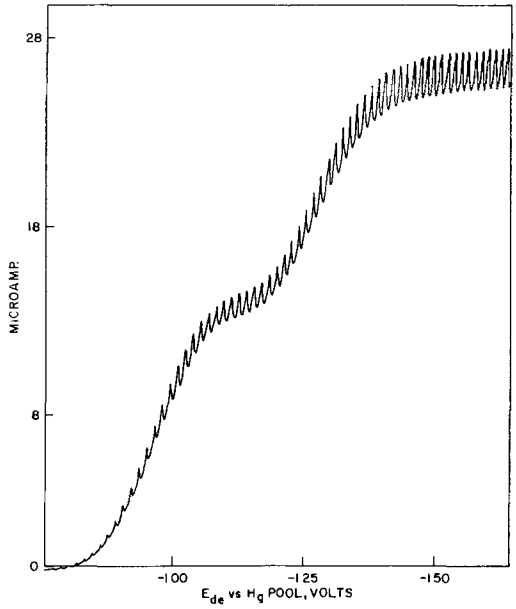

Fig. 1. Polarographic waves of 1.70 mM nitrosoguanidine solution. Britton and Robinson buffer (2X), pH 5.5, 0.001 % methyl red, $m^{2/3}t^{1/6} = 1.45$ mg$^{2/3}$ sec$^{-1/2}$.

that these waves were greatly dependent on the pH and the medium, Therefore, nitro and nitrosoguanidine solutions were studied in Clark and Lubs' and in Britton and Robinson's buffer solutions. The ionic strength of the polarographic solutions was maintained below 0.2M to minimize effects on half-wave potentials. In general, two well-defined waves were obtained over the acid and neutral pH range and one well-defined wave was obtained in alkaline solutions with a pH > 10. The definition of the waves appeared to be better in the Britton and Robinson buffer solutions and a typical polarogram is shown in Fig. 1 for nitrosoguanidine in this system. The first wave is referred to as the more positive in voltage. The effect of pH on the i_d values and the $E_{1/2}$ values of the two individual waves and the total waves, respectively, is shown in Tables I and II. The $E_{1/2}$ values of the first waves increased linearly with an increase in pH to about a pH of 4. The slope of

Table I. Effect of pH on i_d and $E_{1/2}$ of nitroguanidine 1.007 mM nitroguanidine solution containing 0.001% methyl red $m^{2/3}t^{1/6} = 1.45$ mg$^{2/3}$ sec$^{-1/2}$

pH*	$E_{1/2}$ (vs. SCE), v		$i_d/Cm^{2/3}t^{1/6}$	
	1st	2nd	1st	2nd
2.4	—0.73	—1.13	5.28	4.67
3.1	—0.85	—1.45	4.32	3.43
3.7	—0.94	—1.43	3.43	4.53
4.4	—1.16	—1.36	3.43	5.22
4.9	—1.26	—	10.09	—
5.5	—1.26	—	10.09	—
6.3	—1.24	—	10.02	—
6.9	—1.24	—	9.95	—
7.8	—1.22	—	9.95	—
9.1	—1.22	—	9.75	—
10.9	—1.16	—	9.06	—
11.6	—1.15	—	9.06	—
11.8	—1.15	—	8.92	—

* 18 ml Britton and Robinson buffer solutions with 2 ml of stock nitroguanidine solution. pH 2.4 well-defined waves, pH 3.1-4.4 ill-defined waves, pH 4.9-11.8 one well-defined wave.

Table II. Effect of pH on i_d and $E_{1/2}$ of nitrosoguanidine 1.043 mM nitrosoguanidine solution containing 0.001% methyl red $m^{2/3}t^{1/6} = 1.45$ mg$^{2/3}$ sec$^{-1/2}$

pH*	$E_{1/2}$ (vs. SCE), v			$i_d/Cm^{2/3}t^{1/6}$		
	1st	2nd	Total†	1st	2nd	Total†
2.4	—0.73	—1.15	—0.94	7.82	0.66	8.48
2.8	—0.78	—1.19	—0.98	7.02	1.19	8.35
3.2	—0.79	—1.22	—0.98	5.83	2.52	8.35
3.6	—0.84	—1.24	—1.02	5.43	2.98	8.41
4.0	—0.86	—1.26	—1.05	5.17	3.24	8.48
4.6	—0.89	—1.27	—1.06	4.57	3.24	8.15
5.0	—0.89	—1.28	—1.06	3.98	3.38	7.82
5.7	—0.90	—1.20	—1.06	3.64	3.71	7.62
6.1	—0.91	—1.18	—1.06	3.64	3.71	7.62
6.7	—0.89	—1.15	—1.06	3.25	3.84	7.09
7.1	—0.91	—1.15	—1.06	3.05	3.84	6.76
8.0	—0.98	—1.20	—1.04	2.85	3.58	6.43
8.7	—1.00	—1.21	—1.07	1.99	4.24	6.23
9.5	—1.01	—1.19	—1.08	1.39	4.57	5.96
10.8	—	—1.14	—1.14	—	5.56	5.56
11.7	—	—1.12	—1.12	—	5.17	5.17

* 18 ml Britton and Robinson buffer solution with 2 ml of stock nitrosoguanidine solution.
† Total, refers to total diffusion current. pH 2.4-5.0 waves well defined, pH 5.7-8.7 waves ill-defined, pH 9.0-11.7 one well-defined wave.

the $E_{1/2}$ vs. pH plots for nitrosoguanidine (1st wave) is about ½ that for nitroguanidine in this pH range. The diffusion current constants become smaller for the first wave and larger for the second wave with an increase in the pH of the solution. It should be noted (Table II) that in the narrow pH range of 5.7-6.1 the diffusion current constants for each wave of nitrosoguanidine are nearly the same. It appears that nitro and nitrosoguanidine have nearly the same reduction potentials in acid solution with a pH < 2.5. Nitrosoguanidine appears to be slightly the better depolarizer ($E_{1/2}$ more positive) in solutions with a pH > 2.5, although the differences in the $E_{1/2}$ values are very small. Thus, it would seem that if one tried to reduce nitroguanidine electrochemically, any nitrosoguanidine that might form would be immediately reduced further. It should be noted also from the data in Tables I and II that a pH range of 5 to 6 appears to be best for a good separation between the first wave of nitrosoguanidine and the wave of nitroguanidine. Thus, a quantitative analysis of nitrosoguanidine in the presence of nitroguanidine should be possible in this pH range.

Data on the effect of the mercury column height on the diffusion current for each wave of nitro and nitrosoguanidine indicates diffusion controlled processes throughout the entire pH range studied; i.e., the limiting current varies with the square root of the corrected mercury height (Tables VII and VIII).

The effect of concentration on the $E_{1/2}$ and i_d values of nitro and nitrosoguanidine is shown in Table III and was obtained in a Clark and Lubs' buffer solution of pH 6. At this pH a double wave was observed with 1.0 mM solutions of the guanidines but only the total wave was defined well enough for accurate measurement. Over the concentration range of 0.5-6.0 mM the total wave appeared to be proportional to concentration ($i_d = KC$) for nitroguanidine. However, for the total wave of nitrosoguanidine,

Table III. Effect of concentration on $E_{1/2}$ and i_d of nitro and nitrosoguanidine, Clark and Lubs' buffer (2x), pH 6.0, 0.001% methyl red $m^{2/3}t^{1/6} = 1.92$ mg$^{2/3}$ sec$^{-1/2}$

Compound	Concentration, mM	i_d, μa	$E_{1/2}$ (vs. Ha pool), v
Nitroguanidine	0.5	8.15	—1.29
Nitroguanidine	1.4	24.20	—1.33
Nitroguanidine	4.0	66.60	—1.38
Nitroguanidine	6.0	94.20	—1.42
Nitrosoguanidine	0.5	7.29	—1.12
Nitrosoguanidine	1.7	20.20	—1.15
Nitrosoguanidine	4.0	39.90	—1.17
Nitrosoguanidine	6.0	50.70	—1.25

$i_d = KC$ over the shorter range of 0.5-2 mM solutions. Since the $E_{1/2}$ values depend on concentration and become more negative with increasing concentration for both nitroguanidine and nitrosoguanidine solutions, and since plots of log $i/(i_d - i)$ do not give a linear relationship, the over-all reduction process at the cathode appears to be irreversible for each compound.

With solutions containing two or more organic compounds, the possibility exists that one compound may affect the diffusion process of the other compound at a dropping mercury electrode. Table IV gives data on the effect of nitroguanidine on the first wave of nitrosoguanidine. Small amounts of nitrosoguanidine can be determined in the presence of nitroguanidine. However, when the ratio of these compounds exceeds 1:1 there is difficulty in precise measurement of the first nitrosoguanidine wave.

Effect of temperature, solvent, and acid concentration.—In a Clark and Lubs' buffer solution (pH 5.5), the total wave for each compound is lower at 5°C than at 30°C. This is what one would expect, as the diffusion coefficients depend on temperature and are larger at the higher temperatures. However, at the lower temperature the i_d of the first nitroguanidine wave decreased and the i_d of the second wave increased. This may indicate a change in state and concentration of the reducible species in solution with a change in temperature. With nitrosoguanidine solutions, the height of the first wave and the $E_{1/2}$ values, respectively, are nearly the same at 5°C as they are at 30°C. Only the second wave appears to be greatly affected by the change in temperature. This unusual behavior of the polarographic waves with a change in the temperature of the solution is difficult to explain. It may be due to the de-

Table IV. Effect of nitroguanidine on first wave of nitrosoguanidine, Clark and Lubs' buffer (2x), pH 5.5, 0.001% methyl red $m^{2/3}t^{1/6} = 1.92$ mg$^{2/3}$ sec$^{-1/2}$

Nitroguanidine concentration, mM	Nitrosoguanidine concentration, mM	i_d, μa
0.0	1.0	7.2
0.5	1.0	7.0
1.0	1.0	7.1
2.0	1.0	7.5*
3.0	1.0	8.0*

* First wave of nitrosoguanidine not as well-defined.

Table V. Effect of ethyl alcohol on $E_{1/2}$ and i_d of nitroguanidine, 1.40 mM solution of nitroguanidine $m^{2/3}t^{1/6}$ = 1.92 $mg^{2/3}$ $sec^{-1/2}$, 0.001% methyl red

Ethyl alcohol %*	$E_{1/2}$ (vs. Hg pool), v		i_d, μa	
	1st	2nd	1st	2nd
0	—0.93	—1.33	11.7	12.5
10	—1.34	—1.55	13.9	6.0
25	—1.39	—1.61	12.4	5.5
50	—1.49	—1.71	15.2	7.5
75	—1.50	—1.71	17.0	8.2

* Remaining per cent is Clark and Lubs' buffer (2x), pH 6.0.

Table VI. Effect of HCl concentration on $E_{1/2}$ and i_d of nitroguanidine $m^{2/3}t^{1/6}$ = 1.45 $mg^{2/3}$ $sec^{-1/2}$, 0.001% methyl red

Nitroguanidine concentration, mM	HCl normality	$E_{1/2}$ (vs. Hg pool), v		i_d, μa	
		1st	2nd	1st	2nd
1.007	0.1	—0.62	—1.01	9.0	3.9
1.038	0.2	—0.54	—0.95	9.5	3.5
1.038	1.0	—0.39	—0.85	14.7	1.7
1.081	2.0	—0.36	—0.85	14.6	1.1
1.077	6.0	—0.25	—	15.6	—

gree of solvation of different reducible species in solution.

Ethyl alcohol was used to study the effect of a nonaqueous solvent on the waves of nitroguanidine (Table V). Although the separation of the waves is not as sharply defined in the presence of ethyl alcohol, there are two distinct waves for nitroguanidine in these solutions. The $E_{1/2}$ values and i_d values are dependent on the concentration of ethyl alcohol in the medium. It should be noted that the $E_{1/2}$ values are shifted to more negative potentials in the presence of ethyl alcohol, and the i_d value of the total wave appears to go through a minimum around 25% ethyl alcohol. With reducible metal ions an increase in the product $i_d\eta^{1/2}$, where η is the viscosity of the solution, is observed up to about 25% ethyl alcohol (28). However, it can be seen that a decrease in the product $i_d\eta^{1/2}$ is observed with solutions of nitroguanidine up to about 25% ethyl alcohol. Thus, it would appear that with up to 25% ethyl alcohol an increase in the size of the solvated reducible nitroguanidine ion occurred as the activity of water decreased; or that the decreasing dielectric constant favored and caused ion-pair formation and thus an increase in the size of the diffusing species. The increase of "apparent" pH of the final solution with increasing ethyl alcohol concentrations could account also for some difference in wave heights. As the percentage of ethyl alcohol is increased beyond 25% the wave heights of both the total and individual waves increase. The total wave is about the same height in a 70% ethyl alcohol solution as it is in a purely aqueous solution; however, the individual wave heights are just the opposite (first wave height larger and second wave height smaller) in alcohol. These data would seem to rule out ion-pair formation and suggest that the degree of solvation of nitroguanidine was about the same in 75% ethyl alcohol and purely aqueous pH 6.0 buffer solution. Since the first wave height is greater in the 75% ethyl alcohol solution than in the purely aqueous solution, it might also be suggested that nitroguanidine is more highly protonated in the 75% ethyl alcohol solution, and that the first wave is due to the reduction of a protonated species and the second wave is due to the reduction of the unprotonated molecule.

The effect of hydrochloric acid concentration on the $E_{1/2}$ and i_d values of nitroguanidine is shown in Table VI. Again two waves were observed. With a decrease in acid concentration the $E_{1/2}$ value of the first wave became more negative and the i_d value decreased. Only one well-defined wave was observed in 6*N* acid, although a very small second wave was found in 2*N* acid. In strong acid solution a highly protonated specie should predominate, and very little of the unprotonated molecule would be present. In acidic solution a shift of half-wave potentials to more negative values with an increase in pH sometimes can be thought of as a direct reaction of the compound with a proton to form an intermediate ion which is reduced more easily. At the higher pH values the molecule itself is reduced, followed by a reaction of the anion with water as hydrogen ions (29).

Nitro and nitrosoguanidine are weak ampholytes. For nitroguanidine pK_a = 12.20 and pK_b = 14.5, while for nitrosoguanidine pK_a = 11.70 and pK_b = 11.90 (30). As a consequence, different ionic and molecular species may exist in solution depending upon the pH. This fact suggests a possible explanation for the existence of two waves at some pH values and only one wave at other values. For simplicity in explanation of the observed polarographic waves, only the following ionic and molecular forms[2] need to be considered.

[2] Since nitro and nitrosoguanidine molecules may be considered as resonating among various hybrids (8), numerous other forms with various charge separations may also be written, but these are not important in the present discussion.

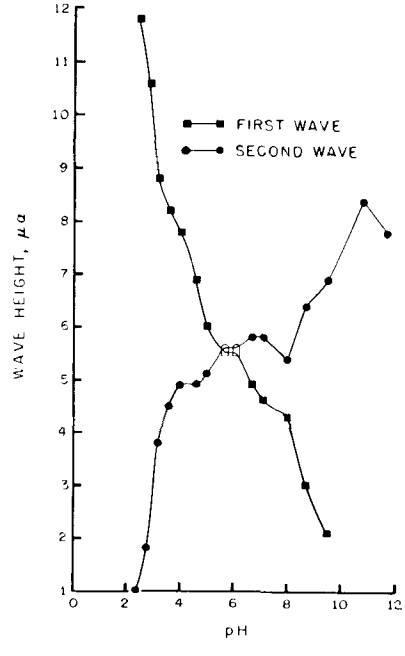

Fig. 2. Effect of pH on i_d of 1.043 mM solution of nitrosoguanidine. Britton and Robinson buffer system (2X).

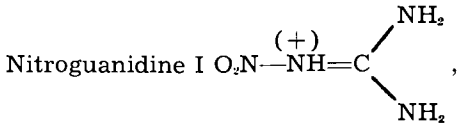

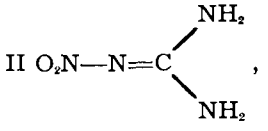

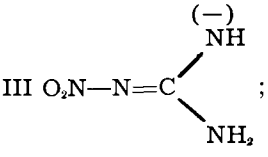

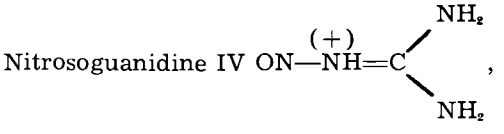

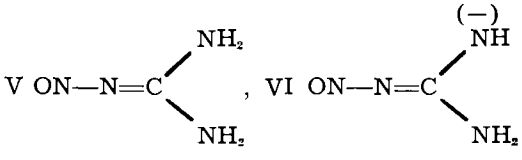

Thus, in 6*N* HCl, forms I and IV would be the predominant species; in *p*H from 1 to 4, I and II or IV and V; about *p*H 7, II and III or V and VI; and at *p*H 8-9 and above, III and VI should be the major forms present. Only one wave was observed in solutions more alkaline than *p*H 9 and more acid than 2*N* acid. In the Britton and Robinson buffer system, the two wave heights obtained with millimolar solutions of nitrosoguanidine vary greatly with *p*H and appear to be of equivalent height around a *p*H of 6 (Fig. 2). Both these waves appear to be diffusion-controlled (i_d varies as $h^{-1/2}$) (Tables VII and VIII) and the $E_{1/2}$ values vary with a change in *p*H. These data would suggest that if the existence of two waves for nitrosoguanidine in this medium is due to two reducible species in solution, then, at a *p*H of 6 forms IV and V probably give rise to the equivalent wave heights shown in Fig. 2 as first wave and second wave, respectively. The two waves obtained with

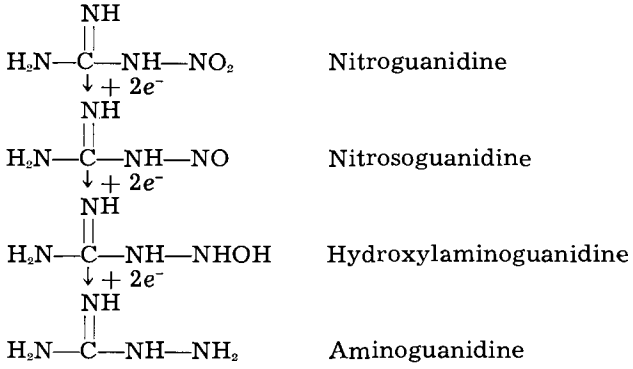

Fig. 3. Possible reduction mechanism for the nitro-nitrosoguanidine system.

Table VII. Effect of mercury column height on i_d of nitroguanidine, Clark and Lubs' buffer (2x), *p*H 6.11, 1.44 mM solution of nitroguanidine containing 0.001% methyl red
$m^{2/3}t^{1/6} = 1.92$ mg$^{2/3}$ sec$^{-1/2}$

Mercury column h, cm	i_d, μa			$i_d h^{-1/2}$		
	1st	2nd	Total	1st	2nd	Total
95.2	12.8	10.2	25.4	1.31	1.05	2.61
71.1	11.3	8.9	22.0	1.34	1.06	2.61
59.7	10.7	8.4	20.4	1.38	1.08	2.63
47.0	9.4	7.6	18.0	1.37	1.11	2.63

Table VIII. Effect of mercury column height on i_d of nitrosoguanidine, Clark and Lubs' buffer (2x), *p*H 5.5, 1.70 mM solution of nitroguanidine containing 0.001% methyl red
$m^{2/3}t^{1/6} = 1.92$ mg$^{2/3}$ sec$^{-1/2}$

Mercury column h, cm	i_d, μa			$i_d h^{-1/2}$		
	1st	2nd	Total	1st	2nd	Total
95.2	13.2	11.9	26.5	1.35	1.22	2.72
87.6	12.5	11.1	25.0	1.34	1.19	2.68
71.1	11.6	10.2	22.8	1.37	1.21	2.70
59.7	11.2	9.5	20.9	1.44	1.23	2.70

solutions of nitroguanidine were not as sharply defined and accurate measurements were not possible in the intermediate *p*H ranges of the buffered systems.

Determination of the n*-value and reduction mechanism.*—The porous diaphragm cell method with magnetic stirring has been used successfully in these laboratories for the determination of the diffusion coefficients (D) of some organic compounds (31). A D value of 2.37 x 10^{-5} cm^2 sec^{-1} was obtained for nitroguanidine by this method in a 2M ammonium sulfate solution. This value for D, when used in the Ilkovic equation ($n = i_d/607D^{1/2}Cm^{2/3}t^{1/6}$), gave an n-value of 3.48 electrons. From the Stokes-Einstein equation, $D(\text{cm}^2/\text{sec}) = 2.96 \times 10^{-7}/\eta(V_m)^{1/3}$ at 25°C, where η is the solution viscosity in dyne seconds per cm^2 and V_m is the molar volume, an n-value of 4.88 electrons was obtained. Since these values were not in agreement and since nitrosoguanidine decomposes rather rapidly in aqueous solutions, a direct and rapid method for the determination of n was thought desirable. With the direct and rapid method for n-values (millicoulometric) that was recently investigated and modified in these laboratories (26, 27), an n-value of 5 was obtained for nitroguanidine in a Clark and Lubs' buffer solution of *p*H 10 where one well-defined wave occurred. Nitroguanidine in a Clark and Lubs' buffer solution of n-value of 3. These values of 5 and 3 are repeatable, and, although the n-values are not 4 and 2 as expected, the 2 electron difference in values indicates that the reduction process of nitroguanidine passes through the nitrosoguanidine state in *p*H 10 buffered solutions (Fig. 3).

It is known that in strong acid solutions nitroguanidine is reduced directly to aminoguanidine (3, 32). In 6*N* hydrochloric acid solutions an n-value of 6 was obtained for nitroguanidine by the millicoulometric technique (26). However, in neutral and alkaline solutions the reduction mechanism appears to be complicated and n-values are of little help in elucidating the over-all process.

The n-value of 5 for nitroguanidine, obtained by millicoulometry in a pH 10 Clark and Lubs' buffer solution, may be explained by a coupling of the products of a 2 and 6 electron reduction respectively (Fig. 3). It has been shown that nitrosoguanidine and aminoguanidine can react to form a tetrazene (33), which should be further reducible. The n-value of 3.5, obtained in the 2M ammonium sulfate solution (pH 4.5) from an experimental D value, would seem to indicate the reduction of nitroguanidine to hydroxylaminoguanidine (Fig. 3) in weakly acidic or neutral solutions. This latter compound was suggested as the end product in the reduction of nitroguanidine in alkaline medium (pH > 12) by Lanza and co-workers (17). Hydroxylaminoguanidine has never been isolated. It would be expected to decompose rapidly to guanidine and hyponitrous acid. It appears that in neutral and alkaline solutions there is more than one process occurring at the dropping mercury electrode. These processes are probably occurring at different rates and the products may undergo "dearrangement." Thus, it is difficult to establish the over-all reduction mechanism of either nitroguanidine or nitrosoguanidine at a dropping mercury electrode in these solutions.

The authors prepared nitrosoguanidine at a mercury cathode in 20% yields by the large-scale electrolysis of nitroguanidine in a 2M-ammonium sulfate solution. Polarographic techniques were used to determine the optimum conditions for the preparation. The addition of nickel II ions to the solutions produced excellent yields of a red nickel-nitrosoguanidine complex salt. The complex salt is extremely stable and attempts to quantitatively recover the nitrosoguanidine from the complex were unsuccessful. The formation of this salt established nitrosoguanidine as the first step in the reduction of nitroguanidine in neutral or weakly acidic solution at a mercury cathode (Fig. 3). As fast as nitrosoguanidine is formed, it complexes with the nickel ions and a bright red precipitate appears in the electrolysis solution.

Acknowledgment

The authors wish to express their sincere appreciation and gratitude to G. B. L. Smith (deceased), Ronald A. Henry, and William G. Finnegan, for their invaluable help and encouragement during this work. The authors also wish to thank Robert D. Weaver for obtaining the n-value data.

Manuscript received March 10, 1958. This paper was prepared for delivery before the Pittsburgh Meeting, Oct. 9-13, 1955.

Any discussion of this paper will appear in a Discussion Section to be published in the December 1959 JOURNAL.

REFERENCES

1. G. Pellizzari, *Gazz. chim. ital.*, **21**, II, 405 (1891).
2. T. L. Davis, *J. Am. Chem. Soc.*, **43**, 669, 2234 (1921); **44**, 2598 (1922).
3. F. K. J. Thiele, *Liebigs Ann. Chem.*, **270**, 1, 383 (1892); **273**, 133 (1893).
4. G. B. L. Smith and V. J. Sabetta, *J. Am. Chem. Soc.*, **54**, 1034 (1932).
5. O. P. Steinbach, Jr., "Reduction of Nitroguanidine," Thesis, Polytechnic Institute of Brooklyn, 1927.
6. C. Hahn, E. Pribyl, E. Lieber, B. P. Caldwell, and G. B. L. Smith, *J. Am. Chem. Soc.*, **66**, 1223 (1944).
7. V. J. Sabetta, D. Himmelfarb, and G. B. L. Smith, *J. Am. Chem. Soc.*, **57**, 1478 (1935)
8. J. H. Bryden, L. A. Burkardt, E. W. Hughes, and J. Donohue, *Acta Cryst.*, **9**, (July 1956).
9. W. D. Kumler, *J. Org. Chem.*, **18**, 676 (1953).
10. W. D. Kumler and P. P. T. Sah, *ibid.*, **18**, 669 (1953).
11. A. F. McKay, M. A. Weinberger, J. P. Picard, W. B. Hatton, M. Bedard, and H. E. Rooney, *J. Am. Chem. Soc.*, **76**, 6371 (1954).
12. S. S. Barton, R. H. Hall, and G. F. Wright, *ibid.*, **73**, 2201 (1951).
13. M. W. Kirkwood and G. F. Wright, *J. Org. Chem.*, **18**, 629 (1953).
14. J. E. DeVries and E. St. Clair Gantz, *J. Am. Chem. Soc.*, **76**, 1008 (1954).
15. A. F. McKay, J. P. Picard, and P. E. Brunet, *Can. J. Chem.*, **29**, 746 (1951).
16 W. W. Brandt, J. E. DeVries, and E. St. Clair Gantz, *Anal. Chem.*, **27**, 392 (1955).
17. P. Lanza, A. Delmarco, A. F. McKay, and G. Semerano, *Sperimentali di Polargrafia*, **2**, 1 (1955).
18. K. Namba and K. Suzuki, *Bull. Chem. Soc. Japan*, **28**, 623 (1955).
19. I. M. Kolthoff and J. J. Lingane, "Polarography," 2nd ed., pp. 373-375, Interscience Publishers, New York (1952).
20. I. M. Kolthoff and J. J. Lingane, *ibid.*, p. 374.
21. N. A. Lange, "Handbook of Chemistry," 8th ed., p. 938, Handbook Publishers, Inc., Sandusky, Ohio (1952).
22. H. T. S. Britton and R. A. Robinson, *J. Chem. Soc.*, **1931**, 1456.
23. T. L. Davis and E. N. Rosenquist, *J. Am. Chem. Soc.*, **59**, 2114 (1937).
24. R. H. Stokes, *ibid.*, **72**, 763 (1950).
25. T. L. Davis, "Chemistry of Powder and Explosives," Vol. I, p. 392, New York (1941).
26. G. F. Reynolds and H. I. Shalgosky, *Anal. Chim. Acta*, **10**, 386 (1954).
27. R. D. Weaver and G. C. Whitnack, *ibid.*, **18**, 51 (1958).
28. L. Meites, "Polarographic Techniques," p. 57, Interscience Publishers, Inc., New York (1955).
29. I. M. Kolthoff and J. J. Lingane, *op. sit.*, p. 627.
30. J. E. DeVries and E. St. Clair Gantz, *J. Am. Chem. Soc.*, **76**, 1008 (1954).
31. G. C. Whitnack, J. Reinhart and E. St. Clair Gantz, *Anal. Chem.*, **27**, 359 (1955).
32. E. Lieber, and G. B. L. Smith, *J. Am. Chem. Soc.*, **59**, 2283 (1937).
33. E. Lieber and G. B. L. Smith, *Chem. Rev.*, **25**, No. 2, 220 (1939).

Electrodeposition of Adherent Titanium Coatings on Induction Heated Cathodes in Fused Salts

B. J. Fortin, J. G. Wurm, L. Gravel, and R. J. A. Potvin

Laval University, Quebec, Quebec, Canada

ABSTRACT

A new electrolytic method for the deposition of adherent coatings of titanium on steel cathodes is described. The procedure involves the use of fused alkali-halide baths composed of eutectic mixtures of lithium, potassium or sodium iodides, bromides, chlorides, and fluorides, with a high-frequency heated cathode and a soluble titanium anode. The bath composed of KI-KF performed best and deposited a very smooth and uniform titanium coating. Conversely, the bath composed of KI-NaI and TiI_4 (2 to 5%) yielded dendritic Ti and is therefore considered more suitable for an electrorefining process. Equipment and operating conditions are described and the microstructure of the coating produced is reported. A series of decomposition voltage curves is included and discussed, and the mechanism of the electrolytic reactions is studied in detail.

A complete literature survey of the electrodeposition of titanium from molten salts has been published recently by Steinberg (1). Ti diffusion coatings were obtained by Straumanis, *et al.* (2, 3) from fused baths containing dispersed Ti crystals or Ti salts. Much remains to be investigated, however, on the deposition of uniform and strongly adherent coatings of Ti.

The present work deals with an electroplating method involving the use of an induction-heated cathode and a soluble Ti anode in fused salt baths. The induction-heated cathode acts at the same time as a heating element to maintain the bath in a molten state. In this manner, the cathode is at a temperature appreciably higher than the surroundings. In fact, the anodic zone, far removed from the cathode area, may be kept much colder. This provides, therefore, means to control the rate of solution of the anode as well as volatilization losses and secondary reactions. The skin effect due to induction current creates a maximum temperature zone on the very surface of the cathode, speeding up degassing and facilitating diffusion of the deposited Ti. Furthermore, the electrolysis may be carried out in a Pyrex or transparent quartz cell which makes it convenient to see directly the phenomena taking place.

Description of Cells

Two types of cells are used. These cells are made up of a Pyrex or quartz tube closed at the bottom and covered at the top by a gas-tight asbestos lid which holds also the electrodes and inert gas ducts.

In the first type, as shown in Fig. 1, the anode is composed of Ti sponge which covers the bottom of the cell: a shielded W wire passing through the molten electrolyte is provided to carry current to the anode. The cathode, in this particular case, is made of steel wire 2-mm diameter and has the form of a ring which is located in the center of the high-frequency coil.

The second type of cell differs from the first one in that the relative positions of the anode and cathode are reversed: the anode is located in the upper portion of the bath and consists of either Ti wire or a cylindrical W grid filled with Ti sponge. The ring-shaped cathode reaches near the bottom of the cell and is held by means of a connecting wire shielded with a Pyrex glass tube. The design of the cell shown in Fig. 1 was found in practice to be preferable. In fact, in this cell, there exists a marked difference in temperature between the anode and the cathode zones, which cannot be obtained in the other type of cell where the cathode, close to the bottom, favors stronger convection resulting in a more uniform heat distribution.

A variety of cathode shapes made of iron or steel were used. These included massive pieces such as threaded rods, flat washers, or lighter pieces made of wire wound in different shapes.

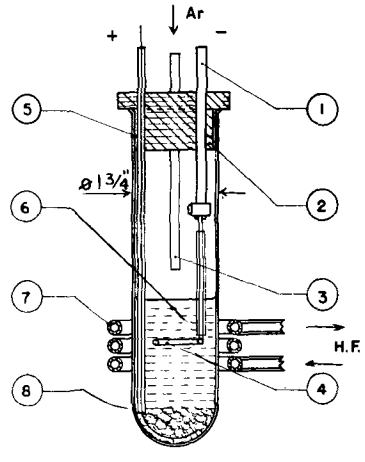

Fig. 1. Electrolytic cell with a heating cathode (Type 1). 1, Cathode holder; 2, asbestos stopper; 3, argon inlet; 4, heating cathode ring; 5, W wire in Pyrex tube; 6, electrolytic bath; 7, high-frequency coil; 8, Ti sponge anode.

Experimental Procedure

Electrolytic baths composed of low-fusing halides of lithium, sodium and potassium were selected. Each bath contained about 150 g of an eutectic mixture of these salts which were placed in the cell tube and melted in a separate furnace for dehydration while flushing with dry argon. Finally, the assembled cell was rapidly transferred to the high-frequency coil. An optical pyrometer was used to observe the cathode temperature, and a thermocouple introduced through the argon outlet tube served to determine the temperature of the bath at different depths. The temperature of the cathode during electrolysis was kept constant within 25°C and was approximately 200°C above the average temperature in the bath.

At the very first stage of electrolysis, the cathode became surrounded with a bluish-violet cloud which within a few minutes extended to the whole bath. At the end of the electrolysis, the cell was cooled rapidly in an air blast while maintaining a difference of potential of about 1 v between the electrodes in order to prevent any interaction between the bath and the deposited Ti. The cathode products and the remainder of the bath after solidification were submitted to a combined chemical and x-ray analysis. It was considered that rapid cooling of the bath after electrolysis minimized postelectrolytic reactions, and therefore it was assumed that analytical results obtained on the solidified melts could serve as a basis for proposing a probable explanation of the mechanism involved.

In some experiments, TiI_4 and K_2TiF_6 were injected into the molten eutectic during electrolysis.

Results

The first series of experiments reported in Table I dealt with electrolytic baths composed of mixtures of halides of eutectic composition, using a soluble anode and a ring-shaped cathode made of a 2-mm steel wire. Cathode current densities were kept fairly constant during the whole of the electrolysis: values from 0.42 to 1.0 amp/cm^2 were used. It was observed that the Ti deposit was mainly dendritic, nonuniform and poorly adherent when the temperature at the cathode was below 850°C, while it was more adherent for higher temperatures; in fact, it was found, in this first series of experiments, that at the start of the electrolysis a compact, adherent and shiny deposit of Ti appeared on the cathode. This deposit grew up regularly for about 10 min, after which some dendritic deposit showed up at various spots and continued to develop, forming an irregular surface or even bridging up to give rise to a spongy layer. This latter effect was more marked for the iodide and bromide baths. At the end of the electrolysis, the zone next to the cathode gave a definitely alkaline aqueous solution while that from the anode was acid. Furthermore, as the electrolysis proceeded the zone near the anode turned from a faint bluish-violet to a reddish-brown in the case of the bromide and iodide baths and to a pale green in the case of the chloride baths. The latter is ascribed to the formation of $NaTiCl_4$ described by Steinberg (1). The current efficiency was high, slightly above 90% in most of the experiments mentioned in Table I. On the other hand, the amount of Ti dissolved at the anode exceeded considerably the theoretical value; this may result in part from the formation of lower valence Ti compounds which have been detected in the bath.

In the second series of experiments, Nos. 9-12 in Table I, small proportions of TiI_4 were injected under argon in baths containing the eutectic mixture NaI-KI. One experiment also is reported on a bath containing KI-KF in which K_2TiF_6 was injected in the same manner. At the end of the electrolysis the baths containing only iodides had a reddish-brown color; as in the previous series, the salts surrounding the cathode gave a very strongly alkaline reaction while those surrounding the anode had a low pH when dissolved in water. The coatings in this series of experiments were in general of a heavier adherent type than in the previous; however, they had a rough and nonuniform surface as may be seen in Fig. 2a. When the temperature of the cathode was increased to 975°C, as in experiment No. 11, the surface became smoother and more uniform but it was found that the amount of anode dissolved during electrolysis was still greater than in the previous series, reaching 215% of the theoretical value based on Faraday's law. This is not surprising in view of the strong reaction between the injected TiI_4 and the anode at a high temperature.

The third series of experiments, Nos. 13-17 of Table I, concerned only baths composed of a KI-KF eutectic mixture using Ti anodes or Zr anodes in the

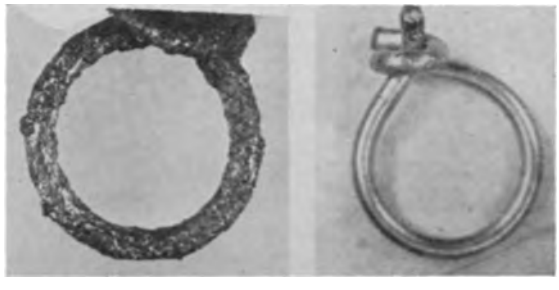

Fig. 2. (a) (left) Rough and nonuniform surface obtained in a KI-NaI bath with TiI_4 addition (Expt. 10, Table I). (b) (right) smooth and uniform coating obtained in KI-KF bath (Expt. 15, Table I). Approx. 2/3 size.

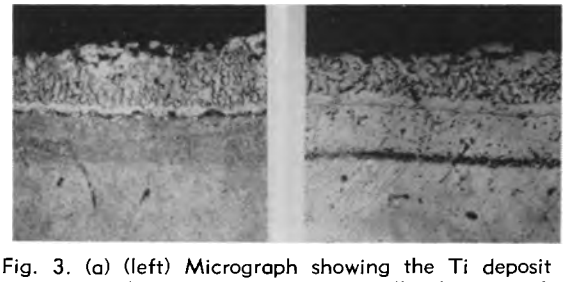

Fig. 3. (a) (left) Micrograph showing the Ti deposit obtained in a KI-NaI bath (Expt. 5, Table I). The HF etch has revealed the more or less granular deposit of Ti crystals separated by a clear white, compact and very hard intermediary zone from a darker etching zone. The Ti at the surface contained below 0.001% metallic elements as determined spectrographically, save for Fe, which reached a value of 11% near the interface. The darker zone is much harder than the low carbon steel of the base as shown by the microindentations in (b) (right), suggesting that Ti has diffused in that zone to the darker line limiting the soft steel and appearing in (b) after a Nital etch. Magnification 300X.

Table I. Electrolytic operating conditions*

Expt. No.	Type of cell	Bath composition, g		Soluble anode**	Volts	Amps	Cat. C.D., amp/cm²	Time, min	Cathode temp, °C	Bath temp, °C	Results
1	Fig. 1	NaCl	85	Ti	6.0	3.0	0.50	18	900-925	725	Very thin, nonuniform, poor coating.
		KCl	65								
2	Fig. 1	NaCl	85	Ti	4.5	2.0	0.50	20	900-925	725	Thin, poor coating, irregular.
		KCl	65								
3	Fig. 1	LiCl	80	Ti	3.5	3.0	0.52	15	875-900	700	Thin, more or less uniform coating.
		KCl	70								
4	Fig. 1	NaBr	79	Ti	2.6	3.0	1.00	18	900-925	725	Uniform coating, with dendritic crystals.
		KBr	71								
5	Fig. 1	NaI	63	Ti	5.0	5.0	0.77	30	925-950	750	Shiny coating with dendritic crystals.
		KI	87								
6	No. 2	NaI	63	Ti	2.5	5.0	0.42	45	900-925	725	Heavy dendritic sponge formation.
		KI	87								
7	Fig. 1	NaI	63	Ti	4.5	3.0	0.53	35	925-950	750	Abundant coating with dendritic shiny crystals.
		KI	87								
8	Fig. 1	NaI	63	Zr	3.5	2.0	0.70	20	900-925	725	Uniform coating with sponge formation.
		KI	87								
9	No. 2	NaI	63	Ti	4.5	3.5	1.0	20	900-925	725	Heavy adherent coating, shiny but nonuniform.
		KI	87								
		TiI_4	7.5								
10	Fig. 1	NaI	63	Ti	2.5	2.0	0.90	30	925-950	750	Heavy adherent coating, shiny but nonuniform.
		Ti	87								
		TiI_4	7.5								
11	Fig. 1	NaI	63	Ti	3.5	2.0	0.40	15	950-975	775	More uniform but thin coating.
		KI	87								
		TiI_4	3								
12	Fig. 1	KF	29	Ti	3.7	3.0	0.40	10	900-925	725	Poor coating.
		KI	121								
		K_2TiF_6	3								
13	Fig. 1	KF	29	Ti	2.5	2.0	0.66	15	900-925	725	Excellent coating, very uniform, no sponge.
		KI	121								
14	Fig. 1	KF	29	Ti	2.5	3.0	0.40	18	925-950	750	Excellent coating, very uniform.
		KI	121								
15	Fig. 1	KF	29	Ti	2.2	2.0	0.70	20	925-950	750	Excellent coating, very uniform.
		KI	121								
16	Fig. 1	KF	29	Zr	2.3	2.0	0.70	20	925-950	750	Uniform coating, some dark spots.
		KI	121								
17	Fig. 1	KF	29	Zr	2.2	2.0	0.70	15	900-925	725	Very uniform coating.
		KI	121								

* Induction heating cathode process.
** Anode: Ti or Zr sponge except for Expts. 6 and 9 where a 2 mm Ti wire was used.

type of cell depicted in Fig. 1. The Ti coatings obtained with this type of bath were adherent, compact, smooth and shiny either on ring-shaped or flat pieces; in all cases, as may be seen in Fig. 2b, they showed no pitting or dark spotted or spongy areas. Contrary to the other two series, the salts surrounding the cathode and the anode both showed an alkaline reaction at the completion of the electrolysis and the bath had a pinkish color. In this latter series also, the inside wall of the Pyrex or quartz cell was free from any Ti mirror which always tends to form in the two other series of experiments; such mirrors have already been observed by Straumanis, *et al.*, on ceramic materials during titanizing experiments (4).

Metallographic examination.—Figures 2-5 illustrate some of the types of Ti coatings obtained with the main baths described above.

Decomposition Voltages and Mechanism of the Electrolytic Reactions

The decomposition voltages were determined for the main eutectic mixtures selected for the above experiments using first an insoluble anode, and then a soluble Ti anode. These decomposition voltages were obtained in the usual way by extrapolating the experimental current-voltage curves to zero current. All measurements were carried out under an argon atmosphere in a graphite crucible containing the molten salts held uniformly at 725°C. The use of a crucible heated in a resistance furnace eliminated the excessive variations brought about by the stirring action obtained in induction heating and, in particular, facilitated the determination of the needed data on the anodic phenomena under the same average bath temperature as in the electroplating experiments described in Table I. The steel cathode was spaced ¾ in. from the anode. Both electrodes were immersed 1 in. into the fused salts. The salts were always submitted to a preliminary electrolysis at 1.8 v for 30 min using graphite electrodes in order to remove the last traces of water. The curves in question are shown in Fig. 6-8. In these figures are also given the current-voltage curves when TiI_4 or, in one case, K_2TiF_6, were injected into the bath prior to measurements.

The extrapolation of curve A in Fig. 6 corresponds to the decomposition of NaCl (3.2 v), indicating that the electrolysis of a NaCl-KCl mixture yields Na as a primary product. On the other hand, when a Ti

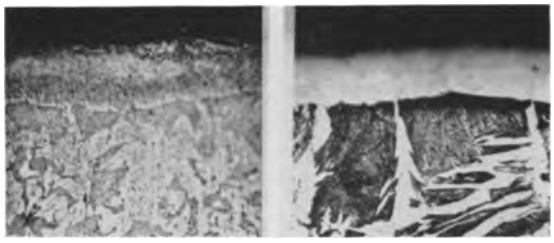

Fig. 4. (a) (left) Micrograph showing the 0.03 mm thick Ti coating built up on the steel cathode (sample appearing in Fig. 2b); the HF etch reveals that interdiffusion of Ti and Fe has taken place in the coating. (b) (right) Micrograph of a section similar to (a), but with a Nital etch to reveal with better contrast the Ti deposit which is left practically unetched and also the coarse Widmanstatten structure of the steel underneath. Magnification 300X.

Fig. 5. Micrograph of a section from a sample plated with Ti in a KI-KF bath (Expt. 15, Table I). The microindentations in the Ti deposit correspond to a hardness of about 180 Vickers which is of high order and possibly results from some diffusion of the steel constituents into the Ti coating at the temperature at which the cathode was held during the electrolysis (950°C).
1% HF + Nital etch Magnification: 500X

anode is used, there is a considerable drop in the decomposition voltage corresponding to 1.7 v as shown by comparison with the extrapolated voltage of curve B. Of the known Ti chlorides, $TiCl_2$ is the one the free energy of which corresponds the closest to the voltage drop mentioned above. It suggests, therefore, the possible following reaction as predominant:

$$Ti + Cl_2 \rightarrow TiCl_2 (E_{725°C} = 1.7 \text{ v}) \qquad [1]$$

It appears also from Fig. 6 that the addition of TiI_4 shifts the decomposition voltage to a slightly lower value for both W and Ti anodes.

Somewhat similar conclusions may be inferred from examination of the decomposition voltage curves of Fig. 7 dealing with KI-NaI baths. In this case, however, the extrapolation of curve A to zero current gives a decomposition voltage of 2.65 which falls between those of NaI and KI. It is therefore likely that K is formed to some extent along with Na as a primary reaction product. On the other hand, since the drop in the decomposition voltage, when using Ti as anode (see curve B), is 0.90 v, it seems that the Ti at the anode, as in the case of the NaCl-KCl bath, also forms a divalent salt; in fact, the voltage drop observed corresponds to the formation of $TiI_2 (E_{725°C} = 0.86 \text{ v})$ which is the Ti iodide having the highest decomposition voltage.

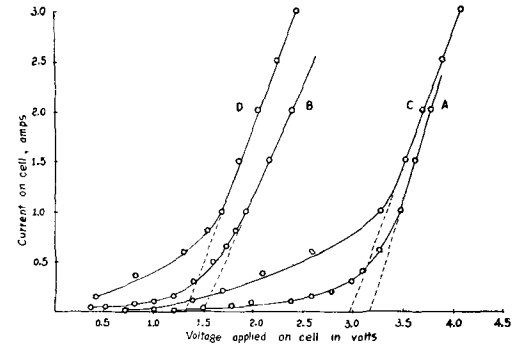

Fig. 6. Decomposition voltage curves of fused KCl-NaCl baths at 725°C with and without addition of TiI_4 using a Fe cathode. A, KCl-NaCl bath, W anode; B, KCl-NaCl bath, Ti anode; C, KCl-NaCl bath + TiI_4 (1.5%), W anode; D, KCl-NaCl bath + TiI_4 (1.5%), Ti anode.

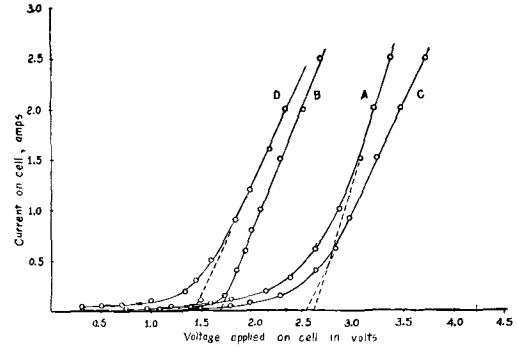

Fig. 7. Decomposition voltage curves of fused KI-NaI baths at 725°C with and without addition of TiI_4 using a Fe cathode. A, KI-NaI bath, Pt anode; B, KI-NaI bath, Ti anode; C, KI-NaI bath + TiI_4 (1.5%), Pt anode; D, KI-NaI bath + TiI_4 (1.5%), Ti anode.

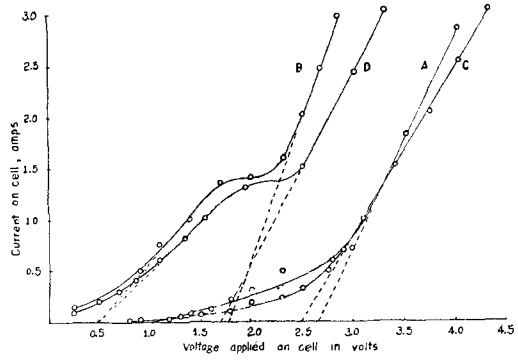

Fig. 8. Decomposition voltage curves of fused KI-KF baths at 725°C with and without addition of K_2TiF_6 using a Fe cathode. A, KI-KF bath, Pt anode; B, KI-KF bath, Ti anode; C, KI-KF bath + K_2TiF_6 (1.5%), Pt anode; D, KI-KF bath + K_2TiF_6 (1.5%), Ti anode.

The extrapolation to zero current of curve A in Fig. 8 indicates that, in the case of a mixed halide bath such as KI-KF, only KI is decomposed because the value of 2.7 v found for the decomposition voltage corresponds closely to the calculated value for KI. Otherwise, a much higher decomposition voltage would be observed (E for KF at 725°C = 4.7 v). When a Ti anode is used, the curve obtained exhibits two distinct branches which may be extrapolated to give two different decomposition voltages; this points to a double type of reaction at the anode. It appears in fact that at low voltage Ti forms only fluorides; formation of such fluorides is highly exo-

Table II. General mechanism of reactions

A—Primary steps

(a) At the Cathode: reduction of an alkali halide.
$M^+ + e^- \rightarrow M$ [7] (Primary cathode reaction according to decomposition voltage curves). where M^+ is an alkali ion in the form of a halide MX contained in the electrolyte and X is the most active halogen.

(b) At the Anode: Formation of Ti ions.
$Ti - ne^- \rightarrow Ti^{n+}$ [8]

B—Secondary steps

(a) At the Anode $Ti^{n+} + nX^- \rightarrow TiX_n$ [9]

(b) At the Cathode $TiX_n + nM \rightarrow Ti + nMX$ [10]

C—Over-all Electrolytic reaction

$$Ti + nMX \underset{b}{\overset{a}{\rightleftharpoons}} TiX_n + nM \quad [11]$$

1. Process: $\overset{a}{\rightarrow}$ The anodic dissolution (endothermic): the Ti anode is attacked and converted into halide.
2. Process: $\overset{b}{\leftarrow}$ The cathodic reaction (exothermic): the Ti halide is decomposed by the free alkali metal formed at the cathode as a primary product

thermic and, consequently, leads to the low decomposition voltage obtained by the extrapolation of the first branch of curve B shown in Fig. 8. The formation of TiF_3 is the most likely to be favored since this salt has a higher decomposition voltage than TiF_2 and TiF_4 and one which is closer to the experimental value inferred from the curves shown in Fig. 8. Furthermore, TiF_2 is not stable even at room temperature because of disproportionation to metal and TiF_3(5) according to the reaction

$$3TiF_2 \rightarrow 2TiF_3 + Ti \quad [2]$$

On the other hand, TiF_4, if formed in the molten bath, would be converted into trivalent fluoride as was shown in a previous paper (6).

When the voltage is increased to a point corresponding about to the extrapolation of the second branch of curve B to zero current, another anodic reaction starts and becomes predominant with increasing voltage, as may be inferred by the shape of the last portion of curve B. The difference between the decomposition voltages corresponding to curve A and the upper branch of curve B is 0.9 v, which is in agreement with the value mentioned in the above paragraph for the formation of TiI_2. It seems, therefore, that the formation of TiI_2 would take place predominantly at the surface of the anode at higher current densities. This TiI_2 would tend, however, to be transformed rapidly in presence of KF according to the reaction

$$TiI_2 + 2KF \rightarrow \underset{\downarrow}{TiF_2} + 2KI \quad [3]$$

TiF_3 (due to reaction [2])

In fact, reaction [3] is very exothermic, and furthermore it was found that the reddish-brown color of TiI_2 did not show up at the end of the electrolysis of the KI-KF bath. To prove reaction [3] by way of similitude, TiI_4 was added to a molten KF bath, and it was observed that the brown color of TiI_4 vanished to form KI as was established by x-ray diffraction analysis; the violet complex of TiF_3 and KF identified as K_3TiF_6 was also found. The following reactions occur

$$TiI_4 + 4KF \rightarrow TiF_4 + 4KI \quad [4]$$

$$TiF_4 + 2KF \rightarrow K_2TiF_6 \quad [5]$$

$$K_2TiF_6 + KF \rightarrow K_3TiF_6 + \tfrac{1}{2}F_2 \quad [6]$$

During the plating operations in the fused salt baths using Ti as anode, there is a transfer of the Ti from the anode to the cathode. As may be seen from the decomposition voltages, this transfer would involve, as a primary step, the reduction of an alkali halide at the cathode and the simultaneous formation of Ti halide at the anode; in turn, the alkali metal would reduce the Ti halide at the cathode where it is deposited (see Table II). As may be inferred from the decomposition voltage curves, the process of cathodic deposition of Ti cannot proceed before some alkali metal has been deposited at the cathode or before some Ti halide has been injected in the bath. This latter condition applies in the case of the experiments in Table I where the addition of Ti salts started earlier the cathode reaction [11](b), Table II.

It may be seen by comparing the curves in Fig. 6-8 that the decomposition voltages for KCl-NaCl or KI-NaI baths using a Ti anode are much higher and the slope indicating the anode polarization much steeper than for KI-KF baths at lower current densities. It results therefore that in the latter bath Ti may be deposited at very low voltages with relatively high current density; energy efficiency is therefore better as also the Ti deposited.

After the electrolysis was completed in the KI-KF baths using a Ti anode, the salt mixture left was submitted to x-ray diffraction analysis (7) and was found to contain besides KI and KF some unidentified compound not described in the available literature which was definitely not K_2TiF_6 nor K_3TiF_6 (6). This compound is most likely the result of the following reaction

$$TiF_3 + n\,KF \rightarrow n\,KF,\ TiF_3 \quad [7]$$

On the other hand, the absence of K_2TiF_6 in the electrolytic bath confirms the view that TiF_4 is not formed at the anode. It follows, therefore, that the reaction at the cathode would be in this particular case

$$TiF_3 + 3K \rightarrow Ti + 3KF \quad [8]$$

The reduced Ti obtained by reaction [8] under the conditions mentioned in Table I produces a smooth and uniform deposit. This is ascribed to the fluidity of the KI-KF bath and to the high temperature of

the cathode which therefore remains clean and free from any excess of K metal on account of its low boiling point (774°C). Conversely, this explains in part the dendritic formation observed in baths containing Li or even Na, the boiling points of which are higher.

Acknowledgment

The authors wish to express their indebtedness to the Defence Research Board of Canada for financial assistance. They also wish to thank Dr. J. Convey, Director, Dr. J. F. Rowland, and Dr. N. F. H. Bright of the Bureau of Mines and Technical Surveys, Ottawa, for their continued interest and collaboration.

Manuscript received Nov. 24, 1958. This paper was prepared for delivery before the New York Meeting, April 27-May 1, 1958.

Any discussion of this paper will appear in a Discussion Section to be published in the December 1959 JOURNAL.

REFERENCES

1. M. E. Sibert and M. A. Steinberg, *This Journal*, **102**, 641 (1955).
2. M. E. Straumanis and P. C. Chen, *ibid.*, **98**, 234 (1951).
3. A. W. Schlechten, M. E. Straumanis, and C. B. Gill, *ibid.*, **102**, 81 (1955).
4. M. E. Straumanis, S. T. Shih, and A. W. Schlechten, *ibid.*, **104**, 17 (1957).
5. L. L. Quill, "Chemistry and Metallurgy of Miscellaneous Materials (Thermodynamics)," p. 126, McGraw-Hill Book Co., New York (1950).
6. J. G. Wurm, L. Gravel, and R. J. A. Potvin, *This Journal*, **104**, 301 (1957).
7. J. F. Rowland and N. F. H. Bright, Internal Report MDT-58-5, Department of Mines and Technical Surveys, Mines Branch, Ottawa.

Electrodeposition Behavior of Trace Amounts of Copper

Richard C. DeGeiso[1] and L. B. Rogers

Department of Chemistry and Laboratory for Nuclear Science, Massachusetts Institute of Technology, Cambridge, Massachusetts

ABSTRACT

Deposition, onto inert electrodes, of copper in amounts insufficient to form a monolayer takes place more readily than predicted using the Nernst equation. The undervoltage is a function of the acidity, the anion present, and the amount of copper deposited. Examination of the literature for silver and for zinc indicated that, as the lattice dimension of the deposited element approached that of the electrode material, the undervoltage increased. Copper undervoltage appears to follow the same trend, but the observed differences are small and open to question.

The electrodeposition of less than a monolayer of an element onto an "inert" electrode sometimes takes place much more readily than one would predict using the Nernst equation (1). For example, deposition of silver from a 10^{-9}M solution onto a platinum electrode takes place at potentials about 0.5 v less cathodic than onto a silver electrode (2). Because silver and copper are quite similar in many chemical and metallurgical properties, a systematic study involving copper was made in the hope of obtaining more information about variables which affect the undervoltage. The fact that copper could be present in more than one valence state was a complication not encountered in the earlier work with silver.

Experimental

Apparatus and Solutions

Deionized water, with conductivity three times less than that of distilled water, was used for all dilutions. In order to insure a minimum of contamination from copper and other elements (as well as organic impurities), all solutions, except concentrated acids, were pre-electrolyzed overnight at —0.8 v vs. S.C.E. using a large platinum gauze cathode.

The concentration of copper in an electrolytic solution was between 10^{-7} and 10^{-9}M. The lower limit was set by the copper impurity in the zinc-oxide cyclotron target (Johnson, Mathey and Co. Ltd.). Copper —61, —63, and —64 produced in the bombardment were much smaller, each being about 10^{-12}M. An upper limit of 10^{-7}M was established by finding no copper in typical tracer solutions when a coulometric procedure, sensitive to somewhat less than 10^{-7}M, was used.

The radio-copper was a mixture of 3.0 hr copper —61 and 12.8 hr copper —64 as shown by half-life measurement, gamma-ray spectrometry, and aluminum absorption analysis. Usually, only 6-10 deposition runs could be completed in the three-day period following isolation of a tracer preparation before its activity became too low to permit precise measurements to be made. As a result, a large number of tracer preparations were used, each of which was undoubtedly somewhat different in concentration of total copper from the others.

Procedures involving electrolysis, anion exchange (3), and solvent extraction were compared briefly as methods for separating the radio-copper from the accompanying zinc and gallium activities. The dithizone extraction procedure, based on that of Haymond, *et al.* (4), was found to be the fastest. The procedure involved dissolution of the target material in concentrated hydrochloric acid, adjustment of the *p*H to 1.0-1.2 by dilution with deionized water, and extraction of the radio-copper using

[1] Present address: Experimental Station, E. I. du Pont de Nemours & Co., Inc., Wilmington, Del.

0.001% dithizone in carbon tetrachloride. The organic extract was washed with 0.1M sulfuric acid and then wet-ashed with a mixture of 1-2 drops of 18M sulfuric acid and 2 ml of 15M nitric acid. After evaporation to dryness, the radio-copper was taken up in 1M perchloric acid. Usually 2 ml of this solution were added to 200 ml of background electrolyte in preparing a solution designated as a "trace" concentration of copper. A pH of 2.0 was used in all depositions unless otherwise stated. Additional amounts of natural copper (II) salt were added if higher concentrations were to be studied.

The electrodes used in this study were of two types. Platinum gauze of approximately 80 cm^2 geometrical area, sealed into 6 mm lead-glass tubing, was used for most of the experiments. In addition, foil electrodes of platinum, palladium, gold, iridium, and rhodium were prepared and had, as nearly as possible, the same geometrical area, estimated to be 29.8 cm^2.

Several procedures for pretreatment of the electrodes were compared and found to give virtually the same results. The procedure finally chosen consisted of rinsing them in ethanol and allowing them to dry in air. They then were immersed in boiling 6*N* nitric acid, rinsed thoroughly with deionized water, and placed directly in the electrolytic cells.

Electrolyses were performed in lipless tall-form beakers, 20 cm tall and 6 cm in diameter. The beakers were covered with Plexiglass to protect the solutions from contamination by atmospheric dust. Salt bridges containing 2M sodium perchlorate connected the reference cell and the working anode with the main electrolytic cell. The ends of the bridges were plugged with unfused Vycor glass which had been previously soaked overnight in sodium perchlorate. The volume of solution in the electrolytic cells was 200 ml in all cases. Nitrogen was bubbled vigorously through the solutions prior to and during the electrolyses in order to keep the oxygen concentration to a minimum. Solutions were stirred by Teflon-covered bars driven by magnetic stirrers.

Immediately after the electrodes had been immersed, a 1-ml sample was removed from the cell. This sample was used as a standard against which all later samples were compared in order to correct for decay of the mixture of radio-copper nuclides. A potential was applied and regulated by potentiostats (5) for the time necessary for the amount deposited to reach a virtually constant value. (For the 80-cm^2 platinum gauze electrodes this time was 1 hr; for the 29.8 cm^2 foils, 3 hr.) At the end of that time, another 1-ml sample was taken and compared with the standard. From the relative difference in activity, the percentage of copper deposited at that potential was calculated. Then the potential usually was changed 0.05 v in the cathodic direction and the procedure repeated. In this manner, the percentage of copper deposited was obtained as a function of cathode potential. Stripping curves were obtained by changing the potential in the opposite direction.

A single-channel differential discriminator coupled through a linear amplifier to a 2-in. well-type, thallium-activated, sodium iodide crystal scintillator was used for measuring the gamma-ray spectrum to characterize the radio-copper. Coupled to an ordinary binary scaler, it was used to count the radio-copper samples in the deposition studies. Usually 3000-3500 counts above background (about 250 cpm) were obtained for each sample. Using the square root of the total counts as an estimate, the standard deviation was about 2%.

The reproducibility of the deposition data was primarily a function of the amount of copper present and the slope of the curve at the potential in question. At the millimolar level, the run-to-run reproducibility was ± 5 mv. Curves at the trace level were reproducible within ± 20 mv (corresponding to an estimated 3-7% variation in observed percentage of copper deposited), although for a given electrode and a particular batch of tracer, the reproducibility was ± 10 mv. Some variability was caused undoubtedly by variation in the copper contamination from one preparation to another.

Potentials for 50% deposition, $E_{50\%}$, in various media, were compared with half-wave potentials, calculated from formal potentials obtained from millimolar copper, using platinum microelectrodes and a Sargent polarograph, Model XXI. Half-wave values could usually be reproduced within ± 10 mv or less.

Results

Perchlorate media

Because a study of the deposition of silver (2) from dilute solutions indicated that the largest undervoltage was obtained in perchlorate medium, 0.1M sodium perchlorate was the first medium studied in the present investigation. Figure 1 shows the deposition behavior of copper in sodium per-

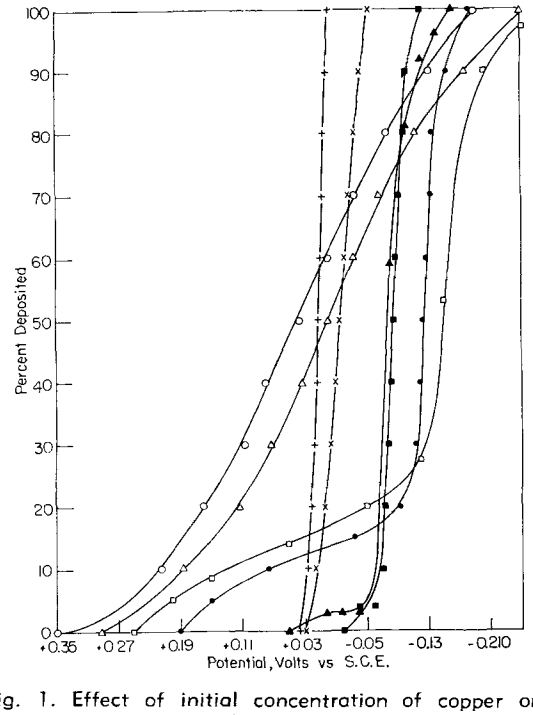

Fig. 1. Effect of initial concentration of copper on its deposition behavior onto 80 cm^2 platinum gauze electrodes from 0.1M sodium perchlorate. ○, trace; △, 1×10^{-6}M; □, 5×10^{-6}M; ●, 1×10^{-5}M; ▲, 5×10^{-5}M; ■, 1×10^{-4}M; ×, 1×10^{-3}M; +, 1×10^{-2}M.

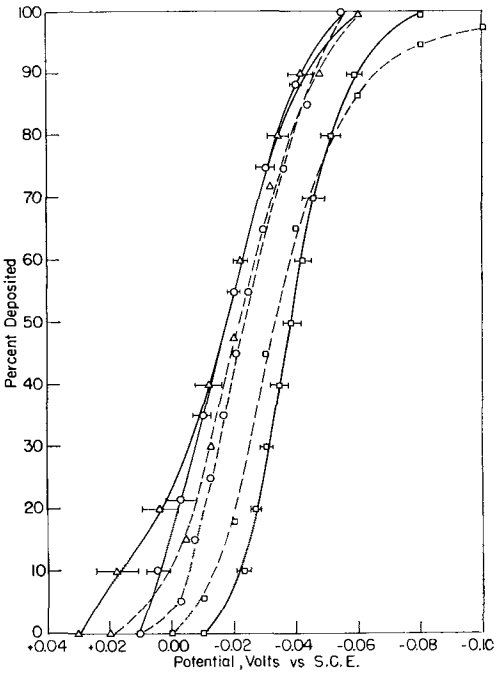

Fig. 2. Effect of pH on the deposition of 10^{-3}M copper from 0.1M sodium perchlorate onto 80 cm² platinum gauze electrodes. pH 0.0: open square with a dot joined by a solid line, deposition, open square with a dot joined by a broken line, stripping; pH 2.0: open triongle with a dot joined by a solid line, deposition, open triangle with a dot joined by a broken line, stripping; pH 5.0: open circle with a dot joined by a solid line, deposition, open circle with a dot joined by a broken line, stripping.

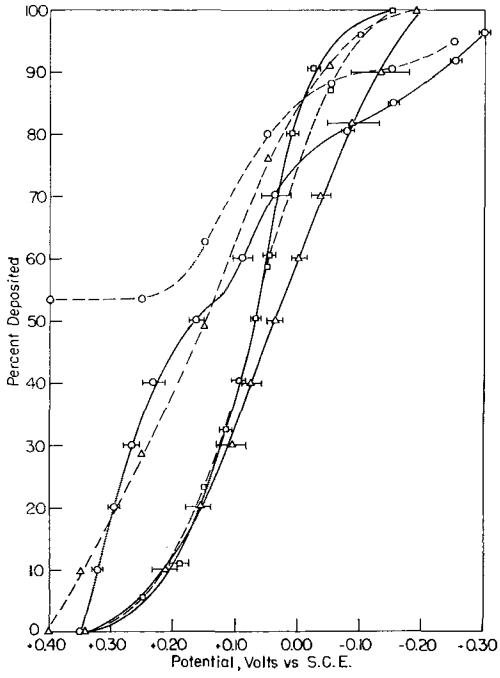

Fig. 3. Effect of pH on the deposition of trace copper from 0.1M sodium perchlorate onto 80 cm² platinum gauze electrodes. pH 0.0: square with a dot joined by a solid line, deposition; square with a dot joined by a broken line, stripping; pH 2.0: triangle with a dot joined by a solid line, deposition, triangle with a dot joined by a broken line, stripping; pH 5.0: circle with a dot joined by a solid line, deposition, circle with a dot joined by a broken line, stripping.

chlorate as a function of copper concentration. Undervoltage effects and changes in curve shape with increasing initial concentration of copper were reminiscent of those obtained for silver. Depositions of copper from 10^{-3}M and 10^{-2}M solutions agreed quite well with predictions based upon the Nernst equation.

The pH always was measured before and after a deposition study. Only in the deposition of millimolar copper from a solution initially at pH 5.0 was a change greater than 0.1 pH unit found, and then it was between 1 and 2 units higher.

Although a change from pH 2.0 to 0.0 had little effect on depositions at the millimolar level (Fig. 2), increased acidity facilitated deposition at the trace level just as it had for silver (2, 6), probably due to its effect on the platinum oxide surface film (Fig. 3). At pH 5.0, deposition appeared to be easiest but, unfortunately, sorption contributed substantially to the observed removal of copper as indicated by the stripping curve and by studies conducted at open circuit. At pH 2.0, however, sorption losses never exceeded 4%. Other effects of pH, particularly those encountered in halide media, are discussed below.

Other Media

A change from perchlorate to complexing media had resulted in lower undervoltages for the deposition of silver. However, Fig. 4 and Table I show the opposite effect for copper in that the ease of deposition increased in the order perchlorate, sulfate, bromide, chloride, and nitrate. The data for nitrate do not fit the trend although it is widely known from macro experiments that depositions from nitrate are difficult to reproduce in the absence of a substance to remove nitrous acid.

The undervoltage for silver had been studied as a function of acidity only in perchlorate medium (2, 6), so a brief study using copper in different media

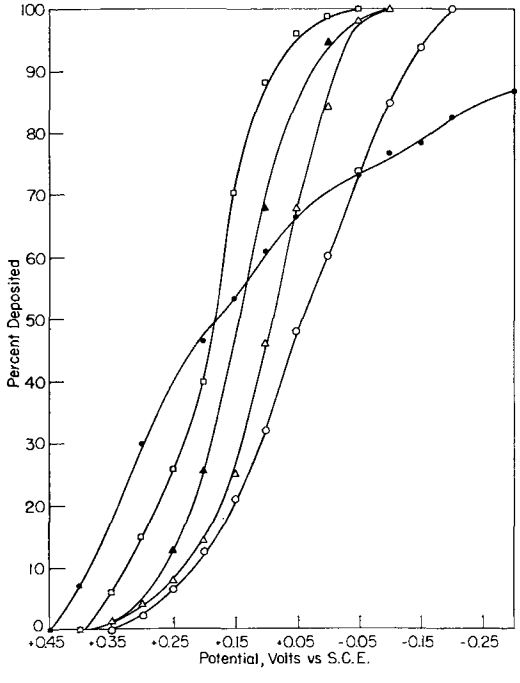

Fig. 4. Deposition behavior of trace copper onto 80 cm² platinum gauze electrodes from 0.1M solutions of sodium perchlorate, sodium sulfate, sodium bromide, sodium chloride, and sodium nitrate. ▲, sodium bromide; □, sodium chloride; •, sodium nitrate; ○, sodium perchlorate; △, sodium sulfate.

Table I. Comparison of experimental $E_{50\,o/o}$ values for trace copper with those predicted for 10^{-7}M solutions from polarographic data on 10^{-3}M solutions

Medium	$E_{1/2}$ for 10^{-3}M, v vs. S.C.E.	Predicted $E_{1/2}$ for 10^{-7}M, v	E_{50}% of trace, v	Undervoltage
$NaClO_4$	—0.03	—0.15	+0.04	0.19
$NaNO_3$	—0.04	—0.16	(+0.18) *	(0.33) *
Na_2SO_4	—0.06	—0.18	+0.09	0.27
NaCl(Cu^+)	+0.14	+0.14	+0.18	0.04
(Cu^o)	—0.25	—0.49	+0.18	0.67
NaBr(Cu^+)	+0.15	+0.15	+0.14	—0.01†
(Cu^o)	—0.26	—0.50	+0.14	0.64

* Unreliable, see text.
† Within experimental error of zero undervoltage.

seemed advisable. For 0.1M sodium perchlorate a change in acidity from *p*H 2 to 1M (in perchloric acid) produced only a 20 mv anodic shift, a change not much larger than the limits of reproducibility. Halide media, however, showed interesting differences. A 0.1M solution of sodium chloride, after being made 1M with hydrochloric acid, gave a cathodic shift of 0.1 v; a similar run in 1M sodium chloride (at *p*H 2) agreed with the 0.1M solution at *p*H 2 (i.e., no shift due to chloride alone). When a *p*H 2 solution of 0.1M sodium bromide was made 1M in hydrobromic acid, a cathodic shift of 0.2 v relative to 0.1M bromide at *p*H 2 was produced. These changes appear to be much too large to be accounted for by changes in activity coefficients or junction potentials. The important factor appears to be not the anion but the hydronium ion. Partial confirmation was obtained by making a 0.1M solution of sodium chloride 1M in perchloric acid and finding a 50 mv cathodic shift. The fact that this same acid produced a slightly anodic shift when added to sodium perchlorate would appear to rule out contamination with copper as the cause for the cathodic shift.

Because the largest undervoltage was observed for deposition from chloride medium, deposition behavior was examined as a function of concentration. Figure 5 shows that a distinct plateau, which extended for 0.2 v, appeared at copper concentrations of 5 x 10^{-6}M and 10^{-5}M. Depositions from 10^{-4}M and 10^{-3}M copper agreed within 0.02 v with the predictions based upon the Nernst equation.

Chloride is known to complex with platinum as well as with copper. It aids in removing oxide films and might also act as a bridging ion. However, preelectrolysis in chloride did not seem to affect the deposition of "trace" copper from 0.1M sodium perchlorate although it is possible that the oxide was first removed in chloride medium and then restored in perchlorate. The following experiment then was performed to study the effect of various amounts of chloride on the deposition of trace amounts of copper from 0.1M sodium perchlorate. The cathode potential was held at +0.15 v vs. S.C.E. in a solution of trace copper in 0.1M sodium perchlorate. At this potential only 21% copper deposited under ordinary conditions. After making this solution 10^{-5}M in chloride, the percentage of copper deposited increased to 24%, a small but possibly significant change. At 10^{-3}M, the per cent increased only to 26%. However, after an increase in chloride concentration to 0.1M, the per cent deposited increased to 38%. This increase, which corresponded to a 0.05 v shift of the entire deposition curve toward less cathodic potentials, seems greater than could be accounted for on the basis of a change in either activity coefficient or junction potential. The fact

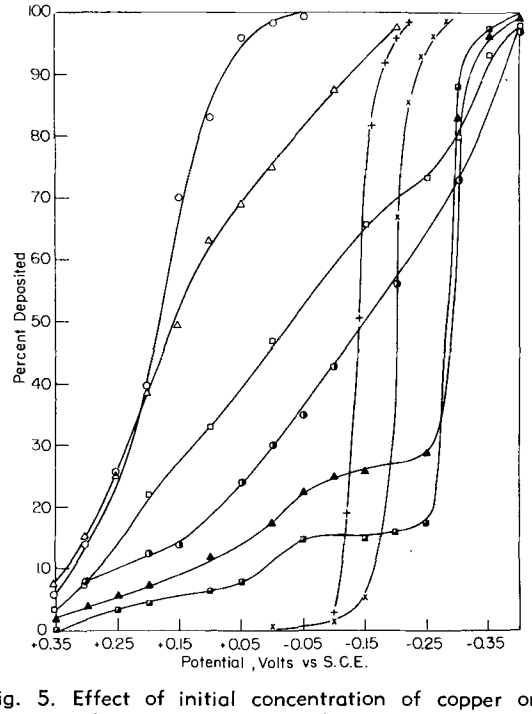

Fig. 5. Effect of initial concentration of copper on its deposition behavior onto 80 cm^2 platinum gauze electrodes from 0.1M sodium chloride. O, trace; Δ, $1x10^{-6}$M; □, $2x10^{-6}$M; •, $3x10^{-6}$M; ▲, $5x10^{-6}$M; ■, $1x10^{-5}$M; ×, $1x10^{-4}$M; +, $1x10^{-3}$M.

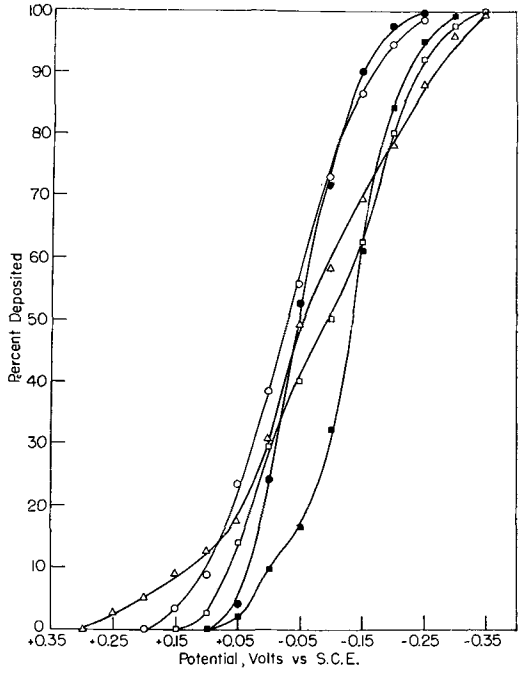

Fig. 6. Deposition behavior of trace copper on 29.8 cm^2 foil electrodes of gold, platinum, palladium, iridium, and rhodium from 0.1M sodium perchlorate. □, gold; O, iridium; •, palladium; Δ, platinum; ■, rhodium.

that the chloride curve in the presence of perchlorate was displaced cathodically from the curve for chloride electrolyte alone may indicate competition for the platinum surface, interference with the discharge reaction, or possibly contamination.

Effects of Electrode Size and Material

Electrodes comparable in size and shape to the standard platinum gauze electrodes were not available for other elements so, in order to be able to make comparisons more easily, foils of platinum as well as gold, palladium, iridium, and rhodium were cut so as to have uniform geometric areas of 29.8 cm^2. As expected (2, 17), a comparison of the deposition curves for the gauze and foil of platinum showed a cathodic displacement for the smaller electrode. A brief comparison of a shiny and a dull platinum foil did not show a difference in behavior greater than the usual experimental error, although it might have on a more extended series of runs (2).

Figure 6 compares the behavior of trace copper using different metal foils. It is interesting that differences could still be observed at the millimolar level (Fig. 7) although, at 10^{-2}M, all experimentally significant differences had disappeared. Calculations show that complete deposition of 10^{-3}M copper would correspond to 1000 layers, assuming a roughness factor of unity. The fact that differences could be observed through many layers is consistent with observations (7) that the early layers of deposit assume the crystal structure of the substrate.

Electrolysis as an Isolation Procedure

Because carrier-free copper deposits so readily, electrolysis should be a suitable method for separating radio-copper from radio-zinc and radio-gallium. It was found that copper could indeed be deposited essentially completely on platinum without depositing zinc or gallium. The following procedure gave radiochemically pure copper activities. It is somewhat more time consuming than solvent extraction but should be adapted more easily to remote operation.

A platinum-gauze electrode was placed in a solution of the target material in 0.5M sulfuric acid. A potential of −0.5 v vs. S.C.E. was applied for 1 hr, following which the electrode was removed, without disconnecting the leads to the potentiostat, and carefully washed by submersion in a beaker containing deionized water. The electrode then was placed in fresh 0.5M sulfuric acid and electrolysis was continued for another hour. A total of three electrolyses were made and, after each one, estimates were made of the activity remaining in solution, the activity in the washings, and the activity on the electrode. The final activity on the electrode was pure radio-copper. Small amounts of zinc and gallium activities present in the washings were presumably carried over by entrainment.

Discussion

Qualitatively, undervoltage appeared to be greater when the lattice dimensions of the electrode material more nearly matched those of the deposited trace element. This was first noted in a re-examination of the data for silver (2) (see Table II and Fig. 8). It was found then that, although quantitative deposition data are not available, qualitative statements for zinc behavior indicate that it follows the same trend. The fact that zinc is normally hexagonal close-packed, while the other metals are face-centered cubes, is probably not as important as the lattice dimensions themselves (8). On that basis, predictions of the order in which the electrode undervoltages would fall were made for copper. Except for rhodium, which also gave anomalous results with silver, the electrode materials fell in the expected order (Fig. 8). Admittedly the differences are small, but they were observed consistently on many batches of copper, the uncertainty being less than ± 10 mv when repeated runs were made using a single preparation of tracer.

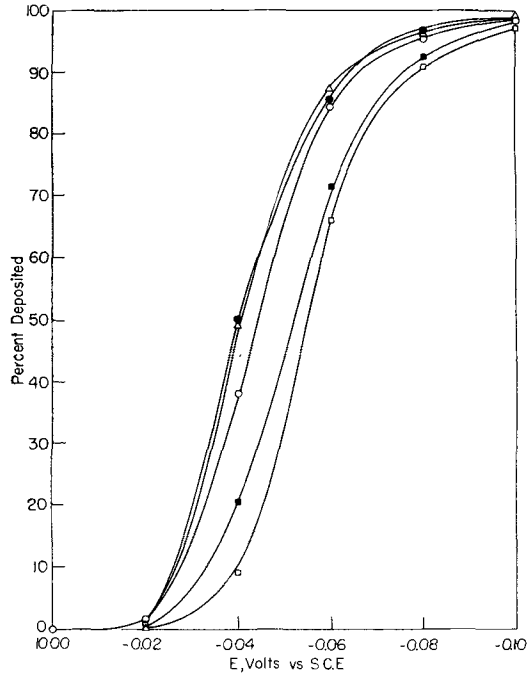

Fig. 7. Deposition behavior of 10^{-3}M copper on 29.8 cm^2 foil electrodes of gold, platinum, palladium, iridium, and rhodium from 0.1M sodium perchlorate. □, gold; ○, iridium; •, palladium; △, platinum; ■, rhodium.

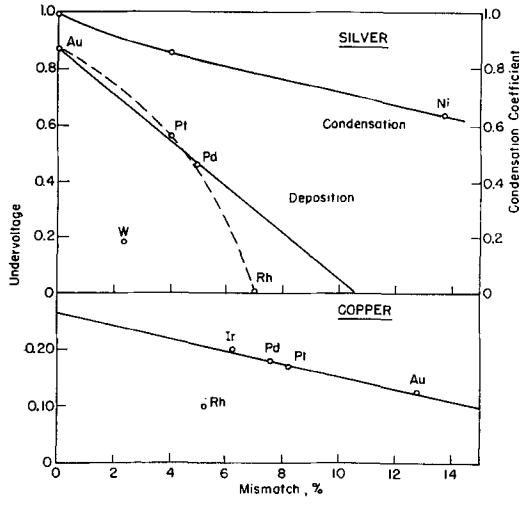

Fig. 8. Undervoltages of silver (2) and copper, and condensation coefficient for silver (10) as a function of lattice mismatch.

Table II. Lattice parameters and deposition data for silver, copper, and zinc

Trace element	Electrode	Nearest neighbor, Å (19)	% Mismatch[a]	Undervoltage[b]
Ag	Rh	2.684	7.0	0.00
	Pd	2.745	4.9	0.46
	Pt	2.769	4.0	0.56
	W	2.816	2.3	0.18
	Au	2.878	0.2	0.87
	Ag	2.882	—	—
Cu	Cu	2.551	—	—
	Rh	2.684	−5.2	0.10
	Ir	2.709	−6.2	0.20
	Pd	2.745	−7.6	0.18
	Pt	2.769	−8.2	0.17
	Au	2.878	−12.8	0.13
Zn	Ni	2.486	6.4	"Slight"[c]
	Cu	2.551	4.0	"Moderate"[d]
	Zn	2.660[g]	—	—
	Pt	2.769	−4.1	"Large"[e]
	Pb	3.493	−31.2	"None"[f]

[a] (Trace metal—Electrode metal)/Trace metal.
[b] Calculated on the basis of 10^{-9}M silver and 10^{-7}M copper in weakly acidic nitrate and perchlorate media, respectively.
[c] Small shift toward nobility at very low initial concentrations.
[d] $E_{50\%}$ remains constant with decreasing initial concentration.
[e] Shift of $E_{50\%}$ toward nobility is inversely proportional to decrease of initial concentration.
[f] Follows Nernst even at very low initial concentrations.
[g] If the value for zinc were 2.75Å (20), the difference in behavior between copper and platinum would be resolved.

On the silver diagram, the discrepancies for tungsten and rhodium are quite probably due to the presence of oxide films which led to anomalous dissolution behavior (2) as well. (Note: the points for rhodium and tungsten have been mislabeled in Fig. 4 of reference 2.) Such films would tend to minimize, or even eliminate (10), the effect of the substrate. While it might be attractive to believe that rhodium fell on a smooth curve, the large percentage of mismatch and the obviously discrepant behavior of rhodium in both the copper and silver series leads one to favor a linear decrease in undervoltage with an increase in mismatch (8).

Extrapolating to zero undervoltage, the silver data give a figure for critical mismatch of about 11%; copper, 23%. [Assuming the data of Yang, *et al.* (10) to be linear rather than curved, one can determine a minimum value of mismatch of about 30%.] Because other determinations of critical mismatch give values in the range from 10 to 20% (11-13) before a continuous film of deposit will fail to form, the limits extrapolated from trace deposition appear reasonable.

That a correlation should exist between mismatch and undervoltage seems plausible on the basis of electron-diffraction and microscopic studies of deposits which have shown that the first few layers tend to follow the structure of the substrate and that smoother deposits are obtained as the lattice parameters of the deposit and electrode approach one another. We are indebted to Taylor and Datz (9) for pointing out the existence of comparable data for the condensation coefficients of silver on different metals (10) and for alkali halides on one another (11, 12).

It is important to note that the undervoltage scale for copper in Fig. 8 is double that for silver. This was done to convert the observed values into slopes equivalent in terms of the decrease in activity of the deposit relative to the standard state. That is, a decrease of 0.060 v for silver corresponds to 0.030 v for copper due to the difference in number of electrons transferred. Even so, the slope for copper was only about half that for silver. Part, if not all, of the difference may be due to differences in surface coverage. The concentration of silver may well have been one hundred times more dilute than the copper, although the sixfold larger geometric area of the electrodes used in the present study would tend to counteract this factor. In any event, it is obvious that a study using the same set of electrodes and as nearly as possible the same concentrations of trace elements would be desirable. At the same time, a reinvestigation of the zinc system to obtain more nearly quantitative data would be valuable, particularly in view of an apparent difference in behavior between copper and platinum electrodes, both of which mismatch about 4%. Zinc falls halfway between the larger platinum lattice and the smaller copper lattice.

There seems to be little question that copper deposited as the element from solutions of perchlorate and sulfate. However, in chloride and bromide media, the respective copper (I) salts probably deposited initially even though their solubility products (particularly for the chloride) were not exceeded. First, the $E_{50\%}$ value for trace deposition corresponded almost exactly with the $E_{1/2}$ for copper (II) to (I) reduction. Second, if one assumes that the nearest neighbors in the copper (I) chloride and bromide are the sums of the radii, values of 2.77Å (0.96 + 1.81) and 2.91Å are obtained. (Platinum is 2.77Å.) Depositions on two batches of copper tracer using both platinum and gold electrodes in both chloride and bromide media indicated somewhat easier reductions in chloride at both electrodes and easier reduction using platinum than gold. The important feature is the qualitative correspondence between ease of deposition and the small mismatch. (Cu-Cl: Pt mismatch 0%; Au, 4.0%, Cu-Br:Pt, 5.1%; Au, 1.4%). If mismatch had been the only factor involved, deposition onto gold from bromide should have been easier than onto platinum, but it was not. Unfortunately, another major program would have been required to explore fully the effects of different electrode materials.

A consideration that has been ignored in the above discussion is the fact that complexing anions, particularly halides in acidic solution, would tend to dissolve oxide coatings, thereby increasing the effective surface area of the electrode. From studies in perchlorate media, an increase in geometric surface area is known to result in easier deposition of copper just as it did in experiments involving silver (14). Comparable studies in fused halide melts would therefore be desirable because oxide films should be virtually absent.

In order to refine the correlations, studies employing the same amount of tracer as well as the same

Table III. Relative volatilities of thin films of metals as a function of lattice mismatch

Substrate	Distance, A		Lead[a]			Bismuth[b]			Polonium[e]		
				% Mismatch			% Mismatch			% Mismatch	
	Nearest	Next	$T_{50\%}$[c]	Nearest	Next	$T_{50\%}$[c]	Nearest	Next	$T_{50\%}$[c]	Nearest	Next
Au	2.88	4.15	770	17.7	18.6	815	20.9	14.0	380	13.6	—24.6
Pt	2.77	3.92	780	20.8	12.0	990	23.9	7.7	—	—	—
Pd	2.74	3.88	1050	21.7	10.9	~1030	24.7	6.6	780[f]	17.8	—16.6
Ni	2.49	3.53	620[d]	28.9	0.9	700[d]	31.6	—3.0	—	—	—

[a] Nearest neighbors 3.50Å; boiling point, 1525°C (21).
[b] Nearest neighbors 3.64Å; boiling point, 1420°C (21).
[c] Temperature in °C for evaporation of 50% of film in 10 min in air.
[d] Nitrogen atmosphere; hydrogen atmosphere gave temperatures lower by 70°C.
[e] Nearest neighbors (22): α-form 3.29Å, β-form 3.35Å; 3.33Å used in calculations of mismatch. Boiling point (23), 962°C.
[f] Palladium-gold alloy.

electrode area would be needed. These conditions might be approached much more closely by comparing several tracer elements using a given electrode at one potential. Such a study was beyond the scope of the present one which was designed to survey the suitability of copper for a comparison of that type.

Another precaution to observe would be the conservative use of lattice parameters, determined for carefully prepared crystals, in interpreting data obtained on foils whose surfaces will reflect, to a greater or lesser extent, the physical treatment encountered in their preparation. An outstanding example of the effect of electrode history has been cited already in an electrodeposition experiment with silver for which a gold crucible was used as an electrode (14). However, the differences incorporated by working a surface generally seem to be much smaller than those between any two elements used in the present comparison. Hence, the use of single-crystal parameters appears valid.

The concept of mismatch appears capable of extension by the use of lattice neighbors more distant than the nearest. For example, a collection of data (15) on the relative rates of volatility of thin metallic films from different substrates is given in Table III along with data on nearest and next-nearest neighbors, the latter calculated on the basis of a face-centered cubic structure. It is important to note, particularly for lead and bismuth, that the direction of change in mismatch using nearest neighbors is directly opposite to that using next-nearest. The latter trend, however, conforms to the concept of stronger sorption for smaller mismatch. The striking exception is nickel, for which the rationalization based on an oxide film seems unlikely because of the great care exercised to exclude air (16). The data for polonium are meager and, unfortunately, fall in a region of large mismatch on both bases. On any given surface, the interatomic distances undoubtedly vary widely and almost continuously so some sorption of any given substance will occur on any surface (8). However, lattice parameters will probably represent modes in a plot of the relative number of sites vs. interatomic distance.

Two other points are worth noting in the lead and bismuth data involving the noble metals. In the first place, although $T_{50\%}$ values for bismuth fall on a straight line when plotted against mismatch, values for lead show a sharp change in slope in going from platinum to palladium. The abrupt change occurs in going from 11 to 12% mismatch, values close to the critical 10% limit above which continuous films did not form in some studies (12, 13). Second, in spite of the fact that bulk bismuth boils 100°C lower than bulk lead, the smaller mismatch of bismuth raised its "50% volatilization" temperature as a thin film to values nearly identical with those for lead films.

The present study emphasizes the similarity between adsorption and trace deposition that has been pointed out earlier (13, 17). However, the presence of inert solute and solvent complicates the picture as they do in adsorptions from the liquid phase. As yet, the effect of changing the solvent remains to be explored, as does the effect of adding small amounts of adsorbable substances. The latter studies should provide a fruitful way of exploring the suggested leveling of activity of sites on an electrode (18), as well as supplementing data from polarographic and electrolytic studies in general.

Acknowledgment

The authors are grateful to the Atomic Energy Commission for partial support of this work.

Manuscript received Jan. 15, 1958. This paper is a part of a thesis submitted by R. C. DeGeiso in partial fulfillment of the requirements for the Ph.D. degree to the Massachusetts Institute of Technology, June 1957.

Any discussion of this paper will appear in a Discussion Section to be published in the December 1959 JOURNAL.

REFERENCES

1. L. B. Rogers, *Record Chem. Progress (Kresge-Hooker Sci. Lib.)* **16**, (3), 197 (1955).
2. L. B. Rogers, D. P. Krause, J. C. Griess, Jr., and D. B. Ehrlinger, *This Journal*, **95**, 33 (1949).
3. K. A. Kraus and G. E. Moore, *J. Am. Chem. Soc.*, **75**, 1460 (1953).
4. H. R. Haymond, R. D. Maxwell, W. M. Garrison, and J. G. Hamilton, *J. Chem. Phys.*, **18**, 258 (1951).
5. R. W. Lamphere, *Anal. Chem.*, **23**, 258 (1951).
6. J. C. Griess, Jr., J. T. Byrne, and L. B. Rogers, *This Journal*, **98**, 447 (1951).
7. G. I. Finch, H. Wilman, and L. Yang, *Discussions Faraday Soc.*, **1**, 144 (1947).
8. D. Turnbull and B. Vonnegut, *Ind. Eng. Chem.*, **44**, 1292 (1952); see also F. C. Frank and J. H. van

der Merve, *Proc. Royal Soc.* (London) **A198**, 216 (1949).
9. E. H. Taylor and S. Datz, Private communication, November 1957.
10. L. Yang, M. T. Simnad, and G. M. Pound, *Acta Met.*, **2**, 470 (1954).
11. L. G. Schulz, *Acta Cryst.*, **5**, 130 (1952).
12. *Ibid.*, **4**, 483 (1951).
13. G. E. Gardham, *Discussions Faraday Soc.*, **1**, 182 (1947).
14. J. T. Byrne, L. B. Rogers, and J. C. Griess, Jr., *This Journal*, **98**, 452 (1951).
15. N. A. Bonner and M. Kahn, "Radioactivity Applied to Chemistry," pp. 154-155, edited by A. C. Wahl and N. A. Bonner, John Wiley and Sons, Inc., New York (1951).
16. E. Holesch, *Sitzber, Akad. Wiss. Wien, Math-Naturw. Klasse, Abt. IIA*, **140**, 663 (1931).
17. J. T. Byrne and L. B. Rogers, *This Journal*, **98**, 457 (1951).
18. E. G. Neal and L. L. Shreir, *Trans. Faraday Soc.*, **53**, 1371 (1957).
19. L. Pauling, "The Nature of the Chemical Bond," p. 409, second edition, Cornell Univ. Press, Ithaca, New York (1944).
20. P. C. L. Thorne and A. M. Ward, "Inorganic Chemistry," pp. 36-37, Gurney and Jackson, London, (1939).
21. *Ibid.*, p. 42.
22. W. H. Beamer and C. R. Maxwell, *J. Chem. Phys.*, **17**, 1293 (1949).
23. L. S. Brooks, *J. Am. Chem Soc.*, **77**, 3211 (1955).

Mechanisms of Hydrogen Producing Reactions on Palladium

VI. Atomic Hydrogen Overvoltage on an α Pd-H Bielectrode

Sigmund Schuldiner

U. S. Naval Research Laboratory, Washington, D. C.

ABSTRACT

An electrochemical system was evolved in which the only reactions occurring on the cathode and anode surfaces of an α Pd-H bielectrode were the formation and ionization of atomic hydrogen, respectively. The atomic hydrogen overvoltage on this bielectrode was determined. A kinetic analysis of the system was supported by the experimental results.

In this paper a bielectrode system is described in which the net reaction, on the cathode side, is the reduction of hydronium ions to hydrogen atoms and, on the anode side, the oxidation of hydrogen atoms to hydronium ions. The electrochemical system consists of two cells in series in which the first cell is connected to the second by means of an α Pd-H bielectrode. In the first cell, the anode reaction is the oxidation of hydrogen atoms, which have diffused through a palladium tube, to hydronium ions. The cathode reaction on the α Pd-H bielectrode is the reduction of hydronium ions to hydrogen atoms. The hydrogen atoms formed on this cathode surface are transported through the α Pd-H bielectrode to the anode surface where they are oxidized to hydronium ions in the second cell. The cathode reaction in the second cell is the reduction of hydronium ions to hydrogen atoms which diffuse through a Pd tube cathode to react with oxygen on the inner surface of the tube.

In such an electrochemical system, for every equivalent of atomic hydrogen oxidized to hydronium ions at the anode in the first cell, an equivalent of hydrogen ions is transported through the bielectrode, and an equivalent of hydronium ions is oxidized to hydrogen atoms which are removed from the system through the cathode in the second cell. Hence, the concentration of hydronium ions in both cells remains constant, atomic hydrogen is consumed as fast as it is produced, and the system can be kept free of molecular hydrogen.

On the cathode side of the bielectrode, the adsorbed atomic hydrogen concentration will increase with increasing current densities, whereas on the anode side of the bielectrode, the adsorbed atomic hydrogen concentration will decrease with increasing current densities. At a limiting current density, the transport of hydrogen through the bielectrode will not be fast enough to furnish enough hydrogen atoms to support the current density on the anode side of the bielectrode. At this point the potential will rise sharply and an oxygen producing reaction also will occur on this surface. No longer will there be a complete transfer of the hydrogen atoms formed on the cathode side to the anode side.

Experimental

The electrochemical system used in this investigation is shown in Fig. 1. It is a modification of a previously described double cell (1). In this system the anode in the right hand cell is a Pd tube with a sealed bottom, 5 cm long, 3 mm in diameter, and with a wall thickness of 0.2 mm. During a run hydrogen gas is circulated through the inside of this tube. Some of the hydrogen diffuses through the wall of the tube and exists as hydrogen atoms on the outer surface in contact with the 2*N* sulfuric acid solution. Virtually all of these hydrogen atoms are oxidized to hydronium ions under an applied current flow. If the flow of atoms to the surface is too slow to support the applied current, an oxygen forming reaction at a sharply elevated positive potential occurs. Hence a determination of the polarization of this electrode indicates whether the reaction is completely the ionization of hydrogen atoms or not. During the runs reported here the maximum

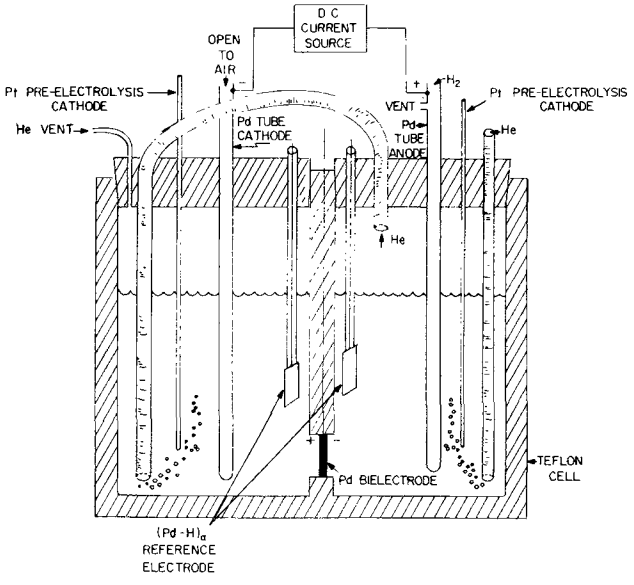

Fig. 1. Electrochemical system

polarization of the Pd tube anode was less than 0.1 v. This indicated that the diffusion of atomic hydrogen through the wall of the anode tube was fast enough to prevent an oxidation reaction other than ionization of atomic hydrogen. There is a possibility that at low current densities some molecular hydrogen could form on this surface of the Pd tube anode. However, even if this did occur the molecular hydrogen would be formed at a slow rate and, since the cells were swept continuously with a rapid stream of helium, the partial pressure of molecular hydrogen in the solutions would always be negligible.

The bielectrode consisted of a Pd diaphragm (0.004 in. thick with an apparent exposed area of 0.14 cm^2) charged to the maximum α phase (H/Pd atom ratio $\sim$ 0.03). During polarization the reaction on the cathode side consisted of the reduction of hydronium ions in the double layer to hydrogen atoms chemisorbed on the cathode surface. The hydrogen atoms formed on this surface are transported to the anode side of the bielectrode where they are oxidized to hydronium ions. A description of the transport mechanism already has been given (2).

The cathode in the left hand cell consisted of a Pd tube of the same dimensions as the anode in the right hand cell. This tube was open to the atmosphere. The reaction on the surface in contact with the solution was the reduction of hydronium ions to atoms which then migrated through the wall of the tube to react with oxygen on the inner surface. Polarization of this electrode for the maximum current applied was less than —0.05 v which indicated that virtually all of the atomic hydrogen formed on the outer surface did diffuse through the wall and react with oxygen on the inner surface of the tube.

The reference electrodes used in this investigation were $(Pd\text{-}H)_\alpha/H_3O^+$ electrodes of the maximum α composition (3).

A run was conducted in the following way. Using previously described techniques (4, 5) the double cell was cleaned thoroughly and about 5 ml of purified 2*N* sulfuric acid solution was added to each compartment. The solution was then "pre-electrolyzed" using the Pt wire electrodes shown in Fig. 1 as the pre-electrolysis cathodes. Purified hydrogen gas was circulated through the cells during the pre-electrolysis. During this treatment all of the Pd electrodes in the cells were anodically cleaned. After a minimum 16-hr pre-electrolysis, the Pt cathodes were removed from the cells (during current flow) by pulling them through the holes indicated in the Teflon stoppers in the cells. These wires then were cleaned by repeatedly dipping them in concentrated nitric acid and heating them white hot in a flame. The Pt wires then were reintroduced into the cells. Hydrogen gas was circulated through the cells until the potentials on the Pd bielectrode and reference electrodes were 0.05 v positive to the Pt/H_2 electrodes in each cell. This usually took from 4 to 6 hr. At this point the hydrogen flow was transferred to the anode tube electrode in the right hand cell and a purified stream of helium was passed rapidly through both cells. The open-circuit potential between the $(Pd\text{-}H)_\alpha/H_3O^+$ reference electrodes and each side of the α Pd-H bielectrode was equal to zero. Steady-state currents then were applied to the double cell in the circuit shown in Fig. 1. Overvoltages were determined under steady-state conditions at increasing current densities only, since at the highest current densities some oxygen formation reaction occurred on the anode side of the bielectrode. Current interrupter (6) measurements were made in order to verify surface cleanliness and to correct for the *IR* drop between the surfaces of the bielectrode and the reference electrodes. The temperature was 27° ± 1°C.

Results and Discussion

Four typical anodic and cathodic overvoltage curves are shown in Fig. 2. Actually about 15 runs

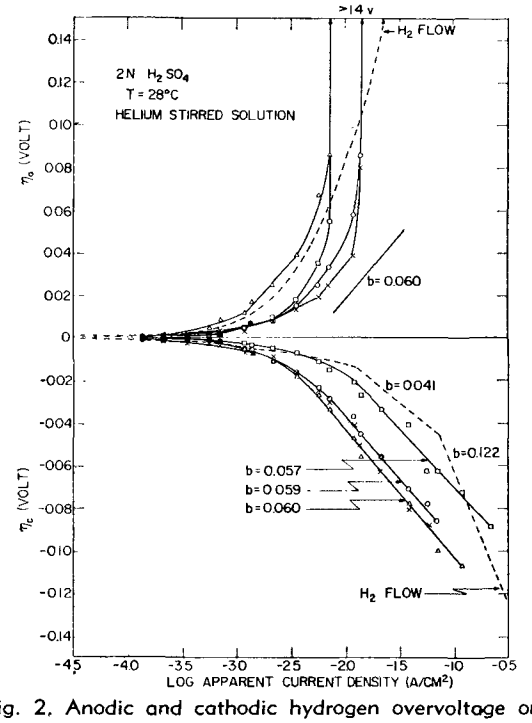

Fig. 2. Anodic and cathodic hydrogen overvoltage on an α Pd-H bielectrode. X, O, △, □ represent experimental points for four separate runs, and • represents the overlapping of three or more points of different runs. Broken line represents overvoltages in the presence of molecular hydrogen (2). The reference electrodes are $(Pd\text{-}H)_\alpha/H_3O^+$ (3).

were made, but the curves shown are representative. The curve with a broken line was taken from a previous investigation (2) and represents the overvoltage curves obtained for the same bielectrode system when molecular hydrogen is present in the system. As can be seen from Fig. 2 the presence of molecular hydrogen does markedly change the polarization behavior on both the anode and cathode sides of the bielectrode. Under open-circuit conditions the potential determining reaction on the α Pd-H electrodes was shown to be an equilibrium between hydronium ions in the solution and protons dissolved in the Pd (3). Upon polarization in a solution containing molecular hydrogen two simultaneous reactions occur on the bielectrode surfaces. The first reaction involves the reduction of hydronium ions to hydrogen atoms on the cathode side of the bielectrode, the transfer of part of the atoms through the bielectrode and the oxidation of the atoms to hydronium ions on the anode side of the bielectrode. The second simultaneous reaction involves the combination of those atoms, which do not migrate from the cathode to the anode sides of the bielectrode, to molecules on the cathode side and an equivalent amount of ionization of molecular hydrogen on the anode side to hydronium ions. Upon polarization in a solution which is free of molecular hydrogen, only the first reaction occurs. Hence all of the hydrogen atoms formed on the cathode side of the bielectrode are transferred to the anode side and there is no second reaction involving the formation or ionization of molecular hydrogen. Therefore, it is obvious that, in the case of the system free of molecular hydrogen, the overvoltage being observed is solely that of atomic hydrogen on the α Pd-H electrode of maximum hydrogen content.

The shapes of the curves shown in Fig. 2 were reproducible. However the effective exchange current density, i_o, values were only reproducible to the extent indicated. This most likely means that the atomic polarization was extremely sensitive to surface conditions. Since previous investigations (5) have shown that for the molecular hydrogen system the effective area remained fairly constant after the initial electrode treatment, this would indicate that the atomic hydrogen electrode in the absence of molecular hydrogen was more sensitive to active centers on the surface. It may be that molecular hydrogen exerts a buffering effect since there is an exchange between molecular hydrogen and hydrogen atoms adsorbed on the surface. When molecular hydrogen is eliminated from the system this source of atomic hydrogen is removed and the effect would be most marked in the low current density region. This would account for the poor reproducibility of i_o.

The rate constants $(-di/d\eta)$ for the over-all reactions found in the low current density overvoltage range in which the overvoltage is linearly dependent on current density varied from 0.14 to 0.33 mhos/cm^2. Since in the presence of molecular hydrogen, $-di/d\eta$ is 0.13 mhos/cm^2 (2), this indicates that the hydrogen transport through the bielectrode is somewhat faster than the surface H_2 evolution or ionization reaction. In the presence of molecular hydrogen 70% of the current was used in transporting hydrogen through the bielectrode and 30% was used forming and ionizing H_2 on the cathode and anode surfaces, respectively (2).

The rate of helium stirring made virtually no change in the overvoltage measurements. Stirring rates were reduced even to zero with no significant change in polarization potentials.

Overvoltage on the cathode side of the bielectrode. —During current flow the reactions occurring on the cathode side of the bielectrode are:

$$H_3O^+ + e^- = H_a + H_2O \qquad [1a]$$

$$H_a \xrightarrow{\text{slow}} H_i \qquad [1b]$$

$$H_i = H_i^+ + e^- \qquad [1c]$$

where H_a denotes hydrogen atoms chemisorbed on sites on the cathode side of the α Pd-H bielectrode; H_i, hydrogen atoms absorbed in the interior of the bielectrode; and H_i^+, protons in the interior of the bielectrode. Equation [1a] represents the formation of chemisorbed hydrogen atoms on the cathode surface. Equation [1b] represents the absorption of the adsorbed hydrogen atoms from the surface through the skin of the metal to some position in the interior of the metal. Equation [1c] represents the donation of hydrogen 1-s electrons to the d band of the metal. The atomic absorption step, Eq. [1b], is considered to be rate determining. Previous work (2) has indicated that the transfer of the hydrogen atoms through the skin of the metal is the rate-determining step in the migration of hydrogen atoms through a Pd bielectrode. The kinetic analysis which follows supports this conclusion since the experimental results are in accordance with the mechanism indicated in Eqs. [1a], [1b], and [1c].

Let us write the kinetic equations for the primary discharge step [1a].

$$\vec{i}_a = \vec{k}_a\,(H_3O^+)\,\exp\,(-\alpha\eta_c F/RT)$$

$$\overleftarrow{i}_a = \overleftarrow{k}_a(H_a)\,\exp\,[(1-\alpha)\eta_c F/RT]$$

where k_a is the rate constant; (H_3O^+), the concentration of hydronium ions; (H_a), the concentration of adsorbed hydrogen atoms on the cathode surface; α, the transfer coefficient; η_c, the cathodic overvoltage; F, the faraday; R, the gas constant; and T, the absolute temperature. Since step [1a] is considered to be virtually equilibrium, $\vec{i}_a = -\overleftarrow{i}_a$ and

$$(H_a) = (\vec{k}_a/\overleftarrow{k}_a)\,(H_3O^+)\,\exp\,(-\eta_c F/RT) \qquad [2]$$

For the rate-determining step [1b]

$$i_c = \vec{k}_a(H_a) + \overleftarrow{k}_a(H_i) \qquad [3]$$

Under conditions where the back reaction in the rate-determining step [1b] is negligible, the net cathodic current density is

$$i_c = \vec{k}_a(H_a), \qquad [4]$$

where $\vec{k}_a$ is the rate constant for the forward reac-

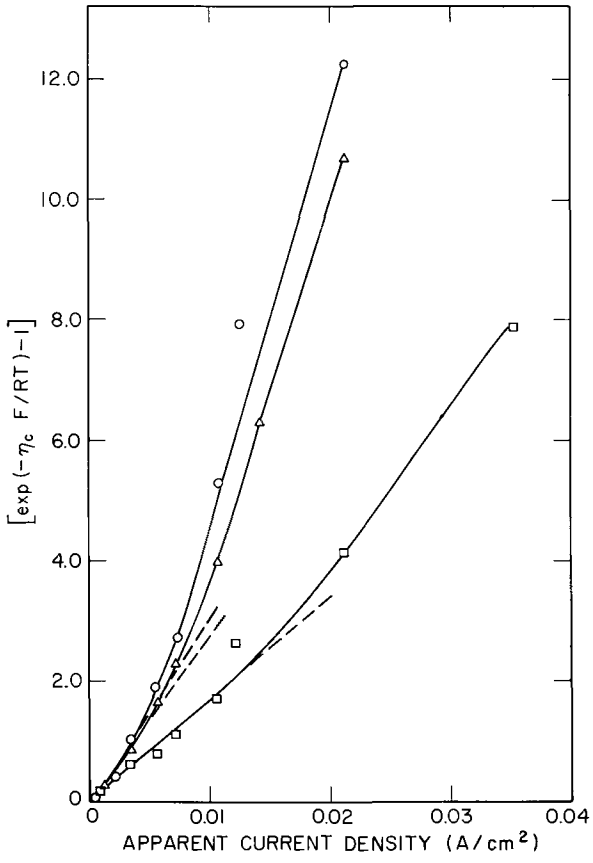

Fig. 3. Relationship between i_c and exp $(-\eta_c F/RT)-1$

tion of the atomic absorption step [1b]. Hence, substitution of Eq. [2] into Eq. [4] yields, after conversion to logarithms,

$$\eta_c = (RT/F)\ [-\ln i_c + \ln \text{const} + \ln (H_3O^+)] \qquad [5]$$

Since (H_3O^+) represents the bulk concentration of hydronium ion, which is constant, the Tafel equation can be written $\eta_c = a - b \log i_c$, where the Tafel constant $b = 2.3\ RT/F$; at 27°C, b = 0.059 v.

Since the Tafel lines found in the cathode overvoltage curves in Fig. 2 are near a 0.059 slope this confirms that the slow step in the hydrogen atom production reaction is the absorption (solution) of hydrogen atoms.

The data in Fig. 2 show that the Tafel lines commence at overvoltages of about −0.02 v. This means that the back reaction in Eq. [3] must vanish at a much lower overvoltage than one would expect. Similar low values for the start of the Tafel slope were found for platinum and palladium (4-6).

From Eq. [3] and [4] one obtains $i_c = K \exp (-\eta_c F/RT) - \overleftarrow{k}_a(H_i)$. From Eq. [1c], $\overrightarrow{i}_{1c} = \overrightarrow{k}_{1c}(H_i)$, and $\overleftarrow{i}_{1c} = \overleftarrow{k}_{1c}(H_i^+)$. Since step [1c] can be considered to be virtually at equilibrium and (H_i^+) is constant at low overvoltages, $(H_i) = K'$. Therefore the net cathodic current is

$$i_c = K \exp (-\eta_c F/RT) - K' \qquad [6]$$

At equilibrium, $i_c = 0$, $\eta_c = 0$, and $K' = K$, hence,

$$i_c = K\ [\exp (-\eta_c F/RT) - 1] \qquad [7]$$

Figure 3 shows a plot of exp $(-\eta_c F/RT) - 1$ vs. i_c for three separate runs which had about the maximum deviation from one another. These curves clearly show that Eq. [7] holds only up to overvoltages of about −0.02 v. This means that $K' = K$ near equilibrium only. The experimental shift to a Tafel slope at about −0.02 v could be accounted for by an increase in K and a decrease in K′ with increasing current density. This implies a larger increase in the forward reaction in the rate-determining step [1b] and a larger decrease in the back reaction. This is owing to the increase in concentration of H_a on the cathode surface.

Overvoltage on the anode side of the bielectrode. —Using a derivation analogous to that for Eq. [6], one finds for the anode side of the bielectrode

$$i_a = K'' - K \exp (-\eta_a F/RT) \qquad [8]$$

where $K'' = K$ at low overvoltages. Hence at low current densities $\eta_a = -\eta_c$. This is experimentally observed in Fig. 2.

The anodic polarization slopes shown in Fig. 2 do not show a clear region in which an 0.059 slope exists, although for a short current density range such a slope can be drawn. This is because in the higher current density range the depletion of adsorbed hydrogen atoms becomes such that it cannot support the current density flowing from the anode. Hence, as the concentration of adsorbed atomic hydrogen approaches zero, there is a sharp rise in potential. At higher potentials (>0.1 v) a secondary reaction involving an oxygen formation reaction occurs in the region shown in Fig. 2 where the anodic potential rises vertically. Equation [8] shows that as a limiting condition, $i_a = K''$. The atomic hydrogen supply on the anode surface is limited by the rate of the deabsorption of atomic hydrogen from the interior of the bielectrode, whereas the limiting step on the cathode surface of the bielectrode is the solution of atomic hydrogen through the skin of the metal. Hence on the cathode side the chemisorbed atomic hydrogen concentration can build up to a large value, whereas on the anode side the depletion of the atomic hydrogen will occur at a relatively low current density, since the atomic hydrogen concentration cannot be larger than that on an α Pd-H reversible electrode of maximum hydrogen concentration.

It should be noted that in the electrochemical system reported here, the interior of the Pd bielectrode is the maximum α Pd-H alloy. This is because this is the alloy at zero current density and this composition is maintained, except at the highest current densities, because hydrogen is dissolved into the interior of the bielectrode from the cathode side at the same rate it is removed from the interior of the bielectrode on the anode side.

In the high current density range a reaction involving oxygen occurs on the anode side of the bielectrode and only part of the current flowing in the interior of the Pd is protonic, the remainder is an electronic current. This would mean that not all of the hydrogen atoms formed on the cathode surface would be transferred through the bielectrode to the

anode side. Most of these excess atoms probably dissolve in the interior of the palladium to form β Pd-H which coexists with the α phase. During the time interval in which measurements were taken in this high current density range (usually less than 1 hr, although in several cases currents were maintained for several hours with no potential change) only a relatively small amount of the β phase would be formed. The atomic hydrogen overvoltage on the cathode side of this two phase alloy does not deviate significantly from the pure α alloy since the cathodic Tafel lines in Fig. 2 show no change in the high current density region.

The anodic curves shown in Fig. 2 indicate that beyond a potential of 0.06 v, the concentration of atomic hydrogen on the surface must be very small. Since the concentration of hydrogen atoms on the surface at zero overvoltage would not be more than ten times higher, it can be concluded that the atomic hydrogen coverage on the maximum α Pd-H alloy under open-circuit conditions is quite small. Also, inasmuch as the potentials on both sides of the bielectrode are dependent on (H_a), one can approximate the change in (H_a) on the cathode side at the maximum overvoltage by use of the Nernst potential equation. Thus, at the maximum measured η_c of about -0.10 v, (H_a) on the cathode side will increase $\sim$50 times. This means that the initial atomic hydrogen coverage must be less than 2%.

Acknowledgment

The author is indebted to Drs. J. C. White and G. W. Castellan of the U. S. Naval Research Laboratory and to Dr. R. A. Marcus of the Polytechnic Institute of Brooklyn for valuable discussions concerning this work.

Manuscript received July 7, 1958.

Any discussion of this paper will appear in a Discussion Section to be published in the December 1959 JOURNAL.

REFERENCES

1. S. Schuldiner and J. P. Hoare, *This Journal*, **103**, 178 (1956).
2. J. P. Hoare and S. Schuldiner, *ibid.*, **104**, 564 (1957).
3. S. Schuldiner, G. W. Castellan, and J. P. Hoare, *J. Chem. Phys.*, **28**, 16 (1958).
4. S. Schuldiner, *This Journal*, **101**, 426 (1954).
5. J. P. Hoare and S. Schuldiner, *ibid.*, **102**, 485 (1955).
6. S. Schuldiner, *ibid.*, **99**, 488 (1952).

Technical Notes

Molybdenum Plating Inside of Large Bore Tubes

Paul L. Raymond

Metallurgical Department, National Research Corporation, Cambridge, Massachusetts

In early 1953 a program was initiated to develop equipment and procedures for coating the inside of alloy steel tubes with a uniform coating of molybdenum. The inside diameter of the tubes was about 1⅝ in. and the coated section was to be about 2 ft long. These tubes when coated were to be subjected to various tests for adhesion, wear resistance, corrosion resistance, etc.

Previous investigations (1, 2) had determined that: (*A*) high-purity molybdenum metal could be deposited at a high rate by the reduction of molybdenum pentachloride with hydrogen; (*B*) the temperature for this reaction ranged between 650° and 1100°C; and (*C*) excess hydrogen was necessary to yield complete reduction and to utilize efficiently the available pentachloride.

Work at this laboratory had shown further that: (*A*) the pressure at which reduction occurred most efficiently was approximately 20 mm Hg; (*B*) the plate followed surface contours without building up at discontinuities; and (*C*) high-purity molybdenum pentachloride required could be obtained by heating commercially pure $MoCl_5$ for an hour at a pressure of 1 mm Hg or less at 100°C.

With this general background it was proposed to coat the interior of tubes with molybdenum by hydrogen reduction of the pentachloride. The size of the tubes precluded the convenient use of an enclosed system for vacuum operation, and it seemed generally desirable to establish a system employing common engineering materials in order that tubes could be inserted rapidly for processing.

Equipment

Schematically, the equipment design for vapor plating is shown in the flow diagram, Fig. 1. Argon from high-pressure cylinders was heated and passed through molten molybdenum pentachloride.

It was then mixed as it passed through the lines with heated hydrogen. The mixture of hydrogen, argon, and molybdenum pentachloride vapor entered the reaction tube where it passed upward through a heated zone. Metallic molybdenum was deposited on the walls in this heated zone by the reduction of the pentachloride by the hydrogen. The reaction gases passed through a filter to remove solid by-products and the gases exhausted to atmosphere through a vacuum pump. The heated zone was

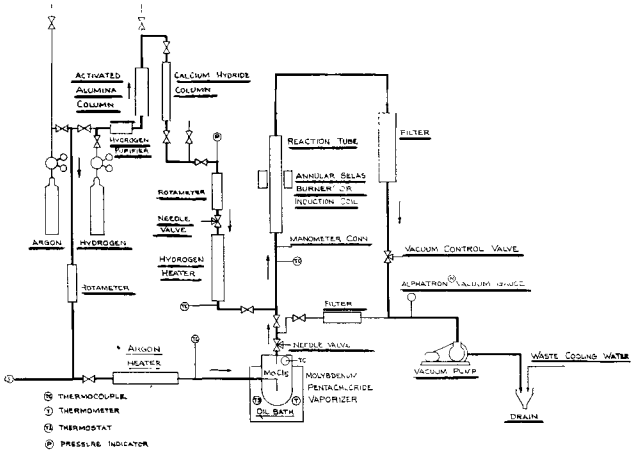

Fig. 1. Flow diagram

slowly moved downward throughout the length of the tube as the plating progressed.

Except for a series of stainless steel valves, the components containing molybdenum pentachloride and the products of the reaction were all mild steel, synthetic, or natural rubber. Operating temperatures of the vaporizer in use at the conclusion of the investigation did not exceed 250°C, so that only a slight amount of iron contamination was observed. A vacuum-tight vacuum system was developed with this equipment and an initial pump-down to 20 μ with the original mechanical vacuum pump was possible throughout the program. Rubber tubing was employed in some cases to facilitate connections to flowmeters and manometers. Experience indicated that the most suitable gasket material for hot connections at the reaction tube was compressed asbestos sheet packing. This material does not flow as do plastic materials and it will withstand high temperatures.

The flow diagram shows the sequence of equipment and operations, starting with the gas system.

Commercially pure water pumped hydrogen in high-pressure tanks was purified by a catalytic purifier followed by a column filled with activated alumina and one filled with calcium hydride lumps. Hydrogen from this system had a dewpoint below −70°C. Argon and helium used for purging and as carriers for molybdenum pentachloride vapor have extremely low dewpoints as-received and were used without further purification. Pressure regulators reduced gas pressures to approximately 1 atm. A manifold permitted the flow of either hydrogen or argon through rotameters to determine the flow rate. A pressure slightly above atmospheric was maintained in this system to preclude air leaking into the system. Needle valves reduced the gas pressure to 5-20 mm Hg and also controlled the flow. As this was generally a steady-state system, only slight adjustments during a plating run were required.

The gases were heated at atmospheric pressure by passing through a spiral finned resistance heater within an asbestos jacketed section of 1¼ in. iron pipe. Exit gas temperature was determined by thermocouples. Variable transformers were used to control power to the heating elements.

The molybdenum pentachloride vaporizer consisted of a 4 in. diameter cylinder about 8 in. long with a hemispherical base and flanged top. The vaporizing gas bubbled through the bath of molten molybdenum pentachloride and out through a pipe in the cover of the assembly. The entire assembly was immersed in a constant temperature oil bath to provide heat of vaporization and to control the vapor concentration.

Throughout the course of the investigation there probably were more changes in the vaporizer than in all other components concerned. In early experiments, heated hydrogen flowed past the molybdenum pentachloride suspended in a glass cloth bag while the outside of the vaporizer, which then consisted of a flanged section of pipe, was heated by gas burners. Poor control of vapor concentration and premature partial reduction of pentachloride resulted from this system.

Next, a mechanical screw-type feeder was employed to regulate the flow of pentachloride crystals to a heated plate where it was hoped that flash evaporation would occur, giving a controlled molybdenum pentachloride-hydrogen ratio. However, premature reduction and disproportionation were observed. Also, the feed screw became jammed frequently, resulting in no vapor flow at all.

The tank-type vaporizer was modified several times before the final model was developed. In the first model, heated hydrogen was passed over molybdenum pentachloride placed on trays in a vaporizer, which picked up the hydrogen vapor. It was hoped that a constant evaporation rate could be maintained throughout the duration of the run, but due to the changing surface conditions of the pentachloride crystals, the vapor concentration in the gas mixture decreased as the run progressed. After several attempts involving minor modifications of the system, it was decided to melt the molybdenum pentachloride before vaporizing. The $MoCl_5$ vapor was picked up in one hydrogen stream and diluted with a second hydrogen stream. Various amounts of partially reduced chlorides were observed in the reaction tube, and the system contained partially reduced chlorides in the form of dust, which at times caused either nonadherent coatings or nodules to be formed in the reaction zone. Through the use of heated argon as a vapor pick-up and carrier, the premature reduction of the pentachloride vapor was eliminated and much closer control of vapor ratio was obtained. In this case, hydrogen for the reaction was added after the argon had passed through the vaporizer and just prior to entrance into the reaction tube. In this way, it was not necessary to control closely the temperature of the diluent hydrogen gas but only to maintain the temperature of the resultant mixture above the dewpoint of the molybdenum pentachloride vapor present.

The use of argon as a means of picking up pentachloride vapor was extremely successful, as it was possible to control the hydrogen:pentachloride ratio sufficiently closely to permit uniform coating conditions throughout extended runs. In an effort to determine whether helium would work as well, two runs were conducted utilizing helium as a carrier

gas. In both of these runs, the coatings deposited were as good as those deposited when argon was utilized.

Measurements and Controls

With the vaporizer operating at approximately atmospheric pressure, near saturation conditions of $MoCl_5$ in argon existed. By varying the temperature of the oil bath or the temperature of the argon entering the vaporizer or both, it was possible to control closely the ratio of molybdenum pentachloride to argon. The diluting hydrogen stream was measured by a rotameter. Thus, the desired molybdenum pentachloride to hydrogen ratio could be maintained through an extended run.

During the project several schemes for actual measurement of the vapor concentration were attempted, but with poor success. Color comparison methods were of little value due to clouding of sight glasses and to variation of color with pressure. Considerable effort was expended in an attempt to develop a dewpoint type of measuring device, but here again, clouded sight glasses prevented precise measurements.

A tap at the reaction tube inlet was connected to a mercury manometer by means of copper tubing to determine the static pressure in the reaction tube. This arrangement functioned very satisfactorily throughout the project. The pressure in the system was maintained by a vacuum pump evacuating the system. The pumping rate was regulated by a globe-type vacuum valve to provide a controllable orifice. Solid products of the reaction frequently caused excessive friction to gas flow until a large area vacuum filter was installed ahead of the control valve.

Reaction Tubes

Most of the plating runs utilized tubes made from commercially drawn steel tubing with an approximate composition comparable to AISI 4620. The internal surface of the tubes was finished to a high polish. Initially, metallic "O" rings were used as gaskets at the tube ends, but experience proved that the asbestos sheet material provided a tighter seal.

The tubes were bored out to 1⅝ in. and were finished to a surface of better than 16 microinches rms. The tubes were approximately 36 in. long over-all permitting a coating length of about 30 in.

Various substrates were used as a basis for the molybdenum plate, in addition to cleaned but otherwise untreated steel. All tubes were carefully degreased with acetone. Electroplates of copper and of nickel and chemical plates of nickel and of cobalt were tested. Chemical plate was produced by the manner outlined by Brenner and Riddell (3) at the National Bureau of Standards. Since cobalt chemical coatings gave the best results in the early stages of development, all tubes used in the later stages were given this treatment.

Heating of the Reaction Tube

An induction heating coil was originally proposed for this study, but it was not possible to secure an adequate power supply in a reasonable time at the outset of the project. For the most part heating of the tube was accomplished by an annular high-temperature gas burner mounted on a moving platform. The burner was of the positive pressure, mixed air and gas type. It was capable of producing a narrow band of intense heat at the exterior of the tube and could be regulated within very close limits.

The burner was moved downward counter to the feed flow in order to allow the molybdenum to be deposited on a clean surface. With a plating run starting at the upper end of the tube, any partially reduced products of the reaction were deposited on the plated surface and could easily be removed.

During the final phase of the project, a 25 kw, 9600 cycle induction generator became available and it was decided to investigate the effect of an extended reaction zone on the process. A heated zone of from 8-10 in. was desired in place of the narrow 2-in. zone available from the gas burner. It was determined that about 2½-3 kw were required to maintain the tube at reaction temperature. This method of heating proved to be extremely successful, clean, easy to control, and produced less scaling on the outside of the tube than the gas burner. The temperature of the external tube surface was measured by a thermocouple and by a radiation pyrometer. Unfortunately, there was time for only four runs utilizing this equipment. Results are discussed later.

For all runs secondary heating by infrared lamps was utilized to maintain the temperature of the reaction tube above the condensation temperatures of molybdenum pentachloride in order to prevent a subsequent vaporization and enrichment of the vapor mixture as the burner traveled down the tube.

Effect of Variables on Plating Quality

Throughout the investigation, the effects of the following variables on plate quality and thickness were studied: total pressure, temperature of reaction zone, vapor concentration, hydrogen flow rate, surface preparation, and direction and rate of travel of the burner. The following were found to be the optimum conditions using the equipment described: (*a*) total reaction pressure 15-20 mm Hg; (*b*) tube temperature of 900°-950°C measured externally; (*c*) rate of travel of burner in the downward direction of 2 in./hr. (*d*) hydrogen flow of 7-9 liters/min measured at standard conditions.

When the pressure in the reaction tube rose above 20 mm, a vapor phase reduction occurred and the deposit became porous and nonadherent due to deposition of molybdenum particles which did not form a continuous coating. Below 10 mm total pressure it was impossible to obtain an adequate concentration of molybdenum pentachloride vapor to provide a sufficiently high rate of deposition. Most of the work was carried out at a pressure of 17 mm Hg.

The external temperature of the reaction zone as determined optically was usually between 875° and 975°C. These temperatures were correlated with measurements made by thermocouples to the internal tube temperature early in the project. Temperatures below 875°C were not high enough to produce a complete reduction at the existing gas velocities. Above 975°C there was an increased tendency to-

ward formation of large amounts of scale and toward decarburization of the exterior tube surface. No improvement in internal plate quality was gained by operating at temperatures in excess of 975°C.

While it was not possible to determine quantitatively the actual molybdenum pentachloride to hydrogen ratio, it was quite evident from the examination of the data that this was one of the fundamental variables of the process. When the vapor concentration was too low, an excessively long period was required to build up an adequate plate thickness. However, when very lean mixtures were used, the plate appeared to be dense and well bonded. With a high ratio of molybdenum pentachloride to hydrogen in the vapor a porous nonadherent coating was deposited. In the latter case there was a tendency for the coating to be much thicker, but because of side reactions, voids were apparent between the molybdenum and the base metal. The maximum plating rate for dense adherent coatings was 0.004 in./hr. When the plating rate was increased by increasing reactant rate or by increasing the vapor concentration, the deposit became less adherent, brittle, and less dense. When a low vapor concentration was used, the deposition rate was low but the quality of the deposit was excellent. Considerable effort was expended in an attempt to establish a means of determining quantitatively the molybdenum pentachloride-hydrogen ratio, but without success.

From the examination of a large number of plating runs, the conclusion was reached that downward travel of the burner consistently produced the best results; as the vapor mixture flowed through the heated zone, the reduction to metallic molybdenum was only partially complete. Some low molybdenum chlorides were also produced, which deposited on the internal tube surface in the cool zone. If the burner were moved concurrent with the flow, these lower chlorides might not be revaporized before they reached reduction temperature. This would result in a porous or powdery deposit with little or no adherence of the subsequent metallic plate. If on the other hand the heater were moved downward, incompletely reduced chlorides would be deposited on plate which had already been laid down and would be subjected to no additional heating. As the heater moved down, the plate would be deposited on fresh clean surface. When necessary, unreduced chlorides were removed with no difficulty by wire brushing.

Because of the reaction of the molybdenum and the carbon of the steel, it was determined early in the research that a barrier must be established to prevent this from taking place. Copper, nickel, and cobalt plates in various thicknesses were tried. The best results were obtained using a cobalt underplate of about 0.00025 in. This plate was easily applied nonelectrolytically and, once in place, provided excellent protection for the internal surface of the tube prior to molybdenum plating.

Time did not permit a more detailed study of the effect of increasing the width of the reaction zone. The results of the last four runs of the project were so much superior to all others that it appears that plating quality and rates could be improved greatly.

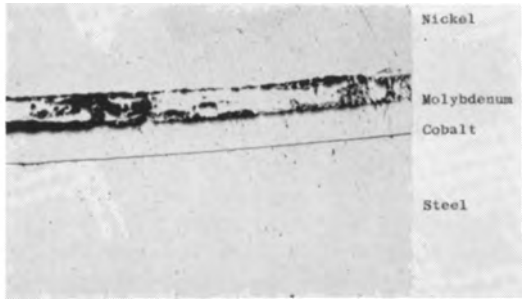

Fig. 2. Photomicrograph of molybdenum on cobalt on steel, unetched. Magnification 100X before reduction for publication. Photograph courtesy of Watertown Arsenal Laboratories.

Examination and Testing

Photomicrographs of coatings and base materials were made regularly to determine quality of the plate. Figure 2 shows the polished, but unetched, tube at 100X magnification (before reduction for printing). On the bottom is the base material of the tube. The line above is the cobalt substrate; next is the molybdenum deposit of about 0.004 in. The specimen was coated with electrodeposited nickel prior to metallographic examination, and the dark area between the molybdenum and the nickel is apparently due to the sample preparation.

Figure 3 shows the etched deposit at 500X. The base material, AISI 4620, is in the lower section, the cobalt interface and the molybdenum. The columnar structure of the deposited metal is readily observed. The protecting nickel coat is shown here as above.

The plated tubes have undergone utilization tests to determine resistance to abrasion and erosion. In addition to the metallographic examination of the coatings, several other tests were made to determine the efficiency of the plating process and the quality of the deposited molybdenum.

Samples of the coatings were subjected to various bend tests to determine the angle to which the plate and base material could be deformed before separation of the plate occurred. The specimen was bent with the plated surface out so that the plate was under tension. It was observed that the heavier the plate, the more readily it fractured. In all cases, the plate fractured when the bending angle exceeded 135° at a bending radius of ½ in. In several instances good plate showed failure at much lower bend angles because of the extreme columnar struc-

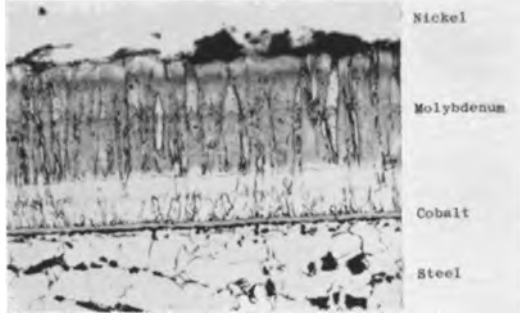

Fig. 3. Photomicrograph of typical molybdenum deposit, etched with alkaline $K_3Fe(CN)_6$. Magnification 500X before reduction for publication. Photograph courtesy of Watertown Arsenal Laboratories.

ture of the deposited material. When this type plate was examined under a low-power microscope, it was evident that the molybdenum failed by separation of the columnar grains as indicated by the many cracks extending from the base material to the outside surface of the plate. In spite of the failure of the molybdenum, it was evident that the cobalt plate below the molybdenum had remained intact during the bend test. Additional indications of quality of the molybdenum plate were obtained by observing the tube when it was sawed for sampling.

To further determine plate quality, various machining operations were performed on coated tubes. Sawing of a tube which had been plated with what was considered to be a high-quality plate produced a rolled-over edge of the coating at the edge of the cut. A poor coating would either flake off or chip away from the base material at the saw cut.

When a piece of coated tube was placed in a shaper and a strip of material removed lengthwise from the tube, good coatings would, as in the case of the sawed sample, remain attached to the section of base material removed from the tube. Poor quality coatings would flake and chip as the tool passed across the coating, and the coating would separate from the base material even though the base material were removed in a clean, even cut from the tube section.

Conclusions

A technique has been developed for the production of relatively heavy molybdenum plates inside of tubes. The best deposits were produced when the vapor concentration was held constant throughout the run. The wide hot zone produced by the induction coil proved superior to the narrow hot zone produced by the external gas burner. It was essential to maintain a large excess of hydrogen in the vapor stream to insure complete reduction, in order to produce dense deposits. Chemically clean surfaces for deposition were necessary to permit good bonding of the plate and substrate.

There should be uses for such plates in the chemical engineering field to take advantage of the mechanical strength and resistance to abrasion and erosion of molybdenum, as well as its high chemical and corrosion resistance. In the presence of air, at elevated temperatures, molybdenum undergoes catastrophic oxidation. However, for many uses in high-temperature, high-pressure reactors, this material could well be the answer to erosion problems where nonoxidizing conditions exist.

Acknowledgment

The author wishes to express his appreciation to the Ordnance Corps, Department of the Army, for permission to publish this information. Dr. Peter R. Kosting, Mr. Murray M. Jacobson, and Mr. Herbert F. Campbell of the Watertown Arsenal Laboratories were very helpful with assistance and suggestions. The author is also indebted to Mr. Morse Hill, the initial project manager, and to Mr. Philip J. Clough, Director, Metallurgical Department, National Research Corporation.

The technical assistance of Messrs. Donald Wilde and Henry Beanland is also acknowledged.

Manuscript received April 22, 1958. This paper was prepared for delivery before the Washington Meeting, May 12-16, 1957.

Any discussion of this paper will appear in a Discussion Section to be published in the December 1959 JOURNAL.

REFERENCES

1. C. F. Powell, I. E. Campbell, and B. W. Gonser, *J. (and Trans.)* Electrochem. Soc., **93**, 258 (1948).
2. W. J. Childs, J. E. Cline, W. M. Kisner, and J. Wulff, *Trans. Am. Soc. Metals*, Preprint 8, 17 pp. (1950).
3. Abner Brenner and G. E. Riddell, "Deposits of Nickel and Cobalt by Chemical Reduction," R. P. 1835, J. Research 39 November (1947) NBS.

Effects of Impurities on the Crystallographic Modifications of Calcium Metal

J. F. Smith and B. T. Bernstein

Institute for Atomic Research and Department of Chemistry, Iowa State College of Agriculture and Mechanic Arts, Ames, Iowa

Previous work at this laboratory (1) has shown that above room temperature very pure calcium exists in only two allotropic forms: f.c.c. between room temperature and 464°C and b.c.c. between 464°C and the melting point. It is the authors' belief that these results represent the behavior of the purest Ca which has been examined to date. This point of view is substantiated by the rapidity and reversibility of the observed transformation since such behavior is representative of high-purity metal. Subtraction of the analyzed impurity content indicated this metal to be 99.96 wt % Ca. No analytical data were available, however, for hydrogen, oxygen, or carbon content.

Indication that these nonanalyzed impurities play an important role in the allotropic behavior of Ca was found in a subsequent examination of a later preparation of Ca. The analytical data for this latter Ca [herein referred to as calcium D (Ca D)] was comparable to that for the original Ca. The values for Ca D were: Mg, <0.01 wt %; N, <0.009 wt %; C, ~0.02 wt %; Si, <0.005 wt %; Mn, Fe, Al, Ba, Be, <0.001 wt %; and Cd, Cu, K, Li, <0.0001 wt %. The observed crystal structures in Ca D showed the low-temperature f.c.c. form and the high-temperature b.c.c. form but showed in addition a h.c.p. modification at intermediate temperatures. This sequence of structures has also been observed by Melsert, Tie-

Table I. Analytical data for those elements showing possible differences in concentration in the two Ca preparations

Element	Analysis of Ca used by Smith, Carlson, and Vest (wt %)	Analysis of Ca D used in the present investigation (wt %)
C	No analysis	0.02
Fe	0.01	<0.001
Mn	0.005	<0.001
Si	Trace	<0.005
Ba	Not detected	<0.001

dema, and Burgers (2). The behavior of Ca D was such, however, that the Ca D must be concluded to be a less pure Ca preparation than the dimorphic Ca used in the original investigation. This conclusion is based on the observation of two-phase regions showing f.c.c. plus h.c.p. and h.c.p. plus b.c.c. The temperature ranges for the occurrence of these two-phase regions was a function of the thermal history of the sample, and indeed the appearance of a single-phase region of h.c.p. could be entirely eliminated after prolonged heating at elevated temperature. On the basis of the phase rule the occurrence of two-phase regions over a temperature range at constant pressure is precluded in a one-component system if the system is at equilibrium. It may be argued that the f.c.c. to h.c.p. transition is mechanistically difficult and that sluggish kinetics may defeat equilibrium; however, a similar argument is not valid for the h.c.p. to b.c.c. transition. In the latter case the transition is conceptually simple and may be visualized as occurring through a region of continuous strain. Such a transition should be rapid and reversible.

It seems evident, therefore, that the behavior of Ca D must be due to some contaminant present to a greater degree in Ca D than in the original Ca. In Table I are shown the analytical data for those elements exhibiting concentration differences in the two Ca preparations. These data were interpreted to mean that carbon or one of the nonanalyzed impurities was most probably responsible for the observed difference in behavior of the two Ca preparations. Substantiation of this point of view was made by re-examination of the only remaining sample of the original Ca preparation. This Ca had been stored for approximately 1½ years in a glass bottle with a plastic stopper. The bottle had been flushed with He and the glass-plastic juncture had been sealed with wax. Visual examination of the Ca taken from the bottle showed that the surface was discolored and obviously contaminated. Instead of the original dimorphic behavior, four structural modifications were observed: f.c.c., a low symmetry form originally reported by Graf (3), h.c.p., and b.c.c. The structural behavior was comparable to the least pure Ca (99.66%) examined in the previous investigation (1). By inference the change in behavior of the

Table II. Summary of diffraction results

Temp, °C	Uncontaminated Ca D	Ca D + oxygen	Ca D + ethane	Ca D + carbon	Ca D + nitrogen	Ca D + boron	Ca D + hydrogen	Uncontaminated Ca E	Ca E + hydrogen
100		Patterns essentially the same as uncontaminated Ca D plus the most intense reflections of CaO at all temperatures	f.c.c. + h.c.p.	f.c.c. + low sym. phase	f.c.c.	Patterns essentially the same as uncontaminated Ca D with some slight shifting of peak positions indicating solid solubility	f.c.c. + h.c.p.	f.c.c.	f.c.c. + h.c.p. + low sym. phase
200	f.c.c.		200°C f.c.c. + h.c.p. + low sym.						
300				300°C low sym.	300°C f.c.c. + low sym.			300°C	
400	350°C f.c.c. + h.c.p.		360°C h.c.p.	350°C h.c.p.	360°C h.c.p.		450°C h.c.p.	f.c.c + low sym. phase 450°C	435°C
500	455°C h.c.p.*		>490°C	>490°C	>490°C				h.c.p. + b.c.c.
	520°C h.c.p. + b.c.c.		h.c.p. + b.c.c. (the temperature limits of these two phase regions were not closely bracketed)				525°C h.c.p. + b.c.c.		550°C
600	560°C		<575°C	<575°C	<575°C		570°C	b.c.c.	
700	b.c.c.		b.c.c.	b.c.c.	b.c.c.		b.c.c.		b.c.c.

* Behavior of Ca D in the temperature region 455°-560°C was a function of the thermal history of the sample since the single phase h.c.p. region could be eliminated by prolonged heating at elevated temperature.

high-purity Ca must have resulted from interaction with atmospheric components (O_2, N_2, CO_2, water vapor) which had diffused through the plastic stopper.

The present investigation was undertaken to determine which contaminants were associated with the appearance of the h.c.p. modification and which with the low symmetry structure. The low symmetry structure had already been shown to be a result of contamination (1) which result is corroborated by the recent work of Schottmiller (4).

Experimental Results

Any attempt to determine which contaminants were associated with the impurity phases by further purification studies seemed impractical because of the limitations of the analytical techniques. Therefore, it was decided to contaminate samples of Ca deliberately to see which impurities caused the appearance of the low symmetry and h.c.p. phases. Calcium D was considered to be satisfactory as a test material for the determination of the impurities associated with the low symmetry phase but, because the h.c.p. phase was already present, Ca D was not suitable for delineating the cause of the h.c.p. phase. Examination of other Ca preparations which were on hand showed one [herein referred to as calcium E (Ca E)] which exhibited the f.c.c., low symmetry, and b.c.c. phases but not the h.c.p. phase. Calcium E was, therefore, satisfactory for the determination of the impurity associated with the h.c.p. phase. Chemical analysis showed Ca E to be high in Mg content but otherwise of good purity: Mg, 0.027 wt %; C, 0.02 wt %; N, <0.009 wt %; Si, <0.005 wt %; Al, B, Ba, Be, Cu, Fe, <0.001 wt %; and Cd, K, <0.0001 wt %.

Oxygen, ethane, carbon, nitrogen, boron, and hydrogen were chosen as contaminants. Boron was included in the list in order to determine whether or not the structural effects were due simply to interstitial atoms. A summary of the diffraction results before and after contamination is shown in Table II. Diffraction patterns were taken with a modified Geiger-counter diffractometer (5) with the samples in the form of small bars. A slowly circulating atmosphere of purified He was maintained in the camera under a slight positive pressure. Temperatures were measured with a Pt-Pt 13% Rh thermocouple spot welded to the sample. It should be emphasized that the transition temperatures shown in Table II are approximate since diffraction patterns were taken at finite temperature increments, and no particular effort was made to precisely bracket a transition.

Gaseous contaminants were introduced into the experimental system by attaching to the system a 200-ml glass bulb filled with the gas. After first checking the sample to see that the structural behavior was typical and that inadvertent contamination had not occurred, the gas was vented into the system through a stopcock. Carbon and boron were added as powders, and contamination was accomplished in the following manner. The powder was sprinkled on a file, and the sample was inverted and lightly abraded across the file until a thin adherent film of the powder had collected on the calcium. The sample was then mounted in the camera and heated to ~500°C to allow reaction to occur.

In all cases the diffraction patterns were checked to determine that the sequence of phases was reversible in temperature. It was observed that in two-phase regions there was a general tendency for the intensity of the diffraction peaks of the low-temperature phase to decrease with increasing temperature with an accompanying inverse effect for the high-temperature phase.

It is evident from Table II that neither oxygen nor boron is responsible for the low symmetry or h.c.p. phases. However, both carbon and nitrogen were found to induce the appearance of the low symmetry phase. Since there might be some question with regard to adsorbed nitrogen on the graphite powder, carbon was also introduced in the form of ethane. Ethane contamination also caused the appearance of the low symmetry phase and, since contamination with hydrogen alone did not produce this result, the evidence indicates that carbon as well as nitrogen can cause the appearance of the low symmetry phase.

It is also evident from Table II that hydrogen is the impurity associated with the h.c.p. phase. Only hydrogen and ethane caused a significant change in the temperature range of stability of the h.c.p. phase in Ca D, and indeed hydrogen induced the appearance of the h.c.p. phase in Ca E. Although hydrogen does not cause the appearance of the low symmetry phase, the stabilization of this phase at lower temperatures in Ca E after hydrogen addition must indicate some degree of hydrogen solubility in the phase.

The effect of the thermal history of the samples on stability of the h.c.p. structure has been noted in the description of the behavior of Ca D. This effect is consistent with the conclusion that hydrogen is responsible for the occurrence of the h.c.p. phase since reduced stability of the phase after high-temperature annealing would be explicable on the basis of volatilization of hydrogen. Hydrogen would be expected to have an appreciable vapor pressure at elevated temperature, and volatilized hydrogen would be carried away by the slowly circulating helium atmosphere.

Discussion

On the basis of the results, there is little doubt that the free energy balance among the various structures is rather precarious and that small variations in the number and type of impurity atoms have significant effects. This sensitivity to nonmetallic impurities, readily available from the atmosphere, must be largely responsible for the disparity in results obtained by different investigators while measuring the physical properties of Ca metal and, in particular, for the diversity in reports concerning the allotropic behavior.

Calcium is known to be a highly reactive metal, especially so in the powdered form which has been used in other structural investigations. In the author's opinion the recent work of Schottmiller (4) on the Ca-Sr phase diagram illustrates this point.

Schottmiller found a marked difference between results obtained by x-ray diffraction using powder samples and results obtained by thermal analysis on massive samples of the same Ca metal. This occurred even though Schottmiller was particularly careful in the handling of his powder samples. The diffraction results showed a f.c.c. to h.c.p. transition at 342°-347°C and a h.c.p. to b.c.c. transition at 607°-612°C. In addition the low symmetry phase was found to exist in the temperature region 300°-345°C; it is not specified whether this was a single-phase or two-phase region. In comparison, the thermal data showed a transition at 281°-314°C which was attributed to the appearance of the low symmetry phase. But only one additional transition was found at 482°-516°C instead of the two transitions to be expected on the basis of the diffraction results.

It seems highly probable that the difference in results observed by Schottmiller was due to reaction of the Ca powder with some contaminant. Water vapor is the contaminant most difficult to exclude from an experimental environment since it adsorbs readily on most surfaces and in addition it will diffuse appreciably through many media.

Svec and co-workers (6, 7) have studied the reaction of Ca with water vapor and have found that the reaction occurs at the surface with the liberation of hydrogen. Hydrogen was found to have a high solubility in Ca and to diffuse rapidly into the metal, while the oxygen remained behind in a thin surface layer. The results provide a ready explanation for a source of hydrogen contamination and hence an explanation for the appearance of the h.c.p. phase in many Ca preparations. The degree of water vapor contamination which may occur before an oxide phase can be detected by x-ray diffraction is a function of the surface to volume ratio and is quite high in the case of powder samples.

In summary, the results of the present investigation show that nitrogen or carbon will induce the appearance of the low symmetry phase in Ca, and hydrogen will induce the appearance of the h.c.p. phase. In fairness, it should be emphasized that in neither case was the initial Ca completely pure and the observed results may have occurred because of a combined effect due to the added impurity plus impurities already present. Nonetheless, by inference the h.c.p. and low symmetry phases are both impurity-stabilized. This leaves f.c.c. and b.c.c. as the allotropic modifications of pure Ca with a transition temperature of ~450°C. The present investigation thus corroborates the results of the previous investigation and, in addition, provides an explanation for the occurrence of the low symmetry and h.c.p. phases. The transition temperature is also in reasonably good agreement with a thermal transition at 440°C listed by Kubaschewski (8) and for which he reports an averaged value for the enthalpy of transition of 0.24 ± 0.04 kcal/mol. Kubaschewski's value is based on a critical survey of available data, and he notes that only one transition is found consistently although an additional transition at lower temperature is also found by some investigators.

Acknowledgments

The authors wish to express their appreciation to Dr. O. N. Carlson for providing the calcium used in this investigation and to Mr. E. D. Gibson for his assistance in the initial stages of the investigation.

Manuscript received Oct. 20, 1958. Contribution No. 675. Work was performed in the Ames Laboratory of the U. S. Atomic Energy Commission.

Any discussion of this paper will appear in a Discussion Section to be published in the December 1959 JOURNAL.

REFERENCES

1. J. F. Smith, O. N. Carlson, and R. W. Vest, *This Journal*, **103**, 409 (1956).
2. H. Melsert, T. J. Tiedema, and W. G. Burgers, *Acta Cryst.*, **9**, 525 (1956).
3. L. Graf, *Physik. Z. vereinigt mit dem Jahrbuch der Radioaktivität und Elektronik*, **35**, 551 (1934).
4. J. C. Schottmiller, Ph.D. Thesis, Syracuse University (1958).
5. P. Chiotti, *Rev. Sci. Instr.*, **25**, 683 (1954).
6. D. S. Gibbs and H. J. Svec, *J. Am. Chem Soc.*, **75**, 6052 (1953).
7. H. J. Svec and C. Apel, *This Journal*, **104**, 346 (1957).
8. O. Kubaschewski, *Z. Elektrochem.*, **54**, 275 (1950).

The Synthesis of Some Pyridyl Glycols by Electrolytic Reduction

M. J. Allen and H. Cohen

Research Department, CIBA Pharmaceutical Products Inc., Summit, New Jersey

The synthesis of the pinacone, 3,3-di(p-aminophenyl)butanone - 2 - dihydrochloride (Amphenone B) (1) with subsequent elucidation of its interesting biological activities (2) led us to continue our investigations in an attempt to find pinacones analogous to Amphenone B which would retain the adrenal inhibitory effect of this compound but not its undesirable side effects.

It was decided to investigate the biological properties of the pinacones (3) prepared from the pinacols of 2-, 3-, and 4-acetylpyridine, but first it was necessary to prepare the respective pinacols. The electrolytic method was chosen for this purpose as it had proved itself quite satisfactory for the preparation of 2,3-bis(p-aminophenyl)-2,3-butanediol, the Amphenone B intermediate (4), as well as for other pinacols (5).

The pinacol of 3-acetylpyridine has been previously described (6). However, the experimental conditions which involved the use of an acidic medium resulted at times in difficulty in isolation of the pinacol with desired purity. Therefore as there is always the possibility of side reactions when using an acidic medium for a cathodic reduction of a ketone to its pinacol, it was decided to utilize basic conditions in our investigation. Although a potassium hy-

droxide medium was found to be quite satisfactory for the 2- and 4-acetylpyridines, the 3-acetylpyridine when electrolyzed in this medium gave extremely poor yields with an excessive amount of tarry material. In this instance a less basic medium, i.e., one containing potassium acetate, proved more satisfactory.

Experimental

The apparatus used for controlled potential electrolysis has been described (7) as has the 1500-ml cell used for the reductions of 2- and 4-acetylpyridine, except a regular paddle stirrer was used instead of a magnetic stirrer (6). The mercury cathode area in this cell was 111.3 cm^2. The reflux-type cell (8) used in the preparation of the 3-acetylpyridine pinacol had a mercury cathode area of 17.2 cm^2. In all the experiments reported the anode chamber contained a nickel anode and an aqueous 40% potassium carbonate solution.

2,3-Bis-(2-pyridyl)-2,3-butanediol. — The catholyte consisted of 100 g 2-acetylpyridine dissolved in 460 ml 1*N* KOH in 50% aqueous ethanol. At a reference potential of —1.6 v vs. S.C.E. the initial current was 5.6 amp and the applied voltage 16 v. The temperature was maintained at 23°-25° throughout the course of the reaction. After 256 min the current plateaued at 1.2 amp at which time the applied voltage was 4.5 v. The heavy precipitate which began to appear 40 min after onset of electrolysis, was filtered, washed with 25% ethanol, and dried. Yield 69 g (68.4%), mp 134°-137°, current efficiency 74.2%. Recrystallization from 50% aqueous methanol mp 138°-139°; anal. found: C, 69.06; H, 6.65; N, 11.77%. $C_{14}H_{16}N_2O_2$ requires, C, 68.82; H, 6.60; N, 11.46%.

2,3-Bis-(3-pyridyl)-2,3-butanediol. — A solution of 6 g 3-acetylpyridine in 35 ml ethanol, 15 g potassium acetate, and 17 ml distilled water was placed in the cathode compartment and the whole maintained at reflux throughout the course of the electrolysis. At a reference potential of —1.5 v the initial current was 8.9 amp and applied voltage, 11.4 v. After 25 min the current plateaued at 0.5 amp with an applied voltage of 2.1 v. The catholyte was distilled to a small volume under reduced pressure and, after chilling, the aqueous phase separated from the solid residue. This solid upon trituration with 20% acetone yielded 4.13 g (68.4%), mp 220°-224°, current efficiency 80.3%. Recrystallization from ethylene glycol gave mp 244°-245° (5).

2,3-Bis-(4-pyridyl)-2,3-butanediol. — The catholyte in this instance contained 100 g of the 4-acetylpyridine in 460 ml aqueous 1*N* KOH. At a reference potential of —2.2 v the initial current was 7.8 amp and applied voltage 12.5 v. After 176 min the current plateaued at 4.2 amp and the applied voltage was 7.0 v. The temperature throughout the course of this reaction was maintained at 23°-25°. The precipitate which had formed during the electrolysis was filtered, washed with water, and dried. Yield 99 g (98.2%), mp 209°-212°, current efficiency 97%. Recrystallization from methanol-ethyl acetate gave mp 219-220; anal. found: C, 68.51; H, 6.63; N, 11.33%. $C_{14}H_{16}N_2O_2$ requires C, 68.82; H, 6.60; N, 11.46%.

Manuscript received Nov. 25, 1958.

Any discussion of this paper will appear in a Discussion Section to be published in the December 1959 JOURNAL.

REFERENCES

1. M. J. Allen and A. H. Corwin, *J. Am. Chem. Soc.*, **72**, 117 (1950); W. Bencze and M. J. Allen, *J. Org. Chem.*, **22**, 352 (1957); J. Korman and E. C. Olson, *ibid.*, **22**, 870 (1957).
2. M. J. Allen, R. Hertz, and W. W. Tullner, *Proc. Soc. Exptl. Biol. Med.*, **74**, 632 (1950); R. Hertz, M. J. Allen, and W. W. Tullner, *ibid.*, **75**, 627 (1950); R. Hertz, *et al.*, *Recent Progr. in Hormone Research*, **11**, 119 (1955); A. E. Renold, *et al.*, *N. Engl. J. Med.*, **256**, 16 (1957).
3. W. Bencze and M. J. Allen, To be published.
4. M. J. Allen and A. H. Corwin, *J. Am. Chem Soc.*, **72**, 114 (1950).
5. M. J. Allen, "Organic Electrode Processes," Reinhold Publishing Corp. New York (1958).
6. M. J. Allen, *J. Org. Chem.*, **15**, 435 (1950).
7. M. J. Allen, *Anal. Chem.*, **22**, 804 (1950).
8. H. A. Levine and M. J. Allen, *J. Chem. Soc.*, **1952**, 254.

Technical Review

The Silver Oxide Electrode

T. P. Dirkse

Calvin College, Grand Rapids, Michigan

ABSTRACT

A review has been prepared of the electrochemistry of the silver oxide electrode. The discussion covers the structure and electrochemistry of the oxides of silver and their behavior in batteries.

With respect to the battery family, silver and its oxides are relatively new arrivals. There was some interest in these oxides for battery use around the turn of the century. In 1910 Morrison was issued several patents (1) covering various phases of the construction of a storage battery using silver oxides as positive plate materials. However, so far as is known, no commercial application was made of these patents.

Around the beginning of World War II interest was again aroused. Andre (2) once again suggested the use of silver oxides in a storage battery. To overcome the problem of a short shelf life he advised the use of a membrane as a sheath around the silver oxide plates. Some work at the National Bureau of Standards showed that silver oxides could serve well in a primary battery. The silver-zinc-alkali system was found to have a relatively high watt hour per pound value. At present this system is available both as a primary and as a secondary battery.

Because of this relatively short history of interest in the silver oxides as active materials for alkaline batteries, there is in the literature of silver and its oxides very little material dealing with the chemical problems peculiar to or associated with the battery industry.

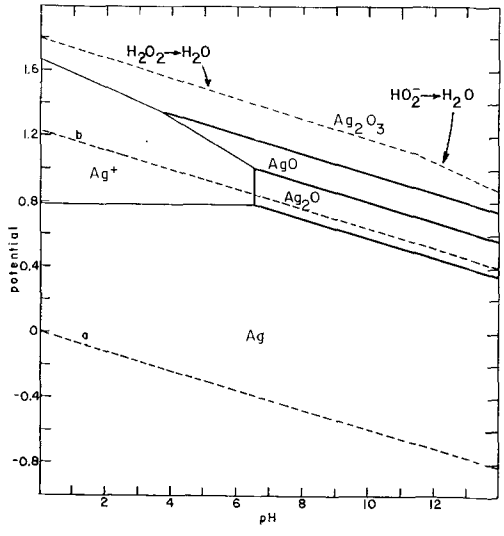

Fig. 1. Potential-pH diagram for silver and its oxides

There are several oxides of silver and, although their use as active materials in batteries has been limited to alkaline electrolytes, there is a good deal of literature dealing with the problem of silver oxides in acid solutions. Figure 1 is a modification of the diagram of Delahay, Pourbaix, and Van Ryssel-berghe (3). It gives a good survey of the relationship of silver to its oxides in a rather wide *p*H range. This diagram, of course, represents equilibrium conditions, and such conditions may not prevail at all areas of electrode-electrolyte interface during the operation of a battery. The areas of Ag, Ag^+, Ag_2O, and AgO seem fairly well defined, but there is uncertainty about the existence of oxides in which silver apparently has an oxidation number greater than two. Line a represents the reduction of H^+ to H_2 and line b the reduction of O_2 to water. For alkaline batteries the region of high *p*H is most significant. Here we find Ag, Ag_2O, and AgO as the thermodynamically stable phases.

Silver

Generally, the oxides used in these batteries are formed by the electrolytic oxidation of silver. Metallic silver is a good electrical conductor, having a specific resistance of 1.59×10^{-6} ohm-cm (4). During discharge, these oxides are reduced to silver, which then makes the plates better electrical conductors.

An interesting characteristic of silver is its ability to allow oxygen to diffuse through it (5). It has been suggested that this is done by the formation of Ag_2O (6).

The crystal structure of silver has been the subject of much investigation. It appears that there is only one crystal form, a face-centered cubic arrangement. The edge of a unit cube has a length of 4.078Å, and the distance between the centers of the nearest silver atoms is 2.884Å (7).

Although the crystal lattice seems fairly well established, there is some question about the electronic

configuration of the silver atoms. The K, L, and M orbits of the silver atom are complete, as are the 4s and 4p orbitals. This leaves 11 electrons to be allocated. One possibility is to assign 10 of these electrons to the 4d orbitals, completing them and leaving one electron for the 5s orbital. This is in agreement with the fact that silver is ordinarily univalent. However, Kaplan (8) contends that the 4d shell does not have the stability of the rare gas shells, and suggests the presence of 3 free electrons per atom in the lattice. This would account for the various oxides and valence states.

When the potential on a silver electrode in alkaline solution is raised, the first product formed is Ag_2O. This reaction proceeds efficiently and can be carried out with a polarization of less than 50 mv. However, only a thin film of Ag_2O is formed. It has been estimated to be of the order of 3 molecules in thickness (9).

Silver(I) Oxide

Silver(I) oxide, Ag_2O, is a rather well-defined substance. It has a deep brown color and gives a definite x-ray pattern. At one time it was suggested that there are two crystal modifications of this substance (10) with different electrode potentials. However, other investigators found no warrant for this (11).

The crystal structure of this oxide is basically the cubic type, the length of an edge being 4.72Å (12). It has a face-centered cubic arrangement of silver atoms or ions interpenetrated by a body-centered cubic arrangement of oxygen ions (13). Consequently, each oxygen ion is in the center of a tetrahedron of silver ions. Apparently then, the formation of Ag_2O does not alter the basic structure of silver but spreads it out a bit, increasing the length of the cube edge. If the basic lattice be divided into octants, the oxygen ions then occupy two octants of the unit cube. The distance between centers of nearest silver ions is 3.336Å and that between silver and oxygen is 2.043Å.

The electrochemical formation of Ag_2O can be represented by Eq. [1]. The variation of E_{Ag-Ag_2O} with hydroxyl ion

$$2Ag + 2\,OH^- \rightarrow Ag_2O + H_2O + 2\,e \qquad [1]$$

concentration is in agreement with this equation. The exact value of E° for this reaction appears to be in some doubt. Hamer and Craig (14) have reviewed the situation, and point out that the lack of reproducibility of the potential of the Ag-Ag_2O couple in alkaline solution is not due to changes in the Ag_2O. They suggest that it is due to a chemisorbed film of oxygen on the silver, which film could be passive. They point out further that no value of E° has been determined for this change by measurement against a hydrogen electrode.

Two properties of Ag_2O limit its effectiveness as the positive active material in an alkaline cell. The first of these is its high electrical resistance. Le Blanc and Sachse (15) give the specific resistance as about 10^8 ohm-cm. This high resistance, or low conductivity, indicates the absence of mobile or unpaired electrons in the Ag_2O lattice. It naturally affects the conductivity of the electrodes in which it is found, and may be the reason why only a thin film of Ag_2O is formed on the Ag. The resistance of this film results in a rise of the applied voltage when such an electrode is charged by a constant current process.

The other property is the solubility of Ag_2O in alkaline solutions. This solubility, at least in the more dilute solutions, is a function of the hydroxyl ion and not of the cation. The solubility product at 25°C is of the order of 2×10^{-8} (16), and it increases with increasing temperature (17). The solubility is due to reaction [2]. A part of the dissolved

$$Ag_2O + 2\,OH^- \rightarrow 2AgO^-\ [\text{or } Ag(OH)_2^-] + H_2O \qquad [2]$$

Ag_2O in alkaline solutions may also be in the form of $Ag_2(OH)^+$. This solubility of Ag_2O is at least partly responsible for the poor shelf life characteristics of the silver cell (18).

Silver(II) Oxide

Silver(II) oxide, AgO, has been investigated in numerous ways and has been studied both in alkaline and acid solutions. It is a grayish black substance and is now available commercially. It can be prepared in many ways, e.g., by the oxidation of silver or silver salts with ozone, persulfate, or permanganate. It is also prepared electrochemically by anodic treatment of silver or Ag_2O in alkaline solutions.

The latter reaction is an efficient one and the polarization is of the order of 100 to 150 mv. Luther and Pokorny (19) state that it proceeds reversibly as well. Jones, Thirsk, and Wynne-Jones (20), however, state that this process is irreversible. They used as their criterion the assumption that the discharge is an efficient process. This, however, is not necessarily the case. On discharge, particularly at appreciable current densities, only a part of the capacity of the AgO is delivered at the higher potential. There is still AgO present at the beginning of the lower voltage level during discharge (Fig. 2). The kinetics or mechanism of this reaction have not been established, but the equilibrium condition is likely represented by Eq. [3].

$$Ag_2O + 2\,OH^- \rightarrow 2AgO + H_2O + 2e \qquad [3]$$

This reaction is similar to [1]. Accordingly, the relation of the potential of [3] to hydroxyl ion con-

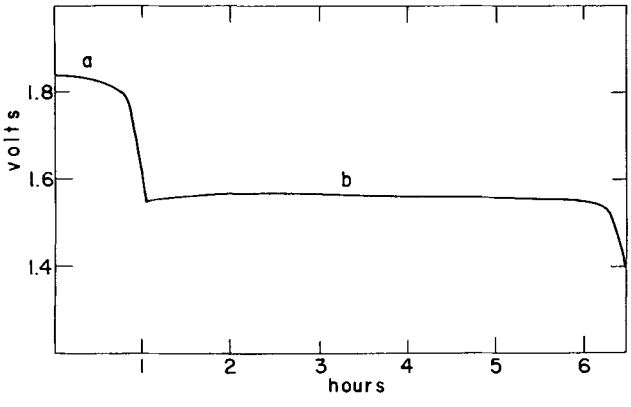

Fig. 2. Discharge curve for silver-zinc alkali cell; (a) reduction of AgO, (b) reduction of Ag_2O.

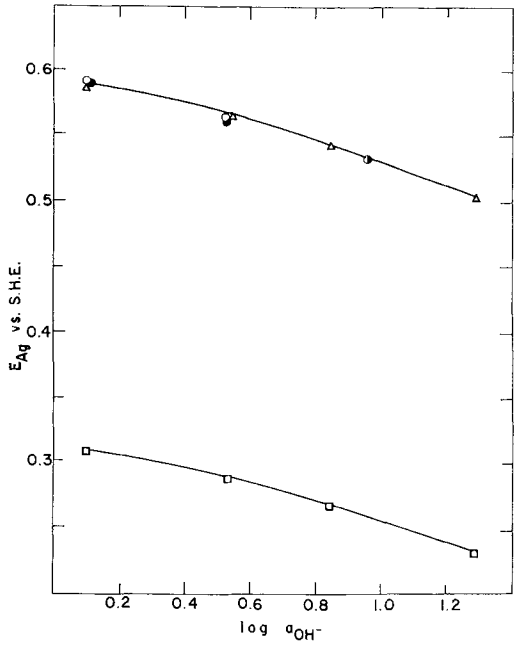

Fig. 3. Electrode potential of silver oxides. O—electrolytically prepared AgO; •—chemically prepared AgO; △—Ag_2O_3; □—Ag_2O.

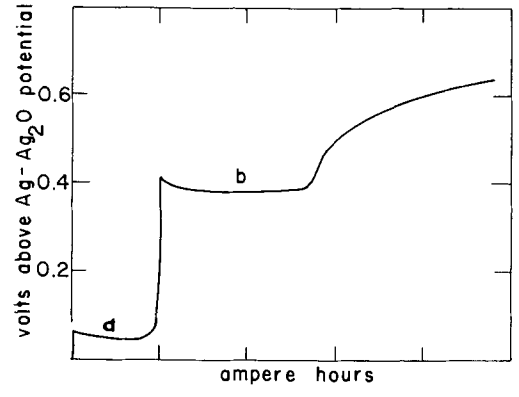

Fig. 4. Charge curve of silver electrode in alkaline solutions; (a) formation of Ag_2O, (b) formation of AgO.

centration is the same as that for reaction [1] (Fig. 3).

The layer of AgO formed in these electrochemical processes is thicker than that of Ag_2O. On Fig. 4, for example, the plateau for the formation of AgO is longer than that for the formation of Ag_2O. At moderate current densities both processes are about 100% efficient (21). Therefore the length of the plateaus is a relative measure of the depth of formation of the oxides. A constant potential charging process can give a product that is completely converted to AgO. In fact, we have produced in this manner products that on analysis appear to be Ag_2O_3. Yet these products have the same electrode potential (Fig. 3) and x-ray pattern that AgO has. It is possible that these products are the AgO plus adsorbed oxygen.

There has been some disagreement as to the mechanism of the transformation of the lower oxide to a higher one. The second plateau of the charge curve is preceded by a small peak (Fig. 4). This peak has been interpreted differently. Hickling and Taylor (9) consider it to represent the formation of Ag_2O_3 which then decomposes to AgO. Jones, *et al.* (20) suggest that this peak is due to the difficulty of forming nuclei of AgO. This could be somewhat similar to a resistive effect of Ag_2O which is decreased as soon as the better conducting higher oxide is formed (22).

Within the past year or so the structure of AgO has been clarified. The work of Scatturin, *et al.* (23) shows AgO to have a monoclinic structure, and the cell parameters have been evaluated. More recently Graff and Stadelmaier (24) have reached the same conclusions. Thus, when Ag_2O is oxidized to AgO the cubic arrangement of the silver atoms or ions is distorted or destroyed.

However, there still are questions concerning the structure of this substance. The material produced from the product obtained by anodizing a silver nitrate solution between platinum electrodes and that produced by extensive ozonization of silver gives a different x-ray diffraction pattern than the monoclinic form of AgO (24, 25). The monoclinic form is the one produced on a battery plate. Jones and Thirsk (26) have interpreted the nonmonoclinic x-ray pattern as revealing a face-centered cubic form of AgO. Graff and Stadelmaier (24) suggest that this may possibly be a higher oxide such as Ag_2O_3. This matter is as yet unresolved.

Various properties of AgO have been studied and the results of the several investigations have differed significantly. Some of this may be due to the fact that many data reported for AgO have been obtained by measurement and study of the nonmonoclinic variety (27, 28). The condition of the silver in the AgO has not been clarified. It has been suggested that there may be two Ag — O distances, and the bonding may be partly ionic and partly covalent (23). The specific resistance of AgO has been reported as 0.012 ohm-cm (26), 15 ohm-cm (29), and 10 ohm-cm (15). In any event, the conductivity is considerably better than that of Ag_2O and this indicates that there are unpaired or mobile electrons present in the solid material. The magnetic susceptibility per mole has been given as $+40 \times 10^{-6}$ (paramagnetic) (30) and -19×10^{-6} (diamagnetic) (29). The latter value was used as evidence for the conclusion that the bonding in the AgO lattice is covalent or metallic and the silver is trivalent. Two of these valences are used for bonding the oxygen atom and the other one for bonding with other silver atoms.

It is generally agreed that the silver in AgO has an oxidation number of +2. Klemm (30) used several criteria to establish this. He considered analytical evidence, oxidative ability, and isomorphism with CuO. To this may be added the fact that electrochemical reduction of this oxide yields two Faradays per mole (31). Addition of acids to this oxide yields oxygen but no hydrogen peroxide. This indicates that AgO is not a peroxide (26).

AgO dissolves in nitric acid to give a dark brown solution which is fairly stable in the cold. This solution has strong oxidizing powers. The color disappears on warming or on dilution. Barbieri (32) suggested that this dark colored solution contained tri-

valent and monovalent silver. However, later work showed that the dissolved silver is primarily bipositive (33). This was determined by a solubility method and by a determination of magnetic susceptibility. The magnetic moment corresponded closely to that calculated on the assumption of one unpaired electron. This then is a 4d electron.

For use in a battery it is necessary that a substance be fairly stable in the electrolyte, in this case an aqueous solution of NaOH or KOH. Denison (31) reported that the oxide is stable in 20-40% KOH solutions. However, pure AgO does decompose very slightly in alkaline solutions at room temperature. At higher temperatures this decomposition is more rapid (34). Practically, in a battery, pure AgO is never produced on charging, and the presence of unoxidized silver in such a plate further hastens the decomposition of the AgO (34).

Because of the higher oxidation state of silver, one would expect the AgO to be more soluble than Ag_2O in alkaline solutions. Some solubility data have been reported (34,35), and it appears that the solubilities of Ag_2O and AgO are not far different from each other in alkaline solutions. The solubility passes through a maximum with time but equilibrium is reached within a few hours (34).

Higher Oxides

Of the various higher oxides of silver mentioned, Ag_2O_3 is the most popular formula. The evidence for the existence of this oxide is, in the main, indirect. It is doubtful whether a pure sample has been isolated. Jirsa (36) claims that Ag_2O_3 can be prepared but cannot exist alone. Furthermore, it is readily decomposed by heating. Braekken (37) attempted to determine the structure by means of x-ray diffraction measurements but reached no conclusion other than that it had a cubic structure. However, the cube edge length seemed to vary with the method of preparation.

Three methods have been used to prepare this material. (*A*) Luther and Pokorny (19) were able to oxidize silver nitrate or sulfate anodically and obtain a product which appeared to be a mixture of AgO and Ag_2O_3. This couple had a potential about 200 mv higher than that of the Ag_2O-AgO couple. They were not able to produce this substance by anodic treatment of AgO in alkaline solutions. Somewhat similar work was done later (38) and it was concluded that Ag_3O_4 or Ag_4O_5 was formed. However, these oxides were not pure but contained $AgNO_3$ or Ag_2SO_4. Later Weber (39) prepared this same material and determined transference numbers of it in a nitric acid solution. On the basis of his results he concluded that at least some of the dissolved silver was trivalent.

(*B*) Yost (40) oxidized silver salts with peroxysulfuric acid and obtained a product which appeared to be $Ag_2O_3 \cdot x\,Ag_2(SO_4)_3$. De Boer and van Ormondt (41) also used acid solutions of persulfates as oxidizing agents and obtained a black precipitate which they considered to be a mixture of Ag_3O_4 and $Ag_2(SO_4)_2$ or $Ag_2S_2O_8$. However, the use of persulfates in alkaline solutions gave only the AgO.

(*C*) The third method for preparing this oxide involves the treatment of silver or Ag_2O with ozone (42), or the treatment of silver salts in acid solution with ozone (43). However, here the trivalent silver, AgO^+, had but a transient existence in solution.

In summary, there seems to be some evidence for the existence of a trivalent state of silver, e.g., Ag_2O_3. However, much of the evidence may also be interpreted in other ways (44). The potential value given for the AgO-Ag_2O_3 couple is very close to that for the formation or reduction of the HO_2^- ion in alkaline solutions or H_2O_2 in acid solutions (Fig. 1). Whatever the interpretation, this higher valence state is of little significance for use in alkaline batteries. This conclusion is substantiated by recent work at the Battelle Memorial Institute (45). Samples of Ag_2O_3 were prepared and used as the positive active material in an alkaline cell. The voltage curves and the ampere-hour capacity obtained from such plates were essentially those of AgO.

Conclusions

Although silver oxides are being used in commercial batteries, the performance of these batteries could stand improvement. Some of the troubles encountered are inherent in the system, e.g., the solubility of the oxides in the alkaline electrolyte. Others are due to or are aggravated by the method of assembly of the components. In order to understand this system better there are at least two areas that need to be more thoroughly investigated.

1. The higher voltage level on discharge, (AgO, Fig. 2), is rather unpredictable, particularly in a secondary battery. The capacity delivered at this voltage is sensitive to a variety of conditions, and it disappears on stand without a loss in total capacity. The latter phenomenon can be accounted for by reaction [4] which can take place readily (34). More work

$$Ag + AgO \rightarrow Ag_2O \qquad [4]$$

is necessary to determine precisely what conditions do affect this part of the discharge curve. It is necessary also that work be carried out to determine the polarization of these various processes, particularly the reduction of AgO to Ag_2O.

2. In a secondary battery the charge acceptance is erratic (44). While the current efficiency is high and the discharge capacity is equal to the charge capacity, the amount of charge capacity varies from cycle to cycle and tends to decrease during the life of the battery. Some of this may be due to design, but it is also possible that there are physical changes in the silver during cycling. This is an area in need of more investigation. Allied with this may be the problem of aging of the oxides during long periods of stand.

REFERENCES

1. W. Morrison, U. S. Pat. 975,980, 975,981, 976,092, Nov. 15, 1910.
2. H. Andre, *Bull. soc. Franc. elec.*, (6) **1**, 132 (1941).
3. P. Delahay, M. Pourbaix, P. Van Rysselberghe, *This Journal*, **98**, 65 (1951).
4. W. M. Latimer and J. H. Hildebrand, "Reference Book of Inorganic Chemistry," 3rd ed., p. 103, Macmillan Co., New York (1951).

5. L. Spencer, *J. Chem. Soc.*, **123**, 2124 (1923).
6. J. H. Simons, *J. Phys. Chem.*, **36**, 652 (1932).
7. R. B. Wilsey, *Phil. Mag.*, **46**, 487 (1923).
8. J. Kaplan, *Z. Physik.*, **52**, 883 (1928).
9. A. Hickling and D. Taylor, *Discussions Faraday Soc.*, No. 1, 277 (1947).
10. H. N. K. Rördam, *Kgl. Danske Videnskab. Selskab., Math-fys. Medd.*, **3**, No. 7 (1920).
11. (a) H. T. S. Britton, *J. Chem. Soc.*, **127**, 2956 (1925); (b) R. F. Newton, *J. Am. Chem. Soc.*, **50**, 3258 (1928).
12. P. Niggli, *Z. Krist.*, **57**, 253 (1922).
13. W. P. Davey, *Phys. Rev.*, **19**, 248 (1922).
14. W. J. Hamer and D. N. Craig, *This Journal*, **104**, 206 (1957).
15. M. Le Blanc and H. Sachse, *Physik. Z.*, **32**, 887 (1931).
16. H. C. Johnston, F. Cuta, and A. B. Garrett, *J. Am. Chem. Soc.*, **55**, 2311 (1933).
17. K. Jellinek and H. Gordon, *Z. physik. Chem.*, **112**, 207 (1924).
18. T. P. Dirkse and F. De Haan, *This Journal*, **105**, 311 (1958).
19. R. Luther and F. Pokorny, *Z. anorg. u. allgem., Chem.*, **57**, 290 (1908).
20. P. Jones, H. Thirsk, and W. F. K. Wynne-Jones, *Trans. Faraday Soc.*, **52**, 1003 (1956).
21. T. P. Dirkse and L. A. Vander Lugt, "A Study of the Oxides of Silver," Techn. Report No. 4 on Contract No. N onr-1682(01), June 30, 1957, Calvin College, Grand Rapids, Mich.
22. T. P. Dirkse, Tech. Report No. 6, Contract No. N onr-1682(01), June 20, 1958, Calvin College, Grand Rapids, Mich.
23. V. Scatturin, P. Bellon, and R. Zannetti, *Ricerca sci.*, **27**, 2163 (1957).
24. W. S. Graff and H. H. Stadelmaier, *This Journal*, **105**, 446 (1958).
25. G. M. Schwab and G. Hartmann, *Z. anorg. u. allgem. Chem.*, **281**, 183 (1955).
26. P. Jones and H. R. Thirsk, *Trans. Faraday Soc.*, **50**, 732 (1954).
27. F. Jirsa and J. Jelinek, *Z. anorg. u. allgem. Chem.*, **148**, 130 (1925).
28. F. Jirsa, J. Jelinek, and J. Srbek, *ibid.*, **158**, 33 (1926).
29. A. B. Neiding and I. A. Kazarnovski, *Doklady Akad. Nauk, USSR*, **78**, No. 4, 713 (1951).
30. W. Klemm, *Z. anorg. u. allgem. Chem.*, **201**, 32 (1931).
31. I. A. Denison, *Trans. Electrochem. Soc.*, **90**, 387 (1946).
32. G. A. Barbieri, *Atti accad. Lincei*, **13**, 882 (1931).
33. A. A. Noyes, K. S. Pitzer, and C. L. Dunn, *J. Am. Chem. Soc.*, **57**, 1229 (1935).
34. T. P. Dirkse and B. Wiers, *This Journal*, **106**, 284 (1959).
35. H. P. Gregor, N. Nakajima, D. H. Gold, E. M. Loebl, G. K. Hoeschele, and R. Gogan, Final Report, Aug. 31, 1954, Contract No. NObs-62383, Polytechnic Institute of Brooklyn, Brooklyn, N. Y.
36. F. Jirsa, *Chem. Listy*, **19**, 3 (1925).
37. H. Braekken, *Kgl. Norske Videnskab. Selskab. Forh.*, **7**, 143 (1935).
38. G. Baborovsky and G. Kuzma, *Z. physik. Chem.*, **67**, 48, (1909).
39. H. C. P. Weber, *Trans. Am. Electrochem. Soc.*, **32**, 391 (1917).
40. D. M. Yost, *J. Am. Chem. Soc.*, **48**, 152 (1926).
41. J. H. De Boer and J. Van Ormondt, Proc. Intern. Symposium Reactivity of Solids, Gothenberg, **1952**, 557.
42. F. Jirsa and J. Jelinek, *Z. anorg. u. allgem. Chem.*, **158**, 61 (1926).
43. A. A. Noyes, J. L. Hoard, and K. S. Pitzer, *J. Am. Chem. Soc.*, **57**, 1221 (1935).
44. C. P. Wales, NRL Report 5167, Aug. 11, 1958, Naval Research Laboratory, Washington, D. C.
45. A. B. Tripler, W. T. Buckingham, L. D. Mc Graw, and C. L. Faust, Final Report, Contract No. DA-36-039-SC-42682, Sept. 1, 1955, Battelle Memorial Institute, Columbus, Ohio.

The Performance of Zinc, Magnesium and Aluminum Primary Cell Anodes. A Review

R. Glicksman

RCA Laboratories, Radio Corporation of America, Princeton, New Jersey

ABSTRACT

In this paper some of the factors involved in the operation of a primary cell anode are presented. The effects of such variables as alloy composition, inhibitors, pH, electrolyte composition, current density, and type of service, on the performance characteristics of zinc, magnesium, and aluminum anodes are discussed.

The number of metals which can be used in a galvanic cell is large in theory, yet in practice only a few have proved satisfactory. The anode materials which are in common use today are those which have standard potentials of an intermediate value and high hydrogen overvoltages such as zinc, cadmium, and lead. Of these, Zn is used most widely in primary cell systems, finding use in both acidic and alkaline cells (1-5). Attempts have been made to use Mg (6, 7) and Al (8) in dry cells, and considerable success has been achieved with Mg anodes.

The requirements for secondary cell anodes are somewhat more stringent than for primary cell anodes in that the electrode reactions have to be reversible. Thus, Mg and Al are unsuitable for use in rechargeable cells. Lead and cadmium, which form insoluble compounds at the anode surface during discharge, find extensive use for this application (9-11). The use of Zn has also proved quite feasible in alkaline cells (12) despite the solubility of $Zn(OH)_2$.

In this paper some of the factors involved in the

Table I. Theoretical data for Mg, Al, and Zn anodes

Metal	Density, g/cc	Reversible electrode potential, v $E°$ acid	$E°$ base	Electrochemical equivalent, amp-hr/g
Magnesium	1.74	2.37	2.69	2.20
Aluminum	2.70	1.66	2.35	2.98
Zinc	7.14	0.76	1.245	0.82

operation of a dry cell anode are discussed, and in particular the performance of Zn, Mg, and Al anodes is considered.

Theoretical

Theoretically, the suitability of a metal for use as a galvanic anode can be ascertained simply from its position in the electrochemical series (13) and its electrochemical equivalent, as shown in Table I. The electrochemical equivalent provides a measure of the quantity of electricity (ampere-hours) contained in a unit weight of the metal and is defined by Faraday's law. On this basis, Mg and Al are more attractive anodes than Zn.

However, because of their protective oxide film, the high reversible potentials of Mg and Al are never achieved. In practice, Mg has anode potentials only 0.3 to 0.6 v higher than those of Zn, while Al is cathodic to Zn in neutral or acidic electrolytes, as evidenced by the data in Table II (14).

Effect of Current Density

The current density affects the anode in two ways: through its effect on the potential and on the current efficiency of the electrode.

Most electrodes used in battery applications are characterized by low polarization as a whole at reasonable current densities. Active metal anodes generally have large activation polarization with respect to hydrogen discharge and, hence, a low self-corrosion, but very little polarization with respect to the oxidation of the metal. Notable exceptions to the latter are Mg and Al in many electrolytes (15). For example, Robinson (16) showed that current density had relatively little effect on the potential of Mg anodes in aqueous chloride and sulfate electrolytes; however, when the electrolyte contains a high concentration of an anion capable of precipitating Mg^{++} ion, e.g., OH^-, $SO_3^=$, anodic polarization occurs. Thus the polarization characteristics of Mg in these electrolytes nullifies an otherwise acceptable electrode potential.

As one might expect from the results of dissolution studies of metal anodes and viscosity studies of cell electrolytes, at low temperatures there is a large increase in polarization with increasing current density and decreasing temperature (17). In order to minimize polarization at the low temperatures, the trend is toward increased electrode area for low-temperature batteries.

Another important index of anode performance which must be considered is the anode efficiency. This indicates how much of the stored electricity is recoverable as useful energy under service conditions. Although theoretically the consumption of Mg per ampere-hour should be only 0.37 times that of Zn, it actually is about 0.6 times. This has been explained by the fact that 40% of the consumed Mg is dissolved by wasteful corrosion during the discharge of the cell as compared to 5-10% for the Zn cell (18).

The effect of a polarizing current on the dissolution rate of a magnesium AZ10A[1] alloy in 2*N* $MgBr_2$ is shown in Fig. 1 (19). When the specimen is made anodic, the observed dissolution rate is the sum of the rate due to the external current and the rate due to local action. It is seen that the local corrosion rate increases with increasing anodic current density. This is known in the theory of corrosion as the negative difference effect. For Mg the magnitude of this effect has been found by Robinson (16) to be dependent on both the electrolyte and anode composition including alloy ingredients and level of impuritites.

[1] This alloy consists principally of magnesium but contains in addition 1% aluminum and 0.5% zinc.

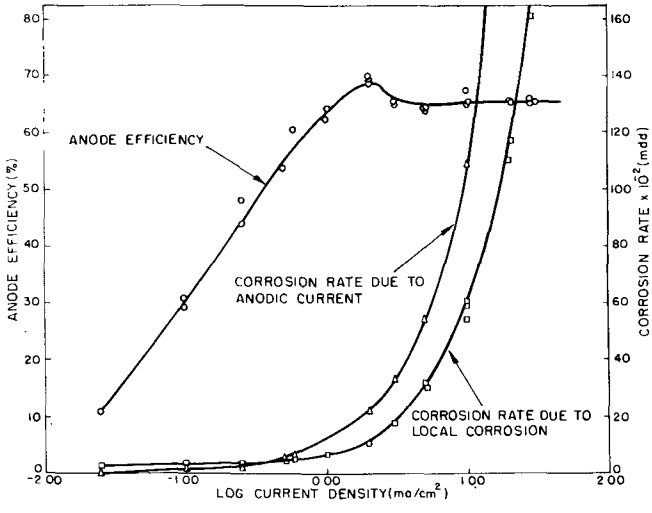

Fig. 1. Effect of current density on the local corrosion rate and anode efficiency of a MgAZ10A alloy dissolving in 2N $MgBr_2$ electrolyte [saturated with $Mg(OH_2)$]. [Glicksman 19)].

Table II. Electrode potentials* of Mg, Al, and Zn in various electrolytes (potentials referred to a standard hydrogen electrode) [Mears and Brown (14)]

Metal	1.0M NaCl	1.0M Na_2SO_4	1.0M Na_2CrO_4	1.0M HCl	1.0M HNO_3	1.0M NaOH	1.0M NH_4OH	St'd $Ca(OH)_2$	St'd $Ba(OH)_2$
Mg	1.38	1.41	0.62	1.34	1.15	1.13	1.09	0.61	0.54
Al	0.52	0.16	0.37	0.46	0.15	1.16	0.46	1.20	1.19
Zn	0.81	0.85	0.33	0.80	0.72	1.17	1.16	1.06	1.15

* Potentials originally reported were referred to a 0.1*N* calomel electrode. They are here corrected to the standard hydrogen electrode scale without making correction for the liquid junction potential.

This type of effect has also been observed on Mg corroding in a 3% NaCl solution (20) and is usually found with very active anode metals covered by a protective layer. The positive effect is found in the absence of a protective layer as in the case of Mg dissolving in HCl (21). Similarly, Al anodes show positive difference effects in certain corrosive electrolytes such as NaOH (22) and HF (23) which can dissolve the protective film, while the negative effect shows up in HCl (23) because of the presence of a film on the metal.

Thus one of the difficulties associated with the use of Al and Mg anodes is their poor current efficiencies, especially at low current densities. Moreover, the efficiency at any given current density has been found to decrease with a more intermittent type of discharge. This increase in corrosion on intermittent discharge is attributed to a change in the surface condition of the anode with alteration of current density. An example of this can be seen in Fig. 2, which shows the change in terminal voltage of Mg/$MgBr_2$/MnO_2 and Zn/NH_4Cl-$ZnCl_2$/MnO_2 dry cells as current pulses of 10 and 50 ma are withdrawn (24). It is seen that the Mg-MnO_2 cells undergo a greater instantaneous voltage fluctuation than the conventional Leclanché cells. (Oscillographic measurements of an Al/$AlCl_3$/MnO_2 cell showed a behavior quite similar to that of the Mg cells.) For Mg cells, the large initial drop is believed due to the resistance of the oxide film on Mg, the voltage rising as the oxide layer is being removed, reaching a steady-state value. When the circuit is opened, the cell voltage rises above the original open-circuit value and then gradually returns to its original voltage.

Thus, immediately after decreasing the current or breaking the circuit, the surface of the Mg is seen to be in a more active form than in its steady state under these same conditions. The question is, then, whether this change in the surface condition influences the over-all rate of hydrogen evolution. Presented in Fig. 3 is a comparison of the rate of hydrogen evolution from two magnesium AZ10A alloy samples in 2*N* $MgBr_2$ electrolyte in the absence of an external anodic current. Prior to the measurements, sample A was discharged for an hour at a current density of 5 ma/cm² and then allowed to corrode normally, while sample B was not discharged at all. The difference in corrosion rates of the two samples for the first 3 hr is attributed to a less effective oxide coating for the previously discharged Mg. At the end of 4-5 hr, there is little or no difference in the corrosion rates, and apparently the oxide coating on sample A is just as protective as that on the undischarged Mg, i.e., sample B. It is thus apparent that the change in surface condition with current density influences the rate of hydrogen evolution at a Mg anode. For Zn, no such problem arises, and it functions at high anode efficiencies for normal current drains and discharge tests.

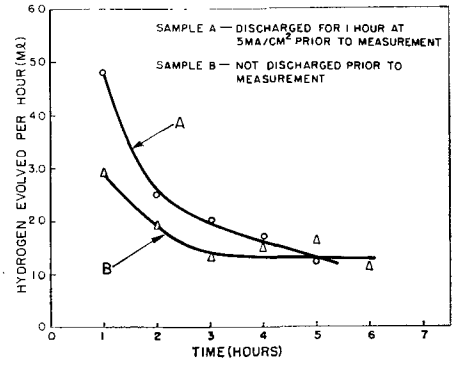

Fig. 3. Corrosion rate of a magnesium AZ10A alloy in 2N $MgBr_2$ electrolyte saturated with $Mg(OH)_2$ (Area 19.6 cm²).

As a consequence of the oxide film, two other problems are encountered in Mg dry cells when current is withdrawn, namely, "delayed action," and impedance. Delayed action is defined as the number of seconds required for the cell voltage to reach a minimum of 1.0 after the circuit is closed. At present this delay is less than 1 sec and apparently is no longer a problem (25). For Al cells using an $AlCl_3$ electrolyte inhibited with potassium chromate, a 1-sec delayed action is found (8).

When a primary cell is considered for use in powering electronic equipment, its impedance values

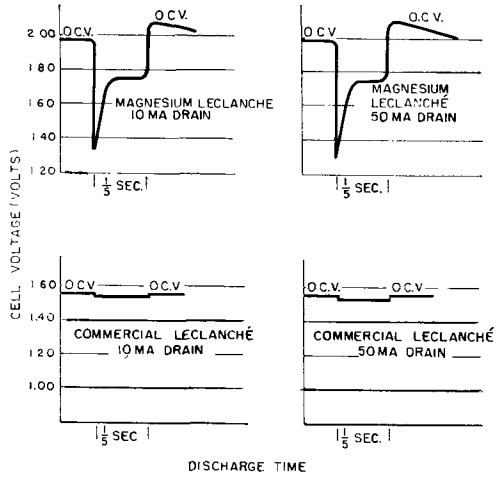

Fig. 2. Oscillographic measurements of change in voltage of AA-size Mg and Zn Leclanche type cells, subjected to 10 and 50 ma constant current drains. [Glicksman and Morehouse (24)].

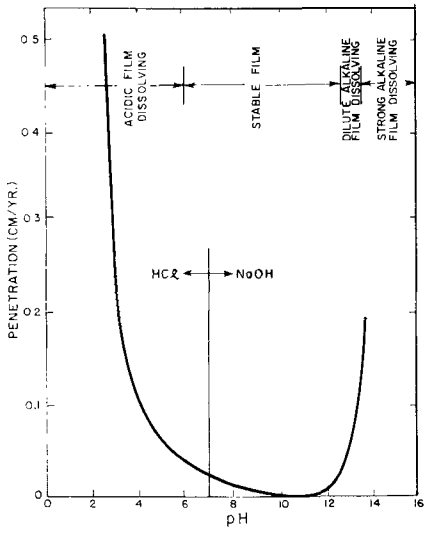

Fig. 4. Effect of pH on the corrosion of Zn by NaOH + HCl [Roetheli, Cox, and Littreal (27)].

under a variety of conditions must also be considered. Impedance measurements (26) for AA-size Mg-MnO_2 and Zn-MnO_2 cells show that the a-c impedance decreases with increasing current density and increasing frequency. At 400 cps the impedance of Mg cells is similar to that of Leclanché cells, whereas at 30 cps the impedance of the Mg cells becomes much greater than that of Leclanché cells at the lighter current drains. The high impedance of the Mg cells and their instantaneous voltage fluctuations with variations in power output, presents a problem as to the use of these cells in some electronic applications. Similar problems would be expected for Al dry cells.

Effect of Electrolyte

The influence of an electrolyte on the electrode potential and corrosion of a metal anode often depends on the nature of the protective film formed on the metal. In the corrosion process these films serve as barriers for the attack of the metal by the corrosive electrolyte. Frequently they are so effective that rapid corrosion proceeds for only a short time, and when the action of the films becomes a predominantly controlling factor, further corrosion is either prevented or the rate is reduced to a small value. Since the pH of the electrolyte has a marked effect on the solubilities and physical characteristics of this film, it is of great importance in choosing a particular electrolyte.

The influence of pH on the corrosion rate of Zn in mixtures of NaCl with NaOH and HCl (27) is shown in Fig. 4. It is seen that Zn is rapidly corroded by solutions whose pH is less than 6 or greater than 12.5 owing to the high solubility of the corrosion product formed. In solutions having pH values from 6 to 12.5 the low corrosion rates are attributed to the presence of adherent protective corrosion-product films. These films are precipitated probably because of the production of high pH's by the corrosion process in the liquid film adjacent to the metal.

In the Leclanché cell, with its NH_4Cl-$ZnCl_2$ electrolyte, the wasteful corrosion of Zn becomes a problem only on long-time intermittent use. For this electrolyte, which has an initial pH [2] of 4 to 5 depending on the concentration of the NH_4Cl and $ZnCl_2$, the corrosion of Zn can be expressed by

$$Zn + 2NH_4Cl = ZnCl_2 \cdot 2NH_3 + H_2 \qquad [1]$$

which represents the over-all reaction.

In alkaline dry cells, it would be expected that the corrosion of Zn would be much faster as the metal is shifted to more anodic potentials due to the low activity of metallic cations brought about by complex ion formation. For example, Zn exists in a sodium zincate solution as $[ZnO_2]^=$, or if the solution is less alkaline, as $[HZnO_2]^-$. However, in strongly alkaline solutions the Zn anodes owe their stability in large part to the addition of zincate salts to the electrolyte in substantially saturating concentration (4). The presence of the zincate ion decreases the rate of corrosion of the Zn anode by the mass action effect.

[2] The pH of the electrolyte increases during cell discharge, attaining values as high as 8 to 10 during heavy continuous service (28).

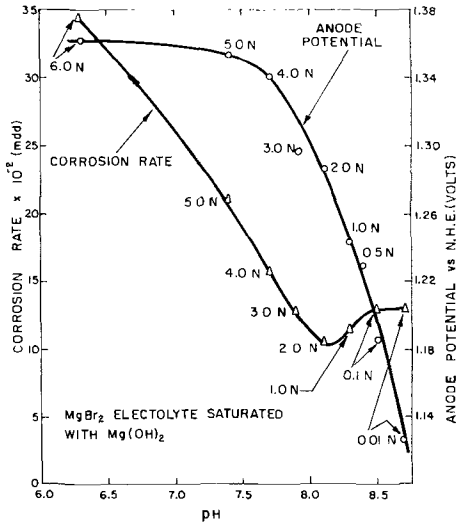

Fig. 5. Effect of pH on the corrosion rate and anode potential of a Mg AZ10A alloy dissolving anodically in various $MgBr_2$ electrolytes [saturated with $Mg(OH_2)$] at a current density of 2.0 ma/cm² [Glicksman (19)].

Aluminum is similar to Zn in that its oxide is soluble in both acid and alkali, and it is attacked by liquids of very high or very low pH value. Analogous curves to that of Zn in Fig. 4 have been obtained for Al, with a minimum near pH 7 (29).

The effect of pH on the corrosion rate of Mg in solutions of NaOH, HCl, and distilled water has been studied by Akimov and Rozenfeld (30). They report that, from pH 3 down, there is a sharp increase in the corrosion rate, while from pH 3 to 11 the corrosion curve slopes smoothly. At pH's of 11 and higher the protective film increases strongly in stability so that corrosion ceases above pH 11.5.

The effect of pH on the corrosion rate and electrode potential of a magnesium AZ10A alloy dissolving anodically in various magnesium bromide electrolytes is shown in Fig. 5 (19). The corrosion rate decreases approximately linearly with increasing electrolyte pH over the range of 6.3 to 8.1 pH units and, at pH's greater than 8.1, approaches a constant value, corresponding to an anode efficiency of 63%. In the weakly acidic solutions the potential varies very slightly with pH, while in the basic pH range the anodic potential falls rapidly with increasing pH and decreasing bromide ion concentration.

These results have been explained in terms of a MgO film on the anode surface, which is more easily penetrable at low pH values because the OH^- ion concentration is too low to maintain an effective oxide film. Thus, at low pH values, high corrosion rates and high anode potentials are observed. At high pH values the OH^- ion concentration controls the precipitation of the Mg^{++} ions produced at the anode, which according to Robinson (16) are precipitated so close to the anode as to stifle the anodic reaction. This results in lower potentials, a decrease in local corrosion, and excessive polarization of the anode.

In an intermediate pH range precipitation of $Mg(OH)_2$ occurs at a sufficient distance from the active anode areas to permit the anodes to function normally. It is in this pH range that other properties

Table III. Electrode potentials of Mg, Al, and Zn in typical electrolytes (potentials referred to a standard hydrogen electrode) [Akimov and Clark (33)]

Metal	3% NaCl		0.1N HCl		0.1N HNO_3		0.1N NaOH	
	1 min	rubbing	1 min	rubbing	1 min	rubbing	1 min	rubbing
Mg	1.418	1.500	1.622	1.596	1.270	1.220	1.086	1.484
Al	0.577	1.221	0.493	0.916	0.320	0.804	1.403	1.386
Zn	0.772	0.818	0.769	0.752	0.688	0.643	1.126	1.123

of the electrolyte, such as the anion present, exert a greater influence over the local corrosion rate and the anode potential.

The effect of the anion present in an electrolyte is often of great importance in dealing with anodes having a protective film. For Al in a solution containing 0.001M K_2CrO_4 and various potassium salts, it was found that small ions show the highest penetration of the oxide film, the order of penetration being Cl^-, Br^-, I^-, F^-, $SO_4^=$, NO_3^-, and $PO_4^{\equiv}$ (31). Evans points out that these differences may be connected not only with size but with solubility and diffusivity as well. What this means in terms of corrosion is seen by the corrosion measurements of Akimov and Glulskova (32) of Al in solutions of NaCl, Na_2SO_4, and $NaNO_3$. Measurements were made over the *p*H range of 0 to 14, and the *p*H being adjusted with NaOH or the acid according to the anion present. In the strongly acid and strongly alkaline regions the rate of corrosion was of the same order, but in neutral or acid solutions the rate of corrosion in the presence of chloride ions was as much as one thousand times greater than in the presence of the sulfate ion.

With metals coated with a protective film, such as Mg and Al, more anodic potentials may be produced by ions which can easily penetrate through this protective film. The fact that aluminum chloride has proved to be the most satisfactory electrolyte for aluminum-manganese dioxide cells (8) is no doubt due to the ability of the chloride ion to penetrate the oxide film and activate the electrode. However, because of their high penetrating power, chlorides are not acceptable for use in conjunction with Mg anodes, and a magnesium bromide electrolyte is used instead.

From an examination of the data in Table II, it is seen that variations in the *p*H of the solution have a pronounced effect on the magnitude of the electrode potential. For the Zn electrode which behaves reversibly except at very high current densities (3), these variations generally follow the Nernst equation. For Al and Mg the influence of *p*H on the electrode potential is essentially due to its effect on the oxide film. Thus, the potential of Al is most anodic in electrolytes of high *p*H in which the oxide film is soluble, but the rate of corrosion is excessive since Al owes its stability in electrolyte to its oxide film.

The influence of protective films on the electrode potentials of Mg and Al is illustrated in Table III (33). Measurements were made by first determining the electrode potentials of the metals in a conventional manner and then during a continuous cleaning of the surface by means of a carborundum rod, which removed much of the original protective film. It is evident that protective films are preserved or formed on metals only when the electrolytes have appropriate characteristics. Thus, a good protecting film is preserved on Al immersed in solutions of NaCl, HCl, and HNO_3, while the film dissolves in NaOH. On the other hand, good protecting films are formed on Mg in NaOH.

Effect of Anode Composition

When hydrogen evolution is the controlling factor in the rate of attack on a metal anode, the effect of low hydrogen overvoltage impurities are important. They produce cathodes from which hydrogen can be evolved rapidly without too much shift in anode potential, so that the conditions for continued corrosion are favorable. The effect of such impurities on the attack of Zn and Al in acid solution is described by Evans (34) while the work of Hannawalt and his co-workers (35) stresses the importance of certain impurities and alloy metals on the corrosion characteristics of Mg alloys in aqueous salt solutions.

For this reason, high-purity Zn (with respect to low hydrogen overvoltage metals) is used in the various zinc-alkaline and Leclanché dry cells. In the case of Mg, although the potential of pure commercial Mg is about 0.04-0.10 v more anodic than the Mg-Al and Mg-Al-Zn alloys, it has been found to be a less efficient anode material than the high-purity alloys (19). It is for this reason that the Mg anodes

Table IV. Electrode potentials* of Al-Zn alloys in various solutions (potentials referred to a standard hydrogen electrode) [Mears and Brown (14)]

Metal	1.0M NaCl	St'd Na_2SO_4	1.0M HCl	1.0M NaOH	1.0M Na_2CO_3	1.0M Na_3PO_4	St'd $Ca(OH)_2$	St'd $CaCO_3$	St'd $CaSO_4$
Al (2S)	0.51	0.16	0.54	1.13	1.01	0.98	1.20	0.70	0.43
Al with 1% Zn (72S)	0.62	0.42	0.68	1.22	1.20	1.19	1.23	0.65	0.36
Al with 5% Zn	0.70	0.48	0.74	1.24	1.16	1.20	1.23	0.71	0.48
Al with 10% Zn	0.71	0.32	0.78	1.24	1.18	1.19	1.24	0.64	0.50
Al with 15% Zn	0.68	0.28	0.78	1.21	1.19	1.15	1.20	0.53	0.46

* Potentials originally reported were referred to a 0.1N calomel electrode. They are here corrected to the standard hydrogen electrode scale without making correction for the liquid junction potential.

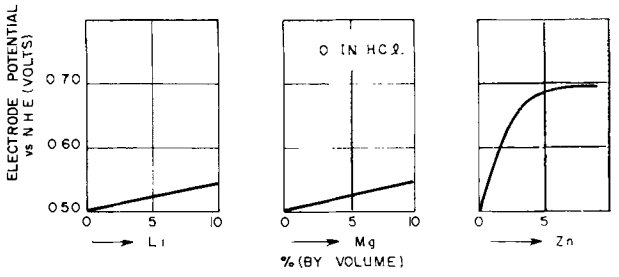

Fig. 6. Electrode potentials of the solid solutions Al-Li, Al-Mg, and Al-Zn. [Akimov and Clark (37)].

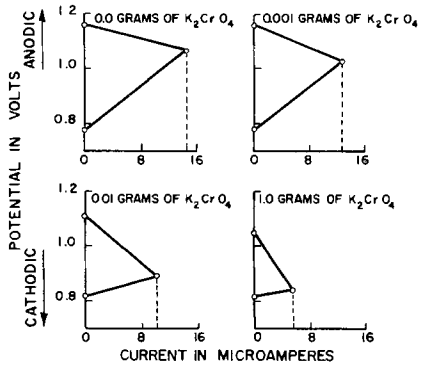

Fig. 7. Effect of concentrations of chromate on local cells on Al in 10% NaCl solution. [Mears and Brown (39)].

used in dry cells have been alloys such as AZ31 and AZ10, the former containing principally 3% Al and 1% Zn, while the latter consists of 1% Al and about 0.5% Zn. The effect of the various alloying ingredients on the anode efficiency of Mg has been reported in detail by Robinson (16). Essentially, the addition of Al permits the removal of the major cathodic impurity, Fe, by precipitation with Mn, while the addition of Zn results in better corrosion distribution and more uniform anode consumption. The latter effect is quite important, for a galvanic anode may operate quite efficiently, but, unless the corrosion is distributed uniformly, segregation losses may be so large as to make operating efficiency a matter of minor concern (36). Recently, it has been found (6) that the addition of small amounts of Ca to the Mg-Al-Zn alloys aids greatly in minimizing "delayed action."

Aluminum dry cells have been fabricated (8) using an Alclad anode which contains an Al 3S alloy on the outside and a 1% Zn-Al alloy on the inside. The effect of Zn is to increase the potential by about 0.1 v. The outer part of the Alclad anode is less anodic than the inner part and serves to prevent pin-hole perforations during normal cell service life and storage. The effect on the electrode potential of alloying Zn to Al has been studied by Mears and Brown (14). They measured the potentials of a series of Al-Zn alloys in various electrolytes and found that in alkaline solutions the potential of Al is high and is not raised greatly by the addition of Zn. However, from the data in Table IV, it is seen that in neutral solutions the addition of Zn raises the potential of Al, and in neutral solutions containing chlorides, the potentials of the Al-Zn alloys approach those of Zn. It was also found by Mears and Brown that, for equal quantities of current supplied by electrodes of such alloys, the Al-base alloys generally lost less than one-third as much weight as did the Zn. Therefore, from the standpoint of metal consumed, the Al-base alloys appear definitely superior to Zn.

Akimov and Clark (37) have made an extensive study of the electrode potentials of solid solutions and have classified them into groups according to the relationship between the potential of a solid solution and its composition. The typical group to which a given system of alloys belongs is defined principally by the nature of (*a*) the components and their interaction, (*b*) the solution, and (*c*) the protective film. They also found that no relationship existed between the potential of a component and the effect on potential produced by this component. Figure 6 presents the influence of three components, Li, Mg, and Zn, on the potential of a corresponding solid solution with Al. It is apparent that Zn shifts the potential of the solid solution in the anodic direction the most and Li the least. This effect is in the reverse relation to the potentials of these three metals.

Corrosion Inhibitors

The corrosion of an anode may be represented as consisting of two parts, an anodic reaction [2], and a cathodic reaction [3].

$$M \rightarrow M^{++} + 2e^- \qquad [2]$$

$$2H^+ + 2e^- \rightarrow H_2 \qquad [3]$$

As long as no external current is present to accept or supply electrons, the two reactions must occur at the same rate. Thus the problem of finding corrosion inhibitors which can retard the corrosion reaction may be accomplished by inhibiting either reaction [2] or [3].

In a dry cell it is desirable that the corrosion of the anode be inhibited by altering the cathodic reaction and not the anodic one, which is necessary for the production of electrical energy in the cell. For example, although organic compounds such as furfural and quinaldine were found to be effective in retarding the corrosion of Zn in dry cell electrolytes, dry cells made with them did not have the expected increase in shelf-life or electrical output (38). The inhibitors either reacted with the paste wall of the cell and decreased its strength or formed a high-resistant film on the Zn. In the latter case, these compounds probably form an insoluble precipitate over the entire surface of the Zn, which stifles not only the undesirable corrosion reaction but also the cell discharge reaction.

The use of soluble chromates, which function as anodic inhibitors, in the electrolyte has proved beneficial for cells during storage. However, they apparently become ineffective when current is drawn from the cell. For Zn the presence of $K_2Cr_2O_7$ in the electrolyte probably passivates the Zn with a very thin chemically resistant film, which, however, breaks down rapidly when current is drawn from the cell. According to Mears and Brown (39) the inhibiting action of sodium chromate on the corrosion of Al in NaCl solution is due to the polarization of local anodes. Chromate functions as an in-

hibitor because it increases anodic polarization in spite of the fact that it decreases cathodic polarization. The latter effect, which is illustrated by the polarization curves in Fig. 7, is to be expected because of the oxidizing properties of the chromate ion.

For Al dry cells which have an aluminum chloride electrolyte, ammonium and alkali chromate inhibitors are used. With potassium chromate a 1-sec delayed action is found, while the Al anode shows no delay with an ammonium chromate inhibitor (8). In general, the concentration of chromate required for protection becomes greater at high chloride concentrations than at low ones and becomes greater still if the temperature is raised (40).

In Mg dry cells, a lithium chromate inhibitor is used in the electrolyte and a small reservoir of an insoluble chromate e.g., barium chromate, is incorporated in the cathode mix to furnish additional soluble chromate as it is used up at the anode. For Mg the lowest chromate concentration which will give adequate corrosion protection is preferred, since delayed action increases with increasing chromate concentration. However, care must be taken since anodic inhibitors like the chromates are dangerous inhibitors when not added to the electrolyte in sufficient quantities. The reason for this is that the area undergoing anodic attack is greatly cut down. If corrosion velocity is controlled exclusively by the anodic reaction, then the anodic attack is cut down in the same ratio, and the intensity of corrosion remains the same. If, however, the velocity is controlled even in part by the cathodic reaction, the corrosion rate will be diminished to a less extent than the corroded area, and the intensity of the attack will be increased (41). In dry cells this localized corrosion causes perforation of the anode can, resulting in loss of electrolyte by leakage and evaporation.

On the other hand, cathodic inhibitors such as mercury are safe in general, as they decrease the total corrosion rate without causing the anodic area to become smaller. For Zn, amalgamation produces an electrochemical couple in which Zn is the anode, but the activation overpotential of hydrogen on mercury is so high as to inhibit the cathodic reaction [3], and thus the corrosion reaction is greatly curtailed. The quantities of mercury than can be used effectively are very limited, seldom exceeding 0.25% because of the embrittlement and loss of strength of the amalgamated metal (1).

For Mg and Al, amalgamation changes both the hydrogen overvoltage and the anodic polarization for the active metal dissolution. The high potentials observed with amalgamated Al and Mg anodes are attributed to the partial removal of the oxide film by amalgamation. For Al this results in a greatly increased rate of corrosion and is therefore undesirable; however, results in this laboratory for Mg dry cells show that the effect of mercurous salts in the electrolyte may be beneficial, especially at low current drains. The use of mercury has a further advantage in that it reduces cell impedance by its interference with the protective oxide coating.

The shelf life of a cell can be considerably increased by storage below ordinary temperatures. The main reasons for this are the lower rates of the corrosion reactions and the increased hydrogen activation overpotential which are associated with decreased temperature. For example, assuming the temperature coefficient of hydrogen activation overpotential at a mercury cathode to be −2.5 mv/°C, Potter (42) calculates that for an amalgamated Zn anode, decreasing the temperature from 40° to 9°C should decrease the current density at the mercury cathode approximately 4.5 times. Thus the shelf life of a cell should be at least 4.5 times as great at 9° as at 40°C. This is in agreement with experimental results.

Cathode Performance

The advantage to the use of a particular anode-electrolyte combination often lies in the effect of the electrolyte on cathode performance. An example of this is illustrated by the coulometric data in Fig. 8 for an electrolytically prepared manganese dioxide.[3] In the more acidic aluminum chloride electrolyte the MnO_2 operates at a potential 0.4-0.5 v higher than in the NH_4Cl-$ZnCl_2$ electrolyte and gives twice the ampere-minute capacity to an end voltage of +0.25 v. This capacity corresponds to a theoretical two-electron change per molecule of MnO_2, indicating that reduction takes place in accordance with the following equation:

$$MnO_2 + 4H^+ + 2e^- = Mn^{++} + 2H_2O \qquad [4]$$

It is also seen that the gain in anode potential derived from the use of a strongly alkaline electrolyte with Zn is offset by the lower operating potential of MnO_2 in this electrolyte. Assuming an end voltage of −0.40 v[4] for MnO_2, the ampere-minute capacity

[3] 85% manganese dioxide.

[4] The potential of Zn is approximately 0.75 v in acidic electrolyte and 1.3 v in strongly basic electrolyte, so that to allow for end voltages of 0.90 v in actual dry cells, half-cell end-potentials of +0.25 and −0.40 v are taken.

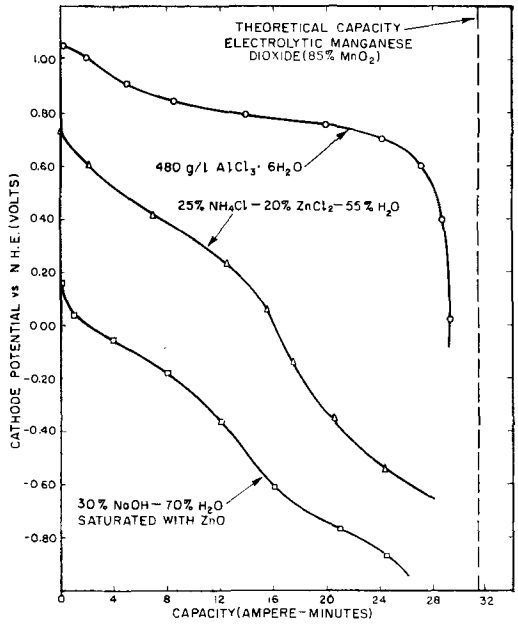

Fig. 8. Effect of electrolyte on the performance characteristics of an electrolytic MnO_2 cathode material.

obtained corresponds to a one-electron change per molecule of MnO_2 in accordance with the following equation:

$$2MnO_2 + H_2O + 2e^- = Mn_2O_3 + 2OH^- \quad [5]$$

It is interesting to note that, under these conditions of discharge, comparable capacities are obtained from MnO_2 in the NaOH and NH_4Cl-$ZnCl_2$ electrolytes. For the use of cathode materials such as mercuric oxide and cupric oxide, however, strongly alkaline electrolytes are necessary because of the solubility of these oxides in acidic solutions.

Conclusions

On the basis of watt-hour capacity per gram, Al and Mg are more attractive anode materials than Zn. The important progress which has been made in the development of Mg dry cells indicates the potential advantages of this anode. However, there are several problems associated with the use of Mg. These are: cost, "delayed action," high impedance, and loss in cell capacity on light intermittent tests. These problems are gradually being solved, and it is predicted that Mg dry cells will achieve commercial significance in the near future. For Al dry cells more research is needed to improve the performance on intermittent tests, as well as to ascertain the shelf life characteristics.

Acknowledgments

The author wishes to express his appreciation to G. S. Lozier and C. K. Morehouse for their helpful suggestions.

Manuscript received Nov. 3, 1958. This paper was prepared for delivery before the Ottawa Meeting. Sept. 28-Oct. 2, 1958.

Any discussion of this paper will appear in a Discussion Section to be published in the December 1959 JOURNAL.

REFERENCES

1. G. W. Heise and N. C. Cahoon, *This Journal*, **99**, 179C (1952).
2. W. S. Herbert, *ibid.*, **99**, 190C (1952).
3. E. A. Schumacher and G. W. Heise, *ibid.*, **99**, 191C (1952).
4. J. M. Booe, *ibid.*, **99**, 197C (1952).
5. P. L. Howard, *ibid.*, **99**, 200C (1952).
6. R. C. Kirk, P. F. George, and A. B. Fry, *ibid.*, **99**, 323 (1952).
7. C. K. Morehouse and R. Glicksman, *ibid.*, **105**, 306 (1958).
8. J. J. Stokes, Jr., Paper presented at ECS Meeting, Pittsburgh, Oct. 10, 1955.
9. E. Willihnganz, *This Journal*, **99**, 234C (1952).
10. U. B. Thomas, *ibid.*, **99**, 238C (1952).
11. G. B. Ellis, H. Mandel, and D. Linden, *ibid.*, **99**, 250C (1952).
12. S. Eidenshon, *ibid.*, **99**, 252C (1952).
13. W. M. Latimer, "Oxidation Potentials," Prentice-Hall, Inc., New York (1952).
14. R. B. Mears and C. D. Brown, *Corrosion*, **1**, 113 (1945).
15. E. Yeager, Abstracts of Papers presented at a Joint Symposium of the Battery and Theoretical Divisions of the ECS, Cleveland, Oct. 1-4, 1956.
16. H. A. Robinson, *Trans. Electrochem. Soc.*, **90**, 485 (1946).
17. A. B. Garrett, Proceedings Tenth Annual Battery Research and Development Conference, p. 4, Power Sources Div., Signal Corps Eng. Labs., Fort Monmouth, N. J.
18. E. C. Potter, "Electrochemistry," p. 370, The Macmillan Co., New York (1956).
19. R. Glicksman, *This Journal*, **106**, 83 (1959).
20. W. O. Kroenig and V. N. Uspenskaja, *Korrosion U. Metallschutz*, **11**, 10 (1935).
21. B. Roald and W. Beck, *This Journal*, **98**, 277 (1951).
22. M. A. Streicher, *J. (and Trans.) Electrochem. Soc.*, **93**, 285 (1948).
23. M. E. Straumanis and Y. N. Wang, *This Journal*, **102**, 304 (1955).
24. R. Glicksman and C. K. Morehouse, *ibid.*, **102**, 273 (1955).
25. R. Kirk, Private communication.
26. G. S. Lozier and C. K. Morehouse, Unpublished work.
27. B. E. Roetheli, G. L. Cox, and W. B. Littreal, *Met. Alloys*, **3**, 73 (1932).
28. N. C. Cahoon, *Trans. Electrochem. Soc.*, **92**, 159 (1947).
29. U. R. Evans, "Metallic Corrosion, Passivity and Protection," p. 213, Longmans, Green and Co., New York (1946).
30. G. V. Akimov and I. L. Rozenfeld, *Doklady Akad. Nauk. S.S.S.R.*, **44**, 211 (1944); *C. A.*, **39**, 0424 (1945).
31. Ref. 29, p. 23.
32. G. V. Akimov and A. J. Glulskova, *Compt. Rend. Acad. Sci. U.R.S.S.*, **49**, 194 (1945); *C. A.*, **40**, 4335 (1946).
33. G. W. Akimov and G. B. Clark, *Trans. Faraday Soc.*, **43**, 679 (1947).
34. Ref. 29, Chap. V.
35. J. D. Hanawalt, C. E. Nelson, and J. A. Peloubet, *Trans. Am. Inst. Mining Met. Eng.*, **147**, 273 (1943).
36. H. A. Robinson, *Corrosion*, **2**, 199 (1946).
37. G. W. Akimov and G. B. Clark, *Trans. Faraday Soc.*, **43**, 685 (1947).
38. C. K. Morehouse, W. J. Hamer, and G. W. Vinal, *J. Research Natl. Bur. Standards*, **40**, 151 (1948).
39. R. B. Mears and R. H. Brown, *This Journal*, **97**, 75 (1950).
40. B. E. Roetheli and G. L. Cox, *Ind. Eng. Chem.*, **23**, 1084 (1931).
41. Ref. 29, p. 545.
42. Ref. 18, p. 365.

Technical Feature

Current Problems in the Production of Magnetic Ceramics

George Economos

Laboratory for Insulation Research, Massachusetts Institute of Technology, Cambridge, Massachusetts

ABSTRACT

Reproducibility of the electrical and magnetic properties while adhering to mechanical tolerances is still the main difficulty in quantity production of magnetic ceramics. This problem is discussed from a developmental viewpoint with suggestions for improving present methods. Older production schemes are compared with newer techniques.

The field of magnetic ceramics has grown by tremendous proportions since its rebirth after World War II. The work by Hilpert (1), Kato (2), Snoek (3), and others came at a time when the need for such materials was not urgent. Television and other high-frequency applications have now brought these materials to the forefront. One of the major difficulties, as in any young industry, is the lack of sufficiently trained technical personnel and of the required "skill in the art." The picture is improving, however, because of the trend in modern ceramics toward a more scientific basis.

The innumerable variables involved in the fabrication of a useful ceramic, from the basic raw materials to a finished electronic component, make it a formidable task to acquire the needed control throughout the production scheme. It must be borne in mind that it is necessary not only to make a product with the proper electrical and magnetic properties, but one that will also meet rather rigid mechanical tolerances of size and shape. The complexity of the problem requires the pooling of many talents. Co-ordination of research and production activities is necessary to utilize the varied skills of the electrical engineer, physicist, chemist, mechanical engineer, ceramist, chemical engineer, crystallographer, and the industrial engineer. There is still considerable inertia in the industry which keeps it from discarding some of the older methods. Present difficulties show the necessity for employing newer and even novel techniques without regard to what is the generally accepted practice.

Achieving reproducibility in the final sintered product necessitates accurate control in all the processing steps. By giving a generalized picture of the various factors involved in the manufacture of these shapes, a critical evaluation of the techniques can be made with suggestions for possible substitutions.

Processing Techniques

General Survey

The "compounding" of ferrites, magnetoplumbites, and other magnetic ceramic materials involves the reaction between various components in the solid state to yield a homogeneous product suitable for forming and sintering into a dense form. A simple outline of the steps required is given below:

1. *Powder preparation*: analysis of the raw materials, weighing the components, mixing, and calcining (reacting).
2. *Ceramic body preparation*: grinding of the calcine, addition of the lubricant and binder, granulating, and drying.
3. *Specimen preparation*: molding, firing (sintering), and testing. An examination of the various steps will give a better insight into the types of problems encountered.

Raw Materials

The choice of raw materials is important in the successful preparation of a homogeneous compound. Extensive information has been compiled on the reactivity between solids (4), which shows that the nature of the reacting species often governs the rate of compound formation. With but few exceptions, the commercial practice is to react the constituent oxides at high temperatures. High-purity oxides are available at relatively low cost, but in using them the manufacturer can defeat one of the prime requisites for high reactivity: high surface area and high-defect crystal structure. Precipitation techniques (5) are available to achieve this end, but they are not competitive at present and find only limited use.

The oxides generally used are products of some decomposition process. Why use the oxide when the original material offers better opportunity for mixing and reacting? This possibility has not been exploited to any extent, even though it could be competitive with the oxides. The result would be a reduction of the calcining temperature and the production of a more friable material for easy grinding.

Comminution Processes

Grinding of the calcine is a major operation in the ceramic body preparation. Ball mills have long been

used, but not until recently have newer type units found extensive use. The attritor and the vibratory ball mill cut the time to a fraction of that needed before. The micronizer (high velocity interparticle impact by air or steam pressure) has not received extensive attention in this field. This unit could accomplish in the dry state what the other methods do in the wet, thus eliminating the expensive dewatering step usually needed.

Dry-Press Body Preparation

The effort expended in the preparation of the dry-press body pays dividends in the behavior of the materials at the presses and in the sintering steps. Lubricants and binders (one or both) are added to the milled material to impart the needed flow properties to this nonplastic material. This is generally done by blending-in these additives in the semiplastic state. For a given amount of additive, the pressing behavior is related to how well each particle is coated by the blending process. The most obvious method is one in which the additives can be dispersed effectively and brought into intimate contact with the solid material. Emulsions are highly dispersed systems, but a molecular or ionic solution is even more so. Using lubricants and binders which are soluble in a liquid medium permits wetting of the solid particles and, on subsequent evaporation of the solvent, a film of the solute remains on the particles.

A word of caution is needed here. In the evaporation of the solvent, it is essential that agitation be continued until evaporation is complete, otherwise capillary activity brings the solute to the surface and destroys the highly dispersed condition originally present. The most effective method to achieve this is to dry the wet mix quickly in as highly divided state as possible. Spray drying effectively accomplishes this. This unit eliminates the dewatering and the binder-blending step after grinding and produces granules suitable for pressing.

Pressing

Most of the problems in the pressing operation usually can be traced to flaws in one of the previous processes. Proper die design and loading, pressing pressure and speed, and other mechanical effects must be worked out for each shape and composition. Most of the difficulties at this stage of manufacture will be overcome by the proper choice of ceramic body preparation.

Firing

The firing or sintering of the molded shapes can be regarded as a three-stage process: (*a*) heating, (*b*) soaking, and (*c*) cooling. The initial stage of the heating period is the careful removal of the additives by evaporation or by burning. The evaporation is not affected by the furnace atmosphere, whereas the burning requires oxidizing conditions. Obviously, the choice of binder will be critical because the mode of its removal can be detrimental to the body, depending on the composition and its behavior in various furnace atmospheres. This initial portion of the heating cycle progresses at a slower rate compared to the rate which follows, generally at more than 300°C.

The proper regulation of the remainder of the heating cycle, the soak period, and the cooling rate will be governed by the size and shape of the pieces, and by the desired end properties. The usual difficulties, such as cracks due to too rapid burn-out and specimen shattering caused by sharp thermal gradients during heating and cooling, must be overcome. Added to this is concern for the oxygen stoichiometry in the fired piece. No set rule can be made on the optimum firing conditions, because these vary widely with the type of material and its properties. Each composition must be treated separately. Tunnel kilns are most efficient for large volume production; however, for special heating and cooling cycles and atmospheres, batch-type kilns are more suitable.

Comparison of Some Production Schemes

Having considered some of the more critical processes and their associated problems, a few typical production flow sheets may be examined and compared. The "dry-process" (Fig. 1) is the most common (5). Two dewatering steps are required: the first is essential for proper mixing of the component oxides, but the second can be eliminated by using the micronizer. This speeds the process and, in the long run, reduces costs. Figure 2 shows the flow sheet of a "wet-process" plant (5) in which the second wet milling could be replaced also. Use of decomposable salts of the cations can be incorporated at the beginning of both these arrangements.

Highly specialized schemes, such as that using the atomizing burner (6) (Fig. 3), cut down the re-

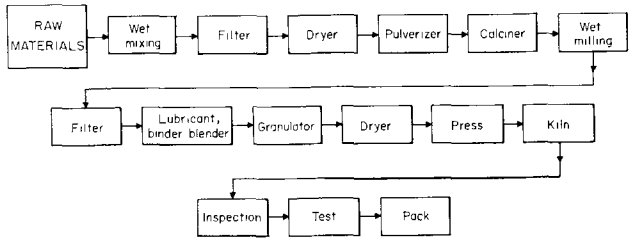

Fig. 1. "Dry-process" flow sheet

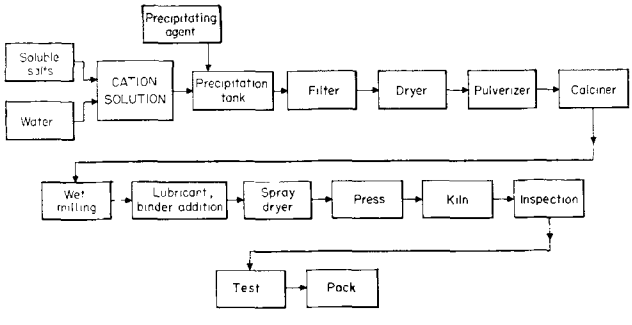

Fig. 2. "Wet-process" flow sheet

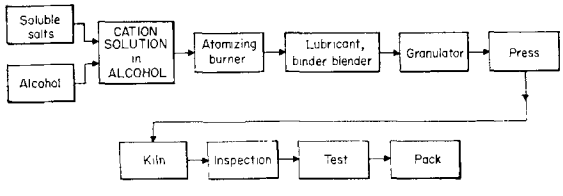

Fig. 3. Atomizing-burner flow sheet

quired number of steps. At present, this technique has found application only where its high cost and low yield can be justified by the special properties of the end product, such as microwave ferrites.

Not to be omitted from this discussion is the present status of the evaluation of the final product. Numerous organizations (Institute of Radio Engineers, Metal Powders Association, American Society for Testing Materials, etc.) have committees which draw up evaluation parameters with acceptable test procedures for these materials. Such factors as shape, size, application, measurement technique, and so on, enter into the picture. Because of the multitude of these factors, no one choice can be expected to win wide acceptance. Some tentative agreements have been reached, but much has to be done before the field is properly covered.

Manuscript received Dec. 1, 1958. This paper was prepared for delivery before the New York Meeting, April 27-May 1, 1958. Work was sponsored by the U. S. Office of Naval Research, the Army Signal Corps, and the Air Force.

Any discussion of this paper will appear in a Discussion Section to be published in the December 1959 JOURNAL.

REFERENCES

1. S. Hilpert, *Ber.*, **42**, 2248 (1909).
2. Y. Kato and T. Takie, *Trans. Am. Electrochem. Soc.*, **57**, 297 (1930).
3. J. L. Snoek, *Philips Tech. Rev.*, **8**, 353 (1946).
4. J. A. Hedwall, "Einführung in die Festkörperchemie," F. Vieweg und Sohn, Braunschweig (1952).
5. G. Economos, *J. Am. Ceram. Soc.*, **38**, 241 (1955).
6. J. F. Wenckus and W. Z. Leavitt, "Preparation of Ferrites by the Atomizing Burner Technique," Papers of the Conference on Magnetism and Magnetic Materials, American Institute of Electrical Engineers, Publication T-91, p. 526 (1957).

Brief Communications

The Ubiquity of Localized Corrosion

R. B. Mears

Applied Research Laboratory, United States Steel Corporation, Monroeville, Pennsylvania

For decades localized corrosion has appeared to be considered more mysterious than uniform or general attack. Many papers have been written pointing out various causes of localized attack, usually implying that uniform corrosion was the expected form and that localized corrosion was exceptional and, therefore, required a special explanation. It now appears that this viewpoint should be changed. Localized corrosion is the form to be expected and uniform corrosion is the form that requires explanation.

Even single crystals of very pure metals contain crystal imperfections. Read and Shockley (1) proposed that localized corrosion (etch pits) occurred at edge dislocations in high-purity aluminum. They stated, "We have proposed that each etch pit originates at a dislocation, where the free energy of the stressed material is somewhat higher than elsewhere; the pit then grows to large size so that it can be observed optically."

Later Vogel, Pfann, Corey, and Thomas (2) showed that etch pits developed in high-purity single crystals of germanium and that the measured spacing of these pits correlated well with spacings predicted from x-ray diffraction. They concluded that individual etch pits are nucleated by single dislocations, with the pit being formed where the dislocation singular line intersects the surface.

Etch pits at dislocation sites have been observed on several other high-purity metals, including iron (3, 4). It now appears that all commercially available metals contain dislocations and that, under appropriate conditions, localized corrosion (etch pits) can develop at dislocation sites. The reason generally given for the formation of these etch pits is still essentially that proposed by Read and Shockley as quoted earlier. However, it should be pointed out that very specific corroding solutions (etchants) must be used to reveal dislocation sites. The majority of corrodents do not give this type of attack. Thus, although following Read and Shockley, we can explain satisfactorily the localized corrosion that occurs in carefully selected etchants, it is much more difficult to explain the more commonly encountered uniform attack.

To complicate matters still further Boswell (3, 4) has pointed out in a private communication that, with the specific etchant he used to reveal dislocation sites in high-purity iron, it was necessary to have between 0.001% and 0.01% carbon in the iron or proper resolution of the dislocation sites did not occur. [Apparently impurity segregation is also necessary for etch pits to be revealed in high-purity Al (5) and Zn (6).]

Metallographers have known for years that grain boundaries, different crystal faces, and dissimilar phases in polycrystalline metals or alloys can be corroded or etched at different rates. Use is made of this "localized corrosion" in examining polished metallic specimens under the microscope.

All metals or alloys used in quantity by industry are polycrystalline and contain dissimilar phases to a greater or lesser extent. The expectation would be, therefore, that all metallic articles when exposed to corrodents would develop localized corrosion.

A New Separator for the Aluminum Dry Cell

N. C. Cahoon[1] and M. P. Korver

Research Laboratories, National Carbon Company, Division of Union Carbide Corporation, Cleveland, Ohio

ABSTRACT

A new and improved separator medium for the aluminum dry cell is described. It provides an adhesive contact with the anode and a satisfactory electrolytic contact with the cathode. The method by which this separator is prepared involves a new technique which is described. The separator layer significantly improves the keeping quality and delayed service performance of the aluminum-manganese dioxide cell.

Aluminum as an anode for primary batteries has received periodic attention during the past 30 years. Recent studies with renewed interest by Stokes and Ruben have shown greater progress (1, 2). As an anode for a battery system, aluminum looks particularly attractive for several reasons. Electrochemically, the aluminum anode theoretically consumes only 0.336 g of metal per ampere hour of electrical output, or about 27% of that consumed by the zinc anode. In addition, drawn aluminum cans offer attractive economic features.

Since any new system imposes many problems, a considerable amount of study was required with this particular system because of the very acidic nature of the altogether new electrolyte employed. Stokes has reported considerable progress on studies of the anode, the cathode, and the electrolyte. These studies have yielded the "Alclad"-type anode and the chloride-chromate type electrolyte (1, 3).[2] Our studies have been concerned primarily with the selection of an improved separator for this system. An effective separator medium is essential if a battery is to operate satisfactorily and to possess acceptable keeping quality.

Experimental

This study has followed a pattern somewhat similar to that previously described for separator studies in the Leclanché cell (4, 5). As in the Leclanché cell, it was deemed advisable to select a separator which would possess the following properties: (*a*) A medium which would contact the cathode satisfactorily and form a positive adhesive contact with the anode; (*b*) A medium which would be compatible with the battery components and nonreactive for a reasonable period of time, i.e. at least one to three years; (c) A separator which would possess adequate wet strength to allow ease of cell assembly.

It has been shown (4) that the usual cereal paste does not meet these requirements satisfactorily, since both starch and flour hydrolyze and break down in an acid electrolyte. The choice of possible separators, therefore, must be made from the field of other natural or synthetic colloids.

First, one must select one or more colloids which satisfy items (*a*) and (*b*) above. Since the depolarizer is the same in both systems, with the background knowledge of the stability of various colloids with manganese dioxide, one may choose colloids which might satisfy item (*a*) when used with an aluminum anode. This group included water soluble methyl cellulose, two types of hydroxypropyl methyl cellulose, Lytron X-887,[3] polyacrylamide 50, locust bean gum, and gum Karaya. Self-supporting films of all colloids of this group except Lytron X-887, locust bean gum, and gum Karaya were prepared. These three materials were difficult or impossible to prepare as self-supporting layers. Therefore, a new technique was used to incorporate the gums into an acceptable separator layer. It involves the suspension of the powdered colloid in a resin solution and is thereby designated the resin-bonded separator. The resin, e.g., polyvinyl acetate, is dissolved in a volatile solvent, e.g., acetone. The colloidal material chosen is then dispersed in this solution. The suspension may be coated onto a paper possessing high wet strength, an anode metal, film, or other support, and dried. In this application high wet strength paper was used.

These prepared films were exposed to the chloride-chromate electrolyte solution, the composition of which is presented in Table I. Periodically they were examined to determine their behavior in the electrolyte. Those materials which absorbed electrolyte to become gel-like and tacky to the touch were locust bean gum, gum Karaya, and polyacrylamide 50. At the end of one week these same materials appeared to have the same bibulous characteristics. The other materials appeared only slightly damp and did not appear to be bibulous enough to act as satisfactory separator media.

[1] Present address: Edgewater Development Laboratories, National Carbon Company, Division of Union Carbide Corporation, Cleveland, Ohio.

[2] The Aluminum Company of America Research Laboratory has been very helpful to us in our work by recommending electrolyte formulations, furnishing cans and helpful technical information.

[3] Lytron X-887, an organic copolymer of maleic anhydride, is an experimental Krilium compound made by the Monsanto Chemical Company.

Table I. Chloride-chromate electrolyte formulation used for experimental studies

Component	Composition, %
$AlCl_3 \cdot 6H_2O$	36
$CrCl_3 \cdot 6H_2O$	12
$(NH_4)_2CrO_4$	12
H_2O	40

Table II. Composition of experimental D-size Al-MnO_2 cells

Electrolyte formulation	African Ore G/cell	African Ore Theor. output amp-hr	Acetylene black g/cell	Electrolyte composition, g/cell $AlCl_3 \cdot 6H_2O$	$CrCl_3 \cdot 6H_2O$	$(NH_4)_2 \cdot CrO_4$	$MnCl_2$	H_2O
Cl-CrO_4	28.6	7.15	5.70	7.64	2.55	2.55	—	16.55
$MnCl_2$	32.71	8.18	6.54	—	—	—	10.90	14.86

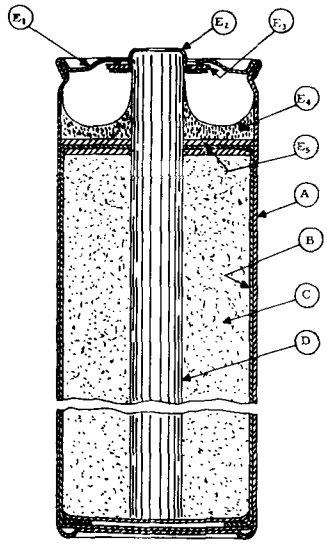

Fig. 1. Cross-section view of a film-lined experimental D-size cell. A, aluminum can; B, film separator; C, cathode; D, carbon electrode; E, cell closure—E_1, cover, E_2, brass cap, E_3, insulating washer, E_4, seal, E_5, washers.

Experimental cells were made evaluating these three separators and also, as a direct comparison, a filter-paper separator.[4] A 5:1::manganese dioxide: acetylene black mix ratio was used with the electrolyte formulation given in Table I. Natural manganese dioxide ore from the African Gold Coast was the depolarizer used. D-size experimental units were assembled which possessed equal weights of the same mix so that the only variable introduced was the different separators. A cross-sectional view of the construction used appears in Fig. 1. In addition, one group of cells was made with manganous chloride electrolyte (2) and assembled with the locust bean gum separator. Comparison of these formulations appears in Table II.

Discussion of Results

Comparative service data on these experimental batteries are presented in Table III. It may readily be seen from these data, especially on delayed and longer term tests, such as intermittent, that the improved separators show a significant advantage. These data show that, although the cells made with manganous chloride give somewhat better initial service than those with the chloride-chromate electrolyte, they do not maintain this service level. The

[4] Filter paper was the separator employed by Aluminum Company of America Research Laboratory in their studies.

Table III. Service summary of experimental D-size Al-MnO_2 dry cells

Separator	Electrolyte	4 Ohm continuous min to 0.75 v Initial	4 Ohm continuous min to 0.75 v 6 Months	4 Ohm continuous min to 0.75 v 12 Months	4 Ohm HIF min to 0.9 v Initial	4 Ohm HIF min to 0.9 v 6 Months
Filter paper	Cl-CrO_4	469	30	Cells failed	402	440
Locust bean gum resin bonded	Cl-CrO_4	479	469	615	368	418
Gum Karaya resin bonded	Cl-CrO_4	429	382	471	322	No cells available
Polyacrylamide 50	Cl-CrO_4	250	343	No cells available	125	286
Locust bean gum resin bonded	$MnCl_2$	694	523	No cells available	400	102

Separator	Electrolyte	4 Ohm LIF min to 0.9 v Initial	4 Ohm LIF min to 0.9 v 6 Months	4 Ohm LIF min to 0.9 v 12 Months
Filter paper	Cl-CrO_4	452	68	Cells failed
Locust bean gum resin bonded	Cl-CrO_4	271	457	401
Gum Karaya resin bonded	Cl-CrO_4	444	420	351
Polyacrylamide 50	Cl-CrO_4	437	315	No cells available
Locust bean gum resin bonded	$MnCl_2$	250	231	No cells available

Separator	Electrolyte	2.25 Ohm LIF min to 0.65 v Initial	2.25 Ohm LIF min to 0.65 v 6 Months	2.25 Ohm LIF min to 0.65 v 12 Months	2.25 Ohm intermittent min to 0.65 v Initial	2.25 Ohm intermittent min to 0.65 v 6 Months
Filter paper	Cl-CrO_4	301	Cells failed	Cells failed	21	35
Locust bean gum resin bonded	Cl-CrO_4	355	289	361	427	355
Gum Karaya resin bonded	Cl-CrO_4	333	357	274	206	332
Polyacrylamide 50	Cl-CrO_4	No test run	216	No cells available	No test run	No test run
Locust bean gum resin bonded	$MnCl_2$	500	279	No cells available	285	162

chloride-chromate electrolyte, because of the chromate present, would be expected to possess better keeping quality. With the improved separator medium present to maintain adequate anode contact coupled with satisfactory stability of the separator, it is evident that the aluminum dry cells will operate satisfactorily even after 12 months shelf storage at 21°C.

The mechanism by which the resin-bonded separator operates is twofold. As the separator absorbs electrolyte the polyvinyl acetate bond hydrolyzes to form polyvinyl alcohol which absorbs electrolyte of the composition, given in Table I, to a very limited extent. This action releases the colloid present, e.g., locust bean gum, which then absorbs electrolyte. This combination provides a stable adhesive mass which readily contacts the aluminum anode, allowing the battery to have both good keeping quality and delayed service characteristics. The paper serves a dual purpose. It serves as a carrier for the resin-bonded film and as a barrier layer to maintain the colloid layer at the anode.

Although only a limited number of batteries was available with the polyacrylamide film, which was not of the resin-bonded type, the data show that it is a satisfactory film separator for this system. These data show that it is not completely the equivalent of the resin-bonded gum separator but could be employed if less stringent service requirements are demanded.

Conclusions

It is believed that these studies have contributed materially to the improvement and advancement of the aluminum dry cell. The establishment of a satisfactory separator medium removes one additional limitation of this system. The discovery of a separator which will provide adequate stability and improved keeping quality should permit further progress and study of the other phases of the aluminum-manganese dioxide system.

Manuscript received Dec. 5, 1958. This paper was prepared for delivery before the Ottawa Meeting, Sept. 28-Oct. 2, 1959.

Any discussion of this paper will appear in a Discussion Section to be published in the December 1959 JOURNAL.

REFERENCES

1. J. J. Stokes, "The Aluminum Dry Cell," paper presented at the Pittsburgh Meeting of The Electrochemical Society, Oct. 10, 1955.
2. S. Ruben, U. S. Pat. 2,638,489, May 12, 1953.
3. J. J. Stokes, U. S. Pat. 2,796,456, June 18, 1957; U. S. Pat. 2,838,591, June 10, 1958.
4. N. C. Cahoon, U. S. Pat. 2,534,336, Dec. 19, 1950.
5. N. C. Cahoon and M. P. Korver, *This Journal*, **105**, 292 (1958).

On the Internal Resistance of Dry Cells

A New Pulse Method

Ralph J. Brodd

National Bureau of Standards, Washington, D. C.

ABSTRACT

The internal resistance of Leclanché cells of various sizes and manufacture was measured by imposing a current pulse on the cell and observing the instantaneous *IR* drop in the cell. The internal resistance of Leclanché cells was determined also as cells were discharged on various standard tests and on continuous or momentary current drains. The increase in internal resistance of the cells on discharge depended on the type of discharge, cell size, and manufacture. The use of the internal resistance of a Leclanché cell to estimate the life expectancy of the cell is suggested.

The internal resistance of Leclanché cells and its measurement have been controversial subjects for many years. In one of the oldest and probably the most universal method (1) the internal resistance of a cell is determined by employing the equation:

$$\text{Internal resistance} = \frac{V - V'}{I} \qquad [1]$$

where V is the open-circuit voltage of the cell and V' is the voltage when current I flows in through the cell. The resistance measured in this fashion is a sum of the resistances of all parts of the cell plus the resultant of any emf including polarizations generated in the cell. Also the resistance depends on the current, age of the cell, temperature, and degree of exhaustion of the cell. In a similar method in wide use today (2) the short-circuit current (SCC) is measured with a critically damped ammeter having a total resistance including the leads of 0.01 ohm. In this instance the ratio V'/I in Eq. [1] is replaced by 0.01. The Wheatstone bridge and the method of charging capacitor are other d-c methods that have been used to measure the resistance of a cell.

Recently, a new d-c method for measuring the internal resistance of dry cells has been reported (3). The *IR* drop of a cell occurring in 10^{-3}-$^{-4}$ sec was measured on an oscilloscope when current pulses were drawn from the cell. The internal resistance of the cell could be calculated by applying Ohm's law, knowing the current in the pulse. In recent years a-c bridge techniques (4-6) for measuring resistance have been employed in an effort to eliminate errors caused by polarization of the electrodes of a cell.

A method for measuring the internal resistance of

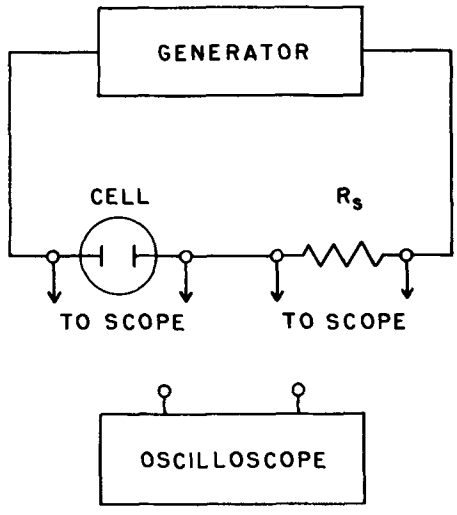

Fig. 1. Schematic diagram of circuit

dry cells is described below wherein the errors caused by polarization of electrodes are reduced to a minimum. The usefulness of this method will be illustrated by measuring the internal resistance of Leclanché cells as they are discharged on momentary drains, on various standard tests, and through constant resistance.

Experimental

A schematic diagram of the circuit used to determine the internal resistance of Leclanché cells is shown in Fig. 1. The pulse generator was a Hewlett-Packard Model 212. The oscilloscope was a Tektronix Model 532. The resistance standard was a deposited carbon resistor of known value. To measure the internal resistance of a Leclanché cell, the oscilloscope leads were connected across the dry cell in Fig. 1 and the instantaneous *IR* drop measured at the trailing edge of the pulse. The instantaneous drop of the oscilloscope pattern occurred in 10^{-7} sec or less. The oscilloscope was connected across the resistance standard, the instantaneous *IR* drop of the resistor was noted, and the current in the pulse was calculated by applying Ohm's law. From this value of the current in the pulse, the resistance of the dry cell was calculated by applying Ohm's law to the *IR* drop in the cell in the first measurement. Typical oscilloscope traces for these measurements are shown in Fig. 2.

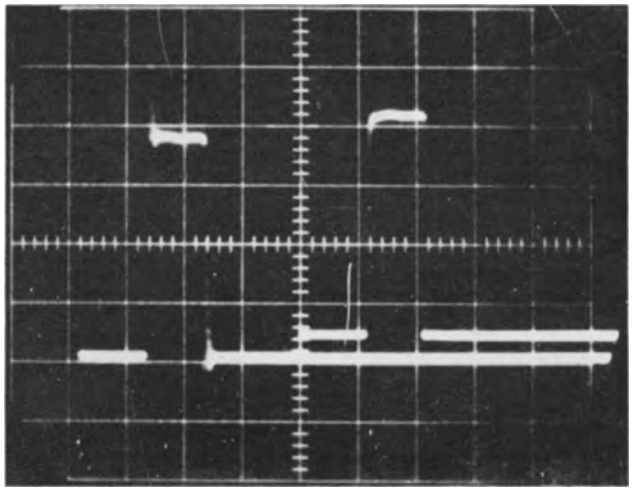

Fig. 2. Typical oscilloscope traces: trace of current pulse through cell on left (0.05 v/cm), trace of current pulse through standard resistor (10 ohms) on right (5.0 v/cm), pulse length 3 μsec.

The effects of both momentary and continuous current drain (in addition to the constant drain by the generator of about 10^{-4} amp) on the internal resistance of Leclanché cells were also investigated. In these cases a loading resistor was connected across the cell. The current drain was calculated by measuring the voltage drop in the resistor with a potentiometer and applying Ohm's law. The internal resistance of the cells was determined in the fashion described above. However, in this case the loading resistor and cell were in parallel. In investigating the effect of momentary drain, measurements of the internal resistance and current drain were made as rapidly as possible so the capacity of the cell would remain essentially unchanged. Measurement of the highest drain was made first; the lowest drain was made last. This procedure was then reversed. The internal resistance with no load was measured after each current drain.

The internal resistance of Leclanché cells was determined also as the cells were discharged on the general purpose 4-ohm intermittent test (4-ohm test), the general purpose 2.25-ohm test (2.25-ohm test), and the light industrial flashlight test (LIF test) (7).

Results and Discussion

When the resistance of a circuit, in this case a Leclanché cell, is determined it is necessary to ascertain whether the measured resistance includes other impedance components than the purely resistive component. In order to establish that the resistance of Leclanché cells measured by the pulse technique had the characteristics of a purely resistive element, the effects of varying various experimental parameters on the value of the measured internal resistance of the cells was investigated first. The current in the pulse was varied from 0.008 to 3.96 amp with no change in the internal resistance of the cell. Likewise there was no change in the internal resistance of the cell when the direction of the pulse was reversed or when the repetition rate of the pulse was altered from 100 to 5000 pulses per second. The measured internal resistance of the cell did not change when the pulse length was varied from 1 to 10 μsec. Thus, the measurement of the internal resistance of Leclanché cells by this method appears to fulfill the conditions for the measurement of the resistive portion of the cell; that is, the current pulse and the voltage pulse have the same shape and the ratio *E/I* is independent of variations in magnitude and sign of the current, repetition rate, and length of the pulse.

The internal resistance of fresh undischarged AA-, C-, and D-size cells (R_i) is found in Table I. The group number has no significance from one cell size to the other. Also reported in Table I are the open-circuit voltage (OCV), the short-circuit current

Table I. Characteristics of various Leclanché cells, standard specification tests

Group	R_i, ohm	OCV, v	SCC, amp	LIF P.T., min	LIF R_f, ohm	2.25-ohm P.T., min	2.25-ohm R_f, ohm	4-ohm P.T., ohm	4-ohm R_f, ohm
D-size cells									
1	0.146	1.58	8.6	696	0.2	581	0.7	805	0.5
2	0.147	1.60	8.7	709	0.5	486	1.0	807	—
3	0.152	1.58	7.0	616	1.1	420	1.6	618	—
4	0.153	1.61	7.7	789	0.4	518	—	873	—
5	0.178	1.59	6.9	870	0.3	631	1.5	1014	1.0
6	0.180	1.57	6.7	471	0.6	323	0.8	575	—
7	0.186	1.64	6.8	657	0.4	473	0.7	808	0.9
8	0.196	1.61	6.1	828	0.3	647	—	931	1.2
C-size cells									
1	0.196	1.59	6.3					407	1.2
2	0.271	1.61	5.0					468	0.9
3	0.353	1.62	3.7					405	1.0
AA-size cells									
1	0.167	1.64	4.1					146	0.5
2	0.192	1.56	5.2					127	0.6
3	0.232	1.57	4.7					117	0.8
4	0.379	1.58	3.2					136	0.6
No. 6 size cells									
1	0.0465	1.64	27.4						
2	0.031_8	1.65	30.3						
3	0.038_0	1.59	32.9						

(SCC), the performance on test (P.T.), and the internal resistance at the cutoff voltage (R_f) of the cells when discharged on the LIF, 2.25-ohm, and 4-ohm tests. All values in Table I are the arithmetic mean of three or more cells. The values of the R_f should be considered only as an indication of the internal resistance of the cell at the cutoff voltage as some of the cells were discharged past the cutoff voltage before their internal resistance could be measured. An examination of Table I fails to reveal a general relation between R_i and R_f of a cell and its performance on test. In general, the SCC increases as the internal resistance decreases. It is also noted that the internal resistance of all the cells increased on discharge. The internal resistance computed from the SCC and OCV is always larger than the internal resistance measured by the pulse method.

The effect of current drain of momentary duration on the internal resistance of an undischarged cell is shown in Table II. After each drain, the internal resistance of the cell with no load was measured. The internal resistance with no load remained constant. The internal resistance of the cells in Table II remained essentially constant at all current drains with a slight tendency to increase at the highest current drain. These results do not confirm the work of other investigators (3, 8) who reported that the internal resistance of Leclanché cells decreased as the momentary current drain increased.

Table II. Effect of momentary current drain on the internal resistance of Leclanché cells

D-size cells		C-size cells		AA-size cells	
Drain, ma	Internal resistance, ohm	Drain, ma	Internal resistance, ohm	Drain, ma	Internal resistance, ohm
0	0.180	0	0.220	0	0.274
1.54	0.180	1.52	0.220	0.42	0.273
15.4	0.180	15.1	0.220	14.1	0.273
32.4	0.178	32.0	0.220	29.6	0.272
149.	0.180	146.	0.221	133.	0.276
508.	0.180	480.	0.225	426.	0.282
1156.	0.186	1141.	0.230		

These investigators interpreted their results by postulating an adsorbed film of hydrogen on the zinc electrode. It is possible that the oscillations observed at the leading edge of the pulse in Fig. 2 are caused by the destruction of an adsorbed film of hydrogen on the zinc electrode. If this is the case, there is no conflict in results.

The discharge behavior of AA, C, and D cells from one manufacturer was determined. The typical behavior of AA- and C-size cells as they were discharged on the 4-ohm test is shown in Fig. 3 and 4, respectively. The typical behavior of D-size cells as

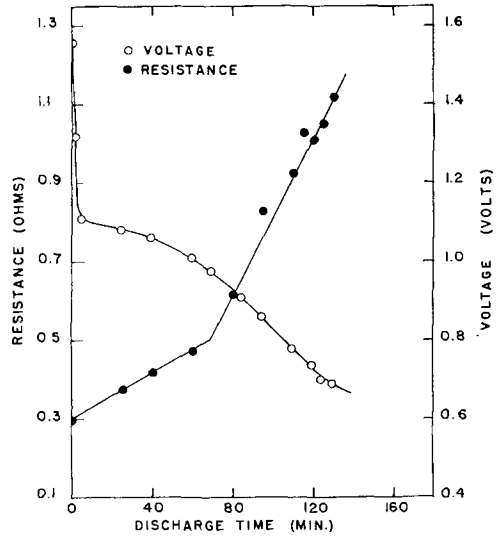

Fig. 3. Behavior of AA-size cell on the 4-ohm test.

Table III. Discharge characteristics of Leclanché cells from one manufacturer

	AA-size cells, 4-ohm test		C-size cells, 4-ohm test		D-size cells, LIF test	
	A.M.	σ_s	A.M.	σ_s	A.M.	σ_s
P.T. (min)	117.	7.6	373.	71.	648.	21.
R_i (ohms)	0.269	0.042	0.215	0.027	0.188	0.012
R_f (ohms)	0.85	0.12	0.915	0.093	0.415	0.042
ΔR (ohms)	0.589	0.076	0.70	0.11	0.227	0.39
$S \times 10^{-4}$ (ohms/min)	28.3	3.4	9.3	3.4	3.46	0.61
T_b (min)	71.0	5.9	243.	56.		
R_b (ohms)	0.470	0.042	0.44	0.10		
E_b (volts)	0.981	0.17	1.05	0.05		

they were discharged on the LIF test is shown in Fig. 5. A summary of the results of discharges of 6 cells of each size is given in Table III, where the arithmetic mean, A.M., and the standard deviations, σ_s, are given for P.T., R_i, R_f, the change in resistance during discharge, ΔR, the slope of the plot of discharge time vs. internal resistance, S. In the case of AA- and C-size cells the discharge time, T_b, internal resistance, R_b, and voltage, V_b, are given at the point of departure from initial linear behavior of the internal resistance-discharge time plot. D-size cells were discharged past 0.6 v on the LIF test with no change in the slope, S. P.T. for control samples of each size cell was within 3% of the values in Table III.

In Fig. 6 the behavior of the internal resistance of AA-size cells is shown as they were discharged continuously through the fixed resistances noted in the figures. The arrows indicate the point at which the cell voltage was 0.8 v. If the discharges were stopped at any point, the internal resistance of the cell remained constant even though the cell voltage recovered to its normal value. C-size cells exhibit behavior similar to that for AA-size cells shown in Fig. 6.

A common feature of the discharges through fixed resistances or on the standard tests was the increase in the internal resistance of the cells as the discharge continued. In general, it was found that the lower values of R_i corresponded to the lower values of R_f. One of the most interesting possibilities that the data in Table III suggest is the use of the internal resistance of a cell to estimate life expectancy for a particular test or use. Unfortunately, the variation of the internal resistance of Leclanché cells with group found in Table I makes impossible any general statements. It appears possible, however, to make a calibration for each group of cells, as Table III and Fig. 3, 4, and 5 illustrate, and then to use the calibration for predictions of life expectancy. For instance, if the internal resistance of D-size cells of the same group as those in Table III increased 0.113 ohms from R_i (refer to Table III and Fig. 5) it would have a life expectancy of 324 min on the LIF test. Similar predictions can be made for the C-and AA-size cells allowing for the change in slope of the plot of time on discharge vs. internal resistance. Of

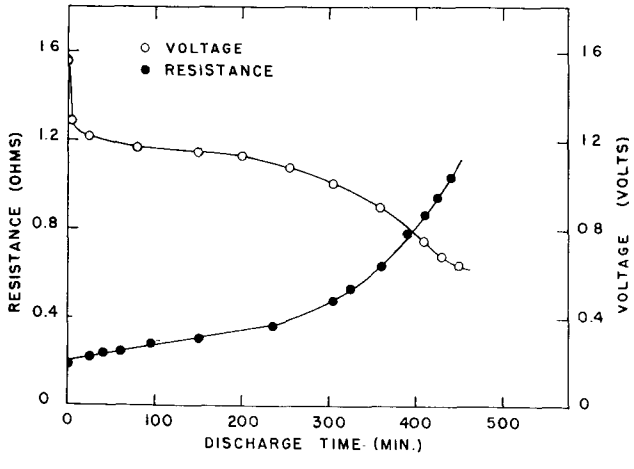

Fig. 4. Behavior of C-size cell on the 4-ohm test.

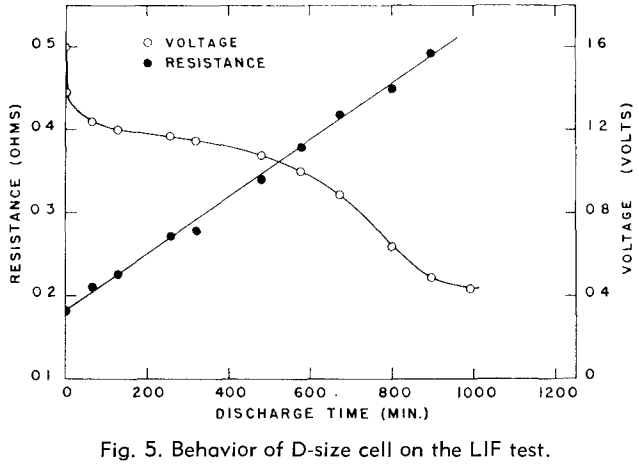

Fig. 5. Behavior of D-size cell on the LIF test.

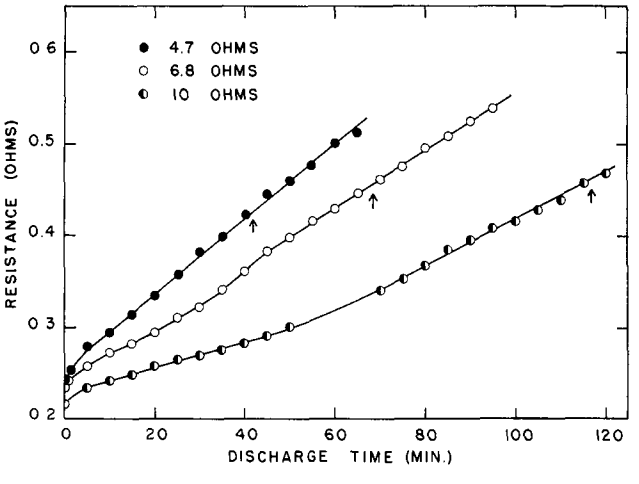

Fig. 6. Behavior of AA-size cells discharged continuously through 4.7, 6.8, and 10 ohms.

course, the predictions are subject to the same statistical errors as the calibration. Investigations are under way to determine if the decrease in life expectancy with age can be predicted from measurements of the internal resistance of the cell. Recently (9) a method for predicting the capacity of a battery has been reported. It is based on repeated short discharges measuring the current and voltage of the battery during discharge.

Acknowledgment

The author wishes to thank H. J. DeWane for his advice and help in conducting the standard specification tests.

Manuscript received Sept. 2, 1958. This paper was prepared for delivery before the Buffalo Meeting, Oct. 6-10, 1957.

Any discussion of this paper will appear in a Discussion Section to be published in the December 1959 JOURNAL.

REFERENCES

1. D. L. Ordway, *Trans. Electrochem. Soc.*, **17**, 341 (1910).
2. G. W. Vinal, "Primary Batteries," p. 133, John Wiley & Sons, Inc., New York (1950).
3. R. Glicksman and C. K. Morehouse, *This Journal*, **102**, 273 (1955).
4. N. C. Cahoon, *Trans. Electrochem. Soc.*, **92**, 159 (1947).
5. W. Heubner, *Elektrotech. Z.*, **61**, 149 (1940).
6. J. Euler and K. Dehmelt, *Z. Elektrochem.*, **61**, 1200 (1957).
7. National Bureau of Standards "Specifications for Dry Cells and Batteries," Circular 559 (1955).
8. W. K. Chaney, *Trans. Electrochem. Soc.*, **29**, 183 (1916).
9. G. B. Ellis, U. S. Pat. 2,853,676, Sept. 23, 1958.

Iodine-Activated Solid Electrolyte Cell for Use at High Temperature

Joseph L. Weininger

Research Laboratory, General Electric Company, Schenectady, New York

ABSTRACT

Iodine-activated miniature cells, Ta(I_2)/AgI/Ag, with solid silver iodide as the electrolyte, have been studied at 150°-550°C. In this range of temperatures the cells have the following characteristics: complete conversion of the consumable silver anode into its electrical equivalent, open-circuit voltage of 0.67 v, short-circuit currents up to 18 ma, capacity of 10 ma-hr, energy output up to 5 mw-hr/cell, a definite activation temperature obtained by selecting a suitable source of iodine vapor, and indefinitely long shelf life below that temperature. The size of the smallest cells is 0.15 cm in diameter and 0.5 cm in length.

Recently halogen-activated solid-electrolyte cells were discussed from a general viewpoint with regard to their history, mechanism, and applications (1). They have the advantage of simpler construction over cells with liquid electrolytes. By reducing the size and weight of individual cells, batteries can be miniaturized. However, solid electrolyte cells have high internal impedance which limits the short-circuit currents to a few microamperes at room temperature. The high-temperature modification α-AgI, which is stable in the range of 146°-552°C is one of the few ionic compounds with large ionic conductivity. Therefore, a study was made of primary cells with an α-AgI electrolyte in that temperature range.

Tantalum-Tube Cells

Figure 1 is a schematic drawing of the cell. The cathode is a tantalum tube containing a "cathode mix," which is a source of the cathode reactant, iodine vapor. The cathode mix may be itself iodine or a suitable chemical system which will produce iodine at a definite elevated temperature. In the course of assembly, the tube is sealed with silver iodide in a stream of dry nitrogen. A silver anode is imbedded then in the iodide, the source of iodine is added, and the other end of the tube is sealed by cold-welding under vacuum. A photograph of one of the first models, which was about 9 mm long, indicates the possibility for miniaturization (Fig. 2). The silver anode can be seen as it protrudes out of

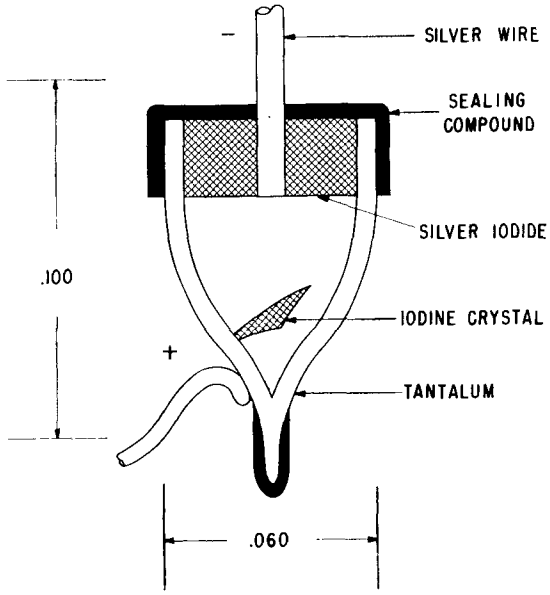

Fig. 1. Schematic of Ta-tube cell

Fig. 2. Photograph of Ta-tube cell

the electrolyte located in the tube. Most of the cell volume is taken up by the iodine reservoir which can be reduced considerably.

The electrode and cell reactions are:

At the anode	$Ag = Ag^+ + e^-$	[1]
At the cathode	$\frac{1}{2}I_2 + e^- = I^-$	[2]
Cell reaction	$Ag + \frac{1}{2}I_2 = AgI$	[3]

Thus, the silver anode is consumed with formation of additional electrolyte, AgI, as the product of the cell reaction.

Preliminary Experiments with Iodine Depolarizer

In preliminary experiments, cells with elemental iodine as the cathode mix as well as cathode reactant were investigated. The following is a typical performance of such a cell, which was 0.477 cm (3/16 in.) long and had an outside diameter of 0.159 cm (1/16 in.): Current-voltage curves at room temperature and at 170°C resulted in the data of Fig. 3. The internal resistance at 170°C was only 40 ohms; hence short-circuit currents were larger than 5 ma. Theoretical open-circuit voltage (0.67 v) also was achieved. With a load of 10 kΩ, 0.11 ma-hr were obtained. This and other cells failed as high temperature was approached because boiling iodine (bp 188°C) burst the cathode tube. For complete cell reaction each cubic centimeter of silver would require the equivalent amount of 1.9 liters of iodine vapor at 1 atm and 200°C. Thus, in the preliminary experiments the cell volume was too small to contain all the iodine vapor. Generally, if maximum capacity, high-temperature operation, and miniaturization are desired, then iodine must be introduced and remain in the cell, as far as possible, in a condensed state.

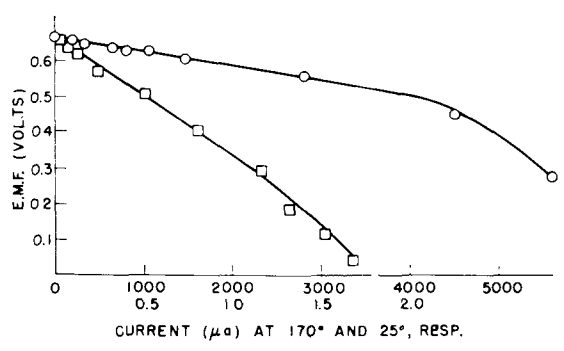

Fig. 3. Current-voltage curves for a cell with iodine as the cathode reactant at 25° (lower curve) and 170°C (upper curve).

Methods of Activating Cells

Two methods were employed to achieve high-temperature stability and gradual evolution of iodine, so that iodine could be used in the cell without building up undue vapor pressure. First, a polyiodide was used which was in thermodynamic equilibrium with iodine over a fairly wide temperature range. In the case of cesium polyiodides, a very thorough study was made by Briggs and co-workers for cesium iodide + iodine + water (3), and for iodine + cesium iodide (4). Second, certain oxidation-reduction reaction mixtures, e.g., Cu_2I_2 + $KMnO_4$, evolved iodine slowly at high temperatures. These systems were investigated by thermogravimetric analyses.

Activation by Decomposition of Iodine Compounds

The following compounds were suitable sources of iodine above the boiling point of iodine: CsI_4, CsI_3, BiI_3, I_2O_5, and CHI_3. In the present work, emphasis was placed on cesium polyiodides as sources of iodine because they decompose at temperatures consistent with their use in tantalum-tube cells.

Preparation of CsI_3 *and* CsI_4

Precipitation from aqueous solutions and crystallization from the melt (in the case of CsI_4) were used to prepare the compounds. As starting material CsI C. P. was added to an aqueous solution of iodine from which precipitation of CsI_3 or CsI_4 took place. Another method involved mixing in stoichiometric ratio 2 mole CsI and 3 mole I_2. This mixture was sealed in a quartz tube under vacuum and raised to 235°C. It was cooled slowly to 135°C and equilibrated at that temperature for 16 hr. Samples were checked for iodine content by wet analysis on a routine basis, and the existence of the tri-iodide and tetraiodide was established in this manner. Samples were also analyzed by x-ray diffraction. The Debye-Scherrer pattern of CsI_4 was not known. In fact, crystals of CsI_4 were identified as I_2O_5. A literature check showed that the pattern given by Hanawalt, *et al.* (5) for I_2O_5, which is accepted as the ASTM standard, also matched the pattern of our sample of CsI_4. To prove our sample as CsI_4, the cesium content was also determined by wet analysis (Table I).

Table I. Analysis of CsI_4 prepared by crystallization from the melt

	Theor.	wt (%)	Found
Iodide content	79.3		78.2
Cesium content	20.7		22.7

Table II. Thermolysis data for decomposition of iodine compounds

Sample	Atmosphere	Primary temp. range, °C	Other temp. ranges, °C	Mechanism	Weight loss	
					Theoretical, %	Experimental (thermobalance), %
I_2O_5	Dry N_2	350-430	—	$I_2O_5 \rightarrow I_2\uparrow + 2\frac{1}{2} O_2\uparrow$	100	98.8
MgI_2	Dry N_2	145-250	300-400	$MgI_2 \rightarrow Mg + I_2\uparrow$	91.1	89.5
BiI_3	Dry N_2	300-359	359-520	$BiI_3 \rightarrow BiI + I_2\uparrow$	43.0	42.9
			80-120			
BiI_3	Dry O_2	285-320	400-480	$BiI_3 \rightarrow BiI + I_2\uparrow$ or	43.0	42.2
			85-95	$2BiI_3 + 1\frac{1}{2} O_2 \rightarrow$		
				$Bi_2O_3 + 3\ I_2\uparrow$	39.0	
CsI_4	Dry N_2	155-230	90-155	$CsI_4 \rightarrow CsI + 1\frac{1}{2} I_2\uparrow$	58.1	57.7
CsI_4	Dry O_2	142-225	95-140	$CsI_4 \rightarrow CsI + 1\frac{1}{2} I_2\uparrow$	58.1	56.8*

* This weight loss determined on analytical balance.

Application of Phase Diagram $CsI-I_2$ *to Solid Electrolyte Cells*

By means of the phase diagram, one can choose a suitable cesium polyiodide as the source of iodine. A composition is required which in the desired temperature range will have a vapor pressure of iodine smaller than 1 atm.

Traces of iodine would be sufficient to produce an appreciable open-cell voltage of the cell $Ta(I_2)/AgI/Ag$, but they could not sustain any current output. Hence, the phase diagram of $CsI-I_2$ may be used to estimate the temperature ranges in which sufficient iodine will be produced to maintain appreciable current density. Thus, iodine first should appear on heating at about 138°C in the case of CsI_4, and at 210° in the case of CsI_3. If it is desired to avoid melts rich in iodine, one can shift the composition of the $CsI-I_2$ mixture toward more CsI, e.g., an over-all composition of 60 mole % CsI and 40 mole % I_2. Such a source of iodine would form less iodine vapor below 306°C than others described previously which also contain CsI_4. The phase diagram of reference (4) refers, however, to the open system $CsI-I_2$ at a pressure of 745 mm, whereas in the cells the polyiodide is in a closed system. In the latter system the iodine pressure increases from vacuum to 1 atm below 306°C as the decomposition reaction proceeds. This difference in the atmospheric environment of the polyiodide will lead to slightly different values for transition temperatures and vapor pressures of the cell as compared to the phase diagram.

Thermolyses of Iodine Compounds

The results of thermobalance measurements of iodine compounds are shown in Table II. Samples were tested in dry oxygen or dry nitrogen to detect any oxidation reactions. In the case of BiI_3 and CsI_4 the oxide was not formed, but decomposition took place in steps. This is indicated in Table II by primary and other temperature ranges. The primary range refers to the temperature interval in which the major part of the decomposition occurred. The other temperature ranges of the next column are those in which smaller weight changes took place. Weight losses to 560°C were considered as final and are compared with calculated values based on the reactions indicated in the table. In each case agreement was very good so that with these compounds the existence of the required iodine-producing reaction is proved.

Activation by Oxidation of Iodides

Mechanism

The second mechanism of activation of tantalum-tube cells is based on the oxidation of an iodide to iodine vapor, e.g.

$$Cu_2I_2 + O_2 \rightarrow 2CuO + I_2\uparrow \qquad [4]$$

This reaction takes place at 240°C, which is the temperature of activation for a cell with Cu_2I_2 as the iodine-source, if oxygen or air is present. If it is desired to achieve a higher activation temperature, one may introduce oxygen chemically bound in compounds such as $KMnO_4$ or KIO_3. These decompose at a higher temperature, and the oxygen formed in the initial decomposition step will react then with Cu_2I_2 above 240°C to produce the necessary iodine vapor, e.g.

$$KIO_3 \rightarrow KI + 3/2\ O_2\uparrow \qquad (\leqq 330°C) \qquad [5]$$

followed by reaction [4] at a temperature above 240°C. Thus, the temperature of activation of tantalum-tube cells may be increased by finding a compound which will give off oxygen at the desired temperature.

Cuprous iodide was used as the source of iodine. When oxygen was added in the form of $KMnO_4$ or KIO_3, the tube was sealed under vacuum. When molecular oxygen was the oxidizing agent, the tube likewise was closed off, but without evacuation. This caused leaks to develop in the cell on heating because of the expanding air. The leaks were necessary to provide a fresh supply of oxygen as the original amount was used up.

Thermolyses of Reaction Mixtures

The thermogravimetric data of iodine-reaction mixtures are listed in Table III. Figure 4 shows the thermobalance curves for cuprous iodide in the presence and absence of oxygen. In dry nitrogen there was 0.6% weight loss at 550°C, which is negligible. The curve of Cu_2I_2 + dry O_2 confirms the temperature of 240°C as the temperature at which reaction [4] takes place (6). In the experiment, 92.2% of the theoretical weight loss corresponding to this reaction had occurred.

Table III. Thermolysis data for iodine-reaction mixtures

Sample	Atmosphere	Primary temp. range, °C	Other temp. range, °C	Mechanism	Weight loss: Theoretical, %	Weight loss: Experimental (thermobalance), %
Cu_2I_2	Dry N_2	No reaction				
Cu_2I_2	Dry O_2	249-330	—	$Cu_2I_2 + O_2 \rightarrow 2CuO + I_2 \uparrow$	58.2	54.0
2.5 Cu_2I_2 + KIO_3	Dry N_2	262-330	332-550	$KIO_3 \rightarrow KI + 3/2\ O_2 \uparrow$ $3/2\ O_2 + 3/2\ Cu_2I_2 \rightarrow 3CuO + 3/2\ I_2 \uparrow$	67.4	66.5
KIO_3	Dry N_2	480-540	540 up	$KIO_3 \rightarrow KI + 3/2\ O_2 \uparrow$	77.6	Reaction not complete at high-temperature limit (620°C)

Figure 5 is the thermobalance curve of a mixture of 2.5 Cu_2I_2 + KIO_3 in dry nitrogen. It shows two separate reaction steps at 260° and 330°C. The weight loss is the result of the oxidation of Cu_2I_2 by oxygen (cf. Fig. 4), but the two steps indicate the successive loss of oxygen from KIO_3, first a partial decomposition to KIO_2, then an accelerated decomposition to KI. This is in agreement with the thermolysis of pure KIO_3, which also takes place in two steps, but at temperatures about 200° higher than in the presence of Cu_2I_2. This lowering of the reaction temperature by a catalyst has been observed in a similar system, that of $KClO_3$ catalyzed by CuO (7). A limitation to a thermogravimetric study of this type is that the oxygen formed would not react entirely with the Cu_2I_2. However, the comparison of the two curves of Fig. 5 and the evidence of the thermolysis of Cu_2I_2 + dry nitrogen, in which Cu_2I_2 did not decompose below 500°C, confirm that KIO_3 decomposes first and then reacts with Cu_2I_2 in the cathode-mix of the solid electrolyte cell.

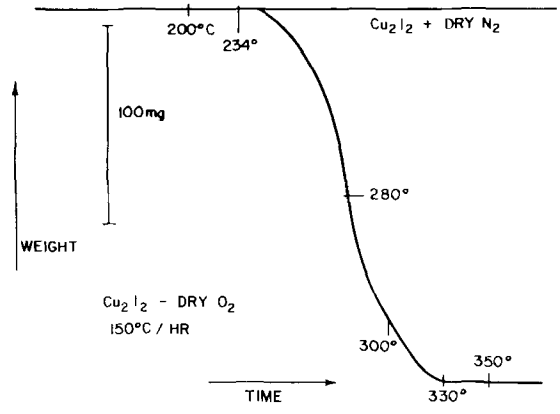

Fig. 4. Thermobalance curves of Cu_2I_2, heated in dry O_2 and N_2, respectively, at 150°/hr (initial wt: 0.3531 g and 0.3205 g, respectively).

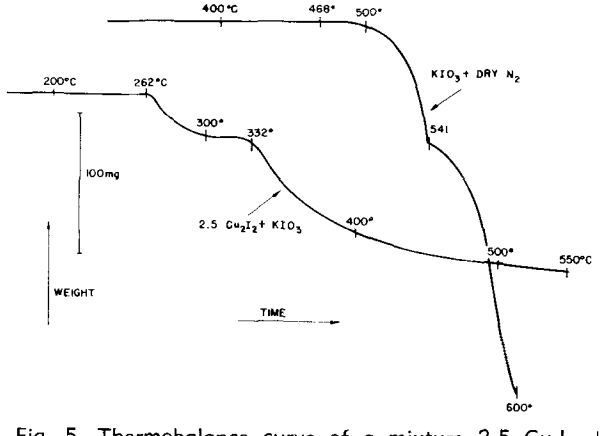

Fig. 5. Thermobalance curve of a mixture 2.5 Cu_2I_2 + KIO_3, (initial wt = 0.3921 g) and KIO_3 + pure N_2 (initial wt = 0.8822 g), heated at 150°/hr.

Another interesting aspect of the thermobalance curve of the mixture Cu_2I_2 + KIO_3 is the weight loss of the mixture, which proceeds quite slowly. This indicates, in comparison with the thermolyses of the individual components, that the production of oxygen is likewise slow. This makes it possible to reach the high-temperature limit of the cell if oxygen is not evolved too rapidly. The reaction mixture of 2.5 mole of Cu_2I_2 per mole of KIO_3 contains an excess of 40% iodide. Assuming that all of the oxygen originally present in KIO_3 is used up in the formation of I_2 from Cu_2I_2, the thermobalance curve shows that at 550°C the reaction was 98.8% complete. This supports the proposed mechanism of decomposition and oxidation.

Results

Performance data.—Cells with the first type of iodine source behaved similarly once the characteristic decomposition of the iodine donor was reached. Besides the iodides listed in Table II, the following compounds were tested successfully as sources of iodine at elevated temperatures: CsI_3, CsI_3 + CsI, Cu_2I_2, CHI_3, and CI_4. Cu_2I_2 reacted with oxygen or oxidizing agents. The organic compounds, CHI_3 and CI_4, were intended primarily as radiation-sensitive iodine compounds which would decompose and trigger off a solid electrolyte cell. For this application CHI_3 and also CBr_4, with the corresponding AgBr electrolyte, are promising, but CI_4 is too unstable at room temperature to act as a radiation detector. Instead, it has a good response to thermal activation in the range 145°-169°C.

In the second type of iodine source, i.e., oxidation couples of iodides, Cu_2I_2 was tested with O_2, $KMnO_4$, and KIO_3, respectively. Results obtained with both types are discussed below.

Temperature response can be obtained from 145° to 500°C. Thus, CsI_4 or CI_4 depolarize satisfactorily at the lower temperature limit; BiI_3, CsI_3, and mixtures of CsI_3 and CsI can be used up to about 320°, and finally, by means of the oxidation couples, e.g., Cu_2I_2 + $KMnO_4$, one can reach the high-temperature limit. Shelf life is unlimited below the activation temperature, because free iodine is absent before

thermal activation of the depolarizer. Capacity and energy-output of cells, whether in series or separately, were as high as 14.4 ma-hr for a single cell of $Cu_2I_2 + KIO_3$ depolarizer or 7.12 ma-hr and 3.62 mw-hr for a battery (four CsI_4 cells in series). Conversion of active cell materials by the cell reaction into their electrical equivalent was nearly complete. The capacity of the cells was limited either by the amount of iodine or silver available to the cell, but generally it is the quantity of silver present as the consumable anode which is limiting. Only in the case of one cell (cathode-mix $Cu_2I_2 + KIO_3$) was the capacity limited by the amount of available iodine. There, 78% of the iodine was converted into its electrochemical equivalent (chemically, into AgI). The open-circuit voltage (OCV) of 0.67 v, equal to the calculated emf of the AgI system based on thermal values at 25°C, was obtained with most cells, although the cells were operated at high temperature. This can be explained qualitatively by the decrease in the free energy of formation of AgI with increasing temperature which is counterbalanced by an increase as a result of higher iodine pressure. This was not the case with oxidation couples. The OCV usually dropped to a lower value after prolonged loading of the cells, but occasionally it recovered to its original value. Complete recovery of OCV was again a question of proper cell design. Likewise, the short-circuit current and internal impedance of cells depended on their structure. Best values of 18 ma and 11 ohms were obtained with a cell of flat tube design (CI_4 depolarizer), but in that case the capacity was only 3.6 ma-hr. It is difficult to estimate a current density for this cell because the dimensions of the silver anode change with time, but at least in its initial operation the surface of the wire anode is known. If 0.159 cm (1/16 in.) is immersed in the solid electrolyte, then the short-circuit current of 18 ma corresponds to about 290 ma/cm^2. The response to activation also depends on the design of the cell. On heating the cell above 145°C from room temperature, the attainment of open-cell voltage required about 1 min or less, whereas proper current response required several minutes of activation.

Tables IV and V show performance data characteristic of the two different sources of iodine. There was considerable variation from cell to cell with regard to internal resistance and capacity, but this is to be expected from the dimensions of the cells, in which the silver anode was a wire 0.127 cm long, imbedded in a solid electrolyte within a tube with inside diameter of about 0.23 cm. The electrochemical equivalent of 0.159 cm (1/16 in.) length of such a silver wire is 5.32 ma-hr. The conversion of silver into the equivalent number of coulombs is described, for brevity, below and in the figures as "percent yield of Ag." Complete utilization of silver can also be demonstrated by microscopic examination of the original locus of the silver anode which has been converted completely into silver iodide. The difference in texture between the original AgI electrolyte and that formed in the course of the experiment gives a clear picture of the cell reaction. A lower but steady output is obtained when one uses smaller diameter tubing. Thus, Fig. 6 shows the discharge

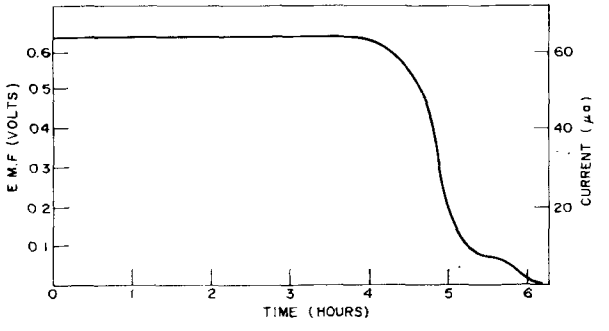

Fig. 6. Ta-tube cell on 10 kΩ load at 300°C; source of iodine: CsI_4; capacity 0.370 ma-hr, theoretical 0.435 ma-hr.

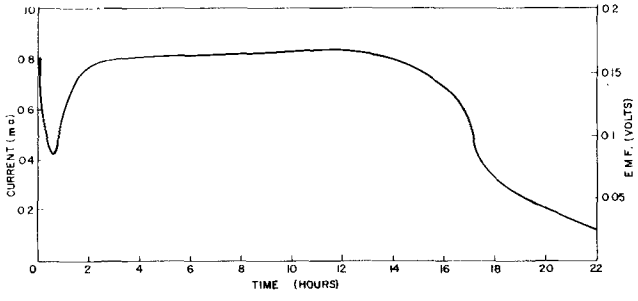

Fig. 7. Ta-tube on 200 Ω load at 258°C; cathode mix: $Cu_2I_2 + KIO_3$; output 14.43 ma hr, 2.32 mw-hr.

Table IV. Performance of AgI cells with thermally activated iodine compounds as iodine sources

No. of cells	OD of Ta-tube, cm	Depolarizer	Temp. of operation, °C	Open-cell voltage, v	Short-circuit current, ma	Internal resistance, ohms	Capacity, ma-hr	Notes
1	0.159	CsI_4	300	0.65	4.0	140	—	
1	0.318	CsI_4	250	0.675	1.5	440	5.23	Discharge at 1 kΩ.
1	0.159	CsI_4	300	0.63	0.5	1510	0.37	3 ma at 0.25 v, per cent yield: 85% Ag, see Fig. 6.
4	0.318	CsI_4	225	2.55	5.8	250	7.19	Energy output 3.62 mw-hr.
1	0.318	CsI_4	265	0.60	11.0	55	3.76	Operated also at 520°C.
5	0.318	CsI_3	250	3.25	6.0	540	0.85	Failure caused by bad contact.
4	0.318	I_2O_5	250	2.75	7.0	130	6.45	
1	0.318	BiI_3	308	0.59	3.0	200	3.22	Temperature may have been slightly too low for BiI_3 the source of iodine.
1	0.318	CHI_3	287	0.63	2.2	320	0.31	
1	0.318	CI_4	170	0.68	6.0	120	10.1	Energy output 1.03 mw-hr.
1	0.318	CI_4	180	0.655	2.4	270	11.2	Energy output 1.43 mw-hr.

Table V. Performance of AgI cells with Cu_2I_2 plus oxidizing agent as iodine sources

Oxidizing agent	Temp. of operation, °C	Open-cell voltage, v	Short-circuit current, ma	Internal resistance, ohms	Capacity, ma-hr	Notes
Air	450	0.95	~34	28	8.58	Two cells in series.
Air	422	0.45	~12	35	5.23	
$KMnO_4$	450	0.60	3.0	120	2.6	
$KMnO_4$	330	0.56	1.2	625	5.5	
$KMnO_4$	450	0.45	—	—	0.53	
KIO_3*	258	0.55	~2.5	200	14.43	Energy output, 2.32 mw-hr.
KIO_3	287 and 360	0.66	>10	11	5.22	1.56 mw-hr. At 360°C obtained capacity of 4.80 ma-hr compared to 0.42 ma-hr at 287°C.
KIO_3	275	0.655	1.2	1320	7.78	Consumed 78% of total iodine present in Cu_2I_2.

* See Fig. 7.

of a cell with small outside diameter across 10-kΩ load. Figure 7 gives the performance of a larger cell. The minimum near the beginning of this discharge curve can be attributed to the relatively low temperature of operation (258°C) for the $KIO_3 + Cu_2I_2$ cathode mix of this cell. The minimum is not a characteristic of the cathode mix or the cell. In other cases, the current terminated abruptly, which indicated that all of the silver anode had been used up.

Comparison of cell performance with thermobalance experiments.—The cells could be operated in definite temperature ranges which were somewhat lower than the temperature of decomposition of the iodine donor obtained from thermobalance curves. This can be explained by the temperature lag between the recording thermocouple and the sample, which would give slightly higher temperature readings in the thermolyses. Also, in the decomposition mechanism an equilibrium or steady-state reaction occurs at constant temperature at which the iodine donor decomposes. The equilibrium may be displaced toward lower temperatures if iodine is removed constantly by the cell reaction.

Thermoactivation current and emf.—By employing a technique similar to that of the thermobalance one can use the solid electrolyte cell as a halogen detector. The cell output is recorded while the temperature is increased in the same manner as the weight is recorded with the thermobalance. This is shown for a cell with CsI_4 in Fig. 8. It is seen that the current rose rapidly starting at about 246°C from 0.3 to 2.9 ma, the steady-state value for this cell at 200 Ω load. Similar curves were obtained for cells with other iodine donors.

Comparison of cell performance with phase diagram of the system CsI-I_2.—On the basis of the phase diagram, it was predicted that a cell with CsI_4 as iodine source should be operable at 190°-245°C, with full activation at the higher temperature. This observation has been confirmed by the thermoactivation current illustrated in Fig. 8. The fact that full current output was not obtained until 257°C was reached can again be explained, as above, by the temperature lag between the recording thermocouple and the cell. It is the temperature at which the increase of current begins that is characteristic of full activation. Below 190°C a current of 0.3 ma is also appreciable for a Ta-tube cell, but the increase in current demonstrated the decomposition of the iodine source. Thus, there is qualitative agreement of cell performance and its prediction from the phase diagram of the open system. The correlation must not, however, be pushed too far, because in the cell we deal with a closed system.

To evaluate different iodine donors, a series of cells was chosen for initial room temperature similarity in structure (0.318 cm OD Ta-tube cells) and internal room temperature impedance (280-500 kΩ). The cells were filled with different iodine sources, namely, iodine, CsI_4, CsI_3, and the mixture of 4 mole CsI_3 + 1 mole CsI, which was discussed previously. The polarization of the cells then was measured at increasing temperatures. Specific values obtained

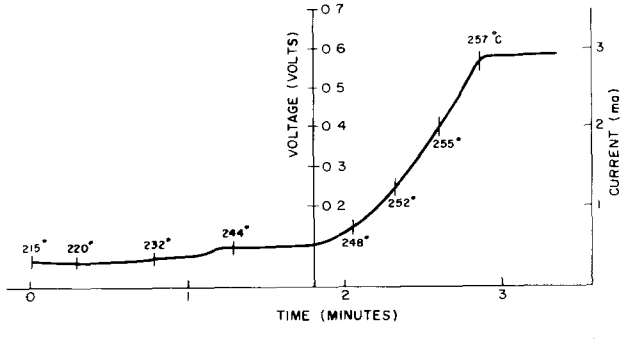

Fig. 8. Thermal activation of a Ta-tube cell, iodine source: CsI_4. Cell on 200 Ω load.

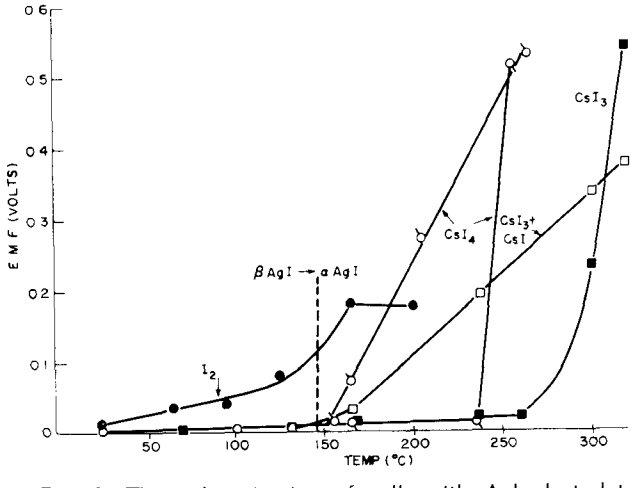

Fig. 9. Thermal activation of cells with AgI electrolyte (emf at 25 kΩ load).

with an external load of 25 kΩ are shown in Fig. 9. Where iodine crystals were the source of iodine vapor the cell responded even below the transformation temperature and broke down at 200°C. This is to be expected because iodine has a boiling point of 188°C. The cell with CsI_3 was not activated fully until 320°C was reached. Two cells with CsI_4 behaved differently; one was activated slowly over the temperature range 155° to 245°C, and the other one attained full output abruptly between 235° and 255°C. Finally, the mixture of $4CsI_3 + CsI$ also was activated slowly from 150°C up and had not reached full activation at 320°C. Despite the discrepancy in the two CsI_4 runs, these curves qualitatively agree with the interpretation of the phase diagram.

Acknowledgments

The author is indebted to D. L. Douglas, W. T. Grubb, A. E. Newkirk, and E. L. Simons for very helpful discussions. Miss I. Aliferis performed the thermolyses, and P. R. Schmidt assisted in the preparation of cells. The x-ray analysis of CsI_4 was performed by the metallography group of the Research Laboratory.

Manuscript received June 25, 1958. This paper was prepared for delivery before the Ottawa Meeting, Sept. 28-Oct. 2, 1958.

Any discussion of this paper will appear in a Discussion Section to be published in the December 1959 JOURNAL.

REFERENCES

1. J. L. Weininger, *This Journal*, **105**, 439 (1958).
2. C. Tubandt and F. Lorenz, *Z. physik. Chem.*, **87**, 513 (1914); K. H. Lieser, *Z. physik. Chem., (n.F.)*, **9**, 302 (1956).
3. T. R. Briggs, J. A. Greenawald, and J. W. Leonard, *J. Phys. Chem.*, **34**, 1951 (1930).
4. T. R. Briggs, *ibid.*, **34**, 2260 (1930).
5. J. D. Hanawalt, H. W. Rim, and L. K. Frevel, *Ind. Eng. Chem., Anal. Ed.*, **10**, 457 (1938).
6. J. R. Partington, "Textbook of Inorganic Chemistry," 5th ed., p. 364, Macmillan and Co., New York (1939).
7. G. B. Kolhatkar and V. A. Sant, *J. Univ. Bombay*, **11**, Pt. 3, 96 (1942); *C.A.*, 37:3325[5].

Studies of the Structure of Anodic Oxide Films on Aluminum, I

D. J. Stirland and R. W. Bicknell

Caswell Research Laboratories, Towcester, Northants, England

ABSTRACT

The influence of the formation voltage on the structure of nonporous anodic aluminum oxide films has been studied by electron microscope and electron diffraction methods. It has been shown that low formation voltages (<100 v) produce an amorphous oxide layer, whereas high formation voltages produce amorphous oxide together with some crystalline γ'-alumina. The location of this crystalline oxide within the anodic layer is discussed.

In general the so-called direct methods for examination of thin films (such as optical and electron microscopy, x-ray and electron diffraction) can provide information regarding the "structure of the films," but it is necessary to define carefully what is meant by this phrase. Conventional microscopical methods can show details of the topography of both surfaces of the film and, providing the film is sufficiently transparent either to light or to electrons, may also reveal bulk physical features within the film. Diffraction methods can be used to determine the crystallographic structure either of a thin surface layer of the film or of the bulk material. These methods thus give two structural parameters, the physical and the crystallographic.

A number of workers (1-5) have investigated these parameters in the case of films formed on aluminum by electrolytic oxidation and have shown that anodic aluminum oxide films can be divided into two classes, determined by the solvent action of the forming electrolyte on the oxide. Electrolytes which dissolve the oxide produce porous coatings whose thickness depends primarily on both formation current and time, whereas electrolytes which do not attack the oxide appreciably produce thin nonporous coatings, whose thickness depends mainly on formation voltage. Although the electrical properties of nonporous films have led to a wide application in the industrial field of electrolytic capacitors, most fundamental investigations of the structure of anodic coatings have dealt with the porous types of oxide only.

This paper presents and discusses the results of electron microscope and electron diffraction studies on both the physical and crystallographic structures of nonporous anodic oxide coatings.

Methods of Examination of Anodic Films

A systematic x-ray investigation of the crystallographic structure of anodic coatings has been made by Taylor, *et al.* (6). Oxide films were formed on 99.8% pure aluminum foil in a variety of electrolytes (giving both porous and nonporous coatings) under differing conditions of temperature and formation voltage. X-ray examination of the oxide films showed that some crystalline alumina was obtained in all cases where the formation voltage exceeded 100 v, and that the amount of crystalline oxide increased with increase in formation voltage. This was determined by comparing the relative intensities of the x-ray diffraction lines given by each specimen.

Taylor, *et al.* do not discuss the significance of the x-ray pattern in detail and, as Burwell (7) has

pointed out, the excessive line broadening of the pattern does not permit conclusive identification of the crystallographic structure of the oxide. We have found that in general only two lines are clear enough for measurement, and these are very broad. A typical x-ray diffraction pattern obtained from an anodic film formed at 525 v on 99.99% pure aluminum (see next section for preparative details) shows two such broad reflections which have d-spacings of 1.97 and 1.39Å. If the observed line broadening is due to the small crystallite size of the alumina, then it might be expected that the smaller equivalent wave length of an electron beam (as compared with an x-ray beam) would give a sharper diffraction pattern suitable for a complete identification of the structure, but it is found that the specimen is then too thick to give any transmission electron diffraction pattern at all. In fact, using a diffraction camera operating at a beam voltage of 50 kv, the practical upper limit to the specimen thickness will be ~400Å, and since for nonporous anodic films the thickness formation voltage ratio is almost constant at ~14Å/v (8), this limits the maximum permissible anodic formation voltage to ~30 v.

However, it is possible to examine higher voltage films in the electron diffraction camera if their thickness can be reduced by some suitable method. It was found that a phosphoric-chromic acid mixture, previously used (9) to dissolve anodic films from aluminum, would also serve to thin down the thick coatings to an appropriate thickness for transmission diffraction. Thus films formed over a wide range of voltages could be examined. Furthermore, these thinned specimens were also suitable for electron microscope examination, providing a direct method of observing the stripping action of the acid mixture on the anodic coatings.

Experimental Details

Aluminum foil of 99.99% purity was used for all the experiments, and in each case the specimens were cleaned prior to anodization by a 3-min immersion in a 3% NaOH solution. They then were washed thoroughly in distilled water and dried in a warm air stream. The anodizing electrolyte consisted of a 3% boric acid-0.05% borax aqueous solution used at 20°C. All specimens were anodized at constant voltage for a set period of 5 min. The acid mixture used to thin down the anodic coatings consisted of 35 cc of 85% phosphoric acid and 20 g of chromic acid per liter of solution used at 80°C.

The investigation was carried out in two parts. (*a*) *Action of the acid mixture.*—Specimens were anodized at 500 v, 20°C, and then immersed for 1, 3, 10, and 20 min, respectively, in the acid mixture. Then they were washed thoroughly and re-anodized at 10 v. One reason for this second anodization was to provide a thin (~150Å) supporting film to hold in position fragments of the original anodic coating which had survived the acid treatment. This 10-v film only formed on the aluminum surfaces exposed by the dissolution of the original coating. Examination of specimens in the electron microscope showed that the second anodization was unnecessary for the lightly attacked films, but the same procedure was adopted for all specimens in order to standardize conditions. The composite film was stripped in small squares from the aluminum by the usual mercuric chloride method (10), washed, and picked up on electron microscope specimen grids for subsequent examination.

(*b*) *Effect of differing formation voltages on the structure of the oxide.*—Specimens were anodized over a range of voltages between 12 v and 500 v at 20°C. They then were immersed in the acid mixture for various times, sufficient in each case to reduce the oxide thickness to less than ~400Å. For example, specimens anodized at 12 and 25 v did not need to be treated at all, the 200-v specimen was immersed for 2 min, and the 500-v specimen for 5 min. The treated specimens were then re-anodized at 10 v and oxide squares prepared for examination as before.

Besides providing a coherent supporting membrane for the remaining parts of the original anodic film, the 10-v oxide film also acted as a normal oxide replica (10) of the exposed parts of the underlying aluminum surface. Thus it was possible to examine, on the same specimen, both the partially dissolved original anodic coating together with an oxide replica of the metal surface from which the coating had been dissolved completely. Since this aluminum had been exposed to the acid mixture, however, it was necessary to investigate whether any reaction had occurred.

A cleaned sheet of aluminum foil was placed in the acid bath for 20 min, and then oxide replicas of its surface were prepared and examined. These showed that the only observable effect of the acid mixture was to produce a small number of easily identifiable etch pits (dimensions ~0.05μ) in the aluminum surface. Since the size of these pits was considerably smaller than that of the surface detail which was being studied, and since the 20-min acid attack was the maximum period employed during the dissolution of the anodic films, it was considered that the effects of the reaction between the acids and the aluminum could be ignored.

Finally, it was found that all the low voltage anodic films (<100 v) dissolved quickly and completely in the acid mixture. For example, squares of oxide removed from foil anodized at 25 v dissolved completely in ~1 min.

Interpretation of Results

Figures 1-7 show typical areas of the anodic layers after different times of immersion in the acid mixture. Figures 1 and 2 demonstrate at once the nonuniformity of the acid attack, which has dissolved the oxide preferentially in cylindrical pores. With a longer attack the pores increase in size and number, and the less soluble parts eventually become thin enough to enable some fine structure to be visible in them (Fig. 3-5, with finely structured areas arrowed on Fig. 4). Figures 6 and 7 show areas in which the high voltage oxide has been dissolved almost completely, and therefore consist mainly of 10-v oxide replicas of the surface beneath the original anodic layer. Micrographs of oxide replicas do not differentiate between identically shaped raised or depressed features, but by metal-shadowing (11) it

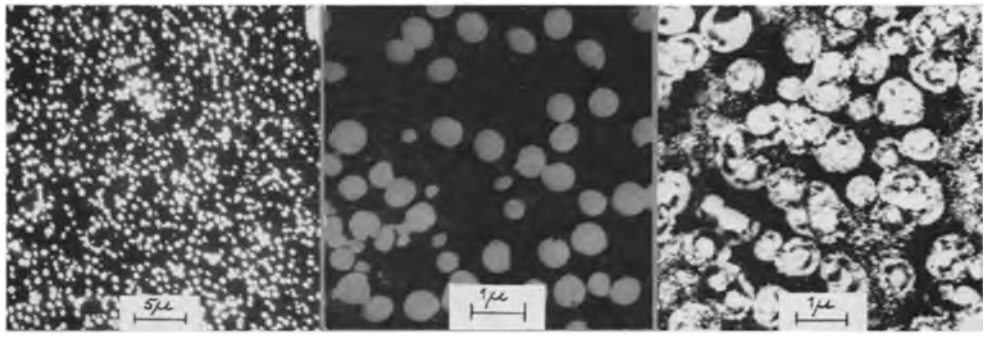

Fig. 1 (left) Fig. 2 (center). Transmission electron micrographs of 500 v anodic oxide film after 3 min in acid mixture. Fig. 3 (right). Transmission electron micrograph of 400 v anodic oxide film after 5 min in acid mixture.

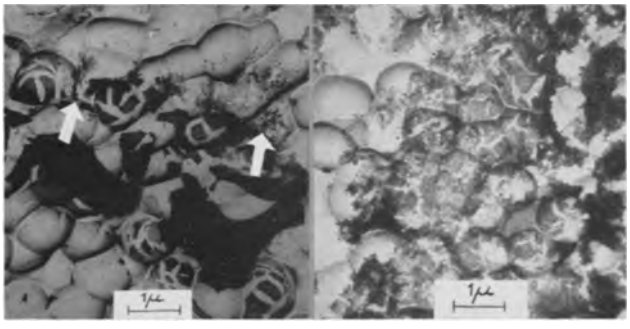

Fig. 4 (left) and Fig. 5 (right). Transmission electron micrographs of 500 v film after 10 min in acid mixture, together with replica of exposed aluminum surface.

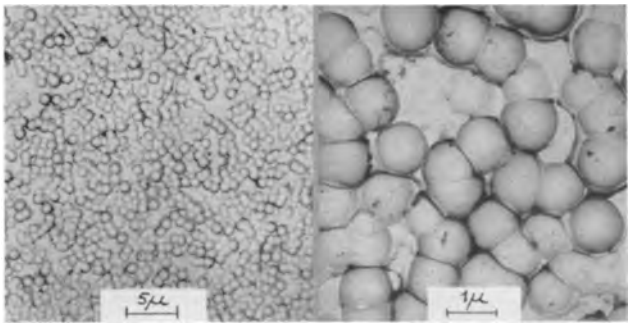

Fig. 6 (left). Cell-base structure beneath a 500 v anodic oxide film, exposed after 20 min in acid mixture. Fig. 7 (right). Transmission electron micrographs of 10 v oxide replica.

has been shown that the features on Fig. 6 and 7 represent shallow craters in the aluminum surfaces.

Electron diffraction examination of specimens containing the areas shown in Fig. 3-5 gave the sharp ring pattern of Fig. 8. Table I gives the indexed reflections, together with their estimated relative intensities, for this pattern. It agrees very closely with x-ray diffraction results obtained by Verwey (12) from anodic aluminum oxides. He identified the material as a face-centered cubic structure of cell-size $a_o = 3.96$Å, and called the oxide γ'-alumina. This is not to be confused with the aluminum oxide which can be prepared by the thermal decomposition of alumina hydrates and has a deficient spinel structure ($a_o = 7.89$Å). In the English nomenclature this oxide is called γ-alumina (13); in American literature it is known as η-alumina (14). Both γ'-alumina and γ (or η)-alumina have in their diffraction spectra two strong lines with d-spacings of 1.97 and 1.39Å; in the case of γ'-alumina these are from (200) and (220) reflections, and in the case of γ (or η)-alumina they are from (400) and (440) reflections. These two may be the only lines capable of measurement on an x-ray pattern, and thus the identification of the oxide structure is not certain. However, the sharp electron diffraction pattern conclusively identified the crystalline oxide as γ'-alumina.

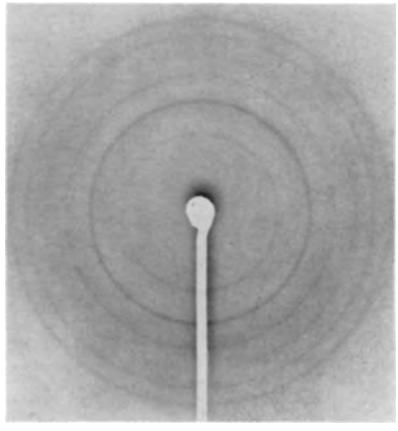

Fig. 8. Electron diffraction pattern from finely structured material present in high voltage anodic oxide films.

Exactly the same diffraction pattern was obtained from all the anodic films formed at voltages greater than 100 v, thus confirming the results of Taylor, *et al.* (6). Films formed below 100 v gave patterns consisting of two broad diffuse rings, typical of those obtained from amorphous materials. Amorphous in this sense is defined as a structure whose crystallite size is less than ~10Å. Electron micrographs of these films appeared to be normal oxide replicas, showing surface detail which could be correlated with that observed by optical examination of the unformed aluminum specimens.

Location of the Crystalline Oxide within the Anodic Layer

It was possible to deduce theoretically and confirm experimentally that the finely structured areas shown in Fig. 3-5 could be identified with the crystalline γ'-alumina. On each micrograph three types of area can be seen; black areas, light gray areas, and the finely structured areas. The black areas cannot give a diffraction pattern since they represent partially dissolved oxide which is still too thick to be penetrated by the electron beam. The light gray areas cannot give a ring pattern because they con-

Table I. Comparison of diffraction spectra of γ'- and γ-alumina

Measured spacings and estimated intensities from Fig. 8		Indexed spacings and intensities of γ'-alumina, according to Verwey (12)			Indexed spacings and intensities of γ-alumina, according to Rooksby (13)		
d_{hkl} (Å)	Intensity	(hkl)	d_{hkl} (Å)	Intensity	d_{hkl} (Å)	Intensity	(hkl)
					4.55	MF	(111)
					2.79	F	(220)
					2.381	MS	(311)
2.287	VVF	(111)	2.281	F	2.271	M	(222)
1.980	S	(200)	1.975	VS	1.973	VS	(400)
					1.517	F	(511)
1.399	VS	(220)	1.397	VS	1.392	VS	(440)
1.193	VF	(311)	Not observed				
1.143	M	(222)	1.140	M	1.138	F	(444)
					1.025	VF	(731)
0.990	F	(400)	0.988	MS	0.987	VF	(800)
Not observed		(331)	Not observed				
0.885	M	(420)	0.883	MS	0.882	VF	(840)
0.805	S	(422)	0.806	S	0.804	F	(844)

sist of the 10-v amorphous film. Hence the remaining areas must be responsible for the γ'-alumina diffraction pattern.

Experimentally this was confirmed by the "selected area diffraction technique." A variable aperture in the electron microscope was adjusted so that only a restricted area of the specimen was visible, and the diffraction pattern from this area was then obtained. On scanning the specimen it was found that the thin film replica areas gave two broad diffuse rings, and the black areas gave no transmission pattern at all. Only the finely structured gray areas produced the γ'-alumina pattern, and hence they indicate the disposition of the γ'-alumina within the anodic layer. These areas are most probably agglomerates of crystallized alumina.

Discussion

The first conclusion which can be drawn from a study of the micrographs is that a short attack by the phosphoric-chromic acid mixture does not dissolve the high voltage anodic coatings uniformly. Instead, a selective dissolution of thin cylindrical columns of material takes place. It was found by examination of the lightly attacked oxide specimens before they had been anodized to give the 10-v replica support film that, in fact, no material was present within the columns after a 3-min immersion in the acid mixture. This means that there is a variation in solubility of the anodic coatings, which in turn implies a variation in their composition. It has been mentioned previously that all the low voltage (that is, amorphous) films dissolved quickly and completely in the acid mixture, and so it is reasonable to propose that the very soluble part of the film consists of amorphous oxide.

Altenpohl (15) used a weighing method to study the action of the phosphoric-chromic acid mixture on nonporous anodic films formed in hot aqueous boric acid electrolytes. From the experimental results he suggested that these anodic films consisted of at least two different types of oxide; an outer layer readily soluble in the acid mixture, and an insoluble layer beneath this. He also found that the relative proportion of insoluble oxide increased with increase of formation voltage. Since the results described in the present paper are not strictly comparable with those obtained by Altenpohl because of the difference in electrolyte temperatures, some preliminary experiments using the boric acid-borax forming electrolyte at 100°C may be mentioned. These showed that 500-v anodic coatings could not be thinned down sufficiently to give any transmission diffraction pattern, even after 30 min in the acid mixture, although in every case of formation at 20°C it was possible to dissolve the oxide completely.

The results obtained with electrolyte at 100°C agree with Altenpohl's observations, but with electrolyte at 20°C it has been shown that all the oxide is removed from the metal. It is not certain whether this is because the cold formation oxide eventually is dissolved completely, or whether dissolution of part of the anodic layer (i.e., the amorphous oxide columns) weakens the adherence of the remainder. Figure 4 suggests that the latter explanation may hold in some cases, since the black fragments on this micrograph have been unattacked during the dissolution of the rest of the film, and yet a further treatment in the acid mixture would result in a film free surface (e.g., Fig. 6 and 7). It is difficult to imagine that these unattacked fragments dissolve completely during the second treatment, if they have already resisted the initial attack, and it seems more likely that they eventually become detached by a weakening of their adherence to the aluminum. The micrographs do demonstrate, however, that the distribution of readily soluble oxide and insoluble (or slowly soluble) oxide is very much more complex than the simple double layer arrangement proposed by Altenpohl.

The electron micrographs also provide information regarding the physical structure of the anodic films. At any instant during its formation the anodic layer is in intimate contact with the aluminum surface beneath it, and so the aluminum must reproduce every topographical detail of the oxide surface. Hence, replicas of the aluminum surface are also replicas of the oxide surface at the metal-oxide interface. This provided Keller, *et al.* (9) with a method of examining the oxide surface of porous anodic coatings, and by using low formation voltages they were also able to examine the stripped films in transmission. From these observations they derived a structure for the porous anodic films. The

Table II. Comparison of cell-sizes for porous and nonporous oxide films formed at 500 v

Forming electrolyte	Forming temp, °C	Cell size at 500 v in μ	Type of oxide
15% Sulfuric acid*	10	0.83	Porous
2% Oxalic acid*	24	0.98	Porous
4% Phosphoric acid*	24	1.03	Porous
3% Chromic acid*	38	1.04	Porous
3% Boric acid, 0.05% borax	20	0.96 ± 0.12	Nonporous

* Data obtained from ref. 9.

basis of this derivation was that the oxide contained a uniformly spaced array of tiny pores surrounded by close-packed hexagonal columns of oxide. These oxide cells had bases with the shape of a spherical section somewhat less than a hemisphere. Measurements of the pore spacings showed that they corresponded with the cell sizes (spacing between cell-base centers) measured from replicas of the aluminum surfaces beneath the coatings. Since the essential feature giving rise to this structure was assumed to be the existence of pores through the anodic films, it is surprising to find that micrographs of the metal-oxide interface of nonporous anodic films (Fig. 6 and 7) are almost identical in appearance with those shown by Keller, *et al.* for the same interface of porous anodic films (Fig. 8 of ref. 9, p. 415). Furthermore, it was possible to show that the similarity between the two structures is also quantitative.

Keller, *et al.* used four different electrolytes, all producing porous films. They found that over a voltage range of 20-120 v a linear relationship existed between cell size and formation voltage. By assuming that this linear relationship continued for higher voltages and by making a large extrapolation, the cell sizes which might be expected for a 500-v formation in each of the four electrolytes could be calculated. These values, compared with the cell size measured directly from micrographs of the 500-v nonporous formation, are shown in Table II.

This remarkably close agreement between the cell-base sizes for both porous and nonporous oxides is indicative of a similarity in physical structure. Franklin (16) has described some aspects of anodic oxidation and suggested that, since nonporous oxide films have a pronounced cell-type of structure, similar growth processes may occur for both types of oxide.

Conclusions

It has been shown that anodic oxide films formed in a boric acid-borax electrolyte contain some crystalline γ'-alumina provided that they are formed at voltages in excess of 100 v; otherwise they consist entirely of an amorphous oxide. The amorphous oxide dissolves more readily in a phosphoric-chromic acid mixture than does the crystalline oxide, and it appears to be present in cylindrical columns penetrating right through the anodic coating. Finally, the nonporous oxide structure is found to be similar in some ways to a structure previously proposed for porous anodic films.

Acknowledgments

It is a pleasure to acknowledge the helpful advice and assistance given to the authors by Mr. R. W. Franklin. They also wish to thank the Plessey Co. Ltd. for permission to publish this work.

Manuscript received Feb. 3, 1958. This paper was prepared for delivery before the Ottawa Meeting, Sept. 28-Oct. 2, 1958.

Any discussion of this paper will appear in a Discussion Section to be published in the December 1959 JOURNAL.

REFERENCES

1. W. G. Burgers, A. Claasen, and J. Zernicke, *Z. Physik.*, **74**, 593 (1932).
2. F. Keller, *Am. Soc. Testing Materials*, **40**, 948 (1940).
3. R. A. Harrington and H. R. Nelson, *Trans. Amer. Inst. Mining Met. Engrs.*, **137**, 62 (1940).
4. E. Brandenberger and R. J. Hafeli, *Helv. Chim. Acta.*, **31**, 1168 (1948).
5. C. J. L. Booker, J. L. Wood, and A. Walsh, *Brit. J. App. Phys.*, **8**, 347 (1957).
6. C. S. Taylor, C. M. Tucker, and J. D. Edwards, *Trans. Electrochem. Soc.*, **88**, 225 (1943).
7. R. L. Burwell, *ibid.*, **88**, 332 (1943).
8. P. D. Lomer, *Proc. Phys. Soc.*, **638**, 818 (1950).
9. F. Keller, M. S. Hunter, and D. L. Robinson, *This Journal*, **100**, 411 (1953).
10. H. Mahl, *Metallwirtschaft*, **19**, 1082 (1940).
11. R. C. Williams and R. W. C. Wyckoff, *J. Appl. Phys.*, **15**, 712 (1944).
12. E. J. W. Verwey, *Z. Krist*, **91**, 317 (1935).
13. H. P. Rooksby, "The X-ray Identification and Structure of Clay Minerals," p. 250, Mineralogical Society, London (1957).
14. H. C. Stumpf, A. S. Russell, J. W. Newsome, and C. M. Tucker, *Ind. Eng. Chem.*, **42**, 1398 (1950).
15. D. Altenpohl, Convention record of I.R.E. Part III, 35 (1954).
16. R. W. Franklin, *Nature*, **180**, 1470 (1957).

Aqueous Uranium Corrosion at 100°C

J. B. Schroeder,[1] D. A. Vaughan, and C. M. Schwartz

Battelle Memorial Institute, Columbus, Ohio

ABSTRACT

The mechanism of aqueous uranium corrosion has been studied using weight loss and hydrogen evolution measurements. Microscopic x-ray diffraction and chemical analyses were made of the corrosion product. The results indicate that uranium corrodes by forming an oxide of the type UO_{2+x}. The lack of chemical balance reported by earlier workers is explained by the existence of metallic uranium in the oxide layer.

Many of the atomic reactors in existence today use a metallic, natural uranium fuel which is cooled with either heavy or light water. The design of some fuel elements is discussed by Gurinsky and Dienes (1) in their review of the first Geneva conference on atomic energy. All of these designs overcome the high corrosion rate of uranium by providing some protective container to prevent the coolant from coming in direct contact with the uranium fuel. The fabrication of reactor fuel elements would be greatly simplified and the potential hazard of contamination resulting from a cladding failure reduced if a corrosion-resistant uranium alloy were available. This study was undertaken to provide information about the mechanism of the aqueous corrosion of alpha uranium to aid in the development of corrosion-resistant alloys.

Previous work on the corrosion of uranium has been summarized in the Reactor Handbook (2) and by Gurinsky and Dienes (1). The early work showed that the uranium corrosion rate below 100°C was lower for oxygen-saturated water than for hydrogen-saturated water. In aerated water, uranium corroded slowly at first and then assumed the higher linear rate for hydrogen-saturated water. The mechanism proposed to account for these observations was that the oxide formed in water containing oxygen was self-healing and, therefore, protective. When the dissolved oxygen was depleted from the water, uranium hydride was believed to form beneath the oxide and break the oxide film. Hydride was identified on samples corroded in steam and water in the temperature range between 150° and 180°C. The formation of UH_3 also was considered necessary in order to account for the small quantity of hydrogen liberated during corrosion.

In the work reported here no evidence was found of either form of UH_3. The observations are explained on the basis of metallic uranium being present in the corrosion produced oxide.

Experimental

The samples were rectangular coupons (½ x ½ x ⅛ in.) of selected, center-cut ingot.[2] Before fabricating into samples the uranium was reduced 50% by rolling in the high alpha region.

Preliminary tests showed that the corrosion rate of uranium in water at 100°C was linear and varied between 2.70 and 3.50 mg/cm²/hr, with an average value of 3.28. Three methods of surface preparation were investigated: electropolishing,[3] abrading through 600 grit paper, and abrading followed by a HNO_3 pickle. Corrosion rates were independent of the method of surface preparation. After this preliminary work all of the samples were electropolished, rinsed in distilled water and alcohol, and tested in boiled, deionized water.

Rate measurements.—Weight loss measurements were made by weighing the sample prior to testing and again after the corrosion-produced oxide had been removed by pickling in concentrated HNO_3. The final weight was corrected for the amount of uranium lost in the pickling step by repeating the pickling step, which was usually of 45-sec duration, and reweighing. The weight lost during the second pickling was added to the final weight in order to calculate the corrosion rate. The average corrosion rate was found to be 3.28 mg/cm²/hr by this method.

Hydrogen evolution during corrosion was measured by bubbling tank argon through the corrodant and drying the gas stream in a $Mg(ClO_4)_2$ train, converting the H_2 to water by passing it through hot CuO, and measuring the weight gain in a $Mg(ClO_4)_2$ absorption tube. The system was flushed until a constant weight was obtained for the absorption tube both before and after the test. The average amount of hydrogen evolved during four 24-hr and four 8-hr tests was 91.5 ± 1.2% of the amount calculated from the weight loss using Eq. [1].

$$U + 2H_2O \rightarrow UO_2 + 2H_2 \qquad [1]$$

Analysis of the Corrosion Product

Microscopic examination.—The oxide produced during corrosion was not adherent after the first few minutes at temperature. Figure 1 is a photomicrograph of the oxide layer after a 24-hr test. Metallographic examination of the metal-oxide interface did reveal some hydride; however, no more hydride was present at the interface after corrosion than was observed in the interior of the sample both

[1] Present address: Ohio Semiconductors, Inc., Columbus, Ohio.
[2] Supplied by Mallinckrodt Chemical Works.
[3] The electropolishing bath was 40% H_2SO_4, 40% H_2O, 10% H_3PO_4, and 10% C_2H_5OH. The open-circuit voltage was 10 v. A more uniform polish was obtained when the bath temperature was maintained below 15°C.

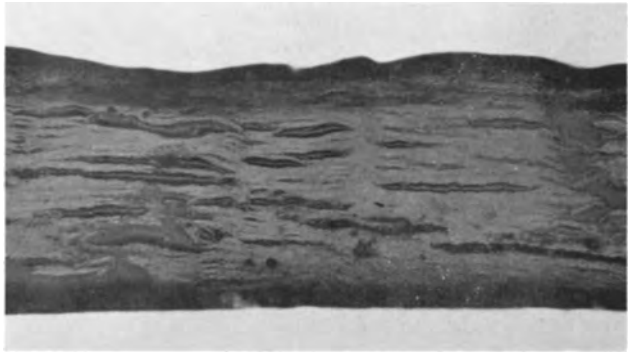

Fig. 1. Oxide layer formed on uranium metal during a 24-hr corrosion test at 100°C.

before and after testing. Vacuum-fusion analysis also failed to detect any increase in the hydrogen content of the metal as corrosion progressed.

X-ray diffraction.—Using copper radiation, diffractometer traces were obtained of the wet sample surfaces after various times during the corrosion tests. These showed alpha uranium and UO_2. After the oxide had grown to such a thickness that it was no longer possible to obtain the diffraction pattern of the metal, the oxide was removed by directing a stream of alcohol or water against the surface. Using this treatment it was possible to remove enough of the oxide to make the metal the most intense phase in the pattern. A hydride phase was not detected.

In both the diffractometer traces and Debye-Scherrer patterns the corrosion produced oxide gave very broad lines, due to extremely small particle size. For this reason it was not possible to obtain accurate lattice parameters of the oxide.

When the corrosion product was reacted with dilute HNO_3 (5%) the UO_2 was attacked preferentially leaving feather shaped particles. These particles were identified by x-ray diffraction as being metallic uranium.

After metallic uranium was detected in the corrosion product, tests were performed which showed that both the metal and the beta hydride could withstand the dilute HNO_3 cleaning and would probably be detected, if present in the corrosion product. Samples which showed no oxide were oxidized to such an extent that only oxide could be seen in the diffraction pattern. This "oxide" was then treated with dilute HNO_3 and the residue examined by x-ray diffraction. The patterns showed a mixture of UO_2 and either the metal or UH_3, depending on the starting material.

Oxygen-to-uranium ratio.—Uranium dioxide, prepared by the hydrogen reduction of higher oxides, is frequently unstable, resorbing oxygen (3-5). This was found to be the case with the corrosion product when it was vacuum dried. The apparent oxygen-to-uranium ratio of the air-dried corrosion product was found by ignition to be 2.40.

The oxygen-to-uranium ratio of oxide samples generally is determined by measuring the weight gain when the sample is ignited to U_3O_8 by heating it in air to 750°C and holding it at that temperature for 15 min. This type of analysis cannot distinguish between oxygen, hydroxyl, or water. Therefore, the valence of the uranium is not necessarily twice the oxygen-to-uranium ratio.

Because of the instability of the dry corrosion product, wet samples were loaded into a controlled atmosphere, differential thermal balance. They were dried overnight in vacuum (5×10^{-5} mm Hg), weighed, heated to constant weight at 750°C, and then ignited to U_3O_8. Three samples lost 3.2, 1.6, and 4.2% of their weight during the drying operation and were found to have oxygen-to-uranium ratios of 2.19, 2.24, and 2.19, respectively. A sample of commercial oxide was placed in a simulated corrosion test and then run through the differential thermal analysis. It was found to lose 0.3% of its weight during the drying cycle and have an oxygen-to-uranium ratio of 2.04, which is in excellent agreement with other measurements.

Mean valence.—The mean valence of the uranium in the corrosion product was determined by a modification of an analytical method developed by Melton (6). It consists of dissolving the sample in a solution of $AgNO_3$ and NH_4F, 1*N* with respect to each. The silver ion acts as an oxidizing agent and produces hexavalent uranium and a precipitate of free silver. The silver is filtered off, dissolved, and measured gravimetrically as silver chloride, and the uranium content determined by a weight-volumetric method employing ceric sulfate.

The mean valence of uranium in the corrosion product was found to be 3.70, which is in good agreement with the hydrogen-evolution experiments. However, when the loose corrosion product was allowed to drop into a cool zone (approximately 25°C), rather than remain in the proximity of the metal, the mean valence was found to be 3.16. A sample of the corrosion product which remained in the boiling solution 24 hr after the metallic sample had been removed gave a mean valence of 3.87.

In order to obtain independent data on uranium valence the x-ray absorption spectrum of the bulk corrosion product was compared with that of UO_2 and UO_3. Spectrometer data were obtained over the range of x-ray wave lengths extending above and below the L_{III} absorption edge of uranium. The powders were briquetted in absorption cells of about the same x-ray density. The corrosion samples were coated with water soluble resin before drying in an attempt to minimize air oxidation. The curve of intensity vs. wave length in the region of the absorption edge was analyzed for maximum, minimum, and point of inflection. The results for the three materials are given in Table I. By each criterion char-

Table I. Characteristic points on the L_{III} x-ray absorption edge of uranium for uranium dioxide, uranium trioxide, and uranium corrosion product

Sample	Maximum absorption, A	Inflection point, A	Minimum absorption, A
UO_2	0.7267_9	0.7226_1	0.7184_1
Corrosion product	0.7263_4	0.7223_2	0.7183_1
UO_3	0.7263_1	0.7222_7	0.7182_4

Note: The absorption-edge wave length was calculated on the basis of a LiF analyzing crystal with an assumed 2d spacing of 4.0275Å.

acteristic values for the corrosion product are intermediate between those of UO_2 and UO_3. These results tend to verify the oxygen-to-uranium ratio measurements and to indicate that the oxide phase should not be considered as stoichiometric UO_2, as written in Eq. [1], but that the valence state of the uranium is somewhat greater than 4.

Solubles.—Samples of the corrodant were filtered and analyzed for solubles. The uranium content of the solid obtained by evaporating the filtered corrodant to dryness was 16%. Spectrographic analysis showed that the major constituents were calcium, magnesium, and chromium. All of these elements were present in the original metal.

The uranium content of the corroding water was measured as a function of time during tests carried out at 60°C. After 50 days the uranium concentration attained a value of 5×10^{-5} mole/l. This is an order of magnitude higher than the solubility data reported (7) for $U(OH)_4$ and is probably due to the formation of complexes. This was considered to be unimportant in the over-all mechanism because samples tested in water containing the dissolved uranium exhibited the same corrosion rates as those run in fresh water.

Effect of Surface Treatments

Oxide films.—Metal samples were heated in low oxygen pressures to form coherent oxide films prior to corrosion testing for study of the protective properties of uranium oxide. Table II presents the results of short term corrosion tests and the heat treatment employed. These data show that the protection of these films increases as the temperature of film formation is increased to 650°C. When the oxide film was removed by electropolishing, the corrosion rate was the same as that for unannealed samples. This demonstrates that the increased corrosion resistance was due to a surface effect and not a bulk effect. When the films were formed at temperatures above the alpha-beta transformation (663°C), deep cracks appeared in the metal, producing discontinuities in the oxide film. All of the samples heated above the alpha-beta transformation corroded at the same rate as untreated samples. Figure 2 shows the results of longer tests on oxide-coated samples. All of the samples used in this test were held for 2 hr at 650°C in an oxygen atmosphere at a pressure of 5×10^{-4} mm Hg. Oxide films were put on only two samples at a time in order to keep them well separated in the furnace. The samples that were coated together are enclosed by one circle in Fig. 2. The spread observed is probably due to minor uncontrolled variations in the conditions used in forming the films. The oxide films failed after approximately 20 hr by developing a few small pits and undercutting. No inclusions were detected at the site of the original failure. X-ray diffraction patterns of the material formed in these pits showed that no hydride was present. Line broadening of the x-ray diffraction pattern showed that the coherent oxide films may have been highly stressed. The failure possibly occurred where the local stress level was sufficient to rupture the film.

Table II. Corrosion results on uranium

Sample No.	Condition of oxide film formation Temp., °C	Pressure, mm Hg	Time in corrosion test, hr	Rate, mg/cm²/hr
90	100	5×10^{-5}	4	2.93
91	100	5×10^{-5}	4	3.04
92	200	5×10^{-5}	4	3.26
93	200	5×10^{-5}	4	3.34
94	300	5×10^{-5}	4	2.78
95	300	5×10^{-5}	4	3.01
96	400	5×10^{-5}	4	3.00
97	400	5×10^{-5}	4	2.71
98	500	5×10^{-5}	4	1.56
99	500	5×10^{-5}	4	2.16
100	600	5×10^{-5}	4	0.68
101	600	5×10^{-5}	4	1.20
102	600	5×10^{-5}	4	1.24
103	600	5×10^{-5}*	4	3.10
104	600	5×10^{-5}	4	1.77
105	600	5×10^{-5}*	4	3.12
108	600	5×10^{-6}	4	Not detectable
109	600	5×10^{-1}	4	Not detectable
110	600	5×10^{-4}	4	Not detectable
111	600	5×10^{-4}	4	Not detectable
112	650	5×10^{-4}	21	0.06
113	650	5×10^{-4}	21	0.10
114	650	5×10^{-4}	21	0.09
122	600	1×10^{-3}	21	0.16
123	600	1×10^{-3}	21	0.28
124	600	1×10^{-3}	21	0.21

* Electropolished after film formation.

It seems likely that the stresses in the oxide film resulted from the difference between the thermal expansion coefficients of the oxide and the metal. In an attempt to reduce the stress and thereby increase the life of the film, samples were run at lower temperatures and, when necessary to obtain a reaction, at higher pressures (10^{-3} to 10^{-2} mm Hg). Above 400°C no change was observed in the line broadening. Below 400°C a mixture of UO_2 and a higher oxide was formed which did not provide protection against aqueous corrosion.

Cathodic charging.—In order to test the effect of surface hydride on corrosion behavior, a hydride layer was produced by cathodic charging in weakly acid (0.5%) solution. By varying the temperature, the structure of the coating could be changed. At

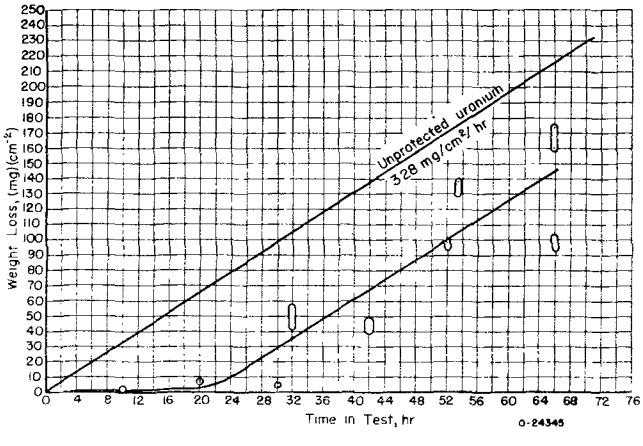

Fig. 2. Effect of oxide film on corrosion of uranium. Samples were held 2 hr at 650°C in oxygen atmosphere at 5×10^{-4} mm Hg. Two samples were coated together and are enclosed by one circle.

temperatures above 80°C only the beta form of UH_3 was produced, while at lower temperature a mixture of alpha and beta UH_3 was formed. No pure alpha coatings were produced.

Corrosion tests were run on samples coated with the beta UH_3 and with the mixture of alpha and beta. When corrected for the amount of uranium in the hydride layer no difference in corrosion rate could be detected between the charged and the uncharged samples.

Discussion of Results

The corrosion product formed when uranium reacts with 100°C water at atmospheric pressure does not offer protection to the underlying metal. In contrast, UO_2 films produced on the metal at temperatures above 400°C in oxygen, temporarily protect the base metal against corrosion in 100°C water. Ignition analyses of the water corrosion product indicate that its composition may be as high as $UO_{2.2}$, and increases to $UO_{2.4}$ after exposure to air at room temperature. Some confirming evidence that the valence state of uranium in the bulk corrosion product is greater than 4 was obtained from x-ray absorption spectroscopy.

This high oxygen-to-uranium ratio is in apparent contradiction to that from hydrogen-evolution measurement which indicates a composition of $UO_{1.9}$. The latter value is in good agreement with valence determination by chemical analysis. However, it is obvious that the oxygen-uranium ratio and the mean-valence and hydrogen-balance measurements are in error, being low by the amount of unattacked metal particles present in the samples. The metal content, although significant in explaining the low values of mean valence, must be considered an extraneous constituent of the corrosion product.

Thus the oxidized product is a phase or phases giving a UO_2-type x-ray pattern. It cannot be concluded from the oxygen-uranium ratio that the material is indeed UO_{2+x}, since, under conditions of reaction in the presence of water, hydrous oxide or the phase $U(OH)_4$ is a likely alternative indistinguishable from UO_{2+x}, by ignition analysis, in the presence of free metal. The solubility of $U(OH)_4$ is known (5), and its powder pattern has been reported to be very similar to that of UO_2 (9). It is possible that the decrease in the oxygen-to-uranium ratio of air-dried corrosion product from 2.40 to 2.21, during vacuum drying, may represent the partial decomposition of $U(OH)_4$. The product cannot be $U(OH)_4$ alone, since this phase would lose weight on ignition, requiring excessive amounts of free metal to compensate. Furthermore, its valence state is not consistent with the x-ray absorption-edge data. Thus, it is suggested that the corrosion product is a mixture of UO_{2+x} and $U(OH)_4$.

Although no hydride was detected in the present investigation, its stability under the conditions of the present tests was verified, and, therefore, it is likely that previous observations (1) of a hydride phase in the corrosion layer were due to hydrogen overpressure in the reaction vessel. It would be of interest to determine the hydrogen pressure required to form hydride in the presence of water and the effect of pressure on the corrosion rate of uranium.

Manuscript received June 21, 1957.

Any discussion of this paper will appear in a Discussion Section to be published in the December 1959 JOURNAL.

REFERENCES

1. D. H. Gurinsky and G. J. Dienes, "Nuclear Fuels," D. Van Nostrand Company, Inc., Princeton, N. J. (1956).
2. "The Reactor Handbook," Vol. 3, Section 1, AECD-3647, U. S. Atomic Energy Commission (1955).
3. D. A. Vaughan, J. R. Bridge, and C. M. Schwartz, To be published.
4. J. S. Anderson, *Bull. soc. chim. France*, **1953**, 781.
5. P. Perio, *ibid.*, **1953**, 256.
6. C. W. Melton, Private communication.
7. K. H. Gayer and H. Leider, *Can. J. Chem.*, **35**, 5 (1957).
8. J. T. Waber, Private communication.

Measuring Equipment for Polarization Studies in Distilled Water

J. E. Draley, W. E. Ruther, F. E. DeBoer, and C. A. Youngdahl

Argonne National Laboratory, Lemont, Illinois

ABSTRACT

A technique of measuring polarization in distilled water is described. The Luggin capillary and the a-c–d-c bridge methods are discussed and judged inapplicable. The decay of polarization voltage (of aluminum) is shown to be relatively slow in this environment. A recording voltmeter and current interrupter suitable for making polarization measurements in low conductivity solutions are described. The important design features of the electrolytic cell are discussed, and polarization data for aluminum in boiling water are given as an experimental example.

A number of articles (1) have discussed the theoretical analysis of metal potential vs. applied current curves for corroding metals. In those cases in which a specific experiment is described, the corroding medium has been of relatively low electrical resistance. Extending these potential-current analyses to a high-resistance medium such as distilled water modifies several of the usual measurement problems and introduces certain new ones.

The most serious problem in high-resistance solutions is that of the solution *IR* drop. Three methods are known for overcoming the solution resistance problem (Fig. 1): (*a*) by use of the Luggin capillary, (*b*) by balancing out this potential with an appropriate bridge circuit, and (*c*) by measuring the metal potential when no current is flowing (the interrupter technique). The Luggin capillary cannot be used in pure water because it shields the metal and because the small leak of the conducting salt at the metal surface would change the results entirely. Furthermore, the Luggin capillary would not eliminate the *IR* drop in so high a resistance medium.

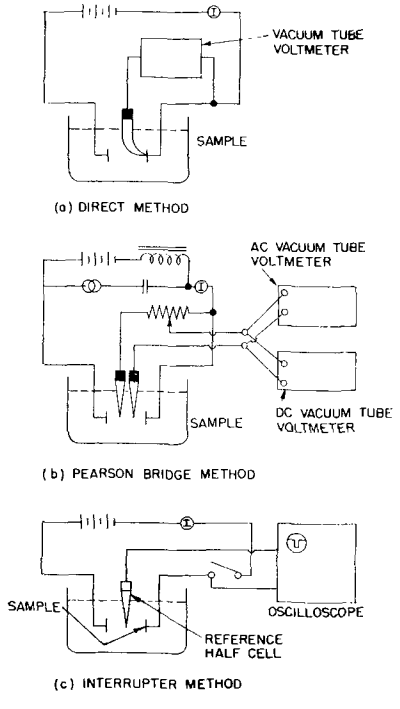

Fig. 1. Methods of overcoming solution IR drop in polarization measurements.

Initially the bridge technique appeared more promising since the circuitry was comparatively simple and the instruments (a-c and d-c vacuum tube voltmeters, etc.) were available from commercial sources. After preliminary experimentation several serious sources of trouble due to the high-resistance solution became apparent. As a result, attention was directed to the third or interrupter technique. A brief description of the experimental difficulties encountered with the bridge circuit is presented before the detailed discussion of the interrupter equipment to illustrate some of the unusual aspects of the problem.

Bridge Circuit

Various modifications of the Pearson (2) circuit were tried. It is assumed that the large specimen-solution pseudocapacitance effectively bypasses the electrode resistance for alternating currents, leaving only the solution resistance. Various impedance bridge circuits may then be devised, using a.c., to balance the solution *IR* drop with an equivalent external *IR* drop. Thus, when the current is changed to d.c., only the polarized potential of the specimen is measured in the previously balanced arm of the bridge. In distilled water at least two serious complications were encountered. First, the capacitative portions of the impedances between bridge members in the polarization cell were the same order of magnitude as the resistive component of the impedance in the solution. Balancing the a-c bridge under these conditions required a Wagner ground connection and multiple adjustments. Since a relatively large total d-c voltage (5-20 v) was required to drive the desired small polarizing currents, the a-c bridge had to be set with extreme precision to reduce the d-c error voltage (due to unbalanced *IR* drop) to within a few millivolts. Another difficulty was experienced with the reference electrodes. Since

most reference electrodes contaminated the pure water (a possible, but cumbersome, exception was the platinum-hydrogen electrode in hydrogen saturated water), the area of contact between the solution of the reference electrode and the pure water was deliberately made quite small. This small area resulted in a high-resistance contact shunted by a capacitative reactance. As a result, a-c and d-c impedances through the reference cell were not equal, whereas the analysis of the bridge circuits used demanded that they be equal. Because of these difficulties the work on bridge circuits was suspended.

Interrupter Technique

High solution resistance also complicates the interrupter type of measurement (Fig. 1c). The electronic detector must be sensitive to millivolts with the polarizing current off and yet not be overloaded by solution *IR* drops of up to 20 v with the current flowing. The high impedance of the measuring path between the reference electrode and the specimen makes it susceptible to stray a-c pickup (usually 60 cycles). Also, the input capacitance of the measuring circuit must be minimized to prevent relatively long RC decay times from introducing spurious polarization voltages.

Many circuits have been described for making quantitative measurements during the current interruption period (3). The recent, more complicated circuits have been required for precise measurements in the microsecond range. However, in the case of corroding specimens in distilled water, examination of current interruptions with a Model 531 Tektronix oscilloscope indicated several favorable features. For example, pure aluminum in 100°C distilled water and the simple circuit of Fig. 1c gave the trace shown in Fig. 2. A low resistance reference cell (platinized Pt, H_2 gas) and a special input circuit to the oscilloscope were used to permit viewing in the short time range. Even so, the period up to 60 μsec was obscured by the decay of the *IR* voltage. A very rapid polarization decay reaction, essentially complete in this time, may have occurred, but in view of the subsequent slow decay this seems unlikely. Since the direct method is not feasible we know of no way to eliminate this possibility.

It was also noted that the polarization decay in this preliminary experiment (with hydrogen gas) was about three times more rapid than that obtained in boiling distilled water without deliberate gaseous additions. In the latter more common case with the above polarizing conditions, the polarization voltage (about 300 mv at 0.2 msec) decayed about 6% in 1 sec, 63% in 33 sec, and 86% in 108 sec. It was obvious that this was not a simple RC decay.

The decay time for polarization voltages in distilled water thus appeared longer than that measured in the usual solutions. It was not similar to the usual rapid decay of the overpotential of a reversible system (3b). Since a smooth platinum sample behaved in approximately the same fashion in hydrogen-free water, the slow decay was not associated with the aluminum oxide film. The slow decay was not caused by the particular form of the reference electrode as is evidenced by the fact that the results with aluminum samples were not changed by interchanging reference electrodes (Pt-H_2 and calomel). It is not intended in this paper to discuss the theoretical implications of the observed values; it is hoped that a future publication will cover this aspect of the subject.

While the oscilloscope is an excellent method of obtaining a single piece of polarization data it is not well suited to the recording of complete curves in which both the *I* and *E* vary with time. A special piece of equipment was designed for this purpose.

Electronic Equipment

A thyratron tube with constant plate voltage fires nearly instantly whenever the grid-cathode voltage is more positive than a constant critical firing voltage. Hickling (4) devised a potentiometer circuit for determining the polarization voltage during a brief current interruption using this principle (Fig. 3a). The potentiometer is connected so that the voltage due to the solution resistance drives the grid negative with respect to the cathode (Fig. 3c). Manual adjustment of P_2 to the threshold of oscillation was required for each reading. However, the thresh-

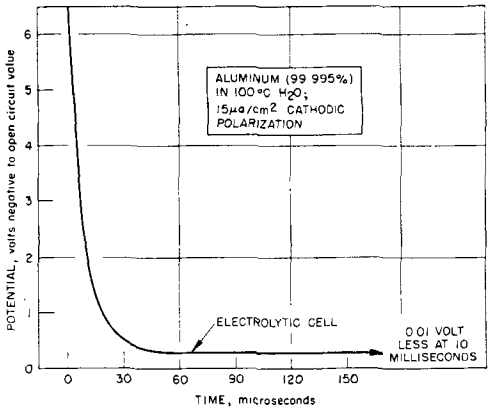

Fig. 2. Oscilloscope trace of current interruption

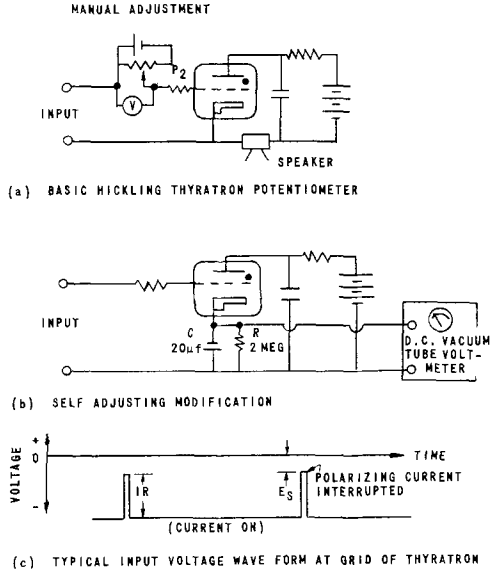

Fig. 3. Basic circuit of self-adjusting polarization voltmeter.

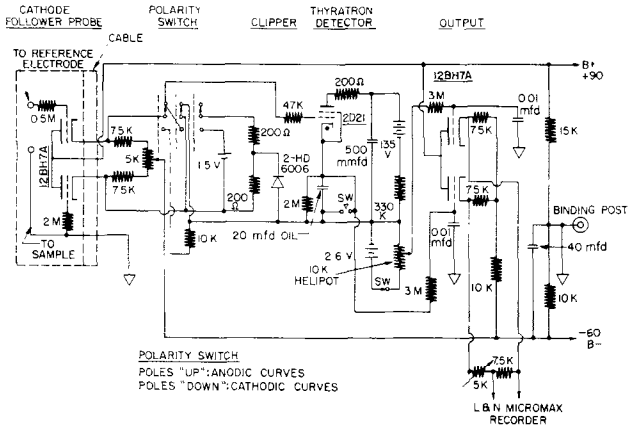

Fig. 4. Circuit diagram of polarization voltmeter

old adjustment can be performed automatically by the RC circuit of Fig. 3b. As the circuit operates as a saw-tooth oscillator, the current through the thyratron charges the condenser C until the grid-cathode potential is just equal to the critical firing potential for the thyratron. If the input voltage to be measured (E_s) changes, the condenser C is charged automatically by renewed oscillation or discharged by leakage through R until the total grid-cathode voltage again equals the critical firing potential. The change in potential across RC (measured with a d-c vacuum tube voltmeter) is therefore the change in the input voltage. This type of detector measures the most positive excursion of the grid potential during the interruption period.

In Fig. 4 the circuit diagram of the complete detector is shown. The cathode follower (12BH7A) provides high input resistance and isolates the sample from voltage pulses generated by the firing of the thyratron detector (2D21). The output circuit (12BH7A) prevents the loading of the RC self-balancing circuit by the L&N recorder. The range of polarization voltage of the specimen that can be handled by the peak detector itself is about 0.6-0.7 v. An adjustable bucking potential arrangement permits extension of this basic range, when it is necessary.

Certain precautions in construction will improve the performance of the instrument materially. The 12BH7A tube used in the cathode follower probe is selected for low grid current. The test is performed by applying +15 v (with respect to ground) to the "reference electrode" connection of the instrument with a galvanometer in series. A maximum of 10^{-9} amp should be drawn by the grid under these conditions.

Permitting the tubes to age for 5-10 days with their filaments operating tends to stabilize their performance, especially the 2D21 thyratron. The 135-v battery in the plate circuit of the 2D21 should be isolated from the instrument chassis to avoid stray leakage currents and large capacitance to ground. The usual care should be taken to isolate signal leads from those carrying 60 cps currents.

The polarizing current is supplied in the normal manner from a multiturn potentiometer and dry cells. The potentiometer may be motor driven, and a large resistance may be in the circuit to provide a

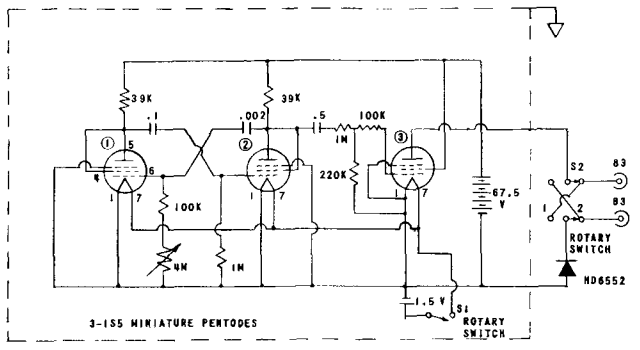

Fig. 5. Battery operated current interrupter

linear rate of change of polarization current when desired. An adjustable, battery operated multivibrator provides the interruption pulses (Fig. 5). The frequency of interruption is about 10 cps. Period of current interruption is adjustable from 1 to 20 msec. A silicon diode in the output lead is used to prevent capacitatively coupled spurious pulses. Reversing switches provide a maximum of flexibility in operation.

Cell Design

The commonly used stop off materials (Bakelite, Lucite, and various waxes) contaminate pure water. As shown in Fig. 6, the sample is clamped tightly against the side of the chamber in a manner similar to that described by Sheff, *et al.* (5) and covers a 1-cm² hole. Only the edge of the thin polyethylene washer is exposed to the solution. The specimen-polyethylene-glass assembly is heat sealed (3 min, 150°C oven) to define the corroding area sharply. Experiments with and without the polyethylene gasket produced identical results within the experimental error.

Contamination of the pure water was also a consideration in choosing materials for construction of the cell. Tygon and Neoprene parts in the water feed line were found to be unsatisfactory where the temperature was high. Teflon parts were difficult to clean properly. Stainless steel appeared to contami-

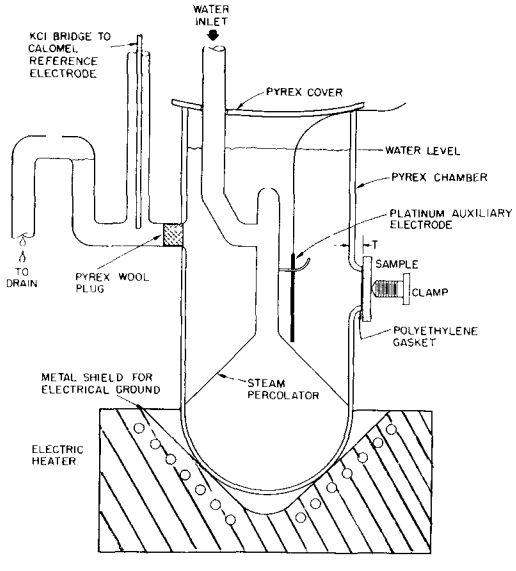

FIGURE 6
TEST CELL USED WITH BOILING DISTILLED WATER

Fig. 6. Test cell used with boiling distilled water

nate the hot water to some extent as judged by its influence on polarization curves. In the present design platinum and Pyrex glass are used throughout, except for the polyethylene gasket.

The 1-cm² hole permits the use of small samples. Any metal which can be ground or otherwise worked to expose one flat surface can be used. These considerations are important when an investigation of a wide range of metals is desired.

A relatively large ratio of water volume (250 cc)/sample area (1 cm²) reduces contamination of the solution by a corroding sample, as does a substantial rate of solution refreshment (10 cc/min).

In order to avoid a stray electrical ground the solution is allowed to form discrete drops at the end of the exit tube and drip into the drain. Also, the cell to ground capacitance is minimized to permit rapid decay of the *IR* voltage pulses.

The calomel cell is used because of its convenience. The slowly leaking salt bridge is constructed by fusing a strand of "Refrasil" insulation in Pyrex. The sweep of distilled water through the cell and the glass wool plug prevent chloride contamination of the sample chamber. On several occasions a portion of the flow was syphoned slowly from the chamber and collected for analysis. No chloride was found (sensitivity better than 0.1 ppm Cl^-).

Dimension T (Fig. 6) should be controlled. If it is made too small, the current distribution is nonlinear to a significant extent. If it is too large, the solution *IR* voltage can exceed +20 v. Under these conditions the grid of the input tube draws current and spurious polarization in the reference path occurs.

To evaluate the problem of nonuniform current distribution a Pt test probe was made by mounting a piece of 2.8 mm OD rod through a piece of Teflon and grinding the exposed face flush with the surface. This probe was mounted on the test cell in place of the usual specimen, and the resistance between the Pt working electrode in the cell and the small probe face was measured with an a-c impedance bridge as the probe was moved from edge to center of the 1 cm² opening. A maximum variation of 4% was found for 100°C distilled water with $T = 1.5$ mm. If greater uniformity were desired, T could be varied so that the maximum *IR* drop did not exceed 20 v or alternatively the input stage to the polarization voltmeter could be operated with higher plate voltage. Experiments have shown that up to 100 v *IR* can be tolerated using this latter technique.

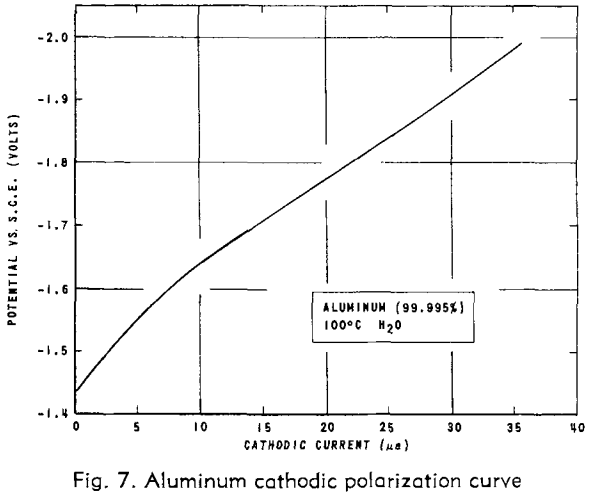

Fig. 7. Aluminum cathodic polarization curve

Annoying fluctuations in the current and voltage measurements were traced to steam bubbles moving across the face of the specimen. The present percolator design provides good temperature distribution, aids in degassing the replenishing water, sweeps the corrosion product away from the sample, and eliminates the steam bubble problem.

Experimental Example

The distilled water (resistivity —1.1 to 1.5 x 10^6 ohm-cm at 28°C) is usually slightly electrolyzed between Pt plates prior to its entry into the polarization chamber. When high-purity Al is used as the sample, this pre-electrolysis causes a slight decrease in the initial slope of the E vs. I cathodic curve and also prevents a sharp bend in the E-I curve at about 30 μa of cathodic polarization current. It is usually thought (6) that this pre-electrolysis takes some impurities out of the solution, but it is not clear that this mechanism applies here. The design of the pre-electrolysis cell and the amount of current do not seem to be critical.

Figure 7 is a trace of the recording of one experiment of potential (vs. saturated calomel electrode at room temperature) against applied cathodic current for high-purity Al in boiling water. The current was increased linearly with time ($\Delta I/\Delta t = 0.08$ μa/sec). This rate had little effect on these curves within the range investigated (0.04 to 0.11 μa/sec) and was controlled easily within this range. A 5-msec interruption period was used. The curve of Fig. 7 is one of thirteen similar curves. For this group of curves the average deviation at $I = 0$ is 0.006 v, that at 35 μa is 0.027 v; the maximum deviation at $I = 0$ is 0.011 v, that at 35 μa is 0.054 v. The slope of the straight line part (15 μa to 30 μa) is 14.4 x 10^3 v/amp with an average deviation of 1.1 x 10^3 v/amp. Samples were prepared by wet grinding pieces of a single stock of rolled and annealed sheet. They were exposed to the boiling water for about 20 hr (to an approximately constant value of open-circuit potential) before these measurements. Great care must be exercised to exclude impurities, since a small amount of contaminant corresponds to a large percentile change in the impurity level of the solution.

Reproducible E-I curves are being obtained for a variety of metals in distilled water at 100°C. Certain other variables of sample preparation are yet to be evaluated before a theoretical interpretation of the data is made.

Manuscript received Oct. 10, 1958. This work was done under the auspices of the U. S. Atomic Energy Commission.

Any discussion of this paper will appear in a Discussion Section to be published in the December 1959 JOURNAL.

REFERENCES

1. For example see: (a) U. R. Evans, "Metallic Corrosion, Passivity, and Protection," pp 47ff, 348ff, Longmans, Green & Co., New York (1948); (b) C. Wagner and W. Traud, *Z. Elektrochem.*, **44**, 391 (1938); (c) M. Stern and A. L. Geary, *This Journal*, **104**, 56, 559, 600, 645 (1957).

2. J. M. Pearson, *Trans. Electrochem. Soc.*, **81**, 485 (1942).
3. For example see: (a) S. Schuldiner and R. E. White, *This Journal*, **97**, 433 (1950); (b) D. Staicopoulos, E. Yeager, and F. Havorka, *ibid.*, **98**, 69 (1951).
4. A. Hickling, *Trans. Faraday Soc.*, **33**, 1540 (1937).
5. S. Sheff, H. C. Gatos, and S. Zwerdling, *Rev. Sci. Instr.*, **29**, 531, (1958).
6. A. M. Azzam, J. O'M. Bockris, B. E. Conway, and H. Rosenberg, *Trans. Faraday Soc.*, **46**, 918 (1950).

Electroplating of Nickel from the Pyrophosphate Bath

S. K. Panikkar and T. L. Rama Char

Electrochemistry Laboratory, Department of Inorganic and Physical Chemistry, Indian Institute of Science, Bangalore, India

ABSTRACT

The pyrophosphate bath has been found to be satisfactory for the plating of nickel. It gives good quality deposits over a wide range of operating conditions and has some advantages over the Watts bath.

Nickel is commonly plated from the sulfate-chloride or choride baths, and the fluoborate and sulfamate types have been established recently for industrial work. These solutions are all right in most respects, but they have a poor throwing power and are not suitable for direct plating on zinc. A complex salt bath suggests itself as an alternative. Brockman and Nowlen (1) have plated nickel on zinc from the triethanolamine bath. Langbein (2) cites an alkaline nickel pyrophosphate solution, and there is a patent (3, 4) on the zialite bath, containing nickel in the form of ammoniacal pyrophosphate and citrate complexes, for plating the metal on zinc. In view of the meager information available in literature, the plating of nickel from the pyrophosphate bath was studied in detail. The initial work has been reported briefly from this laboratory (5, 6), and a general review of plating metals and alloys from the pyrophosphate bath was made recently (7, 8).

Experimental

Plating solutions were prepared in the early work (5) by the addition of alkali pyrophosphate to a wet precipitate of nickel pyrophosphate obtained from nickel sulfate and pyrophosphate. Alkali chloride was then added to facilitate anode corrosion. It was necessary to add at least 6 g/l potassium chloride to the solution; otherwise the anode efficiency was zero. The bath preparation was therefore altered, potassium pyrophosphate being added to nickel chloride. The potassium salt was chosen in place of the sodium in view of the beneficial effects of the former as in other plating solutions. The pyrophosphate content of the bath was always in excess of that required for complex formation. Physicochemical measurements have shown (9) that the molar ratio of pyrophosphate to nickel in the complex is 2 as well as 1, the instability constant as determined from spectrophotometric data being of the order of 10^{-4}. There was no immersion deposition of nickel on zinc.

In solutions containing more than 0.3M nickel there was a tendency for precipitation after electrolysis. Ammonium citrate was added as a bath constituent since it was beneficial from the viewpoint of stability and buffering of the solution, quality of the deposits, cathode efficiency, and limiting c.d. (current density). Solutions with 0.3M nickel were titrated electrometrically with alkali using the glass electrode. Figure 1 shows that the precipitation pH is raised slightly by citrate, the best buffering action being imparted by 20 g/l of the salt. It was not advisable to increase the citrate content of the solution, thereby making it a mixed bath. The concentration of citrate was proportional to the nickel content of the solution, the ratio being 66.6 g/l ammonium citrate for 1M (58.7 g/l) nickel. Figure 2 shows that the resistivity of the solution is slightly decreased by citrate.

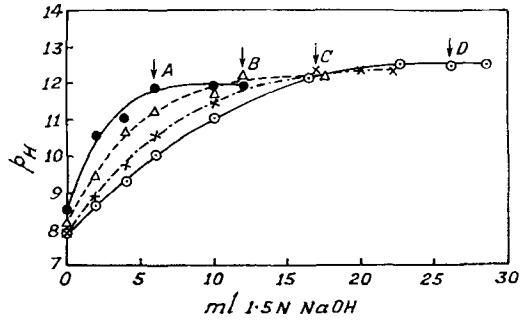

Fig. 1. Electrometric titrations. Ni 0.3M, ratio (i.e., ratio of pyrophosphate to metal by weight) 8. (A) am.citrate nil, (B) am.citrote 10 g/l, (C) am.citrate 20 g/l, (D) am.citrate 30 g/l. Each arrow shows the precipitation point for a curve, and the letter above it refers to the curve.

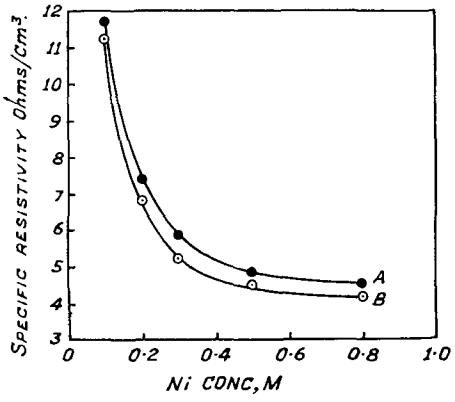

Fig. 2. Specific resistivity. Temp. 60°C, ratio 8. (A) am.citrate nil, (B) am.citrate 66.6 g/l for 1M Ni.

Fresh solutions, 200 ml, were taken for each experiment. Nickel anodes[1] (3 x 1 x ⅛ in.) and copper sheet cathodes (3 x 1 x 1/32 in.) were used, the inter-electrode distance being 1 in. and the immersed area of each electrode 2 in.^{2}; plating time for an experiment was 10-45 min. The experimental details concerning cleaning of electrodes, plating equipment, current efficiencies, temperature, agitation, pH, resistivity, and electrode potentials were the same as described before (10). The pH was varied by the addition of potassium hydroxide or hydrochloric acid. Conditions were carefully controlled to obtain electrode potential values (hydrogen scale) to the accuracy of ± 0.005 v.

The throwing power of the plating solution was measured under optimum conditions with a modification of the Haring-Blum throwing power box (11). The object was to obtain a relative idea of the throwing power of different plating solutions. A cylindrical glass cell 15 cm long and 4.5 cm in diameter was used, with 2 copper cathodes and a perforated nickel anode in between. The distance between the cathodes was 12 cm. The cathodes were weighed after electrolysis and cathode potentials and resistivity of the solution determined. The throwing power was calculated from the Field formula (12) and also from the equation of Gardam (13) for a linear relationship between cathode potential and log c.d., there being no variation of the cathode efficiency with c.d.

Photomicrographs of a thick coating (0.001 in.) of the surface of nickel deposit were taken with a Leitz projection microscope. X-ray powder patterns of the deposit were obtained from a Rich Seifert 13 unit with 57.3-mm diameter camera. Hardness measurements were made on the surface of the deposit with Leitz 1151 Durimet Midget hardness tester.

[1] Supplied by Canning and Co.

Experimental Results

Electrodeposition was carried out under the following conditions: nickel concentration 0.05, 0.1, 0.2, 0.3, 0.4, 0.5, and 0.8M; ratio of pyrophosphate (P_2O_7) to metal (weight) 6, 7, 8, and 10 (3.375 molar ratio); pH 7.8, 8.5, 9, 9.5, and 10.5; temperature 30°, 50°, 60°, and 70°C. Results are presented in Fig. 3-14 and in Tables I-III. All the results have not been covered to avoid overlapping. For the same reason, points corresponding to static potentials have not been marked. The data recorded correspond to good quality deposits. The decomposition potential for the plating solution was 1.8-1.9 v, and the bath voltage 0.9-3.0 v.

Nature of deposit.—The bath gave smooth, white, bright, fine-grained, and adherent deposits of nickel on copper (brass or zinc) cathodes over a wide range of plating conditions. Table I shows the effect of beneficial addition agents on cathode efficiency, potential (where there was a significant change), and quality of the deposit. Among other substances tried, diphenylamine had no effect, and selenium dioxide resulted in a deterioration. Plates 1 to 5 (Fig. 3) show the photomicrographs of the surface of nickel plates obtained under different conditions. Addition of ammonium citrate made the deposit finer grained and brighter, and there was no indication of escape of gas from the surface (plates 1 and 2). Increase of c.d. or temperature (not shown) or addition of cobalt chloride gave a brighter deposit; in the last case there was gas evolution and stress (plates 3-5). X-ray studies showed that the deposit has a f.c.c. structure, with $a = 3.516$Å.

Current efficiencies.—The cathode efficiency was increased by the addition of ammonium citrate, increase of nickel content, or pH of the solution. There was a slight increase with increase of temperature, and decrease with agitation. Most of the addition agents increased the efficiency at higher

Table I. Effect of addition agents on cathode efficiency, potential, and quality of the deposit

Bath composition: Ni 0 5M, ratio 8, ammonium citrate 33.3 g/l; pH 9.5; temperature 60°C, still plating. The first figure under c.d. gives the cathode efficiency % and the second (in parentheses) gives the cathode potential (-ve sign) in volts in H scale. Quality of deposit: A—marked improvement, B—slight improvement.

Addition agent	Conc. g/l	c.d., amp/dm^2 0	4	6	8	10	Brightness of deposit
Nil	—		92	86	65		—
		(0.41)	(1.08)	(1.18)	(1.24)		
Cobalt chloride	4.8		93	93	87	72	A
Cadmium chloride	0.8		89	88	86	83	B
Lead acetate	1.0		88	83	79	75	A
		(0.40)	(1.08)	(1.12)	(1.14)	(1.18)	
Zinc pyrophosphate	1.5		82	82	81	80	B
Sodium sulfite	0.5		90	89	82	82	A
Sodium bisulfite	0.2		90	89	89	87	A
Thiourea	0.5		78	71	55	32	B
		(0.52)	(0.94)	(1.07)	(1.14)	(1.24)	
Gelatin	0.5		78	69	59	56	B
		(0.46)	(1.21)	(1.29)	(1.36)	(1.48)	
β-naphthol	0.05		81	81	77	62	B
		(0.43)	(1.02)	(1.10)	(1.11)	(1.36)	
Coumarin	0.5		86	80	78	72	A
α-nitroso β-naphthol	0.1		79	79	79	76	A
Azoxybenzene sulfanilamide	0.1		96	93	86	82	A
Sodium β-naphthalene sulfonate	0.1		91	88	85	76	B
Triethanolamine	0.1 ml/l		90	85	85	82	B

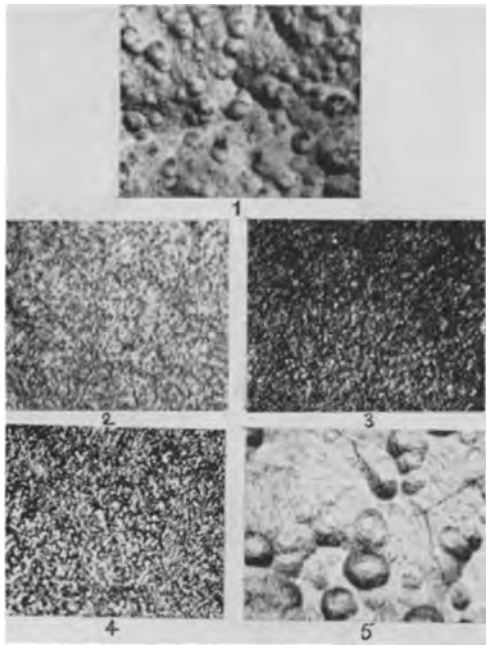

Fig. 3. Phatomicrographs of deposits. Temp. 60°C, Cu cathode, magnification 1 x 700. Plate 1—Ni 0.3M, ratio 8, 1 amp/dm²; Plate 2—Ni 0.3M, ratio 8, am.citrate 20 g/l, 1 amp/dm²; Plate 3— Ni 0.5M, ratio 8, am.citrate 33.3 g/l, 2 amp/dm²; Plate 4—Ni 0.5M, ratio 8, am.citrate 33.3 g/l, 4 amp/dm²; Plate 5—Ni 0.5M, ratio 8, am.citrate 33.3 g/l, cobalt chloride 4.8 g/l, 2 amp/dm².

c.d. In the majority of cases the values were from 80 to 94% (Table I and Fig. 4-8). The deposits were satisfactory even though the efficiency was less than 100%. It was possible to work the bath up to 10 amp/dm² with addition agents. The anode efficiency was about 100% throughout, and the values have therefore not been recorded under different conditions (Fig. 8). There was some sludge formation at the anode. The corrosion was, however, quite normal even beyond the limiting cathode c.d.

Potentials.—The cathode potential decreased[2] with increase of nickel or citrate content of the solution, temperature or agitation, and decrease in the ratio or pH (not shown). However, the potential changes were not very marked. The values were decreased by the addition of lead acetate, thiourea, beta-naphthol, and selenium dioxide (0.15 v decrease), and increased by gelatin (Table I and Fig. 9-11). The effect of the variables on the anode potential was in general similar to that on the cathode side (not recorded). Figure 12 shows that the chloride ion promotes anode corrosion.

[2] "Decreased" means that the potential has become more noble, i.e., has shifted toward the potential of a gold electrode.

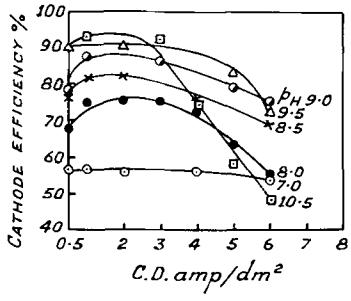

Fig. 4. Effect of pH on cathode efficiency. Temp. 60°C, Ni 0.3M, ratio 8, am.citrate 20 g/l.

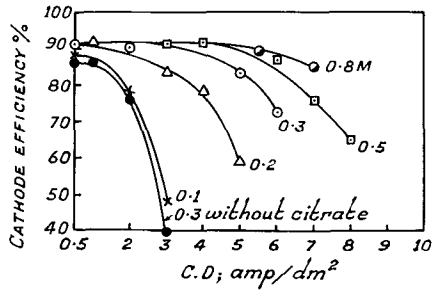

Fig. 5. Effect of nickel concentration on cathode efficiency. Temp. 60°C, ratio 8, pH 9.5, am.citrate 66.6 g/l for 1M Ni.

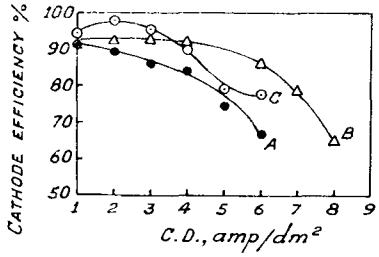

Fig. 6. Effect of ratio and am.citrate on cathode efficiency. Temp. 60°C, Ni 0.5M, pH 9.5. (A) ratio 8, am.citrate 20 g/l, (B) ratio 8, am.citrate 33.3 g/l, (C) ratio 6, am.citrate 33.3 g/l.

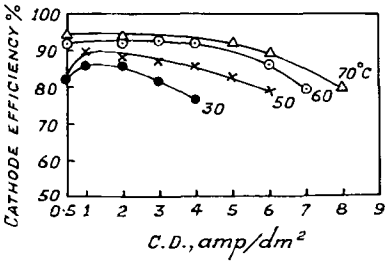

Fig. 7. Effect of temperature on cathode efficiency. Ni 0.5M, ratio 8, pH 9.5, am.citrate 33.3 g/l.

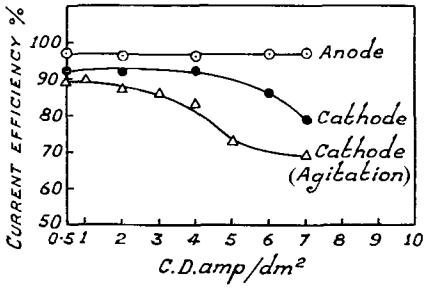

Fig. 8. Effect of agitation on cathode efficiency and anode efficiency. Temp. 60°C, Ni 0.5M, ratio 8, pH 9.5, am.citrate 33.3 g/l.

Throwing power.—Table II gives the results on throwing power measurements for the pyrophosphate, Watts (4), and chloride (14) baths under optimum conditions. The throwing power decreased with increase of c.d., and increased to some extent with increase in the linear ratio. There was reasonable agreement between the values calculated from the Field and Gardam equations. The reciprocal of the slope of the plot of the metal ratio against linear ratio, called the throwing index (15), gives a direct measure of the throwing power. Figure 14 gives this plot for the three baths; the index values are given in Table II.

Table II. Throwing power

ρ sp. resistivity ohm/cm³; b slope of cathode potential- log c.d. curve; N throwing number = $b/2\rho$; L, M, and R linear, metal, and current ratios, respectively (13)

	ρ	b	N
Pyrophosphate	4.51	0.545	0.0604
Watts	11.60	0.090	0.0039
Chloride	5.48	0.125	0.0114

Bath	c.d., amp/dm²	L	M	R	Throwing field	Power % Gardam	Throwing index
Pyrophosphate	0.5	5	2.11	1.57	57	—	10.0
	1.0	5	2.32	2.00	50	—	
	2.0	5	3.12	2.54	39	41	
	4.0	5	—	3.28	—	27	
	6.0	5	—	3.66	—	20	
	1.0	11	2.53	2.42	74	—	
	1.0	3	1.75	1.66	46	—	
Watts	0.5	5	3.38	3.97	25	—	2.8
	1.0	5	3.80	4.35	17	—	
	2.0	5	4.05	4.64	14	5	
	4.0	5	—	4.81	—	3	
	6.0	5	—	4.87	—	2	
	1.0	11	5.34	8.19	40	—	
	1.0	3	2.59	2.77	11	—	
Chloride	0.5	5	2.98	2.87	40	—	4.7
	1.0	5	3.00	3.55	33	—	
	2.0	5	3.27	4.11	37	14	
	4.0	5	—	4.50	—	7	
	6.0	5	—	4.65	—	5	
	1.0	11	4.27	5.21	43	—	
	1.0	3	2.51	2.45	33	—	

Control and maintenance of bath.—The bath was quite stable under the conditions of operation. In a typical case with a solution containing 0.5M nickel, ratio 8, and ammonium citrate 33.3 g/l, the cathode and anode efficiencies were 92 and 96%, respectively. The changes before and after electrolysis for 1 hr at 4 amp/dm² and 60°C were: nickel 29.8, 29.9; total pyrophosphate (P_2O_7) 234.6, 234.5 g/l; pH 9.50, 9.52; specific resistivity 4.51, 4.50 ohm/cm³; orthophosphate nil. A freshly prepared solution could be used for several runs with consistent and satisfactory results. Ageing of the electrolyte up to six months had no effect on the performance.

Testing of deposits.—Satisfactory coatings of any desired thickness from 0.0003 in. onward, calculated from area and weight, could be obtained. Bending and breaking tests indicated excellent adherence of the electroplate to the copper base. Deposits were free from porosity as shown by the electrographic method. A filter paper moistened with a 5% solution of sodium nitrite is applied to a coating of nickel on brass, and a sheet of platinum is placed on top. The test specimen is made the anode and the metal plate the cathode while a current of 2 ma/in.² is passed for 3 min. The paper is then developed for 1 min in a solution of 50 g/l potassium ferrocyanide and 30 g/l glacial acetic acid. Porosity is shown by brown spots on the paper. The hardness of deposits, 0.001 in. thick, increased with increase of c.d. from 1 to 6 amp/dm²: 380 to 450 Vickers, and decreased with increase of temperature from 50° to 80°C: 470 to 240.

Comparison of pyrophosphate and acid baths.—Table III gives the plating characteristics under optimum conditions for the pyrophosphate, Watts, and chloride baths for nickel plating. Data for the last two have been obtained experimentally for typical commercial compositions (4, 14).

The pyrophosphate bath is comparable to the acid baths in all important characteristics. The advantages of this bath over the others are: low metal content, high throwing power, and ability to plate directly on zinc.

Discussion

Experimental results show that the pyrophosphate bath is satisfactory for the plating of nickel. The solution mentioned by Langbein (2) contains nickel pyrophosphate 19.5 and sodium pyrophosphate 79.4 g/l; it is operated at 0.5 amp/dm², the bath voltage being 3.5 v. The zialite bath (3) consists of nickel in the form of pyrophosphate and citrate complexes, sodium and ammonium sulfates, chlorides, and free ammonia. It has been used for plating on zinc at 21°-35°C, pH 7.5-9.0, and current densities up to 2.5 amp/dm². The current efficiency

Table III. Comparison between pyrophosphate and acid baths

	Pyrophosphate		Watts		Chloride	
Composition g/l	Nickel chloride ($NiCl_2$, $6H_2O$)	118.9	Nickel sulfate ($NiSO_4$, $7H_2O$)	300	Nickel chloride	300
	Pyrophosphate (P_2O_7)	234.8	Nickel chloride	60	Boric acid	30
	Ammonium citrate	33.3	Boric acid	38		
	Nickel (0.5M)	29.4	Nickel	77.5	Nickel	74.1
pH	9.5		5.5		3.8	
Temp, °C	60		50		54	
Sp. resistivity, ohm/cm³	4.51		11.60		5.48	
Bath voltage, v	1.3-2.6		0.8-2.5		0.6-1.9	
Cathode c.d. (max.), amp/dm²	6		6		8	
Anode c.d. (max.), amp/dm²	8		8		8	
Cathode efficiency %	86-93		87-100		85-100	
Anode efficiency %	96-97		100-104		94-102	
Cathode polarization, v 0.5-6.0 amp/dm²	0.43-0.78		0.33-0.40		0.18-0.32	
Throwing power %, Gardam, 2 amp/dm²	41		5		14	
Hardness of deposit Vickers, 2 amp/dm²	390		200		350	

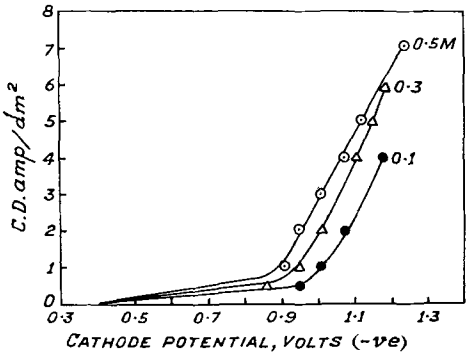

Fig. 9. Effect of nickel concentration on cathode potential. Temp. 60°C, ratio 8, pH 9.5, am.citrate 66.6 g/l for 1M Ni.

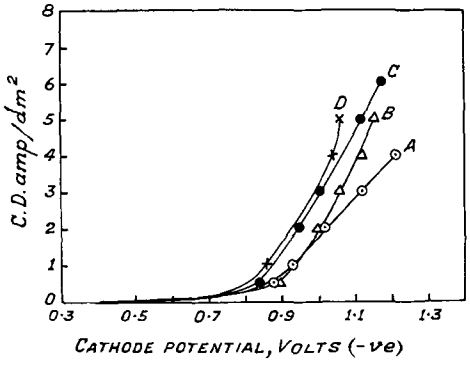

Fig. 10. Effect of ratio, am.citrate concentration and agitation on cathode potential. Temp. 60°C, Ni 0.5M, pH 9.5. (A) ratio 8, am.citrate 20 g/l; (B) ratio 10, am.citrate 33.3 g/l; (C) ratio 8, am.citrate 33.3 g/l, (D) ratio 8, am.citrate 33.3 g/l, agitation.

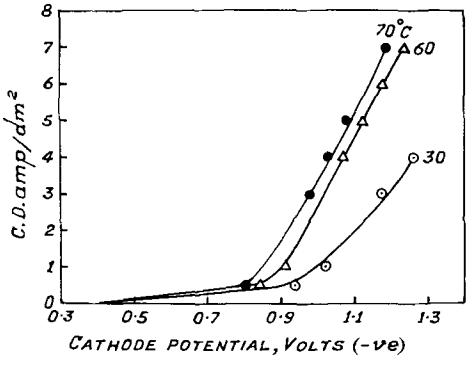

Fig. 11. Effect of temperature on cathode potential. Ni 0.5M, ratio 8, pH 9.5, am.citrate 33.3 g/l.

is 92% at 1.5 amp/dm², the values decreasing with increasing c.d. Solutions used in the present investigation are simple in composition, and even at 30°C the limiting c.d. is 4 amp/dm².

Most of the addition agents given in Table I act as brighteners in the Watts bath. Sodium sulfite and bisulfite have also been used in the zialite bath (3) and the pyrophosphate (16) and cyanide (4) baths for copper. The beneficial effects of ammonium citrate are similar to those obtained in the deposition of copper (16) and zinc (17) from the pyrophosphate bath. Brighteners in other baths include: gelatin and beta-naphthol in zinc (17) and tin (10) pyrophosphate, and lead acetate, sodium beta-naphthalene sulfonate and triethanolamine in copper (16) pyrophosphate baths. Cobalt, lead, and zinc codeposit with nickel from this bath. All these

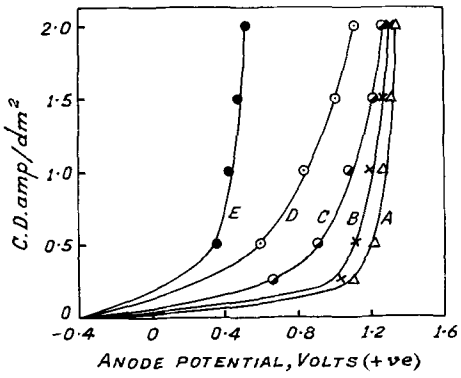

Fig. 12. Effect of chloride on anode potential. Bath prepared from: (A) to (D) nickel pyrophosphate, (E) nickel chloride and potassium pyrophosphate. Temp. 60°C, Ni 0.5M, ratio 8, pH 9.5 om.citrate 33.3 g/l, (A) KCl nil, (B) KCl 3 g/l, (C) KCl 6 g/l, (D) KCl 10 g/l.

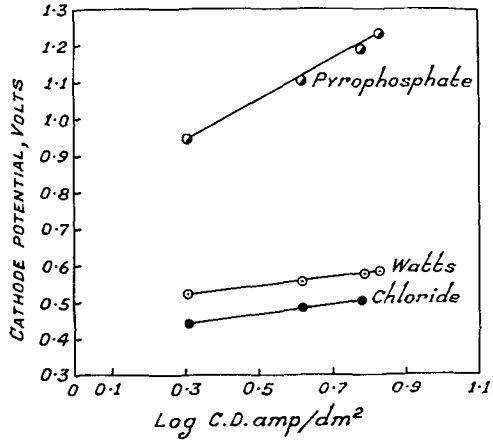

Fig. 13. Cathode potential—Log c.d. lines. Pyrophosphate bath—nickel chloride 118.9, pyrophosphate 234.8, am.citrate 33.3 g/l; pH 9.5, 60°C. Watts bath—nickel sulfate 300, nickel chloride 60, boric acid 38 g/l; pH 5.5, 50°C. Chloride bath—nickel chloride 300, boric acid 30 g/l; pH 3.8, 54°C.

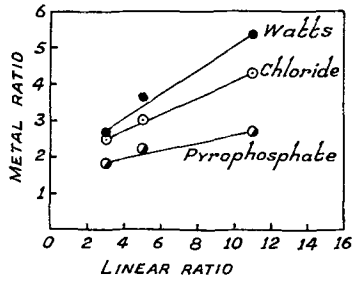

Fig. 14. Throwing index. L and M values at 1 amp/dm² from Table II.

substances belong to three broad types from the viewpoint of the current theories of addition agent action (18): complex formation, codeposition, and the formation of compounds which may exist as adsorbable colloids in the cathode film or function as brighteners on the analogy of their acid pickling inhibiting tendency.

The nickel electrode did not give reproducible potentials; this has been observed by other workers. It appears to be due to a passive film on the metal surface, giving a more noble potential. The passage of nitrogen or a freshly deposited nickel surface

changed the static potential in a negative direction, and a combination of these two gave the most satisfactory value. In a 0.5M nickel solution the potential values were: —0.1 under normal conditions, —0.4 for deposited surface, and —0.5 v for deposited surface under nitrogen. Taking the last value the instability constant for the complex (molar ratio of pyrophosphate to metal 2) was of the order of 10^{-9}, indicating a fairly stable complex. The static potential values including those given in Table I correspond to the deposited condition.

Cathode polarization was high, as in the deposition of other metals from this bath (7). Polarization is considerable during the deposition of nickel from the sulfate and sulfamate (19) baths; in the former case it is about 0.2 to 0.3 v. In the pyrophosphate bath the polarization was in the range 0.4 to 0.9 v. The relationship between cathode potential and log c.d. is linear under optimum conditions for the pyrophosphate, Watts, chloride (Fig. 13), and sulfamate (19) baths, and fine-grained deposits are obtained. This is in accordance with the views of Gardam (20) that the logarithmic relationship is an indication of frequent formation of new nuclei. Similar results have been obtained in the plating of tin (10), zinc (17), and copper (7) from the pyrophosphate bath. The slope of the potential-log c.d. straight line was 0.55, much greater than the values for the Watts and chloride baths (Fig. 13 and Table II). For the pyrophosphate bath the slope of the plot of polarization under agitation, against log c.d., was 0.34 (from Fig. 10, curve D). Calculations from the Tafel equation gave a value of the order of 10^{-4} amp/cm^2 for the exchange current density, and 0.1 for alpha under these conditions. The corresponding values reported in literature (21) for nickel from sulfate bath are 10^{-9} amp/cm^2 and 0.5, respectively.

The bath possesses good throwing power. In view of the greater slope of the potential-log c.d. lines and the lower resistivity the throwing power of this bath is much better than that of the acid baths. The throwing index is also greater.

The anode potentials of nickel in pyrophosphate solutions indicate the phenomenon of passivity (Fig. 12). The passive anode shows a potential of 1.2 v., close to the oxygen evolution value. Increasing additions of potassium chloride change the potentials to more negative values, and finally at the chloride concentrations used for plating the potential is 0.4 v, the active value. Unlike the partial passivity in acid solutions, the nickel anode is totally passive in the pyrophosphate bath. Addition of chloride raises the efficiency from 0 to 100%. Anode polarization was rather high, 0.8-0.9 v, but the values cannot be regarded as accurate in view of the sludge formation.

The electrodeposition of alloys of nickel with tin, copper, zinc, cobalt, iron, manganese, tungsten, and molybdenum from this bath has been reported elsewhere (8, 22-24).

Acknowledgment

Our thanks are due to Professor K. R. Krishnaswami, Head of the Department, for his keen interest in the work. One of the authors (S. K. Panikkar) is grateful to the Government of India for the award of a Senior Research Scholarship during the period of the investigation.

Manuscript received May 20, 1958. This paper was prepared for delivery before the Ottawa Meeting, Sept. 28-Oct. 2, 1958.

Any discussion of this paper will appear in a Discussion Section to be published in the December 1959 JOURNAL.

REFERENCES

1. C. J. Brockman and J. P. Nowlen, *Trans. Electrochem. Soc.*, **69**, 541 (1936).
2. G. Langbein, "Electrodeposition of Metals," p. 318, Hodder and Stoughton, London (1920).
3. R. L. Tuttle, U. S. Pat. 2,069,566 (1937).
4. A. G. Gray, Editor, "Modern Electroplating," John Wiley & Sons, Inc, New York (1953).
5. S. K. Panikkar and T. L. Rama Char, *J. Sci. Ind. Research, India*, **14B**, 603 (1955).
6. S. K. Panikkar and T. L. Rama Char, Symposium on Electrodeposition and Metal Finishing, 1957, India Section, Electrochemical Soc., under publication.
7. T. L. Rama Char, *Electroplating and Metal Finishing*, **10**, 347 (1957).
8. T. L. Rama Char, *ibid.*, **10**, 391 (1957).
9. J. Vaid and T. L. Rama Char, *Bull. India Sect., Electrochem. Soc.*, **7**, 5 (1958).
10. J. Vaid and T. L. Rama Char, *This Journal*, **104**, 282 (1957).
11. H. E. Haring and W. Blum, *Trans. Electrochem. Soc.*, **44**, 313 (1923).
12. S. Field, *J. Electrodepositors' Tech. Soc.*, **9**, 144 (1934).
13. G. E. Gardam, *Trans. Faraday Soc.*, **34**, 698 (1938).
14. W. A. Wesley and J. W. Carey, *Trans. Electrochem. Soc.*, **75**, 209 (1939).
15. R. V. Jelinek and H. F. David, *This Journal*, **104**, 279 (1957).
16. S. K. Panikkar, R. P. Singh, and T. L. Rama Char, *Bull. India Sect., Electrochem. Soc.*, **6**, 69 (1957).
17. J. Vaid and T. L. Rama Char, *J. Sci. Ind. Research, India*, **15B**, 509 (1956).
18. J. A. Henricks, *Trans. Electrochem. Soc.*, **82**, 113 (1942).
19. S. Sathyanarayana and T. L. Rama Char, *J. Sci. Ind. Research, India*, **16A**, 78 (1957).
20. G. E. Gardam, *Discussions Faraday Soc.*, **1**, 182 (1947).
21. J. O'M. Bockris, "Modern Aspects of Electrochemistry," p. 217, Butterworths Scientific Publications, London (1954).
22. S. K. Panikkar and T. L. Rama Char, *J. Electrochem. Soc., Japan*, **25**, E121, 573 (1957).
23. S. K. Panikkar and T. L. Rama Char, *J. Sci. Ind. Research, India*, **17A**, 95 (1958).
24. Vasanta Sree and T. L. Rama Char, *Bull. India Sect., Electrochem. Soc.*, **7**, 72 (1958).

Phase Equilibria and Fluorescence in the System $Zn(PO_3)_2$-$Mg(PO_3)_2$

J. F. Sarver and F. A. Hummel

Department of Ceramic Technology, College of Mineral Industries, The Pennsylvania State University, University Park, Pennsylvania

ABSTRACT

The equilibrium diagram for the system $Zn(PO_3)_2$-$Mg(PO_3)_2$ was established as a solid solution type by quenching and solid-state methods. About 10 mole % $Mg(PO_3)_2$ was found soluble in β-$Zn(PO_3)_2$ at 850°C, but less than 2 mole % was soluble in α-$Zn(PO_3)_2$ at 650°C. Solid solution of $Zn(PO_3)_2$ in $Mg(PO_3)_2$ was extensive, ranging from approximately 35 to 100 mole % $Mg(PO_3)_2$.

The cathodoluminescence of compositions in the three solid-solution series was examined for peak emission and brightness when activated with manganese. A shift in the position of the emission peak from 6000 to 6200Å in the magnesium metaphosphate solid-solution series has been interpreted in terms of the difference in influence between magnesium and zinc ions on the polarizability of oxygen ions in the neighborhood of the manganese activator.

Equilibrium relationships in the system $Zn(PO_3)_2$-$Mg(PO_3)_2$ were established as an aid to the identification and understanding of the host lattices which are responsible for the luminescence of preparations in the system ZnO-MgO-P_2O_5. It is well known that the ortho-, pyro-, and metaphosphate compounds of zinc and magnesium are bases for several phosphors which emit in the red portion of the visible spectrum and a few others which emit in the orange or green portion.

Two previous papers have dealt with the phase relationships in the system ZnO-P_2O_5 (1) and the emission characteristics of the manganese-activated zinc phosphate compounds under cathode ray excitation (2).

Berak (3) has established the melting points and eutectic compositions and temperatures in the system MgO-P_2O_5. The fluorescence of the magnesium phosphate compounds has not been explored as extensively as that of their zinc phosphate counterparts, probably due to the generally low brightness obtained with manganese activation. No equilibrium data have been published for the ternary system ZnO-MgO-P_2O_5.

Experimental Procedure

Compositions Used for Determination of Equilibrium Relationships

Ten-gram batches of the compositions shown in Table I (weighed to 0.0001 g) were made from C.P. ZnO, C.P. basic magnesium carbonate, and C.P. $(NH_4)_2HPO_4$ and were melted to glasses in platinum crucibles for use in quench determinations.

To minimize P_2O_5 volatilization during melting, the batch materials were reacted in the solid state at about 800°C for 24 hr. The batches were melted then in platinum crucibles for 10 min between 900° and 1200°C. The glasses were air quenched, crushed in a steel mortar, and passed through 100 and 120 mesh sieves. The fraction retained on the 120 mesh screen was reserved for index of refraction measurements, and the minus 120 mesh material was used for quench experiments after magnetic removal of traces of metallic iron introduced by the crushing process.

Heat Treatment and Physical Measurements

The melting, quenching, solid-state reactions, phase identification, differential thermal analyses, and measurement of emission spectra were carried out as described in previous papers (1, 2). Calibration of thermocouples used in the quench work was done using Li_2SiO_3 (1201°C), Au (1063°C), and Ag (961°C); the accuracy of temperature measurement was generally ±2°C.

CuKα radiation was used for x-ray identification

Table I. Composition and refractive indexes of metaphosphate glasses

Comp. No.	Mole % $Zn(PO_3)_2$	Mole % $Mg(PO_3)_2$	Refractive index, n_D ± 0.001 Sodium light, λ = 5890Å
1	100.0	0.0	1.517
2	95.0	5.0	1.517
3	90.0	10.0	—
4	85.0	15.0	1.515
5	80.0	20.0	—
6	75.0	25.0	1.513
7	70.0	30.0	—
8	65.0	35.0	1.511
9	55.0	45.0	1.508
10	45.0	55.0	1.505
11	35.0	65.0	1.503
12	25.0	75.0	1.500
13	15.0	85.0	1.496
14	5.0	95.0	1.492
15	0.0	100.0	1.491

Table II. X-ray diffraction data for the metaphosphate compounds

α-$Zn(PO_3)_2$			β-$Zn(PO_3)_2$			$Mg(PO_3)_2$		
2θ	d	I/I_0	2θ	d	I/I_0	2θ	d	I/I_0
13.5	6.56	5	16.5	5.37	5	14.5	6.11	10
13.7	6.46	15	17.3	5.13	5	19.5	4.55	45
13.8	6.42	55	17.6	5.04	5	21.0	4.23	25
14.4	6.15	5	19.6	4.53	10	25.4	3.51	15
19.3	4.60	5	20.1	4.42	10	26.5	3.36	25
20.0	4.44	55	21.8	4.08	40	27.8	3.21	45
20.8	4.27	50	23.1	3.85	10	28.2	3.16	35
25.2	3.53	5	23.4	3.80	30	29.9	2.99	100
25.8	3.45	55	24.0	3.71	15	31.3	2.86	20
26.4	3.38	5	25.5	3.49	45	32.9	2.37	5
27.1	3.29	—	25.8	3.45	100	35.0	2.56	20
27.6	3.23	5	26.2	3.40	25	37.9	2.37	15
28.1	3.18	5	27.2	3.28	10	39.7	2.27	5
29.3	3.05	15	27.8	3.21	15	40.2	2.24	5
30.1	2.97	95	29.8	3.00	—	41.5	2.18	10
30.7	2.91	100	31.8	2.81	10	43.3	2.09	20
31.2	2.87	5	32.5	2.75	10	46.7	1.940	5
31.7	2.82	20	33.6	2.67	10	47.2	1.925	5
34.8	2.58	5	35.4	2.54	—	48.4	1.887	5
35.5	2.53	5	36.3	2.47	5	51.0	1.791	5
37.3	2.41	45	37.4	2.40	10	53.1	1.728	5
37.7	2.39	10	37.7	2.39	10	54.3	1.689	5
38.2	2.36	25	39.6	2.28	10	55.8	1.650	5
42.4	2.13	10	40.0	2.25	5	56.6	1.626	10
42.9	2.11	10	40.8	2.21	5	57.2	1.610	10
43.8	2.07	25	41.2	2.19	10	60.3	1.535	10
45.1	2.01	10	41.5	2.18	5	61.2	1.514	10
45.4	2.00	10	44.1	2.05	5	62.0	1.497	5
46.8	1.94	5	44.3	2.04	15	67.9	1.380	10
47.9	1.90	20	47.8	1.90	5	Other reflections		
50.1	1.82	—	48.2	1.89	5			
50.6	1.80	—	48.7	1.87	5			
51.0	1.79	10	49.6	1.84	5			
52.0	1.76	—	51.4	1.78	5			
52.4	1.75	5	53.9	1.70	10			
53.5	1.71	5	Other reflections					
56.6	1.63	10						
56.9	1.62	10						
57.5	1.60	10						
59.6	1.55	10						
60.1	1.54	50						
60.7	1.53	5						
Other reflections								

of crystalline materials. Petrographic microscope determinations of refractive indexes of glasses and crystals were accurate to ±0.001 using index oils which had been calibrated with an Abbé refractometer. Cathodoluminescent emission spectra were determined on a demountable tube using an electron beam with a current density of 2.0 μamp/cm² and an accelerating potential of 16 kv.

Results and Discussions

Magnesium Metaphosphate

Although it was already known that ortho-, pyro-, and metaphosphate compounds of magnesium exist, the system was briefly re-examined by solid-state reactions and the three compounds were confirmed. Then further work was carried out on the thermal behavior of $Mg(PO_3)_2$ to check for possible inversions and the nature of melting. The congruent melting point was determined by quenching experiments to be 1165° ±5°C which agrees well with that reported by Berak (3).

No inversions were detected after extensive solid-state, quenching, D.T.A., and dilatometric experiments. Crystals prepared by devitrification of $Mg(PO_3)_2$ glass were found to be biaxial negative with $n_\beta = 1.585$ and 2 v equal to about 30°C. The x-ray diffraction data for $Mg(PO_3)_2$ and the two forms of $Zn(PO_3)_2$ are given in Table II.

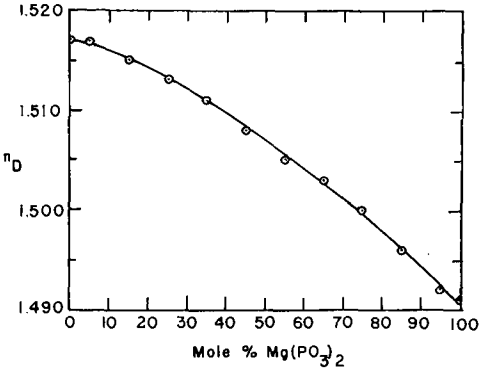

Fig. 1. Indexes of refraction of metaphosphate glasses

Phase Equilibrium Relationships in the System $Zn(PO_3)_2$-$Mg(PO_3)_2$

The refractive index curve for the metaphosphate glasses is shown in Fig. 1. These data were used extensively during the petrographic examination of the many quenches made in the system. The important quench data are summarized in Table III and the equilibrium diagram based on these data is shown in Fig. 2. The starting material for the quench work was a glass, and all phase identifications were made with the petrographic microscope, except for composition No. 16. In this case the starting material was batch which had been reacted below 650°C and the phase identifications were made by x-ray diffraction.

The system is characterized by two small regions of solid solution near the $Zn(PO_3)_2$ compound, a large region of $Mg(PO_3)_2$ solid solutions, and a mis-

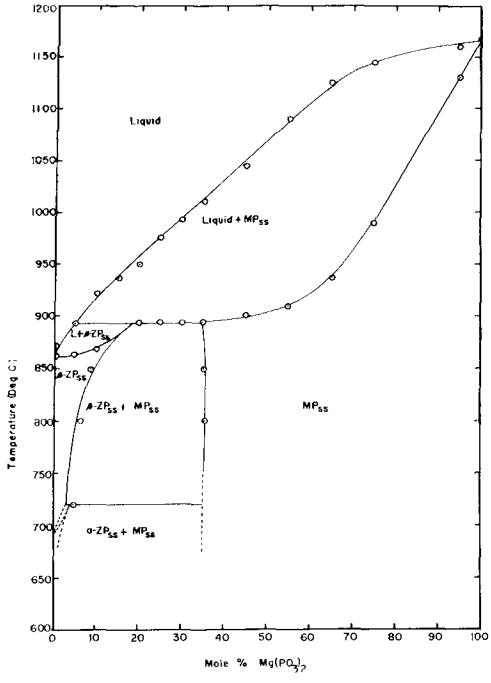

Fig. 2. Equilibrium relationships in the system $Zn(PO_3)_2$-$Mg(PO_3)_2$.

Table III. Quench data for the system $Zn(PO_3)_2$-$Mg(PO_3)_2$

Comp. No.	Mole % ZP	Mole % MP	Quench temp, °C	Time, min	Phases*	Remarks
1	100	0	860	30	β-ZP	
	100	0	865	15	G+β-ZP	
	100	0	871	15	G+β-ZP	Trace crystals
2	95	5	838	30	β-ZP_{ss}	
	95	5	859	30	β-ZP_{ss}	
	95	5	864	30	G+β-ZP_{ss}	Trace glass
	95	5	878	20	G+β-ZP_{ss}	
	95	5	890	20	G+β-ZP_{ss}	Trace crystals
	95	5	895	15	G	
3	90	10	861	30	β-ZP_{ss}	
	90	10	865	30	G+β-ZP_{ss}	
	90	10	872	30	G+β-ZP_{ss}	
	90	10	920	20	G+MP_{ss}	Trace crystals
	90	10	925	15	G	
4	85	15	870	30	β-ZP_{ss}	
	85	15	875	30	G+β-ZP_{ss}	Trace glass
	85	15	881	30	G+β-ZP_{ss}	
	85	15	888	30	G+MP_{ss}	
	85	15	935	20	G+MP_{ss}	
	85	15	940	20	G	
5	80	20	892	30	β-ZP_{ss}+MP_{ss}	
	80	20	896	30	G+MP_{ss}	
	80	20	902	30	G+MP_{ss}	
	80	20	918	30	G+MP_{ss}	
	80	20	937	30	G+MP_{ss}	
	80	20	944	20	G+MP_{ss}	
	80	20	949	20	G+MP_{ss}	Trace crystals
6	75	25	893	30	β-ZP_{ss}+MP_{ss}	
	75	25	897	30	G+MP_{ss}	Trace glass
	75	25	912	30	G+MP_{ss}	
	75	25	965	15	G+MP_{ss}	
	75	25	973	15	G+MP_{ss}	Trace crystals
	75	25	976	15	G	
7	70	30	892	30	β-ZP_{ss}+MP_{ss}	
	70	30	897	30	G+MP_{ss}	Trace glass
	70	30	910	30	G+MP_{ss}	
	70	30	916	30	G+MP_{ss}	
	70	30	922	30	G+MP_{ss}	
	70	30	982	15	G+MP_{ss}	
	70	30	992	15	G+MP_{ss}	Trace crystals
8	65	35	890	30	MP_{ss}	
	65	35	898	30	G+MP_{ss}	
	65	35	911	20	G+MP_{ss}	
	65	35	963	20	G+MP_{ss}	
	65	35	981	20	G+MP_{ss}	
	65	35	1003	15	G+MP_{ss}	Trace crystals
	65	35	1008	20	G	
9	55	45	898	30	MP_{ss}	
	55	45	910	30	G+MP_{ss}	
	55	45	914	30	G+MP_{ss}	
	55	45	930	30	G+MP_{ss}	
	55	45	1033	15	G+MP_{ss}	
	55	45	1038	15	G+MP_{ss}	
	55	45	1041	15	G+MP_{ss}	Trace crystals
	55	45	1068	15	G	
10	45	55	908	20	MP_{ss}	
	45	55	912	20	G+MP_{ss}	
	45	55	917	20	G+MP_{ss}	
	45	55	1080	10	G+MP_{ss}	
	45	55	1087	10	G+MP_{ss}	
	45	55	1092	12	G	
11	35	65	932	30	MP_{ss}	
	35	65	940	15	G+MP_{ss}	Trace glass
	35	65	1122	15	G+MP_{ss}	
	35	65	1126	15	G	
12	25	75	977	30	MP_{ss}	
	25	75	987	30	MP_{ss}	
	25	75	1004	30	G+MP_{ss}	
	25	75	1012	30	G+MP_{ss}	
	25	75	1140	15	G+MP_{ss}	
	25	75	1144	15	G+MP_{ss}	
	25	75	1149	15	G	
14	5	95	1115	30	MP_{ss}	
	5	95	1130	30	MP_{ss}	Trace glass
	5	95	1157	15	G+MP_{ss}	
	5	95	1163	15	G	
15	0	100	1161	15	G+MP	Trace glass
	0	100	1168	15	G	
16	95	5	687	20 hr.	α-ZP_{ss}+MP_{ss}	
	95	5	701	20 hr.	α-ZP_{ss}+MP_{ss}	
	95	5	716	24 hr.	α-ZP_{ss}+MP_{ss}	
	95	5	725	24 hr.	β-ZP_{ss}+MP_{ss}	

* G, glass; ZP, $Zn(PO_3)_2$; MP, $Mg(PO_3)_2$; ss, solid solution.

cibility gap involving β-$Zn(PO_3)_2$ and $Mg(PO_3)_2$ solid solutions. At 850°C, the two-phase region extends from about 10-35 mole % $Mg(PO_3)_2$.

Further confirmation of the nature and extent of solid solution was obtained on a series of well-crystallized compositions which had been prepared by devitrification of glasses at 800°C for 24 hr. Diffraction patterns shown in Fig. 3 were obtained with a rotating specimen holder and a goniometer speed of 1°/min. An examination of the patterns of compositions containing 100-35 mole % $Mg(PO_3)_2$ showed that there was practically no change in peak positions, but only a change in intensity for certain 2θ reflections, notably those at 14.5°, 19.5°, 21°, and 27.8°.

A more detailed examination of the $Mg(PO_3)_2$ solid-solution series was made by obtaining diffraction patterns at a goniometer speed of ¼° (2θ)/min. When the patterns of the end members of the solid-solution series (Fig. 3a) were compared [$Mg(PO_3)_2$ vs. $(Mg_{0.35}Zn_{0.65})(PO_3)_2$], the maximum shift in position of any particular high angle reflection was 0.05°, indicating a very low order of magnitude of change in lattice dimensions. With increasing amounts of zinc in solid solution, the small shift was toward lower angles, indicating only the slightest increase in lattice dimensions.

When attention is focused on the patterns of compositions containing 30-10 mole % $Mg(PO_3)_2$ (Fig. 3b), it is evident that two solid solutions are present in this range. The strong lines of $Mg(PO_3)_2$ at 29.9°

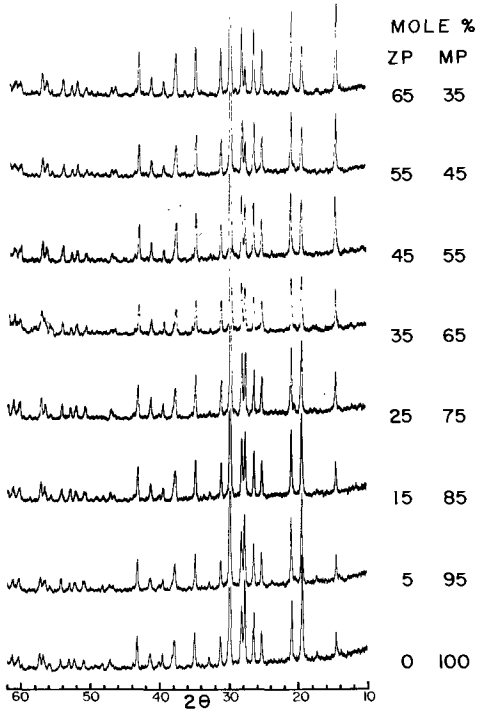

Fig. 3a. X-ray diffraction patterns of $Mg(PO_3)_2$ solid solutions.

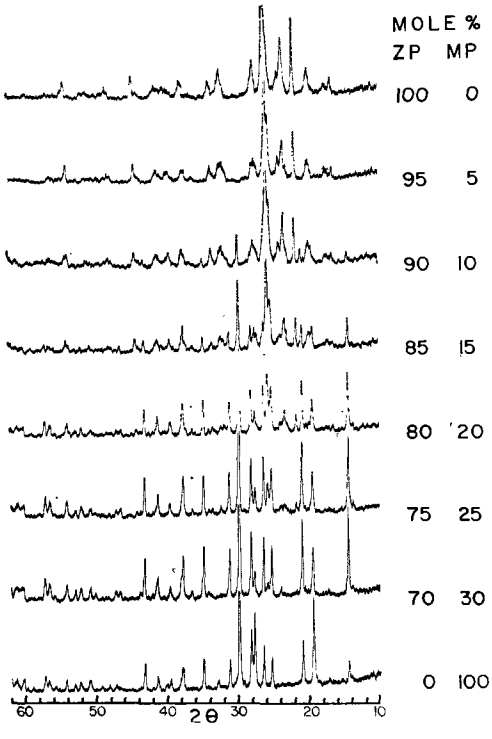

Fig. 3b. X-ray diffraction patterns of β-$Zn(PO_3)_2$ solid solutions and mixtures of β-$Zn(PO_3)_2$ solid solution and $Mg(PO_3)_2$ solid solution.

and 21.0° persist in this region as do the characteristic 25.8° and 21.8° lines of β-$Zn(PO_3)_2$. The relative intensities of the reflections of each of the two solid solutions do not change in this range, indicating constancy of composition.

Finally, it should be noted (Fig. 3b) that only the relative intensities in the 5 mole % $Mg(PO_3)_2$ pattern change when compared to the pattern for pure $Zn(PO_3)_2$, indicating that it is a solid solution having the structure of the beta form of zinc metaphosphate.

Table IV. Peak emission and brightness of metaphosphate phosphors

Comp., mole % ZP	Comp., mole % MP	°C/hr	Phases	Peak emission, Å	Brightness (f-L)
100	0	850/24	β-ZP	5700	33.9
95	5	850/24	β-ZP_{ss}	5700	17.0
85	15	850/24	β-ZP_{ss}+MP_{ss}	5900	18.2
100	0	650/48	α-ZP	6300	1.0
97.5	2.5	650/48	α-ZP_{ss}	6300	0.8
95	5	650/48	α-ZP_{ss}+MP_{ss}	6300	1.6
55	45	850/24	MP_{ss}	6000	25.2
45	55	850/24	MP_{ss}	6100	23.3
35	65	850/24	MP_{ss}	6100	23.0
25	75	850/24	MP_{ss}	6100	21.1
15	85	850/24	MP_{ss}	6100	18.9
5	95	850/24	MP_{ss}	6200	12.1
0	100	850/24	MP_{ss}	6200	9.8
NBS standard β-$Zn_3(PO_4)_2$				6380	36.0

Note: In the MP_{ss} series, one would expect the peak emission to vary systematically and continuously rather than in steps as shown (6200, 6100, 6000). However, the spectroradiometer curves could not be read with greater accuracy than that listed in the table.

It is conceivable that the brightness values listed above may have been affected by the method of preparation (settling in an aqueous medium) since metaphosphates are known to have relatively poor chemical durability.

It had been shown previously that pure α-$Zn(PO_3)_2$ could never be obtained by devitrifying a glass (1). A mixture of α and β forms always resulted from the crystallization. Likewise, from the glass containing 5 mole % $Mg(PO_3)_2$, a mixture of the α and β forms of $Zn(PO_3)_2$ and a $Mg(PO_3)_2$ solid solution always resulted from devitrification below 700°C. Quench work with this crystalline mixture showed that this assemblage could be converted to β-$Zn(PO_3)_2$ plus a $Mg(PO_3)_2$ solid solution between 716° and 725°C. Due to the uncertainties about the increase in the α and β inversion temperature with increase in Mg $(PO_3)_2$ in solid solution, the phase boundaries in this region of the diagram are showed in dashed lines.

Luminescence Studies

On the basis of the phase relationships determined above, the compositions shown in Table IV were selected for the preparation of manganese-activated phosphors. To each composition 0.01 mole MnO/mole (ZnO + MgO) was added, and heat treatments were carried out at subsolidus temperatures as listed in Table IV. The constitution of the phosphors was checked by x-ray diffraction patterns as shown in the fourth column of Table IV.

β-$Zn(PO_3)_2$ solid solutions.—The β-$Zn(PO_3)_2$ phosphors did not show any shift in their peak emission positions (5700Å). However, there was a noticeable decrease in brightness with increasing magnesium content. In the composition 85 $Zn(PO_3)_2$, a second phase was present, a $Mg(PO_3)_2$ solid solution. Its emission dominated that of the β-$Zn(PO_3)_2$ phosphor, raising the apparent brightness, and causing the peak emission to lie at 5900Å.

An interesting observation was made regarding the brightness of the β-$Zn(PO_3)_2$ phosphor. Katnack (2) prepared this phosphor by additions of 1 wt % MnO to preformed $Zn(PO_3)_2$ and obtained a brightness of 4.8 ft-L as compared with 33.9 obtained in this work. His preparation was fired 50°C lower than

the β-$Zn(PO_3)_2$ listed in Table IV, but the greatest part of the difference probably was due to starting materials.

α-$Zn(PO_3)_2$ *solid solutions.*—These phosphors do not exhibit a shift in the position of peak emission (6300Å) with increasing magnesium content. Magnesium seems to lower the brightness (Table IV), and with as little as 5 mole %, $Mg(PO_3)_2$ solid solution appears as a second phase.

The α-$Zn(PO_3)_2$ phosphors had a second emission band with a peak around 4000Å, but of much lower intensity than that at 6300Å.

$Mg(PO_3)_2$ *solid solutions.*—This is the most interesting series, since the $Mg(PO_3)_2$ lattice accommodates 65 mole % $Zn(PO_3)_2$ in solid solution without appreciable change in dimensions. However, there is a significant shift in peak emission from 6200Å for pure $Mg(PO_3)_2$ to 6000Å for the $(Zn_{0.55}Mg_{0.45})(PO_3)_2$ solid solution (Table IV).

Fonda (4) recently reviewed the influence of activator environment on the spectral emission of isomorphous compounds and solid solutions and indicated that lattice dimensions and polarizability of the ions are major factors which determine the position of the peak emission.

Since changes in cation to anion distances in this series of solid solutions are apparently extremely small, an explanation of the shift in peak emission might be based on the polarization of oxygen ions in the structures.

Unfortunately, the crystal structure of $Mg(PO_3)_2$ is not known. However, it is reasonable to assume that some kind of P-O unit forms the basic network and that zinc isomorphously replaces magnesium in MO_6 groups in the $Mg(PO_3)_2$ structure. If there were no difference in polarizing power between Zn^{2+} and Mg^{2+} and the ions acted as rigid spheres, some increase in lattice dimensions would be expected with increasing substitution of zinc (0.83Å) for magnesium (0.78Å). However, due to its 18 electron shell, the zinc ion distorts the oxygen ion, resulting in a Zn-O distance which gives essentially the same effective size for ZnO_6 and MgO_6 groups. Addition of manganese results in MnO_6 groups which are adjacent to MgO_6 groups in $Mg(PO_3)_2$ and to an increasing number of ZnO_6 groups as one proceeds to the $(Zn_{0.55}Mg_{0.45})(PO_3)_2$ solid solution. The electron density distribution in the oxygen around the manganese ion is controlled by the relative amount of zinc and magnesium in the solid solution. Substitution of zinc for magnesium apparently lowers the electron density around the Mn^{2+}, causing a change in the energy of electronic transitions and a resultant shift toward shorter wave lengths.

The change in energy required for the electronic transitions due to substitution of Zn^{2+} ions for Mg^{2+} ions is attended by an increase in brightness of these phosphors from 9.8 ft-L for $Mg(PO_3)_2$:Mn to 25.2 ft-L for $(Zn_{0.55}Mg_{0.45})(PO_3)_2$:Mn.

Summary

1. The solid solubility of $Mg(PO_3)_2$ in β-$Zn(PO_3)_2$ increases from about 3 mole % at 725° to about 10 mole % at 850°C. Increasing solubility of $Mg(PO_3)_2$ decreases the cathodoluminescent brightness of manganese-activated solid solutions which have a peak emission at 5700Å.

2. The solid solubility of $Mg(PO_3)_2$ in α-$Zn(PO_3)_2$ is very low, probably less than 2 mole % at 700°C. Manganese activated α-$Zn(PO_3)_2$ solid solutions have a very low cathodoluminescence brightness with a maximum at 6300Å.

3. Solid solubility of $Zn(PO_3)_2$ in $Mg(PO_3)_2$ is very extensive, ranging from 100-35 mole % Mg $(PO_3)_2$. The peak emission of manganese-activated cathodoluminescence varies from 6200Å for pure $Mg(PO_3)_2$ to 6000Å for a $(Zn_{0.55}Mg_{0.45})(PO_3)_2$ solid solution. Brightness increases with increase in Zn $(PO_3)_2$ in solid solution.

Acknowledgment

Emission curves were obtained through cooperation of Marjorie Brines of the Chemical Products Plant, General Electric Co. The investigation was made possible by the support of the Chemical Products Plant, General Electric Co., Cleveland, Ohio.

Manuscript received Dec. 3, 1958. This paper was prepared for delivery before the Philadelphia Meeting, May 3-7, 1959. Contribution No. 58-42 from the Department of Ceramic Technology, College of Mineral Industries, The Pennsylvania State University, University Park, Pennsylvania.

Any discussion of this paper will appear in a Discussion Section to be published in the December 1959 JOURNAL.

REFERENCES

1. F. L. Katnack and F. A. Hummel, *This Journal,* **105,** 125 (1958).
2. F. A. Hummel and F. L. Katnack, *ibid.,* 528.
3. Józek Berak, *Roczniki Chem.,* **32,** 17 (1958); *Chemical Abstracts* (June 25, 1958).
4. G. R. Fonda, *J. Optical Soc. America,* **47,** 877 (1957).

Chemical Etching of Silicon

I. The System HF, HNO_3, and H_2O

Harry Robbins and Bertram Schwartz

Hughes Semiconductors, Newport Beach, California

ABSTRACT

The kinetics of the etching of silicon in the system HF, HNO_3, and H_2O was studied as a function of the composition of the etchant at 25°C. A triaxial plot of the etch rate vs. composition of the etchant shows two extreme modes of behavior. In the region of high nitric acid compositions, etch rates are functions only of the hydrofluoric acid concentration. In the region of high hydrofluoric acid compositions, nitric acid concentration determines the etch rates. The kinetic behavior in the latter region is complicated by autocatalysis in which the reduction products of nitric acid are involved.

The reaction proceeds by an oxidation step followed by the dissolution of the oxide. In the high hydrofluoric acid region the oxidation step is rate limiting. In the high nitric acid region the dissolution step is rate limiting. In both regions the flow of reagent to the surface by diffusion determines the etch rates. A plot of the etch rates as a function of the concentration of the rate-limiting reagent indicates an exponential relationship between the etch rates and the concentration. This relationship has been explained qualitatively on the basis of a second, nonchemical autocatalytic factor, the heat of reaction.

This study was undertaken for the purpose of elucidating the physical and chemical processes that determine the behavior of an acid etching solution. The system HF, HNO_3, H_2O was chosen for study because it is the simplest, from the point of view of composition, of all the acid etching systems used on silicon. It was felt that an understanding of the simple system was a prerequisite for the understanding of the more complicated systems containing additives such as acetic acid, bromine, or heavy metal salts.

Experimental Procedure

The kinetics of the etching system was studied as a function of the composition of the etchant at constant initial temperature (25°C), and data were taken over the composition range where the decrement in die thickness exceeded 0.1 mil/min. Silicon specimens were ⅛ x ⅛ x 0.025 in. n-type dice of approximately 3 ohm-cm resistivity. The two large surfaces of the die were 111 oriented with an accuracy of about 90 min, while the remaining four surfaces were not oriented with respect to any crystal plane. All surfaces had been lapped with an abrasive grit and were work damaged to a depth of about ¼ mil.

The dice were etched, one at a time, in 10 cc of solution in a small Teflon beaker. Agitation was provided by an electric stirring motor equipped with a polyethylene paddle. The reaction was quenched at the proper time with a large volume of water. The dice were then rinsed in distilled water, dried, and measured with a micrometer.

All dice were etched three times, and each etch was performed in a fresh portion of the same solution. Since each etching period had been selected to remove from 4 to 6 mils from the specimen, it may be assumed that the work damage had been removed after the first etch. The third etch was performed in the presence of a few milligrams of $NaNO_2$, for reasons which will be explained later.

All etching was performed in a Teflon beaker immersed in a constant temperature bath regulated at 25°C. The heat transmission of the beaker was so poor, however, that the temperature of 25°C could not necessarily be maintained in the etch solution. Since the etching period was generally shorter than 1 min, and quite often of the order of only several seconds, it is extremely unlikely that thermal equilibrium was maintained, and the reaction may be considererd to have been run under essentially adiabatic conditions.

A triangular coordinate system was set up to represent the composition of the etchant. One vertex was arbitrarily chosen to represent the composition of the stock HNO_3 used to make up the solutions, and another vertex was similarly used to designate the stock HF. The third vertex, therefore, represents only the amount of added water, not the total amount of water present. This normalization of the axes results in a representation of the data valid only for one particular set of concentrations of reagents. However, the representation of the data in mole fraction units, which is free from this objection, led to identical conclusions.

In the preparation of the etching solutions, HF was weighed out to ±0.01 g. The weights of HNO_3 and water were converted to volumes and measured out in a buret to ±0.01 cc. Control of the composition of the etching solutions was established by analysis of the stock acids from which the solutions were to be made and adjustment of these stock acids to the proper concentration, which was arbitrarily taken as the analysis of the initial batch of reagents.

In order that the effect of crystal orientation and

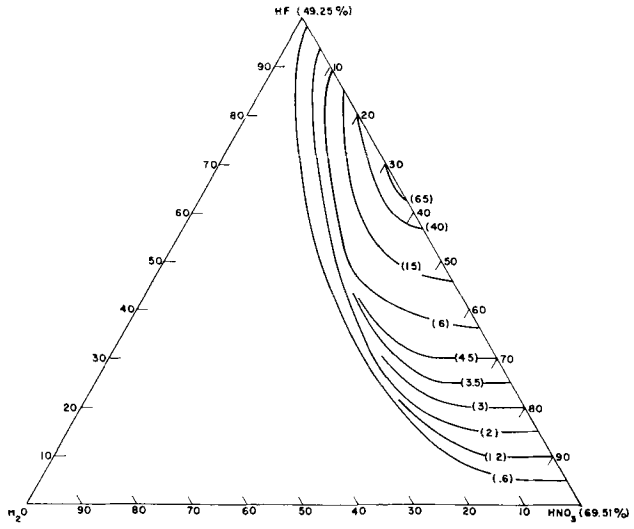

Fig. 1. Curves of constant rate of change of die thickness (mils per minute) as a function of etchant composition (weight per cent in the system 49.25% HF, 69.51% HNO_3, and water).

resistivity type on the etch rates might be checked, specimens of both p-type and n-type Si oriented along the 111, 110, and 100 planes, as well as small Si spheres, were etched in several compositions chosen at random.

Results and Discussion

Figure 1 is a plot of the etch rate (numbers in parentheses are the decrement in die thickness in mils per minute) as a function of the composition of the etchant. The reagents used in this study were the normally available concentrated acids, i.e., 49% HF and 70% HNO_3. It will be shown later that the range of compositions accessible through the use of these reagents was insufficient to clarify the mechanism in the HF-rich region, so that it was necessary to extend the range by employing more concentrated reagents, i.e., 60% HF and 90% HNO_3. Data corresponding to this system are plotted in Fig. 2.[1]

[1] Note that the 20%-added-water line of Fig. 2 corresponds approximately with the no-added-water line of Fig. 1.

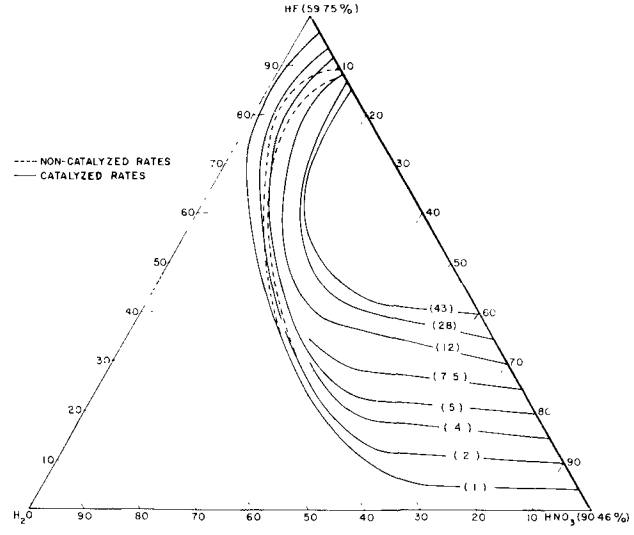

Fig. 2. Curves of constant rate of change of die thickness (mils per minute) as a function of etchant composition (weight per cent in the system 59.75% HF, 90.45% HNO_3, and water).

Rate-Limiting Reagents and Autocatalysis

The contours shown are lines of constant etching rate. In the high HNO_3 compositions the contours run parallel with lines of constant HF concentration, indicating a dependence of the rates only on the HF concentration. The slight inclination of the contours with respect to lines of constant weight per cent HF does not indicate a slight dependence of the rates on HNO_3, as a plot of the same data in mole fraction units results in an inclination of the contours in the other direction. In either case the inclination can be shown to be in the direction of constant molarity, which is kinetically a more significant unit, but which cannot be represented on a triaxial plot.

In the upper region of Fig. 2 there is a strong tendency for the contours to run parallel with lines of constant HNO_3 concentration, indicating that in this region only the HNO_3 concentration determines the rates. However, the behavior of the system is complicated by a second factor, autocatalysis. Rates shown by the dotted curves are second etch rates. They represent the action of fresh solution on a surface from which the work damage has been removed. The solid curves represent what shall be called catalyzed third-etch rates. These etches were performed in the presence of a trace of $NaNO_2$. Sodium nitrite decomposes in acid solution to yield oxides of nitrogen which are apparently catalysts for the reaction (1), as shown by the displacement of the solid contours in the direction of decreased HNO_3 concentration. At all compositions within the area bounded by the innermost dotted contour the added catalyst had no effect on the measured rates. The reaction is believed to require the presence of catalyst throughout the entire composition range. For the majority of compositions, however, the rates are sufficiently high that adequate catalyst is generated to assure its availability for the reaction, and other factors come into play to mask the effect of the catalyst concentration on the etch rates. It is only when the rates are very slow and HNO_3 dependent that the amount of generated catalyst is a prime factor in rendering the reaction self-sustaining.

Many etchant compositions have been found that attack a work-damaged surface readily but fail to re-etch the specimen after the work damage has been removed. This is another manifestation of the influence of the generated catalyst. Etch rates are initially more rapid on a work-damaged surface. The catalyst is either generated in adequate amounts or trapped in surface crevices, and the reaction rate can build up to the steady-state value. When the surface is free from work damage the initial reaction rate is very slow, and it is possible for the reaction products to be dispersed before they can become involved in the propagation of the reaction. The addition of oxides of nitrogen to the solution by any means, such as the addition of $NaNO_2$ or even a chip of work-damaged Si, will supply sufficient impetus to get the reaction started, and once it is started it will usually attain the same steady-state rate as a damaged specimen.

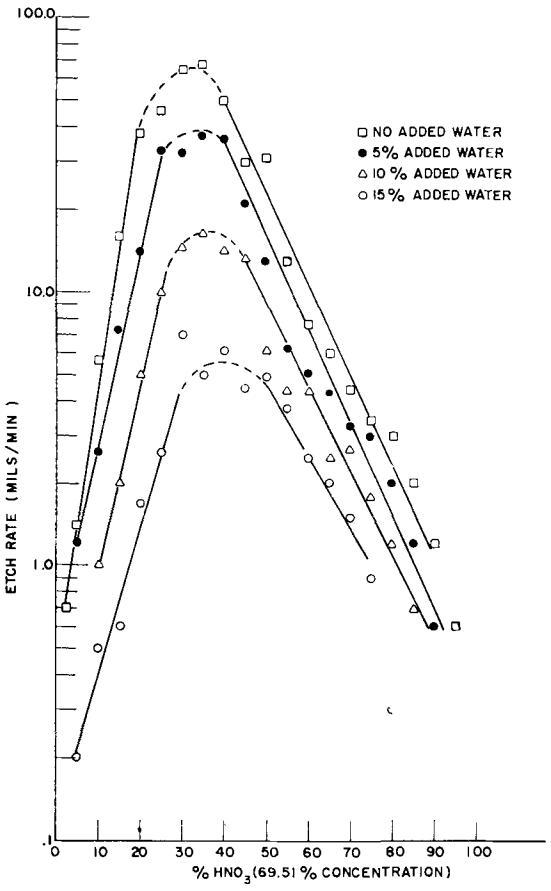

Fig. 3. Logarithm of the rate of change of die thickness as a function of the concentration of HNO_3.

In Fig. 2 the etch rates are initially insensitive to the addition of substantial amounts of water in both the high HF and the high HNO_3 regions, provided that the concentration of the rate-determining species in the region under consideration remains constant. However, at a fairly definite composition the system suddenly becomes critical with respect to the addition of water, and the etch rates rapidly vanish with a slight increase in the water concentration. It will be shown below that the etch rates are determined by the rate of diffusion of the kinetically important species to the Si surface in the regions where the system is insensitive to the addition of water. For this reason the etch rates do not respond to the concentration of added catalyst or to changes in the oxidizing potential of the HNO_3 resulting from the addition of the water. However, at the critical concentration of water, the oxidation potential of the solution has been reduced to the extent that the surface of the Si is no longer a nearly perfect sink for the HNO_3, and the etch rates decrease slightly. At this point the catalyst concentration begins to play a kinetic role. A slight decrease in the etch rates is amplified by the decreased production of the catalyst so that on further addition of water the etch rates rapidly vanish, even though the rate-determining reagent remains at the same concentration. It should be pointed out that the regular concentrated HF contains just the critical amount of water, so that the slope of the etch-rate contours in the very high HF region is just beginning to turn parallel with lines of constant HNO_3 concentration (see Fig. 1). It is for this reason that it was necessary to go to the more concentrated system, where the amount of water is less than critical.

Reaction Mechanisms

Figure 3 is a plot of the logarithm of the etch rate as a function of the concentration of HNO_3 for various levels of added water, i.e., in a direction parallel with the HF-HNO_3 axis of Fig. 1. A similar family of curves may be plotted for the more concentrated acid system. In the latter system the curves corresponding to compositions containing 0-20% added water and to the left of the maximum would coincide. To the right of the maximum the curves for both systems would coincide throughout if the data were plotted as a function of the HF concentration. In this region the displacement of the curves is the result of the varying amount of water in the etchant, which does not permit the simultaneous representation of the concentration axis in terms of both HF and HNO_3.

To the left of the maximum the etch rates are dependent on the HNO_3 concentration and on the amount of added water. Hydrofluoric acid is present in considerable excess, and decreasing amounts of that reagent are still sufficient to sustain increasing rates. The surface of the Si may be considered to be essentially stripped of oxidized Si until the composition corresponding to the maximum etch rate is approached. Then the rate of the reaction becomes sufficiently great, and the concentration of HF sufficiently reduced that a skin of oxidized Si begins to form. This skin renders the surface less accessible to HNO_3 so that the rate of the reaction decreases as the concentration of HNO_3 is increased still further. Beyond this point the rates are dependent only on the rate at which HF can attack the oxidized film.

The kinetics suggest a two-step process. In the first step the Si is oxidized by the HNO_3. This step is followed by a metathesis-type reaction in which the oxidized Si is attacked by the HF. In the composition region to the left of the maximum the oxidation step plays a rate-limiting role, and in the composition region to the right of the maximum the metathesis reaction plays a rate-limiting role.

The conformance of the data to a straight-line relationship indicates that the rates are possibly exponential functions of the concentration of the type $R = e^{ac+b}$. It is interesting to note that the logarithms of the maximum etch rates, when plotted against the concentration of water, also give a straight-line relationship. The constants a and b remain constant only as long as the etch rates are strictly diffusion limited. Thus the curves to the left of the maximum in the weaker acid system do not have the same slopes, although the exponential form of relationship is retained.

The exponential relationship between the etch rates and the concentration of the rate-limiting reagent suggests autocatalysis. As we have indicated above, the chemical catalyst cannot be expected to enhance the rate of a diffusion-governed process, and so we are obliged to postulate the existence of a physical factor which is capable of operating on the

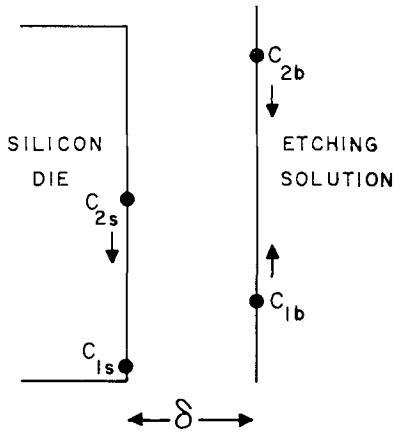

Fig. 4 Model used to explain the diffusion mechanism of the reaction.

diffusion mechanism. This factor is the heat of reaction, which sets up a thermal gradient in the vicinity of the specimen and therefore causes the diffusion coefficient to become a function of the distance from the reacting surface.

In favor of diffusion-governed kinetics is the evidence that differently oriented surfaces, as well as p- and n-type silicon of different resistivities, all appeared to etch at the same rate, whereas large differences in the etch rate of these surfaces are generally observed in other etching systems. Furthermore, the fact that the etch rates are insensitive to the concentration of added catalyst or to the variation of the oxidation potential of the solution, as explained above, supports the theory. The heterogeneous nature of the reaction also requires the consideration of transport phenomena as being kinetically important (2).

In Fig. 4 is shown schematically the surface of a Si specimen immersed in an etching solution under the condition of violent agitation. A thin layer of relatively immobile liquid of thickness δ adheres to the specimen as the solution moves past it. Since the amount of reaction is negligible relative to the total amount of reagents in solution, the bulk solution provides a constant source for reagents. The surface of the Si provides a nearly perfect sink for one of the reagents, the one that is rate limiting. The flow of the other reagent adjusts itself to the stoichiometric requirements of the reaction. Thus, if the stoichiometry of the reaction is assumed to be

$$3Si + 12HF + 4HNO_3 = SiF_4 + 4NO + 8H_2O$$

then the flow rate of HF will have to be three times that of the HNO_3.

In addition to the concentration gradients across δ there will exist a thermal gradient, because of the flow of the heat of reaction away from the surface. Our calculations show that the temperature profile across δ is linear, and the slope is proportional to the amount of heat dissipated, i.e., to the reaction rate. In the absence of the temperature gradient the concentration gradients across δ would also be linear, because of the assumption of the steady state. However, the temperature gradient causes a distortion of the concentration profile toward steeper gradients and thus enhanced reaction rates.

Let us now identify subscript 1 with HNO_3 and subscript 2 with HF, and let us consider the change in the reaction rate as the proportion of HF to HNO_3 is decreased at a given constant level of added water. As C_{1b} increases, the concentration gradient, and thus the reaction rate, also increases. C_{2b} falls because the sum of the two reagents $C_1 + C_2$ is constant. C_{2s} will also fall in a manner that takes into consideration both the fall of C_{2b} and the stoichiometry of the reaction, and will approach C_{1s}, which remains stationary. The finite surface concentration C_{2s} reflects the condition that the HF is present in excess, for the flow rate can be increased by a decrease in C_{2s}. As the maximum etch rate is approached, C_{2s} approaches C_{1s}, and the rate of the dissolution of the oxidized Si can no longer keep ahead of the rate of oxidation. The oxide coating thus impedes the HNO_3 reaction, and the decreased flow rate of HNO_3 is reflected in a rise in C_{1s}. The point where the two surface concentrations cross over marks the transition from a HNO_3 dependent rate to a HF dependent rate. Further increase in the proportion of HNO_3 causes a decrease in the reaction rate by virtue of the resultant decrease in C_{2b}, which is now rate determining.

It is interesting to speculate that if the diffusion coefficients of the two reagents are equal and if the stoichiometry indicated above is correct, then the composition of the fastest etching solution at a given level of added water would have to contain 3 molecules of HF per molecule of HNO_3. On the HF-HNO_3 axis, this composition corresponds to 56 wt % HF, which is not much removed from the observed 65%.

Acknowledgment

The authors wish to express their indebtedness to S. Pryor for her assistance in the experimental work and to F. Ludwig, S. Watelski, and P. Walker for most stimulating discussions and many helpful comments.

Manuscript received April 30, 1958. This paper was prepared for delivery before the New York Meeting, April 27-May 1, 1958.

Any discussion of this paper will appear in a Discussion Section to be published in the December 1959 JOURNAL.

REFERENCES

1. H. Remy, "Treatise on Inorganic Chemistry," Vol. 2, p. 712, Elsevier Publishing Co., New York (1956).
2. Ibid., p. 749.

Preparation of Crystals of InAs, InP, GaAs, and GaP by a Vapor Phase Reaction

G. R. Antell and D. Effer

Research Department, Metropolitan-Vickers Electrical Co. Ltd., Manchester, England

ABSTRACT

Small crystals of InAs, InP, GaAs, and GaP have been grown from a vapor composed of the monochloride or mono-iodide of the metal and phosphorus or arsenic. Crystal growth took place at from 100° to 300°C below the melting points of the compounds. Whiskers of InAs up to 2 cm long also have been grown.

Indium monochloride tends to disproportionate in some of its reactions forming the trichloride and a compound of indium. The reaction of indium monochloride and arsenic vapors to form InAs therefore seemed a practical possibility. $AsCl_3$ would not form as it is unstable at the temperatures of such a reaction.

The reaction was of practical interest especially as we had established that chlorine had little or no effect on the electrical properties of InAs. Crystals of InAs in fact were deposited by this reaction and the principle was extended to the preparation of crystals of GaAs, InP, and GaP, even though the solubility of chlorine or iodine in these latter compounds is not yet known.

Theory

From the free energies of formation of the indium halides at 298°C the free energy change of reactions [1] and [2] are small but negative.

$$3InCl \leftrightarrows InCl_3 + 2In \qquad [1]$$

$$2InCl \leftrightarrows InCl_2 + In \qquad [2]$$

As the temperature rises the free energy change becomes more positive and the reactions tend to go from right to left.

If arsenic vapor is added to reaction [1], the following becomes possible:

$$3InCl + \tfrac{1}{2}As_4 \leftrightarrows InCl_3 + 2InAs \qquad [3]$$

The decrease in free energy due to the formation of InAs should lead to a reasonable yield of InAs crystals.

Equation [3] is strictly applicable only if the pressure of arsenic equals the dissociation vapor pressure of InAs at the temperature of the reaction. For arbitrary pressures of arsenic vapor, the InAs formed might be expected to be associated with an indium or arsenic-rich liquid as shown in the phase diagram (1, 2). Hence, a more general description of the reaction in Eq. [3] is:

$InCl + As_4$ (arbitrary pressure) in equilibrium with $[InCl_3 + (InAs + liquid)]$

It should be noted that Eq. [1]-[3] have been used merely to illustrate the principle and that the actual reaction is not known.

Arguments similar to the above can be applied to the bromides and iodides of indium and to the chlorides, bromides, and iodides of gallium together with the cases where phosphorus replaces arsenic.

Crystal Growth

All the crystals were grown in evacuated silica reaction tubes approximately 20 cm long and having volumes of about 50 cm^3.

Method 1.—The reaction tube containing the reactants on the left hand side of Eq. [3] was heated uniformly. Initially the temperature was maintained high enough to prevent any crystals forming and was lowered gradually until nucleation occurred.

Method 2.—The reaction tube contained a small amount of chloride or iodide of gallium or indium or only iodine itself, together with a sample of the appropriate $A_{III}B_V$ compound. The tube was placed in a furnace which had a temperature gradient of between 40° and 70°C over the length of the tube, the sample of the compound being at the hotter end. As the temperature of the whole furnace was lowered slowly, crystals nucleated at the cool end. The furnace was held at this temperature, and it was possible to transport the whole of the sample of the compound from the hot to the cool end of the tube.

This result follows from the fact that Eq. [3] is a

Table I

Reaction number	Initial reactants	Temp. of growth, °C	Pressure of atmospheres: Halide	Pressure of atmospheres: As_4 or P_4
1	InCl, As_4	725	8	1.2
2	InI, As_4	690	8.2	1.65
3	$InCl_3$, As_4	No growth	3.1 (800°C)	1.8 (800°C)
4	InI_3, As_4	No growth	3.1 (800°C)	1.35 (800°C)
5	GaI, P_4	1050	5.0	2.6

Table II

Reaction number	Initial reactants	Temp. of sample, °C	Temp. of growth, °C	Press. atm of halide
6	InAs, $InCl_3$	890	840	1.6
7	InAs, InI_3	875	830	1.6
8	InP, InI_3	915	860	1.65
9	GaAs, I_2	1070	1030	2.15

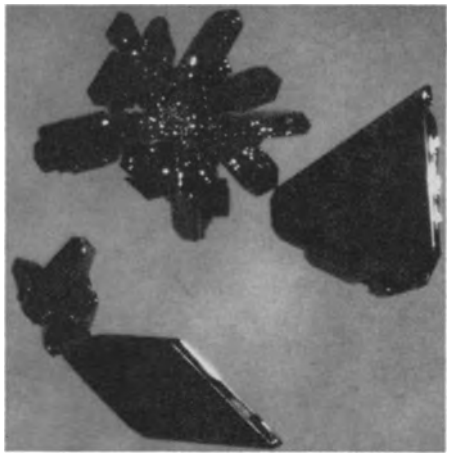

Fig. 1. InP crystals grown by reaction 8. Magnification 27X.

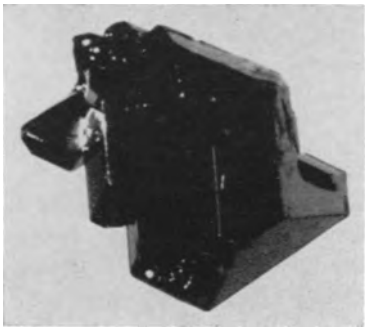

Fig. 2. GaAs crystals grown by reaction 9. Magnification 27X.

reversible reaction. At the hot end of the reaction tube the reaction tends to go from right to left and is reversed at the cool end.

Results

Table I gives a list of experiments that were performed according to method 1. The pressures that are listed are the partial pressures that the reagents would have at the temperature of growth but before they have reacted. Table II covers experiments that were performed by method 2. The pressure of the halide has been calculated as that which it would have been if the tube were at a uniform temperature equal to that of the cool end.

Crystals that have been grown by the reactions listed in Tables I and II are shown in Fig. 1-4.

Growth of InAs *Whiskers.*—Conditions under which whisker growth may be expected are not entirely clear, but it appears that there must be a low pressure of halide present in the tube and also a fairly rapidly falling temperature.

The whiskers always seemed to grow from what appeared originally to have been a molten globule.

The whisker shown in Fig. 4 was grown by reaction 6, Table II when the density of $InCl_3$ molecules was about $10^{18}/cm^3$. Whiskers up to 2 cm in length were grown by a combination of reactions 2 and 4 in Table I. The iodide vapor consisted of InI_3 at a pressure of about 3 atm at 800°C together with a trace of a lower iodide.

X-ray and electron diffraction data.—InAs crystallized mainly as flat plates which in many cases

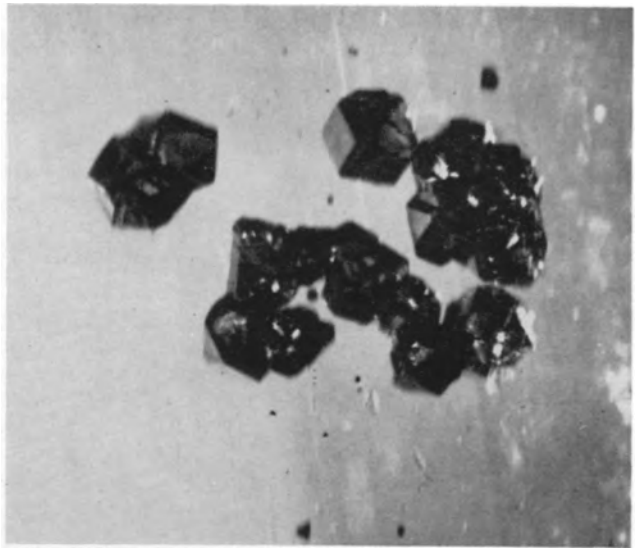

Fig. 3. GaP crystals grown by reaction 5. Magnification 40X.

Fig. 4. InAs whiskers grown by reaction 6. Magnification 40X before reduction for publication.

were up to 5 mm across. A sample was mounted in an electron diffraction camera and a "Kikuchi line" pattern was obtained by reflecting an electron beam at a glancing angle from the flat face of the crystal. From this it was deduced that the flat face was a (111) plane. This also was found to be the case with two other crystals.

The edge of the elementary cell was measured for each compound by the x-ray powder method using a copper anode and a nickel filter. The determinations are listed below together with other published results in brackets.

InAs	$a_o = 6.058_5$Å	[6.058$_4$Å] (1)
InP	$a_o = 5.868_8$Å	[5.869Å] (3)
GaAs	$a_o = 5.654_1$Å	[5.653$_4$] (4)
GaP	$a_o = 5.451_4$Å	[5.450$_5$] (4)

The close agreement between these determinations and previously published values shows that the various compounds have indeed been formed in all cases.

Acknowledgments

The authors are indebted to Mr. P. Worthington for his electron diffraction measurements, and to Miss K. Whitehead and Mr. L. Brownlee for the determination of unit cell sides.

We should also like to thank Dr. R. W. Sillars and Mr. R. P. Chasmar for their helpful criticisms of the manuscript and to Sir Willis Jackson, Director of Research and Education, and Dr. J. M. Dodds, Manager of Research Department, Metropolitan-Vickers Electrical Co. Ltd., for permission to publish this paper.

Manuscript received Nov. 3, 1958.

Any discussion of this paper will appear in a Discussion Section to be published in the December 1959 JOURNAL.

REFERENCES

1. T. S. Liu and E. A. Peretti, *Trans. Am. Soc. Metals*, **45**, 677 (1953).
2. J. von der Boomgaard and K. Schol, *Philips Research Repts.*, **12**, 127 (1953).
3. W. N. Reynolds, *et al.*, *Proc. Phys. Soc.*, **71**, 416 (1958).
4. G. Von Giesecke and M. Pfister, *Acta Cryst.*, **11**, 369 (1958).

Oxide Nucleation and the Substructure of Iron

E. A. Gulbransen and K. F. Andrew

Research Laboratories, Westinghouse Electric Corporation, Pittsburgh Pennsylvania

ABSTRACT

Electron optical studies were made of the initial stage of reaction of oxygen with pure iron. Oxidation occurred in a discontinuous manner with the oxide structure orienting to the metal grain. The sites for oxide nucleation depend on the initial pretreatment atmosphere. Thus, a vacuum annealing treatment showed a random arrangement of nucleation sites, while a hydrogen annealing treatment showed a highly ordered arrangement of nucleation sites.

Since iron was embrittled by annealing in dry and moist hydrogen and not by vacuum annealing, the nucleation sites probably show the substructure of iron responsible for embrittlement.

The theory of oxidation as developed by Wagner (1, 2), Mott (3), and others is based on the diffusion of metal or oxygen atoms and ions through interstitial sites or through cation and anion defects in the oxide film. The oxide film is assumed to be uniform while the metal underlying the oxide is assumed to be structureless over a particular grain. Recent developments in metal physics have shown that crystal orientation, dislocations, and other defects determine the mechanical properties of the metal. These factors also may determine the nature of chemical reactions on metal surfaces. The purpose of this paper is to show the effect of annealing environment on the oxide nucleation pattern for pure iron and to indicate a possible relation between the nucleation pattern and the mechanical properties of the metal.

The fact that iron reacts with oxygen in a nonuniform manner is well known. Early electron optical work was reviewed by Phelps, Gulbransen, and Hickam (4). These authors, in addition, studied the structure of oxide films formed on mechanically polished specimens of pure iron using electrochemical stripping methods for removal of the oxide film. Electron optical studies showed the oxide to consist of many small crystals several hundred to a thousand angstroms in size. The oxide crystals were nearly randomly oriented with respect to the metal grain.

Bardolle and Bénard (5) used carefully polished and annealed specimens of Armco iron to study oxide nucleation processes at temperatures between 650° and 850°C at low pressures of oxygen. At 850°C and a vacuum of 10^{-3} mm Hg, a few well oriented oxide nuclei of definite crystal habit were formed. Many nuclei were formed at pressures of 10^{-2}-10^{-1} mm Hg. Light micrographs of thick oxide films formed under these conditions showed the oxide film on a single metal crystal to consist of many similarly oriented crystals. In no case was a single crystal of oxide observed to form on a single crystal of iron.

Gulbransen, McMillan, and Andrew (6) extended the work of Bardolle and Bénard (5) by controlling conditions of oxidation and by use of electron optical methods. The latter method makes possible observation of finer details of the crystal habit.

Thermodynamic conditions for oxidation.—Since the formation of an oxide film, as well as its crystal habit, depends on the relative importance of one or more chemical reactions, it is necessary to consider the thermodynamic equilibria of these reactions. For iron at 650°-850°C, the more important reactions are the following: (*a*) direct oxidation of iron to FeO, (*b*) reaction of carbon in the metal with the surface oxide to form carbon monoxide and the metal, and (*c*) solution of oxygen in the metal.

Calculations show the dissociation pressure of oxygen over FeO and Fe to be $10^{-17.6}$ atm at 850°C (6). The extent of the oxygen reaction is limited only by the oxygen available and the time of reaction.

Under conditions of low pressure, carbon in the metal reacts with the surface oxide. To minimize this reaction, the concentration of carbon should be less than 0.005% by weight (6). The kinetics of this reaction has been shown by Gulbransen and Andrew (7) to be feasible above 610°C.

Several recent values exist for the solubility of oxygen in alpha-iron. Seybolt (8) found a value of 0.022 wt % at 850°C. Sifferlen (9) has shown that for iron recrystallized by a rigorous thermal treatment the solubility does not exceed 0.002 wt % at 850°C. Considering the low values for the solubility and that oxygen pressures of 10^{-2}-10^{-3} mm Hg were used, we feel that the amount of oxygen dissolving in the metal is small.

Good conditions for studying the initial nucleation process and the effect of pretreatments on iron are as follows: (*a*) carbon content of less than 0.005 wt %, (*b*) oxygen pressures of less than 0.01 mm Hg, (*c*) electropolished and annealed metal, and (*d*)

low concentration of other impurities such as Mn, S, P, Si, etc.

Structural factors in matter.—Four factors are important in discussing structural factors in the oxide nucleation process. These are as follows: (*a*) crystal structure or atomic geometry of the unit cell, (*b*) crystal size and shape, (*c*) particle size and shape, and (*d*) orientation of the oxide particles with respect to the underlying metal crystal.

The crystal structure is studied by electron diffraction while crystal size and shape and orientation factors are studied by the electron microscope.

Experimental

Samples.—"Puron" [1] iron was used for all of the experiments. The iron contains about 0.001% metallic impurities. Of nonmetallic impurities there exists about 0.04% oxygen, 0.005% C, and virtually no sulfur, phosphorus, or nitrogen.

The following steps were used in the preparation of specimens for this study: (*a*) mechanical polishing using polishing papers up to 4/0 under purified kerosene, (*b*) cleaning with soap and water, distilled water, petroleum ether, and absolute alcohol, (*c*) electrolytic polishing using Jacquet's solution, (*d*) washing in distilled water and absolute alcohol.

The following pretreatments were used: (*a*) annealing at 875°C for 24 hr in vacuum of 10^{-7} mm Hg plus 1-hr annealing in hydrogen passed through a palladium tube at 2.4 cm Hg pressure to remove any oxide formed in vacuum annealing, cooled in vacuum, (*b*) annealing at 850°C for 20 hr in 1 atm of hydrogen purified by passing over hot copper and dried with $CaCl_2$, cooled in hydrogen, (*c*) annealing at 850°C for 23 hr in tank hydrogen passed over a dry ice trap at −78.5°C at 59 cm Hg, cooled in vacuum, (*d*) annealing at 875°C for 21 hr in hydrogen passed through a palladium tube at 59 cm Hg pressure, cooled in vacuum, (*e*) same as (*d*) except with an additional annealing for 20 hr in vacuum of 10^{-7} mm Hg plus 1 hr in palladium purified hydrogen at 2.3 cm Hg pressure to remove any oxide formed, cooled in vacuum, and (*f*) annealing at 875°C for 23 hr with hydrogen passed through a palladium tube at 59 cm Hg plus 0.2 cm Hg of pure nitrogen, cooled in vacuum.

Reaction with oxygen.—Strips of 0.013 cm thick iron weighing about 0.1 g and having a surface area of 2.5 cm^2 were reacted in the microbalance system. Specimens were introduced singly and the system pumped overnight. A vacuum of better than 10^{-6} mm Hg was obtained. The furnace at the desired temperature was raised around the Mullite furnace tube. A given quantity of oxygen was introduced by means of a gas handling system. Weight changes were followed with the microbalance. Although the oxygen reacted very rapidly with the metal, the metal was kept in contact with the gas atmosphere for 25 min. Following reaction the residual gases in the system were evacuated, the furnace lowered, and the specimen allowed to cool in the vacuum.

The following facts were observed or calculated for each nucleation experiment: (*a*) weight of oxygen reacting, (*b*) average thickness of oxide film, (*c*) color of oxide, (*d*) crystal structure of oxide, (*e*) size and shape of oxide crystallites, and (*f*) crystal habit and orientation of oxide with respect to the metal grain.

Examination of crystal habit and structure.—The crystal structure of the oxide crystallites was studied by transmission electron diffraction while the crystal habit was studied by electron microscopy of the stripped oxide film. Electron diffraction patterns were taken with the electron diffraction adapter of the EMB-4 electron microscope. Polystyrene-silica replicas shadowed with chromium were prepared in the conventional manner. Stripped oxide films were prepared in an electrochemical stripping apparatus similar to one previously described (4). To support the oxide crystallites, the oxidized surface was covered with a Parlodion film.

Several modifications were made in the electron microscope to obtain large fields at low magnifications. A special internal screw mechanism was used for removing the projector-pole piece for carrying out studies in the range of 400X to 1600X. Most of electron micrographs were made at 1080X to 1600X and enlarged two to eight times.

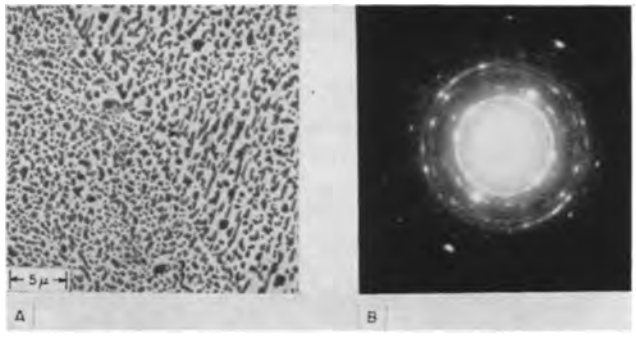

Fig. 1. Oxide film (453Å) stripped from vacuum pretreated Puron. Vacuum, 875°C, 20 hr.

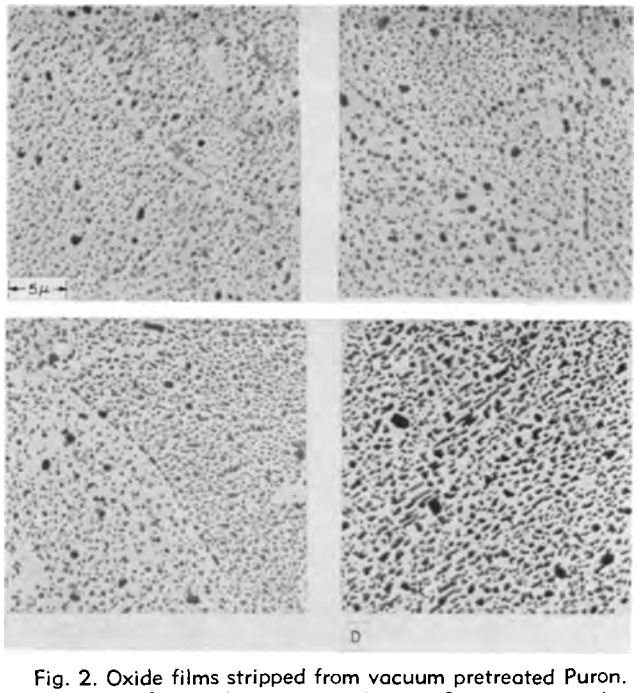

Fig. 2. Oxide films stripped from vacuum pretreated Puron. Vacuum, 875°C, 20 hr. A, upper left, 64Å; B, upper right, 106Å; C, lower left, 230Å; D, lower right, 453Å.

[1] "Puron" is a proprietary name for a grade of pure iron manufactured by Westinghouse Electric Corporation.

Table I. Summary of vacuum pretreatment experiments

Pretreatment	Nucleation conditions	Oxide thickness $\mu g/cm^2$	Å	Color	Crystal size, μ	Remarks
For all experiments: 10^{-7} mm Hg, 875°C 24 hr, plus 1 hr H_2 at 2.4 cm Hg at 875°C, cooled in vacuum	O_2 at 5 x 10^{-4} mm Hg, 850°C, 25 min	0.92	64	Bright	<0.15 few larger	Random nucleation, oriented growth
	O_2 at 1 x 10^{-3} mm Hg, 850°C, 25 min	1.5	106	Nearly bright	<0.25 few larger	Same
	O_2 at 2 x 10^{-3} mm Hg, 850°C, 25 min	3.29	230	Blue-gray	<0.30 few larger	Same
	O_2 at 5 x 10^{-3} mm Hg, 850°C, 25 min	6.46	453	Blue-gray	<0.50 few larger	Same

Results and Discussion

Vacuum pretreatment.—Table I and Fig. 1 and 2 show the pretreatment and nucleation conditions and results. Figure 1A shows a typical electron micrograph of the stripped oxide film formed by low pressure oxidation at 850°C using oxygen at a pressure of 5 x 10^{-3} mm Hg. For this condition a blue-gray film was formed having an average film thickness of 453Å. The electron diffraction pattern shown in Fig. 1B shows a highly oriented oxide film of FeO and Fe_3O_4. The electron micrographs suggest that, although the oxide is highly oriented to the metal, the sites at which oxide nucleation takes place are nearly random.

Figure 2, A, B, C, and D, shows the effect of the amount of oxidation on the nucleation and growth processes. The average oxide film thickness varies from 64 to 453Å. The oxide crystal size increases with the amount of oxidation. In each experiment electron diffraction patterns showed oriented oxide crystals while the electron micrographs showed a random arrangement of the oxide nucleation sites.

Figures 1 and 2 show several interesting facts about the mechanism of oxidation when the specimen was annealed in high vacuum. (*A*) Single crystals of oxide do not form on a single crystal of metal. This confirms the results of a light micrograph study of Bardolle and Bénard (5) for a later stage of the reaction. The fact that many nucleating centers exist on a metal surface may be related to dislocations and defects in the structure of the metal. (*B*) The oxide structures were oriented to the metal structure. (*C*) Except for the grain boundaries, nearly random distribution of nucleation sites were observed. (*D*) The grain boundaries of the metal were not preferentially attacked.

Pretreatment with tank hydrogen passed over hot copper.—Table II shows details of pretreatment and oxide nucleation conditions together with information on the thickness and color of the oxide crystallites. Fig. 3, A and B, shows electron micrographs of the oxide film formed at 850°C by dosing with O_2 at 2 x 10^{-3} mm Hg and the oxide film formed at 750°C by dosing with O_2 at 1 x 10^{-3} mm Hg. Figure 4, A and B, shows similar results for the film formed at 650°C. A surface replica was included to check the film stripping technique.

Electron micrographs of specimens pretreated in partially purified hydrogen and cooled in hydrogen showed some similarities with and some differences from the results of vacuum annealing. For both pretreatments, a discontinuous oxide film was formed.

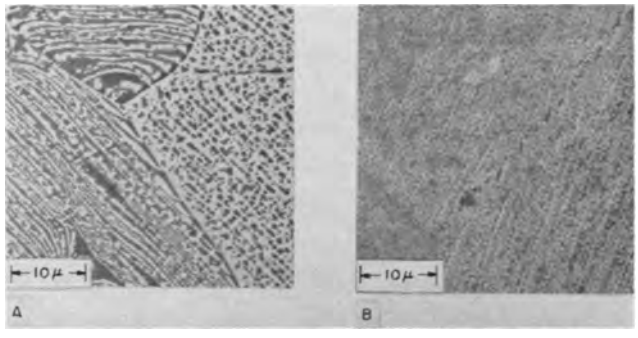

Fig. 3. Oxide film stripped from Puron annealed in hydrogen passed over hot copper. H_2, 850°C, 20 hr, cooled in H_2. A, 752Å thick oxide, 850°C; B, 322Å, thick oxide, 750°C.

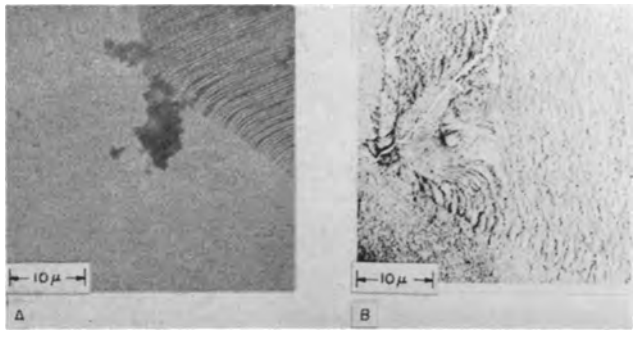

Fig. 4. Oxide film stripped from Puron annealed in hydrogen passed over hot copper and surface replica. H_2, 850°C, 20 hr, cooled in H_2. A, 252Å thick oxide, 650°C; B, surface replica.

Electron diffraction studies of the oxide films in both cases show orientation of the oxide structure to the metal. In addition, the particle size of the oxide crystals for the same degree of oxidation was nearly the same.

Several major differences were observed: (*a*) nucleation sites were not random but highly ordered in certain directions determined by the orientation of the metal grain; (*b*) spacings of these lines of nucleation sites were relatively constant over a given distance; (*c*) lines of nucleation were usually bent at the grain boundaries and join with lines of oxide growth of other metal grains, and (*d*) circular growth patterns were frequently seen. This is shown in Fig. 5. The circular growth patterns probably were related to inclusions or other local defects in the metal structure.

To test the influence of annealing in dry hydrogen, tank hydrogen was dried by passing through a dry ice trap at —78.5°C. Details of the experiment were

Table II. Summary of hydrogen pretreatments, tank hydrogen passed over hot copper

Pretreatment	Nucleation conditions	Oxide thickness $\mu g/cm^2$	Oxide thickness Å	Color	Crystal size, μ	Remarks
1 atm, 850°C, 20 hr, cooled in H_2	O_2 at 2 x 10^{-3} mm Hg, 850°C, 25 min	10.73	752	Light blue	1	Directed-nucleation pattern, oriented growth
1 atm, 850°C, 20 hr, cooled in H_2	O_2 at 1 x 10^{-3} mm Hg, 750°C, 25 min	4.59	322	Blue spots	0.5	Same
1 atm, 850°C, 20 hr, cooled in H_2	O_2 at 1 x 10^{-3} mm Hg, 650°C, 25 min	3.60	252	Blue spots	0.3	Same
56 cm, 850°C, 23 hr, cooled in vacuum dew point—78.5°C	O_2 at 5 x 10^{-3} mm Hg, 850°C, 25 min	6.35	451	Blue	1.0	Partially directed nucleation pattern, oriented growth

given in Table II. Figure 6, A, B, and C, shows three electron micrographs, while Fig. 6D shows an electron diffraction pattern of the oxide crystals. Although an ordered pattern of oxide nucleation was observed, the amount of order was smaller than that shown in Fig. 3, 4, and 5. The electron diffraction pattern showed oriented oxides of FeO and Fe_3O_4 were formed.

Pretreatment with hydrogen passed through palladium.—Table III and Fig. 7, 8, and 9 show details of pretreatment and nucleation conditions together with a summary of the results.

Figure 7, A and B, shows an electron micrograph and an electron diffraction pattern of a specimen pretreated in hydrogen passed through palladium and cooled in vacuum. The sample was oxidized at 850°C in O_2 at 5.0 x 10^{-3} mm Hg. The electron diffraction pattern shows a highly oriented structure while the electron micrograph shows a partially ordered oxide nuclei. Ordering of nucleation sites was not as well developed as for specimens annealed and cooled in less pure hydrogen.

Figure 8 shows an electron micrograph and an electron diffraction pattern of a specimen pretreated in palladium purified hydrogen and then held in a vacuum for 20 hr at 875°C before cooling. The electron micrograph shows a partial ordering of oxide nucleation sites.

Figure 9, A and B, shows electron micrographs of a specimen treated in palladium purified hydrogen plus a small amount of pure nitrogen. Nucleation sites show only a small amount of ordering. Nitrogen, as an impurity in the hydrogen, does not have an important influence on the ordering process.

We conclude from these experiments that water vapor in hydrogen is primarily responsible for ordering of nucleation sites for oxide formation.

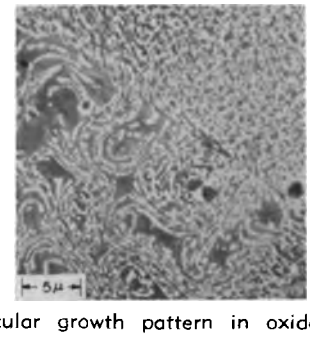

Fig. 5. Circular growth pattern in oxide film (752Å) formed on Puron annealed in hydrogen passed over hot copper. H_2, 850°C, 20 hr, cooled in H_2.

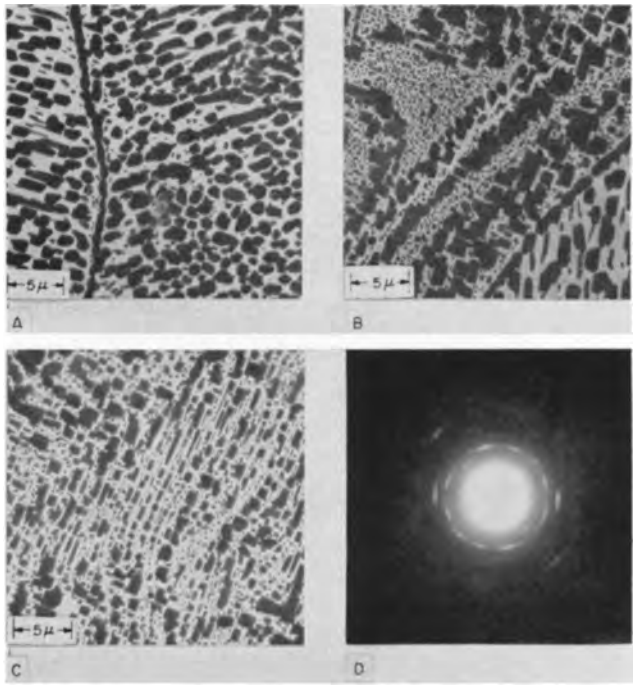

Fig. 6. Oxide film stripped from Puron annealed in hydrogen passed over hot copper and dried (—78.5°C). H_2, 850°C, 23 hr, cool in vacuum.

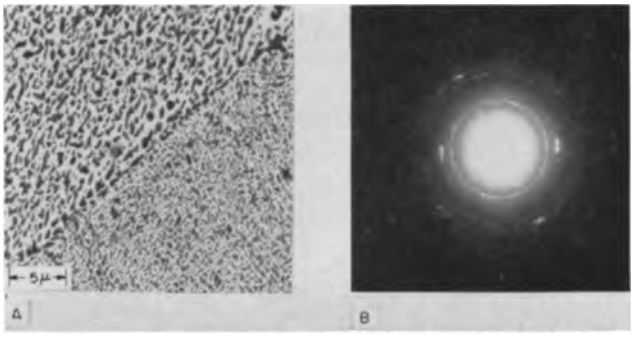

Fig. 7. Oxide film (417Å) stripped from Puron annealed in hydrogen passed through palladium. H_2, 875°C, 24 hr, vacuum cooled.

Discussion

It is of interest to note that the density of oxide crystallites in Fig. 1 is of the same order of magnitude as the density of dislocations in a well annealed metal crystal, i.e., of the order of $10^8/cm^2$. The growth of oxide nuclei may be related to the number and arrangement of dislocations in the metal crystal. Normally, these nucleation centers are random in arrangement. However, if iron is annealed

Table III. Summary of hydrogen pretreatments, palladium purified hydrogen

Pretreatment	Nucleation conditions	Oxide thickness $\mu g/cm^2$	Oxide thickness Å	Color	Crystal size, μ	Remarks
59 cm Hg, 875°C, 21 hr, cooled in vacuum	O_2 at 5.0 x 10^{-3} mm Hg, 850°C, 25 min	5.96	423	Blue-black	0.3 few larger	Partially directed nucleation pattern, oriented growth
59 cm Hg, 875°C, 21 hr + 10^{-7} mm Hg, 20 hr + H_2 2.3 cm Hg, 1 hr, cooled in vacuum	O_2 at 5.0 x 10^{-3} mm Hg, 850°C, 25 min	6.36	452	Blue-black	0.3 few larger	Same
59 cm Hg + 0.2 cm Hg N_2, 850°C, 23 hr, cooled in vacuum	O_2 at 5.0 x 10^{-3} mm Hg, 850°C, 25 min	6.05	430	Purple	1.0	Same

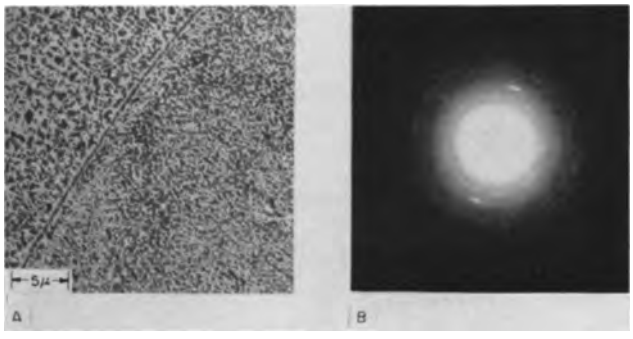

Fig. 8. Oxide film (445Å) stripped from Puron annealed in hydrogen passed through palladium. H_2, 875°C, 24 hr plus vacuum, 875°C, 20 hr.

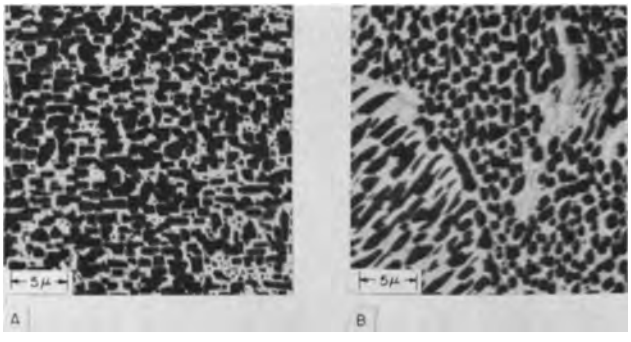

Fig. 9. Oxide film stripped from Puron annealed in palladium hydrogen plus nitrogen. H_2 + N_2, 850°C 23 hr, vacuum cooled.

in impure hydrogen, these nucleation centers become ordered along definite crystallographic directions. The mechanism of ordering is not clear. However, low pressure oxidation offers a new method for the study of the fine structure of iron not observable by light microscopic studies of low temperature etched surfaces.

These results may lead to an understanding of the effect of annealing treatments on the mechanical properties of Puron and other pure irons. Stanley (10) has made a thorough study of the embrittling of Puron when heated in high vacuum and in dry and moist hydrogen atmospheres at temperatures of 700°-1100°C. Puron is embrittled in dry hydrogen atmospheres at a dew point of −65°C in 10 hr for the temperature range of 700°-1150°C. In moist hydrogen, Puron was embrittled in about an hour. Vacuum annealing did not lead to embrittlement. Light micrographic studies showed only minor changes in metal structure.

Stanley's observations on the embrittlement of iron at 700°C and our studies on the effect of hydrogen and its impurities on the oxide nucleation pattern at 700°C appear to be related. Atmospheres which embrittle iron give ordered nucleation sites for oxide growth while atmospheres which do not embrittle iron give random nucleation patterns for oxide growth.

Manuscript received Dec. 2, 1958. This paper was prepared for delivery at the Philadelphia Meeting, May 3-7, 1959.

Any discussion of this paper will appear in a Discussion Section to be published in the December 1959 JOURNAL.

REFERENCES

1. C. Wagner, *Z. physik. Chem* (B), **21**, 25 (1953).
2. C. Wagner, Diffusion and High Temperature Oxidation of Metals in "Atom Movements," American Society for Metals, Cleveland (1951).
3. N. F. Mott, *Trans. Faraday Soc.*, **36**, 472 (1940).
4. R. T. Phelps, E. A. Gulbransen, and J. W. Hickman, *Ind. Eng. Chem., Anal. Ed.*, **18**, 391 (1946).
5. J. Bardolle and J. Bénard, *Rev. met.*, **49**, 613 (1952).
6. E. A. Gulbransen, W. R. McMillan, and K. F. Andrew, *Trans. Am. Inst. Mining Met. Engrs.*, **200**, 1027 (1954).
7. E. A. Gulbransen and K. F. Andrew, *J. Phys. & Colloid Chem.*, **53**, 690 (1948).
8. A. Seybolt, *J. Metals*, **6**, 641 (1954).
9. C. M. Sifferlen, [see discussion by R. Collongues of paper by W. R. McMillan and E. A. Gulbransen, *J. chim. phys.*, 643 (1956)].
10. J. K. Stanley, *Trans. Am. Soc. Metals*, **44**, 1097 (1952).

The Separation of Hydrogen and Deuterium by the Reaction of Iron with Water

Hilton A. Smith, Carl O. Thomas,[1] and John C. Posey[2]

Department of Chemistry, University of Tennessee, Knoxville, Tennessee

ABSTRACT

In the decomposition of water by reaction with iron, as in the electrolysis of water, the residual water is enriched in deuterium. Since the separation factor is an inverse function of the temperature, an attempt was made to increase the reaction rate at low temperatures. Introduction of cathodic surfaces by partial plating of cathodic impurities on steel increased the reaction rate by a factor of 2 to 4 at 98°-100°C. Separation factors from 4.8 to 6.1 were observed for the chemical reaction of these partially plated samples with water. In electrolysis experiments vigorous agitation of the electrolyte caused an increase in the separation factor.

An important part of the development of nuclear power is the procurement of heavy water which is used as a moderator in some types of nuclear reactors (1). Since the natural concentration of deuterium in water is approximately 1 part in 7000 and since separation factors are generally small for isotope separation processes, it is necessary in the initial concentration stages to process very large quantities of water (2). One of the largest separation factors is obtained in the electrolysis of water. However, the energy cost is high, and the method is practical economically only when a market exists for electrolytic hydrogen or when the method is used for the final concentration of water which has been enriched by a less expensive process (2).

Separation of the isotopes is obtained in the direct chemical reaction of a variety of metals with water or steam (3-5). Smith and Posey (6) reported separation factors of 3.2 to 1.4 for the reaction between iron and steam at 118°-340°C. The reaction rate in this temperature range is low for a practical production technique. Moreover, the commercial production of hydrogen by the reaction between iron and steam requires temperatures of 800°-1000°C (7).

Since the separation factor is an inverse function of the temperature (8), temperature requirements for a useful separation factor and a useful rate in the reaction of metals with water or steam appear to be mutually exclusive. The principle of sacrificial corrosion protection suggested the possibility that the reaction rate might be increased without increasing the temperature, so that the advantage of the larger separation factor at the lower temperatures could be retained. The present paper discusses reaction rates and separation factors in the direct chemical reaction of water with iron samples some of which had plated on a portion of their surfaces a variety of cathodic materials. The effect of vigorous stirring on the concentration gradient at the cathode also is discussed.

[1] Present address: Bell Telephone Laboratories, Murray Hill, N. J.
[2] Present address: Union Carbide Nuclear Company, Oak Ridge, Tenn.

Experimental

Reaction rates.—Reaction rate data were obtained by measuring the rate of hydrogen evolution at constant volume or at constant pressure. The constant volume apparatus is shown in Fig. 1. The liquid and gas-phase volumes were approximately 10 ml each. Since the apparatus is very simple and compact, as many as ten runs could be conducted simultaneously in a 5-gal thermostat. Constant-pressure apparatus is shown in Fig. 2. The volume of the reaction flask was approximately 500 ml. Before each run the receiving flask was evacuated. The check valve was set to operate at 85 cm Hg.

The electrolyte was ferrous chloride which was prepared by the reaction of hydrochloric acid with an excess of iron powder. In order to conserve heavy water, reaction rates were investigated using ordinary water only.

Iron samples were prepared from the following materials: Merck and Company iron powder (re-

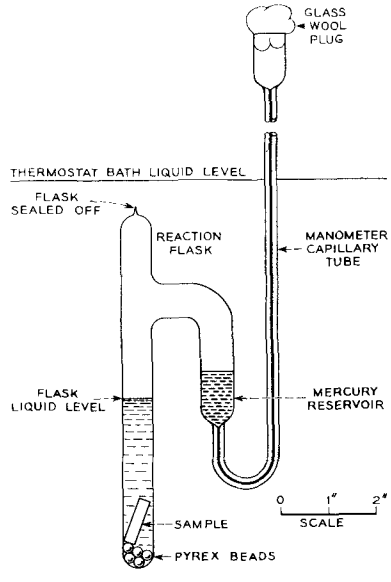

Fig. 1. Constant volume apparatus for measuring rate of hydrogen evolution.

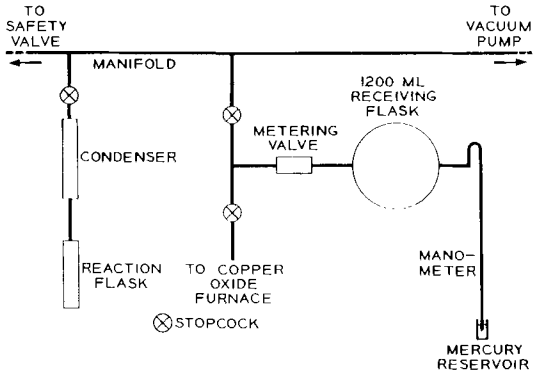

Fig. 2. Constant pressure apparatus for determining separation factors and rates of hydrogen evolution.

duced by hydrogen); J. T. Baker's and Baker and Adamson's reagent grade iron wire (size AWG-36); extremely pure bulk iron (9) provided by the Bell Telephone Laboratories and the Battelle Memorial Institute; and ordinary low-carbon steel plate, rod, and tubing. Iron powder was used as received. Wire samples approximately 1 meter in length were wound into spirals approximately 5 mm in diameter and 3 cm in length. Rectangular and cylindrical samples of the remaining materials were prepared by machining.

All of the samples except the iron powder were cleaned by washing with hot C.P. toluene and then by sulfuric acid pickling. Following cleaning, the absence of hydrophobic contaminants was verified by the wetting properties of the surface as exhibited by the contact angle of water droplets at the surface.

The surface area of the iron powder was measured by the BET-nitrogen-adsorption method and the krypton-adsorption method. The values found by these two methods were 3.5 $m^2\ g^{-1}$ and 3.4 $m^2\ g^{-1}$, respectively. In order to obtain a comparison between the reaction rates observed with powder and with bulk samples, the rate of hydrogen evolution was calculated in cm^3 atm of gas per cm^2 of substrate per minute, corrected to 30°C. For all of the samples, except the iron powder, the reaction rate was constant throughout the runs. Since the surface roughness of the bulk samples changed visibly during the runs, the rate per unit area for the bulk samples was calculated from their physical dimensions, arbitrarily assuming unit roughness factor.

For all of the samples, except iron powder, runs were made with a cathodic surface plated onto approximately 50% of the sample surface. Plating was accomplished by displacement, thermal decomposition, and electroplating.

Table I summarizes the reaction-rate data for a variety of conditions. It can be seen that the rate of hydrogen production may be increased by the application of cathodic metals to a portion of the surface of the iron samples. The data presented in Table I include rate values obtained with both types of apparatus. This suggests that the difference in the reaction rates at constant pressure and at constant volume is not significant.

Some measurements of the reaction rate, not included in Table I, were made with samples of wire, Bell Telephone iron, Battelle iron, and low-carbon

Table I. Rate of hydrogen production in 1M ferrous chloride solutions at 98°-100°C

Substrate	Cathode	10^4 Reaction rate, (cm^3 atm) $cm^{-2}\ min^{-1}$
Iron powder	—	0.39 (0.01)‡
Iron powder	—	0.10 (0.01)
Iron wire (JTB)	—	1.54 (0.01)
Iron wire (B&A)	—	1.55 (0.05)
Pure iron (Battelle)	—	1.17 (0.07)
Pure iron (BTL)	—	1.04 (0.07)
Low carbon steel	—	1.07 (0.05)
Low carbon steel	Au*	4.3 (0.7)
Low carbon steel	Ag*	2.8 (0.4)
Low carbon steel	Cu*	3.1 (0.4)
Low carbon steel	Brass*	3.3 (0.4)
Low carbon steel	Ni*	3.9 (0.4)
Low carbon steel	Cd*	2.5 (0.4)
Low carbon steel	Pt†	4.1 (0.5)

* By electroplating 50% of surface.

† By thermal decomposition on 50% of surface.

‡ Average error in parentheses, defined as $\pm\Sigma d/n\sqrt{n}$, where d is the deviation of a single measurement from the arithmetical average, and n is the number of measurements.

steel which were partially plated by displacement with mossy deposits of platinum, palladium, and copper. In general, the initial rates were several times larger than those which were obtained with unplated samples. However, the hydrogen evolution rates dropped off rapidly and approached the values which were obtained with the unplated samples. The mossy deposits had a tendency to become detached from the iron, and they collected a layer of reddish-brown oxide very quickly. The oxide layer eventually turned black. The reproducibility of the rate measurements with this type of cathode surface was very poor.

Rates with iron powder were initially relatively rapid but decreased rapidly, presumably due to stifling by the reaction products. Prereduction of the powder, coating with copper, or use of other salts such as sodium chloride, ammonium chloride, sodium sulfate, ferrous sulfate, and zinc sulfate did not prevent the decrease in rate as the reaction proceeded.

Separation factors.—Ferrous chloride solutions of twice the desired strength were prepared as described above. A calculated amount of heavy water was added in order to produce a salt solution of the appropriate concentration which also contained approximately 45 mole % of heavy water. The heavy water[3] was reported to be 99.8% pure.

The reaction was carried out in the apparatus shown in Fig. 2. The hydrogen-deuterium mixture which was collected in the receiving flask was subsequently oxidized by copper oxide at 300°C in a Pyrex-tube furnace. The water which was produced by this reaction was collected in a cold trap. The method has been described in detail by Posey (6).

Approximately 130 ml of salt solution was used in each of the runs. The amount of water which was consumed in the reaction was small in comparison to the total amount of water present. However, the change in the composition of the residual water during a run was large enough to affect the calcu-

[3] Obtained from the Stuart Oxygen Company.

Table II. Separation factors in the reaction of cathodically coated steel samples with 1M ferrous chloride solutions at 98°-100°C

Cathode*	Separation factor
Uncoated steel	6.1 (0.5)†
Au	5.7 (0.4)†
Ag	5.6 (0.7)†
Cu	6.0 (1.0)†
Brass	6.0 (0.7)†
Ni	4.8 (0.9)†
Cd	5.3 (0.7)†
Fe powder	5.2 (0.1)†

* By electroplating on 50% of surface.
† Average error.

lation of the separation factor. Therefore, the arithmetical average of the compositions at the beginning and at the end of the run was used for the calculation of the separation factor. A small sample of the salt solution was taken before and after each run. The samples were vacuum distilled, and the water was collected in a cold trap. The isotopic compositions of the various water samples were determined by the falling-drop method of Combs, Googin, and Smith (10).

Steel tubing was used for these runs since it provided the most convenient form for plating, for obtaining a large surface area, and for physically supporting the samples in the reaction flask.

Table II lists the separation factors which were obtained in the reaction of 1*M* ferrous chloride solutions (45 mole % heavy water) at 98°-100°C with unplated and with partially plated samples of steel tubing. Separation factors were calculated by means of Eq. [1]

$$\alpha = (D/H)_e/(D/H)_g \qquad [1]$$

where D and H are the mole fractions of deuterium and of hydrogen, the subscript *e* refers to the electrolyte, and the subscript *g* to the gas produced by the reaction.

Separation factors also were determined in a series of electrolysis experiments with an external emf of 4 v and a current density of 0.06 to 4 amp cm^{-2}. All electrolysis experiments were conducted in 1*M* ferrous chloride solutions containing approximately 45 mole % heavy water. The only heating was that produced by the electrical-power dissipation in the cell, which established an operating temperature of 30°-45°C. The purpose of these runs was to determine the effect of vigorous stirring on the separation factor. Three levels of stirring were investigated: that provided by hydrogen evolution at the cathode, that provided by vigorous mechanical agitation, and that provided by ultrasonic agitation. The mechanical agitation was obtained in the apparatus shown in Fig. 3. The cathode, to which an off-balance weight was attached, was rotated at 1800 rpm, with consequent vigorous vibration. The ultrasonic generator[4] produced sufficient energy to create a Nujol-water emulsion in a test tube in approximately 1 min.

[4] Manufactured by the Crystal Research Laboratories, Hartford, Conn.

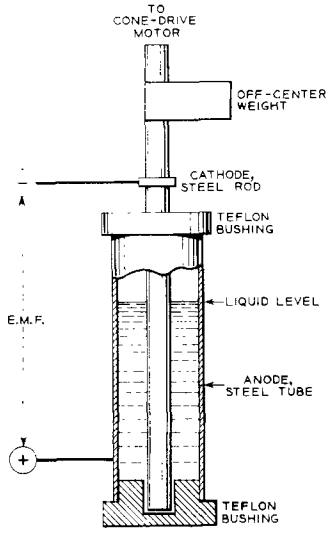

Fig. 3. Electrolysis cell with rotating off-balance cathode

A much larger fraction of the water was decomposed in the electrolysis runs than in the direct chemical reaction runs. Therefore it was not necessary to collect the hydrogen and deuterium. Instead, the separation factor was determined from the initial and the final concentrations of the reacting water by means of Eq. [2]

$$\alpha \ln (H_o/H) = \ln (D_o/D) \qquad [2]$$

where H_o and D_o are the initial concentrations, and H and D are the final concentrations of hydrogen and deuterium in the reacting material. The separation factors for the three types of electrolysis experiments are presented in Table III.

Discussion

The rate of hydrogen production per unit surface area of unplated sample was approximately the same for all of the materials, except iron powder. Therefore, for reasons of convenience, steel was chosen as the substrate material for the investigation of plated cathodic surfaces.

The increase in the reaction rate which was produced by the artificial introduction of galvanic couples was lower than expected. It is possible that cathodic polarization prevented the rates from being much larger. Since hydrogen was the desired product, it was not possible to take advantage of oxidative depolarization of the cathode in order to increase the rates. In fact, the preparation and handling of the salt solutions was done in such a manner as to minimize the amount of dissolved air, and the

Table III. Separation factors in the electrolysis with steel electrodes of stirred 1M ferrous chloride solutions at 30°-45°C

Method of stirring	Separation factor
Hydrogen evolution at cathode	7.23 (0.09)*
Rotating off-balance cathode	7.61 (0.08)*
Ultrasonic agitation	8.32 (0.07)*

* Average error.

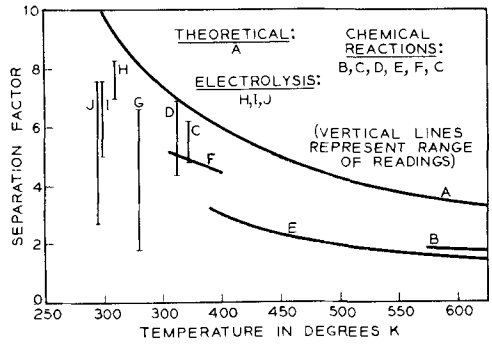

Fig. 4. Separation factors for reaction of metals with mixed protium oxide and deuterium oxide. A, Theoretical, Eyring and Cagle (8); B, Henderson and Bernstein (5); C, massive iron, present work; D, Hughes, Ingold, and Wilson (12); E, Smith and Posey (6); F, iron powder, present work; G, Johnston and Davis (13); H, electrolysis, present work; I, electrolysis, Topley and Eyring (11); J, electrolysis, Topley and Eyring (14).

ferrous chloride solutions were continually in contact with excess metal. The solutions were always blue-green in color.

Separation of hydrogen and deuterium by chemical or electrical decomposition of water depends on differences in the reaction rates of the two species. Therefore, the kinetic separation factor normally should be calculated by use of Eq. [2]. This was done in the electrolysis experiments where a relatively large fraction of water was decomposed. Since a very small fraction of the water was decomposed in the direct chemical reaction between iron and water, steady-state conditions were approximated, and it was possible to calculate the separation factor by use of Eq. [1].

The average values of the separation factors in the chemical reaction of iron with water vary from 4.8 for a brass cathode to 6.1 for uncoated steel. The values of the separation factors are not sufficiently precise to show conclusively any variation due to the nature of the cathode. From the data in Table II a composite separation factor of 5.7 may be calculated with an average error of ± 0.2.

No variation in the separation factor could be observed in the electrolysis experiments as a function of current density.

Topley and Eyring (11) discussed in detail the effect on the observed separation factor of a concentration gradient in the thin film of liquid at the cathode surface. They concluded that the effect should be small. The data in Table III show that efficient stirring can increase the separation factor.

The direct chemical reactions and the electrolysis experiments were performed at different temperatures and cannot be compared directly. In Fig. 4 the separation factors obtained in this investigation are compared with selected values from the literature. Figure 4 also includes the theoretical curve of separation factor vs. temperature which was calculated by Eyring and Cagle (8).

Acknowledgment

The authors are indebted to the U. S. Atomic Energy Commission for support of this work.

Manuscript received Oct. 1, 1958. This paper is taken from theses submitted by Carl O. Thomas and John C. Posey in partial fulfillment of the requirements for the Ph.D. degree in chemistry at the University of Tennessee, Knoxville.

Any discussion of this paper will appear in a Discussion Section to be published in the December 1959 JOURNAL.

REFERENCES

1. R. Stephenson, "Introduction to Nuclear Engineering," pp. 102-105, McGraw-Hill Book Co., Inc., New York (1954).
2. H. K. Rae, *Chemistry in Can.*, **7**, No. 10, 27 (1955).
3. W. Bleakney and A. J. Gould, *Phys. Rev.*, **44**, 265 (1933).
4. J. Horiuti and A. L. Szabo, *Nature*, **133**, 327 (1934).
5. W. G. Henderson and R. B. Bernstein, *J. Am. Chem. Soc.*, **76**, 5344 (1954).
6. H. A. Smith and J. C. Posey, *ibid.*, **79**, 1310 (1957).
7. W. L. Faith, D. B. Keys, and R. L. Clark, "Industrial Chemicals," John Wiley & Sons, Inc., New York (1950).
8. H. Eyring and F. W. Cagle, *J. Phys. Chem.*, **56**, 889 (1952).
9. G. A. Moore, *J. Metals*, **5**, 1443 (1953).
10. R. L. Combs, J. M. Googin, and H. A. Smith, *J. Phys. Chem.*, **58**, 100 (1954).
11. B. Topley and H. Eyring, *J. Am. Chem. Soc.*, **55**, 5058 (1933).
12. E. D. Hughes, C. K. Ingold, and C. L. Wilson, *J. Chem. Soc.*, **1934**, 493.
13. H. L. Johnston and C. O. Davis, *J. Am. Chem. Soc.*, **64**, 2613 (1942).
14. B. Topley and H. Eyring, *J. Chem. Phys.*, **2**, 217 (1934).

The Role of the Electrokinetic Potential in Some Surface Tension Phenomena

Lawrence Baylor Robinson

Space Technology Laboratories, Inc., Los Angeles, California

ABSTRACT

The Wagner-Onsager-Samaras theory (without adjustable constants) allows one to calculate the surface tension of an aqueous electrolyte solution as a function of concentration. It predicts that an electrolyte added to water would increase the surface tension. Precise measurements of the surface tension by the capillary rise method give an initial decrease and a minimum in the surface tension-concentration wave. Theory and experiment can be reconciled by taking the electrokinetic effects into account.

The available evidence indicates that a knowledge of the electrokinetic (commonly called zeta) potential is required for an interpretation of surface tension measurements of electrolyte solutions made with the capillary rise technique. The basic contributions to the theory of the surface tension of (Debye-Hueckel) electrolytes were made by Wagner (1) and by Onsager and Samaras (2). The quantitative discussions were limited to 1-1 electrolytes such as KCl. An extension of the theory to the case of asymmetrical electrolytes has been carried out by Thacher (3), and numerical results are given for 2-1 (e.g., $BaCl_2$) electrolytes and 3-1 (e.g., $LaCl_3$) electrolytes. More drastic approximations in the theory, used by Robinson (4), gave results for 2-1 and 3-1 electrolytes not too different from those obtained in Thacher's more refined treatment. The essential result in all of the cases is that the surface tension turns out to be an increasing monotone function of the concentration; the addition of any amount of a neutral salt to water will increase the surface tension according to theory.

Meanwhile, the theory of surface tension had received a serious challenge by the precise measurements of Jones and Ray (5) with a capillary rise apparatus which gave the ratio of the surface tension of an electrolyte solution to that of water. Their measurements indicated that the surface tension of water decreased sharply as a result of the addition of a small amount of a salt; the surface tension-concentration curve passed through a broad minimum at about 0.001 equivalents per liter for all electrolytes tested. Following this, the curve increased with concentration at a rate about that predicted by theory.

Jones and Ray initially interpreted the decrease in the surface tension as resulting from the interaction of the polarized water molecules (dipoles) with the ions of the electrolyte. They pointed out that these forces are neglected in the usual theoretical treatments, in which the principal effect is attributable to the presence of a boundary (so-called image forces). They postulated that the addition of ions to water would disturb the systematic arrangement of water dipoles. The electric forces among the water molecules, opposing this disturbance, would tend to thrust the disturbing ions into the surface. This initial positive adsorption was taken as the cause of the decrease in surface tension in the extremely dilute range.

Several other proposals were put forward by various theoreticians to account for the observed minimum in the surface tension-concentration curve. The interpretation given by Irving Langmuir (6) attracted more attention; it is subject to quantitative checks. Langmuir advanced the suggestion that the results obtained by Jones and Ray represented an instrumental effect rather than a pure surface tension property. He contended that the film of the liquid in the capillary above the meniscus was not of negligible thickness as was generally assumed, but could assume thicknesses which would be appreciable when compared with the radius of a tiny capillary. The thickness of the wetting film was postulated as being dependent on the nature and concentration of the electrolyte and especially on the potential existing at the interface between the capillary wall and the solution. This is essentially the so-called zeta-potential, the potential existing at the boundary between a flowing liquid and the layer of liquid attached to the wall. The film was supposed to be much thicker for water than for solutions of electrolytes of moderate concentrations, and the film evidently becomes negligible for concentrated solutions. Jones and Frizzell (7) developed the theory more rigorously so that the original surface tension data of Jones and Ray could be corrected in the manner proposed by Langmuir.

A significant result is that a connection is established between the surface tension and the electrokinetic potential. In principle, one can invert the problem and calculate the zeta potential from a static phenomenon. At the time of Langmuir's suggestions, reliable zeta potential measurements were very few. At present, reliable results have been made on a variety of electrolytes by Rutgers and De Smet (8) and by Jones, Wood, and Robinson (9). The results of these two groups of workers are in complete agreement.

The application of the correction, as suggested by

Langmuir, puts the results of Jones and Ray in substantial agreement with the theory.

Surface Tension by Capillary Rise

The method employed by Jones and Ray measured the ratio of surface tensions of solutions to that of water, by measuring relative rises in a capillary tube. The surface tension is given by

$$\sigma_c = h\ (d_c - \beta)\ gr_c/2 \qquad [1]$$

where d is the density of the solution, h is the height to which the liquid rises in the capillary, β is the density of air, g is the acceleration of gravity, and r_c is the radius of the capillary containing the liquid. The relative surface tension is

$$\sigma = \frac{\sigma_c}{\sigma_o} = \frac{h_c}{h_o}\,\frac{(d_c - \beta)}{(d_o - \beta)}\,\frac{r_c}{r_o} \qquad [2]$$

where the subscript zero refers to water. Jones and Ray assumed that $r_c = r_o$. Langmuir's suggestion that a wetting film (of significant dimensions) forms in the capillary requires that the original data of Jones and Ray be multiplied ("corrected") by a factor of $(r - \Delta r_c)/(r - \Delta r_o)$ where Δr is the thickness of the film.

The wetting film is established from the equilibrium of various forces at the meniscus. For films which are thick in comparison with the diameter of the water molecule, one may neglect short range forces. The other forces considered have their origin as follows:

1. The hydrostatic pressure exerted by the main body of the liquid in the capillary exerts a downward force (per unit area) on the film which tends to make this film thinner; this pressure has magnitude $-(d - \beta)\ hg$, where d is the density of the solution, β the density of air, h the capillary rise, and g the acceleration of gravity.
2. The surface tension in the inner surface of the annular wetting film tends to contract the entire inner surface, and hence make the film thicker; the pressure exerted has magnitude $p = \sigma/r = (d - \beta)\ hg/2$.
3. The difference between the osmotic pressure in the bulk solution and at the air-solution interface tends to make the film thicker in attempting to dilute the solution comprising the film; this pressure has magnitude

$$\Sigma_i\, n_i\, kT\left\{\exp\left(-\frac{Z_i \epsilon \Psi}{kT}\right) - 1\right\}$$

where n_i is the number of ions per cubic centimeter of the ith species in the main part of film (assumed to be the same as that in the bulk solution), Z_i is the number of electronic changes on the ion, and the other symbols have their usual significance. The above expression is a result of Vant Hoff's simple law that the osmotic pressure is $P = nkT$ (where n is the total number of ions per cubic centimeter), and from the assumption that the ions in the wetting film are in a Boltzmann distribution governed by the potential Ψ. At equilibrium, the sum of all of these pressures is zero, and therefore

$$\Sigma_i\, n_i\, kT\left\{\exp\left(-\frac{Z_i \epsilon \Psi}{kT}\right) - 1\right\} - (d - \beta)\ hg/2 = 0 \qquad [3]$$

where the potential Ψ is evaluated at the air-film interface. It is also assumed that at the air interface

$$\nabla \Psi = 0 \qquad [4]$$

The above two boundary conditions, plus the Poisson-Boltzmann equation

$$\nabla^2 \Psi = \frac{d^2\Psi}{dr^2} + \frac{1}{r}\,\frac{d\Psi}{dr} = \Sigma_i\, n_i\, \epsilon Z_i \exp\left(-\frac{Z_i \epsilon \Psi}{kT}\right) \qquad [5]$$

constitute the problem to be solved. The problem is to find the Δr consistent with the boundary conditions and the specified potentials.

Equations [3] and [4] provide a means of determining both the function Ψ and its slope, respectively, at the air-solution boundary. Some refinements have been offered at various times to improve the theory, especially as far as Eq. [4] is concerned; the evidence suggests that the theory as proposed is substantially correct as long as the potential at the film-quartz interface (i.e., the zeta potential) is large in comparison with the potential at the air-film interface. This condition prevails in the cases of KCl and $BaCl_2$, but is not so for $LaCl_3$. In fact, in two of the $LaCl_3$ solutions studied, the air-film interfacial potential (as calculated) turned out to be larger than the zeta potential. Presumably, the wetting film thickness is zero in such cases; in any circumstance this film thickness would have to be calculated in some other way. Evidently the results for $LaCl_3$ are not as reliable as those for KCl and $BaCl_2$.

Electrokinetic Potentials

In order to carry out the corrections as suggested by the wetting film theory, one must have reliable values of the zeta potential. Recently significant gains have been made in regard to the experimental knowledge concerning this potential. Hitherto there has been no agreement among the various experimenters (10) in this field, and the reliability of much of the data is open to question. Many experimenters have not characterized their methods and instruments adequately and, therefore, a valid evaluation of their results is difficult. A hopeful indication that reliable information has been obtained concerning these potentials is furnished in the work of Rutgers and De Smet (8) at Ghent (Belgium) and Jones, Wood, and Robinson (9) at Harvard. This is perhaps the first time that systematic agreement has been obtained by different investigators, using different experimental techniques. Rutgers and De Smet, using both the method of electroendosmosis and of streaming potentials, studied the ζ-potential of solutions of a great variety of salts in contact with Jena 16 III glass, whereas the Harvard experimenters studied solutions of metallic chlorides in contact with quartz. The latter group used only the streaming potential method. It is remarkable that the results were practically identical.

An interesting regularity was observed in both sets of data. Instead of the curves passing through maxima, as shown in most textbooks (11), the potentials decreased in a more or less linear fashion

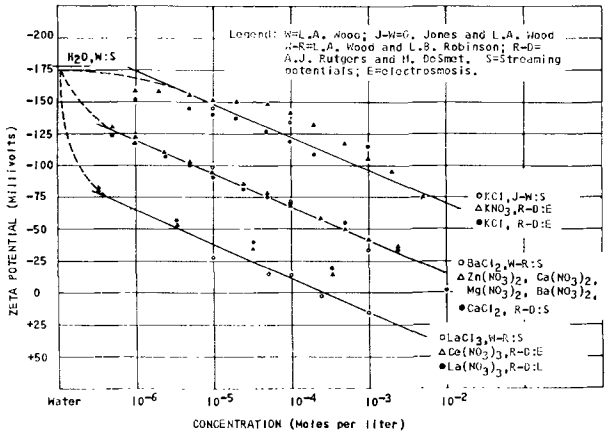

Fig. 1. Zeta potentials of neutral electrolyte solutions

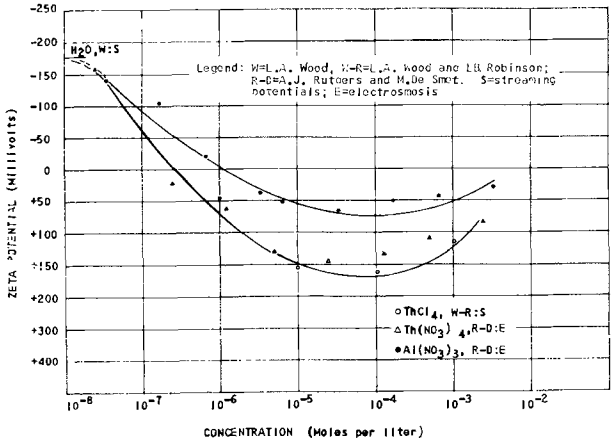

Fig. 2. Zeta potentials of hydrolyzable electrolyte solutions

with the logarithm of the concentration. Both groups of workers found out that thorium salts did not fit the general behavior pattern. This is also true of aluminum chloride. Hydrolysis and other effects with these salts gave their solutions properties not common to the other electrolytes.

Typical results for neutral electrolyte solutions are given in Fig. 1. One observes that all of the data of both groups of workers can be correlated very simply. Actually, only one slope and one intercept are needed to correlate all of the phenomena. The broken lines in the figure are used to give some indication of the expected behavior of the zeta potential in the very dilute range. The three solid lines represent the following equation:

$$\zeta(\text{mv}) = -336 + 55.0\, Z_+ + 26.3 \log c \qquad [6]$$

where Z_+ is the number of charges on the positive ion, and c is the concentration of the salt in moles per liter. The above formula describes the results accurately to about ±10 mv, which is the order of the experimental accuracy. Many times, reversing the direction of flow of the solutions gives an asymmetry potential of this order. In Eq. [6], the symbol c could represent the concentration of the anions (well within the experimental accuracy). There is perhaps some significance in that Eq. 6 can be rewritten as

$$2.27\,\zeta\ (\text{volts}) = \zeta' = -0.760 + 0.1235\, Z_+ + 2.303\,\frac{kT}{\epsilon}\log c \qquad [7]$$

where k, T, and ϵ have their usual significance.

The above equation makes ζ' immediately amenable to an electrochemical interpretation in which the ratio of the viscosity to the dielectric constant (η/D) in the double layer has been increased by a factor of 2.27 over this ratio in pure water. The zeta potential, as calculated both from streaming potential data and from electroendosmosis (electroosmosis) involves this (unknown) ratio as well as experimentally evaluated parameters. Remarks similar to this were made by Robinson (5) some time ago. It seems as though some independent determination of this ratio would be a very worthwhile contribution to the subject of electrokinetic phenomena.

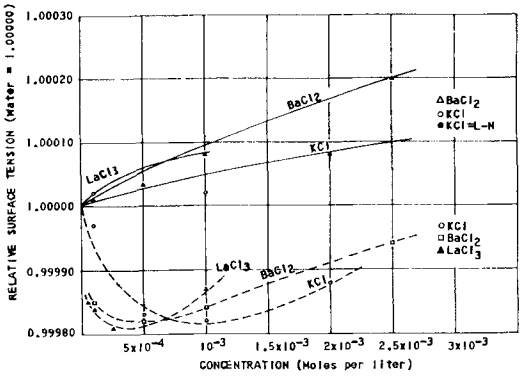

Fig. 3. Relative surface tension of some electrolyte solutions. Solid lines are calculations by H. C. Thacher, Jr.; broken lines connect experimental points of G. Jones and W. A. Ray. Points above 1.00000 (except the one solid circle) are the "corrected" experimental points. The one solid circle is an experimental point of F. A. Long and G. C. Nutting.

Figure 2 shows a different type of behavior for electrolytes which hydrolyze. An interesting problem here would be an attempt to determine the degree of hydrolysis of these salts from the data given

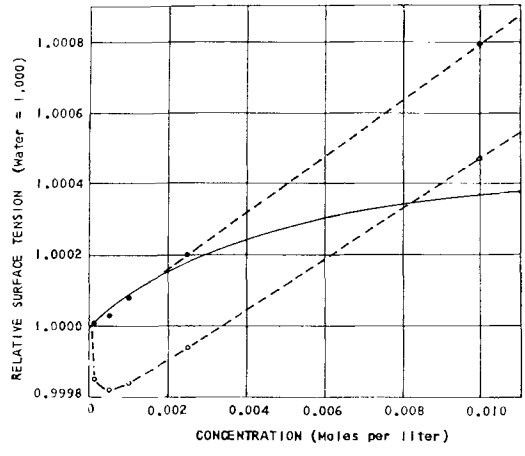

Fig. 4. Comparison of surface tension data of solutions of barium chloride with theories. Open circles are the measurements of Jones and Ray; solid circles are the "corrected" experimental points. The solid line is an approximation to the limiting law of Onsager and Samaras by L. B. Robinson. The upper broken line coincides with a linear extrapolation of the calculations of H. C. Thacher, Jr.

Table I. Wetting film thickness in the Jones-Ray capillary apparatus

Concentration $BaCl_2$	Δr (A)	
	Reported previously	New
2.50×10^{-3}	87	88
1.00×10^{-3}	112	110
5.00×10^{-4}	152	135
1.00×10^{-4}	223	240
$LaCl_3$		
1.00×10^{-3}	56	277
1.00×10^{-4}	18	78

by Rutgers and De Smet for HCl and KOH and a formula similar to Eq. [6]. It is interesting to note that one single curve can represent the streaming potential data for $ThCl_4$ as well as the electroosmosis data for Th $(\eta O_3)_4$. Such all around agreement as exhibited in Fig. 1 and 2 increases confidence in the reliability of both sets of measurements.

Results

Numerical results for the thickness of the wetting film as a function of the zeta potential have been reported by Jones and Frizzell and by Jones and Wood for 1-1 electrolytes, by Wood and Robinson for 2-1 electrolytes, and by Robinson for 3-1 electrolytes. In every case, the approximation was made that one could replace the Laplacian for a region of cylindrical symmetry by the one dimensional Laplacian operator. When this is done, the solution of the problem for the case of 1-1 and 2-1 electrolytes can be obtained in terms of elliptic function. For the case of 3-1 electrolytes, in addition to the approximation of the one-dimensional case, another approximation of a computational nature has to be made; the solution involves hyperelliptic integrals and these were approximated in terms of elliptic integrals. Since the publication of these results, a numerical analysis group at the Ramo-Wooldridge Corporation has assisted Robinson in obtaining numerical integrations of the differential equation involving the Laplacian in cylindrical coordinates. These new results show that the one-dimensional approximation is entirely justified for the 2-1 case; for the 3-1 case, the new wetting film thicknesses are larger by a factor of about four or five than those previously reported. The larger wetting films, however, made no significant difference in the qualitative behavior of the "corrected" surface tension-concentration curves. Table I shows the old and new results for $BaCl_2$ and $LaCl_3$ as well as the old results for KCl. No additional calculations have been made for KCl.

Figure 3 shows the original data of Jones and Ray, the theoretical curves as given by Thacher, and the "corrected" data of Jones and Ray for KCl and $BaCl_2$ solutions. The agreement between various aspects of theory and experiment is good for these two cases. One data point is given from the work of Long and Nutting; they did not have points at lower concentrations (12).

Figure 4 shows the results for $BaCl_2$ in more detail. In the very high dilution range, the calculations of Thacher and Robinson agree. Thacher's calculations were carried up to a concentration of 2.5×10^{-3} moles/l of $BaCl_2$. Figure 5 shows the corresponding results for $LaCl_3$. The only specific thing one can say in regard to the corrected data is that none of these corrected relative surface tensions is less than that of water.

The evidence suggests that the theory of the surface tension of electrolytes is satisfactory, and the minimum in the surface tension-concentration curve is an instrumental effect.

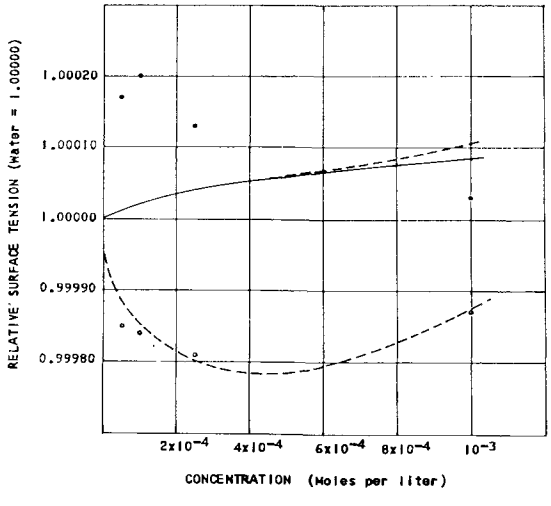

Fig. 5. Comparison of surface tension data of solutions of lanthanum chloride with theories. Open circles are the measurements of Jones and Ray; solid circles are the "corrected" measurements; solid line is the calculation given by H. C. Thacher, Jr. The calculation given by L. B. Robinson coincides with this below 6×10^{-4} moles/l; the broken line continues Robinson's results beyond this point.

Acknowledgment

The author is indebted to Dr. Henry C. Thacher, Jr. for allowing him to make use of the results of his thesis.

Manuscript received June 17, 1958. This paper was prepared for delivery before the New York Meeting, April 27-May 1, 1958.

Any discussion of this paper will appear in a Discussion Section to be published in the December 1959 JOURNAL.

REFERENCES

1. C. Wagner, *Physik Z.*, **25**, 474 (1924).
2. L. Onsager and N. N. T. Samaras, *J. Chem. Phys.*, **2**, 528 (1934).
3. H. C. Thacher, Jr., Ph.D. Thesis, Yale University, 1949 (unpublished).
4. L. B. Robinson, Ph.D. Thesis, Harvard University, 1946 (unpublished).
5. G. Jones and W. A. Ray, *J. Am. Chem. Soc.*, **59**, 187 (1937); **63**, 288 (1941); **63**, 3262 (1941); **64**, 2744 (1942).
6. I. Langmuir, *Science*, **88**, 430 (1938); *J. Chem. Phys.*, **6**, 894 (1938).
7. G. Jones and L. D. Frizzell, *J. Chem. Phys.*, **8**, 986 (1940).
8. A. J. Rutgers and M. De Smet, *Trans. Faraday Soc.*, **41**, 758 (1945); **47**, 102 (1947).
9. G. Jones and L. A. Wood, *J. Chem. Phys.*, **13**, 106 (1945); L. A. Wood and L. B. Robinson, **14**, 251 (1946); *J. Am. Chem. Soc.*, **69**, 1862 (1947).
10. H. Lach and J. Kronman, *Bull. Int. de L'Acad. Polonaise d. Sci. d. Let. (A), Sci. Math.*, 289 (1925); H. Freundlich and G. Ettish, *Z. physik. Chem.*, **116**, 401 (1925); H. R. Kruyt and van der

Willigen, *Kolloid Z.*, **45**, 307 (1928); Furutani, Kurokochi, and Asoda, *Jap. J. Gastroent.*, **2**, 148 (1930); H. Lachs and J. Biczyk, *Z. physik. Chem.*, **A148**, 441 (1930); R. duBois and A. H. Roberts, *J. Phys. Chem.*, **40**, 543 (1936); A. J. Rutgers, E. Verlende, and M. Moorkens, *Proc. K. Ned. Akad. Wetensch. Amsterdam*, **41**, 763 (1938); A. J. Rutgers, *Trans. Faraday Soc.*, **36**, 69 (1940).

11. H. A. Abramson, "Electrokinetic Phenomena," p. 203, Chemical Catalogue Co. (1934); S. Glasstone, "Text-Book of Physical Chemistry," p. 1201, D. Van Nostrand Co., New York (1940); S. Glasstone, "Introduction to Electrochemistry," p. 534, D. Van Nostrand Co., New York (1942).
12. F. A. Long and G. C. Nutting, *J. Am. Chem. Soc.*, **64**, 2476 (1942).

Technical Notes

Enhanced Surface Reactions

IV. The Adsorption of Hydrogen on $ZnO \cdot Cr_2O_3$

M. J. D. Low and H. A. Taylor

Nichols Laboratory, New York University, New York, New York

Recent experiments on gas-solid interactions (1-3) were explained in terms of a mechanism (4) intimately connected with the Elovich equation (4)

$$dq/dt = ae^{-\alpha q}$$

q being the amount of gas adsorbed at time t. It was thought of interest to study the change of the constants a and α with initial gas pressure, P_o, and temperature. The adsorption of hydrogen on $ZnO \cdot Cr_2O_3$ was measured using previously described techniques (3-6). The unreduced catalyst (33.4 g) (7) was reduced in flowing hydrogen at 1 atm at 450°C for 20 hr. Between runs the catalyst was degassed at 450° for 16 hr to $\leqq 10^{-6}$ mm Hg.

Most q-log t plots showed isothermal discontinuities (4) and were described precisely by the Elovich equation. At 147° and 200°C the change in slope corresponded to a decrease in α; at 257°, to an increase in α. Table I summarizes the data, numbered according to the order of their execution. The subscripts 1 and 2 refer to the a and α values calculated (8) before and after the break at time t_b and adsorption amount q_b.

Plots of $\alpha_1 - P_o$ show breaks, α_1 varying more rapidly with a change in P_o at low temperature, less rapidly at higher pressures. In contrast to previous studies, this break seems to be temperature dependent, changing from 16 cm at 147° to 20 cm at 257°C. Conversely, the breaks in q-log t plots occur approximately at $q = 8$ ml regardless of P_o or temperature. Further, the break occurs at $q = 8$ ml, whether the change in slope corresponds to an in-

Table I. H_2 adsorption on $ZnO \cdot Cr_2O_3$

Run	P_o cm Hg	α_1	$\alpha_1 = n \cdot 10^x$ n	x	ln $a_1\alpha_1$	α_2	$\alpha_2 = n \cdot 10^x$ n	x	ln $a_2\alpha_2$	t_B, min	q_B, ml
						147°C					
13	16.1	3.03	1.5	10	10.66						
14	10.6	3.59	5.0	9	10.26						
15	7.4	3.77	3.6	9	11.10						
16	23.6	2.91	3.0	9	9.90	2.30	1.5	7	7.55	20	8.85
17	30.7	2.80	3.0	9	9.89	2.13	8.0	6	7.25	13	9.00
						200°C					
9	5.0	2.84	3	5	5.90	1.34	89	0	2.08	21	5.8
10	19.1	2.25	1	6	6.45	0.69	18	0	1.10	17	7.8
11	35.2	2.20	8	5	6.19	0.71	41	0	1.46	15	8.5
12	16.5	2.32	8	6	7.72	1.04	370	0	2.58	16	8.4
18	14.3	2.42	4	6	6.93	0.82	53	0	1.64	13	7.6
19	10.7	2.07	3	5	5.82	0.67	14	0	0.98	21	7.9
						257°C					
2	41.5	0.77	5.2	2	2.60	2.88	2	12	12.25	8	10.5
3	24.0	0.77	3.2	2	2.40	2.56	5	9	10.11	8.7	10.0
4	11.1	0.97	2.0	2	2.29	2.71	5	7	8.12	8	7.7
5	37.7	0.80	3.3	2	2.42	2.58	3	8	8.92	3	8.4
6	6.3	1.07	2.1	2	2.35	8.52	2	26	27.22	17	7.7
7	18.3	0.82	3.1	2	2.41	3.15	2	11	11.84	8.5	9.3

Table II. H_2 on $ZnO \cdot Cr_2O_3$—Kubokawa and Toyama

°C	α	q_1	a
0	0.20	9.8	36.2
20	0.66	11.4	2.9×10^3
80	1.17	16.4	1.9×10^5
110	1.05	16.0	1.8×10^7
140	0.96	16.0	5.7×10^6
170	0.71	16.0	1.2×10^5
200	0.56	15.8	1.1×10^4

crease or decrease in α. Such behavior is similar to that found by Decrue and Susz (9) in part for the same system, but even more so for the system H_2-WS_2. A peculiar effect of initial pressure is discernible in the earlier work with hydrogen on zinc chromite by Taylor and Strother (10). At ¼ atm of hydrogen they calculated energies of activation which increase monotonously with the amount of hydrogen adsorbed over the range 80°-218°. At ½ and at 1 atm the change in the calculated energy of activation is different for the ranges 80°-110° and 110°-184°. The adsorption isobar showed a maximum around 184°. No energies of activation at temperatures higher than 184° at ½ or 1 atm are given. Kubokawa and Toyama (11) have called attention to this effect as different from their findings, remarking that "the reason for the difference is not yet clear." That they did not observe the effect is no doubt to be attributed to the low pressure, 6 cm, in their work. The low pressure would account also for the absence of breaks in the q-log t plots of their data, since none was found at the lowest pressures at 147° in the current study. Their data satisfy an Elovich treatment, Table II listing the calculated parameters. The value q_1 is the amount adsorbed after 1 min, obtained by extrapolation of the data given, and used to calculate the initial rate a from the integrated Elovich equation, $q = (2.3/\alpha) \log (1 + a\alpha t)$. From 0° to 80°C a increases steadily, but from 80° to 200°C a decreases. If the Arrhenius equation is applied to these values the energy of activation so calculated is 37 kcal in the first temperature interval, and −26 kcal in the second interval. If the a_1 values in Table I are similarly treated, an average energy of activation of −63 kcal is found. Similar negative activation energies have been pointed out by Decrue and Susz. The numerical discrepancy can undoubtedly be attributed to a difference in the catalytic activity of the adsorbent. At 140° Kubokawa and Toyama found 21 ml hydrogen adsorbed on 12.37 g catalyst at ≈6 cm pressure; the α value was ≈1.0. In the present study at 147° 33.4 g adsorb only 10 ml at that pressure, while α_1 is 2.1.

The a_2 values in Table I decrease in going from 147° to 200°C but increase from 200° to 257°C. It is obvious that the temperature dependence of the adsorption after the break is completely different from that before the break. Patently, at least two types of adsorption are involved, and much more kinetic data from other adsorbent-adsorbate systems are required to unravel the complexity. It may be noted, parenthetically, that the activation energies calculated from the times required to adsorb definite amounts of gas, in the ranges 3-4 or 7-13 ml found by Taylor and Strother and also by Kubokawa and Toyama, do not have the significance which these authors claim.

The Elovich equation shows adsorption to be a decelerating process, to an extent dependent on the value of α, which is itself temperature and initial-pressure dependent. To apply the Arrhenius equation to rates at constant amounts adsorbed disregards whatever is responsible for the parameter α. In view of the previously discussed mechanism the deceleration is the result of spontaneous site decay and hence, for the adsorption of a constant amount of gas, a different proportion of the surface sites has decayed at different temperatures, and thus the stages of reaction are not comparable.

Manuscript received May 13, 1958.

Any discussion of this paper will appear in a Discussion Section to be published in the December 1959 JOURNAL.

REFERENCES

1. M. J. D. Low and H. A. Taylor, *This Journal*, **104**, 439 (1957).
2. M. J. D. Low, *ibid.*, **105**, 103 (1958).
3. M. J. D. Low and H. A. Taylor, *ibid.*, **106**, 138 (1959).
4. H. A. Taylor and N. Thon, *J. Am. Chem. Soc.*, **74**, 4169 (1952).
5. M. J. D. Low and H. A. Taylor, *Canadian J. Chem.*, May 1959.
6. L. Leibowitz, M. J. D. Low, and H. A. Taylor, *J. Phys. Chem.*, **62**, 471 (1958).
7. H. S. Taylor and S. C. Liang, *J. Am. Chem. Soc.*, **69**, 2989 (1947).
8. J. N. Sarmousakis and M. J. D. Low, *J. Chem. Phys.*, **25**, 178 (1956).
9. J. Decrue and B. Susz, *Helv. Chim. Acta*, **39**, 619 (1956).
10. H. S. Taylor and C. O. Strother, *J. Am. Chem. Soc.*, **56**, 586 (1934).
11. S. Y. Kubokawa and O. Toyama, *J. Phys. Chem.*, **60**, 833 (1956).

Formation of Silicon Carbide Crystallites

Allen H. Smith

Research Division, Raytheon Manufacturing Company, Waltham, Massachusetts

A unique approach to the problem of growing silicon carbide crystals has produced free falling crystallites. This SiC "snow" is transparent and clear in typical hexagonal or triangular platelet form. The snow forms in a pressurized furnace containing an argon atmosphere.

Silicon carbide is known to sublime at elevated temperatures. Near 2700°C (1) decomposition takes place forming an atmosphere of silicon vapor and a solid residue of graphite. This experiment utilizes decomposition rather than sublimation. The Lely process (2,3) employs sublimation as the principal mechanism. The argon pressure of about 80 psi was established empirically. This pressure controls the diffusion rate of the silicon vapor rather than operation at some arbitrary point on a phase vs. pressure diagram.

Figure 1 shows the apparatus for this experiment in a schematic drawing. The essential parts include the pressure envelope of steel, with water cooling coils soldered on; graphite heater tube with graphite piston sliding fit; thermal insulation of lampblack; and a viewing port at the bottom through which the temperature is taken and events viewed. A neoprene "O" ring and a lavite washer electrically isolate the top electrode. The "O" ring also serves as the pressure seal around the water-cooled electrode. Argon circulates throughout the furnace for flushing and gives a supporting upward draft for the flakes at the point of entry. The furnace uses about 4 kw of power at 600 amp to maintain 2700°C. A saturable core reactor with a stepdown transformer supplies the power. Manual control regulates the power for temperature changes. The temperature remains at a constant value for a given power setting, as determined by a L&N optical pyrometer.

The operating zone, ¾ x 4 in., contains the graphite capsule with its supply of silicon carbide (see Fig. 2). A dense form of graphite[1] must be used for this capsule to prevent breakage when the silicon vapors react with it. The silicon vapor does not attack other parts of the system as much as the capsule. Spectroscopic grade[2] graphite works well for the piston, base, and heater sleeve. The capsule support with three thin legs minimizes heat loss by conduction to the base. A radiation shield above the capsule cuts radiation losses from the capsule top to the much cooler piston.

A simple concept of this experiment assumes the equilibrium reaction:

$$Si + C \rightleftarrows SiC$$

Silicon combines with carbon from 1600°C up to the decomposition temperature. As silicon carbide is very stable, the silicon remains localized until released at the decomposition temperature. As the silicon vapor builds up in the capsule, it streams out

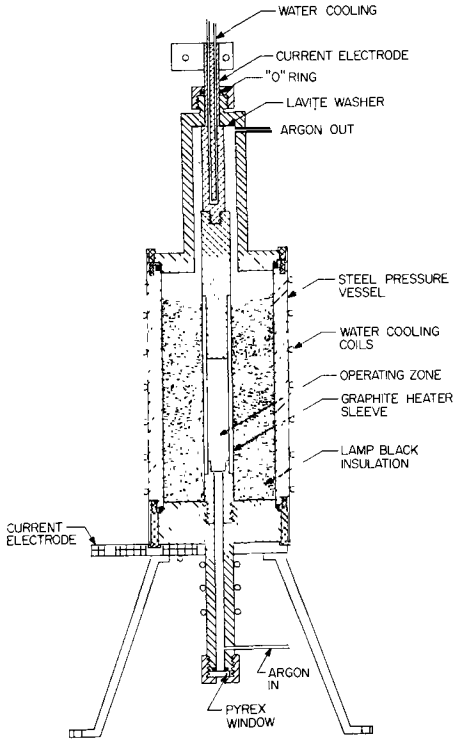

Fig. 1. Longitudinal section of the graphite pressure furnace for growing SiC crystals; one inch equalled 40 mils before reduction for publication.

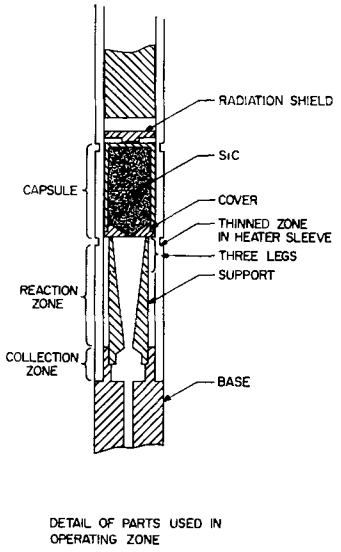

Fig. 2. Detail of parts used in operating zone

[1] For example, "Graphitite," Graphite Specialties Co., Niagara Falls, N.Y.

[2] United Carbon Products, Bay City, Mich.

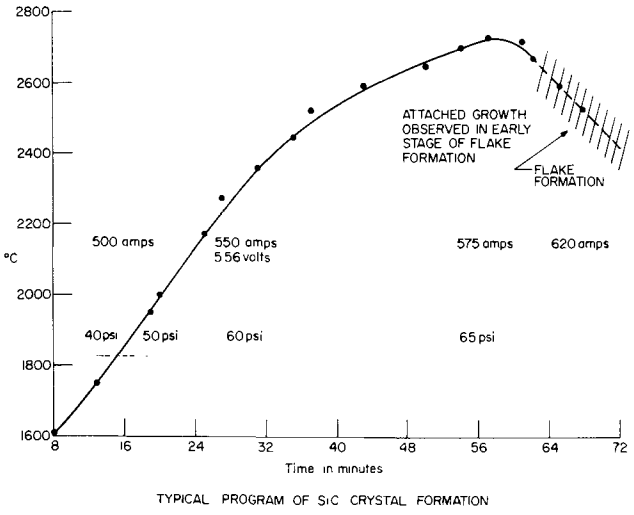

Fig. 3. Typical program of SiC crystal formation

a small hole in the cover. In the upper part of the reaction zone the silicon combines with carbon at a temperature just below decomposition. The inner wall of the support becomes coated with silicon carbide crystals. However, a thinned zone in the heater sleeve creates a "hot spot" from which carbon atoms evaporate readily. This carbon can react with silicon before it reaches the side walls of the reaction tube. When this happens free falling crystals occur.

The actual mechanism of the reaction has not been studied. Possibly intermediate carbides form before a silicon carbide crystal develops. A clear understanding of the reaction would help make a more efficient process. Three important observations lead to the mechanism suggested. The release of silicon from the silicon carbide has been abrupt enough to separate the cover from the capsule. The shape of the original sintered mass of silicon carbide remains in the soft, spongy, graphitic mass. The flutter of flakes visible in the pyrometer occurs abruptly about 2750°C at 80 psi. Those runs in which conspicuous erosion of the heater sleeve takes place, are most productive of silicon carbide crystals.

A run lasts for a little over an hour as shown in the typical program, Fig. 3. The drop in temperature at the end of the run comes from the masking effect of the silicon carbide snow, between the pyrometer and the reference surface. An upward flow of argon

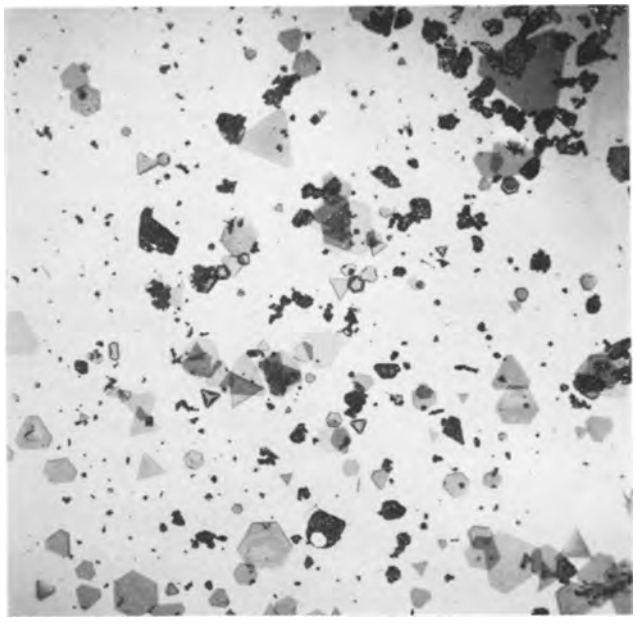

Fig. 4. Display of SiC crystallites as they fell in the furnace. Graphite dust and silicon spheres are also present. One inch equals 40 mils.

maintains the flakes in the reaction zone until they become large enough to fall under gravity. Typical shapes are shown in the display of Fig. 4. The largest dimensions observed are between 20 and 30 mils. Measurements on these crystals are very difficult because of their extreme thinness (~0.3 mil). The size of the crystals is limited largely by the small size of the reaction zone. Crystals which hit the side walls adhere and are no longer free falling. Further work on these free falling crystals is planned with a larger reaction zone so that larger crystals can form.

Manuscript received Nov. 18, 1958. This paper was prepared for delivery before the Ottawa Meeting, Sept. 28-Oct. 2, 1958.

Any discussion of this paper will appear in a Discussion Section to be published in the December 1959 JOURNAL.

REFERENCES

1. Hansen, "Constitution of Binary Alloys," p. 378, McGraw-Hill Book Co., New York (1958); possible phase diagrams of SiC from p. 378.
2. J. A. Lely, *Ber. deut. keram. Ges.*, **32**, 229 (1955).
3. D. R. Hamilton, *This Journal*, **105**, 735 (1958).

Corrections

In the paper by William T. Allen and C. H. Bachman, "Changes in Trapping Levels of Zinc Sulfide Phosphors Resulting from Positive Ion Bombardment," which appears in the March 1959 issue of the JOURNAL, in Figure 1, page 213, the curve labeled 350°K should read 280°K and the curve labeled 280°K should read 350°K.

In the Brief Communication by G. J. Schafer and P. K. Foster, "The Role of the Metal-Ion Concentration Cell in Crevice Corrosion," which appears on page 468 in the May 1959 JOURNAL, Reference 5 should read: R. V. Jelinek, *Chem. Eng.*, **65**, No. 17, 125 (1958).

The Diffusion Coefficient of Lead Ion in Fused Sodium Chloride-Potassium Chloride Eutectic

Richard B. Stein[1]

Ecole Nationale Supérieure d'Electrochimie et d'Electrométallurgie, Grenoble, France

Work in progress in this Laboratory (1) has indicated that the fused sodium chloride-potassium chloride eutectic displays an ideal behavior; the molten bath is completely ionized and solvation is absent. Electrode reactions taking place in this fused electrolyte are being investigated at present by the method of oscillographic polarography. The diffusion coefficient of the discharging metal ion can be measured directly by this method.

In the case of oscillographic polarography the discharge current is given by (2)

$$i = \pi^{1/2}\, n\, F\, A\, \beta^{1/2}\, D^{1/2}\, C^{\circ}\, \phi\, (\beta t)$$

where A is the surface of the electrode, D is the diffusion coefficient, C° is the bulk concentration of the diffusing species, and $\phi(\beta t)$ is a complex function relating the discharge current, electrode potential, and rate constant. Once the electrode surface and bulk concentration are known, the diffusion coefficient can be obtained from the polarographic wave and the above equation.

Experimental

The polarographic reduction of Pb^{++} in the fused electrolyte was followed by means of a polarograph especially conceived for this system. The reduction cell consists of a cathode in the form of a microelectrode, made from a 0.5 mm platinum wire sealed into a quartz tube ($A = 1.89 \times 10^{-3}$ cm^2), and the Ag/AgCl electrode of Coriou, Dorian, and Hure (3).

The preparation and purification of the solvent bath have already been described (1). The lead chloride used to make up the electrolyte was purified by a flash distillation under vacuum. The dissolution of the lead chloride in the purified solvent was accomplished under a rigorously controlled inert atmosphere, and the resulting solution was electrolyzed immediately in such a manner that no impurities were introduced from the atmosphere. The polarographic cell was placed in a graphite resistor furnace where the temperature was regulated to $\pm\frac{1}{2}$ °C. Polarograms were taken at four different temperatures for a solution ($C^{\circ} = 2.187 \times 10^{-2}$ mmole Pb^{++}/g solvent) in order to determine the energy of activation of the diffusion process.

[1] Present address: 219 Grace Dr., South Pasadena, Calif.

Table I. Diffusion coefficient of Pb^{++} ion in fused NaCl-KCl eutectic

Temp, °C	Diffusion coefficient x 10^5, cm^2/sec
701	2.4±0.3
746	3.1±0.4
777	3.8±0.5
807	4.4±0.6

Discussion

If the solvent is considered as being a continuous medium in which the laws of classical hydrodynamics are applicable, then the diffusion coefficient can be calculated from the Stokes-Einstein equation. For the diffusion of the lead ion having a radius of 1.21Å, and using the viscosity data of Smithells (5), the diffusion coefficient is calculated at 780°C as $D = 4.6 \times 10^{-5}$ cm^2/sec. From Table I it is seen that the measured and calculated values for the diffusion coefficient are approximately equal, and it can be concluded that the solvent possesses the structure of a simple ionic fluid.

The energy of activation for the diffusion process as obtained from the experimental values is 12.5 kcal/mole. This value can be compared with the value of 13 kcal found by Nachtrieb and Steinberg (6) for the diffusion of Pb^{++} in a complex nitrate bath.

Manuscript received Dec. 29, 1958.

Any discussion of this paper will appear in a Discussion Section to be published in the December 1959 JOURNAL.

REFERENCES

1. R. B. Stein, *C. R. Acad. Sci.*, **246**, 2611 (1958).
2. P. Delahay, "New Instrumental Methods in Electrochemistry," Chap. 6, p. 126, Interscience Publishers, New York (1954).
3. H. Coriou, J. Dorian, and J. Hure, *J. chim. phys.*, **52**, 479 (1955).
4. L. Pauling, "The Nature of the Chemical Bond," 2nd ed., p. 345, Cornell University Press, Ithaca, N. Y. (1940).
5. C. J. Smithells, "Metals Reference Handbook," 2nd ed., Vol. 2, p. 635, Butterworths, London (1955).
6. N. H. Nachtrieb and M. Steinberg, *J. Am. Chem. Soc.*, **72**, 3558 (1950).

Brief Communications

Rectification by Zircaloy 2 in High-Temperature Water

J. N. Wanklyn and R. Aldred

Atomic Energy Research Establishment, Harwell, Berkshire, England

Recent corrosion tests of Zircaloy 2 under heat transfer in water at pH 10.5, 280°C, were vitiated by rectification effects. Strips of the material were heated by the passage of a large 50 cps alternating current, and this involved a voltage of about 12 v rms between the specimen and the wall of the apparatus. Corrosion was unexpectedly great, white oxide forming in less than 200 hr, and much hydrogen was taken up by the Zircaloy 2.

Polarization experiments with unheated Zircaloy 2 specimens in the same apparatus at 250°C, and in simpler apparatus at 20°C, showed that, as expected from work by Carmody (1), rectification occurred, producing a cathodic direct current. As shown in Fig. 1, there was a "barrier" voltage below which no significant d.c. flowed, and above this the curve rose to a final linear portion. At room temperature, curves for unalloyed zirconium lay to the right of those for Zircaloy 2, but had the same linear slope. Experiments in solutions of different concentrations showed the slope to be predominantly controlled by the electrolyte resistance. The "barrier" value was virtually unaffected by changing from a 1 g/l KOH solution to 50 g/l KOH and to a dilute Na_2SO_4 solution. The lower barrier for Zircaloy 2 (which contains iron among other additions) is interesting in view of Carmody's finding (1) that the addition of Fe^{++} to his electrolyte (H_2SO_4) lowered the barrier for unalloyed zirconium.

Similar curves were obtained at 250°C, but the currents were more variable, and the curves changed appreciably with time when sufficient polarization was applied to cause white oxide to form. Analysis after 100 hr at 12 v rms showed that the hydrogen entering the metal was about 15-25% of that equivalent to the charge passed cathodically. Micrographs showed precipitated hydride throughout the material and, generally, a "case" of massive hydride at the surface. The increased corrosion accompanying cathodic charging with hydrogen is presumably related to the similar effect of d-c polarization of zirconium alloys in high-temperature water (2).

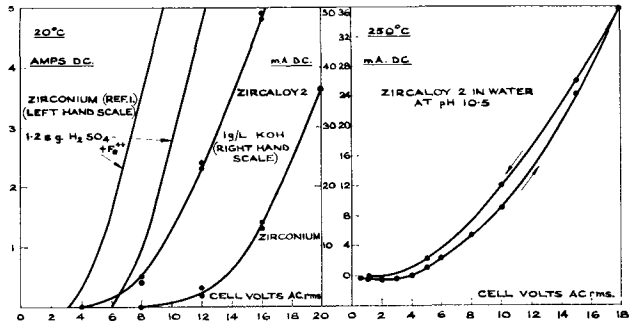

Fig. 1. Rectificotion curves of zirconium and Zircaloy 2

In contrast, virtually none (<1%) of the cathodic hydrogen entered zirconium and Zircaloy 2 polarized at 12 v rms at room temperature.

Provided the conductivity was at least several hundred μ mho/cm, variation of it, at 20°C, merely altered the linear slopes; but if it fell below roughly 100 μ mho/cm, little or no d.c. flowed even up to 50 v rms although, considering only the electrolyte resistance, there was sufficient voltage to produce a measurable current. Likewise, in neutral water at 250°C the currents were low, and the curves, although rather irreproducible, suggested that the barrier was raised to about 10-15 v rms and that the linear slopes were lower than corresponding merely to the reduced conductivity, compared with that at pH 10.5. No hydrogen was taken up in 100 hr at 12 v rms. In dilute solutions behavior appears to be determined by complex phenomena, probably in the oxide/solution interface.

Manuscript received Feb. 19, 1959.

Any discussion of this paper will appear in a Discussion Section to be published in the December 1959 JOURNAL.

REFERENCES

1. W. R. Carmody, *This Journal*, **91**, 309 (1947).
2. J. N. Wanklyn and B. E. Hopkinson, *J. Appl. Chem.*, **8**, 496 (1958).

Heater Cathode Breakdown

R. J. Jaccodine

Allentown Laboratory, Bell Telephone Laboratories, Inc., Allentown, Pennsylvania

This communication concerns a method of studying heater-cathode insulation breakdown (1). It further proposes a mechanism for this breakdown.

In some electron tubes, the heater is a helix of tungsten wire coated to several mils thickness by spraying with fine Al_2O_3. These heaters are then baked at high temperature prior to being inserted into the cathode sleeve. During use this insulating coating degrades allowing leakage, and in extreme cases a short develops between heater and cathode.

In order to study these phenomena under more controlled conditions, the following method is used. A regular sprayed heater is mounted vertically in a standard tube press. Coiled about this heater is another uncoated tungsten heater or a thin strip of metal (Fig. 1). This outside heater acts in the same manner as the cathode sleeve in an actual tube. This arrangement allows the environmental condition of a portion of the insulation to be controlled. If the effects of various metals or impurities are to be tested, they are applied on thin strips and wound in place of the uncoated heater. The current in each heater can be controlled separately and a d-c potential can be applied between the two heaters. This allows a wide range of temperature, potential and environmental conditions to be studied.

Using the above technique, breakdown was shown to occur only under the wound outside heater (Fig. 1); the appearance of the alumina varied from light gray to black. Under conditions where the heater voltage was 15% higher than normal rated voltage and the heater-cathode potential was 10% higher, breakdown was accelerated. Shorts occurred which caused a glassy, cratered appearance in the insulator probably due to large amounts of current passing through degraded spots raising the local temperature of these spots to the melting point.

In the course of studying factors influencing this breakdown, it was found that oxygen, in the form of metal oxides, caused the degradation process to occur in a fraction of the normal time. The alumina in tubes in which either of the tungsten heaters was oxidized broke down in a short time. In still other tubes, a source of oxygen was included in the form of a separate tungsten filament coated with cupric oxide. Heating this filament gently released oxygen. The alumina in these tubes, after the oxygen was released, broke down in the same order of time as

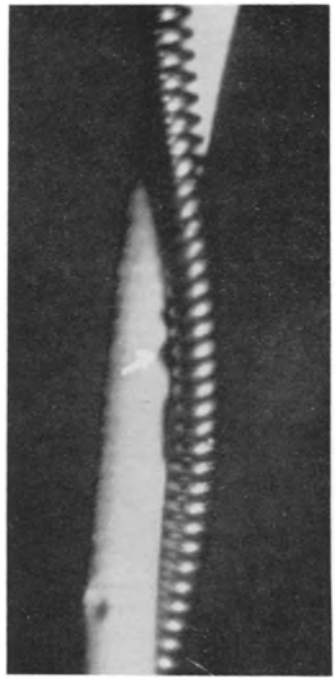

Fig. 1. Experimental arrangement showing "breakdown" region under outside tungsten heater.

the previous group. Heaters subjected to three and five times the normal processing time in dry hydrogen however have not degraded and are still on life.

It is proposed that in an actual tube, a metallic oxide is formed either of nickel or of tungsten depending in part on the polarity of heater-cathode potential. The oxide reacts with the Al_2O_3 to form a spinel (aluminum tungstate in the case of tungsten oxide).[1] It is this product that degrades the insulating quality of the alumina and allows leakage and eventually a short.

[1] In a paper by Rodinhuis, *et al.* (2), they mention that identification of the breakdown product has been made as aluminum tungstate.

Manuscript received Feb. 13, 1959.

Any discussion of this paper will appear in a Discussion Section to be published in the December 1959 JOURNAL.

REFERENCES

1. G. Metson, E. Rickard, and F. Hewlett, *Proc. Inst. Elec. Engrs., London*, **B102**, 678 (1955).
2. K. Rodinhuis, H. Santing, and H. J. M. Van Tol, *Philips Tech. Rev.*, **18**, 181 (1956).

Discussion Section

This Discussion Section includes discussion of papers appearing in the JOURNAL of The Electrochemical Society, 104, No. 5 (May 1957), and 105, No. 1, 5, 6, 7, and 11 (January, May, June, July, and November, 1958). Discussion not available for this issue will appear in the Discussion Section of the December 1959 JOURNAL.

Throwing Index; A New Graphical Method for Expressing Results of Throwing-Power Measurements

R. V. Jelinek and H. F. David (pp. 279-281, Vol. 104)

S. A. Watson[1]: One point which is not made clear in the experimental details given by the authors is that the distance between the anode and the nearer of the two cathodes must be kept constant if the metal distribution ratio at a given average current density is to be a linear function of the linear or primary ratio.

At a fixed average current density, the relationship between the metal distribution ratio, M, and the linear ratio, L, was found by the authors to be of the form $L = kM + C$ where k = Throwing Index and C is some constant. From this, it follows that throwing power expressed by Field's formula,

$$T^F = \frac{(k-1)+C}{(k+1)+C-2} = \text{a constant.}$$

But Gardam[2] showed that

$$T^F = \frac{1}{1+\frac{2dl_2}{N}}$$

where d is the average current density, l_2 is the distance from the anode to the nearer cathode, N is a constant related to solution resistivity and cathode polarization, and clearly T^F is constant at a fixed current density only if l_2 is constant. Therefore, Throwing Index is constant only if l_2 is constant.

The dependence of Throwing Index on the value of l_2 can be shown using data published by Wesley and Roehl[3] by taking advantage of the fact that $M = 1$ at $L = 1$. In Fig. 1 of this discussion, values of M determined at current densities of 0.01, 0.02, and 0.04 amp/cm^2 in a nickel chloride/boric acid solution are plotted against linear ratio and the lines for $l_2 = 10$ cm are extrapolated. Throwing Index is seen to be higher when $l_2 = 2.9$ cm than when $l_2 = 10$ cm at all three current densities. From similar data of Wesley and Roehl obtained with a hard nickel solution and a Watts solution (pH 2.0) at a current density 0.04 amp/cm^2, it can be shown that Throwing Index increases as l_2 decreases with these solutions, too, though the effect is smaller than in the chloride bath.

Although the influence of l_2 on the results obtained by Jelinek and David cannot be estimated from the data given in their paper, the data published by Pan[4] which they quote does show the effect of change in l_2. Pan's data for a cadmium cyanide solution at a current density 0.01625 amp/cm^2 are plotted in Fig. 2 of this discussion. Throwing index is seen to increase as l_2 is decreased. Throwing index can also be shown to vary with l_2 for the acid-zinc and nickel baths which Pan used.

The plots of Wesley and Roehl's data in Fig. 1 show that a threefold increase in l_2 may affect Throwing Index as much as a fourfold increase in current density, which emphasizes that l_2 must be kept constant during determinations of Throwing Index.

R. V. Jelinek: We certainly appreciate Mr. Watson's interest in our paper and his effort to offer constructive criticism. Unfortunately, his mathematical argument is rendered invalid by what appears to be an error in algebra. Using Mr. Watson's symbols, if we substitute the linear Throwing Index relationship

[4] L. C. Pan, *Trans. Electrochem. Soc.*, 58, 423 (1930).

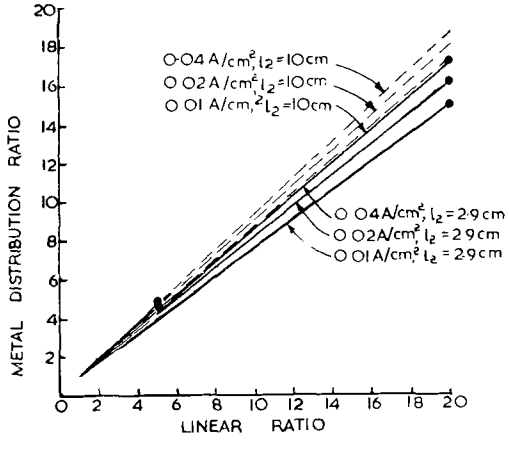

Fig. 1

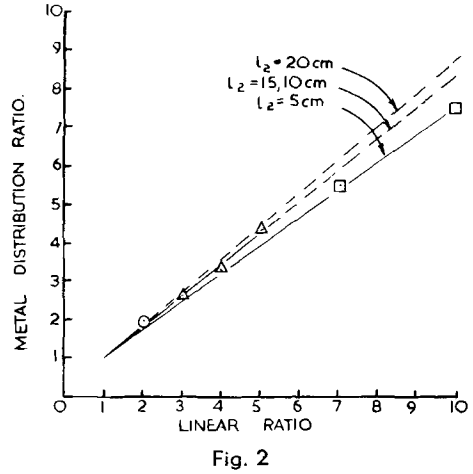

Fig. 2

[1] Electrodeposition Section, The Mond Nickel Co. Ltd., Birmingham, England.
[2] G. E. Gardam, *Trans. Faraday Soc.*, 34, 698 (1938).
[3] W. A. Wesley and E. J. Roehl, *Trans. Electrochem. Soc.*, 86, 79 (1944).

$$L = kM + C$$

into Field's formula [Eq. (III) of our paper], the correct result is

$$T_F = \frac{kM + C - M}{kM + C + M - 2} = \frac{M(k-1) + C}{M(k+1) + C - 2}$$

and not the equation stated by Mr. Watson. Since M remains in the equation T_F is clearly not a constant.

The data of Wesley and Roehl and of Pan, as interpreted by Mr. Watson, do appear to indicate some dependence of Throwing Index on electrode spacing. However, his rather ambitious extrapolation of some of the points is questionable at best. When we originally examined Pan's results, we noticed some drift in the cadmium cyanide data, but in preparing our Fig. 2 we thought it best to draw a single line through the points. We do not believe that the three separate lines in Mr. Watson's second figure are really justified. Also, we question seriously the 10-cm lines on his first figure.

Our own results were obtained by keeping the cathodes fixed at the ends of the throwing-power box and moving the anode. Thus, in successive runs, the spacing between the anode and both of the cathodes was varied; i.e., Mr. Watson's 1_2 was definitely not kept constant in our measurements.

Perhaps a careful evaluation of geometric factors and their influence on Throwing Index would be an interesting subject for study. However, we should remember that the rectangular throwing-power box is simply a convenient empirical device with many theoretical limitations. Throwing Index is offered principally as an interpretive tool, which we believe more convenient in practice than the various Throwing Power formulas in the literature, for the reasons stated in our paper.

The Anodic Oxidation of Cadmium, I. Mechanism of Film Formation

P. E. Lake and E. J. Casey (pp. 52-57, Vol. 105)

Indra Sanghi[5]: I was deeply interested in the paper by Lake and Casey as we also happen to be carrying on some investigations on the constant current polarization of Cd in our laboratory. Preliminary results were presented at the XLV Indian Science Congress Session.[6]

During our studies, we found that the behavior of Cd was more complicated than appears from the paper of Lake and Casey. The time-voltage curves obtained during anodic polarization with constant current show more than one arrest. The method adopted by us was similar to that already reported in connection with our studies on Zn[7] and generally resembled the procedure adopted by Lake and Casey. Cd rods or sheets (electrolytic 99.99% purity) were machined out and all the surface except the experimental portion was stopped off with suitable plastic coatings. The prepolarization preparation of the surface consisted of successive mechanical polishings with 0 to 6/0 grades of emery moistened with ethanol. Hg/HgO/KOH was used as the reference electrode and Philips GM 6010 type VTVM to read the potential variations. Both stirred and unstirred solutions were studied at room temperature (35°C) but no attempts were made to keep the solutions air free. Various current densities and concentrations of KOH solutions ($N/5$ to $5N$) were tried and some of the curves obtained are reproduced in Fig. 1 published here.

From these figures, it will be seen that sudden or single-step passivation, similar to that of Zn[7] and as reported by Lake and Casey, was not observed by us in the case of Cd. Also, if only one oxidation compound, CdO, is electrochemically formed and effective, then the reasons for the observed arrests in the neighborhood of −0.6 v with reference to the Hg/HgO/KOH electrode are not clear. Also, a uniform gradual variation of potential, as is observed with Al and other barrier layers, is not to be expected in the case of Cd. Moreover, the potential at which the polarization curve becomes horizontal appears to vary considerably from 0.2 to 1.2 v with different concentrations and current densities, more than can be accounted for on the basis of $(OH)^-$ concentration. All these points could be checked only if the authors had given actual detailed polarization curves obtained by them.

The authors do not give the order of variations in t_p experimentally observed by them. General experience has been that good reproducibility of t_p is obtained only when t_p is small and not greater than a few minutes.[8] There may be risks in taking average values for quantitative calculations, and we were not successful in getting satisfactory reproducibility in similar experiments, either with Zn or Cd. Accordingly, the discussed paper, based almost entirely on It_p measurements, appears to depend on rather uncertain grounds for deriving final conclusions. It would have been helpful if the authors had specifically mentioned the actual method of measuring t_p in cases of prolonged polarization wherein the curves would not steeply rise, clarifying particularly whether the determining criterion was a low slope or atttainment of a particular potential (say 1.1 v). Also in Table I of the discussed paper, measured It_p value for KOH is shown to be 0.52; but the concentration of the electrolyte and the current density are not clearly mentioned. If a low slope determines t_p, then, in our experiments, It_p varies from 0.004 to 0.20 in KOH depending on current density and concentration.

Quantitative calculations and electrometrics depend on the assumption that all oxide films are reduced before hydrogen evolution starts. But it has been suggested, and some evidence adduced, that in some cases hydrogen is actually liberated even on thin oxide films,[9] and hence it is necessary to check this point in the particular case of Cd. It is possible that metals like Zn and Cd are never completely free of oxide films in aqueous solutions, as suggested also by Huber.

The authors have presented only the derived

[5] Central Electro-Chemical Research Institute, Karaikudi, India.
[6] I. Sanghi and R. Rao, *Proc. Indian Sci. Congr., 45th Congr.*, 1958, Part II, p. 202, Abs. No. 423.
[7] I. Sanghi and W. F. K. Wynne-Jones, *Proc. Indian Acad. Sci.*, 46A, 309 (1957); *ibid.*, 47A, 49 (1958).
[8] Bicri, Ph.D. Thesis, Berne University, Switzerland (1949); P. Delahay, *Anal. Chem.*, 27, 478 (1955).
[9] I. Sanghi, *et al.*, Paper presented at C.I.T.C.E. 10th Reunion (1958), In press.

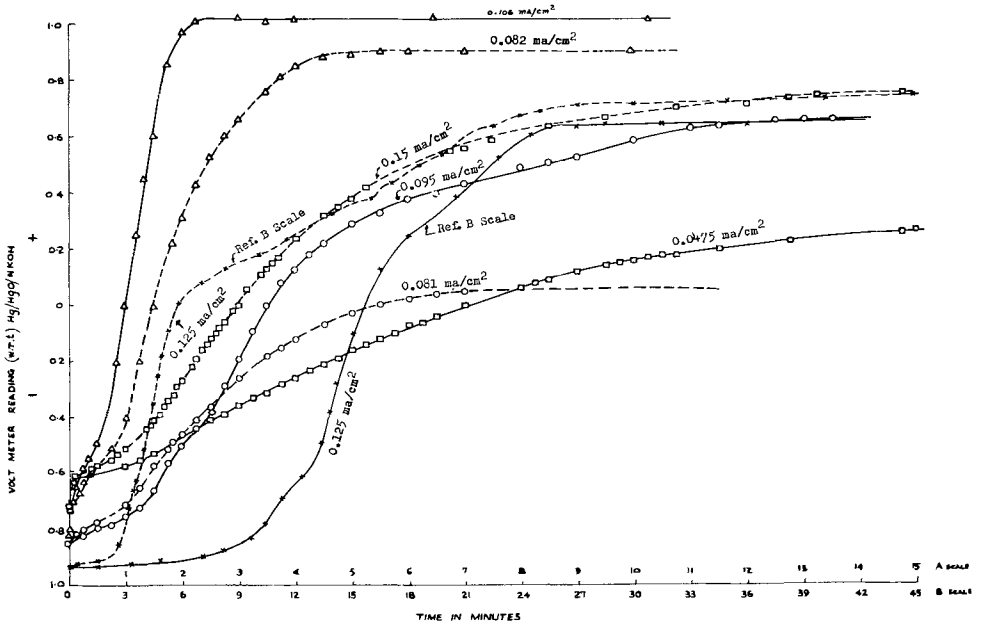

Fig. 1. Some current densities and concentrations of KOH solutions: - - - - -, stirred; ————, unstirred; X, 5N KOH; triangle with dot, 2N KOH; O, 1N KOH; □, 0.2N KOH.

graphs and have not reported the direct measurements. This has resulted in some loss of clarity. For example, in Fig. 1 of the discussed paper, the dotted gas evolution curve appears to indicate that oxygen is discharged in the negative region of potential itself and that as much as 40% of current goes toward oxygen evolution at as low a potential as 0 v with respect to Hg/HgO/KOH. This is not possible in view of the high oxygen overvoltage on Cd and in view of the definite minimum potential required for the reaction $2\overline{OH} \rightarrow H_2O + O$. Also, on page 54 of this paper, the full significance of Fig. 5a and b in connection with the depassivating reaction is not quite clear. Some average rate of depassivation R_2 has been discussed, and probably what the authors imply is that $R_2 = \frac{I\,t'_p}{t_s\,t'_p}$. Similarly, on page 56 (bottom of column 1), it is stated that "if $R'_2 >> R_1$ initially, the CdO film may build up even before supersaturation is reached." This does not appear to be correct, and perhaps there is a typographical error and it should read "$R'_2 << R_1$."

Ionic conduction through very thin oxide films is governed by the high field theory[10] and would be expected to assist the oxide film growth. However, correct ideas about this can be had only by measuring current growth and decay transients or by applying square wave polarization.

Stirring appears to have very interesting effects in the present case. Generally, stirring is expected to delay the passivation considerably, but we find that stirring decreases t_p for 0.2N and N-KOH but increases it for 2N and 5N-KOH. This aspect has perhaps not been considered by Lake and Casey. Also, there appear to be certain difficulties and limitations in evaluating the kinetics of electrode processes and in measuring the rate of film thickening or growth by constant current polarization alone. It has been suggested that potentiostatic measurements are more fruitful[11, 9] and are, therefore, being carried out in these laboratories.

P. E. Lake and E. J. Casey: *Potential arrests.*— Preliminary work showed that extra prolonged potential arrests exist if the current density distribution through the electrode is not uniform and/or constant. In all of the electrometric work reported, a cylindrical cell of which the electrodes formed the ends was used and, within the limits of sensitivity of the multipoint recorder used (±0.005 v, 4 points per min), the extra steps were no longer present. Dr. Sanghi's instrumentation may have detected a real "fine structure." However, if this fine structure is not reproducible, one must consider that the current distribution may be changing from run to run.

Reproducibility of the value of It_p was not as good as could be desired, as was reported in the paper. Best reproducibility was obtained by us if the surface was first cleaned with nitric acid and then prereduced. The possibility that all oxide was not removed was suggested in the paper but accepted as a possible small constant error. When parallel-plate geometry was used, the determination of the value of It_p was usually reproducible to ±10% in experiments done within the fiftyfold range of current densities reported. If successive experiments disagreed by a larger amount, some extraneous factor, such as peeling of the stop-off lacquer, could usually be found to be the reason. However, at Dr. Sanghi's room temperature of 35°C (if this is indeed not a misprint!), the conversion reaction would be expected to be more rapid than at the temperatures (≦25°C) used in the study reported by us, and would probably lead to irreproducible passivation. This comment is strengthened by the further facts that the solubility of $Cd(OH)_2$ in KOH is much higher[12] than is usually supposed, even at 25°C, and

[10] N. F. Mott and N. Cabrera, *Repts. Progr. in Physics*, 12, 163 (1948); D. A. Vermilyea, *This Journal*, 104, 426 (1957).

[11] M. Fleischmann and H. R. Thirsk, *Trans. Faraday Soc.*, 51, 71 (1955); M. Fleischmann and H. R. Thirsk, Paper presented at C.I.T.C.E. 10th Reunion (1958), In press.

[12] P. E. Lake and J. M. Goodings, *Can. J. Chem.*, 36, 1089 (1958).

that the electrolyte can supersaturate during the oxidation. The effect of the supersolubility on potential is simply not known because there are no activity data available.

For the above reasons, the use of It_p as a quantitative measure of the depth to which Cd is oxidized before passivation is certainly justified on the basis of reproducibility. Its variation, as OH^- is replaced by $CO^=_3$ at constant $[K^+]$, is real and can be described in terms of the mechanism proposed in the paper. An interesting further fact, the one which suggested the reported study, is that the changes in It_p with experimental conditions are amplified, sometimes up to tenfold, in the sintered negative plate of the Ni-Cd battery. We are driven to the conclusion that the amplification is due to an important factor not usually considered, *viz.*, the effective volume of the reaction product. It is considered that the product could, in favorable circumstances, seal off at the neck the pores which contain still-unoxidized Cd.

Passivation.—The criterion for choosing t_p was low value of $d\,E/dt$ following the onset of oxygen evolution. To choose a definite potential over so wide a range of experimental conditions would have been meaningless, as Dr. Sanghi's graph testifies. However, it is necessary to restate that sharp passivation depicted in Fig. 1 of the original paper is typical of the behavior of pure Cd at 25° and below.

Dr. Sanghi has simply misinterpreted Fig. 1 in his discussion of gas evolution rate. It is the time base which is common to both the potential and the O_2 evolution rate. What the graph shows, for example, is that a small fraction of the current goes into O_2 evolution while the average potential of the electrode is still below 0 v w.r.t. Hg/HgO (this is not surprising because the potential distribution on the actively corroding metal is probably not completely uniform), and that gas evolution accounts for 40% of the current by the time the rapidly rising potential has reached 1.1 v. What is interesting is the fact that, in the experiment reported in Fig. 1, for some hours *after* passivation a small fraction of the current continued to split off to oxidize Cd and to keep in repair the CdO film which is continually etched away by the conversion reaction.

New work.—A study of the decay of overpotential before, during, and after passivation has recently been completed and will be submitted shortly. At any time after passivation, the decay is of the form usually found for gas electrodes and referred to as activation overpotential decay. However, at times before passivation, after an *IR* drop has been separated the first part of the decay is *exponential* in time. The exponential part is not described by activation theory and is tentatively interpreted as the decay of an inner double layer of $O^=/OH^-$, of fixed dimensions, in the CdO layer at the CdO-electrolyte interface. Passivation occurs when the field strength across this inner double layer increases to the value at which OH^- discharge to OH occurs more easily than the ionization reaction $OH^- \rightarrow O^= + H^+$.

The role of adsorption of OH^- on the CdO surface thus becomes quite important, and is manifested through unexpected variations of overpotential with activity of KOH. In general, the new work supports and extends the mechanism of passivation already proposed:

$$\mathrm{Cd} \xrightarrow{R_1} \mathrm{CdO} \xrightarrow{R'_2}$$

$$\text{Soluble Complex} \xrightarrow{R_2''} \begin{matrix}\mathrm{Cd(OH)_2}\ \text{or}\\ \mathrm{CdCO_3}\end{matrix}$$

where R_1 refers to the oxidation process, and R_2 to the conversion.

In fact, the proposed mechanism, which incidentally has been strengthened by recent work of Huber,[13] has proven to be quite versatile. For instance, poor reproducibility at high temperatures and low currents is predictable when considered in terms of the role of the conversion reaction and the new information on solubility. At high temperatures, the conversion reaction is fast; a thick and probably loose layer of product is built up on the surface before passivation occurs. The first evolution of oxygen may simply undermine the protecting film of product, and force the process to start over again. At very low currents, the solubility is high enough that the product can actually be transported to and plated out on the negative electrode, and the passivation time will be longer than expected, probably will be irreproducible, and indeed the electrode may never passivate. Stirring will obviously have its greatest effect at low current densities, by aiding dissolution of the CdO layer and aiding transport of complex to the negative where it can be plated out.

The supposed role of adsorption of OH^- on the CdO layer predicts longer passivation times for increasing a_{KOH}, because the decrease in pH in the pores of the conversion product will be less the higher the a_{KOH}. Stirring should shorten t_p in low concentrations by raising the pH in the pores. On the other hand, increased a_{KOH} increases the rate of the conversion reaction and, once the CdO surface is saturated with OH^-, stirring should lengthen t_p as the a_{KOH} is further increased. It is encouraging that Dr. Sanghi has observed that t_p is shortened in low concentrations of KOH and lengthened in high concentrations.

General.—The conditions under which the values in Table I were obtained could have been approximated from Fig. 4a; they were 0.07 ma/cm^2 and 7.2*N* electrolytes.

As Dr. Sanghi has kindly pointed out, on page 56, line 15, the misprint should read $R_2' << R_1$.

We agree with Dr. Sanghi's comment that the reaction is a complicated one on which further work is necessary.

Uncommon Valency Ions and the Difference Effect

M. E. Straumanis (pp. 284-286, Vol. 105)

Ph. Brouillet, I. Epelboin, and M. Froment[14]: In his article, Dr. Straumanis expresses surprise that the Δ-effect has not been considered to explain the deviations from faradaic yield in the anodic dissolution of certain metals. However, examination of experiments carried out in recent years shows that the Δ-effect cannot explain the anomalous yields obtained in certain electropolishing procedures.

[13] K. Huber, *Z. Elektrochem.*, **62**, 675 (1958).

[14] Laboratoire de Physique, Faculté des Sciences de Paris, Paris, France.

The Δ-effect supposes that in the absence of current there is a protective film on the metal, and that this film is disrupted in certain spots on passing anodic current.

We have observed the surface of metals undergoing anodic dissolution with a noninverting metallographic microscopic whose objective was immersed in the electrolyte. Examination was made in two ways: (*a*) with an interferometric arrangement using two polarized waves (Nomarski system), and (*b*) with ordinary polarized light. The first method gives a resolution of a few dozen angströms; the second makes evident the existence of crystalline layers as they are formed at the anode surface. The results have been observed visually, and recorded by means of microphotography and microcinematography.[15-17]

We have established that during electropolishing the surface becomes more and more uniform and can become perfectly smooth within a few dozen angströms. If polishing is continued on such a surface, its appearance does not change. The homogeneity of the dissolution seems to contradict the Δ-effect, heterogeneous by definition.

The polishing sometimes can be accomplished without the appearance of a layer on the anodic surface. But, if it appears (and it is clearly visible in polarized light), it is quite homogeneous, and an important fact is that it disappears on interrupting the current. Optical examination, as well as chemical analysis,[16] shows that this film has nothing in common with the oxide film which is formed when the anode is just below the polishing potential; this oxide film disappears when the polishing range is attained.

From a chemical point of view, the reactions involved in the mechanism of the Δ-effect raise additional difficulties.

In the experiments to which we refer, for example the anodic dissolution of pure Al in solutions containing ClO_4^- ions,[18-22] the electrode does not undergo any "spontaneous" dissolution when there is no applied current. In electropolishing, no gas evolution is apparent. If, according to the argument of Straumanis, a "spontaneous dissolution" occurs on parts of the metal made bare by anodic dissolution, one must indeed consider the possibility of unusual chemical reactions, for example the reduction of perchlorate to chloride on the metal surface. According to authors who have studied this question,[23] the reduction is difficult, even if the surface has been "made bare" by amalgamation.

We have explained the appearance of reduction products in the electrolyte by the return to their stable valence of ions formed at the anode in a lower and unstable valence state. Quantitative analysis has confirmed this hypothesis, [10,21,22,24] and the work of others with quite different solutions[25] has shown that the reduction products can be formed at some distance from the electrode.

In addition, we have described[22,26] the precise measurement of the electrode potential with respect to a reference electrode. The anodic overpotential is considerable, and it is difficult to postulate a reasonable mechanism of reduction at the electrode surface. Even if this chemical reaction exists, we do not see how it could explain the constancy of the yield when such parameters as time of electrolysis and current density are varied. We have observed a yield constant to about 1% as both parameters were varied over a range of 1 to 20.[22,24]

On the other hand, the importance of the "spontaneous dissolution" ought to vary if the potential of the electrode is changed, with a consequent change in the yield. Now, experiment has shown that the anomalous yield is not modified by change in the polishing potential.[16,24,27] Even on changing the potential by incorporating the metal studied in an alloy, for example Al-Ni,[16,24,27] the Al retains the same abnormal valence. In this case, the electrochemical potential is changed as much as 500 mv, without any external polarization. Again, we do not see how the Δ-effect can explain these results.

Finally, we wish to point out, in response to a question of the author, that we have measured the yield of anodic dissolution during electropolishing of most of the common metals.[10,22,24] With certain metals, the valence calculated from these measurements has been the lowest customary value: Mo^{3+}, Bi^{3+}, V^{2+}, Mn^{2+}, Zr^{2+}, Fe^{2+}, Cd^{2+}, Co^{2+}, Ni^{2+}, Sn^{2+}, Pb^{2+}, Ga^{+}, In^{+}, Hg^{+}, Ag^{+}, Cu^{+}, Li^{+}. With others, we have found a valence lower than the lowest accepted values: La^{+}, Ce^{+}, Ti^{+}, Zn^{+}, U^{+}, Mg^{+}, Al^{+}, Be^{+}. The values found are in no case greater than a known valence, and they are never less than unity.

M. E. Straumanis: The negative difference effect is found when the rate of *self-dissolution* of a metal electrode increases while under an anodic current, and the positive Δ-effect—when under the same conditions this rate decreases. From the loss of weight of the electrode and from the time and strength of the current passing the anode, the valency of the metallic ions pushed into solution can be calculated. If, now, the difference effect (that is, the increase or decrease of self-dissolution rate during the flow of current) is disregarded, one will calculate in the first case a decrease in the valency of ions going anodically into solution (because the weight of the metal which dissolved outside the faradaic current was not taken into consideration), and, vice versa, an increase in the ionic charge in the second case.

Both effects were studied by the author[28] and they also were observed by others, e.g., the negative effect by Heumann and associates during the anodic

[15] I. Epelboin, M. Froment, and G. Nomarski, *Rev. Métall.*, 55, 260 (1958).
[16] M. Froment, Thesis 1958, *Corrosion et anti-corrosion*, 6 (Nov. 1958).
[17] "Etude Microscopique du Polissage Electrolytique," Film prepared by I. Epelboin and M. Froment (with the assistance of G. Nomarski).
[18] I. Epelboin and M. Froment, *Comp. rend.*, 238, 2416 (1954).
[19] Ph. Brouillet, I. Epelboin, and M. Froment, *Compt. rend.*, 239, 1795 (1954).
[20] M. Froment, Dissertation, Paris (1954).
[21] Ph. Brouillet, Thesis 1955, *Métaux (Corrosion-Indus.)*, 30, No. 356—April, No. 357—May, No. 358—June (1955).
[22] I. Epelboin, *Z. Elektrochem.*, 59, 691 (1955).
[23] W. R. King and C. S. Garner, *J. Phys. Chem.*, 58, 29 (1954).
[24] I. Epelboin and M. Froment, 73rd Colloque International du C.N.R.S., Paris, 1956, *Métaux (Corrosion-Indus.)*, 32, 55 (1957).
[25] M. D. Rausch, W. E. McEwen, and J. Kleinberg, *J. Am. Chem. Soc.*, 77, 203 (1955).
[26] Ph. Brouillet and F. Monnot, *Bull. soc. franc. électriciens*, 8, 498 (1958).
[27] M. Froment, *Bull soc. franc. électriciens*, 8, 505 (1958).
[28] M. E. Straumanis, *This Journal*, 105, 284, 286 (1958).

passivation of Cr[29] and on stainless steel by Tomaschow.[30] Both effects are proportional to the current density, meaning that the ratio of the rate of self-dissolution and of enforced rate (through current) is constant, and independent of the *p*H of the solutions.

In the case of Al corroding in KCl, the increase in rate of self-dissolution while the anodic current was on could be directly observed. Besides, it could be seen that the protective (oxide) layer on Al broke down under the impact of anodic current. Thus, the increase in self-dissolution could be attributed to the scale breakdown. It is not said that the latter should in all cases be an oxide scale; it can be a salt layer as well. Even a metal without any scale at all could produce a Δ-effect if the metal in the surface becomes activated by the anodic current. The same effect could be produced by a decreasing thickness of the scale while under anodic current. If in the experiment with Al in KCl the increase in self-dissolution is disregarded, a valency lower than 3 can be calculated for Al ions from the experimental data. This, in the opinion of the author, happened in the work of Drs. Brouillet, Epelboin, and Froment.

Although the discussors state that in an electrolyte containing ClO_4^- there was no gas evolution (at the anode) during electropolishing, and that the reduction of ClO_4^- is difficult by the metal, they nevertheless write in the next paragraph that there are reduction products present but produced by the Al ions of lower valency. Is it not simpler to write: $Al + 3H^+ \rightarrow Al^{3+} + 3H$ (self-dissolution while under anodic current, Δ-effect) and then $ClO_4^- + 8H \rightarrow Cl^- + 4H_2O$?[31]

The (active) hydrogen has a certain solubility in water and may act at some distance from the electrode; no lower valency Al-ions are necessary for the reduction. In addition, no such ions were obtained by the discussors when electropolishing was made in solutions containing phosphoric acid, chlorides, or fluorides.[32] It is clear that there was no negative Δ-effect, but probably a positive one during the passage of current, as it is well known that the effect may change its sign if a metal is anodically dissolved in different electrolytes.[33]

Furthermore, in the last paragraph of the discussion, two series of metal ions are given. Is it not surprising that the metals which supposedly produce ions of lower valency during electropolishing all are *the most active metals* (Zr^{2+} should be transferred into the second series because its most common valency is 4)? These metals react with the electrolyte (self-dissolution) as soon as the protective layer is removed or changed (e.g., by the anodic current, Δ-effect). Even ions with a valency lower than 1 can be found by calculation in such cases.[34] More noble metals exhibit only very slight Δ-effects[30] and, therefore, no ions of unusual valency (1st series) were found by the discussors with such electrodes.

Finally, the assumption of the discussors, that during anodic polarization ions of lower valency are going into solution, is contrary to experience gained in passivation experiments. For instance, Fe or Cr,[29] as it, e.g., follows from the recent work of Pourbaix,[35] at small current densities go into solution with low but normal valencies and with the valency increasing at higher current densities (or potentials), which is in accordance with our theoretical considerations.

Of course, if the discussors can show that there is absolutely no change in the rate of self-dissolution of an anode made of an active metal during polarization (no Δ-effect), then their conclusions should be regarded as correct (or *see* last sentence in the discussed paper).

Studies of Natural Convection at Vertical Electrodes

N. Ibl and R. H. Müller (pp. 346-353, Vol. 105)

G. Wranglén[36]: This paper is of great interest since it shows that the velocity profiles obtained in the rigorous numerical solutions of the boundary layer equations by Ostrach and by Sparrow and Gregg can be realized also in electrolysis experiments under ideal flow conditions just as they already have been realized in experiments on thermal boundary layers. In addition, a new contribution is the application in the approximate analytical treatment, according to von Kármán, of velocity profiles that are in agreement with theoretical expectations and experimental findings. The method adopted by the authors is to vary certain parameters in the velocity and concentration functions so that the calculated values of u_m and τ fit the experimental data. However, this method will not admit a comparison between a purely theoretical solution and experimental results. This comparison can be made if the functions introduced are adapted instead to the profiles obtained by a rigorous numerical treatment. It should further be emphasized that any functions will give results that are correct dimensionally. Only the numerical coefficients in the expressions for maximum flow velocity, limiting current density, diffusion layer thickness, concentration difference, etc., will differ. However, exact values of these coefficients can easily be obtained by comparison with the rigorous numerical solutions for the appropriate Schmidt (or Prandtl) number.

According to these principles, the discussor has performed calculations, the main results of which were recently published in a short communication.[37] While the concentration profiles used were the conventional ones, corresponding to Eq. (V) of the paper discussed, the following approximation was used for the velocity profile, *viz.*,

$$u = 3.375\, u_m \frac{y}{\delta}\left(1 - \frac{y}{2\delta}\right)^2 \qquad [1]$$

for

$$0 \leqq y \leqq 2/3\ \delta$$

[29] Th. Heumann and W. Rösener, *Z. Elektrochem.*, **59**, 722, 730 (1955); Th. Heumann and F. W. Diekötter, *ibid*,. **62**, 745, 748 (1958), however, the authors do not mention the words "difference effect," but that there was such an effect follows from the description.
[30] N. D. Tomaschow, *Z. Elektrochem.*, **62**, 717, 725 (1958).
[31] I. Epelboin, *Z. Elektrochem.*, **59**, 689, 690 (1955).
[32] I. Epelboin, *Z. Elektrochem.*, **62**, 813, 815 (1958).
[33] M. E. Straumanis and Y. N. Wang, *This Journal*, **102**, 304 (1956).
[34] M. D. Rausch, W. E. McEwen, and J. Kleinberg, *J. Am. Chem. Soc.*, **77**, 2093 (1954).
[35] M. Pourbaix, *Z. Elektrochem.*, **62**, 670 (1958).
[36] Div. of Applied Electrochemistry, Royal Institute of Technology, Stockholm 70, Sweden.
[37] G. Wranglén, *Acta Chem. Scand.*, **12**, No. 4 (1958).

Table I

Quantity	Constant liquid density A.A.	Constant liquid density R.N.	Constant current density A.A.	Constant current density R.N.
u_m	1.18	0.98	1.33	1.1
$\delta_{0.99}$	3.48	3.54	3.00	3.09
τ	2.32	2.69	2.00	(2.1)
i_{11m}	0.575	0.499	—	—
$/c_o - c_e/$	—	—	1.50	1.59

Fig. 1. Transition from laminar to turbulent flow in the electrode film in electrodeposition of Cu under free convection conditions.

and

$$u = 0.070\, u_m\, Sc^{-1/3}\left(1.5\, Sc^{1/3} - \frac{y}{\delta}\right) \qquad [2]$$

for $2/3\ \delta \leqq y \leqq 1.5\ Sc^{1/3}\ \delta$. In these expressions, $\delta = \delta_{0.99}$ is defined as the value of y for which $/c - c_e/ = 0.99/c_o - c_e/$. This definition also allows an exact meaning to be assigned to δ. Eq. [1] implies that u_m is reached at 2/3 δ, which is approximately true for high Schmidt numbers. Eq. [2] takes into account the fact that the thickness (1) of the hydrodynamic boundary layer is a function of the Schmidt number. Generally, $1 \simeq \delta \cdot Sc^{1/3}$.

For the numerical constants of interest here, the results listed in Table I were obtained. They refer to Sc = 1000, which is a good mean value for aqueous electrolytes, particularly if higher temperatures are also considered.

A.A. means approximate analytical solution and R.N. rigorous numerical solution. The table shows that the approximate profiles introduced, although comparatively simple, are a satisfactory substitution for those obtained in the rigorous numerical treatments. This can also be shown by plotting the respective profiles in the same diagram. In a comparison with experimental results, the constants derived from the numerical solutions should be used. Experimental values for the coefficients are: 1.04 for u_m, 1.63 for τ (at constant c.d.), and 0.505 for the limiting c.d.[38]

The fact that the flow becomes turbulent at relatively low values of the Grashof number is illustrated by Fig. 1 published here which was obtained by a schlieren technique without lenses.[39] A cathode in a 1M $CuSO_4$-solution was placed in a beam of parallel light and the shadow was photographed. The electrode, filling the whole cross section of the electrolyte, was 180 mm high and the photograph was taken between $x = 80$ and $x = 140$ mm. The current density was 1.5 amp/dm² and the temperature 20°C. While laminar flow on the lower part of the cathode is evident from the constant deviation of light and a regular vertical motion in the bright band, the conditions on the upper part of the cathode are clearly turbulent. The transition from laminar to turbulent flow under the conditions mentioned occurs at $x \simeq 100$ mm both at the cathode and the anode. The same result was obtained with electrodes, 1000 mm in height. These results seem to agree with those reported in the paper under discussion. They obviously imply that in full-scale electrolysis (e.g., copper refining) the free convective flow is turbulent over the main part of the electrodes. Calculations, based on an assumption of laminar flow, are then of qualitative value only. This situation stresses the need for at least empirical relations for mass transfer under turbulent free convection conditions.

N. Ibl: The interesting results reported by Wranglén on the onset of turbulence in natural convection are in agreement with the findings of R. Müller. In our optical experiments, the flow became turbulent[40] for instance at a height of 8 cm with a current density of 20 ma/cm² and at a height of 14 cm with a current density of 4 ma/cm². This corresponds to a Rayleigh number, Ra (Ra = Sc x Gr) of roughly 4×10^{11} (compared to a Ra of 2×10^9 reported by Saunders[41] for the transition to turbulence in heat transfer). As Wranglén points out, the question arises as to how far the relations hitherto derived are still valid with tall electrodes, of the kind used in technical cells. M. G. Fouad has studied experimentally in our laboratory the mass transfer by natural convection at Rayleigh numbers above 10^{11}. His unpublished experiments show that the limiting current has a tendency to become almost independent of the height with tall electrodes. The slope of the line log Nu vs. log Ra is somewhat larger than ¼. In this investigation, the cathodic limiting current was measured in the usual way with electrode heights up to 100 cm and $CuSO_4$-solutions acidulated with H_2SO_4, the concentration of the $CuSO_4$ ranging from 0.01 to 0.73M.

Concerning the question of the profiles as discussed by Wranglén, there is no doubt that the results obtained by von Kármán's method should become better with increasing accuracy of the profiles employed. However, it is interesting to note that the profiles hitherto commonly used in the application of von Kármán's method to natural convection [Eq. (V) and (VII) of the discussed paper], although they are far from true, yield limiting currents which differ by only 2%[42] from those derived from the rigorous treatment given by Ostrach. In the case of the maximum flow velocities, the agreement is less good but

[38] C. R. Wilke, M. Eisenberg, and C. W. Tobias, *This Journal*, **100**, 513 (1953).
[39] E. Schmidt, *Forsch. Gebiete Ingenieurw.*, 3, 181 (1932).
[40] R. H. Müller, Dissertation No. 2668, Swiss Federal Institute of Technology, Zurich (1956).
[41] R. Saunders, *Proc. Roy. Soc. (London)*, **A157**, 278 (1936).
[42] C. R. Wilke, C. W. Tobias, M. Eisenberg, *Chem. Eng. Progr.*, **49**, 663 (1953); S. Ostrach, *Nat. Advisory Comm. Aeronaut., Technote Note 2635* (1952).

the difference is still not very large, the numerical coefficient in the equation for the flow velocities being 0.98 for the rigorous method[43] and 0.77 in the case of von Kármán's approximation using the above profiles (Table I of the discussed paper). It was thus felt worth while to study in some more detail the influence of the assumed profiles on the results obtained with von Kármán's method. This was achieved by varying the parameters of Eq. (VIII) to (X) of the discussed paper. It was found that the results depend greatly on the assumption made on the relative location of the velocity maximum and the shape of the velocity profile up to the maximum, but, within a wide range, they are almost not affected by a variation of the slope of the velocity profile beyond the maximum. This might help to understand how it is possible that Eq. (V) and (VII) give good results in spite of the fact that they are quite wrong in the outer parts of the boundary layer. It might be noted that, with velocity profiles of the type used by Wranglén, the results are also practically independent of the slope beyond the maximum. This slope is in this case inversely proportional to $Sc^{1/3}$, which is roughly 10 in aqueous solutions. However, if a value of 5 or 20 is used instead of 10, the calculated maximum of the flow velocity at constant liquid density, for instance, is changed by less than 2%.

In the discussed paper, the measured velocities were not compared with the values obtained by the rigorous method, since the extrapolation to high Schmidt numbers of the velocity distributions shown graphically by Sparrow and Cregg[44] for a few Prandtl numbers between 0.1 and 100 appeared inaccurate. It is encouraging that the figure of 1.1 given in Wranglén's discussion for the numerical coefficient of the equation for the flow velocity (which was extrapolated to Sc = 1000 from more accurate values of the rigorous solution communicated by Sparrow and Cregg) is in very good agreement[45] with the experimental value of 1.04.

A Contribution to the Theory of Stress Corrosion in Al-4% Cu Alloys

W. H. Colner and H. T. Francis (pp. 377-384, Vol. 105)

G. J. Schafer and T. Marshall[46]: The comments regarding H_2O_2 concentration variability during tests are of great interest. Partly for this reason, we have much greater confidence in the acid chloride gas evolution test for intercrystalline corrosion susceptibility than in the salt-peroxide test. It has been shown[47] that important composition variables remain constant during the former test.

We do not entirely agree with the interpretation of some of the results presented by the authors. The polarization curves in Fig. 7 and 8 of the discussed paper indicate mixed rather than cathodic control. Cathodic control implies a large difference in polarization curve slopes with the cathode polarization curve being relatively much steeper. Again, in Fig. 6, current is only influenced by cathode area at large cathode: anode ratios, which indicates mixed control.

The area effect demonstrated in Fig. 2 of the paper does not necessarily support the contention that the grain boundary-grain center corroding cell is under cathodic control. In the case of the specimens not connected to auxiliary electrodes, the ratio of grain-center to grain-boundary areas is constant. Therefore, the failure time vs. exposed area curve must be explained purely on the basis that, when a larger specimen area is exposed, more grain-boundary trenches are formed in the stressed metal surface, and the time required for a given deflection is therefore shorter.

The disappearance of the area effect when auxiliary electrodes were used is not very relevant. It is shown in Fig. 8 that stressed 2024 is anodic to unstressed 2024 (this effect of stress has been observed on other materials),[48] so, when a stressed specimen is electrically coupled to an unstressed specimen, the system under consideration is equivalent to a bimetallic couple and has no simple relation to a stressed specimen by itself. Auxiliary electrodes of any more noble metal having appropriate polarization characteristics would have a similar effect on times to failure of the stressed specimens.

We would appreciate the authors' comments on our interpretation of their data.

H. T. Francis and W. H. Colner: It is conceded that Fig. 7 and 8 could be interpreted as indicating mixed control rather than cathodic control. In the couples of Fig. 6, however, the current was determined by the total cathode area when the anode area was held constant (C curves). Conversely, the current was unaffected by changes in anode area when the cathode area was held constant (A curves). This we interpret as cathodic control.

With regard to the area effect demonstrated in Fig. 2, we agree that the ratio of grain-center area to grain-boundary area is constant in any given specimen. For small specimens, however, we contend that the cathodic area is insufficient to produce enough total anodic attack to promote cracking. With larger specimens, the total cathodic area promotes rapid enough attack on *some* of the anodic zones to permit cracking. Reference is made to the work of Mears, Brown, and Dix on this point.[49]

We agree that coupling to other suitable cathode material would cause small-area specimens to crack. The question then remains: Why do small-area specimens not fail by themselves? We know they possess anodic grain-boundary zones, since they crack readily when coupled to auxiliary cathodes. The conclusion then must be that they cannot in themselves provide sufficient cathodic action to cause cracking.

[43] The K value of 0.98 indicated on the third line of Table I of the discussed paper is equal to the rounded numerical coefficient in Wranglén's equation for the flow velocity at constant liquid density along the interface [*Acta Chem. Scand.*, 12, 1143 (1958)]. The figure of 0.98 was directly obtained from the value of F' (η) given by Ostrach for a Prandtl number of 1000, the method used in the derivation being probably very similar to that employed independently by Wranglén (G. Wranglén, *Trans. Roy. Inst. Technol., Stockholm*, In press).

[44] E. M. Sparrow and J. L. Cregg, *Trans. Am. Soc. Mech. Engrs.*, 78, 435 (1956).

[45] The numerical factor of 2 in the right-hand side of Eq. (XXIII) of the discussed paper is a misprint and should be omitted.

[46] Dept. of Scientific and Industrial Research, Dominion Lab., P. O. Box 8023, Wellington, New Zealand.

[47] T. Marshall and G. J. Schafer, *J. Appl. Chem. (London)*, 8, 303 (1958).

[48] U. R. Evans, "Metal Corrosion Passivity and Protection," p. 471, Edward Arnold & Co., London (1937).

[49] R. B. Mears, R. H. Brown, and E. H. Dix, Jr., "Symposium on Stress-Corrosion Cracking of Metals," ASTM-AIME, 323-337 (1944).

Fundamentals of the Theory of Electrodes and Galvanic Cells

E. Lange and P. Van Rysselberghe (pp. 420-428, Vol. 105)

Patrizio Gallone[50]: I would like to take the liberty to submit some very modest considerations about some particular points of this paper, which deserves the most careful study by all electrochemists wishing to keep abreast with the fundamentals of their subject.

[2.3] About the last statement made by the authors in this paragraph of their paper one may object that "if chemical forces were alone effective" the "corresponding reaction" could only be spontaneous, so that in this hypothetical case A would only be positive.

[2.7] The electrochemical affinity is defined as the sum of the chemical affinity and of a term derived from the galvanic tension. This term, which also has by consequence the dimension of an affinity, is, among all the physical quantities considered by the authors, the only one that has not been given its own name. From the concepts underlying the definition of the Galvani tension, one may deduce that such nameless quantity should be called *Galvani affinity*, or *inner electric affinity*, or *electrostatic affinity*.

[2.9] With regard to the sign of the reversible Galvani tension of a given electrode, one may note that the way in which this quantity has been defined under [2.5] is clearly based on the spontaneous reaction, *viz.*, either α or β, as the case may be, irrespective of considering the electrode x or its reverse y. This is the reason for the change in sign when considering the reverse electrode. Consequently, the statement that the Galvani tension "is the same whether the electrode reaction is regarded as being α or β," instead of adding any further clarification, may seem to be at variance with the definition of the Galvani tension itself, which is based on the consideration of the spontaneous reaction only.

These same considerations essentially apply also to the sign of the corresponding chemical tension.

[4.11] As to the mutual interdependence of the cell tension U and the electromotive force E, may it be emphasized that we "always" have $U = -E$ provided that the equilibrium conditions of the reversible process are satisfied. For a better understanding of the reciprocal behavior of U and E, as well as of their different nature, it can be noted that these two tensions are in the same relationship as an acting and a reacting force in a mechanical system. The chemical tension, or electromotive force, E of the Galvanic cell can be compared to a static pressure exerted by a fluid against the wall of its container, and the electrostatic tension U is comparable to the reaction force opposed by the vessel. Whenever the reaction force is decreased, e.g., by establishing a metallic connection between the two cell electrodes, or by opening an aperture through the wall of a fluid-containing vessel, a new equilibrium of a dynamic sort comes about, with a flow of electric charges or of fluid and the consequent appearance of forces having a dissipative nature.

A mechanical comparison such as the above may sound somewhat trivial at the higher stages of theoretical standing, but it is extremely helpful at the lower ones in giving more concreteness to the fundamental concepts expounded by the authors.

E. Lange and P. Van Rysselberghe: The authors appreciate Dr. Gallone's interest in their paper.

The statement made about paragraph [2.3] is erroneous. The chemical affinity of an electrode reaction will be positive or negative according to the direction in which the reaction is written.

In connection with paragraph [2.7], we agree that an expression such as *electric affinity* could well be used. This has, in fact, been suggested in the 1958 version of the report on Electrochemical Nomenclature and Definitions of the International Committee of Electrochemical Thermodynamics and Kinetics (C.I.T.C.E.).

The statement made about paragraph [2.9] is erroneous. Paragraph [2.5] defines the chemical tension, not the electric or Galvani tension. Moreover, the direction in which these tensions, chemical and electric, are taken corresponds to the manner in which the phases are counted and not to the direction in which the electrode reaction may be spontaneous.

We agree that the analogy developed by Dr. Gallone in connection with paragraph [4.11] may be of some help in an elementary discussion of electrochemical equilibrium and of the departure from this equilibrium.

The Mechanism of Passivating-Type Inhibitors

M. Stern (pp. 638-647, Vol. 105)

H. H. Uhlig[51]: The electrochemical mechanism for passivation of metals by oxidizing passivators, as outlined by Dr. Stern, is a reasonable proposal and, in my opinion, fits the facts as we now know them. In a paper by Dr. King and myself, presented at this same meeting (ECS, Ottawa, September 1958), we have arrived at essentially the same mechanism. Dr. Stern appears to lean toward a definition of passivity which excludes nonoxidizing passivators. I concur in the advantages of such a definition, especially if the metal admitted to be passive exhibits a Flade potential. But many investigators have traditionally defined passivity on the basis of a low corrosion rate (Definition II, "Corrosion Handbook") which includes as passivators nonoxidizing substances like pickling inhibitors, Na_3PO_4, Na_2SiO_3, and carbon monoxide. Perhaps we are now at the point where a clearer definition of passivity can be formulated, and, in this regard, Dr. Carl Wagner has already moved in this direction.[52]

Of course, oxidizing property is not the only factor that enters passivation even in the presence of a

[50] Oronzio de Nora, Impianti Elettrochimici, Milan, Italy.

[51] Corrosion Lab., Massachusetts Institute of Technology, Cambridge 39, Mass.

[52] C. Wagner, International Symposium on Passivity, Jugenheim, West Germany, September 1957.
A metal is called passive if: (*a*) on increasing the electrode potential toward more noble values, the rate of anodic dissolution in a given environment as a function of electrode potential under steady-state conditions is found to be less than the rate at a lower, less noble potential; or (*b*) if, on increasing the concentration of an oxidizing agent in an adjacent solution or gas phase, the rate of oxidation without flow of external electrical current under steady-state conditions is found to be less than the rate at a lower concentration of the oxidizing agent.

strong oxidizer. In an experiment we did some years ago, 18-8 stainless steel in 10% ferric chloride was found to corrode by pitting at a very high rate, but, on addition of 3% sodium nitrate, the corrosion rate fell to less than one millionth its original value. It is not possible that the nitrate ion contributed to the cathodic depolarizing action of the ferric ion; instead, the nitrate ion probably adsorbed on anodic areas displacing chloride ion and thereby reduced the critical current density required for passivity of 18-8. This mechanism fits in with the general picture outlined by Dr. Stern. Incidentally, it is difficult in this instance to conceive of any mechanism involving build-up of thick oxide films as cause of the tremendous decrease in corrosion rate.

With regard to Fig. 2, it is unfortunate that point E is described in the text as the Flade potential. This potential is not the same as the critical potential observed on decay of passivity first described by F. Flade, and after whom the Flade potential is named. Point E includes an unknown increment of potential caused by concentration polarization and *IR* drop through temporary thick films of anodic corrosion products. Such films are not present and do not cause error in measurement of the true Flade potential when passivity decays.

Whether a critical concentration of passivator exists with accompanying sudden shift of potential to the passive value, or instead the shift in potential is more gradual on increasing the passivator concentration, depends on the rapidity with which the passivator can be cathodically reduced. If reduction is slow, as is apparently the case with chromates, chromate can adsorb increasingly on the metal surface (thereby producing more cathodic area) in accord with the Langmuir adsorption isotherm. If reduction is rapid, a critical concentration should be found above which, but not below, passivity is observed. For the latter case, a Langmuir adsorption behavior of potential vs. passivator concentration may then be found only on a surface already passive. This situation probably obtained in the course of Geary's measurements showing a Langmuir relationship for 18-8 and titanium in sulfuric acid in presence of Cu^{++} and Fe^{+++}. It is my conclusion that the passive film in presence of ferric or cupric sulfate is essentially an adsorbed film of oxygen in accord with the ideas described in the paper by Dr. King and myself, on top of which Cu^{++} or Fe^{+++} is adsorbed in amount dependent on concentration.

It is not entirely clear what experimental conditions of Okamoto led to a constant corrosion potential of iron short of 10^{-3} moles chromate/liter and a passive potential thereafter. Careful work of Heyn and Bauer[53] shows a gradual change of potential on increase of chromate concentration more nearly in accord with data of Geary.[54,55] The lower purity iron used by Okamoto is not the cause,[56] and it is not certain whether Okamoto's use of beeswax-rosin to shield a portion of his electrode surface reduced some chromate at the wax-metal interface and produced a passive-active cell which disturbed the potential.

It is true that Fig. 4 indicates that the corrosion rate in a passivator solution should be the same as that which occurs when the metal is passivated by anodic polarization to the same potential, but with one important provision. This provision is that the anode to cathode ratio should be the same in the passivator solution as during anodic polarization. This situation may or may not prevail in practice, depending on the metal and the passivator.

From data of Fig. 8, it is probable that chemical equivalents of passive film substance on Ti are less than 0.02 coulomb/cm^2 in view of the fact that Ti corrodes rapidly in boiling sulfuric acid before passivity is achieved. The calculated coulombs under these conditions partly include those measured in forming an insulating reaction product film preceding build-up of the true passive film. The situation is analogous to Fe where the measured coulombs in sulfuric acid are found to be 1.6/cm^2 [57] which includes build-up of ferrous sulfate or similar film before passivity is achieved. But as Weil[58] observed, the true passive film accounts for only about 0.008 coulombs/cm^2 of the 1.6 coulombs/cm^2. It well may be, therefore, that the chemical equivalents of passive film substance on Ti are also consistent with the value of about 0.01 coulomb/cm^2 for Fe, which is the value found for the passive film on Cr-Fe and 18-8 stainless steels.[57,59]

With respect to Fig. 6, Dr. Stern states that, when the redox system is essentially at equilibrium on the passive surface, there is no net reduction of inhibitor. Thermodynamically, of course, the total system still tends to react and hence some corrosion undoubtedly occurs. The actual situation is probably one in which the net reduction of the redox system is finite, but nevertheless so small that the conditions of equilibrium are not appreciably upset.

The effect of oxygen on passivity of Fe in presence of molybdates and tungstates (and also on the rate of passivation in presence of chromates), in addition to factors mentioned by Dr. Stern, is a probable increase in the cathode to anode ratio favoring anodic passivation of the smaller anodic areas. This factor is mentioned in our paper.

Finally, I should like to mention that Dr. Stern's paper helps clarify our understanding of passivity and passivation, and is a welcome contribution. It comes at a time when serious effort is being made, as was evident at the International Symposium on Passivity held at Jugenheim, West Germany, in September 1957, to arrive at a more satisfactory knowledge of the structure and composition of passive films in general in metals and alloys.

E. E. Nelson[60]: This paper is another example of Dr. Stern's excellent discussions of previous publications and of his original work on electrode processes. The explanations of the roles of the reversible poten-

[53] E. Heyn and O. Bauer, *Mitt. Materialprüfungsamt. Berlin-Dahlem*, 26, 95 (1908).
[54] Although relative values of potential are reported correctly in the paper by Uhlig and Geary, absolute values are apparently too active by about 0.1 v.
[55] H. H. Uhlig and A. Geary, *This Journal*, 101, 215 (1954).
[56] G. Okamoto, Private communication.
[57] R. Olivier, "Proceedings 6th Meeting, International Committee for Electrochemical Thermodynamics and Kinetics," p. 314, Butterworths, London (1954).
[58] K. Weil, *Z. Elektrochem.*, 59, 11 (1955).
[59] H. Uhlig and P. King, Unpublished data.
[60] Socony Mobil Oil Co., Inc., 412 Greenpoint Ave., Brooklyn 22, N. Y.

tials, the exchange currents, and concentrations of oxidizing agents will aid greatly in the eventual complete understanding of passivity.

In this discussion, the relationship of Stern's arguments to particular anode-cathode reactions will be considered. It is believed that this supports Stern's conclusions and develops some additional information. The particular reactions were discussed by Pryor and Evans[61] and were named "autoreduction" by them. Later, they have been studied by Oswin and Cohen,[62] Buob, Beck, and Cohen,[63] and Nelson.[64]

"Autoreduction" is the combination of reactions (I) and (II) given below.

$$Fe_2O_3 + 6H^+ + 2e \leftrightarrows 2Fe^{++} + 3H_2O \qquad (I)$$

$$Fe \leftrightarrows Fe^{++} + 2e \qquad (II)$$

Pourbaix[65] shows that in the pH range of about 2 to 8, the equilibrium potential of reaction (II) is negative to the equilibrium potential of reaction (I). Therefore, when ferric oxide is in metallic contact with Fe in solution, reaction (II) will be mostly in the anodic direction and reaction (I) will be mostly in the cathodic. Footnotes 61, 62, and 63 give proof that this actually does occur. Many writers have felt that passivation is due to a covering of ferric oxide over the metallic Fe. The theory of "autoreduction" indicates that an extensive film of ferric oxide can not start forming until the Fe anode is polarized to the equilibrium potential for reaction (I).

Some authorities feel that passivity is due to absorbed oxygen rather than to an oxide. The arguments here could apply also to absorbed oxygen, but the work on autoreduction seems to favor the oxide theory.

Referring to Fig. 2 of Dr. Stern's paper, the corrosion rate of Fe increases along the curve from A to B. The reduction of ferric oxide would predominate over its formation at point A. These two rates would approach each other and become equal at point B. As the potential becomes more positive, the formation of the oxide increases and its reduction decreases. In the region from B to E, the coverage of the oxide increases. This decreases the anode area and also the total corrosion rate. The corrosion rate per unit of active anode is probably increasing in this area. This would account for the tendency for steel to pit in an inhibitor solution of a concentration below a safe minimum. At point E, the film development is completed and maximum protection is achieved.

In many of the figures of Dr. Stern's paper, current is plotted rather than current density. This has the advantage of showing the decrease in anodic current (and the total amount of corrosion) as passivity is developing. However, it fails to show that the current density on the active anode is probably increasing up to the establishment of a complete film. If current density is considered, the curve would look more like Fig. 1 of the original paper. This would avoid the multiple intersections between the polarization curves for the oxidizing agent and for the Fe anode. It seems probable that only one of these intersections represents an electrochemical state. The other is due merely to the method of plotting the data. The current density of the Fe anode, of course, cannot be plotted since we do not know the true anode area. This does not alter the above reasoning, however, At least if this concept is kept in mind, the curves in the original paper are no longer ambiguous.

The Discussion indicates that, for passivity to start, the cathodic curve for the oxidizing agent must intersect the anodic curve for Fe at a potential more positive than the oxidation-reduction potential of Fe_2O_3. For complete passivity, the intersection must be more positive that the abrupt break in potential (E in Stern's Fig. 2). This agrees with Dr. Stern's conclusions.

The combination of Dr. Stern's position with autoreduction" correlates well with certain known facts about inhibitors. For instance, at room temperature, sodium hydroxide requires dissolved oxygen in order to reduce corrosion. According to Pourbaix,[65] the difference between the equilibrium potential of reactions (I) and (II) decreases with increasing pH. Adding sodium hydroxide increases the stability of any ferric oxide that forms, but it does not produce any ferric oxide. For Fe_2O_3 to result, there must be some oxidizing agent, such as dissolved oxygen, present. At higher temperatures, water alone can probably oxidize iron to Fe_2O_3.

Sodium nitrite acts as an oxidizing agent to produce the higher Fe oxide. Also, the reduction of sodium nitrite provides a cathodic reaction so that a high anodic current is possible on the Fe anodes. This polarizes the Fe anodes to a more positive potential than the equilibrium potential of Fe_2O_3. At this more noble potential, a protective film of ferric oxide can develop.

Chromate ions probably have an additional action. They produce an oxide film and also permit a high anodic current to flow and polarize the Fe anode. Additionally, the reduction product of chromate has an oxidation-reduction potential more negative than that of bare Fe.[65] Therefore, chromate can form a stable film even though the Fe anode is not greatly polarized. This stable film reduces the anode area and aids in producing a condition where ferric oxide becomes stable.

D. M. Brasher[66]: We have read with much pleasure Dr. Stern's illuminating exposition of the electrochemical principles underlying the passivity of metal surfaces brought about by oxidizing inhibitors.

In his reference to the amount of inhibitor associated with the passivated surface, the author states that the amounts reported have "varied considerably from system to system." With regard to surfaces passivated in chromate, it is probable that this variation in the amount of Cr^{51} found (by radiometric means) is due to the fact that some workers have determined Cr^{51} on the surface without reference to the variation of this quantity both with time of immersion of the specimen, and also with "age" of the

[61] M. J. Pryor and U. R. Evans, *J. Chem. Soc.*, 1950, 1259.
[62] H. G. Oswin and M. Cohen, *This Journal*, 104, 9 (1957).
[63] K. H. Buob, A. F. Beck, and M. Cohen, *This Journal*, 105, 74 (1958).
[64] E. E. Nelson, Paper submitted to *Corrosion* for publication.
[65] M. Pourbaix, *Corrosion*, 5, 121 (1949).
[66] Dept. of Scientific and Industrial Research, National Chemical Lab., Teddington, Middlesex, England.

surface oxide film before immersion. In this laboratory, in work on steel, we have shown that adsorption of the inhibitor (presumably as $CrO_4^=$ ions) is followed by "logarithmic" growth of a film containing Cr_2O_3.[67] The work has also demonstrated the logarithmic growth of an oxide film on steel, both in air[68] and also in other inhibitive solutions such as sodium nitrite, aerated fenzoate, phosphate, etc.,[69] at rates comparable to that occurring in chromate solution.

The logarithmic nature and similarity in rates of film growth in all these environments has led us[70] to suggest a common mechanism, based on theories of Mott, and Hauffe and Ilschner,[71] whereby electron transfer through the film is the rate-controlling step in the growth of the film. It would be of much interest to know whether this logarithmic growth can be alternatively accounted for on the electrochemical principles set forth in Dr. Stern's paper.

Milton Stern: Before commenting on the above discussion, it should be mentioned that the description of passivity in the subject paper was devised in order to obtain a *useful* description of passivity. The mechanism proposed is kinetic in character and relies on simple, measurable parameters which determine the corrosion rate and electrode potential of the system. Descriptions of passivity which embrace films of one type or another are still embryonic in character and do not promise utility for some time.

I heartily agree with Professor Uhlig's suggestion that a clearer definition of passivity is in order. Dr. Wagner's definition appears quite reasonable and is consistent with the mechanism of passivity in the subject paper. I further agree that it is unfortunate that point E in Fig. 2 is described as the Flade potential—not necessarily for the reasons given by Professor Uhlig, since the figure is schematic, but rather because of the special nature of Flade's experiments. I would prefer to let the term "Flade potential" decay to nonexistence and believe point E would best be called the critical potential for passivity. This point, then, divides the potential scale into active and passive regions.

Since "oxidizing" is a relative term, it should be clear that a passivating-type inhibitor must exhibit a redox potential more noble than the critical potential for passivity of the metal. This is why a metal like Fe, which exhibits particularly noble critical potentials for passivity, requires rather strong oxidizing agents, whereas a metal like Ti, which exhibits relatively active critical potentials for passivity, is passivated by only mildly oxidizing solutions. As described in the text, many factors other than the oxidizing nature of the inhibitor are also pertinent to determining whether passivity is achieved.

The subject description of the mechanism of passivating inhibitors requires that a critical concentration of passivator exist which is accomplished by a sudden shift of potential from active to passive values. The data of Geary are not consistent with this since they show a gradual change of potential with inhibitor concentration. However, since the data do not appear to traverse the critical potential for passivity, they cannot be considered a test of the theory since the electrochemical picture also shows a gradual change of potential with inhibitor concentration in either the active or the passive potential region.

Miss Brasher's interesting work with Cr[51] deserves considerable attention and careful study. The electrochemical description of passivating inhibitors is consistent with her observation that Cr associated with the surface is in the reduced form. It is also consistent with the observation that the amount of Cr found on the surface is not dependent on the concentration of the chromate solution provided the mixed potential is between points E and F of Fig. 2. The mechanism further predicts that in the presence of oxygen the amount of Cr associated with the surface should be less than that found in the absence of oxygen.

There is some evidence that current in the potential region between E and F (Fig. 2) is time dependent and actually decreases in magnitude in a manner which is logarithmic with time.[72] This has been observed for stainless steel. If it is also true for Fe, then Miss Brasher's observations and this electrochemical description (modified to consider time effects) may be considered completely compatible.

Mr. Nelson's suggestion that current density be substituted for current is not clear, since it is necessary to plot polarization diagrams on a current basis in order to have the intersection of anodic and cathodic curves represent the mixed potential. I believe it is not only correct to show multiple intersections between polarization curves, since this is a characteristic of passive systems, but also that this is highly desirable and represents one of the characteristic features of this description. Note, for example, that the diagram in Fig. 10 shows an abrupt change in potential would occur when the limiting diffusion current for reduction of inhibitor exceeds the critical current for passivity. Fig. 9 illustrates this behavior experimentally.

The introduction of area effects into the electrochemical description of passive systems could probably be accomplished in the manner described for systems controlled solely by activation polarization.[73] However, this additional complexity was not introduced (along with possible time effects) because it was believed it would mask the more elementary and equally important features of the description and because these effects could not (at the time) be handled in a quantitative manner.

[67] D. M. Brasher, A. H. Kingsbury, and A. D. Mercer, also D. M. Brasher and C. P. De, *Nature*, **108**, 27 (1957); D. M. Brasher and A. H. Kingsbury, *Trans., Faraday Soc.*, **54**, 1214 (1958).

[68] D. M. Brasher, A. H. Kingsbury, and A. D. Mercer, *Nature*, **108**, 27 (1957).

[69] "Chemistry Research 1957," p. 12, Her Majesty's Stationery Office, London (1958).

[70] O. Kubaschewski and D. M. Brasher, In press.

[71] N. F. Mott, *J. Inst. Metals*, **65**, 333 (1939); *Trans. Faraday Soc.*, **35**, 1179 (1939). K. Hauffe and B. Ilschner, *Z. Elektrochem.*, **58**, 382 (1954).

[72] M. Stern, *This Journal*, **106**, 376 (1959).

[73] M. Stern, *Corrosion*, **14**, 329t (1958).

A New Experimental Technique for the Study of Films Produced at Electrochemical Interfaces

B. D. Cahan and P. Rüetschi

Research Center, The Electric Storage Battery Company, Yardley, Pennsylvania

ABSTRACT

A new experimental technique for the study of the corrosion films at electrochemical interfaces has been developed. It consists of applying a square wave current superimposed on a constant d-c current. The a-c current charges and discharges the double layer capacity at a high frequency. From the voltage transients produced by this current, as observed with an oscilloscope, the nature of the electrode interface can be studied. The instrumentation is described in detail, and experimental results for corrosion films on lead are presented. Capacities were measured with a precision of better than 3% and voltages to 1 mv during transients lasting only a few seconds.

The formation or precipitation of films at electrochemical interfaces occurs in many systems. A good example is found in the behavior of lead in sulfuric acid. During constant current anodization a film of lead sulfate is built up. If the current exceeds a critical value, the electrode passivates and the potential rises quickly to very high values and arrives finally at a steady-state oxygen overvoltage value. The characteristics of electrochemical interfaces have been studied in the past by a variety of different techniques. These characteristics include the electrode potential, electrode double layer capacity, and ohmic resistance.

The oldest technique used in electrochemical investigations is the measurement of the steady-state voltage-current relation (1, 2). This procedure naturally ignores any initial transients. Initial transients have been studied by the application of a single current step function (3). In this manner ohmic resistance and electrode capacity can be determined. However, this procedure permits the determination of only one value in a particular state requiring many measurements for the study of one transient phenomenon. This applies also to experiments based on a constant voltage step function (4, 5).

On the other hand, a-c techniques allow continuous measurements during a transient (6-8). The use of an a-c bridge permits precise, but not necessarily accurate, determinations of electrode capacities and resistances. This technique involves the superposition of a small sine wave on the polarizing d.c. The bridge is balanced by using an equivalent RC network. Capacities and resistances are generally found to be frequency dependent and nonlinear. The balancing operation takes a certain amount of time, and it is difficult to obtain measurements in the short times involved in some transient phenomena.

A very useful technique is the application of a current interrupter (9-12). The polarizing d.c. is interrupted periodically for very short periods of time and the potential decay is followed with an oscilloscope. The ohmic drop, due to R_1 in series with R_2C network of the electrode interface,

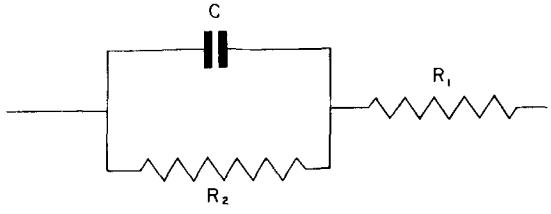

is separated out and easily determined by this technique. For this reason, the interrupter is useful in overvoltage measurements at high current densities. If the electrode interface is represented rigorously by the network shown above where R_2 and C are assumed linear, then a plot of the logarithm of the electrode potential vs. time would be a straight line. Experimentally, this is not always the case. Moreover, only the product R_2C can be evaluated from this plot. A complicating factor is that, if faradaic currents and strongly adsorbed species are involved, the potential decay becomes logarithmic with time. This is due to the fact that the discharge current of the capacitor C is then an exponential function of potential (13).

At high frequencies the reactance of the double layer capacity C is much smaller than the parallel resistor R_2 and the latter can be neglected. In the present investigation, an a-c coupled square wave current is superimposed on the polarizing d.c. The double layer capacity is charged and discharged by the square wave current. The initial portion of the square wave represents high-frequency harmonics of the base frequency, and the initial slope of the voltage-time trace gives then a direct measure for the effective double layer capacity, since one measures effectively the charge and discharge of the capacitor at constant current.

Experimental Technique

Figure 1 shows the electrolytic cell used in our investigation. The body of the cell is constructed from two sections of a 1½-in. glass pipe. Two

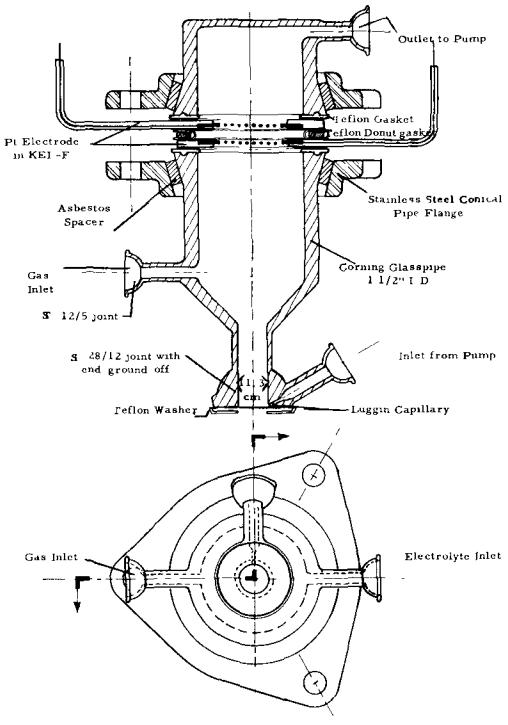

Fig. 1. Electrolytic cell

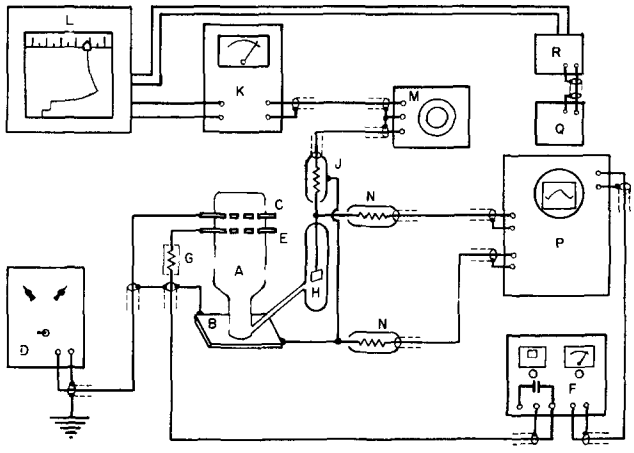

Fig. 2. Block diagram of electronic circuit: A, electrolytic cell; B, sample; C, upper platinum electrode; D, constant current supply; E, lower platinum electrode; F, square wave generator; G, noninductive resistor; H, reference electrode; J, 9mΩ scope probe; K, electrometer; L, high speed recorder; M, bias box; N, 4mΩ scope probes; P, oscilloscope; Q, camera; R, relay.

platinum gauze electrodes, imbedded at the edges in Kel F, are gasketed with Teflon between the two sections of the cell. Kel F coated platinum wires are used as current connectors. Inlets for gas bubbling and electrolyte are provided with ball joints. The electrode sample to be investigated is pressed with a clamp against an opening in the bottom of the cell and gasketed with a thin Teflon washer. The bottom of the cell is ground flat and a Luggin capillary to the reference electrode intersects the wall in the immediate vicinity of the electrode surface. In this manner ohmic drops are minimized. The electrode area exposed to the electrolyte is 1 cm^2. The narrowed section at the bottom of the cell provides a uniform current density. The samples investigated were of pure lead and were microtomed at the exposed surface as described in previous publications (14).

Figure 2 shows a block diagram of the instrumentation used. The electrolytic cell is shown at A with the sample B pressed against the bottom of the cell. A constant d-c current is applied between the sample and the upper platinum electrode C by the constant current supply D. An a-c square wave current is applied between the sample and the lower platinum electrode E. The constant voltage output of the square wave generator F is converted to constant current by a noninductive resistor G. The electrode potential is measured against a reference electrode H which was in our particular case Hg/Hg_2SO_4 in the same solution. The d-c component of the electrode potential is measured through a 9mΩ scope probe J with an electrometer amplifier K. This electrometer amplifier drives a high-speed recorder L. A bias box M is used to adjust the zero level of the d-c voltage. The a-c component of the electrode potential is measured through two 4mΩ scope probes N with a high-gain, wide-band differential input oscilloscope P, which is synchronized externally with the square wave generator F. A robot camera Q is mounted on the oscilloscope. A side marker pen on the recorder L is synchronized to the camera by an electronic relay R, triggered by the flash contacts of the camera.

The use of a square wave signal has, as pointed out before, the advantage that the capacities can be measured accurately, independent of frequency.

It is necessary to avoid carefully any ground loops in the circuit. Any portion of the circuit where currents or voltages may pass through two separate paths in parallel, in particular paths through ground, must be eliminated; otherwise spurious a-c voltages may be generated by inductive or capacitive pick up. All connecting wires in the circuit must be shielded to eliminate hum and noise. The shields of the coaxial cables used can be grounded only at one point. For the input of the electrometer amplifier, amphenol noise-free cables were used. This eliminates spurious noises due to flexing of the cables.

All coaxial cables have a natural resonant frequency and if a square wave is applied, the cable will produce a damped oscillation called ringing which distorts the desired signal. Pick up of a.c. in the cable to the d-c generator is minimized by the use of the upper platinum electrode rather than the lower one. In this manner the d-c supply electrode is kept outside of the a-c field in the electrolyte. In the cables to the electrometer amplifier and to the oscilloscope, ringing is minimized by the use of the scope probes.

The square wave frequency is adjusted for the particular electrode capacity range to be investigated. A high frequency is desired to minimize the voltage swing of the electrode and the frequency dependence. The upper limit is set by the response of the oscilloscope and by the available output current of the generator. The square wave current is set by the choice of the noninductive resistor and using the maximum output voltage of the generator,

which in our case, was 50 v. A low leakage capacitor is used to block out the d-c component. This capacitor must be large enough to pass the lowest frequencies involved with a drop of less than 2%.

The differential input of the oscilloscope assures rejection of any stray pick-up. The two scope probes must be a matched pair to preserve the differential characteristics of the scope. The trimming of the frequency compensating capacitors and the differential balance controls in the oscilloscope must be done with the probes connected to achieve the lowest noise level and best resolution.

The constant current generator has been described in an earlier paper (14). It is capable of delivering currents from 1 μa to 10 ma with a regulation better than 0.5%. The shield of the output cable is the common ground for the whole circuit. The bias box consists of a helipot potentiometer across a 5-v mercury battery. The desired bias voltage is obtained between one end of the pot and the slide contact. This voltage is in series with the input voltage of the General Radio 1230-A Electrometer. The electrometer output drives a Minneapolis-Honeywell ½ second Recorder. The electrode potential can be followed in this manner with an accuracy of 1 mv or 0.25%, whichever is greater.

The square wave generator is a Hickok model 710. The rise time of the generated square wave is 0.1 microsec, and the frequency range is 20 cycles to 1 M cycle. The maximum output voltage is 50 v peak to peak, and the maximum current output 50 ma. In the experiments to be described, the current limiting resistor was 10,000 Ω which adjusted the square wave current to 5 ma. The d-c blocking capacitor was 5 μF.

The oscilloscope is a Textronic model 535 with a 53/54 D plug-in preamplifier. The camera was a DuMont model 352. This is a Robot camera which is able to take up to 6 pictures per second. In our experiments, the camera was triggered manually, but a solenoid was provided which allowed remote or automatic triggering. The flash contact available on the camera was used to trigger a marker pen on the recorder through a sensitive transitorized relay. In this way the time of each exposure was exactly correlated to the voltage recordings.

Results and Discussion

Figure 3 shows a selection of oscilloscope traces obtained during an anodization run on pure lead in 4.40M H_2SO_4 at 30°C. The anodizing d-c current was 1 ma/cm^2. The square wave current was 5 ma peak to peak with a frequency of 6250 cps. The sweep speed of the oscilloscope was 20 μsec/cm, or 200 μsec full screen. The voltage scale factor was varied from 5 to 25 mv/cm, depending on electrode capacity. The initial slope of the traces is a measure of the electrode capacity. The capacity C is determined by the equation

$$C = \frac{i}{(\delta V/\delta t)}$$

where i is the square wave current and $\delta V/\delta t$ the voltage time slope.

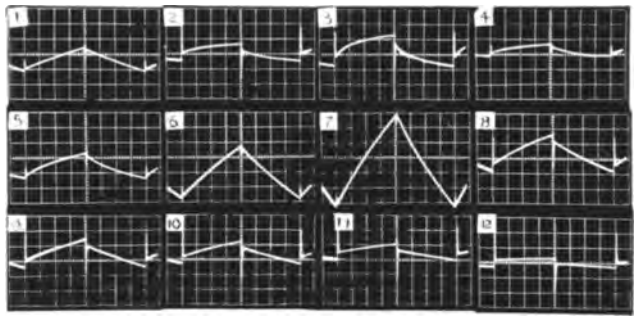

Fig. 3. Selection of oscilloscope traces. DC current 1 ma. Square wave current 5 ma peak to peak. Frequency 6250 cps. Sweep speed of oscilloscope 20 μsec/cm (before reproduction of photograph). Photograph 1: hydrogen evolution, at scale factor 25 mv/cm; 2: after 15 sec anodizing, scale factor 5 mv/cm; 3: after 47 sec, 5 mv/cm; 4: after 53 sec, 25 mv/cm; 5: after 54 sec, 25 mv/cm; 6: 55 sec 25 mv/cm; 7: 105 sec, 25 mv/cm; 8: 122 sec, 5 mv/cm; 9: 126 sec, 5 mv/cm; 10: 129 sec, 5 mv/cm; 11: 137 sec, 5 mv/cm; 12: 129 sec, 5 mv/cm.

The first trace was taken during cathodization with hydrogen evolution, at 1 ma/cm^2 at 25 mv/cm. The steepness of the slope shows that the capacity here is fairly small, amounting to about 10 μF/cm^2. Trace 2 is taken 15 sec after reversal of the current. At this point metallic lead is being converted to lead sulfate, a reaction which proceeds with extreme ease. The capacity, as determined from the initial slope, is 40 μF/cm. It is interesting to observe that the trace is highly curved indicating a nonlinearity in the apparent electrode capacity. This shows that at this point the electrode does not behave like an ideal condenser, but that a faradaic current is also flowing. The "exchange current" of the conversion of lead to lead sulfate is large, so that even with a small polarization a large faradaic current is produced. The curvature accounts for the frequency dependence usually observed with a-c bridge techniques. The initial portion of the trace is representative of the high-frequency range, whereas the later portions correspond to the lower frequency range.

Trace 3 is taken further along the lead-sulfate plateau and shows that the capacity is now decreasing, which is due to a blockage of the surface with lead sulfate. Traces 4, 5, 6, and 7 are taken during the rise of the electrode potential toward the oxygen evolution value. In this portion, the capacities are extremely small, in the range from 1 to 3 μF/cm^2. Film resistance, on the other hand, is increased considerably as shown by the ohmic drop. The electrode is substantially covered with a passivating layer of lead sulfate. Traces 8, 9, 10, 11, and 12 show the gradual build up of capacity as a surface film of PbO_2 is built up and oxygen is evolved. It is interesting to note that the traces are quite straight in this region, indicating a small faradaic component which means that the exchange current is small.

At the points where the current reverses, small peaks are observable on the oscilloscope traces. These peaks result from high-frequency pick-up by the unshielded capillary to the reference electrode. They could have been eliminated by proper shield-

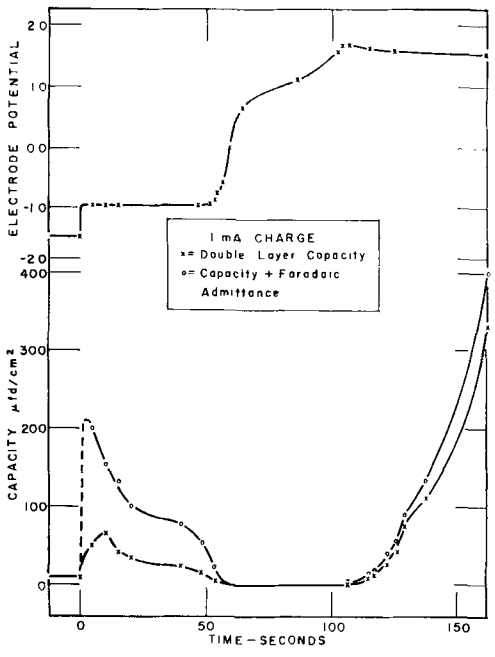

Fig. 4. Electrode potential and double layer capacity as function of time during build-up of an anodic corrosion layer on lead at 1 ma/cm².

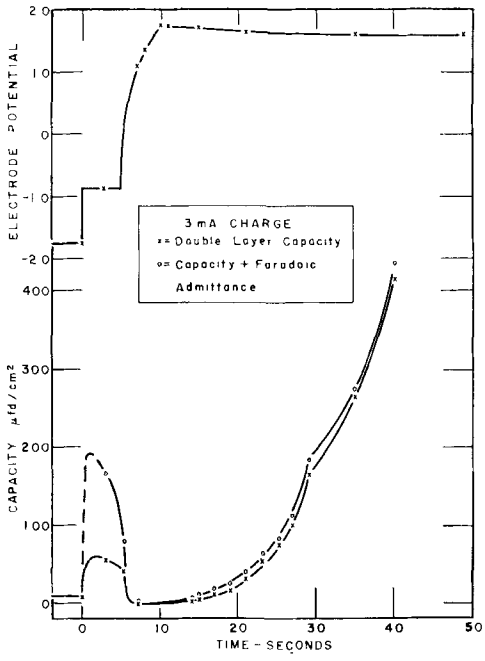

Fig. 5. Electrode potential and double layer capacity as a function of time during build-up of an anodic corrosion layer on lead at 3 ma/cm².

ing, but they did not interfere with the accuracy of the measurements. In fact, they turned out to be quite useful in checking the particular voltage scale factor used.

Figure 4 shows a plot of the electrode potential vs. the Hg/Hg_2SO_4 reference electrode and of the capacities as a function of time during anodization at 1 ma/cm². The lower curve with the crosses is the capacity as determined from the initial slope of the traces, and the curve with the circles shows the capacity including a faradaic component, as determined from the average slope of the traces and shows the regions where this component is large. In particular, it is seen that the faradaic component is large during the reversible oxidation of lead to lead sulfate. The first voltage plateau corresponds to this reaction. As the electrode is covered with lead sulfate, the capacity decreases and drops sharply to a very small value at the point where the potential starts to rise. As the oxidation of lead sulfate to PbO_2 proceeds and oxygen is evolved, the electrode potential drops somewhat and the capacity gradually increases to very high values. A hump in the capacity curve is observed at a point where the potential stops falling and could possibly correspond to the completion of the oxidation of lead sulfate to β PbO_2 and the start of oxygen evolution and production of α PbO_2 from the metallic lead.

The resistance of the electrolyte path from the electrode to the Luggin capillary is about 0.3 ohm in the electrolyte used. Such a low value could not be achieved with an arrangement whereby the a-c potential is measured between the electrode and a much larger platinum counter electrode in the same solution (15).

Figure 5 shows similar curves for an anodization at 3 ma/cm². Again, one observes a large faradaic component during the conversion of lead to lead sulfate, the low capacity during passivation where the ohmic drop is high, in the order of 1 ohm, and the hump at the end of conversion of $PbSO_4$ to β PbO_2.

Figure 6 shows the electrode potential and capacity curves during discharge at 1 ma/cm² of the PbO_2 layers formed after 180 sec of anodization at 1 ma/cm². On the potential plot one recognizes the $PbO_2/PbSO_4$ plateau, the $PbSO_4/Pb$ plateau, and a

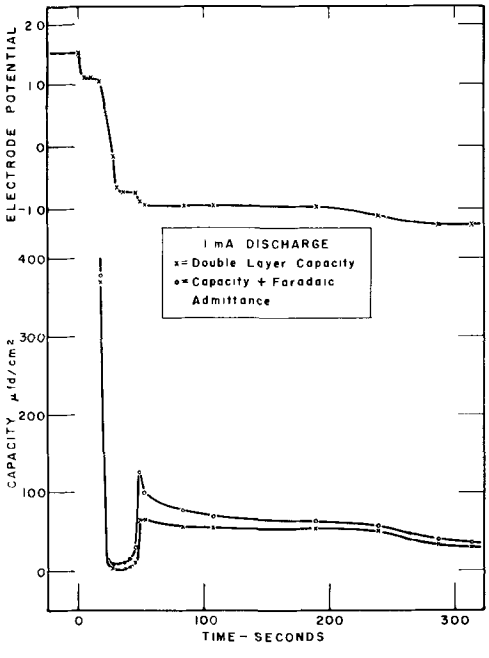

Fig. 6. Electrode potential and double layer capacity as a function of time during discharge of an anodic film on lead at 1 ma/cm².

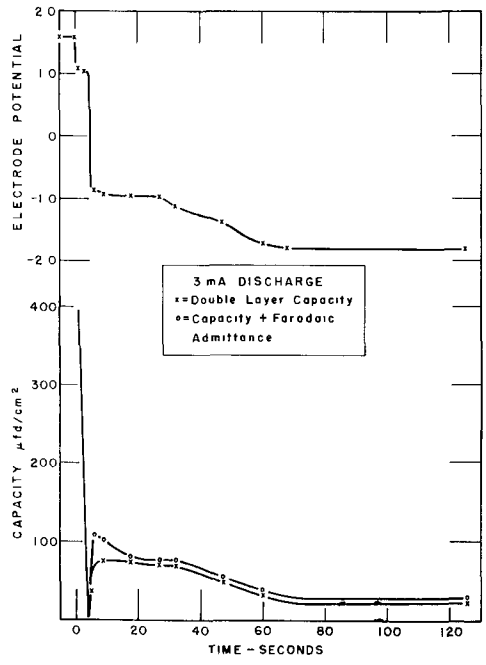

Fig. 7. Electrode potential and double layer capacity as a function of time during discharge of an anodic corrosion layer on lead at 3 ma/cm².

slow decrease of potential toward the hydrogen overvoltage value. During the PbO_2 step the capacity is extremely high, 500-1000 μF/cm, but decreases rapidly toward the end of the plateau to a very low value. This indicates a passivation of the PbO_2 film as it is covered by $PbSO_4$. During the $PbSO_4$/Pb plateau the capacity is again much higher and decreases again toward the end of the plateau. It is interesting to note that there exists a potential plateau at about −0.73 v vs. Hg/Hg_2SO_4 during which the capacity remains quite small. This could correspond to the formation of a discharge product underneath a partially protecting sulfate layer, for instance PbO, or polarized α PbO_2.

Figure 7 shows a discharge curve at 3 ma/cm after 300 sec of anodization at 3 ma/cm². Quite similar phenomena are observed. The ohmic resistance again increases sharply at the end of the PbO_2 discharge step, indicating passivation.

These results show the usefulness of this technique in studying transient film phenomena on electrodes. The capacities can be measured with a precision of better than 3% and the voltages to 1 mv during processes lasting only a number of seconds.

Manuscript received Dec. 22, 1958. This paper was prepared for delivery before the Ottawa Meeting, Sept. 28-Oct. 2, 1958.

Any discussion of this paper will appear in a Discussion Section to be published in the June 1960 JOURNAL.

REFERENCES

1. P. Delahay, "New Instrumental Methods in Electrochemistry," Interscience Publishers, New York (1954).
2. J. O'M. Bockris, "Modern Aspects of Electrochemistry," Butterworths Scientific Publications, London (1954).
3. T. Berzins and P. Delahay, *Z. Elektrochem.*, **59**, 792 (1955); *J. Am. Chem. Soc.*, **77**, 6448 (1955).
4. H. Gerischer and W. Vielstich, *Z. physik. Chem. N. F.*, **3**, 16 (1955).
5. W. Vielstich and H. Gerischer, *ibid.*, **4**, 12 (1955).
6. B. W. Erschler, *Discussions Faraday Soc.*, **1**, 269 (1947).
7. J. E. B. Randles, *ibid.*, **1**, 11 (1947).
8. H. Gerischer, *Z. Elektrochem.*, **59**, 604 (1955).
9. A. Hickling, *Trans. Faraday Soc.*, **33**, 1540 (1937).
10. S. Schuldiner and R. E. White, *This Journal*, **97**, 433 (1950).
11. S. Schuldiner, *ibid.*, **99**, 488 (1952); **101**, 426 (1954).
12. D. Staicopoulos, E. Yeager, and F. Hovorka, *ibid.*, **98**, 68 (1951).
13. P. Rüetschi, R. T. Angstadt, and B. D. Cahan, *ibid.*, **106**, 547 (1959).
14. P. Rüetschi and B. D. Cahan, *ibid.*, **104**, 406 (1957).
15. R. J. Brodd and N. Hackerman, *ibid.*, **104**, 704 (1957).

Oxygen Overvoltage and Electrode Potentials of Alpha- and Beta-PbO_2

P. Rüetschi, R. T. Angstadt, and B. D. Cahan

Research Center, The Electric Storage Battery Company, Yardley, Pennsylvania

ABSTRACT

Buildup and decay of oxygen overvoltage on α- and β-PbO_2 has been studied. Layers of the two PbO_2 modifications were electrodeposited on Pt wires, sealed at both ends into glass. Initial buildup of oxygen overvoltage at constant current is linear with time, and decay on open circuit is logarithmic with time. The results are explained on the basis of a generalized theory of overvoltage. Electrode potentials of α- and β-PbO_2 have been measured as a function of pH.

Lead dioxide exists in two modifications, the tetragonal β-PbO_2 and the orthorhombic α-PbO_2. The latter was identified only a few years ago by Zaslavsky, *et al.* (1). Previously, an unidentified oxide of lead had been described by several authors (2, 3). Bode and Voss (4) and Rüetschi and Cahan (5), found α-PbO_2 independently in battery and corrosion research. Recently, other authors have mentioned the occurrence of α-PbO_2 (6-8).

The exact electrode potentials of α- and β-PbO_2 in

H_2SO_4 have been determined recently (9) by the authors.[1] The potentials of the α-PbO_2-$PbSO_4$ and the β-PbO_2-$PbSO_4$ couples are 1.7085 ± 0.0005 v and 1.7015 ± 0.0005 v, respectively, vs. H_2 in 4.4*M* H_2SO_4 at 31.8°C. This value of the β-PbO_2 electrode is in good agreement with that reported by Hamer. Other measurements of electrode potentials of α-PbO_2 have also been reported (10).

In spite of the fact that the potentials of the PbO_2 electrodes are much higher than the potential of the oxygen electrode and that the PbO_2 electrodes must, therefore, thermodynamically oxidize water to oxygen, the PbO_2 potentials can be measured over long periods of time with good reproducibility. Thus, PbO_2 electrodes have a very high degree of metastability, which is the reason that these electrodes can be used in the lead-acid battery.

Experimental

Electrodes of α- and β-PbO_2 have been prepared by electrodeposition onto a platinum rod, sealed at both ends into glass. The exposed length of the platinum rods was 20.0 mm and the diameter 1.30 mm.

The plating solution for the α-PbO_2 electrode was prepared by making up a stock solution of lead plumbate (500 cc of saturated sodium acetate, 100 cc of saturated lead acetate, 1000 cc of carbonate-free saturated KOH and 500 cc of water). Prior to plating, the solution was diluted 1:1 with water. Triple-distilled water was used throughout the experiments.

For the β-PbO_2 electrode, the plating solution was lead perchlorate-perchloric acid. A stock solution was prepared by dissolving 500 g of PbO in 1000 cc of 30% perchloric acid. The PbO was obtained by precipitating from a lead nitrate solution at slightly alkaline *p*H, adjusted by the addition of KOH. The precipitate was dried at 170°C. Prior to plating, the stock solution was diluted 4 parts to 1 part H_2O. The plating of both electrodes was performed in a two-compartment cell, joined at the bottom with a capillary, in a water bath held at 30°C. The plating current was 1 ma, the plating time 6 days. The plating bath was renewed every two days. PbO_2 was deposited to a depth of 0.1 mm.

Certain precautions must be observed when making PbO_2 electrodes. For instance, during the electrodeposition of α-PbO_2 it was observed that a too strongly alkaline solution would permit the growth of red Pb_3O_4 crystals on the electrode. Further, at the end of the plating period, the electrodes must be washed carefully so as to be free of Pb^{++} ions, which would otherwise form deposits of $PbSO_4$ which can rupture the electrodeposits physically or form passivating layers. Also, particular care must be taken that during washing temperature fluctuations are kept to a minimum. Rapid evaporation of water by a stream of air might chill the electrode sufficiently to cause cracking, and even the smallest crack or exposure of the underlying platinum to the solution results in rapid deterioration of the electrodes.

Electrodes prepared in this manner, and for which the above precautions were observed, were stable over extended periods of time (up to one month) and their potentials were reproducible to within 1 mv.

Constant currents were obtained by a generator described earlier (5).

Electrode potentials were measured against hydrogen and Hg/Hg_2SO_4 in the same solution. Electrode potentials were followed with a precision of 1 mv, current drains less than 10^{-11} amp and with a response of 1 mv in 20 msec.

Figure 1 shows a photograph of two electrodes prepared in the described manner. This picture was taken at the end of all the measurements reported herein and after a surface film of the electrodes had been stripped off in ammonium-acetate solution. The texture of the α electrode is quite smooth and shiny, whereas the surface of the β electrode appears polycrystalline.

Results

Figure 2 shows the dependence of the α- and β-PbO_2 electrode potentials on *p*H. The first point

[1] Since this paper was submitted for publication, electrode potential measurements on α-PbO_2 electrodes by S. J. Bone, Battery Symposium, Signals Research and Development Establishment, Ministry of Supply, Christchurch, Hampshire, England, Oct. 21 to 23, 1958, have been brought to the attention of the authors by M. Barak.

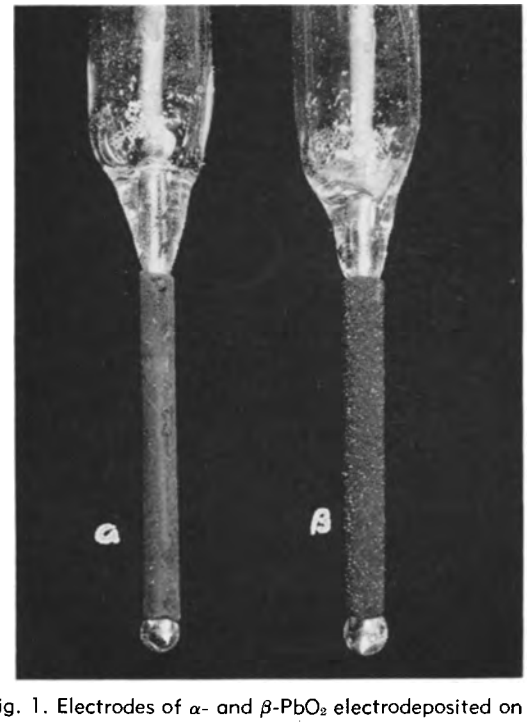

Fig. 1. Electrodes of α- and β-PbO_2 electrodeposited on Pt

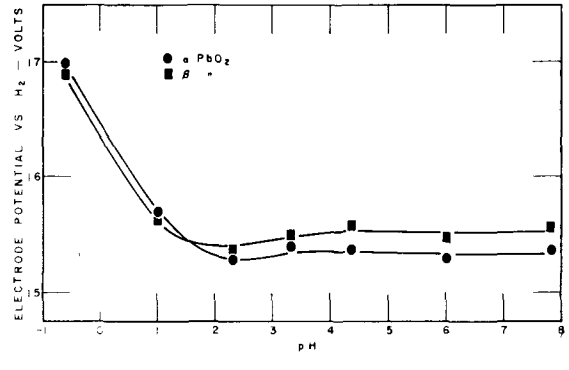

Fig. 2. Electrode potentials of α- and β-PbO_2 as a function of pH vs. a hydrogen electrode in the same solution at 30.0° ± 0.02°C.

(at pH −0.6) was measured in 4.4*M* H_2SO_4. Subsequent measurements were made in solutions where the ($SO_4^=$) concentration was maintained at 1/10M. For pH 1, a 1/10M solution of H_2SO_4 was used. For other pH values, various amounts of a solution, which was 1/10M in KOH and 1/10M in K_2SO_4, were mixed with a 1/10M solution of H_2SO_4. In this manner, the sulfate ion concentration was kept at 1/10M in all the experiments. After mixing, the solutions were saturated with $PbSO_4$, and pH values were determined accurately with a glass electrode. Figure 2 shows that above pH 2 the potentials tend to vary only little with pH. This behavior is, of course, in contradiction to the normally written electrode reaction involving hydrogen ions. However, one has to remember that $PbSO_4$ starts to become soluble at high pH values. Soluble lead species might set up a mixed electrode potential. Also, the H_2SO_4-K_2SO_4-KOH system is not a very good buffer, and in the pH range from 2 to 9 the hydrogen ion concentration is not well stabilized.

Figure 2 shows that in strongly acid solutions the α-PbO_2 has a potential 7 mv above that of the β-PbO_2, but that there is a crossover in the region between pH 1 and 2 where the β-PbO_2 becomes more positive than the α-PbO_2. The electrode with the lower potential is naturally the more stable one, hence it follows that in solutions more alkaline than pH 2, α-PbO_2 is formed in preference to β-PbO_2. The crossover point might be influenced by the particular anion of the solution. In our case only $SO_4^=$ and OH^- were present.

The crossover in electrode potentials is of practical importance in lead-acid battery manufacture. The interior of positive plates is known to remain basic during the initial periods of formation, providing one condition conducive to the formation of α-PbO_2. It is also known that corrosion of metallic lead at elevated potentials tends to form α-PbO_2. This might also be due to a pH effect underneath a protecting sulfate layer. The combination of the two conditions provides an explanation for the observation that newly formed positive plates usually show more α-PbO_2 in their interiors than in their surface layers.

After measuring the potentials through the pH series, the electrodes were replaced in 4.40*M* H_2SO_4, and the potentials were observed to return to within 1 mv of their previously observed values. This was repeated with the same result, demonstrating the stability of the electrodes. Also, concerning stability, on occasion the electrodes were polarized slightly below their open-circuit values for very short time periods whereby some lead sulfate was formed; after removing the polarizing current the electrodes returned slowly to their original open-circuit values.

After prolonged open-circuit stand of these electrodes in 4.40*M* H_2SO_4, the slow oxidation of water, as mentioned earlier, produced some self-discharge and the buildup of some lead sulfate on the surface. If the electrodes are subsequently anodized at an appreciable rate (where the electrode potential is raised substantially), this lead sulfate is oxidized to β-PbO_2. This treatment, therefore, does change an α-PbO_2 electrode into an electrode containing a mixture of α- and β-PbO_2. During open-circuit periods an exchange current is always maintained. A finite amount of PbO_2 is converted into $PbSO_4$ and *vice versa*. This exchange establishes the reversible potential. In the case of an α-PbO_2 electrode, this means that $PbSO_4$ must convert back to α-PbO_2 at the rate of the exchange current even in acid solution. The fact that α-PbO_2 is formed rather than β-PbO_2 must be explained in that the activation energy required for the nucleation of β-PbO_2 must be greater than the activation energy required for the deposition of α-PbO_2 on α-PbO_2. During anodization, the electrode potential is raised sufficiently that the activation energy for the formation of β-PbO_2 is exceeded and the β phase can be formed. Without anodization, the electrodes maintain their particular structures over extended periods of time. This has been determined both by their maintenance of distinctly different and reproducible potentials and by x-ray diffraction analysis. The difference in electrode potentials between α- and β-PbO_2 in the same solution must be a measure of the difference in free energy of the two crystalline modifications. The crossover of the potentials could mean that the free energies of the two materials are a function of the hydrogen (or hydroxyl) ion concentration of the electrolyte. The oxygen deficiency and/or possibly the OH^- or H^+ content of either crystalline form of PbO_2 can change with the pH of the solutions with which they are in equilibrium. In other words, the free energy (or electrode potential) varies with the oxygen deficiency and/or OH^- or H^+ content in the crystals.

This becomes particularly evident in oxygen overvoltage studies. Figure 3 shows the buildup of oxygen overvoltage on the β-PbO_2 electrode at constant current. The electrode had been anodized previously at 10 μa over a prolonged period of time and then left on open circuit for 24 hr prior to the curve identified 20 μa. After each anodization the electrode was allowed to decay to a value slightly above the reversible potential and then anodized at the next higher current. In this manner no $PbSO_4$ was allowed to be formed on the electrode. The formation of lead sulfate would have changed the surface area of the electrode upon subsequent anodization. The currents in Fig. 3 refer to the total electrode area.

The buildup of oxygen overvoltage at constant current involves four processes which proceed at

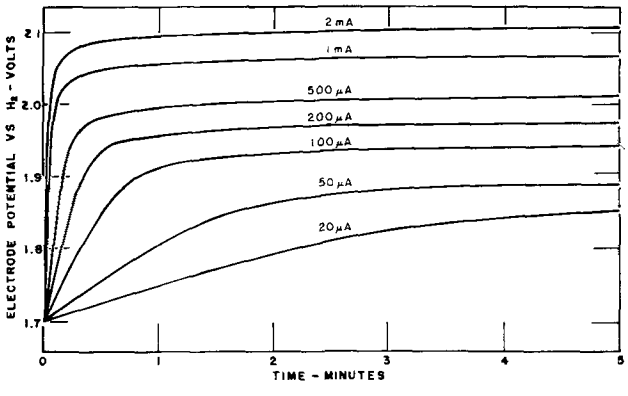

Fig. 3. Buildup of oxygen overvoltage on β-PbO_2 at constant current in 4.40M H_2SO_4 at 30.0°C.

different rates. The fastest process occurs first and is the buildup of a double layer, whereby only free electrons of the electrode and hydrated ions of the solution are displaced. This process occurs during the initial few microseconds and was observed using an oscillographic technique. The apparent double-layer capacity of this first process is of the order of 100 μF/cm^2 of the true surface area.

The buildup of the double layer is paralleled by the much slower process of oxygen deposition onto the surface of the electrode. This process becomes predominant after the initial few milliseconds and after a rise of potential of 5-10 mv. During this second step (which is shown in Fig. 3) the potential rises linearly with time. The process involves the buildup of a layer of adsorbed, negatively charged oxygen species. This can be expressed again as an apparent capacitance. Also, this capacity is apparently constant over a considerably potential region. If the current density is divided by the slope of the linear portion of the curve, one obtains a value for this apparent capacity of 20,000 to 30,000 μF/cm^2 of apparent geometric area. This capacity is independent of the charging current.

As the oxygen content on the surface continues to increase, two further processes become apparent. Oxygen molecules are formed from the activated adsorbed species and oxygen is removed by evolution as a gas. The process of oxygen removal becomes increasingly faster with the number of adsorbed species and finally approaches asymtotically the rate of oxygen deposition onto the surface.

Consideration has been given to a fourth process: oxygen may diffuse into the bulk of the PbO_2 electrodes and slowly saturate it. Because of the relatively slow rate of the last process, the steady-state value of oxygen overvoltage on PbO_2 electrodes is reached slowly.

Figure 4 shows the steady-state oxygen overvoltage on α- and β-PbO_2 in 4.4*M* H_2SO_4 at 30°C. The Tafel slope of the α electrode is 0.07 and that of the β electrode is 0.14. This would indicate a different mechanism of oxygen evolution on the two electrodes. The slopes were quite reproducible and were measured several times with increasing and decreasing currents. The values of the slopes remained constant after anodization periods of up to 5 days which demonstrates the absence of any changes in modification during anodization. It is of interest to note that the absolute overvoltage value of β-PbO_2 is higher than the value for α, although the reverse is true of the reversible potential on open circuit. Tafel slopes for oxygen overvoltages on α- and β-PbO_2 reported earlier (9) were obtained without thoroughly saturating the electrodes by previous anodization.

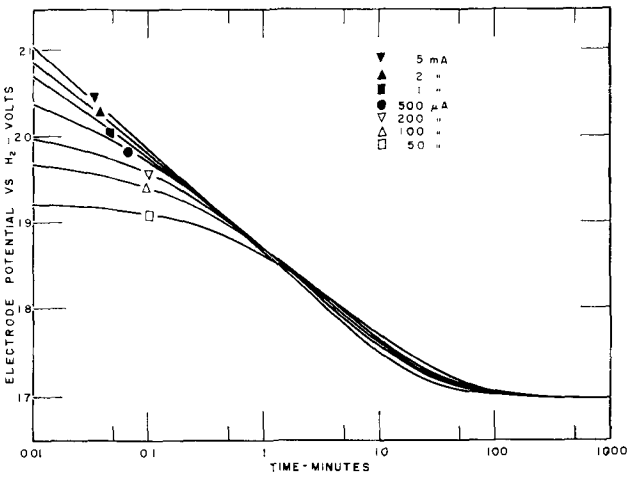

Fig. 5. Decay of oxygen overvoltage on open circuit of a β-PbO_2 electrode at 30.0°C in 4.40M H_2SO_4.

The decay of oxygen overvoltage on open circuit is shown in Fig. 5.

The decay tends to become logarithmic with time, and the slope of the voltage-log time plot is (within experimental errors) the negative of the Tafel slope.

Figure 6 shows the plot of the open-circuit decay of potential vs. log time for the α electrode.

That the slopes of the potential vs. log time plot are the negatives of the Tafel slopes can be explained by the following: The electrode potential is a linear function of the surface concentration of oxygen (11-13). The rate of oxygen evolution and desorption is an exponential function of the electrode potential; therefore one obtains

$$i = K_1 \cdot \exp\left(-\frac{V\alpha Ze_0}{KT}\right) = \text{const.} \cdot \frac{d[O^=]}{dt} = K_2 \frac{dV}{dt} \quad [1]$$

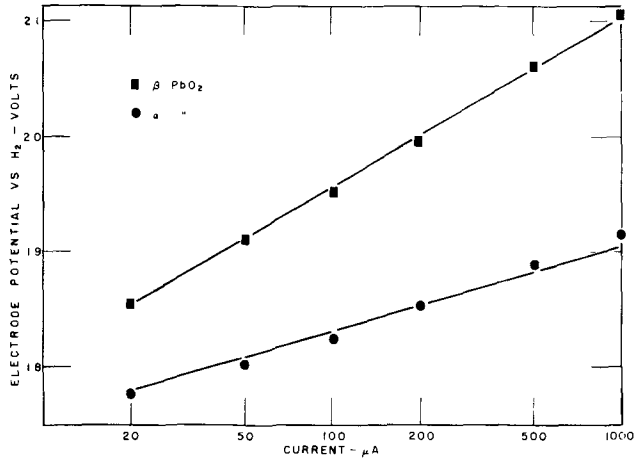

Fig. 4. Steady-state Tafel curves for α- and β-PbO_2 electrodes at 30.0°C in 4.40M H_2SO_4.

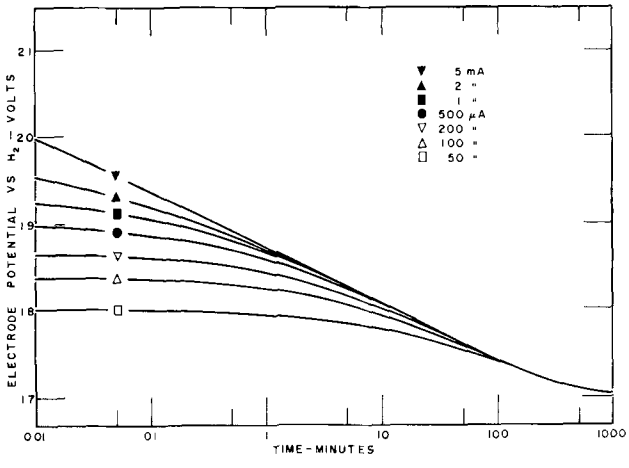

Fig. 6. Decay of oxygen overvoltage on open circuit of α-PbO_2 electrodes at 30.0°C in 4.40M H_2SO_4.

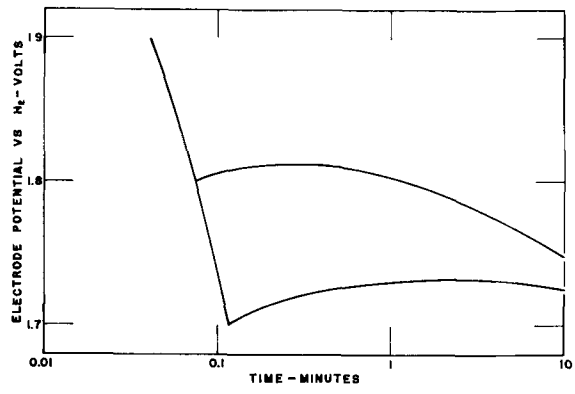

Fig. 7. Recovery of overvoltage after discharge to a lower potential value.

where i is the current density, V the electrode potential, $[O^=]$ the oxygen concentration on the surface, and K_1 and K_2 are constants.
Integrating, one obtains

$$t = \frac{K_2}{K_1} \cdot \frac{KT}{\alpha Ze_0} \left[\exp\left(\frac{V\alpha Ze_0}{KT} \right) - \exp\left(\frac{V_0 \alpha Ze_0}{KT} \right) \right] \quad [2]$$

After the potential has decayed about 50 to 100 mv, the second exponential may be neglected and one obtains:

$$V = \frac{KT}{\alpha Ze_0} \cdot \ln t - \frac{KT}{\alpha Ze_0} \cdot \ln \frac{K_2}{K_1} \cdot \frac{KT}{\alpha Ze_0} \quad [3]$$

or

$$\frac{dV}{d(\ln t)} = \frac{KT}{\alpha Ze_0} \quad [4]$$

which is the negative of the Tafel slope (11).

The presence of the adsorbed (activated) oxygen on and/or in the PbO_2 lattice was demonstrated by the following experiment. The oxygen overvoltage of the β electrode at 2 ma was forced down toward the open-circuit potential by application of a reversed current of 2 ma. The current was interrupted after the potential reached a given value. Figure 7 shows the voltage-time curves for two different runs. In the first one the potential was forced to 1.8 v and in the second to 1.7 v (that is, the reversible open-circuit value). At the point where the electrode reached these potentials, the current was interrupted. The voltage-time curve showed a recovery of overvoltage of more than 30 mv after interruption of current before the potential slowly decayed to the open-circuit value. At higher reversal currents, the recoveries observed were much greater, in the order of 100 mv. This phenomenon, which has not been described previously, shows that the electrode potential is maintained by the strongly adsorbed or absorbed species. A reversal of current would definitely destroy a diffuse ionic type double layer.

Acknowledgment

The authors would like to thank Mr. C. G. Grimes, Director of Research of the Electric Storage Battery Company, for permission to publish this paper.

Manuscript received Jan. 14, 1959. This paper was prepared for delivery before the Ottawa Meeting, Sept. 28-Oct. 2, 1958.

Any discussion of this paper will appear in a Discussion Section to be published in the June 1960 JOURNAL.

REFERENCES

1. A. I. Zaslavsky, Y. A. Kondrashov, and S. S. Tolkachev, *Doklady Akad. Nauk. SSSR*, **75**, 559 (1950).
2. N. Kameyama and T. Fukumato, *J. Soc. Chem. Ind. Japan*, **49**, 154 (1946).
3. T. Katz, *Ann. Chim. 12th Ser.*, **5**, 5 (1950).
4. H. Bode and E. Voss, *Z. Elektrochem.*, **60**, 1053 (1956).
5. P. Rüetschi and B. D. Cahan, *This Journal*, **104**, 406 (1957).
6. J. Burbank, *ibid.*, **103**, 87 (1956).
7. J. Burbank, *ibid.*, **104**, 693 (1957).
8. M. Fleischmann and M. Liler, *Trans. Faraday Soc.*, **54**, 1370 (1958).
9. P. Rüetschi and B. D. Cahan, *This Journal*, **105**, 369 (1958).
10. W. Singh, Thesis, Durham University, 1956, mentioned by reference (8).
11. E. Baars, *Marburger-Sitzungsberichte*, **63**, 214 (1928).
12. A. L. Pitman and G. W. Work, NRL Report 5031, Naval Research Lab., Washington, D. C. (1957).
13. P. Rüetschi, *This Journal*, being reviewed.

On an Ion-Exchange Property of Manganese Dioxide

Akiya Kozawa

Department of Applied Chemistry, Faculty of Engineering, Nagoya University, Nagoya, Japan

ABSTRACT

When manganese dioxide is shaken with an electrolyte solution, the cation is adsorbed and hydrogen ion is released: an ion exchange reaction takes place on the surface of the manganese dioxide. A simple method based on zinc ion exchange reaction is proposed to measure the ion exchange capacity of various manganese dioxides. Results have been compared to the surface area of those samples measured by the B.E.T. method based on nitrogen gas adsorption, and a fairly good proportionality was found between them. The mechanism of the ion exchange is correlated with the structure of a surface complex.

If manganese dioxide is shaken with a salt solution, some cations are adsorbed on the dioxide, and simultaneously hydrogen ions are released to the solution. This ion-exchange property of MnO_2 has been known since 1926 (1, 2). Sasaki (3) and Johnson and Vosburgh (4) have emphasized the importance of this ion-exchange property in conjunction with measurements of the electrode potentials of MnO_2, since the potential depends on the *p*H of the solution. The ion-exchange capacity of MnO_2 varies widely from sample to sample and also is affected by various factors which determine the suitability of certain manganese dioxides for dry-cell use. The ion-exchange capacity of MnO_2 usually is known as "the *p*H of the manganese dioxide." In Japan this statement is taken to mean the change in the *p*H value of a salt solution after shaking it with the dioxide. The *p*H values can be used to evaluate manganese dioxides for dry cell use (5) and have a close relationship with the corrosion of the zinc anode. Up to the present time only water and ammonium chloride solution (3) have been used for the determination of the *p*H value.

In the present paper, a new method is proposed for comparing the ion-exchange capacities of various manganese dioxides. Manganese dioxide is shaken with an NH_4Cl solution in which ZnO is dissolved, and the solution then is analyzed for zinc and hydrogen ion by volumetric methods. The results for various samples of manganese dioxide are compared with the surface areas of these samples as obtained by the B.E.T. method. In addition, in order to clarify the mechanism of the ion-exchange reaction, several additional experiments have been carried out.

Special Property of Ammonium Chloride Solution in Which Zinc Oxide Is Dissolved

In preliminary experiments it was found that the adsorption of cations on MnO_2 depends on both the *p*H of the salt solution and the concentration of the cation. Therefore, these conditions must be kept constant if the relative ion-exchange capacities of manganese dioxides are to be measured. Ammonium chloride solution in which ZnO is dissolved has a *p*H of about 7 and, in addition, has very good buffer action. When this solution is titrated with HCl, a nearly constant *p*H is maintained until the point where the same number of equivalents of HCl are added as that of ZnO added to the solution. At this point the *p*H changes suddenly. Two moles of NH_4Cl and about 0.1 mole of ZnO were dissolved in a liter of water. The zinc content was determined by the E.D.T.A. method: 5 ml of the solution was titrated with a 0.02 m/l E.D.T.A. (ethylenediaminetetracetic acid disodium salt) standard solution using Eriochrom Black T as the indicator (before titration, the *p*H was adjusted to about 9.5 using an NH_4Cl-NH_4OH buffer).

Figure 1 shows the titration curves for the zinc solution (2 m/l NH_4Cl, 0.1073 m/l ZnO) using 0.100*N* HCl as the standard solution. It is evident from the titration curves that the zinc solution has a remarkable *p*H buffer action. At the point where exactly the same number of equivalents of HCl is added as that of zinc in the solution, the *p*H changes suddenly from 5 to 2.8. This feature of the zinc solution makes it possible to determine the zinc ion adsorption on MnO_2 at a constant *p*H of 7 and also to measure the released hydrogen ion by titration of the resulting solution with HCl.

This property also can be used to determine a small amount of ZnO existing in $ZnCl_2$ as an impurity. In most cases, $ZnCl_2$, even the analytical reagent, contains a small amount of ZnO. A concentrated $ZnCl_2$ solution (7.63 m/l from zinc analysis)

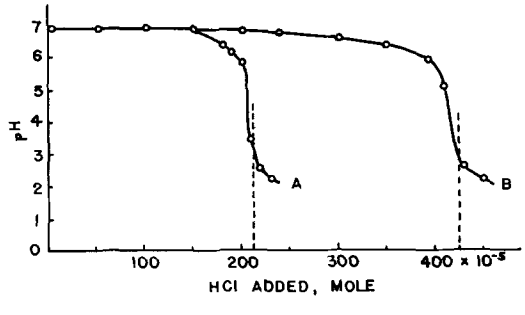

Fig. 1. Titration curves of the Zn solution (2 m/l NH_4Cl, 0.1073 m/l ZnO). 10 or 20 ml of the Zn solution was titrated, corresponding to curve A or B, respectively. Broken lines indicate the points where the ratio of the amount of HCl to that of Zn^{++} is $H^+ : Zn^{++} = 2:1$.

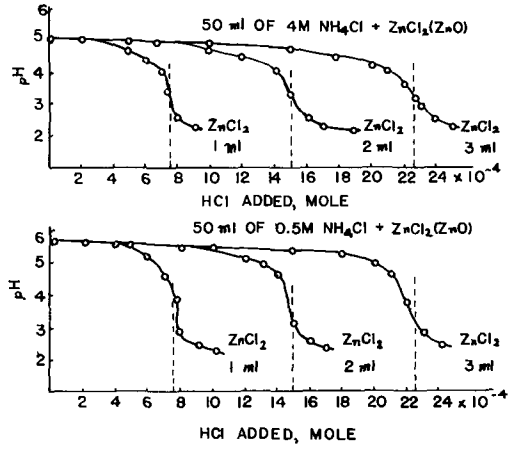

Fig. 2. Titration curves of the solutions of NH_4Cl (0.5 and 4.0 m/l), into which 1 to 3 ml of $ZnCl_2$ (7.63 m/l) solution containing ZnO were added. Broken lines indicate the points where mole ratio H^+ added: ZnO contained in the $ZnCl_2$ = 2:1.

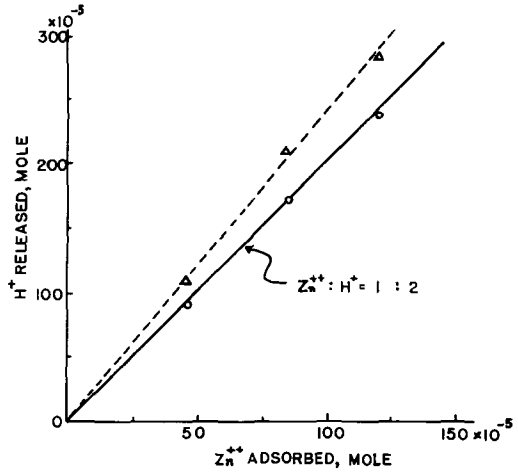

Fig. 3. Zn^{++} adsorbed and H^+ released by the ion-exchange reaction on electrolytic MnO_2. The three points correspond to 1, 2, and 3 g of MnO_2 taken as samples. △, experimental values; O, experimental results corrected for free acid in the MnO_2.

containing a small amount of ZnO was prepared. One to five ml of this solution was added to 50 ml of 0.5, 2.0, and 4.0 m/l NH_4Cl solution. These solutions then were titrated with a standard solution of HCl, using a *p*H meter to measure *p*H values. Results for the 0.5 and 4.0 m/l solutions are shown in Fig. 2. In spite of the large difference in NH_4Cl and $ZnCl_2$ concentration, an abrupt *p*H change was noted and, as more of the $ZnCl_2$ solution containing ZnO was taken, proportionally more HCl was consumed.

From very careful analysis of the $ZnCl_2$ solution the ratio Zn:Cl = 1:1.900 was determined. Therefore, the original $ZnCl_2$ contained ZnO in the amount of 1/20 of the total zinc. Dotted lines in Fig. 2 indicate the equivalent amounts of HCl as calculated from this analysis.

From the previous studies (6,7) of the $ZnCl_2$-NH_4Cl-H_2O system, the above described behavior of the zinc solution can be understood. In the zinc solution containing 2 m/l NH_4Cl and 0.1 m/l ZnO, the species $[ZnCl_4]^{2-}$, $[Zn(NH_3)Cl_3]^-$, $[Zn(NH_3)_2Cl_2]$, $[Zn(NH_3)_3Cl]^+$, $[Zn(NH_3)_4]^{2+}$ are present, with $[Zn(NH_3)_2Cl_2]$ being the predominant complex at *p*H 7. The equations describing the formation and dissociation of this complex ion (neglecting intermediate species) are:

$$ZnO + 2NH_4Cl \rightarrow [Zn(NH_3)_2Cl_2] + H_2O \quad [1]$$

$$[Zn(NH_3)_2Cl_2] + 2H_2O + 2Cl^- \rightleftharpoons [ZnCl_4]^{2-} + 2OH^- + 2NH_4^+ \quad [2]$$

When HCl is added to the zinc solution the OH^- is neutralized and all the $[Zn(NH_3)_2Cl_2]$ is converted to $[ZnCl_4]^{2-}$.

Proposed Method for Determination of the Ion-Exchange Capacity of MnO_2

If MnO_2 is shaken with the zinc solution described above, zinc ion is adsorbed and hydrogen ion is released, but the ion-exchange reaction proceeds at a nearly constant *p*H value. A portion of the supernatant solution (or the filtrate) then is titrated with a standard solution of HCl (0.100*N*) using methyl orange as the indicator. The difference between the amount of HCl consumed in this procedure and that consumed by the original solution corresponds to the amount of hydrogen ion released by the ion-exchange reaction. Another portion of the supernatant solution is analyzed by the E.D.T.A. method to determine the zinc ion adsorption.

Samples of 1, 2, and 3 g of MnO_2 (prepared by electrodeposition and ground so as to pass through a 100 mesh sieve) were added to 50-ml portions of 2 m/l NH_4Cl + 0.1 m/l ZnO solution contained in 100-ml flasks fitted with rubber stoppers. The resulting suspensions then were shaken for 6 hr by machine and allowed to stand overnight. Then 5-ml portions of the supernatant liquid were analyzed for Zn^{++} and H^+ as described above. Thus, the amount of adsorbed Zn^{++} and released H^+ were determined. Results are shown in Fig. 3. The MnO_2 used contained some free H_2SO_4. Therefore, the released H^+ value must be corrected. After complete decomposition of the dioxide by concentrated HCl, the $SO_4^=$ in the solution was determined as $BaSO_4$. The correction is shown in Fig. 3. The corrected values show that the ratio adsorbed Zn^{++}:released H^+ is very nearly equal to 1:2, and that the ion-exchange values are proportional to the amount of MnO_2 used. Thirty minutes shaking followed by filtration gave the same results within 5%.

To measure the Zn adsorption of a very small sample of MnO_2 (15-50 mg), a more dilute Zn solution (0.5 m/l NH_4Cl, 0.005 m/l ZnO; *p*H about 7.2) is recommended. In this case 0.01-0.005 m/l E.D.T.A. standard solution should be used. This micromethod for the zinc adsorption measurement has been shown to give the same results as that of the above method within a few per cent. The micromethod has been applied to MnO_2 electrodeposited on graphite rods (8).

Since the Zn adsorption value is not affected by free acid, NaOH, or Na_2CO_3 present in the sample, it, rather than the amount of H^+ released, may be taken as a measure of the ion-exchange capacity of MnO_2. If the MnO_2 sample has heavy metal ions adsorbed on the surface, these should be washed off

Table I. Various samples of MnO_2 (ground to pass through 100 mesh sieve) for measurement of ion-exchange capacity

	x in MnO_x	MnO_2, %
No. 1 prepared by electrodeposition from $MnSO_4$ bath at 97°-98°C with a current density of 1.74 amp/dm²	1.98	84.94
No. 2 No. 1 treated with Na_2CO_3 solution	1.98	87.58
No. 3 No. 2 washed with 6N H_2SO_4 at 60°C, then with water	1.94	89.23
No. 4 cryptomelane prepared by autoclaving No. 2 with NH_4Cl solution at 170°C	1.95	89.31
No. 5 Mn_2O_3 prepared by heating No. 2 at 630°C for 5 hr	1.50	50.01
No. 6 No. 5 heated at 250°C with dilute NaOH solution followed by washing with water	1.53	55.95
No. 7 prepared by thermal decomposition of $Mn(NO_3)_2$	2.00	100.07
No. 8 natural ore (pirica)	2.00	86.05
No. 9 natural ore (kawai)	1.96	76.88

by dilute H_2SO_4 prior to the ion-exchange capacity measurement.

The method for obtaining the ion-exchange capacity described above was applied to various samples of MnO_2, including natural ores, artificial manganese dioxides, and a series of heated manganese dioxides (see Table I). Some of the results were corrected for free acid. Results shown in Fig. 4 indicate that ion-exchange capacities thus measured are distributed over a very wide range depending on the origin of the dioxide, the electrolytic manganese dioxides having the largest capacity.

In Fig. 4, most of the points are above the theoretical line of $Zn^{++}:H^+ = 1:2$. There are two causes for this: free acid and impurities such as Ca and Mg, the ions of which behave like Zn^{++} in the E.D.T.A. method. Natural ores especially contain the latter impurities. The effect of these impurities is to decrease the apparent adsorption of Zn^{++}.

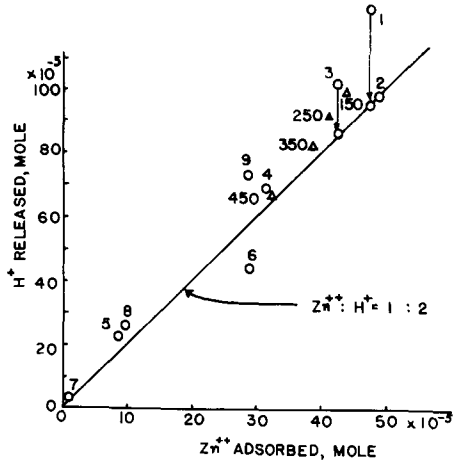

Fig. 4. Ion-exchange capacities of 1.00 g of the various manganese dioxides listed in Table I. The numbers near the points correspond to the ones in Table I. The triangles show the results for sample 1 on heating at the various temperatures indicated in the figure for 3 hr. Samples 1 and 3 were corrected for free acid, the length of the arrows indicating the amount of the correction.

Sasaki (5) and Johnson and Vosburgh (4) have shown that MnO_2 is able to exchange NH_4^+. For the case under consideration here, however, any contribution of NH_4^+ need not be taken into consideration, since the amount of H^+ released can be explained experimentally by the amount of Zn^{++} adsorbed. Therefore, in the competitive adsorption of Zn^{++} and NH_4^+, divalent Zn^{++} seems to be far superior to monovalent NH_4^+ in spite of the large difference in the bulk concentrations.

Relation between Ion-Exchange Capacity and Surface Area

The surface areas of various manganese dioxides including electrolytic MnO_2 heated at various temperatures have been measured by the B.E.T. method using nitrogen gas adsorption at liquid nitrogen temperatures. In these experiments, prior to the gas adsorption, out-gasing of all the samples (except the unheated and 90°-heated samples) was carried out by heating at 165°C for 2 hr under evacuation in the adsorption vessel followed by 4-hr evacuation at room temperature. The unheated and 90°-heated samples were evacuated to 2×10^{-4} mm Hg for 24 hr at room temperature.

As shown in Fig. 5, the surface area of the electrolytic MnO_2 decreases with heating temperature above 250°C. Although the surface areas for the unheated and 90°-heated samples appear to be slightly smaller than that for the 160°-heated sample due to their greater water content (several per cent), the surface areas per net MnO_2 content remain constant up to 160° heating.

The relationship between the surface areas and the Zn ion-exchange values of the various kinds of MnO_2 is shown in Fig. 6. In spite of the variety of samples, there is a fairly good proportionality between the surface area and the Zn adsorption value. The adsorption of 1×10^{-3} mole Zn^{++} corresponds to 140 m² of the surface of MnO_2 with an approximate error of 10-15%. These results suggest a method for determining the approximate surface area of MnO_2 by the Zn adsorption method described above.

In a previous paper (9) it was reported that heat-treatment of MnO_2 forms lower oxides on the surface of the sample. Thus, the cause of the decrease of the Zn^{++} ion-exchange of MnO_2 on heating can be consid-

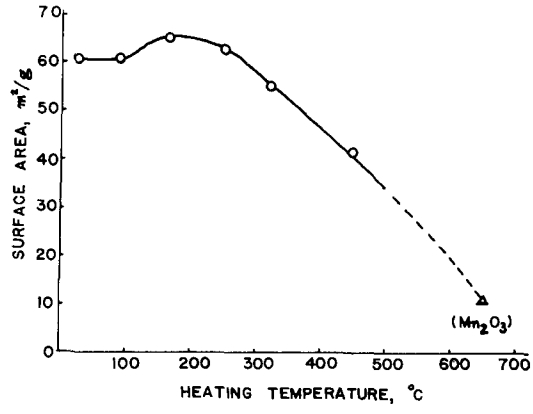

Fig. 5. Surface-area change of electrolytic MnO_2 on heating. Each sample was heated at the temperature indicated for 3 hr under air in an electric furnace.

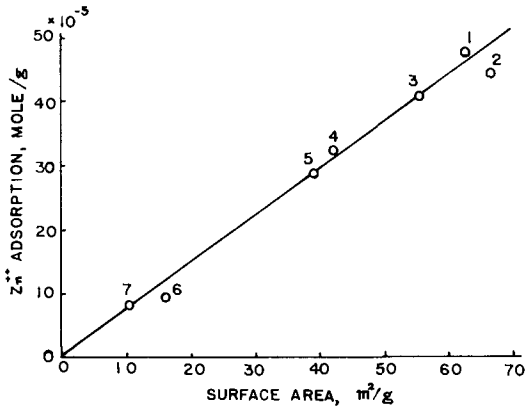

Fig. 6. Relation between the surface area measured by the B.E.T. method and the Zn adsorption from the 2 m/l NH_4Cl, 0.1 m/l ZnO solution: 1, electrolytic MnO_2; 2, No. 1 heated at 165°C; 3, No. 1 heated at 320°C; 4, No. 1 heated at 450°C; 5, natural ore; 6, natural pyrolusite; 7, Mn_2O_3 prepared from electrolytic MnO^2 by heating at 650°C for 6 hr.

ered as twofold: change of the surface area and change of the surface oxidation state of the manganese dioxide. The former factor appears to predominate, since points for Mn_2O_3 and 450°-heated MnO_2, which has considerable lower oxide on its surface, fall on the straight line shown in Fig. 6.

If the pore size of electrolytic MnO_2 is extremely small, the zinc adsorption method might not give the true surface area. Therefore, the pore size distribution of electrolytic MnO_2 was measured using the mercury method (10, 11). The results (see Fig. 7) show that the sample has a fairly homogeneous pore size with a predominant pore radius of 180Å and with no extremely fine pores. This is in accord with the fact that the Zn ion-exchange reaction attains equilibrium within a short period of time.

Mechanism of the Ion-Exchange Reaction

The following five experimental facts are important for consideration of the mechanism of the ion-exchange reaction occurring on MnO_2:

1. The ratio of the adsorbed Zn^{++} to the released H^+ is 1:2 (Fig. 3 and 4).

2. The Zn^{++} adsorption isotherm on MnO_2 was measured as follows: 2:00-g samples of electrolytic MnO_2 were washed with dilute H_2SO_4 and shaken at 25° ± 1°C with various concentrations of the zinc solution (0.01-0.1 m/l ZnO in 2 m/l NH_4Cl, *p*H 7.0) using enough solution to furnish 5×10^{-3} mole of total zinc ion.

The results, shown in Fig. 8, seem to indicate a typical chemi-adsorption process. The ratio of the number of Mn^{IV} atoms present on the surface of the MnO_2 to the number of Zn ions adsorbed on the surface for the highest concentration in Fig. 8 is Mn^{IV}: $Zn^{++} = 5.9 \times 10^{20}$ *: 3.0×10^{20} * = 2:1.

The number of Mn^{IV} atoms on the surface was calculated using the formula, number of atoms = $(d \times N/MnO_2)^{2/3} \times 100^2 \times S$, where d is the density of the MnO_2 (4.4 for this sample), S is the surface area as measured by the B.E.T. method using N_2 adsorption (60.7 m^2/g for this sample), N is the Avogadro number, and MnO_2 is the formula weight.

* Refer to 1 g MnO_2.

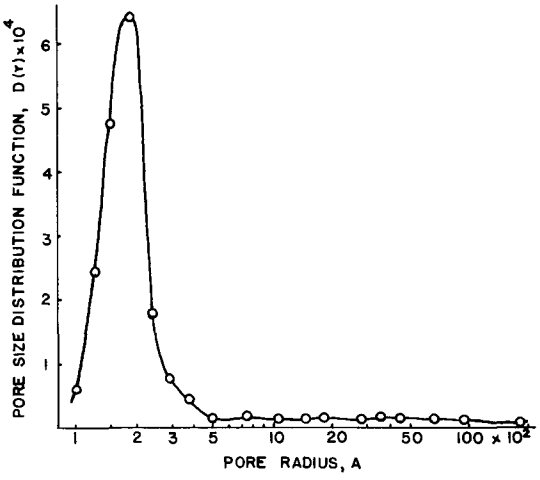

Fig. 7. Pore size distribution of electrolytic MnO_2 (No. 2 in Table I).

3. The ion exchange of various metal ions on MnO_2 was examined by shaking the electrolytic MnO_2 with various divalent metal sulfate solutions, 2×10^{-3} m/l in $M^{II}SO_4$, buffered to *p*H 5.5 with a sodium acetate-acetic acid buffer solution. Results are given in Table II. In the formation of divalent metal chelate compounds, for example:

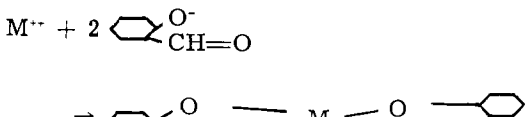

$$K = \frac{(MKe)}{(M^{++})(Ke)^2}$$

there is a well-established order in the stability constant (or log K) for the divalent metal ions (12), Cu > Ni > Co > Zn > Mg. Adsorption values for MnO_2 show a similar order, although the position of Ni is slightly different.

4. Combined water molecules (13) and OH groups contained in the MnO_2 samples might be expected to be the source of the released H^+. However, the electrolytic MnO_2 loses almost all H_2O when heated above 300°C: the original H_2O content is 8.7% and after heating above 300°C it is only 0.4% or less (13). Nevertheless, this heated MnO_2 has a

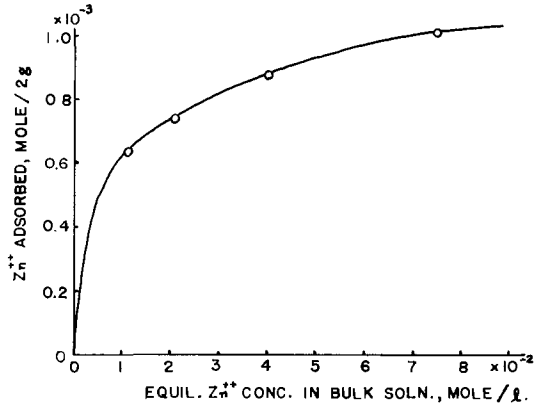

Fig. 8. Zn^{++} adsorption isotherm. Zn^{++} adsorption by 2 g of the electrolytic MnO_2 in the zinc solution.

Table II. Adsorption of various divalent ions on MnO_2 in the solution of pH 5.5 buffered with HAc and NaAc

Cu^{++}	88×10^{-5} Mole/2 g MnO_2
Co^{++}	37
Zn^{++}	26
Ni^{++}	19.5
Mg^{++}	0.5

considerable ion-exchange ability, or in other words a considerable amount of H^+ ion is released. Thus, the source of the released H^+ may be H_2O molecules from the solution adsorbed on the surface of the MnO_2. This is supported by the fact that the amount of H^+ ion released is proportional to the surface area of the MnO_2.

5. Wadsley (14) has considered the ion-exchange reaction of various hydrous MnO_2 samples. Sodium contained in the hydrous oxides was irreversibly replaced by various metal ions. However, the electrolytic MnO_2 used in the above experiments was found by using a flame photometer to be free from Na and K. Also, it was found that the adsorbed Zn can be desorbed reversibly by lowering the pH of the solution. Figure 9 shows the reversibility. The pH of the Zn solution was raised by adding NH_4OH and then lowered by HCl. For each experimental point the mixture of MnO_2 and Zn solution was shaken for a few hours in order to attain the ion exchange equilibrium.

In conclusion, the author would like to propose the mechanism shown in Fig. 10 for the ion-exchange reaction occurring on the surface of MnO_2. This mechanism satisfies all five of the experimental facts described above. In order for the complex ions in the zinc solution to be adsorbed preferentially on the MnO_2, it is necessary that the adsorbed forms be more stable than the form existing in the solution. In the proposed mechanism, the adsorbed zinc forms a six-membered ring with the MnO_2 surface with adsorbed water. It is a well-known fact of chelate chemistry that 5- or 6-membered rings are more stable than complex ions having groups such as Cl^-, OH^-, NH_3, and H_2O as the ligands.

Acknowledgment

The author would like to thank Professor K. Sasaki for his valuable suggestions during the course of this work. The author is indebted to Dr. H. Saito, Nagoya University of Japan, for the pore size distribution measurement. Thanks are also due to Professor E. Yeager, Western Reserve University, and Professor W. C. Vosburgh, Duke University, for their encouragement and comments.

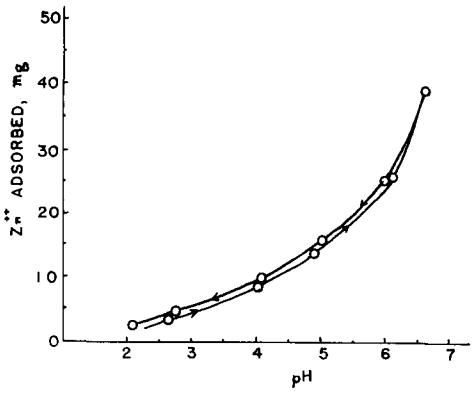

Fig. 9. Reversibility of the Zn^{++} ion adsorption on MnO_2

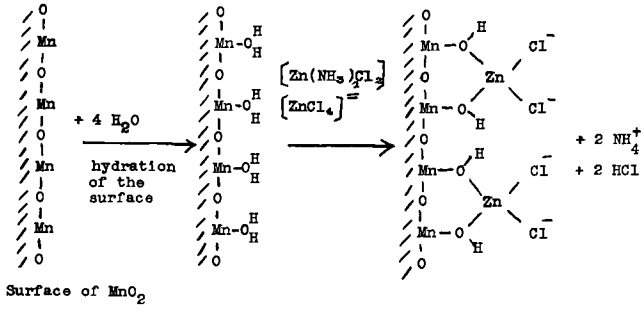

Fig. 10. The mechanism of the ion-exchange reaction on the surface of MnO_2.

Manuscript received Jan. 7, 1959. This paper was prepared for delivery before the Ottawa Meeting, Sept. 28-Oct. 2, 1958.

Any discussion of this paper will appear in a Discussion Section to be published in the June 1960 JOURNAL.

REFERENCES

1. B. N. Ghosh, *J. Chem. Soc.*, **1926**, 2605.
2. B. N. Ghosh, S. N. Chakravarty, and M. L. Kunder, *J. Indian Chem. Soc.*, **28**, 319 (1951).
3. K. Sasaki, T. Kurano, and Y. Fuseya, *J. Electrochem. Soc. Japan*, **4**, 67 (1936).
4. R. S. Johnson and W. C. Vosburgh, *This Journal*, **99**, 317 (1952).
5. K. Sasaki, *Mem. Fac. Eng., Nagoya Univ.*, **3**, No. 2, 84 (1951).
6. T. Takahashi and K. Sasaki, *J. Electrochem. Soc. Japan*, **25**, 58 (1957).
7. T. Takahashi and K. Sasaki, *ibid.*, **24**, 221 (1956).
8. A. Kozawa and W. C. Vosburgh, *This Journal*, **105**, 59 (1958).
9. A. Kozawa, *ibid.*, **106**, 79 (1959).
10. H. L. Ritter and L. C. Drake, *Ind. Eng. Chem. Anal. Ed.*, **17**, 782 (1945).
11. L. C. Drake, *Ind. Eng. Chem.*, **41**, 780 (1949).
12. A. E. Martell and M. Calvin, "Chemistry of the Metal Chelate Compounds," p. 184, Prentice-Hall Inc., New York (1952).
13. K. Sasaki and A. Kozawa, *J. Electrochem. Soc. Japan*, **25**, 115 (1957).
14. A. D. Wadsley, *J. Am. Chem. Soc.*, **72**, 1781 (1950).

The Significance of the Flade Potential

M. J. Pryor

Metallurgical Laboratories, Olin Mathieson Chemical Corporation, New Haven, Connecticut

ABSTRACT

Previous explanations of the Flade potential have been reviewed critically. A new explanation based on a single phase passive film of γ-Fe_2O_3 having non-uniform defect concentration and type is advanced. The potential determining reaction is considered to be that between excess oxygen in the outer p-type layers and hydrogen ions and electrons. The inner n-type oxide is destroyed by reductive dissolution in acid media and by exchange of oxygen ions with hydroxyl ions in solution having pH values higher than 3.0.

Previous Explanations of the Flade Potential

If iron is polarized at progressively more noble potentials in sulfuric acid, the onset of passivity will be observed at a reproducible potential. If the potential of iron which has been passivated either by anodic means or by inhibitors is permitted to decay by switching off the passivating current, or by adding corrosive agents to the passivating solution, a similar well-defined potential arrest is again often observed. This potential arrest was first observed by Flade (1) whose name it now bears. Later workers (2) in the field have characterized the pH dependency of the Flade potential by the equation

$$E = 0.58 - 0.059\ pH \qquad [1]$$

Since the early work of Flade, Weil (2) has proposed that the Flade potential is an equilibrium potential when no current is passing through the film and when no oxidation-reduction system is available in the electrolyte. This view has been supported by Cartledge (3) following a study of the formation of passive films in osmium (VIII) oxide.

If the postulate that the Flade potential is an equilibrium potential is accepted, its pH dependency, under conditions of potential decay (with no external current passing), implies that the basic reaction involved is an electrochemical reduction of the type

$$O + 2H^+ + 2e = H_2O \qquad [2]$$

Depending on the state of association of the oxygen, ferric ions in an iron oxide film also may be reduced to the ferrous condition.

The main problem lies in the fact that the oxygen would appear to be necessarily contained in or otherwise associated with an oxide of iron on the passive surface. Attempts to reconcile a value of $E_F = 0.58$ (Eq. [1]) with the standard state free energies of reduction of known bulk oxides of iron to an intermediate state or to the metal have been unsuccessful. In order to reconcile this difficulty "sandwich" oxides often possessing unusual properties have been suggested almost universally. Investigators favoring a thermodynamically reversible reaction have pictured the reaction giving rise to the Flade potential as occurring within such sandwich films.

For instance, Cartledge (3) postulated the formation of a duplex passivating oxide on iron immersed in osmium (VIII) oxide. He assumed, consistent with past electron diffraction investigations (4-6), that the outer layer was composed of γ-Fe_2O_3. He also assumed that an inner two dimensional layer of "abnormal" ferrous oxide existed between the γ-Fe_2O_3 layer and the iron. By assigning arbitrarily an unusual value of free energy of formation of -73.6 kcal mole^{-1} to the inner layer of abnormal "FeO" (the free energy of formation of bulk FeO is actually -58.4 kcal mole^{-1}) he was able to derive a potential determining reversible electrode process in the film as follows

$$Fe_2O_3 + 2H^+ + 2e = 2\text{"FeO"} + H_2O \qquad [3]$$
$$\Delta F_o = -26.7 \text{ kcal}$$

A fit with the $E_F = 0.58$ v for the Flade potential is obtained only because of the assumption of the unusual free energy of formation for abnormal "FeO". This is somewhat similar to the approaches used by several investigators of passivation mechanisms of iron who have postulated the presence of layers of energy-rich and unknown oxides of iron (7, 8).

Vetter (9, 10), Weil (2), and Gohr and Lange (11) also pictured the passive layer on iron as being duplex, with a Fe_3O_4 layer next to the metal interface being overlayed by a second layer of γ-Fe_2O_3. Using this model Vetter (10) proposed that the Flade potential was, in fact, an irreversible potential. He suggested that the reaction

$$Fe + 4Fe_2O_3 = 3Fe_3O_4 \qquad [4]$$

occurs irreversibly and completely giving rise to a potential difference of 0.66 v in the resulting magnetite layer. This is the difference between the theoretical and experimental values which is otherwise difficult to explain. Vetter proposed that the destruction of the duplex layer involved the slow dissolution of the γ-Fe_2O_3 film. He considered that once the γ-Fe_2O_3 was consumed it was succeeded by an extremely rapid dissolution of the magnetite layer during which the iron became spontaneously activated.

Past explanation of the Flade potential have all been based on Eq. [1] in which $E_F = 0.58$ v. Recently, however, Uhlig and King (12) have shown that the values of the Flade potential in inhibitive solutions such as nitrite, chromate, tungstate, molyb-

date, and ferrate are constant in that they do not vary with time, but that the absolute values vary by up to 0.14 v with the passivating medium. Using these facts, Uhlig and King have reasoned that the Flade potential observed during passive potential decay is an equilibrium potential due to the reduction of chemisorbed oxygen atoms and molecules ($0 \cdot O_2$) on the surface of iron or on a nonprotective oxide covering the iron surface.

Critical Examination of Previous Models of Passive Films on Iron and Their Relation to the Flade Potential

One of the most fundamental questions left unresolved by previous considerations of the Flade potential is whether this is a thermodynamically reversible or an irreversible potential. Direct experimental proof of either concept has so far not been obtained. Consequently, it appears that one procedure based on existing knowledge involves obtaining a suitable model for the reactions occurring during passive potential decay and from this determining the magnitude of the local-cell currents involved in these reactions. The magnitude of these currents then may suggest whether or not the overall reaction occurs at a potential close to the equilibrium value. The first part of this approach involves setting up the most reasonable model for the reactions involved during passive potential decay on iron. In order to achieve this a critical consideration of previous suggested models is in order.

Previous models of duplex passivating films proposed by investigators of the Flade potential fall primarily into the following classes:

(*a*) $Fe/Fe_3O_4/\gamma\text{-}Fe_2O_3$ (2, 9-11)

(*b*) Fe/"FeO"/Fe_2O_3 (3)

(*c*) The model of Uhlig and King (12) involving chemisorbed oxygen atoms and molecules on the iron surface.

Model (*a*) as stated by its supporters appears difficult to maintain for passive potential decay in acid electrolytes. Here it has been shown (13-15) that films of γ or α Fe_2O_3 formed on iron by exposure to air at different temperatures are destroyed rapidly by reductive dissolution according to the equations

$$Fe = Fe^{++} + 2e \qquad [5a]$$

$$Fe_2O_3 + 6H^+ + 2e = 2Fe^{++} + 3H_2O \qquad [5b]$$

$$Fe + Fe_2O_3 + 6H^+ = 3Fe^{++} + 3H_2O \qquad [5]$$

The rate of reaction [5] is very great so that up to 800Å of film may be destroyed in 1-2 sec in either 1*N* HCl or 1*N* H_2SO_4. The reaction proceeds by fairly uniform inward thinning from the oxide-solution interface. Similar films, when detached from the iron, are virtually unattacked for prolonged periods by similar acid electrolytes.

In examining model (*a*) it is first necessary to determine why the outer portion of the duplex film has apparently greater stability toward H_2SO_4 solutions than γ-Fe_2O_3 films formed by exposure of iron to air. One possible reason might lie in a higher electronic resistance which might make reaction [5*b*] slower or in higher ionic resistance which would make reaction [5*a*] slower. Either factor would tend to decrease the rate of over-all reductive dissolution of the film.

However, it has been pointed out previously (16) that the passive films on iron are good electronic conductors and that they cover the surface of the metal completely. Therefore, enhanced electronic resistance cannot provide the reason for the greater stability of the thin (100Å) passive films. Values of leakage current determined during anodic passivation of iron in H_2SO_4 (2) show that the initial ionic resistance of the passive films so formed is fairly high. However, if the passivating conditions are disturbed, the ionic resistance of thin oxide films on metals can be reduced very rapidly, even at 25°C, by n-type defects introduced into the oxide film by exchange between O" in the oxide lattice and monovalent anions such as OH' (17) and by the introduction of H^+ into the lattice. Therefore, it also appears that enhanced ionic resistance cannot account for the relative stability of the outer γ-Fe_2O_3 layer in H_2SO_4 electrolytes. This greater stability is presumably the result of special properties or structural characteristics not described to date by the supporters of model (*a*).

The suggestion that an inner layer of Fe_3O_4 is present in the passive films formed anodically in H_2SO_4 is also hard to reconcile with previous work on thermal films unless unusual properties are again ascribed to it. If the structure of the film was duplex as suggested by Lange (11) and Vetter (10), the initial destruction of a conventional γ-Fe_2O_3 film by reductive dissolution would be fast in acid solution. Magnetite as formed in duplex thermal Fe_3O_4/Fe_2O_3 films cannot easily be cathodically reduced by local-cell corrosion currents in acid solutions or by impressed cathodic currents of the order of 15 $\mu a/cm^2$ in neutral or slightly alkaline electrolytes (18). Therefore, the subsequent direct dissolution of magnetite would be slower than the reductive dissolution of the outer γ-Fe_2O_3 layer. This is exactly opposite to the mechanism suggested by Vetter (11). Therefore, it appears that the applicability of model (*a*) to passive potential decay in H_2SO_4 logically requires the postulation of radically different characteristics both for the γ-Fe_2O_3 and to the Fe_3O_4 layers than are experienced in thermal films.

Model (*b*) and Eq. [3] as put forward by Cartledge also lack experimental support. Certainly in solutions having *p*H values lower than 3.0 the reaction shown in Eq. [3] has not been observed experimentally. A considerable volume of experimental evidence (15, 19) shows that reduction of thermal ferric oxide films proceeds completely to soluble ferrous ions rather than to "FeO" (normal or abnormal) whose existence, even in transient form, has never been detected during cathodic reduction of oxide films on iron. Recent precise and successive quantitative cathodic reduction of duplex Fe_3O_4/Fe_2O_3 thermal films on iron (18) at *p*H = 7.65 has revealed in turn α-Fe_2O_3, γ-Fe_2O_3, and Fe_3O_4 in that order but with no suggestion of any "FeO" compound either normal or abnormal. Again successful application of model (*b*) requires the description of the Fe_2O_3 layer in markedly different terms to those normally attributed to thermal films. If it was at-

tempted to apply the Cartledge model to acid solutions, it would suffer the same additional disadvantage experienced above by model (*a*).

The mechanism suggested by Uhlig and King (12) appears to be more consistent with previous knowledge of the reactions of iron oxide films than those outlined above. Doubtless, adsorbed oxygen is present on the surface of many passive films, and it would appear necessary to reduce this in some manner before further reactions involving the film could occur. The time factor for one seems to argue against this mechanism being primarily responsible for the Flade arrest. For instance, Evans (21) in his early work on anodic passivation showed that a layer of oxygen absorbed on the surface of an iron oxide film[1] prevented its reductive dissolution but only for a fraction of a second. Therefore, it is evident that a certain period of immunity toward reductive dissolution of the film may be obtained by virtue of oxygen supersaturation on its surface; supersaturation of this type could result from the formation of the oxide by the anodic discharge of oxygen or by the action of strong oxidizing agents. It is also equally clear that this short period of immunity against reductive dissolution observed earlier by Evans is not sufficient to account for the rather long periods of metastable passivity observed by many investigators. The model of Uhlig and King also fails to account for the slow appearances of ferric ions in sulfuric acid electrolytes during the early stages of passive potential decay (25). Further it implies that passivation processes in the inhibitors studied are invariably associated with the layer of adsorbed oxygen atoms and molecules ($O \cdot O_2$) which is generally contrary to the existing direct experimental evidence.

Proposed Model for Passive Layers on Iron

It is believed that the subsequent model reconciles many of the difficulties outlined above and is more consistent with known experimental facts on the properties of thermal oxide films on iron. It postulates structural differences between thermal and passive oxide films which can account for their different behavior in many electrolytes and for the Flade potential. The passive films on iron have been shown in many cases to consist largely of γ-Fe_2O_3 (4-6). Accordingly, it is most consistent with past experimental evidence to propose that the passive films are crystallographically single phase. These films may, of course, contain minor inclusions of hydrated oxide (5, 6) when formed in nearly neutral inhibitors, but these compounds in small amounts of less than a few per cent do not affect the arguments advanced below.

Whereas the gross crystallographic structure of passive films is held to be uniform, the defect concentration of passive films having thicknesses of the order of 100Å will be far from uniform and will result in marked departure from stoichiometry. For instance Fig. 1 shows schematically the effect of a metal interface on the concentration of metal excess, n-type, defects in the oxide near to the oxide-metal interface. The investigations of Grunberg and Wright (20) on photosensitized electron emission strongly suggest that the excess metal concentration in this interfacial region is due to considerable numbers of oxygen ion vacancies where electrons are trapped. Defect concentrations at the oxide-metal interface may presumably approach values of 10^{20}-10^{21}/cc. The strong effect of the oxide-metal interface largely disappears at a distance of around 50Å. Thereafter, the film is capable of assuming a more conventional defect structure and concentration (10^{14}-10^{17}/cc) except at the outer interface between the oxide and the passivating medium. Here, if strongly oxidizing conditions exist, it is reasonable to propose that the surface layers of oxide contain excess oxygen. By similar reasoning to that above this is probably due to metal ion deficiency resulting in a p-type structure although the existence of interstitial excess oxygen cannot be ruled out.

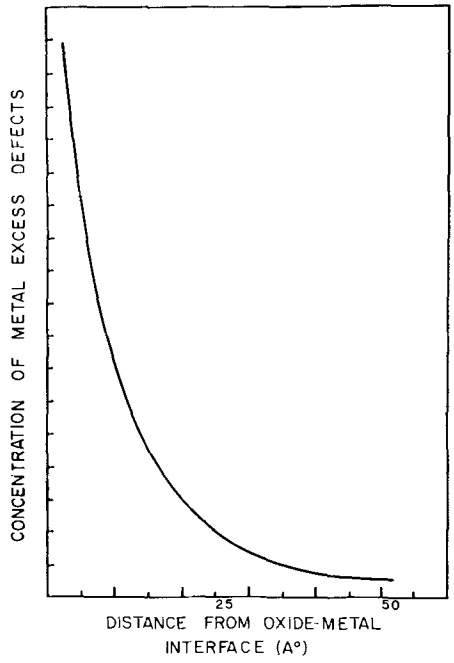

Fig. 1. Schematic representation of the concentration of metal excess defects in an oxide film on iron as a function of distance from the metal interface.

The concentration of excess oxygen ions plus bound positive holes in the outer portion of the film usually should distinguish passive from thermal films. In the former case films are produced at low temperatures when cation diffusion is relatively slow and also under conditions where the concentration of oxidant is high. Such conditions seldom apply to thermal films since appreciable thickening must be the result of raising temperature in which case cation diffusion is speeded. The chance of producing a high concentration of excess oxygen plus bound positive holes in the outer portion of a thermal film is thus greatly reduced. Here, therefore, it appears possible to use the new model to account for logical differences in defect structure between air-formed and passive films as will be shown below. This can

[1] Oxygen dissolved in the bulk electrolyte cannot depolarize reaction [5b] at pH values less than 3.0 because the local cell corrosion currents are sufficiently high that O_2 depletion occurs at the cathode surface and because the reduction of dissolved molecular oxygen is a gas electrode reaction which suffers from high activation polarization. These effects offset the more favorable free energy considerations involved.

in turn relate to differences in behavior on immersion in certain electrolytes.

The resulting model of a p-n semiconductor has many aspects in common with the duplex oxides postulated by Cartledge and Vetter. However, it does not involve gross crystallographic changes throughout the oxide and provides a means of eliminating many of the difficulties encountered with the other models.

Application to the Flade Potential

Using this model it is first necessary to explain why such a single phase film of p-n γ-Fe_2O_3 will resist rapid reductive dissolution when exposed to electrolytes more acid than pH 3.0. The explanation should rely logically on factors other than an adsorbed layer of oxygen to retard reductive dissolution of the film.

The most probable means by which reductive dissolution of γ-Fe_2O_3 could be prevented involves the excess oxygen contained in the outer p-type portion of the passive film. This excess oxygen which consists of oxygen ions plus bound positive holes could be reduced by the following electrochemical reaction:

$$O'' + \boxed{+\atop +} + 2H^- + 2e = H_2O \qquad [6]$$

crystal lattice; bound positive holes

with the electrons being supplied by the anodic passage of ferrous ions through the film.

By employing the new model outlined above in conjunction with reaction [6] a ready distinction is obtained between the electrochemical characteristics of passive and thermal oxide films on iron based on the concentration of excess oxygen ions plus bound positive holes in the outer layers. It has been suggested above that passive films on iron contain a much higher concentration of excess oxygen than thermal films due to their formation at lower temperature often under strongly oxidizing conditions. Consequently, the higher concentration of excess oxygen may confer substantial periods of immunity against reductive dissolution (Eq. [5]) which would not be experienced with thermal films of similar crystallographic structure.

An equilibrium potential may be written for reaction [6] as follows

$$E = E_0 + \frac{RT}{2F} \log (H^-)^2 (O'') \left(\boxed{+\atop +}\right) \qquad [7]$$

where (O") and $\left(\boxed{+\atop +}\right)$ are the activities of excess oxygen ions and bound positive holes, respectively, in the outer p-type layer. Reaction [6] is considered to be potential determining during the thinning of the outer p-type γ-Fe_2O_3. Therefore, the relationship between the equilibrium potential of reaction [6] and the Flade potential may now be considered with a view to determining how closely the two will approach.

It is known from past work on the reductive dissolution of oxide and sulfide films on iron (13), copper (19), and silver (22) that cathodic removal of oxygen and sulfur from the oxide and sulfide lattices is accompanied by a high degree of polarization. However, calculation of local-cell currents during reductive dissolution of thermal oxide films on iron in 1N H_2SO_4 shows that these are of the order of 50 ma/cm^2. Currents of the order of 0.5 to 1.0 ma/cm^2 often have been employed for the quantitative cathodic reduction of oxide films on iron and copper in neutral electrolytes. Severe cathodic polarization of the reductive dissolution at these high current densities normally would be anticipated. However, Price (23) has pointed out that as the applied current density is reduced the reduction potential will approach the calculated equilibrium value asymptomatically.

Typical values of local-cell current flow may be calculated for reaction [6]. Assuming the outer p-type layer of γ-Fe_2O_3 is 50Å thick, that it contains an average of 0.1 at. % of excess oxygen, and that it is subjected to a combination of reduction (Eq. [6]) and dissolution as described later for 100 sec, local cell currents of the order of only 0.2 μa/cm^2 are required to reduce the excess oxygen by reaction [6]. The extremely small current flow involved when combined with Price's observation (23) strongly suggests that the degree of polarization of reaction [6] should be very small. Consequently, the Flade potential and the equilibrium potential for reaction [6] may be regarded as being identical to the first approximation. Of course, the Flade potential must always be somewhat less noble than the E value in Eq. [7] and the difference between the two will be related to the film structure and the length of the Flade arrest. Based on the calculations above, the differences appear to be very small so that the Flade potential will be regarded through the rest of the paper as approximately representing the equilibrium potential of reaction [6].

The success of the new model, therefore, depends to a considerable degree on the accuracy with which it represents experimental observations on the Flade potential and the behavior of oxides of iron exposed to aqueous solutions. If Eq. [7] is compared with Eq. [1] it may be deduced that

$$E_F = E_0 + \frac{RT}{2F} \log (O'') \left(\boxed{+\atop +}\right) \qquad [8]$$

Using this model it becomes erroneous to treat E_F as a standard state thermodynamic potential because it is uncorrected for the activities of the components of the excess oxygen. Equation [8] also implies that reproducible values of the Flade potential will be obtained only if the method of formation of the oxide film is such that a relatively reproducible defect structure is formed in the outer layers. The considerable variation in E_F found by Uhlig and King (12) when passive films were formed in different inhibitors can be ascribed logically to variations in the defect structure of the outer layers of passivating oxides formed under different conditions.

The potential determining step outlined in Eq. [6] fits well with previous work concerning the mechanism of direct dissolution of bulk ferric oxide (24).

Here it was found that direct solution of α-Fe_2O_3 occurred rapidly only at surface defects associated with oxygen vacancies. Once these had been "leached out" further attack on more perfect portions of the oxide was very slow. It is reasonable, therefore, to picture a slow reduction of excess oxygen at a surface layer resulting in conditions where apparent stoichiometry is approached by the production of surface layers which contain missing ferric and oxygen ions in approximately equal proportion. By analogy with previous mechanism of direct solution of ferric oxide (24) the disruption of the electric field within the oxide lattice accompanying removal of oxygen ions should permit the more rapid removal of remaining oxygen ions by combination with hydrogen ions adsorbed from solution. The latter is a direct dissolution process with iron entering solution in the ferric condition rather than a reduction process. Some iron should enter solution in the ferrous condition since the electrons in reaction [6] presumably are supplied by the anodic formation of ferrous ions. Calculation of the amount of ferrous ions so produced, using the assumptions put forward previously for calculation of local cell currents required for reduction of excess oxygen, indicates that this is only of the order of 5×10^{-9} g Fe^{++}/cm^2. This accords well with the recent observations of Weil (25) who demonstrated that iron found in solution during the initial stage of the potential decay in 1.0N H_2SO_4 decay was in the ferric condition with any ferrous ions being below the limit of detection of the ferricyanide test.

The sequence of reduction followed by direct solution of the defective surface layer outlined above may occur until such a time as the depolarizing influence of excess oxygen in the p-type surface layer is exhausted. When the p-type oxide has been removed as outlined above, the reaction proceeds on the n-type metal-excess oxide which can be destroyed almost instantaneously in acid solutions by reductive dissolution as shown in Eqs. [5a & b]. Here the product of both the anodic and cathodic reactions is ferrous ion as has also been observed by Weil (25). Since it has been pointed out previously that local-cell corrosion currents involved during the rapid reductive dissolution of n-type γ-Fe_2O_3 films to soluble ferrous ions are of the order of several milliamperes per square centimeter, reaction [5b] is highly polarized. Therefore, on exposure of the n-type γ-Fe_2O_3 and on initiating reaction [5b] an immediate and substantial shift in potential in the active direction must be observed. This, of course, coincides with the end of the Flade plateau.

The pH dependency of reaction [6] is clearly consistent with the Flade potential. Furthermore, the over-all reaction is consistent with past work on the direct and reductive dissolution of iron oxides. However, the value of $E_F = 0.58$ v for the Flade potential, with or without the deviations observed by Uhlig and King (12), is still a problem which defies precise solution. If the above model is accepted, it is clearly meaningless to attempt to calculate E_F in terms of free energies of formation of bulk oxides. This is because no reliable estimates of free energy of formation of energy rich, highly defective oxide films have been developed, and because E_F cannot be corrected to the standard state without a knowledge of the activity of excess oxygen in the outer p-type layer. However, the latter problem is one that can be investigated experimentally using semiconductor techniques. If the activity of the excess oxygen ions in the outer layers was known, it would then be possible to calculate the E_0 value for Eq. [8]. Subsequent calculation from this value and from the free energy for the reduction of molecular oxygen would give the standard state free energy for the reaction

$$\tfrac{1}{2}\,O_2 \rightarrow \underset{\text{crystal lattice}}{O''} + \underset{\text{bound positive hole}}{\boxed{+\\+}} \quad \Delta F = 110 \text{ kcal} \quad [9]$$

i.e., the partial ionization of gaseous oxygen into a different dielectric and would throw light on the bond energy between the excess oxygen ions and the bound positive holes. This in turn would assist the understanding of the structure of defect and energy rich surface oxides on iron.

The mechanism outlined above proposes that the Flade potential should be observed only if an oxygen excess p-type layer of γ-Fe_2O_3 is formed during passivation. Formation of films of γ-Fe_2O_3 less than around 50Å thick would appear to preclude the possibility of this type of outer layer defect structure. It is, therefore, of interest to note that thin films formed by very short time anodic passivation of iron in H_2SO_4 appear to be destroyed almost instantaneously once the passivating current is switched off. No evidence of a Flade arrest is found in this case and it is probable that the film is destroyed by reductive dissolution in a similar manner to thermal oxide films.

Whether the same sequence of passive film breakdown can occur in p-n γ Fe_2O_3 films at pH values higher than 3.0 is less certain. It is known that the inner n-type oxide could not undergo reductive dissolution due only to the flow of local-cell corrosion currents (13). Instead it is probable that the ionic resistance of the n-type inner layer is reduced progressively by hydroxyl ion exchange which will be more rapid at the higher pH values.

However, there appears no reason why the reduction and dissolution of the outer p-type layer of oxide, which is believed to give rise to the Flade potential, should not proceed by the same mechanism as that outlined above. At the same time it must be borne in mind that the higher electrolyte pH magnifies the importance of exchange between oxygen ions in the oxide and hydroxyl ions from solution. This exchange will be accompanied by a decrease in ionic resistance since each exchange creates an n-type defect. A decrease in ionic resistance due to this reaction will be accompanied by a shift in potential in the active direction similar to that which accompanies activation of the iron in acid electrolytes by reductive dissolution of the n-type inner layer. These two processes, therefore, have a similar total

effect, differing only in rate. On occasion, however, the exchange reaction could presumably occur before the outer p-type oxide was completely removed by reaction [6] and the accompanying dissolution reaction. In this case, the decrease in ionic resistance accompanying the exchange reaction may well mask the Flade potential. Therefore, it is of interest to note that well-defined Flade arrests do not always occur at the higher pH values (26). Instead, there is sometimes a range of erratic potentials spreading over as much as 400 mv. From these, it is impossible to typify a well-defined Flade potential.

Rapidly fluctuating potentials such as these are characteristic of the nonuniform reduction of ionic resistance and accompanying increase in local-cell currents such as would accompany oxygen-hydroxyl ion exchange. Potential-time curves of this type are, therefore, believed to be characteristic of the exchange reaction masking the true effect of the Flade potential.

Acknowledgments

The author wishes to acknowledge the many helpful suggestions offered by Dr. D. A. Vermilyea, Dr. J. F. Murphy, Dr. J. J. McMullen, and Mr. C. E. Michelson.

Manuscript received Sept. 29, 1958. This paper was prepared for delivery before the Philadelphia Meeting, May 3-7, 1959.

Any discussion of this paper will appear in a Discussion Section to be published in the June 1960 JOURNAL.

REFERENCES

1. F. Flade, *Z. Phys. Chem.*, **76**, 513 (1911).
2. K. G. Weil, *Z. Elektrochem.*, **59**, 711 (1955); U F. Franck, *Z. Naturforsch.*, **4a**, 378 (1949).
3. G. H. Cartledge, *J. Phys. Chem.*, **60**, 1571 (1956).
4. J. E. O. Mayne and M. J. Pryor, *J. Chem. Soc.*, **1949**, 1831.
5. J. E. O. Mayne, J. W. Menter, and M. J. Pryor, *ibid.*, **1950**, 3229.
6. J. E. O. Mayne and J. W. Menter, *ibid.*, **1954**, 103.
7. W. D. Bancroft and J. D. Porter, *J. Phys. Chem.*, **40**, 37 (1936).
8. K. F. Bonhoeffer, *Z. Elektrochem.*, **59**, 594 (1955).
9. K. J. Vetter, *Z. Phys. Chem. N. F.*, **4**, 165 (1955).
10. K. J. Vetter, "Internationales Kolloquien uber die Passivitat der Metalle II," p. 5 Heiligenberg (1957).
11. H. Gohr and E. Lange, *Naturwissenschaften*, **43**, 12 (1956).
12. H. H. Uhlig and P. F. King, *This Journal*, **106**, 1 (1959).
13. M. J. Pryor and U. R. Evans, *J. Chem. Soc.*, **1950**, 1259.
14. M. J. Pryor and U. R. Evans, *ibid.*, **1950**, 1266.
15. M. J. Pryor, *ibid.*, **1950**, 1274.
16. K. G. Weil, "Internationales Kolloquien uber die Passivitat der Metalle II," p. 5 Heiligenberg (1957).
17. M. J. Pryor, *Z. Elektrochem.*, **62**, 783 (1958).
18. K. H. Buob, M. Cohen, and A. F. Beck, *This Journal*, **105**, 74 (1958).
19. U. R. Evans and H. A. Miley, *J. Chem. Soc.*, **1937**, 1295. *Carnegie School Mem. Iron & Steel Inst.*, **25**, 197.
20. L. Grunberg and K. R. H. Wright, *Proc. Roy. Soc.*, **A232**, 403 (1955).
21. U. R. Evans, *J. Chem. Soc.*, **1930**, 478.
22. L. E. Price and G. J. Thomas, *J. Inst. Metals*, **63**, 29 (1938).
23. L. E. Price, *Trans. AIME*, **133**, 248 (1939).
24. M. J. Pryor and U. R. Evans, *J. Chem. Soc*, **1949**, 3330.
25. K. G. Weil, Private communication.
26. G. H. Cartledge and R. F. Sympson, *J. Phys. Chem.*, **61**, 973 (1957).

Potential Studies on Passivity to Corrosion Induced by Pretreatment Processes

II. Comparative Study of Chromate Treatment and Chromate Inhibition

K. S. Rajagopalan and K. Balakrishnan

Central Electrochemical Research Institute, Karaikudi, South India

ABSTRACT

The mechanism of passivation of zinc by chromate treatment is compared with that of chromate inhibitor in this paper. The part played by soluble chromate in enhancing passivation by chromate treatment is elucidated in terms of the kinetic approach made in a previous paper.

It was shown earlier (1) that potential and polarization studies are very helpful in elucidating the mechanism of passivation of aluminum by chemical oxidation processes. The present paper attempts to throw more light on the mechanism of inhibition of corrosion of zinc by chromate treatment as well as chromate inhibitor.

Experimental

Commercially pure zinc (1/16 in. thick) was cut into 1 x 1 in. and 3 x 2 in. specimens. The metal specimens were abraded with 120 emery until a uniform finish was obtained, degreased with methanol, hot benzene, and hot acetone, and subjected to chromate treatment, where necessary, in Cronak (2) composition (200 g of potassium dichromate + 6 cc of H_2SO_4/l) at room temperature for 30 sec. Specimens were rinsed in cold water and dried by cold compressed air after treatment.

Sodium chloride solutions of various concentrations were used. The chloride solutions were air-saturated by bubbling air through solution for 15

Table I. Initial and steady potentials* of chromate-treated and untreated zinc in sodium chloride solutions

Condition of metal	Conc. of NaCl, %	Initial potential[α] vs. SCE	Form of potential time curve	Steady potential[β] vs. SCE
Untreated	0.001	—0.94	Becomes 50 mv more negative and recovers to initial potential after 2 weeks	—0.94
Untreated	1.0	—1.02	Same as above	—1.01
Chromate-treated	0.001	—1.05	Rises slowly over 2 weeks to a potential 100 mv more positive	—0.95
Chromate-treated	1.0	—1.03	Rises slowly over 2 weeks to a potential 40 mv more positive	—0.99

* Mean of duplicate determinations which did not differ from each other by more than ±20 mv. α—measured after 5 min; β—measured after 2 weeks.

min before each test and were exposed to air afterward. All inhibition experiments were done using 500 ppm sodium chromate in the solutions.

Methods.—These have been described (1). All experiments were carried out at 35°C. The potential values are given the negative sign according to the European convention (3). The potential decreases in anodic polarization curves and increases in cathodic polarization curves.

The 3 x 2-in. specimens were suspended in triplicate in 1 liter of solution contained in a tall form beaker such that the upper edge of the specimen was 3 in. below liquid level. At the end of test period, the specimens were taken out, cleaned in 20% sulfate-free chromic acid at 80°C (8), and reweighed. Weight of film was deducted from the initial weight for calculation of the loss in weight due to corrosion in the case of treated metal. The mean of the triplicate determinations made in each solution did not differ from the individual values by more than 20%. Mean values are given in Table II.

Results

Potential-time studies.—Initial and steady potentials of untreated and chromate-treated zinc in 0.001% and 1% NaCl solutions and the forms of the potential-time curves are shown in Table I. It is seen from Table I that the potential of untreated zinc varies little with time and that its potential in 0.001% NaCl is 70 mv more positive. Nearly the same potential as that of untreated metal is recorded by chromate-treated zinc after it is allowed to reach a steady value. The potential obtained immediately after immersion is, however, about 100 mv more negative in 0.001% NaCl solution. As compared to these, rapid changes are observed in the potential of untreated metal in the presence of chromate inhibitor (see Fig. 1). At the lowest chloride concentration, viz., 0.001% NaCl, the initial potential becomes immediately more positive by

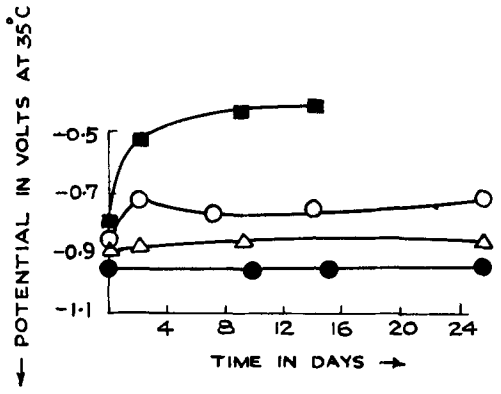

Fig. 1. Potential-time curves of untreated zinc in NaCl solutions containing 500 ppm chromate. ■ in 0.001% NaCl; ○ in 0.01% NaCl; △ in 0.1% NaCl; • in 1% NaCl. Potentials were measured against saturated calomel electrode.

nearly 200 mv, and this increases in the next few days to a value of 500 mv more positive. The ennobling effect is observed again in 0.01% NaCl but to a lesser extent. In the case of 0.1% NaCl, the initial potential is slightly more positive to start with, but there is hardly any change with time. In 1% NaCl solution, the behavior of untreated zinc is reproduced.

Polarization studies.—Potential-current density curves obtained with untreated and chromate-treated zinc, a few hours after immersion, in solutions containing different concentrations of chloride ions are shown in Fig. 2 and 3. Figure 4 gives poten-

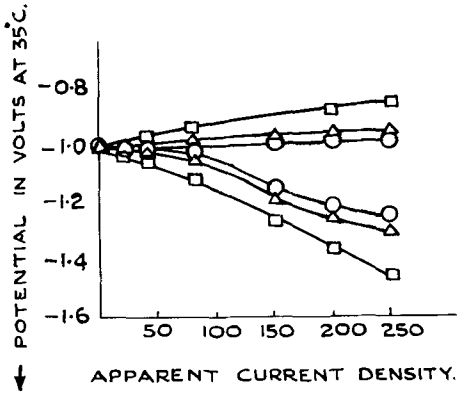

Fig. 2. Potential-current density curves of untreated zinc in NaCl Solutions. □ In 0.001% NaCl; △ in 0.1% NaCl; O in 1% NaCl.

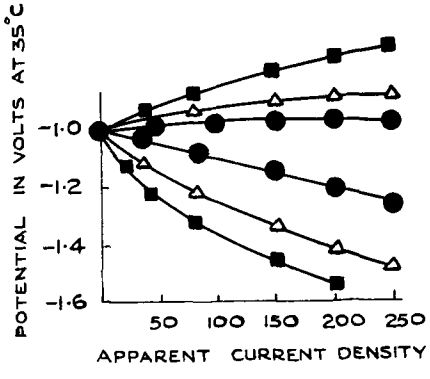

Fig. 3. Potential-current density curves of chromate-treated zinc in NaCl solutions. ■ In 0.001% NaCl; △ in 0.01% NaCl; • in 1% NaCl.

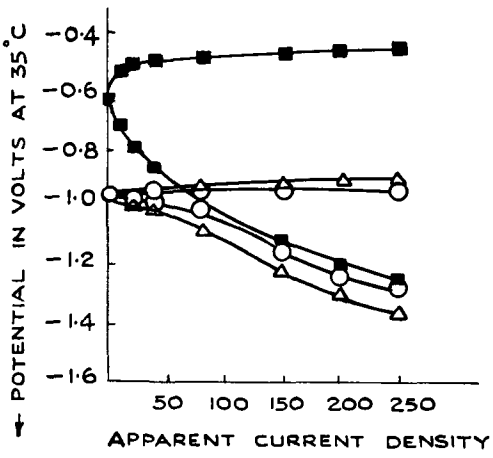

Fig. 4. Potential-current density curves of untreated zinc in NaCl solutions containing 500 ppm of chromate. ■ In 0.001% NaCl, △ in 0.1% NaCl; O in 1% NaCl.

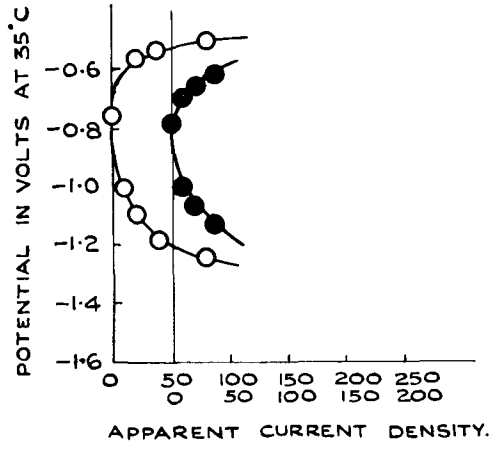

Fig. 5. Potential-current density curves of chromate-treated zinc. • After immersion for a week in 0.001% NaCl; O in 0.001% NaCl + 500 ppm chromate immediately after immersion. Potentials were measured against saturated calomel electrode. Current densities are given in $\mu a/in.^2$.

tial current density curves for untreated zinc in chloride solutions to which chromate has also been added. A common initial potential has been taken where the potentials do not differ from each other considerably to avoid overlapping of the curves and to compare the slopes.

The points given in the curves, therefore, indicate only the observed shifts. It is seen from Fig. 2 that at the highest concentration of chloride, i.e., 1% and 0.1%, there is practically no polarization of untreated metal. Slight polarization is observed in 0.001% NaCl solutions. The initial potential is itself changed considerably (c.f. Fig. 1) in 0.001% solution containing inhibitor, and the metal shows considerable cathodic as well as anodic polarization with externally applied current. Chromate-treated metal shows slight polarization in 1% solution. This increases considerably as the concentration falls to 0.01%. This is further increased at 0.001% concentration when the metal is polarized both anodically and cathodically to a much greater extent than untreated metal. Slopes of the polarization curves suggest that cathodic polarization is somewhat greater than anodic polarization at all concentrations.

Table II. Rate of corrosion of treated and untreated zinc in NaCl solutions in the presence and absence of chromate

Solution	Whether untreated or treated	Loss in weight in mg/dm² (16 in.²) of metal at the end of: 2 days	4 days	11 days
1% NaCl	Untreated	58	86	183
1% NaCl	Treated	22	39	34
1% NaCl + $CrO_4^=$	Untreated	49	60	57
1% NaCl + $CrO_4^=$	Treated	16	36	35
0.1% NaCl	Untreated	35	—	109
0.1% NaCl	Treated	6	8	11
0.1% NaCl + $CrO_4^=$	Untreated	10	31	26
0.1% NaCl + $CrO_4^=$	Treated	Neg.*	4	17
0.01% NaCl	Untreated	28	56	126
0.01% NaCl	Treated	Neg.	3	7
0.01% NaCl + $CrO_4^=$	Untreated	4	2	6
0.01% NaCl + $CrO_4^=$	Treated	Neg.	Neg.	4
0.001% NaCl	Untreated	31	56	154
0.001% NaCl	Treated	Neg.	Neg.	5
0.001% NaCl + $CrO_4^=$	Untreated	Neg.	2	4
0.001% NaCl + $CrO_4^=$	Treated	Neg.	Neg.	Neg.

* Below 0.5 mg.

Figure 5 compares the potential-current density curves obtained with treated metal after immersion in 0.001% NaCl solution for a week with that given by treated metal immersed in solution containing chromate in addition to chloride immediately after immersion. The close resemblance in the shapes of the two curves may be noted.

Corrosion tests.—Losses in weight of untreated and chromate-treated zinc in the various solutions considered are given in Table II. It is seen from Table II that, at all concentrations, chromate treatment gives better protection than inhibitor and the corrosion rate falls to a negligible value in 0.01% and 0.001% solutions. It is also seen that even at 1% concentration of NaCl, corrosion rates of both treated metal and untreated metal in the presence of inhibitor fall with time. The combined effect of inhibitor and chromate-treatment is greater than that of either.

From the loss in weight data given in Table II, the current flowing through the local cells was calculated. The calculation shows that at the highest chloride concentration of 1% this current is of the order of 10 $\mu a/in.^2$ in the case of chromate-treated metal and 30 $\mu a/in.^2$ for untreated metal. In the other solutions, it is much less. Polarization studies thus have been carried out at similar and greater current densities.

Discussion

A comparison of Fig. 1 and Table I shows that, while the presence of chromate inhibitor in solution is accompanied by considerable shifts in potential in the nobler (positive) direction, no such shift in potential is observed in the case of chromate-treated metal. On the other hand, the initial potential of chromate-treated zinc is slightly more negative than that of untreated metal. But it is seen from Table II that, in both cases, the corrosion rate becomes almost negligible in chloride solutions of low concentration, i.e., 0.01% and 0.001%. The irreversible character of these potentials thus is

brought out. An understanding of such potentials has, however, been facilitated by the mechanism of inhibition put forward by Mears (4) based on local cell theory of corrosion and Evans' diagram. According to Mears, corrosion inhibition will be accompanied by shifts of the over-all electrode potentials such as those measured here in the nobler (positive) direction when the polarization of the local anodes alone is increased, in the negative direction if only cathodic polarization is increased, and no shift in potential will take place when the polarization of both anodes and cathodes is increased. That this approach is very helpful is readily seen in the case of chromate treatment where the treated metal shows more cathodic as well as anodic polarization. When we come to polarization curves in the presence of chromate inhibitor, however, we find that there is marked cathodic polarization and the anodic polarization is not very significant unless we take into account the initial shifts also. Mears' mechanism does not, therefore, lend itself to an explanation of the changes in potentials with time, as has been pointed out (1). The other drawbacks of this approach, viz., the need for reproducing the local cell by indirect methods which themselves are suspect and the lack of quantitative relationship between changes taking place on the metal surface and potential, were also referred to earlier (1). It was also shown that the behavior of aluminum subjected to a wide variety of passivation treatments could be explained satisfactorily if a kinetic approach based on the theory of rate processes is made. This approach was shown to result in an equation which enabled changes in potentials being interpreted in terms of log ratio of the anodic and cathodic areas on the metal surface under identical experimental conditions (5, 1). A similar equation has also been derived by other workers (6, 7). It will be shown presently that this approach is equally helpful in explaining the behavior of zinc and that it also enables us to get an intimate knowledge of the mechanism by which chromate ions inhibit corrosion in the present case, information which may be of use in other cases of chromate inhibition as well.

No appreciable shift in potential following chromate treatment is explained on this basis as arising from a reduction in the anodic as well as cathodic areas. Polarization data given in Fig. 2 confirms this conclusion. A much lower anodic and cathodic polarization observed at higher chloride concentration shows that, due to the penetrating effect of chloride ions, both anodic and cathodic areas are increased. This is also reflected in the increased corrosion rate. No appreciable change in potential with time is expected in the case of treated zinc, as both anodic and cathodic areas are increased by the chloride ions. This is what is observed (see Table I). Similarly, no change in potential is expected with time in the case of untreated zinc as it does not form a protective oxide film (cf. aluminum). Coming to untreated zinc in solution containing chloride and chromate, the smaller rise in potential with increase in chloride concentration is to be attributed either to the breakdown of the film covering the anodic area, if a film is formed, or due to the greater solubility of insoluble zinc chromate formed at the anodic areas in the higher chloride concentrations. The first rapid rise in potential immediately after immersion in 0.001% NaCl is followed by a slow rise for several days. It is likely that in the presence of the inhibitor the following reactions take place at the anodes and cathodes which result in the diminution of both the anodic and cathodic areas.

$$3Zn + 3CrO_4^{=} \rightarrow 3ZnCrO_4 \text{ (insoluble)} + 6e^- \quad [1]$$

$$6e^- + 2CrO_4^{=} + 5H_2O \rightarrow Cr_2O_3 + 10(OH^-) \quad [2]$$

Thus, the chromate ion may be expected to act like oxygen both as a depolarizer at the cathode and as a suppressor of the anodic reaction. According to the above mechanism, the first rapid rise in potential indicates the preponderating coverage of the anodic areas by the reaction of adsorbed chromate ions at the anodic points, and the later slow rise is to be attributed to the coverage of the cathodic areas also according to Eq. [2]. Potential-current density data for untreated zinc in 0.001% NaCl solution containing chromate confirms this view. Considerable anodic polarization is indicated by the rapid rise in potential in the presence of chromate even without application of current. But increase in cathodic polarization is also observed indicating that, in the presence of the chromate ion, the cathodic areas also are affected. It may be seen from Table II that, in 1% NaCl, corrosion of the metal is suppressed to some extent in the presence of the inhibitor when the test is prolonged to 11 days. The potentials of the two systems, however, remain nearly the same (cf. Table I and Fig. 3). This is also to be attributed to partial coverage of both anodic and cathodic areas by the formation of insoluble reaction products. Figure 5 compares the potential-current density curves obtained with treated metal after immersion in 0.001% solution for a week with that given by treated metal immediately after immersion in solution containing 500 ppm of sodium chromate in addition to chloride. A close resemblance in the shape of the two curves is observed. This similarity arises from the fact that the two systems are nearly identical since the former system also contains hexavalent chromium ions in solution at the end of one week due to its getting leached out from the film. Since, as already pointed out, the treatment predominantly diminishes cathodic areas and addition of chromate predominantly diminishes anodic areas, increased anodic and cathodic polarization is observed in the above two systems. It may, therefore, be expected that under these conditions, the corrosion rate will also be further reduced. Corrosion resistance data given in Table II confirms this view.

Conclusions

According to the local cell theory of corrosion and the equation derived earlier (1), inhibition of corrosion will be most satisfactory when both anodic and cathodic areas are diminished. This condition is

obtained satisfactorily when zinc is chromate-treated and immersed in an aqueous solution containing hexavalent chromium.

Acknowledgment

The authors wish to express their gratitude to Professor K. S. G. Doss, Director, Central Electrochemical Research Institute for his valuable suggestions and encouragement.

Manuscript received Sept. 25, 1958.

Any discussion of this paper will appear in a Discussion Section to be published in the June 1960 JOURNAL.

REFERENCES

1. K. S. Rajagopalan, *This Journal*, **106**, 113 (1959).
2. E. A. Anderson, *Proc. Am. Electroplater's Soc.*, **30**, No. 6, 6 (1943).
3. T. P. Hoar and F. Wormwell, *Chem. and Ind.*, **1955**, 642.
4. R. B. Mears and R. H. Brown, *This Journal*, **97**, 75 (1950).
5. K. S. Rajagopalan and K. S. G. Doss, *Naturwissenschaften*, **44**, 631 (1957).
6. M. Takahashi, *J. Electrochemical Soc. Japan*, **25**, No. 4, E 6 (1957).
7. M. Stern, *Corrosion*, **14**, 329t (1958).
8. E. A. Anderson and C. E. Reinhard, *Proc. Am. Soc. Test. Mat.*, **39**, 691 (1939).

Anodic Behavior of Aluminum at Low Potentials

J. V. Petrocelli

Research Laboratory, The International Nickel Company, Inc., Bayonne, New Jersey

ABSTRACT

Electrode potentials, differential capacities, and anodic polarization curves have been determined for aluminum in sulfuric acid solutions. It is shown that the anodic behavior in the region of low potentials (—1.0 v to +3.0 v, S.C.E. scale) follows the relationship $i = \alpha \exp [\beta F]$. Differential capacity measurements show that the capacitance is inversely proportional to the potential. The analysis of the experimental data indicates the existence of a very thin film on the aluminum in this low potential region. It is suggested that the passive behavior of aluminum is due to the presence of a thin, compact, and continuous "oxide like" film on its surface. This film is formed and/or modified by the electrochemical action which takes place between the aluminum and the electrolyte.

The role played by films, especially oxide films, on metal surfaces in electrode processes is of increasing technical and scientific interest. The greatest advances have perhaps been made in the study of the oxidation of metals in air. The foundation of these advances was the idea introduced by Wagner (1) that metal ions and electrons diffuse through the oxide layer and react with the oxygen at the oxide-gas interface.

Verwey, Mott, and others (2-7) have extended the theories of dry oxidation to the formation of anodic films by electrolytic action. The rate of both types of processes are supposed to depend on the kinetics of the movement of ions, usually metallic ions, into and through the film under the influence of an electrostatic field. Experimental work and theoretical developments have been concerned primarily with the so called "valve" metals such as tantalum, aluminum, hafnium, niobium, titanium, vanadium, and zirconium. Most of these studies have dealt with the formation of relatively thick oxide films, circa 2000Å or more, formed at 100-600 v (8-16). The work of Guntherschulze and Betz (17) contains an excellent compilation of results up to 1936. Johansen, *et al.* (18) give a comprehensive bibliography for the more recent work on anodization.

Although under certain conditions of formation some thick anodic coatings may be porous, there are strong indications that many of them are relatively compact and nonporous and that even the thicker porous coatings have a compact, nonporous "barrier" layer film underneath which may be from 10Å to 200Å thick (15, 19, 20).

It has been suggested that the above "valve" metals as well as chromium, nickel, and iron, which exhibit passive behavior at relatively low voltages, have a compact, nonporous film on their surface under conditions usually encountered in corrosion and finishing (21-23, 24). These metals exhibit passive behavior in that they do not react or react extremely slowly with aqueous solutions despite the extremely favorable thermodynamic conditions. Although there are several schools of thought as to the nature of these films which exist on passive metals (25), it is very likely that they are similar, if not identical, to the barrier layer type which form during anodization of the metal in question (10, 11, 27).

In some cases the film is formed in air, hence preexists prior to exposure to the aqueous medium. For other cases the entire film forms after immersion in the electrolyte. In either case the final thickness of the film will be governed by the electrochemical action which occurs in the electrolyte. On open circuit, without external polarization, film growth is promoted by an electrostatic field set up across the film by the local electrochemical action. The anodic reaction consists of the migration and diffusion of ions (the metallic ions in many cases) through the film while the cathodic reaction involves the reduction of oxygen, hydrogen, or other reducible substance present in the solution. The kinetics and mechanism are very similar to that which occurs

during anodization by application of an external current.

It is the object of this work to determine the presence of such a film on Al on open circuit and in the low voltage region, −1.0 to +2.0 v. Previous work on the behavior of Al with oxidation-reduction systems strongly suggested the presence of such a film on this metal (21).

Some investigators have explored this low voltage region for some of the film forming metals. Vermilyea (26) has shown that it is possible to form a film on Ta even when its electrode potential is negative to the hydrogen electrode in dilute solutions of HNO_3 and NaOH. Young (10) studied the anodization of Nb in the 0.0 to 10 v range in Na_2SO_4 and H_2SO_4. He found that in this voltage region films ranging from about 20Å to a few thousand angstroms thick formed on the metal. Johansen, *et al.* (18) studied anodic film formation on Ta, Al, Ti, Hf, V, Nb, and Cr in boric acid-ammonia solutions in the potential region below oxygen evolution. Except for Cr and V they found that films did form and determined some of the electrolytic parameters involved.

Experimental Technique

Differential capacity measurements, strictly speaking impedance measurements, were adopted in this work for detecting and studying the film on Al. Measurements of the capacity of electrodes covered by anodic oxide films have been used successfully for obtaining an estimate of film thickness (10, 13, 17). The oxide film functions as the dielectric of a parallel plate condenser of which the basis metal and the solution form the plates. It is likely that this model is oversimplified and Young (10) has treated some of the possible complicating factors which may be involved.

It is well known, however, that the capacity of clean metallic surfaces in electrolytes varies with the electrode potential in such a manner that the minimum capacitance is about 16 $\mu F/cm^2$ and that this value is that characteristic of the double layer (28, 29). It is reasonable to assume that the presence of a thin film on the surface will yield lower capacity values and that the capacity should decrease as the film thickens. The results obtained do in fact strongly indicate that the capacity values measured at high frequencies are very close to, if not identical with, the capacity of a barrier layer film.

The apparatus was practically identical to that used by Grahame (29) and Robertson (30). A mercury-mercurous sulfate half-cell was used as a reference electrode, and a glass tube filled with the solution being studied served as a salt bridge. One end of this tube was drawn down to a fine capillary which was pressed close to the back of the Al electrode. An H-type electrolysis cell with two separate compartments was used. One compartment contained the Al electrode, the capillary tipped tube, and a large (75 cm^2) platinized Pt electrode which functioned as an auxiliary electrode for the a-c measurements. The other portion of the cell contained a Pt electrode which served as a cathode in the d-c circuit.

All experiments were performed at constant temperature of 25.0°C. Although no appreciable difference was observed between results obtained in air-free solutions and air-saturated solutions, purified nitrogen was used in most of the experiments. The data presented were obtained with stationary electrodes and unstirred solutions.

The values of the electrode potentials, E, are given with reference to the saturated calomel electrode, increments in the electrode potential, ΔV, are referred to the open-circuit potential of Al in any given experiment.

Pure Al (99.99) sheet, 0.25 mm thick was used, and all solutions were made up from redistilled water and reagent grade sulfuric acid.

Generally the experimental procedure was as follows: The sheet aluminum was thoroughly cleaned and then polished with No. 0000 metallographic paper. It was then cleaned in hot acetone and thoroughly rinsed in distilled water, alcohol, and dried. All but a defined rectangular area, 0.10 cm^2 to 1.0 cm^2, was coated with an inert resin. The electrodes were then stored in a desiccator for one or two days prior to use.

Polarization experiments were conducted by making the Al the anode of a d-c circuit and impressing a predetermined current density. Unless noted otherwise, each potential reported is a steady-state value. The a-c impedance bridge could be connected to the Al and the platinized Pt auxiliary electrode at any time for the measurement of the a-c impedance. The impressed a-c voltage never exceeded 10 mv and was usually less.

The a-c impedance was measured on the bridge as a capacitance ,C_s, in series with a resistance, R_s. The impedance at the metal-solution interface is probably best represented by a capacitance in parallel with the film resistance (14). Therefore the values C_s and R_s obtained on the bridge were converted to the corresponding values C_p and R_p as shown in Fig. 1 where R_L is the resistance of the electrolyte. This choice does not effect the results reported because C_s and C_p are identical at the higher frequencies used in this work (10-15 kc).

The resistance due to the electrolyte was obtained by extrapolating R_s to infinite frequency. The values so obtained were checked in the following manner: a small platinized Pt electrode having the same shape, size, and exposed area as the Al was substituted for the Al electrode and the conductivity of the system measured with the a-c bridge in the conventional manner. The resulting values compared very well with those obtained above. The electrolyte resistance is designated by R_L.

Many exploratory experiments showed that neither the electrode potential nor the capacitance was appreciably sensitive to the exact position of the capillary tip and/or the auxiliary Pt electrode. Sev-

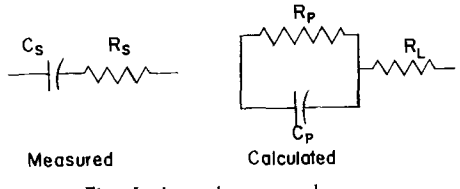

Fig. 1. Impedance analogues

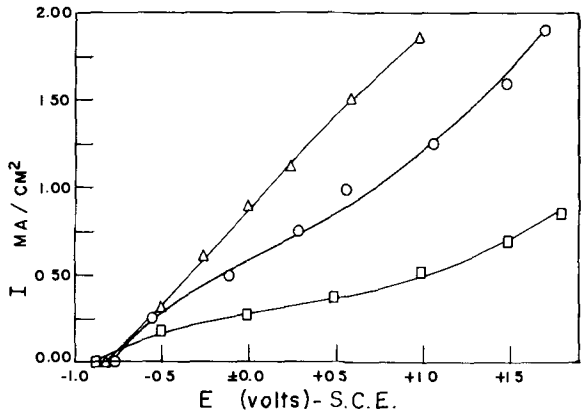

Fig. 2. Anodic polarization of Al. △—10N H_2SO_4; ○—5.0N H_2SO_4; □—1.0N H_2SO_4.

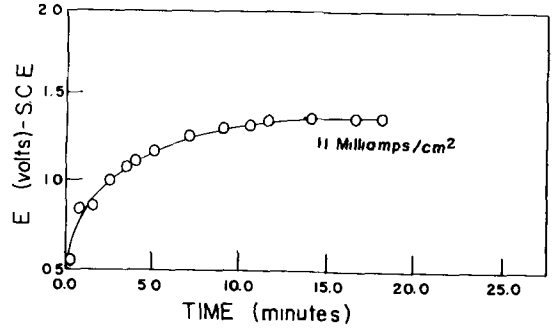

Fig. 3. Change of electrode potential with time at a given anodic current density in 3.0N H_2SO_4.

eral experiments were performed without the use of an insulating resin in order to determine if this resin had an effect on the capacitance values. No significant effect was ever found.

Experimental Results

The potential of Al on immediate immersion was about −0.2 v and changed to more anodic values with time, becoming fairly steady in about 1 hr. The steady-state value was about −0.9 v in all solutions. While any given specimen maintained a steady-state potential within a few centivolts, the steady-state potential of different specimens varied within 0.1 v.

When anodically polarized, Al reaches a steady potential at any given current density in about 15 min. The actual time required depends on the previous current density as well as the current density in question. The behavior is that generally found for film forming metals.

The curves shown in Fig. 2 and 3 show typical behavior in H_2SO_4. Curves obtained with many different specimens all had about the same general shape. Variation in potential for any given current density was about ±0.2 v.

The polarization at any one current density could be prolonged for 1 or 2 hr without changing the form of the curve to any appreciable extent.

No visual evidence of gas evolution was detected throughout the voltage range investigated.

If the Al is polarized rapidly (each reading taken within 30 sec), subsequently depolarized, and the process repeated several times, the following behavior, shown in Fig. 4, is observed. The first polarization curve lies somewhat above the remaining curves, curve A in Fig. 4. The subsequent curves,

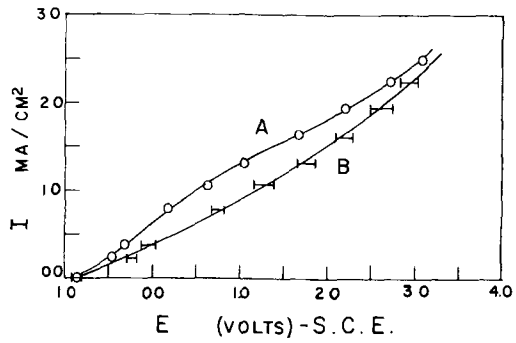

Fig. 4. Rapid anodic polarization in 5.0N H_2SO_4 hysteresis effect.

as well as the steady-state curve, lie within the brackets of curve B in Fig. 4. After the first rapid polarization all subsequent curves including the steady-state one are identical within the experimental error.

Although instrument limitations did not allow accurate readings for times less than about 30 sec, indications were obtained that if depolarization potentials were obtained in very short time intervals a considerable hysteresis effect would be noted. A specimen which had been polarized at steady-state values up to about 1.0 ma/cm^2 showed a pronounced hysteresis on rapid depolarization. The potential retained its noble value for several seconds while the current diminished to very low values.

An Al specimen which had been polarized up to +1.0 v in 5N H_2SO_4 and removed from the solution without interrupting the current exhibited noble behavior in a weaker, 1N H_2SO_4, solution. The open-circuit potential was about −0.6 v, and the anodic polarization obtained in the latter solution had a higher slope, (dV/di).

Several specimens were polarized at various current densities for 30 min in 5.0N H_2SO_4 and tested in the dry state for the presence of an insulating film. A metallic probe was pressed against the surface, and 1.0 v d.c. was applied across the probe and the Al.

Insulating films were obtained on specimens which had been polarized at more noble potentials than +1.0 v. The conduction did not depend on the polarity of the probe.

The anodic behavior described above strongly indicates that Al forms a film on the surface and that its thickness depends on the potential and current density.

The differential capacitance varied with the frequency as shown in Fig. 5. In all cases it became constant at about 8 kc. It may be assumed that the C_p measured at 10 kc or greater is the true, or very close to the true, value of the parallel plate capacity of the oxide (10). Unless otherwise noted, all values reported were measured at 15 kc.

At any given current density the capacitance changed with time in about the same manner as the potential. On open circuit the capacitance increased in value as the potential became more anodic (negative with respect to S.C.E.). At any given current density the capacitance decreased with time as the potential became more noble, both values becoming fairly steady at about the same time.

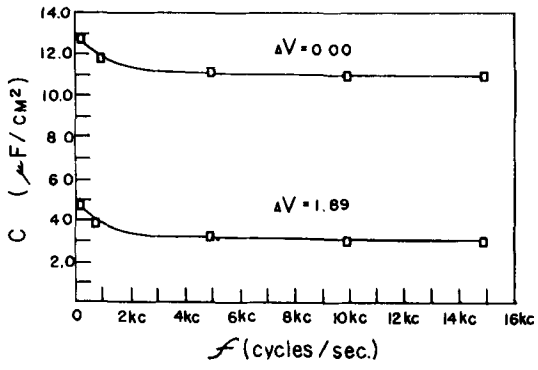

Fig. 5. Variation of capacitance with frequency in 1.0N H_2SO_4.

In any one experiment the capacitance varied from about 13 $\mu F/cm^2$ on open circuit to about 2 $\mu F/cm^2$ at $\Delta V = +3.0$ v. On open circuit the maximum variation from one specimen to another was about 1 $\mu F/cm^2$; this variation decreased with applied current to a few tenths of a microfarad per square centimeter. It is very likely that variations in capacitance values were predominately due to variations in the surface roughness factor, since this probably approached unity as the surface film thickened (9).

Generally the capacitance was lower in 1N H_2SO_4 than in the 5N and 10N acid. No significant differences were observed in 5N and 10N H_2SO_4.

A fairly well-defined linear relationship was found between $1/C$ and ΔV. Typical results are shown in Fig. 6.

Assuming that an oxide film is present on the surface we may follow the ideas of Mott and Cabrera (5) and others (8, 9) and express the current density as follows:

$$i/Ar = \alpha\, e^{\beta F} \qquad [1]$$

where α and β are constants and F is the field strength across the film.

If we let $F = V/x$, where V is the potential difference across the film and X the film thickness, we obtain

$$i/Ar = \alpha\, e^{\beta V/x} \qquad [2]$$

Expressing the current density in terms of the current per unit of apparent area, A, we have

$$i/A = \frac{Ar}{A}\,\alpha\, e^{\beta V/x} \qquad [3]$$

where Ar/A is the roughness factor.

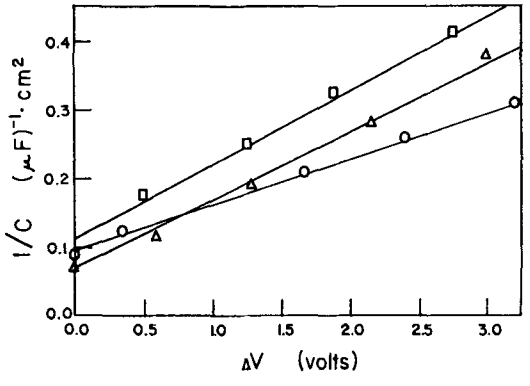

Fig. 6. Variation of the reciprocal capacitance with potential. □—1.0N H_2SO_4; ○—5.0N H_2SO_4; △—10.0N H_2SO_4.

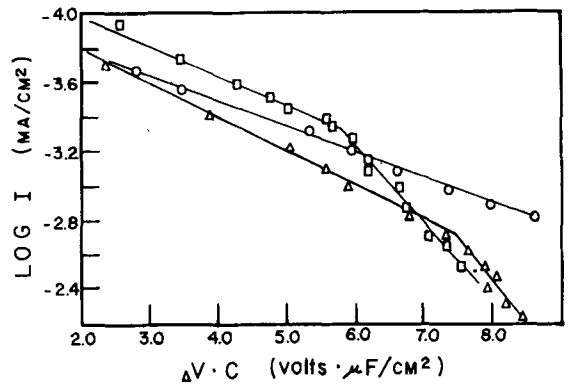

Fig. 7. Variation of the product $\Delta V \cdot C$ vs. log of current density. □—1.0N H_2SO_4; ○—5.0N H_2SO_4; △—10.0N H_2SO_4.

Since the measured electrode potential of the Al will differ from the actual electrical potential difference at the Al-solution interface by some constant, we will, for purposes of convenience, refer most of our potentials to that of the Al on open circuit, V^0.

$$i/A = Ar/A\ \alpha \exp\left[\beta(V^0 + \Delta V)/x\right] \qquad [4]$$

Assuming that the roughness factor is one, we finally have:

$$\Delta V/x = \frac{2.3}{\beta}\log i/A - \frac{2.3}{\beta}\log \alpha - V^0/x \qquad [5]$$

If the film on the surface acts as the dielectric of a parallel plate condenser, the capacity should be related to the film thickness as follows:

$$C = \frac{D\,Ar}{4\pi x} \qquad [6]$$

or

$$C = k/x \qquad [7]$$

where C is the capacitance and D the dielectric constant.

Substituting the above into Eq. [5], we have

$$\Delta V \cdot C = 2.3\ k/\beta \log i/A - 2.3\ k/\beta \log \alpha - V^0 \cdot C \qquad [8]$$

If we assume that α and β do not differ appreciably from the values found for thick films, where $\alpha \cong 5 \times 10^{-18}$ amp/cm² and $\beta \cong 5 \times 10^{-6}$ cm/v (8, 9), it is reasonable to expect that the relatively small variations in the product $V^0 \cdot C$ will not affect expression [8] to any appreciable extent. Hence if our concepts and assumptions are correct, $\Delta V \cdot C$ should be a linear function of log i/A.

Figure 7 shows that the product $(\Delta V \cdot C)$ plotted vs. log i/A yields straight lines as predicated by Eq. [8].

The data obtained in 5N H_2SO_4 always resulted in one line, whereas those obtained in 1N and 10N H_2SO_4 invariably showed a break with two straight lines of different slopes. This tendency for the current to increase more rapidly at high field strengths has been observed by others for both Al and Ta (8, 9), and a "heating effect" was suggested as the possible cause.

It is difficult to understand why this phenomena was not observed in 5N H_2SO_4, and no satisfactory explanation can be offered at this time. It is possible, of course, that the proper conditions of current and solution composition for producing a heat effect were encountered in 1N and 10N acid and not in the 5N H_2SO_4.

The average value of the slope $d(\Delta V \cdot C)/d \log i$

obtained on several different specimens in 5*N* H_2SO_4 was 6.0, with an average deviation of 5%. The slopes in 1*N* acid were 6.0 and 2.1 and in 10*N* acid 4.3 and 2.3. The average deviation was about 10% in both cases.

Discussion

Since the capacity of the auxiliary platinized Pt electrode was about 2000 μF, we may assume that the measured capacitance is very close to the true value of the capacitance of the Al electrode. The experimental results may be interpreted, at least in a qualitative manner, as indicating the presence of a film on the Al surface. The film is present at all potentials including open-circuit conditions and apparently thickens as the potentials are made more noble.

A quantitative interpretation of capacitance in terms of a film thickness is complicated because of the following factors. The true capacity of the film is somewhat greater than the measured value because of the capacitance of any diffuse double layer at the oxide-solution interface. While the film is probably fairly uniform in thickness, it is not entirely so, and our measurements correspond to some average thickness. The surface roughness factor is not known, although as previously mentioned, it probably approaches unity as the film increases in thickness. Finally, we do not know the exact composition nor the dielectric constant of the film.

However, the data do strongly indicate a film thickness which varies linearly with the potential, and it is interesting to obtain at least some qualitative idea of the probable thickness.

If we rewrite Eq. [6] as

$$C = \frac{8.84\ D}{x \cdot 10^{8}} \qquad [9]$$

where C is in μF/cm^2 and x in centimeters, we see from Eqs. [7] and [8] that the slope, S, of the $\Delta V \cdot C$ vs. log i curve is

$$S = \frac{20 \times 10^{-8}\ D}{\beta} \qquad [10]$$

If we take the value of $\beta \cong 0.5 \times 10^{-6}$ cm/v as calculated by Verwey (2), we obtain a value for the dielectric constant, D, of about 15 which is the right order for Al_2O_3.

Higher values of β as reported for thick films (4, 8, 9) would yield values of D which are unreasonably high.

If we take $D \cong 15$, and calculate x we obtain film thickness of the order of about 10Å on open circuit to about 50Å at +3.4 v in 5*N* H_2SO_4; and in 1*N* and 10*N* acid in lower voltage region.

Since it is not known whether β, D, or both change to cause lower values of the slope at the higher voltages no attempt will be made to calculate thicknesses in these cases. It should be noted, however, that a change in β from 0.5×10^{-6} to about 1.5×10^{-6} is all that is necessary to account for the change in the slope with the same dielectric constant.

The results obtained on Al in this study and on some of the other film forming metals mentioned in the introduction strongly indicate that, at least for these metals, the presence of a very thin, compact, and continuous "oxide-like" film on the surface is responsible for their passive behavior. The film thickness and characteristics will be governed by the electrochemical action which occurs between the metal and the electrolyte. This action exists on open circuit and does not differ in kind from that induced by external anodic polarization.

It is, in fact, a self-anodic polarization. The electrons are removed by the cathodic reduction of some reducible substance present in the solution.

Acknowledgment

The author wishes to express his appreciation to the Patent Button Company for permission to publish that portion of the work which was carried out in its laboratory.

Manuscript received Jan. 2, 1959. This paper was prepared for delivery before the Ottawa Meeting, Sept. 28-Oct. 2, 1958.

Any discussion of this paper will appear in a Discussion Section to be published in the June 1960 JOURNAL.

REFERENCES

1. C. Wagner, *Z. Physik Chem.*, **B21**, 25 (1933); **B32**, 447 (1936).
2. E. J. Verwey, *Physica*, **2**, 1059 (1935).
3. S. Anderson, *J. Appl. Phys.*, **15**, 477 (1944).
4. N. F. Mott, *Trans. Faraday Soc.*, **43**, 429 (1947).
5. N. Cabrera and N. F. Mott, *Rep. Progr. Phys.*, **12**, 164 (1948-49).
6. H. E. Haring, *This Journal*, **99**, 30 (1952).
7. J. J. Dewald, *ibid.*, **102**, 1 (1955).
8. A. Guntherschulze and H. Betz, *Z. Physik.*, **92**, 367 (1934).
9. L. Young, *Trans. Faraday Soc.*, **50**, 153 (1954).
10. L. Young, *ibid.*, **51**, 1250 (1955).
11. L. Young, *ibid.*, **52**, 503 (1956).
12. L. Young, *ibid.*, **53**, 841 (1957).
13. D. A. Vermilyea, *This Journal*, **102**, 655 (1955).
14. W. Van Geel and J. W. Scholte, Philips Research Repts., **6**, 54 (1951); **8**, 47 (1953).
15. M. S. Hunter and P. Fowle, *This Journal*, **101**, 481 (1954).
16. R. B. Mason and P. E. Fowle, *ibid.*, **101**, 53 (1954).
17. A. Guntherschulze and H. Betz, "Elecktrolyt-Kondensatoren," M. Krayn, Berlin (1937).
18. H. A. Johansen, G. B. Adams, Jr., and Pierre Van Rysselberghe, *This Journal*, **104**, 339 (1957).
19. Charlesby, *Proc. Phys. Soc.*, **B66**, 317, 533 (1953).
20. F. Keller, M. S. Hunter, and D. L. Robinson, *This Journal*, **100**, 411 (1953); A. J. Dekker and H. M. Urquhart, *Can. J. Research*, **28**, 541 (1950).
21. J. V. Petrocelli, *This Journal*, **97**, 10 (1950); **98**, 183 (1951); **99**, 513 (1952).
22. U. R. Evans, *Nature*, **168**, 853 (1951).
23. T. P. Hoar and U. R. Evans, *This Journal*, **99**, 212 (1952).
24. D. M. Sowards and Norman Hackerman, *ibid.*, **102**, 297 (1955).
25. Y. M. Kolotyrkin, Internationales Kolloquium Uber Die Passivitat Der Metalle, p. 131, Darmstadt 1957.
26. D. A. Vermilyea, *This Journal*, **101**, 389 (1954).
27. M. Maraghini, G. B. Adams, Jr., and Pierre Van Rysselberghe, *ibid.*, **101**, 400 (1954); **102**, 502 (1955).
28. J. O'M. Bockris, "Modern Aspects of Electrochemistry," p. 43, Butterworths Scientific Publication, London (1954).
29. D. C. Grahame, *J. Am. Chem. Soc.*, **63**, 1207 (1941); **68**, 301 (1946); **71**, 2975 (1949); **78**, 3577 (1956).
30. W. D. Robertson, *This Journal*, **100**, 194 (1953).

Kinetic Studies on Corrosion Systems

I. Polyelectrodes under Activation Control

Franz A. Posey

Oak Ridge National Laboratory, Oak Ridge, Tennessee[1]

ABSTRACT

Electrochemical kinetics has been applied to the case of corroding polyelectrodes under activation control for the situation where the rates of partial processes vary over the surface of an electrode. Explicit expressions have been derived for rate and potential in the simplest polyelectrode systems. The kinetics of galvanic couples under activation control has been derived with emphasis on the significance of measurable quantities. The use of steady-state polarizability measurements, potentiostatic measurements, and galvanostatic measurements in the study of polyelectrode systems has been outlined.

Numerous investigators have contributed to the foundations[2] and experimental applications of electrochemical kinetics and comprehensive reviews of this work have been published (4-6). Much of the existing theory treats the case of a single over-all reaction under activation control[3] at an electrode-solution interphase [e.g., a metal-metal ion equilibrium, or a redox reaction at an inert electrode (8)], and one of the most general treatments of such a system[4] has been presented by Parsons (9). Wagner and Traud (10), Kimball (11), and Audubert (12) have been among the few to examine corrosion systems from a systematic kinetic viewpoint. However, in the study of some of the more complex electrochemical situations, such as those occurring in many corrosion systems, there appears to be a need for a more extensive treatment suitable for interpreting the phenomenology. In the present report, an elementary electrochemical kinetic treatment of two-phase polyelectrode systems[5] and galvanic couples under activation control has been developed, and the application of the theory to the analysis of corroding polyelectrodes has been outlined for several types of steady-state measurements. The results of an experimental investigation on a particular polyelectrode system will be presented in a subsequent report.

[1] Operated by Union Carbide Corporation for the U. S. Atomic Energy Commission.

[2] The source equations of electrochemical kinetics may be found in the works of Butler (1), Bowden and Rideal (2), and Erdey-Gruz and Volmer (3).

[3] Use of the term, activation control, here corresponds to the sense of the designation, "Durchtrittsüberspannung," as employed by Vetter (7) to distinguish between cases where the charge transfer step in an electrochemical reaction or partial process is rate-determining and those where the higher activation energy of a precursor step or a subsequent step in the reaction determines the rate.

[4] The designation, system, is used here to refer to an electrode plus its liquid environment.

[5] The term, polyelectrode, as used here, refers to the situation where more than one chemically distinct individual or partial process is occurring at the same electrode-solution interphase. The term, two-phase polyelectrode system, denotes a metallic polyelectrode in contact with a nonmetallic environment in the liquid state. The case of intervention of a third phase (e.g., an oxide film) between metal and solution is not considered explicitly, although the kinetics of some three-phase systems is indistinguishable from that of the two-phase systems treated here. This latter situation may occur if all rate-determining charge transfer steps in a three-phase system proceed at the same interphase (e.g., an oxide-solution interphase).

Definitions and Fundamental Relations

The present theory, in addition to treating the case where several partial processes under activation control occur at the same electrode-solution interphase, attempts to take account (at least in a formal manner) of the experimentally demonstrable fact that the rates of each of the partial processes may vary over the surface of the electrode. As a consequence of these variations, three current quantities present themselves for consideration in a kinetic analysis. The first of these quantities is given by the equation:

$$j_i = \lambda_i F \overline{k_i} \pi (C_i^{p_i}) \qquad [1]$$

wherein the current density, j_i (units of amp/cm^2), of the i^{th} charge transfer step at a very small (differential) element of area, dS, on the surface of an electrode is related to the absolute value of the number of charges transferred across the interphase (λ_i) during the i^{th} charge transfer step, Faraday's constant (F), an electrochemical specific rate constant ($\overline{k_i}$), and the product of the concentrations of the reactants (symbolized by $\pi(C_i^{p_i})$, where p_i denotes the kinetic order of the i^{th} charge transfer step with respect to the species of concentration, C_i).[6]

Since the energy barrier of a charge transfer step may be traversed in either direction, it is pertinent

[6] In this definition, the significance of the current density of a charge transfer step is assigned to j_i, instead of the current density of a partial process. This is done so that Eqs. [2], [3], and [7] will be general in that they include all the charge transfer steps of any two-phase polyelectrode system. However, the current density of a charge transfer step is not necessarily identical to the current density of the associated partial process, except for partial processes under pure activation control (cf. footnote 3) having a mechanism with only one charge transfer step. A partial process may involve several steps (i.e., the surmounting of several energy barriers), of which at least one step will be a charge transfer step. Furthermore, the charge transfer step(s) of a partial process may or may not be rate-determining (viz., the "slow recombination" mechanism of the hydrogen evolution reaction), but each charge transfer step will obey Eq. [1] in which $\overline{k_i}$ is the electrochemical specific rate constant of the charge transfer step and $\pi(C_i^{p_i})$ involves all species participating in the step, whether they be identifiable reactants or products of the partial process or intermediates of transitory existence. In general, the current density of a partial process which has a mechanism with m energy barriers involving charge transfer is equal to m times the net current density crossing each of the energy barriers. In applying Eqs. [1], [2], [3], and [7] to the cases discussed in the rest of the report, however, it will be assumed that all partial processes are under pure activation control and involve only one charge transfer step; in other words, only the simplest electrode processes will be assumed present in the system.

to define the anodic and cathodic current densities, $j_{i,a}$ and $j_{i,c}$.[7] With this convention, a second current quantity is given by the equation:

$$j_\sigma = \sum_i (j_{i,a} - j_{i,c}) \qquad [2]$$

This is the net current density (j_σ) at a differential element of area (dS) on an electrode surface and is the difference between total anodic and total cathodic current densities at dS. It will be shown later that the sign and magnitude of j_σ depend on the kinetics (i.e., on the energetics and on the number of reactive particles) of the various processes occurring both at dS and over the rest of the electrode surface, as well as on the sign and magnitude of any current applied to the electrode from an external source.

The third important current quantity is the applied current, i_P, which for steady-state conditions is given by:

$$i_P \equiv \int_S j_\sigma \, dS = \int_S [\sum_i (j_{i,a} - j_{i,c})] dS \qquad [3]$$

on integrating j_σ over the surface area, S, of the electrode. The applied current, of course, is an experimentally measurable quantity.

Further consideration of polyelectrode systems necessitates the assignment of a particular form to the electrochemical specific rate constants, $\overline{k_i}$. It will be assumed that the rate constants are given (13) by:

$$\overline{k_i} = \tau_i \left(\frac{kT}{h}\right) e^{-\frac{\overline{\Delta\mu_i}^\ddagger}{RT}} \qquad [4]$$

where (kT/h) has its usual significance of the decomposition frequency of activated complexes (14), τ_i equals $\kappa_i \dfrac{\pi(\gamma_i^{p_i})}{\gamma_i^\ddagger}$ (in which κ_i is the transmission coefficient of the i^{th} charge transfer step (15), $\pi(\gamma_i^{p_i})$ symbolizes the product of the activity coefficients of the reactants, and $\gamma_i^\ddagger$ is the activity coefficient of the activated complex), and $\overline{\Delta\mu_i}^\ddagger$ is the change in the electrochemical potential of the system required for the formation of one mole of activated complex from reactants. $\overline{\Delta\mu_i}^\ddagger$ is a partial molar quantity in the usual thermodynamic sense.

The rate constants for anodic and cathodic charge transfer steps may be obtained from Eq. [4] on introducing the definition of electrochemical potential due to Lange (16, 17), $(\overline{\mu_n})_\beta = (\mu_n)_\beta + Z_n F \phi_\beta$ (in which $(\overline{\mu_n})_\beta$ is the electrochemical potential of species n in phase β, $(\mu_n)_\beta$ is the chemical potential of n in β, Z_n is the charge on n, and ϕ_β is the inner or Galvani potential of the phase β), in a manner similar to the procedure used by Parsons (9) in deriving the rate constant of a partial process. The electrochemical specific rate constants become:

$$\overline{k_{i,a}} = \tau_{i,a} \left(\frac{kT}{h}\right) e^{-\frac{\Delta\mu_{i,a}^\ddagger}{RT}} e^{+\frac{\alpha_{i,a}\lambda_{i,a}F}{RT}\Delta\phi_H} \qquad [5]$$

$$\overline{k_{i,c}} = \tau_{i,c} \left(\frac{kT}{h}\right) e^{-\frac{\Delta\mu_{i,c}^\ddagger}{RT}} e^{-\frac{\alpha_{i,c}\lambda_{i,c}F}{RT}\Delta\phi_H} \qquad [6]$$

for anodic and cathodic charge transfer steps, respectively. Here, $\Delta\mu_{i,a}^\ddagger$ and $\Delta\mu_{i,c}^\ddagger$ are the changes in the chemical potential of the system required for the formation of one mole of activated complex from reactants for anodic and cathodic steps, respectively. $\alpha_{i,a}$ and $\alpha_{i,c}$ are the symmetry factors of the charge transfer steps while $\Delta\phi_H$ is the inner potential difference between the interior of the metallic element of volume, dv (one surface of which is the element of area, dS, in contact with the solution), and the innermost portion of the diffuse double layer in the solution.[8,9] Many of the preceding definitions are offered mainly to establish a nomenclature for the treatment of polyelectrode systems rather than as new propositions, and the presentation resembles Parsons' derivation (9) of similar expressions for partial processes. For convenience in reference, a list of frequently used symbols and their definitions is appended to this report.

From Eqs. [1], [3], [5], and [6], the current applied to a polyelectrode system in a steady state is given by:

$$i_P = F\left(\frac{kT}{h}\right)\int_S \sum_i \Big[\lambda_{i,a}\tau_{i,a}\pi(C_i^{p_i})_a \, e^{-\frac{\Delta\mu_{i,a}^\ddagger}{RT}} e^{+\frac{\alpha_{i,a}\lambda_{i,a}F}{RT}\Delta\phi_H} - \lambda_{i,c}\tau_{i,c}\pi(C_i^{p_i})_c \, e^{-\frac{\Delta\mu_{i,c}^\ddagger}{RT}} e^{-\frac{\alpha_{i,c}\lambda_{i,c}F}{RT}\Delta\phi_H} \Big] dS \qquad [7]$$

Equation [7] is the fundamental expression of the present model of two-phase polyelectrode systems; it includes all the charge transfer steps occurring at an electrode-solution interphase, whether rate-determining or not. Since $\Delta\phi_H$ of Eq. [7] is not an experimentally measurable quantity, it is appropriate to modify this equation to a form containing a measurable potential difference. Figure 1 shows a typical circuit for the measurement of cell or electrode potentials. Here, the measurable potential difference, V, is the potential difference corresponding to the difference in the electrochemical potential of electrons in the two ends of a potentiometer slidewire of uniform composition, i.e., $V = (\phi_{l'} - \phi_{l''})$. Hence, $V = (\phi_{l'} - \phi_M) + (\phi_M - \phi_S) - (\phi_{l''} - \phi_R) - (\phi_R - \phi_S)$, where $(\phi_{l'} - \phi_M)$ is the potential difference due to electronic equilibrium between one potentiometer lead (l') and the metallic volume element, dv, at the surface of the electrode, $(\phi_M - \phi_S) = \Delta\phi = \Delta\phi_H +$

[7] Here and elsewhere, subscript a refers to an anodic charge transfer step, entailing a transfer of positive charge from electrode to solution or of negative charge in the reverse direction; likewise, subscript c refers to a cathodic charge transfer step, with transfer of negative charge from electrode to solution or of positive charge in the reverse sense. Current densities are denoted by j, currents by i. Currents and current densities of charge transfer steps are considered as positive quantities, and positive or negative signs are affixed according to whether the particular charge transfer steps are anodic or cathodic, respectively. The signs of all other current quantities and derived functions, such as that of the externally applied current, are fixed by this procedure.

[8] If ϕ_M is the inner potential of the metallic volume element, dv, and ϕ_S is the inner potential at the outermost portion of the diffuse double layer in the solution, $\Delta\phi \equiv \phi_M - \phi_S$ is the over-all inner potential difference between metal and solution at dS. However, the specific rate constant of a charge transfer step is a function of the potential difference across the Helmholtz double layer, $\Delta\phi_H \equiv \phi_M - \phi_H$, where ϕ_H is the inner potential at the outermost portion of the Helmholtz or "fixed" double layer or (we shall assume also) at the innermost portion of the diffuse double layer. The inner potential difference of the diffuse double layer is then $\psi \equiv \phi_H - \phi_S$, and it follows that $\Delta\phi \equiv \phi_M - \phi_S = \Delta\phi_H + \psi$.

[9] The inner potential of electrochemistry should not be confused with the inner potential of electron diffraction theory. For the distinction, see Parsons' article in reference (4).

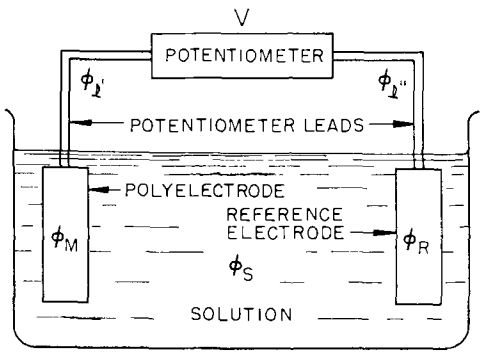

Fig. 1. Schematic diagram of typical circuit for the measurement of electrode potentials of polyelectrodes.

ψ (cf. footnote 8) is the electrode-solution potential difference at dS, $(\phi_{l''} - \phi_R)$ is the potential difference due to electronic equilibrium between the other potentiometer lead (l'') and the reference electrode, and $(\phi_R - \phi_S)$ is the potential difference between the reference electrode and the solution. If $(\phi_{l''} - \phi_R) + (\phi_R - \phi_S) = (\phi_{l''} - \phi_S)$ is denoted by $\Delta\phi_{\text{ref.}}$, and $(\phi_{l'} - \phi_M)$ is replaced by $\frac{1}{F}[(\mu_e)_{l'} - (\mu_e)_M]$, $\Delta\phi_H$ of Eq. [7] is given by $\Delta\phi_H = V - \psi + \Delta\phi_{\text{ref.}} + \frac{1}{F}[(\mu_e)_M - (\mu_e)_{l'}]$. Here, $[(\mu_e)_M - (\mu_e)_{l'}]$ is the difference in the chemical potential of electrons in the metallic volume element, dv, and in the potentiometer lead (l'). Equation [7] then becomes:

$$i_P = F\left(\frac{kT}{h}\right)\int_s \sum_i \left[\lambda_{i,a}\tau_{i,a}\pi(C_i^{p_i})_a\, e^{+\frac{\alpha_{i,a}\lambda_{i,a}F}{RT}(\Delta\phi_{\text{ref}} - \psi)} \right.$$

$$e^{-\frac{(\Delta\mu_{i,a}^{\ddagger} - \alpha_{i,a}\lambda_{i,a}[(\mu_e)_M - (\mu_e)_{l'}])}{RT}}\, e^{+\frac{\alpha_{i,a}\lambda_{i,a}F}{RT}V}$$

$$- \lambda_{i,c}\tau_{i,c}\pi(C_i^{p_i})_c\, e^{-\frac{\alpha_{i,c}\lambda_{i,c}F}{RT}(\Delta\phi_{\text{ref}} - \psi)}$$

$$\left. e^{-\frac{(\Delta\mu_{i,c}^{\ddagger} + \alpha_{i,c}\lambda_{i,c}[(\mu_e)_M - (\mu_e)_{l'}])}{RT}}\, e^{-\frac{\alpha_{i,c}\lambda_{i,c}F}{RT}V} \right] dS \quad [7']$$

Two assumptions are implicit in Eq [7']. First, it is assumed that currents flowing in the electrode, whether externally applied or existing as a result of variations in the rates of processes over the electrode surface, can have no significant effect on $[(\mu_e)_M - (\mu_e)_{l'}] = F(\phi_M - \phi_{l'})$. This assumption is surely an excellent approximation since it is well known that metals and metallic contacts are quite unpolarizable; certainly the assumption will be valid for currents encountered in systems having partial processes under activation control. Second, it is assumed that ϕ_S is constant everywhere in the solution, and hence that the measured value of V will be independent of the position of the reference electrode (or its Luggin capillary) with respect to the corroding polyelectrode (i.e., no significant "IR drop" exists in the solution). For systems under activation control, this condition usually can be met experimentally by employing a large excess of an indifferent electrolyte in the solution. The presence of a large excess of inert electrolyte is advantageous also in that the diffuse double layer potential difference (ψ) is suppressed, is approximately independent of the overall electrode-solution potential difference ($\Delta\phi$) at potentials sufficiently far from that of the electrocapillary maximum and is approximately independent of the concentration of reactive species.

It should be noted that $\Delta\phi$ (or ϕ_M) has not been presumed to be constant over the polyelectrode surface. Constancy of $\Delta\phi$ is expected only when the polyelectrode is a metal of uniform composition, although even in this case the rates of processes may vary over the surface because of, for example, the presentation of various crystal faces to the solution. Measurements of V do not necessarily give any information on the variation of $\Delta\phi$ over a polyelectrode surface, although a change in V corresponds to an identical change in $\Delta\phi$ everywhere on the surface, under the conditions of validity of the two assumptions mentioned above. The terms, $\Delta\mu_{i,a}^{\ddagger}$ and $\Delta\mu_{i,c}^{\ddagger}$, of Eq. [7'] frequently are not independent of $(\mu_e)_M$ since electrons must be considered as reactants in some charge transfer steps; the exact dependence is a function of the particular charge transfer step.

In applying Eq. [7'] to cases of practical interest, several further assumptions will be made. First, it is assumed that all partial processes are under pure activation control and that each has only one rate-determining charge transfer step. Second, it will be presumed that concentrations of solution species which enter into the terms, $\pi(C_i^{p_i})_a$ and $\pi(C_i^{p_i})_c$, are approximately the same as the concentrations of the same species in the bulk of the solution. Third, a large excess of an indifferent electrolyte will be presumed present, so that the diffuse double layer potential difference (ψ) is suppressed. And fourth, it will be assumed that the electrochemical transfer coefficient ($\alpha_i\lambda_i$) of the i^{th} charge transfer step does not vary significantly over the polyelectrode surface, even though the energetics of the step may vary greatly, as from one metallic crystal face to another.[10] With these assumptions, Eq. [7'] may be modified to give:

$$i_P = \sum_i \left[Q_{i,a} I_{i,a} e^{+\frac{\alpha_{i,a}\lambda_{i,a}F}{RT}V} - Q_{i,c} I_{i,c} e^{-\frac{\alpha_{i,c}\lambda_{i,c}F}{RT}V} \right] \quad [8]$$

where

$$Q_{i,a} \equiv F\left(\frac{kT}{h}\right)\lambda_{i,a}\tau_{i,a}\pi(C_i^{p_i})_a\, e^{+\frac{\alpha_{i,a}\lambda_{i,a}F}{RT}(\Delta\phi_{\text{ref.}} - \psi)}$$

$$Q_{i,c} \equiv F\left(\frac{kT}{h}\right)\lambda_{i,c}\tau_{i,c}\pi(C_i^{p_i})_c\, e^{-\frac{\alpha_{i,c}\lambda_{i,c}F}{RT}(\Delta\phi_{\text{ref.}} - \psi)}$$

$$I_{i,a} \equiv \int_s e^{-\frac{(\Delta\mu_{i,a}^{\ddagger} - \alpha_{i,a}\lambda_{i,a}[(\mu_e)_M - (\mu_e)_{l'}])}{RT}} dS$$

$$I_{i,c} \equiv \int_s e^{-\frac{(\Delta\mu_{i,c}^{\ddagger} + \alpha_{i,c}\lambda_{i,c}[(\mu_e)_M - (\mu_e)_{l'}])}{RT}} dS$$

In Eq. 8, $Q_{i,a}$ and $Q_{i,c}$ are considered independent of dS, whereas the exponential terms under the integral signs of $I_{i,a}$ and $I_{i,c}$ are functions of dS. Remembering the approximate nature of the assumptions which led to the development of Eq. [8], it is possible to proceed with a derivation of formulas which

[10] See, however, the work of Busing and Kauzmann (18), who consider the possibility of a rather large variation of the electrochemical transfer coefficient over an electrode surface.

describe the behavior of certain of the simpler polyelectrode systems satisfying the conditions discussed above.

Rate and Potential in Simple Polyelectrode Systems

Frequently, and especially in corrosion systems, the situation is encountered where only two chemically distinct partial processes, one anodic and one cathodic, contribute a significant portion of the total current crossing an electrode-solution interphase. Such might be the case for the hydrogen-evolution-type corrosion of a metal. From Eqs. [5]-[8] it is seen that $\Delta\mu_{i,a}^{\ddagger}$ and $\Delta\mu_{i,c}^{\ddagger}$ are most important factors in determining rates of partial processes, and the effect of variations in these quantities over a polyelectrode surface is of interest. Variations in $\Delta\mu_{i,a}^{\ddagger}$ and $\Delta\mu_{i,c}^{\ddagger}$ are expected to occur on a real polyelectrode surface because of a number of well-known structural factors, e.g., the presence of impurities and lattice imperfections in the metal, the presentation of various crystal faces to the interphase, the existence of grain boundaries, etc. If Eq. [8] holds for such a system with two distinct partial processes, the measurable potential (V) for the case of no externally applied current ($i_P = 0$, "spontaneous" corrosion) is given by:[11]

$$V = \frac{RT}{(\alpha_a\lambda_a + \alpha_c\lambda_c)F}\left[\ln\left(\frac{Q_c}{Q_a}\right) + \ln\left(\frac{I_c}{I_a}\right)\right] \quad [9]$$

Equation [8] is soluble explicitly for V (for arbitrary values of $\alpha_a\lambda_a$ and $\alpha_c\lambda_c$) only for the present case where $i_P = 0$, but various workers have reported solutions for other specialized cases (19-21). The potential (V) of this simple corroding polyelectrode system is not related directly to the rates of the partial processes (except through the condition that $i_a = i_c$) but, apart from concentration terms, is a function primarily of the difference in the "activation energies" of the two partial processes, $\Delta\mu_a^{\ddagger} - \Delta\mu_c^{\ddagger}$. Thus, if $\Delta\mu_a^{\ddagger}$ and $\Delta\mu_c^{\ddagger}$ were constant over the polyelectrode surface, $\ln(I_c/I_a)$ would contain a term in $(\Delta\mu_a^{\ddagger} - \Delta\mu_c^{\ddagger})/RT$. If, in addition, both partial processes referred to the same over-all chemical reaction, Eq. [9] would reduce to the familiar Nernst equation of thermodynamics.

The corrosion current of this polyelectrode system, which is a measurable quantity, is given by:

$$i_a = i_c = Q_a^{\theta_c} Q_c^{\theta_a} I_a^{\theta_c} I_c^{\theta_a} \quad [10]$$

on substituting the result of Eq. [9] into the appropriate rate equations for i_a and i_c expressed in terms of V. Here, $\theta_a \equiv \dfrac{\alpha_a\lambda_a}{\alpha_a\lambda_a + \alpha_c\lambda_c}$ and $\theta_c \equiv \dfrac{\alpha_c\lambda_c}{\alpha_a\lambda_a + \alpha_c\lambda_c}$

The integrals, I_a and I_c, determine the effect of the variations in activation energies of the partial processes on the observable kinetics. Terms in $(\Delta\phi_{ref} - \psi)$, which appear in the definitions of Q_a and Q_c (cf. Eq. [8]), in order to relate the rates of partial processes to the measurable potential (V), cancel out in the result of Eq. [10]. The symmetry of this equation and the interdependence of the kinetic parameters of the two partial processes in determining rates is rather striking. Whereas the potential, V, was found to be a function primarily of the difference in the activation energies of anodic and cathodic processes, the corrosion current is a function primarily of the sum of the activation energies. Thus, if $\Delta\mu_a^{\ddagger}$ and $\Delta\mu_c^{\ddagger}$ were constant over the polyelectrode surface, i_a would be proportional to $e^{-\frac{(\theta_c\Delta\mu_a^{\ddagger} + \theta_a\Delta\mu_c^{\ddagger})}{RT}}$

When Eq. [9] is solved for $e^{+\frac{\alpha_a\lambda_a F}{RT}V}$ and $e^{-\frac{\alpha_c\lambda_c F}{RT}V}$ and these quantities are substituted into the appropriate form of Eq. [2], the net current density at dS (j_σ) is given by:

$$j_\sigma = Q_a^{\theta_c} Q_c^{\theta_a}\left[\left(\frac{I_c}{I_a}\right)^{\theta_a} e^{-\frac{(\Delta\mu_a^{\ddagger} - \alpha_a\lambda_a[(\mu_e)_M - (\mu_e)_{i'}])}{RT}} - \left(\frac{I_a}{I_c}\right)^{\theta_c} e^{-\frac{(\Delta\mu_c^{\ddagger} + \alpha_c\lambda_c[(\mu_e)_M - (\mu_e)_{i'}])}{RT}}\right] \quad [11]$$

This interesting relation shows that the net current density at dS is a function not only of the anodic and cathodic activation energies at dS but also of the kinetic variables over the rest of the polyelectrode surface. Depending mainly on the values of I_a, I_c, $\Delta\mu_a^{\ddagger}$, $\Delta\mu_c^{\ddagger}$, and $(\mu_e)_M$, j_σ may be either positive or negative. j_σ is the kinetic counterpart of the "local cell currents" of classical corrosion theory. For the case of a polyelectrode consisting of a metal of uniform composition, but with various crystal faces exposed to solution, $(\mu_e)_M$ and $\Delta\phi$ are expected to be constant over the electrode surface, whereas j_σ is free to follow the variations of $\Delta\mu_a^{\ddagger}$ and $\Delta\mu_c^{\ddagger}$ of Eq. [11]. Equation [11] provides a kinetic basis for a definition of "anodic" and "cathodic" areas on an electrode surface. At anodic areas, j_σ is positive, whereas at cathodic areas, j_σ is negative. In this definition no reference is made to the value of $\Delta\phi$ at anodic as compared to cathodic areas. It will become evident in the kinetic treatment of galvanic couples (to be discussed later) that, in fact, $\Delta\phi$ at anodic areas may be more positive, more negative, or the same as $\Delta\phi$ at cathodic areas. This may be seen also from Eq. [11] on replacing the term $[(\mu_e)_M - (\mu_e)_{i'}]$ by $F[\Delta\phi - (\phi_{i'} - \phi_S)]$, so that j_σ (and its variation over the surface) is not determined uniquely by $\Delta\phi$ (and its variation over the surface), but is a function of $\Delta\mu_a^{\ddagger}$, $\Delta\mu_c^{\ddagger}$, and $\Delta\phi$. Thus, there is no kinetic necessity for variations in the net current density (or the "local cell current") to follow (or to be "in phase" with) variations in $\Delta\phi$ over a polyelectrode surface.

As a corollary of Eq. [11], if the actual distribution of $\Delta\mu_a^{\ddagger}$, $\Delta\mu_c^{\ddagger}$, and $(\mu_e)_M$ were specifiable in algebraic form, so that I_a and I_c could be evaluated, the locus[12] of all elements of area on the electrode surface where $j_\sigma = 0$ could be obtained from:

$$(\Delta\mu_a^{\ddagger} - \Delta\mu_c^{\ddagger}) - (\alpha_a\lambda_a + \alpha_c\lambda_c)[(\mu_e)_M - (\mu_e)_{i'}] = RT\ln\left(\frac{I_c}{I_a}\right) \quad [12]$$

[11] Subscript i will be dropped in the presentation of equations pertaining to systems with only one anodic and one cathodic partial process.

[12] If $\Delta\mu_a^{\ddagger}$, $\Delta\mu_c^{\ddagger}$, and $(\mu_e)_M$ are expressed in Cartesian coordinates as functions of x and y, the values of these quantities at the point (x, y) will be considered as referring to those at the rectangular element of area dS, two adjacent sides of which have the lengths, $(x + dx) - x$ and $(y + dy) - y$. Hence, the coordinates of the point (x, y) are defined as the locus of the element of area, $dS = dxdy$.

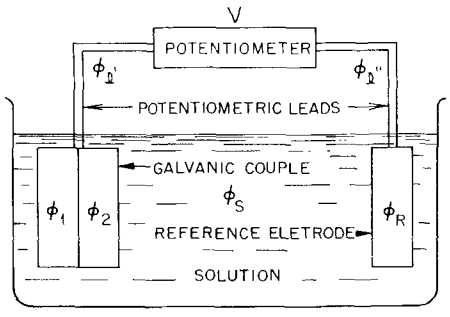

Fig. 2. Schematic diagram of typical circuit for the measurement of electrode potentials of galvanic couples.

In the more general case of externally applied current ($i_P \neq 0$), values of j_a, and thus the locus of elements of area where $j_a = 0$ (hence also the ratio of anodic to cathodic areas, defined as above), are functions of i_P. For purposes of illustration, a numerical example based on a continuous distribution of activation energies of partial processes over a polyelectrode surface is presented in the appendix to this paper.

Kinetics of Galvanic Couples under Activation Control

The kinetics of a special case of a polyelectrode system wherein two metallic electrodes may be connected together (shorted) in the same solution as a galvanic couple can be derived on the basis of propositions discussed above. An appropriate circuit for electrode potential measurements on a galvanic couple is presented in Fig. 2. Here (cf. Fig. 1), the measurable potential difference is $V_n = (\phi_{l'} - \phi_{l''}) = (\phi_{l'} - \phi_n) + (\phi_n - \phi_S) - (\phi_{l''} - \phi_R) - (\phi_R - \phi_S)$, where subscript n refers to metal 1 or metal 2. On setting $(\phi_{l'} - \phi_n) = \frac{1}{F}[(\mu_e)_{l'} - (\mu_e)_n]$ because of electronic equilibrium between one potentiometer lead (l') and the metal n, setting $(\phi_n - \phi_S) \equiv \Delta\phi_n$, and setting $(\phi_{l''} - \phi_R) + (\phi_R - \phi_S) \equiv \Delta\phi_{ref}$, it follows that $V_n = \frac{1}{F}[(\mu_e)_{l'} - (\mu_e)_n] + \Delta\phi_n - \Delta\phi_{ref.}$.

It will be assumed that only two partial processes under activation control, one anodic and one cathodic, occur at each electrode, and that all the assumptions considered in the derivation of Eqs. [9]-[12] apply here also. In addition, it is assumed that the rate constants of the partial processes are constant over the surface of each of the electrodes (although different rate constants will be assumed for each electrode). With these conventions, it is possible to derive formulas for quantities of interest for the cases in which each electrode is isolated and in which both electrodes are shorted together. The anodic (corrosion) current ($i^0_{n,a}$) and the cathodic current ($i^0_{n,c}$) of the metals in the unshorted state[13] are given by:

$$i^0_{n,a} = S_n K_{n,a} e^{+\frac{\lambda F}{2RT}\Delta\phi^0_n} \qquad [13]$$

and

$$i^0_{n,c} = S_n K_{n,c} e^{-\frac{\lambda F}{2RT}\Delta\phi^0_n} \qquad [14]$$

[13] Superscript zero refers to quantities pertaining to the unshorted electrodes, while superscript asterisk pertains to the shorted state.

Here, S_n is the area of metal 1 or metal 2, $K_{n,a}$ and $K_{n,c}$ include activation energies and concentrations of reactants,[14] and $\Delta\phi^0_n$ is the metal-solution potential difference of metal 1 or metal 2 in the unshorted state. It is assumed that the symmetry factors and the electrochemical transfer coefficients of all partial processes in the system are identical; specifically, α equals ½ and λ is common to all partial processes. Since $i^0_{n,a} = i^0_{n,c}$ for metals 1 and 2 when unshorted, it follows from Eqs. [13] and [14] that:

$$\Delta\phi^0_n = \frac{RT}{\lambda F}\ln\left(\frac{K_{n,c}}{K_{n,a}}\right) \qquad [15]$$

The measurable electrode potential (V^0_n) of the unshorted metals is given by:

$$V^0_n = \frac{1}{F}[(\mu_e)_{l'} - (\mu_e)_n] - \Delta\phi_{ref.} + \frac{RT}{\lambda F}\ln\left(\frac{K_{n,c}}{K_{n,a}}\right) \qquad [16]$$

When the result of Eq. [15] is substituted into Eqs. [13] and [14], $i^0_{n,a}$ and $i^0_{n,c}$ are given by:

$$i^0_{n,a} = i^0_{n,c} = S_n(K_{n,a}K_{n,c})^{1/2} \qquad [17]$$

From Eqs. [15] and [16], the difference in the measurable potentials of the unshorted metals is related to the difference in the interfacial potential differences or to the K's by:

$$(V_2^0 - V_1^0) = \frac{1}{F}[(\mu_e)_1 - (\mu_e)_2] + (\Delta\phi_2^0 - \Delta\phi_1^0) = \frac{1}{F}[(\mu_e)_1 - (\mu_e)_2] + \frac{RT}{\lambda F}\ln\left(\frac{K_{1,a}K_{2,c}}{K_{2,a}K_{1,c}}\right) \qquad [18]$$

It is apparent from Eq. [18] that the sign of $(V_2^0 - V_1^0)$ is not necessarily the same as the sign of $(\Delta\phi_2^0 - \Delta\phi_1^0)$ and that, in fact, measurements of $(V_2^0 - V_1^0)$ alone give no information about $(\Delta\phi_2^0 - \Delta\phi_1^0)$. If $(V_2^0 - V_1^0)$ is positive, then $(\Delta\phi_2^0 - \Delta\phi_1^0)$ may be negative provided $\frac{1}{F}[(\mu_e)_1 - (\mu_e)_2]$ is sufficiently positive. On the basis of Lange's definitions (16, 17) and on the condition that the metals be nonpolarizable, the term $[(\mu_e)_1 - (\mu_e)_2]$ depends only on the composition and structure of the two metals in contact and is independent of the environment and of the events occurring at the metal-solution interphases.

When the two electrodes are connected together, the measurable electrode potential of the resulting galvanic couple (V^*)[13] is given by:

$$V^* = V_1^* = V_2^* = \frac{RT}{\lambda F}\ln \frac{\left[S_1(K_{1,a}K_{1,c})^{1/2}e^{+\frac{\lambda F}{2RT}V_1^0} + S_2(K_{2,a}K_{2,c})^{1/2}e^{+\frac{\lambda F}{2RT}V_1^0}\right]}{\left[S_1(K_{1,a}K_{1,c})^{1/2}e^{-\frac{\lambda F}{2RT}V_1^0} + S_2(K_{2,a}K_{2,c})^{1/2}e^{-\frac{\lambda F}{2RT}V_2^0}\right]} \qquad [19]$$

[14] In terms of previously defined quantities,

$$K_{n,a} = F\left(\frac{kT}{h}\right)\lambda\tau_{na}\pi(C_i^{p_i})_{n,a}e^{-\frac{\Delta\mu^{\ddagger}_{n,a}}{RT}}e^{-\frac{\lambda F}{2RT}\psi_n}$$

and $K_{n,c} = F\left(\frac{kT}{h}\right)\lambda\tau_{nc}\pi(C_i^{p_i})_{n,c}e^{-\frac{\Delta\mu^{\ddagger}_{n,c}}{RT}}e^{+\frac{\lambda F}{2RT}\psi_n}$. $K_{n,a}$ and $K_{n,c}$ have the dimensions of current density and, from Eqs. [13] and [14], are merely the current densities of the respective partial processes when $\Delta\phi_n = 0$.

Equation [19] gives the electrode potential of a galvanic couple in terms of the electrode potentials of the unshorted metals and the currents crossing the interphases of the metals when unshorted (cf. Eq. [17]). If metals 1 and 2 were both reversible electrodes when unshorted, the terms $S_1(K_{1,a}K_{1,c})^{1/2}$ and $S_2(K_{2,a}K_{2,c})^{1/2}$ would be merely the exchange currents of the respective systems. If $S_1(K_{1,a}K_{1,c})^{1/2} > S_2(K_{2,a}K_{2,c})^{1/2}$, V^* will have a value nearer to V_1^0 than to V_2^0. In the limit, if $S_1(K_{1,a}K_{1,c})^{1/2}$ is much larger than $S_2(K_{2,a}K_{2,c})^{1/2}$, then V^* will be approximately the same as V_1^0.

The total anodic (corrosion) current or total cathodic current of both electrodes in the shorted state is given by:

$$i_a^* = i_{1,a}^* + i_{2,a}^* = i_c^* = i_{1,c}^* + i_{2,c}^* =$$

$$\left[S_1^2 K_{1,a}K_{1,c} + S_1S_2\{K_{1,a}K_{1,c}K_{2,a}K_{2,c}\}^{1/2}\left\{ e^{+\frac{\lambda F}{2RT}(V_2^0 - V_1^0)} + e^{-\frac{\lambda F}{2RT}(V_2^0 - V_1^0)} \right\} + S_2^2 K_{2,a}K_{2,c} \right]^{1/2} \quad [20]$$

In terms of $(\phi_1^* - \phi_2^*)$, the difference in the inner potentials of metals 1 and 2 in the shorted state, Eq. [20] becomes:

$$i_a^* = i_c^* = \left[S_1^2 K_{1,a}K_{1,c} + S_1S_2\left\{ K_{1,a}K_{2,c}\, e^{+\frac{\lambda F}{2RT}(\phi_1^* - \phi_2^*)} + K_{2,a}K_{1,c}\, e^{-\frac{\lambda F}{2RT}(\phi_1^* - \phi_2^*)} \right\} + S_2^2 K_{2,a}K_{2,c} \right]^{1/2} \quad [20']$$

The term $(\phi_1^* - \phi_2^*)$ of Eq. [20'] is equivalent to $(\Delta\phi_1^* - \Delta\phi_2^*)$, the difference in the interfacial potential differences of the two shorted metals. For the case that $V_1^0 = V_2^0$, no change would occur in the system on shorting the metals, and Eq. [20] reduces to $i_a^* = i_c^* = S_1(K_{1,a}K_{1,c})^{1/2} + S_2(K_{2,a}K_{2,c})^{1/2} = i_{1,a}^0 + i_{2,a}^0 = i_{1,c}^0 + i_{2,c}^0$. In the limiting case where $S_1(K_{1,a}K_{1,c})^{1/2}$ is very much greater than $S_2(K_{2,a}K_{2,c})^{1/2}$, Eq. [20] reduces to $i_a^* \cong S_1(K_{1,a}K_{1,c})^{1/2} = i_{1,a}^0$, in which case the corrosion rate of metal 1 would be scarcely changed on shorting to metal 2. The term $F(\phi_1^* - \phi_2^*)$ of Eq. [20'] may be replaced by $[(\mu_e)_1 - (\mu_e)_2]$, which is a constant depending only on the composition and structure of the two metals in contact.

In the shorted state, the net current crossing the interphase of metal 1 ($i_{1,N}^*$) is equal but of opposite sign to the net current crossing the interphase of metal 2 ($i_{2,N}^*$). These net currents are given by:

$$i_{1,N}^* = i_{1,a}^* - i_{1,c}^* = -i_{2,N}^* = i_{2,c}^* - i_{2,a}^* = \text{(see below)}$$

In terms of $(\phi_1^* - \phi_2^*)$, Eq. [21] becomes: (see [21'])

$$\frac{S_1S_2\left\{K_{1,a}K_{1,c}K_{2,a}K_{2,c}\right\}^{1/2}\left\{ e^{+\frac{\lambda F}{2RT}(V_2^0 - V_1^0)} - e^{-\frac{\lambda F}{2RT}(V_2^0 - V_1^0)} \right\}}{\left[S_1^2 K_{1,a}K_{1,c} + S_1S_2\left\{K_{1,a}K_{1,c}K_{2,a}K_{2,c}\right\}^{1/2}\left\{ e^{+\frac{\lambda F}{2RT}(V_2^0 - V_1^0)} + e^{-\frac{\lambda F}{2RT}(V_2^0 - V_1^0)} \right\} + S_2^2 K_{2,a}K_{2,c} \right]^{1/2}} \quad [21]$$

Equation [21'] shows that, for a galvanic couple, the sign of the net current $i_{1,N}^*$ (which is equivalent to the "local cell current" of classical theory) is a function of, but certainly is not uniquely determined by, the sign of $(\phi_1^* - \phi_2^*)$, or its equivalent $(\Delta\phi_1^* - \Delta\phi_2^*)$, the difference in the interfacial potential differences of the shorted metals. If $i_{1,N}^*$ is positive, $\Delta\phi_1^*$ may be more positive than $\Delta\phi_2^*$ provided the K's have appropriate values, even though V_2^0 is more positive than V_1^0. If $V_1^0 = V_2^0$, then obviously $i_{1,N}^* = -i_{2,N}^* = 0$. For the case where $S_1(K_{1,a}K_{1,c})^{1/2}$ is very much greater than $S_2(K_{2,a}K_{2,c})^{1/2}$, then from Eq. [19] metal 2 is polarized nearly to the potential of unshorted metal 1 and Eq. [21] reduces to $i_{1,N}^* \cong S_2(K_{2,a}K_{2,c})^{1/2}\left\{ e^{+\frac{\lambda F}{2RT}(V_2^0 - V_1^0)} - e^{-\frac{\lambda F}{2RT}(V_2^0 - V_1^0)} \right\}$, so that the net current here depends primarily on the current crossing the interphase of unshorted metal 2 and the difference in the unshorted potentials.

$$i_{1,N}^* = -i_{2,N}^* = \frac{S_1S_2\left\{K_{1,a}K_{2,c}\, e^{+\frac{\lambda F}{2RT}(\phi_1^* - \phi_2^*)} - K_{2,a}K_{1,c}\, e^{-\frac{\lambda F}{2RT}(\phi_1^* - \phi_2^*)}\right\}}{\left[S_1^2 K_{1,a}K_{1,c} + S_1S_2\left\{K_{1,a}K_{2,c}\, e^{+\frac{\lambda F}{2RT}(\phi_1^* - \phi_2^*)} + K_{2,a}K_{1,c}\, e^{-\frac{\lambda F}{2RT}(\phi_1^* - \phi_2^*)}\right\} + S_2^2 K_{2,a}K_{2,c} \right]^{1/2}} \quad [21']$$

From Eqs. [20] and [21], the ratio of the current flowing between the shorted metals to the total anodic (corrosion) current is given by:

$$\frac{i_{1,N}^*}{i_a^*} = -\frac{i_{2,N}^*}{i_a^*} = \frac{i_{1,N}^*}{i_c^*} = -\frac{i_{2,N}^*}{i_c^*} = \text{(see [22] below)}$$

The value of this ratio may lie anywhere between 0 and 1, depending on the values of the various kinetic parameters. A similar expression in terms of $(\phi_1^* - \phi_2^*)$ is derivable from Eqs. [20'] and [21'].

The anodic (corrosion) current of metal 1 in the shorted state is given by:

$$i_{1,a}^* = S_1(K_{1,a}K_{1,c})^{1/2} \frac{\left[S_1(K_{1,a}K_{1,c})^{1/2} + S_2(K_{2,a}K_{2,c})^{1/2} e^{+\frac{\lambda F}{2RT}(V_2^0 - V_1^0)} \right]^{1/2}}{\left[S_1(K_{1,a}K_{1,c})^{1/2} + S_2(K_{2,a}K_{2,c})^{1/2} e^{-\frac{\lambda F}{2RT}(V_2^0 - V_1^0)} \right]^{1/2}} \quad [23]$$

From Eqs. [17] and [23], the ratio of the corrosion current of shorted metal 1 to the corrosion current of the same metal in the unshorted state is:

$$\frac{S_1S_2\left\{K_{1,a}K_{1,c}K_{2,a}K_{2,c}\right\}^{1/2}\left\{ e^{+\frac{\lambda F}{2RT}(V_2^0 - V_1^0)} - e^{-\frac{\lambda F}{2RT}(V_2^0 - V_1^0)} \right\}}{\left[S_1^2 K_{1,a}K_{1,c} + S_1S_2\left\{K_{1,a}K_{1,c}K_{2,a}K_{2,c}\right\}^{1/2}\left\{ e^{+\frac{\lambda F}{2RT}(V_2^0 - V_1^0)} + e^{-\frac{\lambda F}{2RT}(V_2^0 - V_1^0)} \right\} + S_2^2 K_{2,a}K_{2,c} \right]} \quad [22]$$

$$\frac{i_{1,a}^*}{i_{1,a}^0} = \frac{\left[S_1(K_{1,a}K_{1,c})^{1/2} + S_2(K_{2,a}K_{2,c})^{1/2} e^{+\frac{\lambda F}{2RT}(V_2^0 - V_1^0)}\right]^{1/2}}{\left[S_1(K_{1,a}K_{1,c})^{1/2} + S_2(K_{2,a}K_{2,c})^{1/2} e^{-\frac{\lambda F}{2RT}(V_2^0 - V_1^0)}\right]^{1/2}} \quad [24]$$

For the limiting case where $V_2^0 >> V_1^0$, Eq. [24] becomes:

$$\frac{i_{1,a}^*}{i_{1,a}^0} \simeq \left[\frac{S_2(K_{2,a}K_{2,c})^{1/2}}{S_1(K_{1,a}K_{1,c})^{1/2}}\right]^{1/2} e^{+\frac{\lambda F}{4RT}(V_2^0 - V_1^0)} \quad [25]$$

Equation [25] shows how the corrosion current of metal 1 increases on shorting to a metal of much higher (measurable) electrode potential. For the limiting case where $V_1^0 >> V_2^0$, Eq. [24] becomes:

$$\frac{i_{2,a}^*}{i_{1,a}^0} \simeq \left[\frac{S_1(K_{1,a}K_{1,c})^{1/2}}{S_2(K_{2,a}K_{2,c})^{1/2}}\right] e^{-\frac{\lambda F}{4RT}(V_1^0 - V_2^0)} \quad [26]$$

This case corresponds to "cathodic protection" of metal 1 on shorting to another metal of much lower (measurable) electrode potential.

For the case, $V_2^0 >> V_1^0$, the corrosion current of shorted metal 1 ($i_{1,a}^*$) is found from Eq. [23] or from Eqs. [17] and [25] to be:

$$i_{1,a}^* \simeq (S_1S_2)^{1/2}(K_{1,a}K_{1,c}K_{2,a}K_{2,c})^{1/4} e^{+\frac{\lambda F}{4RT}(V_2^0 - V_1^0)} \quad [27]$$

It may be seen also from Eqs. [20] and [21] that, for this same assumption ($V_2^0 >> V_1^0$), $i_{1,a}^* \simeq i_{1,N}^* \simeq i_a^*$. That is, provided the kinetic parameters have suitable values and metal 1 is shorted to a second metal of much higher electrode potential, the corrosion current of shorted metal 1 is virtually identical to both the net current flowing from metal 1 and the total corrosion current of both electrodes. This limiting case apparently corresponds to situations which led to the development of the classical "local-cell" hypothesis of the corrosion of metals in solution. It should be noted that Eqs. [19]-[27], containing V_1^0 and V_2^0 (which are measurable quantities), also contain the factors, $S_1(K_{1,a}K_{1,c})^{1/2}$ and $S_2(K_{2,a}K_{2,c})^{1/2}$. These latter factors may be replaced by their equivalents, $i_{1,a}^0$ and $i_{2,a}^0$ (cf. Eq. [17])[15]. The quantities $i_{1,a}^0$ and $i_{2,a}^0$ (the corrosion currents of the respective metals in the unshorted state) are measurable in principle by either direct chemical or electrochemical means. Hence all these equations may be expressed in terms of measurable quantities.

The equations derived above may be considered as special cases of the more general treatment discussed earlier. In particular, appropriate forms of Eqs. [9], [10], and [11] are equivalent to Eqs. [19], [20], and [21], respectively. It should be remembered that the expressions derived in this section pertain only to one of the simplest possible cases of a galvanic couple and that drastic assumptions about the values of particular kinetic parameters were invoked in order to obtain explicit equations for the various quantities of interest. However, it is expected that systems of greater complexity will behave in a manner qualitatively similar to that predicted by the present analysis.[16,17] In this sense, it is hoped that the ideas presented will prove to be useful as a kinetic basis for interpreting studies on galvanic couples.

[15] For example, in terms of $i_{1,a}^0$ and $i_{2,a}^0$, Eq. [20] assumes the simple form: $i_a^* = \left\{(i_{1,a}^0)^2 + (i_{1,a}^0)(i_{2,a}^0)\left\{e^{+\frac{\lambda F}{2RT}(V_2^0 - V_1^0)} + e^{-\frac{\lambda F}{2RT}(V_2^0 - V_1^0)}\right\} + (i_{2,a}^0)^2\right\}^{1/2}$.

Polarizability of Polyelectrode Systems

The remainder of this paper is concerned with the interpretation of some types of steady-state measurements on polyelectrode systems under activation control. It is often convenient to perform three complementary operations on a system; these are: (*a*) polarizability measurements, (*b*) potentiostatic measurements, and (c) galvanostatic measurements. The equations presented below which describe these operations are expressed in terms of the surface average current densities of the respective partial processes, $\overline{j_i} \equiv \frac{1}{S}\int_s j_i dS$ (see Eq. [1] for definition of j_i). With this convention, and the assumptions leading to Eq. [8], the applied current of a polyelectrode system is given by $i_P = S\sum_i[\overline{j_{i,a}} - \overline{j_{i,c}}]$ and the applied current density is $j_P = \sum_i[\overline{j_{i,a}} - \overline{j_{i,c}}]$.[18]

The "polarizability" of an electrode will be defined here as the derivative of the (measurable) electrode potential, V (cf. Fig. 1), with respect to any one of the four quantities: (*a*) the applied current (i_P), (*b*) the applied current density (j_P), (c) the logarithm of the applied current, and (*d*) the logarithm of the applied current density. Differentiation of Eq. [8] for the above cases and substitution of the definitions of $\overline{j_{i,a}}$ and $\overline{j_{i,c}}$ lead to the equations:[19]

$$\left(\frac{\partial V}{\partial i_P}\right) = \frac{RT}{F}\left[S\sum_i\{\alpha_{i,a}\lambda_{i,a}\overline{j_{i,a}} + \alpha_{i,c}\lambda_{i,c}\overline{j_{i,c}}\}\right]^{-1} \quad [28]$$

$$\left(\frac{\partial V}{\partial j_P}\right) = \frac{RT}{F}\left[\sum_i\{\alpha_{i,a}\lambda_{i,a}\overline{j_{i,a}} + \alpha_{i,c}\lambda_{i,c}\overline{j_{i,c}}\}\right]^{-1} \quad [29]$$

[16] See, in this connection, the interesting analysis of Shultin (22) on the relative importance of the several factors (e.g., activation and diffusion control of partial processes and ohmic resistance of the solution) which influence the corrosion rate of a galvanic couple.

[17] The preceding analysis should hold also for the appropriate case where an active metal (two-phase system) is shorted to a passive metal (three-phase system) if all the rate-determining charge transfer steps in the passive metal system occur at the same interphase (e.g., the oxide-solution interphase).

[18] Using the nomenclature of Eq. [8] $\overline{j_{i,a}} = \frac{1}{S}Q_{i,a}I_{i,a}e^{+\frac{a_{i,a}\lambda_{i,a}F}{RT}V}$ and $\overline{j_{i,c}} = \frac{1}{S}Q_{i,c}I_{i,c}e^{-\frac{a_{i,c}\lambda_{i,c}F}{RT}V}$. The assumptions of Eq. [8] equated the current density of a charge transfer step, j_i, to the current density of the associated partial process. However, Eqs. [28]-[30], subject to the assumption that the electrochemical transfer coefficients of charge transfer steps are invariant, also describe the more general case where mechanisms of partial processes involve several charge transfer steps. In this case, $\overline{j_{i,a}}$ and $\overline{j_{i,c}}$ may be interpreted as the surface average current densities of the respective charge transfer steps.

[19] $\left(\frac{\partial V}{\partial \ln i_P}\right)$, of course, is equal to $\left(\frac{\partial V}{\partial \ln j_P}\right)$, and the electrode area, S, cancels out in the derivation of Eq. [30].

$$\left(\frac{\partial V}{\partial \ln i_P}\right) = \left(\frac{\partial V}{\partial \ln j_P}\right) = \frac{RT}{F} \frac{\sum_i [\overline{j_{i,a}} - \overline{j_{i,c}}]}{[\sum_i \{\alpha_{i,a}\lambda_{i,a}\overline{j_{i,a}} + \alpha_{i,c}\lambda_{i,c}\overline{j_{i,c}}\}]} \quad [30]$$

Polarizability measurements usually find importance in the determination of the rates and the electrochemical transfer coefficients ($\alpha_i\lambda_i$) of partial processes. If, in some range of electrode potentials, the rate of one partial process ($\overline{j_x}$) greatly exceeds those of all other processes occurring at the same interphase, Eq. [30] reduces to:

$$\left|\left(\frac{\partial V}{\partial \ln j_P}\right)\right| = \frac{RT}{F} \cdot \frac{1}{\alpha_x\lambda_x} \quad [31]$$

Equation [31] is just the differential form of the well-known Tafel relation. Generally, however, for systems with several partial processes of comparable rates, there may exist no accessible range of electrode potentials where the rate of one process predominates, so that the more general relationship, Eq. [30], must be used.

A relationship between the polarizability of a corroding polyelectrode and its corrosion rate, $\overline{j_{corr}}$, at the steady-state corrosion potential ($V_{corr.}$) is derivable from Eq. [29]. If it is assumed that all anodic processes are corrosion processes, and ξ_a and ξ_c are dimensionless constants such that $\sum_i \alpha_{i,a}\lambda_{i,a}\overline{j_{i,a}} \equiv \xi_a \cdot \sum_i \overline{j_{i,a}}$ and $\sum_i \alpha_{i,c}\lambda_{i,c}\overline{j_{i,c}} \equiv \xi_c \cdot \sum_i \overline{j_{i,c}}$, then, on recognizing that $\overline{j_{corr.}} = \sum_i \overline{j_{i,a}} = \sum_i \overline{j_{i,c}}$ at V_{corr}, Eq. [29] can be rearranged to give:[20]

$$\overline{j_{corr.}} = \frac{RT}{F} \cdot \frac{1}{(\xi_a + \xi_c)} \cdot \frac{1}{\left(\frac{\partial V}{\partial j_P}\right)_{V_{corr.}}} \quad [32]$$

Here, the term $(\xi_a + \xi_c)$ has a value which is of the order of magnitude of unity for corroding polyelectrodes under activation control. For a simple polyelectrode system having only one anodic and one cathodic partial process, $(\xi_a + \xi_c) = (\alpha_a\lambda_a + \alpha_c\lambda_c)$. The exact value of $(\xi_a + \xi_c)$ is a function of the particular system, depending both on the identity of the metal and on the composition of the solution. Equation [32] may be used to estimate corrosion rates from polarizability measurements to an accuracy of a small numerical factor for corroding polyelectrode systems under activation control. Alternatively, in studying relative corrosion rates of a series of alloys of similar compositions, it may be possible to determine the factor $\frac{RT}{F} \cdot \frac{1}{(\xi_a + \xi_c)}$ experimentally and to use the resulting value in Eq. [32] to estimate corrosion rates for the series in a constant environment.[21]

Potentiostatic Measurements on Polyelectrode Systems

This section and the following one are concerned with the information obtainable from electrical measurements on polyelectrode systems when the concentration of one of the reactants in the system can be varied. One of the important parameters of electrochemical kinetics is the kinetic order (p_x) of a partial process with respect to the concentration of one of its reactants (C_x).[22] For a situation in which V is held constant while the concentration of one of the reactants (C_x) in the system is varied, it can be shown from Eq. [8] that p_x is given by:

$$\left(\frac{\partial \ln |\, i_P - i_{P,0}\,|}{\partial \ln C_x}\right)_V = p_x \quad [33]$$

Here, i_P is the current applied to the polyelectrode which is necessary to maintain the (measurable) electrode potential (V) constant in the presence of some amount, C_x, of the reactant under study. $i_{P,0}$ is the applied current at the same potential before additions of x (or for a known amount of x already present). Precautions are necessary that additions of x do not change appreciably the ionic strength of the solution or the structure of the double layer at constant V; i.e., experiments should be performed in an excess of an inert electrolyte. The procedure embodied in Eq. [33] is equivalent to the method of isolation long used to determine reaction orders in ordinary chemical kinetics.

An assumption implicit in Eq. [33] is that electrode processes other than x proceed independently of C_x, at constant V. It is in providing an experimental test of this assumption that potentiostatic experiments find considerable value. Plots of $\ln |\, i_P - i_{P,0}\,|$ vs. $\ln C_x$ can exhibit linearity only if $i_{P,0}$ is independent of C_x; i.e., linearity will be obtained if the processes initially present in the system proceed with unchanged rates regardless of the value of C_x. Nonlinearity of the plots does not necessarily obviate the model for a given electrode system but may merely indicate that new paths are being provided for the reactions initially present in the system on the introduction of x.[23] A series of potentiostatic experiments conducted at various potentials yields a spectrum of relations among V, C_x, and $\overline{i_x}(\equiv |\, i_P - i_{P,0}\,|)$. These data lead immediately to the same information ($\alpha_x\lambda_x$ and $\overline{i_x}$ as a function of V) obtainable from the usual procedure of direct analysis of the rates of partial processes and use of the Tafel relation, Eq. [31].[24]

[20] An expression similar to Eq. [32] has also been derived by Stern (23) for the case of a simple corroding polyelectrode with one anodic and one cathodic partial process

[21] An inverse relationship between corrosion rate and polarizability at V_{corr} was noted by Bonhoeffer and Jena (24), Simmons (25), and Skold and Larson (26). The data of Bonhoeffer and Jena on the corrosion of iron and carbon steels in acid environments are described well by Eq. [32]. The systems studied by Skold and Larson apparently were not under pure activation control (and probably were not simple two-phase systems), and Eq. [32] describes their data only qualitatively.

[22] Subscript x will be used in this section and the following one to denote both the reactant and the partial process in which it participates. C_x and p_x are as defined in the discussion of Eq. [1].

[23] Conceivably the situation may arise where more than one new partial process is encountered on additions of x (e.g., x may react by alternative paths of comparable rates). In this case, Eq. [33] will contain additional terms (as can be verified by solving Eq. [8] for such a situation) which may cause plots of $\ln|i_P - i_{P,0}|$ vs. $\ln C_x$ to consist of two (or perhaps more) linear portions, if the new, alternative paths possess different orders (p_x) with respect to C_x. If, in addition, the alternative paths possess different electrochemical transfer coefficients ($\alpha_x\lambda_x$), the projection of the point(s) of intersection of the linear portions of these plots on the concentration axis will vary with V, the potential chosen for observation.

[24] Equation [33] holds also in the event that the reaction of x proceeds by alternative and/or consecutive charge transfer steps (if each step has the same value of p_x). However, two (or perhaps more) linear portions in the Tafel-type plot of V vs. $\ln \overline{i_x}$ (at constant C_x) may then be obtained, and for this case the observed value of $\frac{F}{RT}\left|\left(\frac{\partial V}{\partial \ln \overline{i_x}}\right)\right|$ on any one linear portion may not equal the electrochemical transfer coefficient ($\alpha_x\lambda_x$) of a single step in the partial process (cf. Eq. [31]) but may be a function of the values of the electrochemical transfer coefficients of two (or more) charge transfer steps of the partial process, as has been demonstrated by workers in the field of hydrogen overvoltage.

Galvanostatic Measurements on Polyelectrode Systems

It is known that the addition of oxidizable or reducible substances to polyelectrode systems affects the electrode potential. It has been found in some cases (27, 28) that the electrode potential of a corrosion system increases linearly with the logarithm of the concentration of the added (reducible) constituent, at least at higher concentrations. This behavior is predictable for polyelectrode systems under activation control. Let the current density applied to a polyelectrode be given by the expression, $j_P = \sum_i \bar{j}_{i,a} - \sum_i \bar{j}_{i,c} \pm \bar{j}_x$, where $\bar{j}_x$ is the (surface average) current density of the added constituent[18,22] and plus or minus signs denote an anodic or cathodic partial process, respectively. Then the slope of the relationship between V and $\ln C_x$ at constant applied current density (j_P) is given by:

$$\left(\frac{\partial V}{\partial \ln C_x}\right)_{j_P} = \pm\frac{RT}{F}\left[\frac{\bar{p}_x \bar{j}_x}{\sum_i\{\alpha_{i,a}\lambda_{i,a}\bar{j}_{i,a} + \alpha_{i,c}\lambda_{i,c}\bar{j}_{i,c}\} + \alpha_x\lambda_x\bar{j}_x}\right] \quad [34]$$

Here, the minus or plus sign is employed according to whether the additional partial process is anodic or cathodic, respectively. Generally, the magnitude of the slope, $\left(\frac{\partial V}{\partial \ln C_x}\right)_{j_P}$, is a function of C_x, but for certain important special cases, it may be a constant; some of these special cases are noted below.

Consider the case of a simple polyelectrode system having only one anodic and one cathodic partial process, but in which a third cathodic process is introduced by the addition of a reducible constituent (x). Equation [34] then becomes:

$$\left(\frac{\partial V}{\partial \ln C_x}\right)_{j_P} = \frac{RT}{F}\left[\frac{p_x\bar{j}_x}{\alpha_a\lambda_a\bar{j}_a + \alpha_c\lambda_c\bar{j}_c + \alpha_x\lambda_x\bar{j}_x}\right] \quad [35]$$

As C_x is increased, $\bar{j}_x$ may become much larger than $\bar{j}_c$, so that j_P is given approximately by $j_P \simeq \bar{j}_a - \bar{j}_x$, and Eq. [35] becomes:

$$\left(\frac{\partial V}{\partial \ln C_x}\right)_{j_P} \simeq \frac{RT}{F} p_x\left[\alpha_x\lambda_x + \alpha_a\lambda_a\left(1 + \frac{j_P}{\bar{j}_x}\right)\right]^{-1} \quad [36]$$

It can be seen from Eq. [36] that, for zero applied current, $\left(\frac{\partial V}{\partial \ln C_x}\right)_{j_P=0}$ is independent of C_x when $\bar{j}_x >> \bar{j}_c$ and is a function only of $\alpha_a\lambda_a$, $\alpha_x\lambda_x$, and p_x. However, both $\alpha_x\lambda_x$ and p_x are obtainable from a series of potentiostatic measurements, as noted in the previous section. Hence, the electrochemical transfer coefficient of the anodic partial process ($\alpha_a\lambda_a$) is calculable from Eq. [36] and potentiostatic data on the same system. If the applied current is large and negative ($j_P << 0$), for the case $\bar{j}_x >> \bar{j}_c$, then $\bar{j}_P \simeq -\bar{j}_x$, and Eq. [36] becomes:

$$\left(\frac{\partial V}{\partial \ln C_x}\right)_{j_P} \simeq \frac{RT}{F}\cdot\frac{p_x}{\alpha_x\lambda_x} \quad [37]$$

Under these conditions, the galvanostatic measurements can provide a check on the results of potentiostatic measurements on the same system.

The preceding kinetic analysis has been limited to two-phase polyelectrode systems in a steady state having partial processes under pure activation control. As such, it obviously is not applicable quantitatively to every polyelectrode system or galvanic couple which may be encountered in the laboratory, since no account has been taken of the influence of diffusion or other situation of mixed rate control of partial processes. It can be expected to serve as a starting point for the treatment of systems of greater complexity, however, and as a kinetic basis for the qualitative interpretation of observations on corrosion systems. The results of an experimental investigation on a particular corroding polyelectrode system, using the theory and techniques outlined here, will be presented in a subsequent report.

APPENDIX I

Numerical Example of Polyelectrode with Continuous Distribution of Partial Process Activation Energies

Consider the case of a two-phase simple polyelectrode system with one anodic and one cathodic partial process. For the particular case that $\alpha_a\lambda_a = \alpha_c\lambda_c = \alpha\lambda$, explicit expressions are derivable from Eq. [8] for various quantities of interest as a function of the applied current (i_P). These are given by the equations below in which the function, Z, appears. Z takes account of the influence of the integrals, I_a and I_c, and of the applied current on the system, and the use of Z leads to simple forms of the equations for the various quantities of interest. The electrode potential of the system may be derived from Eq. [8] as:[25]

$$V = \frac{RT}{\alpha\lambda F}\ln Z$$

where

$$Z \equiv \left(\frac{i_P + \sqrt{i_P^2 + 4Q_aQ_cI_aI_c}}{2Q_aI_a}\right) \quad [38]$$

The total anodic and cathodic currents in the system are given as a function of Z and thus of i_P by:

$$i_a = Q_aI_aZ \quad [39]$$

$$i_c = \frac{Q_cI_c}{Z} \quad [40]$$

The net current density at dS (j_σ) is given by:

$$j_\sigma = Q_aZ\,e^{-\frac{A_a}{RT}} - \frac{Q_c}{Z}e^{-\frac{A_c}{RT}} \quad [41]$$

where A_a and A_c are given in the nomenclature of Eq. [8] by $A_a \equiv \Delta\mu_a^\ddagger - \alpha\lambda[(\mu_e)_M - (\mu_e)_{i'}]$ and $A_c \equiv \Delta\mu_c^\ddagger + \alpha\lambda[(\mu_e)_M - (\mu_e)_{i'}]$, so that $I_a \equiv \int_s e^{-\frac{A_a}{RT}}\,dS$ and $I_c \equiv \int_s e^{-\frac{A_c}{RT}}\,dS$. Finally, the equation of the locus of elements of area on the electrode surface[12] where $j_\sigma = 0$ follows from Eq. [41] as:

$$A_a - A_c = RT\ln\left(\frac{Q_a}{Q_c}Z^2\right) \quad [42]$$

[25] The minus sign is omitted before the square root symbol in the function, Z, of Eq. [38] since $Z = e^{\frac{\alpha\lambda F}{RT}V}$ must be a positive quantity for all values of V.

Table I. Certain quantities pertaining to numerical example

i_P (applied current), amp	V, v	i_a (corrosion current), amp	$i(+) \equiv \int_S j_\sigma(+)dS$, amp	$\frac{i_a}{i(+)}$	Locus where $j_\sigma = 0$, cm
$+6 \times 10^{-3}$	+0.307	6.72×10^{-3}	6.00×10^{-3}	1.12	—
$+1 \times 10^{-3}$	+0.261	2.75×10^{-3}	1.45×10^{-3}	1.90	0.504
±0.00	+0.249	2.20×10^{-3}	8.09×10^{-4}	2.71	0.371
-1×10^{-3}	+0.237	1.75×10^{-3}	3.47×10^{-4}	5.05	0.237
-3×10^{-3}	+0.216	1.16×10^{-3}	0	$+\infty$	—

When $i_P = 0$, Eqs. [38]-[42] become the appropriate cases of Eqs. [9]-[12], respectively.

In the construction of the present model, $\alpha = \frac{1}{2}$, $\lambda = 1$, $T = 25°C$, $Q_a = Q_c = 6 \times 10^{17}$ (amp/cm²), and the electrode area (S) is 1 cm². A_c is taken to be constant over the electrode surface and equal to 25 kcal/mole. It is assumed that A_a is of the form, $A_a = A_{a,0} + B_a \cdot x$, where $A_{a,0} = 30$ kcal/mole, $B_a = 2$ kcal/mole-cm, and x is one of the coordinates of the set (x, y) which describe the locus of elements of area on the electrode surface ($0 \leqq x \leqq 1; 0 \leqq y \leqq 1$). A_a thus varies linearly from 30 kcal/mole at $x = 0$ to 32 kcal/mole at $x = 1$ cm. From the previous information and Eqs. [38]-[42], it is possible to calculate the properties of this simple polyelectrode system.

Table I lists the values of some of these quantities as a function of the applied current. Figure 3 shows the rather enormous variation of j_σ over the electrode surface as a function of the applied current. The fourth column of Table I lists values of $i(+)$, the net positive current flowing from the electrode, obtained by integration of j_σ over that region of the electrode where it has positive values. When $i_P = 0$, it is noteworthy that the total corrosion current of the electrode (i_a) is about a factor of three greater than would have been estimated from $i(+)$, the current flowing between anodic and cathodic areas (as defined by Eq. [11]). Column six of Table I shows how the "boundary" between anodic and cathodic areas on the electrode varies with applied current; for large positive applied currents, no cathodic areas exist on the surface, while for large negative applied currents, no anodic areas exist. Because of the 1 cm² area of the electrode, the values recorded in column six are also equal to the fraction of the surface area which is anodic. The relatively large variation of j_σ over the surface corresponds to a variation in A_a of only 6-7%, so that the importance of variations in the activation energies of partial processes over the surface of a polyelectrode is evident.

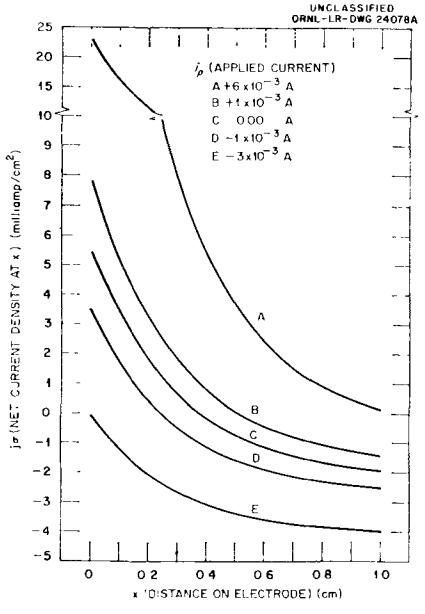

Fig. 3. Plot of j_σ vs. position on electrode surface for model of numerical example (see Appendix I for description of model).

APPENDIX II

List of Frequently Used Symbols

j_i = current density of i^{th} charge transfer step at element of area, dS, on polyelectrode surface.

λ_i = number of charges transferred across interphase during i^{th} charge transfer step.

$\overline{k_i}$ = electrochemical specific rate constant of i^{th} charge transfer step.

$\pi(C_i^{p_i})_a, \pi(C_i^{p_i})_c$ = product of reactant concentrations raised to appropriate kinetic orders for anodic and cathodic charge transfer steps.

j_σ = net current density at element of area, dS.

i_P = current applied to polyelectrode from external source.

τ_i = equal to transmission coefficient of i^{th} charge transfer step (κ_i) times product of activity coefficients of reactants raised to appropriate kinetic orders ($\pi(\gamma_i^{p_i})$) divided by activity coefficient of activated complex ($\gamma_i^{\ddagger}$).

$\Delta\mu_i^{\ddagger}$ = "activation energy"; change in chemical potential of polyelectrode system required for formation of one mole of activated complex from reactants for i^{th} charge transfer step.

$\Delta\phi$ = interfacial inner potential difference at dS, between metallic volume element dv at polyelectrode surface and outermost portion of diffuse double layer in solution ($\Delta\phi = \Delta\phi_H + \psi$).

$\Delta\phi_H$ = inner potential difference across Helmholtz double layer at dS.

ψ = inner potential difference across diffuse double layer at dS.

α_i = symmetry factor of i^{th} charge transfer step.

$\phi_{l'}, \phi_{l''}$ = inner potentials of potentiometer leads, l' and l'' (cf. Fig. 1).

V = measurable cell or electrode potential; $V = \phi_{l'} - \phi_{l''}$.

ϕ_M, ϕ_R, ϕ_S = inner potentials of metallic volume element, dv, on polyelectrode surface, of reference electrode, and of solution, respectively.

$(\mu_e)_M, (\mu_e)_{l'}$ = chemical potentials of electrons in metallic volume element, dv, on polyelectrode surface and in potentiometer lead, l', respectively.

$\Delta\phi_{ref}$ = equal to $(\phi_{l''} - \phi_R) + (\phi_R - \phi_S)$.

$Q_{i,a}, Q_{i,c}$ = contain decomposition frequency of activated complexes, concentrations of reactants, reference electrode potential ($\Delta\phi_{ref.}$), and other quantities presumed independent of dS; defined in Eq. [8].

$I_{i,a}, I_{i,c}$ = exponential integrals containing chemical potentials (which may vary over polyelectrode surface); defined in Eq. [8].

i_a, i_c = total anodic (corrosion) current and total cathodic current of polyelectrode.

$\theta_a, \theta_c =$ equal to $\frac{\alpha_a\lambda_a}{\alpha_a\lambda_a + \alpha_c\lambda_c}$ and $\frac{\alpha_c\lambda_c}{\alpha_a\lambda_a + \alpha_c\lambda_c}$; occur in treatment of simple polyelectrode system.

$V_1^0, V_2^0 =$ measurable electrode potentials of metals 1 and 2 (cf. Fig. 2) when disconnected from each other; occur in treatment of simple galvanic couple.

$\Delta\phi_1^0, \Delta\phi_2^0 =$ netal-solution potential differences of metals 1 and 2 when disconnected.

$i_{1,a}^0 = i_{1,c}^0, i_{2,a}^0 = i_{2,c}^0 =$ anodic and cathodic currents of metals 1 and 2 when unshorted.

$S_1, S_2 =$ areas of metals 1 and 2 of simple galvanic couple.

$K_{1,a}, K_{1,c}, K_{2,a}, K_{2,c} =$ include activation energies and concentrations of reactants for anodic and cathodic partial processes on metals 1 and 2 of galvanic couple; defined in footnote 14.

$(\mu_e)_1, (\mu_e)_2 =$ chemical potentials of electrons in metals 1 and 2 of galvanic couple.

$V^* = V_1^* = V_2^* =$ measurable electrode potential of galvanic couple formed by shorting metals 1 and 2.

$i_a^* = i_c^* =$ total anodic (corrosion) and cathodic currents of galvanic couple.

$\phi_1^*, \phi_2^* =$ inner potentials of metals 1 and 2 when shorted as a galvanic couple.

$i_{1,N}^* = -i_{2,N}^* =$ net currents from metals 1 and 2 when shorted as a galvanic couple.

$i_{1,a}^*, i_{1,c}^*, i_{2,a}^*, i_{2,c}^* =$ anodic and cathodic currents of metals 1 and 2 when shorted as a galvanic couple.

$\bar{j}_{i,a}, \bar{j}_{i,c} =$ surface average current densities of anodic and cathodic partial processes.

$\bar{j}_{corr.} =$ corrosion current density of polyelectrode (surface average).

$V_{corr.} =$ steady-state (measurable) electrode potential of corroding polyelectrode with no externally applied current.

$Z =$ function taking account of effect of i_P, I_a, and I_c on properties of simple polyelectrode system; defined in Eq. [38] of Numerical Example.

$A_a, A_c =$ functions of activation energies of anodic and cathodic partial processes of Numerical Example.

Acknowledgment

The author wishes to express his appreciation to Dr. G. H. Cartledge, Dr. R. E. Meyer, and Dr. A. L. Bacarella, all of this Laboratory, for their kind encouragement in the present endeavor.

Manuscript received Jan. 16, 1958.

Any discussion of this paper will appear in a Discussion Section to be published in the June 1960 JOURNAL.

REFERENCES

1. J. A. V. Butler, *Trans. Faraday Soc.*, **19**, 734 (1924).
2. F. P. Bowden and E. K. Rideal, *Proc. Roy. Soc., London*, **A120**, 59, 80 (1928).
3. T. Erdey-Gruz and M. Volmer, *Z. physik. Chem.*, **A150**, 203 (1930); **A157**, 165 (1931).
4. J. O'M. Bockris, "Modern Aspects of Electrochemistry," pp. 180 ff., Butterworths, London (1954).
5. K. J. Vetter, *Z. Elektrochem.*, **59**, 596 (1955).
6. H. Gerischer, *ibid.*, **59**, 604 (1955).
7. K. J. Vetter, *Z. physik. Chem.*, **A194**, 284 (1950); **A199**, 300 (1952).
8. J. V. Petrocelli, *This Journal*, **98**, 187, 291 (1951).
9. R. Parsons, *Trans. Faraday Soc.*, **47**, 1332 (1951).
10. C. Wagner and W. Traud, *Z. Elektrochem.*, **44**, 391 (1938).
11. G. E. Kimball, *J. Chem. Phys.*, **8**, 199 (1940).
12. R. Audubert, *J. chim. Phys.*, **49**, C97 (1952).
13. R. Parsons and J. O'M. Bockris, *Trans. Faraday Soc.*, **47**, 914 (1951).
14. S. Glasstone, K. J. Laidler, and H. Eyring, "The Theory of Rate Processes," McGraw-Hill Book Co., New York (1941).
15. J. O. Hirschfelder and E. Wigner, *J. Chem. Phys.*, **7**, 616 (1939).
16. E. Lange and K. P. Miscenko, *Z. physik. Chem.*, **A149**, 1 (1930).
17. E. Lange, *Z. Elektrochem.*, **55**, 76 (1951).
18. W. R. Busing and W. Kauzmann, *J. Chem. Phys.*, **20**, 1129 (1952).
19. E. Lange and K. Nagel, *Z. Elektrochem.*, **53**, 21 (1949).
20. R. Audubert, *J. chim. Phys.*, **49**, C97, C106 (1952).
21. J. O'M. Bockris, "Modern Aspects of Electrochemistry," p. 253, Butterworths, London, 1954.
22. A. I. Shultin, *J. Appl. Chem. U.S.S.R.*, **29**, 241 (1956).
23. M. Stern and A. L. Geary, *This Journal*, **104**, 56 (1957).
24. K. F. Bonhoeffer and W. Jena, *Z. Elektrochem.*, **55**, 151 (1951).
25. E. J. Simmons, *Corrosion*, **11**, 255t (1955).
26. R. V. Skold and T. E. Larson, *Corrosion*, **13**, 139t (1957).
27. G. H. Cartledge and R. P. Yaffe, "Chem. Semiann. Prog. Rep. June 20, 1953," ORNL-1587, p. 13.
28. G. H. Cartledge and R. P. Yaffe, "Chem. Semiann. Prog. Rep. December 20, 1953," ORNL-1674, p. 11.

Kinetic Studies on Corrosion Systems

II. The Reduction of Cupric Ion on Passive Stainless Steel Electrodes

Franz A. Posey, G. H. Cartledge, and R. P. Yaffe[1]

Oak Ridge National Laboratory, Oak Ridge, Tennessee[2]

ABSTRACT

The reduction of cupric ion on the surface of passive stainless steel electrodes in aerated, dilute sulfuric acid medium has been investigated using potentiostatic, galvanostatic, and tracer techniques. The independent simultaneity of the electrode reactions has been demonstrated. A mechanism is advanced for the reduction of cupric ion on the oxide surface. The data are interpreted on the basis of electrochemical kinetics.

The first paper in this series (1) (hereinafter referred to as I) treated two-phase polyelectrode systems under activation control, including corrosion systems, on the basis of electrochemical kinetics. It was shown in I that the results of steady-state potentiostatic and galvanostatic measurements can be interpreted in terms of the rates, the kinetic reaction orders, and the electrochemical transfer coefficients of the individual partial processes proceeding at the metal-solution interphase of a polyelectrode system under activation control. The present report deals with the results of some measurements of these types on a real corroding polyelectrode system. Specifically, the effect of additions of cupric ion to solution on the electrode potential and the rates of the partial processes of the system, passive stainless steel in aerated, dilute sulfuric acid solution, has been examined and compared with theoretical expectations.

The effect of additions of oxidizable and reducible substances to solution on electrode potentials and corrosion rates of metals has been studied by several workers in recent years (2-9). Numerous exploratory experiments, performed in this laboratory, have been concerned with the effect of additions of reducible ions (and some uncharged species) on the electrode potential of passive stainless steel in dilute sulfuric acid solution (3, 4, 9). A summary of these results is presented in Table I. Here the addition slope, $\left(\frac{\partial V}{\partial \log C_x}\right)$, refers to the slope of the linear portion of plots of the stainless steel electrode potential (for zero applied current) against the logarithm of the additive concentration for those ions causing significant potential changes (> 40-50 mv for concentrations up to about 10^{-3} M) and for which the linear $V - \log C_x$ relation holds (cf. Part A). Part B lists ions of "noble" metals which, even at low concentrations ($10^{-7} - 10^{-6}M$), cause large changes in electrode potential. However, in this concentration region, it appears that steady states are not attained with the ions of Part B. Electrode potentials may increase with time for long periods, and the observations suggest that the specific rate constants of one or more partial processes change markedly with time. The reduction rates of ions in Part B are large (much larger than the reduction rates of ions in Part A) and at higher concentrations ($10^{-5} - 10^{-4}M$) it appears that a metallic phase is soon produced on the electrode surface. Following the appearance of a metallic phase, potentials no longer

Table I. Summary of the effect of additions of various ions to solution on the electrode potential of passive stainless steel in aerated, 0.10N H_2SO_4 at 85°C*

A. List of ions (and uncharged species) which cause significant potential changes and for which linear plots of electrode potential vs. logarithm of additive concentration are obtained.

Added group	Addition slope, $\left(\frac{\partial V}{\partial \log C_x}\right)$ (V)	Number of experiments averaged
BrO_3^-	0.072	1
Cu^{++}	0.051 ± 0.004	12
Fe^{+++}	0.104 ± 0.012	9
$HCrO_4^-$	0.098 ± 0.008	10
H_2O_2	0.139 ± 0.005	4
IO_3^-	0.080	1
IO_4^-	0.160 ± 0.005	2
OsO_4	0.137 ± 0.003	3
$S_2O_8^=$	0.035	1

B. List of ions which cause significant potential changes but for which, at low concentrations, steady states are not attained and which, at high concentrations, produce a metallic phase on the electrode surface:
Ag^+, Au^{+++}, Hg_2^{++}, Hg^{++}, Pd^{++}, $PtCl_6^=$

C. List of ions which cause slight potential changes:
La^{+++}, Sn^{++}, UO_2^{++}, Zr^{++}, Zn^{+2}

D. List of ions for which no appreciable effect is detected:
AsO_4^{-3}, BiO^+, Ca^{++}, Cd^{++}, Ce^{+3}, Cr^{+3}, Cl^- (caused loss of passivity at high concentrations), ClO_3^-, ClO_4^-, F^-, $Co(NH_3)_6^{+3}$, I^-, Mn^{++}, Na^+, Ni^{++}, NO_3^-, PO_4^{-3}, ReO_4^-, Tl^+, TcO_4^-

* Medium: 150-400 ml of 0.10N H_2SO_4 at 85°C stirred at ca. 600 rpm; pO_2 = 0.2 atm. Electrodes: flag-shaped type 347 stainless steel sheet electrodes (abraded surface) of 2-4 cm^2 geometrical area, stems lacquered with baked G. E. Glyptal. Initial electrode potentials, before additions, occupied region + (100-200) mv vs. S.C.E. at 25°C and were sensibly constant (±3 mv/hr). 2.303 RT/F at 85°C = 0.071 v.

[1] Present address, Department of Chemistry, San Jose State College, San Jose, Calif.

[2] Operated by Union Carbide Corporation for the U. S. Atomic Energy Commission.

change with time, steady states are attained rapidly, and the addition slopes, as well as the potentials, correspond closely to those expected for equilibrium between oxidized and reduced (metallic) forms of the additives. Part C lists ions which cause very slight potential changes (< 10-20 mv for concentrations up to about $10^{-3}M$) and, finally, Part D lists those ions which cause no detectable change in stainless steel electrode potential.

In order to inquire further into the significance of the addition slopes, one of these systems was chosen for more detailed examination by the methods outlined in I. The effect of additions of cupric ions to the chosen stainless steel electrode system was studied potentiostatically at a number of potentials in the passive region. From the resulting information the kinetic order of the reduction reaction with respect to the concentration of cupric ions was determined as well as the (electrode potential)-(current density) relationship for the reduction of Cu^{++} as a function of concentration. In addition, the independent simultaneity of the electrode processes was demonstrated. The results of galvanostatic experiments, together with the results of the potentiostatic experiments, permitted a calculation of the (electrode potential)-(current density) relationships for the anodic oxidation reaction of passive stainless steel and for the cathodic reduction reaction of oxygen dissolved in solution, these being the interphase reactions present in the system before additions of Cu^{++}. Tracer experiments were performed with labelled cupric sulfate (using isotope of atomic weight 64) which yielded information of interpretive value. The results of these experiments are reported below and analyzed on the basis of an electrochemical kinetic model.

Experimental

The experimental vessel was a five-necked spherical reaction flask of 500-ml capacity fitted with a short, vertical condenser to which was attached a mercury-seal stirrer operated by a Bodine motor (type KYC-23) with a step-up gear at 600 rpm. Standard taper (24/40) entry ports provided space for a thermometer, the entry of air, an auxiliary platinum polarizing electrode, and for the insertion of a stainless steel electrode. A vigorous supply of air was effused into the solution through a sintered glass disk. Standard taper joints and glass apparatus were used throughout the experimental assembly. Temperature was controlled by means of a Glascol heating mantle operated from a Variac supplied with regulated a.c. The constancy of the ambient temperature permitted control of the solution temperature by this means from room temperature up to the boiling point to within $\pm 0.5°C$. The efficiency of the condenser was such that no significant change in solution volume occurred for many hours, even at temperatures close to the boiling point.

Measurements of electrode potentials were performed using a L&N *p*H Indicator (No. 7664) as a potentiometer coupled with a Brown recorder. The input impedance of this instrument is very large compared to the polarizability of stainless steel electrodes under almost any conditions. Potentials were measured and recorded with time by the direct method, using a Luggin capillary bridged (with $0.10N$ H_2SO_4) to a Ag/Ag_2SO_4 (sat'd. in $0.10N$ H_2SO_4) reference electrode maintained at room temperature. Currents were measured with time by recording the voltage drop across precision resistors in the polarizing circuit. Current-interrupter and other incidental studies proved ohmic potential drops in solution between the stainless steel electrode and the tip of the reference electrode capillary to be negligible even at the highest externally applied currents employed. External polarizing current was provided through high resistances by means of high voltages supplied by an Oregon Electronics Variable Voltage Regulated Power Supply (model A3A).

Experiments were performed using abraded[3] electrodes of 4 cm^2 geometrical surface area prepared from a type 347, Ta-stabilized stainless steel sheet of 20 ml thickness. Stainless steel electrodes were attached to a stainless steel rod lead and all portions of the rod, the junction of the rod with the electrode, and a part of the electrode (except 4 cm^2) were covered with an insulating coat of G.E. Glyptal Clear Baking Varnish No. 1202 which was baked at 110°C to a tough, acid-resistant finish. Electrodes were allowed to passivate for many hours in the environment, 400 ml of aerated, $0.10N$ H_2SO_4 (prepared from redistilled water) at 85°C, until constancy (± 3 mv/hr) of electrode potential was observed. The choice of the experimental temperature, 85°C, rested on the fact that steady states are attained very much more readily here than at room temperature as a consequence of the higher rates of the partial processes at the higher temperature.

In the potentiostatic experiments, following the attainment of a steady-state potential, the electrode potential was maintained constant ($\pm$ 1 mv) at any desired value with an electromechanical potentiostat (10) or with a sensitive manual device. Additions of aliquots of a concentrated stock solution of $CuSO_4 \cdot 5H_2O$ in $0.10N$ H_2SO_4 were made to the solution by micropipettes and the externally applied current necessary to maintain the chosen potential constant was recorded with time. In the galvanostatic experiments, a similar procedure was followed except that the electrode potential was recorded continuously with time at constant externally applied current.

For the tracer experiments, previously irradiated[4] $CuSO_4 \cdot 5H_2O$ was dissolved in $0.10N$ H_2SO_4 to form a stock solution, and aliquots of this were added to the stainless steel electrode system. In these experiments, eight stainless steel electrodes, each of 2 cm^2 area and prepared as above, were present in the dilute acid environment. Electrodes were removed periodically from solution at various cupric ion con-

[3] Abrasion as a method of electrode surface preparation is subject to obvious objections from the standpoint of distortion of the surface structure of the metal. However, for use with the stainless steels, the method was found to permit a good degree of reproducibility among different electrode specimens with respect to initial steady-state potentials in the passive region and polarizability in the environment used here. These are characteristics of considerable importance in a series of galvanostatic experiments using different electrodes. However, it should be made explicit that current quantities measured here pertain only to the real electrode surface used.

[4] The authors are indebted to G. W. Leddicotte of the Analytical Chemistry Division of this Laboratory for his kind cooperation in irradiating samples of $CuSO_4 \cdot 5H_2O$ in the graphite reactor for use in this work.

centrations, rinsed thoroughly in distilled water, dried in a jet of air, and assayed for ^{64}Cu in a standard well-type scintillation counter. Specific activity of the experimental solution at the end of an experiment was found by counting small aliquots of the solution which had been evaporated to dryness on an abraded stainless steel surface.

Results and Discussion

Potentiostatic Experiments

It was shown in I that potentiostatic measurements permit the determination of the kinetic order of an individual partial process in a polyelectrode system with respect to the concentration of a reactant in this process, provided the reactant concentration can be varied without affecting the concentrations of other reactants in the system and provided two (or more) partial processes of the system have no common kinetic orders with respect to the reactant under examination. Thus, the kinetic order (p_x) of a reaction (denoted by subscript x) with respect to the concentration of one of its reactants (C_x) is given by:

$$\left(\frac{\partial \ln \mid i_P - i_{P,0} \mid}{\partial \ln C_x}\right)_V = p_x \qquad [1]$$

Here, i_P is the externally applied current in the presence of an amount, C_x, of the reactant and $i_{P,0}$ is the initial applied current at the chosen electrode potential (V) before additions of the reactant (or for a known amount of reactant already present). Figure 1 presents graphically the results of experiments of this type on the addition of Cu^{++} to a passive stainless steel electrode system. From the unit slopes obtained in Fig. 1, it is evident that the reduction reaction is first order with respect to (Cu^{++}) over the whole potential range investigated (−158 to +283 mv vs. S.C.E.) and over a thousandfold variation in (Cu^{++}).

The ionic strength of the solution was essentially constant at $\mu = 0.15$ throughout the experiments except for the very highest concentrations, hence changes in activity coefficients have been neglected in the interpretation of the results. Two observations attest to the independent simultaneity of the electrode reactions (i.e., the presence of the additional partial process due to the reduction of Cu^{++} does not significantly affect the rates of the initial partial processes in the system): (*a*) i_P does not vary with time at the various (Cu^{++}), except for the very highest concentrations at the lowest potentials studied;[5] (*b*) the measured values of $i_{P,0}$, for each potential, are exactly the current quantities necessary to confer linearity on the plots of log $\mid i_P - i_{P,0} \mid$ vs. log (Cu^{++}).

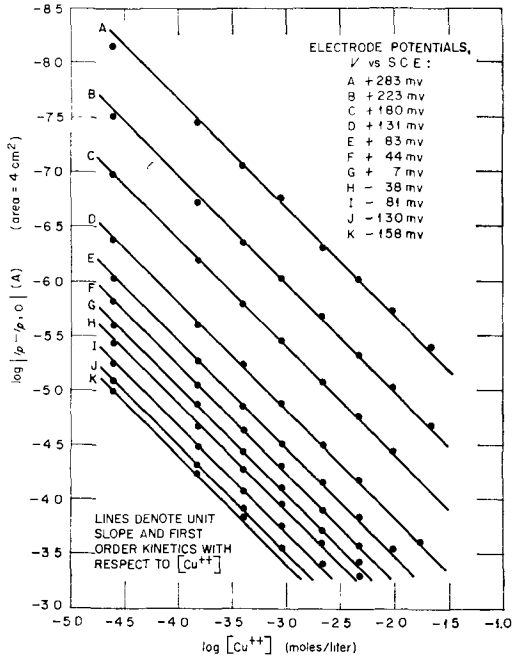

Fig. 1. Results of potentiostatic experiments on the reduction of cupric ion at the surface of passive stainless steel in aerated, 0.1N H_2SO_4 at 85°C.

In Fig. 2, a Tafel-type plot, experimental points corresponding to log $\mid i_P - i_{P,0} \mid$ at constant (Cu^{++}) from Fig. 1 have been plotted against electrode potential, V. Solid lines are drawn through experimental data referring to constant (Cu^{++}). Lines of slope $-RT/F$ and $-4RT/F$ have been provided for comparison with theoretical expectations. The present system is limited with respect to the experimentally accessible potential region. At higher potentials than those studied, currents due to the reduction of Cu^{++} are small and difficult to measure accurately except for very high (Cu^{++}), where changes in ionic strength become important. At lower potentials than those in Fig. 2, Cu^{++} is reduced so rapidly that the electrode surface cannot long be

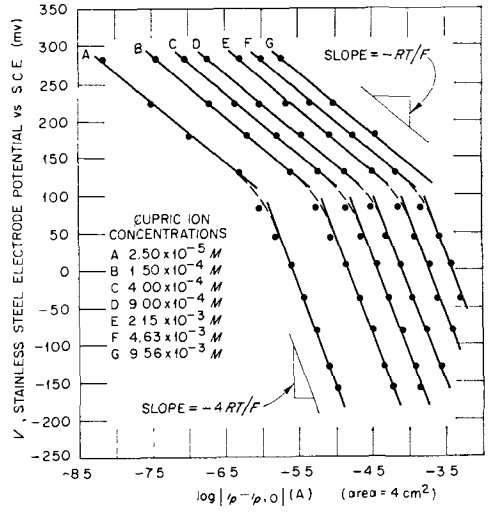

Fig. 2. Electrode potential-current density curves for the reduction of cupric ion at the surface of passive stainless steel in aerated, 0.1N H_2SO_4 at 85°C.

[5] Variations of i_P with time were observed at the lowest potentials at high (Cu^{++}); i_P became more negative linearly with time at constant (Cu^{++}). If, following the onset of this behavior, the (cathodic) applied current was interrupted, the electrode potential was observed to assume very rapidly the value of the reversible Cu^0/Cu^{++} potential for the environment and to maintain that value for periods of the order of minutes before changing to more noble potentials characteristic of passive stainless steel in the presence of Cu^{++}. This phenomenon was not observed at potentials much above S.C.E. even for the highest (Cu^{++}) studied and did not occur at lower potentials unless i_P was observed to change with time at constant (Cu^{++}). For electrodes held at still lower potentials than those of Fig. 2, the addition of Cu^{++} soon produced a visible metallic copper phase, and on release of applied current, these electrodes also showed the above behavior. Precautions were taken in studies at the lower potentials of Fig. 1 to minimize the effect of this additional complication by conducting experiments as rapidly as possible and the data of Fig. 1 contain no significant error from this source.

considered that of passive stainless steel, i_P changes very rapidly with time, and a metallic copper phase is soon produced, the properties of which are not of primary interest here. For partial processes under pure activation control and involving a single charge transfer step, such plots of V vs. log $|i_P - i_{P,0}|$ ($\equiv$ | current due to added constituent |) yield straight lines of slope $\left|\frac{RT}{F}\cdot\frac{1}{\alpha_x\lambda_x}\right|$ (cf. Eq. [31] in I). Here, α_x is the symmetry factor of the energy barrier in the charge transfer step of the partial process, and λ_x is the number of charges transferred across the interphase during the charge transfer step.

The change of slope of the curves in Fig. 2 implies the existence of alternative and/or consecutive charge transfer steps in the mechanism for the reduction of Cu^{++} on the electrode surface.[6] Numerous mechanistic schemes have been examined for the purpose of finding one or more which predict the type of behavior observed in Fig. 2. Mechanisms involving partial diffusion and partial activation control (assuming Fick's first law and linear diffusion) or partial "reaction" (12) and partial activation control, with a single charge transfer step, were found to be inconsistent with experiment in that they do not allow a constant slope at lower potentials, but predict an asymptotic approach to a limiting current as $V \to -\infty$. It can be shown that when the slope of the (electrode potential) - (logarithm of current density) curves for these mechanisms is twice that of the upper portion, where activation is effectively rate controlling for a cathodic partial process, the current at this point equals half the limiting current. Inspection of Fig. 2 shows that at the lowest potential studied the current is already a factor of about ten larger than that at the point where the slope is twice the slope of the high potential region, with no indication of an approach to a limiting current. Furthermore, a calculation of the expected effect of concentration polarization on the results at the lowest potentials of Fig. 2, using probable values of the diffusion coefficient of cupric ion and of the thickness of the Nernst diffusion layer (13), shows that little error is involved in neglecting changes in cupric ion concentration at the electrode surface for the currents used here. A mechanism consisting of two simultaneous simple reaction paths (e.g., a "two-electron" path simultaneous with a "one-electron" path) is incapable of explaining the data, for it requires that the slope of the higher potential region of the (electrode potential) - (logarithm of current density) relation be greater than that of the lower potential region, whereas the reverse is observed here.

Without discussing additional mechanisms examined in relation to this problem, one mechanism is presented which is consistent with the data. This reaction sequence is given by:

$$Cu^{++}(\text{d.l.}) \underset{\overline{k_2}(-e^-)}{\overset{\overline{k_1}(+e^-)}{\rightleftharpoons}} Cu^{+}(\text{d.l.}) \xrightarrow{\overline{k_3}(+e^-)} Cu^{\circ}\,(\text{oxide}) \qquad [2]$$

[6] R. Parsons (11), among others, has discussed cases of simultaneous mechanisms for the hydrogen evolution reaction.

The symbol Cu^{++}(d.l.) refers to cupric ions at the innermost portion of the diffuse double layer at the interphase, the concentration of which, for the experimental conditions of this work (large excess of inter electrolyte), must be essentially equal to the concentration in the bulk of the solution. Because of the well-known multivalency of copper in aqueous solutions, it does not seem unreasonable to presume that the cuprous state is energetically accessible as an intermediate in the over-all process for the reduction of Cu^{++}, and the symbol Cu^{+}(d.l.) refers to the postulated intermediate at the interphase. Cu^{+} (d.l.) is produced from Cu^{++}(d.l.) by the "one-electron" step of electrochemical specific rate constant $\overline{k_1}$ and (surface average) current density $\overline{j_1}$. It may react further either by reoxidation back to Cu^{++}(d.l.) (via the "one-electron" anodic step of rate constant $\overline{k_2}$ and current density $\overline{j_2}$) or by moving across the interphase to a position in the stainless steel oxide lattice. This latter cathodic step is characterized by rate constant $\overline{k_3}$ and current density $\overline{j_3}$. The product of the partial process is symbolized in Eq. [2] by Cu° (oxide), although the observable kinetics gives no information on the identity of the species, which may be Cu^{+}(oxide).

Designating the over-all (surface average) current density of the reduction process by $\overline{j_x}$, $\overline{j_x}$ is given as a function of $\overline{j_1}$, $\overline{j_2}$, and $\overline{j_3}$ by:

$$\overline{j_x} = \overline{j_1} - \overline{j_2} + \overline{j_3} \qquad [3]$$

Denoting the concentration of Cu^{++}(d.l.) (or the equivalent concentration of Cu^{++} in the bulk of the solution) by (Cu^{++}), and denoting the concentration of Cu^{+}(d.l.) by (Cu^{+}), Eq. [3] becomes:

$$\overline{j_x} = \overline{k_1}(Cu^{++}) - (\overline{k_2} - \overline{k_3})\,(Cu^{+}) \qquad [4]$$

Assuming that (Cu^{++}) is constant with time, that (Cu^{+}) very soon reaches a steady-state value, and that the reaction product on the oxide surface builds up continuously with time (i.e., no back reaction), the steady-state concentration of Cu^{+}(d.l.) is given by:

$$(Cu^{+}) = (Cu^{++})\,\frac{\overline{k_1}}{\overline{k_2} + \overline{k_3}} \qquad [5]$$

The over-all current density of the reduction process is given from Eqs. [4] and [5] by:

$$\overline{j_x} = (Cu^{++})\,\frac{2\overline{k_1}\overline{k_3}}{\overline{k_2} + \overline{k_3}} \qquad [6]$$

The electrochemical specific rate constants of the respective steps in the mechanism of Eq. [2] are assumed to be given by:

$$\overline{k_1} = k_1\, e^{-\frac{\alpha_1\lambda_1 F}{RT}V} \qquad [7]$$

$$\overline{k_2} = k_2\, e^{+\frac{\alpha_2\lambda_2 F}{RT}V} \qquad [8]$$

$$\overline{k_3} = k_3\, e^{-\frac{\alpha_3\lambda_3 F}{RT}V} \qquad [9]$$

The terms, k_1, k_2, and k_3 are presumed independent of the value of V, the measurable electrode potential, α_1, α_2, and α_3 are the symmetry factors of the steps in the mechanism of Eq. [2], and λ_1, λ_2, and λ_3 are the numbers of charges transferred across the interphase during the respective charge transfer steps ($\lambda_1 = \lambda_2 = \lambda_3 = 1$ is assumed in the mechanism of Eq. [2]). Substitution of Eqs. [7], [8], and [9] in Eq. [6] and differentiation of the resulting expression for $\overline{j_x}$ with respect to V, with use of the relations $\frac{d\overline{k_1}}{dV} = -\frac{\alpha_1\lambda_1 F}{RT}\overline{k_1}$, $\frac{d\overline{k_2}}{dV} = \frac{\alpha_2\lambda_2 F}{RT}\overline{k_2}$, $\frac{d\overline{k_3}}{dV} = -\frac{\alpha_3\lambda_3 F}{RT}\overline{k_3}$, and $\frac{dV}{d\ln \overline{j_x}} = \overline{j_x}\cdot\frac{dV}{d\overline{j_x}}$, leads to:

$$P_x \equiv \left(\frac{\partial V}{\partial \ln \overline{j_x}}\right)_{(Cu^{++})} = -\frac{RT}{F}\left[\frac{\overline{k_2} + \overline{k_3}}{(\alpha_1\lambda_1 + \alpha_2\lambda_2 + \alpha_3\lambda_3)\overline{k_2} + (\alpha_1\lambda_1)\overline{k_3}}\right] \quad [10]$$

The behavior of the function, P_x, depends on the ratio of $\overline{k_2}$ to $\overline{k_3}$; this ratio increases rapidly with increasing V. Thus, when $\overline{k_2} >> \overline{k_3}$ at high potentials, P_x becomes $P_x^+ = -\frac{RT}{F}\cdot\frac{1}{(\alpha_1\lambda_1 + \alpha_2\lambda_2 + \alpha_3\lambda_3)}$; and when $\overline{k_2} << \overline{k_3}$ at low potentials, P_x becomes $P_x^- = -\frac{RT}{F}\cdot\frac{1}{\alpha_1\lambda_1}$. The former slope ($P_x^+$) corresponds, in the present set of experiments (cf. Fig. 2), to that in the potential region from +100 to +300 mv vs. S.C.E., while the latter slope (P_x^-) corresponds to that in the region from +100 to −200 mv vs. S.C.E.[7] Equations [6] and [10] adequately describe the present data on the reduction of Cu^{++} at the surface of passive stainless steel in the chosen environment.

Before calculating values of electrochemical transfer coefficients from the results of Fig. 2, on the basis of the mechanism of Eq. [2] and the kinetic deductions of Eqs. [6] and [10], it is necessary to recognize the existence of three phases in the present passive metal system. The over-all electrode-solution potential difference may be considered to be composed of three parts: (*a*) the metal-metal oxide potential difference; (*b*) any potential difference existing between the inner and outer boundaries of the oxide on the passive metal; and (c) the oxide-solution potential difference. In the absence of a quantitative kinetic theory of the passive state which takes into account all the above potential differences, a theoretically exact interpretation of the system studied here does not seem possible at the present time. However, the values of the electrochemical transfer coefficients calculable from the present data and Eq. [10] do find a reasonable interpretation on the basis of a model developed in collaboration with Meyer of this laboratory (14).

In the model it is assumed that the rate constants for the transport of positive ions and oxide ions through the passive oxide layer on stainless steel are quite large compared to the rate constants for the transfer of positive ions from metal to oxide and from oxide to solution. Hence it is assumed that any potential difference between the inner and outer boundaries of the oxide is negligible compared to the potential differences at the metal-metal oxide interphase and at the oxide-solution interphase. It is assumed also that the concentration of metal ions is essentially constant everywhere in the oxide. The current density for the transfer of positive ions from metal to oxide is assumed to be given by:

$$\overline{j_M} = K_M e^{+\frac{\alpha_M\lambda_a F}{RT}\Delta\phi_M} \quad [11]$$

Here, $\overline{j_M}$ is the (surface average) current density of the transfer step, K_M contains the potential-independent portion of the specific rate constant of the charge transfer step and the concentration of ions in the metal, α_M is the symmetry factor of the energy barrier at the metal-oxide interphase, λ_a is the charge of the metal ions, and $\Delta\phi_M$ is the inner potential difference between metal and oxide. The current density for the transfer of positive ions from oxide to solution ($\overline{j_S}$) is given by:

$$\overline{j_S} = K_S e^{+\frac{\alpha_S\lambda_a F}{RT}\Delta\phi_S} \quad [12]$$

Here, K_S is analogous to K_M of Eq. [11], α_S is the symmetry factor of the energy barrier at the oxide-solution interphase, λ_a is as defined in Eq. [11], and $\Delta\phi_S$ is the oxide-solution potential difference. It is assumed that the back reactions corresponding to Eqs. [11] and [12] can be neglected. Since it has been presumed that the potential difference through the oxide is negligible, the total metal-solution potential difference ($\Delta\phi_T$) is given by:

$$\Delta\phi_T = \Delta\phi_M + \Delta\phi_S \quad [13]$$

Equations [11], [12], and [13] may be solved simultaneously and, for steady-state conditions ($\overline{j_M} = \overline{j_S}$), lead to the current density of the anodic process ($\overline{j_a}$), which is given by:

$$\overline{j_a} = \overline{j_M} = \overline{j_S} = (K_M)^{\frac{\alpha_S}{\alpha_M+\alpha_S}}(K_S)^{\frac{\alpha_M}{\alpha_M+\alpha_S}} e^{\left(\frac{\alpha_M\alpha_S}{\alpha_M+\alpha_S}\right)\frac{\lambda_a F}{RT}\Delta\phi T} \quad [14]$$

Furthermore, the current density of a cathodic partial process ($\overline{j_r}$) under pure activation control with one charge transfer step and proceeding at the oxide-solution interphase may be written as:

$$\overline{j_r} = K_r e^{-\frac{\alpha_r\lambda_c F}{RT}\Delta\phi_S} \quad [15]$$

Here, K_r is analogous to K_M and K_S of Eqs. [11] and [12], α_r is the symmetry factor of the barrier at the oxide-solution interphase, and λ_c is the charge trans-

[7] No evidence was found in this system for the existence of a significant direct "two-electron" reduction path for Cu^{++}. If a path of this type is included in Eq. [2], it is found that P_x (cf. Eq. [10]) can then possess four constant values in four ranges of potential, and the plot of V vs: log $\overline{j_x}$ for the mechanism possesses the aspect of an inclined "W", in which the two inner portions (or "legs") are described by Eqs. [6] and [10] and the two outer portions refer to the additional "two-electron" path. Thus either the experimentally accessible range of electrode potentials for this system does not permit observation of regions at very high and very low potentials corresponding to predominance of a "two-electron" path, or else such a path is nonexistent.

ferred across the interphase during the cathodic charge transfer step. Equation [15], together with the value of $\Delta\phi_S$ obtained by simultaneous solution of Eqs. [11], [12], and [13], leads to:

$$\bar{j}_r = K_r \left(\frac{K_S}{K_M}\right)^{\frac{\alpha_r\lambda_c}{(\alpha_M+\alpha_S)\lambda_a}} e^{-\left(\frac{\alpha_r\alpha_M}{\alpha_M+\alpha_S}\right)\frac{\lambda_c F}{RT}\Delta\phi_T} \quad [16]$$

It is evident that, for this case, the "over-all" symmetry factor for the anodic partial process is given by $\frac{\alpha_M\alpha_S}{\alpha_M+\alpha_S}$, so that, if the energy barriers are symmetrical (i.e., $\alpha_M = \alpha_S = \frac{1}{2}$), the over-all symmetry factor is $\frac{1}{4}$, instead of the $\frac{1}{2}$ observed frequently for two-phase polyelectrode systems. Likewise, the over-all symmetry factor for the cathodic partial process, $\frac{\alpha_r\alpha_M}{\alpha_M+\alpha_S}$, is also $\frac{1}{4}$ if $\alpha_r = \alpha_M = \alpha_S = \frac{1}{2}$.

If it is assumed that the preceding model holds for the case of passive stainless steel, and that α_1, α_2, and α_3 of Eqs. [7]-[10] are "over-all" symmetry factors having values of $\frac{1}{4}$, while $\lambda_1 = \lambda_2 = \lambda_3 = 1$ in accord with the mechanism of Eq. [2], the values of P_x calculated from Eq. [10] for the higher and lower potential regions of the (electrode potential)-(logarithm of current density) plot (cf. Fig. 2) are $P_x^+ = -1.33\ RT/F$ and $P_x^- = -4\ RT/F$, respectively, compared with the observed values of $-1.14\ RT/F$ and $-3.71\ RT/F$. The agreement seems satisfactory since exactly symmetrical energy barriers are not necessarily expected. The slope of the higher potential region in Fig. 2 (P_x^+) is $P_x^+ = -0.082\ (V)$; hence it follows that $(\alpha_1\lambda_1 + \alpha_2\lambda_2 + \alpha_3\lambda_3) = 0.87$. The slope of the lower potential region is $P_x^- = -0.263\ (V)$, leading to a value of $\alpha_1\lambda_1 = 0.27$; and if λ_1 is presumed equal to unity as in the mechanism of Eq. [2], $\alpha_1 = 0.27$, in good agreement with the assumption of two fairly symmetrical energy barriers for the anodic process in the system. From the values of $\alpha_1\lambda_1$ and of P_x^+, it follows that $(\alpha_2\lambda_2 + \alpha_3\lambda_3) = 0.60$, and if λ_2 and λ_3 are also equal to unity, $(\alpha_2 + \alpha_3) = 0.60$, also in reasonable agreement with the mechanistic conceptions outlined above. No further separation of $(\alpha_2 + \alpha_3)$ into its constituents appears possible from these data.

Galvanostatic Experiments

An elementary theory of the effect of additions of a reducible constituent to solution on the electrode potential of a polyelectrode system with only one anodic and one cathodic partial process initially present was presented in I. There it was shown that the slope of the (electrode potential)-(logarithm of additive concentration) plot is given by:

$$\left(\frac{\partial V}{\partial \ln C_x}\right)_{j_P} = \frac{RT}{F}\left[\frac{p_x \bar{j}_x}{\alpha_a\lambda_a\bar{j}_a + \alpha\lambda_c\bar{j}_c + \alpha_x\lambda_x\bar{j}_x}\right] \quad [17]$$

Here, $\bar{j}_a$ and $\bar{j}_c$ are the (surface average) current densities of the anodic and cathodic partial processes initially present in the system; in the system studied here these are the oxidation of stainless steel constituents and the reduction of molecular oxygen dissolved in solution. The current density of the added reducible constituent is denoted by $\bar{j}_x$, where $\bar{j}_x$ is defined for the present system by Eq. [3], $\alpha_x\lambda_x$ is given from Eq. [10] by $-\frac{RT}{F}\cdot\frac{1}{P_x}$, and p_x is as defined in Eq. [1]. The appropriate values of α_a, α_c, and α_x for use in Eq. [17] are the "over-all" symmetry factors of the respective processes, as discussed in the previous section. The applied current density is given by $\bar{j}_P = \bar{j}_a - \bar{j}_c - \bar{j}_x$, so that when $\bar{j}_x >> \bar{j}_c$ (at higher concentrations of the added reducible constituent), $j_P \simeq \bar{j}_a - \bar{j}_x$, and Eq. [17] reduces to:

$$\left(\frac{\partial V}{\partial \ln C_x}\right)_{j_P} = \frac{RT}{F} p_x \left[\alpha_x\lambda_x + \alpha_a\lambda_a\left(1 + \frac{j_P}{\bar{j}_x}\right)\right]^{-1} \quad [18]$$

Equation [18] predicts a constant slope when $j_P = 0$, in accord with experimental observations. The potentiostatic experiments have shown that p_x equals unity for the reduction of Cu^{++} on the surface of passive stainless steel.

Figure 3 presents the results of galvanostatic experiments on the present system and Fig. 4, constructed from the data of Fig. 3, shows how the slope, $\left(\frac{\partial V}{\partial \log C_x}\right)_{j_P}$, varies with C_x for various values of j_P. For comparison with theory, the analogous behavior of an idealized system is shown in Fig. 5 and 6. For the construction of these theoretical diagrams,

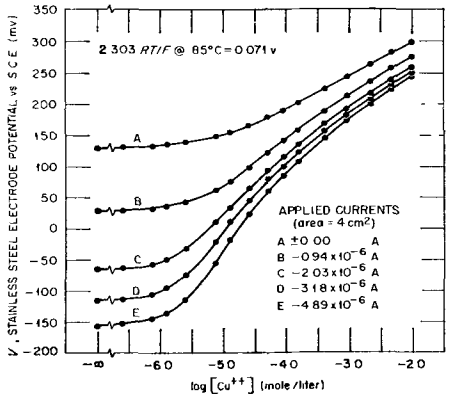

Fig. 3. Variation with applied current of the effect of cupric ion on the electrode potential of passive stainless steel in aerated, 0.1N H_2SO_4 at 85°C.

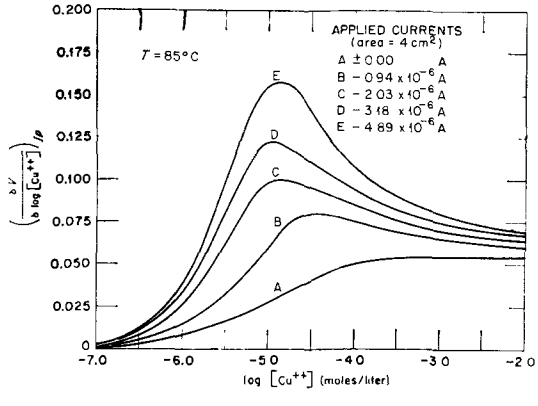

Fig. 4. Variation with applied current of the slope, $(\partial V/\partial \log [Cu^{++}])_{j_P}$, for the effect of cupric ion on the electrode potential of passive stainless steel in aerated, 0.1N H_2SO_4 at 85°C.

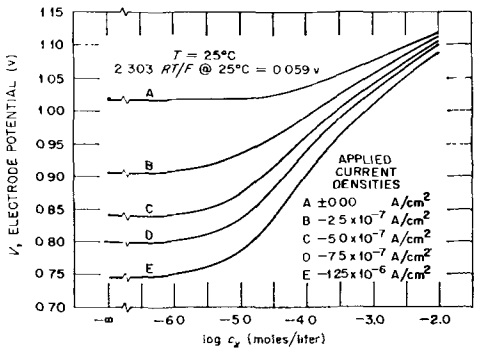

Fig. 5. Theoretical variation with applied current of the effect of an added reducible constituent on the electrode potential of a polyelectrode system (see text for description of model).

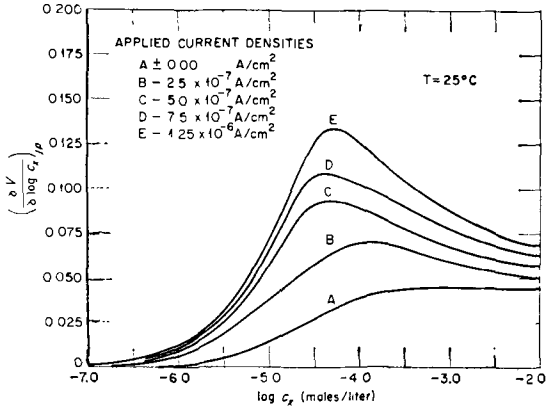

Fig. 6. Theoretical variation of the slope, $(\partial V/\partial \log C_x)_{j_P}$, with the applied current density and with the concentration of an added reducible constituent for a polyelectrode system.

a model was used having the following electrochemical kinetic parameters. k_1, k_2, and k_3 of Eqs. [7]-[9] were assumed to be given by the relations: $k_1 = 44.3$ and $k_2/k_3 = 8.59 \times 10^{-9}$. In accord with the mechanism of Eq. [2] and with the dual barrier model discussed in the previous section, $\alpha_1 = \alpha_2 = \alpha_3 = \frac{1}{4}$ and $\lambda_1 = \lambda_2 = \lambda_3 = 1$. The current density of the anodic process was assumed to be of the form of Eq. [14]; specifically, $\overline{j_a} = 1.21 \times 10^{-15}\, e^{+\frac{\alpha_a \lambda_a F}{RT} V}$ with $\lambda_a = 2$ and α_a (the over-all symmetry factor equal to $\frac{\alpha_M \alpha_S}{\alpha_M + \alpha_S}$ of Eq. [14]) $= \frac{1}{4}$. Likewise, the current density of the cathodic process was assumed to be of the form of Eq. [16]; specifically, $\overline{j_c} = 9.55 \times 10^{-3}\, e^{-\frac{\alpha_c \lambda_c F}{RT} V}$, with $\lambda_c = 1$ and α_c (the over-all symmetry factor equal to $\frac{\alpha_r \alpha_M}{\alpha_M + \alpha_S}$ of Eq. [16]) $= \frac{1}{4}$. These parameters were selected to correspond closely, except for temperature ($T = 25°C$), with those calculable from the results of the potentiostatic experiments on the reduction of Cu^{++} and with those calculable from the polarizability of the system before additions of Cu^{++}. The agreement between the forms of the curves for theoretical and experimental systems seems satisfactory.

The linearity, at high (Cu^{++}), of curve A in Fig. 3 is evidence for the independent simultaneity of the two partial processes, oxidation of steel constituents and reduction of Cu^{++}, in agreement with evidence from the potentiostatic experiments. In this linear region, the reduction current of dissolved oxygen is negligible compared to that for the reduction of Cu^{++}, hence the latter current very nearly equals the current for the oxidation of the steel constituents. Therefore, from the results of Fig. 2 and 3, the (electrode potential)-(logarithm of current density) relationship for the anodic (corrosion) reaction can be calculated. This is found to be linear and to exhibit a slope of $\left(\frac{\partial V}{\partial \log \overline{j_a}}\right) = 0.164$; hence it follows that $\alpha_a \lambda_a = 0.43$. This result is consistent with a value of λ_a (an average value since stainless steel is composed of three important oxidizable species) in the vicinity of two and slightly asymmetrical energy barriers for the anodic process (cf. Eq. [14] with $\alpha_a = \frac{\alpha_M \alpha_S}{\alpha_M + \alpha_S}$).

Knowledge of $\alpha_a \lambda_a$ and $\overline{j_a}$ as a function of V permits a calculation of the corresponding quantities for the reduction reaction of dissolved oxygen from the polarization curve for passive stainless steel in the absence of Cu^{++}. The (electrode potential)-(logarithm of current density) plot for this reaction was found to possess a slope of $\left(\frac{\partial V}{\partial \log \overline{j_c}}\right) = -0.275$; hence $\alpha_c \lambda_c = 0.26$, in agreement with a "one-electron" process for the reduction of oxygen and an over-all symmetry factor for the process of approximately $\frac{1}{4}$. The values of $\alpha_a \lambda_a$ and $\alpha_c \lambda_c$ are seen to be consistent with the dual barrier model discussed above which was invoked to interpret the potentiostatic experiments on the reduction of Cu^{++}. If the values of $\alpha_a \lambda_a$ and $\alpha_x \lambda_x$ reported above are substituted into Eq. [18], $\left(\frac{\partial V}{\partial \log C_x}\right)$ has the value 0.054 (V) when $j_P = 0$. This value is identical to that observed experimentally, as seen in Fig. 3 and 4. If the values of $\alpha_a \lambda_a$ and $\alpha_x \lambda_x$ found in this work are substituted into Eq. [18] for the temperature, 25°C, a slope of 0.046 (V) is predicted. This value compares favorably with that [0.048 (V)] obtained on plotting data [in a V vs. log (Cu^{++}) diagram] of other workers (5) on the effect of Cu^{++} on the electrode potential of 18-8 stainless steel in 0.2N H_2SO_4 at 25°C. An increase in cupric ion concentration from zero to $10^{-2}M$ in this system, with $j_P = 0$, increases the corrosion rate of passive stainless steel from 2.9×10^{-8} amp/cm² to 3.0×10^{-7} amp/cm².

Part A of Table I lists those ions for which a linear relationship between electrode potential and logarithm of additive concentration is observed for zero applied current. The model of the passive stainless steel interphase outlined above also assists in the interpretation of the values of the addition slope, $\left(\frac{\partial V}{\partial \log C_x}\right)$, for some of these systems. Thus, as-

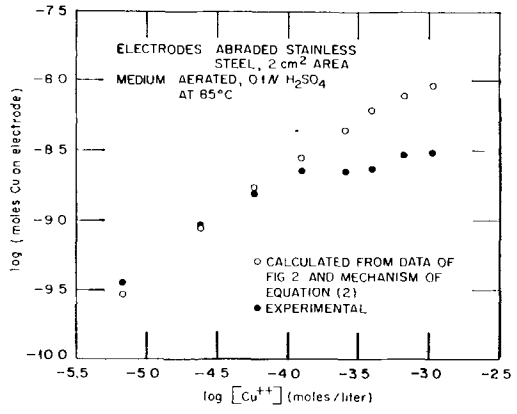

Fig. 7. Typical results of tracer experiments using $^{64}Cu^{++}$—relationship between amount of copper retained by electrode surface and $[Cu^{++}]$ in solution.

suming over-all symmetry factors of $\alpha \simeq 1/4$ for the reduction processes of each of the additives and the value of $\alpha_a\lambda_a$ reported above, the following approximate values of λ_x are calculable from the addition slopes and Eq. [18] for $j_P = 0$: $Fe^{+++} = 1$; $HCrO_4^- = 1$; $BrO_3^- = 2$; and $IO_3^- = 2$. These values seem in reasonable agreement with known facts about the solution chemistry of these ions. The other groups in Part A, consisting of peroxy species and ions of high oxidation state, may involve complicated reaction sequences for reduction, instead of simple one-step mechanisms necessarily assumed in the calculations for the above ions ($HCrO_4^-$ may also belong in this category).

Tracer Experiments

A typical set of tracer results is shown in Fig. 7. Calculated values of the amount of copper reduced by the path of specific rate constant $\overline{k_3}$ of the mechanism suggested in Eq. [2], as a function of (Cu^{++}) in solution, are included for comparison. Calculated and experimental values are in good agreement below $(Cu^{++}) = 10^{-4}M$; at higher concentrations, the order of magnitude is still correct, but the numerical agreement is poorer (theoretical and experimental values differ by a factor of about three at $(Cu^{++}) = 10^{-3}M$).[8] Although the results of the tracer experiments offer some support for the mechanistic conceptions outlined above, the quantity measured is not particularly well defined, as the procedures followed in rinsing and drying electrodes for assay of radioactivity may have involved unknown errors. Nevertheless, these tracer experiments and some other tracer studies on the amount of copper retained by the electrodes as a function of time at constant (Cu^{++}) do support the contention that the product of the final reduction step, the path of specific rate constant $\overline{k_3}$ in Eq. [2], builds up continuously with time on the oxide surface. Further tracer studies have demonstrated the "irreversibility" of the final step in the mechanism of Eq. [2]. If galvanostatic experiments at zero applied current are performed with $^{64}Cu^{++}$, in which the solution is subsequently replaced with fresh, copper-free solvent, the electrode potential returns to its initial value observed before additions of Cu^{++}. However, the amount of copper retained by the electrodes in the copper-free solution is identical, within expected experimental error, to that retained by similar electrodes withdrawn from solution before changing solvents.

The potentiostatic, galvanostatic, and tracer experiments, together with the mechanism of Eq. [2] and a dual barrier model for the anodic (corrosion) reaction of passive stainless steel, offer a self-consistent picture of the present polyelectrode system and afford a mechanistic basis for interpreting the results of experiments like those reported in Table I. There seems little doubt that similar studies, involving the theory and techniques outlined in I and used here in a concerted study of a single system, would prove valuable in analyzing other corroding polyelectrode systems.

Manuscript received Jan. 16, 1958.

Any discussion of this paper will appear in a Discussion Section to be published in the June 1960 JOURNAL.

[8] The discrepancy between theory and experiment in Fig. 7 at higher (Cu^{++}) may be removed by assuming additional paths for the destruction of the cuprous intermediate in the mechanism of Eq. [2], such as diffusion of the intermediate away from the interphase before it can react at the surface or reaction of the intermediate with molecular O_2 from the solution. The additional paths are not included in Eq. [2], however, since this would complicate the analysis unduly.

REFERENCES

1. F. A. Posey, *This Journal*, **106**, 57 (1959).
2. J. V. Petrocelli, *ibid.*, **98**, 183 (1951).
3. G. H. Cartledge and R. P. Yaffe, "Chem. Semiann. Prog. Rep. June 20, 1953," ORNL-1587, p. 13.
4. G. H. Cartledge and R. P. Yaffe, "Chem. Semiann. Prog. Rep. December 20, 1953," ORNL-1674, p. 11.
5. H. H. Uhlig and A. Geary, *This Journal*, **101**, 215 (1954).
6. A. C. Makrides, N. M. Komodromos, and N. Hackerman, *ibid.*, **102**, 363 (1955).
7. H. C. Gatos, *Corrosion*, **12**, 322t (1956).
8. H. C. Gatos, *This Journal*, **103**, 286 (1956).
9. G. H. Cartledge, *ibid*, **104**, 420 (1957).
10. R. W. Lamphere and L. B. Rogers, *Anal. Chem.*, **22**, 463 (1950).
11. R. Parsons, *J. chim. Phys.*, **49**, C82 (1952).
12. H. Gerischer and K. J. Vetter, *Z. physik. Chem.*, **197**, 92 (1951).
13. C. V. King, *This Journal*, **102**, 193 (1955).
14. R. E. Meyer, "Chem. Ann. Prog. Rep. June 20, 1958," ORNL-2584, p. 69.

Effects of Chloride on the Orientation of Nickel Deposits

B. C. Banerjee and A. Goswami

National Chemical Laboratory, Poona, India

ABSTRACT

The effects of chloride ions in a nickel bath have been studied. Chloride ions generally counterbalance the outgrowth condition due to impurities and favor lateral growth; this is attributed to the desorption of the impurities from the cathode, which facilitates the electron-transfer process.

In a series of papers (1-3) Goswami and his coworker have shown that the preferred orientation of an electrodeposit can be altered by an appropriate change in the bath conditions such as *p*H, current density (c.d.), temperature, rate of stirring, bath compositions, additives, etc. Finch, *et al.* (4, 5) first recognized that the crystal orientations were related to the modes of ways in which crystals were growing and these were loosely termed as (*a*) out growth deposits, when the most densely packed atom rows of deposit crystals were normal to the substrate-surface, (*b*) lateral growth deposits, when a densely packed lattice plane containing the most densely packed lattice rows was parallel to it, and (*c*) other types of growth exhibiting complex orientations. In f.c.c. metals, out growth deposition condition is denoted by the appearance of {110} orientation, whereas lateral growth is denoted by {100} or {111}. The last orientation was never observed during electrodeposition of nickel but was observed (6) during chemical reduction from a nickel hypophosphite bath. The mixed {211} + $\{10\bar{1}0\}_{hex}$ which come primarily from the initial {100} orientation have also been shown (7, 2) to be of lateral growth type.

In preliminary experiments it was observed that the out-growth condition of nickel deposition in presence of impurities as reported (8) earlier can be modified to lateral growth type by addition of sodium chloride. Since chloride ion is known to increase the bath conductivity (9-11) and also facilitate electron transfer process (12, 13) at the cathode, it was deemed necessary to study its effect on the structure of nickel deposited from impure baths and gain an insight into the mode of cathodic crystal growth process.

Experimental

Nickel was deposited on mechanically polished brass substrates from baths containing $NiSO_4$, $7H_2O$ 280 g/l and H_3BO_3 31 g/l in presence of varying amount of aluminum sulfate, chromium sulfate, chromic acid, benzaldehyde, nitrobenzene, glycine, gelatine, benzene disulfonate, and 1:3:6 sodium salt of naphthalene trisulfonate at constant c.d. ($\simeq$10 ma/cm^2) and temperature ($\simeq$24°C).

Deposition was carried out to well beyond the stage where polycrystalline deposits developed preferred orientations characteristic of bath conditions. The *p*H of the solution was adjusted so that the deposits were lateral growth type in the absence of impurities (8). After each addition of impurities or sodium chloride the deposit orientation was determined by electron diffraction (reflection method) in the usual way. Other experimental conditions such as *p*H adjustment, method of deposition, etc., were similar to those already described (1-3).

Results and Discussion

Electron diffraction studies revealed that the polycrystalline deposits, which were initially unorientated, developed one or another orientations depending on the amount and also on the nature of the additives. The results (Table I) showed that with increasing amount of impurities, at high *p*H region, the deposit crystals favored {110} orientation, but {210} at low *p*H values. This later orientation has been ascribed to hydrogen adsorption (2, 3) by the deposit crystals. The addition of sodium chloride suppressed these orientations and eventually led to {100} or {211} + $\{10\bar{1}0\}_{hex}$ or a mixture of them. This, however, signifies that the crystal growth process was considerably modified to give lateral growth deposits (2, 7). Both the out-growth or lateral growth conditions of deposition could be induced by the alternate addition of suitable amount of impurities or sodium chloride. This is demonstrated clearly with chromic sulfate and gelatine in the results marked with asterisks (Table I) and is likely to be true for others also.

Factors which control the crystal growth process at the cathode have been described by various workers (1-5). An important feature in the growth process in the present cases is the adsorption of basic salts or hydroxides of the inorganic impurities (8) or of the organic compounds which are good surface active agents (14, 15). The deposition will, however, be influenced both by the extent of equilibrium coverage of the cathode surface area and also by the rate of adsorption/desorption process (16). In any case, the result will be the out-growth deposition condition either due to depletion of metal ions at the cathode surface region as discussed in the previous paper (8) or to an increase in c.d. resulting from the decrease in surface area. That high c.d. favors {110} orientation even at different *p*H and bath composition is evident from Table II. Increase in c.d. also raises the cathode polarization. The interdependency between modes of crystal growth process or the preferred orientation and cathode polarization in presence of or-

Table I. Effect of concentration of sodium chloride on the orientation of nickel deposited from baths containing various impurities

pH	Impurity: Name	Conc. g/l	Conc. of NaCl g/l: 0	20	40	60	80	100
3.1	Aluminum sulfate	0	100					
		0.8	100 + 210					
		1.0	210	210	210 + 100	100 + 211 + $10\bar{1}0$		
5.2		0	100					
		1.2	100 + 210					
		1.4	210	210 + 100	100 + 211 + $10\bar{1}0$			
3.1	Chromic sulfate	0	100					
		0.3	210	210	210	210	211 + $10\bar{1}0$	
5.05		0	100					
		0.35	100 + 110					
		0.45	110					
		0.65	110	110	100 + 211* + $10\bar{1}0$			
		+0.2*	110	211 + $10\bar{1}0$	211 + $10\bar{1}0$			
5.9	Chromic acid	0	211 + $10\bar{1}0$					
		0.07	211 + $10\bar{1}0$ +110					
		0.12	110	110	110	211 + $10\bar{1}0$	211 + $10\bar{1}0$	
3.1	Gelatine	0	100					
		0.02	100 + 210					
		0.03	210	210 + 110	110 + 100	211 + $10\bar{1}0$		
5.2		0	100					
		0.06	110	211 + $10\bar{1}0$*				
		+0.08*	110	110	211 + $10\bar{1}0$			
4.4	Nitrobenzene, Benzaldehyde	0	100					
		0.30	110	110	110	110	211 + $10\bar{1}0$	211 + $10\bar{1}0$
	Naphthalene trisulfonate	0	100					
		0.1	Pattern not clear	110	211 + $10\bar{1}0$			
5.8	Glycine	0-4	100					
		6	110	110	110	110	110	110

* Chromic sulfate and gelatine added.

Table II. Effect of current density on the orientation of nickel deposits

Bath	pH: c.d. in mA/cm²	10	20	40	70	100	200	300
A	3.1	100	210	210 + 110	110	110		
	5.1	100	100 + 210	210 + 110	210 + 110	110		
B	5.1	211 + $10\bar{1}0$	211 + $10\bar{1}0$	211 + $10\bar{1}0$	210	210	110	110
C	3.7	100	100 + 210	210	210 + 110	110	110	

A — $NiSO_4 \cdot 7H_2O$ 280 g/l + H_3BO_3 31 g/l.
B — $NiCl_2 \cdot 6H_2O$ 150 g/l + H_3BO_3 31 g/l.
C — $NiSO_4 \cdot 7H_2O$ 280 g/l + $NiCl_2 \cdot 6H_2O$ 48 g/l + H_3BO_3 31 g/l.

ganic brighteners in nickel baths has been pointed out by one of us (A.G.) in a recent paper (2).

Sodium chloride seems to suppress completely or at least minimize the effect of factors such as (*a*) adsorption of compounds at the cathode, (*b*) film formation in the catholyte resisting the supply of ions and hindering the electron transfer process, (c) complex ion formation, etc., which contribute to out-growth deposition condition. Hoar (17) has emphasized that adsorption is essentially a dynamic process and equilibrium may be shifted by altering additives. That sodium chloride facilitates the desorption process is clearly shown from the results with naphthalene trisulfonate. The deposits were highly lustrous with this additive, but did not yield any clear diffraction patterns which were only ill-defined and

diffuse. By the addition of sodium chloride, the deposit crystals became less and less lustrous and finally became dull and even blackish, similar to those obtained from a chloride bath (3). Such surfaces yielded clear diffraction patterns, revealing that the deposits had developed $\{211\} + \{10\bar{1}0\}_{hex}$ orientations. That the loss of details of electron diffraction pattern in the above was not due to non-crystallinity, but due to adsorption of organic compounds, was shown from x-ray pattern of the stripped films, which consisted of rings indicating the crystalline nature of deposits. X-rays, because of their higher penetrating power, are scattered by the underlying metals, whereas electrons are scattered by surface layers which in the present case contained adsorbed additives. The alternate addition of naphthalene trisulfonate and sodium chloride made the deposits bright and dull, with their characteristic surface structures as discussed above.

These results suggest that chloride ions facilitate the desorption process of the surface active compounds at the cathode surface and produce more sites for depositions, thus reducing the current density and hence contributing to lateral growth. The depolarization of cathode potential in a gelatine-copper sulfate bath with halide ions has been explained similarly (18). In the competition between chloride ions and surface active agents or other impurities to get adsorbed at the growing cathode surface, it is likely that the former, because of its polarizability (19), prevails over the others. This will also help the electron transfer process and favor lateral growth condition. The observation that chloride ions facilitate the deposition of metals (9-11) and the suggestion that the formation of chloro or aquo-complexes helps the electron transfer process during nickel deposition (12, 13) are also in agreement with our results.

Acknowledgment

The authors thank Professor G. I. Finch, F. R. S. and Dr. A. B. Biswas for their interest.

Manuscript received Oct. 1, 1957.

Any discussion of this paper will appear in a Discussion Section to be published in the June 1960 JOURNAL.

REFERENCES

1. B. C. Banerjee and A. Goswami, *J. Sci. Ind. Res. (India)*, **14B**, 322 (1955).
2. A. Goswami, *ibid.*, **16B**, 315 1957).
3. B. C. Banerjee and A. Goswami, *This Journal*, **106**, 20 (1959).
4. G. I. Finch, H. Wilman, and L. Yang, *Discussions Faraday Soc.*, **1**, 144 (1947).
5. G. I. Finch and D. N. Layton, *J. Electrodepositors' Tech. Soc.* **27**, 215 (1951).
6. A. Goswami, Unpublished work.
7. A. Goswami, *J. Sci. Ind. Res. (India)*, **15B**, 322 (1956).
8. B. C. Banerjee and A. Goswami, *ibid.*, **16B**, 144 (1957).
9. E. Muller and H. Barchmann, *Z. Elektrochem.*, **39**, 341 (1933).
10. R. Pointelli, *J. chim. phys.*, **45**, 288 (1949).
11. R. Pointelli, *J. Inst. Metals*, **19**, 99 (1951).
12. E. H. Lyons, Jr., *This Journal*, **101**, 372 (1954).
13. E. H. Lyons, Jr., *ibid.*, **101**, 376 (1954).
14. G. E. Gardam, *Proc. 3rd. Int. Conf. (London)*, P-203 (1947).
15. P. K. Frolick, *Trans. Am. Electrochem. Soc.*, **46**, 67 (1924).
16. E. G. Neal and L. L. Shreir, *Trans. Faraday Soc.*, **52**, 703 (1956).
17. T. P. Hoar, *Trans. Inst. Met. Finishing*, **29**, adv. copy No. 11 (1953).
18. L. Mandelcorn, *et al.*, *This Journal*, **99**, 84 (1952).
19. J. Heyrovsky, *Discussions Faraday Soc.*, No. 1, 212 (1947).

On the Jet Etching of N-Type Si

Paul F. Schmidt and David A. Keiper

Research Division, Philco Corporation, Philadelphia, Pennsylvania

ABSTRACT

The rate of jet electropolishing of low resistivity n-Si is controlled by two factors: supply of injected minority carriers and rate of dissolution of the SiO_2 film. The current through the oxide changes from ionic to electronic, i.e., the silicon becomes passive, if the oxide thickness increases beyond a critical value. The hole supply determines the amount of etching which can occur when the Si is not passivated by a thick oxide layer.

A general description of this process has been given before (1). The present paper is concerned with the mechanism of the etching process and with the rate and quality of etching, which is important from the economic point of view; not only is it necessary to etch fast, but the resultant surface also must be polished completely for subsequent device applications.

Anodic dissolution of a metal involves the removal of positive ions from the metal lattice under the action of the applied electrostatic field. In n-type semiconductors having an appreciable width of the forbidden gap there are no positive ions, except the few donor atoms and the very few lattice ions corresponding to holes in the valence band. In principle, the hole concentration can be increased by raising the temperature of the system. However, this approach is of no help on heavily doped n-Ge because of the very small hole concentration in this material at room temperature. The hole concentration at 100°C has not increased sufficiently to maintain any appreciable etching currents. (For 0.1 ohm-cm n-Ge the electron concentration is $n = 2.0 \times 10^{16}$ cm^{-3}. The intrinsic product for Ge at room temperature is $n_i^2 =$

$n \cdot p = 6.25 \cdot 10^{26}$, so that $p = 3.7 \times 10^{11}$ cm^{-3}. At 100°C the intrinsic product has increased to 2.6×10^{29} cm^{-3}. Assuming that $n_{25°}$ is approximately the same as $n_{100°}$, $p_{100°}$ would be approximately 1.3×10^{18} cm^{-3}.) With increasing bias, therefore, either discharge of anions in the electrolyte or breakdown of the surface barrier of the n-Ge must occur. This breakdown is usually very undesirable because it does not occur evenly over the anode surface and thus leads to pitting. Use of higher boiling electrolytes than water is not readily possible because of the low solubility of the reaction products in nonaqueous electrolytes. Also viscosity problems are troublesome. On Si with its wider gap appreciable thermal generation of hole-electron pairs is almost out of the question for jet operation.

For these reasons hole-electron pairs are generated by optical excitation of electrons from the valence band, and strong illumination is employed in the etching of both n-Ge and n-Si. This need for strong illumination is a common feature in the etching of n-Ge and n-Si. Differences in behavior are caused on one hand by the smaller gap of Ge and on the other by the relatively good solubility of GeO_2 in water as compared to SiO_2.

Mechanism of electropolishing.—Electropolishing proceeds under conditions of strong polarization. Differences in work function of the individual crystal faces, or due to degree of crystal perfection, or differences in conductivity of semiconductor material, must be small compared to the overpotential of the process; otherwise preferential etching would result.

On metals which form very stable oxides, the necessary polarization during electropolishing can be provided by an oxide having such a rate of dissolution in the given electrolyte that rate of anodic film growth and rate of dissolution of the film can be balanced.

The applied electric field pulls ions through the film, cations from the metal, and anions from the electrolyte interface; they combine to form more oxide [the older theory of anodic oxide growth by Mott and Cabrera regards only the cations as mobile: recent evidence favors the mobility of both cations and anions, at least for some systems (2, 3)]. At the same time the oxide dissolves in the electrolyte; under steady-state conditions the oxide thickness does not change. The differences in work function[1] of the individual crystal faces are small compared to the activation energy for migration through the oxide film,[2] which in turn is small compared to the activation energy necessary for migration through the oxide at a point not favored by the presence of a vacancy or other defect.

An increase in current density at any spot would increase the rate of film growth there; the rate of dissolution by the electrolyte would not increase as readily (it may increase somewhat because of a local rise in temperature and greater disorder of the film structure; cf. however, discussion on "Characteristics of SiO_2 films"). For a given applied bias, the field strength in the oxide decreases very rapidly with increasing thickness. The rate of reaction at this spot must therefore decrease to its old value. Thus there results a complete masking of local differences in etch rate of the metal surface itself.

It is hoped to present here evidence that an oxide film is present on Si during electropolishing in aqueous solvents, but it has not been shown that the oxide film must be present and that other anions, e.g., halides, cannot play the same role as oxygen.

Electropolishing of N-Si

The jet electropolishing of Si is possible in aqueous or alcoholic solutions containing fluoride ions. Prior to this investigation the jet etching of n-Si was done with a 0.2*N* solution of NaF + 5 cc 48% HF/1000 ml H_2O. Under illumination with a Bausch and Lomb reflector lamp electropolishing currents not higher than 3.0 ma were possible with a 10 mil jet. A further increase in light intensity did not increase the etch rate.

This limitation of the etching currents could be due to (*a*) an insufficient hole supply, or to (*b*) a slow chemical step, or to both.

In order to check the first possibility, it was necessary to know (*a*) the absolute intensity of illumination expressed in number of photons of energy greater than the gap width, and (*b*) what fraction of this number is available for the etching process, allowing for the unavoidable losses by reflection and by bulk and surface recombination.

Experimental Methods

The intensity of illumination was determined by shining the focused beam of a 1 kw projector lamp through a narrow opening in the lid of a Dewar flask into a dilute solution of india ink in water. A water filter of 2 cm thickness inserted in the path of the beam cut off wave lengths greater than 1.2 μ which do not create hole-electron pairs in Si. The lid of the Dewar consisted of cork, covered with reflecting aluminum foil both on the inside and the outside. The india ink solution was stirred gently to obtain a uniform temperature distribution. The rise of temperature with time of illumination was measured, as was the drop of temperature with time after switching off the light. The total energy absorbed thus could be calculated from the known heat capacity of the solution and could be corrected for heat losses during illumination. The latter correction proved to be very small.

Knowing the color temperature of the tungsten filament, approximately 3200°K, the total energy input, and assuming that the energy distribution vs. wave length for the tungsten filament is essentially the same as for a black body radiator, the total number of photons of wave lengths shorter than 1.2μ can be calculated. This also gives the number of photons/cm^2 x sec for a given size of the illuminated area.

Knowing the reflectivity of the Si the number of photons is obtained which penetrate into the Si and create hole-electron pairs.

The next step was to determine experimentally the fraction of the injected holes that are lost by bulk or surface recombination before they can be collected by the anode process. Since the rate of

[1] Work for removal of a positive ion from the crystal.

[2] At least in the "high field" case which is realized in jet etching (2).

recombination could change at very high light intensities, it was also necessary to determine the hole flux that could be collected as a function of light intensity. This was done by shining light of a known intensity on the front surface of a photodiode on n-Si, while maintaining a reverse bias of 0.25 v across the diode. Light intensity was varied by inserting Kodak-Wratten neutral density filters in the path of the light beam.

Since illumination introduces a forward bias of the diode, the applied reverse bias had to be increased in order to maintain the effective bias at 0.25 v. This procedure does not take into account the change in voltage drop with current across the base contact and across the bulk of the diode; it is, therefore, only a rough approximation. However, the current under illumination does not depend strongly on the magnitude of the applied reverse bias for the given resistivity of the Si.

Before the hole current collected can be compared to the hole current injected a further correction must be applied because the diode collects holes not only from the area directly in front of it but also from the surrounding area by lateral diffusion of holes.[3] The absolute amount of this contribution to the current increases with the circumference of the contact. The relative importance, however, depends on the ratio of contact radius to diffusion length for holes. For the photodiode employed it will increase the current by a factor of about 2. Collection of holes by the jet also differs from collection of holes by the photodiode in that the concentration of injected holes is greatest immediately underneath the Si surface; it must be expected therefore that the jet will be a more efficient collector than the photodiode. Thus the experiments with the photodiodes only give a lower limit for the supply of holes which may be expected to be available for the anode process.

Results

Determination of light intensity.—Total energy input into calorimeter by 1 kw projector lamp, with water filter inserted, was equal to 0.70 w. The light beam was focused uniformly over an area of 0.08 cm^2. For this setting, which also was used in the experiments with the photodiodes and during jet etching, a total number of photons of 5×10^{19}/sec x cm^2 in the wave-length region 0.3-1.2μ is calculated from the color temperature of the tungsten filament (3200°K).

Corrections for reflection losses and for collection of holes by lateral diffusion.—Table I gives the pertinent data for the n-Si photodiodes employed. For the diode area of 1.9×10^{-4} cm^2 the photon flux is 9.5×10^{15} sec.

[3] Provided the illuminated area is larger than the diode area, as was the case in our experiment.

Table I

Bulk lifetime after alloying, μ sec	Material	Resistivity, ohm-cm	Base thickness in front of recrystallized region, μ	Area of contact
9	n-Si alloyed Al contact	0.7 to 1.3	5.0	1.9×10^{-4} cm^2

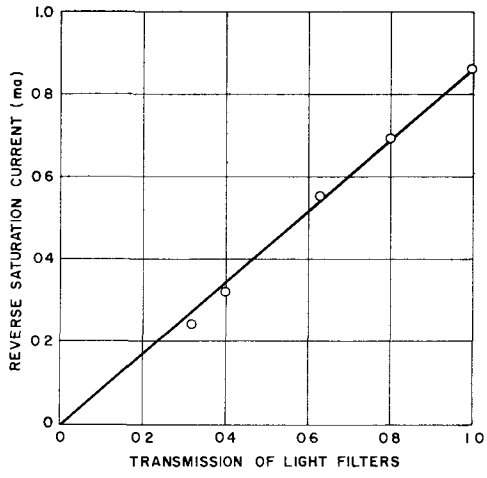

Fig. 1. Response of photodiode on n-Si vs. light intensity

The reflectivity of Si as a function of wave length in the visible has been given by Coblentz (4). Taking into account the change of reflectivity with wave length it was found that for the energy distribution of the tungsten filament an average reflectivity of 29% can be employed for the spectral region 0.3-1.2μ.

An average reflectivity[4] of 29% converts the number of 9.5×10^{15} photons/sec incident on the diode area to 6.8×10^{15} photons penetrating into the silicon, equivalent to a hole current of 1.1 ma.

Due to the above mentioned affect of lateral diffusion, however, a current of about 2.2 ma may be expected.

Diode response vs. light intensity.—Figure 1 shows diode current vs. light intensity and also indicates the transmission factors of the filters used.

The diode response is practically linear. As already mentioned, this can be only an approximation because the change in voltage drop with current across bulk of the diode and base contact has been neglected.

At the highest light intensity the diode response was 0.87 ma, i.e., about 40% of the injected holes reached the collector.

Correction for reflection losses during jet etching.—Since under our experimental conditions of jet etching the light was not perpendicularly incident on the Si surface but within 15° of the perpendicular, and because additional reflection losses are introduced by the jet stream, the above figure needs a further correction before it can be used to estimate the expected etch rate. It was found that the diode current decreased by about 40% when an electrolyte jet was directed against the front surface of the diode and the light was incident within 15° of the perpendicular.

Applying the above corrections indicates that at least 1 out of every 3 incident photons should be available to the etching process, based on the etched area.

Discussion

From the fact that there is no levelling off of the photodiode response at very high light intensity, and

[4] Actually, the reflectivity may also depend somewhat on intensity of illumination (5, 6).

from the fact that there is a definite correlation between low light intensity and etching currents below 3 ma/10 mil jet, it may already be concluded that the limitation of 3 ma is imposed by a slow chemical step and not by an insufficient hole supply (at very high light intensities).

As a check, we can now compare the hole supply and therefore also the expected etching current under illumination with the 1 kw projector lamp to the highest etching current obtained experimentally (with 10 mil ϕ jet and 0.2*N* NaF + 5 cc 48% HF/liter solution).

At low current densities (3 ma) the diameter of the etch pit is normally about twice the jet diameter (it increases to about 4 times the jet diameter at large current densities, i.e., the current density does not increase as rapidly as the jet current.)

The photon flux on an area of 2×10^{-3} cm^2 (= 20 mil ϕ) is 1×10^{17} sec^{-1}, equivalent to a hole current of 16 ma. Reflection losses under actual jet-etching conditions reduce this figure to 6.8 ma. Two corrections must again be applied: increase of the available number of holes due to lateral diffusion, and decrease because of surface and bulk recombination. It can be estimated that the first factor will increase the current by about 60% of its value in the absence of lateral diffusion.[5] Recombination losses ought to be considerably less than in the case of the photodiode, because the holes are generated in the space charge region of the surface barrier and are immediately collected by the strong field. The two factors should at least balance. It is therefore justified to assume a hole supply sufficient to maintain an etching current of at least 6 ma. Experimentally, however, the electropolishing current was found to be limited to 3.0 ma.

It must therefore be concluded that the hole supply under intense illumination is sufficient to maintain quite large etching currents, but that a slow chemical step controls the etch rate for the given electrolyte.

Dissolution of SiO_2 *Film as the Rate-Controlling Process During Jet Etching of* N-Si *Under Intense Illumination*

Characteristics of SiO_2 *films.*—Slow dissolution of a SiO_2 layer appeared as the most likely cause of slow etching under the above mentioned conditions. In work on the anodic formation of oxide films on Si in inert electrolytes it had been found (7) that the current through the SiO_2 during forming is mostly electronic and not ionic (e.g., 99% electronic at 7 ma/cm^2). The same is true apparently also for the SiO_2 film present during electropolishing; thus if for a given electrolyte the rate of formation of SiO_2, i.e., the current density, is higher than the rate of dissolution of the SiO_2 by the electrolyte, the oxide film will increase in thickness, and the silicon will become passive because the current through the SiO_2 changes from ionic to electronic.

It might be thought that the chemical dissolution of the oxide would continue at the same rate after passivation so that the Si must again become active. This, however, is not the case: once the silicon has become passive, it remains passive at the given current density. An explanation for this phenomenon may be sought either along the lines of passivation of iron, which dissolves rapidly as long as the surface is covered by Fe_3O_4 only, but becomes passive when a layer of Fe_2O_3 appears in addition (8), or along the lines of the work of Engell (9) who showed that the dissolution rate of bulk oxides like FeO or Fe_3O_4 depends strongly on an applied potential. But it may also be that the enormous electrostatic pressure on the SiO_2 film at the very high current densities of the jet process is of importance. The oxide is strongly disordered while ionic current is flowing through it (10). Any strongly disordered structure will have a higher rate of dissolution than an ordered structure. When the Si passivates, ionic current flow through the SiO_2 stops almost completely. According to Le Chatelier's principle the electrostatic pressure should decrease the number of interstitials and vacancies, thus decreasing the volume and leading to a decreased rate of dissolution.

If the slow dissolution of an SiO_2 film is indeed rate determining, an increase in acidity and in temperature should permit faster etching (under intense illumination).

Effect of acidity and temperature on etching speed.—In order to accelerate the dissolution of the SiO_2 both the temperature and the HF content of the electrolyte were increased. A solution containing 30 cc of 48% HF + 8.4 g NaF/1000 H_2O, heated to 70°C, was found suitable for electropolishing at 30 ma with a 10 mil jet under the above quoted high light intensity. The resulting etch pit had a diameter of 0.1 cm. The photon flux on the area of the etch pit, 7.8×10^{-3} cm^2, is equivalent to a hole current of 26.8 ma, allowing for reflection losses. For the relatively large area of the etch pit (radius $> L_p$) the contribution by lateral diffusion of holes is becoming less important and may be estimated to amount to about 14%, which increases the expected electropolishing current to 30.5 ma. This good agreement between expected and experimentally determined electropolishing current may be somewhat accidental (compensation of errors), but essentially it means that surface and bulk recombination of holes are suppressed by the strong field of the jet contact. Another solution, 40 g NH_4HF_2 + 8 g NaF/liter, proved very satisfactory at room temperature.

Shape of etch pits.—Assumption of slow dissolution of an SiO_2 film as the rate-determining step permits understanding of the factors governing the shape of the etch pit. Si, in contrast with Ge, usually yields very flat-bottomed etch pits. The current density should be highest in the center of the etch pit if potential distribution alone were decisive. However, as was shown above, a very high current density leads to a thickening of the SiO_2 film, which in turn increases the electronic current component. The center region also cannot collect as many holes as the periphery which profits from lateral diffusion of holes. Thus a balance can be achieved with the periphery etching at about the same rate as the center. Mounds

[5] These estimates are based on the assumption that the number of laterally collected holes decreases to $1/e$ at distance $\chi = L_p$ from the geometric edge of the diode.

formed in the center of the etch pit can be explained by the same reasoning. Typically, it was found that under conditions of high HF content and high light intensity the resulting etch pits are rounded. Thus, a delicate balance of all contributing factors is required to obtain flat-bottomed etch pits at high etch rates.

What causes the pitting at too high current density is not yet completely clear. Crystal defects are an obvious possibility, but it seems that other causes like dielectric breakdown of insulating layers or removal by the electric field of positively charged donor atoms, aggregated at dislocations, and thus causing a catastrophically high local etch rate, may also be involved. Correlation between pitting and dislocation density is, of course, very pronounced.

Pitting is reduced markedly when the light intensity, current density, and pH of the solution are correctly adjusted; it is also possible to add certain complexed cations (such as K_4 [Fe(CN)6]) in their lower valence state to the electrolyte; apparently they are then oxidized to a higher valence at a lower field strength than is required for the production of "pin-holes."

Valence state of dissolved Si.—No lattice structure is revealed by the anodic electropolishing of Si; the same holds true for the anodic electropolishing of Ge. On the other hand, the cathodic jet etching of Ge[6] (reaction product GeH_4) results in etch pits corresponding to the given orientation, i.e., formation of distorted hexagonal etch pits on the {100} plane. Clearly sufficient polarization is absent in the cathodic etching of Ge but is present in the anodic polishing of Si (and Ge). The polarization factor could be either a thin oxide layer on the Si or diffusion control in the electrolyte, specifically diffusion of fluoride ions through the diffusion layer to the interface (12). Actually the two mechanisms may describe the same physical picture, namely, the presence of a thin oxide layer on the Si. This question can perhaps be decided if the current efficiency during jet electropolishing of Si is known. In the absence of an oxide layer one would expect the Si to go into solution initially in the divalent state. If a layer of SiO_2 were present, then the Si should definitely go into solution in the quadrivalent state. A third possibility is suggested by the work of Bockris (to be published) who has shown by galvanostatic measurements that the surface of Ge during anodic polarization is covered by a monolayer of GeO; yet the Ge ions which have gone into solution are found to be in the quadrivalent state. Results of related studies (11) show that the Si dissolves in the quadrivalent state in the high current density region. This, together with the high potential values observed, with the need for free HF in order to electropolish, and with the passivation of the Si at too high current densities for a given HF content seems to establish definitely the presence of a thin SiO_2 film during electropolishing in aqueous solutions. In order to obtain the best polish, the dissolving power of the electrolyte must be neither too low nor too high.

[6] Discovered by A. Topfer of Philco Corporation.

Acknowledgments

This work was supported in part by the U. S. Army Signal Supply Agency under contract number DA-36-039-SC-72705.

The authors are greatly indebted to Mr. Joseph Walsh and Dr. Ruth Schwarz for many valuable discussions, and to Mr. Ralph Mossman[7] for experimental work on p-Si and n-Ge; information obtained in work on these materials was of considerable help in interpreting the results on n-Si.

Manuscript received April 2, 1958.

Any discussion of this paper will appear in a Discussion Section to be published in the June 1960 JOURNAL.

[7] Now with the Hughes Products Co., Los Angeles, California.

REFERENCES

1. J. W. Tiley and R. A. Williams, *Proc. Inst. Radio Engrs.*, **41**, 1706 (1953).
2. J. F. Dewald, *This Journal*, **104**, 244 (1957).
3. O. Flint and J. H. O. Varley, *Nature*, **179**, 145 (1957).
4. "Handbook of Chemistry and Physics," p. 2714, Chemical Rubber Publishing Co. (1957).
5. J. Filinsky, *Phys. Rev.*, **107**, 1193 (1957).
6. F. R. Kessler, *Z. Naturforschung*, **13a**, 295 (1958).
7. P. F. Schmidt and W. Michel, *This Journal*, **104**, 230 (1957).
8. K. E. Heusler, K. G. Weil, and K. F. Bonhoeffer, *Z. physik. Chem., Neue Folge*, **15**, 149 (1958).
9. H. T. Engell, *ibid.*, **7**, 158 (1956).
10. J. F. Dewald, *Physics and Chemistry of Solids*, **2**, 55 (1957).
11. P. F. Schmidt and M. Blomgren, Submitted to this Journal.
12. D. R. Turner, *This Journal*, **105**, 402 (1958).

Uniform Resistivity p-Type Silicon by Zone Leveling

E. D. Kolb and M. Tanenbaum

Bell Telephone Laboratories, Inc., Murray Hill, New Jersey

ABSTRACT

Silicon single crystals nominally 1 cm in diameter and 16 cm long have been grown with aluminum doping in a floating zone apparatus. Crystals have been prepared with nominal p-type resistivities of 0.3 and 5 ohm-cm with variations of 5% or less along the crystal length. Variations of resistivity with rotation rate, growth rate, ambient gas flow rate, and other growth variables have been studied. Zone volume variations were also measured.

The wide use of diffusion techniques for the production of silicon devices has led to a need for large quantities of single crystalline Si of uniform resistivity. Past experience with germanium zone refining and leveling (1) demonstrated that this is a practical method of obtaining large quantities of uniform resistivity single crystals.

By the use of the floating zone technique (2) Si single crystals can be grown and zone refined. The process can be adapted easily to zone leveling. Figure 1 illustrates a typical zone leveling experiment. A zone of molten semiconductor, A, is formed between a single crystal seed, B, and a pure polycrystalline ingot, C. The impurity is added to the molten zone. The molten zone is moved to the right freezing out impurity doped semiconductor onto seed B and melting pure polycrystalline semiconductor from ingot C. The newly grown single crystal will contain a concentration of impurity kC_L, where k is the effective distribution coefficient of the impurity, and C_L is the impurity concentration in the molten zone. If k is very small (e.g., < 0.01), the amount of impurity frozen into the single crystal is sufficiently small so that C_L is not significantly altered even after several zone lengths have been traversed.

In addition to having a small k, a suitable doping element must be nonvolatile if a uniform concentration is to be maintained. It must be of high purity since trace elements having a larger distribution coefficient would have a detrimental effect on the leveling process. Further, since control is often desirable over several orders of magnitude of impurity concentration, it is desirable to be able to use both alloys of the impurity with the semiconductor as well as the elemental impurity itself. Aluminum fulfills these requirements and was used for these experiments.

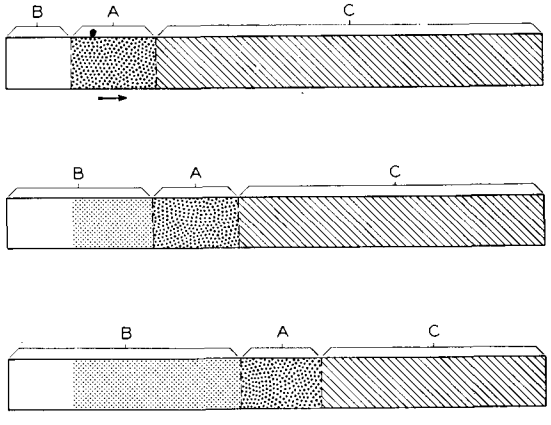

Fig. 1. Typical zone leveling experiment

Experimental

The floating zone machine used for the experiments has been described by Buehler (3). It is necessary to keep the zone volume constant during zone leveling to keep C_L constant. In order to minimize zone volume changes, the zone volume was monitored during the leveling operation. This was done by measuring the zone length with a cathetometer, assuming that the zone diameter and liquid-solid interface shape remain essentially constant, and manually adjusting the rf induction heater to compensate for any observed changes. Zone length variations did not exceed ±7% for the growth conditions studied.

Zone leveling was studied with crystals that ranged from 14 to 18 cm in length, were between 0.9 and 1.2 cm in diameter with diameter variations in individual rods of ±3% or less. They were all p-type with resistivities at the seed ends in the range from 80 to 175 ohm-cm and 30 to 165 ohm-cm at the opposite ends.

Crystals were doped to nominal resistivity levels of 0.3 and 5 ohm-cm. The 0.3 ohm-cm crystals were grown by doping with elemental Al. A small piece of 99.998% Al weighing approximately 0.5 mg was placed in a 0.025 cm slot, cut at approximately a 45° angle in the seed end of the pure crystal, where the starting zone was to be established (Fig. 2a).

The 5 ohm-cm rods were grown by doping with cylinders of floating zone leveled Al doped Si of approximately 0.038 ohm-cm resistivity. These were placed between the seed and the undoped starting rod where the starting zone was to be established (Fig. 2b). It was important to assure that the seed, the doping cylinder, and the starting rod were coaxially aligned prior to the zone-leveling operation. Any eccentricity tended to increase the diameter variations during zone melting and thus increase the uncertainty in the zone volume. It was possible to achieve conditions where the diameter fluctuations increased from an original average of ±3% to final values of ±7% or less.

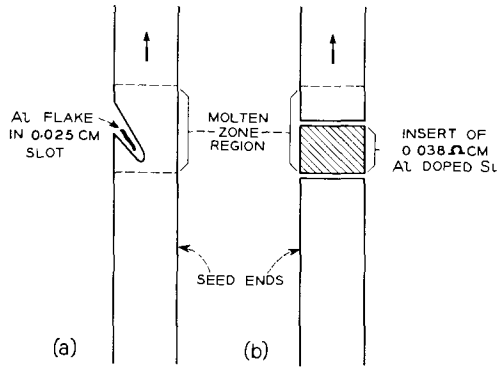

Fig. 2. Aluminum doping schematic

All the experiments were performed in a hydrogen atmosphere. Oxygen was removed from the hydrogen by passing through a Deoxo purifier and the hydrogen dried to a dew point of $< -100°C$ by passing over Linde molecular sieves (No. 5A) at liquid nitrogen temperature. This purification was necessary to insure a minimum loss of aluminum from the molten zone by oxidation.

The resistivity of the zone leveled crystals was measured on bars 0.625 cm by 0.625 cm in cross section cut from the center of a crystal. Current electrodes were rhodium and copper plated on the ends of the bars, and a constant current was passed along their length. Two movable points spaced 0.025 cm apart were driven mechanically along the length of the rod and the potential difference between the points was plotted on a L&N Speedomax recorder. Resistivities were calculated from the potential profiles. These measurements showed a background noise level which appeared as the points were dragged along the surface of the crystal. By repeating the measurements several times on a particular crystal, it was determined that the measurements were reproducible but, due to the noise, variations in resistivity less than ±3% could not be determined.

Results

The following variables were studied: stirring of the molten zone, growth rates, loss of Al from the molten zone, and ambient gas flow rate.

The molten zone is stirred by rotating the seed crystal while holding the undoped portion of the rod stationary. The effect on resistivity of seed rotation speeds between 40 and 110 rpm was determined to be negligible at the 0.3 ohm-cm level. A crystal was grown at both 0.0021 and 0.0058 cm/sec with rotation speeds of 40 and 110 rpm. Figure 3 is a resistivity profile obtained from a typical stirring experiment. Distance along the crystal axis in centimeters is plotted along the vertical coordinate while resistivity in ohm-cm is plotted along the horizontal coordinate. It can be seen that the resistivity is virtually unchanged by changing the rotation rate at either growth rate. A closer comparison of the resistivities at the 0.0021 cm/sec growth rate showed the 110 rpm region to be ~7% higher than the 40 rpm region. Since this increase occurred gradually, and there was no abrupt change when the stirring rate was changed, it is believed that this is not a result of stirring but is due to some unknown variable.

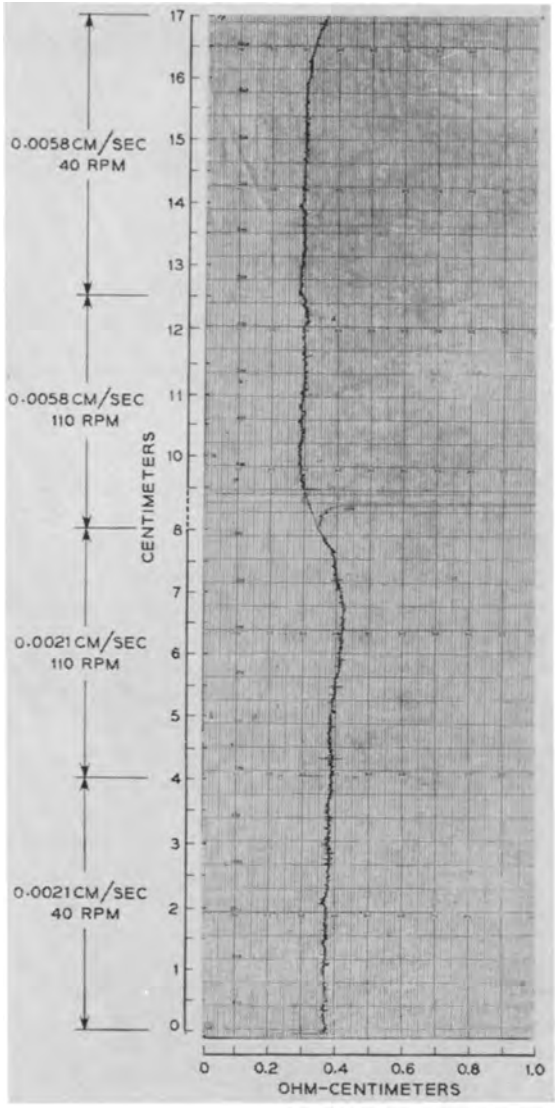

Fig. 3. Resistivity profile of 0.3 ohm-cm stirring and growth rate experiment.

Changing the growth rate produced the largest effect of any of the variables studied. Increasing the growth rate from 0.0021 cm/sec to 0.0058 cm/sec decreased the resistivity approximately 25% at the 0.3 ohm-cm level and 35% at the 5 ohm-cm level. Measurements of zone length and crystal diameter indicated that the maximum change in zone volume between the above growth regions was not more than ±3%. Figure 3 is the resistivity profile of a typical 0.3 ohm crystal. The decrease in resistivity is in the direction expected from the Burton-Prim-Slichter (4) diffusion layer theory. At the faster growth rate, less of the rejected impurity is able to diffuse away from the growing interface, and the effective distribution coefficient increases.

It is interesting to note that a comparison of uniformity of resistivity vs. growth rate shows that at resistivity levels of 5 ohm-cm and growth rates of approximately 0.0021 cm/sec the resistivity variations are ±10%. In the region grown at 0.0058 cm/sec the resistivity varied less than ±5%. Zone volume changes as measured by the cathetometer readings between the slow and fast growth rate regions did not exceed ±3% for each region and cannot ac-

count for the observed resistivity variations. It appears that at the higher resistivity levels the resistivity is more uniform at the faster growth rates. At the lower resistivity levels, the resistivity uniformity is not affected over the range of growth rates studied. The reason for this difference is not known.

Loss of Al from the molten zone by evaporation or reaction with the protective atmosphere was studied by stopping the zone travel approximately halfway through the pass, holding the zone stationary for an hour with the seed rotating (puddling), and then proceeding at the original growth rate. Loss of Al from the molten zone would produce higher resistivity after puddling. By comparing the resistivity measurements in the first half of a 0.3 ohm-cm crystal with those in the second half it was observed that the resistivity level upon resuming growth is equal to that prior to the puddling interval within the measurement error. Thus the loss of Al from the molten zone at the 0.3 ohm-cm level is negligible. Two additional puddled crystals doped to 1.5 and 5 ohm-cm resulted in resistivity levels upon resuming growth that were 5% and 12% higher, respectively, than the levels prior to the puddling, indicating some loss of Al. The loss of Al may be due to variations in the control of the H_2 dew point resulting in oxidation of Al from the molten zone. In this case the total loss of Al would depend only on the water content of the ambient hydrogen atmosphere and would be independent of the Al concentration in the molten zone. At higher resistivity levels the loss of a constant amount of Al from the molten zone would be more noticeable since it is a larger fraction of the total Al concentration added initially to the molten zone.

Finally, the effect of the H_2 gas flow rate between 100 and 1000 cc/min on resistivity level was determined to be negligible at the 0.3 ohm-cm level. A crystal was grown at 0.0028 cm/sec. The resistivity in the region of 100 cc/min of H_2 was within measurement error of $\pm 3\%$, while the resistivity varied $\pm 8\%$ in the 1000 cc/min region. The reason for this difference is not known.

Measurements of the resistivity variations through the cross sections of the zone leveled crystals were made on rods 0.0125 cm by 0.0125 cm in cross section cut diagonally from the 0.625 cm cross section of the square rods that had been used for the longitudinal measurements. Maximum resistivity variations through the cross section were $\pm 7\%$ and seldom exceeded $\pm 5\%$ in any of the growth conditions studied.

Values for the effective distribution coefficient of Al in Si at the concentration levels and with the growth variables studied ranged between 2.0×10^{-3} and 9.0×10^{-3}. Burton (5) has reported an equilibrium distribution coefficient value for Al in Si at the melting point of Si $> 4.0 \times 10^{-3}$. The values obtained from the present work are based on Al concentrations in the molten zone calculated from the concentration of Al added and corrected for zone volume changes measured along the crystal length. The concentration of Al in the leveled crystals and in the doping alloys was obtained from the respective resistivity measurements using mobility data of Prince (6).

There is some uncertainty in Prince's mobility data below 1.0 ohm-cm, and an extrapolation was made to the 0.038 ohm-cm level. Calculations of the effective distribution coefficient were also made using the recent values of hole mobility determined by Backenstoss (7). These resulted in distribution coefficients as large as 1.5×10^{-2}. These values are much larger than any previous estimate of the distribution coefficient of aluminum. Furthermore, if the distribution coefficient was this large, zone leveling with Al should not be as effective as is actually observed. This indicates that the mobilities reported by Backenstoss may be too low at low resistivities.

Minority carrier lifetime determined by photoconductivity decay measurements (8) ranged from 10-20 μsec at the 0.3 ohm-cm level, and from 50-200 μsec at the 5 ohm-cm level.

Conclusions

For the growth parameters studied, changes in growth rate have the largest effect on resistivity level. Increasing the growth rate from 0.0021 cm/sec to 0.0058 cm/sec produced a decrease in the resistivity level of approximately 25% at the 0.3 ohm-cm level and 35% at the 5 ohm-cm level. Changes in stirring rate or gas flow rate do not produce significant effects on resistivity level over the range that was explored. Also aluminum evaporation is not significant. This suggests that satisfactory zone leveling of Al in Si requires close control of growth rate while moderate variations in rotation rate and ambient gas flow rate can be tolerated.

Crystals doped with Al can be grown in the present apparatus with resistivity variations along the length of $\pm 5\%$ or less at the 0.3 ohm-cm level at growth rates between 0.0021 cm/sec and 0.0058 cm/sec and at the 5 ohm-cm level at 0.0058 cm/sec. Crystals doped to the 5 ohm-cm level and grown at approximately 0.0021 cm/sec have variations along the length of $\sim 10\%$. Resistivity variations through the cross section of all crystals studied were less than $\pm 7\%$.

Acknowledgments

The authors wish to express their appreciation to Miss A. D. Mills who made all the resistivity and lifetime measurements.

Manuscript received Feb. 24, 1959. This paper was prepared for delivery before the New York Meeting, April 27-May 1, 1958.

Any discussion of this paper will appear in a Discussion Section to be published in the June 1960 JOURNAL.

REFERENCES

1. W. G. Pfann, *Metall. Rev.*, **2**, 65 (1957).
2. P. H. Keck, W. Van Horn, J. Soled, and A. MacDonald, *Rev. Sci. Inst.*, **25**, 331 (1954).
   R. Emeis, *Z. Naturforsch.*, **9a**, 67 (1954).
   H. C. Theurer, *J. Metals*, **8**, 1316 (1956).
3. E. Buehler, *Rev. Sci. Inst.*, **28**, No. 6, 453 (1957).
4. J. A. Burton, R. C. Prim, and W. P. Slichter, *J. Chem. Phys.*, **21**, 1987 (1953).
5. J. A. Burton, *Physica*, **20**, 845 (1954).
6. M. Prince, *Phys. Rev.*, **93**, 1204 (1954).
7. G. Backenstoss, *ibid.*, **108**, 1416 (1957).
8. R. L. Watters and G. W. Ludwig, *J. Appl. Phy.*, **27**, No. 6, 489 (1956).

Simple Method of Determining Crystal Perfection

H. K. Herglotz

Pigments Department, E. I. du Pont de Nemours & Company, Inc., Wilmington, Delaware

ABSTRACT

An optical analogy leads to a simple x-ray method of determining crystal perfection. Although furnishing only semiquantitative information at present, this can be developed into a quantitative method. For some applications it is considered superior to existing techniques such as etch pit counts or x-ray rocking curves. This method is combined with the determination of the crystal orientation since it is based on a slightly modified Laue back reflection method.

It is not necessary to stress the importance of crystal perfection for semiconductor devices since it has been emphasized by several authors (1, 2). Many of the properties of the solid state can be understood only if a deviation from the regular arrangement of matter in crystals is assumed (3). The status of this knowledge has been summarized (4, 5).

The methods commonly used for the determination of single crystal perfection are etch pit counts (6), copper precipitation (7), and x-ray rocking curve measurements (8, 9). These procedures have limitations with respect to ease of handling, reproducibility, or interpretation.

This paper describes a simple x-ray method which eliminates some of the drawbacks of the methods mentioned above. The objective of this method is an over-all characterization of the crystal with respect to reticular orientation (Ref. 4, p. 411) but not to lattice defects of atomic dimensions. Other x-ray methods of perfection studies are available (10-12).

This part of the publication presents a qualitative description of the method, an outline of the evaluation procedure, and some preliminary results. Part II will deal with some quantitative considerations and more examples of application.

Experimental Procedure

A model with visible light is helpful in explaining this x-ray method (13). The reference article shows a well grown rock salt cube which, although far from being an ideal single crystal, might represent here a single crystal. It is completely transparent which means that no internal surfaces reflect light from a light source into the eye of the observer. However, it became dull and opaque after it had been deformed by exercising some pressure on it in a hand press. The crystal has kept its external shape, but the deformation has created internal reflecting surfaces. This rock salt cube with internal surfaces might serve as a model for a mosaic crystal.

Consider an analogous experiment using x-rays, for which practically all materials are to some extent transparent, particularly silicon or germanium. X-rays are also a more sensitive probe due to their short wave lengths. The inherent differences between x-ray diffraction and optical reflection must be kept in mind in spite of the frequent informal use of the expression "x-ray reflection."

Due to the selectivity of x-ray diffraction a stationary single crystal permits reflections by the lattice planes only if a variety of wave length (bremsstrahlung) is used so that the crystal can select those which satisfy Bragg's equation: $n\lambda = 2d \sin \theta$.

Monochromatic radiation, however, has a chance for reflection only if a variety of angles are used so that the crystal can select those very few which satisfy Bragg's equation. It is well known that this is achieved by rocking or rotating a single crystal. In the case of a powder or polycrystal without preferred orientation, a large variety of lattice planes is present, whose normals point to all directions of radii of the sphere around the crystal. This large number of planes offers such a variety of incident angles that in any case a sufficient number of planes are in glancing position. The geometrical shape of all rays reflected by one type of planes forms a cone with an apex of 4θ or $360\text{-}4\theta$, respectively. The polychromatic bremsstrahlung is in the case of a powder reflected in all directions because of the variety of both λ and θ and contributes to the background only.

The oriented polycrystals such as rolled sheets or electrolytically grown whiskers, to name two of many examples, hold a position between the well grown single crystal and the irregular powder, which mark the extremes. Also, a place between, although closer to the single crystal, must be attributed to the distorted single crystal (mosaic crystal) as represented by the opaque rock salt cube.

Since the mosaic crystal, the most common form of "single crystal," is a hybrid between the perfect monocrystal and a polycrystal, a method should be available to determine how much of each component is present. One possible way is to take an x-ray pattern under conditions for both mono- and polycrystal and find out what traces of polycrystallinity it contains.

As stated previously, it is proper to use the bremsstrahlung to obtain a pattern of a stationary single crystal (Laue pattern). A tungsten target x-ray tube serves best for this purpose, since the radiation from such a tube consists almost exclusively of the polychromatic x-ray spectrum.

For powder patterns, however, the bremsspectrum is not only useless, but even adverse, since it gives rise to excessive background. The radiation of a copper target is used mostly for this case since it com-

bines a very intense characteristic radiation with little bremsstrahlung due to the relatively low atomic number of copper. To make Debye-Scherrer diagrams even clearer, other wave lengths besides the desired Kα-doublet are suppressed or eliminated by filters, monochromators, or pulse height discriminators.

However, the purpose is served best by the unfiltered radiation of a copper target, since it offers a certain amount of a polychromatic radiation plus a strong monochromatic component. Thus, conditions for both single and polycrystal are met simultaneously. Furthermore, the unfiltered radiation from a copper target is obtainable in the simplest fashion.

Registration by counters (Geiger, proportional, scintillation), which offers tremendous advantages in many cases in comparison to photographic methods, is not very suitable in this case because the scanning nature of these devices makes registration of a Laue pattern of a single crystal uneconomical. A recorder should register a maximum of diffracted rays and offer an over-all view of the crystal. The ideal situation would be to have a spherical film around the crystal. The closest approximation to this, which permits rolling off the film into a plane, is the double cone suggested by Regler (14, 15).

The appearance of undeformed and deformed rock salt in double cone patterns is illustrated by Fig. 1 and 2, respectively. The film from regular cones has the shape of a semicircle and permits simple evaluation of the readings on the film.

Figure 1 shows a Laue pattern of a single crystal with spots from the bremsstrahlung and hardly any diffraction of the copper radiation. This corresponds to the reflectionless appearance of the crystal in visible light. Distortion of the crystal lets monochromatic reflections appear in the form of lunates on the back reflected part and causes the Laue spots on the transmitted part to degenerate to curves, (Fig. 2). This is closely related to the multiple reflections of the visible light which make the crystal appear dull.

In using these facts for crystal perfection studies,

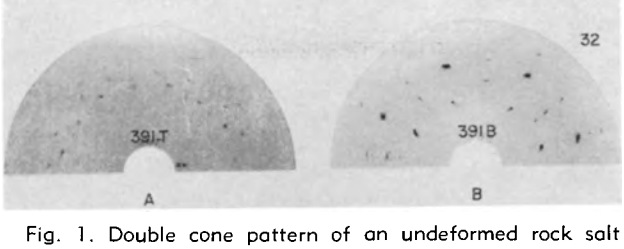

Fig. 1. Double cone pattern of an undeformed rock salt crystal: (A) transmitted part, (B) back-reflected part. The figure next to the back reflected pattern indicates the perfection value in arbitrary units (see Fig. 7).

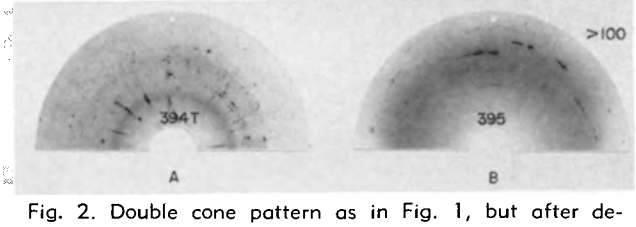

Fig. 2. Double cone pattern as in Fig. 1, but after deformation of the rock salt crystal.

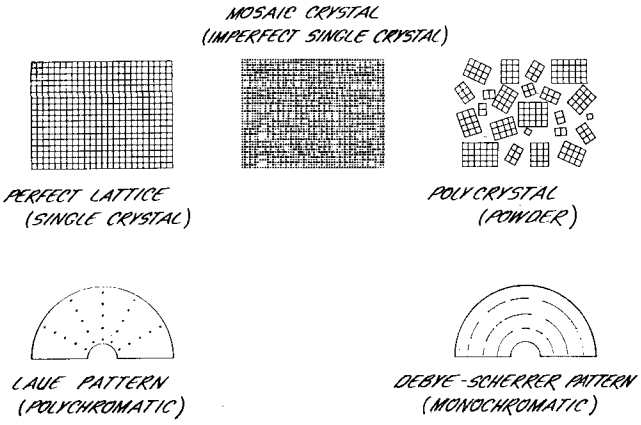

Fig. 3. Summary of perfection method

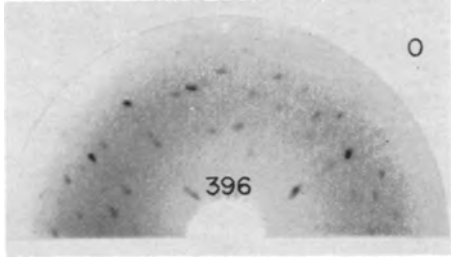

Fig. 4. Cone back reflection pattern of a diamond (perfection value 0).

it is found the back reflected cone furnishes all the information we need and permits nondestructive testing. Restriction to the back reflected part of the diffraction pattern is, therefore, no disadvantage since it offers simplicity with no sacrifice of information. This is the reason all routine work on perfection studies has been carried out with the single cone back reflection method only.

As compared to the plane film method, the advantages of the cone back reflection method for the task under consideration consist of: (a) focusing, which reduces exposure time by making use of a wider aperture; (b) recording of all glancing angles $45 < \theta < 90$ on the entire circumference of the diffraction cones.

Figure 3 summarizes the situation. A perfect lattice, symbolized by an undistorted network (left), furnishes only a Laue pattern from the bremsstrahlung. A completely irregular polycrystal with small sized crystallites furnishes only Debye-Scherrer circles, the bremsstrahlung disappearing in the continuous background. The mosaic crystal, symbolized by an irregular network, is a hybrid between the two.

Even with the small divergence of the primary beam which offers a small variety of angles to the crystal, no traces of Debye-Scherrer lines should be found on the Laue back reflection pattern of an ideal single crystal. This is proved by Fig. 4, a pattern from a 3 x 3 mm clear diamond chip. Diamond is known to have the most nearly perfect lattice. In spite of the divergence of about 5° of the primary beam, no reflection from the copper K radiation can be observed. The diamond chip was not cut in a major crystallographic direction; therefore, no simple symmetry relations can be seen on its Laue pattern.

To demonstrate the opposite extreme from this diamond lattice, a pattern taken under the same con-

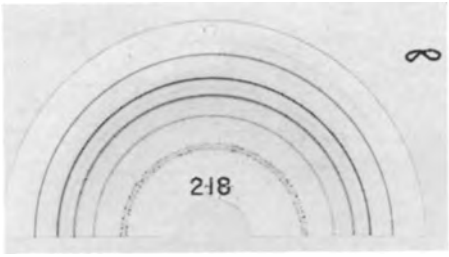

Fig. 5. Cone back reflection pattern of a polycrystalline piece of silicon (perfection value ∞).

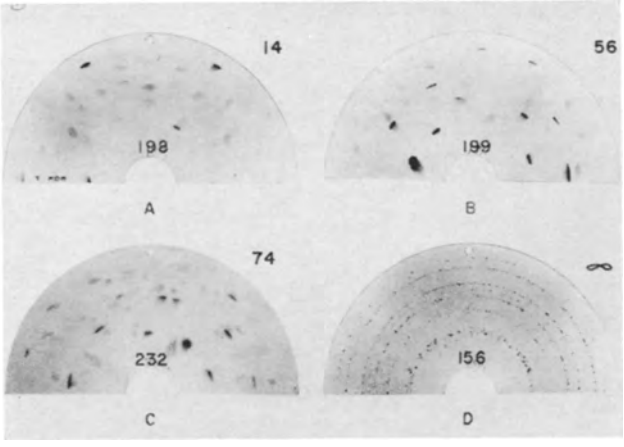

Fig. 6. Various degrees of "singularity" between the extremes of Fig. 4 and 5. A, B, Czochralski crystals with perfection values of (14) and (56), respectively; C, floating zone crystal, twinned (74); D, silicon needle from the zinc reduction of silicon tetrachloride (∞).

ditions as for Fig. 4 was obtained with a piece of silicon (Fig. 5). The silicon was obtained by vapor decomposition of its chloride. It is an example of a finely polycrystalline aggregate without any preferred orientation furnishing full Debye-Scherrer circles (degenerated into half circles after rolling off the film). No Laue spots from the bremsspectrum can be observed.

Between these two extremes belong the photographs of Fig. 6 (A-D). Figure 6A is taken from a well grown Si-Czochralski crystal, "B" from a less perfect Si single crystal, "C" is the pattern from an early unsuccessful attempt to grow a float zoned single crystal, and "D" stems from a silicon needle deposited from the vapor phase. The latter approaches Fig. 5, but the crystalline individuals are large enough to furnish Laue spots instead of continuous background from the bremsspectrum. A necessary consequence of this is that the Debye-Scherrer circles are broken into single reflections and are not continuous as in Fig. 5.

Evaluation of Perfection Numbers

These experiments make it clear that conclusions about the perfection of the single crystal can be drawn by counting the number of monochromatic reflections and by taking into account the size of the lunates, in other words, estimating the fraction of the Debye-Scherrer circle which is blackened. This leads to semiquantitative results in arbitrary units, good for comparison of crystals but not of significance in an absolute sense. A scale for arbitrary units is suggested in a later part of this paper (Fig. 7).

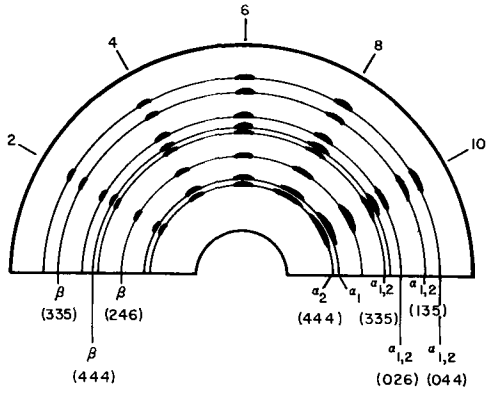

Fig. 7. Scheme of a rough scale for evaluation in arbitrary units. The size of the lunates is rated from 2-10. The reflecting planes are marked (in parentheses) from both Kα and Kβ. If the doublet appears, the number should be doubled. The β-reflections are weaker than the α-reflections because of the lower intensity of the β wave length.

Perfection numbers measured in these arbitrary units are shown for the back reflection patterns of Fig. 1, 2, 4-6, 13. This figure in arbitrary units is derived from the planes (111), (013), (011), (135), (335), (123), which appear on the back reflection pattern of silicon with the radiation from a copper target (see Fig. 7).

The method applied in this way is semiquantitative and does not take strict account of several factors such as, for example, the divergence of the primary beam and the intensity of the Debye-Scherrer lunates (correlated with each other). The method, however, furnishes a very dependable relative measure of perfection as demonstrated by a few examples below. A chip of a clear industrial diamond serves as a standard marking the zero point of the scale. A perfect single crystal represents the value 0 in this scale, while the powder or polycrystal with continuous Debye-Scherrer circles is designated as infinity. The method can be developed into a quantitative one leading to the stereographic projection of the poles of all planes appearing on the back reflection pattern. The number of planes registered can be increased by using alloyed targets (14). This development will be described in a future paper. For almost all practical purposes encountered with semiconductor single crystals, evaluation in arbitrary units yields adequate information and is preferred because of the rapidity of the method.

A few more detailed instructions about this proposed semiquantitative scale in arbitrary units is given below to facilitate its application.

Figure 7 is a rough sketch of a cone back reflection pattern of silicon with copper radiation. The full semicircles, pictured in thin lines, are the Debye-Scherrer reflections from the following planes (111) IV. Order, (335), (013) II. Order, (135), (011) IV. Order, (335), and (123) II. Order. These reflections are obtained by the α_1, α_2 doublet and/or by the β line of the characteristic copper K spectrum. At glancing angles near 90°, the α-doublet is clearly resolved into its components (444 reflection). In the case of an imperfect single crystal, fractions of these Debye-Scherrer circles appear on the pattern on the place of a Laue spot. Fractions from all possible

Debye-Scherrer circles can appear. This is verified for example in Fig. 13B, where practically every Debye-Scherrer circle is represented by a fraction. There is a correlation between the peripheral width of the lunate, its glancing angle θ, and the fluctuation of the normal vector of the reflecting plane. This will be covered in more detail in Part II of this paper. A small fraction on any of the Debye-Scherrer circles points to a relatively small misorientation of the lattice. A number of 2 is arbitrarily attributed to such a small lunate pictured on the left side of Fig. 7. Increasing size of the lunate points to larger misorientation and is represented on subsequent rows, from left to right, Fig. 7, by increasing "imperfection values" ranging from 2-10. A double lunate of both α_1 and α_2 radiation indicates a rather serious misalignment of the crystal since the probability of reflection of a monochromate radiation by a single crystal is small; to reflect two monochromatic wave lengths of 4 XU wave-length distance is still more improbable. If it happens, the crystal must be significantly distorted. Therefore, such a double lunate should be counted double. The reproductions do not give all the details visible on the originals, particularly with respect to these double lunates. In Fig. 13, a full evaluation of these patterns is carried out, leading to the "perfection" values at the right side of the patterns.

The significance of the intensity of a lunate should also be considered when evaluating the photographs. A very intense lunate of small peripheral width evidently stems from a small fluctuation of the normal vector of a "shattered plane," but spread over a large part of the crystal. On the other hand, one occasionally finds large fractions of the Debye-Scherrer circle of very weak intensity (Fig. 6C, clearly visible on the original photograph). Such a case points to a serious misorientation with large fluctuations of the normal vector but only in small areas of the crystal.

Admittedly, the perfection figures are dependent on some individual judgment varying from person to person. However, it has been established empirically

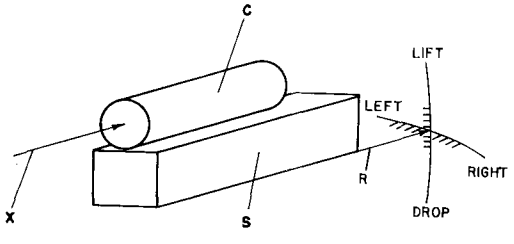

Fig. 8. Device for crystal orientation and cutting: X, x-ray beam; S, support; C, crystal; R, reference direction for corrections (turn left—turn right, and lift—drop).

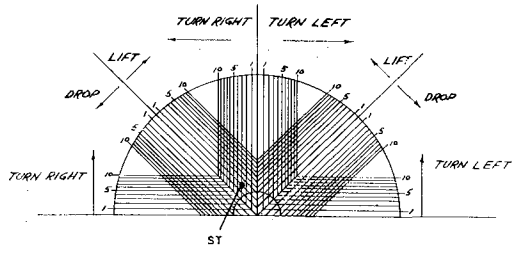

Fig. 9. Mask for orientation (correction values in degrees)

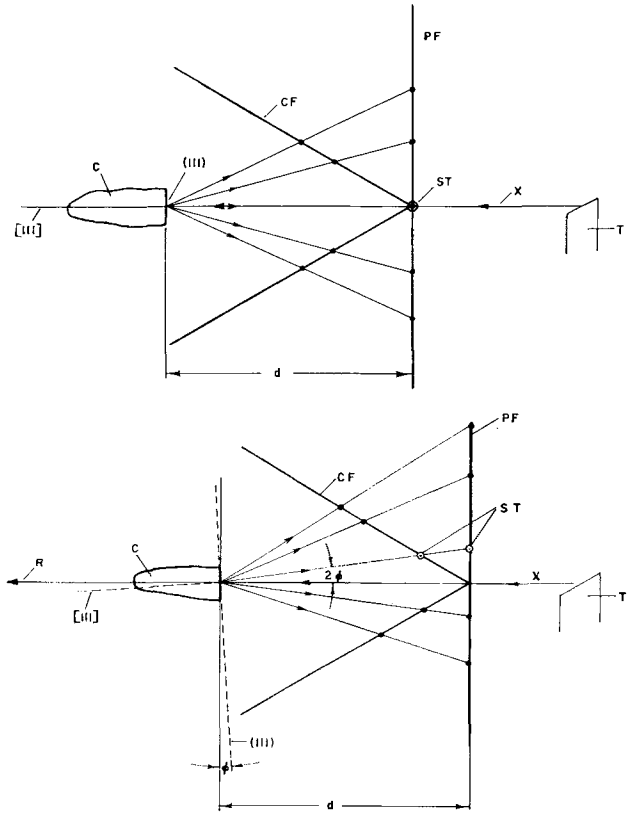

Fig. 10. Scheme of Laue back reflection method on plane and cone film from a perfectly oriented crystal (A) (top) and a crystal misoriented by the angle ϕ (B) (bottom) C = Crystal. [111], Crystallographic direction, X, x-ray beam, T, x-ray target. (111), crystallographic plane, d, crystal-film distance. CF, cone film, ST, starpoint, PF plane film.

that a laboratory assistant, after proper instruction, will assign figures differing not more than a few points from those of the writer in most cases. A deviation of several points is rare. It is significant that the relative values assigned by a given observer are self-consistent, based on numerous cases, although the absolute figures may vary slightly.

Crystal Orientation

The method furnishes crystal orientation simultaneously. If the direction of the x-ray beam is a major direction of the lattice, for example the [111]-direction, the Laue spots of zones with zone axes perpendicular to the x-ray beam intersect in the center of the cone (Fig. 1b). If the crystal direction is a few degrees off, the intersection does not occur in the center of the film (Fig. 13). If the crystal is fixed on a support as demonstrated in Fig. 8, correction values can be derived with respect to a direction of reference. Whereas the monochromatic reflections are used for evaluation of the perfection, the polychromatic Laue spots are an excellent means of determining how much a crystal grown in a certain crystallographic direction deviates from this direction. Figure 9 shows a mask which enables one to read correction values with respect to the reference direction of Fig. 8. These corrections can be incorporated when the support shown in Fig. 8 is fastened on the diamond saw. The mask is derived from the geometry of the particular cone camera and a definite sample distance (see Fig. 10).

If the starpoint (intersection of spots from zones with zone axes perpendicular to the x-ray beam) is at the position marked in Fig. 9, a movement of the R-direction (Fig. 8) 2° upward and 3° to the right will bring the crystal into a position such that the x-ray beam is in accord with the [111]-direction of the lattice, which was the direction of growth in this case.

Figures 10-12 illustrate more in detail how the mask of Fig. 9 and the correction values are obtained. Consider a Laue plane film back reflection pattern, the more familiar case. It is then easy to change to the less common cone film.

The macroscopic axis of the crystal might be the [111]-direction and the x-ray beam may impinge perpendicularly to the (111)-plane (Fig. 10A). Then we obtain the Laue pattern sketched in Fig. 11A. If the [111]-direction does not coincide with the macroscopic crystal axis but is inclined by the angle ϕ (Fig. 10B), we obtain the Laue pattern of Fig. 11B or C, respectively, depending on whether the deviation is vertical or horizontal. The [111]-direction can deviate in an arbitrary manner, of course, but this case can be resolved into a vertical plus horizontal deviation.

The mirror can be used as an analogy. To bring the crystal (or mirror, respectively) of Fig. 11B or C into a position to furnish a Laue pattern of Fig. 11A, turn it by the angle ϕ_V in the vertical or ϕ_H in the horizontal direction, respectively. Use of a mask facilitates evaluation of the films (Fig. 12). This mask or the one for the cone film can be obtained by geometrical construction using Fig. 10 for a given distance, d, and varying angles, ϕ.

Figure 12 shows a Laue plane film back reflection pattern on top of the mask. The crystal from which this diagram stems could be oriented by a movement of the R direction (Fig. 8) 2° upward and 2° to the left.

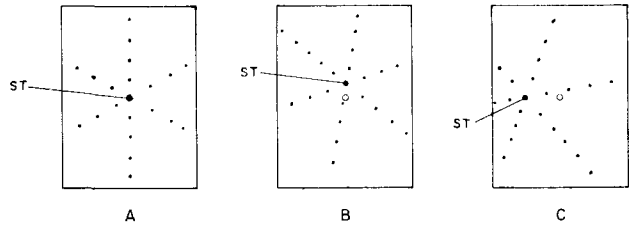

Fig. 11. Schematic Laue plane film patterns from a perfectly oriented crystal (A), a vertically misoriented crystal (B), and a horizontally misoriented crystal (C); ST, star point.

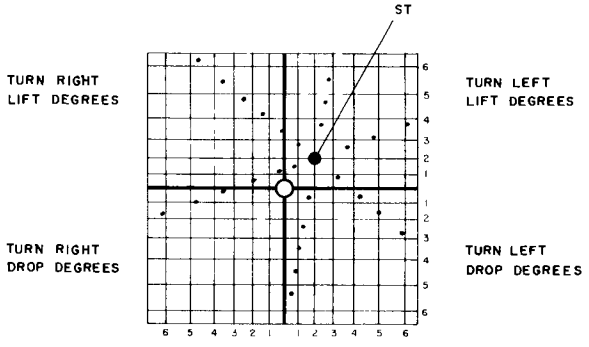

Fig. 12. Evaluation mask for a plane film at a given distance d (Fig. 10). On top of mask, a sketched Laue pattern from a misoriented crystal.

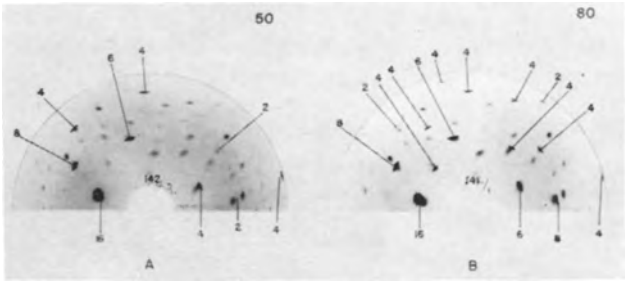

Fig. 13. Cone back reflection pattern of the top (A) and bottom (B) of a Czochralski crystal. The crystal axis is about 9° off the [111]-direction. Degree of perfection evaluated according to Fig. 7.

The shift from these plane film considerations to the case of a cone is very simple. The symmetry of the photograph is unchanged. Rolling off the film cone, however, compresses the 360° picture of the plane film into the 180° of a semicircle. It also compresses the mask of Fig. 12 to our mask of Fig. 9. Simple geometrical considerations show that the starpoint of Fig. 11 and 12 is split in two when the cone film is rolled off into a semicircle, but only the one lying within the film semicircle is realistic and can be used for evaluation purposes.

In this discussion, no consideration has been given to orientation of the crystal by rotation about its axis of growth. This is evident from the random direction of radii of the star in Fig. 11 A-C. If orientation with respect to rotation about the crystal axis of growth is desired, this can readily be done by measuring the angle necessary to rotate the star in order to bring it to the desired position.

No attention has been paid to the attainable precision of this orientation method. The accuracy of the cutting tool for which the orientation figures were used was inferior (±1°). Therefore, no need existed for more accurate x-ray orientation, which can be achieved easily.

Results of Perfection Studies

Results of the new method generally agree with information obtained by etch pit counts (see Table I). Disagreement, however, was experienced in some cases, where the etched plane did not coincide with the (111) plane nor with any other low indices plane.

The decrease in perfection of a Czochralski crystal from top to bottom is demonstrated in Fig. 13. Whereas the part next to the seed can be characterized by a number in arbitrary units of 50, the bottom represents a number of 80. The same or a similar observation was made in many other cases. However, this rule appears to be invalid in cases of crystals

Table I. Comparison of etch pit counts with x-ray values

Crystal slice	Etch pits	Perfection No. (Fig. 7)
A	$1 \times 10^4/cm^2$	30
B	$2 \times 10^4/cm^2$	46
C	$1 \times 10^4/cm^2$	32

with good orientation and good perfection.

The influence of sawing and sanding on the x-ray picture was demonstrated in another experiment. A large crystal disk sawed from a Czochralski crystal was covered with wax. The wax was successively removed from different quarters and the crystal leached every time so that the 4 quarters were exposed 0, 1, 2, 5 min to the etchant (HF, HNO_3, COOH, equal parts, about 40°C). The thickness change of the four sectors was: 0, 0.04, 0.06, 0.1 mm. X-ray patterns taken from each of the 4 sectors demonstrated that, after removal of 0.04 mm, the pattern did not change by further removal. In other words, the thickness of the damaged layer was less than 0.04 mm. Higher intensity of the pattern from the unleached part of the crystal, clearly visible on the photographs, is another criterion of distortion (secondary extinction) (3, 4) but can be observed only in a case like this where photographs were taken under identical conditions before and after removal of the damaged surface layer.

Other conclusions from corresponding experiments were:

(*A*) The average crystal grown in good accord with a major lattice direction is of better perfection than the average crystal poorly oriented during growth.

(*B*) Pictures taken before and after heat treatment showed only slight differences which were not consistent from crystal to crystal. The heat treatment consisted of heating the crystal in argon and holding at 1100°C for 30 min, cooling in the furnace to 700°C, and removing from the furnace.

(*C*) The average perfection of large diameter crystals is better than the one of small diameter crystals. This rule was found true in the range $\frac{3}{8}$ in. $< d < 1$ in. (d = diameter). Different results, however, have been reported in the case of germanium crystals. Since the perfection of Czochralski crystals depends on many factors such as geometrical arrangement, gradient of supercooling, and skill of the operator, a rather complex correlation might be obtained if other variables besides the diameter in the limited range between $\frac{3}{8}$ in. and 1 in. are varied.

(*D*) A multipass float zoned crystal from which all impurities other than boron had been removed was of very high perfection. Whether this is a general rule could be established only after a series of experiments, but it appears to be very logical.

(*E*) A Czochralski crystal grown with poor heat control due to failure of the automatic heat control was of very poor perfection. What has been said in the former example about establishing this as a general rule applies here.

It is inherent in the method that it integrates over the whole volume of the crystal hit by the slightly divergent beam. Therefore, localized imperfections such as those close to the surface can be detected only under certain conditions.

The photographs were taken almost exclusively under the following conditions: radiation: Cu-target, 35 kvp, 20 ma; exposure time: 10 min; size of pinhole: 0.6 mm.

Manuscript received Nov. 12, 1958. This paper was prepared for delivery before the Ottawa Meeting, Sept. 28-Oct. 2, 1958.

Any discussion of this paper will appear in a Discussion Section to be published in the June 1960 JOURNAL.

REFERENCES

1. H. Y. Fan, "Valence Semiconductors, Germanium and Silicon"; F. Seitz and D. Turnbull, "Solid State Physics," Vol. 1, p. 315, Academic Press, New York (1955).
2. E. Paskell, "Semiconductor Abstracts," Vol. 3, John Wiley & Sons, Inc., New York (1955); References under "Dislocations" and "Lattice Defects."
3. C. G. Darwin, *Phil. Mag.*, **27**, 675 (1914).
4. W. Shockley, J. H. Hollomon, R. Maurer, and F. Seitz, "Imperfections in Nearly Perfect Crystals," John Wiley & Sons, Inc., New York (1952).
5. W. T. Read, Jr., "Dislocations in Crystals," McGraw Hill Book Co., New York (1953).
6. P. Lacombe, "Report of Conference on Strength of Solids," p. 91, Physical Society, London (1948).
7. W. C. Dash, *J. Appl. Phys.*, **27**, 1193 (1956).
8. A. D. Kurtz, S. A. Kulin, and B. L. Averbach, *J. Appl. Phys.*, **27**, 1287 (1956); *Phys. Rev.*, **101**, 1285 (1956).
9. A. H. Compton and S. K. Allison "X-Rays in Theory and Experiment," p. 726, D. Van Nostrand Co., Inc., New York (1935).
10. P. J. Holmes, *J. Electronics*, **1**, 324 (1955).
11. W. Cochran, *Acta Cryst.*, **9**, 259 (1956).
12. A. Merlini and A. Guinier, *Bull. soc. franc. minéral. et crist.*, **53**, 147 (1957).
13. H. Herglotz, *Radex-Rundschau*, **1953**, 106.
14. F. Regler, *Z. Phys.*, **74**, 547 (1932).
15. H. Herglotz, *Z. Metallkunde*, **46**, 620 (1955).

The Anodic Oxidation of Zinc and a Method of Altering the Characteristics of the Anodic Films

H. Fry and Marjorie Whitaker

The British Non-Ferrous Metals Research Association, London, England

ABSTRACT

Preliminary work on anodizing zinc in a variety of alkaline solutions led to some smooth white or gray films. A detailed study was made of the anodic oxidation of zinc and zinc alloys in one electrolyte the results of which suggest similarities but also some differences between anodic films on aluminum and on zinc. Autoclaving in silicate solutions improved the resistance to corrosion and abrasion and changed the chemical composition of the anodic films without altering their appearance greatly.

Systematic work previously has been done on the kinetics of the oxidation of zinc in air (1) and of the initial stages of the anodic oxidation of zinc in sodium hydroxide solutions as well as on the characteristics of films on zinc produced by anodic oxidation at low voltages in a variety of solutions (2-7). Considerable variations in the properties of the films were observed in the earlier work. It was therefore of interest to study some aspects of the nature and growth of a wider variety of anodic films on zinc, including particularly films formed at higher field strengths. In view of the poor chemical resistance which zinc oxide films were expected to have, the possibility was examined of converting the films to zinc silicate by reaction of the anodic film with a silicate solution at elevated pressure and temperature.

Experimental

The following materials were used: high-purity Zn strip (99.95%), 4.3 mm thick, main impurity 0.02% Pb; die-cast flat plates of Mazak 3,[1] 2.8 mm thick; chill-cast Zn-4% Al and Zn-12% Al alloys, made from 99.99% pure metals. Their grain size and microstructure were coarser than those of the die-cast alloy. In the 4% Al alloy the primary phase is the Zn-rich β solid solution, containing about 1% Al (light gray in Fig. 1A). In the 12% Al alloy the primary phase is the α solid solution, and it separates on cooling to a mixture of α and β phases; this is the slightly darker constituent in Fig. 1B. The electrolytes were made up with demineralized water using "Analar" chemicals if available or purest commercial grade of chemicals.

Preparation of specimens.—Strips of the material to be anodized (1 x 8 cm) were bolted to copper strips. An area of 3 x 1 cm of polished surface on one side was left exposed for anodizing and the remainder coated with an insulating lacquer. The zinc was electropolished in a solution of 250 g/l chromic acid, 12 g/l boric acid, and the alloys were buffed.

Anodizing procedure.—Fresh electrolyte at 20°C was used for each experiment, unless otherwise stated, and stirred during anodizing. Specimens were immersed for 15 sec before applying the potential. Temperature rises of up to 3°C were observed during anodizing. The anode potential relative to a saturated calomel electrode was measured as a function of time.

[1] Zamak 3 in U.S.A. High purity Zn-4.1% Al-0.04% Mg.

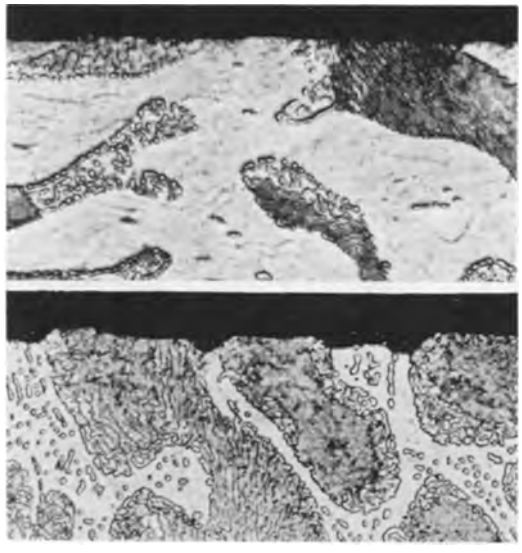

Fig. 1. Microsections through the anodized surface of chill-cast alloys showing (A) (top) even attack on Zn-4% Al and (B) (bottom) preferential attack on the eutectic in Zn-12% Al. Both etched nital. (The films, which are about 5 mm thick at this magnification, are not visible in the photographs.) Magnification X100.

In constant-current tests the selected current density was reached almost instantaneously and was maintained to within 1%. In constant-anode-potential tests the selected potential was reached in about 10 sec and was maintained to within 1%. In some tests the mains voltage was applied across the cell in series with a fixed external resistance.

After-treatment.—Anodized specimens were autoclaved in various solutions in a stainless steel autoclave.

Isolation of films and density measurements.—Film thicknesses were measured on microsections to $\pm\frac{1}{4}\mu$ at a magnification of 1000. The apparent density was determined by weighing isolated films of known area (6). The method involved an experimental error of about $\pm 10\%$.

Abrasion resistance.—The abrasion resistance of the films was measured by a method due to Schuh

and Kern (8) in which a stream of 60 mesh fused alundum particles falls on to the film from a height of 1 m through a tube of 0.5 cm internal diameter. The film was judged to be worn through when electrical contact could be made with the basis metal over an area which was just sensibly greater than a single point with a hardened steel probe having a radius of curvature of 1/16 in. Results of abrasion tests, expressed in terms of the volume of abrasive required to penetrate the coating, appear to be reproducible to within ±10%.

Results

Preliminary Work

Dark films and white films.—Black coatings were obtained by anodizing zinc in *N* NaOH solution at a current density of about 200 ma/cm² and a cell voltage of about 5 v. These coatings were smooth and uncracked and in this respect differed from those prepared by Huber at a cell voltage of 2.5 v (4).

In various solutions containing Na_2CO_3 and NaOH, dark films were formed at low anode potentials and white films at higher potentials. Films formed under the latter conditions were transparent when thin.

Formation of smooth anodic films.—Using a constant voltage source and constant external resistance, zinc was anodized in a series of mixtures made from 0.2*N* NaOH and one other 0.2*N* solution. When the second solution was sodium borate or sodium succinate, translucent and smooth opaque white films were obtainable. The latter type of film was obtainable when the second solution was sodium carbonate or sodium oxalate and the former type when it was sodium hydrogen phosphate.

Some of the white films had areas with small, partly or wholly detached flakes. Flaking depended on the solution composition and on conditions and duration of formation of the film. From NaOH-Na_2CO_3 solutions smooth white films were obtained only when the composition was 0.146*N* NaOH, 0.054*N* Na_2CO_3, but the films flaked if, under certain conditions of anodizing, the time exceeded a certain maximum or if the solution had been used previously.

The tendency to form flakes increased with increasing temperature, voltage, and current density. For example, at 0°C incipient flaking occurred only in samples anodized at a constant voltage of 120 v, whereas at 50°C flaking occurred even at 15 v.

Electrical breakdown of anodic films in the electrolyte.—In experiments at constant current, the anode voltage rose until there was an arrest or reversal of the original current-voltage trend accompanied by audible and sometimes visible sparks. Experiments usually were stopped at this stage. The sparking voltage depended on the composition of the electrolyte, a maximum voltage of about 170 v being reached in certain alkaline borate electrolytes while about 110 v was typical for NaOH-Na_2CO_3 solutions.

In the experiments in a solution of 0.146*N* caustic soda 0.054*N* sodium carbonate the sparking voltage in constant current tests was about 130 v at 0°C and 120 v at room temperature, independent of current density under both conditions, while at 50°C it was 3 v at 50 ma/cm² and about 80 v at 183 ma/cm². In later experiments, described below, the mean sparking voltage was about 100 v for zinc anodized in the same solution at an initial temperature of 20°C.

Abrasion resistance of smooth anodic films.—The abrasion resistance of smooth films on zinc varied from about 300 to about 3500 ml of abrasive, i.e., by a factor of about 10. The values for anodized aluminum lay between 8000 and 9000 ml for a 4μ thick sealed anodic film. The abrasion resistance of films formed under one set of conditions increased with thickness, but in general the abrasion resistance per unit thickness was found to depend in a complex manner on the anodizing conditions and on the composition of the solution.

Chemical resistance of anodic films.—A few tests were made of the corrosion resistance provided by anodic films on zinc under humid conditions and the results were invariably poor, white corrosion product appearing after about 1 day's exposure. The anodic films also were attacked by several dye solutions acidified with oxalic acid to pH values lying between 6.4 and 3.2.

Systematic Study of Anodic Oxidation of Zn *and* Zn-Al *Alloys in a Solution of 0.146N Sodium Hydroxide, 0.054N Sodium Carbonate*

Constant current experiments.—When the current flowing through the cell was kept constant during anodizing, smooth white films were formed on zinc and Mazak 3 at current densities in the range 50-200 ma/cm². Curves of anode potential against time are reproduced in Fig. 2A (zinc) and 2B (Mazak 3). They show that after an initial period the anode potential increased linearly with time. The shape of the curve suggests that the initial period, which became shorter as the current density increased, is associated with the formation of black films.

The mean rate of increase of the anode potential with time, obtained by measuring the slope of the straight part of the curve, became greater as the

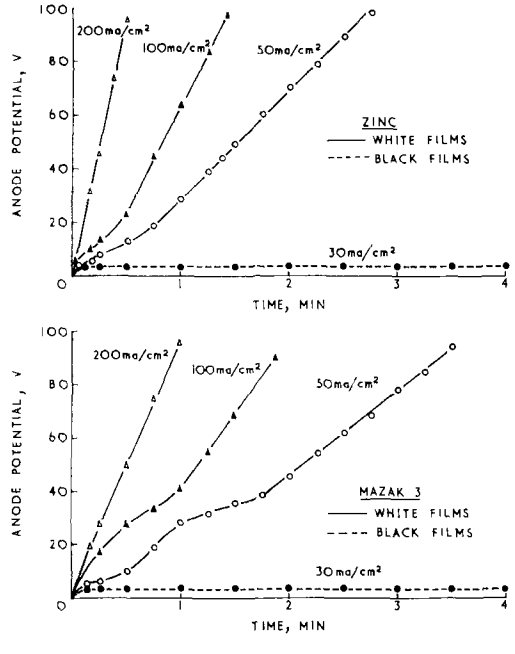

Fig. 2. Anode potential as a function of the time during the formation of black and white films at constant current density (A) (top) zinc, (B) (bottom) Mazak 3.

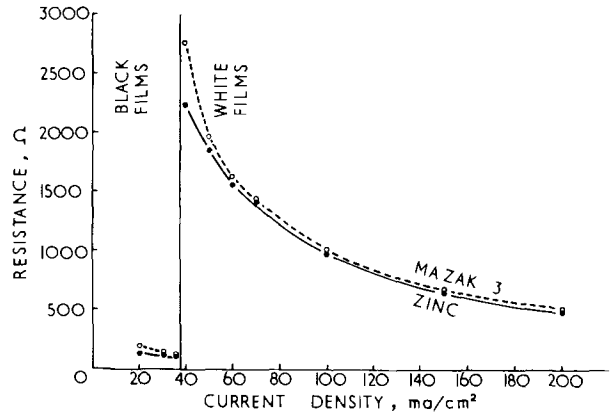

Fig. 3. Effective wet resistance per unit area of a completely formed film as a function of current density in constant-current tests.

current density increased, but the rate of increase of the effective wet resistance (the anode potential divided by the current) was nearly independent of current density. The rate of increase of the effective wet resistance at each current density was greater for zinc than for Mazak 3. Although the reproducibility was low (±20% for zinc and ±25% for Mazak 3 in five tests) the corresponding results for the two materials did not overlap.

There was a spread of about 20 v in the potential at which conditions became unsteady in replicate tests, and the mean was about 100 v, independent of current density for both zinc and Mazak 3 anodes. The effective wet resistance of the complete film was approximately inversely proportional to the current density as shown by the hyperbolic shape of the curves in Fig. 3.

At low current densities, 20 to 35 ma/cm², the anode potential reached a maximum in the range 1.8 to 4 v after several minutes and then fell slightly. The films on both materials were black. Curves showing the relationship between anode potential and time at 30 ma/cm² are given in Fig. 2. The effective wet resistance of completely formed black films, i.e., at the maximum voltage, decreased slowly as the current density was increased within the range 20 to 35 ma/cm² and it was greater for Mazak 3 than for zinc (Fig. 3).

At current densities between 35 and 50 ma/cm² the results were unpredictable. Some films remained dark, some quickly became white, and others remained dark for several minutes and then became white, a fairly sudden increase in resistance being associated with the change.

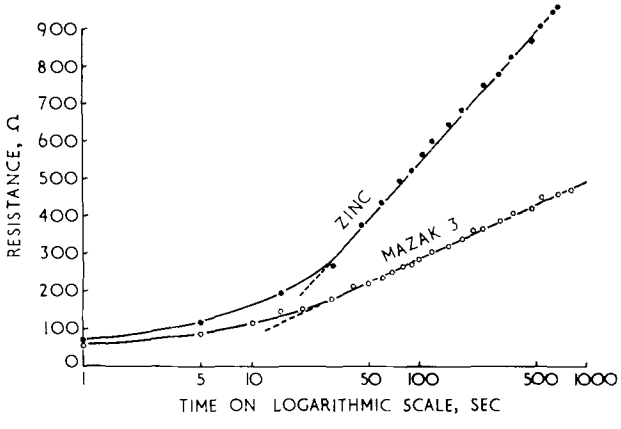

Fig. 4. Typical curves showing the effective wet resistance per unit area of film as a function of the logarithm of time in constant-voltage tests. Zinc and Mazak 3 at 16 v.

With chill-cast Zn-4% Al alloy the rates of increase of anode potential at constant current were close to the corresponding values for Mazak 3, and it was concluded that the results were not influenced by the difference in grain size and microstructure of these two materials.

The Zn-12% Al alloy formed a black film at 30 ma/cm², with effective wet resistance (110 ohm/cm²) similar to that of films on zinc and Mazak 3. Smooth white films were obtained at 70 and 150 ma/cm² but the anode potential did not increase linearly with time; after a continuous rise at a rate which decreased with time the potential became unsteady at a value between 50 and 80 v.

Constant-voltage experiments.—When the anode potential was kept constant during anodizing smooth white films were obtained on zinc and Mazak 3 at anode potentials in the range 4 to 60 v. The point at which fluctuations first occurred in the resistance of the film was taken as indicating the completion of film growth. Figure 4 shows that the effective wet resistance increased linearly with the logarithm of the time after an initial period of slower growth which is probably associated with the formation of black films. The current density at the point of completion, taking the mean of several tests, is plotted against anode potential in Fig. 5, and the effective wet resistance is plotted against anode potential in Fig. 6. At each anode potential in the white-film region the completely formed films on zinc had greater resistance than films on Mazak 3. The scatter of the resistance values was within ±30% in replicate tests, six at each voltage, but the probability that the difference between the two materials at each anode potential (Fig. 6) could have arisen by chance was 2 in 100, which is conventionally accepted as indicating that the difference is significant.

Black films were formed on both materials at anode potentials 1.5-3.5 v. The current reached a minimum after several minutes and then increased, sometimes only slightly. The minimum current is plotted against anode potential in Fig. 5. The effective wet resistance of films on Mazak 3 increased by about 40% at the boundary between dark and white films, and the corresponding increase for zinc was about 100% (Fig. 6).

Relative rates of anodic attack on the different constituents in zinc-aluminum alloys. — Metallographic examination of sections through anodized Mazak 3 and chill-cast Zn-4% Al mounted in a cold-setting acrylic resin revealed no differential attack or penetration at the surface (Fig. 1A). At the surface of the Zn-12% Al alloy, however, the eutectic was attacked more rapidly than the primary dendrites[2] (Fig. 1B). The primary dendrite areas (the slightly darker gray constituent) remained flat in the center during anodizing and did not project through the film at any point.

Thickness of white films on zinc and Mazak 3.—

[2] The buffed surface (before anodizing) was flat.

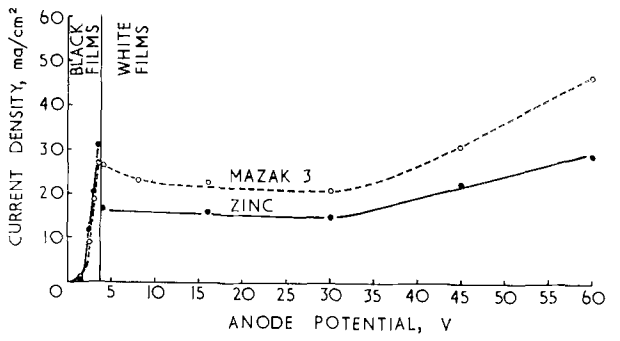

Fig. 5. Current density on completion of film formation as a function of anode potential in constant-voltage tests.

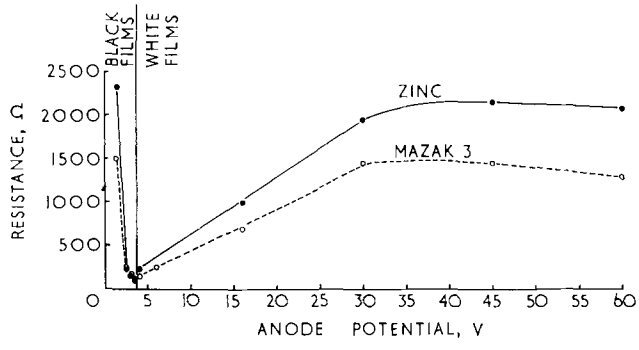

Fig. 6. Effective wet resistance of a completely formed film as a function of anode potential in constant-voltage tests.

Specimens were anodized at 20°C until just before the resistance of the film was known to become unsteady. The thickness of films on zinc (see Table I) appeared to be largely independent of current in constant-current tests (mean about 4μ) and independent of anode potential in constant-voltage tests (mean about 2.5μ). Films on Mazak 3 were thicker than those on zinc. Films on the chill-cast Zn-4% Al alloy were not significantly different in thickness from those on Mazak 3. Exceptionally thick films on Mazak 3 (7-8μ) were formed at 40-50 ma/cm^2 in constant-current tests and at 16-30 v in constant-voltage tests. These films took much longer to form than any of the others.

Rather thicker films were formed at 0° than at 20°C both at constant voltage and constant current, but the thicknesses of films formed at 50°C were the same as those of films formed at 20°C.

Analysis.—Specimens were dried over silica gel for several days. On ignition at 700°C films produced by anodizing zinc at 60 ma/cm^2 lost about 15% by weight. This was mainly water, including combined water, and it probably included a trace of carbon dioxide. The zinc content of these films before ignition, determined microchemically by a titrimetric dithizone procedure, was equivalent to 84% zinc oxide.

The x-ray diffraction pattern of films removed from zinc indicated the presence of zinc oxide in the film; the lines were diffuse, suggesting that the crystal size was small, possibly between 10^{-5} and 10^{-6} cm. No further information was obtained from electron diffraction examination although the diffraction pattern was less diffuse.

Porosity and cell structure of white films on zinc:

Table I. Thickness and porosity of films formed at 20°C

Anodizing conditions	Films on Mazak 3 Thickness,* μ	Films on zinc Thickness,* μ	Films on zinc Porosity,* %
Constant current density, ma/cm^2			
40	7.5	3.8	45
50	6.3	4.3	43
60	5	5.6	43
70	4	4	45
100	3.3	3.5	38
150	5	4.3	54
200	4.5	3.1	40
Constant voltage, v			
16	6.9	2.2	50
30	6.6	2.3	—
45	3.8	2.5	48
60	4	2.4	45

* Mean of duplicate tests.

Electron microscopy.—In many cases carbon replicas of the outer surfaces of anodic films on zinc could not be interpreted, but some evidence of an hexagonal cell structure was obtained from a film formed at 45 v as shown in Fig. 7, the cell width being about 3000Å.

Very thin films examined by direct-transmission appeared to be porous (see Fig. 8). Three constant-current films formed by anodizing zinc for 1 sec and 2 sec at 60 ma/cm^2 and for 0.6 sec at 200 ma/cm^2 were examined in this way; the distance between the pores was about 500Å in each case, with no detectable difference between the two current densities.

Determination of porosity from the apparent density.—Apparent densities were in the range 1.8-3.5 g/cm^3. In calculating the porosity a correction was made for the presence of 15% water in the films, and the density of zincite (5.60 g/cm^3) was taken to be the density of the nonporous oxide. The porosities of duplicate films from zinc anodized at a range of constant-currents and constant-voltages are given in Table I. Within the limits of the experimental error (±15%) the porosity, with a mean value of 45%, appeared to be independent of anodizing conditions.

After-treatment of anodic films on zinc: Composition of autoclaved films.—The films for analysis were made by anodizing in a solution of 0.146*N* sodium hydroxide, 0.054*N* sodium carbonate to just before the sparking voltage and they were autoclaved in a solution of 200 g/l sodium silicate "Q79" containing 8.8% Na_2O, 29% SiO_2, 62.2% H_2O for 30 min at 150°C. The films were isolated (6) and then analyzed in the same way as anodized films. Silica was determined spectrophotometrically as reduced silicomolybdate.

The total water content of films produced at constant current density was about 10%. The ZnO:SiO_2 ratio increased from 2:1 to nearly 3:1 as the current density was increased from 60 to 200 ma/cm^2, although films formed to completion at 60 ma/cm^2 and 200 ma/cm^2 resembled each other closely in thickness and porosity.

Only lines corresponding to zinc oxide were identified in x-ray and electron diffraction photographs.

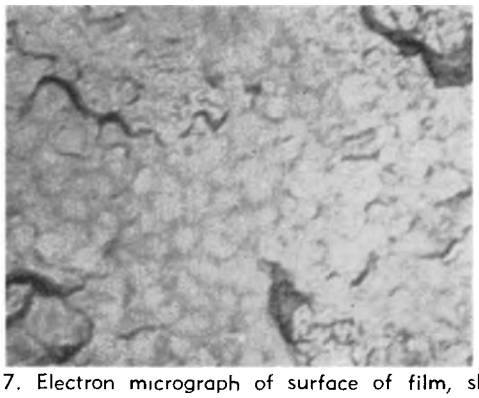

Fig. 7. Electron micrograph of surface of film, showing cell structure. Zinc anodized 1 min at 45 v. X 10,000

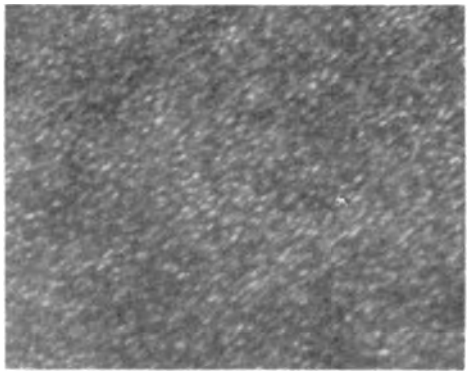

Fig. 8. Direct transmission electron micrograph of film, showing pores. Zinc anodized 2 sec at 60 ma/cm^2. X 32,500

In view of the change of the chemical properties of the film on autoclaving it would be surprising if silica had not entered into chemical combination with zinc oxide to some extent.

Properties of autoclaved films:

Appearance and abrasion resistance.—Films were generally smooth and off-white after autoclaving in a variety of different silicate solutions at 150°C for 30 min. For a given autoclave treatment the abrasion resistance of the films depended in a complicated way on the anodizing conditions, the ratio of abrasion resistances before and after autoclaving varying from 1 to 7. For a given set of anodizing conditions, e.g., 0°C and 50 ma/cm^2, the abrasion resistance of the autoclaved samples increased roughly linearly with the thickness, the duration of the anodic treatment, and the maximum anodic voltage. The highest values of abrasion resistance (about 7000 ml of abrasive) were obtained by using an autoclaving solution with a relatively high SiO_3:Na_2O ratio (about 3.3-3.6) at a relatively high concentration of about 400 g/l sodium silicate (water glass).

The autoclaved films accepted some dyes from acidified solutions, the intensity of the color produced generally increasing as the *p*H of the dye decreased. Dyeing was aided by boiling autoclaved samples in a solution of chromium oxalate the *p*H of which had been adjusted to 7.4 with NaOH.

Corrosion resistance.—Anodized and autoclaved samples suffered hardly any deterioration after 1 week's exposure to humid conditions in contrast to unautoclaved samples which corroded quickly. After 96 hr in an atmosphere of 95% relative humidity containing 3% sulphur dioxide the samples were attacked strongly as were some samples of chromated zinc and of anodized aluminum.

After treatment of anodized zinc alloy die-castings.—Films on zinc alloy were affected adversely during autoclaving in some solutions in which the corresponding films on pure zinc remained intact. The adverse effects included flaking and darkening which occurred particularly when anodizing had been carried out in solutions containing borates. By adding phosphoric acid to the normal autoclaving solutions or by using solutions of lower alkaline content, flaking, but not darkening could be avoided. In some cases a fine mottled effect was observed; the pattern of flow marks was usually found on treated commercial die-castings. Smooth, almost white films were obtained when certain anodized films were autoclaved in a solution of 400 g/l sodium silicate "Q79" (*p*H 11.1) but not for all conditions of anodizing.

The abrasion resistance of anodized and autoclaved samples of zinc alloy was about 3500 ml of abrasive for samples anodized in a NaOH-Na_2CO_3 solution with a fixed external resistance of 1000 ohms and autoclaved in water glass containing phosphoric acid, but this value was not accurately reproducible.

The ability of treated zinc alloy to accept dyes is similar to that of treated zinc.

A few tests suggest that the corrosion resistance of treated zinc alloys resembles that of treated pure zinc. Some anodized and autoclaved zinc alloy die-castings were attacked considerably when exposed to an industrial atmosphere for several months.

Discussion

Composition, Structure, and Color of Anodic Films on Zinc

The results of chemical and x-ray diffraction analysis indicated that the white anodic films consisted essentially of zinc oxide. The same result was obtained by Huber for a white film formed under different conditions (6).

Huber found that loose white coatings were formed when zinc was anodized at cell voltages up to 2 v in *N* NaOH solution and that white or dark films were formed and oxygen was evolved at voltages between 4 and 6 v, the color of the film depending on composition and *p*H of solution. The present results show that continuous white films are formed at still higher voltages in a variety of similar solutions.

The dark appearance of certain films is due to the presence of finely divided zinc (4); such films turn white if heated in air because the free zinc is oxidized. The resistivity of normal zinc oxide, an excess metal semiconductor, is of the order of 10 ohm-cm, and this increases to 10^7 ohms when the oxide is kept for 30 hr at 900°C in 120 atm pressure of oxygen (9). Dried white anodized films on zinc had a resistivity of more than 10^{10} ohm-cm indicating that the composition of such films approaches still more closely that of stoichiometric zinc oxide, ZnO.

The transmission electron micrograph in Fig. 8 demonstrates the porosity of films about 100Å thick

whose structure was probably that of black films. The distance between pores was independent of current density. Huber and Bieri (5) found that films formed in *N* NaOH solution did not develop any porosity till they were about 2000Å thick. In thick anodic films on aluminum the distance between pores was also independent of current density (11), but thin anodic films on aluminum appear to be different, in that the distance between pores increased with the forming voltage (10, 11).

The porosity of thick anodic films on zinc calculated from measurements of the apparent density (Table I) was about 45% independent of electrical conditions of formation, while that of anodic films on aluminum has been calculated from data on the number and diameter of pores to vary from about 50% at 10 v to less than 2% at 100 v (10). Some evidence has been found for a hexagonal cell structure similar to that on certain anodic films on aluminum, the cell size of about 3000Å in a film formed at 45 v being of the same order as that of the largest cells observed in films on aluminum.

In view of the large porosity of the films the resistance of the electrolyte in the pores is small and in order to account for the relatively high effective wet resistance it is necessary to postulate a nonporous barrier layer adjacent to the basis metal.

The Barrier Layer

The wet resistance of the black films is seen in Fig. 6 to drop rapidly with increasing voltage. This suggests that the concentration of metallic zinc in the barrier layer of the black film increases with increasing voltage, rapidly at first and then more slowly.

The slope of the curves of resistance vs. voltage and vs. current density changes its direction at 4 v and at 40 ma/cm^2, respectively. The change in the nature of the barrier layer which is responsible for this reversal is presumably the same as that which is known to take place at this stage in the porous part of the layer, viz., the oxidation of metallic zinc. This change is accompanied by a change in the mechanism of conduction which, in white films, is dependent on the presence of interstitial zinc ions.

The changes in the wet resistance of the film cannot, however, be interpreted solely in terms of changes in the thickness of the barrier layer, i.e., without taking into account the changes in resistivity which probably occur. The resistivity is influenced by the concentration of interstitial zinc ions, and, since this concentration may be expected to increase with increasing field strength the resistivity probably falls as the field strength increases (12). Another factor, which also tends to cause a fall in the resistivity of the barrier with increasing field strength, while it is being formed, is the increasing amount of heat evolved (13, 14).

For these reasons the rate of increase of the thickness of the barrier layer of white films with increasing voltage is probably greater than the rate of increase in the wet resistance of the film (Fig. 7).

In constant-current tests the increase in resistance at any given current density (directly proportional to the increase in voltage in Fig. 2A and 2B) may be a fair measure of the increase in thickness, since the concentration of interstitial zinc ions is presumably constant and a mean equilibrium will be quickly established. Fig. 2A and 2B suggest that the thickness of the barrier layer increases linearly with time after an initial period during which it appears to increase more slowly.

Influence of Aluminum on the Barrier Layer

In the anodizing of Mazak 3 the linear and logarithmic rates of increase of the effective wet resistance were less than the corresponding rates for zinc.

It seems likely that aluminum enters the barrier layer and changes its properties and its rate of growth. The presence of aluminum in zinc reduces the rate of atmospheric oxidation—0.1 at. % Al reducing the rate of oxidation 100-fold at 390°C (15), and Wagner's theory of oxidation attributes this to the displacement from the lattice of interstitial zinc ions whose diffusion is the rate-controlling process in atmospheric oxidation. It is reasonable to suppose that the rate of growth of the barrier layer in anodic oxidation is controlled by the same process, and it would follow that the layer should grow more slowly on Mazak 3 than on zinc.

In entering the zinc oxide lattice aluminum ions also increase its conductivity by increasing the concentration of electrons in the conduction band—1 mole % Al_2O_3 increasing the conductivity of zinc oxide 1000-fold at 394°C (16). Although the concentration of aluminum in the barrier layer of anodized films on Mazak 3 is not known, it seems likely that the conductivity of the layer is considerably greater than that of the corresponding layer on zinc.

These two factors explain the lower rate of increase of the resistance of the barrier layer on Mazak 3 in all experiments and the lower resistance of the layer in completely formed films in constant-voltage tests.

Manuscript received June 5, 1958. This paper was prepared for delivery before the New York Meeting, April 27-May 1, 1958.

Any discussion of this paper will appear in a Discussion Section to be published in the June 1960 JOURNAL.

REFERENCES

1. W. H. T. Vernon, E. I. Akeroyd, and E. G. Stroud, *J. Inst. Metals*, **65**, 301 (1939).
2. E. Müller and K. Schwabe, *Z. Elektrochem.*, **38**, 407 (1932).
3. K. Huber, *ibid.*, **48**, 26 (1942).
4. K. Huber, *Helv. Chim. Acta*, **26**, 1037 (1943); **26**, 1253 (1943); **27**, 1443, (1944).
5. K. Huber and B. Bieri, *Helv. Phys. Acta*, **21**, 375 (1948).
6. K. Huber, *This Journal*, **100**, 376 (1953).
7. R. Landsberg and H. Bartelt, *Z. Elektrochem.*, **61**, 1162 (1957).
8. A.S.T.M. D968-51.
9. O. Fritsch, *Ann. Physik*, **22**, 375 (1935).
10. F. Keller, M. S. Hunter, and D. L. Robinson, *This Journal*, **100**, 411 (1953).
11. C. J. L. Booker, J. L. Wood, and A. Walsh, *Brit. J. Appl. Physics*, **8**, 347 (1957).
12. D. A. Vermilyea, *This Journal*, **104**, 427 (1957).
13. L. Young, *Trans. Faraday Soc.*, **53**, 229 (1957).
14. E. E. Hahn, *J. Appl. Physics*, **22**, 855 (1951).
15. C. Gensch and K. Hauffe, *Z. phys. Chem.*, **196**, 427 (1951).
16. K. Hauffe and A. L. Vierk, *ibid.*, **196**, 160 (1950).

A Study of the Silver (I) Oxide-Silver (II) Oxide Electrode

James F. Bonk and Alfred B. Garrett

McPherson Chemical Laboratories, The Ohio State University, Columbus, Ohio

ABSTRACT

A reproducible emf of the cell Ag(c), Ag_2O(c)/NaOH (1M)/AgO(c), Ag_2O (c), Pt is found to be 0.262 v at 25°C. From this value and the known potential of the Ag, Ag_2O electrode, the standard oxidation potential of the Ag_2O, AgO electrode is —0.604 v. The temperature coefficient of the cell is $+2.20 \times 10^{-4}$ v/deg. The free energy, enthalpy, and entropy changes for the cell reaction are —6049 cal, —4537 cal, and 5.07 cal/deg, respectively. From these values and the existing thermodynamic data on Ag and Ag_2O, values of 3463 cal, —2769 cal, and 13.81 cal/deg are calculated, respectively, for the free energy and enthalpy of formation and for the entropy of AgO at 25°C.

The purpose of this research is to present data on the electrode potential of the silver (II) oxide electrode over the temperature range 20°-30°C. Various investigators (1-5) have established in studies of the silver (II) oxide-zinc-alkali battery that a cell having an AgO cathode has twice the capacity of a similar cell having an Ag_2O cathode, but at high current drains the discharge of an AgO cathode to free silver takes place in a single step at a potential corresponding to that of an Ag_2O cathode. At low current drains, however, there occurs a two step reduction in voltage (1) which would be expected in view of the results of a number of earlier studies involving AgO.

Marsh (6) determined the potential of Ag_2O against AgO to be 0.15 v. From this datum and the known oxidation potential for the Ag, Ag_2O electrode of —0.342 v (7),[1] a value of —0.49 v can be calculated for the Ag_2O, AgO oxidation potential. Early studies by Luther and Pokorny (8) indicated a stepwise reduction of $AgO \rightarrow Ag_2O \rightarrow Ag$ at electrode potentials of 0.57 v and 0.344 v, respectively. The preceding values were determined from cells using Hg, HgO reference electrodes and samples of AgO prepared by the anodic oxidation of Ag in alkali. Unfortunately, conflicting values of 0.927 and 0.962 v are given in the original reference for the emf of the cell

$$Hg, HgO/NaOH(1N)/H_2(1\ atm) \qquad [A]$$

The difference of 0.035 v may have led to conflicting values for the Ag_2O, AgO potential. Latimer (9) accepts the oxidation potential obtained directly from Luther and Pokorny's data (—0.57 v). Hickling and Taylor (10), however, correct the original data by 0.04 v so as to produce a value of —0.61 v for the Ag_2O, AgO oxidation potential. No explanation of this 0.04-v correction is given by Hickling and Taylor, but Jones, Thirsk, and Wynne-Jones (11) suggest that the correction may be connected with the potential of the cell

$$H_2/OH^-(N)/calomel \qquad [B]$$

which Hickling and Taylor used in their study. It is also possible that a 0.04-v correction can be made for the 0.035-v inconsistency in the reported emf of cell [*A*]. From studies of Jirsa (12) and Jirsa and Jelinek (13) on cells of the type

$$H_2/NaOH(M)/Ag_2O,Ag \qquad [C]$$

a value of about —0.60 v can be calculated for the Ag_2O, AgO oxidation potential at 25°C.

In view of the inconsistencies which exist with regard to the potential of the couple

$$Ag_2O + 2\ OH^- \rightarrow 2AgO + H_2O + 2e^- \qquad [1]$$

it was deemed advisable to reinvestigate the emf associated with the Ag_2O, AgO electrode. Such an investigation also makes possible the evaluation of some important thermodynamic functions of AgO which at present have not been determined reliably.

Experimental

In this study of the Ag_2O, AgO electrode, cells of the following type were employed

$$Pt,Ag(c),\ Ag_2O(c)/NaOH(1M)/AgO(c),\ Ag_2O(c),\ Pt \qquad [D]$$

The reactions occurring in the cell would be

$$(Cathode)\quad 2AgO + H_2O + 2e^- \rightarrow Ag_2O + 2\ OH^- \qquad [2]$$

$$(Anode)\quad 2Ag + 2\ OH^- \rightarrow Ag_2O + H_2O + 2e^- \qquad [3]$$

Thus, the over-all cell reaction for 1 faraday may be considered to be

$$AgO(c) + Ag(c) = Ag_2O(c) \qquad [4]$$

As this reaction indicates, it is not practical to replace the platinum contact by a silver contact in this cell since reaction [4] can then occur completely at the cathode. Confirmation of this was obtained in a preliminary study of the cell

$$Ag,\ Ag_2O/NaOH(1M)/AgO,\ Ag_2O,\ Ag \qquad [E]$$

In less than 1 min the voltage of cell [*E*] dropped from about 0.25 v to less than 0.01 v. In a half hour

[1] Signs given for oxidation potentials in this paper are consistent with those used by Hamer and Craig (7) in their study of the Ag, Ag_2O electrode and with those of Latimer's (9) oxidation potentials. The electrode potential, as defined by The Electrochemical Society and by the IUPAC Stockholm convention, has the opposite algebraic sign.

the voltage had dropped almost to zero. Therefore, it is necessary to use an inert substance such as platinum in the construction of the Ag_2O, AgO electrode.

In constructing cell [*D*], reproducible and highly stable Ag, Ag_2O electrodes, prepared as directed by Hamer and Craig's method number two (7), were used as reference electrodes. The Ag_2O used in the preparation of the electrodes was of certified reagent grade.[2] Two different sources of AgO were employed in the preparation of electrodes: (*a*) "Divasil"[2] and (*b*) AgO prepared from reagent grade chemicals by Kleinberg's method (14), in which $AgNO_3$ was oxidized by $K_2S_2O_8$ in NaOH at 90°C. The resulting AgO was washed numerous times, filtered, and allowed to dry in an atmosphere of nitrogen in a desiccator. Analyses of AgO samples, carried out iodimetrically by Dutta's method (15), averaged 98% AgO for samples of "Divasil" and 99.0 to 99.5% AgO for preparations carried out by Kleinberg's method.

In assembling the cell, an H-type Pyrex glass container was used. The legs were 1.5 cm in diameter by 12.5 cm long and were connected near the top by a cross-tube 5 cm long and 0.8 cm in diameter. In one leg was placed the sample of AgO which had been thoroughly mixed with a small amount of Ag_2O and then repeatedly washed with the 1M NaOH which was to be used in filling the cell. After filling the cell with 1M NaOH, a rubber stopper, through which extended a 5 mm soft glass tube with a Pt-helix sealed into one end, was inserted into the leg of the H-tube in such a way that the Pt-helix was completely covered by the oxide slurry. Into the other leg of the H-cell, the reference electrode was inserted and held in place by means of a rubber stopper. The assembled cell was then placed in a bath in which a desired temperature could be maintained within 0.02°C. All temperature measurements were made with a National Bureau of Standards certified thermometer graduated in 0.02°C intervals in the range from 18° to 30°C. Measurements of emf were made by means of a L&N type K-2 pontentiometer which was calibrated against a Rubicon potentiometer of known accuracy. The standard cell employed was calibrated against a standard cell certified by the National Bureau of Standards.

[2] Supplied by the Merck Chemical Company.

Table I. Electromotive force at 25°C of cell [D]

Cell No.	Emf, v	Type of reference electrode	Type of AgO employed
1*	0.2622	Pasted	Freshly prepared
2*	0.2625	Pasted	Freshly prepared
3*	0.2620	Pasted	Freshly prepared
4*	0.2625	Pasted	Freshly prepared
5	0.2608	Pasted	"Divasil"
6	0.2610	Pasted	"Divasil"
7	0.2618	Pasted	"Divasil"
8	0.2615	Pasted	"Divasil"
9	0.2616	Slurry	"Divasil"
10	0.2614	Slurry	"Divasil"

* Reference Ag, Ag_2O electrode prepared by Hamer and Craig's (7) method No. 2; AgO used was prepared by Kleinberg's (14) method.

Table II. Electromotive force at 25°C of cell No. 4 as a function of time

Time, days	Emf, v	Time, days	Emf, v
0.5	0.2625	7	0.2613
1	0.2622	8	2.2612
4	0.2616	9	0.2611
6	0.2614	10	0.2610

Table III. Electromotive force at various temperatures in order of observation

Cell #1 Temp, °C	Cell #1 Emf, v	Cell #2 Temp, °C	Cell #2 Emf, v	Cell #3 Temp, °C	Cell #3 Emf, v
30.00	0.26327	25.00	0.26252	25.00	0.26198
27.00	0.26261	20.00	0.26142	20.00	0.26087
25.00	0.26217	23.00	0.26208	22.00	0.26131
23.00	0.26173	25.00	0.26252	25.00	0.26198
20.00	0.26108	28.00	0.26318	27.00	0.26242
		30.00	0.26362	30.00	0.26308
dE/dT (mv/°C)	+0.219		+0.220		+0.221

Average value of $dE/dT = 2.20 \times 10^{-4}$ v/deg at 25°C.

In Table I are given the emf's found at 25°C for cell [*D*]. New samples of AgO were prepared freshly by Kleinberg's method (14) for each of the first four cells. The average value for the emf of these cells is 0.2623 ± 0.0002 v. Using 23,060.5 cal/abs volt. g-eq for the faraday (16) in the relation $\Delta F^\circ = -n\mathbf{F}E^\circ$, the standard free energy change for cell reaction [4] is −6049 ± 5 cal at 25°C.

For comparison, four cells (No. 5 through 8) were prepared in the same manner using Merck's "Divasil" instead of our own preparation of AgO. As can be seen in Table I, "Divasil" produces a slightly lower emf of 0.2613 ± 0.0004 v at 25°C. For further comparison, slurry-type reference electrodes prepared by Hamer and Craig's method No. 1 (7) were used in the preparation of two cells, No. 9 and 10. Comparison of the data in Table I for the two types of reference electrodes shows good agreement between them.

The stability of cell No. 4 was investigated by taking emf measurements over a period of ten days at 25°C (Table II). As can be seen, the emf slowly decreases from 0.2625 v to 0.2610 v in this period of time. Aged AgO and "Divasil" seem to produce slightly lower and more stable potentials than freshly prepared AgO.

The effect of temperature on the emf of cells No. 1, 2, and 3 is given in Table III. Readings were taken at each temperature when a constant emf value had been maintained for at least 1 hr. No appreciable emf-temperature hysteresis occurred as is clearly shown by the reproducibility of 25°C emf's in cells No. 2 and 3. The average value for the coefficient at 25°C is $+2.20 \times 10^{-4}$ v/deg which gives ΔS° for cell reaction [4] as 5.07 ± 0.02 cal/deg since $\Delta S^\circ = n\mathbf{F}(dE^\circ/dT)$. The enthalpy ΔH° of cell reaction [4] is −4537 ± 11 cal at 25°C since $\Delta H^\circ = \Delta F^\circ + T\Delta S^\circ$.

Thermochemistry

From the standard value −2586 cal for the free energy of formation of Ag_2O (16) and our value of

-6049 ± 5 cal for the standard free energy of cell reaction [4], a value of 3463 ± 5 cal is calculated for the standard free energy of formation of AgO. The entropy of reaction [4] is given by

$$\Delta S^\circ = S^\circ(Ag_2O) - S^\circ(Ag) - S^\circ(AgO) \quad [5]$$

The values for $S^\circ(Ag_2O)$ and $S^\circ(Ag)$ are, respectively, 29.09 and 10.21 cal/deg (16). From these values and our value of 5.07 ± 0.02 cal/deg for ΔS°, a value of 13.81 ± 0.02 cal/deg is calculated for $S^\circ(AgO)$.

In a similar manner, our value of -4537 ± 11 cal for the enthalpy of reaction [4] together with -7306 cal for the heat of formation of Ag_2O (16) leads to a value of -2769 ± 11 cal for the heat of formation of AgO at 25°C. Latimer (9) gives -6.0 kcal/mole for this heat of formation of AgO which he attributes to the National Bureau of Standards. Actually, Circular 500 (16) gives -6.3 kcal/mole as the heat of formation of Ag_2O_2 (not AgO) from which the heat of formation of AgO would be -3.15 kcal/mole. This value is obtained from thermochemical measurements made by Jirsa (12). Jirsa's studies involved the determination of the heats of solution of Ag_2O and AgO in acids. Taking $HClO_4$ as an example

$$2AgO + 2HClO_4(aq) \rightarrow 2AgClO_4(aq) + H_2O + \tfrac{1}{2} O_2 + 10964 \text{ cal}$$

$$Ag_2O + 2HClO_4(aq) \rightarrow 2AgClO_4(aq) + H_2O + 9964 \text{ cal}$$

By subtraction

$$2AgO \rightarrow Ag_2O + \tfrac{1}{2} O_2 + 1000 \text{ cal}$$

However, Jirsa found that the difference between the two heats of solution was not a constant 1000 cal but varied from 1197 cal to 1956 cal as the acid strength varied from 20% to 70%, respectively. The 1000-cal difference was obtained by a questionable extrapolation of these data to zero concentration of acid. Using 1000 cal as the approximate difference between the heats of solution of the oxides and the known heat of formation of Ag_2O (16), an approximate value of -3.15 kcal/mole can be calculated for the heat of formation of AgO. Thus no great discrepancy exists between Jirsa's value of -3.15 kcal/mole and our more accurate value of -2.769 kcal/mole. The discrepancy becomes even smaller when Jirsa's actual calorimetric values are substituted for his extrapolated value.

Electrode Potential

From our value of 0.262 v for the emf of cell [D] and the value -0.342 v (7) for the oxidation potential of half-reaction [3], a value of -0.604 v can be calculated for the standard oxidation potential of couple [1]. The standard electrode potential of this couple is, therefore, 0.604 v.

Our value of -0.604 v is in poor agreement with -0.49 v calculated from Marsh's data (6). Since no experimental data are given in the reference, it is not possible to make a further evaluation of this discrepancy. Our oxidation potential does agree well with the value -0.60 v calculated from Jirsa's work (12, 13) and with Hickling and Taylor's (10) correction of Luther and Pokorny's (8) data. Although the corrected value does agree well with our data, such a correction does not seem justifiable for a number of reasons.

First, applying a 0.04-v correction to the other data obtained by Luther and Pokorny would give a value of $+0.38$ v for the standard electrode potential of Ag, Ag_2O and a value of $+0.78$ v for the AgO, Ag_2O_3(?) electrode potential. These values are both 0.04 v higher than other determinations (7, 9, 13).

Second, using samples of AgO prepared by a variety of methods, Luther and Pokorny obtained data from which values of -0.56 to -0.60 v can be calculated for the standard oxidation potential of the Ag_2O, AgO electrode. Since the same Hg, HgO reference electrode was used in all these determinations, it seems reasonable to attribute the variation in the standard potential to the method of preparation of AgO. The cell from which the highest oxidation emf value (-0.56 v) was obtained by Luther and Pokorny contained AgO prepared by the anodic oxidation of silver in dilute sulfuric acid. Due to the lack of experimental details, it is not possible to determine the exact method of preparation of the AgO electrode used in their study. However, in view of a later x-ray study (17) it is probable that the AgO electrode contained some free silver or silver in some oxidation state other than +2, which produced the higher oxidation emf value of -0.56 v. Luther and Pokorny's accepted oxidation emf of -0.57 v was determined from samples of AgO prepared by the anodic oxidation of silver in alkali. Denison (1), however, has shown by x-ray studies that this electrolytic method produces AgO which still contains some free silver. Jones, Thirsk, and Wynne-Jones (11) also suggest the presence of a "suboxide" in AgO prepared by this electrolytic method. The lower oxidation emf of -0.60 v was obtained by Luther and Pokorny from cells containing AgO prepared both by the anodic oxidation of $AgNO_3$ and Ag_2SO_4 solutions. This same value can be obtained from Jirsa's (13) data on AgO prepared by the ozonization of powdered silver and from our data on AgO prepared by the alkaline oxidation of Ag(I) by $K_2S_2O_8$.

Thus it would appear that early electrolytic preparations of AgO from silver resulted in high standard oxidation potentials for the Ag_2O, AgO electrode. The other major methods of preparation produce a lower oxidation potential of about -0.60 v. In the case of AgO prepared by the alkaline oxidation of Ag_2O by $K_2S_2O_8$, we have accurately determined this lower oxidation potential to be -0.604 v for couple [1].

In conclusion it is of interest to consider the observations made on the commercial silver(II) oxide-zinc-alkali battery. Most interesting of these is the fact that the emf of the commercial cell on high current drains is the same whether AgO or Ag_2O is used as the cathodic material, but the capacity of a cell containing an AgO cathode is twice that of a similar cell containing an Ag_2O cathode. In light of our study it seems possible to explain this observation in the same manner as Schumacher and Heise (18) explained a similar phenomenon involving the corre-

sponding oxides of another coinage metal, Cu_2O and CuO. The discharge may be considered to be represented by the following reactions

$$2AgO+2KOH+Zn+H_2O=K_2Zn(OH)_4+Ag_2O \quad [6]$$

$$Ag_2O + 2KOH + Zn + H_2O = K_2Zn(OH)_4 + 2Ag \quad [7]$$

Reaction [6] predominates until the amount of Ag_2O builds up at which point reaction [7] predominates. This would be consistent with the observation that a higher voltage is observed for a short time on low current drains (1). The fact that the AgO electrode has twice the capacity of an Ag_2O electrode may be explained by reference to reaction [4]. The Ag_2O used in reaction [7] is regenerated by means of reaction [4] until all the AgO has been consumed. In this way AgO can contribute to the total capacity of the cell without contributing to the potential, once reaction [7] becomes the predominant reaction.

Manuscript received Nov. 10, 1958.

Any discussion of this paper will appear in a Discussion Section to be published in the June 1960 JOURNAL.

REFERENCES

1. I. A. Denison, *Trans. Electrochem. Soc.*, **90**, 387 (1946).
2. J. C. White, R. T. Pierce, and T. P. Dirkse, *ibid.*, **90**, 467 (1946).
3. G. W. Vinal, "Primary Batteries," J. Wiley & Sons, Inc., New York (1950).
4 R. Glicksman and C. K. Morehouse, *This Journal*, **104**, 589 (1957).
5. P. L. Howard, *ibid.*, **99**, 200C (1952).
6. A. L. Marsh, Ref. in *Jahrb. f. Elektrochem.*, **9**, 430 (1902).
7. W. J. Hamer and D. N. Craig, *This Journal*, **104**, 206 (1957).
8. R. Luther and F. Pokorny, *Z. anorg. u. allgem. Chem.*, **57**, 290 (1908).
9. W. M. Latimer, "The Oxidation States of the Elements and Their Potentials in Aqueous Solutions," 2nd ed., Prentice-Hall, Inc., New York (1956).
10. A. Hickling and D. Taylor, *Faraday Soc. Discussions*, **1**, 277 (1947).
11. P. Jones, H. R. Thirsk, and W. F. K. Wynne-Jones, *Trans. Faraday Soc.*, **52**, 1003 (1956).
12. F. Jirsa, *Z. anorg. u. allgem. Chem.*, **158**, 33 (1926).
13. F. Jirsa and J. Jelinek, *ibid.*, **158**, 61 (1926).
14. R. N. Hammer and J. Kleinberg, "Inorganic Synthesis," McGraw-Hill Book Company, New York, **4**, 12 (1953).
15. R. L. Dutta, *J. Indian Chem. Soc.*, **32**, 191 (1955).
16. "Selected Values of Chemical Thermodynamic Properties", National Bureau of Standards Circular 500 (1952).
17. P. Jones and H. R. Thirsk, *Trans. Faraday Soc.*, **50**, 732 (1954).
18. E. A. Schumacher and G. W. Heise, *This Journal*, **99**, 191C (1952).

The Temperature Coefficients of Electrode Potentials

The Isothermal and Thermal Coefficients—The Standard Ionic Entropy of Electrochemical Transport of the Hydrogen Ion

A. J. deBethune, T. S. Licht, and N. Swendeman

Chemistry Department, Boston College, Chestnut Hill, Massachusetts

ABSTRACT

The temperature coefficient of the potential of an electrode can be defined experimentally by reference to (*a*) the potential of the SHE at the same temperature, (*b*) the potential of the same electrode at some fixed temperature. These two definitions give rise to the "isothermal" and "thermal" temperature coefficients of electrode potentials. The isothermal coefficient is $\Delta S/n\mathbf{F}$ where ΔS is the reaction entropy of the "SHE//Electrode" cell. The thermal coefficient is $S^*/n\mathbf{F}$ where S^* is the entropy transported from the hot to the cold heat reservoir by the passage of n faradays of positive electricity through the cell from the cold to the hot electrode (before the onset of thermal diffusion). The entropy S^* is divided into an entropy S^*_E of electrochemical transport which determines the electrode temperature effect, and an entropy S^*_M of migration transport which determines the thermal liquid junction potential.

By assuming that S^*_M is negligible in a saturated potassium chloride bridge, we have deduced that the thermal temperature coefficient of the SHE is +0.871 mv/°C [hot electrode (+) terminal] at 25°C. The standard ionic entropy $S^{*\circ}_E$ of electrochemical transport of hydrogen ion is —4.48 cal/deg. Thermal temperature coefficients are computed for calomel, silver chloride, and copper sulfate electrodes and are compared with experiment. Thermal and isothermal temperature coefficients are computed and tabulated for nearly 300 standard electrode potentials.

The temperature coefficient of electrode potentials[1] can be defined experimentally in two ways, either as an "isothermal" or as a "thermal" temperature coefficient. The isothermal temperature coefficient $(dV/dT)_{isoth}$ is the derivative dE/dT of the emf[2] E of the isothermal cell

$$\text{SHE // Electrolyte / Electrode} \qquad [1]$$

where the left electrode is a standard hydrogen electrode (SHE). In cell [1], the temperature of the two electrodes is varied in the same way.

The thermal temperature coefficient $(dV/dT)_{th}$ is the derivative dE/dT_2 of the emf E of the thermal cell

$$\text{M}(T_1) \,/\, \text{Electrode}(T_1) \,/\, \text{Electrolyte}(T_1) \,/\, \text{Electrolyte}(T_2) / \text{Electrode}(T_2) / \text{Electrode}(T_1) / M(T_1) \qquad [2]$$

in which T_1 is fixed and T_2 varies. When the thermal coefficient, as defined here, is positive, the hot electrode is the (+) terminal of cell [2]. Cell [2] can also be modified by the introduction of salt bridges across the liquid thermal boundary.

The Gibbs-Helmholtz equation (5, 7, 8) yields an expression for the isothermal temperature coefficient in the form

$$(dV/dT)_{isoth} = \Delta S/n\mathbf{F} = (\Delta H - \Delta G)/n\mathbf{F}T \qquad [3]$$

where ΔS, ΔH, and ΔG are the entropy, enthalpy, and free enthalpy (Gibbs free-energy), respectively, of the reaction which transfers n faradays of positive electricity through cell [1] from left to right.

Thermal Temperature Coefficients

Thermal temperature coefficients of electrode potentials have been studied by many investigators (9-36) since the pioneering work of Bouty (9). Much of the early work was reviewed by Lange (10). The electromotive force of a thermal cell (in its initial state) is the resultant of three effects: (*a*) the metallic thermocouple effect, (*b*) the electrode temperature effect, and (c) the thermal liquid junction potential. Effect (*a*) can be eliminated by keeping all metal-metal junctions isothermal, as in cell [2], a technique used by Richards (13), or it can be corrected for, as in the work of Carr and Bonilla (31). Effect (*a*) has a magnitude of the order of 1% of the sum of (*b*) and (c) and will be considered eliminated in what follows.

With the passage of time, a thermal cell is subject to thermal diffusion in the electrolyte (Soret effect) (18) as demonstrated experimentally by Agar and Breck (33). Thermal diffusion tends to concentrate strong electrolytes in the cold region. The resultant concentration gradient further changes the two electrode potentials, and the cell eventually reaches a new stationary state after thermal diffusion has become fully developed. However, most thermal cell

[1] The sign convention to be followed in this paper for single electrodes is that of the Gibbs-Stockholm electrode potential V (1-4) which is positive if the electrode in question is the (+) terminal of a cell whose other electrode is a standard hydrogen electrode (SHE).

[2] The sign convention followed for whole cells is that of the Lewis-Stockholm cell emf E (2-6) which is positive when positive current tends to flow through the cell as written from left to right.

measurements have been conducted under experimental conditions unfavorable to the development of the Soret effect, and the initial state of the cell then has been found to be stable for extended periods of time (up to 24 hr) (13, 30). Only the initial state of thermal cells is considered here.

Thermodynamics of Thermal Cells

The driving force of a thermal cell is the transport (or flux) of entropy from a high-temperature heat reservoir (at T_2) to a low-temperature heat reservoir (at T_1) as is the case for any heat engine. Let the entropy transported in a Carnot engine be S^*. The product $S^*(T_2 - T_1)$ is the useful work output of the engine. This work, divided by the electrical charge transported $n\mathbf{F}$, gives the electromotive force E of the cell, i.e.,

$$E/(T_2 - T_1) = dE/dT = S^*/n\mathbf{F} \qquad [4]$$

The electromotive force is positive for that direction of the current flow which transports entropy reversibly from the hot to the cold heat reservoir. The quantities of heat absorbed by the cell from the hot heat reservoir, and evolved to the cold heat reservoir, are T_2S^* and T_1S^*, respectively (Peltier heats).

The above analysis is too simple, since a thermal cell is the seat of two entropy fluxes: (*a*) a flux of entropy by heat conduction, and (*b*) a flux of entropy accompanying the flux of electricity. The former is irreversible while the latter can be made reversible by the use of a potentiometer. Consider cell [2] connected with a potentiometer. Let $T_2 = T_1 + dT$ where dT is positive. The electrical potentials of the left and right terminals are V and $V + dV$, respectively. Let the current I be positive when it flows through the cell from left to right. The entropy flux J is positive from the hot (right) to the cold (left) heat reservoir.

The irreversible rate of production of Clausius' uncompensated entropy (37, 38) from these two fluxes is

$$\dot{S} = I(-dV/T) + JdT/T \geqq 0 \qquad [5]$$

Following the methods of irreversible thermodynamics (39), one may write the phenomenological equations for the two fluxes:

$$I = L_{II}X_I + L_{IJ}X_J \qquad [6]$$

$$J = L_{JI}X_I + L_{JJ}X_J \qquad [7]$$

where $X_I = -dV/T$ and $X_J = dT/T$. The L's are phenomenological coefficients. By Ohm's law, L_{II} is T/r where r is the total resistance of the circuit. The heat conductance of the system, at zero current, is given by $L_{JJ} - L_{JI}L_{IJ}/L_{II}$, a quantity which must be positive. The interaction coefficients L_{IJ} and L_{JI} serve to measure, respectively, the flow of electricity caused by a thermal gradient when the cell is short-circuited and the flow of entropy caused by an applied emf when the cell is at uniform temperature. By the Onsager relations (40), the conjugate interaction coefficients are equal, i.e., $L_{IJ} = L_{JI}$.

Equation [6] shows the current I as the resultant of two emf's: (*a*) an externally applied emf $-dV = TX_I$ determined by the potentiometer, and (*b*) a thermal emf $dE = TL_{IJ}X_J/L_{II} = L_{IJ}dT/L_{II}$ determined by the applied temperature difference. At the balance point ($I = 0$), the potential difference dV equals the emf dE and

$$-X_I/X_J = dE/dT = L_{IJ}/L_{II} \qquad [8]$$

By the Onsager relations, this becomes

$$dE/dT = L_{JI}/L_{II} \qquad [9]$$

Suppose now that the cell is brought to uniform temperature and a small external emf applied (dV negative). The current flowing is $I = L_{II}X_I = n\mathbf{F}/t$ if t is the time required for the passage of n faradays. At the same time, the entropy flux is $J = L_{JI}X_I = S^*/t$ if S^* is the entropy transported from the right heat reservoir to the left heat reservoir, by the transfer of n faradays of positive electricity through the cell from left to right. And therefore

$$dE/dT = (dV/dT)_{I=0} = (J/I)_{dT=0} = S^*/n\mathbf{F} \qquad [10]$$

an expression derived from the Onsager relations which coincides with Eq. [4], obtained above from a consideration of a thermal cell as a quasi-Carnot engine. The entropy S^* is seen to be the entropy transported from one heat reservoir to the other, by the flow of electricity, in the absence of a temperature gradient.

The entropy S^* is the sum of two terms: (*a*) an entropy S^*_E absorbed by the reaction at the right electrode from its heat reservoir and evolved by the reaction at the left electrode to its heat reservoir (S^*_E will be referred to as the entropy of electrochemical transport); and (*b*) an entropy S^*_M transported through the cell from right to left by electrolytic migration. An equal quantity of entropy then enters the cell from the right heat reservoir and leaves the cell at the left heat reservoir, in order to keep the temperature constant (S^*_M will be referred to as the entropy of migration transport).

Consider cell [2] with two reversible iron-ferrous ion electrodes and a ferrous sulfate salt bridge. For the passage of 2 faradays through the cell from left to right, the reaction at the right electrode is $Fe^{++} + 2e^- = Fe$ and the entropy S^*_E becomes

$$S^*_E = S(Fe) - S^*_E(Fe^{++}) \qquad [11]$$

where $S(Fe)$ is the entropy of metallic iron while $S^*_E(Fe^{++})$ is the ionic entropy of electrochemical transport of the ferrous ion. The entropy S^*_M is

$$S^*_M = t_-S^*_M(SO_4^=) - t_+S^*_M(Fe^{++}) \qquad [12]$$

where the t's are transference numbers, and the S^*_{Mi}'s are ionic entropies of migration transport, of the two ions. The two transport entropies S^*_{Ei} and S^*_{Mi} for an ion[3] do not coincide with its ordinary ionic entropy (based on the standard $S^\circ(H^+) = 0$ at all temperatures) and neither do they coincide with one another. S^*_{Ei} is the entropy transported by an

[3] S^*_{Ei} has been referred to (18, 29, 41) as the "absolute ionic entropy," and S^*_{Mi} as the "entropy of transfer." Agar and Breck (33) have referred to $S^*_{Ei} + S^*_{Mi}$ as the "transported entropy" and to S^*_{Mi} as the "molar entropy of transport." See Temkin and Khoroshin (33).

ion when it sheds its hydration sheath in one place and picks up a new hydration sheath in its new place. S^*_{Mi} is the entropy transported by the ion when it drags its hydration sheath with it across the cell (35, 36). The ionic entropy S^*_{Mi} is equal, in ideal solutions, to $-RT$ times the Soret coefficient of the ion.

The thermal temperature coefficient of the iron-ferrous ion electrode, with a ferrous sulfate salt bridge, should therefore be given by

$$(dV/dT)_{th} = S^*_E/2\mathbf{F} + S^*_M/2\mathbf{F} \qquad [13]$$

where S^*_E and S^*_M are given by [11] and [12] above.[4] The first term in Eq. [13] measures the electrode temperature effect, the second term the thermal liquid junction potential. The separation of a measured thermal emf into these two terms is, strictly speaking, impossible. This separation can be accomplished only with the help of certain arbitrary assumptions.

An estimate of the thermal liquid junction potential.—One such assumption, which we shall make now, is that the thermal liquid junction potential of a saturated potassium chloride salt bridge, as used in the experimental work of Fales and Mudge (14), is zero. This assumption, while arbitrary, can be looked upon as reasonable and approximately valid for the following reasons.

In 1928, Eastman (42) estimated entropies of migration of the ions of hydrogen, and alkali chlorides, in 0.02*N* solutions from measurements on electrolytic thermocouples. From his estimates, the following entropies of migration, and thermal liquid junction potentials (tljp), can be calculated.

0.02M solution	HCl	LiCl	NaCl	KCl	RbCl
S^*_M (cal/deg)	−7.7	−0.03	−0.36	−0.49	−0.54
tljp (mv/deg)	−0.33	−0.001	−0.016	−0.021	−0.023

(23.06 cal/deg = 1 mv-faraday/deg). The negative sign means that the hot end of the thermal liquid junction dipole is negative. While the tljp of hydrochloric acid is significant, the tljp's of dilute alkali chlorides are estimated to be not larger than 0.03 mv/deg.

With the assumption that the tljp of saturated potassium chloride is zero, Fales and Mudge's (14) measurements lead to a value of the entropy of electrochemical transport S^*_E of the hydrogen ion, as will be shown below. This in turn yields the S^*_E values of other ions, and from them, the thermal temperature coefficients of reversible electrodes (without tljp). When these calculated thermal coefficients of electrodes are compared with experimental values, the difference may be used as an estimate of the tljp in the experimental bridge. This study, which is still in progress, will be reported in detail in a companion paper (36). It is possible at this stage, however, to present certain tentative conclusions. The estimated tljp's of a variety of salts, in concentrations ranging from 0.001*N* to 1*N*, fall within +0.08 to −0.08 mv/deg that of a saturated potassium chloride bridge. For potassium chloride solutions, the estimated tljp's are +0.03 to −0.03 mv/deg; for sodium chloride, +0.02 to −0.02 mv/deg; for lithium chloride, +0.05 to +0.07 mv/deg. For strong acids, the estimated tljp's are around −0.3 to −0.4 mv/deg. For strong alkalies, they are around +0.5 mv/deg. The latter two are consistent with the Soret effect in that the cold end of the thermal liquid junction dipole takes on the charge of the faster ion (H^+ or OH^-). Thus it seems probable that our assumption of zero tljp in a saturated potassium chloride bridge will not be in error by more than about 0.03 mv/deg.

Since the saturated potassium chloride salt bridge is used widely in electrochemistry as method of "eliminating the liquid junction potential," since it has been proposed by Scatchard (60) as a practical tool for the definition of single ion activities, since it is part of every cell that measures pH (61) or pCl (62), we felt justified in adopting it as a means of exploring further the subject of thermal temperature coefficients. In particular, our assumption opens up an avenue to the evaluation of the two transport entropy terms which appear in Eq. [13].

Thermal temperature coefficient of the 0.1N hydrogen ion saturated hydrogen gas electrode.—Fales and Mudge (14) investigated the emf of the isothermal cell

Pt/H_2(satd, total pressure 1 atm),

$$0.1M\ HCl/\text{satd KCl}, Hg_2Cl_2/Hg \qquad [14]$$

in the temperature range 5°-60°C. We have calculated the least squares expression

$$E\ (\text{cell [14] at } t°C, \text{mv}) = 310.0 - 0.46793(t\text{-}25) - 0.0020617(t\text{-}25)^2 \qquad [15]$$

which fits their data within the experimental scatter of a few tenths of a millivolt. In addition, Fales and Mudge investigated the emf's of the thermal cells H/C, C/H, H/H, and C/C, where H and C denote the two electrodes of cell [14], with one electrode at 25° and the other at 5°-60°, and with the thermal liquid junction located in a saturated potassium chloride bridge. From their observations, we have calculated least squares expressions for the electrode potential V_t referred to the potential V_{25} of the same electrode at 25°, as follows:

$$(V_t - V_{25})\ (Pt/H_2(\text{satd 1 atm}), 0.1M\ HCl/\text{satd KCl}, \text{mv}) = +0.67273(t\text{-}25) + 0.0018351(t\text{-}25)^2, \qquad [16]$$

$$(V_t - V_{25})\ (Hg/Hg_2Cl_2, \text{satd KCl}, \text{mv}) = + 0.21692(t\text{-}25) - 0.0010547(t\text{-}25)^2 \qquad [17]$$

[4] Equation [13] has been referred to as the Eastman thermocell equation (29) and applies to a thermal cell in its initial state, before the onset of thermal diffusion. Wherever the Soret effect is allowed to develop, it can be shown, by introducing solute diffusion into the set of Onsager fluxes [6-7], that the cell reaches a final steady state in which $2\mathbf{F}(dV/dT)_{th,final} = S^*_E[11] - \frac{1}{2}[S^*_M(Fe^{++}) + S^*_M(SO_4^=)] - \frac{1}{2}[S^*_M(Fe^{++} - S^*_M(SO_4^=)]$. Here the second term gives the effect of the thermally induced concentration gradient on the difference of the two electrode potentials, and the third term gives the final value of the liquid junction potential as a resultant of both temperature and concentration gradients. The whole expression for the final state reduces to $S^*_E[11] - S^*_M(Fe^{++})$. The corresponding equation [13] for the initial state takes the comparable form $S^*_E[11] + S^*_M[12]$.

For an electrolyte which dissociates into $\nu_+ + \nu_- = \nu$ ions, and for the passage of $\nu_i|z_i|$ faradays through electrodes of the metal Me reversible to the positive ion, the molal and ionic entropies are replaced by $\nu_i S(Me)$ or $\nu_i S^*_E(i)$ or $\nu_i S^*_M(i)$ in all of these expressions. The first $\frac{1}{2}$ in the expression for the final state is replaced by ν_+/ν; the second $\frac{1}{2}$ is replaced by ν_-/ν for the positive ion and by ν_+/ν for the negative ion.

Both expressions fit the data well within the experimental scatter of a few tenths of a millivolt.[5] At 25°, the thermal temperature coefficients are +0.217 mv/deg for the saturated calomel electrode, and +0.673 mv/deg for the 0.1*N* hydrogen electrode. Their difference, −0.456 mv/deg, is consistent with the isothermal coefficient −0.468 mv/deg observed for cell [14] (Eq. [15]). The uncertainty of these 25° values appears to be no more than 0.02 mv/deg. Over the temperature range 5°-60°, the isothermal temperature coefficient of cell [14] calculated from Eq. [15] agrees with the difference of the two thermal temperature coefficients calculated from Eq. [16] and [17] within ±0.045 mv/deg.

Correction to unit activity of hydrogen gas.—Fales and Mudge's 0.1*N* hydrogen electrodes were saturated with hydrogen gas under total pressures of 755-770 mm Hg. To correct to the standard state of hydrogen gas (partial pressure equal to 760 mm Hg), the term $(RT/2\mathbf{F}) \ln [p(H_2, \text{mm})/760]$ must be added algebraically to the hydrogen electrode potentials as measured in any of their cells. The partial pressure of hydrogen can be computed by subtracting the vapor pressure of water (which holds very nearly in 0.1*M* hydrochloric acid) from their recorded barometric data. When this correction is applied to their individual data, Eq. [15] is modified as follows

$$E \text{ (cell [14] corrected to } H_2 \text{ p.p. 1 atm, mv)} = 310.3 - 0.43520(t\text{-}25) - 0.00089234(t\text{-}25)^2 \quad [18]$$

while Eq. [16] becomes

$$(V_t - V_{25}) \text{ (Pt/H}_2\text{(p.p 1 atm), 0.1}M \text{ HCl/satd KCl, mv)} = +0.64023(t\text{-}25) + 0.00064334(t\text{-}25)^2 \quad [19]$$

At 25°C, the thermal temperature coefficient of the 0.1*N* hydrogen electrode is +0.640 mv/deg, after correction to unit activity of hydrogen gas.

Correction to unit activity of hydrogen ion.—The Nernst equation for a reversible hydrogen electrode is

$$V = V^\circ + (RT/\mathbf{F}) \ln [(H^+)/(H_2)^{1/2}] \quad [20]$$

The temperature derivative of this equation can be applied to both isothermal and thermal temperature coefficients of electrode potentials. When applied to the thermal coefficient, it yields[6]

$$(dV/dT)_{th} = (dV^\circ/dT)_{th} + (R/\mathbf{F}) \ln [(H^+)/(H_2)^{1/2}] + (RT/\mathbf{F})(d \ln [(H^+)/(H_2)^{1/2}]/dT) \quad [21]$$

[5] Neither of these expressions has been corrected for the thermocouple effect. The status of the correction is not clear from Fales and Mudge's paper. However, the emf's of Hg/Cu and Pt/Cu thermocouples (43) amount to +0.0120 and +0.0068 mv/deg at 25° [hot Cu terminal (+)]. These values fall within the experimental uncertainty of Fales and Mudge's data of about 0.02 −0.04 mv/deg.

[6] Applications of equations such as [20] and [21] come up against the thorny problem of defining the single ion activities which they involve. A practical rule is that of Scatchard (60): "We will define single ion activities as those measured with a use of a saturated potassium chloride bridge. 'Such a definition does not contradict any measurements or theories which do not involve single ion activities.' " A convenient rule for computation applicable to uni-univalent salts is to take the single ion activity equal to the measurable mean ion activity of the electrolyte (7). For multiply charged ions of binary salts, an extension of this rule, consistent with the Debye theory (44), is to take single ion activity coefficients as $\gamma_+ = \gamma_\pm^{-z_+/z_-}$ and $\gamma_- = \gamma_\pm^{-z_-/z_+}$ where z_+ and z_- are the valences (with sign) of the cation and anion, respectively. These rules will be adopted in the present paper.

Fales and Mudge (14) reported their 0.1*M* hydrochloric acid as 0.1003*M*. If one takes $\gamma_+ = \gamma_\pm = 0.7967$ (45), the second term in Eq. [21] becomes equal to (0.1984 mv/deg) log (0.1003 × 0.7967) = −0.218 mv/deg, when $(H_2) = 1$. At constant molality, $d \ln (H^+)/dT$ can be replaced by $d \ln \gamma_\pm/dT$. From data of Bates and Bower (45, Eq. [5] in their paper), $d \log \gamma_\pm/dT = -0.0002181$ deg^{-1}, and the third term in Eq. [21] is equal to (59.16 mv)(−0.0002181 deg^{-1}) = −0.013 mv/deg.

Thermal temperature coefficient of the standard hydrogen electrode.—By taking $(dV/dT)_{th} = +0.640$ mv/deg in Eq. [21], one can obtain the thermal temperature coefficient of the standard hydrogen electrode (SHE) as (+0.640) − (−0.218) − (−0.013) = +0.871 mv/deg at 25°C.

An independent experimental check of this value can be made as follows. The potential of the saturated potassium chloride calomel electrode (SCE) has been deduced from buffer measurements of (*a*) MacInnes, Belcher, and Shedlovsky (46) and of (*b*) Baxter (47) to be: 10°C, +0.2540*b*; 12°, 0.2530*a*; 15° 0.2508*b*; 18° 0.2489*b*; 20° 0.2476*b*; 25° 0.2446*a*, 0.2443*b*; 30° 0.2410*b*; 35° 0.2376*b*; 38° 0.2375*a*, 0.2356*b*; 40° 0.2342*b*. The isothermal temperature coefficient of the SCE at 25°C is obtained as −0.60 mv/deg from set (*a*) and −0.66 mv/deg from set (*b*). These may be contrasted with Clark's (61) earlier estimate of −0.76 mv/deg and Vellinger's (48) of −0.66 mv/deg. The thermal temperature coefficient of the SCE has been observed as +0.217 mv/deg, Fales and Mudge (14); +0.21, Ewing (15); +0.20, Cary and Baxter (25); +0.22, Bjerrum and Unmack (20); +0.234, Wingfield and Acree (23).

The difference thermal minus isothermal coefficient for the SCE should yield the thermal temperature coefficient of the SHE. When this is done, extremes ranging from +0.80 to +1.0 mv/deg are obtained. However, if −0.66 mv/deg is adopted as a preferred isothermal value and +0.22 mv/deg as a median thermal value, for the SCE, the thermal value +0.88 mv/deg is obtained for the SHE, which is very close to our own. The experimental uncertainty in these and other observations still amounts to a few hundredths of a millivolt per degree. It seems best to assign a precision measure of not less than ±0.02 mv/deg and we shall therefore adopt, for the SHE at 25°C:

$$(dV^\circ/dT)_{th}(H_2/H^+) = +0.871 \pm 0.02 \text{ mv/deg} \quad [22]$$

Standard ionic entropy of electrochemical transport of the hydrogen ion.—For the standard hydrogen electrode, the entropy of electrochemical transport $S^{*\circ}_E$ is given by

$$S^{*\circ}_E = S^\circ(H_2) - 2S^{*\circ}_E(H^+) \quad [23]$$

for 2 faradays, and is equal to +0.871 mv/deg × 2**F** = +1.742 mv**F**/deg = 40.17 cal/deg. Since the molal entropy of hydrogen gas is 31.211 cal/deg (6), the standard ionic entropy $S^{*\circ}_E$ of H^+ is computed as −4.48 cal/deg ±0.5 cal/deg. This value may be contrasted with estimates ranging from −1.5 to −6.3 cal/deg reported by several authors (28, 29, 41).

Since the entropy transported by a neutral sub-

stance should be independent of the particular way its entropy is divided into constituent ionic entropies, the standard entropies of electrochemical transport $S^{*\circ}_{Ei}$ of other ionic species can be obtained from their tabulated standard entropies S°_i (referred to $S^\circ(H^+) = 0$ at all temperatures) by the equation

$$S^{*\circ}_{Ei} = S^\circ_i + z(-4.48 \text{ cal/deg}) \quad [24]$$

where z_i is the ionic charge (with sign).

Calomel electrodes.—For the calomel electrode: $2Hg + 2Cl^- = Hg_2Cl_2 + 2e^-$, $V^\circ = +0.2676$ v, the entropy of electrochemical transport S^*_E is

$$\begin{aligned} S^{*\circ}_E &= 2S^\circ(Hg) + 2S^{*\circ}_E(Cl^-) - S^\circ(Hg_2Cl_2) \\ &= 2(+18.5) + 2(13.2 + 4.48) - (46.8) \\ &= 25.56 \text{ cal/deg} = 1.108 \text{ mv}\mathbf{F}/\text{deg} \end{aligned} \quad [25]$$

Division by 2 faradays yields

$$(dV^\circ/dT)_{th}(Hg/Hg_2Cl_2, Cl^-) = +0.554 \text{ mv/deg} \quad [26]$$

The Nernst equation for this electrode and its temperature derivative (applied to the thermal coefficient), are

$$V = V^\circ - (RT/\mathbf{F}) \ln (Cl^-) \quad [27]$$

and

$$\begin{aligned} (dV/dT)_{th} &= (dV^\circ/dT)_{th} - (R/\mathbf{F}) \ln (Cl^-) \\ &\quad -(RT/\mathbf{F})(d \ln (Cl^-)/dT) \end{aligned} \quad [28]$$

By means of Eq. [26] and [28], we have calculated the thermal temperature coefficients of 0.01, 0.1, 1.0, 3.5, and 3.8N potassium chloride calomel electrodes and compared them with experimental observations on thermal cells in which the salt bridge contained the same concentration of potassium chloride as the electrodes (Table I). The second term in Eq. [28] is equal to $+(0.1984 \text{ mv/deg})$ pCl where $pCl = -\log (Cl^-)$, a quantity which can be equated to $-\log m\gamma_\pm$ (62). In the third term, the derivative $d \ln (Cl^-)/dT$ can be replaced, at constant molality, by $d \ln \gamma_\pm/dT$. The latter quantity can be evaluated from data in Harned and Owen (49), the estimates for the two highest normalities are uncertain and have been put in parentheses in Table I. The third term in Eq. [28] amounts to +0.002, 0.000, −0.021, (−0.07), and (−0.075) mv/deg for the five normalities studied. For the first three normalities, the third term could have been neglected without significant error while, for the last two, it is significant but uncertain. For the first three normalities, agreement between calculation and experiment falls by and large within ±0.02 mv/deg, and no deviation exceeds 0.04 mv/deg. For the two highest normalities, better agreement is attained when the third term is neglected. Inclusion of the third term (values in parentheses) leads to calculated values that are about 0.06 −0.07 mv/deg low.

The potential of the saturated potassium chloride calomel electrode (SCE) can be calculated from Eq. [27] with the chloride ion activity set equal to the square root of the activity of the saturated potassium chloride electrolyte. The latter in turn is equal to $\exp(-\Delta G^\circ/RT)$ where ΔG° is the standard free enthalpy (Gibbs free energy) of solution of potassium chloride according to the reaction: $KCl(c) = K^+(aq) + Cl^-(aq)$, and is equal to −1.224 kcal = −0.0532 v-faraday (6). The potential of the SCE is therefore equal to $V(SCE) = V^\circ + \Delta G^\circ/2\mathbf{F} = +0.2676$ v + (−0.0532 v$\mathbf{F}$/2$\mathbf{F}$) = +0.2410 v, a value which is consistent with observed values 0.2446 (46) and 0.2443 (47) at 25°C after correction for the liquid junction potential by means of the Henderson equation. The thermal temperature coefficient of the SCE potential is then given by $(dV/dT)_{th}(SCE) = (dV^\circ/dT)_{th} - \Delta S^\circ/2\mathbf{F}$ where ΔS° is the standard entropy of solution of potassium chloride, and is equal to 17.94 cal/deg = 0.778 mv$\mathbf{F}$/deg (6). We can therefore calculate

$$(dV/dT)_{th}(SCE) = +0.554 - (0.778/2) = + 0.165 \text{ mv/deg}$$

at 25°C. The comparable experimental values already have been quoted above as: +0.217 (14), +0.21 (15), +0.20 (25), +0.22 (20), and +0.234 mv/deg (23). The calculated value here seems to be about 0.05 mv/deg low.

Silver chloride electrode.—For the silver chloride electrode: $Ag + Cl^- = AgCl + e^-$, $V^\circ = +0.2223$ v, the entropy of electrochemical transport S^*_E is

$$\begin{aligned} S^{*\circ}_E &= S^\circ(Ag) + S^{*\circ}_E(Cl^-) - S^\circ(AgCl) \\ &= (10.206) + (13.2 + 4.48) - (22.97) \\ &= 4.92 \text{ cal/deg} = 0.214 \text{ mv}\mathbf{F}/\text{deg} \end{aligned} \quad [29]$$

Division by 1 faraday yields

$$(dV^\circ/dT)_{th}(Ag/AgCl, Cl^-) = +0.214 \text{ mv/deg} \quad [30]$$

This value may be compared with experiments of Tyrrell and Hollis (28) who deduce a value of +0.205 mv/deg for the standard thermal coefficient,

Table I. Thermal temperature coefficients of unsaturated calomel electrodes

Normality of KCl	0.01	0.1	1.0	3.5	3.8
Molality	0.01002	0.1006	1.033	3.93	4.31
$\gamma_\pm$	0.901	0.770	0.607	0.578	0.58
pCl	2.042	1.111	0.203	−0.356	−0.398
$10^4 d \ln \gamma/dT$	−1	0	+8	(+27)	(+29)
$(dV/dT)_{th}$ mv/deg					
Calc.	+0.961	+0.774	+0.573	+0.48[a] (+0.41)	+0.475[a] (+0.40)
Obs.	+0.94[b]	+0.79[b] +0.79[c] +0.792[d]	+0.61[b] +0.59[b] +0.57[f,g]	+0.47[c]	+0.475 exposed[h] +0.394 jacketed[h]

[a] Values exclusive of the third term in Eq. [28]; [b] Richards (13); [c] Sorensen and Linderstrom-Lang (17); [d] Based on Lewis and Randall's (50) observed $dE/dT = +0.152$ mv/deg for the cell: H_2(p.p. 1 atm)/0.1M HCl/Hg_2Cl_2, Hg combined with the thermal value +0.640 mv/deg for the 0.1N hydrogen electrode; [e] Kolthoff and Tekelenburg (19); [f] Burian (21); [g] deBethune, Licht, and Swendeman (36); [h] Wingfield and Acree (23).

Table II. Thermal temperature coefficients of silver chloride electrodes

Normality of chloride	0.001	0.01	0.1	1.0
$\gamma_\pm$	0.965[a,b]	0.90[a,b]	0.77[a] 0.78[b]	0.61[a] 0.66[b]
pCl	3.02	2.04	1.11	0.21[a] 0.18[b]
$10^4\, d \ln \gamma/dT$	−0.6[d] —	−1[a] −1.7[d]	0[a] −3[b]	+8[a] +4[b]
$(dV/dT)_{th}$ mv/deg				
Calc.	+0.81[a] —	+0.621[a] +0.623[b]	+0.434[a] +0.442[b]	+0.235[a] +0.239[b]
Obs.	+0.77[a,c,c]	+0.617[a,f] +0.620[b,f] +0.60[c,e]	+0.431[a,e] +0.449[a,g]	+0.250[a,e] +0.261[a,f] +0.228[b,f] +0.22[a,b,h]

[a] KCl; [b] NaCl; [c] CsCl; [d] from Debye equation; [e] Levin and Bonilla (30); [f] Bernhardt and Crockford (26); [g] deBethune, Licht, and Swendeman (35), satd KCl bridge; [h] Gilbert (27).

from their observations in sodium chloride solutions.

For several nonstandard silver chloride electrodes, thermal temperature coefficients can be computed (neglecting the slight discrepancy between normality and molality of chloride) and compared with experiment (Table II). The temperature effect on activity coefficients was estimated from data in Harned and Owen (49) or from the Debye theory (44). Agreement between calculation and experiment is within ±0.02 mv/deg, the largest deviation is 0.04 mv/deg.

From the calculated values in Table II, the Peltier heat of the silver chloride electrode can be computed as $TS^*_E = Tn\mathbf{F}(dV/dT)_{th} = 4.27$ and 2.98 kcal, in 0.01N and 0.1N potassium chloride, respectively. Lange and Hesse's calorimetrically observed values are 4.52 and 3.32 kcal, respectively (22).

Copper-copper sulfate electrode.—The standard potential of the copper electrode, $Cu = Cu^{++} + 2e^-$, has been assigned values ranging from $V° = +0.3448$ to +0.337 v (5-7, 51-53) at 25°C. In general, the amalgam electrodes proved about 5 mv more noble than the pure metal. Tragert and Robertson (53) investigated the dependence of potential on crystal face orientation. For the most stable (111) plane, they found a potential of +0.3419 v. For unstable (110), (100), and (210) planes, the potential was about 4 mv more active and reverted in time to the (111) value.

The entropy S^*_E of electrochemical transport for the copper electrode is

$$\begin{aligned} S^{*\circ}_E &= S^\circ(\mathrm{Cu}) - S^{*\circ}_E(\mathrm{Cu^{++}}) \\ &= (7.96) - (-23.6 - 2 \times 4.48) \\ &= 40.52 \text{ cal/deg} = 1.757 \text{ mv}\mathbf{F}/\text{deg} \end{aligned} \quad [31]$$

Division by 2 faradays yields

$$(dV°/dT)_{th}(\mathrm{Cu/Cu^{++}}) = +0.879 \text{ mv/deg} \quad [32]$$

Bonnemay (32) has reported a value of +0.81 mv/deg for the standard thermal coefficient from his experimental observations.

For unsaturated copper sulfate electrodes, the thermal temperature coefficient should be given by $+0.879 + (R/2\mathbf{F}) \ln (Cu^{++})$ plus a third term involving the temperature dependence of activity coefficients which will be neglected here. This coefficient was measured by Meyer (12), Burian (21), Ewing (24), and other observers [see Lange (10)]. The bulk of the values, for copper sulfate concentrations from 0.02 to 1M, fall in the range +0.5 to +0.8 mv/deg. The following approximate calculations can be carried out and compared with selected experimental values (Table III). Agreement between calculation and experiment falls here within about ±0.05 mv/deg.

The saturated copper sulfate electrode is a popular reference electrode in corrosion field work (24, 34). Its potential at 25°C is given by $V(\mathrm{Cu/satd\ CuSO_4}) = V° + (RT/2\mathbf{F}) \ln (Cu^{++} \text{ in satd } CuSO_4)$. The activity of cupric ion in saturated copper sulfate solution may be set equal to the square root of the activity of saturated copper sulfate electrolyte. The latter is equal to $\exp(-\Delta G°/RT)$ where $\Delta G°$ is the standard free enthalpy of solution of copper sulfate according to the equation $CuSO_4 \cdot 5H_2O(c) = Cu^{++}(aq) + SO_4^=(aq) + 5H_2O$ and is equal to +4.04 kcal = +0.1752 v$\mathbf{F}$ (6). The potential of the saturated copper sulfate electrode is therefore equal to $V(\mathrm{Cu/satd\ CuSO_4}) = V° - \Delta G°/4\mathbf{F} = +0.3419 \text{ v} - (0.1752 \text{ v}\mathbf{F}/4\mathbf{F}) = +0.2981$ v at 25°C. The latter is in good agreement with data of Hall (54) who observed values ranging from +0.302 to +0.317 on uncleaned copper, and +0.296 to +0.303 after nitric acid etch.

The thermal temperature coefficient then is given by $(dV/dT)_{th}(\mathrm{Cu/satd\ CuSO_4}) = (dV°/dT)_{th} +$

Table III. Thermal temperature coefficients of unsaturated copper sulfate electrodes

Molarity of $CuSO_4$	0.08	0.1	0.5	1.0	1.4
$\gamma_\pm$	0.17	0.16	0.068	0.047	0.04 (est)
pCu	1.86	1.80	1.47	1.33	1.25
$(dV/dT)_{th}$ mv/deg					
Calc.	+0.694	+0.700	+0.733	+0.747	+0.755
Obs.	+0.64[a]	+0.72[b]	+0.75[c]	+0.69[a] +0.79[b]	+0.75[c]

[a] Meyer (12); [b] Burian (21); [c] Ewing (24) found no variation when copper sulfate bridge was replaced by a potassium chloride bridge. Coefficients observed in range 28.5°-51°C. In 0.5M $CuSO_4$, observed value drops to +0.55 mv/deg at 0°C.

$\Delta S°/4\mathbf{F}$ where $\Delta S°$ is the standard entropy of solution of copper sulfate pentahydrate and is equal to -8.92 cal/deg $= -0.3868$ mv**F** (6). We can therefore calculate

$$(dV/dT)_{th}(\text{Cu/satd CuSO}_4) = +0.879 + (-0.3868/4) = +0.782 \text{ mv/deg}$$

This calculated value may be compared with the observed values: Ewing's +0.895 mv/deg (24) observed in the temperature range 0°-50°C with a copper sulfate bridge, and Scott's +0.97 mv/deg (34) observed under field conditions with a soil bridge and a polarized steel structure as the constant temperature reference electrode. Ewing observed a distinct hysteresis in the behavior of the saturated copper sulfate electrode with temperature changes, Scott apparently did not. Although the agreement between calculation and experiment is only within 0.1-0.2 mv/deg, it is sufficiently striking to confirm the validity of the ionic entropies of electrochemical transport deduced in this paper from Fales and Mudge's observations (14) on the 0.1*N* hydrogen electrode together with the assumption that their saturated potassium chloride bridges eliminated the thermal liquid junction potential.

Isothermal Temperature Coefficients

Isothermal temperature coefficients of electrode potentials have already been defined above in terms of cell [1] and Eq. [3]. Consider cell [1] with a reversible iron-ferrous ion electrode at the right-hand end. The entropy ΔS of the reaction which transfers 2 faradays of positive electricity through cell [1] from left to right is

$$\Delta S = S(\text{Fe}) - S(\text{Fe}^{++}) + 2S°(\text{H}^+) - S°(\text{H}_2) \qquad [33]$$

If the iron and ferrous ion are in their standard states, their standard molal entropies are 6.49 and -27.1 cal/deg, respectively, at 25°C (6). Given the standard entropies of hydrogen gas and hydrogen ion as 31.211 cal/deg and zero, respectively, the standard reaction entropy of cell [1] is $\Delta S°[33] = +2.38$ cal/deg $= +0.1032$ mv**F**/deg. Division by 2 faradays yields

$$(dV°/dT)_{isoth}(\text{Fe/Fe}^{++}) = +0.052 \text{ mv/deg}$$

The thermal temperature coefficient of the iron-ferrous ion electrode is determined by the electrochemical transport entropy S^*_E already given in Eq. [11]. If we take $S^{*\circ}_E(Fe^{++}) = -27.1 + 2\ (-4.48) = -36.06$ cal/deg, the standard transport entropy $S^{*\circ}_E$ [11] becomes +42.55 cal/deg $= +1.845$ mv**F**/deg. Division by 2 faradays yields

$$(dV°/dT)_{th}(\text{Fe/Fe}^{++}) = +0.923 \text{ mv/deg}$$

The difference thermal minus isothermal coefficient for the iron-ferrous ion electrode becomes $[S^*_E[11] - \Delta S[33]]/2\mathbf{F} = [S(\text{Fe}^{++}) - S^*_E(\text{Fe}^{++}) - 2S°(\text{H}^+) + S°(\text{H}_2)]/2\mathbf{F} = [-2S^{*\circ}_E(\text{H}^+) + S°(\text{H}_2)]/2\mathbf{F}$, i.e., this difference is equal to the thermal temperature coefficient of the SHE. For the standard iron-ferrous ion electrode, this difference is equal to $+0.923 - (+0.052) = +0.871$ mv/deg, i.e., the numerical value assigned above to the SHE thermal coefficient.

Thus the thermal temperature coefficient of any (standard or nonstandard) electrode potential, when computed according to the methods of this paper, can be converted to the corresponding isothermal temperature coefficient by subtraction of the numerical constant 0.871 mv/deg.

Table of Temperature Coefficients

Table IV lists a number of electrodes, their standard electrode potentials, the thermal temperature coefficients computed according to the methods of this paper, and the isothermal temperature coefficients computed from Eq. [3]. The data refer, except where noted, to 25°C. The entropy data were taken largely from Latimer (6). Whenever entropies were given only to the nearest cal/deg, the coefficients were rounded off to the nearest hundredth of a millivolt per degree. Direct experimental observations, in addition to those discussed above in the text, are noted in parentheses. The agreement is usually within a few hundredths of a millivolt per degree for both thermal and isothermal temperature coefficients.

The temperature coefficient of the emf[2] of any isothermal cell can be computed from the temperature coefficients given in Table IV by taking the algebraic difference of the values listed for the two electrodes in the order: thermal right minus thermal left, or isothermal right minus isothermal left.

Acknowledgment

The authors wish to express their gratitude to those corrosion engineers who persistently asked them the question "What is the effect of temperature on electrode potentials?" They take pleasure in acknowledging their indebtedness to Dr. W. A. Mudge of the International Nickel Company for calling their attention to his experiments (14) on the thermal temperature coefficient of the 0.1*N* hydrogen electrode which have proved basic to this entire study. They also wish to thank the International Nickel Company for a Grant-in-Aid in support of this work.

Manuscript received Aug. 8, 1958. This paper was prepared for delivery before the Philadelphia Meeting, May 3-7, 1959.

Any discussion of this paper will appear in a Discussion Section to be published in the June 1960 JOURNAL.

REFERENCES

1. J. Willard Gibbs, "Collected Works," Vol. I, pp. 332-349, 429, Longmans Green, New York (1928).
2. J. A. Christiansen and M. Pourbaix, *Compt. Rend. 17th Conf. I.U.P.A.C.*, pp. 82-84, Maison de la Chimie, Paris (1954).
3. A. J. deBethune, *This Journal*, **102**, 288*C* (1955).
4. T. S. Licht and A. J. deBethune, *J. Chem. Education*, **34**, 433 (1957).
5. G. N. Lewis and M. Randall, "Thermodynamics and the Free Energy of Chemical Substances," McGraw Hill Book Co., New York (1923).
6. W. M. Latimer, "Oxidation Potentials—The Oxidation States of the Elements and Their Potentials in Aqueous Solutions," 2d Ed., Prentice Hall, New York (1952).
7. D. A. MacInnes, "Principles of Electrochemistry," Reinhold Publishing Co., New York (1939).
8. G. Scatchard, "Thermodynamics and Electrostatic Theory," in E. J. Cohn and J. T. Edsall, "Protein,

Table IV. Thermal and isothermal temperature coefficients of the standard electrode potentials at 25°C

The electrode potential V° is given a positive value if the electrode is the (+) terminal of a cell whose second electrode is the SHE. The thermal temperature coefficient $(dV°/dT)_{th}$ is given a positive value if the hot electrode is the (+) terminal in a thermal cell. The isothermal temperature coefficient $(dV°/dT)_{isoth}$ is given a positive value if the electromotive force of the isothermal cell: SHE // Electrode, increases with the temperature.

Electrode	V°, v	$(dV°/dT)_{th}$, mv/deg	$(dV°/dT)_{isoth}$, mv/deg
(Acid Solution)			
$HN_3(g) = (3/2)N_2 + H^+ + e^-$	−3.40[a]	−0.322	−1.193
$HN_3(aq) = (3/2)N_2 + H^+ + e^-$	−3.09	−0.70	−1.57
$Li = Li^+ + e^-$	−3.045	+0.337	−0.534
$K = K^+ + e^-$	−2.925	−0.209	−1.080
$Rb = Rb^+ + e^-$	−2.925	−0.374	−1.245
$Cs = Cs^+ + e^-$	−2.923	−0.326	−1.197
$Ra = Ra^{++} + 2e^-$	−2.916[a]	+0.28	−0.59
$Ba = Ba^{++} + 2e^-$	−2.906[a]	+0.48	−0.39[5]
$Sr = Sr^{++} + 2e^-$	−2.888[a]	+0.680	−0.191
$Ca = Ca^{++} + 2e^-$	−2.866[a]	+0.696	−0.175
$Na = Na^+ + e^-$	−2.714[a]	+0.099	−0.772
$La = La^{+++} + 3e^-$	−2.522[a]	+0.96	+0.08[5]
$Nd = Nd^{+++} + 3e^-$	−2.431[a]	+0.995	+0.124
$Sm = Sm^{+++} + 3e^-$	−2.414[a]	+1.007	+0.136
$Gd = Gd^{+++} + 3e^-$	−2.397[a]	+1.02	+0.15
$Y = Y^{+++} + 3e^-$	−2.372[a]	+1.05	+0.18
$Mg = Mg^{++} + 2e^-$	−2.363[a]	+0.974	+0.103
$Am = Am^{+++} + 3e^-$	−2.320[a]	+0.960	+0.089
$Lu = Lu^{+++} + 3e^-$	−2.255[a]	+1.064	+0.193
$H^- = (1/2)H_2 + e^-$	−2.25[b]	−0.70[b]	−1.57
$H(g) = H^+ + e^-$	−2.1065[a]	+1.382	+0.511
$Sc = Sc^{+++} + 3e^-$	−2.077[a]	+1.12	+0.25
$Al + 6F^- = AlF_6^{---} + 3e^-$	−2.069[a]	+0.67	−0.20
$Pu = Pu^{+++} + 3e^-$	−2.031[a]	+0.93	+0.06
$Th = Th^{+4} + 4e^-$	−1.899[a]	+1.15	+0.28
$Np = Np^{+++} + 3e^-$	−1.856[a]	+0.817	−0.054
$Be = Be^{++} + 2e^-$	−1.847[a]	+1.44	+0.56[5]
$U = U^{+++} + 3e^-$	−1.789[a]	+0.80	−0.07
$Al = Al^{+++} + 3e^-$	−1.662[a]	+1.375	+0.504
$Si + 6F^- = SiF_6^{--} + 4e^-$	−1.24[a]	+0.22	−0.65
$Ti + 6F^- = TiF_6^{--} + 4e^-$	−1.191[a]	−0.09	−0.96[5]
$Mn = Mn^{++} + 2e^-$	−1.180[a]	+0.79	−0.08
$B + 3H_2O = H_3BO_3(aq) + 3H^+ + 3e^-$	−0.8698[a]	+0.390	−0.481
$B + 3H_2O = H_3BO_3(c) + 3H^+ + 3e^-$	−0.869[a]	+0.632	−0.239
$Si + 2H_2O = SiO_2(quartz) + 4H^+ + 4e^-$	−0.857[a]	+0.497	−0.374
$2Ta + 5H_2O = Ta_2O_5 + 10H^+ + 10e^-$	−0.812[a]	+0.494	−0.377
$Zn = Zn^{++} + 2e^-$	−0.7628[a], −0.7626[c]	+0.962 (+1.[e])	+0.091 (+0.10[c], +0.166[d])
$Tl + I^- = TlI + e^-$	−0.752[a]	+0.721	−0.150
$Cr = Cr^{+++} + 3e^-$	−0.744[a]	+1.339	+0.468
$H_2Te(g) = Te + 2H^+ + 2e^-$	−0.718[a]	+1.151	+0.280
$Tl + Br^- = TlBr + e^-$	−0.658	+0.458	−0.413
$2Nb + 5H_2O = Nb_2O_5 + 10H^+ + 10e^-$	−0.644[a]	+0.48	−0.39
$U^{+++} = U^{+4} + e^-$	−0.607[a]	+2.27	+1.40
$AsH_3(g) = As + 3H^+ + 3e^-$	−0.607[a]	+0.82	−0.05
$Tl + Cl^- = TlCl + e^-$	−0.5568[a]	+0.311	−0.560 (−0.579 amalgam, −0.611 crystal[e])
$Ga = Ga^{+++} + 3e^-$	−0.529[a]	+1.54	+0.67
$SbH_3(g) = Sb + 3H^+ + 3e^-$	−0.510[a]	+0.81	−0.06
$P(white) + 2H_2O = H_3PO_2 + H^+ + e^-$	−0.508[a]	+0.45	−0.42
$H_3PO_2(aq) + H_2O = H_3PO_3(aq) + 2H^+ + 2e^-$	−0.499[a]	+0.51	−0.36
$Fe = Fe^{++} + 2e^-$	−0.4402[a]	+0.923	+0.052
$Cd = Cd^{++} + 2e^-$	−0.4029[a]	+0.778 (+0.788[f])	−0.093 (−0.053[d])
$H_2Se(aq) = Se + 2H^+ + 2e^-$	−0.399[a]	+0.843	−0.028
$Pb + 2I^- = PbI_2 + 2e^-$	−0.365	+0.747	−0.124 (−0.095 amalgam, −0.111 solid[e])
$Pb + SO_4^= = PbSO_4 + 2e^-$	−0.3588[a]	−0.144	−1.015
$Cd(Hg) = Cd^{++} + Hg + 2e^-$	−0.3515[c], −0.3514[c], −0.3516[d]	(+0.62[c])	(−0.252[c], −0.292[c], −0.250[d])
$Pb(Hg) + SO_4^= = PbSO_4 + Hg + 2e^-$	−0.3505[d]	(−0.043[d])	(−0.914[d])
$In = In^{+++} + 3e^-$	−0.343[a]	+1.27	+0.40
$Tl = Tl^+ + e^-$	−0.3363	−0.456 (−0.525[f])	−1.327 (−1.314[d])
$(1/2)C_2N_2 + H_2O = HCNO + H^+ + e^-$	−0.330[a]	+0.283	−0.588
$Pt + H_2S(aq) = PtS + 2H^+ + 2e^-$	−0.327[a]	+0.606	−0.265
$Pt + H_2S(g) = PtS + 2H^+ + 2e^-$	−0.297[a]	+1.039	+0.168
$Pb + 2Br^- = PbBr_2 + 2e^-$	−0.284[a]	+0.530	−0.341
$Co = Co^{++} + 2e^-$	−0.277	+0.93	+0.06
$H_3PO_3(aq) + H_2O = H_3PO_4(aq) + 2H^+ + 2e^-$	−0.276	+0.51	−0.36
$Pb + 2Cl^- = PbCl_2 + 2e^-$	−0.268	+0.396	−0.475 (−0.45 amalgam, −0.47 solid[e])
$Sn + 6F^- = SnF_6^= + 4e^-$	−0.25	+0.178	−0.693
$Ni = Ni^{++} + 2e^-$	−0.250	+0.93[ee]	+0.06
$N_2H_5^+ = N_2 + 5H^+ + 4e^-$	−0.23	+0.03	−0.84
$S_2O_6^= + 2H_2O = 2SO_4^= + 4H^+ + 2e^-$	−0.22	+1.39	+0.52
$HCOOH(aq) + CO_2(g) + 2H^+ + 2e^-$	−0.199[a]	−0.065	−0.936
$Cu + I^- = CuI + e^-$	−0.1852[a]	+0.671	−0.200
$Ag + I^- = AgI + e^-$	−0.1518[a]	+0.587 (+0.414[u])	−0.284 (−0.328[d])

Table IV (Continued)

Electrode	V°, v	$(dV°/dT)_{th}$, mv/deg	$(dV°/dT)_{isoth}$, mv/deg
$Ge + 2H_2O = GeO_2 + 4H^+ + 4e^-$	−0.15	+0.54	−0.33[5]
$Sn(white) = Sn^{++} + 2e^-$	−0.136	+0.589	−0.282
$Pb = Pb^{++} + 2e^-$	−0.126	+0.420 (+0.45[v])	−0.451
$W + 3H_2O = WO_3(c) + 6H^+ + 6e^-$	−0.090[a]	+0.471	−0.400
$PH_3(g) = P(white) + 3H^+ + 3e^-$	−0.063[a]	+0.767	−0.104
$2Hg + 2I^- = Hg_2I_2 + 2e^-$	−0.0405	+0.890	+0.019
$Hg + 4I^- = HgI_4^= + 2e^-$	−0.038[a]	+0.91	+0.04
$H_2 = 2H^+ + 2e^-$ (SHE)	±0.0000	+0.871[g]	±0.000[f]
H_2 (sat'd, t.p. 1 atm) = $2H^+ + 2e^-$	+0.0004[h]	+0.904[g]	+0.033[h]
$Cu + Br^- = CuBr + e^-$	+0.033	+0.426	−0.445
$UO_2^+ = UO_2^{++} + e^-$	+0.05	+1.45	+0.58
$Ag + Br^- = AgBr + e^-$	+0.0713[a], (+0.0711[d], +0.0713[t])	+0.363 (+0.320[x], +0.327[u], +0.38[y])	−0.508 (−0.488[d], −0.500[t])
$SiH_4(g) = Si + 4H^+ + 4e^-$	+0.102	+0.674	−0.197
$CH_4(g) = C(graphite) + 4H^+ + 4e^-$	+0.1316[a]	+0.662	−0.209
$Cu + Cl^- = CuCl + e^-$	+0.137	+0.236	−0.635
$2Hg + 2Br^- = Hg_2Br_2 + 2e^-$	+0.1397	+0.729	−0.142
$H_2S(aq) = S(rhombic) + 2H^+ + 2e^-$	+0.142[a]	+0.662	−0.209
$Np^{+++} = Np^{+4} + e^-$	+0.147	+2.23	+1.36
$2Sb + 3H_2O = Sb_2O_3 + 6H^+ + 6e^-$	+0.152	+0.496	−0.375
$Cu^+ = Cu^{++} + e^-$	+0.153	+0.944	+0.073
$Bi + H_2O + Cl^- = BiOCl + 2H^+ + 3e^-$	+0.160[a]	+0.526	−0.345
$H_2SO_3 + H_2O = SO_4^= + 4H^+ + 2e^-$	+0.172[a]	+1.68	+0.81
$Ag + Cl^- = AgCl + e^-$	+0.2222 (+0.2225[d], +0.22234[j])	+0.213[w]	−0.658 (−0.638[d], −0.653[j])
$Hg + 4Br^- = HgBr_4^= + 2e^-$	+0.223[a]	+0.45	−0.42
$As + 2H_2O = HAsO_2(aq) + 3H^+ + 3e^-$	+0.2476[a]	+0.361	−0.510
$2Cl^- + 2Hg = Hg_2Cl_2 + 2e^-$	+0.2676	+0.554[w]	−0.317 (−0.320[e])
$U^{+4} + 2H_2O = UO_2^{++} + 4H^+ + 2e^-$	+0.330[a]	−0.40	−1.27
$Cu = Cu^{++} + 2e^-$	+0.337 (+0.3419[k])	+0.879[w]	+0.008 (−0.016[t])
$Ag + IO_3^- = AgIO_3^- + e^-$	+0.354[a]	+0.303	−0.568
$Re + 4H_2O = ReO_4^- + 8H^+ + 7e^-$	+0.362[a]	+0.36	−0.51
$HCN(aq) = 1/2C_2N_2(g) + H^+ + e^-$	+0.373[a]	+0.275	−0.596
$2NH_3OH^+ = H_2N_2O_2 + 6H^+ + 4e^-$	+0.387[a]	+0.43	−0.44
$S_2O_3^= + 3H_2O = 2H_2SO_3 + 2H^+ + 4e^-$	+0.400[a]	−0.39	−1.26
$Rh + 6Cl^- = RhCl_6^{---} + 3e^-$	+0.431	+0.73	−0.14[5]
$S + 3H_2O = H_2SO_3 + 4H^+ + 4e^-$	+0.450[a]	+0.21	−0.66
$2Ag + CrO_4^= = Ag_2CrO_4 + 2e^-$	+0.464[a]	−0.287	−1.158
$S_4O_6^= + 6H_2O = 4H_2SO_3 + 4H^+ + 6e^-$	+0.51	−0.44	−1.31
$C_2H_6(g) = C_2H_4(g) + 2H^+ + 2e^-$	+0.52	+0.246	−0.625
$Cu = Cu^+ + e^-$	+0.521	+0.813	−0.058
$Te + 2H_2O = TeO_2(c) + 4H^+ + 4e^-$	+0.529	+0.501	−0.370
$2I^- = I_2(c) + 2e^-$	+0.5355	+0.723	−0.148 (−0.150[e])
$3I^- = I_3^- + 2e^-$	+0.536	+0.657	−0.214
$CuCl = Cu^{++} + Cl^- + e^-$	+0.538	+1.521	+0.650
$HAsO_2 + 2H_2O = H_3AsO_4(aq) + 2H^+ + 2e^-$	+0.560[a]	+0.507	−0.364
$Ag + NO_2^- = AgNO_2 + e^-$	+0.564	+0.606	−0.265
$2H_2SO_3 = S_2O_6^= + 4H^+ + 2e^-$	+0.57	+1.97	+1.10
$Pt + 4Br^- = PtBr_4^= + 2e^-$	+0.581[a]	+1.02	+0.15
$CH_4(g) + H_2O = CH_3OH(aq) + 2H^+ + 2e^-$	+0.588[a]	+0.836	−0.035
$Pd + 4Br^- = PdBr_4^= + 2e^-$	+0.60[a]	+1.11	+0.23[5]
$2Hg + SO_4^= = Hg_2SO_4 + 2e^-$	+0.6151, +0.6119[a], +0.61515[m]	+0.045	−0.826 (−0.802[d], −0.803[m])
$U^{+4} + 2H_2O = UO_2^+ + 4H^+ + e^-$	+0.62	−2.26	−3.13
$Pd + 4Cl^- = PdCl_4^= + 2e^-$	+0.62	+0.75	−0.12
$CuBr = Cu^{++} + Br^- + e^-$	+0.640	+1.331	+0.460
$Ag + C_2H_3O_2^- = AgC_2H_3O_2 + e^-$	+0.643	+0.074[n]	−0.797
$2Ag + SO_4^= = Ag_2SO_4 + 2e^-$	+0.654[a]	−0.311	−1.182
$PtCl_4^= + 2Cl^- = PtCl_6^= + 2e^-$	+0.68	+0.54	−0.33
$H_2O_2(aq) = O_2(g) + 2H^+ + 2e^-$	+0.6824[a]	−0.162[n]	−1.033
$3NH_4^+ = HN_3(aq) + 11H^+ + 8e^-$	+0.695[a]	+0.373	−0.498
$C_6H_4(OH)_2 = C_6H_4O_2 + 2H^+ + 2e^-$	+0.6994	(+0.140[d])	(−0.731[d])
$OH(g) + H_2O = H_2O_2(aq) + H^+ + e^-$	+0.71[a]	+1.411[n]	+0.540
$H_2N_2O_2 = 2NO + 2H^+ + 2e^-$	+0.712[a]	−0.861	−1.732
$Pt + 4Cl^- = PtCl_4^= + 2e^-$	+0.73	+0.64	−0.23
$C_2H_4(g) = C_2H_2(g) + 2H^+ + 2e^-$	+0.731	+0.291	−0.580
$Se(gray) + 3H_2O = H_2SeO_3(aq) + 4H^+ + 4e^-$	+0.740[a]	+0.351	−0.520
$Np^{+4} + 2H_2O = NpO_2^+ + 4H^+ + e^-$	+0.75	−2.26	−3.13
$Ir + 6Cl^- = IrCl_6^{---} + 3e^-$	+0.77	+0.84	−0.03
$Fe^{++} = Fe^{+++} + e^-$	+0.771	+2.059	+1.188
$Ag = Ag^+ + e^-$	+0.7991	−0.129 (−0.22[z], −0.170[z])	−1.000
$N_2O_4(g) + 2H_2O = 2NO_3^- + 4H^+ + 2e^-$	+0.803[a]	+0.978	+0.107
$Os + 4H_2O = OsO_4$ (c, yellow) $+ 8H^+ + 8e^-$	+0.85	+0.438	−0.433

Table IV (Continued)

Electrode	V°, v	$(dV°/dT)_{th}$, mv/deg	$(dV°/dT)_{isoth}$, mv/deg
$H_2N_2O_2 + 2H_2O = 2HNO_2 + 4H^+ + 4e^-$	+0.86	+0.36[n]	−0.51
$CuI = Cu^{++} + I^- + e^-$	+0.86	+1.086	+0.215
$Au + 4Br^- = AuBr_4^- + 3e^-$	+0.87 (60°C)	+0.39	−0.48
$PuO_2^+ = PuO_2^{++} + e^-$	+0.93	+1.58	+0.71
$HNO_2 + H_2O = NO_3^- + 3H^+ + 2e^-$	+0.94	+0.07	−0.80
$NO + 2H_2O = NO_3^- + 4H^+ + 3e^-$	+0.96	+0.899	+0.028
$Pu^{+++} = Pu^{+4} + e^-$	+0.97	+2.27	+1.40
$Pt + 2H_2O = Pt(OH)_2 + 2H^+ + 2e^-$	+0.98	+0.561	−0.310
$NO + H_2O = HNO_2 + H^+ + e^-$	+1.00	+1.574[n]	+0.703
$Au + 4Cl^- = AuCl_4^- + 3e^-$	+1.00	+0.24	−0.63
$IrCl_6^{---} = IrCl_6^= + e^-$	+1.017	−0.24	−1.11
$TeO_2 + 4H_2O = H_6TeO_6(c) + 2H^+ + 2e^-$	+1.02	+1.00	+0.13
$2NO + 2H_2O = N_2O_4 + 4H^+ + 4e^-$	+1.03	+0.860	−0.011
$Pu^{+4} + 2H_2O = PuO_2^{++} + 4H^+ + 2e^-$	+1.04	−0.69	−1.56
$2Br^- = Br_2(l) + 2e^-$	+1.0652	+0.242	−0.629
$2HNO_2 = N_2O_4 + 2H^+ + 2e^-$	+1.07	+0.145[n]	−0.726
$2Br^- = Br_2(aq) + 2e^-$	+1.087	+0.393[n]	−0.478
$Pu^{+4} + 2H_2O = PuO_2^+ + 4H^+ + e^-$	+1.15	−2.95	−3.82
$H_2SeO_3 + H_2O = SeO_4^= + 4H^+ + 2e^-$	+1.15	+1.424	+0.553
$NpO_2^+ = NpO_2^{++} + e^-$	+1.15	+1.45	+0.58
$4Cl^- + C + 4H^+ = CCl_4 + 4H^+ + 4e^-$	+1.18	+0.226	−0.645
$ClO_3^- + H_2O = ClO_4^- + 2H^+ + 2e^-$	+1.19	+0.46	−0.41
$(1/2)I_2 + 3H_2O = IO_3^- + 6H^+ + 5e^-$	+1.195	+0.507	−0.364
$HClO_2 + H_2O = ClO_3^- + 3H^+ + 2e^-$	+1.21	+0.62	−0.25
$2H_2O = O_2 + 4H^+ + 4e^-$	+1.229	+0.025	−0.846
$2S + 2Cl^- = S_2Cl_2 + 2e^-$	+1.23	+0.23	−0.64
$Mn^{++} + 2H_2O = MnO_2 + 4H^+ + 2e^-$	+1.23	+0.210	−0.661
$Tl^+ = Tl^{+++} + 2e^-$	+1.25	+1.76	+0.89
$2NH_4^+ = N_2H_5^+ + 3H^+ + 2e^-$	+1.275	+0.69	−0.18
$HClO_2 = ClO_2 + H^+ + e^-$	+1.275	−0.57	−1.44
$PdCl_4^= + 2Cl^- = PdCl_6^= + 2e^-$	+1.288	+0.42	−0.45
$N_2O(g) + 3H_2O = 2HNO_2(aq) + 4H^+ + 4e^-$	+1.29	+0.544[n]	−0 327
$2Cr^{+++} + 7H_2O = Cr_2O_7^= + 14H^+ + 6e^-$	+1.33	−0.392	−1.263
$NH_4^+ + H_2O = NH_3OH^+ + 2H^+ + 2e^-$	+1.35	+0.34	−0.53
$2Cl^- = Cl_2 + 2e^-$	+1.3595	−0.389	−1.260 (−1.26[e])
$N_2H_5^+ + 2H_2O = 2NH_3OH^+ + H^+ + 2e^-$	+1.42	−0.01	−0.88
$Au + 3H_2O = Au(OH)_3(c) + 3H^+ + 3e^-$	+1.45	+0.665	−0.206
$(1/2)I_2 + H_2O = HIO + H^+ + e^-$	+1.45	+1 29	+0.42[n]
$Pb^{++} + 2H_2O = PbO_2 + 4H^+ + 2e^-$	+1.455	+0.633	−0.238
$Mn^{++} = Mn^{+++} + e^-$	+1.51	+2.10	+1.23[n]
$Mn^{++} + 4H_2O = MnO_4^- + 8H^+ + 5e^-$	+1.51	+0.21	−0.66
$(1/2)Br_2(l) + 3H_2O = BrO_3^- + 6H^+ + 5e^-$	+1.52	+0.453	−0.418
$(1/2)Cl_2 + H_2O = HClO + H^+ + e^-$	+1.63	+0.73	−0.14
$HClO + H_2O = HClO_2 + 2H^+ + 2e^-$	+1.64	+0.32	−0.55
$PbSO_4 + 2H_2O = PbO_2 + SO_4^= + 4H^+ + 2e^-$	+1.685	+1.197	+0.326 (+0.350[d], +0.389[p], +0.349[p])
$MnO_2 + 2H_2O = MnO_4^- + 4H^+ + 3e^-$	+1.695	+0.205	−0.666
$2H_2O = H_2O_2 + 2H^+ + 2e^-$	+1.776[a]	+0.213[n]	−0.658
$NH_4^+ + N_2 = HN_3 + 3H^+ + 2e^-$	+1.96	+0.73	−0.14
$2SO_4^= = S_2O_8^= + 2e^-$	+2.01	−0.39	−1.26
$O_2 + H_2O = O_3 + 2H^+ + 2e^-$	+2.07	+0.388	−0.483
$2F^- + H_2O = F_2O + 2H^+ + 4e^-$	+2.15[a]	−0.313	−1.184
$Am^{+++} = Am^{+4} + e^-$	+2.18	+2.40	+1.53
$Fe^{+++} + 4H_2O = FeO_4^= + 8H^+ + 3e^-$	+2.20[a]	+0.02[a]	−0.85
$H_2O = O(g) + 2H^+ + 2e^-$	+2.422[a]	−0.277	−1.148
$N_2 + 2H_2O = H_2N_2O_2 + 2H^+ + 2e^-$	+2.65[a]	+0.78	−0.09
$H_2O = OH + H^+ + e^-$	+2.85[a]	−0.984	−1.855
$2F^- = F_2(g) + 2e^-$	+2.87	−0.959	−1.830
$2HF(aq) = F_2(g) + 2H^+ + 2e^-$	+3.06	+0.27	−0.60
(Basic Solution)			
$Ca + 2OH^- = Ca(OH)_2 + 2e^-$	−3.02[a]	−0.094	−0.965
$Ba + 2OH^- + 8H_2O = Ba(OH)_2 \cdot 8H_2O + 2e^-$	−2.99[a]	+1.25[n]	+0.38
$H(g) + OH^- = H_2O + e^-$	−2.9345[a]	+0.548	−0.323
$La + 3OH^- = La(OH)_3 + 3e^-$	−2.90	−0.08	−0.95
$Sr + 2OH^- = Sr(OH)_2 + 2e^-$	−2.88[a]	−0.09	−0.96
$Ba + 2OH^- = Ba(OH)_2 + 2e^-$	−2.81[a]	−0.06	−0.93
$Mg + 2OH^- = Mg(OH)_2 + 2e^-$	−2.69	−0.074	−0.945
$Th + 4OH^- = Th(OH)_4 + 4e^-$	−2.48	−0.12	−0.99
$U + 4OH^- = UO_2 + 2H_2O + 4e^-$	−2.39	−0.349	−1.220
$Zr + 4OH^- = H_2ZrO_3 + H_2O + 4e^-$	−2.36	−0.24	−1.11
$Al + 3OH^- = Al(OH)_3 + 3e^-$	−2.30[a]	−0.06	−0.93
$B + 4OH^- = H_2BO_3^- + H_2O + 3e^-$	−1.79	−0.276	−1.147
$Mn + 2OH^- = Mn(OH)_2 + 2e^-$	−1.55	−0.208	−1.079
$Mn + CO_3^= = MnCO_3(c) + 2e^-$	−1.50[a]	−0.361	−1.232
$Mn + CO_3^= = MnCO_3(ppt) + 2e^-$	−1.48	−0.433	−1.304
$Cr + 3OH^- = Cr(OH)_3(c) + 3e^-$	−1.48[a]	−0.11	−0.98
$Zn + S^= = ZnS(wurtzite) + 2e^-$	−1.405[r]	+0.02[r]	−0.85
$Cr + 3OH^- = Cr(OH)_3$ (hydrous) $+ 3e^-$	−1.34[a]	−0.12	−0.99

Table IV (Continued)

Electrode	V°, v	$(dV°/dT)_{th}$, mv/deg	$(dV°/dT)_{isoth}$, mv/deg
$Zn + 4CN^- = Zn(CN)_4^= + 2e^-$	−1.26	+1.19[n]	+0.32
$Zn + 2OH^- = Zn(OH)_2 + 2e^-$	−1.245	−0.131	−1.002
$Cd + S^= = CdS + 2e^-$	−1.175[a]	0.00[r]	−0.87
$HPO_3^= + 3OH^- = PO_4^{---} + 2H_2O + 2e^-$	−1.12	+0.38[n]	−0.49
$S_2O_4^= + 4OH^- = 2SO_3^= + 2H_2O + 2e^-$	−1.12	+0.16	−0.71
$Zn + CO_3^= = ZnCO_3 + 2e^-$	−1.06	−0.293	−1.164
$W + 8OH^- = WO_4^= + 4H_2O + 6e^-$	−1.05	−0.49	−1.36
$Mo + 8OH^- = MoO_4^= + 4H_2O + 6e^-$	−1.05	−0.49	−1.36
$Ge + 5OH^- = HGeO_3^- + 2H_2O + 4e^-$	−1.03[a]	−0.42	−1.29
$In + 3OH^- = In(OH)_3 + 3e^-$	−1.00[a]	−0.10	−0.97
$CN^- + 2OH^- = CNO^- + H_2O + 2e^-$	−0.970	−0.340	−1.211
$Fe + S^= = FeS(\alpha) + 2e^-$	−0.95[r]	−0.10[r]	−0.97
$Pb + S^= = PbS + 2e^-$	−0.93[r]	−0.03[r]	−0.90
$SO_3^= + 2OH^- = SO_4^= + H_2O + 2e^-$	−0.93	−0.518	−1.389
$Se^= = Se + 2e^-$	−0.92	−0.02	−0.89
$2Tl + S^= = Tl_2S + 2e^-$	−0.90[r]	−0.07[r]	−0.94
$2Cu + S^= = Cu_2S + 2e^-$	−0.89[r]	−0.17[r]	−1.04
$PH_3 + 3OH^- = P(white) + 3H_2O + 3e^-$	−0.89	−0.067	−0.938
$Fe + 2OH^- = Fe(OH)_2 + 2e^-$	−0.877	−0.19	−1.06
$Sn + S^= = SnS + 2e^-$	−0.87[r]	−0.14[r]	−1.01
$H_2 + 2OH^- = 2H_2O + 2e^-$	−0.82806[a]	+0.037	−0.8342
$Cd + 2OH^- = Cd(OH)_2 + 2e^-$	−0.809	−0.143	−1.014
$Fe + CO_3^= = FeCO_3 + 2e^-$	−0.756	−0.422	−1.293
$Cd + CO_3^= = CdCO_3 + 2e^-$	−0.74	−0.361	−1.232
$Co + 2OH^- = Co(OH)_2 + 2e^-$	−0.73	−0.193	−1.064
$Ni + 2OH^- = Ni(OH)_2 + 2e^-$	−0.72	−0.17	−1.04
$Hg + S^= = HgS(black) + 2e^-$	−0.69[r]	+0.08[r]	−0.79
$2Ag + S^= = Ag_2S(\alpha) + 2e^-$	−0.66[r]	−0.21[r]	−1.08
$Re + 8OH^- = ReO_4^- + 4H_2O + 7e^-$	−0.584	−0.59	−1.46
$S_2O_3^= + 6OH^- = 2SO_3^= + 3H_2O + 4e^-$	−0.58	−0.27	-1.14_5
$Te + 6OH^- = TeO_3^= + 3H_2O + 4e^-$	−0.57	−0.36	−1.23
$Fe(OH)_2 + OH^- = Fe(OH)_3 + e^-$	−0.56	−0.09	−0.96
$Pb + CO_3^= = PbCO_3 + 2e^-$	−0.506	−0.423	−1.294
$2Bi + 6OH^- = Bi_2O_3 + 3H_2O + 6e^-$	−0.46[a]	−0.343	−1.214
$Ni + CO_3^= = NiCO_3 + 2e^-$	−0.45	−0.400	−1.271
$S^= = S + 2e^-$	−0.447[r]	−0.06	−0.93[r]
$Hg + 4CN^- = Hg(CN)_4^= + 2e^-$	−0.37	+1.65	+0.78
$Se + 6OH^- = SeO_3^= + 3H_2O + 4e^-$	−0.366	−0.447	−1.318
$2Cu + 2OH^- = Cu_2O + H_2O + 2e^-$	−0.358	−0.455	−1.326
$Tl + OH^- = Tl(OH)(c) + e^-$	−0.3445	+0.003	−0.868
$Ag + 2CN^- = Ag(CN)_2^- + e^-$	−0.31	+0.958	+0.087
$Cr(OH)_3(hydr) + 5OH^- = CrO_4^= + 4H_2O + 3e^-$	−0.13	−0.804	−1.675
$Cu + 2NH_3 = Cu(NH_3)_2^+ + e^-$	−0.12	+0.09	−0.78
$Cu_2O + 2OH^- + H_2O = 2Cu(OH)_2 + 2e^-$	−0.080	+0.15	-0.72_5
$TlOH + 2OH^- = Tl(OH)_3 + 2e^-$	−0.05	−0.069	−0.940
$Mn(OH)_2 + 2OH^- = MnO_2 + 2H_2O + 2e^-$	−0.05	−0.458	−1.329
$Ag + CN^- = AgCN + e^-$	−0.017	+0.992	+0.121
$NO_2^- + 2OH^- = NO_3^- + H_2O + 2e^-$	+0.01	−0.388	−1.259
$2Rh + 6OH^- = Rh_2O_3 + 3H_2O + 6e^-$	+0.04	−0.36	−1.23
$SeO_3^= + 2OH^- = SeO_4^= + H_2O + 2e^-$	+0.05	−0.316	−1.187
$Pd + 2OH^- = Pd(OH)_2 + 2e^-$	+0.07	−0.193	−1.064
$2S_2O_3^= = S_4O_6^= + 2e^-$	+0.08	−0.24	−1.11
$Hg + 2OH^- = HgO(r) + H_2O + 2e^-$	+0.098	−0.249	−1.120
$2NH_4OH + 2OH^- = N_2H_4 + 4H_2O + 2e^-$	+0.11[a]	−0.22	−1.09
$Mn(OH)_2 + OH^- = Mn(OH)_3 + e^-$	+0.15[a]	−0.032	−0.903
$Pt + 2OH^- = Pt(OH)_2 + 2e^-$	+0.15	−0.273	−1.144
$Co(OH)_2 + OH^- = Co(OH)_3 + e^-$	+0.17	+0.07	−0.80
$PbO(r) + 2OH^- = PbO_2 + H_2O + 2e^-$	+0.248	−0.323	−1.194
$I^- + 6OH^- = IO_3^- + 3H_2O + 6e^-$	+0.26	−0.291	−1.162
$ClO_2^- + 2OH^- = ClO_3^- + H_2O + 2e^-$	+0.33	−0.60	−1.47
$2Ag + 2OH^- = Ag_2O + H_2O + 2e^-$	+0.345[a]	−0.466	−1.337
$ClO_3^- + 2OH^- = ClO_4^- + H_2O + 2e^-$	+0.36	−0.37	−1.24
$Ag + 2NH_3 = Ag(NH_3)_2^+ + e^-$	+0.373	+0.411	−0.460
$4OH^- = O_2 + 2H_2O + 4e^-$	+0.401	−0.809	−1.680
$2Ag + CO_3^= = Ag_2CO_3 + 2e^-$	+0.47	−0.506	−1.377
$Ag_2O + 2OH^- = 2AgO + H_2O + 2e^-$	+0.607[aa]	−0.246[aa]	−1.117
MnO_2 (pyrolusite) $+ 4OH^- = MnO_4^- + 2H_2O + 3e^-$	+0.588	−0.907	−1.778
$Br^- + 6OH^- = BrO_3^- + 3H_2O + 6e^-$	+0.61	−0.416	−1.287
$ClO^- + 2OH^- = ClO_2^- + H_2O + 2e^-$	+0.66	−0.583	−1.454
$Fe(OH)_3 + 5OH^- = FeO_4^= + 4H_2O + 3e^-$	+0.72[a]	−0.75[a]	−1.62
$N_2H_4 + 2OH^- = 2NH_2OH + 2e^-$	+0.73	−0.94	−1.81
$Cl^- + 2OH^- = ClO^- + H_2O + 2e^-$	+0.89	−0.208	−1.079
$ClO_2^- = ClO_2(g) + e^-$	+1.16	−1.35	−2.22
$O_2 + 2OH^- = O_3(g) + H_2O + 2e^-$	+1.24	−0.447	−1.318
$OH^- = OH(g) + e^-$	+2.02[a]	−1.818	−2.689

[a] Based on Latimer's (6) free enthalpies of formation.
[b] Based on Latimer's estimate for H⁻ [Ref. (6), p. 36].
[c] Harned and Owen (49), p. 741. Thermal values computed from observed isothermal data.
[d] MacInnes (7), p. 201. Thermal values computed from observed isothermal data.
[e] From isothermal cell temperature coefficients of Gerke (55) and the isothermal coefficients of the calomel, silver chloride, silver iodide, and lead iodide electrodes as computed here from Latimer's entropies (6).
[ee] Based on an estimated value of −27 cal/deg for $S°(Ni^{++})$. Observed thermal values reported by Carr and Bonilla (31) in $NiSO_4$ as −0.84 to −0.91 mv/deg (1*M*); −0.70 to −0.92 (0.1*M*); −0.52 to −0.88 (0.01*M*); −0.44 to −0.79 (0.001*M*); −0.31 to −0.62 (0.0001*M*).
[f] By definition.
[g] From Fales and Mudge's (14) observations as recalculated in the present paper. Experimental comparisons discussed in text.
[h] Calculated from the vapor pressure of water.
[i] Harned and Owen (49), pp. 495-496.
[j] Bates and Bower (45).
[k] Tragert and Robertson (53).
[l] From the temperature coefficient of the isothermal cell: $Cu/CuSO_4$, Hg_2SO_4 (c)Hg, −0.81 mv/deg, Tragert and Robertson (53), and the isothermal temperature coefficient of the mercurous sulfate electrode as computed here from Latimer's entropies (6).
[m] Harned and Owen (49), p. 577.
[n] Based on entropies obtained from Latimer's (6) enthalpies and free enthalpies of formation.
[p] Harned and Owen (49), pp. 570-572; Harned and Hamer (58).
[q] Based on $\Delta H° = -115$ kcal, $\Delta G° = -77$ kcal, $S° = 9$ cal/deg for $FeO_4^=$, Wood (56).
[r] Based on $\Delta H° = 7.8$ kcal, $\Delta G° = 20.6$ kcal, $S° = -4$ cal/deg for $S^=$, Kury, Zielen and Latimer (57).
[s] Bonnemay (32).
[t] Agar and Breck (33), standard values averaged from their observations with Cd and Tl amalgam electrodes.
[u] Lange (10).
[v] Gockel (11), standard value computed from his observations.
[w] Experimental comparisons discussed in text of paper.
[x] Tyrell and Hollis (28).
[y] Goodrich, Goyan, Morse, Preston, Young (29), standard values computed from observations in KBr and NaBr.
[z] Burian (21), standard value averaged from observations in $AgNO_3$.
[aa] $E° = 0.2623$ v, $dE°/dT = +0.220$ mv/deg for Ag, $Ag_2O/NaOH/Ag_2O$, AgO/Pt, Bonk and Garrett, *This Journal*, **106**, p. 612 (1959).

Amino Acids and Peptides," Reinhold Publishing Co., New York (1943).
9. E. Bouty, *J. Physique*, **8**, 289, 341 (1879); **9**, 306 (1880); **10**, 241 (1881).
10. E. Lange, *Handbuch Experimental Physik*, **12**, 327-352 (1932).
11. A. Gockel, *Wied. Ann.*, **24**, 618 (1885); **40**, 453 (1890); **50**, 696 (1893).
12. G. Meyer, *ibid.*, **33**, 281 (1888).
13. Th. W. Richards, *Z. physik. Chem.*, **24**, 39 (1897).
14. H. A. Fales and W. A. Mudge, *J. Am. Chem. Soc.*, **42**, 2434 (1920).
15. W. W. Ewing, *ibid.*, **47**, 301 (1925).
16. I. M. Kolthoff, *Chem. Weekblad*, **22**, 332 (1925).
17. S. P. L. Sorensen and K. Linderstrom-Lang, *Compt. rend. trav. lab. Carlsberg*, **15**, No. 6, 1-40 (1925).
18. E. D. Eastman, *J. Am. Chem. Soc.*, **48**, 1482 (1926); **50**, 283, 292 (1928).
19. I. M. Kolthoff and F. Tekelenburg, *Rec. trav. chim.*, **46**, 18 (1927).
20. N. Bjerrum and A. Unmack, *Kgl. Danske Videnskab. Selskab, Math.-fys. Medd.*, **9**, No. 1 (1929).
21. R. Burian, *Z. Elektrochem.*, **37**, 238 (1931).
22. E. Lange and Th. Hesse, *ibid.*, **39**, 374 (1933).
23. B. Wingfield and S. F. Acree, *J. Research Nat. Bur. Standards*, **19**, 163 (1937).
24. Scott Ewing, "The Copper Sulfate Half-Cell for Measuring Potentials in the Earth," Paper presented to the Distribution Conference, American Gas Association, 420 Lexington Ave., New York, Chicago, April 17-19, 1939.
25. H. Cary and W. P. Baxter, Private communication from Dr. A. O. Beckman to M. Dole, quoted in "Glass Electrode," p. 166, John Wiley & Sons, Inc., New York (1941).
26. H. A. Bernhardt and H. D. Crockford, *J. Phys. Chem.*, **46**, 473 (1942).
27. P. T. Gilbert, *Discussion Faraday Soc.*, **1**, 323 (1947).
28. H. J. V. Tyrell and G. L. Hollis, *Trans. Faraday Soc.*, **45**, 411 (1949); **48**, 893 (1952); H. J. V. Tyrell, Chap. 13 in "Electrochemical Constants," National Bureau of Standards Circular 524 (1953); H. J. V. Tyrell and R. Colledge, *Trans. Faraday Soc.*, **50**, 1056 (1954).
29. J. C. Goodrich, F. M. Goyan, E. E. Morse, R. G. Preston, and M. B. Young, *J. Am. Chem. Soc.*, **72**, 4411 (1950).
30. H. Levin and C. F. Bonilla, *This Journal*, **98**, 388 (1951).
31. D. S. Carr and C. F. Bonilla, *ibid.*, **99**, 475 (1952).
32. M. Bonnemay, *Proc. C.I.T.C.E.*, **6**, 68 (1955), *Compt. rend.*, **226**, 1014, 1522 (1948); **232**, 409 (1951); *J. chim. physique*, **48**, 152 (1951).
32a. J. E. B. Randles and K. S. Whiteley, *Trans. Faraday Soc.*, **52**, 1509 (1956).
33. J. N. Agar and W. G. Breck, *ibid.*, **53**, 167, 179 (1957). M. H. Temkin and A. B. Khoroshin, *Z. Fiz. Khim.*, **26**, 500 (1952).
34. G. N. Scott, *Corrosion*, **14**, 136t (1958).
35. A. J. deBethune, T. S. Licht, and N. Swendeman, *Chemistry and Industry* (London), 1364 (1958).
36. A. J. deBethune, T. S. Licht, and N. Swendeman, Unpublished observations.
37. R. J. E. Clausius, "Merchanische Wärmetheorie," Chap. 10, Vieweg und Sohn, Braunschweig (1876).
38. A. J. deBethune, *Ind. Eng. Chem.*, **50**, 129 (1958).
39. S. R. deGroot, "Thermodynamics of Irreversible Processes," North Holland Publishing Co., Amsterdam (1951).
40. L. Onsager, *Phys. Rev.*, **37**, 405 (1931); **38**, 2265 (1931).
41. B. E. Conway and J. O'M. Bockris, "Ionic Solvation," Chap. 2 in J. O'M. Bockris' "Modern Aspects of Electrochemistry," Academic Press, New York (1954).
42. E. D. Eastman, *J. Am. Chem. Soc.*, **50**, 295 (1928).
43. American Institute of Physics Handbook, McGraw Hill Book Co., New York (1957). Values interpolated graphically from Table 4a-5.
44. P. Debye and E. Hückel, *Physik. Z.*, **24**, 185, 305 (1923).
45. R. G. Bates and V. E. Bower, *J. Research Nat. Bur. Standards*, **53**, 283 (1954); **59**, 261 (1957).
46. D. A. MacInnes, D. Belcher, T. Shedlovsky, *J. Am. Chem. Soc.*, **60**, 1094 (1938).
47. W. P. Baxter, Private communication from Dr. A. O. Beckman to M. Dole, quoted in "The Glass Electrode," p. 156, John Wiley & Sons, Inc., New York (1941).
48. E. Vellinger, *Arch. phys. biol.*, **5**, 119 (1926).
49. H. S. Harned and B. B. Owen, "Physical Chemistry of Electrolytic Solutions," 3d ed., Reinhold Publishing Co., New York (1958).
50. G. N. Lewis and M. Randall, *J. Am. Chem. Soc.*, **36**, 1976 (1914).
51. G. N. Lewis and W. N. Lacey, *ibid.*, **36**, 804 (1914).
52. F. H. Getman, *Trans. Electrochem. Soc.*, **26**, 67 (1914); *J. Phys. Chem.*, **34**, 1454 (1930); F. Wetmore and A. Gordon, *J. Chem. Phys.*, **5**, 60 (1937); R. Neilson and D. Brown, *J. Am. Chem. Soc.*, **49**, 2423 (1927).
53. W. E. Tragert and W. D. Robertson, *This Journal*, **102**, 86 (1955).
54. R. E. Hall, "Use of Half Cell Reference Electrodes in Corrosion Measurements," Union Oil Co. of California, Research Div., Brea, California.
55. R. H. Gerke, *J. Am. Chem. Soc.*, **44**, 1684 (1922).
56. R. H. Wood, *ibid.*, **80**, 2038 (1958).
57. J. W. Kury, A. J. Zielen, and W. M. Latimer, *This Journal*, **100**, 470 (1953).
58. H. S. Harned and W. J. Hamer, *J. Am. Chem. Soc.*, **57**, 9, 27, 33 (1935).
59. H. S. Harned and R. W. Ehlers, *ibid.*, **55**, 2179 (1933).
60. G. Scatchard and R. C. Breckenridge, *J. Phys. Chem.*, **58**, 602 (1954); G. Scatchard, *Science*, **95**, 30 (1942); *Rev. Sci. Instruments*, **26**, 395 (1955).
61. S. P. L. Sorensen, *Compt. rend. trav. lab. Carlsberg*, **8**, 1 (1909); W. Mansfield Clark, "The Determination of Hydrogen Ions," p. 455, 3d ed., Williams and Wilkins, Baltimore (1928); R. G. Bates, "Electrometric pH Determinations," John Wiley & Sons, Inc., New York 1954).
62. Jaques Loeb, "Proteins and the Theory of Colloidal Behavior," McGraw Hill Book Co., New York (1922); M. Stern, H. Shwachman, T. S. Licht, and A. J. deBethune, *Anal. Chem.*, **30**, 1506 (1958).

Transport Numbers in Pure Fused Salts

The Alkali Metal Chlorides

Frederick R. Duke and Allen L. Bowman[1]

Institute for Atomic Research and Department of Chemistry, Iowa State College, Ames, Iowa

ABSTRACT

The transport number of the chloride ion has been determined in fused alkali chloride salts by a radiochlorine tracer technique, using a membrane cell. Values obtained (Table I) are compared with theoretical predictions of Mulcahy and Heymann, and of Sundheim.

The transport numbers of the fused alkali metal chlorides have been estimated from comparisons of electrical conductivity data (1, 2) and from purely theoretical considerations (3, 4). Mulcahy and Heymann (1) compared the equivalent conductivities at a corresponding temperature defined as three-fourths of the boiling point. They found that the data could be approximated by the equation $\lambda = K(1/r_A + 1/r_C)$. Bloom and Heymann (2) concluded that the electrical conductance of the alkali halides is due primarily to the small cation. This was based on the fact that the equivalent conductivity changes strongly with change of cation but very little with change of anion. Frenkel (3) suggested that only one of the ions in a molten salt should be responsible for electrical conductance, and that this would in general be the cation because of its smaller radius. Sundheim (4) proposed that the transport numbers in a pure fused salt should be expressed by the equation $t_A = M_C/(M_A + M_C)$ where the M's are the masses of the anion and cation. Sundheim derived this equation by requiring a balance of momentum in a simplified model, assuming no momentum transfer to the apparatus.

If the transport number of an ionic species in a fused salt is defined as the fraction of the current carried by those ions which are moving relative to the bulk of the liquid (5), then this number can be determined by holding a quantity of salt in a thick membrane of very fine porosity where its motion is restricted, and measuring the movement of the ions through this membrane under the influence of an electrical potential. The transport numbers of several pure fused salts have been determined by measuring the volume changes in the electrode compartments resulting from the movement of the ions through the membrane (5-7). The movement of one of the ions can also be measured by the use of a radioisotope (8). This method is particularly convenient for the measurement of the transport number of the chloride ion in any fused chloride.

Experimental

Reagent grade salts were used; they were kept in a drying oven at 150°C and cooled in a desiccator before weighing, except for lithium chloride which was fused and held in this condition in a dry atmosphere for several hours. The chloride isotope, Cl^{36}, was obtained from Oak Ridge National Laboratory as an aqueous solution of hydrochloric acid. The alkali metal salts containing Cl^{36} were prepared by dissolving the salt in water, adding HCl^{36}, and evaporating the solution to dryness. Reagent grade silver wire and granulated lead were used for electrodes.

A 16-in. Marshall Tube Furnace was used with a Brown Indicating Controller to provide the high-temperature region. A d-c power supply capable of delivering up to 350 ma at 35 v was used for electrolysis. The quantity of charge was determined by measuring the fairly constant current with a milliammeter and the time of electrolysis with a Precision "Time-It".

The cells were made from 10 mm ID quartz, in the form of a square U-tube, 2.5 in. wide and 1.5 in. high, with a small bubble on the bottom of each vertical tube to hold the liquid metal electrodes. A membrane of fused quartz, 1.5 mm thick, porosity No. 4, Engelhard Industries, Amersil Quartz Division, was sealed into the center of the horizontal section. The porosity of the membrane was reduced by depositing silica within it. This was done by alternately running ethyl silicate and hydrochloric acid through the membrane and dehydrating the resulting silica gel by baking at 800°C. This treatment was repeated until more than 2 hr was required for 1 ml of water to flow through the membrane under suction. The cathode was a pool of molten lead, with electrical contact through a nichrome wire sealed into a glass tube. The anode was either lead or a silver wire. The same results were obtained with both anodes.

To carry out a run, the cell was filled with solid salt, radiotracer salt was added to the catholyte, the electrodes were inserted, the ends of the cell were capped, and the cell was placed in the furnace at the temperature of the run. As soon as thermal equilibrium was attained and the cell was conducting, a metered d-c current was passed for a measured time (usually 300 ma for 400 sec). The cell was then withdrawn, frozen, and split at the membrane to separate anolyte and catholyte. The two halves of the cell were dissolved in aqueous ammonia. The Cl^{36} was precipitated from the ammoniacal solutions with excess silver nitrate and counted as silver chloride.

[1] Present address: Los Alamos Scientific Laboratory, University of California, Los Alamos, N. Mex.

In order to obtain a smooth, fine-textured precipitate, it was necessary to keep the solution ammoniacal during the precipitation. All samples were corrected to a common weight by the use of a self-absorption curve. The weight of anolyte salt was obtained by weighing the anode portion of the cell before and after the salt was dissolved.

To obtain a relation between experimental quantities and the transport numbers, consider a cell whose anolyte and catholyte are separated by an ideal membrane which permits passage of current-carrying ions only. The number, m, of current-carrying chloride ions which pass through the membrane is equal to (tZ/e) where t is the transport number of the chloride ion, Z is the quantity of charge passed during electrolysis, and e is the electronic charge. Let the catholyte initially contain $(N^*)^\circ$ radioactive chloride ions and a total number N° of chloride ions. After m chloride ions have passed through the membrane during electrolysis, $(N^*)_m$ radioactive chloride ions are found in the anolyte. Then $m = [(N^*)_m/(N^*)^\circ]N^\circ = [(N^*)_m/(N^*)]N$, where N^* and N are the numbers of radiochloride and total chloride ions, respectively, in the catholyte at the end of the run. The second relation follows, since the initial and final ratio of Cl^{36}/Cl in the catholyte must remain the same, if no isotopic fractionation occurs. If the radioactivity found in anolyte and catholyte at the end of the run, C_A and C_C, are expressed in (counts per minute) per milligram, then $(N^*)_m = C_A W_A$, and $(N^*) = C_C W_C$, where W_A and W_C are the total weights of anolyte and catholyte, respectively, in milligrams. This assumes that the samples used for counting are identical in size and composition. But $N = (W_C/M) N_A$, where M is the milliequivalent weight of the salt and N_A is Avogadro's number. Then m can be expressed by $m = (C_A/C_C)(W_A/M)N_A$, and the transport number t of chloride ion by

$$t = em/Z = \mathbf{F}C_A W_A/ZC_C M \qquad [1]$$

where $\mathbf{F}$ is the faraday.

The assumed condition that only current-carrying ions pass through the membrane can be realized in effect by carrying a parallel blank run with no passage of charge, and subtracting the $(C_A)_{blank}$ from the observed values of C_A. It was found experimentally that the blank correction was essentially zero if the membrane was sufficiently fine.

Table I. Transport numbers of chloride ion in fused alkali metal chlorides

Salt	Temp, °C	Observed values (This investigation)	Calculated values	
LiCl	600	0.25±0.03	0.25*	0.16†
NaCl	860	0.38±0.04	0.34	0.41
KCl	830	0.38±0.04	0.42	0.52
RbCl	785	0.42±0.04	0.45	0.71
CsCl	685	0.36±0.04	0.48	0.79

* $t = r_C/(r_A + r_C)$ Mulcahy and Heymann (1).
† $t = M_C/(M_A + M_C)$ Sundheim (4).

Results and Discussion

The values of t obtained in the alkali metal chlorides by following the migration of Cl^{36} are given in Table I and are compared with values calculated from the estimates of other workers.

It is apparent that the transport numbers do not agree with Sundheim's equation (4) nor with the predictions of Bloom and Heymann (2) and Frenkel (3). With the exception of cesium chloride, the experimental values do agree, within experimental error, with the radius dependence of Mulcahy and Heymann (1). However, the latter authors require that the mobility of the chloride ion should be constant at corresponding temperatures. Using the conductivity data of Yaffe and Van Artsdalen (9), the mobility of the chloride ion in these salts at 5% above their melting points varies from 2.9×10^{-4} $(cm^2/sec)/v$ for cesium chloride to 5.6×10^{-4} for sodium chloride. Thus it would appear that the transport numbers of these salts cannot be expressed as any simple function of the mass or radius of the ions.

Manuscript received Nov. 3, 1958.

Any discussion of this paper will appear in a Discussion Section to be published in the June 1960 JOURNAL.

REFERENCES

1. M. F. R. Mulcahy and E. J. Heymann, *Phys. Chem.*, **47**, 485 (1943).
2. H. Bloom and E. Heymann, *Proc. Roy. Soc. (London).*, **A188**, 392 (1947).
3. J. Frenkel, "Kinetic Theory of Liquids," Oxford University Press, London (1946).
4. B. R. Sundheim, *J. Phys. Chem.*, **60**, 1381 (1956).
5. F. R. Duke and R. W. Laity, *ibid.*, **59**, 549 (1955).
6. R. W. Laity and F. R. Duke, *This Journal*, **105**, 97 (1958).
7. F. R. Duke and B. Owens, *ibid.*, **105**, 548 (1958).
8. F. R. Duke and R. A. Fleming, *ibid.*, **106**, 130 (1959).
9. I. S. Yaffe and E. R. Van Artsdalen, *J. Phys. Chem.*, **60**, 1125 (1956).

Technical Notes

Glow Discharge Spectra of Copper and Indium above Aqueous Solutions

Dwight E. Couch and Abner Brenner

Chemistry Division, National Bureau of Standards, Washington, D. C.

An unusual glow discharge was produced between a tungsten electrode and an aqueous solution of cupric or indium salts. This glow was somewhat lambent and almost filled the containing flask. It was not produced with solutions of the other metallic salts which we tried ($BaClO_4$, $CuCN \cdot 3KCN$, H_2SO_4, LiCl, LiI, $LiClO_4$, NaCl, $SrCl_2$ U (VI) Acetate). However, occasional flashes of color were produced with solutions of lithium and sodium chloride. Many studies of the chemical effects of the glow discharge between an electrode and a solution have been made (1-3), but the phenomenon which we observed has not been reported. The glows were characteristic of the spectra of copper and indium. Production of spectra in this manner is unique since spectra are usually obtained by vaporizing the metal or compound at high temperatures.

In these experiments, saturated solutions of cupric perchlorate, chloride, or sulfate or indium(III) chloride were placed in a round, three-necked flask, one- or two-liters in volume, and the flask evacuated through a side neck to 5 or 10 cm Hg. One lead of a high-voltage d-c power supply was attached to a tungsten rod which passed through the center neck of the flask and terminated about 1 in. above the solution level. The other electrode which passed through the remaining neck of the flask was shielded along its length by a glass tube except at the end where the electrode dipped into the solution. A current of 0.05-0.2 amp, which required about 500 v, produced a continuous glow discharge. After a period of about 15 min of discharge a soft green or blue glow developed around the central discharge, depending on the salt used, and grew until it almost completely filled the containing flask. The glow was more easily produced with copper salts than with indium salts. The spectra of the glow were photographed and examined.[1] The atomic lines were excited at about the same intensities as those produced by flame spectra. Spectral lines of OH were also present.

These experiments were repeated using a fused salt bath of lithium chloride, potassium chloride, and

[1] By Marvin Margoshes of the National Bureau of Standards, Washington, D.C.

Table I. Wave lengths and relative intensities of various lines observed in the glow discharge produced between a solid tungsten anode and an aqueous solution cathode of either cupric sulfate or indium trichloride

Emitting species	Relative intensity*	λ	Emitting species	Relative intensity*	λ	Emitting species	Relative intensity*	λ
In	4	2710.27	InCl	1	2672.1†	Cu	2	2961.17
In	4	2713.94	InCl	1	2694.7	Cu	1	3010.84
In	4	2753.88	InCl	1	2717.5	Cu	5	3247.54
In	3	2775.36	InCl	1	2740.6	Cu	5	3273.96
In	4	2836.92	InCl	2 to 3	3419.3	Cu	1	3337.84
In	4	2858.74	InCl	2 to 3	3456.3	Cu	2	4022.66
In	4	2932.62	InCl	2 to 3	3458.5	Cu	3	4062.70
In	3	2957.01	InCl	2 to 3	3499.0	Cu	3	5105.54
In	5	3039.36	InCl	2 to 3	3513.0	CuH	3	4279.6
In	5	3051.25	InCl	2 to 3	3514.6	OH	4	3063.6
Cu	3	3247.3	InCl	2 to 3	3554.0			
In	5	3256.09	InCl	2 to 3	3556.2			
In	5	3258.57	InCl	2 to 3	3596.5			
Cu	3	3273.96						
In	1	3280.69	InCl	2 to 3	3599.2			
In	1	4072.40	probably InO	1 to 3	4102 to 4511			
In	5+	4101.77						
In	5+	4511.32						

* 1 indicates a very faint line and 5 a very strong line.
† Wave lengths listed for molecular emitters are band heads.

cupric chloride, but no similar copper spectra could be produced. Therefore, it was concluded that there was something unique about the aqueous cupric salt solution that caused this green glow around the central discharge. Table I shows the wave lengths of the lines observed.

The first attempt to explain the glow discharge was on the basis of spray or particles being thrown between the electrodes. If this is the explanation, the glow should have been produced with aqueous solutions of other metal salts. To test this hypothesis specifically an apparatus was constructed which consisted of a rotating device which threw a sheet of electrolyte into the space between the two electrodes. This procedure did not lead to results as good as were obtained in the simple equipment consisting of a three-necked flask with electrodes. Further experiments showed that the glow was not caused by salts coating the electrodes, as coated electrodes did not yield a spectrum until they became hot enough to volatilize the deposited salt.

Our explanation of the phenomenon is that a volatile copper or indium compound is formed in the solution. This evaporates into the evacuated space and is responsible for the spectra. This explanation is in accordance with the observations that the glow is less pronounced with chilled solutions and becomes stronger as the solutions become warmer; also it fits with the observation that the glow is not always given immediately with a fresh solution, but may require a brief period of electrical discharge. A somewhat stronger glow was obtained when the solution was cathodic, but, since the glow could be produced also when the solution was anodic, this indicates that the phenomenon was not likely caused by the migration of charged cations into the gaseous space.

Manuscript received Jan. 22, 1959.

Any discussion of this paper will appear in a Discussion Section to be published in the June 1960 JOURNAL.

REFERENCES

1. A. R. Denaro and A. Hickling, *This Journal*, **105**, 265 (1958).
2. L. Ligabue, *Atti soc. nat. Modena*, **68**, 96 (1937).
3. A. Klemenc, *Chimia (Switz.)*, **6**, 177 (1952).

Determination of Activities in Multicomponent Metallic Solutions

Rudolph Speiser and George St. Pierre

Department of Metallurgy, The Ohio State University, Columbus, Ohio

It is generally difficult to determine phase equilibria at high temperatures. Attempts at retaining the high-temperature situation by rapid quenching to low temperatures at which examination is easier are not entirely satisfactory. Diffraction studies are performed at high temperatures with considerable success; however, no knowledge of the activities of the components is obtained from such investigations. The present method allows for the simultaneous determination of activities and phase equilibria at high temperatures.

Thermodynamic Treatment

The vapor pressure and vapor composition over a condensed phase can be used to determine phase equilibria and activities. A direct measurement (static) of the vapor pressure can be made only when the vapor pressure is at least 10^{-2} mm Hg. At lower pressures dynamic methods must be employed. It will be shown that it is not necessary to determine the vapor pressure at all.

The general form of the Gibbs-Duhem (1) equation may be written in the following form:

$$S^q\,dT - V^q\,dP_T + \Sigma_i N_i^q\,d\mu_i = 0 \qquad [1]$$

where N^q_i is the mole fraction of component i in any condensed phase, q, and μ_i is the chemical potential of component i in the system. For each phase, q, there is an equation of form [1]. The first term in Eq. [1], $S^q\,dT$, disappears under isothermal conditions and is not considered further in this paper. The second term, $V^q\,dP_T$, is negligible because the absolute variation of P_T with the composition of the condensed phase is very small. Therefore, Eq. [1] is reduced to

$$\Sigma_i N_i^q d \ln a_i = 0 \qquad [2]$$

(constant T and P_T)

The activity of each component in the condensed phase is related to the vapor phase by the following equations:

$$a_i = \frac{f_i}{f_i^\circ} \cong \frac{P_i}{P_i^\circ} \qquad [3]$$

where f_i° and P_i° designate the fugacity and partial pressure of component i for a standard state of the condensed system. If the vapor is assumed to obey ideal gas laws, then

$$P_T = \frac{P_i}{N_i^v} = \frac{P_1}{N_1^v} = \frac{P_2}{N_2^v} = \ldots \qquad [4]$$

where N_i^v is the mole fraction of component i in the vapor phase. The partial pressure of any component may be expressed in terms of the partial pressure of any other component by the relation

$$P_i = \frac{N_i^v}{N_j^v} \cdot P_j \qquad [5]$$

and the activity of each component may be related to the vapor composition and the relative vapor pressure of one component.

$$a_i = \frac{N_i^v}{N_j^v} \cdot \frac{P_j}{P_i^\circ} \qquad [6]$$

Combination of Eq. [2] and [6] results in the following modification of the Gibbs-Duhem equation

$$\sum_i N_i^q \, d \ln \frac{N_i^v}{N_j^v} P_j = 0 \qquad [7]$$

Solving for P_j in Eq. [7]

$$d \ln P_j = -\sum_i N_i^q \, d \ln \frac{N_i^v}{N_j^v} \qquad [8]$$

which reduces even further to

$$d \ln P_j = d \ln N_j^v - \sum_i N_i^q \, d \ln N_i^v \qquad [9]$$

The integration of Eq. [9] from $N_j^{v(1)}$ to $N_j^{v(2)}$ yields the ratio of the activities in the corresponding condensed mixtures.

$$\ln \frac{a_j^{(2)}}{a_j^{(1)}} = \ln \frac{N_j^{v(2)}}{N_j^{v(1)}} - \sum_i \int_{N_i^{v(1)}}^{N_i^{v(2)}} N_i^q \, d \ln N_i^v \qquad [10]$$

The path of integration in Eq. [10] is of no significance because only exact differentials are involved. If the starting condensed mixture is the standard state ($a_j^{(1)} = 1$), then Eq. [10] gives the a_j at any composition in the system. The integrations involved may be obtained graphically from a plot of N_i^q vs. $\ln N_i^v$ or the integral may be modified as follows,

$$\int N_i^q \, d \ln N_i^v = \int \frac{N_i^q}{N_i^v} \, dN_i^v \qquad [11]$$

Equation [11] has the obvious advantage that both $\frac{N_i^q}{N_i^v}$ and N_i^v do not become infinite.

Equation [10] allows for the determination of activities from a study of vapor composition corresponding to condensed phase composition without any need for the measurement of vapor pressures. There is an equation of form [10] for every component in the system. Before pursuing this aspect any further, attention will be directed at phase equilibria within the condensed system.

Phase Equilibria

Equation [10] indicates that it is necessary to follow the variation in vapor composition caused by variation in the composition of the particular condensed phase, q. If this were so, the method would lose much of its value because it would require sampling and examination of multiphase condensed systems. As previously noted the Gibbs-Duhem equation may be applied to each equilibrium phase in the system. Therefore, from Eq. [9] it follows that

$$\sum_i N_i^\alpha d \ln N_i^v = \sum_i N_i^\beta d \ln N_i^v = \sum_i N_i^\gamma d \ln N_i^v = \ldots = . \qquad [12]$$

where α, β, γ designate particular equilibrium condensed phases. From the above equalities, the following set of equations may be written:

$$\sum_i (N_i^\alpha - N_i^\beta) d \ln N_i^v = 0 \qquad [13a]$$

$$\sum_i (N_i^\beta - N_i^\gamma) d \ln N_i^v = 0 \qquad [13b]$$

$$\sum_i (N_i^\gamma - N_i^\delta) d \ln N_i^v = 0 \qquad [13c]$$

$$\vdots$$

$(p\text{-}1)$ equations

If p designates the number of phases, then there are $(p\text{-}1)$ equations of the above type. From material conservation

$$N_i^T = n_\alpha N_i^\alpha + n_\beta N_i^\beta + n_\gamma N_i^\gamma + \ldots + . \qquad [14]$$

where N_i^T is the mole fraction of i in the system taken as a whole and n_α, n_β, are the fractions of the total moles of the system included in each stable phase. Equation [14] may be modified to

$$N_i^T = n_\alpha (N_i^\alpha - N_i^\beta) + (n_\alpha + n_\beta)(N_i^\beta - N_i^\gamma) + \ldots + N_i^P \qquad [15]$$

and

$$N_i^T - N_i^P = n_\alpha (N_i^\alpha - N_i^\beta) + (n_\alpha + n_\beta)(N_i^\beta - N_i^\gamma) + \ldots + (1 - n_P)(N_i^{P-1} - N_i^P) \qquad [16]$$

If each equation in set [13] is now multiplied by the appropriate factor, [13a] by n_α, [13b] by $(n_\alpha + n_\beta)$, etc., and their sum is taken, it follows that

$$\sum_i (N_i^T - N_i^P) d \ln N_i^v = 0 \qquad [17]$$

and

$$\sum_i N_i^T d \ln N_i^v = \sum_i N_i^P d \ln N_i^v = \sum_i N_i^\alpha d \ln N_i^v = \ldots \qquad [18]$$

The necessity of designating a particular condensed phase in Eq. [10] is, therefore, removed and the general solution becomes

$$\ln \frac{a_j^{(2)}}{a_j^{(1)}} = \ln \frac{N_j^{v(2)}}{N_j^{v(1)}} - \sum_i \int_{N_i^{v(1)}}^{N_i^{v(2)}} \frac{N_i^c}{N_i^v} \, dN_i^v \qquad [19]$$

N_i^c designates the mole fraction of i in either a particular phase or in the condensed system taken as a

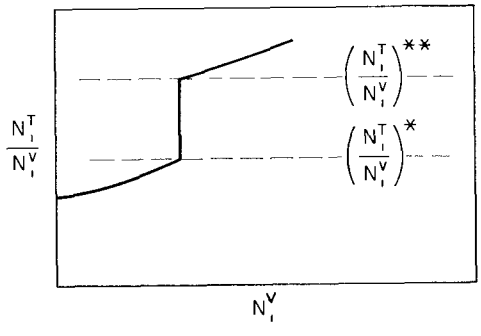

Fig. 1. Schematic representation of vapor composition variation in a binary system.

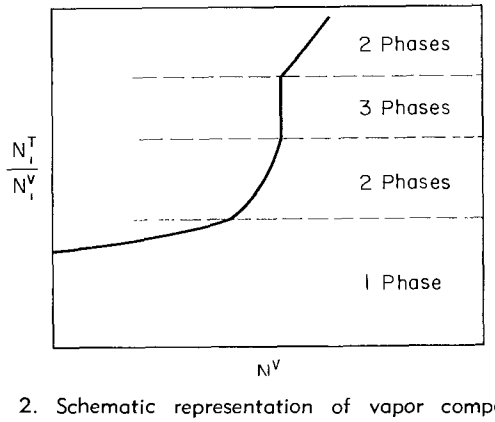

Fig. 2. Schematic representation of vapor composition variation in a ternary system.

whole. The question now arises as to the possibility of detecting phase boundaries from the experimentally determined plots of N_i^v/N_i^v vs. N_i^v. The answer can best be obtained by examination of special systems.

Binary and Ternary Systems

For a two-component system with immiscibility a plot of N_i^T/N_i^v vs. N_i^v would appear as schematically represented in Fig. 1. Within the two-phase region the activities and, therefore, the vapor composition must be invariant and the slope of the curve must become infinite. The composition limits of the region of immiscibility are defined clearly. Thus binary phase diagrams may be determined by isothermal cuts of the variation of vapor composition with total composition.

For a three-component system the situation is similar; however, the vapor composition does not become invariant in a two-phase field except when the total composition varies along a tie line. In a three-phase field the vapor composition is independent of total composition without exception. A traverse of a ternary system could appear as schematically illustrated in Fig. 2. In moving from a one-phase field to a two-phase field a change in slope must occur. If, by coincidence, the total composition varies along a tie line in the two-phase field, then the slope of the curve in the two-phase region will be infinite. This coincidence could be readily detected; however, because the total composition at either end of the two-phase field would then correspond to a boundary between a one-phase and a two-phase field. By several different traverses an isothermal section of the phase equilibria may be determined from plots like Fig. 2.

Experimental Application

Speiser, Jacobs, and Spretnak (2) have applied the method to liquid Fe-Ni alloys at temperatures between 1510° and 1600°C. Analyses of the condensed vapor effusing from a Knudsen cell enabled them to apply a special form of Eq. [19]. Iron and nickel are completely miscible at the temperatures employed so that no phase equilibria were involved. The activity data on Fe-Ni alloys has also been determined by Zellars and Morris (3) at the U. S. Bureau of Mines by a transpiration method which obtained vapor pressures directly. The agreement between the two methods was outstanding.

Acknowledgments

This work received support from the American Iron and Steel Institute.

Manuscript received May 1, 1958. This paper was prepared for delivery before the New York Meeting, April 27-May 1, 1958.

Any discussion of this paper will appear in a Discussion Section to be published in the June 1960 JOURNAL.

REFERENCES

1. J. Willard Gibbs, "The Collected Works of J. Willard Gibbs," vol. 1, Yale University Press, New Haven, Conn. (1948).
2. R. Speiser, A. Jacobs, and J. W. Spretnak, *Trans. Amer. Inst. Mining Met. Engrs.* (1959) to be published.
3. G. R. Zellars and J. P. Morris, *ibid.*

Formation of Hydride Films on Ti, Zr, Hf, Th Dissolving in Hydrofluoric Acid

W. J. James and M. E. Straumanis

Departments of Chemical and Metallurgical Engineering, School of Mines and Metallurgy, The University of Missouri, Rolla, Missouri

During studies on the dissolution of nuclear metals in dilute hydrofluoric acid in our laboratories, the formation of gray to black films on the surface of the dissolving metals has been noted (1). The presence of a black film on the surface of Zr dissolving in HF has also been reported by Baumrucker (2) and by Johnson and Hill (3); and on Ti by Ogawa (4) and Rüdiger, *et al.* (5). Suggestions as to the nature of these films have been made (4) but not corroborated by experimental data.

Small pieces of low Hf content Zr and Ti metal, in separate beakers, were immersed in approximately 0.1*N* HF for about 1 hr. The films were removed with the aid of a rubber squeejee and the black smut washed onto a watch glass. In the case of Zr, immersion of the sample in saturated NH_4F for a short time facilitated the removal of the film. The films were dried and crushed to a powder. Powder diffraction pictures were taken using Cu $K\alpha$ radiation with a Ni filter.

The "d" values of the patterns were compared with data from many sources and were found to agree very well with hydride patterns corresponding to approximately ZrH_2 and TiH_2. The comparison with the three principal "d" values of the hydrides are shown in Table I. Additional lines were also in good agreement with the standards.

In addition to the identification above, the authors have previously reported the formation of ThH_2 on Th dissolving in dilute HCl (6).

A thin grayish film was observed also on Hf dissolving in dilute HF, but attempts to remove the film were unsuccessful. In light of the foregoing the film is probably HfH_2.

These observations appear to indicate that sufficient atomic hydrogen is generated under conditions

Table I. Comparison of samples with ASTM data

Zr Sample		$ZrH_{1.9}$ Standard	
d in Å	I/I_0	d in Å	I/I_0
2.76	100	2.76	100
1.76	100	1.76	100
1.64	90	1.66	100
Ti Sample		TiH_2 Standard	
d in Å	I/I_0	d in Å	I/I_0
2.55	100	2.55	100
1.57	50	1.56	60
1.31	50	1.33	60

of corrosion to produce saturated metal hydrides on the metallic surfaces at room temperature.

Acknowledgment

The above work is part of a major study made possible by funds from the Atomic Energy Commission.

Manuscript received Feb. 2, 1959.

Any discussion of this paper will appear in a Discussion Section to be published in the June 1960 JOURNAL.

REFERENCES

1. M. E. Straumanis and P. C. Chen, *J. Electrochem. Soc.*, **98**, 234 (1951).
2. J. E. Baumrucker, "Dissolution of Zr in HF", ANL-5020, March 31 (1950).
3. A. B. Johnson and G. R. Hill, AECU-3000, 3 (1954).
4. Sh. Ogawa and D. Watanabe, *Sci. Rep. Tokoku U. A.*, **7**, 184 (1955).
5. O. Rüdiger, R. A. Fischer, and W. Knorr, *Techn. Mitt. Krupp*, **14**, 82 (1956).
6. W. J. James and M. E. Straumanis, *Acta Cryst*, **9**, 376 (1956).

Some Morphological Studies of Silver Crystals Electrodeposited from LiCl-KCl Eutectic Melt Containing AgCl

Ling Yang, Chien-yeh Chien, and Robert G. Hudson

Metals Research Laboratory, Carnegie Institute of Technology, Pittsburgh, Pennsylvania

Study of the morphology of metal crystals electrodeposited from molten salt baths is of both fundamental and practical interest. Information available on this subject, however, is very limited (1-7). This note reports some observations made on silver crystals electrodeposited from LiCl-KCl eutectic melt containing AgCl at 500°C.

The electrolyte was made by melting known amounts of AgCl and LiCl-KCl eutectic mixture under dry argon atmosphere in a Pyrex cell shown in Fig. 1 and was purified by electrolysis with dummy silver electrodes according to procedures described previously (8). When electrolysis was carried out with the cathode remaining stationary, the metal pulley shown in the figure was removed, and the iron rod holding the silver cathode was connected to the glass sleeve by a rubber tubing seal, similar to that shown for the anodic side. However, if it was desired to rotate the cathode during electrodeposition, the arrangement shown in Fig. 1 was used, with the metal pulley resting on top of the glass sleeve. The latter fitted closely to the iron rod and acted as a bearing. Any leakage of air into the cell during rotation was prevented by maintaining a slow flow of argon through the space between the iron rod and the glass sleeve. After the electrolysis, the cathode was raised out of the melt to the upper part of the cell and cooled in argon. The silver crystals deposited were freed of occluded electrolyte by washing in dilute (6*N*) NH_4OH, dried, and examined under a microscope.

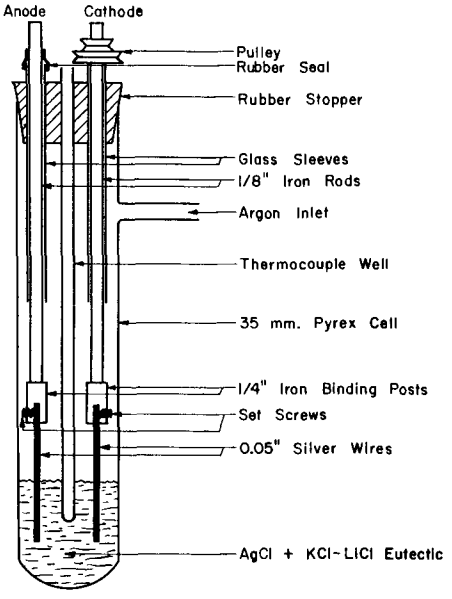

Fig. 1. Cell arrangement for electrodeposition

When the cathode was stationary, the deposits were always dendritic [Fig. 2 (a)], irrespective of the current density (10-1000 ma/cm^2 of original cathodic area) and the concentration of AgCl (3-14 wt %) used. Figure 2(h) and 2(k) are microphotographs taken of these dendrites. It can be seen that the main axis of the dendrite is 60° from the branches at one side and 90° from the branches at the other side. The 60° branches stretch out much farther than the 90° branches which terminate with the formation of definite facets [Fig. 2(k)]. All dendrites examined showed this unsymmetrical feature. X-ray back reflection Laue patterns obtained from these dendrites indicate that the plane of the dendrite is of the most densely packed {111} type, and the main axis of the dendrite is parallel to the <211> directions. The 60° branches are also parallel to the <211> directions, while the 90° branches are parallel to the <110> directions, each being a densely packed atom row in the {111} planes. Thus, the growth of the dendrite is fastest along the <211> directions and slowest along the <111> directions. Since the flow of current is perpendicular to the

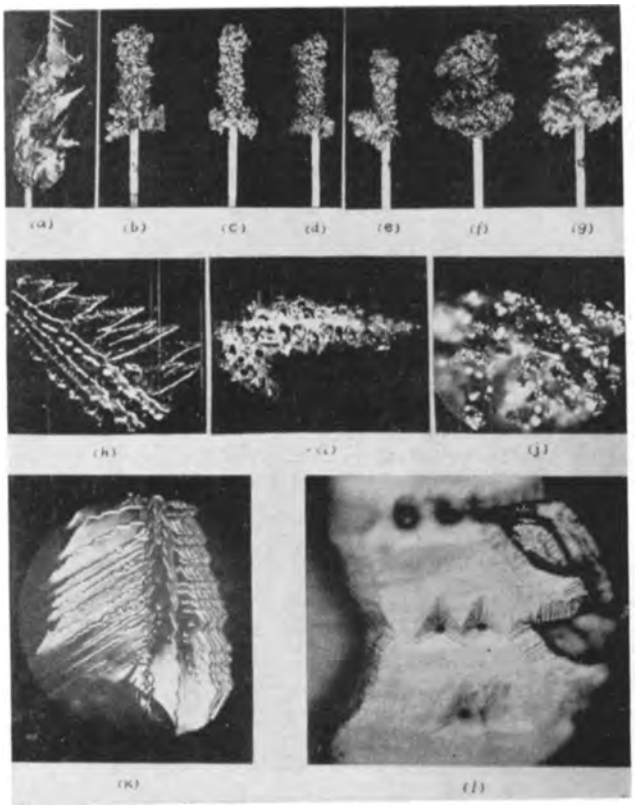

Fig. 2. Ag crystals deposited from LiCl-KCl-AgCl baths

I. Macroscopic appearance (1X), 500°C, 3 hr.

	% AgCl	Current density ma/cm²	Cathode rotation speed, rpm
(a)	4	50	0
(b)	4	50	400
(c)	4	50	1000
(d)	4	50	2000
(e)	4	200	2000
(f)	4	1000	2000
(g)	14	200	2000

II. Microscopic appearance [50X, except (l) 250X], all reduced to one-third of their sizes)
(h) same as (a), (i) same as (b), (j) same as (d), all oblique illumination (k) same as (a) but for a very large dendrite, vertical illumination, (l) triangular etch pits on the (111) plane of the dendrite shown in (k), vertical illumination.

equal potential surfaces, any crystal grain on the surface of the silver cathode with the <211> directions perpendicular to the equal potential surfaces between the electrodes is a favorable site for starting a dendrite. As the dendrite nucleus grows outward, more metal ions are attracted to its tip and edge where the electric field is more concentrated and thus help the formation of branches. The actual current density on the flat {111} planes is thus very small and the growth along the <111> directions probably has to rely on the screw dislocation mechanism.

Close examination of Fig. 2(k) reveals the existence of triangular pits with pipes (some triangular shaped) running down at their centers. On the surfaces of other dendrites, round pits have been observed [Fig. 2(h)]. These pits were probably formed by etching while these dendrites were being freed of the occluded electrolytes by washing in NH_4OH. The favorable locations of these pits are regions in between the dendritic branches [Fig. 2(k)] and along the midrib of the dendrite [Fig. 2(h)], although more drastic etching does produce pits elsewhere. The regions between the dendritic branches are places where large amounts of impurities and imperfections are concentrated. The two sides of the dendrite, grown out of its midrib, may not exactly align with each other crystallographically. These may be the reasons why pits are more likely to form at these places. The fact that some of these pits are triangular and some are round is probably due to the difference in the rate of etching and the presence of different amounts of impurities at these pits. When the impurity contents are high, preferential adsorption on certain faces would lead to the formation of pits showing crystallographic symmetry. On the other hand, if the impurity contents are low and the rate of etching fast, round pits are formed. Figure 2(l) shows the triangular pits at a bigger magnification. The large size of the pipe at the center of the pit is probably associated with the presence of large amounts of impurities along the line defect pointing downward.

If the cathode was rotated during the electrolysis, both the macroscopic and the microscopic appearances of the deposits were modified. When the speed of rotation was low (e.g., 400 rpm, and current density equaled 50 ma/cm²), the branches of the dendrites grew thicker and shorter in the form of polyhedrons showing well-defined facets, although the deposits in general still retained the dendritic shape [Fig. 2(b) and 2(i)]. With the increase of the speed of rotation to 2000 rpm (current density still equaled 50 ma/cm²), the dendritic structures broke up further, and the deposits became granular, each grain being a single crystal polyhendron exhibiting mostly the low index planes [Fig. 2(c), 2(j)]. Since these grains usually were not located in one plane, it was impossible to obtain well-focussed pictures. Rotation continuously moves the dendrite nuclei away from the positions favorable to their growth along the <211> directions. It also helps to even up the current density distribution over the various parts of the dendrite and thus the rate of growth along the different crystallographic directions. High current density and high AgCl concentration were found to favor the dendritic growth, as shown by comparing Fig. 2(d) with Fig. 2(e), 2(f), and 2(g). Periodic reversal of the current (2-sec deposition, 1-sec dissolution; or 20-sec deposition, 10-sec dissolution) did not appear to affect appreciably the macroscopic appearance of the deposit on the cathode. In all cases studied, both the cathodic and the anodic current efficiencies were close to 100%, as determined from the weight loss of the electrodes with the aid of a silver coulometer.

Acknowledgments

The authors wish to thank Dr. G. Derge and Dr. G. M. Pound of Carnegie Institute of Technology and Mr. Frank Kerze, Jr., of the U. S. Atomic Energy Commission, for their interest in this work. We also are indebted to Dr. John P. Hirth and Dr. W. H.

Robinson of Carnegie Institute of Technology for stimulating discussions and to Mr. R. T. Keelan for the x-ray work involved.

Manuscript received March 5, 1959. This work is part of a program sponsored by the U. S. Atomic Energy Commission under Contract No. AT(30-1)-1432.

Any discussion of this paper will appear in a Discussion Section to be published in the June 1960 JOURNAL.

REFERENCES

1. L. T. Lloyd, "Progress in Nuclear Energy, V. Metallurgy and Fuels," p. 71, McGraw Hill Book Co., New York (1956).
2. R. S. Dean, W. W. Gullett, and F. X. McCawley, "The Structure of Titanium Deposits Formed in Electrolytic Cells Using Fused Alkali Chloride Baths," Chicago Development Corp., Riverdale, Md.
3. M. A. Steinberg, M. E. Sibert, and E. Wainer, Chapter on "The Extractive Metallurgy of Zirconium by the Electrolysis of Fused Slats," in "Zirconium and Zirconium Alloys," ASM (1953).
4. S. F. Palgnev, M. V. Smirnov, and S. V. Karopachev, *Zhur. Priklad. Khim.*, **26**, 50 (1953).
5. S. F. Palgnev and M. V. Smirnov, *Zhur. Priklad. Khim.*, **26**, 1166 (1953).
6. W. R. Opie, *Trans. AIME*, **206**, 1192 (1956).
7. B. C. Raynes, J. C. Bleiweiss, M. E. Sibert, and M. A. Steinberg, *ibid.*, **209**, 1373 (1957).
8. L. Yang and R. G. Hudson, "Equilibrium Electrode Potentials of Some Metal-Chlorine Galvanic Cells and Activities of Some Metal Chlorides in LiCl-KCl Eutectic Melt" to appear in *Trans. Met. Soc. AIME*.

The Silver/Silver Chloride/Chlorine Solid Electrolyte Cell

Donald M. Smyth

Sprague Electric Company, North Adams, Massachusetts

ABSTRACT

A $Ag/AgCl/Cl_2$ solid electrolyte cell has been developed in which the chlorine is furnished by the dissociation of potassium tetrachloroiodide, $KICl_4$. These cells can be assembled into batteries which are extremely stable and compact and which deliver currents in the microampere range. The dissociation characteristics of the cathode salt influence the shelf-life, temperature dependence of the open-circuit voltage (OCV), and the change of OCV with aging. The ionic conductivity of the AgCl electrolyte controls the internal resistance of the battery and its temperature dependence. The shelf-life, OCV, and temperature dependence of OCV are strongly dependent on the cathode atmosphere since this can influence the electronic conduction of the electrolyte.

The development of electronic devices which can operate on currents in the microampere range has given rise to considerable interest in electrochemical cells with solid electrolytes. Such cells have potential shelf-lives many times those of conventional systems and lend themselves to extreme miniaturization. This paper describes a cell system with an indicated shelf-life in excess of 20 years and which is easily constructed in sizes of the order of 0.03 cm^3/v.

The choice of a solid electrolyte cell system is based on several factors: (*a*) the electrolyte should have a high ionic conductivity for current delivery and an infinitesimal electronic conductivity for long shelf-life; (*b*) the electrolyte must have suitable mechanical properties for the formation of strong, thin films; (*c*) the component parts must be chemically compatible; and (*d*) a high emf is desirable.

Requirement (*b*) excludes a large majority of ionic salts from consideration as electrolytes. The silver/silver halide/halogen systems meet these requirements quite well, and batteries based on the $Ag/AgI/I_2$ and $Ag/AgBr/Br_2$ systems have been described previously (1-3). The $Ag/AgCl/Cl_2$ system has the advantages of a higher emf [$Ag\text{-}Cl_2$, $E_o = 1.133$ v; $Ag\text{-}Br_2$, $E_o = 1.008$ v; $Ag\text{-}I_2$, $E_o = 0.788$ v (4)], an electrolyte with a smaller electronic conductivity (based on the evidence of silver-halogen tarnishing reactions), and an electrolyte with excellent mechanical properties. Use of potassium tetrachloroiodide, $KICl_4$ as a low pressure source of chlorine vapor has made possible the development of a $Ag/AgCl/Cl_2$ cell which is extremely stable. The cells have an open-circuit voltage (OCV) of 1.04 v at 25°C, and this does not vary more than ±5% over the temperature range +75° to −40°C. The theoretical shelf-life predicted by tarnishing experiments and the shelf-life obtained by extrapolation of accelerated aging data are both of the order of decades of years. The cells have an internal resistance of about 10^5 ohms/cm^2 area at 25°C and this increases by a factor of 60 as the temperature is reduced to −40°C.

Cell Structure

For a system such as the $Ag/AgCl/Cl_2$ cell which contains a corrosive vapor phase, the stability of the cell system depends on the extent to which this vapor can be sealed within the cell and, for this reason, a sealed cup structure has been developed. The cell is constructed from a small silver can which serves as the anode and as the main structural unit. An electrolyte film of AgCl a few microns thick is formed over the anode by exposure to Cl_2 at 200°-300° for about 30 min. The cathode is a conducting mixture of $KICl_4$ and carbon black in 6:1 weight ratio mixed with Kel-F #90 grease[1] to give a putty-like consistency. The cathode is extruded into the anode can which is then sealed with a compression fitted Teflon plug through which extends a tantalum wire that provides electrical contact to the cathode.

Open-Circuit Voltage (OCV)

The emf of the $Ag/AgCl/Cl_2$ system is related to the temperature, T, chlorine pressure, P_{Cl_2}, and the standard free energy, $\Delta F°$, of the reaction

$$Ag + \tfrac{1}{2}\, Cl_2 = AgCl \qquad [1]$$

by the familiar expression

$$E = \frac{-\Delta F°}{F} + \frac{RT}{2F} \ln P_{Cl_2} \qquad [2]$$

This expression yields a theoretical emf of 1.04 v at 25°C using thermodynamic data compiled by Quill (4) for $\Delta F°$ and the data of Smyth and Cutler (5) and Cornog and Bauer (6) for P_{Cl_2}. The observed OCV is in exact agreement with this theoretical value. If Eq. [2] is differentiated with respect to temperature, neglecting the variation of $\Delta F°$ with temperature and assuming that the chlorine pressure over $KICl_4$ can be expressed in the form

$$P_{Cl_2} = Ae^{-B/T} \qquad [3]$$

we obtain an expression for the temperature dependence of the emf,

[1] A product of M. W. Kellogg Co., Jersey City, N. J.

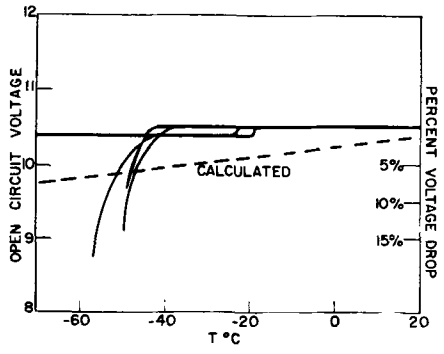

Fig. 1. Temperature dependence of open-circuit voltage. Behavior of several ten cell batteries compared with calculation from Equation IV.

$$\frac{dE}{dT} = \frac{R}{2F} \ln A \qquad [4]$$

in which R is the gas constant in coulombs per mole °K and A is a constant evaluated from the dissociation pressure data (5, 6). Evaluation of this relation gives a predicted temperature variation of OCV of 0.00092 v/°C assuming that the chlorine vapor is always in equilibrium with the solid phase. Figure 1 shows the actual temperature dependence of the OCV of several batteries together with the calculated dependence. It is seen that the observed OCVs lie above the predicted value down to about —50°C. In the vicinity of this temperature, the voltages start to drop off rapidly in many cases, although a few batteries show very little voltage drop even at —70°C. The rapid drop in OCV at very low temperatures is probably related to a relatively increasing importance of the electronic conductivity of the electrolyte with decreasing temperature.

The discrepancy between the observed and calculated temperature dependence of the OCV can be related to the nonreversible dissociation of the polyhalide cathode salt. It has been observed that equilibrium dissociation pressures are obtained only in the direction of increasing temperature for these salts (5). After a decrease in temperature, halogen pressures several times the equilibrium value may be maintained for several days. This is probably related to the formation of a film of solid recombination product over the decomposition residue, with the result that further recombination is hindered. Thus the assumption that the chlorine vapor is in equilibrium with the solid cathode phase is not valid when the temperature is decreased.

Attempts have been made to return the OCV to its equilibrium value by consuming the excess halogen pressure by current drain. The number of electrochemical equivalents of excess pressure is surprisingly high, however, and exceeds that estimated from the cell volume by more than a factor of ten. It is believed that the grease cathode binder and the carbon black act as reservoirs of excess halogen by dissolving and adsorbing large amounts of vapor. This fact reduces the hazard that a slight drop in OCV may result after a small amount of current has been drawn from the cell.

The full, theoretical emf of the electrochemical system will be observed across the cell terminals only for systems in which electronic conduction through the electrolyte phase is negligible compared with the ionic conduction. This requirement is always satisfied in aqueous electrolyte cells, since water solutions have immeasurably small electronic conductivities. Ionic crystals range all the way from essentially pure ionic conductors to essentially pure electronic conductors, however, and the relative magnitudes may depend on the purity and crystallinity of the material, the composition of the ambient atmosphere, and the nature of the electrodes.

As a result of the early work of Tubandt (7), the silver halides were long considered to be classic examples of materials having almost purely ionic conductivity. Wagner was able to show, however, that in the presence of 0.23 atm of bromine at 200°C the total conductivity of AgBr films formed by reaction of silver with bromine is 17% electronic, and that the electronic contribution increases rapidly with decreasing temperature (8). In recent years, Pfeiffer, Hauffe, and Jaenicke have shown that single crystal AgBr is an essentially pure electronic conductor and that the ionic contribution increases with the concentration of grain boundaries (9). Luckey and West (10) and Shamovskii, Dunina, and Gosteva (11) have shown that, in the presence of bromine vapor, single crystal AgBr has an "additional" conductivity which is proportional to the square root of the bromine pressure and which is thus considered to be due to the injection of electron holes into the AgBr in agreement with the theories of Wagner. These properties of AgBr and their possible extension to AgCl and AgI raise a question as to the suitability of the silver halides for electrolytes in solid-state cells of the silver-halogen type. It has been known for several years that such cells do have open-circuit voltages close to the theoretical emf (1-3), and it is necessary to reconcile this fact with the known electrical properties of the electrolytes. The following experiments clarify this point.

It has been found that a Ag/AgCl/Cl_2 cell with a cathode phase consisting of 1 atm of dry chlorine has an equilibrium OCV of about 0.75 v, whereas the theoretical emf is 1.13 v. The OCV also decreases rapidly with temperature. This indicates that a substantial electronic conduction through the AgCl electrolyte is partially short-circuiting the emf and that the relative electronic contribution is increasing with decreasing temperature. When undried chlorine is used, however, the OCV is the same as the thermodynamic emf, and the change of OCV with temperature is greatly reduced. The cell voltage changes rapidly and reversibly with changes in the moisture content of the chlorine. It appears that the moisture content of the chlorine atmosphere is suppressing the electronic conduction through the AgCl. Measurements of the internal resistance of the cell in wet and dry chlorine show that the water vapor has very little effect on the ionic conduction through the electrolyte. These findings led to an investigation of the effect of foreign

vapors on the tarnishing rate of silver in halogen vapor; this work is described in a separate publication (12). It was found that very small partial pressures of water or carbon tetrachloride vapor suppress the reaction rates drastically and that the rate-determining process is an interface phenomenon, since the reaction rate is independent of tarnish film thickness. The suppression of the reaction rate may be taken as an upper limit of the suppression of the electronic current.

It has since been found that cells made with cathodes consisting only of carbon black and $KICl_4$ have voltages less than the theoretical emf, and very poor low-temperature properties. Cells in which the cathode contains a hydrated salt as a source of water vapor or Kel-F grease have the theoretical emf and greatly improved low temperature properties. Thus the Kel-F grease binder used in the cathode serves to stabilize the cell voltage and to extend the theoretical shelf-life by decreasing the electronic conduction through the electrolyte. Tarnishing experiments indicate that the stabilizing vapor is not consumed during the formation of more silver halide.

The stability of the OCV with time as a function of temperature is of great interest for such a potentially long shelf-life item. The shelf-life under ideal conditions will be determined by the rate of consumption of the active materials by the internal tarnishing reaction whose rate is limited by the electronic leakage through the electrolyte. Thus a maximum attainable life of such a system can be estimated from tarnishing data and the amount of active materials in a cell. The reaction rates of silver foils of different purities with the equilibrium halogen atmosphere over $KICl_4$ at 60°C are shown in Fig. 2, in which the square of the weight increase is plotted against time. The two cadmium doped samples appear to follow a parabolic tarnishing expression, whereas high-purity and commercial purity silver have an even greater dependence of reaction rate on film thickness.

Chemical analyses of these films indicate a chloride:iodide atomic ratio of about 19.5:1 whereas the equilibrium dissociation vapor of $KICl_4$ at 60° has a Cl:I ratio of 14.5:1 (5). Thus there may be a slight preferential reaction of chlorine, and the films

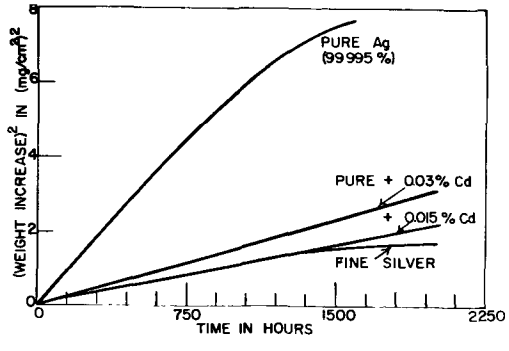

Fig. 2. Tarnishing rates of various silver samples with the dissociation vapor over $KICl_4$ at 60°C. Square of weight increase plotted against reaction time. (Fine silver is nominally 99.9% silver.)

may be considered as a dilute solution of AgI in AgCl.

A calculation based on the assumption that the commercially pure silver reacts according to a parabolic rate expression gives a theoretical shelf-life of 25 years for continuous storage at 60°C for typical cell dimensions and an initial electrolyte thickness of 13 μ. This is a conservative estimate, since the actual reaction rate is decreasing with time more rapidly than indicated by a parabolic expression and also because the reactions were carried out in the room atmosphere without the presence of any rate-depressing vapors such as are present in actual cells. The initial electrolyte film of pure AgCl will also depress the reaction rate to a greater extent than would the same thickness of Ag-$KICl_4$ tarnishing product.

In actual practice, the shelf-life of a solid electrolyte cell is limited by the leakage of active cathode vapor from the cells and by electrical leakage through and over the surface of the encapsulating material. The magnitude of these effects may be determined from accelerated life tests carried out at elevated temperatures. Such tests have been performed with groups of 4-cell batteries stored at 125°, 110°, and 100°C. The end of the battery life has been defined arbitrarily as the time at which the room temperature open-circuit voltage of half the batteries in a group has dropped 5%. Results are summarized in Fig. 3, in which the shelf-life has been plotted logarithmically against the reciprocal absolute storage temperature. The relationship is merely an intuitive guess which seems to fit the extremely strong temperature dependence of shelf-life reasonably well. Although the extrapolation of these data to ordinary storage temperatures cannot be considered accurate, the indication is that satisfactory stability has been attained.

The aging characteristics of a typical battery are shown in Fig. 4, in which the room temperature voltage of a 4-cell battery stored at 100°C is plotted against storage time. It is seen that there are two stable voltage levels: an initial voltage of about

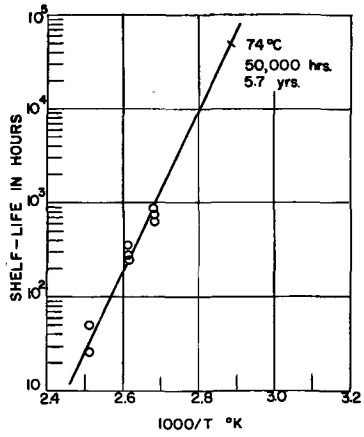

Fig. 3. Accelerated aging data of four-cell batteries, and a possible extrapolation to lower temperatures. Shelf-life defined as time prior to a 5% drop in open-circuit voltage (measured at room temperature) for half of the batteries in a group. The line was fitted to the data by the method of least squares.

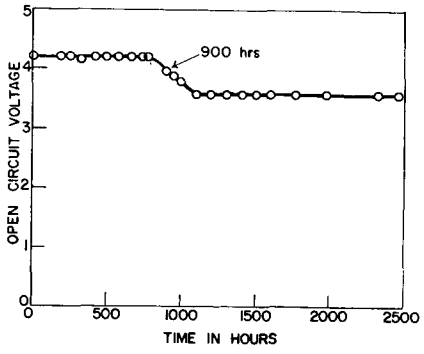

Fig. 4. Aging behavior of a four-cell battery stored at 100°C. Open-circuit voltage measured at room temperature.

1.05 v/cell which is related to a $Ag/AgCl/Cl_2$ cell in which the Cl_2 is furnished by the dissociation of $KICl_4$, and a subsequently stable plateau at 0.89 v/cell. It has been shown that this latter voltage is that of a Ag/AgCl/ICl cell in which the ICl is furnished by the dissociation of $KICl_2$. An earlier publication (5) has shown that $KICl_4$ dissociates in two steps:

$$KICl_4 \rightarrow KICl_2 + Cl_2 \qquad [5]$$

$$KICl_2 \rightarrow KCl + ICl \qquad [6]$$

and that the equilibrium vapor is predominantly chlorine which is thus consumed or lost faster than the ICl. When the chlorine has all been lost, there is still sufficient $KICl_2$ left to maintain the voltage at 0.89 v/cell for a period which is generally longer than the duration of the initial voltage. Note that this second voltage plateau has not been included in the shelf-life definition and thus represents a substantial safety factor for applications that can tolerate a 15% voltage drop. The internal resistances of the cells do not increase appreciably until near the end of the second voltage plateau.

The Internal Resistance

The internal resistance, R_o, is defined here by the expression

$$V = E_o \frac{R}{R+R_o} \qquad [7]$$

in which E_o is the OCV and V is the terminal voltage with load R. The relatively small ionic conductivity of the AgCl electrolyte determines the general magnitude of the resistance and also its temperature dependence. Data reported by Compton (13) show a conductivity of about 3×10^{-9} to 2×10^{-8} ohm^{-1} cm^{-1} at 25°C for undoped AgCl. For a cell area of 0.24 cm^2 and an electrolyte thickness of 0.0013 cm, this gives a calculated resistance range of 2.7×10^5 to 1.8×10^6 ohms which is to be compared with an observed range of 5×10^5 to 5×10^6 ohms for cells with these dimensions. The single-crystal conductivity data reported by Compton may contain an unknown electronic contribution which could account for the observed resistances being slightly higher than the calculated values. The conductivity data predict a resistance increase by a factor of 60 between 25° and −40°. Seventeen 10-cell batteries selected at random showed an average increase by a factor of 57 over this range although there was considerable variation among the group (average deviation of factor = 20).

Compton's conductivity data lie in the impurity-sensitive range below 100°C rather than in the intrinsic range, and the correlation between the temperature coefficients of resistance and resistivity indicate that the cell behavior should also be typical of the impurity-sensitive range. Thus small additions of impurities to the AgCl electrolyte might have considerable influence on the resistance. It is well established that the principal ionic charge carriers in silver halides in this temperature range are silver ion vacancies and that the cation vacancy content of the silver halides can be enhanced by the addition of divalent metallic halides such as those of cadmium or lead. The divalent foreign cation enters the lattice in place of a monovalent silver ion, and another silver ion position is left vacant to maintain electrical neutrality. It has also been established that the impurity content of halide films formed by tarnishing reactions is related to the metallic impurity content of the base silver. Cells have been made from silver anode cans containing various amounts of cadmium, and it was found that a cadmium content of 0.02% causes a reduction in the cell resistance by a factor of three to five over the entire temperature range of battery operation. Larger amounts of cadmium cause the AgCl film to become brittle and less adherent. Aging characteristics, low temperature properties, and other operating characteristics are as good or better for these batteries as for the undoped cells.

In addition to the ionic conductivity of the electrolyte, other factors may influence the apparent resistance of cells during long periods of heavy current drain. The rate of dissociation of the polyhalide salt and the rate of diffusion of the liberated halogen to the electrolyte-cathode interface may eventually limit the current. The importance of these secondary factors may be surmised from a comparison of heavy current drain data with ideal behavior, which takes into account only conductivity effects. In particular it is necessary to allow for the fact that the electrolyte thickness increases with current drain due to the formation of additional AgCl.

The rate of increase in electrolyte thickness with current drain may be expressed as

$$\frac{dx}{dt} = \frac{V}{\mathbf{F}} \frac{\sigma E}{x} \qquad [8]$$

where x is the thickness of the electrolyte, t the time, V the volume of AgCl per equivalent weight, $\mathbf{F}$ Faraday's constant, σ the ionic conductivity of the AgCl, and E the voltage drop across the electrolyte (essentially the emf for near short-circuit conditions). It has been assumed that the current can be expressed as

$$i = \frac{\sigma A E}{x} \qquad [9]$$

where A is the active electrolyte area, and that the product of current drain is essentially pure AgCl.

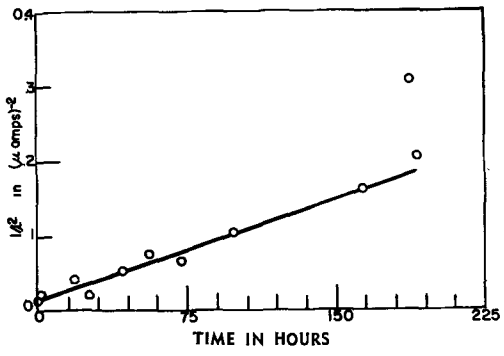

Fig. 5. Short-circuit current of a ten-cell battery at room temperature plotted according to Eq. [10].

Integrating [8] and using [9] to relate thickness to current and expressing σ in terms of i_o and x_o (the initial current and electrolyte thickness) gives

$$\frac{1}{i^2} = \frac{2V}{\mathbf{F}x_o A i_o} \cdot t + \frac{1}{i_o^2} \qquad [10]$$

Thus a plot of $1/i^2$ vs. t should give a straight line of slope $2V/\mathbf{F}x_o A i_o$ and an intercept of $1/i_o^2$, if the electrolyte conductivity is the principal determining factor. An example of this type of treatment is shown in Fig. 5. It is seen that ideal behavior is followed for about 150 hr, after which the current decreases quite abruptly. The scatter of the data is due mainly to fluctuations in room temperature; smoothed discharge data give precise linearity. At the end of 150 hr, the cell had delivered a total of 2 coulombs; after 265 hr of continuous drain the load was removed from the cell and its OCV returned to 85% of its original value in 3 sec and to 95% of its original value in 25 min. When current drain was resumed the current was 5.5 μa, decaying after about a day to the 1.5 μa level reached prior to the initial removal of the load. A more detailed study of the first few minutes of discharge discloses a brief period of high current which amounts to about 0.005 coulombs of charge more than would correspond to a linear $1/i^2$ vs. t plot extrapolated to $t=0$. An evaluation of the slope of this plot gives $x_o = 11.6$ μ and $\sigma = 3.7 \times 10^{-8}$ ohm^{-1} cm^{-1} which agrees remarkably well with the x_o of 13 μ estimated from the time and temperature of the chlorination of the silver cans and with the conductivity range previously quoted from the work of Compton. This correlation is a good indication that the current drain is conductivity controlled even in the near short-circuit range for periods up to about a week.

Typical current drain performance of 10-cell batteries at room temperature and —40°C are shown in Fig. 6 and 7. Voltage recovery after removal of the load is almost instantaneous.

Acknowledgment

The author gratefully acknowledges the advice and guidance of Dr. Kurt Lehovec and the valuable assistance of Mr. Matthew Stefanski.

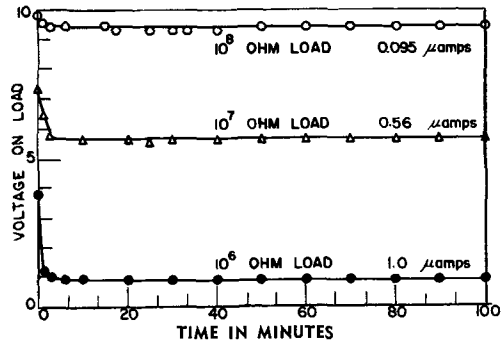

Fig. 6. Terminal voltage of a ten-cell battery with various loads at room temperature (undoped cells).

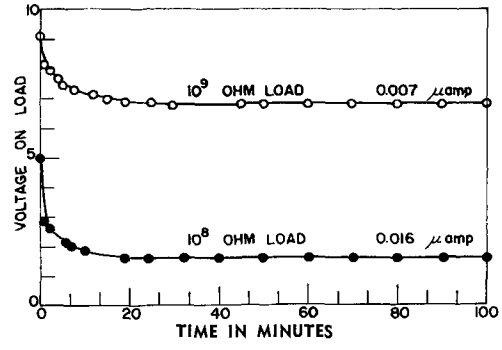

Fig. 7. Terminal voltage of a ten-cell battery with various loads at —40°C (undoped cells).

This work was sponsored by the U.S. Army Signal Research and Development Laboratories under contracts DA-36-039-sc-63151 and DA-36-039-sc-72349.

Manuscript received Jan. 12, 1959. This paper was prepared for delivery before the Ottawa Meeting, Sept. 28-Oct. 2, 1958.

Any discussion of this paper will appear in a Discussion Section to be published in the June 1960 JOURNAL.

REFERENCES

1. K. Lehovec and J. Broder, *This Journal*, **101**, 208 (1954).
2. W. J. van der Grinten, *ibid.*, **103**, 201C (1956).
3. J. L. Weininger, *ibid.*, **105**, 439 (1958).
4. Nat'l. Nuclear Energy Series, Div. 4, *19B*, "Chemistry and Metallurgy of Miscellaneous Materials, Thermodynamics", pp. 76-192, McGraw-Hill Book Co., New York (1950).
5. D. Smyth and M. Cutler, *J. Am. Chem. Soc.*, **80**, 4462 (1958).
6. J. Cornog and E. Bauer, *ibid.*, **64**, 2620 (1942).
7. C. Tubandt and F. Lorenz, *Z. physik. Chem.*, **B7**, 513 (1914).
8. C. Wagner, *ibid.*, **B32**, 447 (1936).
9. I. Pfeiffer, K. Hauffe, and W. Jaenicke, *Z. Elektrochem.*, **56**, 728 (1952).
10. G. Luckey and W. West, *J. Chem. Phys.*, **24**, 879 (1956).
11. L. Shamovskii, A. Dunina, and M. Gosteva, *Soviet Physics, JETP*, **3**, 511 (1956).
12. D. Smyth and M. Cutler, *This Journal*, **106**, 107 (1959).
13. W. Compton, Thesis, University of Illinois (1955).

Surface to Volume Considerations in the Palladium-Hydrogen-Acid System

James P. Hoare

Scientific Laboratory, Ford Motor Company, Dearborn, Michigan

ABSTRACT

The open-circuit potential against a Pt/H_2 electrode in the same $2N$ sulfuric acid solution of a series of palladium electrodes of different sizes and shapes was recorded as a function of time. The electrical resistance in certain cases was also followed as a function of time. It is shown that the time required for charging the palladium with hydrogen is sensitive to the surface-to-volume ratio of the electrode. Charging mechanisms are discussed.

It has been shown (1) that pure palladium metal, when placed in an acid solution saturated with hydrogen gas, will absorb the hydrogen until the maximum α-Pd concentration ($\sim$0.03 H/Pd atomic ratio) has been reached and will exhibit a potential of 50 mv more noble than a Pt/H_2 electrode placed in the same solution. It was stated also that under open-circuit conditions the Pd would not absorb additional hydrogen beyond this maximum α-Pd limit and that the 50-mv potential could be maintained indefinitely in the absence of impurities. The potential of 50 mv has been associated with an atomic-hydrogen potential-determining reaction (2) on the Pd as opposed to the molecular hydrogen reaction on the Pt/H_2 electrode. The solubility limit at H/Pd atomic ratios of about 0.03 has been described (3) in terms of a blocking mechanism due to a variation in the point of zero charge of the Pd as hydrogen was absorbed.

Recently, Ratchford and Castellan (4) have reported that Pd electrodes made from thin metal wires or foils behaved somewhat differently. Such electrodes did not give open-circuit-potential-vs-time curves with a plateau at 50 mv of indefinite length; instead, the plateau at 50 mv was less than 10 hr long after which the potential dropped to a steady value of zero volt. Another interesting feature about these curves is the initial overshooting of the 50 mv value with an immediate return to the 50 mv plateau, analogous to a supercooling curve. Electrodes, which had gone to zero potential vs. a Pt/H_2 electrode, were analyzed for the hydrogen content with ceric sulfate (5) and found to have absorbed hydrogen to the β-phase concentration of about 0.6 H/Pd atomic ratio.

It is the purpose, then, of this investigation to study possible surface to volume effects important to the solution of hydrogen by palladium.

Experimental

Electrodes were made from Pd foil and wire 99.5+% pure. In the first set of experiments the following electrodes were used: (*a*) a 1 cm^2 piece of Pd foil 2 mils thick; (*b*) a 1 cm^2 piece of foil 4 mil thick; (c) a 1 cm^2 piece of 4 mil foil whose surface was nine-tenths covered with a polyethylene film; (*d*) a 3 cm length of wire, 5 mil in diameter; and (*e*) a Pd bead 0.057 in. in diameter and half way covered with polyethylene so that a hemisphere was exposed to the solution.

The Teflon cell was similar to those used before (6). All electrodes were cleaned in hot concentrate HNO_3 and the cell was rinsed repeatedly with water triply distilled in an all-quartz still as described before (6). All measurements were made in $2N$ H_2SO_4 solution made with triply distilled water and saturated with hydrogen purified by a standard multistage purification-train. The hydrogen flow was maintained approximately at a constant rate night and day. Final purification of the solution and electrodes was done by pre-electrolysis overnight with an auxiliary Pt electrode which was removed while the pre-electrolysis current was flowing. The open-circuit potential between the test electrode and a Pt/H_2 electrode in the same solution was recorded as a function of time. At no time in this complete investigation was any electrode cathodized.

A second series of experiments was done in which wires of approximately the same length but of varying diameters were used. These wires were about 11 cm long and had diameters of 5, 10, 15, 20, and 25 mils. Each wire was cleaned as described above and mounted diagonally in a virgin polyethylene cell 19 cm long and 2.5 cm in diameter from the top on one side to the bottom on the other side. Platinum leads were welded to the Pd wire and the weld area as well as about 3 or 4 mm of Pd wire penetrated through the cell wall and was well covered with polyethylene. This was done to assure adequate protection against contact between the weld area or the Pt and solution and against contact between Pd and the external atmosphere. It is to be noted that in all cases throughout this investigation the entire Pd electrode was maintained submerged beneath the solution level so that the Pd was never in contact with the external atmosphere. After a given wire was cleaned electrolytically overnight, the hydrogen stirring was begun and the open-circuit potential vs. a Pt/H_2 electrode in the same solution as well as the electrical resistance of the wire was recorded as a function of time. Zero time is taken when hydrogen flow is begun. The resistance was measured

with a General Electric Portable Double Bridge which is designed to measure resistance from 0.0001 to 22Ω.

These same experiments were repeated with these same wires wound in the form of a toroid on a polyethylene ring and placed in the Teflon cell. The results of this series of experiments were similar to those done in the polyethylene cell.

Results and Discussion

Figure 1 shows the open-circuit potential vs. a Pt/H_2 electrode in the same $2N$ H_2SO_4 solution for a series of Pd electrodes having different values for the ratio of the exposed apparent surface area to the total volume of the Pd as a function of time. The surface area was determined by geometric measurement and the volume by weight measurements using a value of 12.01 g cm^{-1} for the density of Pd. As was observed by Ratchford and Castellan, the open-circuit potential falls from the high positive value produced by anodization to a very flat plateau at about 50 mv. After a time, the potential falls along a sigmoid curve to zero and remains there. The length of the 50 mv plateau and the transition time from the 50 mv plateau to the zero volt plateau are found to be sensitive to the ratio, area/volume (A/V).

In Fig. 2 and 3 are shown the relative resistance-vs.-time curves for a series of Pd wires. Figure 3 shows the initial part of the curves in greater detail. It is seen that a plateau of varying length occurs at about a value of R/R_0 of 1.05. Using Fischer's expression (7), $R = R_0(1.0292 + 0.000668\ V)$, where V is the relative volume of the dissolved hydrogen, this resistance value corresponds to about 31 relative volumes or a H/Pd atomic ratio of about 0.03, the upper limit of the α-phase (1, 7, 8).

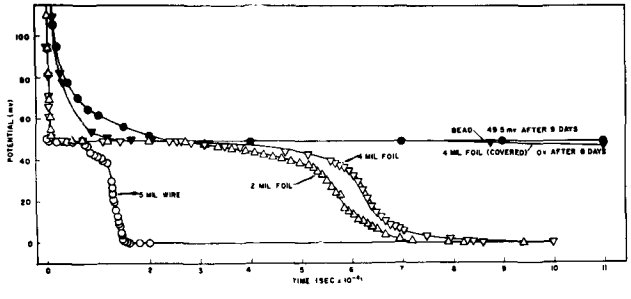

Fig. 1. Open-circuit potentials of Pd electrodes of various sizes in 2N H_2SO_4 solution plotted as function of time. Potential measured with reference to Pt/H_2; temperature, 24°±1°C.

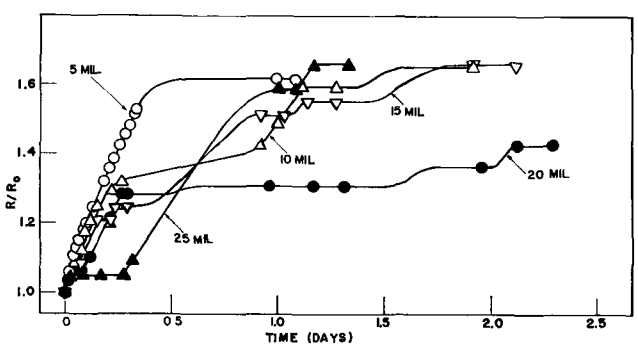

Fig. 2. Relative resistance-vs.-time curves for Pd wires of different diameter; temperature, 24°±1°C.

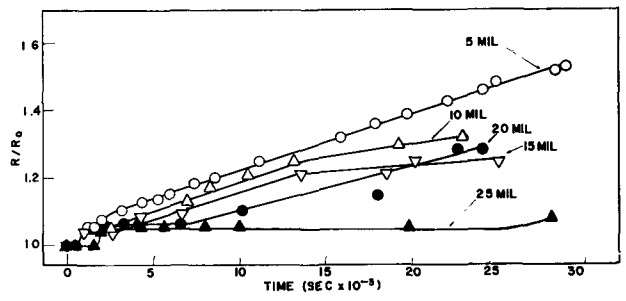

Fig. 3. Initial part of relative resistance-vs.-time curves of Fig. 2 for Pd wires on open circuit in H_2-saturated acid solution.

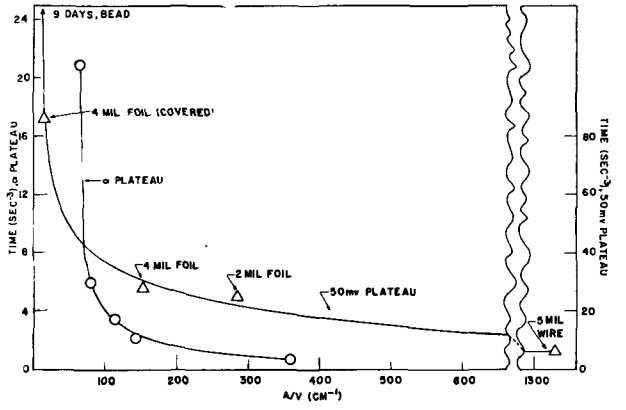

Fig. 4. Length of α plateau found on resistance-time curves for Pd wires is shown by circles and is plotted vs. surface-to-volume ratio. Length of 50 mv plateau found on potential curves for Pd electrodes of various shapes is shown by triangles and also is plotted as function of surface-to-volume ratio.

In general after the α-phase-plateau the resistance increases uniformly to about a value of 1.27 for R/R_0 which corresponds to a H/Pd atomic ratio of 0.29. In Fig. 5 is shown the potential-time curve with the accompanying relative resistance-time curve for only the 5 mil wire case, for the sake of simplicity. Similar curves were obtained for all the other wires. When the relative resistance reaches a value of about 1.35, corresponding to a H/Pd atomic ratio of 0.37, the potential begins to drop away from the 50 mv plateau in all cases. This is in good agreement with the data reported when the wire was charged with hydrogen cathodically (1, 2). When the potential finally reaches a steady value of zero volts, the resistance has come to a steady value somewhat over 1.6 for R/R_0. This is a higher value than was reported for a wire charged with hydrogen cathodically (1, 2) and corresponds to a H/Pd atomic ratio near 0.7.

In order to check the hydrogen content of a wire which had reached zero volts, the amount of hydrogen absorbed was determined using ceric sulfate solution and was found to contain about 0.6 H/Pd atomic ratio.

A plot of the length of the 50 mv plateau vs. A/V is found in Fig. 4. The curve is hyperbolic. Although the experiment with the bead was terminated for convenience after 9 days, it is believed that the potential would have fallen to zero after a sufficiently long time.

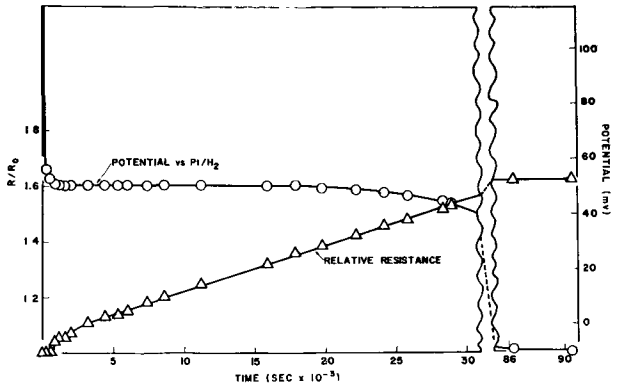

Fig. 5. Potential vs. time and R/R_0 time curve recorded simultaneously for 5 mil wire; temperature, 24°±1°C; solution, hydrogen saturated 2N H_2SO_4.

The length of the α-Pd plateau for the wires is plotted in Fig. 4 as a function of A/V. This plot is also hyperbolic. If the data in Fig. 4 are plotted as a function of V/A instead of A/V, indeed, straight lines are obtained. This indicates that the length of the plateau is directly proportional to the volume and inversely proportional to the area. It is to be noted, though, that the values for the bead and for the 25 mil wire deviate from the respective straight lines toward higher values.

One may conclude from the data in Fig. 5 that hydrogen does not enter the Pd metal until the oxide is removed from the surface. This is indicated by the fact that the resistance does not change until the potential drops from a high positive value to that of 50 mv which is the potential associated with the exposed α-Pd surface of maximum concentration. This same behavior was found in all cases. Once the surface is clear the hydrogen is dissolved by the Pd.

The potential remains at 50 mv until an H/Pd atomic ratio of about 1.37 is reached. At this point, the amount of β-Pd has increased at the expense of the α-phase until now the mixed potential (2), which had, up until now, been dominated by the α-phase potential-determining reaction, is beginning to be dominated by the β-phase reaction. Of course, when the wire reaches a potential of zero volt, it is now a β-phase electrode and the potential determining reaction is the same as that on Pt.

Because of the fact that both the length of the plateau of 50 mv on the potential curves and the length of the α-phase plateau on the resistance curves are sensitive to the ratio, A/V, it is suggested that the penetration of the surface skin of the metal is the rate-determining step in the solution of hydrogen by Pd. This proposal is also supported by the lack of a thickness effect in the transport of hydrogen through a Pd bielectrode (9). Once the hydrogen enters the interior of the metal, it is quite mobile as shown by the nuclear magnetic resonance work of Norberg (10) and spreads evenly throughout the metal. It is postulated here that the β-phase cannot nucleate until the entire body of Pd is converted to the α-phase of maximum hydrogen concentration (H/Pd at ratio ~0.03). It is interesting to note that the resistance makes a very rapid jump to an R/R_0-value of about 1.05 and remains at this value for a length of time dependent on the value of A/V according to the curve shown in Fig. 4. It would appear, then, that the resistance is not a linear function of the hydrogen content until the maximum α-phase concentration is reached throughout the metal. As a matter of fact, Fischer makes this statement, and it appears in the intercept value of 1.0292 in his equation. It is assumed here that the length of the α-phase plateau is the time it takes to change the entire bulk of Pd to the α-phase of maximum concentration and that the resistance is not a linear function of hydrogen content until at least some β-phase is present.

After the α-phase plateau the resistance increases at the same linear rate of 1.67×10^{-5} units sec^{-1} up to a value of about 1.27 for R/R_0 in all cases regardless of the value of A/V. From then on, as shown in Fig. 2, the resistance increases in steps, increasing in length with decreasing values of A/V, except for the 25 mil case. This would seem to suggest that the β-phase nucleates at various centers throughout the metal and then grows according to a domain-type mechanism at the expense of the α-phase. The steps in the resistance may be due to a coalescing of these domains. The rate at which the β-phase nucleates and grows seems to be a function of the history of the electrode preparation as exemplified by the rapid charging of the 25 mil wire. Such steps are not found in the open-circuit potential curves for these wires. These curves are not shown here, but they are similar to the smooth curves shown in Fig. 1. This may have been expected since the resistance is a bulk quantity while the potential is a function of a surface quantity and surface conditions may not necessarily vary linearly with those occurring in the bulk material.

In the case of a very small wire, these effects are at a minimum because of the high surface area and consequently the high rate of penetration of the hydrogen to the interior of the metal. It is with this type of electrode, one with a very high value of A/V, that Ratchford and Castellan worked and so they worked on the right-hand branch of the hyperbolas shown in Fig. 4. On the other hand, Schuldiner and Hoare worked on the left-hand branch by using small beads and pieces of foil

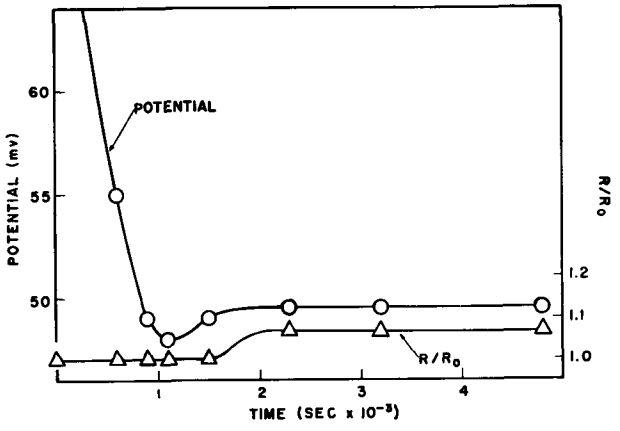

Fig. 6. Potential and resistance curves for 20 mil wire that exhibited overshoot in potential. Potential is measured against Pt/H_2 electrode in same solution.

highly covered with polyethylene films. In this way it is possible to resolve the differences between the two investigations. Even though it is not necessary to resort to a change in the point of zero charge to explain the α-phase plateau, it is still held that the hydrogen enters the metal by way of a hydrogen atom in the double layer being transported to the metal surface through an adsorbed water molecule as described before (3).

It was observed neither by Schuldiner and Hoare nor in this investigation that an electrode made from Pd foil or bead gave a potential time curve with a minimum similar to a supercooling curve. This effect was not observed for the wires stretched along a straight line in the polyethylene cell nor for the same wire wound as a toroid on a polyethylene ring in the Teflon cell. However if the wire was wound in the form of a loose air-cored helix, a minimum may be found as shown in Fig. 6. It is important to note that the resistance does not change from the original hydrogen free value of R_0 until the potential has returned to the 50 mv value. It would appear, then, as the hydrogen removes the oxygen from the surface, by some chance condition of the surface film brought about by an accidental stage in the history of its preparation the surface becomes more platinum-like, that is, a noble metal that does not dissolve hydrogen readily and the potential strives toward zero volt. However, the potential never reaches zero because the hydrogen gradually destroys this unusual surface film. After the film is destroyed and the true Pd surface exposed, the hydrogen begins to dissolve, the resistance increases and the potential returns to the 50 mv plateau. Although the nature of this surface film has not been determined at this time, it is seen that it is reduced by hydrogen, it is conducting, it is a catalyst for the hydrogen reaction, and it most likely contains oxygen since it occurs only after strong anodization.

In view of the results presented here it may be necessary to differentiate between three types of hydrogen-charging mechanisms in the Pd-H system. In previous work (3), it was shown that hydrogen-charged Pd that was obtained from dry Pd exposed to dry hydrogen gas had different properties from that obtained by the cathodic charging of a Pd electrode in an acid solution. A difference was in the hydrogen content of the final stable product which seemed to be a function of the amount of lattice distortion. In the first case the H/Pd atomic ratio was about 0.6 while in the second case it was about 0.36. In the present work, the final product contains hydrogen at 0.6 H/Pd atomic ratio but which exhibits a relative resistance which seems to be much too high and does not lose hydrogen as in the cathodized case. This may indicate that in this case the lattice is distorted in a different manner in absorbing a quantity of hydrogen necessary to raise the H/Pd atomic ratio to 0.6 than in the two previous cases cited above. Apparently the domain-like charging process described here was not permitted in the cathodically charged Pd due to the forcing of the hydrogen into the Pd by electrochemical means as shown by the linear curve in Ref. (1).

One may say, then, that Pd charged with hydrogen to the β-phase by standing on open circuit in a hydrogen-stirred acid solution gives a final result more similar to the dry Pd-H charging than to the cathodic charging. Also, if one wishes to study the properties of α-phase Pd one must use an electrode configuration (e.g., beads) in which the A/V value is such that the rate of change to the β-phase is very slow.

Manuscript received Feb. 20, 1959. This paper was prepared for delivery before the Philadelphia Meeting, May 3-7, 1959.

Any discussion of this paper will appear in a Discussion Section to be published in the June 1960 JOURNAL.

REFERENCES

1. J. P. Hoare and S. Schuldiner, *J. Phys. Chem.*, **61**, 399 (1957).
2. S. Schuldiner, G. W. Castellan, and J. P. Hoare, *J. Chem. Phys.*, **28**, 16 (1958).
3. J. P. Hoare, S. Schuldiner, and G. W. Castellan, *ibid.*, **28**, 22 (1958).
4. R. J. Ratchford and G. W. Castellan, *J. Phys. Chem.*, **62**, 1123 (1958).
5. F. A. Lewis and A. R. Ubbelohde, *J. Chem. Soc.*, 1710 (1954).
6. J. P. Hoare and S. Schuldiner, *This Journal*, **102**, 485 (1955).
7. F. Fischer, *Ann. Physik*, **20**, 503 (1906).
8. D. P. Smith, "Hydrogen in Metals," p. 126, Univ. Chicago Press, Chicago (1948).
9. J. P. Hoare and S. Schuldiner, *ibid*, **104**, 564 (1957).
10. R. E. Norberg, *Phys. Rev.*, **86**, 745 (1952).

The Growth of Barrier Oxide Films on Aluminum

W. J. Bernard and J. W. Cook

Sprague Electric Company, North Adams, Massachusetts

ABSTRACT

The growth of anodically formed barrier oxide films on aluminum has been followed by weight, capacitance, and rate measurements. The increase of film thickness at constant voltage has been calculated and compared to the values obtained by optical measurements. The results have been shown to obey the law $i = \alpha e^{\beta F}$.

Several papers in recent years (1-6) which have dealt with the thickness of anodically formed barrier oxide films on aluminum lead to the conclusion that the thickness is determined precisely by the voltage impressed on the oxide film. This conclusion ignores the generally accepted theory of anodic ox-

ide growth first advanced by Mott (7) and covered more specifically in the case of aluminum by Charlesby (8) and by Nagase (9). It is the purpose of the present paper to show that the relationship between current and field $i = \alpha e^{\beta V/s}$, where α and β are constants, correctly expresses the dependence of the thickness, s, of the oxide film on both ionic current density, i, and the applied voltage, V. It is probably the failure to define the current density in the cited papers, rather than the use of different electrolytic solution, which has led to the variations in reported values of oxide thickness, ranging from 12.7 to 16.5 Å/v. Although it is pointed out by van Geel and Schelen (2) that film growth may continue at constant voltage, they suggest that it is sufficient only to permit the current to decrease to a low (but unspecified) value in order to define the thickness.

In this investigation we have calculated oxide film thicknesses by measurement of the weight of oxide and by the direct measurement through the use of interference fringes. This latter method has been employed previously by Nagase (1).

Barrier films can be formed on Al in any of several different aqueous solutions, most commonly in solutions of boric acid or alkali borates. However, aqueous solutions are characterized by generally poor current efficiency of oxide formation, as a result of oxygen evolution and anodic dissolution of Al. These effects make it difficult to examine only that component of the current which leads to film growth, and we have, therefore, found it convenient to work with solutions of ammonium pentaborate in ethylene glycol. The particular composition chosen by us (30% by weight of salt) is not useful for oxidizing Al to high voltages, but it is characterized by a high current efficiency of formation up to 150 v; within the error of the measurements the efficiency is 100%. The films found in this solution appear to be identical to those found in aqueous solutions of boric acid, as shown by the capacitance of films formed under the same conditions of temperature, voltage, and current density in the two electrolytes.

In order to determine the thickness of a formed film by weight measurements, the density of the oxide and the surface area of the formed metal must be known. The density of such films of Al_2O_3 is not necessarily the same as that of the bulk oxide, and values varying from 3.0 to 5.0 g/cm^3 have been reported. We have, therefore, also carried out a determination of this quantity. The "roughness factor" of the metal surface has been estimated by comparing the formation charge required for foil to that of highly polished Al surfaces where the true area is assumed to be equal to the geometrical area. We have verified the equation for oxide growth by obtaining straight-line plots of log i vs. $1/W$ (W = oxide film weight), and log i vs. capacitance, over the current density range of 10^{-3} to 10^{-7} amp/cm^2 for films maintained at a constant voltage of 150 v.

Experimental

Formations were carried out at 25°C on Alcoa foil of 99.99% purity, with an apparent surface area of 97 cm^2. Before forming the foil was cleaned briefly with cold potassium dichromate-sulfuric acid cleaning solution and washed thoroughly with high-purity water, rinsed in methanol, and dried. The negative electrodes of the formation cell, which were platinized, also served as the subsidiary electrodes for capacitance measurements of the formed films.

The roughness factor of the foil was measured by comparing its formation charge to that of electrodes which were assumed to have a factor of unity. These latter electrodes were prepared by machining high-purity Al plates in the form of disks 2 in. in diameter. One face of each disk was drilled and tapped to accommodate a brass rod which served as an electrical contact. The opposite face was polished, cleaned, and then formed, along with the cylindrical surface, to 400 v in aqueous boric acid. The formed face was repolished to a mirror finish and then given a brief chemical polish in Alcoa "R-5 Bright Dip" solution. The heavy formation on the cylindrical surface of the electrode protected that portion from chemical attack and defined the area for subsequent formation. Several such electrodes were formed to 150 v at 1.0 ma/cm^2, and from the charge passed it was determined that the roughness factor of our foil specimen was 1.03. This low roughness factor is probably not a true measure of the state of the surface before formation but is a result of the smoothing effect of anodizing. This effect has been discussed by Lewis and Plumb (10).

Oxide films were detached from the underlying metal by dissolving the Al in a methanol-bromine solution (11), filtered, washed, and dried at 105°C. All weighings were made on a Brinkmann-Sartorius microbalance.

Density measurements were made by hydrostatic weighing in toluene. About 100 mg of sample was sufficient to give the desired accuracy.

Capacitance readings were made 10 min after removal of voltage, at which time the change in capacity with time is negligible.

Direct determinations of the thickness of films were made by the measurement of the displacement of interference fringes produced by a standard air wedge. Detached flakes of oxide, prepared by Strohmaier's method (12), were mounted on an optical flat and covered with an evaporated layer of silver about 600Å thick. Since the step thus produced on the surface of the optical flat is the same height as the thickness of the oxide film, the observed displacement is the same as that which would be due to the film itself. The displacement was measured at a magnification of 32X with a traveling microscope which was calibrated to read to 0.001 mm. The light source was the Hg 5460Å line.

A constant-current generator[1] was used for the measurement of formation rates at constant current. The range of current of this instrument limited the measurements to between 2.0×10^{-6} and 2.0×10^{-4} amp/cm^2. During the period of measurement the current could be held constant to better than 0.5%.

[1] Constructed by the Test Equipment Department, Sprague Electric Co.

Table I. Current efficiency of oxide formation based on weight measurements

Current density, amp/cm²	10^{-7}	10^{-6}	10^{-5}	10^{-4}	10^{-3}
Total charge, coulombs/cm²	0.388	0.363	0.339	0.318	0.299
Measured wt. gain, μg/cm²	31.9	30.0	28.3	26.8	25.0
Calculated wt. gain, μg/cm²	32.2	30.3	28.1	26.3	24.8
Measured wt. of oxide, μg/cm²	68.0	63.6	59.8	56.5	53.4
Calculated wt. of oxide, μg/cm²	68.4	64.0	59.6	56.0	52.8

Results

The validity of the results is dependent on a knowledge of the current efficiency of oxide formation, i.e., the fraction of the total current which is ionic. Preliminary work with the glycol-borate electrolyte showed a linear rise in voltage with time to slightly higher than 150 v when a constant current of 10^{-3} amp/cm² was maintained. Therefore, an end voltage of 150 v was chosen as a convenient value for our formations. Formations were made at a constant current density with a silver coulometer in series with the cell, the voltage being adjusted manually during formation. At the end voltage, the voltage was held constant, and the current was allowed to decrease to the desired value. Therefore, in each formation 0.299 coulomb/cm² (see Table I) was passed at 10^{-3} amp/cm², the remainder of the charge being passed at a constantly decreasing current density. The measured weight gain of the anode was compared to that calculated from the amount of charge passed, assuming that the production of Al_2O_3 was the only anodic process. In addition, the oxide was removed from the foil, and its weight was also compared to the calculated value. Table I shows that the agreement between the two values is generally within 1%, which is the estimated error of the experiments.

Heating of the oxide to 600°C resulted in no change in weight, indicating that the film contained neither water nor glycol, and the presence of borates could not be detected by chemical analysis. Furthermore, there was no apparent oxygen evolution at any time during formation, nor did the electrolyte contain Al after formation. On the basis of these analyses, we have concluded that the anodic product was solely Al_2O_3 and that the conditions of formation led to 100% current efficiency of oxide formation.

Figure 1 is a plot of log i vs. $1/W$ (the reciprocal of the weight of oxide per unit area), where each point represents the average value of at least three separate measurements. The data at the higher current densities were corrected for iR losses in the electrolyte so that each point corresponds to an applied anodic voltage of 150 v. The slope of the line is $150\beta\,\rho/2.303$ where ρ is the density of the anodic oxide. Four separate density measurements resulted in an average value for ρ of 3.17 ± 0.03 g/cm³. β is then calculated to be 4.8×10^{-6} cm/v. A similar plot of log i vs. capacitance per unit area measured at 120 cps is given in Fig. 2. The slope in this case is equal to $150\beta/2.04 \times 10^{-13}\epsilon$. From the thickness measurements, ϵ is calculated to be 8.4 ± 0.2, and β from this plot has a value of 5.4×10^{-6} cm/v. Extrapolation of the two plots permits an estimation of α, giving 10^{-22} and 10^{-24} amp/cm² in Fig. 1 and 2, respectively. Charlesby (8) reported $\beta = 3 \times 10^{-6}$ and $\alpha = 10^{-18}$, while Nagase (9), who obtained his values from rate measurements, is in better agreement with our figures, giving 4.3×10^{-6} and 10^{-20} for β and α.

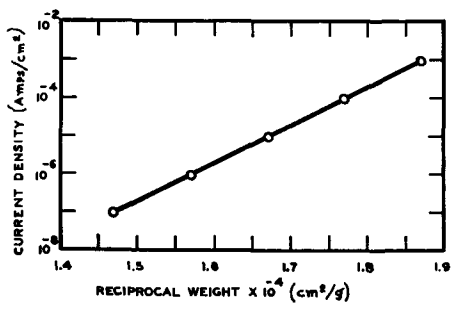

Fig. 1. Current density vs. reciprocal weight of aluminum oxide films maintained at a constant potential of 150 v at 25°C.

Table II shows the thickness, s, calculated for some of the points and compared with those obtained from interferometric measurements, the latter being reliable to about 30Å. Satisfactory agreement was obtained between the two methods.

The increase in oxide thickness which is possible at constant voltage explains the variation in the reported values for anodic aluminum oxide. In the range of currents discussed here, a 150-v film may vary in thickness from 11.3 to 14.4 Å/v. Clearly, then, both voltage and ionic current density must be defined if the value of thickness at some specified voltage is to be significant.

In a recent paper, Winkel, Pistorius, and van Geel (13) suggest a modification of the existing theory for anodic growth. Support for their view is given by their observation that the constant β apparently varies with field. However, the aqueous electrolyte used in their experiments required them to correct the total current for the electronic component, and large corrections of this nature lead to an appreciable degree of uncertainty in the final results. We, on the other hand, have measured these rates in our electrolyte of high current efficiency and plotted in the same manner as Winkel, *et al.*, as shown in Fig. 3. A straight line is produced as predicted by theory. From the slope β may again be calculated and gives the value 4.4×10^{-6}, in good

Table II. Comparison of film thickness at constant voltage as determined by weight and optical measurements

Current density, amp/cm²	Film thickness, cm × 10⁵	
	Weight measurement	Optical measurement
10^{-3}	1.68	1.72
10^{-5}	1.89	1.93
10^{-7}	2.15	2.14

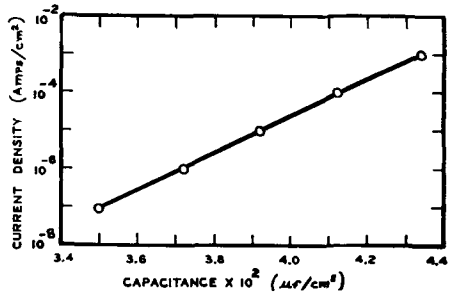

Fig. 2. Current density vs. 120 cps capacitance of aluminum oxide films maintained at a constant potential of 150 v at 25°C.

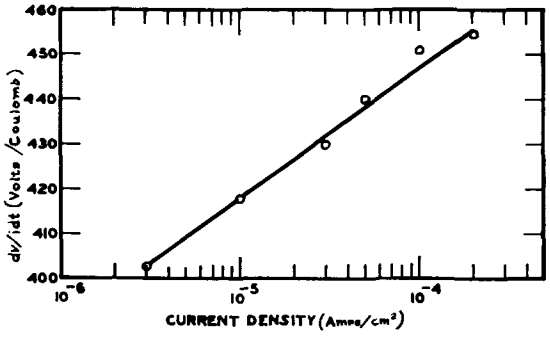

Fig. 3. Increase of voltage per unit charge as a function of the current density of formation at 25°C.

agreement with the values obtained from weight and capacitance measurements.

Rates at all current densities were measured in the voltage range of 120-150 v by first forming at 10^{-3} amp/cm² to 120 v and then reducing the current to the desired level. In this way all rates were measured under the same conditions of surface roughness since nearly the same thickness of oxide was present before the initial readings were taken.

All the work presented here is based on the assumption that even at the lowest current densities used we are dealing solely with ionic current. It may be argued that since the experiments which led to this conclusion were based on formations during which the major portion of the charge was passed at 10^{-3} amp/cm², an appreciable contribution by electronic current would have been unnoticed at the lower currents. If such were the case, however, we would not expect such a good fit to the plots over the whole range. Furthermore, the rate curve (Fig. 3) would then be expected to have the shape obtained by Winkel, *et al.*, rather than a straight line.

Acknowledgments

The authors wish to acknowledge the assistance of Mr. Stanley Szpak, who prepared the special electrodes for surface roughness measurements, and Mrs. Concetta Duval, who carried out the density determinations.

Manuscript received Jan. 19, 1959.
Any discussion of this paper will appear in a Discussion Section to be published in the June 1960 JOURNAL.

REFERENCES

1. K. Nagase, *Mem. Inst. Sci. Ind. Research, Osaka Univ.*, **10**, 66 (1953).
2. W. Ch. van Geel and B. J. J. Schelen, *Philips Research Repts.*, **12**, 240 (1957).
3. M. Hennig, *Z. Physik*, **144**, 296 (1956).
4. W. Walkenhorst, *Naturwissenschaften*, **34**, 373 (1947).
5. G. Hass, *J. Opt. Soc. Amer.*, **39**, 532 (1949).
6. R.C. Plumb, *This Journal*, **105**, 498 (1958).
7. N. F. Mott, *Trans. Faraday Soc.*, **43**, 429 (1947).
8. A. Charlesby, *Proc. Phys. Soc.*, **66B**, 317 (1953).
9. K. Nagase, *Mem. Inst. Sci. Ind. Research, Osaka Univ.*, **12**, 67 (1955).
10. J. E. Lewis and R. C. Plumb, *Intern. J. Appl. Radiation and Isotopes*, **1**, 33 (1956).
11. T. J. Nurse and F. Wormwell, *J. Appl. Chem. (London)*, **2**, 550 (1952).
12. K. Strohmaier, *Z. Naturforsch.*, **6a**, 508 (1951).
13. P. Winkel, C. A. Pistorius, and W. Ch. van Geel, *Philips Research Repts.*, **13**, 277 (1958).

Kinetics of the Dissolution of Copper in Oxygen-Containing Solutions of Various Chelating Agents

J. Halpern,[1] H. Milants,[2] and D. R. Wiles[3]

Department of Mining and Metallurgy, The University of British Columbia, Vancouver, British Columbia

ABSTRACT

The kinetics of the dissolution of copper in stirred oxygen-containing solutions of ethylenediamine and several amino acids have been examined and compared with those found earlier for ammonia. In each case, provided that the partial pressure of oxygen exceeds a critical value (below which its transport to the copper surface may be rate limiting), the rate was found to be zero-order in oxygen and first-order in the complexing agent. The rate-determining process is believed to be the chemical attack of the oxygen-covered copper surface by the complexing agent. At 25°, the rate constants for dissolution by ethylenediamine, glycinate, α-alaninate, and β-alaninate were found to be 2.3×10^2, 49, 59, and 11 mg Cu cm^{-2} hr^{-1} M^{-1}. These follow the same order as the stability constants of the corresponding cupric complexes. In each system there is also another reaction path, independent of the first, which involves the protonated species, i.e., the ethylenediaminium ion and the neutral amino acids. The corresponding rate constants are 5.1×10^2, 31, 36, and 3.5 mg Cu cm^{-2} hr^{-1} M^{-1}.

A kinetic study of the dissolution of copper in oxygen-containing aqueous solutions of ammonia and ammonium salts was described earlier (1, 2). It was shown that the reaction proceeded by two independent paths whose rate-determining steps are the chemical attack on the oxygen-covered copper surface by an NH_3 molecule and an NH_4^+ ion, respectively. Both rates are independent of the oxygen concentration above a critical value when the transport of oxygen to the surface is no longer rate-limiting. Under these conditions the kinetics are of the form

$$\text{Rate} = k_A[NH_3] + k_{AH}[NH_4^+] \qquad [1]$$

At lower oxygen partial pressures a different rate law, first-order in oxygen and independent of the concentrations of ammonia or ammonium salts, was observed; this was attributed to rate control by oxygen transport.

The present paper describes similar measurements using several other complex-forming reagents, notably the chelating agents ethylenediamine, glycine, α-alanine, and β-alanine. These were selected with a view to providing further insight into the role of complex formation in the mechanism of the dissolution process and to correlating the rate of dissolution with the structure and stability of the complexes formed.

Experimental

The apparatus and experimental procedure were similar to those employed earlier (1, 2) with the following minor variations: Agitation was effected by means of a turbine-type impeller whose blades, generally rotating at 770 rpm, swept a cylindrical volume of 8 cm diameter. The exposed surface (generally about 2 cm^2) of the Bakelite-mounted copper specimen was positioned in a vertical plane tangential to this cylindrical volume.

Most of the measurements were made using conductivity-grade (99.97%) copper; no difference in the rate of dissolution was noted when Johnson-Matthey high-purity (99.999%) copper was used instead. Different annealing pretreatments, which resulted in grain sizes ranging from 0.035 to 0.12 mm, were also without effect on the dissolution rate. Before each experiment the copper surface was etched lightly with an ammonia-ammonium persulfate solution, but this procedure also did not appear to be critical.

Ethylenediamine (99%) was obtained from Carbon and Carbide Chemicals Corp. Purification by fractional distillation did not affect the dissolution rate. Glycine, α-alanine, and β-alanine, of Reagent Grade, were obtained from Nutritional Biochemical Corp.

Dissolution rates were determined by analyzing the leaching solution periodically for copper using the carbamate colorimetric method (3). All experiments were performed at 25.0° ± 0.1°C. To avoid the complications due to salt effects found in the previous study (1), the total electrolyte concentration of all the solutions was adjusted (in most cases to 0.1M) with sodium perchlorate.

Results

The chelating agents used and their properties are listed in Table I. Typical rate plots for the various complexing agents are shown in Fig. 1. In all cases these were found to be linear, and the dissolution rates, corresponding to the slopes of the plots, were generally reproducible to about ±2%. It was established that the total dissolution rates were proportional to the copper surface area and independent of the solution volume (generally 2 liters). No cuprous species could be detected in the solutions, the dis-

[1] Department of Chemistry, University of British Columbia.
[2] Present address: Union Minière du Haut Katanga, Jadotville, Belgian Congo.
[3] Present address: Department of Chemistry, Carleton University, Ottawa, Ont.

Table I. Properties of complexing agents and first order rate constants for the dissolution of copper at 25°C

Complexing agent	A or A⁻	Formula	pK* HA⁺	pK* H_2A^{++}	Stability constant of Cu^{++} complex* log K_1	Stability constant of Cu^{++} complex* log K_2	Rate constant (mg cm^{-2} hr^{-1} M^{-1}) k_A	Rate constant (mg cm^{-2} hr^{-1} M^{-1}) k_{AH}
Ammonia	A	NH_3	9.26	—	4.3	3.6	84†	1550†
Ethylenediamine	A	$NH_2CH_2CH_2NH_2$	10.2	7.47	10.7	9.3	2.3×10^2	5.1×10^2
Glycinate	A⁻	$NH_2CH_2COO^-$	9.78	2.35	8.4	6.9	49	31
α-Alaninate	A⁻	NH_2CHCOO^- (CH₃)	9.87	2.34	8.4	6.9	59	36
β-Alaninate	A⁻	$NH_2CH_2CH_2COO^-$	10.4	3.60	7.1	5.5	11	3.5

* From Ref. (4).
† From Ref. (1).

solved copper apparently being predominantly in the form of the tetracoordinated cupric chelate complex, e.g., $Cu(en)_2^{++}$, $Cu(gl)_2$, etc.

For each of the complexing agents, the dependence of the rate of dissolution on the concentration of the reagent and on the oxygen partial pressure (shown for ethylenediamine in Fig. 2) was found to conform qualitatively to the same pattern as observed previously for ammonia. This pattern is characterized by two distinct kinetic regions. At low oxygen pressures, the rate is first order in oxygen and independent of the concentration of the complexing agent. In the case of ammonia, evidence was found that the rate in this region is determined by transport of oxygen to the copper surface. While this interpretation also may apply to the present systems, it appears superficially at variance with the observations that the rate for ethylenediamine in this region (as well as in the region of high oxygen pressure) was unaffected by varying the stirring rate from 550 to 810 rpm and that the rates for solutions of different complexing agents (e.g., ethylenediamine and glycine) differed by as much as 25%. This point was not investigated further, and all the kinetic results to be considered here refer to the region of higher oxygen pressure, where the rate was found to be zero-order in oxygen and first-order in the complexing agent. In this region the rate-determining step is obviously chemical in nature.

In the ethylenediamine system, kinetic measurements extended over ethylenediamine (en) concentrations of 0.05 to 0.5M, ethylenediaminium (enH^+) perchlorate concentrations of 0.00 to 0.03M and oxygen partial pressures of 0 to 7.5 atm. The results are summarized in Table II and Fig. 2 to 4 and, in the high oxygen pressure region, conform to a rate-law analogous to Eq. [1], i.e.,

$$\text{Rate} = k_A[\text{en}] + k_{AH}[\text{enH}^+] \qquad [2]$$

Values of k_A and k_{AH}, given in Table I, were computed from the data in Table II.

Addition of sodium hydroxide to a solution of ethylenediamine resulted in a slight decrease in the rate of dissolution (Table II). This is attributed to passivation of the copper surface by oxide or hydroxide films.

In the glycine, α-alanine, and β-alanine systems, kinetic measurements were made at concentrations ranging from 0.0 to 0.3M each of the free amino acid (AH) and of the corresponding anion (A^-). The results are summarized in Table II. Both

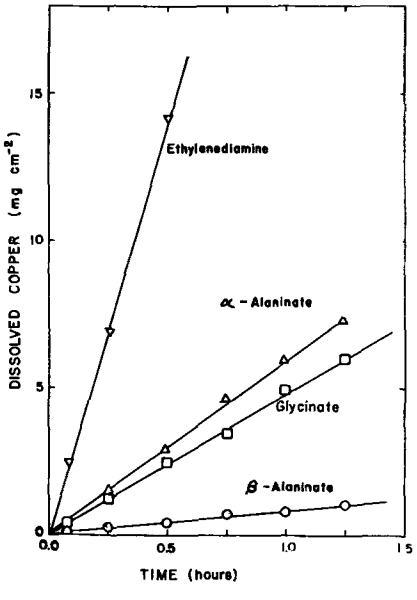

Fig. 1. Typical rate plots for the dissolution of copper in 0.1M solutions of various complexing agents at 25°, 6.5 atm O_2.

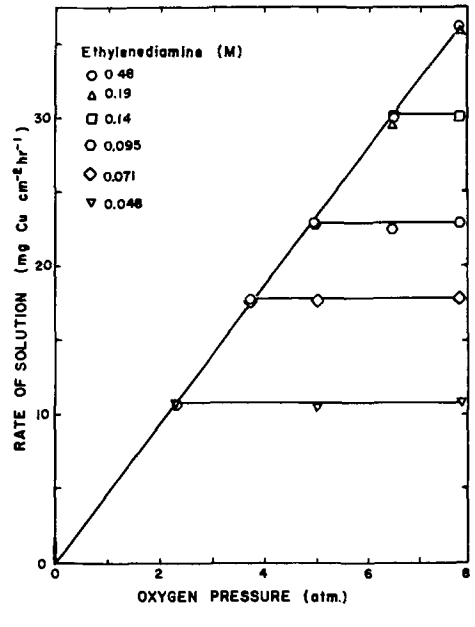

Fig. 2. Dependence of the dissolution rate on the ethylenediamine concentration and the oxygen partial pressure.

Table II. Summary of kinetic data (25°)*

Chelating agent	Concentration (M) A†	AH^+†	AH_2^{++}†	NaOH (M)	pH	Ionic strength‡	Rate of solution (mg Cu $cm^{-2}hr^{-1}$)
Ethylenediamine	0.045	0.002	0.00	0.00	11.5	0.1	11.7
	0.068	0.003	0.00	0.00	11.5	0.1	17.2
	0.091	0.004	0.00	0.00	11.6	0.1	22.8
	0.138	0.005	0.00	0.00	11.7	0.1	31.3
	0.0475	0.010	0.00	0.00	10.9	0.1	17.0
	0.0475	0.020	0.00	0.00	10.6	0.1	22.0
	0.0475	0.030	0.00	0.00	10.4	0.1	27.0
	0.0950	0.00	0.00	0.01	11.8	0.1	20.0
	0.0950	0.00	0.00	0.02	12.2	0.1	19.4
	0.0950	0.00	0.00	0.03	12.4	0.1	18.5
Glycinate	0.097	0.003	0.00	0.00	11.3	0.1	4.8
	0.146	0.004	0.00	0.00	11.3	0.2	9.8
	0.194	0.006	0.00	0.00	11.3	0.3	14.8
	0.00	0.10	0.00	0.00	6.0	0.1	3.2
	0.00	0.15	0.00	0.00	6.0	0.1	4.6
	0.00	0.20	0.00	0.00	6.0	0.1	6.2
	0.00	0.10	0.01	0.00	4.2	0.1	0.2
	0.00	0.10	0.02	0.00	2.7	0.1	0.0
α-alaninate	0.096	0.0037	0.00	0.00	11.3	0.1	5.9
	0.193	0.0074	0.00	0.00	11.3	0.2	11.7
	0.29	0.011	0.00	0.00	11.3	0.3	17.3
	0.00	0.10	0.00	0.00	6.3	0.1	3.6
	0.00	0.20	0.00	0.00	6.3	0.2	7.5
	0.00	0.30	0.00	0.00	6.3	0.3	10.8
	0.00	0.10	0.01	0.00	4.2	0.1	0.2
	0.00	0.10	0.02	0.00	2.7	0.1	0.0
β-alaninate	0.094	0.006	0.00	0.00	11.6	0.1	1.0
	0.187	0.013	0.00	0.00	11.6	0.2	2.2
	0.281	0.019	0.00	0.00	11.6	0.3	3.6
	0.00	0.10	0.00	0.00	6.6	0.1	0.34
	0.00	0.20	0.00	0.00	6.6	0.1	0.69
	0.00	0.30	0.00	0.00	6.6	0.1	1.11
	0.00	0.10	0.01	0.00	4.7	0.1	0.00

* O_2 partial pressure = 7.8 atm for ethylenediamine and 6.5 atm for the other systems.
† $[A^-]$, [AH], and $[AH_2^+]$ in the case of the amino acids.
‡ Adjusted with $NaClO_4$.

species are apparently active in promoting dissolution and the oxygen-independent rate law in each system was found to be of the form

$$\text{Rate} = k_A[A^-] + k_{AH}[AH] \qquad [3]$$

Values of k_A and k_{AH}, computed from these data, are listed in Table I. By analogy with the interpretations accorded to the ammonia and ethylenediamine system it may be concluded that these are the rate constants for the independent attack of the anion and acid species, respectively, on the oxygen-covered copper surface, either process leading to the dissolution of a cupric ion.

The neutral amino acids are present in solution in two forms (5), the zwitterion (e.g., $^+NH_3CH_2COO^-$) and the molecular form (e.g., NH_2CH_2COOH). Since the ratio of the concentrations of the two forms is constant for each acid, the kinetic data provide no information about the relative contributions of the two species to the rate. However, in view of the predominance of the zwitterion form, it is reasonable to conclude that k_{AH} refers essentially to the reaction of this species.

No passivation effect was evident with solutions containing appreciable concentrations of the free amino acid and/or the anion. However, the addition of an excess of H^+, resulting in formation of some protonated amino acid, H_2A^+, was found to inhibit dissolution completely. This is attributed to passivation of the copper surface by an oxide film due to suppression of complex formation in the solution

$$CuA_2 + 2H_2A^+ \rightleftharpoons Cu^{++} + 4AH \qquad [4]$$

[Similarly it was found (2) that copper does not dissolve in a solution containing NH_4^+ if the free NH_3 concentration is very low, despite the fact that the rate constant for the reaction of NH_4^+ is higher than for NH_3 when both are present.] Because of this restriction, measurements could be made only in solutions in which the concentration of the pro-

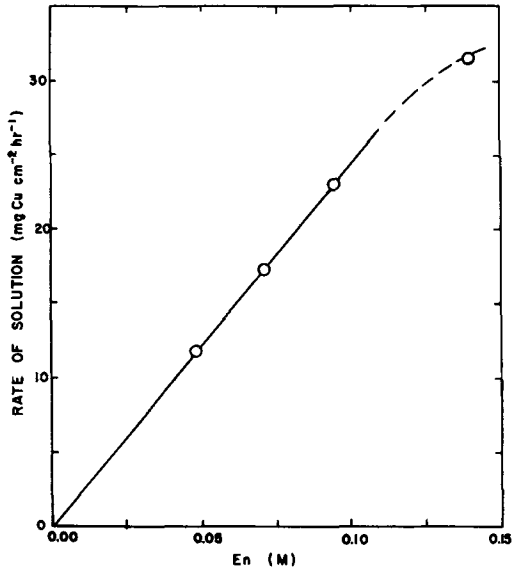

Fig. 3. Dependence of the rate at 7.8 atm O_2 on the ethylenediamine concentration.

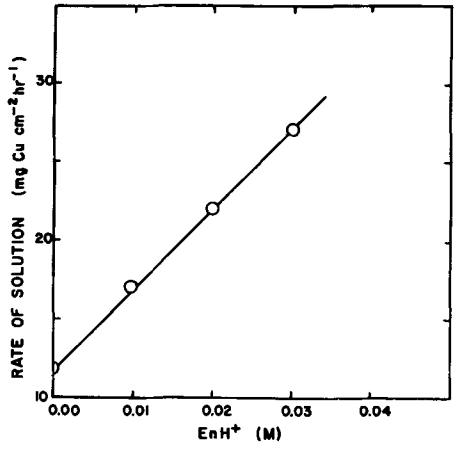

Fig. 4. Dependence of the rate at 7.8 atm O_2 on the ethylenediaminium perchlorate concentration. Solutions also contain 0.048M free *en*. Ionic strength held constant at 0.1M with sodium perchlorate.

tonated amino acid (e.g., $^+NH_3CH_2COOH$) was very low and the rate constant for the reaction of this species could not be determined.

Under the conditions employed in these studies (25°, 6.5 atm O_2) the dissolution of copper in solutions of acetic acid and/or sodium acetate was found to be very slow. This is probably also due to passivation of the copper since the *p*H of these solutions is relatively high and the complexing of Cu^{++} weak.

Conclusions

The same type of mechanism as proposed earlier for the dissolution of copper by ammonia also appears to be applicable to the present systems. This mechanism involves the following sequence of steps

$$\text{(i)}\quad Cu + \tfrac{1}{2}O_2 \xrightarrow{\text{fast}} Cu\ldots O$$

$$\text{(ii)}\quad Cu\ldots O + NH_2R \xrightarrow{\text{slow}} \left[\begin{array}{c} NH_2R \\ \diagup \\ {}^{++}Cu \\ \diagdown \\ O^{=} \end{array}\right]$$

$$\xrightarrow[\text{fast}]{HOH} Cu(NH_2R)^{++} + 2\,OH^- \qquad [5]$$

or

$$Cu\ldots O + {}^+NH_3R \xrightarrow[\text{slow}]{} \left[\begin{array}{c} NH_2R \\ \diagup \\ {}^{++}Cu \quad H^+ \\ \diagdown \\ O^{=} \end{array}\right]^{\cdot}$$

$$\xrightarrow{\text{fast}} Cu(NH_2R)^{++} + OH^- \qquad [6]$$

Examination of the data in Table I reveals the following points of interest:

1. The reactivities of the amines (NH_3 and en) in dissolving copper appear to be significantly higher than those of the amino acids.

2. The higher reactivities of ethylenediamine relative to ammonia, and of α-alanine relative to β-alanine suggest the influence of a chelate effect in the rate-determining step. This implies that both coordinating groups of the chelating agent interact with the metal surface in this step.

3. The rate constants for the four chelating agents follow approximately the same order as the stability constants of the corresponding cupric complexes.

4. In the case of both ammonia and ethylenediamine the protonated species is more reactive than the neutral base ($k_{AH^+} > k_A$). This has previously (1) been attributed to stabilization of the activated complex in the dissolution process by interaction between the extra proton and the incipient oxide ion (Eq. [6]). However, this explanation does not accommodate the present observation that the reactivities of the amino acids are enhanced by *removal* of a proton (i.e., $k_{A^-} > k_{AH}$). It may be of significance that in both cases the higher reactivity is associated with the ionic species.

5. A comparison of the rates of reaction of α- and β-alanine fails to reveal any indication that the presence of a methyl group on the α- position of the amino acid interferes sterically with the reaction.

6. Somewhat unexpectedly, the ratio $k_{NH_4^+}/k_{NH_3}$ (18.5) is much greater than k_{enH^+}/k_{en} (2.1). A possible explanation of this is that dissolution by ethylenediamine involves concerted interaction with the surface of both amine groups and hence is assisted only slightly by protonation of one of the groups.

Acknowledgment

The authors are grateful to the National Research Council (Canada) for financial support.

Manuscript received Dec. 9, 1958.

Any discussion of this paper will appear in a Discussion Section to be published in the June 1960 JOURNAL.

REFERENCES

1. J. Halpern, *This Journal*, **100**, 421 (1953).
2. J. I. Fisher and J. Halpern, *ibid.*, **103**, 282 (1956).
3. E. B. Sandell, "Colorimetric Determination of Traces of Metals," p. 204, Interscience Publishers, Inc., New York (1950).
4. "Stability Constants," Special Publications Nos. 6 and 7. The Chemical Society, London, 1957, 1958.
5. N. Bjerrum, *Z. phys. Chem.*, **104**, 149 (1923).

Electrodeposition of Amorphous Selenium

A. K. Graham, H. L. Pinkerton, and H. J. Boyd

Graham, Savage & Associates, Inc., Jenkintown, Pennsylvania

ABSTRACT

Amorphous selenium coatings have been electroplated in thicknesses up to 30 μ (1.2 mils) on bright nickel cathodes (and thicker coatings can be prepared). Data are given for studies leading to the selection of the optimum bath and operating conditions for the formation of reproducible, uniform, and adherent deposits. It is shown that the plating baths employed and the amorphous deposits obtained are extremely sensitive to a variety of conditions, thus emphasizing the need for further study of the electrodeposition of selenium in the amorphous form.

During recent years an electrophotographic process called xerography (1) has been developed. It is used for the rapid reproduction of photographs. As a photographic process, xerography employs a reusable plate consisting of a thin layer of a photoconductive material, having a high dark resistivity, on an electrically conductive base. The plate is sensitized by electrostatic charging immediately before use and an electrical image formed by exposure of the plate to a light image. The electrical image then is transformed to a powder image by subjecting the plate to an electrically charged powder dispersed in air. Prints are made by transferring the powder image to paper or other material suitable for handling or use.

The photographic plates in use today are composed of a 50 μ (2.0 mils) thick layer of amorphous selenium on an aluminum base. The selenium layers are deposited on the basis metal by a vacuum evaporation process.

This paper presents the results of a research investigation undertaken to produce by electrodeposition amorphous selenium films having the required properties for use as electrophotographic plates.

Both electronegative and electropositive ions of selenium can exist together in alkaline solutions. Crystalline allotropes of selenium include two monoclinic forms and one hexagonal form. The monoclinic variety consists of 8-membered ring molecules (2), and the hexagonal form is built up from chain-molecule spirals (3). The amorphous and monoclinic forms of selenium are nonconductors and are dark red to black and red, respectively. The hexagonal modification is a semiconductor and is generally gray in color.

The semiconducting hexagonal form of selenium has reportedly been electrodeposited both cathodically (4) and anodically (5). However, there is little information concerning the formation of uniform, dense, and adherent amorphous selenium electrodeposits. Von Hippel and Bloom (4) in their work on the electrodeposition of metallic selenium stated that under certain conditions nonconductive selenium was formed which interrupted current flow. They also reported that the electrodeposition of amorphous selenium practically ceases in the dark but could be continued under strong illumination until a thickness of about 0.12 μ was reached. Sella (6) reported obtaining, by electrodeposition, the allotropic forms of selenium by varying the deposition temperature with low temperature (0° - 62°C), apparently producing the amorphous form of the element.

The baths previously reported for electrodepositing selenium ranged from alkaline (for anodic deposition) to strongly acid and, except for anodic deposition, were solutions containing Se IV. It appears from polarographic evidence (7) that Se VI is not reduced in acid media.

Experimental

Plating solutions were prepared in distilled water, using selenium dioxide of high purity.[1] When a wetting agent was used, it was important to follow the sequence of adding the agent to the water first, and then adding the desired amount of selenium dioxide in order to obtain satisfactory reproducibility. The solution was digested 30 min at 80°C, cooled, and filtered through a cellulose filter aid.

The range of spectrographic analyses of three lots of selenium dioxide is shown in Table I.

Except in the preliminary work, the plating so-

[1] Obtained from A. D. Mackay Inc., New York, N.Y.

Table I. Analysis of SeO_2
Range of three lots, %

Cu	-0.005	-0.01
Pb	-0.02	-0.05
Fe	-0.01	-0.1
Si	-0.005	-0.01
Al	-nd*	-0.01
Mg	-0.01	-0.05
Cr	-nd	-0.001
Ca	-0.01	-0.03
Bi	-0.0001	
As	-0.001	
Ag	-0.0005	-0.005
B	-0.0001	-0.0005
Hg	-nd	-0.001
Te	-0.2	
Sb	-nd	-0.001

Sought but not detected—Ni, Mn, Sn, Au, Ga, Ti, V, Mo, Co, Zn.
* Not detected.

lutions were contained in a Lucite Haring cell provided with a ceramic diaphragm. The anolyte was placed in the smaller section; for acid plating baths, 10% (vol) H_2SO_4 was used with lead anodes; stainless steel anodes were used in NaOH solution of bath strength when alkaline plating baths were being studied. Most of the work was done in a cell 17.7 x 10 x 11 cm deep, although a smaller, geometrically similar cell also was used.

The plating solutions were circulated through Tygon tubing by means of a Sigmamotor pump, providing mild agitation of the catholyte. Temperature control was obtained by immersing a considerable length of the Tygon tubing in a constant temperature bath. Storage batteries were used as the current source to provide direct current with zero ripple.

Provision was made for varying the degree of illumination of the cathode from very strong to complete darkness. The very strong illumination was obtained by focusing three 500-w photospot lamps on the cathode surface from a distance of 12½ in. Under these conditions, considerable cooling was required to maintain bath temperatures, especially those below room temperature.

Temperatures from 5° to 40°C were investigated; no higher temperature was studied, since it was deemed inadvisable to approach the transformation temperature amorphous → crystalline too closely.

Exploratory work was done on a beaker scale with a Pt cathode and with the anodes in porous cups. Deposits were made with normal illumination and no agitation at room temperature. In one series, the solution contained 211 g/l SeO_2 and the *p*H, originally about 0.8, was raised successively to 1.5, 2.6, 7.8, 12.8, and 13.7 with NaOH. At the two higher *p*H values, little or no deposit was obtained. From the other baths, at moderate current densities of 0.1 to 0.2 amp/dm², uniform, adherent, glossy deposits were obtained ranging from glossy slate or black below *p*H 3 to dark red above this *p*H. In another series, 350 g/l SeO_2 was dissolved in water or in 1, 2, or 5*N* H_2SO_4. Deposits made in the same way showed the solution without added acid to be the most promising. Further work was confined to the *p*H region of 0.8 to 8.0.

Solutions of selenious acid attack a great many metals, including lead, silver, and gold. Platinum is not attacked, and the attack on rhodium or chromium, if any, is slow. The rate of attack diminishes, naturally, as the *p*H is raised. In all the work reported here, the cathode was connected to the current source before immersion in the plating solution to minimize the effect of the chemical attack.

Using the two baths at the extremes of the selected *p*H range, the limiting current densities on platinum were found to be as shown in Table II. Above these current densities, the deposits became redder, pulverulent, and nonadherent.

Alkaline bath.—Because of its higher limiting current density and the reduced attack on metals other than platinum, the alkaline bath of Table II was chosen initially for evaluation in the Haring cell. The temperature was varied from 5° to 25°C, the current density from 0.05 to 0.25 amp/dm², and strong illumination of the cathode was used. The character of the deposit, as judged by appearance, was extremely sensitive to the cathode material used, which included buffed sheet copper, and electrodeposits thereon of lead, Watts nickel, bright nickel, bright chromium, black chromium, rhodium, and gold. Generally speaking, the limiting current density was lower (about 0.4 amp/dm²) on these cathodes than on platinum. The deposits were redder, with a tendency to be pulverulent, and on copper a black, nonadherent deposit was obtained. With the sole exception of the deposit on platinum, which was amorphous, all deposits from this bath were crystalline, by x-ray diffraction.[2] The addition of wetting agent, the addition of citrate ion, and/or the substitution of ammonium ion for sodium were without effect. No further work was done with alkaline baths.

Table II. Preliminary work with selenium deposits on Pt cathodes for 15 min at 25°C with normal illumination

	Bath	Composition	*p*H	Limiting C. D., amp/dm²	Deposit description below limiting C. D.
A	Acid	350 g/l SeO_2	0.7-0.9	0.4	Amorphous,* uniform dark red to black
B	Alkaline	211 g/l SeO_2 in 2.6*N* NaOH	7.5-8.0	0.85	Amorphous,* uniform, red

* By x-ray diffraction.
Note: The deposits tended to be pulverulent, the more so at the higher current densities.

Acid bath.—From various modifications of the acid bath of Table II, a large number of deposits were obtained which were amorphous according to x-ray diffraction. These varied widely in appearance, and surprisingly, deposits up to 30 μ (1.2 mils) thick were obtained, with no indication that this was an upper limit. Spectrographic analysis of two such deposits showed contamination with copper, nickel, and lead, minor in one case and in major amounts in the other. Possibly because of such contamination, none of the amorphous deposits would retain an electrical charge, and were therefore unsuitable for xerographic purposes. The physical character of many such deposits, however, was excellent, being smooth, glossy black, and adherent. Because of this it is considered worth while to report on their preparation.

The best deposits were obtained from a solution of 350 g/l SeO_2 in distilled water, containing 1 g/l Duponol ME (sodium lauryl sulfate) prepared as described above. The cathode was plated with an undercoat of bright nickel about 0.25 mil thick and was introduced into the bath with the current on, at a current density of 0.1 to 0.4 amp/dm². Room temperature up to 40°C was found to be the best range. Moderate to strong illumination favored the formation of glossy black deposits; the deposits were less glossy and grayer in normal illumination or in total darkness.

[2] Since the authors were interested only in amorphous selenium, the existence of any crystalline diffraction pattern at all amounted to a rejection. No attempt was made to characterize the actual structure of the crystalline deposits from the diffraction data.

Results

At acidities varying between 5*N* H_2SO_4 up to *p*H 1.5, over temperatures from 5° to 40°C, with illumination varying from total darkness to very strong white light, amorphous deposits were obtained, varying only in appearance, on bright nickel-plated cathodes from baths containing wetting agent from 0.01 to 10 g/l. From baths without wetting agent, deposits were sometimes amorphous and sometimes crystalline, for causes not clearly established.

None of these amorphous deposits would retain an electrical charge. Seeking the reason for this, two of the best-looking amorphous deposits and two samples of vacuum-deposited selenium suitable for xerography were sent out for spectrographic analysis, with rather startling results:

	Spec. A	Spec. B	Vacuum-deposited
Ni	0.5	>10.0	nd*
Cu	0.5	>10.0	0.005-0.5
Pb	0.01	1-10	nd-0.0002
Fe	0.001	nd*	0.005-0.01
Ag	0.02	<0.01	nd-0.01

Notes:

1. Specimen B was analyzed by a different laboratory, and the results are believed to be order-of-magnitude only, rather than quantitive.
2. Specimen A was produced in a bath without wetting agent at *p*H 0.7; Specimen B was produced under similar conditions of temperature, current density, and illumination, but the bath contained wetting agent.
* nd, not detected.

An attempt was made to obtain purer deposits by purifying the bath before use and by taking extra precautions to avoid accidental contamination of the bath. Graphite anodes were substituted for the lead anodes previously used; the porous diaphragm of the cell was replaced by a fresh one, and all metallic connections close to the bath were coated heavily with stop-off lacquer, leaving the face of the nickel cathode as the only exposed metal. The freshly prepared bath was carefully neutralized with ammonium hydroxide. The white precipitate which was obtained was filtered off and the *p*H was readjusted to 0.8 with H_2SO_4. Another portion of fresh bath was passed through a bed of Amberlite IR-120,[3] a strong acid cation exchange resin. Baths with and without wetting agents were treated thus. After plates were prepared under conditions presumed to be optimum, the purified baths were purposely contaminated with 10 mg/l each of Cu and Ni and 30 mg/l of Pb as soluble salts, and further plates were made. Plates also were made from a freshly prepared control bath (i.e., untreated) with and without additions of contaminating metals. Generally speaking, the appearance of the deposits from purified baths was less satisfactory than from the control; those from the contaminated baths were slightly improved. Time was not available for x-ray or spectrographic analyses, but retention-of-charge tests showed some very weak ability to hold a charge in about half the plates, but in an entirely haphazard and inconsistent manner from which no conclusions could be drawn.

[3] Rohm & Haas Co. analytical grade.

Effect of substrate.—It has already been observed that from the alkaline bath deposits on platinum were amorphous, but on all the other basis metals tried, they were crystalline. Except on copper, the deposits were dense, uniform, and dark red to reddish black. Copper was so reactive that good deposits could not be obtained.

From the acid bath, deposits on lead and dull nickel were smooth and black; glossy black on bright nickel, but orange-red and pulverulent over chromium and bright nickel that had been passivated by a dichromate dip. All these deposits were amorphous. Black deposits were obtained on platinum, which were amorphous when prepared at room temperature, but crystalline when prepared from the bath at 5°C.

Defective Deposits.—All the remarks above apply to deposits which were not visibly defective. Especially in the early work, good deposits were difficult to obtain reproducibly. During the long plating runs necessary to obtain the thicker deposits, a defect frequently occurred which at the onset appeared like pitting in nickel but as plating progressed, these pits erupted into large crater-like areas of powdery red selenium. These areas invariably gave x-ray evidence of crystallinity, although the good black areas remained amorphous. It was surmised that hydrogen evolution was responsible for the pitting and likewise for the chemical reduction of selenious acid to the metal. Addition of the wetting agent improved the situation and it was found that, if the fresh bath was made up in the manner which has been described, good deposits could be obtained reproducibly until the bath had been operated for no more than about 6 amp-hr/l, when the defect reappeared. All attempts to determine the cause and cure for this behavior were futile. There had been no measurable loss of wetting agent, and depletion of the selenium content of the bath was insignificantly small. During plating, a certain amount of red selenium invariably formed in the bath; when no wetting agent was present, this could be removed by filtration, but in the presence of wetting agent some of it must have been in colloidal form, since even after heavy carbon treatment and filtration through filter aid, the bath had a red tinge. This treatment, followed by replacement of the wetting agent, also failed to restore the bath's ability to produce good plates. Considering what was later learned of the presence of impurities in the deposits, it is thought possible that the depletion by deposition of some of these impurities from the bath may have been responsible. The results of the later attempts to purify the bath in part support this explanation, although replacement of the three major impurities did not again cause good plates to be produced. Time did not permit a fuller exploration of this problem.

Summary

1. Although the production of relatively thick amorphous selenium electrodeposits with photosensitive retention-of-charge properties was not achieved, thick, sound, amorphous deposits were obtained from a bath containing 350 g/l SeO_2 and

wetting agent at current densities of 0.05 to 0.2 amp/dm^2 and temperatures of 20°-40°C.

2. Spectrographic analysis of two of the best-looking amorphous deposits showed metallic contamination, in one case serious, but relatively minor in the other. It was not determined whether this contamination occurred in all cases.

3. A serious drawback was the short life of the bath before defective deposits were obtained. More work needs to be done to discover the cause and cure for this behavior.

4. Equally sound crystalline deposits were obtained from a bath containing 211 g/l SeO_2 and wetting agent in 2.6*N* NaOH (8.0 pH) under similar conditions, but this area was not as extensively investigated.

5. Illumination varying from zero to very strong had no very profound effect.

6. The nature of the cathode material exerts a profound influence on the appearance and structure of the deposits. Bright nickel plating was the best of the substrates examined, which also included lead, silver, gold, rhodium, copper, dull nickel, bright chromium, and black chromium electrodeposits and sheet platinum.

Acknowledgment

The authors wish to express their appreciation to Dr. Harold J. Read, Pennsylvania State University, University Park, Pa., under whose direction the x-ray diffraction and spectrographic analyses were performed, and personnel of the Fort Monmouth Laboratory for several spectrographic determinations.

Manuscript received Oct. 20, 1958. Project carried out under Contract DA-36-039-SC-71228 with U. S. Army Signal Corps, Fort Monmouth, N. J.

Any discussion of this paper will appear in a Discussion Section to be published in the June 1960 JOURNAL.

REFERENCES

1. R. M. Schaffert and C. D. Oughton, *J. Opt. Soc. Am.*, **38**, 991 (1948).
2. P. H. Keck, *ibid.*, **41**, 53 (1951).
3. A. J. Bradley, *Phil. Mag.*, **48**, 447 (1924).
4. A. von Hippel and M. C. Bloom, *J. Chem. Phys.*, **18**, 1243 (1950).
5. M. C. Bloom, U. S. Pat. 2,414,438, Jan. 21, 1947.
6. G. Sella, *Ricerca sci.*, **10**, 1143 (1939).
7. J. J. Lingane and L. W. Niedrach, *J. Am. Chem. Soc.*, **71**, 196 (1949).

Electroclad Aluminum on Uranium

John G. Beach and Charles L. Faust

Battelle Memorial Institute, Columbus, Ohio

ABSTRACT

Electroplating of aluminum was studied at Battelle in 1953-55 as an alternative method for aluminum cladding of uranium fuel elements. Uranium electroclad with 12 mils of aluminum over a 0.5-mil nickel or nickel-plus-copper electroplate resisted corrosion for more than 100 hr in boiling water. Hot pressing the electroclad composite improved the corrosion resistance. Many of the results obtained with aluminum electrocladdings paralleled those obtained with wrought aluminum claddings on uranium.

One method of cladding uranium fuel elements with wrought aluminum involves an intermediate braze layer of aluminum-12.5% silicon alloy (AlSi) or a nickel plate. The purpose of the intermediate layer is to aid bonding, to prevent rapid interdiffusion, and/or to provide a secondary barrier to rapid corrosion by hot water in case of penetration of the aluminum cladding. However, during dip brazing excessive solution of the aluminum cladding in the molten AlSi and selective penetration of the AlSi into the cladding may result if the temperature and time of AlSi dip brazing are not carefully controlled, and porosity of the AlSi brazing layer and unbonded area can also result in an inferior cladding.

This research was undertaken at Battelle to evaluate the possibilities of electrocladding uranium with aluminum. The electrodeposition of aluminum had been developed to the point where commercial applications were technically feasible, but electrocladding of reactor materials had not been explored. New techniques for preparing metal surfaces to be plated with adherent aluminum were needed. The principal characteristics of the electrocladding investigated were the diffusion and the corrosion protection afforded by aluminum plated directly on uranium and also over intermediate coatings plated on uranium. The studies were useful in showing the role of barrier-metal electroplates in preventing deleterious diffusion of uranium with the aluminum and the importance of good bonds between the barrier metal, the uranium, and the aluminum.

Selection of an Aluminum Plating Process

Two types of aluminum electroplating baths were available: fused salt (1) and organic. In this work, the need for deposits thicker than 10 mils (0.010 in.) obviated more than a few cursory tests with fused-salt baths. Two organic-type baths, the ethyl pyridinium bromide bath and the hydride bath, were investigated.

The ethyl pyridinium bromide-aluminum chloride-toluene bath was discovered by Weir and Hurley (2, 3, 4) and developed by Safranek, Schick-

ner, and Faust (5, 6). The following plating bath and conditions are recommended: *bath composition*: Ethyl pyridinium bromide-aluminum chloride fusion product, 32%; toluene (sp gr 0.866), 67%; methyl t-butyl ether, 1%; *plating conditions*: temperature, 86° ± 2°F; current density, 10-20 amp/ft^2 (superimposed a.c.); agitation nitrogen diffuser.

The lithium hydride-aluminum chloride-ethyl ether bath (composition and operating conditions are given later) was discovered by Couch and Brenner (7-9). The hydride bath is relatively easy to prepare. The ether content makes the bath flammable and safety precautions must be followed rigorously. Although explosions with systems containing lithium hydride and ether have been reported (10, 11), the presence of aluminum chloride tends to suppress the volatility of the ether and thus reduces the fire hazard.

Both nonaqueous organic processes produce smooth, dense, mat-type deposits, but electroformed foils, prepared for this work from the hydride bath, were more resistant to boiling water than those made in the ethyl pyridinium bromide bath. After 8 days' exposure to boiling distilled water, 2S aluminum foils and foils deposited in the hydride bath gained about 0.4 mg/cm^2 in weight. The absence of appreciable lithium in the hydride-bath deposit, in view of the high lithium content of the bath and the low weight change, suggests little or no occlusion of the bath constituents in the electrodeposited aluminum. On the other hand, foils deposited in the ethyl pyridinium bromide bath gained 2.0 mg/cm^2 in weight after exposure to distilled water. This greater weight gain is attributed to the hydration of occluded organic matter. Table I shows the results of spectrographic analyses of the aluminum deposits from the two organic plating baths. The aluminum produced in the hydride bath was of somewhat higher purity than that produced in the other bath.

Based on the ease of plating-bath preparation and operation and the higher purity and greater corrosion resistance of the electrodeposited aluminum, the hydride bath was selected for these studies of electrocladding aluminum on uranium.

Table I. Per cent of impurities in aluminum deposits

Contaminant	Ethyl pyridinium bromide bath	Hydride bath
Antimony	*	<0.01†
Arsenic	*	<0.01†
Calcium	*	0.03
Cobalt	*	<0.001†
Chromium	<0.005	0.001
Copper	0.005-0.05	*
Gallium	*	0.0005
Iron	0.05-0.10	0.008
Lead	0.005-0.05	0.001
Lithium	*	<0.005†
Magnesium	0.005-0.05	0.002
Manganese	*	0.001
Molybdenum	*	<0.005†
Nickel	*	0.001
Potassium	*	<0.1†
Silicon	0.05-0.10	0.001
Sodium	*	<0.01†
Tin	*	0.005
Titanium	*	0.003
Tungsten	*	<0.02†
Uranium	*	<0.05*
Zinc	*	0.01

* Not determined.
† Lower limit for this spectrographic analysis.

Adherent Plating of Aluminum on Various Metals

Good adhesion between the aluminum and the uranium is an important factor for satisfactory claddings. But, as shown later, the good as-plated adhesion of aluminum directly on uranium is degraded by diffusion. Thus, adherent plating of aluminum on metals other than uranium was investigated. Adherent plating of aluminum on wrought metals was done preparatory to electrocladding aluminum over intermediate coatings plated on the uranium.

Treatment of clean metal surfaces by rinsing in alcohol, dipping in oleic acid (12), and plating with aluminum produced fairly adherent aluminum deposits on many metals. Wrought metal surfaces were first cleaned and activated by conventional means for aqueous plating and then treated by rinsing in alcohol and oleic acid.

Fatty acids other than oleic acid, such as linoleic acid and ethereal solutions of palmitic acid, were also successfully used to promote adherent plate of aluminum. Since pelargonic acid was not effective, a fatty acid with carbon chain longer than nine carbon atoms apparently is necessary.

Solutions of stearato chromic chloride[1] in isopropyl alcohol were even more effective than oleic acid in promoting adhesion of aluminum to iron and nickel. However, the stearato chromic chloride carried into the plating bath shortened the bath life. Subsequently rinsing in oleic acid was helpful in preventing bath contamination. Oleic acid per se did not shorten the life of the aluminum plating bath noticeably.

Preparation of Metal Surfaces for Plating with Adherent Aluminum

Aluminum.—Preparation of aluminum surfaces was by application of a conventional zincate replacement film and rinsing in water before rinsing in alcohol and oleic acid. The adhesion of the aluminum electroplates on 3S aluminum was tested by peening and by soldering. Peening of the surface was done by a rounded tip tool mounted in a vibrating marking tool. In the second test, the aluminum electrodeposit was copper plated, and a rod was soldered perpendicular to the surface and then pulled loose. Neither peening nor solder testing broke the aluminum-zincate-aluminum bond. The distortion of the peened aluminum plate is apparent in Fig. 1.

Copper.—Clean copper surfaces were activated in a sodium cyanide solution and then rinsed in water before rinsing in alcohol and oleic acid.

Nickel.—Nickel was activated by electropolishing[2]

[1] Quinol, E. I. du Pont de Nemours and Company, Inc.

[2] Proprietary nickel electropolishing process, Battelle Development Corp. U.S. Pat. 2,440,715, May 4, 1948.

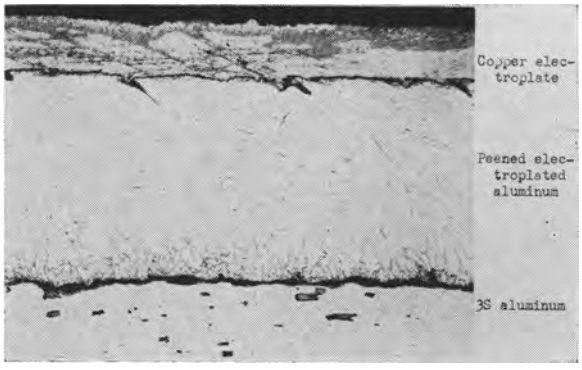

Fig. 1. Aluminum electroplate on 3S aluminum after peening and plating with copper. HF etch. Magnification 50X before reduction for publication.

Fig. 2. Aluminum electroplate on SAE 1020 steel. HF etch. Magnification 250X before reduction for publication.

or anodic etching and strike plating in the high-chloride "Woods" nickel bath and then rinsed in water prior to rinsing in alcohol and oleic acid.

Stainless steel.—Stainless steel was activated by anodic etching and nickel strike plating in the high-chloride "Woods" nickel bath and then rinsed in water before rinsing in alcohol and oleic acid.

Carbon steel.—Carbon steel, Type 1020, was electropolished and then rinsed in water prior to rinsing in alcohol and oleic acid. Chemical etching in hydrochloric acid or anodic etching in sulfuric acid was less satisfactory than electropolishing. Aluminum on carbon steel is shown in Fig. 2.

Electroplating of Aluminum over Metals Electroplated on Uranium

Electroplating of aluminum over electroplated metals on uranium was complicated by the fact that uranium was exposed through discontinuities in the intermediate plated layers which prevented optimum activation of the surface. Nickel, copper, and iron electrodeposits, ½ mil thick, plated adherently on uranium, were not impervious. The thickness of the intermediate metal coating was limited in this study to about ½ mil because of the higher thermal-neutron cross section of nickel, copper, and iron as compared with aluminum.

The best methods for activating solid nickel and steel specimens prior to the organic activation steps were not applicable to nickel- or iron-plated uranium, because these acid treatments attacked the underlying uranium. Therefore, aluminum was electroplated directly on nickel- or iron-plated uranium following rinsing in alcohol and oleic acid. The method for activating clean copper surfaces by immersion in a cyanide solution prior to the organic activation steps was effective in promoting adherent aluminum electroplating over uranium plated with copper or nickel.

The as-plated bond of the aluminum to the nickel or iron plates was inferior to that of aluminum to electroplates of copper or copper over nickel on uranium. Subsequent hot pressing or vacuum heat treating of electroclad specimens having aluminum on nickel- and copper-plated uranium improved the as-electroplated bonds. However, hot pressing of aluminum plate on iron-plated uranium produced brittle alloys that resulted in doubtful adherence.

Electrocladding Uranium with Aluminum

Uranium samples.—Alpha-rolled uranium plate was cold rolled to 90-mil sheet and cut into samples ¾ by ¾ in. square. The edges and corners were rounded to minimize edge buildup. Surfaces were cleaned by grinding or by grit blasting to remove scale. Samples were held in racks made of stainless steel with two point-type contacts on opposite edges. The contact areas were not plated, and thus there were discontinuities in the electrocladding. The racks were coated with Synthetasine,[3] a synthetic resin preparation, which was inert in the bath.

Aluminum-Plating Bath

Preparation.—The lithium hydride-ethyl ether bath was prepared under nitrogen atmosphere in a three-neck flask provided with a stirrer and a cooling bath of dry ice and acetone. Ethyl ether was stirred in the flask while $AlCl_3$ was added through a gooch rubber tube. Next, the LiH was added similarly. Considerable heat was liberated during these additions; however, the temperature was maintained between −25° and −10°C to minimize ether evaporation. The final composition was 400 g $AlCl_3$, 6 g LiH, and ether to make 1 liter.

Baths of 2.5 liters were contained in glass jars and covered with an aluminum dry box into which dry nitrogen gas was bled slowly. Two sets of doors were provided in the dry box for insertion and removal of the cathodes. Figure 3 shows the electroplating setup.

Bath life.—The longest time a hydride type of aluminum bath was operated was 30 days, or 190 amp-hr/liter. About 160 g of aluminum had been deposited from the 2-½-liter bath, or 80% of the amount in the original $AlCl_3$. The bath was then discarded because the electrodeposited aluminum had become brittle, nodulated, and spongy. The cathode current efficiency had increased to 115%. No attempt was made to recondition the bath.

Generally, at the beginning of their use, aluminum plating baths produced ductile, mat aluminum. As the baths grew older the plates tended to become smoother. In some cases, the smoothness was accompanied by small cracks and fissures in the plates. As the plates became smoother they usually tended to loose ductility. Finally, many baths began to produce dark, streaky deposits when they had outlived their usefulness.

[3] Synthetasine Protective Coatings, Inc., New York, N.Y.

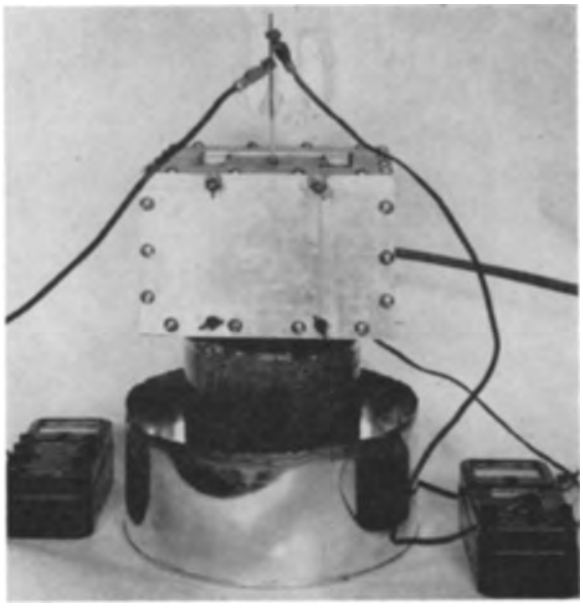

Fig. 3. Aluminum plating bath with dry box and plating rack in place.

Fig. 4. Surface view of crystalline electrodeposited aluminum. Magnification approx. 1000X before reduction for publication.

In some cases the aluminum tended to become satin surfaced, due to aluminum crystals. Figure 4 shows one of these flat surfaces. The tendency to form regular hexagons was outstanding. In Fig. 4 cubic crystals can be seen also.

Aluminum Plated Directly on Uranium

The preparation of uranium for aluminum plating was the same as for conventional aqueous plating, as discussed later. An extra requirement for aluminum plating was that after activation the uranium was dried in alcohol and ether before being immersed in the anhydrous plating bath. As-plated aluminum on uranium is shown in Fig. 5.

Heat treatment of aluminum-plated uranium easily diffused the two metals. The extent of diffusion occurring in 24 hr at temperatures of 200°, 250°, and 300°C is illustrated in Fig. 6, 7, and 8. The diffusion in 24 hr at 300°C was enough to destroy the as-plated bond.

Diffusion of aluminum and uranium at 250°C, and possibly at 200°C, was unexpected based on the observed diffusion between wrought aluminum and uranium. The interface of aluminum plated on uranium probably has less oxides than mechanically

Fig. 5. Aluminum electroplate on uranium as-plated (aluminum thickness, 12 mils). As-polished. Magnification 500X before reduction for publication.

Fig. 6. Aluminum electroplate on uranium after 24-hr diffusion at 200°C (aluminum thickness, 12 mils). As-polished. Magnification 500X before reduction for publication.

Fig. 7. Aluminum electroplate on uranium after 24-hr diffusion at 250°C (aluminum thickness, 12 mils). As-polished. Magnification 500X before reduction for publication.

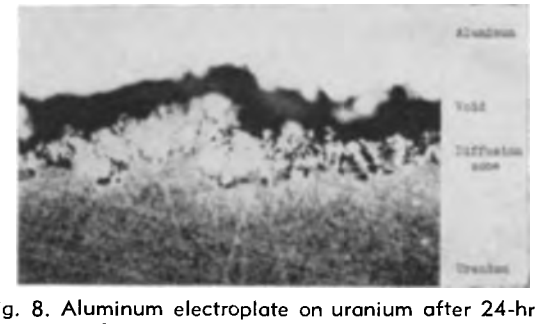

Fig. 8. Aluminum electroplate on uranium after 24-hr diffusion at 300°C (aluminum thickness, 12 mils). As-polished. Magnification 500X before reduction for publication.

prepared diffusion samples, and this difference could explain the difference in diffusion across the aluminum-uranium interface.

Aluminum Plated over Electroplated Metals on Uranium

The observed deleterious diffusion of electroplated aluminum and uranium in 24 hr at 250° and 300°C pointed out the need for an interfacial diffusion barrier. A barrier metal was desired that would prevent diffusion, would be well bonded to both the aluminum and the uranium, and would provide secondary corrosion protection to the uranium when exposed to boiling water through discontinuities in the aluminum. Nickel, copper, and iron electroplates were tried as barrier layers.

The procedure for activating and plating on uranium was as follows:

Descale uranium: (a) surface grind, (b) abrasive blast, or (c) chemical pickle.

Alkaline clean: immersion for 2 min at 180°F.

Rinse

Nitric pickle: 8*N* HNO_3, 80 ± 10°F, 5-10 min.

Rinse

Anodic pickle: 22*N* H_3PO_4, 0.2*N* HCl, 100°F, 50 amp/ft², 10 min

Cold rinse

Nitric pickle: 8*N* HNO_3, 80° ± 10°F, 3-5 min.

Electroplate: (a) Copper (0.5 mil), copper sulfate, $CuSO_4 \cdot 5H_2O$, 210 g/l; sulfuric acid, H_2SO_4, 82.5 g/l; molasses, 2.5 g/l; 20° ± 10°F, 50 amp/ft², 1 min, 25 amp/ft², 20 min.

(b) Iron (0.5 mil), ferrous sulfate, $FeSO_4 \cdot 7H_2O$, 300 g/l; ferrous chloride, $FeCl_2 \cdot 4H_2O$, 40 g/l; sodium formate, NaCOOH, 15 g/l; ammonium sulfate, NH_4SO_4, 15 g/l; boric acid, H_3BO_3, 30 g/l; wetting agent, DuPonol M. E.,[4] 1 g/l; pH 4.1 ± 0.1, 140°F, 60 amp/ft², 1 min, 30 amp/ft², 19 min.

(c) Nickel (0.5 mil), nickel sulfate, $NiSO_4 7H_2O$, 145 g/l; magnesium sulfate, $MgSO_4 \cdot 7H_2O$, 75 g/l; ammonium chloride, NH_4Cl, 15 g/l; boric acid, H_3BO_3, 15 g/l; wetting agent, XXXD,[5] 20 mil/liter; pH 5.5 ± 0.1, 100°F, 30 amp/ft², 1 min, 15 amp/ft², 30 min.

Rinse

Activate: (a) ethyl alcohol rinse, (b) oleic acid rinse.

Aluminum plate (12 mils), aluminum chloride, $AlCl_3$, 400 g/l; lithium hydride, LiH, 6 g/l; ethyl ether, balance; 75° ±5°F, 10 amp/ft², 24 hr.

Rinse and dry.

Treatment after electrocladding.—Heat treating of aluminum-electroclad samples for 5 min at 950°F and hot pressing for 5 min at 950°F with ram pressures up to 5.1 tsi were done to promote diffusion and improve the as-plated adhesion. Heat treating was done in a vacuum tube furnace with a pressure of less than 10 μ.

Hot pressing was done in a closed die. The hot-press assembly, Fig. 9, consisted of a frame and two cover plates of 3S aluminum in which the electroclad sample was encased. A 1-½-mil iron foil was included as a parting compound. The 1-7/16-in.-diameter by ⅜-in. thick assemblies were hot pressed in a tubular die with the ram pressure applied on one face. The 3S aluminum deformed under pressure and heat to fill the contours of the aluminum-electroclad sample. After being hot pressed, the aluminum-electroclad core was peeled off the 3S aluminum casing. A small hydraulic press[6] furnished the pressure.

Corrosion Testing of Aluminum-Plated Uranium

Samples of aluminum-plated uranium were immersed in boiling distilled water for 24-hr intervals or less. The corrosion trend was followed by the weight change and the progressive change in appearance. The relative corrosion resistances of the various cladding systems were based on the hours in test before a weight change of ± 1 mg/cm² was noted. Corrosion for the most part occurred only at contact areas in the aluminum electrocladding. If the bond of the aluminum cladding was not good, corrosion also occurred over the barrier-coated uranium because of penetration of water along the aluminum-barrier metal interface. The best samples

[4] E. I. du Pont de Nemours and Co., Inc.

[5] Harshaw Chemical Company.

[6] Carver Laboratory Press, Fred S. Carver Inc., Summit, N.J.

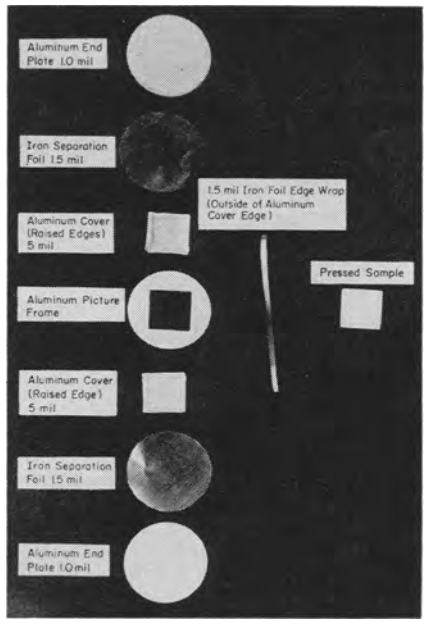

Fig. 9. Assembly for hot-pressing aluminum-clad uranium samples.

Table II. Relative corrosion resistance of aluminum-electroclad uranium specimens having various barrier-metal coatings and postcladding treatments (aluminum 12 mils in thickness)

Barrier metal	Thickness, mil	Postcladding treatment	Corrosion resistance, hr*
Ni	0.5	Hot pressed	63
Ni	0.5	Heat treated	39
Ni + Cu	0.4 + 0.1	Hot pressed	104
Ni + Cu	0.4 + 0.1	Heat treated	64
Ni + Cu	0.25 + 0.25	Hot pressed	50
Ni + Cu	0.25 + 0.25	Heat treated	38
Ni + Cu	0.1 + 0.4	Hot pressed	26
Ni + Cu	0.1 + 0.4	Heat treated	23

* Hours in boiling water until weight change of ±1 mg/cm² occurred. Average of four samples.

Table III. Effects of barrier-metal coating, activity of uranium surface for plating, and pressure applied during postcladding hot pressing on the relative corrosion resistance of aluminum-electroclad uranium (aluminum, 12 mils in thickness)

Barrier metal	Coating thickness, mil	Activity of uranium*	Pressure, tons/in.²	Corrosion resistance, hr†	
Fe	0.5	Active	3.5-4.3	144-77	(95)
Fe	0.5	Passive	0.2-2.2	31-1	(16)
Cu	0.5	Active	3.3-3.9	108-46	(77)
Cu	0.5	Passive	3.5-5.1	46-1	(23)
Ni	0.5	Active	0.6-1.2	38-1	(19)
Ni	0.5	Passive	0.0-4.8	7-86	(46)
Ni + Cu	0.4 + 0.1	Active	1.0-5.1	138-327	(232)
Ni + Cu	0.4 + 0.1	Passive	1.4-4.4	109-80	(94)
Ni + Fe	0.4 + 0.1	Active	2.8-3.5	49-84	(66)
Ni + Fe	0.4 + 0.1	Passive	2.6-4.5	36-1	(18)

* *Active* uranium was that which was pretreated for good as-plated adherence. *Passive* uranium was just pickled in nitric acid and plated with an envelope of the barrier metal. Bonding of the electroplated metal to the uranium depended on the diffusion that occurred during hot pressing.

† Hours in boiling water until weight change of ±1 mg/cm² occurred. Number in parentheses is average of two samples.

showed slight corrosion only at the electroplating contact areas.

Tables II and III show the relative corrosion resistance of uranium electroclad with various barrier metals plus 12 mils of aluminum. The best corrosion resistance was observed for uranium that was plated with adherent 0.4 mil of nickel plus 0.1 mil of copper plus aluminum and hot pressed at 950°F with a ram pressure of 5.1 tsi. This system provided the best adhesion of the aluminum cladding and also provided desirable alloying of the uranium with the nickel as a secondary corrosion barrier. Samples that were not hot pressed nor heated after electrocladding corroded rapidly (within a few hours) along the uranium-electroplate interface.

Manuscript received Feb. 13, 1959. This paper was prepared for delivery before the Ottawa Meeting, Sept. 28-Oct. 2, 1958. Work on this paper was performed under AEC Contract W-7405-eng-92.

Any discussion of this paper will appear in a Discussion Section to be published in the June 1960 JOURNAL.

REFERENCES

1. F. R. Collins, *Iron Age*, **169** (3), 100 (Jan. 17, 1952).
2. F. H. Hurley and T. P. Weir, *This Journal*, **98** (5), 203 (1951).
3. T. P. Weir and F. H. Hurley, U. S. Pat. 2,446,349, Aug. 3, 1948.
4. T. P. Weir, U. S. Pat. 2,446,350, Aug. 3, 1948.
5. W. H. Safranek, W. C. Schickner, and C. L. Faust, *This Journal*, **99** (2), 53 (1952).
6. W. H. Safranek, *et al.*, U. S. Pat. 2,692,850.
7. D. C. Couch and A. Brenner, *This Journal*, **99** (6), 234 (1952).
8. D. C. Couch, *et al.*, U. S. Pat. 2,651,608, Sept. 8, 1953.
9. J. H. Conner and A. Brenner, *This Journal*, **103** (12), 657 (1956).
10. G. Barbaras, *et al.*, *J. Am. Chem. Soc.*, **70**, 877 (1948).
11. Anonymous, *Chem. and Eng. News*, **31**, 2334 (1953).
12. W. C. Schickner, *Steel*, **135**, 125 (Nov. 2, 1953).

Electrolytic Iron Powder from a Caustic Soda Solution

J. Adrien M. LeDuc[1] and Richard E. Loftfield

Electro Chemicals Division, Research Department, Diamond Alkali Company, Painesville, Ohio

and Luther E. Vaaler[2]

Electrochemical Engineering Division, Battelle Memorial Institute, Columbus, Ohio

ABSTRACT

Conditions for electrolytic deposition of iron powder from a slurry of iron III oxide in caustic soda solutions were investigated. The variables that influence the deposition the most were temperature (90°C), caustic soda concentration (600-800 g/l), and low current densities. Results from pilot-plant studies were in good agreement with laboratory findings. Several photomicrographs of the deposits are included. Physical and chemical properties of the powders are listed. Results show that a ductile, dendritic deposit was obtained that could be ground up easily. The size of the dendrites was influenced greatly by conditions of deposition. Particle size distribution, particle shape, ductility, flow rate, purity, and compactability of several powders were examined. Tensile strength and elongation of sintered compacts were also studied.

Iron III hydroxide is soluble to a limited extent in strong caustic soda solution from which metal powder may be deposited in a dentritic and ductile form. The solution is kept saturated by employing an excess of finely divided iron oxide maintained in suspension by agitation.

Estelle (1) first patented such a process in which he recommended a bath consisting of 30% iron III hydroxide, 35% sodium hydroxide, and 35% water, maintained at 100°C. He stated that a gray metallic deposit can be obtained from this solution. Angel (2) showed that finely divided iron ore could be used in place of the pure hydroxide in the same type of medium. Estelle's and Angel's patents defined very few conditions for electrodepositing the iron and did not describe the characteristics of the powder produced. Little attention has been given to this method of producing iron powder. Ljungberg (3) described it in a review of electrolytic methods for making powders and concluded that further work would be necessary to change it from the status of a laboratory curiosity. He considered the method attractive, since the powder is obtained directly from the ore. Mehl (4) stated that a brittle deposit, suitable for crushing, is obtained by Estelle's process, and patented a process (5) in which soluble iron anodes were employed in 50% caustic solution at 100°C. A very fine, dentritic powder was obtained.

The experimental work described in this paper was undertaken to determine conditions of electrolysis, yields, and characteristics of the iron powder produced in an alkaline iron oxide medium.

Experimentation

Laboratory Electrolytic Studies

A bath was prepared consisting of equal parts of water, caustic soda, and finely divided C.P. iron III oxide. This was electrolyzed at cathode current densities ranging from 30 to 90 amp/ft^2 and a tem-

[1] Present address: Exploratory Research Department, Research & Development Laboratories, M. W. Kellogg Co., Jersey City, N.J.

[2] Present address: Research Laboratories, National Carbon Co., Parma, Ohio.

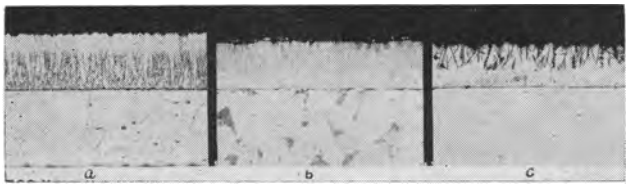

Fig. 1. Effect of agitation: a, iron deposited on flat panel cathode; b, iron deposited on rotating cathode; c, iron deposited from agitated bath. Magnification 500X before reduction for publication.

perature of 120°C in an iron container used as the anode. Gray, metallic deposits were formed from which it was difficult to remove all of the adhering oxide, so that the current efficiencies calculated from the gain in weight were 120%. A photomicrograph of the cross section of a typical deposit is shown in Fig. 1a. Oxide inclusions are evident, except near the surface, where they were washed out. However, if a rotating cathode was used, the calculated current efficiency was reduced to 92%. Figure 1b is a photomicrograph of this deposit, and the amount of oxide occluded is seen to be less than previously. If, in addition, a high-speed impeller was used to agitate the viscous bath, oxide inclusions were further eliminated, as shown in Fig. 1c, and a current efficiency of 70% was obtained.

In addition to its tendency to give deposits containing occluded oxide, the bath was so viscous that drag out was excessive. The viscosity was considerably reduced by decreasing the amount of suspended oxide, and deposition at high current efficiency was still possible if the bath was vigorously agitated. Further experiments were carried out in 1- and 4-liter containers. Nickel or iron anodes 0.5 in. in diameter or larger and 6-7 in. long were used. The iron anodes were corroded slowly during electrolysis. The cathodes consisted of mild-steel sheets that had been slightly roughened. The deposits adhered well to the surface but were easily removed from the electrode by flexing or scraping. The removed chips were reduced to powder by mild grinding. Air agitation was tried in a few experiments but had the disadvantages of producing a large amount of spray and introducing carbon dioxide into the bath. Agitation with a 2.5 in. diameter impeller revolving at about 700-800 rpm was found to be more satisfactory.

Bath stability during electrolysis.—The cathode current efficiency of a freshly prepared bath was found to decrease upon continued electrolysis. In a typical experiment a current efficiency of 90% was obtained during the first few hours of electrolysis, but after 24 hr the current efficiency had decreased to a steady value in the range of 60-80%. The high current efficiency of a freshly prepared solution may be due to the fact that the iron oxide contains an easily soluble fraction that dissolves shortly after the addition to the caustic soda solution.

The character of the deposits also changed during the stabilization period. Deposits from freshly prepared baths were loose and powdery but became more compact as electrolysis was continued. In the progress of the experimental work, successive experiments were run until the bath had reached a stable state.

Table I. Effect of bath temperature on current efficiency. Fe_2O_3-50 g/l; current density, 40 amp/ft²

Temp, °C	NaOH, g/l	Cathode current efficiency, %
30	400	30
35	600	45
50	600	75
60	400	45
70	600	85
80	600	90
90	400	60
90	600	90-95
120	400	70

Effect of temperature.—The effect of temperature was investigated in a bath containing 200-600 g/l of caustic soda and 25-75 g/l of iron III oxide. Electrolysis was carried out at a cathode current density of 40 amp/ft² over a temperature range from 30° to 120°C. The highest temperature was still below the boiling point of the bath.

Results are shown in Table I and indicate a current efficiency of well over 80% in several instances. The effect of temperature was investigated before the need for extensive electrolysis to obtain a stable condition was realized. While the results are generally consistent with one another, some of the values are inconsistent with later work.

The best current efficiency was obtained at the highest temperature for any given caustic concentration. The nature of the deposit also changed with the temperature. As the temperature increased the deposited dendrites increased in size, as shown in Fig. 2a to 2d inclusive. These figures are photomicrographs of polished cross sections of the deposits. The deposit made at 60°C was dispersed somewhat when mounted prior to polishing.

The variation in dendrite size with temperature was even more clearly shown by grinding deposits to −325 mesh, mounting in Lucite, and polishing.

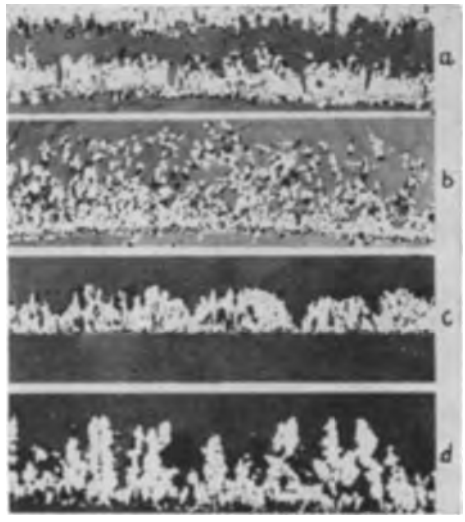

Fig. 2. Influence of temperature on cathode deposits: a, 35°C; b, 60°C; c, 90°C; d, 120°C. Magnification 100X before reduction for publication.

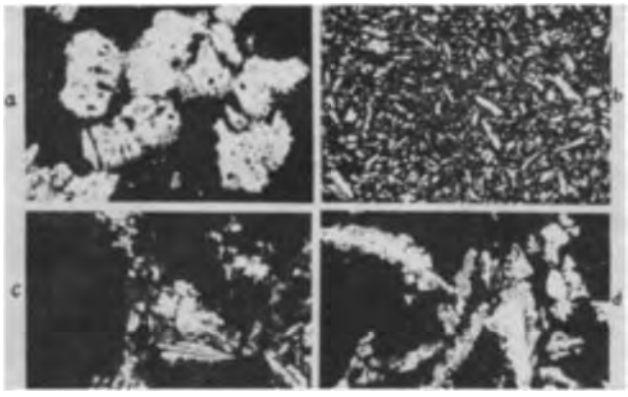

Fig. 3. Effect of bath temperature on iron deposit (caustic soda, 400 g/l; Fe_2O_3, 50 g/l): a, 35°C; b, 60°C; c, 90°C; d, 120°C. Magnification 500X before reduction for publication.

Photomicrographs of the specimens are shown in Fig. 3a to 3d. The large particles appearing in the photomicrograph of the powder deposited at 35°C are not individual dendrites but rather clumps made up of many smaller dendrites. This powder had very poor flow characteristics and balled up on the screen rather than passing through it. The dendrites from the 60°C deposit easily passed a −325 mesh screen. At higher temperatures some of the dendrites were too large to pass a −325 mesh screen and had to be distorted first, requiring a much more severe grinding treatment. However, the flow properties of the powder tended to improve as the temperature of deposition increased.

In all of the photomicrographs, except that of the powder produced at 35°C, fragments with a hexagonal symmetry can be observed, resulting from sectioning through the width rather than the length of the dendrite. Therefore, the dendrites consist of six longitudinal ridges spaced around a longitudinal axis with hexagonal symmetry.

Effect of caustic concentration.—Electrodeposition of iron from iron III oxide slurries in caustic soda solutions of varying concentrations showed that a high caustic soda concentration, in excess of 400 g/l, is required to obtain a current efficiency of over 50%. Representative results are shown in Table II. A bath containing 200 g/l of caustic soda and 50 g/l of iron III oxide was held at a temperature of 90°C and electrolyzed at 36 amp/ft². The first deposits from this bath were obtained at a current efficiency in excess of 60%, but the current efficiency dropped continually as more ampere-hours were put through the bath. Apparently, caustic soda present in a concentration of 200 g/l is not able to solubilize all of the iron oxide.

Table II. Effect of caustic soda concentration. Fe_2O_3-50 g/l; temp, 90°C; current density, 40 amp/ft²

200 g/l NaOH		465 g/l NaOH		765 g/l NaOH	
Amp-hr/l	C.E., %	Amp-hr/l	C.E., %	Amp-hr/l	C.E., %
3.1	68	3.1	91	4.7	80
15.6	40	15.6	86	17.2	85
28.0	22	28	65	26.6	73
50.0	13	47.0	54	36.0	68
59.5	13	50	52	39.2	67

With 465 g/l of caustic soda in the bath, a stable current efficiency of about 55% was obtained. With 765 g/l of caustic soda in the bath, deposits were produced at a current efficiency of 70%.

Effect of iron III oxide concentration.—The slurry concentration of iron III oxide in caustic soda solution was varied to determine whether its concentration affected the current efficiency of electrodeposition and the type of deposit produced. A finely divided, chemically pure iron oxide was selected for use in the bath. Baths containing 25, 50, and 75 g/l of iron oxide and 400-765 g/l of caustic soda were operated at 90°C and a cathode current density of 35-40 amp/ft². The results in Table III indicate that the concentration of oxide could be varied without significantly affecting the electrolysis.

Use of commercial hematite ores containing as high as 86% Fe_2O_3 in place of pure iron oxide gave somewhat inconsistent results. However, the current efficiencies were generally 20-30% lower than with the pure oxide. The use of a magnetite ore (Fe_3O_4) gave current efficiencies below 5%.

Effect of current density.—The effect of increasing the current density was to decrease both the current efficiency of deposition and the size of the dendrites deposited. Current efficiency values are given in Table IV. The decrease in the average size of the dendrites deposited is evident from the photomicrographs of deposit cross sections shown in Fig. 4a to 4g. At 2400 amp/ft² the deposit appears to have been torn off by the hydrogen evolved, except for a thin layer.

As expected, the effect of increasing the current density is opposite to the effect of increasing the temperature. Increasing the current density decreases the concentration of iron in the cathode film, leading to a decrease in the current efficiency and

Table III. Effect of iron oxide concentration on cathode current efficiencies. C.D., 40 amp/ft²; temp, 90°C

400 g/l NaOH						765 g/l NaOH			
25 g/l Fe_2O_3		50 g/l Fe_2O_3		75 g/l Fe_2O_3		25 g/l Fe_2O_3		50 g/l Fe_2O_3	
Amp-hr/l	C.E., %	Amp-hr/l	C.E., %	Amp-hr/l	C.E., %	Amp-hr/l	C.E., %	Amp-hr/l	C.E., %
1.39	46	1.4	66	1.4	74	3.13	83	3.13	73
7.1	55	2.8	63						
8.5	50	31	54	33	57	28.2	68	28.2	64
9.9	60							43.8	73
15.4	68			40	58	94	83		
25.2	60			46	61	163	80	163	73
				49	63	191	73	191	78
				52	48	269	68	269	75

Table IV. Effect of current density on current efficiency. Fe_2O_3, 50 g/l; temp, 90°C

Current density	Current efficiency, %	
Amp/ft²	at 400 g/l NaOH	at 765 g/l NaOH
40	55	80
72	—	75
80	45	—
145	—	68
160	35	—
300	20	—
600	15	—
1200	15	—
2400	3	—

more nucleation. Thus, finer dendrites are formed. An increase in temperature increases the rate of diffusion in the cathode film and probably increases the solubility of the oxide. The result is a higher current efficiency and a tendency to deposit on dendrite surfaces already established, rather than to start new ones.

Conclusions

The experimental results have shown that it is possible to prepare iron powder with an average particle size that can be varied over a wide range. The variables that most influence the electrodeposition of iron from an alkaline bath are temperature, caustic soda concentration, and current density. High temperatures of the order of 90°C are desirable for maintaining current efficiency and producing coarser dendritic deposits. Similarly low current densities, in addition to producing high current efficiencies, bring about coarse dendrites. High caustic soda concentrations in excess of 400 g/l and preferably between 600-800 g/l effect the best current efficiencies. The laboratory scale experiments established the feasibility of depositing dendritic iron from a caustic soda-iron oxide medium.

It is probable that the iron was deposited by the reduction of the soluble sodium ferrite in the solution. The solubility of the ferrite is rather low and deposition would soon cease without constant replenishment of the solution by the suspended oxide. The presence of more oxide particles than are needed to maintain the ferrite ion concentration should not change the results, which explains why the oxide concentration is not critical, at least above a certain minimum value.

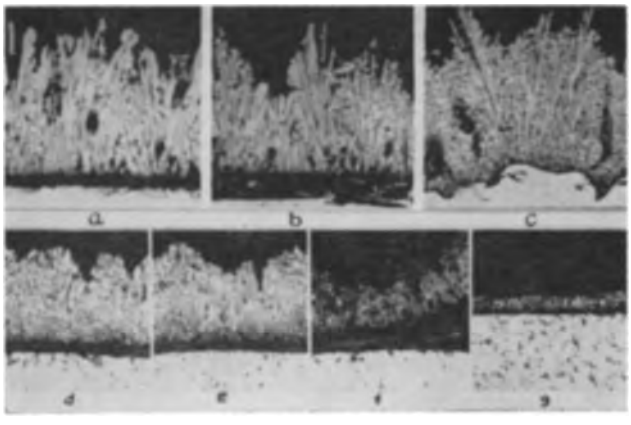

Fig. 4. Effect of current density on cathode deposit: a, 40 amp/ft²; b, 80 amp/ft²; c, 160 amp/ft²; d, 300 amp/ft²; e, 600 amp/ft²; f, 1200 amp/ft²; g, 2400 amp/ft². Magnification 500X before reduction for publication.

Pilot-Plant Electrolytic Studies

On the basis of the laboratory findings establishing the feasibility of the deposition process, pilot-plant studies were undertaken. Pilot-plant studies were to aid in determining the best conditions for continuous electrolysis, to verify efficiencies, to furnish a basis for an economic study of the process, and to make available sufficient quantities of iron powder for chemical and physical property studies, commercial applications and evaluations.

Large-scale studies also offered the possibility for investigating other sources of iron oxide in place of the chemically pure material used in the laboratory. They further aided in determining the technical advantages and disadvantages of the electrodeposition process and gave some knowledge on the design of the cell, grinding equipment, and the over-all production process.

Equipment and procedure.—The cell was constructed of 0.125 in. nickel sheet with base dimensions 18 x 9 in. and a height of 29 in., and had a 20-gal capacity. An inlet and outlet were provided on the side of the cell for the introduction and removal of liquor. Agitation was provided by a high-speed impeller rotating from 1000 to 1500 rpm. The solution was heated from the outside by strip heaters. The walls of the cell served as one anode, and a second anode was hung in the center of the cell. Two cathodes 10 x 24 in. made of 0.25-in. steel plate were inserted on either side of the center nickel anode. The total cathode area was 5.5 ft². D.C. current was supplied by a selenium rectifier.

Caustic soda flakes were dissolved in water to make 16.5 gal of 50% liquor. This electrolyte was used throughout a run, which sometimes extended from 6 to 8 days, with only periodic additions of water to replace evaporation loss. The iron was added as 9 lb of C.P. iron oxide or commercial ores. Periodic additions of approximately 2 lb of oxide were made every 4 hr throughout the run, assuming a current efficiency of 85%.

The cell was operated at 275 amp with an average cell potential of about 2.3 v. The bath temperature was maintained at 85°-90°C, and the solution was agitated to assure intimate mixing of the iron oxide and the alkaline bath.

After each 24 hr of operation the cathodes were removed from the cell. The deposited iron was washed thoroughly with water to remove any excess alkali and metallic oxides adhering to the surface and then scraped off. After the iron was ground in a ball mill, the oxide was removed. The powder was oven dried, sifted through a U. S. Standard 120 screen, and weighed. Samples of each day's production were analyzed for hydrogen loss, total iron, and particle size distribution according to standard MPA methods.

Process evaluation.—Pilot-scale runs were made at conditions which had proven most successful in the laboratory. The correlation between the laboratory work at Battelle Memorial Institute and Dia-

Table V. Pilot Plant Data. 82°-88°C, 275 amp, 45 amp/ft², 2.3 v, 16.5 gal. Capacity cell, 9 lb initial Fe_2O_3 charge followed by 2 lb additions every 4 hr

Run No.	Fe_2O_3 Ore	Current efficiency	Time, hr	Bath age, days	Amp-hr / liter	Ease of stripping deposit	Product analysis: Fe	Product analysis: H_2 loss
17	C.P.	75	8	New	35	Easy		
18	C.P.	80	11	1	83	Easy		
25	C.P.	46	20	New	88	Easy		0.4
26	C.P.	81	20	1	176	Easy	99.66	0.30
27	C.P.	76	21	2	268		99.60	0.33
28	C.P.	72	23	3	369		99.49	0.69
						Composite	99.57	0.43
19	Oolitic hematite	50	12	New	53	Easy when fresh,		
20	Oolitic hematite	52	12	1	106	hard after stand-		
21	Oolitic hematite	46	12	2	159	ing.		
22	Oolitic hematite	58	24	6	273			
23	Oolitic	59	20	New	88	Easy when fresh,		
24	Oolitic	41	20	1	176	hard after stand- ing.	98	2.0

mond Alkali Company and the pilot-plant runs made at Diamond Alkali was excellent. As shown on Table V, using C. P. Fe_2O_3 as a raw material, current efficiencies were in the range of 75-80% and were not appreciably affected by the age of the bath as long as the Fe_2O_3 concentration was maintained by the addition of ore. The chemical quality of the product was excellent, analyzing 99.57% iron and 0.43% hydrogen loss. The type of deposit is shown in Fig. 5, which is similar to that found in bench scale work.

Pilot operation verified that a very simple cell design was sufficient. It was shown that a bath could be used for several days without detrimental effects. It was also shown that after several days of operation the cell could set dormant for several days and be put back in operation without a reduction in current efficiency.

The use of oolitic hematite in place of C.P. ore reduced the current efficiency to approximately 50%. The product quality was also reduced, showing 2% hydrogen loss. The nature of the deposit was altered slightly, and although it was easily removed while fresh, it became difficult to remove if allowed to cool and dry. This was probably due to the presence of silicate, which cemented the deposit. It is possible that with some additional work to improve the technique and by selection of a more suitable natural ore results could be considerably improved.

Fig. 5. Iron deposited on pilot plant cathode, cross section of cathode deposit. Magnification 90X before reduction for publication.

In general, it was shown that the electrodeposition of dendritic iron from a caustic soda bath containing a suspended Fe_2O_3 is chemically and economically feasible. The raw materials are low in cost and can be handled easily. The electrolysis proceeded as planned. And finally, the product could be removed from the cathodes with a minimum of effort, yielding a deposit that could be easily ground in a ball mill.

Physical and Chemical Properties of Iron Powders

A determination of the physical and chemical properties of powders made under all of the conditions tried would be extremely laborious, since there are so many properties of significance in powder metallurgy and other powder uses. However, many of the properties are related inherently to the shape and size distribution of the powder. Therefore, detailed determinations could be restricted to a few representative powders covering the shapes and size distributions encountered during the experimental production of powders. In most of the deposition experiments on a laboratory scale less than 30 g of powder were produced. This amount of material is insufficient to determine several important properties, such as flow rate. Therefore, most of the powders that were examined in detail were made on a

Table VI. Chemical analysis of iron powder. L-Laboratory; P-Pilot plant

Sample No.	Fe_2O_3	H_2 loss, %	Fe, %	FeO, %	Fe_2O_3, %	Total Fe, %
L-82	C.P.	0.05	98.77	0.65	0.49	99.62
L-83	C.P.	0.38	94.22	6.50	0.49	99.62
L-84	C.P.	0.00	97.08	3.05	0.25	99.62
L-85	C.P.	0.12	98.28	2.16	0.05	99.96
L-86	C.P.	0.58	97.08	3.05	0.00	99.45
P-25	C.P.	0.40	—	—	—	—
P-26	C.P.	0.30	—	—	—	99.66
P-27	C.P.	0.33	—	—	—	99.60
P-28	C.P.	0.69	—	—	—	99.49
#8		0.76	—	—	—	—
L-87	Oolitic hematite	1.08	—	—	0.73	96.58
L-88	Oolitic hematite	1.39	—	—	0.47	96.07
P-24	Oolitic hematite	2.0	90.6	7.3	0.6	—

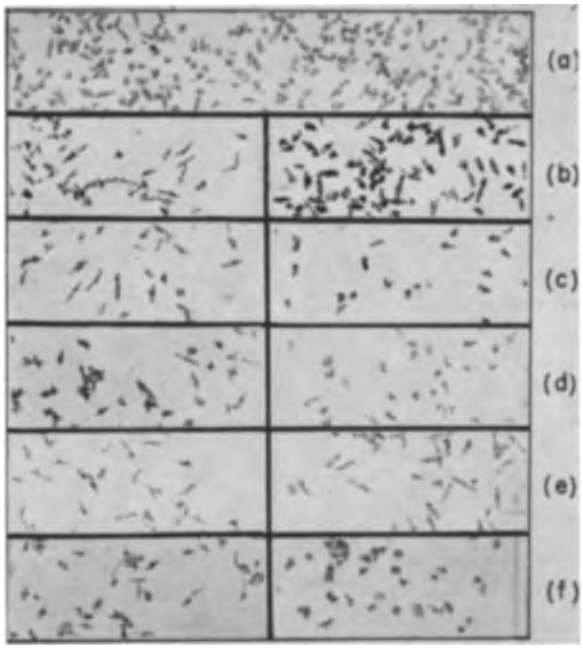

Fig. 6. Photomicrographs of various powders; left, unground; right, ground. a, powder No. 8; b, powder No. 9; c, powder No. 10; d, powder No. 11; e, powder No. 12; f, powder No. 13. Magnification 24X before reduction for publication.

pilot-plant scale. In several cases the operations of stripping from the starting sheet and washing with vigorous agitation were sufficient to reduce most of the deposit to powder. The product is referred to as "unground" powder as distinct from "ground" powder resulting from further comminution in a ball mill or mortar.

Analytical data.—Determinations were made of powders prepared from baths containing either C.P. iron oxide or a commercial iron oxide ore (hematite). Typical results of several experiments are shown in Table VI. Little difficulty was experienced in obtaining a hydrogen loss[3] (oxygen content) of less than 1% when pure oxide was used. However, with oolitic hematite ore the oxygen content was as high as 2%.

Ductility.—All deposits and powders were extremely ductile. When struck with a hammer a deposit was easily deformed without fracture. It was difficult or impossible to fracture particles by grinding. Even a relatively mild grinding deformed the particles as evidenced by the photomicrographs, Fig. 6a-6f, of the same powder, before and after milling. Extensive grinding caused severe deformation. Evidence that the powder is fully ductile as formed and that an annealing treatment does not increase the ductility was obtained as follows: A green compact prepared from powder No. 1 had a density of 5.51 when pressed at 38.7 t.s.i. A green compact made from powder No. 1 annealed in hydrogen at 1,000°C for 1 hr had a density of 5.57, or essentially the same value as the unannealed powder. Had the annealing increased the ductility to any extent, the density of the corresponding compact should have increased.

[3] The term "hydrogen loss" is the loss due to the removal of oxygen during the heating of the specimen in an atmosphere of hydrogen. Procedure in MPA-Standard 2-48 was followed.

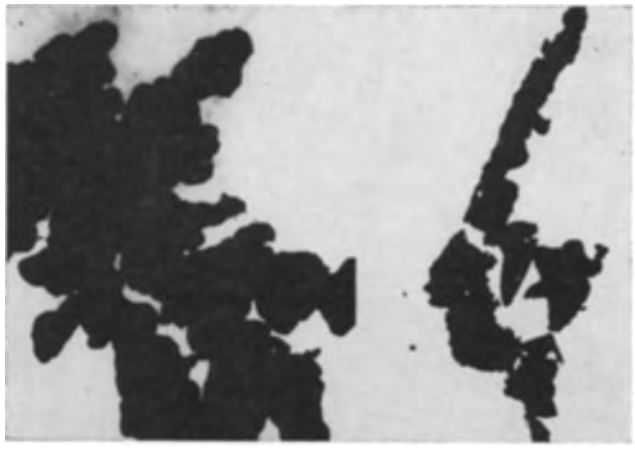

Fig. 7. Electron micrograph showing pattern of growth. Magnification 24,750X before reduction for publication.

Comminution.—The deposits were adherent, and, after they were removed from the bath, excess electrolyte and oxide could be eliminated by spray rinsing. The size of the dendrites and their adherence to each other increased with the temperature of deposition. Many of the 90°C deposits were converted to powder by the stripping and washing operations, particularly the deposits prepared on a pilot-plant scale. A further mild grinding treatment separated the few remaining dendrite agglomerations except for the large nodules formed at the corners and edges of the cathodes. The deposits prepared at 120°C in the laboratory showed a different behavior than the lower temperature deposits. Dendrites were generally too large to pass a 100 mesh screen, and the agglomerates tended to deform under the impact in the ball mill rather than to separate into individual dendrites.

Particle shape.—The dendrites as formed tended to be needle-like, and the particles appeared to become narrower and longer as the current density and temperature were lowered. Powder particles of No. 12, as shown in Fig. 6e, had perhaps the largest length to width ratio of any of the samples examined. Even mild grinding tended to flatten the particles, and extensive grinding distorted the particles into flattened platelets. Individual particles were also examined at higher magnifications. Electron-micrographs in Fig. 7 show the pattern of growth. Growth appears to take place by budding off from a parent stalk.

Particle size distribution.—Sieve analyses were made of powders prepared in both the laboratory and pilot plant. The laboratory results are shown in Table VII. A high proportion of fines was found in all the powders. As the temperature of deposition was increased, more grinding was required to break up the deposit, and the amount of fines became less. At 120°C a firm deposit was obtained that required extensive grinding and resulted in powder particles having a flat, disk-like shape. Similar results were obtained with pilot-plant powders as shown in Table VIII. Again the powders were on the fine side. The results for −325 mesh fractions would appear to be erratic, and this is related to the deformability of the particles on grinding. Table IX indicates this effect clearly. In four of the five examples the frac-

Table VII. Properties of powders prepared in the laboratory

Sample No.	Temp, °C	Current density, amp/ft²	NaOH conc, g/l	Weight of powder, g	Green density, g/cc	Size distribution, Tyler Equivalent					
						+100 %	−100 +150 %	−150 +200 %	−200 +250 %	−250 +325 %	−325 %
1	90	86	400	49.4	5.2	8.8	—	—	5.3	—	85.9
2	90	40	600	26.4	5.5	1.02	0.38	22.6	16.9	23.4	35.7
3	105	40	600	26.2	5.5	0.23	1.5	4.8	5.3	14.7	73.5
4	112	40	600	26.8	5.8	1.06	14.7	13.6	8.3	15.3	47.1
5	116	40	600	24.8	5.8	0.14	17.9	15.3	6.56	14.0	46.2
6	120	40	600	35.7	5.7	12	12.3	18.6	9.6	21.6	26.0
7	120	80	600	49.6	5.4	19.7	2.3	10.7	7.5	19.3	39.8

Notes:
No. 1. Deposits average 0.1 in. in thickness and were ground wet for 2 hr with 1-in. diameter steel balls. Several large pieces from edges and corners of the deposits were not broken up. The large pieces account for most of the 100 mesh material.
No. 2. Deposit loose and crumbly. Ground for 5 min with ½-in. diameter steel balls. Particles were needle-like and tended to agglomerate so that particle size is probably much finer than indicated by sieve analysis.
No. 3. Ground with 0.5 in. diameter ceramic balls, sizing after 5, 15, 30, and 45 min and returning 100 mesh material to the ball mill. Powder definitely dendritic but less so than No. 2.
No. 4. Deposit was firm and adherent but easily ground in a mortar. Particles dendritic but considerably less so than No. 2 and No. 3.
No. 5. More grinding required than with lower temperature deposits and particles were more irregular in shape.
No. 6. Deposit very firm and compact. Ground with 0.625 in. diameter steel balls for 3 hr, removing −100 mesh material frequently. Particles were severely deformed and flattened.
No. 7. Deposit very firm and compact and required over 10 hr of grinding to reduce the bulk to −100 mesh powder. Particles severely deformed and flattened.

Table VIII. Properties of powders prepared on a pilot-plant scale

Sample No.	Current density, amp/ft²	Time, hr	Temp, °C	Thickness, in.	Sieve analysis of ground powders, Tyler screen size					
					+100 %	−100 +150 %	−150 +200 %	−200 +250 %	−250 +325 %	−325 %
8	—	—	—	—	0.06	1.63	11.72	10.52	14.82	61.25
9	45	24	93	3/32	15.1	7.9	11.7	9.1	27.0	29.2
10	45	8	93	1/32	0.5	0.5	2.8	5.5	33.2	57.0
11	90	12	93	1/8	13.4	3.7	6.9	7.1	33.3	35.6
12	33	24	88	3/32	4.6	1.9	7.2	8.2	29.5	48.6
13	45	24	77	3/32	5.0	2.4	5.5	5.4	28.6	53.1
14	45	24	93	—	Trace	8.0	15.3	(37.6)		39.1*

* Part of the fines were removed so that the powder would flow.

tion of fines is decreased by grinding, as the needle-shaped particles are flattened and unable to pass through as fine a screen. Therefore, the amount of grinding is very critical in determining size distribution, since breaking up of agglomerates, tending to reduce screen size, and flattening, tending to increase screen size, occur simultaneously.

The −325 fraction of a laboratory sample was further analyzed by air elutriation (infrasizer) with the results shown in Table X. The results can be considered only very approximate, since the instrument is calibrated for spherical rather than needle-like particles. The average nominal diameter for the particles in the fines appears to be in the range of 20-40 μ, with less material below 10 μ.

Flow rate.—Flow rate tests were carried out on sized fractions of powders prepared in the pilot plant with the results shown in Table XI. None of the powders flowed prior to screening, but all the −325 fractions flowed after screening. Powder No. 14 originally contained much more than 39% fines, but when the fines above this amount were removed, the powder flowed with a standard time of 35 sec, which is commonly accepted in powder specifications.

Apparent density.—The apparent densities of powder No. 8 and No. 14 were 2.29 g/cc and 2.47 g/cc, respectively. The higher value for the latter powder may be because a part of the fines were removed. The values for apparent density are acceptable for metallurgical powders.

Compactability.—Green compacts were made in a single plunger die with a 0.5 in. diameter cylinder. Unless otherwise stated, the pressure used was 30 t.s.i., and 0.5-1% of zinc stearate was added to the powder as a lubricant. In most cases the green density was in the range 5.5-6.0 g/cc (Fig. 8). A

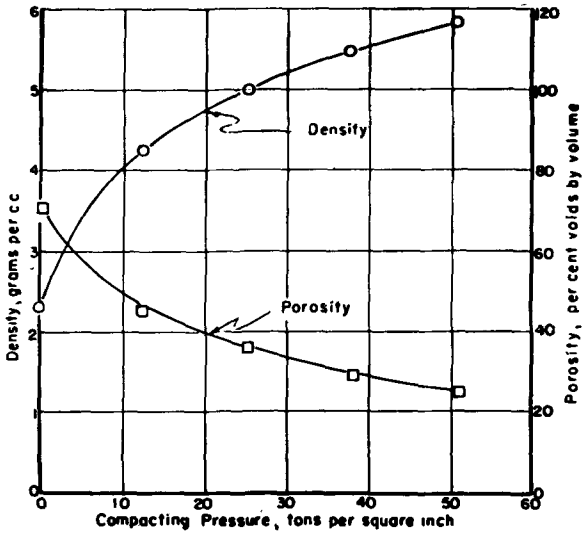

Fig. 8. Green density and porosity of iron powder compacts

Table IX. Change in amount of fines with grinding

Sample No.	Fraction of −325 mesh sample		Grinding time, min
	Unground	Ground	
9	42.5	29.2	40
10	49.5	57.0	30
11	45.5	35.6	60
12	59.4	48.6	25
13	71.2	53.1	30

Table X. Particle size distribution of −325 mesh fraction by air elutriation, powder No. 1

Particle size, microns	Weight fraction, %
0.9	56-84
16.0	42-70
30.6	28-56
25.2	15-42
15.2	9-30
6.7	5-18
3.5	3-15

green density of at least 6.5 would be preferable to meet existing specifications, although tensile tests indicated that such a high density is not necessarily required for strength and ductility.

Green strength.—The standard MPA rattler test was carried out with green compacts of powder No. 8. The value was 2.29% loss, well above minimum requirements.

Tensile strength and elongation of sintered compacts.—Tensile specimens were compacted, sintered,

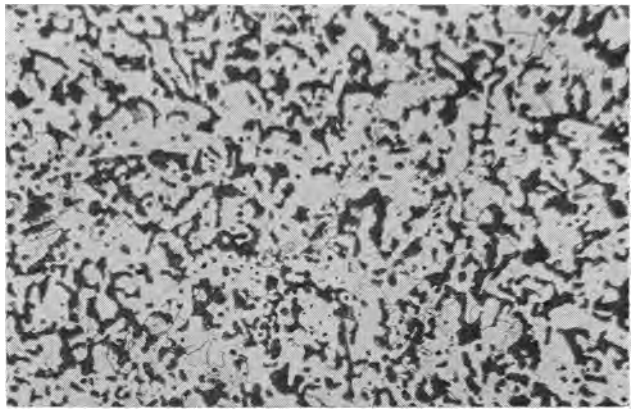

Fig. 9. Sintered powder compact. Magnification 250X before reduction for publication.

and tested according to MPA standard 10-50 T. Results for two experimental powders are shown in Table XII and are compared with several commercially available materials. Powder No. 12 had very long, jagged particles and did not flow. Its sintered compacts had strengths and ductilities comparing favorably with much higher density compacts from other powders. The results with powder No. 14 illustrate the risk in using a standard evaluation test. At a pressure of 30 t.s.i., commonly used for evaluation, results were very poor, but at 50 t.s.i., which is still a practical pressure, much higher strength and ductility were obtained.

A photomicrograph of a sintered compact made from an experimental powder is shown in Figure 9.

Table XI. Properties of powders prepared on a pilot-plant scale

Sample No.	Minus 325 mesh powder, %	Flow rate, sec					Green density, g/cc
		Tyler screen −100 +150	−150 +200	−200 +250	−250 +325	−325	
8	61.25	33.8	33.1	33.5	31.9	NF	5.9
9 (A)	29.2	43.0	39.8	36.8	32.5	NF	5.5
10 (B)	57	—	40.6	40.1	33.5	NF	5.5
11 (C)	35.6	57.3	51.1	44.9	35.2	NF	5.7
12 (D)	48.6	95.3	63.5	55.6	43.9	NF	5.6
13 (E)	53.1	45.8	44.1	41.1	34.7	NF	5.7
14	—	35					—

Table XII. Tensile strength and elongation of iron powder compacts

Powder	Lubricant	Compacting pressure, tsi	Density, g/cc	Tensile strength, psi	Elongation, %
Diamond No. 12	0.5% Zn stearate	30	5.8	22,000	9
		40	—	24,000	10
Diamond No. 14	0.5% Zn stearate	30	6.06	11,100	2.3
		50	6.64	28,000	6.1
British	none	40	6.8	23,000	10.5
	1% stearin	40	7.0	16,000	2.5
European I	—	25.8	6.8	18,000	—
		38.7	7.2	24,000	—
		51.6	—	27,000	—
European II	—	25.8	6.5	24,000	—
		38.7	7.0	31,000	—
		51.6	—	34,000	—
Japanese	—	30	6.4	20,045	10.4
U. S. I	0.5% Zn stearate	30	6.7	21,300	—
		50	7.2	29,200	20
U. S. II	—	18	6.6	23,000	7
		31	7.0	31,000	7
		45	7.3	37,000	10

Intermeshing of particles and grain growth are evident, as are the interstices.

The investigation just discussed was carried out at the Diamond Alkali Laboratories and at Battelle Memorial Institute under the sponsorship of the former.

Acknowledgment

Acknowledgment is expressed to the persons that have carried out the experimental work as follows: Battelle Memorial Institute, Messrs. W. Buckingham, R. Lindsey, and R. Wylle; Diamond Alkali Company, Messrs. A. Barbato, N. Daugherty, D. Goens, C. Hardman, P. Locotosh, T. Norris, and J. Parker. Appreciation is also extended to the Analytical and Metallurgical Departments of both institutions.

Manuscript received Oct. 28, 1958. This paper was prepared for delivery before the Buffalo Meeting, Oct. 6-10, 1957.

Any discussion of this paper will appear in a Discussion Section to be published in the June 1960 JOURNAL.

REFERENCES

1. Estelle, Swedish Pat. 42,849, (1915); U. S. Pat. 1,275,-161, Aug. 16, 1918.
2. Angel, U.S. Pat. 2,622,063, June 30, 1945.
3. Ljungberg, *Stahl u. Eisen*, **74**, 279 (1954).
4. Mehl, *Metal Treatment and Drop Forging*, **117**, 118 (1950).
5. Mehl, U. S. Pat. 2,389,734, Nov. 27, 1945.

Electric Field Enhancement of Cathodoluminescence (Cathodoelectroluminescence)[1]

Philip M. Jaffe

Research Department, Westinghouse Electric Corporation, Bloomfield, New Jersey

ABSTRACT

The application of an alternating electric field to certain cathode-ray excited ZnCdS:Mn,Cl powder phosphors causes the cathodoluminescence to be enhanced. Enhancement is a function of the frequency and strength of the applied field, the beam current density, and the accelerating potential. The indications are that the effect is in reality cathode-ray induced electroluminescence. Similar testing of a ZnCdS:Mn,Au,Cl phosphor results in either enhancement or quenching depending upon the exciting conditions.

Destriau has shown that the Roentgenoluminescence of certain ZnCdS:Mn,Cl (1) and ZnCdS:Mn,-Au,Cl(2) phosphors is enhanced by the application of an alternating electric field. Since then, several similar enhancement effects have been reported (3-14). One of these, described by Cusano (3-5), utilizes a thin film of ZnS phosphor activated by either manganese, arsenic, or phosphorus and coactivated by chlorine. On exciting the film with 3650Å radiation, x-rays, or cathode-rays, the simultaneous application of a d-c field produces an increase in the light output. A similar effect has been reported by Thornton using a wide variety of powdered ZnS phosphors with u.v. radiation and either a-c (6) or d-c (7) fields and by Woods (8) using single crystals. Halsted's enhancement effect (9) has been observed using a-c fields and 2537Å excitation of ZnS:Cu,Al and ZnS:Ag,Cl and 3650Å excitation of ZnCdS (35, 50, 85% Cd): Ag,Cl and ZnSSe (20%Se): Cu,Al phosphor powder samples. Gobrecht and Gumlich (10) have studied the effect of a-c fields on u.v.-excited ZnS:Mn,Cl powder phosphor, while Mattler (11) investigated the same phosphor using excitation by α particles. Neumark (12) has studied the enhancement of thermoluminescence by electric fields. Mention also should be made of the work of Woods and Wright (13) on the enhancement of the cathodoluminescence of MgO by the application of a d-c field.

The present paper deals with a-c field enhancement of the cathodoluminescence of certain ZnCdS:Mn,Cl, and ZnCdS:Mn,Au,Cl powder phosphors. The simultaneous effect of a-c fields and cathode-rays on ZnS:Cu,Al and ZnS:Mn powder phosphors has been reported on by Gobrecht and co-workers (14).

Experimental

The composition of the phosphor mainly used in this work was (70Zn·30Cd)S:0.14Mn,0.5NaCl[2] and is similar to that used by Destriau in his studies on x-ray enhancement (1). Some observations also were made with a (50Zn·50Cd)S:0.5Mn,10^{-4}Au (added as the respective chlorides) phosphor, supplied by Destriau, which shows greater x-ray enhancement than the phosphor without gold (2). In addition, silver-activated ZnS and ZnCdS(30,-70, 85 wt % Cd), Zn_2SiO_4:Mn and a good electroluminescent ZnS:Cu,Cl phosphor were tested. The silver-activated phosphors generally showed quenching of the cathodoluminescence on application of the field. No field response was found for the willemite phosphor, i.e., no enhancement or quenching.

[1] The sections of this paper which deal with the ZnCdS:Mn, Cl phosphor were presented at the Washington, D.C., Meeting of The Electrochemical Society, May 1957, under the title "Electrocathodoluminescence." F. E. Williams in his keynote speech before the Luminescence Symposium of this Society in 1955 suggested that in phenomena of this sort the first prefix indicate the controlling source and the second prefix the power source. As will be shown later, the experimental results indicate that the effect reported on here should be called "Cathodoelectroluminescence" in keeping with Williams' suggestion.

[2] All compositions are on a weight basis. Normally Destriau adds the activators as the chlorides but the presence of the halide is not necessary, at least for Mn alone. He finds, however, that the phosphors without chlorine are not as good as those containing chlorine.

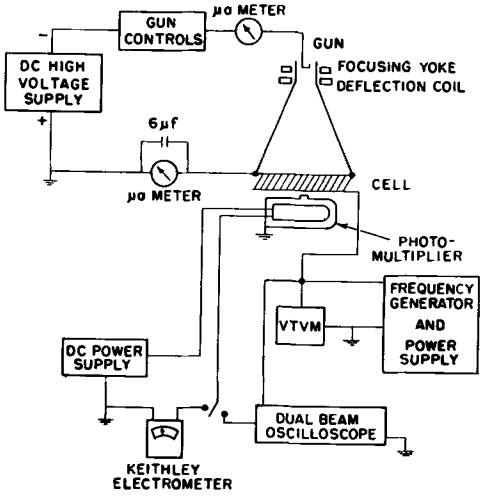

Fig. 1. Block diagram of the circuit used in the cathodoelectroluminescent studies.

The phosphors were made into cells 1 x 1 in. and approximately 2 mils thick using Nylon (DuPont FM6501) as the dielectric. The cells were prepared by coating the conducting surface of tin oxide-coated glass with a clear coat of Nylon, 0.5 mil thick (as measured with a micrometer), on which was superimposed a 1 to 1.5 mil thick layer of Nylon plus phosphor in a volume ratio of 1:1. The cell was completed by evaporating an approximately 1500Å thick layer of aluminum on the Nylon-phosphor layer. The cells were first tested under x-rays for uniform enhancement. The satisfactory cells then were examined in a continuously pumped, demountable cathode-ray tube. The tube was operated with the gun at negative high voltage while the aluminum electrode of the cell and the internal conducting coating of the tube were connected to ground. The gun was of the magnetically focused type, and a constant raster of approximately 5 cm² was used in all the measurements. The light output from the cell was detected with an RCA 1P22 photomultiplier and a Keithley electrometer. Provisions also were made for visual observations of the photomultiplier output on a dual-beam oscilloscope in order to study phase relationships. A block diagram of the test circuit is shown in Fig. 1.

Results

Studies of the enhancement effect were made as a function of accelerating potential, beam current density, and the frequency and strength of the applied field. The results of these measurements as well as several miscellaneous measurements and observations are given below. The results are reported in terms of the enhancement factor, ρ, which is defined by the expression

$$\rho = B/B_{cl} + B_{el}$$

where B is the light output under the action of both cathode rays and the field, B_{cl} is the normal cathodoluminescence and B_{el} is the electroluminescence, if any.

Enhancement as a function of frequency.—The enhancement effect was studied extensively over the range of 60-6000 cps; some measurements were also made between 20 and 60 cps using the ZnCdS:Mn,-Cl phosphor. With the Mn,Cl phosphor, ρ goes through a maximum around 30 cps and decreases toward a limiting factor of unity with increasing frequency (Fig. 2). Also, ρ decreases with increasing frequency for the Mn,Au,Cl phosphor, and, depending on the beam current density and field strength, may be less than unity, i.e., the output is quenched (Fig. 3).

Enhancement as a function of field strength.—The enhancement effect was studied over the range of approximately 10,000 to 60,000 v/in. since the use

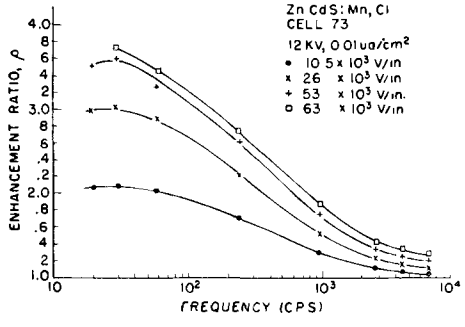

Fig. 2. Enhancement ratio, ρ, as a function of frequency for the (70Zn·30Cd)S:Mn,Cl phosphor at different field strengths.

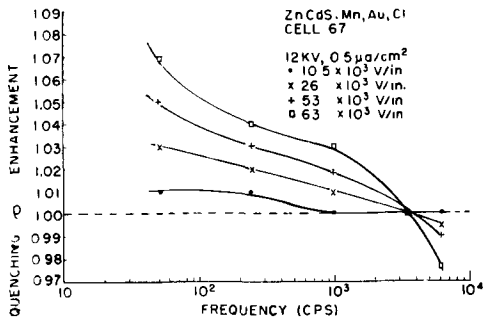

Fig. 3. Enhancement ratio, ρ, as a function of frequency for the (50Zn·50Cd)S:Mn,Au,Cl phosphor at different field strengths. At 12 kv, 0.5μa/cm² and field strengths between 26,000 and 63,000 v/in., quenching is found at frequencies above 3600 cps. Quenching is also found at 4 and 8 kv as discussed in the text.

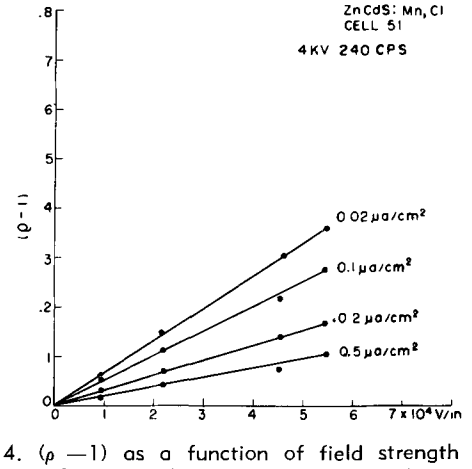

Fig. 4. $(\rho - 1)$ as a function of field strength for the (70Zn·30Cd)S:Mn,Cl phosphor. Notice the decrease in ρ with increasing beam current density over the range 0.02-0.5 μa/cm².

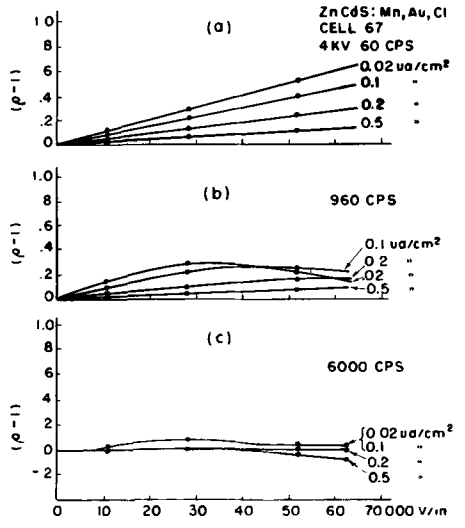

Fig. 5. $(\rho - 1)$ as a function of field strength for the (50Zn·50Cd)S:Mn,Au,Cl phosphor. Note the decrease in ρ with increasing frequency, field strength, and beam current density.

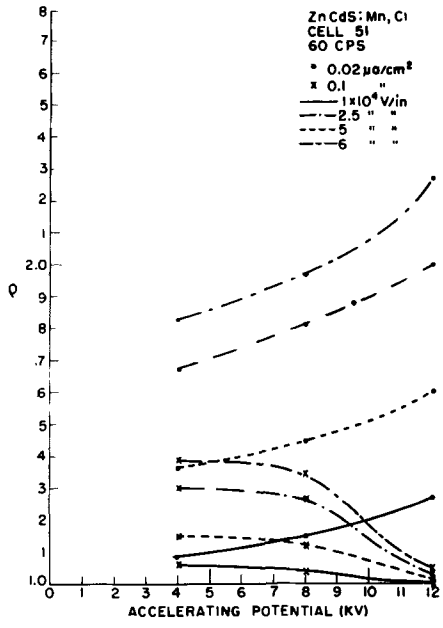

Fig. 6. Enhancement ratio, ρ, as a function of accelerating potential for the (70Zn·30Cd)S:Mn,Cl phosphor. At low beam current densities ρ increases with increasing accelerating potential over the range 4-12 kv; at high beam current densities ρ decreases with increasing accelerating potential. The value of the beam current density at the cross-over point between the two kinds of behavior varies from cell to cell. A similar behavior is observed for the (50Zn·50Cd)S:Mn,Au,Cl phosphor.

of higher fields resulted in arcing which deteriorated the cells. With the Mn,Cl phosphor the quantity $(\rho-1)$ increases linearly with field strength (Fig. 4). The quantity $(\rho-1)$ also increases linearly with increasing field strength for the Mn,Au,Cl phosphor at low frequency (60 cps) and 4 kv. As the frequency increases there is a negative deviation from linearity; the curves obtained at 0.02 and 0.1 μa/cm^2 first show the deviation, but as the frequency increases the 0.2 and 0.5 μa/cm^2 curves also deviate. In the frequency range of 3800-6000 cps there is quenching at high field strengths. This behavior is shown in Fig. 5. At 8 and 12 kv the quantity $(\rho - 1)$ is linear except at 6000 cps where quenching is observed at a beam current density of 0.2 and 0.5 μa/cm^2 and high field strengths.

Enhancement as a function of beam current density.—The effect of beam current density on the enhancement factor was studied over the range of 0.01 to 0.5 μa/cm^2 for the Mn,Cl phosphor and 0.02 to 0.5 μa/cm^2 for the Mn,Au,Cl phosphor. At higher current densities, or for long times of bombardment at the lower current densities there is some decomposition of the Nylon as evidenced by its acquiring a brown discoloration. Because of this, measurements at high current densities were taken after those at lower densities. Between measurements, the current was either lowered or turned off.

The enhancement factor is strongly dependent on the beam current density as can be seen in Fig. 4 and 5. Maximum enhancement occurs at the lower densities and decreases with increasing current density. This decrease in enhancement with increasing incident energy is not limited to the present studies but also is found with several of the other enhancement effects mentioned earlier (3-7, 9).

Enhancement as a function of accelerating potential.—The effect of accelerating potential was studied over the range of 4-12 kv. The results are a little erratic and depend on the beam current density, field strength, and frequency. In general the enhancement factor increases with increasing accelerating potential for low current densities and decreases for high current densities (Fig. 6). The value of the beam current density at the cross-over point between the two kinds of behavior varies from cell to cell, the range being from 0.1-0.5 μa/cm^2.

Brightness waves.—Brightness waves from cells made with the Mn,Cl phosphor were observed on a dual-beam oscilloscope. These were displayed in two different ways. In one method, the photomultiplier output was fed into one set of vertical deflection plates and the alternating voltage across the cell into the other set. The two channels were locked together so that the signals were synchronized. This resulted in a linear trace that showed the time relationship of the two curves. In the second method a trace similar to a Lissajous figure was obtained. This was accomplished by connecting the photomultiplier output to one set of vertical plates and the alternating voltage across the cell to both sets of horizontal plates. The two channels were locked together and the horizontal traces superimposed. In this way one channel, the one having only the horizontal signal, acts as a zero reference while the other shows the brightness wave form as a function of voltage.

The study of the wave form was made at beam current densities of 0.01 and 0.02 μa/cm^2 at variable frequency, field strength, and accelerating potential. The brightness waves show two peaks per cycle of applied voltage, with one peak generally larger than the other (Fig. 7 and 8). The brightness peaks appear after the voltage maxima, as can be seen in the figures. This is similar to the brightness waves obtained during the electroluminescence of Mn-

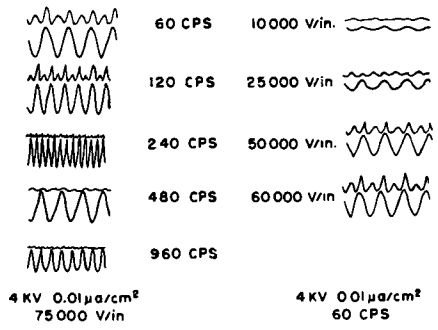

Fig. 7. Linear display of brightness and voltage wave forms for the (70Zn·30Cd)S:Mn,Cl phosphor. The curves on the left showe the influence of frequency and those on the right the influence of field strength. The bottom curve of each pair of curves is the voltage wave form.

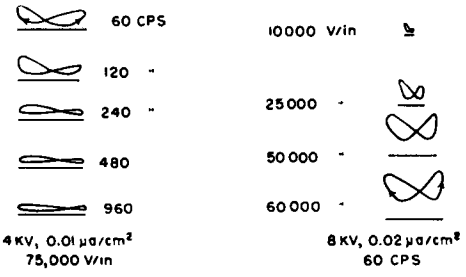

Fig. 8. Lissajous-type of display showing, on the left, the influence of frequency and, on the right, the influence of field strength on the brightness waves of the (70Zn·30Cd)S:Mn,Cl phosphor. The transparent conducting electrode is negative to the left and positive to the right. The direction of the trace is shown by arrows.

activated zinc sulfide phosphors (15). On increasing the field strength both peaks generally increased proportionally. In general the larger peak occurred after the transparent electrode became positive. On increasing the frequency of the applied field, the brightness waves shift slightly to later times, the magnitude of the shift varying from cell to cell. There also appears to be some field strength dependence of the brightness peaks, but the dependence is very erratic. The shift with increasing field strength is also to later times. Variations in beam current density and accelerating potential seem to have little, if any, effect on the waveform relationships.

Examination of the wave form shows the presence of two components, an a-c component superimposed upon a d-c component (Fig. 8). On increasing the field strength, at constant frequency, both the a-c and the d-c components increase, with the amplitude of the former increasing the faster. On increasing the frequency at constant field strength, the d-c component decreases slightly while the amplitude of the alternating component decreases fairly rapidly.

Miscellaneous observations.—In addition to the enhancement effect there is also a Gudden-Pohl effect. Immediately after the application of the field to a cell under cathode-ray excitation there is a rapid increase in brightness to some maximum value followed by a rapid decrease to a constant value which is higher than the initial cathodoluminescence. This permanent increase in light output here has been called the enhancement effect. Removal of the field also causes a transient brightness increase which decreases rapidly to the original field-off value. Both the magnitude and the decay time of the transient component increase with increasing field strength. Equilibrium was usually obtained within 5 sec after the application or removal of the field.

Relative brightness obtained with the enhancement effect.—In order to compare the relative brightness obtained with cathodoelectroluminescence with that of the usual P4 phosphor,[3] cells were prepared using a P4 phosphor (RCA #33Z259). Table I shows the results of brightness measurements (no field) for different beam current densities and accelerating potentials. An RCA 1P22 photomultiplier corrected for eye sensitivity was used in making these measurements. The enhancement ratio used for a given exciting condition is the maximum that was obtained under those conditions, i.e., for any value of frequency. The brightness with field acting was obtained by multiplying the brightness of the ZnCdS:Mn,Cl phosphor, no field acting, by the selected value of the enhancement ratio. As can be seen from Table I, depending on the exciting conditions,

[3] The phosphor used in black-and-white television, designated P4, is in reality a mixture of two phosphors, one (ZnS:Ag) having a blue emission and the other (ZnCdS:Ag) a yellow emission.

Table I. Relative brightness of (70Zn·30Cd)S:Mn,Cl phosphor, with and without field acting, compared to a standard P4 phosphor

Phosphor	Current density, μa/cm²	4 kv			8 kv			12 kv		
		ρ_{max}*	Brightness (B)†	B Enhanced = $\rho_{max}B$	ρ_{max}	B	$\rho_{max}B$	ρ_{max}	B	$\rho_{max}B$
RCA P4	0.01	—	14.7	—	—	176	—	—	750	—
	0.02	—	24	—	—	480	—	—	1,420	—
	0.1	—	163	—	—	2,500	—	—	7,900	—
	0.2	—	310	—	—	4,900	—	—	15,000	—
	0.5	—	770	—	—	11,170	—	—	30,000	—
(70Zn·30Cd)S: Mn, Cl	0.01	2.36	1.16(12.7)‡	2.74(5.38)	3.07	7(25.2)	21.4(8.23)	4.03	25(30)	100.7(7.4)
	0.02	1.99	1.95(12.3)	3.88(6.2)	2.4	17(27.2)	42.3(11.2)	2.36	60(23.5)	141.3(10.0)
	0.1	1.38	7.7(21.2)	10.6(15.4)	1.5	82(30.5)	122.8(20.4)	1.33	220(35.9)	292(27.0)
	0.2	1.26	12.7(24.4)	16(24.2)	1.26	145(33.8)	182.15(26.9)	1.23	360(41.6)	444(33.7)
	0.5	1.13	27.5(28.8)	31.1(28.0)	1.13	300(39)	339(33.0)	1.06	800(37.6)	848(35.4)

* The value of ρ is the maximum under the given accelerating potential and current density.
† Brightness in arbitrary units with no field acting.
‡ The number in parenthesis is the ratio $B_{P4}/B_{ZnCdS:Mn,Cl}$.

Table II. Maximum values of ρ for the ZnCdS:Mn,Cl and the ZnCdS:Mn,Au,Cl phosphors

Accelerating potential, kv	Beam current density, $\mu a/cm^2$	(70Zn 30Cd)S: Mn, Cl ρ	(50Zn·50Cd)S: Mn, Au, Cl ρ
4	0.01	2.36	—
	0.02	1.99	1.85
	1.0	1.38	1.59
	0.2	1.26	1.24
	0.5	1.13	1.14
8	0.01	3.07	—
	0.02	2.40	1.48
	0.1	1.50	1.20
	0.2	1.26	1.15
	0.5	1.13	1.08
12	0.01	4.03	—
	0.02	2.36	1.59
	0.1	1.33	1.18
	0.2	1.23	1.16
	0.5	1.06	1.07

the P4 phosphor is approximately 5-35 times brighter than the field-enhanced ZnCdS:Mn,Cl phosphor.

Discussion

An increase in light output is observed when an alternating electric field is applied to a 2-mil thick cell made with (70Zn·30Cd)S:Mn,Cl phosphor or, under certain conditions, with (50Zn 50Cd)S:Mn,-Au,Cl phosphor which is under cathode-ray excitation. As can be seen from Fig 9, the total light output (B) is greater than the sum of the electroluminescence (B_{el}) and the cathodoluminescence (B_{cl}). The enhancement ratio, ρ, is found to depend on several factors, the most important being the frequency and strength of the applied field, the accelerating potential, and the beam current density. The Mn,Cl phosphor has the brighter cathodoluminescence and also the larger enhancement factor (Table II).

In many respects the behavior of the ZnCdS:-Mn,Au,Cl phosphor is similar to the ZnCdS:Mn,Cl phosphor. The major differences are: (a) quenching occurs with the former phosphor at 4, 8, and 12 kv at high beam current densities, high field strengths, and high frequencies. (b) The quantity (ρ -1) as a function of field strength is linear for the Mn,Cl phosphor but may have a negative deviation from linearity at 4, 8, and 12 kv for the Mn,Au,Cl phosphor depending on the frequency, field strength, and beam current density.

Several characteristics of this effect are similar in nature to ordinary electroluminescence, i.e., the shape and number of brightness waves per cycle of applied field, the increase in ρ with field strength, the effect of frequency on the a-c component of the light output, and the possible shift of the brightness peaks with frequency (16). There are also some dissimilarities, the main ones being the decrease in ρ with increasing frequency and the apparent shift of the brightness waves to later times with increasing field strength.

This new enhancement effect is somewhat similar to some of the other enhancement effects in that there is a decrease in enhancement with increasing high exciting intensity (3-7, 9). The x-ray and

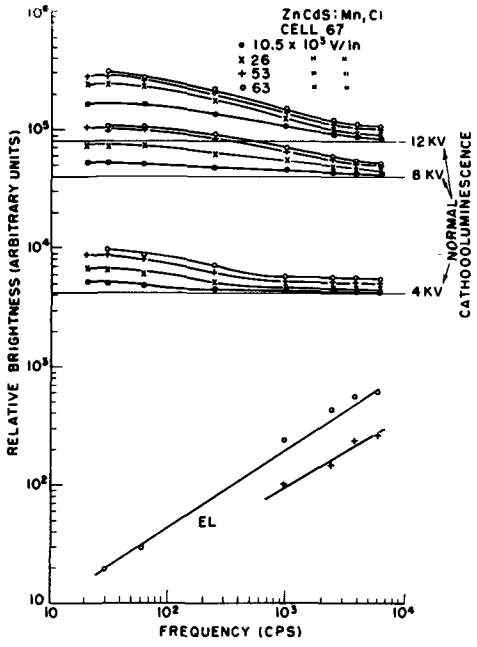

Fig. 9. Relative brightness of the enhanced cathodoluminescence and the electroluminescence of (30Zn·30Cd)S:Mn,Cl phosphor. Beam current density 0.01 $\mu a/cm^2$.

cathode-ray enhancement effects differ with respect to frequency in that there appears to be little frequency dependence for x-ray enhancement. This may be related to the difference in penetration between x-rays and cathode-rays.

Because of the preliminary nature of this work no conclusive theory can be developed at this time for the cathodoelectroluminescent effect. From the general behavior of this effect and the similarity to ordinary electroluminescence, it would appear that the effect is fundamentally radiation-controlled electroluminescence and is similar to the mechanism proposed by Williams for Cusano's and Destriau's enhancement effects (17). Recently, however, Curie (18), Destriau, (19), and Ivey (20) have concluded that the field-enhancement effect observed by Destriau does not have the same mechanism as that observed by Cusano. This presumably can be extended to the effect reported on here. Because of the complexity of cathodoluminescence in general and of the present effect, it may be extremely difficult to elucidate the enhancement mechanism.

Acknowledgments

The writer would like to thank Mr. E.G.F. Arnott and Dr. H. F. Ivey for suggesting this project (21) and Professor G. Destriau for supplying the information relating to the preparation of the ZnCdS:Mn,Cl phosphor and for the sample of the ZnCdS:Mn,Au,-Cl phosphor. Thanks also are due to Mr. G. Scanlon for his help in cell preparation and for obtaining some of the measurements. Acknowledgment should also be made to Drs. H.F. Ivey and W.A. Thornton for their advice and aid in solving some of the circuit problems and for the many valuable discussions held with them.

Manuscript received Dec. 15, 1958. This paper was prepared for delivery before the Washington Meeting, May 12-16, 1957.

Any discussion of this paper will appear in a Discussion Section to be published in the June 1960 JOURNAL.

REFERENCES

1. G. Destriau, J. Mattler, M. Destriau, and H. E. Gumlich, *This Journal*, **102**, 682 (1955).
2. G. Destriau, *Compt. rend.*, **245**, 1913 (1957).
3. D. A. Cusano, *Phys. Rev.*, **98**, 546 (1955).
4. D. A. Cusano, *ibid.*, **106**, 604 (1957).
5. D. A. Cusano, *IRE Trans. Nuclear Science*, NS3, #4, November 1956.
6. W. A. Thornton, *Bull. Am. Phys. Soc.*, **3**, 273 (1958) Abstract SP-1.
7. W. A. Thornton, *ibid.*, Abstract V-11.
8. J. Woods, *J. Electronics and Control*, **3**, 531 (1957).
9. R. E. Halsted, *Phys. Rev.*, **90**, 1807 (1955).
10. H. Gobrecht and H. Gumlich, *J. phys., rad.*, **17**, 754 (1956).
11. J. Mattler, *ibid.*, **17**, 758 (1956).
12. G. Neumark, *Phys. Rev.*, **103**, 416 (1956).
13. J. Woods and J. Wright, *Proc. Phys. Soc. (London)*, **68B**, 566 (1955).
14. H. Gobrecht, H. E. Gumlich, H. Nelkowski, and D. Langer, *Z. Phys.*, **149**, 504 (1957).
15. J. Mattler, *J. Phys., rad.*, **17**, 725 (1956).
16. W. A. Thornton, *Phys. Rev.*, **102**, 38 (1956).
17. F. E. Williams, *ibid.*, **98**, 547 (1956).
18. D. Curie, "Progress in Semiconductors," Vol. 2, 249, John Wiley, New York (1957).
19. G. Destriau, *Compt. rend.*, **245**, 1797 (1957).
20. H. F. Ivey, International Conference on Solid-State Physics, Brussels, 1958.
21. E. G. F. Arnott and H. F. Ivey, U. S. Pat. 2,863,084, Dec. 2, 1958.

Influence of Hydrogen on the Red ZnS-Cu Fluorescence

W. van Gool and A. P. D. M. Cleiren

Philips Research Laboratories, N. V. Philips' Gloeilampenfabrieken, Eindhoven, Netherlands

ABSTRACT

Self-coactivated ZnS-Cu phosphors were made by firing in different atmospheres. When H_2S/H_2 mixtures were used, the red fluorescence decreased with increasing amounts of hydrogen. With A/S_2 or with N_2/S_2 atmospheres no red fluorescence was obtained. These experimental results can be summarized by stating that, in order to obtain the red fluorescence, hydrogen must be incorporated into the phosphor and the sulfur pressure must be sufficiently high. The hydrogen either forms a part of the red center or it destroys or replaces a killer center that prevents the occurrence of red fluorescence when hydrogen is absent. In connection with the high sensitivity of the red fluorescence to small amounts of impurities it is suggested that the concentration of the red centers is much smaller than the amount of incorporated copper.

Some years ago Froelich (1) made an extensive study of the red fluorescence obtained by activating ZnS with Cu without coactivators such as chlorine or trivalent ions. Recently new data on the preparation of these powders and their properties were reported by Aven and Potter (2). In spite of this work it is as yet not possible to give a model of the structure of the centers which would account for this red fluorescence.

In our own investigations, which confirmed the more important facts given by the above-mentioned authors, we wanted to make sure that hydrogen had no influence on the red fluorescence. In view of the fact that most powders had been in contact with an atmosphere containing hydrogen in one way or another, the role of hydrogen should not be disregarded entirely. The experiments indicate that indeed hydrogen must be incorporated into the lattice in order to obtain the red fluorescence, as is described in the next sections.

Preparation of Powders and Firing Conditions

Several phosphors were made in gas atmospheres containing H_2S, S_2, and H_2. A fluorescent grade ZnS, precipitated from an acid $ZnSO_4$ solution, was used. By chemical analysis about 0.4% SO_4 and 0.003% Cl were found in the starting material. Spectrographical analysis showed 0.0005-0.0010% Pb and the other impurities were below their detection limit (all percentages are given by weight). The ZnS was wetted with a $CuSO_4$ solution, dried at 90°C, and mixed. The concentration in these phosphors was 10^{-4} gram atom Cu per mole ZnS.

The H_2S was taken from tanks. In the earlier stages of this research the H_2S was washed with an acid $CrCl_2$ solution to eliminate O_2 (3), with a solution of NaHS to eliminate HCl, and then dried over P_2O_5. At a certain stage of this investigation the red ZnS-Cu emission could not be reproduced. A careful investigation of the working conditions indicated that a change-over from one tank of H_2S to another was the cause of this failure. Further investigation showed that some tanks contained only small amounts of CO_2, whereas others contained about 1% CO_2. For this reason the H_2S was also washed with $Ba(OH)_2$ solution in the later stages of this research. The H_2S gas may contain small amounts of methylene chloride that are not removed by the purification technique used in these experiments. There was, however, no indication from the fluorescence of the powders that this impurity interfered with the result.

Hydrogen, nitrogen, and argon were taken from tanks and were of the purest quality available. In some experiments they were washed with an acid $CrCl_2$ solution, with a KOH solution, and then dried over P_2O_5. In other cases traces of oxygen were re-

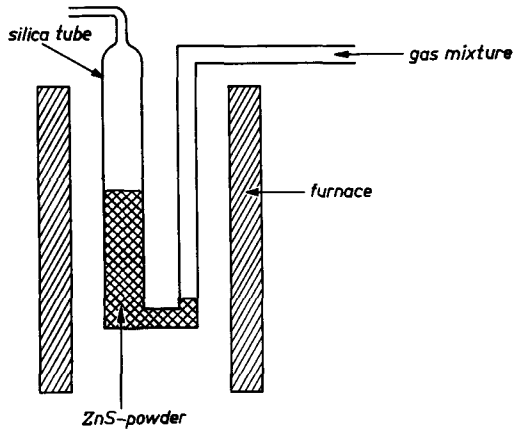

Fig. 1. Firing method used normally

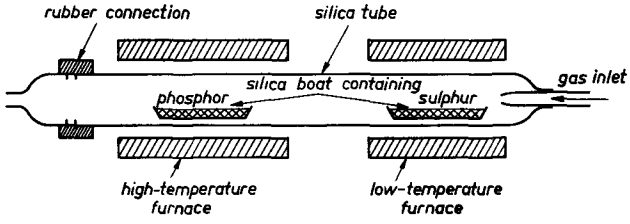

Fig. 2. Firing method used for producing sulfur-containing atmospheres.

moved from the nitrogen by means of a copper oven. When necessary the gases were mixed first and then passed through one purifying set. The sulfur used was of high purity: the only impurity found by spectrographical analysis was 0.00003% (by weight) of Cu.

Two different firing techniques were used. The first one, which was used in most of our experiments, is shown in Fig. 1. The second one, shown in Fig. 2, was used when addition of sulfur to the gases was necessary. By changing the temperature of the sulfur-containing part of the silica tube and the gas-flow rate, different sulfur pressures were obtained. In both firing techniques the tubes with powder were placed in the furnace after the furnace had reached the required temperature; thus the powders reached the firing temperature within a few minutes.

All powders were cooled as rapidly as possible. In the first firing technique this was done by immersing the firing tube in water; in the second one the outside tube was flooded with water.

Several cross experiments were made. Some powders were fired with both setups in order to make sure that no unexpected factors were important. Except for the case already mentioned, no significant differences were found.

Table I. ZnS-10^{-4} Cu fired in H_2S [not passed through $Ba(OH)_2$] 2 hr 1100°C

Phosphor	Firing method	Gas flow, ml/min*
AC 497	Fig. 1	75
AC 510	Fig. 2	200
AC 538	Fig. 2	200

* The gas flow was always measured at room temperature.

Table II. ZnS-10^{-4} Cu, fired in H_2S/H_2, 2 hr 1100°C

Phosphor	Firing method	Gases [no $Ba(OH)_2$ used]	Total gas flow, ml/min	Ratio H_2S/H_2
AC 499	Fig. 1	H_2 not purified	100	7/93
AC 532	Fig. 1	H_2 purified	100	7/93
AC 511	Fig. 2	H_2 not purified	200	7/93
AC 503	Fig. 1	H_2 not purified	100	20/80
AC 501	Fig. 1	H_2 not purified	100	44/56
AC 531	Fig. 1	H_2 purified	100	44/56

Three powders were fired in pure H_2S; some details of the firing conditions are given in Table I.

A second set of fluorescent powders was obtained by firing in H_2S/H_2 mixtures, as detailed in Table II.

A third series of phosphors was made by firing in H_2S/S_2 mixtures (Table III; AC 535, AC 536, and AC 537).

One single phosphor was made by passing pure H_2 over sulfur (Table III, AC 543).

In a fourth series nitrogen or argon were used as carrier gases. Powders AC 528, AC 529, AC 530, and AC 550 were obtained by passing the nitrogen over sulfur. AC 549 was fired in argon carrier gas (Table IV). The powders AC 533 and AC 534 were made by passing a N_2/H_2 mixture over sulfur.

In order to eliminate the effect of contaminations originating from the silica walls, ZnS-10^{-4} Cu was fired in two new vessels (Fig. 1). In each tube four firings were made in purified hydrogen. One tube was cleaned in the normal way after each firing. The second tube was not cleaned between the firings, the powder was merely shaken out (AC 551-AC 557).

Observations and Measurements

The fluorescence of the powders described in the preceding section was studied with 3650Å excitation. Although the relative brightness of the powders could be established easily by visual inspection of the powders, the measurement of the red fluores-

Table III. ZnS-10^{-4} Cu, fired in H_2S/S_2 or H_2/S_2, 1100°C, 200 ml gas/min, firing setup Fig. 2

Phosphor	Gas	Firing time	Evaporated sulfur, g
AC 535	H_2S no $Ba(OH)_2$ used	2 hr	3.418
AC 536	H_2S no $Ba(OH)_2$ used	2 hr	7.228
AC 537	H_2S no $Ba(OH)_2$ used	45 min	7.217
AC 543	H_2 purified	45 min	7.284

Table IV. ZnS-10^{-4} Cu, fired in N_2, N_2+H_2 or A, 1100°C

Phosphor	Gases used	Total gas flow, ml/min	Firing time	Evap. sulfur, g
AC 528	N_2 (copper oven)	200	2 hr	0.0245
AC 529	N_2 (copper oven)	200	2 hr	2.712
AC 530	N_2 (copper oven, P_2O_5)	200	2 hr	3.879
AC 550	N_2 ($CrCl_2$, KOH, P_2O_5)	100	45 min	9.177
AC 549	A ($CrCl_2$, KOH, P_2O_5)	200	2 hr	4.355
AC 533	N_2/H_2 70—30 (N_2 + H_2 — $CrCl_2$, P_2O_5; N_2-copper oven)	200	2 hr	4.575
AC 534	N_2/H_2 90—10 (N_2 + H_2 — $CrCl_2$, P_2O_5; N_2-copper oven)	200	2 hr	4.463

Table V. Relative luminance of phosphor layers, measured with Schott RG1 red filter

Fired in	H_2S		H_2S/S_2		H_2S/H_2		$N_2/S_2/H_2$		H_2, N_2/S_2, A/S_2	
	No. of phosphor	Lum.	No. of phosphor	Lum.	No. of phosphor	Lum.	No. of phosphor	Lum.	No. of phosphor	Lum.
	AC 497	73	AC 535	89	AC 543	38	AC 533	14	AC 551-557	<6
	AC 510	44	AC 536	94	AC 501	25	AC 534	8-10	AC 528-530	
	AC 538	100	AC 537	71	AC 531	19			AC 550	
					AC 503, AC 499, AC 532, AC 511	<6			AC 549	

cence was difficult owing to the weakness of the red light emitted. The best method was to compare the luminance of a phosphor layer with that of a mat surface by means of a Lommer-Brodhun photometer containing a Schott red RG1 filter in the eyepiece. The mat surface was illuminated by an incandescent lamp, and the lamp voltage was varied so as to match the luminance of both surfaces. Every measurement was repeated two or three times, and the average of the lamp voltages was used in the calculation. The red luminance (as seen through a Schott red RG1 filter) of the mat surface at different voltage settings was calibrated with a laboratory luminance meter. The luminance of one phosphor layer (AC 538) arbitrarily was given the value 100. Calculated values of the luminance of the phosphor layers are summarized in Table V.

Phosphors made in low sulfur pressure or made in atmospheres without hydrogen did not show any red fluorescence; this corresponds to the values below the minimum value detectable with the luminance meter (about 6 units). They had a weak green or green-blue fluorescence. This fluorescence was killed when infrared light was shone on the phosphors together with the u.v. at room temperature. No stimulation of an afterglow was found with infrared radiation. At low temperature (77°K) these phenomena were reversed: the fluorescence was not influenced by infrared, but a stimulation of the afterglow was found. During the stimulation, the emitted light had the same color as during u.v. excitation, and not the slightest indication of any red fluorescence was found.

It is well known that the red Cu-fluorescence has the important property that it is much more sensitive to impurities than the fluorescence of normally activated ZnS powders; small amounts of O_2, CO_2, or H_2O all disturb the red fluorescence (1, 2). When adding aluminum in the order of 10 mole % of the added amount of Cu, one finds a blue emission as strong as the red emission. We have confirmed these observations.

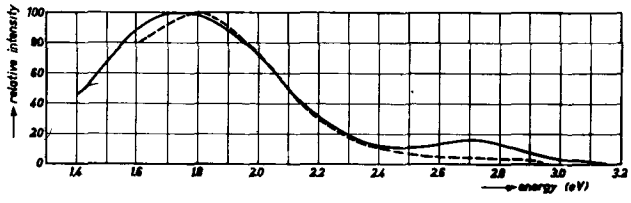

Fig. 3. Spectral distribution of red ZnS-Cu phosphor. ——— AC 538; measured at room temperature; - - - - - spectral distribution measured by Aven and Potter (2), Fig. 3 (x=0).

The spectral energy distribution was measured with the aid of a Leiss (Berlin) double mirror-monochromator with sodium chloride prisms. The 800 cps chopped radiation of the phosphor was imaged on the entrance slit of the monochromator. The output of the detector, amplified by a tuned a-c amplifier with synchronous detection, was recorded automatically as a function of the wave length.

The phosphor was excited by the radiation of a high-pressure mercury discharge lamp (the inner part of a Philips HP 125W lamp with stabilized discharge) from which the long wave length u.v. radiation was isolated by a combination of Schott filters UG11 and BG18. The BG18-filter was used to remove the transmission of the UG11 filter in the red part of the spectrum.

As a detector for the spectral region from 3.5 about to 1.65 ev a selected RCA photomultiplier (type IP28) was used with very high sensitivity in the red. For radiation of lower frequencies a Philips photomultiplier type 51CVP with Cs-O-Ag photocathode was used.

The relative emitted power of the phosphor was found from the recorded photocurrent by calibrating the equipment with the aid of a tungsten ribbon lamp with known spectral distribution. In Fig. 3 the spectral distribution of AC 538 is reported together with one of the distributions given by Aven and Potter (2).

Discussion

In describing the equilibrium system ZnS-sulfur vapor, the sulfur pressure is sufficient to define the oxidation-reduction state of the ZnS crystal. In that case the zinc pressure can be derived from the sulfur pressure according to the equation

$$p_{Zn} \cdot p_{S_2}^{1/2} = K_{ZnS} \qquad [1]$$

When hydrogen is also present in the atmosphere and when hydrogen is incorporated into the ZnS, the value of the hydrogen pressure must also be known in order to define the state of the ZnS powders. In equilibrium it is unimportant whether the presence of the hydrogen is defined by the hydrogen pressure itself, by the H_2S pressure, or by the pressure of some other hydrogen compounds, because these pressures are correlated by a relation of type [2]

$$\frac{p_{H_2}^2 \cdot p_{S_2}}{(p_{H_2S})^2} = K_{H_2S} \qquad [2]$$

A third equation is obtained from the condition that the total pressure is 1 atm, thus

$$p_{Zn} + p_{H_2} + p_{H_2S} + p_{S_2} = 1 \qquad [3]$$

A fourth equation is obtained from the relative amounts of gases or sulfur used during the experiment. In the case of pure H_2S this equation is

$$p_{H_2} = 2p_{S_2} \qquad [4a]$$

When 1 mole gas mixture, introduced in the firing vessel, contains p moles H_2 and $(1-p)$ moles H_2S and when, after establishment of the equilibrium, x moles S_2 have been formed, then we have

$$p_{H_2} = \frac{p + 2x}{1 + x}$$

$$p_{S_2} = \frac{x}{1 + x}$$

Thus, after elimination of x

$$p_{H_2} = p + (2 - p) \cdot p_{S_2} \qquad [4b]$$

In the same way a similar additional equation can be formulated for every experiment. We used $K_{H_2S} = 17 \cdot 10^{-3}$ atm (4) at 1100°C.[1]

The value $K_{ZnS} = 5.4 \cdot 10^{-5}$ atm$^{3/2}$ at 1100°C was calculated from reference (6). Recent measurements by Spandau and Klanberg (7) and Neuhaus and Retting (8) do not permit the calculation of the dissociation constant K_{ZnS}. The total pressures of ZnS, as measured by Spandau and Klanberg, deviate from the values used in (6), but there is no important influence on the main aspects of these calculations. Calculated pressures are given in Table VI.

p_{Zn} is always so small that one can use the equation

$$p_{H_2} + p_{H_2S} + p_{S_2} = 1 \qquad [3a]$$

instead of [3] when only H_2, H_2S, S_2, and Zn are present in the atmosphere. The relation obtained by eliminating p_{H_2S} from Eq. [1] and [3a] is represented by the heavily drawn line in Fig. 4. In the same figure the pressure points of the fired powders are indicated. All pressures were calculated with the assumption that all equilibria were actually established. In some cases the sulfur pressure was lower than the minimum sulfur sublimation pressure of ZnS ($9.1 \cdot 10^{-4}$ atm) and thus the zinc pressure higher than the minimum zinc pressure. Then the question arises whether the gas flow is slow enough to provide sufficient time for the equilibria to be established (9). If this is not the case, the pressure will be stabilized on the minimum sublimation line. This has been indicated in Fig. 4 by arrows pointing to some powders (AC 499, AC 532, AC 511, AC 551-AC 557, and AC 528). As none of these powders has any red fluorescence (see below), the question of the exact localization of the firing conditions in the pressure diagram is not important.

[1] From the tables of (5) a value of $K_{H_2S} = 18.5 \cdot 10^{-3}$ atm was calculated. The difference between this constant and the one we used results in a relatively unimportant change in the pressure calculations.

Table VI. Calculated H_2 and S_2 pressures under equilibrium conditions, $T = 1100$°C

Powder	Gas introduced into the firing vessel	p_{H_2} (atm)	p_{S_2} (atm)
AC 497, AC 510, AC 538	H_2S	0.24	0.12
AC 535	H_2S/S_2	0.21	0.15
AC 536	H_2S/S_2	0.19	0.18
AC 537	H_2S/S_2	0.15	0.26
AC 543	H_2S/H_2	0.46	$2.1 \cdot 10^{-2}$
AC 501-531	H_2S/H_2	0.55	$1.0 \cdot 10^{-2}$
AC 503	H_2S/H_2	0.80	$1.0 \cdot 10^{-3}$
AC 499, AC 532, AC 511	H_2S/H_2	0.93	$1.0 \cdot 10^{-4}$
AC 533	$N_2/S_2/H_2$	0.18	$7.4 \cdot 10^{-3}$
AC 534	$N_2/S_2/H_2$	$4.1 \cdot 10^{-2}$	$3.4 \cdot 10^{-2}$
AC 551-557	H_2		
AC 528	N_2/S_2	—	$3.6 \cdot 10^{-4}$
AC 529	N_2/S_2	—	$3.8 \cdot 10^{-2}$
AC 530	N_2/S_2	—	$5.4 \cdot 10^{-2}$
AC 550	N_2/S_2	—	0.42
AC 549	A/S_2	—	$6.0 \cdot 10^{-2}$

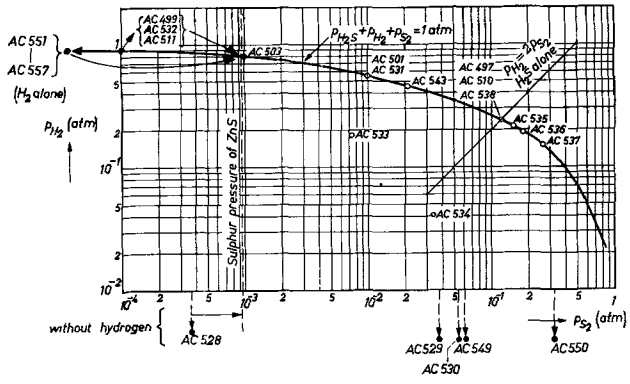

Fig. 4 Sulfur and hydrogen pressures used during preparation of the powders at 1100°C.

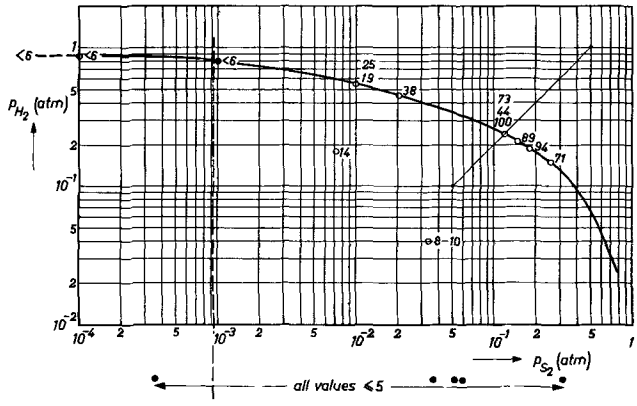

Fig. 5. Measured red fluorescence (in arbitrary units). The location in the pressure diagram corresponds with Fig. 4.

In order to facilitate the review of experimental results, the measured red fluorescence of the powders is inscribed at the respective pressure points in Fig. 5. From this figure it is immediately clear that two conditions had to be fulfilled in order to obtain the red fluorescence: (*a*) there must be hydrogen in the atmosphere, and (*b*) the sulfur pressure must be sufficiently high.

Unless these results are caused by impurity effects (see below), the first condition means that hydrogen is incorporated into the ZnS powders. At this time it is not possible to decide whether the hydrogen forms really a part of the red fluorescent center. The other explanation would be that without hydrogen the red centers would be present but that some other center kills the red fluorescence. Adding hydrogen then would transform the killer center into a harmless one. As there is, however, no evidence in our

work for the presence of the red centers in the powders fired without hydrogen, we prefer the first explanation.

Some doubt may be thrown on this conclusion on the basis of a few experiments described by Aven and Potter (2). They reported that firing ZnS-Cu in hydrogen first gave a blue fluorescence, but that repeated firings in the same vessel finally gave a red fluorescence. The authors interpreted their results with the transfer of a certain impurity (for instance aluminum) from the silica wall to the powder. We have found in some cases that the outside of the sintered powders did show a different fluorescence than the core, but this was restricted to a thin outer shell and the bulk of the powders was always homogeneous. Firing in hydrogen alone produced no red fluorescence, although the firings were repeated four times in the same vessel. Moreover, comparison of the powders AC 499, AC 503, AC 501, AC 543, and AC 497 (Table II) shows that the change in hydrogen pressure is rather small (by a factor of 4), but that the sulfur pressure changes at least by a factor of 100. The red fluorescence disappears completely at lower sulfur pressures in this series, and it seems improbable that a large change in impurity transfer should be brought about by a rather small change in hydrogen pressure. Therefore we believe that in the interpretation of our results we have to assume a direct influence of the sulfur pressure on the formation of the red fluorescence centers.

An important cross experiment is represented by the powders AC 533 and AC 534. With nitrogen no red fluorescence was found and with hydrogen the red fluorescence is decreased, as has been described above. Considering the great sensitivity of the red fluorescence to impurities it would be possible for some harmful impurity to have been introduced by each gas individually. But in using both gases together the red fluorescence was present again and thus the assumption about harmful gas impurities is made very improbable.

Some of the red fluorescent powders mentioned in (1) were made in a CS_2 atmosphere. This result is in conflict with the interpretation given in this paper. However, the experiments in (1) and (2) were not performed with the thought in mind that hydrogen in any form had to be removed carefully, and the experimental details necessary to settle this question are lacking in these papers.

Although the weakness of the red fluorescence as compared with that of strong red phosphors (for example color television phosphors) can be explained by assuming a small recombination coefficient in the kinetic mechanism, the assumption seems more probable that the concentration of the red centers is much smaller (by a factor of 10 to 100) than the added amount of Cu. Hence the occurrence of the red fluorescence centers results only in a minor change in the mechanism by which Cu is built into the lattice without hydrogen. This has three consequences. In the first place, the red fluorescence as such does not provide much useful information about the incorporation of Cu. In the second place, it is difficult to say anything definite about the structure of the red fluorescence centers so long as we do not know exactly the built-in mechanism of Cu. The diamagnetism of these ZnS-Cu phosphors, as found by Bowers and Melamed (10), can be interpreted as a diamagnetism of the majority of the built-in copper atoms. As long as we do not know the concentration of the red fluorescence centers the possibility that these centers are paramagnetic can not be excluded. Finally, this assumption can explain the high sensitivity of the red centers to impurities in a simple manner.

Perhaps one conclusion about the structure of the red fluorescence centers can be reached by comparing the red ZnS-Cu fluorescence with that of ZnS-Ag. According to the results published by Aven and Potter the red silver fluorescence has a spectral distribution different from that of Cu. Since hydrogen is also necessary for the red silver fluorescence the center must contain at least one metal (Ag or Cu) and one hydrogen atom or ion. As to the real nature of the center several possibilities arise depending on whether the impurities occupy substitutional or interstitial positions and on the valencies of these impurities.

In spite of the careful control of the preparative conditions a rather large spread in the luminance of the red phosphors was found, as can be seen from the powders fired in pure H_2S alone. Therefore it is impossible to give quantitative relationships between this luminance and the pressures used. Further investigations are necessary in order to find these quantitative relationships. In our opinion it is premature to give models for the red fluorescent centers as long as the experimental material is scarce and even partly contradictory.

Acknowledgments

The authors wish to express their thanks to Mr. H. J. M. Heyligers for his aid in the gas purifications and furnace construction. The assistance of Dr. P. M. van Alphen and Mr. A. H. C. Vliegen with the luminance measurement and of Dr. A. Bril with the measurement of the spectral distribution is gratefully acknowledged.

Manuscript received Jan. 7, 1959. This paper was prepared for delivery before the Philadelphia Meeting, May 3-7, 1959.

Any discussion of this paper will appear in a Discussion Section to be published in the June 1960 JOURNAL.

REFERENCES

1. H. C. Froelich, *This Journal*, **100**, 280 (1953).
2. M. H. Aven and R. M. Potter, *ibid.*, **105**, 134 (1958).
3. Gmelins Handbuch, Systemnummer 9 (Schwefel) Teil B Lieferung 1, S. 14, Verlag Chemie GmbH (1953).
4. *Ibid.*, p. 6.
5. W. H. Evans and D. D. Wagman, *J. Research Natl. Bur. Standards*, **49**, 141 (1952).
6. Gmelins Handbuch, Ergänzungsband Zink, 8. Auflage Verlag Chemie GmbH, S. 920 (1956).
7. H. Spandau and F. Klanberg, *Z. anorg u. allgem. Chem.*, **295**, 309 (1958).
8. A. Neuhaus and W. Retting, *Z. Elektrochem.*, **62**, 33 (1958).
9. J. Bloem and F. A. Kröger, *Z. Phys. Chem.*, **7**, 15 (1956).
10. R. Bowers and N. T. Melamed, *Phys. Rev.*, **99**, 1781 (1955).

The Fluorescence of Binary and Ternary Germanates of Group II Elements

H. Koelmans and C. M. C. Verhagen

Philips Research Laboratories, N. V. Philips' Gloeilampenfabrieken, Eindhoven, Netherlands

ABSTRACT

The fluorescence of binary and ternary germanates of Ca, Sr, Ba, Mg, and Zn with different activators was investigated. Germanate phosphors activated with Pb, Ti, and Mn are described. The ternary composition triangles are given together with the x-ray powder-diagrams of 23 hitherto unknown germanates.

A great deal of the research on inorganic phosphors has been concentrated on silicates. In contrast to this the germanates, which are closely related to the silicates, have drawn little attention. Only the orthogermanates of Mg, Zn, and Be have been investigated to some extent (1). For this reason it seemed worth while to investigate the fluorescence of germanates, also because nowadays pure GeO_2 is commercially available.

The work described in this article was done along the same lines and in close connection with the work of Klasens, Hoekstra, and Cox (2) on binary and ternary silicates. Most of the new germanates found are isomorphous with the corresponding silicates.

Preparation.—The starting materials used were reagent grade $CaCO_3$, $SrCO_3$, $BaCO_3$, $MgCO_3$, ZnO, and GeO_2. The activators, which included Pb, Ti, Mn, Sn, Ce, Bi, and Re, in form of solutions of their salts, were added in the required amounts to the raw materials. The suspension formed was evaporated to dryness and milled in a runner mill for 15 min. The blends were then heated in alundum crucibles in air at 1050°-1250° for 1 or 2 hr. In all cases 2 or 4% of the Ca-, Sr-, or Ba-carbonates used as base materials were substituted by the corresponding fluorides.

X-ray diagrams showed that this fluoride substitution greatly aided in quickly completing the reaction. It was shown by chemical analysis that after firing only a negligible amount of the fluoride was retained in the phosphors. The activator content was usually about 0.5 mole %. In order to prepare efficient phosphors an excess of free GeO_2 had to be avoided because GeO_2 absorbs u.v. radiation below 3150Å without giving any appreciable luminescence. The same is true for several of the germanates, especially those with a high GeO_2 content. This complication necessitated a careful choice of the composition with the aid of the phase diagrams to be discussed in section 3. X-ray diagrams of the fired powders were made with a North American Philips Geiger counter x-ray diffractometer using Co-K_α radiation.

Binary germanates.—The binary germanates found are listed in Table I together with the known binary silicates. The compounds labeled with the same letter in Table I are isomorphous. Our x-ray powder diagrams of the orthogermanates (2-1) of Ca, Sr, Ba, and Mg essentially correspond to those published by Ludekens (3). In contrast to Ludekens, who obtained only orthogermanates irrespective of the ratio of basic to acid oxides, we also found other compounds. Our mixtures were probably more reactive, especially because of the fluoride flux. The x-ray powder diagrams of the new 1-1, 2-3 and 1-2 germanates are given in Table II.

Ternary germanates.—The ternary germanates found are given in Table III together with the known ternary silicates. Table III shows that with the exception of the 2-1-2 BaMg- and BaZn-germa-

Table I. Binary germanates and silicates of Ca, Sr, Ba, Mg, and Zn. Identical letters in the columns denote that the corresponding compounds are isomorphous. Temperatures given are the firing temperatures in °C

Component oxides		Mole ratios of base to acid oxides							
		2-1		3-2	1-1		2-3	1-2	
CaO	GeO_2	a	1150°	—	d*	1200°	e 1100°	f	1150°
	SiO_2	b		c	d*		—	—	
SrO	GeO_2	g	1125°	—	h	1150°	—	i	1150°
	SiO_2	g		—	h		—	—	
BaO	GeO_2	g	1100°	—	h	1100°	—	i	1075°
	SiO_2	g		—	h		—	j	
MgO	GeO_2	k	1150°	—	m	1150°	—	—	
	SiO_2	l		—	n		—	—	
ZnO	GeO_2	o	1050°	—	—		—	—	
	SiO_2	o		—	—		—	—	

* $CaGeO_3$ is isomorphous with $\beta CaSiO_3$ (wollastonite); no other modifications of $CaGeO_3$ were found.

Table II. X-ray data of the binary germanates

$CaGeO_3$		$SrGeO_3$		$BaGeO_3$		$MgGeO_3$		$CaGe_2O_5$		$SrGe_2O_5$		$BaGe_2O_5$		$Ca_2Ge_3O_8$	
d (Å)	I	d (Å)	I	d (Å)	I	d (Å)	I	d (Å)	I	d (Å)	I	d (Å)	I	d (Å)	I
5.10	20	3.65	30	3.80	30	4.75	40	5.10	40	3.65	100	3.66	100	4.95	25
4.10	10	3.45	60	3.60	25	4.41	40	4.00	27	3.27	6	3.21	20	4.65	12
3.90	15	3.00	100	3.12	100	3.35	90	3.58	24	2.83	70	2.90	65	3.42	10
3.85	5	2.63	30	2.72	25	3.22	95	2.84	100	2.70	90	2.73	80	3.20	45
3.60	20	2.13	20	2.22	30	3.00	65	2.75	16	2.43	20	2.48	10	3.13	50
3.57	5	2.09	45	2.20	70	2.95	100	2.67	13	2.09	16	2.17	14	3.00	100
3.37	30	1.95	10	2.05	25	2.91	25	2.42	13	1.95	18	1.98	18	2.77	6
3.27	25	1.82	10	1.90	15	2.79	15	2.36	14	1.82	20	1.83	14	2.64	80
3.17	25	1.71	10	1.80	25	2.58	100	2.31	13	1.76	22	1.79	16	2.60	35
3.05	100	1.63	10	1.71	20	2.53	55	2.22	9	1.64	25	1.67	14	2.53	25
2.98	15	1.57	15	1.64	30	2.48	20	2.00	7	1.49	10	1.52	10	2.32	12
2.68	10	1.49	5	1.56	20	2.05	15	1.79	5	1.415	12	1.43	8	2.28	6
2.56	20	1.38	5	1.44	10	2.02	30	1.77	13	1.345	10	1.37	10	2.05	8
2.39	5	1.32	10	1.39	30	1.73	15	1.75	15					2.03	10
2.21	5					1.65	15	1.67	13					1.70	15
1.98	5					1.64	15	1.60	9					1.69	25
1.88	10					1.55	15	1.555	9					1.65	18
1.81	10					1.52	30	1.515	9					1.64	18
1.76	5					1.49	20	1.485	9					1.575	15
1.66	10					1.42	15	1.42	11					1.535	10
1.58	5							1.315	12					1.50	8
1.57	5													1.485	6
1.53	10													1.36	8

Table III. Ternary germanates and silicates of Ca, Sr, Ba, Mg, and Zn. Identical letters in the columns denote that the corresponding compounds are isomorphous. The temperatures given are the firing temperatures in °C

Component oxides		Mole ratios of base to acid oxides									
		2-1-2		1-1-1		1-2-2		3-1-2		1-1-2	
CaO, MgO	GeO_2	—		q	1100°	—		—		s	1100°
	SiO_2	p		q		—		v		s	
CaO, ZnO	GeO_2	p	1150°	—		—		—		s	1100°
	SiO_2	p		—		—		—		—	
SrO, MgO	GeO_2	p	1100°	—		—		v	1150°	s	1100°
	SiO_2	p		—		—		v		—	
SrO, ZnO	GeO_2	p	1150°	—		—		—		t	1050°*
	SiO_2	p		—		u		—		—	
BaO, MgO	GeO_2	p	1100°	—		—		v	1100°	t	1100°
	SiO_2	v		—		w		v		—	
BaO, ZnO	GeO_2	p	1100°	x	1100°	w*		—		—	
	SiO_2	v		x		w		—		—	

* $BaZn_2Ge_2O_7$ and $SrZnGe_2O_6$ are rather unstable. Lines of other compounds, especially of Zn_2GeO_4, also occur in the x-ray diagrams of these powders.

nates all corresponding germanates and silicates are isomorphous. This was confirmed by the formation of uninterrupted series of solid solutions. The x-ray powder data of the new ternary germanates are given in Tables IV-VII. The 2-1-2 germanates (Table IV) are all isomorphous with $Ca_2ZnSi_2O_7$ (hardystonite) and $Ca_2MgSi_2O_7$ (akermannite) which are tetragonal. The diagrams could readily be indexed. Cell dimensions are given in Table VIII in which it is seen that the corresponding Zn- and Mg-compounds have practically the same cell dimensions.

The 3-1-2 compounds occur only in the systems containing magnesium. $Sr_3MgGe_2O_8$ and $Ba_3MgGe_2O_8$ are isomorphous with $Ca_3MgSi_2O_8$ (merwinite) which is orthorhombic. With this knowledge the x-ray diagrams could be indexed (Table V) and the unit cell dimensions could be calculated.

$Sr_3MgGe_2O_8$	a = 5.5	b = 9.6	c = 7.3
$Ba_3MgGe_2O_8$	a = 5.7	b = 10.0	c = 7.4

$CaMgGe_2O_6$, $CaZnGe_2O_6$, and $SrMgGe_2O_6$ (Table VI) are isomorphous with $CaMgSi_2O_6$ (diopside), which is the only compound with this structure in the ternary silicate systems. $SrZnGe_2O_6$ and $BaMgGe_2O_6$ are isomorphous but have no diopside structure.

Sufficient firings were made to construct the composition phase triangles shown in Fig. 1. The final phases produced by the firing of compositions falling on conjugation lines are given by the compounds at the end of the lines. The final phases produced by the firing of compositions falling within the triangles are given by the compounds at the apexes of the triangles.

Activation with Pb.—The binary germanates did not give efficient phosphors with Pb activation. Of the ternary compounds the 2-1-2 BaMg-, SrMg-, BaZn-, and SrZn-germanates gave u.v. emitting phosphors. The emissions are given in Fig. 2 together with those of the corresponding silicates. The phosphors are excited strongly only with 2537Å. It is

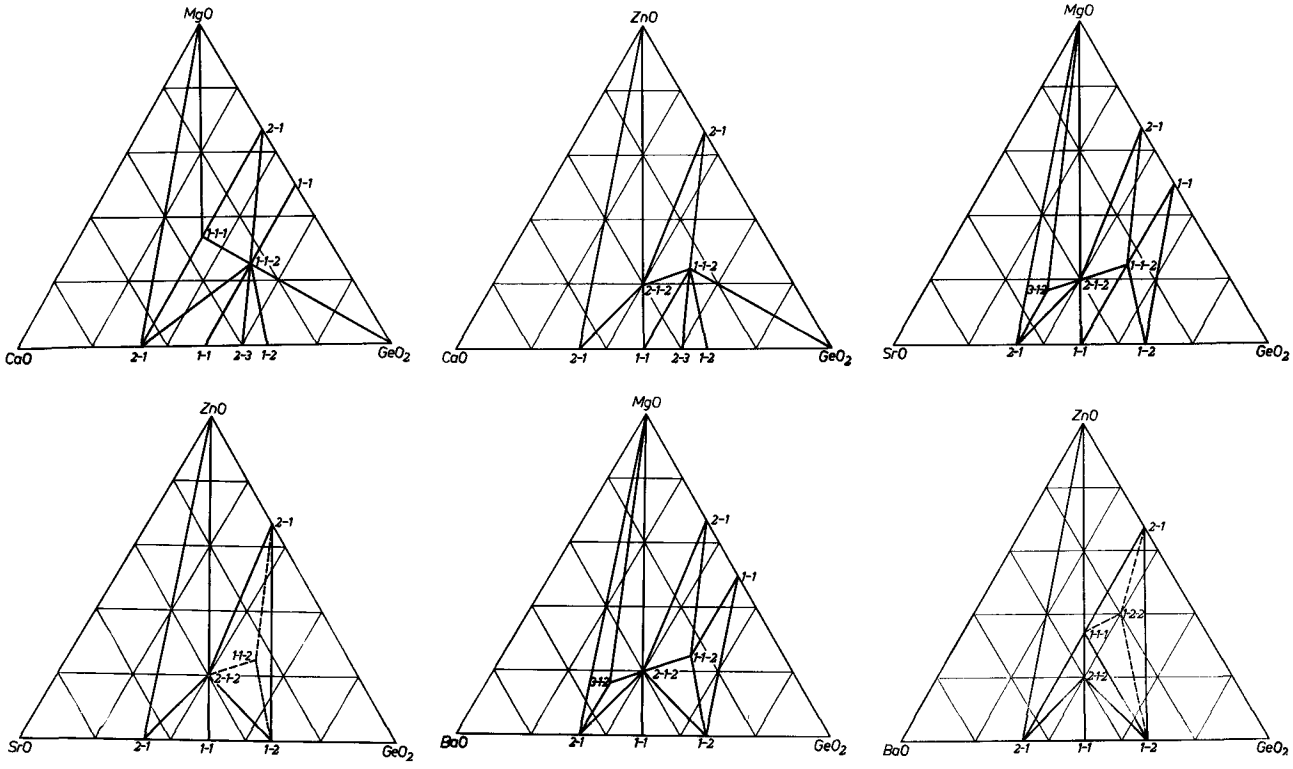

Fig. 1. Composition phase diagrams of the ternary germanate systems.

seen from Fig. 2 that the peak of the Pb emission in the germanates is at several hundred Å longer wave lengths than it is in the silicates. The 2-1-2 Pb-activated BaMg- and SrMg-germanates can be made with about the same efficiency as the corresponding silicates. The efficiency of the Pb-activated 2-1-2 BaZn-, SrZn-, and CaZn-germanates is much lower. An explanation for this can be given easily with the aid of Fig. 3, where the shaded parts are the triangles which contain one or more phases with an inefficient u.v. absorption. These phases are given by circles at the apexes. This means that compositions falling in the shaded areas have a low efficiency due to the presence of those undesired phases. It is also seen from Fig. 3 that in the Zn-containing compounds the whole area around the 2-1-2 com-

Table IV. X-ray data of the 2-1-2 germanates

Indices hkl	$Ca_2ZnGe_2O_7$		$Sr_2MgGe_2O_7$		$Sr_2ZnGe_2O_7$		$Ba_2MgGe_2O_7$		$Ba_2ZnGe_2O_7$	
	d (Å)	I	d (Å)	I	d (Å)	I	d (Å)	I	d (Å)	I
110	5.15	40	5.80	22						
101	4.35	8	4.49	5						
111	3.79	9	3.93	9	3.90	10	4.18	10	3.15	5
210	3.54	20								
201	3.15	20	3.25	20	3.20	22	3.30	20	3.35	12
211	2.92	100	3.04	100	3.00	100	3.10	100	3.10	100
220	2.80	6	2.90	3	2.87	8				
002	2.58	12	2.67	10	2.65	12	2.76	8	2.80	12
310	2.50	48	2.59	26	2.57	30	2.64	17	2.65	40
221	2.46	10	2.53	6	2.52	7				
301	2.34	5	2.42	7	2.40	3	2.50	5	2.50	12
311	2.26	30								
212	2.03	2	2.15	4	2.14	3	2.23	10	2.24	10
400	1.99	2	2.04	18	2.03	4	2.09	9	2.09	8
410	1.90	10	1.96	4	1.95	5	2.03	9	2.03	10
330	1.87	7	1.93	20	1.92	6	1.97	10	1.97	11
312	1.80	40	1.85	32	1.84	36	1.92	22	1.92	27
411							1.90	21	1.90	15
420	1.77	8	1.83	3	1.82	7	1.86	5	1.87	10
103, 322	1.68	4	1.72	3						
213	1.55	2	1.595	15	1.59	11	1.66	26	1.66	20
332			1.56	6	1.55	4	1.61	16	1.61	12
223	1.47	7	1.51	6	1.505	4	1.57	5	1.57	9
521	1.42	7	1.46	19	1.45	13	1.50	25	1.50	20
512					1.39	3	1.395	5	1.395	18
531			1.36	7	1.355	4				
004			1.32	7	1.32	5	1.365	11	1.37	12

position is shaded. Since in our firing experiments the reaction was never entirely complete, nonluminescent absorbers could not be avoided in these cases. In the systems containing Mg there are unshaded triangles around the 2-1-2 composition. In fact the efficient Mg-containing phosphors were made by firing compositions falling within these favorable triangles.

Activation with Ti.—Of the binary and ternary germanates only $Ca_2Ge_3O_8$ gave an efficient emission with Ti. The spectral distribution with 2537Å excitation is given in Fig. 4 which shows that the emission of the $Ca_2Ge_3O_8$-Ti closely corresponds to that of blue-emitting, Sb-activated calcium halophosphate (Cl/F = 1). The quantum efficiency of the germanate phosphor is the same as that of the halophosphate or slightly better. The activator was added from a solution of $TiCl_4$ in a mixture of alcohol and water. The intensity of the emission does not vary much between 0.05 and 0.5 mole % of Ti, a concentration of about 0.1 mole % being the optimum. In the preparation of the phosphor a slight excess of GeO_2 was taken, because the occurrence of small amounts of the 2-1 germanate (cf. Fig. 1), which also gives a fairly strong emission, is less harmful than the occurrence of the 1-1 compound which does not give an appreciable emission with Ti. The phosphor was made in one single firing at 1150°C for 1 hr. The $Ca_2Ge_3O_8$-Ti is not efficiently excited by cath-

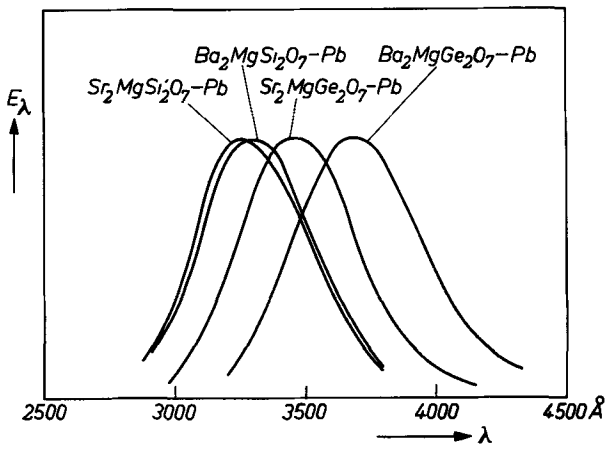

Fig. 2. Spectral distribution curves of Pb-activated 2-1-2-BaMg- and SrMg- germanates and silicates. Excitation with 2537Å at room temperature.

Table V. X-ray data of the 3-1-2 germanates

Indices	$Sr_3MgGe_2O_8$		$Ba_3MgGe_2O_8$	
hkl	d (Å)	I	d (Å)	I
111	4.00	22	4.15	36
002	3.50	15	—	—
012	3.25	15	—	—
102	3.02	25	3.10	18
112, 022	2.86	85	2.98	80
130	2.80	100	2.88	100
040	2.48	15	—	—
013	2.35	18	2.46	12
221	2.29	20	2.35	20
222	2.00	45	2.06	40
310			1.86	20
241			1.82	8
	1.685	9	1.73	12
	1.62	27	1.67	35
	1.605	28	1.655	30
			1.55	6
			1.48	12
			1.43	16
	1.39	15	1.41	12
			1.37	10
			1.35	10
			1.31	16

Table VI. X-ray data of the 1-1-2 germanates

$CaMgGe_2O_6$		$CaZnGe_2O_6$		$SrMgGe_2O_6$		$SrZnGe_2O_6$		$BaMgGe_2O_6$	
d (Å)	I	d (Å)	I	d (Å)	I	d (Å)	I	d (Å)	I
4.90	24	4.90	4	—	—	3.60	25	3.65	8
—	—	4.50	13	4.65	4	3.20	100	3.35	100
3.43	45	3.40	12	3.50	17	2.91	75	3.03	75
3.30	16	3.30	7	3.40	30	2.84	15	2.96	25
3.06	100	3.06	100	3.12	100	2.70	30	2.79	37
3.00	25	3.00	21	3.02	60	2.47	30	2.66	23
2.63	47	2.63	60	2.68	30	2.37	15	2.46	12
2.60	60	2.60	80	2.65	95	1.97	20	2.04	20
2.44	5	2.43	5	2.47	15	1.85	80	1.91	30
2.40	12	2.40	3	2.42	20	1.74	18	1.80	18
2.30	7	2.30	6	2.32	10	1.56	25	1.60	27
2.25	6	2.25	5	2.26	8	1.49	10	1.53	10
2.08	10	2.08	13	2.13	28				
2.06	15	2.06	6	2.10	12				
2.01	6	—	—	—	—				
1.91	8	1.91	3	1.92	10				
1.77	7	1.77	4	1.79	6				
1.71	10	1.70	7	1.73	10				
1.67	18	1.67	13	1.69	20				
1.585	5	1.58	10	1.615	10				
1.575	6	1.57	5	1.60	18				
1.545	7	1.54	5	1.58	13				
1.47	8	1.47	6	1.49	10				
1.44	7	1.44	6	1.465	17				
1.43	7	1.43	7	1.45	6				
1.375	8	1.38	8	1.39	12				
1.33	5	1.33	5	1.34	12				

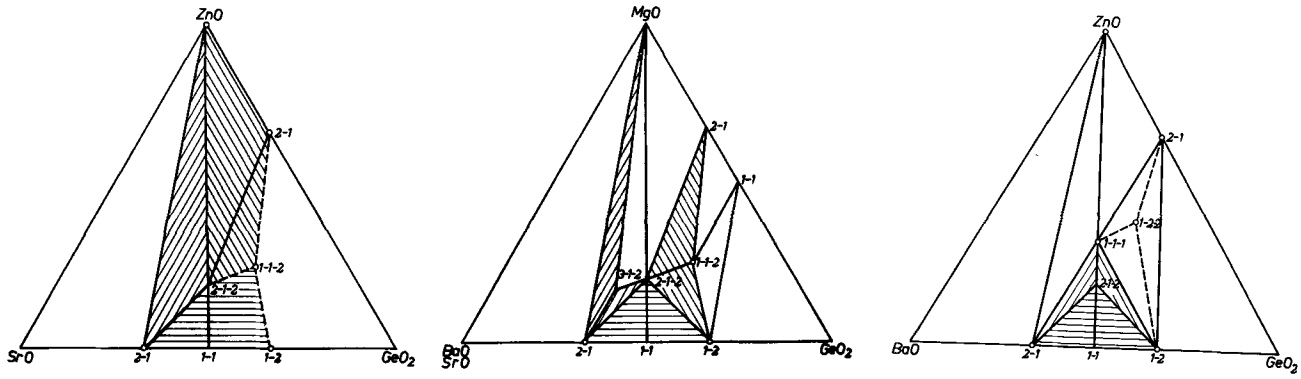

Fig. 3. Part of the phase diagram around the 2-1-2 compounds. Shaded parts contain one or more phases with an inefficient u.v. absorption given by circles at the apexes.

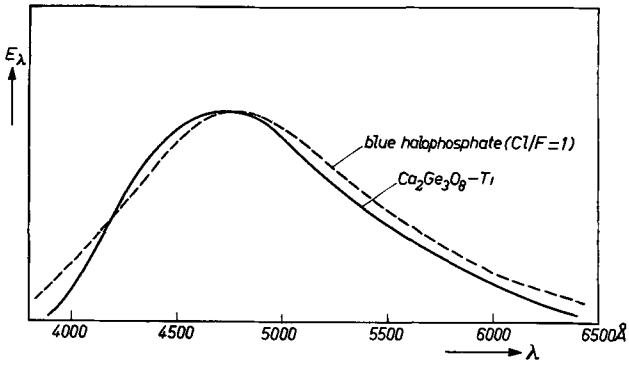

Fig. 4. Spectral distribution curve of the fluorescence in $Ca_2Ge_3O_8$-Ti with 2537Å excitation at room temperature.

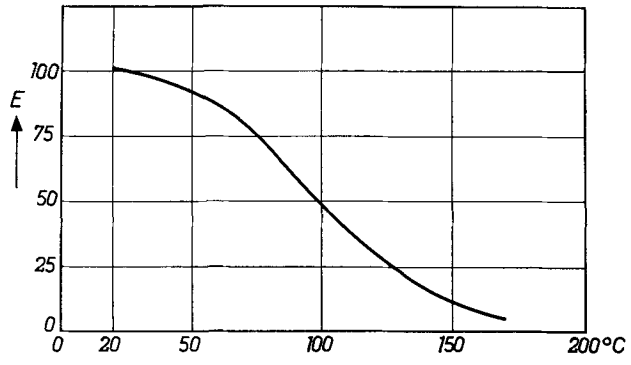

Fig. 5. Temperature dependence of the Ti-emission in $Ca_2Ge_3O_8$-Ti. Excitation 2537Å.

Table VII. X-ray data of the 1-1-1 and 1-2-2 germanates

$CaMgGeO_4$		$BaZnGeO_4$		$BaZn_2Ge_2O_7$	
d (Å)	I	d (Å)	I	d (Å)	I
5.61	25	4.75	15	3.30	100
4.55	25	4.15	30	3.23	75
4.25	70	3.21	100	3.06	75
3.95	25	3.12	20	2.94	18
3.75	25	2.68	85	2.56	45
3.23	30	2.49	40	2.48	15
3.05	20	2.06	45	2.33	33
2.73	100	1.99	20	2.16	21
2.64	70	1.82	10	1.98	21
2.58	30	1.71	40	1.80	9
2.43	15	1.65	20	1.70	10
2.28	20	1.63	60	1.64	6
2.07	5	1.60	5	1.60	25
1.86	20	1.55	15	1.535	6
1.78	15	1.51	5	1.425	8
1.73	25	1.40	10	1.41	6
1.69	10	1.37	15	1.31	12
1.61	30	1.34	10		
1.59	15	1.29	10		
1.52	10				
1.42	10				

Table VIII. Cell dimensions of the tetragonal 2-1-2 germanates

	a (Å)	b (Å)
$Ca_2ZnGe_2O_7$	7.94	5.16
$Sr_2MgGe_2O_7$	8.18	5.28
$Sr_2ZnGe_2O_7$	8.13	5.27
$Ba_2MgGe_2O_7$	8.40	5.46
$Ba_2ZnGe_2O_7$	8.40	5.46

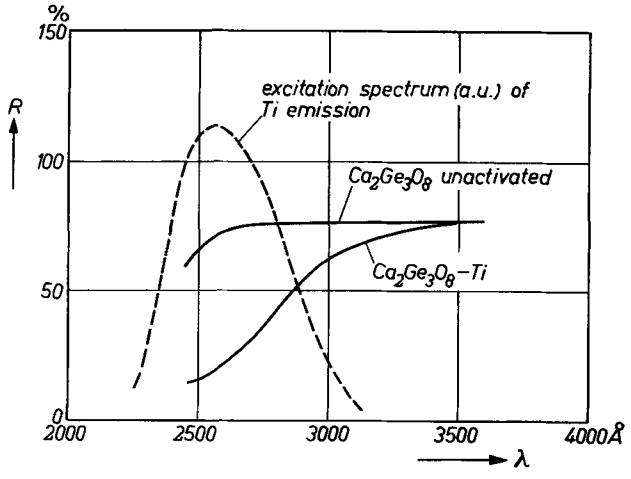

Fig. 6. Reflection spectra (solid lines) of unactivated and Ti-activated $Ca_2Ge_3O_8$ at room temperature. Excitation spectrum (dashed curve, arbitrary units) of $Ca_2Ge_3O_8$-Ti at room temperature.

ode rays or long-wave u.v. In samples activated with Ti and Mn no sensitization of a Mn emission by the Ti was found. The temperature dependence of the Ti emission is shown in Fig. 5. The reflection spectrum of the unactivated and activated phosphor together with the excitation spectrum of the Ti emission are given in Fig. 6.

Activation with Mn.—Of the other activators tried in the binary and ternary germanates, e.g., Mn, Sn, Ce, Bi, and Re, only Mn gave a noticeable emission in $Ca_2Ge_3O_8$ with cathode-ray excitation. The peak of the emission is in the orange-yellow region; the en-

ergy efficiency is about 2%. The optimum Mn concentration is about 0.8 mole %. In order to obtain proper incorporation of the Mn the phosphors had to be fired in N_2.

Conclusions

The fluorescence of binary and ternary germanates of group II elements has been investigated. $Sr_2MgGe_2O_7$-Pb and $Ba_2MgGe_2O_7$-Pb proved to be good u.v. emitting phosphors. $Ca_2Ge_3O_8$-Ti was found to be a good blue emitting phosphor.

Manuscript received Jan. 28, 1959. This paper was prepared for delivery before the Philadelphia Meeting, May 3-7, 1959.

Any discussion of this paper will appear in a Discussion Section to be published in the June 1960 JOURNAL.

REFERENCES

1. H. W. Leverenz, "An Introduction to Luminescence of Solids," John Wiley & Sons, New York (1950).
2. H. A. Klasens, A. H. Hoekstra, and A. P. M. Cox, *This Journal*, **104**, 93 (1957).
3. W. L. W. Ludekens, *J. Inorg. Nucl. Chem.*, **3**, 281 (1956).

Thermoluminescence and Shallow Traps In ZnS:Cu:Co

B. Goldstein[1] and J. J. Dropkin

Polytechnic Institute of Brooklyn, Brooklyn, New York

ABSTRACT

Trapping states of the hexagonal ZnS:Cu 10^{-4}:Co 10^{-6} phosphor were investigated by thermoluminescence as functions of the time and temperature of ultraviolet (u.v.) excitation and of the time and temperature of spontaneous or *IR* induced decay. The main copper (chloride) and cobalt peaks are complex, and retrapping takes place in both.

In connection with some work on photoconductivity, quenching, and stimulation of the ZnS:Cu-10^{-4} mole %:Co 10^{-6} mole % phosphor, we found it advisable to investigate the shallow trap structure and used thermoluminescence as one of the methods(1-4). This paper reports the results of the glow curve work on the nature of the shallow trap distribution. Some estimate of the trap energies is obtained from the initial slope of the glow curves (4). The presence of retrapping was shown by temperature recycling experiments(3). Some of the properties of the *IR* sensitivity of the traps were studied. A measure of the complexity of the trap distribution was obtained by varying the time and temperature of excitation as well as by introducing a delay time for decay of the trap population before running the glow curves.

Experimental Details

The apparatus used in our glow curve work is illustrated in Fig. 1. This was a metal-glass Dewar with a thin layer of the phosphor powder mounted in the vacuum in contact with a brass block which was cooled or heated by liquid nitrogen or a nichrome heater. The heating rate was 3.6°C/min.

The Dewar was so situated that the phosphor and a photomultiplier were located at conjugate foci of a spherical mirror. The phosphor was excited by 3650Å u.v. radiation or stimulated by *IR* from a monochromator through a hole in the mirror. The luminescence reaching the photomultiplier first was filtered so that only the characteristic green Cu emission was measured.

The phosphors used were prepared by firing at 1100°C with NaCl flux in an atmosphere of H_2S to eliminate the effect of oxygen on the trap structure (4).

[1] Present address: Radio Corp. of America, Princeton, N. J.

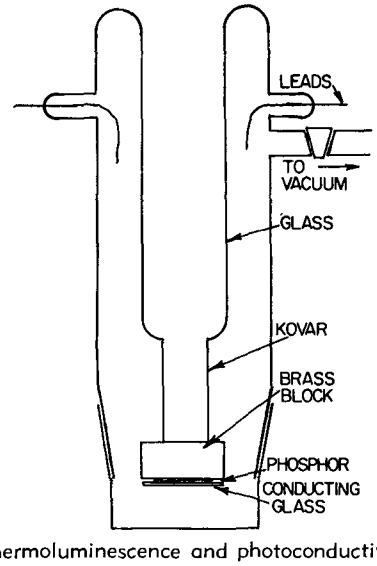

Fig. 1. Thermoluminescence and photoconductivity Dewar

Results

Effect of time and temperature of excitation.— Figure 2 shows some typical glow curves taken under saturation conditions of excitation for excitation at −178° and at −60°C. Curve A is the glow curve after 30-min excitation and 13 min of decay at −178°C. The low-temperature peak, attributable to copper (3) or to chloride (4),[2] is at −123°C and seems simple as in Hoogenstraaten's work (4). The high-temperature peak, attributable to Co (5), is at + 60°C and shows some structure. The activation energies derived from the initial rising portions of these peaks under the assumption either of trap saturation or of no retrapping are 0.16 ev and 0.20 ev, respectively. With the phosphor excited at −60°C, cooled to −178°C, and then warmed, curve

[2] In what follows, we will refer to the lower temperature glow peak found in ZnS:Cu (NaCl flux) as the Cu peak.

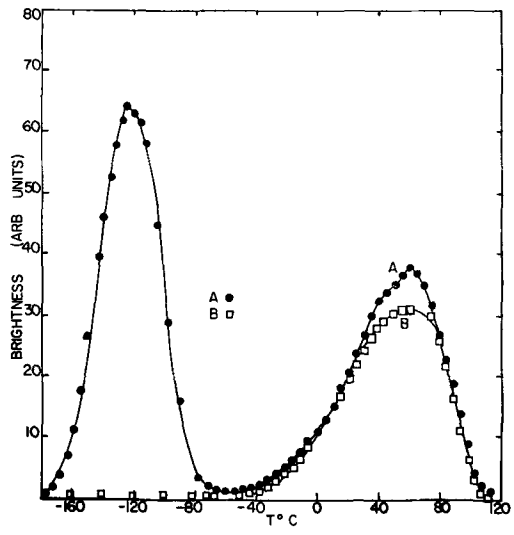

Fig. 2. ZnS:Cu:Co glow curves. A, Excitation: —178°C for 30 min, decay of 13 min at —178°C before glow curve run; B, excitation: —60°C for 30 min, cooled to —178°C before glow curve run.

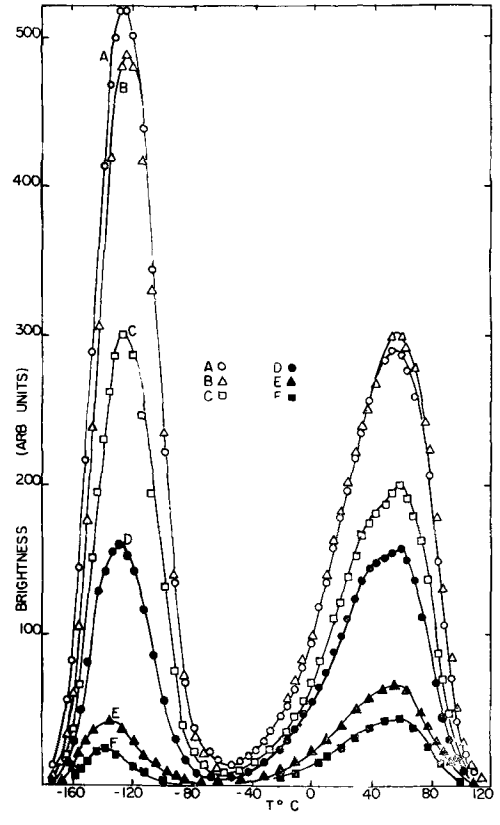

Fig. 3. Effect of time of excitation on ZnS:Cu:Co glow curves: A, 60 min; B, 5 min; C, 1 min; D, 10 sec; E, 5 sec; F, 2 sec (all at —178°C).

B is obtained. The first peak has disappeared, and now with no interference from the trailing edge of the lower temperature peak, the rising portion of the Co peak gives an activation energy of 0.38 ev.

When we studied how this trap or group of traps fills under excitation and empties under decay or *IR* stimulation, the simple structure apparent in the smooth shape of the Cu peak turned out to be nonexistent.

We investigated first the trap filling process by exciting the phosphor at — 178°C for various lengths of time from 2 sec to 60 min. The results are given in Fig. 3. Saturation is seen to occur in approximately 5 min. We note that, as the excitation time was reduced, the Cu peak shifted to lower temperatures and the ratio of the Cu peak area to the Co peak area decreased.

The latter point seems to indicate either that the Co trap has a larger cross section for u.v. excited electrons than the Cu trap or that Co traps retrap electrons released from Cu traps. The former suggests that the Cu glow peak is due to a trap distribution rather than a single trap. A single trap which did not retrap liberated electrons would produce an unchanged glow peak. A single trap which did retrap liberated electrons would have a *higher* temperature glow peak when only partly filled than when completely filled. Activation energies obtained from the initial portions of the respective glow curves vary from 0.11 ev for 2-sec excitation to 0.16 ev for saturation.

The Co peak does not shift with excitation time. Activation energies obtained from the leading edge do vary from 0.21 ev for saturation to 0.23 ev for 2-sec excitation, but the effect of the trailing edge of the Cu peak could not be eliminated in any of these cases.

In order to study the trap distribution of the Cu peak by another means, the phosphor was excited at successively higher temperatures and then cooled to — 178°C before warming. Figure 4 shows the glow curves obtained with excitation at — 178°, — 140°, —120°, and — 100°C before running the glow curves from — 178°C. These glow peak temperature shifts could be consistent with the behavior of a partly filled set of traps all of the same energy if they could retrap released electrons. However, in view of the previous results these

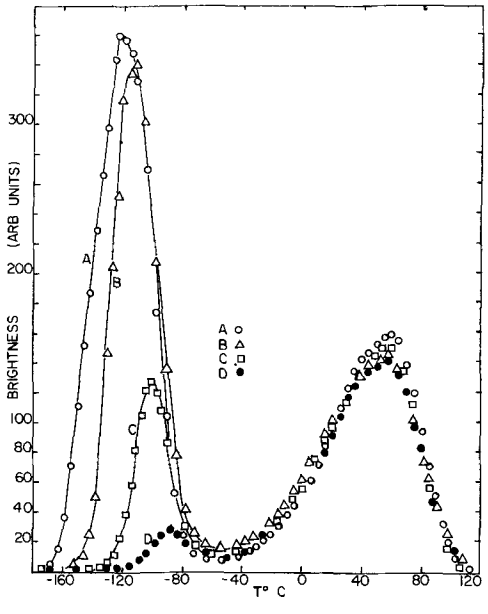

Fig. 4. Effect of temperature of excitation on ZnS:Cu:Co glow curves. Temperature of excitation for: A, —178°C; B, —140°C; C, —120°C; D, —100°C (all glow curves run from —178°C).

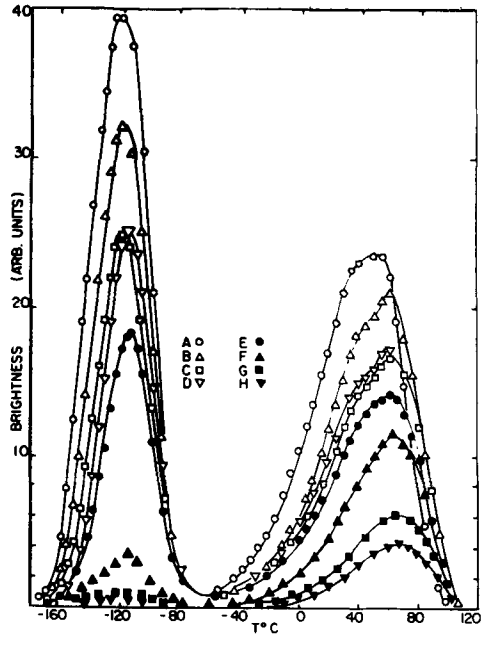

Fig. 5. Effect of infrared radiation on ZnS:Cu:Co glow curves. Wave length of IR for: A, No IR; B, 1.6μ; C, 1.4μ; D, 1.2 μ; E, 1.0 μ; F, 0.9 μ; G, 0.8 μ; H, 0.7 μ.

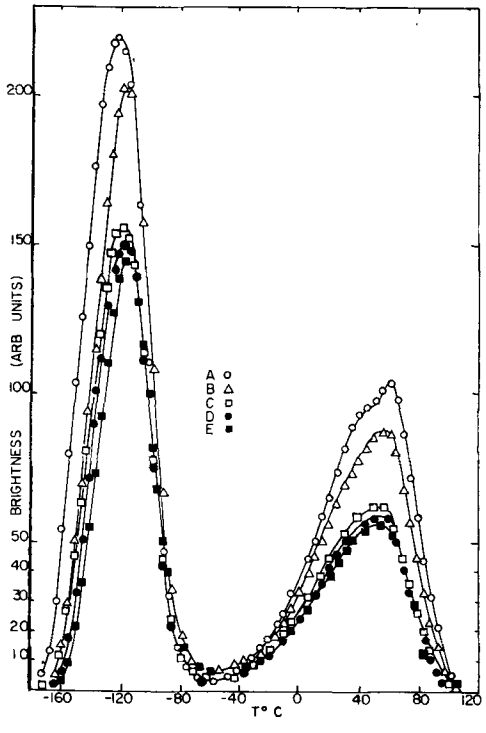

Fig. 6. Effect of decay time on ZnS:Cu:Co glow curves. Decay time at —178°C for: A, 11 min; B, 21 min; C, 36 min; D, 64 min; E, 122 min.

curves are better interpreted by the presence of a distribution of traps of different energy. The effect of higher temperatures of excitation is to leave occupied only those deeper traps of the distribution which are relatively more stable at the higher temperatures. The Co peak is unchanged throughout.

Effect of infrared radiation.—The wave-length dependence of the effect of *IR* on the thermoluminescence curves was studied by exciting the phosphor to saturation with u.v. for 30 min at —178°C and then irradiating the phosphor for 5 min with *IR* of a particular wave length at —178°C prior to running the glow curve. This was repeated for a number of *IR* wave lengths, keeping the incident *IR* intensity constant. Results are shown in Fig. 5. These curves seem to indicate that electrons trapped in either the Cu or the Co traps may absorb *IR*. All we observe, however, is the decrease of luminescence. The actual emptying of either or both traps may be an absorption of *IR* by the electron or alternatively may be part of an indirect process (such as one involving the luminescent center).

Effect of time of decay.—In the thermoluminescence obtained by allowing the phosphor to stand for a time after excitation before running the glow curves, we observed an interesting anomaly which also may indicate that both traps are linked to the luminescent center. Figure 6 shows the glow curves obtained by allowing the phosphor to decay for successively longer times at —178°C after excitation for 30 min at —178°C. The Cu peak temperature shifts slightly from —123°C after 11 min decay to —119°C after 21 min decay, and remains unchanged thereafter, except for a decrease in area for all longer decay times. There is little change in area from 36-min decay time to 120-min decay time. What is unusual, however, is that, although the decay takes place at —178°C, the Co peak, which should be stable, decreases in area also. In fact, the ratio of Cu peak area to Co peak area remains constant to within 2% over the entire decay time interval. This ratio was also found to be constant for these same decay times after excitation of 1 min, i.e., below saturation. This effect is not consistent with the removal of electrons from traps, but more likely with the filling of ionized luminescent centers by electronic transitions to these centers.

Effect of CdS.—We repeated the work of Hoogenstraaten (4) and found that both glow peaks shifted linearly to lower temperatures as CdS was added.

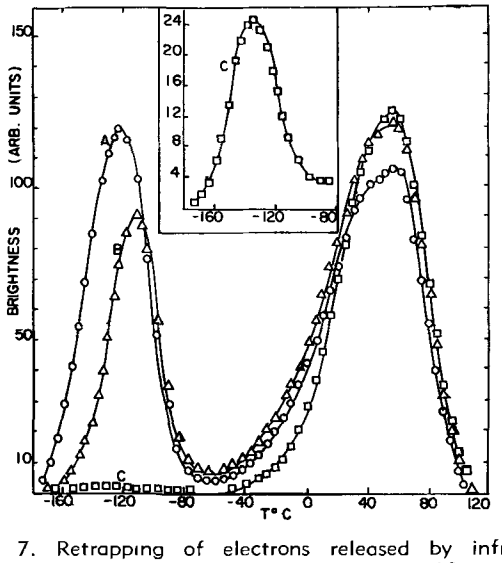

Fig. 7. Retrapping of electrons released by infrared. ZnS:Cu:Co glow curves: A, u.v. 1 min at —178°C, no IR; B, u.v. 1 min at —178°C, IR 1 min at —178°C; C, u.v. 1 min at —60°C, IR 1 min at —178°C. Insert: Portion of curve C replotted with enlarged scale.

In addition, the emission during thermal glow shifted to longer wave lengths with increased CdS content.

Retrapping.—After exciting at −60°C so that the Cu traps were empty (see Fig. 2), and for only 1 min so that the Co traps were only partially filled (see Fig. 3), the phosphor was cooled to −178°C and then irradiated with intense 1.2-μ radiation.[3] Results shown in Fig. 7 indicate that retrapping can occur in either the Cu or the Co trap. The insert shows the retrapping in the Cu peak on a larger scale. A comparison of curve A with curve B shows that retrapping occurs in the Co traps as well. It should be noted that this increase in the Co peak by retrapping of electrons released from the 1.2-μ deep trap occurs over and above the *IR* sensitivity of the Co traps shown in Fig. 5.

Summary

The shallow trap structure of ZnS:Cu 10^{-4}:Co 10^{-6} which produces thermoluminescence consists of two different groups of traps, one associated with copper or chloride, the other with cobalt. Each of these is capable of retrapping electrons that are released. The copper traps have a distribution of energy levels.

[3] In connection with photoconduction studies, we have found a 1.2-μ sensitive storage center in ZnS:Cu:Co. (See final report N6onr 26313, "Photoconduction in Phosphors.")

Acknowledgment

The authors wish to thank Professor E. Banks and his assistant, A. Ferretti, of the Chemistry Department of the Polytechnic Institute of Brooklyn, for the preparation of the samples used in this work.

Manuscript received Jan. 19, 1959. This paper was prepared for delivery at the Chicago Meeting, May 2-6, 1954, and is part of the Ph.D. dissertation of one of the authors (B. G.). Work on this paper was supported by the Office of Naval Research Contract N6onr 26313.

Any discussion of this paper will appear in a Discussion Section to be published in the June 1960 JOURNAL.

REFERENCES

1. F. Urbach, *Sitz. Ber. Akad. Wiss., Wien, Math. Naturw. Klasse,* **139**, 353 (1930).
2. J. T. Randall and M. H. F. Wilkins, *Proc. Roy. Soc., London,* **A184**, 366 (1945).
3. G. F. J. Garlick and D. E. Mason, *J. (and Trans.) Electrochem. Soc.*, **96**, 90 (1949).
4. W. Hoogenstraaten, Electron Traps in Zinc-Sulfide Phosphors, Thesis of Univ. of Amsterdam (1958).
5. E. S. Krylova, *Doklady Akad. Nauk S.S.S.R.*, **64**, 495 (1949).

Arrays of Inorganic Semiconducting Compounds

A. J. Cornish

Research Laboratories, Westinghouse Electric Corporation, Pittsburgh, Pennsylvania

ABSTRACT

Arrays of compounds related to the periodic chart of the elements can be prepared. These arrays aid in estimating the physical and chemical properties of compounds, including semiconducting properties. Many compounds included in the arrays may not exist; however, if the compound does exist, the value of its melting point, energy gap, and electron mobility generally fit into a uniform pattern related to adjacent compounds. The crystal structure of semiconducting compounds is shown to be of only second-order importance. Grouping semiconducting compounds by crystal types loses the over-all relations that exist between many compounds.

Braun (1) observed the rectifying action of metallic sulfides, and since then many attempts have been made to relate the phenomena of semiconductivity to chemical bonds and structure for the purpose of discovery of new semiconducting compounds. In 1925 Wherry (2), using a copper cat's whisker, a simple crystal set, and a mineral collection, found 75 minerals capable of being used as radio detectors. Since 1925 numerous tables of inorganic semiconducting compounds have been published (3-5); however, the number of compounds has not increased materially. Winkler's (3) list published in 1955 contains slightly under 100 inorganic semiconducting compounds. The reason for the lack of greatly expanded tables of semiconducting compounds is not because workers in the field are unaware of the large number that exist, but rather the lack of experimental work confirming the existence of a large number of suspected semiconducting compounds.

The recent expansion of semiconductor materials into the infrared detector, thermoelectric device, and other fields of application has led to a new interest in expanding the list of available compounds. Such an expansion involves the selection of compounds likely to be semiconductors, the careful preparation, and the measurement of properties of these compounds. Arrays of compounds, related to the periodic chart of the elements, serve a very useful purpose in the selection, preparation, and estimation of properties of semiconducting compounds. With these arrays, it is possible to estimate melting points, energy gaps, and possibly electron mobilities.

Crystal structure.—The idea that semiconductivity is found in only a few different types of crystal structures has been disproved during the past few years. Table I lists over 35 crystal structures containing inorganic semiconducting compounds. Many more are known to exist. Fischer and Pearson (6) and Mooser and Pearson (7) have shown relation-

Table I. Structures of semiconducting compounds

Structure	System	Semiconducting compounds
B1* (NaCl)	Cub.	PbS, SrS, $AgSbSe_2$, etc.
B3 (ZnS)	Cub.	AlSb, In_2Te_3, $CdZnSe_2$, etc.
B4 (ZnO)	Hex.	ZnO, CdS, ZnS, AgI, etc.
B8 (NiAs)	Hex.	MnTe, FeS, CrSe, etc.
B9 (HgS)	Hex.	HgS
B18 (CuS)	Hex.	CuS, CuSe
B29 (SnS)	Ortho.	GeS, SnS, $PbSnS_2$
B32 (NaTl)	Cub.	Li_2MgSn
B37 (TlSe)	Tet.	TlSe
C1 (CaF_2)	Cub.	Mg_2Pb, $GeLi_5P_3$, LiZnN, etc.
C2 (FeS_2)	Cub.	FeS_2, CoAsS, $MnSe_2$
C3 (Cu_2O)	Cub.	Cu_2O
C4 (TiO_2)	Tet.	TiO_2, SnO_2
C6 (CdI_2)	Hex.	SnS_2
C13 (HgI_2)	Tet.	HgI_2
C18 (FeS_2)	Ortho.	$FeAs_2$, $CoAs_2$, $NiAs_2$
C33 (Bi_2Te_3)	Rhomb.	Bi_2Te_3, Bi_2Te_2S, Sb_2Te_3
$D0_3$ (BiF_3)	Cub.	Li_3Bi
$D0_{21}$ (Cu_3P)	Hex.	Cu_3As
$D5_1$ (Al_2O_3)	Rhomb.	Fe_2O_3
$D5_2$ (La_2O_3)	Hex.	Mg_3Sb_2, Mg_3Bi_2
$D5_3$ (αMn_2O_3)	Cub.	Mg_3As_2
$D5_9$ (Zn_3P_2)	Tet.	Zn_3P_2, Cd_3As_2
$E0_7$ (FeAsS)	Mon.	FeAsS, FeSbS
$E1_1$ ($CuFeS_2$)	Tet.	$AgInTe_2$, $ZnGeP_2$, etc.
$E3_1$ (Ag_2HgI_4)	Tet.	Cu_2HgI_4, $HgIn_2Te_4$, etc.
$E3_3$ ($FeSb_2S_4$)	Ortho.	$FeSb_2S_4$
$F5_6$ ($CuSbS_2$)	Ortho.	$CuSbS_2$, $PbSb_2S_4$, etc.
$H1_1$ ($MgAl_2O_4$)	Cub.	Fe_3O_4, $HgIn_2S_4$
$H2_4$ (Cu_3VS_4)	Cub.	Cu_3VS_4
$H2_5$ (Cu_3AsS_4)	Ortho.	Cu_3AsS_4, Cu_3SbS_4
$H2_6$ (Cu_2FeSnS_4)	Tet.	Cu_2FeSnS_4

* "Strukturbericht" symbols.

ships between many of the different structures. It now appears that semiconductivity could be found in any crystal structure except the close-packed, high coordination number structures. In the latter structures, the large number and nearness of neighboring atoms generally insures an overlapping of the bands and therefore metallic characteristics.

Too much emphasis has been placed on the relationship between semiconductivity and crystal structure. The crystal structure which a compound assumes is a minimum energy orientation of atoms in space satisfying a particular bond scheme. The bond scheme is determined by the distribution of electrons between atoms in the compound; this same distribution determines the position of the valence and the conduction band. Although it is true that certain crystal structures commonly exhibit semiconductivity, the more basic property is the nature of the bonds. As the bonds change in a series of compounds, different crystal structures become preferred. In some examples an increase or decrease in ionic contribution to the bond changes the structure; in other examples radius ratio rules forbid certain orientations. However, in a chemically related series of compounds, even these structural changes form a more or less continuous spectrum, the crystal structures of adjacent compounds being the same as, or related to, the crystal structure of its neighbors. Thus listing and discussing semiconductors by crystal structure types hides the over-all relationships of properties that exist between structure types.

Melting points.—Attempts have been made to correlate the melting points of semiconducting compounds with bond strength and energy gap. Considerable caution should be taken in such work. The melting point of a compound may or may not be related to the strength of the bonds providing semiconducting properties. When germanium melts, covalent bonds are broken and the liquid becomes a denser metallic material. In tin, metallic properties appear following a solid-state phase change. The melting point is a transition from a metallic solid to a metallic liquid. Weak van-der Waal bonds are broken at the melting point of selenium; the covalent bonds giving rise to semiconductivity exist at temperatures well above the melting point. Compounds frequently behave like tin or selenium. The occurrence of phase changes and low melting points greatly reduce the number of usable semiconducting compounds. For chemically related compounds we expect melting points to decrease as the molecular weight increases. When this trend is reversed we look for a complicated bond structure.

Energy gaps.—At the present time it is not possible to predict satisfactorily the energy gap of a compound chosen at random. For related compounds, however, Pauling and Goodman have provided us with a means of understanding many of the measured values. Pauling (8) proposed that bond energies were inversely proportional to the equilibrium interatomic distance for the Group IVB elements C, Si, Ge, and αSn as well as groups using covalent bonds other than sp^3.

Goodman (9), in a speculative paper, assumed that the bond energy was proportional to energy gap. He also assumed the measured energy gap was the sum of two terms: a covalent contribution which is a function of the interatomic distance, and an ionic contribution which is a function of the electronegativity differences. The Group IVB elements, having no ionic contribution, gave values of the "covalent" energy gap as a function of interatomic distance. Values of the second term can be obtained for Group III-V compounds knowing the interatomic distance and the measured energy gap. Goodman was then able to show that an increase in the ionic contribution to the energy gap was proportional to an increase in the ionicity. When a series of chemically related compounds are compared the energy gap increases when: (*a*) the compounds become more ionic or less metallic, (*b*) the covalent bond length decreases, (*c*) the molecular weight decreases.

Electron mobilities.—The experimental values of electron mobilities are so sensitive to crystal perfection that it is difficult to put much faith in the present values. They appear to increase with increasing molecular weight and reach a maximum value in compounds possessing a small ionic component to the binding.

Periodic Arrays of Compounds

Knowing only the general trends of the melting points, energy gaps, and electron mobilities as the molecular weights, ionicities, and bond lengths change, we should look for some method of tabulat-

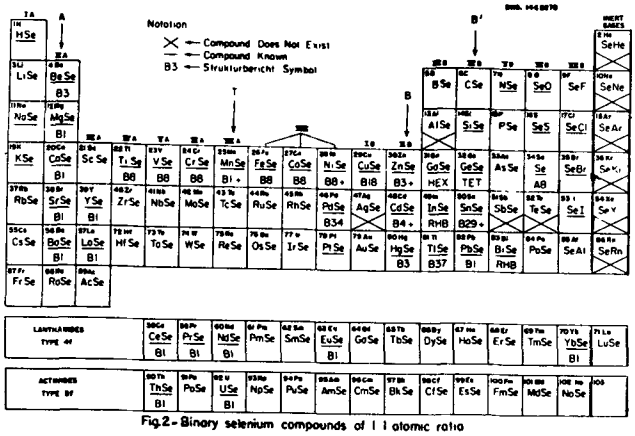

Fig. 1. Binary selenium compounds of 1:1 atomic ratio

ing or arranging compounds in order to make maximum use of this knowledge. The periodic chart of the elements is such an arrangement for the elements. Similar charts can be constructed for compounds. One such chart, a periodic chart of binary selenium compounds of 1:1 atomic ratio is shown in Fig. 1. The complete chart illustrates the principles involved but does not conveniently permit the listing of physical properties. Reduced charts or arrays of compounds including crystal structures, melting points, energy gaps, and electron mobilities will be used to discuss semiconducting compounds. Obviously many charts similar to Fig. 1 may be drawn considering that there are 102 elements and a large number of common stoichiometric ratios. The number of possible arrays increase rapidly when ternary and higher component systems are considered.

Figure 1 is similar to the elemental periodic chart in many ways. Cations occupy their normal positions as in the periodic chart of elements. The number of electrons increases as it does for the elements, and electronegativity differences between positions in the table are the same as for the elements. Definite trends in properties should and do exist as adjacent compounds in the same group (column) or period (row) are compared. These trends are more uniform in an array of binary compounds, such as Fig. 1, than in the periodic chart of elements. The common element, selenium, in this chart tends to moderate the effect of a change in the cation. In higher component systems where more than one atom is constant throughout the table this moderating effect is even more pronounced.

The compounds underlined in Fig. 1 are known to exist. Many not underlined probably exist, but sufficient work has not been done to establish the compound. When the phase diagram is known and a compound of 1:1 atomic ratio does not occur an x is placed in the appropriate square.

Relationships between crystal structures of adjacent compounds can be shown. In the alkaline earth column (IIA) the Bl (NaCl) structure occurs except for BeSe where the radius ratio forces a lower coordination number structure. The hexagonal B8 (NiAs) structure taken by many transition metals acts as a bridge structure, adjusting its c/a ratio in such a manner that it forms an almost continuous transition between adjacent compounds. Many compounds lying close to the tetrahedrally bonded B3 and B4 structures have related structures such as the B37 (TlSe) and B18 (CuSe). Similar relations exist between other physical properties which depend primarily on the bond between the cation and nearest selenium atoms.

Since selenium requires two electrons to fill its outer shell, selenium compounds are most stable when the element forming the cation can, by losing or sharing two electrons, form a stable kernel. This occurs whenever the element possesses two electrons above a stable electron configuration such as a filled or half-filled shell. Most semiconductors are compounds which obey this rule of stability and can conveniently be written as normal ionic compounds. A few important exceptions do exist, e.g., CuSe and BiSe. These would be missed if we limited ourselves to the abbreviated arrays that follow. They do appear on a periodic chart of compounds of the type shown in Fig. 1.

Columns A, T, B, and B′ in Fig. 1 indicate some of the places where this maximum stability occurs. Elements in Column A can lose 2 electrons and leave a stable filled p-shell (an s-shell in the case of Be). These elements form compounds which are largely ionic as their outer electrons are easily lost. Elements in Column T are transition metals. They are able to lose two electrons and have remaining a stable half-filled d-shell. Column B contains the usual B Group elements which tend to share two electrons leaving a filled d-shell, the two shared electrons being s-electrons. The B′ column elements are capable of losing two electrons leaving filled s- and d-shells. Many elements in other columns show a valence of two, but only those in columns designated A, T, B, and B′ are discussed in this paper.

The arrays that follow are, therefore, portions of periodic charts of compounds. The other anions in each anion group are included in such a manner that maximum use can be made of the relations that exist between chemically similar compounds.

It is obvious from Fig. 1 that, if we were forming compounds with a Group VB anion (N, P, As, Sb, or Bi) which require three electrons to fill their outer shells, the column marked A, T, B, and B′ would move one space to the right. In like manner, columns of other valence can be designated.

Table II shows an array of Group II-VI compounds with melting points, crystal structures, energy gaps, and electron mobilities taken from the literature. Compounds of beryllium, radium, and carbon have been omitted since they are not at present of great interest as semiconductors. Using the general relations discussed in the previous section, estimates can be made to fill in many of the missing experimental values. In the A column we generally expect the melting points to decrease with increasing molecular weight thus mp MgO > mp MgS > mp MgSe > mp MgTe and mp MgO > mp CaO > mp SrO > mp BaO. Similar series should

Table II. Properties of group II VI compounds

A					T					B					B'				
Comp.	mp, °C	Str.	ΔEg, ev	μe, cm²/v. sec	Comp.	mp, °C	Str.	ΔEg, ev	μe, cm²/v. sec	Comp.	mp, °C	Str.	ΔEg, ev	μe, cm²/v. sec	Comp.	mp, °C	Str.	ΔEg, ev	μe, cm²/v. sec
MgO	2800	B1	6												SiO				
MgS		B1													SiS		?		
MgSe		B1													SiSe		?		
MgTe		B4													SiTe		Cub.		
CaO	2572	B1			MnO	1650	Cub.	0.5		ZnO	1975	B4	3.4	1000	GeO	700			
CaS		B1			MnS	1580	B3+			ZnS	1850	B3+	3.6	100	GeS	530	B16	1.8	
CaSe		B1			MnSe		B1	0.1		ZnSe		B3	2.58	~100	GeSe	680	Tet.		
CaTe		B1			MnTe	1175	B8			ZnTe	1238	B3	2.2		GeTe	725	B1+		
SrO	2430	B1			TcO					CdO		B1		120	SnO		B10		
SrS		B1	4.1		TcS					CdS	1750	B3	2.42	210	SnS	882	B29		
SrSe		B1			TcSe					CdSe	>1350	B3	1.74	700	SnSe	860	B29		
SrTe		B1			TcTe					CdTe	1041	B3	1.4	300	SnTe	790	B1		
BaO	1923	B1	4.20		ReO					HgO		RHB			PbO	888	B11+		
BaS		B1	3.6		ReS					HgS	583	B3+		700	PbS	1114	B1	0.34	800
BaSe		B1			ReSe					HgSe	690	B3	0.16	15,000	PbSe	1088	B1	0.25	1200
BaTe		B1			ReTe					HgTe	650	B3	0.1	25,000	PbTe	905	B1	0.22	2100

exist for the T column. Occasionally in the B column and more frequently in the B' column we find deviations from this general rule. These deviations are attributed to a more complicated bonding picture than simple cation-anion interaction. The B' group elements, and to some extent, the B group elements are capable of forming covalent bonds between themselves. This means a competition between bonding types exist in the solid. Many of these compounds melt to give covalent liquids. Their melting points are irregular.

Energy gaps follow the general rules already discussed. The gaps in the A group of Table II are too large to be classed as semiconductors; they are ionic insulators. The decrease in energy gaps with increasing molecular weights leads to predictions such as 6 ev > Eg (CaO) > Eg (SrO) > 4.2 ev, and 3.6 ev > Eg (BaSe) > Eg (BaTe). In the T group the gap of MnO of about 0.5 ev indicates that all the other compounds that exist in that group will have a gap of less than 0.5 ev. In fact it might indicate the ReSe and ReTe, if they exist as compounds, could be metallic. In the B group, the gaps are quite regular with the exception that ΔEg (ZnO) < ΔEg(ZnS). This inversion of the general rule could possibly be the 2nd order effect of crystal structure. In the B group the measured gap of 1.8 ev for GeS indicates that 1.8 ev > Eg GeSe > Eg GeTe and also 1.8 ev > Eg SnS > 0.34 ev.

Mobilities of compounds in Table II follow the rules except for the high value of ZnO and the low value of CdTe. It should be pointed out again that electron mobilities are so dependent on crystal perfection that all measured values are open to question. The large mobilities of HgSe and HgTe confirm the statement that maximum mobilities occur with slight ionicity.

Table III shows an array of Group III_2VI_3 compounds; boron and nitrogen compounds have been omitted. The trends in melting points and energy gaps are similar to those for the Group II-VI compounds. The value of 2.3 ev for the energy gap of Fe_2O_3 and 2.5 ev for Al_2O_3 indicates that the remaining compounds in both groups will have energy gaps below 2.3 and 2.5 ev, respectively. The energy gap of As_2Se_3 should be above 1.2 ev, the value for Sb_2Se_3, and below 2.2 ev, the value for As_2Se_3. It is expected that higher mobilities will be found, especially in the lower portion of the B group of compounds.

Ternary compounds and higher component systems require elaborate arrays if all possibilities are to be included. Figure 2 shows the possible substitutions that can be made to form compounds of the type I III VI_2. All possibilities do not exist, however many of the compounds do occur. In a single array, the effect of having more than one atom in

Table III. Properties of group III_2 VI_3 compounds

A					T					B					B'				
Comp.	mp, °C	Str.	ΔEg, ev	μe, cm²/v. sec	Comp.	mp, °C	Str.	ΔEg, ev	μe, cm²/v. sec	Comp.	mp, °C	Str.	ΔEg, ev	μe, cm²/v. sec	Comp.	mp, °C	Str.	ΔEg, ev	μe, cm²/v. sec
										Al_2O_3	2050	$D5_1$+	2.5		P_2O_3	23.8	Mon.		
										Al_2S_3	1100	Hex.			P_2S_3	290			
										Al_2Se_3	950	B_{4}+			P_2Se_3				
										Al_2Te_3	890				P_2Te_3				
Sc_2O_3		$D5_3$			Fe_2O_3	1565	$D5_1$+	2.3		Ga_2O_3	1740	$D5_1$			As_2O_3	315	Cub.+		
Sc_2S_3		?			Fe_2S_3		?			Ga_2S_3	1255	$B3_1$			As_2S_3	310	Mon.	2.2	
Sc_2Se_3		?[1]			Fe_2Se_3					Ga_2Se_3	1020	~B3			As_2Se_3	307			
Sc_2Te_3		?			Fe_2Te_3	780	B8			Ga_2Te_3	790	~B3			As_2Te_3	360	Mon.	1.0	170
Y_2O_3	2410	$D5_3$			Ru_2O_3		?			In_2O_3	>2000	$D5_3$			Sb_2O_3	652	$D5_{11}$+		
Y_2S_3	1600	Mon.			Ru_2S_3					In_2S_3	1095	Hl_1+			Sb_2S_3	550	$D5_8$	1.7	
Y_2Se_3	?	?[1]			Ru_2Se_3					In_2Se_3	890	~B3	1.2	30	Sb_2Se_3	575	$D5_8$	1.2	15
Y_2Te_3					Ru_2Te_3					In_2Te_3	667	~B3	1.0		Sb_2Te_3	629	C33	0.3	
La_2O_3	2315	$D5_2$			Os_2O_3	?	?			Tl_2O_3	717	$D5_3$		>100	Bi_2O_3	860	$D5_{12}$+		
La_2S_3	2150	$D7_3$			Os_2S_3					Tl_2S_3	260				Bi_2S_3	745	$D5_8$	1.3	200
La_2Se_3		?[2]			Os_2Se_3					Tl_2Se_3	274				Bi_2Se_3	706	C33	0.35	600
La_2Te_3					Os_2Te_3					Tl_2Te_3	—	—			Bi_2Te_3	573	C33	0.15	800

[1] Isomorphous with Er_2Se_3, Yb_2Se_3.
[2] Isomorphous with Ce_2Se_3, Pr_2Se_3, Nd_2Se_3.

Table IV. Properties of Group I(Cu) III VI_2 compounds

A					T					B					B′				
Comp.	mp, °C	Str.	ΔEg, ev	μe, cm^2 / v. sec	Comp.	mp, °C	Str.	ΔEg, ev	μe, cm^2 / v. sec	Comp.	mp, °C	Str.	ΔEg, ev	μe, cm^2 / v. sec	Comp.	mp, °C	Str.	ΔEg, ev	μe, cm^2 / v. sec
$CuBO_2$															$CuNO_2$				
$CuBS_2$															$CuNS_2$				
$CuBSe_2$															$CuNSe_2$				
$CuBTe_2$															$CuNTe_2$				
$CuAlO_2$															$CuPO_2$				
$CuAlS_2$		El_1	~2.4												$CuPS_2$				
$CuAlSe_2$		El_1													$CuPSe_2$				
$CuAlTe_2$		El_1													$CuPTe_2$				
$CuScO_2$					$CuFeO_2$					$CuGaO_2$					$CuAsO_2$				
$CuScS_2$					$CuFeS_2$	950	El_1	0.53		$CuGaS_2$		El_1			$CuAsS_2$	625	~B3	>1	
$CuScSe_2$					$CuFeSe_2$	800		0.16		$CuGaSe_2$	1040	El_1	1.6		$CuAsSe_2$	415	~B3	>1	
$CuScTe_2$					$CuFeTe_2$	773		0.10		$CuGaTe_2$	840	El_1	1.0		$CuAsTe_2$	360			
$CuYO_2$					$CuRuO_2$					$CuInO_2$					$CuSbO_2$				
$CuYS_2$					$CuRuS_2$					$CuInS_2$		El_1	1.2		$CuSbS_2$	535	$F5_6$	>1	
$CuYSe_2$					$CuRuSe_2$					$CuInSe_2$	990	El_1	1.07	1000	$CuSbSe_2$	460		>1	
$CuYTe_2$					$CuRuTe_2$					$CuInTe_2$	700	El_1	0.95		$CuSbTe_2$	520			
$CuLaO_2$					$CuOsO_2$					$CuTlO_2$					$CuBiO_2$				
$CuLaS_2$					$CuOsS_2$					$CuTlS_2$		El_1			$CuBiS_2$		$F5_6$	0.6	
$CuLaSe_2$					$CuOsSe_2$					$CuTlSe_2$	405	El_1			$CuBiSe_2$	590			
$CuLaTe_2$					$CuOsTe_2$					$CuTlTe_2$	375				$CuBiTe_2$	510			

common moderates the trends in properties to a greater degree than in the binary systems.

Table IV shows an array of Group I III VI_2 compounds in which copper is used as the Group I element. Similar arrays exist for each of the other Group I elements. The few measured properties shown in Table IV confirm in general the trends expected. A similar chart with the Group I element silver instead of copper should have very similar properties with slightly lower melting points, energy gaps, and higher mobilities.

Similar arrays can be drawn up for other stoichiometric ratios of binary, ternary, and higher component systems following a pattern similar to that shown in Fig. 2.

One guide to other possible arrays could be a list of semiconducting compounds similar to Table I. For example Zn_3P_2 suggests II_3V_2, $ZnGeP_2$ suggests II IV V_2 and $HgIn_2Te_4$ suggests II III_2 VI_4. Goodman (10) has outlined a procedure which would aid in the selection of types of compounds which could be expanded into arrays. If the properties of some of the compounds in an array are known, the properties of others can be estimated.

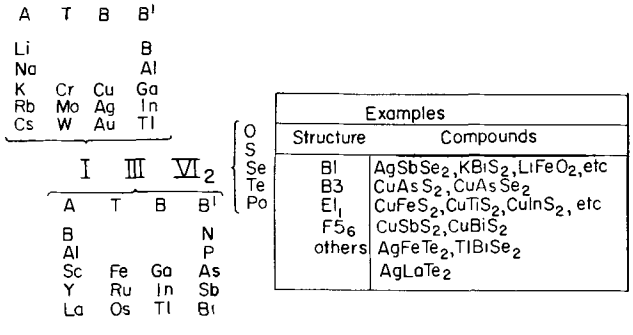

Fig. 2. Possible Group I III VI_2 semiconducting compounds

Acknowledgment

The author is indebted to Dr. R. L. Longini for his encouragement and helpful comments on this work.

Manuscript received Feb. 9, 1959. This paper was prepared for delivery before the Ottawa Meeting, Sept. 28-Oct. 2, 1958.

Any discussion of this paper will appear in a Discussion Section to be published in the June 1960 JOURNAL.

REFERENCES

1. F. Braun, *Pogg. Ann.*, **153**, 556 (1874).
2. E. Wherry, *Amer. Mineral.*, **10**, 28 (1925).
3. U. Winkler, *Helv. Phys. Acta.*, **28**, 633 (1955).
4. E. Mooser and W. B. Pearson, *J. Chem. Phys.*, **26**, 893 (1957)
5. R. L. Sproull, Section 5e, "American Institute of Physics Handbook," McGraw-Hill Book Co., New York (1957).
6. G. Fischer and W. B. Pearson, Compound Semiconductors, Proceedings of the Symposium on the Role of Solid State Phenomena in Electric Circuits, Polytechnic Institute of Brooklyn (1957).
7. E. Mooser and W. B. Pearson, *Phys. Rev.*, **101**, 1608 (1956).
8. L. Pauling, *J. Phys. Chem.*, **58**, 662 (1954).
9. C. H. L. Goodman, *J. Elect.*, **1**, 115 (1955).
10. C. H. L. Goodman, *Physics and Chem. Solids*, **6**, 305 (1958).

Glycerol Baths for the Electrodeposition of Molten Indium or Indium-Cadmium Alloy

A. J. Certa, T. J. Manns, G. L. Schnable, and H. S. Segal[1]

Lansdale Tube Company, Division of Philco Corporation, Lansdale, Pennsylvania

ABSTRACT

Plating baths employing glycerol as a solvent are described, from which ellipsoidal beads of molten indium or indium-cadmium alloy of approximately eutectic composition are electrodeposited onto whisker wires used as leads to electrodes of transistors. The In-Cd eutectic consists of 75% In and 25% Cd by weight and melts at 123°C. The glycerol baths for electrodepositing molten In-Cd alloy, which are solutions of $InCl_3$, $CdCl_2$, and NH_4Cl (and in some cases ethylenediaminetetraacetic acid) in glycerol, are usually operated at 140°C. Carbon anodes are used. With 24 v d.c. applied, a 15 μg ellipsoidal bead of In-Cd alloy of approximately eutectic composition can be electrodeposited on the end of a 0.05-mm nickel wire in about 2 sec. The effects of bath composition and of plating conditions on alloy composition, plating rate, and bath life are discussed. The plating baths are capable of serving as effective fluxes during soldering of whisker wires to electrodes of transistors.

In the manufacture of many types of semiconductor devices, electrical connections must be made to the electrodes. Indium metal, mp 156°C, is a convenient solder for devices where a soldering temperature of about 170°C can be employed.

In the fabrication of surface-barrier transistors, electrical connections must be made to indium emitter and collector electrodes. Indium-cadmium eutectic alloy (75% In, 25% Cd, by weight), which melts at 123°C (1), can be used to solder whisker wires to emitter and collector electrodes without melting the In metal. Soldering temperatures of about 140°C are employed. Indium-cadmium alloys in the approximate range from 50% In-50% Cd to 80% In-20% Cd by weight have been found to flow at temperatures below 130°C and thus are considered satisfactory solders for In metal. The advantages of In-Cd alloys as solders for semiconductor devices have been described previously (2).

Electrodeposition of Molten Solders

Metals electrodeposited in molten form are smooth, dense, and nonporous (2, 3). When molten metal or alloy is electrodeposited on a small wire, a bead forms at the end of the wire in a location highly suitable for a subsequent soldering operation (3). Deposition can be very rapid since high current densities can be used. Such current densities would generally cause dendritic growths in ordinary aqueous electroplating solutions.

The glycerol baths for electrodepositing molten In or In-Cd alloy are particularly suitable for rapidly plating small amounts of metals or alloys which may readily be used as solders. In contrast to the fused salt bath described previously (2), the glycerol bath is capable of acting as a soldering flux in the temperature range from room temperature to about 200°C. Thus in some applications, for example, on the automatic whisker attacher machines (4), the coating of plating solution which remains on plated whiskers withdrawn from the bath serves as a satisfactory flux during a subsequent soldering operation.

[1] Present Address: Amchem Products, Inc., Ambler, Pa.

Experimental Results

Glycerol solvent.—In the electrodeposition of molten metals, a solvent is required which has a boiling point above the liquidus temperature of the metal or alloy electrodeposited. While it was found possible to electrodeposit molten In metal from solutions of anhydrous indium trichloride in a wide variety of polar organic compounds including ethylene glycol, 1, 2-propanediol, 1, 2, 4-butanetriol, N, N, N′, N′-tetrakis (2-hydroxypropyl) ethylenediamine, phenol, d-sorbitol, acetamide, ethylene glycol monobutyl ether, benzoic acid, phthalic anhydride, diethylene glycol, triethanolamine and ammonium formate, glycerol was the most suitable solvent. Glycerol, which has a boiling point of 290°C, is relatively nonvolatile at the usual operating temperatures of the plating baths, and its thermal decomposition rate at these temperatures is comparatively low. Glycerol fumes are nontoxic.

Materials.—Materials used in the preparation of In and In-Cd alloy plating baths are: glycerol (assay 95%, sp. gr. 1.25), A.C.S. reagent; cadmium chloride, anhydrous, powder, minimum assay 99%, A.C.S. reagent; indium trichloride, powder, anhydrous, minimum assay 96%, 0.02% maximum metallic impurities;[2] ammonium chloride, granular, A.C.S. reagent; ethylenediaminetetraacetic acid (EDTA), powder, reagent grade.[3]

Preparation of solutions.—Formulations of the glycerol solutions for electrodeposition of molten

[2] From Consolidated Mining and Smelting Co. of Canada, Trail, B.C., or Indium Corp. of America, Utica, N.Y.

[3] J. T. Baker Chemical Co., Phillipsburg, N.J., or Fisher Scientific Co., Fair Lawn, N.J.

Table I. Formulations, properties and typical operating conditions of glycerol solutions for electrodeposition of molten indium or indium-cadmium alloy

Description	Solution I: Solution for electrodeposition of In metal		Solution II: Solution for Electrodeposition of In-Cd alloy			Solution III: Complexed solution for electrodeposition of In-Cd alloy		
Formulation, % by weight								
$InCl_3$	12.0		6.0			5.2		
$CdCl_2$	—		1.7			1.5		
EDTA	—		—			12.6		
NH_4Cl	8.0		10.6			9.3		
Glycerol	80.0		81.7			71.4		
Electrolytic conductivity								
Specific conductance at 140°C, mho/cm	0.035		0.040			0.035		
Typical operating conditions								
Operating temperature, °C	140	165	140	140	140	140	140	140
Bath life, hr	8	4	8	8	8	8	8	8
Applied potential, v	15-24	3-24	10	18	24	12	18	24
Composition of the electrodeposited alloy, % In by weight	100	100	75-80	75-80	67-75	66-70	66-70	70-75
Approximate plating time to obtain a 15-μg deposit, sec	—	—	—	—	2	—	—	5
Approximate current density, amp/cm²	—	—	—	—	50	—	—	25
Approximate cathode current efficiency, %	—	—	—	—	20	—	—	15

In or In-Cd alloy are given in Table I. Solutions are prepared by stirring a mixture of the constituents for 30 min, breaking up any lumps, and then heating the resulting slurry with continuous stirring at 140°C for 10 min, or at 160°C for 10 min in the case of Solution III, to form a clear solution. The solution is allowed to cool to 100°-120°C and vacuum filtered through a coarse-porosity sintered glass filtering funnel.

While it is possible to dissolve all of the indium trichloride, cadmium chloride, and ammonium chloride in the glycerol at 25°C, the EDTA is only slightly soluble. Rapid dissolution of the solids is not possible below 135°C.

The glycerol baths are clear, light amber solutions which are somewhat more viscous than glycerol. Densities average roughly 1.35 g/ml at 25°C. The baths, which are prepared, stored, and operated in Pyrex or Kimax glass vessels, are stable for years at room temperature.

The reproducibility of numerous batches of plating solutions made by several different operators was quite satisfactory in terms of specific conductance at 140°C and in terms of plating rate (with 18 or 24 v applied) at 140°C, both initially and after 5 hr at 140°C.

Glycerol baths for Electrodeposition of Molten In *and* In-Cd *Alloy*

Properties and typical operating conditions of the various solutions are given in Table I.

Ammonium chloride increases the electrical conductivity of the plating solutions considerably and improves wetting by making the solutions more effective fluxes for the base metal to be plated (for example, nickel) as well as for the molten metal being deposited. (The specific conductivity at 140°C of a solution consisting of 13% $InCl_3$ and 87% glycerol was roughly 0.001 mho/cm, compared to 0.035 mho/cm for Solution I.) Cadmium chloride and indium trichloride are present in Solutions II and III in the ratio of 1:3.54 by weight, so that the ratio of Cd to In (as metal) in the baths is 1:3 by weight. Sufficient EDTA is present in Solution III to complex all In and Cd (assuming one mole of either metal per mole of EDTA) with 35% EDTA in excess.

Inert anodes of carbon (spectroscopic graphite) were used in all experiments. During electrolysis bubbles of oxygen and/or chlorine are evolved at the anode. The carbon anode should have sufficient area so that there is no appreciable polarization or local heating at the anode during electrolysis. One or more carbon rods 1/8 in. in diameter are used as anodes. The distance between cathode and anode is generally on the order of 1 cm.

In all of the experiments described, nickel wire 2 mils (0.05 mm) in diameter was used as a cathode. Under typical operating conditions the wire was immersed 1 to 2 mils (0.025 to 0.05 mm) below the plane of the surface of the plating solution. The hot plating baths normally wet the whisker wires far above the level of immersion. For example, a 2-mil nickel whisker wire immersed 1 to 2 mils below the plane of the surface of a glycerol plating solution at 140°C is wetted and plated along approximately a 10-mil length at the tip.

Under normal electrodeposition operating conditions, some hydrogen gas is evolved at the cathode during electrolysis of the solution.

The cathode area of immersed wires increases rapidly with the growth of the electrodeposited ellipsoidal beads of molten metal. For example, under typical operating conditions an ellipsoidal bead of molten In-Cd alloy 5 mils in diameter and 10 mils long is deposited on a 2-mil wire in about 2 sec. At the end of the 2-sec plating period, the surface area of the molten In-Cd alloy is several times

as great as the original immersed area of the wire. As the surface area of the molten solder increases during electrolysis, the current drawn at constant applied voltage also increases. For this reason, operating conditions are specified in terms of applied voltage rather than current density. Approximate current densities are given in Table I for several operating conditions.

Operating temperature and voltage of the baths are not particularly critical. Samples plated from Solution II at 120°C with 6 to 36 v applied, and at 160°C with 12 to 36 v applied, flowed at 130°C or less. The flow temperature of In-Cd alloys plated from Solution III at 140°C using 1.5 to 30 v was 130°C or less.

Bath life.—The average amount of In-Cd alloy deposited on the 2-mil nickel wires used in the fabrication of surface-barrier transistors is of the order of 10 to 20 μg. Under ordinary operating conditions, bath life is limited by decomposition reactions which occur in the bath at the operating temperature, usually 140°C; depletion of Cd and of In is negligible.

Since the ratio of Cd to In both in the plating baths and in the eutectic alloy is 1:3 by weight, the ratio of Cd to In in the bath remains essentially unchanged even when large amounts of alloy are electroplated from the bath.

Although thousands of whiskers can be plated from a 25-ml sample of plating bath without any evidence of decomposition of the plating solution due to anodic oxidation, prolonged electrolysis of these baths at high currents can accelerate decomposition reactions considerably.

Normally the principal limitation of bath life arises as a result of increase in viscosity with time at operating temperature. Increased viscosity results in lower electrolytic conductance and thus lower plating rates (with a constant plating voltage applied). Eventually, baths operated at 140°C become sufficiently viscous that plating rates are significantly lower than they had been initially, and the plated deposit tends to be somewhat erratic in size or location.

Tests have shown that these solutions frequently lose several per cent of their weight during 3 hr at 140°C due to volatilization.

No changes have been observed in flow temperatures of In-Cd alloys plated from solutions held at operating temperature for various periods of time up to 16 hr.

Effects of Bath Composition and Plating Conditions on Plating Rate and Bath Life

In a series of experiments to determine the effect of variations in bath composition, the relative amounts of $CdCl_2$, $InCl_3$, and EDTA were kept constant and were in the mole ratio of 1:2.94:5.36, respectively. The independent solution composition variables were thus per cent by weight ($CdCl_2$+$InCl_3$+EDTA) as a constant mole ratio group, and per cent by weight ammonium chloride, the remainder of the bath being glycerol. Specific conductance measurements at 100°C indicated that solutions consisting of the group ($CdCl_2$+$InCl_3$+EDTA) and glycerol in the weight ratio of 1 to 3 or 4 had a maximum specific conductivity. Decrease in the concentration of such solutions resulted in less ions available for electrolytic conductance and thus lower specific conductivity. Increase in the concentration of such solutions decreased the specific conductivity because the viscosity of these solutions increased considerably with concentration. [Generally, dissolved electrolytes increase the viscosity of glycerol solutions (5).] The viscosity of the glycerol solutions increased considerably with increase in concentration of the group ($CdCl_2$+$InCl_3$+EDTA); change in the concentration of the ammonium chloride had little effect on the viscosity of the solution.

Baths which were more concentrated than Solution III had a rather sharp decrease in specific conductivity with evaporation of glycerol and thus had a limited bath life. Solution III, which has approximately the concentration at which maximum specific conductivity is obtained, is relatively insensitive to changes in specific conductivity resulting from evaporation of glycerol. Solution III has an operating life at 140°C of approximately 8 hr whereas a more concentrated bath, consisting of 2.5% $CdCl_2$, 8.9% $InCl_3$, 21.4% EDTA, 6.1% NH_4Cl, and 61.1% glycerol, by weight, had an operating life of 2-3 hr at 140°C.

Increase in the ammonium chloride content of the bath increased the specific conductance and thus increased the plating rate at a given applied voltage. However, the solubility limit of ammonium chloride in the bath at about 20°C cannot be exceeded if the bath is to be stored at room temperature.

In some cases a small amount of surface-active agent is added to glycerol baths for plating molten metals and alloys. This addition lowers the surface tension of the solution, causing the bubbles formed at the cathode during electrolysis to be smaller. For example, 0.05% by weight of decyl benzene sodium sulfonate is effective in considerably reducing the surface tension of the Solution II at 140°C. The presence of a surface-active agent, by making the bubbles smaller, results in steadier plating currents and thus more reproducible plating rates.

Composition of Electrodeposited In-Cd *Alloys*

Flow temperatures were determined by immersing whiskers, on which the beads of In-Cd alloy had been flattened, into a flux such as 9% ammonium chloride in glycerol at 130°C. If the alloy flowed at 130°C or less, the bead returned to an ellipsoidal shape.

The composition of electrodeposited In-Cd alloys was determined by quantitative spectrographic analysis. Weighed samples of clean, dry, plated whiskers were treated with about 0.6 ml of 4*N* HCl to dissolve the In-Cd alloy. The stripped whiskers were rinsed, dried, and reweighed. The solution was diluted to a concentration of 0.50 mg of In-Cd alloy/ml and analyzed spectrographically by comparison with solution standards. About 50 plated

whiskers were used to prepare each sample solution for analysis. Generally duplicate determinations were made.

Local Heating at the Cathode during Electrolysis

In some cases considerable local heating occurs at the cathode during electrolysis. For example, molten In-Cd alloy was plated on a 2-mil nickel wire immersed in Solution III, operated at a temperature of 70°C, using 18 v for electrolysis. In this case, the temperature at the cathode rose more than 50°C above the operating temperature of the bath. In one experiment, with 90 v applied to a 2-mil wire immersed about 5 mm, molten In-Cd alloy was electroplated from Solution III at room temperature (25°C), indicating a temperature rise of approximately 100°C at the cathode.

Molten In metal can be deposited on 2-mil nickel wire from Solution I operated at 140°C with 18 v applied or at 120°C with 24 v applied. Molten In-Cd alloy can be plated on 2-mil nickel wire from Solution II operated at 100°C with 24 v applied.

The principle of employing local heating at the cathode to plate molten metals or alloys from a solution operated at a temperature considerably below the liquidus temperature of the metal or alloy is of interest in applications where long bath life or minimum fuming is desired.

Chemical Plating

Small pieces of Cd and of In metal were added to both Solution II and Solution III at 140°C. With both solutions the Cd became coated with a molten alloy, indicating that chemical plating of In had occurred. The In metal was etched by both solutions but no visible deposition of Cd occurred.

Conclusions

The chemical plating experiments indicate that In is more noble than Cd at 140°C in both the complexed and the uncomplexed solutions for plating molten In-Cd alloy. Such a result might be expected from a comparison of the single electrode potentials of In and of Cd in the acid electromotive series of the elements (in aqueous solution), where $E^\circ = -0.34$ v for In and $E^\circ = -0.40$ v for Cd (6).

Increase in plating solution viscosity with time at operating temperature is believed to be due to evaporation of glycerol and/or water and to condensation polymerization of glycerol to form polyglycerides, which are more viscous than glycerol (7). Since formation of polyglycerides appears to be catalyzed by anhydrous indium trichloride, the solutions listed in Table I are less susceptable to this type of degradation than more concentrated solutions.

Both Solution II and Solution III are used in the production of semiconductor devices. Solution II deposits In-Cd alloy more than twice as fast as Solution III, but the latter is less volatile at 140°C and electrodeposits In-Cd alloys of suitable solder composition over a wider range of operating conditions than the uncomplexed solution (8).

Acknowledgment

The authors wish to express their thanks to M. Sadowsky for his interest and encouragement, to E. Murt, who performed the spectrographic analyses, and to W. Hillegas, Jr., for excellent assistance in the experimental work on the uncomplexed In-Cd plating solution.

Manuscript received July 9, 1958. This paper was prepared for delivery before the Buffalo Meeting, Oct. 6-10, 1957.

Any discussion of this paper will appear in a Discussion Section to be published in the June 1960 JOURNAL.

REFERENCES

1. E. A. Peretti, "Constitution of Indium Alloy Systems," p. 15, Indium Corp. of America, Utica, N. Y. (1956).
2. G. L. Schnable and J. G. Javes, *This Journal*, **105**, 84 (1958).
3. G. L. Schnable (to Philco Corporation), U. S. Pat. 2,818,375, Dec. 31, 1957.
4. "Soldering Whiskers on Transistor Pellets," in "Production Techniques," J. Markus, Editor, Electronics, **29**, 270 (1956).
5. "Physical Properties of Glycerol and its Solutions," by J. B. Segur in "Glycerol," C. S. Miner and N. N. Dalton, Editors, p. 285, Reinhold Publishing Corp., New York (1953).
6. W. M. Latimer, "The Oxidation States of the Elements and Their Potentials in Aqueous Solutions," 2nd Ed., Prentice-Hall, Inc., New York (1952).
7. "Chemical Properties and Derivatives of Glycerol" by J. B. Segur in "Glycerol," C. S. Miner and N. N. Dalton, Editors, pp. 366-8, Reinhold Publishing Corp., New York (1953).
8. T. J. Manns and A. J. Certa (to Philco Corporation), U. S. Pat. 2,818,374, Dec. 31, 1957.

Potential Measurements during Jet Etching of P-Type Ge and P-Type Si

Paul F. Schmidt and Maire Blomgren

Research Division, Philco Corporation, Philadelphia, Pennsylvania

ABSTRACT

Potential measurements have been made during jet etching, and the feasibility of the method has been established. Potentials during jet etching have been compared with those obtained in bath operations by other authors.

Jet etching and plating have become increasingly important for the fabrication of semiconductor devices. The current densities employed are well beyond the usual range of bath operation. Thus it appeared very desirable to investigate jet etching and plating by potential measurements. Development of special techniques was required for the peculiar geometry of the jet method. The method has been applied to p-Ge and p-Si so far, but should be applicable also to other systems.

Experimental

Jet-etching apparatus.—The apparatus consisted of a transparent plastic enclosure with removable lid; the jet and anode were inserted into the plastic chamber from opposite sides, both making an angle of 45° with the perpendicular (Fig. 1). The jet was rigidly fixed in its position. The anode consisted of a Ge or Si wafer mounted on a nickel or stainless steel disk, which in turn was screwed into a holder. Three micrometer screws permitted the movement of the holder perpendicular and parallel to the jet axis. In the direction parallel to the jet axis the accuracy was 0.2 mil, in the two perpendicular directions the accuracy was about 1 mil.

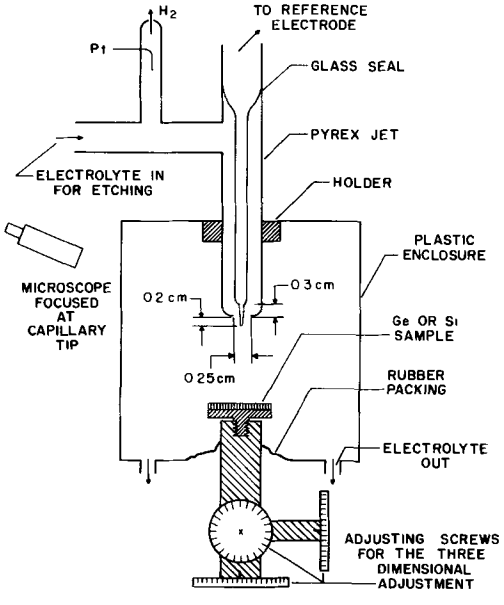

Fig. 1. Schematic of jet etching apparatus

A pocket microscope was mounted in such a fashion that it could always be brought to exactly the same position and could be focused simultaneously on the jet nozzle and on its mirror image at the shiny Ge or Si surface. Magnification by the microscope was 60X. Two drainage tubes at the bottom of the plastic chamber permitted the withdrawal of the electrolyte during etching. A lid was placed on the plastic chamber when large jet sizes were used.

The jet.—Two sizes of jet nozzles were employed: 30 and 100 mil diameter (7.6×10^{-2} and 2.5×10^{-1} cm). Inserted in the center of the jet, by means of a glass seal, is a smaller tube which tapers off to a capillary, about 0.5 cm long, 2.5 mil (6×10^{-3} cm) OD, and 1.5 mil (3.7×10^{-3} cm) ID. The capillary is located accurately in the center of the jet nozzle and extends 0.15 to 0.2 cm beyond it. The inner tube is connected to a saturated calomel electrode. The electrolyte in the outer tube was used for jet etching. The electrolyte in the inner tube, connected to the reference electrode, was usually the same as that in the outer tube except for those experiments which involved the use of free HF for jet etching. In this case the *p*H of the electrolyte in the inner tube was kept neutral in order to avoid excessive attack on the capillary. Only capillaries without any faults could be used; if the tip of the capillary was damaged in any way, the electrolyte from the inside would form droplets at the tip thus making it impossible to position the Ge or Si sample accurately (compare below). Also the potential values would be quite erratic with faulty capillaries.

The electrolyte for jet etching was introduced into the outer tube of the jet through a side arm. The latter in turn was connected to a small tube partially open at the tip. Inserted in this small tube was a Pt wire which served as the auxilliary electrode. Any hydrogen bubbles forming at the wire were swept out at the tip and thus did not enter the main jet stream.

Anode set up —The anode, as already mentioned, consisted of a Ge or Si wafer mounted on a nickel or stainless steel disk which in turn could be screwed into the sample holder. When positioning the sample, the anode was moved toward the jet nozzle by means of the micrometer screws until

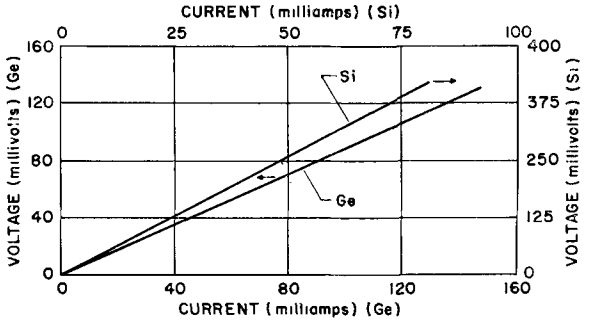

$R_{bulk\ Ge}$. 0.5 ohms $R_{bulk\ Si}$. 0.6 ohms
$R_{measured}$. 0.9 ohms $R_{measured}$. 5.2 ohms
$R_{each\ contact}$. 0.2 ohms $R_{each\ contact}$: 2 3 ohms

Fig. 2. I-V of ohmic base contacts to Ge and Si

both the tip of the capillary and its mirror image were simultaneously in the focus of the microscope. In this fashion it was possible to make the distance between the tip of the capillary and the semiconductor surface less than 1.2×10^{-3} cm.

Preparation of Ge *and* Si *samples.*—Ohmic base contacts to the p-Ge wafers (resistivity 1 ohm-cm, lifetime about 100 μsec, thickness 0.05 cm) was obtained by sand blasting the whole back surface of the wafer and soldering pure tin to the sand blasted area. The stainless steel disk was then pressed against the tin while heating. This resulted in a good electrical and mechanical contact. In the case of p-Si (ρ about 1 ohm-cm, τ about 20 μsec, thickness = 0.05 cm), Al was evaporated onto the back surface of the chemically polished wafer and was then alloyed by heating at 850°C for 30 sec. The Al was then painted with silver paste, which again resulted in a good contact when mechanically pressed against the metal disk.

In order to check that the contact was truly ohmic, the front surface of some wafers was given the same treatment as the back surface and I.V. curves were taken. Figure 2 shows that completely ohmic contacts were obtained both on p-Ge and on p-Si. The contact resistance for each contact is about 0.2 ohm on p-Ge, and 2.3 ohm on p-Si.

In order to obtain a homogeneous current density during jet etching it was necessary to mask the Ge or Si surface except for a hole of the same size or smaller than the jet employed. The hole had to be a perfect circle without fuzzy edges; otherwise, the resulting etch pit would be of very poor quality. The masking material must also meet the requirements of being quite inert to the electrolytes employed, and of being so thin that it would not obstruct the view of the mirror image of the capillary tip when the sample is brought into position. For measurements of current efficiency it was also essential that the masking material should be easily removable without changing the weight of the Ge or Si wafer. All these requirements were met by a Teflon tape with pressure sensitive silicone adhesive.[1] The tape was applied to the chemically polished surface of the semiconductor.

[1] Produced by the Minnesota Mining and Manufacturing Co. (pressure sensitive tape No. 549).

Potential measurements.—A voltage regulator supply, model 3-150 L, of the Dressen-Barnes Corporation served as a power source. The voltage was applied between the auxilliary electrode in the side arm of the jet and the ohmic base contact of the Ge or Si wafer. A standard resistor was inserted in the circuit and the voltage across this resistor applied to one axis of a Moseley X-Y recorder. The voltage between the reference electrode and the ohmic base contact was applied to the input of a Keithley electrometer, model 210, and from there to the other axis of the X-Y recorder. Use of the Keithley electrometer was necessary because of the high resistance in the capillary (about 10^9 ohm). The response time of the recorder is 1 sec full scale on either axis.

It was found that the potential values did not depend on the speed with which the curves were taken, i.e., for times of the order of a few seconds, except, of course, for the additional *RI* drop introduced if the etching process at high current densities increased the distance between capillary and Ge surface by an appreciable amount. Usually the current was increased to its maximum value in 10 sec and decreased to zero in the same time.

Owing to the small distance between the tip of the capillary and the semiconductor surface, the *RI* drop in the electrolyte up to current densities of about 0.1 amp/cm^2 is negligible ($\leqq$ 10 mv). This was checked by experiments in which the distance between capillary and Ge surface was increased successively in steps of 0.5 mil (1.3×10^{-3} cm).

At high current densities, however, this *RI* drop must be taken into account. It is then necessary to consider the distance by which the Ge or Si surface has receded from the capillary due to the etching action. Knowledge of the current efficiency over the current range investigated, of changes in the resistivity of the solution due to heating effects, and of the total amount of charge passed at each point of the curve would be required in order to apply an accurate correction. The amount of charge passed could be determined if the current had been increased linearly with time. The current in our experiments was increased manually and therefore not quite linearly with time. Therefore it is not justified to apply a correction in this manner.

No corrections have been applied to any of the curves shown in this paper, except those applied to Fig. 3; they are stated below in the text. However, from the known resistivities of the electrolytes employed it can be calculated that the additional *RI* drop introduced by recession of the semiconductor surface during etching is less than 1 v (at 10 amp/cm^2) if the etching current is raised linearly with time over a period of 10 sec from 0 to 10 amp/cm^2. When comparing this value to the potentials obtained at 10 amp/cm^2, roughly 10 v, it can be seen that the error even at the largest current densities is less than 10%. It can be shown that the additional *RI* drop under the above conditions increases with i^2; the error at lower current densities is therefore much smaller. The *RI* drop due to the original distance between the tip of the capillary

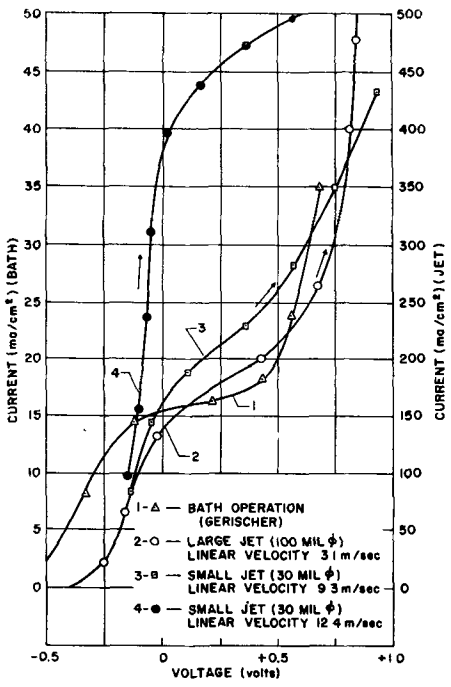

Fig. 3. Current-potential curves on p-Ge for bath operation (Gerischer and Beck) and for jet-operation using the same electrolyte. 1 ohm-cm p-Ge, 0.1M $NaClO_4$ + 0.02 M NaOH; flow rate: 3.1 m/sec.

and the semiconductor surface is about 0.5 v at 10 amp/cm^2.

The curves shown are typical of a very large number of experiments; the reproducibility was quite good. The potentials always refer to the saturated calomel electrode, except in Fig. 3 where they have been referred to the N-calomel electrode. All measurements were done at room temperature.

Since the experiments were performed on p-type material only, saturation effects inside the semiconductor are not expected to occur, and except for their appreciable resistivity Ge and Si can be treated in this respect much like metals.

Measurements of current efficiency.—These measurements were done in parallel to the potential measurements. The weight of the Ge or Si sample before and after etching was determined with a Mettler microbalance, sensitivity ± 1 μg. Before weighing, the samples were kept in a dessicator for 1 hr. It was again necessary to mask the Si or Ge wafers except for a small hole facing the jet in order to deal with a defined current density. In control runs it was found that applying the masking tape to the sample, exposing it to the electrolyte stream (without applying a bias), removing the tape and washing the sample with chloroform or CCl_4 did not change the weight of the wafer by more than ± 10 μg. The amount of charge passed during each run was chosen so as to remove 400 μg. It is believed therefore that the result of the weighings should be accurate to at least ± 5%. However, the amount of charge passed was obtained simply from the product time x constant current. This reduces the accuracy somewhat more. For accurate determinations a coulometer should be employed.

The electrolytes.—The electrolytes used had the following composition and resistivity (at room temperature):

On p-Ge: 0.1M $NaClO_4$ + 0.02M NaOH; ρ = 79.3 ohm-cm
0.2N H_2SO_4; ρ = 21 ohm-cm
0.2N H_2SO_4 + 1 cc Hyamine/1; ρ = 24.9 ohm-cm.
On p-Si: 40 g NH_4F + 8 g NaF/1; ρ = 16.4 ohm-cm
0.2N NaF + 5 cc 48% HF; ρ = 61.8 ohm-cm

The electrolyte was forced through the jet by pressure from a nitrogen tank. In separate experiments it was shown that removing dissolved oxygen from the electrolyte did not effect the potential measurements within the limit of accuracy except close to zero current.

The nitrogen pressure was 2 psig when the 100-mil jet was employed, and either 2.5 or 5 psig when the 30-mil jet was used. The corresponding linear jet velocities were 3.1 meters/sec (100-mil jet, 2 psig), 9.3 meters/sec (30-mil jet 2.5 psig), and 12.4 meters/sec (30-mil jet, 5 psig). The flow rate of the electrolyte has a very marked effect on the I.V. curves as would be expected.

Results

1. *Potentials during jet etching of p-Ge with 0.1M $NaClO_4$ + 0.02M NaOH solution, and comparison to the potential values obtained by Gerischer and Beck (1) with the same electrolyte in a stirred bath.*—Figure 3 shows the current potential curves for three different jet flow rates. For the sake of comparison the curve obtained by Gerischer and Beck is also shown. Unfortunately, the stirring rate for this curve is not given in the preliminary publication by Gerischer and Beck.

The jet curves in Fig. 3 are corrected for the total *RI* drop between base contact and tip of capillary in the following way: (*a*) From the experiments on contact resistance (Fig. 2) the resistance of the base contact is known to be about 0.2 ohm. (*b*) For the contact jet/Ge the spreading resistance inside the Ge is calculated from the formula (2): $R = \frac{1}{4a\sigma}$ (where a = radius of the contact, σ = conductivity of the Ge) to be 4.0 ohm for the large, and 6.5 ohm for the small jet. (In the experiments with the large jet the unmasked area of the Ge was 50 mils ϕ = 0.13 cm ϕ.) (*c*) From the resistivity of the solution (79.3 ohm) and an assumed distance of 1.3 x 10^{-3} cm, the resistance of the electrolyte layer between the tip of the capillary and Ge surface is calculated to be 23.1 ohm for the small jet (30 mil ϕ), and 8.1 ohm for the large jet (effectively 50 mil ϕ). (No correction has been applied for increase of the distance with etching because the curves were taken so rapidly that the additional distance is negligible compared to the original distance.)

It can be seen from Fig. 3 that the shapes of the curves are quite similar. However, the current

plateaus occur at much higher values for the jet operation, and the plateaus are not so flat.

It is evident that the vigorous stirring action of the jet causes a decrease in thickness of the Nernst diffusion layer. The fact that the position of the current plateaus depends strongly on the jet speed shows that concentration overpotentials are very pronounced in jet operation in this current density range.

The current plateaus obtained with the jet are not as horizontal as in the bath. This is due to the fact that the current density is not exactly homogeneous over the etching area, as can be seen from the slightly rounded bottom of the etch pit obtained with prolonged etching.

The current plateaus of curve 2 (100 mils ϕ jet, 50 mils ϕ etching area, 3.1 m/sec linear jet velocity) and of curve 3 (30 mils ϕ jet, 30 mils ϕ etching area, 9.3 m/sec linear jet velocity) occur at not greatly different current densities, whereas the current plateau of curve 4 (30 mils ϕ jet, 30 mils ϕ etching area, 12.4 m/sec linear jet velocity) is shifted to a much higher current density.

The thickness of the Nernst diffusion layer, which determines the position of the current plateau, is apparently smaller in the case of curve 2 than would be expected from the average flow rate of the jet (measured as volume/time). This must be due to the fact that the 50 mils ϕ etching area is exposed to the higher flow velocity in the center of the 100 mils ϕ jet. The small distance between jet nozzle and Ge surface (2 mm = 80 mils) is apparently not sufficient to suppress the velocity profile of the jet stream.

A rough calculation indicates that the thickness of the Nernst diffusion layer is about 25 times smaller for curve 4 than for curve 1.

The agreement between curve 1 (bath operation) and curves 2-4 (jet operation) is satisfactory when considering the deviations from ideal conditions mentioned above and shows that essentially the same electrode process takes place in jet etching as in bath operation.

As to the interpretation of the curves, reference is made to the publication by Gerischer and Beck (1). According to these authors the anode reaction

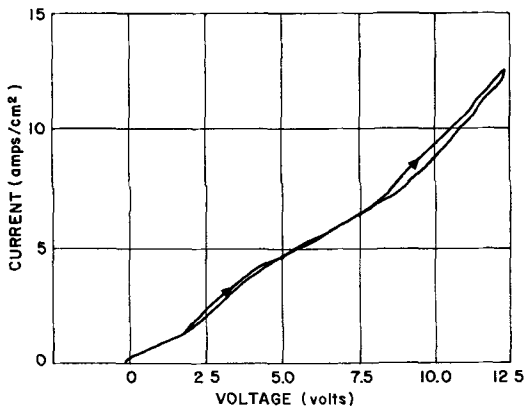

Fig. 4. Current-potential relationship at high current densities. Same electrolyte as in Fig. 3. 1 ohm-cm p-Ge, 0.1M $NaClO_4$ + 0.02M NaOH; flow rate: 12.4 m/sec.

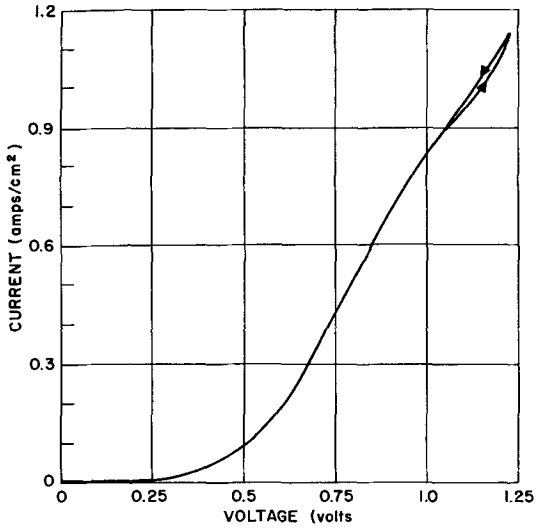

Fig. 5. Current-potential relationship in dilute H_2SO_4 at low current densities. 1 ohm-cm p-Ge, 0.2N H_2SO_4; flow rate: 9.3 m/sec.

on the first ascending branch is between Ge and OH^- ions, and on the second ascending branch between Ge and H_2O molecules. The current plateau indicates depletion of OH^- ion supply at the surface.

This solution (0.1M $NaClO_4$ + 0.02M NaOH) is not an electropolishing solution on Ge. It does not reveal crystal structure, but neither does it remove any surface structure present prior to jet etching.

Figure 4 shows an experiment (with the 30 mil ϕ jet at a flow rate of 12.4 m/sec) in which the current density was increased to 13 amp/cm^2. The additional *RI* drop caused by etching at high current densities is clearly seen on this graph from the difference of the potentials on the way up and down. In addition, a second levelling of the current is observed at about 5 amp/cm^2. This levelling marks the beginning of oxygen evolution (as indicated by current efficiency measurements), and is probably connected with the buildup of an oxide layer. At current densities much below 5 amp/cm^2 there is no indication of an increase in thickness of a hypothetical oxide layer with time: the current can be held constant without causing an increase of potential within a reasonable length of time. Above 5 amp/cm^2 an increase of potential with time at constant current is observed but cannot be distinguished easily from an additional *RI* drop caused by etching unless transient techniques were to be employed.

These remarks also apply to the current levels observed at very high current densities with the other electrolytes employed in this investigation.

2. *Current-potential curves obtained with a 0.2N solution of* H_2SO_4.—Figure 5 shows the curve obtained with 0.2*N* H_2SO_4 at low current densities, and Fig. 6 at high current densities. A second levelling of the current is again observed in Fig. 6, but it is remarkable that in the region of the levelling the current for a given potential is larger on the way down than on the way up. At higher current densities the curve taken upward coincides with

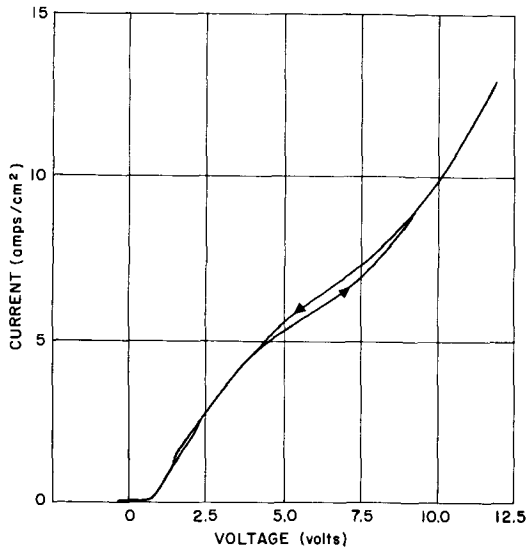

Fig. 6. Current-potential relationship in dilute H_2SO_4 at high current densities. 1 ohm-cm p-Ge, 0.2N H_2SO_4; flow rate: 9.3 m/sec.

the downward curve. This suggests that in this region the additional *RI* drop caused by etching is compensated by a decrease of potential with time at constant current. The shape of the curve in the region of low potentials is markedly different from the one obtained with the $NaClO_4$/NaOH solution and gives evidence that differences in electrode processes can be observed by potential measurements with the present jet technique.

Sulfuric acid has distinct electropolishing properties on Ge, but it still takes time for initially present surface structures to disappear.

3. *Current-potential curves obtained with 0.2N H_2SO_4 with the addition of a wetting agent.*—Figure 7 shows the current-potential curves obtained with a 0.2 *N* H_2SO_4 + 1 cc/liter of Hyamine 2389 [Alkyl (C_9-C_{15}) tolylmethyltriethyl ammonium chloride

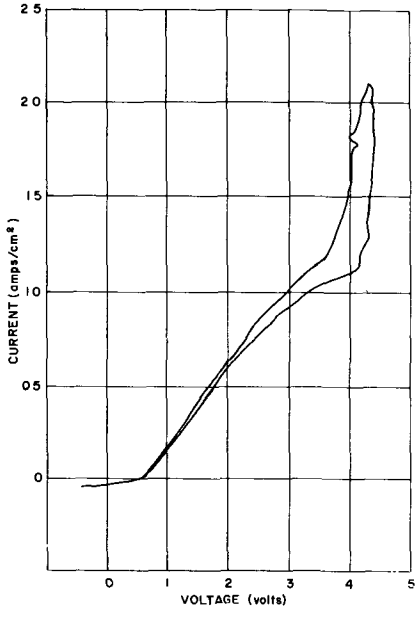

Fig. 7. Effect of addition of hyamine to dilute sulfuric acid. 1 ohm-cm p-Ge, 0.2N H_2SO_4 + 1 cc hyamine/liter; flow rate: 9.3 m/sec.

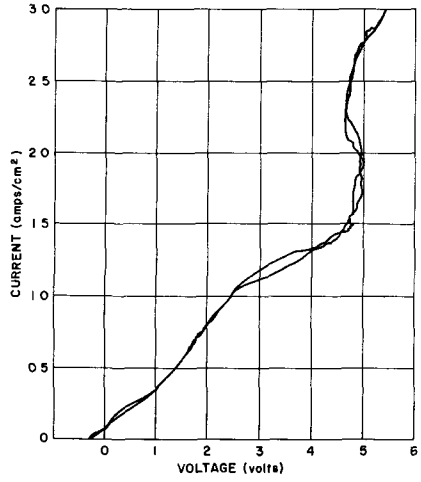

Fig. 8. Current-potential curves on p-Si in acidic fluoride solution. 1 ohm-cm p-Si, 8 g NaF + 40 g NH_4HF_2/liter; flow rate: 9.3 m/sec.

50%, H_2O 50%; Rohm & Haas Company]. The high anode potentials are remarkable. It is known that aromatic amines are adsorbed to an appreciable extent also on an anodic surface, and that they are desorbed at high anode potentials (3). The sudden jump in current at + 4.2 v suggests that the organic agent is partially desorbed at this potential, causing the current to approach the value for a clean Ge surface.

4. *Effect of crystal orientation.*—No difference in potential values was observed for the {111} and the {110} plane.

5. *Current-potential curves during jet-etching of p-Si with a solution of 40 g NH_4HF_2 + 8 g NaF/liter H_2O.*—Figure 8 shows a typical current-potential curve in the low, and Fig. 10 in the high current density range. In the region between 4 and 5 v the potential varies irregularly and rather violent fluctuations occur if the current in this region is held constant. The amplitudes of the oscillations are damped if the curves are taken with higher

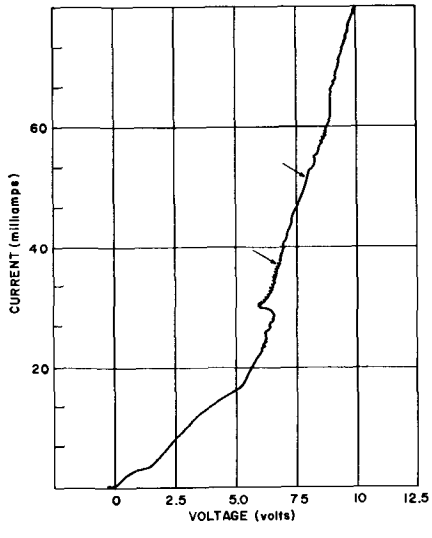

Fig. 9. Increasing size of etched area relative to jet size does not affect the general shape of the curve. 1 ohm-cm p-Si, 8 g NaF + 40 g NH_4HF_2/liter; flow rate: 12.4 m/sec; etching area 16 times jet size.

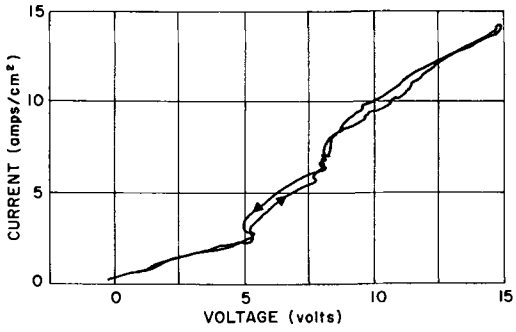

Fig 10. Current-potential curves in the same electrolyte at high current densities. 1 ohm-cm p-Si, 8 g NaF + 40 g NH_4HF_2/liter; flow rate: 12.4 m/sec.

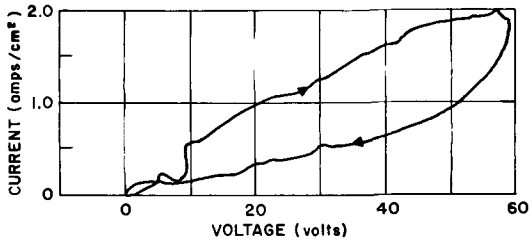

Fig. 11. Current-potential curves in an electrolyte containing less acid. 1 ohm-cm p-Si, 8 g NaF + 5 cc 48% HF/liter; flow rate: 9.3 m/sec.

speed. Also the jet flow rate has some influence. It was of interest to find out whether the fluctuations are caused by phenomena occurring at the edges of the masking tape. In Fig. 9 the diameter of the unmasked Si surface was 4 times the jet diameter; the contribution by phenomena at the periphery may therefore be expected to be less. The fluctuations nevertheless show up very clearly. Also in Fig. 9 two points are marked at which the current was held constant for 5 sec each without causing oscillations. Under the conditions of this experiment the oscillations are confined to the region between 16 and 31 ma.

A similar region of current-potential instability in the anodic oxidation of Si has been reported by Turner (5). No "run-away" region of decreasing potential with increasing current as noted by Turner was observed in our experiments presumably because the resistance of the electrolyte jet is so high (several K-ohms) that variations in electrode potential do not affect the current noticeably.

Potentials below 1 v were not very reproducible; this is probably connected with the ability of Si to form a thick oxide film in contact with air. Thus potentials in this region depend on the previous history of the sample, especially on the time elapsed since the wafer was polished chemically (with CP 4).

A thick air-formed film will not etch away rapidly before a critical potential is reached, as can be seen from the following experiment. Photodiodes on n-Si which had been exposed to air for a long time after their manufacture were biased reversely (+ 0.25 v), and light was shone through the running electrolyte jet aimed accurately at the front surface of the photodiode. (The diode area in these experiments was 30 square mils, the jet diameter was 20 mils, and the front surface of the Si had not been masked; the diode contact on the reverse side was, of course, insulated against contact with the electrolyte.) The saturation current of the photodiode increased to a value determined by the light intensity. An increasing anodic current was now applied between the Si base contact and an auxiliary electrode in the jet, so that the jet should now also act as a collector for the holes injected by the light. Until a current of 7 ma was reached, the current of the diode was quite independent of the jet current, proving that up to 7 ma the discharge of oxygen, i.e., the injection of majority carriers (electrons) was the main anodic process. Beyond 7 ma the diode current decreased abruptly to near the reverse saturation current in darkness, the jet now collecting practically all the injected holes.

If the electrolyte jet (same NH_4HF_2/NaF composition as above) is aimed at the Si surface without application of a current, a thin, semitransparent white film is formed, but the reaction is very slow and the Si is not attacked appreciably within 20 min. It is therefore more likely that the air-formed SiO_2 film rather than the formation of this whitish compound is responsible for the poor reproducibility of the potentials below 1 v. In our experiments the current density range 0-25 ma/cm² was usually traversed within 1 sec or less.

If, on the other hand, jet etching is done on purpose at a constant current density of 25 ma/cm² for a prolonged period of time, the Si is etched deeply and the surface becomes covered with a firmly adherent colorless compound, which is not soluble in water, slowly in CP 4, and dissolves slowly in strong NaOH with evolution of a gas, presumably hydrogen. The substance is thus similar to but not identical with the one described by Turner (5).

At large current densities (about 6 amp/cm²) oxygen evolution occurs as a side reaction, as shown by the current efficiency measurements (see below).

6. *Current-potential curves obtained with a solution of 8.4 g* NaF + *5 cc 48%* HF/*liter.*—This solution had been used extensively in practice but was satisfactory only at very low current densities. Figure 11 shows convincingly that at high current densities a high resistance SiO_2 film is formed which does not disappear quickly even when the current density is lowered.

7. *Measurements of current efficiency in the jet etching of p-Ge and p-Si.*—When etching p-Ge with dilute sulfuric acid the current efficiency based on a valency of +4 is usually close to 100% or just below, regardless of whether the Ge surface is masked or not. Up to moderately high current densities the current efficiency does not seem to depend much on current density; at high current densities oxygen is discharged as a side reaction and the current efficiency drops.

In solutions containing halide ions, more complex phenomena occur if the surface is not masked. Cur-

Table I

Electrolyte: 40 g NH_4HF_2 + 8 g NaF/liter; Flow rate: 3.1 m/sec

Current density range, amp/cm²	≦0.025	0.05< × <0.5	0.5< × <2	2< × <15
% Current efficiency	>>160	485-115	115-95	95-75
Remarks	Etched area covered with adherent white deposit, actual loss of Si therefore much greater, i.e., current efficiency >> 160%. Surface badly pitted under the deposit.	Shiny but not polished surface; at higher current densities transition to electropolishing.	Good electropolish at higher current densities	Electropolishing concommitant with O_2 evolution

rent efficiencies as high as 120% can be observed in HCl solution. This may well be due to the "edge-effect" described by Jirsa (4) who found that Ge goes into solution +4 valent over the whole current density range and in all electrolytes investigated by him (HCl, H_2SO_4, KOH, NH_4OH), but that at the interface solution/air/Ge divalent Ge ions are formed by the reaction: $Ge^{4+} + Ge \rightarrow 2\ Ge^{2+}$.

In contradistinction to the behavior of Ge very large deviations from a current efficiency of 100% were observed on Si. Table I summarizes the results.

It is very remarkable that apparent current efficiencies > 400% are obtained at low current densities. This rules out any explanation based on dissolution of Si as ions of lower valency. It seems in fact that an explanation must be sought along the lines of the negative difference effect investigated by Straumanis (6). A corresponding effect is not found on Ge which is more noble than hydrogen. This lends support to the assumption that current efficiencies > 200% are caused by current flow between local anodes and cathodes. The local cathodes are evidently created by an impressed anodic current in the manner described by Straumanis (6). The effect disappears at larger anodic potentials because the hydrogen evolution reaction is then suppressed on the Si surface.

At very large current densities oxygen evolution occurs but in the given electrolyte Si does not passivate, at least not below 20 amp/cm², the highest current density investigated.

Acknowledgments

The authors are greatly indebted to Dr. E. Blomgren of the University of Pennsylvania for valuable discussions and advice, and to Professor J. O'M. Bockris of the University of Pennsylvania for valuable discussions of semiconductor electrode kinetics. Our thanks are also due Mr. Larson at the University of Pennsylvania for solving the difficult task of preparing the Haber-Luggin capillaries and inserting them in the jets.

Manuscript received Sept. 24, 1958.

Any discussion of this paper will appear in a Discussion Section to be published in the June 1960 JOURNAL.

REFERENCES

1. H. Gerischer and F. Beck, *Z. Phys. Chem., N. F.*, **13**, 389 (1957).
2. H. C. Torrey and C. A. Whitmer, "Crystal Rectifiers," p. 24, McGraw-Hill Book Co. (1948).
3. E. Blomgren and J. O'M. Bockris, *J. Phys. Chem.*, in press.
4. F. Jirsa, *Z. anorg. u. allgem. Chem.* **268**, 84 (1952).
5. D. R. Turner, *This Journal*, **105**, 402 (1958).
6. M. E. Straumanis, *ibid.*, **105**, 284 (1958); M. E. Straumanis and Y. N. Wang, *ibid.*, **102**, 304 (1955).

Junction Delineation on Silicon in Electrochemical Displacement Plating Solutions

D. R. Turner

Bell Telephone Laboratories, Incorporated, Murray Hill, New Jersey

ABSTRACT

Antimony, copper, silver, platinum, and gold can be deposited on silicon by electrochemical displacement. The displacement plating process induces potential differences between abraded and polished n- and p-type silicon. This results in metal being deposited at different rates on the four types of silicon surfaces which in turn produces p-n junction delineation. The process also shows up abrupt changes in the impurity concentration at the surface. The maximum resolution between junctions in a multiple junction crystal is about 2 microns.

A number of chemical treatments have been developed to show up p- and n-regions on the surface of silicon single crystals. The first was devised by Fuller (1) and consisted of treating the Si in HF solutions containing a small amount of HNO_3. This solution stains p-type regions darker than the n-type. Silverman and Benn (2) were able to portray junctions on Si with Au deposited by electrochemical displacement from a gold cyanide plating solution in the presence of light. Recently Whoriskey (3) has improved on the reproducibility of the HF stain method by eliminating the HNO_3 and illuminating the junction with white light. He also reports good junction delineation using white light and a copper nitrate solution containing a small amount of HF. Iles and Coppen (4) obtained junction delineation on Si in a dilute silver-fluoride solution. They reported that Ag deposited preferentially on the lower conductivity material regardless of conductivity type in the dark or with room light.

The purpose of this paper is to describe a method of obtaining very sharp p-n junction delineation on Si in acid fluoride displacement plating solutions without the aid of light. Waltz (5) and Wang (6) have deposited metals on Si by electrochemical displacement from acid fluoride solutions for the purpose of making ohmic contacts. Their solutions are not suitable for junction delineation.

Electrochemical displacement plating on Si.—One metal plates on another by electrochemical displacement when the depositing metal is more noble (electropositive) than the metal receiving the deposit. Plating is literally by displacement, for each milligram-equivalent of metal depositing on Si at cathodic sites, 1 mg-equivalent of Si dissolves at anodic sites. The total anode current, therefore, equals the total cathode current. The rate of metal deposition by displacement can be controlled by regulating the rate of the anode reaction. Silicon dissolves anodically by first forming an oxide. Unless the electrolyte is capable of dissolving the oxide, the anode reaction will stop after the oxide becomes a few atom layers thick. Displacement plating also will stop under these conditions. Silverman and Benn (2) were able to deposit Au on Si by displacement from a gold cyanide plating solution because hot strongly alkaline solutions dissolve silicon dioxide forming a soluble silicate complex:

$$SiO_2 + 2KOH \rightarrow K_2SiO_3 + H_2O$$

For the same reason, Cu can be deposited on Si by displacement in a hot alkaline Cu plating solution.

Hydrofluoric acid dissolves SiO_2 by forming a soluble silicofluoride complex:

$$SiO_2 + 6HF \rightarrow H_2SiF_6 + 2H_2O$$

The rate of Si dissolution at anodic sites, and therefore the metal deposition rate at cathode sites, in acid fluoride displacement plating solutions can be regulated by controlling the rate of mass transfer of HF from the solution bulk to the anode sites. This is done easily by adjusting the bulk HF concentration in the plating solution.

Experimental Methods and Results

Five different metals were deposited on Si by electrochemical displacement: Sb, Cu, Ag, Pt, and Au. The aqueous solutions contain simple metal salts plus different amounts of HF as shown in Table I. They are all used at room temperature. The metals in Table I are arranged according to the electromotive series. Antimony is the most electronegative of the group while Au is the most electropositive. The amount of HF used in each solution is believed to be optimum for the sharpest junction delineation. A 2-min treatment is usually sufficient to portray p-n junctions in the solutions of Table I. At lower HF concentrations, the time required for delineation increases, and the deposit often is not uniform. Higher HF concentrations result in rapid metal deposition on both sides of the p-n junction so that delineation is poor or impossible. At a given HF concentration, the rate of metal deposition by displacement on Si increases the more electropositive the metal. Therefore, Au will deposit faster than the other metals. Rates of metal deposition may be equalized, however, by decreasing the HF concentration as the metal becomes more electropositive as shown in Table I.

Table I. Solutions for junction delineation on Si

Metal deposited	Metal salt	g/l	cc 48% HF/l
Sb	SbF_3	400	500
Cu	$CuSO_4 \cdot 5H_2O$	200	10
Ag	$AgNO_3$	40	4
Pt	$H_2PtCl_6 \cdot 6H_2O$	3	2
Au	$AuCl_3$	10	0.3

Experiments were carried out with single crystal bars of n- and p-type Si, half-sections of crystals with pn junctions, and bars with either single or multiple rate-grown junctions. The surface was prepared by either lapping with No. 600 SiC on glass or bright etching in an acid mixture containing HNO_3, HF, and acetic acids.[1] Silicon samples are used immediately after lapping or etching.

Adhesion of metals deposited by electrochemical displacement is relatively poor as compared to electroplated deposits. This is due, at least in part, to the undermining action of the anodic reaction which tends to dissolve Si from under the metal deposited by displacement. As expected, the adhesion of displacement plated metals is better on abraded than on polished Si surfaces. The most adherent deposits were obtained with Sb and Cu on abraded surfaces. The relative adhesion of displacement plated metals on Si is lower the more noble the metal. Gold deposits have the poorest adhesion and on polished surfaces the deposit is usually pulled off by the surface tension of the solution as the sample is removed. Adhesion of the other metals deposited on chemically polished silicon was adequate for the purpose of portraying junctions.

The best resolution of pn junctions was obtained with Cu and Ag. Most of the experimental work was done with the aqueous solution containing 200 g/l $CuSO_4 \cdot 5H_2O$ and 10 cc 48% HF/l. For the remainder of the paper, it will simply be called the Cu solution.

The solutions in Table I will deposit metal uniformly on n- or p-type Si specimens with either abraded or polished surfaces. If the Si contains a p-n junction and the surface is either all abraded or all chemically polished, metal again deposits fairly uniformly, and junction delineation is poor if discernible at all. This can be improved if the p-n junction area is illuminated with white light (2-4).

In order to obtain sharp p-n junction delineation on Si in the displacement plating solution without using light, it is necessary that the surface be partly polished[2] and partly abraded. An example of the results obtained is shown in Fig. 1. The photograph at the left shows a slice of a single crystal of Si about 2 x 2 x 0.2 cm thick, containing a grown p-n junction. The junction is visible as an inverted U with p-type on top. First, the entire slice was chemically polished and then the left half was abraded by rubbing with No. 400 Aloxite paper. The sample was immersed in the Cu solution for 2 min after which it

[1] The exact composition of the chemical polishing solution is: 5 parts by vol. conc. HNO_3, 3 parts by vol. 48% HF, and 3 parts by vol. glacial acetic acid. This is identical with the etching solution known as C.P.-4 except no bromine is added.

[2] Either a chemically or a mechanically polished surface is satisfactory. A chemically polished surface was used in most of the work to be described here.

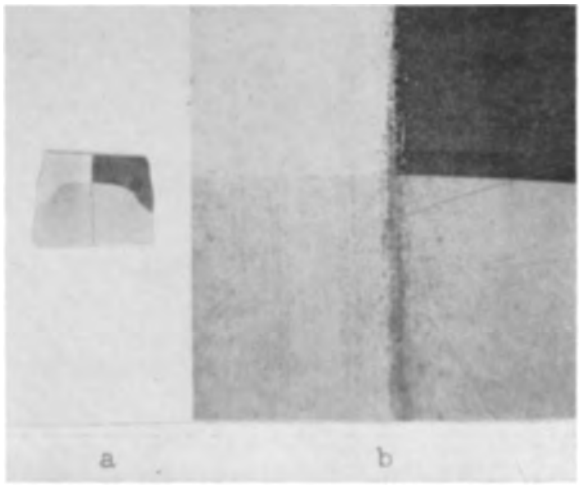

Fig. 1. P-N junction delineation on Si in the $CuSO_4$-HF solution with partly abraded and partly polished surfaces; p-region is the top half of crystal; left side is abraded while the right side is chemically polished. (a) View of large slice 2 cm x 2 cm; (b) magnified view of central region of (a).

was rinsed in water and air dried. The heaviest Cu deposit appeared at the top left on abraded p-Si while the least amount was on polished p-Si. An intermediate amount of Cu deposited on both abraded and polished n-Si. An enlarged view of the center of the specimen is shown in Fig. 1b. Good junction delineation is evident on both abraded and polished surfaces, but the greatest contrast is on polished Si.

If the junction area is illuminated with a strong light in the displacement plating solution, the results on abraded surfaces are about the same as without light. On the polished side of the crystal, however, the pattern is reversed and more Cu deposits on p-Si than on n-Si but only where the surface is illuminated. Polished areas that are not strongly illuminated behave as shown in Fig. 1. Whoriskey (3) and Iles and Coppen (4) reported that, under strong illumination, metal deposits more rapidly on n- than p-type Si. These results are obtained only when the Si is covered with a thin layer of plating solution. If the Si is immersed in a large volume of solution, a heavier deposit appears on p- than on n-Si with illumination as described previously. The reason for this reversal is not understood at present.

There is another way of obtaining sharp junction delineation on polished Si without using light or abrading part of the surface. This method requires a metal electrode connected to the p-type Si by means of an ohmic contact. The metal electrode should be the same as the metal deposited by displacement and is immersed in the plating solution along with the Si. An example of junction delineation obtained by this process in the Cu solution is shown in Fig. 2. This is a highly magnified view of the surface of a Si bar containing multiple rate-grown p-n junctions. Copper has deposited on the n-regions but not on p-type Si. This example also demonstrates the high resolution of junction delineation which is possible in displacement plating solutions. The narrow n-region in the center of the photograph is about 10 μ wide at the extreme left and is clearly visible down

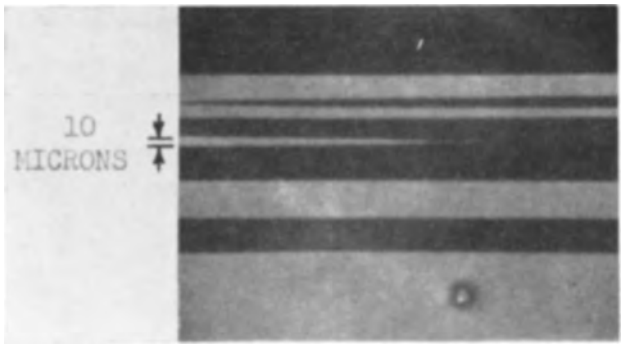

Fig. 2. An example of the high resolution of junction delineation on polished Si in the $CuSO_4$-HF solution. Surface of sample contains multiple rate-grown pn junctions. Copper deposit appears only on n-Si (light areas).

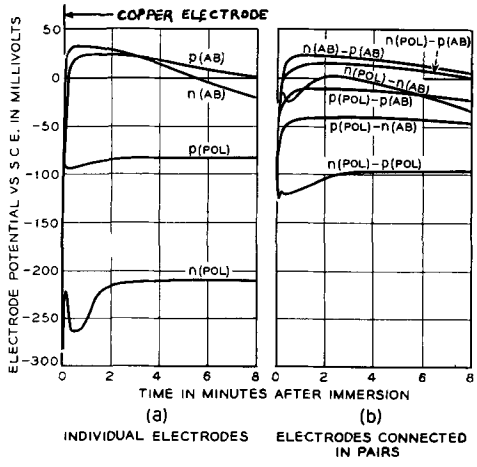

Fig. 3. Electrode potential-time curves of abraded and polished n- and p-type Si in the $CuSO_4$-HF solution.

to about 2 μ as it tapers to the right. The process also shows up abrupt changes in the impurity concentration at the surface of a Si crystal.

Junction Delineation on Germanium

Attempts were made to produce sharp pn junction delineation on Ge in the same displacement plating solutions used for Si. The results on Ge were not good as the junction was poorly defined if detectable at all. Some improvement was obtained with higher HF concentrations. The inherent differences in the electrochemical and semiconductor properties of Ge and Si probably make it impossible to obtain as sharp junction delineation on Ge as is obtained on Si in displacement plating solutions.

Mechanism of Junction Delineation

Electrochemical displacement plating on Si involves Si dissolution as well as metal deposition. It has been found that, if Si is attacked by an electrolyte, a large excess of holes and electrons is produced at the surface (7). These excess holes and electrons diffuse into the Si and change the concentration gradient of the minority current carrier between the surface and the Si bulk. The net result is to shift the measured potential of p-type Si toward more positive values while n-type Si changes in the negative direction. A similar effect is observed if excess holes and electrons are produced at the Si with illumination. The magnitude of the potential change is a function of the resistivity of the Si and the minority carrier lifetime.

The potentials of individual electrodes of n- and p-type Si with abraded and polished surfaces were measured against a saturated KCl calomel reference electrode (SCE) in an unstirred Cu solution. The electrodes were single crystal 0.7 ohm-cm n-type and 1.5 ohm-cm p-type Si. Number 400 Aloxite paper was used to prepare abraded surfaces while the polished electrodes were obtained by etching in the modified C.P.-4 solution previously described.

The recorded potentials vary with time as shown in Fig. 3a. The results show that there are considerable potential differences between abraded and polished Si and also between polished n- and p-type Si in the Cu solution. The potential of a Cu electrode in the Cu solution vs. SCE is also included in Fig. 3a for the purpose of comparison. A Cu electrode was used instead of abraded Si to bring out the junction in the experiment illustrated in Fig. 2.

All four Si electrodes exhibit large initial transients in potential. The two polished electrodes appear to reach steady potentials about 130 mv apart after 3 min immersion in the Cu solution. After the initial maximum, the potential of the abraded electrodes gradually became more negative and approached the steady potential values of polished Si electrodes. The reversal in potential between abraded n- and p-type Si after about 3 min is reproducible and is consistent with experimental results. On abraded Si, metal begins to deposit more rapidly on the n-side of a pn junction but later the rate of metal deposition becomes greater on p-Si than on n-Si.

In a voltaic cell, the negative electrode is the anode. Then according to the results of Fig. 3a, polished n-type Si is anodic to all the other electrodes. If all four types of Si electrodes are connected together in a single crystal, one would expect the least amount of Cu deposited on polished n-type Si. In actual practice, as demonstrated in Fig. 1, the least amount of metal is deposited on polished p-Si. The reason for this apparent anomaly is indicated by the results of connecting the electrodes of abraded and polished n- and p-type Si together in pairs as shown in Fig. 3b. The mixed potentials obtained are recorded as a function of time after immersion in the Cu solution. The three voltaic cells involving polished n-Si as the anode have mixed potentials very near the individual potentials of the cathode. This means that the current flowing between the electrode pairs is controlled by a polarizing effect at the polished n-Si. The effect is illustrated more clearly in Fig. 4 which shows the potential-current density relation of polished n-Si as the anode and polished p-Si as the cathode of a voltaic cell in the Cu solution. These curves were obtained by connecting the two electrodes together through a variable known resistance. The current between the electrodes was determined by measuring the *IR* drop across the shunting resistor while the electrode potentials were measured against the saturated calomel reference electrode. Initially a large resistance was placed be-

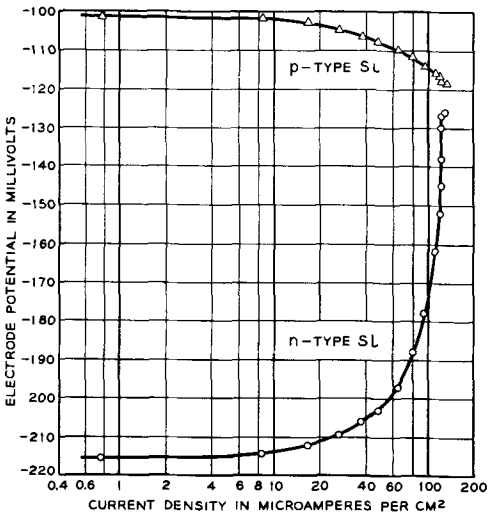

Fig. 4. Electrode potential-current density curves of polished n-Si anode and polished p-Si cathode of a voltaic cell in the $CuSO_4$-HF solution.

tween the two electrodes so the current flowing between them was small and the potentials were essentially those at open circuit. As the current between the electrodes was increased, by decreasing the shunting resistance, the potential of n-type Si acting as an anode changed more rapidly than p-type Si acting as a cathode. The maximum current flowing between the two electrodes therefore is determined primarily by the anodic polarizing effect on n-type Si.

Brattain and Garrett (8) and others have shown that holes are required to carry out anode processes on semiconductors. There is also evidence that cathodic processes on semiconductor electrodes require electrons (8-10). If the only source of holes and electrons at the surface of n- and p-type Si, respectively, is by diffusion from the bulk, then the saturation current of n-Si made anode and p-Si made cathode should be only a few microamperes per square centimeter. The results shown in Fig. 4 indicate that there must be another source for holes and electrons at the surface. As described earlier, holes and electrons are produced as a result of displacement plating. The additional holes available at the surface of the polished n-type Si electrode studied in the Cu solution allowed a maximum anode current density of about 130 $\mu a/cm^2$ when connected with a suitable cathode such as: polished p-Si, abraded Si, or a Cu wire. The maximum or saturation anode current density in the dark is a function of the equilibrium hole density and the diffusion length for holes in the surface region of the n-type Si electrode (9). This current flowing between n- and p-type Si should tend to deposit more Cu on p-Si than on n-Si. There are two electrolytic currents involved, however; one is between n- and p-type regions as just described and the other is between local anode and cathode areas that result in displacement plating. The reason that junction delineation is not obtained on an all polished Si crystal in the absence of strong light is that the rate of Cu deposition over all surfaces by electrochemical displacement is much greater than the deposition of Cu at different rates on n- and p-Si as a result of the potential difference. The displacement plating current density can be estimated from the total weight of Cu deposited in a given time. The amount of Cu deposited in 2 min from the Cu solution corresponds to an average current density of about 1.5 ma/cm^2, assuming equal anode and cathode areas and a Si dissolution valence of 4. This current density is about ten times the maximum current density between polished n-Si and polished p-Si when connected together as shown in Fig. 4. Shining light on the junction provides more holes on n-Si which increases the current flowing between n- and p-areas. This results in more Cu being deposited on p and less on n, thereby increasing the sharpness of junction delineation.

Polished p-type Si is cathodic to polished n-Si but is anodic to both abraded n- and p-Si and Cu as shown in Fig. 3a. Since holes are the majority current carrier in a p-type Si electrode, it can function as an anode up to relatively high current densities without the surface becoming depleted in holes. The current between polished and abraded p-type Si, therefore, can be about the same as the displacement plating current which results in a heavier Cu deposit on abraded p-Si and a corresponding lighter amount on polished p-Si. A Cu electrode, connected to polished p-type Si by means of an ohmic contact, behaves in the same manner as abraded p-Si in contact with polished p-Si in the Cu solution.

On the basis of the individual electrode potential measurements, abraded n-type Si should be as good a cathode in the Cu solution as abraded p-Si with respect to polished p-Si. However, current must flow between abraded n-Si and polished p-Si in the Si across the pn junction in the blocking direction to complete the electrical circuit. This limits the current between the two regions to a few microamperes and explains why the amount of Cu deposited on abraded n-Si is not as heavy as that obtained on abraded p-Si.

Summary and Conclusions

Electrochemical displacement of metals such as Cu and Ag and to a lesser extent, Sb, Au, and Pt can be used to delineate Si p-n junctions. Junction delineation is possible because of potential differences that are established between abraded and polished n- and p-type Si in displacement plating solutions. On the basis of these potential differences alone, the least amount of metal should deposit on polished n-type Si. This is not confirmed experimentally. Instead, polished p-type Si receives the least amount of metal. This is because polished n-Si cannot function as an anode at a high enough current density in the voltaic cell between n- and p-areas relative to the displacement plating current density. Shining light on the junction improves the junction portrayal because additional holes are produced by the light in n-type Si which increases the current in the voltaic cell between n- and p-surfaces.

Polished p-Si is capable of sustaining an anode reaction at relatively high rates without the aid of light. If connected to a suitable cathode, such as abraded p-Si or a Cu electrode in the Cu solution,

very little if any Cu deposits on polished p-Si while a substantial amount deposits on n-Si due to displacement plating. This produces a sharp junction delineation between n- and p-type Si.

Acknowledgment

The author wishes to acknowledge the assistance of George Peranteau in the experimental phase of the work and to U. B. Thomas for his helpful comments and discussion.

Manuscript received Feb. 2, 1959. This paper was prepared for delivery before the Ottawa Meeting, Sept. 28-Oct. 1, 1958.

Any discussion of this paper will appear in a Discussion Section to be published in the June 1960 JOURNAL.

REFERENCES

1. C. S. Fuller and J. A. Ditzenberger, *J. Appl. Phys.*, **27**, 550 (1956); C. S. Fuller, U.S. Pat. No. 2,740,-700, April 3, 1956.
2. S. J. Silverman and D. R. Benn, *This Journal*, **105**, 170 (1958).
3. P. J. Whoriskey, *J. Appl. Phys.*, **29**, 867 (1958).
4. P. A. Iles and P. J. Coppen, *ibid.*, **29**, 1514 (1958).
5. M. C. Waltz, U.S. Pat. No. 2,814,589, Nov. 26, 1957.
6. P. Wang, Recent News Paper, Electrochem. Soc. Meeting, New York (1958).
7. D. R. Turner and J. F. Dewald, To be published.
8. W. H. Brattain and C. G. B. Garrett, *Bell System Tech. J.*, **34**, 129 (1955).
9. J. B. Flynn, *This Journal*, **105**, 715 (1958).
10. D. R. Turner, Paper submitted to *This Journal*.

Diffusion of Radioactive Antimony in Silicon

J. J. Rohan, N. E. Pickering, and J. Kennedy

Radiochemistry Section, Electronic Material Sciences Laboratory, Electronics Research Directorate, Air Force Cambridge Research Center, Air Research and Development Command, Bedford, Massachusetts

ABSTRACT

The diffusion coefficient of radioactive Sb-124 in Si has been investigated in the temperature range 1190° to 1398°C, with use of a technique involving measurement of the residual integrated activity of the 0.602 Mev gamma before and after removing successive 2- to 4-μ layers perpendicular to the diffusion path. Results are compared to literature data obtained via p-n junction measurements. The diffusion coefficients are on the average about 85% higher than the literature values, while the activation energies are essentially the same. The temperature dependence of the diffusion coefficient is given by $D = 12.9 \exp(-91{,}700/RT)$ cm^2 sec^{-1} with an average error of ±12%. Surface concentrations of Sb were in the range of 10^{19} to 10^{20} atoms cm^{-3}.

Studies of the diffusivities of donor and acceptor elements in semiconductors by means of radiotracers have been supplanted largely in recent years by methods involving the measurement of p-n junction distances. These methods (1, 2) which depend on the formation and location of p-n junctions within the crystals are faster and far less tedious than methods employing radiotracers. Up to the present, no comparison of results obtained by the two techniques appears to exist for diffusion in silicon. In germanium a radiotracer method gave diffusion coefficients for Sb which were 20 to 40% higher than those given by a p-n junction method (1, 3). Some indication that this might be the case for Sb in Si was noted in this laboratory in a study of the effect of various pressures of Sb_2O_3 vapor on the surface concentration of Sb on Si during diffusion anneals. With use of the data and techniques of Fuller and Ditzenberger (4), it was found in all cases that p-n junction measurements gave much larger values for the surface concentration, C_o, of Sb than radioactivity measurements when similar amounts of diffusant were heated in evacuated quartz tubes containing p-type single-crystal Si slabs. In these and the following experiments, boundary conditions were such that diffusion proceeded according to the error function complement equation. From p-n junction measurements then, the surface concentration, C_o, in atoms cm^{-3}, was calculated from:

$$C_x = C_o \operatorname{erfc} \frac{x}{2\sqrt{Dt}} \qquad [1]$$

where C_x is the concentration in atoms cm^{-3} of Sb at a junction located x cm from the surface of Si; D is the diffusion coefficient in cm^2 sec^{-1}, and t is the time in seconds at constant temperature. The diffusion coefficient, D, was presumed to be only temperature dependent and the surface concentration, C_o, presumed to be constant. Radioactivity measurements, described more fully later, gave C_o in terms of the total number of atoms N_T of Sb which diffused through one face of the Si slab. This is given by integration of Eq. [1] so that

$$N_T = GR_T = A\,C_o \int_0^\infty \operatorname{erfc} \frac{x}{2\sqrt{Dt}}\,dx = 1.13\,AC_o\sqrt{Dt} \qquad [2]$$

where R_T is the total activity, A is the area of the diffusion plane introduced here to account for the total number of diffused atoms, and G is a factor which relates activity to the number of atoms of Sb.

An example of the large discrepancies noted for values of C_o as found by both methods is given for a

diffusion anneal at 1380°C. From radioactivity measurements a value of $C_o = 4.3 \times 10^{19}$ atoms cm^{-3} was obtained while p-n junction measurements gave $C_o = 3.4 \times 10^{21}$ atoms cm^{-3}. The latter is consistent with a mean value obtained by Fuller and Ditzenberger (4) at the same temperature with similar amounts of Sb_2O_3, but is inconsistent with the expected solid solubility of Sb in Si even if saturation had been reached. The binary alloy system Sb-Si belongs to a class whose liquid phases are "regular" solutions and whose solid phases exhibit the phenomenon of retrograde solubility, as has been shown by Thurmond and Struthers (5). They have also shown that the logarithm of the distribution coefficient k of the solute (Sb in this case) between the solid and liquid phases of such systems is a linear function of the reciprocal of absolute temperature near the melting point of the solvent. Extrapolation of this line to the k corresponding to the melting point of the solvent (Si) gives the maximum value or segregation coefficient. The latter has been found by direct measurement to be 0.04 for Sb in the Sb-Si system (6). However, a value of 1.4 is calculated for the distribution coefficient of Sb in Sb-Si at 1380° from the C_o obtained by p-n junction measurement and the solubility of Sb in the liquid phase at this temperature (5, 7).

Apparently then C_o values for Sb in Si calculated from p-n junction measurements and the values of D given by Fuller and Ditzenberger can be too high by one or two orders of magnitude. One explanation for this is that too low values of D were used in the calculation. In the preliminary work and in much of Fuller's, the quantity $x/2\sqrt{Dt}$ had a numerical value of 2 or greater; relatively small changes in the value of erfc in such cases can lead to very large changes in C_o as calculated from Eq. [1], which is apparent on examination of tables of the error function. For example, a 50% increase in D at constant x and t can effect a tenfold reduction in C_o as calculated by Eq. [1] (p-n junction), whereas with Eq. [2] (radiotracer) the effect is to reduce C_o by only 20%. In view of the foregoing observations, it was decided to re-examine the diffusion of Sb in Si using radiotracer Sb-124 exclusively.

Discussion of Methods

Where the concentration of radioactive diffusant does not change appreciably over short distances (several microns) along the diffusion path, a method based on counting the activity in thin parallel segments of the matrix ground onto emery paper, or similar abrasive, has been used successfully for the determination of diffusion coefficients in highly impenetrable single crystals. Such concentration profiles require that the penetration parameter $\sqrt{Dt}$ be of the order of 10^{-3} cm, or greater, to insure any degree of precision and were accomplished in the case of Sb in Ge with anneal times of less than 10 days (3). However, in the case of Si in which Sb is one of the slowest diffusing elements, it would take up to 100 days to produce comparable penetrations; hence, a more suitable procedure was desired.

An alternate method for the radioassay of diffused Sb-124 in Si is to count the integrated gamma activity of a crystal following removal of thin layers parallel to one surface. On decay of Sb-124, beta particles and gamma rays are emitted. Of the several gamma rays emitted the principal one has an energy of 0.602 Mev and is virtually unabsorbed by the small thicknesses of Si encountered here. The count rate of the 0.602 mev gamma rays is therefore directly proportional to the total number of Sb atoms at all depths within the Si crystal. When the edges and one face of the crystal have been removed by grinding to depths below which the concentration of Sb is negligible, only unidimensional diffusion need be considered. The number of residual Sb atoms, N_x, in the crystal lapped down to a plane x cm below and parallel to the remaining original surface is

$$N_x = GR_x = A\,C_o \int_x^\infty \operatorname{erfc} \frac{x}{2\sqrt{Dt}}\,dx$$

$$= A\,C_o \sqrt{Dt}\left[\frac{2}{\sqrt{\pi}} \exp\left(-\frac{x^2}{4Dt}\right) - \frac{x}{\sqrt{Dt}} \operatorname{erfc} \frac{x}{2\sqrt{Dt}}\right] \qquad [3]$$

where R_x is the residual 0.602 Mev gamma activity.

If C_o is known, D can be obtained directly from Eq. [3] by successive approximations using tables of the error function and its first derivative (8), (the first term inside the bracket). Since C_o is usually not known, the integral count rates, R_1 and R_2, at two depths, x_1 and x_2 may be combined to give:

$$\frac{N_1}{N_2} = \frac{R_1}{R_2} = \frac{\phi_1}{\phi_2} \qquad [4]$$

where ϕ represents the terms inside the bracket of Eq. [3], and is a function of x only. Again, by successive approximations, a value for D is found which satisfies the ratios of Eq. [4].

Experimental

Samples of single-crystal Si, 200 ohm-cm n-type, 8 mm on a side and 1 mm thick, were prepared by hand lapping on glass through 3200-mesh abrasive suspended in water. They were then brought to a semi-mirror finish by a short final lapping with ¼-μ Diamet Hyprez on a silicon flat; in all cases the flatness of the samples, measured optically, was at least ± 0.1 μ out to the edges. After cleaning, the samples were washed successively in conc HNO_3 and conc HF. Two such specimens were sealed at 10^{-5} mm of air in quartz ampules containing 200 to 500 μg of radioactive Sb_2O_3. In the latter, obtained by neutron irradiation at Brookhaven National Laboratory, about 1 at. in every 10^5 at. of Sb was Sb-124. Before irradiation, the impurity content of the oxide was determined by spectroscopic analysis; the impurity content was low enough not to give rise to undesirable extraneous radioactivity. The samples were annealed in a graphite-resistor vacuum furnace which was maintained at constant temperature by a Minneapolis-Honeywell Radiamatic unit. This unit was calibrated against the melting points of Cu, Si,

and Ni contained in quartz ampules. Temperature measurement and control was ±4°C. Temperature rise and decay times in this furnace were such that no time correction was needed for samples diffused over 24 hr. At the highest temperature investigated (1398°C), the anneal was done in a globar-heated tube furnace where the samples could be introduced and withdrawn quickly. In nearly all cases, times were chosen so that the value of $\sqrt{Dt}$ would be at least 5 x 10^{-4} cm, in order to insure that count rates would not change by over three orders of magnitude while lapping through a depth of 15 μ or more.

After removal from the furnace, the samples were washed in 48% HF to remove possible oxides. The edges and one of the faces were ground off to a depth far below that at which no change in count rate was observed and autoradiographs of the active faces were taken. The samples were then weighed to constant weight on a microbalance and an initial count rate for each sample was determined. A layer of uniform thickness (2 to 4 μ in most cases) was then ground off each sample by hand lapping with 3200-mesh abrasive on glass. This process effects a clean separation between matrix and ground-off material; no extraneous activity on the matrix due to adhesion of ground-off layers was noted.

The process of grinding, weighing, and counting was repeated until the activity dropped to a value below which further processing would be impractical. All counting was done in a well-type gamma scintillation detector coupled to a single-channel spectrometer. All sample count rates were compared to the count rate of a standard of known total Sb content; backgrounds were determined at least twice a day. In most cases total counts were collected so as to give a counting error of 1% or less with 95% confidence.

Results

Evaluation of D.—The thickness of sample layers removed at each cut was calculated from the weight loss and the cross-sectional area of the sample using a density of 2.33 for Si[9]. All of the data from six temperature anneals are too bulky to reproduce here; however, an example of the basic data used in calculating D for the run at 1330°C is given in Table I.

The ratio of successive count rates and the corresponding values of x were substituted from Table I into Eq. [4] and D's were calculated for successive combinations as shown in Table II. The mean value of the D's thus calculated was taken as the final value for each sample.

Evaluation of C_o.—The surface concentration C_o was calculated from Eq. [2], substituting the mean value of D found for each sample and the corresponding total number of Sb atoms. This could be done in all cases where no extraneous surface activity was found on the samples as checked by autoradiography.

The results of six temperature anneals are summarized in Table III.

The temperature dependence of the diffusion coefficient of Sb in Si found in these experiments is expressed by the following equation:

$$D = 12.9 \exp(-91{,}700/RT) \text{ cm}^2 \text{ sec}^{-1} \quad [5]$$

which is the least squares equation of the data in Table III, omitting the data from the run at 1355°C. The solid line in Fig. 1 is a plot of Eq. [5]; the experimental points represent the mean D value of the two samples at each temperature. The latter fall on or are close to the line except the point correspond-

Table I. Example of basic diffusion data*

Cut No.	Wt. loss per cut, μg		Total depth (x), μ		Count rate (R), counts min^{-1}	
	A	B	A	B	A	B
0	—	—	—	—	119,138	96,361
1	515	241	5.92	3.07	65,127	70,980
2	246	244	8.74	6.19	44,084	47,819
3	359	179	12.9	8.48	22,738	36,092
4	374	248	17.2	11.65	10,266	22,276
5	387	269	21.6	15.1	4,155	11,553
6	304	290	25.1	18.8	1,725	5,180
7	170	297	28.2	22.6	794	2,396
8	356	325	32.3	26.7	248	790
9	—	141	—	28.5	—	514

* Temperature, 1330°C; time, 49 hr;
Sample A: Area 0.373 cm^2, G 3.825 x 10^{11} at. count^{-1} min^{-1}
Sample B: 0.336 cm^2, 4.390 x 10^{11} at. count^{-1} min^{-1}.

Table II. Example of method for obtaining mean value of D*

Combination	Sample A D (cm^2 sec^{-1})	Sample B D (cm^2 sec^{-1})
1-2	4.01 × 10^{-12}	4.10 × 10^{-12}
2-3	3.80 × 10^{-12}	4.69 × 10^{-12}
3-4	3.77 × 10^{-12}	4.10 × 10^{-12}
4-5	3.93 × 10^{-12}	3.40 × 10^{-12}
5-6	3.84 × 10^{-12}	3.32 × 10^{-12}
6-7	3.85 × 10^{-12}	4.10 × 10^{-12}
7-8	3.69 × 10^{-12}	3.36 × 10^{-12}
8-9	—	4.10 × 10^{-12}
Mean	3.84 × 10^{-12}	3.90 × 10^{-12}
σ (rms)	±0.09 × 10^{-12}	±0.46 × 10^{-12}
% σ (rms)	±2.34	±11.8

* Temperature, 1330°C; time, 49 hr;
Sample A: Area 0.373 cm^2, G 3.825 x 10^{11} at. count^{-1} min^{-1}
Sample B: 0.336 cm^2, 4.390 x 10^{11} at. count^{-1} min^{-1}.

Table III. Summary of results

Sample	Temp, °C	Time, hr	D x 10^{13} cm^2 sec^{-1}	C_o x 10^{-19} at. cm^{-3}
A	1190	144	2.46 ± 0.25	2.4
B	1190	144	2.83 ± 0.48	1.9
A	1230	144	5.81 ± 0.91	—[a]
B	1230	144	5.82 ± 0.82	—[a]
A	1280	93	16.2 ± 3.8	4.5
B	1280	93	16.2 ± 1.0	5.0
A	1330	49	38.4 ± 0.9	4.9
B	1330	49	39.0 ± 4.6	4.5
A	1355	24	104 ± 7	3.5
B	1355	24	103 ± 8	3.5
A	1398	2	135 ± 18	3.1
B	1398	2	—[b]	3.2[c]

[a] Surface contamination; [b] sample destroyed in processing; [c] calculated from the N_T of B and the D of A.

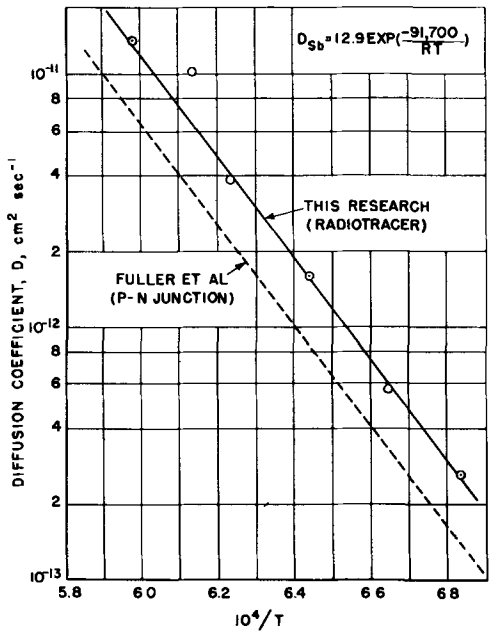

Fig. 1. Diffusion coefficients of Sb in Si plotted against reciprocal of absolute temperature.

ing to the 1355°C run. It is probable that this deviation was caused by the temperature being much higher than recorded, since some difficulties were experienced with the temperature controller during that run. For comparison a plot of the temperature dependence of the diffusion coefficient of Sb in Si as given by Fuller and Ditzenberger's equation (4),

$$D = 5.6 \exp(-91{,}000/RT) \text{ cm}^2 \text{ sec}^{-1} \quad [6]$$

is shown (dashed line). It can be seen that, whereas both tracer and p-n junction methods gave ΔH values which are in essential agreement, the values of D obtained by the tracer method averaged about 85% higher than those by the p-n junction method in the temperature range studied.

Discussion of Results

It is difficult to analyze quantitatively the effect of all possible errors on the values of D, C_s, and ΔH reported here. The error in counting has been mentioned previously; however, this error is based on the statistics of random process. A more practical error to consider here is that of reproducibility. In our counting assembly, count rates were reproducible to ±2% which leads to errors of ±4% in the ratio of Eq. [4]. Cumulative weighing errors of ±2 μg lead to errors in the estimation of lapping depths of ±0.02 μ; such precision, however, means little in view of the fact that parallel lapping was assumed but not proved.

The most serious errors in the value of D could be due to nonparallel lapping; the effect of misalignment of the plane of lapping with respect to the plane of the original crystal face can result in a value for D which is high compared to the true value in all cases. By assuming various geometries of misalignment it is possible to estimate the error in D due to this source. This was done for various geometries and degrees of misalignment, and it was found that the worst conceivable situation would produce an error in D of about +25%. However, toward the end of this work it was possible to check the geometry and degree of misalignment by means of a Zeiss optimeter capable of measuring thicknesses with an accuracy of ±0.2 μ. These measurements indicated that the degree of misalignment was indeed small and that confidence in the inherent simplicity of hand lapping was justified. Experiments with various machines and jigs led to the conclusion that these could introduce systematic errors which would be more serious than the random errors produced by hand lapping.

Errors might also accrue due to loss of sample surface by evaporation. It was felt that such losses would be small in a closed system; this was confirmed both by micrometric measurements and by the fact that the original semi-mirror finish of the samples was preserved (although some pitting was noticed). The question of whether the diffusion coefficients obtained are truly representative of bulk diffusion has not been fully resolved. This question arises from the fact that the samples were not etched after grinding flat. It is possible that the worked surfaces and the layers immediately below might provide an easier path for diffusant penetration than would the bulk material. Indeed it was found that values of D calculated from the data of cut combinations 0-1, 0-2, etc., were much higher than the mean value in all cases. Such values for D, therefore, were not included in calculating the mean; however, it will be noted from the representative data of Tables I and II that this effect was not noticeable beyond a depth of a few microns. Samples were left in the ground state because even the most rigorously controlled etching always produced uneven surfaces that would be very poor planes of reference for such relatively shallow diffusion penetrations.

The over-all effect of all the possible errors, as well as the assumptions made in carrying out these experiments, may be illustrated by comparing the experimental diffusion of Sb into Si with that predicted by Eqs. [2] and [3]. These equations may be combined to express the fraction of total diffused atoms remaining in the crystal, i.e., after grinding down to a plane x cm below the surface, as follows:

$$\frac{N_x}{N_T} = \frac{R_x}{R_T} = \frac{\phi}{1.13} \quad [7]$$

Figure 2 is a plot of theoretical residual atom fractions at various depths calculated from Eq. [7], substituting for $\sqrt{Dt}$ the value 8.26×10^{-4} cm corresponding to the mean value found from the diffusion anneal at 1330°C (Table II). The points are the experimentally determined count rate ratios; it is apparent that these follow the theoretical curve within experimental error. For the sake of clarity only one such curve is shown in Fig. 2, viz., that which may be verified by the data given; however, for other temperature anneals the fit of the experimental penetration with the theoretical was even more striking. Despite the fact that the rms deviations in the value of D's of the two samples in any temperature run varied considerably between samples, it

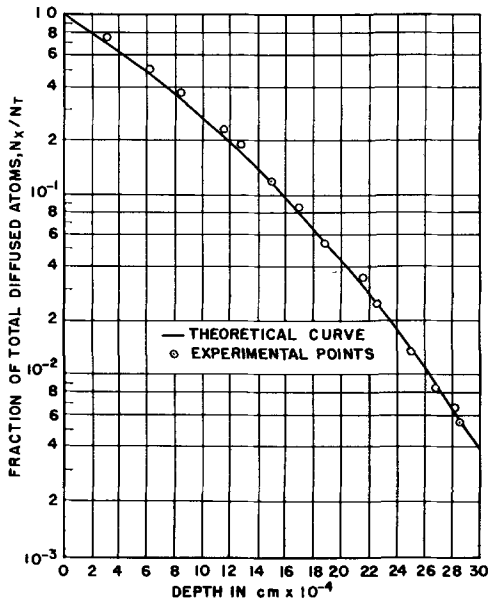

Fig. 2. Plot comparing experimental with theoretical diffusion of Sb in Si at 1330°C.

should be noted that the mean D values of both samples were in very close agreement (Table III). Such agreement, coupled with the good fit of the experimental penetration with the theoretical, seems to indicate that all of the assumptions made were vindicated and that the D's represent true bulk diffusion with an average error of ±12% which represents the mean of all the individual sample errors. From this and the closeness of the experimental points to the log D vs. $1/T$ line in Fig. 1, the estimated error in ΔH is about 1%.

Errors in C_o reflect the errors in D and the conversion factor G. The latter, from a series of calibrations, is estimated to be about ±5%. Thus, the error in C_o is about 12%.

Conclusion

Diffusion coefficients of Sb in Si measured by a radiotracer technique were found to be considerably higher than those reported in the literature where a p-n junction technique was used. The results confirmed the belief that p-n junction measurements gave too low values for D, since abnormally high values for the surface concentration of Sb on Si are calculated when p-n junction values of D are used. Surface concentrations calculated from the diffusion coefficients found in this investigation were found to be within the range expected for unsaturated Si surfaces. No explanation is offered at this time for the disagreement between the results as obtained by the two methods pending the completion of further studies using tracer acceptor elements as diffusants.

Since this work was completed, it has come to the attention of the authors that the diffusion of Sb in Si has been investigated using Sb-124 (10). Details of these experiments are insufficiently explicit to warrant comment; however the results of the work, expressed by the equation $D = 0.112 \exp(-66{,}000/RT)$ cm^2 sec^{-1} is in complete disagreement with both the authors' results and those of Fuller and Ditzenberger.

Acknowledgments

The authors are indebted to Mrs. Thelma B. Salmas for assistance in sample preparation and checking calculations; to Henry M. DeAngelis for stimulating discussions; and to Joseph R. O'Connor for furnishing the single-crystal silicon.

Manuscript received Feb. 2, 1959. This paper was prepared for delivery before the New York Meeting, April 27-May 1, 1958.

Any discussion of this paper will appear in a Discussion Section to be published in the June 1960 JOURNAL.

REFERENCES

1. W. C. Dunlap, Jr., *Phys. Rev.*, **86**, 615 (1952); D. E. Brown and W. C. Dunlap, Jr., *ibid.*, **86**, 616 (1952); W. C. Dunlap, Jr. and D. E. Brown, *ibid.*, **86**, 417 (1952).
2. C. S. Fuller, H. C. Theuerer, and W. VanRoosbroeck, *ibid.*, **85**, 678 (1952); C. S. Fuller, J. D. Struthers, J. A. Ditzenberger, and K. B. Wolfstirn, *ibid.*, **93**, 1182 (1954).
3. W. C. Dunlap, Jr., *ibid.*, **94**, 1531 (1954).
4. C. S. Fuller and J. A. Ditzenberger, *J. Appl. Phys.*, **27**, 544 (1956).
5. C. D. Thurmond, *J. Phys. Chem.*, **57**, 827 (1953); C. D. Thurmond and J. D. Struthers, *ibid.*, **57**, 831 (1953).
6. R. N. Hall, *ibid.*, **57**, 836 (1953); J. A. Burton, *Physica*, **20**, 845 (1954).
7. M. Hansen, "Aufbau der Zweistofflegierungen," Springer, Berlin (1936).
8. "Tables of the Error Function and Its Derivative," National Bureau of Standards Applied Mathematics Series 41, 1954.
9. W. C. Dunlap, Jr., "An Introduction to Semiconductors," John Wiley & Sons, Inc., New York (1957).
10. D. A. Petrov, IV. M. Shashkov, and I. P. Akimchenho, Transactions of the Second Conference on Semiconductors (Questions of the Metallurgy and Physics of Semiconductors. Akademiia Nauk Press, Moscow, 1957, ed. D. A. Petrov) Needham Heights, Mass: M. D. Friedman, Inc.

The Relation of Gas Composition to Current Efficiency in an Aluminum Reduction Cell

T. R. Beck

Metals Division Research, Kaiser Aluminum & Chemical Corporation, Permanente, California

ABSTRACT

Experience with a 10,000-amp aluminum reduction cell indicates that the previously accepted equation relating current efficiency and cell gas CO_2 concentration is an oversimplification. A modified equation, % CE $= g[50 + \frac{1}{2}(\%\ CO_2)] - Z$, fits the data more satisfactorily. The new terms, g and Z, respectively, account for: (*a*) less than 100% initial CO_2 and/or reaction of CO_2 with carbon, and (*b*) a certain percentage of current inefficiency by oxidation or loss of some cathode products without involvement of CO_2. The experiments showed g to be somewhat larger than unity and to vary with the bake temperature of the anodes and Z to be somewhat larger than 3.5%.

This paper describes work done on a 10,000-amp experimental aluminum reduction cell. The cell was established for studying process variables that could not be studied satisfactorily in any other way. It was of such a size that results could be scaled up to apply directly to the present commercial cells. Although it was only 1/6 to 1/10 the size of present commercial cells, it was comparable in size to the commercial cells of three decades ago (1). Because it was operated as an independent unit with its own power supply and was not tied to a production schedule, experiments and measurements could be made and an accuracy obtained that would be virtually impossible to attain under plant conditions. Significantly smaller self-sustaining cells operating at commercial current densities are difficult to operate because of proportionately higher heat losses for their greater surface-to-volume ratio. Scale-up from still smaller externally heated bench scale cells to full scale plant cells is open to question.

In construction and dimensions it was equivalent to placing the two ends of a commercial prebaked-anode cell together after removing the center section. Dimensions of the cavity were approximately 43 in. x 65 in. cross section by 14 in. deep. Plant anodes and superstructure hardware were used. Anode dimensions were 15½ in. x 19½ in. cross section by 12 in. high.

Early in the program a test was made to evaluate the effect of anode-bake temperature on carbon consumption. Routine cell gas analyses for CO_2 and CO were made in order to determine what fraction of the carbon consumption could be attributed to the electrochemical reaction. Correlation of these gas analysis data with current efficiency was the basis for this paper.

Experimental

Anodes for use in this study were pressed and baked at the Corporation's Mead Works near Spokane, Washington. Thermocouples were installed in the baking pits to determine the maximum temperatures reached during the bake. From these data maximum-temperature-isotherms were drawn for the pits, and anodes were segregated into suitable bake temperature ranges for use in the 10,000-amp cell tests.

Each test lasted four weeks and consumed approximately 19 anodes. Each of the four anodes in the cell was changed every six days on a regular schedule. A one-week transition period between tests was used to install a new complement of anodes.

Cell conditions were held as constant as possible during the test series. Anode-cathode distance was maintained at 2 in. for all but the last three runs at which it was 1½ in. Bath composition was 89% cryolite at 1.5 NaF: AlF_3 ratio, 8% calcium fluoride, and 3% alumina. Bath temperature was maintained at 975°-985°C. Current varied from 9500 to about 11,000 amp during the course of the experiments because the power input was increased to compensate for increased heat losses as bath penetrated the insulation and because the last three runs were made at a lower anode-cathode distance.

Gas composition was measured with an Orsat gas analyzer at 2-hr intervals half way between hourly feedings of alumina. The cell gas was collected through a steel bell placed on the crust of the cell as shown in Fig. 1. The gas was drawn through Inconel and rubber tubing to the gas analyzer. The

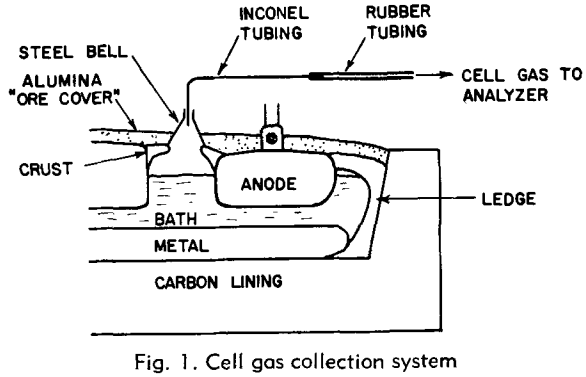

Fig. 1. Cell gas collection system

Table I. Experimental data for various bake temperature anodes. Each point represents one four-week test

	Current eff.	% CO_2	Avg. est. anode bake temp, °C	
Low-bake-temperature anodes	85.5	69.3	946	959
	86.9	71.8	972	
Medium-bake-temperature anodes	86.7	77.4	1071	1070
	88.9	79.7	1070	
High-bake-temperature anodes	86.8	80.7	1142	Approx. 1150
	85.5	78.5	1110-1190	
	86.4	79.0	1110-1190	
	88.2	81.1	1110-1190	
	86.5	78.7	1110-1190	
	84.4	77.4	1110-1190	
	84.1	75.9	1110-1190	

crust, composed of frozen cryolite, was continuous except for the single vent which was used for feeding and gas collection so there was a negligible leakage of air into the system. Reaction of the cell gas within the Inconel sample tube appears unlikely because the measured gas composition did not vary with the rate that the gas was sampled. The gas was cool before it entered the rubber tubing.

Results

The experimental data are presented in Table I and Fig. 2. Current efficiency did not vary significantly with anode-bake temperature, but per cent of CO_2 in the cell gas increased with increasing bake temperature. The low-bake-temperature-anode data are above the previously accepted Pearson and Waddington correlation (1, 2), and the high-bake-temperature-anode data are below it. There is a certain scattering of the data, but there is an unmistakable trend with anode bake temperature. For a given bake temperature, the data roughly parallel the Pearson and Waddington correlation although the slope appears to be slightly steeper.

The first four groups of anodes were run in random order to cancel the effect of cell aging. The remaining seven groups were run in the order listed.

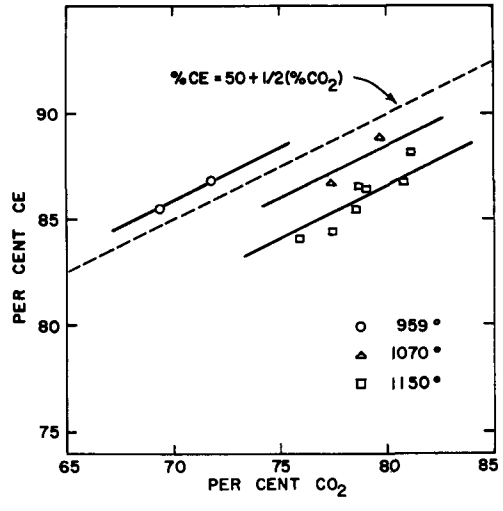

Fig. 2. Experimental data for various bake temperature anodes. Each point represents one 4-week test.

The range of current efficiency from 85.5 to 88.9% can be attributed to small changes in the operating conditions, unavoidable in an aluminum reduction cell. The 84% current efficiency in the last two runs was the result of the lower anode-cathode distance. Despite some variations in cell conditions the data for each bake temperature fell on its characteristic line. The regular deviation suggested that there were some factors ignored in the original derivation of the Pearson and Waddington equation so a more comprehensive equation was derived.

Discussion

The Pearson and Waddington equation

$$\% \text{ CE} = 50 + \tfrac{1}{2}(\% \text{ CO}_2)$$

is based on the following assumptions: (*a*) initial anode product is 100% carbon dioxide, and (*b*) carbon monoxide is produced by reduction of carbon dioxide by cathode products, i.e.,

$$CO_2 + \left\{\begin{matrix}2Na,\\ Al^{+},\\ 2/3Al,\\ \text{etc.}\end{matrix}\right\} \rightarrow CO + \left\{\begin{matrix}2Na^{+},\\ Al^{+++},\\ 2/3Al^{+++}\\ \text{etc.}\end{matrix}\right\} + O^{=}$$

A plot of the Pearson and Waddington equation is shown in Fig. 3 with the directions of the deviations due to errors in the assumptions.

Case I is a decrease in per cent CO_2 without a change in current efficiency. This can result from primary and/or secondary formation of CO. These are inseparable in the data presented here but could perhaps be separated using a radio-carbon technique. It must be borne in mind that there is always the possibility of introduction of air during sampling which will give a low apparent CO_2, especially with plant cells which often do not have a continuous solid crust. It is felt that this error is not significant in the work with the Permanente cell because of the continuous solid crust. The nitrogen content of the samples was usually less than 1%. Small amounts of other gases have been found in reduction cell gas but not in sufficient amount to affect the results presented here significantly. Hydrogen, hydrogen sulfide, and carbonyl sulfide have been found in concentrations of a few tenths of a per cent or less (3). Formation of fluorocarbons appears to be limited to periods of anode effect (3).

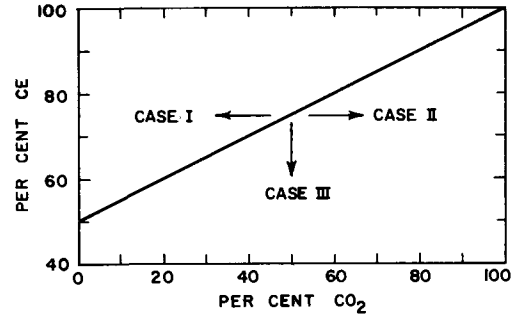

Fig. 3. Deviations due to errors in derivation assumptions for Pearson and Waddington equation.

Case II is an increase in per cent CO_2 without a change in current efficiency. A possible reaction is the formation of free carbon and CO_2 by disproportionation of CO as the pot gas temperature is reduced. No measurable amount of this free carbon formation was found with the Permanente cell.

Case III is a decrease in current efficiency without a change in the gas composition. There are a number of mechanisms that can lead to this condition. The more important possibilities are as follows. (*a*) escape of sodium from the cell or oxidation of sodium by air (Pockets of sodium metal are frequently found in the crust of the Permanente cell, substantiating this mechanism.); (*b*) direct oxidation of sodium, monovalent aluminum, or "metal fog" at the anode without the intervention of CO_2; (*c*) electronic conduction through the bath or through short circuits between anode and cathode by metal splashing or accumulated carbon "dust;" (*d*) formation of sodium and/or aluminum carbides with the lining; and (*e*) oxidation of aluminum during tapping.

Case IV, an increase in current efficiency without a change in gas composition, is not possible because it would require more than Faraday's equivalent of metal formed at the cathode.

The deviations of the experimental data in Fig. 2 can be explained by these reactions. For all three sets of data, the deviation below the Pearson and Waddington line due to Case III would be expected to be about the same. Anode quality would hardly be expected to affect significantly the factors that make up Case III. The shift in the lines to the left with lower-bake-temperature anodes can be explained by Case I.

The more general relation between current efficiency and gas composition is derived as follows:

Initial cell reaction

$$2Al_2O_3 + (6-n)\,C \rightarrow 4Al + nCO_2 + (6-2n)\,CO \quad [1]$$
$$0 \leqq n \leqq 3$$

Equivalent inefficiency reaction

$$2/3Al + CO_2 \rightarrow 2/3Al^{+++} + CO + O^{=} \quad [2]$$

Reaction of CO_2 with carbon

$$CO_2 + C \underset{y_2}{\overset{y_1}{\rightleftarrows}} 2CO \quad [3]$$

$$\% \text{ CE} = \frac{A - C - D}{A + B} \times 100 \quad [4a]$$

where A = equivalents of Al (or Na, etc.) initially formed; B = equivalents of electrons carried by electronic conduction; C = equivalents of Al reoxidized by CO_2; and D = equivalents of Al lost or reoxidized without CO_2.

To simplify the derivation the following transformation is made

$$A' = A + B$$
$$E = D + B$$
$$\therefore \% \text{ CE} = \frac{A' - C - E}{A'} \times 100 \quad [4b]$$

* The subscript *p* represents material produced, subscript *r* indicates material reduced, and the numerical subscripts refer to Eqs. [1], [2], and [3].

$$\% \text{ CO}_2 = \frac{CO_{2(p,1)} - CO_{2(r,2)} - CO_{2(r,3)}}{CO_{2(p,1)} + CO_{(p,1)} - CO_{2(r,2)} + CO_{(p,2)} - CO_{2(r,3)} + CO_{(p,3)}} \times 100 \quad [5]^*$$

Per each Eq. [1], assume x Eq. [2] and y Eq. [3]. (Note: y is the net number of CO_2's lost, i.e., $y = y_1 - y_2$ since the reaction is reversible.) $\therefore A' = 4$, $C = (2/3)\,x$, and $E = 4Z/100$, where Z is percentage of current lost by Case III.

$$\therefore \% \text{ CE} = 100\left(\frac{4 - (2/3)x - 4Z/100}{4}\right) \quad [6a]$$

and

$$\% \text{ CO}_2 = 100\left(\frac{n-x-y}{n+6-2n-x+x-y+2y}\right) = 100\left(\frac{n-x-y}{6-n+y}\right) \quad [6b]$$

Eliminating x from [6*a*] and [6*b*] gives

$$\% \text{ CE} = \frac{6-n+y}{3}\,[50 + \tfrac{1}{2}(\% \text{ CO}_2)] - Z \quad [6c]$$

The fraction of the initial CO_2 reacting by Eq. [3] is $f = y/n$

$$\therefore \% \text{ CE} = \frac{6-n+nf}{3}\,[50 + \tfrac{1}{2}(\% \text{ CO}_2)] - Z \quad [7]$$

$$\% \text{ CO}_2 \text{ in primary gas} = 100\left(\frac{n}{6-n}\right) \quad [8]$$

Substituting the value for n [Eq. 8] in Eq. [7]

$$\% \text{ CE} = 2\left[\frac{1 + f\left(\frac{\text{initial } \% \text{ CO}_2}{100}\right)}{1 + \frac{\text{initial } \% \text{ CO}_2}{100}}\right][50 + \tfrac{1}{2}(\% \text{ CO}_2)] - Z \quad [9]$$

Because it is difficult to separate the effect of initial anode gas composition and the reaction of CO_2 with carbon, Eq. [9] may be simplified by letting

$$g = 2\left[\frac{100 + f(\text{initial } \% \text{ CO}_2)}{100 + \text{initial } \% \text{ CO}_2}\right]$$
$$\therefore \% \text{ CE} = g[50 + \tfrac{1}{2}(\% \text{ CO}_2)] - Z \quad [10]$$

This equation reduces to the Pearson and Waddington equation for 100% initial CO_2, no reaction of CO_2 with carbon, and no loss of cathode products other than by reaction with CO_2.

The theoretical limits for g are $g = 1$ to 2. A value of $g = 1$ means initial $CO_2 = 100\%$ and no reaction of CO_2 with carbon. A value of $g = 2$ means that undiluted gas leaving the cell is pure CO and no CO_2 reduction by metal has occurred. Except when the cell is on anode effect, the value of g appears to be closer to unity. The value of g would be less than 1 for Case II in Fig. 3, but Case II appears to be negligible for the Permanente experimental cell.

The theoretical limits for Z are $Z = 0$ to 100.

The preceding sections show that (*a*) less than 100% initial CO_2 or reaction of CO_2 with carbon, and (*b*) loss of metal without reacting with CO_2 tend to shift actual pot data to opposite sides of the Pearson and Waddington line. It appears that the relation of per cent CO_2 to current efficiency found by prior investigations (2, 4) was due to a fortuitous combination of these two effects.

In Fig. 2 it is seen that the line for the highest bake-temperature anodes is about 3.5% below the Pearson and Waddington line within the range of the experimental data. Since even the highest bake-temperature anodes used probably gave a g value greater than one, Z must have been greater than 3.5%. The lines through the data in Fig. 2 were drawn as an example with a value of $Z = 5.0$. The corresponding values of g are as follows:

Anode bake temp, °C	g
959	1.070
1070	1.040
1150	1.020

In future tests it is hoped that Z can be evaluated, or at least its variation with cell variables determined. While the value of Z was probably relatively constant in these tests, there are indications from later tests that it varies significantly with bath NaF/AlF_3 ratio.

Measurement of the per cent CO_2 in cell gas has been advocated as a means of determining instantaneous values of current efficiency (4). Results in this work indicate that this is a very questionable practice.

Summary and Conclusions

Current efficiency and cell gas composition were measured on a 10,000-amp experimental aluminum reduction cell for operation with groups of anodes baked at temperatures from 950° to 1190°C. The following are the conclusions from this work:

1. Current efficiency did not vary significantly with anode bake temperature.

2. The percentage of CO_2 in the cell gas varied with anode bake temperature, increasing with increasing bake temperature.

3. This produced deviations from the previously accepted equation:

$$\% \text{ CE} = 50 + \tfrac{1}{2}(\% \text{ CO}_2)$$

4. The data could be correlated by a new equation:

$$\% \text{ CE} = g\,[50 + \tfrac{1}{2}(\% \text{ CO}_2)] - Z$$

5. Some oxidation or loss of cathode products by other than reaction with CO_2 is indicated by a value of Z that is at least 3.5%.

6. The value of g was greater than unity and increased for low-bake-temperature anodes, which indicates less than 100% initial CO_2 and/or reaction of initially formed CO_2 with carbon in cell.

7. Use of the oversimplified equation, $\% \text{ CE} = 50 + \tfrac{1}{2}(\% \text{ CO}_2)$, to calculate current efficiency from gas analyses is a questionable practice.

Acknowledgment

The author wishes to thank Bernard Porter and other members of the Research staff for helpful criticisms and Kaiser Aluminum & Chemical Corporation for permission to publish this work.

Manuscript received Dec. 22, 1958. This paper was prepared for delivery before the San Francisco Meeting, April 29-May 3, 1956.

Any discussion of this paper will appear in a Discussion Section to be published in the June 1960 JOURNAL.

REFERENCES

1. T. G. Pearson, Royal Institute of Chemistry, Lectures, Monographs and Reports, No. 3, pp. 36-63 (1955).
2. T. G. Pearson and J. Waddington, *Discussions Faraday Soc.*, No. 2, 307 (1947).
3. J. L. Henry and R. D. Holliday, *J. Metals*, **9**, 1384 (1957).
4. E. Pruvot, *Alluminio*, **22**, No. 6, 721 (1953).

December 1959 Discussion Section

A Discussion Section, covering papers published in the January-June 1959 JOURNALS, is scheduled for publication in the December 1959 issue. Any discussion which did not reach the Editor in time for inclusion in the June 1959 Discussion Section will be included in the December 1959 issue.

Those who plan to contribute remarks for this Discussion Section should submit their comments or questions in triplicate to the Managing Editor of the JOURNAL, 1860 Broadway, New York 23, N. Y. *not later than September 1, 1959.* All discussions will be forwarded to the author(s) for reply before being printed in the JOURNAL.

Electromotive Force Series of Metals in Fused Salts and Activities of Metal Chlorides in 1:1 Molar KCl-NaCl Solutions

S. N. Flengas and T. R. Ingraham

Mines Branch, Department of Mines and Technical Surveys, Ottawa, Ontario, Canada

ABSTRACT

The potentials of a series of metal-metal chloride systems in an equimolar mixture of molten potassium and sodium chlorides have been measured against a silver-silver chloride reference electrode. An electromotive force series of metals at different temperatures has been established for this particular solvent. Experiments with a chlorine electrode have shown that the solutions of silver chloride in the KCl-NaCl solvent are ideal, and hence, deviations from ideality of the other chlorides in this solvent can be attributed directly to the formation of complexes in the melts. Three types of behavior have been observed for the salts studied in this solvent: ideality, and positive and negative deviations from ideality. The theoretical aspects of complex formation in melts are discussed.

The work reported in this paper is the culmination of experiments begun in 1956 for the purpose of establishing electromotive force series of metal-metal chloride systems in a solvent consisting of 1:1M KCl-NaCl, at temperatures between 650° and 900°C. In the initial experimental work, a thermodynamically reversible, diffusion-free, silver-silver chloride reference electrode (1) was developed. This electrode was used to obtain the standard potentials of several systems (2-5). In this paper, the data have been used to establish emf series of metals at various temperatures.

A theoretical interpretation of these data required the definition of an "ideal" reference standard state. By choosing the pure metal chlorides at the temperatures of experiment as the standard state, it was observed that the experimental standard cell potentials showed pronounced deviations from ideality. To resolve the differences, a chlorine-chloride ion electrode was constructed, and the properties of the silver-silver chloride electrode were investigated in detail. Having established the properties and thermodynamic functions of the silver chloride solutions, the activity coefficients and other related thermodynamic properties of the remaining chlorides were calculated.

Standard Electrode Potentials in Fused Salts

Experimental

The preparation of materials and the detailed experimental procedure for electrode potential measurements in fused salts has been described in detail in previous publications (1-5). The potentials of the systems Mn-$MnCl_2$, Zn-$ZnCl_2$, Cr-$CrCl_2$, Tl-TlCl, Cd-$CdCl_2$, Fe-$FeCl_2$, Pb-$PbCl_2$, Sn-$SnCl_2$, Co-$CoCl_2$, Ni-$NiCl_2$, and Cu-CuCl were investigated with cells of the type

M	$MCl_n(x_2)$			
(-)	KCl-NaCl (1/1 Mole)			
	(Indicator electrode)			
Asbestos	$AgCl(x_1)$			Ag
fiber	KCl-NaCl (1/1 mole)			(+)
	(Reference electrode)			

[*A*]

A typical design of the all-silica cell is given in Fig. 1. In this cell the reference electrode solution is

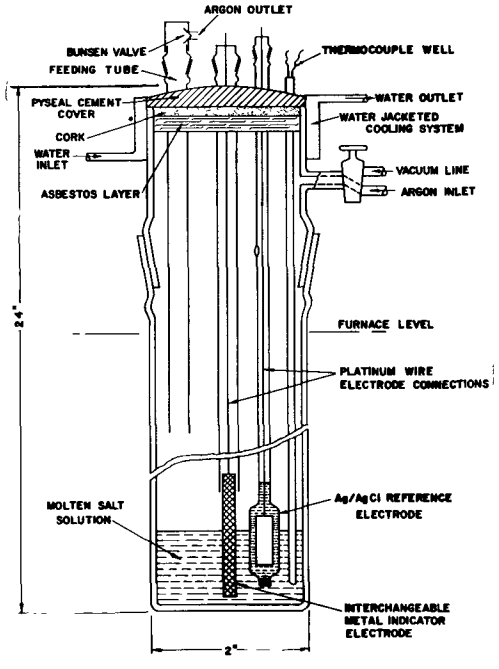

Fig. 1. Cell design for metal electrode potential measurements: Cell [A]

M	$MCl_n(x_2)$		Asbestos		$AgCl\ (x_1)$	Ag
(—)	KCl-NaCl	‖	fiber	‖	KCl-NaCl	(+)
	(1/1 mole)				(1/1 mole)	

separated from the solution in the indicator electrode by a small asbestos fiber sealed into the end of the silica tubing of the reference electrode. The fiber absorbs the salts and makes a good electrical contact between the two solutions while hindering diffusion. Analysis of the solutions from both electrode compartments indicated that this method of separation was effective. For dilute salt solutions, the presence of a large excess of the same ionic melt on both sides of the junction effectively eliminated junction potentials.

The reaction for a cell of the type shown above is:

$$M\,(s) + n\,Ag^+(AgCl \text{ in KCl-NaCl}) = M^{n+}(MCl_n \text{ in KCl-NaCl}) + nAg(s) \quad [A']$$

The relationship between the cell potential and salt concentrations in the melt is given by the Nernst equation in the expanded form

$$E(\text{cell A}) = E^\circ(Ag/Ag^+) - E^\circ(M/M^{n+}) + (RT/n\mathbf{F}) \ln \frac{x_2}{x_1^n} - (RT/n\mathbf{F}) \ln \frac{\gamma_2}{\gamma_2^n} \quad [1]$$

where $E^\circ(M/M^{n+})$ is the *standard electrode potential* [with the IUPAC Stockholm sign convention (16)] of M in the metal chloride MCl_n and $E^\circ(Ag/Ag^+)$ is the *standard electrode potential* of Ag in AgCl. The γ and x are, respectively, the mean activity coefficients and mole fractions of the metal chlorides taking part in the cell reaction. If the E° are referred to the standard chlorine-chloride electrode at the same temperature (see below), they become equal to *minus the formation potentials* of MCl_n and AgCl, respectively, in their standard states (pure salt at the temperature of the experiment) as defined by Hamer, Malmberg, and Rubin (6). Mole fractions are defined in the usual way, which is

$$x_i = n_i/\Sigma n_j \quad [2]$$

where n_i is the number of moles of the i^{th} constituent.

From Eq. [1], assuming that the activity coefficients for dilute solutions are constant, it is possible to calculate a cell potential which proved to be independent of concentration. This is done simply by subtracting the term $(RT/n\mathbf{F}) \ln (x_1^n/x_2)$ from the experimentally obtained potential, E (cell A). The potential thus derived is constant over the range of concentrations for which the activity coefficients are constant and will be called the "apparent standard cell potential," $E^{\circ\prime}$ (cell A). From Eq. [1], the apparent standard cell potentials are given by

$$E^{\circ\prime}(\text{cell A}) = E^\circ(Ag/Ag^+) - E^\circ(M/M^{n+}) + (RT/n\mathbf{F}) \ln (\gamma_1^n/\gamma_2) \quad [3]$$

The standard cell potential E°(cell A) would be given by Eq. [3] without the activity coefficient term.

Apparent standard cell potentials can be obtained in either of two ways: by the graphical method, which involves the interpolation (or extrapolation) of the log x_2/x_1^n vs. E(cell A) curve to zero log-value (Fig. 2), or by calculation from the Nernst equation. In the latter method the Nernst curves must be linear, and the slopes of the straight lines must be identical with the theoretical values of $(2.303\ RT/n\mathbf{F})$. From Eq. [3] it is seen that the experimentally derived apparent standard cell potential $E^{\circ\prime}$(cell A) includes, in addition to the standard electrode potentials, the dilution effect as an activity coefficient term. Since standard electrode potentials are known (6), Eq. [3] can be used to calculate activity coefficients in melts.

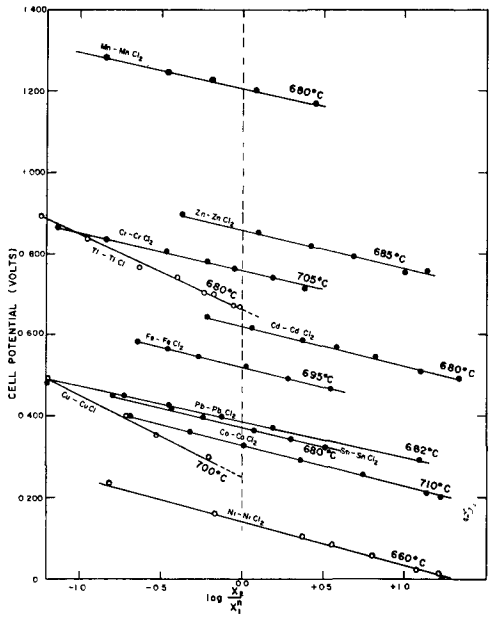

Fig. 2. Electromotive force of Cell [A] for different metals as a function of log (x_2/x_1^n) at constant temperature. ($x_1 = 6.235 \times 10^{-2}$).

Results

The results of potential measurements with these cells at different salt concentrations are given in Fig. 2. In this graph the experimentally obtained cell potentials E(cell A) are plotted vs. the logarithm of the mole fraction ratio in the two half-cells, following the Nernst equation [1]. It will be observed that the relationship is linear, which justifies the assumption made for the definition of the apparent standard cell potential $E^{\circ\prime}$(cell A) of Eq. [3]. This linearity indicates that the activity coefficients of the metal chlorides are either unity or constant for the concentration range of the experiments. The apparent standard cell potentials for each system, obtained by graphical interpolation or extrapolation at zero log-term, are indicated by the intercepts with the dotted line in the center of Fig. 2.

The slopes of the straight lines are in most cases in good agreement with the Nernst equation, with the exception of the Ni-$NiCl_2$ system in which a slope of 0.107 is obtained instead of 0.096. Cell potentials in Fig. 2 are corrected for small thermoelectric forces. These were measured separately on the bimetallic systems of the electrodes (with their connections) and are given in Fig. 3.[1]

[1] Potentials given in some of our previous publications (1-4) have not been corrected for thermoelectric effects. For such corrections, reference should be made to Fig. 3.

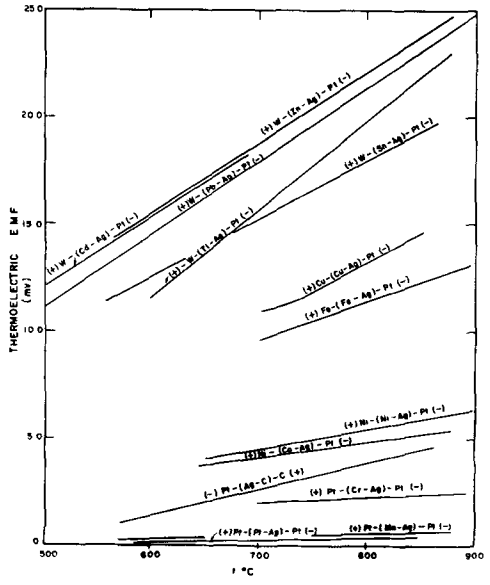

Fig. 3. Thermoelectric electromotive forces of the bimetallic systems of the various types of electrodes used in this study.

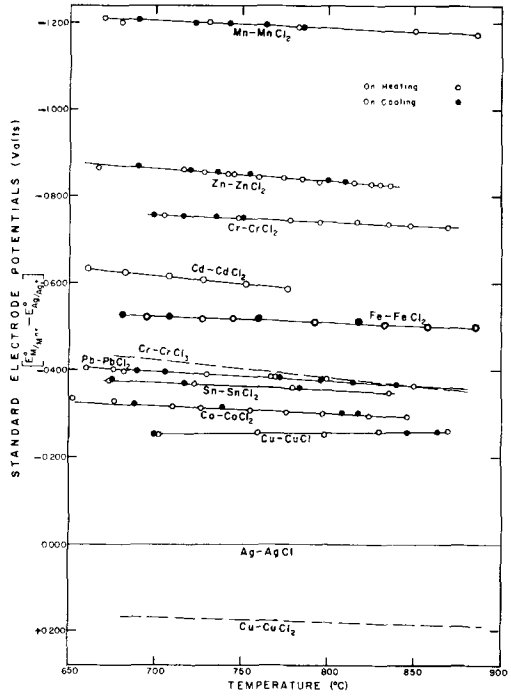

Fig. 4. Variation of standard electrode potentials with temperature.

The effect of temperature change on the apparent standard cell potentials $E^{o\prime}$ (cell A) was also measured; the results are summarized in Fig. 4. It is seen that between 650° to 900°C the relationship of temperature and apparent standard cell potential is linear and the temperature coefficient is small. Standard cell potentials for the systems Cu-$CuCl_2$ and Cr-$CrCl_3$ are shown in the graph by dotted lines to indicate that these values were not obtained experimentally but were calculated using a process described previously (4). In fact, neither of these potentials could be measured directly because of a spontaneous reduction of the higher valency chlorides by the corresponding metal electrodes.

The emf series derived in the present investigation at temperatures of 700°, 800°, and 900°C are given in the first three columns of Table I from our observed values of $E^{o\prime}$ (cell A). In the same tabulation are also included the standard potentials, calculated from E^{o} (cell A) values derived from thermal data by Hamer, Malmberg, and Rubin (6). A third set of data is included to demonstrate the agreement between the standard electrode potentials obtained in this study in the presence of 1/1M KCl-NaCl solvent and those published recently by Laitinen and Liu (7) in the KCl-LiCl eutectic solvent. Since the latter were determined at 450°C, it was necessary to extrapolate our values to this temperature.

Table I. Standard electrode potentials[a] of metals in fused 1:1 KCl-NaCl

	E^{o} (M/M^{n+}) − E^{o} (Ag/Ag^{+}), v							
	This study			Hamer, *et al.*[b]			At 450°C	
Electrode	700°C	800°C	900°C	700°C	800°C	900°C	This study[c]	Laitinen and Liu[d]
Mn, $MnCl_2$	−1.206	−1.190	−1.172	−1.010	−0.981	−0.955	−1.230	−1.212
Zn, $ZnCl_2$	−0.860	−0.835	−0.810	−0.665	−0.650	−0.630	−0.930	−0.929
Cr, $CrCl_2$	−0.758	−0.740	−0.728	−0.565	−0.526	−0.505	−0.810	−0.788
Tl, TlCl	−0.665	—	—	−0.665	—	—	—	—
Cd, $CdCl_2$	−0.620	−0.580	—	−0.415	−0.367	—	−0.630	−0.679
Fe, $FeCl_2$	−0.520	−0.510	−0.498	−0.305	−0.292	−0.270	−0.560	−0.534
Cr, $CrCl_3$	−0.425	−0.385	−0.345	−0.385	−0.380	−0.375	−0.525	−0.523
Pb, $PbCl_2$	−0.390	−0.376	−0.355	−0.315	−0.286	−0.270	−0.447	−0.464
Sn, $SnCl_2$	−0.370	−0.354	−0.340	−0.405	−0.435	−0.450	−0.410	−0.445
Co, $CoCl_2$	−0.324	−0.300	−0.275	−0.195	−0.155	−0.135	−0.372	−0.354
Cu, CuCl	−0.260	−0.256	−0.260	−0.140	−0.145	−0.152	−0.240	−0.214
Ni, $NiCl_2$	−0.140	—	—	−0.095	—	—	—	−0.158
Ag, AgCl	0.0	0.0	0.0	0.0	0.0	0.0	0.0	0.0
Cu, $CuCl_2$	+0.170	+0.180	+0.192	+0.410	+0.430	+0.450	+0.200	+0.189
Cl_2, Cl^-	+0.845	+0.820	+0.795	+0.850	+0.826	+0.794	+0.905	+0.853

[a] It will be noted that the sign of the electrode potentials is in accord with the recommendations of the IUPAC Stockholm Convention [See Licht and deBethune (16)]. The potentials are referred to Ag/AgCl.
[b] Standard potentials calculated from thermal data.
[c] Extrapolated values from our experimental data obtained at temperatures between 650° to 900°C in 1:1 KCl-NaCl.
[d] Values obtained by Laitinen and Liu (7) in KCl-LiCl at 450°C.

From Table I, it is readily seen that both the sequence and the magnitude of the potentials in the experimentally derived emf series of metals are different from those calculated by Hamer, Malmberg, and Rubin (6). These differences are due to the effects of solvent on the salts, as expressed by the γ term in Eq. [3]. On the other hand, standard potentials obtained experimentally in this study and by Laitinen and Liu (7) are in substantial agreement. The small differences in the magnitude of the potentials should be attributed to the difference in solvents and to the error in extrapolating our data to 450°C. It should also be noted that standard potentials determined by Laitinen and Liu are given without thermoelectric force corrections. The corrections are probably a few millivolts only and should be added to the measured potentials. The agreement should therefore be, in most cases, even better than that shown in Table I.

Thermodynamic Properties of Solutions of Silver Chloride in 1/1M KCl-NaCl

The standard cell potentials obtained in cell [A] represent the difference between the individual standard electrode potentials of the reference and indicator electrode systems. Consequently, it is not possible to calculate individual activities of the metal chlorides in solution unless the thermodynamic properties of one species are known. Although preliminary results (1) indicated ideality of the AgCl (KCl-NaCl) system, it was necessary to confirm this by determining the activities of silver chloride in solution. The thermodynamic properties of pure silver chloride have been studied by several investigators (8-10, 17), using silver-chlorine cells of various designs. The agreement between the different data is quite good. On the other hand, there is little information on the properties of solutions of silver chloride in fused salt solvents. Stern (11, 12) investigated the systems AgCl-KCl and AgCl-NaCl, at 800°C and showed that, whereas the former deviates from ideality positively, the latter deviates negatively. Takahashi (13) investigated the system AgCl(KCl-LiCl) and found a small deviation from ideality. In these studies the pure silver chloride state was also chosen as the standard state for reference.

In the present investigation, a cell consisting of silver-silver ion and chlorine-chloride ion electrodes was developed and used to measure the thermodynamic properties of solutions of silver chloride in the 1/1M KCl-NaCl solvent at temperatures varying between 650°-900°C.

Experimental

The cell used to measure the potentials of silver chloride in the molten salt solution was of the following type:

Ag (-)	AgCl (x) KCl-NaCl (1/1 mole)	‖		
Asbestos fiber	KCl-NaCl 1/1 mole	‖	Cl_2 (1 atm) C (graphite)	(+) [B]

The cell consisted of a chlorine-chloride ion reference electrode and a silver-silver ion indicator electrode. The cell reaction is simply the formation of silver chloride in solution, i.e.:

$$Ag(s) + \tfrac{1}{2}Cl_2(g) = Ag^+Cl^-(\text{in KCl-NaCl}) \quad [C]$$

The relationship between the cell potential and the mole fraction of silver chloride (x), is given by the Nernst equation in the expanded form:

$$E(\text{cell } B) = E^\circ(Cl^-/Cl_2) - E^\circ(Ag/Ag^+) - (RT/\mathbf{F}) \ln (x\gamma) \quad [4]$$

where the E° are the *standard electrode potentials* in pure silver chloride (which is the standard state), and x and γ are, respectively, the mole fraction and mean activity coefficient of silver chloride in solution in the potassium-sodium chloride solvent.

The actual cell design is shown in Fig. 5. The lower part of this cell was constructed from silica tubing and the upper part from Pyrex tubing. The two parts were joined by a graded seal. The over-all dimensions of the cell were 2 in. x 20 in. The silver electrode was a rod of pure silver wire (99.99%) connected to the potentiometer by platinum wire.

The inert electrode for the chlorine-chloride ion system was a ¼ in. diameter rod of spectrographically pure graphite. A 20,000-ohm resistance in series with the electrodes was used as an additional precaution to reduce the potentiometric current and prevent any polarization phenomena. One of the features of this cell is the activation of the graphite electrode before use. The end of the rod was coated with a concentrated sucrose solution and then carbonized in a chlorine atmosphere at 800°C for 24 hr. The result was a thin, porous, and highly absorbent carbon deposit. This cell, like all the others used in this investigation, was fitted with a small asbestos fiber to separate the two solutions. It will be noted

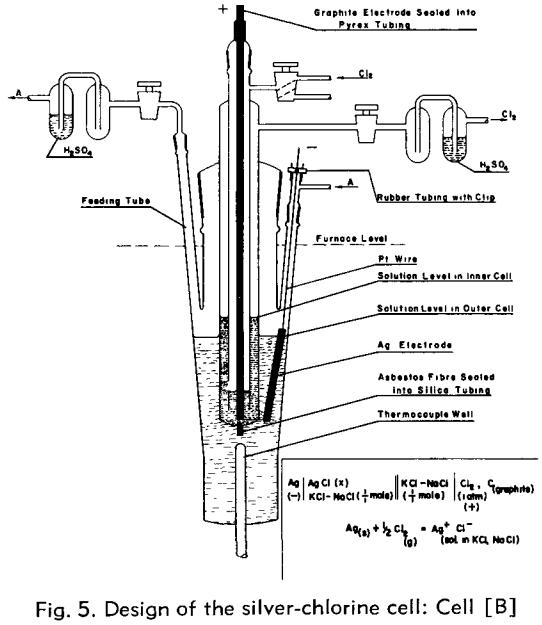

Fig. 5. Design of the silver-chlorine cell: Cell [B]

Ag (—)	AgCl (x) KCl-NaCl (1/1 mole)	‖	Asbestos fiber	‖	KCl-NaCl (1/1 mole)	Cl_2 (1 atm) (+) C (graphite)

that the main significant differences between this cell and those used by other investigators (8, 9) are (*a*) the effective separation between the two half-cells by the asbestos fiber, and (*b*) the simple method of activating the carbon electrode.

Prior to a run, the dry potassium-sodium chloride mixture was added to both the inner and outer half-cells, the amounts being arranged so that when the contents were molten the height in the inner cell would be greater than that in the outer cell. After the salts had melted, the graphite electrode was placed in position, and dry pure chlorine gas was introduced into the cell and permitted to escape after bubbling through the melt. To obtain steady and reproducible potential measurements, it was necessary to leave the cell in operation for about 24 hr before taking potential readings. A sulfuric acid outlet trap prevented air from leaking into the cell and also provided a means of estimating the chlorine gas flow. It was found that the cell potential was independent of the rate of chlorine gas flow, and the cell was operated normally under a very slow flow (about 30 cc/min).

Solutions of silver chloride were prepared *in situ* by adding weighed amounts of silver chloride to the molten salt solvent and mixing well with a small electrically-operated platinum stirrer. To insure that true equilibrium had been attained after each addition of solute, the cell was allowed to stand for about 24 hr during which the potentials were checked several times. It was observed that with vigorous stirring, equilibrium was attained in a short time and that afterward the potentials remained practically unchanged. Small fluctuations of the potentials, of the order of ±0.4 mv, did actually occur and were attributed to local temperature changes in the cell. Thus, a complete run lasted several days, during which the chlorine electrode was in continuous use. The silver electrode was immersed in the solution only while potential measurements were being made. It was then withdrawn into the space above the solution. Purified argon was used to provide an inert gas protection for the silver electrode compartment.

The chlorine-chloride ion electrode may be regarded as a standard reference electrode for potential measurements in fused chloride salts. Unfortunately, in comparison with the silver-silver chloride electrode, it has the disadvantage of being rather fragile and complicated in design.

Results

The results of the experiments in which the electromotive forces of the silver-chlorine cell were measured as a function of temperature at various mole fractions of silver chloride, are shown in Fig. 6. All potentials have been corrected for small thermoelectric effects. It is apparent that the cell potential varies linearly with temperature over the temperature range between 650° to 900°C.

The variation of E(cell B) with log x, according to the Nernst equation [4], is shown in Fig. 7, for 700°, 800°, and 900°C. The relationship over most of the curves is linear, and the slopes of the straight

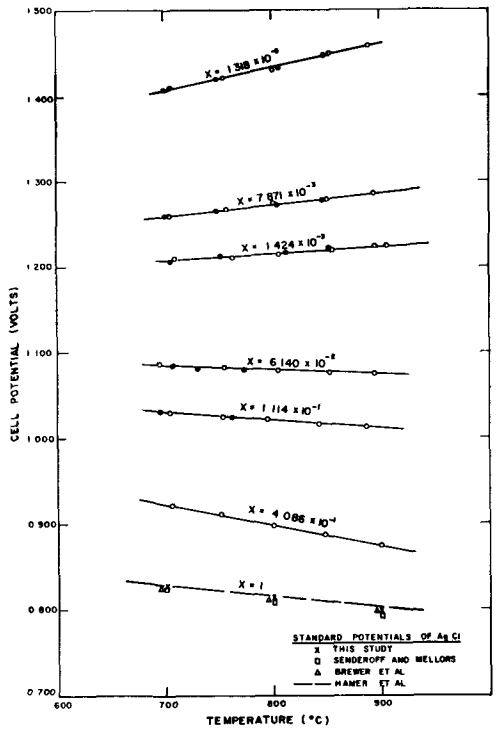

Fig. 6. Variation of emf with temperature for Cell [B]

lines agree very well with the calculated slopes from the Nernst equation at these temperatures for a one-electron electrode reaction. The standard cell [B] potential is obtained by graphical extrapolation of the straight lines in Fig. 7, to zero log x. These potentials, according to Eq. [4], would include the activity coefficient term of the Nernst equation, if any. It will be observed, in Fig. 7, that one of the experiments was continued to higher concentrations of silver chloride than the others. At a mole fraction of about 0.5, which corresponds to a log x term of about −0.2, the curve deviates from linearity. This is attributed mainly to the generation

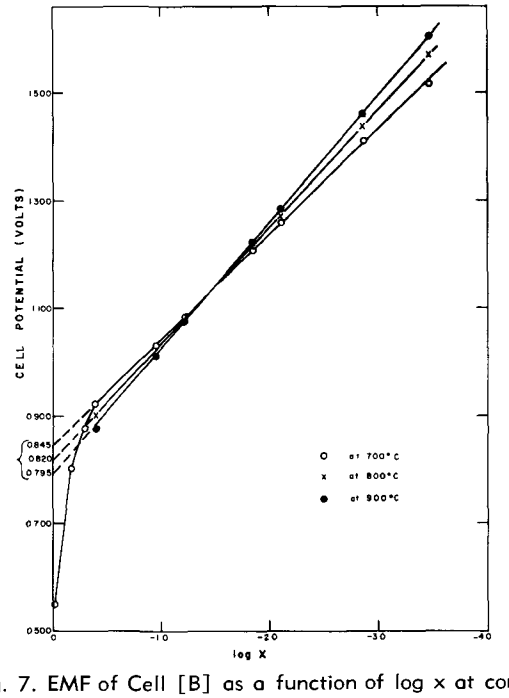

Fig. 7. EMF of Cell [B] as a function of log x at constant temperature.

of a junction potential at high silver chloride concentration. On this basis, it can be calculated that the junction potential between pure silver chloride and the potassium-sodium chlorides is about 300 mv. This junction potential decreases rapidly as soon as some of the potassium-sodium chloride mixture has been added to the silver chloride side, and at a mole fraction of about 0.5 it disappears completely.

However, it should be pointed out that part of this potential, which is termed a junction potential, could be due to a difference in the chloride ion activities in the two half-cell solutions. The activity of chloride ion in the potassium-sodium chloride half-cell, is equal to the activity of chloride ion in the silver chloride half-cell only for dilute silver choride solutions.

To investigate the combined effects of chloride ion activity and junction potential, a silver-chlorine cell without transference was operated. This was done by simply removing the asbestos fiber that separated the two half-cells and thus permitting free mixing of the solutions. The observed electromotive force initially was only 2 mv less than in the corresponding cell of the closed type, for the same chloride ion concentration (0.32*M*). After a short time, however, the potential of the open cell became erratic and this was attributed to the chemical depolarization of the silver electrode caused by small amounts of chlorine gas dissolving and migrating in the molten mixture. Hence, further experiments with this type of cell were discontinued. However, the initially observed difference of 2 mv, which is almost within the area of experimental error for the method, indicates that the effects of chloride ion activity coefficient had almost disappeared even in this rather concentrated silver chloride solution.

In Fig. 6 the dashed line at a mole fraction $x = 1$ indicates the formation potential of pure silver chloride at different temperatures, as calculated from thermal data by Hamer, Malmberg, and Rubin(6). The triangular and square points along this line represent the experimental results obtained by Senderoff and Mellors (9), and the potentials calculated from the free energy functions as tabulated by Brewer, *et al.* (10) for the Ag-AgCl system. It is evident from Fig. 6 that the potentials calculated by Hamer and co-workers are a little larger than the experimental ones, although the agreement with the calculations of Brewer is good. Deviations between the potential data are probably due to the uncertainty of the thermal data. The crosses along this line represent standard formation potentials derived experimentally in the present study, in the presence of solvent, and the agreement between the experimental data by the different methods is striking.

From the data in Fig. 6, using the well-known equations,

$$\Delta F^\circ = -E^\circ \mathbf{F} = -RT \ln K \qquad [5]$$

$$d \ln K/dT = \Delta H/RT^2 \qquad [6]$$

$$\Delta F = \Delta H - T\Delta S \qquad [7]$$

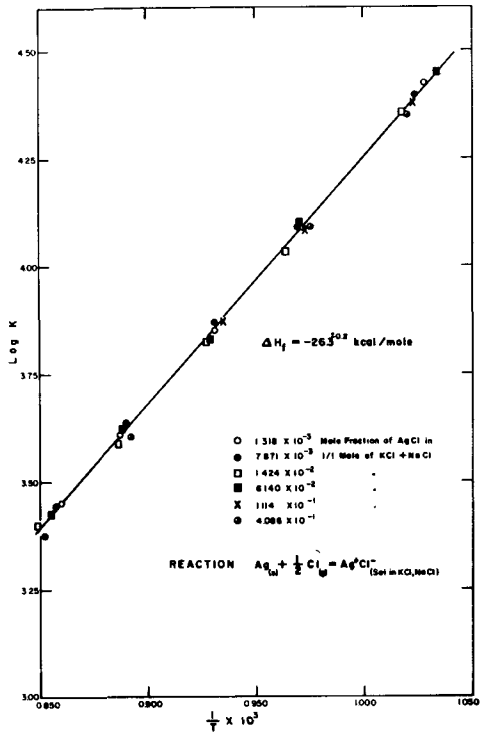

Fig. 8. Variation of log K with the reciprocal of absolute temperature of the reaction:

$$Ag(s) + \tfrac{1}{2}Cl_2(g) = Ag^+Cl^- \text{ (in KCl-NaCl)}$$

it is possible to calculate the enthalpies and entropies of formation of silver chloride in the presence of solvent. The results of the calculations are shown in Fig. 8, in which the logarithm of the equilibrium constant for the formation reaction of silver chloride is plotted against the reciprocal of absolute temperature. It will be noted that the agreement between the different sets of data from which these points were calculated is very good. The relationship is linear for the range of temperature, i.e., between 650°-900°C. From the slope of the straight line the heat of formation of silver chloride is calculated as: $\Delta H_f = -26.3 \pm 0.2$ kcal mole^{-1}. The summary of all thermal data for silver chloride is given in Table II.

From Table II it can be readily derived that the standard partial molal free energy of mixing of silver chloride with the potassium-sodium chloride

Table II. Thermal data for silver chloride

Temp, °C	Standard free energy of formation, kcal mole^{-1}	Standard enthalpy of formation, kcal mole^{-1}	Standard entropy of formation, cal. deg^{-1} mole^{-1}
700	−19.48[a]	−26.3[a]	−7.1[a]
	−19.42[b]	−25.3[b]	−6.1[b]
	−19.35[c]	−26.0[c]	−6.8[c]
800	−18.91[a]	−26.3[a]	−7.0[a]
	−18.79[b]	−25.3[b]	−6.1[b]
	−18.84[c]	−26.0[c]	−6.7[c]
900	−18.33[a]	−26.3[a]	−6.9[a]
	−18.19[b]	−25.3[b]	−6.1[b]
	−18.31[c]	−26.0[c]	−6.6[c]

[a] This study. Data obtained from solutions of silver chloride in KCl-NaCl solvent.
[b] Senderoff and Mellors (9). Data obtained on pure silver chloride.
[c] Brewer, *et al.* (10). Data obtained on pure silver chloride.

molten salt solvent is of the order of only −0.05 to −0.15 kcal mole^{-1}, a value surprisingly low and well within the area of experimental error of the data used for comparison. Accordingly, for all practical purposes, the activity coefficient of silver chloride in the 1/1M KCl-NaCl solution is unity ($\gamma = 1.0$). From the data in Table II, it can also be derived that the standard partial molal entropy of mixing is of the order of −0.9 to −0.3 cal/deg mole, the value again depending on the data used for the comparison. The indication is that the standard entropy change accompanying the process of solution is very small and in the area of experimental error of these measurements. Thus, the solution of silver chloride will be considered to be ideal over the temperature range of 650°-900°C and for the range of concentrations from very dilute up to 0.5*M*.

Discussion

By taking the state of the pure metal chlorides at the temperature of the experiments as the standard state, Eq. [3] can be applied to measure the activity coefficients of the metal chlorides in the fused salt solution. By setting the activity coefficient of silver chloride (γ_i) equal to unity, Eq. [3] can be rearranged to read

$$\log \gamma\,(MCl_n) = ({}_n\mathbf{F}/2.303RT)\,[E^\circ - E^{\circ\prime}] \quad [8]$$

where $E^{\circ\prime}$ is the apparent standard cell [A] potential experimentally obtained in this study, and E° is the calculated standard cell [A] potential from tabulated formation potentials given by Hamer, Malmberg, and Rubin (6) (cf. Table I).

Hence, the activity coefficients can be readily calculated by using Eq. [8] and the data given in Tables I and II. The accuracy of the values thus obtained depends on the accuracy of our observed potentials and on the accuracy of the thermal data from which Hamer's standard potentials have been calculated. The results of these calculations are given in Table III. Also shown in Table III are the range of concentration, for which the activity coefficients were found to be constant and the variation of activity coefficient with temperature. It is obvious from the table that only the solutions of silver chloride and thallous choride in this solvent behave ideally. For all the other metal chloride solutions studied, a marked deviation from ideality is observed.

For metal chloride solutions such as $MnCl_2$, $ZnCl_2$, and all the others for which the activity coefficients are less than unity, the formation of complexes can be postulated. It would appear that these salts in solution are complexed to the extent that only about 1/100 to 1/1000 of the amount present is free to contribute to the electrode potential. For these chlorides the activity coefficients show the expected behavior, i.e., they increase with increasing temperature. The constancy of the activity coefficients in dilute solutions, for the range of concentrations investigated, indicates that in these solutions the complex species remain unchanged.

Two notable exceptions to the general pattern of complex formation are represented by chromic and stannous chloride. For these salts the activity coefficients are larger than unity. On the assumption that no phase changes are involved, this behavior would indicate that the solvent has a bond-loosening effect on the solute.

In Table III, the standard partial molal free energies of mixing are calculated from the data, using the equation:

$$\overline{\Delta F^\circ}_{mix} = RT \ln \gamma = + n\mathbf{F}\,[E^\circ(\text{cell A}) - E^{\circ\prime}(\text{cell A})] \quad [9]$$

The quantity defined by Eq. [9] represents the difference between the free energy of the salt in its hypothetical standard state as a solute [i.e., a solution containing unit mole fraction of the salt but having in all other respects the thermodynamic properties of the state of infinite attenuation of the solute, as defined by Lewis and Randall (18)] minus the free energy of the salt in its actual standard state as the pure salt. It is of interest to note that the effect of temperature on the standard partial molal free energies of mixing is, in most cases, very small. Only in the cases of stannous chloride and chromic chloride is the change significant. For chromic chloride the "ideality" of the solutions is closely

Table III. Activity coefficients, standard partial molal free energies and entropies of mixing of metal chlorides in 1:1M KCl-NaCl

Salts	Range of mole fractions, $10^4\,x$	Activity coefficients γ_x			$\overline{\Delta F^\circ}$ (mixing), cal mole^{-1}			$\overline{\Delta S^\circ}$ (mixing), cal deg^{-1} mole^{-1}		
		700°C	800°C	900°C	700°C	800°C	900°C	700°C	800°C	900°C
$MnCl_2$	5.87-107.0	0.0093	0.011	0.014	−9,040	−9,640	−10,000	3.6	3.7	3.5
$ZnCl_2$	22.20-717.0	0.0091	0.018	0.028	−8,990	−8,530	−8,300	−2.0	−2.3	−2.0
$CrCl_2$	2.84-93.5	0.010	0.010	0.013	−8,900	−9,820	−10,280	8.9	8.9	8.8
TlCl	36.10-603.0	1.0	—	—	0.0	—	—	—	—	—
$CdCl_2$	23.40-835.0	0.0075	0.010	—	−9,460	−9,820	—	6.1	5.8	—
$FeCl_2$	8.85-138.0	0.0059	0.0089	0.011	−9,920	−10,050	−10,520	4.4	4.1	4.4
$CrCl_3$	4.00-90.0	0.24	1.18	2.4	−2,770	+350	+2,070	−22.0	−22.2	−22.0
$PbCl_2$	3.25-628.0	0.17	0.14	0.19	−3,460	−4,150	−3,920	3.7	3.8	3.9
$SnCl_2$	6.32-125.0	2.3	5.7	8.9	+1,610	+3,730	+5,070	−15.1	−11.7	−9.8
$CoCl_2$	7.60-612.0	0.046	0.043	0.063	−5,950	−6,690	−6,460	3.9	4.2	3.9
CuCl	10.80-391.0	0.24	0.30	0.34	−2,770	−2,570	−2,560	−0.7	−0.8	−0.8
$NiCl_2$	5.94-666.0	0.34	—	—	−2,080	—	—	—	—	—
AgCl	3.37-6850.0	1.0	1.0	1.0	0.0	0.0	0.0	(−0.5)	(−0.5)	(−0.5)
$CuCl_2$	10.0 -390.0	0.0033	0.0045	0.0061	−11,070	−11,530	−11,900	5.5	5.4	5.5

related to temperature. At about 800°C the solutions are almost "ideal," but with increasing temperature a positive deviation from ideality is evident.

From the dependence of the standard partial molal free energies of mixing on temperature, the standard partial molal enthalpies and entropies of mixing can be calculated for the systems shown in Table III. The latter are also given in this table.

The standard partial molal entropies of mixing, as shown in the last three columns of Table III, also suggest that complex ions are present in all of these systems. It is necessary here to define the term "complex" as used throughout this study. In a very broad sense a "complex" in an ionic melt should be defined as a group of atoms for which the binding forces are stronger than the forces tending to separate them. The latter type of forces obviously includes the interactions between similar groups of atomic aggregates and also the interactions with the solvent. In terms of structure, a "complex" in solution should be a group of atoms in which the immediate neighbors of any atom are arranged in some orderly way, but the arrangement becomes more random gradually with increasing distance from the center of the complex. The definition is almost that on a liquid, with the difference that there is a distinction between the random distribution of atoms or ions in the solvent, and the locally more ordered distribution of atoms in a complex.

Although the presence of finite complexes in melts has been demonstrated both by potentiometric (14) and by spectrophotometric measurements (15), it seems reasonable that in ionic metals there should exist several intermediate states of aggregation between the so-called "noncomplexed" ionic state and the type of finite complexes found in aqueous solutions.

The actual values of the activity coefficients, and of other thermodynamic functions which characterize these complexes in solution will depend entirely on the definition of a noncomplexed state. A completely different set of data would be obtained if, instead of choosing the pure metal salt as the standard state, the state of infinite dilution were chosen. In fact, only the existing differences between any two states are measured directly, and a thermodynamic definition of a noncomplexed state is quite arbitrary. Even the "ideal solution" appears to arise from cancelling out of opposing effects in the binding forces within the complex itself.

In support of this view is the behavior of the solutions of silver chloride in alkali chlorides. Stern (11,12) found that the partial molal free energy of mixing of silver chloride in potassium chloride is negative, and that of silver chloride in sodium chloride is positive. In the present investigation it was found that in a solution of silver chloride in 1/1M mixture of potassium and sodium chlorides, the standard partial free energy of mixing is zero and the solutions are "ideal." It is apparent that by regulating the composition of the solvent and temperature it is possible to obtain solutions with positive, negative, or zero deviation from ideality. Thus, one may conclude that what is theromdynamically an "ideal" state is not necessarily a noncomplexed state.

Acknowledgment

The authors wish to acknowledge the help of Mr. P. Hernandez, Mines Branch glassblower, in constructing the silica apparatus used in the foregoing experiments.

Manuscript received Nov. 28, 1958. This paper was prepared for delivery before the Ottawa Meeting, Sept. 28-Oct. 2, 1958.

Any discussion of this paper will appear in a Discussion Section to be published in the June 1960 JOURNAL.

REFERENCES

1. S. N. Flengas and T. R. Ingraham, *Can. J. Chem.*, **35**, 1139 (1957).
2. S. N. Flengas and T. R. Ingraham, *ibid.*, **35**, 1254 (1957).
3. S. N. Flengas and T. R. Ingraham, *ibid.*, **36**, 780 (1958).
4. S. N. Flengas and T. R. Ingraham, *ibid.*, **36**, 1103 (1958).
5. S. N. Flengas and T. R. Ingraham, *ibid.*, **36**, 1063 (1958).
6. W. Hamer, M. Malmberg, and B. Rubin, *This Journal*, **103**, 8 (1956).
7. H. A. Laitinen and C. H. Liu, *J. Am. Chem. Soc.*, **80**, 1015 (1958).
8. E. J. Salstrom, *ibid.*, **55**, 2426 (1933).
9. S. Senderoff and G. W. Mellors, *Rev. Sc. Instr.*, **29**, 151 (1958).
10. L. Brewer, *et al.*, as reported by L. L. Quill in "Chemistry and Metallurgy of Miscellaneous Materials," Paper 6, McGraw Hill Book Co., New York (1950).
11. K. H. Stern, *J. Phys. Chem.*, **60**, 679, (1956).
12. K. H. Stern, *ibid.*, **62**, 385 (1958).
13. M. Takahashi, *J. Electrochem. Soc., Japan*, **25**, 432 (1957).
14. S. N. Flengas and Sir E. K. Rideal, *Proc. Roy. Soc., London*, **A233**, 443 (1956).
15. D. M. Gruen, "Spectrophotometry Applied to the Analysis of Fused Salts," Paper presented at the 11th Annual Summer Symposium, Division of Anal. Chem., Amer. Chem. Soc., June 19, 1958.
16. T. S. Licht and A. J. deBéthune, *J. Chem. Ed.*, **34**, 443 (1957).
17. J. H. Hildebrand and E. G. Salstrom, *J. Am. Chem. Soc.*, **52**, 4650 (1930); **54**, 4257 (1932).
18. G. N. Lewis and M. Randall, "Thermodynamics," Ch. XXII, McGraw-Hill Book Co., New York (1923).

The Oxygen-Evolution Reaction at Gold Anodes

I. Accuracy of Overpotential Measurements

Sidney Barnartt

Research Laboratories, Westinghouse Electric Corporation, Pittsburgh, Pennsylvania

ABSTRACT

The oxygen-evolution reaction at gold anodes was studied in 0.1M H_2SO_4 at 25°C. The factors affecting the accuracy of overpotential measurements and a new cell design for improved accuracy with a Luggin-Haber capillary are described. Current distribution in the cell, limitations imposed by competing reactions and by the *IR* drop included in the measurement, overpotential-time curves at constant current density, and the accuracy with which Tafel's equation is obeyed are presented. The current density range for accurate measurements was found to be 3×10^{-6} to 10^{-2} amp cm^{-2}. Overpotential measurements taken with decreasing and increasing currents were reproducible to ±1 mv, and deviations from the Tafel line were within this variation. At constant current density the gold anodes oxidized to hydrated Au_2O_3 following the linear law, and the current density dependence of the oxidation rate indicated a blister mechanism.

The steady-state overpotential measurements necessary for distinguishing possible rate-determining steps in anodic oxygen evolution have been compiled by Bockris (1). Data reported to date, however, have shown little consistency. Inherent experimental difficulties are probably greater than, and certainly have not been as intensively investigated as, those for the hydrogen evolution reaction (2, 3).

Platinum anodes have been studied in greatest detail (2). For this electrode there is general agreement that anodic oxygen evolution follows Tafel's equation (4):

$$\eta = a + b \log i \qquad [1]$$

where η is the steady-state overpotential at the applied current density (c.d.) i. The Tafel constants a and b reported by various authors are discrepant. Recently Bockris and Huq (5) investigated platinum in sulfuric acid solutions under conditions of extreme purification. Greater consistency in the Tafel plots was reported; the slope b was reproducible to ±12% or better. In the absence of applied current, a reversible oxygen electrode was apparently obtained for the first time.

This paper reports a detailed study of the accuracy attainable for oxygen overpotential measurements at gold anodes in 0.1M H_2SO_4 at 25.0°C. The various sources of error in overpotential measurements are evaluated, a new cell design for uniform current distribution described, and the c.d. limits determined for measuring η to ±1 mv. It will be seen that Tafel's equation is obeyed within this deviation.

Sources of Error

The following is a general outline of the sources of error involved in the experimental measurement of steady-state overpotential.

Current distribution.—When measurements are made by the direct method (while current is flowing) with a Luggin-Haber capillary (6), the current distribution over the test electrode should be uniform (7). With cell geometries having nonuniform distribution, the c.d. at the point of measurement generally will not be a constant and known fraction of the average c.d. at all values of overpotential (8-10). Even when interrupted currents are used and the potential is measured very rapidly after the interruption, it is desirable to use a cell having uniform current distribution (11).

It is recognized that a mechanically polished electrode surface will contain fine scratches and a large number of sharp micro peaks. In the primary current distribution (that in the absence of electrode polarization) the current density approaches infinity at sharp peaks. When the electrode is polarized, however, the distribution (secondary) is more uniform. The greater the ratio of Wagner's characteristic length parameter $\kappa \left| \partial\eta/\partial i \right|$, where κ is the solution conductivity, to the average scratch depth λ, the more uniform the current distribution (10). If Tafel's equation applies, $\left| \partial\eta/\partial i \right|$ decreases and the distribution becomes less uniform as the c.d. is increased, since

$$\partial\eta/\partial i = \pm 0.4343\ b/i \qquad [2]$$

where the plus sign refers to anodic and the negative sign to cathodic reactions. For even roughly polished electrodes in most electrolytes, the ratio of Wagner's characteristic length to average scratch depth is expected to be sufficiently large that the current distribution over the surface will be essentially uniform. The surface roughness, however, must be taken into consideration in calculating the true current density.

Shielding by the capillary.—It has been shown that large errors in overpotential can result from shielding of the electrode at the point of measurement, unless the capillary tip is either sufficiently far removed from the electrode surface (12, 13) or is

against the electrode and has a properly designed opening (14-16). For an open tip capillary of diameter d, negligible shielding will occur if the distance between the tip and electrode surface is $2d$ or greater.

IR-drop corrections.—Where a Luggin-Haber capillary with open tip is used, correction must be made for the IR voltage drop (V_{IR}) in the electrolyte between the tip and the electrode. These corrections can be appreciable, even in solutions of moderately high conductivity. For example, at 10^{-2} amp cm^{-2}, the following values of V_{IR} in 0.1M H_2SO_4 ($\kappa = 0.046$) were calculated for a capillary tip of diameter d positioned a distance $3d$ from a plane electrode:

d(cm):	0.5	0.1	0.02
V_{IR}(v):	0.290	0.058	0.012

These values were obtained from the equation:

$$V_{IR} = (3d - d/3)\, i/\kappa \qquad [3]$$

which is based on the observation (12, 13) that the potential inside the capillary is equal to that at a distance $d/3$ closer to the electrode in the undistorted field.[1] The above example illustrates the general requirement of positioning the capillary very close to the electrode and, hence, for using a capillary with small outer diameter in order to avoid shielding errors.

Where a coating forms on the electrode surface, as often occurs during anodic overpotential measurements, the resistance of the coating must be evaluated. This is done by actual measurement of the total IR drop included in the overpotential measurement, from which the IR drop in the electrolyte, calculated as above, is subtracted to obtain the IR drop within the coating.

Roughness factor.—For an electrode surface with roughness factor q (ratio of true area to apparent area), Tafel's equation may be written in the form

$$\eta = a + b \log(i'/q) = a' + b \log i' \qquad [4]$$

where i' is the apparent c.d. and $a' = a - b \log q$. If q remains constant throughout the measurements, the correct slope b is obtained when η is plotted against log i'. The apparent a-value from this plot, however, is the value a'; this is too small, as compared with the true a, by the amount $b \log q$.

For systems in which the roughness factor changes with changing c.d., the measurements may appear to follow a Tafel line, but both the slope and the a-value will be in error. This type of error should be revealed by a drift of the apparent Tafel line when determined with decreasing, then with increasing, current densities.

There is evidence that the roughness factor of a polished metal may vary by an order of magnitude, depending on subsequent treatments (17, 18). Therefore, where the electrode surface undergoes change, e.g., by oxidation during anodic oxygen evolution, prepolarization to a stable surface should precede the overpotential measurements.

[1] This observation refers (12) to a capillary tip with ID = 2/3 OD; the capillaries used in the apparatus to be described conformed to this geometry.

Impurities.—Trace impurities, present in the electrolyte or adsorbed on the electrode surface, may produce large errors in overpotential (5, 19-21). The observable effects of impurities on η-measurements include: (*a*) prolonged potential drift with time, (*b*) irreproducibility of steady-state potentials, and (c) depolarization accompanying increased agitation, particularly at low c.d., resulting from competing reactions involving impurities.

Competing reactions.—Any competing reaction depolarizes the electrode reaction under study, i.e., the measured overpotential corresponds to a current smaller than the observed total current. Competing reactions may occur even in highly purified systems; during anodic oxygen evolution, for example, metal dissolution and oxide formation often proceed simultaneously. Soluble products of the cathode reaction can diffuse to the anolyte and depolarize the anode reaction, and vice versa.

Potential-time variations.—The use of arbitrary polarization times has often resulted in failure to attain the steady-state η-values, as has been emphasized for anodic oxygen evolution by the work of Hickling and Hill (22). In general it is preferable to approach the steady state from two directions, e.g., with increasing and with decreasing current density, in order to avoid errors resulting from slow drifts or temporary potential arrests.

Concentration polarization.—Concentration changes at the electrode surface impose an upper limit to the c.d. range over which accurate overpotentials can be measured. The maximum permissible c.d. will generally be considerably lower than the so-called limiting current (at which the current efficiency begins to fall). An appreciable concentration change of any dissolved substance which affects the electrode potential will contribute to concentration polarization. In most cases the accompanying potential changes will be complex and not amenable to accurate calculation. Therefore, the fractional concentration change at the electrode should be maintained small by the use of increased agitation, a more concentrated solution, or a lower c.d. range.

From the mathematical theory of diffusion, the concentration at the electrode, C_e (mole cc^{-1}), of any solution constituent under steady-state conditions is given by the relation (23-25):

$$C_e - C_o = f\, l/D \qquad [5]$$

where C_o is its bulk concentration, l the thickness of the diffusion layer (cm), D its diffusion coefficient (cm^2 sec^{-1}), and f its flux at the electrode boundary (mole cm^{-2} sec^{-1}). The flux is equal to the rate at which the constituent is added at the electrode surface by the electrode reaction and by electrical transference.

In most practical systems involving forced convection of a complex nature, Eq. [5] is applied as a first approximation, with the assumption that the only effect of convection is a decrease in the parameter l. Quantitative theoretical predictions for convective effects in several simplified systems have been reviewed (26).

Experimental Procedure

Materials.—Reagent-grade sulfuric acid was distilled in an all-Pyrex still. Distilled water was treated with small amounts of KOH and $KMnO_4$ and redistilled in an all-Pyrex still. In each case the first portion of the distillate was rejected and the middle fraction used.

Oxygen gas was purified by passage through a column of cupric oxide heated to 700°C in a Vycor tube, then into an all-Pyrex system through bubblers containing 1M NaOH and 1M H_2SO_4, and finally through a fritted Pyrex tube to trap droplets. The purified gas was led into the cell through a short length of flexible, unplasticized polytrifluorochloroethylene (Kel-F) tubing.

Anodes of solid gold and of gold-plated copper were used. The solid electrode was machined from pure gold rod (99.98% Au, principal impurities Ag and Pt metals). The plated electrode was prepared by electroplating gold at 2 ma/cm^2 and 70°C from the following solution (reagent-grade chemicals): 0.05M K $Au(CN)_2$, 0.2M, KCN, and 0.1M K_2CO_3. The surface was alternately plated and polished until a gold layer 75 μ thick was achieved. Diamond polishing compound with a particle size of 3 μ was used for the final polish on each electrode.

The following surface treatments of the gold electrodes, prior to insertion in the cell, were standardized. Precleaning involved degreasing in solvents, treatment cathodically in hot 3M NaOH, then immersion in 10M HNO_3. The final treatment of the plated electrode consisted in electroplating an additional 3 μ thickness of gold to produce a smooth, matte surface. The solid gold electrode was made anodic in 1M H_2SO_4 at 5 x 10^{-2} amp cm^{-2} for 5 min to produce a very thin brown oxide, then the latter was dissolved in 5M HCl; the final surface remained almost mirror bright.

Two saturated calomel electrodes (SCE), of the type having a Pyrex salt-bridge junction tube containing a controlled diffusion crack (27), were used to follow potential changes. These were checked periodically with each other and with a third electrode; the voltage between any two never exceeded 0.1 mv.

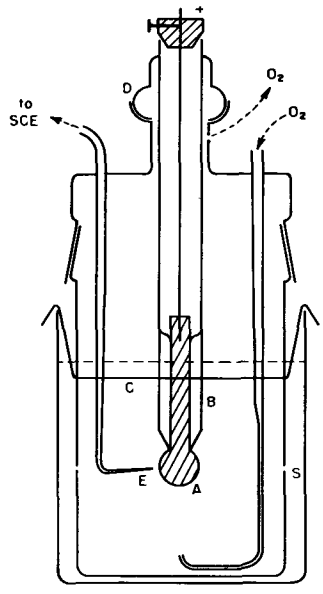

Fig. 2. Cell I

Cell design.—Two cells were used, both designed for uniform current distribution and based on concentric spherical geometry with conical sectioning (7), as indicated in Fig. 1. The following two distortions were introduced in the actual cells. (*A*) The insulator was shortened, as shown in Fig. 1 by the broken vertical lines, so that the 60° angle was maintained only for a distance r_o, where r_o is the radius of the inner electrode. In the cells used the inner electrode was the anode with $r_o = 0.50$ cm. (*B*) It was assumed that, provided the cell diameter exceeded 10 r_o, the outer spherical electrode (cathode) could be highly distorted with little effect on current distribution at the anode. For this reason the cathode was removed to an external compartment, and the diameter of the anode compartment was made 12 r_o in cell I (Fig. 2) and 16 r_o in cell II (Fig. 3). These distortions were expected to produce relatively small non-uniformities of current distribution at the anode A.

The cells were constructed of Pyrex glass. The 60° conical insulator was ground from precision-bore tubing B, and the rod portion of the anode was machined to fit snugly into the bore. The ball joint D

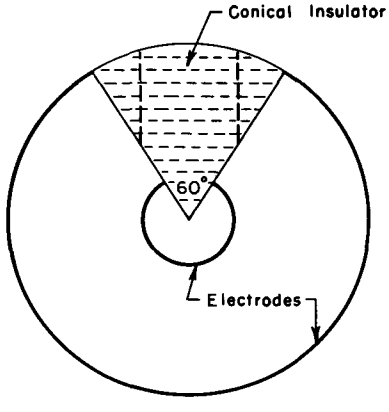

Fig. 1. Conical sectioning of concentric spheres

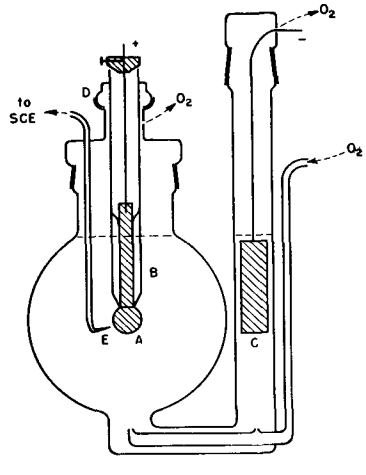

Fig. 3. Cell II

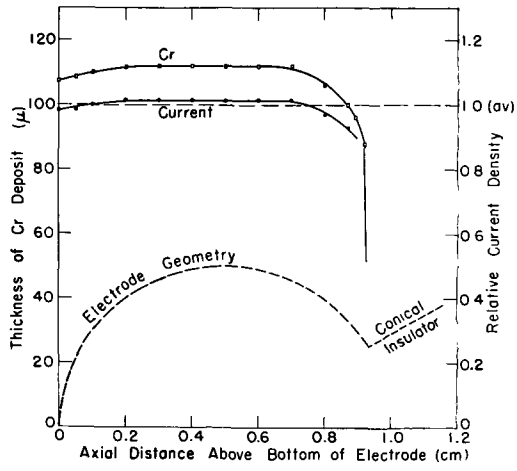

Fig. 4. Current distribution over the anode determined by electrodeposition of chromium.

permitted accurate positioning of the anode with respect to the fixed capillary tip E. A tip of diameter $d = 0.20$ mm was used and was positioned at a distance of about $3d$ from the anode.

In cell I the anolyte boundaries were cylindrical, 12 r_o in diameter and 12 r_o in height. Contact with the catholyte was made through a slot S, 0.5 mm wide, which was concentric with the anode. The cathode C was a platinum wire ring situated near the top of the catholyte. The primary current distribution over the electrode surface in this cell was obtained by measuring the distribution of chromium, electroplated under conditions shown previously (28) to yield good agreement with the primary distribution as measured by the potential-mapping method. Figure 4 shows the measured distribution of chromium over a copper electrode, and the current distribution calculated from it using the current efficiency data of Dubpernell (29). It may be concluded that the current distribution in this cell is sufficiently uniform for overpotential measurements, and that negligible error is incurred when one uses the average c.d. instead of that directly opposite the capillary tip.

In cell II the anolyte was approximately spherical in shape, of diameter 16 r_o. This cell incorporated the following improvements over cell I. (*A*) Both compartments were covered, with only a small hole for escape of oxygen. (*B*) The cathode, a platinized-platinum cylindrical gauze, had much larger surface area. (*C*) Oxygen was bubbled around the cathode as well as the anode, thus tending to sweep out any hydrogen formed at high c.d. The uniformity of current distribution was not measured in cell II, but was assumed to be just as satisfactory as in cell I. Cell II with the solid gold anode was used for measurements reported below except where otherwise stated. The reference compartment of each cell was, of course, filled with the solution under study. Traces of KCl entering this compartment from the reference electrode had a long diffusion path to the capillary tip.

Measurement of overpotential.—Polarizing current was drawn from a 30-v lead-acid battery source, through a resistance box designed to allow a sudden change in current to a preselected value without breaking the circuit. The anode-SCE voltage, E_{obs}, was measured with a shielded potentiometer (L&N Co. model K3) and a current-sensitive galvanometer having sensitivity of 1.3×10^{-9} amp/mm. The sensitivity-selecting switches of the potentiometer were replaced by four push-button switches in an external shielded circuit, by means of which a resistance of 10^9, 10^8, 10^7, or 10^6 ohms was inserted in series with the voltage being measured. With this circuit it was possible to prevent the out-of-balance current drain from exceeding 10^{-9} amp during a voltage measurement.

The reversible voltage E_1 between the SCE and a hydrogen electrode of the Hildebrand type was measured in the solutions used in the present study and the overpotential for the oxygen-evolution reaction was then given by:

$$\eta = E_{obs} + E_1 - 1.229 \qquad [6]$$

where 1.229 v represents the reversible emf between the oxygen and hydrogen electrodes in a given solution at 25°C (30).

Results and Discussion

Oxide formation.—In dilute sulfuric acid, gold anodes become covered with hydrated Au_2O_3 (31, 45). At very low c.d. Au_2O first forms, then converts through AuO to Au_2O_3 before oxygen evolution commences (32). The color of the oxide changes from yellowish brown to reddish brown as it thickens.

A coating was prepared at 10^{-2} amp cm^{-2} for 23 hr and was carefully flaked off the electrode. Chemical analysis for Au and H_2O (and oxygen by difference) indicated $Au(OH)_3$; some change in hydration could have occurred, however, during removal of the coating. X-ray diffraction patterns of the oxide were attempted with a Guinier focusing camera (33); no diffraction lines were obtained, although the instrument had high sensitivity and gave good patterns for evaporated gold films 100Å thick.

The kinetics of oxide growth at constant c.d was investigated at 10^{-3} and 10^{-4} amp cm^{-2} apparent anodic c.d. It was found that the amount of oxide on the spherical anode could be determined by dissolving it in 10 ml of 5M HCl, then analyzing the solution for Au spectrophotometrically (absorption peaks in the ultraviolet at 226 and 314 mμ). Oxide layers 1Å in average thickness are detectable by this method.

Figure 5 presents the oxidation rate measurements. Linear oxidation curves were obtained, corresponding to constant current efficiency for oxide formation. In 0.1M H_2SO_4, the oxidation rates at 10^{-3} and 10^{-4} amp cm^{-2} are 143 and 6.8 Å/hr, respectively, corresponding to current efficiencies for oxide formation of 1.13% at 10^{-3} amp cm^{-2} and 0.53% at 10^{-4} amp cm^{-2}. Such low current efficiencies would have negligible depolarizing effects. Measurements were made also in 0.05M H_2SO_4 at 10^{-3} amp cm^{-2}; as seen in Fig. 5, the change in acid concentration had no appreciable effect on the oxidation curve.[2]

[2] Armstrong, Himsworth, and Butler (44) found linear oxidation curves for gold in 0.1M H_2SO_4, as determined by cathodic reduction of the oxide, with a current efficiency of 0.9% independent of c.d.

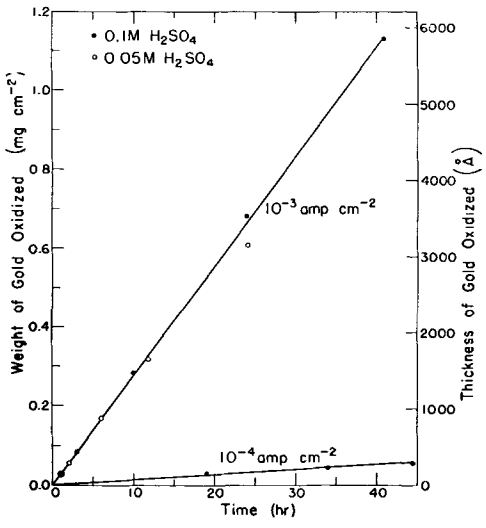

Fig. 5. Anodic formation of gold oxide in sulfuric acid solutions, 25°C.

Linear oxidation curves may be interpreted as resulting from a blister mechanism, in which local separation occurs at the oxide-metal interface in a manner similar to that postulated for gas-metal reactions (34). In support of this mechanism, it was noted that the oxide exhibited poor adhesion, and the thicker coatings could be readily flaked away from the gold substrate.

The blister mechanism may be used to explain the increase in current efficiency for oxide formation with increasing c.d. According to this mechanism, localized interfacial separation occurs when the oxide layer has grown to a critical thickness, such that the local adhesive force is exceeded by the compressive force in the oxide at that point. A blister forms, the distorted oxide cracks, the electrolyte then contacts the exposed metal surface, and rapid oxidation begins there again. In the absence of gas evolution, the oxidation rate should increase with c.d.; it would tend to be roughly proportional to c.d. if the critical oxide thickness for blistering is very small, as appears to be the case for gold anodes where linear oxidation occurs even at low film thicknesses (Fig. 5). The effect of simultaneous gas evolution, however, is to increase the oxidation rate by causing increased rate of blistering. Gas pressure can build up within the blisters, because the surface tension of the liquid tends to prevent the escape of gas through the small cracks in the blistered oxide layer. The gas pressure within a local blister helps to overcome the adhesive force at adjacent areas, thus increasing the rate of blistering and decreasing the critical oxide thickness. Since the rate of gas evolution is proportional to c.d., the higher the c.d. the greater the increase in oxidation rate resulting from this gas-evolution effect. Thus the blister mechanism is qualitatively consistent with the observed fact that the current efficiency for oxidation increased with c.d.

Potential-time variations.—In 0.1M H_2SO_4, oxygen-saturated but before any electrolysis, a clean gold electrode assumes a potential of 0.83 v vs. RHE,[3]

[3] Single electrode potentials refer to the reversible hydrogen electrode in the same solution.

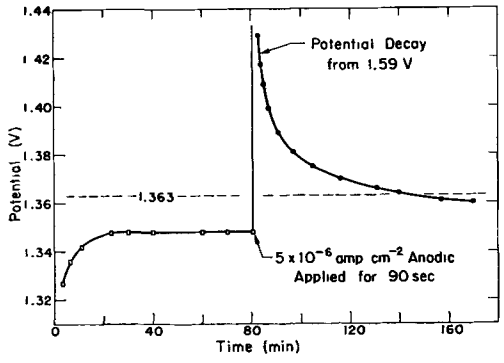

Fig. 6. Potential behavior of a fresh gold electrode in pre-electrolyzed 0.1M H_2SO_4, 25°C. Potential referred to reversible hydrogen electrode (RHE) in same solution.

which is 0.4 v less than the reversible oxygen potential. After prolonged electrolysis of the solution (roughly 0.2 coulomb/ml), however, the typical behavior of a clean gold electrode is that shown in Fig. 6. Upon immersion (zero time) the potential rises quickly to a value higher than the reversible oxygen potential and approaches the reversible Au/Au_2O_3 (hydrated) potential, 1.363 v (35, 36), indicating that gold tends to oxidize in the electrolyzed solution. After the electrode is made anode for a short time at very low c.d., the potential decay curve tends to arrest at the same value.

When a clean gold surface was made anode at 10^{-3} or 10^{-4} amp cm^{-2}, the potential increased to a value 3 to 5 mv higher than the steady-state value, then decreased to the steady value after passage of about 1 coulomb cm^{-2}. The potential was followed for an additional 40 hr, and remained constant to ±0.5 mv as the oxide layer thickened. It was concluded that no deleterious impurities were diffusing into the cell from the reference compartment.

In the procedure that was adopted for determining the η-i relationship, a relatively heavy oxide coating was first formed at a c.d. near the upper end

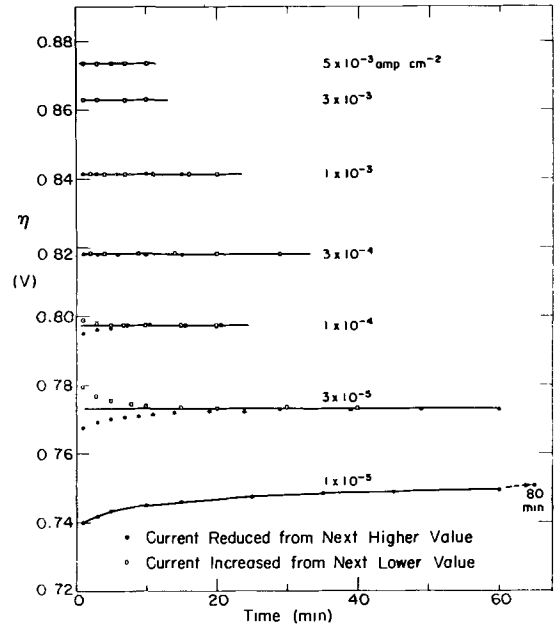

Fig. 7. Overpotential vs. time for oxygen evolution at gold anode in 0.10M H_2SO_4, 25°C.

of the range (at least 40 coulomb cm^{-2} passed). Then the current was decreased in steps to the minimum value and finally increased in steps to the maximum value. A typical set of η vs. time curves are shown in Fig. 7. The steady-state overpotentials obtained with decreasing or with increasing current were the same within ±0.5 mv. One experiment was continued through a second cycle of decreasing followed by increasing current densities, and the steady-state overpotentials remained the same within ±1 mv. Preliminary electrolysis of the solution with an auxiliary anode produced no appreciable change in the steady-state η-i curve.

The constant current curves of Fig. 7 exhibit a time effect at low current densities. When the current is decreased from a higher value the overpotential is initially lower than the steady-state value, and when the current is increased from a lower value η exceeds the steady-state value initially. This is a reproducible effect.

At 10^{-5} amp cm^{-2} the potential drift with time was prolonged (Fig. 7). The value of η after 1 hr was still 3 mv below the extrapolated η-log i curve. This behavior was characteristic of all runs, hence $i = 3 \times 10^{-5}$ was chosen as the lower limit for steady-state overpotential measurements. The interpretation of this time effect is considered in the next section from the standpoint of competing reactions.

Competing reactions.—The reversible single electrode potentials, referred to the standard hydrogen electrode (SHE), at 25°C for possible reactions at gold anodes, and for possible cathodic reactions, in dilute sulfuric acid solids are given in Table I.

Table I. Reversible electrode potentials at 25°C referred to SHE*

(a) $O_2 + H^+ + e^- = HO_2$; $E = -0.13 - 0.0592\ pH + 0.0592 \log [O_2]/[HO_2]$

(b) $2H^+ + 2e^- = H_2$; $E = -0.0592\ pH - 0.02\% \log [H_2]$

(c) $O_2 + 2H^+ + 2e^- = H_2O_2$; $E = 0.682 - 0.0592\ pH - 0.0296 \log [O_2]/[H_2O_2]$

(d) $O_2 + 4H^+ + 4e^- = 2H_2O$; $E = 1.229 - 0.0592\ pH + 0.0148 \log [O_2]$

(e) $Au(OH)_3 + 3H^+ + 3e^- = Au + 3H_2O$; $E = 1.363 - 0.0592\ pH$

(f) $Au^{+3} + 3e^- = Au$; $E = 1.50 + 0.0197 \log [Au^{+3}]$

(g) $Au^+ + e^- = Au$; $E = 1.7 + 0.0592 \log [Au^+]$

(h) $HO_2 + 3H^+ + 3e^- = 2H_2O$; $E = 1.7 - 0.0592\ pH + 0.0197 \log [HO_2]$

(i) $H_2O_2 + 2H^+ + 2e^- = 2H_2O$; $E = 1.77 - 0.0592\ pH + 0.0296 \log [H_2O_2]$

(j) $S_2O_8^{-2} + 2e^- = 2SO_4^{-2}$; $E = 2.01 + 0.0296 \log [S_2O_8^{-2}] - 0.0592 \log [SO_4^{-2}]$

(k) $O_3 + 2H^+ + 2e^- = O_2 + H_2O$; $E = 2.07 - 0.0592\ pH + 0.0296 \log [O_3]/[O_2]$

(l) $OH + H^+ + e^- = H_2O$; $E = 2.8 - 0.0592\ pH + 0.0592 \log [OH]$

* Standard electrode potentials are from Latimer (30), except for reaction (e) (35, 36). Potentials follow the IUPAC-Stockholm sign convention. [ ] denotes activity.

Reactions (a) to (c) are possible cathodic processes which yield products that would depolarize the oxygen evolution reaction at the anode. Of these, H_2O_2 is expected to be the primary depolarizer produced at low currents, hydrogen gas at high currents. The latter tends to be swept out of the solution by oxygen bubbling and has been shown to have no appreciable depolarizing effect at moderate current densities (37). Hydrogen peroxide was detected in the solution, at the end of an η vs. i run, with titanium sulfate reagent; spectrophotometric analysis indicated a concentration of 5×10^{-6}M. The maximum c.d. for H_2O_2 oxidation at the anode, corresponding to this concentration, can be computed from Eq. [5]; thus with $l = 5 \times 10^{-3}$ cm for gas-bubbling conditions (38), $D \approx 10^{-5}$ cm^2 sec^{-1}, and $C_e = 0$, one obtains $f = 1 \times 10^{-11}$ mole cm^{-2} sec^{-1}. This corresponds to a diffusion current density, $i_d = 2\mathbf{F}f$, of 2×10^{-6} amp cm^{-2}, which would result in measurable depolarization at an applied c.d. of 3×10^{-5} amp cm^{-2} or less. Actually the measured H_2O_2 concentration was determined soon after electrolysis at high c.d.; after prolonged electrolysis with gradually decreasing currents the H_2O_2 concentration would be less than the measured value, and the c.d. for observable depolarization would be less than 3×10^{-5} amp cm^{-2}. The typical potential-time curves in Fig. 7 indicated depolarization beginning at 1×10^{-5} amp cm^{-2}, hence this may be attributed to the presence of cathodically produced H_2O_2.

Of the possible simultaneous anodic reactions which could lower the current efficiency, (e) to (l) in Table I, oxide formation (e) and metal dissolution (f) tend to occur at low overpotentials. The rate of the former reaction has already been shown to be insignificant. The metal dissolution rate is expected to be small because of the relatively low solubility of the oxide in dilute acids (30):

$$Au(OH)_3 = Au^{+3} + 3OH^- \quad K = 8.5 \times 10^{-45} \quad [7]$$

This was confirmed in 0.1M H_2SO_4; the average current efficiency for gold dissolution at 10^{-3} amp cm^{-2} over a 24-hr period was found to be 0.007%.

At high values of η water tends to oxidize anodically to H_2O_2 and HO_2 by reactions (i) and (h), but these substances are very unstable with respect to further anodic oxidation, i.e., reactions (a) and (c). Peroxidisulfuric acid can be produced by reaction (j) and ozone by reaction (k); these products have greater stability in the anolyte, as shown by the fact that they can be generated at the anode in large quantities in more concentrated H_2SO_4 solutions (39, 40).

Thermodynamically, either of the latter two products is capable of oxidizing a fresh gold electrode, as indicated by the reactions:

$$2Au + 3H_2S_2O_8 + 6H_2O = 2Au(OH)_3 + 6H_2SO_4, \quad \Delta G^\circ = -90 \text{ kcal} \quad [8]$$

$$2Au + 3O_3 + 3H_2O = 2Au(OH)_3 + 3O_2, \quad \Delta G^\circ = -98 \text{ kcal} \quad [9]$$

where the values of ΔG°, the standard free energy change at 25°C, were calculated from the standard electrode potentials of Table I. Hence one of these substances might have produced the effect shown in Fig. 6, in which a fresh gold electrode in a used solution assumes a potential higher than the reversible oxygen potential and approaching that of the $Au/Au(OH)_3$ electrode. It may be noted that H_2O_2, which accumulated in the solution as found above, would not produce such high potentials (41). Attempts to detect $H_2S_2O_8$ in the solution after prolonged electrolysis, by the use of $Ni(OH)_2$ reagent (sensitivity approximately 5 ppm), were negative. More significantly, it was found that the potential of a clean gold surface in un-electrolyzed 0.1M H_2SO_4 remained constant at about 0.83 v when $K_2S_2O_8$ was added to the solution, even in concentrations as high as 0.002M.

The effect of ozone was determined qualitatively in the following manner. A platinum wire was placed inside a small Pyrex tube through which the purified oxygen gas passed before entering the cell. An induction coil (laboratory leak tester) was used to produce sparking to the platinum wire for a period of 9 min, thus introducing a little ozone into the oxygen gas bubbling around the electrode. At the end of this period the potential of the gold electrode had risen to 1.30 v, which is above the reversible oxygen potential but below the $Au/Au(OH)_3$ potential. Thus oxidation of an appreciable fraction of the gold surface was indicated.

From the above evidence it was concluded that ozone is an anodic by-product at the higher current densities, and is responsible for the marked change in potential behavior of a fresh gold electrode produced by pre-electrolysis of the solution.

IR-drop measurements.—An upper limit to the c.d. range may be imposed by the accuracy with which the *IR* drop included in the overpotential measurement is determined. To calculate the *IR* drop within the solution for a capillary of diameter d positioned at a distance $3d$ from the electrode, Ohm's law in the form $i = -\kappa dV/dn$ was integrated for concentric spheres, from $n = r_o$ to $n = r_o + 3d - d/3$, to give the equation:

$$V_{IR} = (ir_o^2/\kappa)\ [1/r_o - 1/(r_o + 3d - d/3)] \quad [10]$$

This assumes that the potential inside the capillary is equal to that at a distance $d/3$ closer to the electrode in the undistorted field, as was observed for parallel planes (12), a good approximation for concentric spheres with $3d << r_o$. The maximum allowable magnitude of V_{IR} was taken to be 10 mv for experimental error ±1 mv. Substitution of this value into Eq. [10] yields i_{max}, the highest c.d. at which accurate correction can be made for the *IR* drop in the electrolyte. For 0.1M H_2SO_4 ($\kappa = 0.046$) in the cells used ($d = 0.02$, $r_o = 0.50$), one obtains $i_{max} = 1 \times 10^{-2}$ amp cm^{-2}.

In order to determine *IR* drops within the oxide coating, the total *IR* drop included in the measured overpotential was evaluated directly at 10^{-2} amp cm^{-2} in 1.0M H_2SO_4, with an oxide of typical thickness preformed over the anode. The interrupted-current method was used: the electrode was polarized to the steady-state potential, the applied current was switched off by means of a rapid electronic switch, and the anode vs. SCE voltage-decay curve displayed on an oscilloscope.[4] The "instantaneous" voltage decay agreed with that calculated from Eq. [10] within 1 mv. Thus the *IR* drop within the oxide was negligible at 10^{-2} amp cm^{-2}, or at any lower c.d. Similar measurements were not made in 0.1M H_2SO_4, but the same conclusion was drawn from the absence of appreciable deviations from Tafel's equation as described below.

Table II. Overpotential-current density relationship for oxygen evolution at gold anodes in 0.100M H_2SO_4, 25.0°C

Electrode	Cell	Tafel constants a'	Tafel constants b
Plated	I	0.977	0.0461
Plated	II	0.977	0.0450
Solid	II	0.976	0.0445
Solid	II	0.976	0.0447
Mean Tafel line		0.977	0.0450

Concentration changes at the anode surface.—The increase in acid concentration at the anode surface may be estimated from Eq. [5]. At any current density i, $f = (1 - t_+)i/2\mathbf{F}$, where t_+ is the cation transference number. For 0.1M H_2SO_4, $t_+ = 0.82$ (42), $D = 1.9 \times 10^{-5}$ cm^2 sec^{-1} (43), $l = 0.005$ cm (38), and the calculated concentration change at $i_{max} = 0.010$ amp cm^{-2} is $C_e - C_o = 0.002_4$ mole l^{-1}, a change of only 2.4%. Therefore concentration polarization effects were expected to be negligible in these experiments.

Overpotential-current density relationship.—Over the c.d. range for precise measurements as defined above, 3×10^{-5} to 10^{-2} amp cm^{-2}, Tafel's equation was accurately obeyed. The Tafel constants for various runs are given in Table II, and Fig. 8 shows a typical Tafel line. In each run the points obtained with decreasing and then increasing current densities all fell on the line within ±1 mv. Essentially the same Tafel constants were obtained in all runs; substitu-

[4] Tektronix, Inc., Portland, Oreg., type 545 oscilloscope with type 53/54D amplifier.

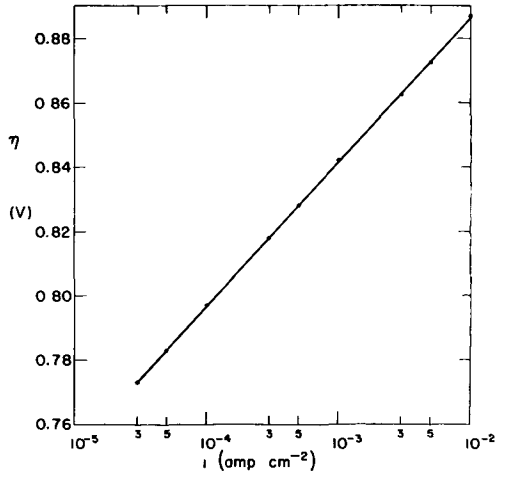

Fig. 8. Typical Tafel plot for oxygen evolution at gold anode in 0.1M H_2SO_4, 25°C.

tion of the slot cell for cell II or of the plated gold electrode for the solid one had no appreciable effect.

The Tafel constants in Table II are based on the apparent surface area; roughness factors were not measured. It was anticipated that the roughness factor for the dull oxide surface on the plated electrode (q_p) would be greater than that (q_s) for the solid electrode (bright oxide surface which reflected clear images). If $q_p = 2q_s$, for example, the effect on the Tafel a constant would be 0.015 v. The fact that no appreciable effect was found indicated that oxide growth on these two surfaces produced the same roughness factor, in spite of the large difference in surface brightness.

The mean value, $b = 0.045$ at 25°C, does not coincide with the predicted value for any mechanism of anodic oxygen evolution given in the compilation of Bockris (1). The exchange current density:

$$i_o = 10^{-(a/b)} = (1/q)\ 10^{-(a'/b)} \qquad [11]$$

has the unusually low value $2 \times 10^{-22}/q$. In addition to the Tafel constants, the measurements required to fix the mechanism of anodic oxygen evolution include the effects of pH and neutral salts on the overpotential. Conclusions concerning the mechanism, therefore, must be deferred to a future paper in which such measurements will be presented.

Manuscript received Oct. 13, 1958. This paper was prepared for delivery before the Ottawa Meeting, Sept. 28-Oct. 2, 1958.

Any discussion of this paper will appear in a Discussion Section to be published in the June 1960 JOURNAL.

REFERENCES

1. J. O'M. Bockris, *J. Chem. Phys.*, **24**, 817 (1956).
2. J. O'M. Bockris, Editor, "Modern Aspects of Electrochemistry," p. 226, Butterworths Publications, Ltd., London (1954).
3. J. O'M. Bockris in "Electrochemical Constants," p. 243, National Bureau Stds. Circular 524 (1953).
4. J. Tafel, *Z. physik. Chem.*, **50**, 641 (1905).
5. J. O'M. Bockris and A. K. M. S. Huq, *Proc. Roy. Soc.*, **A237**, 227 (1956).
6. F. Haber, *Z. physik. Chem.*, **32**, 208 (1900).
7. C. Kasper, *Trans. Electrochem. Soc.*, **77**, 353 (1940).
8. C. Kasper, *ibid.*, **78**, 131 (1940).
9. C. Kasper, *ibid.*, **78**, 147 (1940).
10. C. Wagner, *This Journal*, **98**, 116 (1951).
11. S. Barnartt, *J. Chem. Phys.*, **21**, 2090 (1953).
12. S. Barnartt, *This Journal*, **99**, 549 (1952).
13. R. Piontelli, G. Bianchi, U. Bertocci, C. Guerci, and B. Rivolta, *Z. Elektrochem.*, **58**, 54 (1954).
14. R. Piontelli and G. Bianchi, *Gazz. chim. ital.*, **80**, 581 (1950).
15. R. Aletti, U. Bertocci, G. Bianchi, C. Guerci, R. Piontelli, G. Poli, and G. Serravalle, "Proceedings of the Third Meeting of the International Committee of Electrochemical Thermodynamics and Kinetics," p. 30, Bern (1951).
16. R. Piontelli, G. Bianchi, and R. Aletti, *Z. Elektrochem.*, **56**, 86 (1952).
17. F. P. Bowden and E. K. Rideal, *Proc. Roy. Soc.*, **A120**, 59, 80 (1928).
18. F. P. Bowden and E. A. O'Connor, *ibid.*, **A128**, 317 (1930).
19. J. O'M. Bockris and B. E. Conway, *Trans. Faraday Soc.*, **45**, 989 (1949).
20. A. M. Azzam, J. O'M. Bockris, B. E. Conway, and H. Rosenberg, *ibid.*, **46**, 918 (1950).
21. A. Hickling and W. H. Wilson, *Nature*, **164**, 673 (1949).
22. A. Hickling and S. Hill, *Disc. Faraday Soc.*, **1**, 236 (1947).
23. H. J. S. Sand, *Z. physik. Chem.*, **35**, 641 (1900).
24. H. J. S. Sand, *Phil. Mag.*, **1**, 45 (1901).
25. T. R. Rosebrugh and W. L. Miller, *J. Phys. Chem.*, **14**, 816 (1910).
26. C. W. Tobias, M. Eisenberg, and C. R. Wilke, *This Journal*, **99**, 359C (1952).
27. G. A. Perley, *Trans. Electrochem. Soc.*, **92**, 497 (1947).
28. S. Barnartt, *This Journal*, **98**, 311 (1951).
29. G. Dubpernell in "Modern Electroplating," A. G. Gray, Editor, 2nd ed., p. 145, John Wiley & Sons, Inc., New York (1953).
30. W. M. Latimer, "Oxidation Potentials," 2nd ed., Prentice Hall, New York (1952).
31. J. W. Mellor, "A Comprehensive Treatise on Inorganic and Theoretical Chemistry," Vol. 3, p. 580 (1923).
32. S.E.S. El Wakkad and A. M. Shams El Din, *J. Chem. Soc.*, **1954**, 3098.
33. A. Guinier, "X-ray Crystallographic Technology," Hilger and Watts, London (1952).
34. U. R. Evans, *Trans. Electrochem. Soc.*, **91**, 547 (1947).
35. R. H. Gerke and M. D. Rourke, *J. Am. Chem. Soc.*, **49**, 1855 (1927).
36. T. F. Buehrer and W. E. Roseveare, *ibid.*, **49**, 1989 (1927).
37. A. Rius, J. Llopis, and P. Gandia, *Annales Real Soc. Esp. Fis. Quim.*, **B46**, 225 (1950).
38. C. V. King, *This Journal*, **102**, 193 (1955).
39. J. W. Mellor, "A Comprehensive Treatise on Inorganic and Theoretical Chemistry," **10**, p. 418 (1930).
40. F. Fischer and K. Bendixsohn, *Z. anorg. Chem.*, **61**, 13, 183 (1909).
41. J. O'M. Bockris and L. F. Oldfield, *Trans. Faraday Soc.*, **51**, 249 (1955).
42. W. J. Hamer, *J. Am. Chem. Soc.*, **57**, 662 (1935).
43. E. A. Hollingshead and A. R. Gordon, *J. Chem. Phys.*, **8**, 423 (1940).
44. G. Armstrong, F. R. Himsworth, and J. A. V. Butler, *Proc. Roy. Soc.*, **A143**, 89 (1933).
45. F. Jirsa and O. Buryànek, *Z. Elektrochem.*, **29**, 126 (1923).

Electrokinetic Measurements on Stainless Steel Capillaries

B. Levy and A. R. Fritsch

Radiation & Nucleonics Laboratory, Materials Engineering Departments, Westinghouse Electric Corporation, East Pittsburgh, Pennsylvania

ABSTRACT

Electrokinetic potentials of stainless steel in HCl, H_2SO_4, and $K_2Cr_2O_7$ solutions have been measured by the streaming current technique. Negative zeta potentials are obtained in H_2O and in low acid concentrations. Isoelectric acid concentrations occur between 10^{-4} and $10^{-3}N$. At higher concentrations positive potentials are obtained. $K_2Cr_2O_7$ adsorbs irreversibly at its isoelectric concentration of 10^{-3}M as evidenced by the inability of water washing to return the sample to its original negative zeta potential.

A technique has been developed recently by Hurd and Hackerman (1, 2) making it possible to measure the electrokinetic potentials of bulk metals. Prior to this all quantitative measurements have been made on metal sols (3). The experiments performed by Hurd and Hackerman involved platinum, silver, and gold capillaries and water solutions of KCl and KOH in the concentration range from 10^{-6} to 10^{-2}M. In all cases the electrokinetic potential was found to be negative. The magnitudes of the potentials were explained on the basis of the relative strengths of the metal oxide and the oxide-counter ion bonds, the larger negative potentials being obtained with the metals forming the stronger oxide bonds. In the present study, electrokinetic potentials of types 304 and 347 stainless steel were measured in HCl, H_2SO_4, and $K_2Cr_2O_7$ solutions. The purpose of the work is to determine if changes in the electrical double layer of adsorbed ions, as determined by electrokinetic measurements, can be correlated with such factors as corrosion, corrosion inhibition, and formation of deposits on metal surfaces. This paper is in the nature of a report on the progress that has been made thus far.

Experimental

The technique developed by Hurd and Hackerman was employed in making the measurements. It consists of measuring the streaming current due to liquid flow through a metal capillary. Unless special precautions are taken, part of this streaming current will flow through the walls of the capillary, thus obscuring the results. In order to eliminate this difficulty an external shunting resistor is placed in series with a pair of Pt electrodes located close to, but not touching, the ends of the metal capillary. It has been shown by Hurd and Hackerman that, if the outside walls of the capillary are isolated from the solution, then the "apparent" resistance of the Pt, Au, and Ag capillaries is large compared to an external resistor ranging from 10^4 to 10^5 or 10^6 ohms. This effect has been verified for the stainless steel capillaries in the present study and is probably due to polarization at the ends of the capillary (Table I, sample 4).

A L&N No. 9835 D-C microvolt amplifier and Varian G-10 recorder are used to measure the voltage drop across this resistor, thus making it possible to calculate the streaming current and thereby the zeta potential from the following equation:

$$I = \frac{\Delta P r^2 D \zeta}{4 \eta l}$$

where I is streaming current, statamp; ΔP the pressure drop across the capillary, dynes/cm^2; ζ the zeta potential, statvolts; η the viscosity, poises; D the dielectric constant of the solution; r the radius of the capillary, cm; and l the length of the capillary, cm.

A check on the operation of the equipment is shown in Fig. 1, where the voltage drop across a 40-k external resistor is plotted against the pressure drop (ΔP).

All of the solutions used in the experiments were prepared from reagent grade chemicals using singly distilled water. The steel capillaries were used as received or treated with acetone, boiling NaOH, and HNO_3. The results were similar qualitatively regardless of pretreatment as is seen in Table I, samples 1-4.

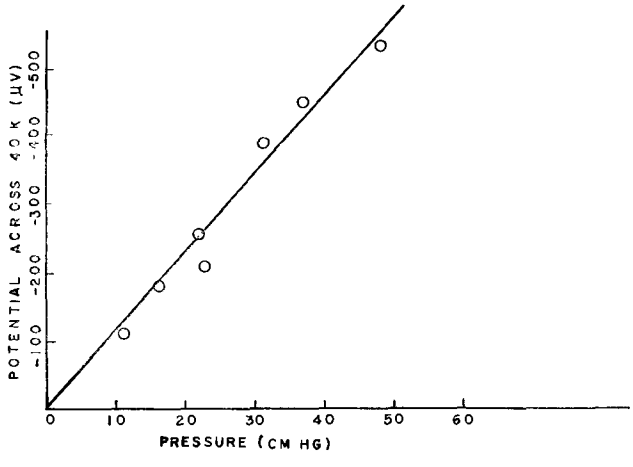

Fig. 1. Potential vs. pressure across 40 K external resistor, sample 2; type 304 stainless steel; r = 1.46 x 10^{-2} cm; l = 2.54 cm, solution H_2O.

Table I. Zeta potential of type 304 stainless steel in H_2SO_4 solutions

Sample 1. l = 2.22 cm, r = 1.40 x 10^{-2} cm, external resistor = 40 K

Solution	Zeta potential, mv
H_2O	−12.8
$10^{-6}N$ H_2SO_4	−4.32
$10^{-5}N$ H_2SO_4	−2.27
$10^{-4}N$ H_2SO_4	−0.27
$10^{-3}N$ H_2SO_4	+13.2
$10^{-2}N$ H_2SO_4	+84.0

Sample 2. l = 2.54 cm, r = 1.46 x 10^{-2} cm, external resistor = 40 K

Solution	Zeta potential, mv
H_2O	−88.0
$10^{-5}N$ H_2SO_4	−28.1
	−25.8
Avg	−27.0
$10^{-4}N$ H_2SO_4	−0
$10^{-3}N$ H_2SO_4	+31.7
	+54.5
Avg	+43.1
$10^{-2}N$ H_2SO_4	+37.2
$10^{-1}N$ H_2SO_4	+24.9

Sample 3. l = 3.60 cm, r = 1.60 x 10^{-2} cm, external resistor = 20 K

Pretreatment: acetone, NaOH, HNO_3 (each reagent was followed by ½-hr refluxing with H_2O in a Soxhelet extractor)

Solution	Zeta potential, mv
H_2O	−64.1
	−64.4
	−69.2
	−65.3
	−56.5
	−63.8
Avg	−63.9
$10^{-5}N$ H_2SO_4	−32.5
	−29.6
	−34.0
	−35.4
	−33.9
Avg	−33.1
$10^{-4}N$ H_2SO_4	−17.3
	−11.1
	−7.58
	−9.61
Avg	−11.4
$10^{-3}N$ H_2SO_4	+38.0
	+41.4
Avg	+39.7
$10^{-2}N$ H_2SO_4	+128
	+143
	+140
Avg	+137

Sample 4. l = 3.54 cm, r = 1.64 x 10^{-2} cm

Pretreatment: ½-hr acetone followed by ½-hr H_2O

Concentration	Zeta potential, mv external resistor = 10^4 Ω	Zeta potential, mv external resistor = 10^5 Ω	Zeta potential, mv external resistor = 10^6 Ω
H_2O	−75.3	−71.8	−70.1
	−61.9	−67.1	−67.1
	−64.5	−62.1	−61.9
	−56.5	−46.4	−46.4
	−49.7	−50.8	−47.6
	−42.6	−46.9	−46.0
Avg	−58.4	Avg −57.5	Avg −56.5
$10^{-6}N$ H_2SO_4	−42.3	−42.8	−43.1
	−35.3	−30.2	−30.8
	−43.1	−29.8	−48.1
	−42.8	−46.0	−45.7
	−55.4	−42.8	−30.1
	−46.6	−28.4	−57.2
	−42.3	−43.8	−38.3
		−43.8	−42.4
		−42.3	−42.6
			−31.7
Avg	−44.0	Avg −38.9	Avg −41.0
$10^{-5}N$ H_2SO_4	−30.0	−22.6	−28.4
	−27.0	−20.9	−24.6
		−25.9	−23.2
		−28.3	−26.5
		−25.1	−28.2
		−26.7	−25.8
Avg	−28.5	Avg −24.9	Avg −26.1
$10^{-4}N$ H_2SO_4	Both positive and negative values		
$10^{-3}N$ H_2SO_4	Both positive and negative values		
H_2O	−44.8	−45.6	−46.0
	−54.8	−49.1	−47.7
	−16.5	−25.6	−23.6
Avg	−38.7	Avg −40.1	Avg −39.1
$10^{-2}N$ H_2SO_4	+393	+401	
	+394	+394	
Avg	+394	Avg +398	

Results and Discussion

Table I lists the results, in the order performed, on type 304 stainless steel capillaries as a function of H_2SO_4 concentration. As is seen, the agreement between the samples is not too good except insofar as the isoelectric point is concerned. This occurs at a concentration close to $10^{-4}N$ H_2SO_4. The lack of quantitative agreement is probably not too surprising. Since the zeta potential of the metal is apparently that of an oxide layer, differences in the nature and extent of oxide film buildup will affect the magnitude of the zeta potential but may not affect the isoelectric point.[1] The transformation from a negative to a positive zeta potential may provide a sensitive indication of the first signs of metal corrosion.

If Grahame's model (4) for the electrical double layer is assumed, the situation at the metal-H_2O interface may be pictured schematically as in Fig. 2. The zeta potential is, by definition, the potential at the surface of shear of the double layer as compared to that of the solution. This surface of shear is generally assumed to coincide with the boundary between the outer Helmholtz layer and the diffuse layer. The sign of the zeta potential is determined by the excess charge in the combined inner and outer Helmholtz layer. Experimentally, type 304 stainless steel has a negative zeta potential in H_2O. Therefore, Fig. 1 shows an excess of OH^- ions in the Helmholtz layer located at sites adjacent to metal atoms. The oxygen atoms would appear to be ideal sites for the adsorption of protons. Perhaps the reason that stainless steel does not have a positive

[1] Suggested by one of the reviewers of this paper.

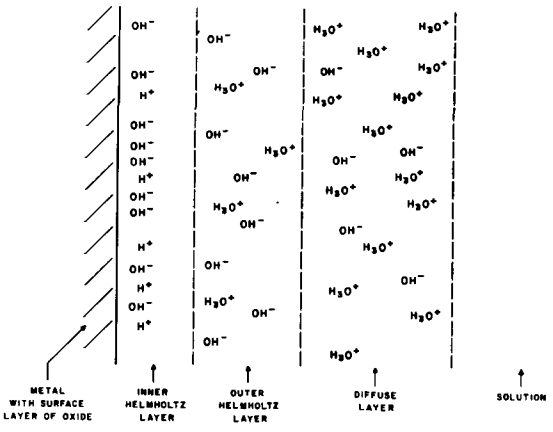

Fig. 2. Structure of the electrical double layer

zeta potential in water is the relatively high dehydration energy that must be supplied in order for the protons to enter the inner Helmholtz layer as compared to the similar process with OH^- ions. As H_2SO_4 is added to the solution there are fewer OH^- ions in the solution and correspondingly more H_3O^+ ions. This leads to a decrease in negative potential due to: (*a*) a decrease in the number of OH^- ions available for adsorption in the inner Helmholtz layer, (*b*) adsorption of protons at oxygen sites, and (c) partial decomposition of the oxide by protons accompanied by the formation and adsorption of positively charged metal ions.

These processes proceed with continued increase in acid concentration until a point is reached where there are an equal number of positive and negative ions in the Helmholtz layer. Further addition of acid causes the zeta potential to become positive.

In Table II the results are given for type 304 stainless steel in HCl solutions. Once again the zeta potential changes from negative to positive with increased HCl concentration. The isoelectric point occurs between 10^{-4} and $10^{-3}N$ HCl. Potentials with HCl were found to be more erratic than with H_2SO_4 solutions, possibly due to the ability of the Cl^- ions to penetrate the surface film which in turn may

Table II. Zeta potential of type 304 stainless steel in HCl solutions

Sample 5. l = 3.19 cm, r = 2.56 x 10^{-2} cm, external resistor = 40 K

Solution	Zeta potential, mv
H_2O	−15.2
	−13.2
	−18.6
	−6.98
	−14.0
	Avg −13.6
$10^{-5}N$ HCl	−9.79
	−11.2
	−12.2
	Avg −11.1
$10^{-4}N$ HCl	+8.93
	+7.64
	+12.6
	Avg +9.72
H_2O	−24.0
	−21.1
	Avg −22.6
$10^{-3}N$ HCl	+48.8
	+58.4
	+55.3
	Avg +54.2
H_2O	−37.0
	−45.5
	Avg −41.3
$10^{-2}N$ HCl	Values ranged from +4.9 to +146
H_2O	−30.0
	−29.5
	Avg −29.8
$10^{-1}N$ HCl	Avg +239
	Values ranged from +166 to +392
H_2O	−35.0

Table III. Zeta potential of type 347 stainless steel in H_2SO_4 solutions

Sample 6. l = 3.30 cm, r = 3.94 x 10^{-2} cm, external resistor = 10 K

Solution	Zeta potential, mv		
H_2O	−102		
	−98.0		
	−96.8		
	Avg −98.9		
$10^{-5}N$ H_2SO_4	−58.1		
	−63.8		
	−68.9		
	−68.9		
	−69.4		
	Avg −65.8		
$10^{-4}N$ H_2SO_4	−41.3		
	−40.2		
	−41.3		
	−44.9		
	−45.2		
	Avg −42.6		
$10^{-3}N$ H_2SO_4	+15.7		
	+16.6		
	+16.6		
	+14.1		
	+15.6		
	+19.8		
	+15.2		
	+19.5		
	Avg +16.6		
H_2O	−54.3		−89.6
	−49.7		−77.8
	−53.0		−87.3
	−53.0	after stand-	−71.5
	−51.3	ing over	−61.0
	Avg −51.5	weekend	−82.2
			−83.6
			−82.4
		Avg	−79.4
$10^{-3}N$ H_2SO_4	+6.2		
$10^{-2}N$ H_2SO_4	Very slightly positive, same result after standing overnight		
H_2O	−133		
	−149		
	−148		
	−186		
	−151		
	−108		
	Avg −146		
$10^{-1}N$	Erratic		

give rise to active corrosion. These special properties of Cl^- ions are evidenced by their ability to cause stress corrosion cracking (5).

Tables III and IV give the results for type 347 stainless steel in H_2SO_4 and HCl solutions, respectively. In H_2SO_4 the isoelectric point occurs between 10^{-4} and $10^{-3}N$. In HCl it is probably closer to $10^{-3}N$. For both solutions the results are somewhat more erratic than with the type 304 stainless steel.

The effects of the acid on the metal surface do not appear to be permanent since the shift to positive potentials with high acid concentration can be reversed easily to negative values by flowing H_2O through the capillary in most instances. This offers support to the generally accepted view that an oxide layer is formed quickly on clean metal surfaces (6), if it is assumed that the acid treatment completely dissolved the oxide layer.

Table V gives the results of a series of experiments that have been run with type 304 stainless steel in $K_2Cr_2O_7$ solutions. The zeta potential was found to be negative in concentrations from 10^{-5} to 10^{-4}M. At 10^{-3}M $K_2Cr_2O_7$ and above, the potentials obtained appear to become insensitive to pressure changes and alternate erratically between low positive and low negative values. Powers and Hackerman (7) have demonstrated by tracer techniques that S.A.E. 1020 steel forms distinct anodic and cathodic areas, accompanied by the deposition of a nonadherent film, in 10^{-4}M Na_2CrO_4. They find that at concentrations of 10^{-3}M Na_2CrO_4 the steel is passivated, and chromate is deposited uniformly on the steel surface and cannot be removed by any physically nondestructive means. King, Goldschmidt, and Mayer (8) have demonstrated a significant decrease in the corrosion rate of iron in 10^{-3}M $K_2Cr_2O_7$ as compared to that found at lower concentrations. The results of the zeta potential determinations in $K_2Cr_2O_7$ at concentrations greater than 10^{-4}M may be the result of the masking, by polarization, of anodic and cathodic areas. Measurements were made with a fresh sample of type 304 stainless steel at successively higher concentrations of $K_2Cr_2O_7$. At 10^{-3}M $K_2Cr_2O_7$ the zeta potential becomes zero. The apparatus was then rinsed with distilled water and a determination made using the same capillary in H_2O. The sample remained at the isoelectric point. Previous measurements showed that there was no apparent permanent change in the behavior of the metal when treated with HCl and H_2SO_4 solutions. Evidently there is a very strong irreversible attachment of the Cr_2O_7 equal to the steel surface, in agreement with the data of Powers and Hackerman. To test this point still further, a new sample of type 304 stainless steel was treated first with H_2O, then 10^{-3}M $K_2Cr_2O_7$, and finally with H_2O. Once again the 10^{-3}M solution caused the zeta potential to go to zero and remain there after treatment with H_2O. Still another series of experiments were performed with a new sample of stainless steel. The order of the experiments consisted of runs with H_2O, 10^{-4}M $K_2Cr_2O_7$, and H_2O. The zeta potential remained negative in the 10^{-4}M $K_2Cr_2O_7$ solution.

Table IV. Zeta potential of type 347 stainless steel in HCl solutions

Sample 7. l = 3.32 cm, r = 1.20 x 10^{-2} cm, external resistor = 10 K

Solution	Zeta potential, mv
H_2O	−86.6
	−86.6
	−95.5
	−116
	−92.0
	Avg −95.3
$10^{-6}N$ HCl	−131
	−115
	−169
	Avg −138
$10^{-5}N$ HCl	Erratic results
H_2O	−84.4
	−94.7
	−82.9
	−105
	−105
	Avg −94.4
$10^{-5}N$ HCl	−69.2
	−81.9
	−71.9
	−67.8
	Avg −72.7
$10^{-4}N$ HCl	−11.7
	−12.5
	Avg −12.1
$10^{-3}N$ HCl	+0.42
$10^{-2}N$ HCl	+106 followed by erratic results
H_2O	−106
	−104
	−76.1
	−139
	−109
	−73.4
	Avg −101
10^{-1}N HCl	+2060 then erratic, no change in potential with change in direction or flow rate
H_2O	No response to direction or rate of flow

Gatos (9) has measured the supression of the polarographic maxima by corrosion inhibitors in systems containing either dissolved O_2, Ni^{++}, or Pb^{++}. At cathodic potentials lower than those at which the polarographic maxima occur, the dropping mercury electrode is assumed to be nonpolarized. When the potential of the polarographic maxima is reached and at higher potentials where the diffusion current is the controlling factor, the dropping mercury electrode is generally considered to be polarized. Enhanced corrosion inhibition is often considered to be due to polarization of the metal by the inhibitor. Gatos has shown a distinct correlation between the supression of the polarographic maxima and corrosion inhibition, and thereby has given strong support to the theory of corrosion inhibition by adsorption of polarizing substances. He has pointed out that,". . . capillary active anions and negative colloids in general preferentially suppress (polarographic) maxima appearing on the positive side of the electrocapillary zero (positive maximum)

Table V. Zeta potential of type 304 stainless steel in $K_2Cr_2O_7$ solutions

Sample 8. l = 3.20 cm, r = 1.48 x 10^{-2} cm, external resistor = 20 K

Solution	Zeta potential, mv
H_2O	−38.6
	−38.1
	−36.6
	Avg −37.8
	After standing over weekend
	−13.5
	−4.33
	−9.81
	−14.1
	−13.4
	−12.6
	−13.8
	−15.0
	−16.0
	−16.5
	Avg −12.9
10^{-5}M $K_2Cr_2O_7$	−19.3
	−16.5
	−19.3
	−17.8
	−17.5
	−16.0
	−16.4
	Avg −17.5
10^{-4}M $K_2Cr_2O_7$	−12.5
	−11.9
	−13.0
	−12.0
	−13.0
	Avg −12.5
10^{-3}M $K_2Cr_2O_7$	+ and − values finally zero
10^{-2}M $K_2Cr_2O_7$	+ and − values finally zero
10^{-1}M $K_2Cr_2O_7$	+ and − values finally zero

Sample 9. l = 3.54 cm, r = 1.59 x 10^{-2} cm, external resistor = 20 K

Solution	Zeta potential, mv
H_2O	−46.9
	−48.0
	−42.3
	−45.9
	−49.2
	−45.9
	Avg −46.4
10^{-5}M $K_2Cr_2O_7$	−47.3
	−47.3
	−42.6
	Avg −45.7
10^{-4}M $K_2Cr_2O_7$	−33.8
	−37.7
	−31.6
	−24.7
	Avg −32.0
10^{-3}M $K_2Cr_2O_7$	+ and − values finally zero
H_2O	+ and − values finally zero

Sample 10. l = 3.69 cm, r = 1.64 x 10^{-2} cm, external resistor = 20 K

Solution	Zeta potential, mv
H_2O	−24.6
	−20.6
	−22.2
	Avg −22.5
10^{-3}M $K_2Cr_2O_7$	First — finally zero
H_2O	Zero

Sample 11. l = 3.68 cm, r = 1.57 x 10^{-2} cm, external resistor = 20 K

Solution	Zeta potential, mv
H_2O	−47.3
	−40.6
	Avg −44.0
10^{-4}M $K_2Cr_2O_7$	−24.8
	−22.7
	Avg −23.8
H_2O	−61.6

whereas capillary-active cations and positive colloids are effective with the negative (electrocapillary) maxima."

The electrokinetic data with $K_2Cr_2O_7$ solutions bear a certain similarity with that of Gatos in that both are concerned with the electrical double layer of adsorbed material at the metal-solution interface. When a concentration is reached at which the isoelectric point is observed in the streaming current experiments, the nature of the metal-solution interface must be similar to that which occurs at the electrocapillary maxima with the dropping Hg electrode, since both correspond to a net zero charge of adsorbed ions at the surface. It may therefore be assumed in the electrokinetic studies that the metal is polarized at the isoelectric point and thereby passivated. As Gatos has pointed out, the polarographic technique for screening corrosion inhibitors is nonspecific in that a substance which is effective in suppressing the polarographic maxima may prove to be a good inhibitor for one substance and be a poor one for another. The electrokinetic technique makes it possible to run tests on the material of immediate interest and to correlate the results with corrosion data on systems containing the identical type of metal, corrosion solution and inhibitor.

Summary

1. The zeta potentials of type 304 and type 347 stainless steel were measured in H_2SO_4 and HCl solutions in the concentration range of from 10^{-6} to $10^{-1}N$. Steel samples go through the isoelectric point at concentrations between 10^{-4} and $10^{-3}N$.

2. The irreversible adsorption of 10^{-3}M $K_2Cr_2O_7$ was demonstrated by electrokinetic measurements and found to be in agreement with the data in the literature.

Acknowledgment

The authors wish to express their sincere appreciation to Drs. W. E. Wallace, K. H. Sun, G. R. Taylor, and D. G. Gardner for their many helpful discussions and suggestions, and also to the Pennsylvania Advanced Reactor Project jointly sponsored by Westinghouse Electric Corp. and Pennsylvania Power and Light Co. for supporting the work.

Manuscript received Aug. 1, 1958. This paper was prepared for delivery before the New York Meeting, April 27-May 1, 1958.

Any discussion of this paper will appear in a Discussion Section to be published in the June 1960 JOURNAL.

REFERENCES

1. R. M. Hurd and N. Hackerman, *This Journal*, **102**, 594 (1955).
2. R. M. Hurd and N. Hackerman, *ibid.*, **103**, 316 (1956).
3. H. R. Kruyt, "Colloid Science," Vol. 1 pp. 168-170, 208-209, 233, Elsevier Publishing Co., New York (1952).
4. D. C. Grahame, *Chem. Rev.*, **41**, 441 (1947).
5. See, for example T. P. Hoar and J. G. Hines, *J. Iron Steel Inst.*, **182**, 124 (1956).
6. H. A. Smith and K. A. Allen, *J. Phys. Chem.*, **58**, 449 (1954).
7. R. A. Powers and N. Hackerman, *This Journal*, **100**, 314 (1953).
8. C. V. King, E. Goldschmidt, and N. Mayer, *ibid.*, **99**, 423 (1952).
9. H. C. Gatos, *ibid.*, **101**, 433 (1954).

Brief Communications

Electron Diffraction of Zinc Silicate Phosphor

S. Yamaguchi

The Institute of Physical & Chemical Research, 31 Kamifuji (Hongo), Tokyo, Japan

A commercial sample of zinc silicate phosphor (Zn_2SiO_4:Mn), in powder form and of unknown history, was studied by electron diffraction using two different wave lengths (0.029 and 0.0455Å) (1). Electrons accelerated to 150 kv or more can penetrate thick grains to a depth of about 3000Å, whereas soft electrons at about 50 kv can only graze their surfaces. The thickness of the surface layer which can be penetrated by the latter electrons is about 200Å. The diffraction patterns observed at the same spot of the sample with the soft and hard electrons are shown in Fig. 1 and 2, respectively. For convenience in comparing these two figures, the negatives were enlarged 2.3 and 3.7 times, respectively. This is the approximate ratio of ring diameter at the two wave lengths.

Estimation of grain size.—A phosphor of practical use is as a rule granular, and it is of significance to estimate the grain size. A discontinuous diffraction ring [for the interplanar spacing 4.04Å, the (300) diffraction from the hexagonal pseudocell of Zn_2SiO_4 (2)] found in Fig. 2 was utilized for a rough estimation of the grain size. In this ring we can count about 80 spots diffracted from individual crystallites. The cross section of the incident beam used was about 0.05 mm. If we assume that the diffraction spots (4.04Å) correspond to sixfold symmetry of each crystal, we obtain the grain size of the sample

$$S = \frac{50}{80/6} = 4\mu$$

Diffraction intensity.—In comparing the figures we recognize that the intensity of certain diffraction spots found in Fig. 1 is distinctly stronger than that of the corresponding spots in Fig. 2. This implies that on the surfaces of the phosphor grains there

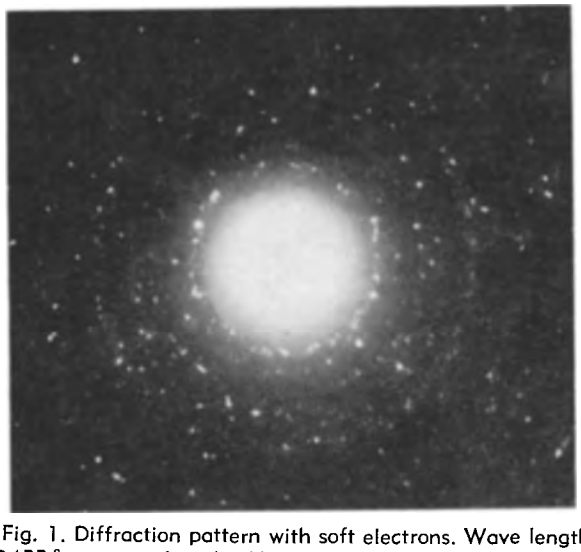

Fig. 1. Diffraction pattern with soft electrons. Wave length, 0.0455Å; camera length, 495 mm; positive enlarged 2.3X.

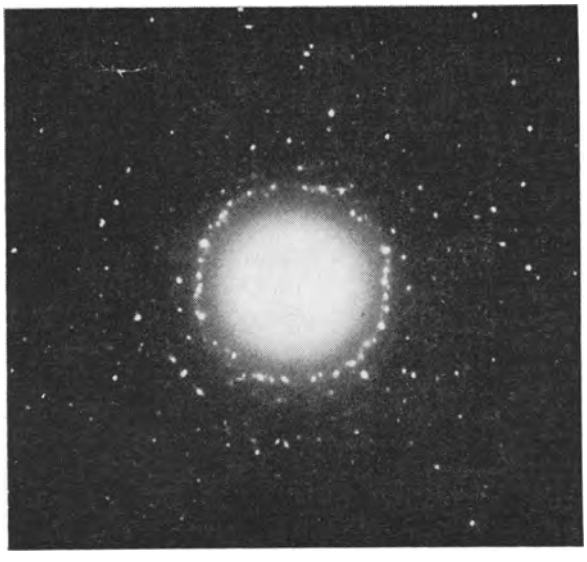

Fig. 2. Diffraction pattern with hard electrons. Wave length, 0.0290Å; positive enlarged 3.7X.

are lattices which are not only distinguishable from those of the substrate, but also are suitable for diffracting soft electrons. The number of diffraction spots found in Fig. 1 is roughly proportional to the number of crystallites able to diffract the soft electrons. Since the electrons used for a television screen are rather slow (about 10 kv), the diffraction phenomenon taking place on this screen is quite similar to that in Fig. 1. An important problem to be studied in the future, is whether electroluminescence depends on the coherent scattering of the incident electrons or not.

Manuscript received March 2, 1959.

Any discussion of this paper will appear in a Discussion Section to be published in the June 1960 JOURNAL.

REFERENCES

1. S. Yamaguchi, *J. Chem. Phys.*, **27**, 1114 (1957).
2. R. W. G. Wyckoff, "Crystal Structures," Vol. II, Chap. VIII, p. 57, Interscience Publishers, Inc., New York (1951).

Influence of Crystallographic Orientation on the Pitting of Iron in Distilled Water

Jerome Kruger

National Bureau of Standards, Washington, D. C.

A review paper by Greene and Fontana (1) indicates that pitting is random with respect to surface structure. Recent work in our laboratory indicates, however, that this is not true for pit formation on iron in distilled water. Initially this work was carried out with an Armco iron single-crystal sphere ⅜-in. in diameter which had flat surfaces cut parallel to the {111}, {110}, and {100} planes. These surfaces were prepared by mechanical polishing prior to chemical polishing using MirroFe[1] solution. When the crystal thus prepared was immersed for 3 hr in distilled water at room temperature, it was observed that the {110} plane had the greatest number of pits per unit area. The {100} had approximately one-half as many pits as the {110}, and the {111} had only around one-quarter as many as the {110}. The number and location of pits was not always the same for a given time interval of immersion. The order of pitting activity, {110}> {100}>{111}, however, remained the same in every one of the seven runs carried out. Figure 1 illustrates this order of activity on the three different planes cut on the same iron crystal.

In order to see if the use of MirroFe for polishing was responsible for the effect observed, the surfaces after mechanical polishing were etched with a dilute solution of HCl prior to carrying out a run. The results were the same as for the surfaces polished with MirroFe. The effect of orientation of the corroding surface, horizontal or vertical, was also checked, and again the same order of pitting activity was observed for the crystallographic planes studied.

[1] Manufactured by MacDermid Inc., Waterbury, Conn.

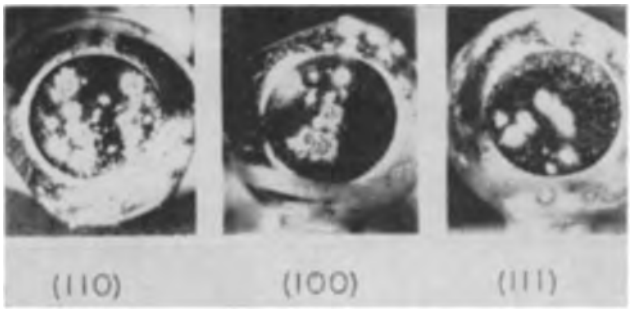

Fig. 1. Three different crystallographic planes of an iron single crystal corroded in distilled water for 3 hr at 25°C. 2.5X.

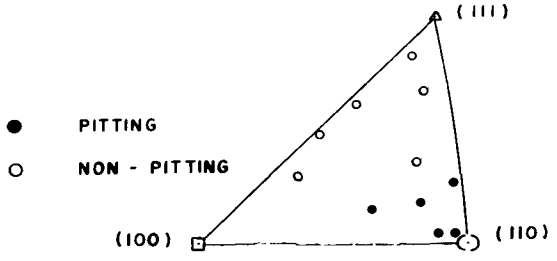

Fig. 2. Stereographic triangle showing pitting on grains of iron having different crystallographic orientations.

Other studies were carried out using a purer iron than Armco (235 ppm of impurities to 2460 ppm for Armco). Here a specimen containing large grains of many different surface orientations were used. As Fig. 2 shows, all those grains whose orientations were near that of the {110} crystallographic plane pitted every time or every time but one, while those which were nearer the {111} or {100} orientations pitted only once or not at all during the course of five runs.

As with the Armco iron, those surfaces having an orientation nearer the {110} exhibited the greatest amount of pitting. Irrespective of crystallographic orientation, the general level of pitting attack was lower for the purer iron.

Acknowledgment

The author is indebted to R. S. Smethurst, Jr., who carried out some of the experimental work and to the Corrosion Research Council who supported this work in part.

Manuscript received April 22, 1959.

Any discussion of this paper will appear in a Discussion Section to be published in the June 1960 JOURNAL.

REFERENCE

1. N. D. Greene and M. G. Fontana, *Corrosion*, **15**, 41 (1959).

Titanium and Zirconium As Primary Cell Anodes

Milton A. Thompson, Allen B. Scott, Donald Chittick, and Paul M. Gruzensky

Department of Chemistry, Oregon State College, Corvallis, Oregon

ABSTRACT

Polarization, chemical corrosion rates, and the anodic electrochemical equivalence for titanium and zirconium were measured in several electrolytes, chiefly fluoride solutions. Titanium exhibited satisfactory electrode characteristics in dilute HF, containing added NH_4F, except for somewhat excessive chemical corrosion. Zirconium was corroded severely by fluoride solutions in which its electrode characteristics were otherwise satisfactory and was somewhat less suitable as an electrode in H_2SO_4 solutions in which chemical corrosion was not serious. The Ti-HF, NH_4F-MnO_2 cell operated stably during discharge with good anode utilization but is probably limited to use as a reserve cell chiefly because of the deleterious effects of fluoride upon the MnO_2 electrode.

The experiments described in this paper were undertaken in order to determine the suitability of titanium and zirconium as negative electrodes in primary cells. Both metals are characterized by large negative electrode potential, corrosion resistance in many electrolytes, galvanic corrodibility in some of these solutions, and relatively low equivalent weight and equivalent volume. On the other hand, both may be rendered passive by oxide films when anodized under certain conditions. While the cost of the metals is still high compared to that of zinc, magnesium, and aluminum, it is decreasing rapidly and continually, and even now an amount of Ti electrochemically equivalent to the Zn contained in a flashlight D cell costs only 4.5 cents.

Electrochemical data for Ti and Zr are given in Table I; data for Zn are also given as a comparison.

Considerable information is available concerning the corrodibility of Ti and Zr in the more common electrolytes (3). Both metals are highly resistant to corrosion under a variety of conditions; however, Ti is attacked by H_2SO_4 above 5% concentration, HCl above 5%, H_3PO_4 above 30%, certain organic acids and HF at all concentrations. Zirconium is corroded by H_2SO_4 above 80%, $FeCl_3$ and $CuCl_2$ solutions, and HF at all concentrations. Straumanis and Gill (4) reported that the addition of NH_4F increased the dissolution rate of Ti in HCl and H_2SO_4 up to a concentration of 4M NH_4F, above which the metal was rendered practically passive. In HF, the effect of NH_4F was to reduce the dissolution rate at all NH F concentrations.

Table I. Comparison of Ti, Zr, and Zn as anode materials

	Ti	Zr	Zn
Eq. wt[a]	11.97	22.8	32.69
Eq. vol, cm^3	2.66	3.50	4.59
Amp min/g	134.	70.6	49.4
Cost (1), \$/lb	2.05	7.50	0.10
Standard oxidation potential,[b] (2) v	1.19	1.53	0.76

[a] Based on oxidation to tetravalent Ti and Zr.
[b] For couples: $Ti\text{-}TiF_6^{--}$, $Zr\text{-}ZrO^{++}$, and $Zn\text{-}Zn^{++}$, respectively.

Schlain and co-workers (5) studied galvanic corrosion of Ti and Zr. When coupled with several other metals in a variety of electrolytes, both were usually cathodic; however, Ti was anodic to stainless steel in H_2SO_4 and to Al after several days in a deaerated H_2SO_4 solution.

Several studies of electrode potentials of Ti and Zr have been reported. Botts and Krauskopf (6) and more recently Sato and Yamane (7) attempted to obtain the standard electrode potential of Ti in $Ti_2(SO_4)_3$ solutions. The values obtained, e.g., −0.355 v in the latter experiment, were far different from the value −1.30 v calculated from thermodynamic data (2), showing that the electrode was not reversible. Other experiments (5, 8) generally support the conclusion that potentials of these electrodes in many electrolytes are variable with time, sensitive to degree of aeration, and that the electrodes are highly irreversible. Straumanis and Chen (8) found that the Ti electrode potential in HF becomes more negative with increasing HF concentration up to 0.20*N*, beyond which it was constant at −0.768 v. Addition of NH_4F resulted in a potential of −0.95 v.

Anodic polarization and oxide film growth during anodization of Ti and Zr have been extensively investigated (9). Passivity is usually attributed to a layer of TiO_2 or ZrO_2.

The only application of either Ti or Zr in a primary cell, to our knowledge, involves a positive electrode of porous Ti coated with depolarizer (10). Schlain (5) obtained a current as high as 11 ma from a Mg-Ti couple in which Ti was cathodic.

In the course of this investigation the following quantities were determined: (*a*) electrode potentials for Ti and Zr as a function of anodic current density in a variety of electrolytes; (*b*) average charge of the ion produced by the anode reaction in several electrolytes and at several current densities; (c) characteristics of more than a hundred primary cells having either a Ti or Zr anode and either a Pb-PbO_2 or C-MnO_2 cathode.

Experimental

Titanium sheet,[1] 0.25 mm thick, was cut to the desired size and polished with emery paper for use as electrodes. Titanium tubing,[2] 3.17 cm O.D., was used for the construction of dry cells. Zirconium sheet, 0.25 mm thick, was either Iodide Process[3] or Kroll Process.[4] No significant differences were observed in the behavior of the two types of Zr. All reagents were C.P. or Analytical Reagent grade.

Single electrode potentials were measured by means of a L&N Type K potentiometer. Cell voltages were measured either potentiometrically or by means of a vacuum-tube voltmeter. Current densities were computed from the measured area of electrodes without application of a roughness factor. The electrode area was regulated by coating the entire electrode with paraffin and cleaning off the desired area on one side of the electrode, finally polishing the exposed area with emery paper.

C-MnO_2 electrodes were of the commercial D-cell type.[5]

In order to select an electrolyte and a usable cathode for detailed tests, the behavior of Ti and Zr coupled to other electrodes in about 40 electrolytes was studied. The open-circuit voltage and the voltage of the couples connected by a 12-ohm resistor were measured. The electrolytes were principally solutions of H_3PO_4, HF, H_2SO_4, $FeCl_3$, NH_4F, and combinations of these. The other electrodes were Cu, Al, Pb, stainless steel, and MnO_2. Most of the couples exhibited either a low open-circuit voltage or severe polarization under load; however, Ti coupled with the MnO_2 electrode in 1*N* HF gave 1.37 v open circuit and 0.600 v under load. A Zr-MnO_2 couple, with 0.1*N* HF, gave 1.60 v open circuit and 0.89 v under load. The highest current drawn was 75 ma, using an anode area of 2 cm^2.

It is evident that acid fluoride solutions are the most effective in reducing polarization under load in the case of both Ti and Zr. The C-MnO_2 electrode, although undoubtedly adversely affected by fluoride, was selected for detailed investigation because of the high voltage observed when coupled with Ti and Zr in many different acid fluoride solutions.

Polarization Measurements

Titanium or zirconium was made the anode in electrolytes composed chiefly of HF, NH_4F, KCl, and in some cases H_2SO_4. The single electrode potential was measured by means of a reference normal calomel electrode, as a function of current density. The single electrode potentials of replications agreed within 1% at current densities less than 1 ma cm^{-2} and within 5% at the highest current densities. Representative curves are presented in Fig. 1 and 2. Potentials are taken with respect to the standard hydrogen electrode.

In the case of Ti (Fig. 1), as the current density was increased, a point was attained at which the electrode potential suddenly became strongly positive. The current density at which this occurred is indicated by the broken vertical portion of the polarization curve, and electrodes which have undergone the sudden positive change in potential will be referred to as passive. In this condition, oxygen is evolved and the electrode is presumably covered by a protective film. The current density for passivation, i_p, was not very reproducible, even though the electrode potentials prior to passivation were quite so. This arose from the fact that i_p depended markedly on the rate at which the current was increased. The curves were selected to show typical passivity behavior.

Zirconium electrodes generally showed less tendency to become passive. However, in solutions containing only HF, or dilute mixed solutions of HF and NH_4F, i_p was lower for Zr than for Ti, as shown in Fig. 2. NH_4F was very effective in eliminating passivation of Zr, even in the absence of HF.

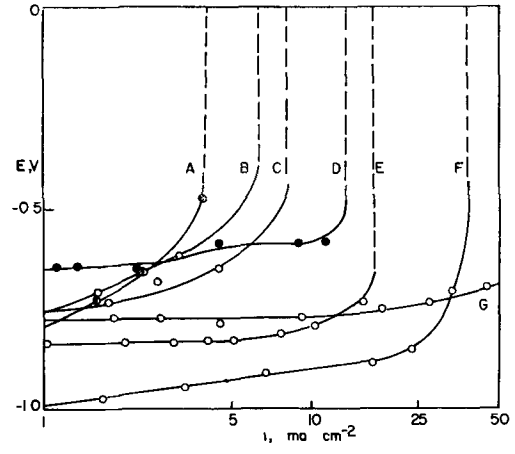

Fig. 1. Polarization and passivation of Ti in fluoride solutions. Curve A, 0.05N HF; B, 0.075N HF; C, 0.1N HF; D, 1N HF, 20% NH_4F; E, 0.2N HF; F, 0.075N HF, 0.1N KCl, 6% NH_4F; G, 1N HF. i_p for 1N HF was 110 ma cm^{-2}.

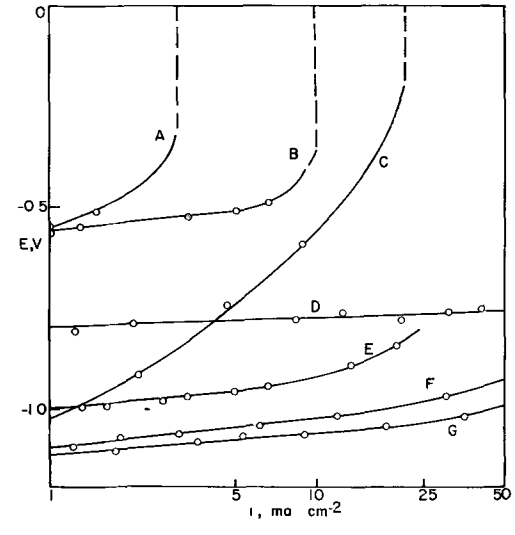

Fig. 2. Polarization and passivation of Zr in fluoride solutions, and Zn in Leclanche electrolyte (curve D). Curve A, 0.1N HF; B, 1N HF; C, 0.1N HF, 1% NH_4F; E, 8% NH_4F; F, 0.075N HF, 4% NH_4F; G, 0.075N HF, 8% NH_4F. Passivity did not occur in E, F, or G, even though in G i was taken as high as 180 ma cm^{-2}.

[1] Supplied by Titanium Metals Corp. as Ti-75A.

[2] Supplied by Superior Tube Co.

[3] Supplied by Foote Mineral Co.

[4] Supplied by the Carborundum Metals Co.

[5] Supplied by the National Carbon Co.

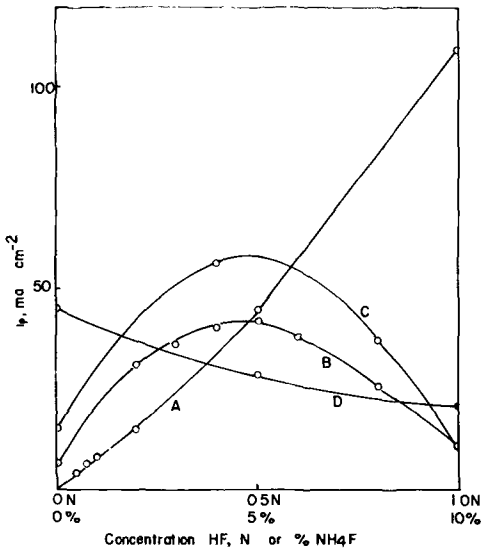

Fig. 3. Dependence of the passivation current density of Ti on HF and NH_4F concentration. A, HF only; B, 0.075N HF, added NH_4F; C, 0.2N HF, added NH_4F; D, 0.5N HF, added NH_4F.

Returning to Fig. 1, we note in particular the effect of HF concentration on the slope of the E vs. i curve for Ti and on the value of i_p. Even more important is the beneficial effect of added NH_4F in dilute HF solutions on the potential, polarization, and passivation current density for Ti, as illustrated by the difference between curves B and F. (KCl had a very minor effect on electrode behavior and was added to several electrolytes for the purpose of increasing conductivity.) Although i_p was somewhat uncertain, enough values were at hand to allow an approximate evaluation to be made of its dependence on electrolyte composition. In Fig. 3, the passivation current density is plotted against the concentration of HF (with no NH_4F), or against % NH_4F at fixed HF concentration. NH_4F exerts a beneficial influence up to about 5% in dilute HF (0.2N) but a deleterious effect at higher HF concentrations. This is also clearly shown by curves D and G of Fig. 1. In 1N HF i_p was reduced from 110 ma cm^{-2} to 8.1 ma cm^{-2} by the addition of 20% NH_4F. In NH_4F solutions with no HF (except that arising from hydrolysis), i_p was very low, e.g., 2.6 ma cm^{-2} in 8% NH_4F.

Considering also the chemical corrosion of Ti which increases rapidly with HF concentration and is inhibited by NH_4F, we conclude that the best electrolyte to be used with Ti is 0.075N HF containing 5-6% NH_4Cl and about 0.1N KCl. For brevity this solution is designated solution A. The potential of Ti in solution A is −1.02 v (about 0.2 v more negative than Zn in the usual dry-cell electrolyte) and remains below −0.8 v up to a current density of 28 ma cm^{-2}.

This current density may be compared with typical values at the Zn electrode in the Leclanché cell. During discharge of a fresh D-cell under 4-ohm load the anodic current density is about 6 ma cm^{-2}, and during operation of an ordinary 2-cell flashlight it is about 20 ma cm^{-2}.

There were too few cases of passivity for Zr to permit the same kind of correlation between i_p and electrolyte composition. Curve G of Fig. 2 shows, however, that the most satisfactory electrolyte for Zr from the standpoint of polarization was 0.075N HF with 8% NH_4F. The addition of KCl caused no significant difference. In this electrolyte the potential of Zr is superior to that of Zn (curve D, Fig. 2) in a solution containing 26% NH_4Cl, 8.8% $ZnCl_2$, and a trace of $HgCl_2$ (a common dry-cell electrolyte) at all current densities up to 200 ma cm^{-2}.

Corrosion

The corrosion rates of Ti and Zr were measured in electrolytes which appeared promising from polarization studies and in several other solutions used in the experimental cells described later. Solutions were in contact with air at room temperature, but not stirred. The favorable effect of added NH_4F on the corrosion of Ti by HF, previously reported (4), was confirmed. The rate for Ti in electrolyte A was 22 mdd, which, while not excessive, sets an upper limit of about six months on the life of a 0.25-mm sheet anode in this electrolyte.

On the other hand, Zr corroded rapidly in all acid fluoride solutions investigated, and the addition of NH_4F was of no benefit. The rate was 6000 mdd in electrolyte A and 800 mdd in 8% NH_4F alone. Small concentrations of Pb, Zr, and chromate ions reduced the corrosion rate in 0.1N HF, but not to a useful level. $Na_2Cr_2O_7$ reduced significantly the corrosiveness of H_2SO_4 on Zr, the rate in the case of 80% H_2SO_4, 1% $Na_2Cr_2O_7$ being only 2.3 mdd.

Anode Reaction

The number of faradays to dissolve a mole of metal, z, when Ti or Zr was made the anode was measured over a series of current densities and with varying electrolyte composition.

Electrolytes used with Ti were all mixtures of NH_4F, KCl, and HF, containing from 4 to 8% NH_4F, 0.1N KCl, and from 0.075 to 0.1N HF. Current densities ranged from 1 to 20 ma cm^{-2}. There was no observable dependence of z on either composition or current density. The average of 16 measurements of z which lay between 3.93 and 4.18 was 4.04.

Electrolytes used with Zr included 0.05 to 0.2N HF, 5 to 10% NH_4F, mixtures of HF and NH_4F, $CuCl_2$, $FeCl_3$, NH_4Cl, and HCl of several concentrations each. Current densities were higher than in the case of Ti in order to reduce the time required and thus the error due to chemical corrosion, ranging from 50 to 140 ma cm^{-2}. At 100 ma cm^{-2}, the anodic corrosion rate is 2 x 10^5 mdd. z did not depend on either composition or current density. The average of 14 measurements of z, which lay between 3.25 and 4.44 was 3.90.

It is clear that the only reaction of significance in these cases is oxidation of the metal to the tetravalent state. Chemical corrosion during the measurements has the effect of reducing z below the actual value; this may account for the somewhat smaller average value for Zr, since in some electrolytes the chemical corrosion rate was in the neigh-

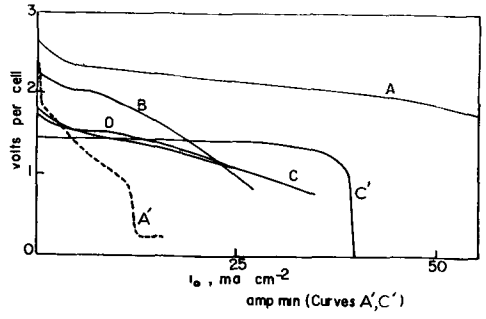

Fig. 4. Characteristics of primary cells. Curve A, A', Ti-0.07N HF, 0.1N KCl, 9% NH_4F, 1.6% H_2SO_4-PbO_2; B, Zr-90% H_2SO_4, 1% $Na_2Cr_2O_7$-PbO_2; C, C', Ti-soln. A-MnO_2; D, Zr-soln. A-MnO_2. Soln. A = 0.075N HF, 0.1N KCl, 6% NH_4F.

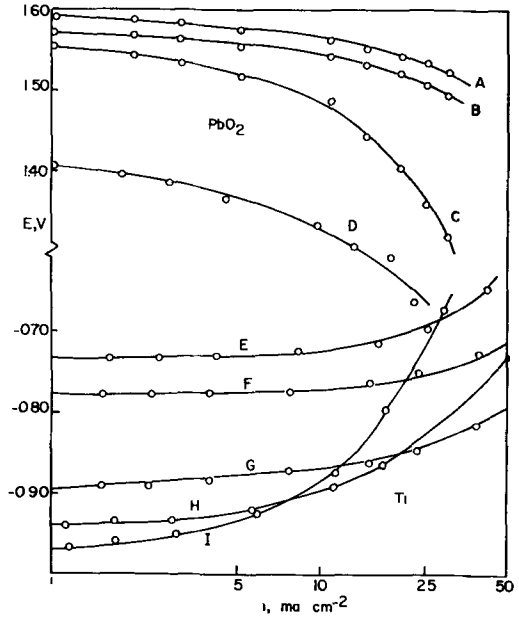

Fig. 5. Effect of H_2SO_4 on Ti and PbO_2 electrodes. Composition given as ratio: vol. soln. A/vol. of 15% H_2SO_4. Curve A, 1/99; B, E, 25/75; C, F, 50/50; D, G, 75/75; H, 90/10; I, 99/1.

borhood of 3% of the anodic corrosion rate. Oxygen was evidently not produced in a significant quantity.

Primary Cells

Cells were made in open beakers using Ti or Zr anodes and either PbO_2 or MnO_2 cathodes. The principal electrolytes used were solution A (0.075*N* HF, 6% NH_4F, 0.1*N* KCl), mixtures of A with H_2SO_4 and additional NH_4F, H_2SO_4, and H_2SO_4 containing $Cr_2O_7^{--}$. Th PbO_2 electrodes were made with commercial positive grids, pasted and formed in the laboratory according to the method described by Vinal (11). Representative data for four types of cells are shown in Fig. 4. Curves A through D were obtained by measuring the cell voltage during very short periods of discharge through a variable load. The drain is given by i_a, the anodic current density. In all cases the cathode was of much greater area than was the anode.

Curves C and C' represent the behavior of a Ti-MnO_2 cell containing solution A. The open-circuit voltage was 1.75. When discharged at $i_a = 10$ ma cm^{-2} the voltage remained about 1.4 for delivery of 25 amp min, and dropped to 1.0 v at 39 amp min. This corresponded to 81% utilization of the anode. The behavior of these cells was not very reproducible, and the example cited here was representative of several of the best cells studied. Unfortunately, fluoride solutions affect MnO_2 electrodes deleteriously, so that even the open-circuit voltage of such cells would fall to zero after 2 or 3 days.

The use of PbO_2 in place of MnO_2 resulted in a much higher initial open-circuit voltage (2.2 to 2.7 v). The addition of a small concentration of H_2SO_4 to the electrolyte increased the PbO_2 potential. Titanium became more positive with increasing H_2SO_4 concentration, but the polarization characteristics were improved. These effects are illustrated by Fig. 5. However, the polarization of Ti with time during continuous discharge was more severe in solutions containing H_2SO_4. Thus we find that, although the voltage remained high for high drain of short duration (curve A, Fig. 4), the discharge characteristics were disappointing (curve A'). Much of the decrease in voltage during discharge was due to failure of the PbO_2 electrode in fluoride solution. At the end of the discharge, the PbO_2 single electrode potential had fallen from an original value of 1.4 v to 0.6 v.

Zr-MnO_2 cells containing solution A were similar (see curve D, Fig. 4) to the Ti cells except for the much greater chemical corrosion of the anode. Many cells of the type Zr-H_2SO_4-PbO_2 were tested, to several of which chromate was added to reduce corrosion. The performance of the best of these is illustrated by curve B, Fig. 4. Discharge characteristics were generally inferior to the Ti-PbO_2 cells.

"Dry" cells were constructed from Ti tubing or Zr sheet, commercial MnO_2 electrodes, and a starch paste containing solution A. These cells polarized completely at low current density, probably because the polarization product was held mechanically in contact with the electrode, while in the open-beaker cells it was allowed to drop off.

Other electrolytes used in experimental cells were chosen with the purpose of eliminating water or reducing its activity markedly in the hopes of avoiding the formation of oxide layers on the Ti or Zr electrodes. Fused hydrates of NaOAc, $FeCl_3$, $CaCl_2$, and KF, and the nonaqueous solvents glacial acetic acid, fused alkali halides, fused KI_3 methanol, diethyl ether, nitrobenzene, SCl_2, S_2Cl_2, formamide, acetone, acetic anhydride, and dioxane all gave unsatisfactory results. Cells containing H_2SiF_6 in aqueous solution were moderately successful but corrosion was severe.

Polarization Product

The nature of the product responsible for polarization of Ti in solution of HF and NH_4F was not ascertained. Colors commonly observed on polarized electrodes were black, blue, or white and were due to material which could be readily scraped off. X-ray diffraction photographs of four products obtained under different conditions showed that no two were identical, nor were any to be identified with compounds for which data are tabulated by ASTM (12). While TiO_2 is undoubtedly a major

component of the polarization product under many conditions, in no case studied did it appear as a pure product.

Acknowledgments

The work described here was supported by contract with W. J. Kroll, whose generosity and technical advice are gratefully acknowledged. We wish to thank the National Carbon Company, the Carborundum Metals Company, the Titanium Metals Corporation of America, the Foote Mineral Company, and the Burgess Battery Company for gifts of materials used in this study. Thanks are also due N. C. Cahoon and Miss M. P. Korver, with whom valuable discussions were held, Miss Judith Skow and Mrs. Celia Rockholt, who made many of the measurements.

Manuscript received March 2, 1959. This paper was taken, in part, from the Ph.D. Thesis of one of the authors (M.A.T.), Oregon State College (1957).

Any discussion of this paper will appear in a Discussion Section to be published in the June 1960 JOURNAL.

REFERENCES

1. *Chem. Eng. News*, **36**, No. 40, 92 (1958).
2. W. Latimer, "Oxidation Potentials," Prentice-Hall, New York (1953).
3. W. J. Kroll, "Corrosion Handbook," H. H. Uhlig, Editor, p. 347, John Wiley & Sons, Inc., New York (1948); L. B. Golden, I. R. Lane, and W. L. Acherman, *Ind. Eng. Chem.*, **44**, 1930 (1952); J. Schmets and M. Pourbaix, "Proceedings of Sixth Meeting, C.I.T.C.E.," p. 167, Butterworths, London (1955); T. Smith and G. R. Hill, *This Journal*, **105**, 117 (1958).
4. M. E. Straumanis and C. Gill, *This Journal*, **101**, 10 (1951).
5. D. Schlain, *U. S. Bur. Mines Repts. Invest. 4965* (1953); D. Schlain, C. Kenahan, and D. Steele, *This Journal*, **102**, 102 (1955); *U. S. Bur. Mines Repts. Invest. 5189* (1956); *ibid., 5201* (1956).
6. E. Botts and F. Krauskopf, *J. Phys. Chem.*, **31**, 1404 (1927).
7. S. Sato and K. Yamane, *Repts. Sci. Research Inst. (Japan)*, **32**, 8 (1956).
8. M. E. Straumanis and P. Chen, *Z. Technik, Industrie, U. Handel*, **7**, 85 (1953).
9. C. D. Hall and N. Hackerman, *J. Phys. Chem.*, **57**, 262 (1953); G. B. Adams, Jr., P. Van Ryssel-berghe, and M. Maraghini, *This Journal*, **102**, 502 (1955).
10. A. L. Fox (to Manganese Battery Corp.), U.S. Pat. 2,631,115, Mar. 10, 1953.
11. G. W. Vinal, "Storage Batteries," p. 27-46, John Wiley & Sons, Inc., New York (1950).
12. "Numerical Index of X-ray Diffraction Data," American Society for Testing Materials, Philadelphia (1950).

Investigation of the Electrochemical Characteristics of Organic Compounds IV. Quinone Compounds

R. Glicksman and C. K. Morehouse

Semiconductor and Materials Division, Radio Corporation of America, Somerville, New Jersey

ABSTRACT

A study of the electrochemical characteristics of various quinone compounds shows that the cathode potential of these compounds during current flow is dependent on the type and position of substituent groups in the molecule, the pH of the electrolyte, and the nature of the quinone itself. Experimental data are presented for dry cells containing 2,5-dichloro-p-quinone and p-quinone-dioxime as cathodes coupled with a magnesium anode.

Most oxidation and reduction reactions in organic chemistry are irreversible. An exception to this is the group of reactions involving quinoid-benzenoid equilibria. One of the best known of these is the quinone-hydroquinone system, whose potential has been reported by Hovorka and Dearing (1) to be

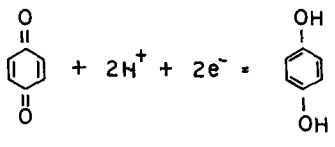

[1]

In this paper the effect of such factors as group substitution, aromaticity, and pH on the operating potential and coulombic capacity of various quinone compounds are presented and their use as cathode materials in primary cells is considered.

Experimental Data and Discussion of Results

Apparatus and Technique

A technique, previously described (2), has been used to measure the operating potential during current flow and the coulombic capacity of the various quinone-type compounds. This technique consists in discharging at a constant current drain of 0.005 amp/g, in a large volume of electrolyte, a 0.5-g sample of the quinone-type cathode material mixed with 0.05 g of Shawinigan acetylene black. The change in cathode potential with time was measured with a L&N type K potentiometer using a saturated calomel reference electrode. The measured potentials were corrected for the *IR* drop associated with the apparatus and electrolyte by means of an oscillographic technique (3).

All half-cell potential data reported in this paper are referred to the normal hydrogen electrode and include a liquid junction potential, which in most cases is small and can be neglected. For most of the measurements an aqueous magnesium bromide electrolyte and a magnesium anode were used, while in studying the effect of pH on potential, a zinc anode was employed with the acidic NH_4Cl-$ZnCl_2$-H_2O and basic NaOH-H_2O electrolytes.

Half-Cell Potential Studies

Effect of aromaticity.—Figure 1 gives half-cell discharge curves for a series of quinones derived from benzene and other polynuclear hydrocarbons. The ortho quinones have higher operating potentials than their corresponding para quinone compounds. In addition, both the ortho- and para quinones show a marked dimunition in cathode potential as one goes to the bicyclic and tricyclic quinone compounds. For example, a comparison of p-quinone with its corresponding naphthoquinone indicates a difference in potential of 200-300 mv, in agreement with standard potential measurements. Fieser and Fieser (4) attribute the markedly diminished energy content of the bicyclic compounds to the fact that the quinoid double bond is incorporated in the aromatic nucleus and hence is relatively inert. In anthraquinone both the otherwise reactive quinoid double bonds participate in benzenoid ring systems and the potential of the quinone is lower yet. Similarly, because of the higher energy content of the orthoquinones as compared to the isomeric paraquinones the standard potentials of the ortho compounds are 85-95 mv higher.

If the standard potentials of a series of quinones are compared, the change in potential will be dependent on the change in free energy in going from the quinone-hydrogen system to the hydroquinone, according to the following equation

$$E^\circ = -\frac{\Delta F^\circ}{nF} = -\frac{\Delta H^\circ}{nF} + \frac{T\Delta S^\circ}{nF} \qquad [2]$$

It has been found that the temperature coefficient of the standard potential is approximately the same for a large number of quinones and is equal to about 0.7 mv/deg. This temperature coefficient, which corresponds to an entropy change of −32 cal/deg for the hydrogenation of a quinone, corresponds roughly to the entropy of the mole of hydrogen lost in the reaction. Thus the change in potential in a series of quinones will represent the change in the relative heat contents of the quinone and hydroquinone through the series (5). The change in bond energies in the reduction represented by Eq. [1] is the same for all quinones and is small compared to the benzene resonance energy gained on the hydroquinone side. Thus it would be expected that resonance effects would be a controlling factor in the magnitude of the potential. Since the largest contribution to the resonance energy is due to the equivalent Kekule forms, the relative numbers of such equivalent forms may be used as a quantitative estimate of the relative energy of the oxidized and reduced forms.

The relationship between the number of contributing resonance forms in the quinone and hydroquinone and the standard potential of the system has been demonstrated by Branch and Calvin (5). They obtained a straight line relationship between the standard potential of para quinones and the ratio of the contributing forms n_q/n_h.[1] A still better relationship was obtained when the expression $(n_h - n_q)/(n_h + n_q)$ was used instead of the simple ratio and when allowance was made for steric and ortho effects in quinones of polynuclear structure. Similarly, Berliner (6) computed the difference in empirical resonance energies of a number of quinones and their respective hydroquinones from known experimental data and found a linear relationship exists between the oxidation-reduction potential and the difference in resonance energies of the quinones and the respective hydroquinones.

To test the above relationship for electrodes undergoing discharge, the cathode potentials of the quinones after 1 amp-min of discharge were plotted vs. $(n_h - n_q)/(n_h + n_q)$, as shown in Fig. 2. In agreement with the results of Branch and Calvin a straight line relationship was found between the potential and the ratio of the number of resonance forms in the quinone and hydroquinone compounds. In addition a similar line is obtained for the orthoquinones but displaced upward about 0.1 v and parallel to the paraquinone line.

[1] n_q and n_h are the number of forms of the quinone and hydroquinone. For p-quinone there is only one such form, while in hydroquinone there are two Kekule forms. In 1, 4-naphthoquinone there are two, while in the corresponding hydroquinone there are three.

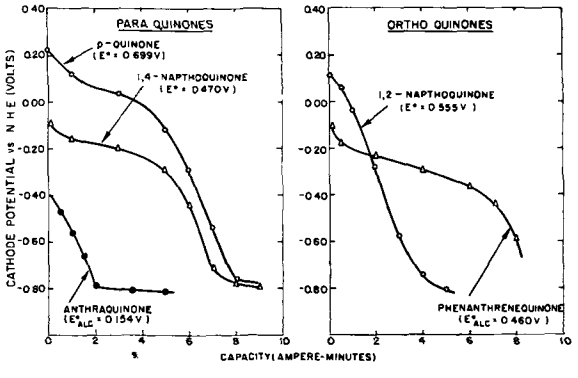

Fig. 1. Half-cell potential studies of various ortho and paraquinone compounds discharged at a rate of 0.005 amp/g in 250 g/l $MgBr_2 \cdot 6H_2O$ electrolyte.

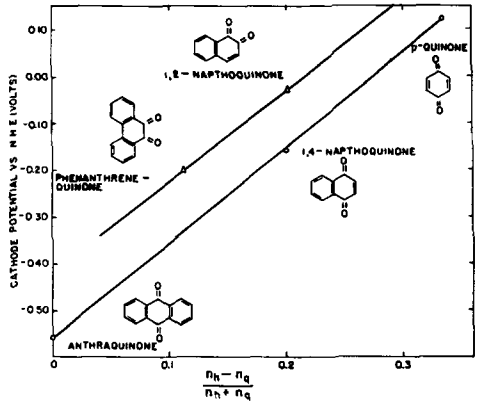

Fig. 2. Relationship between the number of contributing resonance forms in the quinone and hydroquinone and the half-cell potential as measured at a rate of 0.005 amp/g in 250 g/l $MgBr_2 \cdot 6H_2O$ electrolyte.

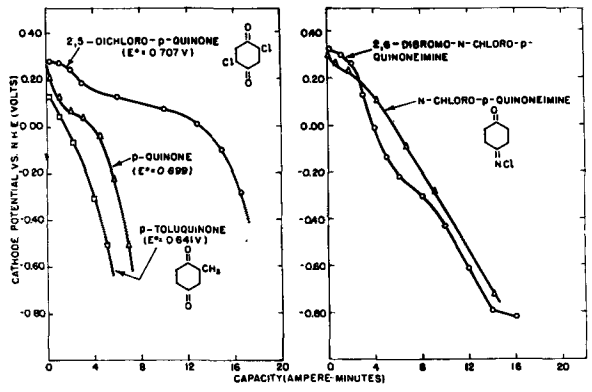

Fig. 3. Effect of group substitution on the cathode potential of p-quinone and N-chloro-p-quinoneimine discharged at a rate of 0.005 amp/g in 250 g/l $MgBr_2 \cdot 6H_2O$ electrolyte.

Effect of group substitution.—Presented in Fig. 3 are discharge curves for various para quinone and chloroimide compounds illustrating the effect of substituent groups on the operating potential of these compounds. It is seen that an electron-attracting halogen group raises the potential while an electron-repelling methyl group lowers the potential of the parent compound. This type of effect closely parallels the effect of these constituents on the standard potentials of quinones, as well as on the operating potential of aromatic nitro compounds (7).

The effect of substituent groups on the standard potentials of quinone compounds has been studied extensively by Fieser (8, 9). Most of the determinations were carried out in alcoholic solution, but the results would be expected to apply closely to aqueous solutions. In general, it was found that electron-attracting groups, such as $-NO_2$, -CN, -COOH, and halogens, raise the potential of the parent quinone, whereas a potential-lowering effect is exerted by electron-repelling groups such as $-NH_2$, -OH, and $-CH_3$. This is in agreement with the data presented in Fig. 3. These relationships are those expected from the course of aromatic substitutions. Electron-attracting groups tend to decrease the electron density in the vicinity of the oxygen atoms and thus to increase the attractive power of the system for external electrons, rendering the compound a stronger oxidizing agent. Conversely electron-repelling substituents decrease the affinity for electrons and hence lower the potential.

When the substituent is not in the quinoid ring its effect is much smaller and depends to a large extent on its position with respect to the quinoid ring. For example, Fieser (8) has shown that substituents in the 1 or 3 position of phenanthrenequinone have a considerable effect on the potential of phenanthrenequinone while in the 2 or 4 positions they are practically ineffective. The importance of the position of substituent group on the electrode potential of an organic compound has also been shown for both aromatic nitro (7) and nitroalkane compounds (10), and it depends essentially on its effect in altering the electron density in the vicinity of the reducible group.

Effect of electrolyte pH.—For the quinone-hydroquinone system the variation of the oxidation-reduction potential with hydrogen ion concentration is relatively simple in acidic electrolytes, but in alkaline solutions allowance must be made for the ionization of hydroquinone, which can function as a dibasic acid. Thus in acidic electrolyte $dE/d(pH) = 0.059$ for this system, while at pH's higher than about 8 the slope of the potential-pH curve becomes 0.030 to a pH of approximately 11 and is zero in more alkaline solutions (11).

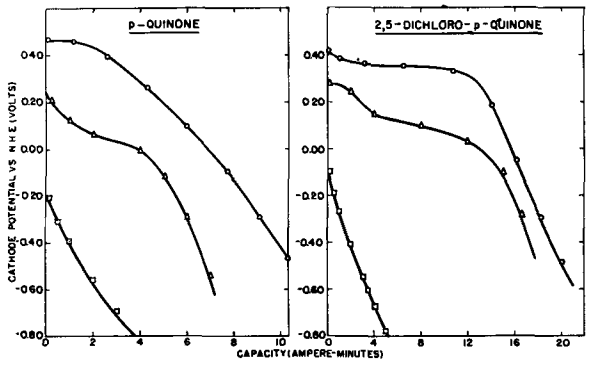

Fig. 4. Effect of pH on the cathode potential of p-quinone and 2, 5-dichloro-p-quinone when discharged at a rate of 0.005 amp/g in various electrolytes. O—25% NH_4Cl, 20% $ZnCl_2$, 55% H_2O; Δ—14% $MgBr_2$, 86% H_2O; □—30% NaOH, 70% H_2O, saturated with ZnO.

Taking into account the effect of pH on potential, it is seen from Fig. 4 that both p-quinone and 2,5-dichloro-p-quinone have initial operating potentials close to their reversible values in the NH_4Cl-$ZnCl_2$ (pH = 4.5) and $MgBr_2$(pH = 8.2) electrolytes. Similarly, the initial operating potentials of the quinone compounds previously presented in Fig. 1 and 3 are also reasonably close to their reversible values in the magnesium bromide electrolyte. However, in the strongly alkaline sodium hydroxide electrolyte, the operating potentials of p-quinone and 2,5-dichloro-p-quinone show a considerable deviation from their reversible values. This is attributed to the decomposition of both the quinone and hydroquinone by atmospheric oxygen in this alkaline electrolyte (12).

Various N-analogues of quinone.—In addition to the various quinone compounds discussed above there are a number of analogous organic compounds containing quinoid structures which are of scientific interest. Many of these compounds are employed as oxidation-reduction indicators in biological applications. Presented in Fig. 5 are discharge curves of

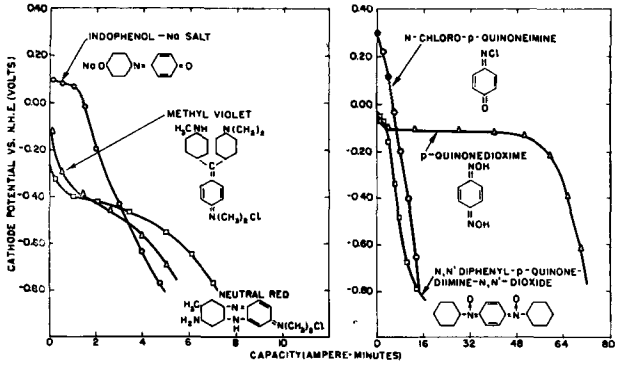

Fig. 5. Half-cell potential studies of various quinone-type compounds discharged at a rate of 0.005 amp/g in 250 g/l $MgBr_2 \cdot 6H_2O$ electrolyte.

three typical indicators, indophenol-Na salt (indophenol group), neutral red (azine group), and methyl violet (triphenylmethane group). As with the other quinones both indophenol-Na salt and neutral red operate at potentials close to their theoretical values (13) after corrections are made for the *p*H of the solution.

Also shown in Fig. 5 are discharge curves of three other N-analogues of p-quinone, which contain in addition to the quinoid structure additional reducible groups in the molecule. Of the three, N-chloro-p-quinoneimine which contains a positive halogen and p-quinonedioxime with two reducible oxime groups are of the most interest, as the amine oxides in N,N'-diphenyl-p-quinonediimine-N,N'-dioxide are reduced very difficultly (14, 15). Only the N-chloro-p-quinoneimine compound has a higher operating potential than p-quinone and, as evidenced by the data in Fig. 3 for 2,6-dibromo-N-chloro-p-quinoneimine, it would appear that the effect of substituent groups on the operating potential of chloroimides is similar to that of the quinones.

Capacities of Quinone Compounds

Presented in Table I are theoretical capacities and electrode efficiencies of various quinone-type compounds as calculated from the half-cell discharge data in Fig. 1, 3, and 5. It is seen that on the basis of theoretical capacity in ampere-minutes per gram the quinone compounds are superior to manganese dioxide, the cathode material now used in conventional Leclanché dry cells. However, because of the low densities and poor electrode efficiencies of these organic compounds a manganese dioxide cathode would give markedly superior performance when rated on the basis of ampere-minute output per cubic centimeter. As seen from the half-cell potential data in Fig. 4 the use of a more acidic NH_4Cl-$ZnCl_2$ electrolyte has no appreciable effect on the electrode efficiency of the quinones, and no advantage could be gained for the organic compounds in going to this electrolyte.

Table I. Theoretical capacities and electrode efficiencies of various quinone compounds discharged in 250 g/l $MgBr_2 \cdot 6H_2O$ electrolyte at a rate of 0.005 amp/g

Compound	Capacity, amp-min/g		Efficiency, %
	Theoretical	Actual*	
Manganese dioxide†	18.5	10.3	65.6
p-quinones			
p-quinone	29.8	6.4	21.5
1, 4-naphthoquinone	20.4	5.8	28.4
anthraquinone	15.5	—	—
p-toluquinone	26.4	4.6	17.4
2, 5-dichloro-p-quinone	18.2	17.2	94.5
o-quinones			
1, 2-naphthoquinone	20.4	2.3	11.3
phenanthrenequinone	15.5	6.5	41.9
N-Analogues			
N-chloro-p-quinoneimine	45.5(4)‡	10.4	22.9
N-chloro-p-quinoneimine	22.8(2)	10.4	45.6
2, 6-dibromo-N-Chloro-p-quinoneimine	21.5(4)	9.6	44.7
2, 6-dibromo-N-Chloro-p-quinoneimine	10.8(2)	9.6	88.9
p-quinonedioxime	69.9(6)	65.2	93.3
N, N'-diphenyl-p-quinone-diimine-N, N'-dioxide	11.1(2)	6.6	59.5
indophenol-Na salt	14.6	2.8	19.2

* Capacities calculated on basis of an end voltage of −0.40 v.
† Electrolytic manganese dioxide (85% MnO_2 content).
‡ Values in parentheses indicate the electron change.

More promising for use as cathodes in primary cell applications are some of the quinones which contain reducible groups in addition to the quinoid structure. These compounds not only have higher theoretical capacities than the quinones but also operate at higher electrode efficiencies. Of particular interest is p-quinonedioxime which has a theoretical capacity of 69.9 amp-min/g and which operates under these conditions of discharge at an electrode efficiency of 93.3%. On the basis of these results and the polarographic data of Elofson and Atkinson (16) it is believed the over-all reduction of p-quinonedioxime takes place with a 6 electron change, the actual reduction probably proceeding through the intermediate diimino stage as shown here:

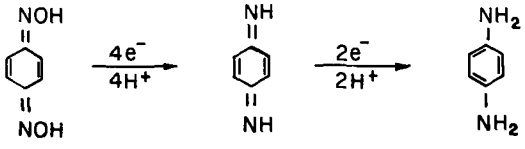

[3]

Experimental Dry Cell Data

The use of quinone compounds in primary batteries was suggested previously by Arsem (17) who referred to the coupling of a zinc anode with an organic oxidizing agent such as quinone. More recently Tripler and McGraw (18) evaluated tetrachloroquinone as a cathode material in both acid and basic electrolyte using zinc and lead anodes. In the present study the quinones were coupled with a magnesium anode to take advantage of the higher potential of this electrode.

Experimental dry cells containing 2,5-dichloro-p-quinone and p-quinonedioxime cathodes were assembled in the usual manner using an impact extruded magnesium AZ10A alloy AA-size can as anode, and a 500 g/l $MgBr_2 \cdot 6H_2O$ electrolyte. The cathode mix (weighing approximately 4.5 g) consisted of one part by weight of the quinone compound to two parts by weight of Darco carbon black G-60.

Performance characteristics of these cells on a 4- and 50-ohm continuous discharge test are shown in Fig. 6. Included for comparison are performance

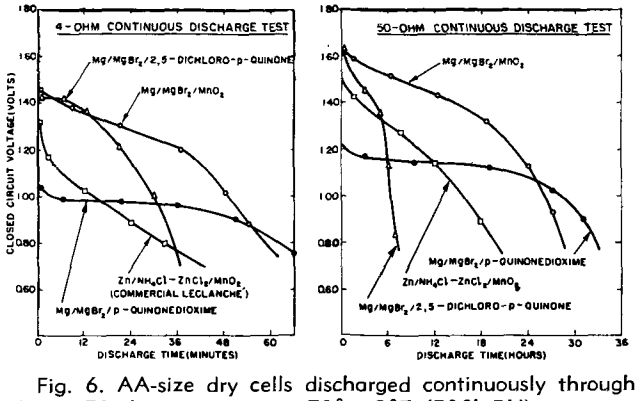

Fig. 6. AA-size dry cells discharged continuously through 4- and 50-ohm resistances at 70° ±2°F. (50% RH).

data for comparable-size commercial Leclanché and magnesium-manganese dioxide dry cells (19) of the type being developed by the Dow Chemical Company. It is seen that the performance of the magnesium-p-quinonedioxime cell is superior to the Leclanché cell on both these tests, while the magnesium-2,5-dichloro-p-quinone cell performs better only on the higher current drain test. Compared to the magnesium-manganese dioxide cell, the quinone cells give inferior performance on these tests. However, the flat voltage discharge curve of the p-quinonedioxime cell is advantageous for some applications.

Summary

An investigation of the electrochemical characteristics of various quinone-type compounds show these compounds to operate close to their reversible values during current flow. The operating potential of these compounds has been found to be dependent on the type and position of the substituent groups in the molecule as well as the pH of the electrolyte, electron-attracting groups and low pH's favoring higher potentials. The operating potential of the quinones is also dependent on the nature of the compound; for example, the ortho quinones operate at potentials approximately 0.1 v higher than their isomeric para quinones, while a decrease in potential is found as one goes to bicyclic and tricyclic members in any given series.

Compared to the conventional inorganic cathode materials the quinone compounds, in general, are not as good. However certain quinone-type compounds containing other reducible groups in the molecule, such as p-quinonedioxime, show some advantages when coupled with a magnesium anode in a magnesium bromide electrolyte.

Manuscript received Feb. 13, 1959. This paper was prepared for delivery before the Ottawa Meeting, Sept. 28-Oct. 2, 1958.

Any discussion of this paper will appear in a Discussion Section to be published in the June 1960 JOURNAL.

REFERENCES

1. F. Hovorka and W. C. Dearing, *J. Am. Chem. Soc.*, **57**, 446 (1935).
2. C. K. Morehouse and R. Glicksman, *This Journal*, **103**, 94 (1956).
3. R. Glicksman and C. K. Morehouse, *ibid.*, **102**, 273 (1955).
4. L. F. Fieser and M. Fieser, "Organic Chemistry," 3rd ed., p. 712, Reinhold Publishing Corp., New York (1956).
5. G. E. K. Branch and M. Calvin, "The Theory of Organic Chemistry," pp. 303-314, Prentice-Hall, Inc., New York (1941).
6. E. Berliner, *J. Am. Chem. Soc.*, **68**, 49 (1946).
7. R. Glicksman and C. K. Morehouse, *This Journal*, **105**, 299 (1958).
8. L. F. Fieser, *J. Am. Chem. Soc.*, **51**, 3101 (1929).
9. L. F. Fieser and M. Fieser, *ibid.*, **57**, 491 (1935).
10. R. Glicksman and C. K. Morehouse, *This Journal*, **106**, 288 (1959).
11. S. Glasstone, "Introduction to Electrochemistry," pp. 291-295, D. Van Nostrand Co., Inc., New York (1942).
12. G. Kortum and J. O'M. Bockris, "Textbook of Electrochemistry," Vol. I, p. 291, Elsevier Publishing Co., New York (1951).
13. W. M. Clark, *J. Appl. Phys.*, **9**, 97 (1938).
14. E. Ochiai, *J. Pharm. Soc. Japan*, **69**, 1 (1949).
15. R. Glicksman and C. K. Morehouse, *This Journal*, **105**, 613 (1958).
16. R. M. Elofson and J. G. Atkinson, *Can. J. Chem.*, **34**, 4 (1956).
17. W. C. Arsem, U. S. Pat. 2,306,927, Dec. 29, 1942.
18. A. B. Tripler, Jr., and L. D. McGraw, *This Journal*, **105**, 179, (1958).
19. R. C. Kirk, P. F. George, and A. B. Fry, *ibid.*, **99**, 323 (1952).

The Cathodic Reduction of Manganese Dioxide in Alkaline Electrolyte

N. C. Cahoon[1] and M. P. Korver

Research Laboratories, National Carbon Company, Division of Union Carbide Corporation, Cleveland, Ohio

ABSTRACT

A study of the mechanism of the reduction of manganese dioxide in strongly alkaline electrolytes has shown that the rather complex process may be considered as occurring in three steps. The first is the simultaneous reduction to form a divalent manganese compound, presumably, $Mn(OH)_2$ and an intermediate oxide tentatively identified as Mn_4O_7; the second step is the electrochemical reduction of Mn_4O_7 to form both Mn_3O_4 and $Mn(OH)_2$; the final step is the electrochemical reduction of Mn_3O_4 to $Mn(OH)_2$. Both chemical and x-ray diffraction analyses of cathodes at various stages of reduction are presented.

The cathodic reduction of manganese dioxide in Leclanché cells (1) has been examined previously and a mechanism proposed to account for the experimental observations. The need of a similar examination of the cathodic reduction of MnO_2 in alkaline electrolytes was recognized some years ago. Accordingly, a study was undertaken to determine the mechanism of the reaction when MnO_2 is used as the cathodic depolarizer in an alkaline cell. The approach to this problem followed the lines of earlier studies in that the products of the cathodic reductions were separated into two fractions by a differ-

[1] Edgewater Development Laboratories, National Carbon Company, Cleveland, Ohio.

Table I. Extent of reaction of cathodes of experimental alkaline cells during the course of discharge

Cell No.	Initial free MnO_2 content, g	Theoretical* capacity, amp min	Actual electrical output, amp min	Output equivalent to Mn^{II}		Output associated with insoluble cathode product, amp min	Last cell reading, v
				Amount present, amp min	% of total output		
1	0.5938	14.64	2.22	1.16	52.3	1.06	1.26
2	0.5174	12.78	4.14	2.41	58.2	1.73	1.19
2a	0.6029	14.88	4.20	1.71	40.3	2.49	1.20
3	0.4642	11.46	6.12	3.79	61.9	2.33	1.09
4	0.5292	13.08	8.09	5.06	63.7	3.03	1.03
5	0.5342	13.20	9.39	5.11	54.5	4.28	0.96
6	0.3949	9.78	8.87	3.25	37.6	5.62	0.63

* The theoretical capacity is calculated on the basis of the reduction of the free MnO_2 to Mn_3O_4.

ence in solubility. The soluble and insoluble fractions were studied separately by both chemical and physical methods. This paper presents some significant results obtained in the course of the work.

Experimental

A series of experimental cells was prepared from electrolytic grade MnO_2, acetylene black, and an electrolyte containing 7.6*N* KOH. An excess of amalgamated powdered Zn was used in a compressed pellet as the anode, and an adequate supply of electrolyte was provided so that the cathodic depolarizer would be the only service limiting factor. The composition of a representative cell follows: electrolytic MnO_2 0.5128 g, acetylene black 0.1923, KOH (7.6*N*) 0.2949, amalgamated Zn 4.0 (approximately). The parts of the cells were assembled in a bench-type cell of a circular cross section with a cross-sectional area of 2.58 cm^2 (0.40 $in.^2$). A cellulosic separator 0.0208 cm (0.0082 in.) thick was employed. The cell was closed with a close-fitting plunger and throughout the test the unit was maintained under a mechanical pressure equivalent to 4.32 kg/cm^2 (61.5 $lb/in.^2$) of cell area. A continuous load of 30 ohms was placed across the cell, and cell voltage readings were taken periodically with a recording voltmeter.

One cell was removed after each of the following service levels had been reached: 2.20, 4.14, 4.19, 6.12, 8.09, 8.87, and 9.39 amp min. Immediately following the removal from test, the cell was quickly dismantled and the cathode mix was suspended in 500 cc of an aqueous solution of 25% NH_4Cl. The *p*H of this suspension was quickly measured and ½*N* HCl added with adequate stirring to reduce the *p*H to 5.4. The suspension was stirred mechanically for 2 hr at room temperature to permit the solution of any divalent manganese that may have been formed in the cell discharge. Previous studies had shown that MnO_2, $Mn_2O_3 \cdot H_2O$, and Mn_3O_4 are all stable under these conditions and that substantially no complicating reactions would occur at this *p*H. Following the leaching operation, the residue was separated from the filtrate and thoroughly washed. The combined washings and filtrate were made up to one liter and aliquot samples of 100 ml were analyzed for manganese content by the method of Lingane and Karplus.(2)

The residue was dried at 100°-110°C and then subjected to examination by standard x-ray diffraction techniques to identify the solid phases remaining in the cathode. Another portion of the residue was analyzed for available oxygen and total manganese contents by conventional analytical methods.

Discussion

The discharge curve characteristic of this group of cells is shown in Fig. 1. Cells 1 to 5 gave substantially the same discharge curve as shown by the upper line in Fig. 1, while cell 6, which had a somewhat smaller cathode but was otherwise the same as cells 1 to 5, gave a discharge curve shown by the lower line in the same figure. Data obtained from the discharge of the cells and analyses of the soluble portion of the depolarizers are given in Table I. The conditions used for leaching the discharged cathodes were chosen so that any divalent manganese, presumably present as manganous hydroxide, would be dissolved. The amounts of divalent manganese leached from the cathodes in this manner have been calculated to equivalent ampere minutes on the basis of the following reaction:

$$MnO_2 + 2e + 2K^+ + 2H_2O \rightarrow Mn(OH)_2 + 2KOH \quad [1]$$

From this reaction 1 amp min of energy results from the reduction of 0.027 g MnO_2 to form 0.0173 g of

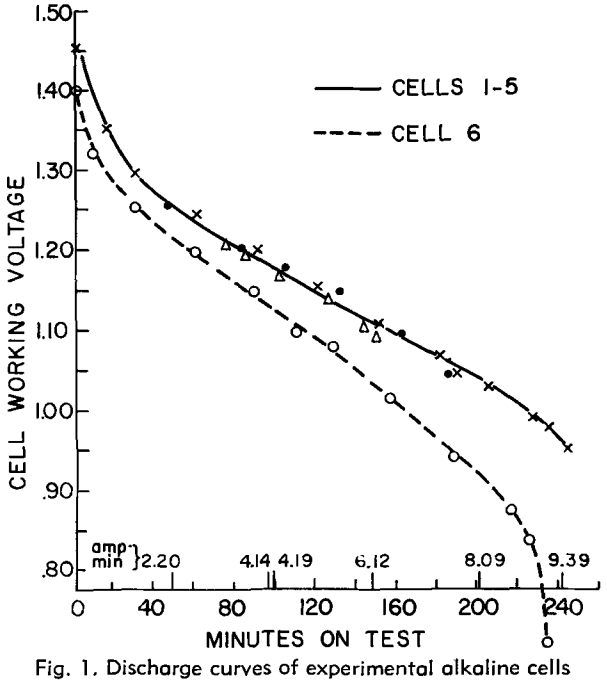

Fig. 1. Discharge curves of experimental alkaline cells

Table II. Composition of the insoluble cathode products during discharge of experimental alkaline cells

Cell No.	Initial depolarizer content: Weight, g	Initial depolarizer content: Free MnO_2, g	Amount free MnO_2 converted to $Mn(OH)_2$, g	Amount free MnO_2 in insoluble cathode product, g	Chemical composition of insoluble cathode product: MnO_2, %	Mn, %	x in $MnOx$	Free MnO_2, %
1	0.7056	0.5938	0.0313	0.5625	55.33	40.21	1.879	47.04
2	0.6148	0.5174	0.0651	0.4523	55.04	39.83	1.883	47.05
2a	0.7164	0.6029	0.0461	0.5568	55.52	39.88	1.888	47.94
3	0.5516	0.4642	0.1023	0.3619	51.42	39.62	1.819	40.16
4	0.6288	0.5292	0.1365	0.3927	—	—	—	—
5	0.6348	0.5342	0.1380	0.3962	42.79	36.66	1.738	27.57
6	0.4692	0.3949	0.0878	0.3071	26.55	42.91	1.391	None

Note: The electrolytic MnO_2 used in these tests contained 86.36% total MnO_2, 55.89% total Mn which can be calculated to 84.16% free MnO_2.

Table III. Relationship between the insoluble reaction product and the electrical output

Cell No.	Initial depolarizer weight, g	Free MnO_2 converted to $Mn(OH)_2$, g	Remaining depolarizer: Weight, g	Remaining depolarizer: Percent free MnO_2	Remaining depolarizer: Free MnO_2 content, g
1	0.7056	0.0313	0.6743	47.04	0.3172
2	0.6148	0.0651	0.5497	47.05	0.2586
2a	0.7164	0.0462	0.6702	47.94	0.3213
3	0.5516	0.1023	0.4493	40.16	0.1804
4	0.6288	0.1365	0.4923	—	—
5	0.6348	0.1380	0.4968	27.57	0.1370
6	0.4692	0.0878	0.3814	—	—

Cell No.	Amount free MnO_2 in insoluble cathode product, g	Free MnO_2 present at end of test, g	Free MnO_2 consumed in test, g	Output obtained, amp min	Free MnO_2 consumed per amp min, g
1	0.5625	0.3172	0.2453	1.06	0.2314
2	0.4523	0.2586	0.1937	1.73	0.1120
2a	0.5568	0.3213	0.2355	2.49	0.0946
3	0.3619	0.1804	0.1815	2.33	0.0779
4	—	—	—	—	—
5	0.3962	0.1370	0.2592	4.28	0.0606
6	0.3071	—	0.3071	5.62	0.0546

manganese as manganous hydroxide. The proportion of the total output in ampere minutes represented by the manganous hydroxide found and calculated on the above basis is shown in Fig. 2. It is evident from these data that while about half the reaction product is in this form, a sudden decrease in the proportion occurs between 8.09 and 9.39 amp min output. However, the finding that $Mn(OH)_2$ constitutes a large proportion of the cathodic reduction product is not in accord with previously published data (3) which indicate that the product is an orange-red Mn_2O_3.[2]

[2] We are unable to rationalize these earlier data with our findings.

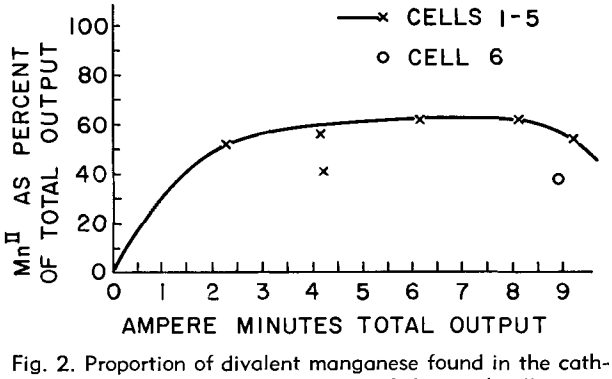

Fig. 2. Proportion of divalent manganese found in the cathodic reaction product as a percentage of the total cell output throughout the test.

Table I shows the depolarizer contents of the five experimental cells in terms of the free MnO_2[3] content and the equivalent theoretical cell output if all this MnO_2 were converted to Mn_3O_4 according to the following cathodic reaction:

$$3MnO_2 + 4K^+ + 4e + 2H_2O \rightarrow Mn_3O_4 + 4KOH \quad [2]$$

In this way 0.0405 g of MnO_2 provides 1 amp min of energy. This basis has been used for general calculation of cell output since work in this laboratory had previously shown that a variety of MnO_2 types was, at least in part, reduced to this compound. Table I also shows the actual electrical output of each cell as well as that portion of the output in equivalent ampere minutes that can be accounted for by the formation of $Mn(OH)_2$. The ampere minute output which must therefore be associated with a change in composition of the insoluble residue is listed. Table II also shows the compositions of these cathode residues. Table III combines the data of Tables I and II and shows the amount of free MnO_2 consumed per ampere minute for that portion of the output associated with the formation of the insoluble cathodic product. The values obtained are calculated on the assumption that only a single insoluble reaction product is formed in each case. By comparison of these values with the amounts of MnO_2 consumed per ampere minute for the reduction to the various lower oxides, some helpful correlations may be found. Thus, in reaction [2] 0.0405 g MnO_2 is required per ampere minute to form Mn_3O_4. Similarly 0.027 g MnO_2 (reaction [1]) and 0.054 g MnO_2 are needed per ampere minute to form $Mn(OH)_2$ and Mn_2O_3, respectively.

Figure 3 shows the ampere minutes per gram of free MnO_2 lost by the residue plotted against the ampere minute output associated with this residue taken from the last two columns in the second part of Table III. The values fall on a smooth curve which approaches the value of 0.0405 characteristic of reaction [2]. However, the three intermediate values for cells 2, 2a, and 3 fall too close to one another to attribute to experimental error. One possible cathodic reaction that gives a value approaching these points is the following:

$$4MnO_2 + 2K + 2e + H_2O \rightarrow Mn_4O_7 + 2KOH \quad [3]$$

This reaction consumes 0.108 g MnO_2/amp min which is not too far from the 0.112 g/amp min obtained from cell 2.

[3] Free MnO_2 is the amount of MnO_2 in the depolarizer available to react electrochemically.

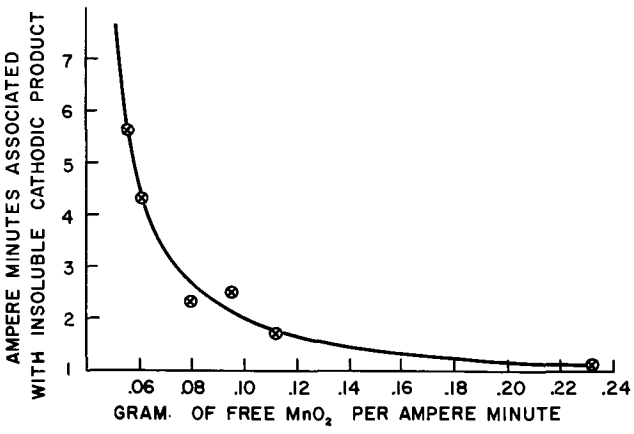

Fig. 3. Relationship between free MnO_2 consumed per ampere minute in the insoluble cathodic product and the extent of discharge.

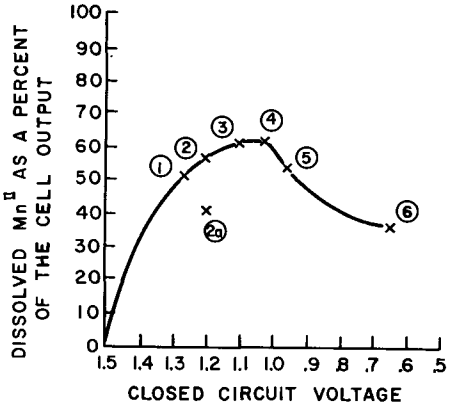

Fig. 4. Relationship between the proportion of divalent manganese found in the cathodic reaction product and the last cell voltage reading.

Data for cell 6, shown in Tables I, II, and III, differ somewhat from that for cells 1 to 5. A lower discharge curve for cell 6 is shown in Fig. 1, and it will be noted that the closed circuit voltage of this unit fell to 0.63 v at the time the test was terminated. The lower voltage of cell 6 probably is the result of the smaller quantity of depolarizer contained in the unit as shown in the tables. When the amount of the cell output represented by the divalent manganese removed from the cathode is plotted on Fig. 3, the point is somewhat lower than the curve given by the data of cells 1 to 5. At this time it appears that the fact that the discharge progressed relatively so much farther in cell 6 than in cells 1 to 5 is probably responsible for this situation. Added evidence to this viewpoint is given by Fig. 4 where there is a sharp break in the curve relating Mn^{II} as a per cent of total output to the last closed circuit voltage reading.

From a consideration of the results of these analyses of the cathode residues, it is concluded that the intermediate oxide is probably Mn_4O_7. However, the evidence we have presented for the existence of this manganese oxide needs further confirmation. The fact that it is cathodically reduced to Mn_3O_4 is not unknown with other manganese oxides. For example, $Mn_2O_3 \cdot H_2O$ when used as the sole depolarizer in experimental cells similar to those used in these tests is electrochemically reduced to $Mn(OH)_2$ and Mn_3O_4 simultaneously. On the other hand, Mn_2O_3 on reduction yields only $Mn(OH)_2$.

The identification of the insoluble cathodic product may also be studied by x-ray diffraction methods since many oxides of manganese possess characteristic patterns. The difficulties inherent in a precise comparison of a possible mixture of manganese oxides are well recognized. However, the results of such a study often yield valuable primary and confirmatory evidence for the existence of a particular solid phase and thereby indicate the reaction by which it may have been formed. A close examination of Fig. 5 showing the actual diffraction patterns of the insoluble residues from the experimental cells shows some rather startling differences. The original electrolytic MnO_2 is a typical gamma structure with the characteristic gamma "hump" and additional characteristic lines. From Fig. 5 it is evident that the shape of the gamma hump changes during the cell discharge from a rounded to a nearer square shape with a wider base and in the last pattern it almost disappears. The charts given in Fig. 5 indicate that each of the so-called gamma humps are topped by a number of small peaks located at specific "d" values. It could be interpreted that the gamma hump itself is only the result of the near coincidence of these specific peaks and many peaks of lesser intensity which are interspersed among them. Attention is drawn to a comparison of the "d" values from 3.0 to 6.0 for the six diffraction patterns. In trying to compare such patterns, considerable care must be taken to avoid misinterpreting random variations in the background counting rate or instrumental hunting as actual but small individual peaks. However, the remarkable regularity shown in the "d" values of the specific lines which occur in several of the gamma hump patterns in Fig. 5 strongly suggest the predominant peaks could represent true diffraction lines.

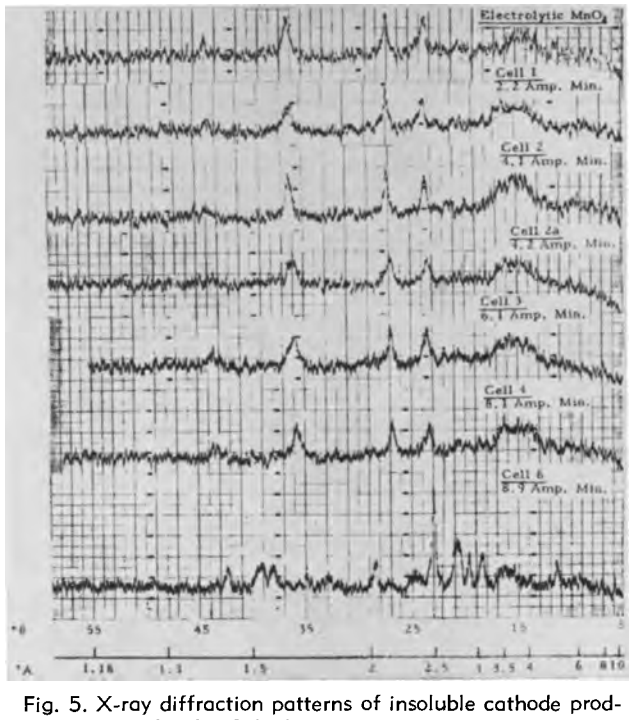

Fig. 5. X-ray diffraction patterns of insoluble cathode products at various levels of discharge.

Table IV. D values of x-ray diffraction patterns of MnO_2 shown in Fig. 5

Electrolytic MnO_2		Cell 1		Cell 2		Cell 3		Cell 4		Cell 6	
d	I	d	I	d	I	d	I	d	I	d	I
5.03	6	4.77	5	6.00	7	4.69	3	4.62	5	4.90	13
4.90	6	4.44	4	5.41	5	4.47	6-7	4.51	7	4.58	6
4.86	8	4.30	4-5	5.12	5	4.44	5	4.21	9	4.12	6
4.25	8	4.24	5	4.98	5	4.15	3	4.11	7	4.06	5
4.07	8	4.12	5-6	4.54	7	4.12	10	4.09	5	4.00	6
3.97	6	4.07	8	4.30	6-7	4.09	5-6	3.97	4	3.81	6
3.89	5	4.02	5	4.12	4-5	4.00	4	3.81	4	3.74	6
3.81	6	3.92	5	4.07	10	3.95	4	3.74	7	3.65	8
3.79	8	3.82	4	3.97	10-11	3.79	7	3.51	7	3.58	7
3.69	4	3.74	3	3.92	10	3.76	11	3.49	8	3.51	8
3.55	5	3.65	9	3.84	8-9	3.69	7	3.45	9	3.49	8
3.37	6	3.62	3	3.76	5	3.65	6	3.35	4	3.45	7
3.29	3	3.60	3	3.67	6	3.58	6	3.26	7	3.37	4
3.09	4	3.53	5	3.65	6	3.51	6	3.13	5	3.31	3
2.91	4	3.51	7	3.60	7	3.49	5	3.02	7	3.27	7
2.78	5	3.49	7	3.51	5	3.41	4	2.84	4	3.08	14
2.55	4	3.45	6	3.49	5	3.37	3	2.75	6	3.03	14
2.49	3	3.43	7	3.41	5	3.29	6	2.71	4	2.97	4
2.43	15	3.35	2	3.29	5	3.17	5	2.69	4	2.87	15
2.41	14	3.29	6-7	3.24	6	3.03	4	2.65	4	2.78	18
2.35	5	3.24	5	3.20	4	2.97	4	2.58	5	2.69	18
2.32	3	3.13	6	3.12	5	2.84	4	2.54	5	2.48	47
2.22	4	3.02	3	3.00	4	2.76	6	2.49	9	2.35	5
2.13	18	3.00	3	2.86	5	2.71	4	2.46	14	2.31	5
2.12	18	2.91	3	2.84	5	2.61	5-6	2.44	15	2.27	7
		2.79	5	2.76	6	2.60	5-6	2.39	8	2.19	7
		2.71	6	2.73	5-6	2.48	7-8	2.33	5	2.14	7
		2.69	2-3	2.68	5	2.44	17	2.28	5	2.11	7
		2.55	5	2.63	8	2.43	17	2.15	18	2.04	16
		2.51	3	2.42	16	2.41	15			2.02	14
		2.42	13	2.33	5	2.28	5				
		2.40	13	2.18	5	2.18	7				
		2.35	7	2.13	16	2.15	15				
		2.28	5	2.12	21	2.14	18				
		2.22	5			2.10	5				
		2.18	5			2.04	7				
		2.15	7								
		2.13	18								

Note: I indicates the relative intensity of the lines and is a measure of the height of divisions above the background.

It seems clear from Fig. 5 that the relatively simple diffraction pattern of the original electrolytic MnO_2 becomes much more complex as the discharge proceeds. It is quite easy to identify the major new component in cell 6, which was discharged to the lowest voltage, as Mn_3O_4. There is some evidence of the characteristic diffraction pattern lines of this material in the chart for cell 4 also, thus indicating that Mn_3O_4 begins to form after the cell reaches the 0.9-1.0 v level. However, it is in the intermediate range of discharge that the real question arises as to what insoluble cathodic product is present.

In view of the crystallographic difficulties involved in interpreting the significance of the gamma band in the pattern of electrolytic MnO_2, it seems unwise to attempt to assign exact diffraction spacings to the new phase which developed during the cell discharge. More extensive data would be required to establish the presence of such a new phase. Therefore, attention is drawn to the fact that a group of diffraction lines appears in the "d" value region of 3.7 to 3.3 which could be associated with the presence of the intermediate oxide tentatively designated Mn_4O_7. Added emphasis to this general point of view is furnished by the fact that some of these diffraction lines become reduced in intensity as the discharge proceeds and Mn_3O_4 is formed. An alternative explanation of these new diffraction lines would be that they might represent a solid solution of certain reduced manganese compounds in manganese dioxide. No conclusive evidence for solid solutions of manganese oxides in Leclanché dry cells has been published although the concept of a solid solution has been suggested in the absence of definitive data.

Perhaps the most complete analysis of the x-ray diffraction patterns of gamma MnO_2 is that of Cole, Wadsley, and Walkley (4) who postulate gamma, gamma I, and gamma II varieties. Their analysis of the gamma I type, electrolytic MnO_2, gives only the 3.94, 2.57, 2.41, 2.33, 2.11, 1.62, 1.41, and 1.37 lines. The 3.94 line apparently refers to the peak of the gamma band mentioned earlier in this paper. From the data presented in Fig. 5 and Table IV, there seems to be no indication that a change from the electrolytic MnO_2 to either of the other phases described by Cole, Wadsley, and Walkley occurs in the discharge of the experimental cells. The diffraction spacings presented in this paper do not conform with any of the patterns of reduced manganese

Table V. X-ray diffraction patterns for MnO_2 reduction by-products

Mn_2O_3		γ-Mn_2O_3		$Mn_2O_3H_2O$		$Mn_2O_3H_2O$		$MnO_{1.88}$		Mn_3O_4		Mn_3O_4		$MnxOy$		$HMnO_2$	
d	I/I_1	d	I/I_1	d	I/I_1	d	I/I_1	d	I/I_1	d	I/I_1	d	I/I_1	d	I/I_1	d	I/I_1
3.86	10	4.93	40	3.40	100	3.40	100	6.99	25	4.86	70	5.10	80	5.1	20	5.36	10
2.72	100	3.08	60	2.64	60	2.63	60	4.91	25D	3.05	50	3.09	20	4.39	100	4.17	100
2.35	10	2.74	70	2.53	5	2.53	40	3.99	10D	2.87	20	2.63	100	4.12	100	3.462	10-20
2.01	20	2.48	100	2.41	20	2.41	70	3.502	10D	2.74	90	2.51	15	3.34	20	2.798	60
1.84	30	2.39	40	2.28	50	2.26	40	3.132	75D	2.47	100	2.17	15	2.46	100	2.675	60
1.66	90	2.03	20	2.23	5N	1.77	50	2.755	10D	2.34	50	1.77	10	2.35	50	2.524	10
1.45	20	1.83	30	2.20	5	1.71	40	2.392	100	2.02	60	1.67	20	2.06	35	2.369	60
1.42	60	1.79	20	1.783	20	1.68	70	2.152	75D	1.812	10	1.53	18	1.74	50	2.303	50
1.39	20	1.59	30	1.708	40	1.64	20	2.086	10D	1.779	50			1.62	50	2.210	20
1.35	10	1.55	60	1.672	30	1.50	40	1.633	25	1.689	20			1.58	35	2.008	10
1.28	10			1.636	40	1.44	40	1.542	50D	1.629	15			1.50	20	1.957	5
1.19	5			1.502	20			1.425	50	1.571	60			1.30	20	1.932	10
1.18	10			1.437	30			1.368	25D	1.537	80			1.27	35	1.798	5
1.16	10			1.326	10			1.358	25D	1.462	10					1.763	20
1.14	10			1.297	10			1.348	25D	1.434	50					1.732	10
				1.256	5					1.405	10					1.692	50
				1.24	20S					1.378	10					1.603	40
				1.21	20S					1.340	20					1.559	0
				1.183	10					1.323	30					1.515	30
				1.162	10					1.238	10					1.465	10
				1.139	40					1.226	30					1.448	10
				1.116	20					1.215	10					1.435	20
				1.10	20S					1.189	30					1.398	10
				1.08	20S					1.175	30					1.367	5-10
				1.029	30					1.142	10					1.345	10
				1.01	—S					1.128	40					1.304	5
				0.993	10					1.095	10					1.286	10
				0.932	20S					1.075	50					1.281	10
				0.890	20S					1.053	30					1.267	10
				0.878	20S											1.258	10
				0.867	20S											1.220	10
				0.860	20S											1.212	10
				0.835	20S											1.202	10
																1.153	20
																1.134	10-20
Mineralogical designation		Bixbyite		Manganite						Ref: McMurdie & Golovato, J. Res. Nat. Bur. Stds., 41, 589 (1948)		Ref: Cowley & Walkley, Nature, 161, 173 (1948)				1.107	10
																1.086	5
																1.077	5
																1.068	30
																Ref: Gruener, Am. Min., 32, 654 (1947)	
																Groutite	
										Hausmannite							

compounds as shown in Table V which are possible products under the conditions used for testing. These compounds include manganite, $Mn_2O_3H_2O$, bixbyite, Mn_2O_3, and groutite, MnOOH (5).

Conclusion

A mechanism for the electrochemical reduction of electrolytic manganese dioxide in strongly alkaline electrolytes is proposed which consists of the several steps listed below.

Step 1.—The manganese dioxide is electrochemically reduced according to the two following reactions which occur simultaneously:

$$4MnO_2 + 2K^+ + 2e + H_2O \rightarrow Mn_4O_7 + 2KOH$$

$$MnO_2 + 2K^+ + 2e + 2H_2O \rightarrow Mn(OH)_2 + 2KOH$$

Step 2.—The intermediate insoluble oxide product formed in Step 1 then becomes the depolarizer which is electrochemically reduced by the following two reactions:

$$3Mn_4O_7 + 10K^+ + 10e + 5H_2O \rightarrow 4Mn_3O_4 + 10KOH$$

$$Mn_4O_7 + 6K^+ + 6e + 7H_2O \rightarrow 4Mn(OH)_2 + 6KOH$$

Step 3.—The insoluble product of the second step then becomes the depolarizer and is electrochemically reduced in this manner:

$$Mn_3O_4 + 2K^+ + 2e + 4H_2O \rightarrow 3Mn(OH)_2 + 2KOH$$

Step 1 occurs during the first part of the discharge while the working voltage falls from the initial value of 1.46 to 1.20. Step 2 apparently operates in the working voltage range of from 1.20 to 0.95. Step 3 occurs in the range below 0.95 v to the complete reduction of the oxide to $Mn(OH)_2$. Much of this last part of the discharge often occurs at a working voltage of 0.4-0.5 v or lower.

Manuscript received March 10, 1959. This paper was prepared for delivery before the Ottawa Meeting, Sept. 28-Oct. 2, 1958.

Any discussion of this paper will appear in a Discussion Section to be published in the June 1960 JOURNAL.

REFERENCES

1. N. C. Cahoon, R. S. Johnson, and M. P. Korver, *This Journal*, **105**, 295 (1958).
2. J. J. Lingane and Robert Karplus, *Ind. Eng. Chem., Anal. Ed.*, **18**, 191 (1946).
3. W. S. Herbert, *This Journal*, **99**, 190C (1952).
4. W. F. Cole, A. D. Wadsley, and Allan Walkley, *Trans. Electrochem. Soc.*, **92**, 133 (1947).
5. J. W. Gruener, *Am. Min.*, **32**, 654 (1947); Cyrus Klingsberg, "The System Mn-O-OH," Ph.D. Thesis, Pennsylvania State University, 1958.

High-Temperature Reaction Rates of Several Metals with Hydrogen Chloride and Water Vapor

Milton Farber

Research Laboratories, Rocket Power Inc., Pasadena, California

ABSTRACT

An experimental study has been made of the high-temperature reaction rates of various metal filaments with HCl and H_2O vapors and mixtures of the two. Measurements were made by an electrical method in which the change in resistance of the metal filament was related to the loss in pure metal due to the vapor-metal reaction. Measurable reaction rates were determined for both nickel and iron in a temperature range from 1000° to 1600°K. Specific reaction rate constants and apparent activation energies are presented. The reaction rates of tungsten with H_2O vapor were measured in a temperature range from 1600° to 2000°K. The reaction rates of chromium, Inconel, stainless steel 18-8, and tungsten did not proceed at a measurable rate in either pure HCl or in mixtures of HCl and H_2O. Nickel, copper, Inconel, and stainless steel 18-8 did not react appreciably with water vapor at temperatures approaching the melting points. The reaction rates for iron in pure HCl varied from 0.03 to 0.04% area loss per second over the temperature range investigated with an apparent activation energy of 10.5 kcal/mole. The reaction rates of iron in mixtures of HCl and H_2O varied from 0.08 to 0.17% area loss per second in the same temperature range with an apparent activation energy of 8.5 kcal/mole. Reaction rates of nickel in pure HCl varied from 0.005 to 0.03% area loss per second in the temperature range of 1000° to 1600°K with an apparent activation energy of 13 kcal/mole. The reaction rates of nickel in the HCl and H_2O mixtures varied from 0.004 to 0.03% area loss per second in the same temperature range with an apparent activation energy of 22 kcal/mole below 1300°K and 13 kcal/mole above this temperature. Reaction rates of iron in H_2O vapor varied from 0.002 to 0.05% area loss per second from 1120° to 1415°K with an activation energy of 28 kcal/mole. Reaction rates of tungsten in H_2O vapor varied from 0.02 to 0.03% area loss per second from 1700° to 2000°K with an activation energy of 14.5 kcal/mole.

In the field of high-temperature reactions of gases and metals, reaction rates are measured in terms of seconds as compared to days and years for reactions between metals and gases at conventional temperatures. This paper is the third in a series of investigations of the reaction rates of several metals with the combustion products of chemical propellants. Previous papers (1, 2) include the study of several metals with H_2S, SO_2, and NO at a temperature range from 1000°-2000°K.

Concerning the reactions of metals with HCl some previous work of a qualitative nature has been reported. A few investigators have studied this reaction by allowing the metal to remain in the HCl atmosphere for a period of time and obtaining the corrosion rate by the loss in weight of the metal (3, 4). Brown, DeLong, and Auld (5) studied the corrosion rates of nickel, platinum, gold, Inconel, stainless steel, Monel, copper, iron, and several nickel and chromium alloys in dry HCl and also in a mixture of HCl containing 0.2% H_2O. They found that nearly all the metals, with the exception of gold and platinum, are corroded quite readily at fairly low temperatures and that the addition of the water vapor increases the corrosion rate only slightly.

When a metal is corroded in an atmosphere of either dry or wet hydrogen chloride, the reaction products are usually the metal chloride and hydrogen as:

$$M + HCl = MCl + \tfrac{1}{2}H_2$$

In the presence of water vapor the reaction can become quite complicated because of the possible formation of other compounds of the metal besides the chloride.

The dissociation of water to H_2 and OH radicals is less than 1% at temperatures below 2000°K, while

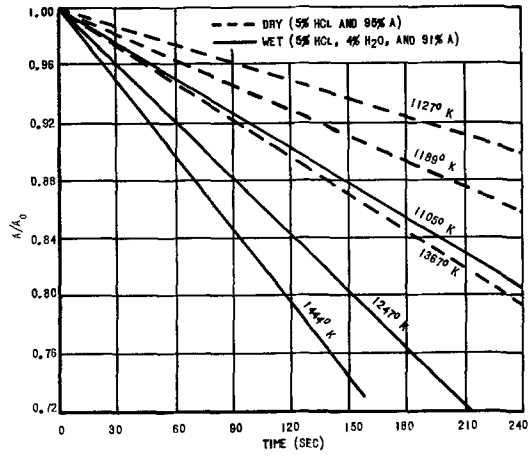

Fig. 1. Corrosion rate of Fe with dry and wet HCl vs. time

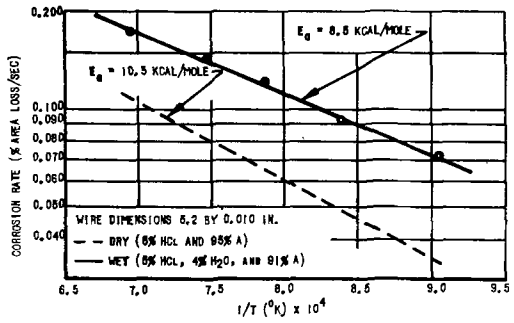

Fig. 2. Corrosion rate of Fe with dry and wet HCl as function of 1/T.

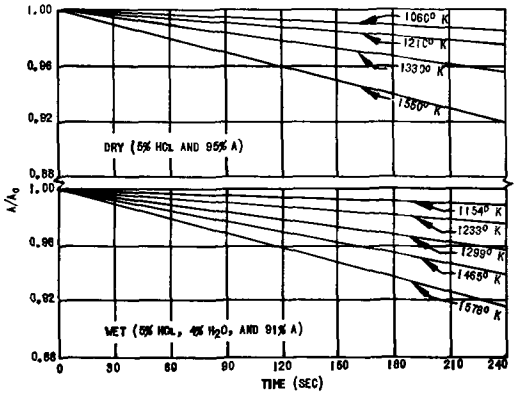

Fig. 3. Corrosion rate of Ni with dry and wet HCl vs. time

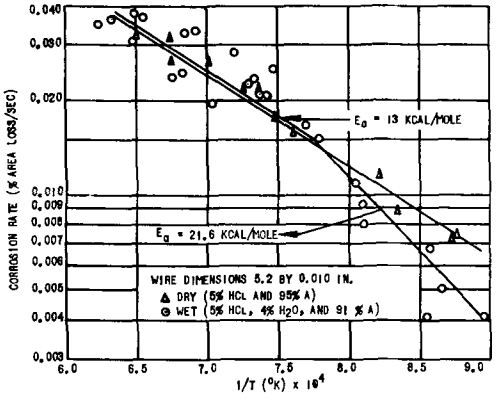

Fig. 4. Corrosion rate of Ni with dry and wet HCl as function of 1/T.

the dissociation of water to O_2 and H_2 does not become appreciable below 3000°K.

Experimental Procedure

The author (1, 2) has previously employed the method presented in this paper for measuring the reaction rates of various metals with H_2S, SO_2, and NO and the apparatus has been described. Garner, Gray, and Stone (6) studied the reaction rate of copper with oxygen by measuring the increase in resistance of a copper film which was plated on the walls of a glass bulb. Wilson (7) and Hudson (8) studied corrosion rates by measuring the change in electrical conductivity of flat metal strips. The method employed here and described in detail earlier (1) is concerned with the measurement of the change in resistance of a metal filament (hot wire) of 0.010 in. diameter in a corrosive medium. Since the corrosion rate is obtained directly from the resistance change, a recording mechanism is necessary to indicate the current and voltage across the filament. The arrangement of the equipment used to conduct rate experiments has been described previously (2).

In order to obtain uniform corrosion of the wire, it is necessary to use filaments which have been accurately machine-drawn. Thus, hot spots can be eliminated and consistent burnout times obtained, justifying the resistance method for measuring corrosion rates.

Theoretical corrosion rate laws have been derived (2) for these cylindrical wires. These resulted in the following rate laws for

Table I. Initial reaction rates of Fe and Ni with dry and wet HCl

Metal	T, °K	(1/T) x 10^4	k, % area loss/sec
Gas mixture: 95% argon and 5% HCl			
Iron	1127	8.87	0.037
	1184	8.44	0.042
	1198	8.34	0.053
	1222	8.18	0.064
	1300	7.69	0.068
	1305	7.66	0.083
	1388	7.20	0.087
Nickel	1060	9.44	0.0053
	1140	8.76	0.0073
	1146	8.73	0.0073
	1195	8.37	0.0087
	1210	8.27	0.0113
	1313	7.61	0.0153
	1330	7.52	0.0173
	1355	7.38	0.0213
	1373	7.28	0.0213
	1419	7.07	0.0260
	1486	6.73	0.0260
	1550	6.48	0.0320
Gas mixture: 91% argon, 5% HCl, and 4% H_2O			
Iron	1105	9.05	0.075
	1186	8.43	0.092
	1274	7.84	0.122
	1335	7.49	0.142
	1444	6.93	0.172
Nickel	1115	8.97	0.0042
	1154	8.67	0.0050
	1162	8.60	0.0067
	1167	8.57	0.0042
	1231	8.12	0.0080
	1233	8.11	0.0092
	1241	8.05	0.0108
	1255	7.97	0.0075
	1283	7.80	0.0150
	1299	7.70	0.0167
	1333	7.50	0.0233
	1340	7.47	0.0250
	1347	7.42	0.0208
	1354	7.38	0.0192
	1355	7.38	0.0208
	1360	7.35	0.0233
	1391	7.19	0.0283
	1445	6.92	0.0333
	1460	6.85	0.0325
	1528	6.55	0.0367
	1543	6.48	0.0308
	1543	6.48	0.0375
	1578	6.33	0.0358
	1608	6.22	0.0341

parabolic

$$A/A_o = 1 - 2\sqrt{\frac{2\pi kt}{A_o}} + \frac{2\pi kt}{A_o} \qquad [1]$$

rectilinear

$$A/A_o = 1 - 2(\pi/A_o)^{1/2} kt + \pi/A_o k^2 t^2 \qquad [2]$$

logarithmic

$$A/A_o = 1 - 2(\pi/A_o)^{1/2} \ln (1+kt) + \pi/A_o \ln (1+kt)^2 \qquad [3]$$

The results obtained for the metals studied yield an experimental rate law of

$$A/A_o = 1 - k/100\, t$$

where: A is the cross-sectional area of wire remaining at time t, A_o is the initial area of wire, and k is per cent area change per second.

This expression is similar to the logarithmic rate law for thin coatings and also to the rectilinear rate law for initial corrosion, wherein the third term is small compared to the second.

It was shown in the previous papers (1, 2) that the conductivity of oxide coatings was negligible in comparison to that of the pure metal even at high temperatures (9). However, in the case of the chlorides, metal chlorides are usually in the vapor phase at the temperatures in question and the surface remains essentially clean during the course of the experiment.

The effect of the solubility of the gases on the resistance of the metal filaments investigated was negligible since there was no discernible change in their resistance at temperatures just below the point of corrosion. However, it was not possible to study the corrosion rates of metals such as zirconium or titanium because the solubility of oxygen and nitrogen changed their resistivities to such an extent that the change in resistance due to corrosion could not be measured.

Results

Reaction Rates of Metals with HCl

Reaction rates of iron with HCl.—Corrosion rates of iron were investigated in both dry HCl (95% A-5% HCl) and wet HCl (91% A-5% HCl-4% H_2O) over a range of temperature from 1100° to 1450°K. The results of the corrosion rates are shown as a function of time in Fig. 1. As may be seen from this figure, the corrosion rate of iron in the wet HCl is slightly faster than in the dry HCl. This fact would tend to indicate that the presence of water speeds up the reaction. In Fig. 2, the logarithm of the rate is plotted against the reciprocal of the absolute temperature. The activation energies are 8.5 and 10.5 kcal for the wet and the dry HCl, respectively. The rate constants as functions of the temperature are given in Table I.

Reaction rates of nickel with HCl.—The corrosion rate of nickel was also investigated in both dry and wet HCl mixtures over a temperature range from 1050° to 1600°K. The rates are given in Fig. 3. The corrosion of nickel with dry HCl shows a slightly higher rate than with wet HCl, particularly in the lower temperature range, as can be seen from the plot of the logarithm of the corrosion rate as a function of the reciprocal of the absolute temperature shown in Fig. 4.

The activation energy for the wet HCl is of the order of 22 kcal/mole for temperatures below 1300°K and decreases to 13 kcal/mole above this temperature. This latter value is approximately the same as for the dry HCl over the entire temperature range covered. The rate constants for the corrosion rates of nickel in both dry and wet HCl are given in Table I. The rates are of the order of approximately 20% of those for iron in the same gas mixtures.

Table II. Initial reaction rates of Fe and W with H_2O

Metal	T, °K	(1/T) x 10^4	k, % area loss/sec
Gas mixture: 95% argon and 5% H_2O			
Iron	1122	8.91	0.0020
	1195	8.36	0.0070
	1202	8.31	0.0085
	1253	7.98	0.0105
	1280	7.81	0.0195
	1314	7.46	0.0260
	1415	7.06	0.0475
Tungsten	1685	5.93	0.0170
	1780	5.61	0.0233
	1800	5.55	0.0185
	1860	5.37	0.0200
	1870	5.34	0.0194
	1965	5.08	0.0313
	1995	5.01	0.0313

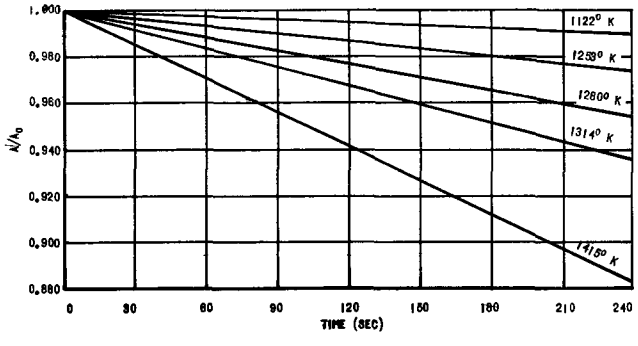

Fig. 5. Corrosion rate of Fe with H_2O vs. time

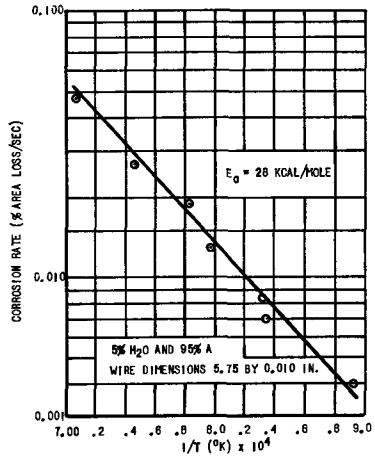

Fig. 6. Corrosion rate of Fe with H_2O as function of 1/T

Table III. Activation energies and rate constants of several metals with reactive gases[a]

Metal	Gas (Pressure = 1 atm) 5% HCl-95% A E_a (kcal/mole)	a	5% HCl-4% H_2O-91% A E_a (kcal/mole)	a	4% H_2O-96% A E_a (kcal/mole)	a
Fe	10.5 (1120 to 1400°K)	4.14	8.5 (1180 to 1430°K)	3.46	28 (1030 to 1400°K)	9.98×10^2
Ni	13.0 (1140 to 1540°K)	2.34	21.6 (1140 to 1300°K)	69.4	—	—
	—	—	13.0 (1300 to 1560°K)	2.41	—	—
W	—	—	—	—	14.5 (1700 to 2000°K)	1.25

[a] E_a = activation energy; a = exponential constant; $k = ae^{-E_a/RT}$.

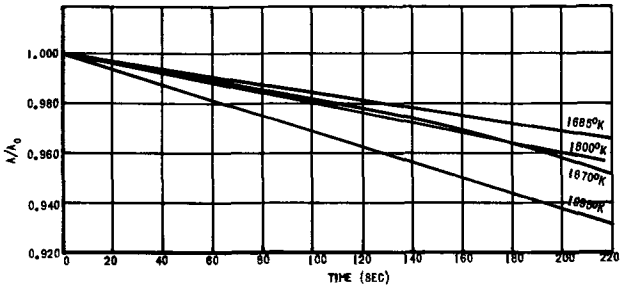

Fig. 7. Corrosion rate of W with H_2O vs. time

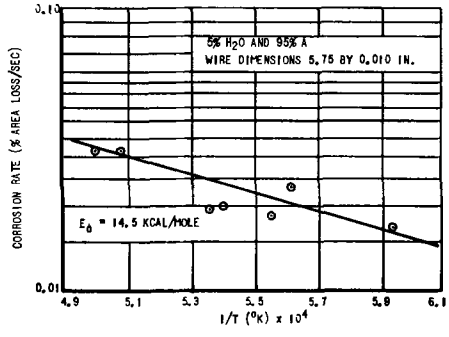

Fig. 8. Corrosion rate of W with H_2O as function of 1/T

Reaction Rates of Several Metals with Water Vapor

Several metals including iron, tungsten, nickel, copper, Inconel, and stainless steel 18-8 were tested in a gas mixture containing 95% A and 5% H_2O vapor. Iron and tungsten were the only metals of the group that corroded at a measurable rate at temperatures approaching the melting points.

Reaction rates of iron with water vapor.—Corrosion rates of iron in a mixture of 95% A and 5% H_2O vapor were measured in a temperature range of 1100° to 1400°K. Corrosion rates are plotted against time in Fig. 5. A plot of the logarithm of the corrosion rate against the reciprocal of the absolute temperature gives an activation energy of 28 kcal/mole (Fig. 6). The rate constants k, which are listed in Table II, vary from 0.0020 (% area loss/sec) at 1120°K to 0.047 at 1415°K.

Reaction rates of tungsten with water vapor.—The corrosion of W in H_2O does not become appreciable until temperature of 1600°K is attained. The corrosion rates of tungsten in a gas mixture of 95% A and 5% H_2O vapor were measured in the temperature range from 1685° to 1995°K. At the higher temperatures the dissociation of H_2O to H_2 and OH is in the neighborhood of 0.1%. The curves of corrosion rate vs. time are shown in Fig. 7. The plot of the logarithm of the rate vs. $1/T$ gives an activation energy of 14.5 kcal/mole (Fig. 8). The rate constants listed in Table III vary from 0.0170 (% area loss/sec) at 1685°K to 0.0313 at 1995°K.

Manuscript received Aug. 9, 1957. Some of the laboratory work for this paper was performed at the Jet Propulsion Laboratory, California Institute of Technology under Contract No. DA-04-495-ORD 18, sponsored by the Department of the Army, Ordnance Corps.

Any discussion of this paper will appear in a Discussion Section to be published in the June 1960 JOURNAL.

REFERENCES

1. M. Farber and D. M. Ehrenberg, *This Journal*, **99**, 427 (1952).
2. M. Farber, A. J. Darnell, and D. M. Ehrenberg, *ibid.*, **102**, 446 (1955).
3. W. Z. Friend and B. B. Knapp, *Trans. Am. Inst. Chem. Engrs.*, **39**, 731 (1943).
4. B. Pershke and L. Pecherkin, *Khimstroi*, **6**, 140 (1934).
5. M. H. Brown, W. B. DeLong, and J. R. Auld, *Ind. Eng. Chem.*, **39**, No. 7, 839 (1947).
6. W. E. Garner, T. J. Gray, and F. S. Stone, *Proc. Roy. Soc. London*, **A197**, 294 (1949).
7. E. Wilson, *Proc. Phys. Soc. London*, **39**, 15 (1926).
8. J. C. Hudson, *ibid.*, **40**, 107 (1928).
9. S. Veil, Thesis, Paris (1920); International Critical Tables, 4, p. 153.

The Electrochemical Behavior and Passivity of Titanium

Milton Stern and Herman Wissenberg

Metals Research Laboratories, Union Carbide Metals Company, Division of Union Carbide Corporation, Niagara Falls, New York

ABSTRACT

In the active condition, corrosion of titanium is controlled by activation polarization. The metal presents a surface with a low exchange current for a variety of electrochemical reactions. Low exchange currents are not conducive to establishment of passivity. However, this is overcome by unusually active critical potentials for passivity. This accounts for the ease with which titanium is passivated by many substances which are only slightly oxidizing. It also explains the ease with which the metal can be protected anodically by galvanic coupling to other metals and alloys. Anodic deposition of thick titanium oxide films is observed under some experimental conditions.

The mechanism of passivating-type inhibitors has been described (1) solely in terms of the kinetics of the various electrochemical processes which occur, without the necessity for reference to the nature of the passive film. The environmental parameters which are pertinent to the achievement of passivity are the exchange current, Tafel slope, and limiting diffusion current for cathodic processes. Passivity is favored by high values of exchange current and limiting diffusion current and by low values for the Tafel slope. The important parameters related to the metal are the critical anodic current and the critical potential for passivity. A low value of critical anodic current and a relatively active critical potential favor passivity.

Titanium shows active-passive behavior similar to stainless steel except that it is not affected adversely by chloride ion and does not exhibit transpassive behavior. This work was done to obtain data which would relate the anodic behavior of Ti to the parameters of temperature and acid concentration. Such information should help in understanding passivity of Ti and permit more efficient use of passivating inhibitors.

Experimental Procedure

Electrodes, glass cells, and methods for measuring potential were generally the same as those reported elsewhere (2) except that anodic polarization measurements were conducted with an Analytical Instruments Company[1] potentiostat, an electromechanical device. It was necessary to use the same material for the test electrode and for a potentiostat reference electrode and to place the two electrodes in the same solution, since the potentiostat does not operate properly if a high impedance exists between these electrodes. Auxiliary electrodes of the same material as the test electrode were placed directly in the cell. All electrodes were aged for about 30 min in the solution before the first measurement. Potentials were measured by means of a Luggin probe to minimize errors caused by *IR* drop. Potentials were measured against a saturated calomel electrode external to the cell at room temperature. No effort was made to correct for liquid junction potentials or temperature effects when the solution was hot.

In systems where hydrogen was used, the gas was purified with Cu at 500°C followed by Pt and Pd catalysts. The solution was further purified by pre-electrolysis for 3 hr on a Ti cathode held at −1.0 v vs. saturated calomel with the potentiostat. The current density during pre-electrolysis was greater than 80 ma/cm^2. In this case, auxiliary electrodes were external to the cell and connected to it by salt bridges.

The Ti metal was of commercial purity containing 0.032% C and 0.13% oxygen.

Behavior of Hydrogen-Saturated H_2SO_4

Figure 1 shows anodic and cathodic polarization curves for Ti in hydrogen-saturated 20% H_2SO_4 at

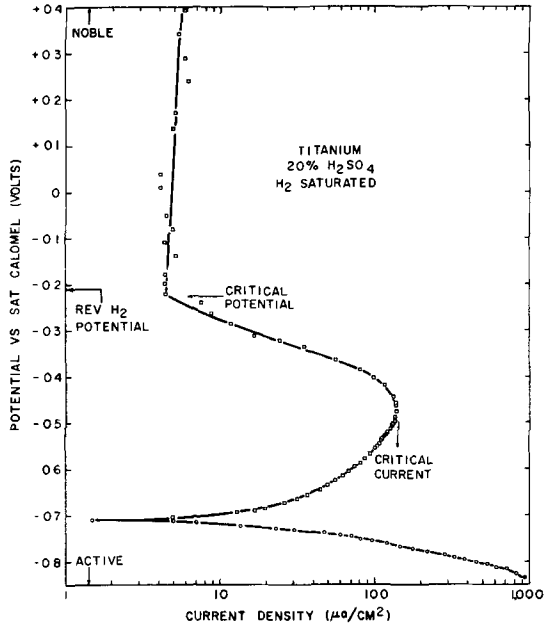

Fig. 1. Anodic and cathodic behavior of Ti in room-temperature, hydrogen-saturated 20% H_2SO_4.

[1] Bristol, Connecticut.

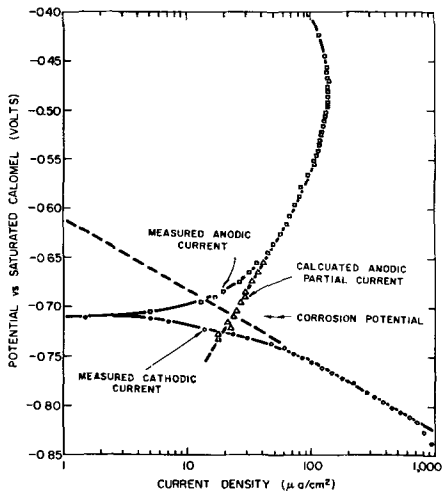

Fig. 2. Expanded view of Fig. 1 showing the calculated anodic polarization curve of Ti.

room temperature. The reversible hydrogen potential of this solution, measured with platinized Pt, is —0.21 v vs. saturated calomel. Polarization data were obtained with the potentiostat by starting at a potential of —0.85 v and gradually increasing the potential in the noble direction. The cathodic curve exhibits a Tafel slope of 0.07 v and an exchange current of only 1.9 (10^{-12}) amp/cm². Relatively small changes in Tafel slope will have a marked effect on exchange current, since extrapolation to the reversible hydrogen potential is made over a potential range of about 0.6 v. Thus, the measured exchange current could be in considerable error. It is evident, however, that the hydrogen ion reduction reaction on Ti is accompanied by a high overvoltage (approaching that of Hg) because of the extremely small exchange current. This agrees with other observations (3, 4).

The anodic data show a critical current for passivity of 140 μa/cm². The critical potential for passivity is about —0.23 v vs. saturated calomel which is 20 mv more active than the potential of Pt in the hydrogen-saturated 20% H_2SO_4 solution. If one defines passivity as the state where the potential of a metal is more noble than the critical potential shown in Fig. 1, then it becomes evident that Ti can show stable passive behavior in solutions which contain a redox system no more oxidizing than the hydrogen ion-hydrogen gas system. Passivity in hydrogen-saturated solutions is an unusual phenomenon which is not observed in Fe- or Ni-base alloy systems. The relatively active critical potential exhibited by Ti explains, in part, the ease with which this metal is passivated by many oxidizing inhibitors.

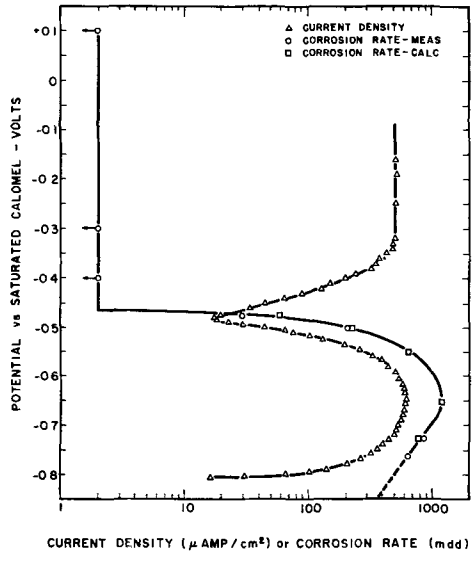

Fig. 3. Current density and corrosion rate at controlled potentials for Ti in boiling 2% H_2SO_4 containing 5% Na_2SO_4.

The data of Fig. 1 permit an examination of the dissolution kinetics of Ti in the active potential region to determine if they are consistent with presently accepted views on electrode kinetics involving activation overvoltage. Figure 2 shows an expanded view of the data close to the corrosion potential. Calculated values of the dissolution rate of Ti as a function of potential are shown as triangles. The methods used for this calculation are similar to those already described (2). The points more noble than the corrosion potential were obtained by summing the extrapolated rate of hydrogen reduction and applied anodic current at any given potential. The points on the active side of the corrosion potential were obtained by subtracting the applied cathodic current from the extrapolated rate of hydrogen reduction at any given potential.

It is evident that in this potential region the dissolution kinetics are controlled by activation polarization with a Tafel slope of 0.22 v. While this value is high, the kinetics near the corrosion potential cannot be considered unusual. Thus, the phenomena associated with passivity are not evident near the corrosion potential but become significant near the potential region associated with the critical current for passivity.

Correlation of Polarization Data with Weight Loss Measurements

An anodic polarization curve, such as that shown in Fig. 1, is expected to represent the dissolution rate of Ti as a function of potential, except in the region close to the corrosion potential where the measured current is significantly less than the dissolution rate as illustrated in Fig. 2. To check this, data were obtained with Ti in boiling 2% H_2SO_4 containing 5% Na_2SO_4, where corrosion rates are higher than at room temperature and more easily measured.

Figure 3 shows the anodic polarization curve obtained. The portion below the critical potential for passivity is as expected. The current rises to some maximum value (the critical current for passivity) and then falls to a low value at the critical potential for passivity. Weight loss measurements in the same environment utilized separate electrodes, each held at a controlled potential for 18-24 hr. Continuous recording during these measurements revealed long-time current variations. These are attributed to changes in the environment caused by accumulating corrosion products from the sample, the auxil-

iary electrodes, and the potentiostat reference electrode. Assuming that Ti corrodes to form trivalent ions, integration of each current-time curve leads to a calculated corrosion weight loss which is also plotted on Fig. 3 (squares) along with the measured weight loss (circles).

It is evident from Fig. 3 that dissolution rate as a function of potential closely parallels the anodic polarization curve in the potential region more active than the critical potential for passivity. Quantitative agreement between the measured corrosion rates and the anodic polarization curve is precluded by differences in experimental procedure. For example, each point on the polarization curve represents only 3 min at that potential contrasted to a minimum of 18 hr for a weight loss measurement.

Unexpected behavior is found in the anodic polarization curve above the critical potential for passivity. Rather than remaining relatively constant with increasing potential as shown in Fig. 1, the current again rises and finally reaches a limiting value. This does not represent the anodic behavior of Ti, but is an artifact resulting from the experimental procedure used. This can be shown in the following manner. Electrodes held at constant potential in this region show a considerable weight gain and develop a thick oxide coating which is not particularly adherent. Scraping the oxide off accounts for all of the weight gain within the error of the technique, and the final sample shows a corrosion rate of less than 2 mdd. Therefore, anodic current measured in this region does not represent oxidation of metal but rather represents a different oxidation process. The most likely process is electrodeposition of oxide in accordance with a reaction of the type $Ti^{+3} + 2H_2O \rightarrow TiO_2 + 4H^+ + e$. It is quite possible that this is not the specific reaction which occurs, since lower oxides could also have been produced. In any event, it is clear that corrosion products are plated onto the anode surface in the form of oxides. The vertical line on the polarization curve probably represents the limiting diffusion current for the process.

The current associated with oxide deposition may obscure the true value of the critical potential for passivity. The critical potential shown in Fig. 3 could be slightly more active than the true value. This error is probably not significant as evidenced by the weight loss data.

Since the corrosion rate of Ti in the potential region of oxide deposition was less than 2 mdd (the experimental error in weight change), the points on Fig. 3 are shown at 2 mdd with arrows indicating the rate is less than this value. Thus, above the critical potential for passivity, the dissolution rate is very slow.

Cotton (5) has measured corrosion rate as a function of potential for Ti in 40% H_2SO_4 at 60°C. His data are similar to those shown here and extend to 2 v more noble than the saturated calomel electrode.

Anodic Polarization by Galvanic Coupling

Anodic passivation of Ti by means of an externally applied potential is described above. Titanium can also be passivated by galvanic coupling (5-7) with some metal or alloy whose potential is more noble than the critical potential for passivity of Ti in the given environment. The mixed potential of the resulting couple must also be more noble than the critical potential. Since the couple mixed potential is dependent on cathodic polarization, large cathode areas should favor passivation of Ti.

Table I. Effect of galvanically coupling titanium to various cathodic materials in boiling H_2SO_4 solutions

Couple	Area ratio A (Ti) / A (Cathode)	Weight loss of titanium (mdd) Boiling* 1% H_2SO_4	Boiling† 3% H_2SO_4 + 5% Na_2SO_4	Boiling‡ 5% H_2SO_4 + 5% Na_2SO_4
Ti		1400	1800	2900
Ti-(18-8)	1	0		
	2	10		
	6.6	6		
Ti-(Hastelloy alloy F)	1	0		
	12	2		
Ti-C	0.2	0	0	3600
	0.5		0	
	1		1200	
Ti-Pt	0.25			21
	1			65
	2			65
	4			108
	35			1700

* Critical potential for passivity of Ti is −0.45 v vs. saturated calomel.
† Critical potential for passivity of Ti is −0.42 v vs. saturated calomel.
‡ Critical potential for passivity of Ti is −0.34 v vs. saturated calomel.

Table I shows the effect of coupling Ti to Pt, C, 18-8 stainless steel, and Hastelloy alloy F in several environments as a function of the ratio of Ti area to cathode area. All the above materials exhibit potentials in these environments which are more noble than the critical potentials for passivity of Ti. In these experiments, no effort was made to estimate surface roughness factors, and all areas are calculated from geometric measurements assuming smooth surfaces. Results show that all of these materials can passivate Ti if sufficient cathode area is present. The more aggressive the environment, the greater the cathode area necessary to passivate. It is important to note that stainless steel and Hastelloy alloy F are both electrochemically active in boiling 1% H_2SO_4. However, their active mixed potentials are still sufficiently more noble than the critical potential for passivity of Ti to produce passivity when galvanically coupled to this metal.

Effect of Temperature on Dissolution Kinetics

Since temperature is known to affect the behavior of passivating inhibitors, it is important to establish how temperature affects those metal dissolution parameters which determine when stable passivity can be achieved.

Figure 4 shows the anodic polarization behavior of Ti in hydrogen-saturated 5% H_2SO_4 containing 5% Na_2SO_4. The critical current for passivity increases considerably as temperature is increased from 50° to 95°C. The critical potential for passivity is not significantly affected. In general, temperature

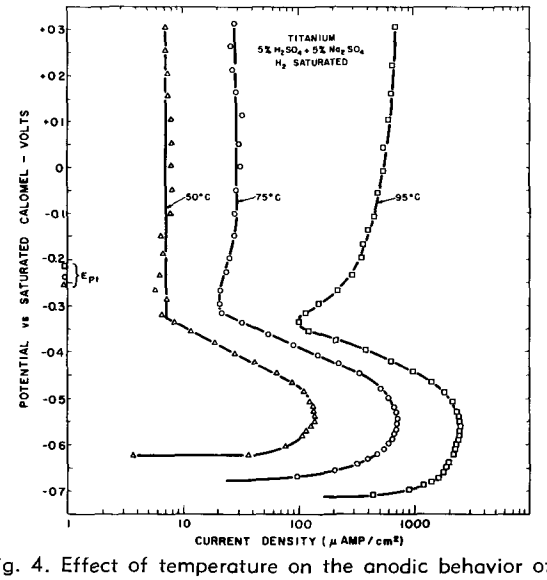

Fig. 4. Effect of temperature on the anodic behavior of Ti in hydrogen-saturated 5% H_2SO_4 containing 5% Na_2SO_4.

serves only to increase reaction rates, shifting the curves to higher current values with an increase in temperature.

At 95°C, where corrosion product build-up is faster, oxide deposition is again observed as evidenced by the shape of the polarization curve in the passive region. At 50° and 75°C, the oxidation rate of corrosion products is probably not significant, and passive currents represent the dissolution rate which also increases with temperature.

The measured potential of platinized Pt as a function of temperature is also shown on Fig. 4. It is important to note for subsequent discussion that the critical potential for passivity of Ti is again more active than the reversible hydrogen potential for this system.

Effect of Acid Concentration on Dissolution Kinetics

Figure 5 shows the anodic polarization behavior of Ti in various concentrations of boiling H_2SO_4

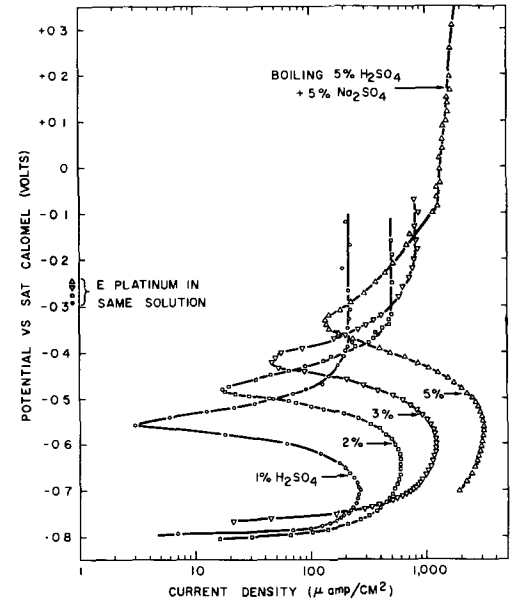

Fig. 5. Anodic behavior of Ti in boiling H_2SO_4 solutions containing 5% Na_2SO_4.

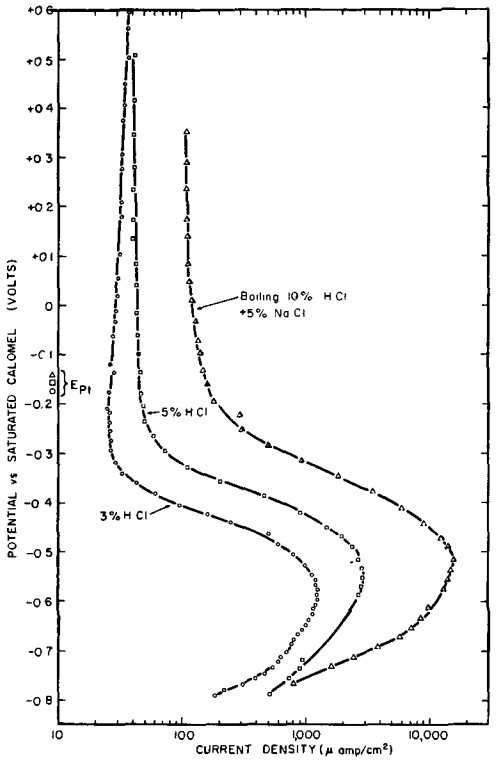

Fig. 6. Anodic behavior of Ti in boiling HCl solutions containing 5% NaCl.

containing 5% Na_2SO_4. Paralleling the effect of temperature, increasing acid concentration markedly increases the critical current for passivity. However, the critical potential for passivity and the potential at the critical current are shifted in the noble direction.

Corrosion product build-up in the solution is sufficiently fast at the boiling point to cause oxide deposition in the passive region. Thus, as described above, anodic current in the passive region does not represent the effect of acid concentration on passive corrosion rate. Rather, the vertical section probably represents the limiting diffusion current for the deposition process which increases with acid concentration because corrosion product build-up increases.

Oxide deposition is not observed in HCl as shown in Fig. 6, where it is evident that the passive corrosion rate increases with acid concentration.

Discussion and Conclusions

In the active condition, corrosion of Ti is controlled by activation polarization. The metal exhibits a particularly high hydrogen overvoltage (low exchange current). In general, it presents a surface with a low exchange current for a variety of electrochemical reactions as evidenced by measurements of rates of ferric ion reduction and oxygen evolution (8). Low exchange currents are not conducive to establishment of passivity. However, this is overcome by unusually active critical potentials for passivity. The critical potential for passivity of Ti is about 0.6 v more active than the corresponding value for Fe and about 0.1-0.2 v more active than the value for stainless steel. The exact differences, of course, are dependent on the environment used

for comparison. This, in large part, accounts for the ease with which Ti is passivated by many substances which are only slightly oxidizing. It also explains the ease with which the metal can be protected anodically by galvanic coupling to other metals and alloys.

Potentiostatic measurements in H_2SO_4 containing corrosion products of Ti show that increasing anodic polarization of Ti in the passive potential region results in an increasing current. This current is caused by anodic deposition of titanium oxide rather than an increasing Ti corrosion rate.

Data presented here show that, as temperature increases, the concentration of inhibitor required to passivate increases. Since the inhibitor concentration must provide a limiting diffusion current greater than the critical current for passivity (1), measurements of the type presented here permit an estimate of the minimum concentration of inhibitor required to attain passivity of a given system as temperature is raised.

The situation is similar for an increase in acid concentration except that, since the critical potential for passivity becomes more noble, the inhibitor must exhibit a greater oxidizing character (more noble reversible potential) for more acid environments.

For anodic protection of Ti by galvanic coupling to a cathodic metal or alloy, data presented here assist in the determination of the couple area ratio required to produce passivity of Ti. The cathodic polarization behavior of the cathode member of the couple also must be known and its area made sufficiently large so that the mixed potential of the couple is more noble than the critical potential of Ti in the environment.

Acknowledgment

The authors acknowledge the skillful assistance of E. J. Bartolomei who obtained much of the data presented here.

Manuscript received April 6, 1959. This paper was prepared for delivery before the Columbus Meeting, Oct. 18-22, 1959.

Any discussion of this paper will appear in a Discussion Section to be published in the June 1960 JOURNAL.

REFERENCES

1. M. Stern, *This Journal*, **105**, 638 (1958).
2. M. Stern, *ibid.*, **102**, 609 (1955); **104**, 391, 559 (1957).
3. S. Tajima, Y. Nakamura, and T. Mori, *J. Electrochem. Soc. Japan*, **22**, 513 (1954).
4. M. E. Straumanis, S. T. Shih, and A. W. Schlechten, *J. Phys. Chem.*, **59**, 317 (1955).
5. J. B. Cotton, *Chemistry & Industry*, p. 68, Jan. 18, 1958.
6. W. R. Buck, III and H. Leidheiser, *Nature*, **181**, 1681 (1958).
7. N. D. Tomashov, *Z. Elektrochem.*, **62**, 717 (1958).
8. M. Stern, *This Journal*, **104**, 600 (1957).

The Influence of Noble Metal Alloy Additions on the Electrochemical and Corrosion Behavior of Titanium

Milton Stern and Herman Wissenberg

Metals Research Laboratories, Union Carbide Metals Company, Division of Union Carbide Corporation, Niagara Falls, New York

ABSTRACT

Alloying of titanium with small amounts of noble metals markedly improves its corrosion resistance in reducing-type acids without any impairment of its high resistance to oxidizing media. The mixed potentials of titanium noble metal alloys are more noble than the critical potential for passivity of titanium in the same environment. Passivity is observed in hydrogen-saturated systems without the presence of a redox system more oxidizing than the hydrogen electrode. The mixed potential of titanium noble metal alloys is much more sensitive to traces of oxidizing agents than unalloyed metal.

Previous work (1) proposed that passivating-type inhibitors function primarily by creating a mixed potential more noble than the critical potential for passivity of the metal involved. The establishment of a potential more noble than some critical value is a basic concept which applies not only to inhibitors but also to the phenomenon of anodic protection (2) and prevention of corrosion by galvanic coupling to suitable cathode materials (3-5).

Anodic polarization under a variety of conditions shows that Ti exhibits unusually active values of critical anodic potential (5). Often, this potential is even more active than the reversible hydrogen potential of the solution. This permits establishment of passivity by alloying with elements having low overvoltage characteristics.

The purpose of this work is to describe the corrosion and electrochemical characteristics of these alloys.

Theory of Noble Metal Alloying to Obtain Passivity

According to what has already been described, passivity is obtained by producing a condition which results in a potential more noble than the critical potential for passivity. Without an externally applied potential, a metal in solution can attain a passive mixed potential only if the solution contains a redox system with a reversible potential more

noble than the critical potential for passivity of the metal. This is a necessary, but not sufficient, condition for stable passivity (1).

Alloying can contribute to the passivation of metals by two distinctly different principles:

1. Alloy addition may affect those metal dissolution parameters (the critical anodic current and the critical anodic potential) which, in turn, determine the ease of passivation. This is the effect which Cr has on Fe in the stainless steels. Increasing Cr content decreases the critical anodic current (6) and moves the critical anodic potential in the active direction (7,8).

2. Alloy addition may influence the reduction kinetics of the cathodic process. Mixed potentials in the passive potential region are favored by an increase in exchange current and a decrease in the cathodic Tafel slope (1).

An example of cathodic process influence was described by Tomashov (9). Alloying of 18% Cr-8% Ni stainless steel or 27% Cr stainless steel with Pt or Pd markedly improves corrosion resistance in room-temperature H_2SO_4 by facilitating the cathodic reaction. While it is not clear whether these experiments were done with intentional aeration of the acid, oxygen was most likely present in solution.

Passivation by alteration of cathodic process kinetics is of special interest when the critical anodic potential of the metal is more active than the reversible hydrogen potential of the solution. Under these circumstances, passivity theoretically can be achieved with the presence of a redox system no more oxidizing than the hydrogen electrode. Under conditions where the metal exhibits a relatively high hydrogen overvoltage, a passive mixed potential may not be obtained directly. However, passivity can be accomplished by alloying such a metal with an element which is essentially insoluble in the environment and which exhibits a high exchange current for the hydrogen ion reduction process. A small amount of corrosion should leave the alloy addition essentially in elemental form on the surface. The surface is now a bi-electrode, or galvanic couple, with one of the constitutents presenting a low-hydrogen overvoltage surface. This is shown schematically in Fig. 1 which may be considered typical of the behavior of Ti. The exchange current for the hydrogen reduction reaction of Ti is very small (5) resulting in an active mixed potential. When alloyed with a metal like Pt, regions with very high exchange currents are produced on the surface creating a mixed potential in the passive potential range. This results in a markedly reduced dissolution rate. Evidence for this is presented below.

Procedures

In general, electrochemical techniques and procedures were similar to those reported previously (5). Alloy buttons were prepared in an argon atmosphere by nonconsumable arc melting on a water-cooled Cu hearth. The buttons, weighing approximately 50 g, were melted three times, reduced in thickness about 50% by cold-rolling, and heat-treated at 1000°C in vacuum for 18-24 hr followed by furnace-cooling.

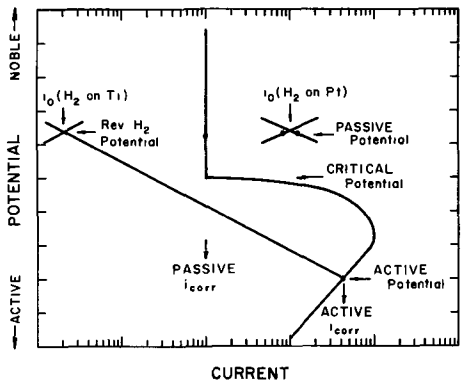

Fig. 1. Schematic diagram showing how alloying with a noble metal produces a passive mixed potential and a marked reduction in corrosion rate.

Corrosion Behavior

Table I shows the effect of ten alloy additions on the corrosion rate of Ti in boiling H_2SO_4 and HCl. Corrosion resistance is markedly improved in many cases. The best results are produced by Pt, Pd, Rh, and Ru; Os, Ir, and Re are intermediate in effect; Au is beneficial only in higher concentrations, while Ag and Cu are detrimental. As expected, the effectiveness of the various additions is roughly in the same order as their hydrogen overvoltage. Generally, Pt and Pd exhibit very low-hydrogen overvoltages, whereas Au, Ag, and Cu may be considered the relatively high-hydrogen overvoltage elements of those evaluated. The approximate exchange current densities (10) in HCl for the various metals are Pt (10^{-3}), Pd(10^{-3}), Rh(10^{-4}), Au(10^{-5} to 10^{-6}), Ag (10^{-7}), Cu(10^{-7}) amp/cm^2.

Table I. Effect of various alloy additions on corrosion resistance of Ti

Composition	Weight loss in 24 hr* (mil/yr)			
	Boiling H_2SO_4		Boiling HCl	
	1%	10%	3%	10%
Titanium	460	3950	242	4500
Ti + 0.064% Pt	<2	145	<2	128
Ti + 0.54% Pt	<2	48	3	120
Ti + 0.08% Pd	<2	166	3	100
Ti + 0.44% Pd	<2	45	<2	67
Ti + 0.1% Rh	<2	26	5	96
Ti + 0.5% Rh	3	48	<2	55
Ti + 0.1% Ru	3	187	5	280
Ti + 0.5% Ru	<2	48	<2	113
Ti + 0.11% Ir	<2	359	3	120
Ti + 0.60% Ir	<2	45	3	88
Ti + 0.10% Os	5	480	3	1820
Ti + 0.48% Os	<2	82	3	208
Ti + 0.11% Re	235	—	345	—
Ti + 0.36% Re	9	—	30	—
Ti + 0.11% Au	1050	—	1500	—
Ti + 0.48% Au	3	—	9	146
Ti + 0.04% Ag	500	—	334	—
Ti + 0.34% Ag	—	—	—	4850
Ti + 0.17% Cu	470	—	340	—
Ti + 0.44% Cu	660	—	550	—

* The possible weighing error of these tests is ±2 mil/yr.

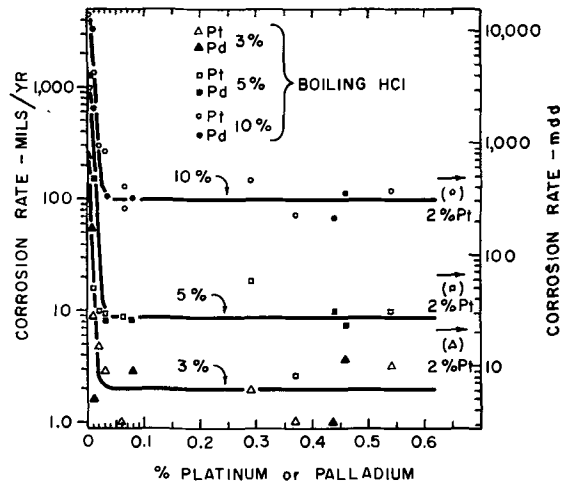

Fig. 2 Effect of Pt and Pd additions on corrosion rate of Ti in boiling HCl solutions.

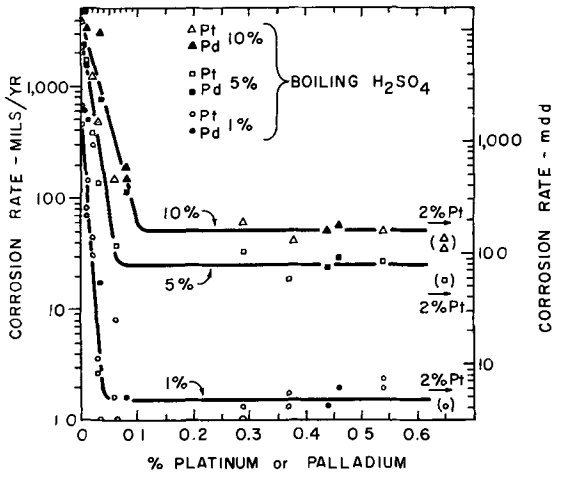

Fig. 3. Effect of Pt and Pd additions on corrosion rate of Ti in boiling H_2SO_4 solutions.

The qualitative theory of noble metal alloy additions described above does not permit an estimate of the alloy concentration required to produce a maximum effect. However, one would predict that, in a given environment, increasing the alloy concentration and noting the effect on corrosion rate should reveal a composition above which no additional benefit is produced. This is the concentration sufficient to produce a mixed potential more noble than the critical potential for passivity. One would also expect that insufficient alloy addition would be detrimental, since the mixed potential would move in the noble direction, yet remain in the active potential region.

Figure 2 shows the effect of Pt and Pd additions to Ti on corrosion rate in boiling HCl solutions. Both of these alloying elements apparently behave in a similar manner, and this observation was used to combine the data on one plot. It is evident that about 0.05% Pt or Pd reduces the corrosion rate by a factor of from 50 to 100. Increased concentrations of noble metals are not additionally beneficial. These data are the results of 24-hr corrosion tests. The sample size was such that a corrosion rate of about 2 mil/yr is within the possible weighing error of the test.

Figure 3 shows similar data in boiling H_2SO_4. In this case, it appears that more noble metal is required to achieve the maximum beneficial effect. Also, in this environment, Pd appears to be not quite as effective as Pt, although only one line is drawn through the points in each H_2SO_4 concentration.

As expected, alloy additions above some critical concentration do not further reduce corrosion rate. However, contrary to expectations, very small alloy additions do not increase the observed corrosion rate. This is because the observed corrosion rate is an average value for a 24-hr test. As will be shown below, these alloys are initially active and probably corrode at an accelerated rate. However, they become passive during the test so that the average corrosion rate is between that of active and passive Ti.

Data not presented here show that such alloying is not detrimental to behavior in highly oxidizing media, such as concentrated HNO_3 or ferric chloride. This is expected since Ti does not exhibit a transpassive potential region where the dissolution rate increases at quite noble potential values. Similar alloying in the case of stainless steels (9) is expected to be detrimental under highly oxidizing conditions because of the transpassive behavior of such alloys.

Electrochemical Behavior

Figure 4 shows potential-time data in boiling 1% H_2SO_4 for Ti and a series of Ti alloys containing various amounts of Pt. The data were recorded continuously using high impedance instrumentation. Note that all Pt-bearing alloys reach the passive potential region during the 24-hr test period. Those alloys containing the higher concentrations of Pt are passive from the very beginning of test, whereas the more dilute alloys remain active for some time prior to becoming passive. It is believed that during this active period the surface concentration of Pt is increasing as a result of corrosion until the area ratio is sufficient to produce a noble mixed potential. Anodic polarization of Ti in this environment, Fig. 5, shows a critical current of about 1000 μamp/cm^2

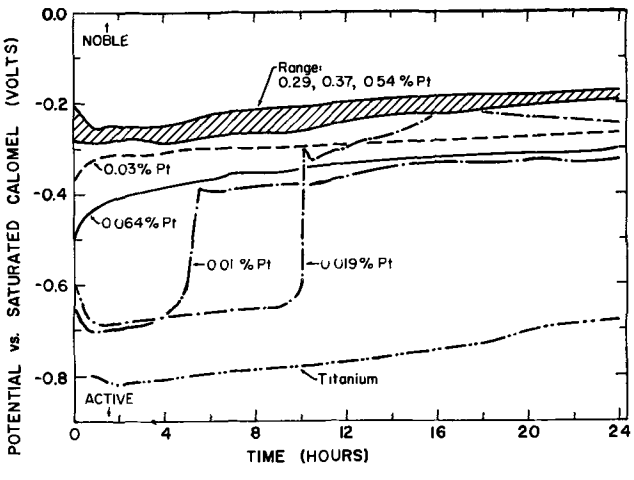

Fig. 4 Potential as a function of time for Ti alloyed with various concentrations of Pt in boiling 1% H_2SO_4.

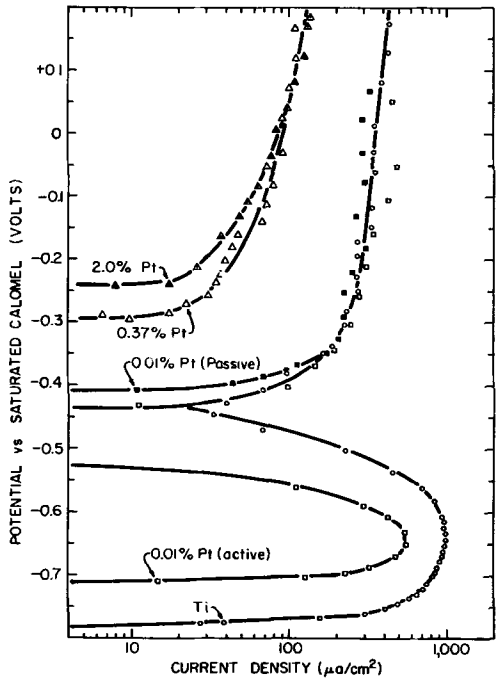

Fig. 5. Anodic polarization of Ti and Ti-Pt alloys in boiling 1% H_2SO_4.

at a potential of —0.64 v vs. saturated calomel. The critical anodic potential is about —0.44 v on the same scale. It is interesting to note in Fig. 4 that the two dilute alloys, 0.01% Pt and 0.019% Pt, which are active for a relatively long period, rapidly pass through the potential region where the polarization curve of Ti has a negative slope. Also, the rapid change in potential occurs when the electrodes have reached values of about —0.64 v. This indicates that this potential region is unstable for these alloys.

Figure 5 shows anodic polarization data for three alloys in boiling 1% H_2SO_4 compared with that of unalloyed Ti. If such measurements are conducted with the 0.01% Pt alloy soon after it is immersed in solution while its potential is still relatively active (see Fig. 4), the polarization curve (open squares) is essentially that of a typical active metal. However, if this alloy is immersed in solution overnight prior to anodic measurements, the data (solid squares) closely parallel the behavior of unalloyed Ti in the passive region. The 0.01% Pt alloy, initially in the active condition, shows negative (cathodic currents) in the potential region between about —0.53 and —0.44 v. This phenomenon has been described adequately by Edeleanu (2), and this observation is consistent with his explanation, since this alloy is expected to exhibit a higher exchange current for the hydrogen ion reduction reaction than unalloyed Ti.

Titanium alloys containing 0.37% or 2% Pt are passive very soon after immersion. Anodic polarization shows only passive behavior as expected. As shown earlier (5) in H_2SO_4 solutions containing appreciable quantities of corrosion products, measured currents in the passive potential region represent the rate of titanium oxide deposition rather than metal oxidation. Thus, currents observed for the 0.37% and 2% Pt alloy are less than that for Ti or the 0.01% Pt alloy because corrosion product build-up in solution (from the sample and the auxiliary electrodes) is slower.

According to the mechanism of protection obtained by noble metal alloying described above, one would expect that cathodic polarization of a Pt-containing alloy would cause a marked increase in corrosion rate. This was found with the 0.37% Pt alloy in boiling 1% H_2SO_4. The potential of this alloy is normally in the passive range between about —0.2 and —0.3 v. It was held at a potential of —0.55 ±0.05 v (see Fig. 5) for 19 hr with a potentiostat. The cathodic current required to accomplish this was very high (0.2-0.3 amp/cm²), presumably because of the high Pt content of the surface. The corrosion rate for this period was 110 mil/yr compared with normal corrosion rate of less than 2 mil/yr in this environment. This supports the mechanism proposed.

Ease of Passivation

Titanium alloyed with noble metals should show another particularly beneficial property. Such alloys should become passive in aggressive environments with concentrations of oxidizing agent insufficient to passivate unalloyed Ti.

A schematic polarization diagram which illustrates this property is shown in Fig. 6. The solid cathodic curve originating from i_{01} represents hydrogen ion reduction on Ti and produces an active mixed potential E_1. The solid cathodic curve originating from i_{02} represents reduction of an oxidizing agent on Ti which produces either a passive potential at E_2' or an active potential E_2. Oxidation and reduction of the oxidizing agent on the alloy surface, where the noble metal content markedly raises the exchange current, are shown at i_{03}. In this case, only one passive mixed potential, E_3, is obtained (1). Evidence for this behavior was obtained in the following experiments.

Corrosion measurements were obtained in H_2SO_4 and HCl at 190°C (374°F). Samples with areas of 2-3 cm² were sealed in heavy wall Pyrex tubes containing 40 ml acid solution. Prior to sealing the tubes, a stream of nitrogen was bubbled through the acid for about 2 hr and continued while the tube

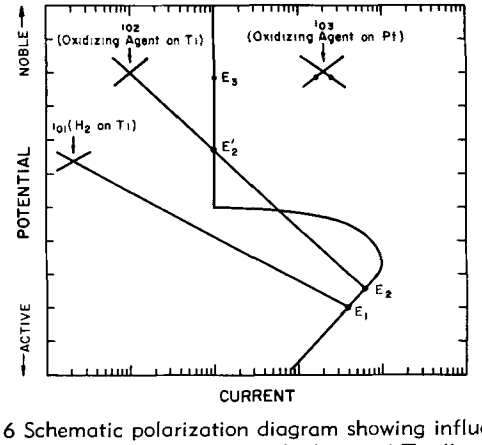

Fig. 6 Schematic polarization diagram showing influence of an oxidizing agent on the potential of Ti and Ti alloyed with a noble metal.

Table II. Effect of Pt and Pd alloy additions on the corrosion resistance of Ti in oxygen-free H_2SO_4 and HCl at 190°C (374°F)

Composition	Weight Loss,* mil/yr						
	H_2SO_4				HCl		
	1%	5%	10%	20%	3%	5%	10%
Ti	515	—	—	—	2250	—	—
Ti + 0.03% Pt	<2	<2	3.4	Diss	—	—	—
Ti + 0.29% Pt	<2	<2	3.3	11.5	<2	<2	890
Ti + 0.08% Pd	<2	<2	3.5	Diss	—	—	—
Ti + 0.44% Pd	<2	<2	5.0	12.0	<2	<2	1120

* One-period tests, 44-64 hr duration. The possible weighing error in these tests is ±2 mil/yr.

was being necked down. Although the gas inlet tube was removed just prior to sealing, the solutions cannot be considered completely oxygen-free. The tubes then were heated in a pressurized autoclave. The weight loss results for Ti and Ti alloyed with Pt and Pd are shown in Table II. Unalloyed Ti corrodes at very high rates, whereas Pt and Pd additions are quite effective in rather high concentrations of acid. The persistence of the noble metal effect at this high temperature is in itself quite important and can be explained in view of evidence (5) showing that temperature does not markedly affect the critical potential for passivity of Ti. What is most significant about these data is that the corrosion rates observed are considerably less than those obtained at the boiling point of the acids. Small quantities of oxygen present during the test are believed responsible for the lower corrosion rate at the higher temperature.

These data alone are probably not sufficient evidence for the general conclusion that noble metal alloying improves the susceptibility to passivation by oxidizing agents. More direct evidence was obtained by a combination of electrochemical and corrosion data. It was observed that in 20% H_2SO_4 at room temperature, unalloyed Ti shows unstable passivity when the solution is oxygen-saturated. This is shown in Fig. 7A. The potential oscillates in an unpredictable manner from a value only slightly more noble than the critical potential for passivity (shown in Fig. 7B) to an active value. The relatively active value of the passive potential of unalloyed Ti is due primarily to a particularly small

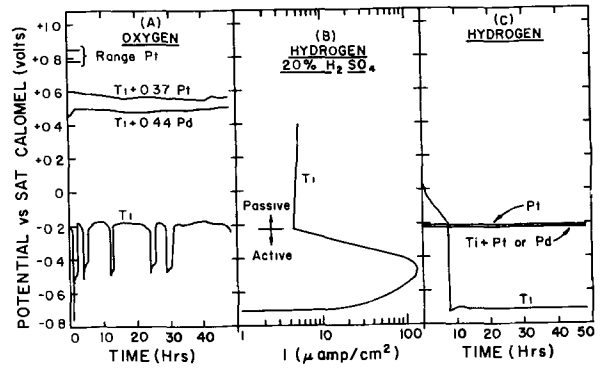

Fig. 7. Anodic behavior of Ti and electrode potential of Ti and Ti alloyed with Pt or Pd in 20% H_2SO_4 at room temperature.

value of exchange current for oxygen reduction on the Ti surface. Alloys containing Pt and Pd are 0.7-0.8 v more noble than unalloyed Ti and only about 0.3 v more active than Pt in the same solution. These data are an ideal illustration of the mechanism shown in Fig. 6.

Figure 7C shows potential-time behavior in hydrogen-saturated solution. Platinum exhibits the reversible hydrogen potential. Potentials of Ti containing Pt and Pd are within 25 mv of this value. The potential of unalloyed Ti, which initially had an air-formed film, is active. This illustrates the basic mechanism of noble metal alloy additions shown in Fig. 1.

Note in Fig. 7 that relatively stable potentials are not observed in the potential region where the anodic polarization curve has a negative slope. When the potential of passive Ti reaches the critical potential, it moves rapidly to active values. When active Ti reaches potentials close to that at the critical current, it moves rapidly to passive values. Also note that the potential of active Ti in oxygen-saturated solution is more noble than active Ti in hydrogen-saturated acid because of the combined cathodic reduction of oxygen and hydrogen ions.

Weight loss data for the electrodes whose behavior is described in Fig. 7A and C are shown in Table III. Alloys containing Pt or Pd are passive and exhibit negligible corrosion rates in either hydrogen- or oxygen-saturated acid. Unalloyed Ti is active in hydrogen-saturated solution and is intermittently active in oxygen-saturated solution. In the latter case, the weight loss is between that observed for the active and passive conditions.

These experiments in 20% H_2SO_4 support the concept that Ti containing noble metal alloy additions is much more sensitive to oxidizing agents than unalloyed metal. Data, which show that this extends to trace concentrations of oxidizing agents, were obtained by measuring the mixed potential of Ti and Ti alloys containing Pt as a function of ferric ion concentration in boiling 1% H_2SO_4. Measurements which were conducted in the manner described previously (1) are shown in Fig. 8. Titanium, which is initially active, requires a ferric ion concentration of about 0.2 mg/ml to passivate. Platinum-containing alloys which are already electrochemically passive in this environment (see Fig. 5) without ferric ion additions respond markedly to concentrations of the oxidizing agent which

Table III. Effect of O_2 and H_2 on corrosion resistance of Ti and Ti alloys in room temperature 20% H_2SO_4

Alloy	Gas	Weight loss, mil/yr
Ti	O_2	4*
	H_2	29
Ti + 0.37% Pt	O_2	<2†
	H_2	<2
Ti + 0.44% Pd	O_2	<2
	H_2	<2

* Passive during most of test. See Fig. 7A.
† The possible weighing error of these tests is ±2 mil/yr.

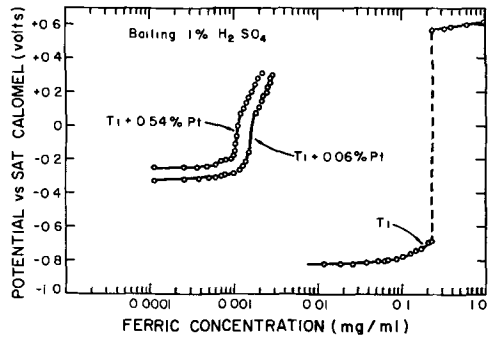

Fig. 8 Effect of ferric ion concentration in boiling 1% H_2SO_4 on the potential of Ti and Ti-Pt alloys.

are less than one-hundredth of that necessary to passivate Ti.

Conclusions

1. Alloying Ti with small amounts of Pt, Pd, Re, Ru, Ir, Os, Rh, and Au markedly improves corrosion resistance to H_2SO_4, HCl, and other reducing-type media.

2. The mixed potentials of Ti-noble metal alloys which exhibit low corrosion rates are more noble than the critical potential for passivity of Ti in the same environment. Anodic polarization of these alloys shows only passive behavior, whereas cathodic polarization into the active potential region produces an increase in corrosion rate.

3. Electrochemical passivity is observed in hydrogen-saturated systems without the presence of a redox system more oxidizing than the hydrogen electrode.

4. The mixed potential of Ti-noble metal alloys is much more sensitive to traces of oxidizing agents than unalloyed metal.

5. The above observations are consistent with the theory of noble metal alloying proposed. Titanium is particularly susceptible to improvement by alloying because it exhibits unusually active values of critical potential for passivity in a variety of media.

6. Alloying Ti with noble metals is not detrimental to behavior in oxidizing media, such as HNO_3 or ferric chloride. This is expected since Ti does not exhibit a transpassive potential region where the dissolution rate increases at quite noble potential values. Similar alloying in the case of stainless steels is expected to be detrimental under highly oxidizing conditions because of the transpassive behavior of Fe-Cr-Ni-type alloys. Thus, the addition of small amounts of noble metals to Ti produces a material with unusually broad corrosion resistance to both oxidizing and reducing-type media.

Manuscript received April 6, 1959. This paper was prepared for delivery before the Columbus Meeting, Oct. 18-22, 1959.

Any discussion of this paper will appear in a Discussion Section to be published in the June 1960 JOURNAL.

REFERENCES

1. M. Stern, *This Journal*, **105**, 638 (1958).
2. C. Edeleanu, *Metallurgia*, **50**, 113 (1954); *J. Iron Steel Inst.*, **186**, 122 (1958).
3. W. R. Buck, III, and H. Leidheiser, *Nature*, **181**, 1681 (1958).
4. N. D. Tomashov, *Z. Electrochem.*, **62**, 717 (1958).
5. M. Stern and H. Wissenberg, *This Journal*, **106**, 755 (1959).
6. H. H. Uhlig and G. E. Woodside, *J. Phys. Chem.*, **57**, 280 (1953).
7. T. Heumann, "Passivierende Filme und Deckschichten," p. 276, H. Fischer, K. Hauffe, and W. Wiederholt, Editors, Springer-Verlag, Berlin (1956).
8. M. Prazak, V. Prazak, and V. L. Cihal, *Z. Elektrochem.*, **61**, 739 (1958).
9. N. D. Tomashov, *Uspekhi Khim.*, **24**, 453 (1955); *Corrosion*, **14**, 229t (1958).
10. J. O'M. Bockris, "Modern Aspects of Electrochemistry," p. 180, Butterworth Scientific Publication, London (1954).

High-Temperature Sulfiding of Iron Alloys in Hydrogen Sulfide-Hydrogen Mixtures

E. W. Haycock

Shell Development Company, Emeryville, California

ABSTRACT

Rates of sulfide scale formation on pure iron and a series of chromium steels have been measured over the temperature range 400°-550°C in H_2S-H_2 mixtures at a total pressure of 600 psi with an H_2S partial pressure of 0.6 psi for exposure periods up to 500 hr. A mechanism of scaling, involving the depletion of a barrier scale layer by recrystallization and grain growth processes, is proposed and substantiated by laboratory studies of the structural properties and mode of formation of scales grown on the various materials studied. A single kinetic equation, based on this mechanism, is shown to satisfy the rate curves over the complete range of conditions studied. A solid defect structure, protons trapped at metal ion vacancies, is suggested to explain the effect of hydrogen on the scaling process. The term "E" center is suggested to describe such a lattice irregularity.

Interest in the high-temperature steel-hydrogen sulfide reaction has been stimulated in recent years by scaling problems experienced in high-temperature refining operations of the petroleum industry. Corrosion due to presence of H_2S in hydrorefining processes has been unexpectedly severe, chromium steels containing up to 9% chromium scaling equally as rapid as carbon steel. Several investigations of

this reaction have been reported (1). Of these investigations, those carried out under well-controlled conditions have, for the most part, involved relatively short duration exposures and have been performed at or near atmospheric pressure. The primary objective of the investigation reported here was to study the kinetics and mechanism of scaling under conditions similar to those experienced in refinery operations. This has involved scaling experiments at elevated pressures and with exposure times beyond the range reported by previous investigators. In the present investigation, corrosion rates of pure iron and iron-chromium alloys have been compared with those of commercial steels and scaling rates studied as a function of chromium content.

Dravnieks and Samans (2) recently have suggested a mechanism for the steel-hydrogen sulfide reaction. Mechanistic studies of the iron-H_2S reaction have been reported by Delahay and coworkers (3). The interpretation of kinetic data in these studies is complicated by the thermodynamic possibility that FeS_2 could be formed as well as FeS. In the present work the H_2S/H_2 mole ratio has been maintained at a sufficiently low value to insure that over the entire range of conditions studied FeS was the only stable product phase. As a result of the present kinetic and mechanistic studies a new mechanism of the reaction is proposed. Although the present studies confirm certain hypothetical features of the Dravnieks-Samans mechanism, our kinetics analysis differs significantly from that of the above authors and allows the experimental data to be explained by a single rate equation over the entire range of conditions studied.

Experimental Rate Measurements

The rates of scaling of pure iron, ½% Mo steel, and a series of chromium steels were measured over the temperature range 400°-550°C in H_2S-H_2 mixtures at a total pressure of 600 psi with an H_2S partial pressure of 0.6 psi. On the basis of thermodynamic data published by Rosenqvist (4), FeS is the stable product under these conditions. The compositions of the alloys studied are given in Table I. Two pure irons, Armco and Ferrovac E, were used, and no significant differences were observed in the relatively long exposure scaling rates studied. Commercial ½% Mo steel was used rather than carbon steel to avoid hydrogen attack of the metal.

The experiments were made in the apparatus shown schematically in Fig. 1. Metal specimens were

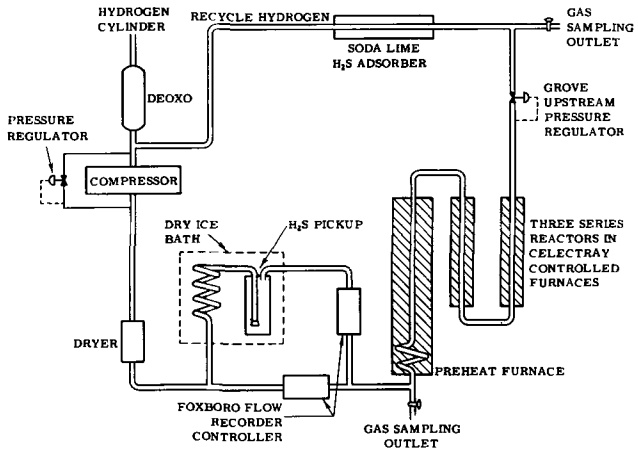

Fig. 1. Schematic diagram of apparatus used to measure metal scaling rate in H_2S/H_2 mixtures at 600 psi.

exposed in three stainless steel reactor tubes heated by electric furnaces which were maintained at chosen temperatures ±2°C by a Celectray indicator-controller. The temperature controller was actuated by iron-constantan thermocouples situated in thermowells close to the metal specimens.

Cylinder hydrogen (99.8% H_2, 0.15% O_2, 0.05% N_2) was led through a Deoxo catalytic cartridge and drying column to remove oxygen. The desired H_2S-H_2 mixture was obtained by dividing the hydrogen stream and passing part of it through liquid H_2S in a dry ice bath. The divided gas stream then was remixed and passed through a preheat column into the reactors. Division of the hydrogen stream to the desired extent was achieved by the use of Foxboro flow recorder-controllers. The total flow of gas over the scaling specimens was maintained at a sufficiently high rate to keep the effluent H_2S concentration to within 10% of the inlet concentration. The gas composition at both the inlet and outlet was checked at frequent intervals, and in many experiments the difference in inlet and outlet composition was considerably less than this amount. For ease in long term continuous operation, H_2S was removed from the effluent gas in soda lime towers and the hydrogen recycled.

The metal specimens studied were in the form of cylindrical rings approximately ½ in. long, ⅝ in. O.D., with 3/32 in. wall thickness. Ring specimens were chosen primarily to insure that scale samples would be obtained *in situ* on the metal surface for subsequent examination by metallurgical microscopic techniques. The scales formed under com-

Table I. Alloy compositions

Nominal alloy composition	Weight % constituents								
	Cr	Ni	Mo	C	Mn	P	S	Si	Cu
Armco iron	—	—	—	0.03	0.02	0.003	0.02	0.01	—
Ferrovac E*	<0.02	—	—	0.01	<0.02	0.004	0.001	<0.03	<0.01
½% Mo steel	—	—	0.55	0.20	0.56	0.018	0.025	0.22	—
5% Cr, ½% Mo steel	4.76	—	0.54	0.10	0.35	0.002	0.011	0.33	—
9% Cr, 1% Mo steel	8.44	—	1.01	0.09	0.42	0.012	0.015	0.36	—
12% Cr, type 410	12.31	0.50	0.11	0.13	0.65	0.010	0.009	0.55	0.03
18% Cr, 8% Ni, type 304	18.43	10.36	—	0.054	1.71	0.014	0.010	0.48	—

* Vacuum melted pure iron.

pression on the inside of the rings remained intact, whereas in many cases the scales on the outer surfaces of ring specimens or on flat specimens would spall on cooling from the reactor temperatures. Up to ten specimens could be supported in each reactor tube.

The experimental procedure adopted was as follows. Prior to exposure, specimens were ground smooth and sharp edges removed with 180 grit abrasive followed by soft rubber erasing. Specimens then were washed with acetone, weighed, and loaded into preheated reactor tubes under nitrogen. Final temperature adjustments were made as the nitrogen was swept out with hydrogen and the pressure brought up to 600 psi. The hydrogen sulfide-hydrogen stream then was introduced and scaling allowed to proceed for various exposure times up to 500 hr. Experiments were terminated by stopping flows to the reactors, venting, and purging with nitrogen. To determine the extent of metal consumption after each exposure, the specimens were descaled in an electrolytic cleaner in 5%w sulfuric acid, dried, soft rubber erased, and weighed. Duplication of alloy specimens allowed additional sampes for scale analyses and microscopic examination.

Experimental Results and Discussion

The rate curves obtained were similar in form to those obtained for carbon steel by Dravnieks and Samans (2). For all of the alloys studied, the rate of scaling was observed to be high initially and gradually decrease over the first 20-30 hr to approach an essentially constant value.

The scaling rate curves for pure iron, ½% Mo steel, and 5% Cr, ½% Mo steel are illustrated in Fig. 2, 3, and 4 for exposures up to 500 hr. The shapes of these curves are typical of all of the alloys studied including 18-8 stainless steel. Several ex-

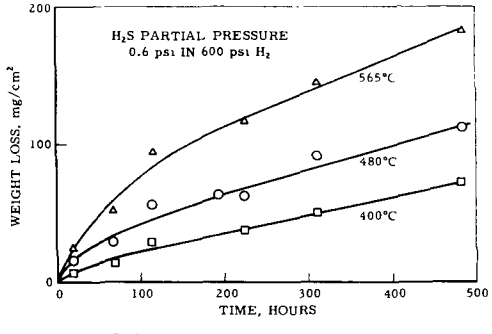

Fig. 2. Sulfiding rate curves for pure iron

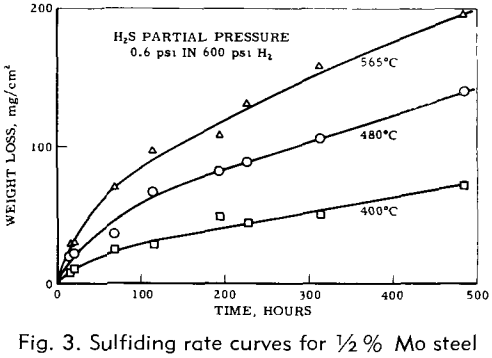

Fig. 3. Sulfiding rate curves for ½% Mo steel

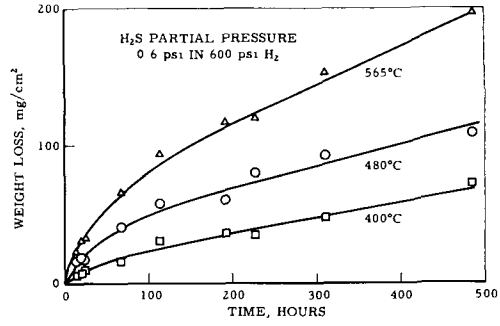

Fig. 4 Sulfiding rate curves for 5% Cr-½% Mo steel. Curves are plots of Eq. 1 with the following rate constants

Temp, °C	K_p	K_1
400	1.1	0.14
480	5	0.23
565	18	0.31

periments with pure iron-chromium alloys, made by vacuum melting "Ferrovac E" pure iron with electrolytic chromium, showed no significant difference in scaling properties between these materials and the corresponding commercial alloys. A large number of scaling experiments, which will not be reported in detail here, have been made under varying partial pressures of H_2S and H_2. These experiments have confirmed previously reported (1) observations that, within the thermodynamic limits of FeS stability, the over-all scaling rate depends on the partial pressure of H_2S and is not affected by changes in the partial pressure of H_2.

Scale structure and composition.—Scales formed on all of the materials investigated consisted of two well-defined layers. The scales resembled those described by Delahay (3) for the pure iron-H_2S product and by Dravnieks (2) for the carbon steel corrosion product. The layer next to the metal consisted of small disorganized crystallites and was coherent and adherent. The second layer adjacent to the gaseous environment consisted of a columnar array of relatively large crystals with pores extending from the gas interface to the surface of the adherent sulfide layer. The scale structure illustrated by the photomicrograph shown in Fig. 5 is typical of that obtained on all of the materials studied.

Chemical analyses of the individual scale layers showed that, for pure iron and the low chromium steels, the main constituent of both layers was metal deficient ferrous sulfide. Similar results for pure iron have been reported by Delahay (3). This was confirmed by power x-ray analyses, the iron sulfide

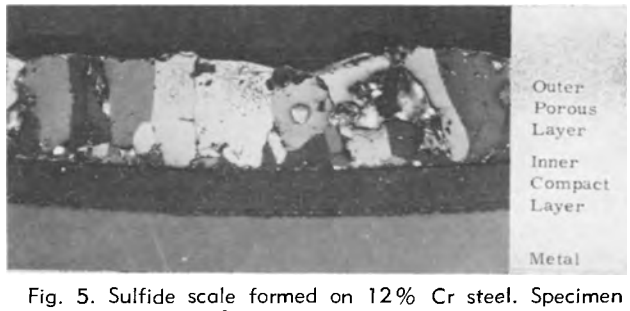

Fig. 5. Sulfide scale formed on 12% Cr steel. Specimen scaled 400 hr at 565°C, partial pressure, H_2S 0.3 psi in 600 psi H_2. Magnification 100X before reduction for publication.

super lattice (α') pattern being obtained in all cases. This structure is associated with the FeS composition range 50-50.74 at. % sulfur. Similar x-ray patterns have been reported by Bruns (5). For the chromium alloys, chemical analyses showed that chromium and molybdenum were retained in the scale layer next to the metal. Other trace metals present such as nickel and manganese were found to be distributed throughout both layers, although some tendency to retain nickel in the inner layer was observed. Silicon and carbon were found to accumulate in the inner layer. For the higher chromium steels and for low chromium steels which had been exposed sufficiently long to allow a significant concentration of chromium to be built up in the inner scale layer, an x-ray pattern corresponding to the spinel structure $FeCr_2S_4$ was observed. Although no thermodynamic data are available for this compound, by comparison with the analogous oxygen compound, it would be expected to have a high negative free energy of formation and its occurrence accounts for the retention of chromium in the inner scale layer.

Mechanism of scale formation.—Microscopic study of scale structure strongly suggests that the outer porous scale layer is formed at the expense of the inner layer by a recrystallization and grain growth mechanism. This is indicated by the sharpness of the interface between the scale layers and the change in crystal size and orientation from one layer to the other. It is also in keeping with the observation that for pure iron both layers are identical within the limits determinable by chemical and x-ray analyses.

To obtain confirmation of this general model, inert marker experiments were performed on 1% Cr, ½% Mo steel, and ½% Mo steel scaled under the conditions previously described for the rate measurements. Three marking materials were used: chromium oxide, aluminum oxide, and platinum metal dust. The positions of the chromium oxide and platinum markers were studied by metallographic techniques and aluminum oxide by chemical analyses of the scale layers. In all cases markers were found distributed throughout the outer scale layers and on the outermost scale surface. Some markers, particularly in the case of chromium oxide, were found at the interface between the scale layers, and the relative number and appearance of these markers suggested that the chromium oxide was not entirely inert and that some inhibition of the processes taking place at the interface between the two scale layers was occurring. The fact that no markers were found in the inner layer or at the metal surface clearly indicates that the inner scale layer was formed by sulfide ion diffusion to the metal surface. The general scattering of markers through the outer layer suggests that continuous rearrangement takes place in this layer, and this is in keeping with the proposed model of its formation by recrystallization and grain growth processes.

The growth of the inner layer by sulfide ion diffusion to the metal surface necessitates that this layer be formed under high compressive stress. The molar volume of ferrous sulfide is considerably greater than that of the parent metal and, except for some relief due to slight plastic deformation, the product sulfide is confined beneath existing scale to the same volume as that initially occupied by the parent metal. It seems probable that the stress in the inner scale layer is the main driving force for nucleation and growth of the outer scale layer. The phenomenon of stress induced recrystallization is well known, particularly in metal systems. A pertinent example of this is the observation that the growth of single crystal tin "whiskers" from polycrystalline tin is greatly enhanced by the application of a compressive stress (6).

The difference in the mechanism of scale formation in hydrogen sulfide environments as compared to sulfide formation in sulfur vapor studied by Birchenall (7) is dealt with later when interaction of hydrogen with metal deficient ferrous sulfide is discussed.

Kinetic analysis of rate data.—Microscopic examination of sulfide scales formed in hydrogen sulfide environments indicates that the porosity of the outer scale layer is sufficiently high to render it ineffective as a solid diffusion barrier between the metal and the gas phase. The main resistance to reaction appears to reside in the inner barrier layer scale. The simplest kinetic model which adequately explains the experimental observations is one to which a combination parabolic-linear law may be applied in which the linear component of the rate is associated with the process occurring at the interface between the compact and the porous scale layers. By comparison with other solid-state interface transformations, the proposed recrystallization process for the formation of the porous layer would be expected to occur at a linear rate and the interfacial area will remain sensibly constant throughout the reaction. The barrier layer scale therefore will grow by the diffusion of sulfide ions to the metal surface and be depleted at a constant rate by the process forming the porous outer scale layer. If it is assumed that diffusion across the inner scale layer determines the rate of metal consumption, then this rate will be inversely proportional to the inner scale thickness. The rate of scaling will start therefore at a high value and decline as the inner scale thickens. When the rate of metal consumption approaches the rate of recrystallization, the inner scale layer will approach a constant thickness and the scaling rate will approach a constant value. This model leads to the expression

$$x = \frac{K_p}{K_l} \ln \frac{K_p}{K_p - K_l(x - K_l t)} \qquad [1]$$

for the metal weight loss as a function of time, where x equals metal weight loss, t, time, K_p is a rate constant associated with the parabolic diffusion process by which the barrier layer is formed, and K_l a rate constant associated with the linear recrystallization rate by which it is depleted.

Equation [1] is a general expression for the rate of scaling of any system in which a diffusion barrier, which would normally be formed parabolically,

is depleted at a constant rate by any secondary process. Its derivation, which is an extension of the work of Loriers (8) and Wagner (9), will be given in more detail in the following paper (10) where it is applied to systems other than sulfiding.

The close correspondence between the present experimental data and the theoretical rate curves obtained from Eq. [1] for the range of conditions studied is shown in Fig. 4 for 5% Cr, ½% Mo steel. Similar agreement has been found for the other alloys studied.

Equation [1] is based on a model of an ideal system. The assumptions made in its derivation are: (*a*) the consumption of metal is controlled solely by diffusion processes in the compact layer, i.e., no surface or interface reaction influences the primary reaction; (*b*) the diffusion coefficient of the rate-determining species is constant throughout the reaction; (c) the secondary interface reaction giving the porous scale layer depletes the diffusion barrier at a uniform rate; and (*d*) both scale layers begin to grow at $t = 0$ and have constant density throughout the reaction. For the early stages of scaling on pure iron and the low chromium steels, these requirements apparently are obeyed reasonably well. However, at long exposure times deviations are to be expected and the results of some of these are apparent in scales formed in long term experiments in both laboratory and refinery plant equipment. The presence of nonmetallic materials (carbon and silicon) in the steels may introduce a changing additional resistance to the consumption of metal at the metal-scale interface. The enrichment of certain alloy constituents in various locations in the scale gradually will effect the diffusion coefficient of other constituents. The outer scale layer, as it thickens, may offer a gradually increasing resistance to gas flow to the interface between the two scale layers. Thus, at the base of pores of the outer scales, the ratio of H_2 to H_2S may increase as the porous scale grows and gaseous diffusion paths to the reaction zone become longer. The compact diffusion barrier may develop stress cracks as the reaction proceeds. The scale interface reaction, which is thought of basically as a recrystallization process, could be affected by changes in concentration of foreign materials at the interface.

Experimental observations of scale layer thicknesses made in the present study indicate that the inner scale layer thickens over the first 24-hr exposure to a value which remains essentially constant for 70-100 hr. A slight but continuous thickening of the inner layer takes place for 100-500 hr exposure and this is accompanied by a slight decrease in the rate of thickening of the outer porous layer. These deviations from the theoretical model do not appear to be of sufficient magnitude to prevent the experimental rate curves being fitted adequately by Eq. [1].

Values of K_p and K_l, plotted as a function of temperature according to the Arrhenius equation, are shown in Fig. 6 and 7. Straight lines were obtained in all cases, which adds support of internal consistency to the proposed mechanism and kinetic

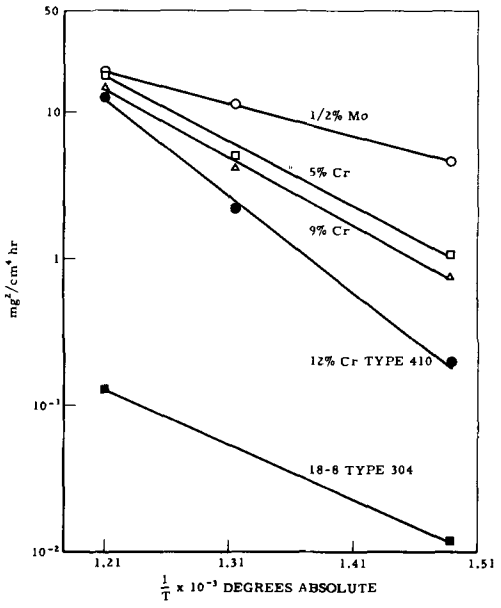

Fig. 6 Arrhenius plots for K_p

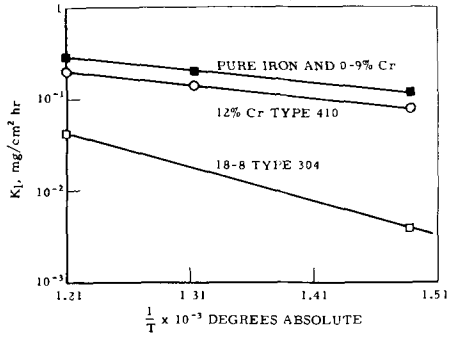

Fig. 7. Arrhenius plots for K_l

analysis. For the purpose of clarity, the pure iron K_p plot has been omitted from Fig. 6 and the lines for various alloys have been grouped in Fig. 7. Activation energies and pre-exponential factors determined from the data for each individual metal are given in Table II for the diffusion and recrystallization processes. The accuracy with which weight losses could be determined and the deviations of individual points from the theoretical curves obtained from Eq. [1] set a limit of accuracy of ±1 kcal on the reported activation energies for all alloys except 18-8 stainless steel. In this case weight losses were very small and the experimental data more widely scattered. The data given for 18-8

Table II. Activation energies and pre-exponential factors for parabolic and linear processes
$K = Ae^{-E/RT}$

Alloy	Parabolic rate constant, K_p		Linear rate constant, K_l	
	Activation energy, E, kcal/mole	Pre-exp. factor, A, mg^2/cm^4 hr	Activation energy, E, kcal/mole	Pre-exp. factor, A, mg/cm^2 hr
Iron	12.5	2.1×10^4	7	10
½% Mo	10	7.7×10^3	7	10
5% Cr, ½% Mo	19	1.6×10^6	7	10
9% Cr, 1% Mo	20	2.4×10^6	7	10
12% Cr, type 410	28	2.9×10^8	7	22
18-8, type 304	17	3.7×10^7	16	7×10^8

stainless steel therefore could be considerably in error and should be taken for comparison in a qualitative rather than quantitative sense. It will be seen that, with the chromium alloys, the activation energy for the diffusion process increases as the chromium content of the steel increases. The activation energy of the recrystallization process, however, stays essentially constant until the 12% chromium alloy is reached and then increases sharply for the 18% Cr, 8% Ni stainless steel.

These activation energy data serve to illustrate several practical features of the scaling process. Since, on the basis of the proposed model, the ultimate rate of scale formation is determined by the recrystallization rather than the diffusion process, the constancy of the activation energies and preexponential factors for the recrystallization process are to be expected since practical experience has shown that chromium additions of less than 12% to steel are not beneficial in lowering the long-term scaling rate (1). The fact that the activation energies for the diffusion process increase with chromium content implies that, if the scaling process involved the diffusion-controlled formation of the barrier scale only, then low percentage chromium additions would be beneficial in reducing scaling. This is in keeping with experience in oxidation of chromium steels where no porous scale layer is produced and low percentage additions of chromium lower the scaling rate. It is anticipated that additions of chromium would be beneficial in the pure sulfur vapor scaling system.

Effect of Hydrogen on Ferrous Sulfide Scale Formation

The effect of hydrogen in high-temperature sulfiding of iron can be appreciated best by comparison of the scaling processes in hydrogen sulfide and in pure sulfur vapor. In hydrogen sulfide environments the rate of scaling is high initially and falls to an essentially constant value. A two-layer scale is formed, the inner layer growing by sulfide ion diffusion to the metal surface. In contrast to this, the iron-sulfur vapor reaction follows a parabolic rate law (7). A single layer scale is formed and has been shown by Birchenall to grow by iron ion diffusion from the metal surface to the scale-gas interface. Since the product in both cases is iron deficient ferrous sulfide, it is evident that hydrogen plays an important role in the mechanism of scale formation in hydrogen sulfide environments.

To obtain a quantitative measure of the interaction of hydrogen with ferrous sulfide, the all glass apparatus shown schematically in Fig. 8 has been used. In a typical experiment a sample of ferrous sulfide in bulb A was equilibrated with a reservoir mixture of approximately 6% hydrogen sulfide in hydrogen at atmospheric pressure for 15 hr at 500°C. This gas composition was suitable to maintain ferrous sulfide thermodynamically stable against bulk reduction at this temperature. The adsorption chamber A was then evacuated to 10^{-6} mm Hg at 500°C for 8 hr. A known amount of H_2S-H_2 mixture was introduced into the system from the reservoir, and the adsorption of gases fol-

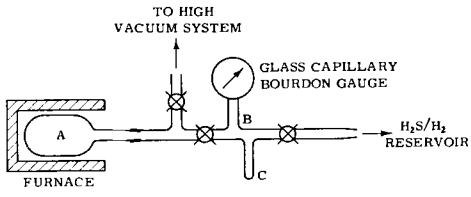

Fig. 8. Schematic diagram of apparatus used to measure absorption of hydrogen by ferrous sulfide.

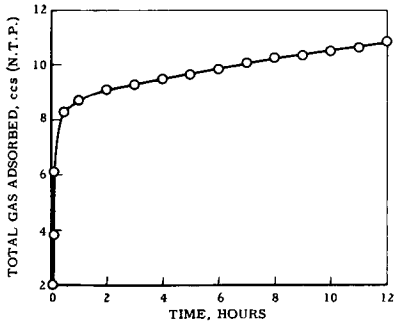

Fig. 9. Adsorption of H_2S/H_2 mixture on ferrous sulfide at 500°C. Weight of ferrous sulfide, 75.6 g; surface area (after experiment), 0.11 m^2/g; gas pressure at zero time, 40.8 cm Hg; gas pressure after 12 hr, 15.8 cm Hg; initial composition of H_2S/H_2 mixture, 6.15% H_2S; gas composition after 12 hr, 10.9% H_2S; hydrogen adsorbed after 12 hr, 10.4 ccs (N.T.P.); hydrogen sulfide adsorbed after 12 hr, 0.34 ccs (N.T.P).

lowed by the reduction in pressure measured with a glass capillary bourdon gauge (11). At any stage of the adsorption a part of the ambient gas could be isolated in section B of the apparatus and the H_2S condensed out in the ampoule C. This allowed a measurement of the H_2S/H_2 volume ratio existing above the adsorbent at any given time. The volumes of the various sections of the apparatus were calibrated with helium. Furnace temperatures were controlled to ±2°C. The surface area of the sulfide was determined after each experiment to allow for any sintering which might occur. Surface areas were measured by the B.E.T. method using nitrogen. A typical adsorption isotherm is shown in Fig. 9 with the pertinent primary and calculated data for the experiment. It will be seen that the system had not reached equilibrium even after 12 hr. Even if it is assumed that the evacuation treatment before adsorption removed all of the hydrogen associated with the ferrous sulfide, the total measured amount of hydrogen adsorbed after 12 hr exceeds the value expected for a monolayer. The slow, essentially linear, adsorption observed after 1 hr is attributed to the solution of hydrogen into the bulk sulfide.

The adsorption of hydrogen by metal deficient oxides, materials known as p-type semiconductors, has been studied extensively and it is known that the adsorption of hydrogen is accompanied by a decrease in electrical conductivity (12). It is anticipated therefore that the adsorption of hydrogen by ferrous sulfide and incorporation into the lattice would be accompanied by a decrease in the concentration of positive holes. From a chemical point of view this is equivalent to adsorbed hydrogen reducing the number of ferric ions in the metal deficient ferrous sulfide lattice. Assuming this to be

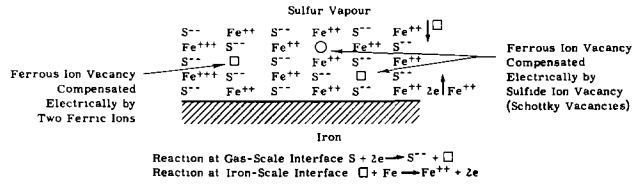

Fig. 10. Growth of iron-deficient ferrous sulfide in the iron-sulfur system.

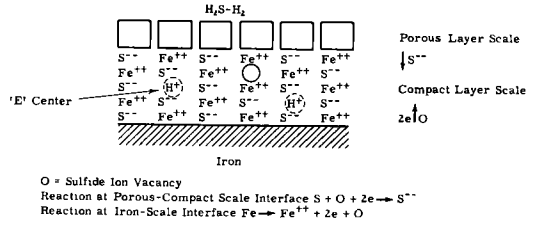

Fig. 11. Growth of iron-deficient ferrous sulfide modified by hydrogen.

the case, and recognizing the difference in scaling mechanism observed in hydrogen sulfide and sulfur vapor, i.e., scale formation by diffusion of sulfide rather than iron ions, it appears that hydrogen is incorporated in the ferrous sulfide lattice as protons associated with metal ion vacancies. As illustrated schematically in Fig. 10, iron deficient ferrous sulfide formed by the reaction of iron with sulfur vapor would be expected to contain metal ion vacancies, of which a part are compensated for electrically by sulfide ion vacancies and a part by the existence of ferric ions. It is suggested that interaction of hydrogen with this system results in a structure shown in the reaction scheme illustrated in Fig. 11. In addition to chemisorbed hydrogen at the surface, protons will be incorporated into the lattice reducing the number of ferric ions. This structure can be regarded as equivalent to a number of HS^- ions incorporated in the lattice, these ions being dissociated to an extent dependent on temperature. Since metal ion vacancies carry an effective negative charge, they would be expected to be efficient traps for protons in the lattice. It is proposed to name the defect structure of a proton trapped at a metal ion vacancy an "E" center. A previous suggestion of such a structure has been made by Caplan and Cohen (13) to explain the inhibiting effect of water in the high temperature oxidation of iron-chromium alloys. An "E" center would be expected to have certain properties similar to those of the well-established "f" center, i.e., an electron trapped at an anionic vacancy. The effective diameter of protons trapped at metal ion vacancies would increase with temperature and, under the scaling conditions studied, an "E" center could be expected to present an effective barrier to the migration of metal ions.

The recrystallization phenomena observed with sulfide scaling in the presence of hydrogen suggest that, in addition to blocking iron ion diffusion, the interaction of hydrogen enhances the mobility of the relatively bulky sulfide ions. This is readily understood on the basis of the above model since the presence of singly charged HS^- ions will tend to loosen the close packed sulfide ion lattice. Surface mobility of sulfide ions would be expected to increase since the energy required to transfer an HS^- ion from the bulk sulfide to a surface adsorbed state would be considerably less than for a S^{--} ion. Such surface mobility is the process considered to be important in recrystallization and grain growth processes.

The enhanced surface ionic mobility in the presence of hydrogen has been demonstrated by sintering experiments. Powdered ferrous sulfide with an initial B.E.T. surface area of 0.5 sq meter/g was maintained in a vacuum of 10^{-6} mm Hg for 5 hr at 500°C. No detectable change in surface area occurred. Heating the powder at the same temperature in a hydrogen-7% H_2S atmosphere for 2 hr reduced the surface area to a half of its initial value, and the powder had visibly sintered to a porous plug.

On the basis of hydrogen interacting with the ferrous sulfide product to (*a*) retard metal ion diffusion, and (*b*) accelerate surface and bulk diffusion of sulfide ions, it is possible to account for the difference in mechanisms observed when steel is scaled in hydrogen sulfide and in sulfur vapor.

The general similarity in oxide and sulfide systems suggests that the effects of hydrogen interaction discussed here for iron sulfide would also apply to metals oxidized in water vapor, although similar effects might be expected to occur over different temperature ranges due to the difference in stability of OH^- and SH^- ions. The study by Gulbransen (14) of the orientation of oxide crystals formed on iron lends support to the suggestion that the interaction of hydrogen with iron oxides will enhance the mobility of oxide ions. It was shown that iron scaled in pure oxygen produced a poorly oriented surface oxide. However, iron scaled in water vapor was found to form a highly oriented film. The bulky anions in the presence of hydrogen apparently possessed sufficient mobility to achieve a desired orientation in the time of oxide formation. The system Fe-H_2O-H_2 has been studied by Chaudron and co-workers (15), and these authors describe a double scale formation similar to that observed in the iron-hydrogen sulfide reaction. Further experimental work will be required, involving measurement of cation and anion diffusion rates in metal deficient oxides and sulfides in the presence of hydrogen, to firmly establish the effects suggested by the present study.

Acknowledgment

The author is indebted to Mr. W. H. Sharp for obtaining the rate data used in this article and to Mr. H. S. MacKinnon for his assistance in the remainder of the experimental work. Helpful discussions by Mr. R. S. Treseder and Dr. A. Wachter are also gratefully acknowledged.

Manuscript received Oct. 13, 1958. This paper was prepared for delivery before the Ottawa Meeting, Sept. 28-Oct. 2, 1958.

Any discussion of this paper will appear in a Discussion Section to be published in the June 1960 JOURNAL.

REFERENCES

1. G. Sorel, *Corrosion*, **14**, 33 (1958).
2. A. Dravnieks and C. H. Samans, *This Journal*, **105**, 183 (1958).

3. F. Hügli, C. M. Hudgins, Jr., and P. Delahay, Paper presented API Division of Refining, Los Angeles, California, May 1958.
4. T. Rosenqvist, *J. Iron Steel Inst., London*, **176**, 37 (1954).
5. F. J. Bruns, *Corrosion*, **13**, 27t (January 1957).
6. R. M. Fisher, L. S. Darken, and K. G. Carroll, *Acta Met.*, **2**, 370 (1954).
7. R. A. Meussner and C. E. Birchenall, *Corrosion*, **13**, 79 (1957).
8. J. Loriers, *C. R. Acad. Sci., Paris*, **231**, 522 (1950).
9. W. W. Webb, J. T. Norton, and C. Wagner, *This Journal*, **103**, 107 (1956).
10. E. W. Haycock, *This Journal*, **106**, 771 (1959).
11. Constructed by S. G. Yorke, The University, Bristol, England.
12. F. S. Stone, "Chemistry of Solid State," Ch. 15, W. E. Garner, Editor, Academic Press, Inc. New York, Butterworths Scientific Publications, London (1955).
13. D. Caplan and M. Cohen, *J. Metals*, **4**, 1057 (1952).
14. E. A. Gulbransen and R. Ruka, *This Journal*, **99**, 360 (1952).
15. R. Collongues, R. Sifferlen, and G. Chaudron, *Rev. Met.*, **50**, No. 10, 727 (1953).

Transitions from Parabolic to Linear Kinetics in Scaling of Metals

E. W. Haycock

Shell Development Company, Emeryville, California

ABSTRACT

A general rate equation is derived for a model of a barrier scale layer being formed by a diffusion process and simultaneously being depleted at a constant rate by a secondary process. The equation, derived to satisfy rate curves for sulfide scaling of iron in hydrogen sulfide, is shown to be applicable to the oxidation of aluminum and hafnium over ranges of conditions where two or three rate equations have been used previously to explain the experimental data. The validity of this equation emphasizes the importance of secondary processes, such as scale recrystallization, in determining the over-all rate of high-temperature corrosion reactions.

An important part of fundamental studies of the mechanism of high-temperature corrosion is the fitting of theoretical rate equations, derived from mechanistic models, to experimental scaling data. The basis of nearly all kinetic treatments of scaling processes, beyond the thin film range, is the simple, diffusion-controlled formation of a barrier product layer. The accepted mechanism by which the barrier scale grows according to a parabolic rate equation is attributed mainly to Wagner (1) and has been described exhaustively in recent review texts (2, 3). Many scaling systems, however, do not follow a parabolic equation except over limited ranges of temperature. Other rate equations such as linear, cubic, exponential, or combinations of these have been shown to fit experimental rate data for various systems, and a number of mechanisms have been suggested to account for these deviations from parabolic behavior (2, 3).

For the oxidation of most metals, an intermediate temperature range has been observed over which a parabolic rate law is reasonably well obeyed. At low temperatures a tendency toward logarithmic laws has been noted, while linear kinetics are favored at elevated temperatures. The apparent need for more than one theoretical rate equation to satisfy experimental data over a range of temperatures usually has been ascribed to transitions in the mechansim of scaling.

Systems which have not received an adequate quantitative treatment are those whose rates begin at a high value and then decrease over a certain time period to follow linear kinetics for the remainder of the scaling reaction. In these systems the linear portion of the rate curve may begin close to the origin or may not be apparent until the scaling reaction is well advanced, depending on the temperature of reaction. The purpose of this paper is to develop a quantitative approach which yields an equation capable of satisfying rate curves of this type over a wide range of conditions.

Mechanisms Associated with Linear Kinetics

Linear rate laws generally are associated with one of two mechanistic features. Surface reactions occurring at either the metal-scale or scale-gas interface can be considered in some cases to be slow and therefore rate determining. If the interface has a constant area throughout the reaction, then an overall linear rate law would be expected. The second mechanism giving rise to linear kinetics depends on the formation of an "open" or porous scale structure. This includes systems where volatile products are formed. Early investigators of oxidation systems associated a porous scale with metals, such as the alkaline earth metals, whose oxides have a smaller molar volume than the parent metal. The oxides of these systems were supposed to be formed under tension, and hence crack and shear as the scale thickened to give access of reactant gas to the metal surface at a constant rate. This is the basis of the well-known Pilling-Bedworth (4) rule. An improved understanding of the mechanism of oxide formation, however, has shown that the Pilling-Bedworth rule is without theoretical foundation (5, 6) for scales formed by metal ion diffusion. A more reasonable explanation, discussed by Evans (7), is that cracking, shearing, etc., can occur as a result of stresses

in the product scale but that the rate of metal consumption is determined by diffusion across a thin barrier layer on the metal surface which builds up to and then maintains a constant thickness. Such a mechanism can apply equally well to systems whose oxides have a molar volume greater or less than that of the parent metal.

Following a study of the oxidation of cerium, Loriers (8) suggested that the observed linear kinetics could be explained by the formation of a porous CeO_2 layer on top of a nonporous Ce_2O_3 barrier layer. The outer scale layer was observed to grow at the expense of the barrier layer at a constant rate while the consumption of metal was controlled by a diffusion process in the barrier layer. The barrier layer approached a constant thickness as the rate of its formation became equal to the rate of formation of the outer porous layer. The over-all rate of reaction therefore was high initially and decreased to approach a constant value. Similar reasoning has been applied by Wagner (9) to the oxidation of tungsten, and it appears that the same mechanistic approach can be used for the oxidation of uranium (10) and thorium (11). In all of these cases a two-layer scale is formed. The outer layer is porous and is a higher oxide of the metal than the compact inner barrier scale. In these systems it is reasonable to assume that the porous layer is formed at the expense of the barrier layer by nucleation and growth of a different chemical phase.

There are other scaling systems, such as iron-H_2S (12), and the oxidation of aluminum (13, 14), hafnium (15), calcium (16), and magnesium (17), where linear rate curves are obtained over certain temperature ranges. In these cases, however, where two scale layers have been observed, both layers have been found to be chemically the same material. In these systems it seems logical to extend the kinetics described qualitatively by Loriers (8) and to attribute the formation of the porous second layer to recrystallization and grain growth processes. Such a mechanism is treated in the following section.

Proposed Scaling Mechanism

By extending the qualitative arguments of Evans (7) and Loriers (8), the mechanistic model illustrated in Fig. 1 can be described in a quantitative manner.

A barrier layer scale AB is formed on the metal surface, its rate of formation being governed by ionic diffusion. Simultaneously, a secondary process is superimposed upon this primary process which depletes the barrier layer at a constant rate. In Fig. 1 this secondary process is shown to give the scale layer BC which is assumed to be sufficiently porous so that it offers no significant barrier to the availability of reactive gas at the interface B. The rate of metal consumption will be inversely proportional to the thickness of the compact barrier layer and will be given by the standard parabolic equation (18).

$$dx/dt = ak_p/2\mu \qquad [1]$$

where x is metal weight loss at time t; μ, thickness of compact layer at time t; k_p, parabolic rate constant;

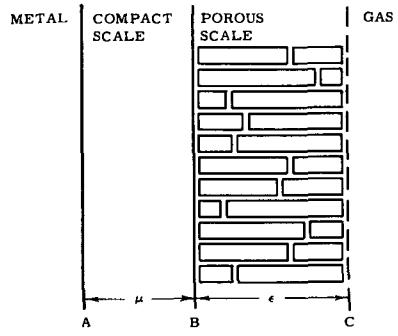

Fig. 1. Schematic model for derivation of rate equation

and a, a conversion factor relating the thickness of metal reacted to the thickness of the compact scale produced. In an unhindered, single scale forming reaction governed entirely by a parabolic kinetic law, a would be defined by $x = a\mu$. In addition to the usual assumptions of constant diffusion coefficient and uniform area at interface A, Eq. [1] assumes that layer AB has a constant uniform density.

Let ϵ be the thickness of the porous layer at time t. As a first approximation we assume the recrystallization process to begin at $t = 0$. Then

$$\epsilon = k_i t \qquad [2]$$

where k_i = linear rate constant of the interface reaction forming BC. We write

$$x = a\mu + b\epsilon \qquad [3]$$

where a and b are the density conversion factors from metal to the two scale types. This introduces the assumption that the porous layer has a constant density throughout the reaction. Substituting in Eq. [3] from Eq. [1] and [2], μ and ϵ in terms of x and t, we obtain

$$\frac{dx}{dt} = \frac{K_p}{x - K_i t} \qquad [4]$$

where

$$K_p = a^2 k_p/2$$

$$K_i = bk_i$$

Integration of Eq. [4] yields the equation giving metal weight loss as a function of time

$$x = \frac{K_p}{K_i} \ln \frac{K_p}{K_p - K_i(x - K_i t)} \qquad [5]$$

In the general case, the process which depletes the barrier layer may be either vaporization of the primary reaction product or, as in the case illustrated, the formation of a solid second scale layer. If a solid second layer is formed, it must either be porous and offer negligible resistance to the availability of reactive gases at the interface between the two-scale layers or it must have a structure such that solid diffusion rates in it are very rapid compared to those in the barrier layer. Mechanical processes such as cracking, spalling, etc., can be considered as possible mechanisms of porous second layer scale formation. However, the general smoothness of linear rate curves and conformance with the Arrhenius

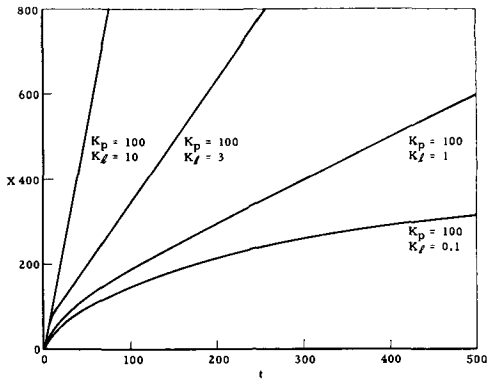

Fig. 2. Theoretical rate curves. $X = \frac{K_p}{K_1} \ln \frac{K_p}{K_p - K_1(X - K_1 t)}$

equation as a function of temperature are considered evidence against such an unpredictable process as mechanical cracking being important in more than a few cases. In instances where the porous and barrier layers are chemically identical, the most reasonable mechanism of porous scale formation appears to be recrystallization and grain growth.

If we eliminate x and ϵ from Eq. [1], [2], and [3] we obtain

$$\frac{d\mu}{dt} = \frac{K_p}{a^2\mu} - \frac{K_l}{a} \qquad [6]$$

The inner scale grows, i.e., $d\mu/dt$ is positive, as long as $K_p/a^2\mu > K_l/a$. As μ approaches a thickness given by $K_p/a^2\mu = k_l/a$, then $d\mu/dt$ approaches zero. The inner layer, therefore, approaches a constant thickness $\mu = K_p/aK_l$. It should be pointed out that mathematically this occurs at infinity. However, for practical purposes, the inner scale layer can be considered to become essentially constant after it has achieved 95% of its ultimate thickness. Equation [6] has been derived by Wagner and co-workers (9) for the oxidation of tungsten.

A plot of Eq. [5] yields a curve which approaches the straight line $K_p - K_l(x - K_l t) = 0$. The general shape characteristics of the curve are determined by the relative values of K_p and K_l. When K_p is large compared with K_l, the parabolic features of the equation are emphasized and the plot is considerably curved for short exposure time. As K_l increases relative to K_p, the linear portion of the plot begins closer to the origin of reaction. These variations are illustrated by the theoretical rate curves shown in Fig. 2.

In the following sections, Equation [5] is applied to systems where scale recrystallization appears to be the mechanism of porous second layer scale formation, and sufficient data are available to test the equation. The K_p and K_l values reported for these systems were obtained from the experimental data in the following way. A trial asymptote was drawn to the final stages of the rate curve. As stated above, this line should follow the equation $K_p - K_l(x - K_l t) = 0$, and hence the gradient was an approximate value of K_l and the intercept on the x axis an approximate value of K_p/K_l. The approximate values of K_p and K_l obtained in this way were then adjusted slightly to give the best coincidence with the experimental data. The number of significant figures to which values of K_p and K_l are reported is an indication of the sensitivity with which the experimental rate curves could be fitted.

Application of Proposed Mechanism and General Rate Equation

Iron-hydrogen sulfide reaction.—In the preceding paper (19), Eq. [5] was shown to satisfy sulfiding rates of iron and a series of chromium steels over a range of environmental conditions. For this system two scale layers are formed. Both layers consist of iron deficient ferrous sulfide. The inner barrier layer is formed by the diffusion of sulfide ions to the metal-scale interface. Since this involves the formation of ferrous sulfide beneath existing scale, it is expected that the barrier layer would be formed under high compressive stresses. The formation of the porous layer is attributed to stress induced recrystallization of the inner scale layer.

Oxidation of aluminum.—An apparent kinetic transition from parabolic to linear oxidation of aluminum has been observed at 475° to 500°C by Gulbransen (13) and Smeltzer (14). Hunter and Fowle (20) have shown that oxide films on aluminum consist of two layers, a barrier layer and a porous outer layer. Vermilyea (6) has suggested that recrystallization qualitatively could account for the formation of the porous layer and explain the transition to linear kinetics.

Equation [5] is fitted to the experimental data of Gulbransen (13) in Fig. 3. The three lower curves in this figure have been fitted with a parabolic equation by Gulbransen, while no attempt was made to satisfy the upper curve. It can be seen that Eq. [5] is capable of fitting all the curves over the apparent transition range. The rate constants K_p and K_l obtained from Fig. 3 have been plotted according to the Arrhenius equation in Fig. 4. Straight lines are obtained, and this is an indication of internal consistency in the application of Eq. [5] to the aluminum system. The experimental activation energy of 23 kcal for K_p is identical to that obtained by Gulbransen from parabolic rate constants of the lower temperature curves and is of the order of magnitude expected for the movement of metal ions in an oxide system. The activation energy of 49 kcal for K_l is similar to the value of 50.5 kcal obtained by Leontis and Rhines (17) for the linear high tem-

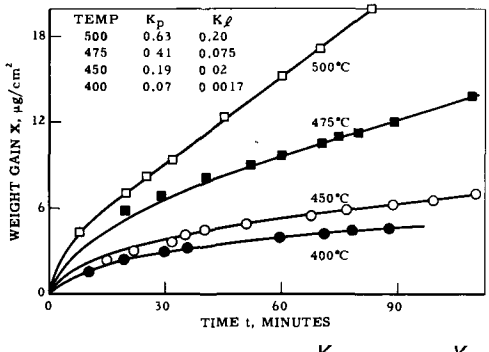

Fig. 3. Application of equation $X = \frac{K_p}{K_1} \ln \frac{K_p}{K_p - K_1(X - K_1 t)}$ to aluminum oxidation rate data. Experimental data taken from Ref. (13).

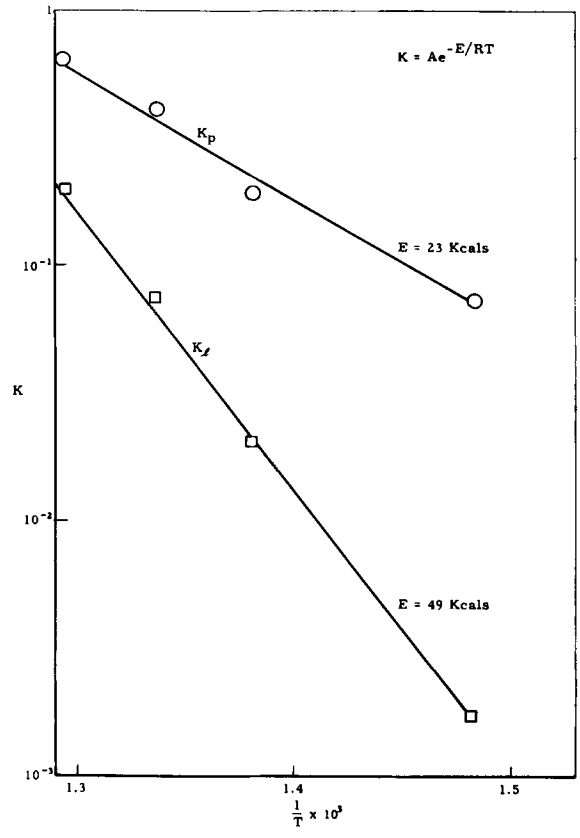

Fig. 4. Arrhenius plots for the oxidation of aluminum

perature oxidation of magnesium. It would be expected that the rate of recrystallization in aluminum oxide would be controlled by the surface mobility of the relatively bulky oxide ions. A high activation energy for this process would be expected for refractory oxides such as alumina and magnesia which are known to be difficult to sinter even at very high temperatures.

On the basis of our previous discussion of the effects of the relative values of K_p and K_l on the shape of the plot of Eq. [5], it would be expected that the apparent transition from parabolic to linear kinetics would occur over a small range of temperature for systems in which K_l has a high temperature coefficient compared with K_p. This effect is well illustrated by the oxidation of aluminum.

The successful application of Eq. [5] to the oxidation curves shown in Fig. 3 emphasizes that short term experiments can be misleading in mechanistic studies. If the mechanism associated with Eq. [5] is correct, then the low temperature curves in Fig. 3 would become straight lines if the experiments were continued for sufficient time. The application of parabolic equations to these curves is misleading, especially if a particular mechanism is associated with the parabolic law. It is important that the correct mechanism and kinetic equations be established if the kinetic data are to be used for theoretical absolute rate calculations such as those attempted by Gulbransen (21).

Oxidation of hafnium.—The oxidation of hafnium from 350° to 1200°C has been studied recently by Smeltzer and Simnad (15). The mechanism appears to be very similar to that of the iron-H_2S system. A two-layer scale is formed. Both layers consist of HfO_2, and the outer layer is very porous. Inert marker experiments indicate that the barrier layer is formed by diffusion of oxygen from the gas-scale interface to the metal surface and hence would be formed under a high compressive stress. The above authors have used an exponential, parabolic, and linear law successively to satisfy empirically the experimental data over the temperature range studied. The scale thickness measurements reported by Smeltzer and Simnad support the mechanism used to derive Eq. [5]. They have shown that the barrier layer approaches a constant thickness which can be expressed in terms of the rate constants K_p and K_l.

The application of Eq. [5] to the experimental results of Smeltzer and Simnad is shown in Fig. 5. It can be seen that the equation explains the data previously fitted by three equations. There is no theoretical evidence therefore of "transitions" occurring over the temperature range studied. As a further test of internal consistency, the straight-line Arrhenius plots, for values of K_p and K_l obtained from Fig. 5, are shown in Fig. 6. The activation energy of 36 kcal obtained for K_p is identical to the value reported by Smeltzer and Simnad from parabolic rate constants obtained by approximating portions of the experiment rate curves to parabolas over the temperature range 470°-1200°C. The activation energy of 18 kcal for K_l is somewhat lower than the value of 26 kcal reported by the above authors from linear rate constants obtained from portions of the experimental rate curves in the temperature range 900°-1200°C. This difference results because, in our analysis of the experimental rate curves, only the 1200°C curve was considered to have reached the final linear stage. The curves presented by Smeltzer and Simnad for 900° and 1000°C were considered not to have reached the final linear rate of reaction in the exposure time studied. Since Smeltzer and Simnad illustrated the growth of the barrier layer oxide by oxide ion diffusion, the activation energy of 36 kcal is associated with the bulk mobility of oxide ions in polycrystalline hafnia. On the basis of a recrystallization process determining the rate of formation of the outer porous scale layer, the activation energy of 18 kcal is associated with the surface mobility of ions. Since, in this case, the temperature coefficient of K_p is greater than that of K_l, apparent transitions in short term exposures are spread over a wide temperature

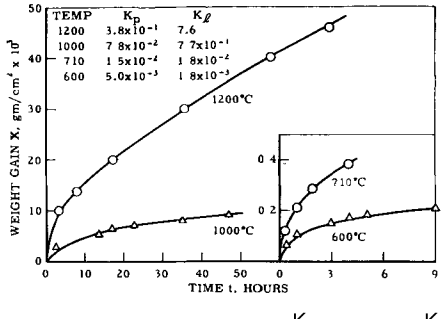

Fig. 5. Application of equation $X = \frac{K_p}{K_l} \ln \frac{K_p}{K_p - K_l(X - K_l t)}$ to hafnium oxidation rate data. Experimental data taken from Ref. (15).

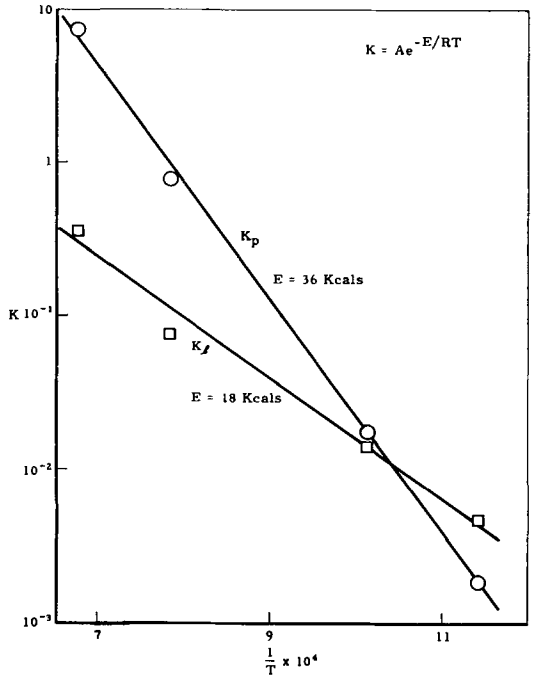

Fig. 6. Arrhenius plots for the oxidation of hafnium

range. The closest approximation of the rate curves to parabolas occurs at the highest temperatures.

A possible extension of the proposed kinetic treatment is that Eq. [5] will be modified in some cases to include the possibility that the secondary process does not begin at $t = 0$. In cases similar to those discussed, this would correspond to the requirement that a minimum stress level be reached before formation of the porous layer begins. This modification yields a rate equation of the form

$$\frac{dx}{dt} = \frac{K_p}{x - K_l(t + t_o)} \qquad [7]$$

where t_o is the time at which the secondary process begins. Such an equation would be expected to apply to systems such as the oxidation of niobium studied recently by Cathcart, Campbell, and Smith (22).

Conclusions

It has been shown that a single rate equation can replace the need for multiple equations in several systems for which sufficient experimental data are available to test its validity. It is probable that, when more data are available, it will be possible to show its general applicability to other scaling reactions. For the systems discussed, the concept of transitions in mechanism occurring over certain temperature ranges has been shown to be an unnecessary complication of previous kinetic treatments. The present analysis emphasizes the fact that short duration experiments can be misleading in studies of scaling mechanisms.

The general validity of Eq. [5] for the systems discussed indicates that secondary processes, such as scale recrystallization, can be of considerable importance in determining the rate of scaling processes. The application of Eq. [5] in future studies, and further development of the mechanistic concept associated with it, should be helpful in improving our understanding of the mechanism of corrosion at high temperature.

Acknowledgment

The author is indebted to Mr. H. S. MacKinnon for valuable assistance in the analysis of the rate data reported and to Mr. R. S. Treseder and Dr. A. Wachter for encouragement and helpful discussions.

Manuscript received Oct. 13, 1958. This paper was prepared for delivery before the Ottawa Meeting, Sept. 28-Oct. 2, 1958.

Any discussion of this paper will appear in a Discussion Section to be published in the June 1960 JOURNAL.

REFERENCES

1. C. Wagner, *Z. physik. Chem.*, **B21**, 25 (1933); *ibid.*, **B32**, 447 (1936).
2. T. B. Grimley, "The Chemistry of the Solid State," Ch. 14, Editor, W. E. Garner, Academic Press, Inc., New York, Butterworths Scientific Publications, London (1955).
3. O. Kubaschewski and B. E. Hopkins, "Oxidation of Metals and Alloys," Butterworths Scientific Publications, London (1953).
4. N. B. Pilling and R. E. Bedworth, *J. Inst. Metals*, **29**, 529 (1923).
5. E. A. Gulbransen, *Ind. Eng. Chem.*, **41**, 1385 (1949).
6. D. A. Vermilyea, *Acta Met.*, **5**, 492 (1957).
7. U. R. Evans, *This Journal*, **91**, 547 (1947).
8. J. Loriers, *C. R. Acad Sci., Paris*, **231**, 522 (1950).
9. W. W. Webb, J. T. Norton, and C. Wagner, *This Journal*, **103**, 107 (1956).
10. J. Loriers, *C. R. Acad. Sci., Paris*, **234**, 91 (1952).
11. P. Levesque and D. Cubicciotti, *Am. Chem. Soc.*, **73**, 2028 (1951).
12. A. Dravnieks and C. H. Samans, *This Journal*, **105**, 183 (1958); F. Hügli, C. M. Hudgins, Jr., and P. Delahay, Paper presented API Div. of Refining, Los Angeles, California, May 1958.
13. E. A. Gulbransen and W. S. Wysong, *J. Physik. chem.*, **51**, 1087 (1947).
14. W. W. Smeltzer, *This Journal*, **103**, 209 (1956).
15. W. W. Smeltzer and M. T. Simnad, *Acta Met.*, **5**, 320 (1957).
16. D. Cubicciotti, *J. Am. Chem. Soc.*, **74**, 557 (1952).
17. T. E. Leontis and F. N. Rhines, *Trans. Am. Inst. Mining Met. Engrs.*, **166**, 265 (1946).
18. Reference (3), p. 41.
19. E. W. Haycock, *This Journal*, **106**, 764 (1959).
20. M. S. Hunter and P. Fowle, *This Journal*, **103**, 482 (1956).
21. E. A. Gulbransen, *Annals. N. Y. Acad. Sci.*, **58**, 830 (1954).
22. J. V. Cathcart, J. J. Campbell, and G. P. Smith, *This Journal*, **105**, 442 (1958).

The Effect of Halides on the Capacity and Resistance of the Magnesium Electrode in Aqueous Solutions

G. R. Hoey and M. Cohen

Division of Applied Chemistry, National Research Council, Ottawa, Ontario, Canada

ABSTRACT

A study of potential-time decay curves at anodically and cathodically polarized magnesium by the d-c current interrupter method is presented. Potential-time oscillograms and polarization curves were determined for magnesium electrodes in buffered and unbuffered aqueous solutions containing chloride, bromide, iodide, and fluoride. Film capacity, solution double layer capacity, and resistance data determined from the oscillograms using the electrical analog

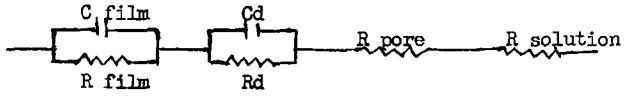

is presented where Cd and Rd are the capacity and resistance of the Helmholtz-Gouy double layer. The effect of specific adsorption of anions and the physical nature of the film on the magnesium electrode are discussed.

Local corrosion (1-3) and electrochemical formation of Mg^{+} (4-10), Mg_2^{++} (11), and $Mg \cdot Mg^{++}$ (3) have been suggested to explain the negative difference effect observed for magnesium. The existence of the ions Mg^{+}, Mg_2^{++}, and $Mg \cdot Mg^{++}$ has not been definitely established, and the negative difference effect of Mg may, in fact, be explained solely on the basis of local corrosion. It can be stated with certainty, however, that even if Mg^{+} is formed, local corrosion must also occur. This conclusion follows from the experimental facts: (*a*) values of the apparent Mg valency (determined coulometrically) less than unity as well as greater than unity have been observed; (*b*) a positive difference effect is observed for Mg at low anodic current densities in solutions containing HCl or NH_4Cl (9, 12). Observed Mg valencies greater than unity may be explained by electrochemical formation of Mg^{++}, either directly or via the reaction, $Mg^{+} \rightarrow Mg^{++} + e$ (5).

From the above considerations it may be concluded: (*a*) the potential of Mg is a mixed anodic-cathodic potential, and (*b*) although the mechanism of the local anodic reaction is uncertain it consists, in part, of the electrochemical formation of Mg^{++}, either directly or via monovalent Mg. The local cathodic reaction is generally the hydrogen evolution reaction but may under some experimental conditions consist both of the h.e.r. and the oxygen adsorption reaction (13, 14).

The potential of the Mg electrode may be under anodic, cathodic, or mixed control depending on the experimental conditions. In acid solutions (*p*H's < 3 in unbuffered solutions) the corrosion reaction is probably under cathodic control; the potential becomes more noble with increasing hydrogen ion concentration (15) and the corrosion proceeds under H_3O^{+} diffusion control (16, 17). At high *p*H's (*p*H $>$ 11 in unbuffered solutions), the potential increases sharply in the more noble direction with increasing *p*H and anodization causes passivation (15) which indicates that at high *p*H's the reaction is under anodic control. In the intermediate *p*H range the potential of Mg is practically independent of *p*H and a transition from cathodic to anodic control probably occurs. Film formation at high *p*H's undoubtedly plays a major role in the transition from cathodic to anodic control and there are indications that transport phenomena through surface film may be partly rate controlling even at low *p*H's (18). Although the chemical composition of the surface film is reasonably well established (19-23), little is known concerning such important factors as the conductivity and porosity of the film. The Mg electrode potential is dependent on the nature and concentration of inactive anions in solution (24) which suggests that specific adsorption effects of anions on the electrode might also be important.

This study was undertaken in order to gain further information on the roles of specific adsorption of anions and film formation in the electrochemical behavior of Mg. It was felt that a comparison of the effect of halide ions on the Mg electrode capacity, resistance, and polarization curves would provide information on specific adsorption and film effects. A limited amount of data exists in the literature which might be used for predicting the adsorption behavior of halide ions on Mg. Cl^{-1}, Br^{-1}, and I^{-1} form soluble salts with Mg, whereas MgF_2 is insoluble leading to passive films. The order of increasing adsorption of these ions on mercury are $F^{-1} < Cl^{-1} < Br^{-1} < I^{-1}$ (25). The fluoride ion is not considered to be specifically adsorbed on mercury. On platinum, I^{-1} is probably more strongly adsorbed than Cl^{-1}; the minimum in the Pt electrode capacity vs. potential curve for solutions containing I^{-1} is more cathodic than that for solutions containing Cl^{-1} (26). The same order of

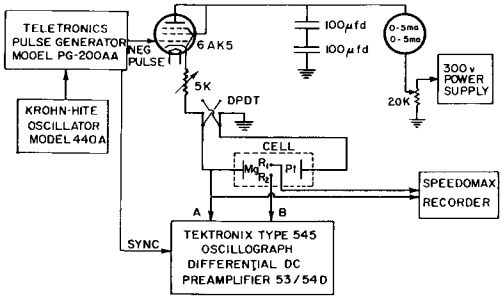

Fig. 1. D-C current interrupter apparatus

adsorbability of Cl^{-1}, Br^{-1}, and I^{-1} might be expected for Mg as for Hg and Pt.

Experimental

Polarization capacity and resistance was determined by the d-c current interrupter method. The current interrupter technique used was similar to that of Shuldiner and White (27). The circuit is given in Fig. 1. The cell was polarized by means of a constant current supplied in the plate circuit of the pentode 6AK5. The pentode was hooked up as a triode. By reversing the DPDT switch the Mg electrode could be made anodic or cathodic. The potential of the Mg electrode was continuously recorded on a Speedomax recorder. Potential-time oscillograms were determined as follows. A negative pulse with a rise time of 0.1 μsec was supplied to the grid of the pentode which shuts off the tube for the pulse interval; the Teletronics pulse generator was used to give interruption times from 1 μsec to 1 msec, and a Tektronix type 161 pulse generator was used for pulse widths from 1 msec to 0.1 sec. The pulse generator could be triggered by the oscillator to give from 0.1 pulses/sec to 5000 pulses/sec; repetition rates less than 0.1 pulses/sec could not be recorded on the oscilloscope. The pulse generator was triggered to a Tektronix type 545 oscilloscope which recorded the potential-time changes occurring at the Mg electrode during the current interruption. The maximum sensitivity of the Tektronix type 53/54D preamplifier was 1 mv/cm. Oscilloscope traces were photographed with a type 299 Dumas oscilloscope recording camera.

Potential-current polarization curves were determined using the constant current method. The Mg electrode was anodically polarized at 0.4 ma/cm² for 12 hr during which time the potential reaches a steady value. The current was then changed in steps lasting about ½ hr from 0.4 ma/cm² anodic to 0.4 ma/cm² cathodic and back again to 0.4 ma/cm² anodic in steps. At each setting of the current the potential was recorded on the Speedomax recorder and potential-time oscillograms were taken. The electrolytic cell was machined from Lucite, cylindrical in shape, with a slit along the top through which the reference electrodes could be immersed in the solution. The distance of the reference electrode from the Mg electrode could be varied along the length of the cell. The working electrode was platinized platinum; the reference electrode (R_1) was a silver-silver halide electrode; and R_2 was a Mg wire reference electrode (Fig. 1).

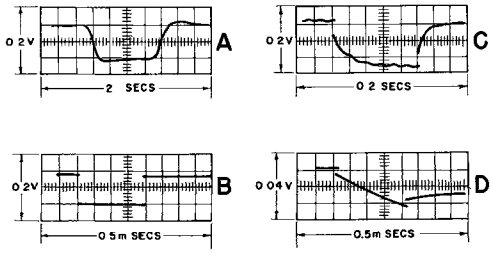

Fig. 2. Potential-time decay curves of anodically polarized Mg; A, B, and C; solutian, 0.05M NaOH, 0.186N H_3BO_3; 0.1M NaCl; pH = 8.9; 0.4 ma/cm². D; solution 0.1M NaF; 0.035 ma/cm².

The Mg test electrode (area = 5 cm²) was machined from commercially distilled pure Mg. This material was supplied to have a minimum purity of 99.96% with a total Fe, Ni, and Cu content not greater than 0.005%. The Mg electrode surface was prepared by polishing on silicon carbide papers followed by a 1 min etch in 10% HNO_3 acid solution. The optical and electron microscopes revealed a clean surface preparation. By electron diffraction examination the film remaining on the Mg electrode after the chemical etch was shown to be MgO and $Mg(OH)_2$.

Solutions were prepared from reagent grade salts. During a run fresh solution was continuously supplied to the cell solution by means of an overflow system.

Results

Typical potential-time decay curves are given in Fig. 2, 3, and 4. The potential-time curves are interpreted in terms of the equivalent electrical circuit:

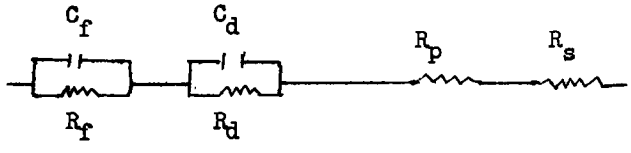

C_f is the capacity of the electrical double layer with the film as dielectric and R_f is the polarization resistance of the film; C_d and R_d are the capacity and polarization resistance of the solution electrical double layer; R_p is that part of the pore resistance of the film which is noncapacitive; and R_s is the resistance of the solution between the reference electrode and the magnesium electrode.

The equivalent electrical circuit is based on the model of the metal electrode given in Fig. 11 which

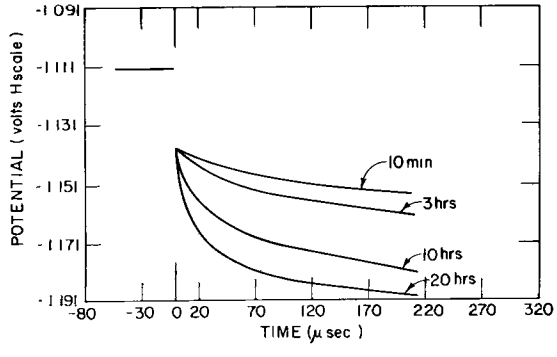

Fig. 3. Potential-time decay curves of anodically polarized Mg after various polarization times in a solution containing 0.1M NaOH; 0.1M H_3BO_3, and 0.1M NaBr; 0.4 ma/cm²; pH = 11.

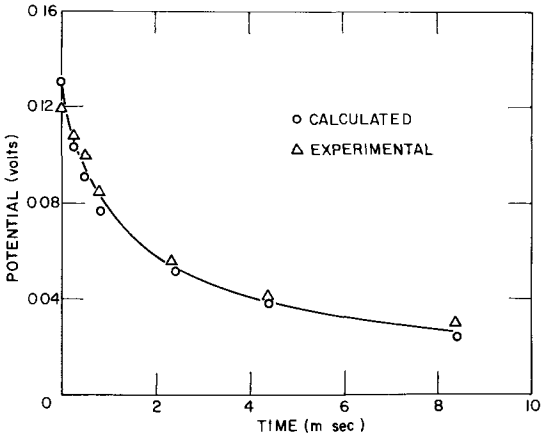

Fig. 4. Calculated and experimental potential-time decay curves of anodically polarized Mg in solution containing 0.05M NaOH, 0.186 H_3BO_3, and 0.1M NaCl; 0.4 ma/cm²; pH = 8.9.

is described in the Discussion. The solution double layer (Fig. 11) is considered to be in a pore of a nonconducting type film. The comparison of the electrical double layer of the electrode with an equivalent circuit is not strictly correct, but it is a simple and convenient manner in which to express the results of this type of experiment.

The components of the equivalent circuit are determined from the potential-time oscillograms. The potential drop which occurs in the first 0.3 μsec of the interruption in Fig. 2A, which will be called the series polarization, is the sum of the potential drops across elements of the equivalent circuit with time constants < 0.3 μsec; the series resistance (R_x) is equal to the series polarization divided by the value of the current before interruption. R_x is equal to the sum of R_p and R_s and will also include R_f and R_d if R_fC_f and C_dR_d is < 0.3 μsec. The residual series resistance exclusive of the solution resistance is obtained by measuring the series polarization at various points from the Mg electrode; R_s is a function of the distance of the reference electrode from the Mg electrode whereas R_f and R_p are not. Typical plots of the series resistance vs. the distance of the reference electrode from the Mg electrode are given in Fig. 5; the residual series resistance for both cases is 25 ohm-cm². For the experimental conditions studied in this work the contribution of the residual series resistance to the overpotential of the Mg electrode is less than 5% in active solutions and less than 1% in passive solutions.

The capacity of the Mg electrode (C) is defined by the expression:

$$C = -i^\circ/(dE/dt)_{t=0} \qquad [1]$$

where i° is the current at the moment of interruption and $(dE/dt)_{t=0}$ is the slope of the potential-time decay curve taken at $t = 0$.

The rate of potential decay across the capacitive part of the equivalent circuit is

$$dE/dt = -(E_f/R_fC_f + E_d/R_dC_d) \qquad [2]$$

where E_f and E_d are the potentials across the film and solution double layer circuits, respectively. At $t = 0$, $E_f/R_f = E_d/R_d = i^\circ$

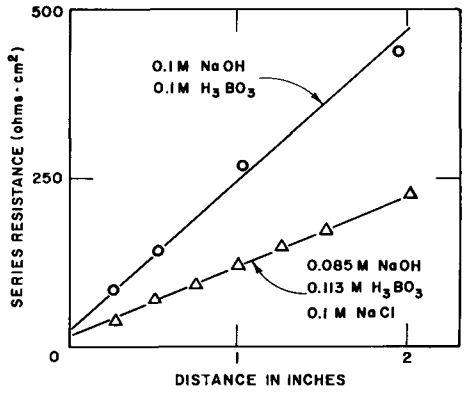

Fig. 5. Series resistance as a function of distance of the reference electrode from the Mg electrode: 0.4 ma/cm².

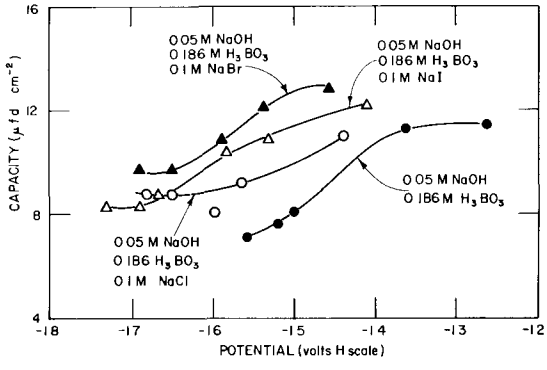

Fig. 6. Magnesium electrode capacity as a function of polarization potential; pH = 8.9.

$$(dE/dt)_{t=0} = -i^\circ(C_f + C_d)/C_fC_d \qquad [3]$$

and

$$C = C_fC_d/(C_f + C_d) \qquad [4]$$

Equation [3] is simplified when the time constants R_fC_f and R_dC_d are quite different, and then

$$(dE/dt)_{t=0} = -i^\circ/C_f \qquad [5a]$$

$$\text{or} \qquad = -i^\circ/C_d \qquad [5b]$$

depending on the time range studied by the oscilloscope. Magnesium electrode capacity data are given in Fig. 6 and Table I. The experimental capacities are correlated with the components of the equivalent electrical circuit in the discussion.

The parallel polarization resistance is obtained from the potential time oscillograms using the equation:

$$R_{f,d} = -\frac{|\Delta E|_{t=0}^{t=t}}{C} \Big/ |dE/dt|_{t=0}^{t=t} \qquad [6]$$

where $R_{f,d}$ is the parallel polarization resistance of either the film or the solution double layer; $|\Delta E|_{t=0}^{t=t}$ is the difference in potential and $|\Delta dE/dt|_{t=0}^{t=t}$ is the difference in rate of potential decay at times $t = t$ and $t = 0$. Equation [6] is valid when the time constants for decay across the film and solution double layers are equal or when one of the two decay rates is small compared to the other. Resistance data for the solutions studied are given in Table I. The reproducibility of $R_{f,d}$ determinations using Eq. [6] is about ±50%.

Potential-current polarization curves of Mg in buffered and unbuffered solutions with halide addi-

Table I

Solution	pH	Current ma/cm²	Polarization potential, v-H scale	Rest potential (E_c), v-H scale	Series polarization, v	Parallel resistance, ohm-cm²	Capacity, μf/cm²
0.05M NaOH, 0.186M H_3BO_3	8.9	0.39(a)	—1.40	—1.61	0.038	40	11.2
0.1M NaCl		0.40(c)	—1.72	—1.61	0.038	55	8.8
0.05M NaOH, 0.186M H_3BO_3	8.9	0.40(a)	—1.18	—1.48	0.125	60	11.0
0.0002M NaCl		0.40(c)	—1.72	—1.48	0.150	85	7.2
0.05M NaOH, 0.186M H_3BO_3	8.9	0.40(a)	—1.37	—1.63	0.038	40	12.2
0.1M NaI		0.19(c)	—1.70	—1.63	0.016	25	8.2
0.05M NaOH, 0.186M H_3BO_3	8.9	0.40(a)	—1.41	—1.63	0.052	70	12.8
0.1M NaBr		0.40(c)	—1.75	—1.63	0.040	135	9.4
0.05M NaOH, 0.186M H_3BO_3	8.9	0.40(a)	—1.15	—1.48	0.12	50	11.2
		0.42(c)	—1.70	—1.48	0.14	80	7.0
0.05M NaOH, 0.186M H_3BO_3	8.9	0.21(a)	4.5	—1.5	0.030	2500	0.30
0.1M NaF		0.28(c)	—2.4	—1.5	0.040	1150	0.36
0.085M NaOH, 0.113M H_3BO_3	10.0	0.40(a)	—1.35	—1.62	0.033	90	10.0
0.1M NaCl		0.40(c)	—1.79	—1.62	0.036	300	7.4
0.10M NaOH, 0.10M H_3BO_3	11.2	0.37(a)	2.42	—1.38	0.065	110	0.2
0.10M NaOH, 0.10M H_3BO_3 0.1M NaCl	11.1	0.36(a)	—1.23	—1.41	0.028	65	0.5
0.10M NaOH, 0.10M H_3BO_3 0.1M NaI	11.0	0.35(a)	—0.86	—1.45	0.030	250	0.2
0.10M NaOH, 0.10M H_3BO_3 0.1M NaBr	11.0	0.38(a)	—1.12	—1.40	0.036	75	0.4
0.10M NaOH, 0.10M H_3BO_3	10.9	0.14(a)	9.0	—1.42	0.012	600	0.32
0.1M NaF		0.20(c)	—2.27	—1.42	0.020	850	0.53
0.1M NaCl	10.6	0.36(a)	—1.21	—1.44	0.090	55	9.0
0.1M NaBr	10.5	0.38(a)	—1.32	—1.50	0.040	70	5.6
0.1M NaI	10.5	0.4(a)	—1.34	—1.45	0.038	55	6.0
0.1M NaF	9.9	0.14(a)	13.7	—1.63	0.004	3250	0.28
		0.50(c)	—2.29	—1.63	0.018	1500	0.44

(a) Anodic polarization; (c) Cathodic polarization.

tions are given in Fig. 7, 8, 9, and 10. The reproducibility of potential measurements for the experimental conditions of Fig. 7, 8, and 9 is 30 mv and for Fig. 10 the reproducibility is 0.2 v. Cathodic polarization measurements of Mg in solutions buffered at pH = 11 containing NaCl, NaBr, or NaI and unbuffered solutions containing NaCl, NaBr, or NaI are nonreproducible and are not presented.

Discusssion

An exact theoretical treatment of the potential time curves observed in this work is not possible; the current density is probably nonuniform over the electrode surface and the electrochemical mechanism is complicated and uncertain. However, a semiquantitative and perhaps fortuitous agreement between the current interrupter theory and experiment was found.

An equation for the potential-time decay curves is derived in the following manner. Assume the rate-controlling reaction is:

$$Mg = Mg^{n+} + ne \qquad [7]$$

The forward current ($\vec{i}$) and the reverse current ($\overleftarrow{i}$) of reaction [7] are given by the equations (28),

$$\vec{i} = i_o \exp(\alpha n\mathbf{F}\,\Delta E_c/RT) \exp(\alpha n\mathbf{F}\,\Delta E/RT) \qquad [8]$$

$$\overleftarrow{i} = i_o \exp(-(1-\alpha)n\mathbf{F}\Delta E_c/RT) \exp(-(1-\alpha)n\mathbf{F}\Delta E/RT) \qquad [9]$$

$$i = \vec{i} - \overleftarrow{i} - i_{corr} \qquad [10]$$

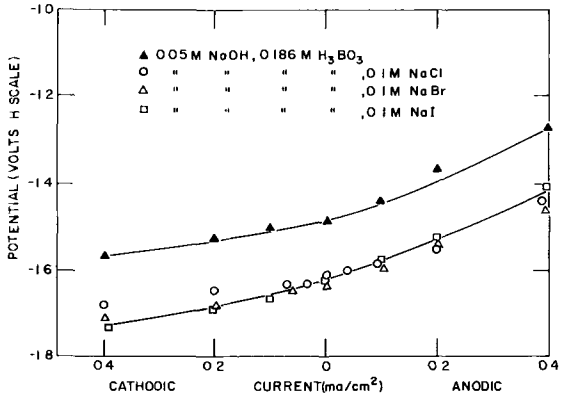

Fig. 7. Anodic and cathodic polarization curves of Mg corrected for series polorization; pH = 8.9.

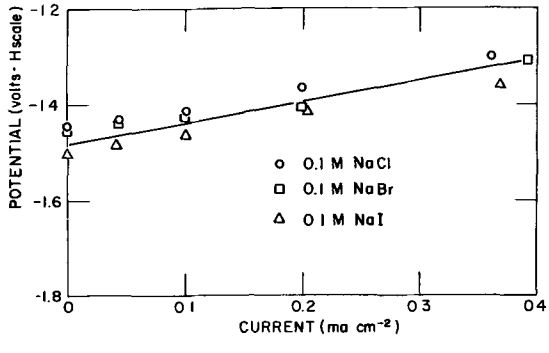

Fig. 8. Anodic polarization curve of Mg corrected for series polarization; pH = 10.5.

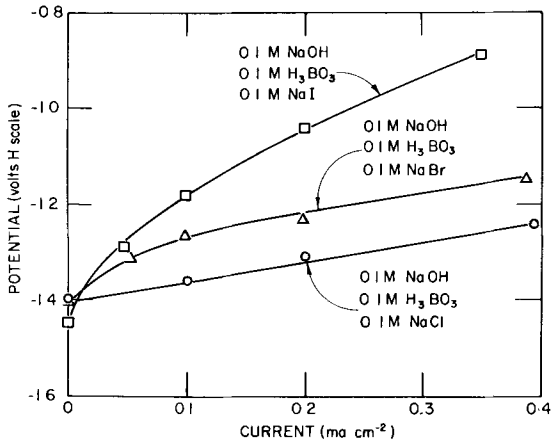

Fig. 9. Anodic polarization curve of Mg corrected for series polarization; pH = 11.

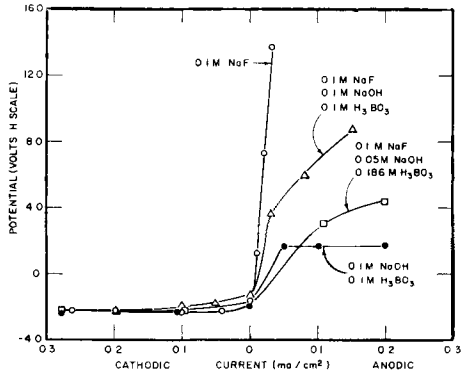

Fig. 10. Anodic and cathodic polarization curves of Mg corrected for series polarization; •, pH = 11; □, pH = 8.9; △, pH = 11; ○, pH = 10.

where $\Delta E = E - E_c$, and $\Delta E_c = E_c - E_o$; i_o is the exchange current and α is the transfer coefficient for reaction [7]; **F** is the Faraday; R is the gas constant; T is the absolute temperature; E is the polarization potential; E_c is the corrosion potential at zero applied current; E_o is the equilibrium potential for reaction [7]; i is the applied current and i_{corr} is the corrosion current. The current efficiency for the anodic dissolution of Mg assuming $n = 2$ (3) is independent of current density at high current densities ($i > 0.05$ ma/cm²) which indicates that the corrosion current is directly proportional to the applied current. Thus, it may be assumed that $i_{corr} = (K - 1)\, i$ where K is a constant ($K > 1$) which is independent of the applied current.

Since

$$dE/dt = -\, i/C \qquad [11]$$

then

$$\int \frac{d\,\Delta E}{\underset{i}{\rightarrow} - \underset{i}{\leftarrow}} = -\int (1/CK)\,dt \qquad [12]$$

where it is assumed that E_c and E_o are independent of applied current. Integration of Eq. [12] by Grahame's method (29) using the assumptions $\alpha = \frac{1}{2}$, $\exp(\alpha n\mathbf{F}\Delta E_c/RT) \approx 1$, and C is independent of ΔE yields the equation

$$\Delta E = \frac{2RT}{n\mathbf{F}} \ln \frac{1 + \exp(-n\mathbf{F}i_o(t + t^1)/RTCK)}{1 - \exp(-n\mathbf{F}i_o(t + t^1)/RTCK)} \qquad [13]$$

t is measured from the moment of interruption and t^1 has the meaning that ΔE would be infinite at $t = -t^1$. The assumption that $\exp(\alpha n\mathbf{F}\Delta E_c/RT) \approx 1$ may set a fictitious value to the equilibrium potential for reaction [7], i.e., $E_o \approx E_c$, when Eq. [13] is applied to a corroding Mg electrode; the simultaneous occurrence of the cathodic and anodic reactions on anodically polarized Mg could have the effect of displacing the experimental potential of the electrode from the potential of the anodic reaction toward the potential of the cathodic reaction if an appreciable ohmic potential drop exists between the reaction paths of the cathodic and anodic reactions.

Equation [13] was derived for an electrode with a uniform current density over the surface. In active solutions at pH = 8.9 a uniform attack occurs on Mg which indicates a uniform current density. The general form of the potential-time decay curves for Mg in this type of solution is represented by Eq. [13]. In Fig. 4 the potential-time decay curve for anodically polarized Mg calculated from Eq. [13] using assumed values of n, t^1, K, and i_o ($n = 2$, $t^1 = 0.1$ msec, $K = 2$, and $i_o = 0.024$ ma/cm²), and $C = 10$ μ f/cm² from initial slope compares well with the experimental potential-time decay curve. The rate of reaction [7] calculated from Eq. [10] is within an order of magnitude of the rate of dissolution of Mg in this particular solution at the same current (10^{-8} moles/cm²/sec).

In view of the many simplifying assumptions necessary for the derivation of Eq. [13] further interpretation of the results in terms of this equation would be unwarranted. The remainder of the discussion will be concerned with qualitative interpretation of the capacity and potential data in terms of the equivalent electrical circuit previously given and the following concept of the structure of the Mg electrode interface.

The structure of the Mg electrode interface will be assumed to be of the form schematically represented in Fig. 11. Positive and negative polarization refers to polarization relative to the potential of the zero point of charge. The anodic and cathodic reactions are assumed to occur at the barrier film-solution interface. In Fig. (11B) the electrode is considered to be sufficiently polarized to completely suppress the anodic reaction. The nature of the film is pH dependent. A thin nonporous barrier film is assumed to be present at all pH's. In active solutions, at pH's $\gtrsim 10.5$, thick white films (10^{-4} cm) are formed on Mg; at pH's < 10.5 thin films ($< 10^{-5}$ cm) are formed. The discontinuity in film formation is due to precipi-

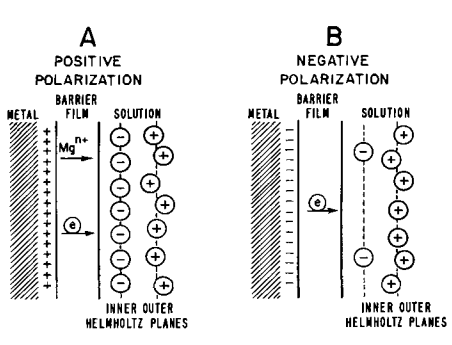

Fig. 11. Schematic diagrams of the electrical double layer of positively and negatively polarized Mg.

tation on the Mg at pH's $\geqq 10.5$ of $Mg(OH)_2$ from solution (3). At the low field strength used in this work transport of ions and electrons through the thick film would not occur for nonpassive films.

The capacity of the barrier film is a decreasing function of pH and polarization current since these factors would tend to increase the barrier film thickness. The polarization resistance of the barrier film is dependent on thickness and chemical and physical structure of the film; the latter factor controls the type of transport (ionic or electronic). The capacity of the solution double layer which includes the fixed double layer and the diffuse double layer is a complex function of potential; several maxima and minima are sometimes observed (25). In the simplest case the capacity of the solution double layer reaches a minimum at the potential of the zero point of charge and increased polarization increases the capacity due to the decrease in effective distance between the outer Helmholtz plane and the barrier film. The electrode capacity per unit of apparent area is directly related to the pore area and the polarization resistance of the electrode is inversely proportional to the pore area.

Specific adsorption of anions on Mg would have the effect of increasing the capacity of the solution double layer and displacing the potential of the zero point of charge to more cathodic potentials. Specific adsorption of anions provides a means of explaining the negative difference effect of Mg. Increased anodic polarization causes increased adsorption on the barrier film which results in an increased positive charge on the diffuse double layer and a closer proximity of the diffuse double layer to the barrier film. Hydrogen ions in the diffuse double layer are therefore more easily discharged at the barrier film by increased anodic polarization.

In the following sections a satisfactory explanation of the experimental results is presented in terms of the pore theory.

Buffered Solutions at pH = 8.9

The halide additions affect the polarization curves of the buffer solutions but no specific effect of the anions Cl^{-1}, Br^{-1}, or I^{-1} are apparent (Fig. 7). The shift in potential observed in solutions without halide additions is probably due to higher Helmholtz-Gouy double layer impedance corresponding to the lower conductivity of the buffer solution. The Mg electrode capacity is probably the solution double layer capacity (C_d) since the capacity increases as the anodic polarization is increased (Fig. 6). Thus, it appears that the time constant for decay across the barrier film at pH = 8.9 is less than 0.3 μsec. Specific effects of each of the halides on the capacity are not evident within the reproducibility of the experiments. The borate ion is apparently preferentially adsorbed on Mg in these solutions.

Cathodic polarization in the range studied does not effect a change in sign of the charge on the metal surface from positive to negative (Fig. 11) since the capacity did not go through a minimum on cathodic polarization. The rate of dissolution of cathodically polarized Mg in these solutions is quite large which serves to maintain the Mg metal surface positively charged or perhaps neutral (there is the possibility that the minimum in the capacity vs. potential curves was reached at the most cathodic potentials studied).

Buffered Solutions at pH = 11

The capacity of the Mg electrode at pH = 11 is considerably lower than the capacity at pH = 8.9 (Table I). A decrease in capacity of both the barrier film and the solution double layer is expected due to the decreased reacting area of the electrode and increased barrier film thickness. The formation of the porous film or barrier film is a slow process; the Mg electrode capacity changes from 2 $\mu f/cm^2$ at 10 min polarization to 0.4 $\mu f/cm^2$ at 20 hr polarization (Fig. 3). Trends of the observed capacity at pH = 11 with specific halide ion or potential may be hidden due to the low reproducibility of capacity measurements in these solutions. Therefore, it is not possible to decide whether the experimental capacity is C_f, C_d, or the series capacity, $C_f C_d/(C_f + C_d)$:

Buffered solutions at pH = 11 without a halide additive exhibit passive potentials on anodic polarization in contrast to solutions buffered at pH = 8.9 (Fig. 10). Halide additions destroy this passivity (Fig. 9). The order of increasing effectiveness of the halide ions as depassivating ions is $I^{-1} < Br^{-1} < Cl^{-1}$. The depassivating effect of halide additions on the passivity of Mg at pH = 11 is explicable in terms of the pore theory if it is assumed that the pore size is large enough for penetration by halide ions and too small for penetration by BO_3^{-3} ions. The relative depassivating effect of the halide ions may be due to the relative mobilities of the halide ions which follow this same order, i.e., $I^{-1} < Br^{-1} < Cl^{-1}$.

Unbuffered Solutions

The film formed on Mg in unbuffered solutions of NaCl, NaBr, and NaI is similar to that at pH = 11 but the pH in the pores is probably lower than the bulk pH of the unbuffered solution. The reacting area of the Mg metal surface is increased over that in buffered solutions at pH = 8.9 by a change in type of attack from general to pitting and film formation in unbuffered solutions tends to decrease the reacting area of the barrier film. Without a knowledge of relative roughness factors of the electrode it is impossible to compare observed capacities in unbuffered solutions with those in buffered solutions. The capacity of the Mg electrode in NaCl solution is significantly greater than for solutions of NaBr and NaI, which indicates that the Cl^{-1} ion is more strongly adsorbed on Mg than either the Br^{-1} ion or I^{-1} ion which is the reverse of what might be expected from data on Pt and Hg (25, 26). If this is true specific adsorption of anions does not produce significant changes in the potential of Mg (Fig. 8). The capacity of the Mg electrode in 0.1M NaCl solution determined by Tomashov, *et al.* (13) using the a-c bridge method (500-5000 cps) is 7-8 $\mu f/cm^2$ which is in good agreement with this work (9 $\mu f/cm^2$).

Sodium Fluoride Solutions

Magnesium in NaF solutions exhibits high anodic polarization (Fig. 10); the rest potential is active yet the corrosion rate is small. These facts may be ex-

plained by a pore theory with the following assumptions: the barrier film is nonporous MgF_2 with inclusions of porous film; the area of the porous film is small compared with the area of the nonporous film; and the nonporous film becomes charged on anodic polarization, but electrochemical reaction both cathodic and anodic occurs only at the porous areas. Thus, at zero applied polarization the corrosion of Mg occurs at a slow rate at the pores which explains the active rest potential observed; anodic polarization would partially fill up the pores with MgF_2 at a rate proportional to the applied polarization current and raise the potential in the pores to passive potentials. The anodic overpotential of Mg is less in buffered solution of NaF than in unbuffered solutions. Evidently the BO_3^{-3} ion has a similar effect on the passivity of Mg in NaF solution as Cl^{-1}, Br^{-1}, and I^{-1} have on the passivity of Mg in the buffer solution at pH = 11 but to a much lesser degree. Partial filling up of the pores with $Mg(OH)_2$ explains the fact that the anodic overpotential is higher for NaF solutions buffered at pH = 11 than at pH = 8.9. The relatively lower overpotential for the cathodic polarization indicates that cathodic polarization does not reduce the pore area.

The capacity in buffered and unbuffered solutions of NaF varied from 0.3 to 0.5 $\mu f/cm^2$ over the entire potential range studied. The invariance of the capacity over the large range of potentials suggest that the capacity is due to the nonporous areas of the film, the effective thickness of which is independent of potential. The double layer with the nonporous areas of the film as dielectric discharges through the pores in the film.

Resistance Measurements

In solutions containing fluoride the parallel polarization resistance ($R_{f,a}$) varied from 600 ohm-cm^2 to 3200 ohm-cm^2; in all other solutions the parallel resistance varied from 25 ohm-cm^2 to 250 ohm-cm^2. Little significance can be given to the values of $R_{f,a}$ due to the poor reproducibility except to state that the relative magnitude of $R_{f,a}$ for Mg in NaF solution indicates that the pore area is smaller than for the other solutions.

The contribution of the ohmic potential drop to the total overpotential of Mg in the passivating solutions studied in this work is less than 1% which is in general agreement with the work of Epelboin, *et al.* (30). By application of a circuit breaking technique Epelboin, *et al.* (30) have shown that the high potentials observed in passivating, anodic oxidation, and electrolytic polishing experiments are not due to diffusion overvoltage or ohmic drop but are probably due to adsorption effects of anions at the metal surface.

Acknowledgment

The authors wish to express their appreciation to Mr. L. T. Bradley for assistance in the design of the d-c current interrupter apparatus, and to Dr. P. B. Sewell and Mr. E. G. Brewer for examination of the magnesium surface preparation used in this work by electron diffraction and the electron microscope.

Manuscript received Jan. 23, 1959. This paper was prepared for delivery before the Ottawa Meeting, Sept. 28-Oct. 2, 1958.

Any discussion of this paper will appear in a Discussion Section to be published in the June 1960 JOURNAL.

REFERENCES

1. H. A. Robinson, *Trans. Electrochem. Soc.*, **90**, 485 (1946); "Cathodic Protection, A Symposium" p. 104, N.A.C.E. Houston (1949).
2. N. D. Tomashov, V. S. Komissarova, and M. A. Timonova, *Trudy Inst. Fiz. Khim., Akad. Nauk S.S.S.R.*, **4**, 172 (1955).
3. G. R. Hoey and M. Cohen, *This Journal*, **105**, 245 (1958).
4. M. D. Rausch, W. E. McEwen, and J. Kleinberg, *J. Am. Chem. Soc.*, **76**, 363, 3622 (1954); **77**, 2093 (1955).
5. W. E. McEwen, J. Kleinberg, D. L. Burdick, W. D. Hoffman, and J. Y. Yang, *ibid.*, **78**, 4587 (1956).
6. J. H. Greenblatt, *This Journal*, **103**, 539 (1956).
7. W. Beetz, *Pogg. Ann.*, **27**, 115 (1866).
8. P. Brouillet, I. Epelboin, and M. Froment, *Compt. rend.*, **239**, 1795 (1954).
9. D. V. Kokoulina and B. N. Kabanov, *Doklady Akad. Nauk. S.S.S.R.*, **112**, 692 (1957).
10. B. N. Kabanov and D. V. Kokoulina, *ibid.*, **120**, 558 (1958).
11. S. Bodforss, *Z. Physik Chem.*, **153**, 83 (1931).
12. B. Roald and W. Beck, *This Journal*, **98**, 277 (1951).
13. E. N. Paleolog, G. V. Akimov, N. P. Tomashov, and K. S. Korotkova, "Problemy Korozii i Zashchity Metallov," *Inst. Fiz. Khim., Akad. Nauk S.S.S.R.*, 237 (1956).
14. N. D. Tomashov and T. V. Matveeva, *Trudy Inst. Fiz. Khim., Akad. Nauk S.S.S.R.*, **2**, Zssledovaniza po Korrozii Metal No. 1, 146 (1951).
15. G. V. Akimov and I. L. Rozenfeld, *Compt. rend. acad. sci. U.R.S.S.*, **44**, 193; *Doklady Akad. Nauk. S.S.S.R.*, **44**, 211 (1944).
16. C. V. King and W. H. Cathcart, *J. Am. Chem. Soc.*, **59**, 63 (1937).
17. G. E. Coates, *J. Inst. Metals*, **71**, 457 (1945).
18. E. J. Casey and R. E. Bergeron, *Can. J. Chem.*, **31**, 849 (1953).
19. R. Faivre and A. Michel, *Compt. rend.*, **208**, 1008 (1939).
20. C. Brouchere, *J. Inst. Metals*, **71**, 131 (1943).
21. K. Huber, *This Journal*, **100**, 376 (1953).
22. N. A. Shishakov, *Zhur. Fiz. Khim.*, **26**, 358 (1952).
23. S. Yamaguchi, *J. Appl. Phys.*, **25**, 1437 (1954); *J. Chem. Soc. Japan*, **61**, 887 (1940).
24. J. Van Muylder and M. Pourbaix, Centre Belge D'Etude De La Corrosion Rappt. Tech. No. 39 (1956).
25. D. C. Grahame, *Chem. Revs.*, **41**, 441 (1947).
26. J. N. Sarmousakis and M. J. Prager, *This Journal*, **104**, 454 (1957).
27. S. Shuldiner and R. E. White, *ibid.*, **97**, 433 (1950).
28. M. Stern, *ibid.*, **104**, 56 (1957).
29. D. C. Grahame, *J. Phys. Chem.*, **57**, 257 (1953).
30. I. Epelboin, P. Brouillett, and M. Froment, *Proc. Intern. Comm. Electrochem. Thermodynam. and Kinet.*, 7th Lindau 26 (1957).

Use of Nickel-Aluminum Alloy Coatings for the Protection of Molybdenum from Oxidation

W. Beck[1]

American Electrometal Corporation, Yonkers, New York

ABSTRACT

Coatings produced by electrodeposition of aluminum on nickel-plated molybdenum protect this metal effectively against high-temperature oxidation. Information about composition and distribution of the Ni-Al phases formed in the coating was obtained from a metallographic analysis of a layer created by deposition of aluminum from the cryolite bath on a sheet of high-purity nickel.

Effective protection of molybdenum against high-temperature oxidation by a coating consisting of nickel aluminides has been reported recently by Couch, Shapiro, and Brenner (1). The coating was produced in an unorthodox fashion by electrodeposition (1, 2) of aluminum from a fused cryolite bath onto nickel, which had been plated from an aqueous solution onto chromium-plated molybdenum. Some years ago, the author of this report (3) succeeded in imparting to Mo, protection against high-temperature oxidation by converting its surface into a Mo-Al alloy, created during electrodeposition of Al from the cryolite bath.

This paper is concerned with the production of Ni-Al coatings on Mo, removal of bath salts from the coating, testing of the effectiveness of the alloy layer to protect Mo against high-temperature oxidation, and the metallographic studies of a Ni-Al diffusion couple.

These investigations were completed some years ago but were not published until now.

Experimental Procedures and Results

Specimens and pretreatment.—The specimens consisted of rods of Mo of 99.9% purity, ¼ in. in diameter and 6 in. long. The ends were rounded in order to avoid sharp angles, ground with a green wheel, and finally polished on a hard rubber wheel.

Various pretreatments were used to achieve satisfactory adhesion of the Ni plate to the Mo surface, including an anodic treatment in HF-HCl mixture and immersion in aqua regia. The latter method, which gave the best results, consisted of a 1-min dip in the acid mixture, followed by cleaning the specimen with cotton under streaming water. This procedure was repeated several times. Immediately following the last immersion and cleaning, the specimen was Ni plated.

Nickel plating.—Nickel was electrodeposited from a Watts-type bath. The average plating thickness was 0.8 mil.

Aluminum plating.—Aluminum was deposited on the Ni plating from a eutectic mixture of 75% cryolite with 25% NaF at a temperature of 1005° ± 5°C. A uniform coating was obtained only when the total concentration of Al in the bath was kept above a minimum value. The Al used up during plating was replaced when necessary by recharging the crucible containing the bath with Al_2O_3 (saturated concentration of Al_2O_3 in the eutectic mixture at 982°C is 15%).

After keeping the rods in the bath for 1 min, Al was plated at a current density of 0.15 amp/cm^2. The approximate total thickness of the aluminide layer, after a plating time of 15 min, was 1.8 mil.

All coatings were produced in a graphite crucible which served as the anode. Bath components were fused by means of high-frequency heating.

Leaching of excess Al and bath salts and testing for protection against high-temperature oxidation.—To avoid premature breakdown of the coatings in the blast burner test to be described below, it is of the utmost importance to remove from the surface excess Al and cryolite without attacking the coating itself.

Numerous attempts were made to solve this problem; some of the results are reproduced in Table I. Most effective and least damaging is apparently a 20% HCl solution when used at room temperature.

After leaching, the rods were fastened securely in holders and about 1 in., measured from the tip of the rod, was inserted in the oxidizing cone of an air-gas blast burner. The temperature of the specimens in the flame was determined by optical measurements to be approximately 800°C. They were kept in the flame until the coating broke down and the Mo began to oxidize, evidenced by a change in color of the flame from reddish orange to bright yellow, which is caused by the oxidation products of Mo. The times to breakdown recorded on specimens leached in different solutions are listed in Table I.

Microscopic examination of the nickel-aluminide coating, as plated and after breakdown.—Two sections were taken through each rod after breakdown had occurred, section A about ¼ in. from the tip of the rod, section B approximately 1 in. from section A.

The specimens were mounted in a mixture of amber Bakelite and phenolic resin which has been found to be particularly suitable for coated material,

[1] Present address: Aeronautical Materials Laboratory, Naval Air Material Center, Philadelphia 12, Pennsylvania.

Table I. Time to breakdown of coated Mo specimens exposed to blast burner after leaching of excess Al and bath salts

Composition of coating	Average thickness of alloy coating, 1.8 mil Leaching solution	Appearance of solution or coating after leaching	Time to breakdown in hours in blast burner, Temp. of specimens about 800°C
Ni-Aluminide	Specimen quenched without delay in 20% HCl	Solution showed in all cases green color [1]	Max. 435 Min. 208[2]
Ni-Aluminide	Specimen cooled to room temperature and leached in 20% HCl	In some cases, solution showed slight green color	Max. 1100 Min. 100[2]
Ni-Aluminide	Specimen cooled to room temperature and leached in 37% (conc.) HCl	No change in color became visible	Max. 200
Ni-Aluminide	Specimen cooled to room temperature and leached in 20% NaOH[3]	Coating changed color from dark to black	Max. 100
Mo-Aluminide	Dip in alkali melt[4] followed by leaching in 20% HCl	No change in color became visible	Max. 600
Ni plated from aqueous solution	—	—	Max. 24

Notes:
[1] Leaching time in HCl in all cases was 2 hr; leaching solution was frequently renewed.
[2] Total number of leached specimens was in all cases 10; 80% of specimens had maximum lifetime.
[3] Leaching time was at least 4 hr.
[4] Alkali melt consisted of 60% NaOH and 40% Na_2CO_3 and was used at 540°C.

polished in the conventional manner, etched with Kellers (4) reagent, and then repolished. Subsequently, photomicrographs were taken.

Figures 1 to 3 are photomicrographs of section A. Figure 1 pictures a specimen in the as plated condition. Micrographs shown in Fig. 2 and 3 are taken on specimens after 100- and 540-hr exposure to the blast burner. The coatings represent single phase systems and a number of breakdowns can be distinguished. The coating thickness decreases slightly with increasing oxidation time.

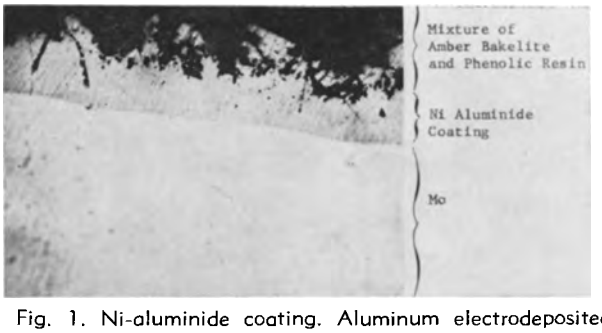

Fig. 1. Ni-aluminide coating. Aluminum electrodeposited from eutectic NaF-cryolite bath on Ni plated on Mo; as plated; leaching in 20% HCl; Keller's etch. Magnification 500X before reduction for publication.

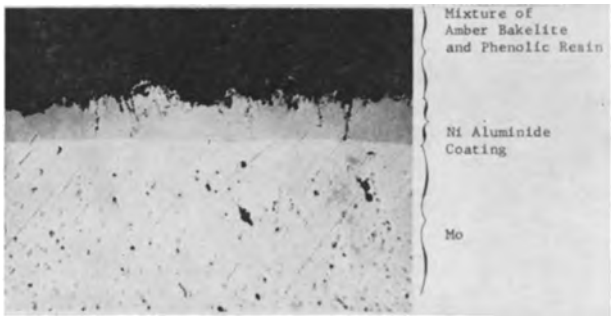

Fig. 2. Ni-aluminide coating. Breakdown after 100-hr exposure to oxidizing flame at approx. 800°C; leaching in 20% HCl; Keller's etch. Magnification 500X before reduction for publication.

Figure 4 exhibits the characteristic "oxidation fingers" which are formed after the coating has broken down and the unprotected Mo is exposed to oxidation. There were no startling differences between the A and B sections.

Phase identification in a Ni-Al *diffusion layer.*— Various attempts to identify the phases formed in the nickel aluminide layer on Mo were not successful, therefore, a different approach was used. Aluminum was electrodeposited from the cryolite bath saturated with Al_2O_3 onto a sheet of A nickel (5),

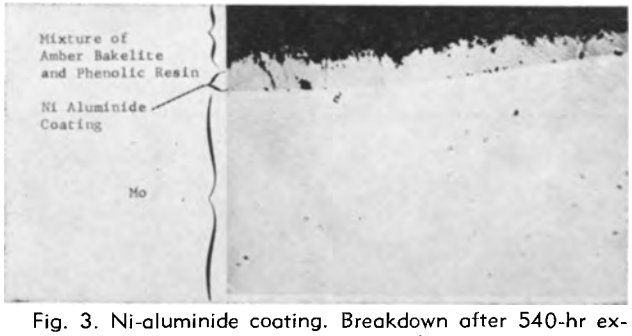

Fig. 3. Ni-aluminide coating. Breakdown after 540-hr exposure to oxidizing flame at approx. 800°C; leaching in 20% HCl; Keller's etch. Magnification 500X before reduction for publication.

Fig. 4. Type of oxidation fingers formed by oxidation of Mo on breakdown points of Ni-aluminide coating at 800°C. Magnification 500X before reduction for publication.

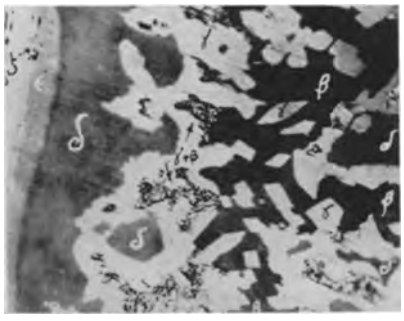

Fig. 5. Phases and phase distribution in Ni-Al diffusion layer produced by electrodeposition of Al from a eutectic NaF-cryolite bath (saturated with Al_2O_3) on a sheet of A Ni. Excess Al was removed in 20% HCl, anodic etch in 1 part conc. HCl with 3-5 parts ethyl alcohol, 1 v, 0.5 amp/in.^{2}, 10 sec. Magnification 1000X before reduction for publication.

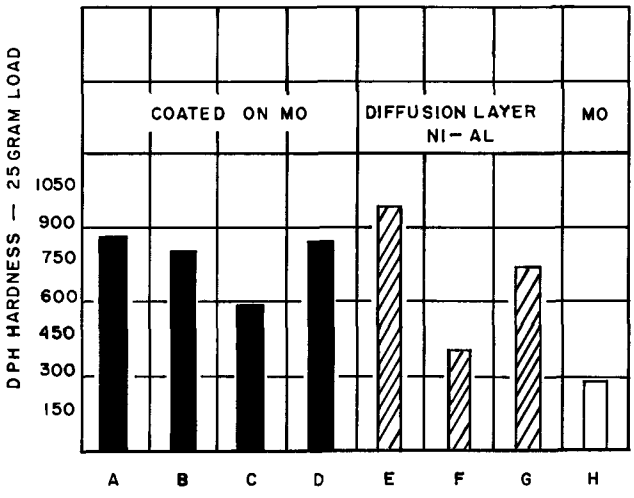

Fig. 6. Hardness measurements made at room temperature: A, Al on Ni, as coated; B, Al on Ni, exposed for 540 hr at 800°C; C, Ni on Al, as plated; D, Ni on Al, exposed for 540 and 1000 hr at 800°C; E, δ phase; F, γ phase; G, β phase; H, Mo.

which was polished to a mirror finish and degreased prior to plating.

The longest time of electrolysis was 5 hr. A number of experiments were made with shorter exposures; however, this did not produce any essential change in the phase distribution shown in Fig. 5. The current density was the same as that used to deposit Al on Ni-plated Mo. After removal from the cryolite bath, the specimen was cooled in ambient air and the coating etched anodically (6).

At the current density and plating time employed, it has to be inferred that the Al diffuses essentially from the liquid phase into the solid Ni after being formed at the cathode, by "direct" electrochemical reduction of an Al donor (7, 8). The Ni is thus in contact with superheated molten Al at a temperature a little above two-thirds of its melting point. By reference to the phase diagram (9), it may be ascertained that Ni may take upwards of about 6 w/o (or 12 a/o) approximately of Al to form the solid solution phase zeta (ζ). This may be assumed to take place by the simple dissolving action of molten Al on Ni, a mutually interpenetrating action between the Al and Ni caused by their comparatively equal atomic sizes, unit cell structure, high temperature, and driving force of the current in the electrolytic cell.

The intermediate phases or secondary solid solutions ε, δ, and γ (10), occur in sequence as the distance from the surface of the Ni is increased. These may be assumed to have been nucleated by a diffusion process dependent on the operation of Fick's law at the environmental conditions obtained in the cryolite cell. The basis of the identification of these various secondary solid solution phases lies in their proximity, or lack of it, to the surface of the Ni cathode, their comparative hardness determined by microhardness tests (to be presented in the next section), and their obviously different etching characteristics.

On removal of the Ni cathode from the cryolite bath, an interface between the γ secondary solid solution and molten Al would be formed. On cooling, as may be seen from the phase diagram (9), the incongruently melting phase β would be formed by the peritectic reaction of the γ and molten Al.

This is believed to be the origin of the mixed black and white areas which appear as islands interspersed in the γ secondary phase. A peritectic reaction would also explain the proximity of the free β phase to these areas. The β phase was also identified by its comparative hardness.

Hardness measurements.—Hardness measurements were made with the Bergsman hardness tester and are presented in Fig. 6. These values are the averages of 3 determinations. Nickel aluminides of three different compositions, Ni_2Al_3, NiAl, and $NiAl_3$, were made by casting (11) and their hardnesses determined. Hardness values of some of the phases formed when Al was deposited on the Ni sheet were determined also. Comparison of these values with those of the cast nickel aluminides was then used as one method of identifying the γ, δ, and β phases in the diffusion coating.

As may be seen from Fig. 6, the hardness values determined on the coatings on Mo did not correspond directly to any Ni-Al system. However, the hardness of the coatings in the as-plated condition and after oxidation periods of 540 and 1000 hr was close to that of the very hard, high melting δ phase.

That the coatings contained ample Ni and Al was proven by chemical analysis of a strong HCl solution in which the coatings had been stripped anodically.

Coatings of Ni on diffused Al.—The adhesion of Ni plated on Mo covered with a molybdenum aluminide coating produced by electrodeposition of Al from the cryolite bath was excellent. The molybdenum aluminides are characterized by good electrical conductivity and, therefore, Ni can be plated on them easily from an aqueous solution. The author has succeeded in identifying by x-ray diffraction (3) the two brittle intermetallic systems, Al_2Mo and Al_5Mo, in the coating and, as could be expected, the oxidation life of specimens covered with a molybdenum aluminide layer, overplated with nickel, was rather limited.

Further work to improve the effectiveness of the protection of Mo against high-temperature oxidation by coatings containing Ni and Al, the latter being

electrodeposited from the cryolite bath, should, therefore, be restricted to the nickel aluminides.

Acknowledgment

The author is much indebted to Dr. Paul Schwarzkopf and Dr. Robert Steinitz for the great interest taken in this study, to Mr. Larry Kaufman, and to Mr. William Sipes (Aeronautical Materials Laboratory) for their assistance with the metallurgical and metallographic evaluations.

Manuscript received Feb. 2, 1959.

Any discussion of this paper will appear in a Discussion Section to be published in the June 1960 JOURNAL.

REFERENCES

1. D. E. Couch, H. Shapiro, and A. Brenner, *This Journal*, **105**, 485 (1958).
2. D. E. Couch and J. H. Connor, WADC Tech. Report 58-5, Part I, March 1958, NBS Report 5894, May 1, 1958.
3. W. Beck, *Metal Ind.*, **86** (Jan. 21) 43 (1955).
4. "Metals Handbook," ASM, 1948 Ed., p. 800.
5. *Ibid.*, p. 1047.
6. R. L. Wachtell, WADC Tech. Report 52-291 (1952).
7. M. Feinleib and B. Potter, *This Journal*, **103**, 235 (1956).
8. J. O'Mara Bockris, Liquid Metals and Solidification, p. 172, A Seminar held during the 39th Metal Congress, Chicago, 1957, published by ASM (1958).
9. "Metals Handbook," 1948 Ed., p. 1164.
10. L. S. Castleman and L. L. Seigle, *Trans. Met. Soc. AIME*, **212**, No. 5, 589 (1958).
11. W. A. Alexander and N. B. Vaughan, *J. Inst. Metals*, No. 2, **61**, 248 (1937).

Electroplating Metal Contacts on Germanium and Silicon

Dennis R. Turner

Bell Telephone Laboratories, Incorporated, Murray Hill, New Jersey

ABSTRACT

Various metals have been plated on germanium and silicon. These semiconductors usually have oxide layers on them which could interfere with the intimate contact required between metal and semiconductor for good adhesion and the desired electrical properties. Oxide films and residues from chemical etching on germanium can be removed by cathodic reduction prior to metal deposition in many plating solutions. Sixteen different metals were plated on n- and p-type germanium. Since oxide films on silicon are difficult to reduce cathodically, other methods of removing the oxide film are employed to produce adherent electrodeposits on silicon.

Solid-state electronic devices made from semiconducting materials require some kind of electrical contact to the semiconductor. Electroplating techniques have been used to make ohmic contacts to semiconductors for many years. More recently, good rectifying contacts have been made by electroplating small metal spots ($\sim 10^{-3}$ cm^2) on germanium and silicon (1-4). Much of this work was carried out using a jet plating technique. One of the best types of plating baths, cyanide solutions, was avoided completely. This paper discusses the results of experiments which sought to determine the solutions and conditions that give high quality, large area deposits with maximum adhesion on Ge and Si. Either ohmic or rectifying contacts can be obtained by electroplating the proper metal on Ge and Si.

Germanium

Semiconducting materials usually have oxide layers on them which could interfere with making an intimate contact between plated metal and the semiconductor. Some oxides on metals can be removed by electrochemical reduction. For example, Linford and Feder (5) have shown that copper oxide layers up to about 650Å thick are completely reduced electrochemically prior to nickel deposition. Turner (6) demonstrated that the continuous monolayer of oxide formed on Ge during anodic dissolution is reduced cathodically in acid solutions prior to hydrogen gas evolution. Many residues from chemical etching and oxide films thicker than a monolayer on Ge can also be reduced electrolytically. This is demonstrated in Fig. 1. If a Ge electrode is chemically polished in C.P.-4 solution,[1] rinsed in distilled water and then subjected to a cathodic treatment in 0.1*N* H_2SO_4, a cathodic reduction curve is obtained. The number of coulombs in the potential arrest stage corresponds to about 2 atom layers of oxide.[2] The cathodic reduction curve obtained on a Ge electrode previously anodized in a fused salt bath (34% $LiNO_3$ + 66% KNO_3, mp $\sim$ 155°C) to produce a thicker oxide layer

[1] Composition of C.P.-4 etch: 5 parts by vol. conc. HNO_3, 3 parts by vol. 48% HF, 3 parts by vol. glacial acetic acid, and 10 drops liquid bromine/50 cc of acid mixture.

[2] Acid fluoride solutions may actually leave a fluoride film on the surface.

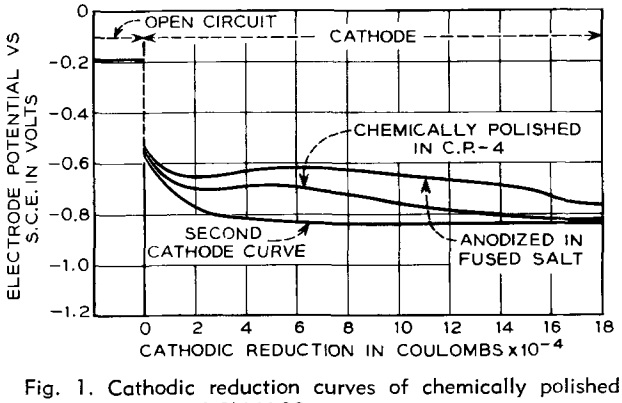

Fig. 1. Cathodic reduction curves of chemically polished and anodized Ge in 0.1N H_2SO_4.

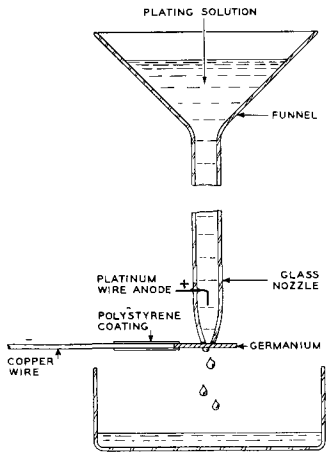

Fig. 2. Experimental arrangement for plating metal spots on Ge.

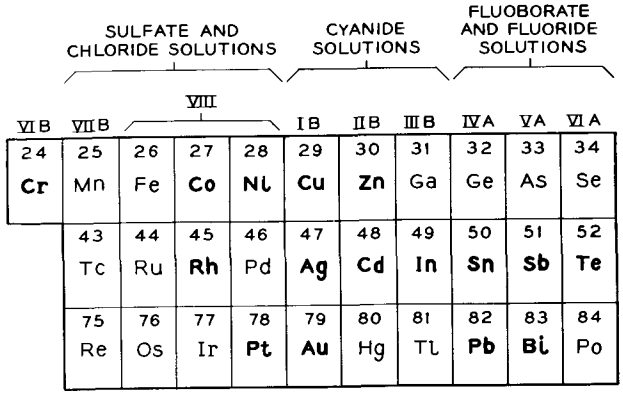

Fig. 3. Metals plateable from aqueous solutions. Bold lettered metals were plated on Ge. Preferred plating solutions are indicated above table.

is also included in Fig. 1. The length of the potential arrest corresponds to about 4 atom layers of oxide. The second cathodic curve obtained in each experiment is included to show that all reducible material is removed in the first cathodic treatment and that the reduced material in the initial curve is not due to some solution impurity. Schmidt (7) has found that thick layers of GeO_2, formed anodically in N-methylacetamide, can be reduced in the same solvent.

These results suggest that the best choice of metals and solutions for electroplating intimate metal contacts on Ge are those which deposit metal only after all oxide films or residues from chemical polishing are removed by cathodic reduction.

Experimental

The experiments were carried out with Ge electrodes about 1 cm square by 1 mm thick. These were cut from two single crystals, one 4-ohm cm n-type Ge and the other 3-ohm cm p-type Ge. An ohmic contact was made to the Ge by abrading one edge and soldering it to a 1.3 mm (0.050 in.) diameter copper wire using a standard lead-tin solder and an acid zinc chloride flux. The solder joint and about 2 cm of the copper wire were coated with polystyrene cement to protect them from the acid etches used later. Prior to plating, the surface of the germanium was chemically polished in the C.P.-4 solution. After a thorough water rinse the Ge was placed against a glass nozzle as shown in Fig. 2. This procedure confined the area of metal plated mainly to the inside diameter of the nozzle tip. A Pt wire sealed into the glass about 2.5 cm above the nozzle tip served as the anode. A glass or polyethylene funnel served as the solution reservoir. Plating solutions that work best above room temperature were preheated prior to filling the funnel. A section of Tygon tubing connected the funnel to the nozzle. Relatively high plating current densities were possible since the solution flowed continuously during plating. About 0.025 mm (0.001 in.) of metal was plated for the contact studies. After plating, the samples were water rinsed and given a brief etch in a suitable acid solution to remove the feather edge around the main spot of metal. This acid etch after plating was often essential for good rectifying contacts.

Sixteen different metals were plated on n- and p-type Ge. They represent practically all of the readily plated metals. The section of the periodic table containing all the elements plateable from aqueous solutions is shown in Fig. 3. The bold lettered metals were plated in this study. The preferred solutions, with a few exceptions, are indicated above the chart. A sulfate solution was used to plate indium instead of the cyanide bath because it was more stable chemically. As a rule the cyanide solutions are to be preferred in this application since metals deposit in them at potentials considerably more negative than that required to reduce oxide films on Ge. Electrodeposits from cyanide baths also are usually of good quality, i.e., smooth and dense. The chromium spots were plated from a standard chromic acid sulfate bath. Bismuth was plated from a perchlorate solution (8) while the tellurium deposits were obtained from a fluoride-sulfate solution (9).

Only technical grade chemicals were available for some of the plating baths. These solutions were purified electrolytically to remove metallic impurities. Overnight electrolysis with a dummy Pt cathode at 2 ma/cm^2 current density was usually sufficient.

Electrical contact to the plated metal spot was made by touching it with a loop of gold wire. Measurements of the electrical properties of the metal-germanium junction consisted first of observing the E-I pattern on an oscilloscope screen using a conventional display circuit and then making a point by point plot of both the forward and reverse E-I characteristic using d. c.

Results of Plated Metal Contacts on Ge

All the plated metals tested except antimony produced rectifying contacts on n-type Ge and ohmic contacts on p-type Ge. Electroplated Sb contacts behaved just the opposite, i.e., they were ohmic on n- and rectifying on p-type Ge. Borneman, *et al.* (3) reported that all plated metals gave rectifying contacts on n- and ohmic contacts on p-type Ge. The reverse voltage-current curves of the sixteen metals plated on n-type Ge are shown in Fig. 4. These results were obtained with circular metal spots about 2 mm in diameter. Most of the curves have the same general shape but are displaced from one another along the current axis. The large differences in the

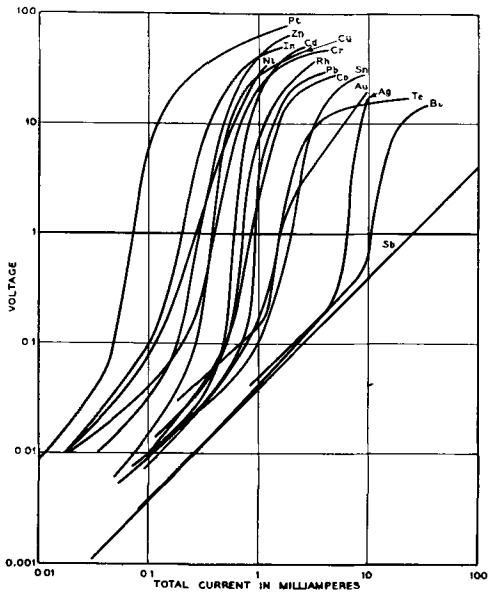

Fig. 4. Reverse curves for 2 mm diameter plated metal contacts on n-type Ge (measured in room air).

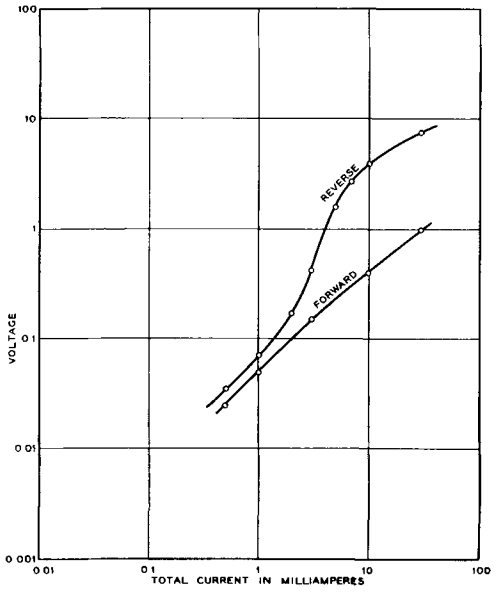

Fig. 5. Forward and reverse curves for a 2 mm diameter plated Sb spot on p-type Ge.

saturation currents are attributed to variations in the state of the surface after etching and also to differences in the adhesion of the various electrodeposits on Ge. In general, the poorer the adhesion the higher the saturation current. The silver deposits on Ge had the poorest adhesion of all and one of the highest saturation currents. Plated 2 mm diameter Sb contacts on n-type Ge were ohmic up to the highest current passed through the contact, 200 ma.

When the results with Sb were obtained, it was thought that perhaps all the metals in groups VA and VIA of the periodic table would behave the same way. Initial tests with Bi and Te in fact did give nearly ohmic contacts to n-type Ge. After the Bi and Te plating solutions were purified by electrolysis, however, both metals produced rectifying contacts on n-type Ge as shown in Fig. 4.

An interesting effect was observed with nickel plating on Ge when the solution was at room temperature. The Ni deposit often curled up at the edges a short time after plating and attached to the Ni were large pieces of Ge. There is a certain amount of hydrogen codeposited with Ni which produces a stress in the deposit. Since the adhesion between electroplated Ni and Ge is good, the stress in the deposited Ni is transmitted to the Ge. The stress apparently is sufficient to crack the Ge under the Ni and the peeling is actually due to this rupture in the Ge. The effect was eliminated when a hot (~60°C) Ni plating solution was used. An increase in the plating solution temperature presumably decreases the amount of codeposited hydrogen in the Ni which reduces the stress transmitted to the Ge under the deposit.

Antimony, the only metal found to give rectifying plated contacts on p-type Ge, was plated from a fluoborate solution. It was prepared by dissolving 6 g of technical grade antimony fluoride in 100 ml of solution containing 10 g of fluoboric acid. As made up, the solution produced Sb-plated spots which were ohmic on both n- and p-type Ge. After electrolytic solution purification, the antimony deposits on n-type Ge remained ohmic but those on p-type Ge became rectifying. Figure 5 shows the forward and reverse voltage-current curves for a 2 mm diameter plated Sb spot on p-type Ge. This represents the first time a rectifying characteristic has been obtained by electroplating a metal contact on p-type Ge. The saturation current in the blocking direction probably could be lowered by the use of plating solutions made from very pure materials. Schmidt (7) reports that a lithium pressure contact on p-type Ge is rectifying. This is attributed to the diffusion of donor lithium atoms into the Ge which converts the surface region to n-type.

Silicon

Metals electroplated on polished Si using ordinary plating techniques have poor adhesion and the deposits usually blister. Wurst and Borneman (4) plated small metal dots on Si using the jet electroplating technique and reported good adhesion. Using their pretreatment procedures and plating solutions, metal electroplated on polished Si specimens with about 2 cm^2 surface area always blistered. The poor adhesion is attributed to a surface oxide layer which cannot be reduced cathodically in aqueous solutions prior to metal deposition as it is on Ge. Archer (10) has estimated the oxide layer thickness on Si after etching to be about 10Å or 2 to 3 atom layers. To improve the adhesion between plated metal and Si, the oxide film must be removed or at least reduced in thickness. Silicon dioxide is soluble in both strong alkaline solutions and HF.

One method which has been found effective in improving the adhesion considerably is to subject the Si to a brief etch in a hot concentrated potassium or sodium hydroxide solution prior to metal plating in a hot cyanide plating bath. Hot, strongly alkaline solutions attack Si vigorously. The Si is transferred quickly from the hot alkaline solution to the plating bath without rinsing and with current on as the Si enters the plating solution. By not rinsing the Si, the corroding effect of the hot alkaline solution continues

until metal deposition begins. By this process, metal plates over at most a monolayer of oxide, and in some places there is direct contact between plated metal and semiconductor.

Another method which gives adherent Ni deposits on Si makes use of a Ni plating bath containing HF. The Si is allowed to soak in the plating solution for about 1 min before the plating current is started. Hydrofluoric acid dissolves silicon dioxide, but the surface may not be clean since there is some evidence that the fluoride simply replaces the oxide on the surface (11). Whatever the mechanism, the adhesion of a subsequent Ni deposit is greatly improved by this procedure. A Ni plating solution developed for plating Ni on Mg (12) was found to be satisfactory: HF (48%) 78 cc/l, citric acid 30 g/l, basic nickel carbonate 130 g/l, wetting agent (sodium lauryl sulfate) 20 drops/l.

Six metals were plated on chemically polished Si using one of the preplating procedures just described. Results are summarized in Table I. The plating solutions used were of standard composition. A "strike" plating technique improved the adhesion of Cu and Zn deposits but not the others. The high initial current density in Cu and Zn plating was reduced after a few seconds to deposit the bulk of the metal. Copper deposits were the most adherent, while Zn gave the poorest results by comparison. The test for adhesion consisted simply of cutting through the deposit by scratching with a sharp object. Even Zn plating, however, did not show signs of the blistering which is common when metals are deposited on Si by ordinary procedures.

The electrical properties of these metal contacts on n- and p-type Si are also given in Table I. These results were obtained with metal spots 1 mm in diameter. Qualitatively they agree with those reported by Wurst and Borneman (4) except for Cu and In on n-type Si, which gave opposite results.

Effect of Semiconductor Electrode

The semiconducting properties of Ge and Si have not been a factor in the electroplating results discussed thus far. Brattain and Garrett (13) have shown that holes are required to carry out anodic processes on semiconductors and electrons are necessary for cathodic reactions. An adequate supply of electrons are present at the surface of n-type semiconductors, under cathodic bias, since they are the majority current carrier. Relatively few electrons are available in p-type Si. If the surface of p-type material is abraded, additional electrons become available at the surface due to a large increase in the generation-recombination rate of hole-electron pairs. A light of high intensity directed at the Si will also raise the minority carrier concentration at the surface. The comparatively few electrons at the surface of chemically polished p-type semiconductors exposed to subdued room light are depleted in a cathodic reaction at very low current densities. This surface depletion of electrons results in a space charge region in the semiconductor. It can be thought of as a concentration polarization of electrons in the semiconductor. Attempts to increase the cathode current by applying more voltage to the cell merely result in increasing the depth of the space charge region in the semiconductor. The current barrier at the surface of the semiconductor eventually breaks down, allowing more current to flow, if the applied voltage is high enough.

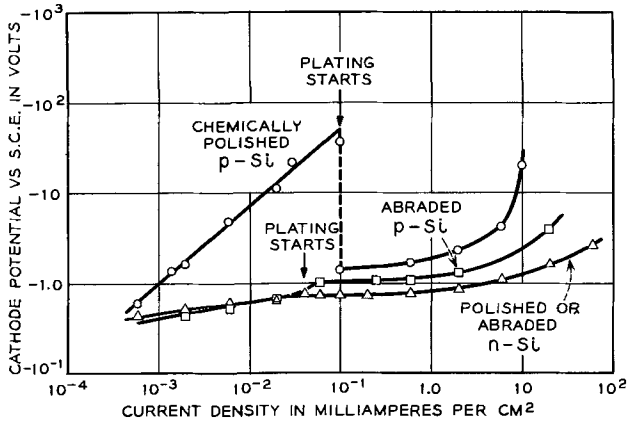

Fig. 6. Cathode potential-current density curves for Ni plating on abraded and polished n- and p-type Si.

An example of what may be encountered in attempting to plate metals on chemically polished p-type semiconductors is illustrated in Fig. 6. It is a log-log plot of the cathode potential vs. current density of 1Ω cm n- and 12Ω cm p-type Si with abraded and polished surfaces in a Ni plating solution. These data were obtained by increasing the current in steps. The current was held constant at each setting and the electrode potential measured when it appeared to reach a steady state. The plating bath was a standard "cold" Ni solution containing nickel chloride, ammonium chloride, and boric acid. Below about 0.1 ma/cm², the cathode reaction is the discharge of hydrogen ions. The E_c-i curves for abraded and polished n-type Si are identical. An abraded

Table I. Metals electroplated on Si with good adhesion and their electrical properties as contacts

Metal	Solution type	Current density, ma/cm²	Relative adhesion	Electrical properties of contact	
				n-Si	p-Si
Cu	Cyanide	200-75	Very good	Ohmic*	Rectifying
Au	Cyanide	15	Good	Rectifying	Ohmic
Ni	Fluoride	40	Good	Rectifying	Rectifying
In	Cyanide	30	Fair	Rectifying*	Rectifying
Sn	Stannate	20	Fair	Ohmic	Rectifying
Zn	Cyanide	100-30	Poor	Ohmic	Rectifying

* Result different from Wurst and Borneman.

p-type Si electrode has about the same E_c-i curve as n-type up to the current density where Ni starts depositing. The potential difference between the two curves is attributed to a small rectifying barrier between plated Ni and the abraded p-type Si.

Polished p-type Si deviates from the other curves even at very low current densities. The experiment was carried out in subdued room light. Most of the voltage applied to the plating cell appears across the space-charge region in the Si. As shown in Fig. 6, the cathode potential can reach as much as 50 v without plating any Ni.[3] At the critical cathode potential (the value is different for each Si electrode), Ni begins to deposit. The start of Ni plating is probably coincident with a local breakdown of the potential barrier at the surface of the Si. The cathode potential drops slowly as Ni covers the Si. The drop in cathode potential at a constant current density is attributed to hole injection by the electroplated Ni contact on the Si. This collapses the space-charge region which reduces the potential drop in the semiconductor.

If the plating solution is capable of corroding the Si, even at a moderate rate, the large polarization effect inside polished p-type Si made cathodic is not observed. This is due to the fact that excess holes and electrons are produced at the surface of Si whenever it is corroded (14). Both strong alkaline and acid fluoride plating solutions will etch Si. The number of electrons produced at the surface in these solutions in the etching process is sufficient to carry out cathode reactions up to current densities where metal deposition begins without surface depletion. Germanium is corroded to some degree in most aerated aqueous solution (15) so that the "internal" polarization effect may not be observed with polished p-type Ge.

Summary and Conclusions

Oxide films and chemical polishing residues on Ge are cathodically reduced in plating solutions prior to metal deposition if the potential at which metal starts depositing is more negative than that required to reduce the surface films. Cyanide plating solutions are usually preferred for this reason. All electroplated metal contacts except Sb gave rectifying contacts on n-type Ge and ohmic contacts on p-type Ge. Antimony behaved just the opposite.

Oxide films on Si are not reduced cathodically in aqueous solutions. When special preplating techniques are used, the adhesion of electrodeposits on Si is improved considerably. Plating solutions that corrode Si serve a double purpose: (*a*) they remove or reduce the oxide layer thickness prior to metal deposition, and (*b*) they prevent the formation of a large polarization effect due to electron depletion inside the Si.

[3] In one experiment, more than 200 v had to be applied to the plating cell before Ni would deposit on polished p-type Si.

Acknowledgments

The author wishes to acknowledge the help received from H. E. Haring and W. A. Sunder in the work on germanium and to G. H. Peranteau for his assistance with the study of contacts on silicon. Thanks are also due to U. B. Thomas for his comments and discussion of the work.

Manuscript received March 30, 1959. This paper was prepared for delivery before the Ottawa Meeting, Sept. 28-Oct. 2, 1958.

Any discussion of this paper will appear in a Discussion Section to be published in the June 1960 JOURNAL.

REFERENCES

1. R. Bray, Purdue University Report, p. 27, Sept. (1950).
2. J. H. Tiley and R. A. Williams, *Proc. Inst. Radio Eng.*, **41**, 1706 (1953).
3. E. H. Borneman, R. F. Schwarz, and J. J. Stickler, *J. Appl. Phys.*, **26**, 1021 (1955).
4. E. C. Wurst and E. H. Borneman, *ibid.*, **28**, 235 (1957).
5. H. B. Linford and D. O. Feder, *Plating*, **45**, 349 (1958).
6. D. R. Turner, *This Journal*, **103**, 252 (1956).
7. P. F. Schmidt, Private communication.
8. H. Harbaugh and F. C. Mathers, *Trans. Electrochem. Soc.*, **64**, 293 (1933).
9. F. C. Mathers and H. L. Turner, *ibid.*, **54**, 293 (1928).
10. R. J. Archer, Private communication.
11. M. M. Atalla, E. Tannenbaum, and E. J. Scheibner, *Bell System Tech. J.*, **38**, 749 (1959).
12. H. K. DeLong, U. S. Pat. No. 2, 728, 720, December 1955.
13. W. H. Brattain and C. G. B. Garrett, *Bell System Tech. J.*, **34**, 129 (1955).
14. D. R. Turner, work to be published.
15. W. W. Harvey and H. C. Gatos, *This Journal*, **105**, 654 (1958).

On the Research and Development of Electron Emitting Substances for Gas Discharges

D. M. Speros

Lamp Research Laboratory, Lamp Development Department, General Electric Company, Cleveland, Ohio

ABSTRACT

Criteria for the stability and chemical behavior of electron emitting substances in gas discharges are obtained by means of thermodynamics. Theoretical analysis is supplemented by means of experimental methods intended for the study of processes at elevated temperatures, such as thermogravimetry and differential thermal analysis. The application of the above permits some insight into the processes of formation, activation, and detrition of electron emitting compositions, guiding the development of a number of improved cathodes.

The purpose of this work was to develop cathodes meeting the requirements of new gas discharge devices. To effect this, a better understanding of the fundamentals involved was necessary. Therefore, a major portion of this work was devoted to the chemical and thermochemical aspects of electron emitting substances, which are but poorly understood at present.

The concern of the theoretical part is to evaluate a degree of relative stability for these materials (with respect to dissociation, sublimation, chemical interaction, physical state, and sputtering) and to predict the processes expected during their history, (such as formation, activation or reduction, and normal detrition) without extended experimentation of a trial and error nature. This part of the work forms an extension or generalization of the thermochemical calculations of Rittner (1) which were concerned primarily with the reduction reaction of the oxide cathode. From the chemical point of view, thermodynamic considerations are obvious in many of their aspects; however, since they appear to be of general usefulness in cathode research, they are outlined in this paper.

The chemical processes occurring in cathodes belong to the realm of solid-state chemistry. Therefore, experimental methods designed for the study of reacting solids were applied to supplement the theoretical analysis and provide information when thermodynamic and kinetic data were lacking.

Procedure

Theoretical basis.—A cathode system is defined as one consisting of α moles of substance A, β moles of substance B, γ moles of substance C, etc., and is represented as follows:

$$A_\alpha B_\beta C_\gamma \ldots .$$

A binary system $A_\alpha B$, where α is the number of moles of A per one mole of B, is for the purpose at hand a sufficient approximation to a large number of actual cathodes. For example, $A_\alpha B$ could represent a common form of the oxide cathode for A = BaO and B = SrO; for A = La and B = B, the boride cathode; for A = Th and B = W, the thoriated cathode, and so on.

The process of formation in each case is as follows:

$$\alpha A(c) + B(c) \rightarrow A_\alpha B(c) \qquad [1]$$

which involves a free energy change:

$$\Delta F = F_{A_\alpha B(c)} - \alpha F_{A(c)} - F_{B(c)} = \Delta H - T\Delta S \qquad [2]$$

As already implied in the above examples, Eq. [1] may represent a chemical reaction, the formation of a solid solution, a process of adsorption, or a combination of more than one of these processes. Since at a temperature T:

$$\Delta F = \Delta F^\circ + RT \ln \frac{A_\alpha B(c)}{A(c)^\alpha B(c)}$$

and at equilibrium $\Delta F = 0$ and

$$\ln \frac{A_\alpha B(c)}{A(c)^\alpha B(c)} = \ln K = -\frac{\Delta F^\circ}{RT}$$

the standard free energy change for the formation of $A_\alpha B$ from its components αA and B was used as a quantitative criterion for the stability of electron emitting substances $A_\alpha B$ with respect to dissociation.

In nearly all cases of interest the vapor pressure of one of the components, B, and of the compound $A_\alpha B$ is negligible in comparison to that of the component A. Therefore, the process of sublimation proceeds for all practical purposes as follows

$$A_\alpha B(c) \rightarrow \alpha A(g) + B(c) \qquad [3]$$

The accompanying free energy change is

$$\Delta F_2 = \alpha F_{A(g)} + F_{B(c)} - F_{A_\alpha B(c)} \qquad [4]$$

The process of sublimation of pure A and the corresponding free energy change are as follows

$$\alpha A(c) \rightarrow \alpha A(g) \qquad [5]$$

$$\Delta F_1 = \alpha F_{A(g)} - \alpha F_{A(c)} \qquad [6]$$

Since obviously:

$$\Delta F_1 - \Delta F_2 = \Delta F \qquad [7]$$

Table I. The $\Delta F^\circ = f(T)$ relations for a number of processes of interest

Process	$\Delta F^\circ = f(T)$	T range of applicability
$CaO\ (c) + SiO_2\ (c) \rightarrow CaSiO_3\ (c)$	$-21{,}300 + 0.12T$*	298-1483
$SrO\ (c) + SiO_2\ (c) \rightarrow SrSiO_3\ (c)$	$-23{,}000 + 0.9T$	298-1600
$BaO\ (c) + SiO_2\ (c) \rightarrow BaSiO_3\ (c)$	$-26{,}800 + 0.1T$*	298-1600
$BaO\ (c) + Al_2O_3\ (c) \rightarrow BaAl_2O_4\ (c)$	$-24{,}500 + 0.3T$	298-2100
$BaO\ (c) + MoO_3\ (c) \rightarrow BaMoO_4\ (c)$	$-59{,}900 + 0.3T$	298-1068
$CaO\ (c) + WO_3\ (c) \rightarrow CaWO_4\ (c)$	$-40{,}600 + 0.6T$	298-M.P.
$SrO\ (c) + WO_3\ (c) \rightarrow SrWO_4\ (c)$	$-58{,}300 + 0.6T$	298-M.P.
$BaO\ (c) + WO_3\ (c) \rightarrow BaWO_4\ (c)$	$-74{,}300 + 0.6T$	298-M.P.

* Available in this form in the literature (2).

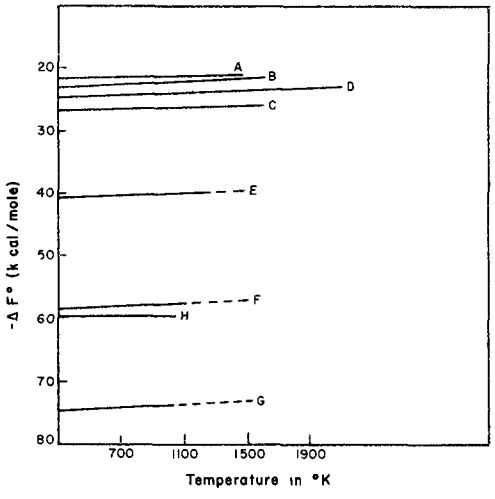

Fig. 1. Standard free energy change as a function of temperature for the formation of some interoxide compounds from the oxides: A, $CaSiO_3$; B, $SrSiO_3$; C, $BaSiO_3$; D, $BaAl_2O_4$; E, $CaWO_4$; F, $SrWO_4$; G, $BaWO_4$; H, $BaMoO_4$.

the free energy change ΔF for the formation of $A_\alpha B$ from its components αA and B is also useful in determining the comparative stability with respect to sublimation of each component A from its combination with a given component B.

The standard free energy change as a function of temperature is shown in Table I for a number of processes of interest which lead to the formation of interoxide compounds.[1] These were evaluated using data in references (2) and (3); since however these calculations involved, in some instances, estimates of entropy and heat capacity values, they are to be considered accurate only in their relative magnitude. These $\Delta F^\circ = f(T)$ functions are plotted in Fig. 1. In accordance with the above, the lower the $\Delta F^\circ = f(T)$ relation for a given compound in this figure, the more stable the compound with respect to dissociation and sublimation.

A third area in which the considerations leading to Fig. 1 are of importance is that of chemical interaction between $A_\alpha B$ and other substances with which it may come in contact. Since all systems tend toward a state of minimum free energy, all substances as shown in Fig. 1 will be thermodynamically unstable in the presence of the free oxides of substances below them in the $\Delta F^\circ = f(T)$ diagram. Further, since in most instances each A may tend to form a number of different combinations with B, an interoxide compound in Fig. 1 will be unstable in the presence of another one if the change of the free energy for their interaction is favorable. Finally, interoxide systems may combine to form a solid solution or compound such as, for example, $Ca_2Al_2SiO_7$.

These considerations also govern the interaction between a component of A or B and a third reagent. In general it can be shown that their combination increases their stability toward chemical attack. For example, it will be seen that $BaO \cdot Al_2O_3$ (or $BaAl_2O_4$) is, for all practical purposes, completely inert in the presence of tungsten, while BaO is not.

If the relative amounts of the components of an emission material are known, the above are useful for the understanding of the nature of cathode coatings and of the interface composition between the coating and the supporting electrode.

Not much is known about the quantitative aspects of sputtering of composite surfaces. However, the process represented by

$$x(\text{solid}) \rightarrow x(\text{gas})$$

will involve the same amount of energy regardless of the path the process follows, the efficiency involved, or the agent causing it. Therefore, from basic considerations alone it can be expected that the separation of an atom or molecule from the surface will involve, as one factor at least, the energy of sublimation regardless of whether this "sublimation" is achieved thermally or by ionic bombardment. Thus it is not surprising that important recent studies on sputtering (4) have succeeded in interrelating, empirically at least, this phenomenon with the heat of sublimation, among other factors. Therefore the criterion ΔF, used for the stability with respect to sublimation, dissociation, and chemical reactivity was used also for the stability with respect to sputtering as the best alternative at the present state of knowledge.

The physical state of $A_\alpha B$ as a function of temperature, the nature of the combination $A_\alpha B$ as a function of α and temperature, and an estimate of the magnitude of the thermodynamic quantities involved were obtained from the study of the appropriate phase diagram.

The application of the above considerations to actual systems involves the well-known limitations of thermodynamics. The experimental work indicated,

[1] The oxides that combine to form these substances do not differ enough in their acidic character to justify the term "oxygen salts" nor do they exist in such a loose combination as to correspond to "mixed oxides." The term "interoxides" is proposed to define this class of materials.

however, that the activation energy and diffusion barriers were of lesser magnitude than should have been expected from solid-state reactions. Therefore, these limitations were of lesser importance than would have otherwise been the case.

Experimental Methods

The awareness of the importance of the thermochemical history of the electron emitting materials led to the application, in this work, of thermal methods of experimental investigation such as thermogravimetric analysis (T.G.A.), and differential thermal analysis (D.T.A.)

The basis for the application of these methods is as follows: It has been shown in the previous section that if A and B will form a combination A_aB such as to increase the stability of A, the sign of ΔF for the process of this combination will be negative.

Since the entropy change for processes in the solid state is small,[2] then

$$\Delta F \cong \Delta H$$

If the change in heat content ΔH is unknown, the next best thing is to determine its sign. By means of D.T.A., the temperature range at which the process takes place, the exothermic or endothermic nature of the process, as well as a very approximate magnitude of ΔH are determined.

This method was also used in order to obtain an indication of the rates at which the thermodynamically predicted processes take place.

Phase diagrams and thermodynamic data for the binary sytems A_aB of interest are few; for the ternary systems resulting from the processes exemplified by Eq. [8], below, are virtually nonexistent. Hence, once the A_aB system was evaluated, D.T.A. provided the means of determining whether the process of Eq. [8] produced a system of increased stability.

The difficulties of interpretation of D.T.A. records can often become formidable when a complex process, such as that of the activation of an emission material, is being studied. Other methods such as x-ray diffraction, mass spectroscopy, microscopy, and T.G.A. were then applied in conjunction with D.T.A.

The maximum temperature attainable by the conventional D.T.A. apparatus used was 1500°C.[3] Therefore, approximate melting point determinations of compounds melting at higher temperatures were performed in inert atmospheres inside a tungsten wound furnace. The temperature was determined by means of a calibrated micropyrometer focused at a "blackbody" cavity formed by a tungsten container into which a small crystal of the compound was placed.

The thermionic behavior of selected materials was examined by means of high vacuum diodes for academic purposes; since it is unknown whether thermionic or secondary processes predominate in a given gas discharge, greater reliance was placed on results obtained by studying the breakdown voltage and the cathode drop in the actual gas discharges for which these cathodes were intended.

[2] This is also true for the evaluation of stability with respect to sublimation, since the difference $\Delta F_1 - \Delta F_2$ cancels out the large increase of entropy on sublimation of αA.

[3] For substances containing excess barium, the D.T.A. apparatus could not be used above 950°-1000°C because of severe chemical attack on the Pt-Pt:13% Rh thermocouples.

Interoxide Systems As Electron Emitting Substances

Interoxide systems $(M_xO_y)_a \cdot (R_zO_w)$, where M_xO_y represents an "emissive" oxide, BaO for instance, and R_zO_w a refractory oxide such as Al_2O_3, if used as such, form poor lamp cathodes even if $\alpha > 1$. Their behavior as cathodes however improves appreciably if an excess of the emissive metal M is introduced. This was done by chemically reducing part of the M_xO_y component as follows:

$$(M_xO_y)_a \cdot (R_zO_w) + \beta R \rightarrow \left(\beta \frac{wx}{zy}\right) M \cdot \left(\alpha - \beta \frac{w}{zy}\right) M_xO_y \cdot \left(\frac{\beta}{z} + 1\right) R_zO_w \quad [8]$$

where the left hand side of the equation represents the emission mixture while the right hand side represents the activated cathode. The reducing agent R used was the same, in each case, as the R of the refractory oxide. This was done in order to obtain, after activation, the simplest possible chemical species hence the easiest to study.

The type of cathode thus produced was controlled by adjusting the following variables: (*a*) selection of the interoxide system; (*b*) selection of the reducing agent; (*c*) amount of the reducing agent; (*d*) state of subdivision of the reducing agent.

In cases where it was desirable that the reduction reaction proceed in a short time, a potent reducing agent (1)[4] in fine powder form was mixed with the powder of the interoxide substance. In the other extreme, the reducing agent was alloyed with the cathode support.

It may be noted that, in all cases, the process of activation, being a chemical reaction in the solid state, does not involve evolution of gases (see below, Process of Activation), nor does it necessitate any particular atmosphere or lack of it for its progress. If the composition of the interoxide system is such that $\alpha \leqq 1$, the emission mixture is stable in the atmosphere for extended periods of time as shown in Fig. 2. Finally, the reduction in volume of the emission mixture upon activation is much less than if, for instance, it had involved the decomposition of carbonates, a helpful fact, as it will be seen when the system is used in conjunction with a refractory metal sponge or compact.

The electron emitting behavior of interoxide systems in lamps parallels that found in this work and by others (5, 6) by means of measurements of the thermionic emission constants of interoxide systems consisting of BaO and a number of refractory oxides. An inspection of these results brings out the possibility that the value of the work function ϕ, or more precisely the slope of the Richardson plots, is approximately the same and in the vicinity of 1.6 e.v. at 750°-850°C regardless of the refractory oxide (Al_2O_3 or ZrO_2, etc.) and, except at the two extremes of

[4] In general, however, it should be remembered that now the ΔF reduction = $\Delta F_R + (\Delta F'' - \Delta F')$ where ΔF_R is the free energy of reduction of M_xO_y to M and R_zO_w, and $\Delta F''$, $\Delta F'$ are the free energies of formation from the oxides of the final and original interoxide substances, respectively.

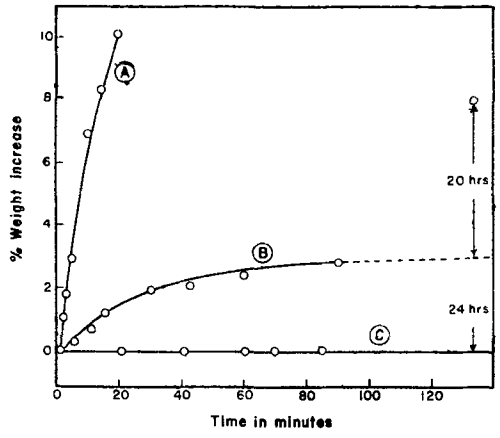

Fig. 2. Weight gain of cathode materials on exposure to air of relative humidity as stated. A, BaO; relative humidity: 70%; B, 0.76 $BaO \cdot BaAl_2O_4$; relative humidity: 80%; C, $BaAl_2O_4$; relative humidity: 80%.

composition, regardless of the BaO content of the interoxide system. In this work the emission coatings were applied on cathodes made of molybdenum, tungsten, and nickel; hence to this extent this value of ϕ is independent of the cathode base. Furthermore, the value of A in the Richardson equation

$$i = AT^2 e^{-e\phi/kT}$$

seems dependent on the amount of Ba present in excess of the stoichiometric formulas for the interoxide system, being very small for the pure substances and increasing with the Ba content.

This evidence points to the hypothesis that the work function in interoxide systems is determined by the nature of the emissive sites involved (BaO-Ba in this case, see also below, Process of Activation) while the saturated current density is determined by the number of these sites per unit area.

If the above is true, then the role of the refractory component is simply to increase the stability of the BaO-Ba emissive sites, as explained, and to increase the amount of Ba that may be combined with the BaO-refractory oxide matrix, as will be explained.

Preparation of Starting Materials

Interoxide substances usually are prepared by heating a mixture of alkaline earth carbonates or oxalates, nitrates, sulfates, etc., with the oxides, hydrates, or other compounds of the refractory component to the point of melting.

In this work the interoxide substances of interest were prepared by the direct combination of the two oxides in the solid state,

$$\alpha M_xO_y + R_zO_w \xrightarrow{\text{heat}} (M_xO_y)_\alpha \cdot (R_zO_w) \qquad [9]$$

In most instances the reactions proceeded at relatively low-temperature ranges and rather short reaction times as shown in the D.T.A. records of Fig. 3. At a heating rate of 15°C/min, it is seen that $BaAl_2O_4$ is formed between 400° and 500°C; $BaZrO_3$ between 200° and 800°C; and $BaThO_3$ between 200° and 900°C. The over-all effect is exothermic. It is interesting to note that in all three cases depicted the reactions proceed in three main stages although these stages may occur at different temperature ranges

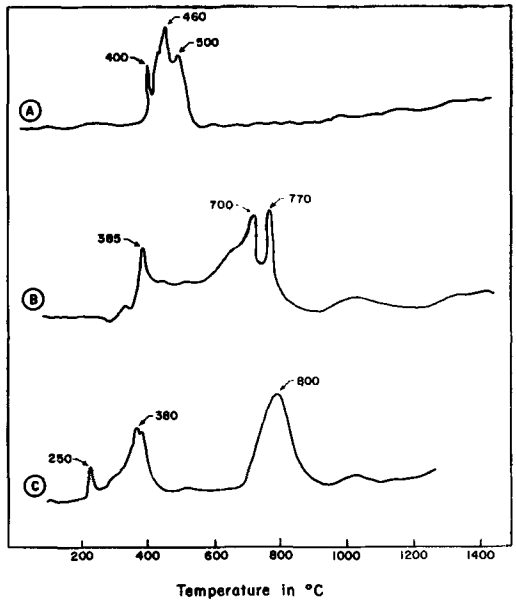

Fig. 3. D.T.A. curves for the formation of some interoxide systems from their component oxides.

(A) $BaO(c) + Al_2O_3(c) \rightarrow BaAl_2O_4(c)$
(B) $BaO(c) + ZrO_2(c) \rightarrow BaZrO_3(c)$
(C) $BaO(c) + ThO_2(c) \rightarrow BaThO_3(c)$

in each case. The reaction leading to the formation of $BaThO_3$ does not proceed to completion in the 50 min of heating as shown, but the other two apparently do proceed to completion: if the aluminate or zirconate samples are taken out of the apparatus after the last stage, reground, replaced in the apparatus, and heated again, no evidence of further reaction is observed. Melting point determinations, chemical analysis, and x-ray diffraction data confirm this to the extent that published data are available. X-ray powder pattern data have been obtained for $BaAl_2O_4$ prepared as described above, which is presented in Table II compared with the data in A.S.T.M. card No. 2-0545. It is seen that the A.S.T.M. intensity values,[5] with the exception of the intensity of the principal line at $d = 3.17$, are approximately twice those determined[6] in this work. As the value assigned to all intensities is relative to that of the principal line (which is assigned the value of 100), we believe, as suggested by Dr. Addamiano, that the values given by the A.S.T.M. card for $BaAl_2O_4$ are higher than the actual ones by a constant factor because of film saturation by the principal line reflection.

Preparation of Cathodes

The interoxide substance is ground and mixed with the powder of the reducing agent. Then, depending on the particular intended application, the mixture is either suspended in a comparatively volatile organic liquid such as butyl acetate, or used as the dry powder. The liquid suspensions may be used for coatings by dipping, spraying, or painting in the usual manner.

The dry powder may be used to provide very thin coatings of the mixture on the electrodes or to form dispersions in refractory metal compacts (or sponges). In connection with the former use it has

[5] Obtained from photographic film recordings.
[6] By means of a Geiger counter detector.

Table II. X-ray diffraction data of $BaAl_2O_4$

This work		ASTM	
d-spacings	Intensities	d-spacings	Intensities
4.57	35		
		4.56	80
4.18	15	4.06	20
4.05	5		
3.75	7	3.17	100
3.16	100		
2.62	39	2.62	80
2.51	6	2.51	20
		2.46	10
		2.26	20
2.25	30	2.24	70
2.20	18	2.20	20
		2.19	10
2.01	25	2.01	60
1.98	21	1.977	20
		1.951	10
1.71	11	1.71	20
1.68	18	1.68	30
1.64	5	1.64	20
1.595	29	1.594	60
1.577	13	1.577	30
1.508	18	1.507	40
		1.477	10
		1.465	10
		1.428	10
		1.395	20
1.392	8	1.389	10
		1.351	35
1.350	14		
1.307	8	1.307	20
		1.279	30
1.276	12		
1.253	7		
1.243	11		
1.227	7		
1.207	14		
1.123	6		
1.112	7		
1.102	6		
1.066	4		
1.010	10		
0.9868	9		
0.9212	6		
0.8385	6		
0.8183	8		
0.7991	5		
0.7968	5		

been found that some of these mixtures, for instance, that of $BaAl_2O_4$ and Al, will adhere to clean metals if the mixture contains a slight excess of BaO or $BaCO_3$ (see below, Chemical Processes). For some uses a thin coating, visible to the naked eye only by direct comparison of the coated and uncoated portions of the electrode, is sufficient to provide desirable performance.

In connection with the latter use the interoxide substance and its reducing agent are mixed in powder form with a chemically inert (see below) refractory metal powder, usually tungsten, the latter being in large excess, as for example 9:1 by weight, for one of the applications reported here. The resulting mixture is pressed without benefit of binders, lubricants, or other additives into compacts of the desired shape and dimensions. A pressure of 6000 kg/cm^2 is sufficient for simple shapes such as that of a short cylinder. The compacts then are placed in refractory firing boats and fired at a temperature of

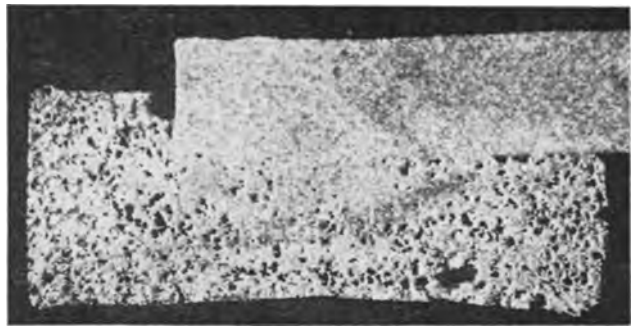

Fig. 4. Photomicrograph of cross section of pellet cathode bottom attached by means of spot welding to the tungsten electrode shown at the top. (Specimen and photomicrograph by K.S.G. Pertwee of Large Lamp Department.)

1050°C in dry hydrogen or an inert atmosphere for at least 20 min. This treatment causes the compacts to sinter into hard, porous pellets of a density range of 8.5 to 9.5 g/cm^3. If the tungsten content is more than approximately 60% by weight, the resistance of the pellets is very low; therefore it may be spot welded directly on a metal lead to form one type of cathode as shown in Fig. 4.

The purpose of the above procedure is primarily to sinter the tungsten particles; for, as will be seen, the activation process involves lower temperatures and shorter times than those mentioned above. The resulting structure is quite similar to cathodes already reported (7), the basic difference being that, due to the choice of $\alpha \leqq 1$ for the interoxide system and to the incorporation of R, the activation is independent of the tungsten sponge which serves simply as a physical support (see below, Chemical Processes).

After activation the coatings obtained from liquid suspensions and the thin dry powder coatings are unstable in the ordinary atmosphere; the sintered tungsten compacts however are stable even if stored for several weeks under saturated humidity conditions (see below, Chemical Processes).

The Process of Activation

The D.T.A. records of Fig. 5 indicate that Eq. [8] describes in reality a complex, multistage process.

From a practical point of view the low temperatures and short times[7] of "activation" are convenient in that the cathodes become activated while lamps are being processed in ovens.

From the theoretical point of view it is interesting to note that the similarities observed in the reactions of formation of the interoxide compounds, Fig. 2, have a parallel in their reactions of reduction. These consist of two main processes: a low-temperature sharp exothermic reaction and a process at higher temperature proceeding at a slower rate and having a hump-like appearance. An increase in β (Eq. [8]) causes an increase in the height and area of the peaks as shown in Fig. 5A. Both processes decrease in intensity and are displaced toward higher temperatures as α is decreased to the extent of necessitating longer time intervals for their completion than indicated by Fig. 5. Finally for $\alpha < 1$ the low-tem-

[7] The D.T.A. experiments were performed in argon at atmospheric pressure at a heating rate of approximately 15°C/min.

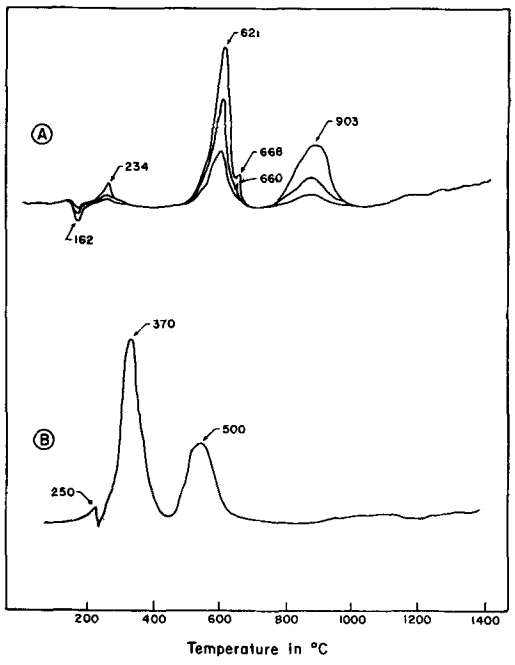

Fig. 5. D.T.A. curves for the reduction (activation) processes
(A) $1.76BaO \cdot 1Al_2O_3$ + various amounts of Al
(B) $9BaO \cdot 1ZrO_2 + 2.3Zr \rightarrow 3.3(1.33BaO \cdot 1ZrO_2 \cdot 1.39Ba)$

perature process begins to become endothermic while the higher temperature hump has still an exothermic appearance.

Repetition of the runs using various proportions of reactants, x-ray diffraction studies, mass spectroscopic work, and chemical analyses were of assistance for the interpretation of the records of Fig. 5 as follows.

At approximately 160°C the small amount of water adsorbed by the powders begins to separate causing the endothermic peak at 186°C on the record for the aluminate case. As the water vapor diffuses out of the sample it attacks the reducing metal it encounters causing the formation of refractory oxide and hydrogen. This exothermic process occurs in the aluminate near 280°C. In the zirconate case this reaction begins at a lower temperature to the extent of balancing the endothermic effect of the desorption of water.

The main reduction reactions then follow peaking at 370° and 620°C for the zirconate and aluminate, respectively. In the case of the aluminate, when the temperature attains the value of 660°C, the melting point of aluminum, the remaining quantity of unreacted aluminum melts, impregnates the sample, and reacts causing the small exothermic peak at 668°C. The area corresponding to the peak at 620°C where aluminum is presumed still solid is far larger than that at 668°C. As this is also the case in the zirconate-zirconium reaction, it may be concluded that the reactions are capable of proceeding in the solid state and it is not necessary to assume the formation of (reducing metal)-(barium) eutectic compositions, which are liquid at the reaction temperatures, in order to explain the progress of these reactions in the short reaction times and low temperatures observed.

The reduction reaction is always followed by a slower exothermic process appearing as a hump on the D.T.A. records. Neither this process nor the unexpectedly exothermic behavior[8] of the peaks attributed to the main reduction reaction have been completely understood to date; however, work in progress has permitted interesting glimpses into their nature which may be summarized as follows.

When the reduction reaction begins, the reducing metal, which is present in excess at the particle interface with the interoxide compound, will reduce a larger quantity of barium oxide than that intended by Eq. [8]. Soon a gradient will be established across the reaction front which in the case of $(BaO)_a$ (Al_2O_3)-Al reaction, for instance, involves the series: Al Al_2O_3 $BaO \cdot 6Al_2O_3$ $BaO \cdot Al_2O_3$ $3BaO \cdot Al_2O_3$ with the quantity of barium produced increasing in the same order as that of aluminum oxide. As shown in the reactions of formation in Fig. 3, the interdiffusion rate of these species is appreciable and a series of exothermic reactions are thermodynamically predictable to take place; as for example,

$$5Al_2O_3 + BaO \cdot Al_2O_3 \rightarrow BaO \cdot 6Al_2O_3$$

Since these reactions depend on the diffusion of molecules bulkier than Al or Al_xBa_y, they would manifest themselves on the D.T.A. record as humps rather than as sharper peaks as the reduction reaction does.

It is suspected that the above explains the hump process only in part and that this process, as well as that causing the sharper peak at lower temperatures, also involves the exothermic interaction between the Ba formed by the reduction reaction and the resulting interoxide substance. Thus, for instance, the 0.31 g of Ba that is theoretically produced by 1 g of a mixture of $BaAl_2O_4$ and Al according to

$$BaAl_2O_4 + 0.4Al \rightarrow 1.2(0.34BaO \cdot 1Al_2O_3 \cdot 0.5Ba)^9 \quad [10]$$

is not detected by means of x-ray diffraction techniques; hence it does not exist in the elementary crystalline state. This is confirmed by thermogravimetric experiments using a Chevenard thermobalance. Except for a weight loss of approximately 1.8% between 70° and 300°C, which has previously been shown to be due to the evolution of water and hydrogen, there was no other significant weight change up to 1050°C, the maximum temperature attainable by the apparatus used. The experiments were performed in a flow of purified argon (600 cc/min) at atmospheric pressure, using 1-g samples of powder consisting of the mixture shown by the left hand side of Eq. [10]. On the average, the sample was at a temperature above 710°C, the melting point of Ba, for at least 2 hr.

In order to overcome the limitations imposed by the inability to perform these experiments in vacuum, and also in order to obtain an indication of the

[8] Thermochemical calculations show most of these reactions to be slightly endothermic within the limits of uncertainty of the available data.

[9] In addition to Eq. [10], the following give specific examples involving actual cathodes.

$$BaZrO_3 + 0.25Zr \rightarrow 1.25(0.4BaO \cdot 1ZrO_2 \cdot 0.4Ba) \quad [11]$$

$$BaThO_3 + 0.2Th \rightarrow 1.2(0.5BaO \cdot 1ThO_2 \cdot 0.33Ba) \quad [12]$$

nature of the apparent combination between barium and the interoxide system, the thermogravimetric experiments were repeated in a flow of hydrogen instead of argon. The behavior in the 70°C range was nearly the same as in the case of argon; however, an increase in weight was observed at 650° to 700°C because of the formation of barium hydride. This permitted the estimation of a maximum for the heat of the combination Ba-X as follows:

$$Ba - X(c) \rightarrow Ba(c) + X(c) \quad \Delta H = ? \quad \Delta F = ? \quad [13]$$

where ΔH is the quantity to be estimated. This process is the sum of

$$Ba - X(c) + H_2(g) \rightarrow BaH_2(c) + X(c) \quad \Delta H_1 = ? \quad \Delta F_1 = ? \quad [14]$$

and

$$BaH_2(c) \rightarrow Ba(c) + H_2(g) \quad \Delta H_2 = +40.9 \; \Delta F_2 = ? \quad [15]$$

therefore $\Delta H = \Delta H_1 + 40.9$ and $\Delta F_1 + \Delta F_2 = \Delta F$.

Reaction [14] proceeds spontaneously and to an appreciable extent even if the flow of H_2 is stopped. Hence $\Delta F_1 \leqq 0$ and therefore $\Delta F \leqq \Delta F_2$ or $\Delta H - T\Delta S \leqq 40.9 - T\Delta S_2$. Since ΔS refers to a reaction involving solids only, it will be small; ΔS_2 refers to a reaction resulting in a gaseous product and will therefore have a larger positive value. Hence $\Delta S_2 > \Delta S$ and therefore $\Delta H \leqq 40.9$ kcal/mole, thus establishing an upper limit for Ba — X.

Subject to further verification this evidence indicates that at least a part of the barium formed is not in a "free" state. This contributes to the explanation of Fig. 5 and the stability of the postulated Ba-BaO-refractory oxide electron emitting sites.

Chemical Processes Involving Refractory Sponge Cathodes

It was seen that the reasons for the choice of equimolar proportions for the composition of the starting interoxide materials included stability in air, low temperatures of activation, lack of copious gas evolution during activation, and ease of control of the chemistry involved in their selection, preparation, and activation.

A further reason is their reduced reactivity toward the refractory metal of the cathode support. As the activation of the interoxide substance is controlled by the reducing agent, it is not necessary that further reduction be made to occur; nor is this desirable because this interaction will result in the creation of an interface concentration gradient and its associated problems.

The pairing of the electron emitting materials and metal supports involves the theoretical considerations at the beginning of this paper. Below, these are applied to the pair $BaAl_2O_4$ — W as an example pertinent to this work. This application necessitates the knowledge of the initial and final states of reactants and products. It was shown in the previous section that the exact state of the barium produced by the reduction process, and hence the final state of the products, are in doubt. Therefore, for comparison purposes, the final state of barium will be taken as being gaseous, because this state offers a common basis for the relative evaluation of the pairs of interest.

The vapor pressure of barium produced in a number of processes was evaluated and is given in Table III. Once again, by necessity, estimates of thermo-

Table III. Theoretical vapor pressures of barium produced by a number of processes of interest

Process or reaction	$\log P_{Ba} = f(T)$
$Ba(c) \rightarrow Ba(g)$	$\log P_{Ba} = \frac{-9730}{T} + 7.83$*
$Ba(c) \rightarrow Ba(g)$	$\log P_{Ba} = \frac{-9340}{T} + 7.42$*
$BaO(c) \rightarrow Ba(g) + \frac{1}{2}O_2(g)$	$\log P_{Ba} = \frac{-25{,}750}{T} + 9.62$
$\frac{4}{3}BaO(c) + \frac{1}{3}W(c) \rightarrow Ba(g) + \frac{1}{3}BaWO_4(c)$	$\log P_{Ba} = \frac{-18{,}650}{T} + 6.50 + 0.74 \log T$
$BaAl_2O_4(c) + \frac{2}{3}Al(c) \rightarrow Ba(g) + \frac{4}{3}Al_2O_3(c)$	$\log P_{Ba} = \frac{-14{,}720}{T} + 6.72 + 0.29 \log T$
$BaAl_2O_4(c) + \frac{2}{3}Al(\;) \rightarrow Ba(g) + \frac{4}{3}Al_2O_3(c)$	$\log P_{Ba} = \frac{-14{,}460}{T} + 6.30 + 0.27 \log T$
$2BaO(c) + \frac{1}{3}W(c) \rightarrow Ba(g) + \frac{1}{3}BaWO_6(c)$	$\log P_{Ba} = \frac{-14{,}730}{T} + 6.10 + 0.74 \log T$†
$BaAl_2O_4(c) \rightarrow Ba(g) + \frac{1}{2}O_2(g) + Al_2O_3(c)$	$\log P_{Ba} = \frac{-29{,}200}{T} + 9.66$
$\frac{4}{3}BaAl_2O_4(c) + \frac{1}{3}W(c) \rightarrow Ba(g) + \frac{1}{3}BaWO_4(c) + \frac{4}{3}Al_2O_3(c)$	$\log P_{Ba} = \frac{-25{,}640}{T} + 6.86 + 0.73 \log T$†
$2BaAl_2O_4(c) + \frac{1}{3}W(c) \rightarrow Ba(g) + \frac{1}{3}Ba_3WO_6(c) + 2Al_2O_3(c)$	$\log P_{Ba} = \frac{-25{,}000}{T} + 6.86 + 0.73 \log T$

* Available in this form in the literature (2).
† See also references (8) and (9).

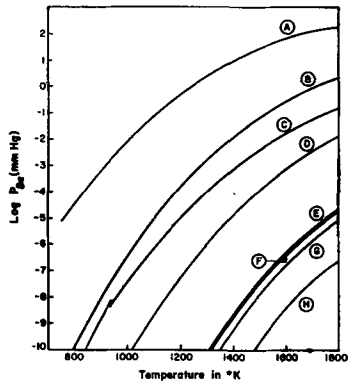

Fig. 6. Logarithm of the theoretical vapor pressure of barium, produced by a number of processes of interest, as a function of temperature.

(A) $Ba(c, l) \rightarrow Ba(g)$

(B) $2BaO(c) + \frac{1}{3} W(c) \rightarrow Ba(g) + \frac{1}{3} Ba_3WO_6(c)$

(C) $BaAl_2O_4(c) + \frac{2}{3} Al(c, l) \rightarrow Ba(g) + \frac{4}{3} Al_2O_3(c)$

(D) $BaO(c) + \frac{1}{3} W(c) \rightarrow Ba(g) + \frac{1}{3} BaWO_4(c)$

(E) $2BaAl_2O_4(c) + \frac{1}{3} W(c) \rightarrow Ba(g) + \frac{1}{3} Ba_3WO_6(c) + 2Al_2O_3(c)$

(F) $BaO(c) \rightarrow Ba(g) + \frac{1}{2} O_2(g)$

(G) $\frac{4}{3} BaAl_2O_4(c) + \frac{1}{3} W(c) \rightarrow Ba(g) + \frac{1}{3} BaWO_4(c) + \frac{4}{3} Al_2O_3(c)$

(H) $BaAl_2O_4 \rightarrow Ba(g) + \frac{1}{2} O_2(g) + Al_2O_3(c)$

chemical data had to be made. Results are plotted in Fig. 6. It is seen that the vapor pressure of barium produced by the reaction between $BaAl_2O_4$ and W resulting in the formation of $Ba_3WO_6(c)$ is comparable to that produced by the thermal decomposition of BaO(c). As is well known with respect to cathode activation, the latter is negligible. The vapor pressure of barium produced by the reaction resulting in the formation of $BaWO_4(c)$ from $BaAl_2O_4$ and W is even less. When these are compared with the vapor pressure of barium produced by the total[10] reduction of $BaAl_2O_4$ by Al it is concluded that the activation of the $BaAl_2O_4$ + 0.4Al + 13.2 W mixture[11] is independent of the tungsten sponge and that the formation of an interface composition of tungstates is unlikely.

The above was confirmed by means of D.T.A. work: no evidence of a reaction was observed on heating finely powdered mixtures of $BaAl_2O_4$ and W up to 1500°C.

In contrast, the reaction between BaO and W and also that between interoxide systems containing BaO in excess of the equimolar composition is thermodynamically favored to nearly the same extent as that between $BaAl_2O_4$ and Al.[12] However, in these cases the role of the tungstate interface becomes apparent. Thus, although the reaction resulting in the formation of Ba_3WO_6 is more favorable than that resulting in the formation of $BaWO_4$, the former is less favorable kinetically since it and the accompanying production of barium depends on the diffusion of the reactants through the $BaWO_4$ interface. Therefore, a pellet cathode of this kind will depend on concentration gradients and hence, delicately, on the cathode temperature, the control of which for directly heated lamp cathodes is not conveniently effected. This is particularly true, of course, in intermittently pulsed discharges where the bulk of the cathode is only slightly above room temperature.

The stability in air after activation of the pellet cathodes containing interoxide materials is interpreted as follows: Upon exposure to the water and carbon dioxide of the atmosphere barium hydroxide and carbonate form on the surface pores of the pellet, with an accompanying large increase in volume of the emission material that has thus been attacked. As these surface pores were already filled with the interoxide substance inasmuch as the activation did not involve any appreciable reduction in volume, the formation of these impervious "plugs" prevents further penetration of vapors and gases and therefore further attack below the surface. If substances such as the usual carbonates had been used for the formation of the pellets, their activation would have been accompanied by a large decrease in volume making the pellets more susceptible to atmospheric attack. The above constitutes an additional reason for the choice of interoxide systems for the pellet cathodes.

[10] Used here as a limiting case; the vapor pressure of Ba from the actual activating process used (Eq. [9]) is substantially higher, $BaAl_2O_4$ and $BaO \cdot 6Al_2O_3$ being the end products rather than Al_2O_3.

[11] Usually employed to manufacture the compacts.

[12] The theoretical vapor pressure of Ba from the reaction between BaO and W resulting in the formation of Ba_3WO_6 is nearly two orders of magnitude higher than determined experimentally (9), either because the enthalpy estimated in this work for the formation of Ba_3WO_4 from its component oxides is too high or because, as shown in this section, the Ba formed by the reduction reaction becomes at least partly bound into the interoxide lattice.

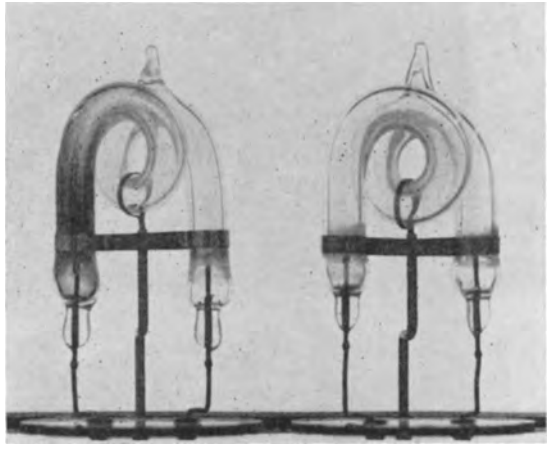

Fig. 7. Left: Standard electronic flashtube after 2500 flashes (near end of life). Minimum average breakdown voltage: 400 v. Right: Lamp identical to that above but using emission materials shown by Eq. [11] (thin film application on tungsten electrode) after 70,000 flashes. Minimum breakdown voltage constant at 285 ±5 v. Both lamps were operated at 125 watt-sec (or Joules) per flash.

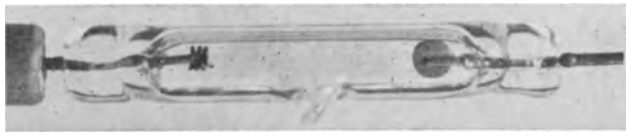

Fig. 8. A new type of repetitive electronic flashtube (used, for instance, for stroboscopic purposes) using pellet cathode of emission materials shown by Eqs. [10] or [11] or [12]. The life of these tubes is several million flashes.

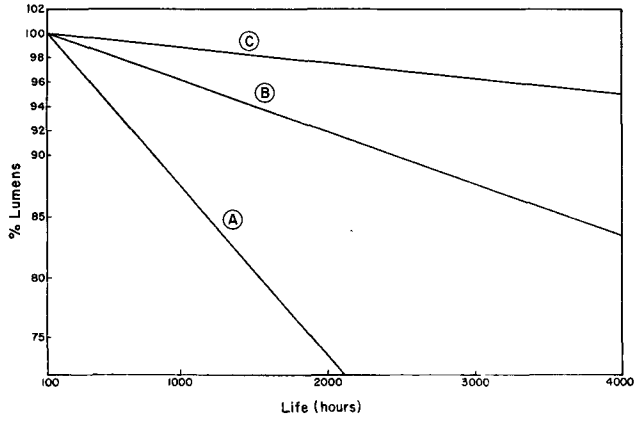

Fig. 9. Maintenance (in per cent of lumen output at 100 hr) vs. life in hours, of: A, standard 400-w high-pressure mercury discharge lamp; B, same as A, but with electron emitting materials as shown by Eqs. [12] or [13] (from liquid suspension); C, same as B, but with modified electrodes.

After manufacture into lamps, the pellet surface is reactivated either thermally or by sputtering. The ease with which this can be accomplished indicates that the attack, even after severe exposure, was very superficial. In the case of thermal reactivation, the formation of tungstates may be expected on the surface. D.T.A. experiments show that barium carbonate and W react at a high rate at 760°C (and slower well below this temperature). T. G. A. work with several interoxide pellets in each experiment failed to detect any weight loss (due to the accompanying evolution of CO) thereby confirming the above results of lamp behavior. This indicates that the formation of tungstates is insignificant. It may become significant, however, when the dry thin coatings mentioned earlier are used on a tungsten base. It will be recalled that these thin coatings adhere tenaciously to the tungsten base and provide good cathode performance if a slight excess of BaO or $BaCO_3$ is introduced. Probably the formation of tungstates to an extent of forming a number of "anchoring" sites but not to the extent of forming an interface could account for this.

Performance Characteristics

In addition to the requirement of ease of manufacture and use already mentioned, lamp cathodes must meet certain standards of performance. These are long life, low breakdown or starting voltage of the lamp, good lamp efficiency (number of lumens output per watt input), and good lamp "maintenance."

Improvements in performance obtained by the use of various forms of interoxide cathodes as described in this paper are shown in the examples of Fig. 7, 8, and 9.

Acknowledgments

The writer is indebted to Drs. J. S. Saby, J. M. Lafferty, V. L. Stout, and Mr. D. E. Elmendorf of this company for their encouragement and discussions. He is also indebted to Mr. R. L. Woodhouse for performing the D.T.A. runs, to Dr. E. G. Zubler for mass spectroscopic work, to Dr. R. P. Taylor for chemical analyses, and for the x-ray diffraction studies to Miss J. R. Cooper and Dr. A. Addamiano, all of this laboratory. For the T.G.A. runs, indebtedness is expressed to Dr. R. C. Griffis of Lamp Metals & Components Department and to Messrs. S. L. Slomski and E. C. Martt of Photo Lamp and Large Lamp Departments, respectively, for tests on lamp performance and general assistance. For discussions on various matters associated with this paper and critical reading of the manuscript, thanks are tendered to Drs. M. D. Gibbons, L. V. McCarty, A. E. Newkirk, H. A. Liebhafsky, T. A. Vanderslice, and J. E. White of this company and E. S. Rittner of Philips Research Laboratories.

Manuscript received March 16, 1959.

Any discussion of this paper will appear in a Discussion Section to be published in the June 1960 JOURNAL.

REFERENCES

1. E. S. Rittner, *Philips Research Repts.*, **8**, 184 (1953).
2. O. Kubaschewski and E. U. Evans, "Metallurgical Thermochemistry," John Wiley & Sons, Inc., New York (1956).
3. F. D. Rossini, *et al.*, National Bureau of Standards, Circ. 500 (1952).
4. G. K. Wehner, *Phys. Rev.*, **102**, 690 (1956); **108**, 35 (1957).
5. D. A. Wright, *British J. Appl. Phys.*, **5**, 391 (1954).
6. H. Huber and J. Freytag, *LeVide*, **54**, 310 (1954).
7. P. P. Coppola and R. C. Hughes, *Proc. IRE*, **44**, 351 (1956).
8. E. S. Rittner, W. C. Rutledge, and R H. Ahlert, *J. Appl. Phys.*, **28**, 1468 (1957).
9. W. C. Rutledge and E. S. Rittner, *ibid.*, **28**, 167 (1957).

The Calcium Silicate Mn + Pb Phosphor Phase Relationships and Preparation

D. E. Harrison and Mary V. Hoffman

Lamp Wire & Phosphors Department, General Electric Company, Cleveland, Ohio

ABSTRACT

Phase relations were examined in the vicinity of $CaSiO_3$ in the system to pseudowollastonite inversion temperature. Addition of $MnSiO_3$ to (Ca,Pb) $CaSiO_3$-$MnSiO_3$-$PbSiO_3$. Lead solid solutions in $CaSiO_3$ lower the wollastonite SiO_3ss markedly lowers the solubility of lead in (Ca,Mn,Pb)SiO_3ss and causes a change in structure from pseudowollastonite to wollastonite. Application of the phase data is used to demonstrate how the synthesis technique can be varied to produce major differences in particle size of the phosphor.

The properties of the $CaSiO_3$:Mn + Pb phosphor are described by Froelich (1), Merrill and Schulman (2), Schulman, Ginther, and Evans (3) and Fonda and Froelich (4). Various synthesis techniques are described by Steadman (5), Schulman (6), and Froelich (7). Phase data pertinent to the phosphor composition are limited. Glasser (8) recently re-examined the system $CaSiO_3$-$MnSiO_3$ and, in general, he confirmed the earlier results of Voos (9), although differing in many details. No data are reported in either the binary system $PbSiO_3$-$CaSiO_3$ or the ternary system $CaSiO_3$-$PbSiO_3$-$MnSiO_3$.

The object of this study was to examine the pertinent phase relationships in the vicinity of $CaSiO_3$ composition and in particular to determine the extent of the solubility of lead in $CaSiO_3$ and its effect on the inversion temperature. Phase data were used as a basis for the interpretation of the reactions which occur during synthesis of the $CaSiO_3$:Mn + Pb phosphor.

Experimental Procedure

The raw materials used for phosphor synthesis were Mallinckrodt Special Bulky silicic acid, silicic acid prepared from tetraethylorthosilicate, and reagent grade $PbSO_4$ and $MnCO_3$. The $CaCO_3$ was prepared by Chemical Products Plant of the General Electric Company. Compositions in the system $CaSiO_3$-$PbSiO_3$ were made from silicic acid prepared by hydrolysis of tetraethylorthosilicate; all other compositions were made with Mallinckrodt silicic acid.

Preparation of compositions and heat treatments.—The ingredients were ground in either an agate or a glass mortar with reagent grade acetone until dry. Calcines were prepared in either platinum or fused silica crucibles at temperatures ranging from 1000° to 1200°C for 3 hr to one month. Ternary compositions were prepared from preformed $CaSiO_3$, $MnSiO_3$, and $PbSiO_3$. The compositions examined are listed in Table I.

Apparatus and techniques.—(*a*) Phase identification was made with a General Electric recording diffractometer using $Cu_{k\alpha}$ radiation ($\lambda = 1.540$Å) filtered with Ni.

(*b*) Microscopic examinations were made with a petrographic microscope.

(*c*) A quench technique was used to examine the solid solution regions by procedures similar to those described by Shepherd, Rankin, and Wright (10). Thermocouples were calibrated using lithium metasilicate (mp 1201°C) and gold (mp 1063°C).

(*d*) Particle size distribution curves of phosphor powders were calculated from settling rates of particles in water by application of Stokes law using the technique of Rabatin and Gale (11).

Results and Discussion

α(Ca,Mn)SiO_3 fluoresces a weak green and β(Ca,Mn)SiO_3 fluoresces a strong orange with cathode ray excitation. Fonda and Froelich showed that Mn-activated wollastonite, the low-temperature form of $CaSiO_3$ called (β), and not pseudowollastonite, the high-temperature modification called (α), could be sensitized to 2537Å radiation by lead. Therefore, β(Ca,Mn,Pb)SiO_3 is the species implied by the notation $CaSiO_3$:Mn + Pb.

Phase Relationships

Preliminary studies showed that in the vicinity of the $CaSiO_3$ composition, the system CaO-MnO-PbO-

Table I. Composition of $CaSiO_3$-$PbSiO_3$-$MnSiO_3$ mixtures

Mole % Sample No.	Composition		
	$CaSiO_3$	$PbSiO_3$	$MnSiO_3$
1	99.5	0.5	—
2	99.0	1.0	—
3	97.0	3.0	—
4	94.0	6.0	—
5	92.0	8.0	—
6	96.5	0.5	3.0
7	96.0	1.0	3.0
8	95.5	1.5	3.0
9	93.5	0.5	6.0
10	93.0	1.0	6.0
11	92.5	1.5	6.0
12	90.5	0.5	9.0
13	90.0	1.0	9.0
14	89.5	1.5	9.0
15	87.5	0.5	12.0
16	87.0	1.0	12.0
17	86.5	1.5	12.0

SiO_2 can be regarded as a 3-component system $CaSiO_3$-$MnSiO_3$-$PbSiO_3$. Consequently, examination of the binary systems $CaSiO_3$-$PbSiO_3$ and $CaSiO_3$-$MnSiO_3$ (after Glasser), and the solid solution region β(Ca,Mn,Pb)SiO_3 provided data necessary to understand many of the reactions which occur during synthesis of the $CaSiO_3$:Mn + Pb phosphor.

A discussion of the pertinent phase data follows:

The inversion temperature of calcium metasilicate.—The literature shows conflicting claims on the temperature of the dimorphic inversion in calcium metasilicate. Voos, for example, reports that the inversion occurs at 1210°C whereas Osborn and Schairer (12) give a value of 1125°C. Our attempts to prepare β-$CaSiO_3$ from $CaCO_3$ and $SiO_2 \cdot XH_2O$ always resulted in a mixture of α- + β-$CaSiO_3$ when fired at temperatures below ca. 1170°C; a sample fired at 1000°C for one month consisted of about 50% α- + 50% β-$CaSiO_3$. At 1180°C or above, only α-calcium silicate formed. α-$CaSiO_3$ will begin very slowly to invert to β-$CaSiO_3$ at 1150°C after several weeks. The data are not conclusive but they indicated that the inversion lies between 1150° and 1180°C.

The system $CaSiO_3$-$MnSiO_3$.—Glasser has recently re-examined the system $CaSiO_3$-$MnSiO_3$ and he is in general agreement with the earlier results of Voos except in many details and the disclosure that the solid solution series extends to 90% $MnSiO_3$ rather than to 100% as reported earlier. He shows that $MnSiO_3$ solid solutions in $CaSiO_3$ raise the inversion temperature to a maximum of 1400°C. The $\alpha \rightleftharpoons \beta$-$CaSiO_3$ inversion temperature was not redetermined in the system $CaSiO_3$-$MnSiO_3$. However, Glasser and Osborn (13) found the $\alpha \leftrightharpoons \beta$-$CaSiO_3$ inversion temperature to occur at 1125°C in the system CaO-Cr_2O_3-SiO_2.

The system $CaSiO_3$-$PbSiO_3$.—Nothing has been reported in the binary system $CaSiO_3$-$PbSiO_3$. The high volatility of Pb limited this investigation to the area around the $CaSiO_3$ composition. Solid-state calcines of preformed $CaSiO_3$ and $PbSiO_3$ were used as starting materials for quench studies. The loss of lead after calcining these mixtures for 6 days at 1050°C is shown in Table II. Since 5 to 7 additional days were required for the samples to reach equilibrium in the quench furnace, further lead losses can be expected, but the magnitudes of these losses were not determined.

The quench data are given in Table III and are shown graphically in Fig. 1. The unusual shape of the two phase area, particularly the flat lower limit, probably reflects the fact that the compositions have shifted from the binary join. Consequently, the phase

Table II. Loss of Pb from $CaSiO_3$-$PbSiO_3$ mixtures

No.	Initial composition Mole % $CaSiO_3$	Initial composition Mole % $PbSiO_3$	Composition after 1050°C/6 days mole % $CaSiO_3$	Composition after 1050°C/6 days mole % $PbSiO_3$	Mole % Pb loss
1	99.5	0.5	99.55	0.45	10.0
2	99.0	1.0	99.27	0.73	27.0
3	97.0	3.0	97.22	2.78	7.3
4	94.0	6.0	94.34	5.66	5.7
5	92.0	8.0	92.14	7.86	1.8

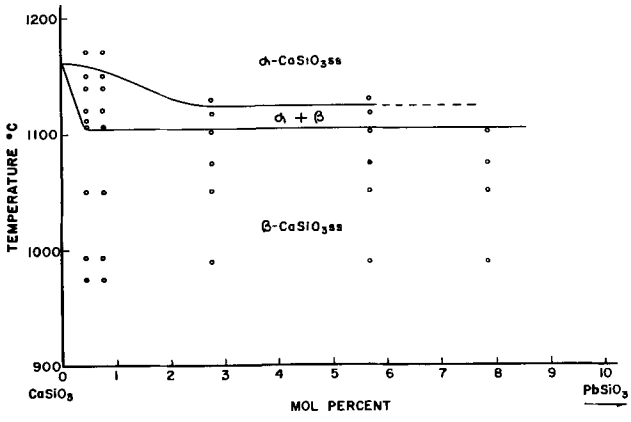

Fig. 1. A portion of the system $CaSiO_3$-$PbSiO_3$

data can be taken only as an approximation of the true equilibrium relationships.

$PbSiO_3$ is soluble in α calcium metasilicate to at least 6 mole % and it lowers the inversion temperature; the addition of 3 mole % $PbSiO_3$ lowers the inversion below 1125°C. Extrapolation of the two-phase area boundaries to pure calcium silicate indicates that the inversion occurs at 1160° ± 10°C.

The (Ca,Mn,Pb)SiO_3 *ss phase region.*—A portion of the plane $CaSiO_3$-$MnSiO_3$-$PbSiO_3$ in the vicinity of $CaSiO_3$ was examined at 1160°C. This temperature was selected because it is near the inversion temperature and also is a practical temperature for phosphor synthesis. Calcines were prepared by heating mixtures of preformed α(Ca,Pb)SiO_3 and $MnSiO_3$ for periods up to three weeks with a thorough grinding every 12 hr.

Lead is much less soluble in β- than in α-$CaSiO_3$ in the presence of $MnSiO_3$. For example, solution of 3 mole % $MnSiO_3$ in α(Ca,Pb)SiO_3 changes it to β(Ca,Pb,Mn)SiO_3 and lowers the Pb solubility from over 6 mole % to less than 1 mole %.

The loss of Pb after various firing times from a typical phosphor composition is shown in Table IV. These data reveal that 8.3% Pb is lost during the formation α(Ca,Pb)SiO_3ss (prepared from PbO + CaO + SiO_2) whereas 33.3% Pb is lost after 4 hr and 53.7% Pb after 16 hr at 1160°C from the reaction of α(Ca,Pb)SiO_3 + $MnSiO_3$ to yield the quaternary composition $\beta(Ca_{0.94-x}Mn_{0.06}Pb_x)SiO_3$. The greater stability of lead in α(Ca,Pb)SiO_3ss than in β(Ca,Mn,Pb)

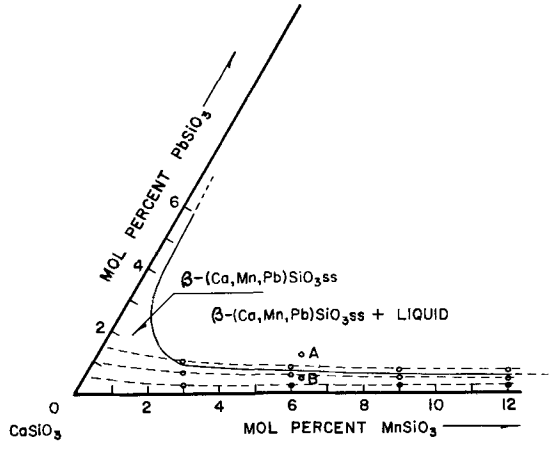

Fig. 2. A portion of the plane $CaSiO_3$-$MnSiO_3$-$PbSiO_3$

Table III. Quench data for the system $CaSiO_3$-$PbSiO_3$

No.	Composition mole % $CaSiO_3$-$PbSiO_3$		Temperature	Phase present
1	99.55	0.45	975	β(Ca, Pb) SiO_3
			994	β(Ca, Pb) SiO_3
			1050	β(Ca, Pb) SiO_3
			1106	β(Ca, Pb) SiO_3 + Trace α(Ca, Pb) SiO_3
			1112	β(Ca, Pb) SiO_3 + α(Ca, Pb) SiO_3
			1121	β(Ca, Pb) SiO_3 + α(Ca, Pb) SiO_3
			1140	β(Ca, Pb) SiO_3 + α(Ca, Pb) SiO_3
			1151	β(Ca, Pb) SiO_3 + α(Ca, Pb) SiO_3
			1165	α(Ca, Pb) SiO_3
2	99.27	0.73	975	β(Ca, Pb) SiO_3
			994	β(Ca, Pb) SiO_3
			1050	β(Ca, Pb) SiO_3
			1106	β(Ca, Pb) SiO_3 + α(Ca, Pb) SiO_3
			1121	β(Ca, Pb) SiO_3 + α(Ca, Pb) SiO_3
			1140	β(Ca, Pb) SiO_3 + α(Ca, Pb) SiO_3
			1151	β(Ca, Pb) SiO_3 + α(Ca, Pb) SiO_3
			1165	α(Ca, Pb) SiO_3
3	97.22	2.78	990	β(Ca, Pb) SiO_3
			1050	β(Ca, Pb) SiO_3
			1075	β(Ca, Pb) SiO_3
			1102	β(Ca, Pb) SiO_3
			1117	β(Ca, Pb) SiO_3 + α(Ca, Pb) SiO_3
			1128	α(Ca, Pb) SiO_3
4	94.34	5.66	990	β(Ca, Pb) SiO_3
			1050	β(Ca, Pb) SiO_3
			1075	β(Ca, Pb) SiO_3
			1102	β(Ca, Pb) SiO_3
			1117	β(Ca, Pb) SiO_3 + α(Ca, Pb) SiO_3
			1128	α(Ca, Pb) SiO_3
5	92.14	7.86	990	β(Ca, Pb) SiO_3
			1050	β(Ca, Pb) SiO_3
			1075	β(Ca, Pb) SiO_3
			1102	β(Ca, Pb) SiO_3

SiO_3ss can be demonstrated qualitatively by a spot test with an acidic solution of KI. α(Ca,Pb)SiO_3ss (Sample B) gave no test for Pb, whereas β(Ca,Mn, Pb)SiO_3 (Sample E) gave a strong test for Pb even after most of the surface Pb had been removed by refiring with NH_4Cl.

The area adjacent to the solid solution region is a liquid plus crystal area. The presence of liquid was detected by quench studies and by its effect on the oxidation state of Mn. Compositions in the crystal plus liquid area had a permanganate pink color and they were sintered into dense agglomerates. In contrast, composition within the solid solution region remained nearly white in body color and did not sinter.

Table IV. Loss of Pb from phosphor composition

Composition	Wt % Pb content	% Pb lost
(A) Batch (CaO + PbO + SiO_2)	1.08	—
(B) 1st Fire, 1140°C/4 hr (Ca, Pb) SiO_3 ss	0.99	8.3
(C) 2nd Fire, 1160°C/4 hr (Ca, Mn, Pb) SiO_3 ss	0.72	33.3
(D) 2nd Fire, 1160°C/ 16 hr (Ca, Mn, Pb) SiO_3 ss	0.50	53.7
(E) 3rd Fire, 1160°C/4 hr + NH_4Cl(Ca, Mn, Pb) SiO_3 ss	0.43	60.2

Because of the volatility of Pb, the quaternary solid solution region reported can be regarded only as a rough approximation to equilibrium conditions. For this reason, the diagram of the plane $CaSiO_3$-$MnSiO_3$-$PbSiO_3$, shown in Fig. 2, has curved dashed lines to indicate the approximate Pb contents.

Preparation of the $CaSiO_3$:Mn + Pb *phosphor*

Synthesis techniques in which all of the components, i.e., CaO+MnO+PbO+SiO_2 are initially fired together require an excess of Pb in order to allow for losses by volatilization. A typical initial composition is indicated in Fig. 2 by point "A" which is in the liquid plus crystal area adjacent to the solid solution region. As the firing progresses the composition gradually shifts to point "B" located within the solid solution region. The metastable liquids formed serve as effective mineralizers, but they promote large particle size and higher oxidation states of Mn. A second firing with NH_4Cl is necessary to remove a surface film of "lead-manganese-silica" which coats the phosphor crystallites.

Certain applications require a phosphor with smaller particle size. In this case it is desirable to avoid formation of metastable liquids. According to the phase data it should be possible to prepare either β(Ca,Mn)SiO_3ss or α(Ca,Pb)SiO_3ss and react each material with either PbO or MnO to form β(Ca,Mn, Pb)SiO_3ss. In this way, metastable liquids are

avoided in the system $CaSiO_3$-$MnSiO_3$-$PbSiO_3$. However, the quaternary solid solution is unstable due to the volatility of lead so that the reaction:

$$\beta(Ca,Mn)SiO_3ss + Pb^{2+} \rightarrow \beta(Ca,Mn,Pb)SiO_3ss \quad [1]$$

cannot be expected to be very successful.

The alternative reaction:

$$\alpha(Ca,Pb)SiO_3ss + Mn^{2+} \rightarrow \beta(Ca,Mn,Pb)SiO_3ss \quad [2]$$

should be more successful due to the greater stability of lead in $\alpha(Ca,Pb)SiO_3ss$ than in $\beta(Ca,Mn,Pb)SiO_3ss$. A sufficiently large excess of Pb can be incorporated initially in $\alpha(Ca,Pb)SiO_3ss$ to allow for losses by volatilization.

Although reaction [2] avoids quaternary liquids, it is still necessary to form $\alpha(Ca,Pb)SiO_3ss$, and low-melting liquids in the system CaO-PbO-SiO_2 cannot be avoided. However, advantage can be taken of the polymorphic inversion from $\alpha(Ca,Pb)SiO_2ss$ to $\beta(Ca,Mn,Pb)SiO_3ss$. Although α- and β-$CaSiO_3$ have about the same densities, a volume change sufficiently large to cause disintegration of agglomerates may be expected in going from $\alpha(Ca,Pb)SiO_3ss$ to $\beta(Ca,Mn,Pb)SiO_3ss$ because of the difference in size between Pb^{2+} and Mn^{2+} ions.

Attempts to prepare $\beta(Ca,Mn,Pb)SiO_3ss$ by reaction [1] did not yield high brightness phosphors since it is not possible to incorporate enough Pb in the phosphor to give sufficiently high absorption for 2537Å.

The preparation of $\beta(Ca,Mn,Pb)SiO_3$ by reaction [2] proved successful. Thus, the preparation of the phosphor involves three steps: (*a*) formation of $\alpha(Ca,Pb)SiO_3ss$, (*b*) formation $\beta(Ca,Pb,Mn)SiO_3ss$, and (c) removal of a surface film of "manganese-lead-silica." Each step is discussed in detail.

(*a*) $\alpha(Ca,Pb)SiO_3$ forms metastably below the inversion temperature so that the reaction proceeds rapidly at temperatures between 1100° and 1200°C. The occurrence of metastable liquids accelerates the reaction and it causes the development of large aggregates having diameters between 30 and 100 μ.

(*b*) The formation of $\beta(Ca,Mn,Pb)SiO_3ss$ requires that both MnO + SiO_2 be incorporated into $\alpha(Ca,Pb)SiO_3ss$. Addition of MnO and SiO_2 as $MnSiO_3$ is impractical since three days or more are required for the reaction to reach equilibrium. This result is not surprising since $CaSiO_3$ and $MnSiO_3$ must have about the same lattice energy as evidenced by their extensive solid solution series. If MnO and SiO_2 are mixed with $\alpha(Ca.Pb)SiO_3ss$, $MnSiO_3$ forms more readily than the quaternary solid solution and again the reaction is very sluggish in reaching completion. However, $\beta(Ca,Mn,Pb)SiO_3ss$ can be formed in 2-3 hr at 1160°C by reacting $MnCO_3$ plus $\alpha(Ca,Pb)$ SiO_3:SiO_2. Using this method it is necessary to add sufficient excess silica in the preparation of $\alpha(Ca,Pb)$ SiO_3ss to account for all of the Mn in the quaternary composition.

Silica is not soluble in $\alpha(Ca,Pb)SiO_3$ at concentrations greater than about 1 mole %, although there may be slight solubility below this amount. Only silica which is in contact with α calcium silicate will react with MnO to form $\beta(Ca,Mn,Pb)SiO_3ss$. Isolated

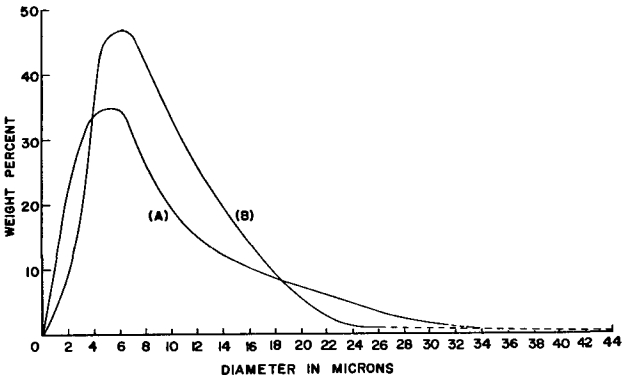

Fig. 3. Particle size distribution curves of $CaSiO_3$:Mn + Pb phosphors. (A) CaO + PbO + MnO + $SiO_2 \rightarrow \beta$(Ca, Pb, Mn) SiO_3 ss; (B) α(Ca, Pb) SiO_3 ss + $Mn^{2+} \rightarrow \beta$(Ca, Pb, Mn) SiO_3 ss.

SiO_2 particles react with MnO to form $MnSiO_3$ which effectively removes Mn from the reaction.

Microscopic examination of samples obtained by quenching after various times clearly revealed the course of the reaction. MnO + SiO_2 diffuse rapidly along grain boundaries of the $\alpha(Ca,Pb)SiO_3$ aggregates. Inversion of $\alpha(Ca,Pb)SiO_3$ begins at the periphery, and as each crystallite of $\alpha(Ca,Pb)SiO_3$ inverts to $\beta(Ca,Mn,Pb)SiO_3$ sufficient contraction occurs to permit the crystallite to separate from the matrix. Thus, this process leads to the disintegration of the aggregates of $\alpha(Ca,Pb)SiO_3$.

(c) The Pb which is volatilized from the quaternary solid solution appears to react with excess silica to form a lead silicate film which causes slight sintering. Sintering can be minimized by employing as short a firing time as possible and by using as little excess silica over stoichiometry as practical.

Lead silicate on the surface of the $\beta(Ca,Mn,Pb)$ SiO_3ss crystals also stabilizes higher oxidation states of Mn. Consequently the surface film serves as a filter which considerably lowers the fluorescent brightness of the phosphor. The film may be removed by refiring with NH_4Cl.

The product obtained has substantially smaller particle size than phosphor produced by initially firing together CaO+MnO+PbO+SiO_2. Phosphor prepared by reaction [2] showed less than 1 wt % oversize on 325 mesh sieve whereas conventional material gave 10-15 wt % oversize. Particle size distribution curves are shown in Fig. 3. It is evident that reaction [2] serves to minimize aggregate growth rather than to yield smaller crystallites since either technique yields a maximum of material in the 5 to 7 μ range. The area under curve "A" for material produced by initially firing together CaO+ MnO+PbO+SiO_2 represents 85-90 wt % of the total material since 10-15 wt % is greater than 44 μ or 325 mesh. On the other hand, curve "B" for phosphor produced by reaction [2] represents 100 wt % since substantially all of the material is less than 325 mesh. Either technique yields phosphor with the same fluorescent properties.

Acknowledgment

The authors thank E. S. Palik for determining the particle size distributions of phosphor powders.

Manuscript received April 1, 1959. This paper was prepared for delivery before the Philadelphia Meeting, May 3-7, 1959.

Any discussion of this paper will appear in a Discussion Section to be published in the June 1960 JOURNAL.

REFERENCES

1. H. C. Froelich, *J. (and Trans.) Electrochem. Soc.*, **93**, 101 (1948).
2. J. B. Merrill and J. H. Schulman, *J. Opt. Soc. Amer.*, **38**, 471 (1948).
3. J. H. Schulman, R. J. Ginther, and L. W. Evans, *ibid.*, **38**, 817 (1948).
4. G. R. Fonda and H. C. Froelich, *J. (and Trans.) Electrochem. Soc.*, **93**, 114 (1948).
5. A. Steadman, U.S. Pat. 2,299,510, Oct. 20, 1943; *Chem. Abs.*, **37**, 1658[3].
6. J. H. Schulman, U.S. Pat. No. 2,474,193, June 21, 1949; *Chem Abs.*, **43**, 6517g.
7. H. C. Froelich, U.S. Pat. 2,542,322, Feb. 20, 1951; *Chem. Abs.*, **45**, 5027a.
8. F. P. Glasser, Private communications.
9. E. Voos, *Z. Anorg. Allgem. Chem.*, **222**, 213 (1935); E. P. Hall and H. Insley, *J. Am. Ceram. Soc.*, **30**, 63 (1947).
10. E. S. Shepherd, G. A. Rankin, and F. E. Wright, *Am. J. Sci.*, 4th Ser., **28**, 293 (1909).
11. J. G. Rabatin and R. H. Gale, *Anal. Chem.*, **28**, 1314 (1956).
12. E. F. Osborn and J. F. Schairer, *Am. J. Sci.*, **239**, 715 (1941).
13. F. P. Glasser and E. F. Osborn, *J. Am. Ceram. Soc.*, **41**, 358 (1958).

The Dielectric Behavior of Solids Embedded in a Homogeneous Medium

Barlane R. Eichbaum

Product Development Laboratory, International Business Machines Corporation, Poughkeepsie, New York

ABSTRACT

Dielectric constant and tan δ of powdered crystal phases of alumina, quartz, and wollastonite were determined. Since it is very difficult to obtain dielectric measurements of very fine (powdered) crystals, a technique of embedding the solids in a homogeneous medium was used. The relationship between particle shape and volume present in the composite to the dielectric properties of such fine powders was in accord with that indicated by Niesel's theory.

The dielectric properties of large single crystals of inorganic materials can be determined since there is sufficient mass present to use standard measuring techniques. Although large single crystals of many inorganic materials are not available, it would be desirable to determine the dielectric properties of granular or pulverized crystallites in order to study their dielectric contribution in composite mixtures. The object of this research is to present a method for determining the dielectric properties of such fine powdered crystallites.

Niesel proposed a theory to compute dielectric properties of solids embedded in a homogeneous medium (1, 2). This theory considers the volume and particle shape of the crystalline materials embedded in the homogeneous medium. In order to overcome the variations which would be encountered if compressed powders were studied, a technique of embedding inorganic powders in a homogeneous medium was devised and used throughout this investigation.

Theory.—Several theories have been developed to predict dielectric properties of polycrystalline mixtures. A theory developed by Lichtenecker (3) in 1926 gives a good approximation for mixtures having a maximum dielectric constant of 10. In 1935 Bruggeman (4) developed equations for determining dielectric constants of mixtures of materials with crystal shapes approximating spheres or lamellae. Niesel (1, 2) gave a method for calculating both the dielectric constant and loss angle of an aggregate consisting of crystals (assumed to be ellipsoids) mixed with a homogeneous material.

The equations derived by Niesel for the isotropic cases of spheres, lamellae, and long cylinders embedded in a homogeneous medium are as follows:

(*a*) Spheres

$$1 - Vi = \frac{\epsilon i - \epsilon}{\epsilon i - \epsilon a} \sqrt[3]{\frac{\epsilon a}{\epsilon}} \qquad [1]$$

(*b*) Lamellae (randomly oriented)

$$= \frac{3\epsilon a + 2Vi(\epsilon i - \epsilon a)}{3\epsilon i - Vi(\epsilon i - \epsilon a)} \qquad [2]$$

(c) Long cylinder (needles)

$$1 - V = \frac{\epsilon i - \epsilon}{\epsilon i - \epsilon a} \frac{(\epsilon i + 5\epsilon a)}{\epsilon i + 5\epsilon} \qquad [3]$$

where ϵi = dielectric constant inside ellipsoid, ϵa = dielectric constant outside ellipsoid, ϵ = resulting dielectric constant, and Vi = volume fraction occupied by ellipsoids.

If δ_1 is the loss angle of the crystal phase and δ_2 that of the medium, then the resulting loss angle δ_{res} is given by

$$\tan \delta_{res} = m_1 \tan \delta_1 + m_2 \tan \delta_2 \qquad [4]$$

If the loss angles of the two ingredients are known it is necessary to determine the values of m_1 and m_2

(energy fractions) which are derived by Niesel to be as follows for the three cases:

(*a*) Spheres

$$m_2 = \frac{(\epsilon_1 - \epsilon)(2\epsilon_2 + \epsilon_1)}{(\epsilon_1 - \epsilon_2)(2\epsilon + \epsilon_1)} \quad [5]$$

(*b*) Lamellae

$$m_2 = \frac{\frac{K_1}{1 + K_1} + 2K_1}{\frac{K_{12}}{1 + K_{12}} + 2K_{12}} \quad [6]$$

(*c*) Cylinder additions

$$m_2 = \frac{\frac{2K_1}{1 + \frac{1}{2}K_1} + K_1}{\frac{2K_{12}}{1 + \frac{1}{2}K_{12}} + K_{12}} \quad [7]$$

where

$$K_1 = \frac{\epsilon_1 - \epsilon}{\epsilon} \quad [8]$$

$$K_2 = \frac{\epsilon_1 - \epsilon_2}{\epsilon_2} \quad [9]$$

$$m_1 + m_2 = 1 \quad [10]$$

and ϵ = dielectric constant of combined phases, ϵ_2 = dielectric constant of glass phase, ϵ_1 = dielectric constant of crystal phase, m_1 = energy fraction of crystal phase, and m_2 = energy fraction of glass phase.

Sample Preparation

In order to test Niesel's theory it was necessary to devise a method of embedding the inorganic crystals in a homogeneous medium; the dielectric properties were then determined. Polystyrene was selected as the homogeneous medium in which to embed the crystals since it has very low loss properties.

Known volumes of five inorganic powders were dispersed in a known volume of polystyrene and carbon tetrachloride solution. This solvent was selected because it has a dielectric constant and tan δ similar to that of polystyrene (5, 6), and, if it should not evaporate completely, little effects would be contributed. The mixtures were completely dried out, then hot pressed into disks having a 1¼ in. diameter and approximately 0.05 in. thick. In all cases the volume of powdered inorganic material does not exceed 65% or the specimen will not be dense, hence, a true evaluation will not be obtained.

The values of dielectric constant and tan δ were determined with the Boonton Q-meter type 160A at 1 megacycle.

Preliminary investigation.—In order to determine the correlation between the theoretical and experimental values for mixtures having known, measured dielectric constant and tan δ, two glasses, Vycor and window glass, were selected for study by embedding in polystyrene. These glasses were ground wet and screened through 100 and 200 mesh sieves prior to combining with polystyrene. The ground glass is considered an isotropic powder material in this case.

Table I. Theoretical and experimental values of dielectric constant and power factor for Vycor glass-polystyrene mixtures

Theoretical

Lamellae			Spheres			Long Cylinder		
Vycor volume, %	ϵ	tan δ	Vycor volume, %	ϵ	tan δ	Vycor volume, %	ϵ	tan δ
0	2.55	0.00022	0	2.55	0.00022	0	2.55	0.00022
10	2.70	0.00030	10.3	2.70	0.00029	10.5	2.70	0.00046
20	2.86	0.00037	21.2	2.86	0.00036	21.0	2.86	0.00050
30	3.02	0.00045	31.4	3.02	0.00043	31.2	3.02	0.00055
40	3.18	0.00051	41.4	3.18	0.00050	41.0	3.18	0.00061
50	3.36	0.00057	52.1	3.36	0.00056	51.8	3.36	0.00064
60	3.53	0.00063	61.7	3.53	0.00062	61.4	3.53	0.00069
70	3.69	0.00068	70.5	3.69	0.00068	70.1	3.69	0.00072
80	3.90	0.00074	81.7	3.90	0.00078	81.5	3.90	0.00077
90	4.09	0.00080	91.5	4.09	0.00079	91.5	4.09	0.00081
100	4.28	0.00084	100	4.28	0.00084	100	4.28	0.00084

Experimental

−200 mesh			−100 mesh		
Vycor volume, %	ϵ	tan δ	Vycor volume, %	ϵ	tan δ
0	2.55	0.00022	0	2.55	0.00022
2.8	2.57	0.00031	4.8	2.57	0.00036
5.5	2.58	0.00039	6.8	2.59	0.00040
9.0	2.62	0.00045	11.3	2.67	0.00047
14.2	2.73	0.00046	18.7	2.83	0.00049
17.7	2.85	0.00048	24.2	2.92	0.00052
26.0	2.91	0.00054	28.9	3.00	0.00054
34.3	3.03	0.00057	37.4	3.12	0.00057
47.1	3.37	0.00065	52.0	3.35	0.00066
58.5	3.55	0.00069	61.6	3.60	0.00068
100	4.28	0.00084	100	4.28	0.00084

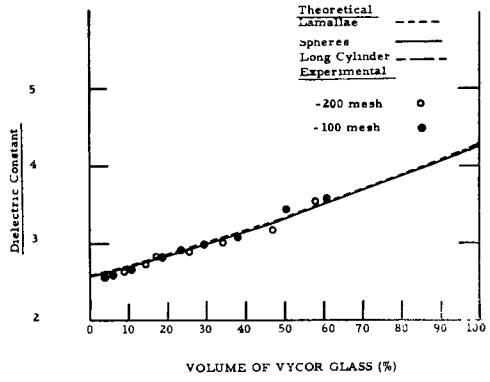

Fig. 1. Volume of Vycor glass on polystyrene vs. dielectric constant and tan δ.

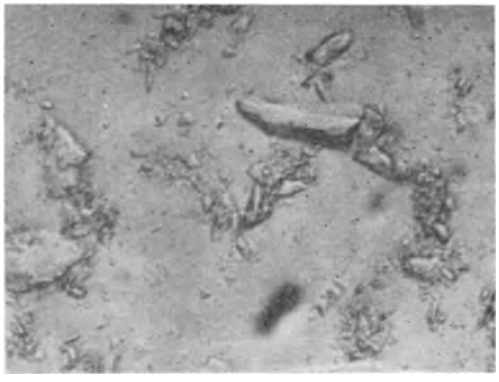

Fig. 2. Photomicrograph of Vycor glass particles. Magnification 1000X.

Two glasses were used because their dielectric properties were quite different and this could be used as a means of verifying the validity of Niesel's equations. Dielectric properties were determined on a square piece of each glass 2 in. by 2 in. by approximately 1/5 in. thick. These glasses were crushed to —100 and —200 mesh grain sizes. Both glasses were investigated using grains of two particle sizes in order to check if the particle size has any effect with either low or high loss glass. Niesel claims that the particle size of the powdered material should have no effect on the results; therefore, it was necessary to substantiate this claim.

Vycor glass-polystyrene mixture.—The two different particle sizes of Vycor glass were embedded in polystyrene. The dielectric properties of the two materials are:

	ϵ	tan δ
Polystyrene	2.55	0.00022
Vycor glass	4.28	0.00084

Since the values for the two end members are known, calculations were made on the basis of lamellar, spherical, and long cylinder (needle) particle shapes in order to determine if the experimental values obtained compare with any of the theoretical curves. Calculated values for the three particle shapes and the experimental value are listed in Table I. All of these values are plotted vs. volume of glass present in Fig. 1.

As can be seen from the graph of Fig. 1, the curves for theoretical dielectric constant are so close together that it is difficult to distinguish between them. The symbols used to denote experimental values for both —100 and —200 mesh sizes follow right in line with the theoretical curves.

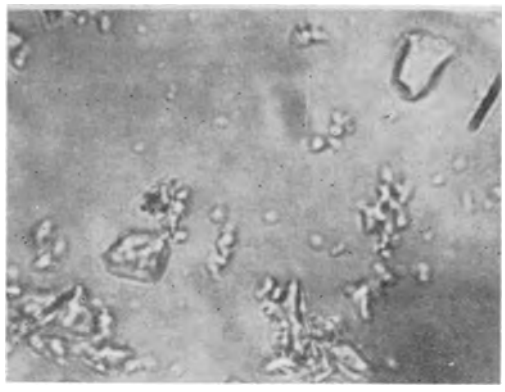

Fig. 3. Photomicrograph of window glass particles Magnification 1000X.

The theoretical curves for tan δ on Fig. 1 are easily differentiated. The curve for spherical particles is almost a straight line, whereas that for randomly oriented lamellae has a greater upward curvature, and the curve for randomly oriented needles has a rapid increase which levels off to almost a straight line. Experimental values obtained for both the —100 and —200 mesh particles fall right in line with the long cylinder addition curve. This was not expected because it was assumed that the particles would most closely approach a spherical shape. However, when examined with a petrographic microscope, many of the particles were noted to be a long needle shape as can be seen in the photomicrograph of Fig. 2.

These results were very enlightening, showing that this difference of particle shape has a definite effect, that the particle size difference has no marked effect, and that the experimental and calculated values of both dielectric constant and tan δ vs. volume per cent are almost identical for the case of the long cylinder shaped additions.

Window glass-polystyrene mixtures.—In the experiments using glass-polystyrene mixtures as with the Vycor glass-polystyrene mixtures both —100 and —200 mesh glass grains were embedded in polystyrene for the determination of dielectric properties.

The values of the 100% product in this case at 1 mc and 25°C are;

	ϵ	tan δ
Polystyrene	2.55	0.00022
Window glass	7.95	0.012

The particle shape of this glass (ground) was investigated and assumed to approach a spherical symmetry as can be seen in Fig. 3. Since the particles did not appear to be elongated as many were in the case of Vycor glass, theoretical calculations were performed only for spherical and lamellar particle shapes. Theoretical values obtained for these two shapes vs. volume per cent as well as the experimental values obtained for the two particle sizes are listed in Table II. Curves plotted for theoretical calculations and symbols designating the experimental values are plotted in Fig. 4.

As can be seen in Fig. 4 the lamellar curves for both dielectric constant and tan δ do not approach

Table II. Theoretical and experimental values of dielectric constant and power factor for window glass-polystyrene mixtures

Theoretical

Spheres			Lamellae		
Window glass volume, %	ϵ	tan δ	Window glass volume, %	ϵ	tan δ
0	2.55	0.00022	0	2.55	0.00022
7.5	2.80	0.00116	25	3.66	0.00051
13.2	3.00	0.00194	50	4.92	0.0081
26.5	3.40	0.00340	75	6.30	0.0105
40.8	4.20	0.00549	100	7.95	0.0120
56.4	5.00	0.00733			
72.8	6.00	0.00921			
87.4	7.00	0.01077			
94.2	7.50	0.01140			
100	7.95	0.0120			

Experimental

−200 mesh			−100 mesh		
Window glass volume, %	ϵ	tan δ	Window glass volume, %	ϵ	tan δ
0	2.55	0.00022	0	2.55	0.00022
6.0	2.68	0.0011	6.2	2.68	0.0011
8.2	2.76	0.0015	9.3	2.78	0.0016
12.6	2.88	0.0017	15.5	2.91	0.0024
18.8	3.01	0.0027	21.3	3.18	0.0031
23.7	3.17	0.0033	26.8	3.30	0.0038
27.3	3.32	0.0039	34.5	3.56	0.0048
31.5	3.48	0.0045	42.6	3.96	0.0055
37.6	3.74	0.0052	29.9	4.40	0.0067
47.7	4.31	0.0064	56.7	4.83	0.0076
53.9	4.69	0.0071	100	7.95	0.0120
60.6	5.22	0.0079			
100	7.95	0.0120			

the experimental values, but both the −100 and −200 mesh particle size symbols are very close to the spherical curves. Calculated values of dielectric constant are slightly larger than experimental values, whereas calculated tan δ values are slightly less than experimental values.

However, the curves, being very close, show that the particle shape of the window glass, approaching sphericalness, can be used to make very close approximations to the true experimental values. This helps to substantiate and justify the use of Niesel's theory as does the case for Vycor glass-polystyrene mixtures.

Since the experimental values obtained for the Vycor glass-polystyrene and window glass-polystyrene mixtures so closely approach the theoretical values obtained with Niesel's equations, the same approach is used to determine the 100% volume values for the three crystalline materials, alumina, quartz, and wollastonite.

Dielectric Properties of Alumina, Wollastonite, and Quartz Crystallites

Since Niesel's equations fit the experimental data for the two cases using glasses as the dispersed ingredient, the same technique was used to determine the dielectric properties of the crystal phases of alpha alumina, wollastonite, and low-temperature quartz.

Alumina-polystyrene mixtures.—A very pure grade of fused alumina[1] was used for determining the dielectric properties by embedding in polystyrene. von Hippel (7) determined the dielectric properties of a clear sapphire[2] to be:

$$\epsilon = 8.6 \pm 0.02, \tan \delta = 0.001$$

perpendicular to the optic axis

and

$$\epsilon = 10.55 \pm 0.02, \tan \delta = 0.001$$

parallel to the optic axis

when measured at one megacycle.

This is a single crystal form of alumina and not a powdered form which is randomly oriented.

The alumina grains used in this study appear to have a spherical shape symmetry (Fig. 5). Since these particles appear to be spherical, calculations were made only for spherical shaped particles and not for the other two shapes. Experimental values were first determined for alumina additions up to 61% by volume as shown in Table III. These dielectric constants and power factors are plotted vs. volume per cent of alumina on Fig. 6. Three of the points at volumes of 10.4, 42, and 50.5%, respectively, which fall on a curve drawn through all

[1] Norton's 38900 (−900 mesh) which is alpha alumina and is 99.86% Al_2O_3.

[2] Linde Air Co. alpha alumina.

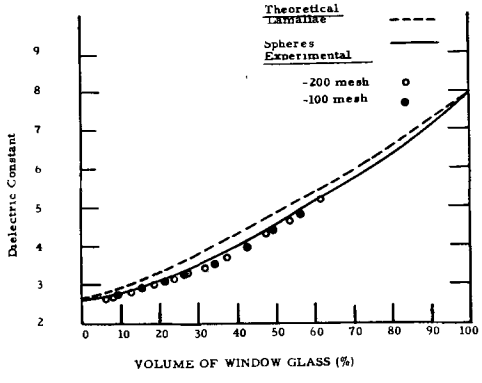

Fig. 4. Volume of window glass in polystyrene vs. dielectric constant and tan δ.

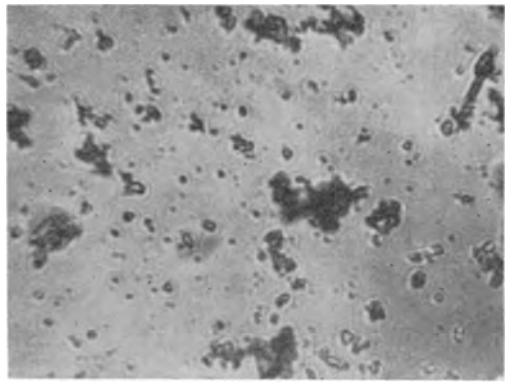

Fig. 5. Photomicrograph of alumina grains. Magnification 1000X.

Table III. Theoretical and experimental values of dielectric constant and power factor for alumina (Norton 38900)-polystyrene mixtures

Experimental					
Alumina volume, %	ϵ	tan δ	Alumina volume, %	ϵ	tan δ
0	2.55	0.00022	0	2.55	0.00022
2.3	2.62	0.00024	10.4*	2.91	0.00027
10.4	2.91	0.00027	25.6	3.55	0.00033
20.9	3.33	0.00031	42.0*	4.36	0.00040
32.0	3.71	0.00036	50.5*	4.82	0.00043
42.0	4.36	0.00040	53.6	5.00	0.00044
50.5	4.82	0.00043	100	8.42	0.00061
61.0	5.29	0.00045			

* Experimental values used to calculate theoretical 100% value.

points, were selected for making calculations of the 100% alumina end point. The calculated values are:

Volume alumina, %	ϵ	tan δ
10.4	8.45	0.00061
42.0	8.42	0.00062
50.5	8.40	0.00060
Avg	8.42	0.00061

With these values other theoretical points were calculated for completing the plot of the theoretical curves on Fig. 6. All theoretical and experimental values are listed in Table III.

As can be seen in Fig. 6 the theoretical curves and symbols for experimental points show good agreement. The dielectric constant and tan δ of these randomly oriented alumina grains approach the values obtained for single crystals by von Hippel.

Quartz-polystyrene mixtures.—Using a very pure grade of low-temperature quartz,[3] which is 99% pure SiO_2, the dielectric constant and tan δ were determined when mixed with polystyrene. Navias (7) determined the average dielectric constant and tan δ of a single crystal of quartz to be

$$\epsilon = 4.44, \tan \delta = 0.00025 \text{ (prism)}$$

$$\epsilon = 4.44, \tan \delta = 0.00024 \text{ (basal)}$$

at 8600 megacycles.

Again, as in the case for alumina, these values are for single crystals and not for fine powders, which

[3] Supplied by Pennsylvania Pulverizing Co.

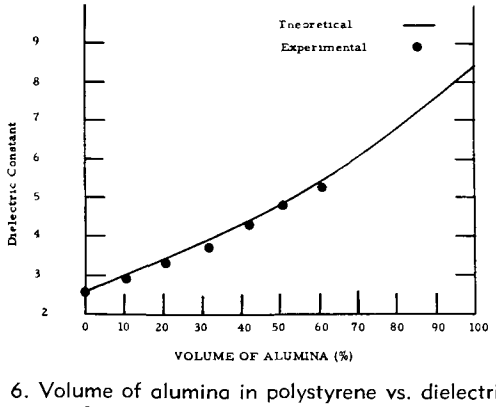

Fig. 6. Volume of alumina in polystyrene vs. dielectric constant and tan δ.

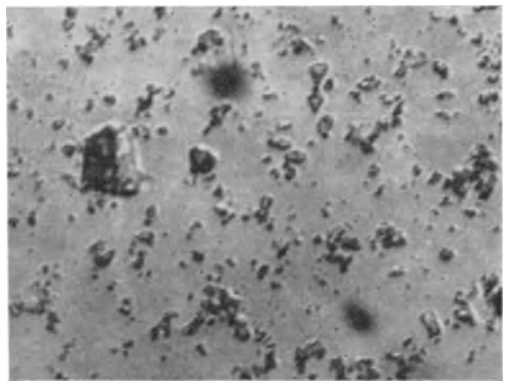

Fig. 7. Photomicrograph of quartz grains. Magnification 1000X.

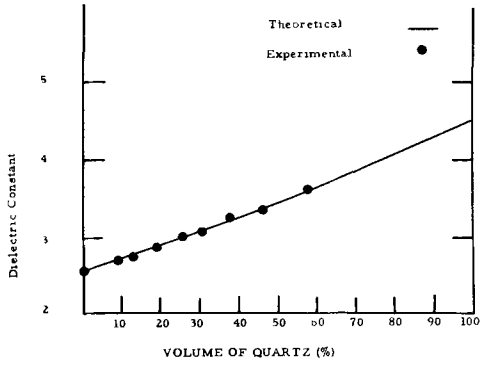

Fig. 8. Volume of quartz in polystyrene vs. dielectric constant and tan δ.

may have similar values regardless of size, but the effects when combined with a continuous phase need to be determined. For the theoretical calculations these quartz grains were considered to be spherical (Fig. 7).

Several experimental values were determined on specimens containing up to 58.3% quartz by volume; these are listed in Table IV. Three sets of values for quartz volumes of 9.6, 25.7, and 58.3% were used for computation to obtain an average dielectric constant of 4.52 and a tan δ of 0.00031 for the quartz grains. Using these values in Niesel's formulas several other theoretical points for quartz volumes up to 100% were calculated and are listed in Table IV. All theo-

Table IV. Theoretical and experimental values of dielectric constant and powder factor for quartz (Pennsylvania Pulverizing Co. —325 mesh)—polystyrene mixtures

Experimental			Theoretical		
Quartz volume, %	ϵ	tan δ	Quartz volume, %	ϵ	tan δ
0	2.55	0.00022	0	2.55	0.00022
9.6	2.71	0.00023	9.6*	2.71	0.00023
13.2	2.76	0.00024	15.7	2.83	0.00024
19.1	2.87	0.00025	21.3	2.90	0.00024
25.7	3.00	0.00025	25.7*	3.01	0.00025
31.0	3.09	0.00026	33.7	3.19	0.00026
38.2	3.26	0.00026	43.2	3.30	0.00026
46.7	3.36	0.00027	52.8	3.49	0.00027
58.3	3.61	0.00028	58.3*	3.61	0.00028
			68.0	3.80	0.00028
			74.6	3.96	0.00029
			86.2	4.20	0.00030
			100	4.52	0.00031

* Experimental values used to calculate theoretical 100% value.

retical and experimental dielectric constant and tan δ values are plotted against volume of quartz on Fig. 8. Both the dielectric constant and tan δ are coincident with the symbols designating the experimental values.

The values of the dielectric properties of these quartz grains are very close to the average values obtained by Navias for single crystals.

Wollastonite-polystyrene mixtures.—Wollastonite has been used successfully as a major ingredient in recently developed low loss insulation. Since no values of the dielectric properties of single crystals of wollastonite are available and synthesis of large wollastonite crystals for measurements would be almost impossible, because pseudo-wollastonite is the stable phase at the high temperature required for synthesis, the values obtained will be considered to approach the average values of a single crystal. The purest commercial grade of wollastonite available[4] was used in this investigation.

The particle shape of C-1 grade wollastonite is shown in Fig. 9. Calculations were made only for long cylinder shape particles in polystyrene because the wollastonite grains are definitely of this shape.

From the several experimental values obtained for the volume of wollastonite in polystyrene listed in Table V three sets of values were selected at 11.0, 24.9, and 62.0% volume for determining the theoretical 100% wollastonite aggregate dielectric properties. The average dielectric constant is 6.15 and the tan δ is 0.00045. Using these values for wollastonite, the theoretical values vs. volume were calculated

[4] Supplied by Godfrey L. Cabot Co.

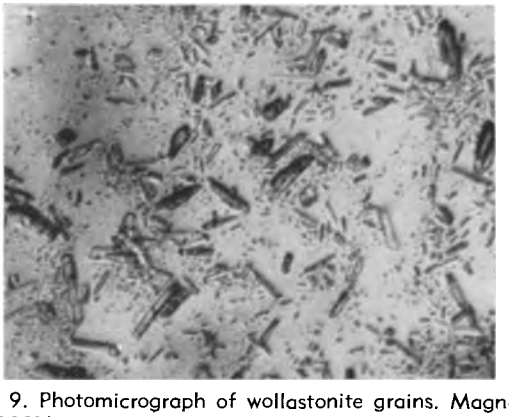

Fig. 9. Photomicrograph of wollastonite grains. Magnification 1000X.

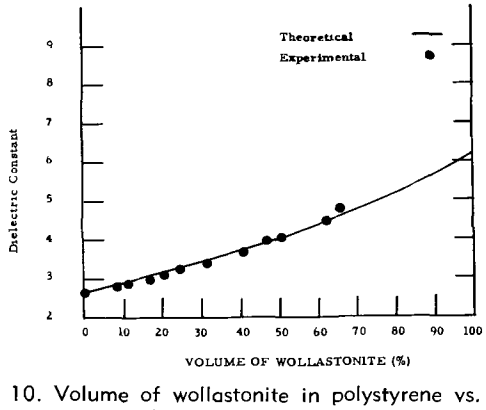

Fig. 10. Volume of wollastonite in polystyrene vs. dielectric constant and tan δ.

Table V. Theoretical and experimental values of dielectric constant and power factor for wollastonite (Godfrey L. Cabot Co. C-1)—polystyrene mixtures

Experimental			Theoretical		
Wollastonite volume, %	ε	tan δ	Wollastonite volume, %	ε	tan δ
0	2.55	0.00022	0	2.55	0.00022
8.5	2.79	0.00024	11.0*	2.84	0.00025
11.0	2.84	0.00025	16.8	3.00	0.00027
16.5	2.98	0.00027	24.9*	3.24	0.00029
20.2	3.08	0.00028	33.0	3.50	0.00031
24.9	3.24	0.00029	47.7	4.00	0.00035
31.7	3.38	0.00030	62.0*	4.50	0.00038
40.2	3.68	0.00033	74.0	5.00	0.00041
46.5	3.99	0.00034	86.8	5.50	0.00043
50.5	4.12	0.00034	100	6.15	0.00045
62.0	4.50	0.00038			
65.8	4.82	0.00038			

* Experimental values used to calculate theoretical 100% value.

and are listed in Table V. These values are plotted on Fig. 10.

Summary

The dielectric properties of solids embedded in a homogeneous medium have been determined with the aid of Niesel's theory which is based on particle shape and volume per cent of the solids. Niesel's theory was first verified by embedding two glasses (one having a high loss and the other a low loss) of 2 specific particle sizes in a homogeneous medium. Since the dielectric properties of both were known (measured) theoretical calculations were made which were almost identical with experimental values on samples with both glasses of 2 different particle sizes. Since such good correlation was observed with these inorganic materials of known dielectric properties the same techniques were used to determine the dielectric properties of alumina, quartz, and wollastonite.

Acknowledgment

The author wishes to acknowledge the U. S. Signal Corps for their sponsorship of this research. He would also like to thank Mr. Sam DiVita, Professor John H. Koenig, Dr. Robert B. Sosman, and Dr. Harold T. Smyth for their assistance and guidance during the course of this research. The author would like to thank Dr. Thomas D. Callinan for his assistance in the preparation of this manuscript.

Manuscript received Sept. 29, 1958. This research was submitted by the author as partial fulfillment for the requirements for his Ph.D. degree at Rutgers University in 1956.

Any discussion of this paper will appear in a Discussion Section to be published in the June 1960 JOURNAL.

REFERENCES

1. W. Niesel, *Ann. Physik*, **6**, [10], 336 (1952).
2. W. Niesel, *ibid.*, **6**, [12], 410 (1953).
3. H. Bruggemann, *ibid.*, **5**, [24], 636 (1935).
4. K. Lichtenecker, *Physik Z.*, **27**, 115 (1926).
5. A. von Hippel, "Dielectric Materials and Applications," pp. 336-362, John Wiley & Sons, New York (1954).
6. *Dielectrics, Trans. Faraday Soc.*, **42A**, 155 (1946).
7. L. Navias, *J. Am. Ceram. Soc.*, **37**, [8], 329 (1954).

Growth of Whiskers by Reduction of Halogenides

H. Wiedersich

Research Laboratories, Westinghouse Electric Corporation, Pittsburgh, Pennsylvania

ABSTRACT

By reduction of $SiCl_4$ with Zn, silicon was produced and similarly by reduction of $FeCl_2$ with H_2, iron. In both cases variations of the growth conditions changed the forms of the crystals from equiaxed into thin, long ones (whiskers). Thermodynamic and kinetic considerations lead to the conclusion that the partial pressure of $SiCl_4$, resp. $FeCl_2$ or HCl determine the growth forms. The hypothesis is suggested that the adsorption of these components makes certain crystallographic plane growth inactive and therefore produces whisker growth.

The phenomenon of filamentary or fibrous growth of metal crystals has been known for more than a hundred years (1). During the past few years these crystals have gained new interest especially due to the discovery that some of them exhibit almost the theoretical strength (2). It became evident that quite a number of different mechanisms are responsible for fibrous growth. Only three basically different categories will be mentioned: (*A*) Growth from the elementary metal: Whiskers grow spontaneous (3) or with applied external pressure (4) from the solid metal or platings. They grow from the root presumably by a dislocation mechanism whereby a stress gradient and/or surface oxidation supplies the necessary energy. (*B*) Growth by reduction of ionic crystals: Compounds inclined to fibrous growth are usually either oxides or sulfides, have a low vapor pressure, and the metal ions have high mobilities in the lattice. The filaments grow from the root. The mechanism suggested by Wagner (5) involves the precipitation of excess metal ions, created by the reduction, at the compound-metal interface. (C) Growth occurs from the vapor phase, either from the elementary vapor (6, 7) or in connection with the reduction of a volatile compound (8-10). The filaments in this group grow from the tip contrary to the two previously mentioned groups.

For growth from the elementary vapor phase, Sears (11) has given a satisfactory theory based on a screw dislocation mechanism. Atoms are adsorbed over the whole surface of the whisker and migrate by surface diffusion to the tip where they attach themselves to a continuous growth step caused by a screw dislocation along the axis of the whisker. Such a whisker should be a perfect crystal apart from one screw dislocation, and its side faces should be atomically smooth.

The present investigation was intended to enlighten the more complex phenomenon of whisker growth by reduction of volatile halides. The following reactions were used:

$$SiCl_4 + 2Zn \rightarrow Si + 2ZnCl_2$$

and

$$FeCl_2 + H_2 \rightarrow Fe + 2HCl$$

which were known to produce whiskers (8-10).

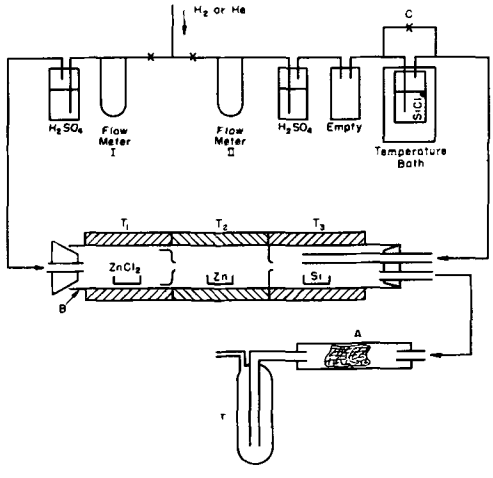

Fig. 1. Experimental setup (schematic)

Experimental

Figure 1 shows schematically the experimental setup for growing silicon crystals. He or H_2, dehumidified by bubbling through concentrated sulfuric acid, was passed through flowmeter I into the left side of the furnace and through flowmeter II and a $SiCl_4$-saturator, which had a bypass C, into the right side of the furnace. The furnace had three separately controlled windings at the positions marked by $ZnCl_2$, Zn, and Si, to provide three different temperature zones for the evaporation of $ZnCl_2$ and Zn, and for the reaction which took place in the zone marked as Si. The interior of the furnace consisted of a Vycor tube with a fixed Vycor baffle between the Zn and Si zones and a removable baffle between the $ZnCl_2$ and Zn zones. There was a short inlet tube for H_2 on the left side and a long one for the H_2-$SiCl_4$ mixture on the right side. The outlet for the gases, on the right side of the tube, leads through chamber A which was filled with glass fibers for the complete removal of $ZnCl_2$, and a trap T immersed in liquid nitrogen to condense the unreacted $SiCl_4$.

The experimental procedure was as follows. The whole tube, B, containing alundum boats filled with $ZnCl_2$ and Zn and an empty boat at the Si location was inserted in the hot furnace to reduce the preheating times and thereby the evaporation of $ZnCl_2$ and Zn before starting the reaction. Then the whole

system was flushed with He before H_2 was introduced. As soon as the furnace was again at the desired temperature the reaction was started by simply closing the bypass C and allowing the $SiCl_4$ vapor to enter the system.

After the run (1 to 4 hr) the bypass C was opened again, the furnace turned off, and the system flushed with He. In order to remove traces of $ZnCl_2$, which precipitated on the grown Si crystals during the cooling period, the boat with the Si crystals was annealed under a vacuum of a few mm Hg at 800°C for an hour. The chemicals used were: Zn (99.99%), $ZnCl_2$(C.P.), and technical $SiCl_4$.

The setup for growing iron crystals was very similar to that described before. The hydrogen was deoxidized by a palladium catalyst and dried by a liquid nitrogen trap. The furnace had a constant temperature throughout. The $SiCl_4$ saturator was omitted, and $FeCl_2 \cdot 4H_2O$ (C.P.) was introduced in place of the $ZnCl_2$ and Zn. In this case the Vycor tube was inserted into the cold furnace, the system connected to the house vacuum, and then heated up to the operating temperature within about 15 min. During this time it was necessary to pass a small flow of hydrogen through the system to prevent condensing of water in the entrance tubes. The water contained in the $FeCl_2$ was practically completely evaporated after the heating-up time, and the flow rates and pressure (1 atm) were adjusted and kept constant throughout the rest of the experiment (6-24 hr).

Results

Silicon.—By controlling the temperature of the temperature bath and the zones T_1 and T_2 of the furnace, the composition of the reacting gases could be controlled. The temperature T_3 of the reaction zone could be fixed independently. The total pressure was practically atmospheric pressure. Table I summarizes the results of the 15 different runs performed. The partial pressures of the different components (indicated by subscripts) in the two entering gases are given by p^*; v_{SiCl_4}, and v_{Zn} are the flow rates of the two different entering gas mixtures. The temperature in the reaction zone is also given. The line before the last states whether whiskers did or did not grow.

All experiments which did not yield whiskers have in common that the initial partial pressure $p^*_{SiCl_4}$ of $SiCl_4$ was comparatively low. The flow rates and the presence or absence of $ZnCl_2$ in the initial mixture do not seem to have an influence. Figure 2 shows silicon whiskers from run XIII. Not all crystals in Fig. 2 can

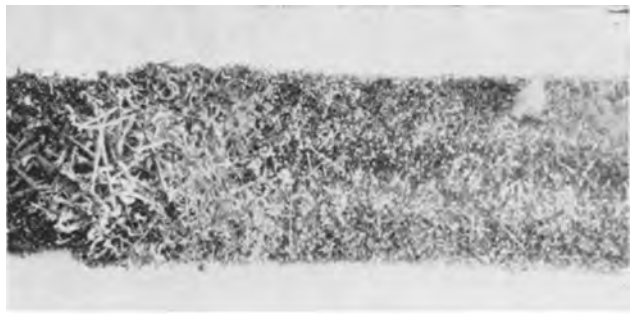

Fig. 2. Silicon whiskers grown in experiment XIII. Magnification 2X before reduction for publication.

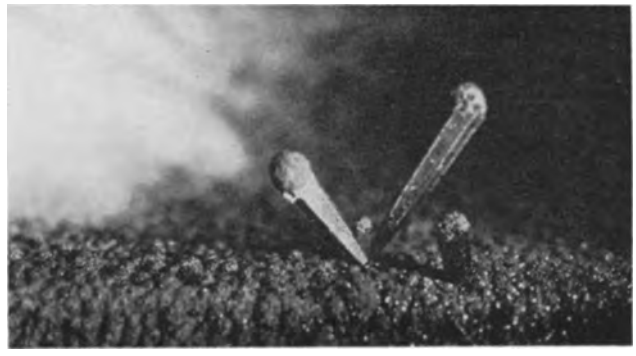

Fig. 3. Silicon crystals grown in experiment X. Magnification 15X before reduction for publication.

be classed as whiskers. Many of those on the left side are not straight and do not have the characteristic smooth surfaces associated with whiskers. However, fine, straight whiskers can be seen. Many of the whiskers, sufficiently large for light microscopic observation, are found to have hexagonal cross section. The diameter of the whiskers ranged from about 5×10^{-5} to 5×10^{-4} cm. Figure 3 shows the types of growth in experiment X. The roughly spherical type of crystals covering the edge of the alundum boat were observed in all experiments which did not yield whiskers but were not observed in those yielding whiskers. Pyramidal crystals were found only in experiment X.

Iron.—Fewer variations in growth conditions were made for iron crystals, since the only aim was to show that the growth mechanism is very much the same as for silicon. Table II summarizes the experiments performed. The symbols used correspond to the ones in Table I. One part of the flow of $H_2(v_1)$ was passed over solid $FeCl_2$ thus converting to the equilibrium mixture of H_2, HCl, and $FeCl_2$ in the presence of solid $FeCl_2$ and Fe. Since the temperature of the furnace was kept constant throughout at $T = 658$°C this mixture had always the composition

Table I. Silicon crystals

Run No.	I	II	III	IV	V, VII, VIII	VI	IX	X	XI, XII	XIII, XIV	XV
$p^*_{SiCl_4}$ [at]	0.077		0.044	0.31	0.31	0.10	0.31	0.31	0.34	0.34	
$v_{SiCl_4} \times 10^6$ [moles/sec]	1.3	2.6	3.9	5.3	5.3	4.1	5.3	5.3	1.1	1.1	0.36
p^*_{Zn} [at]	0.13		0.13	0.13	0.13	0.13	0.29	0.36	0.29	0.29	
$p^*_{ZnCl_2}$ [at]	0.17		0	0	0	0	0	0.41	0	0.28	
$v_{Zn} \times 10^5$ [moles/sec]	1.6	3.2	4.1	4.1	4.1	4.1	5.0	16.1	1.0	1.7	0.55
T, °C	928		928	928	834	834	852	874	830	830	
Whiskers	No		No	Yes	Yes	No	Yes	No	Yes	Yes	
Symbol in Fig. 9	□		■	○	●	△	▲	▽	▼	∅	

Table II. Iron crystals

Run	A	B	C	G	H	I
v_{-1} [moles/sec]	10.6×10^{-5}	21.1×10^{-5}	4.9×10^{-5}	10.6×10^{-5}	10.6×10^{-5}	10.6×10^{-5}
v_2 [moles/sec]	10.8×10^{-5}	10.8×10^{-5}	10.8×10^{-5}	21.5×10^{-5}	3.4×10^{-5}	10.8×10^{-5}
$\frac{v_2}{v_1}$	1.02	0.50	2.18	2.04	0.51	1.02
$p^f_{FeCl_2}$ [at]	2.85×10^{-3}	4.31×10^{-3}	1.39×10^{-3}	1.50×10^{-3}	4.31×10^{-3}	2.85×10^{-3}
p^f_{HCl} [at]	0.082	0.108	0.054	0.053	0.108	0.082
$p^f_{H_2}$ [at]	0.915	0.889	0.944	0.945	0.889	0.915
Whiskers	Some	Many	None	None	Many	Some

Values common to all runs: $p^*_{FeCl_2} = 7.25 \times 10^{-3}$, $p^*_{HCl} = 0.156$, $p^*_{H_2} = 0.837$ at; temperature 658°C; $S_{max} = 1.12$; r_{max} (calc.) = 10^{-14} cm/sec; $r_{exp} = 5 \times 10^{-5}$ cm/sec.

$p^*_{HCl} = 0.156$, $p^*_{H_2} = 0.837$, and $p^*_{FeCl_2} = 7.25 \times 10^{-3}$ at. Equilibrium data of Kangro and Peterson (12) and vapor pressure data of Mayer (13) were used to obtain the values of the partial pressures. Into this mixture pure H_2 was introduced with the flow rate v_2.

A decrease of the ratio v_2/v_1 (this means smaller amounts of H_2 get introduced into a given volume of the equilibrium mixture) causes an increase in the tendency to form whiskers. Figure 4 shows the growth resulting from the runs G, I, and H. Above the centers of the boats an iron wire is suspended from which most but not all of the whiskers grew. Small crystals were found, in all experiments, growing on the boats, the wires, and the surrounding Vycor tubes. They were mostly cubes with indications of (110) and (111) planes as shown in Fig. 5. The whiskers as shown in Fig. 6 and 7 frequently had

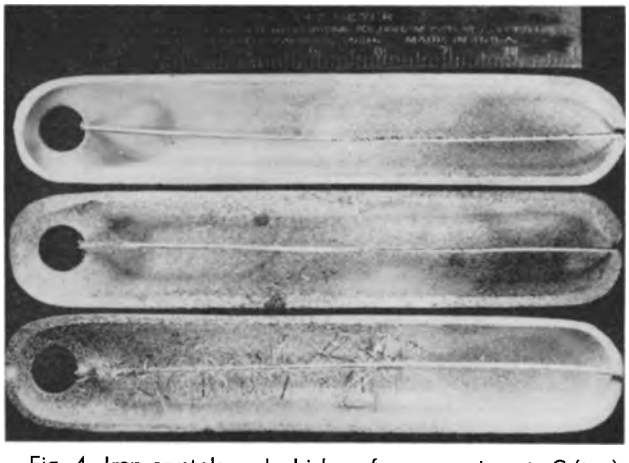

Fig. 4. Iron crystals and whiskers from experiments G (top), I (middle), and H (bottom).

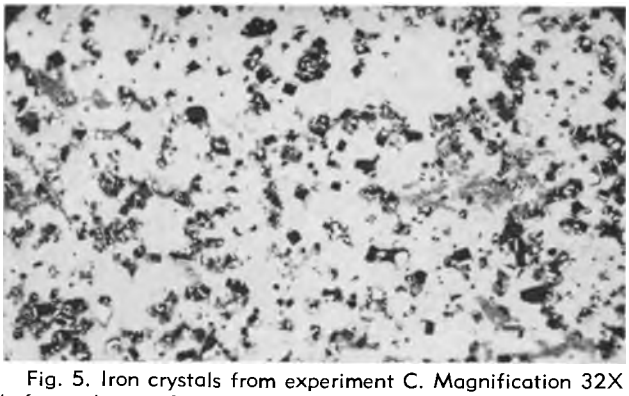

Fig. 5. Iron crystals from experiment C. Magnification 32X before reduction for publication.

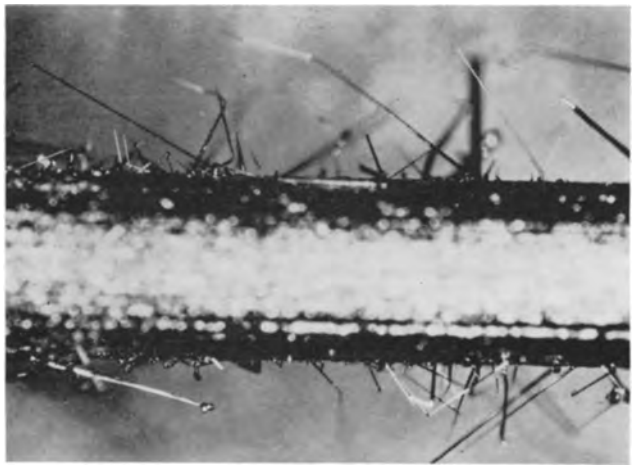

Fig. 6. Iron whiskers from experiment I. Magnification 38X before reduction for publication.

right angle kinks and varied in thickness from about 5×10^{-4} cm to 8×10^{-2} cm. The cross section was usually square or rectangular; a few hexagonal ones were found. Sometimes the cross section decreased toward the tip. Figure 8 shows the tip of a whisker apparently bounded by (100) planes and one (111) plane.

Discussion

There are principally three different processes involved in the growth of the crystals in the present kind of system: (*a*) intermixing of the two incoming

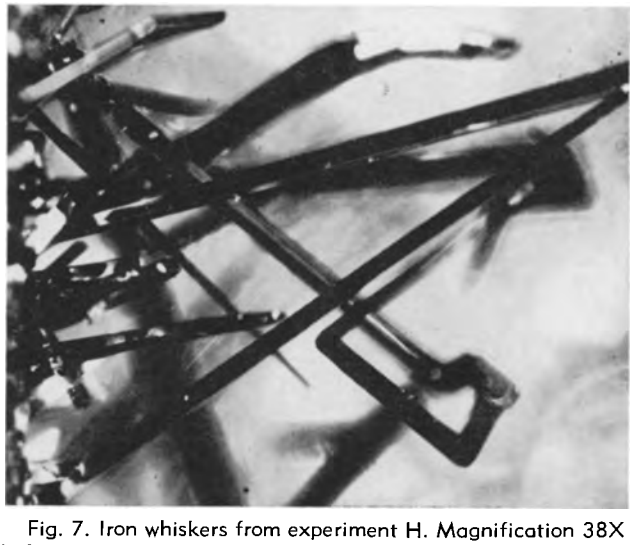

Fig. 7. Iron whiskers from experiment H. Magnification 38X before reduction for publication.

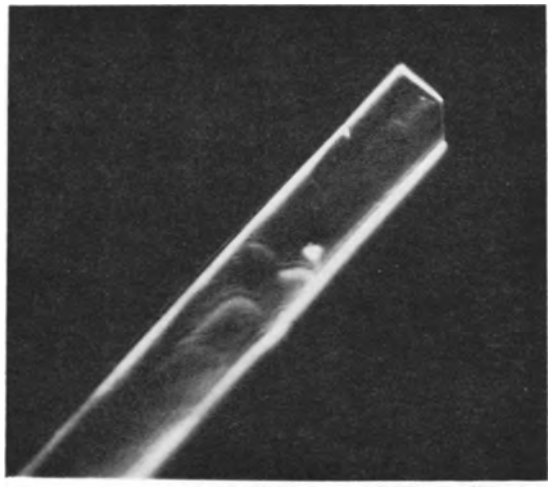

Fig. 8. Tip of an iron whisker. 300X before reduction for publication.

gases by convection and diffusion; (*b*) chemical reactions; and (*c*) precipitation on the growing face of the crystal.

Since no simple way of estimating the intermixing by convection is available, we consider only the process of diffusion. From kinetic gas theory one obtains for the diffusion constant in gases the expression (14)

$$D = \frac{32}{9\pi}\left(\frac{kT}{\pi}\right)^{3/2}\frac{1}{\delta^2 p\sqrt{m}}$$

where k = Boltzmann constant, T = absolute temperature, δ = collision diameter, p = pressure, and m = mass of the molecules. Using reasonable average numbers for these quantities ($T = 1150°K$, $\delta = 3$ Å, $p = 10^0$ dynes/cm^2, $m = 2 \times 10^{-22}$ g); a rough estimate for D is:

$$D = 1.5 \text{ cm}^2/\text{sec}$$

Thus one can expect that for a tube of radius 1 cm complete mixing is achieved in less than 1 sec. This is to be compared with the time the gas mixture remains in the hot part of the reaction zone (≃10 cm), which ranged between 1 and 20 seconds. So the reacting gases are expected to have mixed completely in all experiments, especially since convection is favoring the mixing.

Very little is known about the details of the second of the above mentioned processes, the chemical reaction. We shall asume that it takes place mainly in the gaseous phase and shall try to derive some conclusions about the growth of the crystals which are based on this assumption.

Due to the nature of the experiments it is not possible to derive values of the actual supersaturation S (defined as ratio of the partial pressure in the gas p to the equilibrium pressure p_{equ}) during growth. Yet one can easily obtain an upper limit for S assuming one can apply the ideal gas law.

Silicon.—The main, and probably the exclusive, reaction taking place is

$$SiCl_4 + 2Zn \rightarrow Si + 2ZnCl_2 \qquad [1]$$

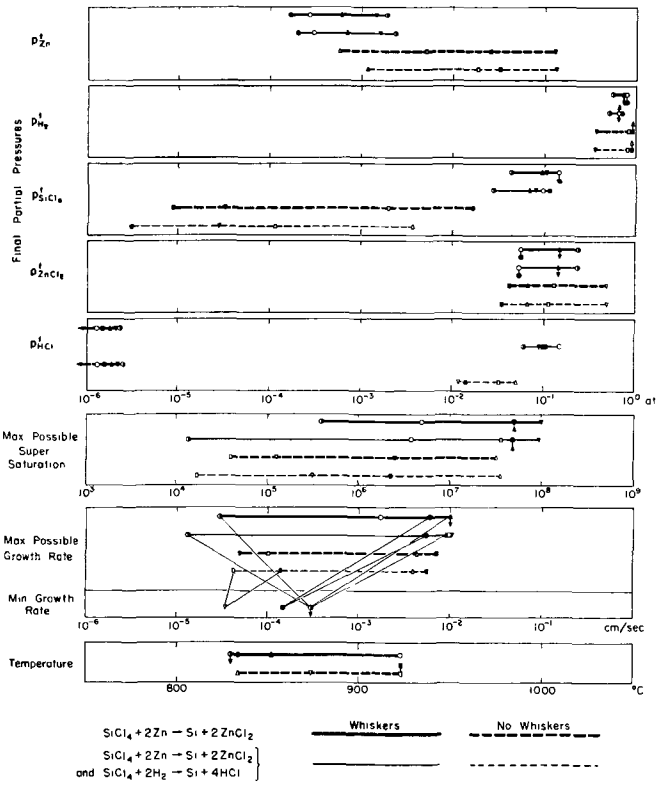

Fig. 9. Range of variables during growth of Si crystals

Preliminary experiments have shown that hydrogen by itself is not able to reduce $SiCl_4$ at the temperatures used even though thermodynamic equilibrium data (15) predict a reaction

$$SiCl_4 + 2H_2 \rightarrow Si + 4HCl \qquad [1a]$$

should yield measurable amounts of Si. In the following it is therefore assumed that only reaction [1] has taken place in the experiments. Yet in Fig. 9 the values obtained by taking in addition [1*a*] into account are added. From Gibbs free energy data given by Kellogg (15) and vapor pressures (14, 16) one obtains the equilibrium constant K^2 [1] in the law of Mass Action for reaction [1]

$$K^2 = \frac{p_{SiCl_4} \times p^2_{Zn}}{p_{Si} \times p^2_{ZnCl_2}} \qquad [2]$$

the p's denote the partial pressures of the chemical Species indicated by subscripts in the gas mixture. A supersaturation $S > 1$ ($S = 1$ means equilibrium between gas and solid phase) is obtained only if the homogeneous reaction in the gas phase is faster than the heterogeneous one of precipitation. The maximum value of S which could be achieved would occur if the first reaction reaches equilibrium before the second has proceeded in any appreciable amount. Taking this into account one derives from [2] in a straight forward way the limits of S:

$$1 \leqq S \leqq \frac{1}{K^2 \times (p_{Si})_{equ}} \frac{p_{SiCl_4} \times p^2_{Zn}}{p^2_{ZnCl_2}} \qquad [3]$$

In case all three components $SiCl_4$, Zn, and $ZnCl_2$ are introduced, one can use on the right side of the Eq. [3] the partial pressures before the reaction since the

[1] The square is used to be in agreement with Kellogg's definitions.

amount reacted in the gas phase to achieve equilibrium is extremely small as long as practically no precipitation has taken place.

In case no $ZnCl_2$ is added, the change in p_{ZnCl_2} due to the reaction has to be taken into account and one obtains:

$$1 \leqq S \leqq \frac{1}{(p_{Si})_{equ}} \sqrt[3]{\frac{p_{SiCl_4} \times p^2_{Zn}}{4K^2}} \qquad [4]$$

Now Eqs. [3] and [4] have to be expressed in terms of the partial pressures p^* in the entering gases. The two gas mixtures characterized by $p^*_{SiCl_4}$ and by p^*_{Zn} and $p^*_{ZnCl_2}$ enter the reaction chamber and mix by convection and interdiffusion. Assuming the diffusion constants are equal (actually they will differ by less than the factor 10) one can obtain the possible upper limit of S in terms of the composition of the entering gases. One volume unit of the final mixture may be composed of "a" units of (Zn, $ZnCl_2$, H_2) and (1 — a) units of ($SiCl_4$, H_2). Then the partial pressures in the final mixture are, neglecting the reaction:

$$p_{SiCl_4} = (1 - a)\, p^*_{SiCl_4}$$

$$p_{Zn} = a\, p^*_{Zn}$$

$$p_{ZnCl_2} = a\, p^*_{ZnCl_2}$$

Inserting these expressions into [3] and [4] and maximizing with respect to "a" gives finally the maximum supersaturations which are possible:

$$S_{max} = \frac{1}{K^2 (p_{Si})_{equ}} \cdot \frac{p^*_{SiCl_4} \times p^{*2}_{Zn}}{p^{*2}_{ZnCl_2}} \qquad [5]$$

$$S_{max} = \frac{0.53}{(p_{Si})_{equ}} \sqrt[3]{\frac{p^*_{SiCl_4} \times p^{*2}_{Zn}}{4K^2}} \qquad [6]$$

The values of S_{max} for the different runs are contained in Fig. 9.

Iron.—Similar considerations lead to

$$S_{max} = \frac{1}{K (p_{Fe})_{equ}} \frac{p^*_{FeCl_2} \times p_t}{p^{*2}_{HCl}} \qquad [7]$$

for the maximum possible supersaturation during the growth of iron crystals. The p^*'s are the partial pressures in the equilibrium mixture entering the reaction chamber, p_t is the partial pressure of the pure H_2 entering (which was always $\simeq$1 at.), and K is defined as

$$K = \frac{p_{FeCl_2} \times p_{H_2}}{p_{Fe} \times p^2_{HCl}} \qquad [8]$$

The value of $K \times (p_{Fe})_{equ}$ was taken from (12, 13). In all experiments S_{max} was equal to 1.12.

One other set of values was obtained by conventional application of the Law of Mass Action. These are the final partial pressures p' in the gas after complete equilibrium with the precipitated phase is achieved. The values of the p''s for the various components are given in Fig. 9 for silicon and in Table II for iron. These values are a good approximation for the partial pressures in contact with the growing crystals so long as the growth proceeds at low supersaturations.

The following should be mentioned in connection with the third of the previously mentioned processes, the precipitation on the growing face of the crystals. From kinetic gas theory one can obtain the number Z of impacts per unit area of a surface per second:

$$Z = \frac{p}{(2\pi\, mkT)^{1/2}} \qquad [9]$$

where p is the partial pressure of the gas. If one assumes every impinging atom sticks at the place it hits, the rate of linear growth would be

$$r = \frac{Zm}{\rho} \qquad (\rho = \text{density}) \qquad [10]$$

The maximum possible growth rate obtained at the maximum supersaturation, r_{max} (calc), is given in Fig. 9 and in Table II and is compared with a rough estimate of the growth rate r_{exp} obtained from some experiments simply by dividing the length of the longest whiskers by the time the experiment lasted. This assumes that the whiskers have grown at a constant rate throughout the experiment and r_{exp} is therefore an estimate of the lower limit of the maximum growth rates in these experiments. Although r_{max} in several cases is larger than r_{exp}, runs XIII and XIV for silicon and the experiments with iron show clearly that one cannot explain the growth of the whiskers simply by the direct attachment of the impinging atoms at the growing face. One has to take into account a surface diffusion process similar to that proposed by Volmer and Estermann (17).

Discussion of Results

A comparison of the experimental range of the values of the variables which could be critical to the form of growth of the Si crystals is made in Fig. 9 for the two observed growth forms. It should be mentioned that the ends of the lines are not necessarily the actual limits for the occurrence of one or the other type of growth; they give only the range which these variables covered in the performed experiments. The final partial pressure of $SiCl_4$ was $\geqq 4.5 \times 10^{-2}$ ($\geqq 2.8 \times 10^{-2}$) at. for all cases where whiskers grew and $\leqq 1.7 \times 10^{-2}$ ($\leqq 3.8 \times 10^{-3}$) for all other experiments. The limits for the case that H_2 should take part in the reaction are added in parenthesis; then the partial pressures of HCl do also not overlap (they have the limits $\geqq 6.4 \times 10^{-2}$, respectively, $\leqq 5.2 \times 10^{-2}$ at.). All the other variables cover, for both growth forms, nearly the same range, or they overlap to a wide extent. This seems to indicate that the silicon tetrachloride (and/or hydrogen chloride) partial pressure has the main influence on the growth form of the Si crystals.

A similar situation was found for the growth of iron crystals. While temperature, maximum supersaturation, and maximum possible growth rate are identical for all experiments, an increase of the final partial pressures of $FeCl_2$ (1.4×10^{-3} to 4.3×10^{-3} at.) and of HCl (0.05 to 0.11 at.) leads from practically no whisker growth to pronounced whisker growth. The small relative change in the final H_2 partial pressure (0.89 to 0.95 at.) would hardly cause the change in growth form. On the basis of the present

experiments it is not possible to decide whether a high $FeCl_2$ partial pressure or a high HCl partial pressure or the combination of both is necessary for whisker growth.

The final partial pressures are a good approximation for the actual partial pressures of these components in contact with the growing crystal as long as the growth proceeds at relatively low supersaturations. The latter is surely true for the growth of iron ($S \leqq 1.12$). It can be shown that the statement that higher $SiCl_4$ partial pressures are necessary to produce whiskers than to produce equiaxed crystals still holds qualitatively, even if silicon grew at high supersaturations.

The findings suggest the following growth mechanism for silicon and iron whiskers: If the density of certain adsorbed species of molecules ($SiCl_4$, $FeCl_2$, or HCl) exceeds a critical value, a further growth of some crystallographic planes gets suppressed. These planes form the side faces of the whisker [(100) for iron, (112) or (110) for silicon]. The growing tip will usually consist of different kinds of planes and hence be able to attach new atom layers. The growth itself may proceed by a screw dislocation mechanism as suggested by Sears (11) for mercury whiskers, yet the possibility that each new atom layer starts with a surface nucleus could not be ruled out by an estimate of the supersaturation necessary for a high enough surface nucleation rate.

Manuscript received June 24, 1957. This paper was prepared for delivery before the Washington Meeting, May 12-16, 1957.

Any discussion of this paper will appear in a Discussion Section to be published in the June 1960 JOURNAL.

REFERENCES

1. G. Bischof, *Ann. d. Phys. (Poggendorf)*, **60**, 285 (1843).
2. C. Herring and J. K. Galt, *Phys. Rev.*, **85**, 1060 (1952).
3. K. G. Compton, A. Mendizza, and S. M. Arnold, *Corrosion*, **7**, 325 (1951).
4. R. M. Fisher, L. S. Darken, and G. K. Carroll, *Acta. Met.*, **2**, 368 (1954).
5. C. Wagner, *Trans. AIME*, **194**, 214 (1952).
6. G. W. Sears, *Acta Met.*, **1**, 457 (1953).
7. R. V. Coleman and G. W. Sears, *ibid.*, **5**, 131 (1957).
8. E. R. Johnson and Y. A. Amick, *J. Appl. Phys.*, **25**, 1204 (1954).
9. A. W. Cochardt and H. Wiedersich, *Naturwiss.*, **42**, 342 (1955).
10. S. S. Brenner, *Acta Met.*, **4**, 62 (1956).
11. G. W. Sears, *ibid.*, **3**, 361 (1955).
12. W. Kangro and E. Peterson, *Z. anorg. Chem.*, **261**, 157 (1950).
13. C. G. Mayer, U.S. Bur. Min., Techn. Paper 360 (1925).
14. S. Dushman, "Scientific Foundations of Vacuum Technic," John Wiley & Sons, Inc., New York (1949).
15. H. H. Kellogg, *Trans. AIME*, **188**, 862 (1950).
16. Landolt-Börnstein, "Physikalisch-Chemische Tabellen," Springer, Berlin (1923-1936).
17. M. Volmer and J. Estermann, *Z. Physik*, **7**, 13 (1921).

Electrolytic Production of Boron

George T. Miller

Hooker Chemical Corporation, Niagara Falls, New York

ABSTRACT

Elemental boron was produced by the fused salt electrolysis of potassium fluoborate. A study was made of anode and cathode materials of construction, particularly the effect of various grades of graphite as anode material. The effect of additives to the electrolyte (including potassium, aluminum, calcium, vanadium, nickel, Inconel, water, and sulfate ion) on boron yield and purity was investigated. A method of passivating elemental boron was developed.

Isotopic boron-10 was produced under contract with the U. S. Atomic Energy Commission by the Hooker Chemical Corporation, using Commission-owned facilities at Model City, New York. The plant was divided into two phases: isotope enrichment and elemental boron production.

The product of the isotope enrichment phase of the plant was a boron trifluoride-dimethyl ether complex. The designed capacity was 40 kg per month of boron-10. Because crystalline elemental boron was required and the isotopically enriched boron in the complex involved considerable cost of manufacture (over $500/lb), an efficient means of reducing the complex to the elemental form was sought. Fused salt electrolysis was investigated and ultimately employed for this purpose.

During the research and development stage and through the process improvement stage, a number of conclusions were reached and also a number of perplexing questions manifested themselves. This paper reviews some of the conclusions and manifested questions believed to be significant.

Basically, the process investigated was the fused salt electrolysis of potassium fluoborate and potassium chloride (1). Based on electrolyte analyses which disclosed the rate of KF production to be approximately 7-8 times that of boron production on a weight basis and on effluent gas analysis which disclosed an F_2 to Cl_2 weight ratio of approximately 3 to 1, the over-all reaction may be expressed by the following equation.

$$4KBF_4 + 2KCl \rightarrow 4B + 6KF + 5F_2 + Cl_2$$

The electrode processes have not been resolved.

The following factors affected cell design. Elemental fluorine and chlorine are produced at ap-

proximately 800°C. The proportion of potassium fluoride in the melt increases during electrolysis. The boron product is removed in solid form because of its high melting point.

General Description (2, 3)

The cell, as finally designed, consisted of a 23 cm ID x 58 cm deep graphite anode crucible protected on the outside by Inconel or nickel. The crucible was heated by a circumferential electrical resistance heater. A Monel cathode was suspended in the potassium chloride, potassium fluoride, potassium fluoborate melt. A reducing atmosphere was maintained above the melt level to avoid corrosion of the cathode. A current of 550 amp, equivalent to approximately 80 amp/dm^2, was used. To provide for periodic cleaning, the whole cell and furnace was mounted on trunnions to permit turning the cell to a horizontal position.

Normal operation of the process involved the addition of 2.5 kg potassium fluoborate to the molten (750°-800°C) electrolyte of 11.5 kg potassium chloride and potassium fluoride. After placement of the cathode, electrolysis at 550 amp and 5-6 v was effected for 3½ hr. The cathode with adherent product was raised above the electrolyte level and precooled to approximately 400°C by an internal flow of air. The cathode was then removed from the cell and quenched in water to effect rapid removal of the product from the cathode. Product was purified by water and acid leaching of the material after crushing operations. Final drying and packaging consummated the operation.

Materials of Construction (2, 4)

Since the purity of the boron would be dependent to a large extent on the materials of construction, this was selected as the subject of initial research work.

Cathode material was selected from a list of nonferrous metals which did not form borides readily. Further, the material had to retain strength at 900°C. Selection narrowed down to copper. To minimize failure due to grain growth, the cathode was cooled internally with nitrogen or carbon dioxide to control its temperature at about 600°-700°C. The copper cathode was satisfactory except for an erratic life of from about 4 to 12 runs, after which it became porous. Subsequently it was found that a Monel cathode developed a protective coating of a very hard and adherent boride. The Monel cathodes did not require cooling and their life was increased to more than 20 runs. Monel was considered a satisfactory material of construction for the cathode.

Since chlorine and fluorine were liberated at about 800°C, graphite was the only suitable material for the anode. The anode material problem soon reduced itself to the selection of the most suitable grade of graphite (Table I).

Note that fine graphite grain size materially improved the quality of boron product as did decreased porosity of the graphite. The comparatively coarse and porous arc furnace electrode graphite spalled badly, rapidly contaminating the electrolyte. For the same grade, graphite yielded a slightly purer product than carbon in addition to the advantages of better electrical conductivity. The ash content of the graphite affected the purity of the boron product adversely. However, the effect due to ash content was secondary to the effect of density and grain size.

Table I. Effect of anode material

Anode material	Ash in %	Apparent density, g/cc	Average % boron in product
Furnace electrode grade graphite	1.9	1.64	69
Extruded high-purity graphite	0.01	1.65	89
Extruded high-density and purity carbon	0.1	1.70	91
Extruded high-density and purity carbon	0.04	1.72	94
Resin impregnated graphite	1.4	1.85	94
Molded — very fine grained graphite	0.1	1.71	97

The highest density, finest grained material obtainable at the time this research was in progress was National Carbon's ATJ grade of graphite. This material yielded the highest purity product of all anode materials tested. However, this graphite was both expensive and not always in stock. When these factors exerted sufficient weight, a compromise was sought. High-purity stock graphite, such as National's AUC or Great Lakes' HPL-9, was machined to shape and then made essentially impervious by the Graph-I-Tite[1] process. This treatment deposits graphite in the voids. The resultant product is most dense near the surface and progressively less dense toward the center. Initial use of the crucible was approximately comparable to National's ATJ grade, but continued operation was not as satisfactory. This was due to corrosion of the surface of the graphite, thus exposing progressively less dense material. The Graph-I-Tite treated material was better than untreated graphite but not as satisfactory as the high density, fine grained graphite, the choice thus becoming one of economics and availability.

Because external electrical heating was employed, a shell was used to protect the Nichrome wire from corrosive salts passing through the anode wall. Initially this shell was made of nickel, which promptly developed cracks. However, after Virgo[2] treatment (fused salt descaling treatment), nickel did not develop cracks and was most satisfactory. Here again the laws of supply and demand were felt and Inconel was substituted. This resulted in contamination of the boron with products of corrosion of the Inconel shell. Most of these contaminations, especially chromium, could be removed by acid leaching. Although more attention had to be paid to the boron purification steps when using Inconel, availability dictated its use. While conducting corrosion tests in molten electrolyte without an applied potential, it was noted that nickel, Inconel, and Hastalloy-B corroded ap-

[1] Graphite Specialties, Niagara Falls, N. Y.

[2] Registered trade name, Hooker Chemical Corp.

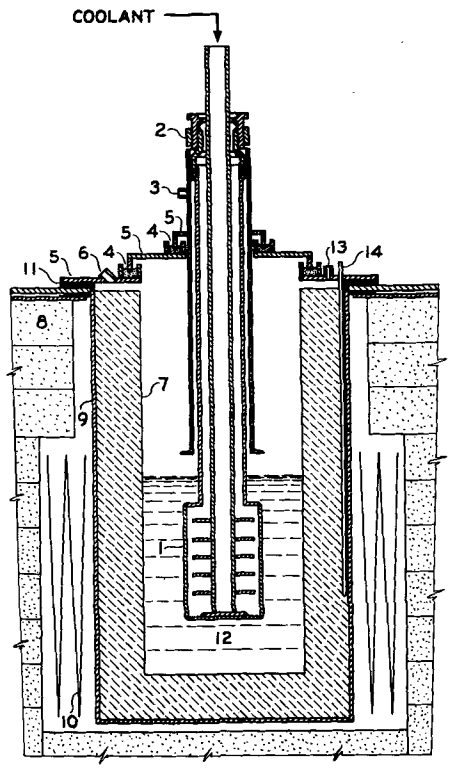

Fig. 1. Electrolytic cell for the production of boron: 1, cathode; 2, quickseal coupling; 3, gas inlet (H_2); 4, salt seal (KCl); 5, cover section; 6, gas outlet; 7, graphite anode; 8, insulating brick; 9, anode shell; 10, heating element; 11, insulating gaskets; 12, cell electrolyte; 13, purge fitting; 14, thermocouple.

preciably only at the liquid-air interface. Under comparable conditions, it was noted that nickel weld rod, ASTM code E3N11, was attacked only slightly.

Cell Design Considerations (2, 3, 4)

Initial laboratory work utilized a hydrogen atmosphere in the cell to minimize oxidation of the graphite. When an inert gas, such as helium, was tried, the copper cathode was rapidly and severely attacked at the electrolyte surface. It soon became evident that chlorine and fluorine liberated in the cell at about 800°C attacked copper vigorously, but HCl and HF did not. The final cathode design is shown in Fig. 1.

Provision was made in this design to concentrate the hydrogen flow at the cathode-electrolyte interface. This proved very effective and permitted satisfactory operation at about 1/3 prior hydrogen flow rates when a nondirected hydrogen flow was used. The cover was sealed by a powdered salt seal ring. This proved an effective and simple technique for control of the cell atmosphere as well as assuring that vent gases would be directed toward the exhaust system. The lack of bolts assured against damage in case of hydrogen failure and a resultant explosion due to air entering the cell. The balance of the structure provided for positioning the cathode above the melt or in the melt, internal cooling, and d-c circuitry. The most desirable temperature control point was found to be in the annular space between the graphite anode and its protective shell.

Table II. Recommended operating details for the electrolytic production of boron

Electrolyte:	70% KCl, 12% KF, 17.8% KBF_4, 0.2% H_2O
Temperature:	750°-800°C
Current:	80 amp/dm²
Voltage:	5-6 v
Power:	55 kwhr/kg
Ampere efficiency:	74%
Cell atmosphere:	H_2 purge directed at electrolyte surface near cathode. Rate: 20 liters/min at 550 amp
Cathode:	Monel
Anode:	High-density, fine grained graphite

Operation (2, 4)

Composition of the electrolyte had a significant effect on yield and/or purity of the boron product (Table II). The first run using a new charge of KCl invariably resulted in poor yield and purity of boron. If the KCl-KF weight ratio was permitted to decrease below approximately 2.5-1, the boron yield decreased. The KCl-KF weight ratio therefore was maintained between 3-1 and 6-1 by partial removal of the electrolyte after a run and replenishing it with KCl.

Purity of the elemental boron was impaired severely when commercial grade KCl was substituted for C.P. grade KCl. A knowledge of the constituent of commercial grade KCl responsible for degrading the boron product was considered desirable in order to effect improvement in purity of normal production. The seemingly obvious approach of determining the foreign material in the product did not yield a solution. Apparently the responsible material entered into side reactions which contaminated the boron product with carbon primarily.

A major difference between technical and C.P. grade KCl is a tenfold difference in the sulfate ion. To ascertain if high sulfate would affect boron purity adversely, 1% of K_2SO_4 in KBF_4 was used. As shown in Table III, it had no apparent adverse effect on the yield or purity of the boron product. The opportunity to explore the effects of bromine was not realized, although the effects of other possible contaminants were investigated.

This work was conducted in three different cells having different grades of graphite. The effect of an additive is thus evidenced by comparing per cent yield and per cent B with product obtained from the same cell without an additive.

Calcium chloride affected the adherence of the product to the electrode causing the deposit to fall out. The purity appeared unaffected. The effect of calcium could be a valuable asset in the design of a continuous cell. Addition of vanadyl sulfate to the electrolyte resulted in decreased purity, apparent decreased yield, and erratic adherence of the product to the cathode.

Aluminum fluoride monohydrate was added in one series of tests and found to yield a dense product of normal yield and purity. Elemental aluminum addition resulted in a slightly higher purity and yield of a very dense product.

The results of drying salts before addition to the melt had given inconclusive results which seemed

Table III. Effect of electrolyte additives

Additive	Concentration in electrolyte		Average % B	Average % yield	Comparison without additive		Cell No.
	g	% by wt			% boron	% yield	
K_2SO_4	25	0.18	95.0	81.5	94.7	75.5	1
$CaCl_2$	100	0.72	93.0	Fell off cathode	92.8	87.8	2
Vanadyl sulfate	66.2	0.47	89.0	48.0	94.7	75.5	1
$AlF_3 \cdot H_2O$	56	0.40	94.7	86.8	95.0	87.0	3
Aluminum	14	0.10	95.5	83.5	94.7	75.5	1
Water	25	0.18	95.8	88.0	94.7	75.5	1
Nickel	38.8	0.28	90.9	73.3	94.7	75.5	1
Inconel	39.2	0.28	88.7	59.2	94.7	75.5	1

to indicate improved yield and purity in the absence of water. It was, therefore, a most surprising result when the addition of 1% water to the KBF_4 before charging resulted in a high density end product of improved yield and purity. This was probably due to a build-up of potassium oxide in the cell which reduced a tendency toward anode effect, a phenomenon otherwise experienced in the cell at approximately 600 amp. This effect of water addition was experienced by Kroll in his work on titanium (5).

Noncathodic nickel or Inconel was severely attacked during electrolysis resulting in decreased cell performance. It clearly confirmed the adverse cell operation that resulted when the graphite anode crucible was porous, cracked, or corroded through.

The first electrolytic run made on a new charge of KCl and KBF_4 resulted in a lower yield and purity of product than the second run. By using a partial charge of KBF_4 and considering the first run as a pre-electrolysis, the yield and purity of subsequent runs could be maintained at acceptable levels. Approximately 30 to 40 runs would be made before total discharge and recharge. The addition of a small quantity of elemental potassium to the pre-electrolysis electrolyte resulted in normal yields and purity of product. Such additions had no discernible effect on subsequent runs. The effect of pre-electrolysis and elemental potassium addition was probably to establish the oxide content referred to under water addition.

Table IV. Effect of drying conditions on purity of boron

Drying conditions	Batch No.	% Boron in dried product: With air purge	With oxygen purge	With argon purge
110°C, 24 hr, no agitation, atmospheric pressure	240	97.0		96.3
	251	97.7		96.8
	213	96.4		94.8
110°C, 1½ hr, agitated, 18 in. vacuum	213	96.4		95.5
100°C, 2.5 hr, agitated, 29 in. vacuum broke vacuum @ 100°C	293	95.3	96.9	
100°C, 2.5 hr, agitated 29 in. vacuum broke vacuum @ 35°C	293	96.2	97.0	
100°C, 24 hr, no agitation, 29 in. vacuum	S-19	94.1	94.4	
100°C, 24 hr, no agitation, atmospheric pressure	S-19	94.0	94.3	

Processing of Cell Product (6)

The product from the electrolytic cell was essentially an agglomerate of boron crystals and electrolyte. To free the boron of soluble impurities, the product was crushed in a rod mill to pass 100 mesh, leached with boiling water and finally boiling HCl. After due washing, rinsing with alcohol, and oven-drying, the product was packaged in polyethylene bags. It was found, when checking analyses for shipping, that the total boron analysis decreased 2-3% after several months' storage. This was traced to boron acting as a getter, adsorbing gases from the air. By drying boron at 100°C in a vacuum oven with an oxygen purge and preferably with agitation for the minimum time needed to effect drying, the boron was passivated. The resultant purity was higher than when dried in an inert atmosphere purged oven (Table IV).

Boron oxide wets elemental boron very well. The observed result of higher boron analysis when using an air or oxygen atmosphere is therefore attributed to a very thin protective film of boron oxide formed on the surface of the boron.

The final product had a size specification of 100% through 100 mesh and 90% through 200 mesh. Approximately 20% passed through 325 mesh and a trace was colloidal. X-ray diffraction demonstrated that the product was mostly crystalline with some scattering due to amorphous material or very fine particle size. When the less than 325 mesh fraction was removed, the remaining material was crystalline.

The purity of the final product was 94-96% boron. Principle impurities were carbon, nickel, chromium, silicon, magnesium, potassium, water, oxygen, and copper.

Acknowledgment

The author wishes to express his appreciation to the U.S. Atomic Energy Commission for permission to deliver this paper, the work discussed having been carried out under USAEC Contract No. AT-(30-1)-1524.

Manuscript received March 23, 1959. This paper was prepared for delivery before the Philadelphia Meeting, May 3-7, 1959.

Any discussion of this paper will appear in a Discussion Section to be published in the June 1960 JOURNAL.

REFERENCES

1. H. S. Cooper (To Walter M. Weil), U.S. Pat. 2,572,248, Oct. 23, 1951.

2. G. T. Miller, U.S.A.E.C. Report NYO-1265, May 31, 1956.
3. G. T. Miller, U.S.A.E.C. Report HEC-79, April 22, 1957.
4. G. T. Miller, U.S.A.E.C. Report HEC-89, May 7, 1958.
5. W. J. Kroll, *This Journal*, **106**, 8C (1959).
6. G. T. Miller, U.S.A.E.C. Report HEC-88, April 18, 1958

Overvoltage and Catalysis

Paul Rüetschi

Research Center, The Electric Storage Battery Company, Yardley, Pennsylvania

ABSTRACT

Analogies between heterogeneous catalysis on solid-gas interfaces and electrochemical kinetics on solid-liquid interfaces are discussed. The surface potential of a solid-gas interface corresponds to the Galvani potential difference of a solid-liquid interface. These potentials depend to a first approximation linearly on the number of adsorbed potential-determining particles. A corresponding linear variation adsorption energy is explained on the basis of electrostatic or induced interaction between adsorbed particles. This behavior is coherent with a logarithmic dependence of the number of adsorbed particles on the bulk concentration or pressure in the liquid or gaseous phase (Temkin isotherm) and a linear dependence of the activation energy of adsorption on the number of adsorbed particles (Becker-Zeldovich equation). It is shown that the Temkin isotherm corresponds to Nernst's formula for electrode potentials and the Becker-Zeldovich equation to Volmer's equation for the rate of electrochemical reactions, and that these equations follow immediately from the theory of charge-transfer adsorption or electrostatic interaction between (activated) potential-determining species or complexes. This treatment leads to a new interpretation of the charge-transfer coefficient and of the influence of the electronic properties of the electrode material and of specifically adsorbed foreign species on hydrogen overvoltage, oxygen overvoltage, and metal deposition overvoltage.

The kinetics and thermodynamics of electrochemical phenomena at solid-liquid interfaces and of catalytic phenomena at solid-gas interfaces are closely related. It is the object of this paper to point out correspondences between the two fields and to derive the fundamental laws of electrochemical thermodynamics and kinetics, in particular the Nernst equation and the Volmer-Tafel equation, from these considerations.

Adsorption and Interaction

The relation between the number of adsorbed species on a solid-gas or solid-liquid interface and bulk concentration (or pressure) of the adsorbable species is described by isotherms. The Langmuir isotherm is derived on the assumption that adsorption occurs at fixed sites and that the energy of adsorption is independent of the number of particles adsorbed. Fixed site adsorption is, however, unlikely for many reactions proceeding on electrodes and catalysts. The energy of adsorption usually decreases with increasing number of adsorbed particles. The Freundlich isotherm is therefore more likely to be obeyed since it allows for the latter effect. However, very few experimental results suggest a logarithmic decrease of the energy of adsorption with increasing number of adsorbed species, as derived from the Freundlich isotherm. Very often the energy of adsorption decreases nearly linearly with the number of adsorbed particles. Such a behavior is accounted for by the Temkin isotherm. The latter can be derived for intermediate ranges of coverage from a fixed site Langmuir-type isotherm by allowing for a linear variation in adsorption energy (1) and, more generally, for mobile adsorption as follows.

Using Boltzmann statistics, the concentration n_i^* (number of particles per cm^3) of species i in the adsorption zone is given by

$$n_i^* = n_i \exp\left[-(w_i^* - w_i)/kT\right] \qquad [1]$$

where n_i is the corresponding concentration in the bulk, and w_i^* and w_i are the energies of a particle i in the adsorption zone and in the bulk, respectively. Here, we assume the entropies of the (mobile) particle in the adsorption zone to be not much different from the entropy of the particle in the bulk. It is now important to consider that, because of the nonideal behavior of the adsorbed particles, n_i^* and w_i^* are connected by an activity function. For such a function of exponential character (activity coefficient varying exponentially with the concentration n_i^* in the adsorption zone), w_i^* becomes a linear function of n_i^* (2) and, neglecting the variation of the term linear in n_i^* compared with the variation of the term exponential in n_i^*, one obtains from [1]

$$n_i^* \cong a \ln n_i - b \qquad [2]$$

where a and b are constants. Equation [2] is the Temkin isotherm.

A linear decrease of adsorption energy with increasing number of adsorbed particles is widely observed. On the other hand, the surface potential solid-gas of the Galvani potential difference elec-

trode-electrolyte depend approximately linearly on the number of adsorbed particles n_i^*. Boudart (3) and Mignolet (4) have discussed the relation between change in surface potential and change in energy of adsorption for solid-gas interfaces. The adsorption energy was expressed in terms of a charge-transfer process, involving the excitation of an electron of the conduction band into a vacant surface orbital provided by the adsorbed species and the surface. The energy difference $w_i^* - w_i$ becomes then a linear function of the surface potential or the Galvani-potential difference

$$\Delta(w_i^* - w_i) = \alpha z_i e_o \Delta(\phi_I - \phi_{II}) \qquad [3]$$

where $\Delta(\phi_I - \phi_{II})$ is the change in surface potential or in Galvani potential difference, $z_i e_o$ the charge of the adsorbed particle i, and α the so-called "structural factor" (5). The latter is a characteristic fraction of the total Galvani potential difference. Experimentally, Boudart finds for adsorption of hydrogen on metals $\alpha \sim \frac{1}{2}$.

It will be shown now that the value of α can be derived from classical electrostatic considerations in a surprisingly simple manner. One can apply the model of a flat-plate electric condenser. For electrochemical interfaces, this model is particularly useful and the capacity of the electric double layer can be determined experimentally. The electrostatic energy content of a charged electric condenser is given by

$$U = \int_o^q V dq = \int_o^V CV dV = \frac{1}{2} CV^2 = \frac{1}{2} qV \qquad [4]$$

where V is the voltage, q the charge, and C the capacity. The energy content per particle with a charge $Z_i e_o$ varies then with the voltage as follows

$$\Delta(Vz_i e_o/q) = \frac{1}{2} z_i e_o \Delta V \qquad [5]$$

This equation is identical to [3] since, by correspondence, $\Delta(Vz_i e_o/q) = \Delta(w_i^* - w_i)$, and $\Delta V = \Delta(\phi_I - \phi_{II})$. This means that α must be equal one-half as long as the adsorption capacity C, due to species i, is independent of voltage or charge. For a variable capacity, Eq. [4] must be integrated, taking into account this dependence which would lead to values of α different from one-half.

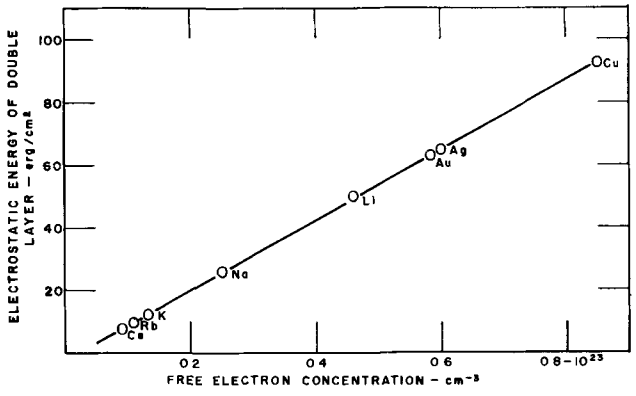

Fig. 1. Electrostatic energy of the double layer on a metal surface against vacuum as a function of free electron concentration.

The interpretation of adsorption on the basis of charge transfer has gained wide acceptance in modern work on catalysis (6, 7). The concepts have been substantiated not only by measurements of changes in work function and contact potential but also by changes in electric resistance (8) and by changes in magnetic behavior (9) of thin solid films during the adsorption process. The surface potential or the Galvani potential difference depends generally on the competitive adsorption of a variety of different species 1, 2, 3—. However, adsorption is generally specific enough to one particular species i such that, at least over limited regions, the variations in adsorption of other species can be neglected. In considering adsorption of the species i on a surface modified by the presence of other species 1, 2, 3— i, the surface potential or the Galvani potential difference, as modified by the presence of these other species, determines according to [3] the adsorption energy of i.

For a bare metal surface against vacuum the electron concentration in the metal is the main parameter characterizing the surface potential barrier. The relation between surface potential and electron concentration becomes evident from Fig. 1. Here, the electrostatic energy of the double layer on a surface against vacuum is plotted against electron concentration.[1] The surface potential (dipole term) is only a relatively small fraction of the total work function (10). Therefore, the work function plays a direct part in the determination of surface potentials and Galvani potential differences only insofar as the dipole term is concerned. However, the dipole term is often a more or less fixed fraction of the total work function.

It has been shown (11) that the energy of cohesion of metals is related to the electron concentration. For alkali metals the energy of sublimation is proportional to $\rho^{2/3}$ where ρ is the free electron concentration. The surface energy is also a function of the electron concentration. According to Breger and Zhukhovitskii (12) the surface energy can be calculated by

$$\sigma = (3\rho/\pi)^{4/3} (\pi h^2/128m) \qquad [6]$$

where h is Planck's constant and m the electronic mass. A recent review on atomic theories of surface energy has been given by Ewald and Juretschke (13). It is known that particularly for solids of the same crystallographic type the surface energy is a fixed fraction of the cohesion energy or heat of sublimation. Since surface potential, cohesion energy, and surface energy are functions of the electron concentration, relations to other quantities depending on electron concentration, e. g., lattice constants, compressibilities, electronic work function (14), are to be expected. For alkali metals one finds, e.g.,

$$L \cong \frac{3}{5} \phi \qquad [7]$$

where L is the sublimation energy and ϕ is the work function (11).

Adsorption energies at zero coverage, calculated on the basis of a charge transfer model, are equally

[1] Data obtained from R. Stratton, *Phil. Mag.*, 44, 1236 (1957).

related to the electronic properties of the metal. For an ionic bond (and electron transfer from the adsorbed particle to the surface) one has used

$$-(w_i^* - w_i) = \phi - I + e_o^2/4K_o r \qquad [8]$$

where I is the ionization energy, r the image force distance (15), and K_o is the Coulomb's Law constant $= 4\pi e_o$ where e_o is 8.854 x 10^{-12} amp sec volt^{-1} m^{-1}. For formation of a negative ion the signs of ϕ and I reverse. Electronic work function and image force distance depend on electron concentration. Adsorption has also been interpreted successfully strictly on the basis of image forces for electrons and protons of adsorbed species for apparent covalent surface bonds (16). The parameter determining the energy of adsorption is then the distance r between the adsorbed particle and the surface mirror plane. For hydrogen atoms on metals, the following equation has been derived

$$-(w_i^* - w_i) = e_o^2/4K_o r)\,(1 + qa_o^2/2r^2) \qquad [9]$$

where a_o is the Bohr radius. The distance r will vary with lattice parameter and electron concentration. For covalent bonds the Pauling formula has been used

$$-(w_i^* - w_i) = \frac{1}{2}D(M-M) + \frac{1}{2}D(A-A) + 23.06(X_M - X_A)^2 \qquad [10]$$

to calculate adsorption energies (17) at zero coverage. Instead of conventional (chemical) electronegativities, the bond moments of the adsorption bonds must be used. The bond moments depend on electron concentration and work function. Stevenson (18) has suggested that $X_M = 0.355\phi$ could be used in Eq. [10], whereas, according to Gordy and Thomas (19), the true (chemical) Pauling electronegativities are related to the work function as follows: $X_M = 0.44\phi - 0.15$. Heats of adsorption can be calculated for any type of bonding from the charge-transfer complex theory as developed by Mulliken (19-21).

As pointed out, Eqs. [8], [9], and [10] refer to the energy of adsorption at zero coverage. The variation of adsorption energy with coverage is due to interaction between adsorbed particles and can, in many cases, be described by Eqs. [3] and [5].

Rate equations describing the kinetics of heterogeneous reactions have hitherto been formulated often without taking into account the activity of intermediate species or activated complexes. However, Horiuti has pointed out that this is incorrect (2). It has been shown above how electrostatic interaction leads to a linear variation of adsorption energy with coverage.

If adsorption energies vary linearly with the number of adsorbed particles, a similar behavior might be expected for activation energies of adsorption (22). Activated complexes formed at interfaces must in fact be considered as adsorbed species. Hereby it is basically immaterial whether the energy level of the species in the adsorbed "activated" state is higher or lower than in the bulk (23). Activation energies of adsorption are (negative) adsorption energies of the activated complex. The activation energy changes then according to [3] linearly with the number of adsorbed "activated" complexes. Therefore the rate of adsorption depends exponentially on the number of adsorbed particles. Such a behavior is indeed widely observed and has been described by Becker (24) and Zeldovich (25) in the form

$$d\theta/dt = a(1-\theta)\exp(-b\theta) \qquad [11]$$

The variation introduced by the factor $1-\theta$ is to be neglected in comparison with the variation introduced by the exponential term. For mobile adsorption $1-\theta$ loses much of its meaning anyway.

We shall now derive the Volmer-Tafel equation for electrochemical reactions from the theory outlined above. The energy difference between a point at the critical distance X^* from the electrode interface, in the region of the activated complex where the electron transfer takes place, is composed of a constant "chemical" term and a variable electric term, respectively. According to [3] and [5] $w_i^* - w_i$ is a linear function of the Galvani potential difference

$$w_i^* - w_i = \alpha Z_i e_o \Delta(\phi_I - \phi_{II}) + \epsilon^* - \epsilon \qquad [12]$$

where $\epsilon^* - \epsilon$ is the "chemical part" of the activation or adsorption energy. The $\Delta(\phi_I - \phi_{II})$ must be measured with reference to the Galvani potential difference $(\phi_I - \phi_{II})_o$, corresponding to the point where n_i^* becomes zero. At this point the charge of the double layer is due to the foreign inert species only. The current of the electrochemical reaction is simply proportional to the number of activated complexes n_i^*, and using [1] and [12] one obtains

$$i = \nu Z_i e_o n_i^* \delta = \nu Z_i e_o \delta n_i \exp[-\alpha Z_i e_o(\phi_I - \phi_{II})/kT] \cdot \exp\{[\alpha Z_i e_o(\phi_I - \phi_{II})_o - (\epsilon^* - \epsilon)]/kT\} \qquad [13]$$

where ν is a frequency factor and δ the thickness of the reaction zone. The exponential dependence of current on voltage described by [18] is the Volmer equation. Over the regions where the charge of the electrode double layer varies predominantly due to accumulation of reacting species and where $(\phi_I - \phi_{II})_o$ remains constant, $(\phi_I - \phi_{II})$ is a linear function of the charge of the double layer condenser due to n_i^*. This illustrates the analogy between the Becker-Zelovich equation [11] and the Volmer equation [13]. Both rate expressions contain a term exponentially dependent on the number of adsorbed particles n_i^*.

The "transfer coefficient" or "structural factor" α can be determined experimentally from the slope of a Tafel-plot. The model from which α has been derived here is different from the one of Volmer (26), who considered the transport of a charge halfway through an electric field without taking into account the interaction with, or energy increase of the other charges of the double layer condenser. The present derivation of the current-voltage relation is more satisfactory.

In order to define an electrochemical equilibrium, at least two (independent) electrode reactions must proceed at an electrode. The two reactions are to produce electrochemical currents in opposite direction at equal rates. If the final products of one reac-

tion are not identical with the initial reactants of the other reaction, a "mixed electrode potential" is established (27). A true equilibrium is observed when the products of the forward reaction are equal to the reactants of the backward reaction. If for the product 1 and the reactant 2 a rate equation of type [13] is valid, one derives for equilibrium ($i_1 = -i_2$) the Nernst equation. Since ($\phi_I - \phi_{II}$) is a linear function of n_i*, the Nernst equation has the form of the Temkin isotherm [2].

The general rate equations for heterogeneous reactions contain the Galvani potential difference $\phi_I - \phi_{II}$. It is pointed out here that they can also be formulated in a similar manner using the experimentally measurable Volta potential differences. Galvani potential differences and surface potentials of condensed phases against vacuum are not measurable but could be calculated in principle on the basis of a sufficiently detailed knowledge of the configuration of the nuclei and electrons in the interior and surfaces of the phases (28, 29). The surface potentials are obtained semi-empirically by comparing the chemical potential μ_i of a charged species i in the bulk of the phase with the experimentally measurable real potential (negative work function) of this species. The surface dipole term is usually a small fraction of the total negative work function and is not appreciably altered by electrostatic surface-charge (10). The surface potential of a condensed phase against vacuum or a gas phase and the Galvani potential difference for this interface have the same physical meaning since a gas phase or vacuum has a zero surface potential. The experimentally measurable Volta potential differences are the result of electrostatic excess charges. They can be induced by changes in surface potentials (30-33).

It has sometimes been assumed that the electrochemical interface is composed of several different double layers. However, it seems that electrostatic interaction (or overlap) is so strong that it is better to consider only one over-all dipole barrier. Also, the Galvani potential difference has been split into a dipole term and an ionic term. However, it is difficult to differentiate these two terms since dipoles can be treated as two separate charges. Furthermore the dipole term should be dependent on the ionic term since dipole adsorption and polarization change with field strength. It is preferred here not to make this differentiation.

Potentials of Zero Charge

Potentials of "zero charge," corresponding to a state of maximum interfacial energy and/or a minimum in electrode double layer capacity (37) are of importance for the interpretation of the term $(\phi_I - \phi_{II})_a$ in the rate equation. The electrode potential at which the charge on the electrode is virtually zero has been determined experimentally for conditions where electron transfer can take place more or less completely (ideal reversible electrode) or is practically impossible (ideal polarized electrode). There is conclusive experimental data that the potential of zero charge is different for the two cases (38).

The electrode potential of ideal polarized electrodes is determined by the externally applied voltage like the tension of a metal-dielectric type condenser. Differences in zero-charge potentials of various electrode metals are to a large extent accounted for by differences in work functions (39, 40) and depend therefore on the particular crystalline face exposed (41). A strict linearity between zero charge potentials and work functions could be expected if adsorption of species at the interface would be purely "electrostatic" in nature (42, 43).

The electrode potential of ideal reversible electrodes is determined thermodynamically by the bulk concentrations of potential-determining species. At the potential of zero charge the concentrations are adjusted such that adsorption of negative and positive ions is balanced to produce a maximum interfacial energy. Some experimental evidence has been accumulated (38, 40) showing that potentials of zero charge of ideal reversible electrodes tend to be independent of the electrode material. This would mean that the electrochemical interface behaves analog to a contact metal-metal. For redox potentials where the emf is (theoretically) independent of the nature of the inert electrode, the state of zero charge would be maintained when the inert electrode is exchanged for some other metal. For a metal electrode in a solution of its own ions, a different ion concentration must be provided for each metal to produce the state of zero charge.

Although the difference in zero charge potentials between polarized and reversible electrodes is due to different adsorption characteristics between "specifically adsorbed" and "inert" species, the physical nature of the state of zero charge is the same in both instances, namely, a state of maximum surface energy. Differences in zero charge potentials are related to differences in the closest approach of the various species to the electrode surface. Potential determining or "specifically adsorbed" ions generally can approach the electrode more closely than "inert" ions. The influence of the nature of the species in the electrolyte and their adsorbability is particularly well demonstrated by the pH-dependence of zero-charge potentials (44). Electrodes which adsorb hydrogen and establish reversible hydrogen potentials show a variation of zero charge potentials with pH. This shows that potential-determining ions are specifically adsorbed.

It should be pointed out that, in analogy to metal-gas interfaces, some sort of strong adsorption forces must always be expected on electrode surfaces. An independence of zero charge potentials of the electrolyte often simply means that the species of the solvent (H^+ ions or OH^- ions or water dipoles) are adsorbed rather than the solute. There is no clear-cut distinction between the two types of zero charge electrodes. The differentiation is in fact one of degree. The process of strong adsorption generally can be considered as an electrode reaction, forming a surface product. The particles taking part in this reaction must be considered as specifically adsorbed, and the electrode potential varies then approximately logarithmically (according to a Temkin isotherm)

with the bulk concentration of these particles (45, 46).

Application to Problems in Electrode Kinetics

In recent discussions on the mechanism of hydrogen evolution a distinction has been made (47-52) between the so-called Volmer-Tafel (discharge-recombination) mechanism

$$2H^+(aq) + 2e^- \rightarrow 2H(ads)$$

$$H(ads) + H(ads) \rightarrow H_2$$

and the so-called Volmer-Horiuti (ion-atom reaction)

$$H^+(aq) + e^- \rightarrow H(ads)$$

$$H(ads) + H^+(aq) + e^- \rightarrow H_2$$

Without specifying the actual configuration and energetic state of the particular activated complex involved and experimental evidence thereof, these formulations are of little help. Any number of other theoretical reaction routes, like for instance (53)

$$2H^+(aq) + 2H(ads) + 2e^- \rightarrow 2H_2$$

$$H_2 \rightarrow 2H(ads)$$

(which does not require the Volmer discharge step) can be postulated. On the basis of the model developed earlier in this paper the differentiation is unnecessary. The electric double layer contains, on the solution side of the interface, protons in various energetic states corresponding to various stages of discharge, which means that their positive charge is shielded to various degrees by overlapping electrons and by negative ions. These adsorbed protons are mobile, like most species in electrochemical double layers. The adsorption follows a Temkin-isotherm and the adsorption (or activation) energy will vary linearly with the number of adsorbed protons. For an approaching proton the surface then looks energetically uniform, and each proton has statistically the same chance to follow the easiest reaction path, which is simply a charging of the double layer condenser. Because of electrostatic interaction there will be no "bare" spots on the surface. The introduction of the degree of coverage θ or the fraction of free surface $1 - \theta$ as a concentration term in the rate equation does not have much meaning. According to the outlined model there is no saturation coverage and the Galvani potential difference keeps increasing more or less linearly (as long as the adsorption capacity is constant) with the number of adsorbed potential-determining ions. This is the reason why the linear relation between logarithm of current and potential prevails to very high rates and why generally no limiting value is reached (54). The metal electrons of the surface are able to be transferred to particles on the solution side over relatively large distances, e.g., during electrochemical reduction of azobenzene on a smooth liquid mercury electrode (55), due to the high electric field at the interface. Recombination of "discharged" protons can occur at various distances as far from the interface as the electron waves can reach (56, 57). The critical distance X^* from the interface where electron transfer takes place may be smaller statistically on one metal than on another. The discharge probability is simply proportional to the number of protons in the double layer.

At this point mention should be made of the stoichiometric numbers ν_i, introduced by Horiuti (58, 59) and commonly defined as number of times the postulated rate-determining step is repeated when the over-all reaction, as represented by the stoichiometric equation, occurs once. In the formulation of Parsons (60) the over-all process requires the formation and decomposition of ν_i activated complexes. Makrides showed from considerations of reaction rates at states close to equilibrium that stoichiometric numbers can take any positive value and are usually equal to the ratio of two small integers (61). If, on the basis of the outlined theory, the activated complex for the hydrogen evolution reaction is assumed to consist of one excited proton only and an electron in the metal, the concentration of activated complexes is immediately given by [1] and [12] and the current-voltage relation by [13]. If the activated complex is considered to consist of two excited protons and two electrons in the metal, one obtains formally the same result since the protons must share the activation energy in equal parts, which can be described alternatively by electrostatic interaction or by the existence of strong resonance between the protons, or by the formation of hydrogen molecule ions. In this manner stoichiometric numbers do not enter the considerations, which is fortunate as can be seen from the recent controversy betwen Horiuti and Bockris (62, 63). From this point of view, the present theory is able to unify various overvoltage theories advanced previously, based on hypothetical existence of atomic hydrogen (64, 65), protons (26), and hydrogen molecule ions (66). The fact that deposition of atomic hydrogen into palladium metal lattice requires a considerable overvoltage would at first suggest that the activated complex consists of single protons rather than molecules. However, on the basis of the present theory strong interaction between adsorbed protons must be present, and with the condenser model all the particles in the interface must actually be included in the activated complex. The interaction between adsorbed particles in the double layer gives also an explanation of the experimentally observed separation factors (67).

It has been shown above that the transfer coefficient α assumes preferably the value $\alpha \cong \frac{1}{2}$. Careful experimental work by Schuldiner (68) on noble metals and noble metal alloys yielded values of α larger than one, or Tafel slopes smaller than 0.058 v at overvoltages below 100 mv. The apparent slope of 0.029 has been explained by the recombination theory of Tafel; however, this explanation is not satisfactory. One must also consider that noble metals have high exchange currents and the backward reaction is of strong influence at low overvoltages. Knorr and co-workers (69) have recently shown that overvoltages below 100 mv on noble metals are

due mainly to diffusion overvoltage of molecular hydrogen.

Bockris and co-workers have developed what they termed "diagnostic criteria" to determine the "rate-controlling step" in hydrogen evolution (70). In deriving their theoretical Tafel slopes they have used $\alpha \cong \frac{1}{2}$ throughout. However, as shown in Eq. [13] α assumes this value only under the special condition that $(\phi_I - \phi_{II})_o$ is constant. The variation in Galvani potential is then due to accumulation of protons only, and the adsorption capacity a constant. The results of the "diagnostic analysis" do not seem to be unambiguous either since on Ni, e.g., electrochemical desorption (71), slow discharge (47) and electrochemical desorption (50) have been named rate determining. The lattice heterogeneity of the electrode surface is not accounted for in the present theory. There are some indications that this heterogeneity is not of primary importance. This is also brought out by MO calculations for adsorption bonds at zero coverage on linear atomic chain models (72).

Some theories have been advanced about electrochemical reduction of water instead of hydrated protons. Usually, it has not been considered that the dissociation equilibrium of water is established with a rate constant of 10^{-5} sec^{-1} and protons are continually produced by this preceding reaction (55, 73). The field effect at the interface can even enhance this reaction rate.

Temkin and Frumkin (74) have suggested that because of the apparent independence of the preexponential factor A in the equation $i = A \exp(-E/RT)$ from the nature of the metal (75), one should expect approximately equal values of the activation energy E for equal current rates i. Generally one should expect a dependence of the frequency factor on the activation energy (76).

In comparing overvoltages of different metals it is necessary to keep the composiiton of the electrolyte the same. This has been taken into account in the work by Rüetschi and Delahay (77) but has not been considered by others (74). Adsorption of anions decreases overvoltage in the sequence $SO_4^{--} < Cl^- < Br^- < I^-$ (43). According to [13] the terms $\epsilon^* - \epsilon$ and $\alpha z_i e_o (\phi_I - \phi_{II})_o$ determine the influence of the electrode material on overvoltage since n_i^* and $\Delta(\phi_I - \phi_{II})$ are constant for a given current. The first term is a measure for the covalent adsorption energy, which can be calculated with [10], omitting electronegativities. Experimental support for a linear relation between covalent adsorption energy and overvoltage has been found (77).

With respect to this conclusion, the present theory gives the same result as considerations of potential energy surfaces according to Horiuti and Polanyi (78). Rüetschi and Delahay used equation [10] without electronegativities to calculate $\epsilon^* - \epsilon$ which is, according to the above argument, the correct procedure. Energetic terms due to polarity of the M-H bond are taken care of by the Galvani potential difference. Bond moments of M-H bonds are anyway quite small. Using bond moments, the last term in Eq. [10] becomes $23.06\ \mu^2$.

Eyring and co-workers (81) have used the value $\mu = 0.46$ for the M-H bond, derived from contact potential measurements by Bosworth (82) for tungsten. However, Mignolet (83) has shown that Bosworth's value is too high. On the basis of Mignolet's results one obtains $\mu = 0.212$ for the tungsten-hydrogen bond and $\mu = 0.183$ for the nickel-hydrogen bond. The moment for the copper-hydrogen bond is even smaller (84). These values show that the contribution of the last term in [10] must be quite small, in the order of one kilocalorie or so. This is the reason why adsorption energies calculated without considering the dipole term agree surprisingly well with experimental results. According to [13] hydrogen overvoltage should generally decrease linearly with covalent adsorption energies $\epsilon^* - \epsilon$ which is in qualitative agreement with Bonhoeffer's experiments (85). The decrease of overvoltage with adsorption energy has recently been derived in a similar manner by Krishtalik (86). It must however be pointed out that exceptions to this rule might be found, since $\epsilon^* - \epsilon$ can contain other terms, e.g., adsorption energies for water.

Various attempts have been made recently to explain an apparent maximum in the curve of overvoltage vs. adsorption energy (50-52), since it had been observed that metals like Mo, Ta, W, Zr, with very high adsorption energies for hydrogen show relatively high values of hydrogen overvoltage. It should be pointed out here that these metals also have an extremely high adsorption energy for other species than hydrogen, e.g., oxygen (and oxygen in water dipoles), and that the experimental hydrogen overvoltage values necessarily refer to somehow oxidized or hydrated surfaces. It is known that cathodic polarization of these metals does not remove the oxide layers completely, which also is related to the fact that these metals cannot be plated out from aqueous solutions. It is pointed out here that hydrogen overvoltage depends not only on the adsorption energy of hydrogen but also on the adsorption characteristics of foreign, inert species, e.g., anions. The influence of the adsorption of foreign inert species which do not take part in the electrode reaction is expressed in [13] by the term $(\phi_I - \phi_{II})_o$. This term is related to the zero charge potentials and electronic work functions.

Since covalent adsorption energies increase according to [10] with the strength of the metallic bond (cohesion energy or sublimation energy) one deduces from [7] a qualitative relation between adsorption energy and electronic work function. On the basis of these considerations Rüetschi and Delahay have explained for the first time the dependence of overvoltage on work function (87), observed empirically by Bockris (47). From equations [6] to [10] it follows that overvoltage can be related to various other electronic properties of the electrode metal, in particular electron concentration, surface energy (88, 89), interatomic distances (90), compressibility (91), cohesion energy (92), melting point (93), and others.

Bockris and Potter (47) had explained the dependence of overvoltage on work function from the fact that the Galvani potential difference of the contact interface between the metal of the reference electrode and the metal of the electrode under investigation changes with the electronic work function of this metal. These authors, and similarly Lorents (91), have not considered that the Galvani potential difference electrode-electrolyte of the reversible hydrogen electrode also changes, in the opposite direction, with the work function of the electrode metal, which becomes apparent from the fact that the (theoretical) hydrogen electrode potential, as measured against a reference electrode, does not depend on the nature of the electrode metal.

Recently, Conway and Bockris (50) have adopted the use of Eqs. [7] and [10] in explaining the relation between electronic work function, adsorption energy, and overvoltage according to Rüetschi and Delahay. However, Conway and Bockris used polar instead of covalent adsorption energies for $\epsilon^* - \epsilon$. Moreover, they used chemical (Pauling) electronegativities for single atoms as given by Gordy and Thomas (94). The present theory shows that the use of large terms of this sort is incorrect, since $\epsilon^* - \epsilon$ is a covalent, chemical term. Any bond moment terms are taken care of energetically by the Galvani potential difference. The present theory is able to account for the influence of specifically adsorbed foreign species, in particular anions, on overvoltage by the term $(\phi_I - \phi_{II})_o$.

Progress in this direction has been made previously by Frumkin, Iofa, Kabanov, and others (54). The considerations have in general been limited to the diffuse part of the double layer (95), whereby the electric work involved, to transfer a hydrogen ion from the bulk to the outer Helmholtz plane, was separated out. However, electrochemical reactions always involve "specific" adsorption and often high electrolyte concentration, and the diffuse part of the double layer (in which the potential depends logarithmically on the charge) is less important than the compact part. The introduction of the adsorption potential of the outer Helmholtz plane also tends to obscure the pH-dependence of overvoltage. According to Frumkin the overvoltage-current relation can be expressed by (54)

$$\eta = a + (2RT/F) \ln i + \psi_I - (RT/F) \ln H^+$$

if one uses $\alpha = \frac{1}{2}$. Since $\psi_I \cong (RT/F) \ln H^+ +$ constant, one would derive a relative independence of η on pH, which is not supported experimentally. Therefore, it is preferred to use the simple condenser model, which accounts for electrostatic interaction of adsorbed protons.

The slow variation of overvoltage with time during prolonged polarization can be explained by changes in the electrode surface area and by dissolution of hydrogen in the metal. With some metals, embrittlement becomes apparent under these conditions. The penetration of atomic hydrogen into the metal lattice changes the electronic configuration, the electron concentration (96), and the covalent adsorption energy. These changes should be taken into account in the interpretation of experiments with bipolar hydrogen diffusion electrodes (97).

It is easy to derive on the basis of the present theory the general laws for build-up and decay of overvoltage. Since at high polarization the electrode potential is simply proportional to the number of adsorbed potential determining species, overvoltage should increase linearly with time under constant current conditions. This is generally observed. On the other hand, overvoltage should decay, after interruption of the polarizing current, logarithmically with time since one derives from [13]

$$n_i^* \sim dn_i^*/dt \sim d(\phi_I - \phi_{II})/dt \sim \exp[-\alpha z_i e_o (\phi_I - \phi_{II})/kT]$$

The slope of the voltage-log time curve must approximate the (negative) Tafel slope of the voltage-log current plot. It is interesting to note that in 1928 Baars formulated the desorption of hydrogen from electrodes analog to the Becker-Zeldovich equation [11]. This early work of Baars (98) is in complete agreement with the present theory.

The presence of the activated adsorbed species at electrode interfaces becomes evident from many experimental observations. The rate of decay and build-up of overvoltage proves the adsorption capacities involved are usually much larger than normally observed for a double layer with inert or nonspecifically adsorbed particles. If the polarizing current is reversed for a very short period of time and the electrode potential forced down rapidly toward the open-circuit potential and then cut off, the overvoltage recovers considerably before the electrode potential falls slowly to the open-circuit value. For very large surface-area porous electrodes, as used in storage batteries, the amount of gas evolved after interruption of current can actually be measured, and it can be shown that the voltage decreases linearly with the amount of desorbed gas (99), which is a direct support for the condenser-theory. The presence of activated species during metal deposition and dissolution has also been demonstrated by Gerischer (100) with potentiostatic techniques. Phenomena relating to adsorption and electrostatic interaction are particularly pronounced in oxygen overvoltage experiments on oxide electrodes (101).

Manuscript received Sept. 17, 1958. This paper was prepared for delivery before the New York Meeting, April 27-May 1, 1958.

Any discussion of this paper will appear in a Discussion Section to be published in the June 1960 JOURNAL.

REFERENCES

1. B. M. W. Trapnell, "Chemisorption," p. 124, Butterworth Scientific Publications, London (1957).
2. J. Horiuti, *J. Research Inst. Catalysis, Hokkaido Univ.*, **4**, 55 (1956).
3. M. Boudart, *J. Am. Chem. Soc.*, **74**, 3556 (1952).
4. J. C. P. Mignolet, *J. Chem Phys.*, **23**, 753 (1955); *Bull. Soc. Chem. Belg.*, **64**, 126 (1955).
5. J. C. P. Mignolet, *Bull. Soc. Roy. Sci. Liege*, **12**, 422 (1954).
6. G. M. Schwab, *Trans. Faraday Soc.*, **42**, 689 (1946).
7. D. A. Dowden, *J. Chem. Soc.*, **1950**, 242.

8. R. Suhrmann and W. M. H. Sachtler, Z. *Naturforschung*, **9a**, 14 (1954).
9. P. W. Selwood, S. Adler, and T. R. Phillips, *J. Am. Chem. Soc.*, **77**, 1462 (1955).
10. F. Seitz, "The Modern Theory of Solids," p. 398, McGraw Hill Book Co., New York and London (1940).
11. H. Frohlich, "Elektronentheorie der Metalle," pp. 256-285, Verlag Julius Springer, Berlin (1936).
12. N. A. Breger and A. A. Zhukhovitskii, *Zhur. Fiz. Khim.*, **20**, 355 (1956).
13. P. P. Ewald and H. Juretschke, "Structure and Properties of Solid Surfaces," p. 82, University of Chicago Press (1953).
14. S. N. Zadumkin, *Zhur. Fiz. Khim.*, **27**, 502 (1953).
15. J. H. de Boer, "Electron Emission and Adsorption Phenomena," p. 81, McMillan Co., New York (1935).
16. F. E. Bellas, Theory of Adsorption of Gases on Metallic Surfaces, Pennsylvania State Univ., Thesis, June 1956.
17. D. D. Eley, *Discussions Faraday Soc.*, **8**, 34 (1950); *J. Phys. Chem.*, **55**, 1016 (1951).
18. D. P. Stevenson, *J. Chem. Phys.*, **23**, 203 (1955).
19. R. S. Mulliken, *J. Am. Chem Soc.*, **74**, 811 (1952).
20. F. A. Matsen, A. C. Makrides, and N. Hackerman, *J. Chem. Phys.*, **22**, 1800 (1954).
21. R. J. Brodd, *J. Phys. Chem.*, **62**, 54 (1958).
22. S. Glasstone, K. J. Laidler, and H. Eyring, "The Theory of Rate Processes," p. 144, McGraw Hill Book Co., New York and London (1941).
23. J. H. de Boer, "Advances in Catalysis, IX," p. 472, Academic Press Inc., New York (1957).
24. J. Becker, *Trans. Am. Electrochem. Soc.*, **55**, 153 (1929).
25. Y. Zeldovich, *Acta. Physicochim. USSR*, **1**, 449 (1934).
26. T. Erdey-Gruz and M. Volmer, *Z. Physik. Chem.*, **150A**, 203 (1930).
27. C. Wagner and W. Traud, *Z. Elektrochem.*, **44**, 391 (1938).
28. P. Rüetschi, *ibid.*, **60**, 29 (1956).
29. P. Rüetschi, *This Journal*, **104**, 176 (1957).
30. E. Lange, *Z. Phys. Chem. N. F.*, **7**, 96 (1956).
31. C. Herring, "The Atomistic Theory of Metallic Surfaces," American Society for Metals, Cleveland (1952).
32. E. Callen, *Am. J. Phys.*, **25**, 138 (1957).
33. P. Klein and E. Lange, *Z. Elektrochem.*, **43**, 570 (1937).
34. K. Huang and G. Wyllie, *Proc. Phys. Soc.*, **62**, 180 (1948).
35. H. Strehlow, *Z. Elektrochem.*, **56**, 119 (1952).
36. N. S. Hush, *Australian J. Sci. Research*, **A1**, 480 (1948).
37. B. W. Erschler, *Erfolge der Chemie, russ.*, **21**, 237 (1952).
38. H. J. Oel and H. Strehlow, *Z. phys. Chem.*, **4**, 89 (1955).
39. A. N. Frumkin, *Colloid Symposium Annual*, **7**, 89 (1930).
40. P. Rüetschi and P. Delahay, *J. Chem. Phys.*, **23**, 697 (1955).
41. B. S. Krasikov and V. V. Syseva, *Dokl. Akad. Nauk. SSSR*, **114**, 826 (1957).
42. A. Frumkin, *J. Chem. Phys.*, **7**, 552 (1939).
43. A. Frumkin, *Z. Elektrochem.*, **59**, 807, 818 (1955).
44. V. L. Kheifets and B. S. Krasikov, *Zhur. Fiz. Khim.*, **31**, 1992 (1957).
45. K. Esin and M. Markov, *Acta Physicochim. USSR*, **10**, 353 (1939).
46. R. Parsons, "Proc. Second International Congress of Surface Activity," Vol. 3, pp. 38, 45, Academic Press Inc., New York (1957).
47. J. O'M. Bockris and E. C. Potter, *This Journal*, **99**, 199 (1952).
48. K. J. Vetter, *Z. Elektrochem.*, **59**, 435 (1955).
49. H. Gerischer and W. Mekl, *ibid.*, **59**, 1049 (1955).
50. B. E. Conway and J. O'M. Bockris, *J. Chem. Phys.*, **26**, 532 (1957).
51. H. Gerischer, *Z. Phys. Chem., N. F.*, **8**, 137 (1956).
52. R. Parsons, *Trans. Faraday Soc.*, **54**, 1053 (1958).
53. J. Horiuti and T. Nakumura, *Z. Phys. Chem. N. F.*, **11**, 358 (1956).
54. A. N. Frumkin, *Trudy Soveschchaniya Elektrokhim, Akad. Nauk SSSR, Otdel Khim. Nauk*, **1950**, 21 (1953).
55. P. Rüetschi, *Z. Physik Chem.*, **5**, 323 (1955).
56. N. I. Kobozev and N. I. Nekrasov, *Z. Elektrochem.*, **36**, 529 (1930).
57. W. Gutt and D. J. G. Ives, *Chem. Soc.*, **1957**, 344
58. J. Horiuti and M. Ikusima, *Proc. Imp. Acad. Tokyo*, **15**, 39 (1939).
59. J. Horiuti, *J. Research Inst. Catalysis, Hokkaido Univ.*, **1**, 8 (1948).
60. R. Parsons, *Trans. Faraday Soc.*, **47**, 1332 (1951).
61. A. C. Makrides, *This Journal*, **104**, 677 (1957).
62. J. Horiuti and H. Sugawara, *J. Research Inst. Catalysis, Hokkaido Univ.*, **4**, 1 (1956).
63. J. O'M. Bockris and E. C. Potter, *ibid.*, **4**, 50 (1956).
64. J. Tafel, *Z. Phys. Chem*, **A50**, 641 (1905).
65. A. Hickling and F. Salt, *Trans. Faraday Soc.*, **38**, 474 (1942).
66. J. Horiuti, T. Keii, and K. Hirota, *J. Research Inst. Catalysis, Hokkaido Univ.*, **2**, 1 (1951).
67. T. Keii and T. Kodera, *ibid.*, **9**, 105 (1958); J. Horiuti and G. Okamoto, *Sci. Papers Inst. Phys. Chem. Res. Tokyo*, **28**, 231 (1936); H. F. Walton and J. H. Wolfenden, *Trans. Faraday Soc.*, **34**, 436 (1938); M. Anbar and H. Taube, *J. Am. Chem. Soc.*, **78**, 3252 (1956).
68. S. Schuldiner and J. P. Hoare, *J. Phys. Chem.*, **61**, 705 (1957); S. Schuldiner, NRL Reports 5091, March 1958, and 5171, July 1958, Naval Research Lab., Washington, D. C.; J. P. Hoare and S. Schuldiner, *J. Phys. Chem.*, **62**, 229 (1958).
69. M. Breiter, H. Kammermaier, and C. A. Knorr, *Z. Elektrochem.*, **60**, 37 (1956).
70. J. O'M. Bockris, "Modern Aspects of Electrochemistry," p. 180, Butterworths Scientific Publications, Ltd. London (1955).
71. J. O'M. Bockris, *Z. Elektrochem.*, **55**, 105 (1951).
72. I. Yasumori, S. Shida, and K. Nakata, *J. Chem. Soc. Japan*, **73**, 892 (1952); K. Fueki, I. Yasumori, and S. Shida, *ibid.*, **76**, 625 (1955).
73. M. Eigen, *Z. Elektrochem.*, **59**, 986 (1955).
74. M. I. Temkin and A. N. Frumkin, *Zhur. Fiz. Khim.*, **30**, 1885 (1956).
75. J. Horiuti, T. Keii, M. Enyo, and M. Fukuda, *J. Research Inst. Catalysis, Hokkaido Univ.*, **5**, 40 (1957).
76. P. Rüetschi, *Z. Phys. Chem.*, **14**, 277 (1958).
77. P. Rüetschi and P. Delahay, *J. Chem. Phys.*, **23**, 195 (1955).
78. J. Horiuti and A. Polanyi, *Acta Physicochim.*, **2**, 505 (1935).
79. D. D. Eley, *Discussions Faraday Soc.*, **8**, 34 (1950); *J. Phys. Chem.*, **55**, 1016 (1951).
80. D. A. Dowden, *Ind. Eng. Chem.*, **44**, 977 (1952).
81. I. Higuchi, T. Ree, and H. Eyring, *J. Am. Chem. Soc.*, **79**, 1330 (1957).
82. R. C. L. Bosworth, *Proc. Cambridge Phil. Soc.*, **33**, 394 (1937).
83. J. C. P Mignolet, *Rec. Trav. Chim.*, **74**, 685 (1955).
84. F. Bloyaert, L. d'Or, and J. Mignolet, *J. Chem. Phys.*, **25**, 53 (1957).
85. K. Bonhoeffer, *Z. Phys. Chem.*, **A113**, 199 (1924).
86. L. I. Krishtalik, *Zhur. Fiz. Khim.*, **31**, 2403 (1957).
87. P. Rüetschi and P. Delahay, *J. Chem. Phys.*, **23**, 1167 (1955).
88. H. Fischer, *Z. Elektrochem.*, **52**, 111 (1948).
89. G. N. Volkov, *Zhur. Fiz. Khim.*, **29**, 390 (1955).
90. H. Leidheiser, *J. Am. Chem. Soc.*, **71**, 3634 (1949); E. N. Khomutov, *Zhur. Fiz. Khim.*, **24**, 1201 (1950); St. G. Christov and N. A. Pangarov. *Z. Elektrochem.*, **61**, 113 (1957).

91. A. K. Lorents, *Zhur. Fiz. Khim.*, **27**, 317 (1953).
92. N. I. Kobozev, *ibid.*, **24**, 113 (1952).
93. N. Chtani, *Sci. Repts. Research Inst., Tohoku Univ.*, **A8**, 399 (1956).
94. W. Gordy and W. Thomas, *J. Chem. Phys.*, **24**, 439 (1956).
95. D. C. Grahame, *Chem. Revs.* **41**, 441 (1947).
96. K. Guminski, *Bull acad. polon. sci.*, **4**, 227 (1956).
97. A. Frumkin, *Z. Physik. Chem.*, **207**, 321 (1957).
98. E. Baars, *Marburger Sitzungsberichte*, **63**, 214 (1928).
99. A. L. Pittman and G. W. Work, NRL Report 5031, Naval Research Lab., Washington, D. C. (1957).
100. H. Gerischer, *Z. Elektrochem.*, **62**, 256 (1958).
101. P. Rüetschi, R. T. Angstadt, and B. D. Cahan, *This Journal*, **106**, 547 (1959).

On the Conductivity of Dispersions

Robert E. De La Rue[1] and Charles W. Tobias

Department of Chemical Engineering, University of California, Berkeley, California

ABSTRACT

Experiments on suspensions of glass beads in electrolytes indicate that Bruggemann's approximation represents the dependence of effective conductance on volume fraction very satisfactorily when the dispersed phase contains a broad range of particle sizes. Data on narrow size ranges fall in between values predicted by the Maxwell and Bruggemann equations. These findings are consistent with the physical assumptions implicit in both theoretical developments.

Presence of gas bubbles or solid dielectrics[2] in electrolytes causes a drop in conductivity relative to the gas- or solid-free condition. Of major interest is the manner in which the effective conductance of the dispersion depends on the volume fraction of the nonconducting phase. In the present study emphasis is placed on particles of spherical shape occupying less than half the volume of the dispersion. Such dispersions occur frequently in industrial electrolytic processes in which gas evolution takes place at one or both electrodes.

According to Maxwell (1) the effective conductivity K_e of random suspensions of spherical particles of uniform diameter and conductivity K_d in a continuous medium of conductivity K_c is related to the volume fraction f of the dispersed phase as follows:

$$\frac{K_e/K_c - 1}{K_e/K_c + 2} = f\frac{K_d/K_c - 1}{K_d/K_c + 2} \qquad [1]$$

If the conductivity of the dispersed phase $K_d = 0$, Eq. [1] simplifies to:

$$\frac{K_e}{K_c} = \frac{1 - f}{1 + \frac{f}{2}} \qquad [2]$$

Rayleigh's treatment (2) of dispersions of spheres of uniform diameter, where the particles occupy cubic lattice positions, leads to an expression identical to Eq. [2] for the case where $K_d = 0$, and $f \to 0$.

In the derivation by Maxwell the assumption has been made that the average distance between the particles of the discontinuous phase is large enough so that the fields around individual particles are undisturbed by the presence of the other particles. This condition is rigorously satisfied only as $f \to 0$. In Fig. 1 we have plotted the potential field around a spherical nonconducting particle, when at large distances from the particle the potential ψ is a linear function of y only, where y is a vector pointing from left to right. In this case

$$\psi = -(S/r^2 - r_o/r)\sin^2\theta \qquad [3]$$

where r_o is the radius of the sphere, $S = -K(dx/dy)_{r\to\infty}$, a constant, r is the distance from the center of the sphere, θ is the angle between r and y, and K is the conductivity of the continuum.

It is apparent from Fig. 1 that the disturbance in the linear field becomes very small at short distances from the sphere. Therefore, in moderately dilute dispersions Maxwell's equation should be an excellent approximation. However, a concentration of $f = 0.25$ already corresponds to an average distance of $0.6\ r_o$ between spheres, and the interaction of fields around the spheres becomes significant. Equation [1] should then no longer represent the relation between volume fraction and conductivity with acceptable accuracy.

Although, according to theory, Eqs. [1] and [2] are subject to limitations, in the past numerous workers have found that experimental data may be

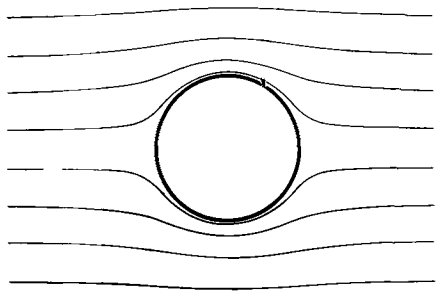

Fig. 1. Potential field around sphere, an insulator, placed in a homogeneous and isotropic conductor. Field is linear at great distances from sphere.

[1] Present address: Stanford Research Institute, Menlo Park, Calif.

[2] Particles exhibiting electronic conduction also may act as insulators, provided the potential gradient in the dispersion is such that the potential difference over a distance corresponding to the largest dimension of the particle in the direction of the field does not exceed the decomposition voltage of the system under consideration.

represented satisfactorily by use of these relations even in moderately concentrated dispersions. Electrical conductivity data obtained on various concentrations of cream in milk were found by Fricke (3) to fit Eq. [2] within experimental error. Eucken (4) reported results of measurements involving the systems water-benzene and water-phenol with KCl and KI, respectively, as solutes. Over the entire range of volume concentrations ($0<f<1$) agreement with Eq. [1] was reported. In a recent review on non-Newtonian fluids Metzner (5) refers to data by Orr and Dalla Valle (6) who measured thermal conductivities[3] of metal shot dispersed in 2% agar gel. Agreement of the experimental data with Eq. [1] within 3% over a large range of volume concentration was again claimed.

Not all investigators found the agreement between the Maxwell-Rayleigh relations and their experimental data satisfactory. Slawinski (7, 8) conducted experimental investigations using enameled metal spheres of approximately 0.5 cm diameter in KCl solutions, in the range of $0.35 < f < 0.6$. His data fitted within 0.4% a curve corresponding to substantially lower effective conductances than would have been predictable by Eq. [2]. This curve corresponded to a relation developed from a physical model in which Slawinski evaluated the integral mean lengths and mean cross sections between spheres arranged in several different lattice orders

$$K_e/K_c=\{1+(f/p)[(1+0.3219p)^2/(1-p)-1]\}^1 \quad [4]$$

where $p = n \cdot f^{2/3}$. Value of parameter n depends on the volume fraction range:

for $0.15 > f$	$n = 0.806$
for $0.15 < f < 0.6$	$n = 0.806 + 0.1333\,f$
for $0.6 < f$	$n = 0.9046$

Data presented by Slawinski for moderate and low volume concentration in random distributions were in far less satisfactory agreement with Eq. [4] than at high concentrations. Unfortunately Slawinski's treatment does not take into account the fundamental principles of the theory of potential, according to which the distribution of potential throughout the conducting medium satisfies the Laplace equation. His equation also contains an adjustable parameter in addition to the volume fraction of the dispersed phase.

More recently Mashovets (9) reported measurements of conductivities of dispersions of glass and hard rubber spheres in $CuSO_4$ solutions where the spheres were fixed in lattice positions. The effective conductances measured were lower than values predictable from Maxwell's equation [2], and by least squares treatment of the data following equation was obtained: $K_e/K_c = 1 - 1.78f + f^2$. Reliability of this equation may be questioned on grounds of lack of adequate description of experiments and failure to indicate reproducibility and confidence limits. It is also doubtful whether the few experimental points taken form an adequate basis for proposal of an empirical equation. Pearce (10) recently presented experimental permittivity values obtained on oil-water emulsions. The data was in good agreement with values calculated by Bruggemann's approximation (11) (see Eq. [6] below). Conductivity measurements on two-dimensional array of metal and bakelite hemispheres submerged in tapwater yielded different results depending on whether the hemispheres occupied lattice positions, or were arranged in a random manner. In the former case Pearce found agreement with Eq. [1], while for random arrangement the Bruggemann approximation seemed to have given a better fit. The two-dimensional model of random arrangement by Pearce, however, does not represent the three-dimensional case accurately enough to base meaningful conclusions on it. Further, Pearce's data on random arrangement of spheres was taken only in the low volume concentration region (up to $f = 0.12$) where, judging from the few experimental points presented in his graphs, the experimental errors may have been comparable to the magnitudes of the possible deviations from Maxwell's or Bruggemann's equations. A comparison of data by the various investigators reveals that the discrepancy between experimental findings is by no means negligible, reaching approximately 10% near $f = 0.5$. Such a large difference in conductivity ratio values cannot be justified on the basis of inherent limitations in the type of measurement. Much rather, one is led to believe that some of the investigators may have taken less caution in defining their systems and in the execution of their experiments than would have been necessary to establish firmly the functional relationship between K_e/K_c and f.

The present work was undertaken with the aim of obtaining data with sufficient confidence in its accuracy to permit the evaluation of the limitations of Maxwell's equation [2] in the range $0 < f < 0.4$. Further, by using a comparatively large range of sizes both in separate fractions and also mixed together within one suspension, it was hoped that differences in conductance behavior between homogeneous and mixed-size dispersions may be detected.

Experimental

Glass beads of excellent shape characteristics[4] were used in the experimental series on spherical nonconducting particles. The beads were separated into size fractions by air elutriation. The diameter range selected for study is given in Table I. Within

[3] Thermal and electrical conductivity of dispersions depend on volume fraction of dispersed phase in an identical manner.

[4] Courtesy Central Research Department of the Minnesota Mining and Manufacturing Co.

Table I

Fraction	Size
	μ
I	49-77
II	107-175
III	175-210
IV	590-840
V*	3100-3400
VI*	6100-6400

VII—Equal volumes of I and VI mixed.
VIII—Equal volumes of fractions I-VI mixed.

* Braun-Knecht-Heimann Co., Catalog No. 13782.

each size range (I-VI) approximately 75% of the beads were within a range of 10% of the mean diameter (Fig. 2a).

The sands[5] were wet-sieved after washing with water and the electrolyte, and only the fraction passing through sieve number 80 and remaining on 100 was used (approximate size range: 0.15-0.175 mm) (Fig. 2b and 2c).

Polystyrene cylinders[6] were cut from fibers of uniform diameter (0.3 mm) to a length of 3 ± 0.3 mm (Fig. 2d).

The specific gravity of the electrolyte was selected to be just slightly below that of the dispersed phase to prevent fast settling. Of the available alternatives, a near saturated solution of $ZnBr_2$ was selected as the continuous phase for the measurements with glass beads and sand. The saturated solution at 20°C has a specific gravity of 2.725 and a conductivity of 0.066 ohm^{-1} cm^{-1}. The specific gravities of the glass beads and of the sand were approximately 2.50 and 2.60, respectively. The density of each size fraction was determined to within unit accuracy in the third decimal figure. For polystyrene cylinders 0.1*N* KCl solution was chosen as the continuous phase.

Conductivity cell.—Following preliminary work with conventional type cells, the main series of measurements were executed with a cylindrical cell (Fig. 3) consisting of two sections, each 2¾-in. long, which could be interconnected by removal of a center electrode. A ¾-in. hole was drilled into Lucite blocks, providing the cylinder sections. Top and bottom electrodes were platinum, surface-welded onto ¼ in. copper plates. Center electrode consisted of a 25 mil platinum plate attached at two sides to ⅛ in. copper bars which served as guides. Sections of the cell were assembled using 1/16 in. Teflon gaskets, and the assembly was held together by bronze studs.

The conventional-type Wheatstone bridge circuit employed in the measurements is illustrated in Fig. 4.

Procedure.—Before each series of measurements the cell was filled with the electrolyte and the cell constants for each cylindrical section determined. Following this, the desired volume fraction of solid phase was weighed on an analytical balance and poured into the cell. The resulting mixture then was stirred with a glass rod for approximately 3 min to remove entrained air. The top electrode was closed and the cell was shaken to insure uniform electrolyte composition and temperature. When the dispersed phase settled below the level of the center electrode, the electrode was closed. Next the resistance of the upper compartment (containing no solids) was

[5] Death Valley Sand or Merck "Sea Sand."

[6] Dow Chemical Company.

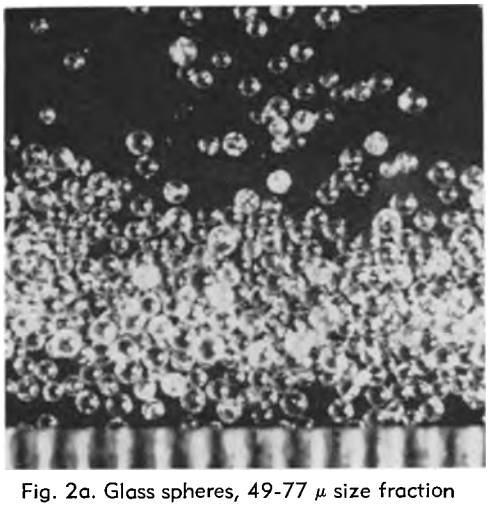

Fig. 2a. Glass spheres, 49-77 μ size fraction

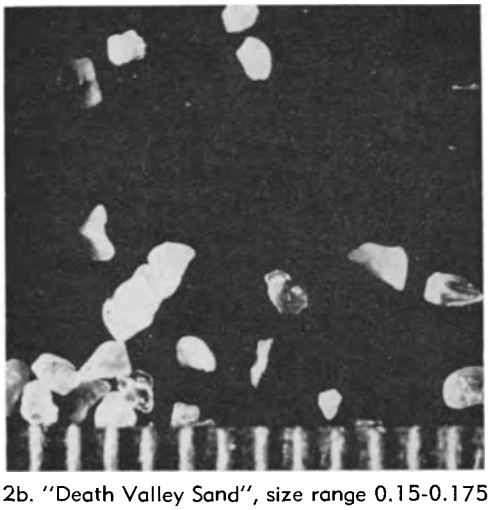

Fig. 2b. "Death Valley Sand", size range 0.15-0.175 mm

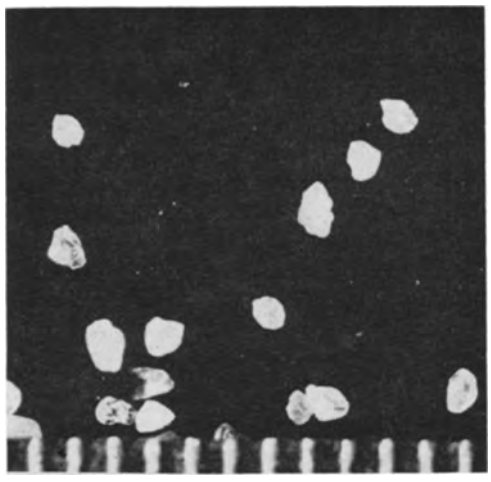

Fig. 2c. " Sea Sand," size range 0.15-0.175 mm

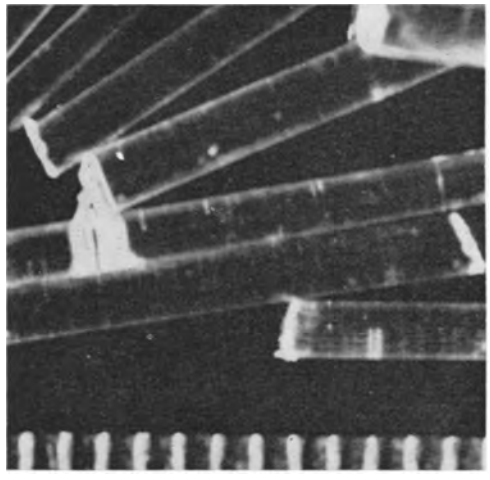

Fig. 2d. Polystyrene cylinders, diameter 0.3 mm, length 3 mm.

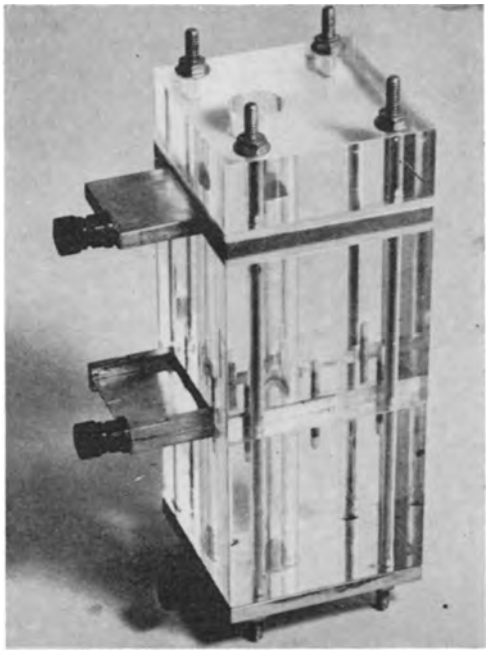

Fig. 3. Assembled conductivity cell, with top and center electrodes in "open" position.

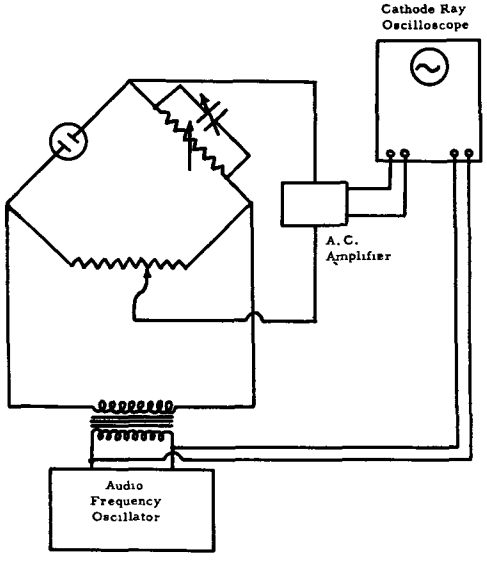

Fig. 4. Schematic diagram of the Wheatstone bridge circuit

measured. The resistance of the lower compartment (containing the known volume fraction of solids) was obtained while the cell was shaken by hand with a rotating, up, down, and sideward motion until a "steady-state" image was obtained on the screen of the cathode-ray oscilloscope. With continued shaking the actual value of the resistance of the dispersions was obtained by adjustment of the slide wire until the image, which was an ellipsoid, would become a line in the vertical gain, the point at which the Wheatstone bridge circuit was balanced.

After the first pair of measurements were completed, to check whether thermal equilibrium existed between the two compartments, the central electrode was opened, and the contents of the compartments thoroughly mixed. Again the solids were allowed to settle into the lower compartment and, after closing the central electrode, conductivity measurement was repeated as described above. In most cases the conductivity ratios obtained by the second pair of measurements were in agreement with those by the first within ±0.2%. If not, the contents of the compartments were again mixed, etc., until the difference between conductivity ratios between two successive measurements was within the limits given above.

Table II. Per cent difference between minimum and maximum values of K_e/K_c measured in three series of runs

f	%
0.1	0.19
0.2	0.17
0.3	1.2
0.4	1.75

To detect any systematic errors such as might be due to weighing and handling of solids, possible imperfect elimination of entrained air, etc., complete series of runs involving measurements at several volume fractions were repeated two or three times. As illustrated in Table II, per cent differences between minimum and maximum values obtained for K_e/K_c at the same volume fractions were only approximately 0.2% at up to f values of 0.2; however at $f = 0.4$ reproducibility was less satisfactory (1.75%).

Data

Figures 5-8 serve to illustrate the results obtained in the 20 series of measurements, each series consisting of four to eight individual measurements of conductivities at approximately evenly spaced volume fractions of solids. On most single- and mixed-size fractions enumerated in Table I and with each sand species and the polystyrene cylinders duplicate measurements were taken. Graphical representation of the data reveals that all the experimental points fall below the line corresponding to Maxwell's equation (Eq. [2]), and this deviation increases with

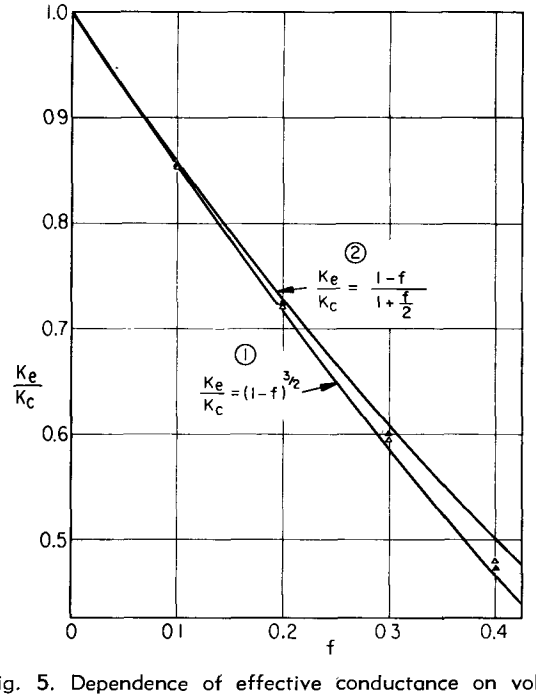

Fig. 5. Dependence of effective conductance on volume fraction of dispersed phase. Size range of spheres: 175-210 μ. ▲, Series I; △, Series II.

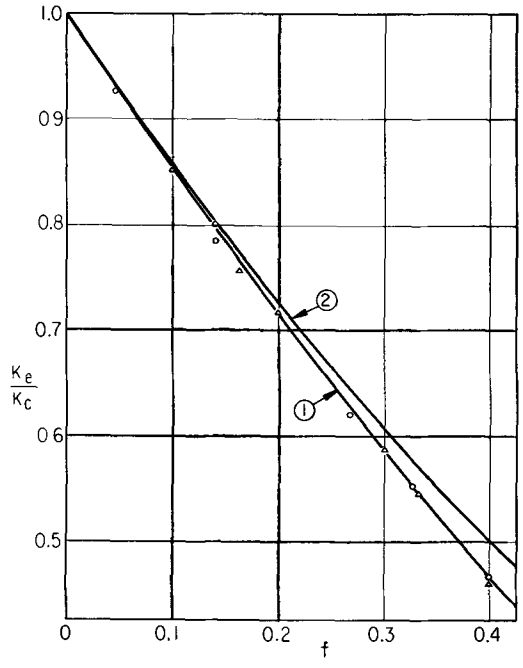

Fig. 6. Dependence of effective conductance on volume fraction of dispersed phase consisting of spherical particles. △, equal weight fractions of size ranges I-VI; ○, equal weight fractions of size ranges I-VI. Curves 1 and 2 as on Fig. 5.

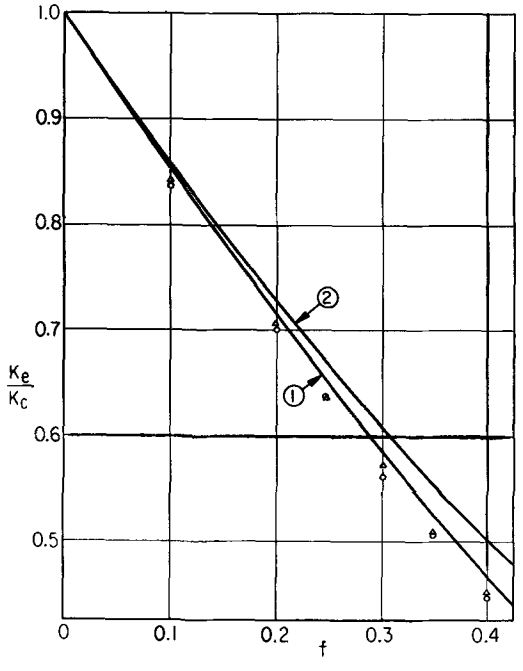

Fig. 7. Dependence of effective conductance on volume fraction of suspended sand. △, "Sea Sand"; ○, "Death Valley Sand." Curves 1 and 2 as on Fig. 5.

volume fraction of the dispersed phase. Further, values of the conductivity ratio on mixed size ranges are slightly but distinctly below the ones obtained on single size ranges. Data on both the polystyrene cylinders and on the two kinds of sands show more substantial differences from Eq. [2] than any on spherical particles.

Best Curves Representing Data

All series were subjected to least squares treatment, using the equation

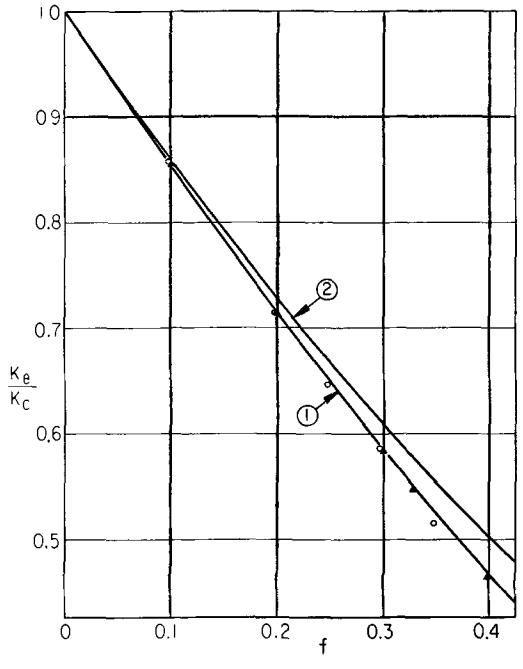

Fig. 8. Dependence of effective conductance on volume fraction of suspended polystyrene cylinders. △, Series I; ○, Series II. Curves 1 and 2 as on Fig. 5.

$$K_e/K_c = X(1-f)^Y \qquad [5]$$

Table III summarizes the least squares values of X and Y. If we assign a value $X' = 1.00$ (which should be satisfied for obvious physical reasons), the modified exponent Y' is obtained. The table also includes the standard deviation S and S'. All coefficients of correlation were greater than 0.998. S and S' are measures of the scatter of data about the curves defined by X, Y, or Y' in units of the ordinate. Twice the standard deviation gives approximately the 95% confidence limits on either side of the curve.

Discussion

While differences between the set of data on single-size fractions and on mixed sizes may be regarded as too small to draw sharp conclusions, the least squares equation representing data on mixed sizes is for all practical purposes identical to the equation proposed on theoretical grounds by Bruggemann (11) in which $Y' = 1.5$ (see Eq. [6] below). That such an agreement for a large diameter range of spherical particles in the dispersed phase confirms reasonable expectations follows from the physical approximations implicit in Bruggemann's mathe-

Table III. Least squares curves representing conductance data in terms of Eq. [5]. X' fixed at 1.00

Dispersed phase	X	Y	S	Y'	S'
I	0.97	1.35	0.010	1.43	0.015
II	0.988	1.47	0.015	1.52	0.014
III	0.998	1.44	0.008	1.45	0.007
IV	0.995	1.45	0.001	1.47	0.002
V	0.988	1.45	0.007	1.48	0.009
VI	0.991	1.48	0.008	1.50	0.008
VII, VIII	0.997	1.50	0.007	1.51	0.007
Death Valley Sand	0.992	1.56	0.005	1.58	0.006
Sea Sand	1.003	1.55	0.010	1.55	0.010
Cylinders	0.994	1.51	0.010	1.53	0.010

matical treatment. If one adds a relatively large spherical particle to a dispersion containing much smaller particles, the disturbance of the field around the large sphere due to the small spheres may be considered negligible. On this basis, the effective conductance of such a system may be evaluated by considering the surroundings of the large sphere as a continuum having an effective conductance K'_e, and apply the Maxwell equation, since the system is "dilute" as far as the large sphere is concerned. The change in K'_e with the volume fraction of the dispersed phase may then be expressed in differential form:

$$dK'_e/df = [-3K'_e/(1-f)][(K'_e-K_d)/(2K'_e+K_d)]$$

Integrating with the boundary conditions $K'_e/K_c = 1$ as $f = 0$ and at the upper limit $K'_e = K_e$, one obtains

$$\frac{K_e/K_c - K_d/K_c}{(K_e/K_c)^{1/3}(1-K_d/K_c)} = 1-f$$

for the case when both phases are conductors, and the Bruggemann equation

$$K_e/K_c = (1-f)^{3/2} \qquad [6]$$

when the dispersed phase is an insulator, or $K_d = 0$. For single sizes or narrow size fractions, the physical conditions necessary for justifying the Bruggemann approximation are not satisfied. Conductivities of such dispersions when $K_d = 0$ must be lower than the value obtained from Maxwell's equation and higher than predicted by Bruggemann's approximation. The series of measurements represented in Table III conform to this qualitatively correct argument.

Size Effect

With the exception of the one series on the 105-177 μ range, where the scatter of data was unusually large, the exponent Y' shows a slight, gradual increase with particle size. There is no reason why particle size should have any effect on the effective conductance, unless the diameter of the spheres becomes comparable to the dimensions of the vessel containing the dispersion. There is no doubt that the larger exponents found for the size fractions V and VI, respectively, reflect wall effects.

It should be noted that while Maxwell's equation is valid strictly only when the dispersed phase consists of spheres of a single diameter, and of course at that only at very low volume concentrations, Eq. [6], both on the basis of the present experimental results and because of the conditions assumed in the derivation by Bruggemann (11), applies best for random distribution of sizes.

Although the present study was not designed to clarify what effects shapes other than spherical would have on the conductivity ratio K_e/K_c, four series of measurements with sand and two with polystyrene cylinders were also performed. The results as presented in Fig. 7 and 8 and in Table III indicate that Eq. [6] again represents the data fairly well. This agreement however should be viewed with caution. The sand particles used were of "smoothed off" polyhedrical shape for which the approximations incorporated in Eq. [6] may be considered to apply rather well. The "Death Valley Sand" gave slightly lower conductivity ratios than the "Sea Sand" reflecting the more elongated shape of the former (12).

As to the cylinders, Fricke's treatment (13) of the conductivities of prolate spheroids in dilute dispersions yields values close to those one obtains by using Eq. [6]. Therefore at least at low concentrations of the solid, the agreement between the present data and Eq. [6] is not surprising. However, at higher volume fraction of the dispersed phase, there is no adequate theoretical basis by which one can safely generalize the agreement found between the data for cylinders of approximately 10:1 length to diameter ratio and the values predictable from Eq. [6], which has been developed for spheres only.

Conclusions

Experiments of reasonably high precision and reproducibility confirmed expectations based on theory, e.g., that the conductivity of electrolytes is lowered by the presence of randomly distributed spherical nonconductors to a larger extent than predictable from the well-known Maxwell relation. Conductivity data obtained on a large size range of glass spheres in aqueous $ZnBr_2$ solutions aligned closely to curves represented by Eq. [5] with $X = 1.00$ and $1.43 < Y < 1.51$. This form of the equation and the upper limit of the exponent find theoretical support in the approximation first proposed by Bruggemann.

It is recommended that for random dispersions of spherical insulators with a large size-range of spheres, such as occurs in gas-electrolyte emulsions, the Bruggemann equation (Eq. [6]) be used to predict effective conductivity. When the size-range of spheres is narrow it may still be used with about the same or lower probable error than the Maxwell equation, although in that case the Bruggemann equation predicts slightly low values for the effective conductance. For shapes other than spherical Eq. [6] is generally not applicable, particularly not if the particles are greatly elongated or when they contain cavities.

Acknowledgment

The authors wish to express their appreciation to Mr. Eugene J. Fenech for work done on the IBM 650 computer and to Mr. Robert E. Meredith and Dr. Thomas Baron for enlightening discussions.

Manuscript received Feb. 9, 1959. This paper was prepared for delivery before the Cincinnati Meeting, May 1-5, 1955.

Any discussion of this paper will appear in a Discussion Section to be published in the June 1960 JOURNAL.

REFERENCES

1. J. C. Maxwell, "Electricity and Magnetism," Vol. 1, 3rd ed., p. 440, Oxford (1892).
2. Lord Rayleigh, *Phil. Mag.*, **34**, 481 (1892).
3. H. Fricke and S. Morse, *Phys. Rev.*, **25**, 361 (1925).
4. A. Eucken, VDI-Forschungsheft, No. 353 (1932).
5. A. B. Metzner, "Advances in Chemical Engineering," Vol. 1, pp. 121-124, Academic Press, Inc., New York (1956).
6. C. Orr and J. M. Dalla Valla, Chem. Eng. Progr. Symposium Ser. No. 9, **50**, 29 (1954).
7. A. J. Slawinski, *Chim Phys.*, **23**, 710 (1926).

8. *Ibid.*, **26**, 368 (1929).
9. J. P. Mashovets, *J. Appl. Chem. (U.S.S.R.)*, **24**, 353 (1951).
10. C. A. R. Pearce, *Brit. J. Appl. Phys.*, **6**, 113 (1955).
11. D. A. G. Bruggemann, *Ann. Physik.*, **24**, 636 (1935).
12. R. E. De La Rue, Master's thesis, University of California (1955).
13. H. Fricke, *Phys. Rev.*, **24**, 575 (1903).

Effect of Gas Evolution on Current Distribution and Ohmic Resistance in Electrolyzers

Charles W. Tobias

Department of Chemical Engineering, University of California, Berkeley, California

ABSTRACT

Volume fraction of gases in electrolyzers increases in the direction of net movement of gases, causing a corresponding variation in the ohmic resistance between electrodes. The resulting nonuniformity in current distribution and the increase in over-all resistance is shown to be characterized by a single dimensionless parameter which incorporates the key process variables. The leveling effect of polarization is shown to be significant.

Although the effect of gas holdup in electrolytic cells on the resistance of the electrolyte has long been recognized (1), quantitative interpretation of the effects observed has not been attempted until recent years. Ipatieff, Schischkin, and Jurieff (2) have presented simple calculations relating the total current to volume of gas present in water electrolyzers. Implicit in their treatment is the assumption that the effective resistivity of the electrolyte between the vertical electrodes does not vary in the vertical direction. While this assumption greatly simplifies the physical model, it also deprives the model used by these workers of reality. In addition to neglecting the current density variation caused by differences in gas concentration, these authors expressed the volumetric effect of gas bubbles on conductivity in an erroneous manner.

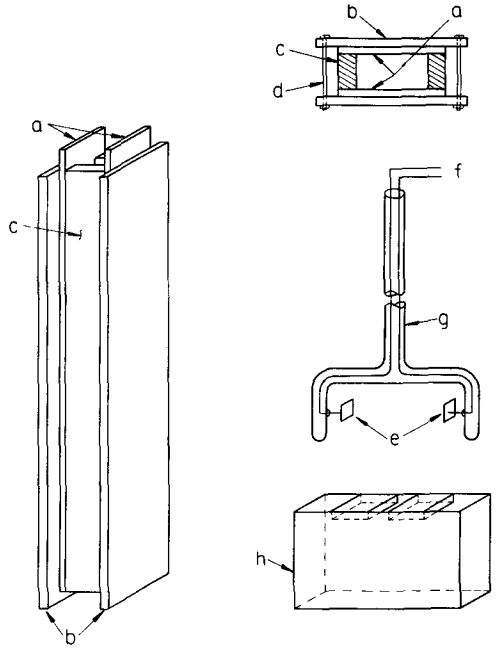

Fig. 1. Experimental cell and conductivity probe used by Baker (2). a, Steel electrodes, 32 x 6 x ⅛ in.; b, Bakelite backing sheets; c, plexiglass separators, 31 x 1 x 1 in.; d, fastening bolts; e, platinized platinum electrodes, 0.5 x 1.0 cm, 7 cm apart; f, shielded leads; g, glass tube, 1 cm OD; h, plexiglass shield fitting over horizontal part of glass tube.

According to measurements of the effective resistance as a function of cell depth (Fig. 1) reported by Baker (3) between parallel electrodes, the volume fraction of gas at a given depth in a given electrolyte is approximately a linear function of current density (Fig. 2). Baker calculated the volume fractions from resistance data obtained by use of a shielded resistivity probe. An experimental plot of the variation of gas volume fraction as a function of distance from cell bottom is shown in Fig. 3.

Current density decrease from bottom to top of a water decomposition model cell was shown by Murakawa and Nagaura (4) by means of direct measurements of branch currents using a "sectioned" electrode (5). Their results conform, at least in a qualitative sense, to expectations based on first principles. When gas evolves along a vertical electrode surface, bubbles ascend under the buoyancy force (and if the electrolyte is in motion, also due to drag forces). The time required for a gas bubble evolved at a point on the surface to reach the surface of the electrolyte will be approximately proportional to the distance of this point from the surface. Consequently the volume fraction of gas in the electrolyte gradually increases with elevation, causing the conductivity of the suspension to diminish along the same direction.

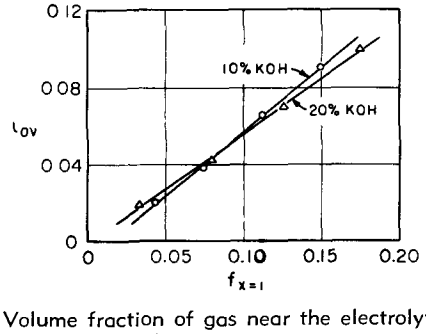

Fig. 2. Volume fraction of gas near the electrolyte surface [from data by Baker (3)].

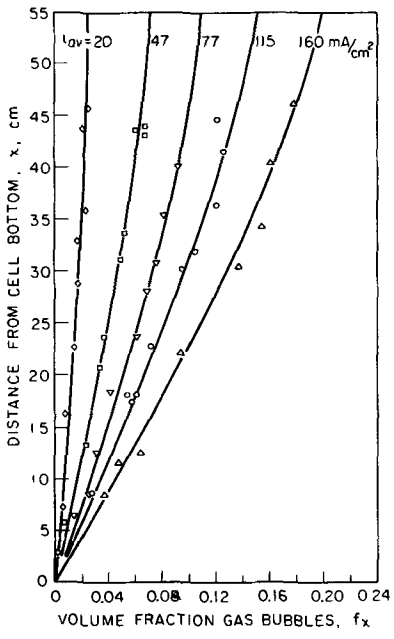

Fig. 3. Experimental volume fractions at different cell depths

The aim of the present work is to establish a theoretical treatment by which the most important design and process variables are combined in functional relationship, quantitatively describing the effect of gas evolution on current distribution and cell voltage. In order to lend clarity and simplicity to the mathematical treatment, certain reasonable physical assumptions must be made, which however should not detract from the general validity of the results.

Nomenclature

b' — $b'_a - b'_c$
b'_a, b'_c — anodic and cathodic linear Tafel slopes, ohm cm²
C — dimensional constant, $RT/PmFs\delta$, cm amp^{-1}
D — bubble diameter, cm
E — portion of applied cell voltage that depends on current, $E = E + i_x R_x$, volts
E_p — current dependent part of polarization voltage, $E_p = b'i_x$
E_D — constant in "linear" Tafel equation, volts approximately the current-independent part of the cell voltage, or the "decomposition" voltage
F — Faraday, coulombs/gram equivalent
f_x — volume fraction of gas in electrolyte at level x, dimensionless
f_{av} — average volume fraction of gas in cell, dimensionless
h — height of electrolyte column in cell (with or without gas), cm (Fig. 4)
I_T — total current passing through cell, amp
i_x — local current density at level x, amp/cm²
i_{av} — average current density in cell, amp/cm²
K — dimensionless parameter $CEh/\rho\delta = RTEh/PmFs\rho\delta^2$
m — number of Faradays passing through the cell, per mole of gas liberated at both electrodes, g-equivalent/mole
P — partial pressure of gas liberated at electrodes, atm, $P = P_T - P_V$
P_T — total pressure (approximated by ambient pressure plus arithmetic mean of hydrostatic pressure in cell)
P_v — vapor pressure of electrolyte at the operating temperature
R — gas constant, cm³ atm/°K g mole
R_e — resistance of gas-free electrolyte between the two electrodes, ohms
r_x — effective resistance of a 1 cm² prism of electrolyte containing gas bubbles, between the two electrodes at elevation x, ohm cm², $r_x = \rho_x\delta = \rho\delta(1 - f_x)^{-3/2}$
R_{eff} — total ohmic resistance of electrolyte and gas in cell, ohms
s — average rising velocity of bubbles, cm/sec
T — absolute temperature, °K
u — velocity of a gas bubble, cm/sec
u_s — steady-state velocity of a gas bubble, cm/sec
dv_x — volume of gas in volume element $w\delta dx$ of electrolyte at level x, cm³ (Fig. 4)
w — width of electrodes, cm (Fig. 4)
X — dimensionless reduced vertical distance, $X = x/h$
x — vertical distance from bottom of electrodes, cm (Fig. 4)
δ — electrode separation, cm (Fig. 4)
θ — time, sec
μ — $b'/\rho\delta$, polarization parameter, dimensionless
ν — dynamic viscosity, g cm^{-1} sec^{-1}
ρ — resistivity of gas-free electrolyte, ohm cm
ρ_x — resistivity of electrolyte containing gas bubbles at level x, ohm cm
σ_e, σ_g — density of electrolyte and gas, respectively, g/cm³
ϕ — cell parameter $\phi = I_T C/w = I_T RT/PmFs\delta w$, dimensionless

Cell Model and Physical Assumptions

The geometry of the cell model is shown in Fig. 4. The following assumptions were made:

1. The electrode on the metal side is equipotential, i.e., there is no "terminal effect."

2. Size distribution of bubbles at all levels is the same, and within the range of current densities this size range and distribution may be regarded as constant.

3. The bubbles assume their steady-state (instantaneous) velocity, u_s, essentially immediately after separation from the surface. It can be shown by the solution of the differential equation from u, the velocity of motion of a gas bubble in the gravitational force field, using Stokes law, that

$$u = u_s[1 - \exp(-18\nu\sigma_e\theta/D^2\sigma g)] \qquad [1]$$

Substitution of reasonable values of the physical constants into Eq. [1] indicates that quasi steady

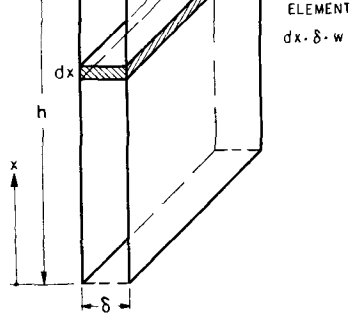

Fig. 4. Model of gas evolution cell

state is reached within 0.01-0.001 sec after release.

4. Velocity of rise is independent of depth. In fact bubbles expand on decrease in hydrostatic pressure. Since the buoyancy force is proportional to D^3 while the drag force is proportional to D^m (where $1<m<2$), ascending bubbles accelerate. In the region of interest velocity of bubbles varies approximately in inverse ratio to the 1/3 to 2/3 power of the pressure; therefore the increase of velocity amounts to only a few per cent, provided the cell depth is not very great. Incorporation of variable velocity into the treatment to be presented, however, would confuse the issue more than it would contribute to the accuracy of the end results.

5. Velocity of rising bubbles is independent of volume concentration of gas. In fact the bubble motion decelerates as the volume concentration of bubbles in the electrolyte increases. Quantitative functional representation of the effect of volume concentration on the departure of velocity from the "free" rate of ascendance however has not been developed so far.[1]

6. Secondary effects on bubble motion, such as those due to coalescence or convection currents in the electrolyte for example, are disregarded.

7. The assumptions under 2-6 above permit the definition of an average velocity, s, at which the gases liberated at the electrodes rise, independent of depth and current density. Within a given electrolyte, however, this velocity depends on pressure, temperature and electrode material.

8. Polarization is linear over the range of current densities occurring within a cell (see Fig. 5). Substitution of a linear relation for a relatively narrow range of current densities has been an accepted technique in treating current distribution problems (6, 7).

9. The flow of current is unidirectional, or at least the curvature of the lines of flow is negligible. It has been shown (6) that for linear geometry this is a good assumption, provided δ/h is small.

[1] Studies by Hanratty, *et al.*, on hindered settling of spherical solids (9) have shown that in the Stokes law region the effective rate of settling may be evaluated if, instead of the density of pure liquid, one substitutes the average density of the suspension (a variable, function of depth), and if one also takes into account the change of effective viscosity with the changing volume concentration. Although the exact functional dependence is more complex, Hanratty's data may be reasonably well represented by $s_x/s_0 = (1 - f_x)^4$ when $f_x < 0.35$, where s_0 corresponds to the free settling rate, and s_x denotes the actual rate of settling at elevation x.

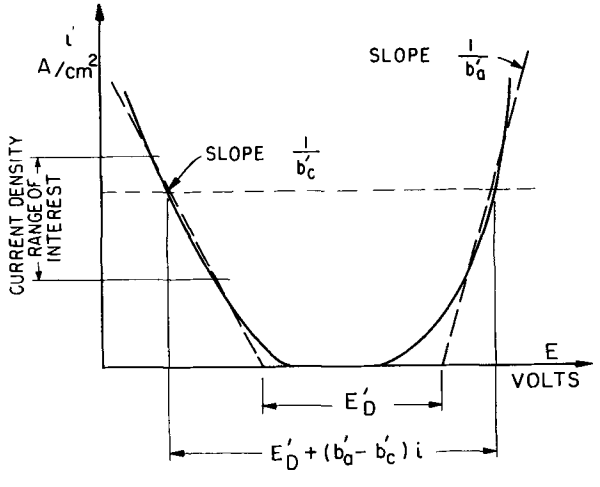

Fig. 5. Linear polarization approximation

Mathematical Treatment

In the steady state, the volume of gas dv_x present in the volume element $w \cdot \delta \cdot dx$ (Fig. 4) is

$$dv_x = (RTwdx/PmFs) \int_0^x i_x dx \qquad [2]$$

Equation [2] may be derived as follows. The quantity w times the integral equals the total current flowing through the cell between the bottom and level x. This current divided by mF gives the total number of moles of gas produced and, multiplied by RT/P, the total volume of gas produced in the cell per second between the bottom and x. This volume of gas is moving upward a distance of s cm in 1 sec. Therefore, the fraction dx/s of it will be in the given volume element at any given instant of time, and this is the volume dv_x. The volume fraction of gas in the same element is then

$$dv_x/w\delta dx = f_x = C \int_0^x i_x dx \qquad [3]$$

For a given geometry, P, T, m, and s, C is a constant having the dimensions of length per unit of current. Equation [3] relates the volume fraction of a gas at height x to the total current passing below that level.[2]

As shown by De La Rue and Tobias (8), dependence of the ohmic resistivity ρ_x at level x on the volume fraction of gas is given by the Bruggemann equation

$$\rho_x = \rho(1 - f_x)^{-3/2} \qquad [4]$$

The current-dependent portion of the electrode potentials E_p may be represented by (Fig. 5)

$$E_p = b' i_x \qquad [5]$$

The dependence of potential on current density, resistance, and polarization is then obtained by combination of [4] and [5]

$$E = (b' + r_x) i_x \qquad [6]$$

Note that, in the present application, E is independent of x by virtue of assumption 1 above. The square centimeter resistance r_x is equal to $\rho_x \delta$.

Substitution and rearrangement of [6] yields

$$E/\rho\delta = [\mu + (1 - f_x)^{-3/2}] i_x \qquad [7]$$

The meaning of the polarization parameter μ has been given by Wagner (7) among others.

The differentiation of [3] yields

$$df_x = C i_x dx \qquad [8]$$

The current density i_x may be eliminated between Eqs. [7] and [8] and the resultant equation integrated

$$(CE/\rho\delta) \int_0^x dx = \int_0^{f_x} [\mu + (1 - f_x)^{-3/2}] df_x \qquad [9]$$

[2] Although constant velocity of rise s has been assumed in this derivation, incorporation of velocity dependence on volume fraction of gases as represented, for instance, by the approximation formula in footnote 1, causes no difficulty. Equation [3] transforms to $f_x(1 - f_x)^4 = C \int_0^x i_x dx$ and the integration of the modified equation replacing Eq. [9] may be readily accomplished. The resulting form however is implicit in f_x, and does not permit therefore derivation of convenient expressions showing the dependence of key process variables. In the following treatment only the simpler relations involving the constant velocity assumption are presented.

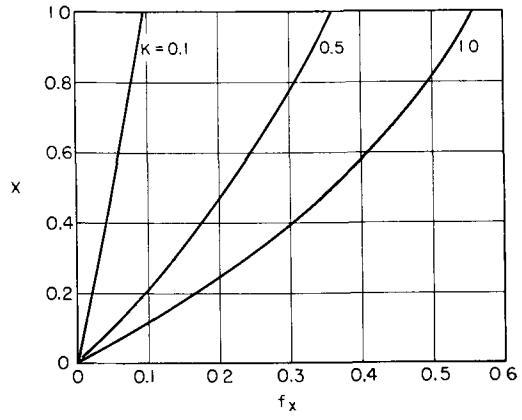

Fig. 6. Volume fraction of gas as a function of reduced height

To obtain a solution in closed form for f_x, let us for the present assign the value $\mu = 0$ (corresponds to constant polarization), and then integrate between the limits given. The solution is

$$f_x = [(KX)^2 + 4KX]/(KX + 2)^2 \qquad [10]$$

where K, the gas effect parameter, and X, dimensionless vertical height, have been introduced to reduce the number of symbols carried. A plot of f_x as a function of X is given in Fig. 6 for $K = 0.1$, 0.5, and 1.0.

Combination of Eqs. [7] and [10] leads to the important relation between local current density and vertical distance

$$i_x = 8K/hc(KX + 2)^3 \qquad [11]$$

Mathematical Results

A number of useful relations may now be derived by simple combinations of the equations derived in the preceding section.

1. The relation between the total current I_T and the current-dependent part of the voltage

$$I_T = i_{av}hw = w\int^h i_x dx = wf_x h/C =$$

$$w(K^2 + 4K)/C(K + 2)^2 \qquad [12]$$

In Fig. 7 the ratio of local to average current density i_x/i_{av} has been plotted by use of Eqs. [11] and [12] for $K = 0.1$, 0.5, and 1.0.

2. Solving [12] for K, we obtain the dependence of K on average current density

$$K = 2[1 - (1 - 1/Chi_{av})^{-1}]^{1/2} - 2 \qquad [13]$$

Equation [13] has been plotted in Fig. 8 The vertical scale is Chi_{av}. Note that for low values of K (<0.15)

$$K \cong Chi_{av} \qquad [14]$$

In this region, K is directly proportional to applied current and depth of cell and, from the definition of C, K is inversely proportional to average velocity of rise of bubbles and to electrode separation.

3. The average effective ohmic resistance of electrolyte R_{eff} relative to gas-free resistance R_e, when the cell depth is the same, is given by

$$R_{eff}/R_e = (K + 2)^2/(K + 4) \qquad [15]$$

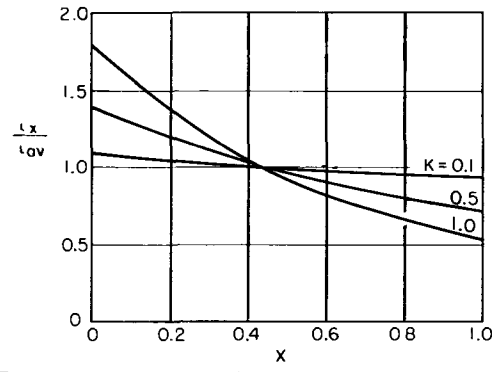

Fig. 7. i_x/i_{av} as a function of reduced height along electrode

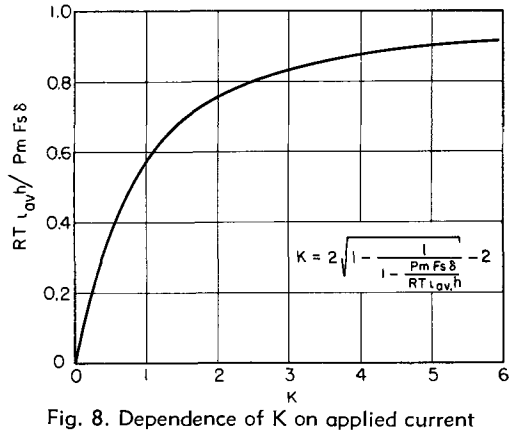

Fig. 8. Dependence of K on applied current

4. The average volume fraction of gases is given by

$$f_{av} = {}_0\int^1 f_x dX = K/(K + 2) \qquad [16]$$

Figure 9 illustrates Eqs. [15] and [16], showing that the per cent effect on resistance is greater than the per cent average gas holdup. Figure 10 shows a plot of f_{av} against a dimensionless grouping ϕ including I_T.

Optimal distance of electrodes.—Because of the effect of gas bubbles on the resistivity of electrolyte, setting the electrodes closer together will not result in a proportionate reduction of ohmic voltage drop. As a matter of fact it is easy to realize that bringing them together below a certain distance should result in an increase of voltage drop. (The volume fraction of gas varies in inverse proportion to the electrode separation, while the effective resistance of the dispersion between the electrodes increases more rapidly than does the volume fraction of gas.) For simplicity's sake let us consider only at what average volume fraction f_{av} of gas the effective ohmic resistance will be at a minimum:

$$R_{eff} = A/f_{av}(1 - f_{av})^{3/2} \qquad [17]$$

where all terms not depending on distance have been grouped into a constant A.

Differentiating with respect to f_{av}, and setting the derivative equal to zero, we obtain $f_{av} = 0.4$, i.e., the ohmic resistance will be at its minimum when the electrodes are at such a distance that the average volume fraction of gas between them is 0.4. Although such a high holdup volume seems to be out of the common design and operational range, it should be noted that the ohmic resistance diminishes rather slowly with distance even when $f_{av}>0.2$. Therefore

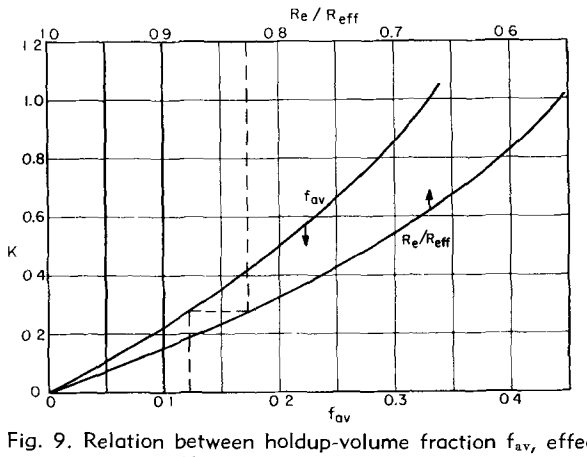

Fig. 9. Relation between holdup-volume fraction f_{av}, effective resistance, and K for gas evolution between plane parallel electrodes.

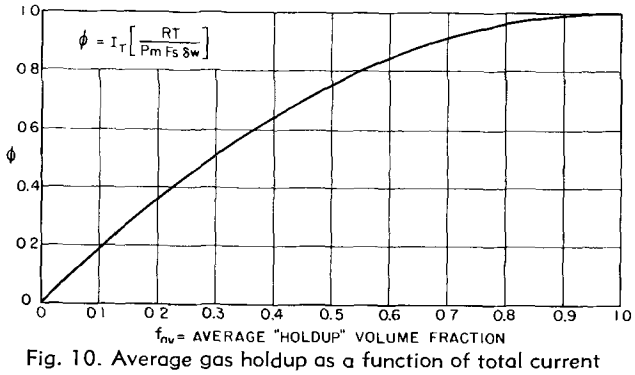

Fig. 10. Average gas holdup as a function of total current

only little can be gained by setting the electrodes closer together than corresponds to $f_{av} = 0.2$.

In attempting to evaluate the effect on the voltage drop of reducing the interelectrode distance, one should keep in mind that in all the developments presented above it has been assumed that the average velocity of gas bubbles is independent of electrode separation. Although for large separations this appears to be a reasonable approximation, it is quite certain that, when the electrodes are so close together, the volume fraction of gas becomes significant, s depends on electrode separation, and the optimal separation will be larger than that corresponding to $f_{av} = 0.4$.

Effect of Polarization

The value $\mu = 0$ has been assigned so far in order to obtain a solution in closed form for the current density distribution, and to show in the manner easiest to follow how the common design and process variable are interrelated.

The relation between X and f_x from the integration of equation [9]

$$KX = \mu f_x + 2(1 - f_x)^{-1/2} - 2 \qquad [18]$$

does not yield an explicit form in f_x and therefore i_x cannot either be expressed in a closed form as a function of X. A reasonable approximation may be obtained however if one replaces[3] the term in Eq. [7] which represents the effect of gas volume fraction on resistance $(1 - f_x)^{-3/2}$ by the first two terms of its binomial expansion $1 + 3/2 f_x$. With this substitution the current density variation as a function of X, K, and μ may be obtained by simple algebraic steps

$$i_x/i_{av} = \frac{3}{2} K[(\mu + 1)^2 + 3KX]^{-1/2} \cdot \{[(\mu + 1)^2 + 3K]^{1/2} - (\mu + 1)\}^{-1} \qquad [19]$$

[3] Use of this expression for conditions where $f_{av} > 0.2$ leads to appreciable errors.

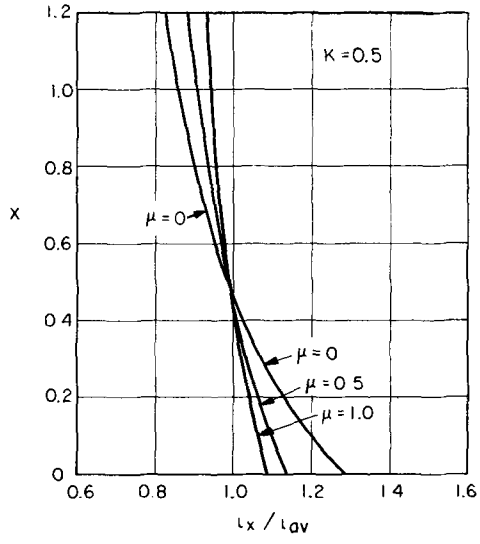

Fig. 11. Leveling effect of polarization on nonuniform current distribution caused by gas evolution.

Figure 11 shows the considerable leveling effect of polarization for a practical range of values of the polarization parameter μ.

When the polarization is strongly dependent on current density and therefore μ is comparable to or larger than unity, the nonuniformity of current distribution is diminished to a significant degree. Under such conditions it is advisable to use Eq. [19] and the correspondingly modified forms of the relations expressing effective resistance, etc.

Note: The fact that the effect of gas evolution on current distribution depends on a single dimensionless parameter should be helpful both in design procedures and when it is desirable to know what effects changes in operational conditions will have.

The foregoing treatment should be regarded as valid only within the physical assumptions made. Therefore, whenever any of the variables (such as size, total current) are changed significantly one must examine whether or not dependent quantities have been affected by phenomena not considered in setting up the physical model. A particularly vulnerable assumption is that relating to the constancy of the average rising velocity of bubbles. Large variations in cell depth or electrode separation will undoubtedly influence s, as will changes in electrode materials. The effect of deceleration of bubble motion due to decrease in bulk density and increase of viscosity cannot be considered quantitatively until further experimental and theoretical developments improve our understanding of the dynamic behavior of suspensions of gases in liquids. The analogy with hindered settling is plausible but not proven. In any case, other factors, such as bulk entrainment of electrolyte and secondary flows caused by descending, relatively gas-free eddies, may so seriously influence bubble motion that conclusions reached by considering the deceleration due to viscosity and density changes alone could be misleading.

The average bubble velocity, s, and its dependence on cell geometry, current density range, and materials used may be established in model experiments. Estimates of s may be obtained by measurement of increase

of electrolyte level due to gas holdup (see Eq. [16]), and the variation of average velocity with total current established by comparing the dependence of K on i_{av} with the values calculated by use of Eqs. [13] and [14].

Manuscript received Feb. 9, 1959. This paper was prepared for delivery before the New York Meeting, April 27-May 1, 1958.

Any discussion of this paper will appear in a Discussion Section to be published in the June 1960 JOURNAL.

REFERENCES

1. V. Engelhardt, "Handbuch der Technischen Elektrochemie," vol. II/I, p. 9, Akademische Verl. M.B.H. 1933).
2. V. V. Ipatieff, V. V. Schischkin, and S. I. Jurieff, *Z. Elektrochem.*, **40**, 713 (1934).
3. W. J. Baker, Master's Thesis, University of California, Berkeley (1951).
4. T. Murakawa and S. Nagaura, *J. Electrochem. Soc. Japan*, **23**, 223, 304 (1955).
5. E. Mantzell, *Z. Elektrochem.*, **39**, 10 (1935).
6. C. W. Tobias and R. Wijsmann, *This Journal*, **100**, 459 (1953).
7. C. Wagner, *ibid.*, **98**, 116 (1951).
8. R. E. De La Rue and C. W. Tobias, *ibid.*, **106**, 827 (1959).
9. T. J. Hanratty and A. Bandukwala, *A.I.Ch.E. Journal*, **3**, 293 (1957).

Technical Note

Preparation and Properties of ZnS-Type Crystals from the Melt

Albrecht G. Fischer[1]

Large Lamp Department, General Electric Company, Nela Park, Cleveland, Ohio

The important semiconducting phosphor materials ZnS, CdS, and ZnSe cannot be melted at normal pressure because they decompose several hundred degrees below their melting points. This tendency is due to the mixed homo-heteropolar nature of their bond. As the diamond lattice requires that the ions be incorporated in a predeformed state and under stress, unstable surfaces result (1, 2).

The first experiments to melt ZnS and CdS in a high-pressure bomb were carried out several decades ago (3), and recently interest has revived in the subject. Accurate values for the melting points and vapor pressures of ZnS and CdS have been reported (4, 5) and a technique of growing crystals of these materials from the melt under high argon pressure has been developed (2, 6).

ZnSe can also be recrystallized from the melt (2). In continuation of earlier work it was found that crucibles of pure graphite and of zirconia can be used. Quartz glass, although rather soft at the melting point of ZnSe, is also suitable as a crucible material since it is not chemically attacked by the melt.

Using a melting point indicator similar to that described in (2) and a Pt-Pt/Rh thermocouple, the melting point of ZnSe has now been determined to be at 1515° ±20°C. $CuGaS_2$ melts at 1280°C.

The vapor pressure at the melting point was determined by a new direct method. A sealed-off evacuated quartz tube filled with ZnSe prefired in vacuum was heated up to the melting point of ZnSe. When the outer pressure in the autoclave was somewhat higher than the decomposition pressure developed in the tube, the walls of the plastic quartz tube were compressed. When, on the other hand, the outer pressure was lower than the inner pressure, the bulb dilated and formed a bubble. In a series of experiments with varying external pressure, it was possible to determine the pressure in the bulb within close limits. In the case of ZnSe it is around 1.8 atm, while it is about 2.5 atm for CdS. This method is also suitable for substances with lower melting points where other glasses have to be used, for instance for certain $A_{III}B_V$ compounds where indirect methods had to be used previously.

The facts that the vapor pressure is comparatively low and that quartz, although already soft at 1500°C, is chemically stable, suggested a new method for the preparation of ZnSe single crystals from the melt. It

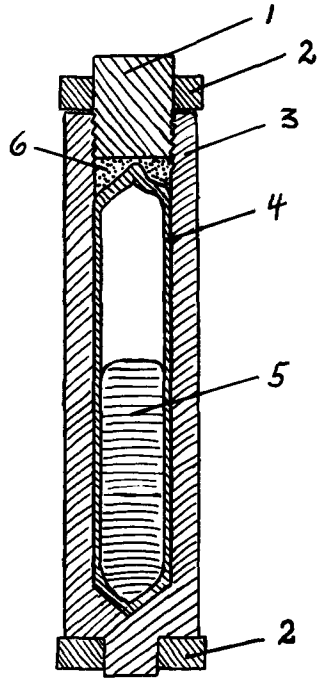

Fig. 1. 1, Graphite stopper; 2, boron nitride rings to prevent electrical shorting of the heater; 3, graphite crucible; 4, quartz bulb; 5, ZnSe or CdS melt; 6, graphite powder.

[1] Present address: RCA Laboratories, Princeton, N. J.

is also suitable for CdS. A quartz tube is filled with ZnSe, heated in vacuum and sealed off. This tube is inserted into a closely fitting thick-walled graphite crucible which can be closed with a plug. The remaining empty space is filled with graphite powder (see Fig. 1). If this assembly is heated up, the softening quartz tube expands, driven by the interior pressure, until the rigid graphite container takes up the mechanical forces and the quartz hull serves merely as a gas-tight lining. The vessel with the molten ZnSe can then be cooled down with any desired temperature gradient in order to crystallize the melt. To prevent devitrification of the quartz it is desirable to use pure graphite with smooth surfaces. Instead of the simple graphite crucible shown in Fig. 1 which has to be destroyed each time a crystal is removed, more elaborately designed vessels can be used which allow disassembly and reassembly.

The method described is expected to find wider application because it allows the growing of large single crystals from the melt in a reproducible way and with simple, inexpensive means; no high-pressure autoclave is needed.

For ZnS or ZnS-rich mixtures, it is better to use high-density zirconia crucibles with stoppers, which are sealed into evacuated, closely fitting quartz tubes and heated in an autoclave. The pressure applied from the outside has to be higher than the decomposition pressure inside. The thermoplastic quartz envelope then forms a gas-tight lining around the ZrO_2 crucible; this permits growing of the crystals in a defined atmosphere and controlling the vacancy equilibrium in the crystals.

It has been found that the pure compounds ZnS, CdS, and ZnSe, or mixtures containing at least about 80% of any one of the constituents, crystallize much more readily than mixtures with lower contents, which have the tendency to stay polycrystalline.

Thermoelectric measurements have shown that undoped ZnSe crystals as well as samples doped with Al and In are n-type, whereas ZnSe crystals doped with Cu or Ag are p-type. The n-type samples are strongly photoconducting, whereas coactivated samples are luminescent.

Solid-state diffusion occurring during the firing of crystals rich in ZnSe or CdS and packed in ZnS powder having the same activator concentration led to spread-band-gap surfaces. This could be observed by a short wave-length shift of the photo- and cathodoluminescence from the interior of the crystals toward their surface. Formation of mixed crystals of ZnSe with ZnTe or GaAs (7) reduces the band gap of ZnSe.

Acknowledgment

It is a pleasure to thank Dr. H. C. Froelich for help with the preparation of this paper.

Manuscript received May 13, 1959.

Any discussion of this paper will appear in a Discussion Section to be published in the June 1960 JOURNAL.

REFERENCES

1. A. Fischer, *Phys. Verh.*, **8**, 204 (1957).
2. A. Fischer, *Z. Naturforschg.*, **13a**, 105 (1958).
3. E. Tiede and A. Schleede, *Ber.*, **53B**, 1717 (1920).
4. A. Addamiano and P. A. Dell, *J. Phys. Chem.*, **61**, 1020 (1957).
5. A. Addamiano, *ibid.*, **61**, 1253 (1957).
6. W. E. Medcalf and R. H. Fahrig, *This Journal*, **105**, 719 (1958).
7. D. N. Nasledov, "Semiconductors and Phosphors," p. 644, Interscience Publishers, Inc., New York (1958).

Technical Review

The Manganese Dioxide Electrode

W. C. Vosburgh

Department of Chemistry, Duke University, Durham, North Carolina

Manganese dioxide has been an important battery reactant since about 1890 when the Zn-MnO_2 cell proposed by Leclanché (1) began to be used in the dry-cell form. Because of the importance of the Leclanché cell and of other uses of MnO_2 a voluminous literature has grown up. A review of the Leclanché cell by Heise and Cahoon (2) was published in 1952 and at the same time reviews of two newer cells with MnO_2 electrodes by Morehouse (3) and Herbert (4). The present review brings together some of the more recent contributions to the structure and properties of MnO_2 and the discharge mechanism of the MnO_2 electrode. Related topics that are not included are the carbon of the Leclanché-cell bobbin, the electrolyte, reactions of the Leclanché cell not closely related to the discharge mechanism, the standard potential and the open-circuit potential of the MnO_2 electrode, and practical features of batteries with MnO_2 electrodes.

Structural Forms of Manganese Dioxide

Reviews of the structure of MnO_2 have been given by Wadsley and Walkley (5) and Brenet (6). Some later contributions have been made by Buser and Graf (7). The large number of more or less differing substances of the approximate composition

MnO_2 (with or without other elements) have been classified as belonging to a relatively few general types which occur naturally. The crystal structures of these have been determined and diagrams of the structures are given in the above references.

The minerals pyrolusite and ramsdellite are MnO_2 with no other element as an essential part of the structure. Ramsdellite in well-crystallized form is rare. Pyrolusite has a more compact crystal structure than ramsdellite (6,8).

Psilomelane is given the type formula $(Ba,H_2O)_2Mn_5O_{10}$ in which the relative amounts of Ba and H_2O are variable (9). The Ba is present as Ba^{++}, and compensation for the charge is made by reduction in the charge of an equivalent number of Mn atoms (9).

The minerals cryptomelane, hollandite, and coronadite are alike except for the additional element present along with the MnO_2, these being K, Ba, and Pb, respectively (10, 11). The type formula is given as KMn_8O_{16}, with K replaceable by other metal atoms, with suitable adjustments of the charge of the Mn.

Lithiophorite and chalcophanite have layer structures in which the MnO_2 forms two layers enclosing other metal ions and water, or hydroxides (12).

Well-crystallized artificial pyrolusite, known also as β-MnO_2, can be prepared. The accepted standard MnO_2 electrode with an acid electrolyte is a β-MnO_2 electrode (13). Well-crystallized ramsdellite has not been prepared, but the artificial material known as γ-MnO_2 and the naturally occurring γ-MnO_2 now usually are considered to be related to ramsdellite (14, 5, 6) although a closer relation of some samples to pyrolusite on the basis of the x-ray diffraction pattern has been pointed out (15). It is suggested (11) that the ramsdellite structure of γ-MnO_2 is partially changed to the more stable pyrolusite structure by as mild a treatment as heating under boiling water. This would make possible a series of disordered intermediate forms. Both natural γ-MnO_2 ores and electrodeposited γ-MnO_2 preparations are used in batteries.

Well-crystallized artificial cryptomelane, or α-MnO_2, has been prepared. Electron microscope photographs of α-MnO_2 showing definite crystal form, are given by McMurdie (16) and Buser, Graff, and Feitknecht (17). In similar photographs of γ-MnO_2 no crystal form can be seen. McMurdie's α-MnO_2 was prepared by the digestion of γ-MnO_2 with NH_4Cl solution either at 100°C or under pressure at 150°C and presumably contained NH_4^+ in its structure. The α-MnO_2 of Buser, Graf, and Feitnecht was prepared with K^+ present.

Electrodeposition of MnO_2 from a bath of $MnSO_4$ and H_2SO_4 gives γ-MnO_2 (14, 6). However, if one of the cations that can take part in the α-MnO_2 structure is present α-MnO_2 may be obtained (18, 19), although Cole, Wadsley, and Walkley (14) obtained γ-MnO_2 in two preparations in which K_2SO_4 was present.

Precipitation processes in which Mn^{++} is oxidized or MnO_4^- reduced (or both) give four different oxides, depending on conditions. The one most commonly formed is γ-MnO_2, but in the presence of K^+ or other similar cations α-MnO_2 or mixtures of α and γ may be formed (14, 20, 21). Some conditions of precipitation give δ-MnO_2 (16), and still other conditions give two forms of a material called manganous manganite (22, 23). As the last name implies, this material contains Mn(II) as well as Mn(IV), and the amount of Mn(II) is variable. Buser, Graf, and Feitknecht (17) showed that δ-MnO_2 and manganous manganite are alike in structure. The crystals are thin plates consisting of two layers of Mn(IV) and O atoms with a variable amount of $Mn(OH)_2$ between the layers. The Mn(II) of the $Mn(OH)_2$ can be replaced by other metals, for example Zn, giving a series of manganites. When the $Mn(OH)_2$ content is small, the material is δ-MnO_2. Compounds $3MnO_2 \cdot Mn(OH)_2 \cdot xH_2O$ and $4MnO_2 \cdot xMn(OH)_2 \cdot 2H_2O$ have been prepared, the latter in well-crystallized form. This preparation indicates that manganous manganite is not a poorly crystallized α-MnO_2 as has been suggested (16,24). Buser and Graf (25) consider that the two forms of manganous manganite are similar in structure to the minerals chalcophanite and lithiophorite, mentioned above. On heating manganous manganite or δ-MnO_2 under water α-MnO_2 is formed if the preparation contains enough K^+, and γ-MnO_2 is formed if the K^+ content is below a certain small minimum (22, 17). Dried δ-MnO_2 containing K^+ was not appreciably converted to α below 300°C (21).

Some Properties of MnO_2

Most of the properties of MnO_2 are well known and need no review here. However, some recent work on certain of the properties should be mentioned.

Changes on heating.—The changes on heating MnO_2 at temperatures between 350° and 450°C serve to show the relative stabilities of the various varieties. Cole, Wadsley, and Walkley (14) represent the changes as follows, most of which they have confirmed. The arrows represent heating at 350° to 450°C except in the one case noted; this

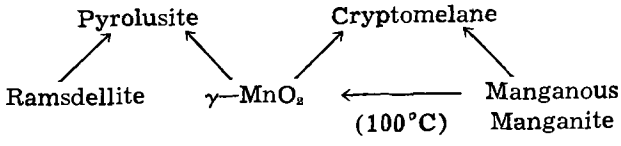

latter change seems to have been carried out only under hot water (17). Pyrolusite, or β-MnO_2, and cryptomelane, or α-MnO_2, are the most stable forms, and of the two α-MnO_2 is much the more stable if it contains K^+ as the additional cation. Whether γ-MnO_2 and manganous manganite are converted to α-MnO_2 or to β-MnO_2 depends on the presence or absence of a suitable cation.

Heating at temperatures of 150° to 350°C affects the properties of γ-MnO_2 (26, 27). The potential of the MnO_2 (that is, the electrode potential when a MnO_2 electrode is made with the material in question, with an ammonium salt electrolyte unless otherwise specified) is decreased by heating. The discharge capacity is also decreased. Combined water is driven off at these temperatures and the

crystal form altered in the direction of increased crystallinity and partial conversion to a pyrolusite structure (11). The decreased discharge capacity may be related to both the decreased water content of the MnO_2 and its change in structure. The electrode potential is determined by the composition of the exterior of the oxide (28). Heating γ-MnO_2 at still lower temperatures, 90° to 140°C, affects the shape of the discharge curve, when electrode potential is plotted against time at constant current (29).

However, when the electrolyte is a solution of HCl and $MnCl_2$ the results are different. Maxwell and Thirsk (21) made electrodes from a number of different MnO_2 preparations, unheated and heated at various temperatures up to 500°C. Heating the MnO_2 either had little effect or caused an increase in the electrode potential, followed by a decrease at the highest temperatures. It is worthy of note also that the various artificial preparations of α-, γ-, and δ-MnO_2 all had electrode potentials higher than artificial β-MnO_2, the differences ranging from 30 to 80 mv.

Surface area.—Measurements of the surface area of MnO_2 by the gas adsorption method have revealed that the area in most cases is very large. For γ-MnO_2 areas of 20-60 m^2/g have been reported (25, 28). This is of the order of 10^5 times the surface of a gram of MnO_2 in the form of a smooth cube. For δ-MnO_2 a surface of 300 m^2/g was found (30), in agreement with the very thin crystal structure proposed for this variety.

The catalytic activity of any one sample of MnO_2 for the decomposition of H_2O_2 is dependent on the surface area, but different samples may differ widely in catalytic activity (5). Variation in the overpotential of similar preparations of electrodeposited MnO_2 electrodes with the temperature and current density of electrodeposition can be explained entirely as caused by variations in surface area (29). However, in general the electrochemical activity of MnO_2 is more dependent on the state of the surface than on the particle size (31).

Ion exchange and isotope exchange.—Manganese oxides, especially when freshly prepared, adsorb a wide variety of cations from solution with liberation of hydrogen ions. This has been considered an exchange adsorption (32), and MnO_2 when hydrated, as most samples are, is a weak acid (33). In the manganous manganites, $4MnO_2 \cdot Mn(OH)_2 \cdot 2H_2O$ and $3MnO_2 \cdot Mn(OH)_2 \cdot xH_2O$, the Mn(II) can be replaced by Zn or various other cations in a reversible ion-exchange reaction (7, 34).

Exchanges between radioactive Mn^{++} and inactive MnO_2 that range from very small to complete have been observed (7). The amount of exchange varies widely with the nature of the MnO_2 and the conditions. With compact lattice structures as in β- and α-MnO_2 and the minerals ramsdellite and chalcophanite exchange of radioactive Mn^{++} takes place only at the surface. There is no diffusion in the lattice. The more open α-MnO_2 structure gives more exchange. Samples of α- and β-MnO_2 having nearly the same surface area per gram gave exchanges of 12% for α and 0.1% for β. In compounds of similar structure and surface area, exchange varies with the amount of disorder. Increase of temperature increases the amount of exchange; a β-MnO_2 that exchanged 2% at room temperature exchanged 15% in a boiling solution (7).

Connected with the ion-exchange property is the observation that each MnO_2 ore or preparation has a characteristic iso-acidic point. This is an electrolyte *p*H of such a value that no change in *p*H takes place when the electrolyte is put in contact with the MnO_2. When MnO_2 is stirred with an electrolyte of higher or lower *p*H than the iso-acidic point the electrolyte *p*H is changed in the direction to approach this point. This change must be taken into account in measuring the change of MnO_2 electrode potential with *p*H. The iso-acidic point is not the same as the isoelectric point which was found to be at the fixed *p*H 6.5 (35).

Magnetic susceptibility.—The magnetic susceptibilities of a number of manganese dioxides have been measured by Selwood, *et al.* (36). Crystalline pyrolusite is a magnetically concentrated substance; that is, the manganese atoms are so close together that they affect each other magnetically. Artificial γ-MnO_2, a gel form of MnO_2, and Gold Coast and Brazilian ores were found magnetically dilute, indicating a more attenuated structure, in agreement with other data. These have the magnetic behavior expected of a Mn(IV) compound. It was found possible to follow the discharge of a dry cell by measurement of its magnetic behavior, since reduction of Mn(IV) causes an increase in susceptibility.

Conductivity.—It is known that MnO_2 is a semiconductor. Four samples of MnO_2 under high pressure (7×10^8 g/cm^2 or 1×10^5 $lb/in.^2$) gave resistivities of 37-77 ohm-cm (37). Electronic semiconductivity is large when electrons can pass easily from one cation to another. This is the case when ions of one element of different electrical charge occupy equivalent positions in the crystal lattice (38).

Activity.—The term "activity" of a MnO_2 sample is used in describing the practical performance of the material in batteries. Brenet (39) states: "A high activity corresponds practically to the possibility of releasing a maximum quantity of electricity with a maximum potential difference at the cell terminals, over as long a period as possible." This is a tentative definition and he points to the need for a satisfactory method of measuring activity other than by making cells and discharging them. Also, the relation of activity to other properties is not well enough understood.

Lower Oxides of Manganese

The lower oxides and hydroxides of manganese are of interest as possible products of the reduction of MnO_2 in the discharge of the MnO_2 electrode. Two forms of the next lower oxide, Mn_2O_3, have been described and are designated as α- and γ-Mn_2O_3 (40). The more stable is α-Mn_2O_3 which is formed by heating β-MnO_2 to constant weight at 600°C

(41, 40). The less stable oxide, γ-Mn_2O_3, is thought to play a part in the discharge of the MnO_2 electrode (42). It is converted to α-Mn_2O_3 by heating in a vacuum at 500°C or on standing for a year at room temperature (40). The x-ray diffraction pattern of γ-Mn_2O_3 is nearly identical with that of Mn_3O_4, indicating a similarity in structure of these two compounds.

The compound MnOOH occurs as the mineral manganite and can be prepared by oxidation of a Mn(II) salt under carefully controlled conditions. It is a final product of the discharge of the MnO_2 electrode (42-45) and of the reduction of MnO_2 with Mn^{++} at *p*H 4 to 5 in the absence of Zn^{++} (46). Heating MnOOH at 250° in a vacuum gives γ-Mn_2O_3 (40).

The compound $ZnO \cdot Mn_2O_3$, or $Zn(MnO_2)_2$, which occurs naturally as the mineral hetaerolite, is another final product of the discharge of the Leclanché cell (45, 47) and is formed in the reduction of MnO_2 by Mn^{++} in the presence of Zn^{++} (46). Conditions for its formation in the dry cell have been studied (47). It cannot be the only product of the discharge, or alternatively not a primary product, because its formation would not involve the increase of *p*H in the bobbin electrolyte that is observed during discharge (44).

All oxides and hydroxides of Mn when heated in air to temperatures in the vicinity of 1000°C are converted to Mn_3O_4, which occurs naturally as the mineral hausmannite.

The compounds MnO and $Mn(OH)_2$ are easily oxidizable by oxygen. It is remarkable that MnO can be oxidized most of the way to Mn_2O_3 before the x-ray diffraction pattern of MnO disappears completely and that of Mn_2O_3 appears (40).

The valence of Mn in some of the lower oxides is a matter on which there is lack of agreement at present. Krishnan and Banerjee (48) measured the magnetic anisotropy of MnOOH and concluded that this compound must be composed of equal parts of Mn(II) and Mn(IV). Brenet (42) prefers to assume only Mn(II) and Mn(IV) in the compounds involved in the MnO_2 electrode reaction. Verwey and de Boer (38) have presented evidence that Mn_3O_4 is composed of Mn(II) and Mn(IV) ions from the electrical conductivity and the crystal structure. On the other hand they presented similar evidence that γ-Mn_2O_3 contains only Mn(III). Since γ-Mn_2O_3 can be prepared by the dehydration of MnOOH in a vacuum at 250°, Mn(III) is suggested for the latter compound, in disagreement with the evidence from magnetic anisotropy. Bhatnagar, *et al.* (41) found a magnetic moment for α-Mn_2O_3 that indicates Mn(III).

The Discharge Mechanism

Early theories.—One of the early theories of the discharge of the MnO_2 electrode was that hydrogen was the primary discharge product, this being subsequently oxidized by the MnO_2. The MnO_2 thus acted as a depolarizer. No definite evidence in favor of this theory has been advanced, and the facts concerning the discharge mechanism can be explained more satisfactorily otherwise.

Another theory involved the formation of Mn^{+4} ions in the electrolyte. Against this is the fact that physical contact between the MnO_2 and the metallic conductor (carbon in the Leclanché cell) is necessary for the effect of the MnO_2 to be detected (49). Also, no appreciable amount of oxidizing substance is found in an NH_4Cl solution digested with MnO_2 (50).

Divers (45) in 1882 explained the polarization of the MnO_2 electrode as the result of the accumulation on the surface of the MnO_2 of the products of the reaction, which he correctly identified as MnOOH and $ZnMn_2O_4$. Divers' explanation of the polarization seems not to have received the attention it deserved. Relatively recent experiments have led to a similar view of the mechanism.

Newer experimental data.—Some of the newer experiments have been carried out on dry cells, but more often special MnO_2 electrodes have been constructed that avoid some of the complications of the dry-cell bobbin. In any case the MnO_2 is brought into intimate contact with either carbon or platinum, by pressure or by electrodeposition of the MnO_2. Except in dry cells, a relatively large volume of electrolyte usually is employed to keep changes in composition small. In what follows it will be assumed that the electrolyte is NH_4Cl solution, with or without added $ZnCl_2$, unless otherwise specified. Potential measurements usually have been made with the help of a reference electrode.

In a dry-cell bobbin an increase in *p*H takes place on continuous discharge, and a decrease takes place near the zinc electrode. The increase in *p*H, resulting from the release of NH_3 in the electrode reaction, is partially compensated by the formation of $Zn(NH_3)_2Cl_2$ and other similar complex salts (44). This increase in *p*H shows that $Zn(MnO_2)_2$ is not the primary product of the discharge of the MnO_2 electrode of the Leclanché cell, as mentioned above.

Even when appreciable *p*H changes are avoided, or corrections made, the electrode potential of a discharging MnO_2 electrode decreases. The decrease is fairly rapid at first and may be slow later. If the circuit is opened the potential rises fairly rapidly at first, then more and more slowly for a period of days, but does not reattain the initial potential (51). The potential decrease during discharge may be described as a decrease in open-circuit potential combined with a rather large polarization. The growth and decay of this polarization is much slower than in most electrode systems, indicating that it is not simple activation polarization or concentration polarization involving the solution (52, 53). Substitution of other ammonium salts for NH_4Cl makes little or no difference (51) and discharges in 4.4M KOH give much the same results (54).

In the absence of $ZnCl_2$ two products of discharge are observed under most conditions. Mn^{++} is found in solution (55-57) and when the discharge is carried to the point of rapid decrease in potential which terminates the useful part of the discharge an oxide (or oxide mixture) of the composition $MnO_{1.6}$ remains (56, 57). In this solid MnOOH can be recognized by its x-ray diffraction pattern (42).

Analysis of the bobbins of discharged dry cells shows Mn in three forms. Some Mn can be extracted from the bobbin material by a solution of NH_4Cl and $ZnCl_2$ and presumably comes from Mn(II) compounds in the bobbin. The insoluble portion contains both MnOOH and $Zn(MnO_2)_2$. The formation of these products by reduction of MnO_2 accounts quantitatively for the current passed in the discharge (58).

Data on the formation of Mn^{++} as a product of the discharge reveal something of the discharge mechanism. With an electrolyte of H_2SO_4 and $MnSO_4$ it is the only discharge product, other than H_2O (59). At *p*H 5 in the discharge of γ-MnO_2 electrodeposited on graphite with NH_4Cl or $(NH_4)_2SO_4$ electrolyte, Mn^{++} is formed throughout the discharge. At *p*H 7.5 or 8 under the same conditions no Mn^{++} is formed in the early part of the discharge (56, 60). The amount of Mn^{++} formed at any one *p*H is independent of the volume of the electrolyte. The presence of Zn^{++} in the electrolyte reduces the amount of Mn^{++} (61).

Changes in the x-ray diffraction pattern of the oxide during a discharge have been observed (42). Starting with γ-MnO_2, the diffraction patterns indicate an expansion of the crystal lattice as the discharge proceeds. With α-MnO_2 the expansion is not as evident, but is believed to take place. After discharge of a little less than half of the theoretical capacity of the MnO_2 a sudden change in the pattern takes place. The new pattern is that of either γ-Mn_2O_3 or Mn_3O_4 (these being nearly the same), and of the two the γ-Mn_2O_3 is considered the more probable. Finally the pattern of MnOOH appears. When β-MnO_2 is reduced electrolytically only the change to MnOOH is observed.

Interpretation of the experiments.—The slow rate of decay of polarization led Coleman (52) to propose that a solid-state diffusion process is involved. Lower oxide formed on the surface of the MnO_2 is thought to cause the polarization, and a diffusion process operates to remove it (51, 56). This involves the assumption that the composition of the surface of the oxide determines the electrode potential (27, 28). The decay of polarization can then be interpreted as an increase in the available oxygen content of the surface as the result of removal of lower oxide. However, another probable contributing factor is discussed below.

The diffusion process involved in the discharge need not be considered an actual diffusion of Mn and O atoms. The same effect can be attained and electroneutrality preserved within the solid by diffusion of protons and electrons only. Since MnO_2 is a semiconductor we may suppose that electrons can pass through it by being transferred between Mn atoms in different stages of oxidation but at equivalent positions in the crystal lattice (38). Protons can be attached to $O^=$ ions to give OH^- ions. If protons can be transferred from surface OH^- ions to underlying $O^=$ ions and at the same time electrons move from surface Mn ions to underlying ones, the lower oxide on the surface has effectively moved and MnO_2 has moved outward. This should cause the expansion of the MnO_2 lattice that is observed, because Mn^{+3} is larger than Mn^{+4} and OH^- is larger than $O^=$.

The changes taking place during discharge can be explained similarly. To reduce MnO_2 requires electrons for the Mn atoms and protons for attachment to the O atoms. Electrons come from the electrode and with physical contact between electrode and oxide they are available anywhere within the MnO_2. Protons are available from NH_4^+ ions of the electrolyte or from H_2O. The reaction may be considered to take place where the electrons and protons meet, for it may be considered that here the oxide is reduced. Qualitatively, the meeting place can be considered to to be at the surface of the MnO_2 exposed to the solution. One reason for postulating this location is the formation of Mn^{++} in the solution. The indications are that the Mn^{++} is dissolved from a surface oxide by action of the electrolyte (61). The reduction reaction on the surface is followed by reaction of part of the lower oxide to give Mn^{++} and inward diffusion of the remainder.

A somewhat different view is that during the discharge the protons penetrate the oxide and meet the electrons in the interior (42, 57). Some of the reaction must still be considered to be on the surface to explain the formation of Mn^{++} and the growth and decay of polarization in terms of an increase in the amount of lower oxide during current flow and its decrease when the circuit has been opened (62).

To decide between the two suggested locations of the reaction one may ask whether diffusion inward from the surface is fast enough to account for the reduction of MnO_2 during a discharge to an oxide of the composition $MnO_{1.6}$. Some recent experiments in the author's laboratory indicate that it is not, and we must assume with Brenet (42) and Naumann and Fink (57) that protons from the solution can penetrate to the interior of the oxide during a discharge.

There is a disagreement as to the valence of Mn in the solid primary product of the electrode reaction. Brenet (42) points to the instability of Mn^{+3} in solution and to the evidence that the final product, MnOOH, is composed of equal amounts of Mn(II) and Mn(IV), and prefers to assume that Mn^{++} [or $Mn(OH)_2$] within the oxide structure is the primary product. This eventually combines with an equivalent amount of MnO_2 to give MnOOH. Others (55, 56) have assumed the formation of a Mn(III) compound as the first step in the reduction. This may be followed by further reduction to Mn^{++}, especially on the surface, accounting for the large fall in potential during discharge.

There can be little doubt that Mn^{+3} is the first reduction product of Mn^{+4}, because the simultaneous entrance of two electrons into a Mn^{+4} ion is improbable. The question is whether this ion is stable on the surface of, or within, a MnO_2 structure or must be immediately reoxidized or reduced to Mn^{++}. While Mn^{+3} is unstable in solution, some of the Mn(III) complexes are quite stable. This is true, for example, of the pyrophosphate complex, which is soluble and sufficiently stable to be the reaction product in a precise titration (63). The bonds to oxygen joining the Mn to the complex must be somewhat similar to the bonds between Mn and O in the solid oxide.

Because there is a possibility of the stable existence of a Mn(IIII) oxide (or oxyhydroxide) on (or in) the MnO_2 it will be assumed in what follows that this is the primary product of the reduction of MnO_2. The discussion would be little different if $Mn(OH)_2$ were assumed.

The discharge mechanism.—A definite discharge mechanism can be formulated on the basis of the above experiments and conclusions. It is constructed to apply to electrodeposited MnO_2 on a graphite rod, but should be easily adaptable to a bobbin.

When current starts, electrons from the electrode and protons from the solution meet at the surface of the MnO_2 exposed to the solution and also beneath the surface, many of the protons penetrating the crystal lattice of the MnO_2. The electrons are retained by Mn atoms and the protons are attached to $O^=$ ions to form OH^- ions.

$$MnO_2 + H^+ + e^- \rightarrow MnOOH$$

The surface of the MnO_2 is very large, so the true current density is small, and with a concentrated electrolyte the ordinary concentration polarization is small. There is no evidence of appreciable activation polarization. However, as the surface composition changes from largely MnO_2 to one containing much MnOOH the electrode potential decreases. This decrease is slow because the surface is large and because much of the lower oxide is formed beneath the surface. There is in addition a diffusion toward the interior where there is less lower oxide. With γ-MnO_2 the decrease in potential is slower than with α-MnO_2 or with γ-MnO_2 that has been heated (29). It may be concluded that in α-MnO_2 and heated γ-MnO_2 the penetration of the protons is less than in the unheated γ-MnO_2, and consequently the surface gains lower oxide more rapidly.

When enough MnOOH has accumulated on the surface of the MnO_2 further reduction to $Mn(OH)_2$ takes place.

$$MnOOH + H^+ + e^- \rightarrow Mn(OH)_2$$

Then Mn^{++} appears in the electrolyte and as the surface is reduced further giving a larger surface concentration of Mn(II) the potential continues to fall.

The lower oxides on the surface will react with the electrolyte if the composition and *p*H are suitable. At *p*H 5 MnOOH can react.

$$2MnOOH + 2H^+ \rightarrow MnO_2 + Mn^{++} + 2H_2O$$

As the *p*H increases the surface must be further reduced to react appreciably.

$$Mn(OH)_2 + 2H^+ \rightarrow Mn^{++} + 2H_2O$$

These reactions are slow and do not come to equilibrium in short discharges (60). They are not dependent on current flow and continue after the circuit is broken. Therefore, more Mn^{++} is formed in an intermittent discharge than in a continuous one (56).

When after a period of discharge the circuit is broken, the excess lower oxide on the surface decreases fairly rapidly at first and then more and more slowly. Inward diffusion of the lower oxide takes place and if conditions are favorable the oxide also reacts with the electrolyte to give Mn^{++}. The potential therefore rises, but since the MnO_2 as a whole now contains less available oxygen than initially the potential never reattains the initial value.

A discharge terminates with a relatively rapid decrease in potential when the formation of reduction products on the surface is considerably faster than their disposal. What causes this condition is not clear. The only suggestion is that the lattice hardens and protons can no longer penetrate it (57).

Daniel-Bek (64) has presented a different theory to account for the polarization and recovery of the MnO_2 electrode. He observed that the potential of graphite or carbon in contact with NH_4Cl solution is very stable and is less than that of MnO_2. Also, a mixture of MnO_2 and carbon in contact with NH_4Cl solution has a smaller potential than MnO_2 alone. This was also observed by Jennings and Vosburgh (50). MnO_2 in contact with carbon and electrolyte is considered to constitute a short-circuited local cell. Such a cell is like a local cell on a metal surface, but with larger resistance in the electronic portion of the circuit. With the electrode as a whole on open circuit the current in the local cell is small because of polarization, but because of the appreciable resistance between MnO_2 and carbon the potential of the carbon is smaller than that of the MnO_2. Both are smaller than the true open-circuit potential of the MnO_2.

When the MnO_2 electrode is discharged the potential of the carbon decreases more than that of the MnO_2 and its surface (which is of low capacity) is partly discharged. The potential of the carbon determines the measured potential of the electrode as a whole. When the external circuit is broken the carbon must be recharged by the local-cell current before a steady state is reattained.

The theory of Daniel-Bek accounts qualitatively for the polarization and recovery of the MnO_2 electrode and is in accord with the effect on the electrode behavior of variation of the surface area of the carbon. It seems probable that both this and the theory based on the changes in composition of the MnO_2 will need to be taken into account in a complete theory of the MnO_2 electrode process.

A mechanism has been proposed by Cahoon and coworkers (55, 58) that differs somewhat from the one described above. They consider the MnO_2 to be reduced electrochemically directly to Mn^{++} which passes into solution. The Mn^{++} then reacts with MnO_2 to give MnOOH, or with MnO_2 and Zn^{++} to give hetaerolite. This is quite similar to the mechanism of Brenet (42). He considers that the electrochemical reaction is reduction to Mn^{++} within the MnO_2 lattice. The Mn^{++} passes into solution (but not necessarily immediately) and forms $Mn(OH)_2$ which is oxidized to MnOOH. More research is needed to reconcile the different theories that have been proposed.

Acknowledgment

The preparation of this paper was supported in part by the Office of Ordnance Research.

Manuscript received Feb. 25, 1959. This paper was prepared for delivery before the Ottawa Meeting, Sept. 28-Oct. 2, 1958.

Any discussion of this paper will appear in a Discussion Section to be published in the June 1960 JOURNAL.

REFERENCES

1. G. Leclanché, *LeMondes*, **16**, 532 (1868); *Compt. rend.*, **83**, 54 (1876).
2. G. W. Heise and N. C. Cahoon, *This Journal*, **99**, 179C (1952).
3. C. K. Morehouse, *ibid.*, **99**, 187C (1952).
4. W. S. Herbert, *ibid.*, **99**, 190C (1952).
5. A. D. Wadsley and A. Walkley, *Revs. Pure and Appl. Chem. (Australia)*, **1**, 203 (1951).
6. J. Brenet, *Bull. Soc. franc. mineral. et crist.*, **77**, 797 (1954).
7. W. Buser and P. Graf, *Helv. Chim. Acta*, **38**, 810 (1955).
8. A. M. Bystrom, *Acta Chem. Scand.*, **3**, 163 (1949).
9. A. D. Wadsley, *Acta Cryst.*, **6**, 433 (1953).
10. J. W. Gruner, *Am. Mineral.*, **28**, 497 (1943).
11. A. Bystrom and A. M. Bystrom, *Acta Cryst.*, **3**, 146 (1950).
12. A. D. Wadsley, *ibid.*, **5**, 676 (1952), **8**, 165 (1955).
13. W. M. Latimer, "Oxidation Potentials," 2nd ed., p. 238, Prentice-Hall, Inc., New York (1952).
14. W. F. Cole, A. D. Wadsley, and A. Walkley, *Trans. Electrochem. Soc.*, **92**, 133 (1947).
15. P. H. Delano, *Ind. Eng. Chem.*, **42**, 523 (1950).
16. H. F. McMurdie, *Trans. Electrochem. Soc.*, **86**, 313 (1944).
17. W. Buser, P. Graf, and W. Feitknecht, *Helv. Chim. Acta*, **37**, 2322 (1954).
18. S. Okada, I. Uei, and H. Chin, *J. Eletrochem. Soc. Japan*, **15**, 79 (1947).
19. I. Nakajima, *ibid.*, **21**, 369 (1953).
20. G. Butler and H. R. Thirsk, *Acta Cryst.*, **5**, 288 (1952).
21. K. H. Maxwell and H. R. Thirsk, Proc. 6th Meeting Intern. Comm. Electrochem., Thermodynam., and Kinet., **1955**, 390.
22. W. Feitknecht and W. Marti, *Helv. Chim. Acta*, **28**, 129, 149 (1945).
23. A. D. Wadsley, *J. Am. Chem. Soc.*, **72**, 1781 (1950).
24. G. Butler and H. R. Thirsk, *This Journal*, **100**, 297 (1953).
25. W. Buser and P. Graf, *Helv. Chim. Acta*, **38**, 810 (1955).
26. G. Brenet and A. M. Moussard-Briot, *Rev. gen elec.*, **61**, 405 (1952).
27. A. Kozawa and K. Sasaki, *J. Electrochem. Soc., Japan*, **22**, 569 (1954).
28. A. Kozawa, *This Journal*, **106**, 79 (1959).
29. A. Kozawa and W. C. Vosburgh, *ibid.*, **105**, 59 (1958).
30. W. Buser and P. Graf, *Helv. Chim. Acta*, **38**, 830 (1955).
31. J. Brenet and A. Herand, *Compt. rend.*, **230**, 1598 (1950).
32. B. Ghosh, *J. Chem. Soc.*, **1926**, 2605.
33. W. Biltz and O. Rahlfs, *Nachr. Ges. Wiss. Göttingen Geschaft., Mitt., Math-physik. Klasse* **1930**, 189. *Chem. Zentr.*, **102 I**, 45 (1931).
34. P. Jordon, *Helv. Chim. Acta*, **34**, 699 (1951).
35. K. Sasaki, *Mem. Fac. Eng. Nagoya Univ.*, **3**, 81 (1951).
36. P. W. Selwood, R. P. Eischens, M. Ellis, and K. Wethington, *J. Am. Chem. Soc.*, **71**, 3039 (1949).
37. R. Glicksman and C. K. Morehouse, *This Journal*, **103**, 149 (1956).
38. E. J. W. Verwey and J. H. de Boer, *Rec. trav. chim.*, **55**, 531 (1936).
39. J. Brenet, *Proc. Intern. Comm. Electrochem. Thermodynam. and Kinet. 7th Meeting, Lindaw 1955* (Pub. *1957*), p. 299.
40. T. E. Moore, M. Ellis, and P. W. Selwood, *J. Am. Chem. Soc.*, **72**, 856 (1950).
41. S. S. Bhatnagar, A. Cameron, E. H. Harbard, P. L. Kapur, A. King, and Bram Prakash, *J. Chem. Soc.*, **1939**, 1433.
42. J. Brenet, *Proc. Intern. Comm. Electrochem. Thermodynam. and Kinetics. 8th Meeting, Madrid, 1956.*
43. N. C. Cahoon, *Trans. Electrochem. Soc.*, **92**, 159 (1947).
44. N. C. Cahoon and G. W. Heise, *This Journal*, **94**, 218 (1948).
45. E. Divers, *Chem. News*, **46**, 259 (1882).
46. H. F. McMurdie, D. N. Craig, and G. W. Vinal, *Trans. Electrochem. Soc.*, **90**, 509 (1946).
47. L. C. Copeland and F. S. Griffith, *ibid.*, **89**, 495 (1946).
48. K. S. Krishnan and S. Banerjee, *Trans. Faraday Soc.*, **35**, 385 (1939).
49. A. Keller, *Z. Elektrochem.*, **37**, 342 (1931).
50. C. W. Jennings and W. C. Vosburgh, *This Journal*, **99**, 309 (1952).
51. D. T. Ferrell, Jr., and W. C. Vosburgh, *ibid.*, **98**, 334 (1951).
52. J. J. Coleman, *Trans. Electrochem. Soc.*, **90**, 545 (1946).
53. A. M. Chreitzberg, Jr., and W. C. Vosburgh, *This Journal*, **104**, 1 (1957).
54. P. D. Lukovtsev and S. A. Temerin, *Trudy Soveshchaniya Electrokhim. Acad. Nauk S.S.S.R., Otdel. Khim Nauk* **1950**, 494 (1953).
55. N. C. Cahoon, *This Journal*, **99**, 343 (1952).
56. A. M. Chreitzberg, Jr., D. R. Allenson, and W. C. Vosburgh, *ibid.*, **102**, 557 (1955).
57. K. Naumann and W. Fink, *Z. Elektrochem.*, **62**, 114 (1958).
58. N. C. Cahoon, R. S. Johnson, and M. P. Korver, *This Journal*, **105**, 296 (1958).
59. S. Yoshizawa and W. C. Vosburgh, *ibid.*, **104**, 399 (1957).
60. A. Sam, Ph.D. Thesis, Duke University, 1958.
61. W. C. Vosburgh, M. J. Pribble, A. Kozawa, and A. Sam, *This Journal*, **105**, 1 (1958).
62. J. Euler, *Z. Elektrochem.*, **60**, 1056 (1956).
63. J. J. Lingane and R. Karplus, *Ind. Eng. Chem., Anal. Ed.*, **18**, 191 (1946).
64. V. S. Daniel-Bek, *Trudy Soveshchaniya Elektrokhim. Akad. Nauk S.S.S.R., Otdel. Khim Nauk* **1950**, 513 (1953).

Brief Communication

Investigations on the Silver-Zinc Alkaline Storage Battery by the Aid of Radioactive Isotopes

Theodore Z. Palágyi

Central Research Institute for Chemistry, Hungarian Academy of Sciences, Budapest, Hungary

The failure of silver-zinc storage batteries is generally caused by the negative electrode, and less often by the separator or the positive electrode (1, 2). Both silver and zinc have isotopes with suitable hard gamma radiation and half-life of about ¾ year; consequently these isotopes can be used easily for labelling of electrodes. This fact induced us to employ Zn^{65} and Ag^{110} isotopes for the purpose of life tests and for investigating processes taking place during storage of the cells.

Our method was based on the hypothesis that, if Zn^{65} isotope is deposited on one of the negative plates of the cell, then the path of the ions while cycling can be followed by the aid of the radioactive contamination of the surface of the nonlabelled plates. The same principle was used to label with Ag^{110} isotope the positive electrode of experimental cells and to follow the path of the dissolved silver ions.

The experiments were performed with cells of 10 amp-hr nominal capacity. Both the zinc and the silver isotopes were deposited on the electrodes by electrolysis. The quantity of the deposited isotope was controlled partly by measuring the activity change of the electrolysis solution and partly by measuring the activity on the electrode itself, with a cylindrical GM-tube, as well as by the autoradiographic method.

The investigations were performed with cells assembled in three different ways: loosely, normally, and more tightly than normal. Each cell contained only one labelled (positive or negative) plate. After formation, some of the experimental cells were cycled and the others were subjected to storage. One charging-discharging cycle lasted 24 hr. After each tenth cycle a measuring discharge was performed.

As far as possible examinations were performed simultaneously on the cells assembled in the three different ways. The cells were opened after the first 20 cycles and after each 20 subsequent cycles, and the degree of contamination of the individual plates with isotope was examined. Then the electrodes were replaced in the cells and the cycling was continued, with the exception of the tightly assembled cells in which the electrodes could not be replaced.

On the basis of contamination with isotope of the nonlabelled electrodes, our experiments show that the zinc ions dissolved from the labelled negative plate can reach not only the other negative plates but the positive electrodes too. The degree of migration of the zinc ions considerably depends on the mode of building in of the electrodes and on the quantity of the electrolyte; in tightly assembled cells having little electrolyte the migration of the zinc ions is of lower degree. The failure of the loosely assembled cells was usually caused by coming to an end of the reversibility of the negative electrode as well as by the formation of acicular zinc crystals, resulting in short circuit. Failure of the tightly assembled cells was caused rather by the separator losing its insulating properties; moreover, the active material of the positive electrode dissolved and reached the negative electrode. Our investigations with Ag^{110} isotope related to this problem and to the storage of cells are still under way.

Manuscript received May 14, 1959.

Any discussion of this paper will appear in a Discussion Section to be published in the June 1960 JOURNAL.

REFERENCES

1. H. H. Bieber, P. F. Bruins, and H. P. Gregor, *Ind. Eng. Chem.*, **50**, 1273 (1958).
2. E. Zöld and L. Kiss, *Magy. Kém. F.*, **63**, 334 (1957).

The Oxide Films Formed on Copper Single Crystal Surfaces in Pure Water

I. Nature of the Films Formed at Room Temperature

Jerome Kruger

National Bureau of Standards, Washington, D. C.

ABSTRACT

A study was made of the nature of the films that formed on carefully prepared surfaces of single crystals of copper immersed in water containing varying amounts of oxygen, with the surrounding atmosphere both controlled and uncontrolled. It was found that the amount of oxidation depended on the crystallographic orientation of the metal surface. Cu_2O was the oxide observed if $pH \leqq 5.7$. Intense white light markedly retarded film formation in water. When Cu_2O was formed, it had a preferred orientation and exhibited epitaxial relationships to the metal similar to those found in high-temperature oxidation. The films formed were not continuous but were composed of small nuclei of Cu_2O. Both Cu_2O and CuO were formed at pH 7 when the water was in equilibrium with an atmosphere of pure O_2. Lowering the pH converted CuO to Cu_2O.

The oxide films that form on a metal surface are one of the very important factors influencing most corrosion processes. These films affect the potential that the surface exhibits and influence the transport of metal ions away from it. Both of these aspects are interrelated and have an important influence on the corrosion of metals. In connection with work on the fundamentals of corrosion sponsored by the Corrosion Research Council, the subject selected for study was the growth of films on metal surfaces in contact with pure water containing oxygen. This system was chosen because most corrosion encountered in practice involves metal, water, and oxygen, plus a number of other substances. Thus if some understanding can be gained of this simple system, it would serve as a basis for study of the complicated systems that are related more closely to practical cases.

The metal chosen to initiate this study was copper, because it has a simple structure, and high-purity metal is available from which single crystals may be prepared easily. Its oxides are few and simple, and a great deal of fundamental data on its properties is available.

Work on the growth of films on Cu in water in the past (1-4) has been done generally on poorly characterized metal surfaces under conditions where the nature of the surrounding atmosphere and the purity of the water was not rigidly controlled. Much work has been done on the corrosion of Cu in aqueous solutions of many different compositions. However, with the possible exception of the work of Miller and Lawless (5) on single crystals, the surfaces used were in general poorly characterized. As a consequence the studies carried out are not as significant from a fundamental standpoint as they should be.

The work described here employs surfaces whose nature is better known than the surfaces used in most of the corrosion studies of Cu in aqueous media. The approach in this investigation was to use single-crystal surfaces, carefully prepared so that they would be as clean as possible and free from strain (6). This paper is concerned with some qualitative studies of the nature of the films formed on Cu in pure water containing oxygen. A subsequent paper will report studies of the rate of film formation.

Experimental Procedure

Materials.—The crystals used in this investigation were grown using OFHC Cu which has a purity of 99.99%.[1] The Bridgman technique of slowly cooling a melt was used to grow crystals in the shape of spheres ⅜ in. in diameter with a cylindrical shaft ¼ in. in diameter and ¾ in. in length. The water was obtained from the Physical Chemistry Section of the National Bureau of Standards and had a conductivity of 7×10^{-7} mhos.

Preparation of the metal surface.—In a number of experiments the as-cast single-crystal sphere was used after following appropriate cleaning and polishing procedures. These consisted in washing the crystal successively in water, ethyl alcohol, diethyl ether, and again in ethyl alcohol and water prior to electrolytically polishing the crystal in a phosphoric acid-water solution 50% by volume. After the electrolytic polishing was completed (1 hr the first time after casting, 10-20 min all times thereafter) the crystal was washed very carefully to remove traces of phosphate ions, following the schedule described by Young, Cathcart, and Gwathmey (6), who found that this washing procedure left a surface that oxidized reproducibly. In the case of experiments carried out in the room atmosphere, the crystal was immediately immersed while still wet in distilled water. When it was introduced into

[1] Spectrographic analysis showed that the Cu used contained 0.001 to 0.01% Ag and < 0.0001% Si, Al, Fe, Mg, Ni, and Pb.

the reaction chamber of the apparatus designed for carrying out the process under controlled conditions, the water remaining on the crystal was evaporated by evacuation of the system. Whenever the crystal was handled, preflamed gold-plated tongs were used to hold the shaft of the crystal.

For some studies three flat surfaces were cut parallel to the {111}, {110}, and {100} crystallographic planes. After cutting these surfaces the crystal was etched in nitric acid to remove the strained layer resulting from this operation. The orientations of the surfaces were checked and corrected, if they differed by more than 2° from the desired orientation. These surfaces then were polished mechanically with metallographic polishing papers through No. 0000 and lapped on a metallographic wheel with a water suspension of Linde B abrasive. From this point on the procedure was as described above.

Reaction apparatus and procedure.—Two different groups of experiments were carried out using Cu crystal surfaces prepared as described above. In the first group the nature of the surrounding atmosphere was not controlled. The procedure in this case was simply to immerse the crystal after electropolishing and washing directly, and while still wet, in 100 ml of distilled water. The crystals were mounted in glass holders and gas washing bottles were used as reaction vessels.

In the second group of experiments the nature of the surrounding atmosphere was controlled by carrying out the reaction in the enclosed apparatus shown in Fig. 1. The crystal, after polishing and washing, was introduced together with the glass crystal holder into the reaction chamber through its top, using a preflamed platinum hook. Introducing the crystal into the apparatus in this manner eliminated the need for greased ground joints with the attendant possibilities for contamination. The top of the chamber then was sealed. An oxy-hydrogen flame was used in the sealing process rather than the ordinary natural gas-oxygen flame because the latter was found to introduce contaminants. The high-purity water was introduced into the freeze-down tube and boiled before sealing and pumping. Half of the water in this tube was distilled in vacuum into the water-introduction tube by placing a Dewar flask of liquid nitrogen around this tube.

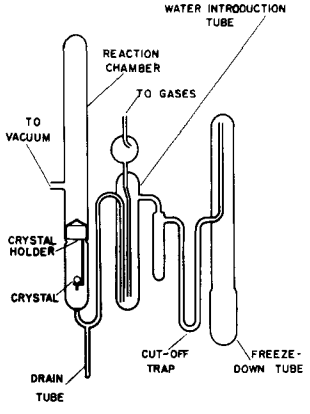

Fig. 1. Apparatus for oxidizing Cu single crystal in water under controlled conditions.

The frozen water so collected was thawed and then pushed into the reaction chamber by helium. The purpose of this part of the procedure was to rinse off any impurities that might have collected on the crystal during the time when it was being placed into the reaction chamber. The water was removed by breaking open the drain tube and pushing it out with a positive pressure of helium. The drain tube then was resealed, and the water remaining in the freeze-down tube was kept frozen in liquid nitrogen until required. Liquid nitrogen also was placed around the cut-off trap as an added measure to prevent any water from reaching the reaction chamber while it was being baked at 500°C overnight at a pressure of 10^{-5} mm. After this baking procedure, with the water still frozen in the freeze-down tube, the crystal was annealed in purified dry hydrogen at 500°C for 2 hr to remove the air-formed oxide film present on the crystal surface. The system then was evacuated, brought to room temperature, and the water in the freeze-down tube distilled over to the water-introduction tube by cooling this tube in liquid nitrogen. This water was thawed, pushed into the reaction chamber by the desired gas (e.g., dry purified oxygen), and the corrosion process allowed to start. To halt the reaction, the water was drained by cracking open the drain tube, resealing, and evacuating the system to dry the crystal. The crystal then was removed for examination by cracking open the top of the reaction chamber.

Results

Corrosion in Water with the Surrounding Atmosphere Uncontrolled

In these experiments, which were essentially preliminary in order to explore and determine the nature and magnitude of the effects to be studied, the Cu was immersed in water that was in contact with the room atmosphere. The spherical single crystal offers an ideal tool for exploratory experiments of this type because all of the crystallographic planes are represented as poles on the surface of the sphere and thus all of them can be studied simultaneously.

The following results were obtained from these experiments:

1. Oxidation was the most readily apparent reaction taking place.

When a crystal was placed in water deoxygenated by boiling, and either hydrogen or helium was bubbled in, no film formation was observed and the crystal remained bright. When oxygen was present, however, a film whose presence was indicated by the appearance of interference colors on the Cu was formed after exposure to the water.

2. At room temperature, oxide films formed on the Cu surface considerably faster in water than in air.

If a Cu crystal was allowed to stand in dry air or oxygen at room temperature no interference colors, which give an indication of the thickness of the films growing on the metal surface, were observed after weeks of standing. In water, however, colors

started to develop after standing only 30 min. Within 6 hr films exhibiting interference colors indicating thicknesses greater than 1000Å were observed.

3. The rate of oxidation varied with the crystallographic plane.

The thickness and thus the color of films formed on Cu exposed to air-saturated water varied with the crystallographic plane on which they were growing. Since all of the crystallographic poles could be observed simultaneously on the spherical crystal these differences could be seen easily. After a given time of exposure a symmetrical pattern made up of many different colors was obtained on the sphere, thus indicating a variation in the amount of film growth with crystallographic orientation. Such a pattern is shown in Fig. 2. Because the patterns formed on the single crystal spheres were extremely sensitive to a very minute change in environment or surface condition, many different patterns were observed unless the nature of the surrounding atmosphere, and the cleanliness of the water and the metal surface, were controlled rigidly. Thus, on the basis of these preliminary experiments carried out in the room atmosphere, it is not possible to list definitely the various crystallographic planes in the order of their relative rates of oxidation.

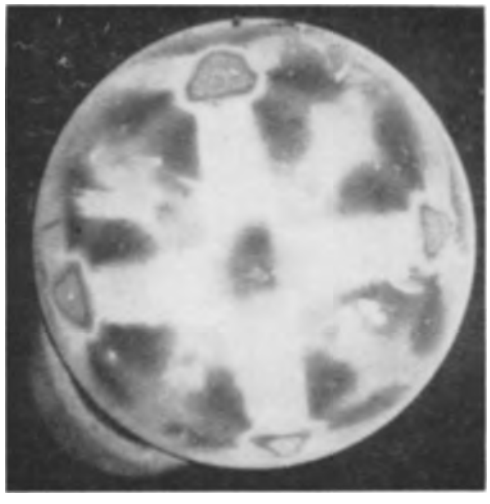

Fig. 2. Pattern formed when Cu single-crystal sphere is corroded in air-saturated distilled water at room temperature.

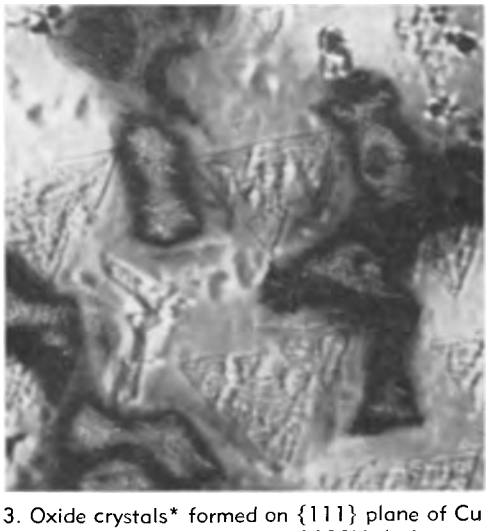

Fig. 3. Oxide crystals* formed on {111} plane of Cu crystal oxidized in water. Magnification 1000X before reduction for publication.

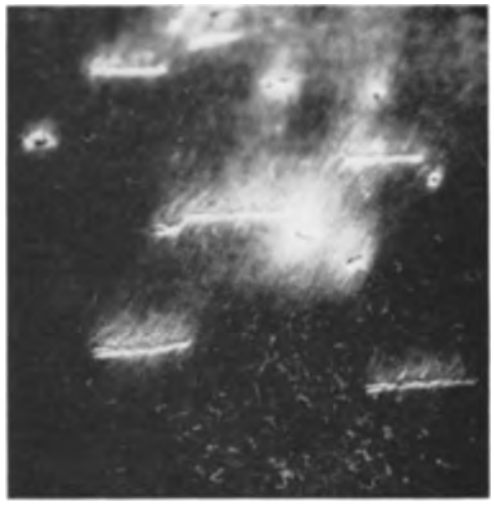

Fig. 4. Oxide crystals* formed on {110} plane of Cu crystal oxidized in water. Magnification 1000X before reduction for publication.

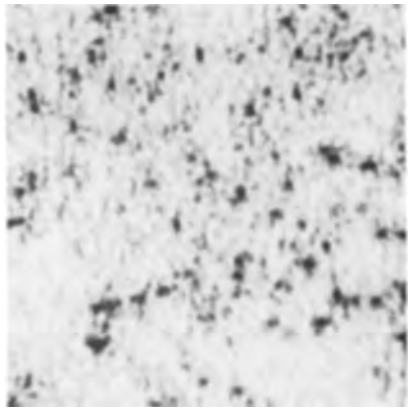

Fig. 5. Oxide crystals* formed on {100} plane of Cu crystal oxidized in water. 1000X.

4. The oxide films were not continuous.

When observed with unaided eye, the oxide films appeared to be uniform. However, microscopic examination indicated that the oxide films were made up of particles or nuclei. Figures 3, 4, and 5 show these oxide nuclei formed on a Cu surface exposed to water on three different crystallographic planes.

5. The degree of orientation and epitaxy of the oxide films depended on the crystal faces upon which they were grown.

X-ray diffraction studies, using the oscillating crystal technique described by Lawless and Gwathmey (7), were carried out to determine the chemical nature of the films and their epitaxial relationship to the metal substrate. Studies of the films formed on Cu crystals exposed to distilled water in an uncontrolled atmosphere for 18 hr showed them to be composed of Cu_2O made up of many crystallites exhibiting a preferred orientation with respect to the Cu substrate. In general, the degree of preferred orientation was higher for the {111} and {110}

* Note that the shape of some of the crystallites are indicative of the symmetry of the crystallographic orientation of the plane on which they are growing.

Table I. Epitaxial relationships between Cu and Cu_2O

Crystal face of Cu	Crystal face of Cu_2O parallel to Cu
{111}	{111}
{110}	{110}
{100}	{111}

planes than that for the {100} plane. The epitaxial relationships, i.e., the mutual orientation relationship between the Cu_2O and the Cu substrate, are shown in Table I.

These relationships agree with those found by others (7-9) on Cu single crystals oxidized in dry oxygen at temperatures considerably above room temperature.

6. Light had a marked influence on the oxidation process in water.

A number of attempts were made to obtain time-lapse motion pictures of the corrosion process of a Cu single crystal in air-saturated water. These were not successful because it was found that the light used to illuminate the crystal had a marked influence on the corrosion process (10). As a consequence, it was decided to study the effect of light on the oxidation process of Cu in water. A water-jacketed vessel, light-tight except for a small hole which allowed light to impinge on half of a crystal sphere, was employed, as shown in Fig. 6. When the crystal was immersed in air-saturated water in this vessel, illuminated by a tungsten 3200°K lamp, and kept at room temperature by the water jacket for 3 hr, the amount of oxidation on the area of the sphere exposed to the light was markedly different from that of the shaded area (see Fig. 7 and 8). Using a simple electroreduction technique similar to that of Miley and Evans (11) to estimate film thickness, it was found that the illuminated part of the crystal had a thickness of roughly 120Å or less,

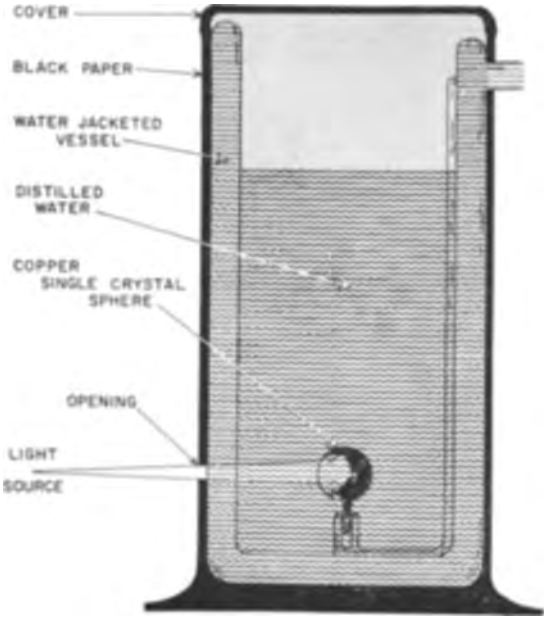

Fig. 6. Apparatus for studying influence of light on oxidation of Cu crystal in water.

Fig. 7. Copper single crystal oxidized in air-saturated distilled water at 25°C. Lower side was exposed to light from a 3200°K tungsten lamp, upper side kept dark.

Fig. 8. Boundary between dark and illuminated areas of Cu single crystal surface oxidized in air-saturated distilled water at 25°C. Upper region kept dark, lower illuminated. 500X.

while the part that was kept dark had an average thickness of approximately 550Å. Further, if light were allowed to impinge on part of a Cu crystal immersed in water and already containing a water-formed oxide film about 1000Å thick or greater, some of the oxide on the illuminated portion dissolved after a period of 2-3 hr and became thinner than the part kept dark. X-ray diffraction studies of the films formed on both the dark and the illuminated parts of the crystal showed that the films were composed of well-oriented Cu_2O.

Mott's theory (12) for Cu-Cu_2O photocells may provide an explanation for this effect. On the basis of this theory, illumination would cause a flow of electrons from the semiconductor film, Cu_2O, into the metal. A flow of electrons in this direction when the film is growing would thus inhibit growth. It is interesting to point out that for Al_2O_3 and Ta_2O_5, which are cation excess semiconductors, illumination enhances oxidation, while Cu_2O, a cation deficient semiconductor, oxidation is inhibited. Besides

this explanation, based on the effect of illumination on the electrons on the solid side of the solid-liquid interface, another explanation based on the influence of light on chemical reactions at the metal-solution interface should be considered also. These reactions may be important, for it is known (13) that light promotes the oxidation of cuprous ions to cupric. Thus any Cu_2O that forms may be oxidized to CuO. Since the latter is the more soluble of the two, it may go into solution rather than form a film, as in the case of the Cu_2O.

Corrosion in Water with Surrounding Atmosphere Controlled

In these experiments the techniques described in the Experimental Section for preparing the crystal surface and reacting it with pure water in a controlled atmosphere were utilized. The results obtained differed considerably from those observed under uncontrolled conditions.

In the controlled experiment the Cu crystal was immersed in high-purity water, which was stirred and kept saturated by bubbling O_2 through it at a rate of approximately 50 ml/min at 1 atm and 25°C. Oxidation was considerably slower in these experiments than in the experiments where the nature of the atmosphere was uncontrolled. It was found that after 1 hr the film thickness was roughly 70Å, and after 8 hr the thickness had not changed appreciably. After 50 hr of exposure the average value of the thickness was about 110Å. Also it was noted that some solid powder had settled to the bottom of the reaction chamber. The electroreduction technique was used to estimate the film thicknesses. This method was not precise enough to allow any definite statements to be made regarding the differences in the thickness of the films on the three crystallographic planes since the differences between them were less than the experimental error.

When the solution, saturated and in equilibrium with 1 atm of O_2, was not stirred but instead allowed to remain quiescent, the corrosion process was quite similar to that in the stirred solution for the first few hours, but after 7 hr a visibly thick brownish black to purplish black film of oxide had formed. This film had a powdery appearance and could be removed partially by wiping with a tissue. Beneath it another film exhibiting interference colors could be observed sometimes.

If the partial pressure of the O_2 in equilibrium with the water were reduced by introducing mixtures of O_2 and He containing varying proportions of these two gases, the time required for the appearance of CuO increased as the partial pressure of O_2 decreased. Thus, with 100% O_2, 7 hr elapsed before CuO was observed by the unaided eye, while with 20% O_2 the time was twice as long, and with 10% O_2, over 24 hr elapsed.

X-ray diffraction examinations of {111}, {110}, and {100} faces, reacted in the presence of oxygenated water under controlled conditions, revealed the presence of polycrystalline randomly oriented CuO. In a few cases Cu_2O also was found to be present along with the CuO. When this was so, the Cu_2O showed the same type of preferred orientation and epitaxial relationships as described for the experiments conducted in uncontrolled atmospheres. This Cu_2O probably was responsible for the film that exhibited the interference colors when the CuO was wiped off. When CuO was present, the film, as observed by the unaided eye and by microscopic examination, was thinnest on the {110} planes and thickest on the {100}, with that on the {111} being intermediate. The electroreduction technique could not be used to measure CuO film thickness because of the great difficulties encountered in reducing the CuO.

It is believed that the reason CuO was not formed on the Cu surface when the solution was agitated was that cuprous ions, on reaching the solid-liquid interface through the Cu_2O film, were caused by the agitation to oxidize in the body of the solution and precipitate as $Cu(OH)_2$ or CuO, whereas under quiescent conditions the cuprous ions were oxidized to cupric ions at the interface and formed CuO there. In all cases Cu_2O is present next to the Cu as CuO is reduced in the presence of Cu.

It is evident that the behavior of the Cu was markedly different when immersed in oxygenated water in the room atmosphere than when the environment was controlled more rigidly. In the first case films of oriented Cu_2O were formed on the Cu surface after a relatively short exposure to water. These films exhibited interference colors and formed beautifully symmetrical patterns. When the conditions were controlled, the Cu oxidized much more slowly and formed dark randomly oriented CuO films. Beneath the CuO films thin films of Cu_2O probably were present also. In an effort to duplicate the experiments in which the water was in contact with the room atmosphere under controlled conditions, it was found that by lowering the *p*H to 5.7 (the *p*H observed in water exposed to the room atmosphere), Cu_2O was observed. The *pH* was lowered by the introduction of CO_2. With still lower *p*H's, Cu_2O also was observed. The influence of CO_2 was demonstrated by an experiment in which CuO was formed on Cu in a closed system by exposing the Cu to water saturated with pure oxygen. Carbon dioxide was bubbled in for 1 min and the corroded crystal then was exposed to this water for 24 hr. At the end of this period, all of the CuO had been converted to Cu_2O. X-ray diffraction examination of the Cu_2O formed in this fashion revealed, however, that it was much more poorly oriented

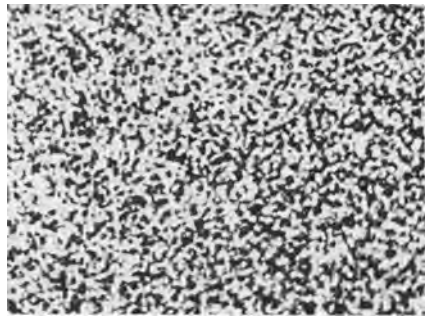

Fig. 9. {100} plane of Cu oxidized in oxygen-saturated water under controlled conditions. 1000X.

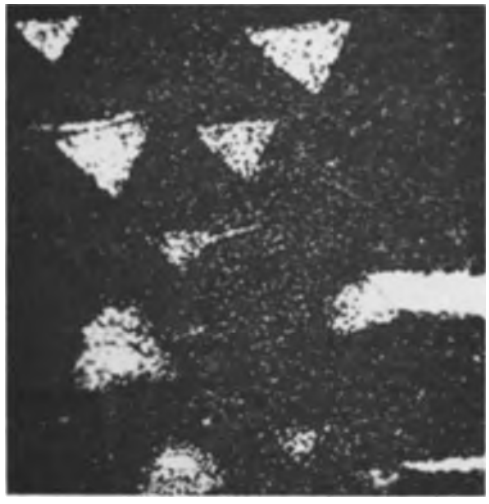

Fig. 10. {111} plane of Cu oxidized in oxygen-saturated water under controlled conditions. Magnification 1000X before reduction for publication.

than where CO_2 was present from the beginning of the oxidation process.

The morphology of the oxide films as revealed by the microscope was of great interest. After the oxidation had proceeded to the point where CuO could be observed, the film on the {110} plane was similar to that on the {100} plane (Fig. 9). Most of the surface of the {111} plane, however, was covered with the black CuO film but, as shown in Fig. 10, there were triangular areas that appeared Cu colored. It is interesting to note that some of the triangles had orientations that are 180° with respect to each other. This indicated that perhaps some nuclei of Cu_2O existed next to the Cu surface. Cu_2O could exist in these two orientations because of the epitaxial relationships found between Cu_2O and a {111} plane of Cu (7). Figures 11, 12, and 13 show the {111}, {110}, and {100} faces, respectively, after the CuO had been converted to Cu_2O by the introduction of CO_2.

Discussion

The first fact which was noted from these studies concerned with the nature of the oxides is that Cu_2O

Fig. 11. Cu_2O formed on {111} plane of Cu by conversion of CuO which was present initially. The change was caused by introduction of CO_2 into aqueous solution. Magnification 1000X before reduction for publication.

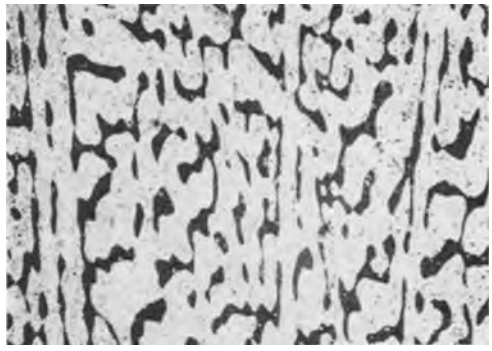

Fig. 12. Cu_2O formed on {110} plane of Cu by conversion of CuO which was present initially. The change was caused by introduction of CO_2 into aqueous solution. Magnification 1000X before reduction for publication.

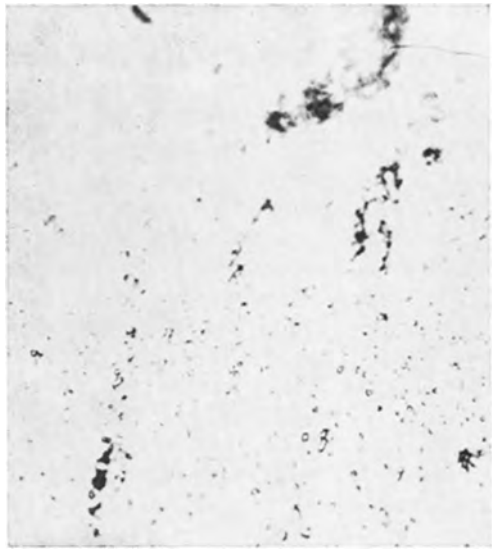

Fig. 13. Cu_2O formed on {100} plane of Cu by conversion of CuO which was present initially. The change was caused by introduction of CO_2 into aqueous solution. 1000X.

was formed when Cu was exposed to water in equilibrium with air, the *p*H of the water being about 5.7. This is the oxide formed initially by dry air oxidation. Further, the epitaxial relationships between the Cu_2O and the metal substrate were the same both for oxidation in solutions and in dry gases. Finally, the extent of oxidation depended on the crystallographic orientation of the surface in both cases.

The one very evident difference between oxidation in air and oxidation in water was that at room temperature oxidation occurred more rapidly in water (exposed to air) than it did in air. It is also known from the work of Miller (14) that, if Cu is immersed in a solution of cupric sulfate, the reaction is even more rapid than if Cu is immersed in pure water. Cu_2O is the product formed in copper sulfate solution and the epitaxial relationships between oxide and metal are the same as those mentioned above. The nuclei contained in films formed during oxidation in solutions were larger than those formed during oxidation in gases. Finally, the influence of light was much more pronounced when oxidation occurred in solutions than when it occurred in gases. A few attempts were made to see if illumination had any influence on the oxida-

tion of Cu in pure oxygen at 250°C but no marked effects were noted.

These differences between oxidation in air-saturated water and oxidation in air, are probably due to the ability of metal ions during aqueous oxidation to move through the water and take part in reactions at sites on the surface that differ from those from which these ions emerged initially. This transport of ions through a solution is, of course, an all-important factor in electrochemical reactions occurring on metal surfaces immersed in an electrolyte. It is not the purpose of this paper to discuss the mechanism of oxidation in water but to be concerned only with the nature of the films formed. However, because of the ability of the water to transport ions, soluble substances can be removed from a surface or insoluble substances can be deposited onto a surface. On account of these processes the oxides formed in water in equilibrium with 1 atm of pure oxygen at room temperature differ from those formed by gaseous oxidation at room temperature. Thus, besides the Cu_2O commonly present at room temperature CuO was also observed.

This has not generally been found in most of the previous studies of the films that form on Cu in contact with aqueous solutions because most of these experiments were carried out under conditions where the presence of CO_2 was not rigorously excluded. The formation of CuO when CO_2 is absent is to be expected on the basis of the diagram of Pourbaix (15). This diagram enables the prediction of the thermodynamically stable phases present under a given set of conditions. On the basis of this diagram it may also be concluded that by lowering the pH and the partial pressure of oxygen there would be a tendency for the CuO to go over to Cu_2O.

However, the thermodynamic considerations on which the Pourbaix diagram is based are not sufficient to allow the prediction of the solid phases present. Thus, for the conditions existing during the oxidation of Cu in water saturated with air and exposed to the room atmosphere (pH = 5.7, $pO_2 = 10^{-0.699}$ atm) the formation of CuO would be expected, although Cu_2O was observed. The rate at which cupric ions build up in solution is also of utmost importance in determining the oxide observed. Thus, if enough time were allowed and if all of the components of the system were kept in intimate contact with each other, CuO would be observed at pH 5.7 in air-saturated water. Actually, what appeared to happen was that at this pH the CuO was soluble to such an extent and the rate of cupric ion formation by oxidation of cuprous ions was sufficiently slow so that only the considerably less soluble Cu_2O was observed.

At a pH of 7, however, the solubility of CuO is less than at the lower pH and with the water in equilibrium with 1 atm of oxygen, the time required to observe the formation of CuO visually was about 7 hr. Experiments with pure water in equilibrium with different partial pressures of oxygen show that apparently the rate of cupric ion formation did depend on the partial pressure of the oxygen, for the time to observe CuO formation increased with a decrease in partial pressure. During this time, before the appearance of CuO, only Cu_2O was observed. When the pH was lowered from 7, after the formation of CuO by the introduction of CO_2, the solubility of CuO was increased and it went into solution.

The Cu_2O that is always next to the Cu was then the only oxide observed and its thickness actually started to increase at the lower pH where it was still quite insoluble. This indicated that the rate of cuprous ion formation was probably faster than the rate of oxidation of cuprous ions to cupric. This question of the rate of film formation and the rate of cupric and cuprous ion formation will be discussed in a more quantitative fashion in the next paper in this series. These details must be investigated before a more nearly complete understanding of the corrosion of Cu can be achieved.

Acknowledgment

The author wishes to thank the Corrosion Research Council which supported this work in part.

Manuscript received Feb. 20, 1959. This paper was prepared for delivery before the Buffalo Meeting, Oct. 6-10, 1957.

Any discussion of this paper will appear in a Discussion Section to be published in the June 1960 JOURNAL.

REFERENCES

1. G. D. Bengough and O. F. Hudson, *J. Inst. Metals*, **21**, 37 (1919).
2. L. W. Haase, *Z. Metallkunde*, **26**, 185 (1934).
3. A. Quartoroli, *Korrosion u. Metallschutz*, **18**, 368 (1942).
4. L. Tronstad and R. Veimo, *J. Inst. Metals*, **66**, 17 (1940).
5. G. T. Miller, Jr., and K. R. Lawless, *J. Applied Phys.*, **29**, 863 (1958).
6. F. W. Young, Jr., J. V. Cathcart, and A. T. Gwathmey, *Acta Metallurgica*, **4**, 145 (1956).
7. K. R. Lawless and A. T. Gwathmey, *ibid.*, **4**, 153 (1956).
8. N. B. Gorney, *Soviet Phys. JETP*, **2**, 687 (1956).
9. E. Menzel, *Ann. Physik (Leipzig)*, **5**, 163 (1949).
10. J. Kruger, *J. Applied Phys.*, **28**, 1212 (1957).
11. U. R. Evans and H. A. Miley, *J. Chem. Soc.*, **1937**, 1295.
12. N. F. Mott, *Proc. Roy. Soc. (London)*, **A171**, 281 (1939).
13. J. W. Mellor, "A Comprehensive Treatise on Inorganic and Theoretical Chemistry," p. 160, Longmans, Green and Co., London (1923).
14. G. T. Miller, Jr., Dissertation, University of Virginia (1958).
15. M. J. N. Pourbaix, "Thermodynamics of Dilute Aqueous Solutions," p. 59, Edward Arnold and Co., London (1949).

An Electron Microscopic Study of the Formation of Oxide on Copper Single Crystals Immersed in an Aqueous Solution of Copper Sulfate

G. Tyler Miller, Jr.[1], and Kenneth R. Lawless

Cobb Chemical Laboratory, University of Virginia, Charlottesville, Virginia

ABSTRACT

Electron microscope and electron diffraction techniques were used for the examination of the different faces of a single crystal of copper which had been immersed in an aqueous solution of $CuSO_4$ containing dissolved oxygen. During the reaction a thin film of Cu_2O was formed initially and continued to grow in the form of well-defined oriented polyhedra of oxide. For immersion times of 24 hr or more, etching of the metal surface and of the oxide polyhedra occurred due to a decrease in the pH of the solution. An attempt was made to interpret the oxide growth in terms of the electrochemical theory of corrosion and the dislocation theory of crystal growth.

Although the reactions of metals with aqueous salt solutions are among the commonest of reactions and have been the subject of many investigations, the influence of surface structure on these reactions is only poorly understood. Most previous studies have been carried out on fine-grained polycrystalline specimens, and the interpretation of the results is complicated by the presence of grain boundaries and by differences in activity of the different crystal faces. In addition to this, an understanding of the reactions involved is frequently difficult because little or no information is available on the structure of the surface before and after the reaction.

This study is concerned with the electron microscopic and electron diffraction examination of the different faces of a carefully prepared single crystal of copper which has been immersed in an aqueous solution of copper sulfate containing dissolved oxygen. During the reaction oxide is formed and some etch pits are developed. The epitaxial relationship of these oxide films with the metal surface as determined in this study are described in detail in another paper (1).

Interesting types of oxide structures were found, and an attempt was made to interpret the oxide growth in terms of the electrochemical theory of corrosion, the structural relationships of the oxide to the underlying metal, and the dislocation theory of crystal growth. The results indicate clearly that the understanding of one of the simplest of reactions, important in an understanding of corrosion, is dependent on a careful study of surface structure.

Experimental Procedure

The experimental procedure consisted of exposing known crystallographic surfaces of copper single crystals to an aqueous solution of cupric sulfate at a known concentration, temperature, and pH. The oxygen concentration in the solution was approximately constant. After definite periods of immersion the surfaces of the specimens were examined with the aid of optical and electron microscopes and by electron diffraction.

Copper single-crystal rods of 99.999% copper were grown from the melt and machined into the form of spheres 5/8 in. in diameter. Flat faces parallel to specific crystallographic planes were cut on the spheres. The surfaces of these crystals were mechanically polished and then electrolytically polished, followed by thorough washing and drying as previously described (2). The Laue back-reflection technique was used to take x-ray diffraction photographs after every three or four experiments to make sure that each face remained within 1° of the desired orientation. Great care was taken in the preparation of these specimens in order to obtain known surfaces as free as possible from chemical contaminations and structural imperfections.

The copper specimens after being washed and dried were placed in a Pyrex reaction chamber. The system was then evacuated, purified hydrogen admitted, and the specimen annealed at 500°C for 1 hr to remove any oxide present on the surface and to relieve any residual strains in the crystal. The specimen was cooled to 25°C in an atmosphere of hydrogen, and then, without exposing it to the air, the crystal was lowered to the bottom of the reaction chamber which was immersed in a water thermostat maintained at 25° ±0.02°C. An aqueous solution of $CuSO_4$ could be admitted into the reaction chamber through a Pyrex tube which was ring-sealed to the base of the chamber. The top end of the tube was ground flat so that a flat face of a crystal could be placed on it and a reaction carried out on only one face. A glass cup was sealed to the upper part of this tube so that the crystal could be suspended within the cup and sufficient solution admitted to cover the whole crystal if desired. After being exposed to the aqueous solution for the de-

[1] Present address: Department of Chemistry, Hampden-Sydney College, Hampden-Sydney, Virginia.

sired length of time, the crystal was removed, washed thoroughly in distilled water to remove any $CuSO_4$, and dried in a jet of nitrogen.

Solutions of $CuSO_4$ were prepared using 50 g/liter of doubly recrystallized reagent grade $CuSO_4 \cdot 5H_2O$ and distilled water. The *p*H of the solution was measured before and after each experiment with a L&N *p*H indicator. The *p*H of the solution initially was 3.8 for all experiments. The oxygen concentration in this solution was approximately 10^{-4} moles per liter.

After reaction the surfaces of the copper crystals were examined using both optical and electron microscope techniques and in many cases electron diffraction techniques. It was not possible to examine the surfaces directly with the electron microscope, and it was therefore necessary to use a replica technique. For all of these studies carbon replicas approximately 100Å thick were made of the surfaces (3). These were removed using a stripping solution such as 10% KCN, 1:1 orthophosphoric acid water or 10% ammonium persulfate. The stripped replicas were mounted on the usual 200 mesh, ⅛ in. diameter grids, and these were then shadowed with Cr, Pt-20% Pd, or Pd (4). The angle of shadowing varied from 5° to 30°, depending on the appearance of the surface as indicated in the optical microscope, the lower shadowing angle being used for the smoother surfaces. The shadowed replicas were examined with the RCA EMU-3B electron microscope operated at 50 or 100 kv.

In a few cases, the reaction product was stripped from the copper surface using a modification of the electrolytic stripping technique described by Harris, Ball, and Gwathmey (5). These stripped films were then examined by transmission electron microscopy and electron diffraction. In order to determine the surface products and their structural relationships to the metal substrate, representative specimens were examined with high voltage electron diffraction (60-80 kv), utilizing reflection techniques (6). In these cases, after reaction, washing, and drying, the specimens were transferred immediately to the diffraction apparatus in order to minimize the possibility of surface contamination.

To determine the importance of copper ions in the solution, several experiments were carried out using a solution of 50 g/liter of K_2SO_4 instead of $CuSO_4$.

Experimental Results

Oxidation of a spherical crystal of copper in dry oxygen gas gave a symmetrical "oxidation pattern" of brilliant colors (2). A black and white photograph of such a pattern is shown in Fig. 1a. Such a pattern was due to the interference colors formed with different thicknesses of oxide on different crystal faces. In the present study, similar oxidation patterns were formed when electropolished crystals were immersed in an aqueous solution of $CuSO_4$ at 25°C which contained dissolved oxygen. With careful surface preparation, these patterns were easily reproducible. A typical oxidation pattern formed under these conditions after an immersion time of 1 min is shown in Fig. 1b. Reflection electron diffraction showed that the surface product was Cu_2O. It was obvious for the immersed specimens that there were differences in the oxidation on the different crystal faces, although the patterns were not as striking as in the case of dry oxidation in oxygen. Transmission electron diffraction studies on stripped oxide films and measurements of shadow heights on electron micrographs of replicas indicated that most of the oxide was greater than 1000Å thick after an immersion time of 5 min in the $CuSO_4$ solution. This is to be compared with an oxide thickness of less than 100Å for dry oxidation of copper at 25°C over a period of months, (7) and of 70Å for oxidation of copper in pure water at 25°C for a period of 8 hr (8). The rate of oxidation was therefore much faster for crystals immersed in $CuSO_4$ solution than for those exposed to dry oxygen or to water containing oxygen at the same temperature.

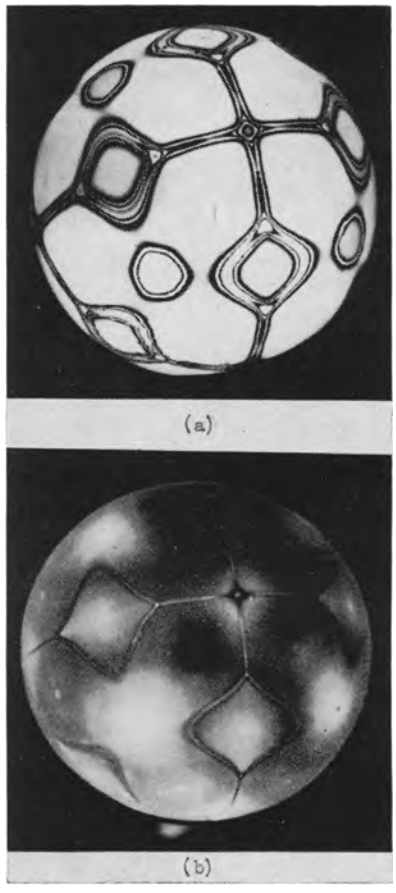

Fig. 1. Oxidation patterns on spherical copper single crystals: a, 20-min oxidation in oxygen at 250°C at atmospheric pressure; b, 1-min oxidation in aqueous $CuSO_4$ at 25°C, pH 3.8.

In order to observe the structural details of the oxide formation on the different crystal faces of copper, flat faces parallel to specific crystal planes were immersed in $CuSO_4$ solutions. In this way differences due to crystal face and the effects of time of immersion could be studied.

Back reflection x-ray diffraction patterns of the flat faces indicated that the cold worked surface layer produced by the mechanical polish was removed by the electropolish. Electron micrographs of

carbon replicas of the metal surface after electropolishing and annealing show no indications of pitting, facet development, or other type of roughness. The surfaces were very smooth with only a slight waviness of the order of 2°. The micrograph is not reproduced here since it would appear only as a plain gray area. Electron diffraction patterns showed sharp Kikuchi lines.

The effect of time of immersion on the oxidation was studied on five crystal faces, the (110), (100), (111), (210), and (311) for immersion times from 30 sec to 90 hr at a solution temperature of 25°C. Figure 2 shows the results of this study on the (110) face for representative immersion times of 30 sec, 24 hr, and 60 hr. Figure 3 shows the results on the (100), (111), (210), and (311) faces for an immersion time of 60 hr. The results at 30 sec and 24 hr for these faces were similar to the (110), the major differences being the shapes of the oxide growths and the relative coverage of the surface by the oxide.

Well-shaped polyhedra of Cu_2O single crystals varying in diameter from 300-3000Å were present on all faces after 30 sec in $CuSO_4$. The coverage of the surface varied from face to face, but in no case was there a complete coverage of the surface by the polyhedra. For oxide crystals 1000Å in diameter the heights of these polyhedra as determined from shadow lengths were roughly 500-700Å. The oxide polyhedra grew larger with time. This growth was both parallel and normal to the copper surface. After 24 hr the oxide polyhedra had grown together so as to give a more complete coverage of the surface, with many individual crystals 20,000-30,000Å in diameter, although some of 1000Å or less were still present. The pH of the solution had changed from 3.8 to 3.4 in this period of time.

After 60 hr in $CuSO_4$, the appearance of the surface was much more complicated. The coverage of the surface was rather uneven, some areas being almost completely covered with large oxide polyhedra which had grown together as in Fig. 3b and 3c. Other areas were only partially covered as in Fig. 3a and 3d, and some areas were almost free of large oxide figures as shown in Fig. 4. These latter regions frequently showed a considerable amount of etching of the metal surface, in addition to small oxide polyhedra. This etching was usually in the form of well-shaped etch pits. This is shown in Fig. 4. It was also apparent that some etching of the larger oxide polyhedra had taken place (Fig. 3c). Some of the oxide crystals were as large as 300,000Å (30 μ) in diameter, whereas others were only of the order of 1000Å. The pH of the solution at the end of 60 hr had changed from 3.8 to 3.2.

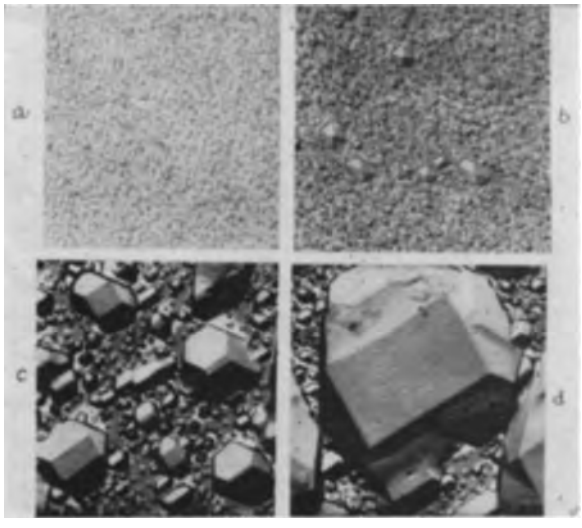

Fig. 2. Effect of immersion time on the oxidation of annealed (110) face of copper in $CuSO_4$ solution at 25°C: a, 30 sec, pH 3.8; b, 24 hr, pH 3.4; c and d, 60 hr, pH 3.2. Magnification 3500X before reduction for publication.

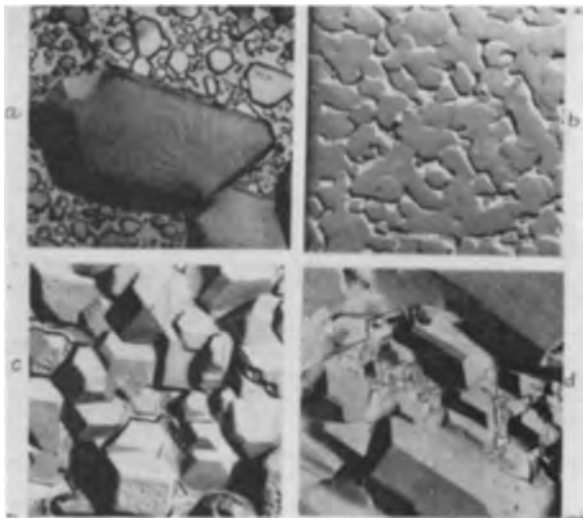

Fig. 3. Appearance of surfaces after 60-hr immersion in $CuSO_4$ solution at 25°C, pH 3.2; a, (100) face; b, (111) face; c, (210) face; d, (311) face. Magnification 3500X before reduction for publication.

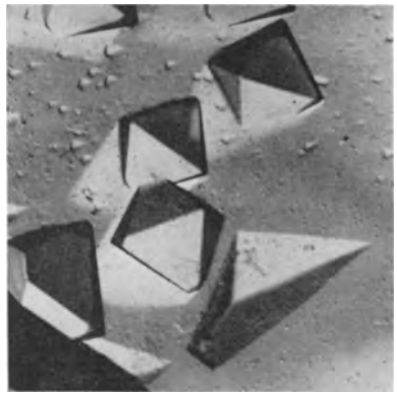

Fig. 4. Etch pits and oxide polyhedra on (210) face after 60-hr immersion in $CuSO_4$ solution at 25°C, pH 3.2. Magnification 6200X before reduction for publication.

After 90 hours' immersion the specimen surfaces were similar to the 60-hr specimens, except that considerably more etching both of the oxide and of the metal surface had taken place.

Both optical and electron microscopic examination of specimens after 24-, 60-, and 90-hr immersion showed that the larger oxide polyhedra usually had complex step and spiral structures present on their surfaces. In most cases the spirals were present on the (111) surfaces of the oxide. The spirals were observed only once on another oxide face, the (100). Figure 5 shows an example of a spiral on the (111)

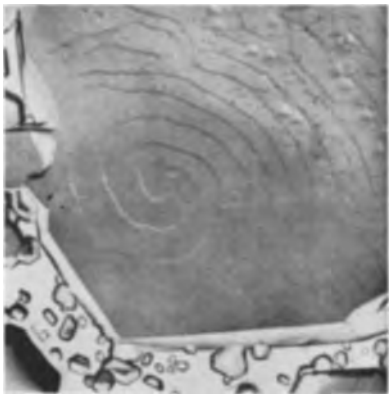

Fig. 5. Spiral growth on (111) surface of Cu_2O formed on the (100) face of copper immersed for 60 hr in $CuSO_4$ solution at 25°C, pH 3.2. Magnification 6200X before reduction for publication.

face of Cu_2O. The step height of the spirals was determined from the shadows and was in the range 100-200Å. No spirals were observed on the smaller oxide growths. In general the spiral systems were more complex than that shown in Fig. 5 and frequently more than one spiral system was present on a given oxide crystal. A more complex spiral system can be seen on the large oxide polyhedron in Fig. 3a.

Both electron diffraction and electron microscopy showed that the oxide grew such that there were specific epitaxial relationships between the oxide and the metal on the different crystal faces. These results will be reported in more detail elsewhere (1). In general the orientation relationships were the same as those previously determined for dry oxidation by Lawless and Gwathmey (9), and for oxidation in pure water by Kruger (8), and Lawless (7).

The very early stages of the oxide growth were studied on specimens which had been immersed for 15 sec. The oxide film was stripped from the copper electrolytically and examined by the electron microscope. Figure 5a shows the appearance of the oxide on the (100) face of copper. The similarity of this to electron micrographs of the early stage of dry oxidation at 150°C (5, 7) was striking. At higher magnifications the dark oxide crystals showed the same shapes as appear in Fig. 3. Electron diffraction (Fig. 6b) indicated that not only well-oriented single crystal particles of oxide but also a continuous polycrystalline thin film of Cu_2O were present. These diffraction studies indicated that the thickness of this thin film was certainly less than 50Å and probably less than 20Å.

Cu_2O also formed on crystals which were immersed in an aqueous solution of K_2SO_4, but at a rate much slower than that for crystals immersed in an aqueous solution of $CuSO_4$. The amount of oxide formed in an hour was of the same order of magnitude as the amount formed on a crystal immersed in distilled water (8).

The oxide on the surface of a copper crystal could be dissolved by dipping the crystal in a 10% HCl solution for about 15 sec. When this experiment was carried out for a crystal on which oxide had been formed by immersion in $CuSO_4$, the oxide dissolved leaving a bright copper surface showing no apparent roughness or etching of the metal surface. When the same experiment was carried out using a crystal with an oxide film of comparable thickness which was formed by oxidation in dry oxygen gas, the surface appeared roughened and faceted.

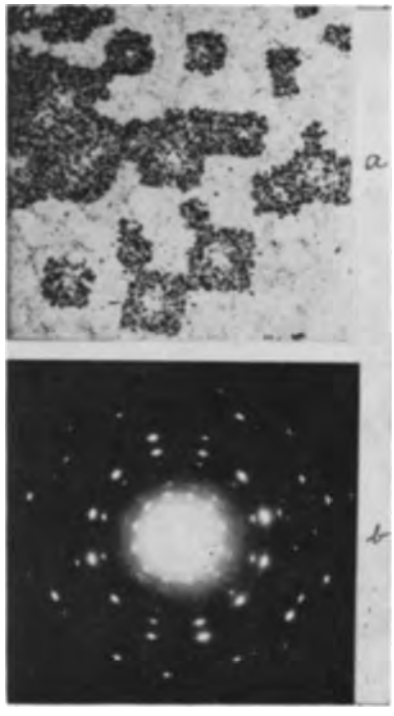

Fig. 6. Oxidation of (100) face of copper in aqueous $CuSO_4$ solution at 25°C, immersion time 15 sec: a, electron micrograph of stripped oxide, magnification 12,000X before reduction for publication; b, transmission electron diffraction pattern of stripped oxide.

Discussion

The results of this study revealed some of the extreme complexities arising in the oxidation of a metal in an aqueous salt solution. Any completely satisfactory mechanism for the reaction of copper in aqueous $CuSO_4$ solution must explain the rapid growth of individual Cu_2O polyhedra, the presence of spirals on the oxide, and the presence of both etch pits and oxide figures on the same surface.

Formation of oxide on the copper immersed in this solution was dependent on the *p*H of the solution. Cu_2O was the only oxide observed in these studies in which the *p*H ranged from 3.8 to 3.2. At a *p*H below 3 only etching of the copper was observed. The results under these conditions do not appear to be important to this discussion and will be treated elsewhere. The formation of Cu_2O only was to be expected on the basis of the work of Pourbaix (10) since this is the only oxide stable in the *p*H range 3.8 to 3.2.

It was obvious from the irregular thickness of the oxide as shown in the micrographs that rate measurements, in the usual sense of the word, would have limited value for reactions of this nature, even when made on carefully prepared single-crystal surfaces. However, it was apparent that the total amount of oxidation on a given area of surface

was much greater when the crystal was immersed in the $CuSO_4$ solution than when immersed in pure water or when oxidized in dry oxygen at the same temperature for the same length of time. The role of the aqueous salt solution is probably a twofold one of providing an easier path for the flow of electrons and ions and a readily available source of copper ions, thus enabling a more rapid oxidation to occur.

A consistent mechanism which can explain the oxide formation can be arrived at from the data available in the micrographs and diffraction patterns and from theoretical considerations. A thin polycrystalline film of Cu_2O, 20-30Å thick, was formed almost immediately, covering the whole metal surface. The electron diffraction patterns indicated that such a film was formed in these studies, and experimental and theoretical work by Hoar and Evans (11) suggested that the formation of a thin compact oxide film was the initial stage for many reactions in aqueous salt solutions. Studies on oxidation in dry oxygen (5) also indicated that the formation of a thin polycrystalline oxide was the initial stage of oxidation in that case.

This initial oxide film contained many grain boundaries and probably a large number of imperfections. In air at 25°C the subsequent growth of this base film was extremely slow, whereas in aqueous $CuSO_4$ solution certain oxide nuclei in the base film continued their growth at a very rapid rate, as seen in Fig. 2-6. Why should certain of these oxide crystals have continued to grow rapidly while others essentially stopped growing or, at best, grew only slowly? First, it was apparent from the diffraction patterns that the crystals which grew rapidly were well oriented with respect to the base metal. Second, during the later stages of growth it was apparent that imperfections in the oxide polyhedra were playing an important role in the continued growth of the oxide. It is probable that imperfections in the initial thin film were important as well. It seems likely, therefore, that the oxide crystals in the base film which continued to grow rapidly were those which had a specific orientation with respect to a particular face, and which had the proper number and type of imperfections necessary for continued rapid growth.

It is now necessary to explain how these specific oxide crystals could grow so much faster in aqueous $CuSO_4$ than in pure water or dry oxygen. The fact that oxide formation was much slower in an aqueous solution of K_2SO_4 than in $CuSO_4$ is an indication of the importance of the copper ions in the solution. In addition, the fact that the metal surface was not roughened appreciably by the formation of a thick oxide is perhaps further evidence that the bulk of the copper ions converted to oxide came from the solution rather than from the metal. It seems likely, therefore, that after the initial formation of the thin oxide film, for which copper ions would be available both from the metal and from the solution, the bulk of the oxide is produced by reaction of copper ions from the $CuSO_4$ solution.

The initial oxide film could be produced either by reaction of copper with oxygen adsorbed on the surface from solution

$$2Cu + \tfrac{1}{2} O_2 \rightarrow Cu_2O \qquad [1]$$

or by reaction of cuprous ions with water or hydroxyl ion

$$2Cu^+ + 2\,OH^- \rightarrow Cu_2O + H_2O \qquad [2]$$

In these experiments it was not possible to distinguish between these possibilities.

The subsequent growth of the oxide could take place either by reaction [2] above or by the reaction of Cu^{++} ions with water at suitable sites on the surface where electrons would be available [3].

$$2Cu^{++} + 2e^- + H_2O \rightarrow Cu_2O + 2H^+ \qquad [3]$$

This is of course essentially the same reaction as [2], only assuming the reduction of cupric ion to cuprous ion at suitable reduction sites on the oxide surface. Since this is a reduction, an oxidation reaction is necessary also. Two possible oxidation reactions are

$$Cu \rightarrow Cu^+ + e^- \qquad [4]$$

and

$$Cu \rightarrow Cu^{++} + 2e^- \qquad [5]$$

According to Hoar and Evans (11) it would be possible for metal ions to go into solution with migration of these ions through an oxide film on the metal surface. This would be expected to take place at imperfections in the oxide such as would be created by lattice defects or grain boundaries, or at very thin regions of the oxide. Since we are concerned with a very thin oxide film, tunnelling of electrons can take place setting up a strong electric field which would assist the movement of metal ions through the oxide (12).

If the copper surface is not completely covered with an oxide film, in addition to reactions [4] and [5], an additional reaction can occur

$$Cu + Cu^{++} \rightarrow 2Cu^+ \qquad [6]$$

Although it seems likely that in the oxygen containing $CuSO_4$ solution a continuous film of oxide would be present on the copper surface, it is not possible from these experiments to conclude definitely that there are no regions on the surface which are free of oxide. There is therefore a possibility that reaction [6] does occur in the aerated solution. The fact that appreciable etching of the copper surface does not occur until the pH has decreased considerably would indicate that the extent of this reaction is at best rather small in the early stages of the reaction. If a copper crystal having a thin air-formed oxide film on its surface is immersed in aqueous $CuSO_4$, additional oxide is formed. This is further evidence that reaction [6] is not important in the early stages of the reaction.

In some preliminary experiments using deaerated aqueous $CuSO_4$ it was found that oxide formed on the copper crystal apparently as rapidly as in the experiments with aerated $CuSO_4$. Similarly, over a

period of 24 hr the pH of the deaerated solution decreased from 3.8 to 3.2. Electron microscope observations of the surfaces of copper crystals immersed in deaerated $CuSO_4$ solution showed the same type of oxide structures as observed with oxygen containing solutions. The regions between the oxide polyhedra seemed, however, to be etched to a greater extent in the experiments with deaerated solution. This could be a result of reaction [6].

The similarity between the behavior of copper in aerated and deaerated $CuSO_4$ solutions indicated that basically the same oxide formation process was occurring in both cases. This is apparently reaction [2],

$$2Cu^+ + 2\,OH^- \rightarrow Cu_2O + H_2O \qquad [2]$$

El Wakkad (13), however, states that the solubility product for this reaction is not exceeded for solutions of the concentration and pH used in these experiments. Since Cu_2O is definitely formed in these experiments it seems probable that the value for K_{sp} of 7.18×10^{-14} taken by El Wakkad (13) is too large and that the value given by Feitknecht (14) of 1.5×10^{-15} is more reasonable.

A calculation of the thickness of oxide formed on the copper based on the stoichiometry of Eq. [2] was made from the pH change and gave a figure of the right order of magnitude. It was not possible to make an exact comparison since the thickness irregularity of the oxide growths made it impossible to get more than an approximate average thickness for the actual oxide formed. The exact concentration of Cu^+ ion in the original solution was not measured, but the maximum concentration possible can be calculated from the solubility product. This amount of Cu^+ ion is less than the amount needed to form the observed amount of oxide and therefore additional Cu^+ ions must be formed either from the metal by reaction [4], from the solution by reduction of Cu^{++} ions at suitable reduction sites on the surface, or by reaction [6] if bare places are available on the metal surface.

It is possible that in the aqueous solution of $CuSO_4$ containing oxygen which was used for most of these experiments that the reaction

$$\tfrac{1}{2}O_2 + H_2O + 2e^- \rightarrow 2\,OH^- \qquad [7]$$

is of importance. This reaction at the oxide surface could produce locally a higher OH^- concentration making it easier to exceed the K_{sp} in aerated solutions. From the experiments with deaerated solutions, however, reaction [7] does not seem to be necessary for the oxide formation in these experiments.

It seems probable, therefore, that reaction [2] is the main process responsible for the oxide formation with either reaction [3], [4], or [6] being responsible for the conversion of additional copper or cupric ions to cuprous ions. This latter point cannot be settled conclusively from the experimental data available at this time. This reaction [2] would lead to a decreased pH as observed. The reaction would take place on the surface of particular oxide crystallites where the oxide growth is energetically most favorable. The oxide will form rapidly since initially copper ions are readily available from the solution for reaction without the necessity for diffusion through the bulk of large oxide crystals. The oxide polyhedra can then continue to grow provided a suitable mechanism for their growth is available.

It has been shown theoretically (15) and experimentally (16) that the emergence of a screw dislocation on a crystal face provides a mechanism for continued rapid crystal growth without the necessity of two-dimensional nucleation on the surface. In this study the larger oxide polyhedra invariably showed spiral or step growth features for times of immersion of 24 hr or more. This indicated strongly that the rapid growth of these polyhedra in the later stages of growth was due to the presence of screw dislocations in the oxide. The presence of complete spirals on the surfaces was also a good indication that the growth was continuing by means of volume diffusion of copper ions and not by surface diffusion or diffusion through the bulk of the oxide. It is probable that the spirals were not observed at the earlier stages of oxidation because of the small size of the oxide particles and the difficulty of shadowing such small step heights. The screw dislocations apparently had large Burgers vectors which were stabilized by the presence of impurities (17). This type of imperfection could arise at any stage in the oxide growth because of stresses in the oxide or the growing together of two or more slightly disoriented oxide crystals.

Copper specimens immersed for 24 hr or more in the $CuSO_4$ solution showed etching of both the metal and the oxide polyhedra. This occurred with an attendant decrease in the pH of the solution. According to reaction [2], a decrease in the pH of the solution was to be expected because of the decrease in hydroxyl ion during the reaction. At a pH of 3.2, a state very close to equilibrium is attained and it might be expected that some solution of the oxide would occur at high energy sites of the oxide. Since the thin oxide film probably consisted of many imperfect crystals with numerous grain boundaries. it would be more subject to attack than the more perfect oxide polyhedra. Thus the thin oxide would dissolve or partially dissolve at specific sites and etching of the metal could occur. The thin oxide film is probably re-formed at these sites fairly rapidly after its solution. Imperfections in the oxide polyhedra would also provide high energy sites which would be subject to attack by the H^+, as observed.

The exact function of the dissolved oxygen in the $CuSO_4$ solution is not understood. It will be necessary to continue experiments in which the oxygen has been removed completely from the solution before this point can be clarified.

Summary

When a copper crystal was immersed in an aqueous $CuSO_4$ solution of pH 3.8, a thin film of Cu_2O, 20-30Å thick, formed immediately over the whole surface. Particular oxide crystals in the base film continued to grow at a rapid rate forming well-defined oriented polyhedra showing only (111),

(100), and (110) faces. Growth spirals were observed on the larger oxide polyhedra after immersion time of 24 hr or more. With long periods of immersion in the aqueous solution the *p*H of the solution decreased to 3.2, and etching of both the metal surface and the oxide occurred. The rapid formation and growth of the isolated oxide polyhedra was explained on the basis of a readily available supply of copper ions, both from the metal and from the solution, an electrochemical mechanism of reaction, and a dislocation mechanism of crystal growth.

This investigation has indicated the importance, and indeed the necessity, of using both electron microscope techniques and carefully prepared single-crystal surfaces if studies of surface reactions are to have any meaning. Details of the metal surface or of the thin oxide film structure, which are too small to be resolved or seen clearly with the optical microscope, can be of the utmost importance in determining the course of a chemical reaction such as oxidation or etching. It is through the study of such structural factors at the high magnifications possible only with the electron microscope, that a better understanding of corrosion processes can be obtained.

Acknowledgment

The authors would like to thank Drs. A. T. Gwathmey, N. Cabrera, and R. E. Cunningham for many discussions pertaining to this work. We would also like to thank Dr. R. H. Kean for carrying out the preliminary studies with the deaerated $CuSO_4$ solutions. This research was supported by a grant from the Office of Naval Research.

Manuscript received Oct. 20, 1958.

Any discussion of this paper will appear in a Discussion Section to be published in the June 1960 JOURNAL.

REFERENCES

1. K. R. Lawless and G. T. Miller, Jr., *Acta Cryst.*, to be published.
2. F. W. Young, J. V. Cathcart, and A. T. Gwathmey, *Acta Met.*, **4**, 145 (1956).
3. D. E. Bradley, J. *Inst. Metals*, **83**, 35 (1954).
4. C. E. Hall, "Introduction to Electron Microscopy," McGraw-Hill Book Co., New York (1953).
5. W. W. Harris, F. L. Ball, and A. T. Gwathmey, *Acta Met.*, **5**, 574 (1957).
6. Z. G. Pinsker, "Electron Diffraction," Butterworths Scientific Publications, London (1953).
7. K. R. Lawless, Unpublished results, University of Virginia.
8. J. Kruger, Private communication.
9. K. R. Lawless and A. T. Gwathmey, *Acta Met.*, **4**, 153 (1956).
10. M. J. N. Pourbaix, "Thermodynamics of Dilute Aqueous Solutions," Edward Arnold and Co., London (1949).
11. T. P. Hoar and U. R. Evans, *This Journal*, **99**, 212 (1952).
12. N. Cabrera and N. F. Mott, *Repts. Progr. Phys.*, **12**, 163 (1948-49).
13. A. R. Tourky and S. E. S. El Wakkad, *J. Chem. Soc.*, **1948**, 740; S. E. S. El Wakkad, **1950**, 3563.
14. W. Feitknecht, *Chimia*, **6**, 3 (1952).
15. W. K. Burton, N. Cabrera, and F. C. Frank, *Phil. Trans.*, **A243**, 299 (1951).
16. A. R. Verma, "Crystal Growth and Dislocations," Butterworth Scientific Publications, London (1953).
17. G. T. Miller, Jr., and K. R. Lawless, *J. Appl. Phys.*, **29**, 863 (1958).

Influence of Silicon on the High-Temperature Oxidation of Copper and Iron

J. W. Evans and S. K. Chatterji

Department of Metallurgy, University of Manchester, England

ABSTRACT

The effects of 1 at. % of silicon on the oxidation behavior of pure copper at 850°-1000°C and of pure iron at 950°-1200°C have been studied by means of a thermobalance. Silicon has a marked effect on the oxidation of iron but relatively little on that of copper. The distinctive behavior is attributed mainly to the different diffusivities of oxygen in the base metals. The depth of subscale formed in the iron alloy suggests that the diffusivity of oxygen in iron is much faster than is commonly supposed.

The high-temperature oxidation resistance of many metals is improved by small additions of silicon. The beneficial effects of Si in steel have been demonstrated frequently and the general pattern of oxidation behavior established (1-5). During oxidation several distinct layers are formed. At the outside surface there is a very thin Fe_2O_3 layer; next to this is a somewhat thicker magnetite layer and this is followed by the thickest layer adjacent to the metal (about 90% at 800°-1000°C) which is wüstite or nonstoichiometric FeO. Because the oxidation of the Fe in the Si steel occurs almost entirely by the outward diffusion of ferrous ions to the surface, the Si concentrates at the oxide-metal interface to form a thin, coherent layer. This layer may consist of fayalite ($2FeO \cdot SiO_2$) or silica, depending on the Si content and temperature.

Silicon has less effect on the oxidation resistance of Cu than it has on Fe. A review of the oxidation behavior of Cu alloys relating to work up to about 1950 has been given by Tylecote (6). The oxidation of a Cu-Si alloy proceeds similarly to that of Fe in

which cationic diffusion outwards of Cu ions occurs. The scale is principally cuprous oxide with a thin outer layer of cupric oxide. Unlike Si in Fe, however, the Si does not invariably concentrate at the oxide-metal interface but may well accumulate in the alloy, the precise behavior depending on the Si concentration initially and the temperature. For example, Preece and Dennison (7) found that a 2% Si-Cu alloy gave a layer of silica at the metal-oxide interface only below 800°C. This layer was absent above this temperature, and above 900°C the Si accumulated in the alloy to such an extent that a liquid Cu-Si phase was formed.

A distinctive feature of the oxidation of Cu alloys is the formation of an extensive subscale caused by the relatively rapid inward diffusion of oxygen into the alloy which precipitates finely disseminated silica throughout the metal matrix. Subscale formation in Cu alloys has been investigated thoroughly by Rhines, Johnson, and Anderson (8), who demonstrated that the depth of subscale was determined principally by oxygen diffusivity. Subscale formation in Fe-Si alloys has been observed but not quantitatively investigated.

In this present work, precise rate laws and their temperature dependence have been determined for pure Cu and Fe. The influence of about 1 at. % Si on the oxidation rate of the pure metals has been studied at temperatures between 800° and 1200°C. The distinctive behavior of Si in each of these metals is shown to be dependent on the extent of subscale formation and this behavior has been partly confirmed by selectively oxidizing Si in the alloys by the use of a controlled gas mixture of hydrogen and water vapor.

Experimental

Materials.—High-purity iron (C, 0.003%; Si, 0.002%; Mn, 0.004%; S, <0.005%; P, <0.001%; Cr, 0.001%; Al, 0.001%) was obtained from the National Physical Laboratory, England.

High-purity (OFHC) Cu and high-purity Fe-Si and Cu-Si alloys containing 0.52% and 0.61% Si, respectively, were supplied by Johnson & Matthey Ltd.

Specimens for oxidation tests were cut from ⅛ in. rolled strip, polished with metallurgical emery paper, and finished with 4-0 grade to give a mirror finish. Specimens were degreased with carbon tetrachloride and acetone immediately before inserting in the furnace.

Oxygen and hydrogen (<10 ppm oxygen) of commercial purity were supplied by the British Oxygen Company.

Apparatus.—The reaction rate of the pure metals and alloys was determined by means of a thermobalance. A Pt-wound resistance furnace was used with an impervious mullite reaction tube mounted vertically. Temperature control was maintained to ±5°C over a 3 in. central zone by means of a mechanical controller operated by a Pt/Rh thermocouple. Connections to the mullite tube were made in Pyrex glass with Araldite cement and these joints were water cooled.

The balance consisted simply of a precision glass spring (obtained from Still and Cameron, London) suspended from the inside of a ground glass joint above the furnace. The sensitivity of the spring was approximately 43 mg/cm extension under a load of 1 g; Hooke's law was obeyed over extensions of several centimeters. The entire spring was maintained virtually at room temperature, and specimens were suspended in the hot zone of the furnace by a fine silica rod; Pt wire was used to support the samples. The weight changes were obtained by measuring the changes in spring extension with a traveling microscope focused on a fine datum mark on the spring. Weight changes of better than 0.1 mg could be observed without difficulty.

The usual arrangements were made for evacuating the furnace tube and for passing dry or wet gases through the system.

The usual procedure for making a measurement was as follows. The furnace was brought to temperature and the ground glass joint removed. The spring with its silica rod and metal sample suspended from it was carefully attached to the hook. While a rapid stream of argon was flowing through the furnace tube, the joint and spring assembly were lowered into position. This could be done in a few seconds and the furnace then was evacuated. The traveling microscope was focused on the mark on the spring to obtain the initial reading. Dry oxygen was admitted and the weight gains followed by adjusting the microscope at suitable intervals to coincide with the datum mark; initially, readings were taken every minute and for longer intervals after the first hour; runs up to 5 hr were made. Pretreatment of certain specimens was carried out by heating them in a stream of hydrogen, saturated with water vapor at room temperature, for 3 hr at the temperature of subsequent oxidation.

Microsections were studied on many specimens and the thickness of various oxide layers estimated.

Results

Pure Copper.—The oxidation of pure Cu followed a smooth parabolic law; results for 906°, 960°, and 1002°C are shown in Fig. 1. The logarithm of the

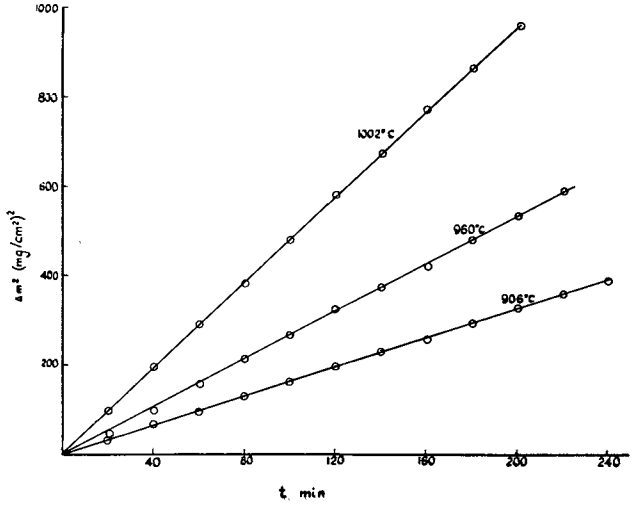

Fig. 1. Oxidation of pure Cu

Table I

Temperature, °C	CuO, mm	Cu_2O, mm
906	0.019	0.286
960	0.003	0.337
1002	0.002	0.622

Table II

Temperature, °C	CuO, mm	Cu_2O, mm	Subscale mm
862	0.003	0.167	0.010
912	0.004	0.257	0.117
952	—	—	0.137
1006	0.002	0.456	0.143

parabolic rate constant is plotted against the reciprocal of the absolute temperature in Fig. 3; from the slope of this line, the usual Arrhenius equation yields an activation energy of 34.8 kcal for the oxidation process. In all cases the oxide scale was firmly adherent and when broken disclosed a dark red layer of Cu_2O underneath the gray-black surface CuO. The relative thicknesses of the two oxide layers are given in Table I.

Copper—0.61% silicon.—As with pure Cu the oxidation of the alloy followed a smooth parabolic law: results for 862°, 912°, 952°, and 1006°C are shown in Fig. 2. The rates are slightly but significantly slower than the corresponding values for pure Cu.

The logarithm of the parabolic rate constant against the reciprocal of the absolute temperature is plotted in Fig. 3. The slope of this line is very close to that for pure Cu, giving a calculated activation energy of 36 kcal for the process.

The oxide scale was similar to that on Cu but was less adherent and tended to flake off during cooling. In addition to the characteristic oxide layers of Cu_2O and CuO, the microstructure of the underlying metal showed a clearly defined subscale, presumably of precipitated silica at grain boundaries.

The relative thicknesses of the various layers are given in Table II.

Copper—0.61% silicon after pretreatment in wet hydrogen.—Even after pretreatment in wet hydrogen, the oxidation proceeded smoothly following a parabolic rate law; results for 952° and 1006°C are shown in Fig. 4. The rates are slower than for both pure Cu and the untreated alloy.

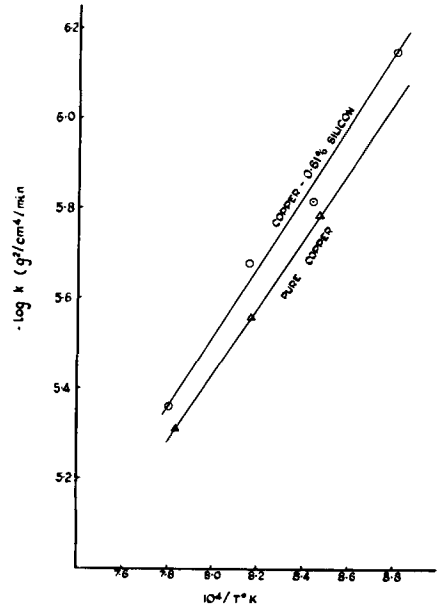

Fig. 3. Log k vs. 1/T for Cu and Cu-0.61% Si

After pretreatment, but before oxidation, the metal surface appeared quite bright and free from a surface film.

Pure iron.—The oxidation curves for pure Fe followed smooth parabolas; results for 810°, 864°, 910°, 984°, and 998°C are shown in Fig. 5. From the graph of the logarithm of the rate constant against the reciprocal of the absolute temperature (Fig. 6), the activation energy for the process is calculated to be 34.3 kcal.

Below 900°C, the surface layer had a velvet, dark red appearance whereas above this temperature the color was metallic gray. The scale was firmly adherent, but it could be removed by light hammering. Microscopically, three oxide layers could be readily distinguished, viz., a very thin outer layer of Fe_2O_3, a thicker layer of Fe_3O_4, and finally a mixed layer of FeO and Fe_3O_4 adjacent to the metal.

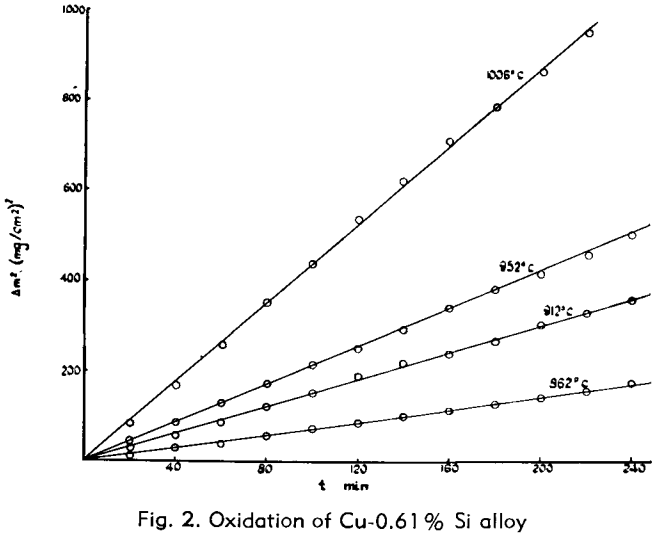

Fig. 2. Oxidation of Cu-0.61% Si alloy

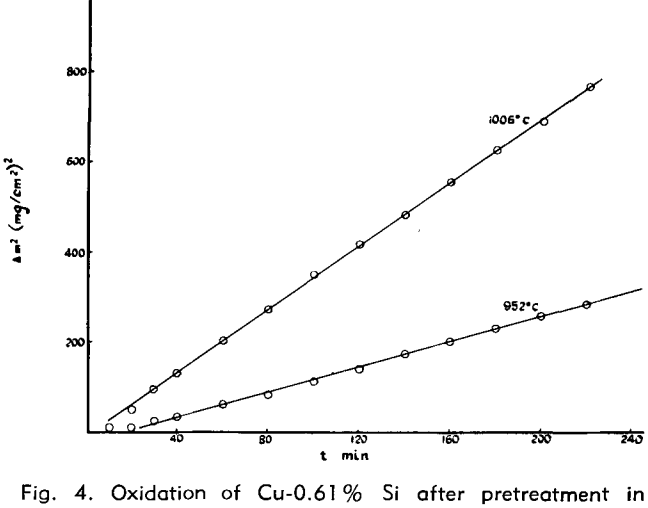

Fig. 4. Oxidation of Cu-0.61% Si after pretreatment in wet hydrogen.

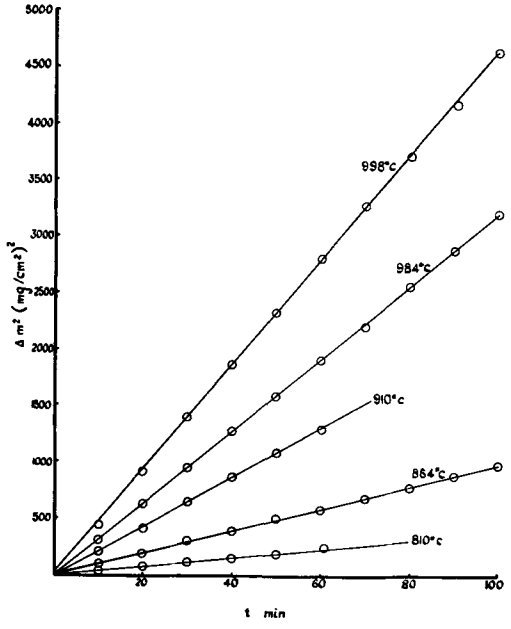

Fig. 5. Oxidation of pure Fe

This latter mixed layer may well result from the partial decomposition of wüstite on cooling. There appears to be no abnormal change in the oxidation process at the α-γ transition in Fe (910°C), but a small difference would be undetected.

Iron—0.52% silicon.—Unlike the behavior of Si in Cu, Si in Fe has a pronounced effect on both the rate and mechanism of oxidation of Fe.

Results for 950°, 998°, 1055°, 1103°, 1131°, and 1165°C are shown in Fig. 7. Up to about 1100°C, the reaction is initially quite slow; after a time depending on the temperature, the oxidation increases, following an approximately smooth curve. At higher temperatures, this initial slow period disappears. At about 1170°-1180°C, the oxidation was catastrophic and no rate data could be obtained above this temperature, because of the melting point of fayalite (1180°C).

The scale was grayish black and closely adherent but could be removed by slight hammering. The exposed metal surface was roughly corroded; there were no obvious signs of silica precipitation at the metal interface, but on the specimen oxidized at

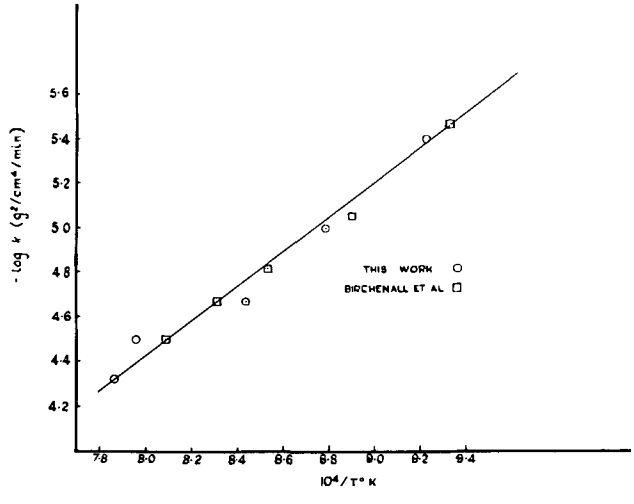

Fig. 6. Log k vs. 1/T for pure Fe

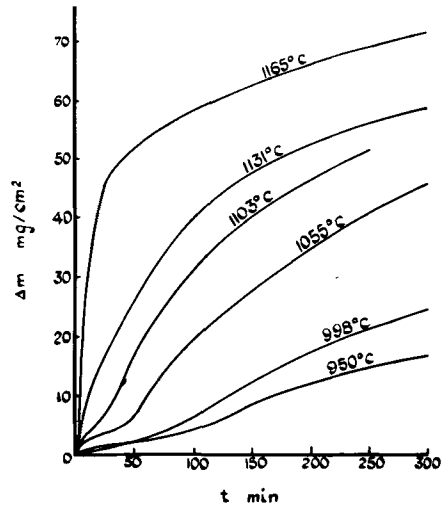

Fig. 7. Oxidation of Fe-0.52% Si

1160°C specks of a partly molten phase could be seen. A microsection of the oxidized specimen showed a number of oxide layers. The external layer was a very thin compact layer of hematite which occasionally showed needle-like growths on specimens oxidized above 1050°C. Beneath this, there was a dense layer of magnetite; below this was a less well-defined and rather more porous structure of wüstite mixed with some magnetite, and finally, adjacent to the metal, there was a thin compact layer of wüstite with fayalite. Within the metal there was a very thin subscale. Approximate relative thicknesses of the various layers are shown in Table III.

Iron—0.52% silicon after pretreatment in wet hydrogen.—After pretreatment in wet hydrogen the oxidation curves showed very similar behavior to that of the untreated alloy, although the rates of oxidation appear somewhat faster. Results are shown for temperatures of 1010°, 1060°, and 1110°C in Fig. 8. The curves are irregular and the oxide scales showed cracking and blistering.

Discussion

Oxidation of Pure Copper and Iron

The parabolic rate constants for pure Cu and Fe derived from the experimental results are:

For Cu (900°-1000°C) $k = 0.076 \exp(-34{,}800/RT)$ $g^2\ cm^{-4}\ sec^{-1}$

For Fe (800°-1000°C) $k = 0.578 \exp(-34{,}300/RT)$ $g^2\ cm^{-4}\ sec^{-1}$

The results for Cu are in general agreement with other workers, e.g., Valensi (9) and Feitknecht (10).

Table III

Temperature, °C	Fe_3O_4, mm	FeO, mm	FeO + Fe_2SiO_4, mm	Subscale, mm
950	0.010	0.060	0.081	0.018
998	0.011	0.072	0.133	0.036
1055	0.020	0.082	0.347	0.030
1103	0.052	0.252	0.131	0.061
1131	0.086	0.361	0.107	0.065
1165	0.253	0.040	0.540	0.120

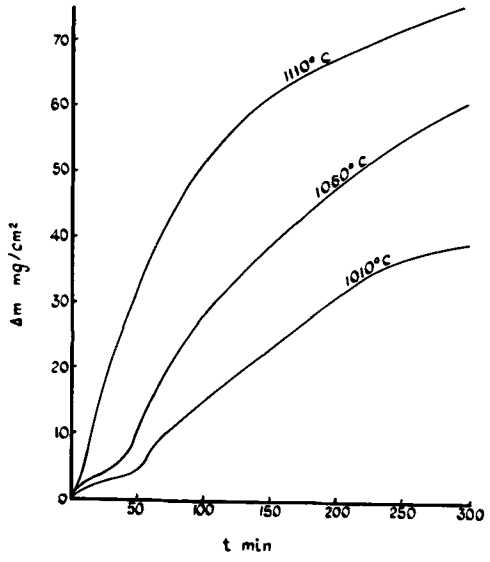

Fig. 8. Oxidation of Fe-0.52% Si after pretreatment in wet hydrogen.

In this temperature region the growth of the oxide layer is controlled by the diffusion of cuprous ions through cuprous oxide. Moore and Selikson (11) measured the diffusivity of Cu^+ in Cu_2O using radiocopper and obtained an activation energy of 36.1 kcal for the diffusion process which agrees reasonably well with the experimental activation energy of 34.8 kcal for the scaling process.

For pure Fe the results compare well with the measurements of Davies, Simnad, and Birchenall (12) in this temperature range; their results are plotted in Fig. 6. Himmel, Mehl, and Birchenall (13) have shown that the controlling process in the oxidation of Fe is the diffusion of ferrous ions in wüstite. They have measured the diffusion rates of cations in the various Fe oxides and obtained a value of 29 kcal for ionic diffusion in wüstite which may be compared with the value of 34.3 kcal for the oxidation process.

Many workers have studied the oxidation of Fe in air, oxygen, and at other controlled oxygen pressures, but the results have not been concordant; part of the discrepancy almost certainly arises from the relative purity of the Fe employed and to a less extent to the use of humid air or oxygen.

When the slight difference in activation energy is taken into account, the parabolic rate constant for the oxidation of Fe is about ten times that for Cu at corresponding temperatures. In both oxides the controlling process is cationic diffusion through a nonstoichiometric oxide, probably via vacant lattice sites. From a consideration of Wagner's theory of parabolic oxidation, it is clear that the difference in scaling rates of the two metals lies in the different ionic conductivities of the two oxides. For FeO the electrical conductivity (13) is 107 ohm^{-1} cm^{-1} for an oxygen partial pressure corresponding to the dissociation pressure of magnetite at 1000°C and the cation transport number is 2×10^{-4}; for Cu_2O the conductivity (14) is 4.8 ohm^{-1} cm^{-1} at an oxygen partial pressure corresponding to the dissociation pressure of CuO at 1000°C and the cation transport number is 4×10^{-4}.

Oxidation of Silicon Alloys

The oxidation of Cu and Fe containing a small amount of Si differs significantly. Silicon in Cu has little effect on the scaling rate of pure Cu, whereas Si in Fe modifies the oxidation mechanism as shown by the irregular oxidation curves. A further point is that the subscale in Cu is substantially thicker than in Fe for the corresponding temperature.

The difference in subscale thicknesses arises principally from the difference in diffusivities of oxygen in Cu and Fe, although the difference in oxygen solubility in both metals, the scaling rate of the base metal, and the relative diffusivities of Si all play their part.

Darken (15) has analyzed the formation of subscale in dilute alloys, and, with certain assumptions, showed that the depth of subscale x during scaling is given by the equation

$$x = (D/r) \ln (1 + u/v)$$

in which D is the diffusivity of oxygen in the alloy, r is the scaling rate, u is the solubility of oxygen in the pure base metal, and v is the initial concentration of Si. This relation shows that the depth of subscale increases with increasing diffusivity and solubility of oxygen and decreases with increasing rate of scaling and Si content of the alloy.

From the diffusivities and oxygen solubilities at 1000°C shown in Table IV, the difference in oxygen diffusivity would appear to be decisive. The very large differences in oxygen diffusivities ought to be reflected in the relative depths of subscale. (Tables II and III, however, show that this is not so.) The value for oxygen in Fe in Table IV is based on one value of Bramley, *et al.* (17), but the depth of subscale in our experiments suggests that their value for diffusivity is at least 1000 times too low. This is partly confirmed by Darken (15) who implies a value for oxygen in iron of the order of 10^{-7} cm^2 sec^{-1} without citing experimental evidence.

The effect of Si in Cu is such that during scaling Si cannot accumulate at the oxide-metal interface but becomes progressively oxidized in depth by virtue of the rapid inward diffusion of oxygen. On the other hand, during the scaling of Fe, Si can diffuse and concentrate at the metal-oxide interface, becoming converted initially to silica which builds up a coherent and partially protective layer. The form of the Si-Fe oxidation curves suggests that, during the initial period of oxidation, silica is first precipitated at the interface and the oxidation rate is appreciably reduced because of the protective nature of the silica (18). However, after this slow initial period the silica undergoes a solid state reaction with FeO to form fayalite. This is itself a semiconductor, and the alloy then begins to oxidize at a

Table IV*

1000°C	D(Oxygen), cm^2sec^{-1}	D(Silicon), cm^2sec^{-1}	Oxygen solubility, wt %
Copper	10^{-5}	0.5×10^{-8}	0.009
Iron	10^{-10}	10^{-8}	0.003

* Data from Metals Reference Book (16).

Table V

	Exptl. gas mixture	Cu-Cu_2O	Fe-FeO	Si(1 at. %)-SiO_2
H_2O/H_2 ratio at 1000°C	2.5×10^{-2}	5×10^{3}	0.5	7×10^{-5}

faster rate by ionic diffusion through this layer. The initial slow period decreases with increasing temperature which would be expected as the solid-state reaction becomes more rapid. A similar two-stage process was observed by Ipatev and Orlova (5) during the oxidation of a Si steel containing 1.4% Si.

Pretreatment in Wet Hydrogen

A controlled gas mixture capable of oxidizing Si but not Cu or Fe was obtained easily by saturating hydrogen with water at room temperature. The H_2O/H_2 ratio under these conditions is 2.5×10^{-2}. Corresponding ratios for the formation of cuprous oxide and ferrous oxide and for the precipitation of silica from a 1 at. % silicon alloy is shown in Table V.

The calculation for silica is based on approximate activity coefficient of Si in both Cu and Fe of 0.01 (19). It is clear from this table that wet hydrogen should, theoretically, readily precipitate silica but not form either copper or iron oxide.

The formation of subscale in the absence of continuous scaling of the base metal has been studied carefully by Rhines, Johnson, and Anderson (8). They studied a number of dilute binary alloys with Cu as the base metal and correlated their results with a theoretical equation which for Si alloys can be expressed:

$$x^2/t = (2D_o c_o - 1.92\, D_{Si}\, c_{Si})/(1.14\, c_{Si} + 0.33\, c_o)$$

where x is depth of subscale; t, time; D_o and D_{Si}, diffusivities of oxygen and silicon in the alloy, respectively; c_o, solubility of oxygen in the base metal and dependent on the external partial pressure of oxygen; c_{Si}, initial concentration of Si in the alloy.

Since c_o is usually much less than c_{Si}, the depth of subscale and indeed whether any subscale forms or not depends on the relative values of $D_o c_o$ and $D_{Si} c_{Si}$, i.e., not merely on the relative diffusivities of oxygen and silicon.

The solubility of oxygen in Cu at the limiting oxygen pressure of Cu_2O is 0.009%. It is reasonable to assume that oxygen dissolved in solid Cu obeys Sieverts' law, viz., the solubility is proportional to the square root of the partial pressure of oxygen. For H_2O/H_2 mixtures this means that the solubility will be simply proportional to the H_2O/H_2 ratio. From Table V it is seen that the maximum oxygen solubility under the experimental conditions is:

$$0.009 \times \frac{2.5 \times 10^{-2}}{5 \times 10^{3}} = 4.5 \times 10^{-6}\ \text{wt \%}$$

By substituting this value for c_o and the other values from Table IV it is seen that $D_o c_o$ is much less than $D_{Si} C_{Si}$ which implies that no subscale can form and Si will, therefore, diffuse to the surface of the alloy forming a layer of silica. The corrosion behavior of pretreated specimens in oxygen shows that they are significantly more resistant than the untreated alloy although a completely protective silica skin has not formed.

For Si-Fe the oxygen solubility under wet hydrogen conditions is

$$0.003 \times \frac{2.5 \times 10^{-2}}{0.5} = 1.5 \times 10^{-4}\ \text{wt \%}$$

With Bramley's value (17) for the diffusivity of oxygen, $D_o c_o$ is again much less than $D_{Si} c_{Si}$ so that no subscale would be expected, and silica should precipitate at the Fe surface. The oxidation of pretreated silicon iron, however, does not confirm this since the oxidation apparently is enhanced after pretreatment. These experimental results suggest that subscale has formed and depleted the surface of the alloy in Si. This could only happen if the diffusivity of oxygen was in fact much faster than Bramley's value or alternatively that the oxygen solubility was much higher.

Conclusions

Small amounts of Si affect the scaling of Cu and Fe in different ways. For Cu, Si in the alloy tends to be precipitated mainly as subscale during external scaling with the result that little or no silica is formed at the metal-oxide interface. Therefore, the oxidation rate compared with pure Cu is lowered only slightly and moreover the mechanism of oxidation is unchanged.

Because of the slower diffusivity of oxygen in Fe, silica tends to precipitate at the metal oxide interface to give some protection during oxidation. However, a solid-state reaction between iron oxide and silica occurs after a comparatively short time depending on the temperature, and the resulting iron silicate is sufficiently conducting to give a fairly rapid scaling rate. The extent of subscale formation in Fe-Si alloys suggests that the diffusivity of oxygen in Fe is much faster than is commonly supposed.

By the use of controlled oxygen pressures it is possible to selectively oxidize Si to form silica on the surface which may give some measure of protection. The conditions for this selective oxidation can be estimated reasonably from a knowledge of diffusivities of oxygen and Si in the metal. Preliminary experiments with higher Si-Cu alloys have demonstrated that a considerable improvement in oxidation resistance can be obtained in this way.

In an Fe-Si alloy it is a relatively easy matter to produce silica only, but as soon as normal oxidation occurs some iron oxide must form and consequently the highly protective silica is converted into the much less protective iron silicate.

Acknowledgment

Thanks are due to the Morgan Crucible Company Limited, London for financial support of this work. The authors are grateful to Dr. O. Kubaschewski for useful discussion.

Manuscript received Jan. 14, 1959.

Any discussion of this paper will appear in a Discussion Section to be published in the June 1960 JOURNAL.

REFERENCES

1. L. B. Pfeil, *J. Iron Steel Inst.*, **119**, 501 (1929).
2. A. Portevin, E. Pretet, and H. Jolivet, *ibid.*, **130**, 219 (1934).
3. E. Scheil and K. Kiwit, *Arch. Eisenhuttenw.*, **9**, 405 (1936).
4. T. Mishima and M. Sugiyama, *Tetsu to Hagane*, **36**, 184, 263, 317, 495 (1950).
5. V. V. Ipatev and O. M. Orlova, *J. Appl. Chem. U.S.S.R.*, **29**, 881 (1956).
6. R. F. Tylecote, *J Inst. Metals*, **78**, 259 (1950).
7. A. Preece and J. P. Dennison, *ibid.*, **81**, 229 (1953).
8. F. N. Rhines, W. A. Johnson, and W. A. Anderson, *Trans. A.I.M.E.*, **147**, 205 (1942).
9. G. Valensi, *Rév. Met.*, **45**, 10 (1948).
10. Feitknecht, *Z. Elektrochem.*, **35**, 142 (1929).
11. W. J. Moore and B. Selikson, *J. Chem. Phys.*, **19**, 1539 (1951).
12. M. H. Davies, M. T. Simnad, and C. E. Birchenall, *J. Metals*, 889 (October 1951).
13. L. Himmel, R. F. Mehl, and C. E. Birchenall, *ibid.*, **5**, 827 (1953).
14. H. Dünwald and C. Wagner, *Z. Phys. Chem.*, **B22**, 212 (1933).
15. L. S. Darken, *Trans. A.I.M.E.*, **150**, 157 (1942).
16. Metals Reference Book, C. J. Smithells, Editor, **2**, 533-560, Butterworth, London (1955).
17. A. Bramley, J. Heywood, W. R. Cooper, and O. P. Watts, *Trans. Faraday Soc.*, **31**, 707 (1935).
13. L. Himmel, R. F. Mehl, and C. E. Birchenall, *ibid.*, 1064 (1958).
19. B. Ellingsaeter and T. Rosenqvist, *J. Metals*, 1111 (August 1956).

Translucent Phosphor Coatings in High-Pressure Mercury-Vapor Lamps

C. H. Haake

Lamp Division, Westinghouse Electric Corporation, Bloomfield, New Jersey

ABSTRACT

The optical conditions in quasi-infinitely thick phosphor plaques and in translucent phosphor coatings of closed lamps are studied. Theory shows, and experiments carried out on magnesium fluorogermanate phosphors activated with Mn confirm, that the correlation between the brightness of plaques and of translucent coatings in closed lamps is rather involved. Although prolonged phosphor firing time monotonically increases the former, the latter reaches a maximum and then decreases. This and other unpredictable results render dubious the value of crude plaque brightness tests of phosphors meant for translucent coatings in lamps. Reliable measurements of phosphors for such coatings must include for the main wave lengths of excitation relative quantum efficiencies, reflectances of quasi-infinitely thick phosphor layers, and also differential reflectivities or absorptivities in a thin phosphor layer of a known density.

The intensity of the visible radiation from the discharge in high-pressure mercury-vapor (HPMV) lamps is about 60% of that of the ultraviolet radiation (1). Therefore, HPMV lamps are good light sources; however, they exhibit a radiation deficiency in the red region of the spectrum. To correct for this deficiency the outer bulb of HPMV lamps is often coated with a layer of an ultraviolet-absorbing, red-emitting phosphor (Fig. 1). The layer is kept so thin that an excessive loss of visible radiation is avoided and yet radiation is added in the red region of the spectrum which amounts to about 8% of the total luminous output of the lamp. (In the future, for the sake of simplicity, we will refer to the radiation of this part of the spectrum as "red-lumens".) Typical such phosphors are magnesium fluorogermanate (2) and magnesium arsenate (3) both activated with manganese.

An inherent difficulty when preparing these phosphors is the judgment of their expected performance. Ultimately one is interested only in the behavior of the phosphor in a coated lamp. Phosphor tests in lamps, however, are rather tedious and in practice one usually restricts the tests to the very conveniently and quickly carried out plaque brightness measurements (emission brightness of quasi-infinitely thick phosphor layers for given excitation conditions) (4). This method is sensible only if a direct correlation exists between the plaque brightness and the red emission of phosphor coatings in a finished lamp such that an increase of the former is concomitant to an increase of the latter.

The purpose of this study is the investigation of the

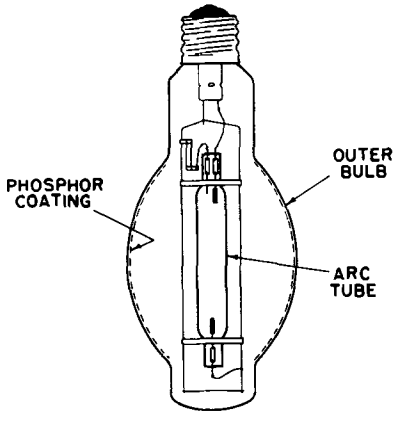

Fig. 1. High-pressure mercury-vapor lamp (Westinghouse JH-1, 400 watts).

behavior of thin phosphor layers in HPMV lamps. Equations which govern the emission from such layers are derived and discussed on the basis of experimental findings obtained from a Mn-activated magnesium fluorogermanate phosphor (MFG) in a Westinghouse 400-watt HPMV lamp. Particular interest is directed toward any possible significance of plaque brightness measurements on phosphors to be used in HPMV lamps.

Theory

The optical conditions of translucent phosphor coatings on plane substrates have been described and discussed by several authors (5, 6). The pertinent equations for the reflectance, transmittance, and absorptance[1] apply to grainy phosphor layers whose thickness is much larger than the average particle size of the phosphor crystals. The average density of the phosphor coating in HPMV lamps is about 1-2 mg/cm^2 and the particle size usually ranges from 3 to 5 μ. However, the particles in the layer do not arrange themselves in anything near a close-packed structure. When viewed under a microscope the layer appears porous and mountainous. The estimated average elevation of the phosphor layer over the surface of the bulb wall is about 30 μ. The coated bulb shows a fair degree of optical scattering and very little transparency. It seems, therefore, that in good approximation the existing equations for translucent phosphor coatings are also applicable to the present case. It will be assumed further that the reflection of the glass substrate for the exciting radiation is much smaller than that from the grainy layer and, therefore, can be neglected.

We will first present the equations for the reflectance, R, the transmittance, T, and the absorptance, A, of plane translucent phosphor coatings (6).

$$R = \frac{(r/p)\sinh(ps)}{\cosh(ps) + [(a+r)/p]\sinh(ps)} \qquad [1]$$

$$T = \frac{1}{\cosh(ps) + [(a+r)/p]\sinh(ps)} \qquad [2]$$

and

$$A = 1 - R - T \qquad [3]$$

where

$$p = \sqrt{a^2 + 2ar} \qquad [4]$$

The layer thickness is given by s, measured either in cm or mg/cm^2. The optical properties of the layer material are described by an absorptivity a and a reflectivity r, both measured either in cm^{-1} or in cm^2/mg, since as and rs are dimensionless arguments. These are the coefficients of absorption and reflection for a phosphor layer of the thickness ds. For practical purposes it is convenient to relate a and r to an easily measurable quantity, the reflectance, R_o, of a quasi-infinitely thick phosphor layer. In this case $\sinh(ps) = \cosh(ps)$ and Eq. [1] gives

$$R = R_o = \frac{r}{p + a + r}$$

from which follow

$$\left.\begin{aligned} \frac{r}{a} &= \frac{2R_o}{(1-R_o)^2} \\ \frac{a}{p} &= \frac{1-R_o}{1+R_o} \\ \frac{r}{p} &= \frac{2R_o}{1-R_o^2} \end{aligned}\right\} \qquad [5]$$

If a thin phosphor layer is applied to the inside wall of the outer bulb of a HPMV lamp, any exciting radiation reflected from the layer will reach the layer somewhere on the opposite side of the bulb, etc. Hence, the effective transmittance of exciting radiation through the bulb becomes approximately

$$\tau = T\sum_{i=0}^{\infty} R^i = T/(1-R) \qquad [6]$$

With Eq. [1], [2], and [5] using exponential terms one finds

$$\tau = \frac{1+R_o}{R_o\exp(-ps) + \exp(ps)} \qquad [7]$$

It is realized that the sum in Eq. [6] is somewhat affected by the uncoated portions of the bulb and the interior parts of the lamp. This effect, however, is small and will be neglected in the calculation, although later in this paper some comments will be made on this matter.

The effective absorptance of the phosphor coating on the bulb is

$$\alpha = 1 - \tau \qquad [8]$$

If $N(\lambda)$, the number of quanta per sec. emitted in the discharge line at λ, the effective absorptances $\alpha(\lambda)$ of the coating and the quantum efficiencies $\eta(\lambda)$ of the phosphor are taken into account, the total quantum emission, I_L of the phosphor coating becomes

$$I_L = \sum_i N(\lambda_i)\,\eta(\lambda_i)\,\alpha(\lambda_i) \qquad [9]$$

On the other hand, the quantum emission of a quasi-infinitely thick phosphor layer under the same excitation conditions is

$$I_p = \sum_i N(\lambda_i)\,\eta(\lambda_i)[1 - R_o(\lambda_i)]\cdot F(\lambda_i) \qquad [10]$$

$F(\lambda_i)$ is the ratio of the radiation generated to the radiation actually escaping the phosphor layer on the side on which the exciting radiation is incident. In the special case of MFG:Mn phosphors the quantum emission I_p is proportional to the plaque brightness since the emission spectrum is independent of the wave lengths of excitation (2).

Experimental Data

For a quantitative discussion of the equations and the dependence of their parameters on the preparation conditions of MFG:Mn, five phosphor samples of the same composition (3.5MgO, 0.5MgF_2, 1GeO_2, 0.01Mn) were studied. These samples were drawn from a large batch:

[1] These equations in a general form were originally derived by Schuster (7) although not specifically for phosphor powders.

Sample A: after 2 hr firing at 1100°C in air

Sample B: after 3 hr ball milling of sample A

Sample C: after 20 hr refiring of sample B at 1100°C in air

Sample D: after 12 hr refiring of sample C at 1100°C in air

Sample E: after 14 hr refiring of sample D at 1100°C in air.

Numerous quantities were measured:

(*a*) The relative plaque brightness, I_p (λ), of the quasi-infinitely thick phosphor layers for λ = 254, 313, 365, 405, and 436 mμ as exciting wave lengths; (*b*) the reflectance, R_o (λ), of the same phosphor layers for the same wave lengths as in (*a*); (c) the relative total lumens, I_T; and (*d*) the relative red lumens, I_R, of a HPMV arc tube with phosphor-coated bulbs; (*e*) the relative total lumens, I_{T_o}, of the same HPMV arc tube with an uncoated bulb; (*f*) the effective transmittance, τ(λ), of the exciting Hg-lines through the coated bulbs; (*g*) the density, *s*, of the phosphor coating on the bulbs.

Methods of Measurement

(*a*) *and* (*b*).—The arc tube of a 400W HPMV lamp (Westinghouse EH-1) served as excitation source whose lines were selected and transmitted through an ultraviolet monochromator onto a thick phosphor layer. The emitted radiation, $I_p(\lambda)$, was measured as photocurrent from a photomultiplier (RCA 1P28). A cut-off filter prevented the exciting radiation from entering the photomultiplier. After this filter was exchanged for one which transmits only the exciting radiation, the reflected radiation was measured as photocurrent. The container with the phosphor was then replaced by a similar one filled with MgO and the photocurrent was read again. Multiplication of the ratio of the former reading to the latter by 0.95 (averaged reflectance of MgO in the wave-length range of interest) gave the reflectance, $R_o(\lambda)$, of the phosphor. The plaque brightness, $I_p(\lambda)$, is proportional to the quantum efficiency, $\eta(\lambda)$, to the exciting radiation absorbed in the phosphor layer, $1 - R_o(\lambda)$, and to the ratio $F(\lambda)$ (see Eq. [10]). An expression for F has been derived by Coltman, *et al.* (5) which, for thick phosphor layers, becomes

$$F(\lambda) = \frac{1}{2} \cdot \frac{1 + R'_o(\lambda)}{1 + p'(\lambda)/p(\lambda)}$$

The primed quantities are those for the emitted radiation. It could be shown that for the five samples studied $F(\lambda)$ did not change by more than 1% at any one particular wave length of excitation. Since in the following the quantum efficiencies η are given relative to those of sample E, the ratio $F(\lambda)$, therefore, need not be considered here.

(*c*), (*d*) *and* (*e*).—Each phosphor sample was ball milled in an equal amount of nitrocellulose for a given length of time under the same conditions. BT-37 bulbs (as used in Westinghouse 400W JH-1 and EH-1 lamps) were coated and lehred for 10 min at about 600°C. They were then sleeved over an EH-1 arc tube mounted in a 60 in. integrating sphere. The arc tube itself was sealed into a slender quartz tube. Relative lumens were measured in a conventional way Weston Photronic cell + Viscor filter #594 Y.R.V., for total lumens and Weston Photronic cell + Viscor filter #594 Y.R.V. + Corning filter #2418 for red lumens).

(*f*).—A double-monochromator with a photomultiplier (RCA 1P28) at its exit slit was placed in front of a small hole in the integrating sphere. A baffle in the sphere shielded the hole from direct light from the lamp. For λ = 313, 365, 405, and 436 mμ, photocurrent readings were taken with the coated bulbs and a clear bulb in place, respectively. The ratio of the two readings gave the effective transmittance, τ(λ), through the phosphor coated bulb. Since the bulb glass does not transmit the 254 mμ line, τ(254) could not be measured.

(*g*).—After completion of the measurements (c) to (*f*) the total amount of phosphor in each bulb was recovered and weighed. The weight divided by the known area coated (500 cm²) gave the coating density, *s*, in mg/cm².

The data obtained are shown in Table I, II, and III. The first six columns of Table II show the sample identification; the wave length of excitation, λ; the plaque brightness, I_p; the reflectance, R_o; the effective transmittance, τ; and the relative quantum efficiency, η, respectively. Since from samples A to E only the relative changes of the values measured or computed are of interest, I_p and η of the sample E were arbitrarily chosen to be 1.00 regardless of the wave length of excitation. In the 7th and 8th column are shown the differential absorptivity *a*, and the differential reflectivity, *r*, which one obtains from Eq. [5] after determining *p* by inserting *s* (Table I), τ and R_o in Eq. [7]. In the 9th column is tabulated $\eta\alpha = \eta(1 - \tau)$. These values show how for each wave length of excitation the emission intensity of the coating in the lamp changes from phosphor A to phosphor E. Since the varying density of the coating with phosphors A to E, as encountered here for experimental reasons, does not lend itself to arriving at general conclusions, one can compute the values of $\eta\alpha$ (listed in Table II as $\eta\alpha^*$) using η, *a*, *r*, and R_o as determined earlier, and $\bar{s} = 1.290$ mg/cm² as mean coating density. If large numbers of lamps were to be prepared with phosphors A to E in the coatings, small variations of the density would cancel out and the averaged values of $\eta\alpha$ for each phosphor at each wave length of excitation would be $\eta\alpha^*$. Likewise on the basis of an averaged density $\bar{s} = 1.290$ mg/cm² computed values of τ are listed in the 11th column as τ^*.

It should perhaps be explained at this point to what extent the values of *a*, *r*, and particularly τ^*

Table I. Density, *s*, of the phosphor coatings

Phosphor	*s* (mg/cm²)
A	1.385
B	1.235
C	1.190
D	1.310
E	1.330

Table II. Measured and computed data for phosphors and phosphor coatings

Samples	λ (mμ)	I_p	R_o	τ	η (rel.)	$a\left(\frac{cm^2}{mg}\right)$	$r\left(\frac{cm^2}{mg}\right)$	ηa	ηa^*	τ^*
A		0.88	0.38	—	0.91	—	—	—	—	—
B		0.90	0.38	—	0.93	—	—	—	—	—
C	254	0.98	0.37	—	0.99	—	—	—	—	—
D		0.99	0.37	—	1.00	—	—	—	—	—
E		1.00	0.36	—	1.00	—	—	—	—	—
A		0.84	0.19	0.15	0.89	1.0	0.60	0.75	0.74	0.17
B		0.85	0.20	0.18	0.90	1.0	0.64	0.74	0.75	0.17
C	313	0.97	0.17	0.23	0.99	0.97	0.46	0.76	0.79	0.20
D		0.98	0.16	0.22	0.99	0.92	0.42	0.78	0.77	0.22
E		1.00	0.15	0.21	1.00	0.95	0.39	0.79	0.78	0.22
A		0.73	0.64	0.59	0.85	0.15	1.5	0.34	0.32	0.62
B		0.72	0.66	0.61	0.88	0.15	1.7	0.35	0.36	0.59
C	365	0.89	0.62	0.66	0.97	0.15	1.3	0.33	0.36	0.63
D		0.94	0.60	0.63	0.97	0.15	1.2	0.36	0.35	0.64
E		1.00	0.59	0.65	1.00	0.15	1.0	0.35	0.34	0.66
A		0.76	0.61	0.67	0.86	0.13	1.1	0.28	0.27	0.69
B		0.77	0.63	0.68	0.90	0.14	1.2	0.29	0.31	0.66
C	405	0.93	0.58	0.73	0.96	0.14	0.90	0.26	0.29	0.70
D		0.95	0.57	0.72	0.96	0.13	0.82	0.27	0.26	0.73
E		1.00	0.57	0.74	1.00	0.12	0.74	0.26	0.25	0.75
A		0.71	0.64	0.65	0.86	0.13	1.3	0.30	0.27	0.69
B		0.72	0.64	0.67	0.87	0.13	1.3	0.29	0.30	0.66
C	436	0.88	0.61	0.74	0.97	0.13	0.99	0.26	0.28	0.71
D		0.94	0.58	0.71	0.97	0.13	0.87	0.28	0.27	0.72
E		1.00	0.57	0.73	1.00	0.13	0.76	0.27	0.26	0.74

and ηa^* are affected by the somewhat idealistic assumption that no exciting radiation reflected from the phosphor coating into the lamp is lost for the process of interreflections, either by absorption in lamp parts or by transmission through the uncoated end parts of the lamp. Actually these losses do occur to some extent and they modify the equations slightly. It can be shown that the values of a and r are somewhat lower than those appearing in Table II. Conversely, within the accuracy desired, the values of τ^* and ηa^* remain unchanged. This is because p (and thence a and r) is obtained from the inverted Eq. [7]. Later after this equation has again been inverted one finds τ^* and thence ηa^* using an average coating thickness $\bar{s}$. Thus a modification of Eq. [7] due to losses has virtually no effect on τ^* and ηa^*.

In Table III are shown the red lumen percentages (based on the total lumens of a clear lamp as 100) of the coated bulbs, and also the per cent loss of total lumens due to absorbed visible radiation in the coating.

Discussion and Conclusion

It can be seen from Eq. [10] that, for constant quantum efficiencies $\eta(\lambda)$, the plaque brightness *increases* with decreasing reflectances $R_o(\lambda)$. On the other hand, an analysis of Eqs. [5] and [7]-[9] shows that, again for constant $\eta(\lambda)$, the emission from a phosphor bulb of a HPMV lamp *decreases* with decreasing reflectance, if, as often is the case, the absorptivity a remains essentially unchanged. This adverse trend of I_p and I_L rules out any meaningful judgment of phosphors based on measurements of plaque brightness, a method which still is widely practiced for selecting phosphors to be used in HPMV lamps [see, e.g., Ref. (4)]. Thus, if one were to choose certain conditions for preparing phosphors merely guided by plaque brightness measurements, phosphors might be discarded which would exhibit an excellent performance in translucent coatings on bulbs, and vice versa.

Table III. Lumen ratios of coated bulbs

Phosphor	$100\ I_R/I_{T_o}$	$100\ (1 - I_T/I_{T_o})$
A	8.5	5.0
B	8.7	5.0
C	8.6	2.5
D	8.9	2.5
E	9.0	2.5

Also in the present case the reflectances $R_o(\lambda)$ decrease (from B to E). At the same time, however, the efficiencies $\eta(\lambda)$ increase. Thus with prolonged firing time ηa^* and, hence, the red lumens emitted from a coated bulb should approach a maximum and then decrease. This maximum is concealed in the values of ηa and I_R/I_{T_o} shown in Table II and Table III, because in the present experiments the coating thickness could not be held constant from A to E. However, the maximum clearly appears in the values of ηa^* as computed for a constant coating thickness. In order to further substantiate this result we coated eight bulbs with MFG:Mn phosphor which had been fired for 10 hr and for 48 hr, respectively. When we measured the red lumen percentage, we actually found a decrease from (9.9 ± 0.1) % for the phosphor fired for 10 hr to (9.2 ± 0.3) % for the phosphor fired for 48 hr. It, therefore, becomes apparent that a limited firing time is required for the

phosphors to obtain optimum performance. There is, however, also the requirement of as high a transmission through the coating for the visible radiation of the discharge as possible. As can be seen from the values of I_τ/I_{τ_0} in Table III this transmission increases slightly from phosphors B to E with firing time, but it soon reaches a saturation at a point where the latter requirement may no longer be conflicting with the former.

There is another interesting phenomenon. The reflectance R_0 at 405 mμ (violet) and 436 mμ (blue) decreases from phosphors B to E. This is tantamount to an increasing yellowish body color of the phosphors which usually is considered objectionable. When used for coatings in HPMV lamps the phosphor will absorb violet and blue radiation of the discharge which is needed for good color rendition. Since phosphor E exhibits a yellowish body color deeper than that of B, one is lead to believe that also in a thin coating phosphor E should show effective transmittances for violet and blue light which are lower than those of phosphor B. It is interesting to note from the values of τ^* in Table II that just the opposite holds true: τ^* (405mμ) and τ^* (436 mμ) *increase* from B to E. This seemingly odd behavior can again be explained by Eqs. [5] and [7]. Since the reflectances $R_0(\lambda)$ decrease from B to E and the absorptivities virtually do not change, p in Eq. [5] decreases and, hence, τ in Eq. [7] increases.

For the purpose of achieving good uniformity of the phosphor the MFG:Mn was ball milled between the first and second firing (sample B). Small pebbles were used whose main action was the breakage of agglomerates. This, as can be seen in Table II, leads to an increase of the reflectance, R_0, to a decrease of the effective transmittance, τ^*, and hence to an increase of the effective absorptance, α^*, of the phosphor coatings. Since also the quantum efficiencies increase, one can expect a rather strong increase of $\eta\alpha^*$ and of red lumens emitted from the phosphor coating. In fact, phosphor B gives the highest values of $\eta\alpha^*$ for $\lambda_{exc} = 365$, 405, and 436 mμ. The increase of η induced by ball milling is rather surprising, as ball milling has a detrimental effect on other phosphors, particularly those of the ZnS type (8). At this time we cannot offer more than a suggestion as to the reason for the increase in η. The arrangement of the oxygen ions which surround the emitter ion (Mn^{+4}) has a strong effect on the efficiency, η, of quantum conversion in the center. Any distortion of the system, possibly frozen in after firing, can result in a small η. It seems feasible that such internal strains are released during mild ball milling of the phosphors.

Summary

Translucent coatings of MFG:Mn phosphors such as are used for color correction in HPMV lamps exhibit performance parameters markedly different from those obtained with quasi-infinitely thick phosphor plaques. By firing the phosphor for a prolonged period of time the emission intensity of the coating increases to a maximum value and then decreases, whereas the emission intensity of the phosphor plaques increases monotonically.

Prolonged firing time will also lead to an increasingly yellow body color of the phosphor plaque, i.e., to an increasing absorption of violet and blue light. Contrary to this, the translucent phosphor coatings in lamps exhibit an increasing effective transmittance for the violet and the blue mercury lines with increasing firing time.

Therefore, a valid judgment of phosphors which ultimately will be used in translucent coatings of HPMV lamps cannot be based on simple plaque brightness measurements. It is mandatory to determine various phosphor parameters whose evaluation will result in the optimum preparation conditions of the phosphor, or to coat bulbs, sleeve them over the same arc tube, and measure the red lumen output.

Manuscript received March 23, 1959.

Any discussion of this paper will appear in a Discussion Section to be published in the June 1960 JOURNAL.

REFERENCES

1. W. Elenbaas, "The High Pressure Mercury Vapor Discharge," North Holland Publishing Co. (1951).
2. L. Thorington, *J. Opt. Soc. Amer.*, **40**, 579 (1950).
3. H. A. Klasens, *Philips Res. Repts.*, **9**, 377 (1954).
4. K. H. Butler and R. W. Mooney, *Sylvania Technologist*, **9**, No. 4 (1956).
5. J. W. Coltman, E. G. Ebbighausen, and W. Altar, *J. Appl. Phys.*, **18**, 530 (1947).
6. I. Broser, *Ann. Physik*, **5**, 401 (1950).
7. A. Schuster, *Astrophys. J.*, **21**, 1 (1905).
8. N. Riehl and H. Ortmann, *Ann. Phys.*, **29**, 556 (1937).

The Use of Organo-Substituted Hydrolyzable Silanes on Silicon Devices

B. Schwartz

Hughes Semiconductors, Newport Beach, California

ABSTRACT

The formation of silicone polymers directly from the monomers, on the surface of silicon diodes, has resulted in devices with low reverse currents. Transistors treated in this way react in different ways due to the conditions imposed by the specific surface potentials involved.

Silicone resins, varnishes, and greases have been used in the fabrication of semiconductor devices, since these materials provide a hydrophobic environment for the device and at the same time have the thermal stability necessary for proper operation. All these materials are in a polymeric form prior to application to the device. This paper concerns techniques for forming a silicone polymer directly on the surface of the device by the use of organo-substituted hydrolyzable silanes so that enhanced electrical properties result (1).

The general formula for an organo-substituted hydrolyzable silane, which is the starting point from which all silicones are derived (2), is $R_{4-i}SiX_i$ (i=1, 2, 3,), while R is an organic radical. For use on semiconductor devices a short-chain hydrocarbon is preferred, since the shorter the chain, the better the thermal stability. The X refers to the hydrolyzable part of the compound and can be a halide, ethoxide, or other radical which will react with water.

In order to see how a silicone polymer is formed from this class of compounds, consider the hydrolysis of the difunctional reagent dimethyldichlorosilane. In the presence of water this compound reacts spontaneously to form dimethyldihydroxysilane and HCl. The dimethyldihydroxysilane is unstable, and by intermolecular dehydration a silicone polymer is formed which in this case would be polydimethylsiloxane. Compounds also are available with either 1 or 3 organic radicals in the so-called monomer, so that not only can linear polymers be made, as just described, but space polymers can be realized also by having some trifunctional silane present during the reaction.

In the case of the ethoxy system, the reaction with H_2O is not so straightforward, and one must provide either an acidic or basic medium for the hydrolysis to proceed. Since most of the silicon device work to be reported on here was done using the chlorosilanes, all reference is to this system. Somewhat analogous results were obtained when the ethoxy system was used in place of the chloro system.

Methods and Results

The techniques that one might use in forming the silicone on the surface are: (*a*) exposure of a premoistened unit to the vapors of the silane mixture (3); (*b*) total immersion of the unit in the silane mixture itself; and (*c*) immersion of the unit in a solution of the silane mixture. The method of total immersion in the silane mixture has given the best results, and this technique is the one preferred to during the rest of this paper.

Figure 1 shows the effect of silaning on the electrical characteristics of a grown p^+n silicon junction. Curve A illustrates the reverse diode characteristics of the unit before etching where the crystal surface contained a good deal of work damage. Curve B illustrates the junction properties after the unit had been acid etched to remove the work damage and baked at 200°C for 15 min. Curve C shows the properties of the same junction after it had been silaned with a mixture of methyl and phenyl chlorosilanes and baked for 1 hr at 250°C. In this particular measurement no attempt was made to reach the full breakdown voltage of the unit, since this device was to be used for a special series of surface experiments which required only a 500 v or better peak inverse voltage.

In Table I the reverse characteristics of 10 experimental large-area evaporative-fused-junction p^+n silicon diodes are listed. E_b and E_s are the voltages necessary to pass 2 and 10 μa, respectively, in the reverse direction; I_b is the reverse current measured at 125 v. For the silaning operation a 50-50 mixture

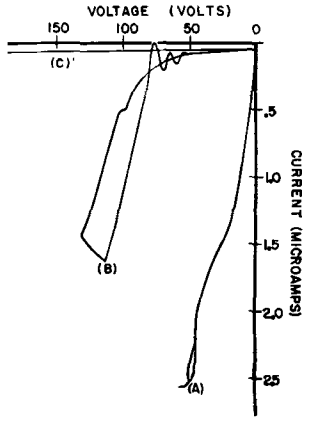

Fig. 1. Reverse characteristics of a group p+n silicon junction diode (A) before etching, (B) after etching in a mixture of hydrofluoric acid and nitric acid, and (C) after silaning.

Table I.

After standard treatment			Silaned with 50% dimethyldichlorosilane-50% methyltrichlorosilane and baked at 100°C for ½ hr		
E_s, v	E_b, v	I_b, mμa	E_s, v	E_b, v	I_b, μa
20	10	>50,000	500+	500+	21
4	2	>50,000	30	10	>50,000
8	3	>50,000	500+	500+	20
500	440	36	500+	500+	21
10	4	>50,000	500+	500+	21
52	20	>50,000	440	400	25
340	320	500	500+	500+	25
14	6	>50,000	32	14	>50,000
4	2	>50,000	500+	500+	22
8	2	>50,000	150	75	5,000

of dimethyldichlorosilane and methyltrichlorosilane was used. One should not attempt to compare the individual units in this table, since they were not tabulated in the same order before and after silaning. Notice that where originally there was only 1 unit with a reverse current less than 100 mμa, there were 7 units with reverse currents of less than 100 mμa after silaning. Again, these units were not tested above 500 v. Other units, similarly treated, were taken out to breakdown, and no adverse effects were noticed unless too much current was allowed to pass in the reverse direction.

Table II shows the necessity of a curing cycle to bring out the improvement in diode properties after silaning. The units were not kept in order so that individual comparisons are not valid. Here again a 50-50 mixture of methyl and dimethylchlorosilanes was used for surface treatment. Initially there were only 3 units that had reverse currents of 220 mμa or less. After silaning, but prior to baking, all the units had poor characteristics; but after baking for ½ hr at 100°C, there were 7 units with reverse currents of 220 mμa or less; in fact, 6 of the units showed less than 50 mμa reverse current.

Heat Treatment and Stability

Some experiments were performed to establish the influence of the baking part of the silane-treatment cycle without the silanes having been applied. Table III shows the results of an experiment where a lot of approximately 700 units, which had been processed simultaneously, was arbitrarily divided in two, and only one half were silaned, using a mixture of mono-, di-, and tri-methylchlorosilanes. Both sets

Table II.

After standard treatment	I_b mμa After silaning but no baking	After silaning and baked at 100°C for ½ hr
100	>50,000	2,000
120	>50,000	50
>50,000	>50,000	30
>50,000	25,000	220
>50,000	>50,000	>50,000
>50,000	>50,000	>50,000
220	12,000	26
>50,000	>50,000	30
>50,000	>50,000	23
>50,000	33,000	20

Table III.

I_b μa, silaned	I_b mμa, control	Percentage less than stated I_b
17	1120	10
24	2000	20
46	4440	50
190	5200	90

of units then were baked at 200°C for 2 hr.

It was also established by experimentation that prolonged air baking, of the order of hours, (i.e., 3 hr or more), at elevated temperatures (approximately 200° to 250°C) would result in improved devices, without silaning, but the reproducibility was poor and further heating might very well cause the units to deteriorate appreciably. Therefore, it is felt that the improvements noted after silaning were due to the formation of the silicone film on the surface of the device and were not merely the result of baking the unit for the stated periods.

Some silaned transistors which have been aging in air for more than two years since they were treated were retested recently. The emitter and collector diode reverse currents on these units were found to be essentially the same as when the units were first silaned, indicating a good stability factor for this type of treatment.

The thermal stability of silaned units was investigated by aging the units at elevated temperatures and periodically checking the reverse current for degradation. At 250°C and below, no noticeable degradation took place; in fact, if anything, the units improved. At 300°C degradation appeared after about 8½ hr of aging. For 350°, 375°, and 400°C, the times for the onset of degradation were approximately 6½ hr, 3½ hr, and ½ hr, respectively.

The solvent resistance of the silaned units was investigated by boiling the units in various solvents for 5 to 15 min, again using the diode reverse current as the indicator of stability. If the units were not properly cured before being exposed to the solvent, degradation was immediate and universal. If the units were cured properly, then boiling in acetone, carbon tetrachloride, benzene, methyl alcohol, or trichloroethylene had no adverse effect.

Surface Channels and Surface Recombination Velocity

In Fig. 2 the effect of silaning on channels (4) on a fused-junction rectifier is shown. To the left of the origin is the p-region and to the right is the n-region. Figure 2A is a plot of the photoresponse of the freshly etched silicon rectifier as a function of distance. The sharpness of the peak indicates the absence of a channel. Figure 2B is a plot of the photoresponse of the same diode after it had been allowed to age in air for two weeks. The channel-type response over the n-region, indicating p-type conversion at the surface, can readily be seen. In Fig. 2C the photoresponse of the same diode is plotted after re-etching and silaning. In Fig. 2D the photoresponse of the same silaned unit after it had been allowed to age in air for six months is plotted; notice the absence of the channel.

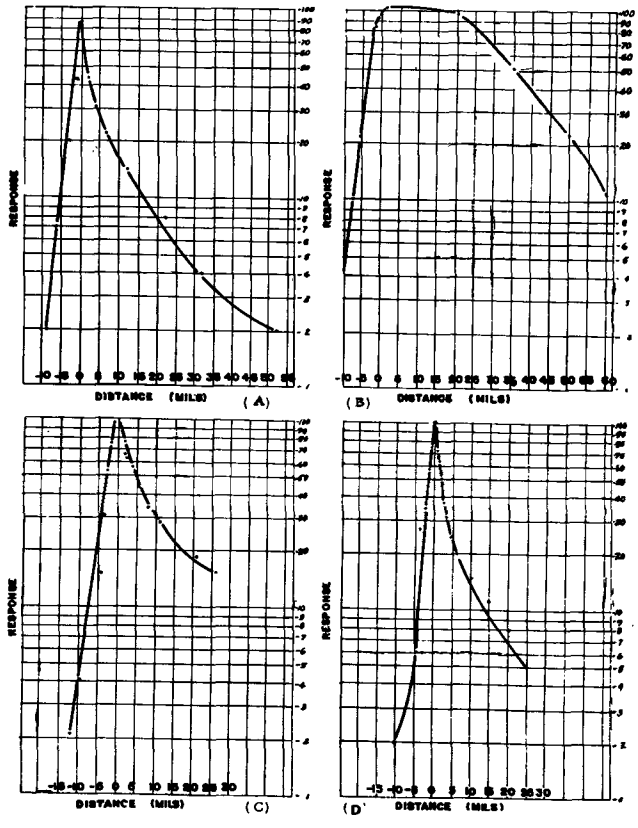

Fig. 2. Photoresponse of a fused p⁺n silicon junction diode as a function of distance from the junction.

A few experiments have been performed where the surface recombination velocity (s) of silicon filaments was measured before and after silaning. Improvement of s was noted, but stability was quite poor and degradation to the initial value occurred within 6 hr. When this treatment was tried on p-n-p transistors, units made by a diffusion technique showed improvement in the current amplification factor while evaporative fused junction transistors degraded in this parameter. These results can be explained on the basis that silaning causes the surface potential to become more positive, i.e., more n-type, a fact which can be seen by observing the results in Fig. 2 and which was verified in a gas cycling study (5). If the surface potential of the base region of the evaporative fused junction transistor is about −0.15 e.v.[1] and considering the relationships between current amplification factor, surface recombination velocity, and surface potential (6-9), then one can, by increasing ϕ_s, produce a decrease in the current amplification factor. It is believed, though, that the base region of the diffused device has a surface potential high enough (i.e., strongly n-type), due to the high doping density at the surface, that the "bell-shaped" functional relationship between surface recombination velocity and surface potential actually can result in an improvement in the current amplification factor by increasing the surface potential. The amount of change in surface potential due to silaning has not been measured as yet, so that more quantitative results cannot be stated at this time.

It has been observed that the structure of the polymer has an important influence on the resulting properties of the device. Long-chain polymers appear to reduce reverse currents more than short-chain systems. Also, stability appears to be structure dependent, and the presence of a tri-functional compound in the system seems to aid in achieving more stable properties in the units so treated. This agrees with the findings of Hall (10), who reports an actual bonding of the film that is formed into the surface of the substrate silicon when a tri-functional compound is present.

In conclusion, it is seen that when organo- substituted hydrolyzable silane monomers are polymerized on a silicon device, creating a silicon coating on the surface, the diode characteristics for the device can be improved. Furthermore, since this approach utilizes the so-called monomers of the silicones, additives and copolymerization agents can be chosen so as to produce additional benefits in semiconductor devices.

[1] "Channel" experiments in this laboratory always have shown conversion of type over the base region of these transistors. Preliminary experiments have shown that the surface potential is of this magnitude when the unit is allowed to age in air. These results will be published at a later date.

Acknowledgment

The author wishes to express his gratitude to Mrs. E. Lu for her assistance in this work, to Mr. A. Drasein for the data used in Table III, and to Mr. M. J. Barrett for the devices used in this study as well as his many helpful comments and suggestions.

Manuscript received June 2, 1958. This paper was prepared for delivery before the New York Meeting, April 27-May 1, 1958.

Any discussion of this paper will appear in a Discussion Section to be published in the June 1960 JOURNAL.

REFERENCES

1. B. Schwartz, U. S. Pat. 2,832,702, April 29, 1958; 2,854,358, Sept. 30, 1958; and 2,874,076, Feb. 17, 1958.
2. E. G. Rochow, "An Introduction to the Chemistry of the Silicones," John Wiley & Sons, Inc., New York (1946).
3. F. J. Norton, *General Electric Rec.*, **47**, p. 6 (1944).
4. A. L. McWhorter and R. H. Kingston, *Proc. I.R.E.*, **42**, 1376 (1954).
5. R. Solomon, Private communication.
6. W. M. Webster, *Proc. I.R.E.*, **42**, 914 (1954).
7. D. T. Stevenson and R. J. Keyes, *Physica*, **20**, 1041 (1954).
8. A. Many and D. Gerlick, *Phys. Rev.*, **107**, 414 (1957).
9. T. M. Buck and F. S. McKim, *This Journal*, **105**, 713 (1958), using a value of the order of 10^8 for the ratio of the capture cross section for holes to that of electrons.
10. T. C. Hall, Private communication.

Arc Decomposition of Rhodonite

Victor Harris, John D. Holmgren, Samuel Korman, and Charles Sheer

Vitro Laboratories, Division of Vitro Corporation of America, West Orange, New Jersey

ABSTRACT

A developmental pilot line for the arc treatment of Colorado rhodonite has been built and operated to investigate the applicability of the high-intensity arc process to the extraction of manganese from siliceous ores. The rhodonite is incorporated into 2-in. diameter electrodes to the extent of 75-85% by weight and vaporized in a d-c high-intensity arc operating in the range 40-60 kw. Vaporization in the arc decomposes the manganese silicate content of the rhodonite to MnO and SiO_2. The product is collected as a mixture of the respective oxides in finely particulated form. The manganese, now readily soluble, is leached from this mixture. The effects of significant process variables are discussed.

This paper describes the design and operation of a developmental pilot plant for the arc decomposition of Colorado rhodonite by means of a new process known as the Sheer-Korman "Hierarc Process" (1, 2). The primary purposes of this program were to demonstrate the technical feasibility of treating rhodonite and to obtain process design and evaluation data.

Rhodonite, a manganese silicate, is found in several sections of the United States and abounds in the southwestern area of Colorado. While deposits represent a significant quantity of Mn, the material is of such a refractory and stable nature that it has never been used as a major Mn source; instead it has been described as worthless gangue material in lead and zinc mining operations. Theoretically, pure rhodonite contains 42% Mn. Mined and milled in conjunction with lead-zinc operations, concentrates ranging up to 33, or perhaps 36% Mn, might be expected.

The Hierarc Process, utilizing the high-intensity arc, serves to decompose the manganese silicate into a mixture of two discreet, finely particulated materials, manganous oxide and silica. In this form, the Mn is readily dissolved by leaching. For example, over 95% of the Mn in samples of arc product dissolved in dilute HCl at room temperature.

Using an anode consisting of an homogeneous mixture of ore and carbon—the ore content may be as high as 80-85%—the high-intensity arc provides an effective means of heating the material to temperatures of decomposition without the necessity of heating crucibles or other containing vessels.

Elements of the Process

The rhodonite, ground to 100% minus 50 mesh, is mixed with carbon source materials, in this case coal and pitch. This mixture, with the addition of an extrusion aid material, is placed in an hydraulic press and ore-bearing electrodes are extruded. These are baked with a controlled schedule rising to a maximum temperature of 900°-1000°C. Electrodes of ⅝-in. diameter are completely baked within 2-3 hr, while 2-in. electrodes are baked 12-20 hr, depending on the desired characteristics.

The pilot plant was operated using electrodes 2 in. in diameter and 44 in. long. A direct current arc was used. Therefore, only the anode is ore-bearing; the cathode is a 1-in. diameter graphite rod. The baked electrode is placed in the arc chamber and the arc current applied. For this application the arc is operated in air at atmospheric pressure. Air, swept into the system, provides excess oxygen to the reaction, rapid quenching of the arc product gases, and arc product transport to the product collector. The arc chamber and product collector are shown schematically in Fig. 1. The simplicity of the system is evident.

Since in this application this process serves only as a means of decomposition, the Mn content of the product will usually be essentially the same as that of the feed material. Generally speaking, the values of recoveries, yields, and processing costs will remain about the same independent of the Mn concentrations in the feed. Over-all process economics, of course, are affected importantly by the Mn content of the feed material.

The arc chamber, 36 in. in diameter and 5 ft high, is ⅛-in. boiler plate; ducts are of 18-gauge galvanized iron. Air is swept into the chamber and circulated in such a way that the chamber wall temperatures do not exceed 200°F when operating at the normal level of around 50 kw.

The homogeneous electrode, being made largely of nonconductive material, has a relatively high electrical resistance, as much as two orders of magnitude greater than a pure carbon electrode. Therefore, to minimize power losses it is necessary to in-

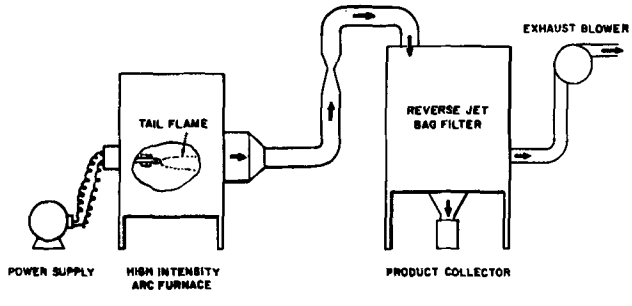

Fig. 1. Arc chamber and product collector

Fig. 2. Anode brush assembly showing anode crater. Graphite cathode can be seen as the smaller diameter electrode.

troduce the arc current as near to the arc crater as possible. A system of sliding brushes is used. Figure 2 shows the brush assembly and also provides a good illustration of the arc crater after the arc is extinguished. The brushes are water-cooled and spring loaded and in this case provided with replaceable graphite shoes. The round plate through which the 2-in. anode projects is water-cooled and electrically neutral, to shield the brush assembly from damage by the arc. The 1-in. cathode in its normal operating position can also be seen.

Operating Data

There are three dependent process variables of primary importance. These are: unit power consumption (in kwhr/lb of anode vaporized), erosion rate (in lb/hr of anode vaporized) and per cent slag (the ratio of the weight of spalled and melted material to the total weight loss of the electrode). These are affected most importantly by the following four independent process variables: anode carbon content (in per cent), arc current (in amperes), anode resistivity (ohm/cm^3), and anode apparent density (g/cc). A comprehensive investigation of the relations of these variables was carried out based on statistical analysis of the results of over 300 test runs. Some typical data are illustrated. Figure 3a shows the effect on unit power consumption of varying arc current and carbon content. This is for electrodes having a specific resistivity in the region of 0.05 ohm/cm^3 and density in the region of 1.75 (g/cc). The heavily inked portions of the curves represent the regions in which experimental data are available. The light portions represent the regions of statistical extrapolation. Curves which are entirely in light ink represent extrapolation of the results obtained with other carbon percentages.

Caution is necessary in viewing the extrapolated data, especially toward the extremes of their extension. They are useful primarily for indicating trends. Referring again to Fig. 3a, it cannot be said, for example, that a 10% carbon electrode can be processed at 300 amp with a unit power consumption of 1 kwhr/lb. However, it can be said that at lower currents the 10% carbon electrode will probably give better results than the higher carbon electrodes, while at higher currents the converse will be true.

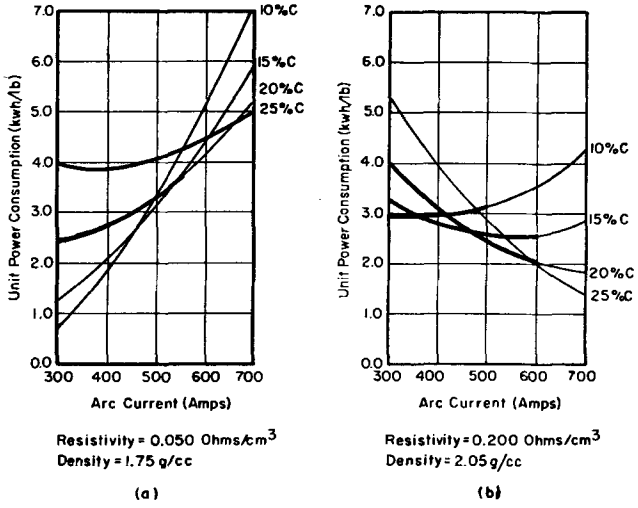

Fig. 3. Effect of arc current and carbon content on unit power consumption.

Figure 3b provides a comparison of the same factors for electrodes having a resistivity of about 0.2 ohm/cm^3 and a density of about 2 g/cc. The considerable difference in character of these curves is apparent. Improved performance is evident. Performance generally improves with current, and under these conditions a 20% carbon electrode provides better operation at higher currents than any of the electrodes in the previous figure.

A comparison of erosion rates can also be made in the same manner. Figure 4a shows the erosion rate for the low resistivity, low density type of electrode in terms of pounds of electrode vaporized per hour. It will be noted that at 600 amp the curves fall in the area below 10 lb/hr. In contrast Fig. 4b shows the same information for the high resistivity, high density anode. In this case it can be seen that at 600 amp operation is in the region of 20 lb/hr.

A similar comparison of per cent "slag" shows that the same conditions which tend to improve unit power consumption and erosion rate tend also to increase per cent slag. This material is not slag in the usual sense. It is material which either spalls from the electrode or melts and drips from the crater without being vaporized. Figure 5a shows the per

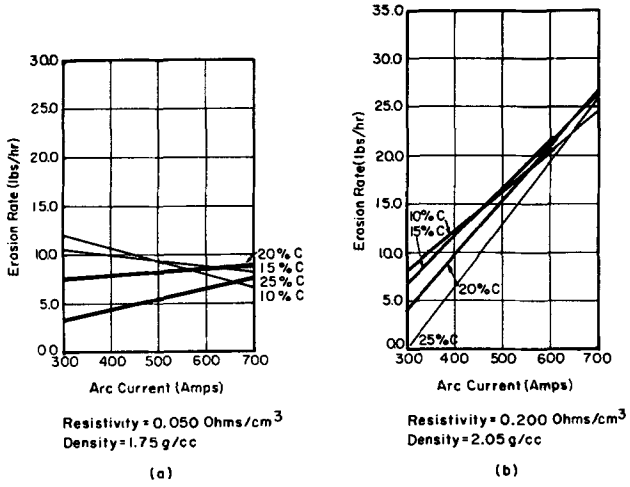

Fig. 4. Effect of arc current and carbon content on erosion rate.

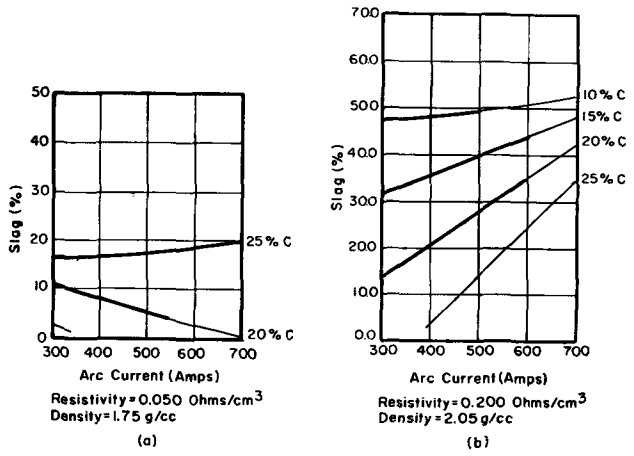

Fig. 5. Effect of arc current and carbon content on "slag" per cent.

cent slag for the low resistivity, low density electrode. The 20% carbon electrode, for example, falls entirely in the region below 10%. In Fig. 5b it is seen that, with the conditions that give better unit power consumption and erosion rate, slag is above 10%.

On the basis of these and other similar data a group of electrode characteristics were evolved as follows: apparent density in the region of 2, specific electrical resistivity in the range of 0.25 to 0.3 ohm/cm³, and carbon content in the range of from 16 to 18% after baking.

Electrodes of these characteristics were subjected to a series of runs extending over half-shift periods of about 4 hr. Typical results are shown in Table I.

Note that the slag per cent is lower than might have been expected from the statistical test results just discussed. This is because those test runs were short, involving considerable on-off operation and corresponding heating and cooling of the system. The sustained runs always exhibit better results and, of course, are more representative of production conditions.

Operations were not carried to the point of actually recycling this slag. However, with its recycling, Mn recovery in the process would be expected to approach 100%, since there is little true loss anywhere in the system. The ore used in these operations contained approximately 25% Mn. Before treatment, on the basis of analysis, over 90% of the Mn in the ore was in insoluble form. After treatment over 90% of the insoluble Mn was found to be converted to soluble form in the arc product.

Table I. Typical operational data

Current	700 amp
Power	50 kw
Anode feed	103 in./hr 24 lb/hr
Slag	16.5 % (wt)
Anode vaporized	20 lb/hr
Unit power consumption (d-c side of generator)	2.5 kwhr/lb of electrode vaporized
Production rate	13 lb/hr of arc product
Cathode consumption	0.5 lb/hr of graphite

It should be emphasized that these results represent a certain stage of development in process application. Further improvement can be expected. Development in the techniques of electrode fabrication for higher strength will permit reduction in slag per cent and operation at higher currents with higher production rates. The use of larger diameter electrodes can be expected to provide some additional improvements in unit power consumption and, of course, also higher production rates. Many other aspects of this development system are subject to engineering refinement. Work in refining the high-intensity arc in process applications is continuing.

Conclusion

This work demonstrates the technical feasibility of applying the Hierarc Process to the decomposition of Colorado rhodonite ore to provide manganese in a readily soluble form. Most importantly, this was done with rapid baked electrodes and over-all values of unit power consumption in the region of 2.5 kwhr/lb.

Acknowledgment

This work was done under contract with the Government by the West Orange Laboratory, Vitro Laboratories Division of the Vitro Corporation of America.

Manuscript received April 1, 1959. This paper was prepared for delivery before the Ottawa Meeting, Sept. 28-Oct. 2, 1958.

Any discussion of this paper will appear in a Discussion Section to be published in the June 1960 JOURNAL.

REFERENCES

1. C. Sheer and S. Korman, "The High Intensity in Process Chemistry," chapter in "Arcs in Inert Atmospheres and Vacuum," W. E. Kuhn, Editor, John Wiley & Sons, Inc., New York (1956).
2. L. Mead, M. A. Marquis, C. Sheer, and S. Korman, "Energy Transfer in the High Intensity Arc, Parts I and II," op. cit.

On the Measurement of the Temperatures of Unenclosed Objects by Radiation Methods

A. G. Emslie and H. H. Blau, Jr.

Arthur D. Little, Inc., Cambridge, Massachusetts

ABSTRACT

The functional relationships between apparent temperature and true temperature for the total radiation pyrometer, the optical pyrometer, the two-color pyrometer, and the two-temperature pyrometer are developed and discussed. It is shown that it is impossible to measure the temperature of an unenclosed object in the range 2000°-4000°K with accuracy greater than about 10% without prior knowledge of the emissivity. If the emissivity is known within 20%, the temperature can be determined within 1 or 2% by means of an optical pyrometer, particularly if the instrument is operated at the blue end of the spectrum. The accuracy obtainable with the other instruments under equivalent conditions is significantly lower.

Since the last war there has been a growing need to operate various devices at higher and higher temperatures in order, for example, to obtain more efficient rocket motors or faster airplanes. As a result a rapid increase is now taking place in research on the properties of all conceivable kinds of materials at higher temperatures. Such tools as the solar furnace, the plasma jet, the pulsed electric discharge, and the shock tube are used in these furnace techniques in several important respects.

An ordinary furnace usually has a fairly uniform internal temperature distribution, including the sample under test, and so the sample temperature can be found quite readily by means of a thermocouple inserted anywhere in the furnace or by an optical pyrometer applied to a sighting hole which emits essentially black-body radiation. With the new methods, on the contrary, there is generally no enclosure at the temperature of the sample, and the sample itself usually has sizeable temperature gradients. Under these conditions it cannot be assumed that the sample acts as a black-body radiator. Also, because of the gradients, it is very difficult to produce an artificial black-body cavity, for example, by drilling a hole in the sample. Thus the optical pyrometer cannot be used routinely to determine the temperature. Furthermore, in many cases of interest the sample temperature is above the limits of measurement by thermocouples.

How, then, can one measure the temperature of a sample under these conditions? The purpose of this paper is to evaluate the various radiometric methods under the assumption that the sample is completely unenclosed and that there is no prior knowledge about the emissivity of the sample.

Total Radiation Pyrometer

In the total radiation pyrometer the radiation from a given area of the sample is integrated over all wave lengths by a thermopile that has been calibrated against a black-body radiator.

The relation between the apparent absolute temperature T_A corresponding to an assumed average emissivity of ½ and the true temperature T corresponding to the real average emissivity $\bar{\epsilon}$ is given by

$$\frac{1}{2}\sigma T_A^4 = \bar{\epsilon}\sigma T^4 \qquad [1]$$

where σ is the Stefan-Boltzmann constant. The fractional error in the absolute temperature is

$$\frac{T_A - T}{T} = (2\bar{\epsilon})^{1/4} - 1 \qquad [2]$$

The graph of this relation, shown in Fig. 1, indicates that an error of about 20% is made when the true emissivity is 0.2 rather than the assumed value of 0.5.

The Optical Pyrometer

In the case of the optical pyrometer, radiation from the sample in a narrow band of wave lengths centered at 0.65 μ is compared with the radiation from a calibrated glowing filament. Assuming as before that nothing is known about the emissivity of the sample and that a value of ½ is guessed, we

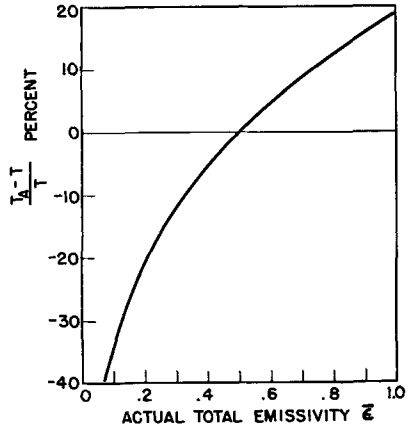

Fig. 1. Error of total radiation pyrometer vs. actual total emissivity for an assumed total emissivity of ½.

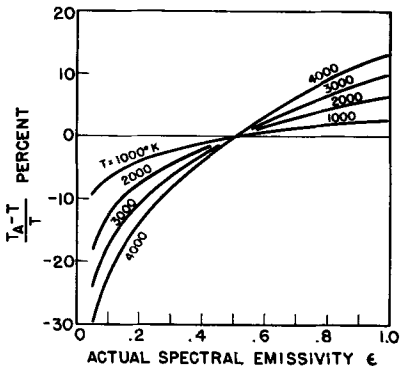

Fig. 2. Error of optical pyrometer vs. actual spectral emissivity at $\lambda = 0.65\ \mu$ for an assumed spectral emissivity of ½.

find from Wien's law the following relation between the apparent and true temperatures:

$$\frac{1}{2}\, e^{-c_2/\lambda T_A} = \epsilon\, e^{-c_2/\lambda T} \qquad [3]$$

where λ is the wave length at the center of the transmission band of the instrument, ϵ is the spectral emissivity of the sample, and $c_2 = 1.44 \times 10^4$ micron degrees.

From Eq. [3] we obtain for the relative error in the temperature

$$\frac{T_A - T}{T} = \frac{(\lambda T/c_2)\ \ln 2\epsilon}{1 - (\lambda T/c_2)\ \ln 2\epsilon} \qquad [4]$$

Figure 2 shows how the error depends on the true spectral emissivity ϵ for various fixed values of the true temperature T. For example, if the true emissivity is 0.2 instead of the guessed value of 0.5, the error is 7.5% at 2000°K and 14% at 4000°K.

Since, according to Eq. [4], the error is approximately proportional to λ, better results would be obtained by operating an optical pyrometer at as short a wave length as possible. At temperatures above 2000°K there should be enough short wavelength radiation to permit the construction of an electronic instrument with a filter in the neighborhood of 0.4 μ.

The Two-Color Pyrometer

The basis of the two-color pyrometer is that the unknown emissivity can be eliminated by taking the ratio of the radiant intensities from the sample at two different wave lengths. Unfortunately, this can only be done if the emissivity is the same at the two wave lengths. If ϵ_1 and ϵ_2 are the actual emissivities at the wave lengths λ_1 and λ_2, the radiated intensities in wave-length bands $\Delta\lambda_1$ and $\Delta\lambda_2$ are

$$\left.\begin{aligned} W_1 &= \epsilon_1 c_1 \lambda_1^{-5} \Delta\lambda_1 e^{-c_2/\lambda_1 T} \\ W_2 &= \epsilon_2 c_1 \lambda_2^{-5} \Delta\lambda_2 e^{-c_2/\lambda_2 T} \end{aligned}\right\} \qquad [5]$$

assuming that λ_1 and λ_2 are both in the region where Wien's law applies. The ratio of the intensities is

$$\frac{W_1}{W_2} = \frac{\epsilon_1}{\epsilon_2}\,\frac{\lambda_1^{-5}\Delta\lambda_1}{\lambda_2^{-5}\Delta\lambda_2}\, e^{(c_2/T)[(1/\lambda_2)-(1/\lambda_1)]} \qquad [6]$$

The apparent temperature T_A is the value derived from the instrument on the assumption that $\epsilon_1 = \epsilon_2$ and is therefore given by

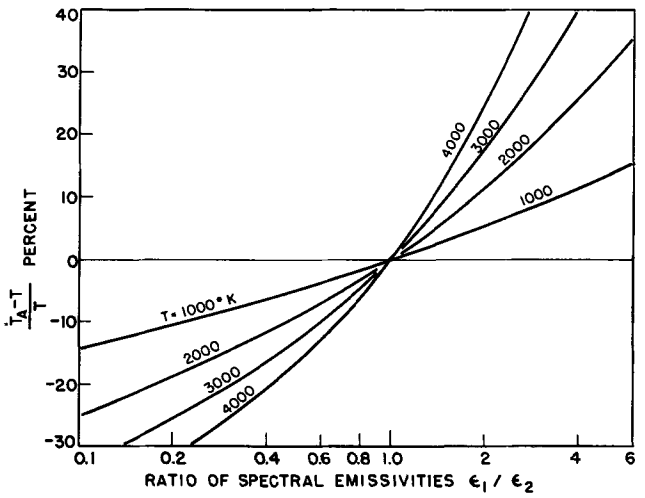

Fig. 3. Error of two-color pyrometer vs. ratio of spectral emissivities at wave lengths of 0.40 and 0.65 μ.

$$\frac{W_1}{W_2} = \frac{\lambda_1^{-5}\Delta\lambda_1}{\lambda_2^{-5}\Delta\lambda_2}\, e^{(c_2/T_A)[(1/\lambda_2)-(1/\lambda_1)]} \qquad [7]$$

The relation between the true and apparent temperature is found by equating [6] and [7]:

$$\frac{1}{T_A} - \frac{1}{T} = \frac{\ln(\epsilon_2/\epsilon_1)}{c_2\left(\frac{1}{\lambda_1} - \frac{1}{\lambda_2}\right)} \qquad [8]$$

The error $(T_A - T)/T$ calculated from this expression is shown in Fig. 3 as a function of the ratio of the spectral emissivities for different values of T, with $\lambda_1 = 0.40\ \mu$ and $\lambda_2 = 0.65\ \mu$.

The error is zero when the underlying assumption that the emissivities are the same is valid. In practice, the ratio of the emissivities at the two wave lengths can differ considerably from unity. If the ratio is 2, for example, the error is 11% at 2000°K and 25% at 4000°K.

It may be thought that the effect of the variation of emissivity with wave length may be evaded by taking the two wave lengths λ_1 and λ_2 very close together. Equation [8] shows that this idea is fallacious. The difference $1/T_A - 1/T$ is clearly proportional to the slope of the chord of the ln ϵ vs. $1/\lambda$ curve. This quantity merely becomes the slope of the tangent to the curve when $\lambda_1 \to \lambda_2$ and there is no *a priori* reason why the tangent should have a smaller slope than the chord.

The idea of the two-color pyrometer can be extended, in principle, to a multi-color pyrometer. A three-color pyrometer, for example, will give the correct temperature if the emissivity varies linearly with wave length. But in general the curvature of the emissivity vs. wave length characteristic is not zero and will produce as large an error in temperature as the slope does with the two-color pyrometer.

Two-Temperature Pyrometer

A new type of pyrometer that we have investigated, and which has also been considered by K. C. Vul'fson (1), depends on the idea that if the spectral distribution of intensity from the sample is measured at two temperatures, the spectral emissivity can be eliminated by dividing one spectral distribu-

tion by the other. Let T and T' be two temperatures. Then the two spectral distributions are given by Planck's law:

$$W = \frac{c_1 \epsilon(\lambda) \lambda^{-5} \Delta\lambda}{e^{c_2/\lambda T} - 1} \quad [9]$$

$$W' = \frac{c_1 \epsilon(\lambda) \lambda^{-5} \Delta\lambda}{e^{c_2/\lambda T'} - 1} \quad [10]$$

The ratio of the distributions is

$$\frac{W'}{W} = \frac{e^{c_2/\lambda T} - 1}{e^{c_2/\lambda T'} - 1} \quad [11]$$

It will be noted that the spectral emissivity has cancelled out.

In Eq. [11] the ratio W'/W can be determined experimentally as a function of wave length λ. Since only two unknown quantities, namely, T and T', appear in the equation, it is sufficient in principle to make measurements at only two wave lengths in order to determine both T and T'. However, more accurate results should be obtainable by using data over the whole spectrum. This can be done by preparing a set of master graphs of the function

$$\frac{W'}{W} = \frac{e^{xT'/T} - 1}{e^x - 1} \quad [12]$$

which is obtained from Eq. [11] by the substitution

$$x = c_2/\lambda T'$$

Figure 4 shows the master graphs of W'/W vs. x for various values of T/T' with x plotted on a logarithmic scale.

To determine T and T' from the experimental data, the experimental values of W'/W are plotted against λ with the same scales as in Fig. 4. The experimental graph is now moved horizontally over the master chart until the best fit with one of the master curves is obtained. By reading any pair of corresponding points on the two abscissas, one finds a value of λ and a value of $c_2/\lambda T'$. Thus T' is found. The matched master curve gives T/T', so T is also determined.

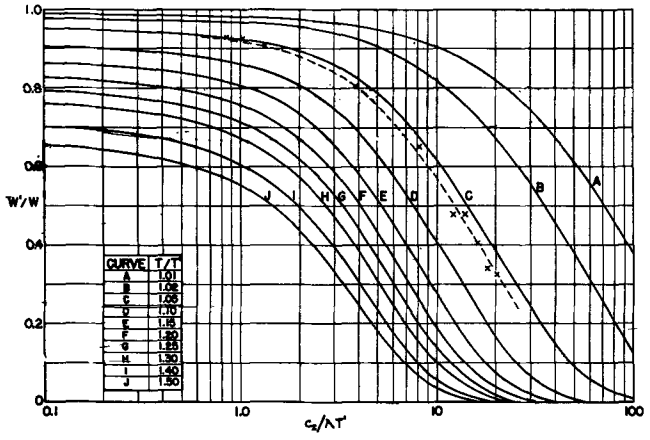

Fig. 4. Master graphs for the two-temperature pyrometer showing intensity ratio for two temperatures vs. $c_2/\lambda T'$. The crosses represent the best fit of experimental data for a hot Globar source.

The crosses on Fig. 4 represent the best fit of experimental data for a hot silicon carbide source taken with a Perkin Elmer infrared spectrometer. The position of the crosses indicates that $T'/T = 1.052$, and the horizontal position of the experimental wave-length scale (not shown in Fig. 4) gives $T' = 1126°K$. The actual temperature determined by a thermocouple embedded in the silicon carbide gave a reading of $T' = 1320°K$. The error is therefore about 15% which is comparable with the errors of the other radiometer methods.

The error in the temperature determination appears to be due to the assumption that the spectral emissivity is independent of temperature. If $\epsilon(\lambda)$ is a function of temperature, then it cannot be divided out by taking the ratio of Eq. [9] and [10].

The effect of the temperature coefficient of emissivity can be calculated most easily for the case of a two-temperature pyrometer that measures the radiation from the sample at only two wave lengths λ_1 and λ_2. For precision in fitting the two-point experimental graph to the master graphs of Fig. 4 the two wave lengths should be on opposite sides of the black-body peak.

The intensity radiated at the shorter wave length λ_1 is given by Wien's law:

$$W = c_1 \epsilon \lambda_1^{-5} \Delta\lambda_1 e^{-c_2/\lambda_1 T} \quad [13]$$

The rate of change with temperature is

$$\left(\frac{1}{W}\frac{dW}{dT}\right)_{\lambda_1} = \left(\frac{1}{\epsilon}\frac{d\epsilon}{dT}\right)_{\lambda_1} + \frac{c_2}{\lambda_1 T^2} \quad [14]$$

The intensity at the longer wave length λ_2 follows Rayleigh's law:

$$W = \frac{c_1}{c_2} \epsilon T \lambda_2^{-4} \Delta\lambda_2 \quad [15]$$

and the rate of change is

$$\left(\frac{1}{W}\frac{dW}{dT}\right)_{\lambda_2} = \left(\frac{1}{\epsilon}\frac{d\epsilon}{dT}\right)_{\lambda_2} + \frac{1}{T} \quad [16]$$

An equation for the true temperature T is obtained by eliminating dT from Eq. [14] and [16]:

$$\frac{\left(\frac{dW}{W}\right)_{\lambda_1}}{\left(\frac{dW}{W}\right)_{\lambda_2}} = \frac{\left(\frac{1}{\epsilon}\frac{d\epsilon}{dT}\right)_{\lambda_1} + \frac{c_2}{\lambda_1 T^2}}{\left(\frac{1}{\epsilon}\frac{d\epsilon}{dT}\right)_{\lambda_2} + \frac{1}{T}} \quad [17]$$

The apparent temperature T_A that would be obtained from the master graphs is found by assuming that the temperature coefficient of emissivity is zero in Eq. [17]. Thus

$$\frac{\left(\frac{dW}{W}\right)_{\lambda_1}}{\left(\frac{dW}{W}\right)_{\lambda_2}} = \frac{\frac{c_2}{\lambda_1 T_A^2}}{\frac{1}{T_A}} \quad [18]$$

On combining Eq. [17] and [18] we find:

$$T_A = T \cdot \left[1 + T\left(\frac{1}{\epsilon}\frac{d\epsilon}{dT}\right)_{\lambda_2} \right] \Big/ \left[1 + \frac{\lambda_1 T^2}{c_2}\left(\frac{1}{\epsilon}\frac{d\epsilon}{dT}\right)_{\lambda_1} \right] \quad [19]$$

The error in temperature is therefore, approximately,

$$\frac{T_A - T}{T} = T\left(\frac{1}{\epsilon}\frac{d\epsilon}{dT}\right)_{\lambda_2} - \frac{\lambda_1 T^2}{c_2}\left(\frac{1}{\epsilon}\frac{d\epsilon}{dT}\right)_{\lambda_1} \quad [20]$$

If $\lambda_1 = 0.4\ \mu$ and $T = 2000°K$, then $\lambda_1 T/c_2 = 0.06$. Thus the short wave-length contribution to the error is negligible compared with the long wave-length contribution and Eq. [20] reduces to

$$\frac{T_A - T}{T} = T\left(\frac{1}{\epsilon}\frac{d\epsilon}{dT}\right)_{\lambda_2} \quad [21]$$

Figure 5 shows a plot of the error vs. $(1/\epsilon)(d\epsilon/dT)$ for various values of T. The circles on the 2000°K line give the errors obtained from published values (2-4) of the temperature coefficients for tungsten, rhenium, and molybdenum. The errors are quite large enough to explain the discrepancy observed in the case of silicon carbide and are of the same order of magnitude as the errors involved in the other radiometer methods.

Conclusions

The general conclusion to be drawn from our analysis is that it is impossible to measure the temperature of an unenclosed sample in the range 2000°-4000°K with an accuracy greater than about 10% by observing only the radiation emitted by the sample and without any prior knowledge of the emissivity. On the other hand, even a 20% measurement of the emissivity at a single wave length will allow determination of temperature to 1 or 2% by means of the optical pyrometer, especially if the instrument is operated at the blue end of the spectrum.

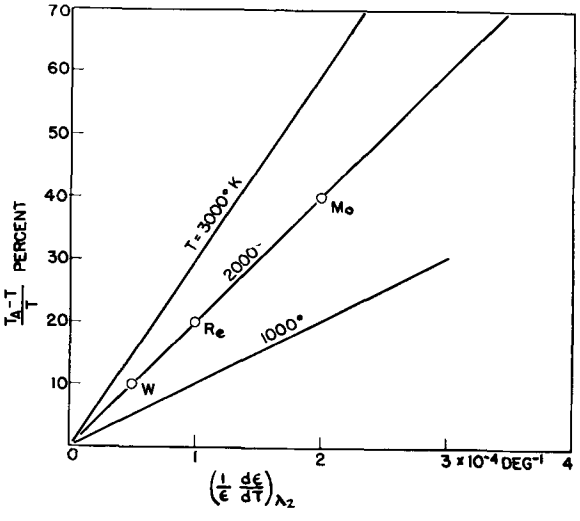

Fig. 5. Error of two-temperature pyrometer vs. temperature coefficient of emissivity. The circles indicate the calculated errors for tungsten, rhenium, and molybdenum at 2000°K.

The problem of measuring the temperature of an unenclosed object therefore hinges on being able to determine the emissivity. Since the emissivity varies quite markedly with temperature it is unsafe to extrapolate low-temperature values to the high-temperature range. Thus the emissivity has to be measured at the high temperature and, since the temperature is unknown, this can only be accomplished by finding the reflection coefficient of the sample at the operating wave length of the pyrometer. If it is assumed that the pyrometer views the surface of the sample at normal incidence, then the reflection coefficient of interest is $\rho_\lambda = I_r/I_o$ where I_o is the intensity of a beam of light at normal incidence and I_r is the intensity of the reflected light integrated over the whole hemisphere. An equivalent arrangement, using the principle of reversibility, is to flood the sample with light uniformly from all directions and measure the reflected light in a small solid angle at normal incidence. In both methods care has to be taken that any specularly reflected light is included in the measurement. Since the hot sample itself emits light in all directions, the reflection experiment requires chopped radiation. The normal emissivity is easily determined from the reflection coefficient by means of Kirchhoff's law $\epsilon_\lambda = 1 - \rho_\lambda$.

In the case of a sample heated in a solar furnace, Laszlo (5) has suggested using reflected sunlight to determine the emissivity. A total radiation pyrometer designed by Gardon is used to determine the incident and reflected radiation fluxes, the ratio of which gives the total reflectivity and hence the total emissivity ϵ_t. The temperature may then be found from the energy balance

$$P = \epsilon_t T^4$$

where P is the incident flux. This equation assumes, however, that the sample loses energy by re-radiation only.

Another method mentioned by Laszlo is use of an optical pyrometer in conjunction with a value of the spectral emissivity ϵ_λ calculated from a measured value of the total reflectivity. It is not clear how a unique value of ϵ_λ can be obtained in this way, except for the case of a gray body.

Manuscript received Sept. 8, 1958. This paper was prepared for presentation before the New York Meeting, April 27-May 1, 1958.

Any discussion of this paper will appear in a Discussion Section to be published in the June 1960 JOURNAL.

REFERENCES

1. K. C. Vul'fson, *Zhur. Eksptl. i. Teort. Fiz.*, **21**, 507 (1951).
2. D. T. F. Marple, *J. Opt. Soc. Amer.*, **46**, 490 (1956) (Rhenium).
3. W. W. Coblentz, *Int. Crit. Tables*, **5**, 242-245 (1929) (Tungsten).
4. W. W. Coblentz, *ibid.*, **5**, 242-245 (1929) (Molybdenum).
5. T. S. Laszlo, *J. Solar Energy Science and Engineering*, **1**, 78 (1957).

The Behavior of Rhenium in Electron Tube Environments

Gordon B. Gaines, Chester T. Sims,[1] and Robert I. Jaffee

Battelle Memorial Institute, Columbus, Ohio

ABSTRACT

Rhenium, tungsten, and rhenium-coated tungsten have been exposed to carburizing atmospheres and to water-cycle attack, rhenium and tungsten to aluminum oxide at 1750°C for 7000 hr, and rhenium to boron-containing atmospheres. It was confirmed that rhenium, unlike most other refractory metals, does not form a carbide. Rhenium forms a boride, which forms a eutectic with another boride or with rhenium, and melts under 2250°C. Thoriated rhenium maintains microstructural and mechanical integrity after long exposure in vacuum at 1750°C in contact with alumina. Rhenium and rhenium-coated tungsten are highly resistant to water-cycle effects.

Extensive work has been reported recently on the metal rhenium, both in this country and abroad (1, 2). Rhenium is a strong, ductile, refractory metal which melts at 3180°C and possesses chemical and metallurgical properties which are in some respects characteristic of the precious metals and in others characteristic of the refractory transition metals. Rhenium is potentially useful in vacuum tubes and other electronic devices. The behavior of Re exposed to reactive environments that might be encountered in such devices at high temperatures is of considerable interest. In this work, Re, W, and Re-coated W have been exposed to carburizing atmospheres and to water-cycle attack; Re and W were heated in contact with aluminum oxide (in commercial vacuum), and Re was heated in boron-containing atmospheres. Following exposure, the materials were evaluated to determine chemical and mechanical stability.

Carburizing Environment

The possibility that Re does not form a carbide was first suggested by Tzyrbiatowski (3). This was confirmed by Hughes (4) who studied arc-melted Re-C alloys and found that the terminal α Re solid solution was in equilibrium with graphite. A eutectic reaction occurs at 2480°C and 16.9 at. % C (1.3 wt %). Rhenium dissolves up to 11.7 at. % C at 2480°C. The solubility of C in Re decreases rapidly with decreasing temperature to about 4.5 at. % at 2000°C. The absence of a compound in the Re-C system is unique among refractory transition metals; W, Ta, Mo, and Nb, all form carbides. In this respect, Re behaves similarly to the Pt-group metals.

In this study, unalloyed Re and W filaments and a Re-coated W wire were heated in the presence of a C-bearing atmosphere to study high-temperature reactivity. The materials used were 0.020-in. annealed Re wire fabricated by conventional techniques, 0.014-in. wrought commercial W wire, and Re-coated W wire prepared by deposition of an 0.007-in. Re coating on the 0.014-in. wrought W by halide decomposition. The deposition process consisted of first preparing rhenium pentachloride by the direct action of chlorine on Re metal at 750°-850°C The rhenium pentachloride then was vaporized in vacuum in the presence of the resistance-heated W wire. The pentachloride was decomposed thermally, depositing Re metal on the hot W wire. During this process, the 0.014-in. W-wire core was resistance heated to a temperature of 900°-1000°C for a period of about 2 hr. The final Re deposit was 0.007 ± 0.001 in. thick, adherent, bright, and quite uniform in thickness along the length of the wire. Some surface roughness was apparent, which is not unusual for coatings prepared by the halide vapor decomposition process.

For carburization, the three different filaments first were heated by self-resistance to 1982°C in flowing hydrogen. Dry hydrogen at the rate of 4.2 l/min and hydrogen-toluene vapor at 0.84 l/min then were passed through the chamber for 2 min. The hydrogen-toluene vapor flow was terminated, and dry hydrogen then was allowed to flow through for an additional 30 sec before cooldown. Thus, the filaments were at temperature somewhat longer than 2 min. Portions of the filaments were mounted for metallographic inspection, and the appearance and the results of Knoop microhardness traverses for unalloyed W and Re, together with a typical wrought structure for unexposed W, are shown in Fig. 1. Uncontaminated, annealed Re wire would have an equiaxed grain structure and an average hardness of about 400-500 Knoop across the diameter.

Upon exposure to the carburizing atmosphere, the W wire recrystallized, and carbide formed at the surface. Recrystallization resulted in a hardness drop to about 400 Knoop throughout the core. The layer on the surface of the W is tungsten carbide, confirmed by the hardness values of about 1900 Knoop. The carbonized W filaments were extremely brittle and fractured at the slightest touch.

The carburized rhenium shown in Fig. 1c retained a single-phase structure. This is supporting evidence that Re does not form a carbide. However, the entire cross section of the wire exhibits rather high hardness for an annealed Re wire of this diameter, and the hardness values are rather scattered. It is believed that C has diffused completely through the Re wire and the structure shown is that of a Re-

[1] Present address: General Electric Co., Knolls Atomic Power Lab., Schenectady, N. Y.

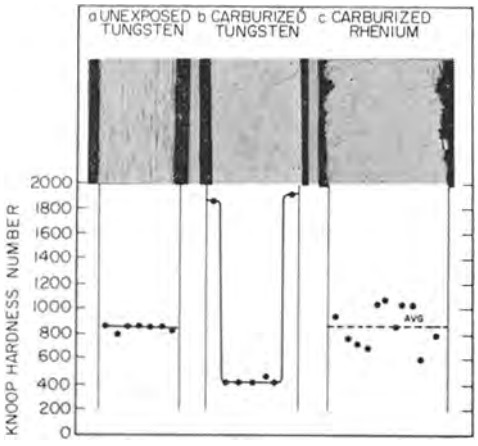

Fig. 1. Appearance and hardness traverses for unexposed and carburized W and carburized Re filaments. Magnification 100X before reduction for publication.

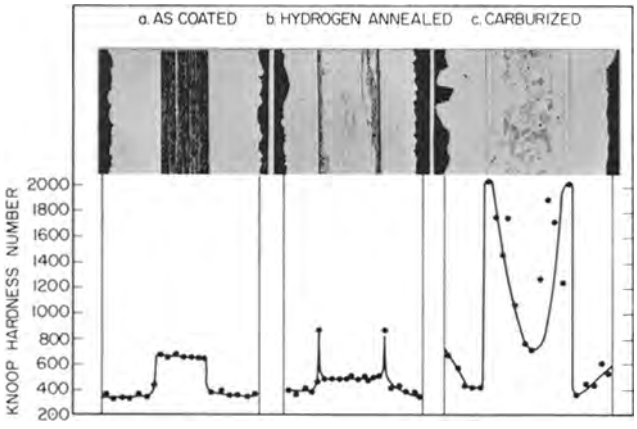

Fig. 2. Appearance and hardness traverses for unexposed, heat-treated, and carburized Re-coated W wire. Magnification 100X before reduction for publication.

base, interstitial-carbon solid solution. The rapid diffusion rate of C through Re is verified by results of the studies of Re-coated W, where W_2C formed underneath a Re layer in a short time period. Thus, although Re does not form a carbide, diffusion of C into Re occurs rapidly with considerable hardening. Although insufficient material was available for quantitative bend tests, the wire showed ductility when bent by hand. This suggests that Re metal is not hardened to the point of embrittlement when heated in carbonaceous atmospheres. This should enhance the usefulness of Re considerably.

A longitudinal section of Re-coated W wire in the as-deposited condition is shown in Fig. 2a. The large-grain, high-purity Re deposited from decomposition of the pentachloride has a somewhat lower hardness (350 Knoop) than fabricated Re filaments (400-500 Knoop). The wrought W core is slightly softer than the W of Fig. 1a, possibly because of stress relief at 900°C during preparation of the Re coating. A portion of the composite wire was exposed in pure hydrogen for 2 min at 1980°C with no C present. The resulting structure and hardness are shown in Fig. 2b. The W core has largely recrystallized, and hardness reduced to about 450 Knoop. The Re cladding is essentially unchanged. A small amount of interdiffusion has commenced between the W core and the Re cladding, causing a narrow, dark layer of a new phase to form at the interface. This phase has a relatively high hardness which may be considerably higher than that shown by measurements as the phase layer is too narrow to yield accurate readings. This new layer probably is either σ-phase (W_2Re_3) or an α-Mn-type W-Re intermetallic, or both (5). Exposure to C, as previously described, results in the structure shown in Fig. 2c. The Re coating hardened from about 350 to 700 Knoop at the surface as a result of C diffusion. This increase is similar to that noted for unalloyed Re wire which hardened from 450 to an average of 850 Knoop. Two new zones were found in the W-Re interface. Using filtered Fe radiation, x-ray diffraction measurement on the new zones showed two major phases, α—W_2C and W_2Re_3 (σ-phase). Weak diffraction lines also observed might have been due to the Re-W-Mn-type phase.

The outer interfacial zone, which has a hardness of over 2000 Knoop, is undoubtedly the W_2C formed from reactions between W and C which diffused through the Re coating. The inner zone, with a hardness of 1500 Knoop, is the diffusion product, W_2Re_3. Thus, Re coatings do not protect underlying W from reactions with ambient C-containing atmospheres, even with thick coatings, as in the present case. Reaction with the underlying W is slowed down, however, and there is no doubt that the carburized Re-coated W filament is not affected so severely by C as unalloyed W, and may be capable of some mechanical service. For instance, the wire was capable of being handled without fracture following carbonization. Although it possessed no measurable ductility, the wire exhibited a room-temperature ultimate tensile strength of 45,000 psi.

Boron-containing Atmospheres

Since Re does not form a carbide, it was thought that it might have somewhat lower reactivity with B than most other refractory metals which form borides. Boron-containing materials are potentially useful in electron-tube technology. If Re does not form a boride, it might be useful for supporting B-containing substances which are good thermionic emitters.

Three individual 0.01-in. Re filaments were heated by self-resistance to different temperatures in an atmosphere of flowing gas, which consisted of a mixture of dry hydrogen and boron trichloride. One filament was heated to 1330°C (black-body temperature), one to 1750°C, and one to 2250°C. During the adjustment of the voltage of the filaments to get the desired temperature, the filaments were in an atmosphere of flowing dry hydrogen. The filaments then were allowed to cool, and boron trichloride was introduced to give a hydrogen:boron trichloride ratio of 7:1. Filament power then was applied for a period of 2 min, following which the filaments were allowed to cool in the B-containing atmosphere.

About 10 to 15 sec after exposure commenced, the filament at 2250°C burned in half. The remaining two filaments lasted for the entire 2-min period.

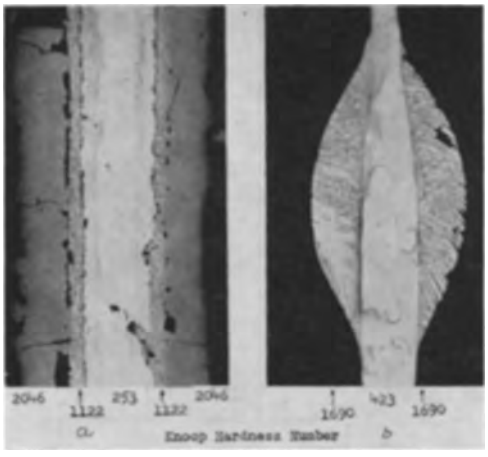

Fig. 3. Longitudinal sections and hardness of unalloyed Re wire exposed to a boron-containing atmosphere under the conditions designated. a, Exposed 2 min at 1750°C; b, exposed 15 sec at 2250°C. Magnification 100X before reduction for publication.

The filaments heated to 1330° and 1750°C appeared to have developed a coated or scaled appearance, while the burned-out filament appeared beaded. A longitudinal section of the filament exposed at 1750°C is shown in Fig. 3a and a similar section of the filament exposed at 2250°C is shown in Fig. 3b, each with pertinent hardness information.

The specimen exposed at 1750°C developed an extremely hard outer crust which readily cracked. A hard intermediate zone also was apparent. An appreciable fraction of the Re core remained unreacted. It is assumed from the appearance and hardness data for the exposed filament that the outer layer shown is a rhenium boride. The intermediate layer may be a solid solution of B in Re or a lower boride, and the inner core is essentially unreacted Re. Thus, Re is not resistant to B at high temperature and undoubtedly forms a boride or borides.

Exposure of the Re wire to B at 2250°C caused melting and burnout. The molten product froze as small beads on the filament, one of which is shown in Fig. 3b. Since the central Re core has a higher hardness than normal, it appears probable that B diffused through the 0.010-in. section at 2250°C. The bead probably is an eutectic mixture of the boride and the phase shown in the intermediate zone of Fig. 3a, which melts below 2250°C.

Life Tests on Thoriated Rhenium and Tungsten Filaments in Contact with Solid Alumina

A 0.020-in. Re-0.85ThO_2 (wt %) wire and 0.015-in. commercial W wire of the type described previously were wrapped on small high-purity (Degussa) Al_2O_3 cylinders and the assemblies were placed in a U-tube container evacuated to a pressure of about 10^{-7} mm Hg. The tube was not gettered. The temperature of the wires was held at approximately 1750°C black-body temperature for 7000 hr. The alumina cylinders were supported by the filaments. The appearance of the test device and the filaments and cylinder surfaces following exposure for 7000 hr are shown in Fig. 4.

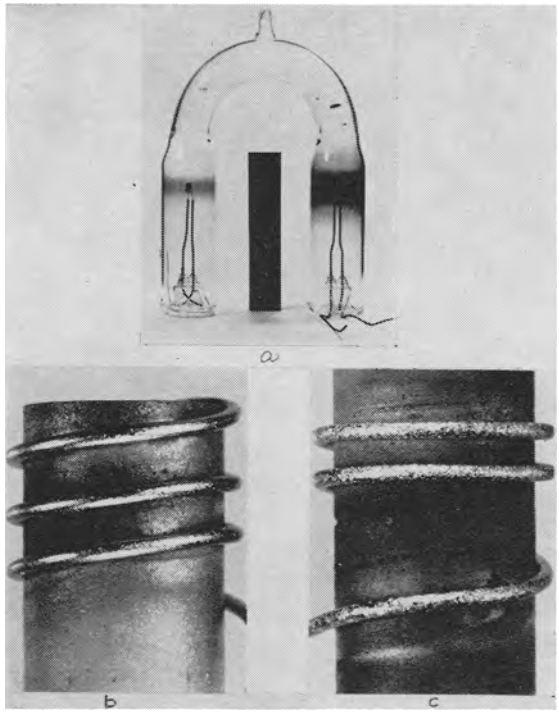

Fig. 4. Appearance of evacuated U-type and of Re and W filaments on alumina sleeves following life testing for 7000 hr at 1750°C. a, Evacuated U-tube; b, Re filament; c, W filament.

The 7000-hr life test resulted in no major changes in geometry or in mechanical or electrical failure. However, a certain amount of local reaction took place, as shown in Fig. 4. At places on the alumina cylinders where physical contact with the filaments was maintained for a long time, eroding of the alumina is evident. The surface appearances of the two filaments had been affected. The W wire possessed a much rougher surface than the Re-ThO_2 wire, although neither was as smooth as drawn wire.

The surface roughing and the black deposits on the glass walls probably are due almost wholly to the water-cycle mechanism. It is known that this mechanism affects Re much less than it does W, and this certainly is suggested by the much larger deposits around the W filament. The water-cycle attack would not be expected to be substantial at a pressure of 10^{-7} mm Hg.[1] However, the tube was ungettered and unbaked, and it is highly probable that the pressure during much of the 7000 hr was of the order of 10^{-5}—10^{-6} mm Hg and that the tube atmosphere contained a substantial amount of water vapor. Another mechanism for explaining the deposits on the tube walls and the grooves in the alumina is a reaction between alumina and tungsten, giving aluminum and tungsten oxide gases. Using published thermodynamic data (6), a simple calculation indicates that, at a pressure of the order of 10^{-6} mm Hg and a temperature of 1750°C, this possibility cannot be ruled out. Unfortunately, an analysis of the deposits was not made, so as to settle this point. It is possible, also, that atomic hydrogen and oxygen, present as a

[1] The authors are grateful to a reviewer for pointing this out.

Table I. Properties of thoriated Re and W filaments

Property	Thoriated Re		W	
	Wrought and recrystallized	Heated 1750°C for 7000 hr[a]	Wrought and recrystallized	Heated 1750°C for 7000 hr[a]
Filament diameter, in.	0.015	0.020	0.010	0.015
Ultimate tensile strength, psi	124,000	115,000	250,000	[c]
Elongation, %	8.5	4	1-4	[c]
Hardness, VHN or KHN	204	277	450	416
Bend ductility, T value[b]	0.0	0.8	1.0	200

[a] Alumina cylinder life test.
[b] T value obtained by dividing smallest successful bend radius by the thickness of the wire; thus, smaller T values mean higher ductility.
[c] Too brittle to be measured.

result of the water-cycle reaction, contributed to the attack of alumina.

The Re-alloy filament did not fracture during its removal from the tube or its handling prior to mechanical testing. The 7000-hr test produced only moderate changes in its over-all mechanical properties as compared to unexposed metal. As shown by the data in Table I, this alloy, which is somewhat less strong and ductile than unalloyed Re, showed only slightly reduced tensile strength as a result of the test. Ductility, as measured by elongation and bend tests, also dropped slightly. As expected, the recrystallized W filament possessed little mechanical integrity compared to Re or to fibered W.

Subsequent microstructure examination showed that the thoria in the Re filament has shown some tendency to agglomerate into larger particles, see Fig. 5. In addition, the W filament developed a heavy concentration of voids scattered uniformly throughout the grain structure, while no voids were found in the Re. No reason for the voids is apparent. Analyses[2] of the W revealed no unexpected or excessive impurities. However, tungsten and alumina are not compatible over about 1400°C (7), and contact with the alumina cylinder may have contributed to the void formation

[2] Impurities in the W by spectrographic analysis were as follows (wt %): Fe, 0.01-0.1; Si, 0.005-0.05; Mg, 0.005-0.05; Mo, 0.001-0.01; Ca, 0.001-0.01; Cu, Ni, K, Mn, <0.001; Th, Na, <0.05; Cr,

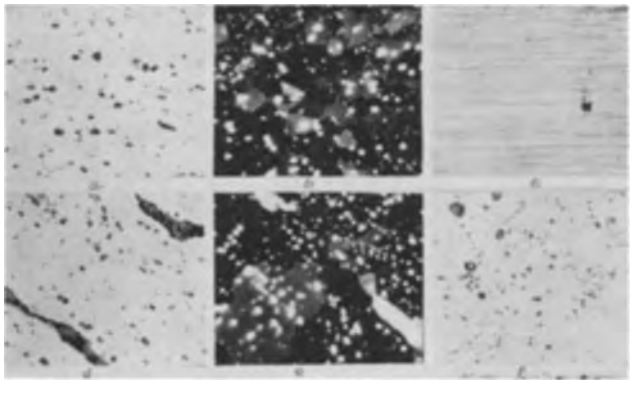

Fig. 5. Appearance of thoriated Re and of W filaments before and after life testing in alumina for 7000 hr at 1750°C. a, Unexposed recrystallized thoriated Re, lightly etched; b, unexposed recrystallized thoriated Re; polarized light; c, unexposed wrought W, etched; d, exposed thoriated Re, lightly etched, e, exposed thoriated Re, polarized light; f, exposed W, etched. Magnifications 500X before reduction for publication.

Water-Cycle Life Tests for Tungsten, Rhenium, and Rhenium-Coated Tungsten

Rhenium is considerably more resistant to the water-cycle effect at elevated temperatures than tungsten, as has been shown previously (8, 9). Accordingly, the possibility of protecting W from this phenomena by Re coatings has been suggested. In the present work, 0.005-in. wrought commercial W, 0.005-in. unalloyed Re, and Re-coated W wires were exposed to water vapor at a pressure of approximately 4×10^{-4} mm Hg[3] at two temperatures, 1300° and 1750°C. The Re coating was applied by the halide-decomposition process, as described previously in the study of attack by carburizing atmosphere. The coating was approximately 0.007-in. thick and was applied to an 0.014-in. W wire. Exposure of all specimens was for 7800 hr, each filament being heated individually by its self-resistance, and all were exposed to the same atmosphere.

Data from the life test are given in Table II. The data confirm that Re is less susceptible to water-cycle attack at all temperatures than W, and the differences is most marked at 1750°C where all of the materials react more severely. Least attack occurs on the Re-coated W, which possessed better water-cycle resistance than unalloyed Re. This is somewhat surprising, particularly since the surface of the Re-coated W was slightly rougher than that of the unalloyed Re wire. The as-deposited Re cladding is probably of higher purity than the unalloyed Re wire, which may account for the difference in rates of attack.

For the conditions of moderate water-vapor attack studied, rather heavy coatings were used in

[3] Vapor pressure over ice at −80°C.

Table II. Weight-loss data for W, Re, and Re-coated W exposed to water-cycle attack for 7800 hr

Material	Exposure temperature, °C		Total wt loss, mg	Attack in 7800 hr, mg/cm²
	Initial	Final		
W	1300	1275	0.5	1.50
	1750	1660	2.6	8.25
Re	1300	1200	0.2	0.65
	1750	1660	0.3	0.98
Re-clad W	1300	1310	0.8	0.48
	1750	1700	1.0	0.57

the present studies. With attack so light, much thinner coatings, such as those applied by electroplating, would probably be adequate protection.

Conclusions

1. It is confirmed that Re metal, unlike most other refractory metals, does not form a carbide. Although C diffuses rather rapidly through Re, causing hardening and some deterioration of mechanical properties, Re maintains dimensional stability and some mechanical integrity. Rhenium coatings on tungsten wire do not prevent carbon from diffusing to the tungsten core and reacting to form tungsten carbide, but the reaction is much slower than that when uncoated tungsten is exposed.

2. Rhenium forms a boride, which forms a eutectic between another boride, or rhenium. The eutectic melts under 2250°C.

3. Thoriated rhenium maintains structural, microstructural, and mechanical integrity after long-time (7000 hr) exposure in vacuum at 1750°C in contact with solid aluminum oxide.

4. Unalloyed rhenium has been shown again to have excellent resistance against the water cycle up to 1750°C, particularly when compared with tungsten. Rhenium coatings protect tungsten from attack by the water cycle.

Acknowledgments

The authors wish to acknowledge with thanks the help given by J. B. Baker, W. W. Kleinschmidt, and W. E. Nexsen, Jr., in carrying out the experiments and by D. F. Rosenbaum in providing rhenium-coated tungsten samples.

The work was supported by the Air Force Cambridge Research Center.

Manuscript received March 19, 1959. This paper was prepared for delivery before the Columbus Meeting, Oct. 18-22, 1959.

Any discussion of this paper will appear in a Discussion Section to be published in the June 1960 JOURNAL.

REFERENCES

1. C. T. Sims, C. M. Craighead, and R. I. Jaffee, *Trans. AIME*, **203**, 168 (1955).
2. C. Agte, M. Alterthum, K. Becker, G. Heyne, and K. Moers, *Z. anorg. u. allgem. Chemie*, **196**, 129 (1931).
3. W. Tzyrbiatowski, *ibid.*, **193**, 311 (1930).
4. J. Hughes, "The Alloy System Rhenium-Carbon," Associated Electrical Industries Report No. A497 (November 1955).
5. P. Greenfield and P. Beck, *Trans. AIME*, **206**, 265 (1956).
6. J. P. Coughlin, "Heat and Free Energies of Formation of Inorganic Oxides," Bulletin 542, U. S. Bureau of Mines, 1954, Supt. of Documents, Washington, D. C.
7. W. Kohl, "Materials Technology for Electron Tubes," Rheinhold Publishing Co., New York (1951).
8. C. T. Sims, *et al.*, "Investigations of Rhenium," WADC TR 54-371 (June 1954).
9. C. Ludington and C. T. Sims, "Rhenium—A High-Temperature Metal," AGET News Bulletin (January 1, 1958).

Oxides on the Silver Electrode

Charles P. Wales and Jeanne Burbank

U. S. Naval Research Laboratory, Washington, D. C.

ABSTRACT

Silver electrodes were studied by means of potentials and x-ray diffraction patterns. The silver was charged anodically in 35% KOH by means of either constant current or constant potential, and discharged at a low or high rate. Attempts were made to form an oxide higher than AgO by means of anodization. The products of anodization of silver in 2*N* H_2SO_4 were determined. The basis for the theory that the oxides of silver are formed by the introduction of oxygen into the octants of the face-centered cubic silver lattice was examined.

Alkaline storage and primary batteries containing positive silver electrodes have been used, in recent years, for special purposes requiring light weight or the ability to discharge at high rates. There is considerable confusion in the literature, however, as to the reactions taking place on these electrodes. In addition the potential distribution and eletcron transfer may be complex on oxide surfaces with different conducting or semiconducting properties.

A typical charge of a silver electrode in alkaline solutions shows three potential plateaus. There is general agreement with the work reported by Luther and Pokorny (1) in 1908 that the first plateau corresponds to the formation of Ag_2O. A possible subsidiary step of short duration was noted by Hickling and Taylor (2) at the beginning of this first plateau, which they suggested may represent some adsorption of oxygen prior to the production of Ag_2O, or may be the formation of a silver suboxide.

The results of Luther and Pokorny further indicate that at the second potential plateau Ag_2O is changed quantitatively and reversibly to AgO. On the other hand, Hickling and Taylor report that an oxide of Ag containing more oxygen than AgO is formed at this second plateau, and that this unstable higher oxide, perhaps Ag_2O_3, decomposes to give AgO; i.e., the AgO forms purely as a secondary product. The results of Jones, Thirsk, and

Wynne-Jones (3) are not in accord with those of Hickling and Taylor but agree partially with those of Luther and Pokorny in that they show the direct oxidation of Ag_2O to AgO. However, Jones, *et al.* claim that only 30% of the current is used to form AgO at this potential, the remaining 70% going to O_2 evolution, and they conclude that the statement about the oxidation of Ag_2O proceeding quantitatively and reversibly (1) is without foundation.

At the third potential plateau the electrode reaction is almost entirely the evolution of O_2. It has been concluded (3, 4) that an oxide higher than AgO is formed at this step, and this Ag_2O_3 potential has been reported by others (5, 6). The present investigation was undertaken to clarify these conflicting statements regarding silver electrodes in alkali. During this work it also became desirable to examine the anodization of silver in sulfuric acid.

Experimental Procedure

The positive (test) electrodes were made by cutting in half silver plates taken from a commercial Ag-Zn storage battery. The test electrodes measured about 28.5 x 66.5 x 0.7 mm and had a capacity of 1.8-2.0 amp-hr. A 3-mm-thick U-shaped plastic frame, with inside dimensions slightly larger than the positive electrode, was wrapped with several layers of separator material of the type used in Ag-Zn batteries. The electrode was then inserted into the frame. This arrangement allowed the electrode to be removed for examination and then to be replaced readily, without unwrapping or tearing the separator. X-ray diffraction patterns were obtained with a General Electric XRD-5 spectrogoniometer using Cu Kα radiation after the electrode was rinsed briefly in distilled water and blotted dry with tissue paper. The x-ray examination of the electrode surface could begin within 5 min after anodic or cathodic treatments and would characterize the deposit within a layer 0.01 mm thick.

The Ag, Ag_2O/OH^- reference electrode used for all of the potential measurements was made by packing Ag_2O into a glass tube which had a Pt wire sealed through its wall, adding a KOH solution as the electrolyte, and, after 24 hr, cathodically reducing part of the Ag_2O onto the Pt, using another Pt wire as the second electrode. This reference half-cell gives a stable potential, after being allowed to stand a few days to establish equilibrium, and electrodes of this type have been used continuously for over two years at this laboratory. The stability of a Ag/Ag_2O electrode was shown recently by Hamer and Craig (7).

A silver screen, wrapped with separator material, served as the negative electrode. The electrodes were assembled in a closed plastic container in an electrolyte of 35% KOH. The instrumentation and techniques previously described (8) were used to measure and record the potential as well as to control the cell current or potential. On a few occasions silver sheet, 0.13 mm thick, was used as the positive electrode in either 35 or 5% KOH, and in addition both types of electrode were anodized in

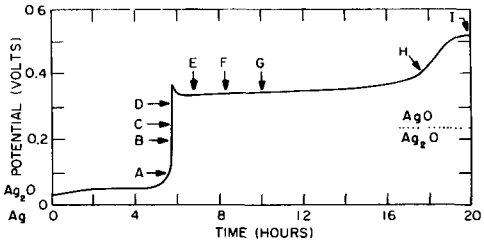

Fig. 1. Typical 100-ma charge of the Ag electrode. Letters refer to points at which x-ray diffraction patterns have been obtained. Potentials are given with respect to a Ag/Ag_2O reference electrode.

2*N* H_2SO_4. All work was carried out in a controlled temperature of 26°-27°C.

Results and Discussion

The three potential plateaus occurred at 0.03 to 0.05 v, 0.33 to 0.37 v, and 0.51 to 0.52 v, positive with respect to the Ag/Ag_2O reference electrode, during a typical 20-hr charge at 100 ma (Fig. 1). The reversible Ag_2O/AgO potential is 0.23 v,[1] and the AgO/Ag_2O_3 potential is 0.39 or 0.40 v, with respect to the reference electrode used here (1, 2).

A discharged silver electrode was charged anodically at 100 ma until its potential was 100 mv above the reference electrode potential (point A, Fig. 1), and the potential then was held at 100 mv. When the charge was interrupted after 21 hr the current had fallen to 0.47 ma, and the electrode was 20% charged (based on the discharge capacity). An x-ray diffraction pattern showed strong Ag lines with weaker Ag_2O lines, but no lines were found which could be attributed to a suboxide. When the potential was held at 200 mv for 6.5 hr, the x-ray diffraction pattern of this anode (point B, Fig. 1) was still strong in Ag, although the amount of Ag_2O had increased. This confirmed the statements that the reaction at the lower potential plateau consists only of the oxidation of Ag to Ag_2O. The same diffraction pattern was obtained when the potential was held at 250 mv for 6.7 hr (C, Fig. 1), 20 mv above what has been believed to be the reversible Ag_2O/AgO potential. It should be noted, however, that in this investigation the Ag_2O/AgO equilibrium potential was normally found to be about 267 mv (measured by charging the electrode to AgO and allowing it to stand until its potential became constant). This is 0.03-0.04 v higher than the value which is usually given (1,2) (see however, Bonk and Garrett, footnote 1).

The potential of the silver electrode then was increased to 308 mv (D, Fig. 1)and held there for 22 hr, but only 0.043 additional amp-hr of charge (2% of the total capacity) could be added. Diffraction patterns, however, showed that some AgO had formed, that the amount of Ag_2O had increased, and that there was now only half as much Ag present on the surface. AgO could not be detected by x-ray diffraction on an electrode held at 275 mv for 175 hr, although the open-circuit potential of 180 mv did indicate the presence of AgO. The fact that AgO

[1] Recent work by J. F. Bonk and A. B. Garrett (7a) indicates that this value should be 0.26 v instead of 0.23 v.

can be formed at a potential well below the Ag_2O_3 potential supports the belief (1,3) that AgO is the primary anodic oxidation product at the second plateau of a charge, but this same fact opposes the theory (2) that the primary product is Ag_2O_3, which then decomposes to AgO.

The concentration of AgO increased rapidly during a charge at the upper potential (E and F, Fig. 1) and at the same time the amount of Ag_2O decreased. It could not be determined from the x-ray patterns whether or not any Ag_2O remained by the time the electrode was half charged (G, Fig. 1), although metallic Ag was still fairly strong. X-ray patterns showed only AgO and metallic silver, both at the end of this potential plateau (H, Fig. 1) and after gassing (I, Fig. 1). When a charge was ended after 5% of the electrode capacity had been added at the second potential plateau (E, Fig. 1), comparison of x-ray patterns before and after the electrode was allowed to stand on open circuit for 24 hr indicated that Ag_2O had increased and the Ag had decreased, while only traces of AgO remained. Similar results required a 7-day stand, after 13% of the charge took place at the second step (F, Fig. 1). This confirms the report (9) that Ag and AgO react during a stand.

The first reaction at the second potential plateau appears to be Ag_2O oxidizing to AgO, since Ag_2O seems to anodize more rapidly than Ag. Then, or perhaps simultaneously, much of the remaining Ag goes to AgO, with any Ag_2O which may be formed in this process being preferentially oxidized to AgO. The reaction $Ag + AgO \rightarrow Ag_2O$ probably does not occur appreciably during a charge, since it appears to be very slow under the conditions of the experiment.

Although trickle charges lasting several days did convert more of the remaining Ag to AgO, overcharges at the normal or even higher rates were more effective in oxidizing the Ag and gave the sharpest diffraction patterns. Strong oxygen gassing appeared to perfect crystallinity. For example, the AgO lines were very sharp after a 200% charge at 100 ma, with only a very small amount of metallic Ag remaining visible in the x-ray diffraction patterns, perhaps arising from the grid mesh. Similar results were obtained by anodizing the charged electrode for 20 hr at 750 ma, at a potential of 0.68-0.71 v. No lines were ever found in the x-ray patterns which could be attributed to a higher oxide, such as Ag_2O_3, despite any of these lengthy treatments well above the equilibrium potential reported for AgO/Ag_2O_3. The transient high open-circuit potentials noted by Jones, *et al.* (3) at the end of a lengthy charge need not be attributed to higher oxides. It seems likely that the transient potentials on silver were probably potentials of the HO_2^--OH^- system. This potential would continue until enough Ag_2O was formed to establish the Ag_2O/AgO equilibrium potential. It was reported by Pleskov (4) that monovalent Ag oxidized to trivalent Ag at high potentials. His results could be interpreted in other ways. This matter is being given further consideration.

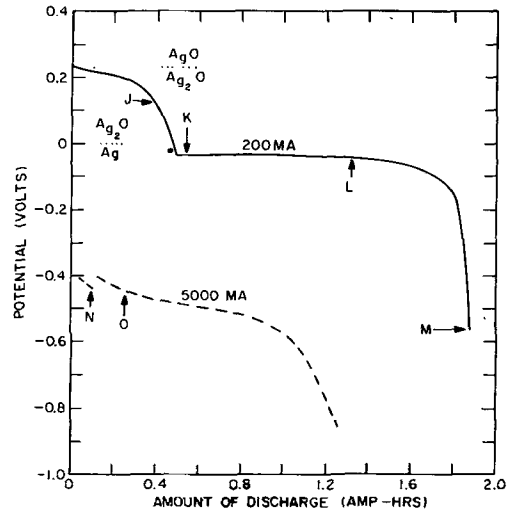

Fig. 2. Discharges of the Ag electrode at the 15-min and 9-hr rates. Letters refer to points at which x-ray diffraction patterns have been obtained. Potentials are given with respect to a Ag/Ag_2O reference electrode.

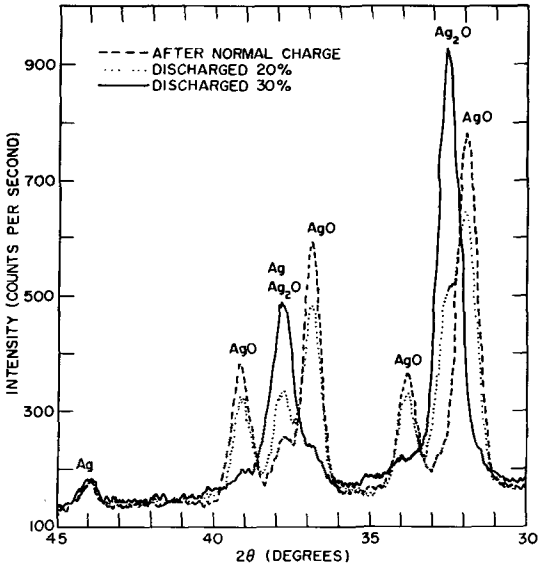

Fig. 3. Spectrogoniometer x-ray diffraction patterns of a charged and partially discharged Ag electrode.

A typical low-rate discharge (Fig. 2) showed the two steps which are associated with silver electrodes. Ag_2O had appeared on the electrode after it was partially discharged at the upper step (J, Fig. 2). The amount of AgO had decreased and metallic Ag remained constant, compared with a charged electrode. The electrode was discharged an additional 10%, reaching the lower potential plateau (K, Fig. 2). X-ray diffraction showed that practically no AgO remained on the surface at this point, and the x-ray pattern of Ag_2O was very strong, with Ag unchanged. The diffraction patterns for this marked change in surface composition are shown in Fig. 3. There is no doubt that the interior of the electrode still contained much AgO, but the x-ray diffraction patterns and the electrode potential only showed what was present near the surface. An electrode discharged 70% showed more Ag than Ag_2O (L, Fig. 2), and at the end of the discharge Ag alone was detected (M, Fig. 2). The only reaction detected

at the upper potential plateau was $AgO \rightarrow Ag_2O$. After the surface is covered with Ag_2O, the surface reaction (which determines the potential) appears to be $Ag_2O \rightarrow Ag$, although there probably is a large amount of AgO in the interior of the electrode which is discharging at this lower potential.

When the electrode was discharged for 7% at a high rate, x-ray diffraction patterns showed that Ag_2O had formed (N, Fig. 2), and after a 20% discharge the amount of Ag_2O had increased (O, Fig. 2). A comparison of the diffraction patterns showed that metallic Ag increased very little if at all during the first 20% of this discharge, despite the fact that the potential of the electrode was more than 0.4 v below the reversible Ag/Ag_2O potential.

Comparison of charge and discharge capacity showed a very high efficiency, in contrast to the report (3) that only 30% of the current charged the electrode at the second potential level. Gas evolution of a commercial 100-amp-hr Ag-Zn storage battery was measured during a 5-amp charge (Fig. 4). The potential changes shown represent changes in the silver plate, since the positive plate became fully charged before the negative one. No oxygen evolution was detected until near the end of a charge. This confirms the earlier report (1) that the oxidation is quantitative and reversible. The contradictory results obtained by Jones, *et al.* (3) may be due to their rapid charging rate.

Structure of Silver Oxides

The structure of Ag_2O had already been established as being a face-centered cube with a side a_o of 4.72Å when Jones and Thirsk (10) described a material thought to be AgO with a similar face-centered cubic structure ($a_o = 4.96$Å), and also gave evidence for a silver suboxide with a cubic structure ($a_o = 4.56$Å). However in 1924 Levi and Quilico (11) had prepared supposed suboxides by several methods, but examination by x-ray diffraction had shown only the patterns of Ag and Ag_2O. Jones, Thirsk, and Wynne-Jones (3) proposed, on the basis of the report of Jones and Thirsk, and of their own

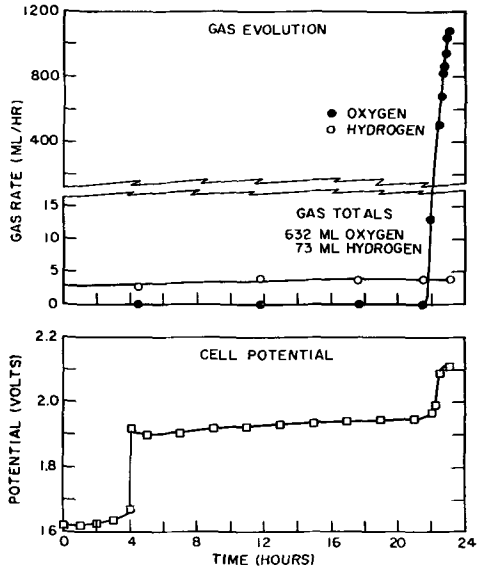

Fig. 4. Potential and gas evolution for a typical low-rate charge of a Ag-Zn storage battery.

work, that the oxides of Ag are formed by the introduction of oxygen into the octants of the face-centered cubic silver lattice, and in order to complete this series they proposed Ag_2O_3 as an intermediate between AgO with half-filled octants and the hypothetical AgO_2 with completely filled octants. The data on which these investigators have based their conclusions may be interpreted otherwise.

There were no diffraction data for AgO in the literature at the time that Jones and Thirsk (10) anodized Ag in H_2SO_4. They assumed that their final product was AgO. In order to check this, they prepared silver peroxynitrate (and presumably boiled it to decompose it), and reacted a silver salt with a persulfate. They reported that all three preparations showed the same x-ray pattern, which they published as AgO. The results of Mulder (12), and Skanavi-Grigor'eva and Shimanovich (13), however, showed that the so-called silver peroxysulfate Ag_7SO_{12} is the product of electrolysis of a Ag_2SO_4 solution. Since the first anodic reaction of Jones and Thirsk was the formation of Ag_2SO_4, it is seen that their second anodic reaction should be formation of silver peroxysulfate.

The two preparations used by Jones and Thirsk for the check of their "AgO" are rather similar. Depending on reaction conditions, a silver salt solution with a persulfate may give either AgO or a compound with a formula like Ag_7SO_{12} (14). The close relationship between silver peroxysulfate and silver peroxynitrate has been noted for many years. Luther and Pokorny (1) prepared these compounds in three ways: by anodizing Ag in dilute H_2SO_4, by electrolysis of a $AgNO_3$ solution, and by electrolysis of a Ag_2SO_4 solution. They used these compounds for the "Ag_2O_3" potential measurements which are so often cited in the literature. It was concluded by Luther and Pokorny that neither the sulfate nor the nitrate was an integral part of these peroxy compounds, since both of the compounds gave the same potential and decomposed cathodically in KOH to AgO, then to Ag_2O, and finally to Ag. Therefore they reported the potential of these compounds with respect to AgO as the Ag_2O_3/AgO potential. However, Sulc (15), Mulder and Heringa (16), Tanatar (17), Watson (18), and Brown (19) all found that the compound, which they obtained by electrolysis of a $AgNO_3$ solution under various conditions, always had the empirical formula Ag_7NO_{11}. In 1954 this was confirmed again by Skanavi-Grigor'eva and Shimanovich (20), and they also reported the similarity in composition and valency of the compounds obtained by anodizing $AgNO_3$ or AgF solutions. This has recently been denied by Graff and Stadelmaier (21), but only on the grounds that a compound with the same structure was obtained by anodizing either AgF or $AgNO_3$ solutions, although they did not report analyses of their products. Yet in 1935 similar x-ray patterns had been found by Brækken (22) for what he considered to be Ag_2O_3 stabilized by either Cl, F, N, or S, with the best results from the compound with N (i.e., Ag_7NO_{11}). The same diffraction pattern for Ag_7NO_{11} has been reported more recently (23, 24), and a similar pattern has been obtained by

Table I. Diffraction data for silver anodized in H_2SO_4 and in $AgNO_3$

"AgO" from H_2SO_4[a]		Ag_7NO_{11}[b]	
d[c]	I/I_o[d]	d	I
2.85	s	2.839	95
2.48	ms	2.459	56
		2.262	15
1.75	s	1.745	98
		1.669	17
1.49	s	1.486	122
1.45	vw	1.422	30
		1.233	28
1.136	ms	1.133	75
1.106	ms		
1.104	ms	1.103	60
		1.006	63
0.953	ms	0.950	86
0.871	vw	0.873	33
0.839	m	0.835	126
0.828	m	0.823	81
0.783	w		

[a] From Jones and Thirsk (10).
[b] From Zvonkova and Zhdanov (23), omitting lines with photometric intensity of 10 or less.
[c] Interplanar spacing in Å.
[d] Relative intensity: s = strong, m = medium, w = weak, v = very.

allowing O_3 to react with Ag and Ag_2O (25). Apparently all of the diffraction patterns reported for silver peroxy compounds are practically identical. Table I shows that the anodic product which Jones and Thirsk (10) reported as AgO has the same lines as Ag_7NO_{11} and probably was in reality the so-called silver peroxysulfate.

In order to check these conclusions a silver electrode was charged at 100 ma in 2*N* H_2SO_4. The initial reaction was $Ag \rightarrow Ag_2SO_4$, as reported (10). Then the potential rose sharply (by 1.3 v), and black spots appeared on the plate. This black material decomposed readily in the acid with vigorous evolution of gas. An electrode which was partially covered with this black material was examined. The diffraction pattern, which was started within 10 min after the end of electrolysis, showed the lines of four substances: Ag, Ag_2SO_4, a compound with lines like those shown in Table I, and traces of AgO. After being allowed to stand in dry air for 8 days, this electrode showed only Ag, Ag_2SO_4, and a strong diffraction pattern for AgO. Obviously the peroxysulfate had decomposed to AgO.

It had been stated by Jones and Thirsk (10) that a minimum of 3 hr elapsed between electrolysis and examination of the specimen. This would allow formation of some AgO before their x-ray diffraction examination. Their patterns may have been similar to those observed in this study: a mixture of Ag, Ag_2SO_4, AgO, and the peroxysulfate. If the lines of the patterns they attributed to "AgO" and those of Ag and Ag_2SO_4 are subtracted from the pattern of the suggested mixture, the lines remaining belong to the true pattern of AgO. Jones and Thirsk appear to have subtracted the lines of Ag_2O from such a remaining pattern, since they stated that Ag_2O was present (although none was found under these conditions in this present study). The lines which then remained were attributed to traces of a face-centered cubic substance having $a_o = 4.56$Å, which was suggested as belonging to a suboxide of silver. Table II shows that the pattern of AgO, by an unfortunate coincidence, contains many of the lines of Ag_2O, and that the remaining lines, none of which are strong, could be indexed as belonging to a cube with $a_o = 4.56$Å. Jones, Thirsk, and Wynne-Jones (3), probably relying on this earlier work, reported only Ag, silver suboxide, and Ag_2O on their fully charged electrode from alkaline solution. It is likely that they actually had Ag and AgO.

The weak Ag_2O line for $d = 3.35$, which is listed in Table II, was never observed at this laboratory. The AgO values given in this table agree closely with those previously reported (21, 25, 26) except that the weak line reported at $d = 2.95$ (21, 26) was not observed on silver anodized in 35% KOH despite repeated attempts with both the sintered silver electrode and a silver sheet, nor was the peak at $d=2.78$ resolved into the two lines which have been reported (21, 26). When sheet silver was charged in 5% KOH this peak could be resolved into two lines, and often the weak peak at $d = 2.95$ could be observed.

The lack of resolution of the $d = 2.78$ doublet on specimens anodized in 35% KOH may be attributed to limited perfection in the crystal lattice, or it may be caused by particle-size broadening of the x-ray lines. A third possible cause of this effect, and of the lack of line $d=2.95$, may be variation in the positions taken up by the oxygen atoms within the electrochemically formed lattices. Scatturin, Bellon, and Zannetti (26) used the line $d = 2.95$ corresponding to (hkl) of (110) to assign the distribution of the oxygen atoms. The lack of this line on specimens anodized in 35% KOH may denote a particular distribution of oxygen in the lattice positions, leading

Table II. Diffraction data for AgO, Ag_2O, and "silver suboxide"

AgO[a]		Ag_2O[b]		"Silver Suboxide"[c]
d	I/I_o	d	I/I_o	d
		3.35	1	
2.78	vs	2.72	100	
2.63	m			2.63
2.42	s	2.36	40	
2.29	m			2.28
1.74	w			
1.701	m			
1.678	w	1.67	24	
1.621	m			1.61
1.478	w			
1.451	mB[d]			
1.409	wB	1.42	16	
1.395	mB			
1.375	m	1.36	3	1.375
1.308	vw			1.316
1.208	vw			
		1.18	1	1.185
1.143	vw			
1.125	vw			
1.104	w			
1.099	w	1.08	2	
1.067	w	1.05	2	1.046

[a] Values observed for Ag specimen anodized in 35% KOH.
[b] From x-ray diffraction data cards ASTM 1950 card No. 1-1041.
[c] Calculated for a face-centered cube with $a_o = 4.56$Å
[d] B indicates a broad diffuse diffraction peak.

to sufficient change in parameter to bring the doublet at $d = 2.78$ into coincidence. The resolution of these questions and their possible relation to the electrochemical activity and utilization of the battery oxide merit further study.

Summary

X-ray diffraction patterns of a silver electrode showed only the lines of Ag and Ag_2O when the electrode was charged anodically at potentials up to 250 mv above the Ag/Ag_2O potential. AgO could be formed at a potential as low as 308 mv, which indicates that the primary product at the second potential plateau is not a higher oxide which then decomposes to AgO. After the Ag_2O on the surface of the electrode oxidizes to AgO, much of the Ag deeper in the electrode then oxidizes. The silver electrode charges efficiently at the first two potential plateaus. Since the reaction $Ag + AgO \rightarrow Ag_2O$ takes place very slowly, it probably has little effect on charges of a silver electrode under normal conditions. At the end of a normal charge, the electrode contained only AgO and a little Ag. The AgO crystallinity was perfected by holding the electrode at potentials well above the gassing potential. No higher oxide was detected, even with lengthy anodization 0.3 v above the reported $AgO/"Ag_2O_3"$ potential.

The surface of a AgO electrode becomes covered with Ag_2O at the time when its potential reaches the lower plateau during low-rate discharges. Even though a high-rate discharge failed to show the first potential level and discharged at least 0.4 v below the Ag/Ag_2O potential, metallic Ag did not form in appreciable amounts during the early parts of this discharge.

The charge of a silver electrode in $2N$ H_2SO_4 goes first to Ag_2SO_4 and then to the so-called peroxysulfate. The latter compound decomposes on standing in dry air to give AgO. Neither Ag_2O nor a silver suboxide was found in acid. The existence of a suboxide on anodized silver is doubtful.

Manuscript received Feb. 27, 1959. This paper was prepared for delivery before the Columbus Meeting. Oct. 18-22, 1959.

Any discussion of this paper will appear in a Discussion Section to be published in the June 1960 JOURNAL.

REFERENCES

1. R. Luther and F. Pokorny, *Z. anorg. Chem.*, **57**, 290 (1908).
2. A. Hickling and D. Taylor, *Discussions Faraday Soc.*, **1**, 277 (1947).
3. P. Jones, H. R. Thirsk, and W. F. K. Wynne-Jones, *Trans. Faraday Soc.*, **52**, 1003 (1956).
4. Yu. V. Pleskov, *Doklady Akad. Nauk S.S.S.R.*, **117**, 645 (1957).
5. G. Rädlein, *Z. Elektrochem.*, **61**, 727 (1957).
6. K. Nagel, R. Ohse, and E. Lange, *Z. Elektrochem.*, **61**, 795 (1957).
7. W. J. Hamer and D. N. Craig, *This Journal*, **104**, 206 (1957).

7a. J. F. Bonk and A. B. Garrett, *ibid.*, **106**, 612 (1959).

8. G. W. Work and C. P. Wales, *ibid.*, **104**, 67 (1957).
9. I. A. Denison, *Trans. Electrochem. Soc.*, **90**, 387 (1946).
10. F. Jones and H. R. Thirsk, *Trans. Faraday Soc.*, **50**, 732 (1954).
11. G. R. Levi and A. Quilico, *Gazz. chim. ital.*, **54**, 598 (1924).
12. E. Mulder, *Rec. Trav. Chim.*, **18**, 91 (1899); **19**, 115 (1900).
13. M. S. Skanavi-Grigor'eva and I. L. Shimanovich, *Zhur. Obshchei Khim.*, **26**, 1540 (1956).
14. J. H. de Boer and J. Van Ormondt, *Proc. Intern. Symposium on the Reactivity of Solids*, Gothenberg 1952, Part I, 557 (1954).
15. O. Sulc, *Z. anorg. Chem.*, **12**, 89, 190 (1896).
16. E. Mulder and J. Heringa, *Rec. Trav. Chim.*, **15**, 1, 235 (1896); E. Mulder, *ibid.*, **16**, 57 (1897).
17. S. L. Tanatar, *Z. anorg. Chem.*, **28**, 331 (1901).
18. E. R. Watson, *J. Chem. Soc.*, **89**, 578 (1906).
19. M. J. Brown, *Trans. Am. Electrochem. Soc.*, **30**, 327 (1916).
20. M. S. Skanavi-Grigor'eva and I. L. Shimanovich, *Zhur. Obshchei Khim.*, **24**, 1490 (1954).
21. W. S. Graff and H. S. Stadelmaier, *This Journal*, **105**, 446 (1958).
22. H. Brækken, *Kgl. Norske Videnskab. Selskab Forh.*, **7**, 143 (1935).
23. Z. V. Zvonkova and G. S. Zhdanov, *Zhur. Fiz. Khim.*, **22**, 1284 (1948).
24. H. E. Swanson, R. K. Fuyat, and G. M. Ugrinic, *Nat. Bur. Stds. Circ. 539*, Vol. IV, 61 (1955).
25. G-M. Schwab and G. Hartman, *Z. anorg. u. allgem. Chem.*, **281**, 183 (1955).
26. V. Scatturin, P. Bellon, and R. Zannetti, *Ricerca sci.*, **27**, 2163 (1957).

Brief Communications

The JOURNAL accepts short technical reports having unusual importance or timely interest, where speed of publication is a consideration. The communication may summarize results of important research justifying announcement before such time as a more detailed manuscript can be published. Consideration also will be given to reports of significant unfinished research which the author cannot pursue further, but the results of which are of potential use to others. Comments on papers already published in the JOURNAL should be reserved for the Discussion Section published biannually.

Submit communications in triplicate, typewritten double-spaced, to the Editor, Journal of The Electrochemical Society, 1860 Broadway, New York 23, N. Y.

Hydrogen Overvoltage on Bright Platinum

III. Effect of Hydrogen Pressure

Sigmund Schuldiner

U. S. Naval Research Laboratory, Washington, D. C.

ABSTRACT

The effect of hydrogen pressure on the hydrogen overvoltage of bright platinum was determined in acid. From the anodic and cathodic overvoltages, kinetic parameters were determined. A mechanism controlled by slow combination of hydrogen atoms adsorbed on the platinum surface fits the experimental data. From the Langmuir adsorption isotherm it is shown that the surface of the active platinum electrode at equilibrium is sparsely covered with hydrogen atoms.

Several investigators (1-6) have established that hydrogen overvoltage η at a given current density in the Tafel region on a cathode evolving hydrogen is related to the hydrogen pressure by the expression $\eta = \eta_o + (RT/2\mathbf{F}) \ln P_{H_2}$, where η is the potential difference between the working electrode and a reversible hydrogen reference electrode in the same solution, η_o is the overvoltage at 1 atm of hydrogen, P_{H_2} is the partial pressure of hydrogen above the solution, and R, T, and $\mathbf{F}$ have their usual significance. Vetter and Otto (6) in an investigation of the effect of pressure on anodic and cathodic overvoltage of an inactive platinum electrode in acid solution were able to determine the kinetic parameters and to establish reaction mechanisms that fitted their experimental findings. This investigation is a continuation of previous work (7, 8) on hydrogen overvoltage on an active, smooth platinum electrode.

Experimental

The general experimental techniques were the same as before (7, 8). The cell was constructed of Teflon and was a simplified version of the one shown in Fig. 1 of reference (8). The platinum (99.99%) cathode was a small sphere at the end of a very short length of exposed wire (apparent area 0.084 cm^2). The solution was in all cases 1M H_2SO_4. Purified gases consisting of either pure hydrogen, a prepared mixture of 5% hydrogen in nitrogen, or mixtures of hydrogen and helium were bubbled through the acid solution in the cell. The hydrogen-helium mixtures were prepared by mixing hydrogen and helium directly from their cylinders through rotameters into the gas purification train. This gave a composition of the two gases which remained constant for any given setting of the flow rates. The pressure of the gas introduced into the cell was always 1 atm. The partial pressure of hydrogen was determined by measuring the potential difference between a reversible hydrogen electrode and a saturated α Pd-H electrode in the cell. Since it was established (9) that the potential-determining reaction on the saturated α Pd-H electrode is independent of hydrogen pressure, the potential difference, E, between it and the reversible hydrogen electrode in the same solution obeyed the Nernst relation $E = 0.05 + (RT/2\mathbf{F}) \ln P_{H_2}$. From this potential the partial pressure of hydrogen flowing through the cell was determined.

After the solution was pre-electrolyzed and the Pt electrode was further cleaned by anodic polarization, the pseudo-capacitance test (7) was used to determine surface cleanliness and also the IR drop between it and the reference electrode (a Pt gauze electrode in the same solution). Repeated measurements were taken at each partial pressure of hydrogen under both anodic and cathodic polarization. Overvoltages at each current density were time independent. The data given are average values of individual runs. The precision of an individual reading was better than 0.5 mv. The spread of each particular reading for a given experiment was ±1 mv. The temperature was 25° ± 1°C.

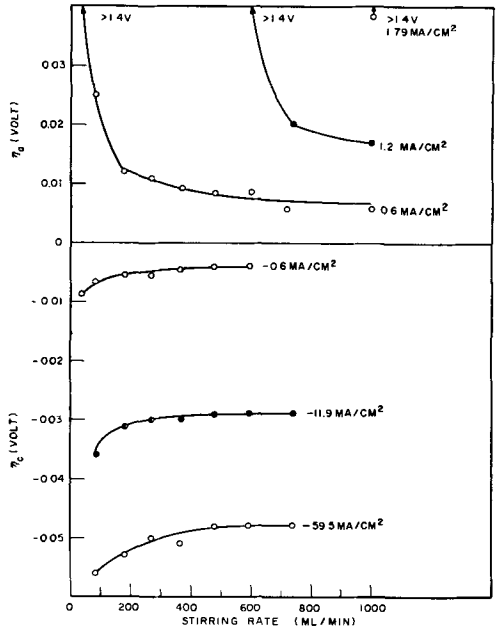

Fig. 1. Effect of stirring rate on η_a and η_c at 1 atm of hydrogen.

Experimental Results

Concentration polarization effects were minimized by stirring the solution with gas at rates for which a further increase in stirring rate would not affect the measured overvoltage. Figure 1 shows the effect of stirring rate on overvoltage for pure hydrogen flowing through the solution. The data show that at the higher current densities flow rates of at least 500 ml/min are required. It should be noted also that the dependence on stirring rate is much more pronounced for anodic than cathodic polarization. This is because for anodic polarization molecular hydrogen must diffuse to the surface at a sufficiently fast rate to maintain a given concentration of atomic hydrogen on the surface. This would be similar to the case described by Frumkin and Aikasjan (10). In the case of cathodic polarization the difference between the hydrogen pressure in the bulk of the solution and at the electrode surface is not as pronounced.

Plots of cathodic overvoltage η_c, vs. logarithm of apparent negative current density at different hydrogen pressures are shown in Fig. 2. It should be noted that the Tafel b slopes are 0.025-0.026 v rather than 0.0295 v expected at 25°C. This confirmed previous results (8). Figure 3 shows plots of anodic overvoltage η_a vs. logarithm of current density. At low currents there is a linear relationship between anodic and cathodic overvoltages and current density (Fig. 4). From experimental data shown in Fig. 2-4, kinetic parameters can be determined and a reaction mechanism suggested.

Derivation of Kinetic Equations

Cathodic overvoltage.—It is assumed that the cathode overvoltage mechanism is primarily a discharge of hydronium ions in the double layer followed by a slow combination of hydrogen atoms to molecules, that is

$$H^+ + e = H \qquad \text{(discharge step)} \qquad [1a]$$

$$2H = H_2 \qquad \text{(combination step)} \qquad [1b]$$

Assuming a Langmuir isotherm, kinetic equations for the discharge step can be written

$$\vec{i}_d = \vec{k}_d(H^+)\,(1-\theta)\,\exp\,(-\alpha\eta_c\mathbf{F}/RT) \qquad [2a]$$

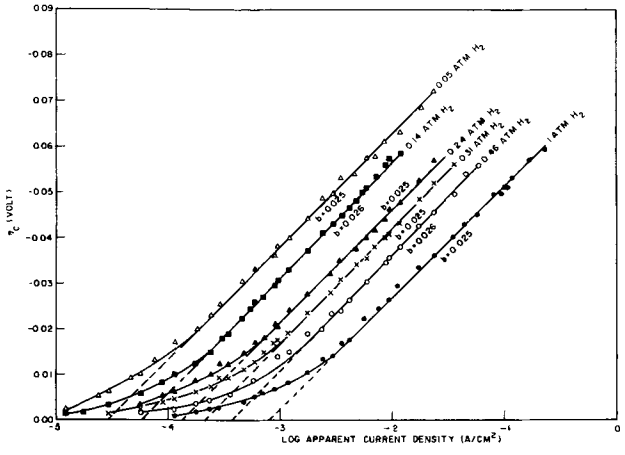

Fig. 2. Relations for η_c vs. log $(-i_c)$ at different partial pressures of hydrogen.

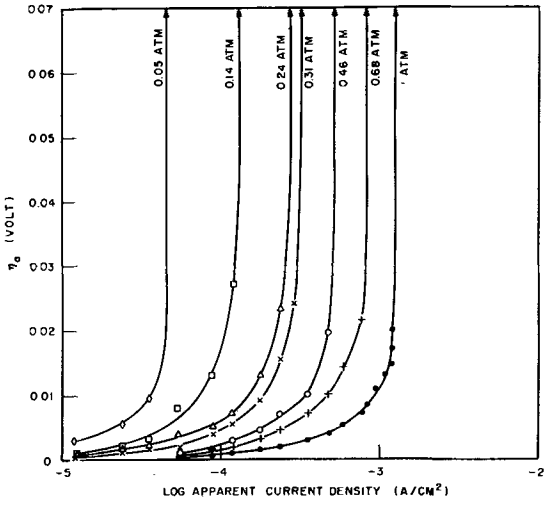

Fig. 3. Relations for η_a vs. log i_a at different partial pressures of hydrogen.

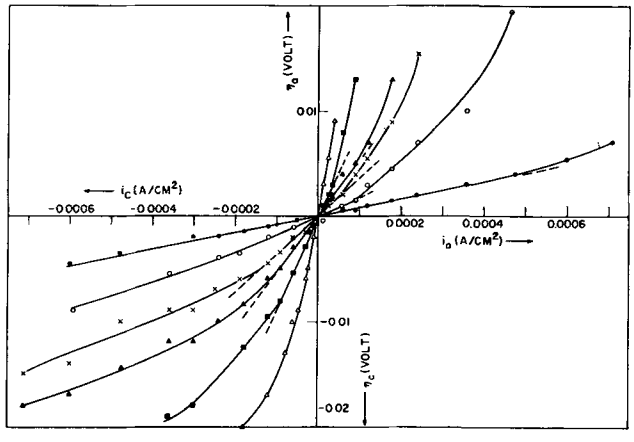

Fig. 4. Low current density relations for η vs. i. Partial pressures of hydrogen as in Fig. 2.

$$\overleftarrow{i}_d = \overleftarrow{k}_d\theta\,\exp\,[(1-\alpha)\eta_c\mathbf{F}/RT] \qquad [2b]$$

where $\vec{i}_d$, $\overleftarrow{i}_d$ represent forward and reverse current densities, respectively. The convention that cathodic current is negative and anodic current is positive is used; $\vec{k}_d$, $\overleftarrow{k}_d$ are forward and reverse rate constants which are negative and positive, respectively. (H^+) is the hydronium ion concentration in the double layer which in 1M H_2SO_4 remains virtually constant in the current density range investigated, θ is the fraction of available surface covered with atomic hydrogen, and α is the transfer coefficient. The discharge step is assumed virtually at equilibrium, hence $\vec{i}_d = -\overleftarrow{i}_d$. Therefore

$$\theta/(1-\theta) = -\mathrm{K}'\,\exp\,(-\eta_c\mathbf{F}/RT) \qquad [3]$$

where K′ is a constant. For the slow combination step

$$\vec{i}_c = \vec{k}_c\theta^2 \qquad [4a]$$

$$\overleftarrow{i}_c = \overleftarrow{k}_c P_{H_2}\,(1-\theta)^2 \qquad [4b]$$

Here the partial pressure of hydrogen at the metal solution interface is considered independent of i_c. This is based on the proposition that the diffusion

of molecular hydrogen is not rate-determining. Hence the net cathodic current density i_c is the algebraic sum $i_c = \vec{i}_c + \overleftarrow{i}_c$, where the magnitude of $\vec{i}_c$ is not less than the magnitude of $\overleftarrow{i}_c$. At equilibrium, i_c is zero, and $\vec{i}_c = -\overleftarrow{i}_c = i_{o,c}$, where $i_{o,c}$ is the cathodic exchange current density (negative). Hence

$$\vec{k}_c\theta_o^2 = -\overleftarrow{k}_c P_{H_2}(1-\theta_o)^2 = i_{o,c} \qquad [5]$$

where θ_o is the fraction of available surface covered with atomic hydrogen at equilibrium. Therefore, from [4] and [5]

$$i_c = i_{o,c}[(1-\theta)^2/\theta_o^2]\{\theta^2/(1-\theta)^2 - \theta_o^2/(1-\theta_o)^2\} \qquad [6]$$

Substituting for $\theta/(1-\theta)$ from Eq. [3], and noting that at equilibrium $\eta_c = 0$ so that $K'^2 = \theta_o^2/(1-\theta_o)^2$, we obtain

$$i_c = i_{o,c}[(1-\theta)^2/(1-\theta_o)^2]\cdot\{\exp(-2\eta_c\mathbf{F}/RT) - 1\} \qquad [7a]$$

At low coverages, the factor involving the θ's reduces to unity. Equation [7a] can be expressed in logarithmic form at 25°C and at low coverages as

$$\eta_c = -0.0295 \log[(i_c/i_{o,c}) + 1] \qquad [7b]$$

This is in effect the equation first derived by Hammett (11).

Anodic overvoltage.—Here the reaction can be written as the inverse of the cathodic case, i.e., a slow dissociation of H_2 followed by ionization of H. The kinetic equations for the ionization step are

$$\vec{i}_i = \vec{k}_i\,\theta\exp(\alpha\eta_a\mathbf{F}/RT) \qquad [8]$$

$$\overleftarrow{i}_i = \overleftarrow{k}_i\,(H^+)(1-\theta)\exp[-(1-\alpha)\eta_a\mathbf{F}/RT] \qquad [9]$$

where $\vec{i}_i$, $\overleftarrow{i}_i$ are forward and reverse current densities for ionization; $\vec{k}_i$, $\overleftarrow{k}_i$ are forward and reverse rate constants and are positive and negative, respectively. The α used here is not the same as before. The ionization step is considered at equilibrium, hence $\vec{i}_i = -\overleftarrow{i}_i$. Therefore

$$\theta/(1-\theta) = -K_i'\exp(-\eta_a\mathbf{F}/RT) \qquad [10]$$

For the slow dissociation step

$$\vec{i}_a = \vec{k}_a P_{H_2}(1-\theta)^2 \qquad [11a]$$

$$\overleftarrow{i}_a = \overleftarrow{k}_a\theta^2 \qquad [11b]$$

The net anodic current density i_a is the algebraic sum $i_a = \vec{i}_a + \overleftarrow{i}_a$, where the magnitude of $\vec{i}_a$ is not less than the magnitude of $\overleftarrow{i}_a$. At equilibrium, i_a is zero, and $\vec{i}_a = -\overleftarrow{i}_a = i_{o,a}$ where $i_{o,a}$ is the anodic exchange current (positive).

Therefore

$$i_{o,a} = \vec{k}_a P_{H_2}(1-\theta_o)^2 = -\overleftarrow{k}_a\theta_o^2 \qquad [12]$$

Following the same analysis as above, one obtains

$$i_a = i_{o,a}[(1-\theta)^2/(1-\theta_o)^2]\{1 - \exp(-2\eta_a\mathbf{F}/RT)\} \qquad [13]$$

At 25°C and low coverages, Eq. [13] reduces to the logarithmic form

$$\eta_a = -0.0295 \log[1 - i_a/i_{o,a}] \qquad [14]$$

Calculation of Kinetic Parameters

The value of $i_{o,c} = -i_{o,a}$ was determined from Eq. [7a] in its limiting low coverage form. The graphs of i_c vs. $[\exp(-2\eta_c\mathbf{F}/RT) - 1]$ for various values of P_{H_2} are shown in Fig. 5. The relationship given by Vetter and Otto (6), which can be derived from Eqs. [4], [5], [11], and [12] when $\theta_o << 1$, is $\theta_o^2 = -i_{a,L}/i_{c,L}$, where $i_{a,L}$ and $i_{c,L}$, the limiting anodic and cathodic current densities, can be used to determine θ_o. It was assumed that $i_{c,L}$ is not algebraically greater than -10 amp/cm^2. This is a reasonable assumption since the Tafel slope in Fig. 2 for pure hydrogen is maintained down to negative currents approaching -1 amp/cm^2. In addition, a calculation by Salzberg and Schuldiner (12) indicated that on a Pt electrode the maximum coverage of the surface with adsorbed atomic hydrogen at -1 amp/cm^2 would be about 2%. Hence using the arbitrary value of -10 amp/cm^2 for $i_{c,L}$ and obtaining $i_{a,L}$ for various hydrogen pressures from Fig. 3, θ_o^2 can be calculated for each pressure. It should be mentioned that $i_{c,L}$ is independent of hydrogen pressure; in other words, $i_{c,L}$ is only dependent on the rate of hydrogen evolution at the cathode. Using θ_o^2 values, which indicate a low coverage with atomic hydrogen, obtained in this way, the rate constant $\vec{k}_c = \overleftarrow{k}_a = -12.08$ was calculated from Fig. 6 using Eq. [5]. The rate constant $\overleftarrow{k}_c = \vec{k}_a = 0.00143$ was calculated using Eq. [5] also. Figure 7 shows the linear relation between P_{H_2} and $i_{o,c}$ which was used to determine this rate constant.

The rate constant $k = \pm(di/d\eta)_{\eta\to 0}$ (negative for cathodic, positive for anodic directions) for the over-all reaction near equilibrium, where there is a linear relation between η and i, was determined from Fig. 4 for various hydrogen pressures. These values

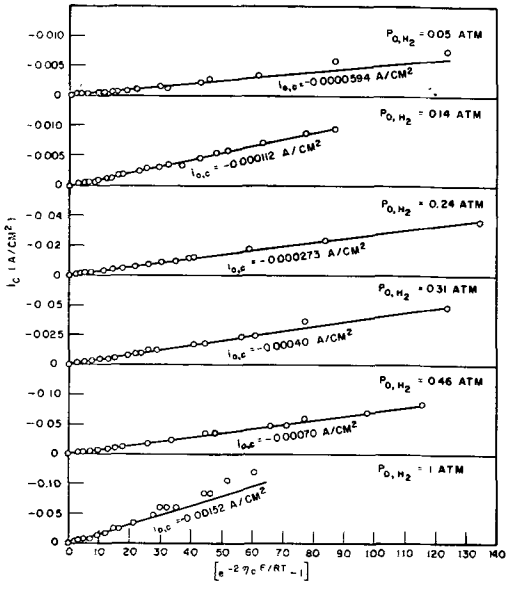

Fig. 5. i_c vs. $[\exp(-2\eta_c\mathbf{F}/RT - 1]$

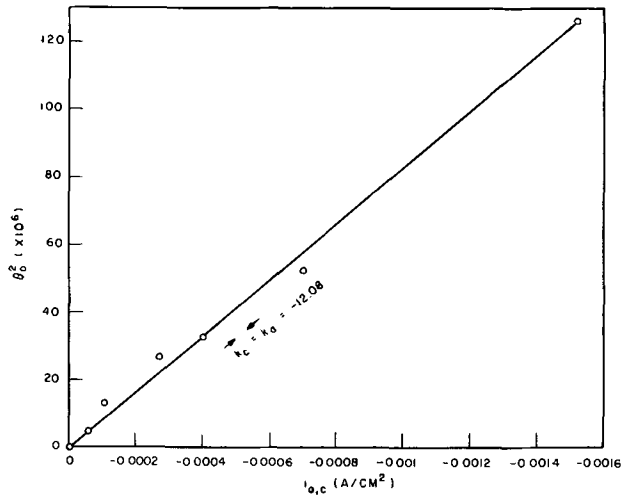

Fig. 6. θ_o^2 vs. $i_{o,\,c}$

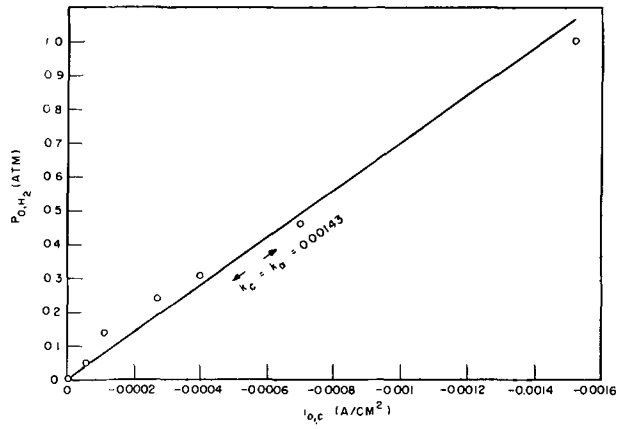

Fig. 7. P_{H_2} vs. $i_{o,\,c}$

are shown in Table I. Also shown are stoichiometric numbers μ calculated from the Horiuti relationship (13) $\mu = 2i_{o,c}\mathbf{F}/kRT$.

Discussion

The assumption that the surface of the active smooth Pt electrode used in this investigation was sparsely covered with atomic hydrogen at equilibrium can be verified by determining the Langmuir adsorption isotherm. This isotherm is $\theta_o^2/(1-\theta_o)^2 = KP_{H_2}$. At low coverages $\theta_o^2 = KP_{H_2}$. The linear data of Fig. 6 and 7 can be combined to give a reasonably good linear isotherm with a K value of 116×10^{-6}. The fact that this isotherm holds throughout the range of hydrogen pressures investigated, with a zero intercept, virtually proves that the surface of the platinum at zero current is only sparsely covered with atomic hydrogen. If one changes $i_{c,L}$ from -10 amp/cm^2 to a value smaller by one to two orders of magnitude, or to any larger value, this still would not affect the linearity of the isotherm, but would merely change K.

The linear relations shown in Fig. 5 confirm the mechanisms assumed, namely, that the hydronium ion discharge is followed by a rate-determining slow combination step. Another way of showing this is to plot anodic and cathodic overvoltages vs. the logarithmic relationships given in Eqs. [7b] and [14]. This should give a straight line with a slope of 0.0295 v. Figure 8 shows this relation for all partial pressures of hydrogen and confirms that the mechanism assumed is a reasonable one. Additional proof is given by the fact that the stoichiometric numbers

Table I. Cathodic kinetic parameters

P_{H_2} atm	$-$ k, mho/cm^2	$-$ $i_{o,\,c}$ amp/cm^2	μ
1.0	0.13	0.00152	0.92
0.46	0.053	0.00070	1.03
0.31	0.027	0.00040	1.15
0.24	0.019	0.000273	1.12
0.14	0.011	0.000112	0.79
0.05	0.0046	0.0000594	1.01
		Av =	1.00

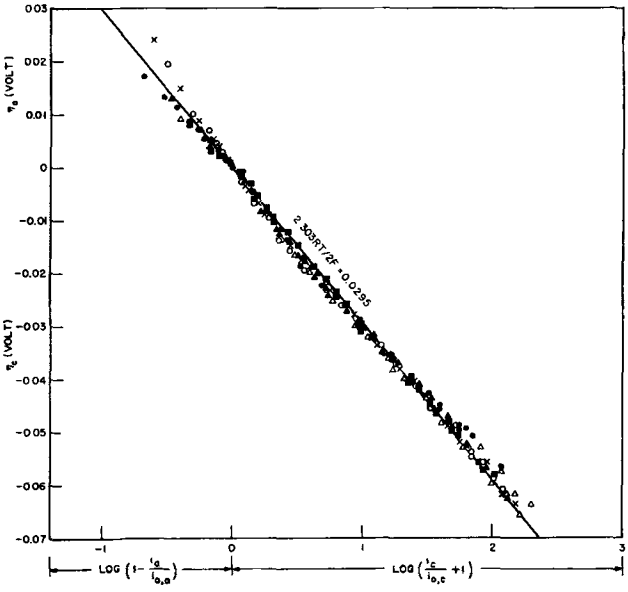

Fig. 8. Hammett relations for η vs. i. Partial pressures of hydrogen as in Fig. 2.

μ for the series of hydrogen pressures shown in Table I are all approximately equal to one.

The Tafel relation derived from the curves in Fig. 2 is only an empirical equation which proves to be compatible with theoretical Eq. [7b]. However at higher current densities one would expect a definite upward curvature from the straight lines shown in Fig. 2. At log $(-i_c) = 0$, the curvature would be such that η_c for 1 atm would be -0.083 v rather than -0.076 v as obtained by extrapolating the linear portion in Fig. 2. Similarly for the other hydrogen pressures there will be an increasing curvature as the pressure is decreased. Experimentally there was an indication of such a deviation at high current densities. However, there exists also a significant concentration overvoltage effect which is undoubtedly owing to the diffusion away of molecular hydrogen from the metal solution interface (14), and it is experimentally difficult to eliminate this effect at higher overvoltages. It should also be noted that an extrapolation of the Tafel lines in Fig. 2 to zero overvoltages give current density values which are much lower than the $i_{o,c}$ values obtained from Eq. [7b].

Acknowledgment

The author is indebted to Drs. J. C. White and G. W. Castellan for their comments and suggestions.

Manuscript received Feb. 5, 1959.

Any discussion of this paper will appear in a Discussion Section to be published in the June 1960 JOURNAL.

REFERENCES

1. S. J. Bircher and W. D. Harkins, *J. Am. Chem. Soc.*, **45**, 2890 (1923).
2. M. Knobel, *ibid.*, **46**, 2751 (1924).
3. H. M. Cassel and E. Krumbein, *Z. physik., Chem.*, **A171**, 70 (1934).
4. G. Schmid and E. K. Stoll, *Z. Elektrochem.*, **47**, 360 (1941).
5. J. O'M. Bockris and R. Parsons, *Trans. Faraday Soc.*, **45**, 916 (1949).
6. K. J. Vetter and D. Otto, *Z. Electrochem.*, **60**, 1072 (1956).
7. S. Schuldiner, *This Journal*, **99**, 488 (1952).
8. S. Schuldiner, *ibid.*, **101**, 426 (1954).
9. S. Schuldiner, G. W. Castellan, and J. P. Hoare, *J. Chem. Phys.*, **28**, 16 (1958).
10. A. N. Frumkin and E. A. Aikazan, *Doklady Ak. Nauk, USSR*, **100**, 315 (1955).
11. L. P. Hammett, *J. Am. Chem. Soc.*, **46**, 7 (1924).
12. H. W. Salzberg and S. Schuldiner, *This Journal*, **104**, 319 (1957).
13. J. Horiuti, *J. Research Inst. Catalysis, Hokkaido*, **1**, 8 (1948).
14. C. A. Knorr, *Z. Elektrochem.*, **59**, 647 (1955).

A Porcelain Reference Electrode Conductive to Sodium Ions for Use in Molten Salt Systems

Roger J. Labrie and Vernon A. Lamb

Chemistry Division, National Bureau of Standards, Washington, D. C.

ABSTRACT

A reference electrode for use in molten salt systems is described. It consists of a porcelain capsule conductive to sodium ions, containing a silver electrode immersed in a melt of silver chloride and sodium chloride. The electrode is reversible to sodium ions. It is stable, reproducible, and temperature-reversible and can be used at temperatures 400° to 500° higher than can similar electrodes made of glass. The capsule-type construction prevents the salt inside the electrode from contaminating the melt under study. Electrodes made from specially prepared porcelains and also from a commercial porcelain were used. Data are presented on the resistivity of the specially prepared porcelains and on the mechanism of conduction by the porcelain.

Accurate data on electrode potentials in molten electrolytes are of importance in electrodeposition from molten salts, corrosion by molten salts, and in studies of the thermodynamic properties of molten salt systems. The amount of research in these fields has increased in recent years because of interest in the production of refractory metals by electrodeposition from molten salt solutions, in the development of molten salt batteries, and in the various applications of molten salt processes in the atomic energy program.

Several types of reference electrodes have been used in previous researches in these fields, such as the Ag/AgCl electrode with a liquid junction (1, 2); the Pt electrode (3, 4); an Ag/AgCl electrode in a graphite sheath for use in fluoride melts (5); the Cl^-/Cl_2 (graphite) electrode (6); and electrodes in glass capsules with the internal electrode in the glass capsule consisting of Na (7, 8), Na-Hg (9), Na-Sn (10, 11), and Ag in a mixture of AgCl-LiCl-KCl (12).

A reference electrode has been developed in this laboratory which is similar to that described by Bockris, *et al.* (12), but differs in that the glass capsule used by them is replaced by a porcelain capsule conductive to sodium ions. The main advantage of the porcelain electrode is that it can be used at much higher temperatures than can glass. In common with the glass capsule electrodes, it also has the advantage that salts in the capsule cannot intermix with those outside the capsule. The porcelain is reversible to sodium ions in the melt under study, and since the inner Ag/AgCl electrode is reversible, the entire electrode system is reversible. Electrodes of the design described below have been used at temperatures up to about 900°C. They should be capable of use at temperatures up to the melting point of silver. If the design were modified to make possible the retention of molten silver, the electrodes might be serviceable at temperatures approaching the softening point of the porcelain.

Preparation of Electrodes

Preparation of porcelain.—The composition of the porcelain from which most of the capsules were made was approximately: Na_2O, 2.5%; SiO_2, 73.1%; Al_2O_3, 24.4%, by weight. The objective in preparing this porcelain was to obtain a material that was nearly free of alkali metals other than sodium and of alkaline-earth metals, with the thought that such porcelain might be conductive only to sodium ions. The sodium content was chosen arbitrarily. In later work, a commercial porcelain and a porcelain containing a higher proportion of sodium were used.

The porcelain containing 2.5% Na_2O was prepared as follows: A glass of the composition $Na_2Al_2Si_2O_8$

was made by dry-milling together in a jar mill with flint pebbles an equimolar mixture of Na_2SiO_3, Al_2O_3, and SiO_2, followed by firing of the mixture at 1100°C, after which the fired mass was reground. A portion of the glass (186 g) then was milled in a 1-gal jar mill with flint pebbles for 10 to 12 hr, together with 388 g of Kentucky ball clay, 520 g of Georgia kaolin, 696 g of flint, 820 ml of water, and 0.5 g of sodium silicate or sodium carbonate. The sodium silicate (or carbonate) was added to effect deflocculation of the slip.

Construction of electrodes.—The construction of the porcelain electrode is shown in Fig. 1. The slip was formed into electrode tubes by slip-casting in a split mold of plaster of Paris, which had been formed over a glass pattern of the electrode tube. The slip-casts were dried in the mold, removed, and usually were fired to 1285°C, but some were fired as high as 1400°C. Although the higher firing temperature caused blisters to form, the tubes still were serviceable.

A T-tube of Nonex glass was sealed to the porcelain tube. At its working temperature, the glass wets the porcelain readily to form a good seal. (The porcelain that contains 10% Na_2O, described in the section on Electrical resistivity of porcelain, was joined to a T-tube of Kovar sealing glass, Corning No. 7052.)

The inner Ag electrode was made as follows: A length of 1 mm W wire, the tip of which had been cleaned by filing, was inserted into a ceramic tube of 1 mm i.d. (McDanel high-temperature porcelain) to within about 1-in. of the end of the tube. The tube was supported vertically in a clamp with the open end upward. A short length of 1 mm Ag wire was inserted into the tube and melted by applying a torch flame, first where the Ag wire touched the W and then higher as the Ag melted, so that the Ag flowed into intimate contact with the W wire and completely filled the tube. Electrical continuity between the Ag and W was checked with an ohmmeter. All of the Ag electrodes used in the cells described in this paper were constructed in this manner, so that the W-Ag thermoelectric potentials cancel. The W wire was then beaded with U glass (Corning No. 3320) and sealed into the T-tube at a position such that the tip of the Ag electrode extended nearly to the bottom of the porcelain bulb. Care must be taken in making this seal to insure that the inner electrode does not touch the inner surface of the porcelain tube. The porcelain is sufficiently translucent so that the location of the inner electrode can be checked by viewing it against a strong light.

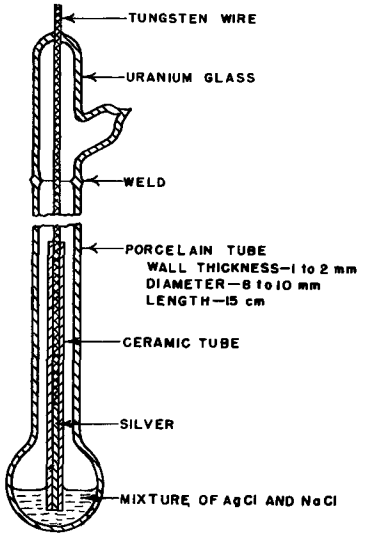

Fig. 1. Construction of porcelain electrode

The assembled electrode was filled with the desired mixture of AgCl and NaCl through the sidearm of the T-tube, which then was sealed off while evacuating the electrode through it. Evacuation and sealing are not essential, but this procedure was preferred. Various proportions of AgCl and NaCl have been used, but a mixture high in AgCl is preferred because of its lower melting point and because fewer capsules break when re-used if they contain such a mixture. Complete cells usually were assembled with two porcelain electrodes and one or two electrodes of some other type, dipped into a melt in a short cylindrical container.

Characteristics of Porcelain Electrodes

Reproducibility and stability.—Reproducibility of the porcelain electrodes was checked by measuring the potentials of cells in which identical electrodes were opposed. In the following cell, P represents the porcelain membrane; the numbers are the mole per cents of each component.

Ag/AgCl 40, NaCl 60/P/AgCl 4.76, NaCl 47.6,

KCl 47.6/P/AgCl 40, NaCl 60/Ag (I)

The results of measurements of the emf of cell (I) are shown in Table I for five replicate electrodes, represented as a to e.

It is seen that there was a difference of 5-7 mv betwen electrodes a and b, which was probably caused by a small difference in the concentrations of the electrode solutions. These were prepared separately, and an error of about one percentage unit in concentration would account for the discrepancy. The temperature of cells c/d and d/e was varied irregularly over long periods. The results show that the emf of the porcelain electrodes was stable and reproducible to within a few millivolts under temperature cycling over a period of nearly six days. These experiments also showed that the

Table I. Electromotive force of cells(I)

Cell a/b			Cell c/d			Cell d/e		
Time, hr	Temp, °C	Emf, mv	Time, hr	Temp, °C	Emf, mv	Time, hr	Temp, °C	Emf, mv
0	720	5.3	0.2	760	1.1	0	760	0.7
0.4	720	6.6	0.5	760	0.4	5	850	0.3
0.7	720	7.1	2.0	760	1.2	22	760	0.3
2.7	720	6.4	4.0	760	0.1	26	850	0.3
3.7	720	6.5	20.0	760	−2.5	27	900	0.4
			21.0	760	0.2	28	850	0.2
			26.0	828	−1.3	29	800	0.2
			29.0	760	1.4	118	770	3.0
						141	800	0.0

porcelain electrode is re-usable since electrode d was used in two separate experiments. This is a distinct advantage for a reference electrode.

The period of time required for the porcelain electrode to reach equilibrium, following a shift in temperature or other disturbance, usually ranged from a few minutes to about 30 min. Occasionally a cell potential did not become stabilized until after several hours. The cause for the variation is not known.

Temperature reversibility.—Temperature reversibility is indicated by the results shown in Table I. Additional experiments bearing on the variation of the emf of the porcelain electrode with temperature are described in this section.

Electromotive forces of the following concentration cell were measured over a range of temperature from 646° to 850°C (numbers are mole per cents).

Ag/AgCl 40, NaCl 60/P/AgCl 9.6, NaCl 45.2,

KCl 45.2/P/AgCl 78, NaCl 22/Ag (II)

The temperature was cycled within this range in a random manner over a period of several days. Repeat readings at the same temperature agreed within about 1 mv. Data are plotted in Fig. 2. The temperature at the break in the curve corresponds reasonably well with the liquidus temperature given in International Critical Tables (ICT) for the AgCl-NaCl system at a mole ratio of 40/60 (from ICT, 675°C; from Fig. 2, 688°C).

The emf of cell (II) may be written

$$E = (2.303\,RT/F)\log(0.78 \times 0.60/0.40 \times 0.22) \quad [1]$$

where mole fractions are used in the log term and activity coefficients are taken as unity. This equation is obtained by combining the equation for the emf of a concentration cell without transference with the equations for the two membrane potentials. The latter are based on the assumption that only sodium ions are transferred through the membranes. With this assumption, the over-all cell (II) process for one faraday is

AgCl (78 mole %) + NaCl (60) =

AgCl (40) + NaCl (22) [2]

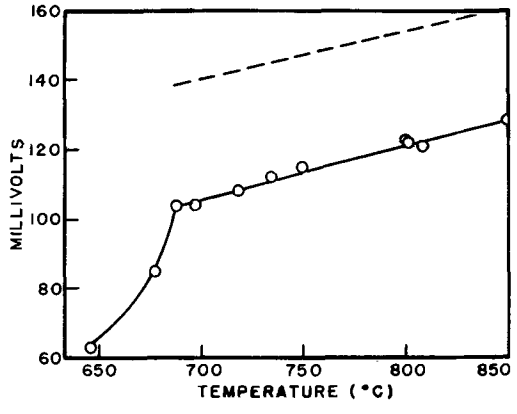

Fig. 2 Emf of cell (II) as a function of temperature. The dashed curve is calculated from Eq. [1].

Equation [1] gives the emf of this process and yields a value of E/T of 0.000144 v/deg. The slope of the curve in Fig. 2 beyond the break, i.e., in the range of temperature at which the salt phase in the left-hand electrode of cell (II) is completely molten, is 0.000148 v/deg. The agreement indicates that the porcelain electrodes behave normally with respect to temperature change.

Theoretically, the curve in Fig. 2 should extrapolate to zero emf at absolute zero. The dashed line shows the position of the theoretical curve calculated from Eq. [1]. It lies about 34 mv above the experimental curve. The difference may be due to deviations of the activity coefficients from unity, or to an effect of the potassium ions in the melt on the membrane potential (see section on Effect of potassium ions in the melt on the potential of the porcelain electrode).

Membrane asymmetry.—Theoretically, the potential of a half-cell including a sodium ion-conductive membrane in contact with a given external melt should be independent of the composition of the membrane. However, it is conceivable that unsymmetrical surface effects might result in an asymmetry potential. To check this point, cells were set up in which two capsule-type electrodes were dipped into the same melt contained in a small crucible. Melts in the two half-cells were identical, but the membranes were different, as shown in cell (III) (numbers are mole per cents).

Ag/AgCl 50, NaCl 50/P/Na-K-Sr

chloride/G/AgCl 50, NaCl 50/Ag (III)

In this cell, the membrane P was a porcelain capsule made from porcelain containing 2.5% Na_2O, fired at 1350°C, and G was a capsule of Pyrex glass. Measurements were made on two additional cells, like cell (III), except that in one cell, capsule G was replaced by a porcelain capsule that had been fired at 1400°C, and in the other by a capsule made from a commercial porcelain. (McDanel high-temperature porcelain in the form of a thermocouple protective tube, 1/2 in. OD, 1/16 in. wall; composition by weight: Al_2O_3, 56.2%; SiO_2, 43.0%; K_2O + Na_2O, 0.32%; C, Mg, and Fe oxides, 0.62%.) Temperatures ranged from about 550° to 750°C, depending on the material of the capsule. The potential of each of these three cells was less than 1 mv.

Since no significant membrane asymmetry potential was found in comparing these unlike membranes, it is unlikely that an asymmetry potential will be a complicating factor in the use of the porcelain-type electrode. The result with the commercial porcelain is especially significant, since the use of commercially available porcelain makes the rather tedious preparation of a special porcelain unnecessary. However, further work on the relationships between the composition of a porcelain and its selective permeability to specific ions might be fruitful.

Effect of the concentration of sodium chloride within the porcelain capsule.—Porcelain electrodes represented as Ag/AgCl(x), NaCl ($1-x$) porce-

lain, in which $1-x$, the mole fraction of sodium chloride, varied from 0.05 to 0.40, have shown reproducible, stable potentials. It is probable that both higher and lower proportions of sodium chloride could be used.

Effect of potassium ions in the melt on the potential of the porcelain electrode.—The effect of potassium ions on the potential of the porcelain electrode was studied by comparing cells having different ratios of sodium chloride to potassium chloride. Data for the following two cells are illustrative (numbers are in mole per cents).

Ag/AgCl 25, KCl 70, NaCl 5/P/

AgCl 50, KCl 45, NaCl 5/Ag (IV)

and

Porcelain electrode/AgCl 75,KCl 20, NaCl 5/Ag (V)

where "Porcelain electrode" designates the left electrode of cell (IV) up to and including the P membrane. The emf values for cells (IV) and (V) at 750°C, were 0.111 and 0.201 v, respectively. By use of assumptions analogous to those employed for calculating the emf of cell (II), the following theoretical values are obtained

	Cell IV v	Cell V v
Porcelain reversible to Na^+ only	0.061	0.097
Porcelain reversible to both Na^+ and K^+	0.097	0.194

The emf values calculated on the assumption that the porcelain membrane is reversible to both Na and K ions are much closer to the experimental values than those calculated from the assumption that only Na ions determine the membrane potential. It must be concluded that the porcelain electrode does not act solely as a Na electrode. However, in view of its stability and reproducibility, this result does not affect its potential usefulness as a reference electrode in any given system.

Current reversibility of the porcelain electrode.—An important property of an electrode is its ability to return to equilibrium after accidental passage of current. To check this property, cell (II) was polarized by passing a current of about 0.1 amp for 20 sec at 800°C. A polarization of 6 mv was measured immediately after passage of current. The polarization decayed to about 1 mv within 5 min. Reversal of the polarizing current gave an equal but opposite polarization, which decayed within 5 min to about 0.3 mv. Within 20 min the residual polarization was less than 0.1 mv. It is concluded that the porcelain electrode is reversible to passage of current.

Electrical resistivity of the porcelain.—Approximate measurements were made of the resistivity of porcelains of two compositions. One of the porcelains had the composition described in the section on Preparation of Electrodes; the other had a higher content of Na_2O. The composition of the latter was Na_2O, 10%; SiO_2, 54%; Al_2O_3, 36% by weight. Sodium was introduced into this porcelain as before in the form of a glass, but in this case the glass was prepared from Na_2SiO_3, SiO_2, and Al_2O_3, plus about one-third of the clays, followed by firing. The clays were added to render the glass less soluble in the slip mixture. The slip-casts were fired at 1170°C. Resistivity was estimated by measuring the voltage drop across the porcelain for a known direct current. The porcelain conductor was an electrode capsule in the case of the low-sodium porcelain. The resistivity of the porcelain containing 10% of Na_2O was so low that a conductor in the form of a U-shaped bar was used. In both cases the porcelain was in contact with a molten mixture of sodium salts having an appropriate melting point. Resistivity data are given in Table II. Even though the results are only approximate, it is believed they are of interest.

The low resistivity of the porcelain containing 10% Na_2O is noteworthy. It is of the order of 100 times that of molten alkali halides and is much lower than that of glasses. For example, the resistivity of soda-glass at 400°C is about 80,000 ohm-cm.

Mechanism of conduction by the porcelain.—Since application of the porcelain membranes to some experiments on conductivity and transference was planned, information on the mechanism of conduction through the porcelain was desired. The cell consisted of a porcelain capsule and a Ag anode dipped into a crucible that contained molten NaCl. The capsule contained a melt of AgCl-NaCl and a Ag cathode. Separate experiments were carried out with the low- and high-Na porcelains. Results are shown in Table III.

The gain in weight shown in the last column was calculated from Faraday's law on the assumption that only sodium ions pass through the porcelain. The agreement is within the limits of experimental error. In the experiment with the low-Na porcelain, examination of the inside of the bulb after the electrolysis showed blackening, probably due to reduction by the Na deposited on the cathode after complete deposition of the silver ion present in the melt. In the experiment with the high-Na capsule, Na was not deposited, and the porcelain was not

Table II. Resistivity of porcelains

Temperature, °C	Resistivity, ohm-cm	
	2.5% Na_2O	10% Na_2O
400		730
450		420
550		140
650		64
700		42
860		25
900	430	20
940	380	
1000	300	

Table III. Ion conductance of porcelain

Porcelain composition	Current, ma	Time, min	Temp, °C	Wt gain, g	Calc wt gain, g
Low-Na	50	300	850	0.215	0.215
High-Na	85	240	850	0.295	0.292

visibly changed, even though the amount of sodium ion transferred was sufficient to replace all of the Na contained in the porcelain.

The above results indicate that the porcelain conducts solely by transfer of sodium ions and not by transfer of electrons or oxygen ions.

Resistance of porcelain electrodes to breakage.— The likelihood of accidental breakage of these electrodes is about the same as that of similar glass electrodes. However, electrodes made with glass capsules usually break on cooling after being used once, whereas the porcelain electrodes usually can be used at least twice. In the course of this work, 26 porcelain electrodes were used. Of this number, 20 operated satisfactorily for one or more experiments, and 6 failed during initial use. Failure was due to breakage of the bulb, breakage of the glass-porcelain seal, or contact defects associated with the Ag-W junction or the porcelain sheath over the Ag. It is probable that improvements in design and construction might make them more durable.

An Application of the Porcelain Electrode

A porcelain reference electrode has been used successfully by another group in this laboratory working on the deposition of Ti from molten salt solutions. In these experiments, changes in the potential of Ti cathodes were followed during electrolyses of solutions of $TiCl_2$ or $TiCl_3$ in a eutectic melt of LiCl-KCl-NaCl at 600°C. The porcelain reference electrode, which was made from the low-Na porcelain, was used repeatedly over a period of five weeks. It was cooled, washed with water, and stored dry during intervening periods of nonuse. At both the beginning and the end of this period, its equilibrium potential against Ti in a fresh, carefully prepared melt was 1.23 v. Since a precision of one centivolt was adequate in these experiments, the data were not recorded to millivolts, but the constancy of the electrode was in fact significantly better than 1 centivolt.

Prolonged immersion of the electrode in the Ti solutions caused a film of Ti to form. A brief dip in a 25% solution of hydrofluoric acid (1 part concentrated HF to 1 part water by volume) removed the Ti film without damage to the electrode.

Acknowledgments

The authors acknowledge the contributions of Gwendolyn B. Wood and Paul A. Krasley, who carried out the work described in the section on Application of the Porcelain Electrode, and of Seymour Senderoff, now at National Carbon Research Laboratories, Parma, Ohio, who initiated this project. Acknowledgment is also made to the Atomic Energy Commission, Division of Research, Chemistry Branch, for financial support and for permission to publish this material.

Manuscript received Jan. 7, 1959. This paper was prepared for delivery before the Ottawa Meeting, Sept. 28-Oct. 2, 1958.

Any discussion of this paper will appear in a Discussion Section to be published in the June 1960 JOURNAL.

REFERENCES

1. S. Senderoff and A. Brenner, *This Journal*, **101**, 31 (1954).
2. S. N. Flengas and T. R. Ingraham, *Can. J. Chem.*, **35**, 1139 (1957).
3. R. A. Osteryoung, *Dissertation Abstr.*, **15** [1], 36 (1955).
4. Kurt H. Stern, *J. Phys. Chem.*, **60**, 1443 (1956).
5. H. Coriou, J. Dirian, and J. Hure, *J. chim. phys.*, **52**, 479 (1955).
6. S. Senderoff and G. W. Mellors, *This Journal*, **105**, 224 (1958).
7. E. M. Skobets and N. S. Kavetski, *J. Gen. Chem. (U.S.S.R.)*, **10**, 1858 (1940).
8. Yu. K. Delimarskii, *Zhur. Fiz. Khim. (U.S.S.R.)*, **24**, 875 (1950).
9. Yu. K. Delimarskii and R. S. Khaimovich, *Ukrain. Khim. Zhur.*, **15**, 340 (1949).
10. Yu. K. Delimarskii and A. A. Kolotti, *ibid.*, **16**, 438 (1950); **24**, 146 (1958).
11. A. A. Kolotti, *Zhur. Fiz. Khim.*, **30**, 508 (1956).
12. J. O'M. Bockris, G. J. Hills, D. Inman, and L. Young, *J. Sci. Instruments*, **33**, 438 (1956).

Galvanic Behavior in Fused Electrolytes

II. Discharge of the System Mg/LiCl-KCl-K_2CrO_4/Ni

Sidney M. Selis[1] and Laurence P. McGinnis

Diamond Ordnance Fuze Laboratories, Washington, D. C.

ABSTRACT

The discharge of the system Mg/LiCl-KCl-K_2CrO_4/Ni at current densities of several microamperes per square centimeter yields a potential-time curve with discrete potential plateaus. Two of the plateau potentials are controlled by nickel oxides formed by the oxidation of nickel by chromate ion. Another plateau potential is controlled by the reduction of hydroxide ion at the cathode.

An effect of added silicon dioxide is the stabilization of initial equilibrium potentials. Another effect of silicon dioxide, or other solid acidic oxides, is the diminution of coulombic output. These effects are attributed to a buffering of oxide ion activity and a removal of hydroxide ion from the electrolyte.

In a recent paper (1), the authors considered the galvanic system Mg/LiCl-KCl/Ni. Lithium chloride is a hygroscopic substance and, if not specially purified, it will contain small amounts of water and hydroxide ion even after it has been melted; the impurity content is on the order of 10^{-3} mole/liter (1-3). The proton of this hydroxide ion is the cathodically reducible material in the above system, and at temperatures below 450°C the cathode half-cell reaction is

$$2\,OH^- + 2e^- \rightarrow H_2 + 2\,O^= \qquad [1]$$

It is of interest to consider the effects of an oxidizing agent stronger than hydroxide ion. Potassium chromate is a convenient choice because it has reasonable thermal stability. Furthermore, it is found that magnesium is not attacked rapidly in the molten electrolyte LiCl-KCl-K_2CrO_4. The investigation of the system including chromate ion has been made by measuring potentials of cells at equilibrium and under resistive load. Relative coulombic capacities have also been determined. Data are presented for cells with and without added solid acidic oxides.

Experimental

Materials.—The chemicals used in this study were all of reagent grade and not purified further. As far as possible they were handled in an atmosphere with a relative humidity of 6% or less. The sheet magnesium and nickel, both 99.5% pure, have been described before (1). The cylindrical magnesium electrodes were machined from stock which was 99.97% pure, the impurities being small amounts of calcium and zinc. The nickel cups were prepared by electrodeposition on a chromium-clad mandrel. The nickel was over 99% pure, the major impurities being cobalt, manganese, iron, and possibly carbon. The sintered nickel, used to prepare nickel-nickel oxide electrodes, has been described by Fleischer (4).

[1] Present address: Research Laboratories, General Motors Technical Center, Warren, Mich.

Procedure.—The procedure followed in studying cells with strip or sheet electrodes has been discussed by Jennings (5) and by us (1). The silver-silver chloride glass reference electrode has already been described (1). The cylindrical cell design is shown in Fig. 1 (for clarity, the horizontal dimension has been exaggerated in Fig. 1). Spacing flanges and a nickel lead wire were welded to the top of the cup, the carefully weighed electrolyte components were added, and the cup was positioned in a Pyrex tube envelope. The latter was then placed in a furnace controlled at 300°C. The sidearms accommodating the wires were sealed, the envelope was capped, and the cup was evacuated to about 20 μ Hg for 18 hr so as to remove excess gas from the elec-

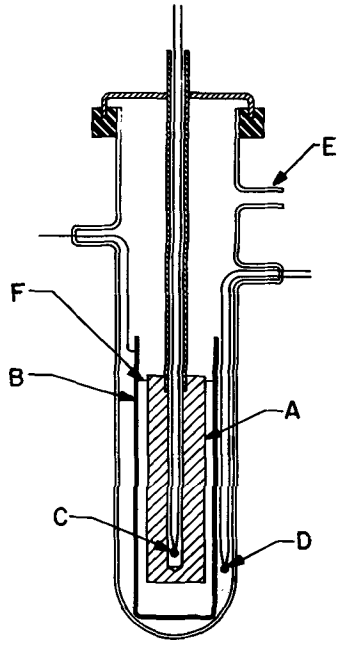

Fig. 1. Diagram of the cylindrical cell. A, magnesium electrode; B, nickel cup cathode; C, measurement thermocouple; D, control thermocouple; E, vacuum sidearm; F, electrolyte level.

trolyte. (This gas is mainly water and hydrogen chloride generated by hydrolytic reactions.) The temperature was then raised to 440°C, thereby melting the salt.

In assembling the anode, a small hole was first drilled nearly through the whole length of a magnesium cylinder of fixed diameter. The upper part of the hole was then enlarged and threaded to accept a threaded brass tube. Through this and the anode could be inserted the measurement thermocouple as distinguished from the control thermocouple located outside the cup (the thermal emf of the magnesium-brass junction was shown to be negligible). The brass tube was then screwed all the way through a threaded hole in the cap shown in the diagram.

After the pre-pumping, the system was opened, and the anode assembly was positioned and properly braced. Using a predetermined reference mark on the brass tube, the anode was lowered to the proper level, and all possible leaks were closed with a wax. The cell was evacuated to 0.5 mm Hg, and final temperature adjustments were made to 440° ± 1°C. Stable initial emf's could be recorded 24 hr later, and the resistive load could then be applied. Available equipment permitted the use of a fixed resistance, and discharge of the cells through this resistance satisfactorily provided the data needed for the discussion presented below.

Voltage-time data were obtained with a recording oscillograph having an input impedance of 9 megohms. Since discharges lasted as long as two days, periodic calibration of the oscillograph was necessary, and the apparatus was calibrated automatically every hour. Additional cell and thermocouple emf measurements were made with a student-type null-balancing potentiometer. Because the changes in cell voltage occurred exclusively at the positive electrode, as will be discussed later, the observed voltages may be considered as electrode potentials referred to the magnesium electrode.

The mixture of electrolyte salts was composed of 55.2 mole % LiCl, 40.0 mole % KCl, 4.83 mole % K_2CrO_4. For each cell, 20.0 ± 0.1 g was used. The amount of added solid oxide was 1 g, which was sufficient to saturate the electrolyte.

The interelectrode distance on the side was 4.4 ± 0.1 mm and was 14.0 ± 0.5 mm at the bottom. After certain runs, the electrolyte level was determined, and from this current densities were estimated for a given potential. Currents were calculated by dividing potential by the external load resistance (it was demonstrated that cell impedances were <1 ohm). For the maximum potential of 1.80-1.81 v, anode and cathode current densities for the 50-ohm load were 552 and 334 $\mu a/cm^2$, respectively; for the 2000-ohm load they were 13.8 and 8.34 $\mu a/cm^2$.

Results and Discussion

A typical potential-time curve for cells discharged across the 2000-ohm load at 440°C is shown in Fig. 2. It will be noted that there is a series of discrete potential plateaus corresponding to 1.80-1.81, 1.76, 1.70, and 1.67 v. A large number of these cells were studied and the plateau potentials were

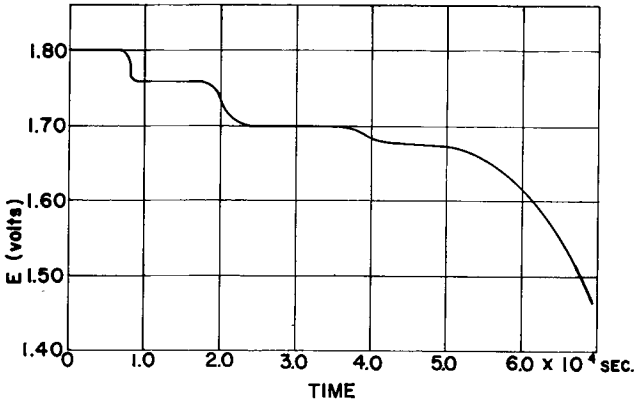

Fig. 2. Potential-time curve for discharge of a cell with SiO_2 through a 2000-ohm resistance.

reproducible to within less than 10 mv. However, as will be shown later, all of the various levels could be obtained dependably only when the electrolyte was buffered by the addition of SiO_2.

Changes in cell potential can be attributed solely to effects at the positive electrode. This was demonstrated by introducing a silver-silver chloride glass electrode in cells with electrodes of sheet magnesium. Measurements of the polarized potentials of these magnesium electrodes, corresponding to the current densities of interest, showed that polarization of magnesium was negligible.

Most of these potentials could be obtained by other means. If, for example, sintered nickel is rubbed with commercially available "black nickel oxide" and its potential is measured against magnesium in the LiCl-KCl electrolyte, the value obtained is 1.76 v. This potential persists for a while and then suddenly falls to 1.70 v. Concurrent with this potential drop, the color of the coating changes from black to green.[2] Green nickel oxide (NiO), rubbed on sintered nickel and measured against magnesium in LiCl-KCl, gives a stable potential of 1.70 v.[3] The 1.67-v potential has been considered before (1); it is obtained with the hydroxide ion-nickel electrode in LiCl-KCl at 440°C.

The following inferences can be made from this work. It is suggested that, during the 24-hr immersion in the electrolyte LiCl-KCl-K_2CrO_4, the nickel becomes coated with successive layers of oxidation products. Next to the metal there is probably a phase which includes nickel (II) ion; upon this, there is nickel in a higher state of oxidation (possibly the dark colored phase already mentioned). To account for the 1.80 v potential there may be nickel in a yet higher state of oxidation, presuming that the chromate ion is a sufficiently strong oxidizing agent so that this phase could be generated. Upon discharge, the potential for the first plateau is determined by the outer layer. As the latter is depleted there is a counter tendency for the higher oxide to be re-formed by the oxidative

[2] Hill, Porter, and Gillespie (6) prepared a "black nickel oxide" *in situ* at 658°C. This was accomplished by bubbling oxygen at unit pressure through a molten Li_2SO_4-K_2SO_4-CaO electrolyte in which was dipped a nickel wire. On decreasing the oxygen pressure, the dark-colored phase behaved in the same way as described above.

[3] The behavior of this electrode has already been measured and discussed (1).

action of the chromate ion. Apparently, however, it is discharged faster than it can be formed. When it eventually disappears, the cell voltage becomes governed by the next lower oxide. Such an explanation is offered for each solid layer. Finally, it is presumed that the cell potential is determined by reaction [1] until the hydroxide ion becomes fairly well depleted.

A few remarks should be made concerning the possible nature of such solid phases. The idea of simple oxides must be discarded. Brewer (7) states in summary that there is only one nickel oxide (nominally NiO with a NaCl-type cubic structure), although its composition range extends to nearly NiO_2. On the other hand, it is a different matter if alkali metal ions can be included in the oxide lattice. Verwey and his co-workers (8, 9) have presented strong evidence that the inclusion of lithium ion in the NiO lattice will induce the formation of Ni(III) ions. Dyer, Borie, and Smith (10) report the preparation of a stable $LiNiO_2$; here the formal valence number is three but the authors suggest that the lattice may actually include a mixture of Ni(II) and Ni(IV) ions. A compound with Ni(IV) ions, i.e., K_2NiO_3, has been characterized by Wahl, Klemm, and Wehrmeyer (11); the evidence is strong for the existence of this phase. But possibly of most pertinence is the observation of Hill, *et al.* already noted above, that a discrete phase producing a higher potential can be formed with oxygen in a fused salt electrolyte.

An explanation has been offered for the observed potential plateaus in terms of different reducible phases at the cathode. Certainly an explanation based on the direct electrochemical reduction of chromate ion would not be reasonable since, in this case, the potential would change continuously rather than in discrete steps. On the other hand, the chromate ion would function in oxidizing the nickel as indicated by reaction [2].[4] Here Cr_2O_3 is shown as a product; it has been identified by x-ray powder diffraction techniques. In any case, the matter is not highly pertinent to the present discussion. Reaction [2] would be followed by the half-cell reaction [3]

$$2xCrO_4^{=}(l) + 3Ni(c) \rightarrow 2xO^{=}(l) + xCr_2O_3(c) + 3NiO_x(c) \quad [2]$$

$$NiO_x(c) + 2(x-y)e^- \rightarrow NiO_y(c) + (x-y)O^{=}(l) \quad [3]$$

For reasons not pertinent to the information presented in this paper, the effects of including silicon dioxide and other solid acidic oxides were studied. One important effect is shown by the data in Table I which presents initial equilibrium voltages for a number of cells with and without SiO_2. The difference in reproducibility of emf is of immediate interest, but the difference of 40 mv in the averages is of doubtful significance.

Another interesting effect was the difference in coulombic delivery with and without added solid acidic oxides. Such comparisons are presented in Fig. 3 and in Table II. Relative coulombic deliveries were obtained to an arbitrary cutoff potential of 0.60 v by measuring the areas under the potential-time curves and dividing these by the external load resistance of 50 ohms. The data presented here were obtained from cells which had an initial potential of 1.80-1.81 v. Table II shows that the coulombic deliveries of cells with added solid oxides is from 38 to 53% of that for cells without added material.

[4] Reactions [2] and [3] have been written in terms of nickel oxide phases. It is to be remembered that these would be stabilized by the presence of alkali metal ions in the oxide lattices.

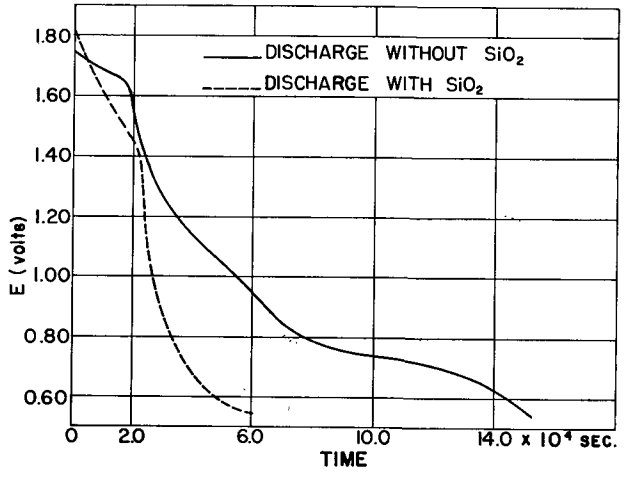

Fig. 3. Effect of added SiO_2 on discharge through a 50-ohm resistance.

To postulate an explanation for these effects of emf stabilization and differences in coulombic delivery, reference is made to reaction [2] in which it is seen that the oxide ion activity is a variable factor. Since it is at least partially governed by originally entrapped water of hygroscopicity, this quantity will depend on the specific batch of lithium chloride used, as well as on room humidity conditions and inadvertent differences in cell preparation. It is possible that, from one cell to the next, variations in oxide ion activity could determine the particular nickel oxide which governs the initial cell emf. But with added silicon dioxide a buffering effect could occur in terms of reaction [4].

$$SiO_2(c) + 2Li^+(l) + O^{=}(l) \rightarrow Li_2SiO_3(s, amorph) \quad [4]$$

Table I. Equilibrium potentials of nickel, with and without silicon dioxide in the melt, referred to magnesium electrode

With SiO_2		Without SiO_2	
Cell	EMF, v	Cell	EMF, v
1	1.82	8	1.70
2	1.80	9	1.80
5	1.82	10	1.85
6	1.80	13	1.80
24	1.82	14	1.77
25	1.81	17	1.79
27	1.81	18	1.76
28	1.80	21	1.72
		22	1.75
Av:	1.81 v	Av:	1.77 v
AD*:	0.010 v	AD:	0.034 v
SD*:	0.013 v	SD:	0.045 v

* AD is average deviation, SD standard deviation from the mean.

Table II. Effect of acidic oxides on the relative coulombic capacities of cells with nickel oxide electrodes

Added material	Capacity (coulombs)
None	3015 ± 115
SiO_2	1145 ± 45
B_2O_3	1585 ± 45
Al_2O_3	1475 ± 55

The presence of solid lithium silicate was confirmed by chemical methods, and an equilibrium involving two solids would fix the oxide ion activity which is the one variable in reaction [2].

The present authors prefer this explanation which involves the concept of different initial potentials being based on different potential-determining couples. An alternative explanation might have been offered in terms of reaction [3] for which potential is conceivably a continuous function of oxide ion activity. However, it is observed, as stated above, that plateau potentials are always reproducible to within less than 0.01 v. If an initial equilibrium potential was less than 1.81 v, then the plateau corresponding to this latter potential was simply never observed.

Regarding the diminution of coulombic delivery due to the addition of solid acidic oxides, a decrease in capacity might be due to the removal of hydroxide ion, and a material such as SiO_2 could provide for this. Hydroxide ion participates in the equilibrium shown in reaction [5],

$$2\,OH^-(l) \rightarrow O^=(l) + H_2O(g) \qquad [5]$$

and the removal of oxide ion by SiO_2 would result in the equilibrium being shifted to the right. In fact, when SiO_2 is added to these electrolytes, the evolution of water is immediately discernible. The authors believe that the added boron oxide or aluminum oxide would behave in a manner analogous to that of silicon dioxide.

Acknowledgment

The authors wish to thank the Dow Chemical Company for the pure magnesium rod used in this work.

Manuscript received March 10, 1959. This paper was prepared for delivery before the Cincinnati Meeting, May 1-5, 1955.

Any discussion of this paper will appear in a Discussion Section to be published in the June 1960 JOURNAL.

REFERENCES

1. S. M. Selis, G. R. B. Elliott, and L. P. McGinnis, *This Journal*, **106**, 134 (1959).
2. H. A. Laitinen, W. S. Ferguson, and R. A. Osteryoung, *ibid.*, **104**, 516 (1957).
3. W. J. Burkhard and J. D. Corbett, *J. Am. Chem. Soc.*, **79**, 6361 (1957).
4. A. Fleischer, *J. (and Trans.) Electrochem. Soc.*, **94**, 289 (1948).
5. C. W. Jennings, *This Journal*, **103**, 531 (1956).
6. D. G. Hill, B. Porter, and A. S. Gillespie, Jr., *ibid.*, **105**, 408 (1958).
7. L. Brewer, *Chem. Rev.*, **52**, 1 (1953).
8. E. J. W. Verwey, *Bull. soc. chim. France*, **1949**, Mises au point D122.
9. E. J. W. Verwey, P. W. Haaijman, F. C. Romeijn, and G. W. van Oosterhout, *Philips Res. Repts.*, **5**, 173 (1950).
10. L. D. Dyer, B. S. Borie, Jr., and G. P. Smith, *J. Am. Chem. Soc.*, **76**, 1499 (1954).
11. K. Wahl, W. Klemm, and G. Wehrmeyer, *Z. anorg. u. allgem. Chem.*, **285**, 322 (1956).

Technical Notes

The Diffusion of Corrosion Hydrogen in Aluminum Alloys

W. E. Tragert

Research Laboratory, General Electric Company, Schenectady, New York

Essentially pure aluminum and many aluminum alloys corrode catastrophically in pressurized water at temperatures above say 275°C. It has been proposed (1) that the resistance of an aluminum—1% nickel alloy (X8001) to such oxidation is due to the presence in the surface of second phase Al_3Ni particles which function as cathodic sites for the evolution of corrosion product hydrogen. Such hydrogen is considered responsible for the usual accelerated oxidation by a mechanism of diffusion through the surface oxide film, discharge at internal pores or grain boundaries in the metal, and resultant blistering of the aluminum and disruption of the otherwise continuous surface oxide film. The local cathodic discharge of hydrogen at the surface thus inhibits entry of hydrogen into the aluminum and prevents catastrophic failure. The present experiment was devised to test the above described hypothesis.

Test samples were aluminum cans, 9.5 in. by 1.44 in. diameter with a wall thickness of 0.030 in. These were filled about 1/3 with distilled water and sealed with solid end plugs which were inert arc welded in place. A small nipple on each plug, pierced with an 0.030-in. hole, served as a vent during welding and was subsequently welded shut. The cans and end plugs were of two alloy compositions, Alloy 1245 (99.45% Al minimum) and Alloy X8001, mentioned above.

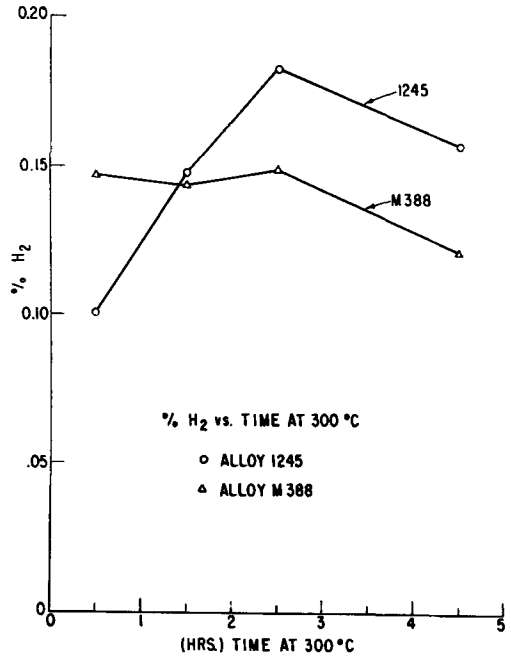

Fig. 1. Hydrogen content of the autoclave atmosphere as a function of time at 300°C.

The experimental procedure was to place a sealed aluminum alloy can in a stainless steel autoclave of internal dimensions 12 in. by 3 in. diameter, and then evacuate and purge the sealed autoclave with pure helium. The autoclave was resistance heated and the water vapor pressure within the aluminum can (inferred from temperature measurements) was compensated by valving helium into the autoclave during heating. When the system had reached 300°C, the atmosphere of the autoclave was sampled periodically, the samples being taken into evacuated 100 cc flasks. The flask contents were analyzed mass spectrographically for water and hydrogen. No water was detected in the several experiments, and data for hydrogen are presented graphically in Fig. 1 as a percentage of the total gas sample collected. The individual values are significant analytically to within 2%. That the proportion of hydrogen appears to diminish with time in these experiments can be attributed to several factors. First, the initial reaction of both aluminum alloys is quite rapid, the rate more or less diminishing as filming occurs; second, the oxide film is thinner and presumably more permeable at the outset than later in the experiment; third, hydrogen is lost from the pressure system by virtue of the samples taken and by diffusive loss through the heated walls of the autoclave.

A blank sample was run on the heated autoclave system and yielded no detectable hydrogen. A second blank was run on the system containing a can of Alloy 1245 that had been filled only with helium and sealed according to the procedure outlined above. No hydrogen was detected prior to heating, during heating, or at 300°C. At the conclusion of each of the corrosion gas sampling experiments, the can was cooled under supporting helium pressure, removed from the autoclave, and cut open. Unfortunately, no measure was made of the residual hydrogen gas pressure in the sample cans. Upon visual examination, there was noted superficial oxidation of the internal surfaces of the X8001 can and extensive oxidation of the 1245 can, although in the latter case one might have expected greater attack than was observed. It has been noted (2) that the transport of corrosion hydrogen appears from these data to be higher than would be expected from published diffusion data (3). It should be further noted, however, that the literature values for Q and D_o are unusually high and may reflect experimental difficulties as judged from the large scatter in the individual diffusion data points.

The present data and observations indicate that corrosion hydrogen diffuses through both Alloy 1245 and X8001. It must be considered, however, that the experimental configuration employed here is not typical of corroding systems; that is, corrosion hydrogen is not usually contained within the material under test. Consequently, it cannot be concluded that under normal conditions of corrosion, where the ambient hydrogen pressure may be small, hydrogen diffuses into either of these alloys to any great extent, although such may in fact be the case. The significance of these data is that, under conditions of hydrogen permeation, Alloy X8001 remained relatively uncorroded while Alloy 1245 was extensively oxidized. According to the galvanic protection hypothesis, the proton flux should have produced accelerated oxidation of both alloys in these tests.

It thus appears that rather than functioning as local cathodes, the second phase particles in Alloy X8001 serve, on oxidation, to alter the nature of the corrosion product film and to render it less permeable to the diffusing reactants. Although the concentration of hydrogen in the oxide film and basis metal may exert an influence on the reaction kinetics, this effect must be considered of secondary importance relative to the rate-controlling mechanism.

Manuscript received April 13, 1959.

Any discussion of this paper will appear in a Discussion Section to be published in the June 1960 JOURNAL.

REFERENCES

1. J. E. Draley and W. E. Ruther, *Corrosion*, **12**, 480 (1956).
2. G. J. Biefer, A.E.C.L., Chalk River, Ont., Canada, Private Communication.
3. C. E. Ransley and D. E. J. Talbot, *Zeit. Metallkunde*, **46**, 328 (1955).

On the Crystallization of Simple Rhombohedral Boron from Platinum

F. Hubbard Horn

Research Laboratory, General Electric Company, Schenectady, New York

Since the report on the preparation of a simple rhombohedral (red) allotrope of boron by pyrolysis of a boron halide or hydride on a filament below a temperature of about 1200°C (1), it has seemed of interest to determine whether this allotrope can be obtained by crystallization from a melt. Requisite to such a process is a solution of boron from which boron and not boron compounds will crystallize below about 1200°C. The boron-platinum system is known to have a low melting eutectic. The remainder of the phase diagram apparently has not been published. A compound PtB or Pt_3B_2 has been reported (2).

Boron-Platinum Alloy System

An attempt to investigate the solidus-liquidus by a normal thermal-arrest procedure was not successful. However, the eutectic was determined by thermal arrest. The crucible was hot-pressed boron nitride which is not appreciably attacked by molten boron (3). The thermocouple was calibrated at the freezing temperature for silver. The eutectic temperature was determined as 825° ± 5°C. The eutectic exists over the composition range explored, from 5 to 87.5 at. % boron. The alloys were prepared from commercial grade platinum and granular boron of 99.8% purity.

The liquidus-solidus for boron-rich alloys was determined by immersing a small boron nitride probe into a melt of predetermined composition and noting the lowest temperature at which the probe could be removed from the melt without any solid (boron) adhering to the probe. In order to assure that the boron freezing on the probe was the first boron to freeze anywhere in the system, it was necessary to approach the liquidus-solidus temperature from a temperature well above it. Once boron had frozen to the probe, the temperature that was just sufficient to melt it could also be determined. With care, it was found possible to reproduce the conditions to about ±5°C. The temperatures measured are probably somewhat higher than true equilibrium temperatures since some additional heat must be supplied to compensate for losses such as those along the probe. Temperature was measured by optical pyrometer sighted on the clean melt surface near the center of the crucible. No correction for emissivity has been made since a calibration of the temperatures obtained by optical pyrometer against those from the embedded thermocouple agreed within 10°C over the temperature range 1200°-1400°C.

Data obtained for the liquidus-solidus line for the boron-platinum alloys investigated are plotted in Fig. 1. A curve through the points indicates a eutectic composition of about 40 at. % boron in platinum. There is no suggestion of compound formation for compositions between the eutectic and pure boron.

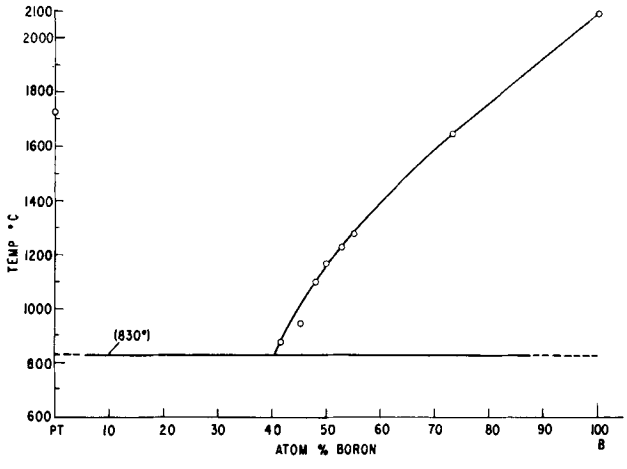

Fig. 1. Phase diagram of boron-platinum system

Attempts to use the probe method to complete the solidus-liquidus line were unsuccessful for alloys richer in platinum than the eutectic composition. The material freezing would not adhere to a boron nitride or graphite probe and probes of Ni, Fe, W, Mo, and Ta were attacked by the alloys.

Crystallization of Simple Rhombohedral (red) Boron

The simple rhombohedral form of boron is stable for a long period of time at 1200°C. It is seen from Fig. 1 that an alloy of about 50 at. % boron in platinum is molten at this temperature. Thus, from such an alloy cooled slowly to the eutectic temperature, boron will crystallize. If the simple rhombohedral form is stable at these temperatures, the boron crystallizing may be of this structure.

Typically, a 50-50 at. % alloy of boron and platinum was prepared from commercial platinum and zone-refined boron. The first melt was allowed to solidify and the surface and sides of the ingot ground away in order to remove a slag found frequently on initial melts. The alloy was transferred to a crucible of boron nitride having a conically tapered bottom. After melting the alloy in vacuum, the crucible was lowered gradually through the high-frequency heating coils. The rate of lowering has been about 0.04 mm/min. As the melt approaches the eutectic temperature it is allowed to freeze suddenly.

A cut and polished section through such a solidified melt shows crystallization of black (boron) in the bottom tip; moreover, regions of translucent red crystals are seen embedded in the remainder of the

section. The red crystals are highly reflecting and may be easily missed in the matrix if with vertical illumination the incident light is not polarized. The red crystals may be recovered by crushing the brittle platinum-boron matrix. They may be separated from the dust of the matrix by performing a gravity separation. The red crystals and some black solids float on bromoform. This fraction is skimmed and the solids allowed to settle by adding acetone. The settled material is rinsed with acetone and dried. Red crystals are readily separated visually from black solids using a microscope.

Powder x-ray diffraction analysis identifies the red crystals as entirely simple rhombohedral boron (4).

Crystals that have been recovered to date are very small, the largest being tenths of millimeters. Thus no attempt has been made to characterize their properties. There is no foreseen reason why larger crystals may not be grown.

It is of interest that the simple rhombohedral boron crystallized is translucent red; this suggests rather high purity. Either the solubility of impurities present must be very small at the low temperatures of formation or some purification may take place during the freezing of the boron in the tip of the ingot prior to crystallization of the simple structure. By x-ray diffraction the identification of the black material that separates with the red crystals or the black material crystallizing in the tip of the ingot is not positive; there is, however, some similarity to the pattern for the complex rhombohedral form of boron. Preliminary results suggest there may be a number of intermediate structures between the complex and simple rhombohedral forms.

Manuscript received May 15, 1959. This paper was prepared for delivery before the Philadelphia Meeting, May 3-7, 1959.

Any discussion of this paper will appear in a Discussion Section to be published in the June 1960 JOURNAL.

REFERENCES

1. L. V. McCarty, J. S. Kasper, F. H. Horn, B. F. Decker, and A. E. Newkirk, *J. Am. Chem. Soc.*, **80**, 2592 (1958).
2. J. H. Puddery and A. J. E. Welch, *Nature*, **167**, 362 (1951).
3. F. H. Horn, *J. Appl. Phys.*, Letter to Editor, in press.
4. B. F. Decker and J. S. Kasper, *Acta Crystallographica*, in press.

Technical Review

Report of the Chlor-Alkali Committee of the Industrial Electrolytic Division for the Year 1958

Clifford A. Hampel

Skokie, Illinois

Nelson J. Ehlers

Columbia-Southern Chemical Corporation, Pittsburgh, Pennsylvania

Chlorine-Caustic

Production and Sales

Consistent with the general chemical sales decline, U. S. chlorine production in 1958 decreased 8.8% from 1957 and was about 3,600,000 tons. For the first time in twelve years, the annual production was lower than that of the previous year. U. S. capacity at the end of 1958 is estimated at near 12,360 TPD, which means the industry operated at about 80% of capacity during the year. Apparent per capita chlorine consumption was 41.2 lb as compared to 22.2 lb in 1948 and 6.7 lb in 1938.

Concerning production in 1959, some sources predict a return to the 1957 production of about 3,950,000 tons and, of course, it is hoped that subsequent annual production tonnages will follow the traditional chlorine growth curve.

Chlorine production in Canada was 268,000 tons in 1958 as compared to 226,000 tons in 1957. Indications are that about 275,000 tons will be produced in 1959.

Caustic soda production for 1958 was at a 4,055,000-ton level, which meant a 6.7% decrease from 1957. Apparent per capita consumption was 44.2 lb compared to 29.9 in 1948 and 11.2 in 1938. Indications are that 1200 TPD lime soda caustic was produced as an average for the first eight months of 1958. This marks an increase for this period of about 260 TPD over the 1957 average and represents about 10.8% of the total caustic production in 1958 as compared to 7.9% in 1957. The Bureau of Census, after August 31, 1958, is not separating lime soda and electrolytic caustic production figures.

In general, the industry was more in balance between chlorine and caustic than in 1957. Again in

Table I. Sources of chlorine

	1957		1958 (preliminary)	
	Tons	%	Tons	%
Cl_2 equiv. of NaOH	3,548,579	89.9	3,234,813	89.9
Cl_2 equiv. of KOH	47,714	1.2	43,717	1.2
Cl_2 equiv. of Na	204,958	5.2	170,002	4.7
Cl_2 equiv. (other sources)	146,417	3.7*	151,182	4.2*
Cl_2 total gas produced	3,947,668	100.0	3,599,714	100.0

* By difference.

1958 soda ash was used to produce lime soda caustic in several plants in the U. S., and Dow Chemical Company, Freeport, Texas, continued to produce soda ash from electrolytic caustic.

Approximately 75.8% of chlorine capacity in 1958 was in diaphragm cells, 18.4% in mercury cells, 5.1% in sodium cells, and 0.7% in nonelectrolytic processes. The estimated sources of chlorine comparing 1958 with 1957 appear in Table I.

New Plants and Expansions

Approximately 640 TPD new U. S. chlorine capacity is estimated to have come on line in the U. S. in 1958, as follows: Columbia-Southern Chemical Corporation, Natrium, W. Va., 160 TPD (Uhde mercury cell); Dow Chemical Company, Plaquemine, La., 300 TPD (Dow bipolar cell); E. I. du Pont de Nemours & Company, Memphis, Tenn., 100 TPD (Downs sodium cell); and Weyerhaeuser Timber Company, Longview, Wash., 80 TPD (DeNora mercury cells).

The Arkansas Louisiana Chemical Corporation started operating the chlorine-caustic plant at Pine Bluff, which is rated at 75 TPD, in 1958, after Diamond Alkali Company terminated its lease.

Among the new plants or expansions to be completed in 1959 are: Diamond Alkali Company, Deer Park, Texas, 200 TPD (DeNora mercury cells); Jefferson Chemical Company, Port Neches, Texas, 150 TPD (Hooker S-3B cells); Stauffer Chemical Company, Niagara Falls, N. Y., 30 TPD (expand and modernize); and Wyandotte Chemical Corporation, Geismar, La., 300 TPD (Diamond diaphragm cell). Diamond Alkali Company announced early in 1959 plans to modernize chlorine cell facilities at Painesville, Ohio.

A listing of U. S. chlorine plants and estimated capacity appears in the March 7, 1959 issue of *Chemical Week*.

In Canada, the estimate of chlorine capacity by the end of 1958 was about 850 TPD. In 1958, among the new plants and expansions were: Shawinigan Chemical Company, Shawinigan Falls, Quebec, 50 TPD (mercury cell); and Western Chemicals Company, du Vernay, Alberta, 20 TPD (diaphragm cell). Dow Chemical Company in Canada has announced an integrated chemical plant at Fort Saskatchewan, Alberta. The chlorine-caustic unit will be built first and other units are to follow. Western Chemicals has announced an additional 20 TPD capacity scheduled to come on the line late in 1959. A chlorine plant for the St. John, New Brunswick area has been announced by K. C. Irving.

Table II. Chlorine—caustic soda end-use pattern

Chlorine*	%	Caustic Soda†	%
Miscellaneous chemicals	83.0	Miscellaneous chemicals	30.6
Pulp and paper	13.0	Rayon and film	16.9
Others	4.0	Pulp and paper	8.3
		Metallurgical	7.5
		Export	6.8
		Petroleum refining	6.3
		Lye and cleansers	4.5
		Textiles	3.7
		Soap	1.6
		Others	13.8
Total	100.0	Total	100.0

* Source, *Chemical Week*, March 7, 1959, p. 116 (for more detailed breakdown, see "Chemical Week," May 26, 1956.
† Source, *Chemical Week*, Jan. 18, 1958, p. 76.

Markets and End-Use Patterns

There appears to be no significant change in the end-use pattern of chlorine and caustic soda during 1958. In the production of ethylene oxide, the oxidation process continues to increase in importance relative to the chlorination process. The reduction in military requirements for titanium adversely affected the demand for chlorine. In 1958, the use of chlorine increased in the pulp and paper, and water and sewage treatment areas. The decline in general business levels reduced the other chlorine uses. Latest end-use patterns appearing in the literature are shown in Table II.

Technical Developments

Some chlorine manufacturers are now using or installing germanium and silicon rectifiers for conversion of a-c to d-c power. Diamond Alkali Company, Deer Park, Texas, is installing germanium rectifiers. Columbia-Southern Chemical Corporation, Natrium, W. Va., has used germanium rectifiers commercially for chlorine production since early 1958. Hooker Chemical Corporation has installed silicon rectifiers at its Niagara Falls, N. Y., plant.

Hooker Chemical Corporation and Diamond Alkali Company continue to offer licenses for their processes to recover blow-off chlorine. The Hooker process calls for dilute chlorine gas to be absorbed in water destined for direct-contact cooling of hot cell gas. In the Diamond process, the gas stream containing chlorine to be recovered contacts carbon tetrachloride in a packed tower under pressure. Further stripping and cooling gives liquid chlorine.

A patent by H. H. Heller (U.S. 2,836,551) discloses the advantages of forcing brine through a mercury type cell at high velocities. A German patent (1,014,080) was issued to Dow Chemical Company for a "slot" type mercury cell.

Platinized titanium anodes were publicized by Imperial Chemical Industries, Ltd., for chlorine, chlorate, and other production uses.[1]

1 "Bright Future for ICI's Newly Developed Electrodes," *Chemical Age*, Jan. 3, 1959, and "Titanium Anodes," *Chemical Trade Journal*, Jan. 2, 1959.

Monsanto Chemical Co. is operating a cell designed by DeNora for recovery of chlorine from hydrochloric acid. The cell is believed to be economically feasible for many situations.

Among articles of interest appearing recently were: "For Cell Operators: What Price Efficiency?" *Chemical Week,* April 19, 1958, p.41-48; A debatable analysis on caustic soda was published in *Chemical Week,* Jan. 18, 1958, p. 69-76, entitled "Caustic—Plenty for Now and Future"; *Chemische Industrie,* June 1958, p. 309, cited research by VEB Farbenfabrik Wolfen to manufacture chlorine by nonelectrolytic means; "Too Much Chlorine," *Barrons,* March 24, 1958, p. 17-19; and "Thermal Data for Chlorine and HCl," *Chemical Engineering,* Feb. 10, 1958, p. 144-146.

Soda Ash

For the last two years, total production of soda ash has decreased. Production in 1958 was 4,955,200 tons, which was 7.1% below 1957. The apparent per capita consumption at 55.73 lb for 1958 was the lowest since 1941. Total domestic consumption in tons per year reached the all-time high in 1955 of 5,444,560 tons and has been on a decline since then. Natural soda ash production for both 1958 and 1957 accounted for 12.6-12.7% of the total soda ash produced. Total capacity of the soda ash plants in the U. S. is near 7,000,000 tons; therefore, it may be concluded that the industry operated at near 70% of capacity.

During 1958, Olin Mathieson Chemical Corporation completed facilities at its Saltville, Va., plant for production of dense ash. Columbia-Southern Chemical Corporation began production of soda ash and sodium sesquicarbonate at a new plant at Bartlett, Calif. The plant reportedly triples the output of an older unit there, now being scrapped. Food Machinery & Chemical Corporation has announced that a major expansion of soda ash production facilities at its Wyoming plant will be completed during the first half of 1959. Solvay Process Division of Allied Chemical Corporation is reported to be doubling dense soda ash capacity at its Baton Rouge, La., plant. Total ash capacity remains the same.

An estimated capacity for U. S. plants appears in *Chemical Week,* May 3, 1958, p. 72. The latest end-use pattern for soda ash appearing in the literature is shown in Table III.

Table III. Soda ash end-use pattern (estimate)*

	%
Chemicals	37
Glass	30
Nonferrous metal refining	10
Pulp and paper	7
Cleansers	3
Water softeners	2
Soap	1
Miscellaneous	10
Total	100

* Source, *Chemical Week,* May 3, 1958, p. 71.

Miscellaneous Chemicals

Potassium hydroxide.—Production of KOH (88-92%) decreased about 8.3%, from 83,898 tons in 1957 to a preliminary figure of 76,870 tons in 1958. Most of the newer caustic potash expansions have been by the mercury cell process. Caustic potash is making gains in the detergent field as a result of greater acceptance of some of the newer types of liquid detergents.

Chlorates.—American Potash & Chemical Corporation started operation of its sodium chlorate plant of 15,000 TPY capacity at Aberdeen, Miss., in early 1959. Reported for American Potash is a company capacity of 45,000 TPY. Hooker Chemical Corporation expanded sodium chlorate production at Columbus, Miss. Standard Chemical Limited announced the start of construction of a plant to produce sodium chlorate at Beauharnois, Que. During 1958, Electric Reduction Company of Canada claimed to be the world's largest producer of sodium chlorate as the result of expansion that doubled capacity of the firm's Buckingham, Que., plant. It has been estimated that U. S. sodium chlorate capacity will exceed 100,000 TPY in 1959 when announced new plants and expansions are on line. Production increased from 59,142 tons in 1957 to 67,247 tons in 1958, about 13.7%.

Perchlorates.—The importance of perchlorates in the production of solid fuels for missiles is highlighted by the announcements of additional plants for their preparation. HEF, Inc., jointly owned by Foote Mineral and Hooker Chemical, began construction on a 4,000,000 lb/yr ammonium perchlorate plant at Columbus, Miss. Pennsalt Chemicals Corporation announced a plant for production of ammonium perchlorate at Portland, Ore.

Two papers on the preparation and use of lead dioxide anodes in the electrolytic conversion of sodium chlorate to sodium perchlorate were published in this JOURNAL by Grigger, Miller, and Loomis of Pennsalt Chemicals Corporation and Schumacher, Stern, and Graham of American Potash & Chemical Corporation. Lead dioxide deposited on tantalum was found to be a suitable substitute for platinum in perchlorate cells.

Miscellaneous Metals

Aluminum.—Electrolysis processes are vital to the production of many of the metals, both old and new, used in this country. The aluminum industry, which consumes 5 to 6% of the total electricity generated in the U. S., continues to grow. At the end of 1957, the aluminum ingot capacity was some 1,842,000 TPY located in 18 plants of 4 companies. By 1960, this will rise to 2,604,000 tons in 23 plants of 6 companies. In Canada, the corresponding tonnages are 821,000 tons at the end of 1957 and 956,000 tons in 1960.

Magnesium.—Consumption of primary magnesium in the U. S. is expected to total about 45,000 tons in 1959. Consumption of scrap and secondary will account for another 10,000 tons or so. Consumption of this order is not a record for peacetime but does represent a resumption of the upward trend

Table IV. 1958 Sodium end-use pattern (estimated)*

	%
Tetraethyl lead	71.0
Sodium cyanide	11.2
Sodium peroxide	6.9
Metal reduction	4.7
Miscellaneous	6.2
Total	100.0

* Source, *Chemical Week*, Jan. 24, 1959, p. 78.

following the recent recession. Production in 1959 will be about 30,000 tons because of a large inventory carry-over. A large inventory was built up in 1957 when Dow Chemical Company was uncertain about the disposition of the then government-owned plant at Velasco, Texas (the plant eventually was sold to Dow, the higher of two bidders). Magnesium uses are roughly 40% structural, 60% nonstructural. Applications are divided about 50-50 between commercial and military.

Sodium.—Capacity for sodium production was reported to be 153,000 TPY as of Jan. 1, 1958. Production in 1958 was 110,298 tons as compared to 132,977 tons in 1957, a decrease of 17%. The Woodstock, Tenn., plant of du Pont for the production of sodium went on the line early in 1959. Capacity was reported as 45,000,000 lb/yr. This new installation, plus recent expansions of other producers, will increase U. S. capacity to about 400,000,000 lb/yr. The general reduction in sodium use since the peak in 1956 is attributed to loss of the fatty alcohol market and the drastic reduction in titanium metal use. The largest use of sodium continues to be in production of tetraethyl lead, and this use is increasing a small percentage each year.

The present status of the sodium industry is given in *Chemical Week*, Jan. 24, 1959, p. 76. The estimated sodium end-use pattern is given in Table IV.

Titanium.—Production of titanium sponge metal in 1958 at 4585 tons was about 27% of the 1957 output; however, the consumption of sponge metal and production and consumption of titanium ingot were, respectively, about one-half that of 1957. Total sponge held by General Services Administration at the end of 1958 was 22,400 tons.

There has been a continued increase in consumption of sponge since early 1958, and by the end of 1958 it was at least 50% of the peak rate in the brightest days of the industry. Use of titanium for its corrosion-resistant properties is increasing.

Zirconium.—The major U.S. production of zirconium metal is for the Atomic Energy Commission program. Carborundum Metals Corporation, Mallory-Sharon Metals Company, and Columbia-National Corporation are the three AEC sponge suppliers. These three producers have contracted to supply about 2,200,000 lb/yr of hafnium-free zirconium sponge.

Mallory-Sharon and Columbia-National began operations in 1958. Carborundum and Columbia-National processes involve the magnesium reduction of zirconium tetrachloride, while Mallory-Sharon uses sodium reduction. Wah Chang Corporation, Albany, Ore., has shut down its zirconium facilities and is now converting hafnium oxide to hafnium metal for the Atomic Energy Commission.

No expansion of zirconium facilities is planned at the present time.

Lithium.—Lithium, made by the electrolysis of fused lithium chloride admixed with potassium chloride, is finding increased use in such fields as the preparation of boron fuels. Olin Mathieson Chemical Corporation has installed electrolytic cells for lithium production at its Model City, N. Y., boron fuel plant, and Foote Mineral Company announced expansion of lithium production.

Manganese.—The use of manganese ore for the production of the metal in the U. S. in 1958 was over 10,000 tons. Production capacity is located in the plants of Foote Mineral Company, Knoxville, and Union Carbide Metals Company, Marietta, Ohio. The electrolytic process is the only one producing pure metal.

Chromium.—High-purity chromium metal is made by electrolysis of ammonium chromium sulfate solution in the Union Carbide Metals Company Marietta plant.

Uranium.—Most uranium metal is derived from the reduction of uranium tetrafluoride with magnesium. While the demand for uranium depends on the scope of the nuclear power plant development and the amount of uranium oxide used in fuel elements, estimates of 50,000-100,000 TPY in 1970 or 1975 have been made. Not only new metal requires magnesium for preparation, but magnesium is also used in reprocessing spent fuel elements.

Beryllium.—Pure beryllium metal is made in the U. S. from the reduction of beryllium fluoride with magnesium. New plants constructed by The Beryllium Corporation at Hazelton, Pa., and The Brush Beryllium Corporation at Elmore, Ohio, produce beryllium metal for nuclear and other applications. Each of these firms had a contract for annual delivery of 100,000 lb each of beryllium ingot to the Atomic Energy Commission, but the contracts were revised and the new production level set at 37,500 lb of ingot per year for each company.

Tantalum and columbium.—Tantalum production was estimated to be 225,000 lb in 1958 and is expected to reach 300,000 lb in 1959. Most of the metal is obtained either by electrolysis of fused potassium fluotantalate or by sodium reduction of this and other tantalum compounds. Columbium, the sister metal of tantalum, reached a production in 1958 estimated at 50,000 lb. While it is made chiefly by reaction between columbium carbide and columbium oxide, it can be made by the process used for tantalum, i.e., sodium reduction.

Stauffer Chemical Company announced construction of a $300,000 semiworks plant to make tantalum and columbium pentachlorides at its Richmond, Calif., research laboratories. National Research Corporation, Mallory-Sharon Metals Company, and Union Carbide Metals Company all had their processes for producing tantalum and/or columbium de-

scribed in articles published in 1958. Each used some form of sodium reduction of metal compounds to produce the metals. Recently, Haynes Stellite Company exhibited the largest tantalum sheet ever produced, the size being 28 x 60 x 0.030 in. The availability of large sheet should increase the use of tantalum in chemical equipment. Other producers of tantalum and/or columbium include du Pont, Fansteel Metallurgical Corporation, Wah Chang Corporation, Kawecki Chemical Company, Kennametal, Inc., and Molybdenum Corporation of America.

Manuscript received June 8, 1959. This paper was prepared for delivery before the Philadelphia Meeting, May 3-7, 1959.

Any discussion of this paper will appear in a Discussion Section to be published in the June 1960 JOURNAL.

Brief Communication

Action of Alkali on Caustic Cell Slimes

S. Wawzonek and P. D. Klimstra

Department of Chemistry, State University of Iowa, Iowa City, Iowa

Used graphite anodes have been the only source of material from which the caustic color compound has been isolated (1, 2). The report (3) that anode graphite slimes from chlorine-alkali cells contained 0.3-0.5% chloride suggested a study of various slimes from diaphragm and mercury cells to determine whether these could serve as a source of the caustic color compound.

Three samples of slimes have been treated with 50% sodium hydroxide at 100° for varying periods of time and the colors produced examined.

A sample of graphite particles removed from the bottom of one of the used anode plates after it had been used for the production of chlorine and caustic soda for approximately six months in a de Nora mercury cell gave the typical bluish-purple color associated with the caustic color compound.

A second sample consisting of graphite particles which were separated from the depleted brine stream after it had flown through the mercury cells gave under similar treatment a cherry red coloration. The possibility that this color was caused by colloidal ferric hydroxide was eliminated by the inability to discharge the color with sodium sulfide solution. This color, however, did not change to the blue on further heating with alkali.

A third sample consisting of the anode slimes from a diaphragm Tucker Windecker Cell operating with untreated anodes gave no color with 50% caustic.

Results obtained indicated that the caustic color compound or its precursor is produced in the mercury cell in the anode compartment but is effectively screened out by the circulating mercury which picks up the sodium in the mercury cell electrolyzer and subsequently releases the sodium as caustic soda in the denuder.

The absence of the caustic color compound in the anode slimes from a diaphragm cell suggests that most of the precursor may have been extracted by the caustic soda.

Acknowledgment

The authors wish to thank C. C. Silsby, Jr., of the Diamond Alkali Company, for the samples which were obtained from the Painesville and Muscle Shoals plants, and for his helpful discussion and advice.

Manuscript received June 12, 1959.

Any discussion of this paper will appear in a Discussion Section to be published in the June 1960 JOURNAL.

REFERENCES

1. H. H. Heller, *Trans. Electrochem. Soc.*, **87**, 501 (1945).
2. S. Wawzonek and D. S. P. Eftax, *This Journal*, **104**, 494 (1957).
3. S. Dahlerus and G. Wranglen, *Svensk Kem. Tidskr.*, **68**, 387 (1956).

Errata

In the September 1959 issue of the *Journal* in the paper by Barlane R. Eichbaum "The Dielectric Behavior of Solids Embedded in a Homogeneous Medium," in Fig. 1, 4, 6, 8, and 10, the tan δ graphs were omitted. Below are the dielectric constant and tan δ curves as they should have been shown.

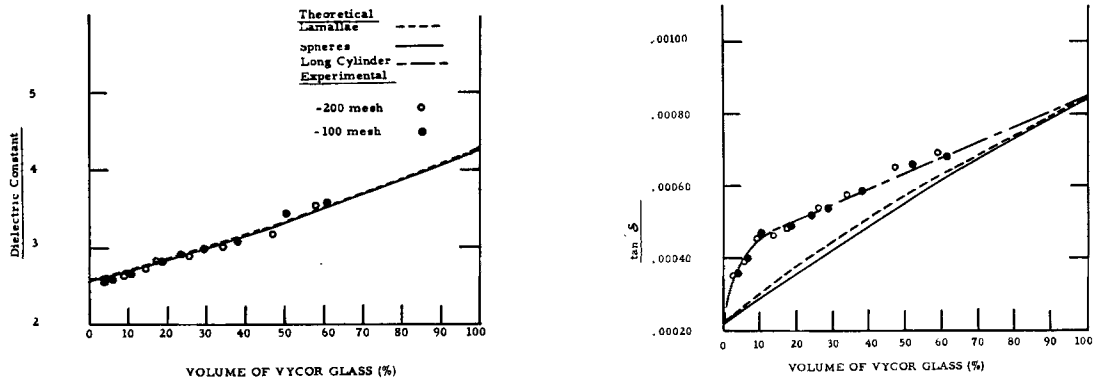

Fig. 1. Volume of vycor glass and polystyrene vs. dielectric constant and tan δ

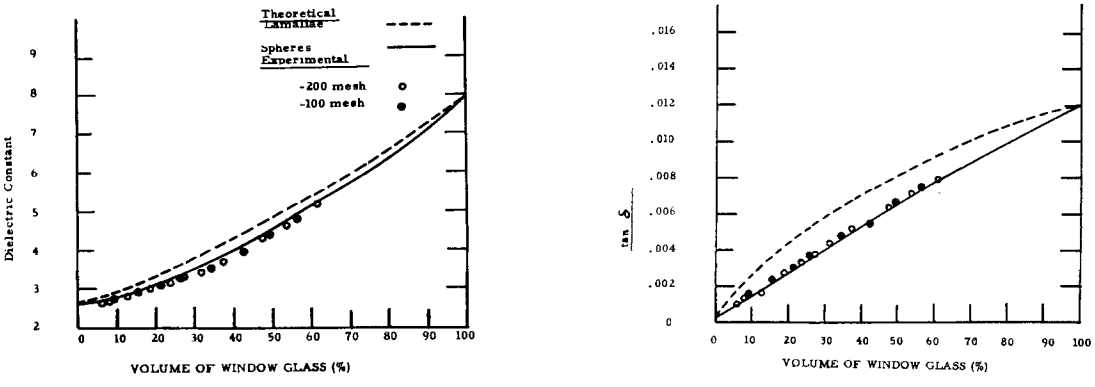

Fig. 4. Volume of window glass in polystyrene vs. dielectric constant and tan δ

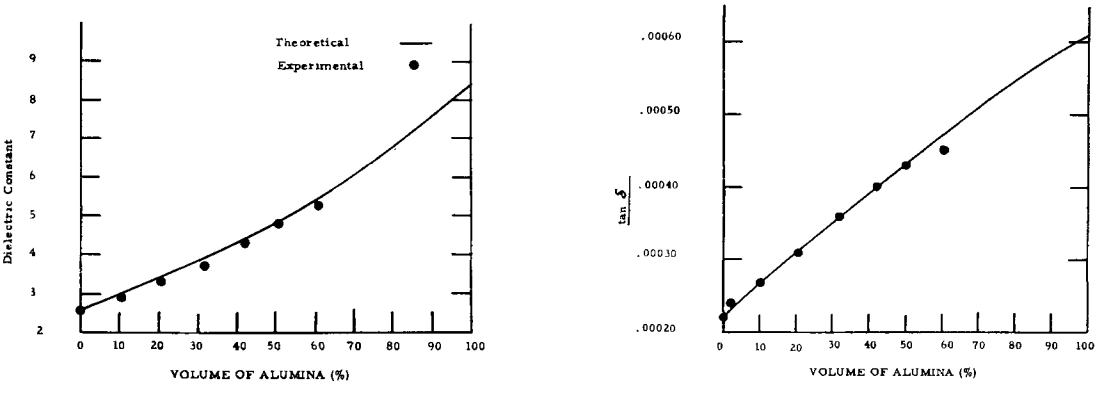

Fig. 6. Volume of alumina in polystyrene vs. dielectric constant and tan δ

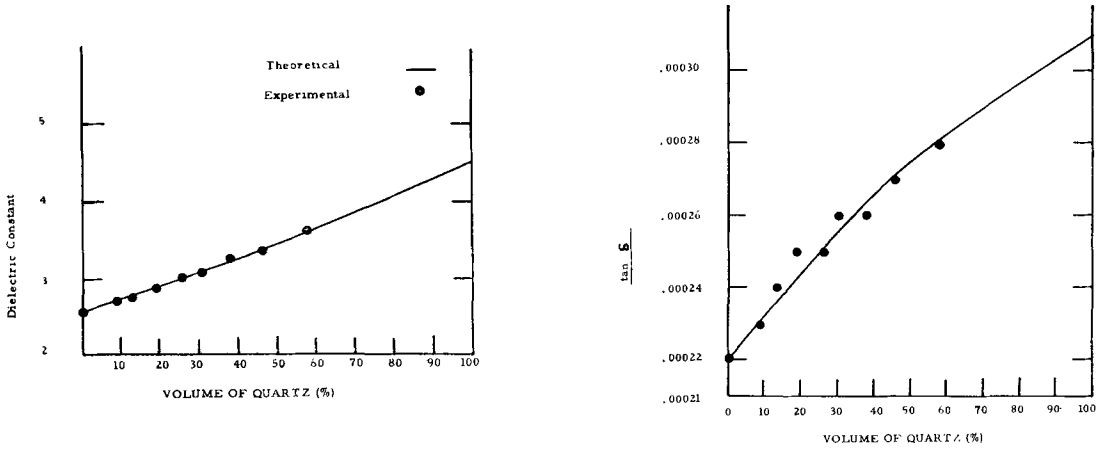

Fig. 8. Volume of quartz in polystyrene vs. dielectric constant and tan δ

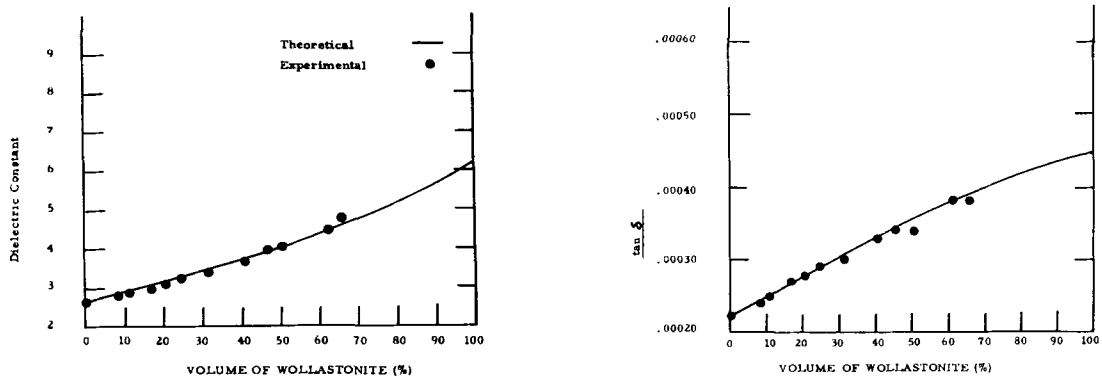

Fig. 10. Volume of wollastonite in polystyrene vs. dielectric constant and tan δ

In the paper by M. J. Pryor, "The Significance of the Flade Potential," which appeared on pp. 557-562 of the July 1959 JOURNAL, Eq. [9] on p. 561 is stated incorrectly. It should read:

$$\tfrac{1}{2}\,O_2 \longrightarrow O'' + \boxed{+\\+} \qquad [9]$$

crystal lattice — bound positive hole

The Anodic Oxidation of Cadmium

II. Electrical Properties of the Film

Phyllis E. Lake and E. J. Casey

Defence Research Chemical Laboratory, Defence Research Board, Ottawa, Ontario, Canada

ABSTRACT

Cadmium electrodes under anodic oxidation in hydroxide and carbonate electrolytes have been examined by analysis of the decay of overpotential after current interruption.

After passivation while oxygen is being evolved, except for a small instantaneous (<1 msec) ohmic drop, the potential decays logarithmically with time in the manner usually found for the decay of activation overpotential of a gas electrode. Before passivation while the metal is actively being oxidized, however, except for the small ohmic drop, the potential decays exponentially with time in two steps. This behavior is not described by activation theory.

Determinations were made of the capacitance of both the oxidizing and the passivated cadmium, both from potential decay curves and from superimposed a.c. All the a-c values correspond to those of a normal double layer, as do those obtained from decay measurements after passivation has occurred. However, the values obtained from decay curves before passivation are two orders of magnitude higher early in the oxidation but drop rapidly toward the a-c values as oxidation proceeds.

It is proposed that next to the Helmholtz double-layer at the CdO-electrolyte interface, there exists a highly polarized inner double-layer in which the reaction $OH^- \rightarrow O^= + H^+$ takes place. When the field strength across the inner double layer becomes high enough for the reaction $OH^- \rightarrow OH + e^-$ to take place instead, oxygen is evolved and the electrode passivates.

The roles of adsorption of OH^- to form the Helmholtz layer and of interference by $CO_3^=$ are discussed in terms of the results.

In a previous paper (1) experimental observation of the anodic oxidation of cadmium in basic solutions was described, and on the basis of the results a general mechanism for the formation of the anodic film was proposed. Two important features of the reaction were recognized: first, conduction of ions must occur through the solid layer of primary reaction product;[1] and second, there exists a rather critical reaction in which the primary reaction product (essentially CdO) is converted to a secondary product [$Cd(OH)_2$ in pure KOH] at a rate which is strongly dependent on electrolyte composition and other experimental conditions. The conversion takes place through the liquid phase. The nature of the cadmium in this phase has since been shown (14) to be $Cd(OH)_4^=$. The purpose of the present work was to investigate the electrical properties of the underlying layer of primary reaction product, and to determine which electrical property is in fact responsible for anodic passivation.

Experimental Method

The samples of cadmium for oxidation were prepared as described previously (1). The test cell was a rectangular lucite box (5 cm long x 3 cm wide x 5 cm high) of which the cadmium anode and nickel cathode formed the ends.

[1] Since the preparation of the present paper, the definitive work of Dr. Croft has appeared (17), in which he found strong evidence (from an entirely different experimental approach involving verification of the laws of film growth) to support the existence of solid-state conduction of ions through reaction product.

Part of the cadmium metal area was covered with stop-off lacquer, which left a square working area of 2.54 cm on a side. The electrode was cleaned in nitric acid and pre-reduced, as described in the earlier work (1).

The potential of the working electrode was measured against a cadmium reference electrode, a piece of charged negative plate from a sintered-plate nickel-cadmium battery chosen because of its large surface area as well as its good voltage stability. Decay curves were recorded on an instrument with an input resistance of at least 10^6 ohms. The open-circuit potential of the electrolytically reduced cadmium test electrode was 0 ± 5 mv. No junction potentials existed in any of the experiments with this arrangement.

Several times during each oxidation experiment the current was interrupted and the decay of the total overpotential η recorded. Two methods were used: (A) Decays of up to 100 msec were displayed on a Tektronix 535 Oscilloscope equipped with type 53/54C preamplifier (input resistance 10^6 ohms), and photographed. Reference voltages were displayed on each trace. (B) Decays up to 5 sec were recorded on a Brush Recording Oscillograph No. BL902, with auxiliary amplifiers (input resistance 1.5×10^9 ohms). Typical voltage traces are shown in Fig. 1(a). Voltages and times were conveniently read off the oscilloscope photographs after enlargement to 8 x 8 in. through a microfilm reader whose

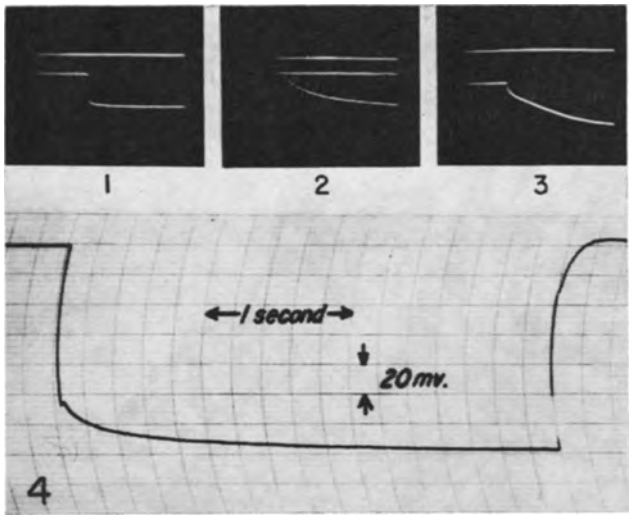

Fig. 1a. Photographs of decay curves, overvoltage vs. time: 1, 2 and 3—oscilloscope traces of curves of type (i), (ii), and (iii). Total sweep 100 msec. (Different vertical scales). 4—oscillograph trace of curve of type (ii). Total decay time 3.4 sec; 200 mv full scale.

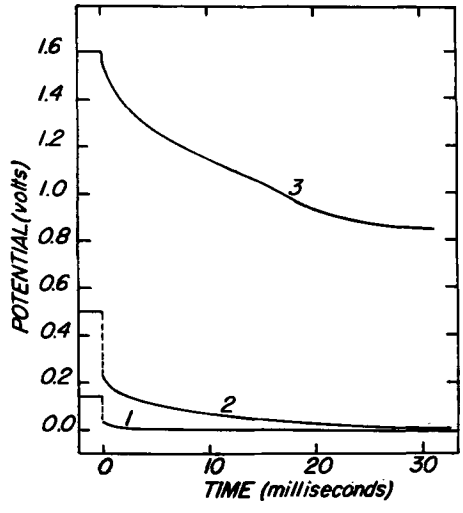

Fig. 1b. Decay curves after transposition (see text): 7.2N-KOH, 0°C, 3.83 ma/cm². For 1, 2, and 3, t/t_p = 0.1, 0.7, and 1.1 respectively.

face plate was equipped with a 2 mm grid; and off the Brush charts through a small hand lens. Figure 1(b) shows the transposed traces.

In addition to measurements of the decay of total overpotential, during several of the oxidation experiments a-c impedance measurements were made using an ESI Model 250 Impedance Bridge. Because of the very high capacitances per unit area of the electrodes, it was necessary to reduce the electrode area to ~1 mm² for these experiments. The error in area thus is appreciable, and this is taken into account in the discussion.

Experiments were done mostly at 25°C, but some were done at O° and −20°C. KOH concentrations ranged from 0.72-14.4N; and K_2CO_3 concentrations from 0.72-7.2N. Oxidation current densities were from 1-15 ma/cm².

Analysis of Decay Curves

The decay curves recorded fell into one of three general types (i) and (ii) before passivation, and (iii) after passivation:

(i) *Resistive decay.*—In all cases during the early stages of the oxidation, and also for longer periods, either in highly concentrated solutions or at low temperatures, the decay consisted principally of an instantaneous (<1 msec) drop plus a very small further decay to a value assymptotic to the open-circuit potential. Other than the determination of the magnitude of the initial drop, no analysis was attempted.

(ii) *Compound decay.*—Throughout most of the oxidation when $t < t_p$, [t_p is time at which passivation occurs (1)], the decay curve after current interruption consisted of an instantaneous drop, followed by a smooth exponential (log E vs. t) decay, which finally went over into a small and slow activation overpotential-like decay toward the open-circuit potential. The form of the tail end of the curve is discussed more fully later.

A plot of the experimental values of η and t, obtained from the oscilloscope trace, as log E vs. t ($E = \eta - E_x$, where E_x is the voltage to which the E has dropped after "infinite" time), it was possible to extrapolate the straight line back to zero time and obtain the value of E just at the instant of current interruption (henceforth called E°_{DL}). Thus it was possible to separate the rapid condenser-like decay from the resistive decay. From the slope of the log E vs. t curve, the value of E°_{DL} and the value of the current density before interruption, an apparent capacitance was calculated.

Inertia of the oscillograph pen rendered unreliable the voltages observed in the first 100 msec after current interruption. Values at $t > 100$ msec were quite reliable, but since voltages were small, and the reading error significant, no firm conclusions could be drawn from these results. It was apparent, however, that the curve changed form in the region of 200 msec and that the initial part of the curve was indeed a continuation of the log E vs. t decay observed on the oscilloscope. The latter part of the curve could be accounted for quite well as either a second slower log E vs. t decay, or as an E vs. log $(t + \theta)$ decay. The voltage obtained by extrapolation of the straight line to zero time (henceforth called E°_{act}), and the calculated capacitances were of the same order for both methods.

(iii) *Activation overpotential decay.*—After passivation, the decay curve was of a different form: a very small instantaneous drop was followed by a long activation overpotential-like decay [i.e. $\eta \propto \log (t + \theta)$; see ref. (4) and (8)], with no evidence of the condenser-like decay. In this respect the decay was normal for that following gas discharge at an electrode. Thus, a plot of the experimental values as η vs. log $(t + \theta)$ permitted graphical separation of the resistive drop from the activation overpotential ($E_{act(O_2)}$) decay. From the slope of the latter decay ($-b$), the value used for θ, and the current density before current interruption, the associated double-layer capacitance was obtained.

Results and Discussion

Components of η°

Concentration overpotential was not considered to be a significant factor determining the course of

the oxidation reaction partly because a log η vs. t relationship for the decay of a concentration polarization would demand that the concentration change as log log c vs. t, which seems most unlikely (10); and partly because values for concentration polarization estimated by Glasstone's method [see ref. (9)] were found to be <1% of η° at 20°C in the highly conducting alkaline solutions under study.

The activation overpotential-like decay at the tail of the decay curves (i.e., between 200 msec and 5 sec) obtained before passivation was small, not very reproducible, and difficult to analyze. An extrapolation of E_{act} to zero time gave the value of E°_{act}, which was between 5 and 20 mv over all the conditions studied. Theta (θ) values and Tafel b values varied considerably from run to run, but with no systematic variation: $0.01 < \theta < 0.6$ sec; $0.005 < b < 0.013$ v per decade of time. Capacitances calculated were always high, the values ranging from 10^4 to 10^5 μfd/cm^2, not unlike those observed on the nickel hydroxide electrode (5) and on some dry, compound oxides (7). Since E°_{act} consistently provided only a small fraction of the total η°, the values obtained need not be discussed further. As mentioned already, a plot of log E_{act} vs. t, actually favored on theoretical grounds for $\eta < 20$ mv, was also linear, and the capacitances obtained were of the same order of magnitude as those obtained from the E vs. log $(t + \theta)$ plot. Similar high values of capacitance at the tail end of decays of cathodic overpotential have been observed and attributed to "the last stages of desorption" (13).

Thus the major portion of the total overvoltage before passivation is made up of a resistive component which decays instantaneously and a capacitive component which decays rapidly and exponentially. Since current must be carried through the underlying CdO film by ions, the resistive part of the decay is assumed to be due to ionic resistance and is referred to as IR_i. Because: (a) Grahame's (4) theory of the capacitance of the electrical double layer predicts a linear log E vs. t plot during decay if forward and backward reactions are of nearly equal magnitude; and (b) in any case, a leaky condenser of fixed dimensions has this type of voltage

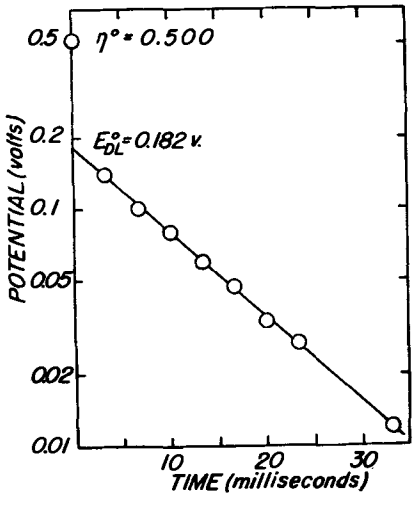

Fig. 2. Analysis of exponential part of decay curve; log $(\eta - E_x)$ vs. t.

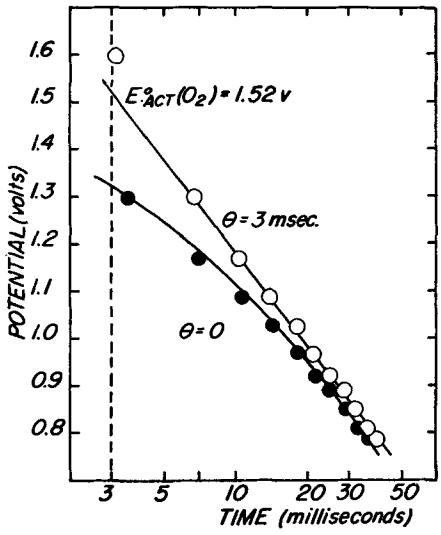

Fig. 3. Analysis of activation overpotential decay after passivation; η vs. log $(t + \theta)$.

decay and later in the paper is considered to be associated with the double-layer in a particular manner: the capacitive part is referred to as E_{DL} during decay or E°_{DL} just at current interruption. Figure 2 illustrates the method used to determine IR_i and E°_{DL} from a particular decay curve.

After passivation the resistive drop was small, there was no evidence of a condenser-like decay, and most of η° was made up of activation overpotential $E^\circ_{act(O_2)}$ associated with oxygen evolution. The small resistive component is thought to be due to only fair electronic conduction across the CdO film and is referred to as IR_e. Figure 3 illustrates the separation of these two components. Since the decay curves of type (iii) follow the theoretical plot for the decay of activation overpotential so rigorously, E°_{DL} after passivation must either (a) be very small compared to $E^\circ_{act(O_2)}$, or (b) refer to the same process and therefore be inseparable from $E^\circ_{act(O_2)}$.

Table I contains the results of determinations of the various components of η° at various times during two experiments, one in KOH and the other in K_2CO_3, both at 7.2N.

Table I. η° and its components during oxidation

Relative time, t/t_p	IR_i, v	E°_{DL}, v	C, μfd/cm^2	IR_e, v	$E^\circ_{act(O_2)}$, v	η°, v
7.2N-KOH, 0°C, 3.83 ma/cm^2; t_p = 26 min						
0.1	0.1	0.015	2850	—	—	0.12
0.7	0.3	0.047	1500	—	—	0.36
0.9	0.32	0.18	245	—	—	0.51
1.1	—	—	54*	0.1	1.7	1.9
* θ = 4 msec; b = 0.65 v/decade of time.						
7.2N-K_2CO_3, 0°C, 3.83 ma/cm^2; t_p = 22 min						
0.3	0.06	0.04	3600	—	—	0.13
0.6	0.16	0.09	2300	—	—	0.25
0.8	0.38	0.62	333	—	—	1.1
0.9	0.50	0.84	300	—	—	1.4
1.1	—	—	126*	0.17	2.0	2.2

* θ = 5 msec; b = 0.35 v/decade of time.

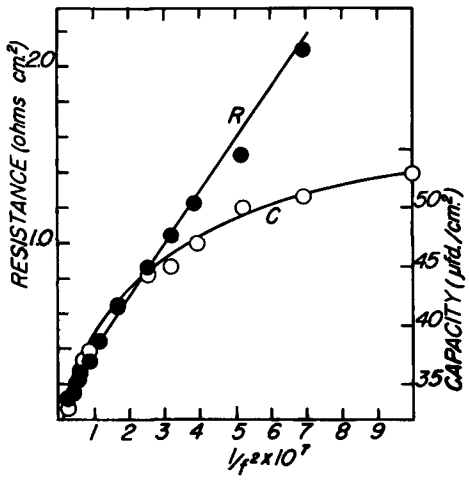

Fig. 4. Variation of series resistance and capacitance with $1/f^2$ for electrode passivated in 7.2N K_2CO_3, at room temperature at 1 ma/cm².

From the results, which are typical of analyses of current interruptions of oxidations at three temperatures, four concentrations, three current densities, and for both KOH and K_2CO_3, it is apparent that the approximate description of the total overpotentials of active (η°_A) and passive (η°_P) cadmium are given by:

$$\eta^\circ_A = IR_i + E^\circ_{DL}$$

$$\eta^\circ_P = IR_e + E^\circ_{act(O_2)}$$

At the moment of passivation then

$$IR_i + E^\circ_{DL} = IR_e + E^\circ_{act(O_2)}$$

and the problem reduces to interpreting E_{DL} and formulating a self-consistent mechanism which permits the transition from cadmium oxidation to oxygen evolution when passivation sets in. Consideration must first be given to capacitance measurements.

Capacitance Measurements

After Passivation: The passivated surface ($t/t_p > 1.0$) is the simplest and will be considered first. The a-c measurements made at 1000 cps during flow of oxidizing current gave values 36-180 μfd/cm²; the values were generally larger the larger the current density used to passivate the electrode. Capacitances determined from the decay of activation overpotential $E_{act(O_2)}$ from $C = 2.3\ i\theta/b$ were about the same, 50-500 μfd/cm². Since Grahame (6) found that double layer capacitances on clean mercury surfaces range up to 40 μfd/cm², a surface roughness factor of 1-5 is suggested for CdO underlayers after the electrodes have been passivated.

Frequency dependence of the series capacitance C_s and resistance R_s associated with the passivated surface also was measured from 1000-6000 cps while current was flowing. Since $R_P^2C_P^2\omega^2 >> 1$, both R_s and C_s should be linear functions of $1/f^2$ if the equivalent circuit for the electrode can be expressed as a pure R and C in parallel. The R vs. $1/f^2$ plot (Fig. 4) was linear, but the C vs. $1/f^2$ plot seems to approach a limiting value at the lower frequencies. Thus abnormally high capacitances at low frequencies are not indicated. Randles (15) found an inverse 0.5 power dependence of double layer capacitance on frequency from 60-1100 cps on clean amalgam electrodes. However, the frequency dependence of C_s on passivated cadmium surfaces studied here follows more closely an inverse 0.28 power dependence (determined from a plot of log C_s vs. log f from 1000-6000 cps) and is not interpretable at present. This property needs further study.

Before Passivation: At times before passivation, the a-c bridge capacitance C_s of the actively oxidizing metal was essentially constant throughout the oxidation, and on any one specimen the capacitance was the same before passivation as after (Table II). Hence there seems to be no essential difference in the composition and dimensions of the Helmholtz double layer before and after passivation.

In contrast, the capacitances obtained from the decay of E_{DL} were two orders of magnitude higher than the a-c values early in the oxidation, but dropped rapidly during the oxidation until at 0.9 t_p they were within a factor of two or three of the a-c values (Table II). [It is recalled that these values result from the experimental fact that the early part of the decay follows a log E vs. t plot, a decay which is far too rapid and with too much curvature to be accountable in terms of concentration polarization in the outer film (10).] The high initial values and the rapid fall of C as oxidation proceeds, the concurrent rapid rise in parallel resistance, and the results of a-c capacitance measurements suggest that the system is one which contains an inner or "crystal" (16) double layer structure in series with the normal Helmholtz double layer: and further that the inner double layer has relatively fixed dimensions and is capable of severe polarization [high dielectric

Table II. Capacitance of cadmium electrode during oxidation. 7.2N K_2CO_3, 25°C.

t/t_p	From decay curves				a-c Impedance bridge							
					1000 cps				3000 cps			
	1 ma/cm²		5 ma/cm²		1 ma/cm²		5 ma/cm²		1 ma/cm²		5 ma/cm²	
	C	R	C	R	C_s	R_s	C_s	R_s	C_s	R_s	C_s	R_s
0	—	—	—	—	51	2.6	—	—	—	—	56	0.17
0.01	5400	6.7	—	—	—	—	—	—	—	—	—	—
0.1	—	—	2700	9.7	50	3.3	74	1.7	26	0.83	60	0.45
0.3	—	—	1200	97	50	3.3	—	—	—	—	—	—
0.5	500	45	500	227	49	2.9	—	—	—	—	—	—
0.9	200	240	—	—	49	2.6	71.2	2.0	28	0.76	—	—
1.1	37	—	46	—	50	2.5	84	1.7	27	0.70	56	0.38

constant (12)] early in the oxidation. Since the inner structure is in series with, and has a capacitance larger than, the outer, it is the latter only which is detected in the a-c measurements. The model which has been most useful in describing qualitatively the experimental results is shown in Fig. 5, and a brief description of a possible mechanism of oxidation, based on this model, follows:

Following reduction prior to the oxidation experiment, the cadmium metal has a double layer due to adsorbed OH^- ions. With the first passage of current, OH^- is activated by removal of H^+ (i.e., $OH^- \rightarrow O^= + H^+$) and a cadmium ion in an active site loses its electrons and forms a CdO "molecule" attached to the surface. This process continues until a monolayer is built up, after which cadmium ions penetrate through the CdO layer to the oxide-electrolyte interface where the film-formation reaction takes place. The Helmholtz double layer then exists at the oxide-electrolyte interface. As the film thickens, after activation oxide ions are in the oxide film, i.e., chemisorbed, forming with the adsorbed OH^- an inner or crystal double layer. When the film is thin, capacitance is high because polarization of $O^=$ is high. As the film grows thicker, and $O^=$ ions diffuse into the film, the field strength (v/cm) across the crystal double layer drops, the dielectric constant decreases, and the capacitance drops. The model suggests that early in the oxidation the slowest step is activation; as film thickens, transport of ions across the film becomes equally slow.[2] Meanwhile the conversion reaction of CdO through soluble complex to $Cd(OH)_2$ or $CdCO_3$ proceeds at the oxide electrolyte interface, gradually building up an outer film, loosely adherent and porous. The activity of OH^- is high enough that the rate of conversion is never transport controlled by ions in solution.

This model accounts for the fact that the impedance bridge methods measure the smaller of the two capacitances in series, in this case the outer double layer. Interruption of the oxidizing current gives a decay of overpotential of which the chief component is the voltage across the inner double layer, whose charge leaks away exponentially with time because of the fixed dimensions.

[2] This point now seems to have been proven by Croft (17).

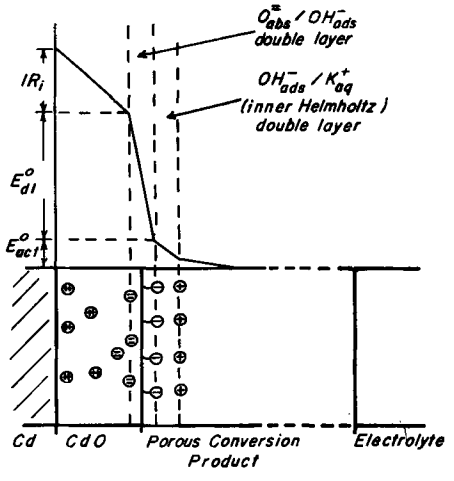

Fig. 5. Model of oxidizing electrode.

Table III. Rate of change of η° and its components with experimental variables

	d/dI	d/dc	d/dT	d/dt $t < t_p$	d/dt $t > t_p$
η°	+	—	—	+	+ small
R_i	+	—	—	+	—
R_e	U	U	—	NM	— small
E°_{DL}	0	—	—	+	NM
C°_{DL}	0	0	—	—	0
E°_{act}	0	NM	U	U	NM
$E^\circ_{act(O_2)}$	+	—	+	NM	+ small
E°_{CP}*	+	—	—	0	0

I, current density; T, temperature; c, concentration of KOH or K_2CO_3; t, time; U, unknown; NM, not measurable; +, positive; —, negative; and 0, nil.
* Rates of change assumed, not measured.

Toward t_p the surface charge of OH^-, which is current dependent, drops off because the film of conversion product closes over near the CdO surface, slows down the escape of complex through the inner Helmholtz double layer, and thus introduces a barrier to OH^- adsorption. The charge separation across the inner double layer increases rapidly until the field strength becomes high enough to remove electrons from OH^- to produce OH and ultimately O_2.

The model suggests further that before passivation E_{DL} decays by $Cd^{++} + O^= \rightarrow CdO$, or by $H^+ + O^= \rightarrow OH^-$ at the $O^=$ site (i.e., without change of dimensions) at a rate which depends on the first power of the concentration of $O^=$; this leads directly to the log E vs. t behavior observed during decay. After passivation, the decay is essentially that of adsorbed OH and/or O, similar to oxygen overpotential decay on a noble metal surface, where complicating films are absent.

Results of Changing Experimental Conditions

Before passivation: Table III is a summary of trends observed from the results of determination of the components of overpotential as a function of current density, electrolyte concentration, temperature, and oxidation time. Detailed examination of this table will reveal that the qualitative facts contained are consistent with the model proposed. Although the details of the results need not be discussed here, it is useful to examine the changes with experimental conditions of the major components involved in the passivation, viz., E°_{DL}, IR_i, and $E^\circ_{act(O_2)}$. Thus Fig. 6a and 6b show how E°_{DL} and IR_i build up as oxidation proceeds toward t_p in KOH and K_2CO_3. Figure 7 shows how E°_{DL} varies with time with increasing concentration of KOH. The value of E°_{DL} remains low until t approaches t_p and then climbs rapidly. It is thus this component which is responsible for the increased potential which ultimately liberates oxygen. At high KOH concentrations the rate of the conversion reaction is higher, and the surface charge density of OH^- remains high longer; hence E°_{DL} has a lower value in the higher KOH concentrations for the same number of coulombs passed. The fact that dE°_{DL}/dI is zero is further support that E°_{DL} is not a common polarization.

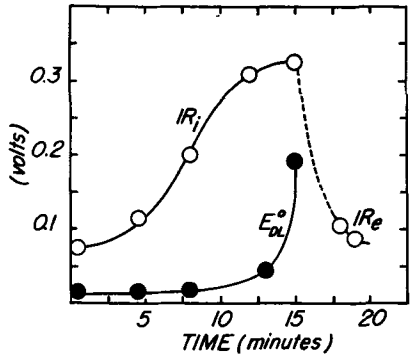

Fig. 6a. Variation of IR_i and $E°_{DL}$ with time, 7.2N KOH, 0°C, 3.83 ma/cm².

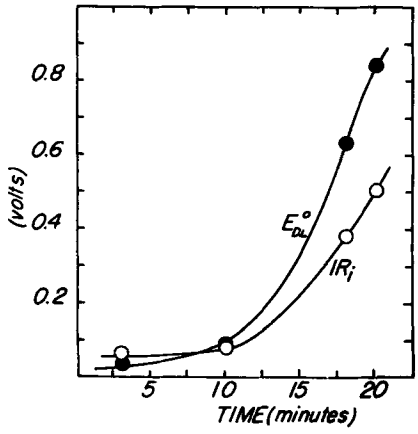

Fig. 6b. Variation of IR_i and $E°_{DL}$ with time, 7.2N K_2CO_3, 0°C, 3.83 ma/cm².

After Passivation: After the electrodes have passivated, it is possible to study properties of the oxide film in a steady-state condition and to compare films formed under different circumstances. A plot of $E°_{act(O_2)}$ vs. log I for an electrode passivated at 0.5 ma/cm² in 7.2*N*-KOH at 25°C was linear, with a slope $b = 0.15 \pm 0.01$ v. This value is close to the value of 0.12 expected (11) for a reaction in which discharge of hydroxyl ions to radicals is rate determining. In Fig. 8 are shown the results of measurements of $E°_{act(O_2)}$ all the points having been determined independently: i.e., on different electrodes, on films which were formed at different current densities, and in both KOH and mixed KOH-K_2CO_3 electrolytes. In terms of the different surface roughness factors of the underlying CdO films formed under such a wide range of conditions, the grouping around the line of slope 0.15 is remarkable.

The *b* values obtained indirectly from the slopes of the decay curves, however, were 2-3 times larger (Table IV) than the values obtained directly by current density variation; that is, the decay was 2-3 times more rapid than was expected. It is suggested that the reason for this is that, in contrast with current variation experiments in which the underlying film of CdO is in a steady-state condition, during voltage decay experiments (following current interruption) the conversion reaction proceeds unchecked at an appreciable rate [~0.3 ma/cm² initially, see Fig. 5 of Ref. (1)]. Thus the CdO layer is being etched away during the decay and carries with it the inner double layer. This chemical attack supplements the normal overpotential decay and increases the *b* value observed. Further, since the complexing reaction is in competition for OH^- with the oxygen discharge reaction, the greater the stability of the complex the greater its ability to decrease the surface activity of OH^- and hence to increase the potential drop across the inner double layer. The facts that the *b*'s from decays in carbonate generally are larger than in caustic and are larger at lower temperature support this view, and support the further

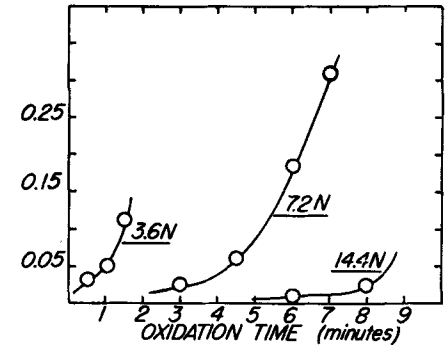

Fig. 7. $E°_{DL}$ vs. time for three concentrations of KOH, 25°C, 7.66 ma/cm².

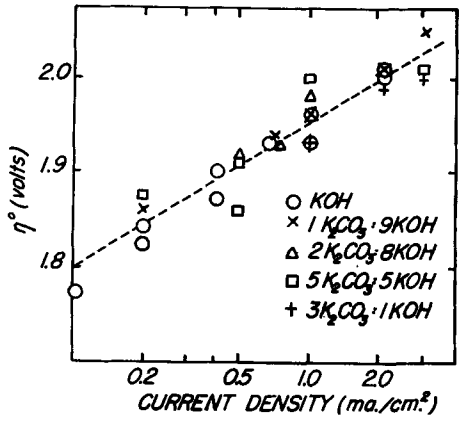

Fig. 8. $\eta°$ vs. log I for electrodes passivated and evolving oxygen in KOH and K_2CO_3-KOH mixtures at various current densities, 25°C. Each point represents a separate oxidation experiment; $\eta° \approx E°_{act(O_2)}$.

Table IV. "*b*" values determined* from decay curves after passivation

	Conc. (*N*)	T, °C	Current density, ma/cm²	*b*
KOH	14.4	25	7.66 ma	0.34
	7.2	25	7.66	0.44
	7.2	25	3.83	0.28, 0.27
	3.6	25	7.66	0.29
	3.6	25	3.83	0.44
	7.2	0	7.66	0.36
	7.2	0	1.53	0.31
	7.2	—20	1.53	0.58
K_2CO_3	7.2	25	3.83	0.35, 0.27
	7.2	25	1.53	0.34
	7.2	0	7.66	0.54
	7.2	0	3.83	0.55, 0.50
	7.2	0	1.53	0.52, 0.50

* $\frac{\partial E°_{act(O_2)}}{\partial \log t} = -b$ [Ref. (8)].

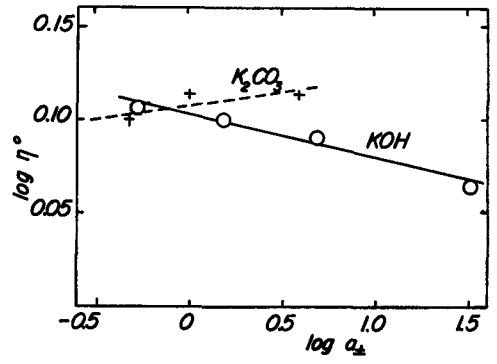

Fig. 9. Freundlich isotherm plot of log $\eta°$ vs. log activity, adsorption of OH^- being assumed to be rate controlling; $\eta \approx E°_{act(O_2)}$.

notion that $E°_{DL}$ rises rapidly at passivation for the simple reason that the rate of absorption of OH^- through the double layer is reduced by the presence of the complex; in other words, the CdO surface becomes poisoned by reaction product which competes for active sites with reactant OH^-. The effect of poisoning should be less the higher the activity of OH^-, and greater the higher the activity of carbonate ion. Figure 9 shows values of $E°_{act(O_2)}$ measured as function of concentration of OH^- and $CO_3^=$, and plotted as a Freundlich adsorption isotherm. The trends are as suggested and support the proposed mechanism. The large (500 mv/factor of ten change in concentration) negative value of $d\eta/d \log a_{OH^-}$ is very difficult to explain on the basis of activation theory, which predicts a value of zero (11).

Further, the fact that the b value of 0.15 is 25% higher than that predicted for a one-electron discharge reaction supports the suggestion of inhibition by reaction products. The higher the current density at which the passivated electrode is being anodized, the greater the surface concentration of still-sorbed complex. The role of adsorption indicated by the electrochemical behavior observed needs further examination.

Summary

The two equations $\eta°_A = IR_i + E°_{DL}$ and $\eta°_P = IR_e + E°_{act(O_2)}$ adequately describe the composition of overpotential when the electrode is active and passivated respectively. In the term $E°_{DL}$ are included the voltage across the normal Helmholtz double layer, as well as that across a second inner or crystal double layer at the outer edge of the film, a charge separation which can build up to high voltages and decay rapidly in the manner of a condenser.

The relative sizes of the components making up the total overpotential are controlled by experimental conditions. It is ultimately the "inner" double layer and the field strength across it which determine when $\eta°_A = \eta°_P$ and the electrode goes from the active to the passivated state.

A mechanism which accounts qualitatively for the experimental results is proposed and discussed.

Acknowledgments

The authors gratefully acknowledge discussions on this work and correspondence with two laboratories: with Professor F. E. W. Wetmore, University of Toronto; and with Mr. U. B. Thomas and his very capable associates, Drs. Baker, Dewald, and Milner, Bell Telephone Laboratories.

Manuscript received May 4, 1959. This paper was prepared for delivery before the Ottawa Meeting, Sept. 28-Oct. 2, 1958. It is a contribution from the Defence Research Chemical Laboratories, Ottawa, Ontario, Canada. Issued as DRCL Report No. 303.

Any discussion of this paper will appear in a Discussion Section to be published in the June 1960 JOURNAL.

REFERENCES

1. P. E. Lake and E. J. Casey, *This Journal*, **105**, 52 (1958).
2. K. Huber, *This Journal*, **100**, 376 (1953); *Z. f. Elektrochem.*, **62**, 675 (1958).
3. D. Grahame, *J. Phys. Chem.*, **57**, 257 (1953).
4. H. B. Morely and F. E. W. Wetmore, *Can. J. Chem.*, **34**, 359 (1956).
5. B. E. Conway and P. L. Bourgault, *ibid.*, **37**, 292 (1959).
6. D. Grahame, *J. Amer. Chem. Soc.*, **68**, 301 (1946).
7. E. J. W. Verwey, "Semiconductor Materials," p. 158, H. K. Henisch, Editor, Butterworths Sci. Pub., Ltd., London (1951).
8. G. Armstrong and J. A. V. Butler, *Trans. Faraday Soc.*, **29**, 1261 (1933); J. O. Bockris, and E. C. Potter, *This Journal*, **99**, 169 (1952).
9. See e.g., J. O. Bockris, "Modern Aspects of Electrochemistry," p. 185, Butterworths Sci. Pubs., London (1954).
10. W. Jost, "Diffusion in Solids, Liquids and Gases," p. 47, Academic Press Inc., New York (1952).
11. J. O. Bockris, *J. Chem. Phys.*, **24**, 817 (1956).
12. C. J. F. Böttcher, "Theory of Electric Polarizations," pp. 201, 422, Elsevier Publishing Co., New York (1952).
13. P. Lukotsev and S. Lewina, *J. Phys. Chem., U.S.S.R.*, **21**, 599 (1947).
14. P. E. Lake and J. M. Goodings, *Can. J. Chem.*, **36**, 1089 (1958).
15. J. E. B. Randles, *Disc. Faraday Soc.*, No. 1, 11 (1947).
16. T. B. Grimley, *Proc. Royal Soc. A*, **201**, 40 (1950); T. B. Grimley and N. F. Mott, *Disc. Faraday Soc.* No. 1, 3 (1947).
17. G. T. Croft, *This Journal*, **106**, 278 (1959).

SYMBOLS

1. η — total overpotential at any time, measured against $Cd/Cd(OH)_2$ reference.
2. $\eta°$ — total overpotential just at current interruption.
3. $\eta°_A$, $\eta°_P$ — total overpotential while current is flowing: electrode active (A), passivated (P).
4. E_∞ — voltage to which exponential part of overpotential has dropped after "infinite" time (~100 msec).
5. E_{act} — value of logarithmic part of overpotential when $t < t_p$ (metal being oxidized).
   $E°_{act}$ — value of E_{act} just at current interruption.
6. $E_{act(O_2)}$ — value of logarithmic part of overpotential when $t > t_p$ (oxygen being evolved).
   $E°_{act(O_2)}$ — oxygen activation overpotential value of $\eta°_P - IR_e$.
7. E_{DL} — $(\eta - E_\infty) - E_{act}$.
   $E°_{DL}$ — value of E_{DL} just at current interruption.
8. IR_i — ionic resistance drop $\eta°_A - E°_{DL}$.
9. IR_e — electronic resistance drop $\eta°_P - E°_{act(O_2)}$.
10. $E°_{CP}$ — concentration polarization.

The Oxidation of the Silver Electrode in Alkaline Solutions

Thedford P. Dirkse

Department of Chemistry, Calvin College, Grand Rapids, Michigan

ABSTRACT

The formation of Ag_2O and AgO was studied by means of constant current and constant potential processes. The efficiency of these oxide formations was determined by measuring the gain in weight of Ag electrodes under various conditions of charge, and the extent of the polarization of these processes was measured by using an interrupted current technique.

The electrolytic behavior of silver in alkaline solutions has been studied, but diverse opinions have been expressed as to the reactions taking place. Luther and Pokorny (1) plated silver on platinized platinum and observed its behavior in 1*N* NaOH solutions. They obtained the typical anodic (Fig. 1) and cathodic curves. They considered the first step of the anodic curve to correspond to the quantitative and reversible change of Ag to Ag_2O, and the second to correspond to the quantitative and reversible change of Ag_2O to AgO. Although they had evidence that a higher oxide, perhaps Ag_2O_3, was stable in alkaline solution, they could not produce it by oxidation of AgO in the NaOH solution. Instead, a third stage of the anodic curve corresponded to the evolution of oxygen.

Denison (2) worked with a system more nearly resembling a battery. His electrodes were made by pasting Ag_2O on a platinum gauze and reducing it to Ag. The electrolyte was a 25% KOH solution. He measured changes in weight of the electrode during anodic and cathodic processes. His results showed that by decreasing the current density a greater amount of weight was gained by the electrode, but he never quite obtained complete conversion to AgO. The anodic potential-time curves occasionally showed peaks but these were not interpreted. These curves also showed that the second stage was longer than the first. Furthermore, his final product always showed the presence of silver, indicating that the anodic process was not completely efficient.

Hickling and Taylor (3) studied an electrode made by plating silver on a platinum wire. The electrolyte was 1*N* NaOH and the results were recorded oscillographically. They found the second stage to be relatively short and interpreted it as due to the formation of Ag_2O_3 which then, being unstable, decomposed to form AgO.

More recently Jones, *et al.* (4) made a similar study of silver wire electrodes in 1*N* KOH solutions. They considered the second stage to be an inefficient one in which both oxidation of Ag_2O and evolution of oxygen occurred. Further, they gave evidence for the formation of Ag_2O_3 but only in small amounts and after completion of the second stage.

The work reported here is an attempt to resolve these differences with respect to the oxidation processes and to suggest a mechanism for them.

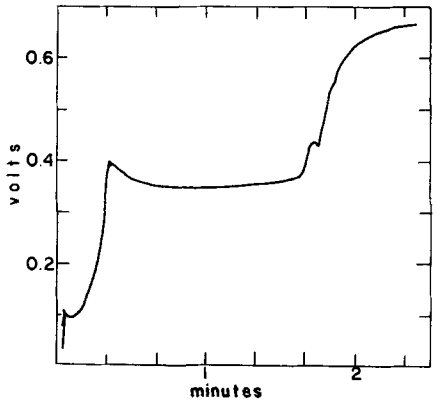

Fig. 1. Charging curve for silver in 15% KOH at room temperature, with a current density of 5 ma/cm^2.

Experimental

The electrodes were subjected to three kinds of treatment. In the first of these, the electrodes were charged at constant potential. The charging circuit is shown in Fig. 2. C is a 1.5-v source, F is a 100-ohm Helipot resistor from which a controlled voltage can be applied to the electrodes. In this way electrode B, the working electrode, can be kept at a definite potential above electrodes A. These latter electrodes were comparatively large electrodes made by pasting Ag_2O on silver screen. E has a resistance of 25,000 ohms so that the loss through this resistor is not large. D is a precision resistor of about 1 ohm which was used in recording the current passed through the system. Although this work was actually carried out at constant cell potential, yet, because of the low current density and relatively large amount

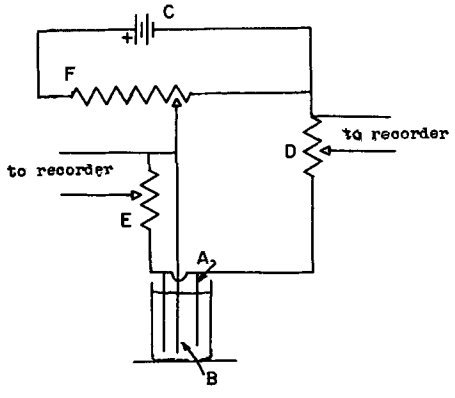

Fig. 2. Schematic diagram for constant-potential charging.

of material on electrodes A, the process in effect was a constant electrode potential one.

The electrodes were also subjected to a constant current oxidation. This circuit consisted of a high voltage source fed through a variable resistor and controlled by means of a Weston Model 534 d-c current relay. In carrying out these runs three currents were used: 1, 5, and 10 ma. The real current densities are unknown since the actual surface area of the silver electrodes was not measured. Four different electrolyte concentrations were used: 8, 21, 28, and 42% KOH.

The third type of treatment involved the use of interrupted current with silver wire electrodes. This technique and procedure have already been described (5).

For the first two methods of oxidation, the working electrodes were made by pasting a small amount of Ag_2O on a platinum screen. The area of the screen covered by the Ag_2O was about 2 cm^2 so that the total area exposed to the solution was about 4 cm^2. The Ag_2O was then reduced to Ag by heating at about 500°C for 15-30 sec. This electrode was placed between the two larger (2.5 cm^2) electrodes A. The 3 electrodes were placed in a polystyrene cell case which held about 35 ml of electrolyte. Unless otherwise indicated, all runs were made at room temperature.

After an electrode had been charged, it was soaked in distilled water for at least 8 hr, then it was dried in a stream of purified nitrogen at room temperature, and finally placed in a desiccator for at least 24 hr. All these operations were carried out in the absence of light. After this the electrode was weighed and the gain in weight was considered to be due to oxygen which had combined with the silver.

In the constant-current process the charging was continued until the voltage reached a certain predetermined value. In the constant-potential process the charging was continued until the current dropped to nearly zero or until 48 hr had elapsed, whichever occurred first.

All voltages are expressed with reference to the Ag-Ag_2O potential in alkaline solution.

Results

Ag *to* Ag_2O.—In the constant current processes the silver electrodes were oxidized until the voltage was 0.2 v. The electrode was then removed, dried, and weighed. Under all the conditions studied, the transformation of Ag to Ag_2O took place at a potential of about 50 to 100 mv. At the highest current densities very little of this transformation took place in the lower electrolyte concentrations. In no case was the Ag completely converted to Ag_2O, even though the current efficiencies (number of Faradays needed to produce the oxygen/number of Faradays actually used) were in the vicinity of 100%. The per cent conversion was usually less than 60%. The actual values will depend to some extent on such factors as the density of the silver.

In general, Ag_2O was produced on the surface of the working electrode. Its presence was verified by x-ray analysis and by emf measurements between the working electrode and the Ag-Ag_2O electrodes. It appears then that the Ag at the electrode-electrolyte interface is converted to Ag_2O, and when this has been completed the voltage increases abruptly and another process takes place—oxidation to AgO. The layer of Ag_2O produced on the Ag undoubtedly increases the electrical resistance of the electrode (5).

There is evidence that this electrical resistance of Ag_2O does limit the electrode process. An electrode similar to those used in this work was prepared using a grid of silver screen rather than of platinum. When this electrode was treated anodically in 20% KOH for some time at the lowest current density used in this work, the voltage rose to the higher level (about 0.35 v) after several days of treatment. Yet when this electrode was removed the surface appeared to be unattacked. It still had the appearance of reduced silver. However, on this material it was found that the active material next to the grid had been oxidized and that formation of Ag_2O seemed to proceed from the grid outward. This, of course, offered resistance to the flow of current from the grid to the surface of the active material and, although there was plenty of unoxidized Ag at the electrode-solution interface, the voltage rose to the level corresponding to the transformation of Ag_2O to AgO.

Another electrode was prepared by pasting a platinum screen with Ag_2O. When this was oxidized (without being reduced first) AgO was formed and, again, it was formed at the grid rather than at the electrode-solution interface. Thus the resistance of the Ag_2O seemed to make it easier for AgO to form at the grid where the amount of electrolyte was small rather than at the electrode surface where there was plenty of electrolyte.

In the constant potential processes Ag_2O was the

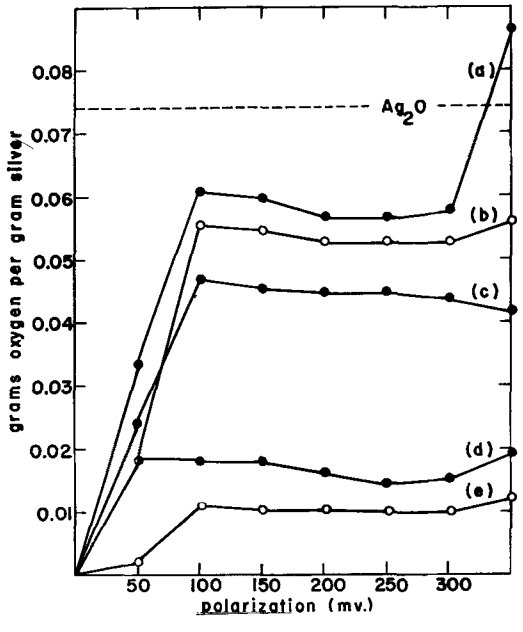

Fig. 3. Weight change for Ag electrode during constant-potential charge for 24 hr in KOH solutions at room temperature: (a) 23% KOH; (b) 20% KOH; (c) 42% KOH; (d) 8% KOH; (e) 23% KOH. Ag grid for (e), Pt grid for others.

product at potentials below 0.3 v. In general, the conversion of Ag to Ag_2O took place with a current efficiency of about 100%. The process appears to be a quantitative one but again, as with the constant current method, the Ag was not completely converted to Ag_2O. The maximum conversion, about 80%, took place in 28% KOH.

In carrying out this constant potential work it was found that on occasion an electrode lost rather than gained weight (6). To investigate this further, a series of experiments was carried out in which several electrodes were charged at constant potential for 24 hr, then dried and weighed. Each electrode was then charged further, without being reduced, at a potential 50 mv higher for 24 hr, and again weighed. This was repeated for several such increments of voltage increase. The results of the weight changes are shown on Fig. 3. It is noted that at potentials under 0.30 v the Ag was not completely converted to Ag_2O. Furthermore, at potentials above 0.10 v there appears to be a loss in weight. This, however, can be traced to a loss of Ag from the electrode. Such a loss was observed in each case and was of the proper magnitude to account for the decrease noted in oxygen content of the Ag_2O. As the electrode is held at a given potential some of the Ag_2O apparently is dissolved from the electrode. However, the results show also that once the initial film of Ag_2O is formed, raising the potential produces no further oxidation until the oxidation of Ag_2O to AgO takes place at potentials above 0.30 v. This is also noted on Fig. 4 where the current accepted by the electrode is practically zero at potentials above 0.10 v. In Fig. 4 each curve represents the current during the series of constant potential charges referred to above and on Fig. 3. The platinum grid is not responsible for this loss in weight. An electrode having a silver grid shows the same behavior, Fig. 3, curve e.

The results heretofore obtained show that the electrochemical oxidation of Ag to Ag_2O is an efficient one. It is the only one taking place under the conditions outlined above. However, the above results were obtained by using Ag pasted on a platinum screen grid. It is possible that the presence of the platinum may modify this process. To check on this, some commercial Ag electrodes were treated anodically under various conditions. These electrodes were about 4 cm square and contained on an average about 6.2 g of Ag. These were treated at 40 and 200 ma. Typical voltage-time curves were obtained. To change all the Ag in these electrodes to Ag_2O would require about 1.5 amp-hr. Using the current rates mentioned above, and KOH concentrations ranging from 8 to 40%, only 0.24 to 0.64 amp-hr were used to oxidize the Ag to Ag_2O. After this the voltage increased and the transformation to AgO took place. Here again the formation of Ag_2O was incomplete, only about 20 to 40% of the Ag being converted to the oxide. However, when this charging was continued at the higher voltage level, the conversion to AgO was above 80%.

Treatment of silver wire electrodes with interrupted current shows that the anodic overvoltage is relatively small while appreciable amounts of unoxidized Ag remain, but the *IR* drop increases as the surface coating of Ag_2O increases, Fig. 5. When a high current density at a temperature of −20°C was used, however, very little oxidation took place and the voltage rose rapidly. Under these conditions the low mobility of the OH^- ion was not sufficient to sustain the reaction.

Ag_2O *to* AgO.—After the oxidation of Ag to Ag_2O no longer takes place, the voltage rises to a higher level where AgO is formed. This is preceded by a peak shown on Fig. 1. The significance of this peak has been discussed earlier (5).

In the constant current processes the electrode containing Ag and Ag_2O was treated until the potential rose to about 0.5 v. The electrode was then removed, dried, and weighed to determine the oxygen gained while the potential ranged from 0.2 to 0.5 v. The amount of oxygen added to the electrode in this voltage range was practically always greater than that added in the range 0 to 0.2 v. The surface material in each case was AgO. This was determined by x-ray analysis. In no case, however, was Ag com-

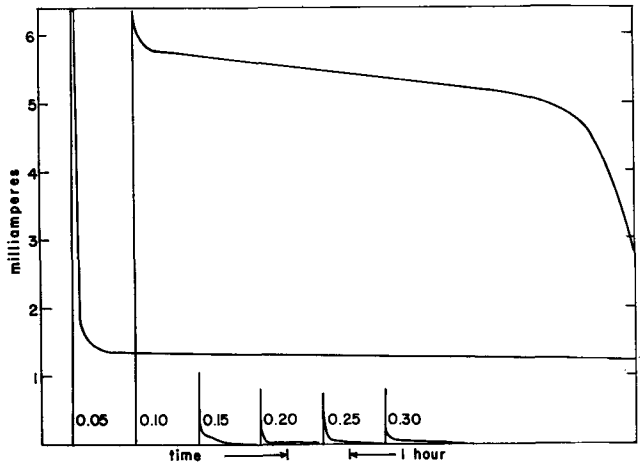

Fig. 4. Variation of current with change in extent of polorization for an Ag electrode in 23% KOH at room temperature. The numbers give the extent of polarization in volts.

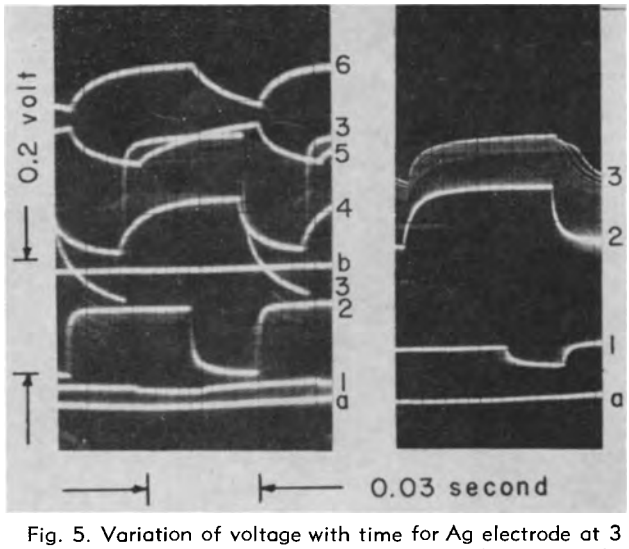

Fig. 5. Variation of voltage with time for Ag electrode at 3 ma/cm²; room temperature. Left picture, 10% KOH; right picture, 5% KOH. (a) Ag-Ag_2O potential; (b) Ag_2O-AgO potential. The numbers give the order in which these curves appeared during the charging process.

pletely changed to AgO. The current efficiencies varied with the current rate. They were about 100% when the process required about 8 hr. They were less at higher and at lower current densities.

With constant potential treatment, no AgO was formed at less than 0.3 to 0.35 v. When the overvoltage was high enough to bring about formation of AgO, the current efficiencies were close to 100% in all KOH concentrations studied. The current was high at the outset, then fell to a low value, then again increased, Fig. 6. The voltage also rose to a peak at the outset and then decreased, Fig. 7.

Furthermore, large amounts of oxygen could be introduced into the electrode by this constant potential process. When the electrode was kept at an overvoltage of 0.40 to 0.45 v for weeks or even months, increasing amounts of oxygen were added to the electrode. In one case, analysis showed a composition corresponding to $AgO_{1.6}$. This is approximately the composition of Ag_2O_3. Yet in preparing this material the electrode was kept at a potential less than that generally considered to be that of the AgO-Ag_2O_3 couple (1, 3). Moreover, the emf of this electrode was the same as that of AgO and the x-ray pattern, although less distinct, showed only lines of AgO, Fig. 8. This preparation was rather stable. A sample kept dry and in the dark showed practically no loss in weight over a period of several months.

The results obtained when a silver wire coated with Ag_2O was subjected to interrupted current showed a difference between this process and the formation of Ag_2O. The shape of the voltage curve was different, Fig. 5, the polarization was greater, and the voltage rise was slower than that for the Ag to Ag_2O transformation. The polarization for this process is 100-150 mv. This was determined over a KOH concentration range of 5-43% and with a variety of current densities. Measurements were also made at 0° and −20°C. At this lowest temperature the polarization was greater and the rate of voltage decay was much slower. This can be attributed to the increased viscosity of these solutions at this low temperature.

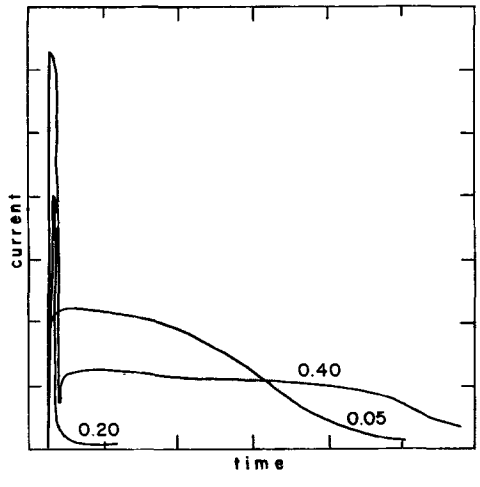

Fig. 6. Variation of current with time during constant-potential charge of an Ag electrode in 30% KOH at room temperature. The numbers give the polarization in volts above the Ag-Ag_2O potential. The scale is not the same for each curve.

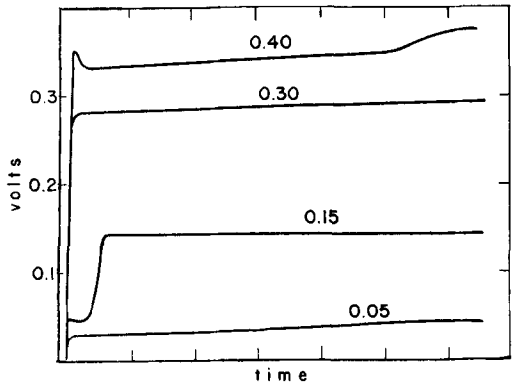

Fig. 7. Variation of potential of Ag electrode during constant-potential charge in 30% KOH at room temperature. The numbers give the polarization in volts above the Ag-Ag_2O potential.

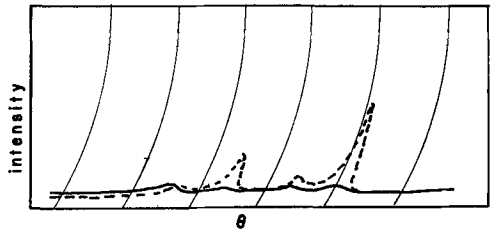

Fig. 8. X-ray patterns for AgO preparations; solid line, $AgO_{1.6}$; dotted line, AgO.

Using the method suggested by Brodd and Hackerman (7), the relative surface areas of Ag, Ag_2O, and AgO are 1 : 2.7 : 7.7. This was determined by measuring the double layer capacitance of a silver wire electrode and then also the capacitance of the same electrode after it was coated with Ag_2O, and finally when it was coated with AgO.

Oxygen evolution.—The third level of the charge curve is associated with the evolution of oxygen. Usually there is a gradual rise in voltage from the second to the third level. However, in experiments with silver wire electrodes it was noted that there were breaks in the part of the voltage curve between the second and third levels. These breaks occurred during a constant current charge and were noted whether the solution was agitated with nitrogen or oxygen, or was quiescent. Two breaks were noted in many instances, Fig. 1, but they did not appear on the discharge curve. These breaks were also observed when a sintered silver plate was charged in excess electrolyte.

When silver wire electrodes were treated with interrupted current, a break was often noted in the decay curve after oxygen evolution had begun, Fig. 5, right panel. This break was at a potential of about 0.4 v at room temperature and 0.33 v at 0°C. These breaks were observed for no more than a second or two, and occurred as the general voltage trend was upward. No such breaks were noted during the closed circuit part of the process.

Discussion

In seeking to account for the behavior of the silver electrode in alkaline solutions it is apparent that the OH^- ions are the solute species involved. They are involved in the oxygen evolution process (8, 9) and

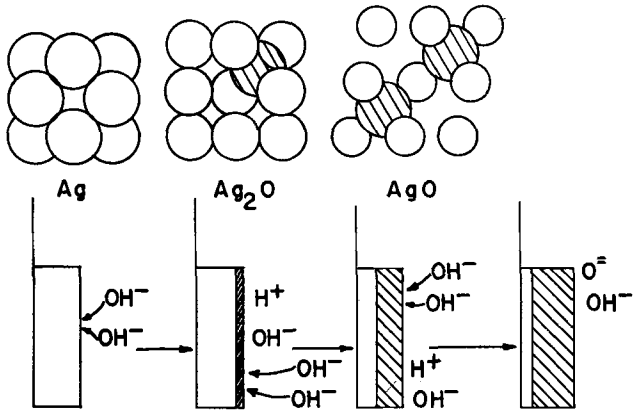

Fig. 9. Possible mechanism for silver oxide formation

are likely also involved in the other reactions. If water were the active species, then at constant current one would expect less formation of Ag_2O, e.g., at high KOH concentrations than at low concentrations. At the high KOH concentrations there would be comparatively fewer H_2O molecules and they would be less mobile because of the increased viscosity of the system. In actual fact, the per cent Ag converted to Ag_2O at constant current was greater in 42% KOH than in 8% KOH at all current densities used.

A possible mechanism for these oxidation processes is illustrated in Fig. 9. The lattice structures in the top panel are drawn to scale (10-12). The open circles represent Ag and the shaded circles oxygen. Since no data could be found for the ionic radius of Ag^{++}, an estimated value of 1.1Å was used. The other ionic radii used are those given by Pauling (13).

As a positive charge is placed on silver, the outermost valence electron is removed from each silver atom, producing Ag^+. This causes an expansion of the silver lattice and allows room for the inclusion of oxygen atoms or ions. The OH^- ions are drawn to this charged silver and the oxygen becomes separated from the hydrogen. The $O^=$ ions are then drawn into the Ag^+ lattice, forming Ag_2O.

	H°, kcal/mole	Reference
$H^+ (g) \rightarrow H^+ (aq)$	−255	(14)
$O^= (g) \rightarrow O^= (aq)$	−125	estimated
$OH^- (aq) \rightarrow OH^- (g)$	+92	(14)
$OH^- (g) \rightarrow O^= (g) + H^+ (g)$	+640	(15*a*)
$OH^- (aq) \rightarrow H^+ (aq) + O^= (aq)$	+352	

The lattice energy of Ag_2O is −715 kcal/mole (15*b*). According to the above data, this separation is energetically allowable.

The $O^=$ ions are rather immobile in this lattice and soon this reaction ceases because no more $O^=$ ions can be accommodated in the Ag^+ lattice. This is indicated also by the behavior of the silver electrode as shown on Fig. 3. This Ag_2O layer acts as a barrier to the flow of electrons and permits no ions to leave it except for a few Ag^+ ions which may go into solution. This accounts for the loss in weight shown on Fig. 3.

To continue the flow of current after the Ag_2O layer is formed, the potential on the electrode must be increased. This withdraws another electron from each Ag^+. There is then a greater repulsive force between the silver ions, and more $O^=$ ions must enter the lattice to preserve electroneutrality. As a result, the silver lattice is further distorted and expanded. Reaction then proceeds and the electrode gains in weight as AgO is formed. Because of the expanded lattice the $O^=$ ions can penetrate more deeply and thus the formation of AgO is greater than that of Ag_2O on the same electrode. This mechanism allows for the possibility that Ag can be transformed to AgO directly without the intermediate formation of Ag_2O. This appears to take place at constant potential charge with a polarization greater than 350 mv, Fig. 7.

The formation of AgO continues until the $O^=$ ions can no longer be absorbed by the electrode material at the rate demanded by the current flow. The potential then rises and another reaction takes place. The rise in potential here is slow compared to that between the formation of Ag_2O and that necessary for the formation of AgO. This rise corresponds to the occurrence of an additional reaction and not the replacement of one reaction by another. This additional reaction is the evolution of oxygen. The increase in potential is not sufficient to remove additional electrons from the Ag^{++} ions. The AgO formed is a fairly good electron conductor and the electrons needed for the flow of current may then arise from another reaction and be transferred through the AgO layer.

The potential rises here because, to continue the flow of current, $O^=$ ions can no longer migrate fast enough and more electrons cannot be removed from the Ag^{++} ions in the lattice. It is possible then that electrons are removed from the OH^- ions which are at the electrode surface,

$$OH^- \rightarrow OH + e \qquad [1]$$

and that these OH radicals then combine to form H_2O_2 which decomposes to give the oxygen.

$$2\ OH \rightarrow H_2O_2 \qquad [2]$$

$$H_2O_2 + OH^- \rightarrow H_2O + HO_2^- \qquad [3]$$

$$HO_2^- \rightarrow \tfrac{1}{2}\ O_2 + OH^- \qquad [4]$$

A serious objection to this mechanism is that the potential needed for reaction [1] is about 1.7 v on the scale used here (15*c*). This is considerably higher than that at which oxygen evolution occurs.

The evolution of oxygen does take place at potentials above that associated with the formation of HO_2^- (16). Furthermore, the breaks in that part of the voltage-time curves corresponding to oxygen evolution, Fig. 1 and 5, also occur at about the potential of the $OH^- - HO_2^-$ or $OH^- - O_2^-$ couples (15*e* and *c*). In general, at low current densities, the break is noted at the lower potential ($OH^- - O_2^-$), while as the current density increases the potential corresponds to the $OH^- - HO_2^-$ couple. Silver catalyzes the decomposition of peroxide and so the evolution of oxygen could easily proceed this way.

These facts suggest two possibilities for the oxy-

gen evolution reaction. Reactions [5]-[7] illustrate a mechanism

$$OH^- \rightarrow O^= + H^+$$

or

$$OH^- \rightarrow O^- + H^+ + e \quad [5]$$

$$2\,O^- \rightarrow O_2^- + e \quad [6]$$

$$O_2^- \rightarrow O_2 + e \quad [7]$$

involving the $OH^- - O_2^-$ couple. It is possible that the $O^=$ or O^- ions may emigrate from the AgO lattice as well as be formed from the OH^- ions in solution.

The other possibility is illustrated by a series of reactions consisting of [5], [8], [4]. Here again the oxygen ions from the solid may be involved.

$$O^- + OH^- \rightarrow HO_2^- + e \quad [8]$$

It is difficult to make a choice between these mechanisms. Both are permissible according to the ideas of Rüetschi and Delahay (8). Perhaps the latter is more consistent with the results and suggestions of Anbar and Taube (9). Measurement of the oxygen overvoltage could conceivably shed some light on this mechanism, but these measurements are, at best, difficult to make.

The ideas suggested here stress the fact that the mobility of the OH^- ion is an important factor in these oxidation processes. When this mobility is impaired, e.g., at low temperatures or at high KOH concentrations, the extent of oxide formation is also less because the OH^- ions cannot migrate fast enough to allow reaction to take place at the rate set by the current.

It has been noted that the polarization necessary to carry out the oxide formation is not very sensitive to current density. This indicates that the cause of the polarization is not primarily resistance. On the basis of the mechanism suggested here, this polarization would be due to the splitting of the OH^- ion. This would appear in the formation of each of the two oxides. In addition to this the formation of AgO would be polarized by the migration of $O^=$ ions in the Ag^{++} lattice.

Acknowledgment

Thanks are due to the Office of Naval Research under whose sponsorship this work was carried out, and to the Yardney Electric Corporation for supplying some of the materials. This work was performed under Contract N onr-1682(01) with the Office of Naval Research.

Manuscript received May 11, 1959. This paper was prepared for delivery before the Columbus Meeting, Oct. 18-22, 1959.

Any discussion of this paper will appear in a Discussion Section to be published in the June 1960 JOURNAL.

REFERENCES

1. R. Luther and F. Pokorny, *Z. anorg. u. allgem. Chem.*, **57**, 290 (1908).
2. I. A. Denison, *Trans. Electrochem. Soc.*, **90**, 387 (1946).
3. A. Hickling and D. Taylor, *Discussions Faraday Soc.*, No. 1, 277 (1947).
4. P. Jones, H. R. Thirsk, and W. F. K. Wynne-Jones, *Trans. Faraday Soc.*, **52**, 1003 (1956).
5. T. P. Dirkse and G. J. Werkema, *This Journal*, **106**, 88 (1959).
6. L. A. Vander Lugt, MS Thesis, Michigan State University, 1959.
7. R. J. Brodd and N. Hackerman, *This Journal*, **104**, 704 (1957).
8. P. Rüetschi and P. Delahay, *J. Chem. Phys.*, **23**, 556 (1955).
9. M. Anbar and H. Taube, *J. Am. Chem. Soc.*, **78**, 3252 (1956).
10. R. B. Wilsey, *Phil. Mag.*, **46**, 487 (1923).
11. P. Niggli, *Z. Krist.*, **57**, 253 (1922).
12. V. Scatturin, P. Bellon, and R. Zannetti, *Ricerca Sci.*, **27**, 2163 (1957).
13. L. Pauling, "The Nature of the Chemical Bond," 2nd ed., p. 346, Cornell University Press, Ithaca (1940).
14. E. J. Garrick, *Phil. Mag.*, **8**, 102 (1929).
15. W. M. Latimer, "Oxidation Potentials," 2nd ed., Prentice-Hall, Inc., New York (1952): *a*, p. 25; *b*, p. 20; *c*, p. 48; *e*, p. 45.
16. T. P. Dirkse and D. B. De Vries, *J. Phys. Chem.*, **63**, 107 (1959).

Effect of Sodium Pyrophosphate on Polarization and Corrosion of Tin

I. A. Ammar[1] and S. Riad

Department of Chemistry, Faculty of Science, Cairo University, Cairo, Egypt, U.A.R.

ABSTRACT

Corrosion rates and corrosion potentials have been measured for tin in eight different acid, alkaline, and neutral solutions. The corrosion potential, measured against the saturated calomel electrode, has been found to increase toward more active potentials with increase of concentration. It has been observed that sodium pyrophosphate decreases the corrosion rate and increases the corrosion potential toward more active values. This increase is proportional to the amount of pyrophosphate added. Cathodic and anodic polarization measurements have been carried out in an attempt to explain the function of sodium pyrophosphate as a corrosion inhibitor. The results have been compared with previous work on the inhibition of iron corrosion by polyphosphates.

Measurements of the rate of corrosion of tin and the related corrosion characteristics are important since tin is used as a protective coating for iron and copper (1). Inhibition of the corrosion of tin in hydrochloric and acetic acid solutions, by incorporating about 5% antimony in tin, was studied by Hoar (2). The corrosion of tinplate and its inhibition by chromate-containing solutions was studied by Kerr (3, 4). Electrodeposited coatings of Sn-Zn (5) and Sn-Ni (6) alloys were found to resist the corrosion of steel. Corrosion of tin in solutions containing chloride ions was studied by Britton and Michael (7) who observed that addition of sodium carbonate, bicarbonate, orthophosphate, chromate, and silicate prevented the corrosion of tin.

The present investigation was undertaken to study the possibility of using sodium pyrophosphate as an inhibitor for the corrosion of tin and to investigate the effect of this substance on the cathodic and anodic polarization measurements. Polyphosphates were found to have an inhibiting effect on the corrosion of iron (8). Pyrophosphate was chosen for the present investigation because it is more stable than metaphosphate (9). The mechanism of inhibition of iron corrosion by polyphosphates sometimes (10) was attributed to the laying down of a calcium carbonate film favored by the presence of polyphosphate. The present investigation, therefore, was extended to study the effect of calcium chloride on the rate of corrosion of tin.

Experimental

The electrolytic cell used for polarization measurements was similar to that used in overpotential work (11). It had two separate compartments for anode and cathode. One of these two compartments was provided with a capillary leading to a salt bridge via a glass tap. The barrel of a syringe, 10 cm long and 1 cm in diameter, was joined to the top of this compartment and was used to lower the test electrode so as to touch the tip of the capillary without introducing air inside the cell. A saturated calomel was used as a reference electrode. The cell was guarded against atmospheric oxygen with the use of ground glass joints and water-sealed taps. A subsidiary platinum electrode, in the form of a disk 1 cm^2 in area, was used in connection with the tin electrode. The cell also was used for the measurements of corrosion potentials. For measurements in air-free solutions, purified nitrogen was introduced into the cell and was divided between the two compartments by means of two taps. Nitrogen was purified by passing it through NaOH and pyrogallol solutions and then over copper heated to 450° to remove traces of oxygen left. Bubbling of nitrogen was stopped during potential measurements.

Tin electrodes were prepared from pure tin foil (over 99.99% Sn) in hydrogen atmosphere. This was carried out in a glass apparatus having a side arm (3 mm ID) containing a piece of platinum wire the middle of which was sealed to glass. After introducing the tin foil, the apparatus was closed by a ground glass joint and was deaerated by passing hydrogen for several hours. The metal then was melted and the melt was introduced into the side arm. The metal was allowed to cool under hydrogen, and the side arm was cut off the main apparatus. Part of the tin electrode was exposed by cutting the appropriate length of glass. The electrode then was sealed to the piston of the syringe, the barrel of which was joined to one of the compartments of the cell.

For corrosion tests, tin rods were prepared as described above and then were rolled into sheets 1 mm in thickness. Specimens (2 x 1.5 cm) were cut. They were abraded to 00 emery paper, degreased in hot benzene, and then were dried and weighed. Corrosion tests were carried out in a wide 100 ml jar provided with a loosely fitting wooden cover from which the electrode was suspended by a thread. In this manner oxygen concentration cells from top to bottom were minimized. All corrosion tests were carried out in aerated unstirred solutions for a period of three days. The specimen then was removed,

[1] Present address: Institut fur anorganische Chemie, Berlin, Germany.

rinsed with conductivity water, swabbed with a towel wetted with benzene, and finally was dried and weighed.

Measurements were carried out in solutions of hydrochloric, acetic, citric, and maleic acids, sodium hydroxide, sodium carbonate, sodium benzoate and sodium chloride. These were chosen to represent some of the solutions which contact tin in its various industrial applications. Solutions were prepared from "Analar" grade reagents and conductivity water. The sodium pyrophosphate[2] used contained 0.1% orthophosphate and 0.025% impurities such as Fe, K, and Pb. Solutions of pyrophosphate were prepared directly before the tests in order to minimize any possible reversion to the orthophosphate. All measurements were carried out at 30° in an air thermostat controlled to ±0.5°. Results were duplicated and the mean was computed. The spread in the corrosion rate was less than 1 mdd. All potentials were recorded vs. the saturated calomel electrode potential. The current density was expressed in amp/cm².

Results

Corrosion rates, in air-saturated solutions, are given in Table I for five concentrations ranging from 0.05 to 1.0M. The effect of sodium pyrophosphate on the corrosion rate was studied in 0.1M solutions for various concentrations of pyrophosphate. Results are given in Table II. Data for the corrosion rate in the presence of 0.01M $CaCl_2$, and in the presence of a mixture of 0.01M $CaCl_2$ and 0.01M $Na_4P_2O_7$ are given in Table III for six different solutions. The effect of $Na_4P_2O_7$ on the *p*H in 0.1M solutions is given in Table IV. The *p*H values in pure 0.1M solutions are included in Table IV for comparison. The *p*H values in presence of $CaCl_2$ are given in Table V. Measurements of the *p*H were carried out under the conditions of corrosion rate measurements.

The dependence of the potential of corroding tin on time was studied in deaerated and air-saturated solutions. Corrosion potentials were measured over a wider concentration range than corrosion rates. Except in Na_2CO_3 solutions, the steady-state corrosion potential E_c is reached within 5 min from the moment the electrode contacts the solution. In all solutions studied, E_c is active with respect to the saturated calomel potential. In deaerated solutions, E_c is more active than the corresponding value in air-saturated solutions. The effect of concentration on the corrosion potential was studied by measuring time-potential relations for five different concentrations in deaerated and air-saturated solutions. Except in NaCl solutions, E_c increases toward more active potentials with increase of concentration. The relation between E_c and log C, where C is the molarity, is linear for both deaerated and air-saturated solutions. Results are shown in Fig. 1 and 2 for aerated and deaerated solutions, respectively. In NaCl solutions (not shown in Fig. 2), E_c remains practically constant (560-570 mv more active than the saturated calomel potential) with increase of concentration from 0.05 to 1.0M. The effect of sodium pyrophosphate on the corrosion potential was

[2] Prepared by Fabrication Alemana, Germany.

Table I. Effect of concentration on corrosion rate in aerated pure solutions

Solution	Corrosion rate (mdd) in 0.05M	0.1M	0.25M	0.5M	1.0M
Hydrochloric acid	3	15	17	22	29
Acetic acid	5	11	14	16	18
Citric acid	13	18	20	23	26
Maleic acid	19	64	212	417	1083
Sodium hydroxide	12	20	23	24	29
Sodium carbonate	5	13	15	27	29
Sodium chloride	2	2	2	3	3
Sodium benzoate	3	3	4	5	6

Table II. Effect of pyrophosphate concentration on corrosion rate in 0.1M solutions

Solution	Corrosion rate (mdd) at different concentration of $Na_4P_2O_7$ 0.01M	0.025M	0.05M	0.25M
Hydrochloric acid	5	4	3	3
Acetic acid	9	7	6	3
Citric acid	17	15	13	10
Maleic acid	37	28	18	7
Sodium hydroxide	20	18	16	11
Sodium carbonate	9	7	6	5
Sodium benzoate	2	2	2	2
Sodium chloride	2	2	1	1

Table III. Effect of $CaCl_2$ on corrosion rate in 0.1M solutions

Solution	Corrosion rate (mdd) in presence of 0.01M $CaCl_2$	0.01M $CaCl_2$ + 0.01M $Na_4P_2O_7$
Hydrochloric acid	3	1
Acetic acid	1	1
Citric acid	4	3
Maleic acid	16	5
Sodium benzoate	1	1*
Sodium chloride	0	0*

* Solution is turbid.

Table IV. Effect of pyrophosphate concentration on the *p*H in 0.1M solutions

Solution	Concentration $Na_4P_2O_7$ Pure 0.1M	0.01M	0.025M	0.05M	0.25M
Hydrochloric acid	1.1	1.2	1.3	2.1	7.6
Acetic acid	2.6	4.0	4.5	5.3	7.8
Citric acid	1.8	2.5	2.8	3.4	6.0
Maleic acid	1.2	1.6	1.9	3.4	7.1
Sodium hydroxide	11.9	12.1	12.1	12.1	12.0
Sodium carbonate	11.1	11.1	11.1	11.0	10.9
Sodium benzoate	7.1	9.6	9.9	9.9	9.9
Sodium chloride	6.3	9.7	9.8	9.8	9.8

Table V. Effect of $CaCl_2$ on the *p*H in 0.1M solutions

Solution	Concentration $Na_4P_2O_7$ 0.01M $CaCl_2$	0.01M $CaCl_2$ + 0.01M $Na_4P_2O_7$
Hydrochloric acid	1.1	1.1
Acetic acid	2.7	3.7
Citric acid	1.9	2.3
Maleic acid	1.4	1.6
Sodium benzoate	7.1	9.3
Sodium chloride	6.3	9.3

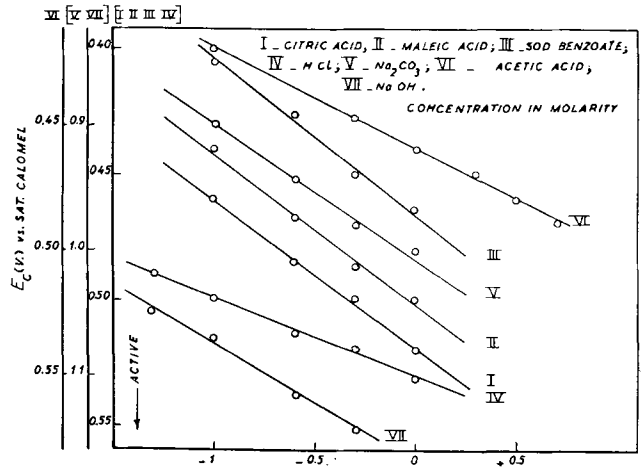

Fig. 1. Effect of concentration on corrosion potentials in aerated solutions.

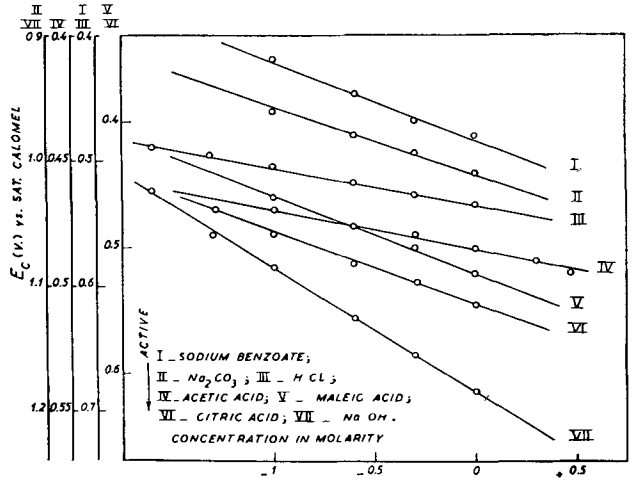

Fig. 2. Effect of concentration on corrosion potentials in deaerated solutions.

studied in 0.1M solutions. In presence of as little as 0.01M $Na_4P_2O_7$, E_c increases toward more active potentials in both deaerated and air-saturated solutions. Furthermore, this effect is proportional to the pyrophosphate concentration as is clear from the results, in deaerated 0.1*N* HCl, shown in Fig. 3.

Cathodic polarization measurements were carried out in deaerated 0.1M solutions of NaOH, HCl, acetic, and maleic acids. Measurements were started from low to high current densities. At each setting of current, the electrode was left polarized until the steady-state potential was reached. This usually took less than 5 min. Results in maleic acid and NaOH are shown in Fig. 4 and 5, respectively. Cathodic polarization curves for HCl and acetic acid are similar to those of maleic acid. It is clear from Fig. 4 and 5 that $Na_4P_2O_7$ increases the cathodic polarization toward more active values. This increase is proportional to the concentration of pyrophosphate added. The relation between cathodic polarization and the logarithm of the concentration of $Na_4P_2O_7$ is similar to Fig. 3. $CaCl_2$, however, does not change the cathodic polarization appreciably (Fig. 4). Similar conclusions are drawn for HCl and acetic acid. Previous work on iron (12) similarly has indicated that polyphosphates increase the cathodic polarization toward more active potentials.

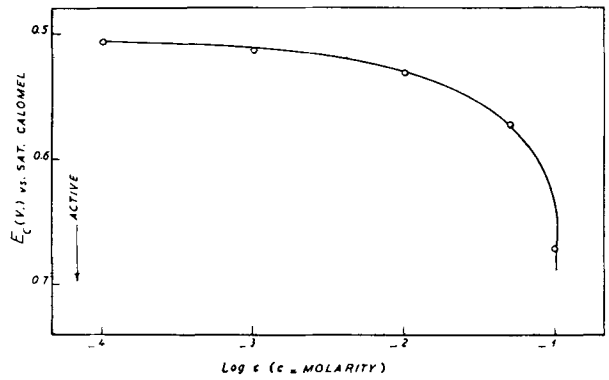

Fig. 3. Effect of pyrophosphate concentration on corrosion potential in deaerated 0.1N HCl.

Anodic polarization measurements were carried out in aerated 0.1M solutions of maleic acid and NaOH. In order to minimize the time effect, the electrode was left unpolarized until the corrosion potential was attained. Polarization then was commenced at a low current density, and the electrode was left polarized for nearly 1 hr until the steady-state potential was reached. With this slow technique, the potential changed from the active to the noble direction. Following this, measurements at higher current densities were taken. Results, at high current densities, are shown in Fig. 4 and 5, from which it is clear that $Na_4P_2O_7$ decreases the anodic polarization (potential becomes less noble) in 0.1N NaOH, and it has no effect on the anodic polarization in 0.1M maleic acid solution.

Discussion

It is clear from the data given in Table I that, in aerated solutions, the rate of corrosion of tin increases with increase of concentration. However, this increase is not marked in NaCl solutions as compared to the results in other solutions studied. The maximum rate of attack is observed in maleic acid solutions. Table II indicates that the corrosion rate, in acid and alkaline solutions, decreases with the increase of pyrophosphate concentration. In NaCl solution, the corrosion rate is decreased only

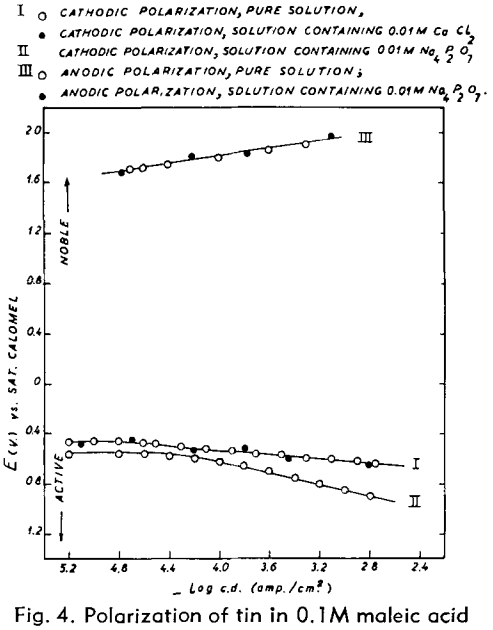

Fig. 4. Polarization of tin in 0.1M maleic acid

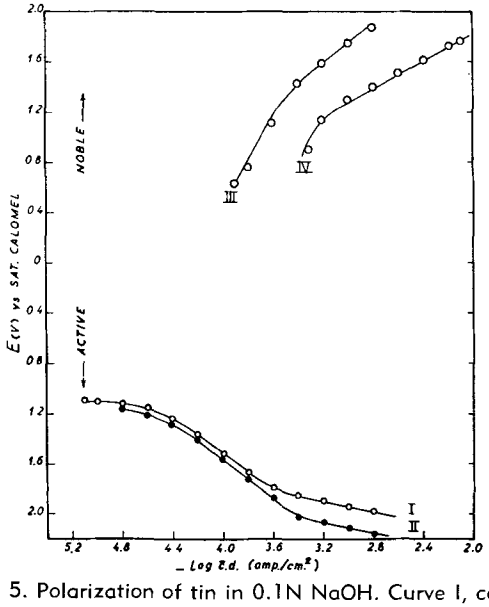

Fig. 5. Polarization of tin in 0.1N NaOH. Curve I, cathodic polarization, pure solution; II, cathodic polarization, solution containing 0.01M $Na_4P_2O_7$; III, anodic polarization, pure solution; IV, anodic polarization, solution containing 0.01M $Na_4P_2O_7$.

by 1 mdd at high pyrophosphate concentrations, whereas in sodium benzoate solution it is independent of pyrophosphate concentration. Hence, pyrophosphate is an effective inhibitor for the corrosion of tin in the acid and alkaline solutions studied. Previous work (8), on the inhibition of the corrosion of mild steel, has shown that polyphosphates are effective corrosion inhibitors in presence of dissolved oxygen. Moreover, it has been observed that addition of $CaCl_2$ accelerates the corrosion of mild steel in presence of dissolved oxygen (8). In the case of tin, $CaCl_2$ decreases the corrosion rate as it is clear from results given in Tables I and III. Addition of pyrophosphates to the solution containing $CaCl_2$ produces a further decrease in the corrosion rate in HCl, citric, and maleic acids (Table III).

The shift of cathodic polarization toward more active values (Fig. 4 and 5), produced by the addition of pyrophosphate, may be ascribed to the adsorption of pyrophosphate on tin cathodes thus lowering the available surface area for the cathodic reaction. Adsorption of pyrophosphate on local cathodic areas also may account for the change of corrosion potentials [given by the point of intersection of the anodic and cathodic polarization curves (13)] toward more active values, observed in solutions containing pyrophosphate. Thus, if the polarization of local cathodes is increased in presence of pyrophosphate (Fig. 4 and 5), while the polarization of local anodes is decreased (Fig. 5) or not affected (Fig. 4), the corrosion potential is shifted toward more active values. In the first case, the corrosion rate may not be affected as it is evident from the results in 0.1*N* NaOH (cf. Tables I and II). On the other hand, when cathodic polarization is increased in presence of pyrophosphate and anodic polarization is not affected, the corrosion rate decreases as is clear from the results in maleic acid solutions, given in Tables I and II.

The present investigation indicates that the rate of corrosion of tin in acid and alkaline solutions is greater than that observed in NaCl and sodium benzoate solutions (Table I). This may be explained on the basis of the amphoteric character of tin according to which tin is expected to dissolve in the acid and alkaline pH range more than in the neutral pH range (cf. Table IV). It is clear from Table IV that addition of pyrophosphate to acid solutions increases the pH to the neutral range, and, hence, it is expected that tin does not go into solution as readily in this pH range as it does in the extreme acid range. In alkaline solutions pyrophosphate has no appreciable effect on pH (Table IV). However, the possibility exists that, in such solutions, pyrophosphate may have a complexing action on tin with the result that the anodic polarization is decreased in presence of pyrophosphate as compared to the values in absence of pyrophosphate (Fig. 5). This effect is, however, compensated by the increase of cathodic polarization in presence of pyrophosphate. In salt solutions, pyrophosphate increases the pH (Table IV) and has no appreciable effect on the corrosion rate (Table II). This increase in pH would require more dissolution of tin, i.e., decrease of the anodic polarization. However, for the corrosion rate to remain constant, this effect also must be compensated by the increase of cathodic polarization.

It is clear from the results of the present investigation that $CaCl_2$ is not necessary for pyrophosphate to function as a corrosion inhibitor, in contradiction to the suggestion of Raistrick (10) that inhibition by polyphosphates is due to the laying down of a calcium carbonate film favored in presence of polyphosphates. However, $CaCl_2$ has no appreciable effect on pH (Table V) and it decreases the corrosion rate (Table III). This is not easy to explain since $CaCl_2$ has no effect on the cathodic polarization measurements (Fig. 4) while its effect on anodic polarization is irreproducible.

Acknowledgment

The authors wish to express their thanks to Professor A. R. Tourky for his interest in this work.

Manuscript received Sept. 11, 1958.

Any discussion of this paper will appear in a Discussion Section to be published in the June 1960 JOURNAL.

REFERENCES

1. U. Evans, "Metallic Corrosion Passivity and Protection," p. 404, Edward Arnold, London (1945).
2. T. P. Hoar, *J. Inst. Metals*, **55**, 135 1934).
3. R. Kerr, *J. Soc. Chem. Ind.*, **65**, 101 (1946).
4. R. Kerr, R. M. Angles, and K. Caulfield, *ibid.*, **66**, 5 (1947).
5. R. M. Angles and R. Kerr, *Engineering*, **161**, 289 (1946).
6. S. Britton and R. Angles, *Bull. Inst. Metal Finishing* (London), **3**, 259 (1953-1954).
7. S. Britton and D. Michael, *J. Applied Chem.*, **7**, 349 (1957).
8. H. Uhlig, D. Triadis, and M. Stern, *This Journal*, **102**, 59 (1955).
9. R. Morgan and R. Swoope, *Ind. Eng. Chem.*, **35**, 821 (1943).
10. B. Raistrick, *Chemistry & Industry*, **1952**, p. 408.
11. I. A. Ammar and S. Awad, *J. Phys. Chem.*, **60**, 837 (1956).
12. J. Mansa and W. Szybalski, *Acta Chem. Scand.*, **4**, 1275 (1950).
13. M. Stern and A. Geary, *This Journal*, **104**, 56 (1957).

Thin Film Formation on Zirconium

Robert E. Meyer

Chemistry Division, Oak Ridge National Laboratory,

operated by Union Carbide Corporation for the U. S. Atomic Energy Commission, Oak Ridge, Tennessee

ABSTRACT

Using an electrochemical method, rates of film growth in oxygenated sodium sulfate solutions have been measured on polycrystalline zirconium at temperatures ranging from 25° to 88°C. The resulting rate-time plots are roughly hyperbolic. A model is proposed which when treated by electrode kinetics is shown to give this type of behavior.

Recently, correlations have been observed between the polarization resistance of a corroding electrode and its corrosion rate (1-3). The polarization resistance of an electrode is defined as the derivative $dE/dI_{E\to E_r}$ where I is the net current flowing through the electrode at a measured potential E, and E_r is the rest potential. Theoretical justification for this correlation has been provided by Stern and Geary (4) who derive the following equation from the Tafel equation for the case where the rest potential of a corroding electrode is determined by the intersection of two logarithmic polarization curves

$$\frac{dE}{dI_{E\to E_r}} = \frac{b_a b_c}{(2.3)(I_{corr})(b_a + b_c)} \qquad [1]$$

Here, I_{corr} is the corrosion rate of the electrode, and b_a and b_c are the Tafel slopes ($dE/d \log I$) for the anodic and cathodic reactions. This equation has been derived from more fundamental quantities by Posey (5), who has presented a complete discussion of the kinetics of polyelectrodes under activation control. If the conditions for the use of Eq. [1] can be met, it provides an excellent method for measuring rates and should be applicable especially to systems whose rates may be too small for weight-loss or analytical methods. Because rates can be measured quickly while the sample remains in the solution without significantly disturbing the system, this method is applicable particularly to the determination of rate-time plots.

In order to use this method, it must be shown that the open-circuit potential is determined by the intersection of two logarithmic polarization curves, one anodic and one cathodic. Furthermore, there must be no oxidation process other than the corrosion process under consideration, i.e., one must make sure that no portion of the anodic current is the oxidation of hydrogen, water, ferrous ion, or other oxidizable species.[1] It should be evident also that the presence of a film does not necessarily preclude the method, for logarithmic potential-current behavior is possible also on film-covered electrodes.

[1] It is, of course, possible in many cases to take a second oxidation reaction into account and determine the corrosion rate from electrochemical measurements alone, but this involves the analysis of far more complex polarization behavior [see Stern (6) and Posey (5)].

In the experiments reported here, this method was applied to the measurement of film growth on zirconium immersed in oxygen-saturated 0.1 F Na_2SO_4 of *p*H 3.5. The reaction believed to occur is the oxidation of zirconium to zirconium oxide (7), ZrO_2. The cathodic or reduction process is therefore the reduction of oxygen and the anodic or oxidation process is the oxidation of zirconium. Because of the great insolubility of ZrO_2, all oxidized zirconium is assumed to be incorporated into the film. Other possible cathodic processes are the reduction of hydrogen ions or water and the reduction of the film. The latter process is thermodynamically improbable at these potentials, and measurements of hydrogen evolution (to be reported in a later publication) showed that the rates are negligible under the conditions encountered in these experiments.

The possible interfering anodic processes are the oxidation of impurities and the oxidation of water. Careful purification of the solution and cell can eliminate the former and also at the same time eliminate impurities that may interfere with the kinetics of the cathodic process. Significant water oxidation on these systems is not observed until one obtains potentials at least 1.5 v above the highest potentials encountered in this work. Therefore, it is probable that the rate of water oxidation is negligible at potentials near SCE.

Typical polarization behavior of this system is shown in Fig. 1. Here it is demonstrated that the reduction of oxygen follows an equation of the form

$$I_c = I_{o,c} \exp \frac{-\alpha_c z_c E\,\mathrm{F}}{RT} \qquad [2]$$

where α_c is the transfer coefficient of the cathodic process, z_c is the charge number, and $I_{o,c}$ is a constant whose numerical value depends on the reference potential to which values of E are referred. This equation is the Tafel equation written in the exponential form with $b_c = RT/\alpha_c z_c \mathrm{F}$.

An analogous equation is assumed for the anodic current, I_a, at constant film thickness, as follows

$$I_a = I_{o,a} \exp \frac{+\alpha_a z_a E\,\mathrm{F}}{RT} \qquad [3]$$

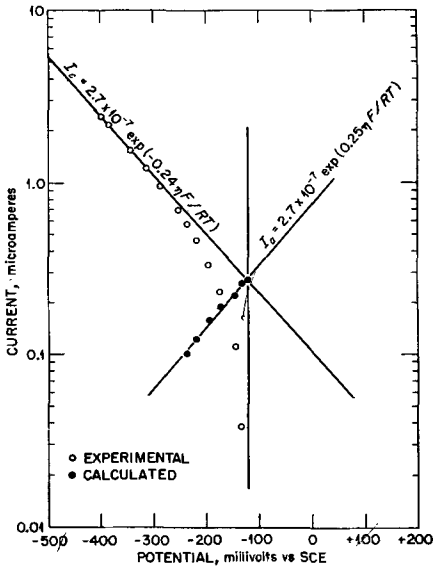

Fig. 1. Experimental current-potential plot in oxygenated Na_2SO_4 solution at 88°C.

where α_a and z_a are the transfer coefficient and charge number, respectively, of the anodic reaction. This assumption is made reasonable by the theoretical considerations described below which led to the derivation of Eq. [6]. An equation of the form of Eq. [3] has been reported valid for the anodizing of zirconium at constant film thickness by Adams and Van Rysselberghe (8).

Equation [1] can be solved for I_{corr} and rewritten in terms of the variables in Eq. [2] and [3] as follows

$$I_{corr} = \frac{dI}{dE_{E\to E_r}} \times \frac{RT}{F} \times \frac{1}{(\alpha_a z_a + \alpha_c z_c)} \quad [4]$$

The quantities $\alpha_c z_c$ and $\alpha_a z_a$ can be determined from Tafel slopes, but generally it is better to determine $\alpha_a z_a$ indirectly. Excessive anodic polarization can affect the surface materially by forming significant quantities of film, and therefore it is best to avoid large anodic polarizations entirely. An indirect method[2] of determining $\alpha_a z_a$ which does not involve excessive polarization is illustrated in Fig. 1. Here the anodic polarization points are determined by the difference between the net current and the extrapolated cathodic current. The Tafel slope, and hence $\alpha_a z_a$, is determined then from the slope of the line through these points. At the end of an experiment, when there is no need for further measurements, it is possible to check the value of $\alpha_a z_a$ by direct anodic polarization. Of course, the voltage rises with time when zirconium is anodized at constant density, but if the current density is small enough, the voltage rise during the measurement will be negligible. At the end of an experiment, these small current densities are sufficient to obtain a Tafel slope, from which $\alpha_a z_a$ may be estimated.

The quantity $dI/dE_{E\to E_r}$ can be determined by plotting I vs. E on a linear scale and by determining the slope at $E = E_r$. Since the I vs. E plot is linear over a short potential range about the rest potential, the slope can be determined very easily from several polarizations at small overvoltages.

In general, $\alpha_a z_a$ and $\alpha_c z_c$ do not vary rapidly in an experiment and therefore need be determined only occasionally. Rate-time curves can be determined therefore by a series of small polarizations, which determine $dI/dE_{E\to E_r}$, along with a few complete cathodic polarization curves.

Normally it is desirable to obtain a longer linear Tafel region than shown in Fig. 1, but concentration polarization is likely to interfere if the current density is further increased. The linear Tafel slope was verified by a great many plots similar to Fig. 1, many of which had considerably longer linear regions.

It should be noted here that this method of measuring rates is independent of mechanism since it only requires that equations of the form of Eq. [2] be obeyed formally over the potential and current ranges used.

Experimental

The measurements were carried out in 100 cc Pyrex cells which contained the zirconium electrode, an inlet and exit for oxygen, a platinum polarizing electrode, and a Haber-Luggin capillary leading through an all-glass closed stopcock to a separate chamber which contained a saturated calomel electrode. Oxygen was introduced through the inlet vigorously in order to provide sufficient stirring and to insure saturation. No greases or waxes of any kind were used in the cell, the only nonglass material used being Teflon. The zirconium electrodes, which were machined from fine-grained ¼ in. crystal bar rod and had an area of 2.2 cm^2, were cylinders ⅜ in. long and ¼ in. in diameter. They were mounted on ¼ in. Teflon rod holders which effectively masked off one end of the cylinder, electrical contact being maintained by a stainless steel rod threaded into the center of the masked-off end of the cylinder. The steel rod was masked completely from the solution by passing it through a hole drilled down the axis of the ¼ in. Teflon rod.

Before immersion in the cell, the electrodes were cleaned and immersed in a H_2O-HNO_3-HF chemical polishing bath long enough to remove several mils of metal. They then were rinsed with triply distilled water several times and finally immersed for 2 min in boiling triply distilled H_2O. This procedure was carried out by rapidly transferring the electrode from beaker to beaker so that the liquid never was allowed to dry on the surface. If the polishing solution were allowed to dry on the surface, a white insoluble residue would be left which defied all attempts at removal except by a repeated immersion in the polishing solution. The electrodes then were placed in a dynamic greaseless vacuum system and annealed for several hours at 750°C. The hottest portion of the furnace contained a supply of zirconium chips which acted as a getter. The electrodes so treated undoubtedly had a residual thin film on the surface even before the 1-min exposure to air during the process of mounting the electrodes on the Teflon holder. The initial rates observed were still

[2] This and another method for determining the anodic Tafel slope knowing the complete cathodic polarization curve have been described by Stern and Roth (9).

faster than could be measured by the methods used, so that there seemed to be no point to taking elaborate precautions to minimize the initial film.

The solutions used were made up from triply distilled water, doubly recrystallized sodium sulfate, and a small amount of C.P. H_2SO_4. One of the water distillations was made from alkaline permanganate solution. The solutions were pre-electrolyzed between platinum electrodes a minimum of 24 hr at about 10 ma before use. At this current the potential of the cathode was well below the lowest potential observed on the zirconium electrode.

The cells were cleaned with ordinary dichromate cleaning solution and with a hot mixture of equal parts of water, concentrated HNO_3, and concentrated H_2SO_4. The latter solution very efficiently removed the last traces of greases and other contaminants from the surface of the cell. The cells then were rinsed thoroughly with triply distilled water, one of the rinses including a 24-hr soaking with hot stirred water.

Potentials were measured with a L&N Model 7664 pH and emf meter which was modified slightly so that its output could be fed into a 10-mv Brown recorder. This whole unit was calibrated periodically with a potentiometer, and the absolute accuracy was about ±1 mv on a 1000 mv range or ±0.5 mv on a 100 mv full-scale range. The high input impedance of the pH meter, about 10^{11} ohms, effectively prevented any polarization of the electrode by the measuring circuit and also made the meter suitable for measuring small currents by measuring the potential drop over high-value resistors.

The small currents used were supplied by a bank of radio "C" batteries connected in series so that up to 230 v could be obtained. In order to maintain constant current a large resistance was placed in series in the polarizing circuit. The resistors were connected to a battery of decade switches so that any resistance from 0 to 10^9 ohms could be obtained quickly. This variable resistance plus a second switch which selected several voltages provided a convenient way of obtaining any necessary current.

A typical experiment was carried out as follows: the cell was cleaned, and the solution and electrode prepared as described above. At the completion of the cooling period after the vacuum anneal the electrodes were mounted quickly on the electrode holder and immersed in the prepared solution with the potential-measuring device on. The potential was recorded continuously during the experiment, and both small and complete polarization curves were taken at appropriate intervals. Care was taken to insure that the polarization did not alter the course of the experiment significantly. In most cases a duplicate experiment was made without any polarization in order to see whether the potential-time behavior duplicated and to compare rates at the end of the duplicate experiment to rates of those experiments which had the normal amount of polarization.

Calculations and Results

Because each of the experiments necessarily involves a large amount of data, results are presented as plots of rates vs. time and the values of the polarization resistance and α will not be given. In order to draw a smooth curve between the experimentally determined points, a semi-empirical method of determining the rates from the potential was used. As was pointed out above, the cathodic current is given by Eq. [2]. Experimentally it was found that the constants $I_{o,c}$ and $\alpha_c z_c$ changed very little in a given experiment (if $I_{o,c}$ is defined always at the same reference potential). Therefore a plot of the corrosion potential vs. the logarithm of the corrosion rate, which is necessarily equal to the cathodic current at the corrosion potential, should be either a straight line of slope $RT/\alpha_c z_c F$ (for the case of constant $I_{o,c}$ and $\alpha_c z_c$) or a gently curving line (for the case of slightly varying $\alpha_c z_c$ and $I_{o,c}$). Such a plot is shown in Fig. 2 for an experiment at 88°C, the open circles on the plot representing points determined from Eq. [4]. Because the potential-time behavior is known from the continuous potential recording, the rate-time curve can be found by combining the rate-potential and potential-time plots. In Fig. 3, the potential-time behavior of this experiment (No. 4) is given along with the potential-time behavior of a number of other experiments at about the same temperature. In Fig. 4 and 5 the rate-time curves are shown for two experiments each at 25°, 46°, 66°, and 88°. Rates are given as total current; current density may be obtained by dividing the numbers in the graph by 2.2 cm^2, the area of the electrodes. The notable features of the rate-time curves are the very sharp initial decline and the gradual leveling off. The shapes of the curves are approximately hyperbolic in time and rate. The open circles on the one 88° experiment in Fig. 5 show points de-

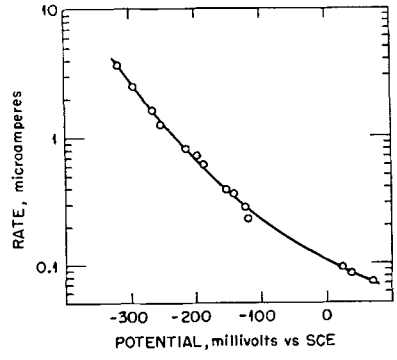

Fig. 2. Corrosion rate vs. open-circuit potential for zirconium in oxygenated Na_2SO_4 solution at 88°C.

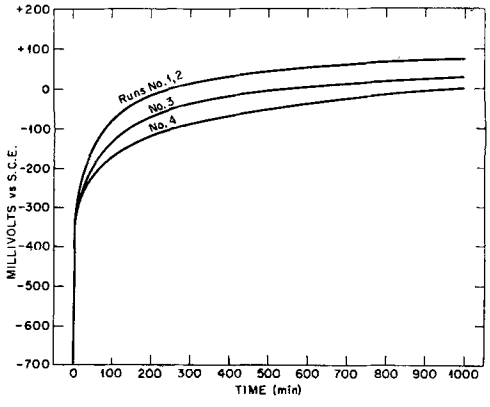

Fig. 3. Potential-time curves for crystal bar zirconium at 88°C in Na_2SO_4 solution.

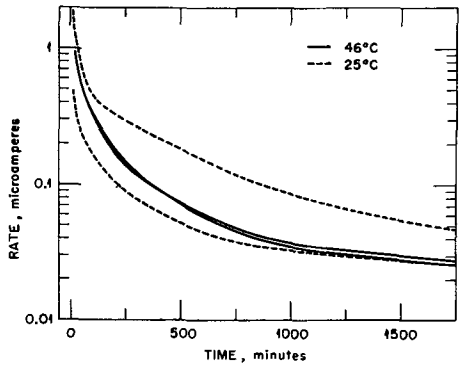

Fig. 4. Corrosion rate vs. time for zirconium in oxygenated Na_2SO_4 solution at 25° and 46°C.

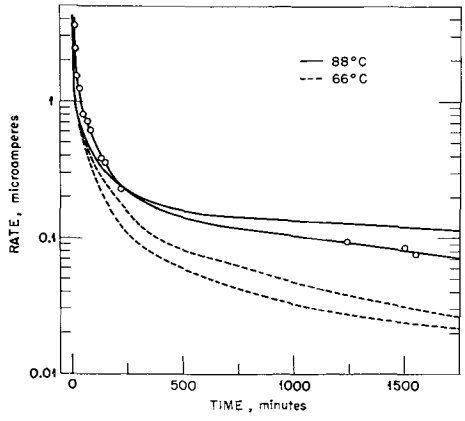

Fig. 5. Corrosion rate vs. time for zirconium in oxygenated Na_2SO_4 solution at 66° and 88°C.

termined directly by Eq. [4]; the rest of the curve was determined by the method described above.

It will be noted from Fig. 3 that the potential time curves do not exactly duplicate, although the general shape is the same. Because the rate changes by one power of ten for about every 300 mv change in potential, it is clear that a difference of 100 mv at a given time is not a serious irreproducibility. It is clearly impossible to duplicate precisely the surface of the electrode or the initial film thickness. The fact that the curves are as smooth as they are is of some significance, since such smooth curves could be obtained only if adequate solution purification and careful electrode preparation were carried out; otherwise jagged potential-time plots were observed.

As mentioned above, the constants $I_{o,c}$ and $\alpha_c z_c$ for the reduction of oxygen stayed fairly constant in a given experiment, i.e., the current-potential plots were almost superimposable. On the other hand, $\alpha_a z_a$ decreased with time, especially at 88°. In a typical experiment at 88°, the first determination of $\alpha_a z_a$ might yield a value as high as 0.3 or 0.35 while after several days $\alpha_a z_a$ might be as low as 0.1.

Discussion

Before attempting to describe the results in any mathematical form, some of the complexities of this system should be discussed. First, one has to be careful about applying the concept of a "single rate-determining step" since there are always two half-reactions present, anodic and cathodic, in any oxidation, and only if one were practically at equilibrium would it be justifiable to say that the other is a single rate-determining reaction. In the system considered here, neither the anodic nor the cathodic reaction is at equilibrium; hence, they both control the rate of the reaction. Furthermore, it is conceivable that in either the anodic or cathodic process there are two or more reaction barriers such that the concepts of consecutive reactions must be considered to analyze the system. Consecutive reactions are especially likely to occur in three-phase systems of the type considered here, when one must consider charged-particle transfer through the metal-film and film-solution interfaces and through the bulk of the film.

Another complexity that very likely occurs is the heterogeneous growth of the film. Variations in thickness and shape of the films can be produced easily by variations in activation energies and other kinetic factors which are caused by the presence of defects, grain boundaries, various exposed crystal faces, etc. Thus the actual growth of a film even in a carefully controlled experiment is very complex. The theoretical treatment of heterogeneous growth is extremely complex and, in common with most treatments of film growth, uniform growth will be assumed here.

The pertinent experimental facts that must be explained are the rapid decrease in rates, the decrease in α_a, and the rise in potential. The basic hypothesis that leads to an explanation of these observations is that a portion of the total potential drop occurs in the film and the field in the film decreases as the film thickens[3] and the potential changes. The field strength will be given by

$$F = \frac{V}{X} = \frac{V}{X_o + R\int Idt} \qquad [5]$$

where F is the field strength, V is the potential drop across the film, X is the film thickness, X_o is the initial film thickness, $\int Idt$ is the total charge passed, and R is the factor relating charge to thickness. If the structure of the film and the area of the electrode are known, R can be calculated easily. It will be assumed that the anodic current is controlled by a field-dependent rate-determining process within the film such that the activation energy will be lowered by the amount $(z_a elV)/(X_o + R\int Idt)$ where $(z_a e)$ is the charge of the moving particle and l is the distance through which the force acts. This rate-determining process could be the movement of an ion from one equilibrium position to another, and the location of the barrier to this movement could be either at one of the interfaces or in the bulk of the film. Neglecting any reverse current in the film, the anodic current will be given by

$$I_a = I_{k,a} \exp \frac{z_a elV}{(X_o + R\int Idt)kT} \qquad [6]$$

This equation, in the simpler form $I_a = A \exp BF$, where A and B are constants, has been verified ex-

[3] Such an explanation was proposed by Cabrera and Mott (11) in their treatment of thin films, but their subsequent treatment is different from that proposed here.

perimentally for the anodizing of zirconium by Charlesby (10); and a similar equation has been derived by Cabrera and Mott (11). The constant $I_{k,a}$ will contain a concentration term, a frequency factor, and an exponential term in activation energy. The assumption that reverse movement of the ions is negligible is good for high field strength or for a very high activation energy for movement in the reverse direction. The latter condition is most probable if the principal barrier to particle movement is at one of the interfaces. If there is a symmetrical energy barrier such as might occur in the bulk of a film, then the reverse current will not be negligible at low field strength.

The reduction of oxygen will entail a flow of electrons through the film against the field. It will be assumed that the height of this potential barrier in the film will determine the flow of electrons in the manner represented by

$$I_c = I_{k,c} \exp(-\alpha_c' eV/kT) \quad [7]$$

The constant α_c' should be distinguished from α_c of Eq. [2] because the former affects only the film potential and the latter affects the total potential including the double-layer potential at the film-solution interface.[4] This assumption is not strictly valid and agrees only approximately with experiment. The experimental α_c value decreases during the course of the experiment although not nearly as much as α_a decreases. This decrease in α_c could easily be due to changes in α_c'. Electronic film resistances are assumed negligible since the films are on the order of 100Å or less thick.

Equations [6] and [7] may be combined with the elimination of eV/kT to give

$$X_o + R\int I dt = -\frac{z_a l \ln(I/I_{k,c})}{\alpha_c' \ln(I/I_{k,a})} \quad [8]$$

recalling that $I_a = I_c = I$ at open circuit.

Differentiating with respect to time, Eq. [8] results in

$$\frac{dI}{dt} = -\frac{\alpha_c' R I^2 [\ln(I/I_{k,a})]^2}{z_a l \ln(I_{k,c}/I_{k,a})} \quad [9]$$

or

$$\frac{dI}{dt} = -AI^2 [\ln(I/I_{k,a})]^2 \quad [9a]$$

where $A = \dfrac{\alpha_c' R}{z_a l \ln(I_{k,c}/I_{k,a})}$.

Equation [9] can be integrated but the result is a series which is not easy to use. It is more convenient to integrate it graphically for various values of $(I/I_{k,a})$. Since the variation in the term $[\ln(I/I_{k,a})]^2$ is small compared to changes in I^2, a useful approximate integration can be made by assuming that $\ln(I/I_{k,a})$ is constant. This assumption may be further improved by the possibility that $I_{k,a}$ may decrease slightly with time along with I. Because particles in low activation energy positions are likely to react first in preference to particles in higher activation energy positions, the over-all average activation energy is likely to be increased and therefore $I_{k,a}$ decreased. If then $\ln(I/I_{k,a})$ is assumed constant, Eq. [9a] integrates to

$$1/I = A[\ln(I/I_{k,a})]^2 t + K \quad [10]$$

where K is an integration constant. Equation [10] is, of course, a hyperbola.[5]

The behavior of these functions is shown in Fig. 6 where Eq. [10] is plotted along with the results of the graphical integration of Eq. [9]. In order to emphasize the differences of the shapes of the curves, the constants are chosen so that all functions will have the same values at currents (rates) of one and 100. There is obviously little difference in the shape of the curves unless $I/I_{k,a}$ is less than about 10^4, which will occur for small fields. Thus these equations would predict that the rate-time behavior is almost hyperbolic at high field strength (or the thickness-time behavior is almost logarithmic). In Fig. 7 it is shown that by the proper selection of the constants, the theoretical expressions can account for experimental plots. For the sake of clarity, only three rate-time curves are shown, but the others can easily be fitted also. Of course, with three arbitrary constants, A, K, and $I_{k,a}$, this is relatively easy, so that all that Fig. 7 shows is the possibility that the theoretical expressions can account for the experimental rate curves.

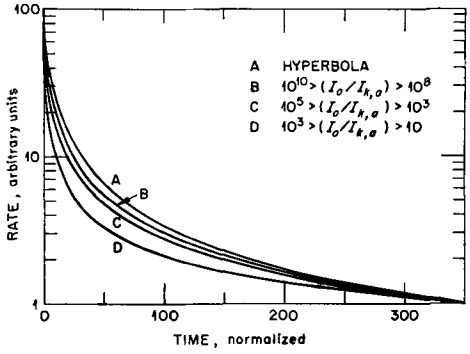

Fig. 6. Theoretical rate-time curves

[4] Experimental evidence obtained by the author suggests that the reduction of O_2 is best represented by a dual-barrier model, one barrier occurring at the film-solution double layer, and the other in the film as described above. For a more complete description of the dual-barrier model see Posey (12).

[5] This derivation is similar mathematically to a derivation presented by Vetter (13) for film growth at constant potential. It is interesting that film growth at constant potential and at open circuit follow essentially the same kinetics.

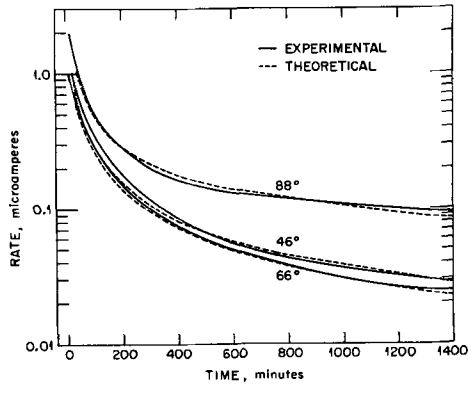

Fig. 7. Comparison of theoretical and experimental corrosion rates of crystal bar zirconium in oxygenated Na_2SO_4 solution.

It is appropriate to estimate the value of the constant A in order to see if it has the correct order of magnitude. This involves mainly an estimate of the quantity R, which relates charge to thickness of film. Assuming the film to be ZrO_2 of density 5.5 g/cc, R is equal to 5.79 x 10^{-5} cc/coulomb ÷ area. For these specimens of 2.2 cm^2, R is equal to 2.63 x 10^{-5} cm/coulomb. The constant α_c' will be assumed to be about one, l will be assumed to be 3 x 10^{-8} cm, z_a will be assumed to be 2 corresponding to oxide ion migration, and the term ln $(I_{k,c}/I_{k,a})$ will be assumed to be of the order of magnitude of ten.[6] Using these values A turns out to be about 40 $coulombs^{-1}$. In Fig. 7, the 46° and 88° runs are fit by the graphically integrated form of Eq. [9] with A equal to 3.4 and 190, respectively, and $I_{k,a}$ assumed to be 1.1 x 10^{-9} A at 88°C and $10^{-12}A$ at 46°. The 66° run was fit by the hyperbola $1/I = 540\ (t + 960)$, t being the time in seconds (the graph gives time in minutes). Since a hyperbola was used, $I/I_{k,a}$ must be greater than about 10^5 and hence $[\ln(I/I_{k,a})]^2$ must be greater than about 130 and A, which is equal to $540/[\ln (I/I_{k,a})]^2$ according to Eq. [10], must be less than about 4. Of course these values depend on how one decides to fit the curve, but they do not change their order of magnitude for various attempts at fitting the curves. The determined values of A therefore seem to be correct as to order of magnitude.

The rise in potential which is observed in these experiments is simply the result of the decrease in anodic current at a given potential due to film thickening. In order that anodic and cathodic currents always remain equal, the potential must rise, since the anodic current must increase and the cathodic current decrease as the potential rises.

The effect of temperature is complicated as can be seen by comparing the rate expressions at various temperatures. In order to obtain meaningful data from the temperature effects, values of $I_{k,a}$ and $I_{k,c}$ would have to be known with considerable precision. However, comparison of the rate-time curves shows that, with the exception of one of the 25° experiments, the rates were considerably higher at 88° than at the other temperatures. There is therefore much more film growth in these experiments, and this accounts for the fact that the decrease in α_a was far more noticeable in the 88° experiments than in the other experiments. The experiments at 25°C should not be given much significance since there was considerably more scatter in the data leading to the (smoothed) rate-time curves shown in Fig. 4.

The expressions given here can account for the shape of the rate-time curves, but it is clear that more information is needed on the mechanisms of the cathodic and anodic processes. Probably such information is obtained best by isolating the individual processes and studying them alone. Such studies now are being carried out, and the reduction of various reducible species on film-covered zirconium will be the subject of a future communication.

[6] This estimate results from the probability that the activation energy for the anodic process is higher than that for the cathodic process. Admittedly this estimate of ten for the value of ln $(I_{k,c}/I_{k,a})$ is only a guess.

Acknowledgment

The kind encouragement and helpful discussions of Dr. G. H. Cartledge, Dr. F. A. Posey, and Dr. A. L. Bacarella, all of this Laboratory, are gratefully acknowledged.

Manuscript received March 2, 1959.

Any discussion of this paper will appear in a Discussion Section to be published in the June 1960 JOURNAL.

REFERENCES

1. K. F. Bonhoeffer and W. Jena, *Z. Elektrochem.*, **55**, 151 (1951).
2. R. V. Skold and T. E. Larson, *Corrosion*, **13**, 69 (1957).
3. M. Stern, *ibid.*, **14**, 440t (1958).
4. M. Stern and A. L. Geary, *This Journal*, **104**, 56 (1957).
5. F. A. Posey, *ibid.*, **106**, 571 (1959).
6. M. Stern, *ibid.*, **104**, 645 (1957).
7. R. D. Misch, "Electrode Reactions of Zirconium Metal," in "The Metallurgy of Zirconium," p. 663, McGraw-Hill Book Co., New York (1955).
8. G. B. Adams, Jr. and P. Van Rysselberghe, *This Journal*, **102**, 502 (1955).
9. M. Stern and R. M. Roth, *ibid.*, **104**, 390 (1957).
10. A. Charlesby, *Acta Metallurgica*, **1**, 340 (1953).
11. N. Cabrera and N. F. Mott, *Repts. Prog. Phys.*, **12**, 163 (1948-1949).
12. F. A. Posey, G. H. Cartledge, and R. P. Yaffe, *This Journal*, **106**, 582 (1959).
13. K. J. Vetter, *Z. Elektrochem.*, **59**, 67 (1955).

The Oxidation of Iron-Nickel Alloys

III. Kinetics of Oxidation of Three Commercial Alloys

R. T. Foley and C. J. Guare

General Engineering Laboratory, General Electric Company, Schenectady, New York

ABSTRACT

Three commercial iron-nickel alloys, containing 30, 41, and 78% nickel, were oxidized over the range 600°-1000°C in two atmospheres, laboratory air, and a 21.7% O_2-78.3% N_2 mixture. The oxidation of these alloys follows a parabolic weight gain-time relationship during the 60-min reaction time. Replicate experiments generally showed that the precision in determining the parabolic rate constants was better in the O_2-N_2 mixture than in laboratory air. This effect is probably the result of day-to-day variations in composition of laboratory air. Temperature dependences of the reaction rates were determined with the Arrhenius-type equation. Both the reaction rates and the apparent energies of activation of the 30-41% alloys are consistent with a rate-determining process of cation diffusion through a spinel structure $Ni_x Fe_{3-x} O_4$. It is hypothesized that the apparent energy of activation for the 78% alloy is due to the influence of the 3.8% Mo on the physical character of the film. Anomalously high rates were observed in both atmospheres at the higher temperatures, and this is discussed with reference to "over-temperatures," resulting from heat generated at the surface by oxidation.

An earlier study (1) had as its objective outlining the mechanism of high-temperature (600°-900°C) oxidation of an iron-nickel alloy containing 42% nickel. It had been pointed out that the iron-nickel system was of theoretical interest because these two elements form a continuous series of substitutional solid solution alloys with both components oxidizable. Furthermore, iron-nickel alloys of various compositions are used industrially for such purposes as glass-to-metal sealing, as magnetic materials, and as materials with special thermal properties. The earlier study demonstrated that the mechanism of oxidation involved diffusion through a nickel ferrite reaction product film, and the variation of activation energies and oxidation rates with surface preparation was explained on the basis of diffusion through ferrite structures of varying percentages of nickel. This study extends this work to two other commercial alloys and special atmospheres. Oxidation was studied over the temperature range 600°-1000°C. The objective of this paper is to report and interpret kinetic data so that ultimately a complete understanding of the mechanism of oxidation of iron-nickel alloys may be realized. It is expected that work reported and underway in two other laboratories (2-4) as well as in our own, will achieve this contribution to general oxidation theory.

Experimental

Oxidation Studies

The oxidations were carried out employing a Chevenard thermobalance. In this instrument the sample to be oxidized is supported on a fused silica rod and the furnace, at the desired temperature, is lowered around it. The change in weight of the sample is recorded automatically as a function of time.

Experiments were run at 600°, 700°, 800°, 900°, and 1000°C. The temperature of the furnace was controlled to ±1.4°C according to a General Electric protable precision potentiometer. This instrument was calibrated to be accurate to 0.05%. Usually the oxidation was allowed to proceed for 60 min. Two atmospheres were employed. The first was static laboratory air. This certainly changed from day to day because of humidity variation and other influences, all of which have not fully been assessed in high-temperature oxidation work. (Some of the experiments described here were made several years apart.) The second atmosphere consisted of a controlled mixture, 21.7% oxygen and 78.3% nitrogen by volume flowing at a rate of 263 ml/min. The dew point of this mixture was −20°F. In all cases at least duplicate, and usually triplicate, samples were oxidized. Weight changes were taken from the thermobalance curve at 6-min intervals and replotted to establish the rate constant. The spread of the parabolic rate constants is apparent from the tables listing the results. Usually this spread was less than ±6% of an average value. Where poorer precision was obtained, the experiment had usually been run in laboratory air. In several instances the first duplicate runs were within 3% of an average value. The experiment repeated several months later gave values with about the same precision. However, the first average might vary from the second by 60%. This must be due to variation in the composition of the atmosphere; experiments are now being run to clarify this point.

Composition of alloys.—The three iron-nickel alloys investigated represent compositions of interest to the electrical and electronics industry. Alloy A was nominally 30% Ni, 70% Fe; Alloy B—41% Ni, 59% Fe; Alloy C—78% Ni, 18% Fe, and 4% Mo.

Complete analyses of these alloy strips before oxidation were given in a previous report (5). Reanalysis for carbon gave a corrected value of 0.001% rather than the 0.01% reported. This agrees with what would be expected from the heat treatments. The alloys were obtained[1] in the form of strip 0.050-0.076 cm thick. The sheared coupons were annealed for 2 hr at 1125°C in hydrogen and then cooled in hydrogen to room temperature. Before oxidation the panels of about 20 cm^2 area were cleaned chemically.

Surface preparation.—The alloy strips were chemically cleaned at 90°C for 2 min in an acid mixture and with a procedure described before (5). The intent was to oxidize a surface free of disturbed metal. Electron diffraction examination of a surface prepared by this method gave only the pattern corresponding to the iron-nickel alloy (1). An objection to acid cleaning a binary alloy might arise from the possibility of selective dissolution. Presumably in an iron-nickel alloy the iron would be selectively dissolved, yielding a nickel-rich surface which would exhibit a lower oxidation rate. The magnitude of this effect was assessed by preparing samples of the 41% nickel alloy for oxidation at 900°C in the controlled O_2/N_2 atmosphere, the only variation in treatment being the time of pickling. The parabolic rate constant varied as follows:

Time in acid bath at 90°C, min	k_p (x 10^{10} g^2cm^{-4} sec^{-1})	
2	4.00, 3.94	avg 3.96
4	3.77, 3.54	avg 3.66
6	3.77, 3.54	avg 3.66

The extended pickling decreased the measured oxidation rate by 7.5%.

Electron Diffraction Analyses of Films

Electron diffraction analyses by the reflection technique were made with a General Electric electron diffraction instrument. This instrument was equipped with an attached high-temperature furnace enabling one to study the oxidation products at the temperature of reaction. These experiments, as well as the equipment, are described in more detail in another report (5).

Treatment of Data

The oxidation rate for these iron-nickel alloys may be represented by the parabolic rate equation:

$$(\Delta m)^2 = b + k_p t \qquad [1]$$

where Δm is gain in weight in g/cm^2 of a sample oxidized for t seconds; k_p is the parabolic rate constant expressed in $g^2cm^{-4}sec^{-1}$; b is a constant (g^2cm^{-4}).

The temperature dependence for the reaction is best described by an Arrhenius type equation as:

$$k_p = Ae^{\frac{-\Delta E^*}{RT}} \qquad [2]$$

in which ΔE^* is termed the apparent energy of activation and A the frequency factor. As discussed below, the significance of ΔE^* derived from the Arrhenius plot must be interpreted with caution at elevated temperatures.

[1] From the Carpenter Steel Company.

Table I. Parabolic rate constants for Alloy A (30% Ni), k_p (g^2 cm^{-4} sec^{-1})

t, °C	Laboratory air	O_2-N_2 mixture
600	1.18×10^{-12} 1.07 1.09	1.26×10^{-12} 1.28
700	1.39×10^{-11} 1.38	1.54×10^{-11} 1.38
800	9.4×10^{-11} 8.4	8.7×10^{-11} 8.2 8.7
900	1.32×10^{-9} 1.25 0.98	5.3×10^{-10} 5.1
1000	a = 1.01×10^{-8} a = 0.98 a = 0.95 b = 1.75 b = 1.65 b = 2.05	3.5×10^{-9} 3.2 3.2

Results

Results for Alloy A (30% Ni)

The parabolic rate constants, k_p in Eq. [1], are listed in Table I. Generally, the precision of the rate constants obtained in the controlled atmosphere is better than of those obtained in laboratory air. For all of the runs with alloy A, the average deviation from the mean for 2 or 3 runs was ±3.0% in the controlled atmosphere and ±5.4% in laboratory air. If duplicate runs were made in laboratory air on the same day, however, the precision would be ±2-3%. At 600°, 700°, and 800°C there is apparently no definite influence of the atmosphere by way of increased or decreased rate. At 900°C the rate in the laboratory air is greater than that in the controlled atmosphere by a factor of 2 and at 1000°C by a factor of 3.

The parabolic relationship gives an excellent representation for the data for all the controlled atmosphere data and most of the data in laboratory air. However, in the latter case at 900°C, there is a slight tendency for the plots to be concave upward. At 1000°C the k_p definitely increases after an oxidation time of about 20 min, and it is necessary to

Table II. Temperature dependence of oxidation reactions

Alloy	Atmosphere	"A" frequency factor, g^2 cm^{-4} sec^{-1}	ΔE^*, apparent energy of activation, cal/mole
A (30% Ni)	Laboratory air	0.044	41,800
	O_2-N_2 mixture	0.024	41,100
B (41% Ni)	Laboratory air	0.082	44,600
	O_2-N_2 mixture	0.020	40,900
	Ref. (1)	0.012	40,800
C (78% Ni)	Laboratory air	1.28×10^{-3}	38,230
	O_2-N_2 mixture	3.10×10^{-4}	35,450

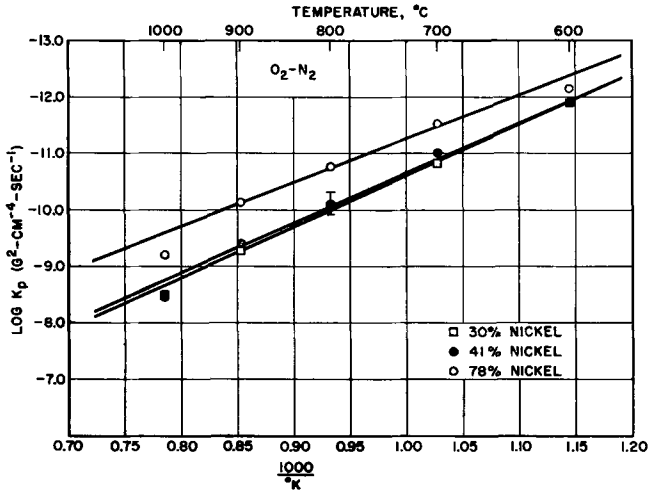

Fig. 1. Temperature dependence of oxidation rate of iron-nickel alloys oxidized in a controlled O_2-N_2 atmosphere.

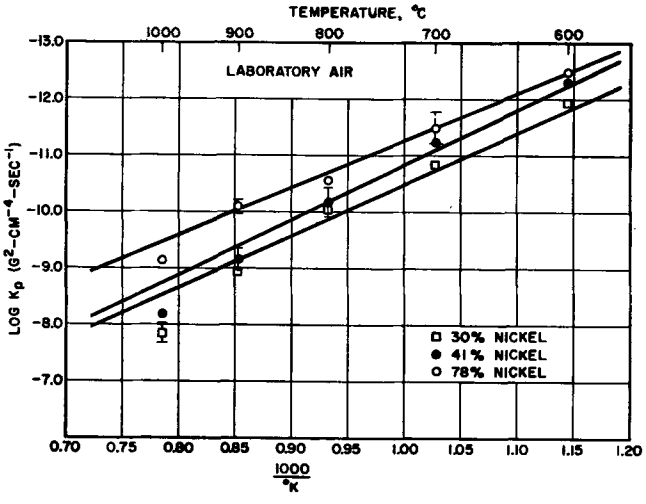

Fig. 2. Temperature dependence of oxidation rate of iron-nickel alloys oxidized in laboratory air.

represent the data by two stages. These two stages are represented by "a" and "b" in Table I. This is a reproducible effect. After the initial oxidation stage the rate almost doubles.

The temperature dependence of the reaction is described by "A" and "ΔE^*" in Eq. [2]. These quantities are given in Table II, and the curves are plotted in Fig. 1 and 2. The 5 points in the O_2-N_2 atmosphere fall close to the linear plot, but the 900° and 1000° points obtained in laboratory air fall in a direction indicating greater reaction. This point is discussed below.

Alloy B (41% Ni)

Rate constants describing the oxidation behavior of the 41% alloy are given in Table III. For comparison, results obtained about 4 years ago (1) on an alloy of almost the same composition are given. (The present alloy contained 40.9% Ni, the former contained 41.8%.) These results agree well with the present and the differences in the results are most likely due to variation in laboratory air.

In all cases excellent representation by Eq. [1] was achieved. The precision of the results obtained in the controlled atmosphere was again better than that of the laboratory air, 4.1% and 7.2%, respectively. In the last case the four 800°C values were considered as two groups. This is a good example of the variation in results, mentioned above, which is sometimes obtained when experiments are run in laboratory air many weeks apart.

The atmosphere effect in this case is not straightforward. Oxidation in laboratory air at 600° and 700°C proceeds at a rate distinctly less than in the controlled atmosphere. At 800° the rates are about the same, whereas at the higher temperature the laboratory air rate is double that in the controlled atmosphere.

The temperature dependence of the oxidation reaction is described in Table II and in Fig. 1 and 2. The actual plot of values obtained in the O_2-N_2 mixture is approximately linear within experimental error. The 900° and 1000°C values obtained in laboratory air fall off in the direction of the higher rate similar to the behavior of the 30% alloy.

Alloy C (78% Ni)

Rate constants for this alloy are listed in Table IV. The precision of runs made in the controlled O_2-N_2 atmosphere was ±6.6%, while that in laboratory air was ±15.2%. The considerable spread in results in laboratory air is explained by the variation in the composition of this atmosphere over the months the experiments were run. These data were represented quite well by a single parabolic equation of the Eq. [1] type with the exception of the 1000°C run in air. In this situation after an oxidation time of about 30 min, the parabolic plot followed a second straight line of lower slope. These two phases of reaction are given by "a" and "b" in Table III.

There was no consistent pattern established on comparison of rates in laboratory air and in the O_2-N_2 mixture. The spread of results in the laboratory air made this comparison difficult.

The temperature dependence of the reaction is given by "A" and "ΔE^*" values in Table II. In both atmospheres the 1000° point falls below the curve, indicating a higher rate of reaction than would be expected from extrapolation from the four lower

Table III. Parabolic rate constants for Alloy B (41% Ni), k_p ($g^2\ cm^{-4}\ sec^{-1}$)

t, °C	Laboratory air	O_2-N_2 mixture	42% Alloy (Ref. 1)
600	5.0×10^{-13} 5.1	1.14×10^{-12} 1.40	9.5×10^{-13}
700	5.6×10^{-12} 6.0	9.6×10^{-12} 9.9	7.9×10^{-12}
800	3.71×10^{-11} 4.40 1.22 1.17	4.87×10^{-11} 1.12 1.19	4.53×10^{-11}
900	4.46×10^{-10} 7.75 8.58 10.8	3.79×10^{-10} 3.89 4.65 4.00 3.94	3.67×10^{-10}
1000	7.2×10^{-9} 6.5	3.51×10^{-9} 3.51	

Table IV. Parabolic rate constants for Alloy C (78% Ni), k_p (g^2 cm^{-4} sec^{-1})

t, °C	Laboratory air	O_2-N_2 mixture
600	4.0×10^{-13}	7.0×10^{-13}
	2.8	7.3
		7.2
700	2.76×10^{-12}	3.17×10^{-12}
	1.96	3.28
	6.1	2.61
	5.9	2.96
800	2.93×10^{-11}	1.62×10^{-11}
	2.71	1.62
	2.76	1.71
	2.77	1.85
900	6.6×10^{-11}	8.5×10^{-11}
	6.3	6.2
	11.0	7.7
	9.8	7.6
1000	a = 8.4×10^{-10}	6.8×10^{-10}
	8.4	5.9
	b = 6.8	5.5
	6.1	

temperatures. The apparent energy of activation lower than that of alloy A or alloy B is significant.

Discussion

The "A" and "ΔE^*" values of Eq. [2] describe the temperature dependence for the oxidation of the three alloys and offer some clue as to the mechanism of oxidation. Based on this work and other work carried out in this laboratory, it is estimated that a value of about 41,000 cal/mole represents the heat of activation of diffusion and the heat of formation of vacancies through a structure of the composition $Ni_x Fe_{3-x} O_4$. This value is approximated by the 30% and 41% alloy. It is recognized that the oxide film on the 30% alloy and the 41% alloy is at least a duplex structure with the spinel growing at the metal-oxide interface and Fe_2O_3 further removed from the metal (1, 5). The composition of the spinel varies, being richer in Ni close to the alloy itself. Because of the duplex nature of the film and because of the variation of Ni/Fe ratio in the spinel, a theoretical derivation of the reaction rate would be difficult.

The rates summarized by the values in Table II indicate that all three of these alloys are more resistant to oxidation than iron, but not as resistant as the so-called "heat resistant alloys," typified by iron alloys containing 18% chromium, 8% nickel. This again is related to the rate-determining process, diffusion through the spinel structure. As has been pointed out by Yearian and co-workers (6), the more resistant alloys form a Cr_2O_3 type film while the more reactive alloys (in the heat resistant class) form spinel type structures upon oxidation. On the other hand, in comparison with pure iron these alloys are oxidation resistant. With alloys containing as much as 30% Ni, the formation of FeO at the alloy-oxide interface is suppressed. Diffusion of cations through the FeO structure is about 20 times as rapid as through Fe_3O_4 (3). Comparison of our results for the 30% alloy with those of Stanley (7) for iron yields rate ratios of 200-1000 rather than 20 expected on this basis. The lower rate is directly related to the Ni substitution in the spinel structure. Therefore, these alloys occupy a position on the oxidation resistant scale intermediate between iron (readily oxidized) and austenitic stainless steels (heat resistant).

The low apparent activation energy of Alloy C must be related to the presence of Mo in the alloy. Apparent activation energies of 40,000-45,000 cal/mole would be expected if the rate-determining step were diffusion through either the spinel structure or NiO, both of which are present in this alloy during oxidation at elevated temperatures. Electron diffraction examination of the alloys at elevated temperature indicates that MoO_3 is probably present in the first formed film (5). This point was not as well established as desired and more work is being done now to clarify this point. However, these prior observations fit those of Iitaka and co-workers (8) who found MoO_3 at the metal-oxide interface after oxidation of alloys of somewhat similar composition. The expectation that MoO_3 will simply evaporate and lead to catastrophic oxidation is an oversimplification. The Mo content, the Fe content, and the temperature all bear on the behavior (9). The effect of Mo, however, may be one of influencing the physical character of the film. This has been demonstrated to be a significant factor in oxidation processes, particularly where thermal cycling is involved (10).

In Fig. 1 and 2 it is very apparent that deviations occur at 900° and 1000°C, from the simple Arrhenius plot. These deviations from the Arrhenius plot may arise from changes in mechanism over the temperature range (11) or the production of local "over temperatures" on the reacting surface (12). Aside from these "experimental" causes, even on a theoretical basis one would not expect ΔE^* to be completely independent of temperature. This has been pointed out by Moelwyn-Hughes (13) and others. It is assumed here, as a first approximation, that, for a given alloy, the mechanism does not change to any considerable extent over this temperature range and an attempt is made to estimate the significance of the "over temperature."

When the reaction

$$\text{metal} + \text{gas} = \text{reaction product}$$

occurs rapidly and is accompanied by a high heat of reaction, it would be expected that the temperature of the sample would rise sensibly during the first few minutes of the reaction. This has been observed, for example, in the oxidation of iron near its melting point (14) and recently measured by Meussner and Birchenall (15). In the latter experimental work a temperature rise of 88°C was observed for the reaction between iron and sulfur at 900°C. In fact, this effect discouraged measurement of the reaction rate over 900°. Schmahl, Baumann, and Schenck (12) measured "over temperatures" during the oxidation of iron in the temperature range of 910°-950°C, to account for deviations from the parabolic law. Direct measurements of the rise in sample temperature were compared with calculated values. The calcu-

Table V. Comparison of calculated and measured over-temperatures

Alloy	Atmosphere		From Arrhenius plot (Fig. 1 and 2)	Calculated
A (30%)	Air	900°	32°	27°
		1000°	126°	106°
	O_2/N_2	900°	0°	31°
		1000°	34°	71°
B (41%)	Air	900°	43°	25°
		1000°	106°	70°
	O_2/N_2	900°	0°	18[b]
		1000°	52°	85°
C (78%)	Air	900°	0°	14°
		1000°	70°	39°
	O_2/N_2	900°	0°	8°
		1000°	92°	34°

lation was based on all of the heat evolved going into heating the iron panel. Following the method of Schmahl, *et al.*, we have calculated temperature rises for the three alloys. The heat evolved equivalent to the amount of oxidation occurring in the first 1½ min—the linear portion of the weight gain-time curve—was calculated. Values for the heats of formation for Fe_3O_4 of 261,700 at 900°C, and 261,800 cal at 1000°C, and for NiO, 56,770 at 900° and 56,650 cal at 1000°C were used (16). Heat capacity data (17) allowed an estimation of the temperature rise in the approximately 4-g sample employed in the experiments. This calculated value was then compared with the value on the basis that the entire deviation from the Arrhenius plot was "over temperature." Table V compares these values and there is a rough correspondence. This treatment introduces large errors, mainly in considering how the heat is dissipated. The assumption that no heat is lost by convection or radiation is obviously an oversimplification and would make the "calculated" values too high. Also, the k_p values given for 900° and 1000°C are based on a 60-min oxidation period rather than the 1½ min initial reaction time. This thermal effect is being studied more exactly because in the 1000°C range it must have an important influence on oxidation rates and their interpretation to develop an understanding of mechanism.

In a qualitative way this would in part account for the greater deviation from the Arrhenius plot observed for the 30% and 41% alloy in the (stagnant) air atmosphere in contrast to that observed in the (flowing) controlled O_2/N_2 mixture. Heat would be carried away in the gas stream in the latter case.

The oxidation of Ni-Fe alloys containing 5, 10, 20, 30% Ni over periods of up to several hundred hours has been reported by Benard and Moreau (18). The kinetics for the 20% alloy is reported up to about 15 hr. The oxidation follows a $y^n = kt$ relationship, y being the amount of oxygen picked up in time, t. At 675°C $n = 2$, indicating agreement with the parabolic relationship. At 800° $n = 2.4$ up to 5 hr and then changes to $n = 1.6$. At 900° the break in the plot is at 2 hr. Up till then $n = 2.6$ and above that 1.22. The authors postulate that during the first stage of the process the controlling factor is the diffusion of iron in the zone of the alloy depleted by a selective oxidation mechanism. During the second phase the controlling rate is the diffusion of oxygen in the superficial oxide layer. Benard and Moreau consider the significant mechanism for the Fe-Ni system to be one of selective oxidation. Some of Sachs's (19) work with low Ni alloys seems to agree in a general way. Their mechanism is based on the reduction of NiO with FeO. In our electron diffraction examination of films we have not seen FeO as a principle constituent and indeed it is rare when the patterns suggest this compound at all. Birchenall, *et al.*, have pointed out that the NiO makes for its instability (3). Our results do not support this selective oxidation mechanism. Perhaps the reason lies in the fact that these investigators have worked with alloys lower in nickel content for long times. Our work deals with relatively thin films. In our work subscale formation was not significant as it was during the lengthy experiments of Benard and Moreau.

We regard the oxidation mechanism for the 30% and 41% alloy as primarily one involving diffusion of cations through a spinel type film and for the 78% alloy diffusion through a film composed of spinel and NiO. In the latter case the MoO_3 enters into the film in a manner as yet unexplained but now under investigation in our laboratory.

Manuscript received Nov. 1, 1956. This paper was prepared for delivery before the Cleveland Meeting, Sept. 30-Oct. 4, 1956.

Any discussion of this paper will appear in a Discussion Section to be published in the June 1960 JOURNAL.

REFERENCES

1. R. T. Foley, J. U. Druck, and R. E. Fryxell, *This Journal*, **102**, 440 (1955).
2. M. J. Brabers, W. J. Heideger, and C. E. Birchenall, *J. Chim. Phys.*, **53**, 810 (1956).
3. M. J. Brabers and C. E. Birchenall, *Corrosion*, **14**, 179 (1958).
4. S. W. Kennedy, L. D. Calvert, and M. Cohen, *Trans. Am. Inst. Mining Met. Engrs.*, **215**, 64 (1959).
5. R. T. Foley, C. J. Guare, and H. R. Schmidt, *This Journal*, **104**, 413 (1957).
6. H. J. Yearian, E. C. Randell, and T. A. Longo, *Corrosion*, **12**, 515 (1956); H. J. Yearian, H. E. Boren, and R. E. Warr, *ibid.*, **12**, 561 (1956).
7. J. K. Stanley, J. von Hoene, and R. T. Huntoon, *Trans. Am. Soc. Metals*, **43**, 426 (1951).
8. I. Iitaka, T. Nakayama, and K. Sekiguchi, *J. Sci. Research Inst. (Japan)*, **45**, 57 (1955).
9. W. C. Leslie and M. G. Fontana, "Pittsburgh International Conference on Surface Reactions," p. 175, Corrosion Publishing Co., Pittsburgh, Pa. (1948).
10. J. F. Radavich, ASTM Special Technical Publication #171 (1955).
11. E. A. Gulbransen and K. F. Andrew, *This Journal*, **106**, 294 (1959).
12. N. G. Schmahl, H. Baumann, and H. Schenck, *Arch. Eisenhüttenw.*, **27**, 707 (1956).
13. E. A. Moelwyn-Hughes, "Physical Chemistry," p. 1111, Pergamon Press, London (1957).
14. W. E. Jominy and D. W. Murphy, *Trans. Am. Soc. Steel Treating*, **18**, 19 (1930).
15. R. A. Meussner and C. E. Birchenall, *Corrosion*, **13**, 677 (1957).
16. J. P. Coughlin, Bureau of Mines Bulletin 542, U. S. Printing Office, Washington (1954).
17. "Thermodynamic Properties of the Elements," American Chemical Society, Washington (1956).
18. J. Benard and J. Moreau, *Rev. Met.*, **47**, 317 (1950); *Compt. rend.*, **232**, 1842 (1951).
19. K. Sachs, *J. Iron Steel Inst.*, **185**, 348 (1957).

Oxidation Studies on the Nickel-Chromium and Nickel-Chromium-Aluminum Heater Alloys

Earl A. Gulbransen and Kenneth F. Andrew

Research Laboratories, Westinghouse Electric Corporation, Pittsburgh, Pennsylvania

ABSTRACT

A systematic study was made of the oxidation resistance of five 80Ni-20Cr heater alloys and one 4Al-19Cr-77Ni alloy. Kinetic and crystal structure studies were made over the temperature range of 500° to 1100°C. The adhesion of the oxide film to the alloy was tested by the strain oxidation technique, and the over-all performance was evaluated by the ASTM useful life tests. The rate of oxidation of the several alloys could not be correlated with the ASTM useful life results, while the strain oxidation tests could be correlated with the ASTM useful life tests. Cr_2O_3 was the major oxide formed on the 80Ni-20Cr alloys at 1100°C. Although Al_2O_3 and Cr_2O_3 were observed below 1000°C on the 4Al-19Cr-77Ni alloy, no Al_2O_3 was observed in the oxide scale at 1100°C. A thermodynamic and kinetic interpretation was made of the results.

Due to their good oxidation resistant properties, the 80 nickel-20 chromium series of heater alloys are used for severe service conditions. The addition of silicon and small amounts of calcium, zirconium, cerium, etc., has resulted in a 600% improvement in the performance of these alloys over the past 40 years as measured by the ASTM useful life test (1) for heater alloys (2-4).

Several studies have been made on these alloys to determine the chemical and physical basis for the improved performance. Using a historical series of alloys, Gulbransen and Andrew (2) showed that the rate of oxidation at constant temperature could not be correlated with ASTM useful life test results. Crystal structure studies (3, 4) of eight alloys also showed no correlation with useful life test results.

This paper presents new studies on the oxidation of the 80Ni-20Cr series of alloys and of a 75Ni-19Cr-4Al alloy. Manganese and silicon compositions were varied in the 80Ni-20Cr series of alloys. These studies include: (*a*) kinetic studies from 500° to 1100°C to determine the rate of oxidation as a function of temperature, (*b*) strain oxidation studies to evaluate the adherence of the oxide to the alloy, and (*c*) crystal structure studies on the oxide scale to determine its structure and composition. These studies are interpreted by thermochemical analyses of the chemical reactions occurring in the system and by oxidation rate theory.

An extensive review of the scientific literature was given in earlier papers (2-4). The technical aspects of heater alloys have been reviewed by Hessenbruch (5). The recent work of Pfeiffer (6) should be noted.

Experimental

Method.—A vacuum microbalance was used for all of the rate studies. Its construction and use have been described (7). In addition to our standard quartz microbalance having a sensitivity of 0.91 μg/0.001 cm deflection, a low sensitivity microbalance of 3.30 μg/0.001 cm sensitivity was used. Two sizes of specimens 0.0127 cm thick were used. The first weighed 0.6826 g and had a surface area of about 14 cm^2. The second weighed 0.5300 g and had a surface area of about 10.5 cm^2.

Samples.—The alloys were prepared, analyzed, and life tested by the Hoskins Company and by the Driver-Harris Company. Table I gives a list of the alloys, their analyses, and the results of the ASTM useful life tests (1). Alloys containing Si were represented by two alloys with a constant Mn content, while alloys containing Mn were represented by three alloys having a given Si composition. Minor changes in composition result in a threefold change in the ASTM useful life value at 1177°C.

Specimens were abraded using 1/0 to 4/0 polishing papers under purified kerosene and then cleaned with petroleum ether, soap and water, distilled water and alcohol.

Table I. Chemical analyses and useful life test data, Ni-Cr and Al-Ni-Cr alloys

Alloy	Classification	Weight %								Useful life,	
		C	Mn	Si	Cr	Ni	Fe	Ca	Al	hrs	T°C
491	Low Mn, intermediate Si	≈0.06	0.05	1.03	≈20.00	Bal.	≈0.25	0.020	0.13	105	1177
492	High Mn, intermediate Si	≈0.06	2.30	1.01	≈20.00	Bal.	≈0.25	0.035	0.15	106	1177
493	Low Mn, low Si	≈0.06	0.04	0.23	≈20.00	Bal.	≈0.25	0.028	0.20	63	1177
494	Low Mn, intermediate Si	≈0.06	0.02	0.82	≈20.00	Bal.	≈0.25	0.040	0.17	124	1177
495	Low Mn, high Si	≈0.06	0.02	2.09	≈20.00	Bal.	≈0.25	0.039	0.15	178	1177
245	High Si, high Al	≈0.03		1.44	≈19.38	Bal.			4.05	>178	1177

Table II. Oxide film thickness and oxide color 7.6 cm of Hg of O_2, 2 hr of reaction except where noted

7.6 cm of Hg of O_2, 2 hr of reaction except where noted

Temp.	Alloy 493 Thickness		Color	Alloy 495 Thickness		Color	Alloy 245 Thickness		Color
	μg/cm²	Å (ρ = 1)		μg/cm²	Å (ρ = 1)		μg/cm²	Å (ρ = 1)	
550	3.66	223	Straw	4.25	259	Purple	—	—	—
650	6.13	374	Purple	6.04	368	Purple	—	—	—
750	6.37	389	Blue	13.8	842	Straw-green	—	—	—
850	17.9	1,092	Blue-gray	35.1	2,141	Blue-green	—	—	—
875	—	—	—	—	—	—	116.0*	7,076	Gray
900	—	—	—	—	—	—	166.0*	10,126	Gray
950	43.1	2,629	Gray	120.0	7,320	Gray	299.0*	18,239	Gray
1000	93.8	5,722	Gray	173.0	10,553	Gray	492.0*	30,012	Gray
1050	169.0	10,309	Gray	277.0	16,897	Gray	675.0*	41,175	Gray
1100	244.0	14,884	Gray	365.0	22,265	Gray	917.0*	55,937	Gray

* 6-hr test.

The furnace tube, reaction system, and gas preparation system have been described (7, 8). Furnace temperature was maintained constant to ±1.5°C.

Strain oxidation.—The ASTM useful life test (1) involves an alternate heating and cooling cycle at 2-min intervals. At 1177°C several hundred thousands of cycles may be required to determine the useful life of a given alloy. The ASTM test involves both a test of the over-all resistance to oxidation and a test of the effect of stress developed by heating and cooling on the oxide-metal interface.

Gulbransen and Andrew developed a microgravimetric test (9) for study of the effect of a single large strain of 2% on the oxidation process. This strain oxidation test involves the following operations: (*a*) oxidizing the alloy to a given weight gain, (*b*) removal of sample from reaction system and straining 1, 2, or 4%, (*c*) reoxidation of the sample to evaluate the effect of strain on the oxidation behavior.

The effect of a strain can be studied quantitatively by comparison of the rate of oxidation before and after application of a strain. Strain can damage the oxide-metal interface and the oxide without visual evidence of cracking.

X-ray diffraction method.—Electrochemical (10) and chemical methods were used for stripping the oxide from the metal. For high Si alloys the oxide films were removed by the iodine-methanol chemical method. Oxide films were washed carefully in distilled water before being rolled on a glass capillary tube for mounting in the x-ray camera.

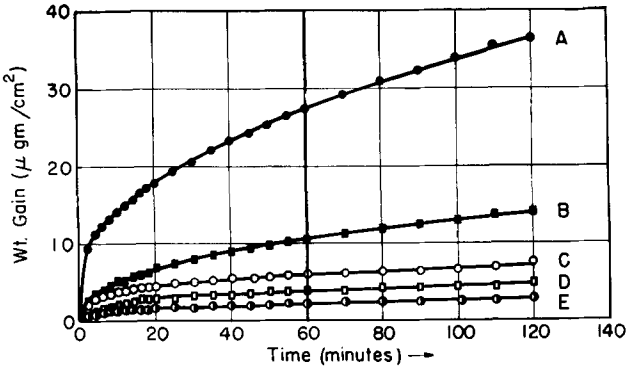

Fig. 1. Effect of temperature on oxidation of Ni-Cr alloy 493, 7.6 cm of Hg of O_2, abraded through 4/0. Curve A, 900°C; B, 800°C; C, 700°C; D, 600°C; E, 500°C.

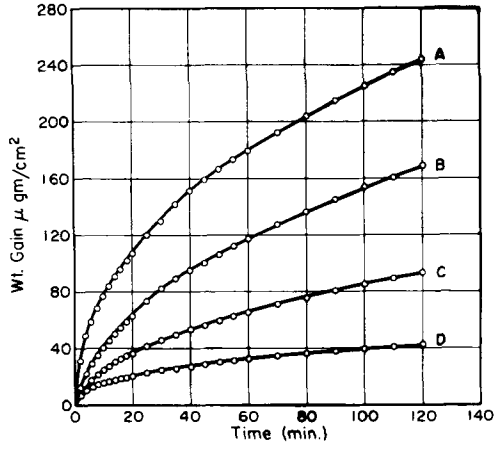

Fig. 2. Effect of temperature on oxidation of Ni-Cr alloy 493, 7.6 cm of Hg of O_2, abraded through 4/0. Curve A, 1100°C; B, 1050°C; C, 1000°C; D, 950°C.

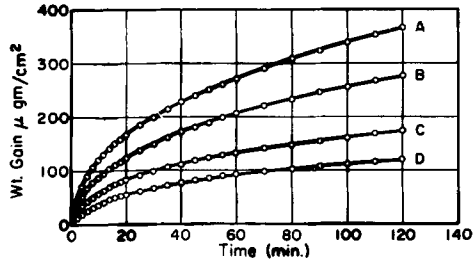

Fig. 3. Effect of temperature on oxidation of Ni-Cr alloy 495, 7.6 cm of Hg of O_2, abraded through 4/0. Curve A, 1100°C; B, 1050°C; C, 1000°C; D, 950°C.

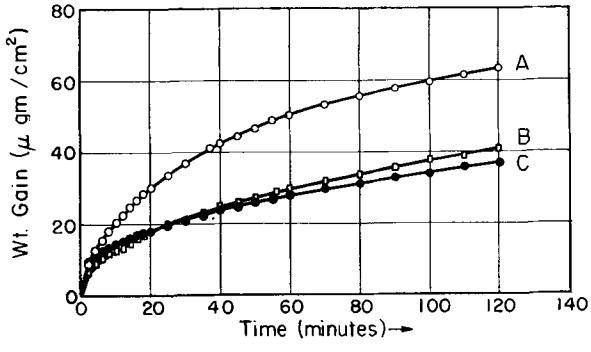

Fig. 4. Effect of Si on oxidation of Ni-Cr alloys, 900°C, 7.6 cm of Hg of O_2, abraded through 4/0. Curve A, 495, 2.09% Si; B, 494, 0.82% Si; C, 493, 0.23% Si.

Table III. Parabolic rate law constants (A) and heats of activation for oxidation of five nickel-chromium alloys at three temperatures

A in $(g/cm^2)^2$/sec, ΔH in calories per mole

Alloy	Analyses	Useful life, hr	750°C A	750°C ΔH	900°C A	900°C ΔH	1100°C A	1100°C ΔH
495	2.09 Si, 0.02 Mn + Ca	178	2.14×10^{-14}	40,850	4.10×10^{-13}	61,200	1.7×10^{-11}	61,200
493	0.23 Si, 0.04 Mn + Ca	63	4.06×10^{-15}	49,730	1.26×10^{-13}	49,730	7.08×10^{-12}	76,350
492	1.01 Si, 2.30 Mn + Ca	106	3.31×10^{-14}	44,850	5.89×10^{-13}	44,850		
491	1.03 Si, 0.05 Mn + Ca	105	1.0×10^{-14}	50,830	2.78×10^{-13}	50,830		
245	1.44 Si, 4.05 Al, 19.38 Cr	>178	1.67×10^{-14}	65,300	1.22×10^{-12}	65,300	5.28×10^{-11}	

Table IV. Summary results effect of strain on oxidation of Ni-Cr alloys oxidized 900°C, 0.1 atm oxygen

Alloy	Class	Film Thickness $\mu g/cm^2$	% Strain	$(g/cm^2)^2$/sec Parabolic rate law constants Before	After	Useful life 1177°C hr
495	High Si, low Mn + trace elements	44.5	2	2.82×10^{-13}	1.6×10^{-13}	178
491	Intermediate Si, low Mn + trace elements	47.1	2	1.97×10^{-13}	1.77×10^{-13}	105
492	Intermediate Si, high Mn + trace elements	43.7	2	5.89×10^{-13}	4.63×10^{-13}	106
493	Low Si, low Mn + trace elements	45.4	2	5.62×10^{-14}	9.81×10^{-14}	63

All of the diffraction patterns were made using filtered CrK_α radiation from a fine focus x-ray diffraction tube. Diffraction patterns were made at room temperature using a 9 cm Unicam camera.

Results

Oxidation studies were made in the vacuum microbalance over the temperature range of 500° to 1100°C. Before oxygen was added, the apparatus was evacuated to a pressure of 10^{-6} mm Hg or less. The furnace was then raised about the sample and furnace tube, and thermal equilibrium was allowed to occur. Above 900°C decarburization of the alloy by the room temperature oxide occurred for some of the alloys (11). Weight gain was calculated in units of micrograms per square centimeter.

X-ray diffraction analyses showed that the oxide scales were Cr_2O_3 and $NiO \cdot Cr_2O_3$. To estimate the thickness in angstroms from the weight gain in micrograms per square centimeter a factor of 61 was used. This factor assumes Cr_2O_3 to be the oxide and a surface roughness ratio of unity.

Kinetic Studies

Alloy 493 (low Si, low Mn).—Figures 1 and 2 show weight gain vs. time curves for the oxidation of alloy 493 for the two temperature ranges 500°-900°C and 900°-1100°C. All of the curves show a rapid initial reaction, with the rate of reaction decreasing as the film thickens. Two series of temper colors were observed on the alloys at 900°C before the gray colored oxide formed. Table II shows a summary of the colors of the oxide films and the thickness after 2 hr of reaction. This alloy showed the lowest rate of oxidation of the series of alloys studied.

Alloy 495 (high Si, low Mn).—Figure 3 shows weight gain curves for alloy 495 for the temperature range 950°-1100°C. The results at 500°-900°C were similar to those for alloy 493. Alloy 495 having a higher Si content oxidizes at a more rapid rate than alloy 493. Figure 4 shows a comparison of three alloys at 900°C. Silicon increases the initial rate of oxidation of the 80 Ni-20 Cr alloys for all temperatures studied. ASTM useful life tests show the high Si alloy to have the longest life.

Effect of Mn.—An earlier study showed that Mn may have a deleterious effect on the oxidation process due to its very high vapor pressure. Small quantities of Mn are probably in the alloy as sulfide and oxide. However, larger amounts of the order of 1 and 2% must be present in solid solution in the alloy.

Since the trace elements Ca, Al, and Zr were not controlled in the earlier study two special alloys were prepared in which only the Mn content was varied. These are alloys 492 and 491 of Table I. Figure 5 shows a comparison at 900°C. The high Mn alloy containing 2.30% Mn and 1.01% Si gave a higher rate of oxidation than alloy 491 containing

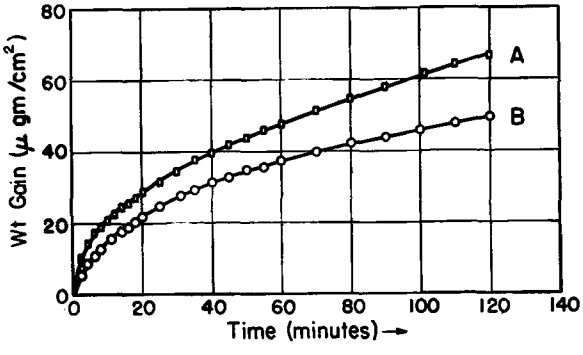

Fig. 5. Effect of Mn on oxidation of Ni-Cr alloys, 900°C, 7.6 cm of Hg of O_2, abraded through 4/0. Curve A, 492, 2.30% Mn; B, 491, 0.05% Mn.

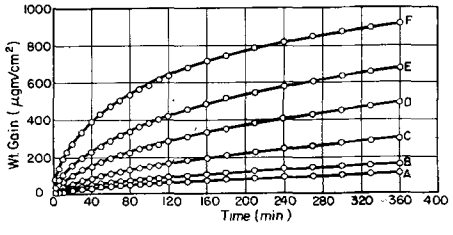

Fig.6. Effect of temperature on oxidation of alloy 245, 7.6 cm of Hg of O_2, abraded through 4/0. Curve A, 875°C; B, 900°C, C, 950°C; D, 1000°C; E, 1050°C; F, 1100°C.

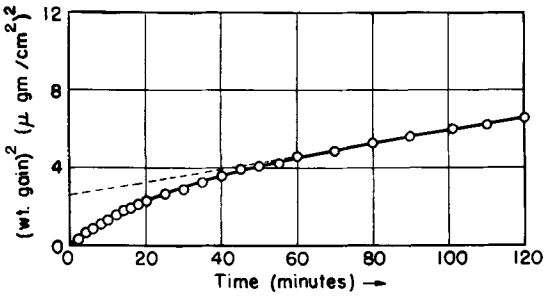

Fig. 7. Parabolic plot oxidation of Ni-Cr alloy 493, 500°C, 7.6 cm of Hg of O_2, abraded through 4/0.

0.05% Mn and 1.03% Si. ASTM useful life data were nearly identical.

Alloy 245 (high Si, high Mn).—Since Al has been shown to greatly improve the Fe-Cr series of heater alloys (12) a special Ni-Cr alloy containing 4.05% Al was studied. Figure 6 shows a 6-hr weight gain curve for this alloy from 875° to 1100°C. A comparison of Fig. 6 with Fig. 2 and 3 shows alloy 245 to oxidize at a more rapid rate than alloys 493 and 495. Table II shows the color of the oxides after 6 hr of reaction and the oxide thickness. Figure 6 shows that the total amount of oxidation after 6 hr is increasing with temperature from 875° to 1100°C. For the 5Al-22Cr-Fe alloys the total amount of oxidation remains nearly constant for the temperature range 950°-1050°C. Addition of Al to the Ni-Cr alloys does not have the marked effect on the oxidation reaction that was found for the Al-Cr-Fe alloys.

Parabolic rate law correlation.—A number of empirical rate laws have been proposed to interpret the rate of oxidation of metals and alloys. The parabolic rate law was used here since it has been derived from fundamental physical concepts involving the formation and diffusion of ions and electrons (13, 14). The equation states that $W^2 = A\,t + C$. Here W was the weight gain, t was the time, and A and C were constants.

Since the composition of the oxide was a function of time and temperature no one rate law could explain the complete time and temperature behavior. We used parabolic rate law plots to indicate changes in the oxide composition and to show whether the protective properties were improving or deteriorating.

To test the application of the parabolic rate law, graphs were made of the square of the weight gain vs. time. Figures 7, 8, and 9 show three plots for alloy 493. The 500°C plot shown in Fig. 7 indicates that the slope decreases continuously. Previous crystal structure studies (4) showed the initial oxide was NiO. After 30 hr of oxidation the oxide was identified as Cr_2O_3. The change in the parabolic rate law constants in Fig. 7 may be related to the change in oxide composition. Figures 8 and 9 at 900° and 1100°C show better agreement with the parabolic rate law after the initial deviation.

Temperature dependence.—To determine the temperature dependence of the parabolic rate law constants A, we use the relation $A = B\,e^{-\Delta H/RT}$. Here ΔH is the heat of activation of diffusion and heat of formation of the defects, B is a constant, and R the gas law constant. More elaborate rate expressions may be used for A so that the entropy terms may be evaluated (15). However, the complex nature of the alloy and oxide makes a complete interpretation very difficult. ΔH was evaluated from log A vs. $1/T$ plots of the rate law data.

Figures 10, 11, and 12 show plots of log A vs. $1/T$ for alloys 493, 495, and 245. All of the alloys gave two or more straight lines. The change in slopes may be related to crystal structure or composition changes in the oxide. Table III shows a summary of the parabolic rate law constants and heats of activation for three temperatures for all of the alloys and a comparison of these data with ASTM useful life tests.

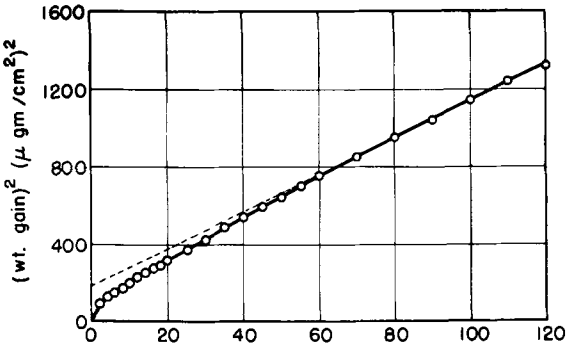

Fig. 8. Parabolic plot oxidation of Ni-Cr alloy 493, 900°C, 7.6 cm of Hg of O_2, abraded through 4/0.

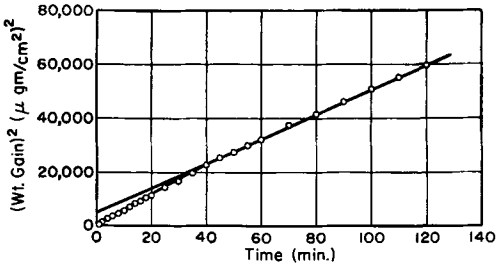

Fig. 9. Oxidation of Ni-Cr alloy 493, 1100°C, 7.6 cm of O_2, abraded through 4/0, parabolic plot. A = 7.08 x 10^{-12} $(g/cm^2)^2$/sec.

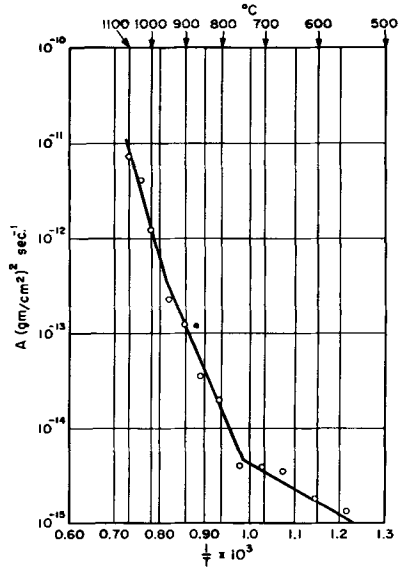

Fig. 10. Oxidation of Ni-Cr alloy 493 (low Si, low Mn), Log A vs. 1/T, ΔH = 76,250 cal/mole (950°-1100°C); ΔH = 49,730 cal/mole (750°-950°C).

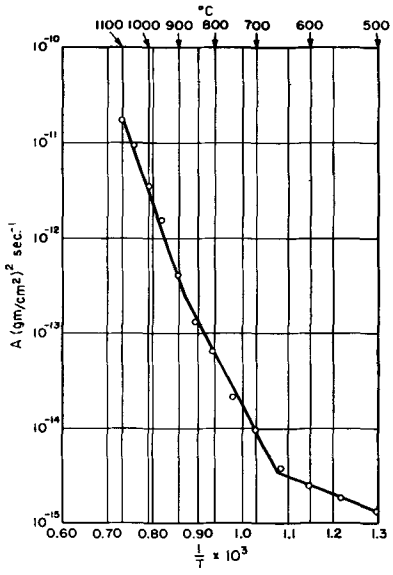

Fig. 11. Oxidation of Ni-Cr alloy 495 (high Si, low Mn). Log A vs. 1/T, ΔH = 61,200 cal/mole (880°-1100°C); ΔH = 40,850 cal/mole (650°-880°C).

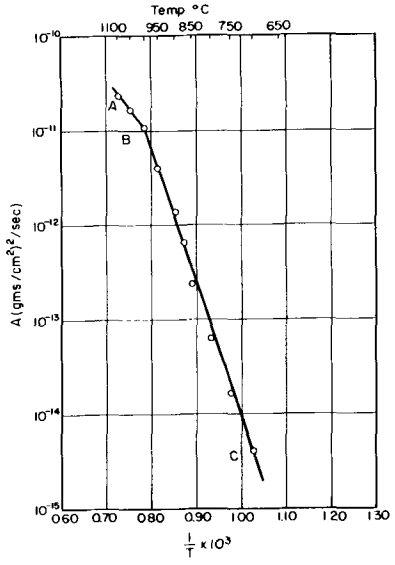

Fig. 12. Oxidation of alloy 245. Log A vs. 1/T, ΔH_{BC} = 65,300 cal/mole.

Strain Oxidation Studies

Samples of alloys 491, 492, 493, and 495 were oxidized individually at 900°C in 7.6 cm Hg of O_2 until a film of 45 $\mu g/cm^2$ was formed. The samples were removed and stretched 2% in a tensile testing machine. The marred surface held in the grips was removed and 4.5-cm length samples used for the reoxidation study.

Parabolic rate law plots of the data show that a 2% strain increased the parabolic rate law constants for the low silicon alloy 493 from 5.73 x 10^{-14} to 9.81 x 10^{-14} $(g/cm^2)^2$ sec^{-1}. A similar plot for the high Si alloy showed the parabolic rate law constants to decrease from 2.82 x 10^{-13} to 1.6 x 10^{-13} $(g/cm^2)^2$ sec^{-1} as a result of the 2 percent strain. Visually 2% strain has not effected the oxide-metal interface.

In addition to the long-term effect on the rate of oxidation a short-term effect was noticed especially on the low Si alloy 493. A rapid pickup of oxygen occurred on reoxidation. This reaction heals some of the damage in the oxide film. A very small short-term effect was noticed for the high Si alloy.

A summary of the effects of strain on the oxidation of the 80 Ni-20 Cr alloys is shown in Table IV.

These experiments indicate that minor elements such as Si and Ca in the alloy can greatly effect the resistance of the oxide and oxide-metal interface to stresses and strains. It is of interest to note that the results of the strain-oxidation test correlate with the ASTM useful life tests.

Crystal Structure Studies

Alloys.—X-ray diffraction studies were made on the alloys to test for the presence of second phases and the effect of minor elements on the lattice parameters of the alloy.

Table V shows the results of x-ray diffraction studies on alloys 493, 495, and 245. The alloys all have the face-centered cubic structure. A trace reflection was found at 2.122Å which suggests the presence of trace amounts of a second phase in the alloy. Three reflections were used in the calculation of the unit cell size a_o. Alloy 495 of the Ni-Cr series had the smallest value for a_o and the best ASTM useful life test. The effect of Al in replacing Ni is to increase the unit cell size.

Table V. Lattice parameters of alloys and pure nickel

Alloy	Composition	Lattice parameter a_o Å
493	Low Si, low Mn + trace elements	3.542 ±0.002
495	High Si, low Mn + trace elements	3.540 ±0.002
245	High Si, high Al	3.547 ±0.002
Ni(16)	Pure	3.52387

Oxide scales.—Crystal structure studies were made on the oxide scales over the temperature range 800°-1100°C. Results are shown in Table VI. A comparison of the crystal structures formed on alloys 493 and 495 shows similar oxide compositions at high temperatures. At 850°C alloy 493 showed Cr_2O_3 plus a trace of NiO while alloy 495 showed Cr_2O_3 alone. Several unidentified reflections were found in both alloys scales. We conclude that small composition differences exist in the oxide films. However, it is unlikely that the observed differences in oxide composition can be correlated with the major differences in performance as measured by the ASTM life test.

Alloy 245 showed $Cr_2O_3 + \alpha - Al_2O_3$ at 850°C. However, at 1100°C the oxide was Cr_2O_3 plus a spinel having a lattice parameter of 8.32Å. The spinel parameter can be compared to a value of 8.32Å for $NiO \cdot Cr_2O_3$ (16) or a value of 8.06Å found for $NiO \cdot Al_2O_3$ (16). The fact that $\alpha - Al_2O_3$ appears in the film at 800°-1000°C and not at 1100°C may be significant. In the 5Al-23Cr-72Fe alloy series Al_2O_3 forms in preference to Cr_2O_3 even at 1100°C.

X-ray diffraction analyses of the oxide scales is subjected to several limitations. (*A*) SiO_2 and other amorphous oxides may not be observed. (*B*) Oxides in amounts of 1-5% or less may not be recorded. (*C*) Oxides may be present in solid solution and not be recorded. (*D*) The chemical or electrochemical

Table VI. Summary crystal structure studies on Ni-Cr and Ni-Cr-Al alloys

Alloy 495, high Si, low Mn		Alloy 493, low Si, low Mn		Alloy 245, high Si, high Al	
Temp, °C	Crystal structures	Temp, °C	Crystal structures	Temp, °C	Crystal structures
1100		1100	Cr_2O_3 s.a. spinel 8.325*	1100	Cr_2O_3 spinel $a_o = 8.32$*
1050	Cr_2O_3 tr. sp. 8.33*	1050	Cr_2O_3 tr. sp. a_o 8.34*		
1000		1000	Cr_2O_3 s.a. sp. 8.33*	1000	Cr_2O_3, NiO spinel $a_o = 8.33$* s.a. $\alpha - Al_2O_3$
950	Cr_2O_3 s.a. sp. 8.33*	950	Cr_2O_3		
900		900		900	Cr_2O_3, NiO spinel $a_o = 8.33$* s.a. $\alpha - Al_2O_3$
850	Cr_2O_3	850	Cr_2O_3 tr. NiO		
				800	Cr_2O_3, $\alpha - Al_2O_3$

* Probably $NiO \cdot Cr_2O_3$; s.a. = small amount; tr. = trace.

stripping techniques also removed carbides, nitrides as well as oxides which can give extraneous reflections in the x-ray diffraction pattern.

Electron diffraction analyses was also attempted for the thinner oxide films. Many unidentified lines were present in addition to the oxide reflections. These we attribute to carbides, nitrides, etc.

Before a complete picture can be obtained of the oxide composition and crystal structure both x-ray diffraction and electron diffraction methods must be improved. Chemical analyses of these films must also be developed.

Discussion

Effects of Alloying Elements in Oxidation

Alloying elements can affect the nature of the oxidation reaction in several ways. First, the alloying element can affect the thermodynamic activity of the various metals in the alloys (17), the phase diagram of the alloy system, and the substructure of the alloy. Second, the alloying element can affect the composition, crystal structure, and physical and chemical properties of the oxide film (4). The alloying element may participate in the oxide film as follows: (*a*) form its own oxide in the outer layer of the oxide film at the oxide-gas interface, (*b*) form a mixed oxide in the outer layer or in the bulk of the oxide film, (c) form a mixed valency oxide changing the electrical and ionic transport properties of the oxide, (*d*) form its own oxide or compound with other oxides at the metal oxide interface, (*e*) remain in the metal at the metal-oxide interface, and (*f*) form a volatile reaction product.

The individual effect of the alloying element depends on its ionic size, charge, mobility, and thermodynamic activity. Since the chemical activity of the several oxides and the mobilities of the several ion species are temperature dependent, the specific effect of an alloying element may change with temperature.

Most of the elements which improve the performance of the 80Ni-20Cr alloy series are those which form very stable oxides and which do not participate in forming spinels or other oxides in the bulk of the oxide scale. These are: Si, Ca, Zr, Th, Ce, etc. To remain at the oxide-metal interface these elements form oxides which do not react with the major metallic components in the alloy.

Thermochemical Calculations

Table VII shows the principle types of chemical reactions which may occur during the oxidation of Ni-Cr and Ni-Cr-Al alloys. The composition of the oxide film and the distribution of the several oxides within the oxide is determined by the thermodynamic equilibria, the rates of the several chemical reactions, and by diffusion processes in the alloy (17). Calculations are made here only for the equilibrium state involving pure oxides and pure metals since information is not available on rates of diffusion of the metals in the alloys and in the oxides or on the chemical activities of the metals in the alloys.

A standard state of unit activity is assumed for the component metals in the alloy. Compared to the

Table VII. Types of surface reactions occurring in Ni-Cr and Al-Ni-Cr alloys

A. Direct oxidation
$2Cr(s) + 3/2\ O_2(g) \rightleftarrows Cr_2O_3(s)$, etc.
B. Solid phase reactions
$2Al(s) + Cr_2O_3(s) \rightleftarrows Al_2O_3(s) + 2Cr(s)$, etc.
C. Formation of spinels
$NiO(s) + Cr_2O_3(s) \rightleftarrows NiO \cdot Cr_2O_3(s)$, etc.
D. Formation of silicates
$Al_2O_3(s) + SiO_2(s) \rightleftarrows Al_2O_3 \cdot SiO_2(s)$, etc.
E. Decarburization
$Cr_2O_3(s) + 3C(\text{solid soln.}) \rightleftarrows 2Cr(s) + 3CO(g)$, etc.
F. Vaporization
$Cr(s) \rightleftarrows Cr(g)$, etc.

Table VIII. Dissociation pressures of the oxides

Temp, °C	$-\text{Log } PO_2$ (atm.)					
	NiO	Cr_2O_3	Al_2O_3	SiO_2	MnO	Fe_2O_3
25	75.4	121.8	184.6	144.6	127.2	85.8
200	43.8	73.4	112.4	87.6	77.4	50.8
400	27.6	48.9	75.7	58.8	52.1	33.0
600	19.0	35.6	55.8	43.2	38.4	23.4
800	13.6	27.3	43.3	33.5	29.8	17.4
1000	9.8	21.6	34.7	26.8	24.0	13.3
1200	7.0	17.4	28.4	21.9	19.6	10.3

Table IX. Solid phase reactions of nickel, chromium, and aluminum oxides

1. $3NiO(s) + 2Cr(s) \rightleftarrows Cr_2O_3(s) + 3Ni(s)$
2. $3NiO(s) + 2Al(s) \rightleftarrows Al_2O_3(s) + 3Ni(s)$
3. $2NiO(s) + Si(s) \rightleftarrows SiO_2(s) + 2Ni(s)$
4. $NiO(s) + Mn(s) \rightleftarrows MnO(s) + Ni(s)$
5. $Cr_2O_3(s) + 2Al(s, g) \rightleftarrows Al_2O_3(s) + 2Cr(s)$

	$Log_{10} K$				
Temp, °C	Reaction 1	Reaction 2	Reaction 3	Reaction 4	Reaction 5
25	69.7	163.8	69.2	25.9	94.2
200	44.4	102.9	43.8	16.8	58.5
400	32.0	72.1	31.2	12.3	40.1
600	25.0	55.2	24.2	9.7	30.2
800	20.6	44.6	19.9	8.1	24.0
1000	17.7	37.4	17.0	7.1	19.7
1200	15.7	32.1	14.9	6.3	16.4

Table X. Vapor pressure of metals

	Log $_{10}K_P$ (atm.)					
Temp, °C	Ni	Cr	Al	Si	Mn	Fe
900	—11.0	—10.17	—7.6	—11.8	—5.3	
1000	—9.6	—8.8	—6.5	—10.3	—4.4	—9.67
1100	—8.2	—7.63	—5.5	—8.9	—3.5	—8.58
1200	—7.2		—4.7	—7.9	—2.8	—7.62

free energy change of the reaction the activity correction is small. Table VIII shows the dissociation pressures of the oxides from 25°C to 1200°C, as calculated from equations given by Kubaschewski and Evans (18). All of the oxides are stable in the oxidation atmospheres used.

Table IX shows calculations on the equilibrium constants for the several solid phase reactions which determine in part the composition of the oxide scale. Nickel oxide is reduced by Cr, Al, Si, and Mn. Chromium oxide is reduced by Al. For the 80Ni-20Cr alloys the equilibrium oxide should be largely Cr_2O_3. Cr_2O_3 was found experimentally by x-ray crystal structure studies shown in Table VI to be the main oxide in the scale. Although thermodynamic calculations cannot be made for the spinels, $NiO \cdot Cr_2O_3$ appears to be a stable compound since it is found also in the oxide scales.

For alloy 245 containing 4.05% Al, thermochemical calculations suggest the oxide should be Al_2O_3. This compound was observed except at 1100° where Cr_2O_3 and $NiO \cdot Cr_2O_3$ were observed.

Table X shows the vapor pressures of the several metals involved in these alloys. The vapor pressures of Ni, Al, Si, and Mn were calculated from the compilation of Stull and Sinke (19). Data for Fe and Cr were taken from a recent work by Gulbransen and Andrew (7).

According to calculations, Al should volatilize at high temperatures from the metal in vacuum or react at the surface to form Al_2O_3 in oxygen. Since Al_2O_3 forms at 800° and 1000°C but not at 1100°C, Al may be lost from the oxide film possibly as a lower oxide of Al.

Orientation Relationships

Tightly adherent oxide scales are one of the important characteristics of high heat resistant alloys. One of the factors in good adhesion is the matching of lattice parameters in the oxide and metal structures. Matching of lattice parameters is also important in determining the epitaxial relationships.

Bénard has suggested two rules for the directing influence of crystal structures in oxidation (20): (*a*) the oxide tends to orient itself to the metal structure to produce as near a coincidence as possible of the repeat distances between the metal atom in the two structures, and (*b*) planes of high atomic density in the oxide tend to orient to high density atomic planes in the metal consistent with the geometry of the two structures.

The orientation relationships of NiO on face-centered cubic Ni has been studied by Lawless, Young, and Gwathmey (21) and by Newkirk and Martin (22). The (111) plane of NiO was found to grow on both the (001) and (111) planes of the metal. A parallelism was found between the [110] directions of oxide and metal. Newkirk and Martin (22) calculate a 15.6% disregistry between the oxide and metal structures. If these relationships are correct, we must conclude that Bénard's simple rules (20) do not hold for NiO on Ni.

We have made an analyses of the simple repeat distances of $NiO \cdot Cr_2O_3$ formed on Ni-Cr-Al and Ni-Cr face-centered cubic alloys following Bénard's rules. A minimum disregistry is found for the growth of the (100) plane of $NiO \cdot Cr_2O_3$ spinel on the (111) plane of the alloy and a parallelism of the [100] direction of the oxide with the [111] direction of the alloy. However, a large disregistry is found for the [110] direction. Due to the influence of atoms outside of the lattice planes involved, the simple picture of coincidence of repeat distances does not apply for face-centered cubic structures. A more detailed picture of the orientation relationships must be developed to explain the good adherence of $NiO \cdot Cr_2O_3$ in Ni-Cr alloys.

We have not made an analyses of the simple repeat distances of Cr_2O_3 formed on the Ni-Cr and Ni-Cr-Al alloys due to the complexities of the Cr_2O_3 structure. Single crystal studies should be made to determine the orientation relationships for the oxides formed on these good oxidation resistant alloys.

Summary

1. Vacuum microbalance measurements were made on the oxidation of a series of 80Ni-20Cr and a 75Ni-19Cr-4Al heater alloys over the temperature range of 500°-1100°C.

2. Silicon and manganese compositions were varied in the 80Ni-20Cr series of alloy.

3. Kinetic studies showed the low Si and low Mn alloy oxidized at a lower rate than the alloy containing 2% Si. No correlation was formed between ASTM heater life tests and the rate of oxidation of a series of heater alloys.

4. Kinetic data were fitted to the parabolic rate law. However, a number of deviations were observed. For all experiments the initial parabolic rate law constant was larger than the final values found for thicker films. This change was attributed to chemical transitions occurring in the oxide films.

5. Parabolic rate law data plotted on a logarithmic plot as a function of $1/T$ showed two or three straight lines. Heats of activation for the several temperature ranges for each alloy were determined.

6. Strain oxidation studies on the alloys showed good correlation with ASTM life tests. This study suggests that the resistance of the oxide-metal interface to stresses or strain is the most important factor in determining the practical performance of heater alloys. Silicon and the other minor elements appear to help the metal resist the effects of stresses or strains at the oxide-metal interface.

7. X-ray diffraction crystal structure studies were made on three alloys over the temperature range. Cr_2O_3 and $NiO \cdot Cr_2O_3$ spinel were the principal oxides formed for the 80Ni-20Cr alloys. α-Al_2O_3 was found, in addition, on the 75Ni-19Cr-4Al alloy at 800° and 1000°C but not at 1100°C. The latter observation was unexpected.

8. Rate data and crystal structure observation were interpreted from thermochemical calculations in the several chemical reactions occurring in the system. Orientation relationships were also discussed.

Manuscript received Dec. 19, 1958. This paper was prepared for delivery before the Philadelphia Meeting, May 3-7, 1959.

Any discussion of this paper will appear in a Discussion Section to be published in the June 1960 JOURNAL.

REFERENCES

1. F. E. Bash and J. W. Harsch, *Am. Soc. Testing Materials Proc.*, **29**, Pt. II, 506 (1929).
2. E. A. Gulbransen and K. F. Andrew, *This Journal*, **101**, 163 (1954).
3. J. W. Hickman and E. A. Gulbransen, *Trans. Am. Inst. Mining Met. Engrs.*, **180**, 519 (1949).
4. E. A. Gulbransen and W. R. McMillan, *Ind. Eng. Chem.*, **45**, 1734 (1953).
5. W. Hessenbruch, "Metalle and Legierungen fur Hohe Temperaturen," Berlin, Julius Springer (1940).
6. H. Pfeiffer, *Werkstoffe u. Korrosion*, **10**, 573 (1957).
7. E. A. Gulbransen, "Advances in Catalysis," Vol. V, pp. 119-175, Academic Press Inc., New York (1953).
8. E. A. Gulbransen, *Trans. Electrochem. Soc.*, **81**, 187 (1942).
9. E. A. Gulbransen and K. F. Andrew, A.S.T.M. Technical Publication No. 171, p. 35, February 2, 1955.
10. E. A. Gulbransen, R. T. Phelps, J. W. Hickman, *Ind. Eng. Chem. Anal. Ed.*, **18**, 391 (1946).
11. E. A. Gulbransen, W. S. Wysong, and K. F. Andrew, *Trans. Am. Inst. Mining Met. Engrs.*, **180**, 565 (1949); T. D. 2438.
12. E. A. Gulbransen and K. F. Andrew, *This Journal*, **106**, 294 (1959).
13. C. Wagner, *Z. Physik, Chem.*, (**B**) **21**, 25 (1933).
14. C. Wagner, "Atom Movements," American Society for Metals, pp. 153-173, Cleveland, Ohio (1951).
15. E. A. Gulbransen, *Ann. N. Y. Acad. Sci.*, **58**, 830 (1954).
16. J. D. H. Donnay and W. Nowacki, "Crystal Data" Memoir No. 60, The Geological Society of America, April 1, 1954, New York.
17. C. Wagner, *This Journal*, **103**, 571 (1956).
18. O. Kubaschewski and E. D. Evans, John Wiley & Sons, Inc., New York (1956) Book.
19. D. R. Stull and G. C. Sinke, "Thermodynamic Properties of the Elements," Am. Chem. Soc., Washington, D. C., November, 1956.
20. J. Bénard, *Bull soc. chim. France*, **13**, 511 (1946).
21. K. R. Lawless, F. W. Young, Jr., and A. T. Gwathmey, *J. chim. phys.*, **53**, 667 (1957).
22. J. B. Newkirk and W. G. Martin, *Trans. Am. Inst. Mining Met. Engrs.*, **212**, 398 (1958).

The Action of Nickel and Cobalt in Electroluminescent Zinc Sulfide Phosphors

Paul Goldberg

Sylvania Research Laboratories, Bayside, New York

ABSTRACT

Nickel and cobalt produce many of the effects in electroluminescent phosphors that are known for photo- and cathodoluminescent zinc sulfide. In addition, these elements bring to electroluminescent phosphors other changes in properties which are of practical and theoretical interest. Among these are (a) enhancement of emittance in blue-emitting phosphors, (b) marked changes in emittance-voltage and emittance-frequency characteristics, and (c) simplification of the brightness wave forms. The frequency and brightness wave effects can be understood in terms of "fast" and "slow" recombination processes which are influenced differently by the iron-group elements. The enhancement of electroluminescence is of uncertain origin but may arise from changes in the photocapacitive properties of the powder crystals due to the iron-group elements. The similarities and differences of nickel and cobalt in both blue and green-emitting phosphors are discussed.

The sensitivity of zinc sulfide phosphors to iron-group elements has a long history (1). Nickel, cobalt, and iron influence the intensity of luminous emission and the rate of luminescence decay in phosphors excited by ultraviolet or cathode rays (2-4). At concentrations much less than the activator content their action is to suppress the emission strongly. Consequently they are termed "killers" or "quenchers." The interpretation of these effects involves trapping and/or recombination of free holes and electrons (3, 5-7) at the killer site. The iron-group elements can influence excitation processes by

introducing absorption bands (8) and also weak emission bands (9).

The purpose of this paper is to discuss the way iron-group elements act in electroluminescent (EL) phosphors. Lehmann already has demonstrated that these elements depress the emittance and induce superlinear emittance-frequency characteristics (10).

In the experiments described below the EL emittance and brightness wave forms were followed as a function of voltage, frequency, and concentration of the iron-group elements. In addition to the effects seen by Lehmann it was found that: (*a*) The emittance of blue-emitting phosphors was increased with additions of 10^{-5} g at./mole or less of the iron-group elements. (*b*) In the range 10^{-5} to 10^{-4} g at./mole of Ni or Co dependencies of emittance on voltage and frequency may undergo marked changes. (*c*) With additions of 10^{-5} to 10^{-4} g at./mole of Ni the brightness waves take on a simplified form.

The ordinary names such as "killers" or "quenchers" given to these elements in the zinc sulfide system are clearly inadequate here. Therefore, in the remainder of this report reference will be made to the elements as "modifiers."

Nickel and cobalt have been shown to influence the dielectric properties of photoluminescent zinc sulfide (11). Also, it is known that the dielectric properties of EL phosphors are of consequence in their response in an electric field (12). Therefore studies were made to trace the importance of these observations on the materials of this report.

Experimental Technique

Phosphors.—The phosphors studied are of the ZnS: Cu,Cl type and contain roughly 3 x 10^{-4} g at. Cu/mole in the case of blue-emitting materials and 1.5 x 10^{-3} g at. Cu/mole for the green-emitting group. The modifiers were introduced during the preparation as aliquots of solutions of the following Johnson-Mathey salts: $Co(NO_3)_2 \cdot 6H_2O$ and $NiSO_4 \cdot 7H_2O$. Not all of the modifier enters the lattice in these preparations as shown in Table I.

For 1 x 10^{-4} g at. Ni/mole and above, the known (8) absorption band of Ni in ZnS appears as a distinct yellow body color.

In subsequent discussions the concentration of modifiers is specified in terms of the amount added in the preparation.

Optical and electrical measurements.—Emittance data were obtained from cells 25 x 25 x 0.125 mm in size with a castor oil dielectric. Brass and transparent conductive glass (500 ohms/square) served as electrode materials. An RCA 1P22 photomultiplier detector was used in conjunction with a Photovolt Model 520 photometer. A rough measure of the emission color was obtained as the blue/green (B/G) ratio with a Corning 4010 filter measuring the green and 5543 and 3389 filters together measuring the blue. The detector for obtaining the brightness waves was a Du Mont 6292 photomultiplier. Dielectric properties of the phosphors were obtained with cells similar to those described above at a field strength too low to give electroluminescent emission. The electrical loss and capacitance data were measured with a *Q* meter (Boonton Radio Co. Model 260-A) in both a dark environment and under room (fluorescent) illumination.

Table I.

Modifier added in the preparation, g at./mole	Ni found in phosphors (green emission) g at./mole	Co found in phosphors (blue emission) g at./mole
Zero (control)	1.3×10^{-6a}	$<8 \times 10^{-7a}$
1×10^{-6b}	1.3×10^{-6}	—
3×10^{-6}	3.6×10^{-6b}	—
1×10^{-5}	0.48×10^{-5}	1.2×10^{-5b}
3×10^{-5}	1.1×10^{-5}	2.3×10^{-5}
1×10^{-4}	0.46×10^{-4}	0.69×10^{-4}
3×10^{-4}	2.3×10^{-4}	1.65×10^{-4}
1×10^{-3}	0.43×10^{-3}	0.49×10^{-3}

[a] Measured by spectrographic analysis, the other data by wet chemical analysis.
[b] The apparent excess found over that added may arise from analytical inaccuracy at low levels of added modifier. The analytical error amounts to ±0.15 x 10^{-5} at the level of 1 x 10^{-5}, and 10% or less at all higher concentrations.

Experimental Results

Frequency Dependence of the Luminous Emittance

Green-emission.—Figure 1 shows the log-log plot of the integrated light output or emittance (*L*) as a function of frequency (*f*) for a family of green-emitting EL phosphors with varying amounts of Ni

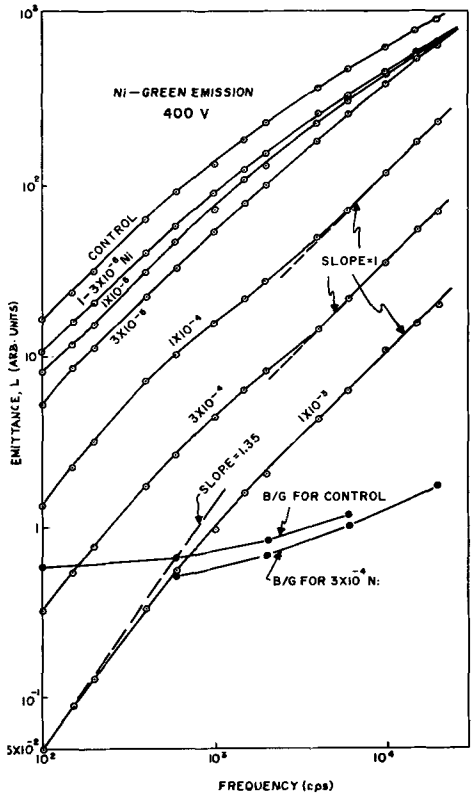

Fig. 1. Emittance-frequency characteristics of green-emitting electroluminescent phosphors with various nickel concentrations, at 400 v. Data for 1 x 10^{-6} and 3 x 10^{-6} g at. Ni/mole are coincident within experimental error.

at 400 v (rms). This family shows many of the characteristics of modifier activity: (*a*) For Ni concentrations up 3 x 10^{-5} g at./mole the *L-f* curves show linearity from 100 cps to nearly 1 kc. At higher frequencies the dependence is sublinear. This is similar to the known behavior of ordinary EL phosphors (15-17). (*b*) The *L-f* characteristics show linear portions at Ni concentrations of 1 x 10^{-4} g at./mole and higher, from frequencies of a few kilocycles up to the limit of measurement at 20 kc.[1] This stands in pronounced contrast to the usual sublinear behavior which sets in at lower frequencies. The effect is approximately independent of voltage. There is a continuing decrease in the average emittance for greater additions of nickel. (c) Superlinearity in the *L-f* characteristics appears at 1 x 10^{-4} g at. Ni/mole and higher. The effect disappears for a given Ni concentration at frequencies above 1 kc and is replaced by the linear behavior described above. The superlinearity is more severe in Co-containing phosphors. As will be shown later, *L* may increase as rapidly as the third power of the frequency. (*d*) There is a convergence at high frequencies of the curves of Ni in range 1 x 10^{-6} to 3 x 10^{-5} g at./mole. (Alternatively, this may be expressed as a decrease in the ability of Ni to suppress electroluminescence as the frequency is increased. The difference in emittance of about 40% between the control sample and that with 1 x 10^{-6} g at. Ni/mole was not found in subsequent preparations.) (*e*) The blue band is quenched more than the green band at higher Ni concentrations. Figure 1 shows the decrease in the B/G ratio upon incorporation of 3 x 10^{-4} g at. Ni/mole. The shift toward the green holds too for phosphors emitting mainly blue light.

The superlinearity and convergence phenomena described above are also brought on by Co. This element however does not provide linear *L-f* characteristics in the kilocycle region for any green-emitting phosphors studied here. Other differences between Co and Ni will be mentioned subsequently.

As a modifier, iron acts somewhat differently. It depresses the brightness with almost no change in the shape of the *L-f* curves. A weak red emission attributable to Fe was observed under field excitation. A similar band was reported previously by Gergely (9) for photoluminescent excitation.

It has been mentioned by others that emittance-frequency investigations should be coupled with temperature studies in order that ambiguous results be avoided (18, 19). However, the shape of the emittance-temperature characteristics of these materials with and without Ni shows a general insensitivity to frequency, except for a scale factor.

Blue-emission.—An analogous pattern to that discussed above is found in EL phosphors emitting mainly blue light. There is however one main difference. The lowest concentrations of modifier effect an enhancement in emittance. Figure 2 shows the *L-f*

[1] The linearity of *L-f* characteristics should be tested with a detector which counts photons. Such results would be unambiguous in spite of color shifts in the emission with frequency. The linearity, e.g., for 1 x 10^{-4} g at. Ni/mole shown in Fig. 1, measured with an RCA 1P22 photomultiplier, is therefore open to some question due to the color shift. In other results, however, e.g. Fig. 3, the linearity is quantitative since color shifts are minimal.

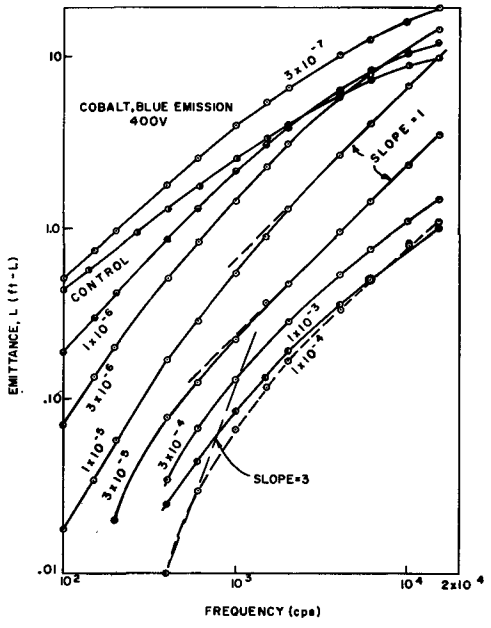

Fig. 2. Emittance-frequency characteristics of blue-emitting El phosphors with various Co concentrations.

characteristics of blue-emitting ZnS:Cu,Cl at various Co concentrations in the range 3 x 10^{-7} to 1 x 10^{-3} g at. Co/mole. The phosphors with 3 x 10^{-7} to 3 x 10^{-6} g at. Co/mole are all brighter than the control at higher frequencies. This increase partially obscures the convergence effect described previously. However, both the superlinearity and linearity relationships are evident. The existence of the enhancement effect has been suggested by Burns (20).

The integrated light output of phosphors containing Ni behave in much the same way as described above for Co although not as strongly. Figure 3 shows a family of curves at various levels of Ni. Cobalt induces superlinearity at 1 x 10^{-6} g at./mole which becomes pronounced at 10^{-4} g at./mole ($L \sim f^3$). Nickel first induces superlinearity at 1 x 10^{-4} g at./mole, and as in Fig. 1, the effect is weak. The emittance enhancement also has been observed for Fe and Cr additions.

The photoluminescence of these materials, in contrast to the electroluminescence, decreases monotonically with increasing modifier content. This is largely in agreement with the work of Arpiarian for the ZnS:Cu, Cl system (2).

A significant difference between Ni and Co in these phosphors is the reappearance of sublinearity in the range 1 x 10^{-4} to 1 x 10^{-3} g at. Co/mole. There is no equivalent to this in the Ni-containing family (cf. Fig. 2 and 3).[2]

Voltage Dependence

The voltage dependence of emittance of EL phosphors can be represented by a variety of empirical formulas. One of these, which receives some support from theory is

$$L = A \cdot f(V) \cdot \exp(-bV^{-1/2})$$

where *L* is the luminous emittance, *V* the rms volt-

[2] The reason the curve for 1 x 10^{-4} Co in Fig. 2 falls below that of 3 x 10^{-4} is not evident. Chemical analyses for Co in the finished phosphors cannot account for it (see Table I) although small temperature gradients during the synthesis may.

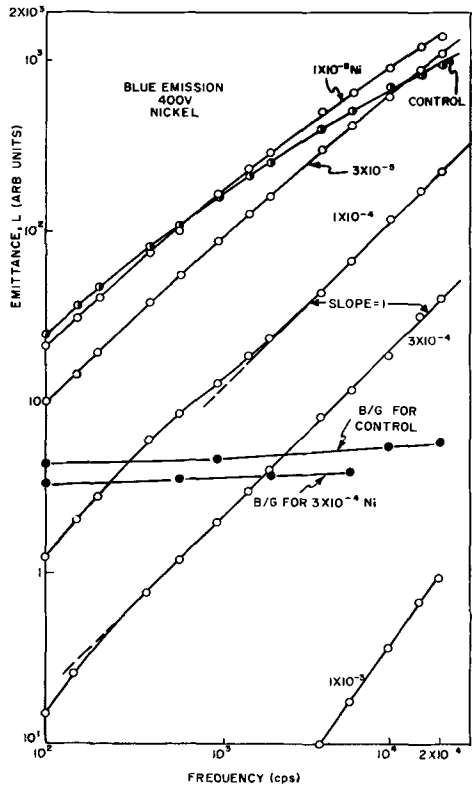

Fig. 3. Emittance-frequency characteristics of blue-emitting EL phosphors with various Ni concentrations.

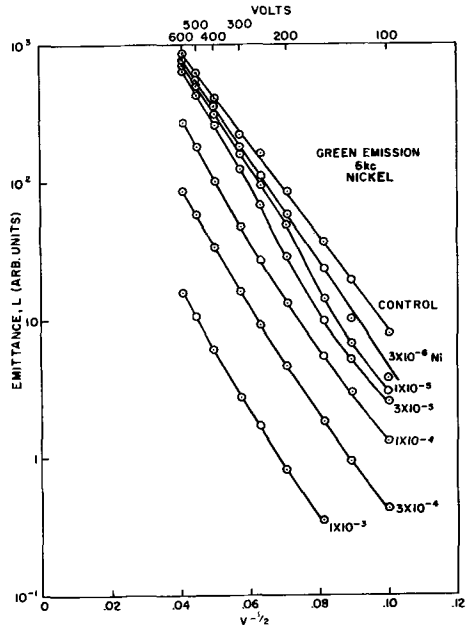

Fig. 4. Emittance-voltage characteristics of green-emitting EL phosphors with various Ni concentrations; $L \sim \exp(-b\ V^{-1/2})$.

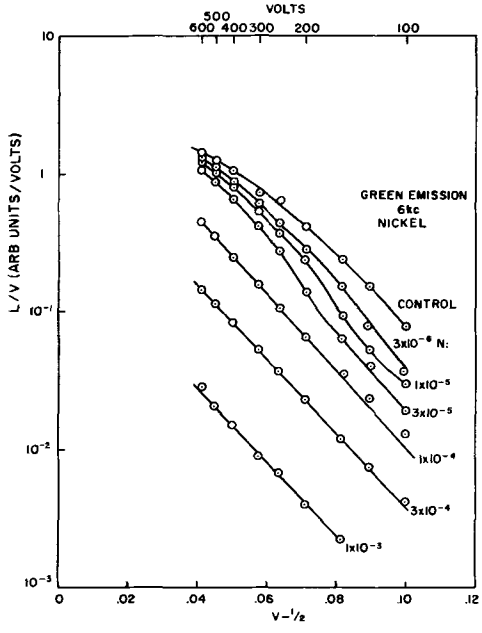

Fig. 5. Data of Fig. 4 plotted according to $L/V \sim \exp(-b\ V^{-1/2})$.

age; A and b are arbitrary constants (15, 18). Experimental work by various investigators shows two functionalities; $f(V)$ = constant (15, 18) or $f(V) = V$ (21). The $f(V)$ term is related to the particular trap distribution in the phosphor (18).

Blue-emission.—Here the behavior on increasing the nickel concentration is almost completely described by changes in the value of the constant A in Eq. [1] with $f(V)$ = const. A similar result was reported by Lehmann for his phosphors (10).

Green-emission.—Phosphors containing either Ni or Co show both functionalities depending on the concentration of modifier. Figure 4 shows the L-V characteristics of the same group of phosphors appearing in Fig. 1, at a constant frequency of 6 kc. It is evident that at Ni contents greater than 1 x 10^{-4} g at./mole, a new voltage dependence has fully developed. This voltage dependence corresponds to $f(V)$ equal to V. Figure 5 presents the data of Fig. 4 replotted such that $f(V)$ equals V (ordinate is L/V). The effect also is found for Co at a concentration one order of magnitude less than for Ni. The change in shape of the voltage characteristic is frequency-dependent. Experiments at 2, 6, and 20 kc all show the effect described above. At 100 and 600 cps, however, no change in shape was detected.

Table II summarizes some of the principal findings on the modifier action on emittance functionalities.

Brightness Wave Forms

Brightness waves have been used widely as a means of following electronic processes relating to electroluminescence in both powders (15, 19, 22-25) and single crystals (26). If the exciting voltage is sinusoidal, the waves show a major (primary) peak and at least one minor (secondary) peak per half cycle of voltage. Also there is usually a continuous component in that the light does not fall to zero at any time during a cycle. Destriau used the intensity of this continuous component as a measure of the mean lifetime of luminescent centers in the excited state (27).

The brightness wave characteristics are changed for phosphors containing modifiers. Figures 6a and 6b show the brightness waves of green-emitting phosphors containing no Ni and 1 x 10^{-4} g at. Ni/mole, respectively, for frequencies of 100 cps, 1 kc and 10 kc at 400 v. The central line in the figures indicates the level of zero light. The principal feature

Table II.

Dominant emission	Frequency dependence	Voltage dependence
Blue—No modifier	Sublinear above 100-200 cps	$L \sim \exp V^{-1/2}$
Low Ni conc., $<10^{-4}$	Sublinear above $\sim$ 600 cps	$L \sim \exp V^{-1/2}$
High Ni conc., $\geq 10^{-4}$	Linear to 20 kc*, superlinear below $\sim$ 400 cps	$L \sim \exp V^{-1/2}$
Low Co conc., $<10^{-5}$	Superlinear below 1 kc	$L \sim \exp V^{-1/2}$
Intermediate Co conc., $\sim 10^{-5}$	Linear to 20 kc, strongly superlinear below $\sim$ 1 kc	$L \sim \exp V^{-1/2}$
High Co conc., $>3 \times 10^{-5}$	Superlinear below $\sim$ 1 kc, sublinear above 1 kc	$L \sim \exp V^{-1/2}$
Green—No modifier	Sublinear above $\sim$ 400 cps	$L \sim \exp V^{-1/2}$
Low Ni conc., $<10^{-4}$	Sublinear above $\sim$ 500-1000 cps	Transition (See Figs. 4, 5)
High Ni conc., $\geq 10^{-4}$	Linear to 20 kc, superlinear below 1 kc	$L \sim V \exp V^{-1/2}$
Low Co conc., $<10^{-5}$ High Co conc., $>3 \times 10^{-5}$	Superlinear below 1 kc, sublinear at higher frequencies	Transition $L \sim V \exp V^{-1/2}$

* 20 kc is the limit of the frequency range examined.

Table III. Dielectric properties of blue-emitting electroluminescent phosphors

	Resistive photocurrent,* μa	ΔK, %	Electro-luminescence enhancement, %, at 15 kc, 400 v	
3×10^{-7} Co [3]	26	6.8	100	(Fig. 2)
No Co [3]	18	29		
1×10^{-6} Ni	10	6.6	45	(Fig. 3)
No Ni	14	30		

* The photocurrent is calculated from the voltage applied by the Q meter oscillator and the equivalent parallel resistance of the test cell.

[3] *Note added in proof*: Activation analyses of these samples show Co concentrations of 1.5 x 10^{-7} g at./mole for "No Co" and 2.0 x 10^{-6} g at./mole for "3 x 10^{-7} Co."

of these curves is the nearly complete absence of secondary peaks and continuous components in the phosphor containing Ni. At lower Ni content an intermediate behavior obtains: reduced height of the secondary peak and also a change in its phase to the descending portion of the primary peak.

The same phenomena result for blue-emitting phosphors. Figures 7a and 7b illustrate equivalent curves for two phosphors previously represented in Fig. 3. The brightness waves of the two Ni-doped phosphors are nearly identical. The phosphors in Figs. 6b and 7b are the same ones which show linear L-f characteristics in Figs. 1 and 3, respectively.

Cobalt-bearing phosphors show a different brightness wave pattern. All phosphors shown in Fig. 2 have brightness waves with a nearly constant continuous component, amounting to about 20% of the amplitude of the primary peaks. At 3 x 10^{-6} g at. Co/mole in that group however, the secondary peak has vanished fully. It reappears again at the same phase angle for all higher Co concentrations.

Dielectric Properties and the Electroluminescent Enhancement Effect

By increasing the matrix dielectric constant one obtains a greater field strength in the phosphor (12). Conversely it may be expected that an increase in the phosphor dielectric constant will reduce the field strength in the phosphor and result in reduced emittance.

In ZnS-type phosphors the dielectric constant increases under photo-excitation (13, 14). It is reasonable that a phosphor, excited to electroluminescence, will absorb part of its own radiation, especially in the blue region. It may then experience the ordinary photocapacitive effect by virtue of that absorption.

Roux has shown that the photocapacitive effect is suppressed by Ni and Co (11). The phosphors in this report which show enhanced emittance in the presence of modifiers may do so because of the suppressed photocapacitive effect and, therefore, because of a resulting higher field strength in the phosphor.

It is difficult to investigate dielectric effects of this sort under conditions of EL excitation because the electrical properties of the cells are dominated by voltage- and frequency-dependent losses (28). However, some information can be obtained by following the dielectric changes in the phosphor induced by external illumination. As mentioned above, this bears a relation to some of the processes in an EL cell, since the emitted radiation itself serves as a source of "external" illumination.

Data given in Table III obtain for phosphors showing electroluminescent enhancement. The results are expressed as the photocurrent and per cent increase in the dielectric constant of the phosphor-matrix mixture on exposure to room light.

The data are consistent with the idea that quenching of the photocapacitive effect is responsible for the electroluminescence enhancement. This is supported by observations that the enhancement occurs almost exclusively in blue-emitting phosphors

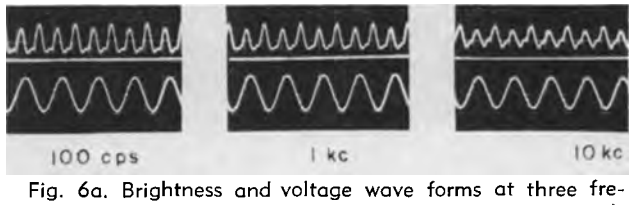

Fig. 6a. Brightness and voltage wave forms at three frequencies for the control phosphor of Fig. 1 (green-emission).

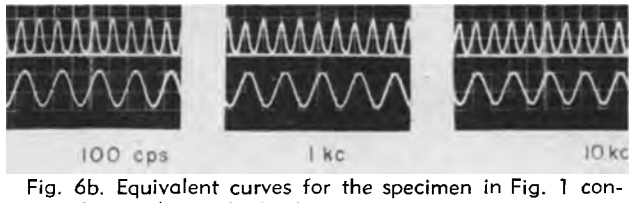

Fig. 6b. Equivalent curves for the specimen in Fig. 1 containing 1 x 10^{-4} g at. Ni/mole.

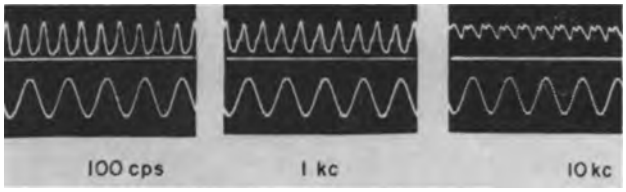

Fig. 7a. Brightness and voltage wave forms at three frequencies for the control phosphor of Fig. 3 (blue-emmission).

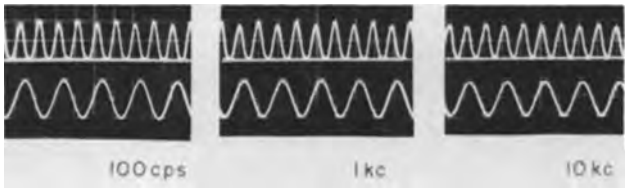

Fig. 7b. Equivalent curves for the specimen in Fig. 3 containing 1 x 10^{-4} g at. Ni/mole.

where self-absorption will tend to be greater than for emission predominantly in the green. Nevertheless, other factors will have to be considered before a definitive explanation of the enhancement is available. Among these are: (*a*) the degree of self-absorption of EL emission in phosphors, (*b*) the effect of such absorption on the phosphor dielectric constant and conductivity, and (c) the detailed field distribution changes within the grains resulting from the self-absorption.

The photocurrent data show that the enhancement is not related to that arising from the photoconductive effects recently reported by Ivey (29) and by Thornton (30). These workers state that external illumination is responsible for shifting the voltage distribution in phosphor crystals in favor of the barrier due to a more conductive bulk. Data in Table I show that the conductivity without Ni is greater than with Ni.

Discussion

Electroluminescence excitation is assumed to arise from impact ionization of luminescent centers by high energy electrons accelerated in a region of high field strength (31, 32). The electrons are swept away from the ionized centers by the field to remote parts of the crystal and contribute to a polarization field or become trapped. The voltage reversal brings many of the electrons back to the excitation region where radiative recombinations occur. The trapped electrons either cannot return at all (deep traps) or return at a later time (shallow traps) following field or thermal release (15, 18, 19, 25). Trapping of these electrons may enhance the continuous component (24). It has been proposed by Zalm, Haake, and others, that electron trapping is responsible for the secondary peak (15, 19).

This physical picture of excitation and recombination will serve as a basis for interpreting the experiments illustrating modifier action. Because Ni and Co behave differently in several respects, e.g., brightness waves and frequency response, they will be discussed separately. We shall refer to an unimpeded electronic recombination as a "fast" process. The delayed emission due to trapping or other causes will be viewed as a "slow" process.

The following model is proposed to account for the experimental result for Ni-bearing phosphors. Nickel offers to both trapped and conduction electrons a radiationless recombination site with a large capture cross section. At intermediate nickel concentrations (1 x 10^{-4} g at./mole) effectively all of the trapped electrons and some conduction electrons are brought back to the activator ground states through these recombination sites. This eliminates the contributions of the slow processes to the brightness waves, namely, the secondary peak and continuous component. Nonradiative escape of electrons from traps in zinc sulfide phosphors containing Ni has been suggested by Leverenz (1) and Kallman and Sucov (33). Only the fast process remains which can follow the field at all audio frequencies. The resulting linear *L-f* relationship of these phosphors up to 20 kc means that the area under each primary peak remains constant with frequency and is dependent only on the voltage. As the frequency is changed, the number of primary peaks per unit of time changes proportionately giving a linear *L-f* response.

At lower Ni concentrations (less than 1 x 10^{-4} g at./mole), the situation is somewhat more complicated. There are not enough recombination sites for all the trapped electrons to be affected. Furthermore, a finite relaxation time is required for the recombination sites to dissipate electronic energy radiationlessly and thereby return electrons to their ground states. The result of this is shown in Fig. 1. At low frequencies (e.g., 100 cps) Ni effects a reduction in brightness at the lowest concentrations. At high frequencies, where the number of conduction and trapped electrons is much larger, the radiationless recombination sites are swamped. The sites are neither numerous enough nor fast enough to be effective. Thus at 10 to 20 kc hardly any quenching action is observed for concentrations up to 3 x 10^{-5} g at. Ni/mole. Further increases in modifier concentration provide sufficient recombination centers, and the emittance is diminished at all frequencies. The concept of rapid capture and relatively slow release by radiationless recombination centers was suggested by Nail, *et al.* (4) as one explanation of superlinear photoluminescence in (Zn,Cd)S:Ag, Cl-Ni.

When large numbers of free electrons are produced by a voltage increase rather than by a frequency increase, the same result is observed. Figure 4 shows that for low modifier levels, the quenching action is more effective at low voltage (small supply of free electrons) than at high voltage (large supply of free electrons).

Zalm suggests that superlinearity in brightness-frequency characteristics is to be expected if the escape of holes to the valence band from ionized centers occurs (15). It is in these terms that the superlinearity seen in Fig. 1, 2, and 3 can be described. The presence of the modifier atom is assumed *ad hoc* to promote the escape of holes. Following this escape the electrons and holes recombine radiationlessly. The escape of holes to the valence band may have an appreciable relaxation time.

When the period of a cycle becomes smaller than this relaxation time superlinearity disappears. This is the case for frequencies above 1 kc in most of the samples studied.

The differences between Co and Ni as a modifier of electroluminescence has a direct counterpart in differences found in photoluminescence (3) and glow curve data (5). It can be argued, although with some reservations, that Ni serves as a recombination center but introduces no new trapping levels of importance to electroluminescence, while Co does both. One can then associate the continuous component and secondary peak in the brightness waves of Co-doped phosphors with this trapping level as well as the return to sublinearity in the L-f curves of Fig. 2. This argument is admittedly incomplete in that sublinearity returns in Fig. 2 at 1×10^{-4} g at. Co/mole while the secondary peak returns at 1×10^{-5} g at. Co/mole.

In one sense Co and Ni act alike. They both are able to change the shape of the voltage characteristic of green-emitting phosphors at frequencies above 1 kc (see Table II). This behavior is then a function of the activator (and/or coactivator) concentration as it is not found in blue-emitting phosphors. Thus it may be related to the particular trap distribution within the phosphor.

Duboc (34) and Klasens (35) discuss the processes in a two-level model which can introduce various functionalities in photoluminescence of photoconduction vs. exciting intensity. In spite of this, it does not seem profitable at the present time to fit the electroluminescence data into the band scheme in detail greater than that already done above. One must make assumptions to fit the models of Duboc and Klasens: (*a*) that the frequency in the electroluminescence case and the exciting light intensity in the photoluminescence case are comparable variables, and (*b*) that ZnS:Cu,Cl-Co/Ni is adequately represented by a two-state band scheme. These assumptions seem too restrictive for the present.

Acknowledgments

It is a pleasure to thank Drs. D. H. Baird, B. E. Bartels, A. L. Solomon, and R. N. Summergrad for many helpful discussions. The able assistance of J. W. Culp, S. Faria, and J. T. Ragusin in the synthesis of phosphors and in carrying out some of the measurements is acknowledged gratefully. Thanks are due J. Cosgrove and R. Weberling for analytical data.

Manuscript received April 17, 1959. This paper was prepared for delivery before the New York Meeting, April 27-May 1, 1958.

Any discussion of this paper will appear in a Discussion Section to be published in the June 1960 JOURNAL.

REFERENCES

1. H. W. Leverenz, "An Introduction to Luminescence of Solids," pp. 333-337, John Wiley & Sons, New York (1950).
2. N. Arpiarian, *J. Phys. Radium*, **17**, 674 (1956).
3. W. Hoogenstraaten and H. A. Klasens, *This Journal*, **100**, 366 (1953).
4. N. R. Nail, F. Urbach, and D. Pearlman, *J. Opt. Soc. Am.*, **39**, 690 (1949).
5. W. Hoogenstraaten, *This Journal*, **100**, 356 (1953).
6. S. Roberts and F. E. Williams, *J. Opt. Soc. Am.*, **40**, 516 (1950).
7. M. Schoen, *Z. Naturforsch.*, **66**, 251 (1951).
8. H. A. Klasens, *This Journal*, **100**, 72 (1953).
9. G. Gergely, *J. Phys. Radium*, **17**, 679 (1956).
10. W. Lehmann, *Phys. Rev.*, **101**, 489 (1956).
11. J. Roux, *J. Phys. Radium*, **17**, 813 (1956).
12. S. Roberts, *J. Opt. Soc. Am.*, **42**, 850 (1952).
13. G. F. J. Garlick, "Progress in Semiconductors—1," p. 99, John Wiley & Sons, New York (1956).
14. S. Roberts, *J. Opt. Soc. Am.*, **43**, 590 (1953).
15. P. Zalm, *Philips Research Repts.*, **11**, 353, 417 (1956).
16. S. Nudelman and F. Matossi, *This Journal*, **103**, 34 (1956).
17. C. W. Jerome and W. C. Gungle, *ibid.*, **100**, 34 (1953).
18. C. F. Alfrey and J. B. Taylor, *Brit. J. Applied Phys.*, Supplement No. 4, S44 (1954).
19. C. H. Haake, *J. Opt. Soc. Am.*, **47**, 881 (1957).
20. L. Burns, U. S. Pat. 2,774,902 (Dec. 18, 1953).
21. F. A. Schwertz, J. J. Mazenko, and E. R. Michalik, *Phys. Rev.*, **98**, 1133 (1955).
22. J. Mattler, *J. Phys. Radium*, **17**, 725 (1956).
23. F. Matossi and S. Nudelman, *Phys. Rev.*, **99**, 1100 (1955).
24. W. A. Thornton, *ibid.*, **102**, 38 (1956).
25. F. F. Morehead, Jr., *This Journal*, **105**, 461 (1958).
26. D. R. Frankl, J. L. Birman, G. F. Neumark, and A. Lempicki, *J. Phys. Radium*, **17**, 731 (1956).
27. G. Destriau, *ibid.*, **16**, 798 (1955).
28. W. Lehmann, *This Journal*, **103**, 24 (1956); **105**, 585 (1958).
29. H. F. Ivey, *Bull. Am. Phys. Soc.*, Ser. II, **3**, 273 (1958).
30. W. A. Thornton, *ibid.*, Ser. 11, **3**, 273 (1958).
31. D. Curie, *J. Phys. Radium*, **13**, 317 (1952).
32. W. W. Piper and F. E. Williams, *Phys. Rev.*, **87**, 151 (1952).
33. H. Kallman and E. Sucov, *ibid.*, **109**, 1473 (1958).
34. C. A. Duboc, *Brit. J. Appl. Phys.*, Suppl. No. 4, S 107 (1954).
35. H. A. Klasens, *J. Phys. Chem. Solids*, **7**, 175 (1958).

Optical Properties of Tin- and Lead-Activated Calcium Metasilicate Phosphors

Richard W. Mooney

Chemical and Metallurgical Division, Sylvania Electric Products Inc., Towanda, Pennsylvania

ABSTRACT

The preparation and optical properties of two new tin-activated calcium metasilicate phosphors are described. The more efficient of these is a β-$CaSiO_3$: Sn phosphor emitting in the visible at about 520 mμ. The optical properties of the tin-activated species are compared to their lead-activated analogues; and from considerations of crystal structure as affected by firing temperature and activator concentration, it is concluded that changes in spectra result from changes in crystal structure and not from the degree of aggregation of the activator ions. It is suggested that the emission spectra correspond to the $^3P_1^0 \rightarrow {}^1S_0$ and the $^1P_1^0 \rightarrow {}^1S_0$ transitions of the lead- and tin-activator centers.

Calcium metasilicate activated by lead and manganese is a well-known phosphor with a visible emission band at 610 mμ and an ultraviolet emission band at about 350 mμ (1-3). A study of the effect on crystal structure (4) showed that the inversion temperature of β-$CaSiO_3$ (wollastonite) to α-$CaSiO_3$ (pseudowollastonite) is raised with increasing manganese concentration in agreement with results reported by Voos (5), who showed that $MnSiO_3$ (rhodonite), being an isomorph of β-$CaSiO_3$, forms mixed crystals with wollastonite. A more recent study (6) of the influence of crystal structure on β-$CaSiO_3$: Pb + Mn showed that at temperatures where both wollastonite and pseudowollastonite are formed, the manganese crystallizes in the wollastonite lattice to the extent that a red shift is produced by the concentration of manganese in the β-$CaSiO_3$, structure. It was shown also that the addition of magnesium oxide to calcium metasilicate increased the inversion temperature of β-$CaSiO_3$ to α-$CaSiO_3$, whereas the addition of strontium oxide lowered the inversion temperature thus favoring the formation of pseudowollastonite.

The calcium silicates activated by lead alone were studied in detail by Studer and Fonda (7). They found several emission bands in the ultraviolet which they attributed to differences in crystal structure as follows: two bands at 300 mμ and 385 mμ to α-$CaSiO_3$: Pb, a 345 mμ band to β-$CaSiO_3$: Pb, and a 334 mμ band to β-Ca_2SiO_4: Pb. The corresponding excitation spectra varied widely with several maxima between 200 and 300 mμ. In a later study of the mechanism of sensitized luminescence of solids, Schulman and co-workers (8) claimed that the differences in emission were due to differences in the nature of the lead activator center rather than to changes in crystal structure. Specifically, they claimed that the emission bands at 290 and 390 mμ in $CaSiO_3$: Pb were caused by Pb^{2+} singlet centers, i.e., Pb^{2+} activator ions which had no other Pb^{2+} nearest neighbors; whereas the single-band emission at 340 mμ observed at higher lead concentrations was attributed to the occurrence of Pb^{2+}-Pb^{2+} doublets or higher aggregates of Pb^{2+} ions, i. e., centers which had 2 or more Pb^{2+} ions in neighboring cation positions.

Due to the similarities in electronic configuration between lead and tin and the resulting similarities in chemical behavior, it was thought that tin also might function as an activator in the calcium silicate system. In addition, previous work on tin-activated phosphates (9) had shown that many of the tin-activated phosphors were moderately efficient. A study of the calcium silicate system activated by tin has shown that there are at least four phosphors present, two having metasilicate structures and two having orthosilicate structures. This paper gives the preparation and properties of tin-activated β-$CaSiO_3$ (wollastonite) and tin-activated α-$CaSiO_3$ (pseudowollastonite) and compares their spectra with their closely related lead-activated analogues. The preparation and properties of the tin-activated calcium orthosilicates will be reported in a later paper.

Experimental Procedure

Calcium carbonate and silicic acid were mixed in a mole ratio of 1.00 to 1.20 together with 0.01-10.0 mole % of stannic or stannous oxide for the tin-activated phosphors, or lead oxide for the lead-activated phosphors. The mixture was pebble-milled in a deionized water slurry, dried at 110°-120°C, and fired in silica trays at temperatures varying from 980°-1320°C depending on the particular crystal form desired. For maximum efficiency it was necessary to fire in a steam atmosphere, and since the tin-activated phosphors luminesce only when the tin is in a lower valence state, a reducing atmosphere, usually a mixture of hydrogen and steam, was maintained. The steam and hydrogen contents of the firing atmosphere were controlled carefully in order to obtain reproducible results.

The crystal structures of the phosphors were determined by conventional x-ray diffraction techniques using CuKα radiation from a Philips Norelco unit. In the majority of cases, identification was made by means of Debye-Scherrer powder patterns taken with large diameter (114.6 mm) cameras. In

Table I. Effect of tin-activator concentration on the inversion temperature for β- to α-$CaSiO_3$*

Firing temperature, °C	Mole fraction of Sn retained in phosphor				
	0	0.00045	0.00075	0.0058	0.042
1150	β	β	$\alpha(\beta)$	$\alpha(\beta)$	α
1120	β	β	β	β	$\beta(\alpha)$

* Minor constituent given in parentheses.

a few cases, diffractometer tracings were taken on a Norelco wide-range goniometer at a scanning speed of 1/4°/min. As would be expected, the two methods were in excellent agreement.

The quantitative analyses for per cent tin and per cent lead were made as follows. For tin the sample was dissolved in HCl, treated with lead to reduce any stannic tin to the stannous state, and then titrated at 10°C with a standard iodine solution. The determination of per cent lead was slightly more complicated. The sample was first decomposed with HF plus H_2SO_4 followed by a Na_2CO_3 fusion. The resulting $PbCO_3$ was dissolved in HNO_3 and precipitated as $PbMoO_4$ by a solution of $(NH_4)_2MoO_4$. The precipitate was filtered, washed, and fired. The activator contents are expressed in this paper as gram-atom tin or lead per gram-mole of $CaSiO_3$, i.e., as mole fraction.

The excitation-emission radiometer[1] used for the measurements of excitation and emission spectra will be described in detail elsewhere (10). Basically, it is a double monochromator system with a high-pressure xenon arc source and a 1P28 photomultiplier detector. A combination of optical and electrical components provides for constant-energy-level illumination of the sample during excitation measurements and gives an emission spectrum which is proportional to the true energy output of the sample regardless of source fluctuations or detector sensitivity as a function of wave length.

Results with $CaSiO_3$: Sn

A preliminary study of firing temperature disclosed that the more efficient β-$CaSiO_3$: Sn phosphor was obtained with good brightness between 1090° and 1150°C, whereas the less efficient α-$CaSiO_3$: Sn phosphor always was obtained at temperatures above 1150°C. Later it was found that the inversion temperature for β- to α-$CaSiO_3$ was dependent on the activator concentration as shown in Table I. In general, the results were in reasonable agreement with the phase diagram of Levin, McMurdie, and Hall (11) who list the inversion temperature of β- to α-$CaSiO_3$ as 1125°C.

It also was shown that the addition of other divalent cations changed the inversion temperature. For instance, the addition of oxides or fluorides of magnesium, zinc, or cadmium increased the optimum firing temperature for β-$CaSiO_3$: Sn to 1200°C and over, thus indicating an increase in the inversion temperature or a stabilization of the wollastonite structure. Conversely, the addition of the carbonates or fluorides of strontium and barium lowered the optimum firing temperature indicating a stabilization of the pseudowollastonite structure. For barium fluoride, for instance, optimum brightness was obtained at 980°C. These results agree in principle with those of Lange and Kressin (6) in that the addition of ions smaller than calcium, such as magnesium, stabilize the β-$CaSiO_3$ structure, whereas the addition of ions larger than calcium, such as strontium, stabilize the α-$CaSiO_3$ structure.

The phosphor β-$CaSiO_3$: Sn emits in the green with a peak of about 518 mμ when excited by 254 mμ radiation. The corresponding excitation spectrum has a maximum at 246 mμ. Plots of emission and excitation spectra of β-$CaSiO_3$: Sn are shown in the top half of Fig. 1. The emission spectrum is non-Gaussian indicating the possibility of a second unresolved emission band on the high-energy side of the peak. All samples identified as β in Table I gave an emission spectrum as shown in Fig. 1 with the exception of the sample containing the least tin (4.5 x10^{-4} gram-atom Sn/$CaSiO_3$) fired at both 1120° and 1150°C, for which an emission peak at 400 mμ as well as the usual peak at 518 mμ was obtained. This peak was not observed in unactivated samples. The excitation spectrum is characteristic of that obtained for tin-activated phosphors, i.e., broad, indicating the presence of several unresolved absorption bands. The fluorescence of β-$CaSiO_3$: Sn persists at low brightness after the exciting radiation is removed. No quantitative measurements of decay time were made.

The phosphor α-$CaSiO_3$: Sn is weakly fluorescent having two emission bands peaking at 562 and 450 mμ as shown in the top half of Fig. 2. All samples identified as α by x-ray diffraction gave the two peaks shown in Fig. 2 again with the exception of the sample having the least tin (4.5 x 10^{-4} gram-atom Sn/$CaSiO_3$). This sample fired at 1205°, 1260°, and 1320°C showed evidence of the 400 mμ band, although its definition was not as good as that obtained with the β-structure due to the 450 mμ band in the α-$CaSiO_3$: Sn phosphor. Those samples identified as a mixture of α- and β-$CaSiO_3$: Sn in Table I gave a broad band emission extending from 562 to

[1] Built by the Perkin-Elmer Corporation, Norwalk, Conn.

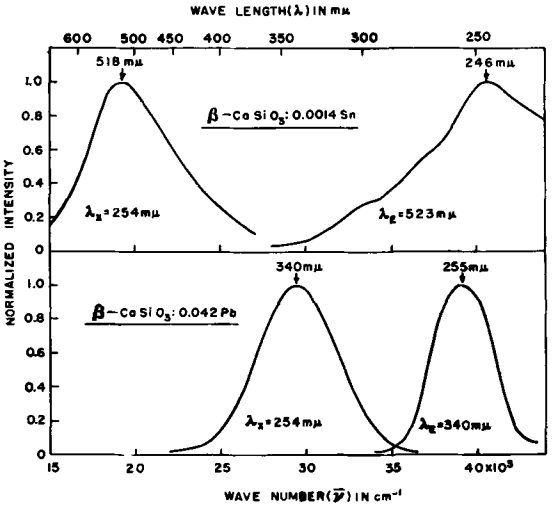

Fig. 1. Excitation and emission spectra of β-$CaSiO_3$:Sn and β-$CaSiO_3$:Pb with activator concentrations given in atoms retained in the fired phosphor per mole $CaSiO_3$.

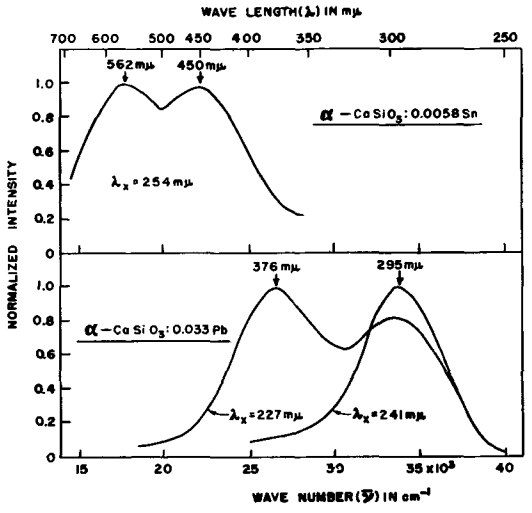

Fig. 2. Emission spectra of α-$CaSiO_3$:Sn and α-$CaSiO_3$Pb with activator concentrations given in atoms retained in the fired phosphor per mole $CaSiO_3$.

450 mμ, since the superposition of the α- and β-$CaSiO_3$:Sn emission gave bands at 562, 518 and 450 mμ which overlapped each other. There was no evidence of the 518 mμ band ascribed to β-$CaSiO_3$:Sn in samples fired at 1205°, 1260°, and 1320°C for the lowest or the highest tin concentration (mole fractions of 4.5×10^{-4} and 4.2×10^{-2}, respectively). The excitation spectra again consisted of several absorption bands as shown in the top half of Fig. 3. It is noteworthy that emission in the lower energy band (562 mμ) is favored by absorption at higher energies, i.e., the excitation spectrum is shifted toward higher energies for fluorescence in the red.

The addition of manganese gave rise to a new emission band at 610 mμ in addition to the band at 518 mμ. Manganese is especially effective in stabilizing the low temperature or β-form of $CaSiO_3$ and, therefore, firing temperatures as high as 1260°C with manganese present still gave the β-$CaSiO_3$ structure. The phosphor β-$CaSiO_3$:Sn + Mn is very similar to the well-known phosphor β-$CaSiO_3$:Pb + Mn (1-3) with the obvious difference in emission between tin- and lead-activation being demonstrated by the presence of the 518 mμ band due to tin rather than the 350 mμ band due to lead. Due to the close proximity of the tin band at 518 mμ and the manganese band at 619 mμ, an increase in manganese concentration produced an apparent shift in the peak emission due to a decrease in intensity of the tin band and an increase in intensity of the manganese band. The tendency of manganese to crystallize in the rhodonite-wollastonite structure stabilized the β-$CaSiO_3$ form over wide Ca/Si ratios (even up to 2.00/1.00 where Ca_2SiO_4 should form) as well as wide temperature ranges.

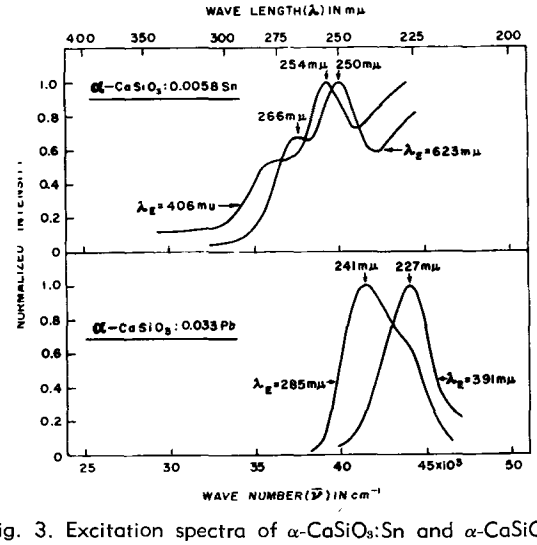

Fig. 3. Excitation spectra of α-$CaSiO_3$:Sn and α-$CaSiO_3$:Pb with activator concentrations given in atoms retained in the fired phosphor per mole $CaSiO_3$.

Results with $CaSiO_3$:Pb

A corresponding study of the lead-activated calcium metasilicates gave very similar results to those obtained on the tin-activated system. Thus, β-$CaSiO_3$:Pb was obtained below 1150°C, whereas the less efficient α-$CaSiO_3$:Pb phosphor always was obtained above 1150°C. Again the particular modification obtained at temperatures close to the transition temperature was dependent on the activator concentration (see Table II).

The β-$CaSiO_3$:Pb phosphor emits in the ultraviolet at about 340 mμ when excited by 254-mμ radiation. The corresponding excitation spectrum has its maximum at 255 mμ. Both the emission and the excitation spectra have Gaussian distributions as shown in the bottom half of Fig. 1. All samples identified as β in Table II had excitation and emission spectra as above. There was no evidence of a second emission band at very low concentrations, but the peak of the emission band did shift slightly from 337 to 350 mμ in going from the lowest to the highest lead concentration.

All lead-activated calcium metasilicates fired above 1150°C had the α-$CaSiO_3$ structure and displayed emission and excitation spectra characteristic of those shown in the bottom halves of Fig. 2 and 3. Thus α-$CaSiO_3$:Pb has two emission bands at 295 and 376 mμ and two corresponding excitation bands at 241 and 227 mμ. It is interesting, however, that irradiation in the lower-energy band at 241 mμ produced the higher energy band at 295 mμ, whereas irradiation in the higher energy band at 227 mμ caused the lower energy band at 376 mμ to appear. That is, the direct energy relationship between excitation and emission that one normally would expect is reversed. Those samples in Table II which were identified as a mixture of α- and β-$CaSiO_3$ gave all three emission bands depending upon the wave length of excitation. However, the greater absorption of β-$CaSiO_3$:Pb compared to α-$CaSiO_3$:Pb at the

Table II. Effect of lead-activator concentration on the inversion temperature for β- to α-$CaSiO_3$*

Firing temperature, °C	Mole fraction of Pb retained in phosphor				
	0	0.001	0.01	0.064	0.085
1150	β	$\beta(\alpha)$	$\alpha(\beta)$	$\alpha(\beta)$	α
1120	β	$\beta(\alpha)$	$\beta(\alpha)$	$\beta(\alpha)$	$\alpha(\beta)$

* Minor constituent given in parentheses.

higher wave lengths made the β-$CaSiO_3$: Pb emission spectra predominant even for the sample containing 0.085 Pb/$CaSiO_3$ fired at 1120°C and identified as primarily α-$CaSiO_3$ (see Table II). Therefore, the emission spectra of lead-activated $CaSiO_3$ fired in the neighborhood of the inversion temperature exhibited the following characteristics with increasing lead content. At very low lead concentrations, the β-$CaSiO_3$: Pb band appeared at 337 mμ. As the structure changed to a mixture of β- plus α-$CaSiO_3$, all three bands appeared, and finally the β-$CaSiO_3$: Pb band now at 350 mμ was again the only band found at high lead concentrations. On the contrary, samples fired at 1260°C having the lowest (0.001) and the highest (0.085) lead concentrations exhibited only the typical α-$CaSiO_3$: Pb bands.

Discussion

The obvious conclusion to be drawn from these results is that the excitation and emission spectra of tin- and lead-activated calcium metasilicates are determined primarily by the particular activator used and the crystal structure of the matrix in which the activator is found. This conclusion is in agreement with the original work on lead-activated calcium metasilicates by Studer and Fonda (7), but is in sharp disagreement with the later work by Schulman, Ginther, and Klick (8), who ascribed the differences in spectra observed on lead-activated calcium metasilicates to the occurrence of singlet Pb^{2+} activator centers at low lead concentrations and doublet Pb^{2+}-Pb^{2+} activator centers at higher lead concentrations.

According to this later work, the singlet Pb^{2+} centers are excited only by absorption in the 235 mμ band, which is shown by Fig. 3 to be in reality two bands peaked at 227 and 241 mμ, and which gives a double-band emission peaked at 290 and 390 mμ (295 and 376 mμ according to Fig. 2). In this work, these paired excitation and emission bands are ascribed to the phosphor, α-$CaSiO_3$: Pb.

The 255 mμ absorption band with single-band emission peaking at 340 mμ was assigned to the presence of Pb^{2+}-Pb^{2+} doublets by Schulman, *et al.* However, while the experimental agreement between the measured spectra is excellent (see Fig. 1), the present work claims that these bands are associated with the β-$CaSiO_3$: Pb phosphor.

The evidence for these assumptions is given by a comparison of the spectra of the lead-activated calcium metasilicates as a function of activator concentration and firing temperature coupled with x-ray identification of the crystal structures of the phosphors. Thus, as related under results, phosphors fired at temperatures close to the inversion temperature (1125°C), i.e., at 1120° and 1150°C, have varying spectra depending upon the activator concentration and its effect on crystal structure. At very low lead concentrations, the spectra are characteristic of β-$CaSiO_3$: Pb as would be expected from the x-ray identification. At intermediate lead concentrations, the spectra are mixtures of that expected from β- and α-$CaSiO_3$: Pb. However, at the highest lead concentrations, the spectra are once more characteristic of β-$CaSiO_3$: Pb, whereas one would expect to find the α-$CaSiO_3$: Pb spectrum in view of the x-ray identification. To explain this result, it must be remembered that with increasing lead concentrations, the phosphors are becoming less efficient due to concentration quenching; and, since the α-$CaSiO_3$: Pb phosphor is inefficient even at low activator concentrations, its emission at high lead concentrations is below the limits of detection of the instrument. These results are in rough agreement with the observation of Schulman, *et al.*, as would be expected, since they used a firing temperature of 1150°C where both β- and α-$CaSiO_3$ may be formed under the right conditions.

The above observations are not convincing proof since the spectra of the phosphors are confused by crystal structure changes. However, it has been noted that firings above 1150°C gave only the α-$CaSiO_3$ structure. If the differences in spectra are due to the occurrence of lead singlet or doublet centers, these differences should depend only upon the activator concentration and not on the firing temperature with its effect upon crystal structure. Therefore, the experimental observation that lead-activated calcium metasilicates fired at 1260°C exhibited only the spectral characteristics of α-$CaSiO_3$: Pb as shown in Fig. 2 and 3 and never the spectrum of β-$CaSiO_3$: Pb as shown in Fig. 1, completely independent of activator concentration leads to the conclusion that the spectra are determined by the crystal structure and not by the degree of aggregation of the activator ions. The same conclusion also may be reached from the results on the tin-activated calcium metasilicate system.

The previous observation (8) that irradiation in the 235 mμ absorption band does not excite the visible Mn^{2+} emission in $CaSiO_3$: Pb + Mn is explained easily by the fact that Mn crystallizes preferentially in the β-$CaSiO_3$ lattice (5, 6) and therefore it is necessary to excite the Pb atoms in β-$CaSiO_3$: Pb, which absorbs at 255 mμ, but not at 235 mμ.

As usual in studies of this type, it is easier to demonstrate the incorrectness of a previous model than it is to propose with any degree of assurance a model which does explain the experimental observations. Due to the complexity of the silicate crystal structures and the resulting complex symmetry of their crystalline fields, it is not possible to explain the results in a quantitative manner as has been done for KCl: Tl (12). However, some rather interesting speculations concerning the nature and origin of the emission bands may be made. For instance, since the electronic configurations of the ground states of Tl II (Tl^+) and Pb III (Pb^{2+}) are identical and that of Sn III (Sn^{2+}) is very similar, having a $5s^2\ {}^1S_0$ ground state instead of the $6s^2\ {}^1S_0$ ground state of Tl II and Pb III, one might expect lead- and tin-activated phosphors to behave generally much like thallium-activated systems.

Therefore, proceeding by analogy with KCl: Tl, the higher energy emission bands in both tin- and lead-activated α-$CaSiO_3$ might be assumed to arise from the ${}^1P_1^0 \rightarrow {}^1S_0$ transition and the lower energy bands to arise from the ${}^3P_1^0 \rightarrow {}^1S_0$ transition of the activator

centers. Similarly, in view of its relative position with reference to the emission bands in the α-structure, the single band in tin- and lead-activated β-$CaSiO_3$ could be assigned arbitrarily to the $^3P_1^0 \rightarrow {}^1S_0$ transition. Such assignments of energy levels are not inconsistent with the trends that one should expect by comparison to the same energy level transitions for the free ions (13). However, the assignment of the $^3P_1^0 \rightarrow {}^1S_0$ transition to the green emission band in β-$CaSiO_3$:Sn is not consistent with the phosphorescence observed, which suggests a forbidden transition, whereas the $^3P_1^0 \rightarrow {}^1S_0$ transition is allowed if the selection rule $\Delta S = 0$ does not hold due to imperfect LS coupling.

In summary, it has been shown that the spectra of tin- and lead-activated calcium metasilicates are associated with the particular structure produced, i.e., α- or β-$CaSiO_3$ and not with the degree of aggregation of the activator ions. Instead it is suggested that the emission bands in both tin- and lead-activated α-$CaSiO_3$ are related to the $^3P_1^0 \rightarrow {}^1S_0$ and the $^1P_1^0 \rightarrow {}^1S_0$ transitions of the activator ions and that the single emission band in β-$CaSiO_3$:Sn or Pb is related to the $^3P_1^0 \rightarrow {}^1S_0$ transition, although the reason for the occurrence of a $^1P_1^0 \rightarrow {}^1S_0$ transition in the α-$CaSiO_3$ structure and not in the β-$CaSiO_3$ structure is not understood.

Acknowledgment

The author is indebted to several of his colleagues for their help with the preparations and measurements. Specifically, the author wishes to thank Mr. F. N. Shaffer for his aid and advice in the preparation of the first Sn-activated metasilicates, Dr. C. W. W. Hoffman for the x-ray identifications, and Mr. G. J. Meisenhelter for the analytical determinations. The author also wishes to acknowledge the advice and encouragement of Dr. J. S. Smith during the progress of this work.

Manuscript received May 18, 1959. This paper was prepared for delivery before the Philadelphia Meeting, May 3-7, 1959.

Any discussion of this paper will appear in a Discussion Section to be published in the June 1960 JOURNAL.

REFERENCES

1. J. B. Merrill and J. H. Schulman, *J. Opt. Soc. Amer.*, **38**, 471 (1948).
2. H. C. Froelich, *This Journal*, **93**, 101 (1948).
3. K. H. Butler, *ibid.*, **95**, 267 (1949).
4. G. R. Fonda and H. C. Froelich, *ibid.*, **93**, 114 (1948).
5. E. Voos, *Z. anorg. u. allgem. Chem.*, **222**, 201 (1935).
6. H. Lange and G. Kressin, *Z. Physik*, **142**, 380 (1955).
7. F. J. Studer and G. R. Fonda, *J. Opt. Soc. Amer.*, **39**, 655 (1949).
8. J. H. Schulman, R. J. Ginther, and C. C. Klick, *This Journal*, **97**, 123 (1950).
9. K. H. Butler, *ibid.*, **100**, 250 (1953).
10. W. Slavin, R. W. Mooney, and D. T. Palumbo, To be published.
11. E. M. Levin, H. F. McMurdie, and F. P. Hall, "Phase Diagrams for Ceramists," p. 48, The American Ceramic Society, Columbus, Ohio (1956).
12. F. E. Williams, *J. Opt. Soc. Amer.*, **47**, 869 (1957).
13. C. E. Moore, "Atomic Energy Levels," Vol. III, NBS Circular #467 (1958).

Phase Equilibria and Manganese-Activated Fluorescence in the System $Zn_3(PO_4)_2$-$Mg_3(PO_4)_2$

J. F. Sarver, Fred L. Katnack,[1] and F. A. Hummel

Department of Ceramic Technology, College of Mineral Industries,

The Pennsylvania State University, University Park, Pennsylvania

ABSTRACT

Determination of the phase relationships on the $Zn_3(PO_4)_2$-$Mg_3(PO_4)_2$ join by the quench method has enabled the previously designated "gamma zinc phosphate" to be identified as a solid solution of zinc orthophosphate in magnesium orthophosphate. $Mg_3(PO_4)_2$ takes 95 mole % $Zn_3(PO_4)_2$ into solid solution at 1000°C. β-$Zn_3(PO_4)_2$ takes a small amount of $Mg_3(PO_4)_2$ into solid solution (about 3 mole % at 1000°) and, in order to satisfy the requirements of the Phase Rule, α-$Zn_3(PO_4)_2$ must take a small amount of $Mg_3(PO_4)_2$ into solution. The previously determined $Zn_3(PO_4)_2$-$Mn_3(PO_4)_2$ relationships are discussed in terms of the new data for the zinc-magnesium orthorphosphate system. Solid solution relationships in the system MgO-ZnO-P_2O_5 are diagrammed and discussed.

Data on peak emission and brightness of the β-$Zn_3(PO_4)_2$ solid solution and the $Mg_3(PO_4)_2$ solid solution were obtained using molar substitutions of manganese as an activator. The brightness of the β-$(Zn,Mg)_3(PO_4)_2$:Mn solid solutions compares favorably with commercial β-$Zn_3(PO_4)_2$:Mn phosphors and the N.B.S. standard. The manganese-activated phosphors near the high zinc end of the $Mg_3(PO_4)_2$ solid solution series are very bright relative to the β-$Zn_3(PO_4)_2$:Mn standard, but they peak near 6280Å, which may in part account for the higher brightness.

This paper is the last of a series which was intended to establish the identity and the manganese-activated emission characteristics of the α, β, and "gamma" zinc orthophosphate family of cathode-ray excitable phosphors. A second purpose in accumulating these data was to establish a general picture of the phase relationships in the system MgO-ZnO-P_2O_5.

The work of Smith (1) led to the development of these red fluorescing T.V. phosphors and the adoption of the alpha, beta, and "gamma" nomenclature.

Katnack and Hummel (2) established the nature of the alpha to beta zinc orthophosphate inversion and later Hummel and Katnack (3) furnished data on the manganese-activated cathode-ray emission characteristics of all the zinc phosphate compounds.

Recent work by Sarver and Hummel (4) established the nature of manganese-activated cathode-ray emission in the system $Mg(PO_3)_2$-$Zn(PO_3)_2$.

Experimental Procedure

Phase relationships.—The equilibrium relationships in the system were established using the seventeen compositions shown in Table I. The raw materials used were C.P. grades of ZnO, basic magnesium carbonate, and dibasic ammonium phosphate, $(NH_4)_2HPO_4$. The starting material for quench determinations in compositions 1-7 was a fused and recrystallized melt which had been held at 750°C for 24 hr. The starting material for the remaining portion of the work (compositions 8-17) was a calcine which had been heated to 200°C for 24 hr.

Phase identifications were made by petrographic and x-ray diffraction examination, using nickel-filtered CuKα radiation for the latter method.

Fluorescence.—Two sets of data on manganese-activated, cathode ray emission were obtained. The first series included data on the β-$(Zn,Mg)_3(PO_4)_2$:Mn solid solutions and a wide range of $(Mg,Zn)_3(PO_4)_2$:Mn ternary solid solutions. The second series included a brief investigation of the manganese activator concentration on the peak emission and brightness of one of the brightest compositions in the high zinc end of the $(Mg,Zn)_3(PO_4)_2$ solid solutions.

Spectral distribution curves were obtained with a demountable cathode-ray tube operating at 16 kv anode potential, 1.0 μa/cm^2 beam current density on a standard scan T.V. raster of 65 cm^2 area.

Brightness under the above conditions was measured using an eye-corrected Weston foot-lambert meter.

Results and Discussion

Phase Relationships on the Orthophosphate Join

The quench and heat treatment data shown in Table I were used to construct the equilibrium diagram shown in Fig. 1. The system is characterized by a small region of β-$Zn_3(PO_4)_2$ solid solutions, a still smaller region of α-$Zn_3(PO_4)_2$ solid solutions, and a very large region of $Mg_3(PO_4)_2$ solid solutions. The x-ray diffraction data for the β-$Zn_3(PO_4)_2$ and

[1] Present address: Radio Corporation of America, Somerville, N. J.

Table I. Compositions, quench data, and heat treatments for the system $Zn_3(PO_4)_2$-$Mg_3(PO_4)_2$

Comp. No.	Mole per cent $Zn_3(PO_4)_2$	Mole per cent $Mg_3(PO_4)_2$	Temp, °C/24 hr	Phases present
1	100	0	900	α-Z_3P
			1000	β-Z_3P
2	99	1	950	β-Z_3P_{ss}
			995	β-Z_3P_{ss}
3	98	2	921	α-Z_3P_{ss} + M_3P_{ss}
			929	β-Z_3P_{ss} + M_3P_{ss}
			933	β-Z_3P_{ss} + M_3P_{ss}
			950	β-Z_3P_{ss} + M_3P_{ss}
			998	β-Z_3P_{ss}
4	97	3	920	M_3P_{ss}
			950	β-Z_3P_{ss} + M_3P_{ss}
			1000	β-Z_3P_{ss} + M_3P_{ss}
			1045	β-Z_3P_{ss}
5	96	4	958	M_3P_{ss}
			995	β-Z_3P_{ss} + M_3P_{ss}
			1035	β-Z_3P_{ss} + M_3P_{ss}
			1045	β-Z_3P_{ss}*
6	95	5	995	M_3P_{ss}
			1035	β-Z_3P_{ss} + M_3P_{ss}
7	94	6	1040	M_3P_{ss}
8	90	10	1050	M_3P_{ss}
9	80	20	1050	M_3P_{ss}
10	70	30	1050	M_3P_{ss}
11	60	40	1050	M_3P_{ss}
12	50	50	1161	M_3P_{ss}
			1180	M_3P_{ss}*
13	40	60	1050	M_3P_{ss}
14	30	70	1050	M_3P_{ss}
15	20	80	1050	M_3P_{ss}
16	10	90	1050	M_3P_{ss}
17	0	100	1050	M_3P_{ss}

* Evidence of melting.

Note: Compositions 1 through 7 and 12 were treated in quenching furnaces. The remaining compositions were heat treated in Globar furnaces.

α-Z_3P = α-$Zn_3(PO_4)_2$
β-Z_3P = β-$Zn_3(PO_4)_2$
M_3P = $Mg_3(PO_4)_2$

α-$Zn_3(PO_4)_2$ phases have been presented in a previous paper (2). The presence of magnesium in solid solution in the α and β phases produced no appreciable shift in the position of the lines in the x-ray diffraction pattern.

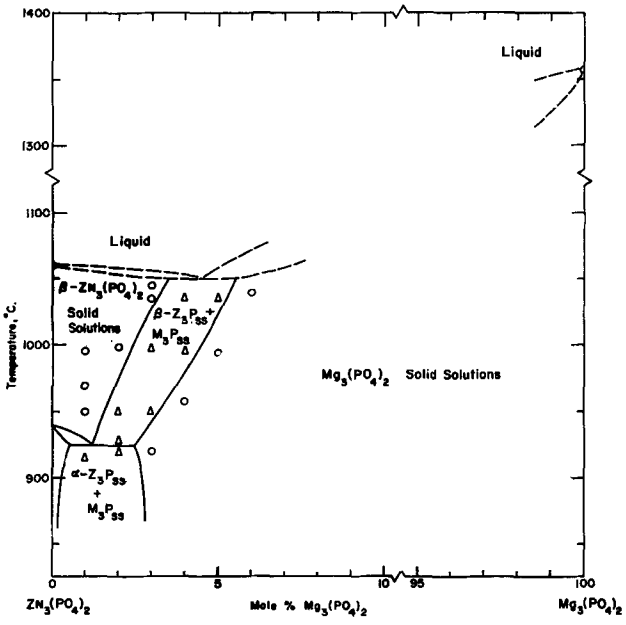

Fig. 1. Phase relationships on the $Zn_3(PO_4)_2$-$Mg_3(PO_4)_2$ join

The x-ray diffraction data for $Mg_3(PO_4)_2$, solid solutions containing 20, 40, 60, 80, and 95 mole % $Zn_3(PO_4)_2$, and the previously reported (3) manganese "gamma zinc orthophosphate" are listed in Table II. The patterns of the magnesium orthophosphate solid solutions are shown in Fig. 2 for convenience in following the changes which occur. A detailed study of the x-ray diffraction patterns of all the members of the $Mg_3(PO_4)_2$ solid solution compositions (7-17) listed in Table I showed that the series was actually continuous from pure $Mg_3(PO_4)_2$ to 95 mole % $Zn_3(PO_4)_2$. Petrographic examination confirmed the one phase nature of the compositions in this region.

Since the system was not glass-forming, the liquidus relationships were not determined and the phase boundaries in the high-temperature region are shown as dashed lines due to this uncertainty. Berek (5) reported the melting point of $Mg_3(PO_4)_2$

Table II. X-ray diffraction data for $(Zn,Mn)_3(PO_4)_2$,* $(Zn_{0.95}Mg_{0.05})_3(PO_4)_2$, Mg_3PO_4, and four intermediate solid solutions

$(Zn, Mn)_3(PO_4)_2$*			$(Zn_{0.95}Mg_{0.05})_3(PO_4)_2$			80Z_3P-20M_3P		60Z_3P-40M_3P		40Z_3P-60M_3P		20Z_3P-80M_3P		$Mg_3(PO_4)_2$		
2θ	d	I/I_o	2θ	d	I/I_o	2θ	I/I_o	2θ	I/I_o	2θ	I/I_o	2θ	I/I_o	2θ	d	I/I_o
15.9	5.57	10												15.9	5.57	14
			20.4	4.35	80	20.4	70	20.4	75	20.4	54	20.4	45	20.4	4.35	32
20.5	4.33	90†	20.6	4.31	37	20.6	41	20.6	59	20.6	46	20.6	37	20.6	4.31	28
21.1	4.21	5	21.1	4.21	8	21.2	12	21.3	19	21.5	22	21.5	27	21.6	4.11	39
22.3	3.99	40	22.1	4.02	40	22.1	31	22.0	33	22.0	40	21.8	27	21.8	4.08	49
23.0	3.87	25	23.0	3.87	25	23.0	27	23.0	40	23.1	48	23.1	61	23.1	3.85	91
24.2	3.68	5	24.4	3.65	5	24.4	5	24.4	6	24.4	6	24.4	15	24.3	3.66	35
26.1	3.41	100	25.9	3.44	100	25.9	100	25.9	100	25.9	100	25.9	100	25.9	3.44	100
27.6	3.23	20	27.6	3.23	26	27.7	26	27.8	29	27.9	26	27.9	22	27.9	3.20	19
29.5	3.03	20	29.5	3.03	27	29.6	26	29.6	30	29.7	26	29.7	22	29.8	3.00	22
30.8	2.90	10	30.7	2.91	10											
31.9	2.81	25	32.0	2.80	10	32.0	17	32.0	9	32.0	9	32.0	17	32.0	2.80	17
32.9	2.72	15	32.8	2.73	13	32.8	10	32.7	9	32.6	9	32.5	8	32.3	2.77	7
34.0	2.64	10	34.1	2.64	5	—	—	—	—	—	—	—	—	—	—	—
35.6	2.52	35	35.6	2.52	51	35.6	54	35.7	55	35.6	22	35.5	21	35.4	2.54	12
35.8	2.51	35	—	—	—	—	—	—	—	35.8	37	35.8	32	35.9	2.50	28
36.6	2.46	55	36.6	2.46	40	36.8	42	37.0	41	37.2	34	37.2	36	37.2	2.42	34

* Hummel and Katnack (3).
† May be a doublet.

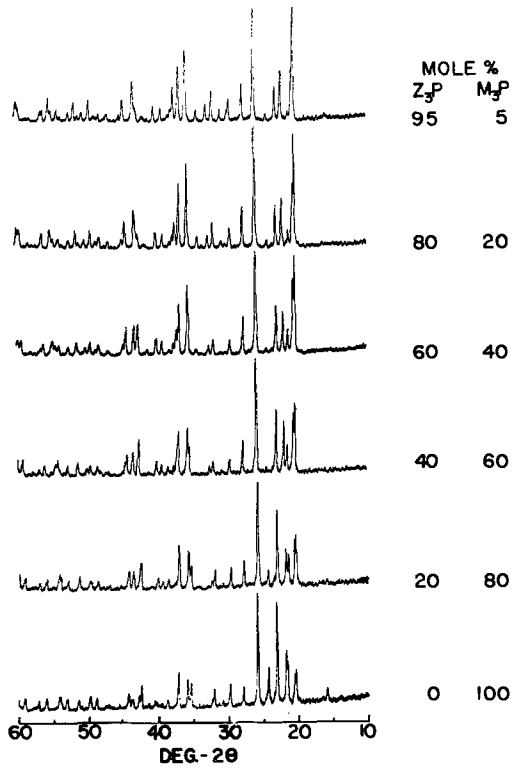

Fig. 2. X-ray diffraction patterns for magnesium orthophosphate solid solutions.

as 1357°C, and this value has been used in constructing Fig. 1.

A word about the previously determined relationships on the $Zn_3(PO_4)_2$-$Mn_3(PO_4)_2$ join (3) is now in order. The close structural relationship between the long series of (Mg, Zn)$_3(PO_4)_2$ solid solutions and the (Zn, Mn)$_3(PO_4)_2$ solid solutions ("gamma zinc orthophosphate") is now apparent from the data in Table II. It had been mentioned (3) and it is well known that oxidation of manganese hinders the complete determination of phase relationships in such a system when working in air. If a pure $Mn_3(PO_4)_2$ phase could be made by synthesis in nitrogen or other protective atmosphere, it is possible that a large range of (Zn,Mn)$_3(PO_4)_2$ solid solutions would exist, analogous to the zinc-magnesium series. Even without the benefit of a protective atmosphere to assure the retention of divalent manganese, it has been shown (3) that quite a broad region of ternary solid solutions do exist.

The Ternary System MgO-ZnO-P_2O_5

The subsolidus solid solution relationships in the ternary system are shown in Fig. 3.

The MgO-ZnO relationships were determined by firing mixtures of the oxides at 1300°C for 8 hr. Using nickel-filtered CuKα radiation ($\lambda = 1.5405$Å) and 10% by weight of silicon metal as an internal standard, diffraction patterns were run at ½° (2θ)/min. The results for MgO and the solid solution limit (ZnO in MgO) are shown in Table III.

The lattice expansion due to the inclusion of 32 mole % zinc oxide was 0.7%. Similar data for compositions near ZnO indicated about 3% of solid solution at 1300°C.

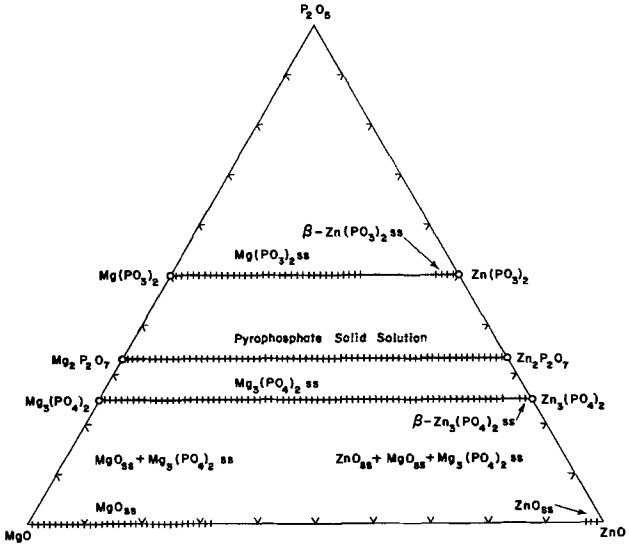

Fig. 3. Subsolidus solid solution relationships in the system MgO-ZnO-P_2O_5 (mole per cent).

Data on the orthophosphate join have been presented above and the data on the solid solutions on the metaphosphate join were presented previously (4).

According to some unpublished data obtained several years ago (6), it is probable that a complete (or nearly complete) series of pyrophosphate solid solutions exist. The generally high solid solubility of the zinc compounds in their magnesium analogues is thus apparent.

Fluorescence

Compositions shown in Table IV were fired at 1000°C for 48 hr, using 1 mole % MnO as an activator.

These results show that a little $Mg_3(PO_4)_2$ added to β-$Zn_3(PO_4)_2$ improves the brightness of the β solid solution, and that excessive amounts will damage brightness. A substantial shift in the position of peak intensity occurs with small additions of $Mg_3(PO_4)_2$.

The $Mg_3(PO_4)_2$ solid solutions containing high amounts of zinc are perhaps brighter than the β-type phosphors, but unfortunately the peak intensities are shifted to the neighborhood of 6300Å. Even the low intensity $Mg_3(PO_4)_2$ peaks at 6320Å.

It appears that there may be a minimum in the position of peak intensity in the solid series in the neighborhood of 70-80 mole % $Zn_3(PO_4)_2$.

Table III. Comparison of unit cell dimensions of MgO and $(Mg_{0.68}Zn_{0.32})O$

			MgO			
hkl	2θ obs.	2θ corrected	d, Å	I	I/I_o	a_o
111	37.00	36.95	2.433	9	11	4.214
200	42.96	42.95	2.104	84	100	4.208
220	62.36	62.36	1.488	44	52	4.209
311	74.75	74.75	1.2689	6	7	4.208
322	78.70	78.70	1.2148	12	14	4.208
			$(Mg_{0.68}Zn_{0.32})O$			
111	36.63	36.73	2.447	25	38	4.238
200	42.55	42.65	2.120	66	100	4.240
220	61.80	61.85	1.4988	33	50	4.239
311	74.10	74.15	1.2777	9	14	4.238
222	78.00	78.05	1.2233	7	11	4.238

Table IV. Brightness and peak intensity of β-$(Zn,Mg)_3(PO_4)_2$ and $(Mg, Zn)_3(PO_4)_2$ ("gamma") solid solutions

Comp. No.	$Zn_3(PO_4)_2$	$Mg_3(PO_4)_2$	Phases	Peak intensity, Å	Relative brightness
1	100.0	0.0	β-Z_3P	6360	116
2	99.5	0.5	β-Z_3P_{ss}	6380	118
3	99.0	1.0	β-Z_3P_{ss}	6400	90
4	98.5	1.5	β-Z_3P_{ss}	6400	105
5	98.0	2.0	β-Z_3P_{ss} + M_3P_{ss}	6300	119
6	95.0	5.0	M_3P_{ss}	6300	133
7	90.0	10.0	M_3P_{ss}	6280	133
8	80.0	20.0	M_3P_{ss}	6260	121
9	70.0	30.0	M_3P_{ss}	6260	87
10	60.0	40.0	M_3P_{ss}	6270	91
11	50.0	50.0	M_3P_{ss}	6290	66
12	40.0	60.0	M_3P_{ss}	6280	43
13	30.0	70.0	M_3P_{ss}	6300	26
14	20.0	80.0	M_3P_{ss}	6300	22
15	10.0	90.0	M_3P_{ss}	6310	14
16	0.0	100.0	M_3P_{ss}	6320	12
N.B.S. Zinc Orthophosphate: Mn				6380	100
G.E. 1092-1, Lot 11 $Zn_3(PO_4)_2$: Mn				6380	117

Table V. Effect of activator concentration on the brightness of $(Zn_{0.95}, Mg_{0.05})_3(PO_4)_2$ solid solution

Comp.	Mole % $Mn_3(PO_4)_2$ substituted for $Mg_3(PO_4)_2$	Heat treatment, °C for 48 hr	Peak intensity, Å	Relative brightness
1	0.01	1000	6300	131
2	0.015	975	6280	123
3	0.020	950	6280	127
4	0.025	925	6280	124
5	Composition 6, Table IV		6300	120
NBS Zinc Orthophosphate: Mn			6380	100
G.E. 1092-1, Lot 11 β-$Zn_3(PO_4)_2$: Mn			6380	124

On the basis of the results shown in Table IV, a series of compositions was made to check the effect of activator concentration in the brightest $(Zn_{0.95}, Mg_{0.05})_3(PO_4)_2$ ("gamma") solid solution, as shown in Table V. These samples were fired at temperatures (see Table V) which were designed to prevent the formation of any unwanted β phase. It must be remembered that the $(Zn_{0.95}, Mn_{0.05})_3(PO_4)_2$ solid solution would transform to the β structure at temperatures around 940°C (3). If fired too high, the intermediate solid solutions would also begin to transform. Unfortunately, this technique does not permit a direct comparison of the brightness of phosphors fired at the same temperature. X-ray diffraction patterns of the fired samples showed them to be pure $Mg_3(PO_4)_2$ solid solutions.

This series of compositions shows that the solid solution is relatively insensitive to large changes in activator concentration. It should be noted that composition 6 when first measured gave a relative brightness of 133 compared to 120 when used as a comparative standard in the series in Table V. These differences are probably mainly due to variations in sample preparation and measuring technique.

The peak intensities hover around 6280-6300Å, indicating not quite as good "redness" as the beta phosphors.

Conclusions

1. "Gamma zinc phosphate" or "gamma zinc orthophosphate" has been shown to be an extended series of solid solutions of zinc orthophosphate in $Mg_3(PO_4)_2$.

2. Analogous series of $(Zn,Mg)_3(PO_4)_2$ and $(Zn,Mn)_3(PO_4)_2$ solid solutions exist in their respective ternary systems and probably form solid solutions in the quarternary system ZnO-MgO-MnO-P_2O_5.

3. The high zinc members of the $Mg_3(PO_4)_2$ solid solutions have good brightness and form the basis of a well-defined series of red cathode-ray phosphors. The brightness and peak emission of these phosphors are relatively insensitive to the amount of Mn^{++} which is substituted for Mg^{++} in the structure.

Acknowledgment

Emission data were obtained through cooperation of Marjorie Brines of the Chemical Products Plant, General Electric Co. The investigation was made possible by the support of the Chemical Products Plant, General Electric Co., Cleveland, Ohio.

Contribution #58-81 from the Department of Ceramic Technology, College of Mineral Industries, The Pennsylvania State University, University Park, Pa.

Manuscript received April 6, 1959. This paper was prepared for delivery before the Philadelphia Meeting, May 3-7, 1959.

Any discussion of this paper will appear in a Discussion Section to be published in the June 1960 JOURNAL.

REFERENCES

1. A. L. Smith, *This Journal*, **98**, 363 (1951).
2. F. L. Katnack and F. A. Hummel, *ibid.*, **105**, 125 (1958).
3. F. A. Hummel and F. L. Katnack, *ibid.*, **105**, 528 (1958).
4. J. F. Sarver and F. A. Hummel, *ibid.*, **106**, 500 (1959).
5. Jozef Berak, *Roczniki Chem.*, **32**, 17 (1958).
6. R. M. Smith and F. A. Hummel, Unpublished data on the pyrophosphate join, 1950.

Cadmium Sulfide Photoconductive Sintered Layers

Martha J. B. Thomas and Edward J. Zdanuk[1]

Engineering Laboratories, Sylvania Electric Products Inc., Salem, Massachusetts

ABSTRACT

The preparation and performance of sintered photoconductive cadmium sulfide layers have been described. Although the photoconductive characteristics are directly dependent on composition, layer preparative techniques, and geometry of the unit, these parameters may be predicted and controlled to give a resultant reproducible layer of desired electrical and optical characteristics.

The use of photoconductive cadmium sulfide in electronic devices, such as light amplifiers and image converters, has increased greatly during the past few years (1-4). These devices usually have necessitated fabrication of photoconductive layers of large surface area. Such layers can be achieved most readily by means of powdered layer (5), sintered layer (1, 3), dielectric imbedment, or evaporated film (7) techniques. Sintered layers have become particularly popular in device fabrication because of their superior sensitivity (5, 8) uniformity, high mechanical strength, and ease of formation (5, 8).

Although a considerable amount of work has been done in determining the electrical and optical characteristics of pure cadmium sulfide and cadmium sulfide matrices in which traces of impurities such as copper and the halogens have been incorporated, these studies were conducted in the main on single crystals (9-11).

This paper describes some of the optical and electrical characteristics of sintered layers of cadmium sulfide and demonstrates the dependence of these characteristics on the initial chemical formulation and on the method of forming the final sintered layer.[2]

Experimental

Figure 1 presents schematically the process involved in the preparation of the sintered layer.

Phosphor quality cadmium sulfide (Sylvania or RCA) and analytical reagent quality cadmium chloride and copper chloride were used. A formulation found to be particularly suitable for general sintered layer application had the following composition:— 1 mole cadmium sulfide; 0.3 mole of cadmium chloride; 8 x 10^{-4} gram atoms of copper added as copper chloride or basic copper carbonate. All components were ground prior to blending. The blended composite, usually 100 g, was given an initial bulk firing for 35 min in covered porcelain crucibles. This resulted in a small amount of sintering and preliminary distribution of activator components into the cadmium sulfide. The partially sintered cadmium sulfide was milled in xylene to insure sufficiently fine particle size to yield a smooth-appearing sintered layer; to the suspension sufficient organic binder (ethyl-cellulose type) was added in order to insure a coherent layer during film formation prior to sintering. Usually this photoconductor suspension was sprayed although layers prepared with flow-on and doctor blade techniques gave identical results.

The sprayed layer was dried at room temperature for at least ½ hr during which most of the organic solvent volatilized. The layer was sintered in an electric muffle furnace in an air atmosphere, normally for 10 min at 550°C. Dependence of layer characteristics on presintering and sintering temperatures is discussed later.

Preparation of Test Cells

Standard cells.—Standard test cells of the geometry indicated in Fig. 2 were used for the determination of the desired characteristics. The cells were made on 1 x 2½ x ⅛ in. Pyrex slides which had been coated with a conductive film of transparent semiconducting tin oxide. The desired electrode structure with ⅛ x ¼ in. gaps was prepared by sand blasting the conductive film through a pattern mask. The slides were then thoroughly washed and dried in an oven at 150°C. The photoconductor suspension was sprayed in square patches between the electrodes using a suitable mask. Each slide had six in-

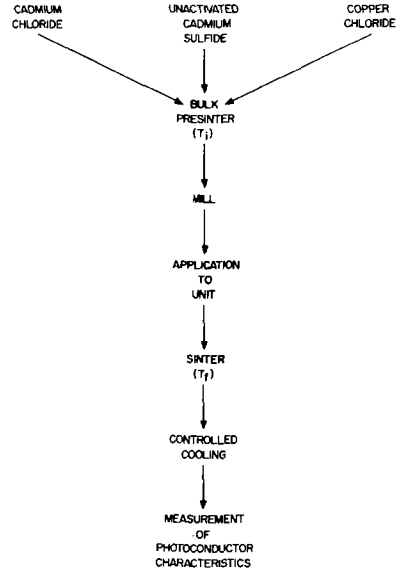

Fig. 1. Flow diagram of preparation of sintered layer

[1] Present address: Research Division, Raytheon Manufacturing Co., Waltham, Mass.

[2] After this paper had been submitted for publication a technical report was issued by Lincoln Laboratories (15). This report, which has limited circulation, describes similar studies of CdS sintered layers and supplements the present paper.

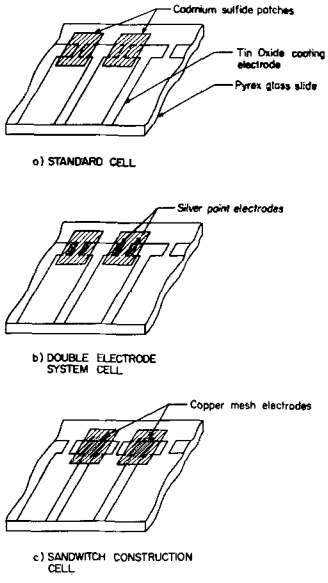

Fig. 2. Types of photoconductive cells used in measurement of photoconductor characteristics.

dividual test cells and measurements of electrical and optical properties of each individual cell were made. Values of the central four cells were found to be reproducible and consistent. The end cells yielded very erratic results, which will be discussed later in the paper.

Double electrode cells.—Double electrode cells (Fig. 2B) were made from the standard test cells by painting silver electrodes (Du Pont air dry conductive silver) on the top surface duplicating the gap structure of the tin oxide electrodes on the undersurface of the photoconductive layer.

Sandwich.—Sandwich cells (Fig. 2C) were also fashioned from the basic standard test cells by applying a ¼ x ¼ in. patch of very fine electroformed copper mesh. This copper mesh, 500 lines to the inch, was applied to the surface by a silicone adhesive. To have the measurement on these sandwich cells reflect only the volume conduction of the photoconductive layer, a mask of an opaque material, e.g., black plastic tape, was applied to prevent activation by light around the edges.

Electrode materials.—All surface conductivity measurements were made with cells having electrodes of semiconducting tin oxide. However, measurements made with cells using fired-on platinum electrodes did not differ significantly. The effect of any reaction of the sintered layer with electrode material as exemplified by the two types of electrodes is apparently confined to the interface between layer and electrode. Such reactions change primarily the resistance of the contact between electrode and layer. This contact resistance is a small fraction of the resistance of the layer and is only slightly photosensitive. Also, it tends to be eliminated in a surface conductivity measurement which is the difference between a light and dark photoresponse. In systems where an asymmetrical electrode system exists and rectifying phenomena are likely, difference in electrode material becomes important.

Techniques and methods of measurement.—The photosensitivity of the prepared layers was measured with a d-c applied voltage of 600 v and with an exciting light of 10 ft-L from a green electroluminescent lamp. For standard measurements this exciting light illuminated the electrode gap from the glass side. Rise and decay characteristics were determined by observing the photoconductor response on an oscilloscope screen. The "dark current" I_{30} was taken as the current measured 30 sec after the removal of the exciting light. Decay time γ_{10} represents the time necessary to reach 10% of photocurrent upon removal of activating light. Spectral response curves were determined using a Beckman D. U. spectrophotometer as a monochromator. By variation of the slit width, an equal quantity of energy at various wave lengths was allowed to excite the photoconductor cell with 600 v d-c applied potential. Slit width variations during measurements gave

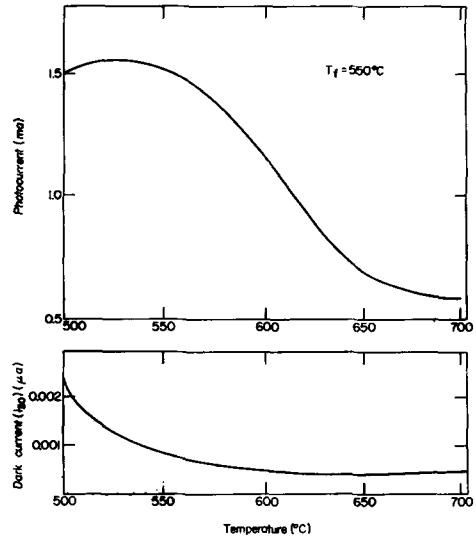

Fig. 3. Effect of presintering temperature on photoconductor characteristics. Final sintering of layer at 550°C for 10 min (600 v d-c potential, 10 ft-L, green El lamp excitation).

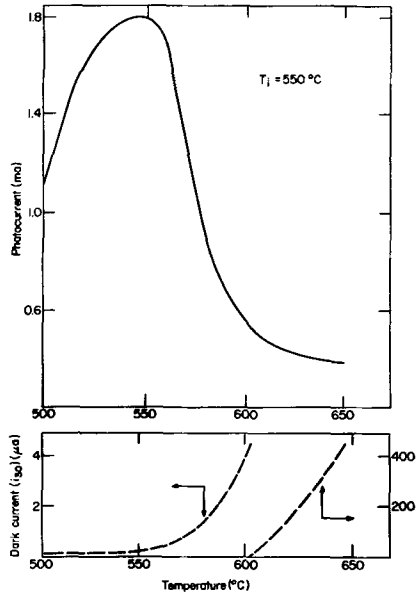

Fig. 4. Effect of sintering temperature on photoconductor characteristic. Presinter of layer at 550°C for 35 min (600 v d-c potential, 10 ft-L green El lamp excitation).

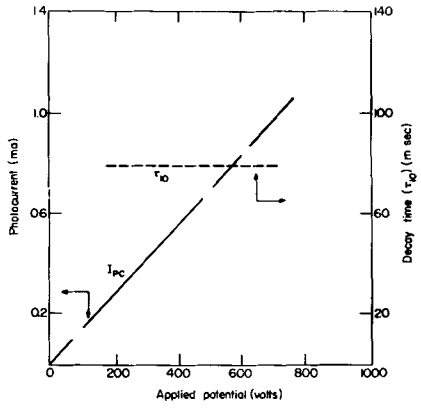

Fig. 5. Effect of applied potential on photoconductor characteristics (10 ft-L green El lamp excitation).

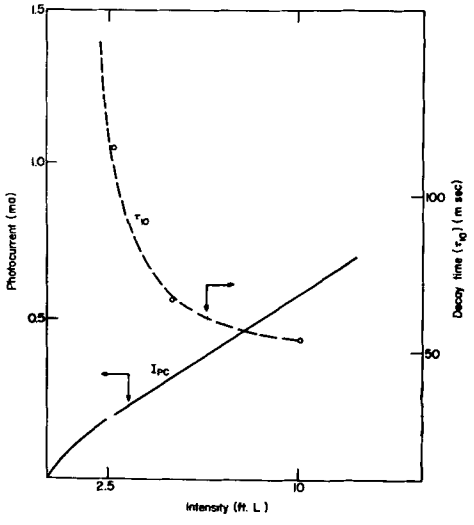

Fig. 6. Effect of intensity of illumination on photoconductor characteristics (green El lamp excitation, 600 v d-c potential applied).

a half intensity band width varying from 14 mμ at 550 to 18 mμ at 700 μ. This small variation of band widths in the peak response region resulted in a negligible shift in peak positions. The response was determined with an RCA electronic microammeter.

Reflectance measurements were made on a modified reflectance attachment to the Beckman D. U. spectrophotometer using basic magnesium carbonate as reference.

Effect of presintering temperature (T_i).—In an effort to establish conditions necessary to obtain maximum photosensitivity, a step-wise variation of the conditions at each part of the process was conducted. Figure 3 represents the effect of the variation of presintering temperature on the photocurrent and dark current. In each case, a 100 g mass of the photoconductor was fired in a covered crucible for a period of 20 min. The final sintering of the test slides was at a temperature of 550°C for 10 min. It will be noted that the greatest ratio of photocurrent to dark current occurs at T_i 550°C. Higher temperatures cause a decrease in the photocurrent while lower temperatures result in a layer which has relatively high dark current. This is probably the result of incomplete sintering combined with a relatively large amount of residual unincorporated $CdCl_2$.

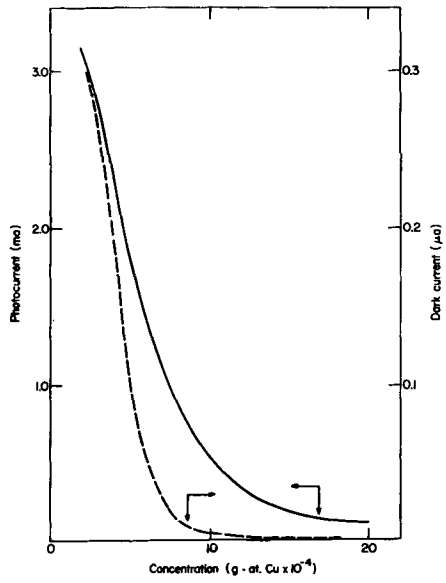

Fig. 7. Effect of copper concentration of photoconductor characteristics. (600 v d-c potential, 10 ft-L green El lamp excitation).

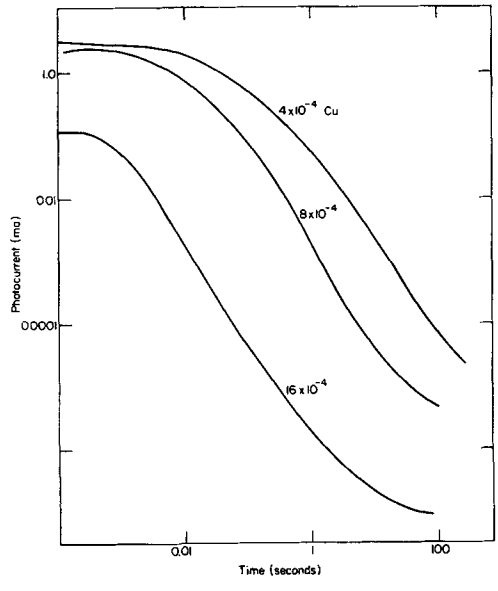

Fig. 8. Effect of copper concentration on decay characteristics of sintered layer cadmium sulfide (600 v d-c potential, 10 ft-L green El lamp excitation).

Effect of sintering temperature (T_f).—The temperature of sintering has a particularly great effect on both the photocurrent and the dark current. In all cases the slides were fired for a period of 10 min at temperatures from 500° to 700°C. With increasing temperatures the dark current increases until the material shows a high dark conductivity with little or no photoconductivity (Fig. 4). As a result of these observations a standard prefiring temperature and sintering temperature of 550°C was chosen for all samples. Cells with layer thickness of about 5 mils prepared under these conditions were used to determine the dependence of the photocurrent and the decay time on the applied voltage and the light intensity. The photocurrent varied linearly with increased voltage over the range of 100-800 v while voltage variation had little or no effect on the decay time γ_{10} (Fig. 5). A linear relationship was also ob-

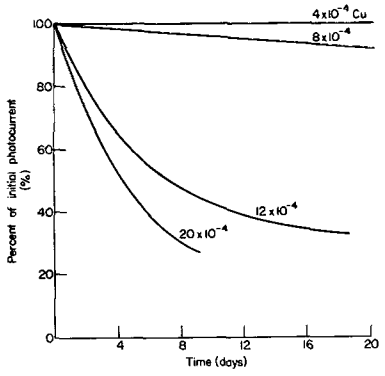

Fig. 9. Effect of copper concentration on shelf life (600 v d-c potential, 10 ft-L green El lamp excitation).

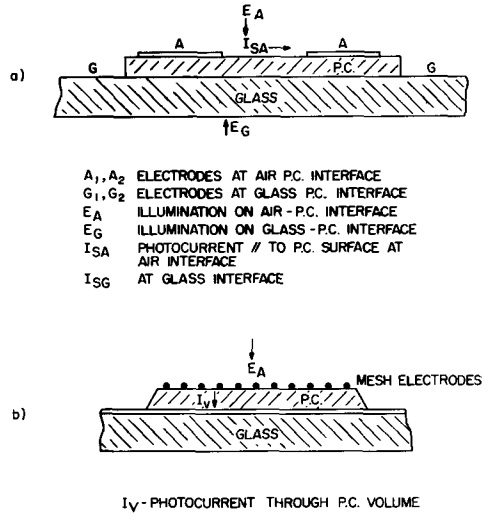

Fig. 10. Notations used describing photoconducting characteristics of layer.

served over most of the intensity range, although at the low intensities some divergence was noted. The decay rate appeared to be quite dependent on the intensity of excitation, being relatively slow at the lower intensities (Fig. 6).

All cell data are reported for excitation with 10 ft-L of green EL light and for 600 v applied potential. Whenever necessary the above linear relationships are applied for conversion to these conditions.

Effect of copper concentration.—Confirming what had been found in single crystal studies, (5, 9, 10, 12, 13), increasing copper concentration results in a decrease of both photocurrent and dark current (Fig. 7) with concurrent change of the body color of the sintered layer from yellow to a black-brown.

Increased copper concentration,[3] although decreasing the photocurrent of the layer, did increase the rate of decay to a considerable (Fig. 8) extent. However, this increased copper effected a decrease of the relative shelf life of the prepared layer (Fig. 9). Test slides measured to obtain these data were subjected to normal laboratory conditions including usual winter humidity variations indoors and fluorescent lighting. Measurements were made in every case at about the same time of day. In all cases the photoconductivity appeared to reach a steady state after the observed decay.

[3] All concentrations expressed in this paper are in units of gram atoms per mole of CdS.

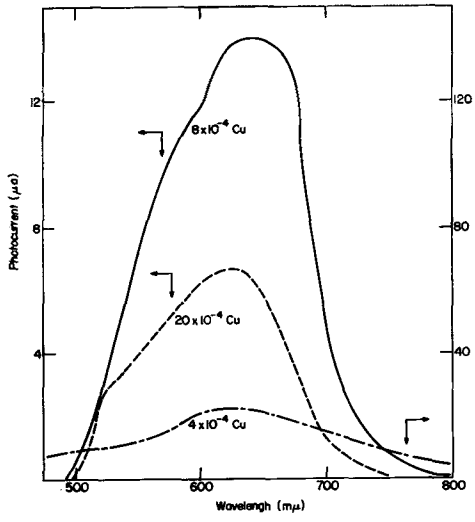

Fig. 11. Spectral response $I_{SG}{}^{G}$ for cadmium sulfide sintered layers (600 v d-c potential).

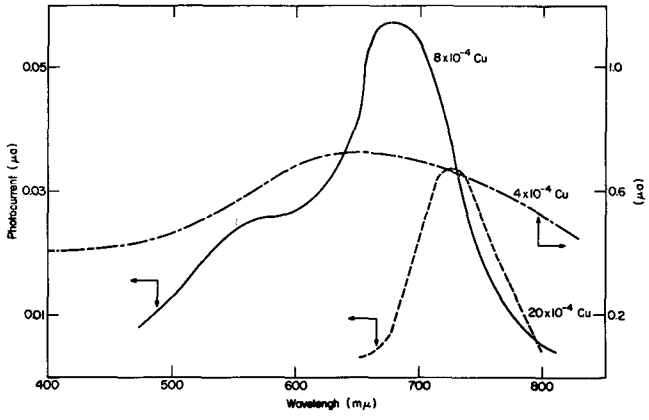

Fig. 12. Spectral response $I_{SG}{}^{A}$ cadmium sulfide sintered layers (600 v d-c potential).

Spectral response.—Although photoconductors have been further classified by the determination of their spectral response, there have been inconsistencies with respect to the published data. Variations in spectral response characteristics of cadmium sulfide photoconductor have been attributed not only to chemical composition but also to its physical state (5) and mode of operation (1). No definitive study of these parameters has been reported.

A consideration of a sintered layer photoconductor reveals the role of the cell structure or geometry on characteristics. Figure 10a represents a magnified view of a test cell showing the arrangement of the various parts involved in the measurement of surface-like conductivity. In the conductivity measurements used to evaluate the effects of different firing temperatures and different copper concentrations, illumination had been in all cases from the glass-CdS interface side (E_G) and voltage had been applied across the tin oxide electrodes in the plane of the same interface. Under these conditions the photocurrent will be designated by $I_{SG}{}^{G}$; the superscript G giving the direction from which the sample is illuminated, in this case the glass side, and the subscript SG indicating a surface-like conduction with voltage across the electrodes in the glass-CdS interface, G.

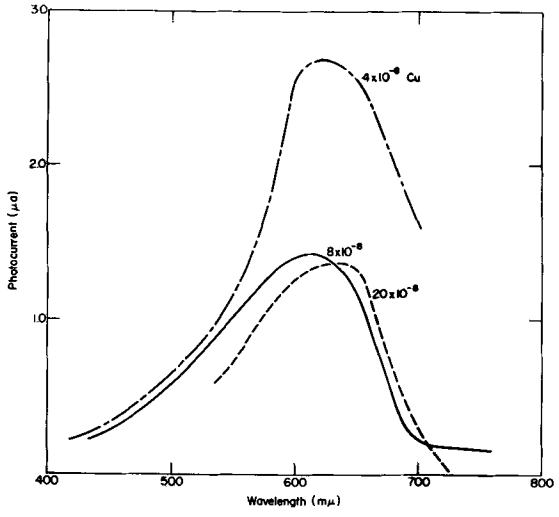

Fig. 13. Spectral response $I_{SA}{}^{A}$ for cadmium sulfide sintered layers (600 v d-c potential).

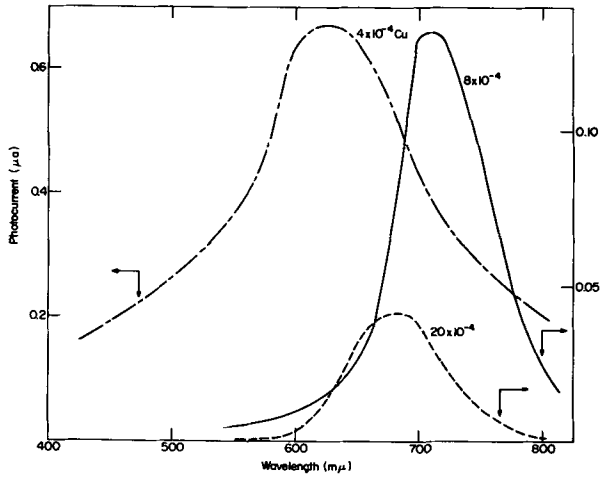

Fig. 14. Spectral response $I_{SA}{}^{G}$ for cadmium sulfide sintered layers (600 v d-c potential).

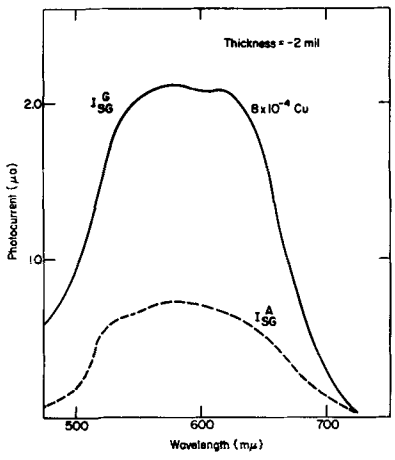

Fig. 15. Spectral response of 2-mil cadmium sulfide layer (600 v d-c potential).

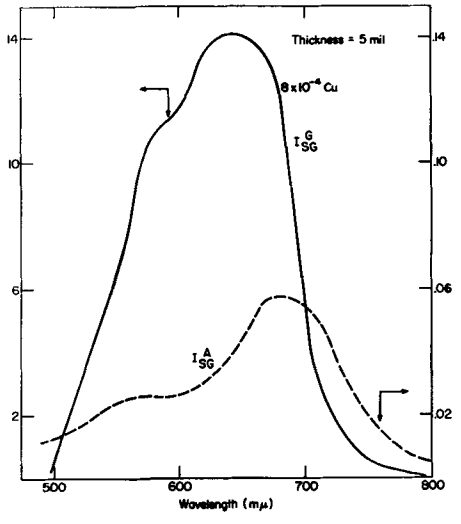

Fig. 16. Spectral response of 5-mil cadmium sulfide layer (600 v d-c potential).

The second surface, i.e., the air photoconductor interface can also be used to evaluate the sintered layer. Voltage was applied across silver electrodes painted on this surface, and the photocurrent $I_{SA}{}^{G}$ produced by exciting from the photoconductor glass side was determined.

Two additional surface type photocurrents may be determined if the direction of excitation is reversed. These currents may be symbolized as $I_{SG}{}^{A}$ and $I_{SA}{}^{A}$ using the same conventions as above.

Thus, the four possible surface photocurrents can be designated by $I_{SA}{}^{G}$, $I_{SG}{}^{G}$, $I_{SG}{}^{A}$, and $I_{SA}{}^{A}$.

In addition to the above surface-like conductivities, the contribution of any current produced within the body of the layer for the particular geometry of the cell should be determined. Using the standard-type cell and adding mesh electrodes to the air surface, the photocurrent through the photoconductor volume may be measured (Fig. 10b). Again, a current may be developed by exciting either through the glass or air interface yielding two possible types of volume currents ($I_V{}^{A}$ and $I_V{}^{G}$).

$I_{SG}{}^{G}$.—The spectral response of photoconductors excited through the glass with voltage applied across electrodes in the glass-photoconductor interface ($I_{SG}{}^{G}$) is shown in Fig. 11. Although the relative magnitude of the photocurrent varies with copper concentration, the optimum wave length or maximum-response occurs in all cases at a wave length of 625 mμ.

$I_{SG}{}^{A}$.—If the excitation occurs at the air-photoconductor interface, spectral response curves for variable copper concentrations show a dependence of the position of their maximum on copper concentration (Fig. 12).

$I_{SA}{}^{A}$,-$I_{SA}{}^{G}$.—The spectral response of the sintered layer as characterized by these two currents is shown in Fig. 13 and 14. There appears to be essentially no shift in the peak response toward longer wave length with increasing copper in these cases.

Effect of layer thickness on photoconductor characteristics.—Since the spectral response of the surface photocurrent appeared to vary with the surface excited, a variation of the chemical composition of the two surfaces might be suspected. If the thickness of the layer were decreased progressively, at some point it might be expected that this surface composition variation should disappear. Figures 15 and 16 represent spectral response curves ($I_{SG}{}^{A}$, $I_{SG}{}^{G}$) using cell layer thicknesses of 2 and 5 mils, respectively. In contrast to the 5-mil layer there is no difference in the shape and maxima of the spectral response

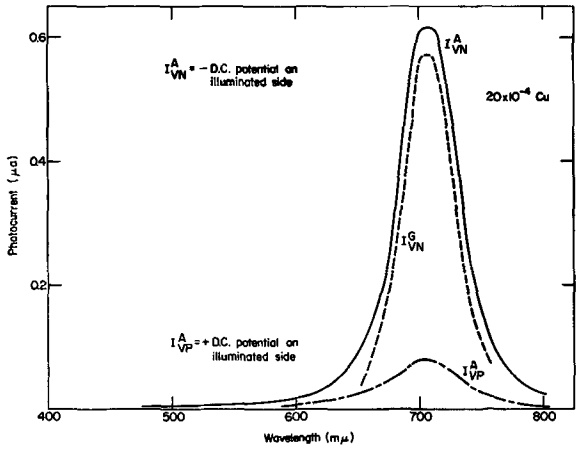

Fig. 17. Spectral response I_V for cadmium sulfide sintered layers (600 v d-c potential 10 ft-L green El lamp excitation).

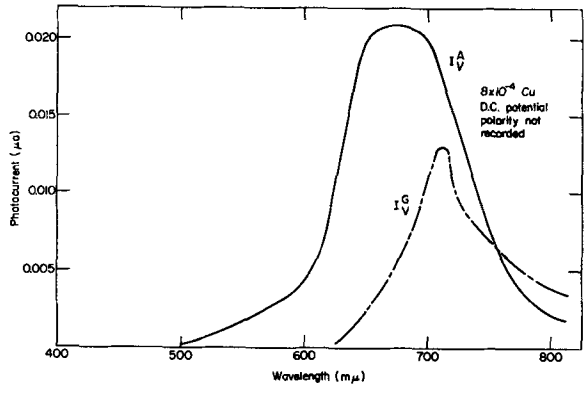

Fig. 18. Spectral response I_V for cadmium sulfide sintered layers (600 v d-c potential 10 ft-L green El lamp excitation).

curves in the case of the 2-mil layer. Also, the body color of thin layers was considerably lighter than that of the 5-mil layer even though the copper concentrations were identical. This difference can be attributed to the loss of a greater amount of chloride from the thin layer. This chloride is necessary for effective incorporation of copper into the lattice.

Volume conductivity I_V.—The spectral response of the volume type current I_V was determined with sintered layers of various copper concentrations. Curves for 8 x 10^{-4} and 20 x 10^{-4} copper are shown in Fig. 17 and 18. The characteristics of these curves are somewhat similar to $I_{SG}{}^A$ and $I_{SA}{}^G$. The layer with the lower copper concentration shows a difference in peak position depending on which side was illuminated. The layer with the higher copper showed no lack of symmetry. It should be noted that Fig. 18 indicates a rectification phenomenon the magnitude of which is dependent on the direction of illumination.

Reflectance curves.—Figure 19 represents the surface (air-photoconductor 5 mil) reflectance of the photoconductive layer. As may be seen from the curves, the body color becomes progressively darker with increased copper concentration.

Effect of firing atmospheres.—The importance of firing conditions with respect to both atmosphere and surroundings was exemplified by the different photoconductive properties associated with the end patches of the standard cells. To determine more ac-

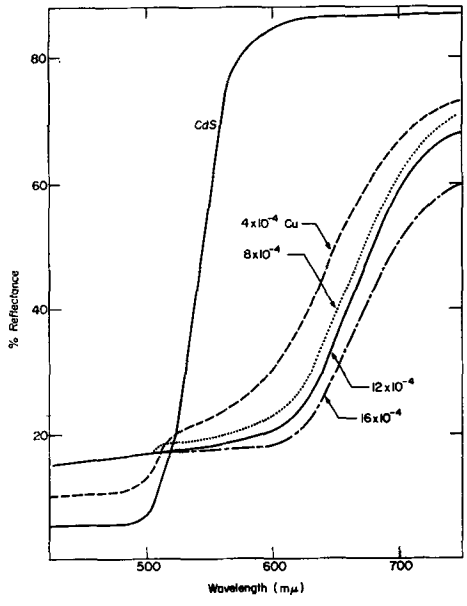

Fig. 19. Reflectance curves of photoconductor layers with variable copper concentrations.

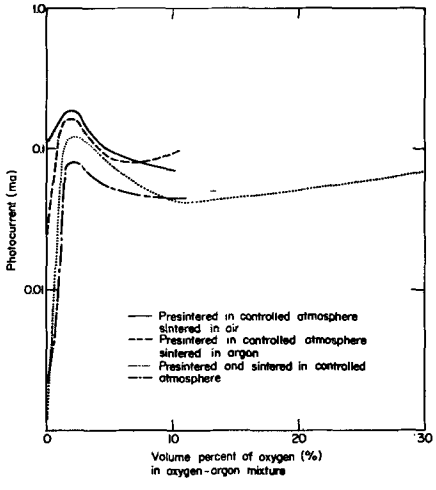

Fig. 20. Effect of oxygen in firing atmosphere on photocurrent $I_{SG}{}^G$ (600 v d-c potential 10 ft-L green El lamp excitation).

curately the importance of the composition of the firing atmosphere, the effect of variations on concentration of (*a*) oxygen and (*b*) cadmium chloride in the firing atmosphere on the photoconductivity of the layers was studied. In the former case, the layers were fired in atmospheres of various oxygen-argon mixtures. There is no doubt that some oxygen is required to achieve an optimum in sensitivity of the cadmium sulfide layer (Fig. 20), but it also appears that the beneficial effect of oxygen may be introduced in the presinter firing or the final sintering. The effect of oxygen on dark current is of importance only when long firing times are used. Some advantage may be gained if the oxygen content of the firing is kept small (about 2%). This is in agreement with improvement of photoconductive characteristics observed with restrictive firings in small volumes. However, conditions close to optimum are achieved simply by firing in air in a small electric muffle furnace for a time and at the temperature indicated earlier.

An atmosphere rich in cadmium chloride or some other chloride-containing compound is also necessary in the fabrication of a sensitive photoconducting layer. When the major portion of the halide is removed by repeated washing of an activated cadmium sulfide material (presintered only) until the wash liquid showed no test for chloride, the resultant sintered layer was pale yellow in color, powdery in character, and low in photoconductive characteristics. However, this same layer may be made sensitive by resintering in a closed volume with cadmium chloride crystals added to provide a suitable atmosphere. A similar effect may be achieved if the layer were exposed to a hydrogen chloride atmosphere prior to resintering. The resintered layer was not only photoconductive, but also the body color was nearly identical to that of the control.

Discussion of Results

Sintered layers of cadmium sulfide photoconductor (copper chloride-coactivated) can be prepared with a sensitivity ratio (ratio of photocurrent and dark current after 30 sec) of 10^7. In general, such layers have characteristics quite similar to those reported with respect to the single crystals. The sintered layer characteristics are, however, directly dependent on the method of preparation and the geometry of the system in which the layer is used.

In the system chosen for investigation, a system which is of practical application to device manufacture, the two surfaces have been shown to be chemically and physically quite different, and hence the optical and electrical responses are dependent on the geometry of excitation. These variations may be explained by differences in the relative activator-coactivator concentrations. During sintering, the halide coactivator is volatilized quite readily. Because of the large excess of cadmium chloride used in formulation, there is sufficient halide available so that some will remain within the photoconducting material itself as well as in the atmosphere surrounding the material. During sintering, the halide volatilizes evenly throughout the layer. Once this halide has diffused to the surface, however, it escapes into the atmosphere. Thus the surface of the layer may be considered as a diffusion boundary between an atmosphere of low chloride concentration and the relatively chloride-rich cadmium sulfide bulk. Upon cooling, some halide is reabsorbed by the surface of the layer. Such processes could explain a concentration variation of halide across the layer. During the sintering the copper concentration would simply equilibrate throughout the layer since copper is not volatile at the sintering temperatures.

Experimentally, the ease of migration of the chloride ion out of the cadmium sulfide lattice has been shown by the successful reactivation of a nonphotoconductive (chloride-free) CdS by means of a simple exposure to cadmium chloride or hydrogen chloride vapors. The unevenness of reabsorptions of the coactivator during cooling is indicated both by the difference in color between the two layer surfaces (especially at higher copper concentrations) and by the dependence of this body color variation on the thickness of the layer.

Assuming that sintering under the conditions used does result in a difference in coactivator concentration within the layer, the spectral response curves may be explained utilizing data obtained in single-crystal work.

Wood (14) ascribed the spectral response peak at 520 mμ to a stimulation of photoconduction resulting from lattice defects in the crystal associated with presence of chloride. The 700 mμ peak on the other hand, was directly associated with copper-type active centers. Considering the $I_{SG}{}^{G}$ spectral energy curves, the peak is in all cases about 625 mμ. This type of curve could result from the combined effects of Cu and Cl centers. Increasing the copper concentration should have little or no effect on the position of the peak response provided that there is sufficient chloride to keep the relative ratio of copper to chloride centers constant. The constancy of ratio would be dependent then on the initial composition of the photoconductor blend, the thickness of the layer, and duplicating of firing times and temperatures of layer.

With respect to the air-photoconductor interface ($I_{SG}{}^{A}$), the spectral response is found to shift toward the longer wave lengths with increasing copper concentration. Again applying the work of Wood, it may be assumed that this shift is the result of a higher ratio of Cu to Cl type centers. This increase in Cu over Cl-type centers would be the result of the lower chloride concentration existing at the surface. Accompanying this increase in the relative number of copper-type centers with respect to the chloride-type centers will be a deepening in the body color of the surface. This body color shift results in a more efficient absorption of longer wave lengths which, combined with the greater effectiveness of activation due to higher copper center concentration, further shifts the spectral response peak toward the red. The copper center concentration is not entirely dependent on initial copper concentration but is interrelated to chloride concentration.

The darkening of the body color associated with increasing copper observed primarily at the air photoconductor interface introduces the possibility of affecting the position of the spectral response peak by a simple filtering action, i.e., modifying the composition of the activating radiation reaching the portion of the layer involved in the conductance measurements by other portions of the layer which are not involved at all or to a much lesser degree.

The greatest effect of this filtering action is observed in the spectral response curves of $I_{SA}{}^{G}$ and $I_{SG}{}^{A}$ type photoconduction. In these cases the most effective wave length will be that which can penetrate through almost the entire layer and activate that part of the layer in the region of the electrodes on the surface opposite the illuminated surface. Since the longer wave lengths are more penetrating, the peak spectral response as measured by these conductances will be further toward the red than the peak responses of the other conductances. In $I_{SA}{}^{G}$ and $I_{SG}{}^{A}$ measurements the easily absorbed shorter wave

lengths will be filtered out by that portion of the layer which is least effective in contributing to the conductance. It will be noted that the peaks of the spectral responses I_{SG}^{A} and I_{SA}^{G} do in fact occur at longer wave lengths. The volume conductance is also dependent on the body color of the layer but to a slightly lesser extent than in the above situation. In this case light absorbed by any part of the layer can contribute effectively to the volume-like photoconduction. The peak response of these spectral response curves lies roughly between the two types of surface conduction responses.

Acknowledgments

Sincere thanks are due to C. Lagos, T. Barry, B. Rybinski, and R. Levitt for the preparation and measurement of many of the photoconducting layers. For frequent and helpful discussions and constructive criticisms the authors are indebted to Dr. K. H. Butler and F. Koury of the Engineering Laboratories as well as M. Zimmerman and R. Billups of the Lincoln Laboratories, M.I.T.

Part of the work reported here was carried out as a cooperative project with the Lincoln Laboratory, a technical center operated by the Massachussetts Institute of Technology with joint support of the Army, Navy, and Air Force under contract.

Manuscript received May 2, 1959. This paper was prepared for delivery before the New York Meeting, April 27-May 1, 1958.

Any discussion of this paper will appear in a Discussion Section to be published in the June 1960 JOURNAL.

REFERENCES

1. G. Diemer, H. A. Klasens, and J. G. Santen, *Philips Research Repts.*, **10**, 401, (1955).
2. J. E. Rosenthal, *Proc. I.R.E.*, **43**, 1882, (1955).
3. E. E. Loebner, *ibid.*, **43**, 1897, (1955).
4. B. Kazan and F. H. Nicoll, *Proc. I.R.E.*, **43**, 1888, (1955).
5. S. M. Thomsen and R. H. Bube, *Rev. Sci. Inst.*, **26**, 664, (1955).
6. G. Kuwabara, *J. Phys. Soc. Japan*, **9**, 992, (1954).
7. E. Schwarz, *Proc. Phys. Soc.*, **62A**, 530, (1949); *ibid*, **63B**, 624 (1950); *ibid.*, **64B**, 821 (1951).
8. B. T. Kalomiets, *Doklady Akad Nauk S.S.S.R.*, **83**, 561 (1952).
9. W. Veith, *Compt. rend.*, **230**, 947, (1950); *Z. angew. Phys.*, **7**, 1, (1955).
10. D. Goerćke, *P. Annalender Tele Communications*, **6**, 325 (1951).
11. J. Gottesman, *J. Opt. Soc. Amer.*, **44**, 368, (1954).
12. R. H. Bube and S. M. Thomsen, *J. Chem. Phys.*, **23**, 15 (1955).
13. F. A. Kroeger, H. J. Vink, and J. van der Boomgaard, *Z. physik. Chem.*, **203**, 1, (1954).
14. J. Wood, *J. Electronics and Control*, **3**, 225 (1957).
15. R. R. Billups, W. L. Gardner, and M. D. Zimmerman, Technical Report #200, Lincoln Laboratory, M.I.T., Lexington, Mass.

The Nature of Alumina in Quenched Cryolite-Alumina Melts

Perry A. Foster, Jr.

Alcoa Research Laboratories, Aluminum Company of America, New Kensington, Pennsylvania

ABSTRACT

The equilibrium primary phases that precipitate from cryolite-alumina melts are cryolite, to the left of the eutectic, and corundum, to the right of the eutectic. No solid solubility of alumina in the cryolite phase was found. Evidence is presented in the form of photomicrographs and x-ray powder patterns that a new alumina phase is obtained by extremely rapid quenching of the liquid. The x-ray pattern of this phase is similar to the aluminum silicate, mullite. It is thought to result from the disproportionation of an oxyfluoride complex in the melt and is perhaps a skeletal arrangement with some of the characteristics of the oxyfluoride precursor. This new alumina phase is metastable and transforms through eta-alumina to corundum on heating.

Although quenching methods are well established and have been used extensively to elucidate the phase relationships in many nonmetallic systems, little use has been made of the technique in studies of the alumina-cryolite system.

Zintl and Morawietz (1) reported that x-ray powder patterns showed only cryolite in quenched cryolite fusion products containing 5 and 10% alumina. Similar experiments with 15% alumina quenches showed corundum as well as cryolite, indicating that the solubility limit had been exceeded at the temperature employed. It is believed this temperature was approximately 1000°C. Zintl and Morawietz (1) also reported that the densities of those quenched products in which no corundum was found were the same as cryolite. Calculated densities, based on a mechanical mixture and the two types of solid solution, ruled out all but the primary or substitutional solid solution model. Zintl reasoned that it was probably impossible to quench fast enough from above the liquidus to preserve the molecular arrangement of that phase field, and that what one obtained was something characteristic of a lower temperature: in this case, a primary solid solution with an alumina dimer (Al_3AlO_6) substituted for Na_3AlF_6 in the cryolite lattice.

Ginsberg and Bohm (2) repeated Zintl's experiments and found that for alumina contents less than 12%, x-ray showed only cryolite in both slowly cooled and quenched samples. However, an aluminum sulfate extraction gave quantitative recovery of alumina for the slowly cooled specimens and a

40% recovery for the quenched specimens. They concluded that alumina is in solid solution at a concentration of 7-8% in the quenched melt.

Grjotheim (3) obtained cooling curves for melts of several compositions from 9 down to 5% alumina at a rather slow cooling rate of 0.7°/min. Eutectic halts were noted for all these compositions. At 2.5%, the halt was not established definitely. Grjotheim felt this might be due either to solid solubility or to the small amount of eutectic which forms at this composition producing an undectable heat effect.

The purpose of the present work is to determine the nature of alumina in alumina-cryolite melts quenched from above the liquidus; to determine the extent of solid solution on the low alumina side of the eutectic; and to obtain information concerning possible new compound formation on the high-alumina side of the eutectic. This is part of a larger program underway in these Laboratories to elucidate the phase relationships in the cryolite-aluminum system.

Experimental

Hand-picked natural Greenland cryolite was employed. The most prevalent impurities are: silicon (SiO_2) 0.14%, potassium (KF) 0.055%, calcium (CaF) 0.01%, and lithium (LiF) 0.035%. The alumina used was Alcoa, A-10 Grade. The most common impurities in this material are: soda, 0.092%, and silica, 0.19%.

The starting materials were prepared by prefusing, under argon, 5-g mixtures of cryolite and alumina in a covered platinum crucible at 1015° ±10°C. The fusion temperature was maintained for 5 min before slowly cooling to room temperature. Weight losses due to moisture and decomposition were of the order of 0.2%. The fused material was crushed to pass 200 mesh and then mixed thoroughly. Two 1-g samples were analyzed for alumina by extraction with a hot aluminum chloride solution. If these two determinations agreed within the usual experimental error, the gross sample qualified as the source material for the 20 mg quenching charge. Prefusing of high alumina samples (14-18%) presented some difficulty. Temperatures higher than 1015°C would be necessary to effect complete solution. However, cryolite begins to decompose above this temperature, evolving $NaAlF_4$, and consequently enriching the melt in NaF. It was found from duplicate alumina determinations of a number of different high alumina compositions that the fine grinding and mechanical homogenizing procedure, after partial fusion at 1015°C, was effective in obtaining a uniform distribution of unreacted and precipitated alumina.

Quenching Procedure

Small platinum tubes, 3-mm ID with 0.01-mm wall, were cut to lengths of approximately 1.5 cm. One end was crimped shut and fused with a Burrell "Kup-L-Weld" Thermocouple Welder, and 20 mg of a prefused, homogenized alumina-cryolite composition was loaded into the tube. The tube was flattened to remove some of the air; then the open end was arced shut. The tube was inserted into a platinum foil envelope, which was threaded with a platinum fuse wire, and suspended from two hooked conductors within 1 mm of a calibrated platinum, platinum-10% rhodium thermocouple (4). This assembly was inserted into a platinum-wound resistance furnace.

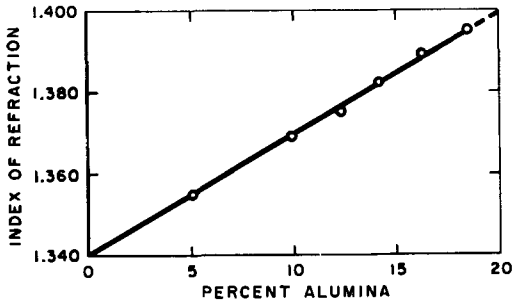

Fig. 1. Variation of the quenched liquid index of refraction with alumina content.

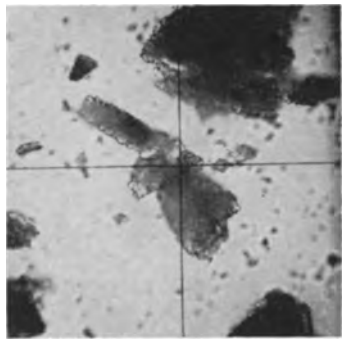

Fig. 2. Quenched liquid, 5% Al_2O_3. X250

The complete liquification of all compositions was insured by initially treating the samples at 1100°C for 30 min. Following this heat treatment, the temperature was lowered slowly to, and controlled at, the level required for that particular investigation. That temperature was maintained for a period of time sufficient to establish chemical and physical equilibrium. The sample was released from the hot-zone of the furnace into a quenching medium by running current through the hooked leads, thereby melting the fuse wire. The optimum time at temperature was determined by experience after microscopic examination of a number of samples.

The index of refraction of the various phases was observed, using the Becke line method. Positive identification was made from x-ray powder diffraction patterns.

Results and Discussion

X-ray powder diffraction patterns of cryolite-alumina melts having alumina contents ranging from 5-18.5%, quenched from above the liquidus, showed only cryolite lines. These observations were in agreement with those of Zintl and Morawietz (1) and Ginsberg and Bohm (2). However, the refractive index increased with increased alumina content (Fig. 1), thus appearing to contradict x-ray findings, which showed a constant parameter regardless of alumina content. The quenched liquid particles were quite opaque and had a fine mosaic crystalline structure (Fig. 2). This feature prohibited obtaining a very precise index. Nevertheless, the increase in re-

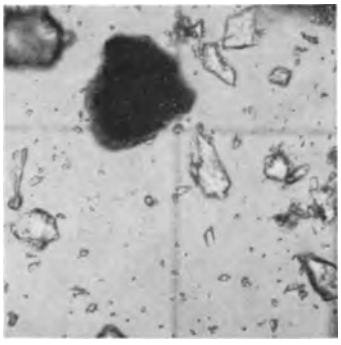

Fig. 3. Primary phase cryolite-quenched liquid, 5% Al_2O_3. X210.

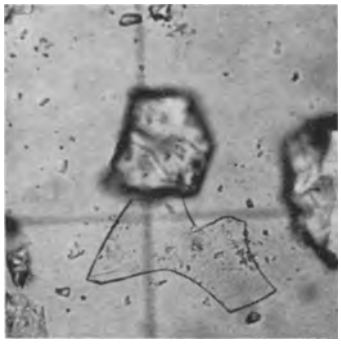

Fig. 4 Sub-solidus cryolite and alumina, 5% Al_2O_3. X210

fractive index above that of cryolite (1.339) was pronounced and nearly linear with alumina content.

If, as Zintl and Ginsberg suggested and the early phase diagram of Roush and Miyake (5) would predict, the primary phase on the low alumina side of the eutectic is a solid solution containing between 7 and 11% alumina, the index of refraction of that phase should be significantly greater than that of cryolite. The indices of refraction of the two phases present in quenches originating slightly below the liquidus along the 5% alumina isopleth indicated that the primary phase is cryolite (the well-formed clear crystals in Fig. 3). The dark, mosaic, quenched liquid particles constitute the other equilibrium phase. Quenches originating from lower and lower temperatures showed an increasing amount of cryolite crystals, as would be expected from the lever arm principle. Quenches from below the eutectic boundary (approximately 960°C) showed microscopically two equilibrium solid phases (Fig. 4). One phase (immediately above the crosshair)[1] is cryolite that precipitates below the liquidus and continues to do so until the composition of the liquid and the temperature of the melt are such (eutectic point) that a second solid phase (flat plate immediately at the crosshair) commences to form. The second phase had the refractive index of corundum. A density separation was performed on a sample quenched from just below the eutectic boundary. Methylene iodide, with a density of 3.33, was used as the separating medium. X-ray analyses showed that the light fraction was principally cryolite and the heavy fraction principally corundum.

Quenches along an isopleth on the high alumina side of the eutectic showed microscopically, and by x-ray, that the primary phase particle is corundum. This was consistent with the preceding observation that corundum appears below the solidus on the low alumina side of the eutectic. It is significant that x-ray diffraction techniques were not sensitive enough to show corundum in a specimen similar to that shown in Fig. 4. This could explain why Ginsberg, employing only x-ray techniques, was unable to observe corundum in either slowly cooled or quenched samples of low alumina content.

Thus it appears possible to quench from above the liquidus and preserve a phase that is not characteristic of anything that occurs at lower temperatures in the diagram. Attention, therefore, is focused on the nature of alumina as it exists in the sample quenched from above the liquidus.

The general consensus in the literature favors some sort of reaction between alumina and cryolite in the molten state to produce oxyfluoride complexes or aluminates, or both. For example, Treadwell (6) proposed $(F_2AlO_2AlF_2)^{=}$; Grunert (7), $AlOF_5^{\equiv}$ and $AlOF_3^{=}$; Boner (8), $AlOF_2^{-}$; Rolin (9), AlO_2^{-} and AlO^{+}; and Forland, *et al.*, (10), $AlO_2F_2^{\equiv}$.

Edwards, *et al.* (11) made density measurements on melts over a range of compositions above the liquidus. These measurements showed that, as the alumina content increased, the density of the melt decreased steadily below that of cryolite towards a minimum, indicating a chemical interaction. Frank and Foster (12), employing radioactive aluminum, demonstrated the complete exchange between the aluminum atoms of cryolite and alumina on fusion. This would not occur if alumina simply dissolved without ionization or dissociation in cryolite. The same workers (13) made density calculations using various possible reaction schemes to get a fit with Edwards' density curve. The best fit was obtained

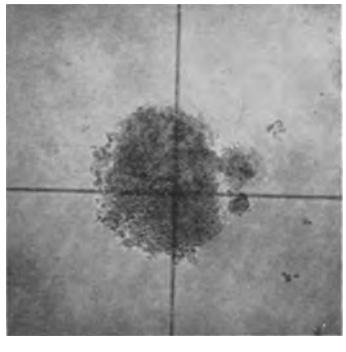

Fig. 5. Mullitized alumina, extracted from quenched liquid. X210.

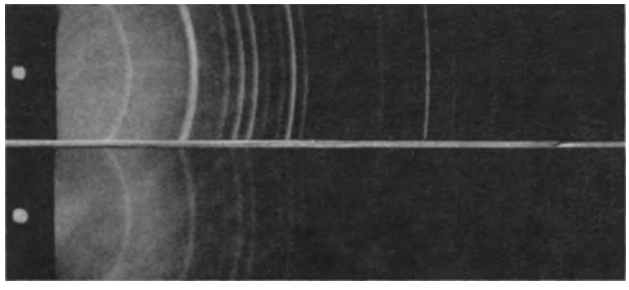

Fig. 6. X-ray powder diffraction patterns of (a) (top) mullite, $3Al_2O_3 \cdot 2SiO_2$, (b) (bottom) m-alumina.

[1] The focus of this particle was sacrificed in order to obtain a definition of the flat corundum plate at the crosshairs.

Table I. *d* Values and relative line intensities

m-Al_2O_3			Mullite, $3Al_2O_3 \cdot 2SiO_2$		
Line No.	*d*, A	I/I_o	Line No.	*d*, A	I/I_o
1	5.45	V. stg.	1	5.42	Med.
2	3.47	V. stg.	2	3.42	V. stg.
3	2.92	Med. wk.	3	2.90	Med. wk.
4	2.72	Stg.	4	2.72	Med.
5	2.59	Stg.	5	2.56	Med.
6	2.46	V. wk.	6	2.44	Wk.
7	2.34	Stg.	7	2.30	Med. wk.
8	2.24	Stg.	8	2.22	Stg.
9	2.15	Med.	9	2.13	Med. wk.
10	2.06	V. wk.	10	1.89	Wk.
11	1.99	V. wk.	11	1.845	Med. wk.
12	1.88	Med. wk.	12	1.71	Med.
13	1.73	Med.	13	1.70	Med.
14	1.61	Med. wk.	14	1.60	Med.
15	1.55	Med. stg.	15	1.58	Wk.
16	1.492	Wk.	16	1.522	Stg.
17	1.461	Wk.	17	1.46	Med. wk.
18	1.41	V. wk.	18	1.445	Med.
19	1.346	Wk.	19	1.426	Wk.
20	1.288	Med. stg.	20	1.409	Med.

with an equilbrium between Na_3AlF_6, $NaAlF_4$, NaF, $Na_3AlO_2F_2$, and $NaAlO_2$.

The identification of the primary phase on the high alumina side of the eutectic as corundum rules out the possibility of a stable solid oxyfluoride compound. X-ray powder patterns of the quenched liquid showed only cryolite, implying that the oxyfluorides are too unstable to retain their configuration on quenching, or are not present in sufficient amounts for detection. Of particular interest, then, is the structural form of the alumina in the quenched liquid particles.

The quantitative separation of alumina in alumina-cryolite fusion products customarily is performed by leaching with hot, 30%, aluminum chloride solution, followed by repeated washing and, finally, ignition of the residue at 1100°C. This procedure yields alumina contents with a precision of ±0.1% with a 1-g sample. With minor modifications, satisfactory precision was also obtained with the small samples, whether quenched or slowly cooled. X-ray diffraction patterns of the ignited residues invariably showed large proportions of corundum, with small amounts of beta- and zeta-alumina, and, occasionally, other forms. To retain the alumina structure as it existed in the quenched liquid, the ignition step was eliminated.

The x-ray patterns of the extraction residues showed a large amount of material that was similar to the aluminum silicate, mullite, $3Al_2O_3 \cdot 2SiO_2$, and a small amount of material resembling the lithium-containing zeta-alumina, although, in this case, the material was lithium free. This was true, regardless of the alumina content, within the concentration range of the experiments. Figure 6 compares Debye patterns of the mullite-like alumina (hereafter referred to as m-alumina for convenience) and true mullite. Table I lists the *d* values and relative line intensities.

Table II. X-ray analyses of heated m-alumina

X-ray analysis of the starting materials	Heating conditions	X-ray analysis after heating
m-Alumina	250°C 1 hr	m-Alumina
m-Alumina	300°C 1 hr	m-Alumina; eta-alumina
m-Alumina	600°C 1 hr	m-Alumina; eta-alumina
m-Alumina	650°C 1 hr	Eta-alumina
m-Alumina	700°C 1 hr	Eta-alumina
m-Alumina	750°C 1 hr	Eta-alumina; corundum
m-Alumina	775°C 1 hr	Corundum

The aluminum chloride extraction residues for compositions on the high alumina side of the eutectic, but originating at a temperature below the liquidus, contained a mixture of m-alumina and corundum. Corundum is the primary phase in this region of the phase diagram. Extraction residues of samples quenched from below the liquidus on the low alumina side of the eutectic contained only the m-alumina. The primary phase in this region, cryolite, is soluble in hot aluminum chloride solution. Residues from quenches originating below the solidus, regardless of their composition relative to the eutectic, contained only corundum, indicating that the amount of m-alumina present is a function of the amount of quenched liquid.

True mullite ($3Al_2O_3 \cdot 2SiO_2$) contains 13.2% silicon. Qualitative spectroscopic analysis of the m-alumina showed a silicon concentration near 1%. This can be accounted for by the accumulation of the silicon present in the original cryolite and alumina. It is not enough, of course, to account for the similarity to true mullite.

The m-alumina was heated at various temperatures to determine its stability. Table II lists the results of x-ray analyses of these materials. The conversion of m-alumina to corundum on heating demonstrates that it is a metastable phase.

Generally, x-ray analysis was too insensitive to detect m-alumina in the quenched liquid. Its occasional detection demonstrated, however, that the m-alumina is a component of the quenched liquid and was not produced during the aluminum chloride extraction. A refractive index of 1.604 ± 0.016 was determined for the extracted m-alumina. A more precise determination was not possible because of the extremely fine particle size of the precipitate (Fig. 5).

Conclusions

The following is offered to explain the observations of this work. Alumina dissolves in cryolite by a reaction mechanism to produce one or more species (perhaps oxyfluorides) that are stable only in the melt. These compounds disproportionate on equilibrium freezing to cryolite and corundum, which then are stable to room temperature. On the cryolite side of the eutectic, cryolite freezes as the primary

phase. If the liquid is rapidly quenched, however, there is insufficient time for the alumina from the disproportionation to recrystallize as corundum. Rather, it assumes the mullite-like configuration, which tentatively might be considered a skeletal arrangement having some characteristics of its oxyfluoride precursor. The quenched liquid is thus an intimate mechanical mixture of cryolite and m-alumina with an observable refractive index that is actually an average index of the two phases, taken in appropriate proportions.

Manuscript received Sept. 9, 1958.

Any discussion of this paper will appear in a Discussion Section to be published in the June 1960 JOURNAL.

REFERENCES

1. E. Zintl and W. Morawietz, *Z. anorg. u. allgem. Chem.*, **240**, 145 (1939).
2. H. Ginsberg and A. Bohm, *Z. Elektrochem.*, **61**, 313 (1957).
3. K. Grjotheim, "Contribution to the Theory of the Aluminum Electrolysis," p. 90, Institute of Silicate Science, Trondheim, Norway (1956).
4. P. A. Foster, *J. Phys. Chem.*, **61**, 1005 (1957).
5. G. A. Roush and M. Miyake, *Trans. Am. Electrochem. Soc.*, **48**, 153 (1925).
6. W. D. Treadwell, *Schweiz. Arch. angew. Wiss. u. Tech.*, **6**, 69 (1940).
7. E. Grunert, *Z. Electrochem.*, **48**, 393 (1942).
8. J. E. Boner, *Helv. Chim. Acta*, **33**, 1137 (1950).
9. M. Rolin, *Ann. Phys.*, Series 12, **6**, 970 (1951).
10. T. Forland, H. Storegraven, and S. Urnes, Symp. sull 'elettrolisi dell 'alluminio, October 12, 1953, Milan, Italy.
11. J. D. Edwards, C. S. Taylor, L. A. Cosgrove, and A. S. Russell, *This Journal*, **100**, 508 (1953).
12. W. B. Frank and L. M. Foster, *J. Phys. Chem.*, **61**, 1531 (1957).
13. W. B. Frank and L. M. Foster, Alcoa Research Laboratories, to be published.

A Study of the Iodide Niobium Process

Robert F. Rolsten[1]

Eastern Laboratory, E. I. du Pont de Nemours & Company, Gibbstown, New Jersey

ABSTRACT

It was established that the rate of deposition of niobium by the thermal decomposition of niobium iodides can be expressed in units of moles of niobium deposited per unit length of a deposition element per unit of time. The rate of deposition of niobium was studied (*a*) with deposition temperatures from 750° to 1100°C, (*b*) with feed material temperatures from 240° to 470°C, and (*c*) with crude niobium with different surface areas.

Van Arkel (1) prepared single crystal tungsten rods by the thermal decomposition of tungsten hexachloride on a resistively heated wire in an evacuated flask in 1923. Van Arkel, deBoer, and Fast (2-7) subsequently extended the technique to the preparation of other metals from their volatile halides. The metal iodides have been used extensively since they exhibit a low thermal stability. In addition, iodine is particularly well adapted as the basis for such a process because it reacts readily with most elements to form compounds which are moderately stable in the vapor state and which dissociate at a high temperature. Furthermore, iodine does not react directly with most oxides.

Fast (8) studied the rate of formation of titanium by the thermal decomposition of gaseous titanium iodides. The temperature of the deposition element was maintained constant while the temperature of the feed material was varied. The deposition rate increased from a minimum at room temperature to a maximum at about 175°C, decreased to a second minimum at about 300°-470°C, and then increased again to 520°C, the highest feed temperature employed in the series of measurements. However, Fast (8) noted, from experiments where the deposition bulb was fabricated from Supermax glass, that the deposition rate at a feed temperature of 620°C was considerably higher than at 520°C. Fast (7), Döring and Molière (9), and Emelyanov, Bystrov, and Evstyukhin (10) observed a deposition rate of zirconium vs. bath temperature curve that was similar in shape to the curve observed by Fast (8) for titanium.

It was reported (11) recently that high-purity niobium[2] could be prepared by an iodide decomposition process. The purpose of the investigation reported here was to determine the effect that such factors as (*a*) deposition and feed temperatures, (*b*) reactivity of the crude (feed) niobium to be refined, and (*c*) the predominant gas and condensed solid phase species would have on the rate of deposition of niobium.

Experimental

The deposition unit employed throughout this investigation is shown in Fig. 1. A 64-mm diameter Vycor cylinder was equipped with a 15-mm OD quartz reentrant tube or finger. The crease or constriction in the deposition bulb was 50 mm in diameter and 45 mm from the bottom of the cylinder. This crease served to position the 50 mm diameter perforated molybdenum retaining cylinder. Molybdenum does not form a volatile iodide under the experimental conditions for deposition and, consequently, is not transferred. The impure niobium was contained in the annular space between the Vycor bulb and the molybdenum cylinder.

[1] Present address: U.S. Borax Research Corporation, 412 Crescent Way, Anaheim, California.

[2] Niobium metal prepared by the thermal decomposition of the niobium iodides can be designated as iodide niobium.

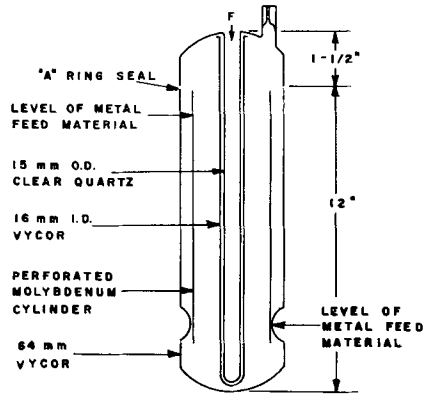

Fig. 1. Reentrant-type apparatus for the preparation of metals.

In a typical experiment, the deposition unit was thoroughly cleaned, charged with impure niobium, and the head assembly attached to the deposition bulb by fusing the Vycor at "A". Thermocouples were fastened to the wall of the deposition bulb, covered with a single layer of ⅛ in. thick asbestos cloth, and wound with 14 gauge Nichrome wire. This unit was positioned centrally in the 6 x 18 in. cavity of the empty salt bath and then connected (glass-to-glass) to a vacuum system composed of a 3-turn glass coil to eliminate fracture due to vibration or expansion, a McLeod gauge, a cold trap, a mercury diffusion, and a mechanical pump. Fifteen grams of resublimed iodine were added to an auxiliary bulb (reservoir) held in dry ice. The space between the steel wall of the salt furnace and the Nichrome heating element was packed with high-temperature insulating wool. The deposition bulb, with the crude metal was vacuum outgassed at 800°-850°C, and heat was supplied from the Nichrome element coiled around the deposition bulb. After the pressure in the system was maintained at 10^{-5} mm Hg or less for 48 hr, the Nichrome element was disconnected, the system cooled to room temperature under vacuum, and the wool insulation removed from the furnace. A salt mixture ($NaNO_3$-KNO_3-$NaNO_2$) was added to the tank of the furnace and was melted with power supplied from the furnace. The liquid salt was agitated with an auger-type screw that lifted salt from the bottom of the tank and distributed it at various levels and directions to the top of the tank. The temperature of the deposition bulb, located 2 in. from the bottom of the tank and 2 in. beneath the surface of the salt, was maintained at ±3°C. Deposition temperatures were attained independently and measured with a platinum-platinum 10% rhodium thermocouple located in the center of the Nichrome wire helical heating element, indicated by "F" in Fig. 1. At the termination of the deposition experiment, liquid salt was siphoned from the salt tank and the residual niobium iodide within the deposition bulb was condensed on the walls of the cold Vycor bulb. The temperature of the deposition element was maintained at 900°-1000°C to prevent any iodide from condensing upon the niobium deposit.

In some experiments, the deposition bulb was positioned centrally within a 100-mm ID furnace. Thermocouples were fastened to the wall of the deposition bulb. Additional thermocouples were located at ½ in. intervals from the top to the bottom of the 24 in. long furnace, and they extended ¼ in. from the inside wall of the furnace into the air gap between the furnace and deposition bulb.

The weight of metal deposited was determined directly by weighing. The Vycor tube with the niobium deposit was compressed between polished stainless steel (No. 316) plates. The ductile deposit deformed while the Vycor tube shattered and thus provided an easy method of separation.

The crude (feed) niobium used in this work was in the form of 4-10 mil sheet and 12 mm diameter by 4 mm thick sintered powder pellets. Both forms are available commercially. Typical analytical results, in weight per cent, of the starting and iodide niobium, are summarized below:

	Oxygen	Nitrogen	Hydrogen	Carbon	Iron	Silicon	Tantalum
Pellets	0.435	0.018	0.0021	0.050	0.05	0.1	~0.5
Iodide (from pellets)	0.064	0.001	0.0008	<0.001	<0.005	0.006	—
Sheet	0.195	0.012	0.0009	0.006	0.01	0.01	~0.4
Iodide (from sheet)	0.043-0.062	<0.001	0.0001	<0.001	<0.005	0.001	0.04-0.18

Oxygen and hydrogen were determined by vacuum fusion analyses utilizing a platinum bath at 1900°C, nitrogen by micro-Kjeldahl, carbon with a Leco No. 515 Carbon Determinator, and iron, tantalum, and silicon by spectrographic analysis.

Results and Discussion

Runnalls and Pidgeon (12) and Döring and Molière (9) reported that the deposition rate of titanium and zirconium, from their respective iodides, was dependent on the surface area of small diameter (0.13 to 0.75 mm) deposition elements. Shapiro (13) reported that the deposition rate of zirconium was independent of the surface area for cylindrical deposition elements with diameters between 2 and 25 mm. This was observed from zirconium (filament) deposition temperatures in the range from 1100° to 1450°C. In addition, Shapiro (13) observed that the rate of deposition of zirconium remained constant at a given bath or feed material temperature and concluded that the vapor pressure, the value of which is determined by the coldest spot in the vessel and which value would thus remain constant for a given feed (bath) temperature, fixed the rate of deposition at a given deposition temperature.

Five deposition experiments were made utilizing a liquid salt bath with the feed temperature and deposition temperature of 244° and 1000°C, respectively. The initial diameter of the Vycor deposition element was 19 mm. Each experiment was made with 450 g of niobium pellets. The results from these five

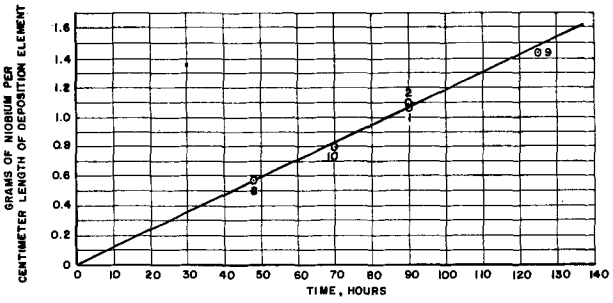

Fig. 2. Deposition element growth vs. time

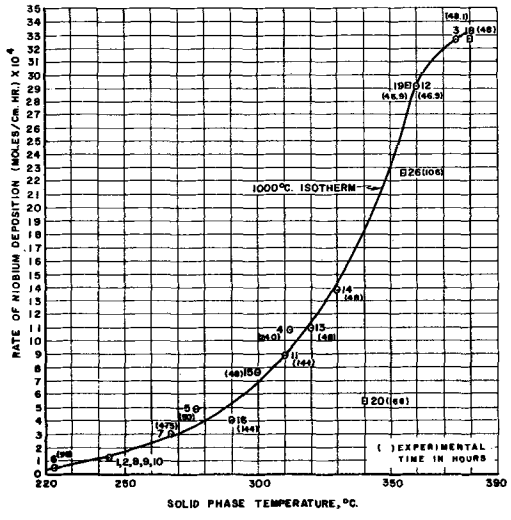

Fig. 3. Dependence of deposition rate on the condensed iodide temperature. Niobium pellet: ⊙ = salt bath; □ = air bath.

experiments, 1, 2, 8, 9, and 10, are shown graphically in Fig. 2, a plot of the grams of niobium deposited per centimeter of length of deposition element vs. the deposition time in hours. These data can be expressed by a straight line over the time interval from zero to 125 hr. Experiments 1 and 2 were made under identical conditions with the deposition time of 90 hr, to indicate the reproducibility of the measurements. The grams of metal deposited per centimeter of length of deposition element were 1.064 and 1.080 for experiments 1 and 2, respectively.

The constancy of deposition rate with time, with the steadily increasing surface area, clearly shows that the decomposition of the iodide on the deposition element cannot be rate controlling. If it were, the increased area of the deposition element would certainly affect the deposition rate. This leaves either (*a*) diffusion of iodide to or iodine from the deposition element or (*b*) the rate of reaction of the liberated iodine with the crude niobium as the possible rate controlling steps.

A total of sixteen experiments (charge of 450 g of niobium pellets) were made in the salt bath with a deposition temperature of 1000°C and feed temperatures from 224° to 375°C. The results from these experiments are summarized in Fig. 3, a plot of the deposition rate in moles of niobium per centimeter of length of the deposition element per hour vs. the condensed iodide[3] temperature. The experimental times, in hours, are reported in parentheses in Fig. 3. The low deposition rate of 0.00005 moles cm^{-1} hr^{-1} was observed at 224°C, and this rate steadily increased to the maximum of 0.00326 moles cm^{-1} hr^{-1} at 375°C, the highest temperature used in this series of experiments. It can be seen that the smooth curve which represents the data changes slope at about 350°C, which indicates that the maximum deposition rate may occur in the temperature range of 380° to 400°C for the 1000°C deposition isotherm.

Sixteen experiments (charge of 450 g of niobium pellets) were made in an air bath with a deposition temperature of 1000°C and at feed temperatures from 335° to 458°C. The results from the experiments for the 1000°C isotherm are summarized in Fig. 4, a plot of the deposition rate vs. feed temperature. The latter temperatures, measured at the surface of the deposition bulb, were about 90°C higher than the temperatures of the air bath. It can be seen that the low rate of 0.00050 moles cm^{-1} hr^{-1} was observed at the lowest condensed iodide temperature (335°C) employed. This rate increased steadily to a maximum of 0.0033 moles cm^{-1} hr^{-1} at about 370°-375°C and then decreased to a second minimum at about 410° to 440°C. From this minimum, the deposition rate again increased to 0.0015 moles cm^{-1} hr^{-1} which was observed at 458°C, the highest condensed iodide temperature employed.

There is a close similarity in the general shape of the deposition rate-temperature curves shown in Fig. 3 and 4. The best agreement occurs in the temperature range from 350° to 380°C, where both sets of data show a maximum in the deposition rate. However, considerable deviation occurs at about 340°C. For example, in experiment 20 (air bath) the observed deposition rate was 0.00054 moles cm^{-1} hr^{-1} while the deposition rate for the corresponding experiment (salt bath) was 0.00178 moles cm^{-1} hr^{-1}. The fact that the individual sets of data given in Fig. 3 and 4 can be expressed by a smooth curve, that is, each set of data are internally consistent but mutually consistent only over a limited range, strongly indicates that some unknown factor entered into the reaction process. In order to make experiment 20 (340°C) agree with the curve shown

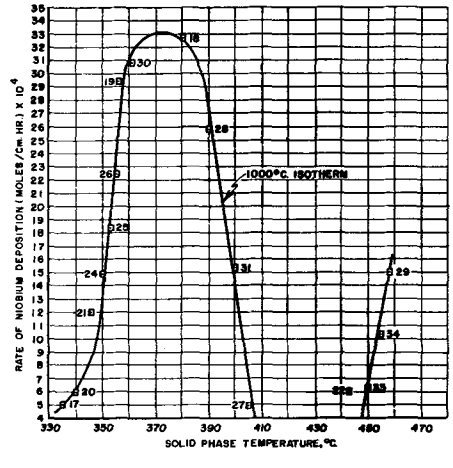

Fig. 4. Dependence of deposition rate on the condensed iodide temperature. Air bath-niobium pellet.

[3] The expressions, "condensed iodide temperature" and "deposition bulb temperature" are considered to be synonymous in this paper.

in Fig. 3, an error in temperature measurement of 50°C would have to be accounted for. It should be remembered, however, that the deposition bulb operated in the liquid salt would be susceptible to more accurate temperature measurement and operation at a more uniform temperature than the deposition bulb operated in the air bath. In addition the wall temperature of the bulb would be much closer to the temperature of the liquid salt.

Twenty-two experiments were made in which each charge consisted of 15 g of resublimed iodine and 500-600 g of 4-10 mil niobium sheet. All experiments were conducted in an air bath, and the temperature of the wall of the deposition bulb was about 70°C higher than the temperature of the air bath. Fifteen of these experiments were made with a deposition temperature of 1000°C and feed temperatures from 310° to 470°C, and five experiments were made with a deposition temperature of 1100°C and feed temperatures from 305° to 405°C. In addition, two experiments, 53 and 55, were made with the deposition temperature of 750° and 900°C, respectively. These deposition rate data are summarized in Fig. 5. It can be seen that the rate data for the 1000° and 1100°C isotherms are quite similar in shape to the curves given in Fig. 3 and 4. All curves start out at a low deposition rate, increase to a maximum rate at about 380°C, and then the rate decreases to a maximum at about 430°C. The deposition rate increases at condensed iodide temperatures greater than 430°C.

The most pronounced difference in the deposition rate data obtained by using sheet (Fig. 5) or pellet niobium (Fig. 4) as the starting material can be seen in the maximum rate of deposition that was attained for the 1000°C isotherms. For example, the maximum rate of 0.00082 moles cm^{-1} hr^{-1} was obtained with sheet niobium feed while the maximum rate of 0.00332 moles cm^{-1} hr^{-1} was obtained with

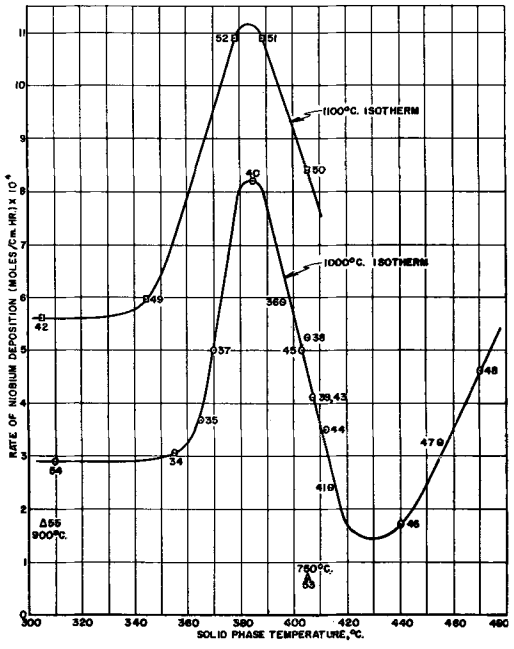

Fig. 5. Plot of deposition rate of niobium vs. condensed iodide temperature, air bath-niobium sheet.

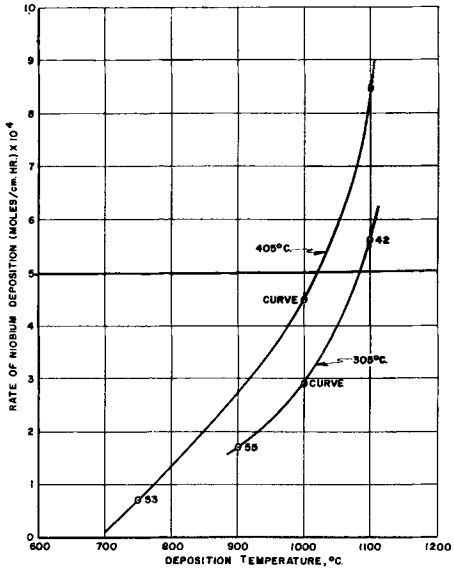

Fig. 6. Plot of deposition rate of niobium vs. deposition temperature.

niobium pellets as feed. Since the conditions under which the above experiments were conducted were identical except for the difference in the feed niobium, it is clear that the reaction of the feed material with the liberated iodine can determine the rate of deposition. Thus, the high surface area niobium pellets can react quickly with the liberated iodine to form iodide. Consequently the iodine pressure does not play as prominent a role in the deposition process when niobium pellets are used as the feed material.

The effect of the deposition temperature on the deposition rate of niobium at constant condensed iodide temperature can be seen in Fig. 6. The condensed iodide isotherm, 405°C, indicated that the deposition rate increased from 0.00007 moles cm^{-1} hr^{-1} at 750°C to 0.00084 moles cm^{-1} hr^{-1} at 1100°C. A similar curve was obtained for the 305°C isotherm. Extrapolation of the 405°C curve to zero deposition rate indicated that the minimum deposition temperature for niobium, that is, the temperature above which the niobium iodides are thermally unstable, would be somewhere in the range of 700°C. The minimum deposition temperature for the 305°C isotherm would, however, be expected to occur at a temperature below 700°C since the total pressure would be less than for the 405°C isotherm. Therefore, the two curves would cross.

In expressing the data given above in Fig. 3, 4, and 5, it was assumed that:

1. The method of expressing the deposition rate, moles cm^{-1} hr^{-1}, was valid for all feed temperatures and not just for the one temperature (244°C) investigated. The feed temperatures, which determine the total pressure in the system, were such as to permit deposition to be controlled by diffusion and the operating conditions did not permit deposition to occur in either the free molecule (lower pressure) or in the diffusion plus convection regions (higher pressure).

2. The deposition mechanism remained the same for all condensed iodide temperatures, that is, for

both the maximum and the minimum total pressures within the deposition bulb.

3. Only iodine and niobium iodides (not oxyiodide or hydrogen, etc.) contributed to the total pressure of the system.

The deposition rate of niobium must certainly be dependent on the availability of niobium iodide(s) at the deposition element. The quantity of gaseous niobium iodide depends on the reactivity of the crude niobium, the stability of the iodides in contact with excess niobium, and the vapor and disproportionation pressures of the various iodides. Therefore, a cursory study of the niobium iodides was made in order to determine the effect of the various iodides on the deposition process.

Niobium pentaiodide was prepared (14) by the reaction of iodide niobium and resublimed iodine in an evacuated tube at 280°-290°C. A high partial pressure of iodine was maintained during the reaction to stabilize the temperature sensitive pentaiodide. The excess iodine was sublimed at 114°C from the large bronze colored, plate-like crystals of the pentaiodide. Niobium was determined as Nb_2O_5 by dissolving and precipitating the sample in freshly filtered NH_4OH, filtering, and igniting in air in a platinum crucible. Iodine was determined by the modified (15) Volhard technique. Anal. calcd. for NbI_5: Nb, 12.77; I, 87.23; found: Nb, 12.81, 12.70, 13.1, 12.70; I, 87.33, 87.55, 87.52, 87.24, 87.17. Crystals of the pentaiodide were placed in a calibrated 10-ml pycnometer (inside a dry box) and the density was determined at 25°C by evacuating the pycnometer bulb containing the pure pentaiodide and then distilling, under vacuum, absolute carbon tetrachloride onto the solid sample. Density values for five different samples were 4.98, 5.04, 5.19, 5.14, and 5.08 g cc^{-1}. This pycnometric density can be compared to the x-ray density of 5.24 g cc^{-1} for the orthorhombic pentaiodide that contains 16 formula weights per unit cell.

A sample of this pentaiodide was placed in a Pyrex tube, equipped with a break seal that was broken under vacuum, and heated at 243°C for 145 hr. Iodine was liberated and the nonvolatile residue was observed to have an I/Nb ratio of 2.97. A second sample of pure pentaiodide was treated in the manner described above, but heated to 250°C. The observed I/Nb ratio was 3.07. X-ray diffraction data obtained from the two niobium iodide samples, $NbI_{2.97}$ and $NbI_{3.07}$, are in essential agreement.

Niobium pentaiodide was heated (16) to 270°C for 48 hr in 0.8 mm pressure of iodine to yield dark gray, metallic-appearing crystals of NbI_4 which were in the form of elongated hexagonal plates and fine needles. Heating a higher iodide to 425°-430°C for 48 hr in a partial pressure of iodine resulted (16) in the formation of pure NbI_3.

Samples of NbI_3 were placed in a Pyrex tube, equipped with a break seal that was broken under vacuum, and heated to 450°C for 123 hr. Material started to sublime at 250° to 260°C, and a brown to bronze colored solid was evolved at a temperature between 430°-450°C. Samples of this residue were observed to have an I/Nb ratio of 1.74. The condensed solid iodide phase removed from the deposition bulb at the termination of an experiment with the condensed iodide and deposition temperatures of 310° and 1000°C, respectively, was observed to have an I/Nb ratio of 2.74. In another experiment, some of the gaseous iodide was removed from the deposition bulb while deposition was in progress and was observed to have an I/Nb ratio of 3.12. The crude niobium was maintained at 430°C with the deposition element at 1000°C. It should be recognized that the solid iodide remaining after a deposition experiment necessarily does not have to be the same as the solid iodide existing during the experiment.

A possible explanation for the shape of the deposition rate vs. feed material temperature curves is now offered. It should be recognized that the following explanation for the deposition of niobium from its volatile iodides parallels the explanation offered by Fast (7, 8) for the zirconium-zirconium iodide and the titanium-titanium iodide systems. Pure niobium pentaiodide is not stable (forms lower iodides) at temperatures of about 200°C in vacuum or when heated in the presence of excess niobium. This thermal instability should be more pronounced inside the deposition bulb where a temperature gradient exists in the crude niobium. Metal at the surface of the molybdenum retaining screen, due to the location of the deposition element (~1000°C), will be considerably hotter than the metal at the wall of the deposition element. Therefore, the niobium at the retaining screen, due to its higher temperature, will be more chemically active toward the liberated iodine. This will prevent the development of a high partial pressure of iodine and this effect will tend to reduce further the thermal stability of the pentaiodide ($NbI_5 \rightarrow NbI_4 + \frac{1}{2} I_2$). The net result is that NbI_5 should not be an important condensed iodide species within the deposition bulb. This seems to have been realized since the solid iodide phase, with the condensed iodide and deposition temperatures of 310° and 1000°C, respectively, was observed to be I:Nb = 2.74.

Solid niobium tetraiodide was not observed in the deposition bulb after any of the experiments and, consequently, it may not be an important condensed iodide species. It should be noted, however, that in the case of tantalum, a compound corresponding to I:Ta = 3.91 was removed from the deposition bulb at the conclusion of a deposition experiment. Corbett and Seabaugh (16) reported that the heating of a higher iodide to 425° to 430°C in a partial pressure of iodine yielded NbI_3. The temperature of the crude niobium at the molybdenum retaining screen within the deposition bulb may be at this temperature level. The fact should not be overlooked, however, that the tetraiodide could enter into the deposition process according to the reactions at 300°C: $NbI_{4(c)} \rightarrow NbI_{4(g)}$ and $2NbI_{4(c)} \rightarrow NbI_{5(g)} + NbI_{3(c)}$. In any event, the quantity of iodide in the gas phase (a low partial pressure) is quite small in the condensed iodide temperature range of 300°-340°C which results in a low deposition rate. In the condensed iodide temperature range where the deposi-

tion rate is at a minimum (~300°C) to the maximum (~380°C), the quantity of iodide in the gas phase was increased as a result of the reactions specified above or for the following: $NbI_{3(c)} \rightarrow NbI_{3(g)}$ and $2NbI_{3(c)} \rightarrow NbI_{4(g)} + NbI_{2(c)}$.

The increase in deposition rate with the condensed iodide temperature in the lower temperature range can be explained on the basis of an increase in vapor pressure of the iodide; however, the behavior from the maximum (~380°C) to the minimum (~400°C) apparently has no simple explanation. Although there is an increase in the quantity of the nonvolatile, thermally stable, lower iodide in the condensed iodide temperature range of 380°-400°C, this alone should not cause the deposition rate to diminish. There can be a pressure over a mixture of solid lower iodides and this pressure, providing there is no solid solubility between the iodide species, will be independent of the quantity of the solid species present. The nonvolatile lower iodide could, however, coat the crude niobium and presumably prevent the iodine liberated at the deposition element from reacting with the crude niobium which would permit the partial pressure of iodine to increase. Thus, any increase in condensed iodide temperature would permit the formation of more lower iodide to coat the crude niobium and prevent the reaction between the niobium and iodine. This would result in a still higher partial pressure of iodine with a necessary shift in the equilibrium and could conceivably permit the iodine to attack and remove niobium from the deposition element. Thus, the net or apparent deposition rate would be quite small.

Upon further increasing the condensed iodide temperature, that is, from about 440° to at least 470°C, the diiodide can enter into the deposition process as a result of the possible reactions:

$$NbI_{2(c)} \rightarrow NbI_{2(g)},\ 2NbI_{2(c)} \rightarrow NbI_{4(g)} + Nb$$
$$\text{and } 2NbI_{2(c)} \rightarrow NbI_{(c)} + NbI_{3(g)}$$

and the deposition rate again increases. In one deposition experiment (sheet niobium was used as the crude) a sample of the gaseous species (iodide and iodine) was removed from the deposition bulb and observed to be I:Nb = 3.12. This would of course indicate that NbI_3 is the principal gaseous iodide within the deposition bulb at condensed iodide temperatures from 430° to 470°C.

The difference in thermal stability of the various niobium iodides manifests itself in that the same deposition rate of niobium can be obtained from at least three different condensed iodide temperatures. For example, the deposition rate of 0.0015 moles cm^{-1} hr^{-1} can be obtained with condensed iodide temperatures of 350°, 399°, and 459°C as shown in Fig. 4.

Acknowledgment

The author wishes to thank the Pigments Department of the Du Pont Company for the use of their facilities for this research program.

Manuscript received May 15, 1959. This paper was prepared for delivery before the Columbus Meeting, Oct. 18-22, 1959.

Any discussion of this paper will appear in a Discussion Section to be published in the June 1960 JOURNAL.

REFERENCES

1. A. E. van Arkel, *Physica*, **3**, 76 (1923).
2. A. E. van Arkel and J. H. deBoer, U. S. Pat. 1,671,-213, May 29 1928.
3. A. E. van Arkel and J. H. deBoer, *Z. anorg. u. allgem. Chem.*, **148**, 345 (1925).
4. J. H. deBoer and J. D. Fast, *ibid.*, **153**, 1 (1926).
5. Idem., **187**, 177 (1930).
6. J. H. deBoer, *Ind. Eng. Chem.*, **19**, 1256 (1927).
7. J. D. Fast, *Z. anorg. u. allgem. Chem.*, **239**, 145 (1938).
8. Idem., **241**, 42 (1939).
9. H. Döring and K. Molière, *Z. Elektrochem.*, **56**, 403 (1952).
10. V. S. Emelyanov, P. D. Bystrov, and A. E. Evstyukhin, *J. Atomic Energy, U.S.S.R.*, **1**, No. 1, 43 (1956); English translation, *J. Nuclear Energy*, **3**, 121 (1956).
11. R. F. Rolsten, *Trans. AIME*, **1959**, 472.
12. O. J. C. Runnalls and L. M. Pidgeon, *J. Metals*, **4**, 843 (1952).
13. "The Metallurgy of Zirconium," B. Lustman and F. Kerze, Jr., Editors, Chap. 5, McGraw-Hill Book Co., New York (1955).
14. R. F. Rolsten, *J. Am. Chem. Soc.*, **79**, 5409 (1957).
15. J. R. Caldwell and H. B. Moyer, *Ind. Eng. Chem., Anal. Ed.*, **7**, 38 (1935).
16. J. D. Corbett and P. X. Seabaugh, *J. Inorg. Nuc. Chem.*, **6**, No. 3, 207 (1958).

Reactions in the Niobium-Hydrogen System

W. M. Albrecht, W. D. Goode, and M. W. Mallett

Battelle Memorial Institute, Columbus, Ohio

ABSTRACT

Equilibria and elevated-temperature x-ray studies show that a solid solution of hydrogen in niobium is produced throughout most of the system. A miscibility gap was found at low temperatures and pressures with a critical point at about 140°C, 0.01 mm of mercury hydrogen pressure, and 0.3 H/Nb. Sorption rates at 300°-550°C were initially linear. At higher temperatures, sorption rates were controlled by diffusion in the metal matrix. Diffusion coefficients at 600°-700°C can be expressed by:

$$D = 0.0215 \exp\left[(-9370 \pm 600)/RT\right]$$

Desorption rates were slower than those predicted by diffusion.

In a previous study (1), the authors investigated the equilibria in the niobium-hydrogen system in the ranges 100°-900°C, 10-1000 mm of mercury hydrogen pressure, and at atomic ratios of hydrogen to niobium, H/Nb, of 0.01-0.85. A single-phase solid solution was produced throughout most of the system. However, the presence of a two-phase region in the system was indicated at low temperatures and hydrogen pressures. The present study was made to establish more definitely the extent of this region. Equilibria were established at pressures lower than those of the preceding work. Equilibrium products were identified by x-ray diffraction. Also, studies were made of the kinetics of the reaction of hydrogen with niobium and of the diffusion of hydrogen in the metal.

Paxton and Sheehan (2) measured the solubility of hydrogen in niobium at 1 atm pressure to establish partially the phase diagram of the system. They also made permeability experiments to measure the rate of diffusion of hydrogen in the metal. Gulbransen and Andrew (3) have reported the kinetics of the reaction of hydrogen with niobium for 200° to 900°C at hydrogen pressures up to 57 mm Hg. Both of these studies have a bearing on the present investigation.

Material

The original niobium bars were cut and fabricated to approximately 0.3 to 0.9 cm rods and to 0.03 cm sheet. Samples for the reaction rate and diffusion studies were vacuum annealed at 1150°C for ½ hr. Analysis of the fabricated niobium after annealing has been reported (1). The major impurities were 0.15 w/o Ta and 0.043 w/o oxygen. All other impurities were below 0.02 w/o.

Pure hydrogen was obtained from the thermal decomposition of uranium hydride prepared from dry tank hydrogen and degassed uranium chips.

Experimental Methods

The method to obtain equilibria data has been described (1). However, for this work, the micro-Sieverts apparatus was equipped with a differential oil manometer to measure pressures in the range 0.1-50 mm Hg. Briefly, data were obtained as follows. A measured amount of hydrogen was added to the calibrated reaction tube containing 3-4 g of sheet (0.03 cm thick) niobium. At the desired temperature, the system was allowed to come to constant (equilibrium) pressure as measured on the differential oil manometer. The equilibrium composition was calculated from the equilibrium pressure, specimen weight, volume of gas addition, and volume capacity of the reaction system at the experimental temperature.

Sorption rates were measured with another modified Sieverts apparatus (4). Essentially, the apparatus consists of a reaction tube, pressure regulator, gas buret, and a high vacuum-pumping system. Cylindrical specimens approximately 0.3, 0.6, and 0.9 cm in diameter and 1-3 cm long were dry abraded through 240-, 400-, and 600-grit silicon carbide paper. Each specimen was weighed, measured, and spot welded to a Pt-Pt + 10% Rh thermocouple. After a light final polish with dry 600-grit silicon carbide paper, the sample was hung in the reaction tube and sealed to the Sieverts apparatus. The system was evacuated to less than 0.01 μ of mercury, then heated to the temperature of the run.

The reaction was initiated by admitting hydrogen through the pressure regulator to the reaction tube. The buret was kept balanced at atmospheric pressure at all times. Readings of the buret were taken at convenient time intervals depending on the speed of the reaction. The amount of gas reacted with the sample was the difference between the volume added from the buret and the volume remaining in the gas phase in the calibrated dead space of the reaction tube.

Diffusion coefficients for hydrogen in niobium were determined from sorption rate data obtained at 600°-700°C. A few experiments were made to determine diffusion rates by a technique based on measuring rates of outgassing of specimens in a vacuum of 10^{-6} to 10^{-5} mm Hg at various temperatures. The apparatus and procedure have been described previously (5, 6). The rates of hydrogen outgassing were measured for 0.6 cm diameter niobium cylin-

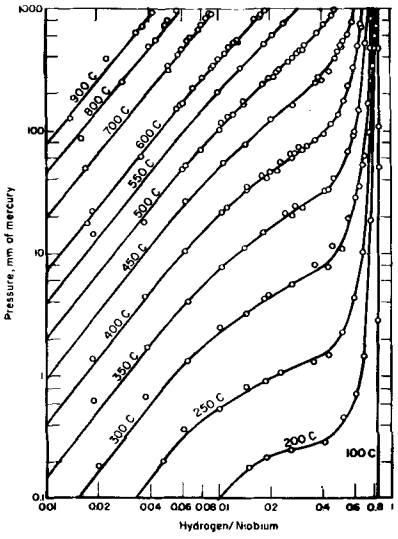

Fig. 1. Logarithmic plot of isotherms in the niobium-hydrogen system.

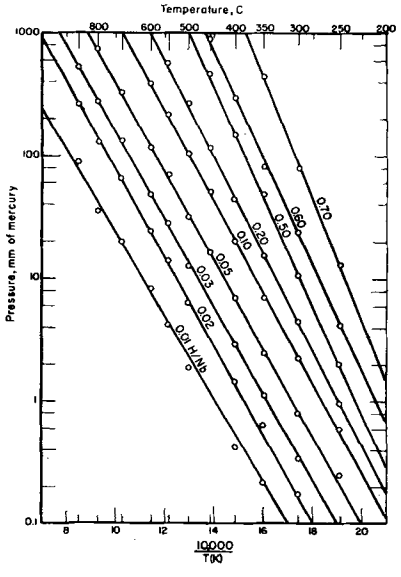

Fig. 2. Representative isopleths for the niobium-hydrogen system.

ders initially containing 0.03 to 0.06 H/Nb atomic ratio.

Results and Discussions

Equilibria

Equilibrium data obtained in the present study have been combined with those previously reported for the niobium-hydrogen system to give comprehensive coverage of the ranges 100°-900°C, 0.1-1000 mm Hg pressure, and 0.01-0.85 H/Nb ratios. Figure 1 is a logarithmic plot of equilibrium pressure against composition for various temperatures. It is seen that none of the isotherms show invariant pressures. This indicates that there is no two-phase region within these ranges. Equilibrium data could not be obtained at lower temperatures and pressures because of the extremely long times required.

Equilibria in the niobium-hydrogen system were interpreted in terms of the conditions required to form various products (solid solutions) having definite H/Nb ratios as discussed in the previous paper

Table I. Thermodynamic data for formation of various niobium-hydrogen compositions

Composition H/Nb ratio	Constants in $\log_{10} P_{mm} = -A/T + B$		$-\overline{\Delta H}$, kcal/mole H_2	$-\overline{\Delta S}$, cal/mole H_2·degree
	A	B		
0.01	3478	4.833	15.90 ±0.20	8.93 ±0.25
0.02	3592	5.490	16.40 ±0.13	11.94 ±0.18
0.03	3567	5.770	16.33 ±0.07	13.22 ±0.09
0.05	3575	6.170	16.40 ±0.11	15.05 ±0.15
0.10	3688	6.801	16.90 ±0.12	17.94 ±0.14
0.20	3953	7.548	18.09 ±0.04	21.36 ±0.06
0.30	4149	8.030	18.99 ±0.05	23.57 ±0.07
0.40	4301	8.403	19.70 ±0.12	25.27 ±0.19
0.50	4424	8.765	20.20 ±0.14	26.93 ±0.23
0.60	4319	8.895	19.80 ±0.29	27.52 ±0.47
0.70	5005	10.670	22.90 ±0.71	35.65 ±0.97

(1). For a given composition, the equilibria can be expressed by the equation,

$$\log_{10} P_{mm} = -[A/T(K)] + B \qquad [1]$$

From plots of the logarithm of the equilibrium pressure against reciprocal temperature, various isopleths are obtained from which the constants, A and B, can be calculated. Several representative isopleths are shown in Fig. 2. Values of the constants determined by the method of least squares are given in Table I. Using the familiar Gibbs-Helmholtz and van't Hoff equations, and defining the activity of hydrogen as equal to the inverse hydrogen pressure in atmospheres, the constants can be defined as,

$$A = -\overline{\Delta H}/2.303\ R \qquad [2]$$

and

$$B = -\overline{\Delta S}/2.303\ R + \log 760 \qquad [3]$$

Partial molar heats of solution, $\overline{\Delta H}$, and partial molar entropies, $\overline{\Delta S}$, calculated from Eq. [2] and [3] are also given in Table I. It is seen that there is a general increase in the magnitude of the partial molar heat of solution and entropy with hydrogen composition.

X-ray diffraction measurements were made at room temperature to 400°C on niobium and on specimens containing 0.097, 0.24, and 0.54 H/Nb ratios. Data were obtained from x-ray patterns of

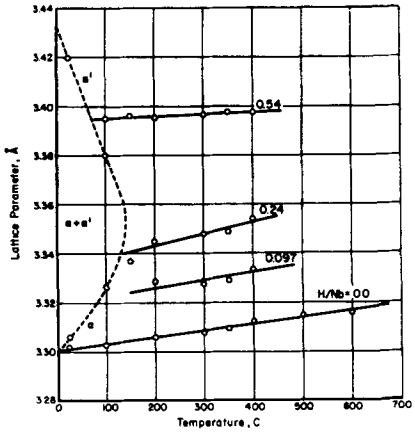

Fig. 3. Variation of lattice parameter with temperature and composition.

the specimens contained in sealed quartz capillaries. In all cases body-centered cubic structures were found. The variation of lattice parameters with temperature and composition are shown in Fig. 3. Specimens having compositions of 0.097 and 0.54 H/Nb contained two phases at room temperature and a single phase at 100°C and above. The specimen having a 0.24 H/Nb ratio showed two phases at room temperature and 100°C and one phase at 150°C and above. In the single phases, the lattice parameters increased with temperature and with hydrogen content. From the data for niobium, the thermal expansion coefficient for the metal was calculated to be 7.9 x 10^{-6}/°C. This is in good agreement with the handbook value of 7.1 x 10^{-6}/°C (7). It can be seen in Fig. 3 that the thermal expansion of the specimens containing hydrogen is approximately the same as that of the metal. The change in lattice parameter with hydrogen concentration was calculated to be 0.0023 ± 0.0002Å/1a/o hydrogen.

X-ray data in Fig. 3 can be used to outline a two-phase region in the niobium-hydrogen system. The limits of the two-phase region were calculated to be 0.024-0.75 H/Nb ratios at room temperature and 0.099-0.52 H/Nb ratio at 100°C. Also, by extrapolating the equilibrium data to lower pressures, isobars of 0.01 and 0.001 mm Hg were calculated which pass through the two-phase region. The phase diagram showing various isobars for the niobium-hydrogen system is presented in Fig. 4. It is seen that the critical point where the two phases become identical is at about 140°C, 0.01 mm of mercury hydrogen pressure, and 0.3 H/Nb ratio. It should be noted that the designation of the high-hydrogen phase which was reported (1) previously as beta has been changed to alpha prime. This is in keeping with the customary nomenclature for solid solutions showing a miscibility gap.

Values for hydrogen solubility in niobium at 1 atm pressure were reported recently by Paxton and Sheehan (2). Their results are compared with those of Sieverts and Moritz (8) and of this study in Table II. It is seen that solubilities of Paxton and Sheehan

Table II. Comparison of equilibria data at 1 atm pressure for the niobium-hydrogen system

Temp, °C	Equilibrium composition, H/Nb		
	Paxton and Sheehan	Sieverts and Moritz	Present study
800	0.047	0.051	0.051
600	0.16	0.15	0.16
500	0.22	0.39	0.42
400	0.55	0.64	0.68
300	0.66	0.73	0.77

below 600°C are considerably lower than those of the other studies. On the basis of the solubility study and high-temperature x-ray data, Paxton constructed a phase diagram for the niobium-hydrogen system showing the presence of the hydrides, Nb_2H having a hexagonal structure, and NbH having a body-centered cubic structure. The presence of the hydride Nb_2H is not indicated in the present study. Such a hexagonal structure has been attributed to impurities, probably nitrides, by Brauer and Hermann (9). The NbH structure of Paxton and Sheehan corresponds to the alpha prime structure of the present study.

Sorption Kinetics and Diffusion

Kinetic data for the sorption of hydrogen by niobium to produce compositions of 0.05, 0.10, 0.50, and 0.70 H/Nb were determined in the range 300°-700°C. Experimental conditions of temperature and pressure were determined from the isopleth (Fig. 2) of the desired product. Representative rate data are shown in Fig. 5 and 6. For every reaction up to 550°C, the initial sorption rate was linear (see Fig. 5). After a time depending on the conditions of the run, the rate decreased and stopped when equilibrium was established. Usually the reactions remained linear until about 40-50% of saturation was attained. At 300° to 450°C only the initial part of the sorption curves were obtained because of the very long times required to reach equilibrium. At 600°-700°C no initial linear rate was noted (see Fig. 6). A summary of all the linear rate constants ob-

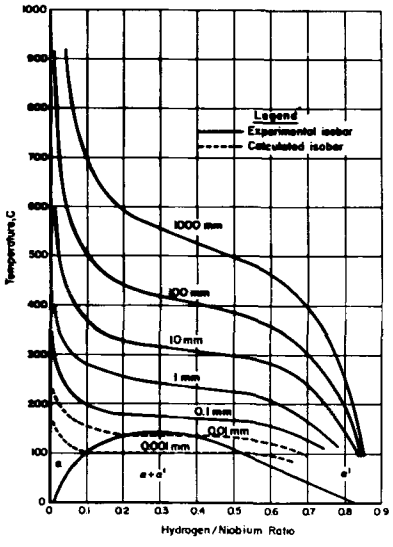

Fig. 4. Phase diagram of the niobium-hydrogen system showing various isobars.

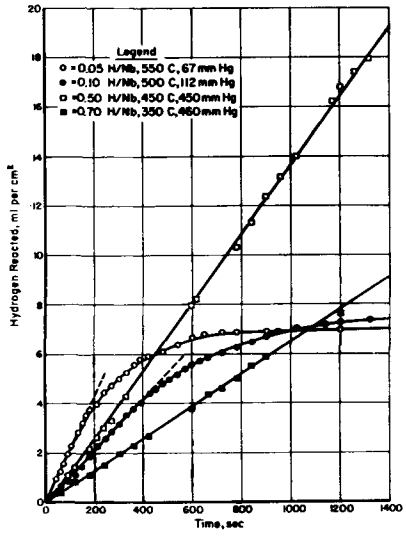

Fig. 5. Representative rate data for the reaction of hydrogen with niobium.

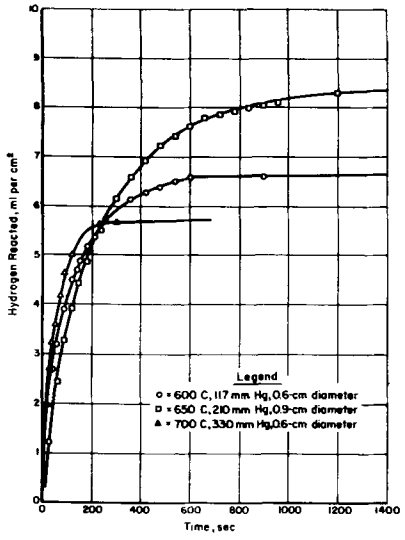

Fig. 6. Representative rate data for reaction of hydrogen with niobium to produce 0.05 H/Nb.

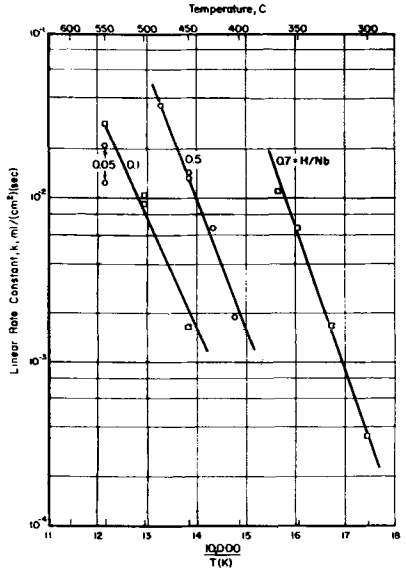

Fig. 7. Variation of linear rate constant with temperature for sorption of hydrogen in niobium.

tained at 300°-550°C is given in Table III. The variation of the initial linear rate constants with temperature for the various compositions is shown in an Arrhenius plot in Fig. 7. Data for the equation,

$$k = A \exp [-Q/RT] \qquad [4]$$

for each composition are given in Table IV. It was found that at a given temperature the initial linear rate increased with increasing hydrogen composition of the product. Also, the activation energies increased with H/Nb ratio.

Gulbransen and Andrew (3) found no consistent rate type for the niobium-hydrogen reaction from 250° to 900°C at pressures up to 5 cm. A linear reaction rate was reported only at 300°C and 21 mm of mercury hydrogen pressure. At these conditions, a composition of 0.6 H/Nb would be produced. The rate constant calculated from their data is 1.6 x 10^{-4} ml/cm²/sec. This rate constant is in line with the present work. However, at 700° and 900°C Gulbransen and Andrew found rather slow reaction

Table III. Summary of linear rate constants for the initial reaction to produce various hydrogen-niobium compositions

Composition, H/Nb	Temp, °C	Pressure, mm Hg	Rate constant × 10^3, ml/cm²·sec
0.05	550	67	21
	550	69	12
0.1	450	52	1.7
	500	112	9.1
	500	114	10
	550	218	29
0.5	400	145	1.9
	425	261	6.6
	450	450	14
	450	480	14
	480	744	37
0.7	300	83	0.35
	325	210	1.7
	350	460	6.7
	366	745	11

Table IV. Rate equations for the initial linear reaction to produce various hydrogen solutions

Composition, H/Nb	Constants in the Arrhenius equation: Frequency factor, A	Activation energy, Q, kcal/mole
0.10	1.32×10^7	32.6 ±1.0
0.50	1.39×10^9	36.4 ±1.3
0.70	2.18×10^{11}	38.7 ±1.5

rates. They show reactions continuing up to 2 hr using 3.3 mil (0.008 cm) thick specimens. In the present study, a specimen 0.6 cm in diameter attained equilibrium solubility in about 5 min at 700°C (see Fig. 6).

At 600°-700°C the sorption curves could be described by a diffusion equation in which sorption is initially parabolic. Modifying the derivation of Demarez, *et al.* (10) the solution of Fick's second law for diffusion in a finite cylinder can be expressed as

$$C/C_o = 1 - \frac{32}{\pi^2} \sum_{n=0}^{\infty} \sum_{m=1}^{\infty} \frac{1}{\beta^2_m (2n+1)^2} \exp\left\{ -Dt \left[\frac{(2n+1)^2\pi^2}{l^2} + \frac{\beta^2_m}{a^2} \right] \right\} \qquad [5]$$

where: C = average hydrogen concentration at time, t; C_o = final equilibrium hydrogen concentration; β_m = a root of the Bessel function, $J_o(\beta)$; D = diffusion coefficient; l = length of cylinder; and a = radius of cylinder.

The cylindrical specimens used in the sorption experiments had a length five times the radius ($l/a = 5$). Substituting $5a$ and l, Eq. [3] becomes,

$$C/C_o = 1 - \frac{32}{\pi^2} \sum_{n=0}^{\infty} \sum_{m=1}^{\infty} \frac{1}{\beta^2_m (2n+1)^2} \exp\left\{ \frac{-Dt}{a^2} \left[\frac{(2n+1)^2\pi^2}{25} + \beta^2_m \right] \right\} \qquad [6]$$

The theoretical curve obtained from Eq. [6] is shown in Fig. 8, in which C/C_o is plotted against

$(Dt/a^2)^{1/2}$ so as to yield a straight line for the initial parabolic behavior. The parabolic rate is followed until about 40% of saturation ($C/C_o = 0.4$) is attained. If the sorption of hydrogen is diffusion controlled, a proper choice of D would result in the experimental curves coinciding with that of theory. The excellent agreement of several experimental curves at 600°, 650°, and 700°C with theory is also seen in Fig. 8. It should be pointed out that the sorption curves obtained at the lower temperatures (350°-550°C) did not follow the theoretical diffusion curve. Probably some surface reaction affected the sorption rates.

The diffusion coefficients that were calculated from sorption and desorption rate data are summarized in Table V. It is seen that the diffusion coefficients from the outgassing (desorption) experiments are somewhat lower than those obtained from sorption rates. There was a poor agreement of the desorption rates with diffusion theory so that diffusion coefficients calculated from desorption are of doubtful worth. The diffusion rates obtained from sorption data give the best values for the diffusion coefficients for hydrogen in niobium.

Diffusion coefficients reported by Paxton and Sheehan (2) and included in Table V are considerably lower than those of the present work. Paxton and Sheehan infer that a slow surface reaction in the

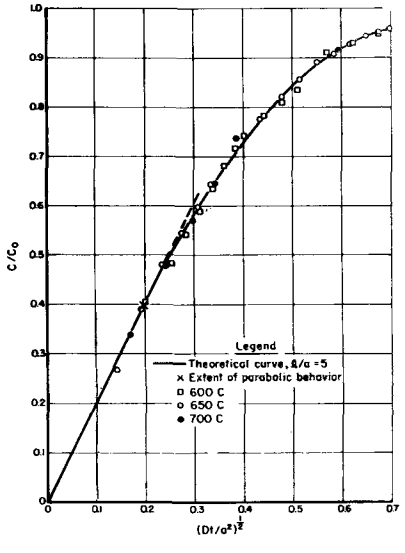

Fig. 8. Theoretical and experimental diffusion curves for sorption of hydrogen in niobium.

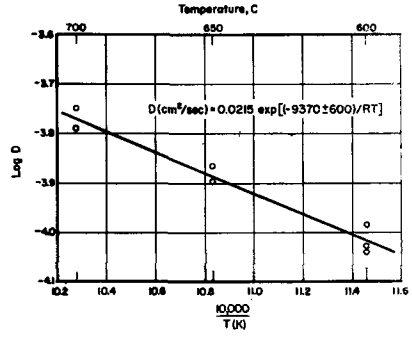

Fig. 9. Temperature variation of diffusion coefficients for hydrogen in niobium.

Table V. Diffusion coefficients for the niobium-hydrogen system

Temp, °C	Diffusion coefficient, $D \times 10^5$, cm² sec⁻¹		
	This work		
	From sorption	From desorption	Paxton and Sheehan (2)
500	—	0.58	0.00011
600	10	2.4	0.00063
600	9.4	—	0.001
600	9.2	—	—
650	14	4.3	—
650	13	—	—
700	16	—	0.0063
700	18	—	0.0036

permeation experiments may have affected their values of D. This is highly probable since they found that the niobium permeation membranes became discolored during their experiments.

The variation of the diffusion coefficient with temperature is described by the equation,

$$D = D_o \exp(-E/RT) \quad [7]$$

Data obtained from sorption rates are shown in Fig. 9. The equation for the best straight line through the points as determined by the method of least squares is

$$D = 0.0215 \exp[(-9370 \pm 600)/RT] \quad [8]$$

where 9370 ± 600 cal/g-atom is the activation energy. The entropy of diffusion can be calculated from D_o and E using the theory of Wert and Zener (11,12) for interstitial diffusion. For a body-centered-cubic lattice

$$D_o = 1/6\, a_o^2\, \nu \exp(\Delta S/R) \quad [9]$$

where a_o is the lattice constant and ν is the frequency of vibration of a solute atom in an interstitial position. The vibration frequency can be approximated from the relationship,

$$\nu = (E/2m\lambda^2)^{1/2} \quad [10]$$

where E is approximately equal to the activation energy, m is the mass of the solute atom, and λ is the distance between the interstitial positions ($\lambda = a_o/2$). From Eq. [7] and [8], ΔS for diffusion of hydrogen in niobium was calculated to be 3.8 cal/g-atom degree. According to theory this low positive value of ΔS is characteristic of interstitial diffusion and not diffusion through grain boundaries or other short circuiting paths.

Conclusions

Equilibria and x-ray studies show that in the ranges 100°-900°C, 0.1 to 1000 mm Hg pressure, and 0.01 to 0.85 H/Nb ratios the niobium-hydrogen system consists of a single-phase solid solution in which the basic body-centered-cubic structure of the metal expands as the hydrogen concentration increases. Equilibria in the system are best described by a series of isopleths since the heat of solution increases with hydrogen content. A two-phase region showing a miscibility gap was found at relatively low temperatures and pressures. Calculations based on the equilibrium and x-ray data place the critical point

where the two phases become identical at about 140°C, 0.01 mm of mercury hydrogen pressure, and 0.3 H/Nb ratio. The two phases, alpha and alpha prime, are both body-centered-cubic structures differing only in lattice parameter and are considered to be solid solutions of hydrogen in niobium.

Rates were obtained for the sorption of hydrogen by niobium to produce several solid solutions having hydrogen compositions of 0.05, 0.10, 0.50, and 0.70 H/Nb. The initial rates determined from 300° to 550°C were linear and increased with temperature and composition. At 600°-700°C sorption rates were diffusion controlled.

The diffusion coefficients obtained from desorption are lower than those obtained for sorption. Actually the desorption curves show a poor agreement with diffusion theory. Apparently some surface reaction influences the desorption rate.

Acknowledgment

The authors wish to express their thanks to Mr. D. A. Vaughan for making the many x-ray measurements. Work on this project was performed under AEC Contract W-7405-Eng-92.

Manuscript received April 27, 1959. This paper was prepared for delivery before the Columbus Meeting, Oct. 18-22, 1959.

Any discussion of this paper will appear in a Discussion Section to be published in the June 1960 JOURNAL.

REFERENCES

1. W. M. Albrecht, M. W. Mallett, and W. D. Goode, *This Journal*, **105**, 219 (1958).
2. H. W. Paxton and J. M. Sheehan, Report No. NYO-8040, Atomic Energy Commission (September, 1957).
3. A. E. Gulbransen and K. F. Andrew, *Trans. AIME*, **188**, 586 (1950).
4. W. M. Albrecht and M. W. Mallett, *This Journal*, **103**, 404 (1956).
5. C. B. Griffith and M. W. Mallett, "Vacuum Metallurgy," p. 147, Electrochemical Society, Inc., New York (1955).
6. W. M. Albrecht and M. W. Mallett, *Trans. AIME*, **212**, 204 (1958).
7. "Metals Handbook," American Society for Metals, Cleveland, Ohio, 1948-20.
8. A. Sieverts and H. Moritz, *Z. anorg. u. allgem. Chem.*, **247**, 124 (1941).
9. G. Brauer and R. Hermann, *ibid.*, **274**, 11 (1953).
10. A. Demarez, A. J. Hock, and F. A. Meunier, *Acta Met.*, **2**, 214 (1954).
11. C. Wert, and C. Zener, *Phys. Rev.*, **76**, 1169 (1949).
12. C. Zener, *J. Appl. Phys.*, **22**, 272 (1951).

Some Investigations of the Ag/AgCl in LiCl-KCl Eutectic Reference Electrode

Ling Yang and Robert G. Hudson

Metals Research Laboratory, Carnegie Institute of Technology, Pittsburgh, Pennsylvania

ABSTRACT

In electrochemical studies of metal chlorides dissolved in LiCl-KCl eutectic melt it is often desired to convert the metal-metal ion oxidation potentials E_a relative to a Ag/AgCl in LiCl-KCl eutectic reference electrode to those E_b based on the chlorine reference electrode. Such conversion can be made by using the emf E_c of the Ag/AgCl in LiCl-KCl eutectic/Cl_2 cell, and involves a correction term ΔE. By using cases where both E_a and E_b can be determined independently, studies have been made of the variation of ΔE with the nature and concentration of the metal ions in the melt, the temperature of the melt, the concentration of AgCl in the reference electrode, and the nature of the membrane separating the reference and metal electrodes. This information gives an estimate of the reliability of data obtained when the two reference electrodes are interchanged.

In electrochemical studies of chloride melts, the thermodynamic properties of metal chlorides dissolved in molten chloride solvents are often calculated from observed potentials between the metal electrodes and a chlorine reference electrode in these melts. The standard potentials may be determined experimentally or calculated from thermodynamic data (1). The information gained has been very helpful to our understanding of the constitution of these systems. There are occasions, however, where the chlorine electrode cannot be used directly. For instance, if the metallic ion of the chloride melt has more than one stable valence state under prevailing experimental conditions and chlorine gas can oxidize it from the lower to the higher state, the potential of the metal and its lower valence ion can be studied only with other reference electrodes. However, for the calculation of thermodynamic properties of the dissolved metal chloride, the observed potential must be converted to the chlorine reference electrode scale.

This problem occurred in our study of thermodynamic properties of polyvalent metal chlorides (MCl_n) dissolved in LiCl-KCl eutectic melt. A suitable reference electrode (2-9) was that suggested by Bockris, et al. (9), namely Ag/AgCl in LiCl-KCl eutectic/Pyrex membrane, which is of interest because of its simple construction. The Pyrex membrane avoids mixing of the electrolytes.

To convert the observed oxidation potential of a metal to such a reference electrode, to that of the same metal to a chlorine reference, we must know

Table I. Observed emf's of cell [c]

Mole fraction of AgCl, N	Temp, °K	Pressure, Cl_2, atm	E_c observed, v	dE_c/dT, v/°C
0.0146	768	0.976	1.1474	$+8.66 \times 10^{-5}$
	801		1.1493	
	823		1.1524	
0.0367	775	0.979	1.0834	-3.00×10^{-5}
	796		1.0825	
	804		1.0826	
	825		1.0818	
0.0452	769	0.968	1.0694	-3.33×10^{-5}
	798		1.0687	
	824		1.0680	
0.1966	767	0.975	0.9835	-1.55×10^{-4}
	803		0.9771	
	823		0.9743	
0.5025	767	0.975	0.9388	-2.33×10^{-4}
	773		0.9346	
	797		0.9294	
	825		0.9203	
1.0000	770	0.980	0.9010	-2.92×10^{-4}
	790		0.8950	
	810		0.8895	
	825		0.8842	

how they are related. Let E_a, E_o, and E_c represent, respectively, the emf's of the cells

M/MCl_n in LiCl-KCl eutectic/Pyrex membrane/AgCl in LiCl KCl eutectic/Ag [a]

M/MCl_n in LiCl-KCl eutectic/Cl_2 [b]

Ag/AgCl in LiCl-KCl eutectic/Cl_2 [c]

The cell reactions are

$M + n\,Ag^+ = M^{+n} + n\,Ag$ [A]

$M + n/2Cl_2 = M^{+n} + n\,Cl^-$ (MCl_n in LiCl-KCl eutectic) [B]

$n\,Ag + n/2\,Cl_2 = n\,Ag^+ + n\,Cl^-$ (AgCl in LiCl-KCl eutectic) [C]

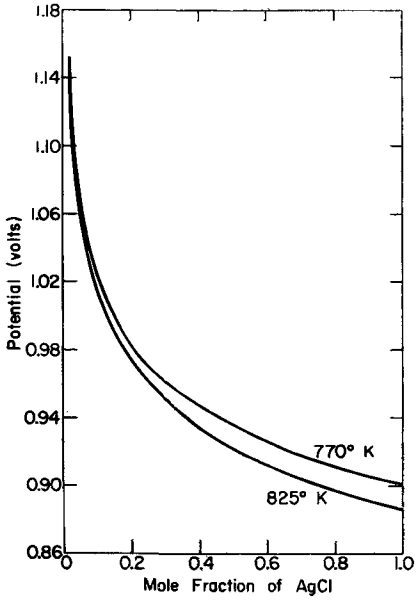

Fig. 1. Emf's E_c of cell [c] for various concentrations of AgCl.

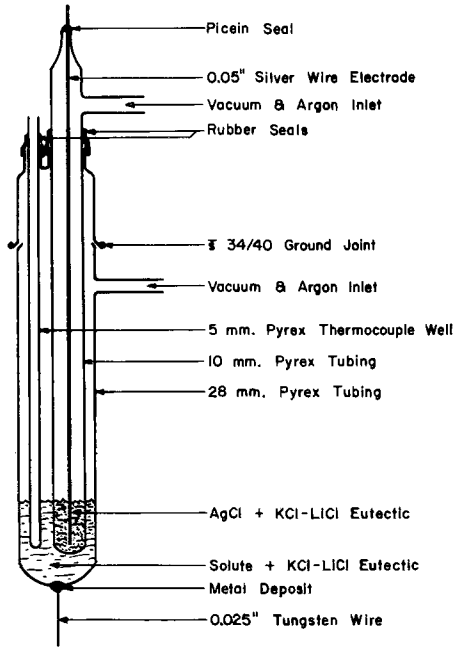

Fig. 2. Cell arrangement for measuring E_a

Define the quantity $\Delta E = E_a + E_c - E_b$. It can be shown from thermodynamics that

$$\Delta E = (1/F)\,[\mu(Cl^-\text{ of } MCl_n \text{ in eutectic}) - \mu\,(Cl^-\text{ of AgCl in eutectic})] + E_m \quad [1]$$

where the μ's are chemical potentials and E_m is the membrane potential in cell [a]. The conversion of E_a to E_b thus requires a knowledge of both E_c and ΔE. Sufficient data do not yet exist to calculate ΔE from Eq. [1]. Our paper attempts an experimental evaluation of ΔE from measured values of E_a, E_b, and E_c.

Determination of E_c

Potentials of metal-chlorine cells have already been studied over a range of temperatures and concentrations (10). The data E_c for the AgCl melts are quoted in Table I. It can be shown from these that mixtures of AgCl and LiCl-KCl eutectic behave as regular solutions, with AgCl deviating positively from Raoult's law.

The derivative dE_c/dT was obtained from the slope of a plot of E_c [after correction to $(Cl_2) = 1$] vs. T, it is essentially constant for a given composition, and its sign changes at a mole fraction N(AgCl) of about 0.03. The data of Table I, after correction to $(Cl_2) = 1$ and to 770° and 825°K, are plotted in Fig. 1. This figure can be used to estimate any value of E_c within or near the concentration and temperature ranges shown.

Experimental Estimation of ΔE

As shown in Eq. [1], ΔE consists of two parts, one due to the difference of chemical potential of chloride ion in the two melts, the other due to the membrane potential E_m. Bockris, *et al.* (9) compared the observed emf's of the concentration cells

Ag/AgCl (0.13M) in LiCl-KCl eutectic/Pyrex membrane/AgCl (0.05-1.3M) in LiCl-KCl eutectic/Ag [d]

with those calculated from the Nernst equation, by assuming the activity coefficient of Ag^+ constant in the range of compositions used. They concluded that the discrepancies were mainly due to the differences of activities of alkali metal ions across the membrane. In general, however, the situation may not be so simple, especially when the metal chloride solute on one side of the membrane is different from that on the other side. Exact evaluation of ΔE is impossible without knowing the conditions prevailing at the two melt-membrane interfaces and that inside the membrane, as well as the transport mechanism through the membrane. So far the study of membrane potential has been confined mostly to aqueous solutions (11); molten salt systems have not received much attention.

In spite of these difficulties, useful information may be obtained on the magnitude of ΔE by studying cases where independent measurements can be made on both E_a and E_b. In our previous investigations (10), measurements have been made of E_b. Therefore if we determine the corresponding values of E_a against AgCl reference electrodes whose E_c evaluated from Fig. 1, we should be able to calculate ΔE and find out how it is affected by the nature and concentration of the metal chloride in the melt, the concentration of AgCl in the reference electrode, the temperature, and the membrane material, e.g. Pyrex, Vycor, or quartz.

Measurement of E_a.—E_a was measured by using the arrangement shown in Fig. 2. The AgCl reference electrode consisted of a 0.05 in. diameter Ag wire (99.99% pure) dipped in a LiCl-KCl eutectic melt containing AgCl of the desired concentration and situated inside a Pyrex (Vycor or quartz) tube.

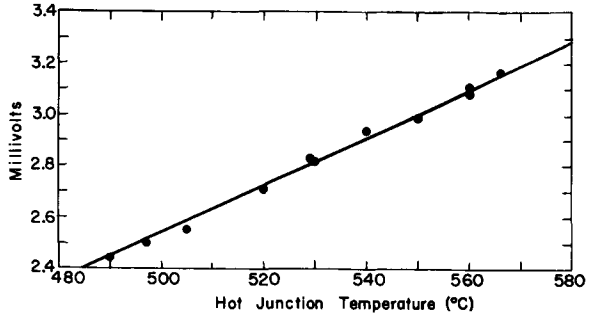

Fig. 3. Tungsten-silver thermal emf, cold junction 0°C, cold terminal of tungsten positive.

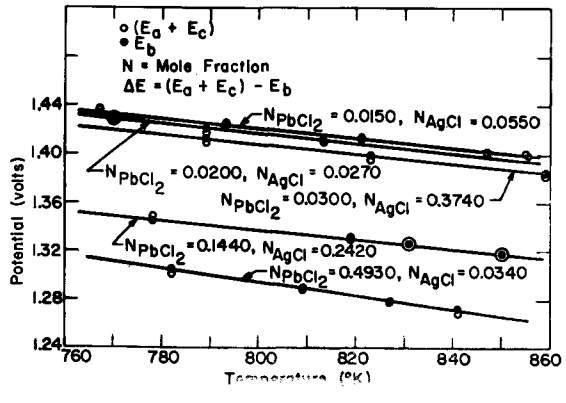

Fig. 4. Comparison of $E_a + E_c$ with E_b; $PbCl_2$ melts.

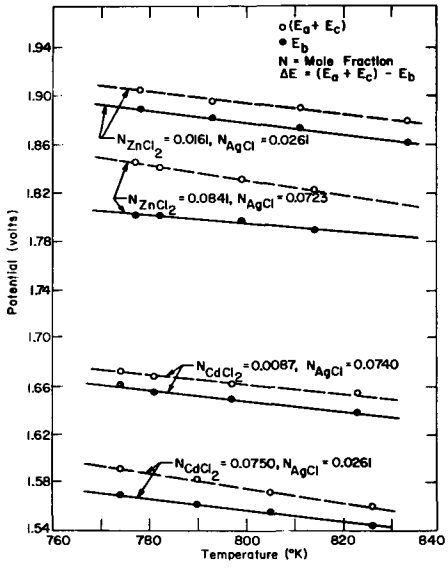

Fig. 5. Comparison of $E_a + E_c$ with E_b; $ZnCl_2$ and $CdCl_2$ melts.

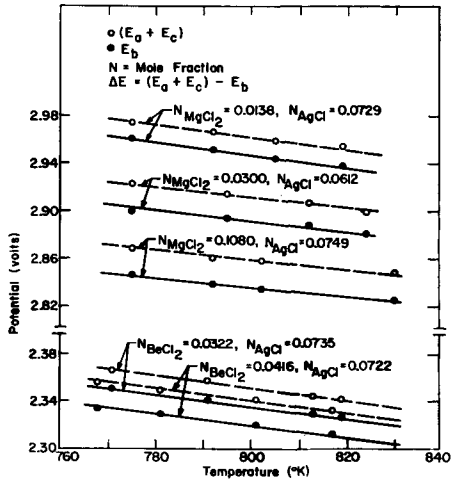

Fig. 6. Comparison of $E_a + E_c$ with E_b; $MgCl_2$ and $BeCl_2$ melts.

The bottom of the tube was sealed and blown thin to form the membrane. The exact thickness of the membrane was unknown but was found immaterial to the results obtained. The metal electrode consisted of the desired metal electrodeposited from the melt containing the metal chloride on a 0.025 in. tungsten wire sealed to the bottom of the cell. Deposition was carried out by using a graphite anode (not shown in Fig. 2) which was then withdrawn. The chlorine gas evolved was removed by pumping and the cell filled with purified argon. The potential between the Ag electrode and the metal electrode was followed to 0.1 mv on a Brown recorder connected in series with a L&N K-2 potentiometer and another potentiometer covering a range of 0-10 v until a steady value was reached. The temperature of the melt, as indicated by a calibrated chromel-alumel thermocouple, was changed to different values and the corresponding steady potentials recorded. Finally the melt was brought back to the original temperature and the steady potential reached was compared with that obtained before. The agreement was usually within ±2 mv. In addi-

Table II. Effect of membrane materials on $\Delta E = E_a + E_c - E_b$

MCl_n	N (MCl_n)	N (AgCl)	Temp, °K	E_a, mv Pyrex	E_a, mv Vycor	E_a, mv quartz	E_c	E_b, mv	ΔE, mv Pyrex	ΔE, mv Vycor	ΔE, mv quartz
AgCl	0.016	0.245	780	0.173	0.183	—	0.970	1141	2	12	—
			787	0.173	0.183	—	0.970	1141	2	11	—
			816	0.183	0.190	—	0.963	1145	1	8	—
$PbCl_2$	0.030	0.136	795	0.411	0.416	0.417	1.003	1410	4	9	10
$ZnCl_n$	0.016	0.026	778	0.800	0.826	0.826	1.104	1888	16	42	42
	0.084	0.072	778	0.802	0.820	0.819	1.042	1806	37	56	55
			799	0.791	0.807	0.808	1.040	1796	35	51	52
			815	0.782	0.799	0.801	1.039	1786	33	52	54

tion, the reversibility of the electrode reactions was established by the close agreement (within ±1 mv) between the steady potential obtained in the above manner and that obtained after a few milliamperes had been drawn from the cell for about 2 min. For metals which attack glass, such as La and Y, the tungsten wire was inserted from the top of the cell so that the metal deposit was not in contact with glass. Although only one Ag/AgCl reference electrode is shown in Fig. 2, in actual measurements, four or five of them can be put in the same melt for the study of the effect of AgCl concentration in the reference electrode or the nature of the membrane material on ΔE. The observed steady potential, after correction for the emf of the Ag-W thermocouple (Fig. 3), is E_a. The correction was made by converting the thermal emf's of Fig. 3 to those for a cold junction at room temperature. Thermal emf data were determined experimentally by coupling the tungsten wire and the silver wire used in this work. Methods for purifying and heating the melts were the same as described previously (10).

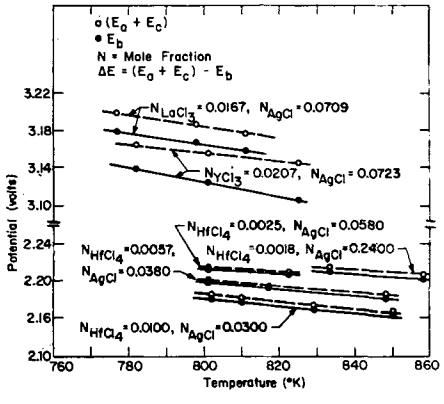

Fig. 7. Comparison of $E_a + E_c$ with E_b; $LaCl_3$, YCl_3, and $HfCl_4$ melts.

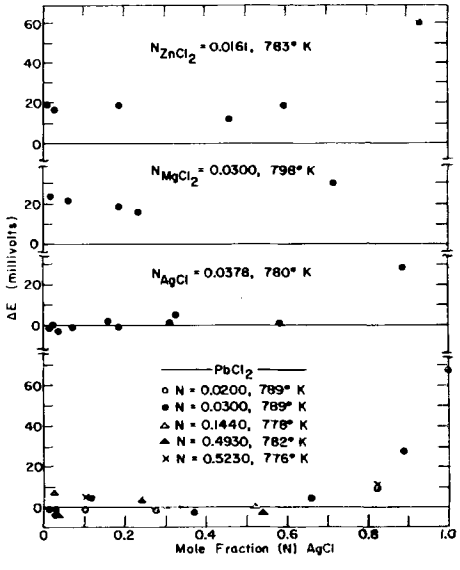

Fig. 8. Effect of AgCl concentration in the reference electrode on ΔE.

After the run, the AgCl reference electrode was raised out of the melt. Both the AgCl and the MCl_n melts were cooled quickly in an argon atmosphere and analyzed. On the basis of the analytical results, E_c was interpolated or extrapolated from Fig. 1, and E_b was taken from our previous data (10). ΔE was then computed from the data.

Variation of ΔE with various factors.—Results obtained are shown in Fig. 4-8, which can be summarized as follows:

1. *Nature of* MCl_n.—ΔE is negligible when MCl_n is AgCl (Fig. 8) and is less than a few millivolts for $PbCl_2$ (Fig. 4). This is true for a wide range of AgCl and $PbCl_2$ concentrations. For the others (Fig. 5-8), ΔE amounts to 5-40 mv. It is interesting to note that melts containing Ag^{++} and Pb^{++} which have less tendency to form complex ions with the chloride ions of the solvent have negligible ΔE, while those containing Be^{++}, Mg^{++}, Zn^{++}, Cd^{++}, which have been shown

Table III. Studies of charge carriers through Pyrex membrane

(a) AgCl, 525°C, 12 v, 5.0 ma, 2.36 hr

	Initial composition, % Ag	Final composition, % Ag	Ag gained, mg exp.	Ag gained, mg calcd.	Ag lost, mg exp.	Ag lost, mg calcd.
Positive side, AgCl (2.0904 g)	28.12	30.29	45.4	47.5		
Negative side, AgCl (2.0434 g)	28.12	25.93			44.8	47.5

(b) $ZnCl_2$, 533°C, 12 v, 8.0 ma, 2.31 hr

	Initial composition, % metal	Final composition, % metal	Zn gained, mg exp.	Zn gained, mg calcd.	Ag lost, mg exp.	Ag lost, mg calcd.
Positive side, $ZnCl_2$ (3.8168 g)	1.70	2.27	21.7	22.6		
Negative side, AgCl (1.2131 g)	11.99	5.97			73.1	74.5

to have a higher tendency to form complex ions exhibit higher ΔE (10).

2. *Concentration of* MCl_n.—For those melts having appreciable ΔE values, ΔE decreases as the concentration of MCl_n decreases (Fig. 5 and 6).

3. *Temperature.*—In the temperature range used in this work, ΔE does not seem to vary appreciably with temperature (Fig. 4-7), except for YCl_3 (Fig. 7).

4. AgCl *concentration of the reference electrode.*—Change of the AgCl concentration of the reference electrode over a wide range does not seem to affect ΔE appreciably (Fig. 8). However, for $N_{AgCl} > 0.6$, ΔE becomes abnormally high (Fig. 8).

5. *Membrane material.*—As shown in Table II, ΔE values for Vycor and quartz membranes are about the same, and they are higher than for Pyrex. Vycor and quartz are therefore less suitable membrane materials than Pyrex.

Some Transport Studies

In addition to the above investigations on ΔE, a few experiments have been performed to determine whether metal ions other than the Li^+ and K^+ are responsible for carrying the current through the Pyrex membrane. These were carried out by using the following cell arrangements with M = Ag or Zn,

M/MCl_n in LiCl-KCl eutectic/Pyrex membrane/

AgCl in LiCl-KCl eutectic/Ag [e]

A known amount of current was passed through each cell so that the Ag or Zn at the left dissolved into the melt while the Ag^+ in the melt at the right deposited out as Ag. The increase in the amount of Ag^+ or Zn^{++} in the melt at the left and the decrease in the amount of Ag in the melt at the right of the glass membrane were then determined by chemical analysis and compared with what would be expected on the basis of the amount of current passed through the cell if the membrane is impermeable to Ag^+ and Zn^{++}. The Ag^+ and the Zn^{++} contents of the melts were determined by precipitation and weighing as AgCl and $Zn(C_9H_6ON)_2$, respectively. The current of electrolysis was controlled manually and its time integral was determined by using a silver coulometer. Results are shown in Table III.

It can be seen that the amount of current carried by the Ag^+ or Zn^{++} through the Pyrex membrane, if any, cannot be more than a few per cent. Spectroscopic analyses of the glass used for making the membrane showed that it contains 0.02% Li_2O, 0.05% K_2O, and less than 0.0005% Ag_2O. The glass membrane in the AgCl cell, recovered after the electrolysis, was found to contain 0.75% Li_2O, 0.12% K_2O, and 0.001% Ag_2O. The large increase in the Li content seems to indicate that Li^+ is the predominant current carrier through the Pyrex membrane.

Reproducibility and Stability

The reproducibility of the Ag/AgCl in LiCl-KCl eutectic/Pyrex membrane reference electrode was studied by comparing the potentials of various reference electrodes made from melts of the same AgCl concentration N(AgCl) = 0.030 or 0.1020. Agreement was found to be within ±2 mv. The stability of this reference electrode was also investigated by following the change of the potential of AgCl concentration cells with N(AgCl) in the range 0.060 to 0.200, in LiCl-KCl eutectic melts with time. It was found that if oxygen and moisture were excluded from the melt, the change in potential was less than a few millivolts after the cells had been maintained at about 800°K for 40 hr.

The investigations described above cover some of the characteristics of the silver chloride-Pyrex reference electrode. Although the information available still does not allow us to calculate ΔE theoretically, these studies may serve to evaluate the reliability of potential data obtained in changing reference electrodes from AgCl to chlorine.

Acknowledgments

The authors wish to thank Drs. G. Derge and G. M. Pound of Carnegie Institute of Technology and Mr. Frank Kerze, Jr., of the U. S. Atomic Energy Commission for their interest in this work and their valuable help. They also are indebted to Drs. C. L. McCabe and P. Fugassi of Carnegie Institute of Technology, Dr. J. O'M. Bockris of the University of Pennsylvania and Dr. S. Senderoff of the National Carbon Company for stimulating discussions. This work is a part of a research program sponsored by the U. S. Atomic Energy Commission under Contract No. AT(30-1)-1432 and was presented at the June 1958 Symposium on Analytical Techniques for Molten Systems, sponsored by the American Chemical Society.

Manuscript received March 5, 1959.

Any discussion of this paper will appear in a Discussion Section to be published in the June 1960 JOURNAL.

REFERENCES

1. W. J. Hamer, M. S. Malmberg, and B. Rubin, *This Journal*, **103**, 8 (1956).
2. S. Senderoff and A. Brenner, *ibid.*, **101**, 31 (1954).
3. S. N. Flengas and E. Rideal, *Proc. Roy. Soc.*, **A223**, 443 (1956).
4. Yu K. Delimarskii and R. S. Khaimovich, *Ukrain. Khim. Zhr.*, **15**, 340 (1949).
5. Yu K. Delimarskii and A. A. Kolotii, *ibid.*, **16**, 438 (1950); **20**, 1169 (1954).
6. K. Hauffe and A. L. Vierk, *Z. Elektrochem.*, **53**, 151 (1949).
7. S. N. Flengas and T. R. Ingraham, *Canadian J. Chem.*, **35**, 1139, 1254 (1957); *This Journal*, **106**, 714 (1959).
8. H. A. Laitinen and C. H. Liu, *J. Am. Chem. Soc.*, **80**, 1015 (1958).
9. J. O'M Bockris, G. J. Hills, D. Inman, and L. Young, *J. Sci. Instrument*, **33**, 438 (1956).
10. L. Yang and R. G. Hudson, to be published in *Trans. Am. Metallurgical Society, AIME.*
11. "Membrane Phenomena," Discussion of the Faraday Society (1957).

The Oxygen-Evolution Reaction at Gold Anodes

II. Overpotential Measurements and Reaction Mechanism in Sulfuric Acid Solutions

Sidney Barnartt

Research Laboratories, Westinghouse Electric Corporation, Pittsburgh, Pennsylvania

ABSTRACT

The oxygen-evolution reaction at gold anodes was studied in sulfuric acid solutions, with and without added potassium sulfate, over the pH range 0 to 2.7 at 25°C. Overpotential measurements were made with an accuracy of ±1 mv in a cell having uniform current distribution over a spherical anode. Within current density limits imposed by the cell and the solution, Tafel's equation was obeyed to ±1 mv. The Tafel slope was $b = 2.303(3RT/4\mathbf{F})$ in each solution. At constant current density the overpotential was independent of pH or neutral salt additions. Several proposed mechanisms of the oxygen evolution reaction predict this independence, but in each case the theoretical Tafel slope is smaller than the observed value.

Overpotential data in the literature relating to the oxygen-evolution reaction have not been sufficiently accurate to settle the reaction mechanism unequivocally. In a previous paper (1) the factors involved in obtaining accurate overpotential measurements were evaluated with reference to a new cell design. Within current density (c.d.) limits dictated by this cell, it was found that steady-state measurements of oxygen overpotential at gold anodes in 0.1M H_2SO_4 were reproducible to ± 1 mv. Within the same deviation the overpotential (η) varied with c.d. (i) in accordance with Tafel's Eq. (2):

$$\eta = a + b \log i = a' + b \log i' \qquad [1]$$

where $i' = qi$ is the apparent c.d., q is the surface roughness, a and b are constants and $a' = a - b \log q$ is the extrapolated overpotential at 1 amp cm^{-2} apparent c.d. These measurements are extended in the present paper to include the effects of pH and neutral salt additions, effects which are diagnostic of the reaction mechanism (3-5).

Experimental Procedure

The experimental procedure was that of the previous paper, cell II and the solid gold electrode described therein (1) being used for almost all of the overpotential measurements. The electrode was polished to an almost mirror-bright surface with diamond polishing compound, ending with 3μ particle size. It was precleaned with solvents, cathodic treatment in hot 3M NaOH and immersion in 10M HNO_3. It was then made anode in 1M H_2SO_4 at 5 x 10^{-2} amp cm^{-2} for 5 min, the thin oxide layer thus formed being dissolved in 5M HCl, after which the electrode was rinsed thoroughly and inserted in the cell.

Sulfuric acid was distilled, and water redistilled from alkaline permanganate, in all-Pyrex stills. Reagent-grade K_2SO_4 was used without further purification; the experiments described below indicated that no deleterious impurities were present. Sulfuric acid solutions of concentration 0.01 to 1M, some with 0.5M K_2SO_4 added, were studied at 25.0°C. Overpotentials were determined by use of a saturated calomel reference electrode, as previously described (1).

The lower limit to the c.d. range for accurate measurements in 0.1M H_2SO_4 has been shown to be 3 x 10^{-5} amp cm^{-2}, and was attributed to cathodically produced H_2O_2 (1). Depolarization by H_2O_2 should depend on the cathode and cell geometry used, and not on solution concentration. Thus the lower c.d. limit of 3 x 10^{-5} was expected for all of the solutions studied, and this was found to be the case.

Although a brown film of hydrated Au_2O_3 formed slowly and continuously over the gold anode in each solution, the current efficiency for film formation was assumed to be sufficiently small to be negligible, as was shown for 0.1M H_2SO_4 (1).

The upper c.d. limit for accurate measurements varies with concentration and is determined either by the IR drop between the capillary tip and the electrode surface (V_{IR}) or by concentration polarization. The IR drop may be computed (1) from the equation:

$$V_{IR} = (ir_o^2/\kappa)\,[1/r_o - 1/(r_o + 3d - d/3)] \qquad [2]$$

where κ is the solution conductivity in mhos per centimeter, $r_o = 0.50$ cm is the radius of the spherical electrode, and $d = 0.02$ cm is the diameter of the capillary tip, the latter being positioned at a distance $3d$ from the electrode surface. The maximum c.d. i_1 for making accurate IR drop corrections is obtained from Eq. [2] by setting $V_{IR} = 0.01$ v (1).

In order to avoid concentration polarization effects an upper limit of 3% was selected as the maximum allowable change in H_2SO_4 concentration at the anode. The c.d. i_2 corresponding to this concentration change was calculated from the equation:

$$\Delta C = 10^3(1 - t_+)\, i\, l/2\mathbf{F}D \qquad [3]$$

by setting $\Delta C = 0.03\ C_o$, where ΔC is the increase in acid concentration at the anode surface, C_o the bulk concentration (mole/l), l the thickness of the diffu-

sion layer, **F** the faraday, D the diffusion coefficient, and t_+ is the hydrogen ion tranference number.[1] For the sulfuric acid solutions studied, the mean values $l = 0.005$ cm for gas-bubbling conditions (7), $t_+ = 0.82$ (8) and $D = 1.9 \times 10^{-5}$ cm^2 sec^{-1} (9) were substituted into Eq. [3] to obtain:

$$i_2 = 0.12\, C_o \qquad [4]$$

Table I lists the calculated values of i_1 and i_2. The smaller of these was taken to be the maximum allowable c.d. for each solution and was not exceeded in this investigation, as shown in the last column.

Results

For each solution studied, oxygen overpotential varied with c.d. in accordance with Tafel's equation. Average values of the measured Tafel constants are given in Table II. The overpotential at an apparent c.d. $i' = 10^{-4}$ amp cm^{-2} ($\eta_4 = a' - 4b$) is included as a reference value within the actual c.d. range studied. Also tabulated is the apparent exchange current density qi_o; this quantity may be calculated from

$$qi_o = 10^{-a'/b} \qquad [5]$$

and is of the order of magnitude of 10^{-22} amp cm^{-2}.

The maximum deviation of the experimental overpotential values from the Tafel lines described in Table II was ± 1 mv, with the exception that at 10^{-2} amp cm^{-2} apparent c.d. the η-values in 1M and 0.5M H_2SO_4 were 3-4 mv high. The latter discrepancy, although small, was reproducible. In each solution, the steady-state overpotential readings obtained with decreasing and increasing currents agreed within ±1 mv and duplicate runs with fresh batches of solution showed the same good agreement previously reported for 0.1M H_2SO_4 (1).

The variation of overpotential with pH at constant c.d. is shown for typical runs in Fig. 1. There is no consistent change in overpotential with acid concentration or with salt addition. The small variations from the mean values (lines of Fig. 1) found for 1M and 0.05M H_2SO_4 reflect changes in the Tafel a and not in the slope b. The mean values yield a linear Tafel plot with deviations ≦ 1 mv, as shown in Fig. 2; the constants from this plot are appended to Table II. The mean slope of 0.045_8 may be closely represented by $b = 2.303\ (3RT/4\mathbf{F})$, which is 0.0443 at 25°C.

The only pertinent[2] data in the literature for gold in sulfuric acid solutions is that of Hickling and Hill (11), for electroplated gold in 0.5M H_2SO_4 at 20°C. These are also plotted in Fig. 2 for comparison, the vertical length of each point representing their stated reproducibility of ± 10 mv. The latter data indicated a slope of 0.07, a value appreciably greater than that found in the present work taking into consideration the 5° temperature difference. The actual experimental points, however, are in good agreement with the curve of Fig. 2 at 10^{-4} and 10^{-3} amp cm^{-2} apparent c.d., taking $\partial\eta/\partial T = -3$ mv/degree (19). The deviation at 10^{-5} amp cm^{-2} indicates depolarization by competing anodic reactions.

[1] Equation [3] is an approximation applicable to ideal solutions. Corrections for deviations from ideality (6) were ignored because only small concentration changes are considered here.

[2] Other work on this system (12-15) did not include studies of steady-state overpotential.

Table I. Upper current density limit imposed by *IR* drop or concentration polarization calculations

Solution	κ, at 25°C, ohm^{-1} cm^{-1}	i_1, V_{IR} = 10 mv, amp cm^{-2}	i_2, ΔC = 0.03 C_o, amp cm^{-2}	Actual c.d. limit studied, amp cm^{-2}
1.00M H_2SO_4	0.39	0.08	0.12	0.01
0.50M H_2SO_4	0.21	0.04	0.06	0.01
0.10M H_2SO_4	0.046	0.01	0.012	0.01
0.050M H_2SO_4	0.025	0.005	0.006	0.005
0.010M H_2SO_4	0.0062	0.001	0.0012	0.001
0.10M H_2SO_4 + 0.50M K_2SO_4	0.099	0.02	0.012	0.005
0.010M H_2SO_4 + 0.50M K_2SO_4	0.085	0.02	0.0012	0.001

Table II. Measured Tafel constants for oxygen evolution at gold anodes in sulfuric acid solutions, 25.0° C

Solution	pH*	a', v	b, v	$\eta_4 = a' - 4b$, v	$10^{22}\, qi_o$,** amp cm^{-2}
1.00M H_2SO_4	0.05	0.988	0.046_3	0.807	5
0.50M H_2SO_4	0.38	0.983	0.046_3	0.798	6
0.10M H_2SO_4†	1.01	0.977	0.045_0	0.797	2
0.05M H_2SO_4	1.28	0.975	0.045_2	0.794	3
0.01M H_2SO_4	1.86	0.975	0.044_8	0.796	2
0.10M H_2SO_4 + 0.50M K_2SO_4	1.63	0.980	0.045_2	0.799	2
0.01M H_2SO_4 + 0.50M K_2SO_4	2.71	0.979	0.045_5	0.797	3
Mean Tafel Line††		0.979	0.045_3	0.798	3

* Standardized with 0.1M HCl, $pH_s = 1.10$ at 25°C (10).
** qi_o is the exchange current per apparent cm^2 of electrode surface.
† Data from previous paper (1).
†† From Fig. 2.

Discussion

Theoretical values of the Tafel slope and of other parameters useful for interpretation of the experimental data have been compiled by Bockris (4) for various mechanisms of anodic oxygen evolution. Three of the mechanisms include rate-determining steps for which overpotential is predicted to be independent of pH or neutral salt additions in acid solutions, in agreement with the experimental results of the present study. These mechanisms are listed in Table III. In each case the predicted slope is smaller than the experimental value.

The theoretical slopes of Table III involve no assumptions as to the value of the symmetry factor β (3, 4), but do involve assumptions concerning the degree of coverage of the electrode surface with adsorbed radicals. The combination mechanism Ib, for example, wherein the slow step is the combina-

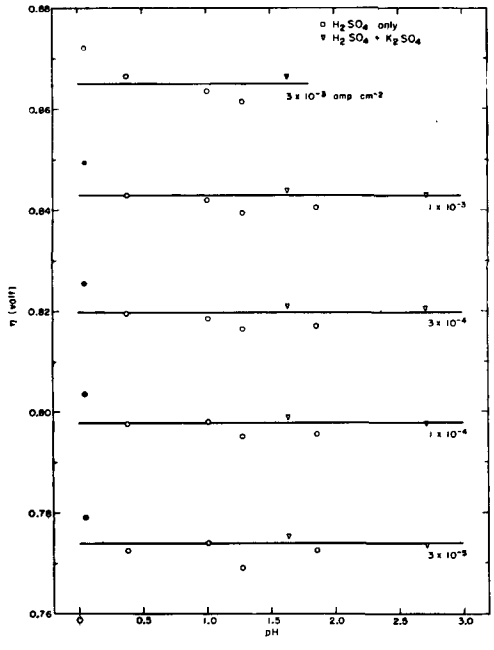

Fig. 1. Variation of oxygen overpotential with pH at constant apparent c.d., gold anodes in sulfuric acid solutions at 25.0°C.

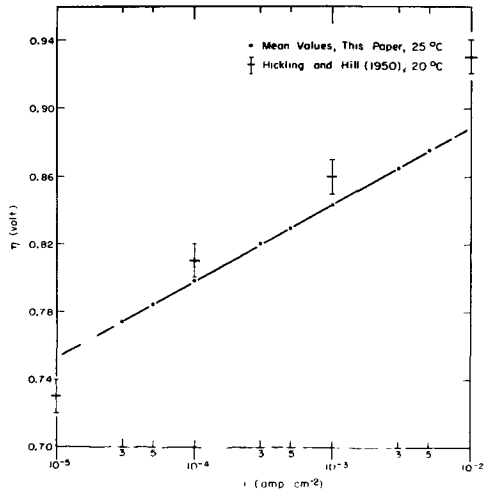

Fig. 2. Oxygen overpotential at gold anodes in sulfuric acid solutions, plotted vs. apparent c.d.

tion of two adsorbed hydroxyl radicals, corresponds to the Tafel slope listed ($RT/2\mathbf{F}$) only when coverage of the electrode surface with OH is very small. If the surface coverage is relatively high, the slope may be greater; this has been shown for an analogous case, the combination mechanism of hydrogen evolution (30). Thus the observed slope of 3/4 $RT/\mathbf{F}$ may correspond to one of the rate-determining steps listed in Table III when adsorption effects are taken into consideration. It may be concluded that the present data for gold are not in strict accord with any one of the mechanisms listed by Bockris (4). Further experimental data are needed to settle the mechanism unequivocally.

Oxygen overpotential at platinum in sulfuric acid solutions has been investigated by Bockris and Huq (16) under conditions of extreme purification (without, however, insuring uniform current distribution over the anode). The mean Tafel slope, measured in H_2SO_4 solutions with and without excess Na_2SO_4, was $b/2.303 = 3RT/2\mathbf{F}$ (± approximately 10%). This is double the value reported here for gold. Not one of the proposed mechanisms predict this slope (4), and the authors assumed that it was sufficiently close to $2RT/\mathbf{F}$ to indicate a discharge mechanism. With the additional assumption of $\beta = 0.5$, measurements of stoichiometric number plus pH and neutral salt effects led to the conclusion that discharge of water molecules is the rate-determining step on platinum.

The value $3RT/2\mathbf{F}$ observed by Bockris and Huq is the same as that previously found for platinum in 1933 by Hoar (17). A slope of less than half this value has been found recently for dilute solutions by Kheifets and Rivlin (29). Several earlier papers (see Table IV), however, reported the value $2RT/\mathbf{F}$, in agreement with the discharge mechanism.

The discharge mechanism is generally assumed also for lead anodes (covered with β-PbO_2) in sulfuric acid solutions on the basis of a slope of $2RT/\mathbf{F}$, although the other confirming parameters have not been measured for this metal. It is interesting that an α-PbO_2 electrode (over platinum) behaved quite differently, giving the slope (3/4) $RT/\mathbf{F}$ which was found here for gold.[3]

Reliable data for oxygen evolution on iron are exiguous. At pH 4, values of both b and i_o found by Wade and Hackerman (18) are remarkably close to those found here for gold. At a slightly lower pH (2.5), however, an appreciable decrease in b and in i_o (the latter by a factor of 10^6) was reported; this strong pH dependence merits confirmation.

In alkaline solutions, oxygen overpotential measurements to date have been discrepant (5). It may be concluded that little basis exists for selecting any one of the currently proposed mechanisms of anodic oxygen evolution as having general applicability for sulfuric acid solutions. There is a pronounced paucity of reliable experimental para-

[3] Revised data of Rüetschi, *et al.* (31) show a significantly higher slope for α-PbO_2 in 4.4M H_2SO_4 at 30°C, namely, 1.2 $RT/\mathbf{F}$.

Table III. Tafel slopes for mechanisms of anodic oxygen evolution in acid solutions, in which overpotential is independent of pH or neutral salt additions

		Mechanism	Rate-determining step	b/2.303
I	1a.	$H_2O \rightarrow OH + H^+ + e$		
	1b.	$2\,OH \rightarrow O + H_2O$	1b	$RT/2\mathbf{F}$
	1c.	$2\,O \rightarrow O_2$	1c	$RT/4\mathbf{F}$
II	2a.	$H_2O \rightarrow OH + H^+ + e$		
	2b.	$2\,OH \rightarrow H_2O_2$	2b	$RT/2\mathbf{F}$
	2c.	$H_2O_2 + OH \rightarrow HO_2 + H_2O$	2c	$RT/3\mathbf{F}$
	2d.	$HO_2 + OH \rightarrow O_2 + H_2O$	2d	$RT/4\mathbf{F}$
III	3a.	$H_2O \rightarrow OH + H^+ + e$		
	3b.	$2\,OH \rightarrow O + H_2O$	3b	$RT/2\mathbf{F}$
	3c.	$O + OH \rightarrow HO_2$	3c	$RT/3\mathbf{F}$
	3d.	$HO_2 + OH \rightarrow O_2 + H_2O$	3d	$RT/4\mathbf{F}$
		Experimental, Au/H_2SO_4 solutions (this investigation)		3 $RT/4\mathbf{F}$

Table IV. Tafel slopes for the oxygen-evolution reaction on various anodes in H_2SO_4 solutions

Anode metal; Oxide surface		H_2SO_4 molarity	t, °C	Apparent c.d. range, amp cm^{-2}	b/2.303 observed	qi_o amp cm^{-2}	Ref.
Au; $Au_2O_3 \cdot 3H_2O$ (1, 24)		0.01 to 1	25	3×10^{-5} to 10^{-2}	$3RT/4F$*	$(2 \text{ to } 6) \times 10^{-22}$	This paper
Pt;	(a)	0.0005 to 0.05	25	10^{-7} to 10^{-4}	$3RT/2F$**	$(1 \text{ to } 3) \times 10^{-10}$	(16)
PtO, $PtO_2\phi$ (25, 26)	(b)	0.05	25	10^{-7} to 10^{-5}	$3RT/2F$	3×10^{-11}	(17)
	(c)	0.05	10 to 30	2×10^{-4} to 5×10^{-3}	$2RT/F$	—	(20)
	(d)	0.04 to 0.5	21.6 (±1)	5×10^{-3} to 10^{-1}	$2RT/3F$***	—	(29)
	(e)	0.1	0 to 80	10^{-7} to 10^{-2}	$2RT/F$	2×10^{-9} (at 35°)	(19)
	(f)	0.5	20	10^{-5} to 1	$2RT/F$	10^{-0}	(22)
	(g)	1	25	5×10^{-4} to 5×10^{-2}	$2RT/F$	—	(21)
Pb;	(a)	1	25	5×10^{-4} to 5×10^{-2}	$2RT/F$	—†	(21)
PbO_2	(b)	3.8	30	not reported	$2RT/F$	10^{-10}	(23)
(Pt) β-PbO_2	(c)	4.4	31.8	7×10^{-5} to 2×10^{-3}	$2RT/F$	6×10^{-10}	(28)
(Pt) α-PbO_2	(d)	4.4	31.8	10^{-4} to 2×10^{-3}	$3RT/4F$	2×10^{-16}	(28)
Fe$\phi\phi$	(a)	pH 4.0	5	5×10^{-7} to 10^{-4}	$3RT/4F$	2×10^{-21}††	(18)
	(b)	pH 2.5	5	3×10^{-6} to 10^{-4}	$RT/2F$	2×10^{-27}††	(18)

* b and η unchanged by addition of excess K_2SO_4.
** b unaffected but η changed by addition of excess Na_2SO_4.
*** b increased rapidly with concentration above 0.5M.
ϕ Probably hydrated (27).
$\phi\phi$ No surface film with properties approaching that of a known bulk oxide.
† qi_o increased continuously with time.
†† $q = 1$; solution contained 0.1M Na_2SO_4.

meters, which are needed to validate a proposed mechanism. Therefore future studies of the oxygen-evolution reaction should stress the accumulation of accurate overpotential measurements.

Manuscript received May 22, 1959. This paper was prepared for delivery before the Philadelphia Meeting, May 3-7, 1959.

Any discussion of this paper will appear in a Discussion Section to be published in the June 1960 JOURNAL.

REFERENCES

1. S. Barnartt, *This Journal*, **106**, 722 (1959).
2. J. Tafel, *Z. physik. Chem.*, **50**, 641 (1905).
3. R. Parsons, *Trans. Faraday Soc.*, **47**, 1332 (1951).
4. J. O'M. Bockris, *J. Chem. Phys.*, **24**, 817 (1956).
5. J. O'M. Bockris, Editor, "Modern Aspects of Electrochemistry," Butterworths Publications Ltd., London (1954).
6. H. S. Harned and B. B. Owen, "The Physical Chemistry of Electrolytic Solutions," 2nd ed., p. 86, Reinhold Publishing Corp., New York (1950).
7. C. V. King, *This Journal*, **102**, 193 (1955).
8. W. J. Hamer, *J. Am. Chem. Soc.*, **57**, 662 (1935).
9. E. A. Hollingshead and A. R. Gordon, *J. Chem. Phys.*, **8**, 423 (1940).
10. R. G. Bates, "Electrometric pH Determinations," p. 47, John Wiley & Sons, Inc., New York (1954).
11. A. Hickling and S. Hill, *Trans. Faraday Soc.*, **46**, 550 (1950).
12. G. Armstrong, F. R. Himsworth, and J. A. V. Butler, *Proc. Roy. Soc.*, **143A**, 89 (1933).
13. G. Deborin and B. Erschler, *Acta Physicochim. URSS*, **13**, 347 (1940).
14. A. Hickling, *Trans. Faraday Soc.*, **42**, 518 (1946).
15. S. E. S. El Wakkad and A. M. S. El Din, *J. Chem. Soc.*, **1954**, 3098.
16. J. O'M. Bockris and A. K. M. S. Huq, *Proc. Roy. Soc.*, **A237**, 227 (1956).
17. T. P. Hoar, *ibid.*, **142A**, 628 (1933).
18. W. H. Wade and N. Hackerman, *Trans. Faraday Soc.*, **53**, 1636 (1957).
19. F. P. Bowden, *Proc. Roy. Soc.*, **126A**, 107 (1929).
20. W. Roiter and R. Jampolskaja, *Acta Physicochim. URSS*, **7**, 247 (1937).
21. P. Jones, R. Lind, and W. F. K. Wynne-Jones, *Trans. Faraday Soc.*, **50**, 972 (1954).
22. A. Hickling and S. Hill, *ibid.*, **46**, 550 (1950).
23. P. Rüetschi and B. D. Cahan, *This Journal*, **104**, 406 (1957).
24. F. Jirsa and O. Buryànek, *Z. Elektrochem.*, **29**, 126 (1923).
25. F. C. Anson and J. J. Lingane, *J. Am. Chem. Soc.*, **79**, 4901 (1957).
26. S. E. S. El Wakkad and S. H. Emara, *J. Chem. Soc.*, **1952**, 461.
27. S. Altmann and R. H. Busch, *Trans. Faraday Soc.*, **45**, 720 (1949).
28. P. Rüetschi and B. D. Cahan, *This Journal*, **105**, 369 (1958).
29. V. L. Kheifets and I. Ya. Rivlin, *Zhur. Priklad. Khim.*, **28**, 1291 (1955).
30. R. Parsons, *Trans. Faraday Soc.*, **54**, 1053 (1958).
31. P. Rüetschi, R. T. Angstadt and B. D. Cahan, *This Journal*, **106**, 547 (1959).

Technical Note

The Formation of Carbides at the Interface of Liquid Germanium and Graphite

A. Epstein[1] and I. G. Geib

Department of Physics, Purdue University, Lafayette, Indiana

In the course of an investigation into the properties of liquid germanium, it was found that Ge solidified in contact with graphite becomes joined to it if a metal soluble in liquid Ge is added. When pure graphite and pure Ge are used, a good mechanical joint is not obtained.

Spectroscopically pure Ge (10-15 g) was placed in a porcelain crucible and heated to about 1000°C at a pressure of about 10^{-6} mm Hg. A hollow spectroscopically pure graphite cylinder of 22 mm internal diameter and about 25 mm height and an inner, concentric cylindrical graphite probe of diameter 3.2 mm were lowered into the molten Ge and were maintained at the stated temperature for periods from 8 to 12 hr. When the entire apparatus was brought to room temperature, the graphite cylinder could be lifted out of the Ge ingot without difficulty. The procedure was repeated with currents of 5-10 amp maintained while the Ge was molten, but the presence of the radial electric field had no effect on the ease of separation of the Ge and graphite.

Either a tungsten rod or a tantalum rod of diameter 0.76 mm (0.030 in.) was placed in the cylindrical arrangement on one of the radii extending from the central graphite probe with its length parallel to the cylinder axis. The arrangement was lowered into the liquid Ge and maintained at about 1000°C for about 8 hr with and without an electric field. On cooling to room temperature, the graphite cylinder and rod could not be separated from the Ge. To examine the area of contact, it was necessary to fracture the ingot and cylinder. The material adhering tightly to the inner wall of the cylinder over the area of contact was examined by x-ray diffraction by obtaining powder patterns of specimens scraped from the inner wall. Ge was removed from the contact by etching with HF, HNO_3, and $Cu(NO_3)_2$ to disclose a layer on the area of contact. Powder patterns were obtained of material from these layers. The Ge-layer-C contact was checked for rectification with area contacts.

With the tungsten rod, the etching revealed a bluish-black layer on the area of contact. A powder pattern of material from this layer showed, in addition to graphite lines, lines which belong to a hexagonal structure, $a = 2.905$Å, $c = 2.839$Å. Westgren and Phragmen (1) found that WC is hexagonal with $a = 2.907$Å, $c = 2.836$Å (calculated from values in kX). Subtraction of these lines and the Ge and graphite lines from the boundary region pattern obtained before etching left 8 lines, 6 of which belong to a hexagonal structure, $a = 3.00$Å, $c = 4.73$Å. Westgren and Phragmen found that W_2C is hexagonal with $a = 2.992$Å, $c = 4.722$Å. This evidence indicates that a layer containing WC and W_2C is formed at the germanium-graphite interface. That the W_2C and not the WC is dissolved by the etchant agrees with a table of solubilities given by Brewer, *et al.* (2).

With the Ta rod, the layer exposed by etching away the Ge has a reddish-brown color. The powder pattern of the reddish-brown material contains a strong pattern, which agrees with that calculated for a NaCl type structure, $a_o = 4.456$Å, in addition to graphite and weak Ge and unknown lines. TaC is cubic (3), $a_o = 4.454$Å.

The Ge-tungsten carbide-C contact gave rectification ratios of better than 200 to 1. The Ge-TaC-C contact gave no measurable rectification. The formation of the carbides must result from the metal dissolving in the Ge, diffusing through the liquid, and reacting with the carbon on coming into contact with it. Qualitative observation of the thickness of the carbide layer indicated that the diffusion or reaction occurred much faster in the presence of an electric field, suggesting that this procedure might be useful for the purification of Ge.

Manuscript received June 15, 1959. This work was supported by a Signal Corps contract.

Any discussion of this paper will appear in a Discussion Section to be published in the June 1960 JOURNAL.

REFERENCES

1. A. Westgren and G. Phragmen, *Zs. f. Anorg. Chemie*, **156**, 27 (1926).
2. L. Brewer, et al., Thermodynamic and Physical Properties of Carbides, in L. L. Quill, Vol. IV-19B of Nuclear Energy Series, p. 40, McGraw-Hill Book Company, Inc., New York (1950).
3. R. W. G. Wyckoff, "Crystal Structures," Vol. I, Interscience Publishers, Inc., New York (1951).

[1] Present address: Monsanto Chemical Company, Dayton, Ohio.

A Study of the Zinc-Noble Metal Couple in Alkaline Solutions

Thedford P. Dirkse and Edwin G. Vrieland

Department of Chemistry, Calvin College, Grand Rapids, Michigan

ABSTRACT

A metal-like coating is formed frequently on copper or silver leads which are attached to the zinc electrodes in commercial zinc-alkaline cells. This coating is zinc or a zinc-rich alloy. The conditions under which this coating is formed have been studied, and several possible mechanisms for its formation are presented and discussed.

It is generally known to those in the battery industry that when silver or copper is coupled with zinc in an alkaline solution, a zinc-like deposit is formed on the noble metal (1). However, so far as is known, no satisfactory explanation has been given for this phenomenon. For that reason, a study of this reaction was undertaken.

Experimental

Thin metal strips about 1 x 5 cm were used, and coupling was accomplished by twisting the ends of the strips together or by wrapping a zinc strip or screen around the noble metal. In some of the runs the entire couple was completely immersed in the KOH solution while at other times a part of the couple was exposed to the air. Nickel, silver, copper, platinum, and lead served as the noble metals, but most of the work was done with Ag and Cu. All runs were carried out at room temperature in 35% KOH. C.P. reagents were used without further purification.

At first there was some difficulty in obtaining a coating on the Ag or Cu. Various anions usually found in commercial KOH, such as Cl^-, $CO_3^=$,$SO_4^=$, HO_2^-, were added to the electrolyte, but had no effect on the formation of the coating. Amalgamating the zinc electrode also failed to influence the formation of this deposit. However, addition of ZnO to the KOH solutions hastened the formation of this coating considerably. Coatings were formed on Ag, Cu, Pb, and Pt, but not on Ni.

The nature of the coating was checked by several methods. The deposit was very thin and, except for Ag, produced no detectable alteration in the x-ray pattern of the noble metal. With Ag, the coating gave two faint lines that could be attributed to a solid solution of Ag in Zn, and one line that is also found in the Zn pattern. The coating produced in 24 hr weighed only about half a milligram. It was removed from the noble metal by treatment with HCl or dilute HNO_3. Ordinary chemical analysis of this solution gave no certain indication of Zn due to the small amount of deposit. Analysis with a Todd Spectranal, however, did give definite evidence for the presence of Zn.

The potential of the coated Cu and Ag in these solutions was within 25 mv of that of pure Zn. This substantiates the suggestion that this coating is Zn or a Zn-rich alloy or solid solution.

When Ni was used as the noble metal it appeared as if a coating was formed on the Ni, but repeated attempts at analysis failed to produce any substantial evidence for Zn. In one experiment three cells were set up under identical conditions using, respectively, Ag, Cu, and Ni as the noble metals in KOH-ZnO solutions which had been deoxygenated. A coating seemed to form on all three electrodes but later, when they were rinsed, the Ni appeared shiny whereas the other two coatings were not affected. These latter coatings did contain Zn, but no certain evidence for Zn could be obtained from the Ni specimen.

There was also evidence that dissolved oxygen tends to hinder the coating process. The coating appeared to form more quickly in solutions which had been deoxygenated.

Discussion

The above results show that Zn is deposited on Cu, Ag, Pb, and Pt when these metals are coupled with Zn in strong KOH solutions containing dissolved ZnO. No such deposit is formed when Ni is coupled with Zn. Any mechanism for this process, then, must allow for a difference between Ni and these other metals. A few possibilities are considered below.

1. The possibility that this phenomenon is due to mere adsorption was ruled out by the fact that strips of Ag and Cu received no coating when they were immersed for 24 hr in a KOH solution containing dissolved ZnO.

2. A more likely explanation involves an electrochemical mechanism, i.e., the potential of reaction [1]

$$Zn + 4\,OH^- \rightarrow Zn(OH)_4^= + 2e \qquad [1]$$

which is the reaction at the Zn electrode, is sufficient to bring about reaction [2]

$$Zn(OH)_4^= + Ag + 2e \rightarrow Zn(Ag) + 4\,OH^- \qquad [2]$$

One requirement of this mechanism is that the energy or potential necessary to reduce Zn onto Ag or Cu is less than that needed to reduce it onto Zn. This is not a case of the simultaneous deposition of Zn and the noble metal (2). The noble metal was always coupled to the Zn and it is difficult to see how any noble metal ions could go into solution. Further, Straumanis and Fang (2) noted the formation of Cu-Zn, Ag-Zn, and Ni-Zn alloys. In our

work Ni definitely did not form an alloy with Zn. Yet Ni and Zn form much the same type of alloy system as do Ag-Zn and Cu-Zn. It is possible that a thin oxide film on the Ni prevents the formation of the Ni-Zn alloy here. However, H_2 is always evolved from the noble metal in such a couple and this could reduce the oxide film. Furthermore, a slight Zn deposit was formed on stainless steel (which also possibly has a thin oxide film) when it was used as the noble metal and coupled with Zn.

It has been shown that there is, in some instances, an undervoltage associated with the deposition of small amounts of metal (3). It was suggested that this undervoltage is dependent on the closeness of approach of the lattice parameters of the noble metal and the deposited metal. Using the data in reference (3) the nearest neighbor in Ag is 2.88Å; in Zn, 2.66Å; in Cu, 2.55Å; in Ni, 2.49Å; in Pb, 3.49Å; and in Pt, 2.77Å. The mismatch then is +31.9% for Pb; +8.3% for Ag; +4.1% for Pt; −4.1% for Cu; and −6.4% for Ni, where + indicates that the parameters are larger for the noble metal than for Zn. These values suggest that Cu and Ni should behave similarly. In both of these metals the atoms are closer together than in Zn. The small difference between Cu and Ni would hardly seem sufficient to account for the fact that Zn deposits readily on Cu but not on Ni. If an undervoltage phenomenon is responsible for this Zn coating, then the extent of the mismatch is not the controlling factor. If it were, then no coating should have been formed on Pb.

The phenomenon of undervoltage is associated with the deposition of thin metallic films such as are deposited on the noble metal of the zinc-noble-metal couple. That only thin films are produced argues for the fact that certain sites on the noble-metal surface are responsible for this undervoltage, and hence the x-ray diffraction pattern of the noble metal is but slightly altered, if at all, by the deposition of the zinc. If, for example, the active sites were submicroscopic pits on the surface, the Zn atoms could fit easily into such pits on Ag, Pb, and Pt, but would do so with difficulty on Ni. In considering the possibility of an undervoltage phenomenon here, it should also be noted that the work in reference (3) was carried out in acid solutions and the shift of potential did depend in part on the pH. The solutions used in this work were approximately 8M KOH. In such solutions the Zn^{++} concentration is only about 10^{-15}M. Any undervoltage associated with this process must be rather small because the Zn-noble metal couple had a potential only about 15 to 25 mv more anodic than that of Zn.

3. Another possible mechanism involves a chemical in addition to an electrochemical reaction at the noble metal surface. When Zn and the noble metal are coupled in KOH solutions, hydrogen gas is evolved at the noble metal, reaction [3].

$$2H_2O + 2e \rightarrow H_2 + 2\,OH^- \qquad [3]$$

The deposition of Zn at the noble metal then can be due to the reduction of the zinc-containing ions or $Zn(OH)_2$ by H_2, Eq. [4].

$$H_2 + Zn(OH)_2 \rightarrow Zn + 2H_2O \qquad [4]$$

However, the reaction does not proceed with molecular hydrogen. Hydrogen gas was bubbled for several hours over a Ag electrode in KOH-ZnO electrolyte, but no Zn was deposited or produced. This suggests that the reduction is accomplished with atomic hydrogen.

At such an electrode surface there is a competition between reactions [5] and [6].

$$2H + Zn(OH)_2 \rightarrow Zn + 2H_2O \qquad [5]$$

$$2H \rightarrow H_2 \qquad [6]$$

Whether or not Zn is deposited at a noble metal electrode in a Zn-noble metal couple will depend on the relative rates of reactions [5] and [6]. According to Bonhoeffer (4) the efficiency of different metals in causing the combination of hydrogen atoms is almost exactly in the reverse order to their overvoltage values, i.e., the higher the hydrogen overvoltage the slower the rate of reaction [6]. It is difficult to find comparable hydrogen overvoltage data for strongly alkaline solutions. However, it has been suggested (5) that the relative overvoltage values are the same in alkaline as in acid solutions. If this is true, then the hydrogen overvoltages vary in the following order: Pb>Cu=Ag>Ni>Pt (5, p. 420). This order is not to be accepted without question. When Zn was coupled with these metals, gas was evolved most copiously at Pb which would indicate a lower overvoltage value. This would favor reaction [6] rather than [5]. But, since Zn was deposited on Pb and Pt, it would seem then that it should also have been deposited on Ni.

It is possible that a third competing reaction enters in. This reaction involves the dissolving of Zn from the coating deposited on the noble metal. It has been noted that a coating that appeared to form on Ni disappeared during rinsing. Furthermore, when a coated Cu strip was placed in water, the Zn redissolved within a day or two. To check this further, Ag-Zn and Cu-Zn couples were allowed to stand in KOH-ZnO solutions for a week. Then the Zn strip was removed from each couple. After standing for a few days the coating began to disappear from the Cu but not from the Ag. After a week the Cu was clean but the Ag was still coated.

When Zn is deposited on a noble metal, a Zn-noble metal couple is formed and reactions [1] and [3] can take place on the coated metal. This, of course, opposes the deposition of Zn on the noble metal. This opposing process appears to occur most readily on Ni, to some extent on Cu, and hardly at all on Ag.

A likely explanation for this concerns the lattice parameters of these metals. As has been noted earlier, Ni has the smallest "nearest neighbor" distance, less than that of Zn. Consequently, Zn is deposited merely on the surface of the Ni and is not held there tenaciously. The "nearest neighbor" distance for Cu is larger than that for Ni but still it is smaller than that for Zn. Zinc, therefore, deposits with less difficulty on Cu than on Ni, is held more firmly, and shows less tendency to reenter the elec-

trolyte. With Ag, Pb, and Pt, the Zn fits easily into pits on the surface and, consequently, is held rather firmly there, perhaps forming solid solutions in which the activity of the Zn atoms is less than one. This reduces the tendency of Zn to reenter the solution.

An attempt was made to verify the suggestion that the Zn is produced by the reduction of $Zn(OH)_2$ or $Zn(OH)_4^=$ with atomic hydrogen. A strip of Ag was placed in KOH-ZnO electrolyte and the potential on this strip was gradually increased until bubbles of gas just became visible on the surface of the metal. The potential of the Ag was then about 20 mv more anodic than that of Zn. The Ag electrode was held at this potential for about 6 hr. Small amounts of H_2 were formed during this interval and, at the same time, a deposit of Zn formed on the surface of the Ag. When the Ag was more anodic than this, no visible deposit was formed.

In summary, it is suggested that the Zn coating formed on the noble metal in a Zn-noble metal couple placed in KOH-ZnO electrolyte results from the reduction of the dissolved Zn species by atomic hydrogen. Whether the Zn coating persists depends on how well the deposited Zn atoms fit into the lattice of the noble metal. The more easily the Zn atoms are accommodated the more likely a solid solution will be formed thereby reducing the activity of the deposited Zn atoms. This reduced activity lessens the tendency of the deposited Zn to redissolve.

The mechanism suggested above is intended to deal only with the first layer or film of Zn deposited on the noble metal. However, very little additional deposit of Zn takes place. The deposition in such a Zn-noble metal couple seems to stop after several hours and the evolution of H_2 practically ceases then also.

Acknowledgment

The authors acknowledge with thanks the helpful comments of S. Eidensohn and W. S. Herbert and the courtesy of the Electric Storage Battery Company in furnishing the materials used in this work.

Manuscript received June 17, 1959.

Any discussion of this paper will appear in a Discussion Section to be published in the June 1960 JOURNAL.

REFERENCES

1. J. M. Booe, *This Journal*, **99**, 197C (1952).
2. M. E. Straumanis and C. C. Fang, *ibid.*, **98**, 9 (1951).
3. R. C. De Geiso and L. B. Rogers, *ibid.*, **106**, 433 (1959).
4. K. F. Bonhoeffer, *Z. physik. Chem.*, **113**, 199 (1924).
5. G. Kortüm, J. O'M. Bockris, "Textbook of Electrochemistry," Vol. II, p. 423, Elsevier Publishing Co., Houston (1951).

The Anodic Dissolution and Electrolytic Polishing of Metals

J. K. Higgins

Metallurgy Division, Atomic Energy Research Establishment, Harwell, Didcot, Berks, England

ABSTRACT

An experimental study has been made, using the potentiostat technique, of the anodic dissolution and electrolytic polishing of nickel in hydrochloric acid. The effect of experimental conditions on the potential/current density curves and the value of the limiting current density has been investigated. Results have been interpreted on the basis of a simple diffusion mechanism, and complications arising from the thick salt films found in the more concentrated solutions have been considered. Some results showing the connection between polishing and passivity have been collected for copper anodes in potassium cyanide solutions containing potassium hydroxide.

Theories of the anodic dissolution of metals under conditions such that electrolytic polishing occurs have been referred largely to the case of copper in phosphoric acid (1). Some authors have emphasized the role played by salt and oxide films during polishing (2, 3). In order to extend the theory to include another metal besides copper the anodic behavior of nickel in hydrochloric acid was studied. Results confirm the general theory and provide clear evidence of the occurrence and importance of salt films during electrolysis. The system was studied by constructing potential/current density (C.D.) curves under various experimental conditions. The potentiostat technique (4) was used in which the anode potential is set at any arbitrary value, the current being controlled by the potentiostat to maintain this value. In order to investigate the relationship between electrolytic polishing and passivity some data on the anodic dissolution of copper in potassium cyanide were obtained under conditions favorable to oxide film formation, in strongly alkaline solution.

Experimental Technique

The electrolytic cell consisted of a 400-ml squat beaker containing 250 cc of electrolyte in all cases. The anodes of projected area 0.15 cm^2 were made by drawing wire (S.W.G. 16) to the appropriate length through a rubber bung in one end of a glass tube and filing the end of the wire flat. The glass tube fitted with the rubber bung and wire anode was mounted vertically, exposing about 2.5 mm of the wire to the electrolyte. The cathode was a Pt spiral of area 1 cm^2 in a tube whose end was closed with a filter paper plug. A Zn/0.1M — $ZnSO_4$ reference electrode was connected to the working electrode by means of a Luggin capillary, and was chosen be-

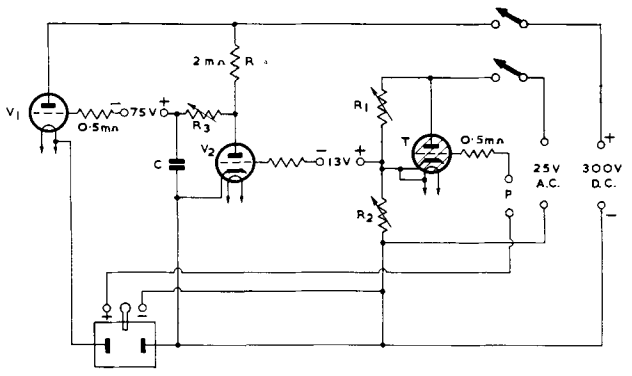

Fig. 1. Potentiostat A. V_1, Osram triode PX25; V_2, Brimar pentode 8 Al strapped as triode; T, Osram thyratron GTIC; C, 8 μF electrolytic condenser; R, 20,000 ohms; R_1, 100,000 ohms; R_2, 1000 ohms.

cause its potential always would be more negative than any it might be required to maintain. The potential of the electrode remained constant at −0.80 v on the hydrogen scale for about 4 weeks. All the anode potentials quoted are expressed on the standard hydrogen scale, the values being obtained by subtracting 0.8 v from the cell voltage of the combination anode (or working electrode)/reference electrode. The electrolyte was usually maintained at 20° ± 0.5°C.

The circuit diagram of the first electronic potentiostat is shown in Fig. 1 and is due to Hickling (4). Upon the application of 300 v d.c. the condenser C charges up through the resistance R, opposes the 75-v negative bias applied to the grid of the triode valve V_1 and thus allows a progressively increasing current to flow through V_1 and the cell. However, C can discharge through V_2 when its negative grid bias of 13 v is opposed by a voltage across V_2; this voltage is developed when the thyratron T fires. T is set 50 times a second by the 25-v a-c supply; it is adjusted to its critical tripping voltage by the automatic biasing potentiometer R_1-R_2. Into the grid circuit of the thyratron are placed the potentiometer P (connected to make the grid more negative) and the working/reference electrode combination in opposition. When the voltage of the electrode combination is greater than that set upon P, then the thyratron will fire, the current through V_1 will drop momentarily and will be controlled to maintain the potential of the working electrode at this point indefinitely. The 300, 75, and 13 v d.c. supplied were obtained from suitable rectifying circuits. The potentiostat could deliver 0.1 amp; its control circuit was sensitive to ± 0.01 v; the current taken from the reference electrode was less than 1 μamp.

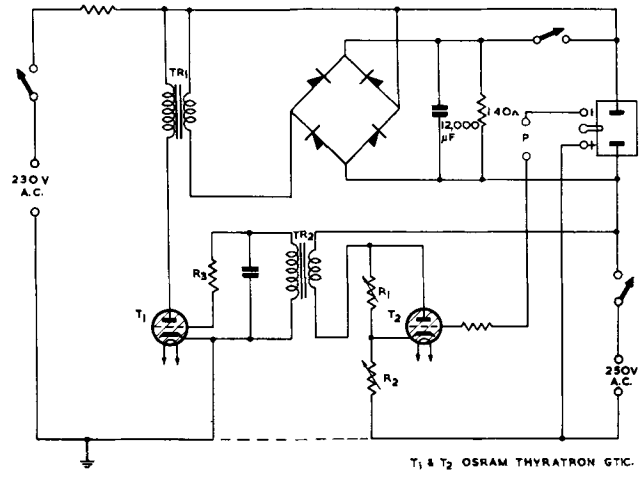

Fig. 2. Potentiostat B

The circuit of the second potentiostat, also due to Hickling, is shown in Fig. 2. The thyratron T_2 is included in a circuit similar to that used in the first potentiostat. When the voltage between the working/reference electrode combination is greater than that set on the potentiometer P, then T_2 fires and induces a voltage across the secondary of TR_2, 180° out of phase due to the condenser; this voltage being applied to the grid of T_1, this valve does not fire.

When the voltage of the working/reference electrode combination is less than that across P then T_2 does not fire, the biasing voltage on T_1 is absent, T_1 fires and induces a voltage across the secondary of TR_1 which is rectified, smoothed, and fed to the electrolytic cell. The current through the cell is thus controlled to maintain the potential of the working electrode indefinitely. In practice it was found that the negative bias on T_1 was not sufficient to withhold any one pulse of electricity, and consequently a 140-ohm resistance was connected across the output to by-pass some of the current. The output current is not limited by having to pass through a triode valve, and an output of several amperes could be obtained with the instrument at low output voltages; but as the output voltage increased the current fell off considerably. The two potentiostats are called A and B, respectively.

Experimental Results

Nickel in Hydrochloric Acid

Potential/C.D. graphs were obtained for nickel anodes in hydrochloric acid of concentration from 0.1*N* to 10.0*N*. The anode potential was increased in steps of 0.2 v, the current becoming constant after a few seconds, when it was read off. The current stabilized to a constant value almost immediately as the anode potential was reduced in steps of 0.2 v to give the descending curve. In Fig. 3A and B are given the curves obtained in 9*N* HCl.

The C.D. was undetectable in Fig. 3A until an anode potential of + 0.15 v was reached, when it rose rapidly for a small increase in potential, attaining a high value of about 0.40 amp/cm^2. As the potential was increased by a further small amount then the C.D. fell, and remained substantially constant with further increase in potential, the limiting C.D. region, until chlorine gas was evolved at about 2.5 v and the C.D. rose. The descending curve followed the ascending curve closely except that the high peak at C on the ascending curve did not recur. Before the limiting C.D. region was reached the anode was etched to a gray matt surface, while in the limiting C.D. region a thick green film formed, the anode being seen to be brightened underneath on removal from the electrolyte.

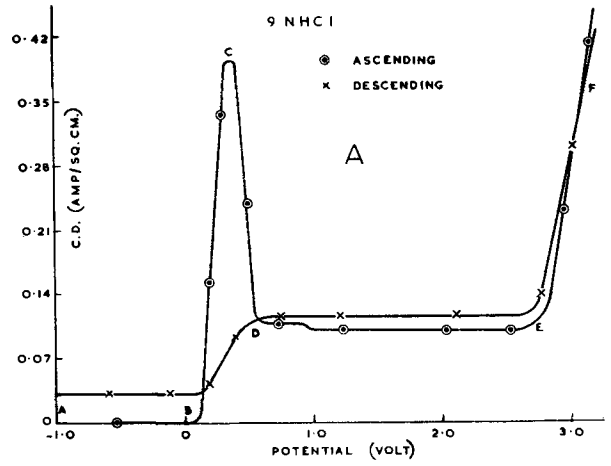

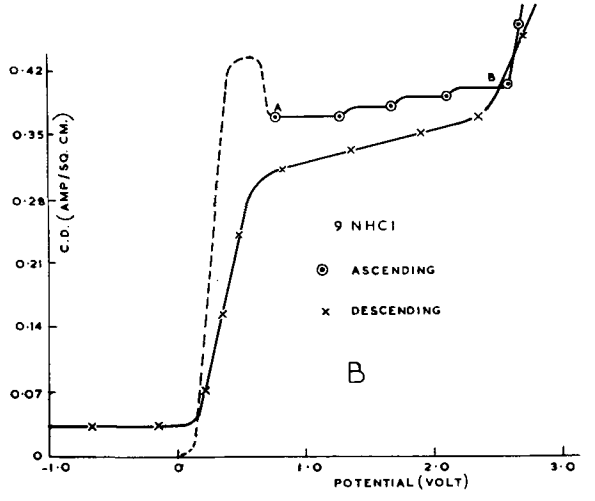

Fig. 3. A and B. Nickel in 9N HCl : Anode C.D. vs. Anode Potential.

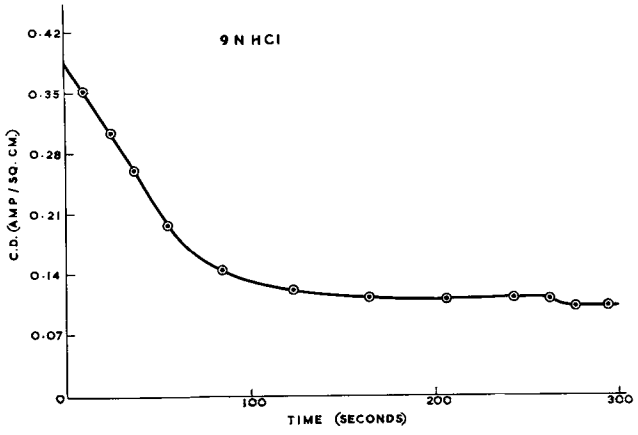

Fig. 4. Nickel in HCl : Limiting C. D. vs. Time

In order to remove the thick green film formed in the limiting C.D. region the following technique was adopted: the anode potential was increased in steps of 0.2 v, up to 1.0 v as in Fig. 3A; the circuit was broken for 1 min, then again completed, the anode potential being 1.0 v, i.e., greater than the potential at which the etching region and high peak value of the C.D. occurred at C in Fig. 3A. The C.D. rose rapidly to about 0.37 amp/cm^2 as recorded in Fig. 3B; the green film fell away to be replaced by a thick green layer of rapidly dissolving salt which streamed away from the anode; the anode was brilliantly polished. The rest of the graph was plotted as Fig. 3A.[1]

It is clear that in this electrolyte there are two limiting C.D.'s of approximately 0.10 and 0.40 amp/cm^2.[2] The operation of raising the potential to 1.0 v, breaking, and remaking the circuit will be called prepolarization.

If a prepolarized anode in 9*N* HCl is electrolyzed in the limiting C.D. region for about 5 min then I_{LIM} sinks gradually to the value for the nonprepolarized anode; the layer of rapidly dissolving salt is replaced by a thick green film. This is shown in Fig. 4, the anode potential being 1.0 v.

The nature of the anodic process occurring in each section of the curve was determined by carrying out constant-potential electrolyses at a series of increasing potentials and comparing the loss in weight of a nickel micro-electrode with the gain in weight of a cathode in a copper coulometer in series with the cell. Results obtained in electrolytes varying from 0.5*N* to 9.0*N* HCl showed that up to a potential of 2.5 v the current efficiency for dissolution of nickel in the nickelous state was practically 100%; above 2.5 v gas evolution set in and the current efficiency dropped.

Influence of experimental factors on I_{LIM}.—The limiting C.D.'s for the ascending curves were found to be reproducible with an accuracy of about ± 5% and ± 7% using potentiostats A and B, respectively.

In Table I are summarized the limiting C.D.'s for solutions of HCl of concentration from 10*N* to 0.1*N*.

The prepolarized values are the greater until the concentration drops below 7*N* HCl when the two sets of figures approximate the same values. Below a concentration of 7*N* HCl the thick green film at the nonprepolarized anodes does not appear, and all the electrodes are surrounded by a thick layer of rapidly dissolving salt streaming away. The limiting C.D.'s for both nonprepolarized and prepolarized anodes increase as the concentration of HCl decreases until 0.5*N* HCl when they decrease rapidly.

Potential/C.D. graphs were constructed for solutions of 7*N* HCl alone and with additions of 5, 10, 20, 25, and 30% glycerol to increase the viscosity, using both nonprepolarized and prepolarized anodes. Results are shown in Fig. 5, I_{LIM} being plotted against the reciprocal viscosity. For the prepolarized

Table I. Influence of concentration of HCl on I_{LIM} at 20°C

Concentration, g mole/l	10	9	8	7	6	4	2	1	0.5	0.1
Limiting C.D., amp/cm^2	0.07*	0.10*	0.24*	0.68*	1.18	1.83	2.37	2.54	1.59	0.19
Limiting C.D., amp/cm^2, prepolarized	0.34*	0.45*	0.54*	0.95*	1.22	1.83	2.24	2.43	1.62	0.19

* Values marked with an asterisk were obtained using potentiostat A, the rest potentiostat B.

[1] The limiting C.D. regions for the ascending and descending curves could not be brought any closer together by leaving the anode potential for 15 sec at each 0.2 v step for both Fig. 3A and B.

[2] When the C.D. passing in the limiting C.D. region is not constant a mean value is taken; the limiting C.D. is denoted in all cases by I_{LIM}.

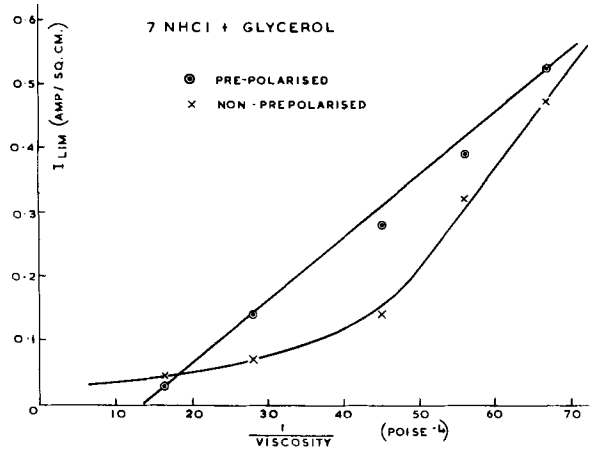

Fig. 5. Nickel in 7N HCl with glycerol additions : Influence of viscosity on limiting C.D.

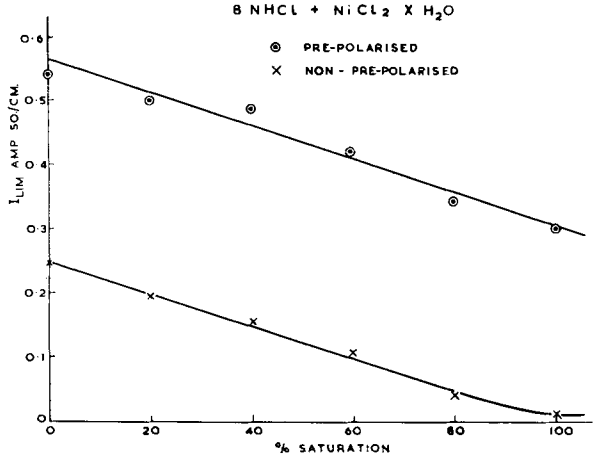

Fig. 6. Nickel in 8N HCl with nickelous ion addition; influence of dissolved nickel on limiting C.D.

anodes I_{LIM} varies linearly as the reciprocal viscosity, but this is not so for the nonprepolarized anodes.

Stirring solutions of 7*N* HCl + 20, 25, and 30% glycerol, at 450 rpm with a glass paddle stirrer, results in an increase in I_{LIM} of 3.9, 5.6, and 4.5 times for nonprepolarized anodes; increases for prepolarized anodes were 3.1, 5.6, and 3.7 times. In the case of 7*N* HCl + 20% glycerol, I_{LIM} increased from 0.09 to 0.35 amp/cm^2 for nonprepolarized anodes and from 0.14 to 0.43 amp/cm^2 for prepolarized anodes.

Rise in temperature from 20° to 70°C caused a rise in the limiting C.D. of 1.5 and 1.9 times for anodes in 0.5 and 6*N* HCl.

Solutions of 8*N*, 4*N*, and 0.5*N* HCl were saturated with A.R. $NiCl_2$. 6 H_2O by mechanical shaking for a few hours; by diluting these with the pure acid, solutions 80, 60, 40, and 20% saturated with nickel salt were obtained. Potential/C.D. curves were of the usual type. Typical curves of I_{LIM} against per cent saturation are given in Fig. 6 and 7 for 8*N* and 0.5*N* HCl.

For the nonprepolarized anodes in 8*N* and 0.5*N* HCl the values of I_{LIM} decrease linearly with per cent saturation of nickel salt; the value of I_{LIM} at 100% saturation is very nearly zero. Although there is a linear decrease in I_{LIM} for prepolarized anodes,

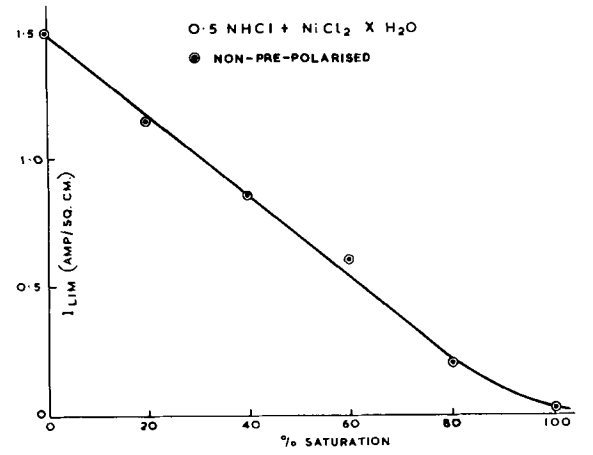

Fig. 7. Nickel in 0.5N HCl with nickelous ion addition; influence of dissolved nickel on limiting C.D.

the graph does not cut the x axis at 100% saturation.

Copper in Potassium Cyanide

The anodic dissolution and electrolytic polishing of copper in potassium cyanide has been discussed in a previous paper (2). An attempt was made to induce passivity gradually by slowly increasing the alkalinity of the electrolyte.

In Fig. 8 is given a typical potential/C.D. graph for a copper anode in 2M KCN. The anode was etched in the rapidly ascending region; it was polished in the limiting C.D. region, although the polish was not comparable in brilliance with those obtained at nickel anodes in hydrochloric acid or copper anodes in phosphoric acid. When the anode potential exceeded 1.0 v a thick brown film formed on it.

In Fig. 9, which is a graph for 2M KCN + 0.5M KOH solution, a pronounced dip occurs in both ascending and descending curves. If the concentration of KOH is increased to 0.75M, then the behavior shown in Fig. 10 is observed. The C.D. attains a high peak value of about 0.09 amp/cm^2 before it drops almost to zero on increasing the potential beyond 0 v; at 1.0 v the next process, formation of the brown film, sets in and the C.D. can again rise. The descending curve does not show a limiting C.D. region but the C.D. remains almost zero until about

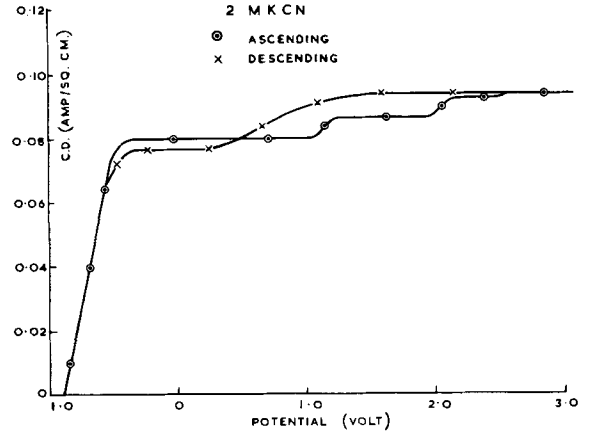

Fig. 8. Copper in 2M KCN; anode C.D. vs. anode potential

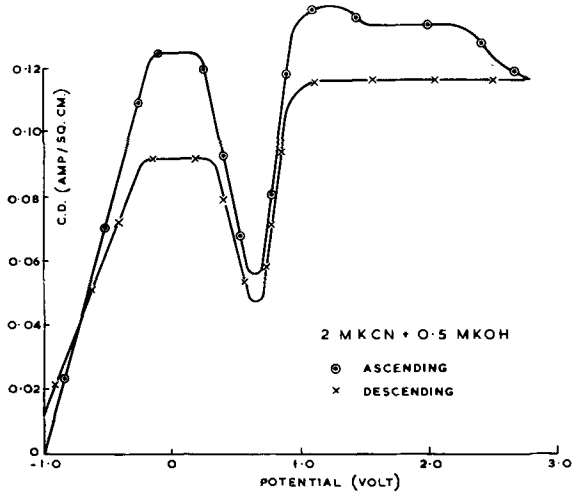

Fig. 9. Copper in 2M KCN + 0.5M KOH; anode C.D. vs. anode potential.

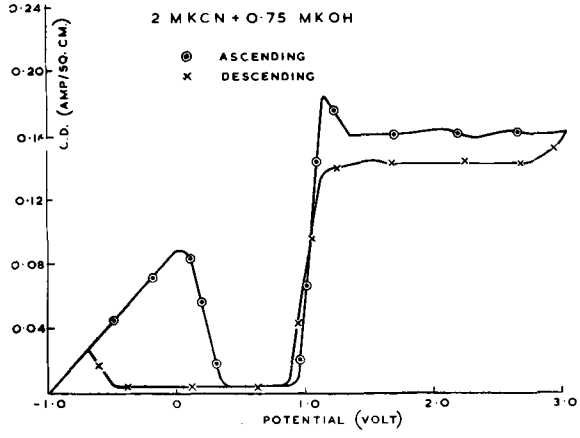

Fig. 10. Copper in 2M KCN + 0.75M KOH; anode C.D. vs. anode potential.

−0.5 v when it rises to the value for the ascending curve.[3]

The behavior in 2M KCN + 0.75M KOH solution up to a potential of 1.0 v is typical of an anode undergoing passivity (5) and the anode was not polished in this electrolyte. Passivity can be induced gradually by increasing the alkalinity of the medium in small steps.

Discussion

The increase in the limiting C.D.'s on stirring and the decrease when the viscosity is increased, together with the effect of temperature, constitute a clear indication that the anodic dissolution of nickel in hydrochloric acid is diffusion controlled at high current densities. The effect on the limiting C.D. of the addition of nickel salts to the solution suggests that it is the diffusion of the nickelous ion away from the anode which is rate determining.

Assuming Fick's law and the existence of a linear concentration gradient over the diffusion layer, the limiting C.D. is given by (2, 6).

$$I_{LIM}\ (\text{amp/cm}^2) = \frac{DFZ\ (C_s - C_o)}{\delta} \qquad [1]$$

[3] The ascending and descending curves in Fig. 9 and 10 could not be brought closer together by leaving the anode potenial for 15 sec at each 0.2-v step.

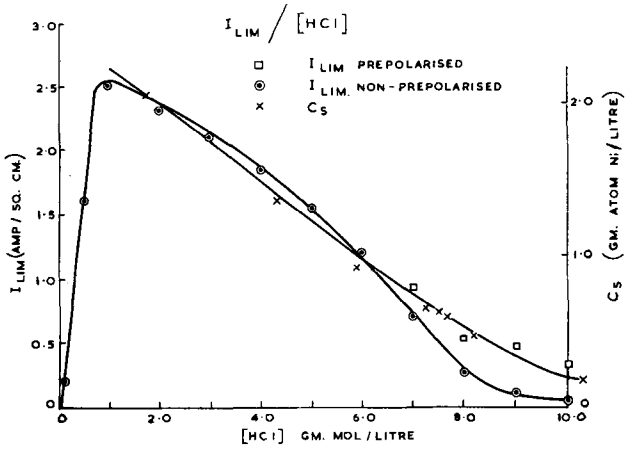

Fig. 11. Comparison of influence of HCl concentration on limiting C.D. and nickel chloride solubility.

where D is the diffusion coefficient of the nickelous ion, $\mathbf{F}$ the Faraday, Z the valency of the dissolving ion, and δ the thickness of the diffusion layer; C_s and C_o (g ion/liter) are the solubility and bulk concentration, respectively, of the nickelous ion. For a solution initially free from nickel $C_o = 0$, and we have

$$I_{LIM} = \frac{DFZ\,C_s}{\delta} \qquad [2]$$

According to Eq. [1] for constant values of C_s any factor such as stirring, tending to decrease δ, should increase I_{LIM}. Increasing the viscosity of the solution should decrease D and therefore I_{LIM}, while increase of temperature should increase D and therefore I_{LIM}. All these predictions are borne out by experiment.

For constant values of D and δ in Eq. [1], I_{LIM} should be proportional to $(C_s - C_o)$ and zero when $C_s = C_o$, i.e., at 100% saturation with nickel salt. This is confirmed experimentally as shown in Fig. 6 and 7 except for prepolarized anodes in 8N HCl.

If Eq. [2] is correct, I_{LIM} should be proportional to C_s in the simple acid solutions. In Fig. 11 the graphs of I_{LIM} and C_s are plotted against concentration of HCl; the shape of the two curves is similar, confirming the above prediction.

By substituting values of D, C_s, and I_{LIM} in [2] it is possible to calculate δ. The values of D were calculated from the equation (6)

$$D = \lambda RT/\mathbf{F}^2 \qquad [3]$$

where λ, reciprocal ohms, is the equivalent conductivity of nickel chloride at 18°C (7). The results obtained using λ values from the International Critical Tables for the solutions shown are: $D = 1.85 \times 10^{-5}$ cm^2/sec^{-1}, 18°C, 10N, 8N HCl; $D = 1.74 \times 10^{-5}$ cm^2/sec^{-1}, 18°C, 7N HCl; $D = 1.63 \times 10^{-5}$ cm^2/sec^{-1}, 18°C, 6N, 1N HCl. Substituting these values in [2] the values

Table II. Thickness of diffusion layer in HCl solutions

Concentration HCl, g mole/l	10	9	8	7	6	4	2	1
δ cm	0.0110	0.0112	0.0070	0.0033	0.0024	0.0024	0.0026	0.0028
δ cm, prepolarized	0.0021	0.0021	0.0030	0.0023	0.0024	0.0024	0.0029	0.0028

of δ for the nonprepolarized and prepolarized anodes are given in Table II for the simple HCl solutions. Apart from the first four values for the nonprepolarized anodes δ is between 0.002 and 0.003 cm; this is much less than the 0.03 cm normally found for cathodic diffusion processes in unstirred solutions. However, at the present vertical anodes and the high C.D.'s encountered there will be a large amount of convective stirring which will decrease δ as discussed by Tobias, Eisenberg, and Wilke (8). Values of δ for nonprepolarized anodes in the concentrated HCl ($> 7N$) solutions are higher than the rest. When the thick salt film is removed, i.e., the anodes are prepolarized, then δ is lowered and is of the same order as the values found in the dilute solutions. It is clear that the simple diffusion mechanism does not hold for the nonprepolarized anodes in the concentrated acid solutions.

The above conclusion is borne out by the graphs of Fig. 11; the I_{LIM} and C, curves agree most closely for the prepolarized anodes. Finally, Fig. 5, where I_{LIM} is plotted against the reciprocal viscosity for solutions of HCl containing glycerol, shows that the linear relationship holds for prepolarized anodes only. This relationship has been found for the anodic dissolution of copper in phosphoric acid and potassium cyanide; both are examples of diffusion-controlled processes (2). It would seem that the process in the dilute ($< 7N$ HCl) solutions is diffusion controlled as it is at the prepolarized anodes in the more concentrated ($> 7N$ HCl) solutions. At the nonprepolarized anodes in the concentrated solutions complications set in due to the formation of thick salt films.

The hydrate of nickel chloride stable in HCl solutions from 1.75 to 7.26N is the hexahydrate, at 7.5N the pentahydrate, and from 7.65 to 10.35N the tetrahydrate (9). It is probable that the thick salt films observed in HCl solutions more concentrated than 7N are films of the tetrahydrate; Fig. 11 shows that this salt, stable in concentrated acid solutions, is less soluble than the more hydrated forms.

If the prepolarized anode in 9N HCl is electrolyzed in the limiting C.D. region for about 5 min, then I_{LIM} sinks gradually to the value for the nonprepolarized anode (see Fig. 4); the diffusion layer is replaced by a thick light green film. It would seem at the prepolarized anode that the nickel first dissolves as an unstable species which then gradually reverts to the sparingly soluble tetrahydrate which forms a film on the anode.

Results for the dissolution of prepolarized anodes in 8N HCl, partly and completely saturated with nickel chloride, are puzzling (Fig. 6). All the evidence suggests that it is the reaction at the prepolarized anodes which is diffusion controlled, and yet it is the nonprepolarized anodes which show nearly zero I_{LIM} in solutions 100% saturated, as would be expected from Eq. [1] for a diffusion-controlled process. It may be because the prepolarized anodes are dissolving as an unstable species that I_{LIM} remains so high in solutions containing nickel chloride; when the nickel goes into solution directly as the stable tetrahydrate (nonprepolarized anodes) then the predictions of Eq. [1] are verified.

On the basis of the diffusion treatment given it is to be expected that in the limiting C.D. region, when the layer of electrolyte adjacent to the anode becomes saturated with salt, a film of salt will be deposited. This film usually dissolves as quickly as it is formed, its thickness depending on the solubility of the salt and its degree of hydration. Williams and Barrett (10) have identified the film formed on copper anodes in phosphoric acid as copper phosphate by electron diffraction measurements. It is invisible during electrolysis as are the films formed in the dilute HCl solutions at nickel anodes. In concentrated HCl solutions at nonprepolarized anodes the salt films are clearly visible, the electrode still being polished underneath.

The smoothing action during electrolytic polishing in the limiting C.D. region can be explained satisfactorily by assuming the absence of a concentration gradient of metallic cations between peaks and cavities in a roughened surface and consequently faster dissolution of the peaks. An additional factor aiding smoothing is the earlier deposition of a salt film in the cavities than on the peaks. However, while this theory is satisfactory for the dilute solutions of HCl, it is not sufficient to explain why nonprepolarized nickel anodes are polished underneath the thick salt film in the concentrated ($> 7N$) HCl solutions; the films are much thicker than the cavity depth of a few microns. Hoar and Mowat (3) have explained the absence of crystallographic etching in the limiting C.D. region by assuming that the metallic cations pass from the metallic surface into vacant sites in an oxide lattice, the oxide dissolving as fast as it is formed. The random distribution of vacant sites would then account for the absence of etch figures. If it is assumed that the oxide film is present underneath the salt film, then the brightening of the nickel in solutions where a very thick film of salt is formed can be understood. Probably both the smoothing and brightening mechanism are present at polishing anodes in dilute solutions.

It is well known from the work of Evans and others (5) that the occurrence of passivity is associated with the formation of a thin, coherent, insoluble oxide film on the anode. The fact that the transition from polishing to passivity behavior can be brought about gradually (Cu in KCN + KOH) by increasing the alkalinity of the electrolyte is evidence for the presence of a dissolving oxide film during polishing and leads to the view that polishing and passivity are two limiting cases of the same general phenomenon.

Conclusions

1. The anodic dissolution of nickel in dilute ($< 7N$) HCl solutions is diffusion controlled.

2. At prepolarized anodes in concentrated ($> 7N$) HCl solutions the dissolution is diffusion controlled.

3. At nonprepolarized anodes in conc. ($> 7N$) HCl solutions the simple diffusion mechanism breaks down.

4. The onset of thick salt film formation in the

more concentrated (> 7*N* HCl) solutions is associated with a decrease in the degree of hydration of the dissolving salt.

5. The state of the prepolarized anode is unstable; it reverts to the nonprepolarized condition in a short time.

6. Polishing in the dilute solutions can be explained satisfactorily by the differential solution of peaks and cavities due to different concentration gradients at peaks and cavities and the deposition of freely soluble salt films.

7. The brightening effect observed under very thick salt films in concentrated acid solutions is best explained by the dissolving oxide theory of polishing.

8. Passivity can be induced gradually in a polishing bath by increasing the alkalinity of the electrolyte in steps and this supports the theory mentioned in 7.

Manuscript received March 3, 1959.

Any discussion of this paper will appear in a Discussion Section to be published in the June 1960 JOURNAL.

REFERENCES

1. P. A. Jacquet, *Trans. Electrochem. Soc.*, **69**, 629 (1936); *Bull. Soc. Chim.*, **3**, 706 (1936); W. C. Elmore, *J. Appl. Phys.*, **10**, 724 (1939); **11**, 797 (1940); H. F. Walton, *This Journal*, **97**, 219 (1950); J. Edwards, *J. Electrodepositors, Tech. Soc.*, **28**, 133 (1952); J. Edwards, *This Journal*, **100**, 189*C*, 223*C* (1953).
2. A. Hickling and J. K. Higgins, *Trans. Inst. Met. Finishing*, **29**, 274 (1953).
3. T. P. Hoar and J. A. S. Mowat, *Nature*, **165**, 64 (1950); *J. Electrodepositors' Tech. Soc.*, **26**, 7 (1950); T. P. Hoar and T. W. Farthing, *Nature*, **169**, 324 (1952).
4. A. Hickling, *Trans. Faraday Soc.*, **38**, 27 (1942).
5. U. R. Evans, *Nature*, **126**, 130 (1930); L. Stephenson and J. H. Bartlett, *This Journal*, **101**, 571 (1954).
6. S. Glasstone, "An Introduction to Electrochemistry," p. 449, D. Van Nostrand & Co., New York (1949).
7. International Critical Tables *6*, 231.
8. C. W. Tobias, M. Eisenberg, and C. R. Wilke, *This Journal*, **99**, 359*C* (1952).
9. Seidel, "Solubilities of Inorganic and Metal Organic Compounds," Vol. 1, p. 1342, D. Van Nostrand & Co., New York.
10. E. C. Williams and M. A. Barrett, *This Journal*, **103**, 363 (1956).

An Investigation of Chemical Variables Affecting the Formation of Films on Copper in Aqueous Solutions

W. H. Davenport, V. F. Nole, and W. D. Robertson[1]

Chase Brass and Copper Company, Waterbury, Connecticut

ABSTRACT

The growth of copper oxide films in aqueous solutions has been studied by an electrometric method. Quantitative data have been obtained on the growth of films as a function of the solution variables; anion type and concentration, *p*H, and oxygen concentration. In air-stirred chloride solutions, film thickness increases with increasing chloride concentration, passes through a maximum in solutions approximately 0.01M, and then decreases. A maximum also is obtained for *p*H dependence in the range *p*H 5.9-9.0. Cuprous oxide is formed below about *p*H 10.5 and cupric oxide predominates at higher values. For equimolar solutions (0.1M), film growth rate in sodium chloride solutions is about double that in sodium sulfate. In both cases the rate is linear and limited by oxygen availability under the conditions described. In high-purity water, in the presence of excess oxygen, the rate of growth is approximately parabolic, but the extremely thin films formed preclude detailed analysis with the present technique.

Many investigators (1-8) have studied the rate of film formation on copper as a result of oxidation in air at various temperatures. The composition of these films, which is affected by environmental factors such as temperature and oxygen partial pressure, has been verified by electron diffraction studies (9-12). A generally accepted mechanism for the reaction relates oxidation rate to the movement of copper cations through vacancies in the oxide lattice and, it has been shown (4, 7, 8) that over a limited range of film thickness or temperature the parabolic equation may be used to express the growth of films with time. In the case of copper, all of the oxidized metal remains on the surface as a film, and a measure of film growth rate is also a direct measure of oxidation rate.

When copper corrodes in an open aqueous solution the rate of reaction is affected likewise by the nature of the corrosion product film formed on the surface. However, in an aqueous solution, all of the products of corrosion do not necessarily remain on the surface; depending on solution composition and *p*H, corrosion products may dissolve in the solution or form at a site removed from the reacting area. Accordingly a study of oxidation of copper in aqueous solution, based on film growth, can become quite complex. This perhaps explains why very little quantitative information is available on this subject.

The growth of films on copper in aqueous potas-

[1] Yale University, New Haven, Connecticut, Consultant.

sium chloride solutions was measured by Hill (13) in a study of the initial corrosion reaction. His tests, however, were limited to the pH range 7.0-8.3 in which the films were essentially insoluble. Kruger (14) studied the effect of illumination on films formed in air-saturated distilled water.

The present paper describes an investigation of the effect of certain solution variables on the growth and composition of films formed on copper in solutions where information appears to be lacking. It is designed to supplement previous work (15) dealing with the effect of the same variables on the corrosion rate of copper under similar conditions.

Experimental Procedure

Specimens.—Rod specimens, 0.125 in. diameter x 12 in. long, were prepared from oxygen-free high-conductivity copper drawn 85%. Chemical composition was: Cu-99.98%, Fe-<0.003%, Ni-<0.005%, Pb-<0.0005%, and Zn-<0.01%. The surface was scrubbed with water and pumice, rinsed in distilled water, and dried in alcohol. Specimens then were inserted in 3/16 in. ID glass tubes through a short section of ⅛ x ¼ in. rubber tubing which served as a gasket. By sliding the rod in or out, the specimen area could be varied. For very thin films the area was adjusted to 4 cm^2. Thicker films were developed on a 2 cm^2 area. Prior to exposure, the projecting portion was etched for 3 min in 10% ammonium persulfate and rinsed in high-purity demineralized water. The specimen assembly then was transferred quickly to the test solution without drying.

This chemical etching technique for preparing the specimen surface was adopted as a reproducible method which minimizes the blank reading that is obtained by other chemical or mechanical methods, not involving preparation in an inert atmosphere. In view of the fact that film growth was to be studied over some considerable period of time, and that the increased thickness is an average quantity, more elaborate methods did not seem warranted for this preliminary investigation of the comparative effects of solution variables.

Film development.—Films were developed at room temperature in the corrosion cell previously described (15), using a continuous flow technique to maintain essentially constant solution composition. The test solution was fed to the bottom of the cell at 220 ml/hr and the appropriate gas stirring mixture was introduced by means of a gas lift side arm at 500 ml/hr (28 bubbles/min). Alternatively, in tests where increased oxygen availability was desired, the stirring gas was supplied to the bottom of the cell through a medium porosity, 10-15 micron pore size, fritted disk (10 mm diameter) at a rate of 250 ml/min.

When gas mixtures other than air were used, the system was kept under a slight positive pressure to maintain the desired atmosphere over the solution.

Three specimen assemblies were inserted in each cell and held in a uniform geometrical arrangement by means of a plastic spacer ring placed approximately at the mid point of the cell.

Air-formed films also were prepared by exposing specimens in an electric furnace equipped with a circulating fan.

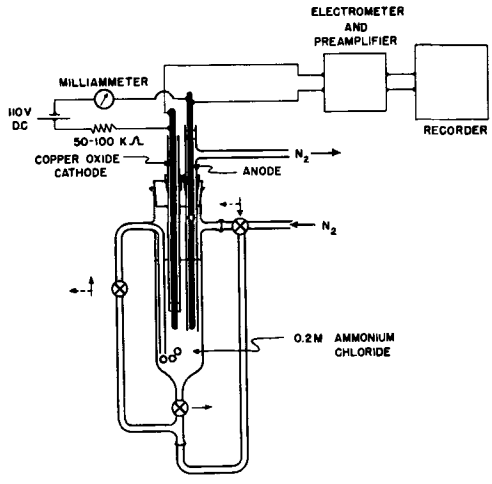

Fig. 1. Electrolytic reduction apparatus

Film analysis.—Following exposure, films were analyzed by an electrometric method, Fig. 1, similar to that used by Miley (4) in his investigation of air-formed films on copper. In principle, the copper compound composing the film is reduced cathodically and the thickness is calculated from the number of coulombs required and the bulk density. This calculation assumes that the surface is a plane and that the film is uniformly distributed. The errors resulting from these assumptions will depend on the magnitude of surface roughness, relative to film thickness, and on the degree of conformity of the contour of oxide and original metal surface. Certainly in the early stages the absolute value of the thickness may be largely in error due to nonuniformity of film and roughness of surface; the error should decrease significantly as the film thickness increases. In the present case the thickness has been used as a measure of changing conditions in the solution usually after 48 hr when a considerable thickness of film has been formed.

Reduction was carried out in a closed glass cell designed so that nitrogen could be either bubbled through the solution or passed over the surface to maintain a protective atmosphere. The film bearing specimen was made the cathode, a copper rod the anode, and 0.2M ammonium chloride was used as the electrolyte. Although the data reported herein were obtained using rod specimens, the apparatus can also be adapted to sheet or tube by using a hooked platinum wire as the cathode and hanging the specimen from this hook.

Current was obtained from a 110 v d-c source consisting of a 90-v "B" battery and a 22½-v "C" battery connected in series. Voltage was applied through a high resistance of 50,000-100,000 ohms. The use of such a large external resistance resulted in a small constant current of 1-2 ma which was unaffected by the relatively minor changes which took place in the cell. The potential developed by the voltage drop across the cell was fed to a Brown electrometer and preamplifier (an instrument which draws no significant current while measuring voltage) and then to a high speed recording potentiometer.

Table I. Oxidation of OFHC copper rod (0.125 in. diameter) in air at 245°C

Time, min	Film thickness, Å: Present data Cu_2O	Present data CuO	Present data Total	Miley Total
3	760	10	770	
5				1100
6	1260	25	1285	
9	1580	0	1580	
10				1450
12	1745	20	1765	
15	1770	55	1825	
20				1900
25				2050
30	1780	385	2165	
43	2145	450	2595	
60	2180	535	2715	2700
90	2365	650	3015	
120	2145	810	2955	
150	2360	900	3260	
300	3000	940	3940	

Prior to analysis the electrolyte was deaerated by bubbling nitrogen for 30 min. The stopcock was turned to pass the gas over the surface and the exposed specimen assembly was inserted.

During the course of reduction the cell potential was followed and recorded to obtain the potential-time curves characteristic of the method. Film thickness then was calculated from the time and current required for reduction using the appropriate factors.

On the basis of Miley's observations and also x-ray diffraction studies, cuprous oxide, Cu_2O, was assumed to be the product which was reduced at a potential of approximately 300 mv and cupric oxide, CuO, the product reduced at 550 mv. Measured against a saturated calomel reference electrode, the corresponding reduction potentials would be 350 mv and 600 mv, respectively.

Experimental Results and Discussion

In order to check the apparatus and the procedure, a portion of Miley's work, dealing with film growth rate in air at 245°C, was repeated. The results are shown in Table I and in Fig. 2.

Good agreement was obtained. Miley's data did not indicate the ratios of cuprous and cupric oxide encountered but, in later work in conjunction with Cruzan (5), they reported that the proportions of the two oxides varied with film thickness. Below 400Å, films contained only cuprous oxide, above 800Å, all films contained a mixture of both, and in the intermediate range some films contained a mixture and others cuprous oxide alone. The films produced in the present work were all too thick to verify the latter conclusions; however, the increase in the proportion of cupric oxide with increasing film thickness does appear to agree with the trend established in the work of Cruzan and Miley.

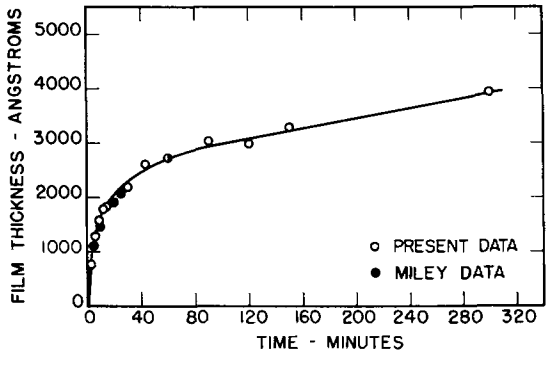

Fig. 2. Oxidation of OFHC copper in air at 245°C

Since the apparatus and analytical procedure proved reliable, the method was applied to the study of film formation in various aqueous salt solutions. The solution variables investigated were anion type and concentration, pH, and oxygen. Reproducibility of results varied with exposure conditions, with the greatest spread, ±5%, appearing in nearly neutral solutions where pH was quite sensitive to small changes in composition. A "blank" corresponding to a film thickness of 20Å is associated with the method and the necessary corrections have been made. The "blank" was traced to air oxidation during specimen preparation and probably could be reduced by preparing specimens in an inert atmosphere.

Effect of Anion Type and Concentration

The growth of films with time in 0.1M sodium chloride and 0.1M sodium sulfate solutions is shown in Fig. 3.

The rate of film growth is considerably higher in sodium chloride solutions and in each case it appears to be approximately linear over the range investigated. In both solutions only cuprous oxide was detected.

Results were about the same in either 0.1 or 0.01M sodium sulfate. However, a change in chloride concentration produced an appreciable change in film thickness as shown in Fig. 4.

For constant time and varying chloride concentration, maxima in thickness are obtained in 0.01M chloride solutions. The effect of chloride ion on film thickness does not correlate with previous observations (15) on the effect of chloride on corrosion rate, where it was shown that corrosion rate increased linearly with increasing chloride ion under the same conditions. The lack of correlation would appear to indicate that corrosion rate is not solely dependent

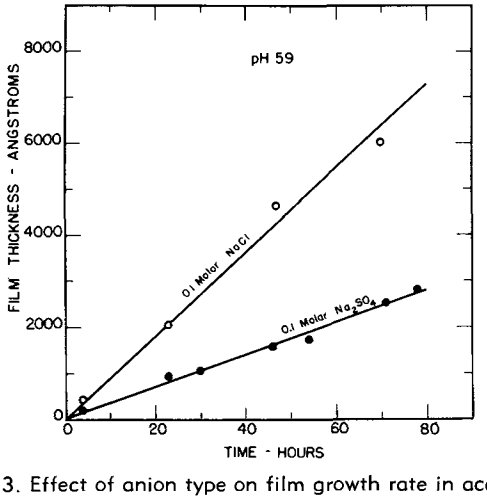

Fig. 3. Effect of anion type on film growth rate in acqueous salt solutions.

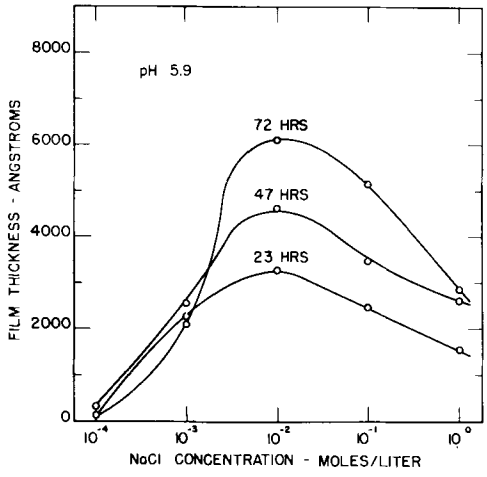

Fig. 4. Effect of concentration on film growth in sodium chloride solutions.

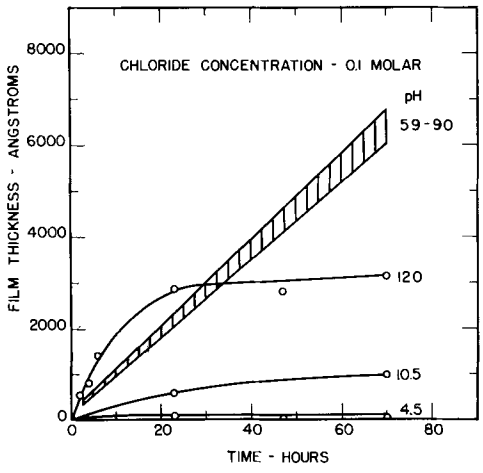

Fig. 6. Effect of pH on film growth rate in chloride solutions

on film thickness for the conditions described. Further studies are being conducted.

Asselin and Rohrman (16) studied the corrosion rate of copper as a function of sodium chloride concentration and reported a maximum at much higher concentrations, 2-3*N*, but none in the range under consideration at present. They attributed the maximum to the net result of the opposing factors oxygen solubility and solution conductivity.

Effect of pH

The effect of *p*H was studied in solutions, 0.1M in chloride ion. Hydrochloric acid or sodium hydroxide was added to sodium chloride solutions as necessary in order to achieve the desired *p*H. It was also necessary to remove carbon dioxide from the incoming air in order to minimize drift in *p*H. Results are shown in Fig. 5.

A fairly flat maximum is obtained in the *p*H range 5.9-9.0. In this range films are essentially cuprous oxide, Cu_2O. Film thickness decreases rapidly below *p*H 5.9, or as the *p*H is raised from 9 to 10.5. At higher *p*H values, however, film growth again starts to increase. Films formed in the high *p*H range, around *p*H 12, are predominantly cupric oxide.

The effect of *p*H is complicated by the fact that the shapes of film growth rate curves vary at different *p*H values as shown in Fig. 6.

Films formed in the *p*H range 5.9-9.0 all fall in the band shown in Fig. 6 and they are still growing after 70 hr. Films formed below or above this range appear to reach a maximum thickness at shorter times and then remain fairly constant. Presumably, in the latter cases, a steady state has been reached where the film formation rate is equal to the dissolution rate.

The absence of measurable films below approximately *p*H 3 is consistent with previous observations (15) and, if the films can be assumed to be partially protective, then the effect of *p*H on films is also consistent with general experience regarding the increase in corrosion rate with decreasing *p*H.

Effect of Oxygen

The effect of oxygen was studied in 0.1M sodium chloride solutions by varying the composition of an oxygen-nitrogen mixture used as the stirring gas. Three mixtures were investigated; 21% (air), 50%, and 100% oxygen. Film thickness increased with increasing oxygen, as shown in Fig. 7, indicating that the process is under oxygen control in every case. The shape of the curve suggests that, at 100% oxygen, conditions were being approached where

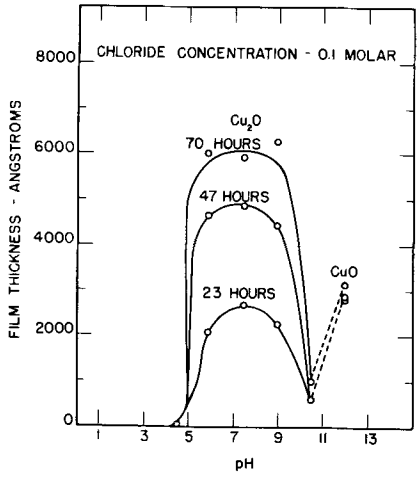

Fig. 5. Effect of pH on film growth in chloride solutions

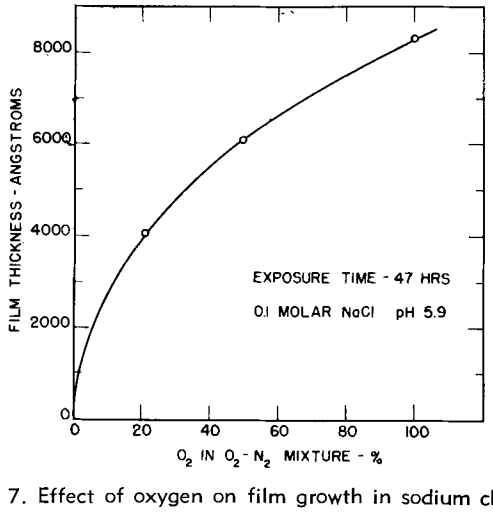

Fig. 7. Effect of oxygen on film growth in sodium chloride solutions.

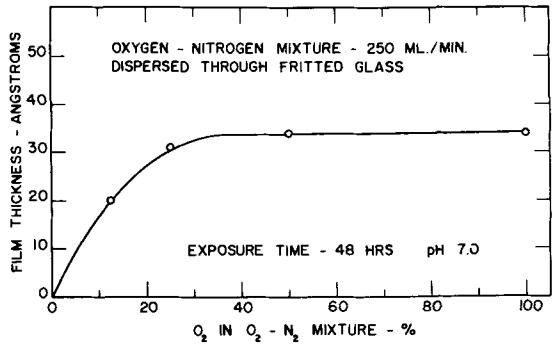

Fig. 8. Effect of oxygen on film growth in high-purity water

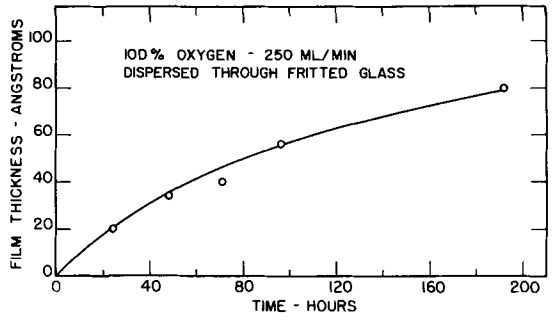

Fig. 9. Film growth rate in high-purity water in the presence of excess oxygen.

rate is independent of further increases in oxygen. This point has not been reached, however, and an increase in stirring rates at this point resulted in films of greater thickness for the same exposure times.

The interdependence of the variables anion concentration, pH, and oxygen makes it difficult to develop a general expression for the growth rate of films on copper in aqueous salt solutions. Thus, a statement regarding the rate in 0.1M chloride solutions must also define the conditions of pH and oxygen availability. In order to obtain a more general expression it was necessary to conduct tests under conditions where variables were either eliminated or reactants were supplied in excess. This was accomplished by using high-purity demineralized water as a corrosive medium. The effect of anions other than the hydroxyl ion present in water was thus eliminated and pH, which was determined before and after test, remained constant at 7.0. An oxygen-nitrogen mixture was supplied to the solution through the medium porosity fritted glass disk which served to increase the availability of oxygen. Under these conditions a mixture containing about 40% oxygen is sufficient to provide an excess of oxygen as shown in Fig. 8.

The film growth rate of copper in high-purity water in the presence of excess oxygen then was determined for times up to 200 hr, Fig. 9. However, under these conditions, the films formed are so thin that the limit of sensitivity of the method is approached. Reproducibility in film formation may also be a factor. Kruger (17) has shown that the nature of oxide films formed in pure water may vary considerably with method of surface preparation and environmental control. The curve is approximately parabolic in form, but the precision of the data, the blank correction, and possible failure of the assumptions involved in the calculations of thickness of thin films preclude detailed analysis of the rate law.

Conclusions

The growth of copper oxide films in aqueous solutions has been studied by an electrometric method. Quantitative data have been obtained on the growth of films as a function of the solution variables, anion type and concentration, pH, and oxygen concentration.

In air-stirred chloride solutions, film growth rate is affected by chloride concentration and pH with a maximum appearing in 0.01M solutions and in the pH range 5.9-9.0. Films are cuprous oxide exclusively except at very high pH values, >10.5, where the rate again increases and cupric oxide predominates.

In equimolar solutions (0.1M) the rate in sodium chloride is about double that in sodium sulfate. In both cases the rate is linear and limited by oxygen availability, even when oxygenation is effected by stirring with a 100% O_2 mixture.

Films formed in high-purity water in the presence of excess oxygen are relatively thin which precludes detailed analysis of the growth rate law from data obtained with the present technique.

Acknowledgment

The authors wish to thank D. K. Crampton and H. L. Burghoff for their interest and suggestions concerning this investigation and to acknowledge the assistance of S. Banisky and other members of the Research and Development Department of the Chase Brass and Copper Co.

Manuscript received April 10, 1959. This paper was prepared for delivery before the Columbus Meeting, Oct. 18-22, 1959.

Any discussion of this paper will appear in a Discussion Section to be published in the June 1960 JOURNAL.

REFERENCES

1. A. B. Winterbottom, *Nature*, **140**, 364 (1937); *Trans. Electrochem. Soc.*, **76**, 327 (1939).
2. B. Lustman and R. F. Mehl, *Trans. Am. Inst. Mining Met. Engrs.*, **43**, 246 (1941).
3. F. H. Constable, *Proc. Roy. Soc.*, **A115**, 570 (1927).
4. H. A. Miley, *J. Am. Chem. Soc.*, **59**, 2626 (1937).
5. C. G. Cruzan and H. A. Miley, *J. Appl. Phys.*, **11**, 631 (1940).
6. W. E. Campbell and U. B. Thomas, *Nature*, **142**, 253 (1938); *Trans. Electrochem. Soc.*, **76**, 303 (1939).
7. N. B. Pilling and R. E. Bedworth, *J. Inst. Met.*, **29**, 577 (1923).
8. J. S. Dunn, *Proc. Roy. Soc.*, **A111**, 241 (1926).
9. U. R. Evans and J. Stockdale, *J. Chem. Soc.*, **1929**, 2561.
10. G. D. Preston and L. L. Bircumshaw, *Phil. Mag.*, **20**, 706 (1935).
11. J. A. Darbyshire, *Trans. Faraday Soc.*, **27**, 675 (1931).
12. C. A. Murison, *Phil. Mag.*, **17**, 96 (1934).
13. G. R. Hill, *This Journal*, **100**, 345 (1953).
14. J. Kruger, *J. Appl. Phys.*, **28**, 1212 (1957).
15. W. D. Robertson, V. F. Nole, W. H. Davenport, and F. P. Talboom, *This Journal*, **105**, 569 (1958).
16. F. J. Asselin and F. A. Rohrman, *Ind. Eng. Chem.*, **32**, 1015 (1940).
17. J. Kruger, *ibid.*, **50**, 55A (March 1958).

The Formation of Porous Oxides on Metals

D. W. Aylmore, S. J. Gregg, and W. B. Jepson

Department of Chemistry, University of Exeter, Exeter, England

ABSTRACT

The porosity of the oxide scales formed on a number of metals during oxidation in dry oxygen has been investigated by measurements of specific surface and of density. The oxides formed during the linear oxidation of the eight metals: calcium, cerium, lead, magnesium, niobium, thorium, tungsten, and uranium are porous whereas those formed during the parabolic oxidation of copper and cobalt are impervious to oxygen gas.

The oxidative behavior of a metal in oxygen depends to a marked extent on the physicochemical properties of the oxide layer formed on its surface. If the layer of reaction product remains continuous during oxidation, reaction can proceed only by the diffusion of either one or both of the reactants in the ionized form through the oxide lattice. In some cases, as with aluminum (1, 2) at 600°C, the rate of oxidation falls off to a negligibly small value as time proceeds, while in others, as for example copper (3) at 1000°C, the oxidation follows a parabolic rate law and the rate of attack is such that a sheet of material is oxidized completely in a few hours.

On the other hand, some metals, usually above a certain characteristic temperature, oxidize at a constant rate which is maintained until the whole of the metal is consumed, a behavior exemplified by magnesium (4) at 500°C. This "linear oxidation" usually is interpreted in terms of the formation of an oxide scale which is porous in the sense that oxygen gas is able to pass freely through its thickness; the rate of oxidation is believed to be controlled by the rate of diffusion either of metal ions or oxygen anions through a thin barrier film of oxide adhering to the metal.

The present study was undertaken in order to provide experimental evidence for the postulated porosity of the oxide layer formed during linear, or almost linear, oxidation and to show that the oxide layer formed during parabolic oxidation is, in fact, impervious to oxygen gas. The metals whose oxides were investigated were calcium, cerium, lead, magnesium, niobium, thorium, tungsten, and uranium, which oxidize at a linear rate, and cobalt and copper which oxidize at a parabolic rate. Two distinct experimental techniques were used to investigate each of the oxide products: the specific surface was measured by the method of krypton sorption (5) at −195°C and the density (6) by immersion in mercury and in carbon tetrachloride, respectively.

Experimental

Each oxide was prepared by oxidizing the metal in dry oxygen at atmospheric pressure in a glass or silica reaction chamber on a thermal balance. The experimental arrangement was the same as that previously described (4) except that the oxygen was further dried by passing it through a column packed with Linde molecular sieves (7).

The percentage purity of the metals was: Ca, >99.4; Ce, >99.99; Co, 99.999; Cu, 99.999; Pb, 99.998; Mg, 99.95; Nb, >99.8; Th, >99.6; W, >99.95; and U, >99.9. Except for calcium, cerium, and lead, the metals were in the form of sheet, 1/32 in. thick for niobium and tungsten and 1/16 in. thick for the others; a sample in the form of a rectangle (4 x 1.5 cm) was cut from the sheet and abraded down to Grade 00 emery under petroleum ether and finally degreased in benzene vapor. The tungsten had to be hot-sheared (8) and the copper after abrasion was etched (9) in a 2.5% aqueous solution of ammonium persulfate for 15 min, washed with water followed by acetone, and finally dried. The calcium was oxidized in the form of a slice, 5 mm thick which was cut from the 1 in. diameter extruded rod; the surface treatment was filing on a "middle cut" file. Lead was oxidized in the molten state in an alumina crucible and cerium in the form of a single lump without surface preparation.

The temperatures of oxidation (Table I) were chosen so as to produce sufficient oxide within a reasonable period of time. The samples of cerium, cobalt, copper, niobium, and tungsten were oxidized to completion, while those of calcium, magnesium, and thorium were only partially oxidized since their oxides spalled from the respective metals on cooling. The oxides of uranium and lead were chipped and scraped from the cooled, oxidized samples.

The apparatus for measurement of krypton sorption (5) at −195°C was designed for the determination of an absolute area of about 1 m^2 of solid with a precision of about ±1%. The use of this quantity of material presented no difficulty with most of the oxides but, as will be seen, there were three whose specific surface was so small that a weight of solid equivalent to 1 m^2 could not be accommodated in the apparatus.

Special experimental techniques (6) were developed for the measurement of the density of the oxide by immersion in mercury and in carbon tetrachloride, respectively, in order to deal with the small amounts of oxide which were available. Briefly, the oxide, contained in a special density bottle, was first outgassed at 110°C to a pressure of 10^{-4} mm Hg and the

bottle then filled with liquid while still in the vacuum system. A quantity of solid equivalent to about 0.3 cm^3 was used for most of the measurements, and both the reproducibility and the absolute accuracy of the method were tested with Iceland spar. With 0.3 cm^3 of solid the density was reproducible to ±0.1% in mercury and to ±0.3% in carbon tetrachloride, and the absolute values agreed with the literature value (10) within these limits.

Results

Kinetic measurements.—The kinetic measurements were of course only ancillary to the main study and the results are described only briefly.

The oxidation curves (of weight gain against time) of magnesium (4) and calcium (11) were the same as those found in earlier work; the former was oxidized for a period such that only the white oxide scale was formed. The cerium was in the form of a single lump of irregular shape so that its oxidation curve could not be classified with certainty; the rate of oxidation at first decreased with time, then reached a constant value [cf. (12) and (13)], but subsequently increased possibly because of self-heating of the metal.

Thorium (Fig. 1) gave a complicated curve consisting of four branches, OA, AB, BC, and CD, over which, respectively, the rate of oxidation decreased, increased, was constant, and decreased; beyond D the rate of oxidation became constant again. Examination of a separate sample which had been oxidized for a shorter period indicated that, as with magnesium, the oxide scale gradually extended laterally over the sample surface. Levesque and Cubicciotti (14), in an experiment covering a much shorter period, found an increase in rate corresponding to branch AB, but the actual weight gains and times were different from those in the present work. The sharp rise in oxidation rate at A probably corresponds to a breakdown of the continuous oxide layer in local regions thus marking the beginning of lateral growth.

Niobium almost from the start of the experiment oxidized at a constant rate of 4.2 mg cm^{-2} hr^{-1} [Baur, Bridges, and Fassell (15) found 6 mg cm^{-2} hr^{-1}] and a breakaway reaction occurred after about 14 hr oxidation. The oxide consisted of a fairly brittle scale together with some powdered oxide, only the former being used for the physical measurements.

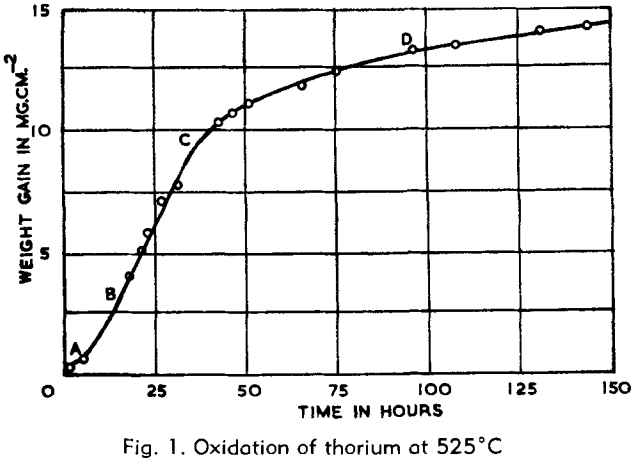

Fig. 1. Oxidation of thorium at 525°C

With tungsten, the rate of oxidation decreased in the very early stages but became constant after about 1 hr, the linear rate of 10.6 mg cm^{-2} hr^{-1} agreeing with the value of 11.5 mg cm^{-2} hr^{-1} found by Webb, Norton, and Wagner (16). The rate of oxidation fell below the linear rate after about 5 hr; the weight gain after this time corresponded to 30% conversion of the metal, and since there was no preferred oxidation at the edges of the sample (8) it is unlikely that the decrease in geometric area is the sole cause.

The rate of oxidation of uranium decreased with time, becoming constant after about 90 hr at 0.8 mg cm^{-2} hr^{-1} [Loriers (17) found 1.0 mg cm^{-2} hr^{-1}]. The oxidation of uranium is complicated by the fact that several oxides probably are involved, perhaps uranium dioxide being first formed and then itself oxidizing (18); at the end of the run the weight gain was in excess of that required for complete conversion to uranium dioxide and yet some metal remained unoxidized. With lead, the rate of oxidation became constant after about 80 hr.

Copper was found to oxidize according to a parabolic rate law ($w^2 = k_p t$), the value of k_p, viz., 238 mg^2 cm^{-4} hr^{-1}, being in good agreement with that calculated from literature data (9) for lower oxygen pressures. The temperature and oxygen pressure were such that both CuO and Cu_2O are stable (19) and the presence of some CuO in the oxide product was confirmed by the fact that the final weight gain

Table I. Values of the specific surface and densities of the oxides[a]

Metal oxide	T,[b] °C	S,[b] m^2 g^{-1}	ρ_m,[b] g cm^{-3}	ρ_o,[b] g cm^{-3}	ρ_o,[b] g cm^{-3}
		A			
Calcium oxide (CaO)	525	6.0±0.05	2.23	3.23	3.37
Cerium oxide (CeO_2)	175	26.3±0.4	5.22	n.d.[c]	7.22
Lead oxide (PbO_2)	575	2.1±0.4	n.d.	n.d.	9.70
Magnesium oxide (MgO)	525	56.0±0.5	0.969	3.33	3.61
Niobium pentoxide (Nb_2O_5)	500	11.3±0.2	4.20	5.15[d]	4.95[e]
Thorium oxide (ThO_2)	525	6.2±0.3	6.43	n.d.	10.04
Tungstic oxide (WO_3)	800	0.92±0.03	5.77	7.17	7.33[f]
Uranium oxide (UO_2) ?	240	6.5±0.3	8.08	9.33	10.96
		B			
Cobalt oxide (CoO + Co_3O_4)	960	<0.01	—	—	—
Copper oxide (CuO + Cu_2O)	960	<0.01	—	—	—

[a] The oxides are classified into Groups A and B according to whether they were formed at a linear or a parabolic rate.
[b] T = temperature of formation, S = specific surface, ρ_m and ρ_o are the densities in mercury and in carbon tetrachloride, respectively, and ρ_o is the theoretical density calculated from the data of Wyckoff (21) unless otherwise stated.
[c] n.d. = not determined because of insufficient material.
[d] This value is significantly greater than the theoretical density. A second determination gave the same result.
[e] Quoted by Gulbransen and Andrew (22).
[f] Calculated from the data of Anderson (23).

was in excess of that required for complete conversion of the metal to Cu_2O; similarly with cobalt, two oxides, CoO and Co_3O_4, are stable (20) under the conditions of the reaction; this may account for the time dependence of k_p which increased from 45 mg^2 cm^{-4} hr^{-1} after 3.5 hr to 49 mg^2 cm^{-4} hr^{-1} after 90 hr oxidation.

Specific surface and density.—The values of the specific surface and of the density in mercury and in carbon tetrachloride are summarized in Table I. The density of each oxide has been calculated on the assumption that the density of the bulk liquid is unchanged at the solid-liquid interface: any error from this source is probably negligible.

With magnesium oxide and niobium pentoxide, it was noticed that the mercury only penetrated the oxide face which had been nearest to the metal. The other oxides did not appear to be penetrated at all by mercury.

Discussion

Group A Oxides

As seen in Table I, the measured specific surface S of the oxides exceeds the geometric surface by several orders of magnitude: the oxides possess an "internal surface" which is made up of the walls of numerous cracks and pores which permeate the solid. A crude but nevertheless useful measure of the degree of dispersion of the oxide is obtained by considering it to be made up of equal-sized cubelets of edge-length l. By simple geometry:

$$l = 6/S\rho_o$$

where ρ_o is the theoretical density of the oxide calculated from the x-ray lattice spacing. The measured surface area then comprises the faces of these cubelets which are accessible to krypton molecules, in other words there are gaps at least two molecules wide between the faces of neighboring cubes: the oxide scale is thus porous to krypton molecules and therefore to oxygen molecules [collision diameters (25): Kr, 4.16Å; O_2, 3.61Å]. The numerical values of l (Table II) cover a wide range, from 3 x 10^2Å for magnesium oxide to 9 x 10^3Å for tungstic oxide.

Somewhat more direct evidence as to the porosity is provided by the data for the density of the oxide in carbon tetrachloride (ρ_c) and in mercury (ρ_m). The difference between $1/\rho_o$ and $1/\rho_c$ or $1/\rho_m$ represents the volume, per gram of oxide, of those pores which are inaccessible to carbon tetrachloride or to mercury, respectively; the volumes of void ϵ_c and ϵ_m, expressed as a fraction of the total volume of the oxide, are thus given by:

$$\epsilon_c = 1 - \frac{\rho_c}{\rho_o}, \qquad \epsilon_m = 1 - \frac{\rho_m}{\rho_o} \qquad [1]$$

Since mercury at 1 atm pressure cannot enter pores of diameter less than about 10^5Å (26) while carbon tetrachloride can penetrate all pores with diameters in excess of about 5Å, ϵ_m and ϵ_c are made up of all the pores finer than 10^5Å and 5Å, respectively. Both values, of course, include those pores which are totally sealed off.

Table II. Calculated void fractions and cube and pore sizes of the Group A oxides

Oxide	α[a]	ϵ_c	ϵ_m	l, Å	δ, Å[b]
CaO	0.28	0.042	0.34	3000	880
CeO_2	0.20	—	0.28	320	73
PbO_2	—	—	—	3020	—
MgO	0.27	0.079	0.73	300	330
Nb_2O_5	0.43	0.00	0.15	1070	120
ThO_2	<0.26	—	0.36	960	310
WO_3	0.62	0.02	0.21	8900	150
UO_2 ?	0.21	(0.149)	(0.263)	(840)	180

[a] Values calculated from the melting points listed in (24).
[b] Calculated from Eq. [2] using ρ_o for ρ.

The values of ϵ_m (Table II) are all relatively large, varying from 0.15 for niobium pentoxide to 0.73 for magnesium oxide, a figure which implies that almost three-quarters of the oxide scale is composed of void. Values of ϵ_c are, as might be expected, considerably smaller and they vary over a narrower range.

The ϵ_m-value of 0.34 for calcium oxide agrees surprisingly well with the 34% porosity which was estimated by Pilling and Bedworth (27) from geometric measurements of the completely oxidized sample. The ϵ_m-value of 0.21 for tungstic oxide is significantly less than the figure of 30% for the porosity quoted by Webb, Norton, and Wagner (16); it is not clear, however, whether their solid had been outgassed.

The data all refer to the oxide scale after it has been cooled down from reaction temperature, but it is reasonable to assume that the state of subdivision of the scale at the temperature of the reaction is not markedly different. It must also be borne in mind that the scale tends to sinter after it has been formed. Such sintering, which would manifest itself in a reduction in specific surface and an increase in density, must come about as a result of either plastic (or viscous) flow or of transport of material through the crystallite by diffusion. Both processes are known to be greatly accelerated at temperatures above a critical value T_c, characteristic of the solid but lying within the range 0.37 T_f to 0.53 T_f where T_f is the mp of the oxide (28). (T_c often is termed the Tammann temperature and sometimes is defined as $T_c = 0.5\ T_f$.) The quantity $\alpha = T/T_f$, where T is the oxidation temperature, is given in Table II for each oxide: that tungstic oxide has the lowest specific surface and with it, the largest crystallite size of all the oxides in Group A, correlates in an interesting way with the fact that its α-value is the highest of the series and well above the Tammann range. It is also satisfactory that the values $\epsilon_c = 0$ and $\epsilon_c = 0.02$ for niobium and tungstic oxides, respectively, are in agreement with their relatively high α-values of 0.43 and 0.62, although it is perhaps surprising that all the fine pores in niobium pentoxide have apparently been eliminated. It is well known that in sintered oxides the measured density does not in general reach the true density unless the oxide is heated for very long periods near its melting point; indeed, sealed-off pores have been

seen with the electron microscope (29). Reference to Table I shows that for niobium pentoxide ρ_c was significantly greater than ρ_o, and it is possible that this oxide was not the exclusive reaction product (22, 30).

Yet another way of expressing the porosity of the oxide scale is to calculate the mean linear separation δ of the cubic blocks of our crude model; we have

$$\delta = 2l\left\{\left(\frac{\rho}{\rho_m}\right)^{1/3} - 1\right\} \qquad [2]$$

here ρ is within the range ρ_o and ρ_c, its exact value being dependent on the relative volumes of sealed and open pores making up the void fraction ϵ_c. Since the oxide scale contains a variety of pores of widely differing shapes and sizes, the numerical values of δ (Table II) can represent no more than the order of magnitude of the gaps within the oxide layer; but they clearly demonstrate the presence of pores sufficiently wide to permit the free passage of gaseous oxygen. A simple calculation, assuming Poiseuille flow, shows indeed that the pores could permit a flow of gas at a rate greater by many orders of magnitude than that actually required by the consumption of oxygen in the reaction.

Group B Oxides

The specific surface of the copper and the cobalt oxides was extremely small, being within the limits of the apparatus and probably representing little more than the geometric surface of the sample.

Conclusions

The findings of the present paper correlate in a satisfactory manner with inferences extant in the literature of metal oxidation as to the porosity of the oxide scale.

Thus the oxides formed during the linear oxidation of calcium, cerium, lead, magnesium, niobium, thorium, tungsten, and uranium are shown to be porous to molecular oxygen which therefore can diffuse freely through the oxide scale; the rate of oxidation probably is controlled by the diffusion, either of metal ions or of oxygen anions, through a thin barrier film of oxide (nonporous to gaseous oxygen) which remains adherent to the metal and whose thickness remains effectively constant.

For parabolic oxidation it generally is accepted that the rate determining step is the diffusion either of interstitial ions or of cation vacancies across the oxide layer which by implication is non-porous to oxygen gas. The present results provide evidence as to this lack of porosity with the oxide layer on copper and on cobalt.

Acknowledgments

Acknowledgment is gratefully made to the U.K. Atomic Energy Authority for financial support, and to Dr. J. E. Antill for some helpful comments.

Manuscript received April 1, 1959.

Any discussion of this paper will appear in a Discussion Section to be published in the June 1960 JOURNAL.

REFERENCES

1. W. W. Smeltzer, *This Journal*, **103**, 209 (1956).
2. D. W. Aylmore, S. J. Gregg, and W. B. Jepson, To be published in *J. Inst. Metals.*
3. C. Wagner, *Z. physik. Chem.*, (B), **21**, 25 (1933).
4. S. J. Gregg and W. B. Jepson, *J. Inst. Metals*, **87**, 187 (1958-1959).
5. D. G. Smith, Thesis, University of Exeter (1958).
6. W. B. Jepson, *J. Sci. Inst.*, **36**, 319 (1959).
7. C. C. Addison, E. Iberson, and J. B. Raynor, *Chem. and Ind.*, 96 (1958).
8. J. P. Baur, D. W. Bridges, and W. M. Fassell, Jr., *This Journal*, **103**, 266 (1956).
9. J. P. Baur, D. W. Bridges, and W. M. Fassell, Jr., *ibid.*, **103**, 273 (1956).
10. T. Batuecas and F. L. Casado, *Z. physik. Chem.*, (A), **181**, 197 (1937).
11. S. J. Gregg and W. B. Jepson, To be published in *J. Chem. Soc.*
12. J. Loriers, *Compt. rend.*, **231**, 522 (1950).
13. D. Cubicciotti, *J. Am. Chem. Soc.*, **74**, 1200 (1952).
14. P. Levesque and D. Cubicciotti, *ibid.*, **73**, 2028 (1951).
15. D. W. Bridges and W. M. Fassell, Jr., *This Journal*, **103**, 326 (1956).
16. W. W. Webb, J. T. Norton, and C. Wagner, *ibid.*, **103**, 107 (1956).
17. J. Loriers, *Compt. rend.*, **234**, 91 (1952).
18. P. E. Blackburn, J. Weissbart, and E. A. Gulbransen, *J. Phys. Chem.*, **62**, 902 (1958).
19. F. H. Smith and H. R. Roberts, *J. Am. Chem. Soc.*, **42**, 2582 (1920).
20. M. Watanabe, *Bull. Inst. Phys.-Chem. Research (Tokyo)*, **12**, 255 (1933).
21. R. G. Wyckoff, "Crystal Structures," Interscience Publishers Inc., New York.
22. E. A. Gulbransen and K. F. Andrew, *This Journal*, **105**, 4 (1958).
23. G. Anderson, *Acta Chem. Scand.*, **7**, 154 (1953).
24. "Handbook of Chemistry and Physics," C. D. Hodgman, Editor, Chemical Rubber Publishing Co., Cleveland (1950).
25. E. H. Kennard, "Kinetic Theory of Gases," p. 149, McGraw Hill Publishing Co., New York (1938).
26. J. F. Goodman and S. J. Gregg, *J. Chem. Soc.*, **1956**, 3612.
27. N. B. Pilling and R. E. Bedworth, *J. Inst. Metals*, **29**, 529 (1923).
28. G. I. Finch and K. P. Sinha, *Proc. Roy. Soc.*, **239A**, 145 (1957).
29. J. E. Bourke, *J. Am. Ceram. Soc.*, **40**, 80 (1957).
30. E. A. Gulbransen and K. F. Andrew, *J. Metals, Trans. AIME*, **188**, 586 (1950).

Galvanic Relationships between Aluminum Alloys and Magnesium Alloys

I. Galvanic Couples

M. R. Bothwell

Metallurgical Laboratory, The Dow Metal Products Company, Midland, Michigan

ABSTRACT

High-purity aluminum has nearly perfect galvanic compatibility with magnesium AZ31B alloy during saline exposure. This compatibility is little changed by additions to the aluminum of magnesium, silicon, or manganese, but it is rapidly and proportionately decreased by the addition of iron, copper, and nickel, and more gradually decreased by the addition of zinc. The addition of magnesium to the alloy or magnesium ion to the environment can greatly suppress the effect of the above deleterious constituents.

Their active potentials and lack of appreciable anodic polarization make magnesium alloys susceptible to galvanic effects during exposure to salt-laden environments. The suppression of these effects by the removal or metallurgical complexing of low hydrogen overvoltage constituents in magnesium alloys is one of the classic examples of the application of local-cell theory to a corrosion problem (1). Due to these operations the commercial magnesium alloys are generally serviceable in salt-laden atmospheres when they are painted with moderate care. However, when these alloys are incorporated in structures with other metals it is frequently not the inherent corrosion resistance of the magnesium alloy which determines the protective system needed, but rather the galvanic characteristics of the macro cells set up between the magnesium alloy and the other metals or alloys in the structure.

Galvanic relationships between magnesium alloys and aluminum alloys are extremely important since the two metals are combined so frequently in light metal structures. Even when the structure is dominantly magnesium, it will often be fastened together by aluminum rivets, for magnesium alloys generally lack the room-temperature plasticity necessary in the cold-driving rivet. Over the years it has been discovered that there is a tremendous range in the galvanic effect of the commercial aluminum alloys on magnesium alloys. Thus, the magnesium-rich aluminum alloys such as 5056 are generally quite compatible with magnesium alloys, whereas the copper-rich aluminum alloys such as 2024 alloy are generally poorly compatible. It is the purpose of this paper to demonstrate some of the principles which determine the compatibility of aluminum alloys toward magnesium alloys and to illustrate how these principles can be used in corrosion control.

Experimental

The cathodic polarization curves for the aluminum materials in Fig. 1 were obtained with an automatically regulated, linear current sweep rate of 30 min from nil to full current and 30 min full to no current. Each aluminum cathode consisted of a 3/8 in. diameter cylinder mounted as a section in a Bakelite holder of the same diameter and located at the axis of a magnesium AZ31B alloy hollow cylinder which was used as the anode. Potentials were recorded in respect to a Beckman Model 1170 saturated calomel electrode which was located in a Luggin capillary salt bridge filled with the corrodent solution. Potentials were recorded by a modified Brown recording potentiometer operating with its chart drive in synchronization with the current sweep. The one aluminum cathode consisted of commercial 2S aluminum rod which contained 0.47% Fe, 0.23% Si, and 0.087% Cu as determined by chemical analysis. The 99.99% purity electrode in these studies was machined from ingot containing 40 ppm respectively of Fe and Cu, 10 ppm Si, and 4 ppm Ni as determined by chemical analysis.

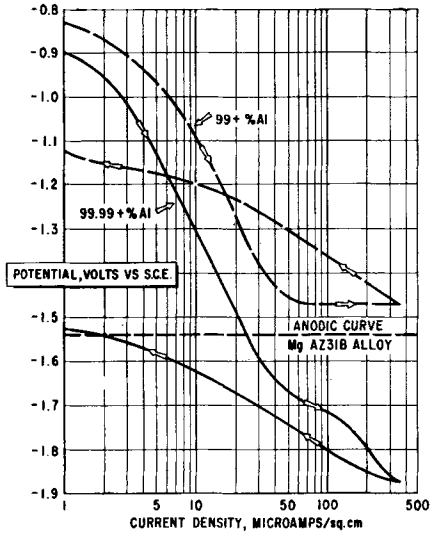

Fig. 1. Cathodic polarization of two grades of aluminum in 3% NaCl solution saturated with air and with $Mg(OH)_2$.

Except where a different base material is indicated, experimental aluminum alloys were prepared

starting with 99.99% purity Al from the same lot mentioned above or from another lot certified by the manufacturer to contain 10 ppm Cu, 20 ppm Fe, 10 ppm Mg, and <10 ppm of any other anticipated impurity. The 99.9% Al contained 300 ppm Fe, 270 ppm Si, 30 ppm Cu, and <100 ppm of any other anticipated constituent. Magnesium was alloyed directly from doubly sublimed material containing 5 ppm Fe. The zinc was also alloyed directly starting with 99.99% purity ingot. The copper, manganese, iron, and silicon bearing alloys were all prepared from master alloys based on 99.99% purity Al and respectively high conductivity, electrolytic copper, electrolytic manganese, high-purity alcoholized iron powder, and silicon of undefined quality. The basic alloying procedure was as follows: pure aluminum was melted in a spectroscopic-grade graphite crucible and heated to 1400°F, after which the alloying constituents were added and stirred in vigorously. This melt was heated to 1500°F for 30 min and then cooled to 1400°F before pouring into spectroscopic-grade graphite molds. Immediately after solidification each casting was water quenched.

Each melt produced two castings, a 1 x 4 x 4 in. miniature rolling slab and a disk specimen for spectroscopic analysis. After its surfaces were removed by grinding on Aloxite cloth, the rolling slab was reduced to sheet of 0.020 in. thickness on carefully cleaned and well-lubricated rolls at 300°F following the schedule, 25% reduction per pass with 15 min reheats at 700°F between passes.

The disk castings of all alloys were subjected to spectroscopic analysis. This was supplemented by chemical analysis in selected cases. Except where the level of an element is specified in the results, analysis has shown it to be negligibly different from the level in the aluminum base stock.

The galvanic corrosion specimens consisted of 2 pieces of the aluminum alloy sheet in the form of squares, ½ in. on the side, which were centrally mounted on the opposite sides of 1½ x 1½ in. squares of commercial, magnesium AZ31B alloy.[1] These specimens were held together by ⅛ in. diameter rivets of a high-purity aluminum-2% magnesium alloy. Prior to assembly the aluminum pieces were ground with fine Aloxite cloth to remove possible cathodic contamination introduced during the rolling, drilling, and shearing operations. The magnesium AZ31B alloy coupons were pickled to a depth of 1 mil per side in a solution of 25½ fluid oz of glacial acetic acid and 6 2/3 oz sodium nitrate per gal of aqueous solution. Following pickling and water rinsing, these magnesium alloy coupons were dried and weighed.

Following the exposure, the test pieces were disassembled and the magnesium alloy coupons were rinsed with gentle scrubbing under tap water. The corrosion product was then removed by immersion for 2 min in a solution of 20% chromic acid plus 1% silver nitrate at 180°F. Following this the specimens were rinsed in tap water, dried, and reweighed to obtain the weight loss due to corrosion. Since tests showed that this method caused <0.5 mg weight change on specimens not previously corroded, no correction for cleaning error was made. All test exposures were made by suspending each specimen in approximately 200 ml of the corrodent concerned. The test temperature was 95° ±2°F. The time of exposure was generally 1 week. However, this period had to be curtailed for those couples with which the galvanic effect was excessively large. The mean deviation for triplicate tests was generally <10% of the average rate and at no time did it exceed 20% of the average rate.

[1] The nominal composition of AZ31B alloy is Mg-3% Al-1% Zn-0.4% Mn.

Results and Discussion

The peculiarity of the pure aluminum cathode in respect to its extremely low limiting current for depolarization by dissolved oxygen has been pointed out by Pryor and Keir (2). It will be seen shortly that their hypothesis of impurity-rich sites as the effective cathodes in the aluminum macro cathode agrees with the data presented here. In fact, it was observation of this same phenomenon in the cathodic polarization of commercial aluminum alloys and a similar analysis of its implications which led to the work to be described here. Hansen and Wetmore (3) arrived at a similar conclusion when they noted that super purity aluminum has a much higher hydrogen overvoltage in acids than does commercial-purity aluminum.

In Fig. 1 can be seen the cathodic polarization curves of 99.99+% purity aluminum and commercially pure aluminum while exposed to 3% NaCl solution saturated with magnesium hydroxide and air. The dotted line represents the potential of magnesium AZ31B alloy which is without significant anodic polarization in this environment. It can be seen that the high-purity aluminum cathode polarizes so readily that it should cause very little galvanic attack to the magnesium alloy, whereas rather severe attack can be expected when the latter is coupled to commercially pure aluminum.

Because of the pronounced hysteresis in the cathodic polarization curves for aluminum and its alloys, the analysis of polarization data was abandoned in favor of measurements on the couples themselves. The configuration of the test couple chosen was felt to meet the following desiderata: (*a*) was easily prepared, (*b*) generally prevented electrolyte entry at faying surfaces, (*c*) invariably maintained contact, (*d*) was sensitive to cathode effects, and (*e*) introduced no significant third electrode effect.

Complete immersion of the test specimen was used rather than the more conventional alternate immersion or salt spray testing in order to utilize more effectively the available cathode and thus make the test more sensitive. While complete immersion testing was believed satisfactory here, since oxygen reduction is relatively unimportant in couples between magnesium alloys and aluminum alloys, such is generally not the case when magnesium alloys are coupled with other metals.

Iron is rarely a deliberate constituent in the commercial aluminum alloys but it is usually present in them to the extent of a few thousand ppm as a major

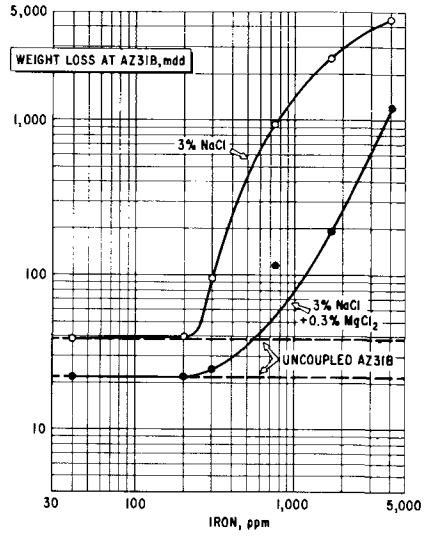

Fig. 2. Effect of iron in aluminum on the corrosion of AZ31B alloy coupled thereto.

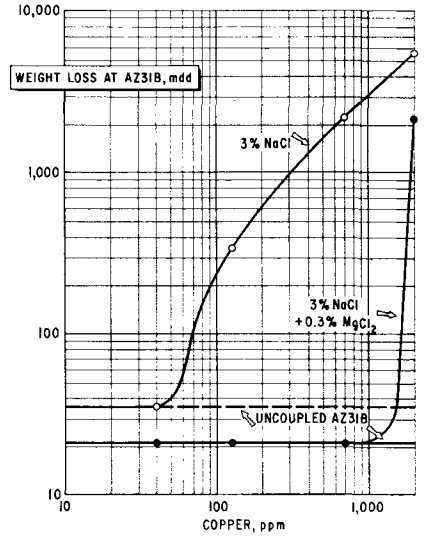

Fig. 3. Effect of copper in aluminum on the corrosion of AZ31B alloy coupled thereto.

impurity. In Fig. 2 it is seen that iron in the aluminum alloy can have a very adverse effect on its compatibility with magnesium AZ31B alloy. Up until the time that the iron content does not exceed 200 ppm, in this particular couple configuration, the iron is without appreciable galvanic effect, but as this level is exceeded, galvanic attack of the magnesium alloy increases rapidly. The addition of 0.3% magnesium chloride to the 3% sodium chloride solution was made to reproduce effects observed in natural seawater. The justification for this will be shown in Part II of this paper (4). Although this addition does not greatly change the iron level at which galvanic attack of the magnesium alloy becomes appreciable, it does greatly reduce such attack once the critical iron level is exceeded.

The results in Fig. 3 are in accord with past observations on the poor compatibility of copper-rich aluminum alloys with magnesium alloys. In the 3% NaCl environment, copper can have a deleterious effect at even lower levels than was seen in the case of iron in the previous figure. However, if 0.3% $MgCl_2$ is added to the environment, copper does not have a significant deleterious effect until it exceeds 1000 ppm.

Table I. Effect of various constituents on the galvanic compatibility of Al toward AZ31B alloy

	Weight loss at AZ31B, mdd	
	3% NaCl	3% NaCl + 0.3% $MgCl_2$
99.9+% Al (unalloyed)	94	24
+ 0.16% Zn	400	59
+ 0.27% Si (0.041% Fe)	78	33
99.99+% Al (unalloyed)	36	22
+ 0.015% Ni	127	
+ 0.30% Mn	34	23
Uncoupled control	38	23

In Table I it can be seen that nickel at low levels has a deleterious effect that is of the same order as that of iron and copper. The effect of nickel has been less extensively studied here because it is not of great importance in aluminum alloys either as a major impurity or a common alloying constituent. Zinc also has a deleterious effect, but it is much milder than that of iron, copper, and nickel. Furthermore, the effect of zinc is very effectively suppressed by the addition of magnesium chloride to the environment. Silicon and manganese have little effect even at moderate levels. Next to iron, silicon is the most prevalent impurity in commercial-purity aluminum and its alloys. Silicon is also an extremely important deliberate constituent in many aluminum alloys as are zinc and manganese as well. Since silicon is innocuous, the marked difference in the cathodic polarization behavior of the two purity grades of aluminum shown in Fig. 1 can be attributed primarily to the iron content of the less pure grade. This is substantiated by couple tests where it is found that the weight loss occasioned by the latter metal is nearly equal to that produced by a high-purity aluminum-iron binary alloy of the same iron content.

Figures 4, 5, and 6 illustrate the basis for the good performance in service of the magnesium-rich alu-

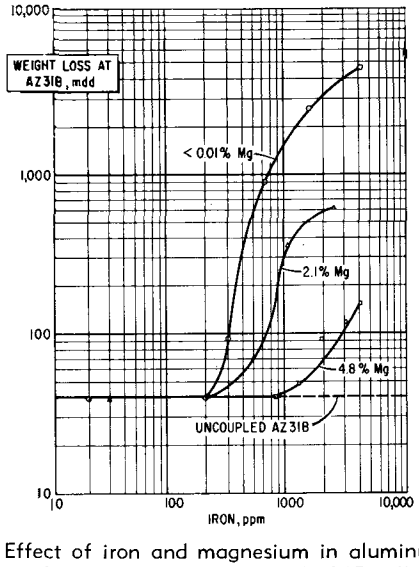

Fig. 4. Effect of iron and magnesium in aluminum on the corrosion in 3% NaCl solution of AZ31B alloy coupled thereto.

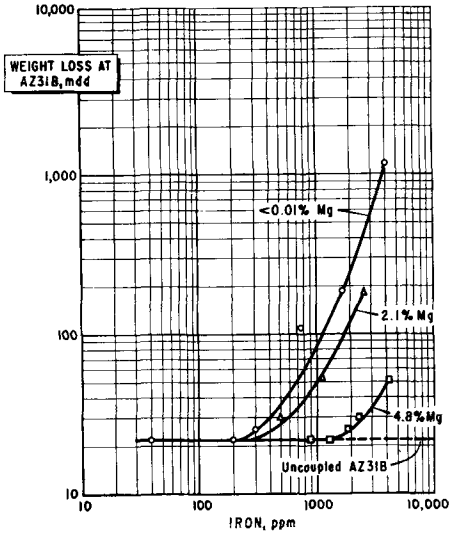

Fig. 5. Effect of iron and magnesium in aluminum on the corrosion in 3% NaCl plus 0.3% $MgCl_2$ solution of AZ31B alloy coupled thereto.

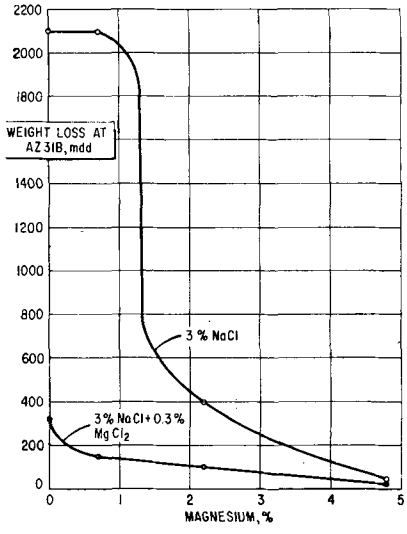

Fig. 6. Effect of magnesium in aluminum plus 0.13% iron on the corrosion of AZ31B alloy coupled thereto.

minum alloys in structures with magnesium alloys. It can be seen that the addition of magnesium to the aluminum alloy greatly improves its tolerance for iron. For example, aluminum 5056 alloy, which has long been used as the standard rivet material for magnesium alloy structures, has a nominal composition of aluminum-5.2% Mg-0.1% Mn-0.1% Cr. Its maximum permissible iron content is 0.4%, but in practice, it will generally be about one-half of this value. The results here indicate that 5.2% Mg should largely suppress the effect of 0.2% Fe and thus 5056 alloy should be a highly compatible material. This conclusion is substantiated by several years of trouble-free service with 5056 alloy rivets in AZ31B alloy structures.

In Table II it can be seen that magnesium can suppress the deleterious effects of copper and of iron and copper in combination. It is also extremely effective in suppressing the mildly deleterious effect of zinc that is observed in couple tests in 3% NaCl solution.

Table II. Suppression by alloyed Mg of the deleterious effects of Cu, Ni, and Zn on the galvanic compatibility of Al toward AZ31B alloy. (Al alloys containing Zn here were coupled with a different lot of AZ31B alloy from that used in remainder of study. Furthermore, duration of exposure to 3% NaCl was only one day.)

	Weight loss at AZ31B, mdd	
	3% NaCl	3% NaCl + 0.3% $MgCl_2$
Suppression of Cu effect		
Al + 0.013% Cu	332	24
Al + 0.014% Cu + 0.36% Mg	40	22
Al + 0.089% Fe + 0.018% Cu + 4.8% Mg	40	24
Al ± 0.078% Fe + 0.74% Cu	>4000	>2000
Al ± 0.078% Fe + 0.74% Cu + 4.5% Mg	81	35
Suppression of Ni effect		
Al + 0.015% Ni	127	
Al + 0.056 ± Ni + 4.8% Mg	46	
Suppression of Zn effect		
Al + 3.6% Zn + 0.05% Fe	3630	43
Al + 4.8% Zn + 0.05% Fe + 3.4% Mg	266	45
Uncoupled control	150	48

On the basis of these results, it can be seen that there is much freedom within which to design aluminum alloys which will have both satisfactory mechanical properties and excellent galvanic compatibility with magnesium alloys. The work hardening aluminum-magnesium alloys and the age hardening aluminum-magnesium-silicon and aluminum-magnesium-zinc alloys are the best prospects to meet these requirements. Contingent upon the magnesium content of the alloy, it may be necessary to reduce its iron content from the levels prevalent in the commercial purity materials.

An example of the effect of iron content on the compatibility of a commercial aluminum alloy is shown in Fig. 7. 6061 alloy is a moderately strong, age-hardening alloy with the nominal composition of aluminum-1.0% Mg-0.6% Si-0.25% Cu-0.25% Cr. The maximum permissible iron content for this alloy is 0.70% and, in practice, about one-half this amount is the general expectation. It can be seen here that this alloy cannot be made completely compatible with AZ31B alloy during exposure to 3% NaCl solu-

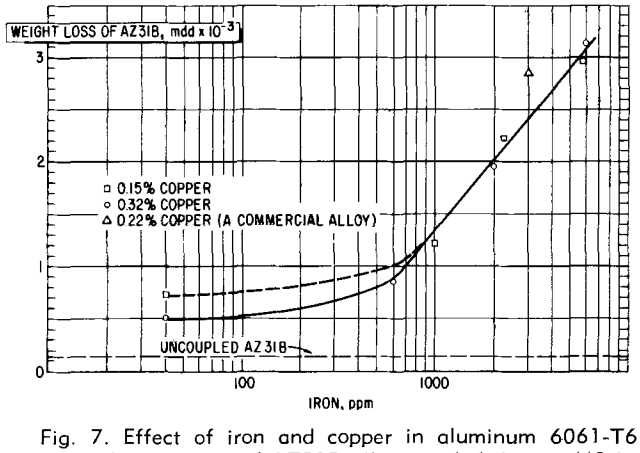

Fig. 7. Effect of iron and copper in aluminum 6061-T6 alloy on the corrosion of AZ31B alloy coupled thereto (48 hr immersion in 3% NaCl).

Table III. Compatibility of 6061-T6 alloy with AZ31B alloy during exposure to substitute ocean water per ASTM designation D-1141-52

	Weight loss at AZ31B, mdd
Commercial 6061-T6 (0.30% Fe, 0.22% Cu)	43
Experimental 6061-T6 (0.005% Fe, 0.15% Cu)	31
Experimental 6061-T6 (0.005% Fe, 0.32% Cu)	33
Uncoupled control	32

tion because the ratio of copper to magnesium is too high. Nevertheless, a decrease in the iron content from the usual levels of the commercial alloys can do much to improve the compatibility. In contrast to the results in 3% NaCl solution, even commercial purity 6061 alloy is highly compatible with AZ31B alloy during exposure to substitute ocean water (see Table III).

It is interesting to note that the constituents which have the greatest deleterious effect on the compatibility of the aluminum alloys with AZ31B alloy are iron, copper, and nickel. Since these are metals with rather low hydrogen overvoltages, it is reasonable to assume that the effective cathodes in an aluminum macro-cathode are regions rich in elements displaying substantially their bulk hydrogen overvoltage characteristics rather than areas in which elements have become incorporated in the film to make it semiconductive as Pryor and Keir have suggested for the case of extremely pure aluminum.

Magnesium constituent in the alloy may suppress the deleterious effect of the above constituents by increasing the resistance of the aluminum alloy to attack by cathodically generated alkali and thereby decreasing their rate of exposure. Since the pH should decrease as the distance from the low overvoltage phase is increased, it is reasonable to expect that enhancement in the alkali resistance of the matrix phase will favor a sharper gradient of cathodic attack and thus favor a higher ratio of impurity undercutting to impurity exposure. This view gains some support from the observation that, at the same deleterious impurity level, the addition of magnesium to the aluminum decreases its cathodic attack as well as the anodic attack of the AZ31B alloy coupled to it. However, this result is not readily resolved in terms of cause and effect. Efforts to confirm this mechanism through a cursory study of the metallography of cathodic attack have been unsuccessful.

Summary

High-purity aluminum causes substantially no galvanic corrosion to magnesium AZ31B alloy during exposure to 3% NaCl solution. The addition of increasing amounts of iron, copper, and nickel to the aluminum results in a rapid loss in compatibility whereas the addition of zinc causes more moderate loss at comparable levels. The addition of magnesium, silicon, and manganese is without noticeable deleterious effect. When magnesium is present in the alloy the deleterious effects of iron, copper, nickel, and zinc are greatly suppressed. The effects of these same deleterious constituents are also suppressed when a small amount of magnesium chloride is added to the corrosion environment. These results are consistent with the view that at the potential of magnesium AZ31B alloy, the bulk of the surface of an aluminum macro-cathode is galvanically inert while the effective cathodes are areas rich in low overvoltage constituents. The beneficial effect of magnesium in the alloy is probably related to its ability to suppress the accumulation of low overvoltage impurities at the alloy's surface.

Manuscript received Jan. 19, 1959. This paper was prepared for delivery before the Buffalo Meeting, Oct. 6-10, 1957.

Any discussion of this paper will appear in a Discussion Section to be published in the June 1960 JOURNAL.

REFERENCES

1. J. D. Hanawalt, C. E. Nelson, and J. Peloubet, *Trans., Am. Inst. Mining Met. Engrs.*, **147**, 273 (1942).
2. M. J. Pryor and D. S. Keir, *This Journal*, **102**, 605 (1955).
3. D. J. Hansen and F. E. W. Wetmore, *Can. Chem. Process Inds.*, **34**, 659 (1956).
4. M. R. Bothwell, *This Journal*, **106**, 1019 (1959).

Galvanic Relationships between Aluminum Alloys and Magnesium Alloys

II. Aluminum Claddings on Magnesium

M. R. Bothwell

Metallurgical Laboratory, The Dow Metal Products Company, Midland, Michigan

ABSTRACT

The cladding of magnesium AZ31A alloy with 99.99% aluminum greatly improves its resistance to saline environments. The protective ability of the cladding is little changed by incorporation therein of magnesium, silicon, or manganese, but it is impaired greatly by iron and copper and more mildly by zinc. The presence in seawater of soluble magnesium salts greatly diminishes the effects of iron, copper, and zinc from that seen in sodium chloride solution. This decrease is probably due to decreased cathodic attack of the aluminum at the lower equilibrium pH of the seawater environment.

While magnesium alloys generally withstand mild weathering very well without recourse to any protection beyond that of their naturally formed film, such weathering is accompanied by the gradual formation of a gray patina which is objectionable in some applications. Furthermore, it would be desirable for some applications to have magnesium sheet which could withstand moderately severe salt exposure when unpainted. Early experimental claddings of aluminum alloys on magnesium alloys showed a substantial improvement in the maintenance of a reflective surface during weathering, but unfortunately, rather than affording any protection to the magnesium alloy during salt exposure, they greatly accelerated corrosion due to strong galvanic effects. The experimental claddings described here were prompted by the recognition that extremely pure aluminum combines its well-known excellent resistance to corrosion in saline environments with remarkable galvanic inertness toward magnesium alloys.

Experimental

The aluminum alloys used here were prepared in the same manner as those in Part I of this paper (1). The aluminum base stocks used were 99.99% purity Al containing 40 ppm Fe, 40 ppm Cu, 4 ppm Ni, 10 ppm Si, and <10 ppm of any other anticipated constituent, and 99.9% purity Al containing 300 ppm Fe, 270 ppm Si, 30 ppm Cu, and <100 ppm of any other anticipated constituent.

Aluminum alloy sheet of 0.020 in. thickness was wire-brushed and then wrapped around 0.250 in. thick, magnesium AZ31A alloy[1] plate. This composite was rolled to 0.040 in. total thickness on clean, well-lubricated rolls according to the schedule described in Part I (1). The resulting thickness of the cladding was slightly over 0.003 in. per side.

These clad composites were cut into 1½ by 2½ in. coupons which were given a 1 min pickle in cold, 10% sodium hydroxide solution. After drying and weighing, they were subjected to alternate immersion testing at 95° ± 2°F in approximately 200 ml of the environments concerned by the method described by Hanawalt, *et al.* (2). Following the exposure, the samples were cleaned for 4 min in the chromic acid cleaning solution mentioned in Part I of this paper (1). Since it was found that individual coupons not previously corroded lost less than 1 mg during this cleaning, no correction for cleaning loss was made. Fortunately this cleaning process is sufficient to remove the corrosion product from all but the most severely corroded specimens, and thus the chromic acid-phosphoric acid baths that are used customarily to remove corrosion product from aluminum corrosion specimens, but which would attack the magnesium alloy wherever exposed, were not necessary.

The mean deviation for quintuplicate tests was generally <10% of the average rate and only rarely exceeded 20% of the average rate.

Results and Discussion

The clad coupons of this study can be considered as galvanic couples with an unusually high ratio of cathode area to anode area, e.g., approximately thirty to one when first exposed. In addition to the anodic attack of the core at the exposed edges, the cathodic attack of the cladding and the exposure of additional core metal thereby must be considered. Experience with galvanic couples shows that the cathodic attack of the aluminum alloy is almost as severe as the anodic attack of the magnesium alloy. Thus, it may be surmised that the aluminum cladding must polarize to the potential of the core with extraordinary ease if the composite is to have useful resistance to saline exposure.

In Fig. 1, it can be seen that a cladding of 99.99% purity Al meets this requirement very well, whereas a cladding of commercial purity aluminum is much worse than no cladding at all. At the edges of the

[1] The nominal composition of AZ31A alloy is Mg-3% Al-1% Zn-0.4% Mn-0.15% Ca.

Fig. 1. Bare, 99% Al clad, and 99.99% Al clad AZ31A alloy after exposures to 3% sodium chloride. Period of exposure 7, 2, and 25 days, respectively.

coupons with 99.99% Al cladding, the AZ31A core exposed during shearing suffers little more than its open circuit corrosion. On the other hand, even beyond the edge damage apparent in Fig. 1, the cores of the coupons with commercial purity cladding were corroded to an average depth exceeding ⅛ in.

Not surprisingly, clad composites are more sensitive to low overvoltage constituents in aluminum than were the galvanic couples of Part I (1). Indeed from the shapes of the curves in Fig. 2 and 3, it may be surmised that even the 40 ppm Fe and 40 ppm Cu levels of the 99.99% Al are producing a significant harmful effect during exposure to 3% NaCl solution and that this level of iron, but not copper, is producing a significant harmful effect during exposure to seawater. However, if the limiting assumption is made that the exposed core alone suffers attack, the steady state rates of Fig. 4 correspond to core corrosion rates of about 180 mdd for sodium chloride exposure and about 120 mdd for seawater exposure. If these rates are compared to the steady-state rates of unclad core metal in each environment, it is deduced that the elimination of all cladding corrosion and all galvanic effects will only produce about a fivefold reduction in corrosion of the composite in either environment. This suggests that further purification of aluminum will yield comparatively small returns.

In Fig. 2 and 3 it can be seen that iron and copper are less deleterious during seawater exposure than

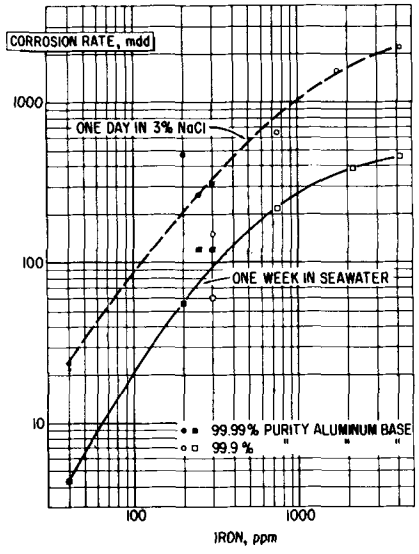

Fig. 2. Effect of iron in cladding on corrosion of Al clad AZ31A alloy sheet.

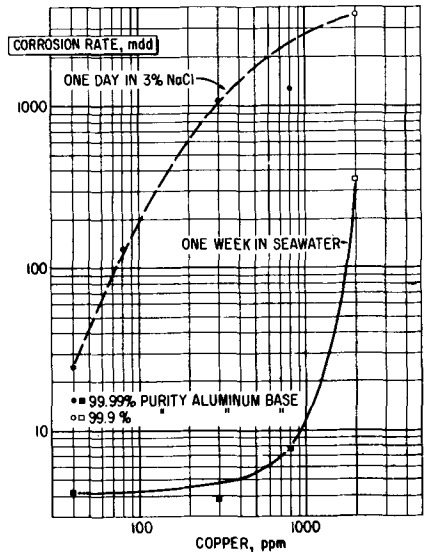

Fig. 3. Effect of copper in cladding on corrosion of Al clad AZ31A alloy sheet.

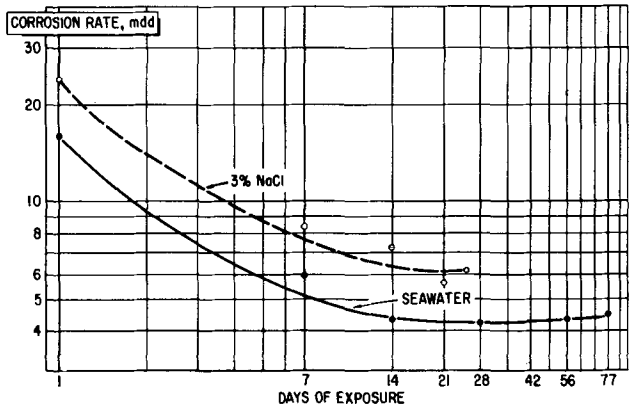

Fig. 4. Decrease in corrosion rate of 99.99+% Al clad AZ31A alloy sheet with time.

they are during exposure to 3% NaCl solution. Although the lesser test time in 3% NaCl solution prevents direct comparison of the environments from these results, there can be little doubt that iron constituent is much less aggressive and copper constituent enormously less aggressive during seawater exposure. Indeed the shorter test time in 3% NaCl was dictated by rapid disintegration of the coupons at the higher iron and copper levels. It is also interesting to note the appearance of a well-defined tolerance for copper in the cladding when exposure is made to seawater.

The effects of some additional cladding constituents are shown in Table I. Zinc is more mildly detrimental than iron and copper during exposure to 3% NaCl solution and, even at very high levels, it has no detrimental effect during seawater exposure. Magnesium, silicon, and manganese are substantially innocuous in either environment.

Difficulties in achieving bonding between magnesium AZ31A alloy cores and aluminum claddings containing large amounts of magnesium prevented a good test of the ability of magnesium constituent to suppress the effects of iron, copper, and zinc here as it did in the galvanic couples of Part I (1). Such an effect is likely in view of the similarity of all other results for the two types of specimens.

Table I. Effect of various constituents on corrosion of Al clad Mg AZ31A alloy sheet

	Corrosion rate, mdd	
	One day—3% NaCl	One week—seawater
99.9% Al	150	60
+0.16% Zn	300	28
+2.05% Zn	800	46
+0.53% Mg	190	86
+1.14% Mg	110	51
+0.10% Si (0.034% Fe)	250	86
+0.10% Si (0.038% Fe)	140	23
+0.27% Si (0.041% Fe)	250	130
+0.58% Si (0.039% Fe)	190	25
+0.05% Mn (0.036% Fe)	340	210
+0.29% Mn (0.042% Fe)	100	110
+0.51% Mn (0.059% Fe)	380	230
99.99% Al	29	4.3
+0.70% Mg	31	4.0
+0.05% Si	30	3.9
+0.30% Mn	69	4.9

The enormous difference in corrosivity between 3% NaCl solution and seawater toward some of the composites is of obvious interest. In Table II are shown the results on the corrosion of a particularly sensitive composite of the addition to 3% NaCl solution of two important seawater constituents, viz., Mg^{++} and $SO_4^{=}$. It can be seen that the addition of 0.3% Na_2SO_4 to the 3% NaCl solution decreases the corrosion of the composite by a small but probably significant amount. When 0.3% $MgCl_2$ is added to the sodium chloride solution, however, the corrosion of the composite is greatly reduced and indeed is nearly the same as the corrosion in seawater. The addition of 0.3% Na_2SO_4 to the above solution of sodium chloride plus $MgCl_2$ appears to have a rather trivial effect.

The difference in corrosivity between sodium chloride solutions and seawater probably depends on the difference in their buffering characteristics as shown in Fig. 5. Because of dissociation of the slightly soluble magnesium hydroxide corrosion product, the sodium chloride solution characteristically buffers at about pH 10.5. However, soluble magnesium salts in the seawater depress the solubility of the magnesium hydroxide and thus cause the system to buffer at a substantially lower pH. The lower bulk pH of the system in turn decreases the attack of the aluminum cladding by cathodically generated alkali. The consequences of this decreased attack of the cladding in order of increasing importance is probably: (a) reduction in the corrosion of the cladding per se, (b) slower exposure of the less resistant core at pits in the cladding, and (c) a smaller accumulation of low overvoltage constituents at the aluminum surface and thus less galvanic attack of the exposed core.

Table II. Effect of constituents in seawater on corrosion of AZ31A clad with 99.99% Al plus 0.08% Cu

Environment	Corrosion rate, mdd Two-day alternate immersion
3% NaCl	1980 ± 100
3% NaCl + 0.3% Na_2SO_4	1320 ± 80
3% NaCl + 0.3% $MgCl_2$	19 ± 1
3% NaCl + 0.3% $MgCl_2$ + 0.3% Na_2SO_4	17 ± 3
Seawater	15 ± 2

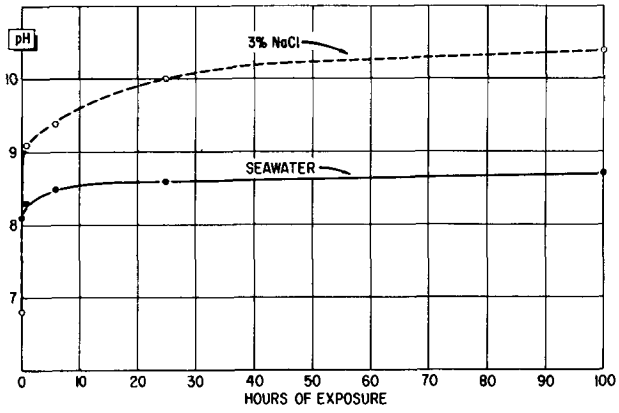

Fig. 5. pH as a function of time during corrosion in 3% NaCl and seawater of AZ31A clad with Al plus 0.08% Cu.

Just as in the case of the addition of magnesium to aluminum in the couples of Part I (1), the reduced galvanic effect from the addition of magnesium ion to the environment probably depends more on the distribution of cathodic attack rather than the total cathodic attack. Thus, a lower bulk pH should produce a sharper decrease in pH as a function of distance from each impurity-rich local cathode, and this should favor a higher ratio of impurity undercutting to impurity exposure.

Summary

High-purity aluminum cladding is extremely effective in protecting magnesium AZ31A alloy during saline exposure. The addition of iron or copper to the aluminum cladding materially impairs this protection by increasing the corrosion of the cladding and by making the cladding more aggressive galvanically toward the magnesium core. Zinc constituent has a milder effect than iron and copper while magnesium, silicon, and manganese are innocuous.

The above deleterious constituents have a much smaller effect during seawater exposure than they have during exposure to 3% NaCl solution because of the presence in seawater of a substantial concentration of magnesium ions which buffer the environment at a lower pH and thereby reduce the corrosion of the cladding by cathodically generated alkali. In addition to prolonging the life of the cladding, this also helps prevent the accumulation of low overvoltage constituents on the cladding surface and thus moderates its galvanic aggressiveness toward the magnesium core.

Manuscript received Jan. 19, 1959. This paper was prepared for delivery before the Buffalo Meeting, Oct. 6-10, 1957.

Any discussion of this paper will appear in a Discussion Section to be published in the June 1960 JOURNAL.

REFERENCES

1. M. R. Bothwell, *This Journal*, **106**, 1014 (1959).
2. J. D. Hanawalt, C. E. Nelson, and J. Peloubet, *Trans. Am. Inst. Mining Met. Engrs.*, **147**, 273 (1942).

Electrical Conduction in Liquid Dielectrics under Pulse Conditions

K. A. Macfadyen and G. C. Helliwell

Department of Physics, University of Birmingham, Birmingham, England

ABSTRACT

The need for a method of measuring conduction in pure nonpolar dielectric liquids under pulse conditions is considered, and details of a measurement technique are given. Experiments with hexane show that currents greater than 10^{-6} amp flow with certain electrode conditions, at a field strength of about 200 kv/cm, although the d-c conduction is much lower. A tentative explanation is offered.

Knowledge of the electrical conduction of dielectrics immediately after the application of an electric field is desirable not only as a means of understanding the mechanism of conduction in general but also to throw light on the breakdown process. This paper reports some experiments with a technique for revealing the time variation of conduction current during the first few microseconds after the application of a pulse of voltage between electrodes immersed in highly insulating liquids. Although applicable equally to polar liquids, the conduction mechanism of which is still not free from doubt (1), the method has so far been applied only to a typical nonpolar liquid (hexane) since views on the processes at work both in conduction and in electrical breakdown show considerable divergence.

Resumé of Present Theories

At low field strengths (about 1 kv/cm) the ultimate conduction in highly purified nonpolar liquids seems to be due to ionization by cosmic rays (2, 3) and other radiation. With stronger fields (over 100 kv/cm) there appears an added component of conduction attributed by different investigators to various forms of electron emission from the cathode with or without the additional influence of collision-ionization of the liquid molecules. Thus, Baker and Boltz (4) pictured thermionic emission from the cathode (without ionization) as the basic mechanism, a view modified in details by LePage and DuBridge (5) and by Dornte (6). Young (7) added the feature of collision ionization, a mechanism put forward earlier by Nikuradse (8). More recently Morant (9) and House (10) have produced evidence favoring a return to the thermionic emission theory. Green (11) considered cathode emission to be due to the combined effects of the applied field and the intense local fields set up by undischarged ions separated from the cathode by a superficial insulating layer.

Experiments leading to the foregoing views were carried out with d-c fields; some (10, 11) involved a lengthy process of "conditioning," whereby stable d-c conduction at field strengths near to breakdown could be obtained. It would clearly help in resolving these divergent views if the value of the conduction current during the first few microseconds after the application of the field, i.e., during the time of transit of an ion between the electrodes, could be established as a function of time. This is one object of the present research.

Apart from its intrinsic interest, the mechanism of conduction has an important bearing on our understanding of electrical breakdown in liquids. It was formerly held that there was no connection between these phenomena. In the case of pure, nonpolar liquids, however, present-day theories of breakdown are based mainly on the assumption that conduction and breakdown are in fact linked.

Thus, Goodwin and Macfadyen (12, 13) have explained their experimental results on the breakdown of various liquids under pulse conditions by a mechanism based on (*a*) a field-dependent cathode emission, and (*b*) intensification of the field at the cathode by positive space charge resulting from collision-ionization.

It is shown that these two relationships constitute a feedback mechanism leading to a catastrophic situation at a certain field strength even though emission and ionization may increase smoothly with field strength. Goodwin (14) later showed by electro-optical means that the predicted intensification of cathode field did in fact occur in certain cases. The breakdown condition is expressed in terms of ionic mobilities, ionization coefficients (Townsend's α), and cathode emission characteristics, all of which are hard to determine at field strengths approaching breakdown. The only estimates are either indirect or based on extrapolation from d-c measurements. Unless the "conditioning" process used by House (10) and by Green (11) is used, the available evidence points to conduction currents of the order of microamperes near breakdown. The object of the present investigation was to develop means for measuring currents of this order during a 5 μsec pulse. The fact that much of the experimental evidence on breakdown is derived from pulse tests is an added reason for the investigation.

The theory of Lewis (15), which has been strikingly successful in correlating breakdown strength with molecular vibration energy levels, does not enable specific predictions regarding conduction current to be made. The criterion here is that breakdown is contingent upon the setting-up of conditions

favorable for ionization by collision. Sharbaugh, Bragg, and Crowe (16), however, on the evidence of the effect of gap width on breakdown strength, suggest more explicitly that breakdown occurs when, on the average, each electron emitted by the cathode undergoes a certain fixed number n of ionizing collisions before reaching the anode. Their experiments suggest that for hexane $n = 9$ approximately. This would result in a current magnification by the factor 8100 (e^9) at breakdown. Cathode emissions of only 10^{-9} amp would thus be expected to yield currents of some microamperes, as in the theory of Goodwin and Macfadyen already considered.

Choice of Method

In order to facilitate interpretation, pulse breakdown measurements are usually carried out with a flat-topped pulse of voltage. The chief difficulty in measuring conduction under such conditions is the presence of very large charging and discharging currents at the beginning and end of the pulse. For example, in applying a 10 kv pulse to a pair of suitably spaced plane parallel electrodes (0.5 cm²) the rate of rise of voltage (10^{11} v/sec) gives rise to a charging current of about 1 amp, which is many orders of magnitude higher than the conduction current expected. In a similar way, irregularities in the pulse-top would produce spurious indication of conduction. Some form of bridge circuit in which the capacitive current is balanced out is necessary.

Gledhill and Patterson (17) in their work on electrolytic conduction at high field strengths used a 3-winding differential pulse transformer to compare the conduction in two cells. This method was tried but found unsuitable for the present work for two reasons: first, a display of conduction current vs. time was required, comparison by null method against a standard resistance or conduction cell being unacceptable for this work; and, second, the above requirement coupled with the smallness of the currents to be measured compared with the large charging current pulses resulted in a transformer design problem impossible of solution with existing materials.

The Schering bridge circuit (Fig. 1) was therefore used, and although a pulse output transformer was ultimately necessary with this circuit the design problem was much less severe, the main requirement being extremely good electrostatic shielding.

In Fig. 1, C_3 represents the capacitance in the conduction cell and i_c the conduction current. C_4 is a compensating condenser and C_2 an adjustable condenser for balancing the stray capacitance C_1. R_0, R_1, and R_2 are equal noninductive high-stability resistors. A flat-topped pulse, negative to ground, was applied to X.

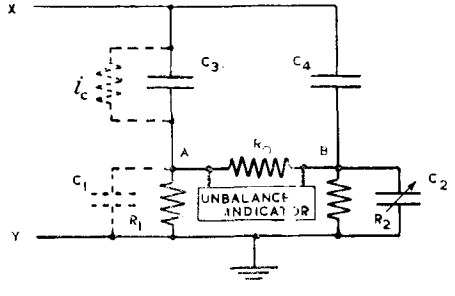

Fig. 1. Schering bridge circuit

An upper limit to the value of R_1 and R_2 was set by consideration of time constants (see below) and a lower limit by tube noise in the ensuing amplifiers. The first form of unbalance indicator to be used was a 2-stage differential amplifier. The requirements were onerous, since pulse potential differences of about a millivolt had to be amplified in the presence of unwanted pulses of some hundreds of volts. The method was abandoned because, whether triodes or pentodes were employed, it was found impossible to avoid spurious indications resulting from interelectrode capacitances. Nonlinearity was also troublesome.

The method of detecting the out-of-balance voltage finally adopted was to use a specially designed screened and balanced pulse transformer followed by conventional wide-band amplifiers and a cathode ray oscilloscope. Details are given below.

The Conduction Cell

The removable parallel plane electrode system (Fig. 2) was enclosed in a borosilicate glass vessel V provided with plane windows for microscopic examination. The vessel was included in a closed-circuit distillation system with a sintered glass filter to exclude particles larger than 1.5 μ in diameter.

The electrode system was designed to be suitable for d.c. as well as pulse measurements. The cylindrical electrodes A, B were supported in accurately milled V-grooves in the blocks C, D. C was highly insulated by its composite quartz-metal mounting E, F, G. Contact with A was made by a spring attached to the rod J. The metal plate F acted as a guard ring to intercept surface conduction over the fused quartz blocks E, G. The quartz-metal joints were made by soft-soldering the chemically silvered quartz blocks to a nickel-iron alloy ("Nilo 36") of low thermal expansion. The bond was strong enough to permit the V-grooves in the block to be milled in one operation. Thus, if A and B were accurately

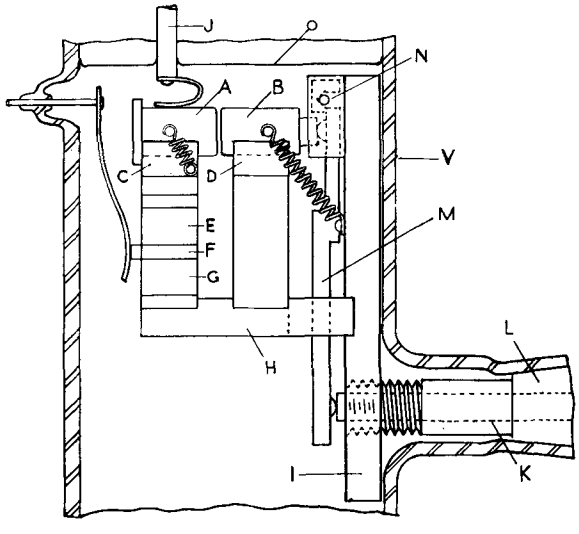

Fig. 2. Electrode assembly in conduction cell. Glass parts are shown in section.

turned, the adjacent surfaces automatically became exactly parallel. In lapping and polishing the end surfaces a special holder was used to preserve accurate geometry.

The pillars supporting A and B were attached to a base plate H. This was supported from the side-plate I which was curved to fit the inside of the glass vessel against which it was held by the screwed sleeve shown. Through this sleeve, to which was attached the cone L, there passed a spring-returned push-rod K sealed by a Neoprene O-ring and operated by a micrometer head (not shown) beyond L. Axial movement of the rod actuated the 10:1 lever M pivoted at N and thus enabled the gap between A and B to be adjusted to an accuracy of 1μ.

A phenomenon inseparable from measuring pulse currents at high field strengths is electrode movement resulting from electrostatic attraction. At a field strength of 1 megavolt/cm this force amounts to about 1 kg-wt/cm^2. With any practicable means of supporting the electrodes their natural frequency of vibration would be no higher than the "near ultrasonic" range; for 5 μsec pulses we may therefore regard the motion as limited by inertia rather than constraint, and attempts at extreme rigidity will be futile.

Solid cylindrical electrodes lightly constrained at the end remote from the gap were employed to make the movement predictable. If a mutual attraction of T dynes cm^{-2} is suddenly set up between the ends of the cylinders at a certain instant, the propagation of the tension pulse in one cylinder results in a steady rate of advance v of its end surface. If Y denotes Young's modulus of the material and ρ is density

$$v = T/\sqrt{(Y\rho)}$$

and since both electrodes move with this velocity the rate of change of capacitance C (in e.s.u.) is

$$\frac{dC}{dt} = 2\,CT/l\sqrt{(Y\rho)}$$

where l is the gap width. The value of T is given by

$$T = \epsilon E^2/8\pi$$

If the voltage, V, is maintained constant while this movement occurs the charging current will be

$$i_c = V\frac{dC}{dt} = E^3\,C\,\epsilon/4\pi\sqrt{(Y\rho)}\ \text{e.s.u.} \qquad [1]$$

where E is the field strength in the gap and ϵ the permittivity of the liquid.

With a 10 kv pulse applied between cylinders 7 mm in diameter with ends 100 μ apart the charging current is 11 μa, the velocity of each electrode surface 0.3 cm sec^{-1} and the velocity of the tension wave 3.4 x 10^5 cm sec^{-1}. With cylinders 0.85 cm long the time of a double passage of the wave from the electrode face to the far end and back is 5 μsec. By this time the required information has been displayed by the oscilloscope. A correction must be applied, according to Eq. [1], for the current due to the electrode movement; this probably sets a lower limit of about 1 μa to the current that can be measured under these conditions. With narrower gaps the charging current is higher, (Eq. [1]).

In principle it is possible to balance out this current by means of a similarly constructed vacuum condenser on the other side of the Schering bridge. It can be deduced from Eq. [1] that if the vacuum condenser has electrode area S'

$$\frac{S'}{S} = \epsilon^{2/3}$$

for equalization of the charging currents.

This procedure has not been necessary in the experiments reported here as measurable currents were found with field strengths at which electrode movement was not serious. Polystyrene parallel plate condensers were used as compensators in the bridge circuit, the design being such as to make plate movement negligible. Bridge balancing was done by fine adjustment of the electrode separation in the conduction cell and by the variable condenser C_2 (Fig. 1).

The Bridge Circuit

Assuming a symmetrical bridge circuit (Fig. 1) with $R_1 = R_2 = R_0$ (=R, say) and other corresponding quantities approximately equal, an analysis of the effect of applying a step-function voltage V_s to the input terminals XY leads to the expression

$$v_{AB} = V_1\,e^{-t/\tau_1} + V_2\,e^{-t/\tau_2} \qquad [2]$$

for the potential of A relative to B at a time t after the application of the step. The time constants are given by

$$\tau_1 = \frac{1}{3}R(C_1 + C_3)$$

$$\tau_2 = R(C_1 + C_3)$$

In the present case τ_1 and τ_2 are about 20 and 60 mμsec, respectively. It is this time which limits the value permissible for R, for in the event of any capacity unbalance the oscilloscope deflection will not be a measure of the conduction current i_c until long after the lapse of time τ_2. Moreover, the indication of changes in i_c will be delayed by a time of the order of τ_2. This sets an upper limit to the value of R which can be used. A lower limit is set by tube noise in the amplifier which amplifies v_{AB}. The conduction current is related to v_{AB} thus

$$i_c = \frac{3\,v_{AB}}{R}$$

The factors V_1 and V_2 in Eq. [2] depend on the degree of capacity unbalance. If C_3 (capacity of the conduction cell) and C_2 are the adjustable capacitances we find

$$\left.\begin{aligned} V_1 &= \frac{3\delta(C_2C_3) - (C_2 + C_3)\delta C_3}{2(C_2 + C_3)^2}\,V_s \\ V_2 &= \frac{-\delta(C_2C_3) + (C_2 + C_3)\delta C_3}{2(C_2 + C_3)^2}\,V_s \end{aligned}\right\} \qquad [3]$$

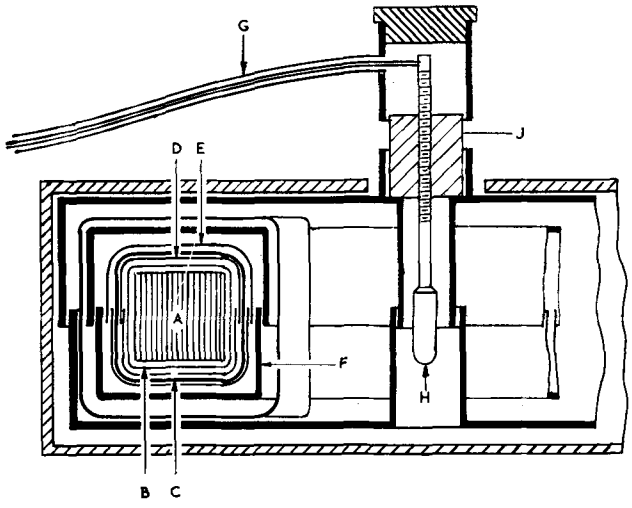

Fig. 3. Section of screened and balanced pulse transformer

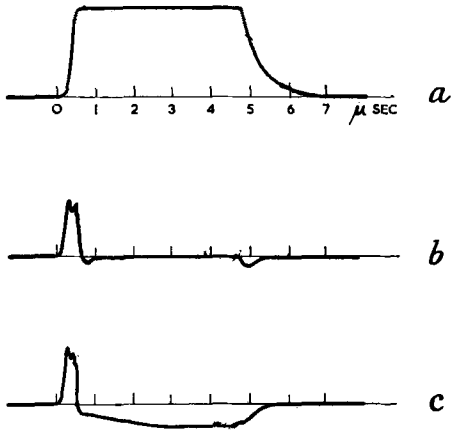

Fig. 4. Oscilloscope traces. (a) Voltage pulse applied to bridge circuit; (b) Output voltage pulse. The residual pulses are probably due to distributed inductance; (c) Output voltage pulse showing conduction current in cell. The shape of the conduction portion depended on the electrode surface conditions.

where δ represents the departure of the quantity in question from the value for perfect balance.

In practice the finite rise-time of the pulse renders Eq. [3] useful only in a general way. The final adjustments of C_2 and C_3 are made experimentally.

As mentioned earlier the essential feature of the unbalance indicator was a screened and balanced pulse transformer. This was wound on a spiral core (A, Fig. 3) of "Supermumetal" ($\mu \sim 50{,}000$) contained in a plastic case B. The primary winding C, occupying only a portion of the circumference, was surrounded by a complete earthed screen F, but in order to avoid spurious secondary emf's due to unbalanced capacity currents from primary to earth, two split foil screens D, E, each part being connected to the appropriate end of the winding, were interposed between the winding and its surroundings. In order to improve the balance still further the primary (52 turns of 38 S.W.G. enamelled wire) was wound back on itself. The final adjustment of balance was achieved by means of a "compensating turn" consisting of a short length of screened cable G leading from one primary terminal to the earthed case by way of a screw-plunger H having very low adjustable capacitance to the case. By joining both primary terminals to (say) point A (Fig. 1) the nut J could be adjusted to give the best discrimination against response to equal potential pulses at A and B simultaneously.

The whole transformer was enclosed in a "Mumetal" case and the entire circuit comprehensively screened. The first two stages of amplification, placed close to the transformer, gave a gain of about 100. When followed by the wide-band amplifier (5 Mc/s) in the oscilloscope (Solartron CD 513) this gave a screen sensitivity of 1 cm/75 μa of cell current.

Procedure

Early tests with the apparatus described were made with brass electrodes, lapped with wet rouge on a pitch block and lightly polished with "Silvo" polish on a "Selvyt" cloth stretched on a plate glass base. Then, after thorough degreasing, a layer of gold 1000Å thick was evaporated *in vacuo* onto the electrode faces. The electrodes were mounted as in Fig. 2 and the whole assembly continuously degreased in cold running refluxed hexane for at least an hour. The unit was mounted in its glass tube and washed out with several changes of hexane which had been dried with phosphorus pentoxide distilled and filtered in the same apparatus. The apparatus was normally filled with dried nitrogen from a cylinder. Microscopic examination of the gap was maintained during tests.

With a 1 kv pulse (Fig. 4a) applied to the bridge, balancing of capacitances was done by adjusting the electrode gap and the condenser C_2 (Fig. 1), giving an optimum oscilloscope trace as in Fig. 4b. The residual pulses were considered to be due to stray inductance in the connections, particularly those in the conduction vessel. Conduction was shown by the displacement of the trace in the center part of the pulse (Fig. 4c) and, although there seems to be some risk that "hangover" from the spurious initial pulse might invalidate this indication, it was possible to eliminate the uncertainty in the course of taking readings with different applied pulse voltages. The residual pulses were proportional to applied voltage while the conduction followed a different law.

Results

With the gold-plated electrodes described above the raising of the pulse input voltage from the balancing value of 1 kv to about 3 kv gave conduction as shown in Fig. 4c. The relatively slow rise of current with time was not an invariable feature.

Figure 5 shows the relationship between peak current and field strength. The two different symbols for the graph points indicate two experimental runs with different capacitance-balance conditions. In both cases breakdown occurred at a pulsed field strength of 0.52 mv/cm.

Similar results, with somewhat smaller currents, were obtained with other pairs of electrodes prepared in a similar way, but currents of this order could not always be obtained. A 5-times enhancement of the emission was obtained on occasion by prolonged exposure of the electrodes to air.

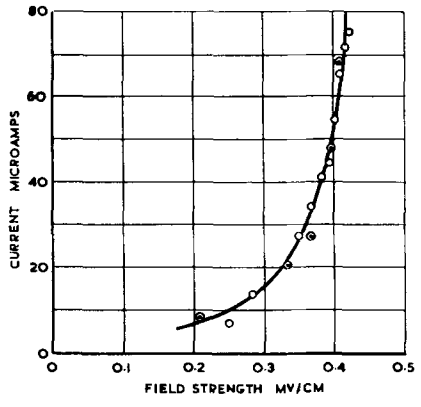

Fig. 5. Conduction characteristic of gold-coated electrodes in hexane. Electrode area: 0.35 cm^2. Electrode separation: 120μ.

With uncoated electrodes the conduction current was much lower. For example, stainless steel, mechanically polished with chromic oxide, gave a barely observable conduction, (about 5 μa). However, after several breakdowns had occurred currents up to about 150 μa were observed.

Experiments carried out to investigate the nature of the conduction included flushing the vessel and refilling with freshly distilled hexane. This produced no substantial change of conduction current. Conversely, when electrodes giving no measurable conduction were used with hexane which had been neither dried nor distilled, no conduction was observable.

Tests with double pulses, the second occurring at times down to 4 μsec after the first, showed no observable difference in behavior on the second occasion.

A further significant result was found in the course of comparing pulse and d-c conduction currents. A pair of electrodes giving a pulse current of 38 μa at 2.2 kv gave a steady conduction of only 0.07 μa with the same voltage and polarity. Furthermore, when the pulse test was again applied after a d-c test of this kind the pulse conduction was found to be reduced by about an order of magnitude.

In a similar way, the enhanced conduction from stainless steel after several breakdowns had occurred was largely suppressed by prolonged d-c testing, e.g., 45 hr with a current of 6 x 10^{-9} amp at 100 kv/cm. Microscopic examination of the electrodes after this treatment showed globular particles about 5μ in diameter mainly clustered around the 70μ craters left by previous breakdowns. These particles were apparently made of the wax-like substance reported by previous observers (5) and assumed to be a polymer resulting from electronic bombardment of the liquid molecules.

Discussion

In view of the preliminary nature of these experiments it would be unwise to attempt to deduce too much from them. The high values of pulse conduction current observed are far greater, having regard to the field strength, than the predictions of any previous measurements or theory. Ionic conduction seems to be ruled out by the dependence of conduction on electrode surface preparation and the lack of correlation between conduction and liquid sample.

Simple calculations show that the total charge during the 5 μ pulse is many orders of magnitude greater than could be explained by orientation of impurity dipoles. Time considerations also make this idea untenable. We are thus led to the conclusion that the conduction current originates at the electrode surfaces, the most likely mechanism being electron emission from the cathode, with or without magnification by collision-ionization in the liquid. The latter point must remain uncertain as conditions prevented a series of measurements with differing gap widths.

The magnitude of the current suggests that it may be limited by negative space charge. An analysis of the case of parallel plane electrodes of separation l and p.d. V volts drawing a space charge-limited current of negative ions having a mobility u cm/sec per volt/cm gives the expression

$$I = \frac{A\,u\,\epsilon}{32\,\pi\,10^{11}\,l^3}\,V^2 \text{ (amp)} \qquad [4]$$

where A is the plate area and ϵ the permittivity. With $l = 0.01$ cm, $\epsilon = 2$, $A = 0.5$ cm^2, $u = 4.4$ x 10^{-4} cm/sec per volt/cm (18) and $V = 4$ kv we find $I = 7$ x 10^{-4} amp, which is only one order of magnitude higher than the observed current. A logarithmic plot of Fig. 5, however, shows a law of variation of about the 5th power, which is different from Eq. [4], but the orders of magnitude of the quantities show that space charge cannot be ruled out as a factor in conduction of this kind, especially when it is remembered that emission from the cathode almost certainly occurs from small areas ($\sim 10^{-4}$ cm^2) as the papers by Dornte (6) and by Goodwin (14) show. Although it can be proved in general that a law of the form $I \propto V^2$ is to be expected for a copiously emitting cathode and an anode, irrespective of their shapes, the argument does not apply when the emission is confined to limited areas on the cathode surface. In this case the influence of negative space charge will be enhanced.

The fact that prolonged exposure to air promoted emission from evaporated gold layers suggests an emission mechanism of the type envisaged by Green (11), namely, extraction of electrons by positive ions on a thin layer, in this case perhaps of CO (19). Some support for this view can be obtained for the high emissions after breakdown and from the effects observed after prolonged d-c conduction. A possible explanation of these phenomena is that a layer of wax (or other material) of suitable thickness results in copious emission according to the mechanism envisaged by Green, but that prolonged conduction results in a wax layer of excessive thickness, reducing emission and ultimately becoming visible under the microscope. Although the present experiments have not been carried far enough for a definite conclusion it seems possible that deposition of solid matter may be an important factor in "electrode conditioning." The experiments are continuing with improved apparatus including a Wagner earth to improve the accuracy of the capacity balance.

Acknowledgments

The authors wish to thank Professor P. B. Moon for placing the facilities of the Physics Department at their disposal. One of the authors (G.C.H.) acknowledges a grant from the British Department of Scientific Industrial Research.

Manuscript received April 8, 1959. This paper was prepared for delivery before the Philadelphia Meeting, May 2-7, 1959.

Any discussion of this paper will appear in a Discussion Section to be published in the June 1960 JOURNAL.

REFERENCES

1. J. Hart and A. G. Mungall, *Can. J. Phys.*, **34**, 491 (1956).
2. G. Jaffé, *Ann. der Phys.*, **29**, 125 (1909).
3. I. Adamczewski, *Nature*, **137**, 994 (1937).
4. E. H. Baker and H. A. Boltz, *Phys. Rev.*, **51**, 275 (1937).
5. W. R. LePage and L. A. DuBridge, *ibid.*, **58**, 61 (1940).
6. R. W. Dornte, *Ind. Eng. Chem.*, **32**, 1529 (1940).
7. D. R. Young, *J. Appl. Phys.*, **21**, 222 (1950).
8. A. Nikuradse, *Arch. Elektrotech.*, **26**, 250 (1932).
9. M. J. Morant, *Proc. Phys. Soc.*, **B68**, 513 (1955).
10. H. House, *ibid.*, **B70**, 913 (1957).
11. W. B. Green, *J. Appl. Phys.*, **26**, 1257 (1955).
12. D. W. Goodwin and K. A. Macfadyen, *Proc. Phys. Soc.*, **B66**, 85 (1953).
13. K. A. Macfadyen, *Brit. J. Appl. Phys.*, **6**, 1 (1955).
14. D. W. Goodwin, *Proc. Phys. Soc.*, **B69**, 61 (1956).
15. T. J. Lewis, *J. Appl. Phys.*, **27**, 645 (1956).
16. A. H. Sharbaugh, J. K. Bragg, and R. W. Crowe, *ibid.*, **26**, 434 (1955).
17. J. A. Gledhill and A. Patterson, Jr., *J. Phys. Chem.*, **56**, 999 (1952).
18. I. Adamczewski, *Ann. phys.*, **8**, 309 (1937).
19. B. M. W. Trapnell, *Proc. Roy. Soc. (London)*, **A218**, 566 (1953).

Luminescence of Copper-Activated Calcium and Strontium Orthophosphates

W. L. Wanmaker and C. Bakker

Light Division, N. V. Philips' Gloeilampenfabrieken, Eindhoven, Netherlands

ABSTRACT

Copper produces a strong luminescence in $Ca_3(PO_4)_2$. Luminescence in $Sr_3(PO_4)_2$ occurs only in the presence of small amounts of foreign ions such as Ca, Zn, Cd, Mg, or Al. These additions give rise to a new crystal phase which is probably isomorphous with β-$Ca_3(PO_4)_2$. The emission peaks under excitation with 2537Å of β-$Ca_3(PO_4)_2$, α-$Ca_3(PO_4)_2$, and of $Sr_3(PO_4)_2$ modified with Al are found at 4800, 5700, and 4950Å, respectively. Sensitization occurs with Mn, giving rise to a red emission peak. The temperature dependence of the fluorescence is good, especially that of β-$Ca_3(PO_4)_2$-Cu and $Sr_3(PO_4)_2$ partly substituted with Mg and Ca. Phosphor application in lamps presents difficulties due to the materials' sensitivity to air at binder bake-out temperatures.

In sulfides, copper is a well-known activator. In this type of phosphor copper does not in general act as a characteristic activator like manganese, but as an indirect one, facilitating the excitation of electrons of the neighboring sulfur ions (1).

In oxygen-dominated phosphors, however, activation by copper is not so generally known. It appears from the survey given by Kröger (2) that carbonates, oxides, halides, phosphates, and silicates may be activated by copper. In some cases copper acts only as an intensifier of the luminescence of the pure substance, as with $ThSiO_4$ described by Leverenz (3). Copper-activated alumino-silicate phosphors were investigated by Claffy and Schulman (4) and found to have a brightness of about one-third of that of calcium tungstate. Recently Wilke (5) also reported the preparation of copper-activated silicates.

Among copper-activated phosphates the following luminescent materials are known: AlBaMg-phosphate glass (6) with a pinkish white fluorescence; calcium apatites giving a blue emission (7); calcium metaphosphate, also with a blue emission (8); and finally the red-emitting magnesium orthophosphate (9).

Quite recently Uehara and Kofuya (10) described the properties of β-calcium orthophosphate activated with Cu and with Cu and Mn. The preparation of β-$Ca_3(PO_4)_2$ modified with the foreign ions Cd, Sr, Mg, and Zn is also given in the patent literature. With manganese, sensitization occurs, giving rise to a red emission band in addition to the blue band due to copper (11).

In this paper the preparation and properties of the efficient β-$Ca_3(PO_4)_2$-Cu and of $Sr_3(PO_4)_2$-Cu phosphors, substituted with small amounts of Al, Mg, Zn, and Cd, are described in some detail. Similar phosphors are prepared by substituting a small part of the Sr by Ca with a resulting green emission. While β-$Ca_3(PO_4)_2$-Cu has a narrow emission peak at 4800Å, the corresponding Sr compound with a small amount of Al has its peak wave length at 4950Å. Incorporation of zinc and magnesium into $Sr_3(PO_4)_2$-

Cu gives rise to an emission peak at about 4900Å, and incorporation of Cd and Ca gives a peak at 5100Å.

Method of Phosphor Preparation

The ingredients used in the firing mixtures were reagent grade $CaHPO_4$, $SrHPO_4$, $CaCO_3$, Cu_2O, $CuSO_4$, Al_2O_3, and $MnNH_4F_3$ or $MnCO_3$. The required amounts of the dry materials were thoroughly mixed and subsequently fired. The firing was done in a special tube furnace, in which alumina boats filled with the firing mixture were gradually passed through the heating zone in a neutral or slightly reducing atmosphere (N_2 with O to 0.5% of pure hydrogen). The furnace exit was provided with a gas lock to prevent the entry of air when the fired samples were removed from the furnace. The best results were obtained by a double firing at temperatures of 1160°-1240°C, in N_2 with 0.03% H_2, for periods of 1 hr each.

Incorporation of the Activator in the Host Crystal Lattice

Air-fired copper-activated phosphors give no luminescence at all or at best a very weak one, whereas firing in a slightly reducing atmosphere produces strongly luminescent materials. With too high a concentration of hydrogen in the firing atmosphere, metallic copper is produced, while too low a concentration of hydrogen gives products with a slightly blue body color, due to divalent copper. This shows that the copper ion should be present in the monovalent state.

Chemical analysis confirmed that, in the strongly luminescent products, all the copper is present in the monovalent state, e.g., in a β-$Ca_3(PO_4)_2$-Cu phosphor ($Cu/P_2O_5 = 0.01$ and $Al/P_2O_5 = 0.10$) the amounts of total and of monovalent copper were both found to be 0.19 wt%. The percentage of monovalent copper was determined by dissolving the phosphor sample in hydrochloric acid in the presence of an excess of potassium dichromate and measuring the amount of unused dichromate by titration with an 0.01*N* Fe^{II}-sulfate solution.

With large amounts of copper, brown colored products are mostly formed, indicating that part of the copper added is not incorporated in the crystal lattice. With the simultaneous addition of Al, the ratio of Cu/P_2O_5 at which the brownish discoloration occurs, increases. Obviously Al facilitates the incorporation of the monovalent Cu^+ ion in the crystal lattice. This phenomenon can be explained easily by the theory of charge compensation, with one Cu^+ and one Al^{3+} ion substituting for $2Ca^{2+}$ or $2Sr^{2+}$ ions, respectively (12).

Although this hypothesis may be applicable to β-$Ca_3(PO_4)_2$-Cu phosphors, other effects must also be taken into account with $Sr_3(PO_4)_2$-Cu.

The β-$Ca_3(PO_4)_2$-Cu phosphor is efficient without the addition of Al, whereas unsubstituted $Sr_3(PO_4)_2$-Cu shows only a very weak, deep blue emission (peak wave length at 4450Å). X-ray analysis showed that the latter substance has the normal $Sr_3(PO_4)_2$ lattice structure (13). However, with $Sr_3(PO_4)_2$-Cu a strong luminescence develops when ions such as Al, Ca, Mg, Zn, and Cd are added. At the same time, the partial substitution of Sr by Al, Ca, Zn, Mg, and Cd gives a pronounced change in the crystal lattice. A new structure appears which is identical with that of $Sr_3(PO_4)_2$-Sn phosphors, where part of the Sr has been replaced by smaller divalent ions like Mg. This structure is similar to the structure of the β-$Ca_3(PO_4)_2$ lattice, as described by Koelmans (14).

Apparently the presence of foreign ions transforms the $Sr_3(PO_4)_2$ structure in such a way that a different structure is obtained which is probably isomorphous with β-$Ca_3(PO_4)_2$ and which gives rise to a strong luminescence with Cu as the activator.

The brightest phosphors are made with a slight excess of P_2O_5, resulting in a total metal to P_2O_5 ratio of about 2.90-2.95. Usually better results are obtained with $CuSO_4$ than with Cu_2O. This may be due to the decomposition of the $CuSO_4$ during the firing process, which forms a more reactive copper compound in the process.

Calcium Orthophosphate Phosphors

$Ca_3(PO_4)_2$ exists in two crystal structures, viz., α-$Ca_3(PO_4)_2$, stable at a temperature above 1180°C, and β-$Ca_3(PO_4)_2$, stable below this temperature. Kroeger found (15) that the transition temperature is raised by the incorporation of small amounts of Ce, Al, or Mn in $Ca_3(PO_4)_2$·Ce,Mn. Similar results were obtained by Butler (16) who also found a high transition temperature with a composition different from the stoichiometric one and in the presence of the activator Sn. From the foregoing it is clear why we obtained the β-$Ca_3(PO_4)_2$ modification in nearly all cases. This compound, when activated with copper, gives a blue emission with a peak at 4800Å (Fig. 1).

It was interesting to investigate the luminescent properties of the α-modification. The α-$Ca_3(PO_4)_2$ structure (as identified with x-ray analysis) was obtained by firing unactivated $Ca_3(PO_4)_2$ at 1270°C

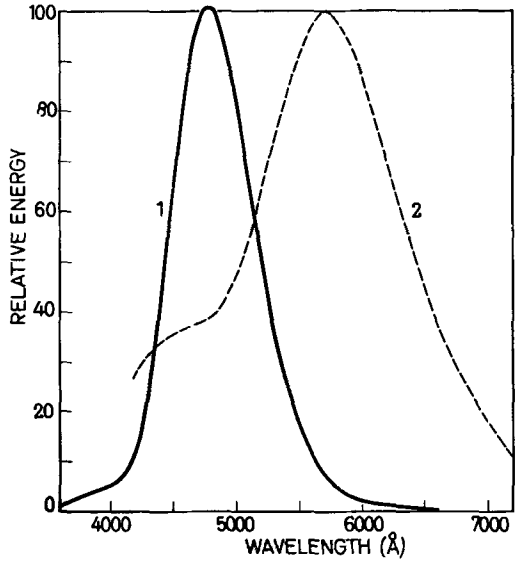

Fig. 1. Spectral energy distribution curves of the emission of β-$Ca_3(PO_4)_2$-Cu [curve 1] and of α-$Ca_3(PO_4)_2$-Cu [curve 2]. Mole ratios: $Cu/P_2O_5 = 0.005$ [2] and 0.01 [1]. $Me/P_2O_5 = 2.99$ [2] and 2.90 [1]. Firing temperature: 1160°C [1] and 1280°C [2]. Firing atmosphere: N_2 with 0.03% H_2.

in air. A low percentage of copper ($Cu/P_2O_5 = 0.005$) in the form of $CuSO_4$ was added to the fired product and the mixture was refired at 1280°C. X-ray analysis showed that the crystal structure did not change during this refiring process and that the crystal structure was entirely the same as that of α-$Ca_3(PO_4)_2$ described by Mackay (17). In this way a nearly white luminescent product (with 2537Å excitation) was prepared, the emission peak lying at 5700Å (Fig. 1). With 3650Å excitation a yellow emission occurs. The small emission peak at 4800Å is attributed to a small amount of β-$Ca_3(PO_4)_2$ in the refired product. When the refiring temperature is lowered to 1100°C only the blue-emitting phosphor is obtained.

With an increase of the amount of copper added, a shift of the emission peak of β-$Ca_3(PO_4)_2$-Cu to longer wave lengths is observed, the crystal structure remaining the same. The shift starts from a Cu/P_2O_5 ratio of 0.05 and reaches an emission peak of 4900Å at a ratio of $Cu/P_2O_5 = 0.20$. In order to obtain the high u.v. absorption desirable for application in fluorescent lamps, a Cu/P_2O_5 ratio of about 0.05 is needed. With the simultaneous addition of Cu^+ and Al^{3+}, the incorporation of the copper ion is obviously facilitated, as deduced from the increase in brightness found. The Al shifts the emission peak to shorter wave lengths and gives a narrower emission band.

With the introduction of manganese, a second emission peak arises at 6550Å. With increasing amounts of manganese, the intensity of the red manganese band is raised and that of the blue copper band is lowered, as is generally known to be the case with sensitized phosphors. This is illustrated in Fig. 2. The brightness of the phosphors activated with copper and manganese is lower than that of the single activated phosphors and falls off rapidly with increasing amounts of manganese. With $Mn/P_2O_5 = 0.08$ a brightness of about 25% of that of Mg-arsenate is reached.

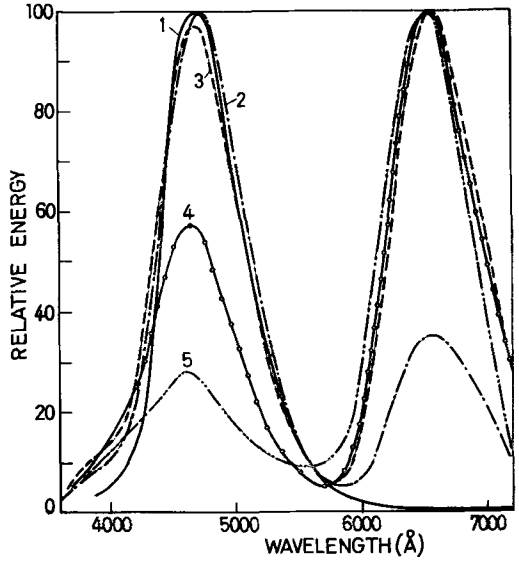

Fig. 2. Spectral energy distribution curves of the emission of β-$Ca_3(PO_4)_2$-Cu·Mn modified with Al, with increasing amounts of Mn. Mole ratios: $Cu/P_2O_5 = 0.02$ and $Al/P_2O_5 = 0.05$

Curve	Mole ratio Mn/P_2O_5
1	0
2	0.02
3	0.04
4	0.06
5	0.08

In contrast to the modified Sr-orthophosphate phosphors the partial replacement of Ca in β-$Ca_3(PO_4)_2$ by foreign ions such as Mg, Zn, and Cd decreases the efficiency of the phosphor. Confirming the results of Uehara and Kofuya (11) the addition of a small amount of Mg and Zn, respectively, was found to shift the emission peak to shorter wave lengths. The partial substitution of Ca by Cd does not change the emission. With addition of La and Ce, a change in the spectral distribution is observed. For example, with a mole ratio of $Al/P_2O_5 = 0.06$, $Cu/P_2O_5 = 0.02$, and $Me/P_2O_5 = 0.25$ (Me = La or Ce), Ce, in addition to its own characteristic band at 3500Å, gives rise to the development of a sensitized Cu-band at 4700Å and La to one at 4900Å.

X-ray diffraction analysis shows that all of the latter substituted $Ca_3(PO_4)_2$ phosphors have the β-$Ca_3(PO_4)_2$ structure. Thus the variations observed in the emission spectra are not caused by a change in the crystal structure but by the perturbing action of the foreign ions on the ground and excited states of the activator ion.

Strontium Orthophosphate Phosphors

$Sr_3(PO_4)_2$ phosphors with Cu give only a very weak deep-blue luminescence with an emission peak at 4450Å. In the presence of even a small amount of Al a strong blue-green emission occurs. With a sufficiently high amount of Al the deep blue emission disappears completely. This effect may be clearly seen from Fig. 3. The brightness of $Sr_3(PO_4)_2$-Cu modified with Al may reach a value of 125% of the brightness of Sb-activated calcium halophosphate.

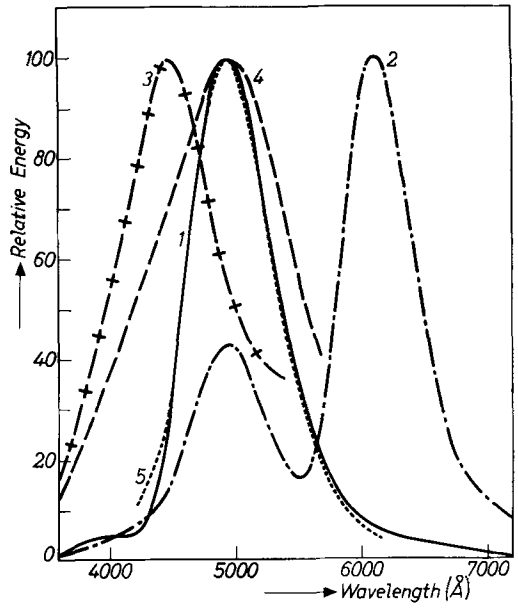

Fig. 3. Emission of Cu- and Cu,Mn-activated Sr orthophosphates. Mole ratio Cu/P_2O_5: curves 1 and 2 = 0.07, curves 3, 4, and 5 = 0.04; Al/P_2O_5: curves 1 and 2 = 0.21, curve 3 = 0, curve 4 = 0.005, curve 5 = 0.02; Mn/P_2O_5: curves 1, 3, 4, and 5 = 0, curve 2 = 0.06.

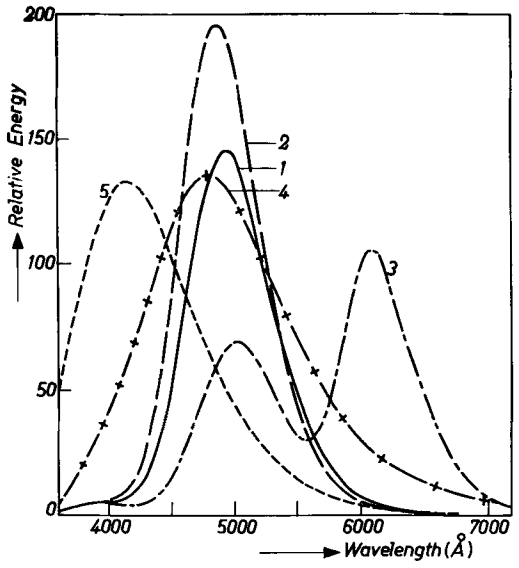

Fig. 4. Emission of Cu-activated Sr orthophosphates, modified with Zn [curve 1], Mg [curve 2], and Cd [curve 3]. The intensities are compared with those of Sb^{3+}-activated calcium halophosphate [curve 4] and of $CaWO_4$ [curve 5]. Composition of phosphors in Table I.

Besides Al, other foreign ions, such as Ca, Zn, Mg, and Cd also give strongly luminescent products, with a brightness higher than that of the known calcium tungstate and Sb-activated calcium halophosphate, as illustrated in Fig. 4. In this figure the intensities of the new phosphors are compared with those of the blue-emitting (Sb-activated) calcium halophosphate and of calcium tungstate. The influence of these foreign ions on the luminescence is due to the effect they have on the crystal structure. Koelmans (14) stated already that the normal Sn-activated $Sr_3(PO_4)_2$ gives only a weak u.v. emission, whereas ions such as Al and Mg cause a transformation into a structure analogous to that of β-$Ca_3(PO_4)_2$. Only the latter structure produces any luminescence. In fact the structures of the Sn-activated phosphors described by Koelmans and of the present Cu-activated ones are identical. As with calcium orthophosphate, the corresponding strontium compound can be activated by Cu and Mn and gives an additional red manganese band at 6100Å (Fig. 3). The intensities of the green Cu and the red Mn bands vary with increasing Mn content in the same manner as already described for the Ca-orthophosphate phosphor.

Modified Orthophosphate Phosphors

Koelmans (14) found that, starting from β-$Ca_3(PO_4)_2$, a gradual replacement of Ca by Sr results in a widening of the β-$Ca_3(PO_4)_2$ lattice until a Ca/Sr ratio of about 0.2 is reached. With more Sr, there is a rather sharp transition to the normal Sr orthophosphate structure and the emission of the Sn-activated phosphor changes from 6200 to 3700Å. With part of the Sr replaced by Ca ($CaO/P_2O_5 = 0.2$) the emission peak of the Cu-activated phosphor lies at 5150Å. The gradual replacement of Sr by Ca shifts this emission peak to shorter wave lengths, until the emission of pure β-$Ca_3(PO_4)_2$-Cu is reached. With the further addition of Al to the SrCa-orthophosphate activated with copper, the emission peak shifts to the blue region of the spectrum.

Table I. Quantum efficiency of Cu-activated orthophosphate phosphors with Al; excitation 2537Å; activator concentration $Cu/P_2O_5 = 0.02$; Al concentration $Al/P_2O_5 = 0.06$; x = Ca, Cd, Zn, and Mg

Phosphor	Activator	x/Sr	Q.R., %
β-$Ca_3(PO_4)_2$	Sn	—	81
$(Sr, Mg)_2(PO_4)_2$	Sn	0.12	87
β-$Ca_3(PO_4)_2$	Cu	—	76
$(Sr, Zn)_3(PO_4)_2$	Cu	0.07	68
$(Sr, Mg)_3(PO_4)_2$	Cu	0.09	82
$(Sr, Ca)_3(PO_4)_2$	Cu	0.11	73
$(Sr, Cd)_3(PO_4)_2$	Cu + Mn	0.11	69

With the partial substitution of Sr by Zn and Mg, respectively, the emission peak is found at 4900Å and at still shorter wave lengths in the presence of additional Al. In accordance with Koelmans' results (14) we found that the amount of foreign ion required to obtain the desired structure of $Sr_3(PO_4)_2$ is smallest with a small substituting ion, e.g., Mg. With the low ratio of $Mg/P_2O_5 = 0.08$ a fluorescence intensity of 70% of that of blue calcium halophosphate is already reached.

The substitution of Sr by Cd gives an emission peak at 5150Å. Besides the foreign ions already mentioned, it was also found that the addition of the rare earth ions La and Ce to $Sr_3(PO_4)_2$ produces luminescent products with an emission maximum at 4500Å. In accordance with Koelmans' results the maximum brightness of the substituted Sr-orthophosphates is achieved with a molar ratio Me/P_2O_5 of about 0.2-0.3 (Me being Mg, Zn, or Cd).

Quantum Efficiency

The efficiencies at room temperature of a number of phosphors, as measured by Bril (18), are given in Table I, together with the values for β-$Ca_3(PO_4)_2$-Sn and $Sr,Mg(PO_4)_2$-Sn, as reported by Koelmans (14). It is seen that the quantum efficiencies of the Cu-activated β-$Ca_3(PO_4)_2$ and of the modified Sr orthophosphates are nearly as high as those of the corresponding Sn-activated phosphors. We cannot state definitely that, for each of the phosphors mentioned in the table, the preparation has been studied sufficiently thoroughly so as to be certain that the figures given for the quantum efficiency are the highest attainable.

Reflection and Excitation Spectra

Figure 5 shows the reflection spectra of some Cu-activated phosphors, together with those of the unactivated product. The small amount of Al which is present does not affect the absorption materially. It may be seen that the introduction of the copper ions produces an absorption in the 2500-3500Å region. The excitation spectra of some phosphors are also shown. From this figure it may be seen that the phosphors investigated are strongly excited by the 2537Å mercury line. Thus this new type of phosphor might be very suitable for low-pressure mercury discharge lamp use, were it not for the difficulty presented by the application of these phosphors. This will be pointed out below. Excitation with cathode rays gives only a weak luminescence, the emission color being the same as with u.v.-excitation.

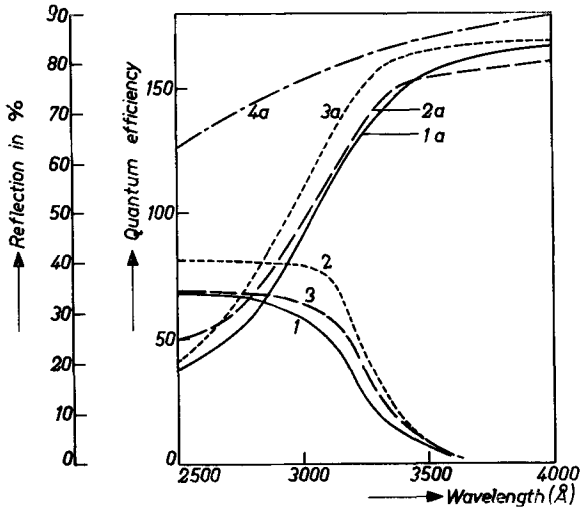

Fig. 5. Reflection (1a-4a) and excitation (1-4) spectra of some Cu- and Cu, Mn-activated Sr orthophosphates. Composition of phosphors in Table I. [1] $(Sr, Zn)_3 (PO_4)_2$ · Cu; [2] $(Sr, Mg)_3 (PO_4)_2$ · Cu; [3] $(Sr, Cd)_3 (PO_4)_2$ · Cu · Mn; [4] $Sr_3 (PO_4)_2$.

Temperature Dependence of Fluorescence

The temperature dependence of the fluorescence of phosphors can hardly be predicted, the behavior of an activator in different matrices varying considerably. Generally speaking, the fluorescence intensity decreases rapidly with increasing temperature when there is a large interaction between the activator ions and the surrounding ions, and vice versa. This is the reason why phosphors with activator ions such as Ce^{3+} and Mn^{4+} with an excited electron in an inner shell generally show a good temperature dependence of the fluorescence. A narrow emission band is, in many cases, evidence for a small disturbing action of the surrounding ions on the activator ion.

As the Cu-activated phosphors described have a band-width of 700-800Å, which is smaller than that of most phosphors, a good temperature dependence of fluorescence of these phosphors could be expected. Figure 6 shows that this is true for β-$Ca_3(PO_4)_2$-Cu and modified $Sr_3(PO_4)_2$-Cu phosphors. With the substitution of some of the Sr in $Sr_3(PO_4)_2$ by other ions, a marked effect on the quenching temperature (i.e., the temperature at which the fluorescence intensity drops sharply) is observed. Figure 6 shows that the quenching temperature decreases in the sequence: Ca, Mg, Zn, and Cd. Similar curves, but with a lower quenching temperature of about 20°C, were obtained with the corresponding phosphors activated with Cu and Mn. It is interesting to note that the ions of group IIa elements of the periodic table (Ca and Mg) have only a small influence on the quenching temperature, whereas the ions of the second sub-series (Zn and Cd) exert a strong one.

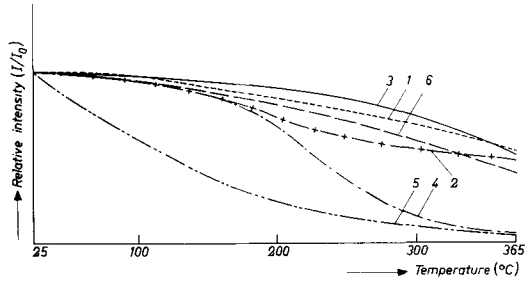

Fig. 6. Variation of fluorescent intensity with temperature for copper-activated calcium orthophosphate [curve 1], and modified strontium orthophosphates [curves 2, 3, 4, 5, and 6]. Composition: moles Me, etc., per 1 mole P_2O_5: Me = 2.90 or 2.95 [curve 2]. Me = Ca(Sr) + Cu + 3/2 Al. Cu = 0.02; Al = 0.06; X = 0.30 (X = Ca, Zn, Cd, or Mg). X = 0.30 (X = Ca, curve 3; Zn, curve 4; Cd, curve 5; or Mg, curve 6).

Obviously the Zn^{2+} and Cd^{2+} ions with a different electronic configuration have a greater disturbing effect on the copper ions than have the Mg and Ca ions. It should be noted that the emission peak of the phosphors investigated shifts to shorter wave lengths at increasing temperatures. An increased activator concentration gives a lower quenching temperature, as was also found with willemite (19) and Mg arsenate (20).

With a constant amount of Cu present, an increase in the Al content improves the temperature dependence of the fluorescence. From the shape of the curves it follows that this type of phosphor may be used in lamps in which good temperature stability is required, namely, high-pressure mercury discharge lamps with an outer bulb coated with a color-correcting phosphor. The difficulties encountered in the application, however, are the same as those met in fluorescent lamps (see below). Moreover the excitation with 3650Å radiation is rather poor (Fig. 5).

Decay of the Cu-Activated Phosphors

The decay of some Cu-activated orthophosphates was measured with the apparatus developed by Bril and Klasens (21). Decay curves are shown in Fig. 7 for Sr orthophosphate modified with Ca and activated with Cu and Mn. Similar curves were obtained with the other Cu-activated orthophosphates. The decay proved to be exponential for Cu, as may be expected for a characteristic activator. The decay constant for Cu in the various phosphors is approximately constant, viz., 40 x 10^{-4} sec. This means that the life time of the excited state is rather long. The decay constant of the Mn emission of some double-activated phosphors was also measured, using an RG 1 filter (transmitting only the radiation with a wave length greater than 6000Å), in order to remove the blue emission produced by the copper ions. For the Mn emission a decay of 1.9 x 10^{-2} was found, in accordance with the figures from the literature for the Mn^{2+} emission in other phosphors.

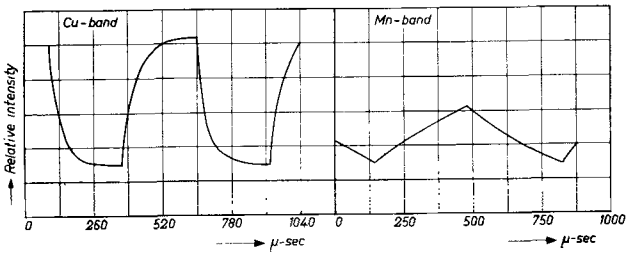

Fig. 7. Build-up and decay of $(Sr, Ca)_3 (PO_4)_2$-Cu, Mn. Composition: Me = 2.90; Cu = 0.02; Al = 0.06; Mn = 0.04; P_2O_5 = 1.

Application

From Fig. 4 and from the quantum efficiencies given in Table I, it is to be expected that this new type of phosphor may be of great importance for fluorescent lamps. In practice, however, serious difficulties arise when the current techniques of lamp making are followed. In order to remove the binder used for applying the phosphor coating, the bulbs are heated to 450°-550°C in air. However, the Cu-activated phosphors are very sensitive to oxidation at temperatures higher than 400°C. Thus after the binder bake-out at 550°C, the phosphor may lose as much as 80% of its efficiency. Phosphors of small grain size are especially sensitive in this respect.

From the foregoing it follows that the phosphors described cannot be applied in the usual way, but special techniques will be required in order to maintain the brightness of the phosphor. The problem of the application of the Cu-activated phosphors is analogous to that of some phosphors which are activated with trivalent cerium, as described by Henderson and Ranby for the calcium halophosphate phosphors (22).

Acknowledgments

The authors wish to express their thanks to Dr. A. Bril for the measurements of the quantum efficiency, the reflection and the excitation spectra of the phosphors; to Dr. H. Koelmans for many helpful discussions regarding the structure of the phosphors; to Mr. E. G. Berns for the determination of the monovalent copper; to Mr. J. Riemens for the measurement of the spectral emission curves; and to Mr. J. G. Verlijsdonk for part of the experimental work.

Manuscript received June 10, 1959. This paper was prepared for delivery before the Philadelphia Meeting, May 3-7, 1959.

Any discussion of this paper will appear in a Discussion Section to be published in the June 1960 JOURNAL.

REFERENCES

1. F. A. Kroeger, *Brit. J. Appl. Phys.*, Suppl. No. 4, 58 (1954).
2. F. A. Kroeger, "Some Aspects of the Luminescence of Solids," p. 266, Elsevier Publishing Co., Amsterdam-New York (1948).
3. H. W. Leverenz, "An Introduction to Luminescence of Solids," p. 192, John Wiley & Sons, New York (1950).
4. E. W. Claffy and J. H. Schulman, *This Journal*, **98**, 408 (1951).
5. K. Th. Wilke, *Z. Phys. Chem.*, **207**, 45 (1957).
6. Brit. Pat. 460,210 (1937).
7. E. Imore, *Sc. pap. Inst. Phys. Chem. Res. Tokyo*, **27**, 1 (1935).
8. D. G. Engle and B. S. Hopkins, *J. Opt. Soc. Am.*, **11**, 599 (1925).
9. J. de Ment, "Fluorescent Chemicals," pp. 76 and 141, Chemical Publishing Co. Inc., Brooklyn (1942).
10. Y. Uehara and Y. Kofuya, Japanese Pat. 1811 and 1812 (1957); *Chem. Abstr.*, **52**, 8754 (1958).
11. Y. Uehara, Y. Kobuke, and J. Masuda, *This Journal*, **106**, 200 (1959).
12. F. A. Kroeger and J. Dikhoff, *Physica*, **16**, 297 (1950).
13. W. H. Zachariasen, *Acta Cryst.*, **1**, 263 (1948).
14. H. Koelmans an A. P. M. Cox, *This Journal*, **104**, 442 (1957).
15. F. A. Kroeger, Unpublished work.
16. K. H. Butler, *This Journal*, **100**, 250 (1953).
17. A. L. Mackay, *Acta Cryst.*, **6**, 743 (1953).
18. A. Bril, Unpublished work.
19. G. R. Fonda, *J. Phys. Chem.*, **43**, 561 (1939).
20. H. A. Klasens, *Philips Res. Repts.*, **9**, 377 (1954).
21. A. Bril, H. A. Klasens, and P. Zalm, *ibid.*, **8**, 393 (1953).
22. S. T. Henderson and P. W. Ranby, *This Journal*, **104**, 612 (1957).

Copper and Tin-Activated Halophosphate Phosphors

B. E. Hunt and A. H. McKeag

Research Laboratories, The General Electric Company Limited, Wembley, England

ABSTRACT

New copper- and tin-activated halophosphate phosphors, fired in mildly reducing atmospheres and of potential practical importance, are described. They include copper- and tin-activated barium chlorophosphates with good thermal characteristics. Copper-activated barium chlorophosphate shows a moderate red fluorescence at ambient temperatures, under long u.v. excitation, which becomes brighter at higher temperatures due to a marked color shift toward the yellow. The same matrix, activated with tin, shows a strong pale green fluorescence at ambient temperatures when excited by 2537Å radiation which is shifted toward the blue at elevated temperatures.

Since the introduction in 1942 of the alkaline earth halophosphate phosphors activated with antimony and manganese (1) a number of additional activators have been described. These include arsenic, bismuth, tin, lead (1), silver (2), uranium (3), and cerium (4). Copper has been mentioned as an activator of hydroxyphosphates (1) but has not been found previously to be very effective as an activator of halophosphates.

This paper describes a number of new copper-activated halophosphates prepared by heat treatment in mildly reducing conditions. Under similar conditions improved tin and tin-manganese activated halophosphates also have been prepared. Some of

these phosphors are of potential importance for use in discharge lamps of both high- and low-pressure mercury vapor types.

Preparation of Copper- and Tin-Activated Halophosphate Phosphors

Phosphors of this type were prepared by conventional halophosphate techniques, but firing treatments were carried out in mildly reducing atmospheres of nitrogen containing a low concentration of hydrogen. Tin-activated phosphors require about 0.5% vol/vol of hydrogen to nitrogen, while copper-activated phosphors, which are more sensitive to reducing conditions than those containing tin, require lower concentrations of hydrogen. With copper, the best results were obtained with about 0.25% vol/vol or less of hydrogen to nitrogen. Excessive reduction of copper and tin compounds is evidenced by discoloration of the samples, and this effect frequently can be corrected by subsequent refiring in "pure" nitrogen. Although nitrogen of the highest commercial purity was used throughout these experiments, it is possible that traces of oxygen present in the gas may contribute to the balance between reducing and oxidizing conditions necessary to maintain copper in the required valency state. It would seem probable that copper in the cuprous state and tin in the stannous state may be the conditions necessary for activation of these phosphors.

The useful ranges for copper and tin are from 0.1 to 1.0% (by weight) for copper and 0.5 to 5.0% for tin. Part of the copper is lost by volatilization during the firing treatment, and this may amount to as much as 50% of the initial quantity added. Preliminary analytical determinations suggest that part of the copper which remains may be present in the cuprous state. Firing temperatures depend on the nature of the halophosphate matrix but were usually in the range of 900° to 1200°C. Samples usually were prefired at a low temperature (900°C) to stabilize the matrix composition of the phosphors.

Fluorescence of Copper- and Tin-Activated Halophosphates

Copper- and tin-activated halophosphates of the alkaline earth metals (Ca, Sr, and Ba) were prepared with varying fluorine and chlorine ratios. X-ray examination of the more interesting phosphors confirmed that the apatite structure had been formed, and no noteworthy matrix impurities other than apatite phases were detected. The results of the various combinations tested are summarized below.

Calcium halophosphates.—Of this group, phosphors with a high chlorine content gives the best results. Copper activation produces a moderate blue fluorescence with short u.v. (2537Å) excitation, and the strongest emission occurs at a fluorine to chlorine molar ratio of 0.3:0.7.Manganese, in addition to copper, modifies the color to orange. Tin, by itself, gives a weak blue fluorescence which is modified to an orange-pink color by the addition of manganese.

Strontium halophosphates.—The best results are obtained in this group with strontium fluorophosphate activated with tin and manganese. Excitation by short u.v. radiation produces a strong yellow-green to orange-yellow fluorescence as the manganese content is increased. Replacement of fluorine by chlorine diminishes the brightness of these phosphors markedly. Copper, alone, (in strontium halophosphates) gives a weak red fluorescence with long u.v. excitation (3650Å).

Barium halophosphates.—These phosphors are more responsive to the effect of copper activation and give a moderately strong orange-red to red emission with long u.v. excitation. Tin, by itself, produces a moderate blue fluorescence in barium fluorophosphate and a strong greenish blue fluorescence with barium chlorophosphate. Manganese, in addition to copper or tin, is ineffective as an activator in these materials.

Among other phosphate combinations which were investigated with copper activation, calcium orthophosphate gives a strong blue fluorescence with short u.v. excitation which is modified to a pink fluorescence by the addition of manganese. This phosphor has also been described by Uehara and Kofuya (5).

Excitation and Emission Characteristics

Copper activation.—Two distinct types of emission are observed in the copper activated halophosphates, a blue or blue green emission in calcium halophosphates excited by short u.v. and a red emission in barium halophosphates excited by long u.v. radiation (Fig. 1, peak values normalized). With barium halophosphates the peak of the excitation curve for the red emission occurs at about 3000Å and declines rapidly at shorter wave lengths. In the presence of sulfate ions (added as copper or barium sulfate) these phosphors also show a weak blue fluorescence when excited by short u.v. radiation (2537Å). A

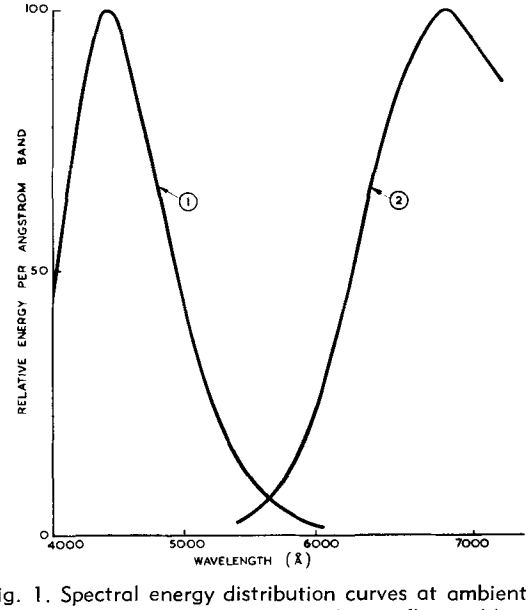

Fig. 1. Spectral energy distribution curves at ambient temperature of: 1. copper-activated calcium fluoro-chlorophosphate excited by 2537Å radiation $3Ca_3(PO_4)_2 \cdot 0.3\ CaF_2 \cdot 0.7\ CaCl_2$ (0.5% Cu by weight of matrix, as introduced), fired at 1200°C (0.1% vol/vol of H_2 to N_2; 2. copper-activated barium chlorophosphate, excited by 3650Å radiation (0.4% Cu, as introduced, fired at 1100°C, 0.25% vol/vol of H_2 to N_2).

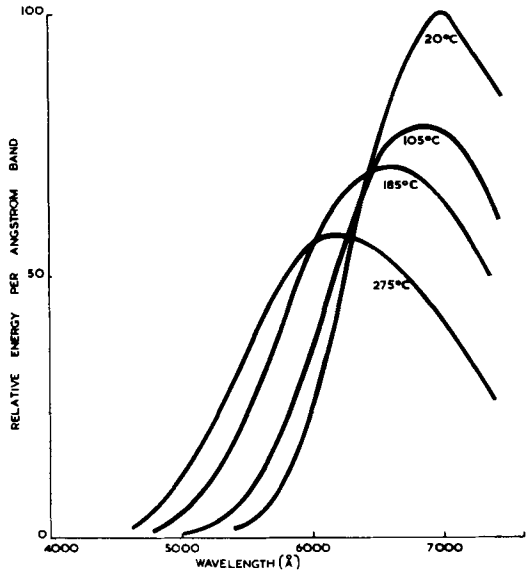

Fig. 2. Change of spectral energy distribution of copper-activated borium chlorophosphote with temperature, excited by 3650Å radiation (0.4% Cu, as introduced, fired at 1100°C, 0.2% vol/vol H_2 to N_2).

weak green emission is also obtained under short u.v. excitation if an attempt is made to compensate for charge difference between the monovalent cuprous ions and the divalent barium ions by the addition of trivalent cations such as cerium or lanthanum.

An unusual feature of the emission spectra of these phosphors is the marked shift in the position of the long u.v. excited band as the temperature of the phosphor is raised. This is most pronounced with barium chlorophosphate (Fig. 2) and is accompanied by an increase in visual brightness due to this shift in color from red toward the yellow.

Brightness-temperature measurements for copper-activated barium halophosphates, shown in Fig. 3, were made visually with a modified Macbeth photometer using suitable matched color filters of known transmission values. Curve 1 was normalized to give a peak value of 100, and curve 2 is relative to curve 1 on the same scale. With copper-activated barium chlorophosphate, the maximum brightness amounts to some three times the brightness at ambient temperatures and the maximum is reached at about 300°C. The corresponding fluorophosphate phosphor

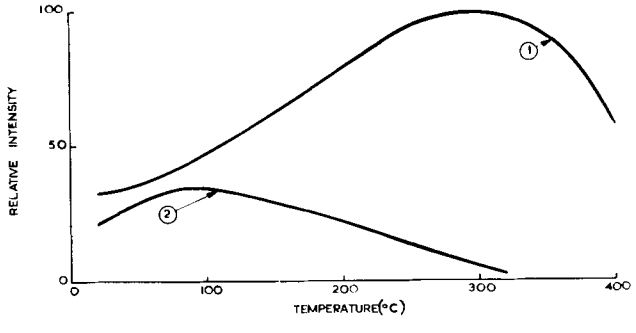

Fig. 3. Variation of visual brightness with temperature of: 1. copper-activated barium chlorophosphate, excited by 3650Å radiation (0.4% Cu, as introduced, fired at 1100°C, 0.2% vol/vol H_2 to N_2; 2. copper-activated barium fluorophosphate, excited by 3650Å radiation (0.4% Cu, as introduced, fired at 1100°C, 0.2% vol/vol of H_2 to N_2).

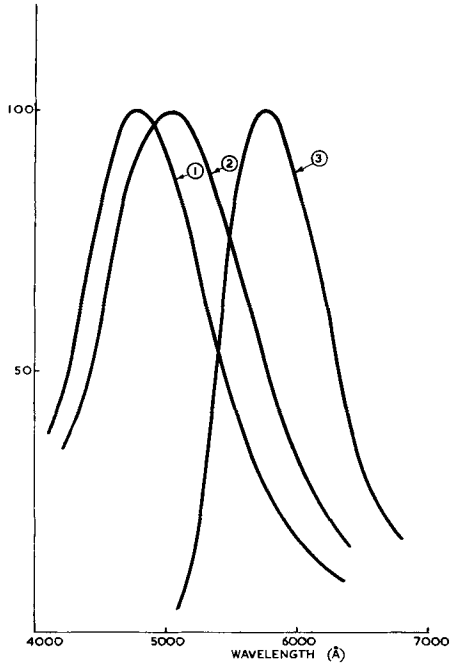

Fig. 4. Spectral energy distribution curves at ambient temperatures of: 1. tin-activated barium fluorophosphate, excited by 2537Å radiation (1% Sn, as introduced, fired at 1200°C, 0.5% vol/vol H_2 to N_2); 2. tin-activated barium chlorophosphate, excited by 2537Å radiation (1% Sn, as introduced, fired at 1150°C, 0.5% vol/vol H_2 to N_2). 3. Tin- and manganese-activated strontium fluorophosphate, excited by 2537 Å radiation (1% Sn, 2% Mn, as introduced, fired at 1050°C, 0.2% vol/vol of H_2 to N_2).

shows a much smaller change in color and has poorer temperature characteristics. These temperature effects are not critically dependent on activator concentration, although somewhat poorer results are obtained with high concentrations of copper. Phosphor samples which were heated in air during these measurements showed no marked permanent deterioration in brightness in the temperature range used for these observations.

Blue fluorescing calcium orthophosphate also shows good temperature characteristics and resembles in this respect certain copper activated aluminosilicates described by Claffy and Schulman (6). Instability of the calcium orthophosphate phosphor itself is evidenced by discoloration which occurs after baking the phosphor in air at temperatures of about 400°C.

Tin activation.—Barium halophosphates activated with tin are strongly excited by short u.v. radiation to give broad emission bands in the blue or blue-green regions of the spectrum (Fig. 4, peak values normalized). Barium chlorophosphate, activated with tin, like the corresponding copper activated phosphor, shows a marked shift in the position of the spectral band toward shorter wave lengths as the temperature is raised (Fig. 5). In this case, however, the shift in color is away from the green, and a reduction in visual intensity occurs (Fig. 6). Nevertheless, the phosphor is superior in temperature characteristics to most other blue emitting phosphors which are relatively poor in this respect, notable exceptions being copper-activated calcium orthophosphate and the aluminosilicates referred to above.

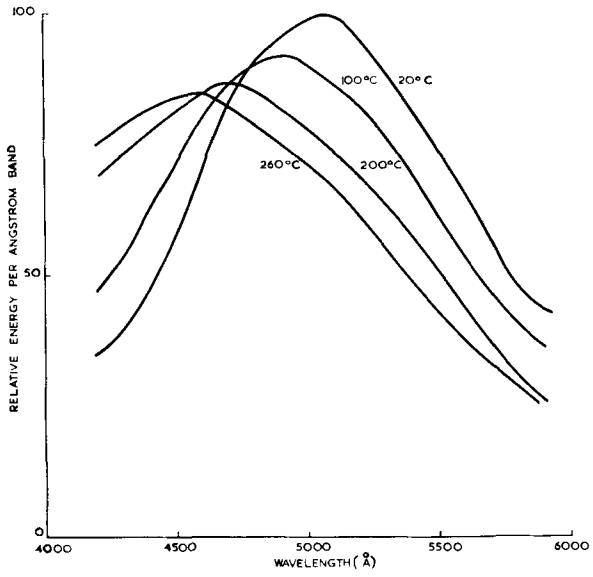

Fig. 5. Change of spectral energy distribution of tin-activated barium chlorophosphate with temperature, excited by 2537Å radiation (1% Sn, as introduced, fired at 1150°C, 0.5% vol/vol of H_2 to N_2).

Strontium fluorophosphate activated with tin and manganese is of potential importance because of the strong yellow emission excited by short u.v. radiation. The spectral energy distribution of a phosphor containing 1% by weight of tin and 2% by weight of manganese, fired at 1075°C, is shown in Fig. 4.

Applications in Lamps

Certain of the phosphors described above are of potential practical interest for use in discharge lamps. Barium chlorophosphate activated with copper, for example, applied to high-pressure mercury lamps is capable of utilizing the longer wave-length u.v. radiation (beyond 3000Å) from these lamps to give improved color rendering properties. In this instance it is an advantage to operate the phosphor at a relatively high temperature (ca. 250°C) in order to obtain the maximum light output.

Of the short u.v. excited phosphors, tin- and manganese-activated strontium fluorophosphates may be useful in mixtures with conventional red emitting phosphors to provide colors suitable for use in lamps of good color rendering qualities of the "De Luxe" types. The chromaticity values of 40-w fluorescent lamps coated with phosphors of varying manganese contents lie on an arc above the black body locus of the C.I.E. chromaticity diagram. The values range from $x = 0.400$, $y = 0.433$ for a phosphor containing 1.0% by weight of Mn to $x = 0.433$, $y = 0.445$ for a similar phosphor containing 2.0% Mn. Phosphors of this type show an appreciable and fairly rapid reduction in brightness when exposed externally to short u.v. radiation from a low-pressure mercury vapor quartz discharge tube. The effect occurs in air or in an evacuated quartz tube and is accompanied by a slight brown discoloration of the phosphor. After the initial reduction in brightness, further exposure produces little subsequent change. The effect is consistent with a chemical change in the surface state of the phosphor produced by the short u.v. radiation and may be similar to the formation of "color centers" produced in other materials by x-rays or cathode rays.

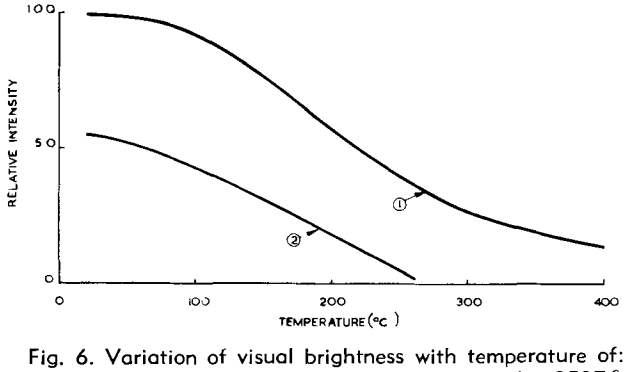

Fig. 6. Variation of visual brightness with temperature of: 1. tin-activated barium chlorophosphate, excited by 2537Å radiation (1% Sn, as introduced, fired at 1050°C, 0.2% vol/vol of H_2 to N_2); 2. tin-activated barium fluorophosphate, excited by 2537Å radiation (1% Sn, as introduced, fired at 1100°C, 0.2% vol/vol of H_2 to N_2).

Lumen maintenance characteristics of lamps coated with these phosphors show a rapid drop in efficiency during the first 100 hr of operation but this is succeeded by a relatively slow depreciation. In 40-w lamps "initial" (100 hr) efficiencies of 40-45 lpw have been obtained with these phosphors. After 4000 hr operation, lamp efficiencies were about 80% of the "initial" values. Of the other phosphors described, tin-activated barium chlorophosphate gives an "initial" efficiency in 40-w lamps of 45 lpw with a chromaticity value of $x = 0.250$, $y = 0.345$. The good temperature characteristics of this phosphor also make it potentially useful in high-pressure mercury vapor lamps.

Discussion

It has been shown that the temperature characteristics of barium chlorophosphates activated with copper and tin are markedly superior to the corresponding fluorophosphates. Both copper- and tin-activated barium chlorophosphates show a pronounced color shift as the temperature is raised. Uranium-activated barium halophosphates (3) also were tested for temperature dependence of fluorescence, but both fluoro- and chlorophosphates were markedly inferior to the copper- and tin-activated chlorophosphates and fluorophosphates. These observations support the view that temperature quenching effects are not a property of the lattice as such but of the emission centers and their surroundings (7). These differences in surroundings produce the marked difference in temperature characteristics between fluoro- and chlorophosphates activated with either copper or tin. As these phosphors are chemically and structurally similar, the differences observed may therefore be associated with the changes in spatial atomic arrangements in the matrix due to the replacement of fluorine by chlorine atoms in the apatite structure.

Besides the question of temperature properties the difference in emission characteristics between the various copper-activated phosphates is also of interest. Blue emission observed in halophosphates and calcium orthophosphate is typical of a number of

other copper-activated phosphors previously reported (1, 6). The long u.v. excited red emission observed in barium and to some degree in strontium halophosphates is more unusual. As both types of emission are obtained under certain conditions of preparation in the same barium halophosphate phosphor, it would seem that two different types of copper centers may be responsible for the blue and red emission bands. As the atmosphere conditions observed in the preparation are the same throughout, it may be assumed that copper is present in the same valency state in these phosphors. If this is so, the possibility of copper atoms occupying alternative sites in the halophosphate lattice might explain the observed differences in excitation and emission characteristics.

REFERENCES

1. H. G. Jenkins, A. H. McKeag, and P. W. Ranby, *J. (and Trans.) Electrochem. Soc.*, **96**, 1 (1949).
2. P. W. Ranby, *This Journal*, **98**, 299 (1949).
3. J. T. Anderson and R. S. Wells, *ibid.*, **98**, 414 (1951).
4. S. T. Henderson and P. W. Ranby, *ibid.*, **104**, 612 (1957).
5. Y. Uehara and Y. Kofuya, *Chem. Abs.*, **52**, 8754 (1958).
6. E. W. Claffy and J. H. Schulman, *This Journal*, **98**, 409 (1951).
7. F. A. Kroeger, "Some Aspects of the Luminescence of Solids," Chap. VI, Elsevier Publishing Co., Amsterdam (1948).

Electrical Properties of High-Purity Silicon Made from Silicon Tetraiodide

L. V. McCarty[1]

Research Laboratory, General Electric Company, Schenectady, New York

ABSTRACT

Resistivities, type of conduction, and lifetimes of minority carriers of single crystals of iodide silicon are recorded as a function of the purification procedure for silicon tetraiodide. Samples of silicon have been prepared by decomposition of silicon tetraiodide on hot tantalum and hot quartz surfaces in vacuum. Distillation in a 12 plate quartz column of silicon tetraiodide prepared from 99.7% silicon results in single crystals of silicon that are uniformly n-type with maximum resistivities at the seed end in the range 0.3-1 ohm-cm. Two recrystallizations from solvents before the distillation step result in both p- and n-type crystals with, respectively, 150-650 ohm-cm and 75-170 ohm-cm resistivity ranges at the seed ends. Distillation of silicon tetraiodide is particularly effective in removing boron, while recrystallization and zone melting are effective for removing group V impurity iodides.

Silicon tetraiodide has been recognized as a potential source of semiconductor silicon for several years. Litton and Andersen (1) first made iodide silicon from silicon powder using iodine vapor in a Van Arkel-de Boer type of apparatus and observed some purification, but, unfortunately, both donor (group V) and acceptor (group III) impurity elements were transferred in the operation. In order to improve the quality of their product they decided to isolate silicon tetraiodide, which probably carried the silicon through the vapor phase of their iodide cells, and to purify it by fractional distillation in an all-quartz column. The electrical properties of their product indicate that they met with considerable success.

Later Szekely (2) reported on the hydrogen reduction of silicon tetraiodide, but electrical data with which one might calculate the purity of the product are not included.

A different approach to the purification problem was adopted by Rubin and his associates (3). They took advantage of the solubility of silicon tetraiodide in toluene from which it can be recrystallized as the first step in their procedure. Their final steps are sublimation and zone melting of the solid, but the electrical properties of silicon made from their purified material are not discussed.

In this work still another sequence of purification steps has been used to prepare silicon tetraiodide for decomposition into silicon and iodine. These techniques include recrystallization from n-heptane and distillation in an all quartz column, and a very brief investigation of zone melting. Electrical properties of single crystals grown from the silicon are interpreted as a measure of crystal purity rather than depending on chemical analyses for individual elements, because the estimated quantity of electrically active impurities is in the range of parts per ten billion for elements that affect the resistivity of this silicon, and even less for those that affect the recombination of holes and electrons. It is true that the electrical properties do not give much detail concerning specific impurity elements, but the tests are more readily made and indicate the presence of broad classes of electrically active impurities. Any one of these would be much more difficult to detect

[1] Present address: Lamp Development Department, General Electric Company, Nela Park, Cleveland, Ohio.

chemically, and, if undetected, might render the silicon quite useless as a semiconductor. The objective of this work was the preparation of the purest silicon possible.

Experimental

Preparation of silicon tetraiodide.—The method of making silicon tetraiodide is quite similar to the one described by Szekely (2). A nitrogen purge was used instead of argon, and a reaction temperature of 600°C was sufficient when the Electrometallurgical Company's 99.7-99.9%, 30-80 mesh silicon powder was used. When DuPont hyper-pure silicon crystals were placed in the reactor, a temperature of 800°C was required to achieve about the same reaction rate. The higher temperature may have been necessary because there is less impurity present to act as catalyst in the latter silicon, but it was also much coarser and did not pack as well.

Recrystallization of silicon tetraiodide.—Silicon tetraiodide was dissolved in sufficient solvent in a Pyrex flask to make a 50 mole % solution at the boiling point. After cooling to room temperature the solvent is drained off, and residual solvent and tetraiodide are transferred to the distillation apparatus after two or more recrystallizations.

Solvents used include Phillips Petroleum 99+% n-heptane, Phillips Petroleum commercial heptane, and reagent grade toluene and benzene.

Distillation of silicon tetraiodide.—The distillation apparatus for most of this work is made entirely of quartz. The smaller column consists of a one liter pot sealed to a 4-ft length of 1 in. OD tubing which is packed with ¼ in. sections of ¼ in. tubing (Raschig rings). The condensing head is a conventional design with a magnetically operated quartz valve to control the take-off, and an electrically heated delivery tube to conduct the tetraiodide into its receiver flask. The larger column is made from a 5 liter pot sealed to a 2 in. OD tube 66 in. long. Both columns have a rectification efficiency equivalent to 12 theoretical plates as tested with a mixture of methycyclohexane and normal heptane. Either is purged with nitrogen before tetraiodide is melted or distilled into the pot, and a flow of 20-30 cc/min is maintained throughout the distillation. The apparatus remains on total reflux overnight before starting the first cut. The minimum reflux ratio is 24:1 while product is taken off at 50-150 g/hr into quartz storage flasks. A first cut of 25% of the charge is discarded, and the second cut, which is later decomposed to silicon and iodine, contains 50% of the tetraiodide.

Decomposition of SiI_4 on tantalum.—The deposition on tantalum is similar in many respects to the technique described by Litton and Andersen (1). A tantalum rod, ⅛ in. in diameter by 3 ft, in the form of a hairpin is suspended in an evacuable chamber by means of a 65/40 ball and socket joint to which are sealed ¼ in. molybdenum electrodes. The 2 in. OD deposition chamber and the reservoir for silicon tetraiodide are an integral unit made of quartz.

After drying the equipment thoroughly, silicon tetraiodide is transferred into its reservoir in a dry nitrogen atmosphere. The tantalum hairpin is placed in position next using silicone grease or, preferably, a silicone rubber gasket on the ball joint. A dry ice bath is placed around a trap to condense iodine and unreacted silicon tetraiodide, and the system is pumped down to about 1 μ. The tantalum rod is heated electrically to 950°C as observed without correction by an optical pyrometer, and, last, the tetraiodide is warmed to about 100°C. The estimated vapor pressure of tetraiodide in the system is of the order of 1 mm.

After all of the iodide in the pot has sublimed, the electrical power is turned off, permitting the silicon and tantalum to cool to room temperature. Cracking noises are heard as the two partially separate due to thermal fracture. When cool, the system is filled with dry nitrogen, and the tantalum rod and silicon are removed and wrapped in a sheet of polyethylene. Gentle flexing separates the silicon from the rod, and the larger spears are broken up. The yield of silicon is about 80-90% in a 20-30 hr run.

Decomposition of SiI_4 on quartz.—For reasons discussed later, tantalum did not seem to be the ideal deposition surface. Quartz is used at much higher temperatures in the crystal growing operation than are needed for the decomposition of silicon tetraiodide, so it seemed reasonable to use it for the latter operation because the requirements are not nearly so severe. Figure 1 shows the kind of equipment designed after preliminary experiments. The silicon tetraiodide storage pot and reactor tube are an integral unit made of quartz. A socket joint is ring sealed into the bottom of the reactor to support a thin walled quartz tube on which deposition actually occurs. The purpose of the tube within a tube construction is to keep the outer portion of the reactor from breaking when the furnace is allowed to cool after silicon has deposited. Silicon adheres to quartz very strongly and, since the coefficients of expansion are different, the deposit and tube fracture on cooling. A tungsten spiral in 1½ in. OD tubes kept fragments from falling into the flask.

The spiral winding on the connection between the decomposition apparatus and the trap is a nichrome ribbon to keep the tube warm and thus prevent condensation of unreacted silicon tetraiodide. The refrigerant usually used around the trap is trichloroethylene-dry ice, and during operation the pressure is of the order of 1 μ or less at the vacuum gauge, but it is much higher in the reactor.

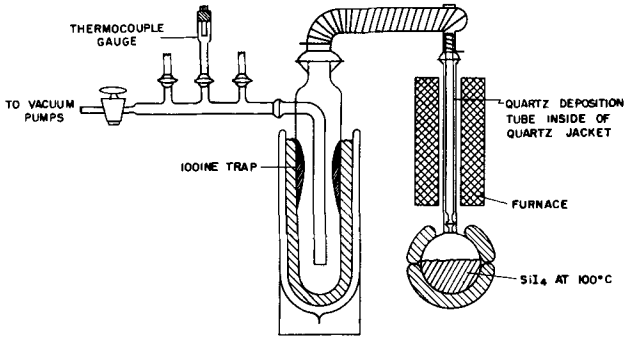

Fig. 1. Apparatus for deposition of silicon on quartz

At the end of a run the silicon with quartz adhering to it is placed in concentrated hydrofluoric acid for a day or two to dissolve the latter. Next it is thoroughly washed with water, then methyl alcohol, and air dried. The yield from 1000 g of SiI_4 is about 70% in a three day run at 1000°C. The reaction probably takes longer on quartz than on tantalum because the corrected temperature for the silicon deposit on the latter may be well above 1000°C.

Cleaning of equipment.—All equipment was thoroughly cleaned after each use with either 1% or 5% hydrofluoric acid followed by rinsing with water and drying by baking wherever possible. The hope was to standardize the surface of the vessels for each experiment rather than making it a function of the history of the equipment.

Crystal growing.—All crystals for this work were prepared in quartz crucibles by the Czochralski technique (4). A stainless steel pull rod held the single crystal seed, and the furnace atmosphere was argon. Heat was supplied to the crucible by a graphite resistance element supplied with a-c power from a Variac stabilized with a Sorensen regulator.

Electrical measurements.—Resistivities were generally measured with a calibrated four-point probe on a lapped surface. Occasionally there was reason to suspect the values obtained, and in these cases resistivities were checked by passing a small current through the sample and measuring the potential drop along the surface.

The relationship between the number of uncompensated impurity atoms per cubic centimeter and the resistivity (above 10 ohm-cm) can be approximated by (5, 6)

$$n = \frac{1}{\rho e \mu_n} \approx \frac{3.6 \times 10^{15}}{\rho} \qquad [1]$$

$$p = \frac{1}{\rho e \mu_p} \approx \frac{1.3 \times 10^{16}}{\rho} \qquad [2]$$

where ρ is the resistivity, e is the charge of one electron in coulombs, and μ_n and μ_p are the mobilities of electrons (~1750 cm^2/v sec) and holes (480 cm^2/v sec) at room temperature, respectively.

Another measurement which typifies the quality of silicon single crystals is the lifetime of the minority carriers. The method used for this measurement has been described by Watters and Ludwig (7) who give detailed data as a function of temperature for sample 3 of Table V, which is referred to as C-Si-170.

Drift and conductivity mobility data for C-Si-170 have also been determined by Ludwig and Watters (8).

Results and Discussion

Spectrographic Data

Impurity elements detected spectrographically in a typical sample of Electromet silicon as received, and after processing by conversion to silicon tetraiodide with subsequent decomposition to silicon, are shown in Table I. The four elements in the right-hand column were detected in a sample of iodide silicon made from unpurified silicon tetraiodide. When recrystallization from solvents or distillation of the tetraiodide were incorporated in the process, the aluminum concentration occasionally dropped so low as to become undetectable. The data show that the iodination and decomposition processes are powerful purification steps in their own right merely from the number of elements rejected. But for semiconductor purposes these spectrographic analyses of iodide silicon have only a very limited value because they are insufficiently sensitive.

Table I. Impurity elements detected spectrographically

Electromet silicon	Iodide silicon
Fe	Fe
Mg	Mg
Cu	Cu
Al	Al*
Ca	
Ti	
Ni	
Sn	
Co	
Cr	
Mn	
Zr	

* Not always detected.

Iodide Silicon Made from Unpurified Silicon Tetraiodide

The most difficult element to remove from silicon by zone melting or crystal growing techniques is boron, and it is almost imperative that it be removed from the compounds used to make silicon before the actual preparation. It is not difficult to recognize a crystal whose resistance is dominated or controlled by boron, however, because its segregation coefficient is about 0.9 (9), and such crystals have a characteristically "flat" resistivity profile.

Because of the importance of removing boron from silicon, it was desirable to determine how the various purification steps affect its removal. In order to establish a base line for comparison purposes, enough silicon was prepared by decomposition of unpurified silicon tetraiodide on quartz so that elements other than boron could be removed by 5 zone passes in a zone melting apparatus. A single crystal grown from the zone melt bar was p-type and had resistivities in the range 0.25-0.14 ohm-cm, about 0.20 ohm-cm on the average. (In this paper the first resistivity quoted will be for the "seed" end of the crystal, while the second number refers to a measurement near the "sprout", or tail end. In general, impurities segregate toward the sprout.) The conductivity mobility, μ_p, for this resistivity range (5) is about 350 $cm^2\ v^{-1}\ sec^{-1}$, and the number of boron atoms per cubic centimeter, p, can be calculated as

$$p = \frac{1}{\rho e \mu_p} = \frac{1}{0.20 \times 1.60 \times 10^{-19} \times 350} = 9 \times 10^{16}$$

or about 1.7 boron atoms per million silicon atoms. Rubin, Moates, and Weiner (3) found considerably more boron than this in their silicon tetraiodide

Table II. Electrical properties of single crystals of iodide silicon prepared from distilled silicon tetraiodide[a]

Sample No.	Type	Resistivity range, ohm-cm
1	n	0.3-0.06
2	n	0.4 max.
3	n	0.7 max.
4	n	0.3 max.
5	n	0.4-0.2
6	n	0.8-0.2
7[b]	n	1-0.4

[a] SiI_4 prepared from 99.7% Electromet Si, distilled in 12 plate quartz column, and decomposed on ⅛ in. Ta rod.

[b] 5 g of KI added to still pot.

which was made from a different grade and different kind of silicon.

Iodide Silicon Made from Distilled Silicon Tetraiodide

In the first attempts in the present experiments at purification of silicon tetraiodide distillation in an all-quartz, 12 plate column was used. Results are shown in Table II. Two things about this data are impressive: all samples are n-type, and the resistivities near the seed end of the crystal (the first number quoted) are reasonably uniform. This means that some group V element, a donor impurity, is the chief contaminant rather than boron. The relatively slow decrease in resistivity along the crystals of samples 1, 5, and 7 indicates a material with a segregation coefficient similar to phosphorus or arsenic (9).

James and Richards have shown that phosphorus can be found in amounts of 0.1 to 10 ppm in iodine (10), and the very careful analysis of 97% silicon performed by the Bureau of Standards (11), as well as the work of Rubin, Moates, and Weiner (3), indicates that this quality of silicon can have as much as 80 ppm of phosphorus. The latter authors (3) also have shown the presence of 150 ppm of arsenic which is mostly eliminated by the iodination reaction.

Either n-type impurity as an iodide might be contaminating the crude silicon tetraiodide. Phosphorus triiodide is more volatile than silicon tetraiodide (1), and it should tend to concentrate in the condensing head of the apparatus. If it were not completely removed from the condenser through faulty technique, the electrical conductivities of Table II ought to show considerable scatter. Since they do not show a broad range of values, it seems more reasonable to believe that the source of n-type contamination is in the crude tetraiodide in the still pot, which should come to equilibrium with the still head during the prolonged initial operation at total reflux. Arsenic triiodide is less volatile than silicon tetraiodide (1). It would concentrate in the still pot, and it may be the n-type impurity responsible for these results.

Potassium iodide was added to the distillation pot of the last sample in an attempt to form complexes with group V iodides which would reduce their vapor pressure.

In order to determine the amount of boron in these samples it is necessary to prepare enough silicon for zone melting to remove n-type impurities. It would have been extremely tedious to do this with the original small quartz equipment, so a large 12 plate Pyrex column was used for the distillation. The use of Pyrex introduces certain complications which will be discussed later, but it is believed that the boron concentration obtained after zone melting represents the maximum amount coming through the distillation step. Sample No. 4 of Table VI was prepared in this way. Its maximum resistivity of 125 ohm-cm, which dropped only gradually over the first part of the crystal, corresponds to about 2 boron atoms per billion silicon atoms. This represents a reduction in the boron concentration by a factor of approximately 850 by a 12 plate distillation. Because of the experimental errors involved, however, it might be better to say that the factor is in the range 500 to 1000.

Litton and Andersen (1) have given a value of 6.8 for the relative volatility of boron triiodide compared to silicon tetraiodide. By assuming that the same relative volatility applies to a dilute solution of boron triiodide at 300°C, one can write

$$\frac{\dfrac{\text{mole fraction of } BI_3 \text{ in vapor}}{\text{mole fraction of } SiI_4 \text{ in vapor}}}{\dfrac{\text{mole fraction of } BI_3 \text{ in liquid}}{\text{mole fraction of } SiI_4 \text{ in liquid}}} =$$

$$\frac{\text{mole fraction of } BI_3 \text{ in vapor}}{\text{mole fraction of } BI_3 \text{ in liquid}} = 6.8$$

since the mole fraction of silicon tetraiodide is within parts per million of being unity in either phase. The number of effective plates realized from the observed separation in the "12 plate" column is:

$$6.8^x \sim 850$$

$$x \sim 3.5 \text{ effective plates}$$

If the total purification achieved in the best samples reported in this study were ascribed to the action of the distillation column, less than 4.5 plates would be required for the removal of boron triiodide to the indicated levels.

Green and Kafalas (12) have shown that the separation factor, α, for dilute solutions of arsenic trichloride in germanium trichloride is remarkably lower than in solutions containing an excess of arsenic trichloride. The α for the system boron triiodide-silicon tetraiodide may behave similarly, in which case many more theoretical plates would be realized than indicated.[1]

There are two other reasons that might be advanced for the discrepancy between the calibrated effectiveness of the column and that actually realized. The mixture of hydrocarbons is so different in physical properties from silicon tetraiodide that our calibration may indicate many more plates than can ever be realized in systems consisting mostly of silicon tetraiodide.[1] The other reason concerns the reduction and solution of boron impurities in quartz boats and crucibles containing molten silicon (13).

[1] The author is indebted to C. S. Herrick and J. G. Krieble for this suggestion.

Table III. Effect of tantalum doping on the electrical properties of silicon

	Type	Resistivity, ohm-cm	Lifetime of minority carriers, μsec
Starting material	p	150	125
Portion of crystal before Ta doping	p	150	150
After doping with 0.1% Ta	p	140	10

This effect may add a small amount of boron which places a limit on what can be achieved experimentally when molten silicon contacts quartz equipment as one of the processing steps.

Tantalum as an Impurity in Silicon

Litton and Andersen (1) have indicated that there is a discontinuous alloy zone formed at the tantalum-silicon interface during deposition. Neutron activation analyses of silicon removed from our tantalum rods showed that tantalum was present, and apparently in variable amounts[2] which supports their observation. In order to determine the effect of occluded alloy or metal, a silicon melt was doped with a small piece of tantalum metal when the crystal was partially grown (14). Table III gives data for the electrical properties of this crystal before and after tantalum doping. There is only a minor change in the resistivity of the silicon, but the lifetime of the minority carriers has dropped rather dramatically.

An n-type impurity in the tantalum metal could conceivably be diffusing through the metal-silicon interface to cause the low resistivities of Table II. Two samples of iodide silicon prepared on tantalum from distilled tetraiodide made from DuPont hyperpure silicon showed that this was not so, however. The resistivity range for an n-type single crystal was 114-8 ohm-cm, while a p-type crystal of another sample was in the range 200-100 ohm-cm.

Because of the tantalum contamination we decided to use another kind of deposition surface to try to avoid any adverse influence tantalum might have on the lifetime properties. Quartz is used at much higher temperatures in the crystal growing operation than is needed for the decomposition of silicon tetraiodide, so it seemed reasonable to use it for the latter operation because the requirements are not nearly so severe. Decomposition on quartz was used for all succeeding samples discussed in this paper.

Iodide Silicon Made from Recrystallized Silicon Tetraiodide

Residual solvent was removed from two samples of recrystallized silicon tetraiodide by heating to the boiling point and distilling a small portion to purge the apparatus. The first sample of Table IV indicates that two recrystallizations from a solvent are more effective than distillation in a 12 plate column, since this material contains less than one-fifth as many excess n-type impurities as the best example of Table II. [The mobility of the current carriers decreases as the resistivity drops in this range (9).] A detailed study of the effectiveness of two recrystallizations from other solvents was not carried out, but we believe that all would be approximately equally effective.

[2] W. W. Schultze performed the neutron activation analysis.

Table IV. Electrical properties of single crystals of iodide silicon prepared from recrystallized silicon tetraiodide[a]

Sample No.	Notes on purification of SiI_4	Type	Resistivity, ohm-cm	Lifetime of minority carriers, μsec
1	Recrystallized twice from toluene as a coarse powder; washed each time with 3 portions of n-heptane	n	5 max.	
2[b]	Recrystallized twice from commercial heptane, and then 6 times from n-heptane	n	94-130-94-22	200-75

[a] SiI_4 made from 99.8% Electromet Si and deposited on quartz.

[b] SiI_4 decomposed at 1200°C.

Eight recrystallizations from two kinds of heptane resulted in the second sample of Table IV which shows that the purity of the tetraiodide is a function of the number of recrystallizations. This sample had the same treatment as No. 4 of Table V except for the distillation step in the latter which seems to have removed the n-type impurity. Superficially the n-type sample appears purer because it has about 4×10^{13} excess carriers per cubic centimeter, while the distilled p-type sample has approximately 7×10^{13} excess carriers. Actually, the n-type sample might have as much as 11×10^{13} n-type carriers of which 7×10^{13} are compensated by p-type carriers.

Table V. Electrical properties of single crystals of iodide silicon prepared from recrystallized and distilled silicon tetraiodide[a]

Sample No.	Type	Resistivity, ohm-cm	Lifetime of minority carriers, μsec
	35 g lots of Si; n-heptane and commercial heptane as solvents:		
1[b, f]	p	420-700-1700	
2[d]	p	150-135-680	
3[c]	n	170-255-220	2000-2500
4[e]	p	200-80	250-75
	200 g lots of Si; n-heptane as solvent:		
5	n	75-30	
6	n	150-140	300-500 (seed end)
7	p	450-180	250-150 (middle-sprout)
8	p	250-50	750-300
	200 g lots of Si; benzene as a solvent:		
9	p	650-425-550	280-230 (seed-middle)
10	p	245-85	110-25

[a] SiI_4 made from 99.8% Electromet Si, recrystallized twice except where noted, distilled in 12 plate quartz column, and decomposed on quartz.

[b] Normal heptane used as solvent.

[c] Commercial heptane used as solvent.

[d] Distilled n-heptane used as solvent.

[e] Recrystallized 2X from commercial heptane, 6X from n-heptane.

[f] Quartz flask used for recrystallization.

If this latter picture is correct, the p-type distilled sample really is the purer, of course.

Iodide Silicon Made from Recrystallized and Distilled Silicon Tetraiodide

Table V contains data for experiments in which two recrystallizations were combined with distillation in a 12 plate quartz column as the purification steps. Comparing these results with those of Table II it is clear that two recrystallizations are exerting a very profound effect on the quality of silicon produced. Apparently the main function of recrystallization is the removal of n-type impurities.

In all but one of the experiments Pyrex flasks were used for the recrystallizations. As the next section shows there is some reason to be concerned about the extraction of impurities from Pyrex, so one set of the recrystallizations was performed in quartz. Sample 1 shows that no marked improvement over other samples was realized by this treatment.

The solvents used might also place a limit on the purification of the tetraiodide. For this reason the n-heptane for sample 2 was carefully distilled before use, but no decrease in impurity content was detected.

Since increasing the number of recrystallizations had improved the quality when this was the sole purification used (cf. Table IV), eight recrystallizations were combined with a distillation for sample 4 for Table V. Apparently two recrystallizations are as effective as more when combined with distillation because sample 4 showed no improvement.

One rather serious criticism of the first three samples of Table V is that they are obviously compensated because the resistivities tend to increase in some portion of the crystal proceeding from seed end to sprout (the portion which freezes last). This difficulty was rather common for the smaller size lots prepared, but it seemed to resolve itself in the larger batches. It may simply reflect a somewhat improved operating efficiency in the larger distillation column.

It was shown that, with very careful preparation of high resistivity crystals, boron contamination from the crucible amounted to only 2 to 3 x 10^{13} atoms/cc of silicon (14, 13). This corresponds so closely to the better resistivities for p-type crystals that contamination from the crucible may limit the results achieved for many crystals of this work. [Data for crystals with higher resistivities, however, are contained in a paper by Herrick and Krieble (15).]

In any event the chief impurity left in our best p-type samples is probably boron. If this assumption is correct, the best sample of Table V has at least 4 boron atoms per ten billion silicon atoms, which is a decrease in the boron content by a factor slightly greater than 4000 compared to the original silicon and represents only a modest improvement over distillation alone for purification.

Iodide Silicon Made from Silicon Tetraiodide Distilled in Pyrex

The distillation column for this work was a Pyrex duplicate of the larger of our quartz columns.

Table VI. Electrical properties of single crystals of iodide silicon prepared from silicon tetraiodide distilled in Pyrex[a]

Sample No.	Type	Resistivity, ohm-cm	Lifetime of minority carriers, μsec
	Recrystallized samples:		
1[b]	p outside n core	3000-120 not measured	
2[c]	p outside n core	1200-1800-25 not measured	
3[d]	p outside n core	2200-3500-250 11-140-35	
	Zone melted samples:		
4[e]	p	125-46	150 (seed end)
5[e, f]	p	200-50	100-10

[a] 12 plate Pyrex still used for all samples

[b] Recrystallized 2X from toluene.

[c] Recrystallized 2X from commercial heptane; decomposition apparatus broke at 800°C exposing sample to air; etched 12% from sample used to grow crystal.

[d] Recrystallized 2X from n-heptane; sample exposed to air at 400°C when decomposition apparatus broke.

[e] No recrystallization step used; Si zone melted with 5 zones.

[f] SiI_4 recovered from first and third cuts of previous distillations.

The complex pattern of electrical resistivities observed in the first three samples of Table VI is probably caused by the presence of traces of both donor and acceptor impurities which segregate at differing rates from liquid silicon as it circulates by the growing crystal to produce compensated p-type crystals near the surface with n-type cores of much lower resistivity. Toluene has not been thoroughly investigated as a solvent for silicon tetraiodide in this work, and, as the notes indicate, difficulties were experienced in handling the other two samples. A single crystal could not be grown from sample 2 before it was etched. In spite of these difficulties we believe that these data are characteristic of iodide silicon made from Pyrex-distilled tetraiodide.

Samples 4 and 5 were zone melted[3] after their preparation from silicon tetraiodide that was purified by distillation in the Pyrex column. This treatment effectively removes n-type impurities and reveals the amount of boron present as a p-type impurity. While the resistivities of these samples are not the best that have been obtained in this work, it is clear that the extraction of boron from Pyrex glass is not a serious problem even though boric oxide is a major constituent of this kind of glass.

Since the first three samples exhibited a kind of compensation which was not observed in comparable samples prepared from tetraiodide distilled in quartz equipment, it seems that the extraction of an n-type impurity from Pyrex is the real problem. Green and Kafalas (12) have shown that germanium tetrachloride can extract arsenic from Pyrex glass, and they have also explained the earlier results of Cluley and Chirnside (16) who found that Pyrex equipment was not suitable for the removal of traces of arsenic even though reasonably effective for relatively large amounts. Assuming that the arsenic is present as the pentoxide in Pyrex, thermodynamic estimates

[3] W. C. Dash performed these operations and evaluated the material.

of the free energy of extraction of arsenic as the triiodide are more favorable for silicon tetraiodide than for germanium tetrachloride. (Of course, it can also be estimated that the free energy for the extraction of boron as the triiodide is favorable.) While the present work does not unequivocally demonstrate the extraction of an n-type impurity from Pyrex, we feel that this is the real problem rather than the extraction of boron even though this may indeed seem like a paradox.

In view of these comments on the use of Pyrex glass for distillation, the use of Pyrex recrystallizing equipment may seem questionable. The best results were obtained when recrystallization was followed by distillation of the silicon tetraiodide, and all that was demanded of recrystallization is an upgrading of the quality of silicon tetraiodide rather than providing the ultimate in purity. If recrystallization alone were to be used for purification it might be desirable to use quartz equipment and specially purified solvents.

Iodide Silicon Made from Silicon Tetraiodide Purified by Zone Melting

The zone melting equipment differs from the kind described by Rubin and Moates (3). The main quartz tube, 2⅜ in. OD by 36 in. long, was held in a horizontal position and was not quite half filled by 2.5 kg of silicon tetraiodide. Alternate freezing and thawing caused no trouble with tube breakage. The rate of zone travel varied between 0.68 and 1.14 iph, but most of the time it was kept very nearly at 0.80 iph. The gas space above the iodide was continuously flushed with 40-50 cc/min of hydrogen.

After ten zones had passed down the tube (two passes of a 5 element heating unit), most of the first 40% of the silicon tetraiodide was a light clear yellow with a small wedge of salmon pink material towards the middle of the tube. The "impure" end of the tube was salmon pink to red in color, and this portion was removed first by rotating the tube 180° about its long axis, tipping slightly, and melting the impure tetraiodide with an air gas flame. The tube was then tipped in the opposite direction and the "pure" tetraiodide was transferred to the apparatus used for decomposition on quartz.

A single crystal prepared from the product was p-type over its entire length and had the following resistivity profile: (seed end) 20-20-20-20-20-100 (sprout end). The relatively uniform resistivity values indicate that boron is the impurity controlling this property except near the sprout end, where compensation results from the segregation of an n-type impurity.

A rather bad feature of the present equipment is the amount of back diffusion occurring in the gas phase as evidenced by needle-like crystals growing above the surface of the refrozen tetraiodide. Impurities that are more volatile than silicon tetraiodide, such as boron triiodide, would contaminate these needles resulting in a smaller degree of purification than actually realized by the zone melting.

In spite of the limitations of the equipment used in this work, the purification achieved is impressive. The n-type impurities have been effectively eliminated, and the boron content has been reduced by a factor of approximately 130 since 20 ohm-cm corresponds to about 1.3 boron atoms per hundred million silicon atoms. If the same ratio continued for ten additional zone passes, the rejection of boron would be impressive indeed.

According to Pfann (17), the boron content will have reached some equilibrium distribution after a sufficient number of zones have passed through a bar of tetraiodide, depending on its distribution coefficient and the ratio of zone length to bar length. In our equipment the zones were approximately one tenth as long as the quartz tube. Rubin, Moates, and Weiner (3) have given two figures for the distribution coefficient of boron in a silicon tetraiodide matrix: 0.16 ±0.07 for the boron contained in a sample of crude tetraiodide, and 0.42 ±0.22 for a boron triiodide doped sample. At equilibrium, zone melting would reduce the average boron content of the first 40% of the bar by a factor 2.3 x 10^7 for the first coefficient, and 4.1 x 10^8 for the second. There is room for a modest amount of improvement or a really significant improvement depending, apparently, on the chemical species containing the boron.

It is interesting, although perhaps superficial, that both recrystallization from solvents and zone melting seem to be particularly effective in removing n-type impurity iodides from silicon tetraiodide.

Acknowledgments

The author is particularly indebted to Dr. C. B. Collins and Dr. F. H. Horn for the preparation of single crystals of silicon, for the measurement and interpretation of the electrical properties, and much valued discussion. Mr. L. C. Landauer and Miss J. M. Binkowski prepared many of the samples of silicon.

Manuscript received April 3, 1959. This paper was prepared for delivery before the New York Meeting, April 28-May 1, 1958.

Any discussion of this paper will appear in a Discussion Section to be published in the June 1960 JOURNAL.

REFERENCES

1. F. B. Litton and H. C. Andersen, *This Journal*, **101**, 287 (1954).
2. Gustav Szekely, *ibid.*, **104**, 663 (1957).
3. B. Rubin, G. H. Moates, and J. R. Weiner, *ibid.*, **104**, 656 (1957).
4. J. Czochralski, *Z. Physik Chem.*, **92**, 219 (1917).
5. F. J. Morin and J. P. Maita, *Phys. Rev.*, **96**, 28 (1954).
6. P. P. Debye and T. Kohane, *ibid.*, **94**, 724 (1954).
7. R. L. Watters and G. W. Ludwig, *J. Appl. Phys.*, **27**, 489 (1956).
8. G. W. Ludwig and R. L. Watters, *Phys. Rev.*, **101**, 1699 (1956).
9. J. A. Burton, *Physica*, **20**, 845 (1954).
10. J. A. James and D. H. Richards, *Nature*, **177**, 1230 (1956).
11. Analysis of Bureau of Standards Sample No. 57, Silicon.
12. M. Green and J. A. Kafalas, *J. Chem. Soc.*, **1955**, 1604.
13. N. B. Hannay, Recent Advances in Silicon, pp. 6-7, chapter in "Progress in Semiconductors," Heywood and Co., Ltd., London (1956).
14. C. B. Collins, Private communication.
15. C. S. Herrick and J. G. Krieble, To be published, *This Journal*.
16. H. J. Cluley and R. C. Chirnside, *J. Chem. Soc.*, **1952**, 2275.
17. W. G. Pfann, *Trans. AIME, J. Metals*, **4**, 747 (1952).

Rare Earth Compound Semiconductors

J. F. Miller, F. J. Reid, and R. C. Himes

Battelle Memorial Institute, Columbus, Ohio

ABSTRACT

Selenides of La, Er, and Y, and tellurides of La, Er, Gd, and Y were prepared by direct reaction of the elements. Measured electrical characteristics indicate semiconducting behavior, with the possibility that a wide range of properties can be obtained within these series of rare earth compounds. Observed room-temperature resistivities, for example, ranged from about 10^{-4} ohm-cm for La_2Te_3 and ErSe to the insulator range for Y_2Se_3. All the compounds prepared possess high melting points (1400°-2000°C) and exhibit good thermal stability. The dissociation pressure of Gd_2Te_3 at its melting point appears to be as low as 0.01 atm.

Semiconductors with interesting and potentially useful properties have been found within a number of classes of intermetallic compounds. Several of these groups of compounds, notably the III-V's and II-VI's, are currently receiving considerable attention. This is the initial report on a study which is concerned with the electrical properties of a group of compounds which has, to date, received little attention—namely, binary intermetallic compounds containing a rare-earth element. Specifically, this paper deals with the preparation and observed electrical properties of the selenides of La, Er, and Y, and the tellurides of La, Er, Gd, and Y.

Preparation

The compounds were first prepared in granular form by reacting selenium or tellurium vapor with filings of the rare earth metal at moderate temperatures. The advantage of increased reaction rate was thought, for these initial experiments, to overcome any disadvantage of contamination through filing. Reactions were carried out in sealed, evacuated Vycor tubes, which were designed so as to maintain physical separation of the liquid selenium or tellurium and the solid rare earth metal. This measure was taken to preclude the possibility of the rapid, violent reaction which takes place on direct contact of the condensed phases. To carry out the desired reaction, vapor of the metalloid was distilled over the rare earth metal filings; temperature was increased slowly to 950°C over a period of about 24 hr and was held at this level for an additional 72 hr.

The granular reaction product was then melted down and cast into ingots to obtain bulk specimens which were suitable for electrical evaluation. The melting was done in tantalum or graphite containers under argon at 1 atm pressure; induction heating was used. Although relatively high temperatures were involved, residence times at temperature were short. Under these conditions, there was little evidence of reaction between the compounds and properly outgassed tantalum (i.e., tantalum which had been outgassed above 1600°C in a hard vacuum). Graphite also appeared to be satisfactory as a container material.

Procedures discussed to this point were used for initial preparations of the compounds. Additional studies concerned with more refined preparation and characterization of the compounds are in progress. Initial work of this type was done with gadolinium telluride. Table II, discussed in greater detail later, includes data for a series of specimens of this compound taken from ingots which were prepared under various conditions noted in the table. The first of these specimens was taken from an ingot which was prepared by distilling tellurium vapor over molten gadolinium metal. Since temperature of the protective quartz envelope was not controlled, the pressure of tellurium vapor prevailing during this initial experiment is not known. The remaining specimens were cut from ingots which were cast by carefully controlled directional freezing under various known pressures of tellurium vapor. Freezing rates varying from ½ in. to 1-½ in./hr were used. In this range, crystallization rate did not appear to have a significant effect on properties of the compound.

Whereas tantalum apparently had been satisfactory as a container material in which simple melting of the compounds could be carried out, the tantalum boats were attacked severely during the prolonged periods of exposure to tellurium vapor encountered in freezing the ingots directionally. Graphite containers appeared to be more satisfactory for this purpose since they were not attacked noticeably.

Physical Properties

Melting points have been determined for three of the compounds. In making the determinations, specimens were placed in a horizontal cylindrical cavity at a depth equal to 12 times the diameter of the cavity so as to obtain near black-body conditions (1). The specimens were of triangular cross section and were supported by contact of the edges with the wall of the cavity. Incipient melting at the edges produced readily detectable movement of the speci-

Table I. Observed electrical properties (measured at room temperature) rare earth selenides and tellurides

Compound	R_H, cm^3 $coul^{-1}$	ρ, ohm-cm	μ, cm^2 v^{-1} sec^{-1}	α, μ v deg^{-1}	η, cm^{-3}
La_2Se_3	Negative	0.024	—	—	$\sim 3 \times 10^{19}$
Er_2Se_3	Positive	7.9	—	—	—
ErSe	Negative	1.7×10^{-4}	—	—	$\sim 10^{20}$
Y_2Se_3			(Insulator)		
La_2Te_3	Negative	1.9×10^{-4}	—	−30	$\sim 10^{20}$
Gd_2Te_3	−3.25	0.019	170	−26	2×10^{18}
Gd_2Te_3	+3.3	0.2	17	>+200	2×10^{18}
Er_2Te_3	Negative	1.1×10^{-3}	—	—	$\sim 10^{19}$
Y_2Te_3	−1400	10.0	140	—	4×10^{15}

mens. Temperatures were measured by means of an optical pyrometer and are estimated to have an accuracy of ± 25°C. Values obtained were: 1520°C for the melting point of Er_2Se_3, 1420°C for Gd_2Te_3, and 1525°C for Y_2Te_3. Indirect observations made in the course of the preparative work indicate that melting points for some of the other compounds may be higher, ranging up to about 2000°C.

Thermal conductivity of Gd_2Te_3 has been determined at room temperature by use of the "Z-meter" (2, 3). Values for n- and p-type specimens were found to be 0.026 and 0.023 watts cm^{-1} deg^{-1}, respectively. Since the lattice component of thermal conductivity usually predominates at room temperature for materials of this type, the nearly identical values are to be expected.

Electrical Properties

Table I presents a tabulation of electrical properties observed for some of the selenides and tellurides in their initial preparations as polycrystalline, cast ingots. It will be noted that resistivities for the sesquiselenides are somewhat higher than those for the corresponding tellurides. In general, resistivities, in both classes of compounds, increase with progression through the rare earth series, the yttrium compounds falling at the end.

The resistivity of Y_2Se_3 appears to be in the insulator range. In attempts to eliminate possible high contact resistance, a number of different methods of contacting specimens of this compound were used. Various techniques explored utilized pressure contacts with probes of Pt, W, Mo, Cu, Fe, Al; contacts of conducting silver paint; leads of Cu, W, Fe applied by spot welding; solder contacts of Pb-Sn, In, Al, Ga applied with various fluxes by both normal and ultrasonic soldering techniques. However, under applied potentials up to 60 v, there was in no instance a detectable current through the sample.

At the other extreme, resistivity for the monoselenide of erbium was found to be quite low. Low resistivities would be expected for the 1:1 compounds if only two of the valence electrons of the rare-earth atom are involved in the chemical bonds, leaving the third free to act as a charge carrier with rather low activation energy. Iandelli (4) also concluded that this was the case through analysis of structures and interatomic spacings for the cerium-group compounds.

Seebeck coefficients were measured over a range of temperatures for specimens of Gd_2Te_3 and La_2Te_3 and were found to remain constant up to 450° and 525°C, respectively, the highest temperatures to which measurements were extended. High-temperature thermoelectric properties of these rare earth compounds may be of practical interest and are being investigated currently.

It will be noted that carrier concentrations for most of the specimens are high. In synthesizing the compounds, high-purity selenium and tellurium were used (i.e., better than 99.99%). However, purity of available rare earth metals is relatively low (i.e., 99⁺%). It is therefore probable that carriers, other than those resulting from excess of one of the component elements, were introduced principally as impurities present in the rare earth metals or as contaminants incorporated during synthesis of the compounds.

Electrical data for specimens of Gd_2Te_3 from ingots cast under various pressures of tellurium vapor (Table II) indicate that, if evolution of tellurium is permitted (specimens 67, 88), *n*-type material is

Table II. Effect of tellurium vapor pressure during casting on electrical properties of Gd_2Te_3

Specimen	Tellurium vapor pressure, atm	Container material	R_H, cm^3 $coul^{-1}$	ρ, ohm-cm	μ, cm^2 v^{-1} sec^{-1}	α, μ v deg^{-1}	η, cm^{-3}
9*	?	Tantalum	−3.25	0.019	170	−26	2×10^{18}
67	~0	Tantalum	−0.11	0.0031	35	−84	6×10^{19}
88	~0	Graphite	−0.1	0.0029	30	−70	6×10^{19}
71	0.5	Tantalum	Pos., small	0.091	(Large, numerous voids throughout ingot)		
73	0.2	Tantalum	+0.16	0.028	6	+160	4×10^{19}
74	0.1	Tantalum	Pos., small	0.68	—	+240	$\sim 10^{19}$
75	0.1	Graphite	Pos., small	0.51	—	+190	$\sim 10^{19}$
77	0.01	Graphite	+3.3	0.20	17	>+200	1.9×10^{18}

* Te distilled over Gd at ~1650°C.

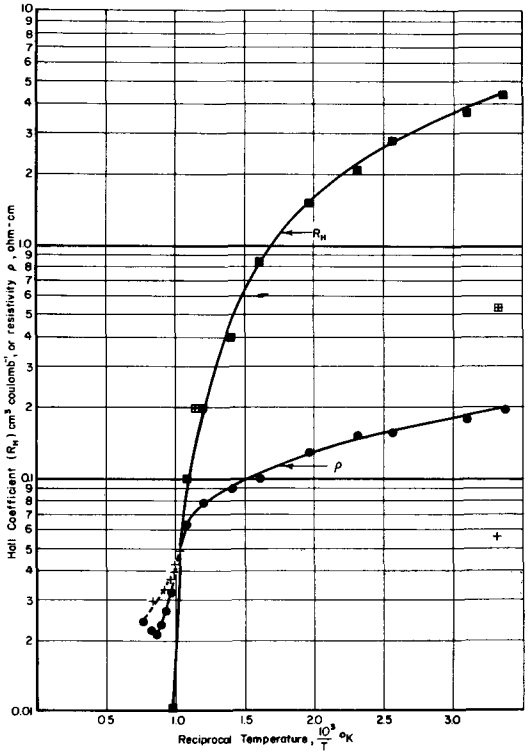

Fig. 1. Resistivity and Hall coefficient as functions of temperature for p-type Gd_2Te_3.

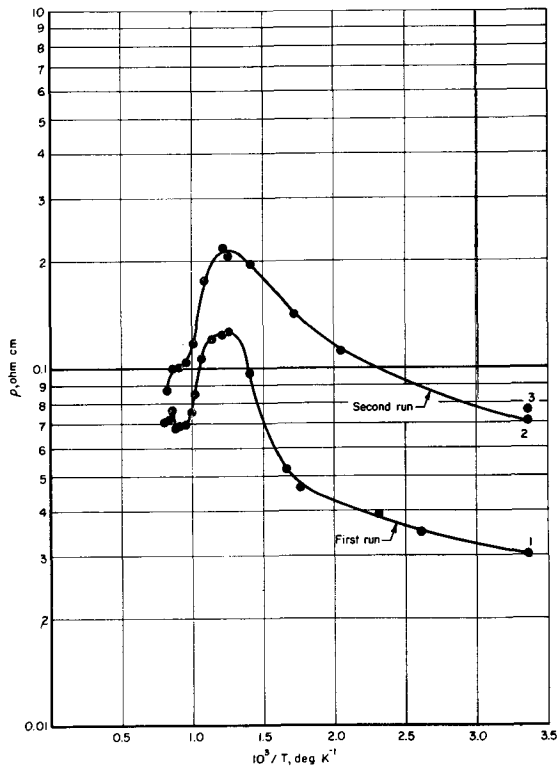

Fig. 2. Resistivity as function of temperature for n-type Gd_2Te_3.

obtained, but in the presence of moderate concentrations of tellerium vapor, (specimens 71-77), p-type material can be cast. However, dissociation pressure of the compound at its melting point appears to be relatively low since it was possible to cast a reasonably good p-type ingot (specimen 77) under only 0.01 atm of tellurium vapor pressure. Similarity of data for specimens from ingots which were cast under similar conditions in tantalum and graphite, (consider specimens 67 and 88, 74 and 75) indicates that any tantalum which may have been taken into solution, as a result of the aforementioned attack, had little effect on electrical properties of the compound at these carrier concentrations.

Figure 1 shows variation of Hall coefficient and resistivity with temperature for a p-type specimen of gadolinium telluride. Up to about 875°C, the curves are typical of those for an impure semiconductor. Above this temperature, however, behavior of resistivity is anomalous. As far as could be determined, the Hall coefficient continued to decrease (up to 950°C) and did not change sign. As temperature was decreased, resistivity followed the dotted curve, and room-temperature values for both Hall coefficient and resistivity were found to be lower following the run. (Points indicated by crosses, for both Hall coefficient and resistivity, were taken as temperature was decreased.) The variation of Hall mobility with temperature for this p-type specimen suggests that impurity scattering is important up to relatively high temperatures (i.e., at temperatures as high as several hundred degrees centigrade).

Figure 2 shows resistivity as a function of temperature for an n-type specimen of gadolinium telluride. Again, what appears to be typical behavior for an impure semiconductor was observed up to about 750°C, and anomalous variation of resistivity with temperature was noted through the range of higher temperatures. An irreversible heat-treating effect was also noted. Room-temperature resistivity was found to be considerably higher (point 2, Fig. 2) after the first temperature run. With the second

Table III. Heat-treatment of Gd_2Te_3 specimens*

Specimen	Heat treatment**	ρ, ohm-cm	μ, cm² v⁻¹ sec⁻¹	η, cm⁻³
67-1, n-type	None	0.0089	16	4×10^{19}
	2 hr at 950°C in vacuum	0.028	10	2.2×10^{19}
9, n-type	None	0.019	170	2×10^{18}
	120°C in vacuum†	0.03		
	950°C in vacuum†	0.072		
	950°C in vacuum†	0.076		
77, p-type	None	0.20	17	1.9×10^{18}
	950°C in vacuum†	0.056	10	1×10^{19}
75, p-type	None	0.51		$\sim 10^{19}$
	2 hr at 950°C in vacuum	0.067	6	1.7×10^{19}
73, p-type	None	0.027	6	4×10^{19}
	740°C in vacuum†	0.031	6	3×10^{19}
	Quenched after 2 hr at 950°C	0.032	6	3.5×10^{19}
	2 hr at 950°C in vacuum	0.037	4	4.2×10^{19}

* Data presented are from room-temperature measurements.

** All specimens cooled slowly except as otherwise noted.

† Heat treatment was that experienced in course of electrical measurements. Temperature given is the maximum attained.

temperature run, the specimen appeared to be approaching a stable condition, as is indicated by the much less pronounced irregularity in variation of resistivity with temperature above 700°C, and the fact that room-temperature resistivity (point 3) returned to approximately its initial value (point 2).

The effects of heat treatment on electrical properties of a number of specimens of gadolinium telluride were studied in an attempt to explain the observed behavior. Data for the heat-treated specimens, which are presented in Table III, indicate that after a sufficiently long period of heat treatment, the samples approach a stable condition.

Because of conflicts in the data (e.g., changes in carrier concentrations vs. changes in mobilities), it is not possible to reach a firm conclusion concerning the nature of heat treating effects. However, it may be seen that for the n-type specimens resistivity is increased and carrier concentration is decreased by heat treatment in vacuum, and for the p-type specimens resistivity is decreased and carrier concentration is increased by the same treatment. Such changes are consistent with loss of n-type impurities. This is a possibility since spectrographic analyses show that relatively high concentrations of Ca, Mg, Fe, Ni, Ta, Si, and Al are present in the specimens.[1] Since tellurium has already been shown to give p-type doping, loss of tellurium is not suspect as a cause for the changes observed.

Manuscript received June 15, 1959. This paper was prepared for delivery before the Philadelphia Meeting, May 3-7, 1959. This investigation was supported by the Rare-Earth Research Group (Davison Chemical Co., Union Carbide Metals Co., Heavy Minerals Co., Lindsay Chemical Div. of American Potash and Chemical Corp., Mallinckrodt Chemical Works, Rare Earths and Thorium Div. of Michigan Chemical Corp., and Molybdenum Corp. of America).

Any discussion of this paper will appear in a Discussion Section to be published in the June 1960 JOURNAL.

REFERENCES

1. I. E. Campbell, "High Temperature Technology," John Wiley & Sons, Inc., New York (1956).
2. T. C. Harman, *J. Appl. Phys.*, **29**, 1373 (1958).
3. T. C. Harman, J. H. Cahn, and M. J. Logan, To be published, *J. Appl. Phys.*
4. A. Iandelli, *Gazz. Chim. Ital.*, **85**, 881 (1955).

[1] Per cent by weight detected: 0:01 Ca, 0.05 Mg, 0.01 Fe, 0.001 Ni, <0.05-5.0 Ta, 0.001 Si, 0.005-0.01 Al.

Diffusion of Cerium and Zirconium in Molten Uranium

Tennyson Smith

Atomics International, A Division of North American Aviation Incorporated, Canoga Park, California

ABSTRACT

Coefficients for the diffusion of cerium in molten uranium have been measured over the temperature range 1170°-1480°C. An equation relating the diffusion coefficient with temperature is: $D = 4.5 \times 10^{-3}\, e - 11{,}000/RT$. At 1200°C the diffusion coefficient for cerium in uranium is $(1.00 \pm 0.17) \times 10^{-4}$ cm²/sec. An estimate of the coefficient of diffusion for zirconium in uranium at 1270°C is $(1.9 \pm 0.9) \times 10^{-4}$ cm²/sec. A discussion of experimental errors involved in measuring diffusion coefficients at high temperatures is given.

A study has been made of the reactions and mechanism involved in the oxide-drossing of fission products from uranium. The oxide-drossing process is a pyrometallurgical method of reprocessing spent uranium with an oxide such as urania, zirconia, or alumina. Those fission products that are more stable than the oxide used are removed selectively from the melt. Elements such as the rare earths react with the oxide, while elements such as cesium, iodine, and the rare gases volatize off.

The diffusion of cerium and zirconium in molten uranium was studied in a preliminary investigation. Cerium and zirconium were selected as representatives of the lanthanide series and high melting elements, respectively. Diffusion characteristics of fission products in uranium are of interest since the mass transfer of these elements to the oxide surface is the first step in the extraction mechanism. A knowledge of the diffusion coefficient for these elements in molten uranium will help determine the slow step in the mechanism.

Most of the studies on the diffusion of metals in molten metals have been done with low melting metals or alloys (300°-700°C) (1). Diffusion coefficients generally range from about 2×10^{-5} to 7×10^{-5} cm² sec^{-1}, which is close to that found for diffusion in other liquids.

At higher temperatures (between 1000° and 1700°C) only a few experiments have been reported, and the diffusion coefficients cover a wider range. Paschke and Hautmann (2) obtained 2.4×10^{-5} cm² sec^{-1} and 10.8×10^{-5} cm² sec^{-1} for the diffusion of silicon in molten iron at 1480° and 1560°C, respectively, and a value of 1.2×10^{-4} cm² sec^{-1} for manganese in iron in the same temperature range. Holbrook, Furnas, and Joseph (3) studied the diffusion of sulfur, manganese, phosphorus, silicon, and carbon in molten iron over the temperature range 1200°-1700°C. The average diffusion coefficients for silicon, phosphorus, sulfur, and manganese was about 1×10^{-4} cm² sec^{-1} in this temperature range. The variation of the diffusion coefficient with tem-

perature was less than the experimental error. They found the diffusion coefficient for carbon in liquid iron to be much larger, about 6 x 10^{-4} cm^2 sec^{-1}. Penetration curves did not correspond well with ideal diffusion curves, probably because of experimental errors such as convection. It is difficult to avoid this problem completely.

A recent paper by Morgan and Kitchener (4) describes an experiment to determine the diffusion coefficients of cobalt and carbon in iron. They obtained D values of 5.5 x 10^{-5} cm^2 sec^{-1} for cobalt at 1638°C and 4.3 to 6.7 x 10^{-6} cm^2 sec^{-1} for the diffusion of carbon in iron, depending on the carbon concentration and temperature. They took particular interest in eliminating the problem of convection.

Experiments to measure diffusion coefficients in molten metals generally have been carried out using one of the three techniques described by Niwa, *et al.* (5). Their third method, used by Kitchener and Morgan (4), was to place a pure metal or an alloy containing the diffusate next to a long, narrow column of solvent. Samples are taken along the length of the metal column after it had been to temperature for a specific time. Morgan and Kitchener point out that this method allows detection of deviations from Fick's law due to convection, etc. This same technique was used in the study reported here, except that metal columns of the order of 7 mm rather than 2 mm diameter were used in order to obtain larger samples for analysis. The larger diameter allowed convection at the higher temperatures which increased the uncertainty of the results at these temperatures (1400°-1480°C).

This paper reports experiments to measure the diffusion coefficient of cerium in molten uranium over the temperature range 1170°-1480°C. An estimate of the diffusion coefficient for zirconium in molten uranium is also given.

Experimental

A slug of natural uranium was machined to fit the crucible, then etched clean with dilute HNO_3. The desired amount of cleaned cerium or Zr-U alloy was placed on top of the uranium, and the unit was placed in the vacuum furnace tube (Fig. 1). The McDanel ceramic tube could be evacuated to 0.1 μ, filled with an inert gas, then placed in a Globar furnace. Three thermocouples were placed in the system so that the temperature could be

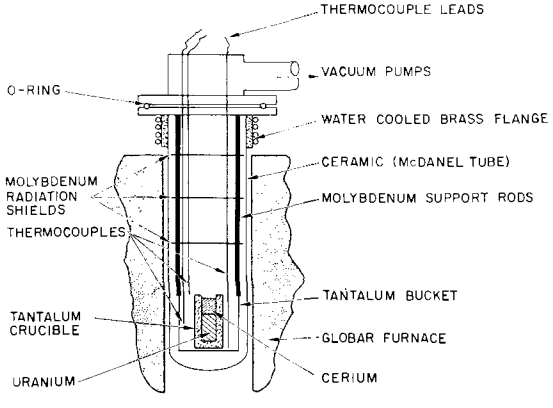

Fig. 1. Furnace assembly

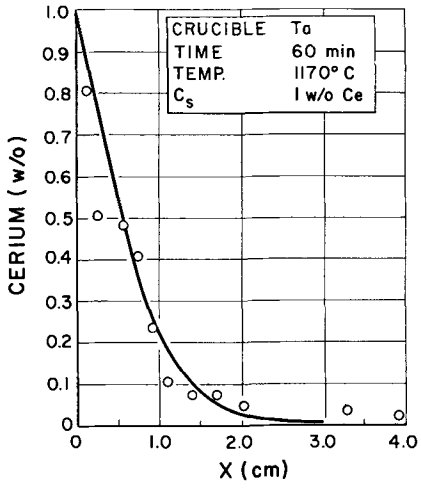

Fig. 2. Penetration curve: cerium diffusion into molten uranium at 1170°C. The solid line is based on an average value of D = 1 x 10^{-4} cm^2 sec^{-1}.

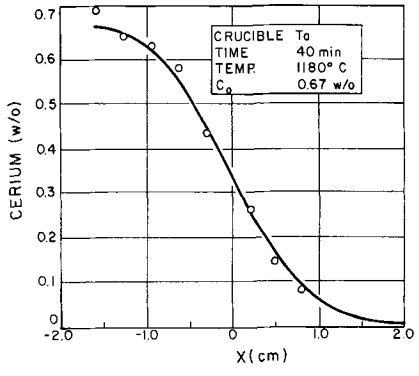

Fig. 3. Cerium diffusion into molten uranium from a Ce-U alloy at 1180°C. The solid line is based on an average value of D = 0.95 x 10^{-4} cm^2 sec^{-1}.

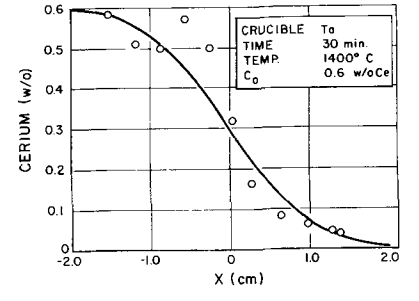

Fig. 4. Penetration curve: cerium diffusion into molten uranium from a Ce-U alloy at 1400°C. The solid line is based on an average value of D = 1.98 x 10^{-4} cm^2 sec^{-1}.

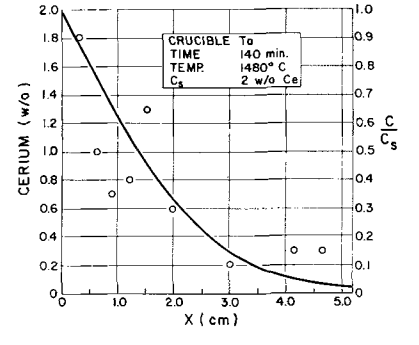

Fig. 5. Penetration curve: cerium diffusion from pure cerium into molten uranium at 1480°C. The solid line is based on an average value of D = 2.54 x 10^{-4} cm^2 sec^{-1}. Scatter of experimental points shows the effect of convection.

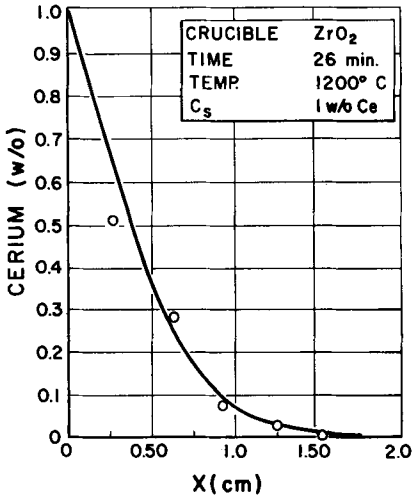

Fig. 6. Cerium diffusion into molten uranium (1200° C) in a ZrO_2 crucible. The solid line is based on an average value of $D = 1 \times 10^{-4}$ cm^2 sec^{-1}.

measured at various points with respect to the sample. The temperature was controlled with a temperature controller and recorded on a millivolt recorder.

In each experiment, the system was first evacuated to about 0.1 μ, then flushed and filled with argon to 1 atm of pressure. The argon was purified by passing it through a uranium trap held at about 600°C. The furnace was brought to the desired temperature, held at temperature for the experiment, then allowed to cool as fast as possible without breaking the ceramic tube. The time to heat the sample from the melting point of uranium to temperature was 3 or 4 min, and the time required to cool the sample below the freezing point of uranium was not more than 4 or 5 min.

Three different crucibles were used in the experiments. A tantalum crucible, 1.5 cm OD by 9 cm high, with a hole 0.75 cm ID and 7.5 cm deep, was used for the experiments reported in Fig. 2, 3, 4, and 5. In two of these experiments (Figs. 3 and 4) a 3 cm slug of uranium-cerium alloy (0.67 w/o, Fig. 3; 0.6 w/o, Fig. 4) was placed on top of a 3 cm slug of pure uranium. In the other two experiments, (Fig. 2 and 5) a thin layer of pure cerium about 2 mm thick was placed on top of a 6 cm slug of pure uranium. The slug of uranium was counter-sunk at the top, with a shallow hole, leaving thin uranium sides and just deep enough to contain the molten cerium when it melted. This was done so that the molten cerium would not run down the sides of the uranium before it melted (mp: Ce, 793°C; U,1133°C) (6).

For the experiment which corresponds to Fig. 6, the uranium was placed in a zirconia crucible approximately 1.5 cm OD x 5.5 cm high, with a hole 1 cm ID and 5 cm deep. In this experiment, pure cerium metal was placed on top of the uranium in the manner mentioned above, and the system was held at 1200°C for 26 min.

Figure 7 gives the results of an experiment carried out in a tungsten crucible at 1350°C for 155 min. Again, the pure cerium metal was placed on the counter-sunk uranium slug. The approximate

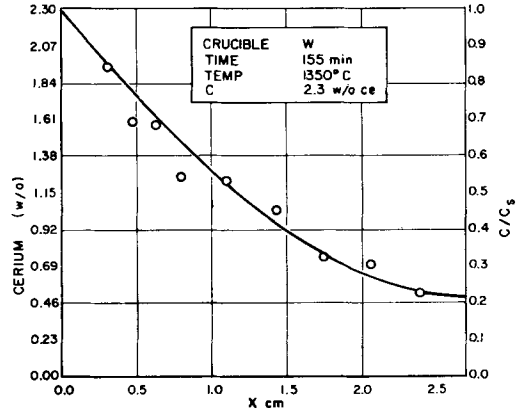

Fig. 7. Penetration curve: cerium diffusing into molten uranium at 1350°C from pure cerium. The solid line is based on an average value of $D = 1.46 \times 10^{-4}$ cm^2 sec^{-1}. The reflection principle was used.

dimensions of the tungsten crucible were: 2.5 cm OD by 4 cm high, with a hole 1.4 cm ID and 3.5 cm deep.

One experiment was conducted with a 3% zirconium-uranium alloy placed on top of pure uranium in the tantalum crucible. The system was held at 1270°C for 40 min.

After each experiment, samples were taken from the uranium at known distances from the top of the slug by drilling lengthwise through the center of the ingot. The samples were washed and dried, then weighed and analyzed. The higher concentrations of cerium were analyzed volumetrically (7) and the low concentrations calorimetrically (8). In two experiments, the cerium had been irradiated, and analysis was accomplished with a gamma-ray spectrometer after extracting the uranium with tributyl phosphate. Analyses for zirconium in uranium was made gravimetrically (9).

Errors and Uncertainties

When taking samples for analysis, there is an uncertainty as to the exact position of the interface due to its shape. The shape of the interface is a function of the interfacial tensions between cerium, uranium, and the crucible wall. Since the interface is not flat, there will be some samples at the interface that will cut both phases simultaneously and will give invalid results.

The uncertainty of the position of the interface generates an error in the value of X, which is increasingly significant as X approaches zero. This is shown by the equation: per cent error (in D) = $100\,(X_1^2 - X^2)/X^2$ where X is the true distance and X_1 is the apparent distance. In the present work, the uncertainty in X is approximately 0.2 cm; consequently, at $X = 0.2$ cm and $X_1 = 0.4$ cm, the per cent error is 300, while at $X = 4$ cm and $X_1 = 3.8$ cm, the per cent error is 10. This same effect is seen for uncertainties in λ (note Eq. [1] below) where λ is small, since $D \propto 1/\lambda^2$. Errors in λ result from uncertainties in the measured variables C or C_s since λ is obtained from a plot of C/C_s vs. λ. C is the concentration of the diffusate in the solvent at any specified time, and C_s is the constant concentration in the solvent at the interface between the solvent and the

Table I. Effect of an uncertainty in C_s on D with distance from the interface*

C_s, wt % Ce	X, cm	Ce, wt %	C/C_s	2	D, cm²/sec x 10^{-4}	% Error
1.1	0.12	0.81	0.737	0.48	0.18	45.5
0.9	0.12	0.81	0.900	0.20	1.00	20.0
1.1	0.59	0.49	0.445	1.05	0.90	10.0
0.9	0.59	0.49	0.545	0.86	1.35	35.0
1.1	1.39	0.07	0.064	2.63	0.77	6.1
0.9	1.39	0.07	0.078	2.49	0.87	6.1
1.1	2.02	0.04	0.036	3.00	1.26	2.3
0.9	2.02	0.04	0.044	2.88	1.37	6.2
1.1	2.30	0.03	0.027	3.15	3.00	32.0
0.9	2.30	0.03	0.033	2.52	4.77	54.0

* From data shown in Fig. 2.

diffusate. Small discrepancies in C or C_s cause increasingly larger uncertainties in λ as λ increases; therefore, large inherent errors are to be expected at small and at large values of X. This is clearly shown in Table I where the per cent error is given as a function of X for a difference of 0.2% in C_s. The most accurate values of D are those calculated for X between 1 and 2 cm.

The residuals for the values of D falling within the above mentioned band are considered random; only the values of D having random residuals are used in the determination of the average value of D.

The per cent error recorded in Table I is based on the assumption that the correct value for C_s is 1%.

It is well known that D, the diffusion coefficient, is rarely a constant with change in concentration; however, it does approach a constant value at low concentrations. Since the concentrations in these experiments were low, the assumption of D constant is good.

Although the uranium and the cerium were cleaned of oxide before each experiment, and the experiments were made in a purified argon atmosphere, it is quite possible that a thin film of oxide existed between the uranium and the cerium in the U-Ce couple. If the film was very thin or if no film existed, the value of C_s should be just the solubility of cerium in uranium at the temperature of the experiment. However, if the oxide film was thick enough to provide a resistance to the diffusion of cerium to the uranium surface, then the value of C_s might be something less than the solubility of cerium in uranium. With or without the oxide, correct values of the diffusion coefficients will be obtained as long as C_s is constant and can be measured.

The curve C/C_s vs. 2λ becomes linear as 2λ approaches zero. The best values of C_s, then, are those obtained by extrapolating the experimental curves of per cent cerium vs. X back to the interface, since $X \propto \lambda$, (note Fig. 2, 5, 6, and 7) this is the manner in which values of C_s were obtained for the calculations.

For the experiments in which an alloy was used instead of pure cerium (Fig. 3 and 4) only values of C_o, the initial concentration of the alloy, was needed rather than C_s. Values of C_o were found before the diffusion experiments were made by analyzing a number of samples from the alloy.

All but two experiments were made in a tantalum crucible. Tantalum is slightly soluble in uranium, and it is to be expected that some interference will result from its presence. Since the two experiments, in which a zirconia crucible and a tungsten crucible were used, gave results consistent with those of the experiments in which tantalum crucibles were used, the effect of the presence of tantalum can be considered to be within the experimental error. It is noted that the use of zirconia crucible will also cause interference, because some of the cerium reacts with the ZrO_2 at the surface. Every known container material would interfere to some extent. The best crucible would be one made of CeO_2, but this was not available for these experiments.

Discussion and Results

Results for diffusion experiments are shown in Fig. 2 through 7 as penetration curves for cerium in molten uranium. The weight per cent cerium plotted as open circles at various distances, X, from the cerium-uranium interface are average values for the concentration of cerium at that position. The length X is the distance from the cerium uranium interface to the center of the sample that was taken for analysis. The solid lines in the graphs are theoretical penetration curves based on average values of the diffusion coefficients.

Diffusion equations.—Diffusion coefficients were measured under three different experimental conditions requiring three separate solutions of Fick's equation.

Case 1.—The simplest experimental situation, that of nonsteady-state diffusion in a semi-infinite media, consisted of two elements in contact, having a sharp boundary between them initially, contained in a cylinder having impermeable sides. Consider only half of such a couple; the dimensions in the direction of diffusion must be large compared to the distance over which measurable composition change occurs during the experiment. The initial concentration of the diffusing element in the semi-infinite media must be uniform, and the surface must be brought instantaneously to some concentration C_s which remains constant during the experiment.

These boundary conditions may be written:

$$C = C_o \text{ at } t = 0 \text{ and } 0 < X < \infty$$

$$C = C_s \text{ at } X = 0 \text{ and } 0 < t < \infty,$$

where C is the concentration of the diffusing species at time, t, C_o is the initial homogeneous concentration of the diffusing species, and X is the distance from the interface in the direction of diffusion.

The solution (10) of Fick's second law corresponding to these boundary conditions and for a constant diffusion coefficient, D, is

$$\frac{C_s - C}{C_s - C_o} = \frac{2}{\sqrt{\pi}} \int_0^{X/(2\sqrt{Dt})} e^{-\lambda^2} d\lambda \qquad [1]$$

where λ is an integration variable. The term on the right is the normalized probability integral or the error function, (erf); its compliment, 1-erf, is known as erfc and is equal to $(C-C_o)/(C_s-C_o)$. Values of

Table II. Variation, with temperature, of the coefficient of diffusion for cerium in uranium

T, °C	$10^4/T$, °K	D (avg), $cm^2\ sec^{-1} \times 10^4$	Avg error $\times 10^4$	$-LnD$	Fig. No.
1170	6.93	1.00	0.21	9.20	2
1180	6.88	0.95	0.13	9.25	3
1200	6.79	1.00	0.17	9.20	4
1350	6.16	1.46	0.15	8.80	5
1400	5.98	1.98	0.73	8.52	6
1480	5.70	2.50	1.60	8.20	7

$(C-C_o)/(C_s-C_o)$ vs. 2λ are tabulated (10) and were used to determine the diffusion coefficients recorded in Tables I and II.

Case 1 is useful for experiments with low melting metals such as cerium and lanthanum where the pure metal is in contact with uranium.

Figures 2, 5, and 6 show penetration curves for cerium in uranium at 1170°, 1200°, and 1480°C, respectively. The experiments for 1170° and 1200°C were made at close to the same temperature but with different types of crucibles, tantalum and zirconia. Both experiments gave an average diffusion coefficient of 1.0×10^{-4} cm^2 sec^{-1}.

In these experiments, pure cerium was contacted with pure uranium and the data were interpreted as in Case 1.

Case 2.—In order to measure the diffusion coefficients of elements such as Zr, Mo, Y, Nb, and Ru that have high melting points, it is necessary to make alloys of these elements with uranium and measure the diffusion from the alloy into pure uranium. The boundary conditions are: $C = C_o$, $X < 0$; $C = 0$, $X > 0$, and $t = 0$. The solution (10) of Fick's second law for these boundary conditions is

$$C(X,t) = \tfrac{1}{2}\, C_o \operatorname{erfc} \frac{X}{2\sqrt{Dt}} \qquad [2]$$

or, $C/(\tfrac{1}{2}C_o) = \operatorname{erfc} \lambda$, which is identical with the expresssion for C/C_s in Case 1. It is seen, then, that the two processes are the same except that, in the second case, $C_s = \tfrac{1}{2}C_o$. It is interesting to note that at $X = 0$ the concentration remains constant, at $\tfrac{1}{2}C_o$, with time.

In order to evaluate D, the experimental value for C/C_s at X is determined and a corresponding value for 2λ is found from the error function tables, then $D = (1/t)\ (X/2\lambda)^2$.

The data reported in Fig. 3 and 4 for cerium and one experiment with zirconium were interpreted as in Case 2 above; pure uranium was contacted with a U-Ce or U-Zr alloy.

Case 3.—One other case must be considered to interpret the data from the experiment shown in Fig. 7. In this experiment the time period was long enough that at $X = l$ (where l is the distance from the interface to the bottom of the crucible), C was not equal to zero as in Case 1. The boundary conditions are:

$$C = C_s, X = 0; C = 0, t = 0; \text{and} \frac{\partial C}{\partial X} = 0, x = l$$

It becomes necessary to use the principle of reflection. The appropriate solution to Fick's second law can be found in Crank's (10) book on diffusion, if his equation 2.54 (section 2.43) has X replaced by $(1-x)$ and C_o replaced by C_s. The equation becomes:

$$C/C_s = \operatorname{erfc} \frac{X}{2\sqrt{Dt}} + \sum_{n=1}^{\infty} (-1)^n \operatorname{erfc} \frac{2nl+x}{2\sqrt{Dt}} - \operatorname{erfc} \frac{2nl-x}{2\sqrt{Dt}} \qquad [3]$$

This equation reduces to Eq. [1] if only the first term is needed, i.e., where x is small or t is short. Only two terms of this equation are needed to interpret the results in Fig. 7:

$$C/C_s = \operatorname{erfc} \left(\frac{X}{2\sqrt{Dt}}\right) + \operatorname{erfc} \frac{2l-x}{2\sqrt{Dt}} \qquad [4]$$

since the other terms are too small to be significant. Diffusion coefficients for the experiment reported in Fig. 7 were obtained by using the family of curves on page 46 of Crank's book (10).

Temperature Effect

Although an attempt was made to reduce thermal convection by controlling the temperature along the diffusion couple, it appears that convection currents did occur, particularly at the higher temperatures. If one assumes that deviation of the experimental points from the theoretical penetration curves is an indication of convective interference (4), it is seen from Fig. 2 through 7 that convection becomes more of a problem as the temperature increases.

Table II reports the average diffusion coefficients which correspond to Fig. 2 through 7 as a function of temperature. This table also gives the values for the average error and LnD.

It is felt that the diffusion coefficients reported in Table II up to 1350°C are accurate to within the error recorded for two reasons: first, the experimental points fall fairly close to the theoretical penetration curves in Fig. 2, 3, 6, and 7; second, even though the experiments reported in Fig. 2 and 3 were conducted in a crucible with different dimensions (0.75 cm ID) than that reported in Fig. 6, (1 cm ID), the diffusion coefficients proved to be the same. However, the experimental points at 1400° and 1480°C deviate considerably from the penetration curves (Fig. 4 and 5). It is thought that this deviation is due to convection and that the resultant average values for the diffusion coefficients are too high.

Data in Table II are plotted in Fig. 8; the open circles are based on the average diffusion coefficients and the solid lines indicate the maximum deviation from the mean. An estimate of the activation energy for diffusion, neglecting the data at 1400° and 1480°C, is 11 kcal $moles^{-1}$, and an equation relating the diffusion coefficient and temperature is: $D = 4.5 \times 10^{-3}\ e^{-11,000/RT}$.

For low melting metals (up to 700°C) activation energies have been reported from 4 to 10 kcal $moles^{-1}$ (1, 4, 11, 12). At higher temperatures (1100°-1500°C) the approximate activation energy reported here for cerium in uranium (11 kcal

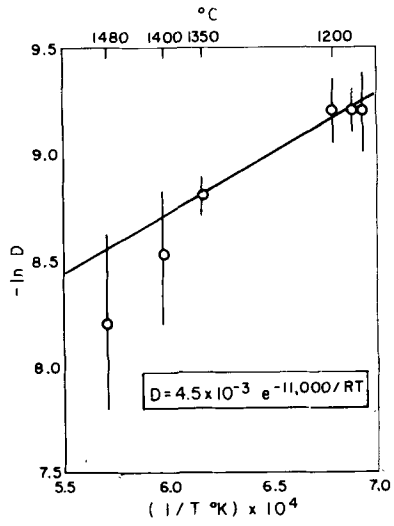

Fig. 8. An Arrhenius plot of the diffusion coefficient of cerium in molten uranium.

mole^{-1}) is close to that reported by Morgan and Kitchener (4) of about 10 to 11 kcal mole^{-1} for cobalt and carbon in molten iron (1350°-1650°C).

An estimate of the diffusion coefficient of zirconium in molten uranium at 1270°C was found from one experiment to be (1.9 ±0.9) x 10^{-4} cm^2 sec^{-1}. The large experimental error for this experiment is attributed to the error in chemical analysis although some turbulence may have had effect.

The diffusion of cerium and zirconium in molten uranium is somewhat faster than diffusion in other molten metal systems. The diffusion coefficients for many elements in molten metals (1) varies between (1 and 10) x 10^{-5} cm^2 sec^{-1}. Most of the work has been carried out below 1000°C, and it may be that the higher melting metals behave differently. Further experimentation with particular attention given to the convection problem is needed for measuring diffusion coefficients in metals at high temperatures.

Manuscript received April 23, 1959.

Any discussion of this paper will appear in a Discussion Section to be published in the June 1960 JOURNAL.

REFERENCES

1. W. Jost, "Diffusion in Solids, Liquids, Gases," Academic Press, New York (1952).
2. M. Paschke and A. Hautmann, *Arch. Eisenhüttenw*, **9**, 305 (1935).
3. W. F. Holbrook, C. C. Furnas, and T. L. Joseph, *Ind. Eng. Chem.*, **24**, 993 (1932).
4. D. W. Morgan and J. Kitchener, *Trans. Faraday Soc.*, **50**, 51 (January 1954).
5. K. Niwa, M. Shimozi, S. Kado, Y. Watanabe, and T. Yokokawa, *Trans. AIME*, **209**, 96 (1957).
6. *"Rare Metals Handbook,"* Reinhardt Publishing Co., New York.
7. C. V. Banks and J. W. O'Laughlin, *Anal. Chem.*, **28**, 1338 (1956).
8. J. Hure nd MMe. R. Saint James Shonberg, *Anal. Chim. Acta*, **9**, 415 (1953).
9. J. J. Klingenberg and R. A. Popucci, *Anal. Chem.*, **24**, 1861 (1952).
10. J. Crank, "The Mathematics of Diffusion," Clarendon Press, Oxford (1956).
11. S. J. Rothman University Microfilms (Ann Arbor Michigan) Publication No. 11, 185, 102 pp. (1954).
12. T. Saito and K. Maruya, *Bull. Research Inst. Mineral Dressing*, Tohoku University, **10**, 167 (1954).

Diffusion-Exchange of Exchange Ions and Nonexchange Electrolyte in Ion-Exchange Membrane Systems

Marvin A. Peterson and Harry P. Gregor

Department of Chemistry, Polytechnic Institute of Brooklyn, Brooklyn, New York

ABSTRACT

The following parameters of cation- and anion-permeable membrane systems were measured: water content; ohmic resistance; exchange capacity; diffusible electrolyte content; concentration potential; rate of exchange-diffusion of electrolytes; rate of diffusion of nonelectrolytes; effect of rate of stirring on diffusive flux. From these were calculated: the thickness of the unstirred film, which varied from 1 to 30 microns; the diffusion coefficient of the potassium ion in a sulfonic acid cation-permeable membrane, which was found to vary from 1.09 x 10^{-7} cm^2 sec^{-1} to twice that value as the ambient solution concentration was changed from 0.001 to 0.1M; the diffusion coefficient of the chloride ion which remained at about 3 x 10^{-7}; the diffusion coefficients of nonelectrolytes. A theoretical treatment showed that diffusion coefficients and other parameters could be estimated from a consideration of pore diameters, a tortuosity factor, and water contents.

Of primary importance in any detailed analysis of free and forced transport of ions across ion-selective membranes is the determination of boundary conditions which define film, membrane or coupled film-membrane diffusion mechanisms as being rate controlling. The appropriate application of Fick's law to diffusion across a membrane and its bounding unstirred films results in an expression which dictates the rate-controlling mechanism under given experimental conditions. The general theory of diffusive processes in ion-exchange resin systems has been described previously by several authors (1-3)

and analyzed by Tetenbaum and Gregor (4). Two different mechanisms, namely, film or particle diffusion, were found to be distinguishable when the resin system was operating in certain limited extremes, and a coupled mechanism was found to be operative in the region between these extremes.

With ion-exchange resin systems it was found that the diffusion coefficient of the exchange ion or the counter ion decreased as the degree of crosslinking or the density of the resin increased and that the diffusion coefficient of nonexchange or co-ions (anions in the case of cation-exchange resins) was proportional to that of the exchange ions and generally somewhat larger (1-6).

Diffusion studies are more complex for ion-selective membrane systems than for ion-exchange resin systems in that two diffusion films are encountered in membrane studies. Matters generally become simplified for the membrane case, however, once concentration gradients are established as compared to the resin system where a point source, nonstationary state prevails. Until steady state has been attained in the membrane system, the application of Fick's law presented by Lowan (7) holds for each of the successive layers, namely, film-membrane-film. Once concentration gradients have been established in each of the layers and a steady state is allowed to prevail, a new set of relations may be developed using Fick's law so as to determine the conditions which will dictate whether film, membrane, or a coupled diffusion mechanism is controlling.

The membrane-system model is characterized by the chain:

Solution' | Film' | Membrane | Film" | Solution"

Subscripts on concentration terms denote ionic species. Primed terms refer to solution' and solution", respectively; o and l refer to interfacial concentrations at $x = 0$ and $x = l$, respectively; a superscript bar refers to concentrations within the membrane phase (see Fig. 1). Assumptions applied to the membrane system include the following: (*a*) steady state prevails; (*b*) the membrane is ideally ion-selective; (*c*) discontinuities at the interfaces present no resistance to interfacial diffusion; (*d*) negligible transfer of solvent occurs; (*e*) the ratio of the diffusion constants of the two diffusing counter ions remains constant throughout the system. The use and validity of these assumptions have been described in detail by many authors including Helfferich (8) and Soldano and Boyd (9).

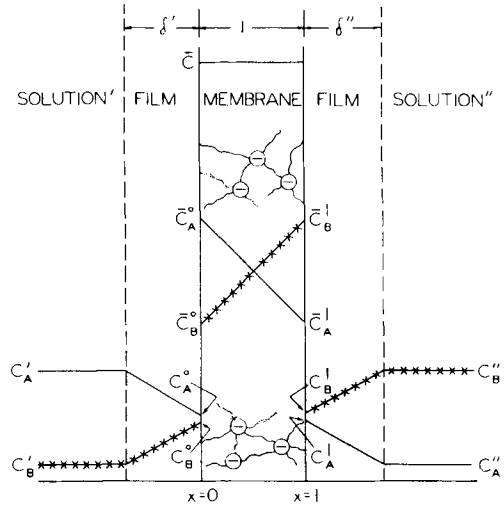

Fig. 1. Concentration profiles for the steady state where a coupled mechanism is rate controlling and where $Z_A = Z_B$ and $\bar{D}_A = \bar{D}_B$. Total membrane capacity is $\bar{C}_A + \bar{C}_B = \bar{C}$ and $C' = C''$.

The flux of ions across a membrane can be defined as the product of mobility, concentration, and driving force. Components of the driving force include gradients of activity, electric potential, and hydraulic pressure. These are summed up algebraically in the Nernst-Planck flux equation and the resulting flux, J, for a cation across a cation-permeable membrane is generally expressed as

$$J_+ = -\bar{U}_+\bar{C}_+\left(\frac{RT}{\bar{C}_+}\frac{d\bar{C}_+}{dx} + Z_+\mathbf{F}\frac{d\phi}{dx}\right) \qquad [1]$$

where $\bar{U}_+$ and $\bar{C}_+$ represent the mobility and concentration of a single ionic species within the membrane and where the potential ϕ is generally taken as $\phi = 0$ at $x = 0$, and where $\mathbf{F}$ is the Faraday. With the aid of the Nernst-Einstein equation it is possible to relate the mobility of an ion in the membrane phase to its self-diffusion coefficient in the membrane phase (10). Direct or modified application of the above expression allows one to calculate interfacial concentrations, but this is a cumbersome approach.

A more direct approach may be made by defining an integral diffusion coefficient, D_{AB},

$$\bar{D}_{AB} = J_A\frac{l}{\bar{C}^\circ_A - \bar{C}^l_A} = J_B\frac{l}{\bar{C}^l_B - \bar{C}^\circ_B} \qquad [2]$$

where the total concentration $C = C_AZ_A + C_BZ_B$ and where similar defining expressions apply for the integral diffusion coefficients in the unstirred films.

Because of discontinuities at the membrane-film interface, a partition coefficient k must be defined for each interface, such that $k_i = \bar{C}_iC/C_i\bar{C}$. For steady-state conditions the flux J for each ionic species remains constant through each layer so that $J_i' = \bar{J}_i = J_i''$.

Application of Fick's law to this model results in the following expressions for the interfacial concentration of ion A at the coordinates $x = 0$ and $x = l$, in the case where $C = C' = C''$,

$$C^\circ_A = C - \frac{k^\circ_AC + \dfrac{D'_{AB}Cl}{\bar{D}_{AB}\bar{C}\delta}C'_B + k^l_A\dfrac{D'_{AB}}{D''_{AB}}C'_B - k^l_AC''_A}{\dfrac{D'_{AB}Cl}{\bar{D}_{AB}\bar{C}\delta} + k^l_A\dfrac{D'_{AB}}{D''_{AB}} + k^\circ_A} \qquad [3]$$

$$C^l_A = \frac{k^\circ_AC + \dfrac{D''_{AB}Cl}{\bar{D}_{AB}\bar{C}\delta}C''_A + k^\circ_A\dfrac{D''_{AB}}{D'_{AB}}C''_A - k^\circ_AC'_B}{\dfrac{D''_{AB}Cl}{\bar{D}_{AB}\bar{C}\delta} + k^\circ_A\dfrac{D''_{AB}}{D'_{AB}} + k^l_A} \qquad [4]$$

Partition coefficients must be determined experimentally. Integral diffusion coefficients can be eval-

uated from flux data by assuming activity coefficients independent of ionic composition and $\bar{D}_i$ constant throughout the membrane phase.

With the aid of these expressions the flux across any layer may be written. For the unstirred film[1] on the side adjacent to solution" and for the case where A and B have equivalent diffusive characteristics ($D_A = D_B = D$) and where $\delta' = \delta''$, the flux for ion A becomes,

$$J''_A = \frac{D}{\delta}(C^l_A - C''_A) = \frac{D}{\delta}\left[\frac{C}{\frac{DCl}{\bar{D}\bar{C}\delta} + 2} - C''_A\right] \quad [5]$$

For the same conditions the flux across the unstirred film on the side adjacent to solution' becomes,

$$J'_A = \frac{D}{\delta}(C'_A - C^\circ_A) = \frac{D}{\delta}\left[C'_A - C\left[1 - \frac{1}{\frac{DCl}{\bar{D}\bar{C}\delta} + 2}\right]\right] \quad [6]$$

These expressions are exact when applied to the unstirred films and dictate whether film, membrane, or a coupled film-membrane diffusion mechanism is controlling. Expressions for the flux of ion B may be written similarly; these must satisfy the electroneutrality assumption inherent in the above derivation. The key parameter in these expressions is $DCl/(\bar{D}\bar{C}\delta)$ which is the ratio of the maximum attainable flux in the unstirred film to that in the membrane and has been used by Helfferich (8).

From these expressions it is noted that if $DCl/(\bar{D}\bar{C}\delta) << 1$, corresponding to a case where, under the same concentration gradient, the flux in the membrane phase is much larger than that in the unstirred film, then where $C'_A >> C'_B$ and $C''_B >> C''_A$ the expression for C°_A simplifies to $C^\circ_A = C/2$. Here the gradient in the unstirred film has reached its maximum value, or pure film control exists. The gradients are almost entirely in the unstirred films, and $C^\circ_A = C^\circ_B = C^l_A = C^l_B = C/2$. Similarly, if $DCl/(\bar{D}\bar{C}\delta) >> 1$, corresponding to cases where the resistance of the film to diffusion is much less than that of the membrane, then $C^\circ_A = C^l_B = C$ and $C^l_A = C^\circ_B = 0$, or the gradients are located almost entirely in the membrane phase. Where the ratio $DCl/(\bar{D}\bar{C}\delta)$ has intermediate values, neither process is purely rate-determining and a coupled mechanism prevails, as shown in Fig. 1. Analogous systems wherein water transport occurs have been described by Schlögl and Schödel (11).

Experimental

Homogeneous interpolymer membranes have been described by Gregor, *et al.* (12-16). These may be prepared by casting a homogeneous film from a solution of a polyelectrolyte and a hydrophobic film-forming polymer in a suitable solvent, allowing the film to dry, and using directly. A series of interpolymer films were examined in a preliminary way to ascertain their characteristics as regards transport phenomena. Transport across ion-exchange membranes proceeds by essentially the same process for all membrane types; however, there are certain basic differences between homogeneous and heterogeneous films as regards the exact mechanisms of transport, particularly of water transport (16). Since there are commercially available membranes of the homogeneous type, ones which show similar properties to the interpolymer membranes, it was decided to carry out the detailed examination of transport processes in commercial membranes. The films selected were quite strong mechanically and capable of withstanding high rates of stirring. The cation-permeable membrane used was the sulfonic acid-type film Nalfilm 1;[2] the anion-permeable membrane was Nalfilm 2, a quaternary ammonium-type obtained from the same source.

The effective exchange capacity of a membrane is the number of acidic or basic exchange sites within the membrane structure which are titrable while leaving the membrane intact. With strong acid (sulfonic) or strong base (quaternary ammonium) membranes simple mass-action exchange of neutral ions (potassium or nitrate) for counter ions (hydrogen or chloride) was utilized to make all exchangeable groups readily titrable (12).

All of the experiments were performed at room temperature, 24°-26°C, unless otherwise stated. In most cases the systems were thermostated at 25.0°C. All data were corrected to 25°C, unless the temperature deviation or the effect of temperature was negligible.

The cation-permeable membranes were equilibrated with 1M hydrochloric acid, washed with water to remove diffusible salt, and then blotted. Elution of the hydrogen ions was accomplished by placing the membrane samples, each having an area of about 100 cm², in 250 ml of 1M potassium chloride; these conditions provided at least a 250-fold excess of potassium ion. After a 24-hr period of shaking (much longer than the time required for equilibrium), an aliquot of the solution was titrated. The molality of this membrane was 2.86 ± 0.02, defined as milliequivalents of hydrogen ions per gram of sorbed water.

The anion-permeable membranes were equilibrated in potassium chloride solutions, the diffusible salts removed by washing with water and blotting, and elution of the chloride accomplished by shaking in 250 ml of 1M potassium nitrate for 24 hr. The membrane was removed, rinsed into the eluate, and the latter titrated potentiometrically with silver nitrate. The anion-permeable membrane was found to have a molality of 4.58 ± 0.04.

The thickness of each membrane was determined, following equilibration in 0.1M potassium chloride, with a micrometer which provided results accurate to ±1%. The water content of each membrane in the same state was determined by first eluting the diffusible salt, blotting with filter paper to remove surface moisture, and weighing immediately. This procedure was shown by Gregor and Sollner (17) to yield accurate and reproducible wet weights. The membranes were then dried at 10 mm Hg and 60°C

[1] The "diffusion layer" of "effective thickness" δ.

[2] Obtained from the National Aluminate Corporation.

for 24 hr and reweighed. Drying for an additional 24 hr under these conditions removed less than 0.2% additional water.

Characterization ohmic resistance measurements were made with a Klett conductivity bridge at 1000 cps on membranes in a plastic flow cell with fixed platinized platinum electrodes and provisions to interpose the membrane (18). The cell resistance was determined for various potassium chloride solutions with and without the membrane. Membrane resistance was calculated from the difference in resistance and consideration of the cell constant and the thickness of the membrane. In the more concentrated solutions the calculated resistance is quite accurate, while in dilute (0.001M) solutions the reliability decreases to ±4%.

Concentration potentials were determined for the chain:

$$\text{S.C.E.} \mid C_2 \mid \text{Memb.} \mid C_1 \mid \text{S.C.E.}$$

where S.C.E. refers to the saturated calomel electrode and where $C_2:C_1 = 2:1$. These measurements were carried out in a plastic cell with provisions for stirring at the membrane-solution interface by means of an air stream. The measuring circuit employed a L&N Type K-2 potentiometer and a Type E galvanometer. Corrections were applied as described by Wetstone (19) to the concentration potential measurements for the salt bridge liquid junction, the S.C.E. asymmetry and temperature. These measurements are summarized in Table I.

Nonexchange of diffusible electrolyte is that which enters the membrane phase in excess of those ions which compensate electrically for the fixed ions. In a cation-permeable membrane system in potassium chloride solution, for example, the mobile potassium ions are designated as counter-ions and the chloride ions as co-ions. Then the molality of co-ions is numerically equal to that of the diffusible electrolyte and is equal to the number of equivalents per gram of sorbed water. Membrane samples approximately 40 cm² in area were equilibrated in 0.100, 0.500, and 1.00M potassium chloride solutions, blotted quickly to remove surface solution, and placed in 25 ml of distilled water with gentle shaking for 24 hr. The amount of eluted diffusible electrolyte was evaluated from resistance measurements of the eluate. Water contents were determined on similar samples in equilibrium with the same solutions. Calculated molalities are presented in Table II.

Table I. Membrane properties

	Cation-permeable membrane	Anion-permeable membrane
Thickness (microns)	96 ±1	84 ±1
Water content		
% by weight	23.5 ±0.2	17.1 ±0.3
% by volume	30.9	20.6
ml. cm^{-2} of membrane ($\times 10^3$)	2.97	1.73
Resistance in ohm-cm^2		
1.0M KCl	8.03	
0.5M	14.5	
0.1M	16.5	28.8
0.01M	20.1	
0.001M	28.0	
Concentration*		
Molality — meq g^{-1} water	2.86 ±0.02	4.58 ±0.04
Capacity—meq cm^{-2} membrane area x 10^3	8.46	7.89
Molarity—meg cm^{-3} membrane	0.882	0.939
Co. P.,† mv (corrected)	15.45	—15.61

* These do not include nonexchange electrolyte.
† Concentration potential of chain: S.C.E. | 0.2M KCl | Memb. | 0.1M KCl | S.C.E. Theoretical, $E_{max} = \pm 16.11$.

Table II. Diffusible electrolyte or co-ion content of cation-permeable membrane

Potassium chloride, M	Area, cm^2	Water content, g cm^{-2}	Molality, meq g^{-1} water
0.100	38.4	0.119	0.0270 ±0.007
0.500	36.9	0.110	0.162 ±0.002
1.00	40.1	0.114	0.474 ±0.009

Ion-exchange membranes, like the ion-exchange resins, show some variation in the properties of different samples. This is particularly the case with materials still in the developmental stage. For a given batch of membranes, a high level of uniformity was encountered; all of the work described in this contribution was carried out on the same batch.

Rate of exchange studies were conducted in an apparatus which consisted essentially of two identical plastic (methylmethacrylate) chambers with a common window such that an interposed membrane was exposed on one side to solution' and on the other side to solution". Each chamber had provisions for an inlet and outlet stream, identical rates of stirring, and cooling coils for precise temperature control. Identical high rates of stirring very near the membrane-solution interface were obtained by means of a 3-bladed flat paddle stirrer which swept the entire exposed membrane area with controlled peripheral linear velocities of 55 to 330 cm sec^{-1} at a distance of

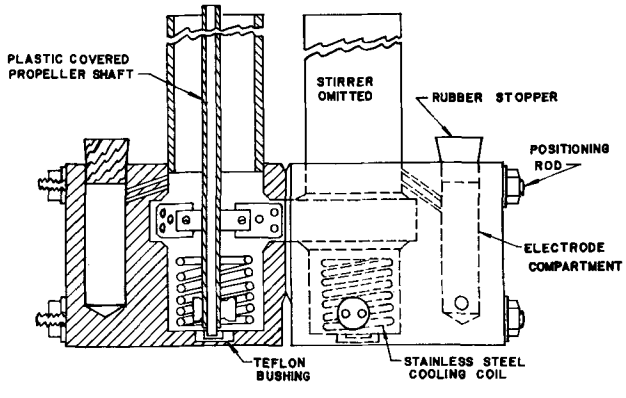

Fig. 2. Cell used for variable, high rates of stirring. The three detachable plastic flat-paddle blades are 0.1 to 0.2 cm from the interposed membrone. The assembly is symmetrical, and each compartment has provision for an entrance and exit stream. Volume of each compartment—115 ml.

1 to 2 mm from the interposed membrane. This cell is illustrated schematically in Fig. 2.

Water can be transported across ion-exchange membrane systems as a result of differences in the activity of water in solution' and solution", or by electro-osmosis. This was recognized by Donnan in his earliest papers, where he suggested the addition of a nonpermeable nonelectrolyte such as sugar to the side of higher solvent activity. Water transport can manifest itself in the measurement of any irreversible phenomenon, including that of a concentration potential, transport number, and diffusion coefficient. Water transport is negligble under almost all experimental conditions (excepting electro-osmosis) with membranes of low water content, such as the homogeneous membranes of Gregor and Sollner (17), the interpolymer membranes (12-16), and the films used in this study. Water contents of about 25% or less usually mean that water transport may be neglected; at water contents of 50% and greater, large effects are observed and have been evaluated by Schlögl and Schödel (11).

Another cell similar to that shown in Fig. 2 was constructed, where the exposed membrane area was about 15 cm^2. One side was maintained at constant volume with a mercury-sealed stirrer, and a capillary permitted direct observation of any volume changes. The imposition of an osmotic concentration difference as large as 1M gave such low rates of water transport as to be neglected.

Three series of runs at solution concentrations of 0.001, 0.1, and 0.5M were made using the cation-permeable membrane with potassium chloride as solution' and ammonium nitrate as solution". These ions resemble one another closely enough to serve as "tracers" for each other. Similar runs including a 0.0001M series were made using the anion-permeable membrane. Each series consisted of a number of runs ranging in time from 10 to 30 min and at stirring rates from 200 to 1200 rpm (corresponding to linear rates of 55 to 330 cm sec^{-1}).

The membranes were equilibrated in the respective potassium chloride solution for 24 hr prior to the rate experiments. Zero time for each run was not critical because essentially no potassium could be detected in the ammonium nitrate solution after a period of 1 hr with no stirring. That the membrane was highly ion-selective was verified when essentially no chloride could be detected in the nitrate solution after 15 min at 800 rpm in the 0.1M series, at which time an appreciable amount of cation-exchange had occurred. Duplicate runs gave essentially identical results.

The cation-permeable membrane contained 0.00846 meq of potassium per square centimeter of surface area. A constant area of 3.422 cm^2 was common to both solutions, so that before steady-state concentration gradients could be established approximately 0.015 meq of potassium (50% of capacity) would, of necessity, be displaced from the membrane sites to the ammonium nitrate cell side in return for the ammonium ion since the membrane was initially equilibrated in 0.001M potassium chloride for the 0.001M series of runs, etc.

Rate data were collected as follows: after a 10-min run both cells were drained and replenished with the original solutions. This was repeated once and followed by a third run for 20 min and a fourth for about 30 min. Once the 0.015 meq of potassium had been displaced it was assumed that the membrane retained a steady-state concentration gradient with respect to potassium and ammonium.

Solutions were analyzed for potassium with a Perkin-Elmer 52A flame photometer. These determinations were accurate to better than ±2% at a solution concentration above 5 x 10^{-4}M. A colorimetric method of analysis was used for chloride, capable of detecting chloride ion quantitatively at concentrations as low as 2 x 10^{-5}M with an accuracy better than 2% (20). The procedure involves the indirect evaluation of the chloride ion by displacement of the chromate ion from silver chromate solution. Analysis of the chromate ion was made using a Beckman DU spectrophotometer at 370 mμ against a

Table III. Exchange-diffusion of potassium

Chain: 0.001M KCl | Cation-Permeable Memb. | 0.001M NH_4NO_3

Elapsed time, min	Final conc soln', M x 10^3	Final conc soln", M x 10^3	Amount in soln", meq x 10^2	Flux, meq cm^{-2} sec^{-1} x 10^6
	Stirring rate—200 rpm			
0				0.236
10	0.946	0.042	0.482	0.234
10	0.948	0.042	0.482	0.234
19	0.910	0.078	0.895	0.224
28	0.880	0.110	1.26	0.197
	Stirring rate—300 rpm			
0				0.318
10	0.933	0.055	0.632	0.308
16	0.910	0.080	0.977	0.280
19	0.888	0.100	1.15	0.280
28	0.850	0.140	1.61	0.249
28	0.848	0.142	1.63	0.260
	Stirring rate—400 rpm			
0				0.386
10	0.923	0.065	0.748	0.365
10	0.925	0.065	0.748	0.365
15	0.894	0.096	1.10	0.343
15	0.895	0.095	1.09	0.334
20	0.868	0.120	1.38	0.308
29	0.825	0.165	1.90	0.281
29	0.823	0.167	1.88	0.271
	Stirring rate—800 rpm			
0				0.664
10	0.876	0.114	1.31	0.638
10	0.875	0.113	1.30	0.632
15	0.824	0.166	1.91	0.595
19	0.784	0.206	2.37	0.574
28	0.699	0.291	3.35	0.530
28	0.698	0.290	3.34	0.524
	Stirring rate—1200 rpm			
0				0.856
10	0.843	0.147	1.69	0.822
10	0.843	0.145	1.67	0.813
15	0.776	0.214	2.46	0.771
19	0.722	0.268	3.08	0.753
28	0.609	0.381	4.38	0.703
28	0.609	0.379	4.36	0.694

$$\text{Flux} = \frac{\Delta M''_{final}\,(115)}{\Delta t_{sec}\,(3.422)}$$ meq cm^{-2} sec^{-1}, where 115 cm^3 is volume of cell, 3.422 cm^2 is membrane area.

suitable standard. The nonelectrolytes employed were analyzed for by standard procedures.

Table III gives the results of a series of exchange-diffusion experiments performed with the solution chain:

0.001M KCl | Cation-Permeable Memb. | 0.001M NH_4NO_3

measured at 25°C and with different rates of stirring. The amount of potassium exchanged was not proportional to the elapsed time at a given rate of stirring because the concentration gradients had changed. The flux for each time interval was evaluated, and by extrapolation to zero time it was possible to calculate the flux under the initial conditions J^*; then $C'_B = C''_A = 0$ and the calculation of δ and $\bar{D}$ followed.

Initial flux values were used to evaluate δ from the following general expression for the case where a coupled-mechanism prevails

$$J = \frac{D(C'_{K+} - C^\circ_{K+})}{\delta} \qquad [7]$$

At the zero time under steady-state conditions

$$C^\circ_{K+} = C\left[1 - \frac{1}{\frac{DCl}{\bar{D}\bar{C}\delta} + 2}\right] \qquad [8]$$

$C'_{K+} = C$ and $k = 1$. The general expression becomes,

$$J^* = \frac{D}{\delta}\left[\frac{C}{\frac{DCl}{\bar{D}\bar{C}\delta} + 2}\right] \qquad [9]$$

or

$$\delta = \frac{DC}{2}\left(\frac{1}{J^*} - \frac{l}{\bar{D}\bar{C}}\right) \qquad [10]$$

In order to evaluate δ as a function of the stirring rate it was necessary to determine $\bar{D}_{K+}$. This was obtainable for the 0.001M system from conductance data using the appropriate application of the Nernst-Einstein equation (10)

$$\bar{\kappa} = \frac{l}{\Omega} = \frac{\mathbf{F}^2}{1000\,RT}(Z_+\bar{D}_+\bar{C}_+ + Z_-\bar{D}_-\bar{C}_-) \qquad [11]$$

and $\bar{D}_+ = 2.66 \times 10^{-7}\,\bar{\lambda}_+/Z_+$ where $\bar{\lambda}_+ = 1000\,\bar{\kappa}_+/\bar{C}_+$ where λ is the equivalent ionic conductance (mho cm^2 eq^{-1}) in the absence of electro-osmosis, κ is the specific conductance (ohm^{-1} cm^{-1}), Ω is the membrane resistance in ohm cm^2, and $\bar{C}$ the concentration (meq cm^{-3}) of the membrane phase. From Table II the concentration of nonexchange electrolyte would be negligible at 0.001M compared to that of the exchange ions and $\bar{D}_+ = 1.03 \times 10^{-7}$ cm^2 sec^{-1} in 0.001M solutions.

Values of δ and $DCl/(\bar{D}\bar{C}\delta)$ as a function of rate of stirring were calculated then, based on the $\bar{D}_+$ value from conductance data, for all experiments performed at 0.001M concentrations. Film thicknesses were found to range from 1 to 30 μ at stirring rates ranging from 1200 to 200 rpm. Values of $DCl/(\bar{D}\bar{C}\delta)$ for this 0.001M series ranged from 18.8 at 1200 rpm to 0.99 at 300 rpm and 0.65 at 200 rpm. Thus, on the basis of these calculations, a coupled mechanism prevailed at all rates of stirring.

Table IV. Evaluation of unstirred film thickness

Rate of stirring—200 rpm (55 cm sec^{-1})
Chain: 0.0001M KCl | Anion-Permeable Memb. | 0.0001M NH_4NO_3
All concentrations are for the chloride ion.

Elapsed time, min	C', M x 10^4	C'', M x 10^4	Amount in soln", meq x 10^2	$C^l - C''_{avg}$, M x 10^4	δ, μ
0	1.00	0.000	0.00		
				0.474	31.3
10	0.948	0.052	0.0598		
				0.435	29.9
15	0.923	0.077	0.0885		
				0.412	31.9
20	0.901	0.099	0.114		
				0.379	30.7
30	0.858	0.142	0.163		

$\delta_{avg} = 30.9 \pm 0.6$.

Experimental results for a series of runs at 0.0001M and 200 rpm are presented in Table IV. Since the parameter $DCl/(\bar{D}\bar{C}\delta)$ equals 0.65 at 200 rpm in 0.001M solution, it was postulated that film control would predominate in 0.0001M solutions at 200 rpm where $DCl/(\bar{D}\bar{C}\delta)$ would equal 0.065 if all values other than C were unchanged. Under these conditions $C^\circ_i = C^l_i$ and the concentrations at the membrane surfaces would be equal to the mean value of C' and C'', or $C/2$. For this determination, an anion-permeable membrane was used because chloride analysis could be performed with greater accuracy at these extreme dilutions. Postulating pure film control, $J = DA/\delta(0.00005 - C''_{avg})$ since C° and C^l are constant and equal to 5×10^{-5}M. Table IV presents calculated values of δ where C''_{avg} is the average concentration of chloride in solution" during the appropriate time interval and A the membrane area.

Table IV shows that δ is 30.9 ± 0.6 μ at 200 rpm, agreeing well with δ as determined in 0.001M solutions wherein the coupled mechanism prevailed, as will be shown later. The constant values of δ over each time interval verifies the assumption that diffusion through the unstirred film was rate determining for 0.0001M concentrations.

The establishment of δ at 200 rpm in the 0.0001M series allowed an independent evaluation of $\bar{D}_+$ for 0.001M solutions from flux data for the 0.001M series, and good agreement was noted between $\bar{D}_+$ (conductance) and $\bar{D}_+$ (flux), as will be shown later.

From consideration of the dimensionless parameter $DCl/(\bar{D}\bar{C}\delta)$ it is seen that membrane control will predominate at values greater than 50, with the film being rate controlling at values less than 0.1. In the system under investigation, $l \cong 0.01$ cm, $\bar{C} \cong 1.0$M, $D/\bar{D} \cong 100$ and $0.0001 < \delta < 0.0030$ cm. Accordingly, film control can be expected at $C <$ 0.00001M at 1200 rpm and $C < 0.0003$M at 200 rpm; deviations from membrane control can be expected at $C < 0.005$M at 1200 rpm and $C < 0.15$M at 200

Table V. Flux of exchange ions

Stirring rate, rpm	δ, μ	J_{K^+} in cation-permeable membrane, meq sec^{-1} cm^{-2} x 10^5		J_{Cl^-} in anion-permeable membrane, meq sec^{-1} cm^{-2} x 10^5	
		0.1M	0.5M	0.1M	0.5M
200	31.0	1.51	1.65	0.850	—
400	14.4	1.53	1.66	0.866	0.99
800	4.25	1.57	1.68	0.894	1.02

Table VI. Chloride exchange-diffusion across cation-permeable membrane

Chain: KCl | Membrane | NH_4NO_3
Rate of stirring—400 rpm

Original conc. C′	Duration of run, min	Chloride conc. C″, M x 10^4	Chloride leak avg flux, meq cm^{-2} sec^{-1} x 10^8
0.100	60	1.90	
			28
0.100	180	2.50	
			28
0.100	300	3.10	
0.500	60	1.90	
			157
0.500	180	5.25	
			163
0.500	300	8.75	
1.000	60	1.90	
			443
1.000	110	5.85	
			443
1.000	160	9.80	

rpm. Intermediate ranges should exhibit a coupled mechanism.

The rate of diffusion-exchange processes in 0.1 and 0.5M solutions was measured with anion- and cation-permeable membranes. Solution concentrations remained essentially constant throughout the experiments, changing by less than one part in 500, and a constant flux was observed over the various time intervals. Table V presents the flux values. Values of δ were assumed to be concentration independent and taken from the 0.001M data. Corresponding data for the diffusion-exchange of chloride ions in the cation-permeable membrane are given in Table VI.

From the general flux expression it is noted that J^* approaches $\overline{D}\,\overline{C}/l$ in the limiting case of $DCl/(\overline{D}\,\overline{C}\delta) >> 1$ where membrane control prevails. The general expression for $\overline{D}$ in the coupled diffusive process is

$$\overline{D}_+ = \left[\frac{\overline{C}}{Jl} - \frac{2\overline{C}\delta}{DCl}\right]^{-1} \qquad [12]$$

From the expression relating specific conductance and diffusion coefficient, the diffusion coefficient for the anion is given by

$$\overline{D}_- = \left[\frac{\overline{\kappa}RT}{\mathbf{F}^2} - \frac{Z_+\overline{D}_+\overline{C}_+}{1000}\right]\frac{1000}{Z_-\overline{C}_-} \qquad [13]$$

Exact values of $\overline{D}_i$ can be calculated from flux data for that ion and values of δ; these can be calculated also from values of the specific conductance of the membrane phase together with values of $\overline{C}_i$ for each ionic species present and values of $\overline{D}_i$ for all other ionic species, subject to the applicability of the Nernst-Einstein equation. Where both kinds of data are available, an independent check is possible. Diffusion coefficients and other parameters for the cation-permeable membrane system are presented in Table VII.

From Table VII it is seen that within experimental accuracy the diffusion coefficients in the membrane phase for a given solution concentration are independent of the rate of stirring. This is not true of the flux unless complete membrane control prevails. As fluxes in the 0.1M solution series decrease, with lower rates of stirring, $\overline{C}/Jl$ increases; however, there is a corresponding increase in the values of $2\overline{C}\delta/(D_{Cl})$ due to an increase in δ, resulting in a constant value of $\overline{D}$. At higher concentrations (C = 0.5M) the film effect is diminished and in the limit

Table VII. Parameters for cation-permeable membrane

Rpm	$\overline{J}_+$ x 10^5, meq cm^{-2} sec^{-1}	$\overline{J}_-$ x 10^5, meq cm^{-2} sec^{-1}	$\overline{C}_+$, M	$\overline{C}_-$, M	$\overline{\kappa}$ x 10^3, ohm-cm^{-1}	$\overline{D}_+$ x 10^7, cm^2 sec^{-1}	$\overline{D}_-$ x 10^7, cm^2 sec^{-1}
			C = 0.001M				
			0.882	(0.000)	0.343	1.03*	
200	0.236					1.09	
			C = 0.01M				
			0.882	(0.000)	0.478	1.44*	
			C = 0.1M				
200	1.51		0.889	0.00832	0.582	1.72	3.24*
400	1.53	0.028				1.69	3.23
800	1.57					1.71	
			C = 0.5M				
200	1.65		0.931	0.0499	0.662	1.73	3.01*
400	1.66	0.160				1.72	3.08
800	1.68					1.74	
			C = 1M				
400		0.443	1.03	0.146	1.197	1.75*	2.91

* Calculated from conductance data.

Table VIII. Value of parameter $DCl/(\overline{DC}\delta)$ for cation-exchange membrane

Stirring rate, rpm	Stirring rate, cm sec^{-1}	$\delta \times 10^4$, cm	Ambient concentration 0.001M	0.1M	0.5M	1.0M
1200	330	1.04	18.8	1120	4930	8650
800	220	4.25	4.59	273	1200	2120
400	110	14.4	1.36	80.5	356	625
300	83	19.7	0.99	58.8	260	457
200	55	30.1	0.65	38.6	170	299

where membrane control is absolute, it is essentially zero and $\overline{D} = Jl/\overline{C}$.

In order to illustrate increasing membrane control with increasing solution concentration, $DCl/(\overline{D}\,\overline{C}\delta)$ values for 0.001, 0.1, 0.5, and 1M solutions are presented in Table VIII. Parameter values ranged from 0.65 at 200 rpm with 0.001M solutions to 8650 at 1200 rpm with 1M solutions.

From values of diffusion coefficients of exchange and nonexchange electrolyte, mobilities and transport numbers can be evaluated. A sequence of concentration potential measurements was made and is presented in Table IX. Good agreement is noted between transport numbers determined from exchange-diffusion studies and those calculated from potential measurements.

From flux data obtained with anion-permeable membranes, values of the anionic diffusion coefficients were calculated to be $(\overline{D}_{Cl})_{0.1M} = 0.78 \times 10^{-7}$ and $(\overline{D}_{Cl})_{0.5M} = 0.85 \times 10^{-7}$ cm^2 sec^{-1}. Subscripts outside the parentheses refer to the ambient solution concentrations.

A calculation of $(\overline{D}_{K+})_{0.1M}$ in this membrane requires either nonexchange electrolyte content and flux data or the former and conductance data. A good approximation of the nonexchange electrolyte concentration can be made by analogy with the ion-exchange resins. Gregor, Gutoff, and Bregman (21), Gregor and Gottlieb (22), and Gottlieb and Gregor (23) measured diffusible electrolyte contents and mean activity coefficients for sulfonic acid cation- and quaternary ammonium anion-exchange resins of different resin phase molalities. Postulating that these systems are comparable, as seems to be the case from nearly all points of view, one can evaluate these parameters for the membranes.

Table IX. Transport numbers in membranes calculated from potential and exchange-diffusion measurements

C_{avg} $C' = 2C''$, M	E_{max}, mv	Cation-permeable membrane E_{corr}, mv	t_+	t_+*	Anion-permeable membrane E_{corr}, mv	t_-
0.0015	17.43	17.42	0.999	(1.000)	—17.42	0.999
0.006	17.14	17.07	0.998		—17.09	0.999
0.015	16.87	16.77	0.997		—16.80	0.998
0.06	16.39	16.08	0.990		—16.13	0.992
0.15	16.11	15.45	0.979	0.983	—15.61	0.985
0.60	15.89	12.17	0.883	0.915	—12.80	0.903
1.5	17.18	10.11	0.794	0.810	—12.43	0.862

t_+*—Transport numbers from exchange-diffusion experiments in 0.001, 0.1, 0.5, and 1M solutions.

Cation-exchange resin mean activity coefficients were calculated from the Gibbs-Donnan equations applied to systems of this type by Gregor, *et al.* (21-25). It was shown that mean activity coefficients for uni-univalent electrolytes defined by the expression $\overline{m}_+\overline{m}_-\overline{\gamma}_\pm^2 = m_+m_-\gamma_\pm^2$ were, for cation-exchange resins, as follows: where $(\overline{m}_+)_{0.1M} = 1.6$, $(\overline{\gamma}_\pm)_{0.1M} = 0.37$; for $(\overline{m}_+)_{0.1M} = 4.0$, $(\overline{\gamma}_\pm)_{0.1M} = 0.31$. For anion-exchange resins, where $(\overline{m}_-)_{0.1M} = 2.9$, $(\overline{\gamma}_\pm)_{0.1M} = 0.32$ and where $(\overline{m}_-)_{0.1M} = 4.6$, $(\overline{\gamma}_\pm)_{0.1M} = 0.28$. Accordingly, $\overline{\gamma}_\pm$ values for both resin types are quite similar when systems of the same resin phase molality are compared.

Since diffusible and nondiffusible electrolyte contents were determined for the cation-permeable membranes, values of $(\overline{\gamma}_\pm)$ could be calculated. These were: $(\overline{\gamma}_\pm)_{0.1M} = 0.273$ at $(\overline{m}_+)_{0.1M} = 2.89$; $(\overline{\gamma}_\pm)_{0.5M} = 0.465$ at $(\overline{m}_+)_{0.5M} = 3.02$; $(\overline{\gamma}_\pm)_{1M} = 0.483$ at $(\overline{m}_+)_{1M} = 3.33$. With the sulfonic acid resins, $(\overline{\gamma}_\pm)_{0.5M} = 0.40$ at $(\overline{m}_+)_{0.5M} = 2.3$, while $(\overline{\gamma}_\pm)_{1M} = 0.44$ at $(\overline{m}_+)_{1M} = 3.1$. Good agreement between the resin and membrane systems is observed.

Accordingly, it is possible to estimate diffusible nonexchange electrolyte contents for the anion-permeable membrane and calculate a $\overline{D}_+$ value from flux data for the anion and conductance data. Having determined $(\overline{m}_-)_{0.1M} = 4.58$, and assuming a value of $(\overline{\gamma}_\pm)_{0.1M} = 0.28$ (since $\overline{m}_-$ is quite constant in dilute solutions), then one can calculate $(\overline{m}_+)_{0.1M} = 0.017$. The calculated value of $(\overline{D}_K)_{0.1M}$ in the anion-permeable membrane was 2.41×10^{-7} cm^2 sec^{-1}, or three times that of the counter-ion.

Measurements were also made of flux values of urea and acetic acid in the cation-permeable membrane in 0.1M potassium chloride solution. In both cases the solution concentration of the nonelectrolyte (also treating the acid as such) was 0.1M. A high rate of stirring was not required since these solutes were not strongly accumulated by the membrane; concentration gradients of these solutes in the membrane phase were about 5% of those found for exchange species. The parameter $DCl/(\overline{D}\,\overline{C}\delta)$, accordingly, increased by a factor of 20, meaning that in all cases where even moderate stirring prevailed, diffusion was almost entirely membrane controlled. Flux values were constant in every case over an interval of several hours. For urea it was found that the flux was 2.37×10^{-10} moles sec^{-1} cm^{-2} from a 0.1M solution stirred at 400 rpm into water across the membrane (0.0096 cm) where the molality of urea in the membrane was 0.180 or its molar concentration was 0.0555 moles liter^{-1} of membrane phase. Then, $\overline{D}_{urea} = 4.11 \times 10^{-8}$ cm^2 sec^{-1}. In free solution, $D_{urea} = 1.36 \times 10^{-5}$ cm^2 sec^{-1}, so that $\overline{D}/D = 0.0030$.

These figures should be compared with those for the diffusion of urea in a sulfonic acid cation-exchange resin system, as measured by Gregor, Col-

lins, and Pope (26). Here $\overline{D}_{urea} = 12.2 \times 10^{-7}$ cm^2 sec^{-1} in a 10% cross-linked resin where the distribution coefficient or $\overline{m}/m = 1.31$, where the water content of the resin was 40%, and where $(\overline{D}_{K^+})_{0.1M\ KCl} = 4.7 \times 10^{-6}$ cm^2 sec^{-1} (4).

For acetic acid, the flux was 3.91×10^{-10} moles sec^{-1} cm^{-2} from a 0.1M solution of the acid in 0.1M potassium chloride. Here a determination of the solution phase molality was not made, but from other sources (26, 27) it appears likely that the distribution coefficient is nearly unity. The diffusion coefficient for acetic acid was calculated to be 3.76×10^{-8}, compared to the free solution value of 1.20×10^{-5} cm^2 sec^{-1}; then $\overline{D}/D = 0.0031$. Manecke and Heller (28) also measured the diffusion of acetic acid across a phenolsulfonic acid-formaldehyde cation-permeable membrane, but diffusion coefficients were not calculated.

Discussion

This discussion is concerned with the cation-permeable membrane systems, unless otherwise stated. Turning first to a comparison between the cation-selective membrane and a cation-exchange resin of the sulfonate type, it is seen that the two systems are quite comparable from almost all points of view. For systems of equal cationic molality, it is seen that the concentrations of diffusible electrolytes vary in the same way with the ambient solution concentration, with respect to both absolute and relative values. These Donnan systems absorb an amount of diffusible electrolyte at low concentrations which is much larger than that calculated for ideal systems. This is presumably because the counter-ion is bound electrostatically to the polymeric chains by their high potential. The system cannot exert its ideal Donnan potential, and excess diffusible electrolyte enters so that low values of mean activity coefficients are calculated.

As additional diffusible electrolyte enters the resin or membrane system with increasing solution phase concentration, the concentration of co-ions increases quite sharply and has a profound influence on the mean activity coefficient. Presumably, at high external solution concentrations the activity coefficient of diffusible electrolyte in the membrane phase would approach that in the solution phase, as was observed with the resin systems.

Turning to the change in the diffusion coefficient of the mobile ions in the cation-permeable membrane phase, it is observed that the diffusion coefficient of the cation rises significantly with increasing concentration of the ambient solution phase, while that of the anion decreases slightly, although the latter effect is within experimental error. This rise in the diffusion coefficient of the counter-ion with increasing ambient solution concentration amounted to a 1.7-fold increase in $\overline{D}_+$; this has been observed by Schlögl (29), Schlögl and Helferich (30), Ishibashi, Seiyama, and Sakai (31), Despic and Hills (32), and Richman and Thomas (33). Some of these authors observed a larger increase in the diffusion coefficient of the counter-ion with ambient solution concentrations than was observed here; this was probably due to their use of systems having a lower fixed-ion concentration and consequently a larger and more variable diffusible electrolyte content. In some cases the resistance due to the unstirred film has been neglected; such calculations are suspect.

In the cation-permeable membrane systems, the diffusion coefficient of the chloride ion was found to be significantly larger than that of the cation, varying by a factor of 3:1 to one of 2:1 as the solutions became more concentrated. At a 0.1M ambient solution concentration, the factor was approximately 2:1. With the anion-permeable membranes, a factor of 3:1 for the co-/counter-ion diffusion coefficients was observed. These differences are expected because the chloride ion is bound significantly to the fixed groups in anion-exchange resin systems and presumably also in anion-exchange membrane systems. The former effect was observed by Gregor, Belle, and Marcus (34). These differences have been observed previously by Schlögl (29) in his study on the diffusion of sodium bromide in an anion-selective membrane system.

As was shown in Table IX, transport numbers calculated from emf data are in good agreement with those calculated from the product of diffusion coefficients and membrane phase concentrations. This agreement is as expected in view of the fact that the solvent transport correction term is negligible in these membranes of low (15-25%) water content.

The absolute magnitude of the diffusion coefficients of the counter- and co-ions is of considerable interest. In dilute solutions (0.001M) the ratio $\overline{D}_+/D_+ = 0.0050$, taking $D_+ = 22 \times 10^{-6}$ cm^2 sec^{-1}, the value for potassium chloride of approximately the same molal concentration ($4M$) as in the membrane. As the ambient solution concentration increased to 0.1M, $\overline{D}_+/D_+$ increased to 0.0078. The value of $\overline{D}_-/D_-$ was 0.014.

It is of considerable interest to compare the diffusion coefficient of an ion in a condensed phase (such as a membrane phase) with the value it has in free solution, and examine each of the factors contributing to the markedly lower diffusion coefficient. Here, three factors must be considered. A large fraction of the membrane area is composed of the matrix polymer and the bulk of the polyelectrolyte. Consequently, ions are free to diffuse only in the interstitial solution, or the true area for diffusion is proportional to the water content; a factor of 0.235 must be applied.

Second, in a membrane system composed of interconnecting pores, a "tortuosity factor" must be applied because presumably only one-third of the pore lengths permit diffusion in a direction perpendicular to the face of the membrane; a factor of 0.333 is assumed. Carman (35) discusses this factor in porous media; Schlögl and Stein (36) have also considered the tortuosity factor.

The third is the so-called "drag factor." The viscous drag on a sphere moving in a homogeneous medium contained in a cylindrical pore will increase as the sphere diameter approaches that of the pore itself. While Stokes' law technically should not be

applied to the motion of an ion in water where both are of comparable size, nevertheless a considerable body of data has shown that Stokes' treatment does apply, although the constant term may be different. The applicability of Walden's rule is a case in point.

The determination of average pore diameters in the same cation-permeable membrane system was made by Gregor and Jacobson (37) who measured the conductivity of the unhydrated quaternary ammonium ions of different size, and applied the equation of Faxen (38),

$$F = \bar{D}/D = 1 - 2.104(s/S) + 2.09(s/S)^3 - 0.95(s/S)^5 \quad [14]$$

where s is the diameter of the sphere, S the diameter of the uniform pore, and F the drag factor. Gregor and Jacobson calculated an effective pore diameter of 6.0Å for a Nalfilm 1 membrane.

From this value of the pore diameter, Gregor and Jacobson (37) were able to calculate the diameter of the hydrated potassium ion *in the same membrane* from its conductivity. While several authors have observed that the conductances of the alkali metal cations in a resin or membrane phase were approximately proportional to their conductances in free solution, the importance of the drag factor was not considered. This proportionality is the result of a diminution in the size of the hydrated ion, proportional to its hydration. Since the velocity of an ion is $v_i \sim F_i/r_i$, where r_i is the hydrated radius, and since F_i increases with r_i, for the alkali metal cations the effect of viscous drag is compensated by an equivalent reduction in the hydrated diameter. An effective hydrodynamic diameter for the potassium ion of 2.5Å was calculated, while for the chloride ion the diameter was 4.0Å. The drag factor for the potassium ion in the cation-permeable membrane was calculated to be 0.54, and for the chloride ion, 0.21.

Accordingly, in the cation-permeable membrane the diffusion coefficient of the potassium ion is calculated to be $22 \times 10^{-6} \times 0.235 \times 0.333 \times 0.54 = 9.3 \times 10^{-7}$. The calculated value for the diffusion coefficient of the chloride ion is 3.6×10^{-7}. Then, the calculated value of $\bar{D}_+/D_+ = 0.042$ and $\bar{D}_-/D_- = 0.016$; in 0.1M solutions, the corresponding experimental ratios are 0.0078 and 0.014. For the co-ion, the agreement is excellent indeed for these ions are not bound electrostatically to fixed charges. For the counter-ions, the experimental value is but one-eighth the calculated value at $M = 0.001$, and one-fifth the value at $M = 0.1$. Obviously, electrostatic binding makes for a significantly higher activation energy for its diffusion.

Since the co-ion can act as a "carrier" for the counter-ions, it is easy to see why it can exert such a strong effect on the diffusion rate of the latter even when present at very low relative concentrations; in 0.1M solution, $\bar{m}_-/\bar{m}_+$ is only 0.01.

Various attempts have been made to calculate from purely theoretical considerations the diffusion coefficient of a counter-ion in a system of fixed charges. These calculations are made difficult by lack of accurate information on the sizes of the fixed and mobile ions and the distance of nearest approach, and on the effective dielectric constant of the system between unlike charges. Robinson and Stokes (39) discuss in some detail the uncertainties in each of these parameters.

Turning to the cation-permeable membrane systems, the average distance between fixed charges cannot be calculated from the molality alone since the fixed charges and the membrane matrix make up a large part of the volume of the system. However, since the actual pore structure is comparable to an ion-exchange resin of the same type and molality, the properties of the latter can be used as a first approximation. The volume of a potassium polystyrenesulfonate resin cross-linked with 6% divinylbenzene and having approximately the same volume of $\bar{m}_+$ as the cation-permeable membrane was found to be 2.02 ml for 5.09 millimoles of exchange groups (21). Assuming that each fixed site is at the corner of a simple cubic lattice, an average distance of separation of 8.7Å can be calculated.

An estimation of the distance of closest approach certainly cannot be made using the conditions that prevail in dilute solution, for in the membrane phase a considerably smaller hydration of the ions occurs. The variation of selectivity coefficients with temperature constitutes direct experimental evidence (40). In dilute solutions the distance of closest approach $\mathring{a}$ for potassium methanesulfonate was calculated from activity coefficient data using the extended Debye-Hückel equation,

$$\log_{10} \gamma_\pm = \frac{0.509\sqrt{M}}{1 + 0.329 \times 10^{-8} \mathring{a} \sqrt{M}} \quad [15]$$

by Fine, Rothenberg, and Gregor (41), and found to be 3.96Å. This compares with 4.0Å calculated from similar measurements with potassium chloride.

It is evident that $\mathring{a} = 4$Å is not a realistic value for this system; the value of 2.5Å (37) is more realistic.

In view of the fact that most of the water present in these membrane systems must be part of hydration spheres, one must take a value of $\bar{\epsilon}$, the dielectric constant in the membrane phase, as being considerably less than its value in dilute solution. The discussion in Robinson and Stokes (39) suggests a value of $20 < \bar{\epsilon} < 60$, which means that the exponential term can vary by e^3 or a factor of about 20. Obviously, agreement between theory and experiment is fortuitous indeed. Actually, in making these calculations an error in $\mathring{a}$ of 0.1Å can alter the result by a factor of two.

That the activation energy for the diffusion of counter-ions is larger than in free solution has been noted by several authors, particularly Boyd and Soldano (5). Frenkel (42) and Carman and Raal (43) have shown that surface diffusion coefficients likewise have higher activation energies.

Turning to any correlation that might exist between the diffusion coefficients of ions and of neutral molecules in the same cation-permeable membrane system, it was found that $\overline{D}_-/D_- = 0.014$, $\overline{D}/D = 0.0030$ for urea and 0.0031 for acetic acid. The relatively greater retardation of urea and acetic acid may be due to their adsorption and immobilization by the matrix, or because they must diffuse *around* the counter-ions. The generally good agreement between the relative diffusion coefficients of all mobile species corroborates our general picture of the relative simplicity of these membrane systems.

Any correlation between diffusion coefficients of counter-ions in systems of different degrees of cross-linking or matrices will depend in large part upon pore diameter data. For example, $\overline{D}_+$ here was 2×10^{-7}, compared to 5×10^{-6} in an approximately 10% cross-linked resin (26). However, the latter system is highly permeable to sucrose molecules, while the pores of our membrane system exclude this solute to a pronounced degree (37).

Acknowledgment

The authors wish to express their thanks to the Office of Saline Water, Department of the Interior and to the National Science Foundation for their support of this study. This paper was abstracted from the thesis of one of the authors (M.A.P.) submitted in partial fulfillment of the requirements for a Ph.D. degree in chemistry at the Polytechnic Institute of Brooklyn.

Manuscript received April 6, 1959. This paper was prepared, in part, for delivery before the New York Meeting, April 27-May 1, 1958.

Any discussion of this paper will appear in a Discussion Section to be published in the June 1960 JOURNAL.

LIST OF SYMBOLS

Subscripts on concentration terms denote ionic species; superscripts on concentration terms denote interfacial solution concentration. The superscript bar refers to parameters within the membrane phase. Primed terms refer to ambient solutions.

A, B — Cationic species.
l — thickness of membrane, cm.
δ — thickness of unstirred film, cm.
C — concentration, molarity, meq cm^{-3} of membrane.
x — spatial coordinate in membrane in cm.
D — diffusion coefficient, $cm^2\ sec^{-1}$.
U — mobility, $cm^2\ sec^{-1}\ volt^{-1}$.
J — flux in equivalents (or coulombs) $cm^{-2}\ sec^{-1}$.
ϕ — potential, volts.
R — gas constant.
T — absolute temperature, °K.
Z — valence.
$\mathbf{F}$ — the Faraday.
k — partition coefficient.
κ — specific conductance, ohm^{-1}, cm^{-1}.
Ω — membrane resistance, ohm cm^2.
λ — equivalent conductance, mho $cm^{-2}\ eq^{-1}$.
m — concentration, molality, meq g^{-1} water.
M — ambient solution concentration, molarity.
$\gamma_\pm$ — mean activity coefficient.
F — drag factor.
s — diameter of sphere in cm.
S — diameter of uniform pore in cm.
ϵ — dielectric constant.
$\mathring{a}$ — distance of closest approach in A.

REFERENCES

1. G. E. Boyd, A. W. Adamson, and L. S. Myers, *J. Am. Chem. Soc.*, **69**, 2836 (1947).
2. T. R. E. Kressman and J. A. Kitchener, *Discussions Faraday Soc.*, **7**, 90 (1949).
3. J. J. Grossman and A. W. Adamson, *J. Phys. Chem.*, **56**, 97 (1952).
4. M. Tetenbaum and H. P. Gregor, *ibid.*, **58**, 1156 (1954).
5. G. E. Boyd and B. Soldano, *J. Am. Chem. Soc.*, **75**, 6091, 6096 (1953).
6. G. E. Boyd and B. Soldano, *ibid.*, **75**, 6105 (1953).
7. A. Lowan, *Duke Math. J.*, **7**, 94 (1935).
8. F. Helfferich, *Discussions Faraday Soc.*, **21**, 83 (1956).
9. B. A. Soldano and G. E. Boyd, *J. Am. Chem. Soc.*, **75**, 6107 (1953).
10. G. Schulze, *Z. physik. Chem.*, **89**, 168 (1914).
11. R. Schlögl and U. Schödel, *Z. physik. Chem.*, **5**, 372 (1955).
12. H. P. Gregor, H. Jacobson, R. C. Shair, and D. M. Wetstone, *J. Phys. Chem.*, **61**, 141 (1957).
13. H. P. Gregor and D. M. Wetstone, *ibid.*, **61**, 147 (1957).
14. D. M. Wetstone and H. P. Gregor, *ibid.*, **61**, 151 (1957).
15. D. M. Wetstone and H. P. Gregor, *Z. Elektrochem.*, **62**, 3, 274 (1958).
16. H. P. Gregor, *Proc. Natl. Acad. Sci.*, Pub. 568, 240 (1957).
17. H. P. Gregor and K. Sollner, *J. Phys. Chem.*, **50**, 53 (1946).
18. J. Andelman and H. P. Gregor, To be published.
19. D. M. Wetstone, Dissertation, Polytechnic Institute of Brooklyn, 1957.
20. L. Isaacs, *J. Biol. Chem.*, **53**, 17 (1922).
21. H. P. Gregor, F. Gutoff, and J. I. Bregman, *J. Colloid Sci.*, **6**, 245 (1951).
22. H. P. Gregor and M. H. Gottlieb, *J. Am. Chem. Soc.*, **75**, 3539 (1953).
23. M. H. Gottlieb and H. P. Gregor, *ibid.*, **76**, 4639 (1954).
24. H. P. Gregor, *ibid.*, **70**, 1293 (1948).
25. H. P. Gregor, *ibid.*, **73**, 642 (1951).
26. H. P. Gregor, F. C. Collins, and M. Pope, *J. Colloid Sci.*, **6**, 304 (1951).
27. R. M. Wheaton and W. C. Bauman, *Ind. Eng. Chem.*, **45**, 228 (1953).
28. G. Manecke and H. Heller, *Discussions Faraday Soc.*, **21**, 101 (1956).
29. R. Schlögl, *Z. Elektrochem.*, **57**, 195 (1953).
30. R. Schlögl and F. Helfferich, *Z. Elektrochem.*, **56**, 644 (1952).
31. N. Ishibashi, T. Seiyama, and W. Sakai, *J. Electrochem. Soc. Japan*, **23**, 182 (1954).
32. A. Despic and G. J. Hills, *Discussions Faraday Soc.*, **21**, 150 (1956).
33. D. Richman and H. C. Thomas, *J. Phys. Chem.*, **60**, 237 (1956).
34. H. P. Gregor, J. Belle, and R. A. Marcus, *J. Am. Chem. Soc.*, **77**, 2713 (1955).
35. P. C. Carman, "Flow of Gases through Porous Media," Academic Press, Inc., New York (1956).
36. R. Schlögl and B. Stein, *Z. physik. Chem.*, **13**, 111 (1957).
37. H. P. Gregor and H. Jacobson, To be published.
38. L. R. Bacon, *J. Franklin Inst.*, **221**, 251 (1936).
39. R. A. Robinson and R. H. Stokes, "Electrolyte Solutions," Butterworth Scientific Publications, London (1955).
40. H. P. Gregor and J. I. Bregman, *J. Colloid Sci.*, **6**, 323 (1951).
41. N. Fine, M. Rothenberg, and H. P. Gregor, To be published.
42. J. Frenkel, "Kinetic Theory of Liquids," Oxford University Press (1947).
43. P. C. Carman and F. A. Raal, *Proc. Roy. Soc.*, **209A**, 38 (1951).

A Method for Evaluating Battery Grade Manganese Dioxide

F. Kornfeil

U. S. Army Signal Research and Development Laboratory, Fort Monmouth, New Jersey

It is well known that, apart from its composition, several factors determine the quality of MnO_2 for use in Leclanché cells. Methods of chemical analysis have, therefore, in the past been supplemented by investigations of the structure of MnO_2, chiefly by studying the diffraction of x-rays and electrons and by measurements of certain magnetic and thermal properties.

In view of the large number of properties which determine the electrochemical behavior of the MnO_2 electrode, it is not surprising that no single test method has as yet been devised which would provide by itself the complete information necessary to predict the performance of the cathode in a dry cell. It is indeed doubtful that such a method will ever be found. Nevertheless, various attempts have been made in recent years to develop relatively simple laboratory techniques for the evaluation of MnO_2 (1, 2). These techniques permit a rather broad classification of the oxides but fail to show a clear quantitative relationship between a measured quantity and the capacities obtained from complete dry cells containing the same oxides.

Experimental

Another method and device for evaluating MnO_2 is suggested in this paper. The principle of operation of this method is quite similar to that of the discharge tests of dry cells. However, the tedious and expensive procedure of manufacturing dry cells for testing purposes is eliminated. Moreover, the length of the discharge period is reduced to approximately one-eighth of the time required in the 16-2/3 ohm continuous drain discharge test on A-size dry cells. The reduction of a 0.500-g compressed pellet of a mixture of MnO_2 and Shawinigan black (weight ratio 10:1) is accomplished in a test cell (Fig. 1) consisting of the two Lucite halves A and B and a plastic piston ("Hysol No. 3110")[1] through the center of which a graphite rod insures good electrical contact with the depolarizer mixture. The pellet is discharged against a circular amalgamated Zn anode to an end-voltage of 1.00 v at 63.5 ma, corresponding to a current density of 50.0 ma cm^{-2} of the cathode-electrolyte interface. The electrolyte is an aqueous solution of 280 g NH_4Cl and 145 g $ZnCl_2$ per liter.

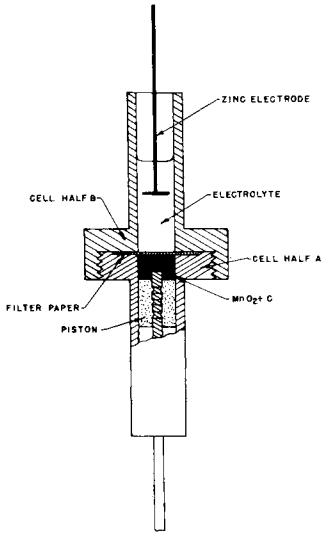

Fig. 1. Completely assembled test apparatus

The test circuit is based on the interrupter principle and is described in detail elsewhere (3, 4). Its essential feature is that the drop of potential due to the internal resistance of the cell is eliminated from the reading of the cell voltage. Therefore, it is not necessary to control some of the factors contributing to the internal resistance, such as the distance between the electrodes, conductance of the graphite rod, and, within a rather wide range, the pressure used in the preparation of the depolarizer pellet.

The results obtained with this method, expressed as length of time required to decrease the cell voltage to 1.00 v (*IR*-drop eliminated), are reproducible within $\pm 2.5\%$. This agreement is remarkably good compared to the results of dry cell tests which normally show a scatter of $\pm 10\%$.

About fifty different samples of MnO_2 were selected for each of which high drain dry cell test results were available of a uniformity considerably greater than $\pm 10\%$. These samples then were discharged in the apparatus at 25°C. Three typical discharge curves are shown in Fig. 2. The results of these tests are plotted against the corresponding dry cell test results (A-size cells) in Fig. 3. The resulting curve was used subsequently to predict the capacities in dry cells of about two hundred additional samples of MnO_2.

The agreement between the present method and the dry cell test results is generally very satisfactory. However, it should be pointed out that, although this method in its present form gives a quantitative measure of the inherent capacity of the

[1] Houghton Laboratories, Olean, N. Y.

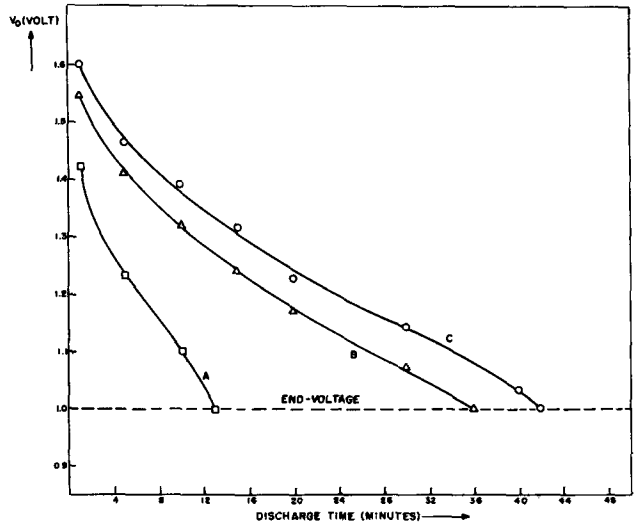

Fig. 2. Discharge curves. Curve A: African ore; Curves B, C: electrolytic manganese dioxides. V_o: Terminal voltage minus IR-drop.

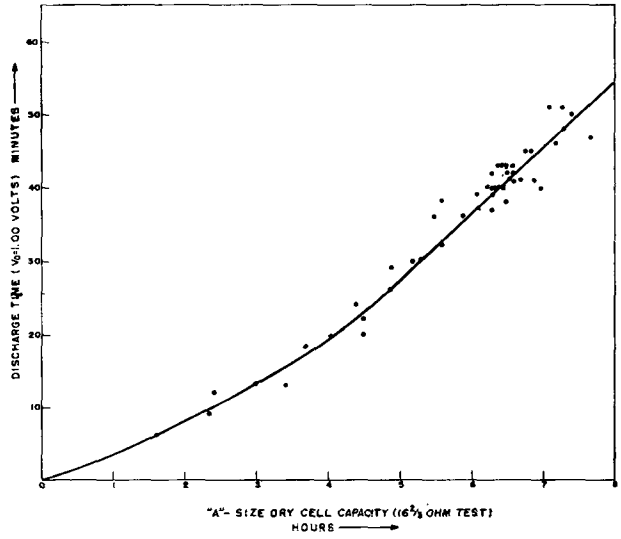

Fig. 3. Correlation between discharge time in test apparatus (end-voltage 1.00 v) and 16-2/3 ohm continuous drain dry cell test.

MnO_2 tested, this capacity need not necessarily be obtainable in an actual dry cell. For example, it has been observed that an oxide of an extremely low apparent density has a lower capacity in a dry cell than would be expected using the curve in Fig. 3, because the dry cell simply contains a comparatively smaller quantity of this particular oxide. This difficulty probably can be overcome by modifying the test procedure so that a constant volume is used instead of a constant mass of the depolarizer.

Acknowledgments

The author wishes to express his appreciation to Mr. H. L. Suchan who carried out a large number of the discharge tests, and to Mr. W. F. Nye, this Laboratory, and Mr. F. Keller, Bright Star Industries, for their continued interest and many helpful suggestions.

Manuscript received Oct. 8, 1958.

Any discussion of this paper will appear in a Discussion Section to be published in the June 1960 JOURNAL.

REFERENCES

1. N. C. Cahoon, *This Journal*, **99**, 343 (1952).
2. C. K. Morehouse and R. Glicksman, *ibid.*, **103**, 94 (1956).
3. A. Marko and K. Kordesch, U.S. Pat. 2,662,211 (1953).
4. F. Kornfeil, Doctoral Thesis, University of Vienna, Austria (1952).

A Study of Stripping Anodized Coatings from an Aluminum Alloy

Walter Beck, John Danovich, and Sara J. Ketcham

Aeronautical Materials Laboratory, Naval Air Material Center, Philadelphia, Pennsylvania

A study has been made of the effect of a HF-HNO_3 mixture in stripping anodized coatings from an aluminum alloy. Comparison of efficacy and amount of metal attack was made with that of the CrO_3-H_3PO_4 solution usually used for this purpose. Information about some of the variables which control the process of film stripping was obtained from weight loss determinations, microscopic and electron microscopic studies.

Experimental Procedure

Pretreatment, anodizing, and stripping.—Unless otherwise reported, panels 5 x 10 x 0.13 cm of 5052 aluminum alloy, which contains 2.5% Mg and 0.25% Cr, were vapor degreased, immersed for 15 min in a nonetching alkaline cleaning solution, and water rinsed. Immediately following this pretreatment cycle, the panels were anodized in a 7% CrO_3 bath, operated at 35°C with air agitation. The average current density was 155 ma/dm^2 and the applied voltage 40 (1). Specimens to be used for weight loss measurements were anodized to a coating weight[1] of 48 mg/dm^2 (450 mg/ft^2). Samples for microscopic studies were buffed to a mirror finish, then anodized to a weight of 113 mg/dm^2 (1050 mg/ft^2), the heavier coating being required to permit metallographic examination at a reasonably low magnification.

The CrO_3-H_3PO_4 solution which contained 0.6N CrO_3 and 1.6N H_3PO_4, was used at 88°C, the HF-HNO_3 solution which contained 0.1N HF and 3.5N HNO_3 at room temperature.

Preparation of specimens for photo and electron micrographs.—Before sectioning and mounting, the

[1] The weight of an anodic coating is determined by weighing the anodized panel, stripping the coating in the CrO-H_3PO_4 acid mixture described here for 10 min, and reweighing the panel. The weight loss represents coating only, as this solution does not attack the base metal in any measurable amount.

specimens were covered with an epoxy resin to protect the anodized film against damage during the preparation for microscopic examination. Specimens were sectioned at an angle of 45° to obtain a greater thickness for study.

For electron microscopic inspection, the panels were cut into 1.59 by 1.59 cm (0.625 by 0.625 in.) squares, cleaned with benzene, and molded between layers of polystyrene at 121°C-149°C (250°-300°F) under 3000 to 4000 psi. The plastic was cut along the edge of the specimen and removed after cooling on dry ice. In order to depict the pore structure of the coatings, silicon monoxide replicas were employed. In this technique, a thick film of silicon monoxide was vapor deposited approximately normal to the surface of the impression. The pores in the impression are represented as peaks, and because of their geometry, they appear as holes in the silicon monoxide replica.

To obtain greater surface detail, a thin carbon replica, shadowed with chromium at an angle of 30°, was employed.

The replicas were floated off the polystyrene impression in benzene, washed twice in this liquid, placed on screen supports, and examined in the electron microscope.

Experimental Results and Discussion

Microscopic and electron microscopic observations. —The photomicrographs in Fig. 1 illustrate the effect of the CrO_3-H_3PO_4 stripping solution, showing the coating as anodized (Fig. 1*a*), after immersion for 10 sec during which the thickness was reduced very slightly but uniformly (Fig. 1*b*), and after immersion for 30 sec during which the coating was completely removed (Fig. 1c).

Results of electron microscope studies are given in Fig. 2. The surface of the aluminum alloy after buffing but before anodizing shows the typical furrow structure of sub-grain boundaries and some contaminants (Fig. 2*a*). The as-anodized surface

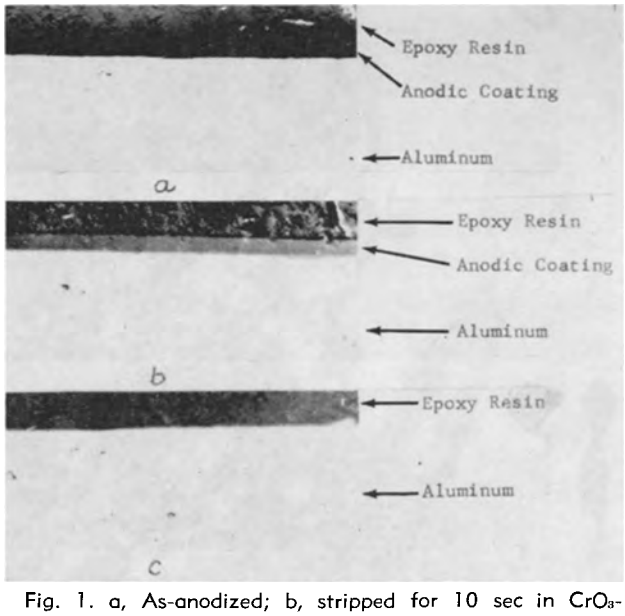

Fig. 1. a, As-anodized; b, stripped for 10 sec in CrO_3-H_3PO_4; c, stripped for 30 sec in CrO_3-H_3PO_4. Magnification 500X before reduction for publication.

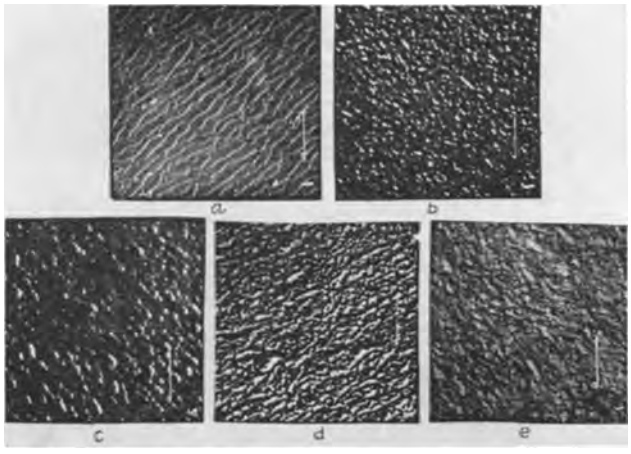

Fig. 2. a, Surface of the aluminum alloy before anodizing; chromium shadowed carbon replica of a polystyrene impression; b, surface of a specimen in as-anodized condition; average pore diameter is 300Å; thick silicon monoxide replica of a polystyrene impression; c, anodized specimen exposed for 10 sec in CrO_3-H_3PO_4; average pore diameter is 600Å; thick silicon monoxide replica of a polystyrene impression; d, same surface as in c; chromium shadowed carbon replica of a polystyrene impression; e, anodized specimen exposed for 30 sec in CrO_3-H_3PO_4; chromium shadowed carbon replica of a polystyrene impression. Magnification 10,000X before reduction for publication.

reveals an average pore diameter of 300Å, the pores being the white areas (Fig. 2*b*). Immersion in the CrO_3-H_3PO_4 for 10 sec enlarged the average pore diameter to 600Å (Fig. 2c), attack of the pore walls is following an elliptical pattern and produces ridges in the coating (Fig. 2*d*). After 30 sec immersion, weight loss measurements (to be discussed in the last section) indicate complete removal of the coating and (Fig. 2*e*) shows that the surface of the base metal has been roughened to a considerable degree, an effect which has been related to the anodizing process (2).

The mechanism which controls the action of the CrO_3-H_3PO_4 system may be discussed in the light of the well-known oxide cell structure of anodized coatings (3). By the attack of the pore walls demonstrated in Fig. 2*d*, the enlargement of the pores, shown in Fig. 2c is achieved (4).

It may be surmised that the enlargement of pores due to the dissolution of oxides which build up the pore walls, in the CrO_3-H_3PO_4 solution, facilitates its access to the barrier at the base of the pores.

The HF-HNO_3 *System*

The electron micrograph depicted in Fig. 3*a* reveals a random attack of the coating which, after an

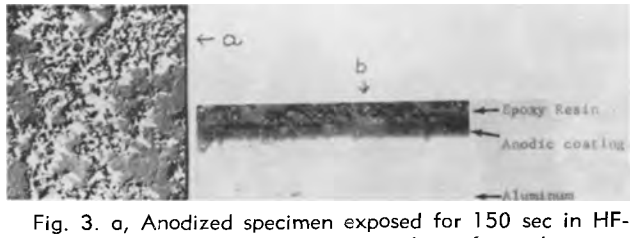

Fig. 3. a, Anodized specimen exposed for 150 sec in HF-HNO_3; chromium shadowed carbon replica of a polystyrene impression, magnification 10,000X before reduction for publication; b, anodized specimen exposed for 450 sec in HF-HNO_3; magnification 500X before reduction for publication.

immersion period of 150 sec, is in a progressive stage of decay; pits can be distinguished in the layer. As depicted in Fig. 3*b*, after an immersion period of 450 sec, the metal underneath the coating is attacked at numerous spots (5) and the layer partially loosened but not yet completely removed.

Figure 3*a* indicates that oxide dissolution is again one of the variables involved in the mechanism which determines the removal of the coating. In addition, as demonstrated in the photomicrograph in Fig. 3*b*, undermining of the coating because of metal attack is another parameter (5). Apparently, in the HF-HNO_3 solution, the rate of oxide dissolution is slower than in the CrO_3-H_3PO_4 solution, and coating removal is partially dependent on film undermining.

Coating Weight Loss

Since the CrO_3-H_3PO_4 stripper does not attack the base metal to any measurable extent, differences in weight found before and after exposure to this solution can be assumed to represent coating weight loss only. However, in HF-HNO_3 solution, the possibility of metal attack had to be considered because immersion of an uncoated specimen in this solution had resulted in considerable weight loss.

After the total weight loss in this solution was obtained for each exposure time, the amount that represented only coating weight loss was determined in the following manner: These specimens were subsequently immersed in the CrO_3-H_3PO_4 acid stripper to see whether any residual coating remained. The weight of this residual coating (if any was present) was then subtracted from the average coating weight of 48 mg/dm^2 (3.1 mg/in.^{2}) to obtain the coating weight loss only. The difference between this figure and the total weight loss was considered to be the amount of metal attack. If no residual coating was present, the amount of weight loss in excess of 48 mg/dm^2 (3.1 mg/in.^{2}) was considered to be the amount of metal attack.

Weight losses plotted in Fig. 4 are the averages of 3 measurements with a maximum deviation not exceeding 6%. With the CrO_3-H_3PO_4 system, a coating weight loss of 25%, determined after a 10-sec exposure, correlates qualitatively with a 10% loss in coating thickness (measured microscopically) and the appreciable increase in pore diameter, as shown in Fig. 2*c*. Also, a coating weight loss of about 75% can be considered to be in a fair agreement with the fact that, after the 30-sec exposure, both the microscopic and the electron microscopic investigation disclosed complete removal of the anodized layer. In the HF-HNO_3 solution, the weight loss determinations and the optical findings indicated a much slower rate of coating removal than in the CrO_3-H_3PO_4 system. Figure 4 also illustrates that almost from the very beginning of the stripping process the removal of the coating is accompanied by the dissolution of metal from beneath the oxide layer when specimens were exposed to the HF-HNO_3 solution. Within an initial period of about 100-sec duration, the rate of dissolution of the aluminum from underneath the anodized layer is considerably slower than that of an uncoated specimen. After exceeding this time interval, the metal is dissolved at a rate similar to that resulting on the unanodized specimen. Also, the electron micrograph 3*a* taken after an immersion of 150 sec showed that the coating was strongly attacked and pitted, while the photomicrograph taken after 450 sec revealed strong metal attack underneath a partially loosened coating. From the last experiments, it has to be concluded that uncritical use of the HF-HNO_3 system may lead to a much greater metal attack than is necessary for coating removal.

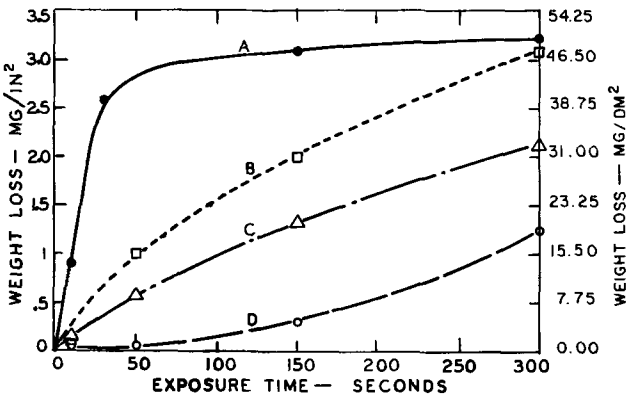

Fig. 4. Plot of weight loss vs. exposure time. Weight loss due to: A, solvation of anodized coating in CrO_3-H_3PO_4; B, removal of anodized coating in HF-HNO_3; C, dissolution of metal from uncoated specimen in HF-HNO_3; D, dissolution of metal from underneath anodized coating in HF-HNO_3.

HF-HNO_3 solutions have come into widespread use for removal of oxide coatings not only from aluminum alloys but also from numerous other metals such as Ti, Mo, Zr, and Ta (6). Metal losses due to over etching are avoidable, and the HF-HNO_3 containing systems should only be used when the concentrations and time of exposure are controlled carefully.

Acknowledgment

The authors are much indebted to Mr. F. S. Williams and Dr. G. K. Holmes, Superintendents of the Metallurgical and Chemical Engineering Divisions, respectively, Aeronautical Materials Laboratory, and Mr. Jack Smith, Head of the Chemical Branch for the great interest taken in this study.

Manuscript received Dec. 29, 1958. This paper was prepared for delivery before the Ottawa Meeting, Sept. 28-Oct. 2, 1958.

Any discussion of this paper will appear in a Discussion Section to be published in the June 1960 JOURNAL.

REFERENCES

1. MIL-A-8625 (issued December 14, 1954).
2. S. Wernick and R. Pinner, "Surface Treatment and Finishing Aluminum and its Alloys," p. 225, Robert Draper Ltd., Teddington Middle Essex, England (1956).
3. F. Keller, M. S. Hunter, and D. L. Robinson, *This Journal*, **100**, 416 (1953).
4. D. J. Stirland and R. W. Bicknell, *ibid.*, **106**, 483 (1959).
5. N. C. Welsh, *J. Inst. Met.*, **85**, Pt. 4, 133 (1956).
6. D. A. Vermilyea, *This Journal*, **104**, 213 (1957).

The Gudden-Pohl Effect of ZnS:Cu

Yoshihide Kotera and Kiyotake Naraoka

Government Chemical Industrial Research Institute, Tokyo, Japan

The Gudden-Pohl effect (1) on the phosphorescence of various ZnS:Cu phosphors was studied by means of an applied alternating electric field. The phosphors were prepared by a method similar to that described by Bube (2). They comprised two series of hexagonal and cubic ZnS:Cu (2% NaCl) phosphors and contained 10^{-6}, 3 x 10^{-6}, 10^{-5}, 3 x 10^{-5}, 10^{-4}, 3 x 10^{-4}, and 10^{-3} moles Cu per mole ZnS. The hexagonal and cubic phosphors were fired at 1200° and 900°C, respectively.

All phosphors were embedded in Acrylite (polymethylmethacrylate) and measured in an electroluminescent cell of common construction. The electric field was obtained from a 50 cps source, and the field intensity was estimated to be about 10,000 v/-cm. The integral of the light flash (i.e., the area under the curve shown in Fig. 1, in which the abscissa is time and the ordinate is the photocurrent from a photomultiplier) during the application of the field was taken as a measure of the magnitude of the Gudden-Pohl effect (Fig. 1). Prior to the measurement the phosphors had been excited with near ultraviolet radiation. The exciting radiation was then removed and the electric field was applied 1 min after removal of the radiation.

The integrals of the light flashes of both hexagonal and cubic ZnS:Cu increased with increasing copper content and reached a maximum at a content of 10^{-5} mole. With further increasing copper contents they decreased again. In general, the effect was stronger with cubic phosphors than with hexagonal ones of the same copper content. The phosphorescent intensity after one minute's decay and the infrared stimulation during illumination with infrared after one minute of normal phosphorescent decay were measured. Results were nearly identical with those reported by Bube (3).

It has been known that the Gudden-Pohl effect may be caused by electrons released from filled traps by the action of a field. Accordingly, from the knowledge of trap characteristics, the existence of a Gudden-Pohl effect might be predicted. Figure 2 shows the temperature dependence of the Gudden-Pohl effect and the thermoluminescence above room temperature. For cubic ZnS:Cu, the effect becomes smaller at rising temperatures between 20° and 120°C. There is no glow peak in this temperature range. In contrast, the effect increases at higher temperatures with hexagonal ZnS:Cu and it reaches a maximum at 70°C, while the glow curve has its peak at 550°C (Fig. 2).

Two glow curves were obtained for hexagonal ZnS:Cu (10^{-5}), one with and the other without previous application of an electric field. It was found that the two glow curves have about the same height.

From the above observations it is concluded that the deeper traps which correspond to a glow peak at 55°C do not produce the Gudden-Pohl effect at room temperature. Rather, the increase of the effect at higher temperatures may be ascribed to the emptying of the deeper traps which are able to release their electrons thermally at higher temperatures.

Manuscript received March 10, 1959.

Any discussion of this paper will appear in a Discussion Section to be published in the June 1960 JOURNAL.

REFERENCES

1. H. F. Ivey, *This Journal*, **104**, 740 (1957).
2. R. H. Bube, *Phys. Rev.*, **80**, 655 (1950).
3. R. H. Bube, *ibid.*, **80**, 764 (1950).

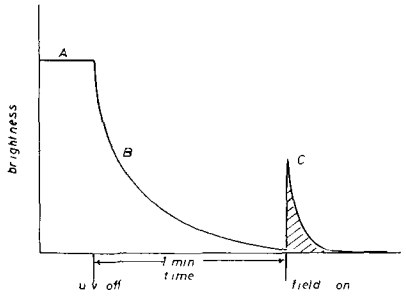

Fig. 1. Schematic representation of the Gudden-Pohl effect. A, Steady luminescence; B, phosphorescent decay; C, Gudden-Pohl effect.

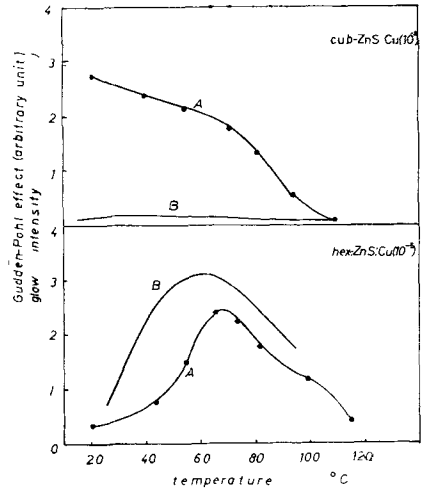

Fig. 2. The Gudden-Pohl effect as a function of temperature (Curves A) and glow curves (B) for ZnS:Cu.

Diffusion of Oxygen in Hafnium

J. Paul Pemsler

Nuclear Metals, Inc., Concord, Massachusetts

Hafnium shares with titanium and zirconium the unusual ability to dissolve large amounts of oxygen in interstitial solid solution. No data have been found regarding the hafnium-oxygen phase diagram other than the existence of a stable oxide HfO_2, and no studies on the diffusion of oxygen in hafnium are reported. The techniques used in this study are similar to those used by the author in a study of the diffusion of oxygen in zirconium (1).

Experimental

The diffusion of oxygen in hafnium was measured by following the rate of dissolution of anodically deposited thin oxide films when annealed *in vacuo*. The thickness of the oxide film was determined periodically during the experiment by observing its color (arising from optical interference) and comparing it with a series of standards.

Reactor grade hafnium samples containing 1.45 w/o Zr and measuring 1.8 x 4.5 x 0.4 cm were obtained from Knolls Atomic Power Laboratory. They were annealed in a vacuum for 1 hr at 800°C, furnace cooled, paper polished on 4/0 emery paper, and then etched for 2 min in a bath of 50% HNO_3, 5% HF, 45% H_2O.

Oxide films were deposited anodically from a 1% KOH solution in distilled water, with the sample as anode and a platinum wire as cathode. Several thicknesses of oxide were deposited on different areas of the same sample. The weight gain on anodization, as measured on a microbalance, was found in separate experiments to be a linear function of the applied voltage over the range studied (0-120 v), and independent of time. Assuming a value of 10.22 g/cm^3 for the density of HfO_2, the oxide thickness deposited during anodization corresponds to 18.9Å/v.

Anodized hafnium samples, sealed off in a Vycor tube, were placed in a horizontal furnace having a view hole for continuous observation of the sample while at temperature. The color of each zone changed with time, indicating a decreasing film thickness. At any given time, the decrease in film thickness was found to be independent of the original film thickness in a particular anodized area; thus identical results were obtained from any one of the color areas.

Results

Microscopic examination of samples which had been anodized and subsequently vacuum annealed revealed that, as in zirconium (1), the dissolution process was not homogeneous, and that, macroscopically, an average process was being observed. A wide range of colors, sharply defined by grain boundaries, was observed under a microscope. The diffusion coefficients calculated are therefore based on a macroscopic, average estimate of color. Variation in the diffusion coefficient by a factor of about two among the differently oriented grains was observed.

The parabolic rate of disappearance of the oxide film on hafnium suggests that the rate-determining step in the dissolution process is the diffusion of oxygen in hafnium metal. The consumption of oxide, generating additional metal, is accompanied by an outward motion of the oxide-metal boundary until the oxide is entirely consumed. Mathematically this case falls within a limited class of moving-boundary diffusion problems, for which solutions are readily found. The diffusion equation is discussed in detail elsewhere (2). From the solution found on the assumption of constant diffusivity, D can be expressed as

$$D = \frac{1}{4b^2}\left(\frac{x'}{\sqrt{t}}\right)^2$$

where b satisfies the equation

$$b\,(1 + \operatorname{erf} b) = \frac{1}{\sqrt{\pi}}\frac{C_o}{m_o}e^{-b^2}$$

Here in time, t, there is a displacement of the oxide-metal boundary, x', which is related to the observed decrease ΔL in thickness of oxide film by the following expression involving the respective molecular volumes

$$x' = \frac{\rho HfO_2}{\rho Hf \text{ saturated}}\,\frac{\text{Formula weight } (HfO_{sat})}{\text{Formula weight } (HfO_2)}\,\Delta L$$

The quantity ρ is the density, and C_o is the difference between the saturated concentration, C_s, and initial concentration of oxygen in the metal. The quantity m_o represents the weight of oxygen removed from the HfO_2 consumed in the generation of unit volume of saturated hafnium (HfO_{sat}), and may be expressed as

$$m_o = \frac{\text{Formula weight } (HfO_2) - \text{Formula weight } (HfO_{sat})}{\text{Formula weight } (HfO_{sat})}\,\rho HfO_{sat}$$

The precise value of the diffusion coefficient cannot be calculated at this time because the saturation concentration of oxygen in hafnium (O_{sat}) is not known. Nevertheless, by considering the titanium-oxygen and zirconium-oxygen systems (saturation oxygen concentration values 34 a/o and 29 a/o, respectively), reasonable estimates of this value may be made. In this work the diffusion coefficient was calculated for each of three saturation values: 20 a/o, 30 a/o, and 40 a/o oxygen in hafnium. Thus,

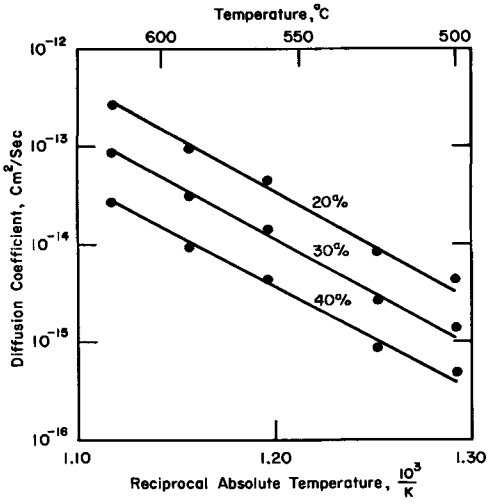

Fig. 1. Temperature dependence of the diffusion coefficient of oxygen in hafnium. The three curves represent results calculated assuming the three indicated oxygen solubilities in hafnium.

$C_o = C_s = 0.30$ g/cm^3, 0.50 g/cm^3, or 0.76 g/cm^3 (the initial concentration was taken as zero); $m_o = 2.07$ g/cm^3, 1.83 g/cm^3, or 1.52 g/cm^3; $x' = 0.657\ \Delta L$ cm, $0.667\ \Delta L$ cm, or $0.678\ \Delta L$ cm; $b = 0.067$, 0.120, 0.218. The density of HfO_2 was taken as the calculated x-ray value equal to 10.22 g/cm^3, and the density of hafnium saturated with oxygen was estimated to be about 13.5 g/cm^3.

A plot of the logarithms of the diffusion coefficients vs. the reciprocal of the absolute temperature for each of the three assumed oxygen solubilities is shown in Fig. 1. The equation for the diffusion coefficient of oxygen in hafnium in the temperature range of 500°-620°C is given by D, cm^2/sec $= 1.4 \exp [(-51{,}850 \pm 200/RT)]$ for 20 a/o; $0.47 \exp [(-51{,}850 \pm 200/RT)]$ for 30 a/o; and $0.14 \exp [(-51{,}850 \pm 200/RT)]$ for 40 a/o oxygen saturation solubility in hafnium.

The diffusion coefficient of oxygen in hafnium is smaller by a factor of about ten than that of oxygen in zirconium, but the energies of activation are identical.

This work was performed under AEC Contract No. AT(30-1)-1565.

Manuscript received April 24, 1959.

Any discussion of this paper will appear in a Discussion Section to be published in the June 1960 JOURNAL.

REFERENCES

1. J. Paul Pemsler, *This Journal*, **105**, 315 (1958).
2. J. Paul Pemsler, "The Diffusion of Oxygen in Zirconium and Its Relation to Oxidation and Corrosion," Report NMI-1177 (1957).

Technical Feature

The Fuel Cell and the Carnot Cycle

Herman A. Liebhafsky

Research Laboratory, General Electric Company, Schenectady, New York

ABSTRACT

To provide a basis for considering the combination of nuclear reactor (or other heat source) and fuel cell, the well-known fact that the fuel cell escapes the Carnot-cycle limitation is reviewed briefly. Then it is shown that the combination cannot escape this limitation and, in some cases, can only approach the Carnot-cycle efficiency.

The Fuel Cell Alone

The fuel cell is an electrochemical device in which the chemical energy of a conventional fuel is converted directly and usefully into electrical work. As has long been appreciated (1), the fuel cell is potentially attractive because the energy conversion it accomplishes is not subject to the Carnot-cycle limitation. This electrochemical conversion can be isothermal: for the Carnot-cycle limitation to operate, heat must flow from a higher to a lower temperature and be partially converted into work.

More precisely, the chemical energy mentioned above is the free energy

$$\Delta G = \Delta H - T\Delta S \qquad [1]$$

of the reaction

$$\text{Fuel} + \text{Oxygen} = \text{Reaction Products} \qquad [2]$$

(In Eq. [1], ΔH is the change in heat content, and ΔS the change in entropy for reaction [2].) Note, however, that the heat $T\Delta S$ absorbed or liberated in reaction [2] is characteristic of the reaction carried

out reversibly. It can be absorbed or liberated isothermally, and it must on no account be confused with heat that is converted into work in a Carnot-cycle process.

A more detailed analysis of this thermodynamic argument is desirable. In Eq. [1], ΔG is the maximum useful work realizable if reaction [2] is carried out isothermally and reversibly. If, instead, we choose to carry out this reaction nonisothermally with no work done, all the chemical energy will appear as heat. Because heat is random in nature, and work is a directed process, a price must be paid to convert heat into work; this price is the Carnot-cycle limitation. To escape this price, it is necessary to avoid randomizing the chemical energy as heat.

The electrochemical cell permits one to avoid this randomization. In such a cell, reaction [2] will occur in two parts (or half-cell reactions) schematically as follows:

Anode Reaction: Fuel = Ions + Electrons [2a]

Cathode Reaction: Oxygen + Electrons = Ions [2b]

When reaction [2] is carried out in this way, randomization never occurs because the electrons liberated at the anode flow unidirectionally to the cathode through the external circuit. They flow in this direction because they are driven by an electromotive force proportional in the limit to the free energy change. Because of this driving force, it is possible to make the electrons do work before they reach the cathode. Randomization of the chemical energy is thus avoided, and the Carnot-cycle limitation does not apply.

If the chemical energy of reaction [2] is randomized as heat that is later converted to work in a heat engine, the maximum useful work recoverable will be the familiar $\Delta H(T_1 - T_2)/T_1$, where the temperatures apply to the heat engine; that is, T_1 might be the inlet temperature of the first stage in a turbine; of course it is less than the temperature under the boiler.

In assessing the possible advantage a fuel cell might have over a conventional power plant, it is thus necessary to compare $\Delta H(T_1 - T_2)/T_1$ with ΔG (Eq. [1]). But the relationship of ΔH to ΔG depends on $T\Delta S$. Now, the sign and magnitude of this last term depend on the heat capacities of the substances in reaction [2] because

$$d(\Delta S) = \Delta Cp\, d\ln T \text{ (at constant pressure)} \quad [3]$$

(Assume ΔCp constant. In general, the integration of this equation also requires the statement about entropy changes at the absolute zero that is known as the Third Law of Thermodynamics. This need not concern us here.)

The three possible relationships of ΔH and ΔG are summarized in Table I.

The present outlook is that all successful fuel cells will use gaseous fuels, hydrogen and carbon monoxide being the most likely. These gases may prove necessary intermediates even when hydrocarbons are used, for the direct anodic oxidation of hydrocarbons to water and carbon dioxide is difficult to accomplish. Because the oxidation of hydrogen and of carbon monoxide to gaseous products reduces the number of gaseous molecules, only Case 3, Table I, is of immediate practical concern. (The sign and magnitude of ΔCp for reaction [2] are determined primarily by the change in the number of gaseous molecules during reaction. Note that this change is zero for the oxidation of methane.)

Table I. Maximum useful work and change in heat content for reaction [2]

Case	ΔCp	Heat exchange*	Arithmetic relationship
1	Positive	Absorbed by cell	$\Delta G > \Delta H$
2	Zero	None	$\Delta G = \Delta H$
3	Negative	Rejected by cell	$\Delta G < \Delta H$

* Heat exchange with environment when reaction [2] proceeds isothermally and reversibly.

To illustrate the relationship between ΔG and ΔH, let us examine the gaseous reaction

$$H_2 + \tfrac{1}{2} O_2 = H_2O \quad [4]$$

for which data (2) are given in Table II.

The ratio in the last column may be compared with $(T_1 - T_2)/T_1$ equals 64%, which is the Carnot efficiency for a good modern steam plant that might attain an actual over-all efficiency of 40%. Table II shows clearly that the potential advantage of this fuel cell over the steam plant will disappear with increasing temperature unless the rejected heat is properly used. This is a much more serious consideration in our day than in Ostwald's (1), when a fuel cell would have been called on to compete with steam plants having an over-all efficiency of only 10%.

Nuclear Reactor and Fuel Cell

As nuclear power bcomes increasingly available, one hears more frequently the suggestion that a fuel cell (or other battery) be combined with a nuclear reactor so as to convert heat into electric energy. Any other source of heat could in principle serve as well. In the fuel cell, for example, elements A and B would be consumed at temperature T_2 to produce electric energy and to form the compound AB, which would flow to the reactor at temperature T_1, where it would be dissociated to regenerate A and B.

The compound AB and its elements may be regarded as a working fluid in a thermal cycle in which heat is changed into work. On general grounds, one is justified in concluding that this conversion of heat into work must be Carnot-cycle limited in accord with the Second Law. The conclusion applies even though the working fluid is un-

Table II. $\Delta G°$ and ΔH for a hydrogen fuel cell

T, °K	ΔH, cal/mole	$\Delta G°$, cal/mole*	$\Delta G°/\Delta H$
400	−58,040	−53,520	0.92
500	−58,270	−52,360	0.90
1000	−59,210	−46,030	0.78
2000	−60,260	−32,310	0.54

* This free energy change, $\Delta G°$, is for all three gases in their standard states (about 1 atm). The superscript must be used also for entropy changes at the standard state ($\Delta S°$), but may be omitted in the present cases from ΔH because this function is virtually independent of volume.

usual in that it undergoes dissociation and recombination. Although the fuel cell alone escapes the Carnot-cycle limitation, the combination of fuel cell and nuclear reactor does not. Detailed analysis is necessary, however, to show whether the Carnot-cycle efficiency can actually be attained.

To make the analysis, let us represent the cycle as follows:

Dissociation in Reactor: AB = A + B at T_1 (I)
Recombination in Fuel Cell: A + B = AB at T_2 (II)

Heat Exchange (connecting link) A and B initially at T_1 (III)
with AB initially at T_2

The maximum efficiency will be attained if the cycle is reversible throughout. We would then have a reversible isothermal process (I) at T_1, which is the reverse of a reversible isothermal process (II) at T_2. The heat exchange process (III) cannot, however, be reversible unless ΔCp is zero.

That a value of ΔCp other than zero lead to irreversible heat flow in process (III) is easily shown. If, for example, ΔCp in process (II) is negative, then the combined molal heat capacities of A and B exceed that of AB. If ΔCp is negative also at T_1, then AB in passing from fuel cell to reactor cannot en route absorb enough heat from A and B to keep infinitesimal the temperature difference between the two legs of the heat exchanger. Consequently, A and B will reach the fuel cell at a temperature above T_2, where the irreversible flow of heat will continue until temperature equilibrium is established.

Because further discussion of such irreversible heat flow is not necessary to the main argument, let us proceed with Table I, Case 3, for which ΔCp is negative.

We need not inquire into the nature of the isothermal reversible processes (I) and (II). We know that each (and the cycle) must obey the Laws of Thermodynamics. We obtain the ideal efficiency in three steps. We postulate A, B, and AB to be in their standard states at T_1 and at T_2.

1. For the two isothermal processes only, with the working fluid initially at T_1, the net maximum useful work under the postulated conditions is

$$\Delta G^\circ_2 - \Delta G^\circ_1 = (\Delta H_2 - \Delta H_1) - (T_2\Delta S^\circ_2 - T_1\Delta S^\circ_1)$$

or

$$\Delta G^\circ_2 - \Delta G^\circ_1 = (\Delta H_2 - \Delta H_1) + (T_1\Delta S^\circ_1 - T_2\Delta S^\circ_2) \quad [5]$$

(Here, as in Table II, the superscripts indicate that standard states are involved. In practice, of course, A, B, and AB are not likely to be in their standard states, but this does not affect the argument.)

2. The heat absorbed from the nuclear reactor is $T_1\Delta S^\circ_1$.

3. The ideal efficiency is

$$\frac{\Delta G^\circ_2 - \Delta G^\circ_1}{T_1\Delta S^\circ_1} = \frac{(\Delta H_2 - \Delta H_1) + (T_1\Delta S^\circ_1 - T_2\Delta S^\circ_2)}{T_1\Delta S^\circ_1} \quad [6]$$

Were our thermal cycle completely reversible, we should expect it to have the Carnot efficiency. The right side of Eq. [6] degenerates to the Carnot efficiency if

$$\Delta H_1 = \Delta H_2 \text{ and } \Delta S^\circ_1 = \Delta S^\circ_2 \quad [7]$$

Noting that

$$d(\Delta H) = \Delta Cp\, dT \quad [8]$$

(assume ΔCp constant)

and considering Eq. [3], we conclude that Eq. [7] is valid if ΔCp is zero. This is true for Table I, Case 2, in which the heat exchange process (III) can be made reversible. With complete reversibility, the combination of nuclear reactor and fuel cell will attain Carnot efficiency.

Let us now examine Table I, Case 3, beginning with a numerical illustration. Let us consider that a hydrogen fuel cell at 500°K(T_2) is combined with a nuclear reactor at 2000°K(T_1). By use of Eq. [6] and of data in Table II, we find

$$\frac{-20{,}050}{\dfrac{-52{,}360 + 32{,}310}{-27{,}950}} =$$

$$\frac{+1990 \qquad -22{,}040}{\dfrac{(-58{,}270 + 60{,}260) + (-27{,}950 + 5910)}{-27{,}950}} \text{ or } 73.3\% \quad [9]$$

This efficiency is less than 75%, the efficiency of a Carnot cycle operating between 2000° and 500°K. Why? Because of the irreversibility in the heat flow process (III), which is traceable to the negative ΔCp.

The difference between 73.3 and 75% subdivides into (*a*) the effect of changing temperature on ΔH and (*b*) the effect of changing temperature on ΔS. (*a*) As Eq. [9] shows, the heat of reaction [4] increases numerically (from −58,270 to −60,260 cal) as the temperature increases from 500° to 2000°K. Consequently, the numerator in Eq. [9] decreases by 1990 cal and this acts to *reduce* the efficiency below the Carnot value. (*b*) Suppose the reduction just described were absent. Then Eq. [6] would yield the Carnot efficiency if ΔS°_2 were replaced by ΔS°_1. What is the effect of this replacement? $T_2\Delta S^\circ_2$ is −5910 cal, and $T_2\Delta S^\circ_1$ is −6990 cal; consequently, the use of the (correct) $T_2\Delta S^\circ_2$ term in Eq. [9] gives a larger (negative) number (by 1080 cal) in the numerator than would the insertion of $T_2\Delta S^\circ_1$, which insertion would yield the Carnot efficiency under the conditions stipulated. On this basis, we may say that the effect of changing temperature on ΔS° tends to *counteract* the analogous effect on ΔH.

It will now be shown that the effect on ΔH is always numerically the larger.

For this to be true, we must have (Eq. [3] and [8])

$$\int_{T_2}^{T_1} \Delta Cp\, dT > T_2 \int_{T_2}^{T_1} \Delta Cp\, d\ln T \quad [10]$$

If we write $T_1 = T_2 + \Delta T$, relation [10] is tantamount to

$$\Delta T > T_2 \ln \frac{T_2 + \Delta T}{T_2} \quad [11]$$

or

$$e^{\Delta T/T_2} > 1 + \frac{\Delta T}{T_2} \quad [12]$$

The correctness of relation [12] is easily established by comparing it with the series

$$e^x = 1 + x + \frac{x^2}{2!} + \frac{x^3}{3!} + \text{- - -} \qquad [13]$$

It follows therefore that the combination of nuclear reactor and fuel cell will, even under ideal conditions, have an efficiency somewhat below the Carnot if ΔCp for reaction [2] is negative. As the foregoing analysis has shown, the difference generally will be small owing to the interaction of the changes in heat content and in entropy.

If ΔCp were positive, A and B could not heat AB to temperature T_1 in the heat exchange process (III). The deficit would have to be made up from the nuclear reactor, and it would therefore appear as an added term in the denominator of Eq. [6]. No doubt detailed calculations for the case of positive ΔCp would also show the Carnot-cycle efficiency to be an upper limit.

Although thermodynamics does not require it, let us examine the combination of nuclear reactor and fuel cell in more detail. Water, especially water vapor, is a poor electrolyte. We shall therefore have to add an electrolyte so that the cell can function. This electrolyte may very well interact with water, and the energy of such interaction will have to be considered. In particular, the work required to separate the water from the salt will have to be subtracted from the work output of the nuclear reactor-fuel cell system. This will reduce the attractiveness of the scheme.

To bring the entire picture nearer reality, we point out, as did Yeager (3), that electrolysis is the simplest process for dissociating AB reversibly and isothermally at temperature T_1. From the electrical energy ΔG_2, ΔG_1 will have to be diverted to accomplish this dissociation. If A and B are gases, electrolysis has the great advantage of separating them at the minimum energy cost, which is ΔG_1. This seems the simplest solution to the separation problem, a problem that can be formidable enough to make the nuclear reactor-fuel cell scheme unattractive.

The energy cost of transferring the gases from reactor to cell and back to reactor has been neglected. No matter how small the cost, the need for this transfer will further reduce the attractiveness of the scheme.

Instead of behaving like water, AB might be stable in state 2 but unstable in state 1. One might then assume that AB does not dissociate until it is passed over a catalyst at temperature T_1, when it dissociates *spontaneously* to regenerate A and B. A substance such as this is unlikely to have a large value of ΔG°_2, and the useful work recoverable from the cycle is likely to be small. Appreciable irreversibility anywhere in the cycle, for example, in the separation of A and B at temperature T_1, will then be a serious matter.

In summary, the combination of nuclear reactor and fuel cell cannot operate at an efficiency exceeding that of a Carnot cycle. It cannot attain this efficiency if the heat capacity relationships among the reacting substances lead to irreversibility in heat transfer. The combination has other limitations that will not usually be offset by factors such as elimination of the need for turbines and generators.

This paper has been restricted to simple fuel cells. In more complex systems (the "redox systems") for the generation of electricity, oxidation-reduction couples are used as intermediates to promote reaction [2]. The conclusions about the Carnot cycle apply to these systems also.

Acknowledgment

The author wishes to thank his colleagues, E. J. Cairns, D. L. Douglas, G. E. Moore, and B. H. Zimm, for helpful discussions of the material in this report.

Manuscript received April 8, 1959.

Any discussion of this paper will appear in a Discussion Section to be published in the June 1960 JOURNAL.

REFERENCES

1. W. Ostwald, *Z.Elektrochem.*, **1**, 122 (1894).
2. J. P. Coughlin, Bureau of Mines Bull. 542, p. 23, U. S. Govt. Printing Office, Washington (1954).
3. E. Yeager, Proceedings 12th Annual Battery Res. and Dev. Conference, Asbury Park, New Jersey, p. 2 (1958); See also R. Roberts, *This Journal*, **105**, 428 (1958).

Discussion Section

This Discussion Section includes discussion of papers appearing in the JOURNAL of The Electrochemical Society, Vol. 105, No. 1, 8, and 9 (January, August, and September 1958), and Vol. 106, No. 1-6 (January-June 1959). Discussion not available for this issue will appear in the Discussion Section of the June 1960 JOURNAL.

The Anodic Oxidation of Zinc and Zinc-Tin Alloys at Very Low Current Density

S. E. S. El Wakkad,[1] A. M. Shams El Din, and H. Kotb
(pp. 47-51, Vol. 105)

M. Prazák[2]: The fact described by Dr. S. E. S. El Wakkad and co-workers, namely that Sn-Zn alloy is more easily passivated than pure zinc or pure tin, is very interesting indeed. According to the binary diagram, two phases exist in this alloy: practically pure tin and zinc. According to x-ray investigation, this is true also for electrolytically deposited alloy. Nevertheless, the electrochemical behavior of the alloy does not correspond to the sum for both components present, as we found in the case of the alloys Fe-Cr-Ni.[3]

We have studied the electrochemical behavior of the Sn-Zn alloy and that of pure zinc and tin in 1*N*-NaOH by means of impedance measurements and also by the potentiostatic method (*see* the polarization curves in Fig. 1 and 2 of this discussion). We found that:

(*A*) The corrosion current in the passive state for the alloy is lower (about 0.5 ma/cm^2) than would correspond to 25% Zn and 75% Sn (2.1 ma/cm^2), as shown in Fig. 1 and 2 at +0.2 to 0.8 v.

(*B*) On pure zinc, two types of passive layers may be found according to the potential imposed. In the range −0.92 to −0.56 v (vs. the normal hydrogen electrode), there exists a colorless thin layer possessing good electron conductance; in the range above +0.2 v, a thicker dark layer grows up, showing a higher corrosion current in the passive state. On this type of layer, oxygen is evolved with an overpotential of about 0.8 v (*see*, also, the paper of

[1] Deceased.
[2] Vyzkumny Ustav Ochrany Materialu, G. V. Akimova, Prague, Czechoslovakia.
[3] M. Prazák, Vl. Cíhal, and M. Holinka, *Chem. listy*, 52, 1693 (1958); *Collection Czechoslov. Chem. Commun.*, 24, 9 (1959).

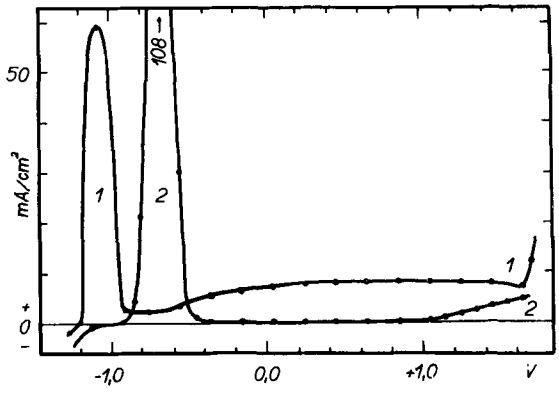

Fig. 1. Potential-polarization curves of Zn (1) and Sn (2) in 1N-NaOH.

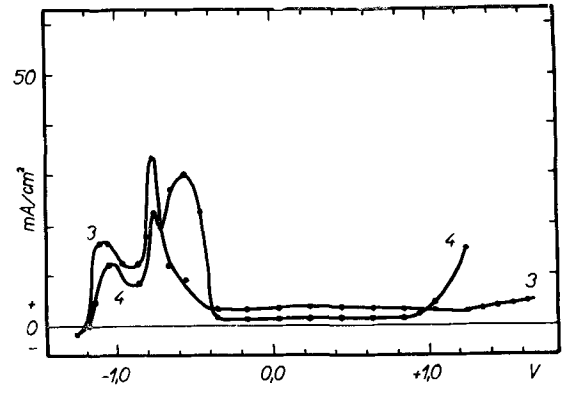

Fig. 2. Potential polarization curves of Sn75-Zn alloy (3—prepared by melting, 4—electrodeposited) in 1N-NaOH.

Landsberg[4]). In the case of the Sn-Zn alloy, this change in the behavior of the zinc component was not found.

To explain these facts, it must be accepted that a homogenous passive layer grows up on the non-homogenous Sn-Zn alloy.

We believe that this and the other works of Dr. El Wakkad and co-workers will do much to clear up the problems concerning passivity of alloys of different types.

Higher Oxides of Silver

W. S. Graff and H. H. Stadelmaier (pp. 446-449, Vol. 105)

J. A. McMillan[5]: Graff and Stadelmaier, in an interesting paper dealing with the higher oxides of silver, have affirmed that Ag_7NO_{11} cannot exist since the same product is obtained from AgF as from $AgNO_3$ solutions. They assume that the x-ray diffraction pattern is due to the presence of silver in an oxidation state higher than two (Ag_2O_3?). The discussor wishes to add that the same pattern is obtained from $AgClO_4$[6] and Ag_2SO_4 solutions. These facts, however, do not necessarily mean that all of the four products are the same oxide with different impurities, as believed by Graff and Stadelmaier, since the patterns could be due to isomorphous substances. The discussor believes that a series of compounds $(Ag_3O_4)_2Ag^IAn$, where An stands for NO_3, ClO_4, F, or SO_4H, exists, on the basis of the following facts.

I. Skanavi Grigoieva and Shimanovich[7] have obtained, during the electrolysis of $AgClO_4$ solutions, a black deposit whose composition was $(Ag_3O_4)_2Ag^IClO_4$.

[4] R. Landsberg, *Zeitschr. f. Physik. Chemie*, 206, 291 (1957).
[5] Instituto de Física de San Carlos de Bariloche, Bariloche, Río Negro, Argentina; present address: Chemistry Div., Argonne National Lab., Lemont, Ill., where the discussor is spending the duration of a Guggenheim Fellowship.
[6] W. S. Graff and H. H. Stadelmaier, *This Journal*, 105, 446 (1958).
[7] M. S. Skanavi Grigoieva and I. L. Shimanovich, *Zhur. Obshchei Khim.*, 24, 1490 (1955): *Chem. Abstracts*, 49, 5165a (1955).

II. de Boer and van Ormondt[8] have obtained, on electrolyzing Ag_2SO_4 solutions under similar conditions, black deposits whose composition was $(Ag_3O_4)_aAg^{II}SO_4$ with $a = 2 - 2.5$. These authors believed that all silver atoms were in higher oxidation states. Nevertheless, if one hydrogen is added (impossible to identify from the results of the analysis) and only the value $a = 2$ is taken into account (values of a greater than 2 correspond to partial decomposition), the formula becomes $(Ag_3O_4)_2Ag^{I}SO_4H$. It should be noted that the oxysalts give insoluble AgO when boiled with water, according to

$$(Ag_3O_4)_2Ag^{I}An \rightarrow 6\,AgO + Ag^{+} + An^{-} + O_2,$$

which permits a straightforward analysis.

III. Kappanna and Talaty[9] have observed a black deposit during the electrolysis of AgF solutions, whose magnetic susceptibility was $+0.37 \times 10^{-6}$ emu/g. Comparing this with the value observed by the discussor[10] in the case of oxynitrate and oxyperchlorate, $+0.41$ and $+0.49 \times 10^{-6}$ emu/g, respectively, it is plausible to infer that the compound was $(Ag_3O_4)_2Ag^{I}F$, earlier reported by Tanatar,[11] and found to exhibit the same x-ray diffraction pattern as the other oxysalts.[6]

IV. $Ag_7NO_{11} = (Ag_3O_4)_2Ag^{I}NO_3$ is a chemical compound that certainly could be questioned until the outstanding papers of Noyes and co-workers, cited by Graff and Stadelmaier, appeared, but not later.

In addition to the above, the discussor's own results[10] support the existence of such a series of compounds. Their space group is $\overline{F}43m - T^2_d$, with $a \cong 10$Å, the anions occupying the tetrahedron (¼, ¼, ¼), the tetrahedron (¾, ¾, ¾) being occupied by monovalent silver atoms. The anions orient as the trigonal axes. Interchanging of different anions gives the different oxysalts. Twenty-four silver atoms center the edges of each of the eight ½a-cubes. Oxygen atoms arrange in two sets of four tetrahedrons each, surrounding anions and monovalent silver atoms, respectively. This structure explains the magnetic behavior.

The interpretation of these patterns is straightforward, and the discussor's experience, in disagreement with Graff and Stadelmaier's, is that quite pure patterns can be obtained, free from AgO lines, at least in the cases of oxynitrate and oxyperchlorate.

With respect to AgO, Graff and Stadelmaier have arrived at the same conclusion as the discussor, although the discussor believes that their values for a, b, and c are more accurate than his own.

Independently, Scatturin, Bellon, and Zannetti[12] have arrived at the same conclusion. Nevertheless, if AgO were a divalent silver oxide, it would be strongly paramagnetic (Ag^{2+} is a $4d^9$ ion), which is not the case. AgO is diamagnetic, its susceptibility having been found to be[13]

$$\chi = -0.15 \times 10^{-6}\ \text{emu/g}.$$

The discussor[10] has modified the structure and adopted the space group $P2_1c - C^5_{2h}$, the oxide then being a silver(I)-silver(III)-oxide, with silver(III) ions coordinated in a planar arrangement with four oxygens (hybridization dsp^2), which explains its diamagnetism.

These results, together with the results on the oxysalts, will be published in detail.

H. E. Swanson[14]: Graff and Stadelmaier have pointed out that the sample we used in reporting the x-ray diffraction powder pattern of argentic oxynitrate $Ag_7O_8NO_3$[15] was not analyzed to show the existence of the NO^-_3 ion and that the nature of the compound was dependent only upon documentation in the literature.[16-20] Graff and Stadelmaier believe this compound to be a higher oxide of silver.

In the four years that have elapsed since our x-ray pattern was prepared, a recent x-ray analysis of the original material shows that it has decomposed, in the vial in which it was stored, into the components AgO and $AgNO_3$, indicating the presence of nitrogen in the original sample. When compared to physical mixtures of AgO and $AgNO_3$, the peak heights of the decomposed sample agree with a six to one molecular ratio mixture.

Graff and Stadelmaier also showed that the $Ag_7O_8NO_3$ is decomposed by boiling in water to AgO. What they did not note was that, when it is so treated, oxygen is released and $AgNO_3$ remains in this solution which may be readily analyzed quantitatively.

This decomposition procedure was used to break down a fresh sample prepared by D. Norman Craig at the National Bureau of Standards. We obtain stoichiometric percentages of 6AgO, O_2, and $AgNO_3$. Oxygen was determined volumetrically over water at 90°C. $AgNO_3$ was obtained by evaporation of the filtrate, and weighed as such.

	AgO	$AgNO_3$	O
Found	785 mg/g	181 mg/g	31.4 mg/g
Calc.	784	179	33.8 oxygen

The reported close similarity of the x-ray patterns of the salts formed by electrolysis of a silver fluoride bath and that of a silver nitrate bath may be easily explained if they are found to be of the same type structure. However, the two patterns published by Graff and Stadelmaier show significant differences in both spacing and intensity values which we feel are due to difference in composition.

We recently have been able to check the similarity in cell dimensions of these two crystals and find about the same values reported by Graff and Stadelmaier.

[8] J. H. de Boer and J. van Ormondt, *Proc. Intern. Symposium on Reactivity of Solids, Gothenburg 1952*, 557 (pub. 1954); *Chem. Abstracts*, **48**, 11972a (1954).
[9] A. N. Kappanna and E. R. Talaty, *J. Indian Chem. Soc.*, **28**, 413 (1951).
[10] J. A. McMillan, Results not yet published.
[11] S. Tanatar, *Z. anorg. Chem.*, **28**, 331 (1901).
[12] V. Scatturin, P. L. Bellon, and R. Zannetti, *J. Inorg. & Nuclear Chem.*, **8**, 462 (1958).
[13] A. B. Neiding and I. A. Kazarnovskii, *Dokl. Akad. Nauk S.S.S.R.*, **78**, 713 (1951); *Chem. Abstracts*, **45**, 8385g (1951).
[14] National Bureau of Standards, Washington 25, D. C.
[15] H. E. Swanson, R. K. Fuyat, and G. M. Ugrinic, *Nat. Bur. Standards Circ. 539*, **4**, 61 (1955).
[16] J. C. Poggendorff, *Ann. Physik.*, **75**, 337 (1848).
[17] O. Sulc, *Z. anorg. Chem.*, **12**, 89 (1896).
[18] E. Mulder and J. Heringa, *Rec. trav. chim.*, **15**, 1, 235 (1896).
[19] A. A. Noyes, D. DeVault, C. D. Coryell, and T. J. Deahl, *J. Am. Chem. Soc.*, **59**, 1326 (1937).
[20] K. Bräkken, *Norske Vidensk. Selskabs*, Forh. 7, p. 143 (1935) as abstracted in *Chem. Zentr.*, **106**, 1, 3634 (1935).

	Silver oxynitrate	Silver (oxyfluoride?)
Graff and Stadelmaier	5.890	5.834
NBS	5.893 at 26°C	5.823 at 25°C

Since Graff and Stadelmaier's paper did not come to our attention until recently, we have not verified the composition of the fluoride bath material as the oxyfluoride counterpart of the oxynitrate. However, we are planning to investigate this portion of the problem further.

W. S. Graff and H. H. Stadelmaier: The authors do not agree that the compound they reported to be a higher silver oxide can be, as McMillan suggests, a series of isomorphous compounds of the type $(Ag_3O_4)_2 \cdot Ag(I)AN$, where AN is NO_3^-, ClO_4^-, F^-, or SO_4H. Our points in answer to McMillan's and Swanson's arguments along this line are as follows.

I. All the preparations reported (Braekken, Swanson, Graff and Stadelmaier, Zvonkova and Zdanov), regardless of the anion present in the preparation (NO_3^-, ClO_4^-, F^-, or $SO_4^=$), yield a substance with a similar diffraction pattern and with lattice constants that differ from each other by no more than 0.5%. We attribute these small differences to varying amounts of absorbed impurities. An additional paper, not cited in our original bibliography,[21] also adds confirmation in that the preparation of a substance that yields the same diffraction pattern is reported from the oxidation of silver in a stream of $O_2 + 5\%$ O_3 with no N_2 present.

The regular presence of anions of such widely differing sizes (NO_3^-, ClO_4^-, F^-, or SO_4H^-) in the lattice as McMillan suggests would likely cause a larger variation in lattice constants than observed, even if we assume that such a series of isomorphous compounds does exist. Furthermore, it seems to us that the structure as postulated by McMillan with Ag(I) and the complex anion tetrahedrally surrounded by oxygen atoms is impossible from the standpoint of Pauling's radius ratio rules. The radius ratio of Ag(I) to $O^=$ is 0.9 and the radius ratio of NO_3^- to $O^=$ is 1.26. These ratios do not appear to be compatible with a coordination number of four.

II. We do not question the validity of Noyes' work in identifying Ag_7NO_{11}; we only feel that after the preparation is washed and dried the resulting decomposition product is the same as can be obtained from other means of preparation (fluoride, perchlorate, etc.) and very probably is a higher oxide of silver.

McMillan's comment on the structure of AgO is very interesting. If the compound is in fact diamagnetic, we agree that this would preclude the existence of a simple Ag^{++} state, because this state would involve an unpaired electron in the bonding with surrounding oxygen atoms and hence would be paramagnetic. Neiding and Kazarnovskii[22] also report that AgO is diamagnetic. This, we agree, indicates that AgO is a more complex structure, and not similar to CuO where Cu^{++} is known to exist.

[21] G. M. Schwab and G. Hartmann, *Z. anorg. u. allgem. Chem.*, **281**, 184 (1955).
[22] A. B. Neiding and I. A. Kazarnovskii, *Dokl. Akad. Nauk S.S.S.R.*, **78**, 713 (1951)

Preparation and Properties of Aluminum Antimonide

A. Herczog, R. R. Hoberecht, and A. E. Middleton
(pp. 533-540, Vol. 105)

H. F. Matare[23]: Four years ago (1953), we[24] produced AlSb-diodes from laboratory-grown crystals. We found a possible use for high-frequency diodes, e.g., as mixer diodes. The characteristic feature was a small diffusion voltage. Blocking voltages were low and corresponding to the order of magnitude given by the authors. Stability over long time periods was not very good. Encapsulation under oil as proposed by the authors was used also.[25]

A. Herczog: In the production of mixer diodes, one has to apply a special surface treatment to bring out the lowest forward resistance. This treatment is known to make the surface rather sensitive and corrosive.

Other treatments capable of producing more stable surface conditions will yield inferior forward characteristic but much higher blocking voltage (85 v).

The Flade Potential of Iron Passivated by Various Inorganic Corrosion Inhibitors

H. H. Uhlig and P. F. King (pp. 1-7, Vol. 106)

G. H. Cartledge[26]: It is gratifying that the authors have independently confirmed the earlier work of Cartledge and Sympson,[27] which showed that the passivating films produced on iron or carbon steel in aerated solutions in inhibitors display the Flade potential upon activation. This indicates that the films have the same electrochemical character, although formed in a variety of ways. In later work, to be published elsewhere, it has been shown that the Flade potential may be demonstrated also on films produced by passivation in an aerated solution containing benzoate ions.

It is not believed that the apparent variation of the activation potential reported by Uhlig and King for different passivators is real. Their measurements were made after the specimens were transferred to unbuffered solutions, whereas those of Cartledge and Sympson were made in the inhibitor solution itself, in which the pH value was accurately determinable. With the exception of the pertechnetate ions, all the inhibitors used have some buffering action. It may be noted in Fig. 2 and 3 of Uhlig and King that the observed points fell on the noble side of the curve of Franck[28] when passivation was conducted in acid media, and on the other side for passivation in alkaline media. The data make one suspicious that the films had some "memory" of their origin, because of incomplete equilibration with the new, unbuffered environment. No such variation was apparent in the observations of Cartledge and Sympson.

[23] Semiconductor Section, Solid State Lab., Sylvania Electric Products Inc., Bayside, N. Y.; present address: Laboratorium Halbleiter, Suddeutsche Telefon-Apparate-, Kabel- und Drahtwerke A.-G., 185 Allersberger Str., Nurnberg, Germany.
[24] Intermetal Corp., Düsseldorf, Germany.
[25] G. Zielasch, *Arch. elektr. Ubertragung, Stuttgart*, **8**, 529 (1954).
[26] Chemistry Div., Oak Ridge National Lab., Operated by Union Carbide Corp. for the U. S. Atomic Energy Commission, Oak Ridge, Tenn.
[27] G. H. Cartledge and R. F. Sympson, *J. Phys. Chem.*, **61**, 973 (1957).
[28] U. F. Franck, *Z. Naturforsch.*, **4a**, 378 (1949).

From the standpoint of theory, if the Flade potential actually corresponds to some electrochemical state that is reproducible, albeit metastable, one should expect to measure it best in as nearly a steady state as possible, rather than during rapid activation. This was the justification of the procedure used by Cartledge and Sympson.

The attempt of the authors to relate the Flade potential to a free energy calculable from data on heat of adsorption of gaseous oxygen on iron powder suffers from the weakness that two entirely different processes are being compared. Adsorption of oxygen in an aqueous medium involves both displacement of adsorbed water and competitive adsorption with all other species present. It would, therefore, be a strange coincidence if the adsorption in the two environments were the same in extent or energy.

The authors' discussion of the passivation process in the presence of a pertechnetate also must be questioned. They suggested that the writer's failure to find more than minute amounts of a technetium compound on the passivated specimen might be due to the formation of a soluble reduction product. This is quite contrary to the facts. Thorough study of the chemistry of technetium in this laboratory has shown that soluble compounds derived from the quadrivalent state (the important one) can be made only by forming complexes in strongly acidic solutions, such as hydrochloric acid of 1*N* concentration or greater.[29] Furthermore, in one experiment on the passivation of cast iron, which reduced an appreciable amount of the inhibitor, a material balance was obtained, within analytical accuracy, by adding the amount found from the beta activity of the specimen to the residual technetium in solution as determined spectrophotometrically as TcO_4^-.

Finally, if one uses the authors' estimate of the free energy of "$Fe{\cdot}O{\cdot}O_2$" in combination with the normal potential of the Tc(VII)-(IV) couple,[30] in accordance with their Eq. [9], it is calculable that 10^{-4} *f* TcO_4^- could passivate by this process only if the pH value were less than 4.9. The corresponding number is 4.0 if Franck's value for the Flade potential is used. As a matter of fact, passivation results best at higher pH values in aerated solutions. It is not believed, however, that such calculations are reliable, in view of the abnormal and unknown free energies of the surface components.[31]

H. H. Uhlig and P. F. King: In view of his extended studies along similar lines, Dr. Cartledge's comments are especially welcome. His comments indicate that he is reluctant to believe that the Flade potential varies with specific passivators, but the facts are quite clear that the observed variations are larger than the experimental error of our measurements, and we believe that the explanations that we have outlined suggest reasons why these variations are to be expected. The observed variation in stability of passivity depending on the passivator used is part of the evidence that differences in Flade potential can be predicted.

It is not likely that the deviations we find can be explained by a "memory" of the electrodes for the pH of the solution in which the electrodes were passivated, as Dr. Cartledge proposes. Other than the fact that each electrode was carefully washed in three separate beakers of distilled water before breakdown of passivity was followed by potential measurements, it is clear from Fig. 2 and 3 that acidity of the solution in which passivation occurred did not appreciably influence the observed Flade potential measurements. For example, iron passivated anodically in 5% H_2SO_4 or in concentrated HNO_3 (16*N*) gave the same Flade potential and the same slope of E_F plotted vs. pH of the solutions in which the passivity decayed despite a large difference in acidity. Furthermore, potassium ferrate solution, which by slow decomposition and hydrolysis was very alkaline, gave the same Flade potential as sodium molybdate or potassium chromate solutions which were near neutral.

We found that the use of buffer solutions is not ideal because of the tendency of some buffer anions in their usual high concentration to accelerate decay of passivity. This probably accounted for our observation that there was a variation in the Flade potential at the same pH when the buffer system was varied.

It is true that, when passivation occurs in an aqueous medium, competitive adsorption is expected to occur, and that this is not the case when oxygen is adsorbed directly on iron. In a subsequent paper,[32] we have shown that the calculated displacement effects amount to about 6000 cal/mole H_2O adsorbed on iron. This corresponds to only a minor part of the free energy accompanying adsorption of oxygen, and hence is not of great significance.

The relative absence of technetium on the surface of iron after passivation by TcO_4^- indicates that either TcO_4^- is not reduced at the surface of iron during passivation, which we discuss as being unlikely, or that the reduction products of TcO_4^- are soluble (or they are dispersed) in the solution. The latter situation is contrary to that for CrO_4^{--} for which chromium ions or compounds tend to remain on the iron surface after passivation and can be counted if the chromium is radioactive. It is difficult to foresee any other possibility explaining lack of Tc on an iron surface passivated by TcO_4^-.

The calculated value for critical pH in accord with our Eq. [9] depends on the particular value of the Flade potential which is assumed to apply to pertechnetates, and hence the calculated pH can be less than 4.9. We are somewhat more optimistic than Dr. Cartledge regarding thermodynamic calculations in which surface reactions are involved, provided that the composition of the surface product and the corresponding free energy are known. The practical use of the Ag-AgCl and Pb-$PbSO_4$ electrodes constitutes proof that thermodynamics also applies rigorously to thin films on metal surfaces. In many cases, of course, composition of surface films is not known, and cannot be readily established by the usual analyses, but potential

[29] R. H. Busey, Personal communication.
[30] G. H. Cartledge and W. T. Smith, Jr., *J. Phys. Chem.*, 59, 1111 (1955).
[31] G. H. Cartledge, *Z. Elektrochem.*, 62, 684 (1958).
[32] H. H. Uhlig and P. F. King, In press, *J. Phys. Chem.*

measurements are still useful nevertheless as a first step in diagnosing the possible composition and structure of such films.

D. M. Brasher [33]: If we have interpreted this paper correctly, Uhlig and King suggest that the very slow film growth on steel in dichromate solutions takes place by means of a dual mechanism. During depolarization of cathodic areas by $Cr_2O_7^{-2}$ ions, deposition of chromic oxide (possibly hydrated) or adsorbed Cr^{3+} ions occurs on these areas; this depolarization causes an equivalent amount of (chemisorbed) $O.O_2$ to be deposited on anodic areas, followed by (it is implied) the gradual conversion of this to Fe_2O_3 with fresh deposition of $O.O_2$.

This is of interest to us as the over-all reaction quoted:

$$Cr_2O_7^{2-} + 8H^+ + Fe_{surface} \rightarrow 2Cr^{3+} + 4H_2O + O{:}O_2$$

with, presumably, in addition

$$2Fe + O.O_2 \rightarrow Fe_2O_3$$

is stoichiometrically equivalent to the reactions we have assumed[34] in the interpretation of film growth in deaerated chromate or dichromate solutions. These reactions have been assumed to be, in the absence of oxygen:

$$2Fe + 2CrO_4^{2-} + 2H_2O \rightarrow Fe_2O_3 + Cr_2O_3 + 4\ OH^- \ (pH\ 7.5)$$

or $$2Fe + 2HCrO_4^- \rightarrow Fe_2O_2 + Cr_2O_3 + 2\ OH^- \ (pH\ 4.2)$$

In each case, the growing film should contain equivalent amounts of Fe and Cr.

In our work,[35] we have shown that Cr uptake, and hence film growth, proceeds as a function of the logarithm of time, and that the rate constant for this growth is similar to that for oxide film growth in dry air. We (Kubaschewski and Brasher) have explained this growth on the basis of theories of Mott, Hauffe, and Ilschner in which electron transfer through the film is the rate-controlling step. It would be interesting to know if Uhlig and King's suggested mechanism, cathodic deplorization with concomitant anodic polarization, can account for logarithmic film growth.

H. H. Uhlig and P. F. King: Miss Brasher's observations are a welcome supplement to our own, and in our opinion comprise a reasonable explanation of what may be expected if iron is passivated by chromates. In fact, similar continuous oxidation should be observed with any of the passivators, such as nitrites, molybdates, etc., for which the Flade potential is approximately the same as for iron anodically passivated in H_2SO_4.

If the passive film formed by passivators is essentially chemisorbed oxygen or an adsorbed oxygen complex, as our data lead us to believe, the further slow oxidation of iron to form iron oxide would be expected to follow a rate curve similar in shape to that observed when iron is exposed to dry oxygen. It has been demonstrated by others that the rate of oxidation in dry O_2 is logarithmic, and the fact that Miss Brasher finds this relation, assuming that reduced chromate is incorporated into the iron oxide film, is confirming evidence that the assumptions and explanations she and her co-workers propose are reasonably correct.

It is not certain that the absolute rates of oxidation should be identical. The presence of chromate adsorbed on the outer boundary of the passive film, and absence of chromate in dry oxidation, may well cause the rates to differ, but the logarithmic equation is expected to hold in either instance.

It may be well to point out that the application of Mott's early derivation of the logarithmic equation relating thin film oxidation to the tunnel effect, and its more recent adoption by Hauffe and Ilschner, is subject to some doubt. The Mott derivation leads to an oxidation rate independent of temperature, and suggests that the logarithmic equation should hold for films not thicker than about 40Å, both being contrary to observation, as Lustman pointed out.[36] A subsequent derivation of Cabrera and Mott based on a quasi-exponential migration of ions in an electric field within the oxide leads to the inverse logarithmic equation instead of the logarithmic equation, and does not account, as we have pointed out earlier, for the observed effects of grain orientation, lattice transformation, and Curie temperature on thin film oxidation rates.[37, 38]

Potential Studies on Passivity to Corrosion Induced by Pretreatment Processes for Metals, I. Aluminum

K. S. Rajagopalan (pp. 113-117, Vol. 106)

S. L. Chisholm[39]: Similar studies of passivating and corrosion inhibitive treatments and compounds have been performed on a variety of aircraft, nonferrous, and ferrous metals, by employing a Beckman *p*H meter and measurement of potentials against silver-silver chloride electrodes made in quantity by fusing silver chloride on strips of pure silver. The purpose was to develop direct screening methods and prospective specification requirements for useful corrosion inhibitors and inhibitive compounds, such as corrosion inhibitive paint films, since development and testing of such materials normally involves inordinate amounts of time for field test exposure. In the case of inhibitive paint primers, such as zinc chromate primer, an interesting variation of the test method is to determine the differential potential of the primed vs. the unprimed metal in separate cells when immersed in ground or saline water. Initial values are of the order of 450 mv on aluminum alloys, which decrease with extended time to a steady state. Increasing salinity increases the initial differential, but also the rate of change. In all of this work, it has been found difficult to obtain exact reproducibility. Replicate samples normally furnish families of similar curves of potential vs. time, as reported and illustrated in the subject paper. By

[33] National Chemical Lab., Teddington, Middlesex, England.
[34] O. Kubaschewski and D. M. Brasher, *Trans. Faraday Soc.*, 55, 1200 (1959).
[35] D. M. Brasher and Kingsbury, *Trans. Faraday Soc.*, 54, 1214 (1958).
[36] B. Lustman, *Trans. Electrochem. Soc.*, 81, 372 (1942).
[37] H. H. Uhlig, *Acta Met.*, 4, 541 (1956).
[38] H. H. Uhlig, J. Pickett, and J. MacNairn, *Acta Met.*, 7, 111 (1959).
[39] U. S. Naval Air Station, North Island, San Diego, Calif.

this method, it is also possible to detect and determine the persistence of nonvisible passivation effects, such as that produced by nitric or chromic acid treatment of corrosion resistant steels.

K. S. Rajagopalan: I am glad to note that observations similar to those made by me have also been made by Dr. Chisholm. Dr. Chisholm is correct in stating that the order of reproducibility of the potential changes observed should be higher from the point of view of using the changes as a method for the assessment of the performance of the pretreatments considered. This aspect has received particular attention in the paper. I think it should be possible to get better reproducibility if the conditions of treatment are better understood. However, it should be noted that the results have an even greater significance from the point of view of the light it throws on the mechanism of passivation of the metal surface. The results show that there are a number of systems where the potential shift is in a negative direction following passivation. The explanation given by the author brings into relief a factor which has not been given adequate attention in the consideration of changes in potential with time and changes in potential with application of external current. This is the important part played by changes in anodic and cathodic areas. It has been shown that, under certain ideal conditions assumed, the potential changes can be attributed either to a change in the ratio of anodic and cathodic areas or a change in the ratio of the velocity factors for the anodic and cathodic reactions. It may be that these two factors cannot be separated ordinarily. But it is possible to visualize the conditions under which one can be studied independent of the other.

Reaction of Aluminum and Carbon Tetrachloride, I

J. D. Minford, M. H. Brown, and R. H. Brown (pp. 185-191, Vol. 106)

R. A. Hine[40]**:** The authors have presented a thorough and most useful study of this reaction, which has considerable practical importance in connection with the use of aluminum vessels and equipment for handling halogenated compounds.

Rather surprisingly, the tremendously increased rate of reaction brought about by mechanical activation has not been referred to; this was first described by Shaw.[41] In our laboratories, we have demonstrated that a very rapid and vigorous reaction takes place when aluminum is abraded, drilled, machined, or filed under the surface of warm carbon tetrachloride. In the case of aluminum powder ground in a mortar and pestle with a little warm carbon tetrachloride, the reaction starts suddenly and may be almost explosively violent with evolution of large amounts of hexachlorethane and aluminum chloride fume. If further portions of liquid and powder are added to the reacting mass, incandescence is reached and a secondary reaction involving direct formation of $AlCl_3$ and liberation of carbon takes place. In the primary reaction, the formation of the red intermediate complex is always strikingly produced.

[40] Aluminium Labs. Ltd., P. O. Box 84, Kingston, Ont., Canada.
[41] M. C. Shaw, *J. Appl. Mechanics*, 15, 37 (1948)

The reaction has been discussed by Grunberg[42] who explains it by taking account of the Kramer and Russell effects (emission of electrons from an abraded metal surface) and formulates the steps as:

$$Cl_3C^+Cl^- + e \text{ (from abraded metal)}$$
$$\rightarrow Cl_3Cl\cdot Cl^- \rightarrow Cl_3Cl\cdot + Cl^-$$
$$Al^{3+} + 3Cl^- \rightarrow AlCl_3$$
$$2Cl_3C \rightarrow C_2Cl_6$$

The above sequence does not explain the formation of the red complex and in my view the present authors' electrochemical theory can be held just as tenable as the free radical theory.

R. H. Brown, E. H. Cook, M. H. Brown, and J. D. Minford: The authors appreciate R. A. Hine's interest in their paper.

It is not surprising that mechanical abrasion of the surface in warm carbon tetrachloride produces a rapid reaction. Our experiments to cathodically protect an aluminum rod whose surface was freshly scratched under boiling carbon tetrachloride were unsuccessful. In order to achieve cathodic protection, it is necessary to supply at least the minimum current as would be calculated from the initial reaction rate at the scratched surface. Because of the high resistance of the solution, such currents could only be obtained with excessively high applied potentials.

Conductivity measurements by the authors indicate the existence of an ionic species before the visible detection of the red complex, and that the conductivity continues to increase after the red complex is detected.

Principles and Applications of the Iodide Process

A. C. Loonam (pp. 238-244, Vol. 106)

A. A. Woolf[43]**:** We wish to comment on Loonam's conjecture that boron and rhenium can be deposited from the vapors of their iodides.

Recent work has confirmed that rhenium iodides cannot be made directly from the elements alone, or in complexing and noncomplexing solvents for iodine, but only indirectly via the hexaiodorhenates (IV).[44,45] The rhenium iodides so prepared are decomposed to rhenium by heating in vacuo without appreciable volatilization of the iodide, indicating that their dissociation pressures are high compared with their vapor pressures. Thus, refining of rhenium is impossible by a continuous iodide process. It is the kinetics, rather than the thermodynamic equilibria, of the reaction of iodine with some elements which limits the method, because reaction only occurs at an appreciable rate at temperatures at which the iodide is no longer stable. Boron is similar in that no appreciable reaction occurs with iodine at temperatures up to 1200°C.[46]

[42] L. Grunberg, *Proc. Phys. Soc. (London)*, **66B**, 153 (1953).
[43] Research Lab., Associated Electrical Industries Ltd., Aldermaston Court, Aldermaston, Berkshire, England.
[44] A. A. Woolf, *J. Inorg. & Nuclear Chem.*, 7, 291 (1958).
[45] R. D. Peacock, A. J. E. Welch, and L. F. Wilson, *J. Chem. Soc.*, 2901 (1958)
[46] H. C. Oldland, Ph.D. Thesis, Imperial College, London (1956); "Gmelins Handbuch der Anorganischen Chemie," 13, 128 (1926).

A. C. Loonam: I am very grateful indeed for Dr. Woolf's comments. However, I believe that they were covered adequately in the paper by the "perhaps" before the "Re" in the statement to which he refers and by the succeeding one: "In some cases, e.g., carbon, it would be necessary to prepare the iodide by an external process," which, of course, includes indirect methods. These would almost certainly be necessary for the preparation of carbon-iodine compounds, since the common forms of this element, graphite and amorphous carbon, in my definite experience, do not react directly with iodine at temperatures up to at least 1100°C.

Formation of a volatile product by the direct action of iodine vapor on metallic rhenium has been reported [47,48] but, even if this should prove to be the oxyiodide found by Dr. Woolf, I would be unwilling to place the metal in the same category with carbon because of recent evidence that other metals ordinarily considered resistant can be made to react with iodine. Not long ago, it was stated that tantalum is resistant to iodine vapor up to 1000°C and that it can be used as a shield in the de Boer-van Arkel process; yet TaI_5 has been prepared by the action of iodine vapor on the metal at temperatures as low as 300°[49] and the metal has actually been refined by the iodide process[50] with bulb temperatures as low as 311°, using commercial sheet as the "crude" material. Moreover, molybdenum, which gives very satisfactory service in iodide process units, can react with iodine under suitable conditions;[51] while the recent announcement by the General Electric Co.,[52] of a compact high-intensity incandescent lamp containing a small amount of iodine to return the volatilized tungsten from the interior surface of the quartz bulb to the filament, shows that even this metal can be attacked and transferred. Even more pertinent to Dr. Woolf's remarks is the report that direct reaction of one form of crystalline boron with iodine at 900° gave as high as 70% yields of the triiodide; and that the vapor of this compound produced deposits of elementary boron at temperatures as low as 800°.[53] Indeed, a new allotropic modification of boron was produced.[54]

Furthermore, the rhenium iodides should be studied in the presence of a high partial pressure of iodine vapor before it is concluded that they cannot exist in the gaseous state. Dr. Woolf's finding of the volatile oxyiodide indicates that the Re-I bond is not excessively weak. Niobium, which forms a similar oxyiodide, has been refined by the iodide process[55] even though heating NbI_5 in an evacuated tube gave results similar to those obtained by Dr. Woolf with the rhenium iodides, the unvolatilized residue being converted slowly to metal at 540° and rapidly at 800°.[56] It is true that evidence for the existence of gaseous NbI_5 was found in these experiments, whereas Dr. Woolf obtained no similar evidence; but this may be due to a lower volatility of the rhenium compounds resulting from the lower valence state and the higher atomic weight of the metal.

I would not be at all astonished to learn that considerable volatilization occurs when the rhenium iodides are heated to 600°-1000° in a stream of iodine vapor at atmospheric pressure. If such proves to be the case, I believe that conditions will be found under which rhenium can be deposited from the vapors of its iodides, perhaps by a "straight-flow" process rather than the conventional de Boer-van Arkel method.

[47] W. Noddack, *Z. Elektrochem.*, **34**, 627 (1928).
[48] H. V. A. Briscoe, P. L. Robinson, and E. M. Stoddart, *J. Chem. Soc.*, 2263 (1931)
[49] R. F. Rolsten, *J. Am. Chem. Soc.*, **80**, 2952 (1958).
[50] R. F. Rolsten, *Trans. Met. Soc. AIME*, **215**, 472 (1959).
[51] T. L. Allen and D. M. Yost, *J. Chem. Phys.*, **22**, 855 (1954).
[52] E. G. Zubler and F. A. Mosby, Preprint No. 19, National Technical Conference, Illuminating Engineering Society, San Francisco, Calif., September 7-11, 1959.
[53] L. V. McCarty and D. R. Carpenter, *Abstracts of Papers, Am. Chem. Soc.*, 135th Meeting, Boston, Mass., April 5-10, 1959, pp. 17M, 18M (2 papers).
[54] L. V. McCarty, J. S. Kasper, F. H. Horn, B. F. Decker, and A. E. Newkirk, *J. Am. Chem. Soc.*, **80**, 2592 (1958).
[55] R. F. Rolsten, *Trans. Met. Soc. AIME*, **215**, 478 (1959).

The System LiF-LiCl, LiF-NaCl, LiF-KCl

H. M. Haendler, P. S. Sennett, and C. M. Wheeler, Jr.
(pp. 264-268, Vol 106)

M. A. Bredig[57]: It appears that the most recent values for the heat of fusion of LiF, NaCl, and KCl were used in the calculations presented in the tables. However, this does not seem to be true for the so-called Clausius-Clapeyron Limit in Fig. 1-3, especially for NaCl in Fig. 2 and above all for both LiF and LiCl in Fig. 1. If for the LiF-LiCl system the latest, correct heats of fusion of 4.80 kcal for LiCl[58] and 6.46 for LiF are used to draw the Clausius-Clapeyron Limit, it becomes apparent that as expected there is no positive deviation from Raoult's Law in this system, but rather very slight *negative* deviations due to the different size of the F^- and Cl^- ions.

H. M. Haendler, P. S. Sennett, and C. M. Wheeler, Jr.: The calculations presented in the tables of this paper used values for the heat of fusion of LiF, NaCl, and KCl listed by Flood. The Clausius-Clapeyron Limit was inadvertently drawn using values for the heat of fusion of these salts as found in National Bureau of Standards Circular 500. These values for, particularly, LiCl and LiF are low and should not be used. Replotting the Clausius-Clapeyron Limit using either the values from Flood or those supplied by Dr. Bredig indicates, as he states, that there is a slight negative deviation in the LiF rich systems.

The Stability and Solubility of AgO in Alkaline Solutions

T. P. Dirkse and B. Wiers (pp. 284-287, Vol. 106)

J. A. McMillan[59]: As Salkind and Zeek[60] have pointed out, the structure of AgO has been of interest to members of the Society, and I should add to chemists in general, during the last years. Dirkse and Wiers, in an interesting paper on the behavior of AgO in alkaline solutions, found that samples of an assumed AgO prepared by different methods ex-

[56] J. D. Corbett and P. X. Seabaugh, *J. Inorg. & Nuclear Chem.*, 6, 207 (1958).
[57] Chemistry Div., Oak Ridge National Lab., P. O. Box X, Oak Ridge, Tenn.
[58] A. S. Dworkin and M. A. Bredig, In press.
[59] Chemistry Div., Argonne National Lab., Lemont, Ill., on leave of absence from Instituto de Física de San Carlos de Bariloche, Bariloche, Río Negro, Argentina, spending the duration of a Guggenheim Fellowship.
[60] A. J. Salkind and W. C. Zeek, *This Journal*, **106**, 366 (1959).

hibit different x-ray diffraction patterns. They have a point, namely: difference in x-ray patterns indicates a difference in structure, or at least the existence of AgO samples with somewhat larger lattice parameters. This latter can be true, but I suspect that the results quoted above stand for the production of a black deposit obtained during the electrolytical oxidation of silver anodes in sulfuric acid medium[61] that should rather be identified with $(Ag_3O_4)_2AgSO_4H$, isomorphous with Ag_7NO_{11}, Ag_7ClO_{12}, and perhaps with Ag_7O_8F (interchanging NO_3, ClO_4, SO_4H, F),[62] also obtained by de Boer and van Ormond[63] during the oxidation of $AgNO_3$ solutions with $K_2S_2O_8$. It should be noted in this respect that the latter method leads to AgO if the medium is alkaline.[64]

The unit cell edge of Ag_7NO_{11} is 9.89Å. This value cannot vary strongly when substitution by other anions takes place. In fact it does not, as can be seen in the table, published here where values of spacings for silver oxinitrate[65,66] and oxifluoride[66] are given. The values found by Jones and Thirsk[61] are quoted in the same table, showing a good agreement with the exception of spacing 1.45Å, presumably due to reflections 311 or 022 of AgO.[67] It should be borne in mind that the oxisalts decompose to give rise to AgO, oxygen, and the corresponding monovalent silver salt. Jones and Thirsk's compound seems to be like the compound obtained by Schwab and Hartmann[68] using ozone for the oxidation, as can also be seen in the table.

I wish to make good use of the opportunity to call to the attention of workers on this problem that the compounds obtained from electrolytical oxidation of silver anodes are not at all clear up to the present time.

T. P. Dirkse and B. Wiers: One of the purposes in reporting on our work with AgO was to show that all that is called AgO is not necessarily AgO. The x-ray data of Schwab and Hartmann, Footnote 68, show that the AgO prepared by decomposition of Ag_7NO_{11} with boiling water is not the same as that prepared by oxidation of $AgNO_3$ with alkaline persulfate. There are also differences in chemical properties between these two substances, such as the effect of boiling water as noted in our article.

[61] P. Jones and H. R. Thirsk, *Trans. Faraday Soc.*, **50**, 732 (1954).
[62] J. A. McMillan, *This Journal*, this issue, Discussion on "Higher Oxides of Silver."
[63] J. H. de Boer and J. van Ormond, *Proc. Intern. Symposium on Reactivity of Solids, Gothenburg, 1952*, 557 (pub. 1954); *Chem. Abstracts*, **45**, 11968f (1954).
[64] J. C. Bailar, "Inorganic Syntheses," p. 12, McGraw-Hill Book Co., New York (1953).
[65] H. E. Swanson R. K. Fuyat, and G. M. Ugrinic, *Nat Bur. Standards Circ. 539*, **4**, 61 (1955).
[66] W. Graff and H. H. Stadelmaier, *This Journal*, **105**, 446 (1958).
[67] J. A. McMillan, *Acta Cryst.*, **7**, 640 (1954).
[68] G. M. Schwab and G. Hartmann, *Z. anorg. u. allgem. Chem.*, **281**, 183 (1955).

Table I. Spacings of some silver oxisalts

Ref., Footnote 66					
Fluoride	Nitrate	Ref., Footnote 65	Ref., Footnote 61	Ref., Footnote 68	HKL
...	...	...			...
2.836	2.855	2.856	2.85	2.85	222
2.457	2.472	2.474	2.46	2.46	400
...	...	...			...
1.483	1.491	1.491	1.49	1.50	622
---	---	---	1.45	---	---
...		...			...
1.230		1.237		1.24	800
...		...			...
1.1261		1.1348	1.136		662
1.0988		1.1062	1.106		840

Water-Stabilized Arc Tests on Nonmetallic Materials

M. Dank, R. A. Nelson, W. R. Sheridan, and W. H. Sutton
(pp. 317-321, Vol. 106)

Charles Sheer[69]: Comment on peak temperatures reported by Burham, Maecker, and Peters in Germany (~50,000°K): "Peak temperatures of this order exist only on the axis of the plasma jet over a very small radial distance (<1 mm). The extreme high temperature region extends a short distance beyond the nozzle opening into the plasma jet, but not enough to be useful in testing samples of materials at these temperatures."

On the subject of temperature measurement in plasma jet environments, rotational temperatures, determined spectroscopically, appear to be abnormally high. However, Stark effect broadening of the hydrogen lines is reported to yield effective temperature measurements with about 10% accuracy.

The Anodic Oxides of Lead

J. Burbank (pp. 369-376, Vol. 106)

P. Rüetschi and B. D. Cahan[70]: *p*H potential diagrams, as developed by Pourbaix, are convenient means to describe the regions of thermodynamic stability of solid phases or ionic species in solution. In applying these diagrams, one must keep in mind that concentration terms other than the H-ion concentration (*p*H) are determining the thermodynamic reversible potentials. For example, in the case of the *p*H-potential diagram of Pb, the nature of the particular anions present is of profound influence. Considering a *p*H of 1, the lead ion concentration could vary over many orders of magnitude with a corresponding shift in potential of several tenths of a volt. This means that, for each anion present, the *p*H-potential diagram might look entirely different.

In Fig. 1 of J. Burbank's paper, the regions of stability of corrosion products *at the solution interface* are given without specifying nature and concentration of other ionic species (in particular anions) present. Looking at the diagram, it is hard to understand the presence of PbO, $Pb(OH)_2$, and αPbO_2 in an acid media of, e.g., *p*H 1, in direct contact with the acid solution. At this *p*H, the existence of PbO, $Pb(OH)_2$, and αPbO_2 are difficult to picture thermodynamically or kinetically. In Fig. 3 of J. Burbank's paper, which refers to a *p*H of 1, no such substances are shown in direct contact with the acid media. Only $PbSO_4$ and βPbO_2 are shown in direct contact with the solution. This is in contrast with the data of Fig. 1.

It should be made clear that the definition of a *p*H *in the interior* of a corrosion layer is ambiguous. The *p*H in the very fine cracks and pores of the cor-

[69] Vitro Labs., West Orange, N. J.
[70] Electrochemistry Div., Electric Storage Battery Co., Yardley, Pa.

rosion layer must be quite different from the pH in the bulk of the electrolyte, due to strong diffusion and depletion effects. It does not make much sense to assume that only H^+ ions and water are penetrating into the layer, since equal amounts of anions and cations must be present in the pores at any time to maintain electroneutrality. In the double layer, an excess charge on the solution side is neutralized by an equal excess charge on the electrode side; however, in any case, the conditions in the interior of the corrosion layer are then not ideal, and the energetic states of the same ionic species in the interior of the corrosion layer and in the bulk must be different.

We feel that the experimental evidence of the presence of PbO, $Pb(OH)_2$, and αPbO_2, which is well confirmed, is connected with a pH effect in the interior of the corrosion layer, due to diffusion effects. It seems that J. Burbank does not sufficiently stress the importance of nonequilibrium conditions with regard to pH in the corrosion film. In a basic media, the formation of PbO, $Pb(OH)_2$, and αPbO_2 would be readily understood. One could visualize a system where the corroding electrode is separated from the solution by a diaphragm, such that the electrode compartment of the corroding electrode has much higher pH than the solution. This diaphragm insulating the electrode from the solution would in practice consist of a $PbSO_4$ or βPbO_2 layer. This would now mean that the corroding electrode would be at a higher pH and thus, for a given impressed over-all electrode potential, the formation of PbO_2 would become possible far below the theoretical thermodynamic value as determined from the bulk pH of the solution. If the undefined virtual pH in the interior of the corrosion layer were effectively basic, then PbO_2 could be formed down to an apparent external potential of 0.6 v or so as can easily be seen from the pH-potential diagram.

In practice, the corrosion of lead might proceed underneath a partially protecting coverage of $PbSO_4$ or βPbO_2 by migration of oxygen species (e.g., OH^-) along the surfaces of the $PbSO_4$ and PbO_2 grains or crystals to produce PbO, $Pb(OH)_2$, or αPbO_2 from metallic lead. The formation of these substances is therefore related to a lack of acid in the interior of the corrosion film.

It has been described by Rüetschi and Cahan[71] that the ratio of α to βPbO_2 in the corrosion layers of lead-antimony alloys in H_2SO_4 depends on the Sb concentration of the corroding grid. It was indicated that with high Sb content generally more βPbO_2 is formed due to the higher porosity of the corrosion film. The Sb, corroding out of the metal, is oxidized to Sb oxide and Sb sulfate.These substances subsequently are leached out of the corrosion film, rendering it more porous and more pervious to H_2SO_4, which is inducive for the formation of βPbO_2 rather than αPbO_2 or PbO. With pure lead or Pb-Ca alloys, one observes often very dense, impervious corrosion films, containing in the interior much PbO. The latter substance can impair, under certain conditions, the contact between grid and active material in positive plates of storage batteries made with Ca-alloy.

J. Burbank prefers not to make any reference to an article of Rüetschi and Cahan[72] where the occurrence of the second modification of PbO_2 (orthorhombic αPbO_2) has for the first time been reported in *corrosion layers of lead.* This material had been described previously in foreign papers, particularly of Russian origin. Its preparation with chemical and with electrochemical plating techniques had been established, but it had not been known as a corrosion product of lead. Prior to the publication date of the article of Rüetschi and Cahan, J. Burbank never mentioned the existence of αPbO_2 in her papers. But since, she also has found αPbO_2 as a corrosion product.

During prolonged corrosion at elevated potentials, αPbO_2 is the major corrosion product. Electrode potentials of α and βPbO_2 in H_2SO_4 solutions have been measured experimentally with good precision by Rüetschi and Cahan in the article referred to, and by S. J. Bone, Symposium of Batteries, Signal Research and Development Establishment, Ministry of Supply, Christchurch, Hampshire, England, October 21, 1958. These measurements agreed very well. In 5M H_2SO_4, e.g., αPbO_2 has an electrode potential 7 mv higher than βPbO_2. The presence of the two different corrosion products has also been demonstrated by the two-step reduction of the corrosion layer.[73] The experimentally determined potential values for α and βPbO_2 do not coincide with the theoretical pH potential diagram of J. Burbank, which is due, as discussed previously, to the presence of other ionic species in the electrolyte.

Recently, Kabonov (*loc. cit.*) has shown that on αPbO_2 less SO_4^{--} ions are adsorbed than on βPbO_2. Inversely, βPbO_2 is formed preferentially in the presence of SO_4^{--} ions, which means at low pH values. Addition of cobalt sulfate to the electrolyte is inducive for the formation of αPbO_2 and to the desorption of SO_4^{--} ions from the surface. Rüetschi and Cahan (*loc. cit.*) have demonstrated that αPbO_2 has a lower oxygen overvoltage than βPbO_2. The lower oxygen overvoltage for αPbO_2 can be associated with a smaller amount of SO_4^{--} ions adsorbed. Oxygen overvoltage is indeed decreased by the addition of cobalt sulfate to the electrolyte.[74]

J. Burbank has not been very consistent with the designations for the various anodic oxides of lead. For instance, she uses intermittently the designations $PbO_t \cdot xPbO_2$ and $PbO \cdot xPbO_2$ for what is apparently the same material. More serious, however, is the use of such composite formulations. The formula $PbO_t \cdot xPbO_2$ is misleading because these substances are not mixtures of PbO_t and PbO_2, but have a definite and separate crystal structure. The designation PbOx is more satisfactory. However, Pb_3O_4 should not be included in the group of PbOx materials. The designation PbOx should be used for substances like Pb_7O_{11} ($PbO_{1.57}$), Pb_5O_8 ($PbO_{1.60}$), Pb_2O_3 ($PbO_{1.50}$), which have a very similar composi-

[71] P. Rüetschi and B. D. Cahan, *This Journal*, **105**, 369 (1958).

[72] P. Rüetschi and B. D. Cahan, *This Journal*, **104**, 406 (1957).

[73] P. Rüetschi and B. D. Cahan, *loc. cit.*, and B. Kabanov, Dokl. *Akad. Nauk S.S.S.R.*, **122**, 1042 (1958).

[74] P. Rüetschi and B. D. Cahan, *loc. cit.*, and D. F. A. Koch, *Electrochemica Acta*, **I**, 32 (1959).

tion, varying only by a few per cent. Also, these substances have basically an orthorhombic symmetry, whereas Pb_3O_4 is tetragonal.

The thermodynamic stability of Pb with regard to PbO_2 (Eq. [1] in J. Burbank's paper) has no practical implication, since both Pb and PbO_2 are unstable at the indicated potential with regard to other possible divalent corrosion products of lead (PbO, $PbSO_4$). Thus, at a potential of, e.g., 0.67 v at *p*H 1, metallic lead *is not stable* thermodynamically even in the presence of PbO_2 since it will form divalent corrosion products first, and the thermodynamic stability of Pb cannot approach that of PbO_2. On the other hand, PbO_2 is reduced to divalent corrosion products not only above 0.67 v but of course also below this value, and metallic lead is unstable above and below this potential. The experimental evidence for the presence of PbO_2 below the thermodynamic theoretical value is more plausibly explained by nonequilibrium concentration (in particular *p*H) in the interior of the corrosion layers.

J. Burbank: This extension of the discussion of the anodic reactions of lead is very interesting. A detailed discussion of ionic equilibria in general is contained in the work of Pourbaix[75,76] and the differences brought about by the presence of sulfates and carbonates was presented in the original lead diagrams.[77] The variations in solubilities among the salts of lead with other anions and the differences in free energies of formation will give rise to as many diagrams.

In the first part of the paper under discussion, solubilities, anions, and ionic equilibria were intentionally and specifically stated to be excluded, and a comprehension of the works of Pourbaix was assumed. The data recorded in Fig. 1 were obtained by diffraction examination of surfaces of anodes as stated in the paper. The picturization of Fig. 3 presented under the heading "anions and passivation" is thought to represent the conditions under which such oxide mixtures are possible—by formation of a salt layer. Fig. 1 must not be read out of context. The text appears clear enough on these points.

It is gratifying to know that Rüetschi and Cahan now accept the appearance of lower oxides of lead on the anode in acid solutions, a fact they were unable to verify at an earlier date. The concept of film formation in the passivation of Pb in H_2SO_4 is rather widely accepted. A change in *p*H toward higher values at local cathodes is a normal expectation of static corrosion phenomena. In the instance under discussion external anodic polarization was applied, and anodic reactions were to be considered. Rüetschi and Cahan did not state by what anodic reaction the area near an anode may become alkaline. The reactions believed to effect an increase in *p*H were not written out in full in the comments so as to permit a more considered analysis of the situation described. No difficulty whatsoever is encountered in visualizing a consumption of hydrogen ion during cathodic reactions, but merely stating that an increase in *p*H occurs adjacent to the film-carrying lead anode does not make it a fact. It would be most convenient if the anodic phenomena could be written off as an increase in *p*H.

Migration of hydroxyl ion along with others through a primary layer of $PbSO_4$ may take place, but it is not clear that a marked increase in *p*H adjacent to an anode may be developed. It is clear that an increase in *p*H can not accompany electrochemical formation of the oxides, oxygen, or similar anodic products.

Experimental work remains to be done to realize a final determination of the mechanisms of the anodic processes on lead, but it is believed that the Hirsch[78-80] effect describes the phenomena encountered with $PbSO_4$ films. If one accepts Hirsch's work, a $PbSO_4$ film is permeable to hydrogen ion and water but not to plumbous or sulfate ion. Furthermore, it appears likely that the charge exchange mechanism of the $PbSO_4/PbO_2$ electrode itself may be elucidated by such a process.

The paper contained no discussion regarding the cited work of Rüetschi and Cahan, but it may be well at this time to indicate that some of the experimental results reported by them may be otherwise interpreted. For one example, the two-step discharge of PbO_2 has been attributed to another phenomenon.[81] It is hoped that Rüetschi and Cahan will continue their experimental work, and that ultimately all experimental facts may be properly interpreted.

The designation $PbO_t \cdot xPbO_2$ should have been uniform through the manuscript; this and several other typographical errors should cause no confusion. It is redundant to reiterate that the stoichiometry Pb_3O_4 is exhibited by at least two structurally different materials. It seems doubtful that a simple mechanical mixture of PbO and PbO_2 could possibly be understood by the definition given for the symbol in the paper.

Some would hesitate to state unreservedly that the equilibrium between Pb and PbO_2 is without "practical" implication. Other factors could prove this to be a most "practical" and significant equilibrium: consider the processing of positives for "dry charge" use.

[75] M. Pourbaix, "Thermodynamics of Dilute Aqueous Solutions," Trans. by J. N. Agar, London (1949).
[76] M. Pourbaix. *Centre Belge d'Etude Corr. R.T. No. 49* (1957).
[77] P. Delahay, M. Pourbaix, and P. Van Rysselberghe, *This Journal*, **98**, 57 (1951).

Role of Thiourea in the Electrodeposition of Copper

B. Ke, J. J. Hoekstra, B. C. Sison, Jr., and D. Trivich
(pp. 382-388, Vol 106)

S. C. Barnes[82] and G. G. Storey[83]: We have studied the effect of thiourea additions to acid copper sulfate solutions on the type of deposit subsequently obtained on electrolysis. All our work has been carried out on flat single crystal cathodes: on which deposits formed at low current densities, from thiourea-free solutions, continue the base orientation

[78] P. Hirsch-Ayalon, *Rec. trav. chim.*, **75**, 1065 (1956).
[79] P. Hirsch-Ayalon, *J. Polymer Sci.*, **23**, 697 (1957).
[80] C. J. Van Oss and P. Hirsch-Ayalon, *Science*, **129**, 1365 (1959).
[81] W. Feitknecht, *Z. Elektrochem.*, **62**, 795 (1958).
[82] Joseph Lucas Lab., Dept. of Industrial Metallurgy, University of Birmingham, Edgbaston, Birmingham 15, England.
[83] Messrs. Joseph Lucas Ltd., Birmingham, England; formerly at Dept. of Industrial Metallurgy, University of Birmingham, Edgbaston, Birmingham, England.

and develop well-defined crystallographic surface structures.[84, 85] The particular surface plane studied in the thiourea investigation was near to {100} on the <110> zone: this develops a sharp straight-edged platelet surface structure (when the deposit is approximately 14 μ thick) at 20 ma/cm^2 and 35°C, and a partially polycrystalline deposit at 40 ma/cm^2.[86] Additions of thiourea in concentrations ranging from 5 x 10^{-10} to 10^{-2}M were made to the bath, and effects on the deposit structures obtained at these two current densities noted. The results obtained from the solution containing an approximately equal amount of thiourea to the one used by Ke, *et al.*[87] (10^{-4}M) were in complete agreement with their observations and conclusions. Our evidence for adsorption was that the overpotential associated with the deposition was considerably increased by the addition of this amount of thiourea, indicating some interference with the normal growth process. However, the results obtained from solutions containing lower concentrations of the addition agent were more interesting. These are briefly summarized below.

At 20 ma/cm^2, 10^{-9} to 10^{-6}M thiourea decreased the overpotential and led to development of deposits characteristic of lower current densities in a thiourea-free solution.[86] 10^{-5}M had negligible effect on polarization but caused a habit change in the deposit: pyramids with sides near {211} developed instead of platelets. Above 10^{-4}M overpotential was increased in proportion to the thiourea content, the deposits becoming increasingly uneven and containing polycrystalline material. With 10^{-2}M thiourea, the deposit was very uneven, nodular, and cracked.

Deposits produced at 40 ma/cm^2 from solutions containing thiourea showed more variations: concentrations from 5x10^{-10} to 10^{-8}M caused an increase in overvoltage and more polycrystalline material to develop. 5 x 10^{-8} to 10^{-6}M reduced overpotential and platelet type deposits were obtained; 5 x 10^{-6} to 10^{-5}M produced deposits with pyramidal habit and only small changes in polarization. These deposits from solutions containing 5 x 10^{-8} to 10^{-5}M, at this current density, were complete continuations of the base, and contained no polycrystalline material. Bright even deposits were produced when 5 x 10^{-5} and 10^{-4}M thiourea was added, that at the higher concentration being almost featureless. At all concentrations above 5 x 10^{-5}M, polarization was increased. 10^{-3}M caused uneven nodular deposits to form, while that obtained from the solution containing the highest concentration studied (10^{-2}M) was covered with needle-like growths at a small angle to the surface. Deposits formed at this current density from solutions containing more than 5 x 10^{-5}M contained polycrystalline material.

This work at present is continuing and an explanation of these, and allied, phenomena is being sought in the relation between relative rates of crystal growth and adsorption of surface active material.

[84] H. J. Pick and J. Wilcock, *Trans. Inst. Metal Finishing, Advance Copy* No. 9, 35 (1958).
[85] H. J. Pick, G. G. Storey, and T. B. Vaughan, In press, *Electrochemica Acta.*
[86] S. C. Barnes, G. G. Storey, and H. J. Pick, In press, *Electrochemica Acta.*
[87] B. Ke, J. J. Hoekstra, B. C. Sison, and D. Trivich, *This Journal*, 106, 382 (1959).

The Role of the Metal-Ion Concentration Cell in Crevice Corrosion

G. J. Schafer and P. K. Foster (p. 468, Vol. 106)

Saul B. Bien[88] and Herbert D. Ayers, Jr.[89]: It was suggested by Schafer and Foster that the metal-ion concentration cell cannot be a cause of crevice corrosion and that crevice mouth attack is a special case of differential aeration. In the case of solder joints, it was clearly demonstrated[90] with autoradiographs made by flux tagged with fluorine-18 that fluoride salts are deposited at the interface between the solder and chromium alloys. We postulated that the crevice mouth attack was initiated by solution through convection and/or diffusion of irregular areas of residue at the interface. Following this, the development of the crevice continues. We discussed[91] the role of the differential aeration cell as described by LaQue[92] and the active-passive cell of Logan[93] in the continued development of the crevice.

A further significant finding was that, after one year of exposure to the room atmosphere in the laboratory, discoloration appeared (at X375) on the polished surface of the cross sections of the solder joints on areas corresponding approximately to those which produced radiopacities on the autoradiographs. The surface was repolished removing all stains. After six months of re-exposure to the air in the laboratory, discoloration again reappeared in the same areas of the surface adjacent to the interface. There is therefore a correlation between the areas of the autoradiographs showing the deposition of fluoride salts at the interface and the discolored areas observed on surface of the cross section of the solder joints. The discoloration appears to result from corrosive action in the areas which were most radioactive. The dissociation of salts deposited at the interface between the solder and the chromium alloy and the movement of ions over the polished surface of the specimen may have been facilitated by moisture from the atmosphere.

G. J. Schafer and P. K. Foster: The investigations of Bien and Ayers[90, 91] are not related to crevice corrosion in the sense used by us in the discussed paper. Their work is concerned with the initiation and propagation of failure at bimetallic soldered joints containing entrapped flux residues. Perhaps it should have been explicitly stated that our concern was solely with the mechanism responsible for maintaining steady-state corrosion in crevices consisting of only *one* homogeneous alloy.

We agree that once a crevice is present between a solder and the base metal due to incomplete bonding in the soldering operation, differential aeration

[88] 76 Union Ave., Lynbrook, N. Y.
[89] Dental Materials Lab., Columbia University School of Dental and Oral Surgery, New York, N. Y.
[90] S. M. Bien and H. D. Ayers, Jr., *J. Dental Research*, 38, 428 (1959).
[91] S. M. Bien and H. D. Ayers, Jr., *J. Am. Dental Assoc.*, 58, 74 (1959).
[92] F. L. LaQue, "Nature of Corrosion of Metals," New York Chapter American Society for Metals, October 10, 1955.
[93] H. L. Logan, *J. Research Nat. Bur. Standards*, 48, 99 (1952).

would have an important effect[91] particularly with stainless steels which are passivated by oxygen. It seems to us, however, that the potential difference between the two different alloys (solder and base metal) should have been considered. Evidence of potential differences is provided by preferential attack of the base metal in Fig. 7 (upper) and Fig. 10 (upper) in the work cited in Footnote 91.

The "crevice corrosion" failures observed by Bien and Ayers[91] may be due to purely physical effects, i.e., the solution of flux from the interface, since "crevice corrosion is characterized by a failure of the bond with little or no macro corrosion of the soldered joints or the solder. In the appliances where the bond failed either clinically or experimentally, there was no obvious corrosion or pitting of any metal."[91]

Alternatively, it may be that a thin layer of a base metal/solder alloy is formed at the interface, and that this layer is anodic to both the solder and the base metal under the conditions of test.[94] This would explain the formation of crevices sufficiently long and narrow to cause separation of the joint without gross corrosion of either the solder or the base metal.

We agree that the experiments cited in the second paragraph of Bien's and Ayer's comments confirm the entrapment of flux at the solder/base metal interface.

On the Internal Resistance of Dry Cells. A New Pulse Method

R. J. Brodd (pp. 471-475, Vol. 106)

J. J. Coleman[95]: I have two specific comments to make on Dr. Brodd's paper, the first specific to the paper, and the second more general in character.

The author's method of measurement involves a comparison of a potential developed across a dry cell, by pulses ranging from 1 to 10 μsec with a potential developed across a simple resistor. This assumes that the "equivalent circuit" in a dry cell is a simple resistor and not, for example, a resistor shunted by a condenser. The author directs his attention to the problem of what *is* a proper "equivalent circuit" in the first paragraph under "Results and Discussion." He found his internal resistance measurement unaffected by a change in the length of the pulse from 1 to 10 μsec and the change in the rate of the pulses from 100 to 5000 pulses per second. He concludes from this, mistakenly I believe, that the "equivalent circuit" can be taken as a simple resistor. Fig. 2 indicates that the pulse is approximately a square wave and the shape of the pulse as exhibited on the experimenter's oscilloscope is more important than its length. Dr. Brodd does not interpret the shape and hence does not come to grips with the problem of determining the "equivalent circuit" of a dry cell.

Now for the second comment, I believe that the method described by the author, and all similar methods, give the same results as conventional methods employing alternating currents. There is a feeling that a short, direct-current pulse is superior to an alternating current because the battery develops direct current and not alternating current. However, the phrases "direct current" and "alternating current" lose many of their usual meanings when applied to very short pulses. These phrases are usually applied to steady states. For example, one may say that a.c. will pass through a condenser and d.c. will not. Certainly this is not true if the d.c. is a very short pulse. A short d-c pulse has much more in common with steady state a.c. than with steady state d.c. This relationship appears mathematically in the Fourier analysis of a square wave. One represents a square wave pulse by the superposition of alternating currents of many frequencies.

Any steady state direct current in a dry cell must flow through the manganese dioxide particles or be coerced in some similar fashion. Alternating current or short pulses of direct current can pass directly from the black to the electrolyte. Hence, I do not regard measurements by short d-c pulses as pertinent to any study of the dry cell as a machine developing electrical energy.

R. J. Brodd: The comments of Dr. Coleman will serve to clear any misunderstanding in my original paper. The purpose of the paper was to report a method for measuring the true internal resistance of the battery. It appears that the method is successful in measuring the pure resistive element of a battery.

Dr. Coleman seems to have missed the significance of my statement concerning the shape of the voltage and current pulses. As was emphasized in the paper, the two traces were identical. The rise and decay of the pulses were instantaneous and the tops of both pulses were flat. This behavior is characteristic of a circuit containing a resistor with no capacitive effects. The ringing at the leading edges of the pulses, as suggested by Dr. Jacopetti,[96] is probably due to lead inductance of the instrument and cell. There is no evidence of a rounding of the leading edge of the pulses as would be expected from capacitive elements. The variation of repetition rate and pulse length without changing the measured resistance supports the conclusion reiterated above that the measuring technique reported in my paper determines the purely resistive element of a dry cell.

The equivalent circuit of a Leclanché cell which results from impedance measurements is

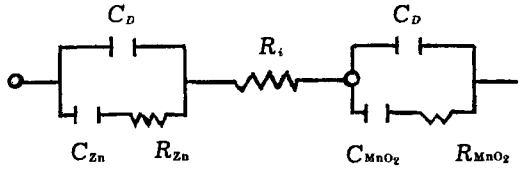

where R_i is the internal resistance, C_D the capacitance of the electrical double layer, C_{Zn}, R_{Zn} and C_{MnO_2}, R_{MnO_2} are the capacitance and resistance of the

[94] J. D. Dowd, *Welding J. (N. Y.)*, 33, 113s (1954).
[95] Burgess Battery Co., Freeport, Ill.
[96] M. M. Jacopetti, Private communication.

zinc and manganese dioxide electrode reactions.[97, 98] As Dr. Coleman mentioned, the pulse method used was essentially a very high-frequency a-c measurement as the pulse may be constructed from a suitable Fourier analysis. The very high-frequency character of the pulse method is emphasized by the 3000 repetition rate of 3 μsec pulse used in the paper. Inspecting the equivalent circuit above, we see that at very high frequencies the impedance of the electrode reactions would be shunted by the capacitance, C_D. At very high frequencies, the impedance of C_D will become negligible. As a result, the pulse measurement of the impedance of the Leclanché cell determines only the resistive element of the circuit R_i, the internal resistance of the cell. Thus, the conclusion reached in the pulse measurement concerning the measured resistive element of a cell is strengthened by results of impedance measurements on the cell.

The comparison of the a-c bridge measurements to the pulse method has been discussed elsewhere.[98] However, a few words of comment are in order. The a-c results reported in the past are often misleading for measurements often were made at only one frequency. The errors involved in this procedure are clearly evident considering the equivalent circuit of a cell. Also, the results of Euler and myself[97, 98] illustrate the effect of frequency on the measured resistance and capacitance of a cell.

It is possible to use the a-c bridge measurements of the resistance and capacitance at various frequencies to calculate the values of all components of the equivalent circuit. My results show that the resistive element R_i determined by the analysis of a-c bridge measurements is identical with the true internal resistance determined by the pulse method

I do not think it is accurate to say, as Dr. Coleman did, that a determination of R_i is not pertinent to the study of dry cells. The resistance polarization of a cell plays an important role in any experimental measurement or use of a cell. The change in R_i as a cell is discharged is interesting as it offers a clue to possible cell reactions and possibly a prediction of cell life. The internal resistance is the most important factor in determining the short circuit current a cell will deliver. The true internal resistance, R_i, is indeed an important part of a cell.

[97] J. Euler and K. Kahmelt, *Z. Elektrochem.*, **61**, 1200 (1957).

[98] R. J. Brodd, paper presented before Columbus Meeting of The Electrochemical Society, October 1959.

June 1960 Discussion Section

A Discussion Section, covering papers published in the July—December 1959 JOURNALS, is scheduled for publication in the June 1960 issue. Any discussion which did not reach the Editor in time for inclusion in the December 1959 Discussion Section will be included in the June 1960 issue.

Those who plan to contribute remarks for this Discussion Section should submit their comments or questions in triplicate to the Managing Editor of the JOURNAL, 1860 Broadway, New York 23, N. Y., *not later than March 1, 1960.* All discussion will be forwarded to the author(s) for reply before being printed in the JOURNAL.